Nineteenth Symposium on

NAVAL HYDRODYNAMICS

Nonlinear Ship Motions
Viscous Ship Hydrodynamics
Hydrodynamics in Ship Design
Wave and Wake Dynamics
Cavitation and Bubbly Flows
Propulsor Hydrodynamics and Hydroacoustics
Frontier Experimental Techniques

sponsored jointly by

Office of Naval Research

Society of Naval Architects of Korea

Naval Studies Board
Commission on Physical Sciences, Mathematics,
and Applications
National Research Council

NATIONAL ACADEMY PRESS
Washington, D.C. 1994

The National Research Council serves as an independent advisor to the federal government on scientific and technical questions of national importance. Established in 1916 under the congressional charter of the private, nonprofit National Academy of Sciences, the Research Council brings the resources of the entire scientific and technical community to bear on national problems through its volunteer advisory committees. Today the Research Council stands as the principal operating agency of both the National Academy of Sciences and the National Academy of Engineering and is administered jointly by the two academies and the Institute of Medicine. The National Academy of Engineering and the Institute of Medicine were established in 1964 and 1970, respectively, under the charter of the National Academy of Sciences.

The National Research Council has numerous operating units. One of these is the Naval Studies Board, which is charged with conducting and reporting on surveys and studies in the field of scientific research and development applicable to the operation and function of the Navy.

A portion of the work done to prepare this document was performed under Department of Navy Contract N00014-87-C-0018 issued by the Office of Naval Research under contract authority NR 201-124. However, the content does not necessarily reflect the position or the policy of the Department of the Navy or the government, and no official endorsement should be inferred.

Printed in the United States of America

FOREWORD

The Nineteenth Symposium on Naval Hydrodynamics, held in Seoul, Korea, from August 23-28, 1992, was organized jointly by the Office of Naval Research (Fluid Dynamics Program), the National Research Council (Naval Studies Board), and the Society of Naval Architects of Korea. This international biennial symposium promotes the exchange of naval research developments of common interest to the countries of the world. The forum encourages both formal and informal discussion of the presented papers, and the occasion provides an opportunity for direct communication between international peers.

More than 200 participants from 13 countries attended the symposium. Ranging from newly graduated students to researchers of established international repute, the attendees represented a mix of experiences and expertise. They presented 48 papers in seven topical areas—nonlinear ship motions, viscous ship hydrodynamics, hydrodynamics in ship design, wave and wake dynamics, cavitation and bubbly flows, propulsor hydrodynamics and hydroacoustics, and frontier experimental techniques—chosen because of recent advances made in these areas. Examples of significant advances presented in the papers are the numerical solution of the nonlinear equations for time-dependent ship motions, the prediction of vorticity flux from surface-piercing accelerating bodies, the design of a novel foil catamaran ship, the emerging understanding of free-surface interactions with vorticity, explanations of acoustic emission from cavitation bubble breakup, the prediction of viscous flow around propellers, and the use of quantitative visualization of large-scale wake structures for a free-running body.

The success of this timely symposium was the result of hard work on the part of many people. The Organizing and Paper Selection Committee consisted of Mr. James Fein, Dr. Patrick Purtell, and myself (Office of Naval Research), Mr. Lee Hunt (National Research Council), Prof. Robert Beck (University of Michigan), Prof. Choung Lee (Pohang Institute of Science and Technology), Prof. Kwang-June Bai (Seoul National University), and Dr. William Morgan and Dr. Justin McCarthy (David Taylor Model Basin). The contribution of this committee was certainly the cornerstone of the symposium's success. However, the organizers would also like to thank Mrs. Susan Campbell and Mrs. Mary Gordon of the Naval Studies Board for their valuable administrative and editorial production support and to express special appreciation to the symposium's host, Prof. Jong-Heul Hwang, chairman of the Local Organizing Committee.

Edwin P. Rood
Office of Naval Research

CONTENTS

Opening Remarks

Technical Sessions

Nineteenth Symposium on

NAVAL HYDRODYNAMICS

Opening Remarks

Jong-Heul Hwang
Chairman, Local Organizing Committee

Ladies and gentlemen, welcome to the Nineteenth Symposium on Naval Hydrodynamics and to Seoul, Korea.

On behalf of the Local Organizing Committee, I would like to express our thanks to the Office of Naval Research and the National Research Council of the United States of America for their kind cooperation for holding this symposium in Seoul.

We are very proud to host the symposium with 36 years of history in providing a forum for frontier subjects in marine hydrodynamics. As all of you will agree with me, the Naval Hydrodynamics Symposia have contributed in the past to inspiring new ideas and approaches to fundamental and challenging problems in marine hydrodynamics, which have been proven by the numerous papers for doctoral dissertation presented in the past symposia.

The present symposium provides a valuable opportunity for the ship hydrodynamics research community in Korea to have direct access to the current state-of-the-art information in marine hydrodynamics research, as well as an opportunity to be acquainted with fellow investigators from all over the world.

We feel very happy, also, for offering a place for our friends from abroad to renew their acquaintance with the friends from other countries who have a common goal of learning more about marine hydrodynamics.

Our sincere gratitude goes to the authors, session chairmen, and participants who will together make the Nineteenth Symposium another successful forum to advance our knowledge in marine hydrodynamics. I would like to take this opportunity to express our appreciation for the support rendered by the Korea Science and Engineering Foundation, the Korean Registry of Shipping, Korea Research Institute of Ships and Ocean Engineering, and the three major shipbuilding companies, namely Hyundai, Daewoo, and Samsung.

Lastly, I wish all of you an enjoyable stay in Korea. Let us know if we can do anything to help make your stay in Korea more pleasant.

Thank you.

Fred E. Saalfeld
Deputy Chief of Naval Research and
Technical Director, Office of Naval Research

Ladies and gentlemen, good morning and welcome to the Nineteenth Symposium on Naval Hydrodynamics. It is my pleasure to see this large number of participants from so many countries. In spite of economic problems in many parts of the world, this participation reflects the recognized need for continuing research and for the exchange of research information in the engineering sciences applicable to marine vehicle technology. It will be demonstrated in the papers to be presented and discussed in this symposium that it is a challenge to predict and control vehicle-related hydrodynamics, and that research must continue in recognition of future naval needs.

As Deputy Chief of Naval Research and Technical Director of the Office of Naval Research (ONR), I am responsible for the basic research effort in the United States that supports the Navy. Naval hydrodynamics is one of the most important of these areas of research, and I have a keen interest in encouraging advancement in this field. I am looking forward to hearing firsthand at this symposium the latest achievements in predicting and controlling marine vehicle hydrodynamics. The Office of Naval Research supports basic research because in the long term there is a direct benefit to naval warfighting capabilities. ONR provides the stability that scientific efforts need to produce beneficial results, even if the outcome cannot be foreseen at the beginning. It is in this spirit that ONR supports this symposium.

The symposium is unique. It is international in character, alternating in location between the United States and a host country other than the United States. This is the nineteenth meeting of the symposium since it began in 1956. As always, the symposium is sponsored by the Office of Naval Research, the National Research Council, and a host institution, in this case the Society of Naval Architects of Korea.

I know this is a long trip for many of us, but it is well worth the effort. Korea is truly beautiful; the people are friendly. I know the effort required to conduct a symposium such as this is immense, and it appears that our hosts have more than accomplished the task. If my experience so far is any indication, the hospitality of our hosts will be unsurpassed.

For this meeting of the symposium, the international flavor is especially significant. Naval ship hydrodynamics have obviously been of military and economic interest for thousands of years. Certainly the basic engineering information is understood, and present-day naval and commercial vessels are efficient and fulfill the purpose for which they are intended. But, in the future there will be an increasing need for vessels that are significantly bigger or faster, and less expensive. There will continue to be a hydrodynamics challenge. The real challenge today is focused on affordability: less expensive to build, operate, and maintain. In our increasingly interconnected world, new demands for maritime transport, together with increased exploitation of the seas, imply a growth in marine vehicle construction. With the increase in maritime activity, there will be an increased need for naval protection.

Many factors enter a nation's decision to design and construct ships. These factors include technological achievement, labor rates, government subsidy, and defense priority. We observe in our world that the nontechnical factors seem to control national shipbuilding efforts. However, the enabling factor is always technology achievement. For example, common to both naval and commercial interests is the need for fast transports. This requires basic understanding of, and prediction capability for, complex turbulent flows and their effects on performance, including propulsive efficiency, noise, and vibration. An enabling technology would be the successful development of useful computer prediction methods incorporating rational turbulence models applicable to a wide range of flow geometries.

Naval hydrodynamics problems are distinguished from aerodynamic problems by the presence of the free surface, the ingestion of turbulent flow by the propulsor, and the phenomenon of cavitation. In spite of the advanced technology associated with aircraft and aerodynamic flow predictions, it has been demonstrated that those methods do not solve naval hydrodynamics problems. Hydrodynamic problems remain unique, requiring special assault. The need is to extend the naval architect's hydrodynamic tools, largely empirical and

based on historical success, to predict hydrodynamic performance beyond the current database, and thus to free the ship designer from the constraints of traditional geometries and conservative assumptions.

Almost surely hull and propulsor designs in the future will be much different from those in use today. The "shaping" of the flow into the propulsor, for example, will become a common feature. To accomplish these goals, one could expect computer predictions that simultaneously consider geometry, hydrodynamics, and performance. In such a scheme, the hydrodynamics codes would be different from those existing today. This is so because the numerical procedure would "sense" the complexity of the flow to be predicted, and would automatically adjust its solution approach consistent with the required accuracy of the results.

Naval hydrodynamics adds additional performance requirements to ship design which demand a broader understanding of the flow physics. Specialty topics of interest in this area include prediction and control of surface ship wakes, acoustic radiation, and the need to design for hydrodynamic loading in high-sea states.

So, what is new for research opportunities? Powerful computers have opened the door for substantial progress in both physical and numerical experiments. We have entered an age where coupled laboratory measurements and flow predictions can be expected to lead quickly to the answer. We are able to measure the whole flow field at an instant, and to compare the results with numerical simulations of the same flow. This gains guidance and validation from the measurements, and spatial and temporal resolution with the simulations.

We are in an era where there is a need to develop technology for the future yet there is a limited supply of resources to conduct the required research. There is an answer, and that is to provide international exchange of information at the basic research level. We all know that the stakes are high in the area of national products. But the engineering science base required to support technology development can be made affordable and timely through open exchange of information. It is in this spirit that ONR sponsors the Symposium on Naval Hydrodynamics.

Forty-eight papers from ten countries will be presented and discussed at this symposium. They were selected from 150 papers submitted for consideration based on relevance and quality. The papers address topics in the areas of nonlinear ship motions, viscous ship hydrodynamics, hydrodynamics in ship design, wave and wake dynamics, cavitation and bubbly flows, propulsor hydrodynamics and hydroacoustics, and frontier experimental techniques. In keeping with the objectives of this symposium, I encourage you to participate in the discussion.

I wish you a successful, meaningful symposium. I know I will enjoy and profit from being able to attend this major scientific event.

George F. Carrier
Professor Emeritus, Harvard University

On behalf of the U.S. National Academy of Sciences, it is my great pleasure this morning to welcome each of you to the Nineteenth Symposium on Naval Hydrodynamics. This symposium series has now served as an international forum for the exchange of ideas and research results in the fields of fluid dynamics and naval architecture for 36 years, and has been convened in the Netherlands, Norway, Italy, France, England, Germany, and Japan in addition to the United States. The success of the series is fitting testimony to the foresight and dedication of Philip Eisenberg and Marshall Tulin of the Office of Naval Research, and the fact that alternate symposia are held outside the United States is due to Marshall's recognition that only in that manner could the series become truly international.

The standards and the vision established by Phil and Marshall have been faithfully preserved in subsequent years by Ralph Cooper, Bob Whitehead, Chung Lee, and Edwin Rood. I am sure that each of them would say that their jobs have been made both easy and pleasant by the cooperation received from the host countries and the international ship hydrodynamics community.

In recognizing the antiquity of this symposium series it is only fitting that the Nineteenth should be held in a country that can trace its own history over nearly 4,000 years. Further, in holding the meeting in the Republic of Korea we pay tribute to the great strides and contributions this country has made in hydrodynamic research, in ship design, and in shipbuilding. And finally, holding this symposium here in your capital city of Seoul is also a tribute to the dedication, the tireless energies, and the respect with which the international community holds Chung Lee. As you know, we were privileged to have Chung serve with the Office of Naval Research prior to his return to Korea.

The technical sessions for the Nineteenth Symposium were prepared by a program committee representing the three organizing institutions—the Society of Naval Architects of Korea, the Office of Naval Research, and the National Research Council of the National Academy of Sciences. On behalf of the three organizers I would like to express our appreciation to the Korean sponsors of this week's activities: the Korean Registry of Shipping, the Korea Science and Engineering Foundation, the Korea Research Institute of Ships and Ocean Engineering, Hyundai Heavy Industries Co. Ltd., Daewoo Shipbuilding & Heavy Machinery, Ltd., and Samsung Heavy Industries. We are most appreciative for their assistance.

Those of you who attended the Eighteenth Symposium at the University of Michigan in 1990 will recall that in his opening remarks, Lee Hunt, as the Academy representative, characterized the period before us as the *Maritime Era*. Incidentally, due to unavoidable conflicts, Lee was unable to attend the meeting this week. He sends his regards and his wish for a successful meeting. He saw the Maritime Era as being driven by a substantial increase in international trade, which, in turn, would place increasing demands not just on shipbuilding, but also on innovative design changes leading to greater transport economy. He also saw the growth of navies to police and protect those shipping fleets.

I not only endorse this vision of the future for the ship hydrodynamics and naval architecture community, but also would like to expand upon it. In the United States, oceanographic research goes back to Benjamin Franklin's observations on the Gulf Stream, and Matthew Fontain Maury's assembling vast amounts of data into nautical charts and sailing directions. But it was not until the 1950s that the international scientific community began a systematic study of the oceans. Since that time our knowledge of the physics, geophysics, geology, chemistry, and biology of the oceans has increased enormously. However, as in all fields of scientific endeavor, every question answered is replaced by two that are yet to be answered. The one thing we have learned is that the oceans play an even greater role in the environment in which mankind lives than we had earlier imagined.

Up until now, and for lack of a technological alternative, we have been practicing vertical oceanography. That is, we have, with limited exceptions, sampled vertical columns of water and extrapolated between the columns. Today—thanks in no small measure to this community—we have the technology to begin practicing horizontal oceanography. I refer, of course, to both remotely controlled and autonomous vehicles capable of

carrying sensor suites to virtually any depths and over meaningful ranges. I also refer to advances in towed side-scan sonars capable of mapping the ocean floor with unprecedented resolution. And I refer to recent proposals for doing a comprehensive survey of the Arctic Basin using a nuclear powered submarine.

The technology is here, and the need is obvious, and I urge the international community of scientists and engineers to get on with the next phase of oceanographic research, made possible in no small measure by the community assembled here this week.

In closing, I would like to make note of the fact that this is my first visit to the Republic of Korea. Therefore I am both pleased and honored to be here this week. I look forward not only to the technical papers the Program Committee has assembled for us, but also to observing as much as time permits of your country, its people, and their culture.

Thank you, and the very best wishes for a successful meeting.

Nineteenth Symposium on

NAVAL HYDRODYNAMICS

Technical Sessions

Session I

Nonlinear Ship Motions

Prediction of Nonlinear Wave/Hull Interactions on Complex Vessels

B. Maskew (Analytical Methods, Inc., USA)

ABSTRACT

A general numerical flow simulation model is used to calculate non-linear free surface/hull interactions on arbitrary configurations. The method is based on a boundary-integral formulation in the time domain, and treats the free-surface deformation and general finite amplitude motions of arbitrary vessels using a time-stepping, mixed Eulerian/ Lagrangian approach.

The boundary element method uses both source and doublet singularity panels on the free surface and on all wetted surfaces of the hull configuration, including, if present, ocean floor, towing tank, etc. The effects of surface boundary layers, lift and vortex wakes may be included in the calculation.

Computed results are presented for a sphere in large amplitude harmonic motion near the free surface. These calculations compare favorably with published results. Initial calculations from an ongoing study of a frigate in large amplitude motion are also presented and include studies of a finite-amplitude wave generator.

NOMENCLATURE

Cp	Pressure coefficient, $(p - p_{REF})/(1/2\ \rho V_{REF}^2)$
dS	Element of surface
Fr	Froude number, $V_{REF}/\sqrt{gL}$
g	Acceleration due to gravity
L	Hull length
NH	Number of active (wetted) panels on the hull surfaces
NPAN	Total number of active panels on the free surface and hull(s)
$\vec{n}$	Unit normal to the surface pointing into the fluid domain
p	Static pressure
p_{REF}	Ambient atmosphere pressure
$\vec{r}$	Position vector in normalized space
L_{REF}	Reference length, L/2
t	Time
$\vec{v}$	Normalized perturbation velocity, $\vec{v}/V_{REF} = -\nabla\phi$
$\vec{V}$	Perturbation velocity, $-\nabla\Phi$
V_{REF}	Reference speed
x,y,z	Normalized Cartesian coordinates, $x = X/L_{REF}$, etc.
X,Y,Z	Cartesian coordinates, dimensional
$\vec{R}$	Position vector in dimensional space
μ	Doublet density, $\phi/4\pi$
σ	Source density, $-(\partial\phi/\partial n)/4\pi$
τ	Normalized time, $t \cdot V_{REF}/L_{REF}$
ρ	Water density
ϕ	Normalized velocity potential, $\Phi/L_{REF}/V_{REF}$
Φ	Velocity potential (units of length^2/time)
$\vec{\Omega}$	Angular velocity

1.0 INTRODUCTION

A general purpose numerical flow simulation method is being developed for treating complex hydrodynamic problems associated with arbitrary vessels moving in or near a free surface. The method is aimed at conditions experienced by modern high performance vessels that are beyond the scope of traditional linearized approaches. The objective is to avoid small amplitude assumptions and other linearizing conditions that leave the free surface essentially flat. Such assumptions would lose the non-linear effects generated by complex hull shaping, flare, etc., during large amplitude motions in heavy seastate.

In recent years, there has been a steady progress towards a non-linear treatment of the hull/ free surface interaction. The early application of Rankine source panel methods by Gadd *(1)* and Dawson *(2)* provided nominally exact boundary conditions on the hull and were developed further in a number of approaches (e.g., Piers *(3)*, Chang and Dean *(4)*, Xia *(5)* and Larsson *(6)*, among others). These approaches still left the free surface essentially flat. A number of researchers pursued a Dawson-like approach, but with higher-order terms in

the free surface boundary condition, e.g., Ogiwara and Masuko *(7)* and Musker *(8)*. A steady non-linear ship-wave problem was solved by Jenson, Soeding and Mi *(9)*, using a simple source distribution located above the free surface. A similar technique was used by Cao, Shultz and Beck *(10)* in a time-domain method for computing non-linear waves, due to underwater disturbances. This so-called "desingularized" approach has several computational advantages when treating simple bodies, but may be difficult to apply to more general surface-piercing bodies having complex lifting appendages. It may also preclude future extension for simultaneous treatment of the air/water regions for surface-effect ship or sailing yacht applications.

Early attempts with panel methods applied to seakeeping problems in the frequency domain were inconclusive because of computational limitations. The recent work by Nakos and Sclavounos *(11)* was more successful, albeit with linearized free surface boundary conditions. King, Beck and Magee *(12)* showed the advantage of a time-domain, rather than a frequency-domain approach to seakeeping calculations. More recently, Lin and Yue *(13)* presented a time-domain approach, which treats large amplitude motions of the hull, but again, the free surface conditions are linearized, consequently, effects due to the changing wetted surface when encountering finite amplitude waves, is missing.

Zhou and Gu *(14)* presented a time-domain non-linear treatment of the free surface that included the motion of simple surface-piercing bodies. The complex problem of the moving water line cutting the surface panels was treated by an interpolation scheme. The scheme chosen may be difficult to apply to a complex shape. The non-linear free surface method presented by Kang and Gong *(15)* used curved panels and a high order integration scheme for the time steps. Results were presented for a submerged sphere oscillating with large amplitude, however, these results, for a single body, took about 14 hours of CRAY 2 time. Powlowski and Bass *(16)* presented a practical method for treating large amplitude ship motions in heavy seas. This uses a method of modal potentials and is based on a weak scatter hypothesis. The time-domain calculations use a set of modal amplitudes which must be predetermined for each vessel and load condition.

For wave/hull interactions in extreme sea state, the effect of bottom-slamming and possibly bow flare-slamming, are matters of concern, not only for predicting vessel behavior, but also for structural loads. The time-domain treatment presented by Troesch and Kang *(17)* based on a doublet panel method, showed very good agreement with experimental measurements for the impact load history in the case of relatively flat bottom-slamming, but gave an overprediction of the load during flare entry. This discrepancy is principally due to a simplification of the free surface boundary condition. In the present project, a more general free surface boundary condition is used, however, practical panel densities for the three-dimensional case may not be sufficient to resolve the water-jet feature of slamming.

The present approach is based on the USAERO FSP program *(18, 19)*. The basic program *(20)* is a time-stepping panel method that has been developed concurrently with the steady VSAERO program *(21)* over the past 15 years. The method uses both source and doublet singularity panels on the free surface and on all wetted surfaces of the configuration, including, if present, ocean floor, towing tank, etc. Doublet singularity panels, which convect with the local flow, represent the transient mean surfaces of wakes shed by lifting components of the configuration; they are also used to model propulsor slipstream effects.

The objectives of USAERO cover a broad range of applications, including helicopter rotor/body interactions, maneuvering aircraft, marine propeller in nonuniform flow, and high-speed train/tunnel simulations. USAERO allows multiple moving frames of reference to be specified, thus allowing study of such problems as transient effects due to control deflection and the mutual interaction of two or more bodies moving relative to each other. Boundary-layer effects are computed and modeled in the surface boundary condition, using the transpiration technique. An optional six-degree-of-freedom flight-path integrator module treats transient problems such as the response of an aircraft flying through a gust or the release of a store from an aircraft, and has been briefly applied to the sink-and-trim calculation on a Wigley hull started impulsively from rest.

Recently, the Free-Surface Program (FSP) was developed as an extension of the basic code. The combined program is referred to as USAERO/FSP. The non-linear free surface treatment uses the mixed Eularian/Lagrangian approach of Longuet-Higgens and Cokelet *(22)* and treats the moving hull(s) and deformable free surface within the time-step loop structure of USAERO. The program

automatically repanels the free surface and the local parts of surface-piercing objects to the changing water line. The free-surface treatment includes a finite amplitude wave generator.

An earlier paper *(18)* presented basic results for a spheroid and a lifting hydrofoil. Both cases were run impulsively from rest below the free surface and included boundary layer calculations. Exploratory calculations for a generic SWATH in a pitch oscillation and also a series 60 hull in open water and in a wave tank simulation were also presented *(19)*.

The ultimate objective of the USAERO/FSP method is to provide a practical, non-linear capability for seakeeping and maneuver predictions. The current effort is directed towards validation and evaluation of the method applied to large amplitude motions. This paper presents results from a discretization sensitivity study based on a sphere oscillating with large amplitude close to the free surface. For a more general case, a frigate hull is examined in a forced, large amplitude harmonic pitch and heave oscillation. One of the issues in these calculations concerns the automatic repaneling of the hull and free surface as the vessel plunges, and particularly when the fore deck becomes wetted. Two bow shapes are considered here: a parent shape and one V3 with a pronounced flare. These are taken from a set of five bow shapes which have been tested in model experiments (O'Dea and Walden *(23)*). As the present study continues, all five shapes will be considered, using the wave tank simulation in the present method. Initial results of the wave tank simulation are presented here, but further work is needed to match the wave profiles in the generated on-coming waves with those of the experiment.

2.0 MATHEMATICAL MODEL

The basic problem to be treated consists of an arbitrary vessel undergoing large amplitude motions in or near the free surface. For generality, the vessel may have fixed or moveable lifting hydrofoils, control surfaces and propulsors. The flow region may extend to infinity or it may be bounded locally in towing tank or canal simulations or in shallow water. A ground-fixed Cartesian coordinate system is used with the X and Y axes in the undisturbed free surface and Z positive upwards, Fig. 1. For the purpose of developing a *practical* mathematical model, it is assumed that the effects of viscosity are largely confined to thin boundary layers on the moving wetted surfaces and that wake vorticity is essentially concentrated in thin vortex sheets and discrete vortices embedded in the fluid. Diffusion and dissipation of vorticity from the wake surfaces and from the free surface into the fluid interior are neglected at this time. Away from the boundaries, therefore, the fluid is regarded as inviscid and irrotational as well as incompressible. The fluid motion can, therefore, be described by a velocity potential, $\Phi(\vec{R},t)$, which satisfies Laplace's equation,

$$\nabla^2\Phi = 0 \qquad (1)$$

Traditionally, Φ is broken down into a number of component parts to aid in the linearizing of boundary conditions. Here, however, since there is no linearization, Φ is left as a whole quantity and will, therefore, encompass such terms as incident wave potential, diffraction potential, radiation potential, etc. The convention adopted here is that the fluid velocity, $\vec{V}$, is the *negative* gradient of the potential, i.e.,

$$\vec{V} = -\nabla\Phi \qquad (2)$$

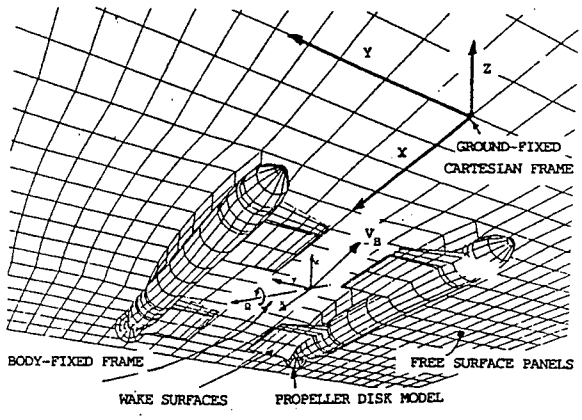

Fig. 1. General Reference System.

It is convenient to non-dimensionalize the problem with respect to certain reference quantities. A reference length, L_{REF} is used to non-dimensionalize the geometry and a reference speed, V_{REF}, is used to non-dimensionalize velocities. (L_{REF} is usually chosen as half the hull length, L, and V_{REF} the mean speed of the vessel relative to the water.) In non-dimensional space, therefore, we have the quantities,

$$\vec{v} = \vec{V}/V_{REF};$$

$$\phi = \Phi/L_{REF}/V_{REF};$$

$$\tau = t \cdot V_{REF}/L_{REF};$$

$$x = X/L_{REF}, \text{ etc.}$$

At any instant of time, the fluid velocities are computed after applying Green's Theorem to the functions ϕ and $1/r$ in the fluid domain, where r is the distance of any point in the fluid from an observe velocity point, P. With $\nabla^2\phi$ (from Eq. 1), the volume integral in Green's Theorem disappears and the flow is then determined by surface integrals of ϕ and its normal derivative, $\partial\phi/\partial n$, over the surfaces bounding the fluid including surfaces enclosing the singularity sheets representing wakes. For a point P on the *wetted* side of a surface, the perturbation potential can be written:

$$\phi_p = \frac{1}{4\pi}\int\int_{S-P} \phi\, \vec{n} \cdot \nabla\left(\frac{1}{r}\right) dS + \frac{\phi_p}{2}$$

$$- \frac{1}{4\pi}\int\int_{S} \frac{1}{r}\, \vec{n} \cdot \nabla\phi\, dS$$

$$+ \frac{1}{4\pi}\int\int_{W} (\phi_U - \phi_L)\, \vec{n} \cdot \nabla\left(\frac{1}{r}\right) dW \qquad (3)$$

where $\vec{n}$ is the outward normal from the surface and r is the length of the vector from the surface element, dS, to the point P. Surface, S, includes all wetted parts of the hull configuration, tank walls, etc., and free surface. W represents the mean wake surfaces. *S-P* signifies that the point P is excluded from the surface integral, the limiting process for the singular point when $r \to 0$ yields the local contribution, $\phi_P/2$.

The first integral in Eq. (3) is the contribution from a surface distribution of normal doublets of strength,

$$\mu = \frac{\phi}{4\pi} \qquad (4)$$

The second integral is the contribution from a surface distribution of sources of strength,

$$\sigma = -\frac{\vec{n} \cdot \nabla\phi}{4\pi} \qquad (5)$$

The third integral in Eq. (3) is the contribution from mean wake surfaces, W. The mean surface of each wake is formed by combining the upper and lower parts of the surface, enclosing the wake singularity sheet, Fig. 2. The resulting surface takes the

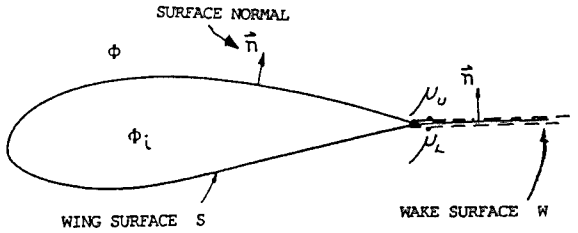

Fig. 2. Section through Wing and its Wake.

upward facing normal and a local strength which is proportioned to the potential jump across the wake:

$$\mu_w = \frac{(\phi_U - \phi_L)}{4\pi} \qquad (6)$$

In combining the wake upper and lower surfaces, the source term has been discarded, which imples that there is no normal flow relative to the wake. In fact, the wake points convect with the flow, so the wake surface is always aligned with the local velocity. (The entrainment effect due to turbulent mixing is neglected for the moment, but could be modeled by leaving the source term on the wake panels and using a free-shear layer entrainment expression.)

Thus, Eq. (3) becomes

$$\int\int_{S-P} \mu\, \vec{n} \cdot \nabla\left(\frac{1}{r}\right) dS - 2\pi\mu_p +$$

$$\int\int_{S} \frac{\sigma}{r}\, dS + \int\int_{W} \mu_w\, \vec{n} \cdot \nabla\left(\frac{1}{r}\right) dW = 0 \qquad (7)$$

This is the basic boundary integral equation, which is solved step by step through time as the vessel moves (see below). At each step, the instantaneous boundaries and their rates of motion are described relative to the ground-fixed frame. Each solution provides the instantaneous doublet and source distribution from which the velocities are

derived. Bernoulli's equation then provides the pressure distribution. This may be written in the form of a pressure coefficient using the non-dimensional quantities.

$$Cp = \frac{P - P_{REF}}{1/2 p V^2_{REF}} = - v^2 - \frac{z}{Fr^2} + 2 \frac{\partial \phi}{\partial \tau} \quad (8)$$

Where p is the local static pressure, p_{REF} is the reference pressure, which is taken here as the ambient atmospheric value. ρ is the water density (constant). z is the height *above* the undisturbed free surface and F_r represents the Froude number, $V_{REF}/\sqrt{gL}$ where g is the acceleration due to gravity. The z/Fr^2 term represents the hydrostatic pressure coefficient.

Equation (8) gives the pressure coefficient at a stationary point in the ground fixed frame; the pressure observed at a point moving with velocity $\vec{v}_s$ relative to the ground-fixed frame is

$$Cp = v_s^2 - v_R^2 - \frac{z}{Fr^2} + 2 \frac{d\phi}{d\tau} \quad (9)$$

where v_R is the fluid velocity relative to the moving point and $d\phi/d\tau$ is the *total* derivative of ϕ experienced by the moving point.

Before Eq. (7) can be solved, certain boundary conditions must be satisfied. For finite time, the condition at infinity is that $\nabla\phi \rightarrow 0$, so the surface integrals in Eq. (7) are performed on the local boundaries only. The free surface is truncated at a "reasonable" distance away from the region of interest. What is a reasonable distance will have to be established by numerical experiment. Edge conditions may be required at the truncated free-surface edge; otherwise, disturbances arriving there may be reflected. So far, this has not been a problem.

On the boundaries representing the "solid" surfaces, the source distribution is determined by the external Neumann Boundary Condition specifying the resultant normal velocity of the fluid. The normalized flow velocity relative to the surface is,

$$\vec{v}_R = \vec{v} - \vec{v}_s + \vec{v}_\infty \quad (10)$$

where $\vec{v}$ is the perturbation velocity in fixed space (Eq. (2)). $\vec{v}_\infty$ is a possible uniform onset flow relative to the stationary frame; this will be assumed zero here, but could be used in the case where the body frame is held stationary with the flow going past.

$\vec{v}_s$ is the velocity of a point on the surface relative to the stationary frame (Fig. 1),

$$\vec{v}_s = \vec{v}_b + \vec{\Omega} \times \vec{R} \quad (11)$$

where $\vec{v}_b(\tau)$ is the body frame velocity and $\vec{\Omega}(\tau)$ is the velocity of rotation about an axis in the body frame. $\vec{R}$ is the position vector of the point in questions relative to any point on the rotation axis.

The normal component of the relative flow is, from Eq. (10),

$$\vec{n} \cdot \vec{v}_R = \vec{n} \cdot (\vec{v} - \vec{v}_s + \vec{v}_\infty) = v_{NORM} + v_{BL} \quad (12)$$

where v_{NORM} is the required resultant normal velocity, which is zero for a solid boundary and positive or negative, respectively, for outflow/inflow in propulsor modeling. v_{BL} is the boundary layer displacement effect using the transpiration technique,

$$v_{BL} = \frac{\partial}{\partial s} (v_e \delta^*) \quad (13)$$

where v_e is the relative flow speed at the edge of the boundary layer and δ^* is the displacement thickness. The derivative is taken with respect to distance in the direction of the local external flow. v_{BL} is zero for stationary boundaries and would be known from the previous step in a time-stepping calculation.

Using Eqs. (2), (5) and (11), the source distribution on the solid boundaries can be written,

$$\sigma = \frac{(v_{NORM} + v_{BL} + \vec{n} \cdot \vec{v}_b + \vec{\Omega} \cdot \vec{R} \times \vec{n} - \vec{n} \cdot \vec{v}_\infty)}{4\pi} \quad (14)$$

The basic unknown on solid boundaries, therefore, is the doublet term which can be obtained from the solution of Eq. (7) at each step.

The wake doublet distribution, μ_W, is essentially known at each step because it is the accumulation of all previous solutions. Basically, at each step a new set of wake elements is created along wake-shedding lines. Each element takes the local jump in potential across the shedding line (Eq. (6)) and

moves along the local mean velocity vector. This satisfies the unsteady Kutta condition, which is obtained after specifying equal pressure (Eq. (9)) across the separation line:

$$\left(\frac{\partial \mu_W}{\partial \tau}\right) + v_M \left(\frac{\partial \mu_W}{\partial s}\right) = 0 \qquad (15)$$

v_M is the mean convection speed and s is measured in the direction of the local mean flow. μ_W is the instantaneous jump in doublet strength across the trailing edge (Eq. (6)), i.e., μ_W is the newly emerging wake strength. Equation (15) essentially states that the rate of change of circulation at the trailing edge must match the transport of circulation into the wake.

The emerging doublet strength is actually unknown at the beginning of each step, so each new wake element is partly involved with the unknown doublet values on the wake shedding surfaces. The strength of each wake element, once created, remains constant for all time as the element convects with the flow. (Diffusion and dissipation are not modeled at this time.)

On the free surface, the initial boundary conditions are that the ϕ and $\partial\phi/\partial n$ (i.e., μ and σ) are zero, and that the pressure is uniform ($Cp = 0$). The ambient pressure is assumed to be transferred directly to the fluid across the free surface, i.e., the effect of surface tension is neglected at this time. From Eq. (8), therefore,

$$\frac{\partial \phi}{\partial \tau} = \left(v^2 + \frac{z}{Fr^2}\right)/2 \qquad (16)$$

the kinematic condition on the free surface is satisfied by moving the particles with the local flow,

$$\frac{d\vec{r}}{d\tau} = \vec{v} \qquad (17)$$

Following a particle, the total derivative of ϕ is

$$\frac{d\phi}{d\tau} = \frac{\partial \phi}{\partial \tau} - v^2$$

Hence, using Eq. (16),

$$\frac{d\phi}{d\tau} = \left(\frac{z}{Fr^2} - v^2\right)/2 \qquad (18)$$

Assuming for the moment that the free surface displacement z and perturbation velocity v are known from the previous step, Eq. (18) can be integrated over a small time step to evaluate the current doublet distribution on the free surface. Given this, Eq. (7) can then be solved for the source distribution (i.e., (*i.e.*, $\partial\phi/\partial n$) on the free surface. This, together with the doublet gradient, provide the instantaneous perturbation velocity in Eq. (17). Integrating Eq. (17) then provides the free surface displacement for the next step, and so on.

In summary, the simultaneous solution of Eq. (7) on the instantaneous locations of the free surface and hull configuration at each time step provides the complete doublet and source distributions from which the flow velocities can be computed. Basically, on the hull the source is known and the doublet is unknown, while on the free surface the doublet is known and the source is unknown. On the wake surfaces, the doublet is essentially known and the source is zero.

With the flow velocities known, the pressure distributions can be evaluated using Eq. (9) and can be integrated over the surface of each part of the configurations to provide the force coefficient,

$$\vec{C}_F = -\iint_S C_p \vec{n} + C_f \vec{V}_R |\vec{V}R| dS \qquad (19)$$

and moment coefficient,

$$\vec{C}_M = \iint_S \left(Cp\vec{n} + C_f \vec{V}_R |\vec{V}_R|\right) \times \vec{r}\, dS \qquad (20)$$

where r is the position vector of a surface element relative to a selected moment reference point, and C_f is the skin friction coefficient from a boundary layer analysis based on the current surface velocity distribution.

Since the geometry has been normalized by L_{REF}, the above coefficients are based on an area of L_{REF}^2 and a moment arm divided the L_{REF}. They include the effect of hydrostatic pressure (the z/Fr^2 term in Eq. (9), and therefore include the buoyancy force and moment. The six-degree-of-freedom response of the vessel to free-surface deformation can therefore be computed by integrating the equations of motion over each time step.

The wetted surfaces of surface-piercing objects, hulls, channel walls, etc. are modified by the deforming free surface and by the movement of the vessel. These effects must be accounted for in the numerical treatment of the model.

3.0 NUMERICAL PROCEDURE

3.1 General

The numerical procedure for treating hydrodynamic problems is outlined in Fig. 3. This is basically the USAERO program *(20)*, plus a coupled free-surface program, FSP. The combined program is referred to as USAERO/FSP.

3.2 Matrix of Influence Coefficients

The main part of the numerical procedure is the treatment of the surface singularity distribution. Basically, the surface integrals in Eq. (7) are discretized using quadrilateral panels as finite surface elements. Uniform doublet and source distributions are assumed on each *surface* panel, while a linear doublet variation (i.e., uniform vorticity) is assumed in the streamwise direction over each *wake* panel. The surface integrals in Eq. (7) can then be performed in closed form over each panel. The resulting panel influence coefficients are evaluated for all active panels (i.e., configuration surface, free surface and wake surface panels) acting at a central control point on each active (i.e., wetted) surface panel on the configuration and free surfaces. Eq. (7) then becomes a summation over all panels and is satisfied at each panel center. This forms a set of simultaneous equations,

$$\sum_{k=1,K\neq J}^{NPAN} (\mu_K C_{JK}) - 2\pi\mu_J + \sum_{K=1}^{NPAN} \sigma_K B_{JK} + \sum_{K=1}^{NWS} \mu_{WK} D_{JK} = 0; \quad J=1,NPAN \tag{21}$$

where μ_K, σ_K are the doublet and source densities, respectively, on panel K.

C_{JK}, B_{JK} are the influence coefficients, respectively, for the uniform doublet and source on panel K acting at the control point of panel J (C_{JK} and B_{JK} are given in Maskew *(21)*.

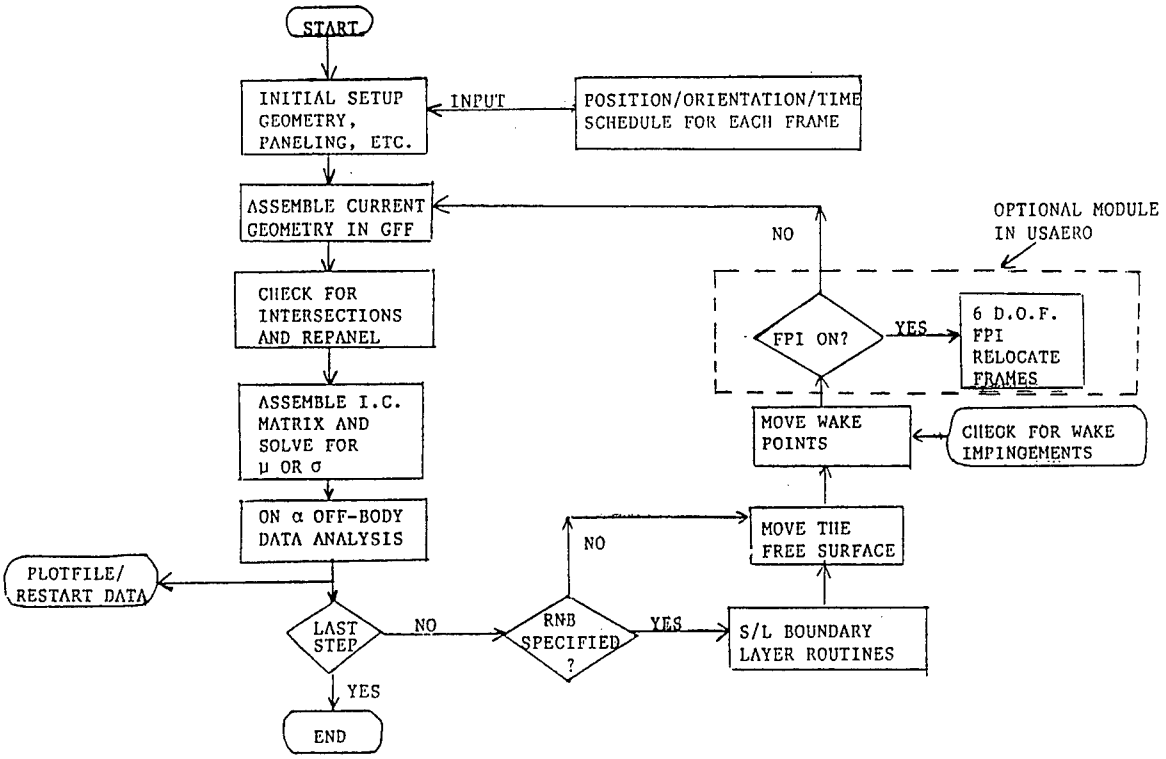

Fig. 3. USAERO/FSP Method Outline.

NPAN is the total number of active panels on all local wetted surfaces, including the free surface. *NWS* is the total number of free, cross--flow wake segments (Fig. 4); this number grows with time. μ_{WK} is the doublet density at the K^{th} wake segment, and D_{JK} is the influence coefficient for the linearly varying strength distribution over the pair of wake panels just upstream and just downstream of the segment. The influences of the wake segments that are about to be created at the shedding lines are combined with the local upper and lower shedding panel influences in the first term of Eq. (21) since these segment strengths are unknown at the start of each step. Some influence coefficients have to be re-evaluated at each time step--these include all wake panels, moving free--surface panels, and any hull panels which have relative motion with other hull panels or which have been modified by the repaneling procedure.

Collecting together "known" and "unknown" quantities in Eq. (21), the following can be written,

$$\sum_{K=1}^{NH} \mu_K C_{JK} + \sum_{K=NH+1}^{NPAN} \sigma_K B_{JK} + E_{JK} = 0 ; \quad J=1,NPAN \tag{22}$$

where

$$C_{JJ} = -2\pi ,$$

$$E_{JK} = \sum_{K=1}^{NH} \sigma_K B_{JK} + \sum_{K=NH+1}^{NPAN} \mu_K C_{JK} + \sum_{K=1}^{NWS} \mu_{W_K} D_{JK}, \text{ and}$$

NH = *number of active panels on the hull.*

Although USAERO has a number of matrix solver options, iterative solvers generally have a problem converging on the free surface equations (which involve the source influence coefficient term). The direct solver is therefore used in this type of analysis. The internal direct solver in USAERO uses the Purcell *(24)* vector method; however, on certain computers, e.g., Cray, Convex, SGI and IBM, USAERO can be directed towards a *system* direct solver which is generally optimized and vectorized. Thus, the penalty for using a direct rather than an iterative solver is not that great unless the number of panels gets well above 3,000.

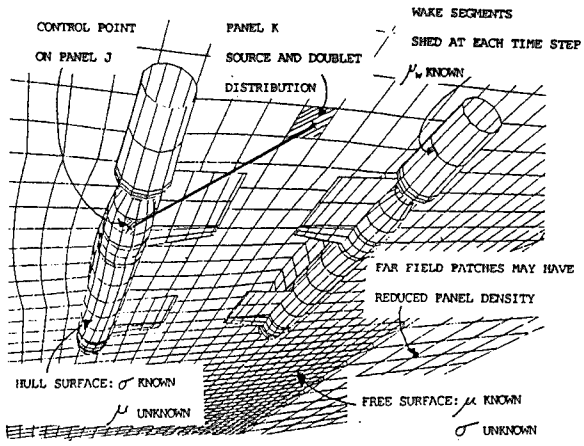

Fig. 4. Panel Influences.

After solution of the singularity values, the perturbation velocities can be evaluated directly on each panel:

$$\vec{v} = v_N \vec{n} + \vec{v}_T \tag{23}$$

The normal component, v_N, is obtained directly from the panel source value,

$$v_N = -4\pi\sigma \tag{24}$$

The tangential component, $\vec{v}_T$, is obtained from the surface gradient of the doublet,

$$\vec{v}_T = -4\pi\nabla\mu \tag{25}$$

The doublet gradient is evaluated in two directions over each panel using a second-order differencing scheme over three panels in each direction. On the "solid" boundaries, the perturbation velocity is combined with the local velocity, $\vec{v}_s$, due to body motion to give the resultant velocity,

$$\vec{v}_R = \vec{v} - \vec{v}_s$$

Hence, the pressure coefficient, Eq. (9), can be evaluated at each panel center. The $d\phi/d\tau$

term is evaluated using second-order forward differencing based on the current and two previous solutions.

Forces and moments (Eqs. (19) and (20)) are evaluated for each part of the configuration by summing the member panel contributions; the pressure and skin friction coefficient are assumed to be uniform over each panel.

3.3 Boundary Layer Calculations

On the moving solid surfaces, families of instantaneous streamlines are computed at each time step using the calculated panel velocity values. These streamlines provide a basis for integral boundary layer analyses, which start with a laminar calculation at the stagnation point or "attachment" point of each streamline.

Laminar boundary layer calculations follow the original method of Curle *(25)*, with modification to solve the unsteady momentum integral equation using a Runge-Kutta method. The turbulent boundary layer method is also based on the unsteady momentum integral equation. Cousteix's *(26)* entrainment relationship and Lyrio/Ferziger's *(27)* skin friction relationship are used for closure. The details of the method are described in Maskew and Dvorak *(28)*, together with tests of the procedure against experimental data and against other methods. These show good agreement.

The calculations provide the boundary layer displacement source term and skin friction coefficient distribution along each of the instantaneous streamlines. These quantities are then redistributed onto the surface panels in the attached flow regions. The skin friction term is included on the analysis of forces and moments (see Eqs. (19) and (20) above). The calculations also provide the location of separation on each streamline. The locus of such points defines separation lines on the body surfaces. At this time, there is no automatic coupling of these data with the wake-shedding routine. Simple cases of separated flow can be treated, but the user must specify the separation line at this time based on the boundary layer prediction.

3.4 Free-Surface Treatment

The free-surface deformation is first evaluated by integrating Eq. (17) over a small time step. A forward Euler scheme is used based on the computed perturbation velocity (Eq. (23)); i.e.,

$$\vec{r}^{(\tau+\delta\tau)} = \vec{r}^{(\tau)} + \delta\tau\vec{v} \tag{26}$$

The z component of $\vec{r}$, together with the square of the perturbation velocity, allows evaluation of the gradient of the potential with respect to time (Eq. (18)). This can then be integrated over the small time step to provide the new doublet distribution on the free surface for the next time step; i.e.,

$$\mu^{(\tau+\delta\tau)} = \mu^{(\tau)} + \delta\tau\left(\frac{d\phi^{(\tau)}}{d\tau}\right)/4\pi$$

The starting conditions for the free-surface integration are that the z component of $\vec{r}$ is 0.0 and ϕ is 0.0.

For the objective of seakeeping predictions, a simple wave generator has been installed which applies an oscillating doublet term at the upstream edge of the free surface,

$$\mu(\tau) = \mu_o \sin\left(\frac{2\pi\tau}{p}\right) \tag{27}$$

where μ_o is the doublet amplitude and p the period of oscillation. (This will later be expanded to include more Fourier terms.) At this time, because of edge conditions, only in-tank conditions have been examined. A simple damper is applied at the downstream end of the tank to absorb wave energy.

3.5 Wake Movement

When a solution has been obtained, velocities are computed at all existing wake points using a summation of all singularity contributions in the model. All wake points are then convected along the local velocity vector for a small time step. Simultaneously, a new set of wake panels is created along the wake shedding lines (Fig. 5).

The current trailing-edge doublet value (the doublet jump across the wake at the trailing edge) is transferred to each newly created wake segment. The doublet strength on each wake segment remains constant for the remainder of the calculation. The wake *vorticity* effectively varies in time and space according to the local stretching or contraction of the wake sheet as the wake points convect at the local velocities. When the new configuration has been assembled in the ground fixed

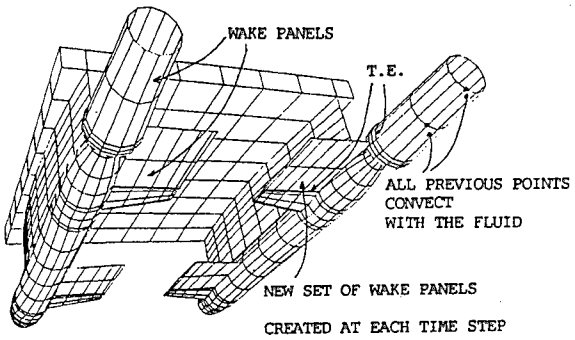

Fig. 5. Wake Model in USAERO.

frame at each step, a routine checks for intersections of the wake segments with the solid surfaces. For the most part, the points convect around downstream obstacles; however, in some cases intersections are unavoidable, e.g., if propeller blades are rotating in the presence of stators. The code deactivates any wake segment (cross-flow or streamwise) that cuts a downstream solid surface.

3.6 Surface Paneling Routines

In USAERO, the surface panels are assembled into a number of patches which have a regular row/column arrangement. User input of each patch requires a number of defining sections to be described using a set of x,y,z offsets which may be digitized from sectional drawings or extracted from a CAD package. A sufficient number of sections must be defined to adequately describe the surface curvature. If the surface is flat or conical, only two sections are required. USAERO will panel up the patch according to simple user input on panel density and form of distribution.

The free surface may be represented by one or more patches facing *downwards*. When the wave pattern remote from the vessel is not of direct interest, it is reasonable to reduce panel density in the outer regions. Usually, a 3:1 reduction in panel number is recommended on neighboring rows of panels across a patch junction. This maintains a correspondence of adjacent panel centers across the junction. A routine can be activated which automatically triangulates the panels on the high-density side, thereby avoiding the chance of a hole appearing in the discretized surface.

The paneling routine in USAERO includes procedures to compute intersections (e.g., at wing-body junctions) and to repanel up to the intersection. This is based on a simple procedure, but is adequate for reasonable panel densities. An extension of the procedure is used at each time step in repaneling the surface-piercing hull elements and free surface to the instantaneous waterline. This treatment is essential for smooth behavior of the time histories of surface pressures and forces; however, the repaneling procedure requires additional treatment for the evaluation of $\partial\phi/\partial t$ in Eq. (9), and a number of surface coefficients have to be re-evaluated. The repaneling becomes quite complicated for extreme-amplitude motions (see later) when the waterline cuts obliquely across a patch.

In USAERO the surface patches may be assembled into one or more components for the convenience of force and moment information. Each component may be assigned to a different moving frame of reference for the treatment of multi-body problems. The reference frames, themselves, may be assigned to other reference frames rather than to the ground-fixed frame directly. This allows individual parts of the vessel to undergo a prescribed motion relative to the parent frame (e.g., for rudder deflection, store release, etc.) during the calculations.

4.0 RESULTS

The following results are from the initial part of an evaluation of the USAERO/FSP approach for nonlinear free surface problems. The evaluation includes validation cases and sensitivity studies. Results are presented here for a sphere oscillating near the free surface and for a frigate in large amplitude motion.

4.1 Sphere

4.1.1 Heave Motion

The force history was computed for a sphere oscillating in heave beneath the free surface. The sphere has unit radius and the motion of its center is described by,

$$z = -2.0 + 0.5 \cos \omega t$$

where ω is the frequency of oscillation and is related to the wave number, K, through

$$K = \omega^2/g$$

In this case, K = 1.

The calculations were performed using the y = 0 plane of symmetry. In the results presented here, two panel densities were used on the half-sphere: a 10 x 10 array and a 15 x 15 array, see Fig. 6. The half free surface, which is truncated at a distance of 16 sphere radii, has 10 panels in the azimuth and 20 in the radial directions. The calculation used 24 time steps per cycle.

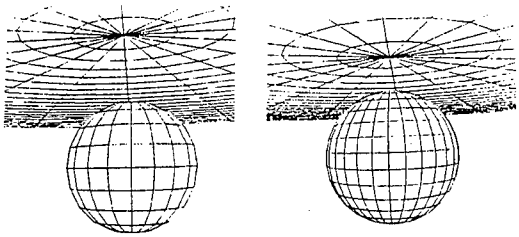

Fig. 6. Sphere Paneling Showing the 10 x 10 and 15 x 15 Arrays.

Figure 7 shows the computed time history of the heave force, which is nondimensionalized by $\rho g K a R^3$. R is the radius of the sphere, 1.0 here, and a is the amplitude of the motion, 0.5. The symbols in Fig. 7 show the values for the low-panel-density case, and these are in very close agreement with the *line* for the higher density case.

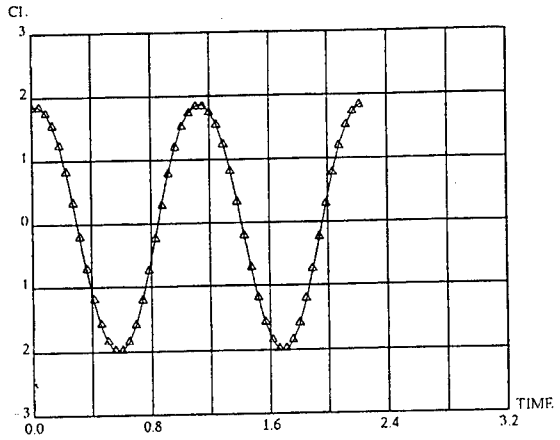

Fig. 7. Computed Heave Force History for a Sphere in Heave Oscillation at one Diameter below Free Surface.

The overall curve agrees very well with that given by Kang and Gong *(15)* and, in fact, the first harmonic terms of 1.846, .264 (cosine, sine, respectively) compare with Kang and Gong's values of 1.843 and .267. The present results give a small mean value of about .9% of the first harmonic magnitude and a sectional harmonic force of 3%. These are low compared with Kang and Gong's values of 1.5% and 6.5%, respectively. As far as sphere panel density is concerned, the present results (a range from 25 panels to 400 panels have been examined separately on the half-sphere) seem essentially converged up to five harmonics. The study is continuing and will consider time-step discretization, free surface discretization, free-surface truncation distance, and a range of frequencies. Computation times on a Silicon Graphics 4DGT workstation were 4.5 minutes per cycle and 10 minutes per cycle, respectively, for the 10 x 10 and 15 x 15 array cases presented here.

4.1.2 Surge Motion

The two sphere cases were run in surge motion described by:

$$x = 0.5 \cos \omega t$$

The sphere center was at z = -2.0 and the wave number, K = 1.0. The time histories of the surge and heave forces are shown in Fig. 8. The symbols show the calculated points for the lower density case and again, they are essentially on the curve for the higher density case. The surge force

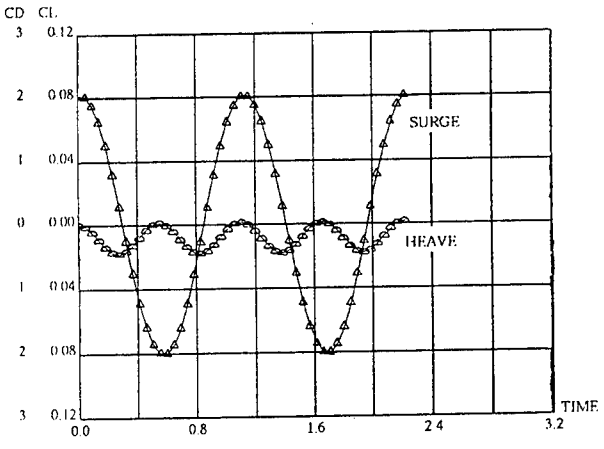

Fig. 8. Computed Surge and Heave Force Histories for a Sphere in Surge Oscillation at One Diameter Below the Free Surface.

history agrees very well with that calculated by Kang and Gong *(15)*, the first harmonic in-phase term being 1.931, compared with 1.928. The present out-of-phase term, however, is .262, compared with a value of .124 from Ref. 15. The heave force is small compared with the surge force, and is dominated by the second harmonic terms. The present values appear to be about half those given by Kang and Gong *(15)*. These discrepancies will be investigated as the study continues.

4.2. Frigate

4.2.1 General

Experimental data are available from a series of tests on a frigate model in steep head waves *(23)*. The results cover fairly extreme conditions, including water on the deck, and compare the effects of five bow shapes, Fig. 9. The ongoing theoretical study, which has just started, will eventually consider the full range of shapes; however, initial calculations for the parent (shown dotted in Fig. 9) and the increased flare shapes are presented here.

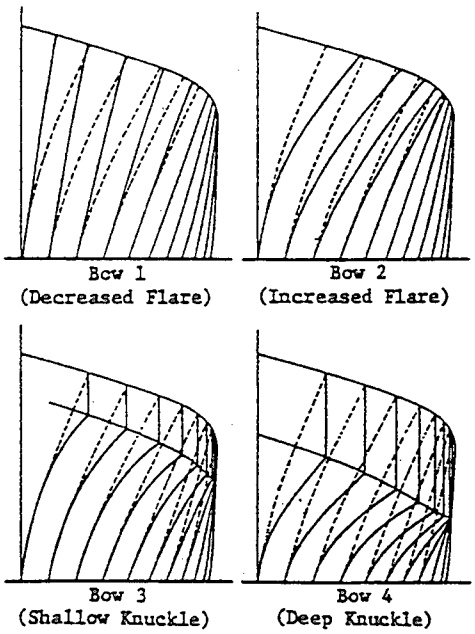

Fig. 9. Alternate Bow Shapes for the Frigate Experiments.

The conditions of the tests are very difficult to treat by purely theoretical modeling, and so the approach has been broken into four steps. First, the pure radiation condition is considered for the hull in large amplitude motion with no forward speed. A simultaneous pitch and heave motion is used to accentuate the bow motion which changes from totally dry to totally wet during the cycle. Although such a calculation is interesting in itself, the main objective here is to quickly explore the behavior of the automatic repaneling procedure in relatively simple conditions before proceeding with the more complex cases which take considerably more computing time.

The second aspect of the problem, which can be examined separately, is the wave generator itself. The present numerical model generates a free-running, finite-amplitude wave system by applying a sinusoidal potential at the upstream "edge" of the free surface. This uses input values for amplitude and period. Just as in a wave tank, whether or not a "regular" wave train is generated depends on the balance between the amplitude and period of the oscillator. Matching an experimental wave pattern is therefore very difficult and an approximation may have to be accepted.

The third aspect of the problem considered separately here is essentially the wave excitation. Again, initial calculations are presented here for the frigate in forced motion through large amplitude waves. The purpose of these calculations is to ensure smooth wave excitation forces before proceeding with the fourth stage, which will let the frigate move freely.

4.2.2 Wave Radiation

The "parent" and "flared" hulls were set in pitch and heave oscillation with sufficient amplitude for the bow keel to clear the mean free surface, and for the foredeck to become submerged during the cycle. The period of the oscillation was equivalent to an incident wave length of 1.2L at Fr = 0.3--a condition which appears critical in the experimental data *(23)*. The calculation used 60 time steps per cycle and took about 4 hours on the Silicon Graphics 4DGT workstation. The case used 1,252 panels on one side of the y=0 plane of symmetry. Figs. 10(a) through (l) show a general view of the parent hull case with free surface elevation contours at key steps in the cycle. Blue indicates a wave peak and red a trough. The motion starts with a positive pitch motion. Fig. 10(a) shows the condition as the bow is about to leave the water. At this stage, the free surface is depressed. As the bow clears the free surface, the

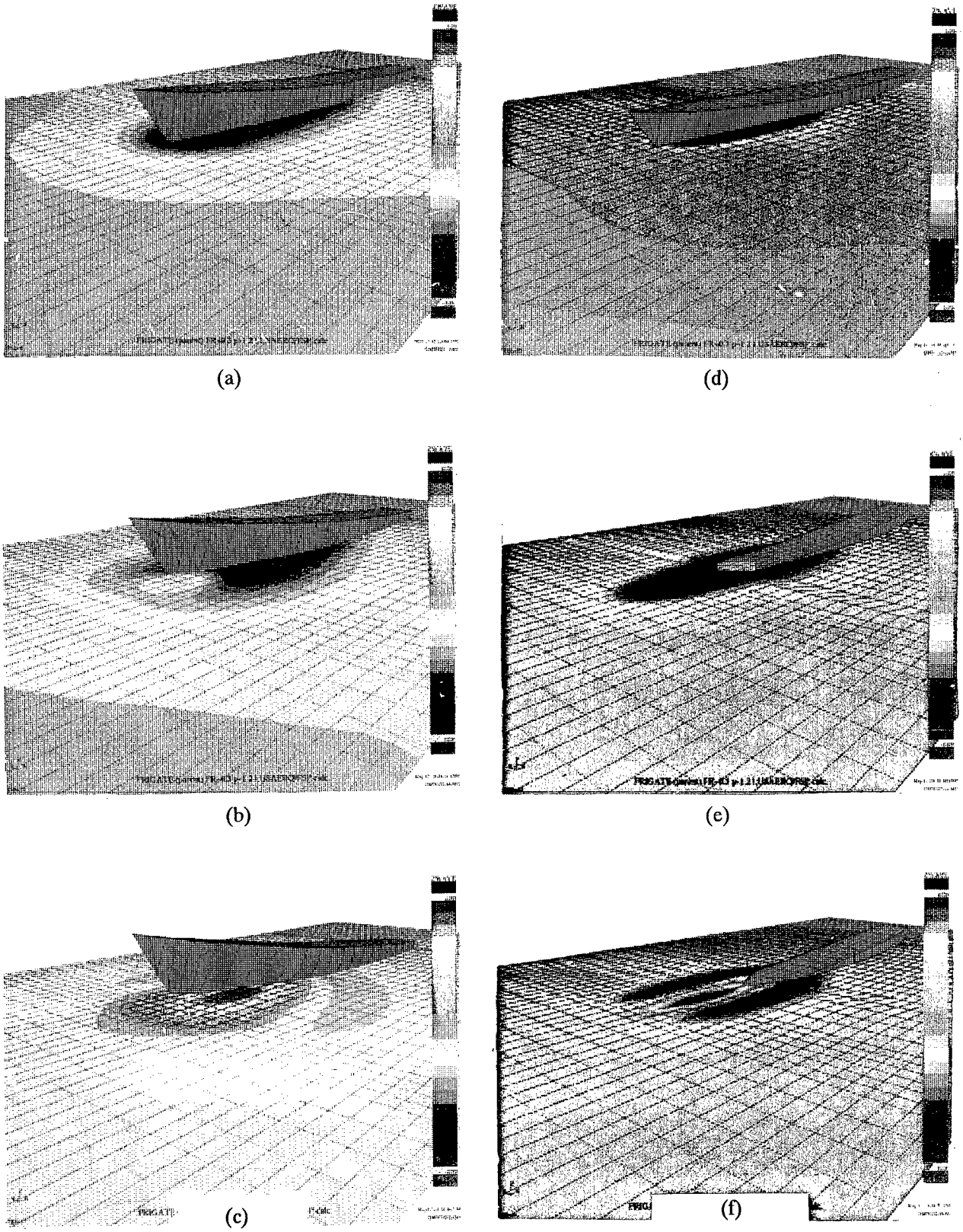

Fig. 10. Calculated Instantaneous Free-Surface Elevation Contours During One Pitch/Heave Cycle of the (Parent) Frigate Hull at Zero Forward Speed.

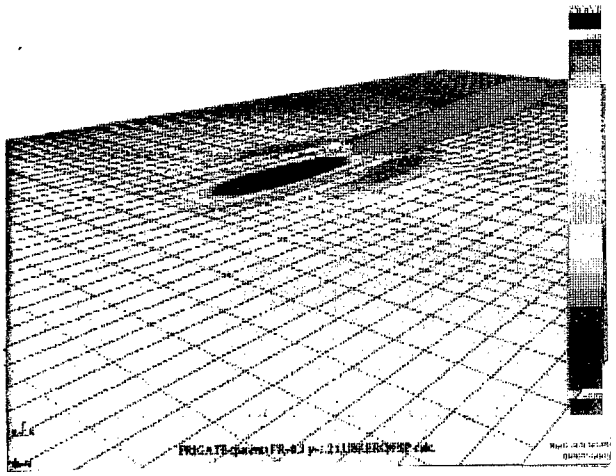

(g)

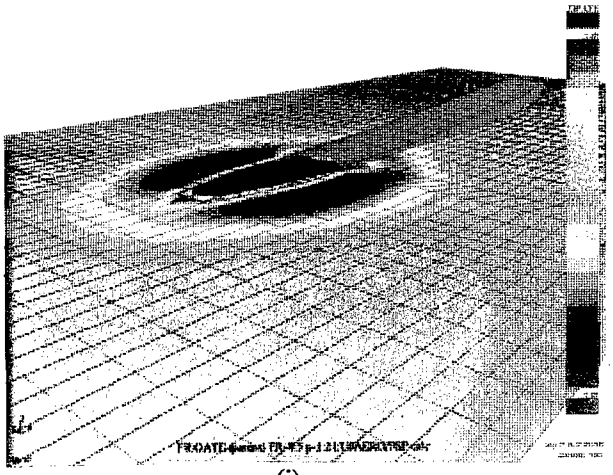

(j)

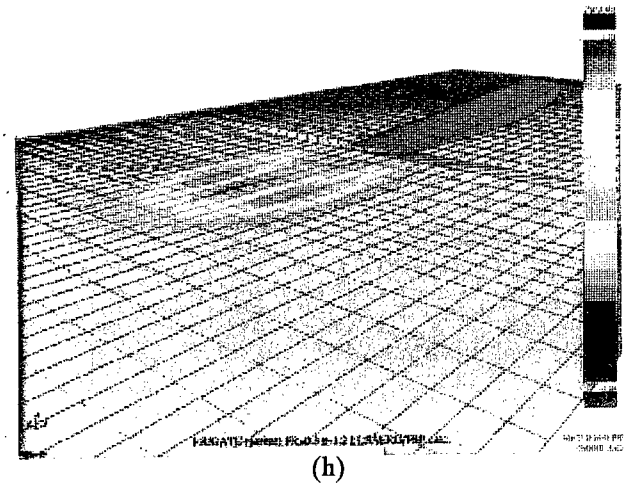

(h)

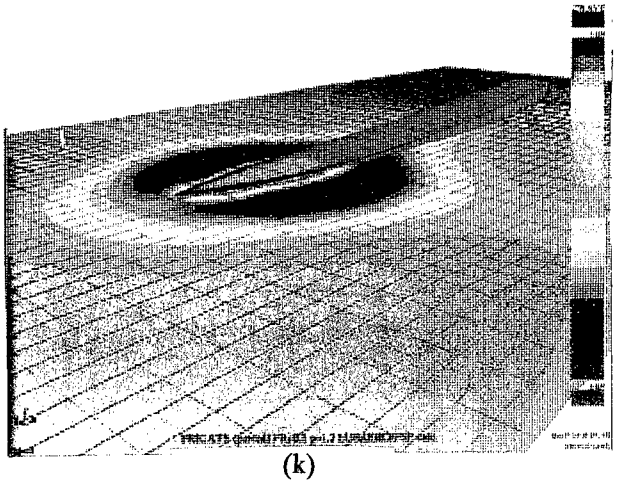

(k)

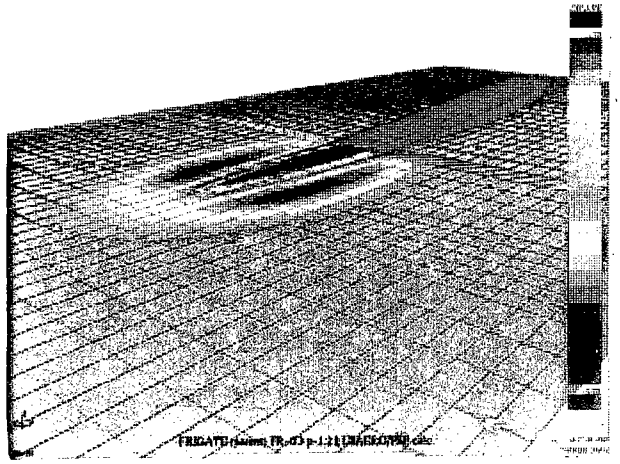

(i)

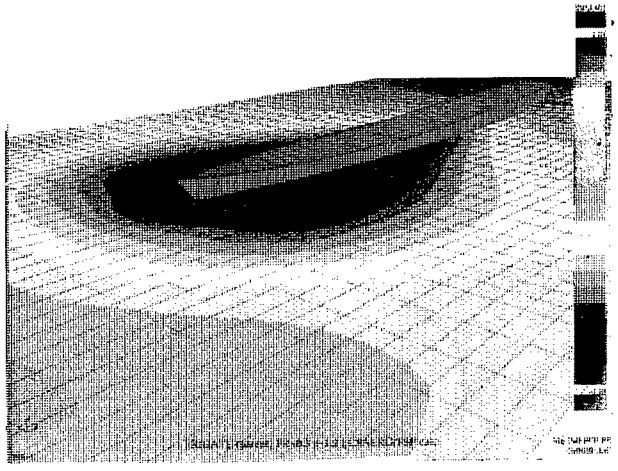

(l)

Fig. 10. Concluded.

depression moves away in a crescent shape, Fig. 10(b), and the free surface under the hull rebounds into a peak, Fig. 10(c). As the bow returns, it reinforces the peak, Fig. 10(d), and is eventually engulfed, Fig. 10(e). Figs. 10(f) and (g) show the condition shortly after submergence; the continued downward movement of the bow creates a local depression in the free surface, and the original wave peak is now divided and proceeds outward. The reverse happens when the bow starts to come back up, Fig. 10(h); the depression is divided by a central peak over the upcoming deck. The central upwelling continues (Figs. 10(i) and (j)) until the deck breaks the surface, Fig. 10(k). The depression in the free surface as the deck continues upwards, Fig. 10(l), is significantly more widespread than during the first part of the cycle (Fig. 10(a)).

During the above calculation, an analysis of the impact loading was performed for three parts of the bow shown in Fig. 11.

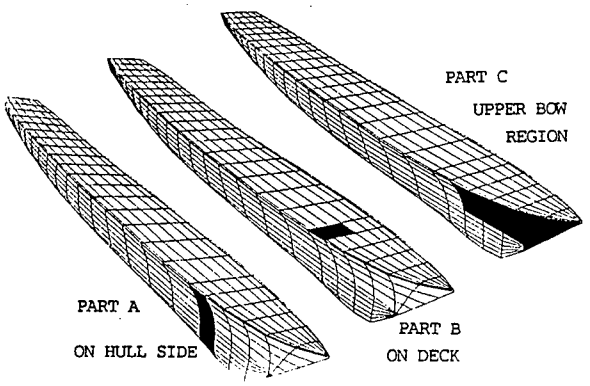

Fig. 11. View of the Frigate Hull Paneling Showing the Separate Parts used for Force Integration Details.

Part A is a vertical strip of panels on the side of the bow and goes down to the keel; Part B is a set of panels on the deck and Part C is a set of panels on the side of the bow above the mean free waterline. The time histories of the integrated loads on these pieces are shown in Fig. 12. The loads are divided by the hull displacement. The line in Fig. 12 is for the parent hull, while the symbols are for the flared blow case. A significantly higher loading is predicted for the flared bow, including the Part B or deck. The flared hull case was repeated with a higher density of panels on the free surface, but gave essentially the same load trace.

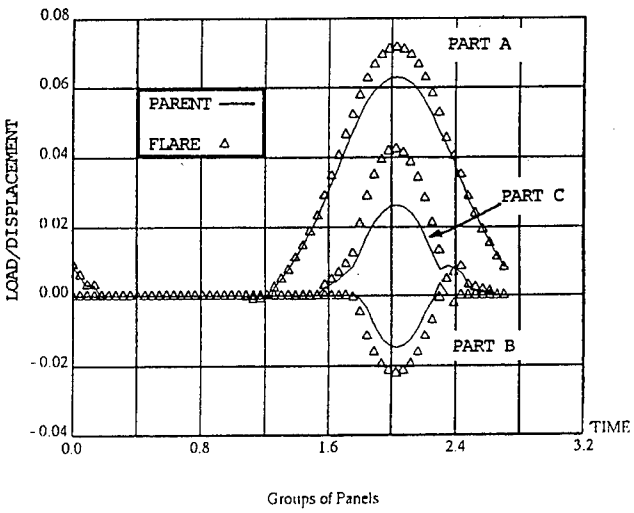

Fig. 12. Comparison between the Parent and Flared Bow Shapes for the Calculated Loads During Extreme Pitch/Heave Oscillation.

Figures 13(a) and (b) show station cuts through the bow and free surface during the submergence of the bow. 13(a) shows the bow going down and the free-surface depression--the symbols display the ZWAVE height value as a separate parameter. 13(b) shows the upwelling conditions as the bow is moving back up. The higher amount of activity for the flared bow case is apparent in both cases. The dotted line in both (a) and (b) shows the free surface location for the flare case using a 50% higher panel density in the lateral direction. This gives somewhat more detail, but

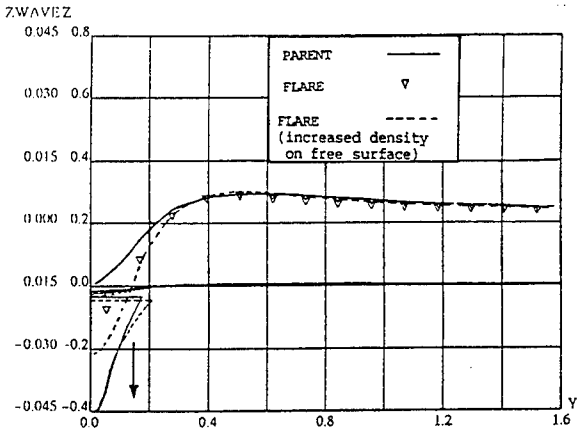

(a) Downward Motion

Fig. 13. Comparison Between Parent and Flare Bow Shapes for Computed Wave Profile at Station Cut through Bow During Extreme Pitch/Heave Motion.

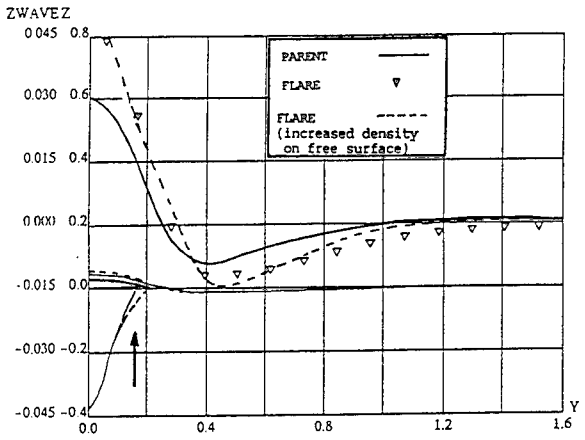

(b) Upward Motion

Fig. 13. Concluded.

does not materially affect the integrated forces. The panel density is not sufficient to capture the rapid rise up immediately adjacent to the hull surface during the downward plunge, and consequently, misses the water jet feature of the slam. It is very unlikely that a sufficiently high panel density could be used in a practical case to capture these features in a fully three-dimensional run (whereas it is possible in the two-dimensional case). Should this omission prove important, a local modeling--somewhat equivalent to a base wake from a bluff body--may be possible.

4.2.3 Wave Generator

A separate wave generator tank model is run to examine the form of the waves prior to running the hull model. Basically, the variables are amplitude and period of the forcing function on the upstream potential; however, time-step size and panel discretization may affect the ensuing wave form.

Figure 14 shows the time history of the velocity potential on a line of free-surface panels running downstream from the generator panel. The oscillating potential is seen to be transferred smoothly onto the neighboring panel with only a small loss in amplitude. The ensuing wave pattern, however, suffers some damping and some distortion as it progresses down the channel, Fig. 15. Figs. 16(a) and (b) display the Vx and Vz perturbation velocity contours on the side of the "tank" in relation to the generated wave some time after the start of the oscillation. The Vx distribution, Fig. 16(a), clearly shows an influence of the tank base presence.

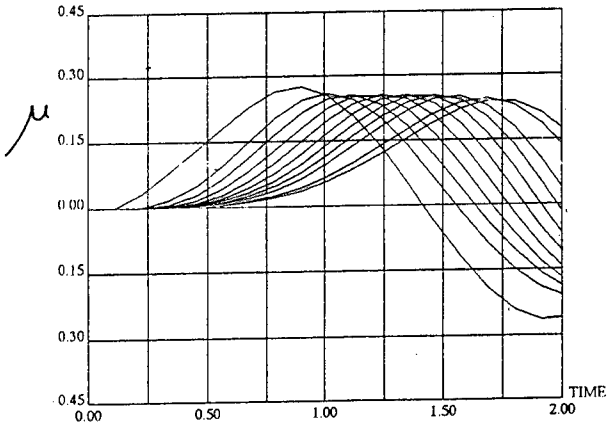

Fig. 14. Time History of the Velocity Potential (i.e., Doublet) on Several Panels Just Downstream from the Wave Generator.

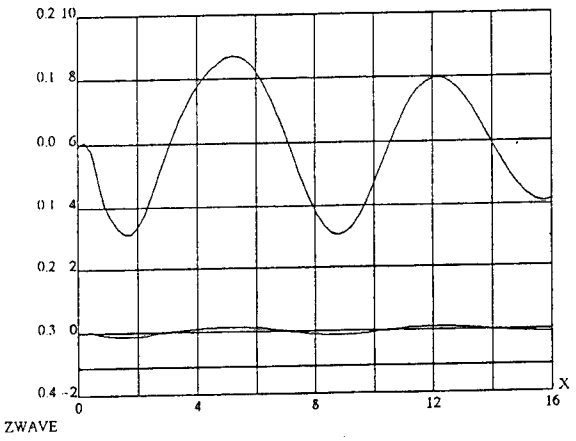

Fig. 15. Computed Wave Profile.

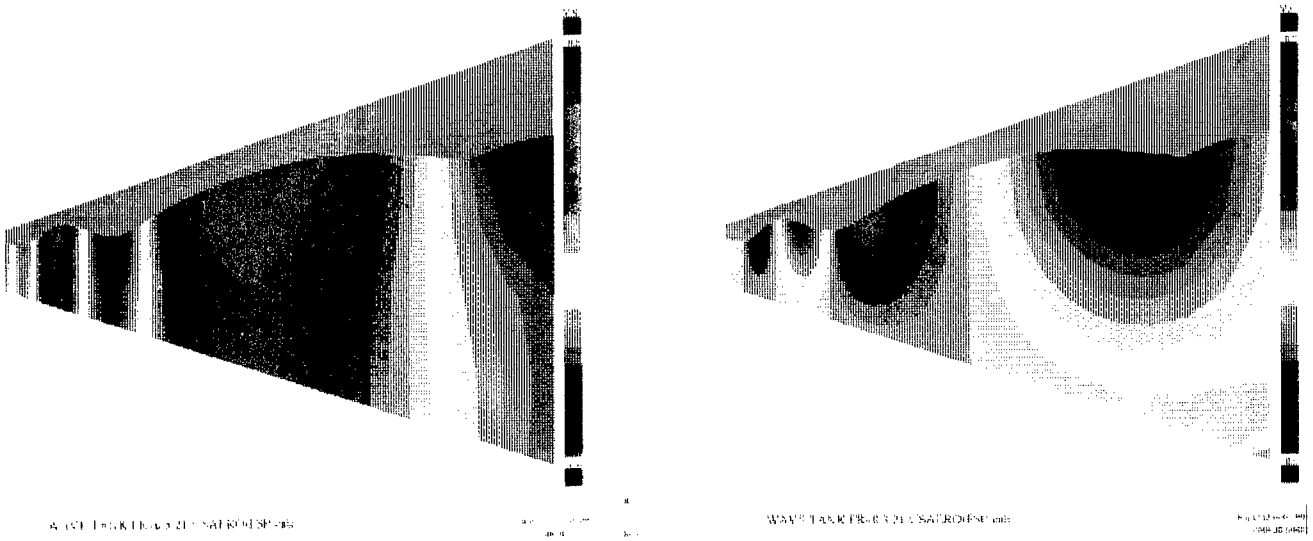

(a) VX Contours (b) VZ Contours

Fig. 16. Numerical Wave Generator Calculations.

4.2.4 Wave Tank Simulation

The setup for the wave tank simulation is as follows. The wave oscillator is first started up, but the hull is left stationary at the downstream end of the "tank". As the waves become established, the hull starts to move up the tank and eventually encounters the generated saves, Fig. 17. At this time, the motion is forced. This allows the wave excitation forces to be examined prior to release of the model for the free pitch and heave calculations. So far, some details of the repaneling procedure have caused minor problems with the $\partial\phi/\partial t$ pressure term, which must be cleaned up

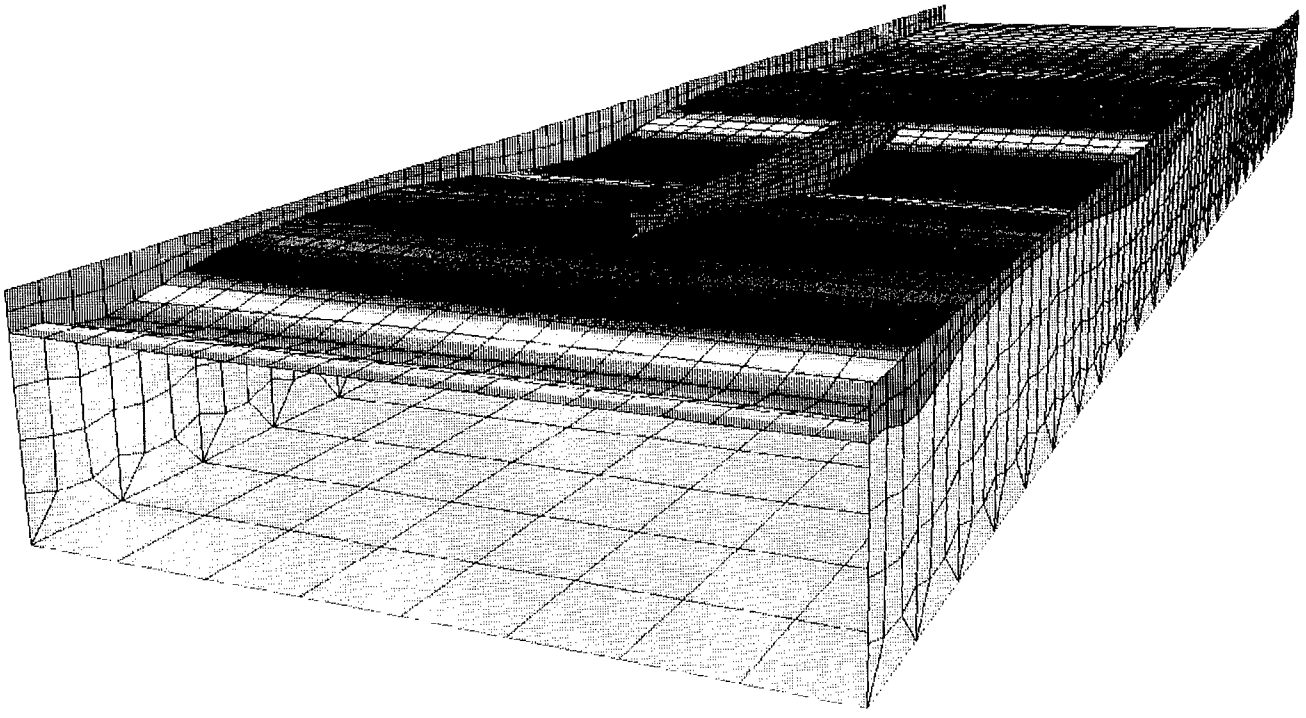

Fig. 17. Initial Calculations for Frigate in Numerical Wave Tank.

before running the model free. Figs. 18(a) and (b) show the good behavior of the velocity potential distribution at two steps during the wave encounter. The extreme variation of the paneling during a wave encounter is clearly visible in these two

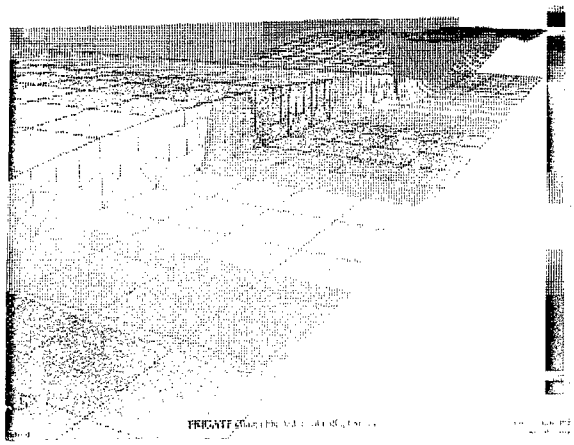

(a) At a Trough

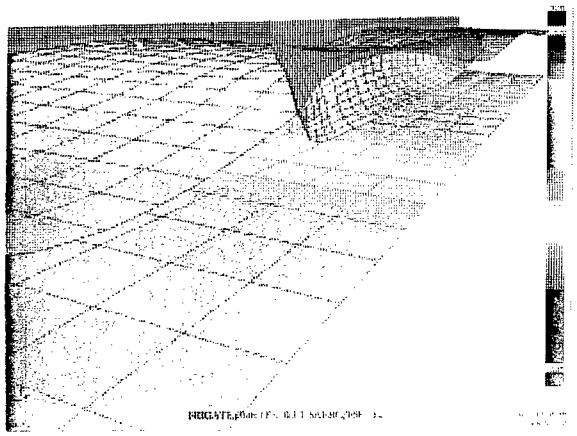

(b) At a Wave Peak

Fig. 18. Cutaway View of Calculated Velocity Potential Distribution During Wave Encounter.

figures. Fig. 19 shows the time history in the dynamic and $\partial\phi/\partial t$ pressure components on a panel near the bow during the wave encounter; these are out of phase with each other. Finally, Fig. 20 shows a station cut through the bow and tank near the end of the run showing a slightly higher wave diffraction for the flared bow--as would be expected. A higher panel density will be employed for the later runs.

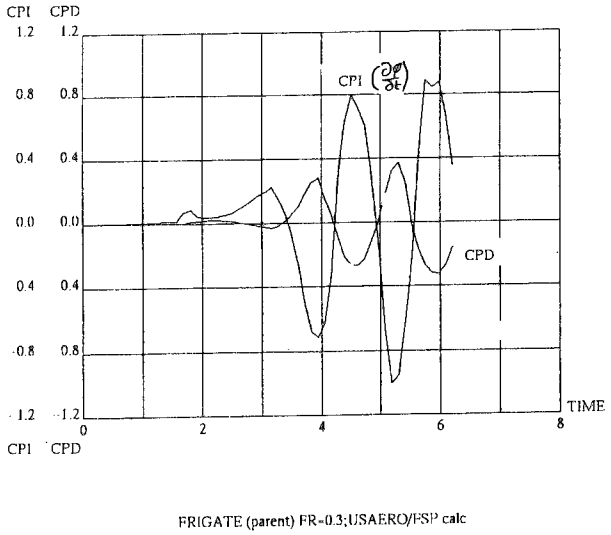

Fig. 19. Computed Pressure Components on a Panel Near the Bow during the Wake Encounters.

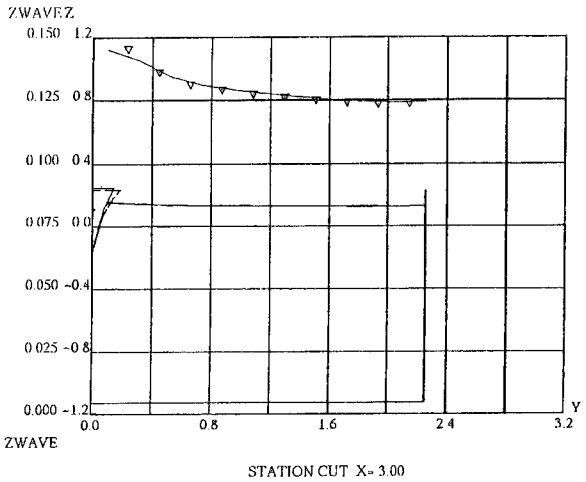

Fig. 20. Computed Wave Elevation for the In-Tank Simulation Comparison between Parent and Flare Shapes.

5.0 CONCLUSIONS

Encouraging progress on the development of a general nonlinear numerical method for wave/hull interaction problems is presented. Basic validation presented here for a sphere case in large amplitude motion is in good agreement with published results, at least for the first harmonic loads. Discrepancies in the smaller higher harmonics will be investigated as the study proceeds. Initial results for a frigate application in large amplitude motion and in the presence of large amplitude wave encounters look promising for

future stages of the ongoing study aimed at comparisons with experimental data on the model in steep head waves.

6.0 ACKNOWLEDGEMENTS

The present results are from a study supported by the Office of Naval Research under the Applied Hydrodynamics Research Program, Contract N00014-90-C-0047.

REFERENCES

1. Gadd, G.E., "A Method of Computing the Flow and Surface Wave Pattern Around Full Forms," *Trans. Royal Asst. Nav. Archit.*, Vol. 113, 1976, p. 207.

2. Dawson, C.W., "A Practical Computer Method for Solving Ship-Wave Problems," 2nd Int'l Conf. Numerical Ship Hydro., U.S.A., 1977.

3. Piers, W.J., "Discretization Scheme for the Modeling of Water Surface Effects in First-Order Panel Methods for Hydrodynamic Applications," NLR Report TR-83-093L, The Netherlands, 1983.

4. Chang, B. and Dean. J.S., "User's Manual for the XYZ Free-Surface Program," Report No. DTNSRDC 86/029, 1986.

5. Xia, F., *Numerical Calculations of Ship Flows, with Special Emphasis on the Free-Surface Potential Flow*, Dissertation, Chalmers, U. Goteborg, Sweden, 1986.

6. Larsson, L., "Numerical Predictions of the Flow and Resistance Components of Sailing Yachts," *Proc. Conf. Yachting Tech.*, U.W. Australia, Australia, 1987.

7. Ogiwara, S. and Masuko, A., "A Method of Computation for Steady Ship Waves by Means of Rankine Sources and Its Application to Hull Form Design," CADMO Int'l Conf., 1986, p. 97.

8. Musker, A.J., "A Panel Method for Predicting Ship Wave Resistance," *Proc. 17th Symp. Naval Hydro.*, The Hague, The Netherlands, 1988.

9. Jenson, G., Soeding, H. and Mi, Z.X., "Rankine Source Methods for Numerical Solutions of the Steady Wave Resistance Problem," *Proc. 17th Symp. Naval Hydro.*, The Hague, The Netherlands, 1988.

10. Cao, Y., Schultz, W. and Beck, R., "Three-Dimensional, Unsteady Computations of Nonlinear Waves Caused by Underwater Disturbances," 18th Symp. Naval Hydro., Ann Arbor, MI, 1990.

11. Nakos, D.E. and Sclavounos, P.S., "Ship Motions by a Three-Dimensional Rankine Panel Method," 18th Symp. Naval Hydro., Ann Arbor, MI, 1990.

12. King, B., Beck, R.F. and Magee, A., "Seakeeping Calculations with Forward Speed Using Time-Domain Analysis," *Proc. 17th Symp. Nav. Hydro.*, The Hague, The Netherlands, 1988.

13. Lin, W.M. and Yue, D.K.P., "Numerical Solutions for Large-Amplitude Ship Motions in the Time Domain," 18th Symp. Naval Hydro., Ann Arbor, MI, 1990.

14. Zhou, Z. and Gu, M., "Numerical Research of Nonlinear Body-Wave Iterations," 18th Symp. Naval Hydro., Ann Arbor, MI, 1990.

15. Kang, C.-G., and Gong, I.-Y., "A Numerical Solution Method for Three-Dimensional Nonlinear Free Surface Problems", Presented at 18th Symp. on Naval Hydro., Ann Arbor, MI, 1990.

16. Pawlowski, J.S., and Bass, D.W., "A Theoretical and Numerical Model of Ship Motions in Heavy Seas", Presented at SNAME Annual Meeting, 1991.

17. Troesch, A.W., and Kang, C.-G., "Evaluation of Impact Loads Associated with Flare Slamming", Presented at Spring Meeting/STAR Symp./3rd IMSDC, June 1988.

18. Maskew, B., "USAERO/FSP: A Time-Domain Approach to Complex Free-Surface Problems," Symp. High-Speed Marine Vehicles, Naples, Italy, 1991.

19. Maskew, B., "A Nonlinear Numerical Method for Transient Wave/Hull Problems on Arbitrary Vessels", Presented at 1991 Annual

SNAME Meeting, New York, N.Y., November 1991.

20. Maskew, B., *USAERO, A Time-Stepping Analysis Method for the Flow about Multiple Bodies in General Motions, Users' Manual*, Analytical Methods, Inc., Redmond, WA, 1990.

21. Maskew, B., "Program VSAERO Theory Document," *NASA CR-4023*, 1987.

22. Longuet-Higgins, M.S. and Cokelet, E.D., "The Deformation of Steep Surface Waves on Water: I. A Numerical Method of Computation," *Proc. R. Soc. London*, A350, 1976, pp. 1-26.

23. O'Dea, J.F., and Walden, D.A., "The Effect of Bow Shape and Nonlinearities on the Prediction of Large Amplitude Motions and Deck Wetness", *Proc. 15th Symp. on Naval Hydro.*, Hamburg, Germany, 1984.

24. Purcell, E.W., "The Vector Method of Solving Simultaneous Linear Equations", *J. Math. Physics*, Vol. 23.180, 1953.

25. Curle, N., "A Two-Parameter Method of Calculating the Two-Dimensional Incompressible Laminar Boundary Layer," *J. Aero. Soc.*, Vol. 71, 1967.

26. Cousteix, J. and Houdeville, R., "Singularities in Three-Dimensional Turbulent Boundary-Layer Calculation and Separation Phenomena," *AIAA J.*, Vol. 19, No. 8, August 1981.

27. Lyrio, A.A. and Ferziger, J.H., "A Method of Predicting Unsteady Turbulent Flows and Its Application to Diffusers with Unsteady Inlet Conditions," *AIAA J.*, Vol. 21, No. 4, April 1983.

28. Maskew, B. and Dvorak, F.A., "Prediction of Dynamic Stall Characteristics Using Advanced Nonlinear Panel Methods," *Proc. Workshop Unsteady Separated Flows*, USAF Academy, August 1983.

DISCUSSION

J. Pawlowsky
National Research Council, Canada

I would like to congratulate the author on his very interesting paper and presentation. As a comment, I think that "the navy secret weapon," i.e., the ship jumping out of the water during a time domain motion simulation shown in the presentation, is probably due to too large a time step used in the simulation. This may result in an excessive force impulse. In other words, the resolution of the modeling of sharp transient loading may be not sufficient. As a question, I would like to ask the author to provide a general description of the procedure used in the modeling of the water flow on decks used in his simulations.

AUTHORS' REPLY

The computed frigate motions shown during the presentation are part of a sensitivity study on the effects of panel size and time step size. The divergent path calculation referred to by the discussor is in fact due to too large a time step size as pointed out in the presentation. An unusually high $\partial\phi$ term was in fact calculated at the stern region due mainly to a poor representation of the transom stern effect at this time.

The modeling of the water on deck has no special treatment at this time. It simply evaporates at the instant the deck recuts the free-surface on the upstroke. This feature and the current omission of the jet on bow keel and bow plane entry, need further consideration in the continued development of the method.

A Nonlinear Theory of Ship Motion in Waves

J. Pawlowski (National Research Council, Canada)

ABSTRACT

The paper presents a systematic approach to the formulation of non-linear boundary value problems of ship hydrodynamics. The approach is based on an explicit use of fluid domain transformations. New forms of the impermeability and free surface conditions are derived. Perturbation formulations of Dawson-like and Neumann-Kelvin problems with steady and unsteady velocity potentials are developed, including second order equations for the latter. A physically justified weak-scatterer hypothesis is introduced and applied to obtain a perturbation and direct formulation of the non-linear ship-wave interaction problem, for which solutions can be obtained using existing computational methods. In the direct formulation a consistent non-linear flow matching (radiation) condition on a control boundary is derived.

INTRODUCTION

The aim of the present paper is to outline a systematic approach to the formulation of non-linear boundary value problems of ship hydrodynamics. It appears that such an approach can be developed by taking explicitly into account the change of a fluid domain D relative to its known reference configuration D_o, which is inherent in those problems. The explicit inclusion of the domain variation is accomplished by defining a one-to-one domain transformation. The transformation depends upon time for time dependent problems. To the domain transformation there corresponds a transformation of the scalar, vector and tensor fields used to define the boundary value problem in D. An application of both transformations allows a reformulation of the governing equations of the problem so that they are applicable on D_o. The second section of the paper describes the domain and field transformations expressible by means of the exponential operator of the directional derivative taken along the domain displacement field which provides the one-to-one mapping between D and D_o. The results constitute in part a restatement of arguments presented in [1] and [2] to justify the usual Euler-like formulations of the boundary value problems [3].

In the third section the domain and field transformations are applied to the governing equations of an irrotational flow of the ideal fluid, influenced by the presence of a free surface, ∂D_F, and of the wetted surface , ∂D_W , of an impermeable body. The presence of a control surface, ∂D_C, on which the continuity of the velocity and pressure fields is required, is also considered. The transformed Laplace's equation, kinematic and kinetic conditions on the free surface, and matching conditions on the control surface are derived. This is followed by the development of the explicit form of the impermeability condition, applicable on ∂D_F and ∂D_W. This form of the impermeability condition takes explicitly into account the domain displacement field. The relation of the explicit condition to its well known implicit counterpart is discussed in the fourth section. In addition, a general form of the condition, which is applicable on the surface of an arbitrarily deformable body, is presented. It is shown that in general for surface piercing bodies the application of a body displacement field in the impermeability condition leads to an inconsistency in the formulation of the boundary value problem on the reference fluid domain.

As described in the fifth section,

a perturbation formulation of a boundary value problem defined on D is obtained by assuming the solution to the boundary value problem transformed to D_o in the form of a perturbation series. The fifth section presents perturbed governing equations on D_o derived by a domain transformation. It is shown that the usual free surface conditions [3], [4], obtained by the Euler-like perturbation procedure constitute a special form of more general equations which do not depend upon the assumption of single-valued wave elevation. Next, perturbations of the double body flow are considered, and the results are compared with the formulation presented in [5]. The main difference between the two sets of governing equations consists in the presence in the equations derived here of additional terms in the impermeability condition on the hull surface. Those terms result from the existance of a waterline for a free surface piercing body, and therefore are here referred to as the waterline correction. A Dawson-like and Neumann-Kelvin formulation of the forward speed problem are shown to follow from two different applications of the same condition on the free surface, and both include terms due to the waterline correction. The Neumann-Kelvin formulation is continued to the second order free surface and impermeability conditions for the steady and unsteady parts of the velocity potential.

In the sixth section, the weak-scatterer hypothesis, [6], is introduced as a physically justified assumption which makes possible to obtain solutions to non-linear time dependent problems of ship hydrodynamics by currently available numerical methods. First, the application of the hypothesis is illustrated in a perturbation formulation for a ship advancing in steep waves. A comparison of computed results with experiment is shown following [6]. Second, the hypothesis is used to derive a more general direct formulation of the problem, in which the solution is sought for directly in an instantaneous fluid domain D bounded by a control boundary ∂D_C. On ∂D_C the solution in D is matched with a perturbation solution in the fluid domain external to D. The domain transformation approach leads to a consistent matching of the velocity and pressure fields on ∂D_C. In other words it allows the construction of a consistent non-linear wave radiation condition.

The presentation throughout the paper is formal and no discussion of the existence and uniqueness of solutions to the considered boundary value problems is undertaken. The tensor notation used is analogous to the dyadic notation explained in [7]. A non-standard notation, $\frac{\partial}{\partial \overline{x}}$ or $\frac{\partial}{\partial \overline{y}}$, is employed for the gradient operator and $\frac{\partial^2}{\partial \overline{x}^2}$ or $\frac{\partial^2}{\partial \overline{y}^2}$ for the Laplace operator.

DOMAIN AND FIELD TRANSFORMATIONS

One of the characteristic features of boundary value problems of non-linear ship hydrodynamics is the dependence upon time of fluid domains on which the problems are defined. The instantaneous configuration (position in space) of the fluid domain boundaries is an unknown in a typical non-linear time dependent problem. In general, for an instantaneous fluid domain D, the boundaries can be categorized generically as an impermeable wetted body surface ∂D_W, free water surface ∂D_F, and control surface ∂D_C. The evolution of configurations of ∂D_W and ∂D_F in time depends on the motion of the impermeable body and on the water flow, and therefore belongs to the solution to the problem. The evolution of the configuration of ∂D_C is prescribed as a part of the formulation of the problem.

A perturbation solution to a non-linear ship hydrodynamics problem can therefore be considered in three steps. First, a transformation of the governing equations of the problem is made from the instantaneous domain D to a reference domain D_o which has a configuration fixed or given in time. Second, the solution to the transformed boundary value problem is sought for in the form of a perturbation series. Third, the perturbation solution on D_o is transformed back into domain D, thus providing a perturbation solution to the original boundary value problem on D. The advantage of such an approach consists in taking explicitly into account the evolution in time of the geometry of D.

In this section domain transformations and corresponding transformations of scalar, vector and tensor fields defined on transformed domains, are discussed. The discussion aims at establishing tools for the required transformations of the boundary

value problems. In part the present discussion restates in a different form arguments that were described in [1] and [2]. Those arguments were used to justify Euler-like approaches to fluid domain perturbations, in which domain transformations are not included explicitly. Here, however, the purpose is to give the domain transformations an explicit consideration. In addition transformations of surfaces defined in the reference domain are discussed as a preliminary step to a formulation of the explicit impermeability condition.

Let $\bar{y}$ denote the radius vector in an instantaneous fluid domain D, $\bar{x}$ signify the radius vector in a reference fluid domain D_o, and t be the time variable. Domain transformations considered here are one-to-one mappings between the two domains, including corresponding boundaries ∂D and ∂D_o. Such mappings can be expressed in the form:

$$\bar{y} = \bar{x} + \bar{\eta}\ (\bar{x}, t) \qquad (1)$$

where $\bar{\eta}\ (\bar{x}, t)$ is a domain displacement field. The domain displacement field is assumed to be sufficiently smooth to guarantee the existence of its derivatives required in further considerations. It is convenient to define the exponential operator for directional derivative $\bar{\eta} \cdot \frac{\partial}{\partial \bar{x}}$:

$$\exp\left(\bar{\eta} \cdot \frac{\partial}{\partial \bar{x}}\right) = 1 + \bar{\eta} \cdot \frac{\partial}{\partial \bar{x}} + \frac{1}{2}\left(\bar{\eta} \cdot \frac{\partial}{\partial \bar{x}}\right)^2 + . \qquad (2)$$

where $\frac{\partial}{\partial \bar{x}}$ denotes the gradient operator and dot indicates the scalar multiplication multiplication. Using (2) mapping (1) can be rewritten as:

$$\bar{y} = \exp\left(\bar{\eta} \cdot \frac{\partial}{\partial \bar{x}}\right) \bar{x} \qquad (3)$$

which defines the domain transformation.

The same transformation by means of the exponential operator can be applied to tensor fields defined on D_o. With $v\ (\bar{x}, t)$ denoting a scalar component of a time dependent tensor field on D_o, the relation becomes:

$$u\ (\bar{y}, t) = \exp\left(\bar{\eta} \cdot \frac{\partial}{\partial \bar{x}}\right) v\ (\bar{x}, t) \qquad (4a)$$

where $u\ (\bar{y}, t)$ is the image of $v\ (\bar{x}, t)$ in D. The assumption is made that $v\ (\bar{x}, t)$ is a real analytic function of $\bar{x}$, although in practice only first few terms of the expansion on the right hand side of (4a) are used. Transformation (4a) has the property:

$$\exp\left(\bar{\eta} \cdot \frac{\partial}{\partial \bar{x}}\right) \Big|_{\bar{x}_2} v\ (\bar{x}) = \exp\left(\bar{\eta}_1 \cdot \frac{\partial}{\partial \bar{x}}\right) \Big|_{\bar{x}_1} v\ (\bar{x}) \qquad (4b)$$

for:

$$\bar{\eta}_1 = \bar{x}_2 - \bar{x}_1 + \bar{\eta}\ (\bar{x}_2) \qquad (4c)$$

Relations (4b) and (4c) imply that for a given $u(\bar{y}, t)$ in (4a) $v\ (\bar{x}, t)$ on the right hand side does not depend on the choice of domain displacement field $\bar{\eta}$.

Since governing equations of boundary value problems are defined in terms of time and space derivatives of basic scalar, vector and tensor fields, such as for instance a velocity potential, it is necessary to establish transformation rules applicable to such derivatives of $u\ (\bar{y}, t)$ and $v\ (\bar{x}, t)$. From (1), (2) and (3) it is found that:

$$du = d\bar{x} \cdot \left(\bar{\bar{I}} + \frac{\partial}{\partial \bar{x}} \otimes \bar{\eta}\right) \cdot \frac{\partial}{\partial \bar{y}}\, u + dt\left(\frac{\partial}{\partial t}\,\bar{\eta} \cdot \frac{\partial}{\partial \bar{y}}\, u + \frac{\partial}{\partial t}\, u\right) \qquad (5a)$$

and

$$du = d\bar{x} \cdot \left(\bar{\bar{I}} + \frac{\partial}{\partial \bar{x}} \otimes \bar{\eta}\right) \cdot exp\left(\bar{\eta} \cdot \frac{\partial}{\partial \bar{x}}\right) \frac{\partial}{\partial \bar{x}}\, v + dt\,[\, \frac{\partial}{\partial t}\,\bar{\eta} \cdot exp\left(\eta \cdot \frac{\partial}{\partial \bar{x}}\right) \frac{\partial}{\partial \bar{x}}\, v + exp\left(\bar{\eta} \cdot \frac{\partial}{\partial \bar{x}}\right) \frac{\partial}{\partial t}\, v\,] \qquad (5b)$$

where $\bar{\bar{I}}$ denotes the unit tensor, and $\otimes$ signifies the tensor multiplication. Since $d\bar{x}$ and dt are independent differentials it follows that:

$$\frac{\partial}{\partial \bar{y}}\, u = \exp\left(\bar{\eta} \cdot \frac{\partial}{\partial \bar{x}}\right) \frac{\partial}{\partial \bar{x}}\, v \qquad (6a)$$

$$\frac{\partial}{\partial t} u = \exp\left(\bar{\eta} \cdot \frac{\partial}{\partial \bar{x}}\right) \frac{\partial}{\partial t} v \qquad (6b)$$

In addition, taking $\frac{\partial}{\partial t} u = u'$ and $\frac{\partial}{\partial t} v = v'$, (3), (6a) and (6b) give:

$$\frac{\partial^2}{\partial \bar{y} \partial t} u = \exp\left(\bar{\eta} \cdot \frac{\partial}{\partial \bar{x}}\right) \frac{\partial^2}{\partial \bar{x} \partial t} v \qquad (6c)$$

By mathematical induction formulae (6) are generalized to:

$$\frac{\partial^{k+\ell+m+n}}{\partial y_1^k \partial y_2^\ell \partial y_3^m \partial t^n} u = \exp\left(\bar{\eta} \cdot \frac{\partial}{\partial \bar{x}}\right) \frac{\partial^{k+\ell+m+n}}{\partial x_1^k \partial x_2^\ell \partial x_3^m \partial t^n} v \qquad (7)$$

where k, ℓ, m and n are 0, 1,...., and y_i and x_i, $i = 1,2,3$, denote respectively Cartesian coordinates in D and D_o. This means that for tensor fields with components u and v related by transformation (4a), their derivatives are related by transformation (7).

The application of relations (4a) and (7) in transformations of governing equations can be generalized by considering u and v as matrix vectors:

$$u = \{u_1, u_2, .., u_k\} \qquad (8a)$$

$$v = \{v_1, v_2, .., v_k\} \qquad (8b)$$

of all the scalar field components and their derivatives occurring in a particular boundary value problem. On the basis of (4a) and (7):

$$u_i = exp\left(\bar{\eta} \cdot \frac{\partial}{\partial \bar{x}}\right) v_i \qquad (9a)$$

$$\frac{\partial^{k+\ell+m+n}}{\partial y_1^k \partial y_2^\ell \partial y_3^m \partial t^n} u_i = \exp\left(\bar{\eta} \cdot \frac{\partial}{\partial \bar{x}}\right) \frac{\partial^{k+\ell+m+n}}{\partial x_1^k \partial x_2^\ell \partial x_3^m \partial t^n} v_i \qquad (9b)$$

Let $F(u)$ be an analytic function of the components of matrix vector u, then:

$$F(u) = exp\left[\sum_{i=1}^{k} (u_i - v_i) \frac{\partial}{\partial v_i}\right] F(v) \qquad (10a)$$

Using (10a) and (9a) it is found that:

$$F(u) = exp\left(\bar{\eta} \cdot \frac{\partial}{\partial \bar{x}}\right) F(v) \qquad (10b)$$

The above formula applies in particular to functions $F(u)$ which are polynomials with respect to their arguments $\{u_1, u_2, ..., u_k\}$.

Another type of functions of special interest in view of the boundary value problem transformations are functions which define surfaces in D and D_o. With:

$$F(\bar{x}) = C \qquad (11a)$$

defining the reference configuration in D_o of a piece-wise smooth surface, the corresponding instantaneous configuration of the surface in D is given by:

$$f(\bar{y}, t) - F(\bar{x}) = 0 \qquad (11b)$$

This leads to the consideration of sufficiently smooth functions defined in D by transformation (1) and relation (11b). It follows from (11b) that:

$$d\bar{x} \cdot \left(\bar{\bar{I}} + \frac{\partial}{\partial \bar{x}} \otimes \bar{\eta}\right) \cdot \frac{\partial}{\partial \bar{y}} f + dt\left(\frac{\partial \bar{\eta}}{\partial t} \cdot \frac{\partial}{\partial \bar{y}} f + \frac{\partial}{\partial t} f\right) = d\bar{x} \cdot \frac{\partial}{\partial \bar{x}} F \qquad (12a)$$

from which:

$$\frac{\partial}{\partial \bar{y}} f = \left(\bar{\bar{I}} + \frac{\partial}{\partial \bar{x}} \otimes \bar{\eta}\right)^{-1} \cdot \frac{\partial}{\partial \bar{x}} F \qquad (12b)$$

and

$$\frac{\partial}{\partial t} f = -\frac{\partial \bar{\eta}}{\partial t} \cdot \left(\bar{\bar{I}} + \frac{\partial}{\partial \bar{x}} \otimes \bar{\eta} \right)^{-1} \cdot \frac{\partial}{\partial \bar{x}} F \tag{12c}$$

where $\left(\bar{\bar{I}} + \frac{\partial}{\partial \bar{x}} \otimes \eta \right)^{-1}$ is the inverse of $\bar{\bar{I}} + \frac{\partial}{\partial \bar{x}} \otimes \bar{\eta}$. The normal vectors on the respective surfaces are defined by:

$$\bar{n} = \frac{\partial}{\partial \bar{y}} f \frac{1}{\left| \frac{\partial}{\partial \bar{y}} f \right|} \tag{13a}$$

and

$$\bar{N} = \frac{\partial}{\partial \bar{x}} F \frac{1}{\left| \frac{\partial}{\partial \bar{x}} F \right|} \tag{13b}$$

Using (12b), the transformation of the normals is given by:

$$\bar{n} = \bar{\bar{K}} \cdot \bar{N} \frac{1}{\sqrt{\bar{N} \cdot \bar{\bar{K}}^T \cdot \bar{\bar{K}} \cdot \bar{N}}} \tag{13c}$$

with:

$$\bar{\bar{K}} = \left(\bar{\bar{I}} + \frac{\partial}{\partial \bar{x}} \otimes \bar{\eta} \right)^{-1} \tag{13d}$$

and $\bar{\bar{K}}^T$ denoting the transpose of $\bar{\bar{K}}$.

When the surface determined by (11a) is parameterized so that:

$$F [\bar{x}(\lambda, \mu)] = C \tag{14a}$$

where λ and μ are real parameters, the differential element of the surface is defined by:

$$\partial \bar{S}_{\bar{x}} = \partial \bar{x}_\lambda \wedge \partial \bar{x}_\mu \tag{14b}$$

with $\wedge$ denoting the vector multiplication,

$$\partial \bar{x}_\lambda = \frac{\partial \bar{x}}{\partial \lambda} d\lambda \tag{14c}$$

and

$$\partial \bar{x}_\mu = \frac{\partial \bar{x}}{\partial \mu} d\mu \tag{14d}$$

The image differential element on the surface determined by (11b) is:

$$\partial \bar{S}_{\bar{y}} = \partial \bar{y}_\lambda \wedge \partial \bar{y}_\mu \tag{15a}$$

with $\partial \bar{y}_\lambda$ and $\partial \bar{y}_\mu$ defined similarly to $\partial \bar{x}_\lambda$ and $\partial \bar{x}_\mu$. Using (1) a relation between $\partial \bar{S}_{\bar{y}}$ and $\partial \bar{S}_{\bar{x}}$ is established:

$$\partial \bar{S}_{\bar{y}} = \partial \bar{x}_\lambda \cdot \left(\bar{\bar{I}} + \frac{\partial}{\partial \bar{x}} \otimes \bar{\eta} \right) \wedge \left(\bar{\bar{I}} + \frac{\partial}{\partial \bar{x}} \otimes \bar{\eta} \right)^T \cdot \partial \bar{x}_\mu \tag{15b}$$

By direct calculation formula (15b) yields:

$$\partial \bar{S}_{\bar{y}} = \left[\left(1 + \frac{\partial}{\partial \bar{x}} \cdot \bar{\eta} \right) \bar{\bar{I}} - \frac{\partial}{\partial \bar{x}} \otimes \bar{\eta} + \frac{1}{2} \sum_{i,j,k=1}^{3} \epsilon_{ijk} \frac{\partial}{\partial x_i} \bar{\eta} \wedge \frac{\partial}{\partial x_j} \bar{\eta} \otimes \bar{e}_k \right] \cdot \partial \bar{S}_{\bar{x}} \tag{15c}$$

with ϵ_{ijk} denoting the sign of permutation and $\bar{e}_k$, k=1,2,3, signifying the unit vectors of the Cartesian system of reference. Also by direct computation it can be shown that:

$$\left(\bar{\bar{I}} + \frac{\partial}{\partial \bar{x}} \otimes \bar{\eta} \right)^{-1} = \frac{1}{1 + \sum_{i=1}^{3} J_i} \left[\left(1 + \frac{\partial}{\partial \bar{x}} \cdot \bar{\eta} \right) \bar{\bar{I}} - \frac{\partial}{\partial \bar{x}} \otimes \bar{\eta} \right.$$

$$+ \frac{1}{2} \sum_{i,j,k=1}^{3} e_{ijk} \frac{\partial}{\partial x_i} \overline{\eta} \wedge \frac{\partial}{\partial x_j} \overline{\eta} \otimes \overline{e}_k]$$

(15d)

so that (15c) is rewritten as:

$$\partial \overline{S}_{\overline{y}} = \left(1 + \sum_{i=1}^{3} J_i\right) \left(\overline{\overline{I}} + \frac{\partial}{\partial \overline{x}} \otimes \overline{\eta}\right)^{-1} \cdot \partial \overline{S}_{\overline{x}}.$$

(15e)

In formulae (15d) and (15e) $J_i, i=1,,2,3,$ denote the scalar invariants of gradient tensor $\frac{\partial}{\partial \overline{x}} \otimes \overline{\eta}$. It should be observed that formula (15d) provides tensor $\overline{\overline{K}}$ in a closed form, an alternative expression for $\overline{\overline{K}}$ can be obtained as the Neumann series:

$$\overline{\overline{K}} = \overline{\overline{I}} - \frac{\partial}{\partial \overline{x}} \otimes \overline{\eta} + \left(\frac{\partial}{\partial \overline{x}} \otimes \overline{\eta}\right) \cdot \left(\frac{\partial}{\partial \overline{x}} \otimes \overline{\eta}\right) + \ldots$$

(16)

which is often more convenient to apply.

Similarly to the differential surface elements $\partial \overline{S}_{\overline{y}}$ and $\partial \overline{S}_{\overline{x}}$, differential volume elements $dV_{\overline{y}}$ and $dV_{\overline{x}}$ can be considered using three space parameters λ, μ *and* γ. Then:

$$dV_{\overline{y}} = \partial \overline{y}_{\gamma} \cdot (\partial \overline{y}_{\lambda} \wedge \partial \overline{y}_{\mu})$$

(17a)

and

$$dV_{\overline{x}} = \partial \overline{x}_{\gamma} \cdot (\partial \overline{x}_{\lambda} \wedge \partial \overline{x}_{\mu})$$

(17b)

It follows from (15e) that:

$$dV_{\overline{y}} = \left(1 + \sum_{i=1}^{3} J_i\right) dV_{\overline{x}}$$

(17c)

TRANSFORMATIONS OF GOVERNING EQUATIONS

Neglecting viscous flow effects, the interaction of a floating body with surrounding water is determined by the fields of flow velocity $\overline{u} = \overline{u}(\overline{y}, t)$ and pressure $q = q(\overline{y}, t)$. Assuming an irrotational flow, both are expressed in terms of a velocity potential $\Psi(\overline{y}, t)$ defined on instantaneous fluid domain D:

$$\overline{u} = \frac{\partial}{\partial \overline{y}} \Psi \qquad in\ D$$

(18a)

$$q = -\rho \left[\frac{\partial}{\partial t} \Psi + \frac{1}{2} \left|\frac{\partial}{\partial \overline{y}} \Psi\right|^2 + g y_3\right] \quad in\ D$$

(18b)

with ρ denoting water density, g the acceleration of gravity, the constant in the Bernoulli's equation taken as 0, and y_3 coordinate axis directed vertically upwards. The velocity field must satisfy the impermeability condition on instantaneous wetted body surface ∂D_w, whereas the pressure field generates fluid loads on ∂D_w.

Velocity potential $\Psi(\overline{y}, t)$ is considered to be related to a scalar field $\Phi(\overline{x}, t)$, defined on a reference fluid domain D_o, by transformation (4a):

$$\Psi(\overline{y}, t) = exp\left(\overline{\eta} \cdot \frac{\partial}{\partial \overline{x}}\right) \Phi(\overline{x}, t)$$

(19a)

Therefore velocity field $\overline{u}$ and pressure field q can be expressed by means of Φ using formulae (7) and (10b):

$$\overline{u}(\overline{y}, t) = exp\left(\overline{\eta} \cdot \frac{\partial}{\partial \overline{x}}\right) \frac{\partial}{\partial \overline{x}} \Phi(\overline{x}, t)$$

(19b)

$$q(\overline{y}, t) = exp\left(\overline{\eta} \cdot \frac{\partial}{\partial \overline{x}}\right) \{-\rho [\frac{\partial}{\partial t} \Phi + \frac{1}{2} \left|\frac{\partial}{\partial \overline{x}} \Phi\right|^2 + g x_3]\}$$

(19c)

In other words it is possible to regard $\overline{u}(\overline{y}, t)$ and $q(\overline{y}, t)$ in D, respectively as images of a velocity field $\overline{v}(\overline{x}, t)$ and pressure field $p(\overline{x}, t)$ defined on D_o:

$$\overline{u}(\overline{y}, t) = \exp\left(\overline{\eta} \cdot \frac{\partial}{\partial \overline{x}}\right) \overline{v}(\overline{x}, t)$$

(20a)

$$q(\bar{y},t) = \exp\left(\bar{\eta}\cdot\frac{\partial}{\partial\bar{x}}\right)p(\bar{x},t) \quad (20b)$$

with

$$\bar{v}(\bar{x},t) = \frac{\partial}{\partial\bar{x}}\Phi(\bar{x},t) \quad (20c)$$

and

$$p(\bar{x},t) = -\rho\left(\frac{\partial}{\partial t}\Phi + \frac{1}{2}\left|\frac{\partial}{\partial\bar{x}}\Phi\right|^2 + gx_3\right) \quad (20d)$$

It follows that scalar field $\Phi(\bar{x},t)$ has the interpretation of a velocity potential in D_o.

The velocity and pressure fields in D must satisfy a set of governing equations. The velocity field complies with the requirement of flow continuity:

$$\frac{\partial}{\partial\bar{y}}\cdot\bar{u} = \frac{\partial^2}{\partial\bar{y}^2}\Psi = 0 \quad in\ D \quad (21a)$$

impermeability of ∂D_w:

$$\left(\frac{\partial}{\partial t} + \frac{\partial}{\partial\bar{y}}\Psi\cdot\frac{\partial}{\partial\bar{y}}\right)f = 0 \quad on\ \partial D_w \quad (21b)$$

where $f(\bar{y},t) = 0$ is the locus of ∂D_w in D, see (11b), and the kinetic condition on ∂D_F:

$$q = 0 \quad on\ \partial D_F \quad (21c)$$

The velocity and pressure fields satisfy also the requirement of impermeability of ∂D_F:

$$\left(\frac{\partial}{\partial t} + \frac{\partial}{\partial\bar{y}}\Psi\cdot\frac{\partial}{\partial\bar{y}}\right)q = 0 \quad on\ \partial D_F \quad (21d)$$

which can as well be written in a form analogous to (21b). On control surface ∂D_c the velocity and pressure fields must be continuous. This leads to conditions:

$$\Psi - \Psi_e = 0 \quad on\ \partial D_c \quad (21e)$$

$$\frac{\partial}{\partial\bar{y}}f\cdot\frac{\partial}{\partial\bar{y}}(\Psi - \Psi_e) = 0 \quad on\ \partial D_c \quad (21f)$$

where Ψ_e is the velocity potential for the flow external to the fluid domain D, and $f = f(\bar{y},t) = 0$ is the locus of ∂D_c in D. For an unbounded D, boundary ∂D_c is placed infinitely far from the floating body and the boundary values imposed by (21e) and (21f) on ∂D_c cannot have an effect upon the flow in D induced by the presence of the ship.

Transformation (10b) applies to the left hand sides of (21a), (21c), (21d) and (21e). Therefore the transformed equivalents of these relations become respectively:

$$\exp\left(\bar{\eta}\cdot\frac{\partial}{\partial\bar{x}}\right)\frac{\partial^2}{\partial\bar{x}^2}\Phi = 0 \quad in\ D_o \quad (22a)$$

$$\exp\left(\bar{\eta}\cdot\frac{\partial}{\partial\bar{x}}\right)\left(\frac{\partial}{\partial t}\Phi + \frac{1}{2}\left|\frac{\partial}{\partial\bar{x}}\Phi\right|^2 + gx_3\right) = 0 \quad on\ \partial D_{oF} \quad (22b)$$

$$\exp\left(\bar{\eta}\cdot\frac{\partial}{\partial\bar{x}}\right)\left(\frac{\partial^2}{\partial t^2}\Phi + g\frac{\partial}{\partial x_3}\Phi + 2\frac{\partial}{\partial\bar{x}}\Phi\cdot\frac{\partial^2}{\partial\bar{x}\partial t}\Phi + \frac{\partial}{\partial\bar{x}}\Phi\cdot\frac{\partial}{\partial\bar{x}}\otimes\frac{\partial}{\partial\bar{x}}\Phi\cdot\frac{\partial}{\partial\bar{x}}\Phi\right) = 0 \quad on\ \partial D_{oF} \quad (22c)$$

$$\exp\left(\bar{\eta}\cdot\frac{\partial}{\partial\bar{x}}\right)(\Phi - \Phi_e) = 0 \quad on\ \partial D_{oC} \quad (22d)$$

where boundaries ∂D_{oF} *and* ∂D_{oC} are, under the transformation inverse to (1), correspondingly the images of boundaries ∂D_F *and* ∂D_C. It follows from (4b) and (4c) that assuming free surface ∂D_F to

be represented by a single valued wave elevation defined on the horizontal plane $x_3 = 0$, the operator $\exp(\overline{\eta} \cdot \frac{\partial}{\partial \overline{x}})$ in (22b) and (22c) can be replaced by $\exp(\eta_3 \frac{\partial}{\partial x_3})$, with η_3 denoting the wave elevation and equations (22b) and (22c) applied on $x_3 = 0$. On ∂D_{oW}, which is the image of ∂D_W, the following condition is obtained:

$$\left[\exp\left(\overline{\eta} \cdot \frac{\partial}{\partial \overline{x}}\right) \frac{\partial}{\partial \overline{x}} \Phi - \frac{\partial}{\partial t}\overline{\eta}\right] \cdot \left(\overline{\overline{I}} + \frac{\partial}{\partial \overline{x}} \otimes \overline{\eta}\right)^{-1} \cdot \overline{N} = O \quad on\ \partial D_{oW} \tag{22e}$$

Formula (22e) is derived from (21b) using (12b), (12c), (13b) and (19a). In the same way relation (21f) gives:

$$\left[\exp\left(\overline{\eta} \cdot \frac{\partial}{\partial \overline{x}}\right) \frac{\partial}{\partial \overline{x}} (\Phi - \Phi_e)\right] \cdot \left(\overline{\overline{I}} + \frac{\partial}{\partial \overline{x}} \otimes \overline{\eta}\right)^{-1} \cdot \overline{N} = O \quad on\ \partial D_{oC} \tag{22f}$$

It should be noticed that if $\overline{\eta}$ and its first spacial derivatives are perpendicular to $\overline{N}$:

$$\overline{\eta} \cdot \overline{N} = O, \qquad \left(\frac{\partial}{\partial \overline{x}} \otimes \overline{\eta}\right) \cdot \overline{N} = O \quad on\ \partial D_{oW} \tag{23a}$$

then (22e) takes the simple form:

$$\left[\exp\left(\overline{\eta} \cdot \frac{\partial}{\partial \overline{x}}\right) \frac{\partial}{\partial \overline{x}} \Phi\right] \cdot \overline{N} = O \quad on\ \partial D_{oW} \tag{23b}$$

A similar statement is valid for condition (22f):

$$\left[\exp\left(\overline{\eta} \cdot \frac{\partial}{\partial \overline{x}}\right) \frac{\partial}{\partial \overline{x}} (\Phi - \Phi_e)\right] \cdot \overline{N} = O \quad on\ \partial D_{oC} \tag{24a}$$

if:

$$\left(\frac{\partial}{\partial \overline{x}} \otimes \overline{\eta}\right) \cdot \overline{N} = O \quad on\ \partial D_{oC} \tag{24b}$$

THE EXPLICIT IMPERMEABILITY CONDITION AND ITS APPLICATION

Condition (22e) imposed on reference wetted surface ∂D_{oW} corresponds to:

$$\left(\overline{u} - \frac{\partial}{\partial t}\overline{\eta}\right) \cdot \overline{n} = O \quad on\ \partial D_W \tag{25a}$$

where $\overline{n}$ is the normal vector on ∂D_W. Taking into account that $\frac{\partial}{\partial t}\overline{\eta} \cdot \overline{n}$ represents the velocity, denoted by u_n, of the instantaneous wetted surface along its normal, (25a) is reduced to:

$$\overline{u} \cdot \overline{n} = u_n \quad on\ \partial D_W \tag{25b}$$

which is the well known form of the impermeability condition. In comparison with (25b), in (22e) the dependence on the domain displacement field $\overline{\eta}$ is made explicit. An equivalent form to (22e) is obtained using (15d). Implying this equivalence, (22e) is named the explicit impermeability condition.

It is important to notice that in (22e) displacement field $\overline{\eta}$ defines the instantaneous normal vector and velocity of wetted surface ∂D_W, and an instantaneous one-to-one mapping between ∂D_{oW} and ∂D_W. The latter property of $\overline{\eta}$ is used in the term:

$$\overline{u} = exp\left(\overline{\eta} \cdot \frac{\partial}{\partial \overline{x}}\right) \frac{\partial}{\partial \overline{x}} \Phi \tag{26}$$

Although (22e) was derived on the assumption that $\overline{\eta}$ represents a displacement field defined on the fluid domain, this assumption is not always necessary. The displacement field due to the motion of an arbitrarily deformable, impermeable body satisfies the properties required of $\overline{\eta}$ to impose (22e) on the wetted surface of the body, if the body remains entirely submerged. The condition of total submergence ensures that $\overline{\eta}$ represents a one-to-one mapping between ∂D_W and ∂D_{oW}.

For a deformable body in motion the

displacement field from a reference configuration can be written as:

$$\bar{\eta}_B(\bar{x},t) = \bar{\alpha}(t) + [\bar{\bar{R}}(t) - \bar{\bar{I}}] \cdot (\bar{x} - \bar{x}_o) + \bar{\bar{R}}(t) \cdot \bar{Q}(\bar{x},t) \qquad on\ D_{oB} \tag{27a}$$

where D_{oB} denotes the reference configuration of the body, $\bar{\alpha}$ is a parallel translation field, $\bar{\bar{R}}(t)$ is a tensor of rotation; $\bar{x}_o$ is the radius vector of the centre of rotation and $\bar{Q}(\bar{x},t)$ is a field of deformation, both of them taken in reference configuration D_{oB}. A simple manipulation gives:

$$\left(\bar{\bar{I}} + \frac{\partial}{\partial \bar{x}} \otimes \bar{\eta}_B\right)^{-1} = \bar{\bar{R}} \cdot \left(\bar{\bar{I}} + \frac{\partial}{\partial \bar{x}} \otimes \bar{Q}\right)^{-1} \tag{27b}$$

Impermeability condition (25a) takes now the form:

$$\left(\bar{u} - \frac{\partial}{\partial t}\bar{\eta}_B\right) \cdot \bar{\bar{R}} \cdot \left(\bar{\bar{I}} + \frac{\partial}{\partial \bar{x}} \otimes \bar{Q}\right)^{-1} \cdot \bar{N} = O \qquad on\ \partial D_W \tag{27c}$$

with:

$$\frac{\partial}{\partial t}\bar{\eta}_B = \dot{\bar{\alpha}} + \bar{\Omega} \wedge \bar{\bar{R}} \cdot (\bar{x} - \bar{x}_o + \bar{Q}) + \bar{\bar{R}} \cdot \frac{\partial}{\partial t}\bar{Q} \tag{27d}$$

where $\dot{\bar{\alpha}}$ and $\bar{\Omega}$ are respectively vectors of linear and angular velocity of the body.

Relation (27c) applies on the instantaneous wetted surface of the body ∂D_W whether the body remains totally submerged or not. The condition is explicit with respect to the body displacement field $\bar{\eta}_B$ with the exception of the mapping of $\bar{u}$. The quantities in (27c) and (27d) related to $\bar{\eta}_B$, and $\bar{N}$, are determined for $\bar{x}_B \in \partial D_{oB}$, that is at points on the boundary of the reference configuration of the body. However, fluid velocity $\bar{u}$ is determined for $\bar{y} = (\bar{x}_B + \bar{\eta}_B) \in \partial D_W = \partial D \cap \partial D_B$, the instantaneous wetted surface of the body. If the body remains totally submerged $\partial D_W = \partial D_B$, that is the instantaneous wetted surface of the body and the instantaneous boundary of the body coincide and both are the image of $\partial D_{oW} = \partial D_{oB}$ under transformation $\bar{\eta}_B$. Therefore (27c) can be rewritten as:

$$\left[\exp\left(\bar{\eta}_B \cdot \frac{\partial}{\partial \bar{x}}\right)\frac{\partial}{\partial x}\Phi - \frac{\partial}{\partial t}\bar{\eta}_B\right] \cdot \bar{\bar{R}} \cdot \left(\bar{\bar{I}} + \frac{\partial}{\partial \bar{x}} \otimes \bar{Q}\right)^{-1} \cdot \bar{N} = O \qquad on\ \partial D_{oW} \tag{28}$$

This is a form of the impermeability condition which is explicit with respect to $\bar{\eta}_B$.

Without the requirement of total body submergence transformation $\bar{\eta}_B$, used in (28), may lead to instances where there are points $\bar{y} \in \partial D_W$ for which $\bar{x}_B \notin \partial D_{oW}$ or $\bar{y} \notin \partial D_W$ for which $\bar{x}_B \in \partial D_{oW}$. In such circumstances the boundary value problem in D is not transformed into a boundary value problem in D_o, and therefore transformation:

$$\bar{u} = exp\left(\bar{\eta}_B \cdot \frac{\partial}{\partial \bar{x}}\right)\frac{\partial}{\partial \bar{x}}\Phi \tag{29}$$

cannot be used in (28). This situation is illustrated in Fig. 1.

In solutions to boundary value problems of ship hydrodynamics $\bar{\eta}_B$ is obtained from equations of body motion. The kinematics of body motion must be taken into account in the impermeability condition. The above discussion indicates that this can be done if the

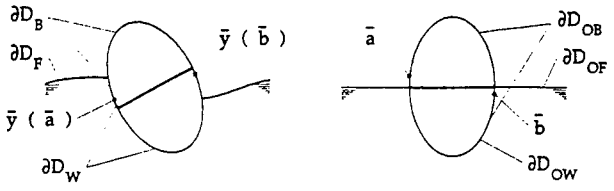

$\bar{y}(\bar{a}) = \bar{a} + \bar{\eta}_B(\bar{a}) \in \partial D_W$ $\qquad \bar{a} \notin \partial D_{OW}$

$\bar{y}(\bar{b}) = \bar{b} + \bar{\eta}_B(\bar{b}) \notin \partial D_W$ $\qquad \bar{b} \in \partial D_{OW}$

Figure 1

solution to a boundary value problem is sought for directly in the instantaneous fluid domain D. Then formula (25b) can be applied. It is convenient to call such formulations of the boundary value problems direct formulations. As explained earlier, boundary value problems formulated in D are transformed into corresponding boundary value problems formulated in D_o to find perturbation solutions. If the impermeable body remains totally submerged impermeability condition (28) is used in the perturbation formulations. In the opposite case it is convenient to consider displacement field $\overline{\eta}$ in (22e) as composed of two displacement fields, one of which is $\overline{\eta}_B$:

$$\overline{\eta}\,(\overline{x}, t) = \overline{\eta}_o\,(\overline{x}, t) + \overline{\eta}_B\,(\overline{x}_B, t) \tag{30a}$$

with:

$$\overline{x}_B = \overline{x} + \overline{\eta}_o\,(\overline{x}, t) \tag{30b}$$

where $\overline{\eta}_o\,(\overline{x}, t)$ is a displacement field defined on ∂D_{oB}. Relations between the displacement fields and transformations they define is illustrated in the following diagram:

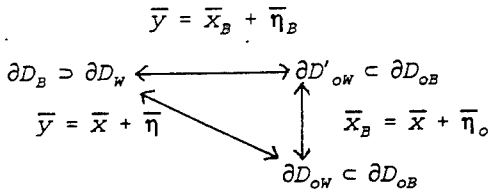

The diagram shows by means of the double arrows the one-to-one mappings induced by the displacement fields, together with their domains. In the diagram $\partial D'_{oW}$ signifies the image of instantaneous wetted surface ∂D_W, in reference body boundary ∂D_{oB}, generated by body displacement field $\overline{\eta}_B$. It is clear from the diagram that for $\partial D'_{oW} = \partial D_{oW}$ displacement field $\overline{\eta}_B$ provides a one-to-one mapping between ∂D_W and ∂D_{oW}. This is always true if $\partial D_B = \partial D_W$ and $\partial D_{oW} = \partial D_{oB}$, that is when the body remains totally submerged, as then $\partial D'_{oW} = \partial D_{oW} = \partial D_{oB}$.

Similar considerations apply to the use of condition (22f). It should be observed that the use of condition (22e) or (22f) is simplified significantly if formula (23b) or (24a) respectively, can be employed.

It follows from relations (4b) and (4c) that Φ in the first term in square brackets in (22e) does not depend on a choice of domain displacement field $\overline{\eta}$. In addition, the outside of the square brackets term is always co-linear with normal vector $\overline{n}(\overline{y})$. Therefore condition (22e) is also satisfied independently of the choice of displacement field. Since by virtue of (4b) and (4c) the same condition applies to all the other transformed governing equations discussed above, solutions to boundary value problems which are formulated with the use of those equations do not depend on domain displacement fields employed.

PERTURBATION FORMULATIONS OF BOUNDARY VALUE PROBLEMS

Perturbation formulations of boundary value problems of ship hydrodynamics are obtained by expressing velocity potential Φ and domain displacement field $\overline{\eta}$, in governing equations (22), by means of perturbation series. A one parameter perturbation formulation is defined by series:

$$\Phi = \sum_{i=0}^{n} \Phi^{(i)} \tag{31a}$$

$$\overline{\eta} = \sum_{i=1}^{n} \overline{\eta}^{(i)} \tag{31b}$$

In (31) indices in brackets indicate orders of magnitude:

$$\Phi^{(i+1)} = o\,(\Phi^{(i)}) \qquad i = 0, 1\ldots, n \tag{31c}$$

$$\Phi^{(i)} = O\,(|\overline{\eta}^{(i)}|) \quad \text{and} \quad |\overline{\eta}^{(i)}| = O\,(\Phi^{(i)}) \qquad i = 1, 2, \ldots, n \tag{31d}$$

In addition it is assumed that differentiation does not change the orders of magnitude.

By applying series (31a) and (31b)

in field governing equation (22a) it is found that:

$$\frac{\partial^2}{\partial \bar{x}^2}\,\Phi^{(0)} = 0 \qquad in\ D_o \tag{32a}$$

$$\frac{\partial^2}{\partial \bar{x}^2}\,\Phi^{(1)} = -\bar{\eta}^{(1)} \cdot \frac{\partial}{\partial \bar{x}}\,\frac{\partial^2}{\partial \bar{x}^2}\,\Phi^{(0)} \qquad in\ D_o \tag{32b}$$

. . . . . .

Therefore potentials $\Phi^{(i)}$ satisfy the Laplace's equation in $D^{(o)}$ for $i = 0, 1, .., n$.

Free surface conditions (22b) and (22c) assume the form of original conditions (21c) and (21d), with respect to $\Phi^{(o)}$. As a result the Laplace's equation and the free surface conditions admit a solution:

$$\Phi^{(o)} = -Ux_1 \qquad in\ D_o \tag{33a}$$

$$x_3 = 0 \qquad on\ \partial D_{oF} \tag{33b}$$

after adjusting the constant in the Bernoulli's equation to $\frac{1}{2}\rho U^2$. Taking for simplicity $U = 0$, conditions (22b) and (22c) yield:

$$\left(\frac{\partial^2}{\partial t^2} + g\frac{\partial}{\partial x_3}\right)\Phi^{(1)} = 0 \tag{34a}$$

$$\eta_3^{(1)} = -\frac{1}{g}\,\frac{\partial}{\partial t}\,\Phi^{(1)} \tag{34b}$$

$$\left(\frac{\partial^2}{\partial t^2} + g\frac{\partial}{\partial x_3}\right)\Phi^{(2)} = -2\,\frac{\partial}{\partial \bar{x}}\,\Phi^{(1)} \cdot \frac{\partial^2}{\partial \bar{x}\partial t}\,\Phi^{(1)} + \frac{1}{g}\,\frac{\partial}{\partial t}\,\Phi^{(1)} \cdot \frac{\partial}{\partial x_3}\left(\frac{\partial^2}{\partial t^2} + g\frac{\partial}{\partial x_3}\right)\Phi^{(1)} \tag{34c}$$

$$\eta_3^{(2)} = -\frac{1}{g}\left[\frac{\partial}{\partial t}\,\Phi^{(2)} + \frac{1}{2}\left|\frac{\partial}{\partial \bar{x}}\,\Phi^{(1)}\right|^2 - \frac{1}{g}\,\frac{\partial}{\partial t}\,\Phi^{(1)}\,\frac{\partial^2}{\partial x_3 \partial t}\,\Phi^{(1)} + \left(\eta_1^{(1)}\frac{\partial}{\partial x_1} + \eta_2^{(1)}\frac{\partial}{\partial x_2}\right)\frac{\partial}{\partial t}\,\Phi^{(1)}\right] \tag{34d}$$

$$\left(\frac{\partial^2}{\partial t^2} + g\frac{\partial}{\partial x_3}\right)\Phi^{(3)} = -2\left[\frac{\partial}{\partial \bar{x}}\,\Phi^{(1)} \cdot \frac{\partial^2}{\partial \bar{x}\partial t}\,\Phi^{(2)} + \frac{\partial}{\partial \bar{x}}\,\Phi^{(2)} \cdot \frac{\partial^2}{\partial \bar{x}\partial t}\,\Phi^{(1)}\right] - \frac{\partial}{\partial \bar{x}}\,\Phi^{(1)} \cdot \frac{\partial}{\partial \bar{x}} \otimes \frac{\partial}{\partial \bar{x}}\,\Phi^{(1)} \cdot \frac{\partial}{\partial \bar{x}}\,\Phi^{(1)} + \frac{1}{g}\,\frac{\partial}{\partial t}\,\Phi^{(1)}\,\frac{\partial}{\partial x_3}\left[\left(\frac{\partial^2}{\partial t^2} + g\frac{\partial}{\partial x_3}\right)\Phi^{(2)} + 2\,\frac{\partial}{\partial \bar{x}}\,\Phi^{(1)} \cdot \frac{\partial^2}{\partial \bar{x}\partial t}\,\Phi^{(1)}\right] + \frac{1}{g}\left[\frac{\partial}{\partial t}\,\Phi^{(2)} + \frac{1}{2}\left|\frac{\partial}{\partial \bar{x}}\,\Phi^{(1)}\right|^2 - \frac{1}{g}\,\frac{\partial}{\partial t}\,\Phi^{(1)} \cdot \frac{\partial^2}{\partial x_3 \partial t}\,\Phi^{(1)}\right]\frac{\partial}{\partial x_3}\left(\frac{\partial^2}{\partial t^2} + g\frac{\partial}{\partial x_3}\right)\Phi^{(1)} \tag{34e}$$

on $x_3 = 0$. The lengthy expression for $\eta_3^{(3)}$ is omitted. Formulae (34a), (34b), (34c) and (34e) are identical with the well known formulae given for instance in [3] and [4] for freely propagating waves. However, the present formulae are derived without making the usual assumption:

$$\bar{\eta} = \eta_3\,(x_1,\ x_2,\ t)\,\bar{e}_3 \qquad on\ x_3 = 0 \tag{35}$$

As a result the second order wave elevation $\eta_3^{(2)}$ determined by expression (34d) contains terms dependent on $\eta_1^{(1)}$ and $\eta_2^{(1)}$ not found in the usual formulations. Those terms indicate for

instance that the free surface of a long-crested wave can be shifted along the crest without changing the wave elevation. It should be noticed that displacement field $\overline{\eta}$ does not effect the dynamic free surface conditions (34c) and (34e). If assumption (35) is made the terms dependent on η_1 and η_2 disappear in (34d) and $\eta_3^{(2)}$ is interpreted as the single valued wave elevation in the perturbed domain. Such an approach is justified by relations (4b) and (4c).

Considering impermeability condition (22e) and taking:

$$\Phi^{(o)} = -Ux_1 + \phi^{(o)} \qquad (36a)$$

in (31a), with $\phi^{(o)}$ independent of time, and:

$$\overline{N} = \overline{N}^{(o)} \qquad (36b)$$

the following impermeability conditions are derived:

$$\overline{N} \cdot \frac{\partial}{\partial \overline{x}} \phi^{(o)} = UN_1 \qquad on\ \partial D_{oW} \quad (37a)$$

$$\overline{N} \cdot \left(\frac{\partial}{\partial \overline{x}} \Phi^{(1)} - \frac{\partial}{\partial t} \overline{\eta}^{(1)}\right) = \left[\left(\frac{\partial}{\partial \overline{x}} \phi^{(0)} - U\overline{e}_1\right) \cdot \frac{\partial}{\partial \overline{x}} \overline{\eta}^{(1)} - \overline{\eta}^{(1)} \cdot \frac{\partial}{\partial \overline{x}} \left(\frac{\partial}{\partial \overline{x}} \phi^{(o)} - Ue_1\right)\right] \cdot \overline{N}$$

$$on\ \partial D_{oW} \qquad (37b)$$

$$\overline{N} \cdot \left(\frac{\partial}{\partial \overline{x}} \Phi^{(2)} - \frac{\partial}{\partial t} \overline{\eta}^{(2)}\right) = \left[\left(\frac{\partial}{\partial \overline{x}} \phi^{(o)} - Ue_1\right) \cdot \left(\frac{\partial}{\partial \overline{x}} \overline{\eta}^{(2)} - \frac{\partial}{\partial \overline{x}} \overline{\eta}^{(1)} \cdot \frac{\partial}{\partial \overline{x}} \overline{\eta}^{(1)}\right) + \overline{\eta}^{(1)} \cdot \frac{\partial}{\partial \overline{x}} \left(\frac{\partial}{\partial \overline{x}} \phi^{(o)} - Ue_1\right) \cdot \frac{\partial}{\partial \overline{x}} \overline{\eta}^{(1)} - \left(\overline{\eta}^{(2)} + \frac{1}{2} \overline{\eta}^{(1)} \overline{\eta}^{(1)} \cdot \frac{\partial}{\partial \overline{x}}\right) \cdot \frac{\partial}{\partial \overline{x}}\right.$$

$$\left. \left(\frac{\partial}{\partial \overline{x}} \phi^{(o)} - Ue_1\right) + \left(\frac{\partial}{\partial \overline{x}} \Phi^{(1)} - \frac{\partial}{\partial t} \overline{\eta}^{(1)}\right) \cdot \frac{\partial}{\partial \overline{x}} \overline{\eta}^{(1)} - \overline{\eta}^{(1)} \cdot \frac{\partial}{\partial \overline{x}} \frac{\partial}{\partial \overline{x}} \Phi^{(1)}\right] \cdot \overline{N}$$

$$on\ \partial D_{oW} \qquad (37c)$$

respectively for potentials $\phi^{(o)}$, $\Phi^{(1)}$ and $\Phi^{(2)}$. According to the preceding discussion of the impermeability condition, for a totally submerged body $\overline{\eta}$ can be replaced by $\overline{\eta}_B$ in the above formulae. Then for a rigid body in motion formula (37b) becomes equivalent to the impermeability condition derived in [8], whereas formula (37c) represents its non-linear extension of the highest order of magnitude.

Impermeability condition (22e) applied on ∂D_{oF}, in conjunction with (36a), gives:

$$\frac{\partial}{\partial x_3} \Phi^{(o)} = O \qquad on\ \partial D_{oF}\ (x_3 = O) \qquad (38a)$$

Formula (22b), with the adjusted Bernoulli's equation constant, results in:

$$\left|\frac{\partial}{\partial \overline{x}} \Phi^{(0)}\right|^2 - U^2 = O \qquad on\ \partial D_{oF} \quad (38b)$$

However, the construction of a perturbation set of governing equations can be continued with a less restrictive assumption:

$$\left|\frac{\partial}{\partial \overline{x}} \Phi^{(o)}\right|^2 - U^2 = O\,(\Phi^{(1)}) \qquad on\ \partial D_{oF} \qquad (38c)$$

On the basis of equations (36a), (37a), (38a), potential $\Phi^{(o)}$ may be taken as a solution to the so called double body problem.

At the next level of approximation, equations (22b) and (22e), or alternatively (22b) and (22c) yield:

$$\left[\left(\frac{\partial}{\partial t} + \frac{\partial}{\partial \overline{x}} \Phi^{(o)} \cdot \frac{\partial}{\partial \overline{x}}\right)^2 + g \frac{\partial}{\partial x_3}\right] \Phi^{(1)} - \frac{\partial^2}{\partial x_3^2} \Phi^{(o)} \left(\frac{\partial}{\partial t} + \frac{\partial}{\partial \overline{x}} \Phi^{(o)} \cdot \frac{\partial}{\partial \overline{x}}\right) \Phi^{(1)}$$

$$= \frac{1}{2} \frac{\partial^2}{\partial x_3^2} \Phi^{(o)} \left(\left|\frac{\partial}{\partial \overline{x}} \Phi^{(o)}\right|^2 - U^2\right) - \frac{1}{2} \frac{\partial}{\partial \overline{x}} \Phi^{(o)} \cdot \frac{\partial}{\partial \overline{x}} \left|\frac{\partial}{\partial \overline{x}} \Phi^{(o)}\right|^2$$

$$on\ \partial D_{oF} \qquad (39a)$$

and:

$$\eta_3^{(1)} = -\frac{1}{g}\left[\left(\frac{\partial}{\partial t} + \frac{\partial}{\partial \bar{x}}\Phi^{(o)} \cdot \frac{\partial}{\partial \bar{x}}\right)\Phi^{(1)} + \frac{1}{2}\left|\frac{\partial}{\partial \bar{x}}\Phi^{(o)}\right|^2 - \frac{1}{2}U^2\right] \quad on\ \partial D_{oF} \tag{39b}$$

Equations (39a) and (39b) are applicable together with impermeability condition (37b) and $\Phi^{(o)}$ taken as the double body velocity potential. The separation of $\Phi^{(o)}$ into a steady part $\Phi_U^{(1)}$ and unsteady part $\tilde{\Phi}^{(1)}$, generates the following sets of governing equations:

$$\frac{\partial}{\partial \bar{x}}\Phi^{(o)} \cdot \frac{\partial}{\partial \bar{x}}\left(\frac{\partial}{\partial \bar{x}}\Phi^{(o)} \cdot \frac{\partial}{\partial \bar{x}}\Phi_U^{(1)}\right) - \frac{\partial^2}{\partial x_3^2}\Phi^{(o)}\frac{\partial}{\partial \bar{x}}\Phi^{(o)} \cdot \frac{\partial}{\partial \bar{x}}\Phi_U^{(1)} + g\frac{\partial}{\partial x_3}\Phi_U^{(1)} = \frac{1}{2}\frac{\partial^2}{\partial x_3^2}\Phi^{(o)}\left(\left|\frac{\partial}{\partial \bar{x}}\Phi^{(o)}\right|^2 - U^2\right) - \frac{1}{2}\frac{\partial}{\partial \bar{x}}\Phi^{(o)} \cdot \frac{\partial}{\partial \bar{x}}\left|\frac{\partial}{\partial \bar{x}}\Phi^{(o)}\right|^2 \quad on\ \partial D_{oF} \tag{40a}$$

$$\eta_{U3}^{(1)} = -\frac{1}{g}\left(\frac{\partial}{\partial \bar{x}}\Phi^{(o)} \cdot \frac{\partial}{\partial \bar{x}}\Phi_U^{(1)} + \frac{1}{2}\left|\frac{\partial}{\partial \bar{x}}\Phi^{(o)}\right|^2 - \frac{1}{2}U^2\right) \quad on\ \partial D_{oF} \tag{40b}$$

and:

$$\bar{N} \cdot \frac{\partial}{\partial \bar{x}}\Phi_U^{(1)} = \left(\frac{\partial}{\partial \bar{x}}\Phi^{(o)} \cdot \frac{\partial}{\partial \bar{x}}\bar{\eta}_U^{(1)} - \bar{\eta}_U^{(1)} \cdot \frac{\partial}{\partial \bar{x}}\frac{\partial}{\partial \bar{x}}\Phi^{(o)}\right) \cdot \bar{N} \quad on\ \partial D_{oW} \tag{40c}$$

for steady potential $\Phi_U^{(1)}$ and steady boundary displacement field $\bar{\eta}_U$. For unsteady velocity potential $\tilde{\Phi}^{(1)}$ and boundary displacement field $\tilde{\eta}^{(1)}$, the corresponding equations are:

$$\left[\left(\frac{\partial}{\partial t} + \frac{\partial}{\partial \bar{x}}\Phi^{(o)} \cdot \frac{\partial}{\partial \bar{x}}\right)^2 + g\frac{\partial}{\partial x_3}\right]\tilde{\Phi}^{(1)} - \frac{\partial^2}{\partial x_3^2}\Phi^{(o)}\left(\frac{\partial}{\partial t} + \frac{\partial}{\partial \bar{x}}\Phi^{(o)} \cdot \frac{\partial}{\partial \bar{x}}\right)\tilde{\Phi}^{(1)} = O \quad on\ \partial D_{oF} \tag{41a}$$

$$\tilde{\eta}_3^{(1)} = -\frac{1}{g}\left(\frac{\partial}{\partial t} + \frac{\partial}{\partial \bar{x}}\Phi^{(o)} \cdot \frac{\partial}{\partial \bar{x}}\right)\tilde{\Phi}^{(1)} \quad on\ \partial D_{oF} \tag{41b}$$

with:

$$\bar{N} \cdot \left(\frac{\partial}{\partial \bar{x}}\tilde{\Phi}^{(1)} - \frac{\partial}{\partial t}\tilde{\eta}^{(1)}\right) = \left(\frac{\partial}{\partial \bar{x}}\Phi^{(o)} \cdot \frac{\partial}{\partial \bar{x}}\tilde{\eta}^{(1)} - \tilde{\eta}^{(1)} \cdot \frac{\partial}{\partial \bar{x}}\frac{\partial}{\partial \bar{x}}\Phi^{(o)}\right) \cdot \bar{N} \quad on\ \partial D_{oW} \tag{41c}$$

The sets of equations (40) and (41) can be compared with those presented and used in [5]. Equations (40b) and (41b) are identical with their respective counterparts.

Equations (40a) and (41a) differ from the corresponding equations in the above mentioned reference by not including terms dependent on $\frac{\partial}{\partial \bar{x}}\left|\frac{\partial}{\partial \bar{x}}\Phi\right|^2$ which, according to (38c), are of $o(\Phi^{(1)})$, and therefore negligible, in the present scheme.

Impermeability condition (41c) is formally identical with the unsteady impermeability condition in [5]. However displacement field $\tilde{\eta}^{(1)}$ in (41c) is composed of unsteady body displacement field $\tilde{\eta}^{(1)}$ and unsteady displacement field $\tilde{\eta}^{(1)}_{o}{}^{B}$ on ∂D_{oB}, as explained in the preceding section, see (30). The impermeability condition in [5] includes only the unsteady body displacement field. The resulting additional term on the right hand side of (41c):

$$\left(\frac{\partial}{\partial t}\bar{\eta}_o^{(1)} + \frac{\partial}{\partial \bar{x}}\Phi^{(o)} \cdot \frac{\partial}{\partial \bar{x}}\bar{\eta}_o^{(1)} - \bar{\eta}_o^{(1)} \cdot \frac{\partial}{\partial \bar{x}}\frac{\partial}{\partial \bar{x}}\Phi^{(o)}\right) \cdot \bar{N} \tag{42a}$$

may be called the waterline correction, since as discussed in the preceding section, it appears as a consequence of the ship not being totally submerged. For a sufficiently small curvature of the wetted surface, displacement field $\bar{\eta}_o^{(1)}$ can be considered as essentially tangential to the hull, and therefore the first two terms in (42a) may be neglected. The same argument can be applied to the third term if the variation of the double body flow velocity on the hull surface is sufficiently small or almost tangential to the hull surface.

The expression on the right hand side of equation (40c) does not have a counterpart in the steady impermeability condition used in [5] or in other formulations of the steady forward speed problem based on a perturbation of the double body flow. Similarly to the unsteady impermeability condition the term consists of a contribution from steady body displacement field $\bar{\eta}_{BU}^{(1)}$, and a contribution from steady displacement field $\bar{\eta}_{oU}^{(1)}$, given by:

$$\left(\frac{\partial}{\partial \bar{x}}\Phi^{(o)} \cdot \frac{\partial}{\partial \bar{x}}\bar{\eta}_{oU}^{(1)} - \bar{\eta}_{oU}^{(1)} \cdot \frac{\partial}{\partial \bar{x}}\frac{\partial}{\partial \bar{x}}\Phi^{(o)}\right) \cdot \bar{N} \tag{42b}$$

The above comments on expression (42a) apply with the appropriate interpretation to (42b). The analogous to (42b) term in (40c), which involves $\bar{\eta}_{BU}^{(1)}$ instead of $\bar{\eta}_{oU}^{(1)}$, may express the influence of sinkage and trim or a steady structural response of the hull, or hull form modification.

With $\phi^{(o)}(\bar{x})$ in (36a) set equal to a constant, potential $\Phi^{(o)}$ satisfies conditions (38a) and (38b) on ∂D_{oF}, and impermeability condition (37a) on ∂D_{oW}, and impermeability condition (37a) on ∂D_{oW} if the following assumption is made:

$$UN_1 = O(\Phi^{(1)}) \qquad \text{on } \partial D_{oW} \tag{43}$$

The free surface governing equations take then the well known forms:

$$\left(U^2\frac{\partial^2}{\partial \bar{x}_1^2} + g\frac{\partial}{\partial x_3}\right)\Phi_U^{(1)} = O \qquad \text{on } \partial D_{oF} \tag{44a}$$

$$\eta_{U3}^{(1)} = \frac{1}{g}U\frac{\partial}{\partial x_1}\Phi_U^{(1)} \qquad \text{on } \partial D_{oF} \tag{44b}$$

of the Neumann-Kelvin problem, for steady potential $\Phi_U^{(1)}$, and:

$$\left[\left(\frac{\partial}{\partial t} - U\frac{\partial}{\partial x_1}\right)^2 + g\frac{\partial}{\partial x_3}\right]\bar{\Phi}^{(1)} = O \qquad \text{on } \partial D_{oF} \tag{45a}$$

$$\bar{\eta}_3^{(1)} = -\frac{1}{g}\left(\frac{\partial}{\partial t} - U\frac{\partial}{\partial x_1}\right)\bar{\Phi}^{(1)} \qquad \text{on } \partial D_{oF} \tag{45b}$$

of the linear wave propagation problem, for unsteady potential $\bar{\Phi}^{(1)}$. For steady potential $\Phi_U^{(1)}$ the impermeability condition on wetted surface ∂D_{oW} becomes:

$$\bar{N} \cdot \frac{\partial}{\partial \bar{x}}\Phi_U^{(1)} = UN_1 - U\frac{\partial}{\partial x_1}\bar{\eta}_U^{(1)} \cdot \bar{N} \tag{44c}$$

whereas for unsteady potential $\bar{\Phi}^{(1)}$ the same condition gives:

$$\bar{N} \cdot \left(\frac{\partial}{\partial \bar{x}}\bar{\Phi}^{(1)} - \frac{\partial}{\partial t}\bar{\eta}^{(1)}\right) = -U\frac{\partial}{\partial x_1}\bar{\eta}^{(1)} \cdot \bar{N} \qquad \text{on } \partial D_{oB} \tag{45c}$$

Again equations (44c) and (45c) differ from their well known counterparts by the presence of free surface corrections and by the body displacement part of the

second term on the right hand side of (44c).

Under the assumption leading to equations (44) and (45), it is found that potential $\Phi^{(2)}$ satisfies the following governing equations:

$$(U^2\frac{\partial^2}{\partial x_1^2} + g\frac{\partial}{\partial x_3})\,\Phi_U^{(2)} = 2U\frac{\partial}{\partial \bar{x}}\Phi_U^{(1)} \cdot \frac{\partial^2}{\partial \bar{x}\partial x_1}\Phi_U^{(1)} - U\frac{\partial}{\partial x_1}\Phi_U^{(1)}\frac{\partial}{\partial x_3}(\frac{1}{g}U^2\frac{\partial^2}{\partial x_1^2} + \frac{\partial}{\partial x_3})\,\Phi_U^{(1)} \quad on\ \partial D_{oF} \tag{46a}$$

$$\eta_{U3}^{(2)} = \frac{1}{g}[U\frac{\partial}{\partial x_1}\Phi_U^{(2)} - \frac{1}{2}\left|\frac{\partial}{\partial \bar{x}}\Phi_U^{(1)}\right|^2 + \frac{1}{g}U^2\frac{\partial}{\partial x_1}\Phi_U^{(1)}\frac{\partial^2}{\partial x_1\partial x_3}\Phi_U^{(1)} + U(\eta_{U1}^{(1)}\frac{\partial}{\partial x_1} + \eta_{U2}^{(1)}\frac{\partial}{\partial x_2})\frac{\partial}{\partial x_1}\Phi_U^{(1)}] \quad on\ \partial D_{oF} \tag{46b}$$

and

$$\bar{N}\cdot\frac{\partial}{\partial \bar{x}}\Phi_U^{(2)} = [U(\frac{\partial}{\partial x_1}\bar{\eta}_U^{(1)}\cdot\frac{\partial}{\partial \bar{x}}\bar{\eta}_U^{(1)} - \frac{\partial}{\partial x_1}\bar{\eta}_U^{(2)}) + \frac{\partial}{\partial \bar{x}}\Phi_U^{(1)}\cdot\frac{\partial}{\partial \bar{x}}\eta_U^{(1)} - \bar{\eta}_U^{(1)}\cdot\frac{\partial}{\partial \bar{x}}\frac{\partial}{\partial \bar{x}}\Phi_U^{(1)}]\cdot\bar{N} \quad on\ \partial D_{oW} \tag{46c}$$

for $\Phi_U^{(2)}$ and $\eta_{U3}^{(2)}$, the steady parts of $\Phi^{(2)}$ and $\eta_3^{(2)}$ respectively, and:

$$[(\frac{\partial}{\partial t} - U\frac{\partial}{\partial x_1})^2 + g\frac{\partial}{\partial x_3}]\,\tilde{\Phi}^{(2)} = -2\frac{\partial}{\partial \bar{x}}\Phi^{(1)}\cdot\frac{\partial}{\partial \bar{x}}(\frac{\partial}{\partial t} - U\frac{\partial}{\partial x_1})\,\tilde{\Phi}^{(1)} + 2U\frac{\partial}{\partial \bar{x}}\tilde{\Phi}^{(1)}\cdot\frac{\partial^2}{\partial \bar{x}\partial x_1}\Phi_U^{(1)} + (\frac{\partial}{\partial t} - U\frac{\partial}{\partial x_1})\,\tilde{\Phi}^{(1)}\frac{\partial}{\partial x_3}\{(\frac{1}{g}U^2\frac{\partial^2}{\partial x_1^2} + \frac{\partial}{\partial x_3})\,\Phi_U^{(1)} + [\frac{1}{g}(\frac{\partial}{\partial t} - U\frac{\partial}{\partial x_1})^2 + \frac{\partial}{\partial x_3}]\,\tilde{\Phi}^{(1)}\} - U\frac{\partial}{\partial x_1}\Phi_U^{(1)}\frac{\partial}{\partial x_3}[\frac{1}{g}(\frac{\partial}{\partial t} - U\frac{\partial}{\partial x_1})^2 + \frac{\partial}{\partial x_3}]\,\tilde{\Phi}^{(1)} \quad on\ \partial D_{oF} \tag{47a}$$

$$\tilde{\eta}_3^{(2)} = -\frac{1}{g}\{(\frac{\partial}{\partial t} - U\frac{\partial}{\partial x_1})\,\tilde{\Phi}^{(2)} + \frac{\partial}{\partial \bar{x}}\Phi_U^{(1)}\cdot\frac{\partial}{\partial \bar{x}}\tilde{\Phi}^{(1)} + \frac{1}{2}\left|\frac{\partial}{\partial \bar{x}}\tilde{\Phi}^{(1)}\right|^2 + \frac{1}{g}(\frac{\partial}{\partial t} - U\frac{\partial}{\partial x_1})\,\tilde{\Phi}^{(1)}\frac{\partial}{\partial x_3}[U\frac{\partial}{\partial x_1}\Phi_U^{(1)} - (\frac{\partial}{\partial t} - U\frac{\partial}{\partial x_1})\,\tilde{\Phi}^{(1)}] + \frac{1}{g}U\frac{\partial}{\partial x_1}\Phi_U^{(1)}\frac{\partial}{\partial x_3}(\frac{\partial}{\partial t} - U\frac{\partial}{\partial x_1})\,\tilde{\Phi}^{(1)} + (\tilde{\eta}_1^{(1)}\frac{\partial}{\partial x_1} + \tilde{\eta}_2^{(1)}\frac{\partial}{\partial x_2})[(\frac{\partial}{\partial t} - U\frac{\partial}{\partial x_1})\,\tilde{\Phi}^{(1)} - U\frac{\partial}{\partial x_1}\Phi_U^{(1)}] + (\eta_{U1}^{(1)}\frac{\partial}{\partial x_1} + \eta_{U2}^{(2)}\frac{\partial}{\partial x_2})(\frac{\partial}{\partial t} - U\frac{\partial}{\partial x_1})\,\tilde{\Phi}^{(1)}\} \quad on\ \partial D_{oF} \tag{47b}$$

$$\bar{N}\cdot(\frac{\partial}{\partial \bar{x}}\tilde{\Phi}^{(2)} - \frac{\partial}{\partial t}\tilde{\eta}^{(2)}) = [U(-\frac{\partial}{\partial x_1}\tilde{\eta}^{(2)} + \frac{\partial}{\partial x_1}\bar{\eta}^{(1)}\cdot\frac{\partial}{\partial \bar{x}}\tilde{\eta}^{(1)} + \frac{\partial}{\partial x_1}\tilde{\eta}^{(1)}\cdot\frac{\partial}{\partial \bar{x}}\bar{\eta}_U^{(1)}) + \frac{\partial}{\partial \bar{x}}\Phi^{(1)}\cdot\frac{\partial}{\partial \bar{x}}\tilde{\eta}^{(1)} + \frac{\partial}{\partial \bar{x}}\tilde{\Phi}^{(1)}\cdot\frac{\partial}{\partial \bar{x}}\bar{\eta}_U^{(1)} - \frac{\partial}{\partial t}\tilde{\eta}^{(1)}\cdot\frac{\partial}{\partial \bar{x}}\bar{\eta}^{(1)} - \bar{\eta}^{(1)}\cdot\frac{\partial}{\partial \bar{x}}\frac{\partial}{\partial \bar{x}}\tilde{\Phi}^{(1)} - \tilde{\eta}^{(1)}\cdot\frac{\partial}{\partial \bar{x}}\frac{\partial}{\partial \bar{x}}\Phi_U^{(1)}]\cdot\bar{N} \quad on\ \partial D_{oW} \tag{47c}$$

for $\tilde{\Phi}^{(2)}$ and $\tilde{\eta}_3^{(2)}$, the unsteady parts of $\Phi^{(2)}$ and $\eta_3^{(2)}$ respectively.

Formulae (46) and (47) illustrate the complexity of the second order

interactions on the free surface and wetted surface. As explained in connection with formulae (22c) and (34d), the steady and unsteady components of $\eta_1^{(1)}$ and $\eta_2^{(1)}$ can be set equal to zero in (46b) and (47b) if $\eta_3^{(2)}$ is interpreted as the single valued wave elevation on $x_3 = O$ in the perturbed domain. In addition, displacement field $\overline{\eta}$ in impermeability conditions (46c) and (47c) has the same interpretations as in impermeability conditions (40c) and (41c).

In order to implement conditions (22d) and (22f) on reference control boundary ∂D_{oc}, it is assumed that ∂D_{oc} consists of the surface of a vertical cylinder extending to reference free surface ∂D_{oF} on the plane $x_3 = O$. Below the free surface the cylinder is closed either by an impermeable bottom, or a horizontal control surface element placed sufficiently deep below the free surface. On the vertical part of ∂D_{oc}, displacement field $\overline{\eta}$ is assumed in the form:

$$\overline{\eta} = \eta_3 \overline{e}_3 \tag{48a}$$

which satisfies condition (23a). This implies that the free surface elevation on ∂D_{oc} and in its vicinity is single valued. On the horizontal part of ∂D_{oc} displacement field $\overline{\eta}$ is defined to be equal to O. On the basis of these assumptions conditions (22d) and (22f) give respectively:

$$\Phi^{(i)} = \Phi_e^{(i)} \text{ on } \partial D_{oc},\ i = 0, 1, \ldots, n \tag{48b}$$

and

$$\frac{\partial}{\partial N}(\Phi^{(i)} - \Phi_e^{(i)}) = O \quad \text{on } \partial D_{oc},\quad i = 0,1,\ldots,n \tag{48c}$$

THE APPLICATIONS OF THE WEAK SCATTERER HYPOTHESIS

A Perturbation Formulation

Using the transformation procedures developed in the preceding sections a formulation of the boundary value problem which represents a ship-wave interaction is sought for by considering the perturbation introduced by the presence of the ship in the flow of steep ambient waves. For the ship advancing with a mean forward speed U, a reference configuration of the ship is defined, relative to a correspondingly advancing coordinate system. This configuration together with the undisturbed water surface at $x_3 = O$ determine the reference fluid domain D_o.

Assuming the ship's hull to be sufficiently slender, the weak scatterer hypothesis is imposed in the perturbation scheme by expressing total velocity potential Φ, as:

$$\Phi = -Ux_1 + \Phi^{(1,0)} + \Phi^{(0,1)} + \Phi^{(2,0)} + \ldots \tag{49a}$$

where x_1 coordinate axis points in the direction of the mean forward velocity of the ship, with:

$$\overline{\eta} = \overline{\eta}^{(1,0)} + \overline{\eta}^{(0,1)} + \overline{\eta}^{(2,0)} + \ldots \tag{49b}$$

defining the perturbation of the fluid domain. In (49a):

$$\Phi_W = \Phi^{(1,0)} + \Phi^{(2,0)} + \ldots \tag{49c}$$

represents the velocity potential of the ambient waves. The following relations define relative orders of magnitude in (49a):

$$\Phi^{(2,0)} = O(\Phi^{(1,0)}),\quad \Phi^{(0,1)} = O(\Phi^{(1,0)}) \tag{49d}$$

and:

$$(\Phi^{(1,0)})^2 = O(\Phi^{(2,0)}),\quad \Phi^{(2,0)} = O(\Phi^{(0,1)}) \tag{49e}$$

Analogous relations are applied to terms in (49b). From relations (49d) and (49e) it is seen that the weak scatterer hypothesis consists in assuming that the induced by the ship disturbance of the flow of the ambient waves, represented by velocity potential $\Phi^{(0,1)}$, is significantly smaller than the disturbance of the calm water condition

due to the ambient wave flow, Φ_w. However, the flow disturbance induced by the ship is not significantly smaller than the non-linear flow effects in the ambient wave field, represented by velocity potential $\Phi^{(2,0)}$.

Starting from formulae (22c) and (22e) it is found that velocity potentials $\Phi^{(1,0)}$ and $\Phi^{(2,0)}$ satisfy equations (45a) and (45b), and equations (47a) and (47b), respectively, with:

$$\tilde{\Phi}^{(1)} = \Phi^{(1,0)} \quad , \tilde{\Phi}^{(2)} = \Phi^{(2,0)} \quad and \quad \Phi_U^{(1)} = O \tag{50a}$$

and

$$\tilde{\eta}^{(1)} = \overline{\eta}^{(1,0)} \quad , \tilde{\eta}^{(2)} = \overline{\eta}^{(2,0)} \quad and \quad \overline{\eta}_U^{(1)} = O \tag{50b}$$

They also satisfy an appropriate bottom impermeability condition, or correspond to a vanishing water velocity at the infinite depth.

Velocity potential $\Phi^{(0,1)}$, which represents the flow disturbance induced by the advancing ship, can be considered as composed of a steady $\Phi_U^{(0,1)}$ and unsteady $\tilde{\Phi}^{(0,1)} = \Phi_S^{(0,1)}$ (scattering) part:

$$\Phi^{(0,1)} = \Phi_U^{(0,1)} + \Phi_S^{(0,1)} \tag{51a}$$

with the corresponding fluid domain perturbation:

$$\overline{\eta}^{(0,1)} = \overline{\eta}_U^{(0,1)} + \overline{\eta}_S^{(0,1)} \tag{51b}$$

Steady velocity potential $\Phi_U^{(0,1)}$ is found to satisfy equations (44) with:

$$\Phi_U^{(1)} = \Phi_U^{(0,1)} \quad and \quad \overline{\eta}_U^{(1)} = \overline{\eta}_U^{(0,1)} \tag{52a}$$

Scattering velocity potential $\Phi_S^{(0,1)}$ satisfies equations (45a) and (45b) with:

$$\tilde{\Phi}^{(1)} = \Phi_S^{(0,1)} \quad and \quad \tilde{\eta}^{(1)} = \overline{\eta}_S^{(0,1)} \tag{52b}$$

On the reference wetted surface the scattering potential must fulfil the impermeability condition:

$$\overline{N} \cdot \frac{\partial}{\partial \overline{x}} \Phi_S^{(0,1)} = \nu_n \qquad on\ \partial D_{ow} \tag{53a}$$

with

$$\nu_n = \overline{N} \cdot \left(\frac{\partial}{\partial t} - U \frac{\partial}{\partial x_1} \right) \overline{\eta}_S^{(0,1)} + \nu'_n \tag{53b}$$

and

$$\begin{aligned} \nu'_n = [& \left(\frac{\partial}{\partial t} - U \frac{\partial}{\partial x_1} \right) \left(\overline{\eta}^{(1,0)} + \overline{\eta}^{(2,0)} \right) \\ & - \left(1 + \overline{\eta}^{(1,0)} \cdot \frac{\partial}{\partial \overline{x}} \right) \frac{\partial}{\partial \overline{x}} \Phi^{(1,0)} \\ & - \left(\frac{\partial}{\partial t} - U \frac{\partial}{\partial x_1} \right) \overline{\eta}^{(1,0)} \cdot \frac{\partial}{\partial \overline{x}} \overline{\eta}^{(1,0)} \\ & + \frac{\partial}{\partial \overline{x}} \Phi^{(1,0)} \cdot \frac{\partial}{\partial \overline{x}} \overline{\eta}^{(1,0)} - \frac{\partial}{\partial \overline{x}} \Phi^{(2,0)}] \cdot \overline{N} \end{aligned} \tag{53c}$$

It follows from (53c) that the weak scatterer hypothesis is equivalent to the assumption:

$$\nu_n' = O(\Phi^{(0,1)}) \tag{53d}$$

if

$$UN_1 = O(\Phi^{(0,1)}) \tag{53e}$$

is satisfied. As a result of adopting the weak scatterer hypothesis scattering velocity potential $\Phi_S^{(0,1)}$ is determined by the solution to the quasi-linear radiation problem, with quasi-linear impermeability condition (53a) imposed on ∂D_{ow} and the linear free surface condition:

$$\left[\left(\frac{\partial}{\partial t} - U \frac{\partial}{\partial x_1} \right)^2 + g \frac{\partial}{\partial x_3} \right] \Phi_S^{(0,1)} = O \qquad on\ \partial D_{oF} \tag{53f}$$

applied on $x_3 = 0$.

To impose impermeability condition (53a) in practical computations and to elucidate its physical meaning it is noticed that ν_n can be rewritten as:

$$v_n(\bar{x}) = [1 + O(\Phi^{(1,0)})]\,[(\bar{v} - \bar{u}_w) \cdot \bar{n} + U\bar{e}_1 \cdot (\bar{n} - \bar{N})] + o[(\Phi^{(1,0)})^2] \tag{54a}$$

where the right hand side is determined at $\bar{y} = \bar{x} + \bar{\eta}$, $\bar{v}$ is the ship velocity relative to the reference configuration, $\bar{u}_w$ is the water velocity induced by the ambient wave field, and $\bar{n}$ is the instantaneous normal vector at $\bar{y}$ *on* ∂D_w. $\bar{N}$ represents the normal vector on ∂D_{ow} at point $\bar{x}$. In deriving (54a) use is made of the relation:

$$\sqrt{\bar{N} \cdot \bar{\bar{K}}^T \cdot \bar{\bar{K}} \cdot \bar{N}} = 1 + O(\Phi^{(1,0)}) \tag{54b}$$

see (13c). On the basis of (53d) and (54a):

$$v_n(\bar{x}) = u_n(\bar{y}) \equiv (\bar{v} - \bar{u}_w) \cdot \bar{n} + U\bar{e}_1 \cdot (\bar{n} - \bar{N}) \tag{55}$$

including all terms up to $O(\Phi^{(2,0)})$. The weak scatterer hypothesis is therefore expressed by:

$$u_n(\bar{y}) = O(\Phi^{(0,1)}) \tag{56}$$

which is the form of the hypothesis applied in [6]. Since the velocity field $\bar{u}_w$ is considered to be given $u_n(\bar{y})$ is easy to determine numerically on the instantaneous wetted surface in a ship motion simulation.

The use of $u_n(\bar{y})$ in impermeability condition (53a) requires that $u_n(\bar{y})$ be mapped onto the reference configuration of wetted surface, ∂D_{ow}. It is possible to accomplish such mapping by approximating $u_n(\bar{y})$ by a finite series of linearly independent, square integrable functions $\Psi_{Ni}(\bar{y})$ defined on the ship's surface:

$$u_n(\bar{y}, t) = \sum_{i=1}^{m} \beta_i(t)\, \Psi_{Ni}(\bar{y}) \quad on\ \partial D_B \tag{57a}$$

where $\beta_i(t)$, $i = 1, 2, \ldots m$, are functions of time. Functions $\Psi_{Ni}(\bar{y})$ are assumed to satisfy the Lipschitz condition:

$$|\Psi_{Ni}(\bar{y}) - \Psi_{Ni}(\bar{y} + \Delta\bar{y})| \le M|\Delta\bar{y}| \quad on\ \partial D_B \tag{57b}$$

on the ship's surface, and to be invariant with respect to displacements of the surface due to the ship motion. Using (1) and (30) the latter condition can be expressed as:

$$\Psi_{Ni}(\bar{y}) = \Psi_{Ni}(\bar{x} + \bar{\eta}) = \Psi_{Ni}(\bar{x} + \bar{\eta}_o),\ i = 1, 2, \ldots m \tag{57c}$$

$$for\ \bar{x} \in \partial D_{ow}\ and\ \bar{y} \in \partial D_w$$

Formulae (57a), (57b) and (57c) lead to:

$$v_n(\bar{x}, t) = \sum_{i=1}^{m} \beta_i(t)\, \Psi_{Ni}(\bar{x}) + O(\beta_i |\bar{\eta}_o|) \tag{57d}$$

Since, on account of the weak scatterer hypothesis $\beta_i = O(\Phi^{(0,1)})$, $i = 1, 2, \ldots m$, and $|\bar{\eta}_o| = O(\Phi^{(1,0)})$, the last term on the right hand side of (57d) is neglected, and impermeability condition (53a) takes the form:

$$\bar{N} \cdot \frac{\partial}{\partial \bar{x}} \Phi_S^{(0,1)} = \sum_{i=1}^{m} \beta_i(t)\, \Psi_{Ni}(\bar{x}) \quad on\ \partial D_{ow} \tag{58}$$

with $\beta_i(t)$ determined from approximation (57a). Applications of condition (58) lead to the computation of scattering potential $\Phi_S^{(0,1)}$ by means of the modal potentials (or equivalent motion) method, [6].

Following the transformation rules explained earlier, perturbation scattering velocity potential $\Psi_S^{(0,1)}$, velocity field $\bar{u}_S^{(0,1)}$ and pressure field $q_S^{(0,1)}$ in the instantaneous fluid domain D are given by:

$$\Psi_S^{(0,1)}\ (\overline{y}, t) = \Phi_S^{(0,1)}\ (\overline{x}, t) \quad (59a)$$

$$\overline{u}_S^{(0,1)}\ (\overline{y}, t) = \frac{\partial}{\partial \overline{x}} \Phi_S^{(0,1)}\ (\overline{x}, t) \quad (59b)$$

$$q_S^{(0,1)}\ (\overline{y}, t) = -\rho \frac{\partial}{\partial t} \Phi_S^{(0,1)}\ (\overline{x}, t) \quad (59c)$$

Forces and moments exerted by the scattering pressure field on the ship hull can be found using formulae (15e) and (27b), which result in:

$$\overline{F}_S^{(0,1)} = \overline{\overline{R}} \cdot \int_{\partial D_{oW}} p_S^{(0,1)}\, \overline{N} dS \quad (60a)$$

and

$$\overline{\Gamma}_{CGS}^{(0,1)} = \overline{\overline{R}} \cdot \int_{\partial D_{oW}} p_S^{(0,1)}\ (\overline{x} - \overline{x}_{CG}) \wedge \overline{N} dS \quad (60b)$$

where $\overline{\overline{R}}$ can be replaced by $\overline{\overline{I}}$, and $\overline{F}_S^{(0,1)}$, $\overline{\Gamma}_{CGS}^{(0,1)}$ denote the force and moment about the instantaneous location of the centre of gravity, denoted by *CG*. In addition $p_S^{(0,1)}$ is defined by the right hand side of (59c).

In figure 2 the effectiveness of the method in predicting scattering forces is illustrated by an example taken from [6]. In the figure a Froude-Krylov and corresponding total (i.e. including scattering) hydrodynamic pitch moment, computed using a numerical implementation of the described perturbation solution, are compared with the total pitch moment record derived from experimental data. The experiment, [11], and numerical simulation, [6], were performed for a low L/B stern fishing trawler advancing unrestrained at 0.2 Froude number, and 30 degrees heading, in steep, close to breaking, periodic waves. As can be seen, the scattering moment reduces the amplitude of the Froude-Krylov moment by about 30%, and significantly changes the pattern of the pitch moment, producing a close qualitative and quantitative agreement with the experimental record. Similar comparisons for the other modes of motion are described in [6].

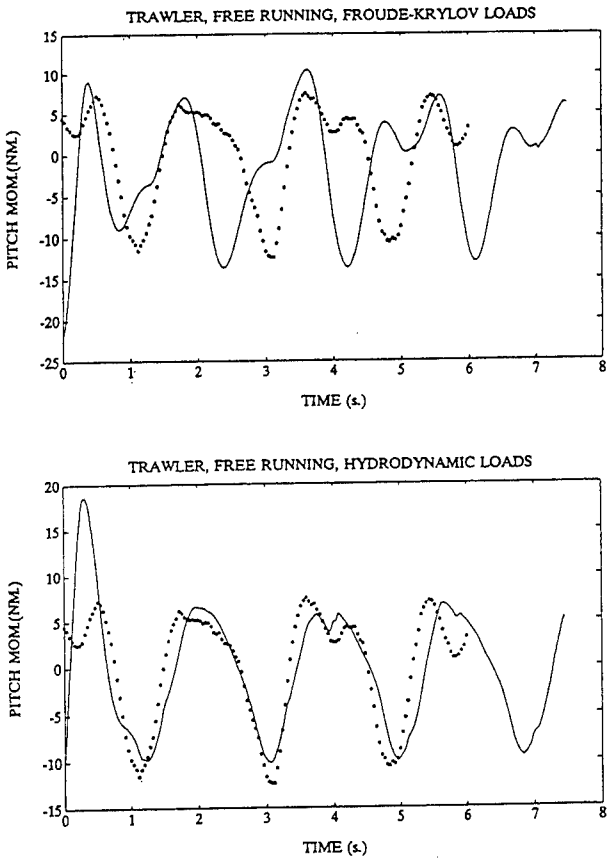

Fig. 2 A comparison of total loads derived from experiment, [11], with computed Froude-Krylov and total loads [6], *** experiment, _____ computation

A Direct Formulation

The described above method of imposing a perturbation impermeability condition on a surface piercing hull can be simplified by shifting its application to a simpler, control boundary. To this end a direct solution to the ship-wave interaction problem is sought for in a bounded control domain *D* and is matched with a perturbation solution in domain D_e, which is external to *D*. The wetted surface of the ship is considered to be at all times entirely contained in *D*. Such an approach leads to a greater generality of the resulting formulation because of the complete (in principle) inclusion of non-linearities in the vicinity (domain *D*) of the hull. It also prompts the development of a consistent radiation condition on a control boundary ∂D_c for the non-linear

time domain boundary value problem.

Instantaneous control domain D is bounded by control surface ∂D_c, which consists of a vertical cylindrical surface extending to the instantaneous free surface ∂D_F. Below the free surface ∂D_c is closed by a horizontal surface element at a sufficient depth. A direct formulation of the problem on D may be obtained by applying Green's formula for harmonic functions to velocity potential $\Psi(\bar{y}, t)$ at time t:

$$\Omega(P,t)\,\Psi(P,t) = \int_{\partial D(t)} [Y(P,Q)\,\frac{\partial}{\partial n_Q}\Psi(Q,t) - \Psi(Q,t)\,\frac{\partial}{\partial n_Q} Y(P,Q)]\,dS(Q) \tag{61a}$$

with $\Omega(P,t)$ signifying the angle subtended at point P by boundary $\partial D(t)$, $\frac{\partial}{\partial n_Q}$ denoting the outward normal derivative taken at point Q, and $Y(P,Q)$ representing the fundamental solution to Laplace's equation. In addition the Cauchy principal value of the integral over $\partial D(t)$ is taken. For point P located on $\partial D(t)$, and with Dirichlet, Neumann, or Robin (mixed) boundary conditions applied on non-overlapping parts of $\partial D(t)$, the formula generates two coupled Fredholm integral equations, of the second kind for the unknown Ψ, and of the first kind with respect to the unknown $\frac{\partial}{\partial n}\Psi$.

On the instantaneous wetted surface of the ship the boundary data in (61a) are determined by impermeability condition (25b). The unknown locus of the free surface and required boundary data on free surface $D_F(t)$ are obtained from initial conditions using evolution equations. The evolution equations can be cast in a Lagrangian or Eulerian form. The Eulerian form is used here, because it imposes the condition of single valued wave elevation which must be satisfied at control boundary ∂D_c to ensure an appropriate matching with the external flow. Therefore:

$$\frac{\partial}{\partial t}\zeta = \frac{\partial}{\partial y_3}\Psi - \frac{\partial}{\partial \bar{y}}\zeta \cdot \frac{\partial}{\partial \bar{y}}\Psi \tag{61b}$$

where ζ denotes wave elevation, and:

$$\frac{d}{dt}\Psi = -g\zeta - \frac{1}{2}\left[\left(\frac{\partial}{\partial y_1}\Psi\right)^2 + \left(\frac{\partial}{\partial y_2}\Psi\right)^2 - \left(\frac{\partial}{\partial y_3}\Psi\right)^2\right] - \frac{\partial}{\partial y_3}\Psi\,\frac{\partial}{\partial \bar{y}}\zeta \cdot \frac{\partial}{\partial \bar{y}}\Psi \tag{61c}$$

with $\frac{d}{dt}$ representing the time derivative at a vertically moving point on the free surface.

Boundary data on control boundary ∂D_c is determined from matching conditions (21e) and (21f). In the application of those conditions velocity potential of external flow Ψ_e is expressed as a transformed potential Φ_e defined on the reference configuration D_{oe} of the horizontally unbounded external domain D_e, which is defined by control boundary ∂D_c and the reference free surface at $x_3 = 0$. The domain displacement field $\bar{\eta}_e$ is assumed to satisfy condition (48a). It follows that matching conditions (21e) and (21f) give:

$$\Psi - \exp\left(\eta_{e3}\frac{\partial}{\partial x_3}\right)\Phi_e = O \quad on\ \partial D_c \tag{62a}$$

and

$$\frac{\partial}{\partial \bar{y}}\Psi \cdot \bar{N} - \exp\left(\eta_{e3}\frac{\partial}{\partial x_3}\right)\frac{\partial}{\partial \bar{x}}\Phi_e \cdot \bar{N} = O \quad on\ \partial D_c \tag{62b}$$

Velocity potential Φ_e is taken in the form:

$$\Phi_e = \Phi_e^{(1,0)} + \Phi_e^{(0,1)} + \Phi_e^{(2,0)} + \ldots \tag{63a}$$

with

$$\Phi_{ew} = \Phi_e^{(1,0)} + \Phi_e^{(2,0)} + \ldots \tag{63b}$$

representing the velocity potential of an ambient steep wave, and $\Phi_e^{(0,1)}$ denoting the scattering velocity potential in D_e. The velocity potentials on the right hand side of (63a) are assumed to satisfy order of magnitude relations analogous to (49d) and (49e), whereas displacement field $\overline{\eta}$ has a representation analogous to (49b).

Taking into account expression (63a) and including consistently terms up to order of magnitude $O(\Phi_e^{(2,0)})$, matching conditions (62) give:

$$\Psi = \exp(\eta_{e3} \frac{\partial}{\partial x_3}) \ (\Phi_{eW} + \Phi_e^{(0,1)}) \quad \text{on } \partial D_c \tag{64a}$$

and:

$$\overline{N} \cdot \frac{\partial}{\partial \overline{x}} \Phi_e^{(0,1)} = v_n \quad \text{on } \partial D_{oc} \tag{64b}$$

with:

$$v_n(\overline{x}) = u_n(\overline{y}) \tag{64c}$$

and:

$$u_n(\overline{y}) = \left[\frac{\partial}{\partial \overline{y}} \Psi - \exp(\eta_{e3} \frac{\partial}{\partial x_3}) \ \frac{\partial}{\partial \overline{x}} \Phi_{ew} \right] \cdot \overline{N} \quad \text{on } \partial D_c \tag{64d}$$

The weak scatterer hypothesis consists in assuming the relation:

$$v_n = O(\Phi_e^{0,1)}) \tag{65}$$

which is satisfied sufficiently far from the ship hull in a three dimensional problem. Relations (64a) and (64b) can be implemented by constructing an appropriate displacement field $\eta_{e3}(\overline{x}, t)$ on ∂D_{oc}, or by employing a mapping technique analogous to the one which leads to relation (58). On reference wetted surface ∂D_{oF} scattering potential $\Phi^{(0,1)}$ must satisfy condition (53f) with $U = O$.

A solution to the external scattering problem may be obtained in terms of the appropriate Green's function, for the infinite depth, by applying the following relation known from so called body non-linear radiation problem formulations, [9], [10]:

$$\begin{aligned}
\Omega(P,t)\,\Phi_e^{(0,1)}(P,t) &= -\int_{\partial D_{oc}(t)} [Y(P,Q) \\
&\quad - Y(P,Q')]\, v_n(Q,t)\, dS_Q \\
&\quad - \int_{-\infty}^{t} \int_{\partial D_{oc}(\tau)} \hat{Y}(P,Q,t-\tau)\, v_n(Q,\tau)\, dS_Q\, d\tau \\
&\quad + \int_{\partial D_{oc}(\tau)} \Phi_e^{(0,1)}(Q,t)\, \frac{\partial}{\partial N_Q} [Y(P,Q) \\
&\quad - Y(P,Q')]\, dS_Q + \int_{-\infty}^{t} \int_{\partial D_{oc}(\tau)} \Phi_e^{(0,1)}(Q,\tau) \\
&\quad \frac{\partial}{\partial N_Q} \hat{Y}(P,Q,t-\tau)\, dS(Q)\, d\tau \\
&\quad - \frac{1}{g} \int_{-\infty}^{t} \int_{\ell(\tau)} [\hat{Y}(P,Q,t-\tau)\, \frac{\partial}{\partial \tau} \Phi_e^{(0,1)}(Q,\tau) \\
&\quad - \Phi_e^{(0,1)}(Q,\tau)\, \frac{\partial}{\partial \tau} \hat{Y}(P,Q,t-\tau)] \\
&\quad V_N(Q,\tau)\, d\ell(Q)\, d\tau
\end{aligned} \tag{66}$$

where $x_i(Q') = x_i(Q)$ *for* $i=1,2$, and $x_3(Q') = -x_3(Q)$, $\hat{Y}(P,Q,t)$ represents the memory part of the time dependent Green's function, [3], $\ell = \partial D_{oc} \cap \partial D_{oF}$ is the instantaneous waterline of ∂D_{oc}, and $V_N(Q,t)$ denotes the normal velocity of the waterline, which results from a prescribed motion of ∂D_c. Formula (66) provides the missing relation between the boundary value data on ∂D_c in the formulation of the direct boundary value problem. Therefore relations (61a) and (66), coupled by means of (64), can be solved to determine the solution, starting from appropriate initial value conditions. It should be noticed that the matching of velocity and pressure fields on control boundary ∂D_c is well defined including terms up to $O(\Phi^{2,0)})$.

CONCLUSION

The above discussion describes and gives examples of the application of a technique for the formulation of non-linear boundary value problems of ship

hydrodynamics. The examples provided indicate the usefulness of the technique in deriving and evaluating formulations of boundary value problems for specific applications. In particular it is shown that consistent formulations of the non-linear time domain problem of ship-wave interaction can be obtained using the described method. The adoption of the weak scatterer hypothesis allows those formulations to be effectively implemented with the application of existing computational means. Also, the method provides a basis for the development of consistent non-linear flow matching (radiation) conditions on control boundaries.

REFERENCES

1. Lebovitz, N.R., "Perturbation Expansions on Perturbed Domains", SIAM Review, Vol. 24, No. 4, 1982, pp. 381-400.

2. Joseph, D., "Domain Perturbation: The Higher Order Theory of Infinitesimal Water Waves", Arch. Rat. Mech. Anal., Vol. 51, 1973, pp. 295-303.

3. Wehausen, J.V., and Laitone, E.V., "Surface Waves", Encyclopedia of Physics, Vol. IX, Springer Verlag, 1960.

4. Newman, J.N., Marine Hydrodynamics, MIT Press, 1978.

5. Nakos, D., and Sclavounos, P., "Ship Motions by a Three-Dimensional Rankine Panel Method", Proc. Eighteenth Symp. on Naval Hydrodynamics, National Academy Press, 1991, pp. 21-40.

6. Pawlowski, J.S., and Bass, D.W., "A Theoretical and Numerical Model of Ship Motions in Heavy Seas", Trans. SNAME, 1991.

7. Milne-Thomson, L.M., "Theoretical Hydrodynamics", Macmillan Comp., 1968.

8. Timman, R., and Newman, J.N., "The Coupled Damping Coefficients of Symmetric Ships", Journal of Ship Research, Vol. 5, No. 4, pp. 34-55.

9. Lin, W.-M. and Yue, D.K.P., "Numerical Solutions for Large Amplitude Ship MOtions in the Time Domain", Proc. Eighteenth Symp. on Naval Hydrodynamics, National Academy Press, 1991, pp. 41-66.

10. Magee, A.R., "Large Amplitude Ship Motions in the Time Domain", Thesis, University of Michigan, 1991.

11. Grochowalski, S., "Investigation into the Physics of Ship Capsizing by Combined Captive and Free-Running Model Tests", Trans. SNAME, Vol. 97, 1989, pp. 169-212.

DISCUSSION

J. Wehausen
University of California at Berkeley, USA

This paper provides the underpinnings of the recent paper by the author and Bass [6]. Because of the rather impressive results reported in that paper, this one deserves some detailed study and comment, more than I can do here. I have not been able to read the whole paper with attention to detail, but shall try to describe my understanding of the author's approach to the problem of the title and some of the difficulties that I have encountered.

In deriving the linearized equations for free-surface flows in the usual Eulerian formulation, one is confronted with the embarrassing situation that one expands the velocity components and pressure (or perhaps a velocity potential if one exists) in a series about a point that does not lie within the fluid and where the quantity in question is presumably not defined. Several ways have been proposed in order to meet this difficulty. One is to assume that the region of definition of the quantity can be extended analytically far enough beyond its natural region of definition to include the point in question. It is seldom, however, that anyone really addresses this problem of analytic extension (but see H. Lewy, Proc. Amer. Math. Soc., vol. 3 (1952), pp. 111-113). Nevertheless, one might argue that if one has proved convergence of the resulting series, one has by that fact established the legitimacy of the analytic extension. Such proofs exist in only a few cases. In 2D potential flow, one may avoid the difficulty by taking (ϕ,φ) as independent variables and solving for $x(\phi,\varphi)$ and $y(\phi,\varphi)$ with domain of (ϕ,φ) known; this stratagem is, of course, not always available. Another procedure is the use of a Lagrangian description of the fluid motion. Then all independent variables are defined on a given domain and presumably one can construct a perturbation approximation without having to leave the reference domain.

Joseph[1], Lebovitz[2], and the author have chosen a procedure that they call Lagrange-like. They start with a given, possibly time-dependent domain D_o as the reference domain (not necessarily the fluid domain at, say, time $t = 0$) and introduce mapping functions from the domain D_o to the domain D(t) of the fluid at time t. The mapping functions are to be determined in the course of solving the problem. Joseph and Lebovitz make it clear from the beginning that they are trying to develop an approach to perturbation approximations that avoids the puzzling situation mentioned above. Also, one of their goals is to relate the (usual) Euler-like procedure to the Lagrange-like one, and indeed they conclude that the Euler-like procedure can be justified, at least formally, on the basis of their approach. Thus, they end up with the same set of boundary-value problems.

The author's approach is more elaborate. Essentially he is developing the Lagrangian equations for a special reference domain that may depend upon the time (i.e., one moving with the mean position of the ship). A perturbation approximation is introduced only fairly late in the paper. The first part is devoted to developing the necessary formulas for expressing the kinematic relationships in terms of the author's form for the mapping from the domain D_o to the fluid domain $D: \bar{y}=\bar{x}+\bar{\eta}(\bar{x},t)$, where $\bar{x}\epsilon D_0$, $\bar{y}\epsilon D$. Unlike its expression in Joseph [1] or Lebovitz [2], η is not considered to be small. The mapping is expressed by means of the operator exp() defined in equation (2). I find the definition ambiguous, for, according to my understanding,

$$(\bar{\eta}\cdot\partial/\partial\bar{x})^2=(\eta i\partial/\partial xi)(\eta j\partial/\partial xj)=\eta i(\partial\eta j/\partial xi)\partial/\partial xj+\eta i\eta j\partial^2/\partial xi\partial xj,$$

and similarly for higher powers. If (3) is to be correct, one must treat $\bar{\eta}$ as a constant in (2). This is true not only here but also later on when the operator $\exp(\bar{\eta}\cdot\partial/\partial\bar{x})$ and $\partial/\partial\bar{x}$ and $\partial/\partial t$ are taken to be commutative, as, e.g., in (6ab) and (19bc). One might think that one motivation for introducing the operator exp() is to exploit exp(-) as its inverse, but this doesn't occur and apparently is not useful. The operator appears to have been introduced chiefly for notational convenience.

An arbitrary scalar function (possibly a component of a vector or tensor) $v(\bar{x})$, defined on D_o, is mapped into $u(\bar{y})$, defined on D, by (4a), i.e., by

$$(*)\qquad u(\bar{y})=u(\bar{x}+\bar{\eta})=v(\bar{x})+(\bar{\eta}\cdot\partial/\partial\bar{x})v+\ldots$$

The series is defined for $\bar{x}\epsilon D_0$, as one wishes. If also $\bar{x}+\bar{\eta}\epsilon D_0$, then the series is just $v(\bar{x}+\bar{\eta})$. Apparently $u(\bar{x}+\bar{\eta})=v(\bar{x}+\bar{\eta})$ when $\bar{x}+\bar{\eta}\epsilon D_0$, not necessarily a useful observation since one is really interested in defining u in D. However, this is

evidently different from the similar-appearing mapping used by Lebovitz, who defines $u(\bar{x}+\bar{\eta})=v(\bar{x})$.

I am not able to verify immediately equations (4b), (4c), and the ensuing statement. If, in fact, the proof is not obvious, it would be some comfort to the reader to be informed of this.

I am interested in the statement that the author did *not* assume (35), the "usual assumption," as he states. In interpret this to mean that, in fact

$$(\#) \qquad \eta = \eta 1 e1 + \eta 2 e2 + \eta 3 e3,$$

and indeed, as pointed out by the author, in (34d) the components $\eta 1^1$ and $\eta 2^1$ do appear. $\eta 3^1$ is determined on ∂D_{0F} by (34b). It would be interesting to see how the expressions for these other components are determined, and under what conditions they are necessary. Also, how does one extend the definition of η to all D_0? One of the conclusions of Joseph [1] and Lebovitz [2] is that the use of domain mappings leads back to the usual equations derived by an Euler-like procedure, although by a path that seems to them more satisfactory. Are the author's equations really different from those that would be derived by the usual Eulerian procedure, and if so, in what way? Perhaps the author can supply some further insight into his reasons for choosing the Lagrangian procedure.

The paper by Nakos and Sklavounas [5] also shows remarkably good agreement between experiment and theory. Following eq. (41) the author gives a detailed description of the differences between his equations and those of [5]. It would be of practical interest to have numerical estimates of these differences, something apparently not too difficult to provide, since computer programs have evidently already been prepared. Since [5] is not presented as a nonlinear theory, are differences primarily a result of the nonlinear aspects of the author's theory?

There is so much detailed analysis in this paper that one cannot be sure of not having overlooked some subtle point or perhaps even an error in calculation. Nevertheless, the impressive comparisons between calculation and experiment shown here in Fig. 2 and more extensively in the SNAME paper [6] suggest that the paper deserves intensive study necessary to understand it fully. There are still many questions to be asked. For example, is the apparent success of the theory attributable chiefly to nonlinearity, to the Lagrange-like approach, or perhaps instead to the weak-scatterer hypothesis? Or are they all intertwined?

AUTHOR'S REPLY

I am most grateful to Professor Wehausen for his insightful questions and comments which give me the opportunity to provide explanations of several topics.

It seems helpful to answer the questions in reversed order, from the more general to the more specific, starting with the question about the contributions of the Lagrange-like mapping method and of the weak-scatterer hypothesis to the formulation and implementation of the non-linear ship/wave interaction model presented in [6].

In the present paper, the Lagrange-like mapping is introduced as a general technique for the formulation of non-linear boundary value problems of ship hydrodynamics. Subsequently, it is shown how main known formulations of such problems can be derived by means of the mapping technique. Then the weak-scatterer hypothesis and its applications in the perturbation and direct formulations of the non-linear ship/wave interaction problem are derived within the previously established framework of the mapping technique.

Therefore, the weak-scatterer formulations do not appear as ad hoc developments. They result from feasible assumptions which are adopted within the framework of the mapping method and in the context of the other formulations organized by the same framework. The consistency achieved in this way cannot be obtained outside of the mapping method. It also allows one to understand and evaluate the weak-scatterer formulations independently of any computational evidence which is always contingent on the numerical tools used and on the data available for comparison. In that sense, the present paper corroborates the results described in [6]. At the level of implementation, the established framework of problem formulation provided a useful guidance in developing the numerical algorithm applied in [6] (see also formulae [57] and [58] here).

In the paper, the derivation of boundary value problems based on the perturbation of double body flow serves as one of the illustrations of the applicability of the mapping method (the others being the non-linear wave propagation and Neumann-Kelvin

perturbations). The comparison with the work by Nakos and Sclavounos [5] is carried out for the double body perturbation but not for the weak-scatterer perturbation model. The reason is that in the weak-scatterer perturbation model forward speed effects are modelled using Neumann-Kelvin approximation by taking the ambient wave flow as the dominant flow feature. In this way, the weak-scatterer hypothesis makes it possible to avoid the complexity of dealing with conditions (47a) and (47c), at the cost of implementing condition (53a).

In a double body perturbation, a disturbance induced by the ship (namely the double body flow) constitutes the dominant flow feature and the ambient wave flow is included in the linear effects of unsteady flow (see equations [41a] and [41c]}. A modelling of flow phenomena which are non-linear with respect to the unsteady flow requires in a double body flow perturbation a consideration of the next, i.e., second, order of magnitude equations. Such equations are not included in [5] and their complexity is at least comparable to that of equations (47a) and (47c).

However, in the paper, the comparison of the double body perturbation formulation with the work presented in [5] brings forward the agreement between the two formulations on the assumption (38c). In the framework of the mapping method, this assumption is the necessary assumption of double body perturbation formulations. A detailed evaluation of double body perturbation formulations of the steady flow (wave resistance) problem in the framework of the mapping method is a subject of a forthcoming PhD thesis. That work will include comparisons of computed results with results obtained from the formulation described in [5].

Let me observe at this point that the above discussion illustrates how the methodology outlined in the paper provides ground for a meaningful comparison and evaluation of existing and possible new formulations of problems of ship hydrodynamics.

Coming to the governing equations of non-linear wave propagation, the interpretation by Prof. Wehausen that the domain displacement field is assumed to contain all three components, none of them a priori taken equal to zero even on the reference free surface, is correct. In a particular application, the three components must be represented in a suitable functional (e.g., polynomial) form as scalar fields on the reference fluid domain. The values which those fields take on the boundaries appear then in their functional representations as unknown parameters which are determined in the course of solving the boundary value problem. This is the approach considered by Joseph [2]. However, Joseph assumes the mapping between the instantaneous and reference configurations of the free surface to be determined by the projection along the normal to the reference free surface. That assumption reduces the mapping field to the vertical component only. Other mappings between the instantaneous and reference configuration of the free surface can be considered and in all of them, including the case examined by Joseph, the equations for free surface elevation (34b), (34d), etc., impose the appropriate constraints on the boundary.

Considering the domain and field mappings as defined in the present paper, they differ from the ones examined by Lebovitz [2] in that fields $v(\bar{x})$ are mapped by analytic expansion from the reference fluid domain to the instantaneous fluid domain, in parallel with domain points and by the same (exponential) operator, to obtain $u(\bar{y})=v(\bar{x}+\bar{\eta})$. Lebovitz, instead, maps fields $u(\bar{y})=u(\bar{x}+\bar{\eta})$ from the instantaneous to reference domain configuration by the identity mapping $u(\bar{y})=v(\bar{x})$ and then expands $u(\bar{y})$ analytically relative to $\bar{\eta}$ in the perturbation process. The mapping procedure presented here avoids the mixing of the mapping itself with the process of arriving at a perturbation solution. This helps to define the mapping procedure clearly including e.g. the impermeability condition. It may also help to address the problem of required analycity of the mapped fields although this problem is not discussed in the present paper.

The proof of equations (4b) and (4c) and of the ensuing statement depends on the assumption that $v(\bar{x})$ is an analytic function. Unfortunately, the proof is too long to be shown here. I intend to provide it in another publication. In addition, the definition of the exponential operator (2) is illustrated by equations (1) and (3), i.e., indeed field $\bar{\eta}$ is assumed to be constant in (2). This is in accordance with the usual notation for Taylor's series in which increments of independent variables are considered as constant although they are functions of the independent variables. However, the notation should have been made more clear in the paper.

In conclusion, I would like to thank Prof. Wehausen again for his discussion.

Nonlinear Effects on High Block Ship at Low and Moderate Speed

Y.-H. Kim (David Taylor Model Basin, USA),
T. Lucas (University of North Carolina at Charlotte, USA)

ABSTRACT

A Rankine panel method is used for the solution of the fully nonlinear free surface problem, in particular for high block ships (C_B greater than 0.75). High block ships usually have a blunt bow and hence experience extreme waves with huge crests followed by deep troughs near the bow region. These phenomena are nonlinear. A new algorithm has been developed, consisting of a nested pair of two iterative procedures: an inner and outer iteration. The inner iteration is to solve the system of nonlinear equations that results from eliminating the unknown wave height from the kinematic and dynamic free surface conditions on the current (outer) free surface. The outer iteration is conducted on the free surface determined from the converged solution of the previous inner iteration. Singularities are distributed on the actual wetted ship hull and the updated free surface location obtained during the outer iteration. The previously reported one parameter family of advection methods is also used. The computations for Series60 with block coefficient 0.80 and Model B at various speeds successfully reveal the details of wave profiles at the bow, hull, and stern. The computational results illustrate the stability, efficiency and accuracy of this approach for all tested hull forms and speeds.

INTRODUCTION

Rankine panel methods have been popular for the solution of steady potential flow problems during the previous two decades. The Rankine source method is straightforward and can handle the details of a complex hull form without numerical difficulties. Gadd[1] and Dawson[2] successfully applied the Rankine panel method to solve ship problems with a linearized free surface condition. Since then several researchers including Xia[3], Ni[4], and Kim[5] attacked the nonlinear free surface problem by applying variations of this method. A major focal point has been the problem of convergence, which has posed difficulties at higher speeds and different hull forms.

Kim and Lucas[6] proposed an iterative algorithm for solving the nonlinear free surface flow problem by using a one parameter family of upstream finite difference methods. The computational scheme developed successfully gave a converged solution and the results demonstrated significantly improved wave profiles as well as wave making resistance for the Wigley and Series 60, C_B=0.60 hulls, compared with those obtained by linearized free surface solvers.

During the presentation at the 18th ONR symposium several discussers suggested investigating the application of the new algorithm to high block coefficient ships with a blunt bow, a case where the nonlinear effects were expected to be more significant. The Series 60, C_B=0.80 hull which has a half entrance angle of 43 degrees was selected. At Froude number 0.25 and lower we can report that the solution converged. But for Froude numbers 0.30 the solution diverged. The wave amplitude grew steadily as the iteration continued and after several iterations the wave amplitude near the bow exceeded the magnitude of the ship draft. Thus modifications are required to solve the fully nonlinear problem for a high block ship. Also it is desirable to use a wetted hull, an improvement that is likely to cause further problems with convergence.

This paper outlines a new algorithm for the solution of the nonlinear free surface problem with more robust convergence properties, even for high block ships. This new approach involves a nested pair of inner and outer iterations. The iteration starts from the solution of the double body flow. The inner iteration is to solve the system of nonlinear equations that results from eliminating the unknown wave height from the dynamic and kinematic free surface conditions within an arbitrary tolerance for a fixed free surface. The outer iteration is conducted on the free surface determined from the converged solution of the inner iteration. Thus if this approach converges, it would give the unique solution to both the free surface and the source coefficients for the nonlinear equations. This approach has shown high accuracy with relatively small computer times as the inner iteration consists of rather cheap matrix solutions while only the outer iteration involves recomputing the influence coefficients at the new free surface. Our computational experience is that with the inner iteration logic, usually

two to four outer iterations give a solution converged to three significant digits in height. In addition to having few outer iterations, each outer iteration is much cheaper than in the more advanced approach since only source terms need be computed, while in the previous approach, the relatively expensive z-partial derivative terms are required.

When we were pursuing the new mathematical analysis we studied a more rigorous convergence criteria: the maximum error in the residual goes to zero (for example be less than 1.0E-9). Here the residual is the error which is found when the result of the current iteration is substituted into the combined kinematic and dynamic equations. We evaluate this error at each control point both in root mean square norm and the maximum norm of the residuals. These measurements of the error are used not only to assess the quality of a given iteration, but also to dynamically choose the underrelaxation parameter λ.

Computations are presented of the wave profiles along Series60,CB=0.80 hull and Model B. A comparison of wave profiles is made with Model B experiments. The results show that the solution converges nicely even for high block ships. Preliminary work is begun on the problem of wave resistance. With the nonlinear solution over a wavy free surface, the pressure is integrated over a wetted hull surface but it is not in final form. Early results for the two full hull forms are presented.

MATHEMATICAL FORMULATION

A Cartesian coordinate system $x_i = (x,y,z)$ fixed on the ship moves with constant forward speed U_0 as shown in Figure 1. The positive x-direction points upstream, the positive z opposing the direction of gravity, and z=0 coincides with the undisturbed free surface. The boundary-value problem will be expressed relative to this moving coordinate system with the flow at infinity consisting of an uniform stream.

The fluid is assumed to be inviscid and incompressible and it's motion is irrotational, governed by a potential function $\phi(x,y,z)$ which satisfies the Laplace equation in the fluid domain

$$\nabla^2\phi = 0 \tag{1}$$

and the velocity field of the fluid V_i can be defined as

$$\vec{V}(x,y,x) = \nabla\phi(x,y,z) \tag{2}$$

On the wetted portion of the ship hull S, the component of the fluid velocity normal to S_0 is equal to the corresponding component of the ship velocity U_o, or

$$\phi_n = U_{on} \tag{3}$$

where $n_i = (n_x, n_y, n_z)$ denotes the outward unit normal vector on the boundary. The fluid domain is bounded by the free surface. The free surface elevation is defined by $z = \zeta(x,y)$ and is subject to the the kinematic boundary condition

$$\phi_x\zeta_x + \phi_y\zeta_y - \phi_z = 0 \quad \text{on } z = \zeta(x,y) \tag{4}$$

The vanishing of the pressure on the free surface combined with Bernoulli's equation leads to the dynamic free surface condition

$$\zeta = -\frac{1}{2g}(\nabla\phi\cdot\nabla\phi - U_0^2) \tag{5}$$

where g denotes the gravitational acceleration. Elimination of ζ from (4) and (5) leads to

$$\nabla\phi\cdot\nabla\left[\frac{1}{2}(\nabla\phi)^2\right] + g\phi_z = 0 \quad \text{on } z=\zeta(x,y) \tag{6}$$

Finally, energy considerations require that the velocity potential approaches the uniform onset flow potential and that there be no waves far upstream of the ship, so that waves always travel downstream.

The problem described in equations (1) thru (5) is nonlinear. The free surface boundary conditions(4) and (5) are nonlinear and furthermore should be satisfied on the true free surface ζ which is unknown a priori and should be obtained as a part of the solution. A straightforward linearization makes the problem tractable. This can be easily achieved by defining

$$E = \phi_x^{o2} + \phi_y^{o2} + \phi_z^{o2}$$
$$F = \phi_x\cdot\phi_x^o + \phi_y\cdot\phi_y^o + \phi_z\cdot\phi_z^o$$

and letting $\phi = \phi^o + (\phi - \phi^o)$. Then substituting into (6) and dropping all terms of power higher than one in $(\phi-\phi^o)$ gives:

$$\frac{1}{2}\left\{\left[\phi_x^o\cdot E_x + \phi_y^o\cdot E_y\right] + (\phi-\phi^o)_x\cdot E_x + (\phi-\phi^o)_y\cdot E_y\right\} + \phi_x^o\cdot(F-E)_x + \phi_y^o\cdot(F-E)_y + g\phi_z = 0$$

which simplifies to:

$$\frac{1}{2}\left[\phi_x\cdot E_x + \phi_y\cdot E_y\right] + \phi_x^o\cdot F_x + \phi_y^o\cdot F_y + g\phi_z = \phi_x^o\cdot E_x + \phi_y^o\cdot E_y \tag{7}$$

an equation linear in ϕ.

The singularity distributions yield equations (1), (3), and (7). The inner iteration continues until the approximate solution to (7) satisfies the exact nonlinear free surface condition (6) to a specified tolerance. The outer iteration then updates the wave profiles by (5) and another inner iteration can begin. Details are provided in a later section. Once the singularity strength distributions

are determined, the wave resistance can be computed by

$$R_W = \iint_S p n_x \, ds \tag{8}$$

where S is the wetted ship hull surface and the fluid pressure p is given by the Bernoulli equation

$$p = -\frac{\rho}{2}[(\nabla\phi)^2 - U_o^2] - \rho g z \tag{9}$$

NUMERICAL SCHEME

The method used here is a boundary element method. Body and free surface are discretized into small panels. A simple Rankine source($1/r$) is distributed across each panel as shown in Figure 2. The velocity potential ϕ at a point $p = p(x,y,z)$ induced by a singularity distributed on S is given by

$$\phi = -\frac{1}{4\pi}\iint_S \frac{\sigma}{r} ds \tag{10}$$

Here

$$r = [(\xi - x)2 + (\eta - y)2 + (\zeta - z)2]1/2$$

and the singularity strength is assumed to vary linearly

$$\sigma(\xi,\eta) = \sigma_o + \sigma_\xi \xi + \sigma_\eta \eta, \tag{11}$$

across the panel, and each panel is approximated as a parabolic element

$$\zeta(\xi,\eta) = \zeta_o + \zeta_\xi \xi + \zeta_\eta + \frac{1}{2}\zeta_{\xi\xi}\xi^2 + \zeta_{\xi\eta}\xi\eta + \frac{1}{2}\zeta_{\eta\eta}\eta^2 \tag{12}$$

where (ξ,η,ζ) are orthogonal coordinates local to S.

The boundary value problem formulated above then reduces to a determination of an unknown singularity distribution $\sigma(x,y,z)$ over the boundary surface of the body and the fluid domain The velocity potential ϕ and its derivatives ϕ_x, ϕ_y, and ϕ_z can be expanded in closed form by using a combination of closed form calculations and recursive relationships. The details are fully included in Johnson[7] and Kim et al.[8].

An algebraically generated waterline-fitted coordinate system, independent of the double model streamline coordinate, is used to create the free surface panel network. The convective terms in the free surface condition involves x and y directional derivatives. A number of researchers have experienced the difficulties in convergence with the four point or three point operator when taking numerical derivatives. Kim and Lucas[6] introduced a one parameter family of four point advection methods to enhance convergence for the free surface problem with great success. This method generalizes both the four point and three point schemes which satisfy a quadratic exactly, and allow for an arbitrary amount of upwind dampening.

We have developed a new approach that consistently gives a converged solution to the nonlinear free surface problem. This approach involves inner and outer iterations. The inner iteration is to solve the linearized system of equations (7) that results from eliminating the wave height from the dynamic and kinematic equations within an arbitrary tolerance for a fixed free surface. The free surface as well as the wetted hull surface is updated from the converged solution of the inner iteration and the outer iteration is applied on the new surfaces. The initial iteration starts from a double body solution. The following section discusses the Inner-Outer Method extensively.

THE INNER-OUTER METHOD FOR NONLINEAR SHIP WAVES

We wish to simultaneously solve the kinematic and dynamic boundary conditions (4) and (5) on an unknown free surface $z = \zeta(x,y)$. Our approach is to first consider the combined equation (6) on the current free surface($z=0$ initially). When linearized about an approximate solution ϕ^o, this gives a new velocity potential of the form $\phi = \phi^o + \delta\phi$ which satisfies (7). In practice we use a standard nondimensionalization where g is replaced by $gL/(2U_o^2) = 1/(2F_n^2)$. Here L is the ship length and F_n is the Froude number. We begin with ϕ^o equal to the double body solution on the flat free surface. The complete inner-outer algorithm is as follows:

Outer Loop:

Iterate on the free surface $z = \zeta(x,y)$ until the z correction satisfies the condition $\Delta z_{max} < \varepsilon_z$, where Δz_{max} equals the maximum change in z over all control points (one per free surface panel). There is an option for recomputing the wetted hull surface. When the option is on, the full influence matrix must be computed once for each outer iteration. When it is off (only the original calm water wetted hull surface is used) again the influence matrix must be recomputed, but the part with the influence of the body singularity panels on body control points may be reused.

Inner Loop:

The inner loop consists of two parts. The first part solves (7) and obtains the source strength distribution for both the ship hull surface and the free surface. In the second part, an optimum underrelaxation factor is determined for the next iteration. Since the influence coefficients do not change on a given free surface, it is straightforward to consider as a tentative solution the previous solution plus any value λ times the Newton correction. The residuals can be calculated by changing λ's and an optimum value of the underrelaxation coefficient can then be determined. The details are as follows:

Here we iterate on equation(6) as follow:

- Using the last value of ϕ for ϕ^o, setup the system (7)
- Solve denoting the result by ϕ'
- Underrelaxation step:
  - For λ = 0, 0.1, 0.2,...,1.1, and 1.2, compute λ

$$\phi(\lambda) = \phi^o + \lambda(\phi' - \phi^o)$$

- Compute two measures of accuracy for each $\phi(\lambda)$:
  - Maximum residual error (ε_0) in (6)
  - Root mean square residual error (ε_2) of (6)
  - Interpolate in λ for the best quadratic fit in these two measures, λ_0 and λ_2
  - Select as the tentative λ_{opt}, the average of λ_0 and λ_2
  - Force λ_{opt} to be no less than 0.33 and no more than 1.2
  - Use $\phi(\lambda_{opt})$ as the next underrelaxed solution
    - Compute ε_0 and ε_2 for $\phi(\lambda_{opt})$
    - If ε_0 is large, abort for excessive residual
- Accept $\phi(\lambda_{opt})$
- If (ε_0 < 5.0E-5 and λ_{opt} > 0.97) or ε_0 < 1.E-7, exit inner loop and compute new ζ (from(5))
- Otherwise repeat inner loop

We have found the use of the underrelaxation method in the inner loop to be extremely helpful. It is inexpensive to use and very efficient in developing converged solutions. In practice λ_{opt} starts out small and works up to 1 or higher. After the first few outer iterations, the inner convergence is rapid. Occasionally we have found it helpful to force completion of the inner loop at say 5 iterations.

RESULTS AND DISCUSSION

To facilitate comparisons, the following non-dimensionalization has been made:

$$C_w = \frac{R_w}{1/2\rho U_o^2 S}$$

$$\bar{\zeta} = \frac{\zeta}{U^2/(2g)}$$

Throughout the computations the ship length is always 2.0, x=1.0 at the bow and x=-1.0 at the stern. All the length scales are nondimensionalized based on the half ship length (L/2), unless otherwise specified. The infinite free surface domain is truncated into a finite computational domain. For all computations we used the same free surface domain, i.e., x spans from 2.0 to -2.6 and y=1.2. We used both the Cray X-MP/216 at DTMB and the Cray Y-MP 8/464 at the NCSC.

For each outer loop, the wave elevation at each free surface control point is computed by using (5) and the new free surface panel network nodal points are fitted bilinearly. When the wetted hull option is on, the intersection point between the hull and the new free surface at each x-station is determined first. The total girth length from keel to intersection point is computed and divided according to the original panel spacing along the girth. The new y- and z- coordinates are determined by cubic spline fitting. A high block ship has a long parallel middle body with a flat bottom and wall side. A smooth cubic spline is not appropriate for this kind of cross section. Therefore we divide the ship hull into two sections: lower and upper sections. The lower section usually covers from hull centerline to about bilge keel and does not change during the iteration. The upper section panels are changed for each wetted iteration.

For a high block ship, care in the free surface panelling at the bow region is critical to have an accurate converged solution. For Model B, the tangential line at the bow is vertical leading to numerical difficulties if some care is not taken. For this reason, the free surface panel network near the bow is algebraically fitted to be close to rectangles with aspect ratios near one. From the ship bow and away, the free surface panel spacing grows as a geometric series. We have found that other paneling arrangements with angles away from right angles, and large aspect ratios inhibit convergence for the nonlinear problem.

Table 1 is the computer printed output and shows the sample runs for the Wigley hull at Fn=0.408. Though the solution converged after the fourth outer iteration, we forced the computation until exceeding the time limits to see the stability of this method. Table 1 uses the following legends:

out	: number of outer loop
in	: number of inner loop
Fn	: Froude number
D1	: residual of (6)
D2	: error
D2a	: error.
ur	: optimum underrelaxation factor 1 for next iteration
angle	: source deviation
change	: change in source strength
size	: total sum of source strength
cond	: influence matrix condition number when solve
Cw	: wave making resistance coefficient (x10^3)

Define Res the residual of equation(6) and superscript "i" stand for the i-th outer iteration and "j" for the j-th inner iteration. NB is the total number of body panels, NF the total number of free surface panels, and NT=NB+NF.

$$D1 = \text{Max.}\ \{\text{abs}(\text{Res})_k\}\quad k = 1,2,\ldots\ldots\ldots,\ NF$$

$$D2 = \text{Max.}\ \left\{(\nabla\phi_k^{i+1,j})^2 - (\nabla\phi_k^{i,1})^2\right\}\quad k = 1,2,\ldots,NF$$

$$D2a = \text{Max.}\ \left\{(\nabla\phi_k^{i,j})^2 - (\nabla\phi_k^{i,j-1})^2\right\}\quad k = 1,2,\ldots,NF$$

$$\text{angle} = \cos^{-1}\left(\frac{\sum_{k=1}^{NT}\sigma_k^{i,j}\bullet\sigma_k^{i,j-1}}{\sum_{k=1}^{NT}(\sigma_k^{i,j})^2\bullet\sum_{k=1}^{NT}(\sigma_k^{i,j-1})^2}\right)$$

$$\text{change} = \sum_{k=1}^{NT}\left(\sigma_k^{i,j} - \sigma_k^{i,j-1}\right)^2$$

$$\text{size} = \sum_{k=1}^{NT}\left(\sigma_k^{i,j}\right)^2$$

140 panels (29 stations and 6 waterlines) are used to represent the Wigley hull and 756 panels(63 x12) for the free surface. The computational results show that the solution is virtually converged by the fourth outer loop.

Table 1. Convergent Test with Wigley Hull

OUT	IN	Fn	D1	D2	D2a	UR	ANGLE	CHANGE	SIZE SC	COND	CW
1	1	0.408	0.1E+00	0.8E-01	0.0E+00	0.79			2.7159	312.	2.33
1	2	0.408	0.3E-01	0.1E+00	0.7E-01	0.90	17.48	0.83	2.7602	299.	2.09
1	3	0.408	0.1E-01	0.1E+00	0.2E-01	0.79	7.99	0.41	2.8720	295.	2.09
1	4	0.408	0.3E-02	0.1E+00	0.9E-02	0.83	2.28	0.12	2.8844	291.	2.09
1	5	0.408	0.3E-03	0.1E+00	0.2E-02	1.02	0.40	0.02	2.8847	304.	2.09
1	6	0.408	0.6E-07	0.1E+00	0.1E-04	1.00	0.02	0.00	2.8847	294.	2.09
2	1	0.408	0.1E-01	0.1E-01	0.1E-01	0.33	26.49	1.30	2.7468	295.	2.11
2	2	0.408	0.1E-01	0.2E-01	0.5E-02	0.33	9.07	0.43	2.7541	299.	2.17
2	3	0.408	0.1E-01	0.2E-01	0.4E-02	0.42	2.05	0.10	2.7702	298.	2.18
2	4	0.408	0.5E-02	0.2E-01	0.6E-02	0.96	0.85	0.04	2.7796	297.	2.19
2	5	0.408	0.5E-04	0.2E-01	0.1E-02	1.00	0.39	0.02	2.7841	300.	2.20
3	1	0.408	0.4E-03	0.6E-02	0.6E-02	0.33	4.50	0.23	2.8514	296.	2.15
3	2	0.408	0.4E-03	0.9E-02	0.4E-02	0.33	0.16	0.01	2.8535	300.	2.15
3	3	0.408	0.4E-03	0.1E-01	0.3E-02	0.38	0.07	0.00	2.8545	300.	2.15
3	4	0.408	0.2E-03	0.2E-01	0.4E-02	0.79	0.04	0.00	2.8550	290.	2.15
3	5	0.408	0.2E-05	0.2E-01	0.1E-02	1.04	0.02	0.00	2.8554	292.	2.15
4	1	0.408	0.1E-02	0.8E-02	0.8E-02	0.33	14.52	0.75	3.0001	282.	2.47
4	2	0.408	0.1E-02	0.1E-01	0.6E-02	0.33	0.80	0.04	3.0058	285.	2.47
4	3	0.408	0.1E-02	0.2E-01	0.4E-02	0.34	0.32	0.02	3.0093	301.	2.48
4	4	0.408	0.8E-03	0.2E-01	0.5E-02	0.64	0.14	0.01	3.0112	288.	2.48
4	5	0.408	0.4E-04	0.3E-01	0.3E-02	1.20	0.09	0.01	3.0126	289.	2.48
5	1	0.408	0.2E-03	0.2E-02	0.2E-02	0.51	2.13	0.11	3.0017	291.	2.44
5	2	0.408	0.7E-04	0.3E-02	0.1E-02	0.75	0.03	0.00	3.0019	290.	2.44
5	3	0.408	0.4E-05	0.3E-02	0.4E-03	1.07	0.01	0.00	3.0020	291.	2.44
6	1	0.408	0.3E-04	0.1E-02	0.1E-02	0.54	0.64	0.03	2.9938	291.	2.43
6	2	0.408	0.2E-04	0.2E-02	0.5E-03	0.65	0.00	0.00	2.9939	291.	2.43
6	3	0.408	0.3E-05	0.2E-02	0.3E-03	1.08	0.00	0.00	2.9939	292.	2.43
7	1	0.408	0.2E-05	0.3E-03	0.3E-03	0.99	0.11	0.01	2.9934	291.	2.42
8	1	0.408	0.2E-06	0.7E-04	0.7E-04	0.99	0.02	0.00	2.9929	291.	2.42
9	1	0.408	0.1E-07	0.2E-04	0.2E-04	1.00	0.01	0.00	2.9929	291.	2.42
10	1	0.408	0.5E-09	0.4E-05	0.4E-05	1.00	0.00	0.00	2.9929	291.	2.42
11	1	0.408	0.3E-10	0.8E-06	0.8E-06	1.00	0.00	0.00	2.9929	291.	2.42

After the fourth outer loop, changes in the wave profiles and wave making resistance are hardly noticeable. The reported[9] measured wave-making resistance coefficient for F_n=0.408 ranges from 0.24 to 0.31. The results indicates that the proposed numerical algorithm is extremely stable. Figure 3 shows the wave profile comparisons between the experiment, linearized free surface computation, and nonlinear free surface computation. The nonlinear solver significantly improves its value except for a noticeable underestimate near the bow. It is not clear why such a nicely converged solution still shows noticeable difference, especially at bow where the viscosity seems not to play any role at all.

Series60, Block 0.80

Todd[10] conducted a methodical series of model experiments with Series 60 and the results were systematically and extensively tabulated and plotted. The experimental data are available in terms of the total resistance coefficients. We computed the total resistance coefficients for this model and compared the computed results with the experimental data. For this high block ship the parallel middle body extends for more than 50 percent of the hull length and at the bow half the entrance angle is 43 degrees. The experiments covered Froude numbers between 0.13 and 0.25. Following Froude's hypothesis, the total resistance coefficient consists of the frictional resistance coefficient C_F and the residual resistance coefficient C_R. C_F is estimated from the ITTC 1957 friction line for a 2D flat plate. C_R includes the wave-making resistance coefficient C_W and the form drag coefficient C_{FD}. C_{FD} may be considered a correction term: the deviation of the hull surface from a flat plate. The following equation is used:

$$C_{FD} = [\ (1+\alpha\ K_p)S/S_o - 1]\ C_F.$$

K_p is the partial form factor introduced by Dawson[11]:

$$K_p = \left[\frac{\iint_S \left(\frac{U}{U_o}\right)^{3.8046} ds}{\iint_S ds} \right]^{0.8559} - 1$$

The parameter α assumes a value of 2.0. The correlation allowance C_A is assumed to be 0.5×10^{-3}. S is the actual wetted surface computed during the iterations and S_o the calm water wetted surface area.

260 panels (26x10) are used to approximate the hull surface and 732 panels (61x12) for the truncated free surface domain. Table 2 summarizes the computed results for six Froude numbers 0.15, 0.17, 0.18, 0.20, 0.25, and 0.30. C_{FD} shows almost a constant value. The wave making resistance coefficient becomes significant when the Froude number exceeds 0.2. For Froude numbers 0.25 and higher the C_W dominants in C_T.

Table 2. Resistance Computation
Series60, C_B = 0.80

($\times 10^3$)

Fn	Computation					Exp.
	C_W	C_F	C_{FD}	C_A	C_T	C_T
0.15	0.40	1.658	0.432	0.500	2.990	3.016
0.17	0.695	1.632	0.435	0.500	3.262	3.108
0.18	1.310	1.620	0.437	0.500	3.867	3.267
0.20	2.210	1.598	0.443	0.500	4.751	3.823
0.25	5.981	1.554	0.450	0.500	8.485	7.835
0.30	12.661	1.519	0.463	0.500	15.143	N/A

These results are preliminary for wave resistance and further work is needed to integrate the wetted logic with the outer iteration and/or to refine the pressure integration. Here our approach has been to rewet the hull on each outer iteration. After the wave amplitude z change was reduced below 1.0E-5 in 9 to 12 outer iterations, C_W still oscillated by 1-3 %, and appears not to be reliable. The wave on hull results, in contrast, converged readily. In Figure 4, the total resistance coefficients are plotted for both experiment and computation. The computation overpredicted the resistance except for low Froude number. Figure 5 depicts the final wetted surface after the solution converged and over which the pressure is integrated to obtain the wave-making resistance.

Model B

Model B is a mathematical hull that Maruo and Ogiwara [12] used when they studied the nonlinear free surface problem. They measured the resistance and also the wave elevations, in particular at the bow and stern of the ship. This happens to be only available measured wave data for high block ships. As shown in Figure 6, the hull shape is unique having a blunt elliptic bow waterline and elliptic frame lines. Also it has a long parallel middle body and a stern with a parabolic shape. The body is divided into two parts; lower and upper part. The upper part covers from the free surface to the half draft and is wallsided throughout the hull length. The block coefficient C_B is about 0.75 and the wetted surface area coefficient is 0.80. 336 panels (28x12), 168 for the lower hull and 168 for the upper hull, are used to represent the hull surface and 756 panels (63x12) for the truncated free surface domain. Experiments were conducted at a Froude number range of 0.14 to 0.25. Wave profiles were measured for three Froude numbers: 0.183, 0.209, and 0.235.

In Figure 7, the measured wave profiles are compared with the computed ones. At the fore body the agreements are excellent for all three Froude numbers. The maximum nondimensionalized wave amplitude is over 0.9. This indicates that at the nose the flow velocity approaches zero since the wave amplitude is 1.0 at the stagnation point. At the aft body, the differences are significant. At the stern the computed wave profiles show the trend growing up continuously while the measured ones seem to level off for all three speeds. For a lower block or fine ship, such as Wigley hull or Series 60, CB=0.60, the wave profile at the stern usually has the same trend as the computation. The differences observed for Model B may be attributed to the viscosity neglected in the computation. We anticipate that the role of viscosity for high block ship and hence the resulting turbulent flow at the stern is more significant than for lower block ships. Figure 8 shows the initial wetted body and the final wetted surface after the solution converged. The preliminary computation of wave-making resistance is obtained by integrating the pressure over the actual wetted surface and the results are compared in Figure 9.

CONCLUSIONS

1. A new approach has been proposed for the nonlinear free surface problem: in addition to iterating on the free surface height, use an inner iteration to first iterate to near exactness over the nonlinear algebraic systems generated by the current free surface. Combined with the one parameter family of advection schemes (Q_{mul} method) of Kim and Lucas[6], this approach has been shown to converge robustly over a wide range of hull forms and speeds. Results for the wave height on hull are excellent, but valid wave resistance calculations require a new wetted hull logic.

2. The inner-outer method is inexpensive to apply as the new part, the inner iteration, consists primarily of cheap matrix solves. We have not found it necessary to compute the more expensive z-partial derivative terms previously favored by many researchers, although they possibly could again be required in future situations. In any case, due to the simplicity of implementing the inner-outer method, it can readily be applied to other outer methods including ones with z-partials.

3. Preliminary work has been completed on adding a wetted hull logic to the above scheme. At any stage of the outer iteration, the ship panels can be redistributed over the currently wetted hull area. This process has been found to be quite helpful, but we are still exploring when in the outer iteration process to rewet the hull. One possibility is to rewet once after 2 or 3 outer iterations and then again after this process converges in z to a specified tolerance. We will report at a later time the change introduced by wetting, in order to determine its relative significance. Our current results show that it plays a more important role for wave resistance then for wave heights.

4. Computer runs were made for two high block ships: Model B and Series 60, Block 0.80. For such high block ships with large entrance angles, especial care is required for the free surface paneling near the bow. In addition a run was made for the Wigley hull at Fn=.408. All runs converged readily in wave heights.

5. The highest value required for Q_{mul} was 5. This gives a partial answer (negative) to some previous concern that for full hull forms the required values of Q_{mul} might become unduly large.

6. Comparison with model experiments of Series60, Block 0.80 were made. The wave on hull converged readily, but C_W still oscillated, and appears not to be reliable. The agreement is poor except for low Froude numbers.

7. Comparison with model experiments of Model B for both wave resistance and wave profiles were made. Experimental data was available for Froude numbers 0.183, 0.209 and 0.235 limited to the fore and aft regions. In the fore body region the wave profiles showed an excellent fit at all three speeds. In the aft region the results were fair to good, but it is now an open question as to why they were not better. Here the results were best at the middle speed, and in general worse near the stern.

8. A run of the Wigley hull with Fn=0.408 was made. The wave on hull pattern is the best ever reported, but shows a noticeable underestimate near the bow. While this effect is common for such codes, an explanation of this would be of some interest, as several possibilities suggest themselves.

9. As noted in our previous paper[6], nonlinear free surface programs add considerably to the accuracy at little total cost. As they become increasingly successful and trusted, interest may well shift to those remaining areas where they do not agree well with experiment, in an effort to understand the cause/better solution. A related question is the timing and payoff in going to codes with more physics.

ACKNOWLEDGMENTS

The authors express their gratitude to Dr. Wen-Chin Lin and Dr. Michael Wilson of DTMB for their valuable suggestions and encouragement during the course of this work. The second author was supported in part by an IPA grant from DTRC and a grant for supercomputer time by the North Carolina Supercomputing Center. The authors also thank Dr. Ogiwara for his kind help providing us Model B offset and valuable experimental data.

REFERENCES

1. Gadd, G.E., "A Method of Computing the Flow and Surface Wave Pattern around Full Form," Trans. Royal Asst. Naval Archit., Vol. 113, 1976

2. Dawson, C.W., "A Practical Computer Method for Solving Ship-Wave Problems," Proceedings of the 2nd International Conference on Numerical Ship Hydrodynamics, Berkeley, Calif., USA, 1977.

3. Xia, F., "Calculation of Potential Flow with a Free Surface,"(amended version), SSPA Rpt. No. 2912-1, SSPA Maritime Research and Consulting, Goteborg, Sweden, 1984.

4. Ni, S.-Y., "Higher Order Panel Methods for Potential Flows with Linear or Non-linear Free Surface Boundary Condition," Chalmers University of Technology, Goteborg, Sweden, 1987.

5. Kim, K.J., "Ship Flow Calculations and Resistance Minimization," Chalmers University of Technology, Goteborg, Sweden, 1989.

6. Kim, Y.H. and T.R. Lucas, "Nonlinear Ship Waves," Proceedings of the 18th Symposium on Naval Hydrodynamics, Univ. of Michigan, Ann Arbor, USA, 1990

7. Johnson, F.T., "A General Panel Method for the Analysis and Design of Arbitrary Configuration in Incompressible Flow," NASA Contract Rpt 3079, Boeing Comm. Airplane Co., Seattle, USA, 1980.

8. Kim, Y.H., S.H. Kim, and T.R. Lucas, "Advanced Panel Method for Ship Wave Inviscid Flow Theory," DTRC-89/029, 1989.

9. Bai, K.J. and J.H. McCarthy, Proceedings of the Workshop on Ship Wave-Resistance Computations, DTNSRDC, Bethesda, Md, USA, 1979

10. Todd, F.H., "Series60, Methodical Experiments with Models of Single-Screw Merchant Ships,", DTMB Report 1712, July 1963.

11. Dawson, C.W., "Calculations with the XYZ Free Surface Program for Five Ship Models," Proceedings of the Workshop on Ship Wave Resistance Computations, DTNSRDC, Bethesda, Md USA, Nov., 1979

12. Maruo, H. and S. Ogiwara, "A Method of Computation for Steady Ship-Wave with Non-linear Free Surface Conditions," Proceedings of the Fourth International Conf. on Numerical Ship Hydrodynamics, Washington, D.C., USA, Sept., 1985

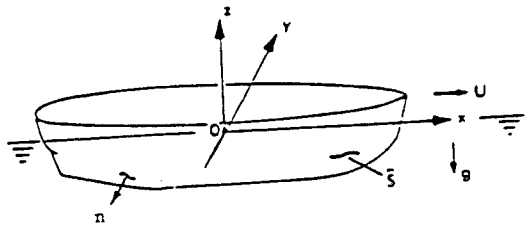

Fig. 1. Coordinate system.

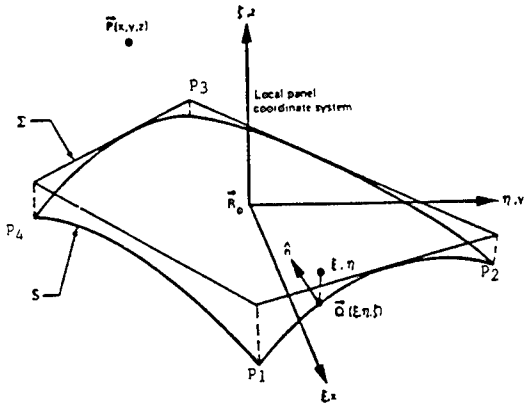

Fig. 2. Field point/panel geometry.

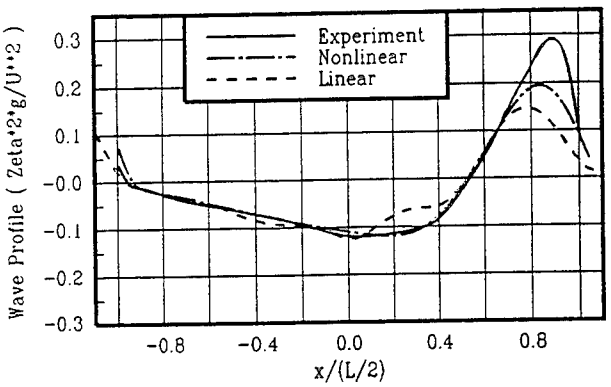

Figure 3. Wave profile at Hull Surface for Wigley Hull at Fn=0.408

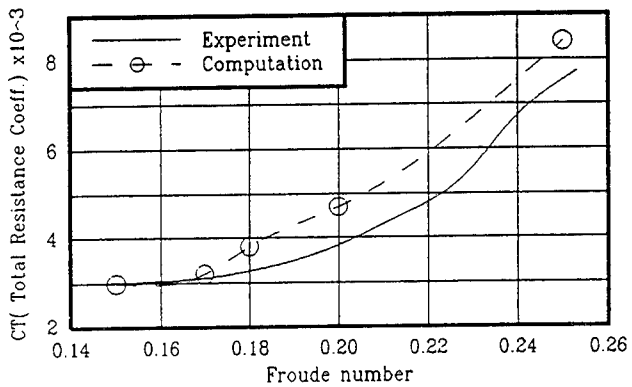

Figure 4. Total Resistance Coefficient Comparison Series60, CB=0.80

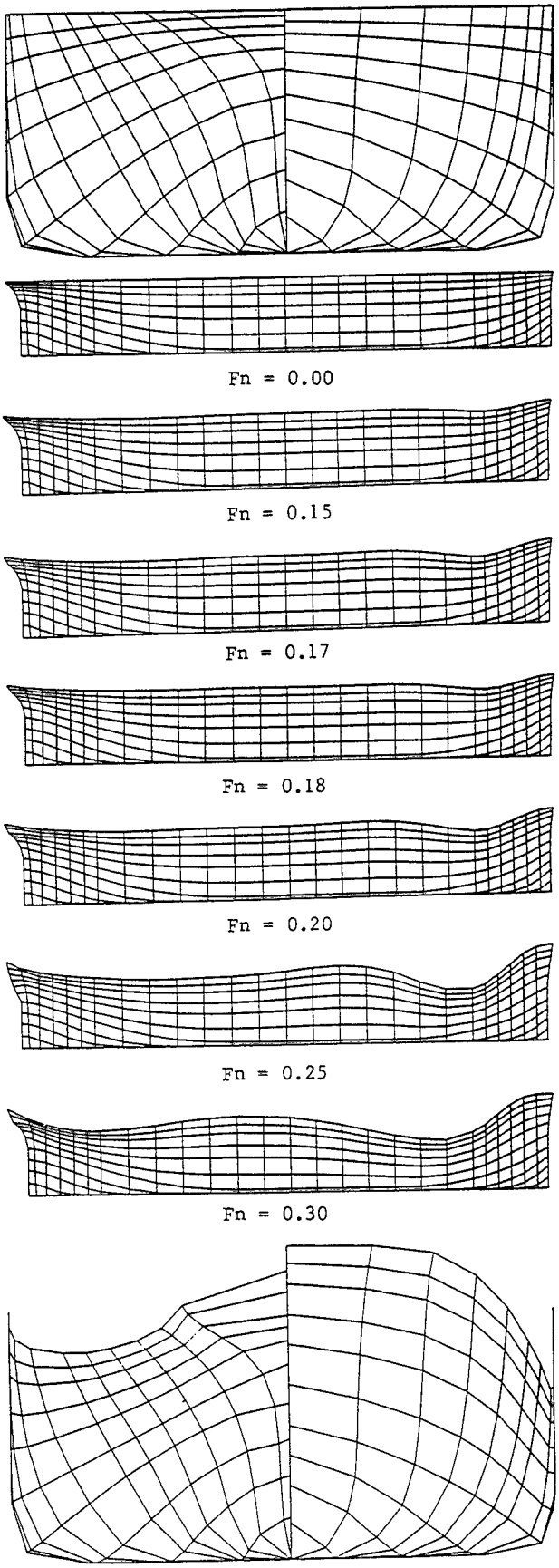

Figure 5 The Wetted Surface of Series 60 after Converged Solution

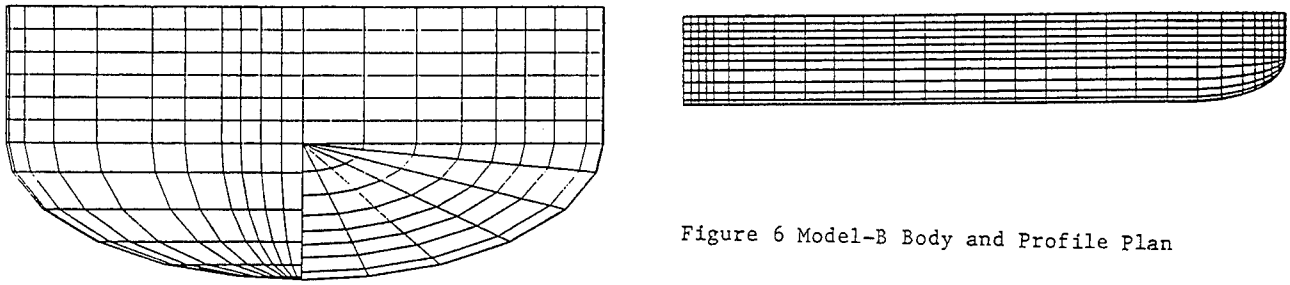

Figure 6 Model-B Body and Profile Plan

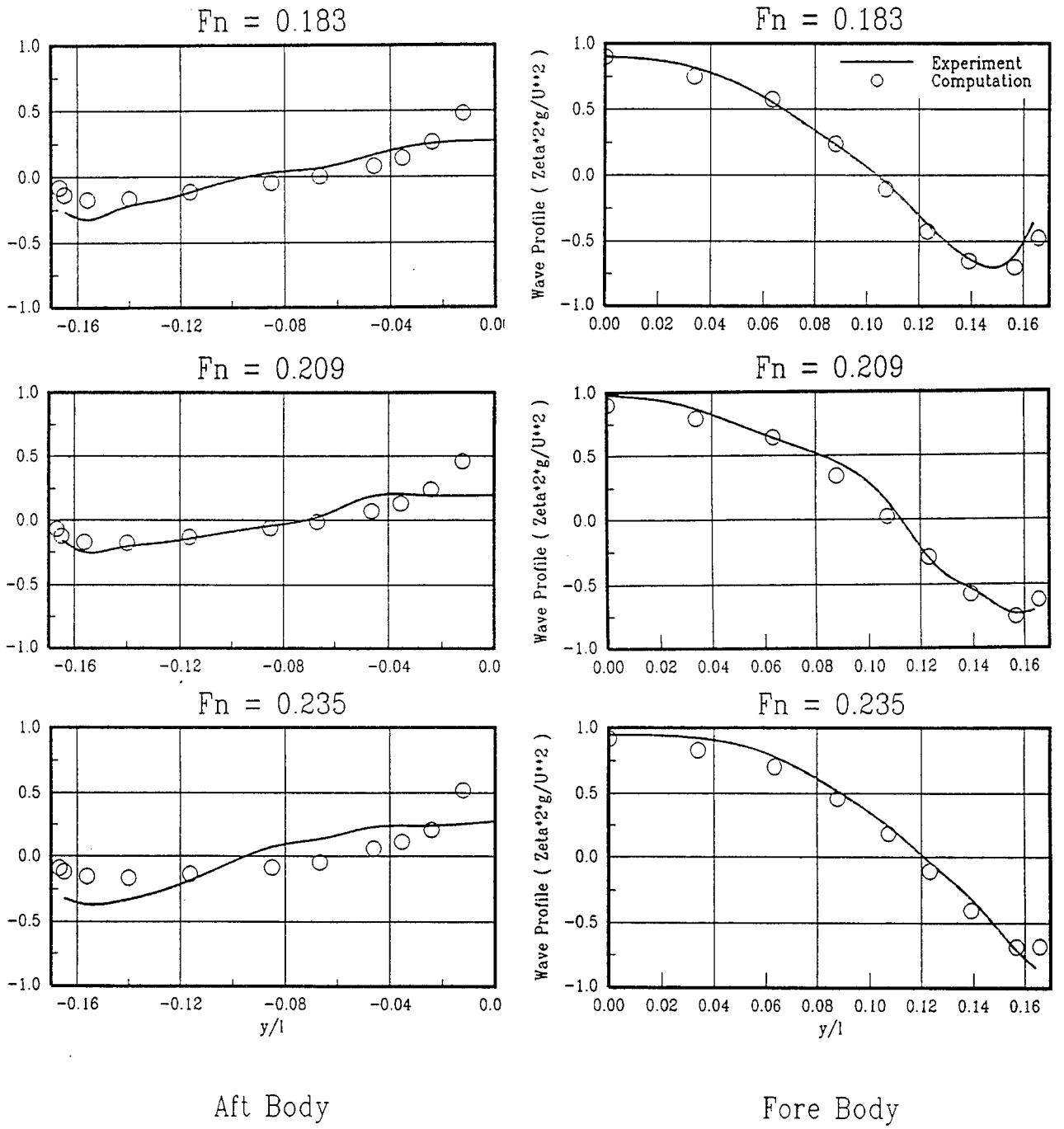

Figure 7 Wave Profile Comparison for Model-B

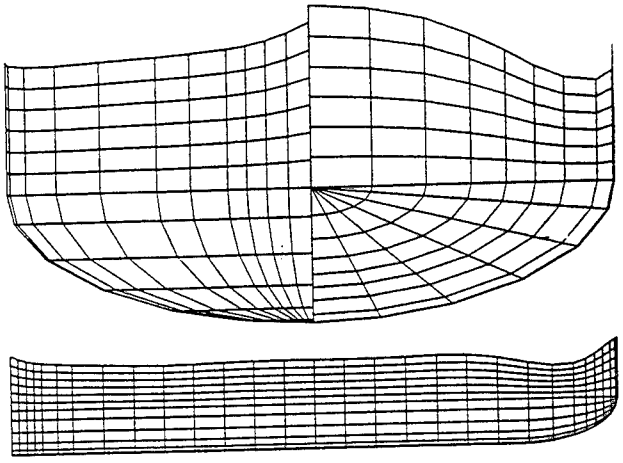

Fn = 0.183

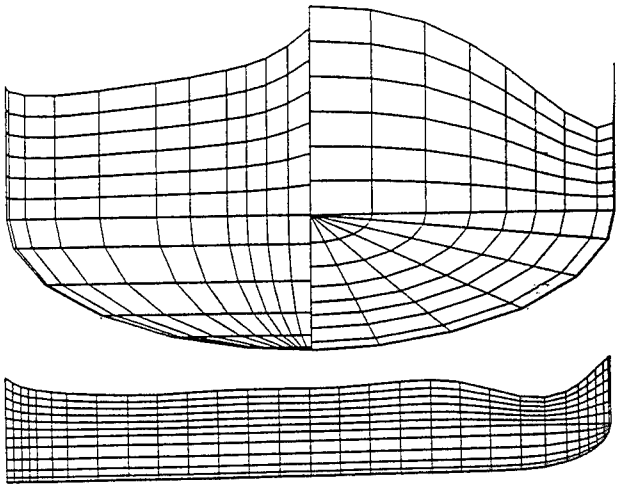

Fn = 0.209

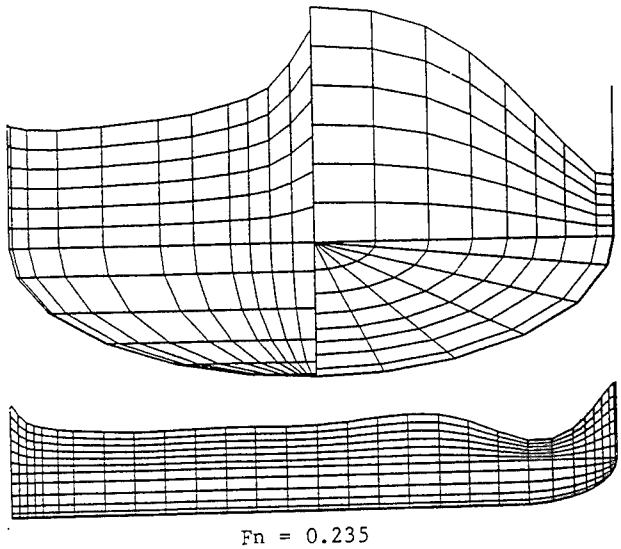

Fn = 0.235

Figure 8 The Wetted Surface of Model-B after Converged Solution

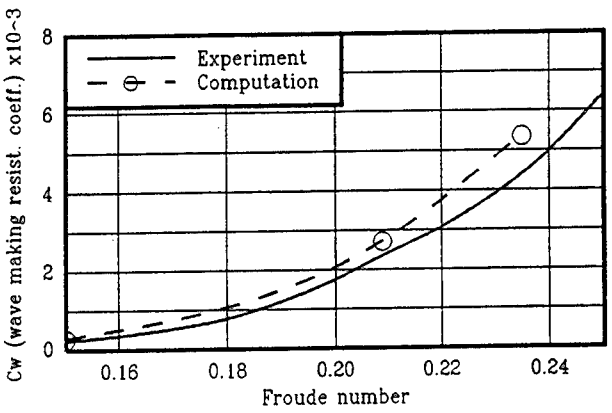

Figure 9. Wave-Making Resistance Coeff. Comparison for Model B

DISCUSSION

H. Raven
Maritime Research Institute Netherlands
The Netherlands

I noticed from your paper that you still use the "Q_{mul}" parameter to get convergence. This method introduces artificial wave damping, which affects the final result. Is not it possible to reduce Q_{mul} to zero in the last iteration, such that the final solution is not unduly damped?

I think the panel density on the free surface is insufficient for the lower Froude numbers in your calculations. E.g., for the Series 6 hull at Fr = 0.15, there are only 4 panels, per wavelength, for the longest waves in the problem! It is useless to apply a *nonlinear* method with such a lack of resolution, since the nonlinearities mainly give rise to higher harmonics which are now not resolved. I suggest you use at least e.g. 12 (higher order) panels per fundamental wave length.

AUTHORS' REPLY

We would like to express our thanks to Dr. Raven for his interest in our paper. When we were developing Q_{mul} parameter to generalize an advection method to enhance convergence, one concern was how to determine Q_{mul} parameter efficiently and effectively. We considered several approaches including one similar to determine an optimum under-relaxation factor for the next iteration by Newton correction reported in this paper. Q_{mul} controls the magnitude of damping, and if Q_{mul} increases the wave amplitude attenuates accordingly along the downstream. If someone is interested in the flow characteristics for downstream, this approach may not be appropriate to apply.

When we developed and studied the inner and outer iteration scheme, several approaches were considered regarding setting Q_{mul}. Two cases of Q_{mul} = 0.0 are tested: (1) Q_{mul} was set to zero at the last iteration of every inner loop and (2) Q_{mul} = 0.0 at the last iteration. For both cases, if solution converged, this adjustment showed improvement in wave amplitude attenuation along the downstream, but the difference in wave-making resistances which is obtained by integrating pressure on the wetted hull surface was insignificant. To obtain converged solution for high block coefficient ship, sometimes Q_{mul} is required to have large value, for example 7, and the generated waves are unrealistically damped. Currently, we are developing a new finite difference operator in hopes of eliminating both numerical damping and dispersion problems. We agree with you regarding number of panels per wavelength.

Session II

Nonlinear Ship Motions

Experimental Determination of Nonlinearities in Vertical Plane Ship Motions

J. O'Dea (David Taylor Model Basin, USA), E. Powers (University of Texas at Austin, USA), J. Zselecsky (U.S. Naval Academy, USA)

ABSTRACT

Experiments have been conducted in regular and random waves of varying severity (steepness) on a model of the standard ITTC hull form. Variation of the heave and pitch transfer functions, as wave steepness was varied, indicate a nonlinear motion behavior for this hull. The response has been modelled as a Volterra functional expansion carried out to include quadratic and cubic terms. The higher order kernels of the expansion have been determined from the regular wave data and have been confirmed by polyspectral analysis of random wave data. The results show how the usual assumption of linearity of response can lead to incorrect predictions, and also show the effect of non-Gaussian random behavior in both the input (waves) and the responses.

NOMENCLATURE

a	Amplitude of first harmonic of waves
g	gravitational constant
$h_j(t_1,..,t_n)$	Volterra response function, jth.
$H_j(\omega_1,..,\omega_n)$	jth order frequency response function.
k	wave number, k= $\frac{2\pi}{\lambda}$
K(m)	Kernel of orthogonal model
Lpp	Ship length between perpendiculars
$\ddot{s}$	Bow acceleration
$S(\omega)$	Spectral density
x(t)	Time history of system input (excitation)
$X(\omega)$	Fourier transform of x(t)
y(t)	Time history of system response
$Y(\omega)$	Fourier transform of y(t)
z	Heave response
Z(m)	orthogonal input vector
Γ(m)	Coherence spectrum
Π_x	Normalized bispectrum
θ	Pitch response
λ	Wave length
σ	Non-dimensional wave frequency, $\sigma = \omega\sqrt{\frac{Lpp}{g}}$
σ_e	Non-dimensional encounter frequency, $\sigma = \omega_e\sqrt{\frac{Lpp}{g}}$
ω	Wave frequency
ω_e	Encounter frequency

INTRODUCTION

For many years the primary analytical tool for analyzing and measuring ship and platform response to wave has been linear system theory, coupled with a narrow band Gaussian model for ocean waves. This approach has been relatively successful in part because typical vehicles are at least quasi-linear in their response, and random waves are at least quasi-Gaussian. The approach is also followed because it greatly simplifies the analysis and allows the use of very general results applicable to linear systems and Gaussian random processes. However, it is also well known that certain types of response to waves are not adequately described by a linear model. In particular, rolling is known to have nonlinear viscous damping and a nonlinear restoring curve, and lateral plane motions are known to be affected by quadratic interactions between the vehicle and waves. In contrast to the generalized techniques used for linear systems, specialized nonlinear methods and approximations have been used to analyze these nonlinear cases.

In the case of rolling motion, the analysis is typically simplified by assuming the dynamics can be modelled as a single degree of freedom ordinary differential equation with constant coefficients and discrete nonlinear terms. It is also usually assumed that the wave excitation is Gaussian and that the roll response is narrow band. Under such assumptions, the statistical properties of the nonlinear motion can be estimated(1). In the case of lateral plane loads, it has long been recognized that there exists a mean value of horizontal force (lateral drift force or axial added resistance) which is quadratic with respect to wave amplitude, and that there is also a quadratic low-frequency component caused by difference frequency interactions between pairs of harmonic components. The mean value of longitudinal force is important in the calculation of total power requirement for ships, while the low frequency drift force can cause significant motions for moored platforms, since the mooring typically results in an underdamped lateral response with a very low natural frequency. Recently, attention has also been directed at quadratic sum and double frequency components which are important in the response of tension leg platforms.

For the purpose of calculating responses to random waves, it is well known that this quadratic behavior can be described as a two-term Volterra functional series(2).

In fact, the linear and quadratic behavior of vehicles in waves are simply the first two terms of a series expansion which, in principle, can be carried to arbitrary order. At each level of such an expansion, the hydrodynamic problem is to determine the Volterra kernels which describe the response characteristics of a particular geometry, while the statistical problem is to use these kernels, together with a proper description of the seaway, to predict the statistical nature of the response. In practice, the first two terms of the expansion have been applied extensively, while there have been relatively few studies covering the cubic term. The statistical aspects of system response up to cubic terms has been studied by Dalzell(3, 4, 5), while the third-order hydrodynamic forces have been calculated for certain simple geometries(6, 7). Nevertheless, it is important to remember that, in terms of harmonic content of nonlinear response, the quadratic term of a Volterra expansion typically accounts for energy outside the frequency band of the waves. That is, for a sinusoidal excitation, the quadratic term accounts for a mean value and a second harmonic, but does not account for any nonlinearity in the first harmonic response. Similarly, for random waves of moderate bandwidth, the quadratic effect accounts for a mean value plus slowly varying (below wave frequency band) and high frequency (above wave frequency band) harmonic content. If there is nonlinear behavior which occurs at the excitation frequency, either a series expansion must be carried to at least cubic order, or a fully nonlinear approach without any series approximation must be used.

The motivation for the present series of experiments was provided by the observation that, in a series of cooperative seakeeping experiments carried out for the International Towing Tank Conference (ITTC) on a standard ITTC hull form designated the S175 hull, there was a rather large scatter in some of the transfer function results for heave and pitch motions in head seas(8). On closer examination, it appeared that this effect was not simply random scatter, but seemed to be a function of wave steepness(9). If this was in fact a variation of the ratio of first harmonic response to first harmonic wave excitation (the ratio which is usually assumed to define the linear transfer function), then a Volterra expansion carried to a least the first odd nonlinear power, i.e. cubic, would be required to describe the wave-motion response system. In order to confirm this, a systematic series of experiments was carried out in 1990 and 1991 at the Hydromechanics Laboratory of the U. S. Naval Academy. The experiments included both regular and random wave conditions, with systematic variation of wave steepness. Analysis of the results included Fourier analysis up to third harmonics for the regular wave experiments, and higher order polyspectral analysis of the random wave experiments as described below.

The experimental determination of the frequency response functions (FRF) from experimental data is a subtle and complex task. For example, to determine cubic frequency response functions (CFRF) requires working in a three-dimensional frequency space. Furthermore, when analyzing model test data one needs to be sensitive to the fact that the recorded time series data contains information not only on the nonlinear wave-ship interaction but also on other "prior" nonlinearities that may have occurred prior to the waves interacting with the ship. These latter nonlinearities may arise because of nonlinear wave interactions or nonlinearities associated with the wavemaker. Prior nonlinearities manifest themselves as a departure from Gaussian random excitation. Unfortunately, the vast majority of nonlinear system modeling techniques in the literature assume Gaussian excitation, primarily because of the associated mathematical simplification, not because it is necessarily a good physical assumption. If one erroneously assumes Gaussian wave excitation, when in fact it is not, one will develop not only incorrect nonlinear models but also incorrect predictions based on these models. The reason for this is the fact that the resulting model includes both the effects of the nonlinear wave-ship interaction and the prior nonlinearities. For the towing tank data used in this investigation, the random wave excitation is not sufficiently Gaussian to make the simplifying Gaussian assumption. (This departure from Gaussianity is discussed later in this paper.) With nonGaussian random sea wave excitation, specially developed algorithms experimentally determine Volterra kernels up to third (i.e. cubic) order. These nonlinear models do an excellent job of predicting the power spectra of heave and pitch motions, for example, due to random seas. In other words, for a given input they predict the correct overall response. power spectrum. However, the price paid for the generality of nonGaussian wave excitation is that the resulting models are nonorthogonal. As will be demonstrated later in this paper, the lack of orthogonality makes it difficult to decompose the total ship response into its constituent linear, quadratic, and cubic components. The recently developed new approach(10), discussed further in the next section, leads to an orthogonal model which is also valid for nonGaussian excitation. It allows the clean decomposition the ship response, such as heave and pitch, into its linear, quadratic, and cubic components.

Recently, with the availability of more powerful computers, there has been a trend toward direct solution of the fully nonlinear equations in the time domain(11, 12) using computational fluid dynamics (CFD). At the present time, these CFD codes are typically being used to predict response to periodic waves of large amplitude in order to emphasize nonlinear behavior, including higher harmonic content. It is hoped that the regular wave results presented below can be used as a data base for validating these codes. Ultimately, if such codes are validated, it should be possible to carry out nonlinear simulations in random waves. However, even in such a case, it will be necessary to propose a system model for statistical analysis; otherwise very large samples will be required in order to establish confidence in statistical measures (especially for extreme values). Therefore, for both experimental data and for large amplitude time domain CFD predictions, it seems reasonable to model the behavior with a three-term Volterra series, which at least has the potential to describe observed nonlinear behavior. It remains to be seen whether higher order terms (beyond cubic) will be required to closely approximate the fully nonlinear results.

NONLINEAR SYSTEM MODELLING

The objective of this section is to overview the nonlinear system identification methodologies utilized to model and quantify vertical plane nonlinear ship motions. The identification, or modelling, of nonlinear systems from excitation and response time series data is a state-of-the-art research area in its own right. For

example, the quantification of vertical plane motion of the S175 hull used in our experimental studies is particularly challenging since the random wave excitation is nonGaussian and the dominant nonlinearities are cubic. Although our initial nonlinear systems model took into account the fact that the random sea wave excitation was nonGaussian, the model was nonorthogonal. As a result, when using such models to estimate the response power spectrum of the ship various "interference" terms appear in the expression for the response. The presence of such terms make it very difficult, and sometimes virtually impossible, to decompose the ship's response its constituent linear, quadratic, and cubic components. This led to our most recent nonlinear system modelling advance, namely, an orthogonal model valid for non-Gaussian excitation. Since the model is orthogonal, the interference terms are eliminated, and we can cleanly decompose the ship response into its linear, quadratic, and cubic components. All of these points are described in greater detail in subsequent sections.

Volterra Functional Series

The classical approach to seakeeping is essentially linear in nature in that the response of ships in a seaway are modelled in terms of a linear frequency response function. Knowledge of such a transfer function then enables one to predict the linear response of a ship to a variety of seawave excitations. St. Denis and Pierson(13) pioneered this linear approach for random seas. Later Dalzell(5) suggested using a Volterra series to extend the linear approach of St. Denis and Pierson to nonlinear seakeeping. In fact, the Volterra series has been and continues to be used to model nonlinear systems in many areas of science and engineering(14). For this reason, we briefly overview the Volterra approach in this section.

Mathematically, the Volterra series representation of a cubically nonlinear system is given by

$$\begin{aligned} y(t) = & \int h_1(t_1)x(t-t_1)dt_1 \\ & + \iint h_2(t_1,t_2)x(t-t_1)x(t-t_2)dt_1dt_2 \\ & + \iiint h_3(t_1,t_2,t_3)x(t-t_1)x(t-t_2)x(t-t_3)dt_1dt_2dt_3 \\ & + e(t) \end{aligned} \tag{1}$$

where $x(t)$ and $y(t)$ represent the observed wave excitation and ship response, respectively. Since no model is absolutely perfect $e(t)$ denotes the error associated with model. The quantities $h_1(t)$, $h_2(t_1,t_2)$, $h_3(t_1,t_2,t_3)$ denote the linear, quadratic, and cubic Volterra kernels, respectively. There are several observations to be made with regard to the RHS of Eq. (1). First note that the first, second, and third terms are linearly, quadratically, and cubically dependent on the wave excitation $x(t)$. Second, note that all the integrals are convolution integrals. For example, the first term on the RHS is the familiar input-output relation for a linear system, namely, the output of a linear system is equal to the input $x(t)$ convolved with the impulse response $h_1(t)$. The second and third terms are generalizations of the linear result and, thus, lead to the interpretation of $h_2(t_1,t_2)$ and $h_3(t_1,t_2,t_3)$ as quadratic and cubic "impulse responses" respectively. The range of these impulse responses in one-, two- and three-dimensional temporal space represent the memory time of the linear, quadratic, and cubic components of the physical system.

If we Fourier transform Eq. (1) term by term, we arrive at the following expression

$$\begin{aligned} Y(\omega) = & H_1(\omega)X(\omega) \\ & + \frac{1}{2\pi}\iint H_2(\omega_1,\omega_2)X(\omega_1)X(\omega_2)\delta(\omega-\omega_1-\omega_2)d\omega_1d\omega_2 \\ & + \frac{1}{(2\pi)^2}\iiint H_3(\omega_1,\omega_2,\omega_3)X(\omega_1)X(\omega_2)X(\omega_3) \\ & \cdot \delta(\omega-\omega_1-\omega_2-\omega_3)d\omega_1d\omega_2d\omega_3 + \epsilon(\omega) \end{aligned} \tag{2}$$

where $X(\omega)$, $Y(\omega)$ and $\epsilon(\omega)$ denote the Fourier transforms of $x(t)$, $y(t)$, and $e(t)$ respectively. Furthermore, $H_1(\omega)$, $H_2(\omega_1,\omega_2)$, and $H_3(\omega_1,\omega_2,\omega_3)$ are referred to as the linear, quadratic, and cubic frequency response functions (LFRF, QFRF, and CFRF) and correspond to the one-, two-, and three-dimen-sional Fourier transforms of $h_1(t_1)$, $h_2(t_1,t_2)$, and $h_3(t_1,t_2,t_3)$. The linear, quadratic, and cubic frequency domain Volterra kernels represent the linear, quadratic, and cubic features of the physical system. Referring to Eq. (2) we observe that the response predicted by the Volterra model at frequency ω is given by the sum of the following terms. The first is the excitation $X(\omega)$ times the LFRF $H_1(\omega)$ evaluated at frequency ω. If the actual physical system is quadratically nonlinear, then pairs of frequencies present in the random seawave excitation will mix to form sum and difference frequencies in the response. This phenomenon is modelled by the second term on the RHS of Eq. (2). The double integral and the delta function indicate that we must consider all frequency pairs in the input wave spectrum that add or subtract to the response frequency ω. The contribution of any given input pair (ω_1,ω_2) to the response is given by the product of their complex amplitudes $X(\omega_1)X(\omega_2)$ times the QFRF $H_2(\omega_1,\omega_2)$ evaluated at (ω_1, ω_2). Thus the QFRF is a direct quantitative measure of the "strength" of the quadratic nature of the physical system being modelled. A similar interpretation holds for the third term, except for the fact that if the physical system is cubically nonlinear, triplets of frequencies in the excitation will mix (i.e., add and/or subtract) to contribute to the model output response at frequency ω. The CFRF is a measure of the "strength" of these cubic interactions. In particular, if the input is at a single frequency ω, then one component of the cubic kernel, $H_3(\omega,\omega,-\omega)$, will result in cubic response at the same frequency as the input.

On the basis of the preceeding discussion we note that one significant advantage of the Volterra series model is that it provides a logical extension of linear system concepts (namely, the frequency response function) to higher order. In this sense the Volterra model provides a logical framework within which to systematically analyze and interpret nonlinear seakeeping experimental data. Nevertheless, since the Volterra series may be interpreted as a Taylor series with memory, it is subjected to the same limitations of a series model. For example, due to the complexity of working in higher-order frequency space it is not practical, at this point in time, to consider models of order greater than three. Such a truncation of the series limits us to considering weakly nonlinear systems. Fortunately, however, many physical systems fall into this category.

Frequency Response Functions

The ability to experimentally estimate the linear, quadratic, and cubic frequency response functions (i.e. the frequency-domain Volterra kernels) is important for several reasons.

1. The linear and nonlinear physics is embedded in the FRF's.
2. The QFRF and CFRF enable us to quantify the "strength" of the quadratic and cubic nonlinearities as a function of frequency.
3. Knowledge of the QFRF and CFRF enables one to track the nonlinear transfer of energy from various frequency bands in the random seawave spectrum to other bands in the ship response(15).
4. Ultimately, knowledge of the Volterra kernels offer the promise of being able to predict the linear and nonlinear ship response to a variety of random seas.

There are essentially two approaches to experimentally determining the FRF's, namely, random and deterministic (usually sinusoidal) signals. For example, it is well known that to experimentally determine a QFRF one needs to probe the actual physical system with two sinusoids at frequency ω_1 and ω_2. One then measures the amplitude and phase of the resulting sum (and difference) frequency response to determine the complex value of $H_2(\omega_1, \omega_2)$. To determine $H_2(\omega_1, \omega_2)$ over the appropriate regions of the bifrequency plane requires repeating the experiment for many different pairs of exciting frequencies, which can be a tedious and time consuming (and hence expensive) process. To determine $H_3(\omega_1, \omega_2, \omega_3)$ one must, of course, probe the system with various triplets of input frequencies and measure the amplitude and phases of the more than twenty intermodulation products that are generated in the response. This procedure must be repeated over and over in order to determine $H_3(\omega_1, \omega_2, \omega_3)$ in the appropriate regions of three-dimensional frequency space. The regular wave experiments discussed below simply identify the components of H_3 for which the three frequencies are equal.

An alternative approach is to excite the system with a broadband random excitation and to record both the excitation and the response. The situation is very complicated, of course, because the total response at any given frequency consists of the sum total of a linear contribution plus many quadratic frequency-pair contributions and many cubic frequency-triplet contributions, as indicated in Eq. (2). However, using the nonlinear system identification techniques based on digital higher-order spectral analysis, which are described in the next section, we are able to determine the linear, quadratic, and cubic frequency response functions.

Third-Order Volterra System Model

NonOrthogonal Model for NonGaussian Excitation

Since we process the observed time-series data of wave excitation - ship response digitally, it is customary to express the third-order Volterra series model of Eq. (2) in discrete notation as follows,

$$Y(m) = H_1(m)X(m) + \sum_{i+j=m} H_2(i,j)X(i)X(j) + \sum_{p+q+r=m} H_3(p,q,r)X(p)X(q)X(r) + \epsilon(m) \quad (3)$$

where $Y(m)$, $X(m)$, and $\epsilon(m)$ are discrete Fourier transforms of the output response $y(t)$ of a ship, the input wave excitation $x(t)$, and the error of the model $e(t)$. The quantities $H_1(m)$, $H_2(i,j)$, $H_3(p,q,r)$ are discrete versions of the linear, quadratic and cubic frequency response functions (LFRF, QFRF, and CFRF), respectively. The integer quantities (m, i, j, p, q, and r) denote discrete frequency. To convert to continuous frequency, one multiplies the value of the integer quantities by the frequency interval $\Delta\omega$, where $\Delta\omega = 2\pi/T$. The quantity T denotes the temporal duration of a data record or realization, and is equal to N (the number of samples per realization) times the sampling interval t_s.

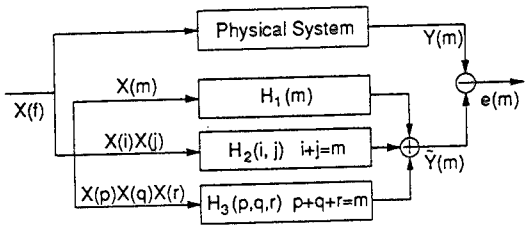

Fig. 1 Third-Order Multi-Input Volterra Model

Notice that Eq. (3) is linear in terms of the FRF's $H_1(m)$, $H_2(i,j)$, and $H_3(p,q,r)$ though the equation is nonlinear with respect to the input wave $X(m)$. Thus, regarding $X(i)X(j)$ and $X(p)X(q)X(r)$ as separate inputs, one can treat the third-order nonlinear system as a multi-input linear system, as shown in Fig. 1. Utilizing such an idea, one can rewrite Eq. (3) in a vector form,

$$\begin{aligned} Y(m) &= \tilde{Y}(m) + \epsilon(m) \\ &= Y_1(m) + Y_2(m) + Y_3(m) + \epsilon(m) \\ &= \mathbf{H}(m)\mathbf{X}(m) + \epsilon(m) \end{aligned} \quad (4)$$

where $\tilde{Y}(m)$ is the total model output which consists of the linear, quadratic, and cubic model outputs ($Y_1(m)$, $Y_2(m)$, and $Y_3(m)$). The bold type in Eq. (4) denotes a vector quantity. The row FRF vector $\mathbf{H}(m)$ and the column input vector $\mathbf{X}(m)$ are given by

$$\mathbf{H}(m) = [\mathbf{H}_1(m), \mathbf{H}_2(m), \mathbf{H}_3(m)] \quad (5)$$

and

$$\mathbf{X}^t(m) = [\mathbf{X}_1^t(m), \mathbf{X}_2^t(m), \mathbf{X}_3^t(m)] \quad (6)$$

The superscript 't' is the transpose of a matrix. In Eq. (5), $\mathbf{H}_1(m)$ is the LFRF, the row vector $\mathbf{H}_2(m)$ is a collection of QFRF $H_2(i,j)(m)$ where $i+j=m$, and the row vector $\mathbf{H}_3(m)$ is a collection of CFRF $H_3(p,q,r)(m)$ where $p+q+r=m$. In addition, $\mathbf{X}_1(m)$ is equal to the input $X(m)$, and the column vector $\mathbf{X}_2(m)$ is a collection of quadratic inputs $X(i)X(j)$ where $i+j=m$. The column vector $\mathbf{X}_3(m)$ is a collection of cubic inputs $X(p)X(q)X(r)$ where $p+q+r=m$. Then, the ith-order model output becomes,

$$Y_i(m) = \mathbf{H}_i(m)\mathbf{X}_i(m) \quad \text{for } i=1,2,\text{and } 3 \quad (7)$$

Though we have restricted ourselves to third order in this paper, obviously one can extend the model description to any higher order.

The FRF's $\mathbf{H}(m)$ which minimize the mean square error $< |\epsilon(m)|^2 >$ are

$$\begin{aligned}\mathbf{H}(m) &= < Y(m)\mathbf{X}^{\Lambda}(m) >< \mathbf{X}(m)\mathbf{X}^{\Lambda}(m) >^{-1} \\ &= \mathbf{S}_{yx}(m)\mathbf{S}_{xx}^{-1}(m) \end{aligned} \quad (8)$$

where $< \cdot >$ is an expected value of a random process, and Λ denotes the Hermitian of a matrix. In Eq. (8), $\mathbf{S}_{yx}(m)$ is the cross-spectral raw vector, and $\mathbf{S}_{xx}(m)$ is the input auto-spectral matrix.

For a linear system, Eq. (8) becomes a scalar quantity so that one can immediately recover the conventional expression of the LFRF $H_1(m)$, where $H_1(m) = S_{yx}(m)S_{xx}^{-1}(m)$, that is, the linear transfer function is given by the cross-power spectrum divided by the auto-power spectrum. For a quadratic Volterra system, the optimum solution for Gaussian inputs was first found by Tick(16), and the general solution of $\mathbf{H}(m)$ for non-Gaussian inputs was studied later by K. I. Kim and Powers(17). For a cubic Volterra system, Hong, Y. C. Kim, and Powers(18) derived the FRF's for Gaussian inputs. Recently, Nam, Powers and S. B. Kim(19) developed a sophisticated way to solve for the LFRF, QFRF, and CFRF for nonGaussian inputs which include novel methods to index and sort the matrix elements and reduce the matrix size using symmetry properties of higher-order spectra.

One of the key issues in nonlinear system identification is how to decompose the total response into contributions from linear and nonlinear effects of different orders. We will discuss now the spectral decomposition problem and derivation of generalized system coherence functions for a cubically nonlinear system.

After the FRF's $\mathbf{H}(m)$ are found, one can estimate the total system model power spectrum using Eqs. (4) and (8),

$$\begin{aligned} S_{\hat{y}\hat{y}}(m) &= \mathbf{H}(m)\mathbf{S}_{\mathbf{XX}}(m)\mathbf{H}^{\Lambda}(m) \\ &= \sum_{i=1}^{3} S_{ii}(m) + 2\sum_{i<j} Re[S_{ij}(m)] \end{aligned} \quad (9)$$

where $Re[\cdot]$ denotes the real part of a complex quantity, and $S_{ij}(m)$ is given by

$$\begin{aligned} S_{ij}(m) &= < Y_i(m)Y_j(m)^{\Lambda} > \\ &= \mathbf{H}_i(m)\mathbf{S}_{\mathbf{X}_i\mathbf{X}_j}(m)\mathbf{H}_j^{\Lambda}(m) \end{aligned} \quad (10)$$

for $i,j = 1,2,\text{and } 3$. Thus, in this nonorthogonal model, the total model output power spectrum consists of not only the linear, quadratic, and cubic model power spectra ($S_{11}(m)$, $S_{22}(m)$, and $S_{33}(m)$), but also interference spectra $2Re[S_{ij}(m)]$, where $i \neq j$, between various order terms. Because of these interference spectra, which result from the use of functional series built upon nonorthogonal basis input vectors, one cannot clearly separate the linear, quadratic, and cubic contributions from the measured output response, though one may write down the output response as in Eq. (4). This is not only a problem in experimental data analysis, but also in theoretical nonlinear dynamics where couplings between different order of nonlinearities are often neglected.

One "figure of merit", which is widely used in the area of signal processing as an index of goodness of a model, is the so-called coherence spectrum. The coherence spectrum $\Gamma(m)$ is defined as the ratio of the model output power to the measured output power,

$$\Gamma(m) = \frac{S_{\hat{y}\hat{y}}(m)}{S_{yy}(m)} = 1 - \frac{S_{\epsilon\epsilon}(m)}{S_{yy}(m)} \quad (11)$$

where $S_{\epsilon\epsilon}(m)$ is the error power spectrum. Obviously, the coherence spectrum is bounded by zero and one. Now one can decompose the total output model coherence spectrum of a cubic system $\Gamma_T(m)$ using Eq. (9) as follows,

$$\begin{aligned} \Gamma_T(m) &= \mathbf{H}(m)\mathbf{S}_{\mathbf{XX}}(m)\mathbf{H}^{\Lambda}(m)S_{yy}^{-1}(m) \\ &= \sum_{i=1}^{3}\Gamma_{ii}(m) + 2\sum_{i<j} Re[\Gamma_{ij}(m)] \end{aligned} \quad (12)$$

where $\Gamma_{ij}(m)$ is given by

$$\Gamma_{ij}(m) = \mathbf{H}_i(m)\mathbf{S}_{\mathbf{X}_i\mathbf{X}_j}(m)\mathbf{H}_j^{\Lambda}(m)S_{yy}^{-1}(m) \quad (13)$$

In Eq. (12) $\Gamma_{11}(m)$, $\Gamma_{22}(m)$, and $\Gamma_{33}(m)$ are the linear, quadratic, and cubic coherence spectra, and $2Re[\Gamma_{ij}(m)]$, where $i \neq j$, are the interference coherence spectra, respectively. Notice that the interference coherence spectra $2Re[\Gamma_{ij}(m)]$ can be negative depending on the phase of the interference spectra $S_{ij}(m)$. Furthermore, $\Gamma_{ii}(m)$ can be greater than one, even though the total system coherence $\Gamma_T(m)$ is bounded by zero and one. This suggests that $S_{11}(m)$, $S_{22}(m)$, and $S_{33}(m)$ are not necessarily purely linear, quadratic and cubic model output power spectra. Such effects cause great difficulty in decomposing the output response into its linear, quadratic and cubic components, and hinders physically meaningful interpretation of the analysis results.

Orthogonal Model for NonGaussian Excitation

Recently S. B. Kim and Powers(20) utilized the concept of conditioned power spectra, which was used previously in multi-input linear system analysis(21), and extended these concepts to higher-order spectra for nonlinear Volterra system analysis. Through conditioning higher-order inputs using an orthogonalization process, they obtained a new orthogonal Volterra system model. This is a generalization of Wiener and Barrett orthogonal functional series which are valid only for Gaussian inputs(22). The new orthogonal model works for arbitrary input statistics (nonGaussian and Gaussian)

and arbitrary spectral shape. Furthermore, after determining the conditioned input vector, each FRF is estimated independently so that one can improve the system model successively by adding the next higher-order term.

In general, the input vectors $\mathbf{X}_1(m)$, $\mathbf{X}_2(m)$ and $\mathbf{X}_3(m)$ are not orthogonal, and thus the cross-spectrum of any two input vectors exists. This is true even for Gaussian inputs (e. g., $\langle \mathbf{X}_1(m)\mathbf{X}_3^{\Lambda}(m)\rangle \neq \mathbf{0}$). Such nonorthogonal input vectors prohibit physically meaningful decomposition as we discussed before. An alternative orthogonal model can be constructed by replacing the original input records by ordered sets of conditioned input records $\mathbf{Z}_1(m)$, $\mathbf{Z}_2(m)$ and $\mathbf{Z}_3(m)$, which are orthogonal to each other.

Consider a third-order Volterra system with nonorthogonal input basis vectors $\mathbf{X}_i(m)$ for $i = 1, 2,$ and 3 as in Eq. (6). Clearly, the system output can be represented with new basis vectors $\mathbf{Z}_i(m)$ for $i = 1, 2,$ and 3, which are generated from any linear combination of the input vectors $\mathbf{X}_i(m)$. Furthermore, we want the new basis vectors $\mathbf{Z}_i(m)$ be orthogonal each other. Then, one can rewrite Eq. (4) as follows,

$$\begin{aligned} \hat{Y}(m) &= \mathbf{H}(m)\mathbf{X}(m) \\ &= \mathbf{K}(m)\mathbf{Z}(m) \\ &= \mathbf{K}(m)\mathbf{L}(m)\mathbf{X}(m) \end{aligned} \tag{14}$$

where $\mathbf{K}(m)$ are the new system FRF's based upon the orthogonalized input vector $\mathbf{Z}(m)$, which are defined as,

$$\mathbf{K}(m) = [\mathbf{K}_1(m), \mathbf{K}_2(m), \mathbf{K}_3(m)] \tag{15}$$

and

$$\mathbf{Z}^t(m) = [\mathbf{Z}_1^t(m), \mathbf{Z}_2^t(m), \mathbf{Z}_3^t(m)] \tag{16}$$

In Eq. (14), $\mathbf{L}(m)$ is a lower triangular orthogonal transformation matrix obtained by Gram-Schmidt orthogonalization process utilizing the orthogonal conditions, $\langle \mathbf{Z}_i(m)\mathbf{Z}_j^{\Lambda}(m)\rangle = \mathbf{0}$, for $i \neq j$.

Considering the orthogonal properties of the conditioned input vectors $\mathbf{Z}(m)$, one can easily find the new minimum mean square solution of the FRF's $\mathbf{K}(m)$ of the conditioned orthogonal system in terms of the orthogonalized input spectral matrices as follows,

$$\mathbf{K}(m) = \mathbf{P}_{yz}(m)\mathbf{P}_{zz}^{-1}(m) \tag{17}$$

On the RHS of Eq. (17) $\mathbf{P}_{yz}(m)$ is a conditioned cross-spectral row vector, and $\mathbf{P}_{zz}(m)$ is a conditioned diagonal auto-spectral matrix.

Now, one can calculate the total model power spectrum $P_{\hat{y}\hat{y}}(m)$ for the orthogonal Volterra model, which becomes

$$\begin{aligned} P_{\hat{y}\hat{y}}(m) &= \mathbf{P}_{yz}(m)\mathbf{P}_{zz}^{-1}(m)\mathbf{P}_{zy}(m) \\ &= P_1(m) + P_2(m) + P_3(m) \end{aligned} \tag{18}$$

where $P_1(m)$, $P_2(m)$, $P_3(m)$ are the orthogonalized linear, quadratic, and cubic model output power spectra, and given by

$$P_i(m) = \mathbf{P}_{yi}(m)\mathbf{P}_{ii}^{-1}(m)\mathbf{P}_{iy}(m) \tag{19}$$

for $i = 1, 2,$ and 3. In Eq. (19), $\mathbf{P}_{ii}(m)$ is the auto-spectra of the ith-order orthogonalized input vector $\mathbf{Z}_i(m)$. Notice that the total model power spectrum $P_{\hat{y}\hat{y}}(m)$ for the orthogonal Volterra model is the same as the total model power spectrum for the nonorthogonal Volterra model $S_{\hat{y}\hat{y}}(m)$, but without the interference spectra.

Accordingly, the total system coherence function $\gamma_T^2(m)$ based upon the orthogonal model, which was defined as Eq. (11), consists of the purely linear $\gamma_1^2(m)$, quadratic $\gamma_2^2(m)$, and cubic $\gamma_3^2(m)$ coherence spectra without the interference terms.

$$\gamma_T^2(m) = \gamma_1^2(m) + \gamma_2^2(m) + \gamma_3^2(m) \tag{20}$$

where $\gamma_i^2(m) = P_i(m)P_{yy}^{-1}(m)$. Notice that each term in Eq. (20) is positive definite, and is bounded by zero and one. Thus, a physical meaningful decomposition is now possible. Furthermore, the total system coherence function $\gamma_T^2(m)$ based upon the orthogonal model is same as the total system coherence function $\Gamma_T(m)$ based upon the nonorthogonal model.

EXPERIMENTS

The experiments were conducted in the U.S. Naval Academy Hydromechanics Laboratory 116 meter long towing tank. This facility has a dual-flap hydraulically driven wavemaker, and a towing carriage driven by shore-mounted electric motors through wire rope and sheaves. The model used was the S175 hull form, used for comparative studies of the ITTC. Principle characteristics of the model are shown in Table 1. The model was towed in head waves by means of a heave staff with a pitch pivot at the center of gravity, as shown in Fig. 2. The lateral plane motions were restrained, as was surge. Heave and pitch were measured with potentiometers. The wave elevation was measured on the tank centerline at a point 1 m ahead of the fore perpendicular, using an ultrasonic probe mounted to the carriage. A vertical accelerometer was installed at a point 0.15 Lpp aft of the fore perpendicular. While the acceleration can be obtained from the rigid body heave and pitch motions, it was felt that an acceleration measurement would be a sensitive way to measure higher harmonics, which would be another indicator of nonlinearity in response.

Length (Lpp)	3.50 m
Beam	0.51 m
Draft	0.19 m
C_B	0.572
R_{yy}/Lpp	0.24
KG	0.20 m
Displacement	193.2 kg

Table 1 S175 model characteristics.

For regular wave testing, the wavemaker was driven by an analog voltage oscillator. The model was towed at two carriage speeds, corresponding to Froude number = 0.200 and 0.275. The regular wave frequencies were as shown in Table 2. The wavemaker gain was varied to obtain wave heights (double amplitude) from approximately 0.03 to 0.18 m. For random wave testing, a computer generated random voltage was generated using standard Hydromechanics Laboratory software. The Bretschneider two-parameter spectral shape was

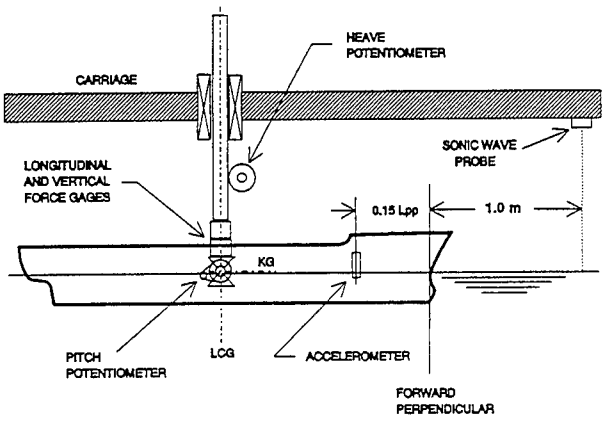

Fig. 2 Test configuration for S175 model.

λ/Lpp	σ	σ_e (Fn=0.20)	σ_e (Fn=0.275)
1.0	2.507	3.764	4.235
1.2	2.288	3.335	3.728
1.4	2.118	3.015	3.352

Table 2 Regular wave conditions.

used as a target spectrum, with a modal period equal to two seconds (peak frequency = 0.5 Hz; or $\sigma_e = 2.582$ at Fn=0.20). This corresponds to a wavelength of approximately 1.8 times the model length. Because of limitations in the wavemaker, the high frequency tail of the spectrum was truncated at 1.0 Hz. The wavemaker drive signal was composed of seventy sine wave components between 0.30 and 1.00 Hz, with random phases. The phases were re-randomized before each carriage run. Three sets of data were obtained with the wavemaker gain set to three levels. The highest level, designated 100%, had a standard deviation of 0.042 m, corresponding approximately to fully developed seas, while the other two were obtained by setting the wavemaker gain at 75% and 50% of the highest gain. For each of the three conditions, twelve carriage runs were made, allowing the collection of data for a total run time of approximately 700 seconds.

Because it was the intention in these experiments to measure deviations from linearity of vertical plane motions which are at least quasi-linear, it was expected that such effects might be an order of magnitude less than the dominant linear part of the total measurement. For this reason, considerable effort was made to minimize various sources of error in test conditions and measurements. The sources of experimental uncertainty are discussed in more detail in the Appendix. While seakeeping experiments and correlations to predictions are typically considered to have a precision of no better than 10-20%(23), it is felt that meaningful indications of nonlinearity have been obtained in the experiments reported here, especially for steep waves where significant changes in both magnitude and phase of the frequency response functions have been observed.

RESULTS

Wave Measurements

The accurate measurement of the incoming wave field is of course at the heart of a seakeeping experiment. An ultrasonic probe was chosen because the high degree of linearity and the fact that is a non-contact device, which will not distort the wave at forward speed as other probes may. The waves themselves may have nonlinear effects (the Stokes wave behavior), appearing as higher harmonics in both regular and random waves. The wave measurements were examined for the presence of such effects, as discussed below. The experiments were done in two series approximately one year apart. In Fig. 3 and subsequent figures showing the regular wave results, the first series data are shown as circular symbols, while the second or more recent series data are shown as square symbols. The random wave experiments were done only during the second series.

Regular Wave Measurements

Regular waves of finite steepness are well known to have higher harmonics. The Stokes wave elevation to third order is given by,

$$\zeta(t) = a\cos(\omega t) + \frac{1}{2}ka^2\cos(2\omega t) + \frac{3}{8}k^2a^3\cos(3\omega t) \quad (21)$$

The measured second harmonic of the wave signal, is shown and compared to the Stokes formula in Fig. 3. The results are presented as a ratio of the second harmonic to the first, as a function of wave steepness ka (with a the first harmonic amplitude of the measured wave). This provides an indication of the ability of the wave probe to resolve a relatively small harmonic in the wave. Equation (21) predicts a third harmonic as well. However, in both the Stokes formula and the measurements, this component is less than one percent of the first harmonic for the maximum steepness in the experiments ($ka = 0.15$). There is also a nonlinear correction to the dispersion relationship,

$$\omega^2 = gk(1 + (ka)^2 + \cdots) \quad (22)$$

For a given wave frequency, this results in a somewhat longer wave length than the linear dispersion relationship would predict. The consequence for a seakeeping experiment is that, for a wave measurement ahead of the model center of gravity, and a phase correction to the motions made on the basis of linear dispersion, there will be a phase lead which increases with wave steepness. For the probe location, wavelengths and steepnesses used in the regular wave experiments, this accounts for less than a 6 degree shift in any motion phase measurements. For both this phase shift, and for the third harmonic amplitude of the waves, the magnitudes involved are considered to be below the minimum threshold for which meaningful results can be obtained from these data.

Random Wave Measurements

The auto-spectra of the wave measurements at the 50%, 75% and 100% wavemaker setting are shown in Fig. 4, plotted against nondimensional encounter frequency. The 1 Hz cutoff frequency in the wavemaker

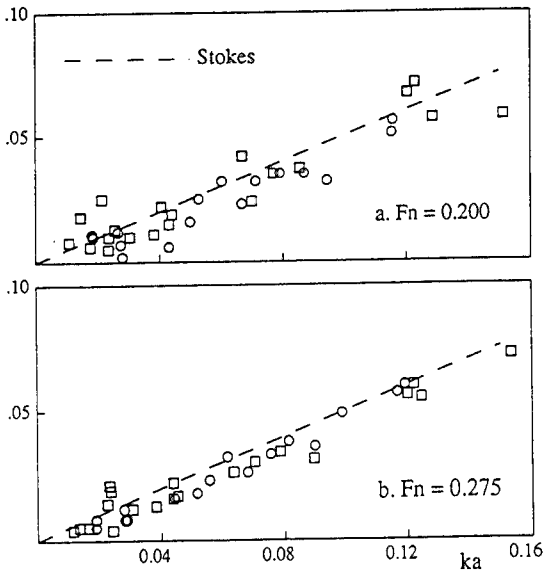

Fig. 3 Regular Wave Second Harmonic
(Ratio of Second to First Harmonic)

drive signal corresponds to a nondimensional encounter frequency,$\sigma_e = 6.6$. A fairly steep attenuation of the spectra is seen at this frequency. Higher frequency energy may be due to a combination of residual wave energy in the towing tank and nonlinear interactions among wave components at lower frequencies.

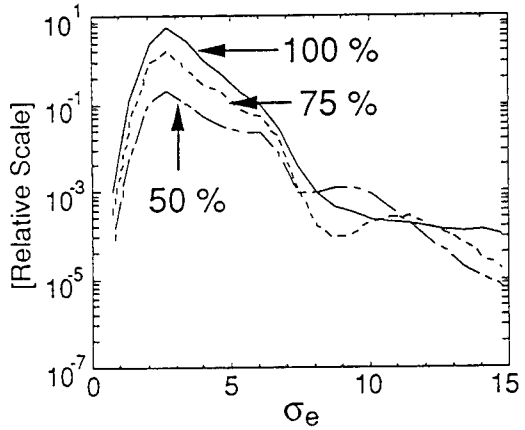

Fig. 4 Wave excitation auto spectra

Test for NonGaussianity of Wave

The effect of nonGaussian wave excitation in ship hydrodynamics is, at the first glance, not quite noticeable especially for linear problems. For example, in the spectral domain, a spectral component at a particular frequency in the excitation is linearly transformed to the output response at the same frequency, and the probability distribution function (PDF) of the output is obtained through a linear transformation of the input wave PDF. However, when one deals with a nonlinear problem, one has to consider couplings between different frequency components via nonlinear interactions. In this case the PDF of the signal contains information on the nonlinearity, since the PDF of the signal will deviate from Gaussian when there are couplings between different spectral components. Thus, a nonGaussian distribution of a stochastic process is a very good indication that such a process is nonlinear.

Conventional methods to test the statistics of a stochastic process do not provide much information on the order of the process. Recently, Rao, Hinich, and others developed stricter test methods for nonGaussianity and nonlinearity of a stochastic process using the bispectrum. Note that the bispectrum in 2-dimensional frequency domain is zero for a Gaussian process. However, this is a necessary condition for a Gaussian process, but not a sufficient condition. In our cubic Volterra system, we need to estimate up to 6th order spectral moments of the wave excitation, but unfortunately there are no general test methods for a Gaussian process for such high order moments. Naively assuming Gaussian excitation without examining the details of the higher order spectral moments or conditional probability functions can lead to misleading Volterra models of a nonlinear system(24).

We have tested the nonGaussianity of the random waves utilized in this experiment by using the test statistic developed by Hinich(25), which, he states, is basically the Subba Rao-Gabr statistic(26) with the asymptotic variance instead of their sample estimate. The test statistic ξ_x is proportional to the normalized bispectrum Π_x as indicated below,

$$\Pi_x = \frac{|B_x(\omega_1,\omega_2)|}{\sqrt{S_x(\omega_1)S_x(\omega_2)S_x(\omega_1+\omega_2)}} \quad (23)$$

$$\xi_x = 2M\Pi_x^2 \quad (24)$$

where $S_x(\omega)$, $B_x(\omega_1,\omega_2)$, and M denote the auto-power spectrum and the auto-bispectrum of the random wave excitation, and the number of ensembles used for the spectral estimation, respectively. The test statistic ξ_x is approximately a central χ^2 variate with 2 degrees of freedom under a null hypothesis, $B_x(\omega_1,\omega_2) \equiv 0$ for a Gaussian process.

The global statistic g_x is defined as the sum of the test statistic ξ_x for ν bifrequency pairs in the principal domain, and is approximately distributed $\chi^2_{2\nu}$. For large ν, Wilson and Hilferty(27) showed that it can be further approximated as a normal distribution if one uses a test statistic Z, where

$$\mathbf{Z} = 3\sqrt{\nu}\,(\sqrt[3]{g_x/2\nu} - 1 + \frac{1}{9\nu}) \sim N(0,1) \quad (25)$$

We have performed the Gaussianity test for three different levels of wave maker gain settings, namely 100%, 75% and 50%. We have tested the null hypothesis $\mathbf{Z} = 0$ for a Gaussian process at the significance level $\alpha = 0.01$, where $\mathbf{Z}_{\alpha=0.01} = 2.33$ for the one-sided test.

In Table 3, test results for variance, skewness, kurtosis, and the statistic Z for the three different settings of the wave maker are tabulated. The bispectrum of the encountered random wave is estimated using the data length of 228 blocks of 70 points sampled at 12.5 Hz, and it is shown in Fig. 5 for the 100% wave setting. If

the random waves are Gaussian, the bispectrum should be ideally zero. In this case it clearly is not zero. The tabulted skewness s and the kurtosis k are the differences from those of a Gaussian process, where s = 0, and k = 3. Thus, we note that these quantities for all three different wave settings are not far from the skewness and the kurtosis of a Gaussian process. However, as one can see in Table 3, the Wilson statistic Z for the three different cases are consistently greater than $Z_{\alpha=0.01} = 2.33$. Thus, one has to reject the null hypothesis of Gaussian process for random waves. Also, notice that Z increases with the wave maker settings. This is consistent with the idea that the wave becomes more nonGaussian as wave amplitude increases. In conclusion, it is very important to test the higher-order statistics in nonlinear system identification in order to verify or reject the Gaussian wave assumption. It has been our experience in using random excitation in nonlinear system identification that very few experimental random signals are sufficiently Gaussian to make use of the simplifying Gaussian assumption(28).

Wave Settings	50 %	75 %	100 %
Variance (cm^2)	4.39	9.87	17.35
Skewness	0.06	0.09	0.04
Kurtosis	-0.19	-0.27	-0.20
Statistic Z	17.5	18.4	27.8

Table 3 NonGaussianity test statistics of wave.

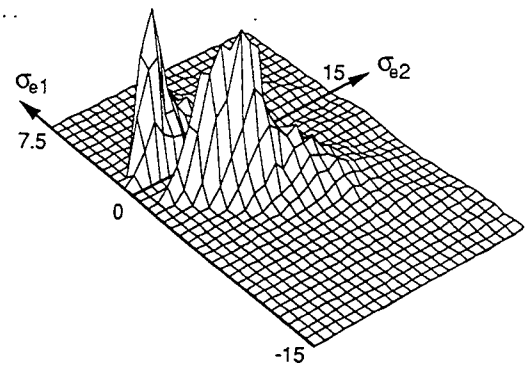

Fig. 5 Auto-bispectrum of wave excitation at 100% wave maker setting

Motion Measurements

First harmonic Frequency Response

The heave, pitch and bow acceleration measurements in regular waves were Fourier analyzed to obtain the amplitude and phase of the harmonic components. In order to do this, approximately ten complete cycles were analyzed for each speed-frequency-amplitude combination. The immediate goal has been to confirm the variation of transfer function (i.e. the ratio of first harmonic response to first harmonic of wave), as a function of wave steepness, which was suspected to be the cause of variation of data in ITTC comparative studies. For this purpose the measured first harmonic results (both magnitude and phase) have been plotted against wave steepness, ka, for three wave lengths shown in Table 2. In computing these quantities, the first harmonic of the wave signal has been used. As noted previously, if the response is truly linear, then both magnitude and phase will be invariant with respect to steepness.

The first harmonic frequency response functions are shown in Fig. 6-17. The magnitudes are in nondimensional form as follows: heave amplitude divided by wave amplitude (z/a), pitch divided by wave slope (θ/ka), and acceleration is nondimensionalized with respect to gravity and length to wave amplitude ratio ($\ddot{s}Lpp/(ga)$). Phases are defined as leads relative to the wave elevation at the LCG, with wave, heave and acceleration defined as positive up and pitch defined as positive bow down. In calculating the phase, the measured wave phase has been corrected with the linear deep water dispersion relationship. As seen in Fig. 6, the magnitude of the heave response at Fn=0.200, especially at $\sigma_e = 3.76$, exhibits a marked drop over the range of wave steepnesses tested. This effect is less pronounced for longer waves (lower frequency). At Fn=0.275, this effect is again seen at approximately the same encounter frequency in Fig. 12 (note that this corresponds to a longer wave length in Table 2, due to the increased encounter frequency shift at higher Froude number. In all cases tested, the variation of heave phase was small, typically not more than 10 degrees, which is not considered significant in terms of the uncertainty in measuring phase angles.

For the case of pitch, the variation in magnitude of response is shown in Fig. 8 and 14 is less pronounced. However, as seen in Fig. 9 and 15, The phase of pitch can shift significantly, as much as 30 degrees over the range of wave steepnesses tested. The acceleration frequency response function shows a variation in both magnitude and phase as shown in Figs. 10-11 and 16-17. This may be expected since the vertical motion at this measurement point (0.15 Lpp aft of the fore perpendicular) is a combination of the rigid body translation and rotation.

Other Harmonic Content

Another quantity which can be taken as an indicator of nonlinearity is the presence of higher harmonics. These are of course present in the waves themselves as discussed above, but in addition can be found in the motions themselves. The harmonic analysis of the heave and pitch shows the presence of second and third harmonics, but they are typically only one or two percent of the magnitude of the first harmonic. Thus, the evidence for higher harmonics in the rigid body displacements is only qualitative. However, the bow acceleration is a more sensitive indication of higher harmonics than the heave and pitch displacements since the second time derivative corresponds to multiplying the displacement harmonics by ω^2, $4\omega^2$, and $9\omega^2$ for the first, second and third harmonics respectively. If the response is properly represented by a Volterra functional series, these harmonics would be expected to vary as the square of

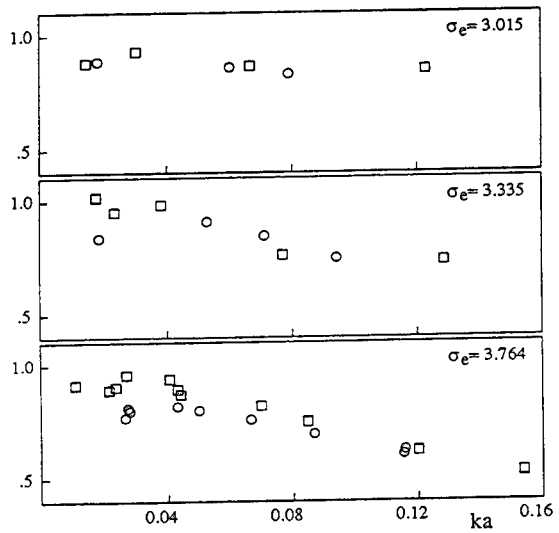

Fig. 6 Magnitude of Heave Response Function, Fn = 0.200

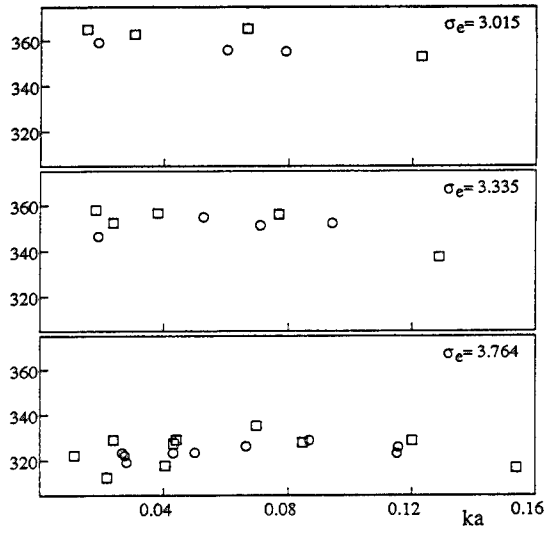

Fig. 7 Phase of Heave Response Function, Fn = 0.200

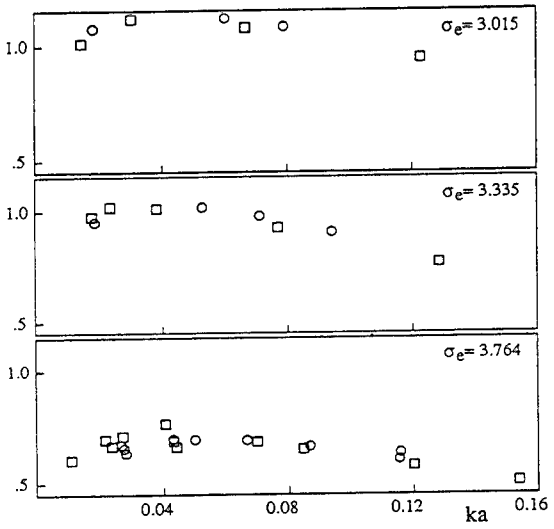

Fig. 8 Magnitude of Pitch Response Function, Fn = 0.200

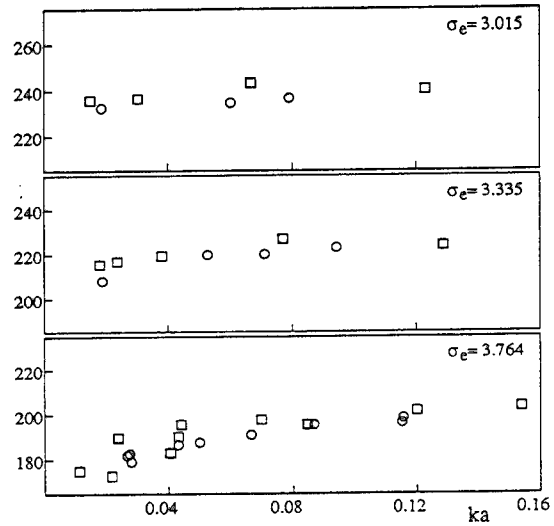

Fig. 9 Phase of Pitch Response Function, Fn = 0.200

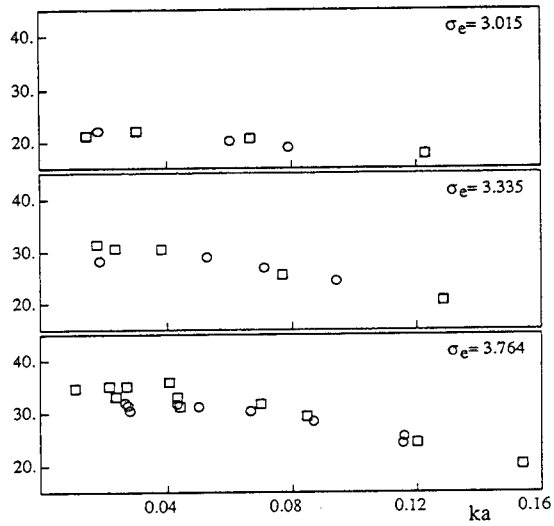

Fig. 10 Magnitude of Acceleration Response Function, Fn = 0.200

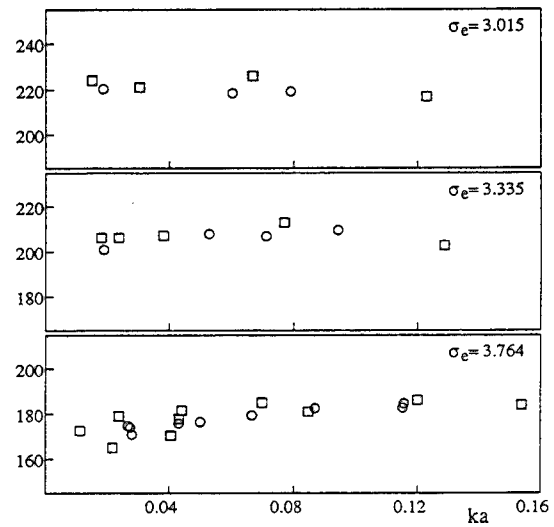

Fig. 11 Phase of Acceleration Response Function, Fn = 0.200

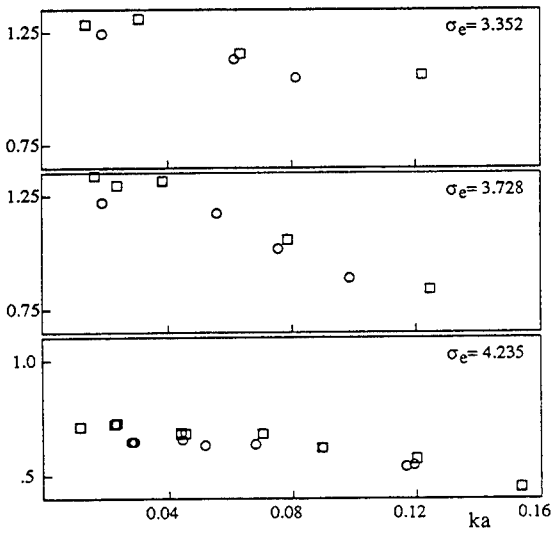

Fig. 12 Magnitude of Heave Response Function, Fn = 0.275

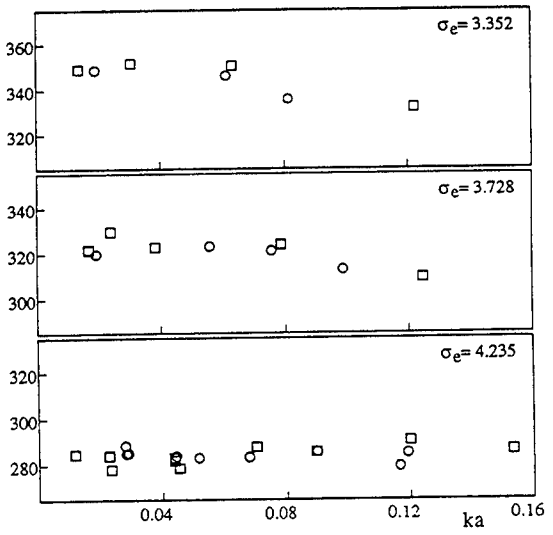

Fig. 13 Phase of Heave Response Function, Fn = 0.275

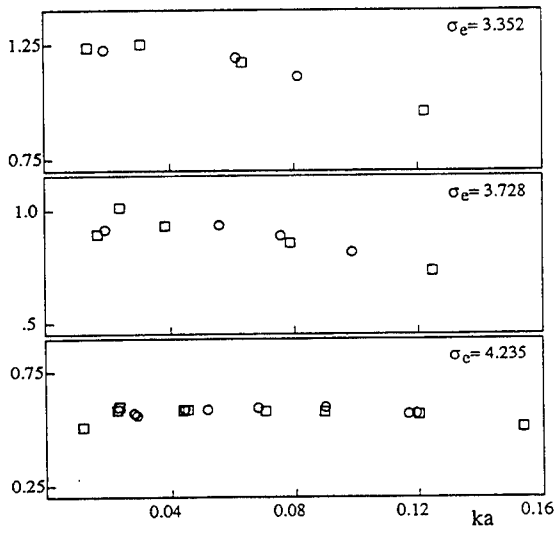

Fig. 14 Magnitude of Pitch Response Function, Fn = 0.275

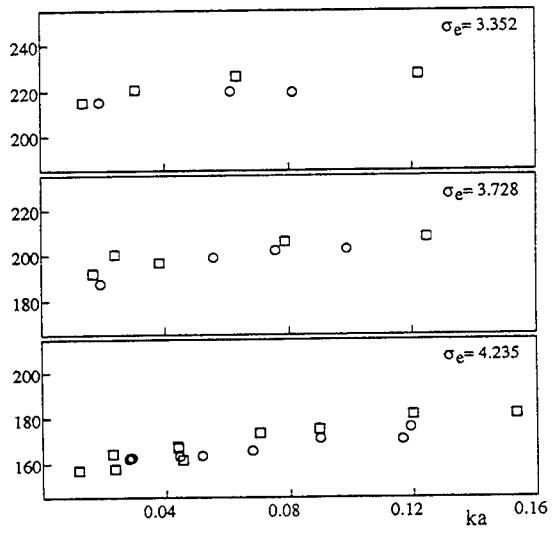

Fig. 15 Phase of Pitch Response Function, Fn = 0.275

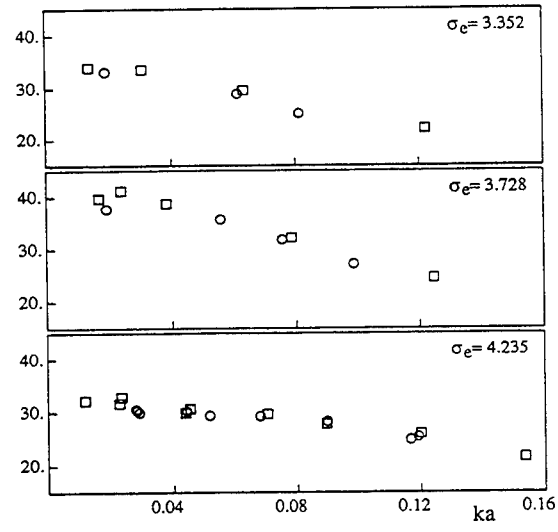

Fig. 16 Magnitude of Acceleration Response Function, Fn = 0.275

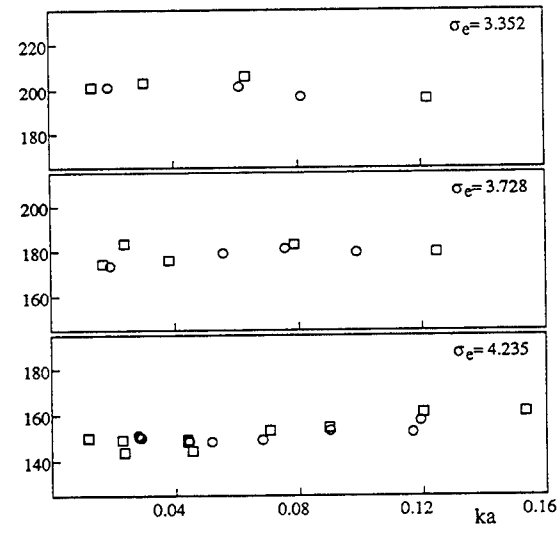

Fig. 17 Phase of Acceleration Response Function, Fn = 0.275

wave amplitude for the second harmonic, cube for the third harmonic, etc. Evidence of this is shown in Figs. 18 and 19 for the acceleration response at σ_e = 3.76 and Fn = 0.200. For this condition, the maximum first harmonic of measured acceleration was approximately 0.5 g, so that these higher harmonic components are a significant percentage of the total. It should also be noted that the second harmonic of acceleration is explained, at least in part, by the "static" component of pitch motion. That is, for the larger values of pitch, the accelerometer actually measures the quantity (g + heave acceleration) times the cosine of the pitch angle, since the accelerometer measurement is perpendicular to the rotating hull-fixed axis. When pitch is large enough for $\cos\theta$ to deviate from 1.0, and second harmonic will be seen. Finally, the data were examined for the presence of mean shifts, relative to steady calm water values. The quadratic term of the Volterra expansion may result in such shifts which may be expected to vary as the square of wave amplitude. However, for the S175 hull these shifts were very small, less than 1 mm for heave and 0.1 degree for pitch.

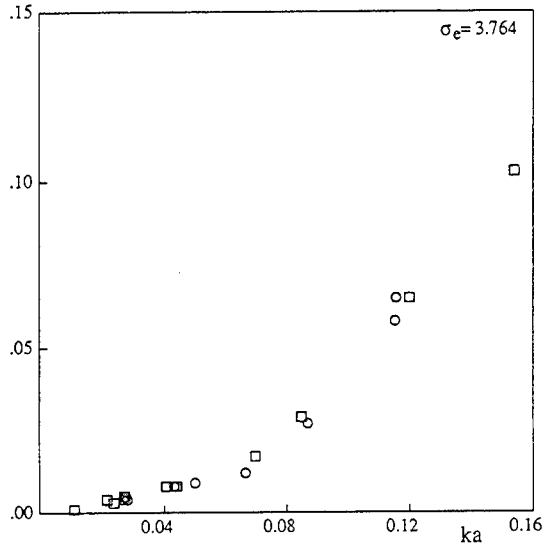

Fig. 18 Acceleration Second Harmonic (G's), Fn = 0.200

Random Waves

The collected data were pre-processed for the third-order Volterra system analysis. Twelve runs of data, which were originally sampled at 25 Hz, for 50%, 75%, and 100% wave maker settings, were used. After removing the starting and stopping transients, we collected 640 data points per each run after decimating the data by a factor of 2. Thus, the new sampling frequency becomes 12.5 Hz. We divided the 640 points of data into 5 blocks (128 points per block) before Fourier transforming using the FFT (fast Fourier transform) algorithm. We also overlapped by 50% to increase the number of blocks of data. Thus, we have total 108 blocks (9 blocks/run × 12 runs) of 128 points data for higher-order spectral estimation.

After the data were Fourier-transformed, we choose a frequency band ($1 < \sigma_e < 15$) appropriate for the higher-order spectral analysis. Then, higher-order spectral components were arranged for the estimation of

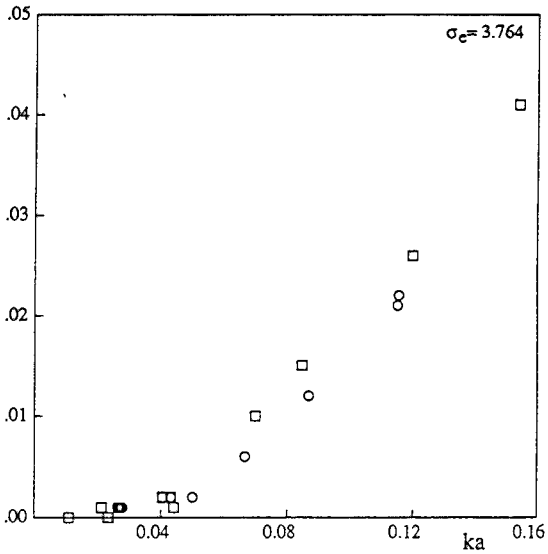

Fig. 19 Acceleration Third Harmonic (G's), Fn = 0.200

the cross-spectral vector $\mathbf{S}_{yx}(m)$ and the auto-spectral matrix $\mathbf{S}_{xx}(m)$. For the nonorthogonal model, an inverse of the auto-spectral matrix $\mathbf{S}_{xx}(m)$ was calculated using the Cholesky decomposition method in order to solve for the FRF's. After the FRF's were obtained, the goodness of the model was tested by calculating the linear, quadratic, cubic, and interference coherence spectra.

For the orthogonal model, first the input vector $\mathbf{X}(m)$ was orthogonalized to generate the conditioned orthogonal input vector $\mathbf{Z}(m)$ using a modified Gram-Schmidt orthogonalization procedure. Then, using the orthogonal input vector $\mathbf{Z}(m)$, we estimated auto- and cross- higher-order spectra and found the new FRF's. Then, we calculated the system model coherence spectra (without interference) according to the formula we described previously in order to check the goodness of the orthogonal model.

The power spectra for heave, pitch, and bow acceleration of the S175 hull are given in Fig. 20 for the 100% case. It is very difficult to conclusively identify the presence of any nonlinearities through examination of the random wave excitation spectrum and the S175 hull response auto-spectra themselves. However, it is seen that for pitch and acceleration, there is measurable energy at frequencies beyond the wave energy band. Also, by calculating the higher order spectral components as discussed in the section on system modelling it is possible to determine the presence of nonlinear components.

First we processed the time series data for 100% random wave excitation and heave response using a third-order Volterra model valid for nonGaussian random seas. In Fig. 21 the corresponding linear, quadratic, and cubic coherence spectra are plotted and denoted by L, Q, C, respectively. Since this model is not orthogonal, interference coherence spectra are also present and are denoted by LQ, LC, and QC respectively. Note that the overall model models the heave response quite well in that the total coherency T is close to unity in the band centered around $\sigma_e \sim 3 - 4$. This indicates that the overall third-order Volterra model accounts for virtually 100% of the observed heave response in this

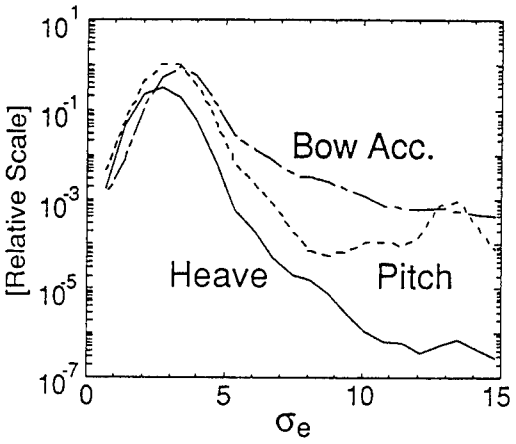

Fig. 20 Auto-power spectra of the heave, pitch, and bow acceleration.

band. The total coherence T slowly drops off at higher frequencies due to the fact that the excitation wave spectrum has progressively less energy, and, thus, the signal-to-noise ratio decreases, which in turn decreases the overall model coherence. Furthermore, observe that the quadratic coherence Q is quite small, suggesting that quadratic effects do not play a major role in the heave response of this hull to random wave excitation.

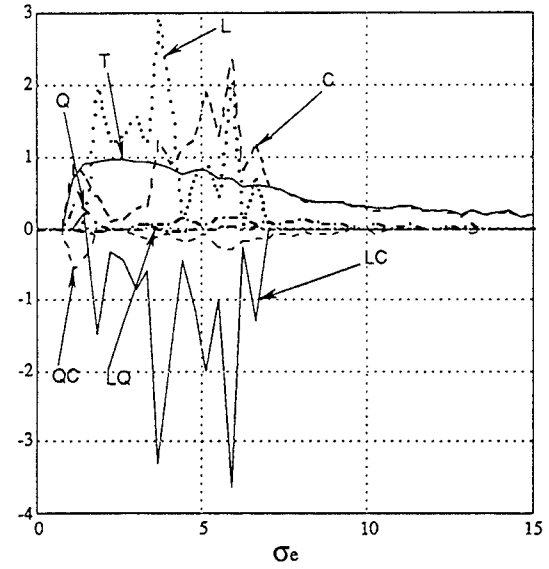

Fig. 21 Overall model coherence spectra for the heave response (nonorthogonal).

Next we note the presence of the interference coherence spectra, particularly LC which takes on relatively large negative valves. By comparison the LQ and QC interference spectra are fairly small. Observe also that the linear L and cubic coherence spectra C often exceed unity, when in fact they should ideally lie between zero and unity as was discussed previously. Thus we see that, although the third-order nonGaussian-excitation Volterra model is a good overall model, the presence of the interference terms prevent us from decomposing the response into its constituent linear, quadratic, and cubic components.

In order to avoid the deleterious interference effects, we utilized the orthogonal third-order Volterra model valid for nonGaussian excitation as discussed earlier in a previous section. The linear (L), quadratic (Q), cubic (C), and total (T) model coherency spectra for heave, pitch, and bow acceleration are plotted in Fig. 22 to 24, for the 100% case. Since we are now dealing with an orthogonal model, there are no interference coherence spectra. Furthermore, the linear, quadratic, cubic, and total model coherence spectra all lie between zero and unity. Thus, we may now interpret L, Q, C as the fraction of power in the observed response accounted for by the linear, quadratic, cubic components of the orthogonal Volterra model. Similarly T accounts for the fraction of power accounted for by the overall model (i.e., $T = L + Q + C$). Some general observations relating to Figs. 22 to 24 follow:

(a) In the band centered at $\sigma_e \sim 3 - 4$, the overall model accounts for approximately 95% of the observed heave, pitch, and bow acceleration response. In this same band, the linear model accounts for approximately 80-90% of the response, while the cubic accounts for 5-10%.

(b) Below and above $\sigma_e \sim 3 - 4$, cubic effects clearly dominate over linear and quadratic effects. In fact for $\sigma_e > 5$, cubic effects account for virtually all the response in heave and pitch, in that cubic coherence C is only slightly less than the total coherence T.

(c) Generally speaking quadratic effects are quite small, accounting for less than 10% of the observed response. An exception is the band centered around $\sigma_e \sim 7$ in the bow acceleration, where the quadratic coherency Q exceeds 10% by a factor of four. This component may again be explained by the large pitch angles as discussed above.

MOTION SIMULATION

The nonlinear response in these experiments on the S175 hull, as show in the harmonic components discussed above, constitutes overall evidence for nonlinearity without directly indicating the specific physical source of the nonlinearity. In order to examine the physics which may cause nonlinear effects, in a preliminary or simplified way, one can begin with the usual linear coupled equations of motion for heave and pitch in head waves:

$$A_{zz}\ddot{z} + B_{zz}\dot{z} + C_{zz}z + A_{z\theta}\ddot{\theta} + B_{z\theta}\dot{\theta} + C_{z\theta}\theta = F_z(t) \quad (26)$$

$$A_{\theta z}\ddot{z} + B_{\theta z}\dot{z} + C_{\theta z}z + A_{\theta\theta}\ddot{\theta} + B_{\theta\theta}\dot{\theta} + C_{\theta\theta}\theta = M_\theta(t) \quad (27)$$

The coefficients A_{zz}, etc. represent the mass plus added mass terms, while the B and C coefficients represent linear wave radiation damping and hydrostatic coefficients respectively. F_z and M_θ represent the exciting force and moment due to incident and diffracted waves. While it is recognized that the added mass terms are not

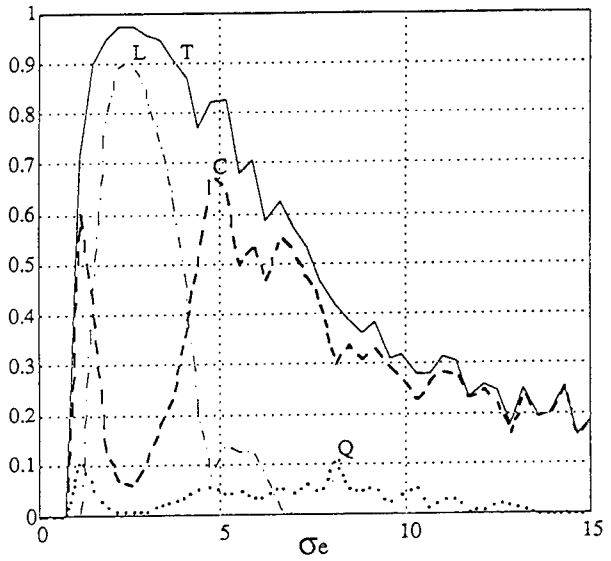

Fig. 22 Linear (L), quadratic (Q), cubic (C), and total (T) coherence spectra for heave (orthogonal model).

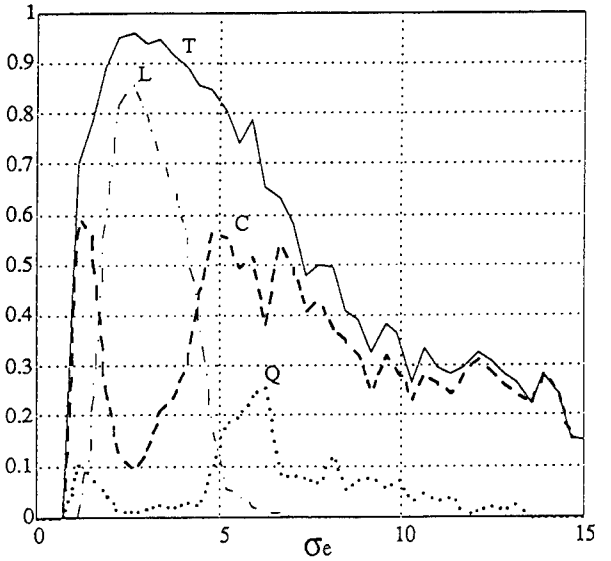

Fig. 23 Linear (L), quadratic (Q), cubic (C), and total (T) coherence spectra for pitch (orthogonal model).

actually constant but functions of frequency, nonetheless this equation may be solved in the time domain if one is only looking at steady periodic motion at one frequency. Solving in the time domain also allows the addition of discrete nonlinear terms to the equations, and a systematic variation of input amplitude to determine their effect. Physically, nonlinear damping may be the result of viscous damping (usually ignored in vertical plane motion calculations), while nonlinear static coefficients may arise when the hull form at the waterline has vertical slope or curvature. A preliminary set of time domain simulation calculations with these equations with cubic nonlinear terms has indicated the possibility of at least qualitatively matching the observed nonlinear behavior in the experiments. This is illustrated in Figures 25-26. Here, the linear coefficients were obtained from strip theory calculations for Fn = 0.200 and $\sigma_e = 3.76$. It is found that simply adding cubic uncoupled static terms of the form:

$$C^{(3)}_{zz} z^3, C^{(3)}_{\theta\theta} \theta^3$$

result in a behavior very similar to the experimental results. That is, there is a large variation in heave magnitude and pitch phase at the first harmonic. Furthermore, the simulated results indicate an extremely small third harmonic component in the displacements (on the order of one percent of first harmonic for $ka = 0.15$). This is consistent with the experimental results. In terms of the Volterra kernels, this means that in the three-frequency domain of the cubic kernel, the kernel $H_3(\omega, \omega, -\omega)$ constitutes a dominant part of the response,noticeably affecting the first harmonic response, while the term $H_3(\omega, \omega, \omega)$ which represents third harmonic response is quite small. The apparent reason for this is that while there may be quite large cubic, third harmonic force or moment components on the left hand side of the equations, the dominant effect of the mass or inertia terms is to force the system to behave similar to a low-pass filter, with small response at high frequency. Of course, these sample results are for only a single frequency of excitation, and do not show how various frequencies may interact. Furthermore, it would be quite surprising (and fortunate) if the nonlinear behavior of heave and pitch could be modelled simply by accounting properly for nonlinear hydrostatics. Nevertheless, this simplified model may be useful for efficiently exploring the cubic behavior over the complete three-frequency space.

DISCUSSION AND CONCLUSIONS

The experimental data for motions of the S175 hull form clearly indicate the presence of nonlinearities in response. By harmonic analysis of the regular wave data, and higher-order statistical signal processing of the random wave data, it is found that the response can be represented by a third-order Volterra functional series, with cubic effects the dominant nonlinearity. The cubic effect appears primarily in the frequency band of the waves, due to interaction of frequency triplets. Higher harmonic response outside the frequency range of excitation is also found, particularly in the acceleration measurement.

It has also been shown that the waves themselves should not be assumed Gaussian, and a new procedure has been developed to identify the Volterra kernels, up to cubic, for nonGaussian random inputs. The ability to measure the kernels up to third order from random wave data eliminates the need to carry out deterministic experiments with a large matrix of three frequency combinations. The ability to obtain these kernels in the frequency domain also means that it should be possible to construct a third order digital filter model, implemented as a parallel combination of linear, quadratic and cubic digital filters. If the sea wave time series is used as an input to this model, the output should provide a more accurate prediction of motions than a purely linear model, especially for extreme values of motion and for acceleration, where the nonlinearities play a prominent part. The digital simulation is also expected to be a useful tool for studying the effect of nonlinearities on the statistical nature of response.

Finally, it should be mentioned that we hope the experimental results presented here will form a useful data base for validating theoretical hydrodynamic models of

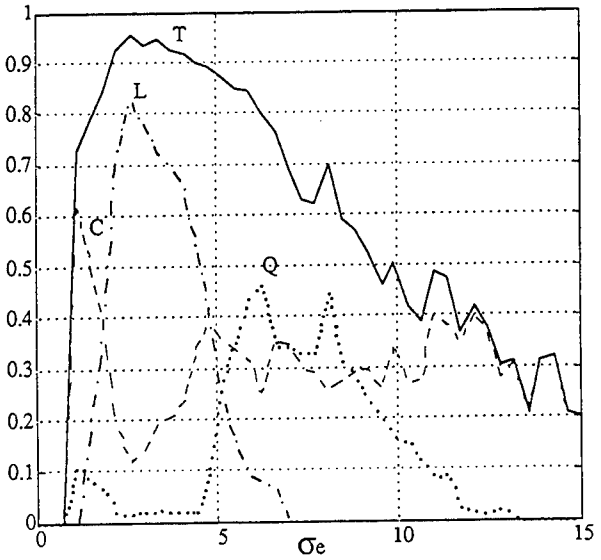

Fig. 24 Linear (L), quadratic (Q), cubic (C), and total (T) coherence spectra for bow acceleration (orthogonal model).

nonlinear wave effects, whether time or frequency domain. It is clear that the standard linear and Gaussian assumptions should not be accepted as strictly correct. As more exact nonlinear theoretical approaches are implemented, and a more powerful method of analyzing measured data, as described here, becomes available, we should be able to provide more accurate predictions of extreme ship motions.

ACKNOWLEDGEMENTS

The series of experiments documented here were carried out at the U.S. Naval Academy while the first author was a visiting professor in the Naval Systems Engineering Department. This exchange program was part of the Independent Research Program sponsored by the Technical Director, Carderock Division, Naval Surface Warfare Center (formerly David Taylor Research Center). At the University of Texas at Austin this work is supported by ONR N00014-88-K-0638 and ONR N00014-92-J-1046. Dr. S. W. Nam developed and implemented the algorithm to determine frequency-domain Volterra kernels up to third order for nonGaussian random excitation, and S. B. Im utilized a modified Gram-Schmidt orthogonalization procedure to implement the conditional orthogonal third-order Volterra modelling algorithm used in this paper to decompose the S175 hull response into its linear, quadratic and cubic constituent components.

REFERENCES

1. Roberts, J.B., "A Stochastic Theory for Nonlinear Ship Rolling in Irregular Seas," J. of Ship Research, Vol. 26, No. 4, Dec. 1982, pp. 229-245.

2. Kim, M.H. and Yue, D.K.P., "Sum- and DifferenceFrequency Wave Loads on a Body in Unidirectional Gaussian Seas,", J. of Ship Research, Vol. 35, No. 2, June 1991, pp. 127-140.

3. Dalzell, J.F., "Estimation of the Spectrum of Non-Linear Ship Rolling: The Functional Series Approach," SIT-DL-76-1894, 1976, Davidson Laboratory, Hoboken, New Jersey.

4. Dalzell, J.F., "Approximations to the Probability Density Of Maxima and Minima of the Response of a Nonlinear System," EW-22-84, 1984, US Naval Academy, Annapolis, Maryland.

5. Dalzell, J.F., "An Investigation of the Applicability of the Third Degree Functional Polynomial Model of Nonlinear Ship Motion Problems," SIT-DL-82-9-2275, Stevens Institute of Technology, Hoboken, New Jersey, December 1982.

6. Vantorre M., "Third-Order Theory for Determining the Hydrodynamic Forces on Axisymmetric Floating or Submerged Bodies in Oscillatory Heaving Motion," J. of Ocean Engineering, Vol. 13, No. 4, 1986, pp. 338-371.

7. Papanikolaou, A., "On the Solution of the Quasi ThirdOrder Problem of TwoDimensional Cylinders

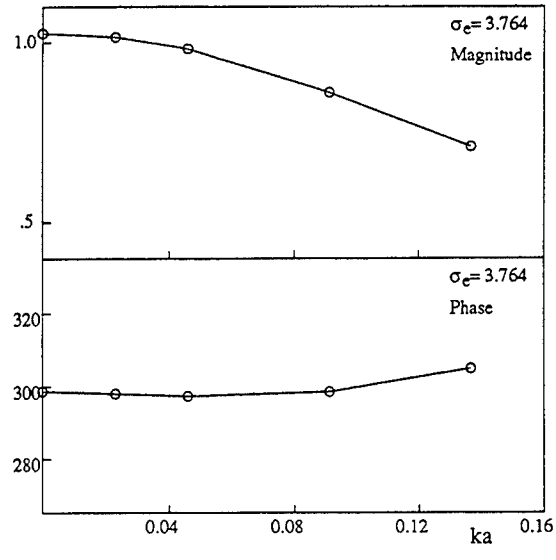

Fig. 25 Amplitude and Phase of Simulated Heave, Fn = 0.200

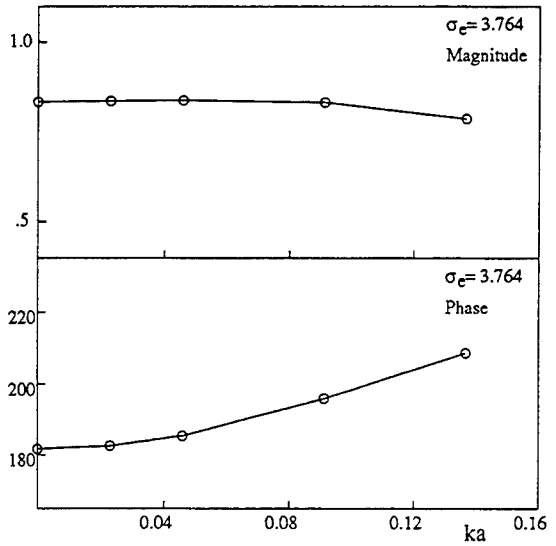

Fig. 26 Amplitude and Phase of Simulated Pitch, Fn = 0.200

in Forced Motion," J. of the Kansai Society of Naval Architecture, Japan, No. 210, 1988, pp. 121-133.

8. Report of the Seakeeping Committee, Proc. of the 18th International Towing Tank Conference, 1987, pp. 401-468.

9. O'Dea, J.F. and Troesch, A.W., "Comparative Seakeeping Model Experiments," Proc. of the 21st American Towing Tank Conference, 1987, pp. 359-368.

10. Kim, S.B. and Powers, E.J., "Orthogonal Representations of Frequency Domain Volterra Models for Arbitrary Inputs," Proc. of the Intl. Signal Processing Workshop on Higher-Order Statistics, Chamrousse, France, July 10-12, 1991, pp. 229-232.

11. Pawlowski, J.S., "A Theoretical and Numerical Model of Ship Motions in Heavy Seas," Trans. of the Society of Naval Architects and Marine Engineers, Vol. 99, 1991.

12. Lin, W-M. and Yue, D., "Numerical Solutions for Large-Amplitude Ship Motions in the Time Domain," 18th Symp. on Naval Hydrodynamics, National Academy Press, 1991, pp. 21-66.

13. St. Denis, M. and Pierson, W.J., " On the Motion of Ships in Confused Seas," Trans. SNAME, Vol. 61, 1953, pp. 280-357.

14. Schetzen, M., " The Volterra and Wiener Theories of Nonlinear Systems," John Wiley and Sons, New York, 1980.

15. Kim, S.B., Powers, E.J., Miksad, R.W. and Fischer, F.J., "Quantification of Nonlinear Energy Transfer to Sum and Difference Response of TLP's," Proc. of the First (1991) Intl. Offshore and Polar Engineering Conf., Edinburgh, U.K. Aug. 11-16, Vol. 1, 1991, pp. 87-92.

16. Tick, L.J., " The Estimation of Transfer Functions of Quadratic System," Technometrics, Vol. 3, 1961, pp. 563-567.

17. Kim, K.I. and Powers, E.J., "A Digital Method of Modeling Quadratically Nonlinear Systems with a General Random Input," IEEE Trans. on Acoustics, Speech, and Signal Processing, Vol. 36, 1988, pp. 1758-1769

18. Hong, J.Y., Kim, Y.C., and Powers, E.J., "On Modeling the Nonlinear Relationship Between Fluctuations with Nonlinear Transfer Functions," Proc. of the IEEE, Vol. 65, No. 8, Aug. 1980.

19. Nam, S.W., Powers, E.J. and Kim, S.B., "On the Identification of a Third-Order Volterra Nonlinear System Using a Frequency Domain Block RLS Adaptive Algorithm," Proc. IEEE Intl. Conf. on Acoustics, Speech and Signal Processing, Albuquerque, New Mexico, 1990, pp. 2407 - 2410.

20. Kim, S.B. and Powers, E.J., "Utilization of Conditioned Higher-Order Spectra for Nonlinear System Identification," IEEE Intl. Conf. on Acoustics, Speech, and Signal Processing, Vol. 5, 1992, pp. 493-496.

21. Bendat, J.S., "System Identification from Multiple Input/Output Data," J. Sound and Vibration, Vol. 49, 1976, pp. 293-308.

22. Billings, S.A., "Identification of Nonlinear System - A Survey," Proc. IEE, Vol. 127, Pt. D, No. 6, 1980, pp. 272-285.

23. Dalzell, J.F., "Experiment - Theory Correlation: Linear Ship Motion and Loading Theory," Proc. of the 18th American Towing Tank Conf., Vol. 2, 1977, pp. 449-462

24. Kim, S.B., Powers, E.J., Miksad, R.W., Fischer, F.J. and Hong, J.Y., " Application of Recent Advances in Digital Nonlinear Time Series Analysis Techniques to TLP Model Test Data," Offshore Engineering (Proceedings of the 7th Intl. Symp. on Offshore Engineering, Rio de Janeiro, Brazil), Pentech Press, London, 1990, pp. 238-256.

25. Hinich, M.H., "Testing for Gaussianity and Linearity of a Stationary Time Series," J. Time Series Anal., Vol. 3, No. 3, 1982, pp. 169-176.

26. Subba Rao, T. and Gabr, M.M., "A Test for Linearity of Stationary Time Series," J. Time Series Anal., Vol. 1, No. 2, 1980, pp. 145-158.

27. Kendall, M., Stuart, A. and Ord, J.K., Kendall's Advanced Theory of Statistics, 5th Ed., Vol. 1, New York, Oxford University Press, 1987.

28. Cho, Y.S., Oh, W.T., Kim, S.B. and Powers, E.J., "Testing for Gaussianity in Nonlinear System Identification," Proc. of the 1990 IEEE Intl. Symp. on Circuits and Systems, Vol. 2, May 1-3, 1990, pp. 1450-1453.

APPENDIX

EXPERIMENTAL UNCERTAINTY

There are a number of factors which contribute to the uncertainty of the measured data, including bias errors (which are constant within an experiment, but which may vary in a subsequent experiment), and precision errors which contribute to the scatter of the data within an experiment. Several of these sources are identified and quantified in this appendix.

Bias Errors

Bias errors by their definition are difficult to detect, since they may be small and are constant throughout an experiment. However, by closely examining various test conditions which are assumed to be constant and known with high accuracy, it is possible to identify several possible sources of bias:

Model Construction and Ballasting

The model was designed with a length of 3.5 m between perpendiculars. The hull designation S175 is based on a full scale design length of 175 m, thus the scale ratio is 1:50. The model was constructed of fiberglass, using an existing wooden model as a mold. When delivered, the model was aligned on a granite surface plate and measured for accuracy. The overall dimensional accuracy (relative to design) was found to be +0.4% in length, and -1% in beam. In terms of hull fairness, the baseline was found to be hogged 3.2 mm, while the side was concave 1.6 mm. In ballasting the model to achieve a design pitch gyradius (R_{yy}) of 0.24 Lpp, an unusual approach was taken in order to achieve maximum accuracy. In normal ballasting of a seakeeping model, the model is often ballasted to a certain yaw gyradius (R_{zz}) by a measurement of the natural yaw period in air with a pendulum arrangement, with the assumption that this is equivalent to the pitch behavior. Alternatively, the model may be oscillated in pitch, but this often requires supporting the model on a pitch table whose inertia may exceed that of the model. In the experiments discussed in this paper, the bare hull (constituting less than 50% of the fully ballasted mass) was suspended and oscillated as a pendulum in air in both pitch and yaw. A computer spreadsheet was then used to calculate the net weight, pitch and yaw inertias as ballast weights were added and adjusted. When the spreadsheet calculations indicated that the required pitch inertia was achieved, the ratio of yaw gyradius to pitch gyradius, as calculated by the spreadsheet, was 1.002. The yaw gyradius of the fully ballasted model was then measured in air. The ratio of the measured gyradius to the calculated gyradius was 1.0004. This check on yaw inertia lends credibility to the calculated pitch inertia. Although the yaw and pitch inertias were very similar in this particular model, the variation may be greater in other test programs, depending on hull proportions and detailed placement of ballast.

Test Environment

In addition to model construction and ballasting, there are a number of parameters which constitute the test environment, and are often considered either to be constant or to have a negligible effect on the results. Among those checked in these experiments were: carriage speed and vibration, the wave dispersion relationship, and heave staff friction. The measured carriage speed, corresponding to nominal Froude numbers of 0.200 and 0.275, had a total variation of ±0.1%. The carriage vibration was measured by observing the harmonic content in a drag gage at the bottom of the heave staff. The natural frequency was found to be approximately 3.6 Hz. This frequency (corresponding to $\sigma_e = 13.5$) corresponds to vibration in the horizontal direction, but may weakly couple into the vertical modes (heave, pitch) at this frequency. As a check on the linear, deep water wave dispersion relationship ($\omega^2 = gk$), the regular wave elevation measured on the moving carriage was used to calculate the actual encounter period. This was then used with the assumed dispersion relationship to estimate the wave frequency. This estimate agreed with the wavemaker oscillator frequency within ±0.2%, confirming the dispersion relationship.

In order to check the effect of heave staff friction, a load cell was installed at the bottom of the heave staff to measure vertical force. In the absence of friction, this would simply be the inertial force corresponding to accelerating the mass of the heave staff. The actual force was found to contain a component similar to Coulomb friction; that is a force opposing velocity, with a magnitude independent of the velocity magnitude. Different heave staffs and bearing arrangements were used in the two test series. The magnitude of this damping force was approximately 4 N in the first series of experiments, and 2 N in the second series. For comparison, the heave damping force (due to wave radiation) estimated from strip theory is approximately 50-300 N in the range of wave frequencies and steepnesses shown in Fig. 6-17. A Coulomb friction term was also introduced into the simulation discussed above, and appears to explain the difference in the results for heave in the two series of experiments, i.e. aproximately 5% for the smallest values of ka, decreasing to approximately 1-2% for the larger magnitudes. For comparison to earlier reported results on this hull, the first series of experiments included a set of runs at $\sigma_e = 3.55$, (λ/Lpp=1.1), and the results for heave are compared in Fig. 27 to published data from Ref. (9) It should be noted that the results taken from Ref. (9) are for a different scale ratio, and the model was self-propelled without a heave staff so that there was no additional heave friction introduced and the model was free to surge. The slight bias between the data sets in this figure is believed to be caused by the heave staff friction.

Precision Errors

Estimates of precision error can be made based on the maximum deviation and standard deviation found in the calibrations. Table 4 lists calibration information for the various transducers. In order to relate the values in this table to the actual ranges of data in the experiments, it is noted that the largest magnitudes measured in the experiments were on the order of 10 cm for waves and heave, 6 degrees for pitch and 0.6 g for acceleration.

In light of light of this information on bias and precision errors, but more importantly on the basis of observed repeatability within each series of experiments, and between both series and other reported results on this hull form, it is felt that for the regular wave experiments, observed magnitude changes greater than ten percent and phase shifts greater than ten degrees con-

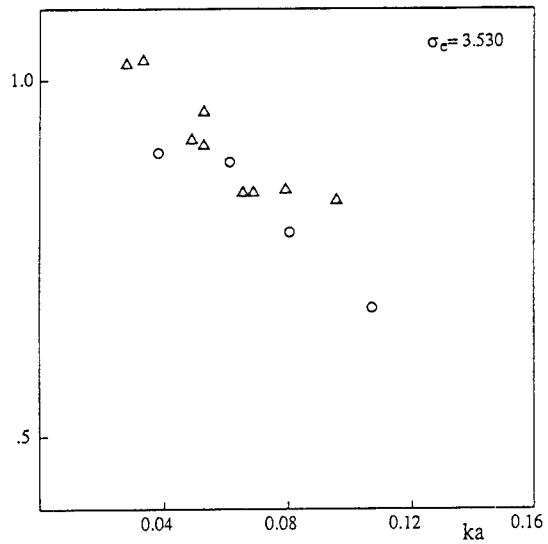

Fig. 27 Comparison of Heave Response to Ref. 9 (△)

Measurement	Units	Full Scale Limit	No. of Points in Cal.	Calibration Statistics Maximum Deviation (%F.S.)	(units)	STD. Dev. (units)
Speed	cm/s	-	29*	-	0.1615	0.0427
Pitch	deg	20	11	0.74	0.15	0.070
Heave	cm	25	8	0.31	0.079	0.051
Wave Height	cm	38	9	0.17	0.066	0.038
Bow Accel.	g's	5	11	0.052	0.0026	0.0013

* Speed statistics represent deviation in speed between tests.

Table 4 Instrument calibration precision information.

stitute firm evidence of nonlinear behavior. For the random wave experiments, it is much more difficult to estimate the accuracy of results because of the inherent statistical variability of finite length records. While guidelines are available for predicting the required length of run to obtain a specified confidence level on certain quantities, these guidelines are invariably based on the assumptions of linear response to Gaussian excitation, which are not supported in the data presented in this paper.

DISCUSSION

C. Calisal
University of British Columbia, Canada

At the University of British Columbia, we are currently testing the same hull (S175) as borrowed from the University of Michigan in a much smaller tank (BCROCC tank). I found your results most interesting. I would like to know if the location of the sonic wave probe is important and is the 1 m distance you use an ITTC recommendation. Secondly, in the analysis of your data in regular waves I assume you used an FFT package. Could you comment if the choice of "windows" was at all important in the determination of magnitudes and phases of the frequency response function. Is there an ITTC recommendation for this procedure? As you showed that the system is nonlinear, shouldn't there be a set of guidelines for uniformity of tank testing and is IIT a suitable process for nonlinear systems. Could you possibly comment on these points.

AUTHORS' REPLY

The objective of the ITTC comparative seakeeping study was to evaluate the level of agreement that can be expected when seakeeping results from different facilities are compared. The study allowed participating facilities to see if their techniques produced results in line with the majority of other facilities. We agree that there should be some specification in future ITTC comparative tests to reduce possible variation due to nonlinearity; this should take the form of a wave steepness specification.

Regarding the position of our wave probe, we moved our probe forward and aft in our earlier (1990) test series to determine if the proximity of the hull had any effect on the measurements. We found no difference between 0.5 and 1.0 m, but 1.0 m is conservative. The phase angles plotted in Figures 7-17 are based on the wave height as calculated at the model's center of gravity using the linear wave dispersion relationship.

The harmonic analysis was carried out using a Fourier series (not FFT) program written specifically for the purpose. The program identified an integer number of cycles in the wave record, using zero crossings to determine the end points of the data to be analyzed. The key feature of this method is that the analysis is conducted over an exact integer number of cycles (± 1 digital sampling interval). In this case, a rectangular window was used.

The random wave data were analyzed using FFT techniques to estimate the required higher-order spectral moments characterizing the random waves to sixth order and the wave-ship interaction to fourth order. The resulting hierarchy of spectral moments was used to estimate the linear, quadratic, and cubic Volterra kernals, which in turn, were utilized to decompose the ship response into its constituent linear, quadratic, and cubic components.

Theoretical and Experimental Study of the Nonlinearly Coupled Heave, Pitch, and Roll Motions of a Ship in Longitudinal Waves

I. Oh, A. Nayfeh, D. Mook
(Virginia Polytechnic Institute and State University, USA)

ABSTRACT

The loss of dynamic stability and the resulting large-amplitude roll of a vessel in a head or following sea were studied theoretically and experimentally. A ship with three degrees of freedom (roll, pitch, heave) was considered. The governing equations for the heave and pitch modes were linearized and their harmonic solutions were coupled with the roll mode. The resulting equation, which has time varying coefficients, was used to predict the response in roll. The principal parametric resonance was considered in which the excitation frequency is twice the natural frequency in roll. Force-response curves were obtained. The existence of jump phenomena and multiple stable solutions for the case of subcritical instability was observed in the experiments and found to be in good qualitative agreement with the results predicted by the theory. The experiments also revealed that the large-amplitude roll is dependent on the location of the model in the standing waves.

1. INTRODUCTION

More than 100 years ago Froude (1) observed that ships have undesirable roll characteristics when the natural frequency in pitch is twice the natural frequency in roll. Only nonlinear equations of motion can explain such behavior; yet the theoretical study of nonlinear coupling began as recently as the 1950s. Paulling and Rosenberg (2) considered a ship (their model) that was only free to pitch and roll. By neglecting damping, the effect of roll displacement on pitch moment, and wave-induced roll moments, and by including wave-induced pitch moments and the nonlinear effects of pitch displacement on roll moments, they found that the roll displacement was governed by a Mathieu equation, which they used to find the boundary, in the excitation amplitude-frequency plane, of the region in which rolling occurs spontaneously. Kinney (3) added a linear damping term to the roll equation and essentially repeated the analysis of Paulling and Rosenberg. Kerwin (4) used the same Mathieu equation to include wave-excited roll motion. Blocki (5) added nonlinear damping and a nonlinear restoring moment to the roll equation and used it to investigate the probability of capsizing.

The possibility of large rolling motions developing in a head sea consisting of regular waves was shown by Grim (6) using a cubic form for the restoring moment. Haddara (7) studied the rolling motion using a quadratic form for damping and a cubic form for the restoring moment. He showed that unstable rolling motion can occur in irregular waves.

The studies mentioned above essentially involve one degree of freedom. There have also been some two-degree-of-freedom models to explain the connection between the frequency ratio and the undesirable roll behavior mentioned by Froude (1). Nayfeh, Mook, and Marshall, and Mook, Nayfeh, and Marshall (8,9) used model equations that account for the coupling between the pitch mode and the roll mode by including the dependence of the pitching moment on the roll displacement. With this approach, the pitch motion is not prescribed but coupled to the roll equation, and consequently, the pitch and roll displacements are determined simultaneously as functions of a prescribed wave-induced excitation in pitch. They clearly showed the significance of the frequency ratio. Moreover, they found a "saturation" phenomenon, nonperiodic responses to periodic excitations, and subcritical instabilities, among other results. Subsequently, Nayfeh (10) investigated the Hopf bifurcations, which can occur under certain conditions, and found period-multiplying bifurcations and chaos in the predicted response.

A vessel in a head or following sea may experience some control problems such as broaching and the loss of course stability, especially in following regular waves. Wahab and Swaan (11) used a linear formulation of the problem with constant coefficients and Froude-Krilov forces as the only wave forces and moments to consider the zero-frequency-

of-encounter case. With this fairly simple model they were able to demonstrate the directional instability when a vessel with fixed controls is positioned anywhere over half of the wave cycle, but particularly when the center of gravity of the vessel is near the steepest part of the wave and the stern near the wave crest. This phenomenon is familiar to vessel operators. Wahab and Swaan also were able to demonstrate analytically that the probability of broaching was greater in steeper waves.

Eda and Crane (12) included hydrodynamic maneuvering coefficients obtained from experiments on models and horizontal plane-wave exciting forces and moments obtained from a strip theory. They also considered very low frequencies of encounter with regular waves and their predicted results of maneuvering performance in regular following or stern quartering waves was in reasonable agreement with model tests on a Series 60 hull. Eda (13) extended this work and demonstrated the same result as Wahab and Swaan, that a vessel which is directionally stable in calm water may not be stable in regular following waves with zero frequency of encounter.

In similar circumstances, a vessel runs a great risk of experiencing large-amplitude motions not only in in-plane modes, such as heave and pitch, but also in out-of-plane modes, such as roll and yaw. The latter phenomenon is caused by the nonlinear interactions among the modes of motion and is the subject of the present investigation.

Blocki (5) considered a ship with only two degrees of freedom (heave and roll). Such a restriction (the elimination of pitch) implies that the ship is symmetric with respect to the midship section (sometimes called fore-and-aft symmetry) and in a beam sea. Attempting to satisfy such limitations, Blocki used a cylindrical model in a beam sea in his experiments. In his analysis, he ignored the wave-induced roll moment, an obvious inconsistency but an approximation that is reasonable when the slope of the waves is small and the wavelength is large compared to the beam.

Following Blocki's work, Nayfeh and Sanchez (14) investigated the qualitative behavior of a ship rolling in longitudinal waves. They used an analytical-numerical technique based on the method of multiple scales to predict the qualitative changes taking place as the amplitude and frequency of the excitation are slowly changed. They confirmed their analytical results by using both analog- and digital-computer simulations.

In the present paper, we describe the real situation more accurately than Blocki (5) and Nayfeh and Sanchez (14). Specifically, we lift the restriction of fore-and-aft symmetry, add a third degree of freedom (pitch), and consider head and following seas both theoretically and experimentally. The heave and pitch motions are assumed to be independent of the roll motion, an assumption that was verified experimentally. Due to the heave-pitch-roll coupling, the amplitudes and frequencies of the heave and pitch motions play the role of an effective amplitude and frequency of the parametric excitation. The parametric term in the roll equation basically accounts for the time-dependent variation of the metacentric height. We investigate the principal parametric resonance in which the excitation wave frequency is twice the natural frequency in roll.

A much more exhaustive review of the literature can be found in the forthcoming doctoral dissertation of I. G. Oh (27).

2. EQUATIONS OF MOTION

Here we consider a model supported on a sting with three degrees of freedom: roll (ϕ), pitch (θ), and heave (z). The equations of motion can be written in the following form:

$$\ddot{z} + 2\zeta_z\dot{z} + \omega_z^2 z = \overline{Z}(t) \tag{1}$$

$$\ddot{\theta} + 2\zeta_\theta\dot{\theta} + \omega_\theta^2\theta = \overline{\Theta}(t) \tag{2}$$

$$\ddot{\phi} + \omega_\phi^2\phi + 2\mu_1\dot{\phi} + 2\mu_3\dot{\phi}^3 - \alpha_3\phi^3 - \frac{1}{2}(K_{\phi z}\phi z + K_{\phi\theta}\phi\theta + K_{\dot{\phi}\dot{z}}\dot{\phi}\dot{z} + K_{\dot{\phi}\dot{\theta}}\dot{\phi}\dot{\theta}) = \overline{K}(t) \tag{3}$$

where ζ_z and ζ_θ are damping coefficients; ω_z, ω_θ, and ω_ϕ are the natural frequencies; μ_1 and μ_3 are linear and cubic roll damping coefficients, α_3 is the constant cubic "stiffness" coefficient, and $K_{\phi z}$, $K_{\phi\theta}$, $K_{\dot{\phi}\dot{z}}$, and $K_{\dot{\phi}\dot{\theta}}$ are the constant coefficients of the quadratic coupling terms. Blocki (5) considered only heave and roll and ignored the kinematic-kinematic coupling; thus, he had only one (static-static) quadratic term: $K_{\phi z}\phi z$. Here we include additional static-static coupling as well as kinematic-kinematic coupling terms.

Assuming simple harmonic wave excitation, we write

$$\overline{Z}(t) = \overline{Z}_0\cos\Omega t \tag{4}$$

$$\overline{\Theta}(t) = \overline{\Theta}_0\cos(\Omega t + \tau_d) \tag{5}$$

where Ω is the frequency of the exciting waves, τ_d is the phase delay of the pitch moment relative to the heave force, $\overline{Z}_0$ is a measure of the amplitude of heave excitation force, and $\overline{\Theta}_0$ is a measure of the amplitude of the pitch excitation moment. $\overline{Z}_0$ and $\overline{\Theta}_0$ are functions of the wave height as well as the position of the mass center in the wave. Since (1) and (2) are uncoupled linear equations, they are solved as

$$z = a_z \cos(\Omega t + \tau_z) \tag{6}$$

$$\theta = a_\theta \cos(\Omega t + \tau_\theta) \tag{7}$$

where a_z and a_θ are the amplitudes of heave and pitch respectively, τ_z and τ_θ are the phase lags of heave and pitch relative to the excitation wave, and τ_θ is a function of ζ_θ and τ_d.

We consider the case in which the ship is in longitudinal waves so that $\overline{K}(t) = 0$ in equation (3). Substituting (6) and (7) into (3), we obtain

$$\begin{aligned}&\ddot{\phi} + \omega_\phi^2\phi + 2\mu_1\dot{\phi} + 2\mu_3\dot{\phi}^3 - \alpha_3\phi^3 \\ &+ [f_1 \cos(\Omega t + \tau_z) + f_3 \cos(\Omega t + \tau_\theta)]\phi \\ &+ [f_2 \sin(\Omega t + \tau_z) + f_4 \sin(\Omega t + \tau_\theta)]\dot{\phi} = 0\end{aligned} \tag{8}$$

where

$$\begin{aligned}f_1 &= -\frac{1}{2} a_z K_{\phi z}, \quad f_2 = \frac{1}{2} \Omega a_z K_{\dot{\phi} z}, \\ f_3 &= -\frac{1}{2} a_\theta K_{\phi\theta}, \quad f_4 = \frac{1}{2} \Omega a_\theta K_{\dot{\phi}\theta}\end{aligned} \tag{9}$$

3. ANALYSIS

An approximate analytical solution of equation (8) can be obtained for small but finite amplitudes. The straightforward expansion shows that resonances occur when $\Omega/\omega_\phi \approx 1,2,4$, etc. The first two cases are known as the fundamental and principal parametric resonances, respectively. It was concluded by Blocki (5) that the most dangerous case is $\Omega/\omega_\phi \approx 2$. Nayfeh and Sanchez (14) presented the bifurcation diagram in terms of the frequency and amplitude of the excitation and showed that the principal resonance occur at the smallest excitation amplitude.

We use the method of multiple scales to determine a first-order approximation to the solution of equation (8). We begin by assuming that an approximation to ϕ can be written in the following form:

$$\phi(t; \varepsilon) \approx \varepsilon\phi_0(T_0, T_1) + \varepsilon^3\phi_1(T_0, T_1) \tag{10}$$

where $T_0 = t$ is a fast time scale, characterizing motions occurring at the frequency Ω; $T_1 = \varepsilon^2 t$ is a slow scale, characterizing the modulation of the amplitude and phase due to the nonlinearity, damping, and resonances; and ε is a dimensionless measure of the amplitude of the motion, which is used solely as a bookkeeping device. By writing expansion (10), we have "scaled" the amplitude of the response. The following analysis provides an approximation that is valid for $\varepsilon << 1$ and, therefore, for small amplitudes of the motion. What the analysis does not provide is a definition of "small." It is not unusual for an analysis such as this one to still be quite accurate at amplitudes of 30 or 45 degrees. The time derivatives are transformed into

$$\frac{d}{dt} \approx D_0 + \varepsilon^2 D_1 \tag{11}$$

$$\frac{d^2}{dt^2} \approx D_0^2 + 2\varepsilon^2 D_0 D_1 \tag{12}$$

$$\text{where } D_0 = \frac{\partial}{\partial T_0} \text{ and } D_1 = \frac{\partial}{\partial T_1} \tag{13}$$

and terms of $0(\varepsilon^3)$ have been neglected. Next we must scale the linear damping and forcing so that all damping and forcing as well as the static restoring moment interact at the same order. We put $\mu_i = \varepsilon^2\hat{\mu}_i$ and $f_i = \varepsilon^2\hat{f}_i$ for i = 1, 2, 3, and 4. The implication of the latter is that small-amplitude pitch and heave motions can produce large-amplitude rolling. In the experiments we observed that waves of very small amplitude did produce large-amplitude rolling, an observation that is consistent with this assumption. Substituting these definitions and equations (10)-(12) into equation (8), and then equating coefficients of like powers of ε, we obtain

$$0(\varepsilon): \quad D_0^2\phi_0 + \omega_\phi^2\phi_0 = 0 \tag{14}$$

$$\begin{aligned}0(\varepsilon^3): \quad &D_0^2\phi_1 + \omega_\phi^2\phi_1 = -2D_0D_1\phi_0 - 2\hat{\mu}_1 D_0\phi_0 \\ &- 2\mu_3(D_0\phi_0)^3 + \alpha_3\phi_0^3 - \hat{f}_1 \cos(\Omega t + \tau_z)\phi_0 \\ &- \hat{f}_2 \sin(\Omega t + \tau_z)D_0\phi_0 - \hat{f}_3 \cos(\Omega t + \tau_\theta)\phi_0 \\ &- \hat{f}_4 \sin(\Omega t + \tau_\theta)D_0\phi_0\end{aligned} \tag{15}$$

The solution of equation (14) can be written as

$$\phi_0(T_0, T_1) = A(T_1)e^{i\omega_\phi T_0} + cc \tag{16}$$

where cc stands for the complex conjugate of the preceding term. The function $A(T_1)$ is an arbitrary complex function of T_1 at this level of approximation. It is determined by imposing the solvability conditions at the next level of approximation.

Because we are considering the principal parametric resonance corresponding to $\Omega \approx 2\omega_\phi$, we introduce a detuning parameter $\hat{\sigma}$ according to

$$\Omega = 2\omega_\phi + \varepsilon^2\hat{\sigma} \tag{17}$$

Then we substitute equations (16) and (17) into equation (15) and find that secular terms are eliminated from ϕ_1 if

$$2i(\dot{B} + \mu_1 B) + (6i\mu_3\omega_\phi^2 - \frac{3\alpha_3}{\omega_\phi})B^2\bar{B} + \frac{f}{\omega_\phi}\bar{B}e^{i\sigma t} = 0 \tag{18}$$

where the overdot denotes the derivative with respect to the original time t, $\sigma = \Omega - 2\omega_\phi$, $B = \varepsilon A$, the unscaled amplitude (here we have eliminated ε by rewriting all the variables in their original form; ε is no longer needed) and

$$f = \frac{1}{2}(f_1 e^{i\tau_z} - f_2\omega_\phi e^{i\tau_z} + f_3 e^{i\tau_\theta} - f_4\omega_\phi e^{i\tau_\theta}) = |f|e^{i\tau_f} \tag{19}$$

Here f is an effective amplitude, due to the combined influence of heave and pitch, and is a complex function of $K_{\phi z}$, $K_{\phi\theta}$, $K_{\dot{\phi}\dot{z}}$, $K_{\dot{\phi}\dot{\theta}}$, a_z, a_θ, Ω, ω_ϕ, τ_z and τ_θ [see equation (9)].

Next, we express the function B in the following polar form:

$$B = \frac{1}{2}ae^{i\beta} \tag{20}$$

where a and β are the amplitude and phase of the response. It follows that

$$\dot{a} = -\mu_1 a - \frac{3}{4}\mu_3\omega_\phi^2 a^3 - \frac{|f|a}{2\omega_\phi}\sin\gamma \tag{21}$$

$$a\dot{\gamma} = a\sigma + \frac{3\alpha_3}{4\omega_\phi}a^3 - \frac{|f|a}{\omega_\phi}\cos\gamma \tag{22}$$

where $\gamma = \sigma t - 2\beta + \tau_f$. It follows from equations (20), (16), and (10) and from the relationship between A and B that

$$\phi(t) \approx a\cos\left[\frac{1}{2}(\Omega t - \gamma + \tau_f)\right] \tag{23}$$

where a and γ are given by equations (21) and (22), and we have made use of equation (17).

For steady-state periodic responses, i.e., fixed-point solutions, we let $\dot{a} = \dot{\gamma} = 0$. There exist two sets of fixed-point solutions: First,

$$a = 0 \tag{24}$$

is always a solution which is actually the solution of the linearized form of equation (3). Second, when $a \neq 0$, manipulating equations (21) and (22) yields a set of algebraic equations which can be solved numerically to determine a and γ. The equation for a is

$$c_4 a^4 + 2c_2 a^2 + c_0 = 0 \tag{25}$$

where

$$c_4 = \frac{9}{4}\mu_3^2\omega_\phi^4 + \frac{9}{16}\frac{\alpha_3^2}{\omega_\phi^2}$$

$$c_2 = 3\mu_1\mu_3\omega_\phi^2 + \frac{3\alpha_3}{4\omega_\phi}\sigma, \qquad c_0 = 4\mu_1^2 + \sigma^2 - \frac{|f|^2}{\omega_\phi^2}$$

The stability of the various fixed-point solutions has been determined by Oh (27).

Equations (21)-(25) yield two types of force-response curves depending on the values of parameters:

Figure 1 shows a typical supercritical-type result when $\mu_1 = \mu_3 = 0.04$, $\alpha_3 = 1.0$, and $\sigma = 0.20$. As the resultant forcing amplitude $|f|$ is increased from 0, there is only the trivial solution until the bifurcation point $|f| = 0.2155$. At the bifurcation point the trivial solution becomes unstable and a nontrivial solution appears. As $|f|$ is increased further, the roll amplitude grows nonlinearly and monotonically.

Figure 2 shows a typical subcritical-type force-response curve, which contains some interesting features. The values of the parameters are the same as those in Figure 1 except the sign of σ has been changed. As the effective amplitude $|f|$ is increased from 0, only one solution is possible; the trivial solution. As $|f|$ passes 0.0957 approximately, three solutions are possible, the trivial solution and two nontrivial solutions. As $|f|$ passes 0.2155 approximately, only two solutions are possible, the trivial solution and a rather large-amplitude nontrivial solution. An analysis of the stability of the various solutions [see Oh (27)] revealed the following: (1) For $0 < |f| < 0.2155$, the trivial solution is stable. For $|f| > 0.2155$, it is unstable. (2) For $0.0957 < |f| < 0.2155$, the large-amplitude nontrivial solution is stable and the small-amplitude nontrivial solution is unstable. (3) For $|f| > 0.2155$, the nontrivial solution is stable.

In an experiment, one would never see motion corresponding to the low-amplitude nontrivial solution in the range $0.0957 < |f| < 0.2155$. For $|f| > 0.2155$, one would always see a rolling motion. In the range $0.0957 < |f| < 0.2155$, one could expect to see one of two possible motions, either no roll at all (corresponding to the trivial solution), or a rather large-amplitude roll. The initial conditions, or external disturbances, determine which motion will develop. The existence of two stable responses to the same excitation is a characteristic of subcritical instability and has been observed in many other systems (15)-(17).

As the effective amplitude $|f|$ is slowly increased from 0, only nonrolling motion will be excited until the bifurcation point $|f| = 0.2155\,(\zeta_2)$ is reached. As $|f|$ is increased further, the trivial linear solution becomes unstable, and the roll

suddenly occurs; i.e., the jump-up phenomenon appears. From there, the "rolling" solution is the only stable response, and its amplitude increases nonlinearly and monotonically as $|f|$ is increased further.

As $|f|$ is decreased slowly from a large enough value, the magnitude of the large-amplitude roll motion decreases nonlinearly, and rolling continues even after the jump-up bifurcation point (ζ_2) is passed. When $|f|$ reaches the second bifurcation point $|f| = 0.0957$ (ζ_1), the large-amplitude roll motion suddenly disappears and the response is roll free; i.e., the jump-down phenomenon occurs.

4. DESCRIPTION OF EXPERIMENTS

A series of experiments was performed in the Ship Dynamics Laboratory at VPI & SU.

4.1 Experimental Setup

The towing basin of VPI & SU is approximately 30m x 1.8m x 2.5m. A plunger-type wavemaker made of a flat steel plate is installed at one end. A set of wave absorbers is placed behind the wavemaker and another set is placed at the other end. There is a towing carriage on the rails of the basin, which is used as a stationary mounting platform for the model in the present experiment. The wooden model of the tanker used in the experiments is approximately 223.5cm x 29.2cm x 19.1cm. The weight of the model and ballast is approximately 54.5kg. The model is supported in such a way that heave, pitch and roll are allowed while surge, sway and yaw are constrained. Pitch and roll motions are possible up to $\pm 22°$ each.

The angular displacements in pitch and roll are measured by two Schaevitz R30D RVDTs, and the linear displacement in heave is measured by a Schaevitz 5000HPD LVDT. The wave heights are measured by capacitance-type Davis WL/WP 03 wave level guages. To control and monitor the movement of the wavemaker, a Temposonics DCTM-36 LVDT is used and its signal is fed into a Tektronix 2230 oscilloscope with the signal from a Wavetek 275 function generator.

A Fluke 8600A digital multimeter, HP 3468A digital multimeter, and a Graphtec SR6335 strip-chart recorder are used to monitor the response of the model. A Data Translation DT 2801 A/D converter is used for digitization, and data acquisitions are done by a commercial software Labtech Notebook installed in an IBM AT personal computer. Most of the analyses of the data are done by two microprocessors: an HP 3562A dynamic signal analyzer and a Rockland 5820B spectrum analyzer.

More details of the experimental setup are to be found in the dissertation of I. G. Oh (27).

4.2 Experimental Procedure

Tests were done without a model to map the frequencies and amplitudes of the wavemaker that produce plane waves in the VPI & SU towing basin. From these tests, it was observed that operating the wavemaker around the frequency of 0.60 Hz produces plane waves for the widest range of amplitudes. Because interest is focused on the principal parametric resonance, weights were distributed inside the model so that the natural frequency in roll (0.32 Hz approximately) is about half of the frequency of the waves (0.6 Hz approximately).

With the model in place, the wavemaker was started at the lowest amplitude available. Then the amplitude was increased very slightly to the next step in the function generator while the behaviour of the model in the waves and various signals were continuously monitored. A period ranging from half an hour to four hours, depending on the amplitude and frequency of waves being generated, was required to achieve a steady state. After reaching the maximal amplitude of the waves available in the present experimental setup, the wave amplitude was slowly decreased.

During this process, the jump-up/down phenomena were observed, and the range of wave amplitudes where roll motions exist was obtained. When the jump up did not occur spontaneously, external disturbances of various kinds were imposed on the model at each different step of wave amplitudes; these disturbances produced large-amplitude stable roll motion in many cases. Video-tape recordings and/or photographs were made during the tests if desired.

5. RESULTS AND DISCUSSION OF EXPERIMENTS

5.1 General Results

Figures 3 and 4 are photographs showing two views of the model rolling in longitudinal regular plane waves. In Figure 4, the view is from the absorber end of the towing basin. The rolling motion (model heeled to the starboard) in longitudinal regular plane waves is clearly evident.

In the following figures, force-response curves are shown. The capital letters are used to denote the sweep-up process of wave amplitudes while the lower-case letters are reserved for the sweep-down process. This practice is followed all the way through from Figs. 5 to 8 except Fig. 6.

As the wave amplitude slowly increased, rolling did not occur until the wave height reached a certain critical value (ζ_2). Then large-amplitude rolling occurred all of a sudden (the jump-up phenomenon). When we increased the wave amplitude continuously beyond the jump-up bifurcation value (ζ_2), the amplitude of the rolling remained almost constant or even decreased instead of increasing monotonically as predicted by the theory.

After reaching the maximum wave amplitude possible in our experimental setup, we slowly reduced the wave amplitude. The large-amplitude rolling continued at wave heights below the jump-up bifurcation value (ζ_2). When the wave amplitude was decreased further to another critical value ($\zeta_1; \zeta_1 < \zeta_2$), the large-amplitude rolling suddenly died out (the jump-down phenomenon), and no discernible rolling existed below ζ_1.

In the range of wave amplitudes between the jump up (ζ_2) and jump down (ζ_1) bifurcation values, the possibility of a stable nonrolling motion coexisted with the possibility of a stable large-amplitude rolling motion, which was sometimes as large as $\pm 20°$ in the present experiment. When the model was not exhibiting any noticeable roll, some disturbances in the roll mode could cause a jump up to large-amplitude steady-state rolling anywhere between ζ_1 and ζ_2. The domain of attraction (i.e., the set of disturbances) for large-amplitude rolling increased as the wave amplitude increased toward ζ_2. This subcritical type of instability was observed at all the locations of the model in the standing waves for a wave frequency of 0.60 Hz in our experiment.

The coexistence of two possible motions for the same wave pattern is further described in Figure 5, which contains a typical force-response curve. The wave frequency is 0.60 Hz at location number 4 (refer to Fig. 6). The sequence of events is marked by arrows from A to H; $A \rightarrow C \rightarrow D \rightarrow E \rightarrow D \rightarrow G \rightarrow H \rightarrow A$. The wave amplitude marked at point H corresponds to ζ_1, and the one at point C corresponds to ζ_2. Just after the wave amplitude passed point C, a sudden jump up to point D occurred. Thereafter, the trivial solution was unstable and only the large-amplitude rolling was stable.

After arriving at point E, the wave amplitude was decreased slowly. The large-amplitude rolling existed below point D, where the jump up occurred during the sweep up. When the wave amplitude was decreased slightly after point G, a sudden jump down to point H occurred and rolling stopped. Between *H* and *C*, two different stable motions exist, the nonrolling motion and the large-amplitude rolling. The motion that develops depends on the initial conditions. It was surprising to observe such large-amplitude rolling of the model in waves of such small amplitudes just before the jump down, but we recall that the theory predicts that small pitch and heave motions can excite relatively large rolling.

The responses in heave and pitch are nearly linear during the whole test, regardless of the magnitude of the roll response and the occurrence of jumps. Figures 5b-d show FFT's and time traces corresponding to a few points on the curves in Fig. 5a. Figure 5b shows the FFT's and corresponding time signals at point B. The first harmonic components of all the responses of heave, pitch and roll are at the same frequency as the wave. The roll is not discernible with the naked eye there. Figure 5c corresponds to point D. (i.e., just after the jump up occurred.) The situation after rolling begins is described in Fig. 5c. The roll response has the largest peak at half the frequency of the waves, which is a dramatic change from Fig. 5b. The heave and pitch continue at the same frequency as the waves. Figure 5d shows the plots of the responses at point H (i.e., just after the jump down occurred). The large peak at half of the frequency of the waves disappeared and the slight rolling returned to the frequency of the waves. The magnitude of roll motion decreased drastically and was not noticeable with the naked eye. The general characteristics of the plots in Fig. 5d are similar to those in Fig. 5b. The responses between 0 and C possess shapes similar to those in the plots of Figs. 5b and d, and the responses between E and G are similar to Fig. 5c.

Figures 5e and f are parts of the long-time records for heave and roll responses recorded continuously on a strip chart recorder. Figure 5e clearly shows the sudden jump up of the roll motion. After the jump, its magnitude almost stays constant while the amplitude of heave varies as the amplitude of the wave is varied. Figure 5f shows the jump down. The small gap is due to an unintentional electric fluctuation that occurred for a very short period of time. Electric fluctuations occurred often because the duration of one test was tremendously long, as much as several days. Thus, the whole process had to be monitored. The same problems sometimes occurred because of thunder storms and automatic cutoff of the electric motor due to overheating.

5.2 Effect of the Location in the Waves

Experiments were conducted to show the dependence of the response on the location of the center of gravity of the model along a wavelength of the standing waves. These results are relevant to the questions of dynamic course instability and instability of motion of a ship when it is navigating with the same speed as the waves so that its encounter frequency is nearly zero. The jump-up

and jump-down bifurcation values (ζ_2 and ζ_1) also varied with the different positions of the model in the waves.

These observations are consistent with the work of Renilson and Driscoll (18). They concluded from experiments conducted in the large circulating water channel (CWC) at the National Maritime Institute in Great Britain that the motion, the magnitude and direction of the side force, and the possibility of a ship broaching while operating in slowly overtaking following or quartering regular waves are dependent on its longitudinal position in the wave system. They actually considered the case of zero frequency of encounter. They found that a longitudinal wave-induced force can lead a ship to a steady-state position relative to the waves; at this point, the ship and the "following" waves are moving at the same speed. They showed that the response of a ship varies over the wavelength and the effects of heel angle due to rolling motion can lead to course instability such as broaching.

We placed the model at various positions along a wavelength of the same standing waves with a frequency of 0.60 Hz. The relative locations are numbered 1-8 in Fig. 6. The node is numbered 1, the antinode is 5, and so on. Changing the location of the ship along the wavelength changes the phase between the pitch and heave motions and, hence, changes the effective amplitude of the parametric excitation of the roll mode.

Figures 7a-c show all the responses in each mode of heave, roll and pitch with the locations of the model as a parameter when the excitation wave frequency is 0.60 Hz. Figures 8a-h show the responses of heave, roll, and pitch in one set at each different location.

The heave motions shown in Fig. 7a possess a systematic order: the heave amplitude is proportional to the wave amplitude at a specific location along a wavelength of the standing waves, which is the linear response as expected. In other words, the amplitude of heave response is largest at the antinode (location number 5) where the wave amplitude is the largest (marks E and e along the curve), the heave amplitude is smallest at the node (location number 1) where the wave amplitude is the smallest (marks A and a), and the heave amplitudes at other locations can be arranged in proper downward order from antinode to node according to the wave amplitudes at specific locations.

The pitch motions, shown in Fig. 7c, also demonstrate a systematic order: the pitch amplitude is proportional to the wave slope at each specific location along a wavelength of the standing waves, which is also expected from the linear results. They are generally opposite in order to the heave responses: The amplitude of the pitch motion is largest at the node (location number 1) where the wave slope is the largest (marks A and a), the pitch amplitude is smallest at the antinode (location number 5) where the wave slope is the smallest (marks E and e), and the pitch amplitudes at other locations can be arranged in proper downward order from node to antinode according to the wave slopes at specific locations.

In Figs. 7a and c, the responses in heave and pitch exhibit linear behaviour very clearly regardless of the existence of jump phenomena and the large-amplitude rolling for all the cases. These results confirm the assumption in the present analysis that roll does not significantly influence pitch and heave for the case considered here.

Figure 7b, which shows the variety of responses in roll, demonstrates the coexistence of multiple stable responses. Some cases in Fig. 7b initially did not show the jump up, but then imposing disturbances externally typically yielded large-amplitude stable rolling.

The effective amplitude of the parametric excitation of the roll mode is produced by the combined role of heave and pitch and hence varies with the location of the center of gravity in the wave form even when the wave frequency is fixed.

Location number 2 produced the seventh largest heave amplitude out of the eight locations considered, the second largest pitch amplitude, and the largest amplitude of the upper-branch roll motion in general. Location number 1 (the node) produced the smallest heave, the largest pitch, and the second largest roll amplitude. Location number 5 (the antinode) produced the largest heave, the smallest pitch, and the third largest roll amplitude in general. Location number 6 produced the second largest heave, the seventh largest pitch, and the smallest roll amplitude, and so on. Hence, the present study significantly extends the work of Blocki (5) and Nayfeh and Sanchez (14). In the real motion, the ship will necessarily experience pitch; therefore, the pitch mode should be included along with the heave in investigating the parametric resonance of the roll mode.

The amplitudes of the upper-branch roll motions are about the same for all eight locations considered in the present experiments. The largest rms amplitude of roll is approximately 9° and the smallest is 7° before the decrease of roll amplitude begins at higher wave amplitudes. In other tests at a wave frequency of 0.80 Hz, the roll amplitude reached 20 ° approximately.

Figures 8a-h show the responses in heave, pitch, and roll for each location of the center of gravity as the amplitude of wave is varied. The

center of gravity of the model was placed in location numbers 1-8 (refer to Fig. 6) along a wavelength of standing waves with a fixed wave frequency of 0.60 Hz. The large-amplitude roll motions exist at all the considered location numbers 1-8 except number 3.

At location number 3, no roll motion was observed although a sufficiently long duration (on the order of hours) was allowed at each step of wave amplitude to obtain the steady-state condition of standing waves. No external disturbances were imposed in this case, and it is possible that there was a subcritical instability with ζ_2 beyond the limits of the experiment. Comparing this case with the other cases in the neighborhood, we expect that rolling would have developed if external disturbances had been imposed on the model during the sweep-up/down procedure.

Jump up occurred for the location numbers 1-5 illustrated in Figs. 8a-e. These correspond to the conditions in which the center of gravity of the model was located between the node and the antinode of the standing waves so that the model was positioned "downhill" on the waves. In these cases, jump down followed during the process of sweep down of wave amplitudes. Location numbers 6-8 (Figs. 8f-h, respectively) yielded no spontaneous jump up to large-amplitude rolling. These correspond to the situation in which the center of gravity of the model was located on the rear part between the antinode and the node of the standing waves so that the model was positioned "uphill" on the waves. External disturbances were used to produce the jump up in these cases.

Figure 7b illustrates that the earliest jump up occurred at location number 4 (mark D) and the latest jump up at location number 1 (mark A) while the latest jump down occurred at location number 5 (mark e) and the earliest jump down at location number 8 (node h). In other words, the smallest wave amplitude that produces the jump up corresponds to the center of gravity of the model being at location number 4. The smallest wave amplitude for which the jump down occurred corresponds to the center of gravity being at location number 5. The upper-branch roll motions for location numbers 6, 7, and 8, which do not show jump up but show jump down only, were obtained by imposing the external disturbances at each step.

The sizes of the domains of attraction of initial conditions for downhill positions of the model were larger than those for uphill positions. The more the center of gravity was behind the antinode, the harder it was to obtain the upper-branch roll motion.

The largest overhang range of wave amplitudes is found for location number 5 (the antinode, marks E and e).

Comparing with the subcritical-type force-response curve of the analytical results, we see that the shape or tendency of the upper-branch shows the largest similarity at location number 2. In other cases, moderate similarities are found. Generally, after the jump up the amplitude of the rolling remains nearly constant for a while and then decreases as wave amplitude continues to increase. The range where rolling has a constant amplitudes varies with the position of the mass center.

Because the wave frequency of 0.60 Hz is slightly smaller than twice the roll natural frequency (2 x 0.32 Hz), the detuning parameter σ is negative, and thus the subcritical-type force-response curves were obtained in these experiments as predicted by the theory (refer to Fig. 2). We could not produce a supercritical-type instability experimentally.

5.3 Miscellaneous Observations

Figure 9 shows the bifurcation wave amplitudes of jump up/down as the location of the model is varied. Vertically above the jump-up curves are the regions where the trivial responses are unstable and the large-amplitude roll motions are the only stable responses. The intervals between the jump-up curves and jump-down curves are the regions where two stable responses (i.e., the trivial and the large-amplitude roll responses) coexist. The regions below the jump-down curves are where the trivial roll motions are the only stable responses. For different wave frequencies, we would expect to find results similar to those in Fig. 9.

If the jump-up bifurcation wave amplitudes are not marked it means the jump up to the large-amplitude roll motions did not occur during the process of sweep up. In such cases, external disturbances were imposed at each step during the sweep-down process, then the jump down followed and its wave amplitude was recorded as shown in Figure 9.

We also observed a penetration phenomenon in the case of a nonstationary excitation. If we increased the wave amplitude fast enough, the jump-up phenomenon occurred at a value of the wave amplitude noticeably higher than the quasi-steady jump-up bifurcation value (ζ_2). The penetration of trivial roll motion into the regime where trivial motion is unstable is due to the nonstationarity of the wave excitation. The higher the sweep rate of wave amplitude was, the deeper the penetration was. A typical force-response

curve theoretically produced by Nayfeh and Asfar (19) is listed in Fig. 10. The observations were in qualitative agreement with this result.

In the present experiments capsize never seemed imminent in any of the tested cases. This can be attributed to having sufficient GM or area under the GZ curve. The effect of GM is not simple because it affects both the natural roll frequency and the static stability. In wave conditions up to the limit of the towing basin at VPI & SU, although the model did not show capsizing in high waves, sometimes the water regularly swept the deck.

5.4 Discrepancies

We found good qualitative agreement between the theoretical and experimental results. However, there exist several discrepancies.

We note from force-response curves that as the wave amplitudes are increased, the magnitude of the large-amplitude roll motions decrease for all the considered cases here. This has also been observed by other investigators; e.g., see Dick, *et al.* (20). In the free model scale experiment performed in the real sea, they showed that when the model was at zero speed in head seas the roll amplitude was almost constant at higher wave heights while the pitch amplitude increased linearly as the wave heights increased.

The discrepancies may be due to one or more of the following four reasons: First, the hydrostatic characteristics of a ship in waves can differ markedly from its characteristics in calm water. Second, while the roll motion causes relatively small waves that reflect from the sidewalls of the tank, the heave and pitch motions generate relatively large waves that do reflect from the sidewalls and form transverse standing waves on both sides of the model. The crests of these waves are a little aft of the midship section of the model, and they always meet the model just before the maximum roll angle occurs. Consequently, the reflected waves also act to limit the roll motion. Third, because the model can pitch as well as heave, the difference in the phases of these two modes might cause the effective amplitude of the parametric excitation to decrease. It is a combination of the heave and pitch motions that produces the effective parametric excitation in the roll equation. Fourth, it is worthwhile to consider the work of Eda, *et al.* (21) and Taggart and Kobayashi (22). They showed that a significant coupling of roll and yaw can develop due to the asymmetry of the underwater hull form of the heeled vessel. This is explained in the following way: the asymmetric form acts as a cambered low-aspect-ratio lifting body, which, together with the forward speed, produces sway forces and roll and yaw moments. When a vessel has relatively small values of GM, this can lead to dramatic increases in roll and yaw motion when the ship is operating in waves, a significant example of the nonlinear process in the responses of a vessel. Thus, in a test when yaw and sway motions are restricted, the reaction forces exerted on the vessel from the sides of the tank could decrease the roll motion.

6. CONCLUSIONS

It has been demonstrated both experimentally and theoretically that a ship in a head or following sea can spontaneously develop severe rolling motion. The energy put into the pitch and heave modes by the wave excitation may be fed into the roll mode by means of nonlinear coupling among those modes. To predict the roll motion, earlier investigators have used the single-degree-of-freedom roll equation and neglected the sometimes pronounced effects of other modes due to nonlinear coupling. These coupling effects often take the form of a parametric resonance, which can lead to a particularly dangerous situation. The nonlinear roll equation is linearized by assuming harmonic pitch and heave motions, and the resulting Mathieu (or Hill) equation is used to determine the conditions for the stability of trivial solutions. With this procedure, however, the predicted roll angle grows exponentially with time, which is unrealistic.

To investigate the loss of dynamic stability and the development of large-amplitude rolling motions of a vessel, we began with a dynamic system of three degrees of freedom (both theoretically and experimentally). The present model to describe the parametrically excited rolling response of a vessel is an improvement over the one used in the previous work of Blocki (5) and Nayfeh and Sanchez (14). Both the pitch and heave modes are used to determine the effective amplitude of the parametric excitation of the roll mode. In the equation for the roll, the kinematic-kinematic nonlinear coupling terms among the three modes are included as well as the static-static terms. Thus, the present approach is closer to reality when the longitudinal asymmetry of a vessel with respect to the midship section is taken into account. Further, in the experiments, the model was placed longitudinally in the towing basin to eliminate the possibility of any external excitation in roll and hence to produce the pure parametric excitation by the regular plane waves.

The principal parametric resonance was considered; the frequency of the wave excitation is approximately twice the natural frequency of the roll mode.

In the analysis, the equations for the heave and pitch modes were linearized, and their harmonic solutions were substituted into the equation for the

roll mode. Due to the heave-pitch-roll coupling, the amplitudes and frequencies of the heave and pitch motions combine to play the role of the effective amplitude and frequency of the parametric excitation. The parametric term in the roll equation basically accounts for the time-dependent variation of the metacentric height. The resulting nonlinear ordinary differential equation with time varying coefficients governs the motion of the roll mode.

The method of multiple scales was used to determine a first-order approximation to the solution. From the solvability condition, two equations were obtained to describe the modulations of the amplitude and the phase of the approximate solution. These modulation equations were used to determine fixed-point solutions and their stability for roll responses. These solutions were verified by numerically integrating the modulation equations using the 5th and 6th order Runge-Kutta-Verner scheme.

Supercritical- and subcritical-type force-response curves were obtained. The latter shows the coexistence of multiple stable solutions, a frequent feature of nonlinear dynamics. Jump phenomena were also found, and in the region between the two bifurcation points of jump up and jump down, two different responses were possible, depending on initial conditions.

The experiments were performed in the towing basin of VPI & SU using a tanker model which was constrained in surge, sway and yaw but allowed to heave, pitch and roll freely. From the basic wave tests, it was decided to use wave frequencies around 0.60 Hz, which produce plane waves for the widest range of amplitudes. The model was ballasted so that the natural frequency in roll is about half of the wave frequency to produce a principal parametric resonance. Wave amplitudes were slowly varied with fixed wave frequencies.

The subcritical instability was found in the experiments which involves jump phenomena between the multiple fixed-point solutions. The amplitude of the roll motion was sometimes as large as $\pm 20°$ in the present experiments. At times when the model was not exhibiting any noticeable roll motion, some external disturbances in the roll mode caused a jump up to a large-amplitude stable roll motion in the overhang region. The large-amplitude roll motion was clear from observations, time traces, and FFT's.

It was observed that the occurrence of large-amplitude roll motion depends on the location of the model along a wavelength of the standing waves. These results can address the cases of dynamic course instability, possible broaching, and instability of the motion of a ship when it is navigating in following seas with the same speed as waves so that its encounter frequency is nearly zero. In this case, both the heave and pitch modes played an equally combined role, rather than only one of the two modes played the more dominant role, to produce the effective amplitude in the parametric excitation of the roll mode. It was also noted that the large-amplitude roll motion occurred more easily when the center of gravity of the model was located in the front part of the standing wave between the node and the antinode.

The present study of ship motion represents a significant extension of the work done by Blocki (5) and Nayfeh and Sanchez (14). In the real situation, the ship will necessarily experience pitch motion and thus the pitch mode as well as heave should be included in investigating the parametric resonance of the roll mode.

The penetration phenomenon was also observed. The penetration of trivial roll motion into the regime where trivial motion is unstable is due to the nonstationarity of the wave excitation.

It was noted that as the wave amplitudes were increased, the large-amplitude roll decreased in magnitude. Moreover, we were not able to produce a supercritical-type instability. Except for these, we observed good qualitative agreement between the theoretical and experimental results.

The discrepancies are conjectured to be due to one or more of the following four reasons: the difference between the hydrodynamic and hydrostatic characteristics in and out of waves, the reflected waves from the sidewalls of the basin, the role of interacting phases between the pitch and heave modes in yielding the effective parametric excitation in the roll mode, and the reaction forces due to the support blocking side motions that would result in a completely free model.

To design more comfortable and safe vessels, one must understand the complicated dynamics of a ship moving in a general seaway. Included among the important dynamic parameters are the ratios of natural frequencies and the nonlinear interactions among the hydrostatic and hydrodynamic forces and moments. The goal of the present effort was to contribute some basic insight toward an eventual entire understanding.

The data obtained in our experiments were voluminous and only some could be given in the present paper. More data and details of the work can be found in the forthcoming dissertation of I. G. Oh (27).

ACKNOWLEDGEMENTS

This work was supported by the Office of Naval Research under Contract No. N00014-90-J-1149.

REFERENCES

1. Froude, W., "Remarks on Mr. Scott-Russell's Paper on Rolling," The Papers of William Froude, published by the Institution of Naval Architects, 1955.

2. Paulling, J. R. and Rosenberg, R. M., "On Unstable Ship motions Resulting from Nonlinear Coupling," Journal of Ship Research, Vol. 3, 1959, pp. 36-46.

3. Kinney, W. D., "On the Unstable Rolling Motions of Ships Resulting from Nonlinear Coupling with Pitch Including the Effect of Damping in Roll," Institute of Engineering Research, University of California, Berkeley, Series No. 173, Issue No. 3, 1961.

4. Kerwin, J. E., "Notes on Rolling in Longitudinal Waves," I.S.P., Vol. 2, 1955, pp. 597-614.

5. Blocki, W., "Ship Safety in Connection with Parametric Resonance of the Roll," International Shipbuilding Progress, Vol. 27, 1980, pp. 36-53.

6. Grim, O., "Zu Stabilität der Periodischen Erzivungenen Rollschwingungen eines Schiffes," Ingenieur Archiv, Band 22, Heft 7, 1954.

7. Haddara, M. R., "On Nonlinear Rolling of Ships in Random Seas," Report, Department of Naval Architecture, University of California, Berkeley, California, Project 713111, 1971.

8. Nayfeh, A. H., Mook, D. T., and Marshall, L. R., "Nonlinear Coupling of Pitch and Roll Modes in Ship Motion," Journal of Hydronautics, Vol. 7, No. 4, October 1973, pp. 145-152.

9. Mook, D. T., Marshall, L. R., and Nayfeh, A. H., "Subharmonic and Superharmonic Resonances in the Pitch and Roll Modes of Ship Motions," Journal of Hydronautics, Vol. 8, No. 1, January 1974, pp 32-40.

10. Nayfeh, A. H., "On the Undesirable Roll Characteristics of Ships in Regular Seas," Journal of Ship Research, Vol. 32, No. 2, June 1988, pp. 92-100.

11. Wahab, R. and Swaan, W. A., "Coursekeeping and Broaching of Ships in Following Seas," Journal of Ship Research, Vol. 7, No. 4, April 1964, pp. 1-15.

12. Eda, H. and Crane, C. L., Jr., "Steering Characteristics of Ships in Calm Water and in Waves," Transactions SNAME, Vol. 73, 1965, pp. 135-177.

13. Eda, H., "Directional Stability and Control of Ships in Waves," Journal of Ship Research, Vol. 16, No. 3, September 1972, pp. 205-218.

14. Nayfeh, A. H. and Sanchez, N. E., "Nonlinear Rolling Motions of Ships in Longitudinal Waves," International Shipbuilding Progress, Vol. 37, No. 411, 1990, pp. 247-272.

15. Sethna, P. R., "Vibrations of Dynamical Systems with Quadratic Nonlinearities," Transactions ASME Journal of Applied Mechanics, Vol. 32, 1965, pp. 576-582.

16. Sethna, P. R. and Bajaj, A. K., "Bifurcation in Dynamical Systems with Internal Resonance," Journal of Applied Mechanics, Vol. 45, 1978.

17. Hatwal, H., Mallik, A. K., and Ghosh, A., "Forced Nonlinear Oscillations of an Autoparametric System-Part 2: Chaotic Motions," Journal of Applied Mechanics, Vol. 50, 1983.

18. Renilson, M. R. and Driscoll, A., "Broaching - An Investigation into the Loss of Directional Control in Severe Following Seas," Transactions RINA, Vol. 125, 1982, pp. 253-273.

19. Nayfeh, A. H. and Asfar, K. R., "Non-stationay Parametric Oscillations," Journal of Sound and Vibration, Vol. 124, No. 3, 1988, pp. 529-537.

20. Dick, D., Eng, C., and Corlett, E. C. B., "The Pan Type Post Office Cable Repair Ship," Transactions RINA, Vol. 119, 1976, pp. 305-322.

21. Eda, H., Falls, R., and Walden, D. A., "Ship Maneuvering Safety Studies," Transactions SNAME, Vol. 87, 1979, pp. 229-250.

22. Taggart, R. and Kobayashi, S., "Anomalous Behavior of Merchant Ship Steering Systems," Marine Technology, Vol. 7, No. 2, April 1970, pp. 205-215.

23. Nayfeh, A. H. and Mook, D. T., Nonlinear Oscillations, Wiley-Interscience, New York, 1979.

24. Nayfeh, A. H., Perturbation Methods, Wiley-Interscience, New York, 1973.

25. Nayfeh, A. H., Introduction to Perturbation Techniques, Wiley-Interscience, New York, 1981.

26. Lewis, E. V., Ed., Principles of Naval Architecture, SNAME, Vol. 3, 1989.

27. Oh, I. G., Theoretical and Experimental Nonlinear Dynamics of Floating Oscillatory Systems, Ph. D. Dissertation, Department of Engineering Science and Mechanics, Virginia Polytechnic Institute and State University, Blacksburg, Virginia, 1992.

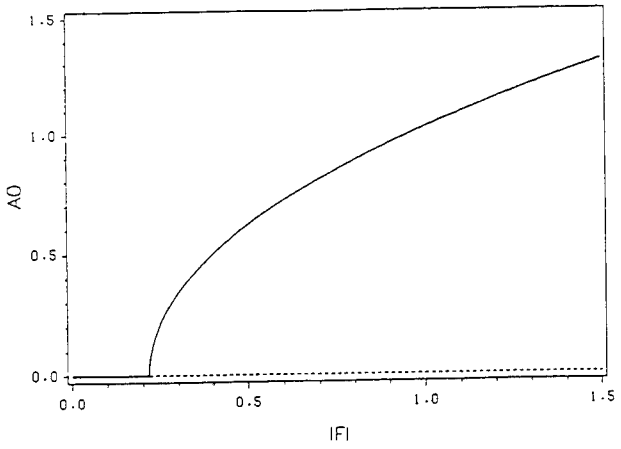

Figure 1. Force-response curve (super-critical type) when $\mu_1 = \mu_2 = 0.04, \sigma = 0.20$. The solid lines (_____) are stable and the broken lines (---------) are unstable solutions.

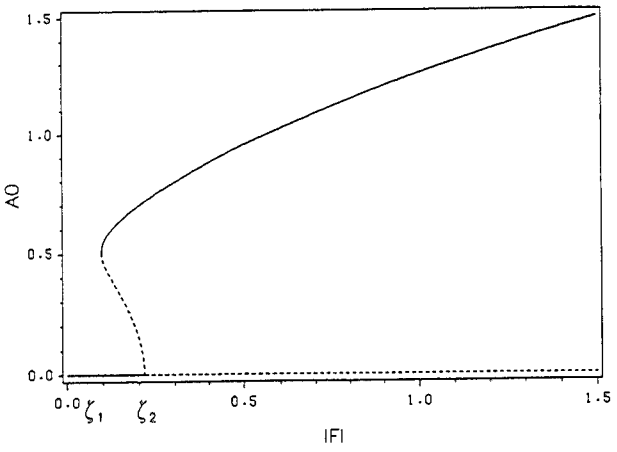

Figure 2. Force-response curve (sub-critical type) when $\mu_1 = \mu_2 = 0.04, \sigma = -0.20$. The solid lines (_____) are stable and the broken lines (---------) are unstable solutions.

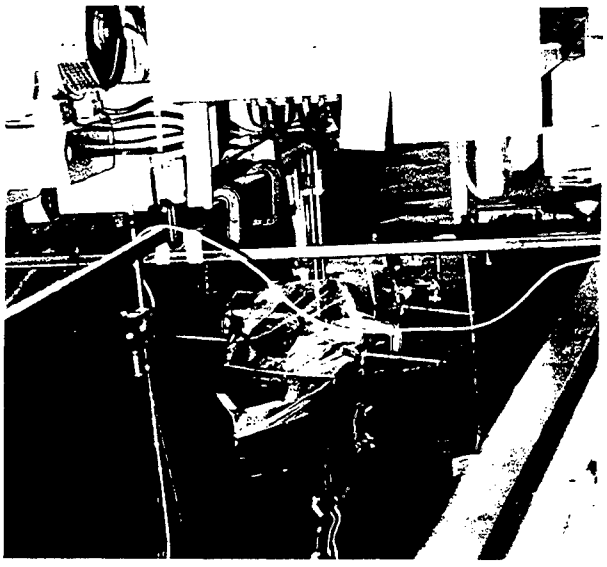

Figure 3. A photograph of the perspective view of the model rolling in the waves.

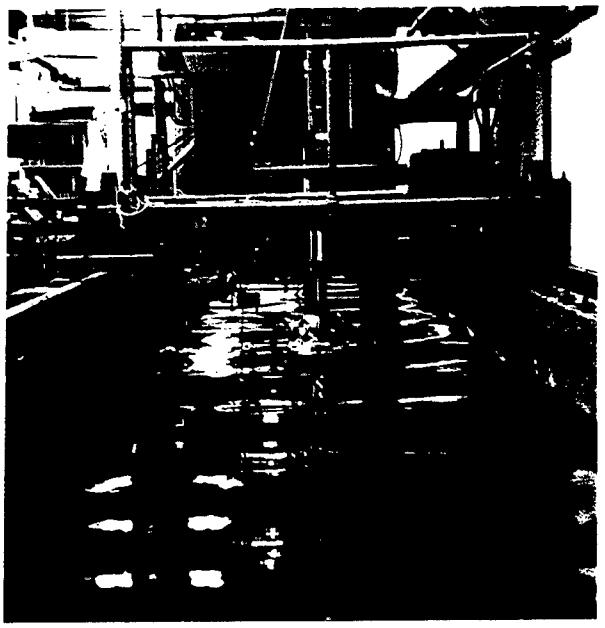

Figure 4. A photograph of the rear view of the model rolling in the waves (heeled to the starboard)

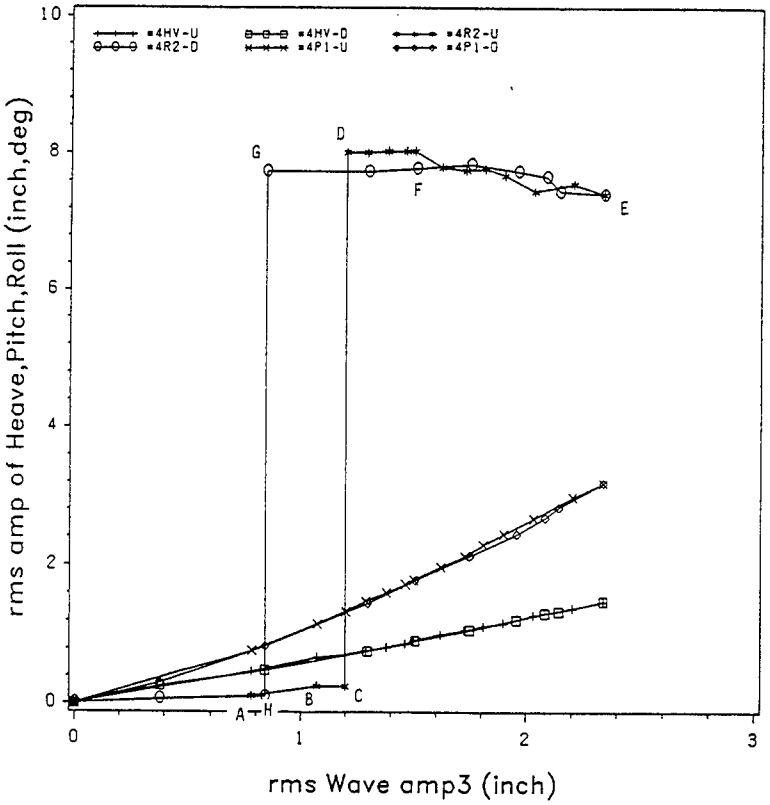

Figure 5 (a). A typical experimental force-response curve : The responses of heave (inch), pitch (°) and roll (°) versus rms amplitude of the wave when the wave frequency is 0.60 Hz and the center of gravity of the model is at location number 4.

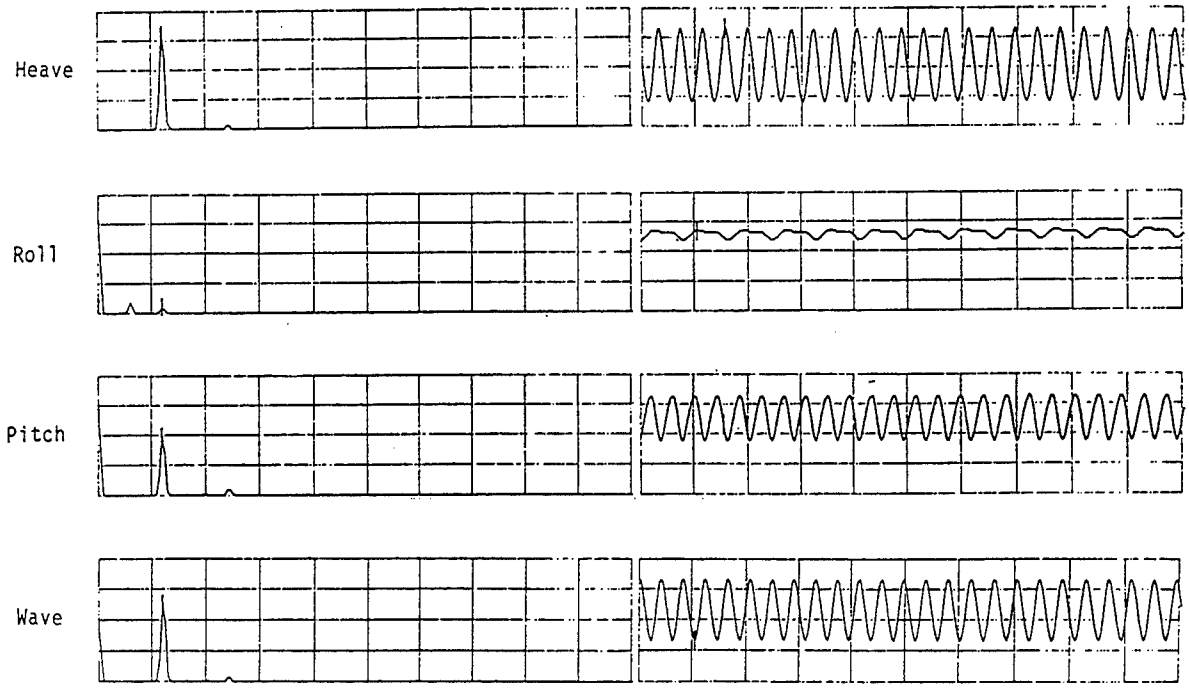

Figure 5 (b). The plots of FFT's and time traces of heave, roll, pitch and wave (from the top) at point B of Fig. 5(a), just before roll motion is initiated. The wave frequency is 0.60 Hz and the center of gravity of the model is at location number 4.

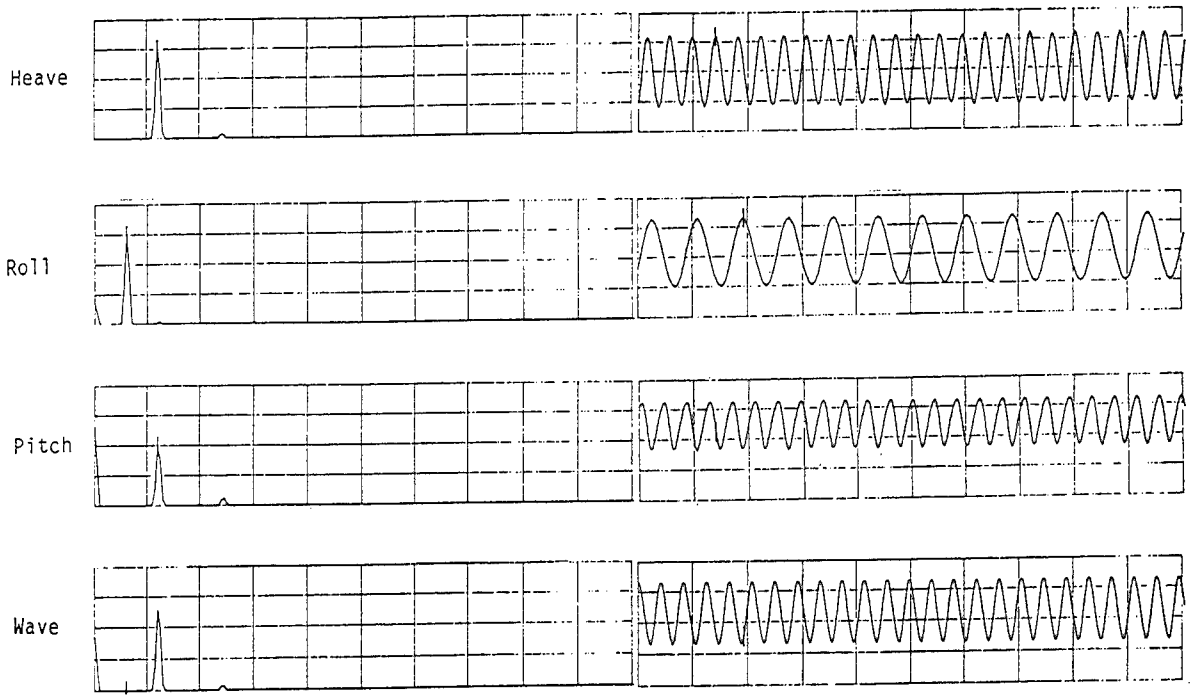

Figure 5 (c). The plots of FFT's and time traces of heave, roll, pitch and wave (from the top) at point D of Fig. 5(a), just after roll has been initiated. The wave frequency is 0.60 Hz and the center of gravity of the model is at location number 4.

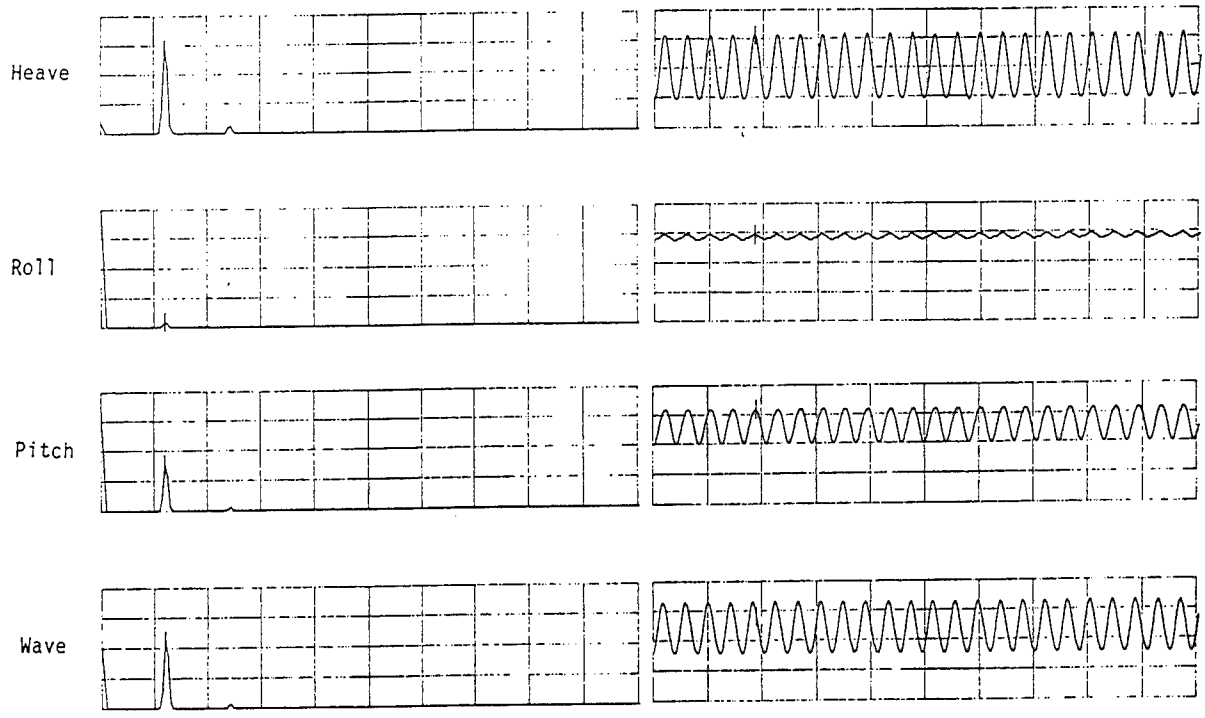

Figure 5 (d). The plots of FFT's and time traces of heave, roll, pitch and wave (from the top) at point H of Fig. 5(a), just after the roll motion has vanished. The wave frequency is 0.60 Hz and the center of gravity of the model is at location number 4.

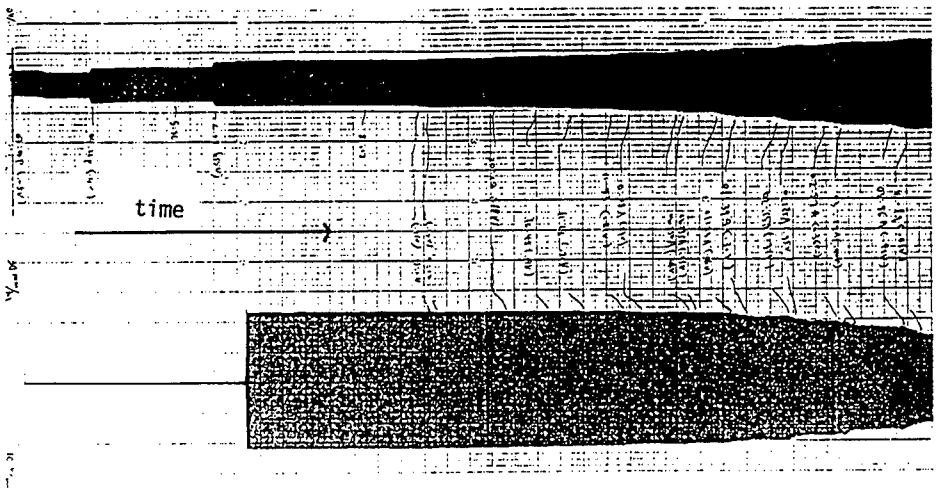

Figure 5 (e). A part of long-time signals of heave (above) and roll (below) recorded on the strip chart recorder: shown here are 15 hours out of a total of 52 hours of the test. The moment of jump up in the roll motion is clearly shown. The wave frequency is 0.60 Hz and the center of gravity of the model is at location number 4.

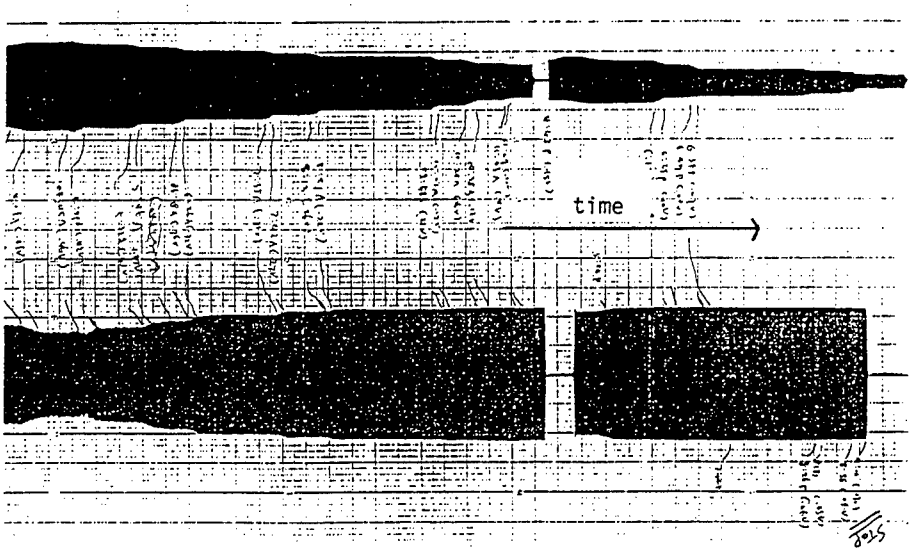

Figure 5 (f). A part of long-time signals of heave (above) and roll (below) recorded on the strip chart recorder: shown here are 19 hours out of a total of 52 hours of the test. The moment of jump down in the roll motion is clearly shown. The wave frequency is 0.60 Hz and the center of gravity of the model is at location number 4.

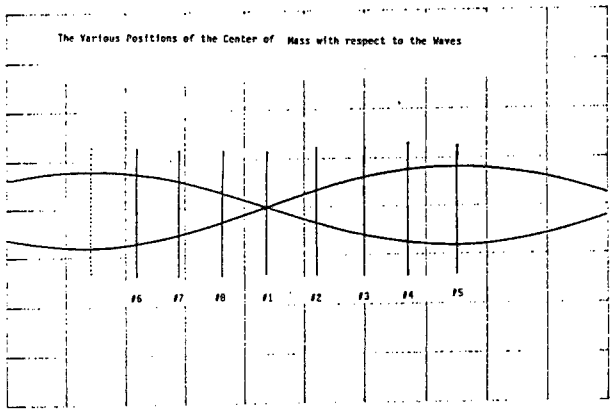

Figure 6. The numbering of the locations of the center of gravity of the model in a wavelength of a typical standing wave: The node is #1, the antinode is #5, etc.. The bow is at the left and the stern is at the right. The wave frequency is 0.60 Hz.

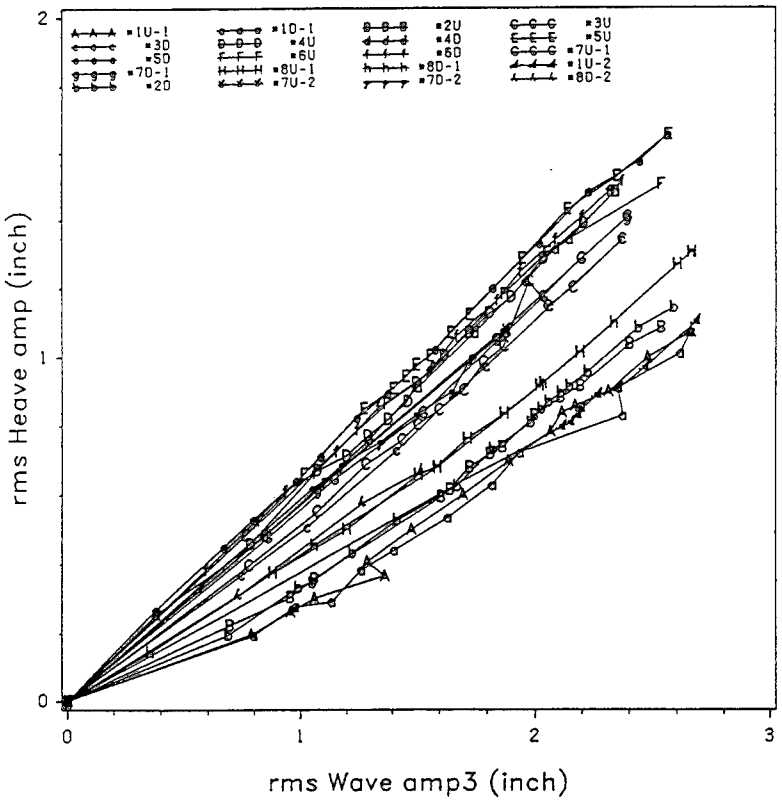

Figure 7 (a). The responses of heave at various locations of the model in the waves; the wave frequency is 0.60 Hz.

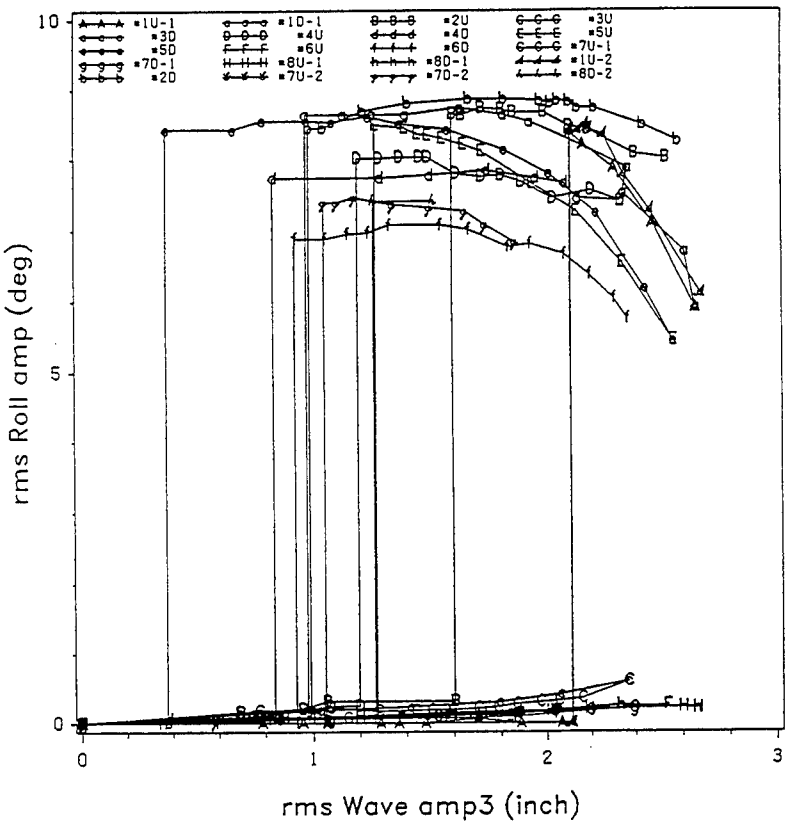

Figure 7 (b). The responses of roll at various locations of the model in the waves; the wave frequency is 0.60 Hz.

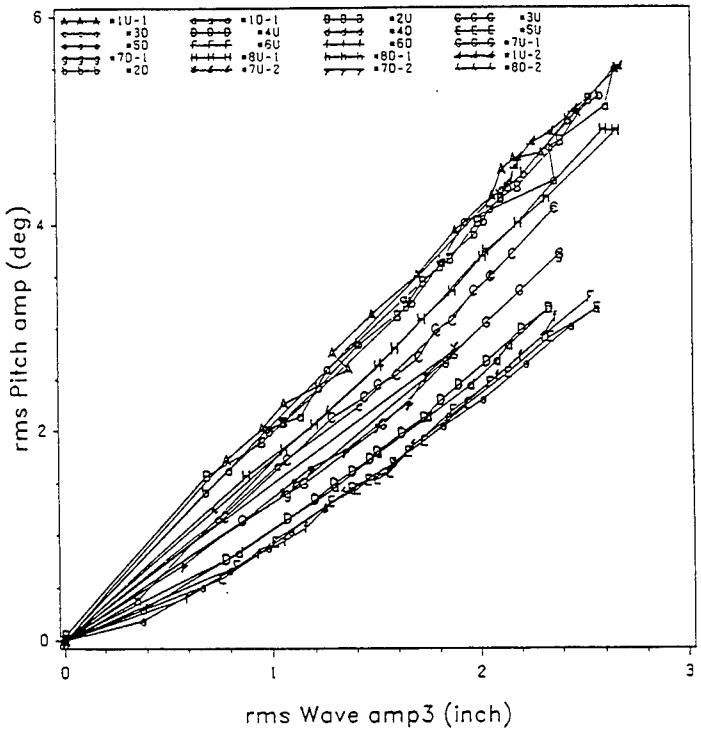

Figure 7 (c). The responses of pitch at various locations of the model in the waves; the wave frequency is 0.60 Hz.

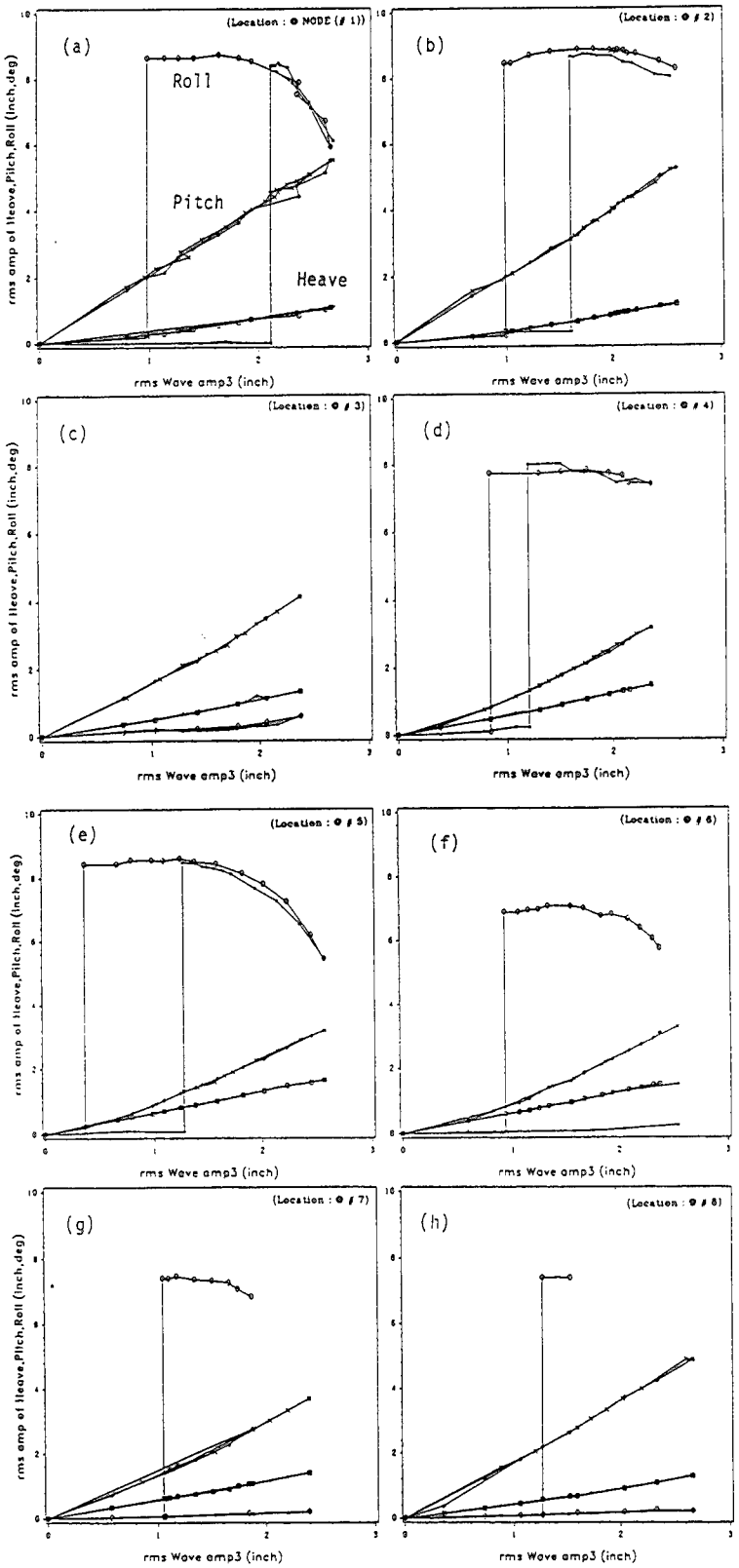

Figure 8. The responses in heave, roll and pitch when the model is at location #1 (a), #2 (b), #3 (c), #4 (d), #5 (e), #6 (f), #7 (g), and #8 (h). The wave frequency is 0.60 Hz.

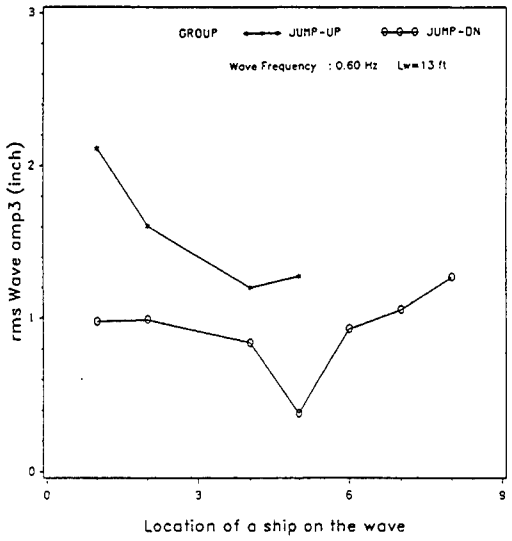

Figure 9. The rms wave amplitude where jump up/down occurred when the model is at various locations. The wave frequency is 0.60 Hz.

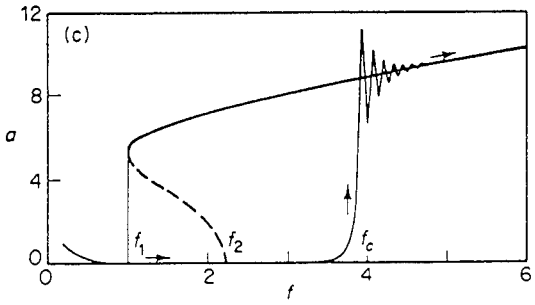

Figure 10. A typical force-response curve with a nonstationary excitation. (from Nayfeh and Asfar (19))

A Localized Finite-Element Method for Nonlinear Free-Surface Wave Problems

K. Bai, J. Kim (Seoul National University, Korea),
H. Lee (Hyundai Maritime Research Institute, Korea)

ABSTRACT

This paper describes a localized finite-element method applied to steady nonlinear wave-resistance problems in three dimensions. The physical model is taken to simulate the towing tank experimental conditions. The exact nonlinear free-surface flow problem is formulated by a weak formulation. In the numerical procedures, two new and notable steps are introduced: the difficulty in the numerical treatment of the radiation condition is overcome by the introduction of an intermediate nonlinear-to-linear transition buffer subdomain. The second notable step is the use of modal analysis in the final stage of the solution procedures and this enables us to save the computation time enormously. As a result, the present method can treat much larger free-surface domain which was not possible previously. As the applications of the present numerical method, we treated specifically, a pressure patch on the free surface and a submerged hydrofoil.

1 INTRODUCTION

The wave-resistance problem is one of the oldest and interesting topics in ship-hydrodynamics. The problem has been generally formulated in the scope of the potential theory. Then the fluid motion can be described by the well-known Laplace equation as the governing equation and appropriate boundary conditions. However, the nonlinear boundary condition on the unknown free surface makes an analytic method of solution intractable. Due to this difficulty this problem has been usually treated by some form of restricted theories where the free-surface conditions are linearized.

From Kelvin(1886) to Ursell(1960) the qualitative features of the downstream wave pattern have been investigated based on the linear dispersion theory and the method of asymptotic expansions. The first theoretical approach to the wave-resistance problem of a ship is the celebrated thin-ship theory initiated by Michell(1898). Although the applicable range of this theory is restricted because of its basic assumptions on the ship geometry, it has provided much information on the wave-making phenomena with its rich theoretical results.

As another effort to apply the linear theory to a more realistic ship, the numerical computations for the Neumann-Kelvin problem satisfying the exact hull-boundary condition has been also made. Many authors treated this problem with various numerical methods. To name a few, Guevel et al.(1977) used Green's function method and Bai(1977) used the localized finite-element method. It can be said that the applicable range of this theory is not so wider than that of the thin-ship theory because of its lack of consistency in treating the free-surface condition.

In the linear theory given above, the basic flow in linearizing the free-surface condition is the uniform flow. The uniform flow cannot be the only choice for the basic flow. For example the flow field generated by a double-body model is used in the slow-ship theory. As a numerical method for this theory, Dawson(1977) used the panel method with the treatment of the convection terms by the forward finite-difference operators. The introduction of the forward difference operator and the resulting numerical damping, make it possible to satisfy the radiation condition numerically. The major advantages of this method are the consideration of the ship geometry in the early stage of the lineariziation and the absence of the water-line integral, which causes computational difficulties in the Neumann-Kelvin theory. However, the numerical damping introduced for the radiation condition makes the result of this method less meaningful at the far downstream.

Recently, the direct numerical analyses on the nonlinear wave-resistance problem has been attempted along with the increasing speed and capacity of the modern digital computers. The numerical methods along this line are the Rankine- source method, the finite-difference method, the finite-element method and the spectral method. The Rankine-source method is an extension of Dawson's method to a nonlinear problem and already

shows a wide engineering application as can be seen in Ni(1987), Raven(1988) and Kim(1990). But this method has a similar drawback as in Dawson's method in treating the numerical radiation condition. Miyata and Nishimura(1986) introduced the finite-difference method for a wave-resistance problem. They solved an unsteady Navier-Stokes equation with the complete consideration of the ship geometry and the free-surface nonlinearity. This method requires an extremely heavy computations with the computing power of the super computers. But their numerical result shows not so much improvements compared to the other methods with more restricted assumptions on the governing equations and the boundary conditions. Because of the high Reynolds number and the complexity of the bow and the stern geometries, and the resulting difficulties in the turbulence modeling and the mesh size required for a high resolution near the hull, there are few numerical methods which gives a satisfactory result even for the problem without the free-surface at present. The spectral method has been applied to the water-wave problems by Dommermuth and Yue(1988). This method has shown the efficiency and the accuracy in many other applications. This method has been applied to the nonlinear wave-resistance problem by an approach in an initial-value problem for the steady waves. Thus much computational time is required to obtain the steady solution.

From the above review on the various numerical methods, we may conclude that a more efficient numerical method for a nonlinear wave-resistance problem should satisfy the following requirements to modify the drawbacks in the previous methods. Firstly, a direct treatment of a steady state problem is more desirable for the computational efficiency. Secondly, the numerical damping should be absent in the treatment of the nonlinear free-surface condition. Lastly, the numerical radiation condition should be still satisfied even after the numerical damping is successfully suppressed. For a linear wave-resistance problem, Bai(1977) developed a localized finite-element method which satisfies the above criteria. In this paper we extend the idea of the localized finite-element method to a nonlinear problem and develop an efficient numerical method for a steady three-dimensional wave-resistance problem to simulate a towing tank experiments..

As the applications of the present numerical method, we treat the steady nonlinear waves generated by a circular pressure patch on the free surface and a submerged hydrofoil. Since the basic properties of the downstream waves generated by the pressure patch do not different from that of the real ship, we can observe the general features of the nonlinear interactions in the Kelvin wave pattern from the results. The shape of the pressure was taken as that treated by Dommermuth and Yue(1988) by the spectral method. Because of the efficiency of our numerical method, we can obtain the steady solution in the domain approximately three times larger than theirs, which enables us to observe the nonlinear wave patterns more clearly in a much larger computed domain. Our result shows the same nonlinear effects as that of Dommermuth and Yue, that is, the widening of the Kelvin angle and the increase in the wave numbers and magnitude of the wave profiles. In our computation we could confirm that the strong nonlinearity near the cuspline is due to the far-field wave interactions. We propose an additional simple analysis based on the generalized Stokes' correction on the dispersion relation and the method of stationary phase. From this analysis we could find that the off-diagonal terms in the wave interaction kernel is important in predicting the correct nonlinear effects along the cuspline.

There is a growing interest in the hydrodynamic phenomena around the submerged hydrofoil as a candidate for an application to a high-speed vessel in the future. The lifting problem of a hydrofoil submerged beneath the free surface has been mainly treated in the scope of a linear water-wave theory in the past. Nishiyama(1965) used a modified lifting-line theory to obtain the hydrodynamic forces acting on the three-dimensional flat hydrofoil with a relatively high Froude number and submergence. Bai(1978) treated the two-dimensional hydrofoil problem with the localized finite-element method. His numerical results show good agreements with the experimental results of Parkin et al. (1956) except a few cases of the extremely shallow submergence. Lew et al.(1991) investigated the free-surface effect on the cavity and the lift of a two dimensional hydrofoil by the lifting surface theory.

In the nonlinear theory for a hydrofoil problem, two lines of the approach have been used. The first line of the approach is by the use of a numerical Navier-Stokes equation solver, based on a finite difference method. In this method the problem is formulated as a transient problem. Two-dimensional problem has been treated by Cordonnier(1985) and Coleman(1986), and three-dimensional problem by Kwag and Mori(1991). In general their results do not show a good agreement with the experimental results despite of the generality in their mathematical formulation and extremely heavy computational efforts. The second line of the approach is based on the potential theory. We can find the examples along this line in Nakatake et al.(1988), Qi and Mori(1990) and Bai and Han(1992). Nakatake et al. used the Dawson's method for two-and three-dimensional problem and showed an agreement with the experiments only for the low Froude numbers. Qi and Mori used the boundary-element method for a three-dimensional transient problem. Bai and Han used the localized finite-element method for a two-dimensional problem and showed some improvements to the previous linear results of Bai(1977).

We treat the lifting problem for a submerged hydrofoil as the second application of the present numerical method. The operating condition of the hydrofoil can be characterized by the high speed with the shallow submergence. Under this condition, the hydrofoil can be effectively modeled by lifting lines, where the chord-wise quantities are treated in a mean sense. Specifically the computations are made for a uniform and elliptic distributions of the sectional circulation. The numerical computations are made for several cases by changing the Froude number, the depth of submergence and magnitude of the circulation. Particularly, we could examine the wave field generated by the free-vortex line, which cannot be obtained in the linear theory. As a more practical application of the present method we calculated the nonlinear corrections on the induced velocities on the bound-vortex line, and the resulting hydrodynamic force components.

2 MATHEMATICAL FORMULATION

We consider the wave elevations and the flow fields generated by a pressure patch translating with a speed U in a towing tank of the depth h and the half width W. The fluid contained in the tank is assumed to be inviscid and incompressible and its motion irrotational. The surface tension on the free surface is neglected. We further assume that the flow is a steady state in the coordinate system Oxyz fixed to the disturbance. The xy-plane is defined as the mean free surface and direction of the z-axis opposite to the gravity. In the scope of the potential theory, we can describe the fluid motion by a boundary-value problem with the governing equation and the boundary conditions given as

$$\nabla^2\phi = 0, \qquad -h < z < \zeta \tag{1}$$

$$\overline{\phi}_n + \nu\,\overline{\phi}_{xx} = -\frac{U}{\rho g} P_x(x,y) - \frac{U}{g}\frac{\partial}{\partial x} N[\overline{\phi}, \overline{\phi}_n, \zeta] \tag{2}$$

$$\zeta = \frac{U}{g}\overline{\phi}_x - \frac{1}{\rho g} P(x,y) + \frac{1}{g} N[\overline{\phi}, \overline{\phi}_n, \zeta] \tag{3}$$

$$\phi_n = 0, \qquad |y| = W \text{ and } z = -h \tag{4}$$

where ϕ and ζ denote the velocity potential and the wave elevation, respectively, and ν is defined as $\frac{U^2}{g}$. The variables $\overline{\phi}$ and $\overline{\phi}_n$ are defined as the velocity potential and its normal velocity on the free surface, i.e.,

$$\overline{\phi}(x,y) = \phi(x,y,\zeta) \tag{5.a}$$

$$\overline{\phi}_n(x,y) = \sqrt{1+\nabla\zeta\cdot\nabla\zeta}\;\phi_n(x,y,\zeta) \tag{5.b}$$

and the nonlinear term $N[\overline{\phi}, \overline{\phi}_n, \zeta]$ is defined as

$$N[\overline{\phi}, \overline{\phi}_n, \zeta] = \frac{1}{2}\left\{\frac{(\overline{\phi}_n + \nabla\zeta\cdot\nabla\overline{\phi})^2}{1+\nabla\zeta\cdot\nabla\zeta} - \nabla\overline{\phi}\cdot\nabla\overline{\phi}\right\} \tag{6}$$

The above boundary value problem may be completed by imposing the following radiation condition at infinity.

$$|\nabla\phi| \text{ is bounded as } x \to +\infty \tag{7.a}$$

$$|\nabla\phi| \to 0 \text{ as } x \to -\infty \tag{7.b}$$

In actual computations, the above radiation condition is too abstract to be utilized. We require a more specific condition, for example, Dirichlet, Neumann or mixed type boundary conditions. However, these types of radiation condition are not available for nonlinear water-wave problems. For linear problems, however, the velocity potential can be expanded by the eigenfunctions and the radiation condition can be given as mixed type boundary conditions or initial conditions for each eigenfunction. Bai(1977) utilized these results and developed a localized finite-element method where the finite element solution defined in the computational domain is matched to the eigenfunction representation in the truncated infinite subdomains. In this paper we extend the idea of the localized finite-element method to the nonlinear problems.

3 METHODS OF SOLUTION

We use finite element method for the spatial discretization to obtain a matrix equation of the discrete velocity potential and wave elevations. Unlike the linear problem, the coefficients of the matrix equation are no longer constants. They are functions of the unknown variables due to the nonlinearities in the variable domain and on the free-surface. Therefore, it is necessary to adopt an iterative scheme in the numerical procedure. We use a kind of fixed-point algorithm as the iterative scheme in which the terms related to the free-surface nonlinearity and the variable domain are evaluated from the result of previous step. Then the remaining operator to be inverted is that of the Neumann-Kelvin problem defined in a separable rectilinear domain. This operator can be simply inverted by the use of modal analysis. Each mode of the finite element solution resembles the exact eigenfunction of the Neumann-Kelvin operator.

The radiation conditions for these modes can be treated as a boundary or an initial condition according to the ellipticity or hyperbolicity of each mode. But this treatment requires the absence of the forcing terms at the end points. This requirement can be accomplished by the introduction of the nonlinear-to-linear transition buffer sub-domain, which will be discussed in the following sub-section.

3.1 Nonlinear-to-Linear Transition Buffer Sub-domain

Here we slightly modify the boundary value problem given in the previous section for a further treatment of the radiation condition. We define a locally-linearizing parameter $\varepsilon(x,y)$ which is a smooth function varying monotonically from 0 and 1. The Equations (1)-(3) and (5.a,b) are modified to

$$\nabla^2\phi = 0, \qquad -h < z < \varepsilon\zeta \tag{8}$$

$$\overline{\phi}_n + \nu\,\overline{\phi}_{xx} = -\frac{U}{\rho g}P_x(x,y) - \frac{U}{g}\frac{\partial}{\partial x}\left(\varepsilon N[\overline{\phi}, \overline{\phi}_n, \varepsilon\zeta]\right) \tag{9}$$

$$\zeta = \frac{U}{g}\overline{\phi}_x - \frac{1}{\rho g}P(x,y) + \frac{\varepsilon}{g}N[\overline{\phi}, \overline{\phi}_n, \varepsilon\zeta] \tag{10}$$

$$\overline{\phi}(x,y) = \phi(x,y,\varepsilon\zeta) \tag{11.a}$$

$$\overline{\phi}_n = \sqrt{1+\nabla(\varepsilon\zeta)\cdot\nabla(\varepsilon\zeta)}\;\phi_n(x,y,\varepsilon\zeta) \tag{11.b}$$

It should be noted in the above equations that the exact nonlinear problem can be obtained when $\varepsilon = 1$ while the well-known linear problem can be recovered when $\varepsilon = 0$. With this in mind, we divide the original fluid domain into the following three subdomains according to the degree of nonlinearities in each subdomain:

$$\begin{aligned} &D_N: \ \varepsilon(x,y) = 1; \\ &D_B: \ 0 < \varepsilon(x,y) < 1; \\ &D_L: \ \varepsilon(x,y) = 0. \end{aligned} \tag{12}$$

Here D_N and D_L denote the nonlinear and linear sub-domain, respectively, and D_B is the nonlinear-to-linear transition buffer subdomain where the free-surface nonlinearities are artificially and monotonically reduced to zero as in the linear problem . All the sources of the disturbances are taken inside the nonlinear subdomain so that the problem to be solved in the linear subdomain becomes a homogeneous Neumann-Kelvin problem. This enables us to treat the radiation condition more effectively, which will be discussed in the later sections.

3.2 Weak Formulation

The differential equations given in the previous section can be equivalently formulated by a weak formulation. The construction of a weak form is based on the scalar product of functions and the integration by parts. This process enables us to choose the candidates for the approximate solution from a wider class of functions. For example, in our problem, the original differential equation requires the velocity potential to have continuous second order derivatives whereas the weakly formulated equation requires the derivatives up to the first order to be square-integrable in any finite region of the fluid domain. The original fluid domain is infinite in our problem, but the actual computational domain will be taken finite after truncating the infinite linear subdomain.

In the present nonlinear problem, the fluid domain is not known a priori as so is the surface. It is advantageous to transform this moving domain to a fixed domain in the numerical computation. For this purpose, we adopt following coordinates transformations

$$\begin{aligned} &(x,y,z) \to (x,y,z'), \\ &z' = z'(z;\varepsilon\zeta) \end{aligned} \tag{13}$$

where z' is a continuous and monotonic function of z defined in the interval $(-h, \varepsilon\zeta)$ with the end values $z'(-h;\varepsilon\zeta) = -h$ and $z'(\varepsilon\zeta;\varepsilon\zeta) = 0$. The linear and/or piecewise linear functions are used as the transformation function here. Examples of these transformations are shown in Fig.1.

If we denote the space of the admissible solutions as H_D and define an auxiliary function space $H_F = \{\overline{\varphi}(x,y) = \varphi(x,y,0) \mid \varphi(x,y,z') \in H_D\}$, the weakly formulated problem can be stated as follows.

Find the functions $\phi(x,y,z') \in H_D$ and $\overline{\phi}_n, \zeta \in H_F$ such that

$$\langle\langle \varphi, \phi \rangle\rangle_{\varepsilon\zeta} - \nu\langle \overline{\varphi}_x, \overline{\phi}_x \rangle = \tag{14.a}$$

$$\frac{U}{\rho g}\langle \overline{\varphi}_x, P(x,y) \rangle + \frac{U}{g}\langle \overline{\varphi}_x, \varepsilon N[\overline{\phi}, \overline{\phi}_n, \varepsilon\zeta] \rangle$$

for all test functions $\varphi(x,y,z') \in H_D$ and

$$< \overline{\varphi}, \overline{\phi}_n > = << \varphi, \phi >>_{\varepsilon\zeta}, \qquad (14.b)$$

$$< \overline{\varphi}, \zeta > = \frac{U}{g} < \overline{\varphi}, \overline{\phi}_x > \qquad (14.c)$$

$$+ \frac{1}{g} < \overline{\varphi}, \varepsilon N[\overline{\phi}, \overline{\phi}_n, \varepsilon\zeta] >$$

for all $\overline{\varphi}(x,y) \in H_F$

where the brackets are used to define the following bilinear functionals.

$$< \overline{\varphi}, \overline{\phi} > = \int\int \overline{\varphi}\ \overline{\phi}\ dxdy \qquad (15.a)$$

$$<< \varphi, \phi >>_\zeta = \int_{-h}^{\zeta}\int\int \nabla\varphi\cdot\nabla\phi\ dz\ dxdy \qquad (15.b)$$

It can be easily shown that Eq.(14.a) is a weak form of Equations (1),(2),(4) and Equations (14.b) and (14.c) are related to Equations (3) and (5.b), respectively. The details of the derivation of the above equations are basically same as that of the linear problem, which can be found in Bai(1977).

It should be noted that Eq.(14.a), which is the main equation to solve, is highly nonlinear equation for the unknown functions. The nonlinearities are due to the nonlinear term, N, in the right-hand side and the variable integral domain of the doubly bracketed term. As mentioned earlier, we treat these nonlinear terms by an iterative scheme. We rewrite Eq.(14.a) as

$$<< \varphi, \phi >>_0 - \nu < \overline{\varphi}_x, \overline{\phi}_x > = \qquad (16)$$

$$\frac{U}{\rho g} < \overline{\varphi}_x, P(x,y) > + \frac{U}{g} < \overline{\varphi}_x, \varepsilon N[\overline{\phi}, \overline{\phi}_n, \varepsilon\zeta] >$$

$$- \{<< \varphi, \phi >>_{\varepsilon\zeta} - << \varphi, \phi >>_0 \}$$

where all the nonlinear terms are on the right-hand side. We evaluate the nonlinear terms by the previous results or an initial guess. Then we can compute new values of the velocity potential from Eq.(13) and $\overline{\phi}_n$, ζ from Eq.(14.a,b). We repeat these iterations until a prescribed convergence condition is satisfied.

3.4 Analysis of the Linear Problem

The variational equation (16) to be solved in each iteration step can be viewed as the Neumann-Kelvin problem with a pressure distribution on the free surface and source distribution in the fluid domain. This problem can be formally given as

$$\nabla^2\phi = -q(x,y,z), \quad -h < z < 0 \qquad (17)$$

$$\phi_z + \nu\,\phi_{xx} = f_x(x,y), \qquad z = 0 \qquad (18)$$

where forcing term q(x,y,z) is originated from the domain nonlinearity and f(x,y) from the pressure distribution and the nonlinear terms in the free-surface condition. The boundary conditions other than the free-surface conditions are same as that of the previous nonlinear problem and omitted here. If we assume that the nonlinear and buffer subdomains are located between x = a and x = b, the forcing terms are zero outside this region or the linear sub-domain, i.e.,

$$q(x,y,z) = f(x,y) = 0, \qquad (19)$$

$$\text{for } x < a \text{ or } x > b$$

The linear problem given above can be formulated as a variational problem. Then the above equation can be replaced by an equivalent problem of imposing a stationary condition on the functional J defined as

$$J = \int L\ dx, \qquad (20.a)$$

$$L = \frac{1}{2}\iint (\nabla\phi\cdot\nabla\phi - 2q\phi)\ dy\ dz \qquad (20.b)$$

$$- \int_{z=0} (\frac{\nu}{2}\phi_x^2 - f\phi_x)\ dy$$

where L is a Lagrangian function.

With the variational formulation given above, we use the finite-element method as the spatial discretization. The computational domain is discretized by the finite number of elements and the velocity potential is approximated by the finite-element basis functions. In the present problem, the domain is rectilinear and the three-dimensional finite-element basis functions can be written as a tensor product of the one-dimensional basis functions. The velocity potential can be approximated as

$$\phi(x,y,z) = \sum_{i,j,k} X_i(x)\ Y_j(y)\ Z_k(z)\ \phi_{ijk} \qquad (21)$$

At this stage, however, we discretize the y- and z-direction only for the further analysis. The velocity potential is alternatively written as

$$\phi(x,y,z) = \sum_{j=1}^{N_y} \sum_{k=1}^{N_z} Y_j(y)\, Z_k(z)\, \phi_{jk}(x). \quad (22)$$

where N_y and N_z are the number of nodes in y- and z-directions. Here, $Y_j(y)$ and $Z_k(z)$ are the finite-element basis functions in each direction. In the present paper, a piecewise linear basis functions are taken. Substituting this equation into Eq.(20.b) and setting the first variation to be zero, we obtain the following linear ordinary differential equations of the discrete velocity potential

$$\sum_{j,l} \{ - F^y_{ij} (F^z_{kl} - \nu D_{kl}) \phi''_{jl} + (G^y_{ij} F^z_{kl} + F^y_{ij} G^z_{kl}) \phi_{jl} \} = q_{ik}(x) \quad (23)$$

$$\text{for } i=1,\ldots,N_y,\ k = 1,\ldots,N_z$$

where the tensors are defined as

$$F^y_{ij} = \int Y_i(y)\, Y_j(y)\, dy, \quad F^z_{kl} = \int Z_k(z) Z_l(z)\, dz,$$

$$G^y_{ij} = \int Y'_i(y)\, Y'_j(y)\, dy, \quad G^z_{kl} = \int Z'_k(z)\, Z'_l(z)\, dz,$$

$$D_{kl} = Z_k(0)\, Z_l(0), \quad (24.a\text{-}f)$$

$$q_{ik}(x) = \int\int q(x,y,z)\, Y_i(y)\, Z_k(z)\, dy\, dz + \int f_x(x,y)\, Y_i(y)\, Z(0)\, dy$$

The differential equations given in Eq.(23) can be viewed as a coupled spring-mass system. They can be decoupled by the modal analysis. We can treat the modal analysis in the y- and z-direction separately since the coefficients are tensor products of each direction. The y-directional modes are represented as the cosine function, whereas the z-directional modes related to each y-modes consist of exponential mode and sinusoidal mode. The signs of the eigenvalues $\{\lambda_{ik},\ i=1,\ldots,N_y;\ k=1,\ldots N_z\}$ are negative for exponential modes and positive for sinusoidal modes. We will call them local modes and wave modes respectively. The properties of each modes are similar to that of the eigenfunctions of the exact linear problem. The details of the modal analysis and the comparison with the eigenfunction expansion are given in Kim(1991). The decoupled equations of each mode, say $\phi(x)$, can be written as

$$-\phi'' + \lambda\phi = q(x) \quad (25)$$

where λ is the eigenvalue of the mode and $q(x)$ is the forcing term originated from $f(x,y)$ and $q(x,y,z)$ terms in Eq.(17) and Eq.(18).

The ordinary differential equation, Eq.(25), can be easily solved with appropriate side conditions. To make the problem well-posed, the side conditions should be treated differently for the wave and the local modes. For the wave modes, initial-value problem is well-posed for the uniqueness. On the other hand, boundary value problem is well-posed for the local modes because of the stability. From the Eqs.(7.a,b) and (19), which can be written as

$$\phi' \to 0 \quad \text{as } x \to +\infty \quad (26.a)$$

$$\phi' \text{ is bounded} \quad \text{as } x \to -\infty \quad (26.b)$$

$$q(x) = 0, \quad x < a \text{ and } x > b \quad (26.c)$$

the side conditions are given as

Local modes ($\lambda > 0$) :

$$\phi'(x) - \sqrt{\lambda}\phi(x) = 0,\ x = a \quad (27.a)$$

$$\phi'(x) + \sqrt{\lambda}\phi(x) = 0,\ x = b \quad (27.b)$$

Wave modes ($\lambda < 0$) :

$$\phi(x) = \phi'(x) = 0,\ x = a \quad (28)$$

The side conditions given above can be obtained from the analytical solutions of Eq.(25). The homogeneous solutions satisfying the radiation condition can be written as

Local modes ($\lambda > 0$) :

$$\phi(x) = e^{\sqrt{\lambda}\, x}, \quad x < a \quad (29.a)$$

$$\phi(x) = e^{-\sqrt{\lambda}\, x}, \quad x > b \quad (29.b)$$

Wave modes ($\lambda < 0$) :

$$\phi(x) = 0, \quad x < a \quad (30.a)$$

$$\phi(x) = A \sin(\sqrt{-\lambda}\, x) + B \sin(\sqrt{-\lambda}\, x), \quad x > b \quad (30.b)$$

It can be shown that the solutions satisfying the end conditions (27) and (28) leads to the homogeneous solutions (29) and (30) in the linear subdomain.

The treatments of the radiation condition are basically same as that of the localized finite-element method of Bai(1977). The only difference is the fact that Bai used the exact normal modes, i.e., eigenfunctions, in the truncated infinite subdomain, while the numerical normal modes are used in the present method.

The numerical solution of the ordinary differential equation (25) can be easily obtained by the finite-element method. The solution of the discretized equation can be easily obtained in a closed form if we use the uniform mesh in x-direction as shown in Kim(1991).

The solution procedures described in the previous sections can be summarized as follows.

(a) Evaluate residuals due to the nonlinear terms from the results of the previous iteration step.

(b) Transform the residuals into the normal mode basis to obtain the forcing terms of each mode.

(c) Integrate the linear ordinary differential equations of each mode.

(d) Obtain the new values of the velocity potential by the inverse operation of (b)

(e) Repeat the above operations until the numerical solution meets a preassigned convergence criteria.

The most computational efforts are made for the procedure (a),(b) and (d). If we denote the number of nodal points in the x-direction as N_x, the number of operations is $O(N_xN_yN_z)$ for the step (a) and $O((N_y+N_z)N_xN_yN_z)$ for the steps (b) and (d). The number of operations for the step (b) and (d) can be further reduced to $O((\text{Log } N_y+N_z)N_xN_yN_z)$, if we use the FFT algorithm in the modal analysis in the y-direction. The number of operations for the present method is much smaller than that in the panel method, where the number of the operation is $O(N_x^2 N_y^2)$ for the assembly of the influence matrix and $O(N_x^3 N_y^3)$ for the matrix inversion.

4 NUMERICAL ACCURACY AND STABILITY

4.1 Linear Analysis

The accuracy of the linear solution by the present method can be determined from the results of the eigenvalues and mode shapes of the numerical normal modes. They can be obtained from the eigenvalue problem of the second order differential equations. The properties of the finite-element approximate solution for this problem are thoroughly investigated in many literature. The qualitative properties of the approximation can be summarized that the approximate eigenvalue gives the upper bound for the exact value and the order of accuracy is the second order of the mesh size if a uniform mesh is used. The quantitative analysis can be found in Bai et al(1989) and Kim(1991).

It can be shown that the modal analysis in the y-direction is related to the following eigenvalue problem.

$$\varphi'' + \mu\varphi = 0, \quad 0 < y < W \tag{31.a}$$

$$\varphi' = 0, \qquad y = 0, W \tag{31.b}$$

The exact eigenvales and the eigenfunctions are given as

$$\mu_n = \left[\frac{n\pi}{W}\right]^2, \qquad n=0,1,2,... \tag{32}$$

$$\varphi_n(y) = \begin{cases} \dfrac{1}{W}, & n = 0; \\ \dfrac{2}{W}\cos\left[\dfrac{n\pi y}{W}\right], & n=1,2,3,... \end{cases}$$

The analytic solution for the finite-element discretized equation gives the mode shapes with the same nodal values of the exact solution given above and the eigenvalues as

$$\mu_n = \frac{6}{\Delta y^2}\frac{1-\cos\left(\frac{n\pi}{N_y-1}\right)}{2+\cos\left(\frac{n\pi}{N_y-1}\right)}, \tag{33}$$

$$n=0,1,2,..., N_y-1$$

where Δy is defined as the mesh size in the y-direction. The maximum eigenvalue, related to the modes with wave length $2\Delta y$, has the value $12/\Delta y^2$ which is about 1.2 times larger than that of the exact value, $\pi^2/\Delta y^2$.

The related eigenvalue problem for the modal analysis in the z-direction can be written as

$$\psi_n'' + (\lambda - \mu_n)\psi = 0, \quad -h < z < 0; \tag{34.a}$$

$$\psi_n' = 0, \qquad z = -h; \tag{34.b}$$

$$\psi_n' + \lambda\nu\psi_n = 0, \qquad z = 0 \tag{34.c}$$

for each n-th y-directional normal modes. The eigenvalues consists of the values of opposite sign with an exception of n=0. The exact eigenvalues and eigenfunctions can be found in Bai(1977). For the infinite depth, the negative eigenvalues are given as

$$\lambda_{n0} = -\frac{1 + \sqrt{1 + 4\nu^2\mu_n}}{2\nu^2} \qquad (35)$$

The eigenvalues μ_n and λ_{n0} are related to the wave number of the wave modes. If we denote the wave number vector in the xy-plane as (k_x, k_y), this can be written as

$$k_x = \sqrt{-\lambda_{n0}}, \qquad k_y = \sqrt{\mu_n}. \qquad (36)$$

The dispersion relation between the wave number components determines the characteristics of the far-field wave patterns. We compare the exact and the numerical dispersion relation and the mode shapes in Fig.2(a) and 2(b), respectively. The numerical test is performed with the a uniform mesh in the y-direction and a quadratic spacing near the free surface for finer meshes are used in the z-direction. The numerical computation are made for W=12, h=2, Δy=0.05 and N_z=13. In the figure, the eigenvalues of first fifty wave modes are given. As mentioned above the approximate value gives the upper bound of the exact value. The difference between numerical and exact values is within a few percents in the computed results.

After the modal analysis is performed, the remaining equations to be solved is a set of linear ordinary differential equations given in Eq.(25). In the previous section the analytic properties of these equations are investigated. But in the actual computation discrete solutions are used. The discretized form of (25) is given as

$$\beta\,\phi_{i-1} + 2\alpha\,\phi_i + \beta\,\phi_{i-1} = q_i \qquad (37)$$

where

$$\alpha = \frac{1}{\Delta x} + \frac{\lambda\Delta x}{3}, \qquad \beta = -\frac{1}{\Delta x} + \frac{\lambda\Delta x}{6}$$

$$q_i = \int X_i(x)\, q(x)\, dx \qquad (38.a,b,c)$$

and $X_i(x)$ is the piecewise linear interpolation function with the mesh size Δx. Like the continuous problem, the solution method of the difference equation (37) depends on the behavior of the homogeneous solutions. The homogeneous solutions can be obtained from the characteristic equation

$$\beta\,\gamma^2 + 2\alpha\,\gamma + \beta = 0 \qquad (39)$$

and given as

$$\phi_i = A\,\gamma_+^i + B\,\gamma_-^i, \qquad (40.a)$$

$$\gamma_\pm = \frac{-\alpha \pm \sqrt{\alpha^2 - \beta^2}}{\beta} \qquad (40.b)$$

The type of the roots of Eq.(39) depends on $\lambda\Delta x^2$, i.e.

(a) $\lambda\Delta x^2 > 0$, $\gamma_\pm$ are real and

$$0 < \gamma_+ < 1, \quad \gamma_- > 1 \qquad (41.a)$$

(b) $-12 < \lambda\Delta x^2 < 0$, $\gamma_\pm$ are complex and

$$|\gamma_\pm| = 1 \qquad (41.b)$$

(c) $\lambda\Delta x^2 < -12$, $\gamma_\pm$ are real and

$$-1 < \gamma_- < 0, \quad \gamma_+ < -1 \qquad (41.c)$$

From these results we can see that the type of the numerical solution is similar to that of the analytic solution for local modes ($\lambda > 0$) but that of the wave modes ($\lambda < 0$) is not. If the magnitude of $\lambda\Delta x^2$ is greater that 12, the wave mode treated as an initial-value problem does not give the bounded solution. A good approximation for the maximum magnitude of λ can be obtained by substituting the maximum y-directional eigenvalue $12/\Delta y^2$ into Eq.(35). From these results the stability condition for the present method can be written as

$$24\,F_{\Delta x}^4 > 1 + \sqrt{1 + 48\,F_{\Delta y}^4} \qquad (42)$$

where the cell Froude numbers are defined as

$$F_{\Delta x} = \frac{U}{\sqrt{g\,\Delta x}}, \qquad F_{\Delta y} = \frac{U}{\sqrt{g\,\Delta y}}. \qquad (43.a,b)$$

The condition (42) can be simplified under the assumption that the cell Froude $F_{\Delta y}$ is sufficiently large. The result is given as

$$\left(\frac{\Delta x}{l}\right)^2 < 3.5\,F_N^2\left(\frac{\Delta y}{l}\right) \qquad (44)$$

where l is defined as the length of the disturbance and the Froude number F_N as $U/\sqrt{gl}$.

With the above stability condition satisfied, the solution of the Eq.(37) can be given in the following recurrence formulas

(a) If $\lambda < 0$,

$$\phi_{i+1} = \frac{q_i - \beta \phi_{i-1} - 2 \alpha \phi_i}{\beta} \qquad (45)$$

(b) If $\lambda > 0$,

$$\phi_i = \phi_i^+ + \phi_i^- , \qquad (46.a)$$

$$\phi_i^+ = \gamma_+ \left[\phi_{i+1}^+ - \frac{q_{i+1}}{\sqrt{\alpha^2 - \beta^2}} \right], \qquad (46.b)$$

$$\phi_i^- = \gamma_+ \left[\phi_{i-1}^- - \frac{q_{i-1}}{\sqrt{\alpha^2 - \beta^2}} \right]. \qquad (46.c)$$

4.2 Nonlinear Analysis

In the present analysis, it suffices to treat only a nonlinear homogeneous problem without including any source of disturbance, i.e. the pressure distribution on the free surface which will be treated in the next section. We consider the following nonlinear problem,

$$-\phi'' + \Lambda \phi = \mathbf{N}[\phi] \qquad (47)$$

where $\phi(x)$ is a vector form of the normal modes and Λ is the diagonal eigenvalue matrix. and $\mathbf{N}[\phi]$ is the nonlinear terms. In the present numerical method it is assumed that the influence of the nonlinear terms, $\mathbf{N}[\phi]$, are weak enough such that they can be treated as the forcing terms determined from the previous step. For the local modes this assumption is thought to be valid since they have the elliptic property, that is, the influence of the forcing terms is localized. The convergence proof for the elliptic problem with a nonlinear forcing is given in Courant and Hilbert(1962).

For the wave modes, however, this assumption causes a difficulty. It is well-known that the leading order of the nonlinear terms in the wave problem is the third order. The dominant feature of the third order nonlinearity is a correction in the wave number. It has been known that the regular perturbation method applied to this problem gives no bounded solution. We faced the same difficulty in our numerical method. However, the situation is not so serious in our case because of the following reasons.

The direct analysis of the nonlinear equation (47) is not easily tractable due to its complexity. Instead, we propose a simplified model where only one wave mode is taken into account. But the essential features of the nonlinearity in the wave modes is included in the model. The mode shape of the wave mode is assumed as exponential function in the z-direction, which is the exact normal mode for an infinite depth of water. Then the reduced nonlinear equation at the downstream, accurate up to the third order, can be written as

$$-\phi'' - (1 + \phi'^2 + \phi^2)\phi = 0 . \qquad (48)$$

after some lengthy algebraic steps and appropriate nondimensionalization. The approximate solution including the third-order correction can be given as

$$\phi(x) = \frac{A}{2} \mathrm{Exp}[\, i\, x \,(\, 1 + \frac{|A|^2}{2}) \,] + \text{c.c.} \qquad (49)$$

where A is a complex amplitude which can be determined in the near field and c.c. denotes the complex conjugate of the first term. The perturbation solution of Eq.(48) has the same behavior of the Taylor expansion of Eq.(49) with respect to A. The complex modulation amplitude function of the secular terms can be given as a Taylor expansion,

$$\mathrm{Exp}[\frac{ix|A|^2}{2}] = 1 - \frac{x^2|A|^4}{8} + \frac{x^4|A|^8}{384} + \ldots \qquad (50)$$

$$+ i \left[\frac{x|A|^2}{2} - \frac{x^3|A|^6}{48} + \frac{x^5|A|^{10}}{3840} + \ldots \right].$$

The terms up to the 2n-th order in $|A|$ gives an approximate complex modulation amplitude of the $(2n+1)$-th order perturbation result or the $(n+1)$-th iteration result of the present method.

In the perturbation method which concerns the solution in the entire domain, the polynomial envelope given in Eq.(50) gives an unbounded solution as x increases. In the present numerical method, however, the nonlinear correction is confined in the finite computational domain. Then if we choose a suitable magnitude of the disturbance and the length of the nonlinear domain, the numerical solution converges within a manageable number of iteration. We use the following two techniques for the convergence. First, we gradually increased the magnitude of the disturbance with the length of the computational domain fixed. Second, we gradually increased the length of the nonlinear subdomain with a given disturbance. In the second method, we could save the computational efforts since the evaluation of the nonlinear terms are not necessary in the converged nonlinear region. In Fig.3 the error of the polynomial approximation given in Eq.(50) is shown.

This can be used as an error estimate of the present iteration method.

5 NUMERICAL RESULTS

5.1 Pressure Patch

As an application of the present numerical method, we treat first a steady nonlinear wave generated by the circular pressure patch. The shape of the pressure patch is given as

$$P(r) = \begin{cases} P_{max}\,\Pi(r/R), & r < R, \\ 0, & r > R \end{cases} \qquad (51.a)$$

$$\Pi(s) = 1 - 462\,s^6 + 1980\,s^7 - 3465\,s^8 + 3080\,s^9 - 1386\,s^{10} + 252\,s^{11} \qquad (51.b)$$

which is identical to that used in Dommermuth and Yue (1988) where the unsteady problem was treated by the spectral method. Here r is defined as the distance from the center of the pressure patch and R denotes the radius of it. Hereafter all the quantities will be non-dimensionalized by the combinations of ρ, g and 2R.

The locally-linearizing parameter $\varepsilon(x,y)$ is taken as

$$\varepsilon(x,y) = \begin{cases} 1, & x < x_1 \\ \cos^2 \dfrac{\pi\,(x - x_1)}{2\,(x_2 - x_1)}, & x_1 < x < x_2 \\ 0, & \text{Othewise} \end{cases} \qquad (52)$$

such that the linear and the buffer subdomains are located only at the downstream. On the upstream, the artificial reduction of the nonlinearity is not necessary since only the exponentially decaying local modes exist.

The Froude number F_N is taken as 0.4 and the depth of the tank as 2. For this case the maximum wave length of the wave modes is about the half of the depth such that the effect of the finite depth can be neglected. The number of nodes in the z-direction, N_Z, is taken as 13 and a quadratic spacing is used for better resolution near the free surface. For the horizontal directions, uniform meshes are used.

One of the major concerns in the present computation is the validation of our numerical radiation condition. For this purpose, we performed the numerical experiment with various size of the computational domain. The tested conditions are tabulated in Table 1.

Table 1 Tested conditions in the numerical computation for a pressure patch

	Δx, Δy	$L^* \times W$	No. of Elements	$x_2 - x_1$
A1	0.05	6 × 3	86,400	1
A2		15 × 7	504,000	2
A3		25 × 12	1,440,000	2

* L denotes the length of the computational domain

In Fig.4 the longitudinal cuts of the wave profiles along the center line are shown for three different sizes of the computational domain. The amplitude of the pressure distribution, P_{max}, is 0.015. We can find that the wave profiles of each case are indistinguishable in the common nonlinear subdomains. In Fig.5 the cuts along the cuspline are shown. On the cuspline, the nonlinear effects are thought to be most apparent since the decay rate of the wave elevation is smaller than the other region. But the same agreements of wave profiles are found in the nonlinear subdomains.

In Fig.6(a) and 6(b) we plotted the computed linear momentum flux, $M_X(x)$, defined as

$$M_X(x) = \frac{1}{2}\int\int (\phi_y^2 + \phi_z^2 - \phi_x^2)\,dydz + \int \zeta^2\,dy \qquad (53)$$

for the linear and nonlinear cases with the amplitude of the pressure patch $P_{max} = 0.016$. The disturbances are located between x = 1 and x=2, and the location of the transition buffer subdomain is x_1=5 and x_2=6 for the nonlinear computation. The momentum fluxes at the downstream are nearly constant which is slightly lower values compared with the computed wave resistances. In the nonlinear subdomain, a small amount of fluctuation in the momentum flux can be found. The reason of the fluctuation can be partially explained by the inaccuracies in evaluating the momentum flux by a numerical quadrature. The presence of the buffer subdomain, introduced for the smooth matching of the nonlinear and linear solution, does not seem to affect the mean value of the momentum flux. It only smoothes out the fluctuation. This is presumably due to the fact that only the nonlinearities are gradually weakened in this region without any introduction of the numerical damping.

Based on these results, we may assert that our treatment of the numerical radiation condition can be effectively applied to the nonlinear water wave problem. This treatment of the radiation condition has already been applied to the 2-dimensional steady wave resistance

problem and transient axisymmetric problem successfully, as can be found in Lee (1990) and Bai and Kim(1992), respectively. The absence of the numerical damping in the present method enables us to perform the calculation in a wider computational domain compared to the existing panel methods, which also gives the meaningless results at the far down stream because of the numerical damping introduced for the radiation condition.

As mentioned previously, the nonlinear wave resistance problem for the circular pressure patch was already investigated by Dommermuth and Yue (1988). They treated this problem as a transient problem and obtained the steady state solution up to the distance from the disturbance, r = 8. From the results with the largest computational domain of the present computation(A3 in Table 1), we obtained steady solution in the region three times larger than theirs. As a result we can investigate the nonlinear effect on the downstream wave pattern with more clarity.

In Fig.7(a) and 7(b) we show the cuts of the wave profiles along the centerline and cuspline, respectively. As shown in Fig. 7(a), the nonlinear effects are not apparent on the center line except in the region near the disturbance. Small amount of phase shift and shortening of the wave length can be found in the nonlinear results. On the cuspline, however, a significant nonlinear effect is found. The difference in the phase between the nonlinear and the linear wave profiles increases almost linearly as the distance from the disturbance does. The wave height also increases with the sharpening of the crests in the nonlinear results, which is a distinct feature of the nonlinear gravity waves. The transverse cuts of the wave profiles at $x - x_c = 10$ and 20 are shown in Fig.8(a) and 8(b), respectively. The outward shift of the wave profiles are found to be more pronounced with increasing distance from the disturbance.

From the above results, the nonlinear effects on the wave patterns near the cuspline can be summarized as the outward shift of the wave profiles and the increase of the wave number and heights. This results agree well with that of Dommermuth and Yue(1988) but differs from the far-field perturbation results of Akylas(1987) along the cuspline where small differences in the phase only were predicted. Dommermuth and Yue argued that this discrepancies are due to the absence of near and intermediate fields in the analysis of Akylas. In the present paper, more information on the nonlinear effects are available from the results with the much larger computational domain.

The solutions of the surface wave problem are composed of wave modes and local modes, as discussed in the previous sections. The nonlinear effects on the downstream waves may be explained to be resulted from the two sources of interactions: namely, the interaction between the wave and the other wave modes, and the wave and the local modes. The dominant effects of the interaction between the wave and the local modes, are refraction of the wave modes under the local convection of the local modes. This phenomena have been well understood in the ray theory of the water wave problem developed by Keller(1979). On the other hand, the dominant feature of the interaction between wave modes are the nonlinear correction of the dispersion relation, which was found by Stokes(1847) and generalized by Longuet-Higgins and Phillips(1962) and Benney(1962). These interactions result in the phase correction of the wave modes but with some distinct properties. The wave-local interaction arise in the near field and give the first order correction on the phase. The wave-wave interaction, on the other hand, prolong up to far-field and give the second order correction on the phase. As a result, the nonlinearities in the downstream wave pattern appear as the mixture of the first order shift of phase and the second order correction of the wave numbers.

The results given in Fig.7 and 8 show that the latter features of nonlinear interaction are dominant for the present case. To confirm the result, we also carried out the numerical computation with the opposite sign for the pressure distribution. The transverse cuts of the wave profiles with the positive and the negative pressure distributions are compared in Fig.9. The phase shifts are in the same direction regardless the signs of the pressure. It is evident that the major nonlinear effect in the present results are caused by the second order phase correction due to the wave-wave interaction.

The arguments given above suggest that the far-field analysis is enough to explain the nonlinear effects of the present results, contrary to the Dommermuth and Yue's argument. It can be also said that the far-field analysis of Akylas has its own defect. As an alternative approach to this problem, we propose a far-field analysis based on the generalized Stokes correction and the method of stationary phase. The details of the analysis can be found in Kim(1991) and the results can be summarized below.

The far-field wave patterns can be represented as a Fourier integral

$$\zeta(x,y) = \varepsilon \int A(k)\, \mathrm{Exp}[\, ix\Psi(k)\,]\, dk + O(\varepsilon^2), \quad (53.a)$$

$$\Psi(k) = G(k) - k\frac{y}{x} \quad (53.b)$$

where ε is now defined as a perturbation parameter, which can be interpreted as the magnitude of the disturbance. Here, k is defined as the y-component of the wave number vector and G(k) is the x-component. The nonlinear relation between the wave number

components, accurate up to the second order, can be given as follows.

$$G(k) = \sqrt{\frac{1+\sqrt{1+4\,k^2}}{2}} \qquad (54)$$

$$+\varepsilon^2 \int_0 K(k,k')\,|A(k')|^2\,dk'$$

where the wave numbers are nondimensionalized by U^2/g. The nonlinear interaction kernel K(k,k') is closely related to that of the progressive waves, whose correct form is given in Benney(1962). The asymptotic behavior of the wave pattern (53.a) can be obtained by the method of stationary phase, which enables us to investigate the geometrical spreading of the wave fields. Especially, the angle of the cuspline can be obtained from the zeroes of the second order derivative of the phase function, $\Psi''(k)$. If we denote the value of the zero as k_c, the cuspline is given as

$$y = G'(k_c)\,x \qquad (55)$$

and the asymptotic form of wave elevation along the cuspline can be written as

$$\zeta \sim \varepsilon \frac{\Gamma(\frac{1}{3})}{\sqrt{3}} A(k_c) \left[\frac{6}{|\Psi'''(k_c)|}\right]^{\frac{1}{3}} \mathrm{Exp}[\,i\Psi(k_c)\,x],$$

$$\text{as } x \to +\infty. \qquad (56)$$

It can be found that the angle of the cuspline, or Kelvin angle, and the geometrical spreading factor on it is related to the first and the third derivative of the phase functions. The above analysis is formally same as that for the linear Kelvin wave pattern, with an exception of the nonlinear correction in the dispersion relation (54). With a careful numerical inspection on the nonlinear interaction kernel K(k,k'), we found that k_c, $G(k_c)$ and $G'(k_c)$ increases but $|\Psi'''(k_c)|$ decreases by the nonlinear correction, independently of the shape of the amplitude function A(k). From these results we can predict the widening of the Kelvin angle and the increase in the wave numbers and magnitude of the wave profiles on it. It has been also found that the correction on the magnitude of the wave profile is pronounced compared to the other quantities.

The result of a simple analysis given above agrees well with the numerical computation, contrary to that given by Akylas. The major difference between two analyses is the treatment of the nonlinear interaction kernel K(k,k'). Akylas considered only the diagonal parts of the interaction kernel under the assumption that the wave fields near the cuspline can be modeled by a modulated wave packet. So only the diagonal part of the interaction kernel was taken into account in his analysis. As shown previously, the increases in the Kelvin angle and the magnitude of the wave profiles are related to the derivatives of the interaction kernel whereas the increase in the wave numbers are related to the values of the interaction kernel itself. As a result Akylas's analysis could not show the nonlinear effects other than the correction of the wave numbers.

In Fig.10 we show the Fourier components of the linear and nonlinear wave profiles with $k = k_c$. No apparent nonlinear effect on the wave amplitude are found although the nonlinear profile along the cuspline shows much larger height than that of the linear case in Fig.7(b). This strongly confirms the fact that the increase in wave height along the cuspline is due to the reduction of the geometrical spreading factor, not to the increase in the amplitude of the wave component.

As the concluding presentation in this section, we show the contour plots of the computed wave patterns in Fig 11(a) ~ 11(d). The solid lines in the figures are the linear cusplines that passes the center of the disturbance. We can vividly see the nonlinear corrections on the far-field wave patterns explained above.

5.2 Lifting Problem

We treat the lifting problem of a submerged hydrofoil as the second application of the present numerical method. As a mathematical model for the problem, the hydrofoil is replaced by the lifting lines with a prescribed sectional circulations. This simplification does not affect the general nonlinear features in the far-field downstream wave-patterns generated by s hydrofoil. For the near-field features, such as the induced velocities and the hydrodynamic forces, the simplified model still provides a good approximation of the original problem. This is due to the fact that the typical operation condition for the hydrofoils can be characterized by the high speed and shallow submergence, under which the chord-wise variation of the physical quantities can be treated in an integral or mean sense.

The lifting lines are expressed as the superposition of the horse-shoe vortex system. Specifically, a single horse-shoe vortex and the vortex system with an elliptic distribution are investigated. The sectional circulation, $\Gamma(y)$, for these cases can be written as

$$\Gamma(y) = \Gamma_0, \qquad -i < y < i \qquad (57)$$

for single horse-shoe vortex and

$$\Gamma(y) = \frac{4}{\pi}\Gamma_0\sqrt{\ell^2 - y^2}, \qquad -\ell < y < \ell \qquad (58)$$

for an elliptic distribution. Here, Γ_0 is the mean circulation and ℓ denotes the half span. Hereafter, all the physical quantities are nondimensionalized by ρ, U and ℓ. For example, the circulation Γ_0 is nondimensionalized by $U\ell$.

The numerical procedure for the present problem is basically same as that for the pressure patch. The velocity potential ϕ is represented as the linear sum of the known analytic potential functions ϕ_v and ϕ_{vi}, for the horse-shoe vortex potential in the unbounded domain and its negative image on the free surface, respectively, and the finite-element numerical solution ϕ_0 to be obtained later, i.e.

$$\phi = \phi_v + \phi_{vi} + \phi_0 \qquad (59)$$

Since the first two analytic functions satisfy the governing equation, only the free-surface conditions are modified in the newly formulated boundary-value problem for the unknown potential ϕ_0. If we treat these modified terms as the forcing terms, the boundary value problem to be solved in each iteration steps leads to the same form of equations (17) and (18).

To validate the accuracy of the present method, we compared the linear numerical results for a single horse-shoe vortex with the analytic solution which can be given as the double layer of the Havelock source potential. The agreement in the wave elevation was remarkably good, as shown in Lee (1992).

Table 2 shows the tested conditions. Here the Froude number, Fn, is defined as $U/\sqrt{g\ell}$. The depth of submergence, d, was taken as 0.125, or one sixteenth of the span. The elliptic sectional distribution is modeled by the superposition of 40 horse-shoe vortices over the span. The maximum strengths of the mean circulation for which we can obtain the converged solutions were 0.025 and 0.06 for the Froude numbers being 0.5 and 1.0, respectively. Hereafter, the presented wave elevations will be normalized by the mean circulation Γ_0.

Table 2 Tested conditions of the numerical computation for the lifting problem

Froude No.	Δx, Δy	L×W×h	No. of Elements	$x_2 - x_1$
0.5	0.05	12 × 6× 3	432,000	1
1.0	0.10	25 × 10× 6	187,500	1

In Fig.12 we present the wave contours of the computed linear and nonlinear wave patterns generated by a single horse-shoe vortex. The Froude number is 1.0 and the mean circulation is 0.06 for the nonlinear case. The nonlinear effects shows the inward and downstream-wise shift of the wave patterns. These shifts are in the same direction of the velocities induced by the free and the bound vortices. By changing the sign of the mean circulation the direction of the shifts reversed. The nonlinear interaction between the wave and the local modes, in the vortex system, seems to play a more significant role than the wave-wave interactions which were dominant in the previous results for the pressure patch. The longitudinal cuts along the centerline and the free-vortex line, and the transverse cuts along $x - x_c = 3$ and 6 are shown in Fig.13(a),(b) and Fig.14(a),(b), respectively, with varying strengths of the mean circulation. In these figures the nonlinear effects described above can be observed more clearly. It can be also found that the nonlinear correction on the phase is a first order to the magnitude of the disturbance. It should be noted that in the linear theory the disturbances by the free-vortex alone do not generate the surface wave since the free-vortex induces no streamwise velocity component. For a nonlinear case, however, the velocity field induced by the free-vortex gives a significant nonlinear correction on the wave profiles.

In Fig.15 the longitudinal cuts of the results of Fn=0.5 are plotted. Since the computational domain contains more waves than that of the previous case, Fn=1.0, we can see the combined feature of the two kinds of nonlinear interactions. The direction of the phase shift, which is backward near the bound vortex line, gradually changes to the forward direction along the downstream. The nonlinear corrections from the wave-wave interaction and the wave-local interaction in the near-field cancels in some degree in this neighborhood. However, in the intermediate field the interaction of the wave-local disturbance becomes more significant.

The results of the elliptic distribution show the same trend of nonlinear effects on the wave profiles. In Fig. 16 we compared the longitudinal cuts of the wave profiles with that of the single horse-shoe vortex system. Some differences can be observed near the bound vortex line due to the difference in the vortex distribution, but in the up- and down-streams both profiles are almost same in magnitude and phase.

Besides the nonlinear effects of the wave profiles, the near-field features such as the induced velocities, the induced angle of attack and the resulting hydrodynamic force components are also calculated. The definition sketches of these are given in Fig.17. In the following we present the computed results of the elliptic distribution, which gives the finite induced velocities at the tip of a lifting line.

In Fig.18 and 19, the nonlinear effect on the induced velocities on the bound vortex line is shown for Fn = 0.5 and 1.0, respectively. Along the x-direction the induced velocity shows relatively high for Fn=0.5 where as that is negligibly small for Fn=1.0. It is of interest to note that the signs of the nonlinear correction are opposite in these two cases of different Froude numbers. For both cases the magnitudes of the nonlinear corrections are within a few percents. Fig.20 shows the induced angles of attack and the opposite tendency in them between the two cases. Fig.21 shows the sectional force ratio, defined as the ratio between the sectional forces with and without the free surface. It can be found that the free-surface effects are negligible in the lift but significant in the drag, with nonlinear corrections within a few percents for both force components. Fig.22 shows the nonlinear effects on the hydrodynamic forces. The lift decreases as the mean circulation increases for both Froude numbers. But drag shows the different tendency depending on the Froude number.

The perspective view of the computed wave patterns for Fn = 0.5 are shown in Fig.23.

In the computation for the case A3 in Table 1, the total number of elements being 1,440,000, the CPU time was approximately 6 hours for the largest magnitude of the pressure by the MIPS RS2030 Workstation. It should be noted that the computation time reduces considerably when the magnitude of the pressure reduces.

6 CONCLUSIONS

The advantages of the present method over the other existing methods may be summarized in the following.

- By the introduction of a more rational matching procedures in the nonlinear-to-linear transition buffer subdomain between the fully nonlinear and linear subdomain, the numerical radiation condition for a nonlinear problem could be treated successfully. It should be noted in the present matching device that not only the fluid domain and the free surface boundary are continuous geometrically but also the differential operator of the boundary condition on free surface boundary is continuous.

- In the present numerical treatment of the radiation condition, the numerical damping is absent.

- By utilizing the modal analysis partially introduced in the computations, the total computation time could be reduced drastically.

- From these major modifications made in the present method, the nonlinear steady wave problems could be treated for a much wider computational domain compared that treated previously.

The present numerical method could be successfully applied to a steady nonlinear wave problem for a pressure distribution and a hydrofoil in three dimensions. From these computed results our findings are a more accurate nonlinear wave patterns in the downstream. We also present a simple nonlinear analysis which supports our numerical results.

Acknowledgment

The authors are grateful for the financial supports from the Korean Science and Engineering Foundation, the Advanced Fluids Engineering Research Center(AFERC) at POSTECH, and Hyundai Maritime Research Institute.

REFERENCES

Akylas, T.R. 1987, "Unsteady and Nonlinear Effects Near the Cusp Lines of Kelvin Ship-Wave Pattern," J. Fluid Mech., Vol.175, pp.333-342.

Bai, K.J. 1977, "A Localized Finite-Element Method for Steady Three-Dimensional Free-Surface Flow Problems," Proc. 2nd. Int. Conf. on Numerical Ship Hydrodynamics, Univ. of Calif., Berkeley.

Bai, K.J. 1978, "A Localized Finite-Element Method for Two-dimensional Steady Potential Flows with a Free Surface," J. Ship Research, Vol. 22, No. 4, pp.216-230.

Bai, K.J. and Han, J.H., 1992, "A Localized Finite Element Method for the Nonlinear Steady Waves due to a Two-Dimensional Hydrofoil," (Submitted to the J. Ship Research)

Bai, K.J. and McCarthy, J.H. (Edited by) 1979, Proc. of the Workshop on Ship Wave-Resistance Computations, DTNSRDC.

Bai, K.J., Kim, J.W. and Kim, Y.H. 1989, "Numerical Computations for a Nonlinear Free-Surface Flow Problem," Proc. 5th Int. Conf. on Num. Ship Hydro., Hiroshima, Japan.

Benney, D.J. 1962, "Non-linear Gravity Wave Interactions," J. Fluid Mech. Vol.14, pp.577-584.

Coleman, R.M. 1986, "Nonlinear Calculation of Breaking and Non-Breaking Waves behind a Two-Dimensional Hydrofoil," Proc. 16th Symp. on Naval Hydrodynamics, pp.51-62.

Cordonnier, J.-P. 1985, "Horizontal Displacement of Hydrofoils Beneath the Free Surface," Proc. 4th Int. Conf. on Num. Ship Hydrodynamics, Tokyo, Japan.

Courant, R. and Hilbert, D. 1962, Methods of Mathematical Physics, Vol. II Partial Differential Equations, Interscience Publishers, pp.367-374.

Dawson, C.W. 1977, "A Practical Computer Method for Solving Ship-Wave Problems," Proc. 2nd. Int. Conf. Num. Ship Hydro., Berkeley,

Dommermuth, D.G. and Yue, D.K. 1988, "The Nonlinear Three-Dimensional Waves Generated by a Moving Surface Disturbance," Proc. 17th Symp. Naval Hydro., The Hague, The Netherlands. pp.523-539

Guevel, P., et al. 1977, "Numerical Solution of the Neumann-Kelvin Problem by the Method of Singularities," Proc. 2nd. Int. Conf. Num. Ship Hydro., Berkeley, pp.107-123.

Keller, J.B. 1979, "The Ray Theory of Ship Waves and the Class of Streamlined ships," J. Fluid Mech., Vol. 91, pp.456-488.

Kelvin, T. 1886, "On Stationary Waves in Flowing Water," Phil. Mag., (5) Vol. 22,1886, pp.353-357, 445-452, 515-530; Vol.23, 1886, pp.52-57.

Kim, J.W. 1991, "A Numerical Method for Nonlinear Wave-Making Phenomena," Ph.D Thesis, Seoul Nat'l Univ., College of Eng., Dep't of Naval Arch. (in Korean)

Kim, Y.H. and Lucas, T. 1990, "Nonlinear Ship Waves," 18th Symp. on Naval Hydro., Ann Arbor, Michigan, USA.

Kwag, S.-H. and Mori, K. (1991), "Numerical Simulation of Free-Surface Flows around 3-D Submerged Hydrofoil by N-S Solver," Ann. Meeting of The Soc. of Naval Arch. of Japan, Univ. of Tokyo.

Leclerc, J. and Salaun, P. (1981), "Unsteady 3-D Lifting Surface Theory with the Free-Surface Effect," Proc. 3rd Int. Conf. on Num. Ship Hydrodynamics, Paris, France.

Lee, H.G. 1992, "Numerical Computations for Hydrofoil-Generated Nonlinear Waves," Ph.D. Thesis, Seoul National University, College of Eng. Dep't of Naval Arch. (in Korean)

Lee, H.S. 1990, "A Numerical Analysis of Two-Dimensional Free-Surface Flow Problem," M.S. Thesis, Seoul National University, College of Eng. Dep't of Naval Arch.

Lew, J.-M., Kim, Y.-G., and Lee, C.-S. (1991), "Analysis of a 2-Dimensional Partially or Super-cavitating Hydrofoils Advancing under the Free-surface with a Finite Froude Number," Spring Meeting of Soc. of Naval Arch. of Korea, Ulsan Univ., Ulsan, Korea.

Longuet-Higgins, M.S. and Phillips, O.M. 1962, "Phase Velocity Effects in Tertiary Wave Interactions," J. Fluid Mech., Vol.12, pp333-336.

Michell, J.H. 1898, "The Wave Resistance of a Ship," Phil. Mag.(5) Vol.45,pp.106-123 also in The Collected Mathematical Works of J.H. and A.G.M. Michell, pp.124-141., 1964.

Miyata, H. and Nishimura, S. 1985, "Finite-Difference Simulation of Nonlinear Ship Waves." J. Fluid Mech., Vol.157, pp.327-357.

Nakatake, K., et al. 1988, "Calculation of the Hydrodynamic Forces Acting on a Hydrofoil," Transactions of the West-Japan Society of Naval Architecs, No.76 (in Japanese).

Ni, S.Y. 1987, "Higher Order Panel methods for Potential Flows with Linear or Non-linear Free Surface Boundary Conditions." SSPA Report No.2912-4,5,6 Division of Marine Hydrodynamics, Goteborg, Sweden.

Nishiyama, T. 1965, "Lifting-Surface Theory of a Fully Submerged Hydrofoil," J. of Ship Research.

Parkin, B.R., Perry, B. and Wu, T.Y., 1956, "Pressure Distribution on a Hydrofoil Running Near the Water Surface," J. Applied Physics, Vol. 27, pp.232-240.

Qi, X. and Mori, K. (1990), "A Boundary Element Method for the Numerical Simulation of 3-D Nonlinear Water Waves Created by a Submerged Lifting Body," J. of Soc. of Naval Arch. of Japan, Vol. 167, pp.25-34.

Raven, H.C. 1988 "Variations on a Theme by Dwawson," Proc. 17th Symp. Naval Hydro., The Hague, The Netherlands. pp.151-171

Stokes, G.G. 1847, "On the Theory of Oscillatory Waves," Trans. Camb. Phil. Soc. Vol.8, pp.441-455.

Ursell, F. 1960, "On Kelvin's Ship-Wave Pattern," J. Fluid Mech., Vol.8, pp.418-431.

Wehausen, J.V. 1973, "The Wave Resistance of Ships," Advances in Applied Mechanics, Vol.13.

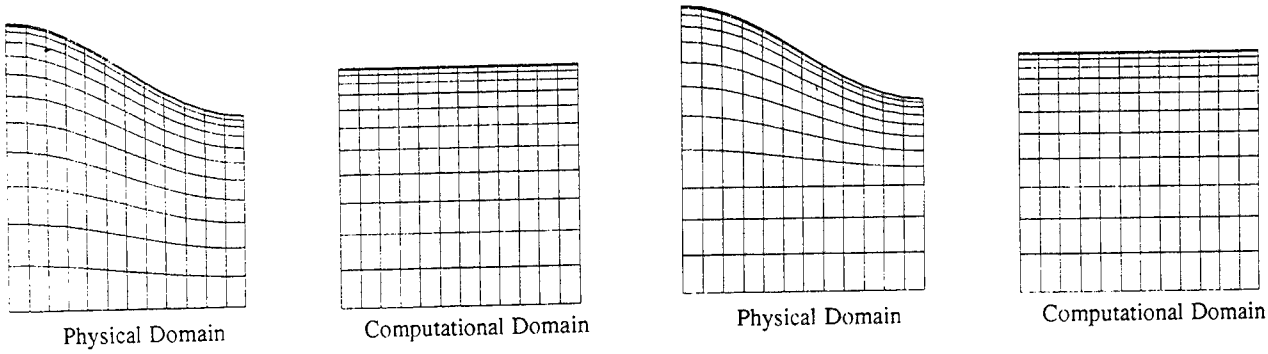

(a) Linear Transformation

(b) Piecewise Linear Transformation

Fig. 1 Coordinate transformations

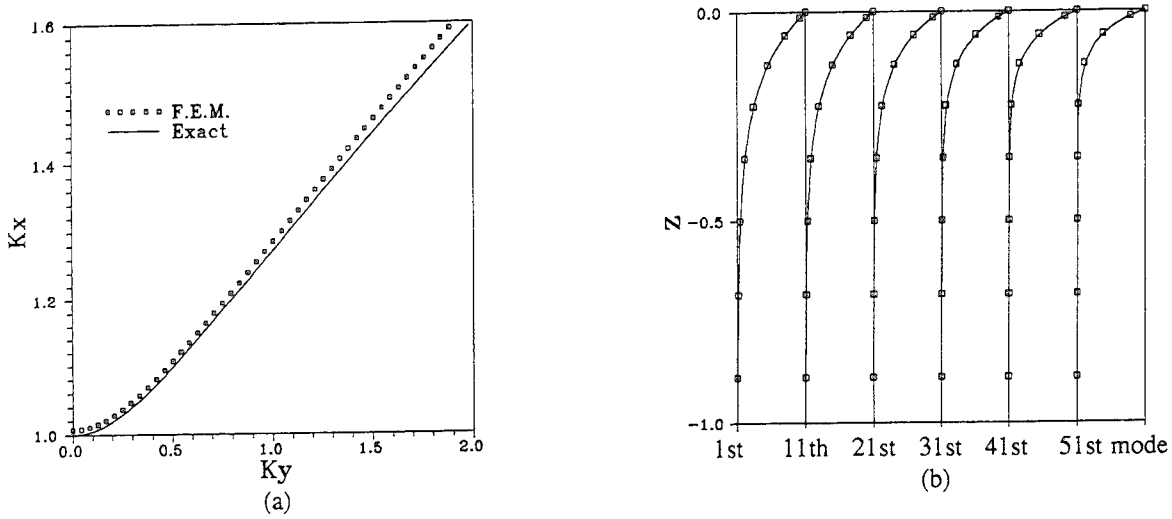

(a)

(b)

Fig. 2 Comparisons of numerical and exact wave modes
(a) Dispersion relation
(b) Mode shapes

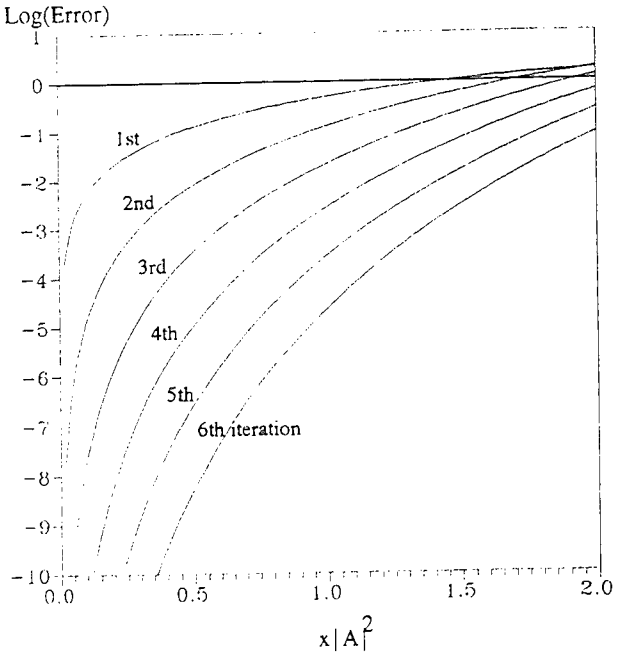

Fig. 3 Estimated error in the fixed point iteration for the nonlinear equation given in Eq.(50)

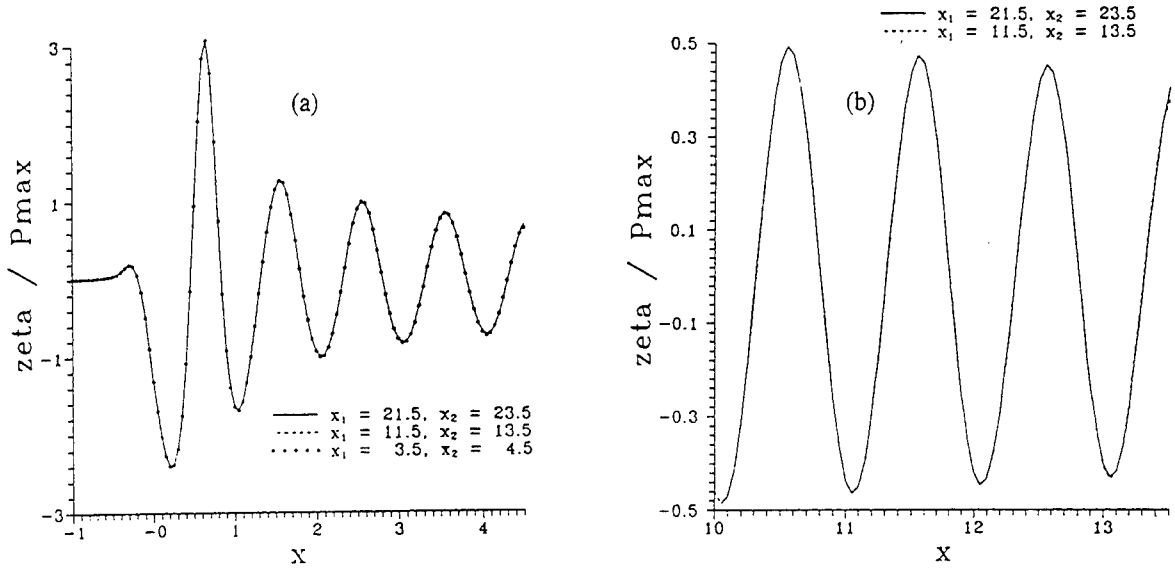

Fig. 4 Effect of buffer region on the wave elevations at y=0. The center of pressure patch is located at x=0.
(a) Wave elevations in -1 < x < 4.5
(b) Wave elevations in 10 < x < 13.5

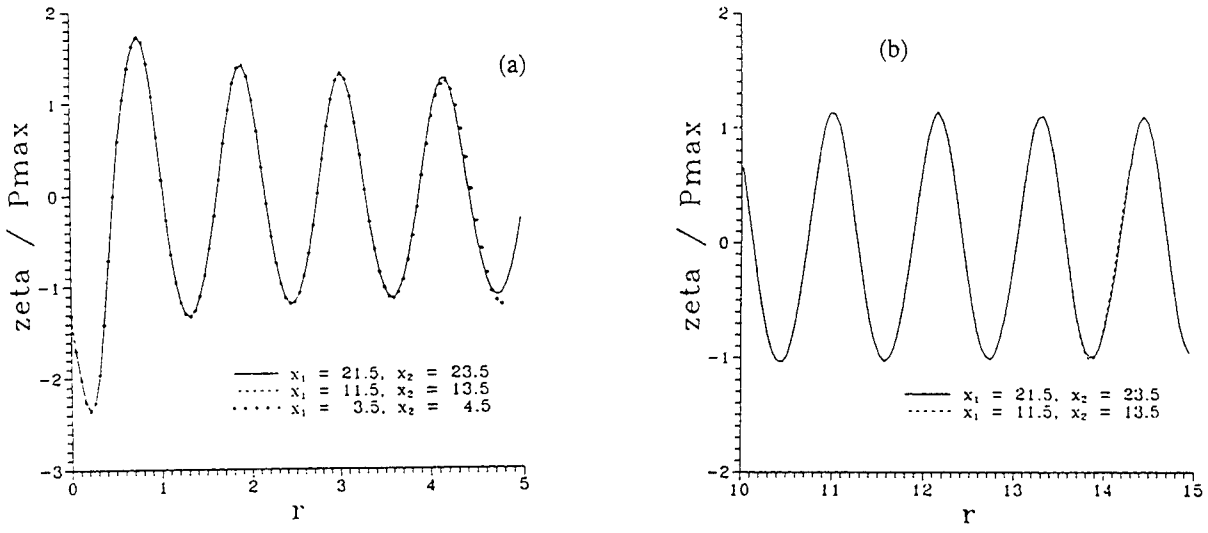

Fig. 5 Effect of buffer region on the wave elevations at cusp line.
(a) Wave elevations in 0 < r < 5
(b) wave elevations in 10 < x < 15

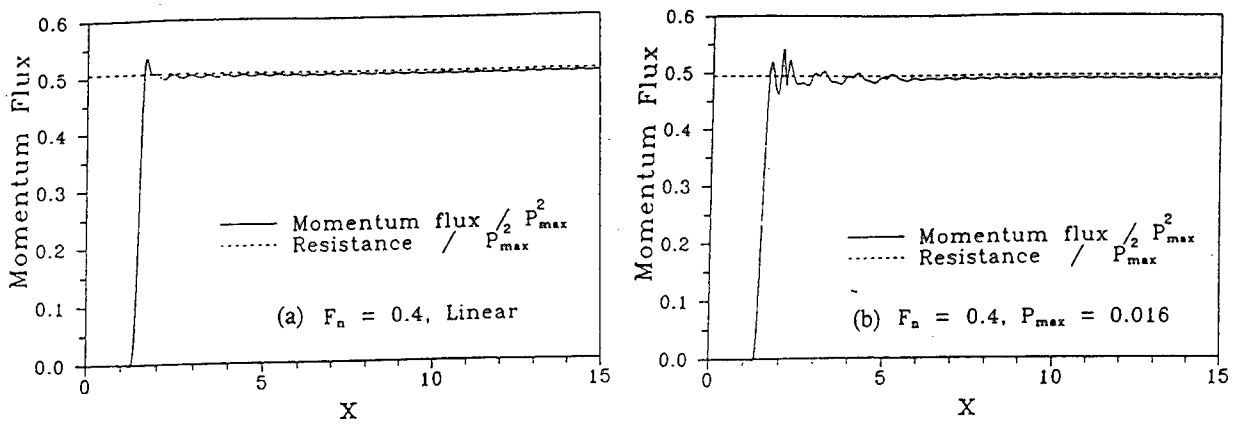

Fig. 6 Momentum flux
(a) Linear case
(b) Non-linear case(x_1=5,x_2=6)

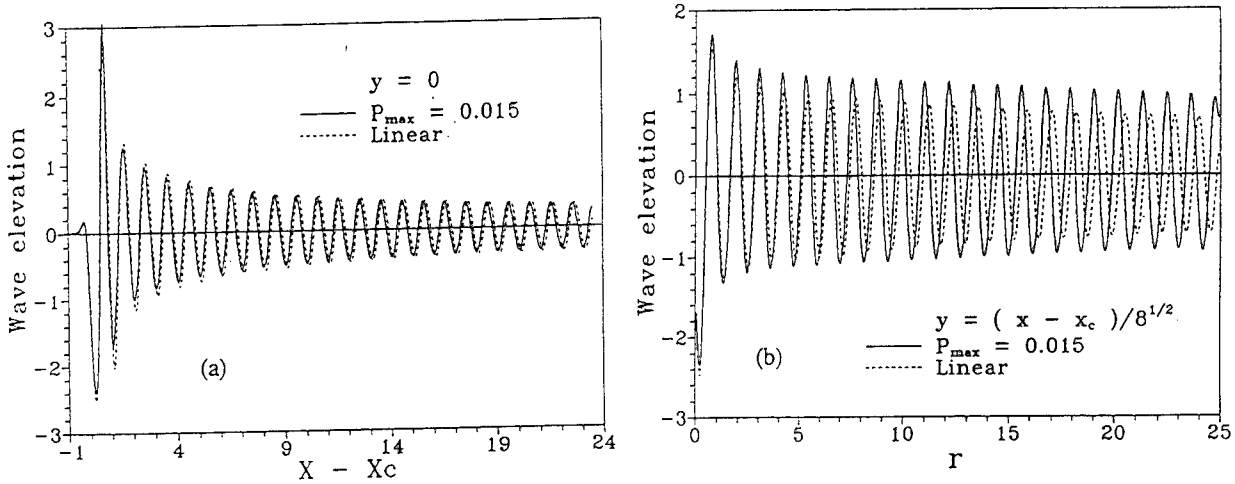

Fig. 7 Non-linear effect on wave profiles.
(a) Center line (y=0)
(b) Cusp line ($y=(x-x_c)/2^{1.5}$)

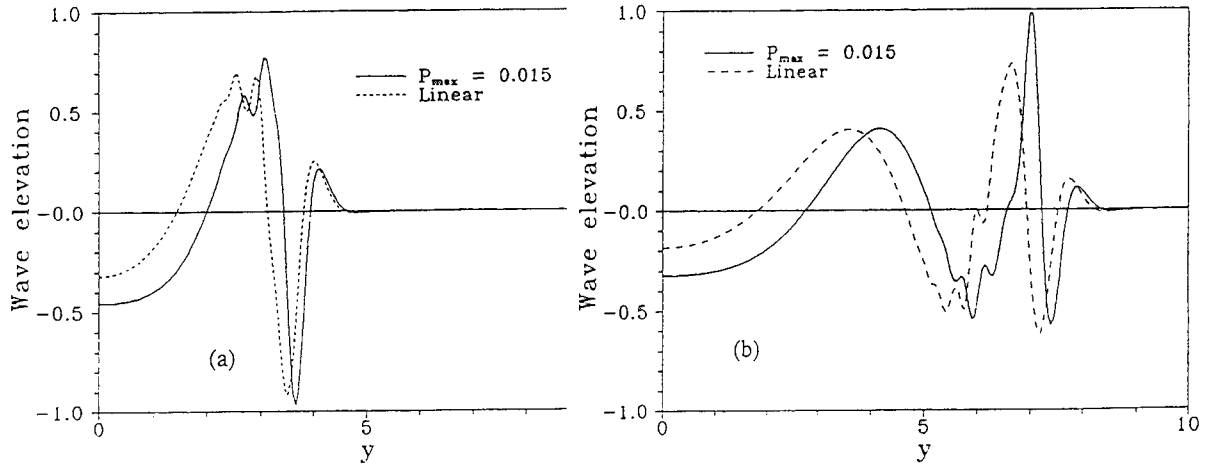

Fig. 8 Transverse cuts of the wave profiles.

(a) $x-x_c=10$ (b) $x-x_c=20$

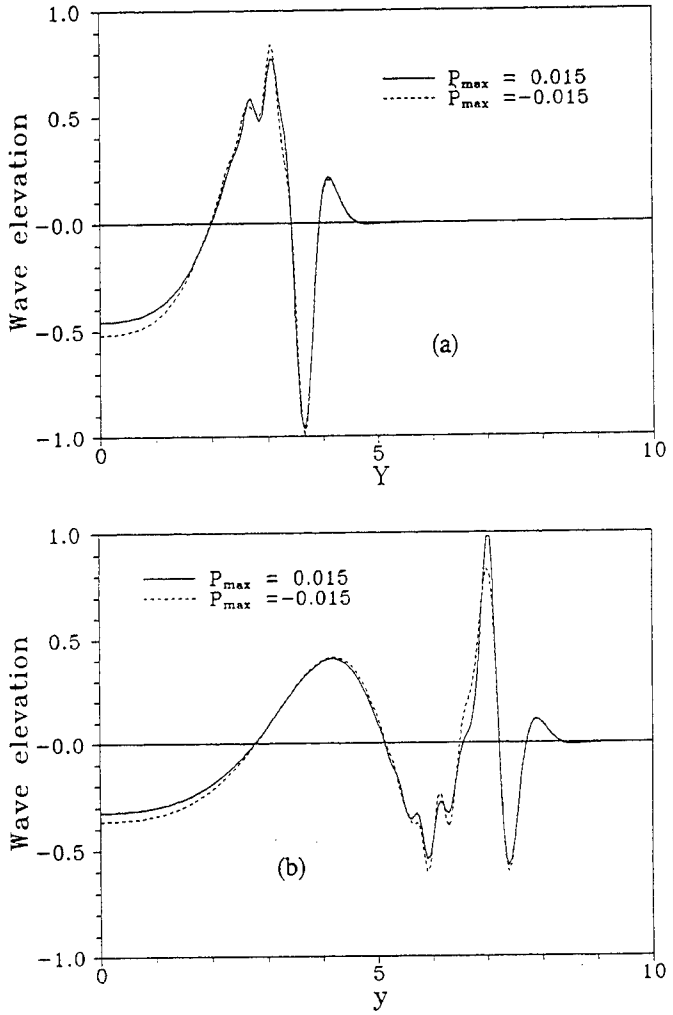

Fig. 9 Transverse cuts of the wave profiles.
(a) $x-x_c=10$ (b) $x-x_c=20$

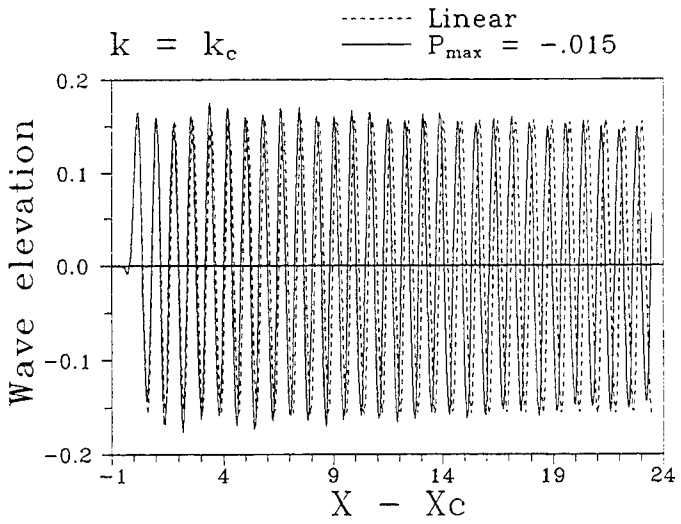

Fig. 10 Fourier component of Linear and nonlinear waves ($k = k_c$)

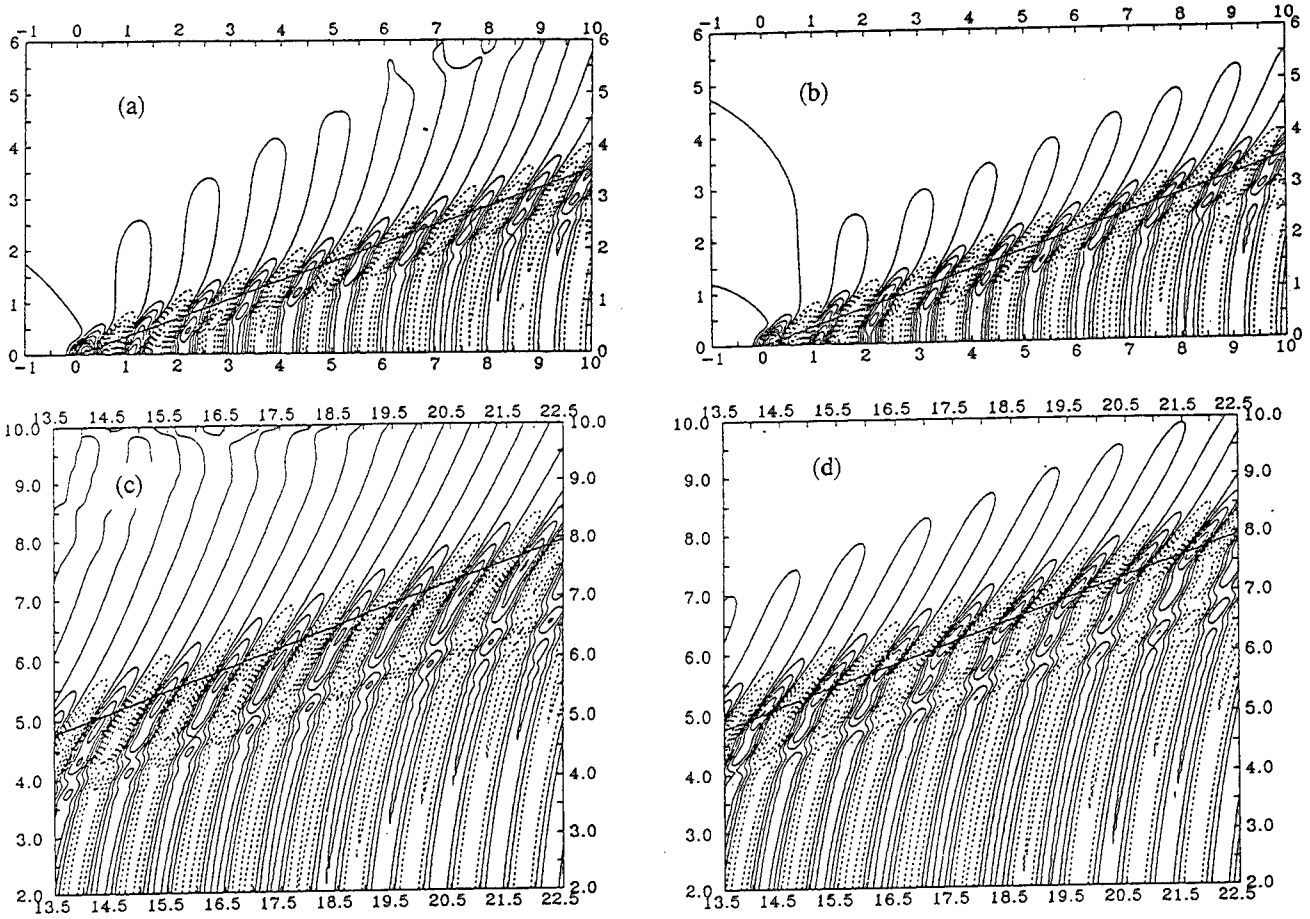

Fig. 11 Linear and nonlinear wave patterns.
Contour levels are 0.2 and 0.3 for (a,b) and (c,d), respectively.

(a),(c): Linear wave patterns
(b),(d): Nonlinear wave patterns

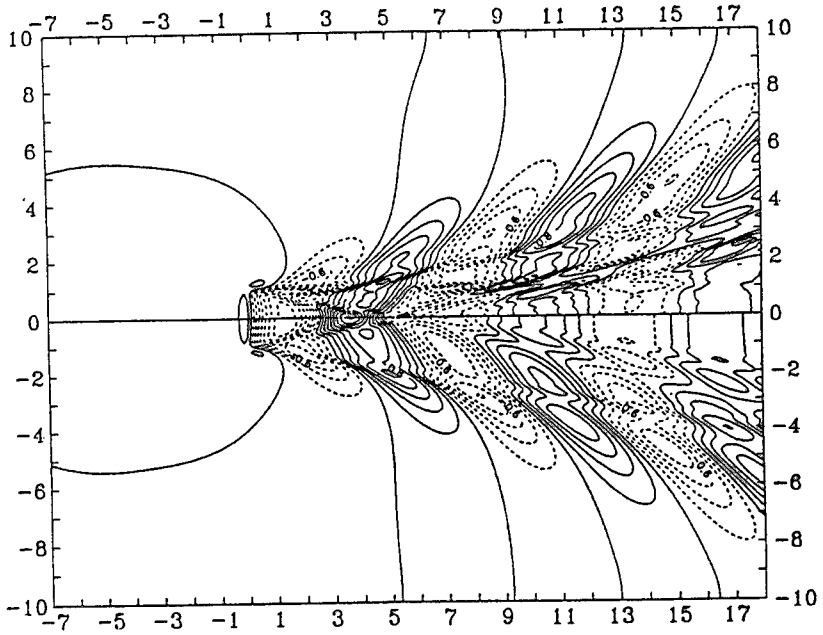

Fig. 12 Linear and nonlinear wave contours for d = 0.125, $\Gamma_0 = 0.06$

above: Nonlinear wave contours
below: Linear wave contours

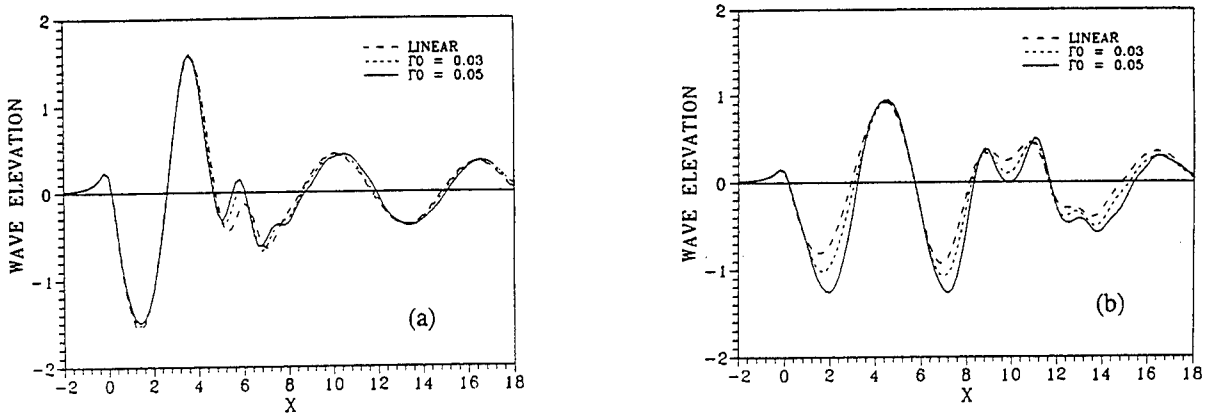

Fig. 13 Nonlinear effect on wave profiles (Fn=1.0)
Uniform circulaton distribution
(a) Center line (Y=0)
(b) Wing-tip line (Y=1)

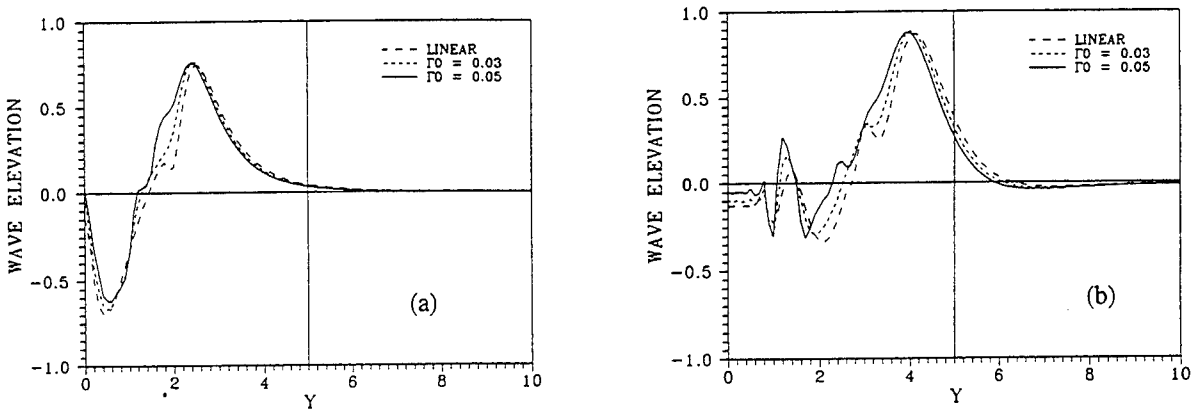

Fig. 14 Transverse cuts of wave profiles (Fn=1.0)
Uniform circulation distribution
(a) $x\text{-}x_c = 6.0$
(b) $x\text{-}x_c = 12.0$

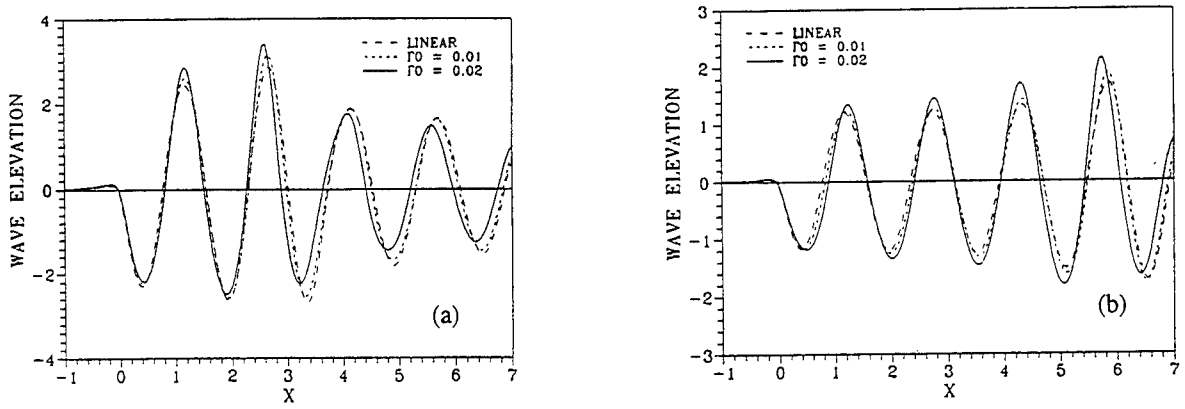

Fig. 15 Nonlinear effect on wave profiles (Fn=0.5)
Uniform circulaton distribution
(a) Center line (Y=0)
(b) Wing-tip line (Y=1)

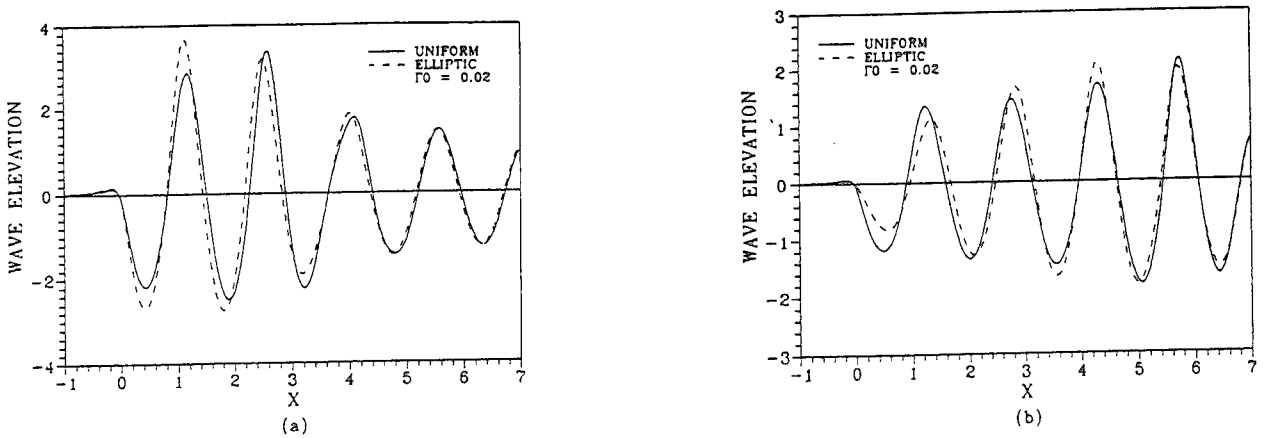

Fig. 16 Circulation distribution effect on wave profiles (Fn=0.5)
(a) Center line (Y=0)
(b) Wing-tip line (Y=1)

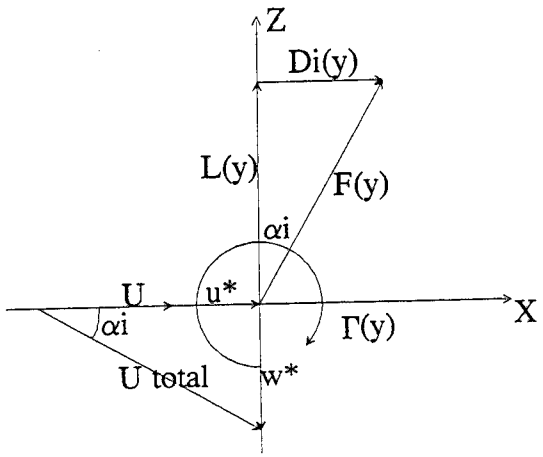

Fig.17 Definition Sketch (Horseshoe Vortex)

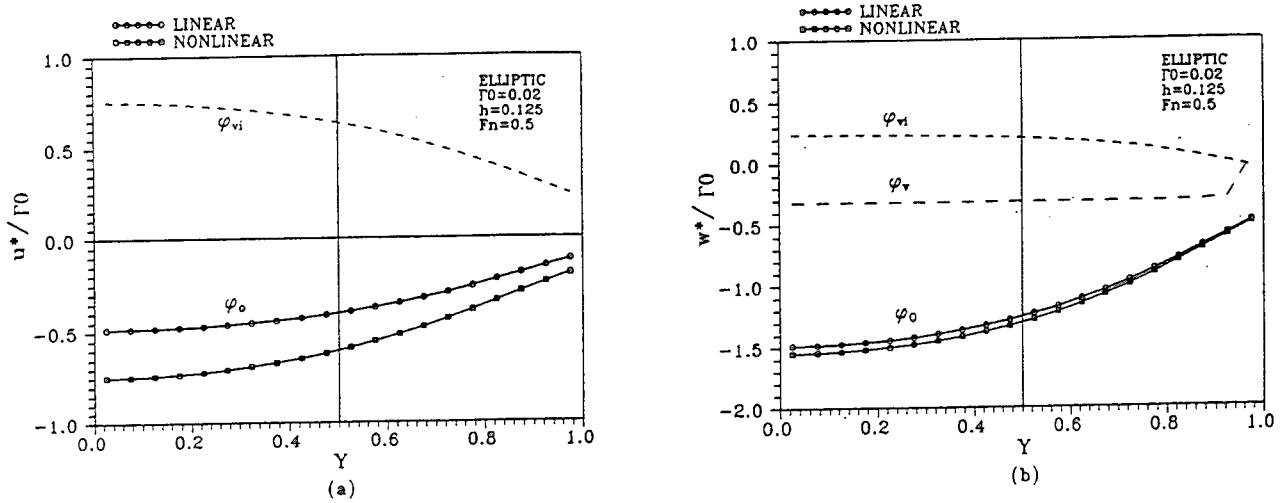

Fig. 18 Nonlinear effect on induced velocity components (Fn=0.5)
(a) x-direction induced velocity
(b) z-direction induced velocity

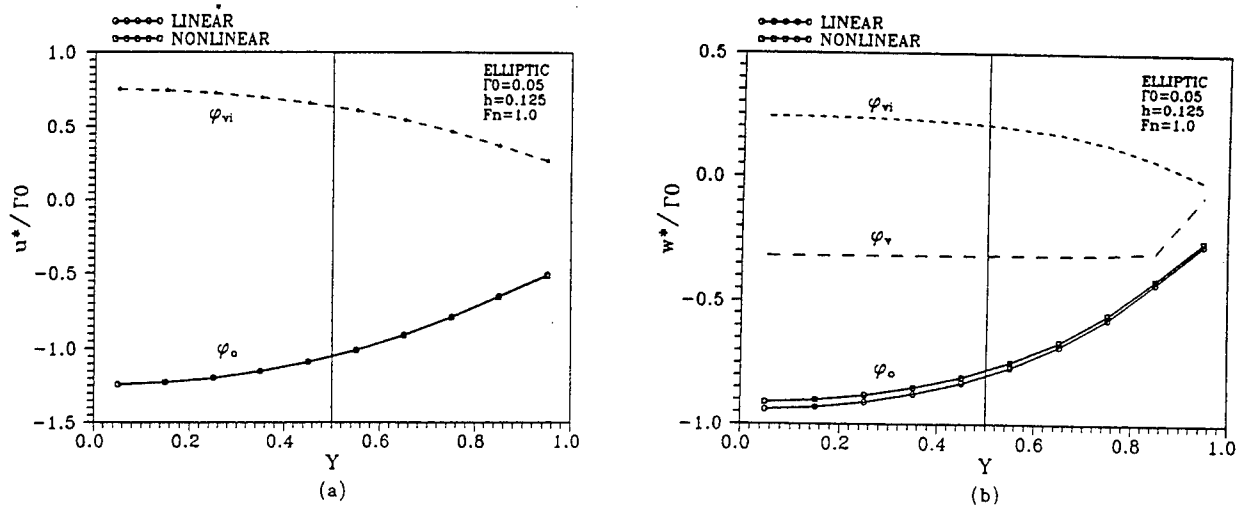

Fig. 19 Nonlinear effect on induced velocity components (Fn=1.0)
(a) x-direction induced velocity
(b) z-direction induced velocity

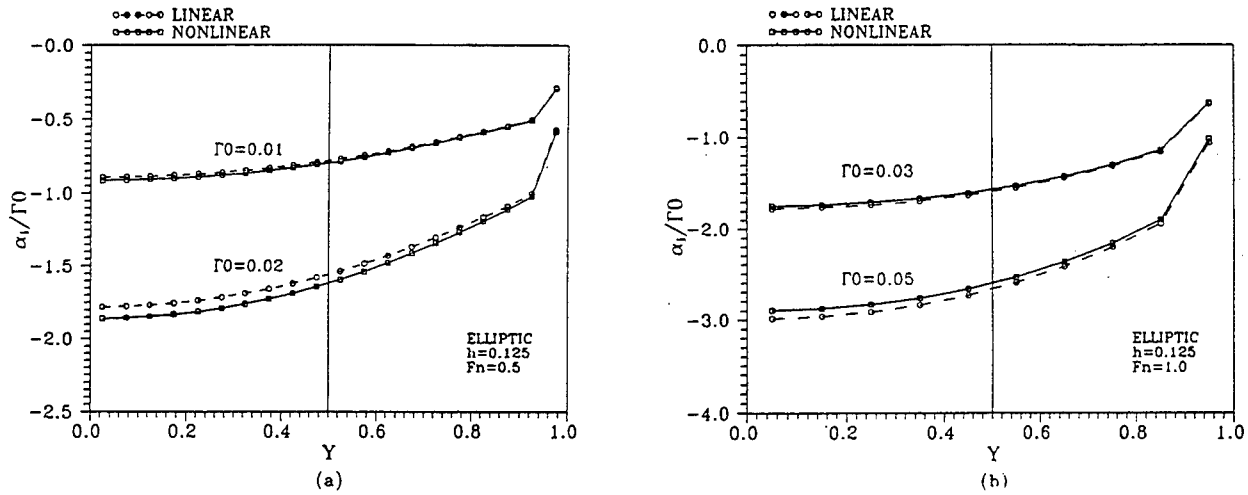

Fig. 20 Nonlinear effect on induced angle of attack
(a) Fn = 0.5 (b) Fn = 1.0

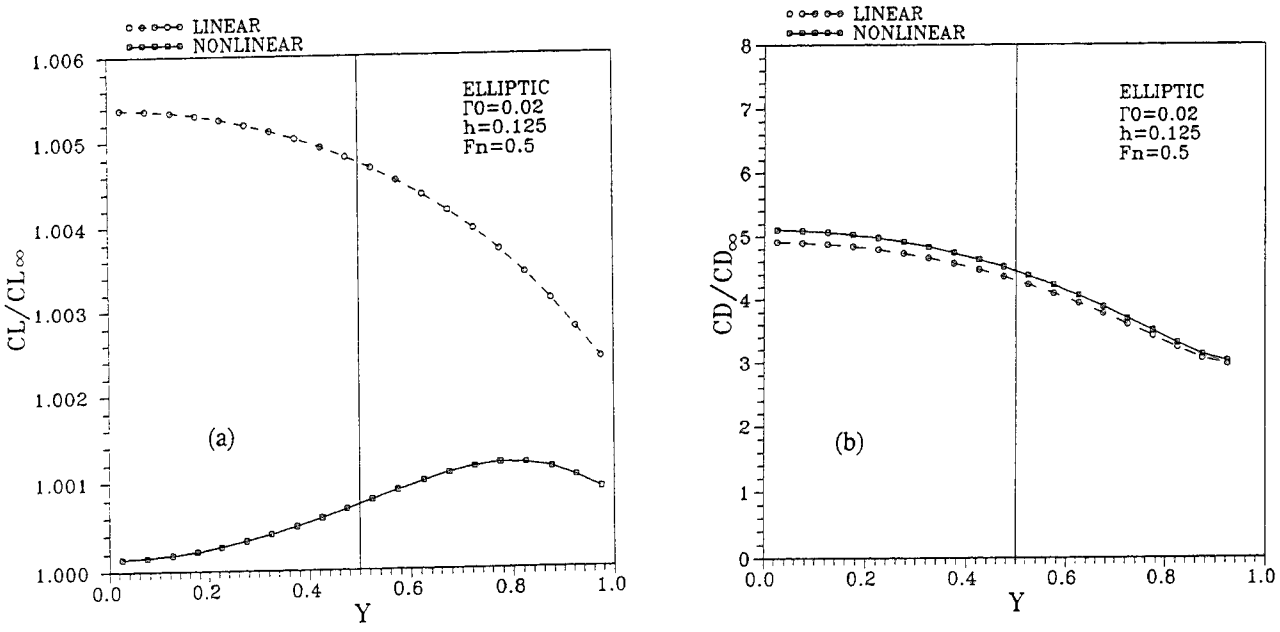

Fig. 21 Nonlinear effect on sectional force ratio (Fn=0.5)
(a) Lift ration (b) Drag ratio

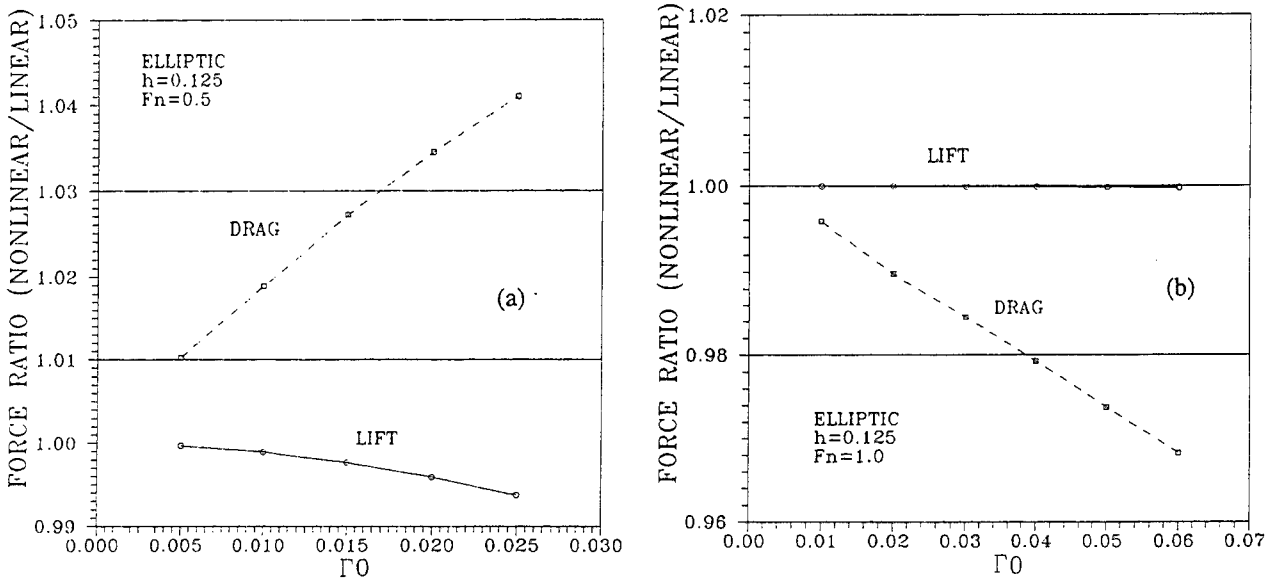

Fig. 22 Nonlinear effect on total force
(a) Fn = 0.5 (b) Fn = 1.0

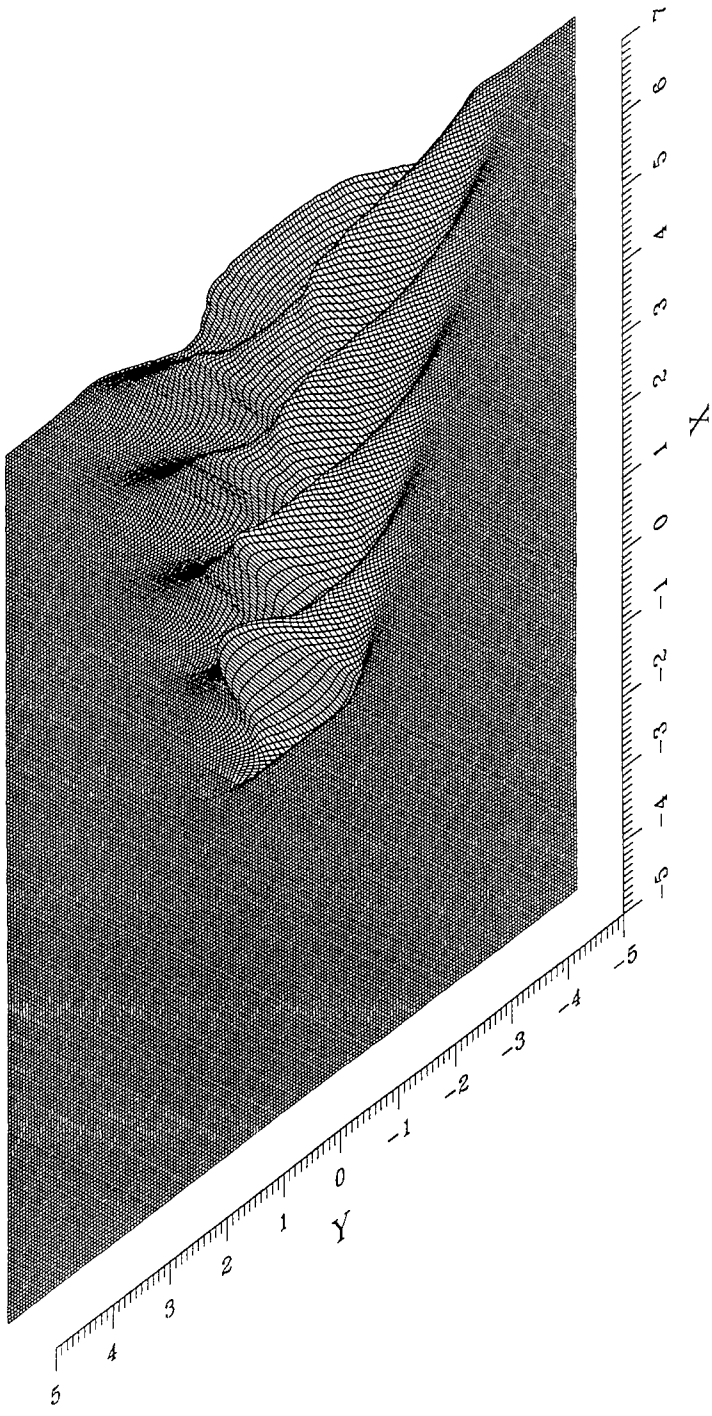

Fig. 23 Perspective view of computed wave patterns
Elliptic circulation distribution
Fn = 0.5, d = 0.125, Γ_0 = 0.02

Paper Title: A Localized Finite Element Method for Nonlinear Free-Surface Wave Problems

First Author: Kwang June Bai

ERRATA SHEET

Place	Present	To be corrected as
Eq(2) and (9)	$-\frac{U}{g}\frac{\partial}{\partial x} N[\bar{\phi},\bar{\phi}_n,\zeta]$	$+\frac{U}{g}\frac{\partial}{\partial x} N[\bar{\phi},\bar{\phi}_n,\zeta]$
Eq (14.a) and (16)	$+\frac{U}{g}<\bar{\varphi}_x,\varepsilon N[\bar{\phi},\bar{\phi}_n,\varepsilon\zeta]>$	$-\frac{U}{g}<\bar{\varphi}_x,\varepsilon N[\bar{\phi},\bar{\phi}_n,\varepsilon\zeta]>$
Eq (14.c)		add $-\frac{1}{\rho g}<\bar{\varphi} P>$
Eq (30.b)	$x > b$	$x \geq a$
Eq (48)	$-\phi'' - (1+\phi'^2+\phi^2) = 0$	$-\phi'' - (1+2\phi'^2+2\phi^2) = 0$
Eq (49)	$\frac{A}{2} Exp[\, i x\, (\, 1 + \frac{\lvert A\rvert^2}{2}) \,]$	$\frac{A}{2} Exp[\, i x\, (\, 1 + \lvert A\rvert^2 \,)\,]$
	$Exp[\, \frac{ix\lvert A\rvert^2}{2}\,] = \ldots$	$Exp[\, ix\lvert A\rvert^2 \,] =$ $1 - \frac{x^2\lvert A\rvert^4}{2!} + \frac{x^4\lvert A\rvert^8}{4!} + \ldots$ $+i\left(x\lvert A\rvert^2 - \frac{x^3\lvert A\rvert^6}{3!} + \frac{x^5\lvert A\rvert^{10}}{5!} + \ldots \right)$
Eq (52)	Othewise	Otherwise
Eq (54)	$\int_0$	$\int_0^\infty$
Fig. 3	$x\lvert A\rvert^2$ (under the x-axis)	$2x\lvert A\rvert^2$
Fig.18 ~ 22	h = 0.125 (in the caption)	d = 0.125

DISCUSSION

Gerhard Jensen
The Hamburg Ship Model Basin, Germany

What is the motivation to use a finite element method (FEM) for potential flow problems instead of a boundary element method (BEM), as the required computational effort seems to be much higher for FEM? There are several BEM published which solve the nonlinear problem very successfully, like those of Ni, Jensen, and Raven.

AUTHORS' REPLY

The discussor's comment is partially true in the sense that the number of unknowns are much larger in FEM than that for BEM. However, the computations of the matrix elements are much easier for FEM than for BEM where the computations are involved with the Green function. As we have already discussed in our paper, the required computational effort in FEM is not so much. For example, the number of operations required to evaluate the influence-coefficient matrix is $O(N_x N_y N_z)$ for FEM and $O(N_x^2 N_y^2)$ for BEM. Thus, less effort is required for FEM when $Nz << N_x N_y$. Often this is the case in practical computations. When we treat a restricted fluid domain, for example, shallow water problems, FEM has more advantages than BEM.

Session III

Nonlinear Ship Motions

Numerical Modeling of Short-Time Scale Nonlinear Water Waves Generated by Large Vertical Motions of Non-Wallsided Bodies

J.-H. Park, A. Troesch (University of Michigan, USA)

ABSTRACT

Various numerical implementations of the boundary integral method (BIM) used in solving the bow flare slamming problem are examined. In particular, the effects on accuracy and numerical stability of different time stepping schemes, different Green functions, and different radiation conditions are considered. Based upon a linear stability analysis using von Neumann or matrix stability methods, it is possible to determine the parameter combinations of temporal and spatial discretizations that lead to stable or unstable behavior. The stability predictions, while derived from the linear free surface conditions, are shown to be valid for simulations of nonlinear waves with small to moderate nonlinearities.

NOMENCLATURE

β	Phase ($k\Delta x$)
Δx	Panel length
Δt	Time interval between time step
ϕ_i^n	Velocity potential of ith location at the nth time step
$\vec{\xi}$	Source point vector (ξ,η,ζ)
η_i^n	Free surface elevation of the ith location at the nth time step
[A],[B]	Induced influence coefficient matrices
c	Green function constant, e.g. $G_{2D}^* = G_{2D} + \ln c$
{f}	Equivalent excitation vector
FSS	Free Surface Stability Number $\left(\frac{\pi g(\Delta t)^2}{\Delta x}\right)$
$G(\vec{x};\vec{\xi})$	Green function
G	Magnification factor $\left(\varepsilon^{n+1}/\varepsilon^n\right)$
k	Wave number
l_B, S_B	2-D, 3-D body surface boundary
l_f, S_f	2-D, 3-D free surface boundary
$l_\infty S_\infty$	2-D, 3-D far-field boundary
$\vec{n}$	Outward unit normal vector on the domain boundary
$\vec{u}$	Velocity vector of the fluid particle
$\vec{V}$	Velocity vector of the body
$\vec{x}$	Field point vector (x,y,z)

INTRODUCTION

Nonlinear ship motions are comprised of several time scales. The long-time scale problem may be defined as large amplitude oscillations at low frequencies. These motions generate relatively well behaved waves with small to moderate wave slopes. The short-time scale problem is characterized by large relative velocities between hull and water surfaces where impact, jet-like flows, and breaking waves are common.

Since bow flare impact forces are local and of short duration, numerical schemes can be formulated using finite domain grids concentrated on the vessel's hull and on the near free surface. The attractiveness of the method lies in its use of a restricted domain resulting in a substantial increase in computational efficiency. This is the approach that Troesch and Kang (1988) took when they approximated the free surface boundary condition as an equipotential ($\phi = 0$) surface and when Kang and Troesch (1988) used the complete nonlinear free surface boundary condition with bodies oscillating beneath the free surface. However, when the nonlinear free surface condition and a surface piercing three-dimensional body are used together, instabilities in the time-stepping simulation appeared.

Sawtooth instabilities in free surface calculations of steep water waves were first encountered by Longuet-Higgins and Cokelet (1976). Since that time numerous researchers have presented numerical results that either do not contain the instability for the problems solved, or contain the instability and have to be smoothed and filtered every few time steps. See for example Faltinsen (1977), Vinje and Brevig (1981), Yeung (1982), Dommermuth and Yue (1987), Hong, et al (1988) or Grilli, et al (1989). Some have suggested that the instability is purely numerical while others claim that it is a manifestation of the actual physics.

A typical strategy in nonlinear water wave computations is to use a mixed Eulerian-Lagrangian method where the boundary value problem (BVP) is solved at some instant in time and the free surface then time stepped to its new position. The procedure is repeated as desired. In this work, the instantaneous BVP is solved using a Fredholm integral equation of the second kind on the body and a Fredholm integral equation of the first kind on the free surface. The spacial discretization form of the integral equation may be written as:

$$[A]\left\{\begin{matrix}\phi,\\ \dfrac{\partial\phi}{\partial n}\end{matrix}\right\}=[B]\left\{\begin{matrix}\dfrac{\partial\phi}{\partial n},\\ \phi\end{matrix}\right\} \qquad (1)$$

Generally, the vector on the right hand side of the equation is known and the vector on the left hand side is unknown. The bold face potentials and bold face normal derivatives of the potentials denote the free surface elements. The vector $\{\phi\}$ on the right side of Eq. (1) is determined through temporal differencing schemes such as staggered implicit/explicit Euler methods or fourth order Runge-Kutta methods. Numerical stability is principally related to the the matrices [A] and [B] and the particular differencing scheme selected. These matrices are functions of the boundary geometry, including the bounding boundary at large distances from the body. If the boundaries are changing, as in the nonlinear problem, then the matrices are also functions of time, implying that the stability is time dependent.

Longuet-Higgins and Cokelet (1976) observed "sawtooth instabilities" on the free surface when they followed the time history of space-periodic irrotational surface waves as can be seen in Fig. 1. This sawtooth instability was found when a deep water progressive wave of finite amplitude was marched in time. The authors speculated that this instability was due, partly, to physical reasons and they applied a smoothing technique to remove it.

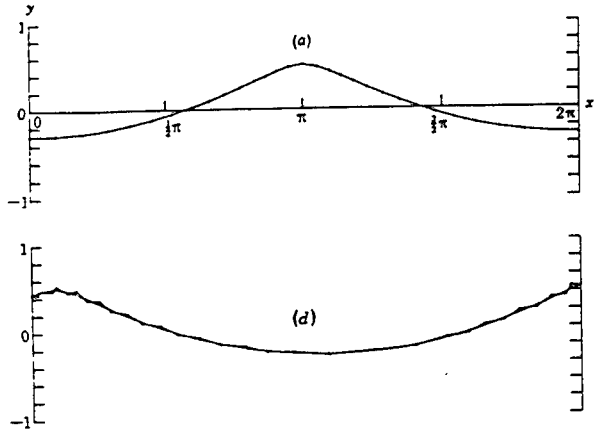

Fig. 1 An example of the sawtooth instability observed by Longuet-Higgins and Cokelet for a steady progressive wave in deep water computed by Pade approximants for Stokes's series (smooth curve) and the corresponding time-stepped profile (unsmoothed). Number of segments, $N = 30$. The profiles are compared at times (a) $t = 0$, (d) $t = \pi$. [Longuet-Higgins and Cokelet (1976)]

Faltinsen (1977), in the numerical solution of two-dimensional nonlinear transient problems, found that his solution procedure sometimes became invalid before the surface waves had reached the far-field boundary. To demonstrate this phenomena, he performed the calculation varying the size of the far-field boundary b. In the calculation, he fixed the length of the free surface elements to $\pi a/14$. As shown in Fig. 2, the force grows rapidly in negative values for the case of $b = 3.24$. This behavior contrasts with that shown in Fig. 1. In Fig. 1, the error has a sawtooth shape as if a high frequency wave-like error is superposed on the onset flow unlike Fig. 2, where the error appears to grow exponentially. These two figures suggest that numerical errors can either grow exponentially when the error magnification factor is greater than 1.0 and pure real, or grow with changing phase when the error magnification factor is complex and has a modulus greater than 1.0.

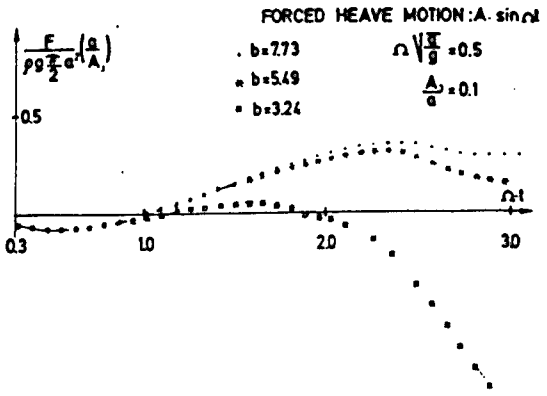

Fig. 2 The vertical force acting on a heaving circular cylinder, an example of the instability observed by Faltinsen. 'b' represents the far-field boundary coordinate, and 'a' the radius of the cylinder. [Faltinsen(1977)]

The two examples shown in Figs. 1 and 2 suggest that a careful analysis of the numerical schemes used to solve nonlinear free surface flows is warranted. The purpose of this paper, then, is to

- evaluate the numerical stability associated with various forms of the boundary value problem formulation,
- formulate stable time-stepping algorithims,
- demonstrate stable nonlinear calculations, and
- discuss significant modeling problems now that numerical stability can be achieved.

PROBLEM FORMULATION

The coordinate system used in this work is depicted in Fig. 3. The figure represents an infinitely long two-dimensional symmetrical body, or a three-dimensional axisymmetric body, either of which is forced to oscillate vertically on a free surface. The body shape is arbitrary and the body motion can be cyclic or linear with constant velocity in the z direction. The free surface is given by $F = (\vec{x},t) = 0$, where $\vec{x}\,(x,y,z)$ is the position vector in the right-handed coordinate system. In this system, the z axis is defined as positive upwards, while the y axis represents the calm water level. The origin is at the intersection of the vertical centerline of the body and the undisturbed water surface. The fluid is assumed to be incompressible and inviscid, and the flow is assumed to be irrotational.

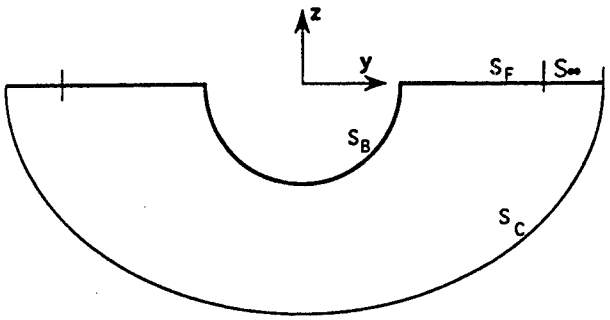

Fig. 3 Coordinates and geometry of the free surface.

The governing equations, boundary conditions, and radation condition are given as

- Governing equation (Laplace's equation)

$$\nabla^2\phi = 0 \qquad \text{in the fluid domain} \qquad (2)$$

- Kinematic free surface boundary condition

$$\frac{D(z-\eta)}{Dt} = \left(\frac{\partial}{\partial t} + \nabla\phi\cdot\nabla\right)(z-\eta) = 0 \qquad \text{on } z = \eta(x,y,t) \qquad (3)$$

- Dynamic free surface boundary condition

$$\frac{D\phi}{Dt} = -g\eta + \frac{1}{2}\nabla\phi\cdot\nabla\phi \quad \text{on } z = \eta(x,y,t)\,. \qquad (4)$$

- Body boundary condition

$$\vec{V}\cdot\vec{n} = \nabla\phi\cdot\vec{n} \quad \text{on the body } S_B(x,y,z,t) = 0 \qquad (5)$$

- Far-field (radiation) condition

$$\frac{\partial\phi}{\partial n} \to 0 \quad \text{as} \quad |r| \to \infty \qquad (6)$$

In the above equations, $\vec{V}$ is the velocity of the body, $\vec{n}$ is the outward unit normal, and $|r|$ is the distance from the origin. The far-field condition is one of the more difficult conditions to apply properly. For the two-dimensional problem, especially, this condition needs to be treated carefully. The far-field truncation effect, properly considered, makes the computational domain finite.

METHOD OF SOLUTION

The method used in this work to solve the boundary value problem of Eqs. 2 - 6 is called the "mixed Eulerian-Lagrangian method" (Longuet-Higgins and Cokelet (1976)). The two step approach is adapted here with different numerical schemes in each step. In Step 1, the governing equation using the Boundary Integral Method (BIM) is solved; and in Step 2, the free surface boundary conditions are satisfied using several different time-stepping schemes.

Green's second identity is employed in the solution of the BIM. The Green function, $G(\vec{x};\vec{\xi})$, is defined as

$$G(\vec{x},\vec{\xi}) = -\frac{1}{2\pi}\ln|\vec{x}-\vec{\xi}| = -\frac{1}{2\pi}\ln r \;\; (2-D) \qquad (7)$$

$$= \frac{1}{4\pi}\frac{1}{|\vec{x}-\vec{\xi}|} \quad = \frac{1}{4\pi r} \qquad (3-D) \qquad (8)$$

Another solution G^* can be obtained by adding any analytic homogeneous solution to the particular solution, Eq. (7) or Eq. (8). One such set of analytic solutions is given as follows

$$G^*(\vec{x};\vec{\xi}) = \frac{1}{2\pi}(\ln r + \ln c) = -\frac{1}{2\pi}\ln rc \quad (2-D) \qquad (9)$$

$$= \frac{1}{4\pi}\left(\frac{1}{r}+\frac{1}{c}\right) \qquad (3-D) \qquad (10)$$

where c is some constant used to normalize the two-dimensional Green function. The integral equations for the velocity potential using G and G^* are derived in principal value form as

$$\phi(\vec{x},t) = -\frac{1}{\pi}\int\left\{\phi(\vec{\xi},t)\frac{\vec{n}(\vec{\xi})\cdot(\vec{x}-\vec{\xi})}{|\vec{x}-\vec{\xi}|^2} + \frac{\partial\phi}{\partial n}(\vec{\xi},t)\ln|\vec{x}-\vec{\xi}|\right\}dl \qquad (11)$$

or

$$\phi(\vec{x},t) = -\frac{1}{\pi}\int\left\{\phi(\vec{\xi},t)\frac{\vec{n}(\vec{\xi})\cdot(\vec{x}-\vec{\xi})}{|\vec{x}-\vec{\xi}|^2} + \frac{\partial\phi}{\partial n}(\vec{\xi},t)\ln c|\vec{x}-\vec{\xi}|\right\}dl \qquad (12)$$

in two-dimensions and in three dimensions as

$$\phi(\vec{x},t) = -\frac{1}{2\pi}\iint\left\{\phi(\vec{\xi},t)\frac{\vec{n}(\vec{\xi})\cdot(\vec{x}-\vec{\xi})}{|\vec{x}-\vec{\xi}|^3} - \frac{\partial\phi}{\partial n}(\vec{\xi},t)\frac{1}{|\vec{x}-\vec{\xi}|}\right\}dS \qquad (13)$$

or

$$\phi(\vec{x},t) = -\frac{1}{2\pi}\iint\left\{\phi(\vec{\xi},t)\frac{\vec{n}(\vec{\xi})\cdot(\vec{x}-\vec{\xi})}{\cdot|\vec{x}-\vec{\xi}|^3} - \frac{\partial\phi}{\partial n}(\vec{\xi},t)\left(\frac{1}{|\vec{x}-\vec{\xi}|}+\frac{1}{c}\right)\right\}dS \qquad (14)$$

where $\vec{x}$ and $\vec{\xi}\in S$, and $\vec{n}$ is an outward unit normal vector.

Two different boundary types are considered here: the near-field closed boundary problem and the far-field open boundary problem. For the near-field closed boundary problem, $S = S_B + S_F + S_C$ where S_C is in the near-field and comprises of the bounding sides and bottom. Either the potential or its normal derivative is given on all surfaces. For the far-field open boundary problem,

$S = S_B + S_F + S_\infty + S_C$. The potential takes the form of a dipole on S_∞ and is assumed to be zero on S_C, the closing contour at infinity.

Once the solution to the above equations are found in the fluid domain, the normal derivatives of the potentials on the free surface and the potentials on the body surface are obtained. With this information, the two free surface boundary conditions are stepped in time to determine the new location of the free surface and estimate the potential on that new surface. For the time stepping algorithms in this work, three different Euler methods are chosen; specifically the explicit, implicit-like, and implicit Euler methods. Two different fourth-order Runge-Kutta methods are also selected which are the explicit and implicit-like methods.

The various Euler difference approximations for the linearized version of Eqs. 3 and 4, the free surface boundary conditions, are shown below:

• Explicit scheme

$$\phi^{n+1} - 2\phi^n + \phi^{n-1} = -g(\Delta t)^2 \phi_z^{n-1}, \tag{15}$$

• Implicit-like scheme

$$\phi^{n+1} - 2\phi^n + \phi^{n-1} = -g(\Delta t)^2 \phi_z^{n}. \tag{16}$$

• Implicit scheme

$$\phi^{n+1} - 2\phi^n + \phi^{n-1} = -g(\Delta t)^2 \phi_z^{n+1} \tag{17}$$

where the superscripts n-1, n, and n+1 represent the values of the potential or its z-derivative at the different time steps. Appendix C of Park (1992) derives the general form of the fourth-order Runge-Kutta algorithm and its discretized forms for the explicit and implicit-like methods.

To apply the free surface boundary condition in the Lagrangian step of the two-step method, the unknown $\phi_n^{\,n}$ on the free surface is calculated using the Boundary Integral Method (BIM), Eqs. (11)-(14). Discretizing the surface with panels (3-D) or line segments (2-D), the potential ϕ at the (i) panel or segment is approximated in generic form as ;

$$\phi_i(\vec{\xi}) \cong -\sum \left\{ \phi_j \int_{\Delta x_j} \frac{\partial G_{ij}}{\partial n_j} dl_j - \left(\frac{\partial \phi}{\partial n}\right)_j \int_{\Delta x_j} G_{ij} dl_j \right\} \tag{18}$$

where ϕ_j : known on the free surface

$\dfrac{\partial \phi_j}{\partial n_j}$: unknown on the free surface

and

ϕ_j or $\left(\dfrac{\partial \phi}{\partial n}\right)_j$: one is known and the other is unknown on the remaining surfaces

For the linear problem, $\dfrac{\partial \phi}{\partial n} \rightarrow \dfrac{\partial \phi}{\partial z}$ on the free surface.

In matrix form, Eq. (18) can be expressed as

$$\begin{bmatrix} A_{ij} \end{bmatrix} \left\{ \begin{array}{c} \vdots \\ \hline \dfrac{\partial \phi}{\partial n} \end{array} \right\} = \begin{bmatrix} B_{ij} \end{bmatrix} \left\{ \begin{array}{c} \vdots \\ \hline \phi \end{array} \right\}$$

or

$$\left\{ \begin{array}{c} \vdots \\ \hline \dfrac{\partial \phi}{\partial n} \end{array} \right\} = \begin{bmatrix} C_{ij} \end{bmatrix} \left\{ \begin{array}{c} \vdots \\ \hline \phi \end{array} \right\} = \left[\begin{array}{c|c} [C^1] & [C^2] \\ \hline [C^3] & [C^*] \end{array} \right] \left\{ \begin{array}{c} \vdots \\ \hline \phi \end{array} \right\} \tag{19}$$

where the first m entries in the left-hand column are the unknown potential or unknown normal derivative values on the bottom boundary, body boundary, and the far-field boundary and the rest of the entries in the left-hand column are the unknown normal derivatives of the potential on the free surface. The $[C]$ matrix is the multiplication of the $[A]^{-1}$ and the $[B]$ matrices (i.e.$[C] = [A]^{-1}[B]$).

A subset of the above matrices is made by retaining only the terms needed to complete the time step on the free surface :

$$\begin{aligned} \left\{ \frac{\partial \phi}{\partial n} \right\} &= \left[[C^3] \; [C^*] \right] \left\{ \begin{array}{c} \vdots \\ \hline \phi \end{array} \right\} \\ &= [C^3] \left\{ \frac{\partial \phi}{\partial n} \text{ or } \phi \right\} + [C^*]\{\phi\} \\ &= \sum_{j=f.s.}^{N} C_{ij}^* \phi_j + \sum_{j=non\,f.s.} C_{ij}^3 \left(\left(\frac{\partial \phi}{\partial n}\right)_j \text{ or } \phi_j \right) \\ &\equiv [C^*]\{\phi\} + \{f\} \end{aligned} \tag{20}$$

where $[C^*]$ is the subset of the influence coefficient matrix $[C]$ which is related to the free surface only. C_{ij}^* is the influence coefficient of the j free surface panel to the i free surface panel. The vector $\{f\}$ is the multiplication of C_{ij}^3 and the known values of ϕ_j or ϕ_{n_j} on all surfaces except the free surface. In this way, the vector acts as a forcing function and consequently does not play a role in determining the linear stability characteristics. This summation form, Eq. (20) is substituted to the Eqs. (15)-(17) to study the numerical stability characteristics of the different time stepping schemes.

As an example of the matrix formulation, if ϕ_n is given and ϕ is unknown on the boundaries excluding the free surface, $[A_{ij}]$ and $[B_{ij}]$ then become

$$[A_{ij}] \left\{ \begin{array}{c} \phi \\ \hline \dfrac{\partial \phi}{\partial n} \end{array} \right\} \equiv \left[\begin{array}{c|c} \dfrac{1}{2} I_{ij} + \displaystyle\int_{\Delta x_j} \frac{\partial G_{ij}}{\partial n} dl_j & -\displaystyle\int_{\Delta x_j} G_{ij} dl_j \end{array} \right] \left\{ \begin{array}{c} \phi \\ \hline \dfrac{\partial \phi}{\partial n} \end{array} \right\} \tag{21}$$

$$\left[B_{ij}\right]\left\{\begin{matrix}\frac{\partial\phi}{\partial n}\\ \hline \phi\end{matrix}\right\} \equiv \left[\begin{matrix}\int_{\Delta x_j} G_{ij}dl_j & \left| \begin{matrix} -\frac{1}{2}I_{ij} \\ -\int_{\Delta x_j}\frac{\partial G_{ij}}{\partial n}dl_j \end{matrix}\right.\end{matrix}\right]\left\{\begin{matrix}\frac{\partial\phi}{\partial n}\\ \hline \phi\end{matrix}\right\} \qquad (22)$$

where I_{ij} is the identity matrix.

STABILITY ANALYSIS AND ITS IMPLICATIONS

Background

The BIM and finite difference equations described previously will not necessarily converge to the solution of the governing equations. Questions about error propagation and convergence should be answered prior to extensive program use.

Similar to Longuet-Higgins and Cokelet (1976), Baker *et al.* (1982) also encountered a numerical instability when the local waves were steep. They used a smoothing operator to reduce the effect of the instability. They also found that this instability was reduced remarkably by the use of a dipole distribution rather than a vortex distribution. There are other researchers who observed no such numerical instability. The instability was apparently removed by Roberts (1983) in his analysis of a body-wave interaction problem using Fourier spectral representations for the position and potential of a free shear layer. The modeling was accomplished by a simple modification of the highest (even) Fourier mode. This method of instability removal was also reported by Dold and Peregrine(1984) extending the idea of Vinje and Brevig(1981) with the addition of the higher time derivatives of the complex potential in the Eulerian step. Using the resulting time integration scheme, they found no apparent short-wavelength instability. Another numerically stable scheme was given by Casulli and Cheng (1990) in their discussion of the stability and error analysis for some finite difference methods of the one-dimensional shallow water equations which consist of a system of quasi-linear hyperbolic equations. They showed that the explicit Eulerian-Lagrangian method with fixed grid is unconditionally stable when the Courant-Isaacson-Rees method is used as a time-stepping scheme.

Dommermuth and Yue (1986) and Dommermuth *et al.* (1988) claimed that the instabilities are not physical but closely related to the accuracy of the velocity calculation for the free surface particles. They postulated that when the mixed Eulerian-Lagrangian scheme is used, the high-wavenumber instability is caused mainly by the concentration of Lagrangian markers in the region of higher gradients. This concentration of the markers, they said, caused a local Courant condition to be inevitably violated for a fixed time step as the waves steepened. They developed a regridding algorithm wherein a new set of equally spaced Lagrangian points on the free surface is created each time step. This regridding algorithm has the disadvantage of the loss of resolution near the region of high velocity gradients where Lagrangian points would otherwise concentrate. Considering another source, Kang (1988) speculated that the numerical error at the intersection point propagates and could generate saw-tooth instabilities.

Few researchers have actually established stability criteria for water wave problems. Yeung (1982) investigated the stability criteria using a *simplified* von Neumann analysis. He assumed $\phi(x,y,n\Delta t)$ to be of the form $\phi^n e^{ikx+ky}$ where k is a wave number; thus $\phi_y^n = k\phi^n$. His calculation for the numerical stability criteria is simple and easy to follow. However, his stability criteria is independent of the panel length Δx and independent of the various boundary conditions.

Dommermuth *et al.* (1988) derived the numerical stability criteria using a "linearized von Neumann stability analysis." They also assumed $\phi_y^n = k\phi^n$. By this assumption and a Taylor-series expansion, they found the stability criteria for the explicit fourth-order Runge-Kutta scheme and the fourth-order multi-step Adams-Bashforth-Moulton predictor-corrector (ABM4) scheme. However, by assuming that the normal derivative of the potential on the free surface is proportional to the potential, the stability will be independent of the BIM algorithm. As will be demonstrated in the example sections, the stability criteria determined in this manner is neither an upper nor lower bound.

Two different types of traditional stability analyses will be discussed here (Richtmyer and Morton (1967) and Anderson *et al.* (1984)). The various methods will be illustrated using the simpler Euler difference approximations, Eqs. (15)-(17). The fourth-order Runge-Kutta methods require a considerable amount of algebraic manipulation and the reader is referred to Park (1992) for details.

von Neumann Stability Analysis

The von Neumann method is well known in the literature. Briefly, the numerical solution is considered to be composed of the exact value and an error. The error, $\varepsilon(\vec{x},t)$, can be assumed to be written as a series of sine and cosine terms. The ratio between the error at the (n) time step and the error at the (n+1) time step is defined as the magnification factor, G. The magnification factor $G\left(=\varepsilon_j^{n+1}/\varepsilon_j^n\right)$ for the (j) point in the computational grid should be less than 1 in magnitude for the numerical algorithm to be stable. The analysis is only approximate since it does not include the effects of the boundaries. The method's chief attributes are its relative simplicity of implementation and its ability to estimate stability characteristics of individual surface elements. By examining the stability of separate panels, strategies can be developed for variable surface discretizations.

For the free surface problem then, the potential ϕ is considered to be composed of an exact value, ϕ_{exact}, and the numerical error, $\varepsilon(x,t)$. The numerical error can be expressed as a Fourier series expansion :

$$\phi = \phi_{exact} + \varepsilon(x,t) \qquad (23)$$

where

$$\varepsilon(x,t) = \sum_{m=1}^{\infty} b_m(t)e^{ik_m x} = \sum_{m=1}^{\infty} e^{at}e^{ik_m x} \qquad (24)$$

and

$$\varepsilon_j^n = e^{an\Delta t}e^{ik_m j\Delta x} \qquad (25)$$

'a' may be complex but k_m is real.

Applying Eqs. (23) - (25) to the linearized free surface boundary conditions using the various Euler schemes results in

$$\phi^{n+1} - 2\phi^n + \phi^{n-1} = -g(\Delta t)^2 \, \phi_z^\gamma \qquad (26)$$

where $\gamma = n - 1$ for the explicit scheme

$\gamma = n$ for the implicit-like scheme.

$\gamma = n + 1$ for the implicit scheme

The potential derivative ϕ_z^γ on the free surface (*i.e.* the right-hand side of Eq. (26)) is obtained through the application of the BIM in Eq. (20) such as:

$$\{\phi_{zi}\}^\gamma = [C^*]\{\phi_j\}^\gamma + \{f_i\}^\gamma \qquad (27)$$

where $\phi_j^\gamma = \phi_{j\,exact}^\gamma + \varepsilon_j^\gamma$, $\{\phi_{zi}\}^\gamma$ is the potential derivative of the (i) panel on the free surface at the n-1, n, or n+1 time step and $[C^*]$ is the submatrix related to the free surface potential $\{\phi_j\}^\gamma$. The submatrix $[C^3]$ forms the equivalent of an external exciting function $\{f\}^\gamma$ through the multiplication of known values and consequently does not affect the linear stability analysis. Substituting Eqs. (23) (25) into Eq. (26) and cancelling common terms yields the equation for the magnification factor $G\left(= \varepsilon_j^{n+1} / \varepsilon_j^n\right)$:

$G^2 - 2G + (1 - \alpha) = 0$ (Explicit scheme)

$G^2 - (2 + \alpha)G + 1 = 0$ (Implicit-like scheme)

$(1 - \alpha)G^2 - 2G + 1 = 0$ (Implicit scheme)

where α is a function of discretized panel length, Δx, time-step size, Δt and the Green function constant, c. The solution of the quadratic equation for the magnification factor G above has two roots. These two roots can have pure real values or complex values and the moduli of the roots are associated with the following stability characteristics :

If $|G| > 1$, then the time stepping algorithm is unstable.
If $|G| = 1$, then the time stepping algorithm is neutrally stable.
If $|G| < 1$, then the time stepping algorithm is stable.

The von Neumann numerical stability analysis of the linearized free surface boundary conditions can also be applied to the fourth-order Runge-Kutta Explicit scheme. See Park (1992) for details.

Matrix Stability Analysis

The disadvantage of von Neumann's approach is that it does not directly include the effects of the boundaries, and therefore gives only approximate stability criteria. A more general, but more computationally intensive way to establish stability criteria is the Matrix Method (Richtmyer and Morton (1967) and Anderson *et al.* (1984)). This method will now be applied to the two linear free surface boundary conditions:

$$\begin{aligned} \frac{\partial \phi}{\partial t} &= -g\eta \\ \frac{\partial \eta}{\partial t} &= \phi_z = [C^*]\,\phi + f \end{aligned} \qquad \text{on } z = 0\,. \qquad (28)$$

The discretized system of the two boundary conditions can be written in general matrix form

$$\begin{Bmatrix} \phi \\ \vdots \\ \eta \\ \vdots \end{Bmatrix}^{n+1} = \begin{bmatrix} & \cdot & \\ & D_{ij} & \\ & \cdot & \end{bmatrix} \begin{Bmatrix} \phi \\ \vdots \\ \eta \\ \vdots \end{Bmatrix}^n + \begin{Bmatrix} 0 \\ \vdots \\ f \\ \vdots \end{Bmatrix}^n \qquad (29)$$

where $[D]$ is a ($2N$x$2N$) matrix and N represents the number of panels on the free surface. If any one of the absolute values of the $2*N$ eigenvalues of $[D]$ is larger than 1, then the marching scheme is unstable (See Richtmyer and Morton (1967) and Anderson *et al.* (1984).) The formation of the $[D]$ matrix is decided according to the choice of numerical schemes. It follows that the eigenvalues of the $[D]$ matrix have a meaning very similar to that of the roots of the magnification factor G in the von Neumann analysis. As examples, consider the explicit and implicit-like Euler schemes:

The difference equations using the explicit Euler scheme is as follows :

$$\begin{aligned} \phi_i^{n+1} &= \phi_i^n - g\,\Delta t\,\eta_i^n \\ \eta_i^{n+1} &= \eta_i^n + \Delta t \sum_{j=1}^{N} C_{ij}^* \phi_j^n + f_i^n \end{aligned} \qquad (30)$$

or combined into matrix form :

$$\begin{Bmatrix} \phi \\ \vdots \\ \eta \\ \vdots \end{Bmatrix}^{n+1} = \left[\begin{array}{cc|cc} 1 & 0 & -g\Delta t & 0 \\ 0 & \ddots & 0 & \ddots \\ \hline & \Delta t\, C^* & 1 & 0 \\ & & 0 & \ddots \end{array}\right] \begin{Bmatrix} \phi \\ \vdots \\ \eta \\ \vdots \end{Bmatrix}^n + \begin{Bmatrix} 0 \\ \vdots \\ f \\ \vdots \end{Bmatrix}^n \qquad (31)$$

As can be seen in Eq. (31), the $[D]$ matrix of the explicit Euler scheme is composed of two identity matrices, one - $g\Delta t^*[I]$ matrix, and the $\Delta t^*[C^*]$ matrix, a subset of the $[C]$ matrix.

The difference equations using the implicit-like scheme are as follows :

$$\begin{aligned} \phi_i^{n+1} &= \phi_i^n - g\,\Delta t\,\eta_i^{n+1} \\ \eta_i^{n+1} &= \eta_i^n + \Delta t \sum_{j=1}^{N} C_{ij}^* \phi_j^n + f_i^n \end{aligned} \qquad (32)$$

with a matrix representation of

$$\left[\begin{array}{cc|cc} 1 & 0 & g\Delta t & 0 \\ 0 & \ddots & 0 & \ddots \\ \hline 0 & 0 & 1 & 0 \\ 0 & \ddots & 0 & \ddots \end{array}\right] \begin{Bmatrix} \phi \\ \vdots \\ \eta \\ \vdots \end{Bmatrix}^{n+1} = \left[\begin{array}{cc|cc} 1 & 0 & 0 & 0 \\ 0 & \ddots & 0 & \ddots \\ \hline & \Delta t\, C^* & 1 & 0 \\ & & 0 & \ddots \end{array}\right] \begin{Bmatrix} \phi \\ \vdots \\ \eta \\ \vdots \end{Bmatrix}^n + \begin{Bmatrix} 0 \\ \vdots \\ f \\ \vdots \end{Bmatrix}^n \qquad (33)$$

To construct the [D] matrix of Eq. (29) using the implicit-like Euler scheme, the inverse of the matrix on the left-hand side of the above equation should be multiplied on both sides. As with the explicit method, the [D] matrix includes the [C^*] matrix.

The fourth-order Runge-Kutta schemes can also be put into matrix form. The detailed procedure for the derivation and formation of the [D] matrix is given in Appendix C of Park (1992).

APPLICATIONS

It is possible to find an analytic solution for the stability region in some very simple cases. Park (1992) derives the closed form expression based upon Eq. (26) for the stability criteria of a *single* free surface panel satisfying the linear free surface boundary conditions. The potential and its normal derivative are known on all other surfaces. This idealized problem is meant as a first step in understanding the complicated behavior associated with more typical free surface problems. When the number of free surface panels is greater than one or when nonlinear boundary conditions are used, the stability criteria must be determined numerically.

In the examples given below, the validity of the method will be demonstrated by comparing estimated stability boundaries with analytical values and the results of numerical simulation thus making the extension to more complex models straightforward. Since it is not possible to obtain an analytic solution for the stability of numerical solutions involving the nonlinear free surface boundary, the stability analysis begins with the linear boundary conditions and linear geometry using the assumption that the nonlinear effect on stability is small in the limit of small wave slope. Within this assumption, the linear stability study becomes the basis for the nonlinear stability analysis. The last example in this section will involve the fully nonlinear free surface conditions with time dependent influence coefficient matrices. This contrasts with the linear calculations, where the influence coefficient matrix does not change during the time interval of interest.

Linear Closed Boundary Problem

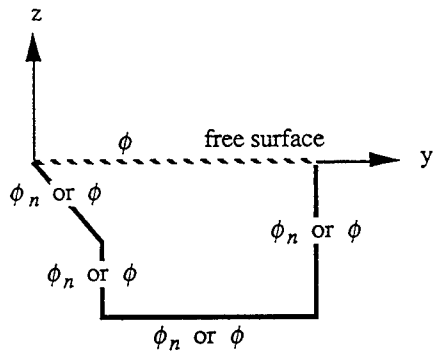

Fig. 4 Model for the closed boundary problem. General polygonal shape

The model geometry and the coordinate system are depicted in Fig. 4. The free surface boundary condition is imposed on top and ϕ or ϕ_n on the other sides. For the purpose of simulation, the initial conditions on the free surface and other boundaries are given as those of a plane progressive wave. This may be thought of as the far-field solution to the wave maker problem.

The first example considered will be a square panel with sides $2a$. One panel is located on the free surface, one panel on the bottom, and one panel on each side. The geometry of the boundary and its coordinate system is shown in Fig. 5.

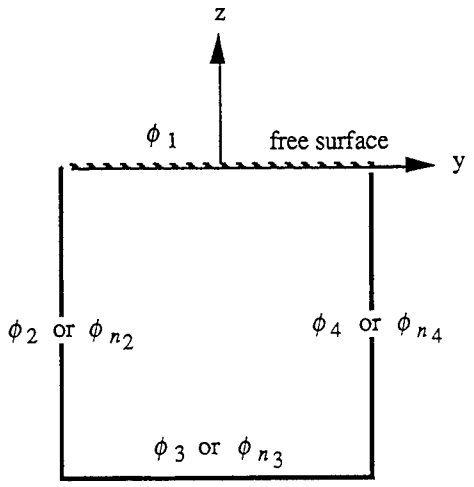

Fig. 5 Geometry of the square panel of the closed boundary problem. The potential ϕ is given on the top panel and ϕ or ϕ_n for the other panels.

For ϕ_n given on the side and bottom panels, following Eq. (20) the solution for the potential is given as

$$\phi_1 = A\frac{\partial\phi_1}{\partial n} + B\phi_2 + C\frac{\partial\phi_2}{\partial n} + B\phi_3 + C\frac{\partial\phi_3}{\partial n} + D\phi_4 + E\frac{\partial\phi_4}{\partial n} \tag{34}$$

$$\phi_2 = B\phi_1 + C\frac{\partial\phi_1}{\partial n} + A\frac{\partial\phi_2}{\partial n} + D\phi_3 + E\frac{\partial\phi_3}{\partial n} + B\phi_4 + C\frac{\partial\phi_4}{\partial n} \tag{35}$$

$$\phi_3 = B\phi_1 + C\frac{\partial\phi_1}{\partial n} + D\phi_2 + E\frac{\partial\phi_2}{\partial n} + A\frac{\partial\phi_3}{\partial n} + B\phi_4 + C\frac{\partial\phi_4}{\partial n} \tag{36}$$

$$\phi_4 = D\phi_1 + E\frac{\partial\phi_1}{\partial n} + B\phi_2 + C\frac{\partial\phi_2}{\partial n} + B\phi_3 + C\frac{\partial\phi_3}{\partial n} + A\frac{\partial\phi_4}{\partial n} \tag{37}$$

where $$A = -\frac{2a}{\pi}(\ln ca - 1) \tag{38}$$

$$B = \frac{1}{\pi}\tan^{-1}2 \tag{39}$$

$$C = \frac{2a}{\pi}\left(\ln\sqrt{5}ca - 1 + \frac{1}{2}\tan^{-1}2\right) \tag{40}$$

$$D = \frac{2}{\pi}\tan^{-1}\frac{1}{2} \tag{41}$$

$$E = -\frac{2a}{\pi} tan\left(ln\sqrt{5}ca - 1 + 2\,tan^{-1}\frac{1}{2} \right) \qquad (42)$$

In matrix form for the case of $(\phi_1, \phi_{n_2}, \phi_{n_3}, \phi_{n_4})$ known and $(\phi_{n_1}, \phi_2, \phi_3, \phi_4)$ unknown, the equations become:

$$\begin{Bmatrix} \frac{\partial \phi_1}{\partial n} \\ \phi_2 \\ \phi_3 \\ \phi_4 \end{Bmatrix} = \begin{bmatrix} \\ C_{ij} \\ \\ \end{bmatrix} \begin{Bmatrix} \phi_1 \\ \frac{\partial \phi_2}{\partial n} \\ \frac{\partial \phi_3}{\partial n} \\ \frac{\partial \phi_4}{\partial n} \end{Bmatrix} \qquad (43)$$

where the unknown normal velocity of the free surface element is

$$\frac{\partial \phi_1}{\partial n} = C_{11}\phi_1 + \sum_{j=2}^{4} C_{1j}\phi_{nj} \qquad (44)$$

and the $[C]$ matrix is the inverse of the $(\phi_{n_1}, \phi_2, \phi_3, \phi_4)$ influence coefficient matrix multiplied by the $(\phi_1, \phi_{n_2}, \phi_{n_3}, \phi_{n_4})$ influence coefficient matrix.

Equation (44) is an analytic solution form for ϕ_n on the free surface assuming that the given potential on the free surface and the normal derivatives on the other surfaces are constant over each panel or segment. Recall that for the linearized problem, the term $\sum_{j=2}^{4} C_{1j}\phi_{nj}$ of Eq. (44) acts as an exciting force in the stability equation and as such plays no role in determining the stability characteristics.

For the explicit Euler scheme, the free surface difference equation for the closed boundaries becomes

$$\phi_1^{n+2} - 2\phi_1^{n+1} + \phi_1^n = -g(\Delta t)^2 \left\{ C_{11}\phi_1^n + \sum_{j=2}^{4} C_{1j}\phi_{nj}^n \right\} \qquad (45)$$

Following a von Neumann stability analysis yields the quadratic equation for the magnification factor:

$$G^2 - 2G + 1 = -g(\Delta t)^2 C_{11}$$

$$\text{or} \quad G^2 - 2G + \left\{ 1 + g(\Delta t)^2 C_{11} \right\} = 0 \quad . \qquad (46)$$

There is no region where $|G| < 1$. Therefore, no stability region exists and the explicit Euler scheme is *unconditionally unstable* for the square panel of the closed boundary problem.

The difference for the implicit-like Euler scheme is

$$\phi_1^{n+2} - 2\phi_1^{n+1} + \phi_1^n = -g(\Delta t)^2 \left\{ C_{11}\phi_1^{n+1} + \sum_{j=2}^{4} C_{1j}\phi_{nj}^{n+1} \right\} \qquad (47)$$

which has the associated quadratic equation for the magnification

$$G^2 - 2G + 1 = -g(\Delta t)^2 C_{11} G$$

$$\text{or} \quad G^2 - \left\{ 2 - g(\Delta t)^2 C_{11} \right\} G + 1 = 0. \qquad (48)$$

The stability region is

$$0 < \frac{g(\Delta t)^2}{2} C_{11} < 2 \qquad (49)$$

Therefore, the implicit-like Euler scheme is *conditionally unstable* in the region where Eq. (49) is satisfied.

The term $1/\Delta x$ appears explicitly in matrix element C_{11}. Define a free surface stability parameter (*FSS*) as $\frac{\pi g(\Delta t)^2}{\Delta x}$. The equations above represent the case of ϕ given on the free surface and ϕ_n given on the other sides. The approach is quite general and the results for other combinations of ϕ and ϕ_n are shown in Table 1. Clearly, the boundary condition type can play an important role in determining the numerical stability limit.

Case	Boundary Condition Type	Stability Limit (*FSS* number)
1	$\phi_1, \phi_2, \phi_3, \phi_4$	5.47
2	$\phi_1, \phi_{n2}, \phi_3, \phi_4$	7.18
3	$\phi_1, \phi_{n2}, \phi_3, \phi_{n4}$	8.14
4	$\phi_1, \phi_{n2}, \phi_{n3}, \phi_4$	10.70

Table 1: Stability limits of the square panel with different boundary condition types. "Boundary Condition Type" represents the known boundary values on each panel. The implicit-like Euler scheme is used.

Time simulations of a plane progressive wave passing through the square panel are performed for the various ranges of the *FSS* number and typical results are shown in Figs. 6 - 9. Fig. 6 is the condition for a very small *FSS* number. In this case, the simulation shows both high levels of accuracy with stability. The *FSS* number is increased to the stability limit to investigate the transition phenomena from a stable to unstable region (Fig. 7). Figure 7 shows the sawtooth contamination on the crest and trough of the sine curve. With an incremental increase in the *FSS* number, (*FSS*=7.185) the simulation diverges drastically as in Fig. 8. In Fig. 9, the *FSS* number is set to a value of 0.01 a highly stable condition, but the $k\Delta x$ value, where k is the plane progressive wave number, is increased to 2.2. Figure 9 demonstrates that stability does not necessarily guarantee accuracy. Without presenting the details here, Park (1992) has shown that the fully implicit Euler scheme is also *conditionally stable* and that the explicit fourth-order Runge-Kutta scheme has approximately double the range of the *FSS* parameter of the implicit-like Euler scheme.

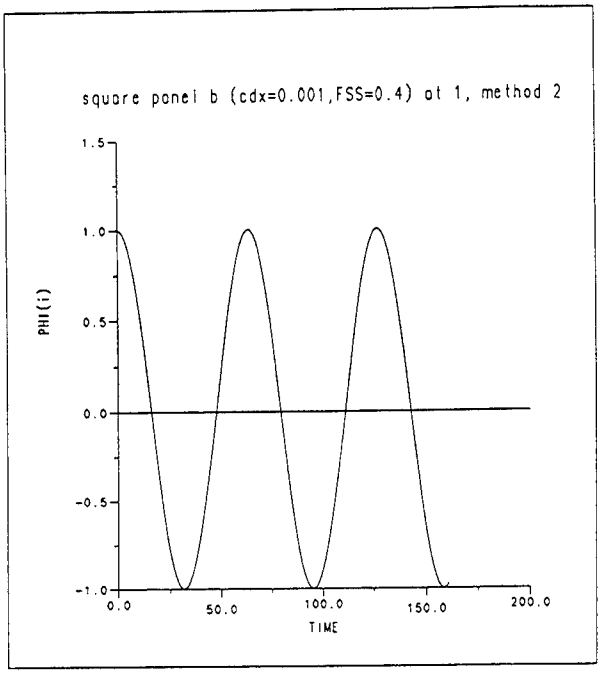

Fig. 6: Time simulation of the square panel. Boundary conditions given as $(\phi_1, \phi_{n_2}, \phi_3, \phi_4)$ with implicit-like Euler scheme for time marching. *FSS* number =0.4.

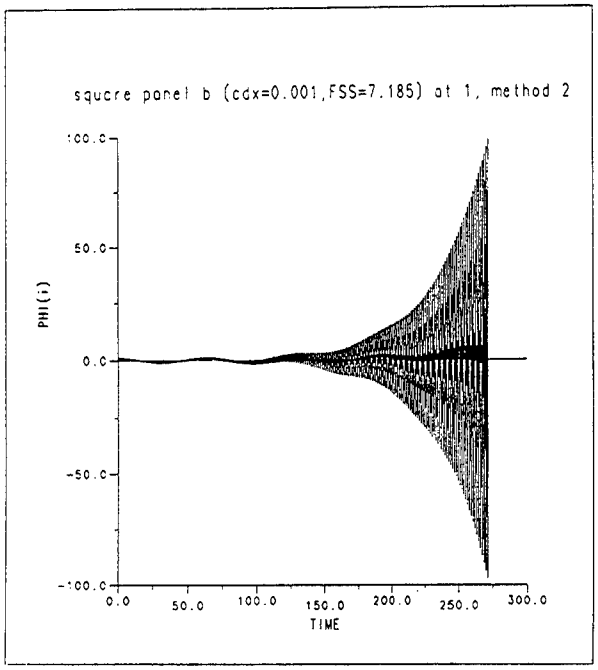

Fig. 8: Time simulation of the square panel. Boundary conditions given as $(\phi_1, \phi_{n_2}, \phi_3, \phi_4)$ with implicit-like Euler scheme for time marching. *FSS* number =7.185.

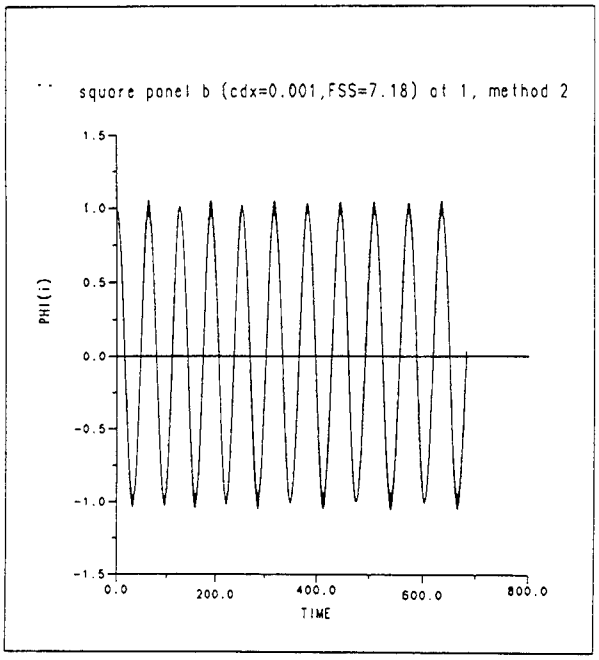

Fig. 7: Time simulation of the square panel. Boundary conditions given as $(\phi_1, \phi_{n_2}, \phi_3, \phi_4)$ with implicit-like Euler scheme for time marching. *FSS* number =7.180.

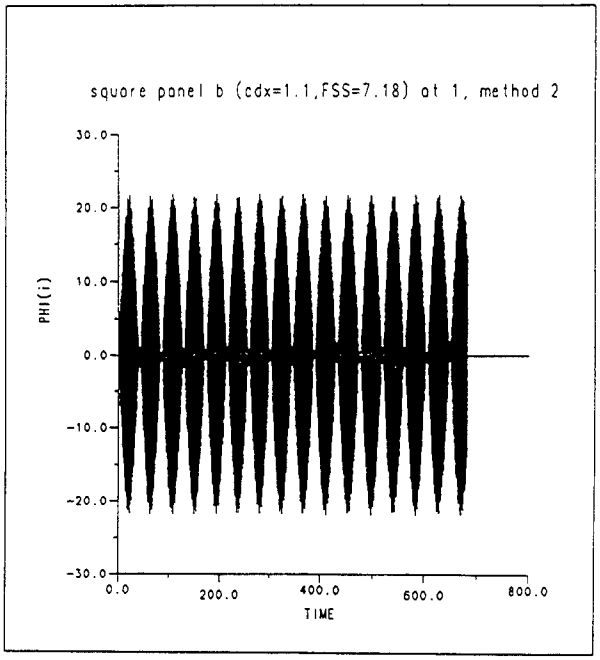

Fig. 9: Time simulation of the square panel. Boundary conditions given as $(\phi_1, \phi_{n_2}, \phi_3, \phi_4)$ with implicit-like Euler scheme for time marching. *FSS* number =0.01 and $k\Delta x$ = 2.2.

Much of the problem formulation and the resulting mathematical equations are the same for the polygonal domain with N panels on the free surface. The geometry of the domain is shown in Fig. 4. For the explicit Euler scheme, the difference equations are found by substituting Eq. (27) into Eq. (26) to find

$$\phi_j^{n+2} - 2\phi_j^{n+1} + \phi_j^n + g(\Delta t)^2 \sum_{m=f.s.}^{N} C_{jm}^* \phi_m^n$$

$$= -g(\Delta t)^2 \sum_{m=non\ f.s.} C_{jm}^3 \cdot \left(\phi_m^n \quad or \quad \phi_{n_m}^n\right) \qquad (50)$$

Following the von Neumann stability analysis, the quadratic form of the magnification factor equation is

$$G_j^2 - 2G_j + 1 + g(\Delta t)^2 \left(\sum_{m=f.s.}^{N} C_{jm}^* e^{i(m-j)\beta} \right) = 0 \qquad (51)$$

with roots

$$G_j = 1 \pm \sqrt{-g(\Delta t)^2 \left(\sum_{m=f.s.}^{N} C_{jm}^* e^{i(m-j)\beta} \right)} \qquad (52)$$

where $\beta = k\Delta x$ and k is the wave number of the Fourier component of the error. The magnitude of at least one of the two roots is larger than 1 ($|G| > 1$); therefore, no region of stability exists. The explicit Euler scheme is *unconditionally unstable* for the multi-panel closed boundary problem, similar to the single-panel closed boundary problem discussed previously.

The implicit-like Euler scheme has the following difference equations for the multi-panel boundary:

$$\phi_j^{n+2} - 2\phi_j^{n+1} + g(\Delta t)^2 \sum_{m=f.s.}^{N} C_{jm}^* \phi_m^{n+1} + \phi_m^n =$$

$$-g(\Delta t)^2 \sum_{m=non\ f.s.} C_{jm}^3 \cdot \left(\phi_m^{n+1} \ or \ \phi_{n_m}^{n+1}\right) . \qquad (53)$$

Based upon a von Neumann analysis, the quadratic form of the magnification factor equation is

$$G_j^2 - \left\{ 2 - g(\Delta t)^2 \left(\sum_{m=f.s.}^{N} C_{jm}^* e^{i(m-j)\beta} \right) \right\} G_j + 1 = 0 \qquad (54)$$

At the (j) panel, the magnification factor G_j, is easily shown to be

$$G_j = 1 - \frac{g(\Delta t)^2}{2} \left(\sum_{m=f.s.} C_{jm}^* e^{i(m-j)\beta} \right)$$

$$\pm \left[-\frac{g(\Delta t)^2}{2} \left(\sum_{m=f.s.}^{N} C_{jm}^* e^{i(m-j)\beta} \right) \right.$$

$$\left. + \frac{g^2(\Delta t)^4}{2} \left(\sum_{m=f.s.}^{N} C_{jm}^* e^{i(m-j)\beta} \right)^2 \right]^{1/2} \qquad (55)$$

The stability region has to be numerically calculated. Therefore, the implicit-like Euler scheme is *conditionally stable* in the region where Eq. (55) is satisfied. Equation (55) can be used to search for the stable region of each panel on the free surface. For each panel, the local maximum FSS number (*i.e.* the largest FSS number before the calculation becomes unstable) is calculated. The smallest FSS number among the local maximum FSS numbers is taken to be the stability limit for entire free surface. As an example, Table 2 shows the distribution of the maximum FSS numbers along the free surface panels

```
40*9*41 RIGHT TRIANGLE:(20011) BOUNDARY CONDITION
                    with Implicit-like Euler scheme
************************************************

  panel no. 51  :  FSSmax = 0.50327953521990E+01
  panel no. 52  :  FSSmax = 0.46935572888574E+01
  panel no. 53  :  FSSmax = 0.46657763639911E+01
  panel no. 54  :  FSSmax = 0.46647364292390E+01
  panel no. 55  :  FSSmax = 0.46654495985777E+01
  panel no. 56  :  FSSmax = 0.46645214740659E+01
  panel no. 57  :  FSSmax = 0.46653739332471E+01
  panel no. 58  :  FSSmax = 0.46646326873699E+01
  panel no. 59  :  FSSmax = 0.46652636309610E+01
  panel no. 60  :  FSSmax = 0.46647314596044E+01
  panel no. 61  :  FSSmax = 0.46651773814673E+01
  panel no. 62  :  FSSmax = 0.46648066659406E+01
  panel no. 63  :  FSSmax = 0.46651111359308E+01
  panel no. 64  :  FSSmax = 0.46648658877095E+01
  panel no. 65  :  FSSmax = 0.46650572343171E+01
  panel no. 66  :  FSSmax = 0.46649158698483E+01
  panel no. 67  :  FSSmax = 0.46650099898935E+01
  panel no. 68  :  FSSmax = 0.46649613650187E+01
  panel no. 69  :  FSSmax = 0.46649653730346E+01
  panel no. 70  :  FSSmax = 0.46650058975132E+01
  panel no. 71  :  FSSmax = 0.46649201553847E+01
  panel no. 72  :  FSSmax = 0.46650525951354E+01
  panel no. 73  :  FSSmax = 0.46648711199720E+01
  panel no. 74  :  FSSmax = 0.46651049612333E+01
  panel no. 75  :  FSSmax = 0.46648142506205E+01
  panel no. 76  :  FSSmax = 0.46651677654242E+01
  panel no. 77  :  FSSmax = 0.46647435023243E+01
  panel no. 78  :  FSSmax = 0.46652480804577E+01
  panel no. 79  :  FSSmax = 0.46646470102447E+01
  panel no. 80  :  FSSmax = 0.46653522313344E+01
  panel no. 81  :  FSSmax = 0.46644836160268E+01
  panel no. 82  :  FSSmax = 0.46654442871698E+01
  panel no. 83  :  FSSmax = 0.46641023690973E+01
  panel no. 84  :  FSSmax = 0.46656975490966E+01
  panel no. 85  :  FSSmax = 0.46661354209918E+01
  panel no. 86  :  FSSmax = 0.46850759928442E+01
  panel no. 87  :  FSSmax = 0.47774251888542E+01
  panel no. 88  :  FSSmax = 0.52561249903248E+01
  panel no. 89  :  FSSmax = 0.72196326036770E+01
  panel no. 90  :  FSSmax = 0.19254511994784E+02
```

Table 2. Maximum FSS number along the free surface on the triangular domain. Boundary conditions given as ϕ on the free surface, ϕ on the vertical boundary, and ϕ_n on the slanted boundary. Implicit-like Euler scheme, c=1.0.

of a right triangular domain. The boundary condition was given as the potential derivatives (ϕ_n) on the longest slanted side. On the free surface and on the vertical side, potentials were given as shown on Fig. 10. Forty panels were located on the free surface, nine panels on the vertical side, and forty-one panels on the slanted side. Panels on the free surface are numbered from the right as 51 to the left as 90. Table 2 reveals that the stability limit is greater near both edges and smaller in the middle indicating that the least stable elements are located near the center.

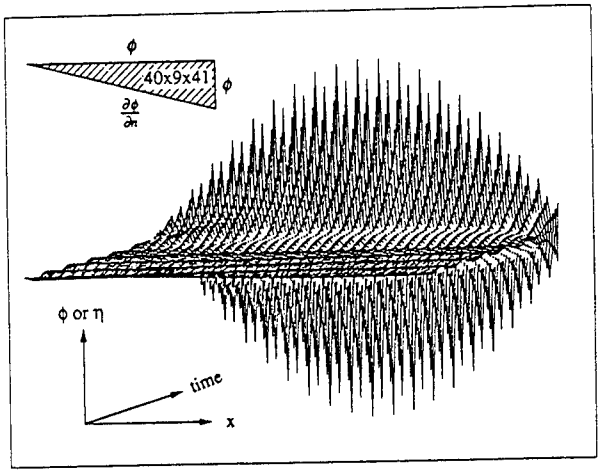

Fig. 10: Free surface simulation for the triangular domain. Boundary conditions given as ϕ on the free surface, ϕ on the vertical boundary, and ϕ_n on the slanted boundary. Implicit-like Euler scheme. FSS number=4.685, c=1.0.

Figure 10 is the time simulation result corresponding to the example of Table 2. The FSS number was fixed at 4.685 which is a stable FSS number for the edges and an unstable FSS number for the middle panels. The figure shows growth in the error of the potential on the middle and the effect propagates to the edges. The matrix method can be used to evaluate the stability of the implicit-like fourth-order Runge-Kutta scheme for the same geometry. Park (1992) calculated that the implicit-like RK-4 algorithm becomes unstable at an FSS number of approximately 5.02.

Linear Open Boundary Problem

The model geometry and the coordinate system for the linear open boundary are depicted in Fig. 3. The fluid is bounded by the free surface S_F and S_∞, by the rigid body S_B, and by the bottom and far-away contour S_C. The surface S changes to a line contour in the two dimensional problem. Following Faltinsen (1977) for the two-dimensional case and Kang (1988) for three-dimensional axisymmetric case, the behavior of the potential ϕ in the far-field is considered to be the same as the value of a vertical dipole at the origin. The strength of the vertical dipole is determined through matching it to the value of ϕ_Z on the last panel at the truncation boundary. The effects of the normalization constant c in the modified Green function (*i.e.* G^*) and the truncation boundary are included and the accuracy of the numerical scheme has been checked with the continuity equation (conservation of mass).

This investigation is essentially numerical. The complexity of the boundary value problem, including boundary conditions and time-stepping algorithms, restricts stability analysis to numerical studies. The matrix method, Eqs. (29) - (33), is used to determine the stability characteristics.

Table 3 shows the numerical stability results as a function of the parameters c, the modified Green function constant, and the FSS number. This analysis was performed with 10 panels on the half wedge-type body which has 45 degree slope (*i.e.* 45 degree wedge half angle) and 20 panels on the free surface. The explicit fourth-order Runge-Kutta scheme was used. The numbers in the table represent the maximum modulus of the eigenvalues in the matrix stability analysis, so the condition which has a value larger than 1 is unstable and the condition which has the value less than or equal to 1 is stable. The stable region is observed by varying c from 1.0 to 0.1 to 0.01. The results suggest that the proper manipulation of c in he modified two-dimensional Green function controls the numerical stability for this linearized problem. The possibility of stability control for other

c	0.01		0.10		1.00	
FSS	w/	w/o	w/	w/o	w/	w/o
1.0	1.0(c)	1.0(c)	1.144(r)	0.9999(c)	1.9067(r)	1.117(r)
2.0	1.0(c)	1.0(c)	1.209(r)	0.9999(c)	1.096(r)	1.169(r)
3.0	1.0(c)	1.0(c)	1.262(r)	0.9999(c)	1.122(r)	1.211(r)
4.0	1.0(c)	1.0(c)	1.308(r)	0.9999(c)	1.138(r)	1.247(r)
5.0	1.0(c)	1.0(c)	1.350(r)	0.9999(c)	1.156(r)	1.280(r)
9.0				0.9994(c)		
10.0				1.255(c)		

Table 3: Magnitude of maximum eigenvalues associated with the forced oscillation, far-field open boundary problem. 45 degree half angle, wedge-shaped two-dimensional body on the free surface with 10 panels on the body, 20 on the free surface. Explicit fourth-order Runge-Kutta scheme. (r) and (c) denote real or complex eigenvalues respectively. w/ : with truncation effect, w/o : without truncation effect.

problems and other numerical schemes is worthy of further investigation.

The effect of the treatment of the truncation boundary on the stability is also demonstrated. Complex eigenvalues referenced to the unit circle are shown in Figs. 11 and 12. As can be seen in Table 3 and Fig. 11, the maximum eigenvalue of 1.144 is pure real while Fig. 12 shows the maximum eigenvalue of 1.255 is complex. Figure 11 implies a diverging error with fluctuation while Fig. 12 implies an exponentially diverging error. A simulation is shown in Fig. 13 for the condition shown in Fig. 11. In these two figures, the truncation effect was included following Faltinsen's far-field model and exhibits instabilities similar to the type of instability shown in the Introduction, Fig. 2.

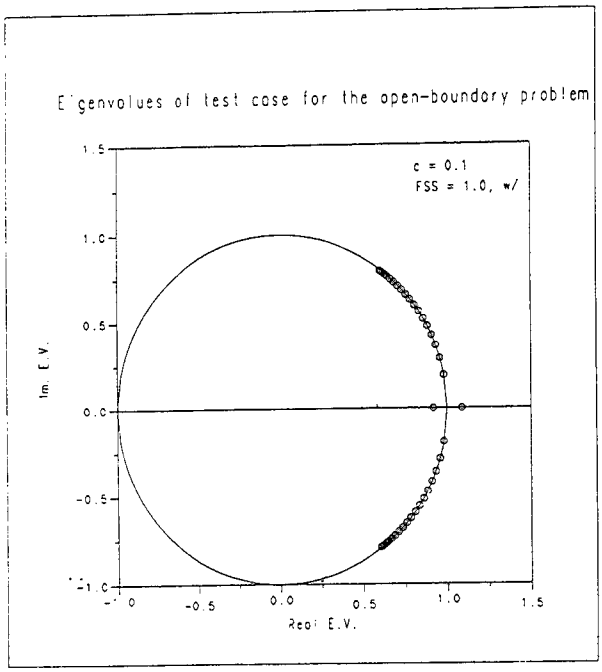

Fig. 11: Eigenvalues of the forced oscillation, far-field open boundary problem 45 degree half angle, wedge-shaped two-dimensional body on the free surface with 10 panels on the body, 20 on the free surface. Explicit fourth-order Runge-Kutta scheme. c = 0.1, 'o' represents the eigenvalues for *FSS* number =1.0 with the truncation effect.

The effects of three dimensionality and increased panel numbers on the free surface are examined next. Consider a cone shaped surface with a 45 degree half angle. The three dimensional modified Green function (Eqs. (12) and (14)) is used to formulate the integral equation of the BIM. Due to the axisymmetric shape, the theta integration is performed in closed form reducing the physical dimensions by one. The influence coefficients in the $[A]$ and $[B]$ matrices will reflect this integration and produce changes in the stability characteristics of the problem. As a far-field closure, the truncation effect is considered by the method of Kang (1988) where the far-field behavior is approximated by a single vertical dipole located at the origin.

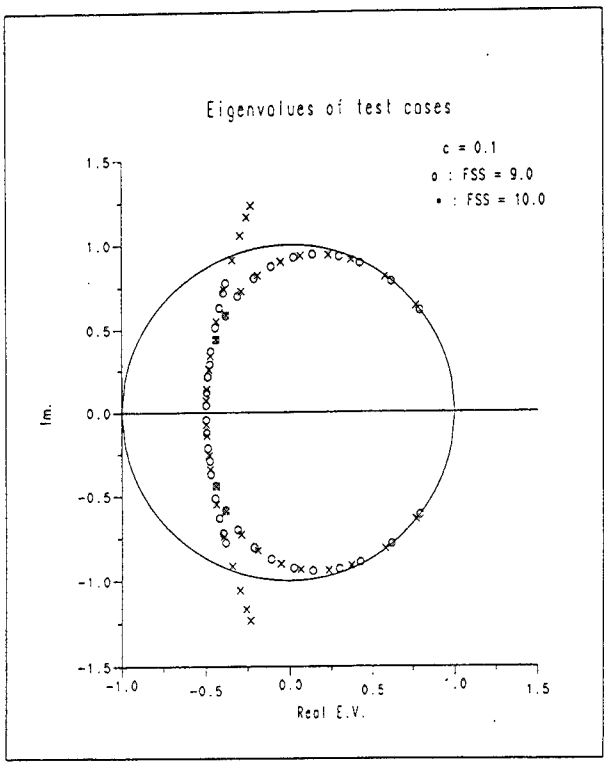

Fig. 12: Eigenvalues of the forced oscillation, far-field open boundary problem. 45 degree half angle, wedge-shaped two-dimensional body on the free surface with 10 panels on the body, 20 on the free surface. Explicit fourth-order Runge-Kutta scheme.c = 0.1, 'o' represents the eigenvalues for *FSS* number =9.0 and 'x' for *FSS* number =10.0 both without the truncation effect.

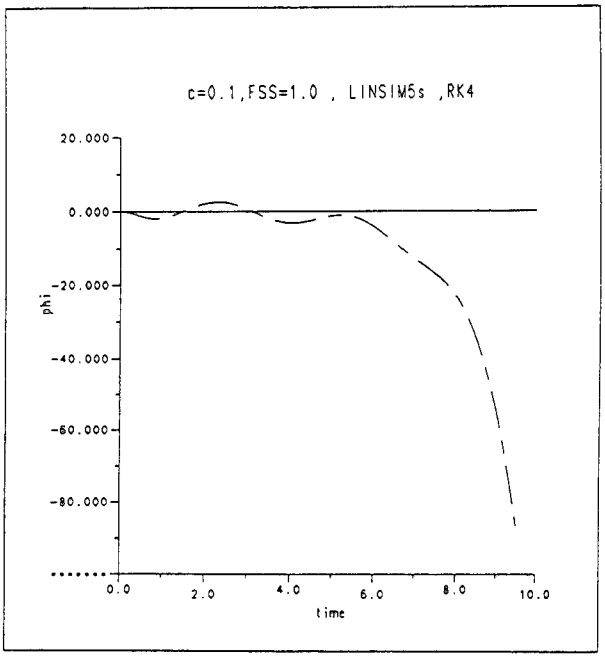

Fig.13: Time simulation for the forced oscillation, far-field open boundary problem. 45 degree half angle, wedge-shaped two-dimensional body on the free surface with 10 panels on the body, 20 on the free surface. Explicit fourth-order Runge-Kutta scheme. c = 0.1, *FSS* number =1.0 with the truncation effect.

Tables 4 and 5 show the numerical stability results for two-dimensional and three-dimensional axisymmetric cases with similar conditions (10 panels on the half-body, 90 panels on the free surface, and the explicit fourth-order Runge-Kutta scheme). From the results presented here, it is found that the far-field closure consideration is not a major factor for the stability analysis of the three-dimensional axisymmetric case. In two-dimensions, as already shown, the stability region can be altered by the far-field closure condition. For the two dimensional case, this appears to be quite reasonable since wave energy propagated from the body is not dispersed radially in the far-field. The proper closure method then becomes much more important than in the three-dimensional case.

The effect of the Green function constant is also very weak in three-dimensions. For two dimensions, c should be less than 0.02 for the computation to be stable. In three dimensions, the stability characteristics, through four significant figures, were unaffected by c. This suggests that little is to be gained by using the modified Green function (*i.e.* Eq. (10)) in three dimensions.

In addition to the examples considered here, Park (1992) also investigated other time-stepping schemes. Several runs with implicit-like fourth-order Runge-Kutta schemes and Kang's fourth-order Runge-Kutta scheme (Kang (1988)) were performed and *no stable regions were found*. In the implicit-like Runge-Kutta scheme, the modulus of the maximum eigenvalues converged to 1.0 in the limit as the *FSS* number went to zero. Hence, for the very small numbered range of the *FSS* number near 0.0, an implicit-like method may also be admissible in the calculation of the impact problem for short-time spans.

The linear stability analysis discussed in this chapter has laid the foundation for understanding the nonlinear calculations. Effects on numerical stability, such as time differencing schemes, boundary formulations and temporal and spatial discretizations have been investigated. While these findings may have to be refined in the cases of steep, breaking waves or jets due to impact, the next chapter will demonstrate that the linear results are valid for moderately nonlinear wave calculations.

Nonlinear Open Boundary Problems

With the basic theory of the linear numerical stability analysis firmly established, the nonlinear numerical stability analysis for the forced oscillation problem can be examined. Most of the problem solving procedures are the same as that described above except that the free surface

c	0.01		0.02		0.10		1.00	
FSS	w/	w/o	w/	w/o	w/	w/o	w/	w/o
1.0	1.0	1.0	1.127	1.0(c)	1.041	1.086	1.027(r)	1.043
2.0	.0	1.0	1.184	1.0(c)	1.058	1.124	1.038(r)	1.062
3.0	1.0	1.0	1.230	1.0(c)	1.072	1.154	1.046(r)	1.076
4.0	1.0	1.0	1.270	1.0(c)	1.083	1.179	1.054(r)	1.088
5.0	1.0	1.0	1.307	1.0(c)	1.093	1.203	1.060(r)	1.099
9.0				1.0(c)				
10.0				1.275(c)				

Table 4: Magnitude of maximum eigenvalues associated with the forced oscillation, far-field open boundary problem. 45 degree half angle, wedge-shaped two-dimensional body on the free surface with 10 panels on the body, 90 on the free surface. Explicit fourth-order Runge-Kutta scheme. (r) and (c) denote real or complex eigenvalues respectively. w/ : with truncation effect, w/o : without truncation effect.

$1/c$	10.0		1.0		0.01		0.00	
FSS	w/	w/o	w/	w/o	w/	w/o	w/	w/o
1.0	1.0	1.0	1.0	1.0	1.0	1.0	1.0	1.0
9.33	1.0	1.0	1.0	1.0	1.0	1.0	1.0	1.0
10.0	1.275	1.275	1.275	1.275	1.275	1.275	1.275	1.275
11.0	1.755	1.755	1.755	1.755	1.755	1.755	1.755	1.755
12.0	2.307	2.307	2.307	2.307	2.307	2.307	2.307	2.307

Table 5: Magnitude of maximum eigenvalues associated with the forced oscillation, far-field open boundary problem. 45 degree half angle, cone-shaped three-dimensional axisymmetric body on the free surface with 10 panels on the body, 90 on the free surface. Explicit fourth-order Runge-Kutta scheme. All values were complex (c) eigenvalues. w/ : with truncation effect, w/o : without truncation effect.

boundary conditions are now nonlinear and the body boundary condition is satisfied on the exact body surface. The Boundary Integral Method (BIM) is used in solving Laplace's equation and the fourth-order Runge-Kutta schemes are used for time-stepping the nonlinear free surface conditions. At each time step, the body and the free surface shape are regridded using modified Lagrangian polynomials (*i.e.* non-uniform parametric blended Lagrangian polynomials). For the fourth-order Runge-Kutta schemes, the influence coefficient matrix may or may not be updated during the intermediate steps depending upon the method used.

Park (1992) describes a number of concerns related to the nonlinear body-wave interaction problem. The stability and closure issues of the previously discussed linear problem are still present. With nonlinear boundary conditions, though, a number of other factors must also be considered, including the body-free surface intersection curve and the effects associated with any regridding algorithm.

At the intersection point, the body boundary condition, usually given as a Neumann type, meets the free surface boundary condition, usually a Dirichlet type. The confluence of these two boundary conditions causes a weak singularity in the integral equation. This weak singularity on the intersection point has a global influence and causes numerical difficulties for the nonlinear problem. For the results presented here, the position and the potential of the computational surface is calculated at the center of the panel in the BIM. By locating the control point at the center of the panel, the logarithmic singularity at the intersection point is removed. However, locating the control point at the panel center introduces the difficulty of tracing the intersection point where a kinematic continuity condition is satisfied. Here the tangential velocity of the intersection point is determined by the modified Lagrangian polynomial interpolation scheme and the normal velocity of the intersection point is determined via the body boundary condition to be the same as the normal velocity of the body (Park (1992)).

After each time step, a new location of the body-wave intersection point is also calculated to get the wetted body length. Starting from the new body-wave intersection point, the total arc length of the free surface is calculated. The free surface is then regridded to have constant panel lengths. For the portion where the high gradient potential exists, more panels are allocated to prevent the possible loss of accuracy due to the regridding algorithm. After the regridding procedure, the new location of the control points and the potential values on the new control points of the free surface are recalculated. To investigate the numerical stability behavior relative to a given *FSS* number, the time step Δt is tuned to keep the *FSS* number constant according to the modified panel length Δx, at every time step.

Since a fully nonlinear stability analysis is very difficult to complete, a local linear analysis is performed while the potential is calculated with nonlinear boundary conditions. The numerical stability analysis, therefore, reflects the nonlinear boundary condition effects in a global sense even though the analysis is locally linear. For moderate wave slopes, the results are consistent with those shown in Tables 3 - 5. The numerical stability analysis, therefore, reflects the nonlinear boundary condition effects in a global sense even though the analysis is locally linear.

Figures 14 and 15 show nonlinear simulations with the same conditions as that given in Table 4. The simulation configuration is as follows: initial depth of body = 1.0, body oscillation amplitude = 0.5, wave number k = 0.1309, number of panels on the body = 10, and number of panels on the free surface = 90. The stability range for the nonlinear simulations was determined to be essentially the same as for linear range indicating that a linear stability analysis is a good estimate of the nonlinear stability characteristics.

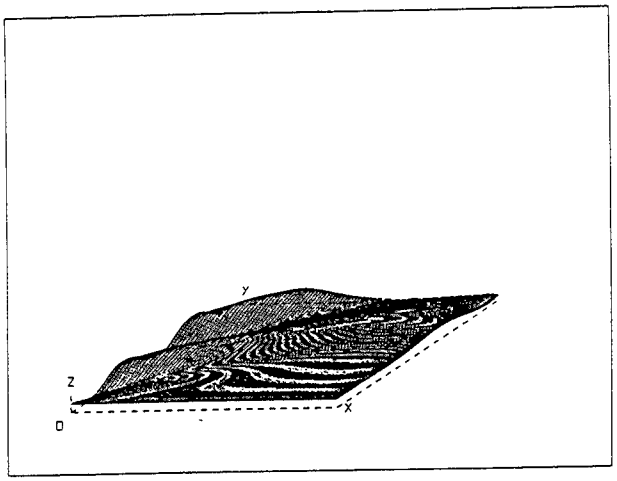

Fig. 14 Time simulation of the nonlinear potential value distribution, stable case. Two-dimensional wedge-shaped body with 45 degrees deadrise angle. 10 panels on the body and 90 panels on the free surface. Amplitude=0.5, k=0.1309, *FSS* number=1.0, c= 0.02, without the truncation effect. Explicit fourth-order Runge-Kutta method.

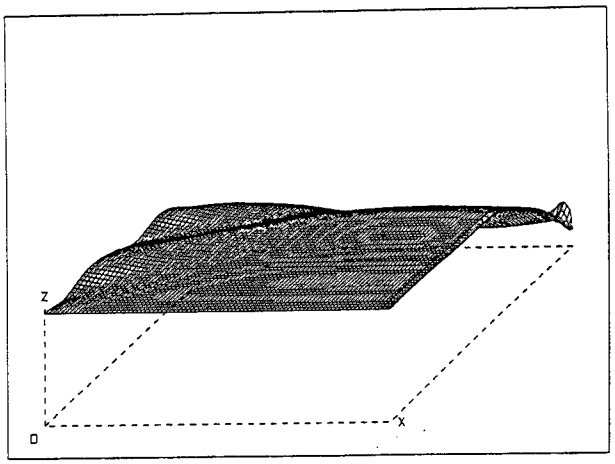

Fig. 15 Time simulation of the nonlinear potential value distribution, unstable case. Two-dimensional wedge-shaped body with 45 degrees deadrise angle. 10 panels on the body and 90 panels on the free surface. Amplitude=0.5, k=0.1309, *FSS* number=1.0, c= 0.02, with the truncation effect. Explicit fourth-order Runge-Kutta method.

SUMMARY AND CONCLUSIONS

The goal of this paper is to better understand the complex behavior of body-free surface interaction problems, specifically the hydrodynamics associated with intersecting, non-wallsided bodies experiencing large amplitude motions. Due to the nonlinearities in the free surface boundary conditions, this problem is generally only tractable through computation and simulation. Previous studies have encountered numerical instabilities restricting the usefulness of this method. Either the simulation program stops due to floating point difficulties or smoothing techniques are applied raising questions about the validity and accuracy of the computed values.

The purpose here is to examine the fundamental causes and solutions surrounding numerical stability and instability and their subsequent effects on hydrodynamic modeling. Analytic determination and evaluation of stability regions have been completed leading to closed form solutions for stability criteria. These criteria have been supported by numerical time simulations.

Initially, simple models for the hydrodynamics are developed yielding basic information on the importance of various parameters and algorithms used in the problem solution schemes. When closed form analytic solutions are not available, this approach gives confidence in numerical results by increasing the level of complexity of the model to finally include the fully nonlinear free surface boundary conditions. Based upon the results presented here, the following conclusions are made:

• By adding a constant to the Green function, the stability characteristics of a particular time stepping algorithim may be changed. This method is effective in two dimensions with open boundary problems, but generally not effective in three dimensions or for closed boundary problems.

• The radiation condition is important to stability considerations in two-dimensional numerical analysis but less so in three dimensions. In the far-field open boundary problem, the effect of the truncation limit plays a significant role in the stability analysis. However, in the three-dimensional problem, no similar effect is observed for the cases studied in this paper. Faltinsen's method (Faltinsen (1977)) for the radiation boundary is apparently unstable but may be approximately valid until the wave propagated from the body reaches the outer boundary.

• The conditional/unconditional stability or instability of various time-stepping schemes has been demonstrated. As shown in the above sections, an explicit Euler scheme is *unconditionally unstable* and other schemes, such as the implicit-like Euler, the implicit Euler, the explicit and the implicit-like fourth-order Runge-Kutta schemes are *conditionally stable.*

• Moderate nonlinearities do not produce significantly different stability regions than equivalent linear problems. This suggests that a preliminary stability analysis can be completed prior to actual simulation of the fully nonlinear problem by applying the von Neumann or matrix methods to linearized boundary conditions on the mean surfaces.

• Based upon axisymmetric flow analysis, three-dimensional problems appear to have larger stability regions than similar two dimensional ones.

• Figure 12 illustrates that errors expanded in terms of the eigen vectors of the $[D]$ matrix have components with different decay rates. Those components that lie on the unit circle neither grow nor decay, while those that are within the unit circle are damped. This suggests the possibility of designing an algorithm that selectively damps unwanted components (*i.e.* frequencies) while minimizing the numerical dissipation of others.

• Numerical stability does not guarantee accuracy in either computation or modeling. For example, bodies characterized by low deadrise angles or high entrance velocities will produce jet-like flows. The computer code that this work is based upon could not successfully calculate such flows. While the time-stepping algorithm is stable, during simulation the formation of a jet near the intersection point leads to numeric overflow. At the intersection point, the free surface forms a thin sheet parallel to the body. The narrow distance between the body surface and the jet surface causes difficulties in the source distribution method since the influence coefficient matrix has large off-diagonal terms. This problem, jet-like impact with and without gravity, has received a considerable amount of attention, but as yet remains unsolved. See, for example Dobrovol'skaya (1969), Hughes (1972), Greenhow and Lin (1985), Greenhow (1987), Miloh (1991), Faltinsen and Zhao (1992), or Vorus (1992).

ACKNOWLEDGEMENTS

This work has been supported by the Office of Naval Research , Applied Hydrodynamics Research Program in Nonlinear Ship Hydrodynamics, Contract No. DOD-G-N0014-90-J-1818.

REFERENCES

1. Troesch, A.W. and Kang, C.G., "Evaluation of Impact Loads Associated with Flare Slamming," STAR Symposium, Pittsburgh, 1988.

2. Kang, C.G. and Troesch, A.W., "Nonlinear Interaction Between Axisymmetric Submerged Bodies and the Free Surface in Water of Infinite Depth," Seminar on Ship Hydrodynamics, Seoul National University, 1988.

3. Longuet-Higgins, M.S., and Cokelet, E.D., "The Deformation of Steep Surface Waves on Water," Proc. R. Soc. Rond. A350, 1976, pp. 1-26.

4. Faltinsen, O.M., "Numerical Solutions of Transient Nonlinear Free-Surface Motion Outside or Inside Moving Bodies," 2nd. Num. Hydr., 1977.

5. Vinje, T. and Brevig, "Breaking Waves on Finite Water Depths, A Numerical Study," Norw. Inst. Tech. & NHL, 1981.

6. Yeung, R.W. , "Numerical Methods in Free-Surface Flows," Ann. R. Fluid Mech. Vol.14, 1982, pp. 395-442.

7. Dommermuth, D.G., and Yue, D.K., "Numerical Simulations of Nonlinear Axi-Symmetric Flows with a Free Surface, JFM, Vol. 178, 1987, pp. 195-219.

8. Hong, S.W., Schultz, W.W., and Graebel, W.P., "An Alternative Complex Boundary Element for Nonlinear Free Surface Flows," University of Michigan Program in Ship Hydrodynamics, Report No. 88-02, 1988.

9. Grilli, S.T., Skourup, J., and Svendsen, I.A., "An efficient Boundary Element Method for Nonlinear Water Waves," Comp. Eng. Anal. with Boundary Elements, 1989.

10. Baker, G.R., Meiron, D.I., and Orzag, S.A., "Generalized Vortex Method for Free Surface Flow Problems," JFM, Vol. 123, 1982, pp. 477-501.

11. Roberts, A.J., "A Stable and Accurate Numerical Method to Calculate the Motion of a Sharp Interface Between Fluids," J. of Applied Math., 1983, 31:13-35.

12. Dold, J.W. and Peregrine, D.H., "Steep Unsteady Water Waves: An Efficient Computational Scheme," School of Math. in U. of Bristol, 1984.

13. Casulli, V. and Cheng, R.T., "Stability Analysis of Eulerian-Lagrangian Methods for the One-Dimensional Shallow-Water Equations," Appl. Math. Modelling, Vol.14, 1990, pp. 122-131.

14. Dommermuth, D.G and Yue, D.K., "Study of Nonlinear Axisymmetric Body-Wave Interactions," Proc. 16th. Symp. on Naval Hydrodynamics, Berkeley, 1986.

15. Dommermuth, D.G., Yue, D.K., Lin, W.M., and Rapp, R.J., "Deep Water Plunging Breakers: A Comparison Between Potential Theory and Experiments," JFM, Vol. 189, 1988, pp. 423-442.

16. Kang, C.G., "Bow Flare Slamming and Nonlinear Free Surface-Body Interaction in the Time Domain," Ph.D. Thesis, University of Michigan, 1988.

17. Richtmyer, R. D. and Morton.K. W., Difference Methods for Initial Value Problems, Interscience Publishers, Inc., 1967.

18. Anderson, Tannaehill, and Pletcher, Computational Fluid Mechanics and Heat Transfer, McGraw-Hill, 1984.

19. Park, J.H., The Numerical Stability of Nonlinear Floating Body Calculations, Ph.D. Thesis, University of Michigan, 1992.

20. Dobrovol'skaya, Z.N., "On Some Problems of Similarity Flow of Fluid with a Free Surface," JFM, Vol. 36, 1969, pp. 805-829.

21. Hughes, O.F., "Solution of the Wedge Entry Problem by Numerical Conformal Mapping," JFM, Vol. 56, 1972, pp. 173-192.

22. Greenhow, M. and Lin, W.M., "Numerical Simulation of Nonlinear Free Surface Flows Generated by Wedge Entry and Wavemaker Motions," 4th Int. Conf. on Num. Ship Hydro, 1985.

23. Greenhow, M., "Wedge Entry into Initially Calm Water," Applied Ocean Research, Vol. 9, No. 4, 1987.

24. Miloh, T., "On the Oblique Water-Entry Problem of a Rigid Sphere," Journal of Engineering Mathematics, 25, pp. 77-92, 1991. 1991.

25. Faltinsen, O. and Zhao, R., "Slamming on the Wetdeck of Multihulls," Seventh International Workshop on Water Waves and Floating Bodies, Val de Reuil, France, 1992.

26. Vorus, W.S., "An Extended Slender Body Model for Planing Hull Hydrodynamics," SNAME Section Meeting, Cleveland, Ohio, 1992.

Slamming Loads on High-Speed Vessels

R. Zhao (MARINTEK, Norway),
O. Faltinsen (University of Trondheim, Norway)

ABSTRACT

Slamming loads on hull cross-sections are studied by a boundary element method, a similarity solution and an asymptotic solution. Pressure distributions on wedges with deadrise angles between 4° and 81° are presented. It is documented that the asymptotic solution is a reliable and practical method for small deadrise angles. The asymptotic method is generalized to wetdeck slamming. The wetted deck area as a function of time is found by solving an integral equation. The results show that the wave slope is important for the slamming load level. The method for wetdeck slamming is incorporated in a time-domain solution for wave induced motions and accelerations of high-speed catamarans. It is demonstrated that the slamming loads on the wetdeck can have an important influence on the vertical accelerations of a catamaran.

NOMENCLATURE

α	=	deadrise angle
λ	=	wavelength of the incident waves
$\eta_j (j=1,6)$	=	motion variables (see Fig. 5)
ζ_a	=	wave amplitude of the incident waves
ζ_{slam}	=	lowest ζ_a-value where wetdeck slamming occurs
ρ	=	mass density of water
C_p	=	pressure coefficient
D_e	=	height of wetdeck relative to mean water level
Fn	=	Froude number = $U/\sqrt{Lg}$
g	=	acceleration of gravity
k	=	wave number
L	=	length between perpendiculars
p	=	pressure
p_0	=	atmospheric pressure
t	=	time variable
U	=	forward speed of the ship
V	=	constant vertical body velocity (positive downwards)
(x,y,z)	=	coordinate system defined in Fig. 5 (also used as local coordinates for one hull and as local coordinate system for wetdeck slamming (see Fig. 7)).
x_1	=	defined by equation (32)

INTRODUCTION

Slamming loads are important in the structural design of high speed vessels. Slamming causes also the ship master to reduce the ship speed. The normal way to predict the voluntary speed loss due to slamming is to first calculate the standard deviations of relative vertical velocity and motion in a vessel-fixed coordinate system at places where slamming is likely to occur. The slamming probability is found by defining a threshold velocity for slamming to occur. An often used criterion is that a typical ship master reduces the speed if slams occur more than 3 of 100 times that waves pass the ship. The conventional way of defining a threshold velocity does not reflect the effect of the structural form. For instance for a high speed vessel with a fine hull form in the bow, the procedure may say that slamming occurs on the bow part of the hull, while it in reality is not a problem. In order to come up with better criteria it is necessary to study theoretical models or performing experiments for water impact against wetdecks and hull shapes typical for high speed vessels. This is also necessary in order to develop rational criteria for operational limits due to slamming. The criteria should be related to average pressures over plate panels on the hulls and the wetdeck that cause plastic deformation of the panels. The occurrence and the magnitude of the slamming pressure are strongly dependent on the relative vertical motions and velocities between the vessel and the waves.

In the following text we will first discuss slamming loads on cross-sections of a hull. Pressure distributions on wedges with deadrise angles between 4° and 81° are presented. A boundary element method,

a similarity solution and an asymptotic solution are used. It is documented that the asymptotic solution is a reliable and practical method for small deadrise angles. The asymptotic method is generalized to wetdeck slamming. The method differs from Kaplan's [1] procedure both in the way that the wetted area and the pressure distribution is found as a function of time. The method for wetdeck slamming is incorporated in a time-domain solution for wave induced motions and accelerations of high-speed catamarans in head sea regular waves. The hydrodynamic loads on the hulls are found by a linear time domain solution. The method is a generalization of Faltinsen & Zhao's [2] frequency domain solution for high speed vessels. It is demonstrated that the slamming loads on the wetdeck can have an important effect on the vertical accelerations of a catamaran. Further that the slamming loads on the wetdeck cannot be estimated by a theory that neglects the effect of slamming loads on the wave induced motions.

SLAMMING LOADS ON HULL CROSS-SECTIONS

Zhao & Faltinsen [3] studied theoretically slamming loads on a two-dimensional body. Three different methods were presented. The assumptions are that no air pocket is created during the impact, the fluid is incompressible and the flow is irrotational. The pressure is set equal to a constant atmospheric pressure on the free surface. The effect of gravity is neglected. This is a reasonable approximation in an impact problem where large fluid accelerations occur.

The three methods can be classified as a boundary element method, a similarity solution and an asymptotic solution. The boundary element method and the similarity solution satisfy the exact free surface and body boundary conditions. The boundary element method is applicable for any body shape and velocity, while the similarity solution is valid for wedges that is forced with constant velocity through the free surface. The asymptotic method is asymptotically valid for small deadrise angles and constant velocity.

The boundary element method assumes that a jet flow is created at the intersection between the free surface and the body surface. The pressure is set equal to atmospheric pressure in the upper part of the jet. The jet flow assumption can be used to simplify the solution. This is done by defining an instantaneous fluid domain Ω that does not contain the whole jet flow. The velocity potential ϕ for the flow inside the fluid domain Ω is represented by Green's second identity. The surface S enclosing Ω consists of AB, CD, S_B, S_F and S_∞ (see Fig. 1). S_∞ is a control surface far away from the body. The angle between the body surface and AB is 90°, while the angle between AB and the free surface is close to 90°. The line AB is in an area where the jet starts and where the pressure can be approximated by atmospheric pressure. CD is constructed in the same way as AB.

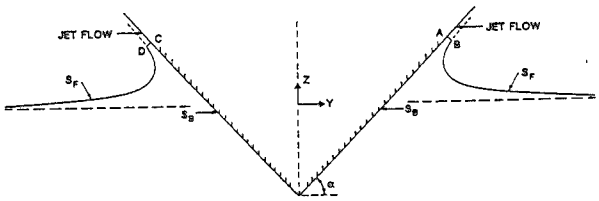

Fig. 1 Definitions of coordinate system and control surfaces used in the numerical solution of water entry of a wedge by means of a boundary element method. α = deadrise angle.

The problem is solved as an initial value problem where the velocity potential and the free-surface elevation are set equal to zero at the initial time. By using the kinematic and dynamic free surface conditions, one can follow how the free surface S_F moves and how the velocity potential changes on the free surface. In the initial phase of the flow AB and CD are not used. When AB and CD are introduced, the motion of AB and CD are found by assuming a one-dimensional flow at AB and CD and integrating the fluid velocity. Since the pressure is assumed to be atmospheric at AB and CD, the dynamic free surface condition can be used to determine the change in ϕ on AB and CD.

At each time instant one solve an integral equation resulting from Green's second identity. On AB, CD and S_F the velocity potential is known and the normal velocity is unknown, while on S_B ϕ is unknown and the normal velocity is known.

Details about the numerical method are described by Zhao & Faltinsen [3]. Important features of the solution method are how the jet flow occurring at the intersection between the free surface and the body is handled and how conservation of fluid mass is satisfied in areas of high curvature of the free surface. The method checks that conservation of mass, momentum and energy are satisfied. Before the segments AB and CD are introduced, conservation of energy and momentum are in general not satisfactory. Conservation of energy are most difficult to satisfy. The reason is numerical difficulties in describing the kinetic energy of the fast moving fluid in the vicinity of the jet flow.

The similarity solution is based on Dobrovol'skaya's [4] work. The solution is not available in explicit form and involves solving a non-linear integral equation. This is particularly difficult for small deadrise angles. Zhao & Faltinsen [3] have presented an iterative scheme to solve the integral equation. They verified the results by checking that

the free surface conditions, the body boundary condition, the far-field representation, conservation of mass, momentum and energy are all satisfied.

The asymptotic solution is based on the work by Armand & Cointe [5] (see also Cointe [6]) who extended Wagner's theory [7] by using matched asymptotic expansions. A simple composite solution for the pressure distribution was presented by Zhao & Faltinsen [3].

Fig. 2 shows numerical predictions of the pressure distribution p on the wetted surface of wedges that are forced with constant vertical velocity V through an initially calm free surface. The deadrise angle α is varied from 4° to 81°. All figures present results by the boundary element method and by the similarity solution. The agreement between these two methods is good. The largest difference occur in how the pressure approaches atmospheric pressure in the jet flow. Reasons to that are believed to be associated with the jet flow approximation used in the boundary element method. At small deadrise angles the pressure is sharply peaked close to the jet flow domain. Calculation of the pressure in this area requires high accuracy both by the similarity solution and the boundary element method. A reason is that the "$\rho\partial\phi/\partial t$"-term ($\phi$ = velocity potential) and the velocity square term in Bernoulli's equation are of different signs and have large and nearly the same absolute value at the jet flow area. This is illustrated in Fig. 3 for α = 20°. It is believed that Zhao & Faltinsen [3] were the first to present similarity solution results for wedges with deadrise angles less than 30°. Dobrovol'skaya [4] presented results for α = 30°, 60°, 81° and higher.

Fig. 2 shows numerical similarity solution results by Dobrovol'skaya [4] for α = 30° and 60° and by Hughes [8] for α = 45°. The agreement with Hughes' results is good while there are some differences between our similarity solution results and Dobrovol'skaya's results, in particular for α = 30°. There must also be a misprint in Dobrovol'skaya's pressure results for α = 30°. The results in Fig. 2 are believed to be correct. A reason for the disagreement may be due to lack of accuracy in Dobrovol'skaya's numerical calculations. Our similarity results agree well with Dobrovol'skaya's results for α = 81°.

Fig. 2 shows also pressure results from the asymptotic theory for small deadrise angles (up to α = 30°). The agreement with the similarity solution is very good for small α-values. The results for α = 4° shows that Watanabe's [9] asymptotic theory differs from our asymptotic theory. Watanabe used a different local jet flow analysis and pressure representation than ours. Reasons why the asymptotic theory deviates for larger deadrise angles are that the quadratic velocity term in Bernoulli's equation is neglected outside the jet flow and that the body boundary condition is not satisfactorily satisfied.

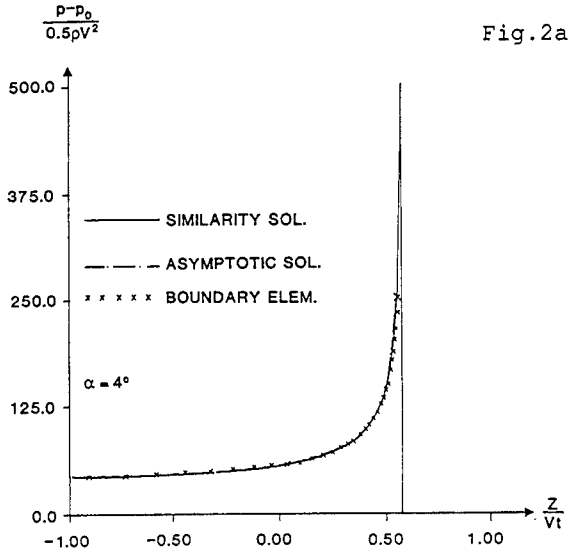

Fig.2a

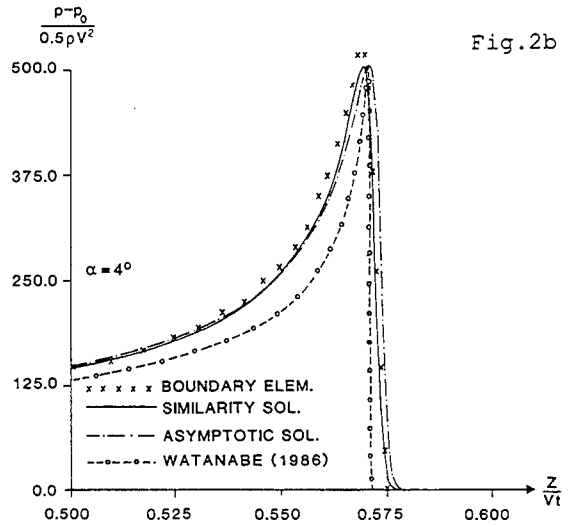

Fig.2b

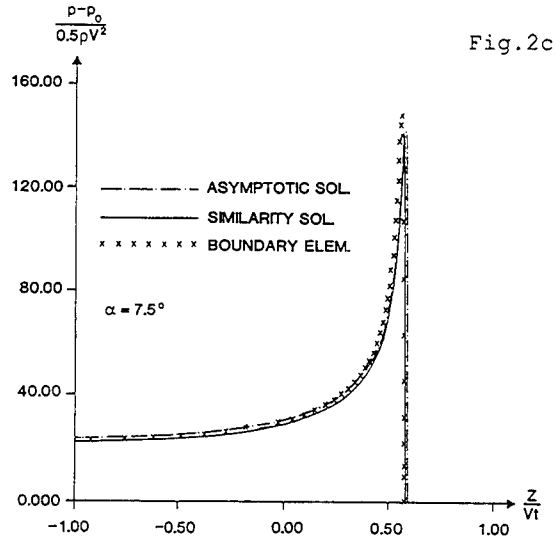

Fig.2c

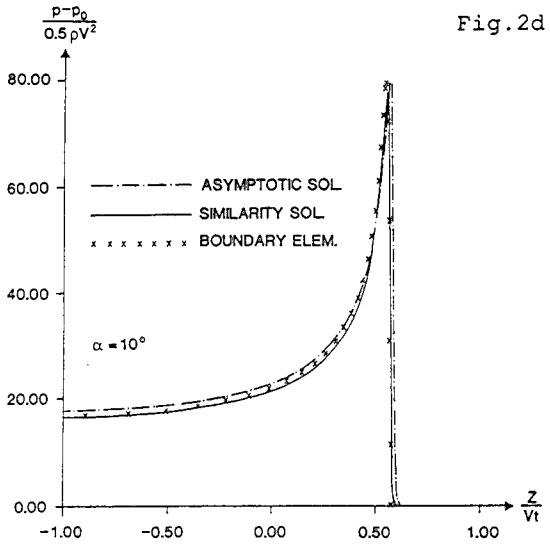

Fig.2d

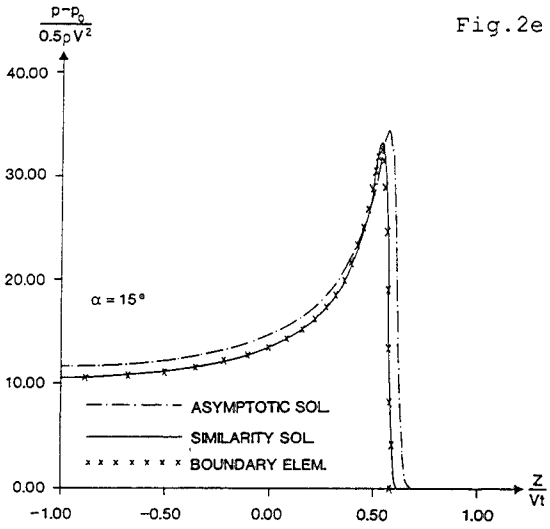

Fig.2e

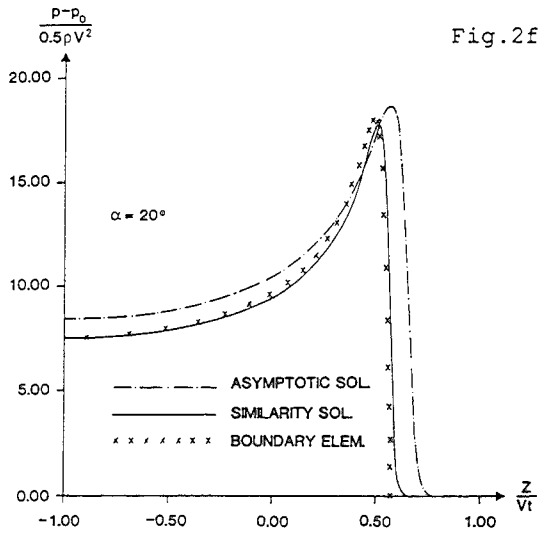

Fig.2f

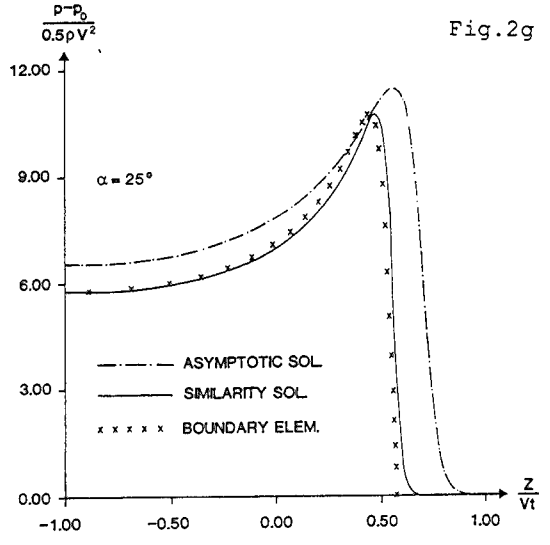

Fig.2g

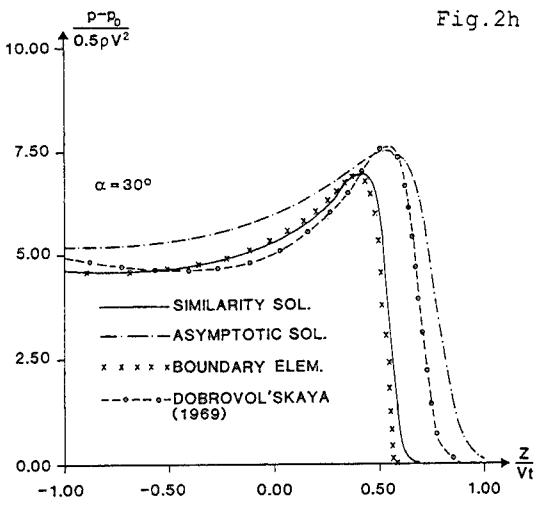

Fig.2h

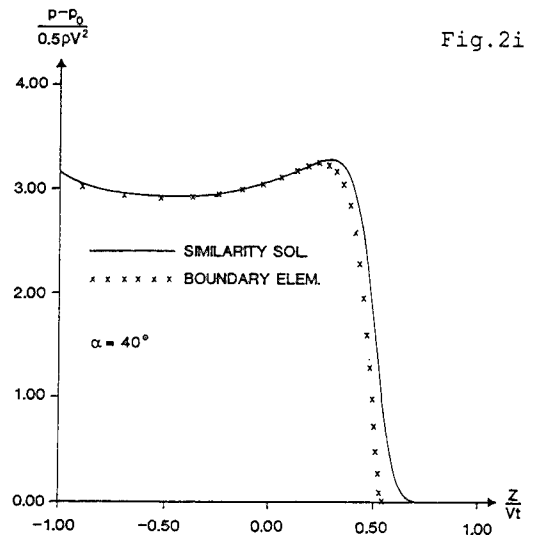

Fig.2i

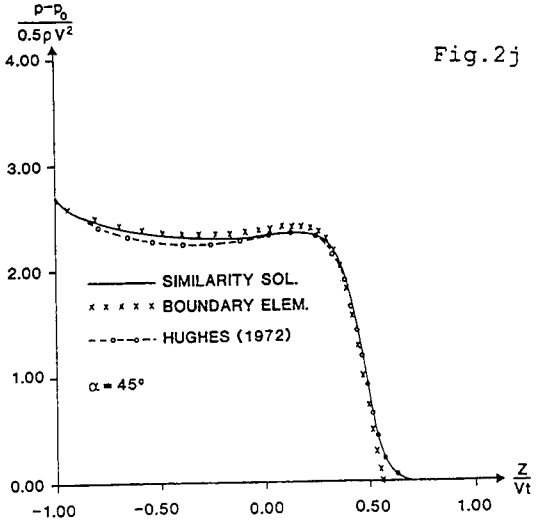

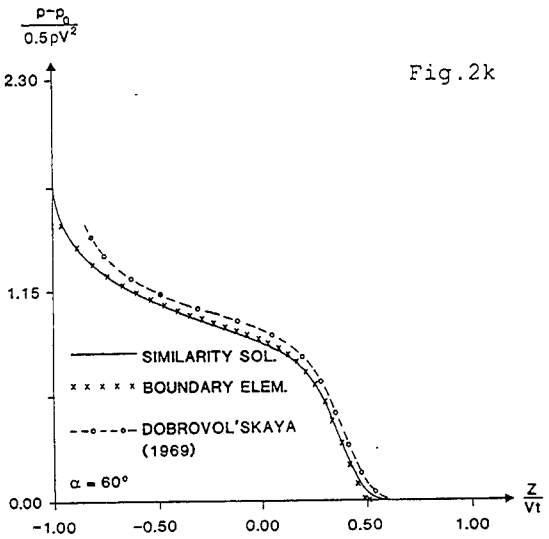

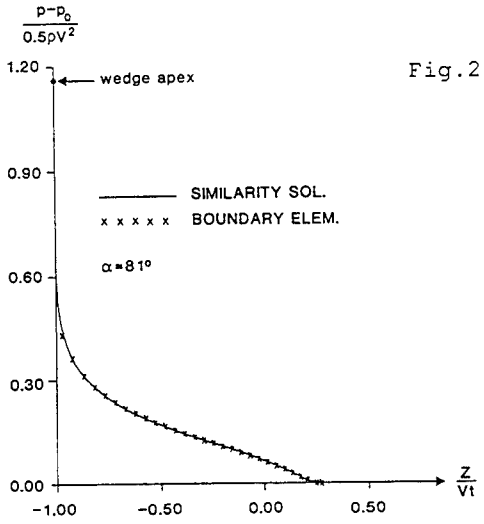

Fig. 2 Predictions of surface pressure distribution p during water entry of wedges with constant vertical velocity V. p_0 = atmospheric pressure. t = time variable. t = 0 initial time of impact. ρ = mass density of water. α = deadrise angle (see Fig. 1).

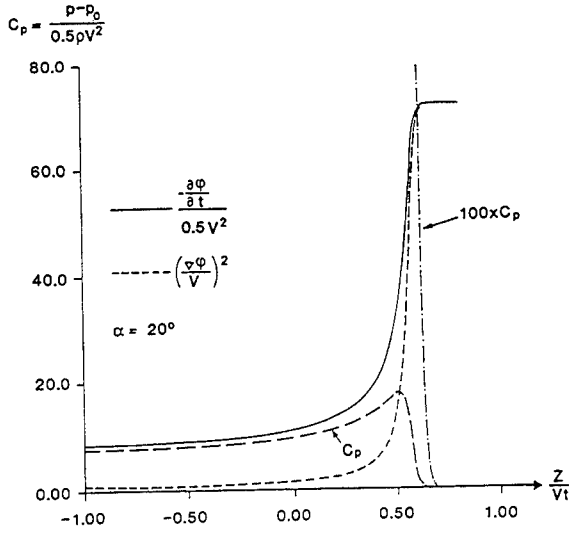

Fig. 3 Contributions to pressure distribution from the $\rho\partial\phi/\partial t$-term and the velocity square term in Bernoullis equation during water entry of a wedge with deadrise angle 20° and constant vertical velocity V. Calculations based on similarity solution.

The pressure results in Fig. 2 show only a typical slamming behaviour for α up to ~30°. By slamming we mean impulse loads with high pressure occurring over a small surface area that changes rapidly with time. Important parameters characterizing slamming are the position and value of the maximum pressure, the time duration and the spacial extent of the slamming pressures.

According to the asymptotic theory the z-coordinate z_{max} of maximum pressure is equal to $(0.5\pi - 1)Vt$ and the maximum slamming pressure p_{max} is given by

$$Cp_{max} \equiv \frac{p_{max} - p_0}{0.5\ \rho V^2} = 0.25\ \pi^2\ cotan^2\alpha \qquad (1)$$

for a wedge. The time duration of slamming can be quantified by considering a fixed point on the body surface and evaluate the time Δt_s it takes from when the pressure is 0.5 (p_{max} - p_0) until it is 0.5 (p_{max} - p_0) again. The spacial extent ΔS_s of the slamming pressure can be found in a similar way (see Fig. 4). Fig. 2 shows that ΔS_s has only meaning when $\alpha \leq$ ~20°. Table 1 shows predictions of Cp_{max}, z_{max}, ΔS_s and the total vertical force F_3 on the wedge for deadrise angles up to 40°. F_3 is based on direct pressure integration. The results in Table 1 show that the boundary element method is in good agreement with the similarity solution. The asymptotic method seems to converge to

the results by the similarity solution when $\alpha \rightarrow 0$. The maximum pressure is well predicted by the asymptotic method even for the larger deadrise angles presented in Table 1. When $\alpha \geq 45°$ (see Fig. 2), the maximum pressure is at the apex of the wedge. According to the similarity solution Cp_{max} will be 2.720, 2.349, 1.810, 1.443 and 1.163 for respectively α = 45°, 50°, 60°, 70° and 81°.

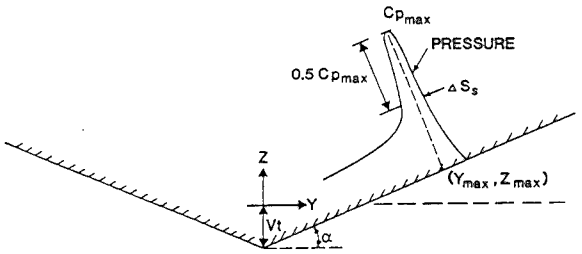

Fig. 4 Definitions of parameters characterizing slamming pressure during water entry of a blunt 2-D body. Cp = pressure coefficient.

The results in Table 1 for ΔS_s at small values of α illustrate that measurement of slamming pressure requires high sampling frequency and "small" pressure gauges. There exists in the literature several reported experimental values for the maximum pressure for wedges and different opinions on how well Wagner's theory for the maximum pressure agrees with experimental results. However, experimental error sources due to the size of the pressure gauge and the change of the body velocity during drop tests are not always considered. Takemoto [10] and Yamamoto [11] did consider these factors and showed good agreement with Wagner's theory for maximum pressure when the deadrise angle was between ~3° and 15°. The reason for the disagreement for $\alpha < -3°$ is due to the air-cushion effect under the wedge.

Equation (1) is often used in practical calculations of slamming pressure for any value of α and is referred to as Wagner's formula. However it has no rational basis for very large α-values where it clearly underpredicts the maximum pressure. For instance at α = 81° Wagner's formula shows Cp_{max} = 0.08, while the similarity solution gives 1.16. It should be noted that the maximum pressure occurs at the apex of the wedge when $\alpha > -45°$ (see Fig. 2). When α is large, the pressure shows a rapid change around the apex.

Table 1 Estimation of slamming parameters by asymptotic method, nonlinear boundary element method and similarity solution during water entry of a wedge with constant vertical velocity V. α = deadrise angle, Cp_{max} = pressure coefficient at maximum pressure. z_{max} = z-coordinate of maximum pressure (see Fig. 4). ΔS_s=spacial extent of slamming pressure (see Fig. 4).c = 0.5 πVt cotanα, F_3 = total vertical hydrodynamic force on the wedge, ρ = mass density of water. t = time (t = 0 initial time of impact).

	Cp_{max}			$\frac{z_{max}}{Vt}$			$\frac{\Delta S_s}{c}$			$\frac{F_3}{\rho V^3 t}$		
α	Similarity	Asymptot.	Boundary element	Similarity	Asymptotic	Boundary element	Similarity	Asymptotic	Boundary element	Similarity	Asymptotic	Boundary element
4°	503.030	504.61	521.4	0.5695	0.5708	0.571	0.01499	0.01576	0.0156	1503.638	1540.506	1491.8
7.5°	140.587	142.36	148.3	0.5623	0.5708	0.558	0.05129	0.05586	0.0526	399.816	423.735	417.9
10°	77.847	79.36	80.2	0.5556	0.5708	0.555	0.09088	0.1002	0.0941	213.980	231.973	220.8
15°	33.271	34.37	32.8	0.5361	0.5708	0.533	0.2136	0.2314	0.226	85.522	96.879	85.5
20°	17.774	18.63	18.2	0.5067	0.5708	0.488	0.4418	0.4270	0.434	42.485	50.639	43.0
25°	10.691	11.35	10.9	0.4709	0.5708	0.443				23.657	29.765	23.7
30°	6.927	7.40	6.94	0.4243	0.5708	0.400				14.139	18.747	13.9
40°	3.266	3.50	3.26	0.2866	0.5708	0.245				5.477	8.322	5.31

SLAMMING LOADS ON THE WETDECK

Consider a multihull vessel in incident head sea waves on deep water. A right-handed coordinate system (x,y,z) fixed with respect to the mean oscillatory position of the vessel is used, with positive z vertically upwards through the centre of gravity of the vessel and the origin in the plane of the undisturbed free surface. The vessel is assumed to have the xz plane as a plane of symmetry in its mean oscillatory position. Let the translatory displacements in the x-, y- and z-directions with respect to the origin be η_1, η_2 and η_3, respectively, so that η_1 is the surge, η_2 is the sway and η_3 is the heave displacement. Furthermore, let the angular displacement of the rotational motion about the x-, y- and z-axes be η_4, η_5 and η_6, respectively, so that η_4 is the roll, η_5 is the pitch and η_6 is the yaw angle. The coordinate system and the translatory and angular displacement conventions are shown in Fig. 5.

The method will be exemplified by considering regular sinusoidal waves where the wave elevation ζ is written as

$$\zeta = \zeta_a \sin(\omega_e t - kx) \tag{2}$$

Here ζ_a is the wave amplitude, k is the wave number, ω_e is the circular frequency of encounter and t is the time variable. The corresponding vertical wave velocity in the free surface zone is

$$w = \omega_0 \zeta_a \cos(\omega_e t - kx) \tag{3}$$

where the circular frequency of oscillation ω_0 of the waves is related to ω_e by $\omega_e = \omega_0 + kU$. U means the forward speed of the vessel.

The instant of slamming between the waves and the wetdeck is found by monitoring the relative vertical motion ζ_R and normal velocity V_{RN} between the deck and the waves. Consistent with linear theory we can write

$$\zeta_R = \eta_3 - x\eta_5 - \zeta \tag{4}$$

$$V_{RN} = \frac{d\eta_3}{dt} - x\frac{d\eta_5}{dt} - U\eta_5 - w \tag{5}$$

Slamming is said to occur when $\zeta_R = -D_e(x)$ and $V_{RN} < 0$. Here $D_e(x)$ is the mean local height of the wetdeck above the mean free surface.

When the waves are in contact with the wetdeck, an additional flow is set up in the water. This is described by a velocity potential ϕ that satisfies the

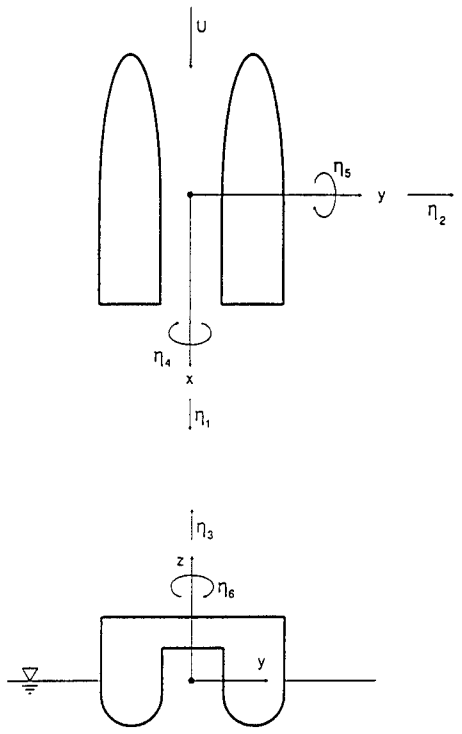

Fig. 5 Coordinate system and definitions of translatory and angular displacements of a catamaran.

body boundary condition

$$\frac{\partial \phi}{\partial z} = V_{RN} \tag{6}$$

We will assume that V_{RN} has a linear variation in the longitudinal direction over the wetted contact area and that ϕ satisfies a two-dimensional Laplace equation in x and z. The flow is divided into an inner and outer flow domain. In the inner flow, the details of the jet flow at the intersection between the free surface and the body are studied. In the outer flow we use the free surface condition $\phi = 0$. The body boundary and free surface conditions are transferred to a horizontal plane (see Fig. 6). The boundary value problem illustrated in Fig. 6 is solved at each time instant by using a local coordinate system (X, Z) where the X and Z-axis are parallel with the x and z-axis. V_{RN} can be written as $V_{RN} = V_1 + V_2 X$. The XZ-coordinate system changes with time. The relationship between X and x is

$$X = x - (a(t) - \ell(t)) \tag{7}$$

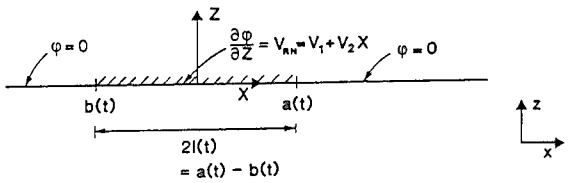

Fig. 6 Definitions of the coordinate systems and illustration of the "outer flow" boundary value problem for the wetdeck impact problem.

By solving the boundary value problem we find that the velocity potential on the body surface at Z = 0 and $|X| \le \ell(t)$ is

$$\phi = (V_1 + 0.5V_2X)\sqrt{\ell^2(t) - X^2} \tag{8}$$

a(t), b(t) and $\ell(t)$ are found by solving the integral equation

$$\int_0^t \left[\frac{-V_1|X|}{\sqrt{X^2 - \ell^2}} + V_1 + V_2X - 0.5sgnX \cdot V_2\left(\sqrt{X^2-\ell^2} + \frac{X^2}{\sqrt{X^2-\ell^2}}\right)\right] dt = \zeta_R(x,t) + D_e(x) \tag{9}$$

where t = 0 is the initial time of contact between the waves and the wetdeck. The integrand is the vertical fluid velocity $\partial\phi/\partial Z$ at Z = 0 for $|X| \ge \ell(t)$. For each time instant equation (9) will be satisfied for two x-values. This determines a(t), b(t) and $\ell(t)$. The integral equation is in general solved numerically. We will show two special cases where analytical methods are possible. In the first case we study an infinitely long horizontal deck with a constant downward velocity V_d impacting on a regular sinusoidal wave. The wave velocity is assumed negligible relative to V_d. In this case $V_1 = -V_d$ and $V_2 = 0$. X will not change with time and X = 0 corresponds to a wave crest. Equation (9) can be written

$$V_d\int_0^t \frac{|X|dt}{\sqrt{X^2 - \ell^2}} = \zeta_a(1 - \cos kX) \tag{10}$$

This integral equation is similar as Wagner [7] set up in studying water entry of two-dimensional bodies. If the right hand side of equation (10) is approximated by $0.5\,\zeta_a k^2X^2$, the solution can be written as

$$\ell(t) = 2\sqrt{V_d t\, R} \tag{11}$$

where $R = (\zeta_a k^2)^{-1}$ is the radius of curvature of the wave profile at the wave crest.

In the second case we will include the effect of the wave velocity. We assume the deck is horizontal, infinitely long and has a constant downward velocity V_d. It is convenient to use a coordinate system (x', z) that follows the wave crest. x' = 0 corresponds to the wave crest. However in the following we will drop the prime in the coordinate notation and use x instead of x'. By using equation (9) we can write

$$\eta_a(x) = \int_0^t \left[\frac{-V_rX}{\sqrt{X^2 - \ell^2}} + V_1 + V_d + V_2X - 0.5V_2\left(\sqrt{X^2-\ell^2} + \frac{X^2}{\sqrt{X^2-\ell^2}}\right)\right]dt \tag{12}$$

where $V_1 = -V_d + (a-\ell)V_2$ and $\eta_a(x)$ is the vertical distance between the deck and the free surface at t = 0 for positive values of x (see Fig. 7). We assume

$$\frac{b}{a} = 1 + F\,a \tag{13}$$

where F a << 1 and F is presently unknown. Further it is assumed that $V_2x << V_d$ and

$$dt \approx (A_r + g_ra + H_ra^2)da \tag{14}$$

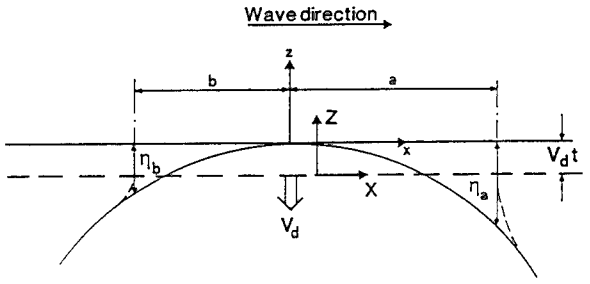

Fig. 7 Impact between a wetdeck and regular sinusoidal waves.

Here A_r, g_r and H_r are unknowns. It is possible to show by integrating equation (12) that

$$\eta_a \approx A_r\frac{\pi}{2}V_d x + g_r V_d x^2 + \left[V_d F\, g_r\left(\frac{4}{3}-\frac{3\pi}{8}\right)+V_d H_r\frac{\pi}{4} - \frac{1}{6}V_2 g_r\right]x^3 \quad (15)$$

Similarly we can do for negative values of x. By assuming

$$dt \approx (A_t + g_t b + H_t b^2)\, db \quad (16)$$

where A_t, g_t and H_t are unknowns, it follows that

$$\eta_b \approx A_t\frac{\pi}{2}V_d|x| + g_t V_d|x|^2 + \left[-V_d F g_t\left(\frac{4}{3}-\frac{3\pi}{8}\right)+V_d H_t\frac{\pi}{4}+\frac{1}{6}V_2 g_t\right]|x|^3 \quad (17)$$

By approximating η_b and η_a by $0.5x^2/R$, where $R = (\zeta_a k^2)^{-1}$ is the radius of curvature of the wave profile at x = 0, we find that $A_r = A_t = 0$, $g_r = g_t = (2RV_d)^{-1}$ and that the coefficients of the x^3-terms in equations (16) and (17) have to be zero. By also using that

$$t = \int_0^a (g_r a + H_r a^2)da = \int_0^b (g_t b + H_t b^2)\, db \quad (18)$$

it follows that $F = 0.125\ V_2/V_d$, $H_r = 1.5\ g_r F$, $H_r = -H_t$. From equations (14) and (16) we can now find a(t) and b(t).

Inner flow regions and matching

The inner flow regions are located near x = a(t) and x = b(t). The velocity potentials in the inner flow are found from Wagner's [7] local jet flow analysis. In the vicinity of x = a(t) the velocity potential on the body is given in parametric form as

$$\phi = -\frac{da}{dt}\frac{\delta_a}{\pi}(1+\ell n|\tau|-|\tau|)+\frac{da}{dt}(x-a) \quad (19)$$

where $0 < |\tau| < \infty$ and the relationship between $|\tau|$ and x is

$$x-a = \frac{\delta_a}{\pi}(-\ell n|\tau|-4\sqrt{|\tau|}-|\tau|+5) \quad (20)$$

δ_a is the jet thickness, that is determined from the matching. A first term outer expansion when $x - a \to -\infty$ is

$$-4\frac{da}{dt}\sqrt{\frac{\delta_a}{\pi}}\sqrt{a-x} \quad (21)$$

This matches with a first term inner expansion of the outer flow solution. We find by using equation (8) and (21) that

$$\delta_a = \pi\,(V_1 + 0.5V_2\ell)^2\, 2\ell\left(4\frac{da}{dt}\right)^{-2} \quad (22)$$

By matching with the local jet flow around x = b(t) we find that the jet thickness δ_b at x = b(t) is

$$\delta_b = \pi(V_1 - 0.5V_2\ell)^2\, 2\ell\left(4\frac{db}{dt}\right)^{-2} \quad (23)$$

Composite pressure solution

In the outer solution a first order approximation of the pressure p_{out} is given by the $-\rho\partial\phi/\partial t$ - term in Bernoullis equation. We find that

$$p_{out}-p_0 = -\rho(V_1+0.5V_2X)\left[\frac{\ell\frac{d\ell}{dt}+X\left(-\frac{d\ell}{dt}+\frac{da}{dt}\right)}{\sqrt{\ell^2-X^2}}\right] - \rho\,0.5V_2\left(-\frac{da}{dt}+\frac{d\ell}{dt}\right)\sqrt{\ell^2-X^2} - \rho\left(\frac{\partial V_1}{\partial t}+0.5\frac{\partial V_2}{\partial t}X\right)\sqrt{\ell^2-X^2} \quad (24)$$

where p_0 is the atmospheric pressure. The pressure p_{in} in the inner flow solution near x = a(t) is given by Wagner [7] as

$$p_{in} - p_0 = 2\rho\left(\frac{da}{dt}\right)^2 \sqrt{|\tau|}\left(1 + \sqrt{|\tau|}\right)^{-2} \qquad (25)$$

where $|\tau|$ is related to x by equation (20). A first term inner flow approximation of equation (24) near x = a(t) is

$$-\rho(V_1 + 0.5V_2X)\frac{\ell\frac{da}{dt}}{\sqrt{2\ell(a - x)}} \qquad (26)$$

This is the same as a one term outer expansion of equation (25). This means we can write the following composite solution for the pressure when $0 \le X \le \ell(t)$.

$$p - p_0 = p_{out} - p_0 + p_{in} - p_0$$
$$+\rho(V_1 + 0.5V_2X)\frac{\ell\frac{da}{dt}}{\sqrt{2\ell(a-x)}} \qquad (27)$$

In a similar way we can construct a composite solution for $-\ell(t) \le X \le 0$. For $|X| > \ell(t)$ we use the jet flow approximation for the pressure.

Fig. 8 shows an example on numerical predictions of pressure by means of the asymptotic method. Equation (9) is used to find a(t), b(t) and $\ell(t)$. The studied problem is a horizontal flat plate that is impacting regular sinusoidal waves propagating along the positive x-axis with phase velocity c. The flat plate has a constant downward velocity V_d. Results for three different time instants are presented. t = 0 corresponds to the time when the flat plate hits the wave crest. It is seen that the pressure is asymmetric about x = ct and that the largest pressure occurs for a positive value of x - ct at each time instant. We can check the results in Fig. 8 qualitatively by using equation (11) for $\ell(t)$. Consistent with the approximation of equation (11) we find that the maximum pressure coefficient is

$$Cp_{\max} \equiv \frac{\left(\frac{d\ell}{dt}\right)^2}{V_d^2} = \frac{\zeta_a}{V_d t} \cdot \frac{1}{k^2\zeta_a^2} \qquad (28)$$

and the minimum value of Cp is

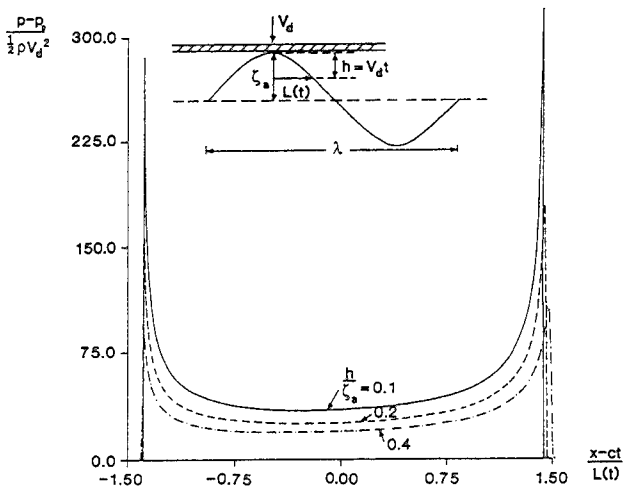

Fig. 8 Pressure distribution caused by a horizontal flat plate impacting on regular sinusoidal waves propagating with phase velocity c along the positive x-axis. V_d = 4 m/s. ζ_a = 1.5 m. The wave length λ = 50 m.

$$Cp_{\min} = 2\sqrt{Cp_{\max}} \qquad (29)$$

Cp_{max} occurs at x-ct = $0.5\pi L(t)$, where L(t) is defined in Fig. 8. Cp_{min} occurs at x=ct. These formulas are in qualitative agreement with the results in Fig. 8.

Equation (27) shows that the pressure goes to infinity when $t \to 0$. In reality the pressure cannot be larger than the acoustic pressure $\rho V_d c_e$, where c_e is the speed of sound in water. Even if the pressure goes to infinity when $t \to 0$, the resulting force on the wetdeck is finite. We can estimate this force by integrating the outer pressure distribution given by equation (24) over a horizontal deck. This gives the following vertical force F_3^{2D} per unit length on the wetdeck

$$F_3^{2D} = -\frac{d}{dt}\left(\rho\frac{\pi}{2}\ell^2 V_1\right) \qquad (30)$$

This shows that the vertical force is independent of V_2. By assuming $V_1 = -V_d$ to be time independent and using equation (11) as an approximation for $\ell(t)$ we find that

$$F_3^{2D} = 2\rho\pi k^{-2}V_d^2/\zeta_a \quad (31)$$

If we imagine that V_d is due to linear wave induced motions, we get the surprising result that F_3^{2D} is linearly dependent on the wave amplitude. However we shall see later in the text that there is an influence from wetdeck slamming on the wave induced motions and accelerations of the vessel.

Equations (27) - (29) show that the magnitude of the slamming loads on a horizontal wetdeck is closely related to the wave slope $k\zeta_a$.

TIME DOMAIN SIMULATIONS OF SLAMMING LOADS AND MOTIONS

To include slamming loads on the wetdeck in the prediction of vessel motions, a time domain formulation is necessary. We consider here a high-speed catamaran in incident waves in deep water. It is assumed that the hydrodynamic loads on the hulls can be approximated by linear theory. Strictly speaking nonlinearities in the incident wave field and the hydrodynamic loads on the hulls may matter. However, these effects are not believed to change the mean conclusions of this paper. The slamming loads on the wetdeck will be included in the way described previously. The method that we use to evaluate the loads on the hulls is a generalization of the frequency domain formulation by Faltinsen & Zhao [2]. It is assumed that the hulls are hydrodynamically independent of each other. This is a reasonable assumption at high speed as long as the hulls are not too close and the waves from one hull do not propagate to the other hull.

In order to solve the problem in the time domain an earth-fixed coordinate system $\mathbf{x}_1 = (x_1,y,z)$ has been used, where

$$x_1 = x - Ut \quad (32)$$

$y = 0$ will in this case correspond to the centre plane of the hull. The problem can be formulated in terms of potential flow theory. The total velocity potential in the vicinity of a hull can be written as

$$\Phi(\boldsymbol{x}_1,t) = \phi_I(\boldsymbol{x}_1,t) + \phi_1(\boldsymbol{x}_1,t) \quad (33)$$

where ϕ_I is the velocity potential of the incident waves. Linear regular incident waves will be used in the present study. By assuming a slender hull and linear response, it can be shown as described by Faltinsen & Zhao [2] that ϕ_1 satisfied

$$\frac{\partial^2\phi_1}{\partial y^2} + \frac{\partial^2\phi_1}{\partial z^2} = 0 \quad (34)$$

in the fluid domain. The body boundary condition on the mean wetted body surface is

$$\frac{\partial\phi_1}{\partial n} = V_n - \frac{\partial\phi_I}{\partial n} \quad (35)$$

where V_n is the body velocity in the normal direction $\mathbf{n}$ to the body surface. Positive normal direction is assumed to be into the fluid domain.

The dynamic and kinematic free surface conditions on the mean free surface in the earth-fixed coordinate system can be written as

$$\frac{\partial\phi_1}{\partial t} = -g\zeta_1 \quad (36)$$

and

$$\frac{\partial\zeta_1}{\partial t} = \frac{\partial\phi_1}{\partial z} \quad (37)$$

where ζ_1 means the wave elevation due to ϕ_1.

To solve the problem in the time domain, Green's second identity is applied for each cross-section and time instant. The velocity potential at a point (y,z) and time t can be written as

$$-2\pi\phi_1(y,z;t) - \int_{S_F+S_B}\left(\phi_1(\eta,\zeta;t)\frac{\partial logr}{\partial N} - logr\frac{\partial\phi_1(\eta,\zeta;t)}{\partial N}\right)ds(\eta,\zeta;t) \quad (38)$$

Here $r = [(y-\eta)^2 + (z-\zeta)^2]^{1/2}$, S_B the mean wetted body surface, S_F the mean free surface, ds a surface element along either S_F or S_B and $\partial/\partial N$ is the derivative along the perpendicular to either S_B or S_F in the cross-plane. Since there are not generated any waves far away from the hull, the contribution from the free-surface integral part of equation (38) can be rewritten. For $|y| > b(x)$, where $b(x)$ is large relative to the cross-dimensions of the hull, we can write

$$\phi_1 \sim A(x_1,t)\ z/(y^2+z^2)+B(x_1,t)\ yz/(y^2+z^2)^2 \quad \textbf{(39)}$$

where A and B are determined as part of the solution. The unknowns in equation (38) are ϕ_1 on the body surface and $\partial\phi_1/\partial N$ on the free surface. When (y,z) approaches points on S_F and S_B in equation (38), the unknowns can be found by solving numerically the resulting integral equations.

The initial conditions $\zeta_1 = 0$ and $\phi_1 = 0$ on the mean free surface at t = 0 are used. The dynamic and kinematic free surface conditions are used to find the free surface elevation ζ_1 and the velocity potential ϕ_1 on the mean free surface.

In the numerical calculations the hull was divided into a number of cross-sections with equal spacing $\Delta x = U\Delta t$, where Δt is the time step in the numerical time integration. A second order Runge-Kutta method was used in the time integration. At each time step the integral equation resulting from equation (38) can be written as a system of linear equations of the form

$$\sum_{j=1}^{N} H_{ij}U_j = I_i \quad \textbf{(40)}$$

where U_j are the unknowns and H_{ij} are only dependent on the element distribution on the body surface and the free surface for each cross-section of the hull. Therefore H_{ij} (and the inverse of H_{ij}) can be calculated prior to the time domain solution.

The hydrodynamic force (F_1,F_2,F_3) and moment (F_4,F_5,F_6) on the catamaran are written as

$$F_i = \rho \int_{S_B} \left(\frac{\partial \phi_I}{\partial t} + \frac{\partial \phi_1}{\partial t} \right) n_i ds - \sum_{j=1}^{6} C_{ij}\eta_j + \begin{cases} 0 & i = 1,2,6 \\ F_{si} & i = 3,4,5 \end{cases} \quad \textbf{(41)}$$

where n_i, i = 1,6 is defined by $\mathbf{n} = (n_1,n_2,n_3)$ and $\mathbf{r} \times \mathbf{n} = (n_4,n_5n_6)$ where $\mathbf{r}$ is the position vector $\mathbf{r} = x\mathbf{i} + y\mathbf{j} + z\mathbf{k}$. $\partial/\partial t$ in equation (41) means partial derivative with respect to time in the earth-fixed coordinate system. Further C_{ij} are restoring coefficients that follows from hydrostatic and mass considerations. F_{si} expresses the slamming load on the wetdeck. Only head sea waves will be considered in the following text. This means that F_2,F_4 and F_6 are zero.

When $V_{RN} < 0$ (see equation (5)) and $\zeta_R \leq -D_e(x)$ (see equation (4)) equation (30) with $V_1 = V_{RN}$ is used to estimate F_{S3}. $\ell(t)$ in equation (30) is determined from equation (11) with V_d replaced by V_{RN}. F_{S5} can be written as $-x_sF_{S3}$ where $x = x_s$ is the mean longitudinal position where slamming occurs at each time instant. Cases where x_s is very close to the fore and aft end of the wetdeck have to be calculated in a different way, but were excluded in the following simulations. When $V_{RN} > 0$, the slamming loads are set equal to zero.

The motions and accelerations of the catamaran can be found by solving

$$\sum_{j=1}^{6} m_{ij}\ddot{\eta}_j = F_i \quad \textbf{(42)}$$

where m_{ij} is the structural mass matrix for the vessel. The pressure distribution due to wetdeck slamming can be found from equation (24).

The numerical program has been tested at different levels. The prediction of hydrodynamic loads on the hulls was tested by convergence tests. This was done by changing systematically the element distribution on the body and free surface, the location of b(x) and number of cross-sections for different vessel speeds and wave frequencies. The results were also compared with the steady results and the unsteady frequency domain results reported by Faltinsen & Zhao [2]. Good agreement was documented.

Numerical results

The simulation model has been used to investigate the effect of wetdeck slamming on catamaran motions, velocities and accelerations in head sea regular waves. The main particulars and the body plan of the catamaran are presented in Table 2 and Fig. 9. The hull geometry is based on an analytical function. This makes it easy to select an arbitrary number of cross-sections and the element distribution on the body surface. The results will be presented in non-dimensional form based on Froude scaling. Important parameters are Froude number Fn, wave slope $k\zeta_a$, ratio between wave length and ship length λ/L and the ratio ζ_a/D_e, where D_e is the mean distance between the mean free surface and the wet deck at the position where slamming occurs. The curvature of the wetdeck at the position of slamming does also matter.

Fig. 10 illustrates how the position of slamming changes with the wavelength. The wave amplitude for each wavelength corresponds to the lowest waves that hit the wetdeck under steady state conditions. The figure shows the relative position of the wetdeck to the incident waves at the time instant of impact. It is strongly wavelength and wave amplitude-dependent how and when the waves hit the wetdeck. This has an important influence on the slamming loads.

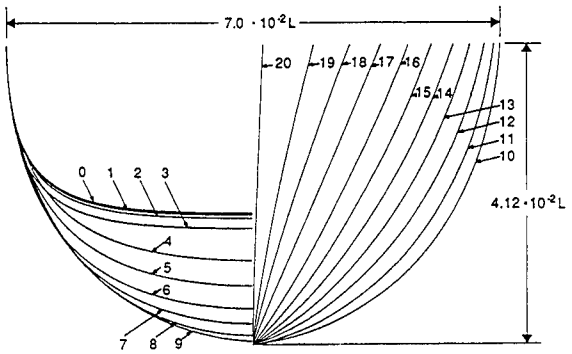

Fig. 9 Body plan of one of the catamaran hulls used in the simulation studies.

Table 2

Main particulars of the catamaran used in the simulation studies

Designation	Value
Length between perpendiculars	L
Beam at waterline midships	0.24L
Draft - even keel	$4.12 \cdot 10^{-2}$L
Displacement	$3.07 \cdot 10^{-3}L^3$
Block coefficient	0.532
Breadth of one hull at waterline amidships	$7.0 \cdot 10^{-2}$L
Centre of gravity above keel	$6.62 \cdot 10^{-2}$L
Center of gravity aft of amidships	$7.1 \cdot 10^{-2}$L
Pitch radius of gyration with respect to axis through centre of gravity	0.25L

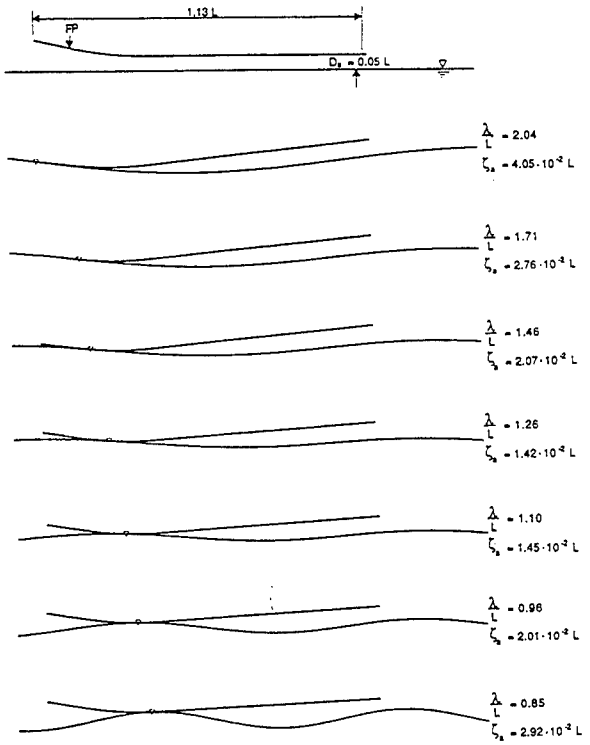

Fig. 10 Position of slamming on the wetdeck of a catamaran in regular head sea waves as a function of wavelength λ. The figure shows a longitudinal cross-section at the centre-plane of the catamaran. Fn = 0.5. $\zeta_a = \zeta_{slam}$ = lowest incident wave amplitude when slamming occurs. L = length between perpendiculars. The catamaran is presented in Fig. 5 and Table 2.

Fig. 11 presents simulations showing the influence of slamming loads on the vertical accelerations, velocities and motions at the forward perpendicular of the catamaran. The wetdeck height D_e was assumed to be constant along the length of the vessel. The wave elevation ζ of the incident waves are given by equation (2). The simulation starts at t = 0 assuming that the vessel is placed in the incident wave system given by equation (2). Results for only one wavelength λ = 0.853 L and one Froudenumber Fn = 0.5 are presented. Two different values of ζ_a/D_e are shown. These corresponds to $(\zeta_a - \zeta_{slam})/D_e$ = 0.0655 and 0.131, where ζ_{slam} is the lowest ζ_a-value where wetdeck slamming occurs. The figure shows vertical accelerations, velocities and motions at FP both with and without the influence of slamming loads. In the start of the simulations when transient linear effects matter, slamming loads were not included. The results show that slamming loads have an influence on the vertical motions and velocities, but that the influence is not as significant as it is for the vertical accelerations. The vertical motions and velocities are nearly periodic, but not sinusoidal, while the maximum vertical accelerations due to slamming change more from period to period. The figures illustrates that slamming loads are restraining the catamaran in its downward motion.

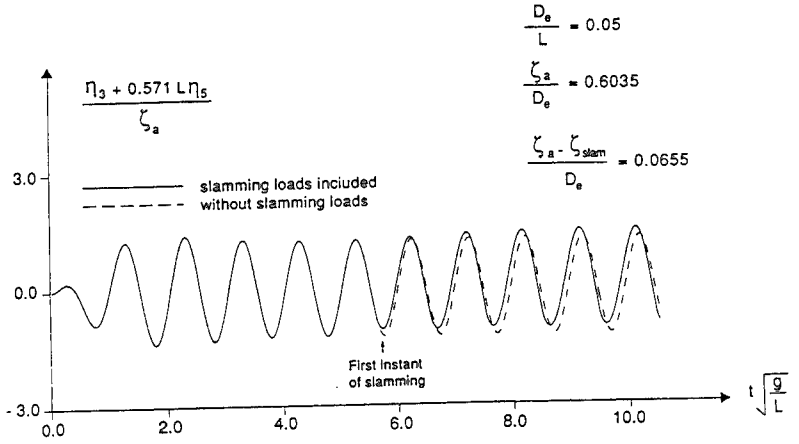

Fig.11a

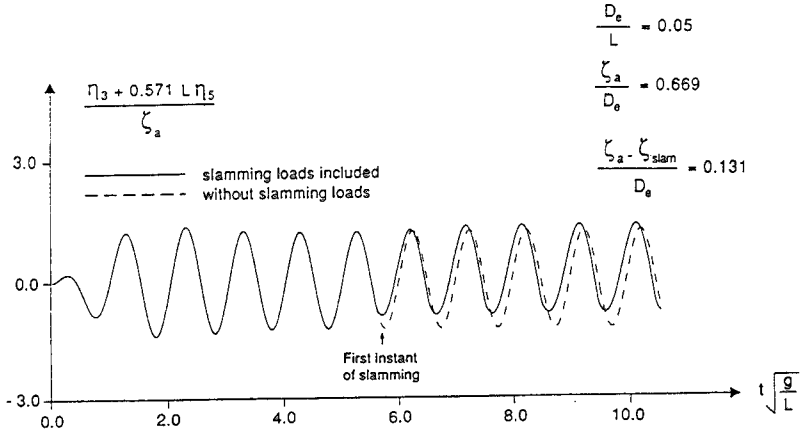

Fig.11b

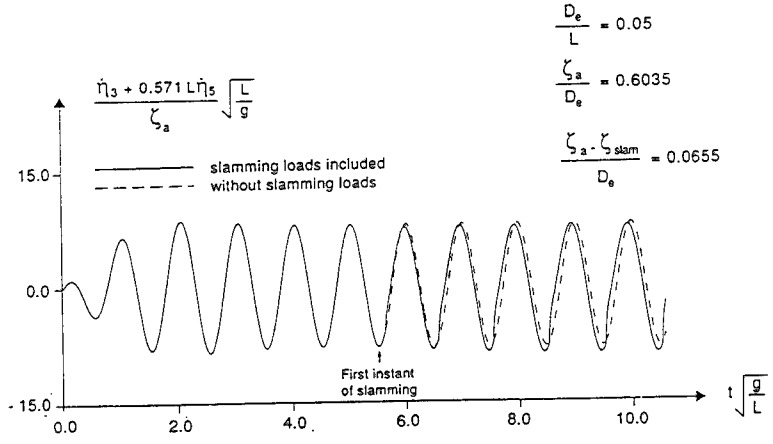

Fig.11c

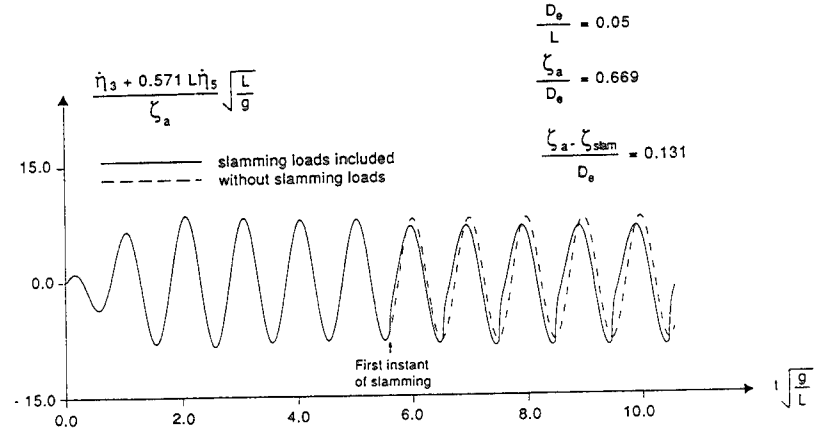

Fig.11d

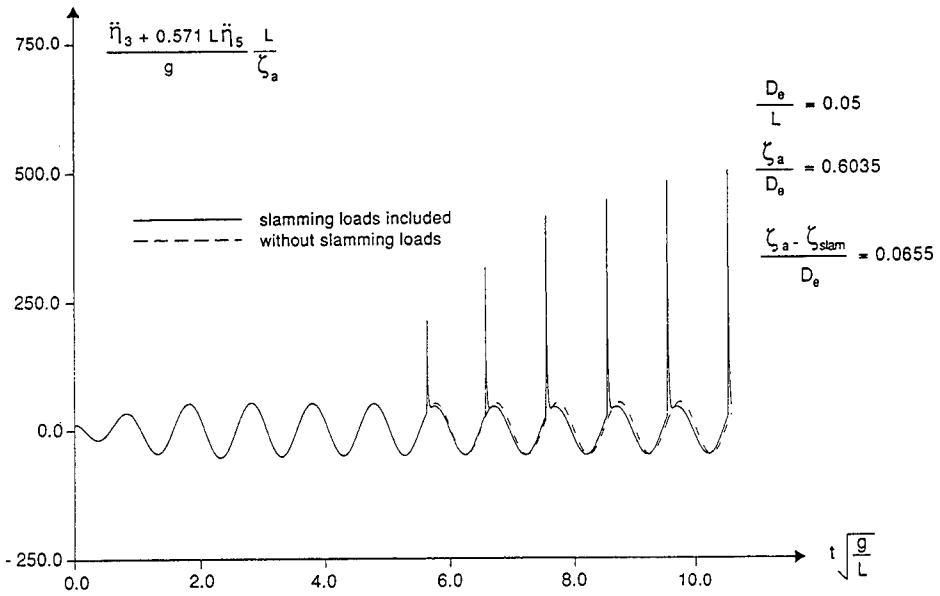

Fig.11e

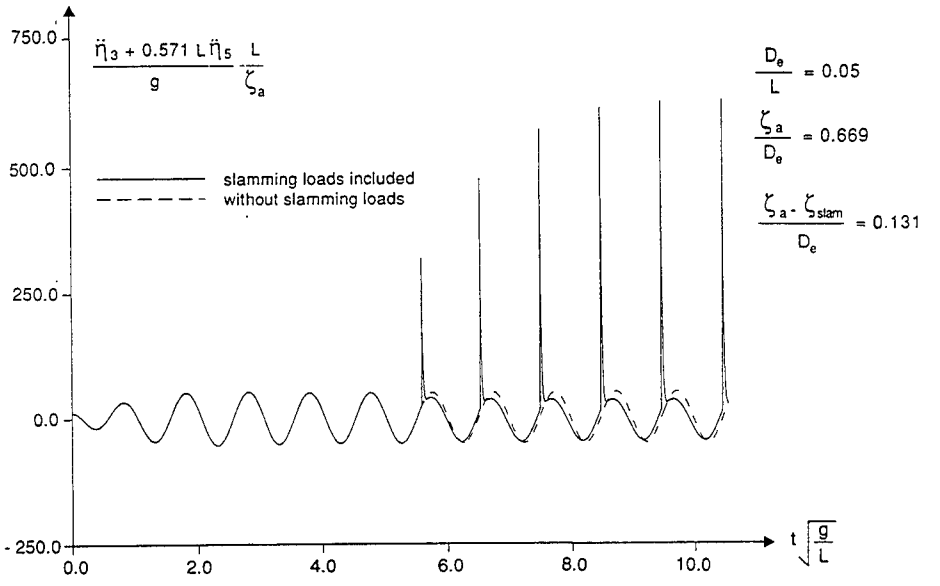

Fig.11f

Fig. 11 Numerical time domain simulations of vertical motions, ($\eta_3 + 0.571\, L\eta_5$), velocities ($\dot{\eta}_3+0.571L\dot{\eta}_5$) and accelerations ($\ddot{\eta}_3+0.571L\ddot{\eta}_5$) at FP of a catamaran in regular head sea waves. Fn = 0.5. $\lambda/L = 0.853$. D_e = mean wetdeck height relative to mean water level. ζ_a = incident wave amplitude, λ = incident wavelength, t = time, L = length between perpendiculars. The catamaran is presented in Fig. 5 and Table 2.

Fig. 12 shows the importance of including the effect of slamming loads on the vertical motions, velocities and accelerations when the slamming force is calculated. The first time the waves hit the wetdeck, the maximum slamming force is independent of that the slamming force is included in the time domain simulation of the motions. However, later on in the time simulation the position of slamming on the wetdeck will change if the slamming force is included. This has an important effect on the magnitude of the slamming force.

The time domain solution outlined above can be generalized to include irregular sea, nonlinear effects in the incident waves and the hydrodynamic loads on the hulls as long as the slamming loads on the wetdeck can be estimated by the two-dimensional theory outlined in this paper. If wetdeck slamming has a more three-dimensional character like in oblique sea, further theoretical developments are necessary. It will also be of interest to study the hydroelastic effect of wetdeck slamming.

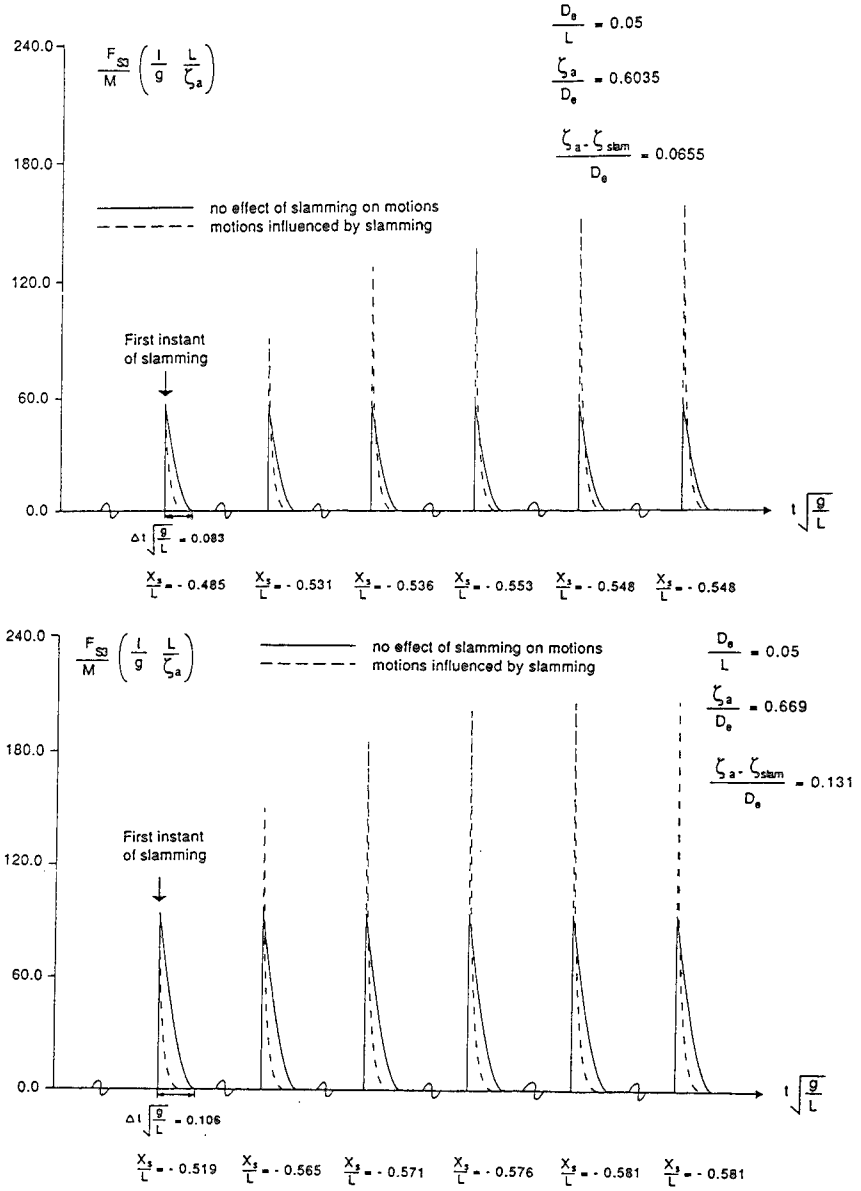

Fig. 12 Numerical time domain simulations of the vertical force F_{s3} on the wetdeck of a catamaran in regular head sea waves. Fn = 0.5. λ/L = 0.853. M = mass of the catamaran. x_s = x-coordinate where the waves hit the wetdeck. L = length between perpen-diculars. B_d = breadth of wetdeck = 0.1L. λ = incident wavelength. ζ_a = incident wave amplitude. D_e = mean wetdeck height relative to mean water level. The catamaran is presented in Fig. 5 and Table 2.

CONCLUSIONS

Slamming loads on hull cross-sections are studied by a boundary element method, a similarity solution and an asymptotic solution. Pressure distribution on wedges that are forced with a constant velocity, are presented. It is documented that the asymptotic solution is a reliable and practical method for small deadrise angles α. When $\alpha > \sim 20°$ the pressure distribution does not show a typical slamming behaviour with sharply peaked pressure close to the jet flow (water spray) area. When $\alpha > \sim 45°$, the maximum pressure occurs at the apex of the wedge.

Slamming loads on the wetdeck are studied by a two-dimensional asymptotic method. The wetted deck area as a function of time is found by solving an integral equation. Approximate solutions show that the wave slope is important for the slamming load level. A composite solution for the pressure distribution is presented. In general the pressure distribution is not symmetric about the midpoint of the two-dimensional wetted area. The pressure distribution in the jet flow (water spray) areas are found by Wagner's [7] analysis.

The method for wetdeck slamming is incorporated in a time-domain solution for wave induced motions and accelerations of high-speed catamarans. Incident head sea regular waves are assumed and the hydrodynamic loads on the hulls are approximated by a linear time domain solution that includes memory effects, diverging wave systems, transom stern effects and neglect transverse wave systems and hydrodynamic interaction between the hulls. It is strongly wavelength and wave amplitude-dependent how and when the waves hit the wetdeck. The slamming loads can have an important effect on the vertical accelerations of the vessel while the effect on the vertical motions and velocities is less pronounced. Slamming loads on the wetdeck cannot be estimated by a theory that neglects the effect of slamming loads on the wave induced motions.

REFERENCES

1. Kaplan, P., Analysis and predictions of flat bottom slamming impact of advanced marine vehicles in waves, *Int. Shipbuilding Progress*. Vol.34, No.391. March 1987, pp. 44-53

2. Faltinsen, O., Zhao, R., Numerical predictions of ship motions at high forward speed, *Phil. Trans. R. Soc.*, Series A, Vol. 334, 1991, pp. 241-252.

3. Zhao, R. Faltinsen, O., Water entry of two-dimensional bodies. In press 1992.

4. Dobrovol'skaya, Z.N., On some problems of similarity flow of fluid with a free surface, *J. Fluid Mech.*, Vol. 36, Part 4, 1969, pp. 805-829.

5. Armand J.L., Cointe, R., Hydrodynamic impact analysis of a cylinder, *Proc. Fifth Int. Offshore Mech and Arctic Engng. Sym. (OMAE)*, The American Society of Mechanical Engineering, Vol. 1, 1986, pp. 609-634.

6. Cointe, R., "Free surface flows close to a surface-piercing body", Mathematical approaches in hydrodynamics, T. Miloh, ed., *Soc. Ind. Appl. Math.*, Philadelphia, 1991, pp. 319-334.

7. Wagner, H., Über Stoss- und Gleitvergänge an der Oberfläche von Flüssigkeiten, *Zeitschr. f. Angewandte Mathematik und Mechanik*, Vol. 12, Part 4, 1932, pp. 192-235.

8. Hughes, O.F., Solution of the wedge entry problem by numerical conformal mapping, *J. Fluid Mech.*, vol. 56, Part 1, 1972, pp. 173-192.

9. Watanabe, T., Analytical expression of hydrodynamic impact pressure by matched asymptotic expansion technique, *Trans. West-Japan Soc. Nav. Arch.*, No. 71, 1986, pp. 77-85.

10. Takemoto, H., Some considerations on water impact pressure, *J. Soc. Nav. Arch. Japan*, Vol. 156, 1984, pp. 314-322.

11. Yamamoto, Y., Ohtsubu, M., Kohno, Y., Water impact of wedge model, *J. Soc. Nav. Arch. Japan*, Vol. 155, 1984, pp. 236-245.

12. Faltinsen, O., Sea loads on ships and offshore structures, Cambridge University Press, 1990.

DISCUSSION

I. Watanabe
Ship Research Institute, Japan

The discussor would like to congratulate the authors on their achievement showing us a theoretical and still practical way of estimating slamming loads and subsequent ship motions of high-speed vessels. There is a short comment to be made. He would like to stress the importance of treating slamming phenomena in a three-dimensional way. You will get infinite pressure when the ship hull hits the water surface flat in a two-dimensional sense. This difficulty can only be avoided by treating the problem in a three-dimensional way or taking longitudinal flow components into account.

Ref. I. Watanabe, 16th Symposium on Naval Hydrodynamics, Berkeley, 1986.

AUTHOR'S REPLY

I agree with Dr. Watanabe's comment about three-dimensional effect in the slamming problem. In our formulation, the pressure will be infinite when the deck hits the water surface, but the integrated force is finite. I should also mention that the air cushion effect is important here.

Computations of Fully-Nonlinear Three-Dimensional Water Waves

H. Xü, D. Yue (Massachusetts Institute of Technology, USA)

Abstract

We extend and generalize the mixed-Eulerian-Lagrangian approach for nonlinear wave-body interactions to full three dimensions. A key to the success of this extension is our development of an efficient and robust high-order boundary-element method based on bi-quadratic curvilinear elements. Extensive convergence tests are performed to validate the accuracy and efficacy of the method.

Our first application of this new capability is the investigation of the kinematics of three-dimensional deep-water plunging breaking waves. To generate such waves, we begin with a plane progressive Stokes wave (wavelength L) and apply a three-dimensional surface pressure (transverse wavelength B) to raise its energy beyond the maximum for a steady Stokes wave. It is found that the resulting kinematics differ *qualitatively* depending on the value of the three-dimensionality parameter $\gamma=B/L$. One of the advantages of the present direct simulation is that entire fields of quantities such as velocity and acceleration can be obtained. Of particular interest is our identification of regions of negative surface normal accelerations in the late stages of wave overturning which are precursors to breakdown of the free surface following a Taylor instability.

Extensions to include finite water depth and boundary walls are completed. With further developments to model also the presence of a moving body, the ultimate capability for the simulation of general three-dimensional fully-nonlinear wave-body interactions can be anticipated.

1 Introduction

Steep, even overturning, three-dimensional (3D) waves are ubiquitous in the ocean environment. The understanding and modelling of steep waves and their interactions are fundamental to free-surface hydrodynamics and ocean engineering applications.

In two dimensions (2D), computational capabilities based on the mixed-Eulerian-Lagrangian (MEL) approach are, since the seminal work of Longuet-Higgins & Cokelet (1976) and Faltinsen (1977), now well established. There are now a fairly large number of 2D MEL results. Notable among these (citing only representative work) are Vinje & Brevig (1981) who developed a Cauchy-integral formulation, and Baker *et al* (1982) who put forward a generalized vortex method, both leading to purely second-kind boundary-integral equations (BIE's); Lin (1984), who addressed the free-surface and body intersection problem; Dold & Peregrine (1986) who developed Taylor methods for time integration; Dommermuth & Yue (1987), who extended MEL to axisymmetric 3D problems including a far-field matching; Dommermuth *et al* (1988), who performed a quantitative comparison to breaking wave experiments; and Cointe (1989), who made a useful and practical numerical wave tank.

Despite these advances in 2D, reliable results for truly nonlinear problems in 3D are still rare. Simulations to date have not been completely successful primarily because of limitations on accuracy/resolution which also affect stability, and computational efficiency and power. One of the

earlier examples is Isaacson (1982), who used an Eulerian formulation but was able to obtain results which are only qualitative and limited to short time and small steepness. Romate (1989) treated the 3D problem using MEL and higher order panels. Again his results were very limited and affected by spurious wave modes possibly resulting from difficulties at free surface and wall intersections. Recently, Yang *et al* (1989) performed 3D MEL wave-body simulations using only coarse discretizations, and the results are likely to be only qualitatively correct. The general realization now is that the road from qualitative to *quantitative* 3D predictions is longer and more arduous then once thought. The impediments to 3D progress, then, in some sense, are largely computational in nature — algorithm innovations and developments are critical, but true success would be difficult without the parallel advances in computer capabilities (see §5).

In this work, we extend boundary-element method (BEM) MEL approach to fully-nonlinear wave-body problems in 3D. The BEM is formulated directly via Green's identity leading to mixed first- and second-kind BIE's. We start with the necessary requirements of overall accuracy and efficiency, and robust and reliable treatment especially at free-surface and body intersections. After extensive evaluation, a quadratic-boundary element method (QBEM) based on bi-quadratic isoparametric curvilinear quadralateral (and triangular) elements is selected and developed. Even for mixed Dirichlet/Neumann boundary conditions with general intersections, QBEM achieves cubic minimax convergence with element size. For the solution of the resulting algebraic system we adopt a GMRES iterative scheme with a SSOR preconditioner. These are presented in §§3 and 4.

To demonstrate the usefulness of the code, extensive validations and convergence tests are performed. Although a number of other results have been obtained, we focus in §4 on the study of the kinematics of 3D deep-water overturning waves. Computational time estimates and potential usefulness of this code for more general applications are discussed in §5.

2 Mathematical Formulation

We consider the ideal, irrotational flow of a fluid bounded by a free surface. An orthogonal reference frame $\vec{x}$ fixed on the earth is chosen with its origin at the undisturbed water level, x and y being the two horizontal directions, and z the vertical direction, positive upward. All variables are nondimensionalized such that the density of water ρ and acceleration due to gravity g are both unity.

2.1 The initial boundary value problem (IBVP)

The flow is described by a harmonic velocity potential $\phi(\vec{x},t)$. The governing equation for continuity is the Laplace equation,

$$\nabla^2\phi(\vec{x},t) = 0, \qquad \vec{x} \in V, \tag{1}$$

where V is the (simply-connected) fluid domain, not necessarily bounded. On prescribed impervious boundaries $S_B(t)$, we require

$$\phi_n \equiv \frac{\partial\phi}{\partial n} = U_n, \qquad \text{prescribed.} \tag{2}$$

On the free surface $S_F(t)$, Bernoulli's equation gives the dynamic boundary condition,

$$\frac{D\phi}{Dt} = \frac{1}{2}|\nabla\phi|^2 - z - P_F, \qquad \vec{x} \in S_F, \tag{3}$$

where $D/Dt = \partial/\partial t + \nabla\phi\cdot\nabla$ is the material derivative following a Lagrangian particle, and P_F is the surface pressure distribution. The kinematic boundary condition is

$$\frac{D\vec{x}}{Dt} = \nabla\phi, \qquad \vec{x} \in S_F, \tag{4}$$

which prescribes the kinematical evolution of the free surface $S_F(t)$. For deep water, the appropriate far-field condition is:

$$\nabla\phi(\vec{x}) \to 0 \qquad \text{as } z \to -\infty, \tag{5}$$

for all times.

The IBVP is complete with the specification of the initial body $S_B(0)$, the free surface $S_F(0)$ and the potential on it $\phi(\vec{x} \in S_F, 0)$.

Applying Green's theorem, we obtain a useful auxiliary condition that the boundary values of

ϕ_n must satisfy the compatibility (Gauss) condition

$$\iint_{\partial V} \phi_n(\vec{x},t)dS = 0, \qquad (6)$$

where $\partial V \equiv S_B \cup S_F$.

2.2 The mixed Eulerian Lagrangian (MEL) approach

The elliptic field equation allows the specification of the entire problem in terms of values on the boundary only. This lends itself to the MEL (Longuet-Higgins & Cokelet 1976) approach via a boundary-integral equation (BIE) formulation. This solution procedure involves two main steps:

1. Given $S_B(t)$, $\phi_n(\vec{x} \in S_B, t)$, $S_F(t)$ and $\phi(\vec{x} \in S_F, t)$, solve the boundary-value problem (BVP) for $\phi_n(\vec{x} \in S_F, t)$, and in particular obtain the velocity $\nabla\phi(\vec{x} \in S_F, t)$.
2. Integrate the dynamic and kinematic free-surface boundary conditions (3) and (4) for $S_F(t+\Delta t)$ and $\phi(\vec{x} \in S_F(t+\Delta t), t+\Delta)$. Repeat the process.

The key to the success of BIE MEL, especially for three-dimensional problems, is the efficient and accurate solution to Step 1, which dominates the computational complexity and effort.

2.3 BIE reformulation of the BVP

We introduce the free-space Green function, $G(\vec{x},\vec{\xi})=r^{-1}$, where $r^2 \equiv |\vec{x}-\vec{\xi}|^2=(x-\xi)^2+(y-\eta)^2+(z-\zeta)^2$. Applying Green's second identity to ϕ and G and taking the limit $\vec{x} \to \partial V$, we obtain the requisite BIE:

$$\alpha(\vec{x})\phi(\vec{x}) + \iint_{\partial V} [\phi(\vec{\xi})G_n(\vec{x},\vec{\xi}) - \phi_n(\vec{\xi})G(\vec{x},\vec{\xi})]dS(\vec{\xi}) = 0, \quad (7)$$

for $\vec{x} \in \partial V$, where the finite part of the singular integral is assumed here and hereafter, and $\alpha(\vec{x})$ is the interior solid angle at $\vec{x}$. For $\vec{x} \in (S_B, S_F)$, the (Neumann,Dirichlet) boundary condition is applied, and (7) is a Fredholm integral equation of the (second,first) kind. A convenient way to evaluate the interior solid angle α in (7) is to observe that (Brebbia *et al*, 1984) for a constant ϕ, (7) reduces to

$$\alpha(\vec{x}) = -\iint_{\partial V} G_n(\vec{x},\vec{\xi})dS(\vec{\xi}). \qquad (8)$$

2.4 Doubly periodic boundary conditions

For many problems, such as the study of 3D overturning waves in nature, it is useful and computationally attractive to impose doubly periodic boundary conditions in both horizontal dimensions. Although it is possible to impose these conditions on (vertical) boundary surfaces, the BIE domain can be greatly reduced by introducing the (free-space) doubly periodic Green function G^p which satisfies:

$$G^p(x-\xi, y-\eta, z-\zeta) = G^p(x+mL-\xi, y+nB-\eta, z-\zeta), \qquad (9)$$

for any integer m, n and periodic domain of dimensions L by B. The BIE (7) can now be reduced to one on S_F only for deep water (plus its image for constant finite depth).

It is important to point out that the far-field behavior of G^p is in general that of a uniform current:

$$G^p = C_\infty |z| + o(1) \qquad \text{as } |z| \to \infty, \qquad (10)$$

where C_∞ is a finite constant. Since G^p does not satisfy the far-field condition (5), the contribution of the integral in (7) over $S_\infty : \{z \to -\infty\}$ must be accounted for. From (5), the non-trivial contribution is from the dipole distribution, where with $\phi \to$constant(t) on S_∞, evaluates to:

$$\iint_{S_\infty} \phi G^p_n dS = C_f(t). \qquad (11)$$

C_f is a nontrivial constant to be determined as part of the BIE solution (from the Gauss condition (6), for example).

Computationally, G^p can be evaluated as a doubly-infinite sum of image sources for which very efficient summation formulas are now available (Breit 1991; Newman 1991).

3 Numerical Method

3.1 The quadratic boundary element method (QBEM)

As pointed out earlier, the success of MEL depends critically on the efficacy of the BIE solver. As part of this research, a range of direct boundary-element methods (BEM's) has been evaluated and compared. These methods differ primarily on the order of approximation of the element (or panel) geometry and ϕ, ϕ_n distributions, and the choice of the collocation point on the element.

One of the simplest choices is the so-called constant-panel method (CPM) (Hess & Smith 1964) which uses (piecewise) plane geometry, constant singularity variations, and centroid collocations. Fig. 1 shows the convergence of CPM for a body with continuous surface normal for an exterior Neumann problem (results for Dirichlet boundary conditions are similar). As expected, the average error decreases approximately quadratically with panel size $\Delta\ell$, while the maximum error is slightly greater. For mixed Dirichlet/Neumann boundary conditions for the sphere, the convergence rate (fig. 2) is appreciably degraded and more so for the maximum error. It should be pointed out that for MEL simulations, the maximum rather than the average is the relevant error measure.

For problems involving mixed Dirichlet/Neumann boundaries with discontinuous slopes at intersection lines (say along $C=S_B \cap S_F$), CPM (using constant panel sizes) fails to converge even for an imposed smooth harmonic solution. This is shown in fig. 3. For a *known* continuous potential, it is possible, in principle, to rendered the solution convergent using variable panel sizes. For general time-dependent problems, however, the solution near the intersection is not known *a priori*, and CPM is likely to be inadequate. The problem is more severe for actual free-surface and body intersection lines, C, where it is known that the solution may be (weakly) singular.

One effective way to avoid the difficulty at the intersection line is to place collocation points on C and specify *both* Neumann and Dirichlet conditions at these 'double' points (*cf.* Lin, *et al* 1984;

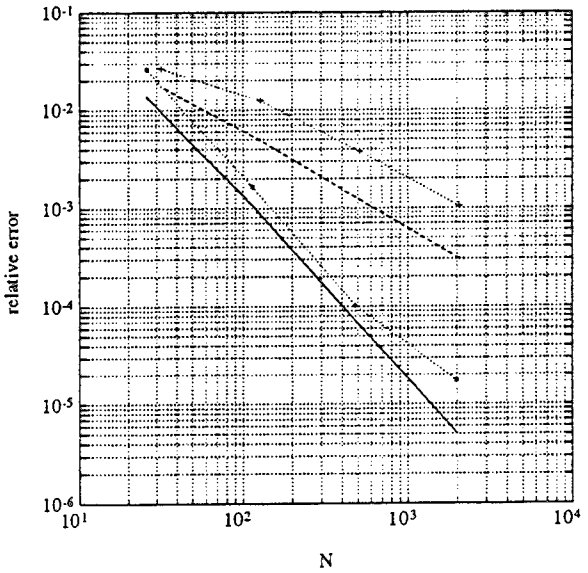

Figure 1: Convergence with the total number of nodes N, for the exterior Neumann problem for (uniform) flow past a sphere. Normalized errors for QBEM —— : average and · · * · · : maximum ; CPM - - - : average and · · + · · : maximum.

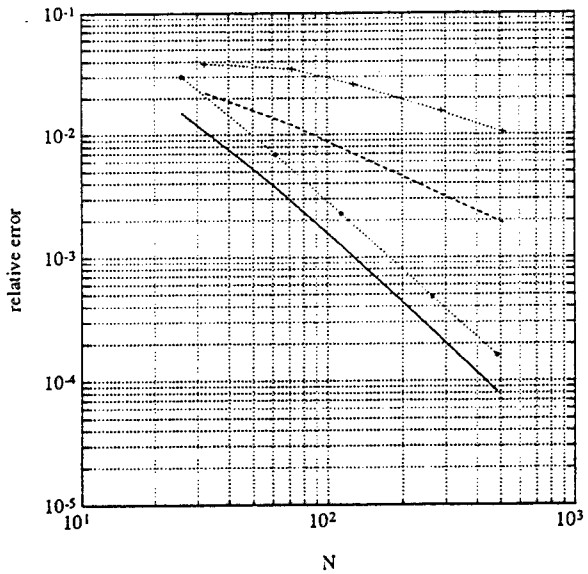

Figure 2: Convergence with the total number of nodes N, for the exterior mixed Dirichlet/Neumann problem for (uniform) flow past a sphere. Normalized errors for QBEM —— : average and · · * · · : maximum; CPM - - - : average and · · + · · : maximum.

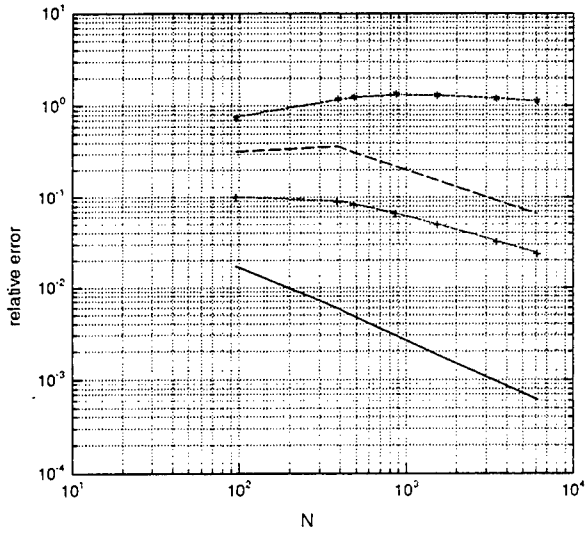

Figure 3: CPM normalized errors as functions of N for the exterior mixed Dirichlet/Neumann problem for a smooth harmonic solution on a cube. —— : average and · · + · · : maximum (Neumann boundary); - - - : average and · · ∗ · · : maximum (Dirichlet boundary).

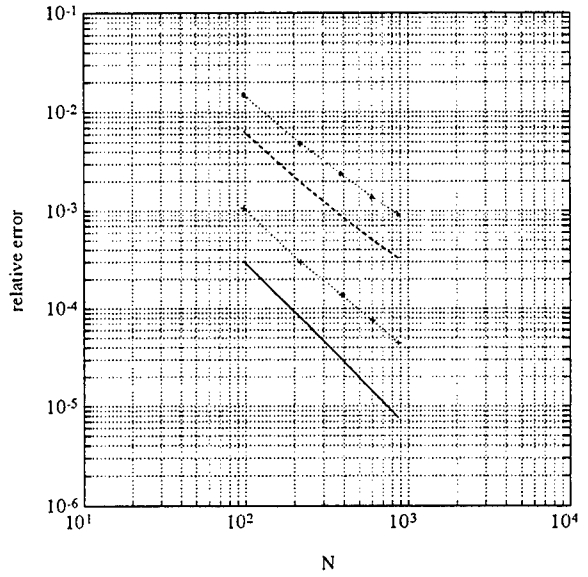

Figure 4: Convergence with the total number of nodes N of QBEM for an interior mixed Dirichlet/Neumann problem for a smooth harmonic solution on a cube. Normalized errors: —— : average, · · + · · : maximum (Neumann boundary); - - - : average, · · ∗ · · : maximum (Dirichlet boundary).

Dommermuth & Yue 1987). One immediate consequence of this is the need for higher order panels — at least linear in the singularity distributions, and, for uniquely defined normals and nodal ϕ_n, geometric approximations with continuous slopes at panel intersections.

After a systematic study of higher order panels including super-parametric elements (geometry based on bi-cubic splines with lower order singularity distributions), we finally decide on a bi-quadratic isoparametric boundary-element method (QBEM) using 9-node curvilinear quadralaterals and 7-node (degenerate) curvilinear triangles. Details of the QBEM implementation including regularization using triangular mapping, adaptive quadrature algorithms and far-field influence integration using multipole expansions can be found in Xü (1992).

Figs. 1, 2 show also the performance of QBEM for respectively the exterior Neumann and mixed Dirichlet/Neumann problem for a sphere. QBEM achieves approximately cubic convergence with panel size for both cases.

Finally, we show the performance of QBEM for the (continuous) solution for a mixed Dirichlet/Neumann problem inside a cube (fig. 4). Difficulties associated with the intersection edges are effectively removed with no appreciable degradation in the convergence rate.

In general, the computational effort for solving the BIE is proportional to N^2, say, CPU$\sim \beta N^2$. Significantly, with proper attention to efficiency and accuracy of the QBEM implementation (Xü 1992), β for QBEM is less than twice that of CPM (both using fully vectorized codes on vector computers). Thus, for a typical required minimax error of 10^{-3}, say, we have from fig. 1, $N \approx 150$ and 2000 respectively for QBEM and CPM, so that QBEM is some two orders of magnitude more efficient than CPM even for the (most favorable to CPM) case of a pure Neumann problem on a smooth boundary.

3.2 Solution of the BIE algebraic equations

The linear algebraic system resulting from the discretization of (7) is in general dense, non-symmetric and, because of the first-kind equa-

tions on S_F, not strongly diagonally dominant. For small numbers of unknowns N, the computational burden is dominated by the evaluation of the BEM influence coefficients (an $\mathcal{O}(N^2)$ effort), so that many existing MEL simulations in 2D (and axisymmetric 3D) simply solve the linear system directly via Gauss elimination (an $\mathcal{O}(N^3)$ effort). For 3D problems, N can be several orders of magnitude greater, and any algorithm requiring $\mathcal{O}(N^3)$ operations is prohibitive.

In this work, we test and demonstrate the efficacy of the generalized minimum residual (GMRES) algorithm (Saad & Schultz 1986) for 2D and 3D MEL BEM. Unlike conjugate gradient methods for symmetric matrices whose convergence rate can be defined in terms of the condition number of the matrix, the corresponding condition for GMRES is not precisely defined, but is given in practice by the *pseudo-eigenvalues* of the matrix (Trefethen 1990).

Fig. 5 summarizes the results of numerical experiments for mixed Dirichlet/Neumann boundary condition matrices using Green's identity (*cf.* (7)). For comparison, results for matrices resulting from completely second-kind equations using Cauchy-integral formulation (Vinje & Brevig 1981) in 2D are also shown. For N up to $\mathcal{O}(10^4)$, the number of iterations (for a tolerance of 10^{-7}) required is approximately given by $N_{it} \approx a_0 N^{1/3}$. For $N > \mathcal{O}(10^3)$, there appears to be an stalling trend for N_{it}.

The next step is to see whether the GMRES iteration can be accelerated by suitable preconditioning of the linear system. Our computational experience indicates that even simplistic preconditioners result in substantial reduction in the number of iterations required. Consider the matrix equation $Ax = b$, a preconditioner is a scaling matrix P, such that the modified equation $P^{-1}Ax = P^{-1}b$ converges more rapidly for the iteration scheme in question.

Two simple preconditioning matrices are tested: (i) diagonal preconditioner (Golub & Van Loan 1989), where $P = D$ (we write in general $A = L + D + U$, where L, D, U are respectively the lower-, diagonal and upper-submatrices of A); and (ii) symmetric successive overrelaxation (SSOR) preconditioner, where $P = (I + \omega L)D^{-1}(I + \omega U)$. The relaxation parameter $\omega \in [0, 1]$ is selected

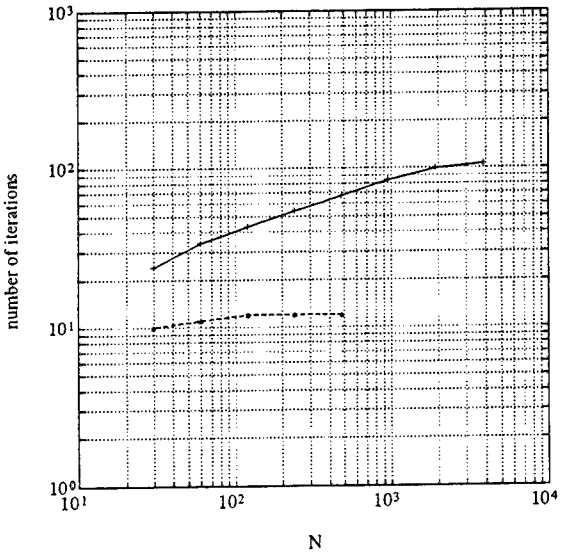

Figure 5: Convergence of MEL matrix solutions using GMRES (tolerance 10^{-7}, no preconditioning). Mixed first- and second-kind BIE's using Green's identity: — + —; purely first-kind equations using Cauchy-integral formulation: · · ∗ · ·.

based on numerical trials. For the present problem, GMRES iterations are reduced by approximately a factor of two ($a_d \approx a_0/2$) using diagonal preconditioner and approximately a factor of five ($a_s \approx a_0/5$) using a SSOR preconditioner ($\omega = 0.5$). Based on these results, we choose GMRES with SSOR preconditioning ($\omega = 0.5$) as our solver for the QBEM linear equation systems.

3.3 Time integration & invariants

Once the BVP at each time is solved and the velocity $\nabla\phi$ on S_F obtained, the free-surface boundary conditions (3), (4) can be integrated in time in a straightforward manner. We adopt a fourth-order Adams-Bashforth-Moulton (ABM4) integrator coupled with a fourth-order Runge-Kutta (RK4) scheme for (re)starting (whenever there is a change in time step size). ABM4 and RK4 require respectively two and four solutions of the BVP per time step.

From (3), we can derive a simple Courant condition for the time step size:

$$\pi \Delta t \parallel \nabla\phi \parallel_F \leq \Delta\ell, \tag{12}$$

where $\| \nabla\phi \|_F$ is the maximum velocity on S_F. This is a necessary condition for stability regardless of the integration scheme. In practice, (12) provides the criterion for dynamic time step control. Since $\Delta\ell$ is in general not constant following Lagrangian points, we adopt the time step formula

$$\pi\Delta t \| \nabla\phi \|_F \leq C_n \Delta\ell_{min}, \qquad (13)$$

where $\Delta\ell_{min}$ is the minimum $\Delta\ell$ on S_F and the Courant constant C_n is a computational parameter to be chosen.

A number of integration invariants can be used to check the global accuracy of the numerical scheme. From mass conservation, we have the Gauss condition (6), which for periodic or fixed-body boundaries, must be valid for S_F alone. Alternatively, we can define the mean water level which must be invariant:

$$S_{F0}\bar{z} = \iint_{S_F} z n_z dS = \text{constant}, \qquad (14)$$

where S_{F0} is the projection of S_F on z=0. In the absence of work done by body boundaries, we require for energy conservation

$$\iint_{S_F} P_F \phi_n dS = \frac{d}{dt}(E_k + E_p)$$
$$= \frac{d}{dt}\left[\frac{1}{2}\iint_{\partial V} \phi\phi_n dS + \frac{1}{2}\iint_{S_F} z^2 n_z dS\right], \qquad (15)$$

where E_k, E_p are respectively the kinetic and potential energies. These mass and energy invariants are evaluated and monitored to typically within 0.5% for all the 3D simulations in §4.

3.4 Removal of saw-tooth instabilities

In numerical studies using MEL where (artificial) damping or filtering is absent, saw-tooth instabilities eventually develop on the free surface as nonlinearity increases. Despite remaining questions regarding their generation and removal, the *inevitable* presence of saw-tooth instabilities can be expected in theory since for any nonlinear system without dissipation, energy cascades from lower to higher wavenumbers and eventually 'accumulates' at the highest wavenumber associated with the discretization.

In the present 3D simulations, saw-tooth instabilities are observed usually near the wave crests even for steep (non-overturning) Stokes waves. To remove these instabilities, we consider 5-point least-square, as well as 5- and 7-point Chebyshev smoothing filters. From numerical tests, and by analysing their wavenumber transfer functions, the optimal scheme appears to be the 5-point Chebyshev formula. This is adopted and applied every N_s (N_s typically 3 or 6) steps.

3.5 Select convergence results

The 3D QBEM MEL code has been tested extensively for accuracy and convergence against exact (longitudinal and oblique) Stokes waves, and existing 2D MEL fully-nonlinear results. For brevity, only select results are given here. More extensive validations can be found in Xü (1992).

First, to test the QBEM BVP solver, we input an exact Stokes wave (Schwartz 1974) profile and surface potential and solve for the surface velocity. Table 1 shows the convergence of QBEM for waves up to near limiting Stokes steepness. Time simulation of such waves for a number of periods varying N_w, C_n and N_s validates the remaining part of MEL and details are omitted. The fractional loss of energy associated with each application of Chebyshev smoothing is typically less than $\mathcal{O}(10^{-4})$.

As a more stringent test, we apply the general 3D MEL program to the relatively well-studied problem of 2D deep-water overturning waves. Following Longuet-Higgins & Cokelet (1976) we apply an asymmetric surface pressure for a short time to a 2D progressive Stokes wave with wavelength L=2π (this defines the length scale) and steepness ϵ=0.4. The fundamental period of this wave is $T_0 \cong 5.806$. The surface pressure distribution is given by

$$P_F = p_0 \sin t \sin(x - ct) \qquad 0 \leq t \leq \pi, \qquad (16)$$

and $P_F = 0$ for $t > \pi$. Here, $c = 2\pi/T_0$ is the

ϵ	N_w	u		w		ϕ_n	
		$\bar{e}$	e_{max}	$\bar{e}$	e_{max}	$\bar{e}$	e_{max}
0.1	8	0.00504	0.01301	0.00516	0.01282	0.00539	0.01348
	16	0.00020	0.00060	0.00134	0.00589	0.00136	0.00593
	32	0.00002	0.00009	0.00033	0.00122	0.00033	0.00121
	64	0.00000	0.00002	0.00009	0.00031	0.00009	0.00031
0.2	8	0.00954	0.02169	0.00660	0.01953	0.00623	0.01891
	16	0.00099	0.00178	0.00205	0.00416	0.00203	0.00432
	32	0.00016	0.00063	0.00064	0.00170	0.00060	0.00162
	64	0.00003	0.00009	0.00017	0.00043	0.00016	0.00041
0.3	8	0.02293	0.05299	0.00578	0.01395	0.00591	0.01602
	16	0.00060	0.00173	0.00288	0.00499	0.00256	0.00512
	32	0.00020	0.00071	0.00065	0.00145	0.00061	0.00148
	64	0.00003	0.00013	0.00027	0.00098	0.00025	0.00089
0.4	8	0.02463	0.05460	0.01165	0.02547	0.01294	0.04134
	16	0.00271	0.00914	0.00581	0.02914	0.00560	0.02453
	32	0.00027	0.00094	0.00126	0.00640	0.00090	0.00503
	64	0.00010	0.00045	0.00055	0.00238	0.00046	0.00197

Table 1: Normalized average ($\bar{e}$) and maximum (e_{max}) errors in the horizontal (u), vertical (w) and normal (ϕ_n) velocities on the surface of a Stokes wave, steepness ϵ. The 3D QBEM solution uses a nonuniform grid with an average of N_w unknowns per wavelength.

phase speed of the Stokes wave, and we choose p_0=0.146 to correspond to the fourth case studied by Longuet-Higgins & Cokelet.

In order to study the convergence with respect to smoothing and temporal discretization, we select three different test cases listed in Table 2. The global invariants after wave overturning are convergent to at least 2 decimal places.

The corresponding wave profiles for the 3 cases (and times) in Table 2 are shown in fig. 6. The overall wave profiles match closely for the 3 cases. Locally, near the overturning jet, detail discrepancies are observable, although the maximum difference in the computed surface velocity is only ~1%.

Our initial condition and surface pressure here are the same as the fourth case studied by Longuet-Higgins & Cokelet (1976). We mention here two comparisons to their results. The height of the overturning wave crest in the present simulation is approximately 0.638 (not accounting for the mean water level). From fig. 11 of Longuet-Higgins & Cokelet, we read the overturning crest

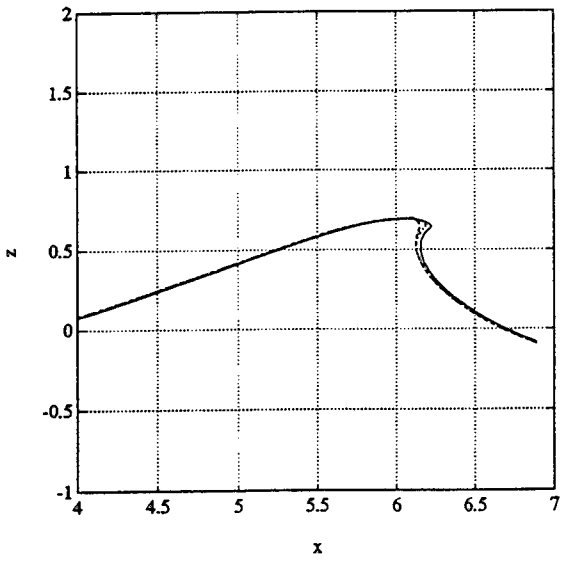

Figure 6: Comparison of overturning wave profiles for the 3 study cases in Table 2. Cases 1: - - -; 2: - - · - -; and 3: ——.

case	N_s	C_n/π	t	E_k	E_p	E_k+E_p	$\bar{z}$
1	6	0.6	4.7510	0.5600	0.3223	0.8822	0.0616
2	3	0.6	4.7506	0.5649	0.3252	0.8901	0.0627
3	3	0.4	4.7493	0.5659	0.3250	0.8909	0.0628

Table 2: Study cases for the convergence of a 2D deep-water overturning wave as a function of time-step control Courant number C_n, and frequency of 5-point Chebyshev smoothing N_s. Minimum and maximum time-step limits $10^{-3} \leq \Delta t/T_0 \leq 10^{-2}$ are imposed. The results are for a specified instant after wave overturning, $t \simeq 4.75$. The initial mean water level is $\bar{z} \simeq 0.0624$.

height at approximately 0.64, so that the discrepancy is less than $\mathcal{O}(1\%)$. The present result for the final total energy density (energy per surface area) is $E/E_{max} \cong 1.91$, where $E_{max}=0.07403$ is the maximum energy for a Stokes wave. This is again in good agreement with the final result of $E/E_{max} = 1.88$ obtained by Longuet-Higgins & Cokelet. Comparisons of the present 3D program to other available 2D MEL codes (*e.g.*, Dommermuth, Yue, *et al* 1988) for a variety of cases show similar quantitative agreement.

4 Numerical Results

Our ultimate goal is the simulation of fully-nonlinear 3D interactions of steep (even overturning) waves with a body undergoing large-amplitude motions. This capability is still some time away, and requires, among other developments, a robust geometry capability involving 3D surfaces and intersections. An immediate and useful application of the present capability is the investigation of the 3D kinematics of steep overturning waves — a problem of both basic scientific interest and practical engineering importance.

4.1 Kinematics of 3D deep-water overturning waves

We extend the 2D fully-nonlinear wave simulation of Longuet-Higgins & Cokelet (1976) and others to three dimensions. Following Longuet-Higgins & Cokelet, we start with a progressive two-dimensional Stokes wave but now apply a *three-dimensional* surface pressure distribution to raise the energy density beyond the maximum for a steady Stokes wave.

The parameters of the Stokes wave are wavelength $L=2\pi$ (this defines the length scale) and steepness $\epsilon=0.4$, which gives a fundamental period of $T_0 \cong 5.806$ and phase speed $c \cong 1.082$. For the imposed surface pressure, the temporal and longitudinal (x) dependences are identical to the 2D form (16) but with a periodic (cosine) transverse variation of wavelength B:

$$P_F = p_0(1+\cos 2\pi y/B)\sin t \sin(x-ct), \quad (17)$$

for $0 \leq t \leq \pi$, and $P_F = 0$ for $t > \pi$. Thus the co-propagating surface pressure is gradually increased from 0 at t=0 to its maximum at $t = \pi/2$ ($t/T_0 \cong 0.271$) and is gradually decreased to zero for $t \geq \pi$. Since (17) is symmetric with respect to y=0 and $\pm B/2$, the doubly-periodic solution (of wavelengths $L = 2\pi$ by B) must also satisfy no normal fluxes on $y_m = mB/2$ for $m=0, \pm 1, \pm 2, \ldots$. Thus the problem can be thought of as one in a wave tank with side walls at any two values of y_m, *i.e.*, a tank with a width which is a multiple of $B/2$. For definiteness, we refer hereinafter to y=0 where $P_F = 2p_0$ is maximum as the 'center', and $y = \pm B/2$ where $P_F = 0$ is minimum as the 'sides'. By selecting $p_0 = 0.073$, the pressure at the center plane has the same longitudinal distribution as the 2D one (16).

The three-dimensionality of the wave is specified by the aspect ratio $\gamma = B/L$. Simulations are performed for a range of γ values (γ=0.5, 1.0, 1.5). Based on convergence tests, we use 64 nodal points per wavelength in the x direction and 48 nodal points in the y direction. Using symmetry and doubly-periodic Green functions, the problem is described by a 65 × 25 grid (384 9-node quadratic elements) in half of the doubly periodic domain ($[0, L]\times[-B/2, 0]$), yielding a total of 1601

unknowns (including the additional unknown constant C_f associated with the far-field dipole integral). A dynamic time step control Courant number of $C_n = 0.6\pi$ is used initially which is reduced to 0.4π after the surface forcing is switched off. Five-point Chebyshev smoothing is applied every 3 time steps. Lagrangian free-surface points (initially distributed unevenly according to the curvature of the Stokes waves) are followed throughout without regridding.

Figs. 7, 8 show the surface profiles and particle velocity components, u, v, w, at times near the final stages of the 3D overturning waves for γ=1.5 ($t/T_0 \cong$0.844) and γ=0.5 ($t/T_0 \cong$and 0.904) respectively. The results for these two γ's are *qualitatively* different. In particular, the 3D wave plunging tip which occurs along the center line for γ=1.5 now develops at the side (where the forcing was minimum) for the narrower case of γ=0.5.

This apparently surprising result can in fact be explained by considering the wave sloshing in the 'tank'. According to linear theory, the sloshing period of the first-mode transverse wave disturbance due to the pressure forcing is given by

$$T_B/T_L = \left[1 + (L/B)^2\right]^{-1/4}, \qquad (18)$$

where T_L (=2π here) is the linear longitudinal period. This corresponds to $T_B/T_L \simeq 0.912$ and 0.669 for γ=1.5, 0.5 respectively. Assuming that this sloshing is established when the applied pressure is removed (at $t_1 = \pi$) (*cf.* figs. 9–14), the disturbance elevation will reach maximum amplitude at the side walls at $t_2 \simeq t_1 + T_B/2$=1.035T_0 and 0.903T_0 respectively. The computed plunging times (which depend in general on the nonlinear energy input and dynamics) are at $t/T_0 \simeq$0.844 and 0.904 respectively (corresponding to figs. 7 and 8). The former is much earlier than t_2 while the latter coincides with the arrival of the cross mode crest. This qualitatively explains the location of the 3D wave plunging especially for 'non-obvious' γ=0.5 case. In general, this location must depend on the period of the transverse dynamics and the time required for the development of the plunging wave. An obvious consequence is the fact that 3D breakers need not develop directly behind the region of maximum (surface or bottom) forcing.

The time development of the wave profiles and surface velocities are plotted in figs. 9, 10 and 11 for u, w and v respectively for the case γ=1.5. Figs. (c) correspond to the instant when the surface forcing is turned off. At this time, changes from the 2D Stokes wave are relatively small, but clear three-dimensional features of this 'initial' condition is evident. In particular, the greater wave elevation and magnitudes of u and w are all appreciably near the center. Eventually, the horizontal velocity on the centerline increases to almost three times its initial value and in the process plunges forward and overturns. In contrast, the magnitudes of the maximum and minimum vertical velocity change insignificantly as the plunging wave develops. A useful parameter to consider is the ratio of maximum u to maximum w as a function of time, $(u/w)_m$, which increases from an initial value of 1.4 to 3.5 at overturning. This indicates that the wave overturning is primarily a result of the longitudinal motion.

The relatively short time to breaking compared to the fundamental transverse oscillation period in this case does not allow significant energy transfer from the center to the sides. This is reflected in fig. 11 for the surface v. By virtue of symmetry, v vanishes at y=0,$\pm B/2$, and is only nonzero in between. This transverse velocity is positive (towards the plunger tip at the centerline) on the front face, and negative near and behind the wave crest. At the last time instant shown, the ratio of maximum u to v is $(u/v)_m$=20.1, so that v plays only a minor role in the dynamics in this case.

The corresponding results for γ=0.5 are given in figs. 12, 13 and 14. Because of the relatively short time of the forcing, the results at the 'initial' time near $t = \pi$ (figs. (b)) are, except for a narrower transverse scale, qualitatively quite similar to the wider tank case (γ=1.5). At this time, u_{max} and w_{max} are ~30% greater than those of the initial Stokes wave while w_{min} at the trough is almost unchanged. As the wave plunges on the side, the magnitude of u approximately triples while $(u/w)_m$ increases from 1.4 initially to 3.6 at wave breaking.

Comparing these figures with those for γ=1.5, we see that the *magnitudes* of the longitudinal and vertical velocity components are comparable. The locations of these maximum velocities and the surface profiles are, however, quite different. In contrast to the γ=1.5 evolution, the transverse energy

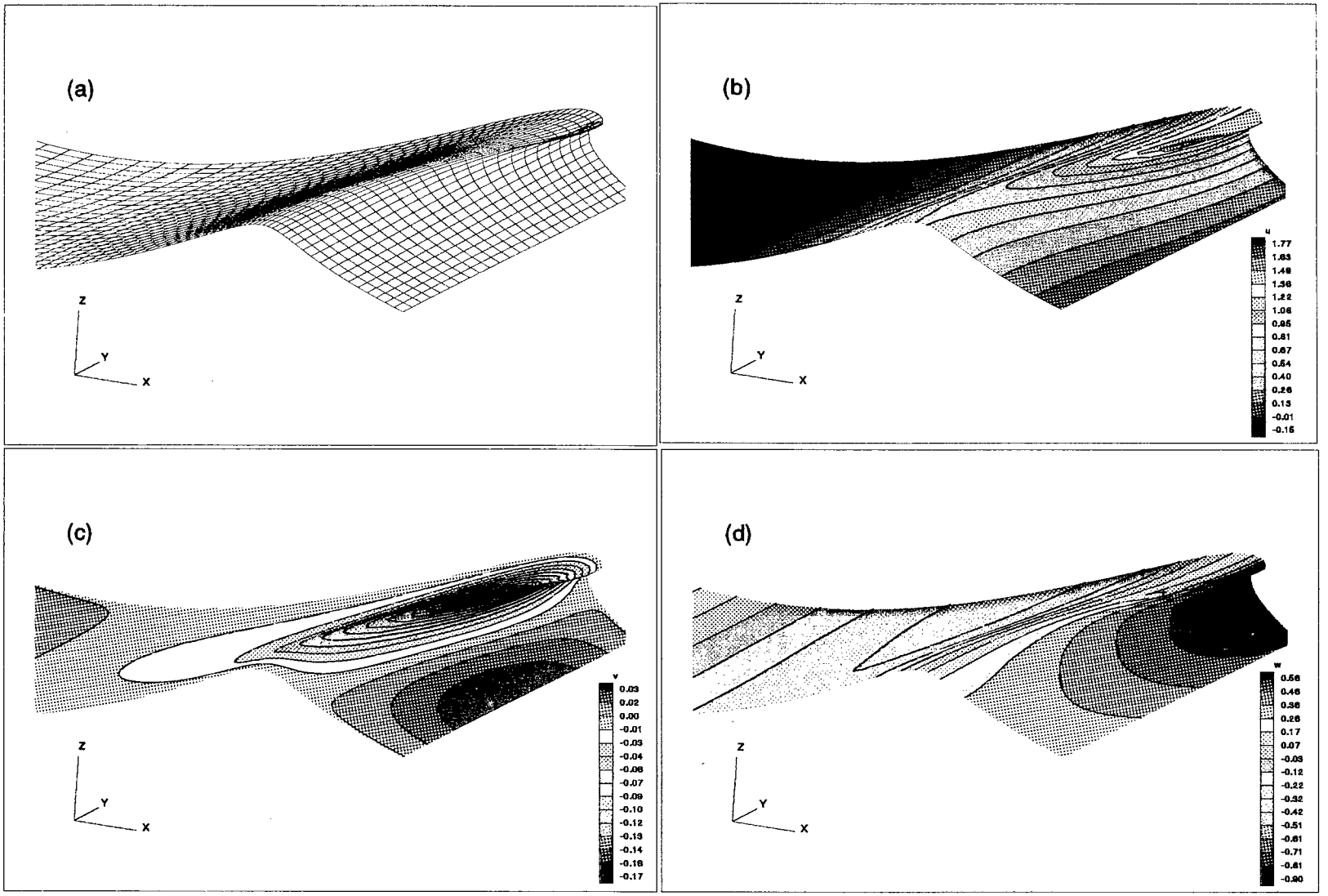

Figure 7: Surface profile (a) and velocity components (b) u, (c) v and (d) w of a 3D deep-water overturning wave for $\gamma = B/L$=1.5 at $t/T_0 \simeq$0.844. Only half of the symmetric transverse domain between the 'center' y=0 (further from the observer) and 'side' $-B/2$ (nearer the observer) and a longitudinal close-up near the crest is shown.

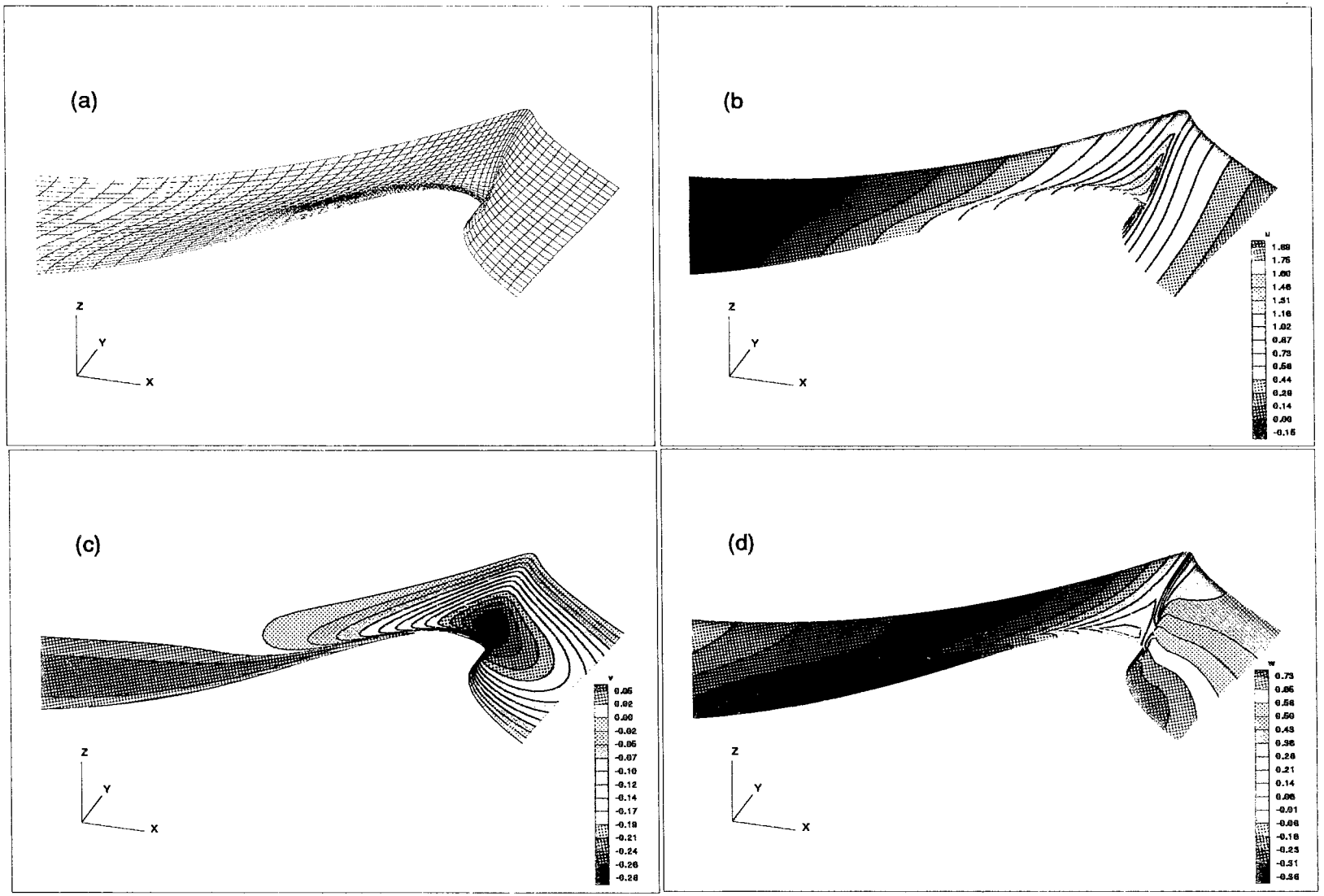

Figure 8: Surface profile (a) and velocity components (b) u, (c) v and (d) w of a 3D deep-water overturning wave for $\gamma = B/L$=0.5 at $t/T_0 \simeq$0.904. Only half of the symmetric transverse domain between the 'center' y=0 (further from the observer) and 'side' $-B/2$ (nearer the observer) and a longitudinal close-up near the crest is shown.

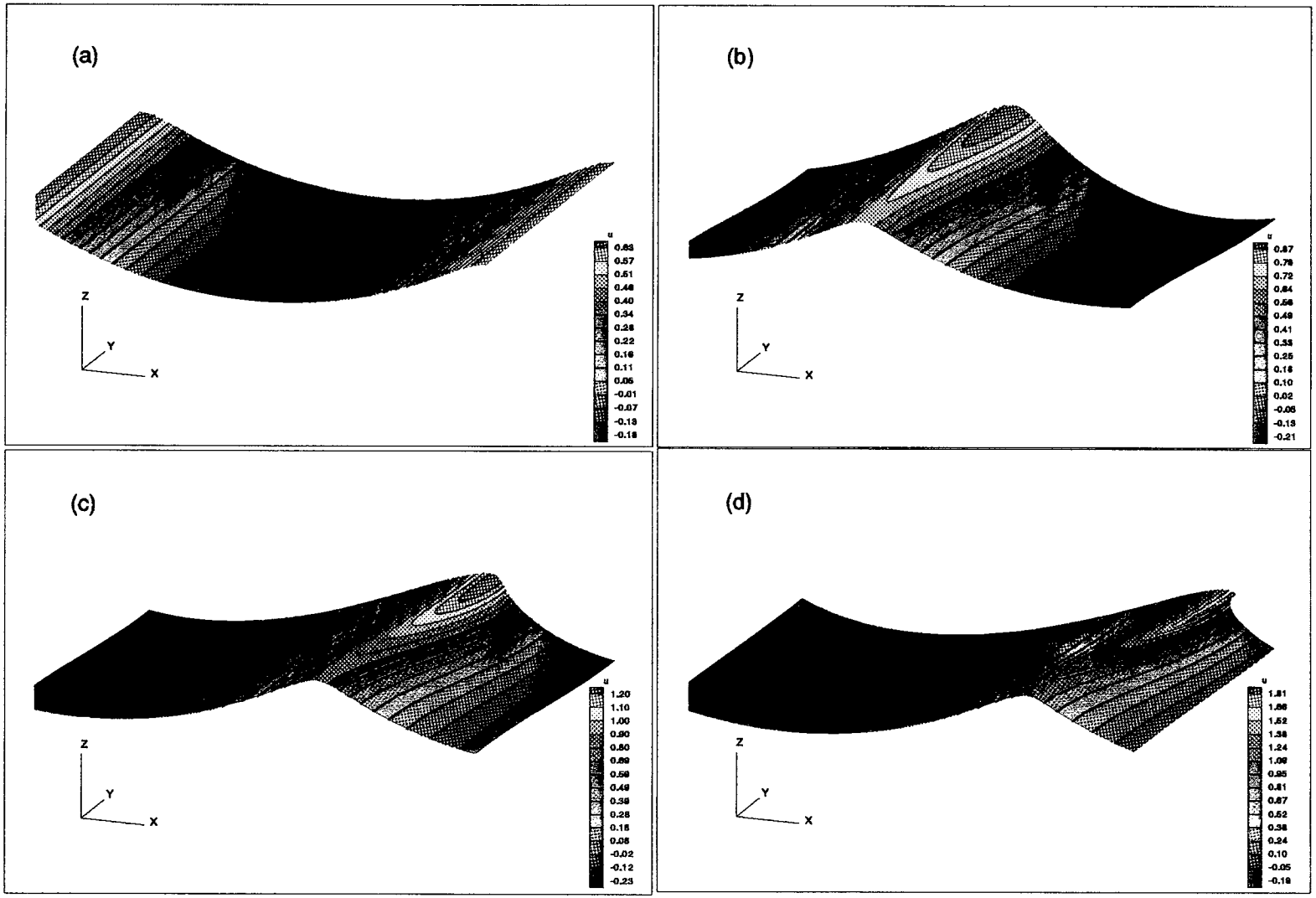

Figure 9: Surface longitudinal velocity u of a 3D deep-water overturning wave, γ=1.5, at t= (a) 0; (b) 3.1568; (c) 4.2521; (d) 4.8166. Only half of the symmetric transverse domain between the 'center' y=0 (further from the observer) and 'side' $-B/2$ (nearer the observer) is shown.

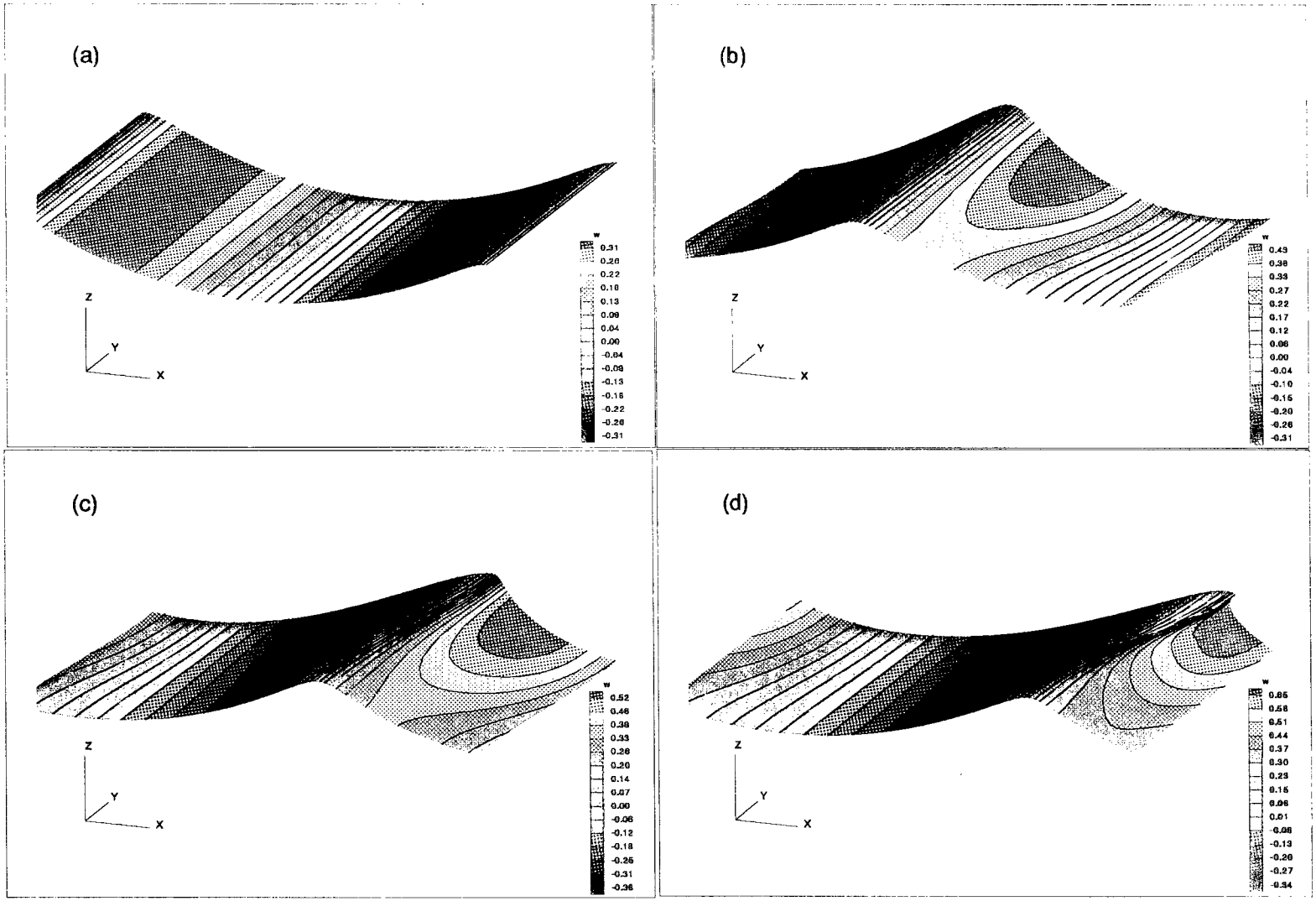

Figure 10: Surface vertical velocity w of a 3D deep-water overturning wave, γ=1.5, at t= (a) 0; (b) 3.1568; (c) 4.2521; (d) 4.8166. Only half of the symmetric transverse domain between the 'center' y=0 (further from the observer) and 'side' $-B/2$ (nearer the observer) is shown.

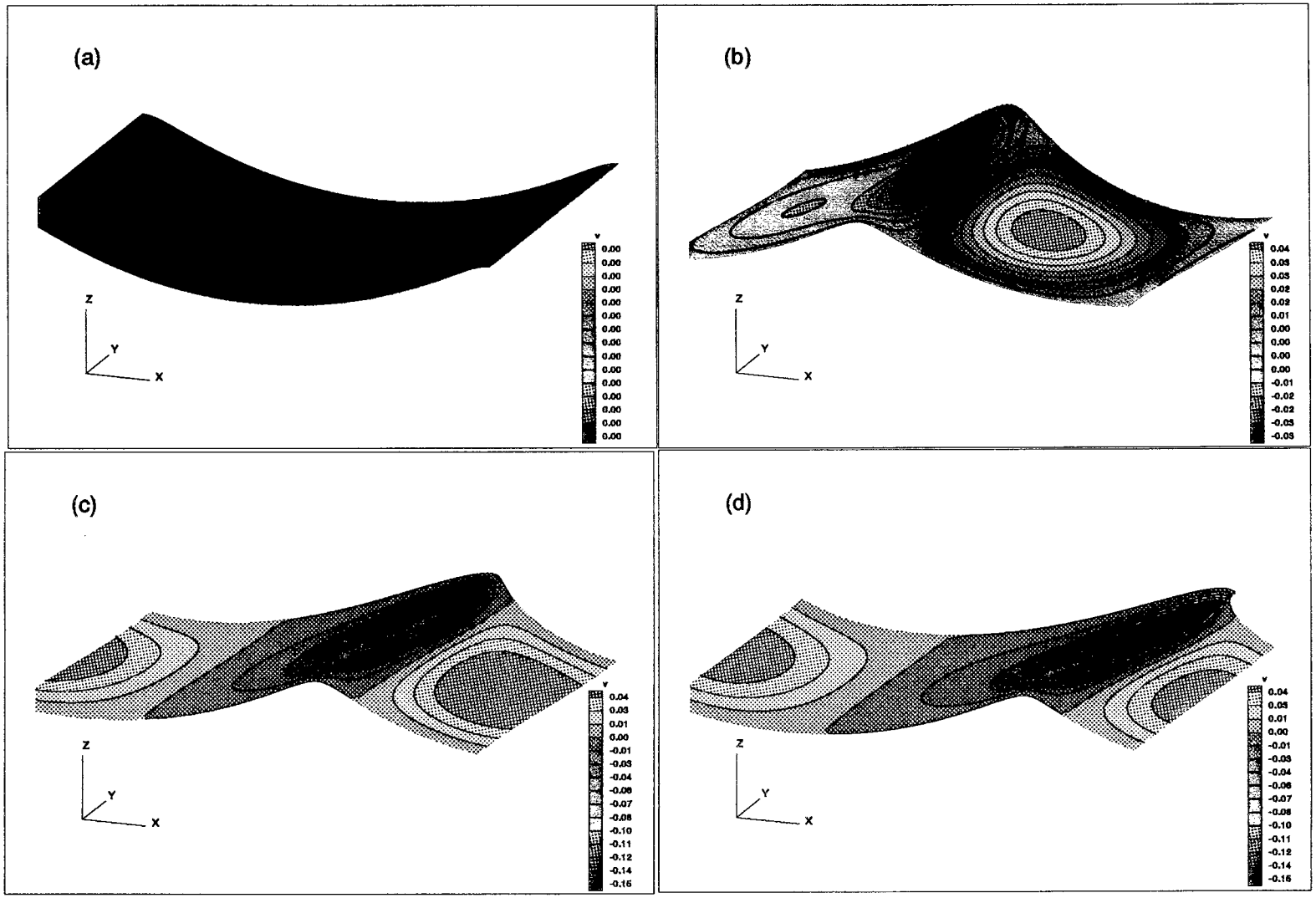

Figure 11: Surface transverse velocity v of a 3D deep-water overturning wave, γ=1.5, at t= (a) 0; (b) 3.1568; (c) 4.2521; (d) 4.8166. Only half of the symmetric transverse domain between the 'center' y=0 (further from the observer) and 'side' $-B/2$ (nearer the observer) is shown.

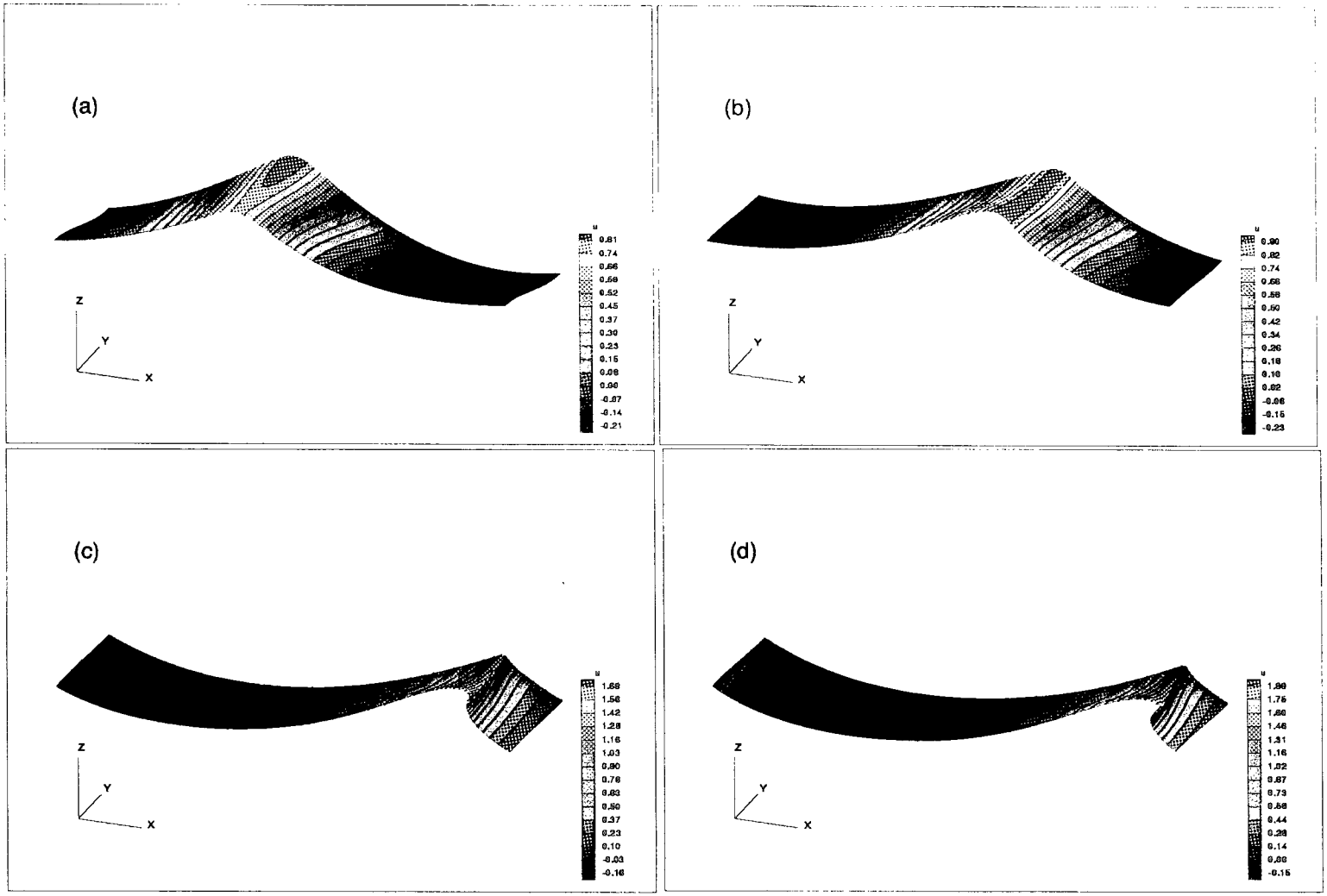

Figure 12: Surface longitudinal velocity u of a 3D deep-water overturning wave, γ=0.5, at t= (a) 3.0136; (b) 39900; (c) 5.0039; (d) 5.2009. Only half of the symmetric transverse domain between the 'center' y=0 (further from the observer) and 'side' $-B/2$ (nearer the observer) is shown.

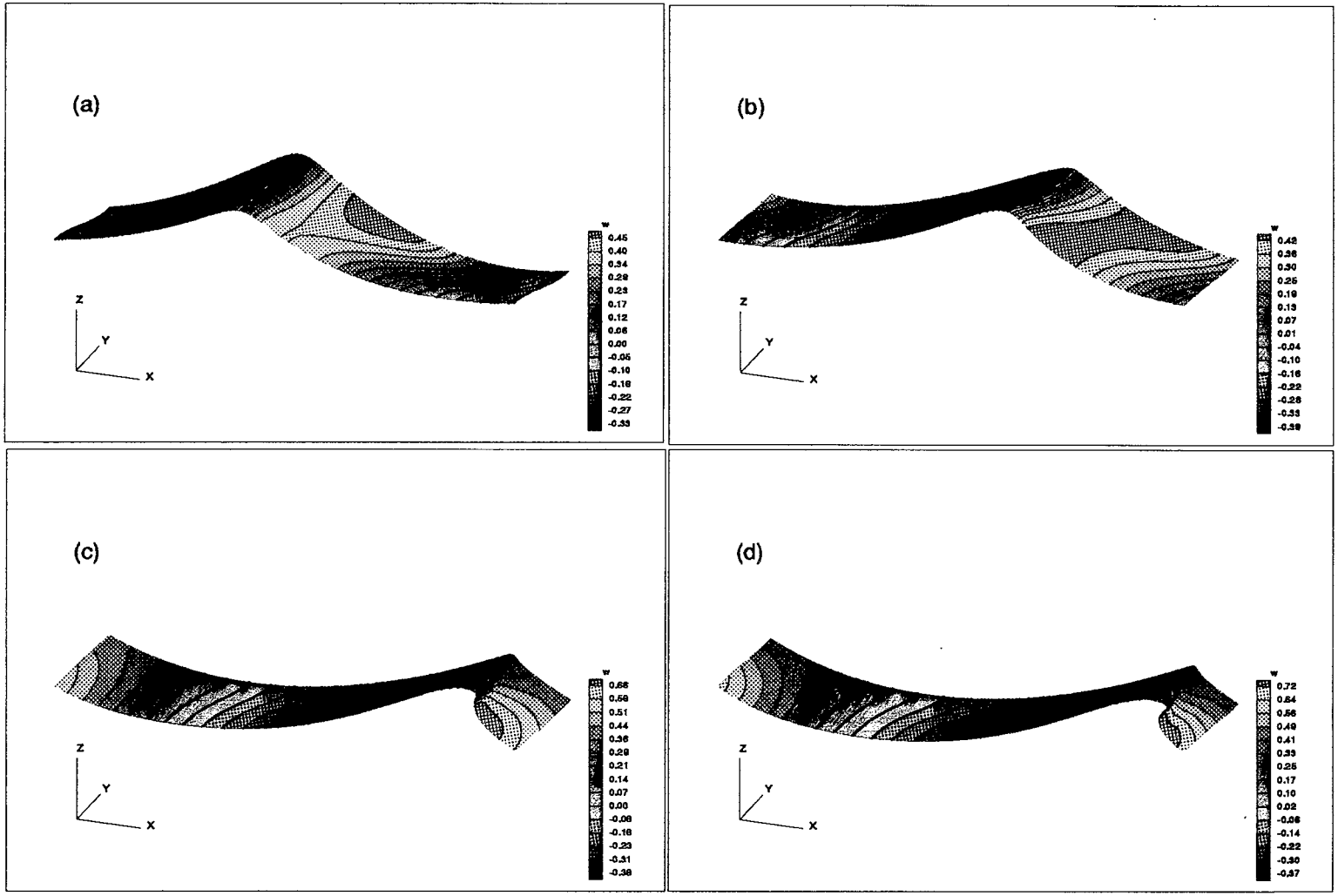

Figure 13: Surface vertical velocity w of a 3D deep-water overturning wave, γ=0.5, at t= (a) 3.0136; (b) 39900; (c) 5.0039; (d) 5.2009. Only half of the symmetric transverse domain between the 'center' y=0 (further from the observer) and 'side' $-B/2$ (nearer the observer) is shown.

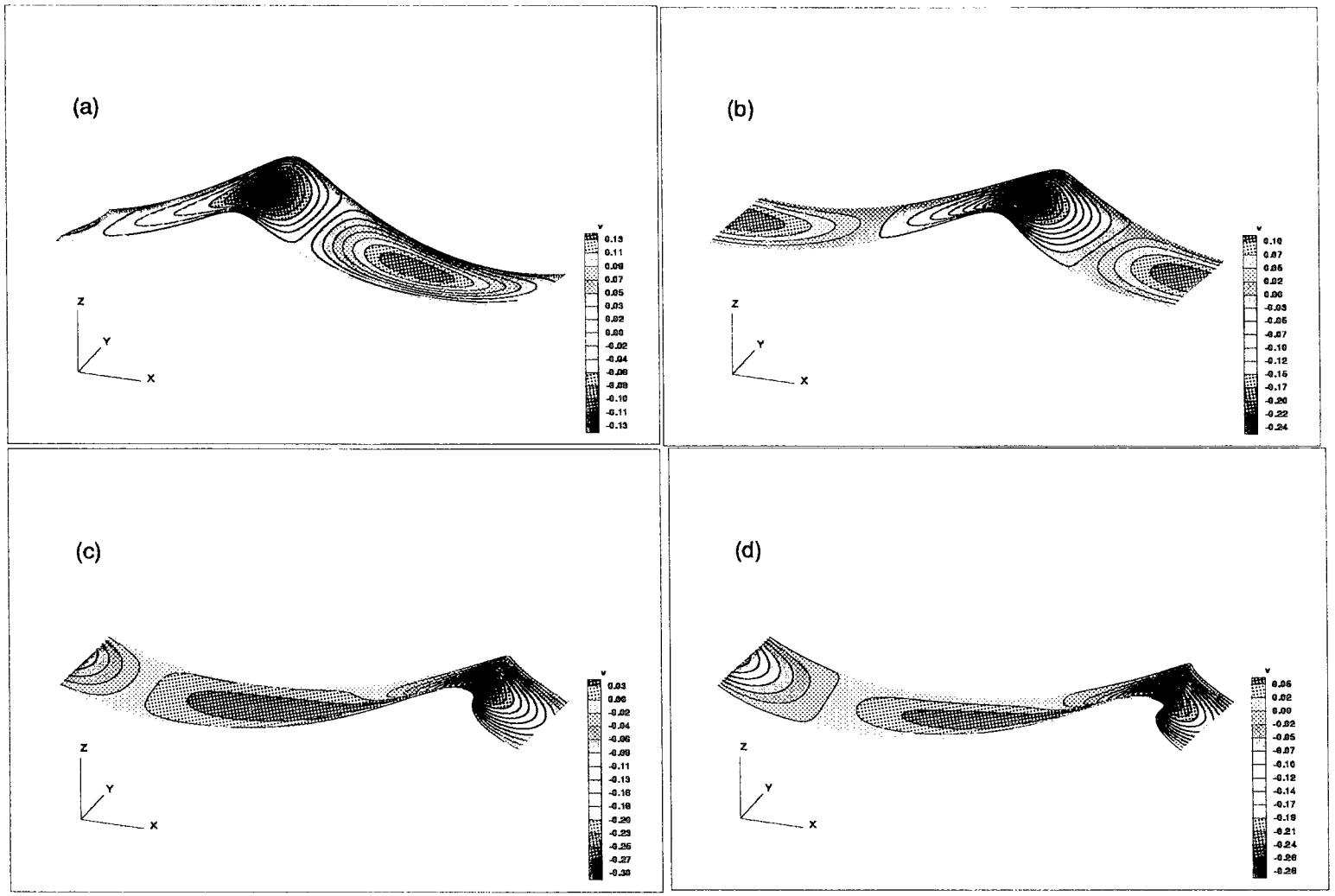

Figure 14: Surface transverse velocity v of a 3D deep-water overturning wave, γ=0.5, at t= (a) 3.0136; (b) 39900; (c) 5.0039; (d) 5.2009. Only half of the symmetric transverse domain between the 'center' y=0 (further from the observer) and 'side' $-B/2$ (nearer the observer) is shown.

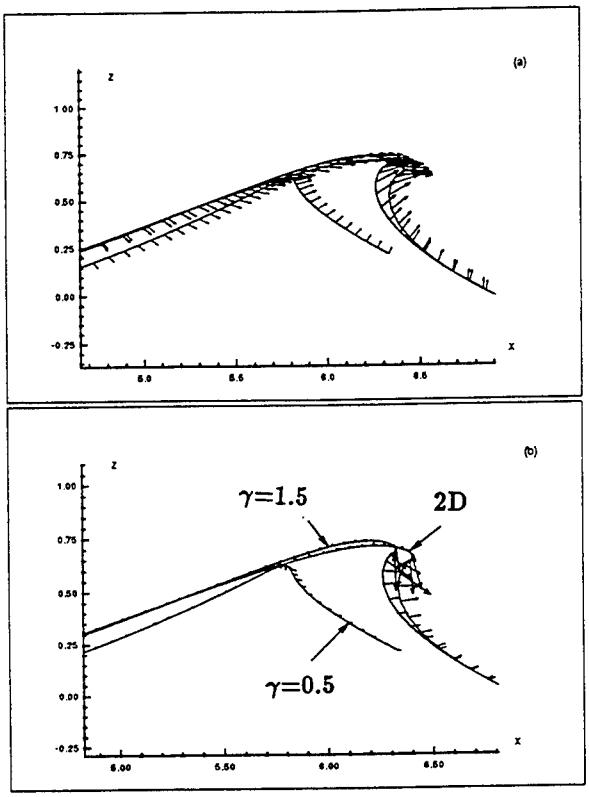

Figure 15: Wave profiles on the centerplane (y=0) at times corresponding to the occurance of maximum u for each case (see Table 3). For clarity, surface particle (a) velocity; (b) acceleration vectors are normalized by their maximum values given in Table 3.

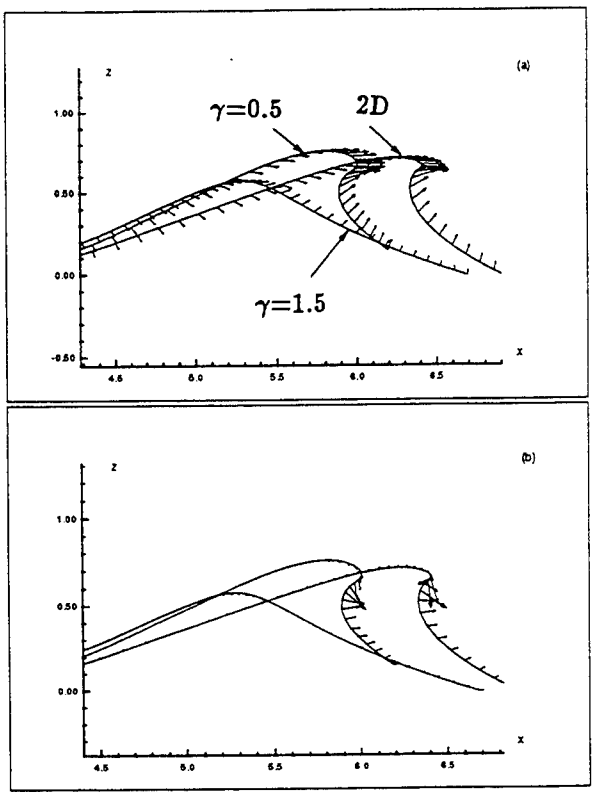

Figure 16: Same as fig. 15 by on the side wall ($y = -B/2$).

transfer plays a critical role here. After the forcing is removed at $t = \pi$, the wave height and u, w velocities near the side section increase rapidly. At $t = 3.9900$ the wave profile looks like a steep plane wave, although the three dimensionality of the w distribution is plainly evident. For $t > 3.9900$, the wave energy continues to be transferred to the side boundary as seen clearly from the w plots. The wave eventually develops into a robust plunging breaker on the side.

The contrast is most clear for v where the transverse velocities for γ=0.5 are negative (towards the side wall) both in front and behind the crest, and positive transverse velocities occur only in the trough region. By comparing figs. 11(d) and 14(d) at the overturning stage, we see that the maximum (negative) transverse velocity v on the crest for γ=0.5 is more than three times that for γ=1.5.

Figs. 15 and 16 show close-ups of the surface profiles, velocity and Lagrangian acceleration vectors on the center plane and side wall respectively for γ=1.5 and 0.5. For comparison, results for the 2D overturning wave (case 3 of Table 2) are also included. For each case, time instants are selected to correspond to when maximum u is reached for the entire evolution (see Table 3) typically relatively late in the overturning phase. The γ=1.5 and 2D cases show only minor differences on the centerplane indicating that the evolution near the centerplane is effectively two-dimensional for γ=1.5. Although the plunger in the γ=0.5 case takes longer to develop, the transfer of energy to the side results in its occurring approximately $L/6$ behind those of γ=1.5 and 2D cases. Despite the difference in the transverse location of breaking, the "cross-section" profiles, particle velocities and accelerations at the respective overturning transverse sections are remarkably similar. For 2D overturning waves, New *et al* (1985) conjectured that local overturning wave profiles must be rela-

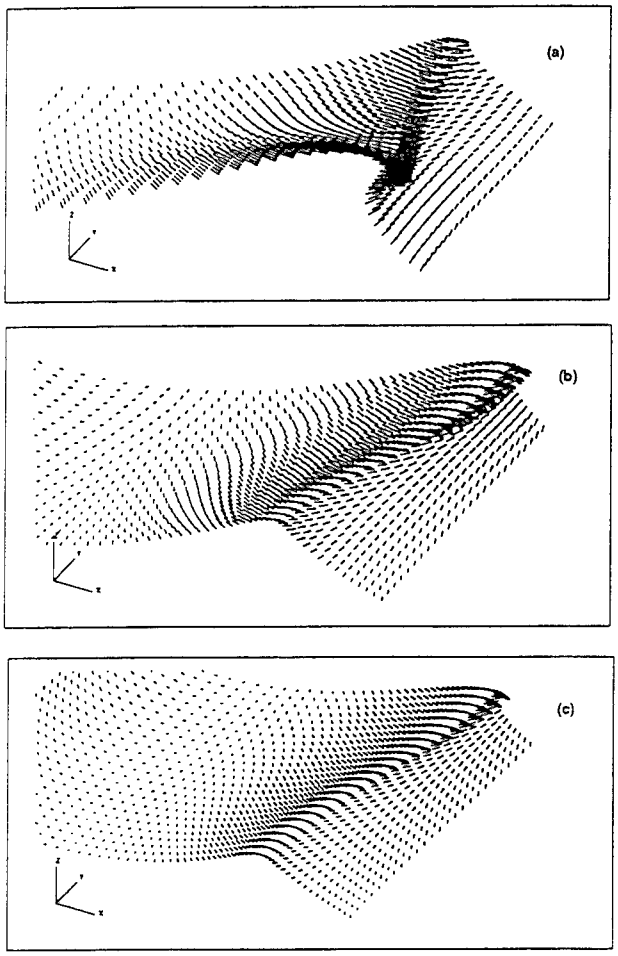

Figure 17: Three-dimensional vector plots of the surface velocity for γ= (a) 0.5; (b) 1.0; and (c) 1.5. The corresponding times and normalizations are given in Table 3.

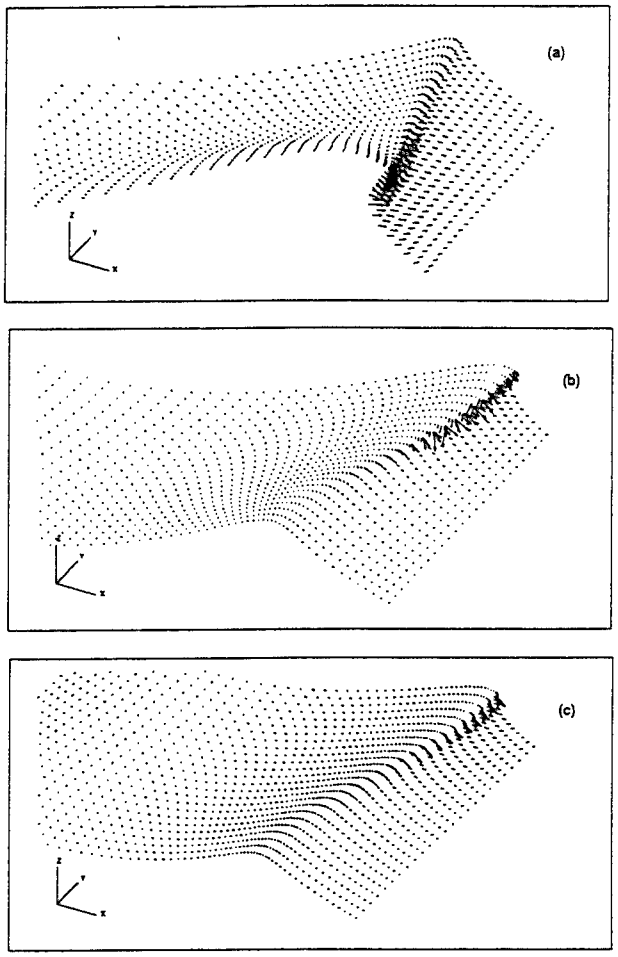

Figure 18: Same as fig. 17 but for the surface Lagrangian acceleration.

tively independent of global dynamics so that local jet solutions (Longuet-Higgins 1982) may be surprisingly useful. The present numerical results suggest that this may be true even for (mildly) 3D plungers.

As mentioned earlier, simulations have also been performed for γ=1.0. This turns out to be qualitatively very similar to the γ=1.5 case. Figs. 17 and 18 show vector plots of the surface particle velocity and acceleration respectively for γ=0.5, 1.0, 1.5. The time instants again correspond to when the respective horizontal velocities are maximum, and for clarity, the velocity and acceleration vectors are normalized by their maxima. These values are summarized in Table 3 together with the maximum and minimum surface elevation.

From Table 3, we note that the wave height, $\eta_{max} - \eta_{min}$, is greatest for γ=0.5 and decreases monotonically with increasing γ, having a minimum value for the 2D case. The overall difference from γ=0.5 to 2D, however, is only ~10%. The maximum velocity magnitudes are approximately twice the phase speed of the original Stokes wave, while the maximum Lagrangian acceleration amplitudes at this time (not necessarily maximum overall in time) are $\mathcal{O}(5.5 \sim 6)$ times that of gravity. Again, the differences among the different cases are relatively small.

As the overturning waves continue to develop

γ	t	$\eta_{max} - \eta_{min}$	$\|V\|_{max}$	$\|a\|_{max}$
0.5	5.2009	1.095	2.038	6.092
1.0	5.0038	1.039	1.958	5.673
1.5	4.8166	1.006	1.954	5.491
2D	4.7754	0.977	2.020	5.593

Table 3: Main parameters of the overturning waves at a time corresponding to when the longitudinal velocity u is maximum for the entire evolution. $|V|_{max}$ and $|a|_{max}$ denote the maximum magnitudes of the surface particle velocity and acceleration at the given times. The 2D data corresponds to case 3 in Table 2.

(shortly beyond the times in figs. 7 and 8), the simulations eventually break down. This occurs typically before the re-entry of the plunging tip and is associated with a Taylor instability (Taylor 1950) of the free surface undergoing increasingly large negative (normal) accelerations. To quantify the Taylor instability, we define the surface normal Lagrangian acceleration

$$a_n \equiv (\vec{a} - \vec{g}) \cdot \hat{n}, \qquad (19)$$

where $\vec{a}$ is the surface particle acceleration, $\vec{g} = (0, 0, -1)$ that of gravity, and $\hat{n}$ the unit normal out of the fluid. Thus, the onset of Taylor instability corresponds to when a_n becomes negative.

For illustration, we consider the case of γ=0.5 and follow 3 surface Lagrangian points whose initial positions on the Stokes wave are $x_i \simeq 1.82\pi$ (just behind the wave crest at 2π), and y_1=$-0.5B$ (on the side wall), $y_2 \simeq -0.35B$ and y_3=0. These points are chosen so that at t=5.2009 (*cf.* Table 3), Points 1 and 2 have respectively the maximum Lagrangian velocity and acceleration (in magnitude) at that time. Point 3 on the centerplane is included as a reference. At this time, $y_2 \simeq -0.41B$, and all three points are on the concave front wall of the overturning wave.

Fig. 19 shows the time evolution of $a_n(t)$ following these three points (only results near the final breakdown are shown). As the plunger develops, Point 2 accelerates out of the fluid rapidly, reaching a maximum value for a_n of almost 10 times gravity at $t \simeq$5.27. After that, a_n decreases dramatically, and eventually becomes negative leading to the break down of the simulation (shortly after the last point shown). (Even before this happens, the dynamic time step control appears in-

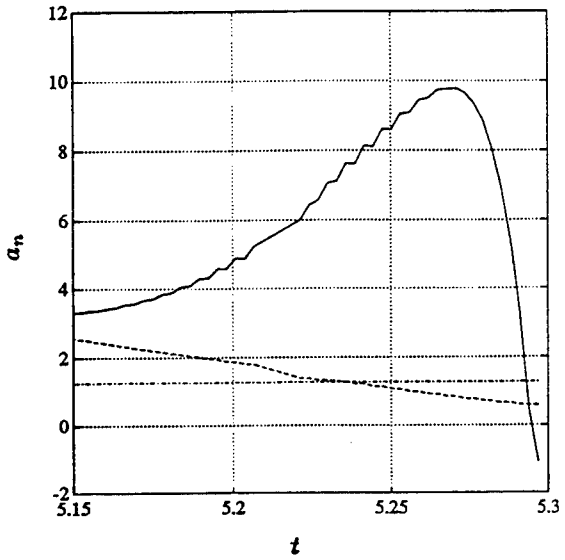

Figure 19: Surface normal Lagrangian acceleration a_n as functions of time for - - - : Point 1; —— : Point 2 and — · — : Point 3.

adequate for Point 2, resulting in small oscillation in a_n during the large accelerations. The corresponding velocities and particle positions are, however, still extremely smooth.) Physically, this rapid increase and decrease in acceleration correspond to the passage of Point 2 from behind to in front of the plunging crest.

The above results for a_n suggest a simple way to identify regions on a breaking wave where instabilities and surface roughness may initially develop. Fig. 20 shows the surface distribution of a_n for γ=1.5 (at $t \cong$4.811) and 0.5 (at $t \cong$ 5.300). In both cases, the (large) negative a_n region is located in a small area along the overturning wave crest where in reality a spray or fingering breakdown can be expected.

Other important results such as the partition of

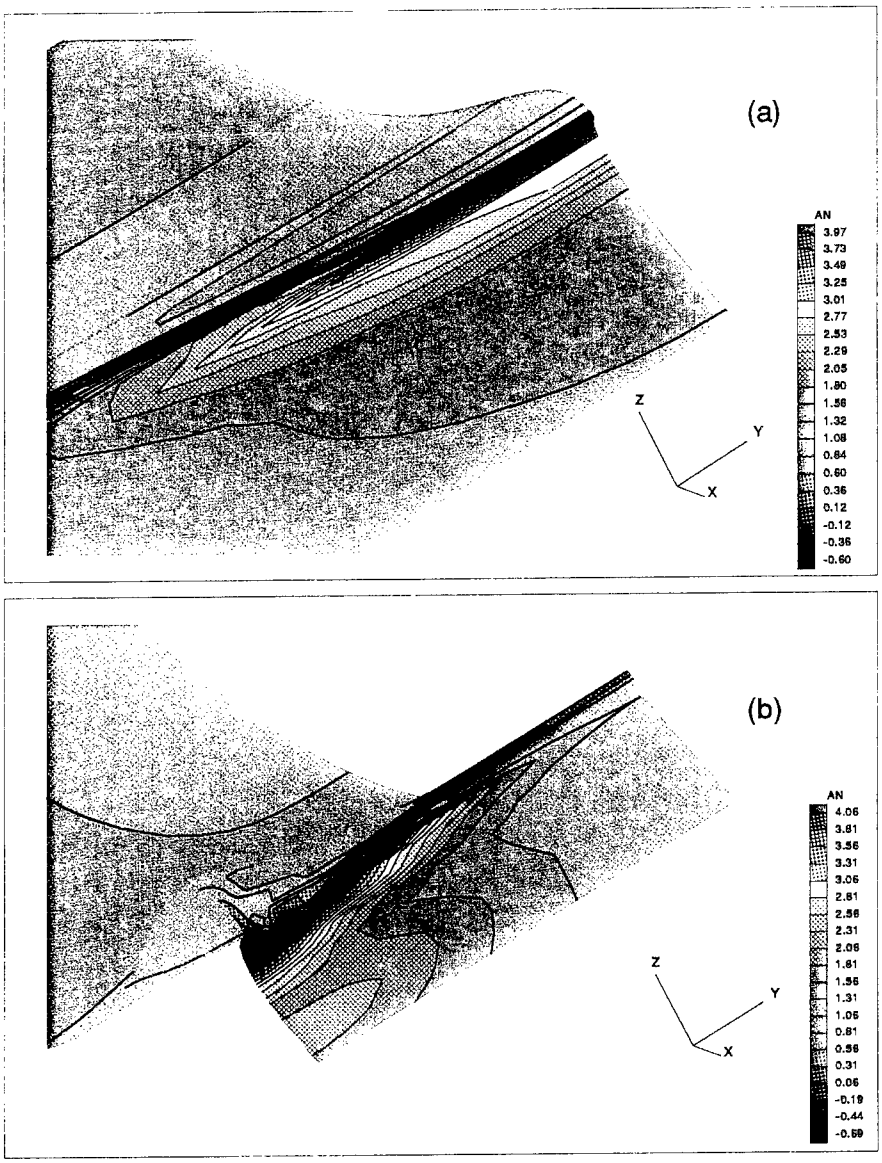

Figure 20: Surface normal Lagrangian acceleration a_n for (a) γ=1.5, $t \simeq$4.811; and (b) γ=0.5, $t \simeq$5.300. The maximum a_n regions are inside the concave loop and almost completely hidden. The minimum/negative a_n are in a small region along the plunging crest.

kinetic and potential energies have also been obtained. Further analyses of the computational results and additional simulations to obtain quantitative dependence of relevant kinematical parameters on γ are now under way. These will be reported in the near future.

4.2 Other results

The present 3D code has also been applied to doubly-periodic problems on finite depth and large-amplitude wave sloshing in a rectangular basin. The latter example, in particular, demonstrates the efficacy of the code in treating free surface and wall intersections. Details can be found in Xü (1992).

5 Conclusions

A robust and powerful numerical method has been developed for the simulation of fully-nonlinear wave and body interactions in three dimensions. The method is based on a mixed-Eulerian-Lagrangian (MEL) approach with the boundary-value problem formulated directly as mixed first/second-kind boundary-integral equations (BIE). The BIE is solved using a new quadratic boundary-element method (QBEM) which demonstrates cubic minimax error convergence with element size for general wave-body boundary conditions and intersections. The resulting linear algebraic system is found to be amenable to and converge rapidly with GMRES iterations with SSOR preconditioning.

To demonstrate the efficacy of this new method we apply it to study the kinematic of 3D deep-water overturning waves. We define a three dimensionality parameter based on the aspect ratio of the problem $\gamma = B/L$. Simulations for different γ are conducted which allow us to map the entire evolution of the wave surface position, velocity and (Lagrangian) acceleration fields as a function of γ. It is found that the results vary qualitatively (*e.g.*, the location of the plunging tip) with γ, although, parameters associated with the local overturning wave (*e.g.*, maximum particle velocity and acceleration) are surprisingly unaffected.

By identifying the surface normal Lagrangian acceleration, a_n, and following its evolution, we are able to locate regions (near the plunging crest) of negative a_n in the late stages of wave overturning. Taylor instabilities rapidly develop in these regions leading to the break-down of the simulations some time before wave reentry. Physically, these surface regions must correspond to areas of initial development of instabilities and roughness on steep waves.

Case	$\mathcal{A}/L^2$	T/T_0	CPU
Validation†	$\mathcal{O}(1)$	$\mathcal{O}(1)$	$\mathcal{O}$ (1)
Fundamental Study†	$\mathcal{O}(1)^*$	$\mathcal{O}(1)$	$\mathcal{O}(10)$
Fundamental Study†	$\mathcal{O}(4)$	$\mathcal{O}(2)$	$\mathcal{O}(40)$
Engineering Appl.	$\mathcal{O}(10)$	$\mathcal{O}(10)$	$\mathcal{O}$ (100)

Table 4: Scenarios and CPU estimates (hours of Cray Y/MP) for quantitative simulations of fully-nonlinear wave-body interactions in 3D. † with wave overturning; * doubly-periodic boundary conditions.

An important consideration for the immediate and potential usefulness of this work is the magnitude of the computational effort required. From numerical experiments, the total CPU time can be estimated by

$$\begin{aligned} \text{CPU} &\sim \mathcal{O}(N^2 N_T) \\ &\approx c_1 c_2^4 c_3 (\mathcal{A}/L^2)^2 (T/T_0), \end{aligned} \qquad (20)$$

where N is the total number of QBEM (surface) unknowns; N_T the total number of time steps; $\mathcal{A}$ the total QBEM surface area; T the total simulation time; and L, T_0 respectively the fundamental (wave) length and period. Our estimates of the computational parameters are $c_1 \sim \mathcal{O}(10^{-7})$ Cray-Y/MP hour ($\sim \mathcal{O}(10^{-6})$ for doubly-periodic boundary conditions); c_2, the number of QBE's per primary wavelength, $\sim \mathcal{O}(10)$ for 1% maximum error ($\sim$16 for 0.5% maximum error); and c_3, the number of time steps per primary period, $\sim \mathcal{O}(60-100)$ ($\sim \mathcal{O}(200)$ with wave overturning).

Table 4 shows the estimated computing time based on (20) for a number of likely applications. Clearly, useful quantitative 3D fully-nonlinear simulations are now feasible but nevertheless still very expensive. Developments that may signif-

icantly improve this situation, in particular the implementation of adaptive multipole algorithms (Rokhlin 1985) that require only $\mathcal{O}(N)$ computational effort (*cf.* (20)), are now underway.

Acknowledgement

This research was financially supported by the Office of Naval Research (ARI in Nonlinear Ship Motions, contract number N00014-90-J-1085; and Fluid Mechanics Program, contract number N00014-90-J-1158). We are grateful to Cray Research, Inc., for the use of their Cray Y-MP/832 and Cray 2S supercomputers. Some computations were also performed on the NSF Pittsburgh Supercomputer Center Cray Y-MP. We thank Y. Liu for valuable graphical help.

References

G.R. Baker, D.I. Meiron & S.A. Orszag. Generalized vortex methods for free–surface flow problems. *J. Fluid Mech.*, 123:477–501, 1982.

C.A. Brebbia, J.C.F. Telles & L.C. Wrobel. *Boundary Element Techniques.* Springer–Verlag, Berlin, 1984.

S.R. Breit. The potential of a rankine source between parallel planes and in a rectangular cylinder. *J. Engng. Math.*, 25:151–163, 1991.

R. Cointe. Quelques aspects de la simulation numérique d'un canal à houle. Thèse de Doctorat de l'Ecole Nationale des Ponts et Chaussées, Paris, 1989 (in French). (See also, R. Cointe. Numerical simulation of a wavetank. *Engineering Analysis with Boundary Elements*, 1991.)

J.W. Dold & D.H. Peregrine. An efficient boundary–integral method for steep unsteady water waves. In K.W. Morton & M.J. Baines, editors, *Numerical Methods for Fluid Dynamics II*, 671–679. Oxford University Press, 1986.

D.G. Dommermuth & D.K.P. Yue. Numerical simulations of nonlinear axisymmetric flows with a free surface. *J. Fluid Mech.*, 178:195–219, 1987.

D.G. Dommermuth, D.K.P. Yue, W.M. Lin, R.J. Rapp, E.S. Chan & W.K. Melville. Deep–water plunging breakers: a comparison between potential theory and experiments. *J. Fluid Mech.*, 189:423–442, 1988.

O.M. Faltinsen. Numerical solutions of transient nonlinear free surface motion outside or inside moving bodies. In *Proc. 2nd International Conf. Num. Ship Hydro.*, 347–357, Berkeley, California, 1977.

G.H. Golub & C.F. Van Loan. *Matrix computations.* Johns Hopkins University Press, second edition, 1989.

J.L. Hess & A.M.O. Smith. Calculation of potential flow about arbitrary bodies. *Progress in Aeronautical Sciences*, 8:1–138, 1964.

M. de St.Q. Isaacson. Nonlinear–wave effects on fixed and floating objects. *J. Fluid Mech.*, 120:267–281, 1982.

W.M. Lin. Nonlinear motion of the free surface near a moving body. Ph.D. thesis. M.I.T. Department of Ocean Engineering. 1984.

W.M. Lin, J.N. Newman & D.K.P. Yue. Nonlinear forced motions of floating bodies. In *Proc. 15th Symp. Naval Hydro.*, 33–49, Hamburg, Germany, 1984.

M.S. Longuet-Higgins. Parametric solutions for breaking waves. *J. Fluid Mech.*, 121:403–424, 1982.

M.S. Longuet-Higgins & E.D. Cokelet. The deformation of steep surface waves on water, I. A numerical method of computation. *Proc. Roy. Soc. London*, A350:1–26, 1976.

A.L. New, P. McIver & D.H. Peregrine. Computations of overturning waves. *J. Fluid Mech.*, 150:233–251, 1985.

J.N. Newman. The Green function for potential flow in a rectangular channel. *J. Engng. Math.*, 1991.

V. Rokhlin. Rapid solution of integral equations of classical potential theory. *J. Comp. Physics*, 187–207, 1985.

J.E. Romate. *The numerical simulation of nonlinear gravity waves in three dimensions using a higher panel method.* PhD thesis, University of Twente, Enschede, The Netherlands, 1989.

Y. Saad & M.H. Schultz. GMRES: A generalized minimal residual algorithm for solving nonsymmetric linear systems. *SIAM J. Sci. Stat. Comput.*, 7:856–869, 1986.

L.W. Schwartz. Computer extension and analytic continuation of Stokes' expansion for gravity waves. *J. Fluid Mech.*, 62:553–578, 1974.

G.I. Taylor. The instability of liquid surfaces when accelerated in a direction perpendicular to their planes, Part I. *Proc. Roy. Soc. Lond.*, A201:192–196, 1950.

L.N. Trefethen. Approximation theory and numerical linear algebra. In J.C. Mason & M.G. Cox, editors, *Algorithms for approximation II.* Chapman & Hall, 1990.

T. Vinje & P. Brevig. Numerical simulation of breaking waves. *Adv. Water Resources*, 4:77–82, 1981.

H. Xü. Numerical study of fully nonlinear water waves in three dimensions. Ph.D. thesis, Dept. of Ocean Eng., MIT, Cambridge, 1992.

C. Yang, Y.Z. Liu & N. Takagi. Time domain calculations of the nonlinear hydrodynamics of wave-body interaction. In *Proc. 5th International Conf. Num. Ship Hydro.*, Hiroshima, Japan, 1989.

DISCUSSION

W. Schultz
University of Michigan, USA

Your statement that "the inevitable presence of saw-tooth instabilities can be expected in theory since for any nonlinear system without dissipation, energy cascades from lower to higher wave numbers..." may be true in most cases, but there is at least one counterexample: a weakly nonlinear Stokes wave is neutrally stable to superharmonics but unstable to subharmonics (Benjamin-Feir Instability). Hence, for small times (at least), the energy "cascades" in this case from higher to lower wave number. Perhaps this is why some nonlinear time marching results have been reported (including your own) without filtering. Can you comment?

Secondly, how general is the Taylor instability criteria developed from (19) considering it is local in space and time and the flow may have an extensional component?

AUTHORS' REPLY

The cascade of energy to the highest wavenumbers represented is unrelated to the stability/instability of high/low wavenumber modes or harmonics. The exchange of energy among these latter modes is in principle uncoupled from the scattering of energy into the much high wavenumber regimes.

The Taylor criterion for instability is a local one. As indicated by Taylor (1950), a component of acceleration in the direction of density gradient is destabilizing. This is true in any local region of the fluid.

DISCUSSION

S. Coakley
University of California at Berkeley, USA

The authors are to be commended on their presentation of a timely and interesting paper. Based on our own ongoing research using isoparametic bi-cubic spline panels, we applaud the authors' selection of a high-order panel method for the overturning wave problem. We have had success with these methods in our investigation of steep waves above a submerged body.

A jump in the velocity vector across panel boundaries is implicit in the bi-quadratic panel formulation, requiring special care in the tangential velocity calculation on the free surface; and the authors have evidently gone to some trouble with this calculation. Bi-cubic spline panels, on the other hand, have no jump and allow direct computation of the tangential velocities on all boundaries. Could the authors comment on this?

AUTHORS' REPLY

For the velocity calculations, we employ Lagrangian polynomial local fits which maintain high-order continuity. Our numerical tests confirm the consistency and effectiveness of this approach.

We have systematically tested the performance of other higher-order panels including iso- and super-parametric elements described by bi-cubic spline geometries before selecting the present QBEM. Consistent with earlier findings (Roberts & Rundle 1972; Sytsma *et al* 1979), our experience with bi-cubic elements in three dimensions indicate that, while they provide somewhat more accurate representations, the computational burden is significantly higher and overall less efficient.

Session IV

Viscous Ship Hydrodynamics

Applications of Boundary Element Methods in Hydrodynamic Problems Relating to Manoeuvring Bodies

W. Price, M.-Y. Tan (The University of Southampton, U.K.)

ABSTRACT

Here we develop a *general, unified viscous boundary element theory and method* to evaluate fluid actions, slow motion derivatives and flow fields associated with a rigid body manoeuvring. It is also shown that this mathematical model has wider applications than initially conceived, extending to rolling motions, propeller theory, viscous fluid-structure interactions, etc.

For a rigid body moving with prescribed unsteady translational and/or rotational motions a non-linear convolution-integral identity is developed from the Navier-Stokes equation, allowing time history effects to be retained in the mathematical model. Central to this model is the fundamental equation, which is a variant of Oseen's equation, and provides the fundamental viscous transient solution.

Analogous to a panel method in potential theory, we replace the potential singularity, ideal fluid and the distribution of singularities over the body's wetted surface area by an appropriate fundamental viscous solution, viscous fluid and distribute the viscous solutions over the body's wetted surface area and into the surrounding fluid. This discretisation of the boundary and domain integrations occurring in the integral equation permits the fluid action and flow velocity disturbance to be evaluated directly in the developed numerical scheme of study.

The applicability of the mathematical model is demonstrated and illustrated through the modelling of a flat plate in a steady flow, oblique tow and rotating arm tests, planar motion mechanism (PMM) experiments, rotating cylinder and a rolling two-dimensional ship like section.

INTRODUCTION

When a body departs from steady motion in a straight line the water exerts a resultant force and resultant moment about the centre of gravity as a consequence of the disturbance. Information on this variation of fluid action to disturbance forms an important role in manoeuvring theory especially in the assessment of the directional stability, manoeuvring and control of the body and in seakeeping studies through oscillatory testing.

In manoeuvring theory, this variation is described in terms of slow motion derivatives and the data are usually obtained from model scale experiments involving steady state oblique tow tests, rotating arm tests and planar motion mechanism (PMM) oscillatory tests. The steady state tests allow velocity and angular velocity derivative data to be evaluated whereas the PMM tests provide information on velocity and acceleration data. The theoretical models and procedures adopted in the experiments are extensively described and discussed in the literature and the techniques developed are now firmly established [1,2].

In fact, such experiments are conceptually simple and readily performed, yet the theoretical modelling of these experiments poses major fundamental problems and confidence in the ability of the models to predict derivative data with a modicum of accuracy remains low. In contrast, seakeeping experiments are more complicated to perform, theoretical modelling is much more advanced and predictive techniques and methods are now well established [3-7]. In these studies, free surface wave disturbances have a dominant influence and although the study of waves is a difficult subject in itself much progress can be achieved by treating the fluid as ideal (i.e. incompressible, inviscid and the motions irrotational) and through simplifications to the mathematical model (e.g. small amplitude waves, linearisation, etc). On the other hand, manoeuvring type problems are dominated by viscous effects and in general, surface wave disturbances are of less importance. Experience shows that because of the dominant influence of the viscous flow component to the fluid actions, especially those associated with velocity derivatives, little theoretical progress can be achieved without quickly being immersed in a non-linear.

It is this latter type of problem which this paper begins to address. Namely the evaluation of fluid actions, their variation to disturbance and the flow around an arbitrary shaped body maneouvring in a viscous fluid. A general theoretical mathematical model is proposed and developed in which the body has prescribed forward velocity and angular velocity [8,9]. Although focused on manoeuvring problems, the proposed method with adaptation is able to describe fluid actions and flow fields around a body rolling in a viscous fluid, a body rolling with forward speed, a propeller rotating in a viscous fluid, the interaction between hull and propeller, etc.

In seakeeping and offshore studies, panel methods have been successfully developed to evaluate the dynamics of quite arbitrarily shaped structures subject to wave loadings [10-12]. A distribution of potential singularities over the panels covering the

wetted surface area of the body provides a framework on which to evaluate the fluid forces assuming the fluid is ideal. Here, we propose to replace the potential singularity and ideal fluid by a fundamental viscous solution and viscous fluid and to distribute the solutions over panels covering the wetted surface area of the body and extending into the surrounding viscous fluid.

Commencing from the Navier-Stokes equation, we derive a convolution-integral identity which allows the fluid forces and disturbed fluid velocity to be determined directly from the mathematical model. The introduction of a convolution time integral process provides a means of retaining time history effects as well as accounting for steady and unsteady or transient translational and rotational prescribed maneouvres. From this non-linear model based on an integral identity involving boundary and domain integrations, it is seen that the Oseen equation or its equivalent plays a central role in its subsequent development [7,8,13,14]; the solution of this equation provides the fundamental viscous solution which is a function of the prescribed translatory and/or rotatory motions of the body.

The fundamental viscous solution chosen depends on the type of problem under investigation e.g. steady state oblique tow, rotating arm, PMM experiment, a combination of unsteady translations and/or rotations, etc. Here we demonstrate through illustrations that, by distributing these fundamental viscous solutions over the panels describing the rigid body's geometry and into the fluid, we can develop a practical, unified viscous boundary element method based on a convolution-integral formulation to evaluate fluid actions and flow fields experienced by two- and three-dimensional shaped bodies undertaking steady or unsteady prescribed manoeuvres.

MATHEMATICAL MODEL

In traditional approaches adopted in studies investigating the manoeuvring capability of an arbitrary shaped marine vehicle, the motions of the rigid body are defined with reference to an orthogonal right handed set of body axes Cxyz. In this axis system C is fixed at the centre of gravity or other convenient position in the body i.e. the stern (say), the positive Cx axis lies in the longitudinal plane of symmetry in the direction of the bow, the Cy axis lies in the transverse direction pointing to starboard and the Cz axis is positive vertically downwards. It is assumed that the body and hence the axis system moves with a translational velocity - $\tilde{\mathbf{U}}(t)$ [$\tilde{\mathbf{U}}(0) = 0$] and rotates with an angular velocity - $\tilde{\Omega}(t)$ [$\tilde{\Omega}(0) = 0$]. The retention of the time dependence in these motions allows unsteady prescribed manoeuvres of the body to be examined.

The Navier-Stokes equation describing the fluid flow velocity $\tilde{\mathbf{V}}(\tilde{\mathbf{r}}, \tilde{t})$ in the incompressible fluid with constant viscosity is given by

$$\frac{\partial \tilde{\mathbf{V}}}{\partial \tilde{t}} + (\tilde{\mathbf{V}} \cdot \tilde{\nabla})\tilde{\mathbf{V}} = -\frac{1}{\tilde{\rho}} \tilde{\nabla}\tilde{p} + \tilde{\nu}\, \tilde{\nabla}^2\tilde{\mathbf{V}} + \tilde{\mathbf{f}} + \dot{\tilde{\mathbf{U}}} + \dot{\tilde{\Omega}}\mathrm{x}\tilde{\mathbf{r}} - \tilde{\Omega}\mathrm{x}(\tilde{\Omega}\mathrm{x}\tilde{\mathbf{r}}) + 2\tilde{\Omega}\mathrm{x}\tilde{\mathbf{V}} \quad (1)$$

and

$$\tilde{\nabla} \cdot \tilde{\mathbf{V}} = \mathrm{div}\, \tilde{\mathbf{V}} = 0 \quad (2)$$

where $\tilde{\mathbf{r}}$ denotes the position vector defined in the body fixed coordinate system and a tilde($\tilde{}$) above a term indicates a dimensional quantity. The variables $\tilde{\nu}$, $\tilde{\rho}$, $\tilde{p}$ and $\tilde{\mathbf{f}}$ represent the kinematic viscosity coefficient, fluid density, pressure in the fluid and an external body force respectively. An overdot denotes an acceleration, ($\dot{\tilde{\mathbf{U}}}$) or an angular acceleration ($\dot{\tilde{\Omega}}$) and the mathematical symbols $\tilde{\nabla}$, $\tilde{\nabla}^2$ have their usual meanings.

In the mathematical model developed herein, the disturbed fluid velocity $\tilde{\mathbf{v}}(\tilde{\mathbf{r}},\tilde{t})$ and the mean pressure $\tilde{p}(\tilde{\mathbf{r}},\tilde{t})$ in the viscous fluid are considered as unknowns. Since $\tilde{\mathbf{V}} = \tilde{\mathbf{v}} + \tilde{\mathbf{U}} + \tilde{\Omega}\,\mathrm{x}\,\tilde{\mathbf{r}}$ and $\tilde{\mathbf{V}}(\tilde{\mathbf{r}},0) = 0 = \tilde{\mathbf{v}}\,(\tilde{\mathbf{r}},0)$, the Navier-Stokes equation governing the disturbed fluid velocity $\tilde{\mathbf{v}}$ is given by

$$\frac{\partial \tilde{\mathbf{v}}}{\partial \tilde{t}} + [(\tilde{\mathbf{U}} + \tilde{\mathbf{v}}).\tilde{\nabla}]\tilde{\mathbf{v}} + \tilde{\nabla}\mathrm{x}\,[\tilde{\mathbf{v}}\mathrm{x}(\tilde{\Omega}\mathrm{x}\tilde{\mathbf{r}})] = \tilde{\nu}\,\tilde{\nabla}^2\,\tilde{\mathbf{v}} - \frac{1}{\tilde{\rho}}\tilde{\nabla}\tilde{p} + (\dot{\tilde{\Omega}}\mathrm{x}\tilde{\mathbf{U}}) + \tilde{\mathbf{f}}\ , \quad (3)$$

$$\tilde{\nabla}.\tilde{\mathbf{v}} = \mathrm{div}\,\tilde{\mathbf{v}} = 0\ . \quad (4)$$

By adopting the Oseen non-dimensional variables

$$\tilde{\mathbf{v}} = \tilde{\mathrm{U}}\,\mathbf{v}, \qquad \tilde{\mathbf{U}} = \tilde{\mathrm{U}}\mathbf{U}, \qquad \tilde{\Omega} = \tilde{\mathrm{U}}\mathrm{Re}\Omega/\tilde{\mathrm{L}}, \qquad \tilde{p} = \tilde{\rho}\,\tilde{\mathrm{U}}^2 p,$$

$$\tilde{\mathbf{f}} = \tilde{\mathrm{U}}^2\mathrm{Ref}/\tilde{\mathrm{L}}\ , \quad \tilde{\nabla} = (\mathrm{Re}/\tilde{\mathrm{L}})\,\nabla,$$

$$\tilde{\mathbf{r}} = \tilde{\mathrm{L}}\mathbf{r}/\mathrm{Re}, \qquad \tau = \tilde{\mathrm{L}}t/\tilde{\mathrm{U}}\mathrm{Re}, \qquad \partial/\partial\tilde{t} = (\tilde{\mathrm{U}}\mathrm{Re}/\tilde{\mathrm{L}})\,\partial/\partial t,$$

where $\tilde{\mathrm{L}}$ is a characteristic length, $\tilde{\mathrm{U}}$ a characteristic speed and $\mathrm{Re} = \tilde{\mathrm{U}}\tilde{\mathrm{L}}/\tilde{\nu}$ is the Reynolds Number, we find that the non-dimensional form of the Navier-Stokes equation is given by

$$\frac{\partial \mathbf{v}}{\partial t} + (\mathbf{U}+\mathbf{v})\ .\ \nabla\mathbf{v} + \nabla\mathrm{x}\,\{\mathbf{v}\mathrm{x}(\Omega\mathrm{x}\mathbf{r})\} = -\nabla\mathrm{p} + \nabla^2\mathbf{v} + \dot{\Omega}\mathrm{x}\mathbf{U} + \mathbf{f} \quad (5)$$

or, if the vorticity $\omega = \nabla \times \mathbf{v}$,

$$\frac{\partial \mathbf{v}}{\partial t} + (\mathbf{U}.\nabla)\mathbf{v} + \nabla\mathrm{x}\{\mathbf{v}\mathrm{x}(\mathbf{v}\mathrm{x}(\Omega\mathrm{x}\mathbf{r})\} = -\nabla(\mathrm{p}+\frac{1}{2}\mathbf{v}^2) + \nabla^2\mathbf{v} + \mathbf{v}\mathrm{x}\omega + \dot{\Omega}\mathrm{x}\mathbf{U} + \mathbf{f}\ , \quad (6)$$

and

$$\nabla.\mathbf{v} = 0 \quad (7)$$

subject to the conditions

$$\mathbf{v}(\mathbf{r},0) = 0, \qquad \mathbf{v}(\infty,t) \to 0, \qquad \nabla\mathrm{p}(\infty,t) \to (\dot{\Omega}\mathrm{x}\mathbf{U}) \text{ and}$$

$$\mathbf{v}(\mathbf{r},t) = -\mathbf{U}(t) - \Omega(t)\mathrm{x}\mathbf{r}$$

on the body's surface.

These non-linear equations contain no direct reference to Reynolds number but as can be seen, its presence remains in the transformation of variables. Furthermore, under the assumption $\Omega(t) = 0$ and $\mathbf{U}(t) = \mathbf{U}$ a constant, the linearised form of these equations produce the classical equations of Stokes [15]:

$$\frac{\partial \mathbf{v}}{\partial t} = \nabla^2\mathbf{v} - \nabla\mathrm{p} + \mathbf{f}, \quad (8)$$

and Oseen [16]:

$$\frac{\partial \mathbf{v}}{\partial t} + (\mathbf{U}.\nabla)\mathbf{v} = \nabla^2\mathbf{v} - \nabla p + \mathbf{f} \qquad (9)$$

In the derivation of the Stokes equation, it is assumed that the Reynolds number is small such that products of $\mathbf{v}$ in equation (5) are negligibly small and therefore neglected in comparison with the first order terms. In the Oseen equation, the constant uniform velocity term is retained and, at large distances from the body, the flow may be regarded as having a parasitic disturbance in the uniform flow under inertial and viscous forces of comparable magnitudes. Thus the Stokes equation is based entirely upon the assumption of small Reynolds number whereas the Oseen equation, though suitable for small Reynolds number, applies to flows in the far field and for any value of the Reynolds number. For these reasons, variants of the Oseen type equation are adopted in the mathematical model to be discussed and developed in preference to the simpler Stokes equation.

Convolution-Integral Identity

By describing the past history of the prescribed manoeuvre of the body through convolution time integrals and using Gaussian integral formulae, we find after a series of mathematical manipulations that the Navier-Stokes equation describing the disturbed fluid velocity $\mathbf{v}$ can be transformed into a convolution-integral equation producing an integral identity. This is achieved by introducing two additional unknown functions $v_{sj}^*(\mathbf{r},t)$ and $p_s^*(\mathbf{r},t)$ where $\mathbf{r} = \mathbf{x}-\mathbf{q}$ represents the position of the field point at $\mathbf{q}$ relative to the source point at $\mathbf{x}$. In this notation, the subscripts i, j, s, etc take values 1, 2 in a two-dimensional problem and 1, 2, 3 in a three dimensional problem. Thus the auxiliary function $\mathbf{v}_s^*$, with element v_{sj}^*, represents a (2x2) or (3x3) matrix depending on the type of problem under investigation whereas $\mathbf{p}^*$, with element p_s^*, is a vector or column matrix containing 2 or 3 elements.

The details of the transformation are omitted but it can be shown that the following integral identity can be deduced from equation (5):

$$\int_\Omega \{\mathbf{v}_s^*\cdot[\dot{\mathbf{v}} + (\mathbf{U}+\mathbf{v}).\nabla\mathbf{v} + \nabla\times\{\mathbf{v}\times(\Omega\times\mathbf{x}\} - \nabla(\nabla.\mathbf{v}) - \nabla^2\mathbf{v} + \nabla p - \Omega\times\mathbf{U} - \mathbf{f}] + p_s^*(\nabla.\mathbf{v})\}d\Omega$$

$$= \int_\Omega \{\mathbf{v}^*\cdot[\dot{\mathbf{v}}_s^* - (\hat{\mathbf{U}}.\nabla)\mathbf{v}_s^* + (\hat{\Omega}\times\mathbf{x})\times(\nabla\times\mathbf{v}_s^*) - \nabla(\nabla.\mathbf{v}_s^*) - \nabla^2\mathbf{v}_s^* - \nabla p_s^*] - [p - (\Omega\times\mathbf{U}).\mathbf{x}]^*(\nabla.\mathbf{v}_s^*)$$

$$+ \mathbf{v}_s^*\cdot[(\mathbf{v}.\nabla)\,\mathbf{v} - \mathbf{f}]\}\,d\Omega + \int_\Omega [v_{sj}^*(\mathbf{r},0)v_j(\mathbf{x},t) - v_{sj}^*(\mathbf{r},t)v_j(\mathbf{x},0)]d\Omega$$

$$+ \int_\Sigma \{\mathbf{v}_s^*\cdot[(\mathbf{U}.\mathbf{n})\mathbf{v} - \mathbf{n}\{(\Omega\times\mathbf{U}).\mathbf{x}\} + \mathbf{n}\times\{\mathbf{v}\times(\Omega\times\mathbf{x})\} - \mathbf{R}] + \mathbf{v}^*\mathbf{R}_s^*\}d\Sigma \qquad (10)$$

Here Ω denotes the fluid domain, Σ represents the boundary surface enclosing Ω, n is a unit normal pointing outwards from the fluid domain Ω and a summation convention is adopted:

$$U_j n_j = \mathbf{U}.\mathbf{n} = \sum_{j=1}^{3} U_j n_j \quad \text{etc.}$$

The asterisk multiplier (*) denotes a convolution operation:

$$\mathbf{a} * \mathbf{b} = \mathbf{b} * \mathbf{a} = \int_0^t a(t-y)\,.\,b(y)\,dy$$

and we define

$$\hat{\mathbf{U}}(t) = \mathbf{U}(\tau-t), \quad \hat{\Omega}(t) = \Omega(\tau-t)$$

to indicate a simple time shift in these parameters.

The term

$$R_j = p_{kj}\,n_k = (-p\delta_{kj} + v_{j,k} + v_{k,j})\,n_k$$

represents the dimensionless force component in the jth direction whereas the variable R_{sj}^* is defined as

$$R_{sj}^* = p_{skj}^*\,n_k = (p_s^*\,\delta_{kj} + v_{sj,k}^* + v_{sk,j}^*)\,n_k$$

where n_k is redefined as the kth component of the unit normal vector at the boundary surface pointing inwards into the fluid domain. In these expressions $v_{j,k} = \partial v_j/\partial x_k$, $v_{sj,k}^* = \partial v_{sj}^*/\partial x_k$, etc and $\delta_{kj} = 1$ when $k = j$, otherwise it is zero.

Fundamental Equation

The functions v_{sj}^* and p_s^* remain undefined in equation (10) and as these variables were introduced into the mathematical model by us, we are at liberty to choose their forms. An examination of the integral identity reveals that a major simplification to this expression occurs if we let these undefined functions satisfy the following equation:

$$\dot{\mathbf{v}}_s^* - \left(\hat{\mathbf{U}}\,.\,\nabla\right)\mathbf{v}_s^* + \left(\hat{\Omega}\times\mathbf{x}\right)\times\left(\nabla\times\mathbf{v}_s^*\right) - \nabla^2\mathbf{v}_s^* - \nabla p_s^* = \delta_s\delta(t)\Delta(\mathbf{r}) \qquad (11)$$

and

$$\nabla.\mathbf{v}_s^* = 0$$

subject to the conditions $v_{sj}^*(\mathbf{r},0) = 0$ and $v_{sj}^*(\infty,t) \to 0$. Here both $\delta(\ )$ and $\Delta(\ )$ denote Dirac delta functions. When this equation is compared with equation (8) we see that apart from the angular velocity term, equation (11) is a variant of the Oseen equation with $f_{sj}^* = \delta_{sj}\,\delta(t)\,\Delta(\mathbf{r})$.

Equation (11) is a general equation applicable to all types of steady and unsteady fluid-structure interaction problems

involving translational and rotational motions of the body. Its solution produces the *fundamental viscous solution* v_s^* which may be derived in analytical form (if possible) or by numerical means depending on the type of problem under examination.

For example, for transient translational motions only (i.e. $U(t)\neq 0$, $\Omega(t) = 0$) equation (11) reduces to

$$\dot{v}_{sj}^* - (\hat{U}.\nabla)\, v_{sj}^* - \nabla^2 v_{sj}^* - p_{s,j}^* = \delta_{sj}\,\delta(t)\,\Delta(r) \qquad (12)$$

which on comparison with equation (8) shows it to have a close affinity to the Oseen equation. By analogy to the term *stokeslet* adopted to describe the fundamental solutions in potential theory for a source and a doublet the fundamental viscous solution of equation (12) might be referred to as a *'transient oseenlet'*. In maritime engineering applications, this fundamental viscous solution is appropriate to model a body undertaking steady or unsteady prescribed motions associated with a steady state towing experiment or a planar motion mechanism (PMM) oscillatory experiment.

For transient rotational motions only ($\Omega(t)\neq 0$, $U(t) = 0$), equation (11) is suitably modified. In this case, the fundamental viscous solution can be used to represent a body rolling, pitching or yawing with no forward speed or a propeller rotating in still water.

For combinations of both translational and rotational motions, in principle, the developed fundamental viscous solution can be adopted to model the rolling, pitching or yawing motions of a body with forward speed, a propeller rotating behind a manoeuvring ship, a helicopter in flight, etc.

2.3 Integral Equation

We shall assume that solutions v_s^* and p_s^* can be obtained from the fundamental equation in either analytical or numerical form. The substitution of these solutions together with their initial conditions into the convolution-integral identity produces an integral equation of the form:

$$C(q)v_s(q,t) = \int_{\Sigma} \left\{ v_s^{*}*\left[R - (U.n)v + n\{(\Omega x U).x\} - nx\{vx(\Omega x x)\}\right] - v^* R_s^* \right\} d\Sigma - \int_{\Omega} v_s^{*}*\left[(v.\nabla)v - f\right] d\Omega \qquad (13)$$

where

$$C(q) = \begin{cases} 0 & \text{if } q \in (\Omega \cup \Sigma) \\ 0.5 & \text{if } q \in \Sigma \\ 1 & \text{if } q \in \Omega \end{cases}$$

This equation relates the disturbed fluid velocity vector $v(q,t)$, with element v_s, to the force R experienced by the body. The boundary Σ in this equation consists of a combination of the boundary around the body, Σ_b, and an outer boundary around the fluid at infinity, Σ_∞, such that $\Sigma = \Sigma_\infty - \Sigma_b$.

Now on Σ_∞ we have

$$v(x,t) = 0, \quad R(x,t) = -np_\infty$$

and

$$\int_{\Sigma_\infty} \{v_s^{*}*[R - (U.n)\,v + n\{(\Omega x U).\,x\} - n \times \{v \times (\Omega \times x)\}] - v * R_s^*\}\, d\Sigma = 0$$

whereas on Σ_b, $v = -U - \Omega \times x$, it can be shown that the following result is valid:

$$-\int_{\Sigma_b} v^* R_s^* d\Sigma = -\{1 - C(q)\}(U + \Omega x q) + \int_{\Omega_b} v_s^{*}*[\dot{U} + \dot{\Omega} x x]d\Omega + \int_{\Sigma_b} v_s^{*}*\{(U.n)\,v + nx[vx(\Omega x x)]\}\, d\Sigma$$

where Ω_b denotes the volume domain of the body. Substituting this result into equation (13) we find the integral equation takes the form

$$C(q)v(q,t) = \{1 - C(q)\}(U + \Omega x q) - \int_{\Omega_b} v_s^{*}*[\dot{U} + \dot{\Omega} x x]d\Omega - \int_{\Sigma_b} v_s^{*}*[R + n\{(\Omega x U).x\}]\, d\Sigma - \int_{\Omega} v_s^{*}*[(v.\nabla)v - f]d\Omega \qquad (14)$$

or,

$$C(q)v(q,t) = \{1 - C(q)\}(U + \Omega x q) - \int_{\Sigma_b} v_s^{*}*[R + n\{(\Omega x U).x\} + n(\dot{U}.x) + \frac{1}{2}x^2\dot{\Omega} x n]d\Sigma + \int_{\Omega_b} (\nabla x v_s^{*})*(\frac{1}{2}x^2\dot{\Omega})d\Omega - \int_{\Omega} v_s^{*}*[(v.\nabla)v - f]d\Omega \qquad (15)$$

Both these non-linear integral equations retain force R and fluid velocity v as the basic unknows which can be obtained directly from the discretised form of these equations. In principle this direct approach should increase the efficiency of any numerical procedure developed as well as enhancing numerical accuracy.

FUNDAMENTAL TRANSIENT SOLUTIONS

The solution of the previous two integral equations depends on deriving the fundamental viscous solution v_{sj}^* in equation (11). In this section we discuss the form of the solutions appropriate to an arbitrary shaped body undergoing unsteady translational and/or rotational motions.

Translations

For a body in translational motion only (i.e. $U(t) \neq 0$, $\Omega(t) = 0$), the equations to be solved to determine the fluid velocity v and force R are:

$$C(q)v(q,t) = \{1 - C(q,t)\}U - \int_{\Omega_b} v_s^* * \dot{U} d\Omega - \int_{\Sigma_b} v_s^* * R d\Sigma -$$

$$\int_{\Omega} v_s^* * \left[(v.\nabla)v - f\right] d\Omega$$

$$= \{1 - C(q)\}U - \int_{\Sigma_b} v_s^* * \{R + (\dot{U}.x)n\}\, d\Sigma -$$

$$\int_{\Omega} v_s^* * \left[(v.\nabla)v - f\right] d\Omega \ , \qquad (16)$$

and

$$\dot{v}_s^* - \left(\hat{U} \cdot \nabla\right) v_s^* - \nabla^2 v_s^* - \nabla p_s^* = \delta_s \delta(t) \Delta(r) \ ,$$

$$\nabla . v_s^* = 0, \qquad (17)$$

together with $v_s^*(r,0) = 0$, $v_s^*(\infty,t) \to 0$.

For a two-dimensional translatory problem (s, j = 1, 2), it can be shown that solutions to equation (17) are of the form:

$$v_{sj}^*(r,t) = \frac{\delta_{sj}}{4\pi t} e^{-(\bar{r}^2/4t)} + \frac{1}{4\pi}\left\{\ln\left(\frac{1}{\bar{r}^2}\right) - E_1\left(\frac{\bar{r}^2}{4t}\right)\right\}_{,sj}$$

$$= \frac{1}{4\pi t}\left\{\delta_{sj} - \frac{\bar{r}_s \bar{r}_j}{\bar{r}^2}\right\} e^{-(\bar{r}^2/4t)} - \frac{\left\{1 - e^{-(\bar{r}^2/4t)}\right\}}{2\pi \bar{r}^2}\left(\delta_{sj} - 2\frac{\bar{r}_s \bar{r}_j}{\bar{r}^2}\right), \qquad (18)$$

$$p_s^*(r,t) = \frac{\delta(t)}{4\pi}\left\{\ln\left(\frac{1}{r^2}\right)\right\}_{,s} \ , \qquad (19)$$

whereas for the three-dimensional translatory problem (s, j = 1, 2, 3) we have

$$v_{sj}^*(r,t) = \frac{\delta_{sj}}{(4\pi t)^{3/2}} e^{-(\bar{r}^2/4t)} + \frac{1}{4\pi}\left\{\frac{1 - \mathrm{erf\,c}(|\bar{r}|/2t^{1/2})}{|\bar{r}|}\right\}_{,sj} \ , \qquad (20)$$

$$p_s^*(r,t) = \frac{\delta(t)}{4\pi}\left(\frac{1}{r}\right)_{,s} . \qquad (21)$$

Here,

$$\bar{r} = r + \zeta, \quad \zeta(t) = \int_0^t \hat{U}(\eta)\, d\eta, \quad r = |x - q|$$

is the distance between the field point x and the source point q, $\bar{r}_s$ is the sth component of the vector $\bar{r}$ and the exponential integral

$$E_1(x) = \int_x^{\infty} \{e^{-\sigma}/\sigma\}\, d\sigma, \qquad |\arg(x)| < \pi$$

and the complementary error function

$$\mathrm{erfc}(x) = (2/\sqrt{\pi}) \int_x^{\infty} e^{-\sigma^2}\, d\sigma \ ,$$

as defined by Abramowitz and Stegun [17].

Rotations

In the case of a body rotating with angular velocity $\Omega(t)$ only (i.e. $U(t) = 0$, $\Omega(t) \neq 0$) the equations to be solved are:

$$C(q)v_s(q,t) = \left\{1 - C(q)\right\}(\Omega x q) - \int_{\Sigma_b} v_s^* * R d\Sigma$$

$$- \int_{\Omega_b} v_s^* * (\dot{\Omega} x x) d\Omega - \int_{\Omega} v_s^* * \left[(v.\nabla)v - f\right] d\Omega \ , \qquad (22)$$

and

$$\dot{v}_s^* + (\hat{\Omega} x x) x (\nabla x v_s^*) - \nabla^2 v_s^* - \nabla p_s^* = \delta_s \delta(t) \Delta(r) \ ,$$

$$\nabla . v_s^* = 0 \ , \qquad (23)$$

and $v_s^*(r,0) = 0$, $v_s^*(\infty,t) \to 0$.

Now for simplicity, and luckily it holds for many practical applications, we shall restrict our solutions to the case in which the axis about which the body fixed coordinate system rotates does not change its orientation in a space fixed coordinate system. That is, $\hat{\Omega}$ can be written in the form

$$\hat{\Omega}(t) = \hat{\Omega}(t)\, m$$

where $\hat{\Omega}$ is a scalar function of time and m is a constant unit length vector.

For a two-dimensional rotatory problem (s, j, k = 1,2) it can be shown that solutions to equation (23) are of the form:

$$v_{sj}^*(r,t) = \frac{\delta_{sk}\cos\Theta + c_{3ks}\sin\Theta}{4\pi}\left\{\frac{\delta_{kj}}{t} e^{-(\bar{r}^2/4t)} + \left[\ln\left(\frac{1}{\bar{r}^2}\right)\right.\right.$$

$$\left.\left. - E_1\left(\frac{\bar{r}^2}{4t}\right)\right]_{,kj}\right\}$$

$$- \frac{\left(\delta_{sk}\cos\Theta + e_{3ks}\sin\Theta\right)}{4\pi} \left[\left(\delta_{kj} - \frac{\bar{r}_k\,\bar{r}_j}{\bar{r}^2}\right)\frac{e^{-(\bar{r}^2/4t)}}{2t} - \left(\delta_{kj} - \frac{2\bar{r}_k\,\bar{r}_j}{\bar{r}^2}\right)\left(\frac{1 - e^{-(\bar{r}^2/4t)}}{\bar{r}^2}\right)\right] , \qquad (24)$$

whereas for the three-dimensional case (s, j, k = 1, 2, 3) we have

$$v_{sj}^*(\mathbf{r},t) = \frac{\left(\delta_{sk}\cos\Theta + e_{ksi}m_i\sin\Theta + m_s m_k(1 - \cos\Theta\right)}{4\pi} \times \left\{\frac{\delta_{kj}e^{-(\bar{r}^2/4t)}}{(4\pi t^3)^{1/2}} + \left[\frac{1 - \mathrm{erfc}(|\bar{r}|/2t^{1/2})}{|\bar{r}|}\right]_{,kj}\right\} \qquad (25)$$

In these expressions we define

$$\Theta(t) = \int_0^t \hat{\Omega}(\eta)\, d\eta ,$$

$$\bar{\mathbf{r}} = \mathbf{r} + (1 - \cos\Theta)\,\mathbf{m} \times (\mathbf{q} \times \mathbf{m}) + \sin\Theta\,(\mathbf{m} \times \mathbf{q}),$$

and the permutation operator $e_{jin} = 0$ if j = i or j = n or i = n, $e_{123} = e_{231} = e_{312} = 1$ and $e_{132} = e_{213} = e_{321} = -1$.

The fundamental viscous solution for steady translational and rotational motions can be derived by integrating these solutions over the whole time domain. That is,

$$v_{sj}^*(\mathbf{r}) = \int_0^\infty v_{sj}^*(\mathbf{r},t)\, dt \qquad (26)$$

For steady translational motions, this mathematical model [8,9,13,14] agrees with a model derived previously by alternative methods [18,19] and also with the fundamental viscous solutions obtained [20-23].

For steady rotational motions, because of the complicated expressions for the integrand in equation (26) there appears to be no easily derived analytic expression and therefore numerical integration is required to obtain a steady state fundamental solution.

NUMERICAL SOLUTIONS AND DISCUSSION

Linear and Non-Linear Models

Equations (13-15) contain a mixture of surface and volume integrals. The latter represents the non-linear convective term which introduces numerical complexities into the numerical scheme of study.

For small Reynolds number flows, the fluid flow can be represented as an Oseen flow and the non-linear convective term in the theory neglected with confidence. This simplifying approximation reduces the computation to a linear one and solutions for the unknowns v and R are relatively simple to obtain requiring only a viscous element distribution and boundary integration over the wetted surface of the body. However, for increasing Reynolds number flows the justification of such an approximation becomes less and less tenuous though, for comparison purposes, we shall retain this approximation and refer to the resulting numerical scheme as the *linearised model.* This does not imply that viscous effects are discarded since these and the non-irrotational nature of the flow are retained in the fundamental viscous solution v_s^*. The findings from this linearised model can be compared to the predictions derived from the *non-linear model* in which we retain in the analysis the fluid domain integral accounting for the contribution of the non-linear convective term.

Fundamental Solutions

In a previous investigation [8], a selection of analytic expressions describing the fundamental viscous solution were derived and their forms discussed. These are solutions to equation (11) and are applicable to steady and unsteady translational and/or rotational problems involving viscous fluid-structure interactions. In principle, equation (11) can be solved numerically but, so far, we have concentrated on solutions which can be derived analytically and have direct relevance to practical problems; they also allow the characteristics of the flow field generated by the fundamental solution to be widely investigated. For example, for an oscillating viscous source the fundamental solution generates an oscillatory vortex wake, a rotating and translating viscous source creates a helical vortex wake, etc. These forms of solution have been illustrated previously and are therefore omitted from the present discussion. Here we focus attention on the range of applicability of the proposed viscous boundary element method to tackle typical steady and unsteady dynamical problems arising in maritime engineering science i.e. resistance, manoeuvring, seakeeping, etc.

Resistance of a Flat Plate

For a flat plate in an uniform steady flow, U(t) = U a constant, figure 1 illustrates the variation of the calculated drag coefficient Cd over the Reynolds number range $0 < Re < 10^6$. These findings are compared with data derived from Blassius' flat plate formula and other analytical expressions [24] dependent on the degree of approximation (i.e. Reynolds number) assumed in the development of the theoretical formula. It is well known that in laminar flows such analytical expressions describe satisfactorily the magnitude of the observed forces on a flat plate but fail when transition and turbulence occurs. The steady state viscous boundary model suffers a similar fate since it is restricted to non time dependent flows and its extension is being further investigated.

From the evidence presented in figure 1, it is clearly seen that the comparison between the non-linear predictions and analytical findings are favourable and hence also with measured data [25]. This comparison confirms with a degree of confidence the ability of the non-linear model to determine magnitudes of fluid actions and flow fields with reasonable accuracy and that the idealisation, convergence and tolerance procedures admitted into the numerical scheme are adequate. Furthermore, no numerical difficulties (e.g. instabilities, etc) were experienced in deriving these results.

Figure 1 also highlights the tendency of the linearised model to overestimate the predicted values derived from the non-linear model but, at low Reynolds number, the contribution

of the non-linear term diminishes and the two models produce comparable results.

An Oblique Towing Test

In this application of the theoretical model, we concentrate on translational motions attempting to model mathematically a typical steady state oblique towing tank experiment to measure slow motion derivatives e.g. heave, sway or surge velocity derivatives. That is, the body is accelerated from rests and then travels at a constant speed along the tank. This experiment is repeated at different drift angles, β, and the variation of fluid action with angle recorded, thus allowing the slow motion derivative to be deduced.

Figure 2(a) illustrates a typical velocity-time history of the prescribed forward motion of the chosen body (i.e. a two-dimensional ellipse of length to beam ratio 10:1); this description of the motion corresponds to the experiment. Although such a test is referred to as *steady state* it contains unsteady (accelerating) and steady (constant velocity) phases. Because of this the two-dimensional transient fundamental viscous solution was used to model the complete numerical experiment. In contrast to previous studies using the steady state model only [13,14], this transient model is less restrictive in its range of application and in its ability to describe flow fields allowing time history effects to be included in the predictive procedures. It also follows that steady state values now correspond to predictions carried out at a large time interval from the start of the experiment when the ellipse is travelling at constant speed, uninfluenced by earlier unsteady fluid motions and the flow around the ellipse and into the wake remains constant with time implying that the interactive influence of the wake on the incoming flow (i.e. feed-back) is constant or zero.

Figure 2(b) shows the time histories of the drag force (β=0) with Reynolds number Re=1000 and Figure 2(c) illustrates the variation of its steady state value with Reynolds number. Again we see the linearised model over-estimates the corresponding values determined from the non-linear model. For Reynolds number Re=200, Figure 2(d) shows the variation of the steady state lift and drag coefficients with drift angle β, from which slow motion velocity derivative data may be deduced.

On passing it is interesting to note that during the initial stages of motion, a starting vortex is created in the flow which sheds from the ellipse into the wake and passes downstream. The strength of this vortex flow depends upon the intensity of the acceleration.

Rotations: Rotating Arm Test

Let us now briefly focus attention on rotational motions and, in the first instance, consider the modelling of a rotating arm experiment. In this test, the attached model is suspended at a fixed distance (radius) along an arm which is set into a circular motion. The model travels a circular path of fixed radius and of known angular velocity which has a time history simililar to the trace illustrated in Figure 1. That is, there is an initial unsteady accelerating phase and a subsequent steady period of constant angular velocity.

Although such experiments purport to measure steady state values, in many ways, they are far less exact and steady compared to the oblique tow test. For example, there is only a limited circumferential path in which the flow onto the model is as defined though unsteady effects in the wake may still influence the fluid actions on the body; after an interval of time, the model passes through its own created wake thus influencing the flow over the body which may be steady but not necessarily as prescribed, etc. In principle, because time histories of the motions are retained in the proposed unsteady mathematical model, the scenarios described can be modelled. However, in the findings presented in Figure 3 such details are not included in the modelling of the numerical experiment. This diagram illustrates the predicted flow field around an ellipse travelling along a circular path and clearly shows the existence of a cross flow over the ellipse and the shedding of vortices into the circular wake.

Oscillatory PMM Experiment

Through the transient fundamental solutions, oscillatory (or random) translational and/or rotational experiments can be modelled. By way of a simple example, let us consider a traditional unsteady sway PMM experiment involving the ellipse. That is, the ellipse is towed along a towing tank at a prescribed forward speed in conjunction with an imposed parasitic transverse oscillatory motion of known frequency and amplitude.

Figure 4(a) illustrates a typical time-history of the unsteady motion; Figure 4(b) shows the vortices shed into the wake and Figure 4(c) illustrates the fluid actions experienced by the ellipse at prescribed conditions defined by the Reynolds and Strouhal numbers. By repeating such numerical experiments at different prescribed conditions a data set can be created from which both velocity and acceleration derivative values may be deduced.

Rotations: Rolling

Two further numerical experiments are briefly discussed in which no prescribed translational motion occurs. Namely, an infinitely long cylinder or two-dimensional disc rotating at constant angular velocity Ω_0 after starting from rest and a two-dimensional representation of an idealised ship section in oscillatory roll motion.

The cylinder problem allows a preliminary validation of the numerical techniques with analytical solutions and, furthermore, to allow speculation as to whether or not the proposed mathematical model can be extended to provide a new viscous flow-propeller theory.

The analytical solution

$$v(t) = -(\Omega_0 a^2/r)\, e^{-r^2/4t}$$

provides information on the tangential flow field at radial distance r measured from the centre of a cylinder of radius a rotating at an angular velocity

$$\Omega(t) = -\Omega_0\, e^{-a^2/4t} .$$

The resultant moment acting on the rotating cylinder by the viscous fluid is given by:

$$M(t) = -4\pi a^2 \Omega_0 [1 + (a^2/4t)]\, e^{-a^2/4t}$$

At $t = 0$, $\Omega = 0$, $v = 0$ and $M = 0$ whereas, the steady state solution obtained in the limit as $t \to \infty$ is given by $\Omega \to -\Omega_0$, $v \to -\Omega_0 a^2/r$ and $M \to -4\pi a^2 \Omega_0$ in accordance with the classical solution obtained by Milne-Thomson [26].

Figure 5(a) shows a comparison between numerically and analytically derived values of these parameters. Their close agreement clearly demonstrates the accuracy of the developed numerical scheme of study and a measure of validation of the proposed mathematical model.

In its simplicity, the disc can be thought of as a very crude idealisation of a propeller. However by changing the geometry of the disc we can achieve a more realistic propeller shape, yet this does not prevent us using the same mathematical model. This needs further investigation, but if proved successful it follows that by introducing the three-dimensional transient rotational fundamental viscous solution into the mathematical model a more realistic propeller geometry-viscous fluid theory can be created.

The rolling of a two-dimensional idealised ship section is analogous to the cylinder problem but now the rotating motion is fully unsteady through the imposed oscillatory or random motion. Figure 5(b) illustrates a selection of flow fields generated around two typical ship like sections and the corresponding excited moments.

The mathematical model may be further extended to include both translational and rotational motions [8] which will be described fully at a future occasion.

CONCLUSIONS

For manoeuvring related viscous hydrodynamic problems involving a body moving with translations and rotations, the proposed general, unified viscous boundary element method based on fundamental viscous transient solutions is found suitable to describe viscous fluid-structure interactions. The results presented are encouraging but further investigations and numerical experiments are necessary to evaluate the range of applicability of the developed mathematical model, its ability to provide a detailed description of the fluid-structure mechanisms in increasing Reynolds number flows and to validate the numerical scheme of study for more complex shaped bodies in steady viscous flows (i.e. body-appendage configurations, three-diemnsional bodies, etc).

The wide range of applicability of the viscous theoretical model demonstrated herein creates optimism and initial indicators suggest that the developed general theory can, with suitable modifications, find application in the wider context of rolling motions, propeller theory, hull-propeller interactions as well as describing the behaviour of a flexible structure distorting in an unsteady viscous flow i.e. a viscous hydroelasticity theory.

ACKNOWLEDGEMENT

We are grateful to Dr. A.J. Musker of the Defence Research Agency (Maritime), Haslar for his encouragement in this project and to DRA for financial support.

REFERENCES

1. Mandel, P. 1967. Ship Manoeuvring and Control. In *Principles of Naval Architecture* (ed. J.P. Comstock). SNAME, New York, 1967, 403-606.
2. Booth, T.B. and Bishop, R.E.D. The Planar Motion Mechanism. *Admiralty Experiment Works*, 1973.
3. Gerritsma, J. and Beukelman, W. The Distribution of the Hydrodynamic Forces on a Heaving and Pitching Ship Model in Still Water. *Fifth Symposium on Naval Hydrodynamics*, 1964, 219-251.
4. Bishop, R.E.D. and Price, W.G. *Hydroelasticity of Ships*. Cambridge University Press, 1979.
5. Newman, J.N. *Marine Hydrodynamics*. Cambridge (Mass): M.I.T. Press, 1977.
6. Price, W.G. (Ed.) *The Dynamics of Ships*. Proceedings of a Royal Society Discussion Meeting. The Royal Society, London, 1991.
7. Faltinsen, O.M. *Sea Loads on Ships and Offshore Structures*. Cambridge University Press, 1990.
8. Price, W.G. and Tan, Mingyi. Fundamental Viscous Solutions or 'Transient Oseenlets' Associated with a Body Manoeuvring in a Viscous Fluid. *Proc. R. Soc. London*, A438, 1992. 447-466.
9. Price, W.G. and Tan, Mingyi. A Viscous Boundary Approach to Evaluate Slow Motion Derivatives. *Int. Symposium on Maneouvring and Control of Marine Craft '92*, University of Southampton, Computational Mechanics Publ. 1992, 437-449.
10. Hogben, N. and Standing, R.G. 1975. Wave Loads on Large Bodies. *Int. Symposium on the Dynamics of Marine Vehicles and Structures in Waves*. Mech. Eng. Publ. London, 1975, 273-292.
11. Faltinsen, O.M. and Michelsen, F.C. Motions of Large Structures in Waves at Zero Froude Number. *Int. Symposium on the Dynamics of Marine Vehicles and Structures in Waves*. Mech. Eng. Publ. London, 1975, 99-114.
12. Bishop, R.E.D., Price, W.G. and Wu, Yousheng. A General Linear Hydroelasticity Theory of Floating Structures Moving in a Seaway. *Phil. Trans. Roy. Soc. London* A 316, 1986, 375-430.
13. Price, W.G. and Tan, Mingyi. The Calculation of Fluid Actions on Manoeuvring Arbitrary Shaped Submerged Bodies Using Viscous Boundary Elements. *Eighteenth Symposium on Naval Hydrodynamics*, 1991, 801-814.
14. Price, W.G. and Tan, Mingyi. The Evaluation of Steady Fluid Forces on Single and Multiple Bodies in Low Speed Flows Using Viscous Boundary Elements. *Dynamics of Marine Vehicles and Structures in Waves* (ed. W.G. Price, P. Temarel and A.J. Keane), Elsevier, 1991, 125-133.
15. Stokes, G.G. On the Effect of the Internal Friction of Fluids on the Motion of Pendulum. *Trans. Camb. Phil. Soc.* 9, 1851, 8-106.
16. Oseen, C.W. Uber die Stokessche Formel und über die verwandte Aufgabi in der Hydrodynamic. *Arkiv Math., Astronomi och Fysck* 6, 1910, 29.
17. Abramowitz, M. and Stegun, I.A. (eds). *Handbook of Mathematical Functions*. New York, Dover Publications, 1972.
18. Kinoshita, T. On the Two Dimensional and the Axi-symmetric Oseen Flow Past an Arbitrary Body. *J. Soc. Nav. Archit. Japan*. 134, 1973, 1-13.
19. Kinoshita, T. The Iterative Method of Solving the Navier-Stokes Equations Based on Oseen Flow. Contribution to the 44th Japanese Towing Tank Conference (Panel 1), 1977.
20. Bessho, M. Study of Viscous Flow by Oseen's Scheme. (Two-dimensional Steady Flow). *J. Soc. Nav. Arch. Japan* 156, 1984, 37-49.
21. Bessho, M. Study of Viscous Flow by Oseen's Scheme. (Two-dimensional Oscillating Flow). *J. Soc. Nav. Arch. Japan*. 157, 1985, 70-81.
22. Bessho, M. Study of Viscous Flow by Oseen's Scheme. (Three-dimensional Steady Flow and Wing Theory). *J. Soc. Nav. Arch. Japan* 157, 1985, 40-47.
23. Bessho, M. Study of Viscous Flow by Oseen's Scheme

(Two-dimensional Oscillating Flow with Uniform Velocity). *J. Soc. Nav. Arch. Japan* 161, 1987, 42-48.

24. Rosenhead, L, *Laminar Boundary Layers.* Oxford University Press, 1963.
25. Todd, F.H. Resistance and Propulsion. *In Principles of Naval Architecture* (ed. J.P. Comstock). SNAME, New York, 1967, 288-462.
26. Milne-Thomson, L.M. *Theoretical Hydrodynamics.* MacMillan, 1962.

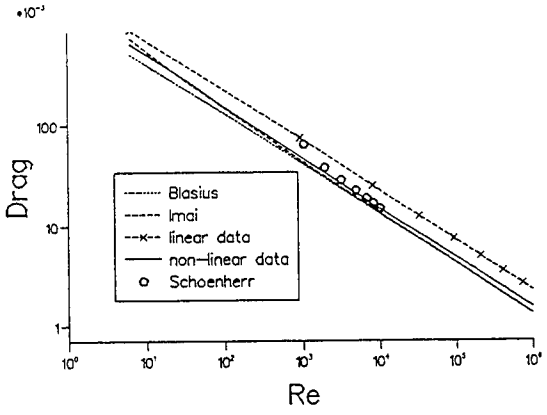

Figure 1: The variation of the drag coefficient for a flat plate against Reynolds number. The figure shows a comparison between analytic solutions [24], experimental data [25] and numerical solutions obtained from the non-linear and linearised mathematical models employing steady state translational oseenlet solutions [8].

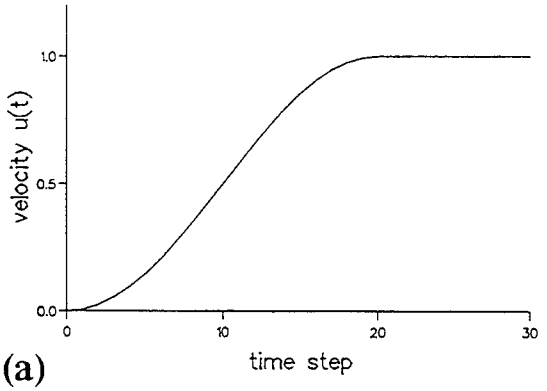

Figure 2: (a) Velocity-time history of the prescribed forward motion of the ellipse.
(b) Variation of the drag coefficient with time (Re = 1000).
(c) Variation of the steady state drag coefficient with Reynolds number.
(d) Variation of the steady state lift and drag coefficients with angle of attack (Re = 200).
In the linearised and non-linear mathematical models the transient translational oseenlet solution described herein is used.

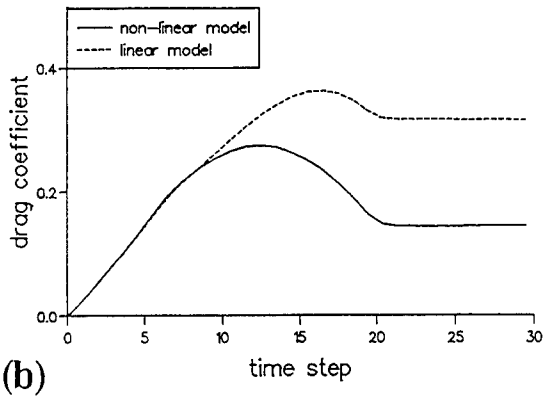

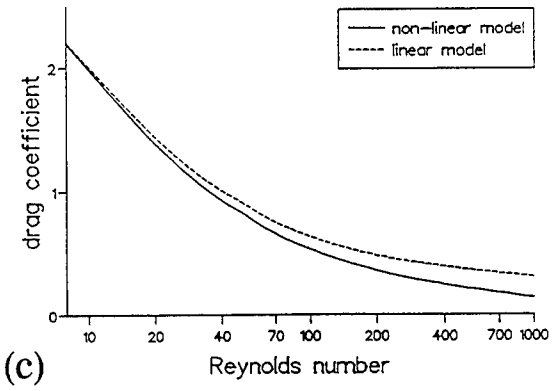

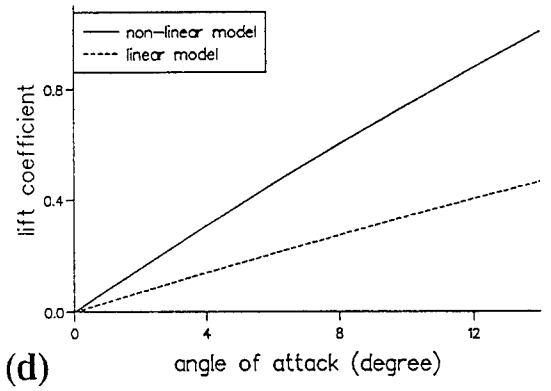

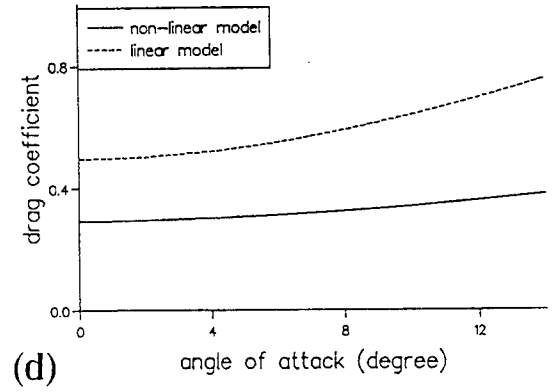

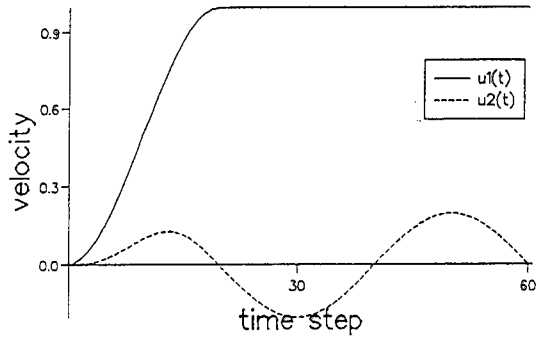

(a)

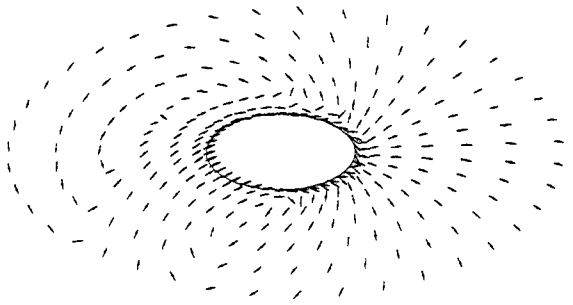

Figure 3: Predicted instantaneous flow field around an ellipse travelling clockwise around a circular path as would occur in a rotating arm experiment. This result is derived from the linearised mathematical model using the transient rotating oseenlet solution.

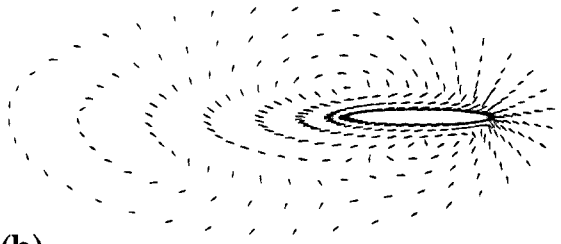

(b)

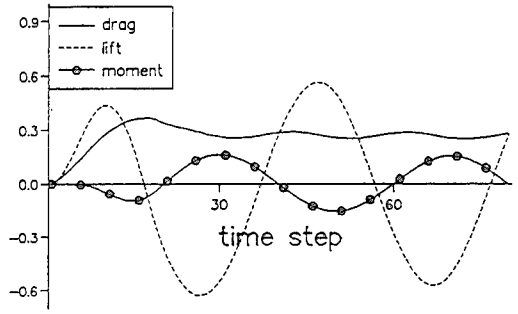

(c)

Figure 4: (a) Velocity time history of the prescribed forward motion, $u_1(t)$, and transverse sinusoidal motion, $u_2(t)$, of the ellipse as would occur in a planar motion mechanism experiment.
(b) Predicted instantaneous flow field around an ellipse undergoing oscillatory and forward motions.
(c) Variation of the fluid actions with time for the described PMM experiment.
These results are obtained from the non-linear mathematical model employing the transient translational oseenlet solution.

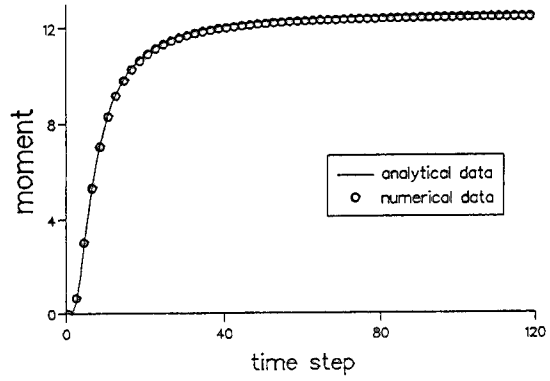

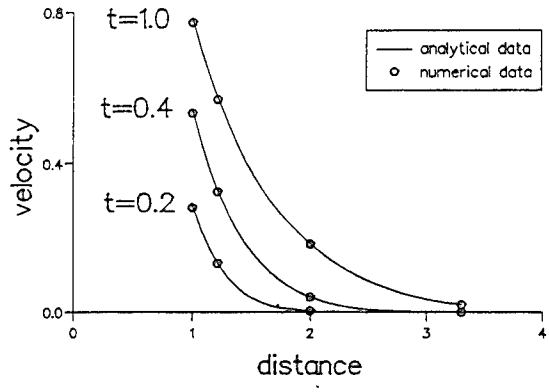

Figure 5: (a) Comparison of analytically predicted and numerically derived results for the variation of the moment with time experienced by an infinitely long, rotating cylinder and the variation of the velocity flow disturbance with radial distance measured from the centre of the cylinder at different instants of time (t = 1.0 corresponds to 50 time steps). The numerical results are obtained from the linearised model employing the transient rotating oseenlet solution.

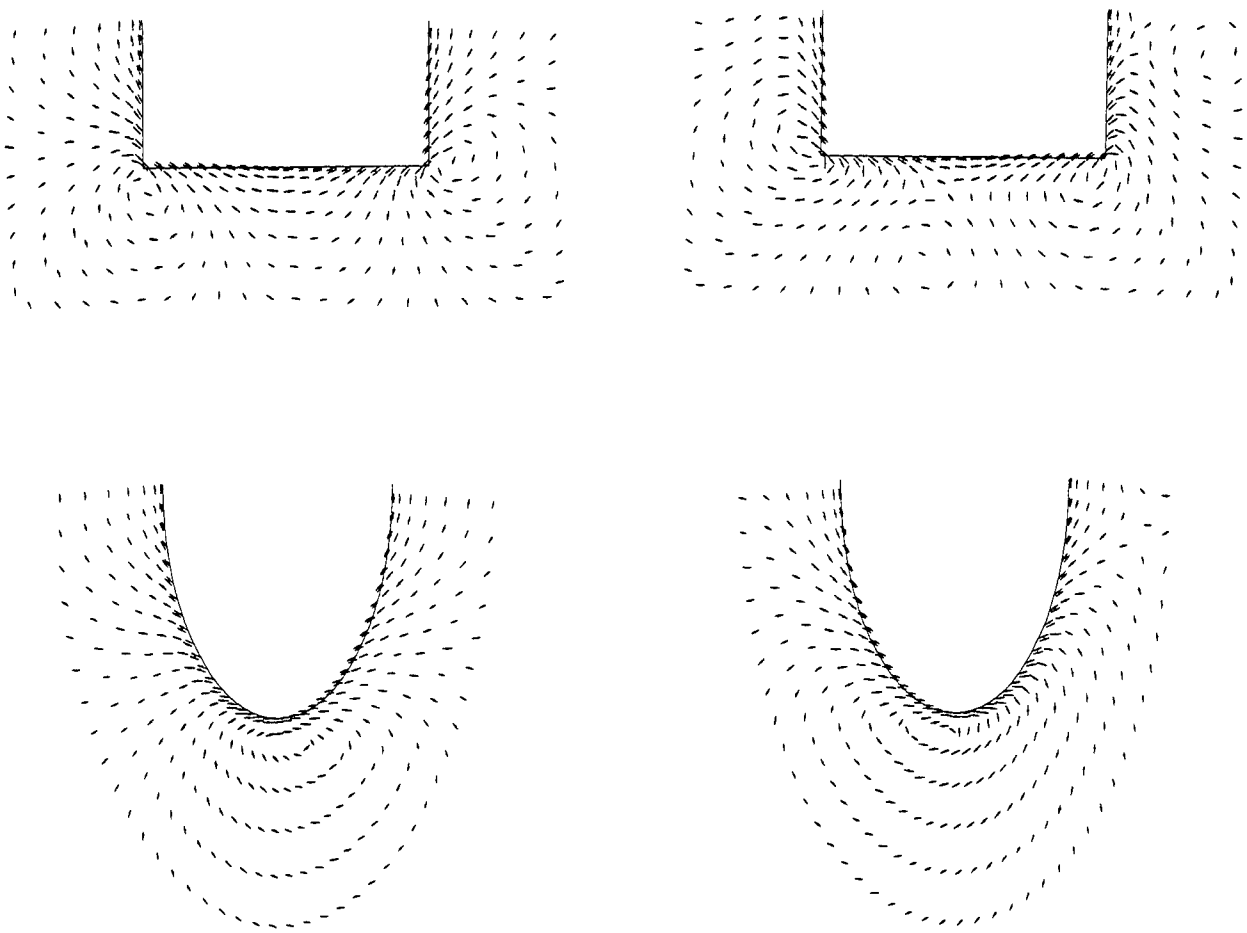

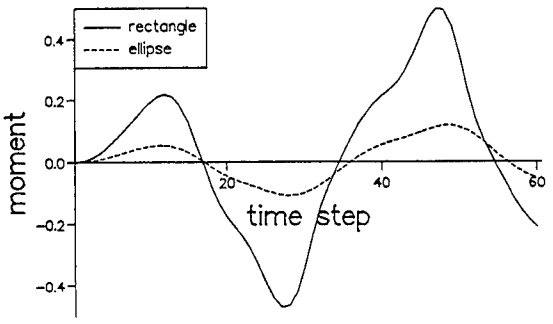

Figure 5: (b) A selection of predicted instantaneous flow fields around a rectangular and a half elliptic two dimensional ship section rolling sinusoidally. Note the clear shedding of vortices with different directions of circulation around the rectangular section and to a lesser extent around the smoother curved section. The corresponding calculated variations of moment against time clearly show marked differences in magnitude caused by form shape and by the visible different intensities of vortex shedding.

DISCUSSION

H. Maeda
University of Tokyo, Japan

I would like to express congratulations for the formulation of a general unified viscous boundary element theory.

I would like to discuss about three subjects.

1. We could not be free from the volume integral term in the right hand side of the equation (13) in this kind of nonlinear problem, which may give us some difficulty for numerical procedure. Especially as to with-uniform-velocity problem, I think we have to extend the volume range for this volume integration according to each time step. Would you please tell me how to decide the volume boundary and how to evaluate this term?

2. I could not follow the derivation procedure of the equation (11) which looks like the Oseen equation, and also the derivation of equation (10) which may be explained in Proc. R. Soc. Lond. Would you please explain briefly the derivation of these equations?

3. The authors treated unsteady problem for instance PMM in time domain, while the same kind of oscillating problems were treated by Bessho in frequency domain. These two domains may be related through Fourier Transformation. In my opinion, time domain procedure is appropriate for problems without uniform velocity, while frequency domain one for problems with uniform velocity. Can I ask your comment on this matter?

DISCUSSION

J. Graham
Imperial College of Science, Technology,
and Medicine, United Kingdom

This is an interesting paper which develops a boundary integral (panel) solution of Oseen's equation for unsteady viscous flow past a body.

My main comment concerns the application of the results because the Oseen equations would not in general be a good approximation to the flow field in the neighborhood of a body for Reynolds numbers much greater than about 5. The two examples given in the paper are special cases for which the Oseen equations give reasonable prediction at all Reynolds numbers. For the case of a steady state boundary layer on a flat plate the Oseen equations subject to a boundary layer approximation give

$$C_f = 2\sqrt{\pi} \cdot R_x^{-1/2}$$

which is similar to but larger than the Blasius result of

$$C_f = 0.664\ R_x^{-1/2}.$$

In the case of the rotating cylinder, the exact result satisfies the Stokes equations and hence the Oseen equations since $U.\nabla U$ is identically zero. Therefore, the agreement shown for these special cases certainly validates the numerical method but not its range of application to general cases. The results for rolling hulls seem to me to be qualitatively realistic and may give useful approximations. However, in my opinion, they cannot be formally correct at significant Reynolds numbers because the nonlinear quadratic velocity term in the Navier Stokes equations which is neglected in the Oseen approximation would be large in the neighborhood of the bilges where the vortex shedding takes place.

Does the addition of the volume integral term (the nonlinear model) incorporate the full nonlinear terms, or does it introduce the next term in the series of which the Stokes/Oseen term is the first? It would be useful to know how easy it is to compute this term for general cases, since it does improve the results.

It would also be useful to carry out further comparisons between the results of the method and exact computations of separated flow.

AUTHORS' REPLY

We are grateful to Professor Graham and Professor Maeda for their valued contributions to our paper.

Before discussing their comments in detail it might be useful to clarify points of presentation and to stress that the paper presents an exact theory to the solution of Navier-Stokes equation applied to a body maneuvering in an unsteady viscous fluid flow. That is, the non-linear mathematical model involving a convolution-integral formulation relating directly force to flow velocity in equation (10) is derived without recourse to simplification through

approximation. Secondly, the fundamental viscous equation in equation (11) evolves directly from this non-linear mathematical model and has been introduced to simplify the mathematical model. Solutions to this equation allow simplifications to the model without approximation but a non-linear relation between force and flow velocity is retained in the integral formulation. Perhaps, on hindsight, it is misleading to the reader to refer to these fundamental viscous solutions as transient oseenlets for there exists the false interpretation that we are studying only solutions to Oseen's equation to describe a body maneuvering in a viscous fluid. This is certainly not what is being investigated. It is coincidential that the fundamental viscous equation is a variant of Oseen's equation and we have brought this to the reader's attention since a large literature exists on this subject. What we are studying and what is described in the paper is the maneuvering of a rigid body in an unsteady viscous flow through an exact non-linear theory based on a boundary element method applied to Navier-Stokes equation. By retaining the quadratic velocity term through the volume integral, full non-linear solutions of the forces and velocity flow field are derived whereas neglect of this quadratic term provides a linear approximated theory and hence linear solutions.

Professor Maeda raises three separate questions.

Firstly, the position of the boundary for the volume integration was judged through a numerical study of the sensitivity of converged solutions to the domain of integration. This problem remains under study but indications clearly show that solutions of forces are far less sensitive to domain of integration than predictions of the flow velocity field. Very small changes occurred in the force results when the domain was restricted to a few body lengths around the body or to a large distance from the body. In contrast, the velocity flow field was much more sensitive to the position of the domain which must be chosen to capsulate the total generation of the wake and hence the converged solutions describing the wake.

In answer to the second question, the application of the integral formula

$$\int_{\Omega} L(\nabla) d\Omega = \int_{\Sigma} L(n) d\Sigma$$

to each term on the left hand side of equation (10) produces the result conveyed in the right hand side of equation (10).

An extended form of the fundamental viscous solutions is given by us in the paper published in the Proceedings of the Royal Society.

We agree with Professor Maeda's interpretation of the appropriate procedures to adopt for the linear approximated theory and non-linear theory.

Professor Graham's contribution focuses on the application of boundary integral solutions of Oseen's equation for unsteady flow past a body. For the reasons stated, we apologize if we have caused confusion or misled him through our presentation. The introduction of the fundamental viscous equation and solution is only a mathematical way of simplifying the non-linear mathematical model without approximation. We agree with his comments about solutions to Oseen's equation but as demonstrated through steady state calculations on a flat plate, the proposed theoretical model produces satisfactory results over a wide range of Reynolds numbers. In fact, from Figure 1, the linear approximated theory gives a solution $C_f \simeq 1.13\, R_x^{-1/2}$ whereas the full nonlinear mathematical model produces the solution $C_f \simeq 0.75\, R_x^{-1/2}$ which is in close agreement with the Blasius result.

We agree with Professor Graham's comments about the numerical validation of the rotating cylinder example and also the qualitative realism of the flow field predicted for the case of a rolling hull. Our previous general discussion applies to these illustrations of rotational motions. Again the full nonlinear theory incorporates the quadratic velocity term through the volume integral based on the solution to the fundamental viscous solution which is used in both the linear approximated theory and full nonlinear theory. Naturally, because of the volume integral, the prediction of nonlinear solutions of force and flow velocities are numerically more difficult and consume more computer time, but this is being addressed as well as comparisons undertaken between the proposed approach, other derived solutions, and experimental data.

Vortical Flows With and Without a Surface-Piercing Body

R. Yeung, P. Ananthakrishnan
(University of California, Berkeley)

ABSTRACT

Unsteady vortical flow about a two-dimensional body translating in a free surface is analyzed, with specific attention paid towards the mechanism of vorticity generation in front of the body. The Navier-Stokes equations with the appropriate free-surface conditions are solved in primitive variables form. Effects of surface tension and surface contaminants are also considered in the analysis. The solution procedure exploits a specially developed variational-based grid-generation algorithm that can handle large-amplitude waves. A projection fractional-step method is used to advance the pressure and velocity fields in time.

Mechanisms associated with the formation of bow vortices are examined by replacing the exact free-surface conditions by (i) free-slip, (ii) no-slip, and (iii) linearized surfactant conditions. Results for these cases suggest that the commonly observed trapped vortex and stagnant flow in laboratory scale would not be present in full-scale. Results based on the fully nonlinear free-surface conditions reveal bow waves of decreasing wavelengths at low draft Froude number. Amplitudes of these short bow waves are suppressed by surface tension. At high Froude number, impulsive start of the body results in a splash; a gentler start leads to a plunging bow wave.

Also considered in the paper is the interaction of a pair of vortices moving upwards normal to the free surface. The fully nonlinear problem for a clean and a contaminated free surface is solved using the same solution method. In the absence of surface contaminants and at low Froude number, short transient waves are generated. The corresponding surface vorticity due to free-surface curvature is not sufficiently strong to alter the courses of the vortices. At intermediate Froude number, steepening of a transient wave is observed. The corresponding layer of secondary vorticity is observed to cause the primary vortices to rebound. Presence of surfactants not only suppresses free-surface deformations but also intensifies the generation of surface vorticity, thereby inducing the primary vortices to rebound even at low Froude number.

1 INTRODUCTION

Breaking of bow waves has been found to increase ship resistance [1]. The turbulent streaks of white waters also leave a distinctive signature in the ship wake. It is the primary objective of this work to examine closely the origin of such breaking. A secondary objective is to understand the behavior of vortical flow near a free surface, particularly in laboratory scale.

Experimental observations of the formation of bow vortices and the consequent separation of the flow upstream of a moving body have been made, for example, by Suzuki [2] and Honji [3]. Experimental results of Mori [4], Takekuma and Eggers [5], Osawa [6], etc. showed that the fitting of a bow bulb would accelerate the flow and reduce the intensity of bow vorticity.

Miyata *et al.* [7] found that at high Froude number, the steep waves generated alongside of the bow were nondispersive and they called them *free-surface shock waves.* Mori [4] analyzed an instability of the waves in the bow region which is quite different from plunging type breaking. Mori called this instability *sub-breaking* and argued that it was caused by turbulence and governed by the velocity-defect and the rate of flow deceleration.

Grosenbaugh and Yeung [8] reported and quantified an oscillatory motion of the bow-wave front which occurs when a certain critical speed is exceeded. In the presence of surface contaminants, they found that the oscillation can occur even below the critical speed. Some of the observations made by them have since been confirmed by Cole and Strayer [9].

Maruo and Ikehata [10] carried out experiments using ship models to study effects of surface tension in bow flows. They were able to reduce the surface tension by applying a surface-active compound. With the reduction of surface tension, they observed spilling type bow-wave breakings. They also argued that the free-surface shear layer is generated primarily by such wave breaking.

Several theoretical analyses were also carried out. First, let us review a few of those that are based on the inviscid-fluid assumption. Dagan and Tulin [11] obtained second-order solutions based on a small draft-Froude number expansion. Arguing that the bow-wave breaking is because of Taylor instability, they obtained a criterion for the breaking of the bow wave. Assuming steady state *a priori*, Tuck and Vanden-Broeck [12], [13] extended the analysis for the nonlinear case. According to these authors, bow- and stern-flow problems could be reversed; that is, if the geometry is just right a splashless, stagnation-type bow wave profile is possible, which would then correspond to a waveless stern flow. Using this approach, Madurasinghe [14] attempted to construct bow geometries that would be of a "waveless" type. More discussions of these may be found in Tuck [15].

Grosenbaugh and Yeung [16] obtained nonlinear inviscid-flow solutions using a mixed Eulerian-Lagrangian boundary-

integral method. Above a certain Froude number, which again depends on the bow geometry, the bow wave was found to be an overturning type. The stagnation point remains trapped beneath the free surface as the wave overturns. However, at low Froude number it was found that the stagnation point reaches the free surface in an oscillatory fashion as the transient waves propagate upstream. Recently, Yeung [17] repeated the above nonlinear calculations using finer node spacings. It was found that the splash occurring at the bow depends on the initial acceleration of the body. By making the initial acceleration of the body sufficiently small, he was able to "suppress" the splash at the bow as well as the breaking of the leading and following waves, thus allowing long-time solutions to be obtained. It was observed that waves of decreasing wavelengths are generated at the bow, implying that a steady-state stagnation-type solution may not exist even at low speed. Based on this inviscid-flow results, Yeung conjectured that these short bow waves could be responsible for the white-water type instability observed ahead of a blunt bow at low speed.

Theoretical studies incorporating the effects of viscosity are very few in number because of several inherent complexities posed by the governing equations. By using the free-surface normal-stress condition and the steady-state double-body potential-flow solution, Patel *et al.* [18] obtained a criterion for the flow separation ahead of the bow. This criterion assumes that surface tension is balanced by the normal component of the viscous stress. Despite these assumptions, experimental observations of [8] seem to suggest a good agreement with this criterion. Using a local expansion of the governing equations, Lugt [19] studied the properties of dividing streamlines at the interface of two fluids. In the case of a free surface, it was shown that the dividing streamline is normal to the interface. Lugt argued that surface tension does not provide any criterion for flow separation. On the other hand, dividing streamlines that are normal to the free surface have not been observed in experiments [8].

With the advent of high-speed and large-capacity computers, direct numerical solution seems to be a viable means to tackle the fully nonlinear viscous-flow problem. However, as we will see later, the governing equations are sufficiently complicated that the numerical analysis is not trivial. Miyata *et al.* [20] obtained bow-flow solutions using a Marker and Cell (MAC) method. In such a method, the free-surface conditions could be implemented only approximately. In particular, it is rather difficult to analyze the effects of surface tension and surfactants. Nevertheless, Miyata *et al.* were able to obtain qualitatively accurate results for large Froude numbers.

Notwithstanding all that has been understood by the above experimental and theoretical studies on bow flows, many issues remain unresolved. Mechanisms leading to the formation of bow vortices especially at low speed, source of white-water wave instability, effects of surface tension and surfactants in bow flows are a few such issues.

A somewhat closely related problem that has drawn the attention of hydrodynamicists in recent years is the interaction of vortices with a free surface. The motivation is to understand the generation of the wake signature behind a ship. For example, Sarpkaya [21] found that two distinct surface patterns are generated by a pair of vortices approaching a free surface, namely, *scars* and *striations*. The experimental findings of Sarpkaya provided impetus to several subsequent experimental and numerical works. Most of the numerical solutions, however, were based on the inviscid-fluid assumption (see Sarpkaya *et al.* [22], Telste [23], Yu and Tryggvason [24], Marcus and Berger [25]). Viscosity effects, leading to the generation of surface vorticity, could alter the flow pattern, particularly the trajectories of the primary vortices. Nonlinear viscous-flow analysis of Ohring and Lugt [26] show that generation of surface vorticity by curvature is strong enough to rebound the primary vortices at intermediate Froude numbers.

Experimental results of Bernal *et al.* [27] show that presence of surfactants could intensify the generation of surface vorticity even at low Froude number. This finding was confirmed by the numerical solutions of Wang and Leighton [28] and Tryggvason *et al.* [29]. However, in these viscous-flow calculations the free surface was assumed to be a rigid surface which is an assumption justifiable only at very low Froude number. Solution of the fully nonlinear problem corresponding to a contaminated free surface has not been attempted thus far.

In this paper, we develop and present solutions of the above two related free-surface flow problems: (1) the translation of a two-dimensional surface-piercing body and (2) vortex-pair and free-surface interaction. These unsteady, nonlinear viscous-flow problems are solved using a finite-difference method based on curvilinear coordinates and are subject to exact nonlinear free-surface conditions that take into consideration the presence of surface tension and of surfactants. The development of the solution method and the analysis of the bow-flow problem constituted the recently completed thesis work of Ananthakrishnan [30].

2 PROBLEM FORMULATION

The first problem to be analyzed is illustrated in Fig. 1. The domain of the fluid is bounded by the free surface $\mathcal{F}$, a far-field open boundary Σ, and the body contour $\mathcal{B}$. The normal and tangential vectors on the boundary are denoted as $\mathbf{n} = (n_1, n_2)$ and $\tau = (\tau_1, \tau_2)$, respectively. The draft of the body is denoted as D and its translational velocity as U. The density of the fluid is denoted as ρ, its coefficient of kinematic viscosity as ν, and the acceleration of gravity as g. The coordinate system is chosen to be inertial with the x-axis along the calm water level and the y-axis pointing against gravity. All field and flow variables, unless indicated otherwise, are nondimensionalized by ρ, D, and U.

2.1 Field Equations

Assuming the fluid to be incompressible, homogeneous, and Newtonian, one can derive the following *nondimensional* Navier-Stokes equations which are applicable to a viscous fluid in a gravitational field:

$$\nabla \cdot \mathbf{u} = 0, \tag{1}$$

$$\frac{\partial \mathbf{u}}{\partial t} + (\mathbf{u} \cdot \nabla)\mathbf{u} = \nabla P + \frac{1}{Re}\nabla^2 \mathbf{u}, \tag{2}$$

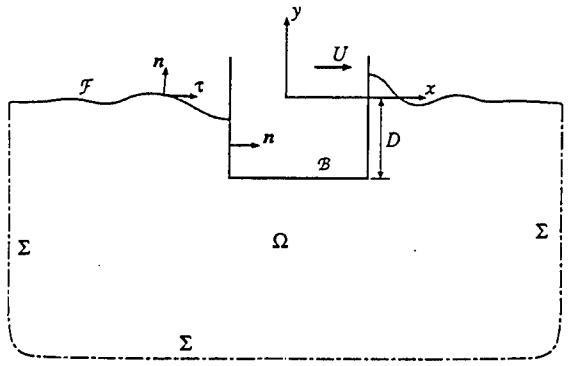

Fig. 1. Flow due to a translating two-dimensional body: coordinate system and notations.

where

$$P = p + \frac{y}{F^2}.$$

Here $\mathbf{u} \equiv \mathbf{u}(\mathbf{x}, t) = (u, v)$ and $p = p(\mathbf{x}, t)$ denote the velocity and pressure fields, respectively. The quantity P represents the dynamic pressure. For a given body geometry, the key parameters are the Reynolds number Re and *draft* Froude number F defined as

$$Re \equiv \frac{UD}{\nu}, \quad F \equiv \frac{U}{\sqrt{gD}}.$$

2.2 Boundary Conditions

Let the free surface of the fluid be denoted by the coordinate $\mathbf{x} \in \mathcal{F}$. Since free surface is a material surface, its evolution is given by

$$\frac{D}{Dt}\mathbf{x} = \mathbf{u}. \tag{3}$$

The above provides a Lagrangian description of the free surface, which would enable one to track $\mathcal{F}$ even if it is multivalued with respect to x.

In the absence of surfactants, continuity of the components of the stress-vector along the normal and tangential directions is given by the following equations (see, for *e.g.*, Wehausen and Laitone [31]):

$$n_1^2(-p + \frac{2}{Re}\frac{\partial u}{\partial x}) + n_2^2(-p + \frac{2}{Re}\frac{\partial v}{\partial y}) + \frac{2n_1n_2}{Re}(\frac{\partial u}{\partial y} + \frac{\partial v}{\partial x}) = \frac{\kappa}{We}, \quad \text{for } \mathbf{x} \in \mathcal{F}, \tag{4}$$

$$\frac{2\tau_1 n_1}{Re}\frac{\partial u}{\partial x} + \frac{2\tau_2 n_2}{Re}\frac{\partial v}{\partial y} + \frac{\tau_1 n_2 + \tau_2 n_1}{Re}(\frac{\partial u}{\partial y} + \frac{\partial v}{\partial x}) = 0, \quad \text{for } \mathbf{x} \in \mathcal{F}. \tag{5}$$

where κ denotes the curvature of the free surface. The Weber number

$$We \equiv \frac{\rho U^2 D}{\sigma_c}, \tag{6}$$

with σ_c being the surface-tension coefficient of a *clean* free surface, represents the ratio of inertia and surface-tension forces.

On the body contour $\mathcal{B}$, the velocity is given by the no-slip condition:

$$u = U, \quad v = 0. \tag{7}$$

At the intersection of the body and the free surface, it is plausible to assume that the fluid slips freely; *i.e.* for a rectangular body as shown in Fig. 1,

$$u = U, \quad \frac{\partial v}{\partial x} = 0. \tag{8}$$

At the far field, we assume that the dynamic pressure is zero for all time:

$$P = 0 \text{ on } \Sigma. \tag{9}$$

It should be emphasized that the above open-boundary condition is only an approximation and could cause spurious reflection of waves incident on Σ. Hence, the flow simulation is aborted once the leading transient wave reach Σ. Velocity components on Σ are determined by extrapolation consistent with the numerical method; this technique will be elaborated later in §3.

2.3 Effect of Insoluble Surfactants

Free surfaces under normal laboratory conditions are always covered with contaminates of one sort or another. Usually these contaminants are surface active, *i.e.* they change the surface tension depending on their concentration. Experimental results have shown that surfactants can alter the dynamics of the flow considerably at low speed (see *e.g.* [27], [8]).

In the present work, we consider only the class of surfactants that is *insoluble* in the fluid. Insoluble surfactants are convected by the flow and diffused (according to Fick's law) only along the free surface. The equation for the conservation of these surfactants can be written as (see Levich [32]):

$$\frac{\partial C}{\partial t} + \frac{\partial}{\partial s}(Cu_\tau) = \frac{1}{R_s}\frac{\partial^2 C}{\partial s^2}, \quad \text{for } \mathbf{x} \in \mathcal{F}. \tag{10}$$

where s denotes the arc-length parameter of $\mathcal{F}$, u_τ the tangential component of fluid velocity, and $C = C(\mathbf{x}, t)$ (where $\mathbf{x} \in \mathcal{F}$) the concentration (mass/area) of the surfactants. And $R_s = UD/\mu_s$, μ_s being the coefficient of surfactant diffusion.

Since the surface tension changes with surfactant concentration, the normal stress condition Eqn. (4) is modified to

$$n_1^2(-p + \frac{2}{Re}\frac{\partial u}{\partial x}) + n_2^2(-p + \frac{2}{Re}\frac{\partial v}{\partial y}) + \frac{2n_1n_2}{Re}(\frac{\partial u}{\partial y} + \frac{\partial v}{\partial x}) = \frac{\kappa}{We}\frac{\sigma}{\sigma_c}, \quad \text{for } \mathbf{x} \in \mathcal{F}, \tag{11}$$

Unlike the case of a clean free-surface, the tangential-stress component is no longer trivially zero. Instead, it now balances the gradient in surface tension induced by the surfactant concentration. Assuming the surface tension to be a function of surfactant concentration alone, one can write,

in replacement of Eqn. (5), the shear-stress condition as (see Levich [32])

$$\frac{2\tau_1 n_1}{Re}\frac{\partial u}{\partial x} + \frac{2\tau_2 n_2}{Re}\frac{\partial v}{\partial y} + \frac{\tau_1 n_2 + \tau_2 n_1}{Re}\left(\frac{\partial u}{\partial y} + \frac{\partial v}{\partial x}\right) = -E\frac{\partial C}{\partial s}, \quad \text{for } \mathbf{x} \in \mathcal{F}. \quad (12)$$

The nondimensional quantity E in the above equation is given by

$$E \equiv \frac{D}{\nu U}\left|\frac{d\sigma}{dC}\right|. \quad (13)$$

where σ denotes the surface-tension coefficient of the *contaminated* free surface. Note that addition of surfactants lowers the surface tension, *i.e.* $d\sigma/dC$ is negative. Modulus of $d\sigma/dC$ is used to define E; hence, a negative *sign* is introduced on the right-hand side of Eqn. (12).

In the present work, we assume that the variation of surface tension with surfactant concentration is linear. Hence, E is a constant which we call here the *Surfactant number*. By integrating Eqn. (13), we can express the right-hand side of the normal stress condition Eqn. (11) as:

$$\frac{\kappa}{We}\frac{\sigma}{\sigma_c} = \frac{\kappa}{We} - \frac{E\,\kappa\,C}{Re}. \quad (14)$$

In the far field, we assume that the concentration of surfactants remains unaltered by the wave motion, *i.e.*,

$$C(\mathbf{x}, t) = C(\mathbf{x}, t = 0) \text{ at } \mathcal{F} \cap \Sigma. \quad (15)$$

On $\mathcal{B}$, the no-flux condition ensures that surfactants are not convected into the body. To prevent the diffusion of surfactants into the body, the following "insulation" condition is imposed

$$\frac{\partial C}{\partial s} = 0 \text{ at } \mathcal{F} \cap \mathcal{B}. \quad (16)$$

To complete the formulation, an initial condition is needed. The body is started impulsively from quiescent state, *i.e.* both velocity field and free-surface elevation are set to zero at $t = 0$.

2.4 Interaction of a Vortex Pair with a Free Surface

The problem corresponding to normal incidence of a vortex pair on a free surface is illustrated in Fig. 2. In this case, the domain of interest is bounded by $\mathcal{F}$, Σ, and the plane of symmetry $\mathcal{S}$. At $t = 0$, the circulation of the (primary) vortex is denoted as Γ, the separation distance between the counter-rotating vortices as a, and their depth of submergence as d. Governing equations are basically the same as the ones stated in §2.1 to §2.3, except for the following minor modifications. The flow variables are now nondimensionalized with respect to fluid density ρ, the separation distance a, and the translation velocity of the vortex pair at $t = 0$ which is equal to $\Gamma/2\pi a$. Therefore, Reynolds, Froude, Weber, and Surfactant numbers are redefined as

$$Re \equiv \frac{\Gamma}{2\pi\nu}, \; F \equiv \frac{\Gamma}{2\pi a\sqrt{ga}}, \; We \equiv \frac{\rho\Gamma^2}{4\pi^2 a\sigma_c}, \; E \equiv \frac{2\pi a^2}{\nu\Gamma}\left|\frac{d\sigma}{dC}\right|,$$

respectively. On the plane of symmetry $\mathcal{S}$, the following conditions are imposed:

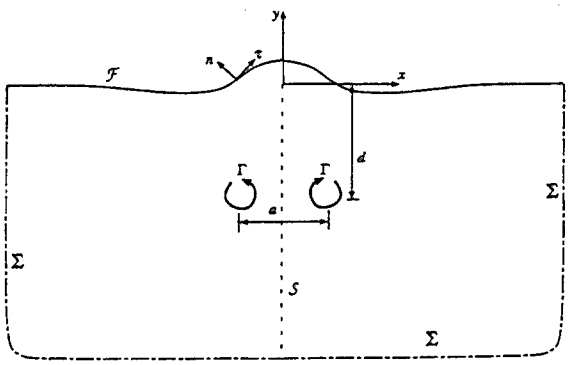

Fig. 2. Interaction of a vortex pair with a free surface: coordinate system and notations.

$$u = 0, \quad \frac{\partial v}{\partial x} = 0 \text{ on } \mathcal{S}, \quad (17)$$

which are equivalent to stating that $\mathcal{S}$ is a free-slip rigid surface.

In the presence of surfactants, we use the following insulation condition

$$\frac{\partial C}{\partial s} = 0 \text{ at } \mathcal{F} \cap \mathcal{S}.$$

to prevent the transport of surfactants across $\mathcal{S}$.

The flow is started impulsively from a quiescent state by the introduction of a pair of Rankine vortices. The velocity field associated with a Rankine vortex can be written in local cylindrical coordinates (r, θ) centered at the vortex core as [33]

$$\begin{aligned} V_\theta(r,\,\theta) &= \Gamma/2\pi r, \quad \text{if } r > \epsilon \\ &= \Gamma r/2\pi\epsilon^2, \quad \text{if } r \le \epsilon \end{aligned} \quad (18)$$

$$V_r(r,\,\theta) = 0$$

where V_θ and V_r are the tangential and radial components of the induced velocity, respectively, and ϵ is a small core radius. Unlike the case of the singular line vortex, the velocity is sufficiently small in the core of the Rankine vortex that the application of a finite-difference method does not require any special treatments.

3 Solution Method

Equations governing the above viscous, free-surface flow problem pose several inherent difficulties. First, the Navier-Stokes equations are nonlinear, with the unknowns p and $\mathbf{u}$ being coupled. While the momentum equation offers a time-evolution type relation for the velocity field, no such relation exists for the pressure field. In an incompressible fluid, pressure acts as a constraint for the velocity field so as to ensure that the equation of continuity is satisfied. Even though this role of pressure is conceptually well understood, numerical implementation of it is not quite straightforward. One could formulate the problem using a vorticity and stream-function formulation and thereby avoid the above complexity. However, implementation of boundary

conditions, especially of the stress type, does not seem, at this time, to be a straightforward task using this latter formulation.

Second, with wave motion present, the stress conditions have to be satisfied on a free surface whose elevation is not known *a priori* but is a part of the solution. Presence of surfactants makes the problem even more difficult. Surfactants are driven by the flow and the flow is affected by the surfactant concentration, thus requiring concurrent solution of both the flow and surfactant equations.

Thirdly, from the viewpoint of field-discretization alone, the present problem poses several complexities. The domain of the problem is continuously evolving because of wave motion and body translation. Since boundary conditions, especially those associated with the surfactants, play a crucial role in determining the dynamics of the flow, they have to be implemented accurately at the exact location of the free surface. Use of boundary-fitted coordinates can overcome these problems. Properly designed, such a method should be capable of resolving the zone of large flow gradients. Special attention, however, is needed to generate a grid system capable of coping with steep surface deformations.

We have just completed successfully the development of a solution method for solving viscous free-surface flow problems accurately [30]. The incompressible Navier-Stokes equations are solved using a fractional-step method in primitive variables form, taking advantage of a grid-generation algorithm developed by us. The fractional-step method is based on the projection method originated by Chorin [34, 35]. As to the generation of the curvilinear coordinates, a variational formulation [36] is used in conjunction with the concept of reference space [37]. This grid-generation procedure is capable of handling steep and overturning free boundaries without suffering from problems such as grid-folding which some other grid-generation methods are prone to (see Steinberg and Roache [37]).

The above solution method has been reported recently also in [38]. For completeness, we provide a brief review of this method in the following subsections.

3.1 Grid Generation

Using curvilinear coordinates, the physical space $(x, y; t)$ is mapped onto a uniform computational space $(\xi, \eta; T)$. The equations governing the physical as well as the grid-generation problem, are also transformed and then solved in the $(\xi, \eta; T)$ space. The transformation relation for the first-order derivatives are given by[2]

$$\begin{aligned} \partial_{,x} &= \frac{1}{J_1}[y_{,\eta}\partial_{,\xi} - y_{,\xi}\partial_{,\eta}] \\ \partial_{,y} &= \frac{1}{J_1}[-x_{,\eta}\partial_{,\xi} + x_{,\xi}\partial_{,\eta}] \\ \partial_{,t} &= \partial_{,T} - x_{,T}\partial_{,x} - y_{,T}\partial_{,y} \end{aligned} \tag{19}$$

and for the Laplacian operator ∇^2 by

$$\partial_{,xx} + \partial_{,yy} = A\partial_{,\xi\xi} - 2B\partial_{,\xi\eta} + C\partial_{,\eta\eta} + P\partial_{,\xi} + Q\partial_{,\eta} \tag{20}$$

[2]For compactness, we use a *comma* in the subscript to denote partial derivatives with respect to the variable(s) following the *comma*.

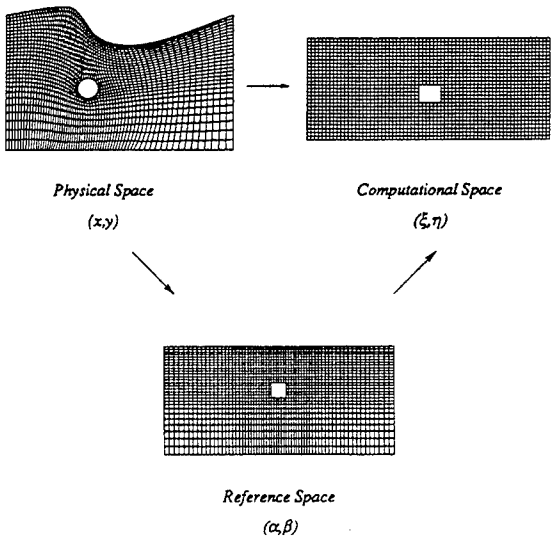

Fig. 3. Generation of boundary-fitted coordinates using reference space.

where

$$J_1 = x_{,\xi}y_{,\eta} - x_{,\eta}y_{,\xi}$$

denotes the Jacobian of the mapping $(x, y) \rightarrow (\xi, \eta)$ and

$$A = \frac{x_{,\eta}^2 + y_{,\eta}^2}{J_1^2}, \quad B = \frac{x_{,\xi}x_{,\eta} + y_{,\xi}y_{,\eta}}{J_1^2}, \quad C = \frac{x_{,\xi}^2 + y_{,\xi}^2}{J_1^2},$$

$$P = \xi_{,xx} + \xi_{,yy}, \quad Q = \eta_{,xx} + \eta_{,yy}.$$

The main idea behind generation of grids using a reference space can be explained as follows. The reference space is an intermediate space that is somewhat similar to the physical space but geometrically so simple that it can be discretized easily by interpolation. In free-surface flow problems, clustered grids are normally required near the free surface and the body boundary to resolve the zones of large flow gradients and to implement the boundary conditions accurately. Requirements such as these are first achieved in the reference space and then transferred to the physical space.

The grid properties (i) coordinate spacings (smoothness) and (ii) cell-area distribution of the reference space are transferable to the physical space by minimizing the following functionals:

$$\begin{aligned} I_s(\xi, \eta) &= \iint d\alpha d\beta \, |\nabla_{x,y}\xi|^2 + |\nabla_{x,y}\eta|^2 \\ &\quad - \iint d\alpha d\beta \, |\nabla_{\alpha,\beta}\xi|^2 + |\nabla_{\alpha,\beta}\eta|^2 , \end{aligned} \tag{21}$$

$$I_c(\xi, \eta) = \iint dxdy \; J_2 \tag{22}$$

respectively. In the above,

$$J_2 = x_{,\alpha}y_{,\beta} - x_{,\beta}y_{,\alpha} \quad J_3 = \alpha_{,\xi}\beta_{,\eta} - \alpha_{,\eta}\beta_{,\xi}$$

denote the Jacobians of the mappings $(x,y) \rightarrow (\alpha,\beta)$ and $(\alpha,\beta) \rightarrow (\xi,\eta)$, respectively. Note that the smoothness integral I_s is a measure of the difference in coordinate spacings, between the physical space and the reference space and I_c is a measure of J_2 which is the Jacobian of the mapping $(x,y) \rightarrow (\alpha,\beta)$.

In addition, orthogonality of the coordinates in the physical space can be ensured by minimizing

$$I_o(\xi,\eta) = \iint dxdy \; \{\nabla_{x,y}\xi \cdot \nabla_{x,y}\eta\}^2 J_1^3, \tag{23}$$

which is a measure of the inner product of the ξ and η coordinates in the (x,y) space. The above formulation for generating orthogonal grids does not require the use of the reference space, and hence corresponds to the direct mapping method of Brackbill and Saltzman [36].

The field (Euler's) equations, in the (ξ,η) space, corresponding to the above functionals are given by:

Smoothness

$$\begin{aligned}
\theta_1 x_{,\xi\xi} - 2\kappa_1 x_{,\xi\eta} + \sigma_1 x_{,\eta\eta} &= -\frac{J_1}{J_3^2}\{(\beta_{,\eta}\chi - \alpha_{,\eta}\mu)x_{,\xi} \\
&\quad +(-\beta_{,\xi}\chi + \alpha_{,\xi}\mu)x_{,\eta}\} \\
\theta_1 y_{,\xi\xi} - 2\kappa_1 y_{,\xi\eta} + \sigma_1 y_{,\eta\eta} &= -\frac{J_1}{J_3^2}\{(\beta_{,\eta}\chi - \alpha_{,\eta}\mu)y_{,\xi} \\
&\quad +(-\beta_{,\xi}\chi + \alpha_{,\xi}\mu)y_{,\eta}\}
\end{aligned} \tag{24}$$

where

$$\chi = \theta_3\alpha_{,\xi\xi} - 2\kappa_3\alpha_{,\xi\eta} + \sigma_3\alpha_{,\eta\eta},$$
$$\mu = \theta_3\beta_{,\xi\xi} - 2\kappa_3\beta_{,\xi\eta} + \sigma_3\beta_{,\eta\eta}\,.$$

The coefficients in the above equations are given by

$$\theta_1 = x_{,\eta}^2 + y_{,\eta}^2, \kappa_1 = x_{,\xi}x_{,\eta} + y_{,\xi}y_{,\eta}, \sigma_1 = x_{,\xi}^2 + y_{,\xi}^2,$$
$$\theta_3 = \alpha_{,\eta}^2 + \beta_{,\eta}^2, \kappa_3 = \alpha_{,\xi}\alpha_{,\eta} + \beta_{,\xi}\beta_{,\eta}, \sigma_3 = \alpha_{,\xi}^2 + \beta_{,\xi}^2.$$

Cell-area distribution

$$\begin{aligned}
&\frac{2}{J_3^2}\{b_{v1}x_{,\xi\xi} + b_{v2}x_{,\xi\eta} + b_{v3}x_{,\eta\eta} + a_{v1}y_{,\xi\xi} \\
&\qquad +a_{v2}y_{,\xi\eta} + a_{v3}y_{,\eta\eta}\} = -J_1^2\frac{\partial}{\partial x}(\frac{1}{J_3^2}) \\
&\frac{2}{J_3^2}\{a_{v1}x_{,\xi\xi} + a_{v2}x_{,\xi\eta} + a_{v3}x_{,\eta\eta} + c_{v1}y_{,\xi\xi} \\
&\qquad +c_{v2}y_{,\xi\eta} + c_{v3}y_{,\eta\eta}\} = -J_1^2\frac{\partial}{\partial y}(\frac{1}{J_3^2})
\end{aligned} \tag{25}$$

where

$$a_{v1} = -x_{,\eta}y_{,\eta},\; b_{v1} = y_{,\eta}^2,\; c_{v1} = x_{,\eta}^2,$$
$$a_{v2} = x_{,\xi}y_{,\eta} + x_{,\eta}y_{,\xi},$$
$$b_{v2} = -2y_{,\xi}y_{,\eta},$$
$$c_{v2} = -2x_{,\xi}x_{,\eta},$$
$$a_{v3} = -x_{,\xi}y_{,\xi},$$
$$b_{v3} = y_{,\xi}^2,\; c_{v3} = x_{,\xi}^2.$$

Orthogonality

$$\begin{aligned}
&b_{o1}x_{,\xi\xi} + b_{o2}x_{,\xi\eta} + b_{o3}x_{,\eta\eta} + a_{o1}y_{,\xi\xi} \\
&\qquad +a_{o2}y_{,\xi\eta} + a_{o3}y_{,\eta\eta} = 0 \\
&a_{o1}x_{,\xi\xi} + a_{o2}x_{,\xi\eta} + a_{o3}x_{,\eta\eta} + c_{o1}y_{,\xi\xi} \\
&\qquad +c_{o2}y_{,\xi\eta} + c_{o3}y_{,\eta\eta} = 0
\end{aligned} \tag{26}$$

where

$$a_{o1} = x_{,\eta}y_{,\eta},\; b_{o1} = x_{,\eta}^2,\; c_{o1} = y_{,\eta}^2,$$
$$a_{o2} = x_{,\xi}y_{,\eta} + x_{,\eta}y_{,\xi},\; b_{o2} = 2(2x_{,\xi}x_{,\eta} + y_{,\xi}y_{,\eta}),$$
$$c_{o2} = 2(2y_{,\xi}y_{,\eta} + x_{,\xi}x_{,\eta})\,,$$
$$a_{o3} = x_{,\xi}y_{,\xi},\; b_{o3} = x_{,\xi}^2,\; c_{o3} = y_{,\xi}^2.$$

One can show that the above field equations corresponding to smoothness and cell-area distribution reduce to those of the direct mapping formulation of Brackbill and Saltzman [36] when the reference space is identical to the computational space, *i.e.* $\alpha = \xi$ and $\beta = \eta$.

Depending on the levels of smoothness, cell-area variation, and orthogonality required in the physical space, a linear combination of the above equations is solved. The grid equations are discretized to second-order spatial accuracy in $(\xi,\eta;T)$ space and solved iteratively using a *mixed over-under relaxation* method. Grids generated by the above procedure for solving a water diffraction problem [39] are shown in Fig. 3. Observe that we are able to transfer the reference space properties to the physical space and thus to obtain clustered grids at the free surface and at the body.

3.2 Fractional-step method for Navier-Stokes equations

A fractional-step method is used for solving the viscous, free-surface flow problems in primitive variables. Accordingly, an intermediate "auxiliary" velocity field is first computed using the momentum equation without the pressure-gradient term. A Poisson equation is then solved to determine the pressure field. Finally, the actual (divergence-free) velocity field is computed using the auxiliary velocity and pressure.

This fractional-step procedure may be explained as follows. Numerical discretization of the Navier-Stokes equations can be written as[3]

$$\mathbf{u}(t_k) = -\delta T\; \nabla P(t_k) + [\mathbf{u}(t_{k-1}) + \delta T\; \mathcal{R}(t_{k-1})] \tag{27}$$

$$\nabla \cdot \mathbf{u}(t_k) = 0 \tag{28}$$

where t_k denotes the instant of discrete time under consideration and δT the time-step size. The symbol $\mathcal{R}(t_{k-1})$ is used to represent the convection and diffusion terms evaluated at t_{k-1}. We use first-order upwind differencing for discretizing the convection terms and central-differencing for the diffusion terms.

With the velocity being known at t_{k-1}, the terms in the square bracket of Eqn. (27) can be readily computed and this is called the intermediate velocity field $\mathbf{u}^*$:

[3]For clarity, we return to the same notations used in §2 to denote differential operators.

$$\mathbf{u}^* = \mathbf{u}(t_{k-1}) + \delta T\ \mathcal{R}(t_{k-1}) \tag{29}$$

By comparing Eqns. (29) and (27), we observe that $\mathbf{u}^*$ can be decomposed into $\nabla P(t_k)$ and $\mathbf{u}(t_k)$ fields:

$$\mathbf{u}^* = \mathbf{u}(t_k) + \delta t\ \nabla P(t_k) \tag{30}$$

The decomposition can be carried out by first solving a Poisson equation for $P(t_k)$, which is obtained by taking the divergence of Eqn. (30):

$$\nabla^2 P(t_k) = \frac{1}{\delta T} \nabla \cdot \mathbf{u}^*. \tag{31}$$

Once known, $P(t_k)$ can be used in Eqn. (30) to obtain $\mathbf{u}(t_k)$. The Poisson equation is discretized by central differencing and the resulting linear system of equations can be solved by direct elimination or iteration.

Since the Poisson equation for pressure Eqn. (31) is not an independent equation governing the flow, some additional boundary conditions have to be constructed in a manner consistent with the numerical method. In implementing the boundary conditions given in §2 and in constructing boundary conditions for the auxiliary velocity field, we take efforts to ensure that the decomposition Eqn. (30) is satisfied even on the boundaries.

Implementation of boundary conditions

On $\mathcal{B}$ (or $\mathcal{S}$ in the case of bow-flow problem), the normal component of the auxiliary velocity is set to be the same as that of the actual velocity $\mathbf{u}(t_k)$:

$$\mathbf{u}^* \cdot \mathbf{n} = \mathbf{u}(t_k) \cdot \mathbf{n} \tag{32}$$

The tangential component is computed as

$$\mathbf{u}^* \cdot \tau \approx \mathbf{u}(t_{k-1}) \cdot \tau + \delta t\ \nabla P(t_{k-1}) \cdot \tau$$

Eqn. (32) together with Eqn. (30) thus implies the following homogeneous Neumann condition for $P(t_k)$ on $\mathcal{B}$ or on $\mathcal{S}$:

$$\nabla P(t_k) \cdot \mathbf{n} = 0$$

On $\mathcal{F}$, the auxiliary velocity is computed using the decomposition relation

$$\mathbf{u}^* \approx \mathbf{u}(t_{k-1}) + \delta T\ \nabla P(t_{k-1}). \tag{33}$$

The free-surface stress conditions written in the computational space are used to obtain a Dirichlet-type condition for P and Neumann-type relations for $\mathbf{u}$. The stress conditions are implemented by a predictor-corrector type scheme. With respect to the implementation of the stress conditions, the solution procedure can be written as follows (see [30] for details):

Predictor:

1. Solution of the pressure Poisson equation with the known pressure at t_{k-1} taken as the Dirichlet condition on $\mathcal{F}$.
2. Evaluation of the actual velocity field in the domain using the decomposition relation Eqn. (30).
3. Evaluation of the actual velocity on $\mathcal{F}$ using the stress conditions written as Neumann condition in the (ξ, η) space.

Corrector:

1. Determination of the pressure on $\mathcal{F}$ using predicted velocity values. This is used as the Dirichlet condition for the solution of the Poisson equation.
2. Calculation of $\mathbf{u}(t_k)$ in the domain using Eqn. (30).
3. Determination of $\mathbf{u}(t_k)$ on $\mathcal{F}$ using the stress relations expressed as Neumann conditions for velocity.

Pressure update:

- Update of the pressure on $\mathcal{F}$ using the normal stress condition with the corrected $\mathbf{u}(t_k)$.

Note that the above procedure requires the solution of the pressure Poisson equation twice at each time step. Concurrently, the free-surface kinematic condition is also implemented by the following two-step predictor-corrector method

$$\begin{aligned} \mathbf{x}(\bar{t}_k) &= \mathbf{x}(t_{k-1}) + \delta T\ \mathbf{u}(t_{k-1}) \\ \mathbf{x}(t_k) &= \mathbf{x}(t_{k-1}) + \frac{1}{2}\delta T\ \{\mathbf{u}(t_{k-1}) + \mathbf{u}(\bar{t}_k)\} \end{aligned}$$

With the velocity and surfactant-concentration values at $t = t_{k-1}$ being known, the surfactant-conservation equation can be solved explicitly for $C(t_k)$. First-order upwind differencing is used for discretizing the convection term and central differencing for the remaining terms of the surfactant equation.

On the open boundary Σ, the approximation given by Eqn. (9) provides an homogeneous Dirichlet condition for the pressure Poisson equation. The auxiliary velocity is evaluated by first-order spatial extrapolation. The decomposition relation is completed to determine $\mathbf{u}(t_k)$ on Σ.

Remarks

The decomposition of a vector field into divergence-free velocity and pressure-gradient fields, as used in the above-mentioned solution method, can be considered as the projection of the incompressible Navier-Stokes equations onto divergence-free velocity and curl-free pressure-gradient fields. Theoretical aspects related to projection of Navier-Stokes equations for rigid-boundary flow problems may be found discussed in Ladyzhenskaya [40], Chorin [34], Temam [41], and Bell *et al.* [42]. In the case of rigid-boundary flow problems, pressure-gradient and velocity fields are orthogonal and hence, strictly speaking, pressure boundary conditions are not required (nor are they available) for the solution of the Navier-Stokes equations. But this is not so in the case of free-surface flow problems. Projection of the Navier-Stokes equation onto divergence-free field would not eliminate the pressure term and the pressure field is determined by the free-surface normal stress condition. Our procedure for treating free-surface flows is therefore original. Other theoretical issues related to viscous free-surface flow problems were investigated by Beale [43].

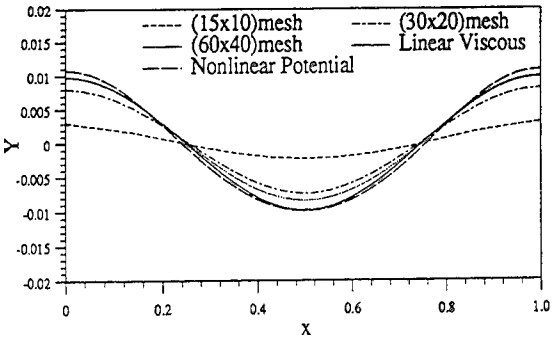

Fig. 4a. Wave elevation at time $t = \hat{T}$ corresponding to $Re = 10,000$ and $\hat{T}/\delta t = 500$. Nonlinear viscous flow results for different mesh sizes are compared with linear viscous and nonlinear potential flow results.

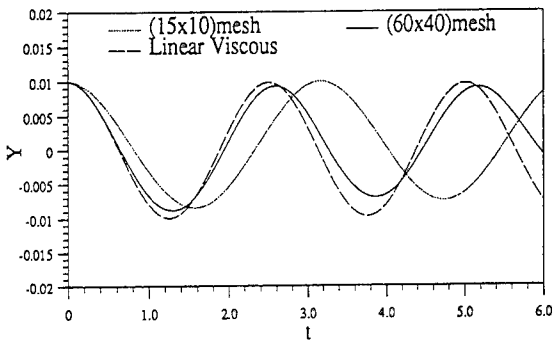

Fig. 4b. Time evolution of the standing-wave at left free-slip wall corresponding to different mesh sizes. $Re = 10,000$ and time step $\hat{T}/\delta t = 500$. For comparison, linear viscous flow result is also given.

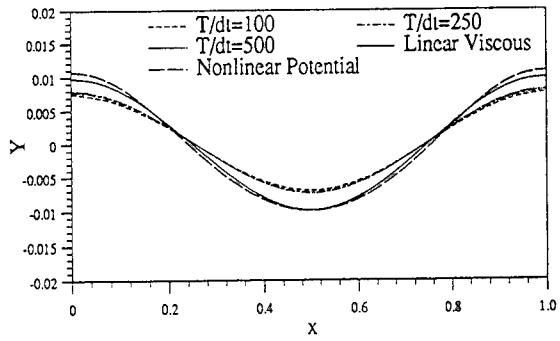

Fig. 4c. Wave elevation at time $t = \hat{T}$ corresponding to $Re = 10,000$, (30×20) mesh. Results corresponding to different time-step sizes $\hat{T}/\delta t = 100, 250, 500$ are compared with linear viscous and nonlinear potential flow results.

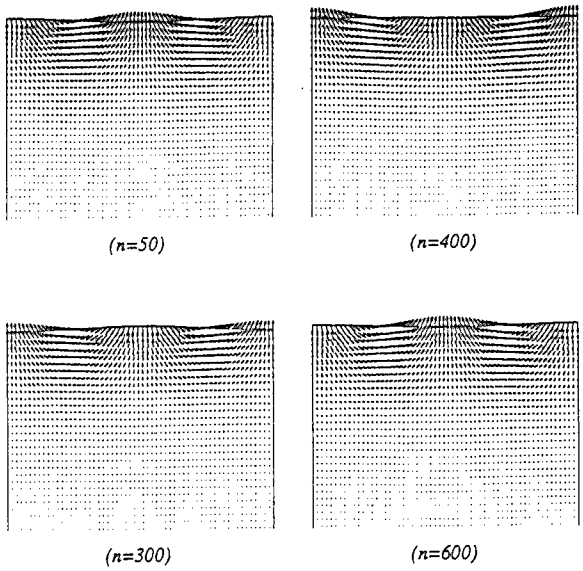

Fig. 4d. Velocity-vector plots at different instants of discrete time n corresponding to nonlinear viscous-flow calculation. $\hat{T}/\delta t = 500$.

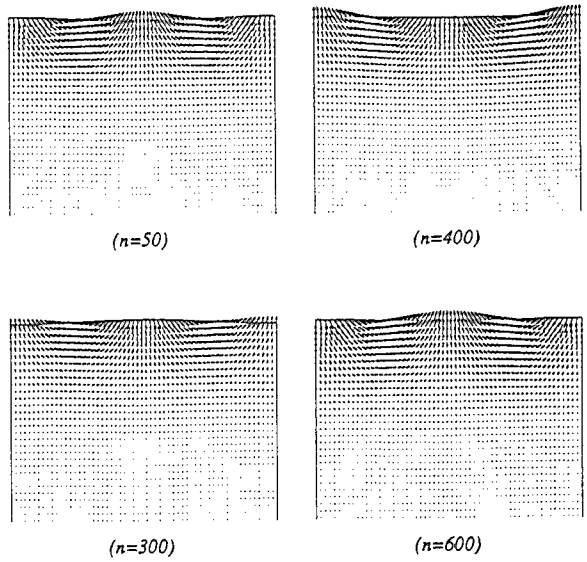

Fig. 4e. Velocity-vector plots at different instants of discrete time n corresponding to nonlinear potential-flow calculation. $\hat{T}/\delta t = 500$.

4 RESULTS AND DISCUSSION

4.1 A Test Case

In order to validate our solution method, especially its convergence properties, we solve a test problem that corresponds to the viscous attenuation of a standing wave.

In this problem, the flow parameters are nondimensionalized with respect to the tank length L, acceleration of gravity g, and fluid density ρ. Length of the standing wave is chosen as unity. Amplitude $a(x,t)$ of the wave at $t = 0$ is taken as 0.01. The Reynolds number, defined in this case by $L\sqrt{gL}/\nu$, is set to 10^4. Effects of surface tension and surface contaminates are not considered in this test case. To eliminate the loss of wave energy due to wall boundary layers, free-slip (zero vorticity) condition is imposed on the tank wall boundaries. The physical space is discretized in such a way that grid spacings are small at the free surface compared to that in the interior. The flow field corresponding to the linear, potential-flow analysis (see *e.g.* Lamb [44]) is used as the initial condition for the nonlinear viscous-flow calculation.

Numerical results obtained by varying the mesh size, *i.e.* for mesh size = 15 × 10, 30 × 20, and 60 × 40, are given in Fig. 4a. The time-step size is set as $\delta T/\hat{T} = 500$, where $\hat{T}$ denotes the wave period. This figure shows the free-surface elevation after the lapse of one period, *i.e.* at $t = \hat{T}$. Also shown for comparison is the free-surface elevation $Y(x,t)$ computed using the following equation, which is based on the linearized Navier-Stokes equations (*i.e.*, with the convective effects neglected) and linearized free-surface boundary conditions:

$$Y(x,t) = a(x,0)e^{-2(2\pi)^2 t/Re}cos(2\pi x)cos(2\pi t). \qquad (34)$$

For additional comparison, the free-surface elevation computed using a nonlinear potential-flow formulation (see [30]) is also given. We can see that the numerical results converge to those predicted by linear viscous-flow theory as the mesh size is refined. The wave amplitude corresponding to the mesh size 15 × 10 is only about 30% of that corresponding to Eqn. (34). However, as can be observed in Fig. 4b, this difference is primarily due to the error in phase. The phase error is large when the mesh is coarse, as to be expected from Fourier-type analysis of our numerical scheme when applied to analogous problems (see *e.g.* Hirsch [45]).

Results obtained by varying the time-step size are shown in Fig. 4c. Here, the mesh size is chosen as 30 × 20. Again, we see that the computed results converge to those given by linear viscous-flow theory as the time-step size is reduced. However, this convergence "rate" is not as rapid as in the case of the mesh-size refinement (Fig. 4a).

Finally, for flow visualization, instantaneous velocity-vector plots are given in Fig. 4d. For comparison, the flow field corresponding to a *nonlinear inviscid flow* model (see [30]) is also presented (Fig. 4e). Generation of vorticity on the wall boundaries is null because of the imposed free-slip condition. Since the free-surface curvature is small, vorticity generated on the free surface is also insignificant. Consequently, the viscous-flow field resembles the one predicted by the inviscid flow model.

4.2 Bow- and Stern-Flow Solutions

All results presented in this section are obtained using a mesh size of 121 × 41. The Reynolds number is set to 10^3. The length of the body is set to unity.

Rigid Free Surface

In order to elucidate the mechanisms associated with the formation of upstream vortices at low speed, we consider three cases in which the exact free-surface conditions are replaced by (i) free-slip, (ii) no-slip, and (iii) linearized contaminant conditions. In all these three cases the vertical component of velocity on the free surface is set as zero. In case (i), the horizontal component of velocity is computed by using the shear-free condition, *i.e.* $\partial u/\partial y = 0$. In case (ii), the no-slip condition $u = v = 0$ is used. In case (iii), a linearized version of the contaminant conditions are used to determine the surfactant concentration and the horizontal component of velocity. In the physical space, the linearized versions of Eqn.(10) and Eqn.(12) are given by

$$\frac{\partial C}{\partial t} + \frac{\partial}{\partial x}(u\,C) = \frac{1}{R_s}\frac{\partial^2}{\partial x^2}C \quad \text{on} \quad y = 0, \qquad (35)$$

$$\frac{\partial u}{\partial y} = -E\,\frac{\partial C}{\partial x} \quad \text{on} \quad y = 0, \qquad (36)$$

respectively. Following Wang and Leighton [28], we set the value of R_s to 10^3, *i.e.* same as that of the flow Reynolds number. We set $E = 0.4$, a typical value of the surfactant number considered in the work of Tryygvason *et al.* [29].

Instantaneous velocity and vorticity fields corresponding to the rigid, free-slip "free-surface" case are shown in Fig. 5.[4]

Vorticities are generated around the body contour because of the no-slip condition. These are swept downstream by the combined action of the flow convection and the viscous diffusion. However, on the bow side, upstream diffusion of vorticity is countered by the flow convection and the vorticity is consequently concentrated only in a thin shear layer. The vorticities generated at the sharp edges merge together to form a "macro" vortex at the stern. In the vorticity-contour plots, one can also notice the generation of secondary vorticity *around* the body contour by the primary vortices peeling off the sharp leading edge.

As to be expected, vorticity is not generated on a flat free-slip surface. Consequently, vortices are not trapped at the bow even though the fluid is stagnant at the junction of the free-surface and the bow. Since surface deformations, generally speaking, are quite small at low speed, the flat free-surface assumption is justifiable in the case of low Froude-number flows. The present results therefore indicate that the bow vortices observed in low Froude-number laboratory-scale experiments are *not* caused by viscosity effects on the free surface.

However, if the generation of vorticity is intense, as in the case of a no-slip surface, formation of trapped vortices in the stagnant zone is possible. This is evident from the

[4] In all the vorticity-contour plots given in this paper, the solid lines denote clockwise vorticity and the dotted lines counter-clockwise vorticity, unless otherwise specified.

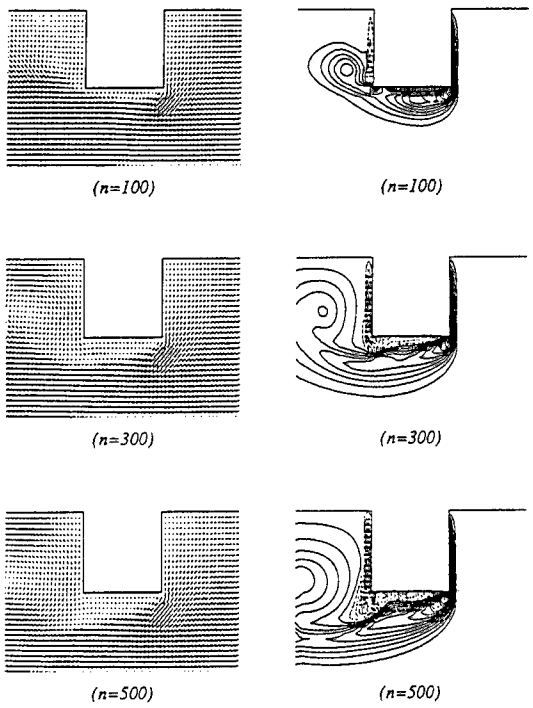

Fig. 5. Velocity-vector and vorticity-contour plots for the free-slip case. n denotes instant of discrete time. $U\ \delta t/D = 0.01$, $Re = 10^3$.

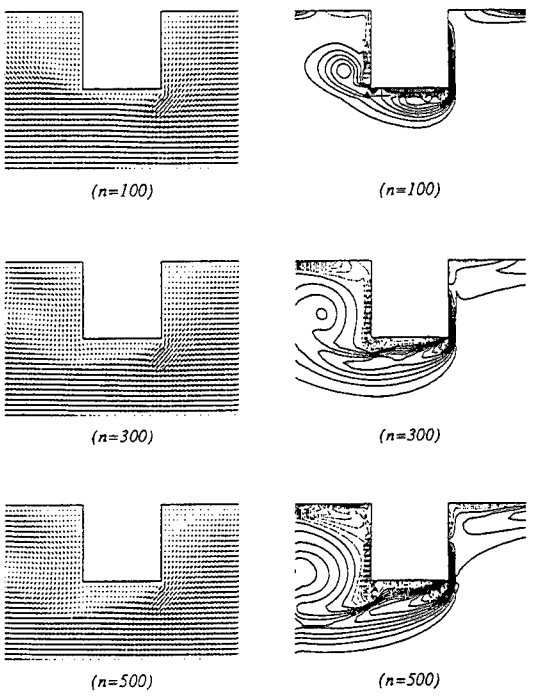

Fig. 6a. Velocity-vector and vorticity-contour plots for the no-slip case. n denotes instant of discrete time. $U\ \delta t/D = 0.01$, $Re = 10^3$.

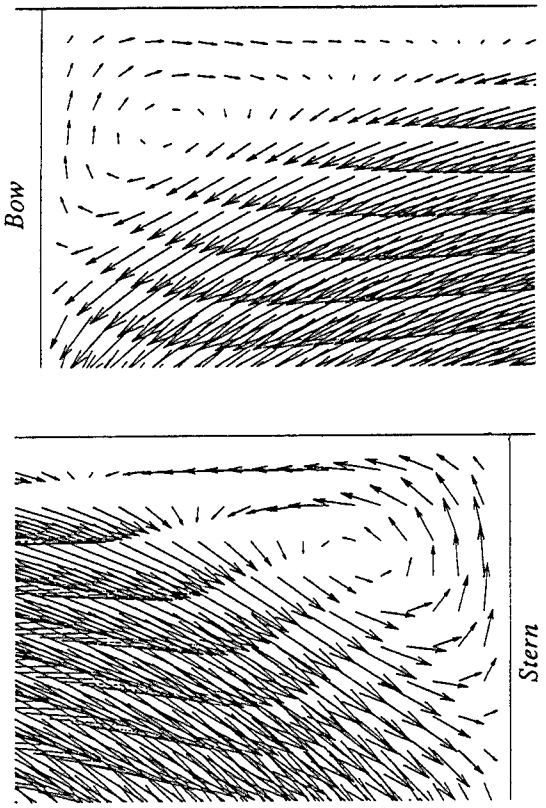

Fig. 6b. The formation of bow and secondary stern vortices in the case of no-slip free surface at $Ut/D = 6.0$.

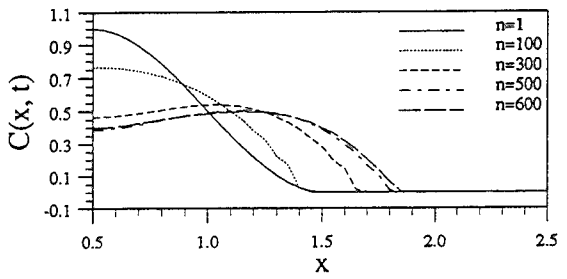

Fig. 7a. Time evolution of the surfactant concentration. n denotes the instant of discrete time with $U\ (\delta t)/D = 0.01$. $x = 0.5$ denotes the bow.

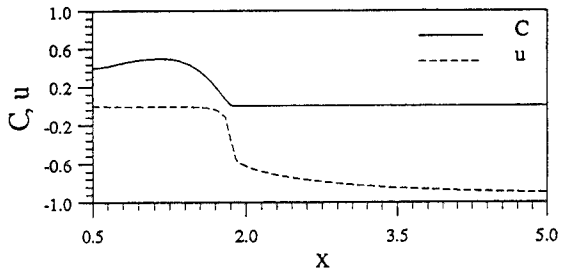

Fig. 7b. Surfactant concentration and the horizontal velocity component at $Ut/D = 6.0$. Bow is at $x = 0.5$.

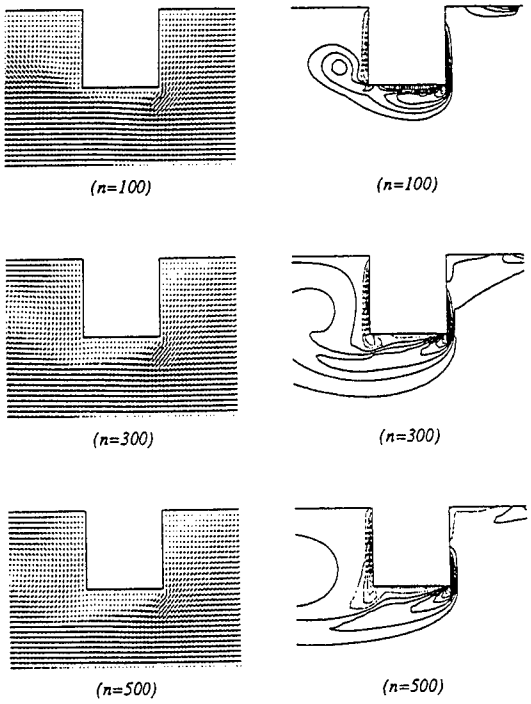

Fig. 8a. Velocity-vector and vorticity-contour plots corresponding to the contaminated-surface case. n denotes the instant of discrete time. $U\,\delta t/D = 0.01$, $Re = 10^3$.

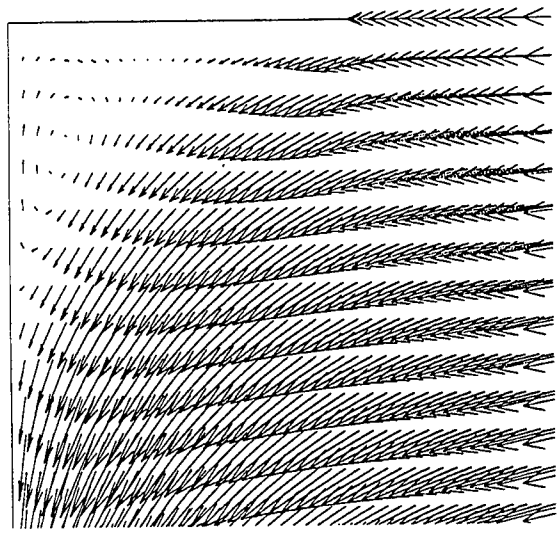

Fig. 8b. Formation of the bow vortex due to the presence of surfactants at $Ut/D = 6.0$.

results presented in Figs. 6a,b. In this case, the approaching flow is seen to decelerate and separate on the free surface ahead of the bow. The separated flow reattaches at the bow near *mid draft.* Consequently, a prominent vortex is seen at the bow (see Fig. 6b). It is interesting to observe that the back flow generated by the primary stern vortex also leads to the formation of a secondary trapped vortex at the junction of the stern and the free surface in a manner similar to that in front of the body.

Results corresponding to the contaminated surface case are presented next in Figs. 7 and 8. It has been observed in low-speed experiments that surface contaminants accumulate at the bow, thereby altering the dynamics of the bow flow (see [8]). In order to simulate this scenario, surfactants are smoothly distributed on the bow-side free surface over one-body length, at $t = 0$ (see $n = 1$ in Fig. 7a). At the stern, the free-slip (no surfactant) condition is imposed on the free surface.

Fig. 7a shows the time evolution of the surfactant concentration. Driven by convection and diffusion, the surfactant concentration changes in time. The area under the surfactant-concentration profile remains, however, constant in time. This indicates that the numerical scheme is able to conserve the mass of the surfactants well. At a later time, the concentration profile reaches a nearly steady state (see curves corresponding to instant of discrete time $n = 500$ and $n = 600$). A graph showing the horizontal component of velocity on the free surface and the surfactant concentration at $n = 600$ is given in Fig. 7b. One observes that the horizontal velocity component (with respect to body-fixed frame of reference) practically vanishes beneath the layer of surfactants when a steady state is reached. Thus, the present results confirm that surfactants accumulating at the bow could behave like an incompressible no-slip membrane.

Instantaneous velocity and vorticity fields corresponding to the contaminated free-surface case are shown in Fig. 8. These plots show that the flow field at the bow resembles that of the no-slip case (see Fig. 6). A close-up view of the bow-flow regime shows the formation of the bow vortex beneath the layer of surfactants (Fig. 8b). The vorticity-contour plots (Fig. 8c) vividly show the generation of surface vorticity and the formation of the bow vortex by the presence of surfactants.

The above flat free-surface flow results thus indicate that the formation of bow vortices observed in low-speed, laboratory experiments (*e.g.* [3], [5]) is because of the presence of surfactants. It also shows that, at low speed, the shear layer generated on a clean surface by surface curvature alone cannot be strong enough to generate bow vortices.

Nonlinear Free Surface

Fully *nonlinear* bow and stern flows are now discussed. Results for $F = 0.2$, $We = \infty$ (*i.e.* zero surface tension), and $Re = 10^3$ are given in Fig. 9. The instantaneous velocity-vector and vorticity-contour plots show that, initially, the stagnation points at the stern and at the bow are located below the mid-draft. On the body, positive vorticity is generated above the stagnation points and negative

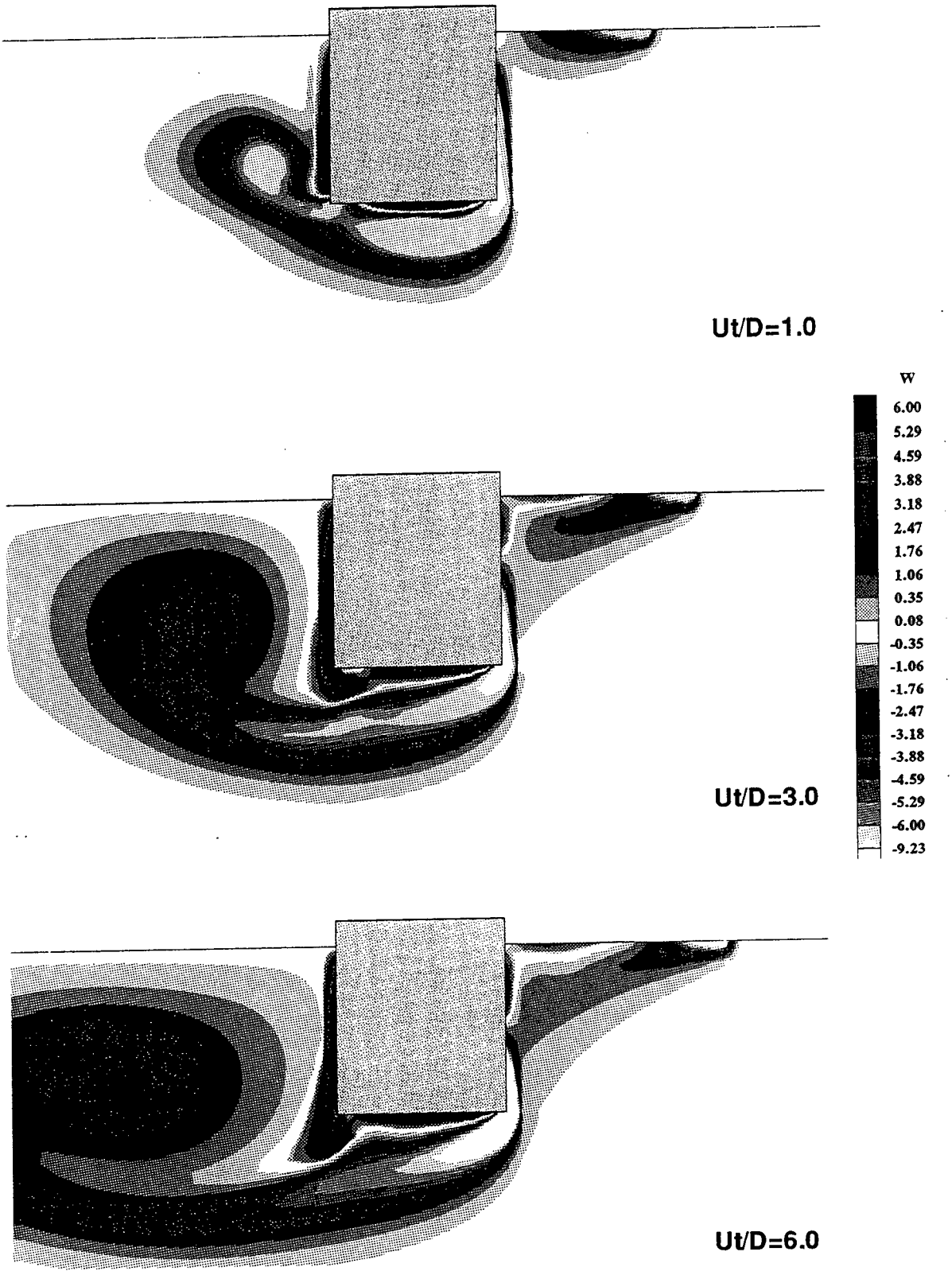

Fig. 8c. Instantaneous vorticity fields corresponding to the flat, contaminated free-surface case: $Re = 10^3$, $E = 0.4$. *White - red* spectrum denotes the clockwise vorticity and *blue-green* spectrum the counter-clockwise vorticity.

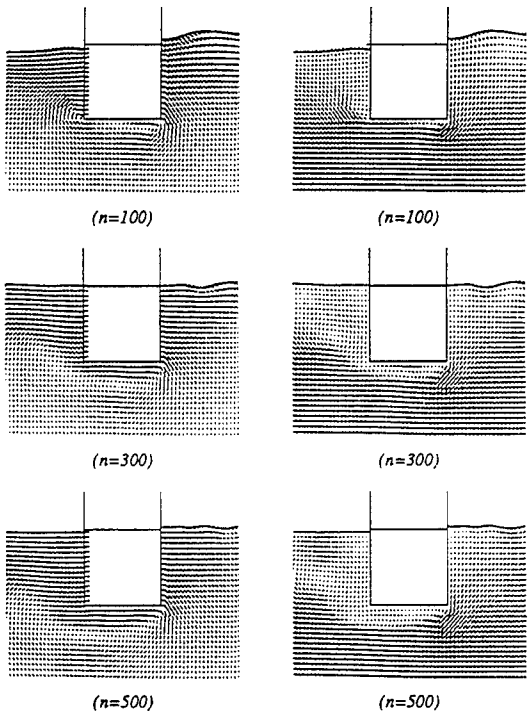

Fig. 9a. Velocity-vector plots in inertial and moving frames of reference for $Re = 10^3$, $F = 0.2$, and $U\ \delta t/D = 0.005$. n denotes the instant of discrete time. The horizontal line in the body near the free surface indicate the mean water level.

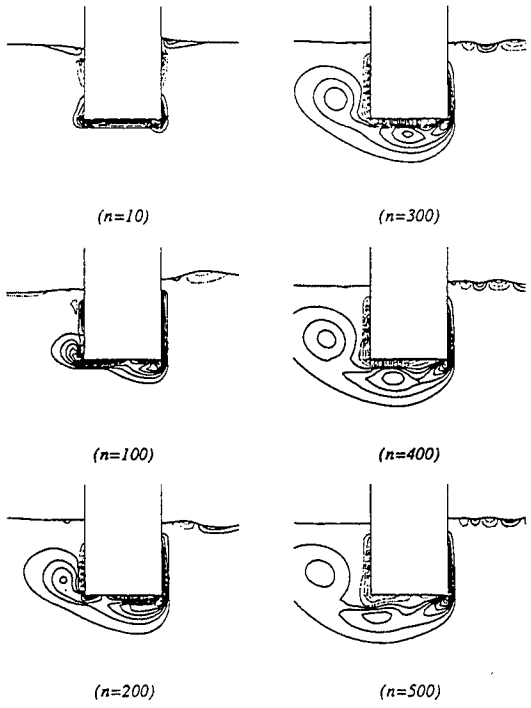

Fig. 9b. Vorticity-contour plots for the case of $Re = 10^3$, $F = 0.2$, $U\ \delta t/D = 0.005$. n denotes the instant of discrete time.

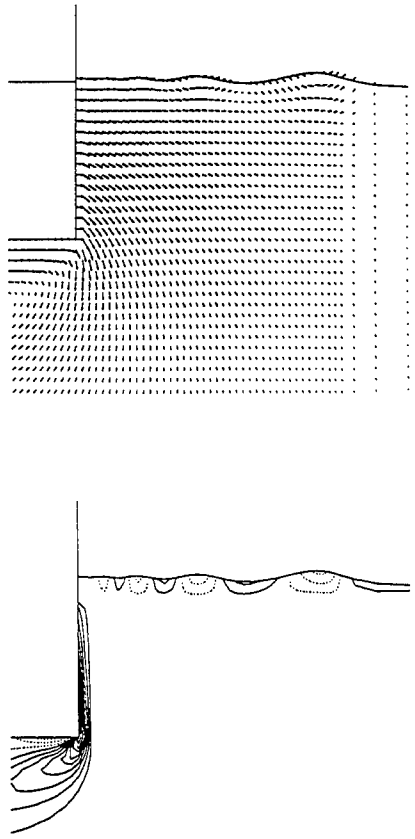

Fig. 9c. Flow field ahead of the body at $Ut/D = 3.0$ for $Re = 10^3$, $F = 0.2$.

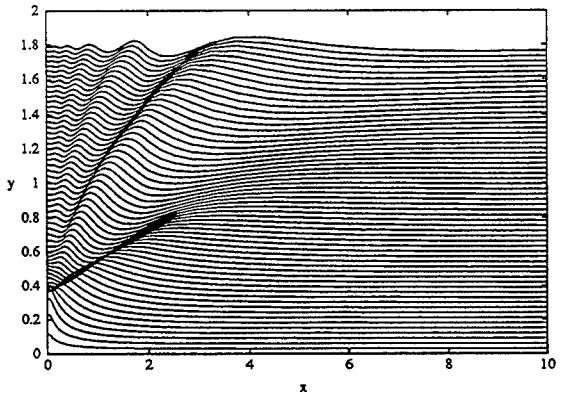

Fig. 9d. Time evolution of bow waves: $F = 0.2$, $Re = 1000$, $We = \infty$, $Ut/D = 0.05(0.05)3.0$. For clarity in display, successive curves are displaced upwards by $\delta y = 0.03$.

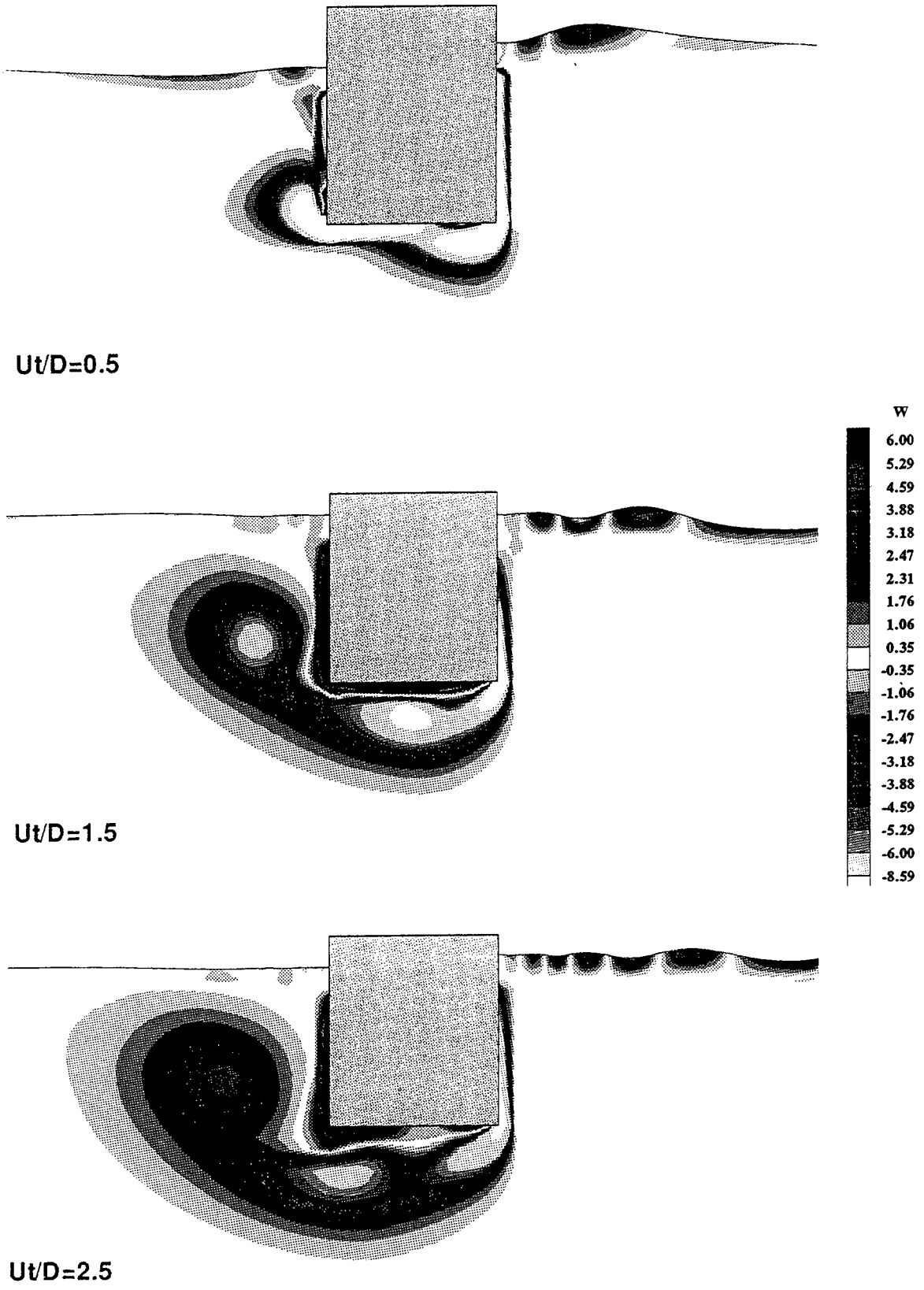

Fig. 9e. Instantaneous vorticity fields corresponding to nonlinear, clean free-surface case: $F = 0.2$, $Re = 10^3$, $We = \infty$. *White - red* spectrum denotes the clockwise vorticity and *blue–green* spectrum the counter-clockwise vorticity.

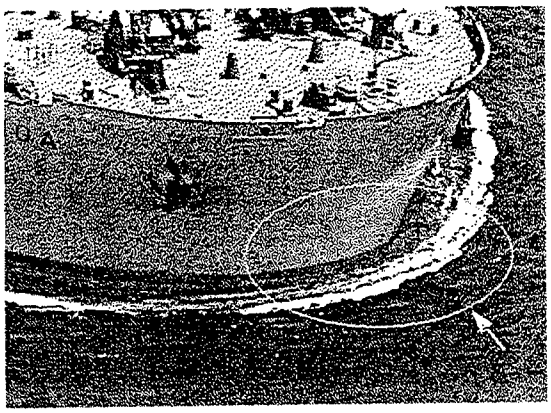

Fig. 10. The formation of short waves ahead of a blunt bow moving at low draft-Froude number.

vorticity below the stagnation points. These stagnation points are then pushed into the fluid by the interaction of the wave field and the body boundary layer. At later times, the flow field beneath the free surface resembles that of the rigid free-slip case discussed earlier (see Fig. 5).

One can observe from the vorticity-contour plots that vorticities of alternating signs are generated on the free surface (see Fig. 9b,e). This is due to the nonzero surface curvature. Near the stern, the free-surface profile becomes quite smooth; hence, vorticity generation becomes vanishingly small at later times. However, at the bow, waves are observed to evolve into decreasing lengths (see Fig. 9d). With the fluid being stagnant relative to the body and the waves being unable to propagate upstream, wave slope steepens in time. This feature is rather different from the conventional Cauchy-Poisson wave system generated by a submerged disturbance, where the short-wave contents eventually trail behind the disturbance. The generation of similar kind of short bow waves has been observed earlier even in the inviscid-flow results of Yeung [17]. It therefore appears that the short bow waves (Fig. 9d) are basically a result of inertial and gravitational effects, and not a result of viscosity.

The strength of such free-surface vorticity generated by free-surface curvature is rather weak (see Fig. 9e). Consequently, we do not observe the formation of bow vortices. However, it is possible that at high Reynolds number, these short bow waves could become unstable and break in the form of spilling. Spilling breakers ahead of full-scale blunt bows are often observed even at low speed. Such breaking can lead to a turbulent vortical structure at the bow (see Fig. 10).

Next, the scale effect of surface tension is analyzed. We retain the Froude number as 0.2. The Weber number (see Eqn. (6)) is set to 55.0. Roughly, this value corresponds to the case of a model of draft $0.1m$ advancing in water at $0.2m/sec$, the surface tension at the air-water interface being $\sigma_c = 0.073N/m$.

Instantaneous "snapshots" of velocity vectors and vorticity contours given in Fig. 11a,b show that the flow field appears to be not much altered by the presence of sur-

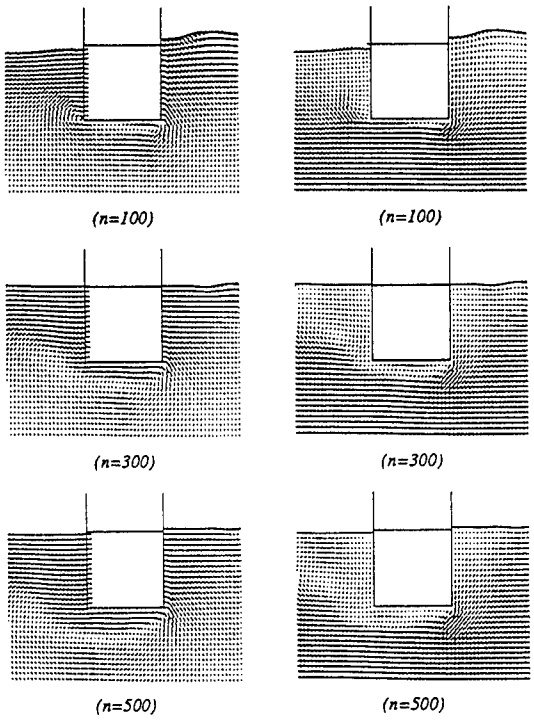

Fig. 11a. Velocity-vector plots in inertial and moving frames of reference for $Re = 10^3$, $F = 0.2$, $We = 55$, and $U\ \delta t/D = 0.005$. n denotes the instant of discrete time. The horizontal line in the body near the free surface indicate the mean water level.

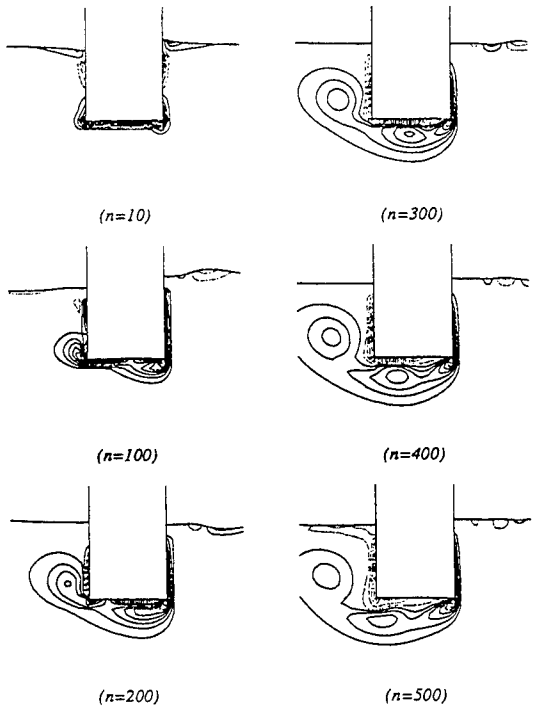

Fig. 11b. Vorticity-contour plots for the case of $Re = 10^3$, $F = 0.2$, $We = 55$, $U\ \delta/D = 0.005$. n denotes the instant of discrete time.

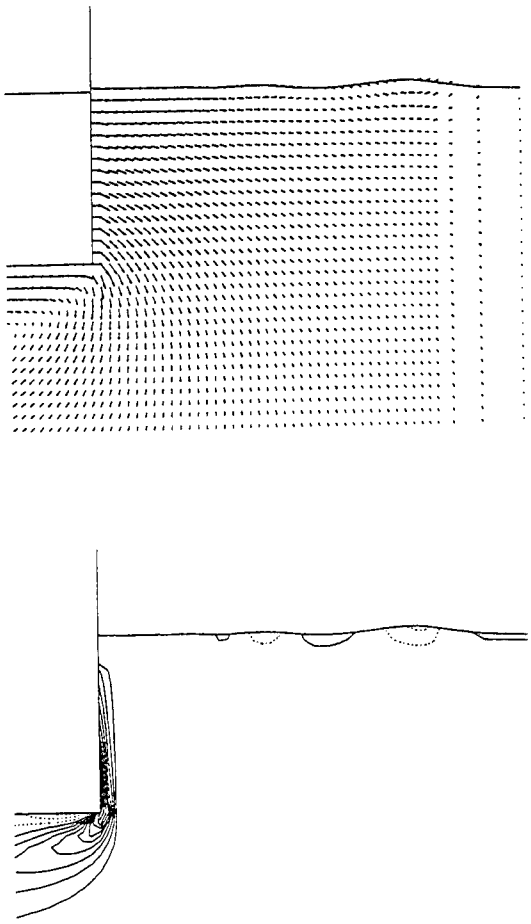

Fig. 11c. Flow field ahead of the body at $Ut/D = 3.0$ for $Re = 10^3$, $F = 0.2$, $We = 55$.

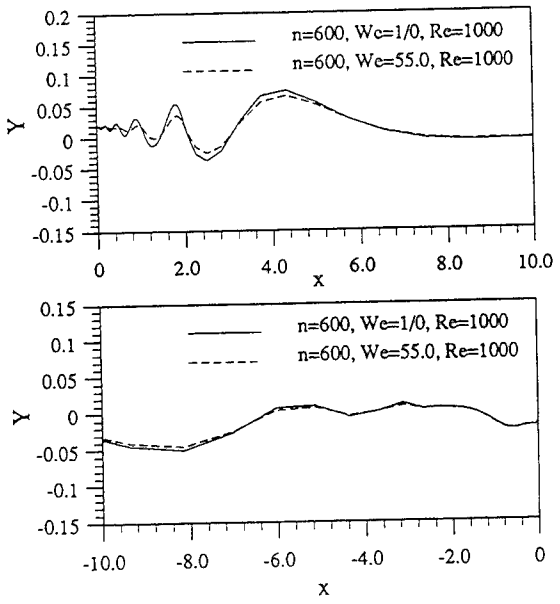

Fig. 12. Profiles of bow and stern waves with and without surface tension at $Ut/D = 3.0$. $x = 0$ denotes the bow in the top figure and the stern in the bottom figure. $Re = 10^3$, $F = 0.2$.

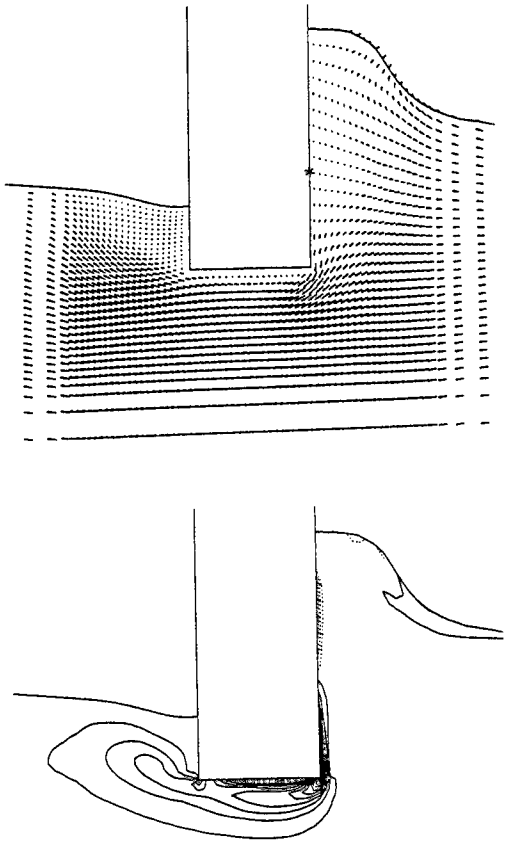

Fig. 13. Velocity-vector and vorticity-contour plots for $Re = 10^3$, $F = 0.8$, $T_s = 2.0$ (gentle start) at $Ut/D = 2.50$.

face tension. However, a close up look (Fig. 11c) reveals that the amplitude of the short bow waves are considerably suppressed. As a consequence, surface vorticity is also mitigated.

In Fig. 12, instantaneous free-surface elevations are compared with those of the case without surface tension. One can see that the wave dampening effect of surface tension is significant near the bow. However, this scale effect is quite weak in the far field ahead of the bow and also behind the body. These results thus resolve the issue of why short bow waves are observed ahead of a full-scale ship operating at low speed but not so distinctly in the corresponding small-scale model experiments, the latter being influenced substantially by the effects of surface tension. Next, results corresponding to a high Froude number ($F = 0.8$) are presented. Impulsive start of the body results in a splash at the bow and thus interrupts the solution process. In order to suppress this behavior, the body is started gently as (see Yeung [17])

$$\begin{aligned} \frac{u(t)}{U} &= (\frac{t}{T_s})^3\{6(\frac{t}{T_s})^2 - 15(\frac{t}{T_s}) + 10\}, \quad \text{if } t \le T_s, \\ &= 1, \qquad\qquad\qquad\qquad\qquad\quad \text{if } t > T_s. \end{aligned}$$

The start-up time T_s is set to 2.0. Results corresponding to this case are shown in Fig. 13. The fluid tends to pile up at the bow as the body is accelerated gently. This pile-up, in effect, reduces the Froude number based on draft. However, at a later time the mound of fluid accumulating

at the bow plunges forward and breaks. During this whole process, the stagnation point at the bow remains trapped at its initial location beneath the free surface.

4.3 Vortex-Pair and Free-Surface Interaction

We present a few representative results corresponding to the nonlinear interaction of a vortex pair with clean and surfactant-covered free surfaces. All boundary conditions used are fully nonlinear. In all cases considered in this section, the Reynolds number $Re = 10^2$ and $d/a = 2.0$ (see Fig. 2). A mesh size of (121×41) with coordinates clustered near the free surface and near the symmetry plane is used for discretizing the physical space.

Clean Free Surface

Instantaneous flow fields corresponding to $F = 0.2$ and *zero* surface tension are shown in Fig. 14 in the form of velocity-vector and vorticity-contour plots. Examining these plots, one can immediately observe that the surface deformations, being drawn to scale, are relatively small at this Froude number. Velocity-vector plots show that the fluid is stagnant at the junction of the free surface and the symmetry plane. From the vorticity-contour plots, one can observe that secondary vorticities, of both positive and negative signs, are generated on the free surface. Generation of these vorticities are due to the zero shear stress condition on the curved surface. Undaunted by these relatively weak secondary vortices, the primary vortex merely stretches beneath the free surface without undergoing any significant rebounding.

Time evolution of the free-surface elevation for the above case is shown in Fig. 15. In this $y-$exaggerated plot, generation of transient waves and a rise in the elevation at the symmetry plane due to the upwelling of the primary vortex can be observed. In the near field next to the prominent surface depression, one can also observe the generation of short waves. Surface vorticities, shown in the previous figure (Fig. 14), are actually generated by the surface depression and the short transient waves.

Instantaneous plots of the velocity and vorticity fields for $F = 0.4$ (see Fig. 16) show that the free-surface deformations are considerably larger compared to the case of $F = 0.2$. Secondary vorticity generated at the free surface is strong enough to rebound the primary vortex. Time evolution of the free-surface elevation, given in Fig. 17, shows that the transient wave developing outboard of the primary vortex becomes steep and eventually breaks because of local instability.

Contaminated Free Surface

Results corresponding to $F = 0.2$, $We = 6.0$, and surfactant number $E = 10.0$ are given in Figs. 18 and 19. Vorticity-contour and velocity-vector plots given in Fig. 18 show that the generation of the surface vorticity is substantially intensified by the presence of surfactants. The generation is primarily due to the *nonzero* shear stress that is needed to balance the gradient of the surface tension induced by the surfactant concentration, see Eqn. (12). Interaction with the secondary vorticity causes the primary

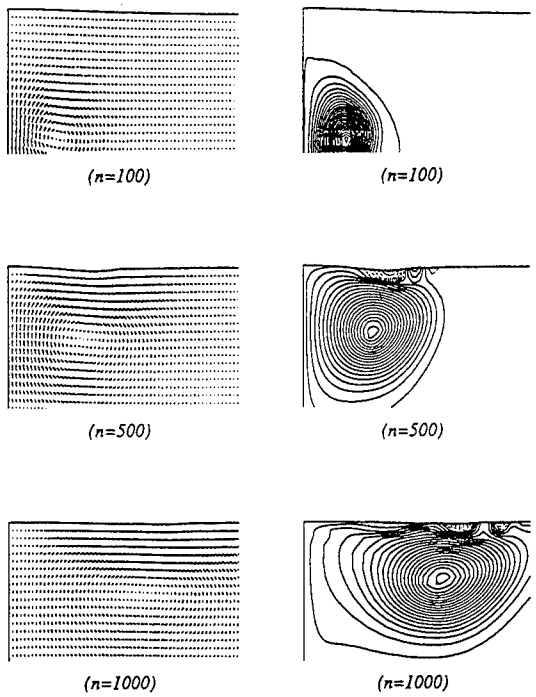

Fig. 14. Nonlinear vortex-pair and free-surface interaction: flow field in the right-half domain for $F = 0.2$, $Re = 100$, and $\Gamma\ \delta t/2\pi a^2 = 0.005$.

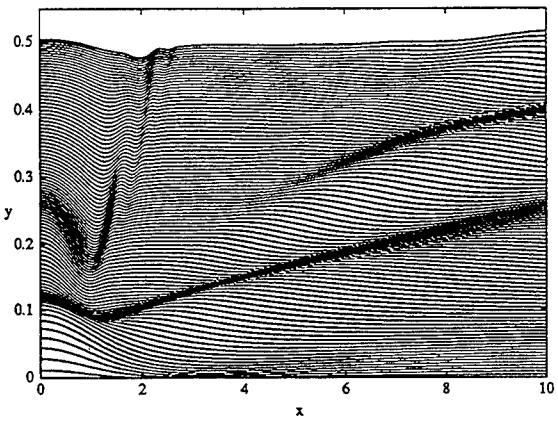

Fig. 15. Time evolution of the clean free-surface elevation to the right of the symmetery plane for $F = 0.2$, $Re = 100$. $\Gamma\ t/2\pi a^2 = 0.05(0.05)5.0$. For clarity in display, successive curves are displaced upwards by $\delta y = 0.005$.

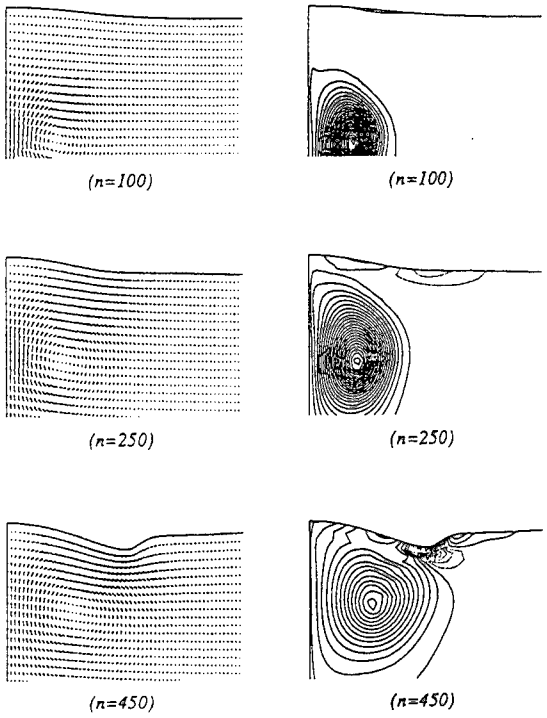

Fig. 16. Flow field in the right-half domain for $F = 0.4$, $Re = 100$, and $\Gamma\ \delta t/2\pi a^2 = 0.005$. n denotes the instant of discrete time.

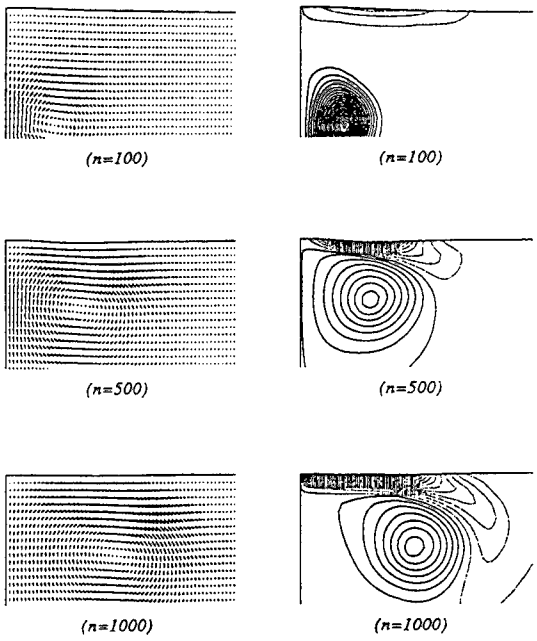

Fig. 18. Interaction of a vortex pair with a contaminated free surface. Flow field in the right-half domain for $F = 0.2$, $Re = 100$, $We = 6.0$, $E = 10.0$, and $\Gamma\ \delta t/2\pi a^2 = 0.005$. n denotes the instant of discrete time.

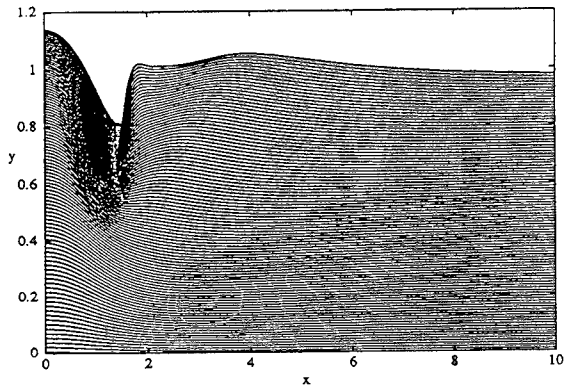

Fig. 17. Time evolution of the clean free-surface elevation to the right of the symmetery plane for $F = 0.4$, $Re = 100$. $\Gamma\ t/2\pi a^2 = 0.025(0.025)2.5$. For clarity in display, successive curves are displaced upwards by $\delta y = 0.01$.

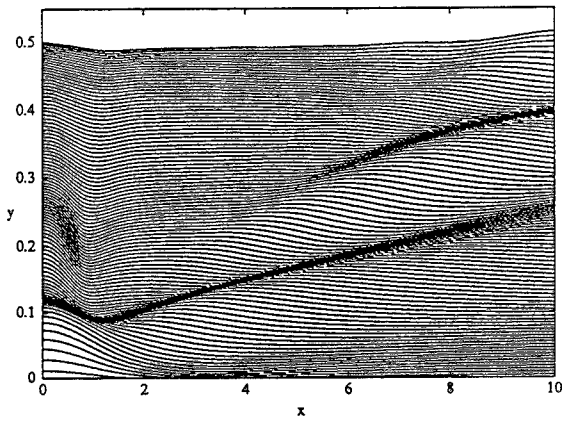

Fig. 19. Time evolution of the contaminated free-surface elevation to the right of the symmetery plane for $F = 0.2$, $Re = 100$, $We = 6.0$, $E = 10.0$. $\Gamma\ t/2\pi a^2 = 0.05(0.05)5.0$. For clarity in display, successive curves are displaced upwards by $\delta y = 0.005$.

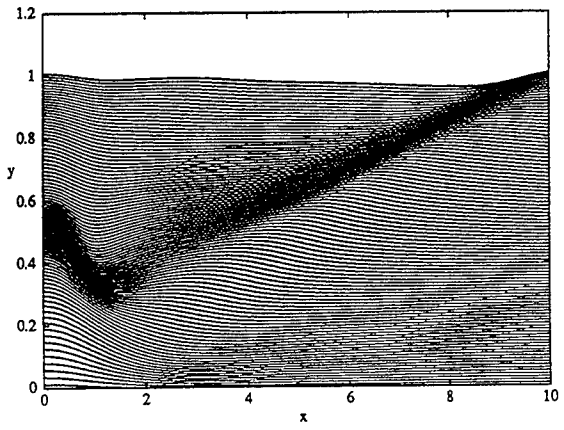

Fig. 20. Time evolution of the contaminated free-surface elevation to the right of the symmetery plane for $F = 0.4$, $Re = 100$, $We = 1.0$, $E = 10.0$, and $\Gamma\, t/2\pi a^2 = 0.05(0.05)5.0$. For clarity in display, successive curves are dispaced upwards by $\delta y = 0.01$.

vortex to rebound as well as to lose its intensity more rapidly. By comparing the free-surface elevation plots given in Fig. 15 and Fig. 19, we observe that the presence of surfactants also suppresses the free-surface deformations, especially the initiation of short transient waves.

The above "free-surface dampening effect" of the surfactants is even more dramatic at $F = 0.4$. Time evolution of the free-surface elevation corresponding to $F = 0.4$, $We = 1.0$, and $E = 10.0$ is shown in Fig. 20. Breaking of the transient wave observed in the case of clean free surface (Fig. 17) is effectively eliminated by the surfactants.

5 CONCLUSIONS

In this paper, we have presented a new theoretical model to analyze the fully nonlinear interaction of vorticity with a free surface. Specifically, we have provided some important new results corresponding to (i) the bow- and stern-flow problem and (ii) the nonlinear interaction of a vortex pair with a free surface. These results have shed light on some of the classic issues that had heretofore remained unresolved. For example, it is now confirmed theoretically that the formation of bow vortices observed in low-speed or small-scale laboratory experiments is because of the presence of surfactants. The present viscous-flow results also confirm that at low speed, waves of decreasing wavelengths are observed at the bow, a feature also observed earlier in the nonlinear inviscid-fluid results of Yeung [17]. The continually steepening of these short waves as they evolve in time could be responsible for the white-water type instability observed ahead of a full-scale blunt bow operating at low speed. The scale effect of surface tension is to suppress the generation of these short bow waves in laboratory scale and hence the white-water instability is rarely distinctly observed in corresponding model tests.

Results corresponding to the vortex-pair and free-surface interaction problem show that rebounding of the primary vortices is not significant at low speed in the absence of surfactants. It has also been observed that, at intermediate Froude number, transient waves generated by the interaction could break because of local instability. The presence of surfactants on the free surface is observed not only to dampen the surface deformations, but also to intensify the secondary vorticity, which results in the rebounding of the primary vortices even at relatively low Froude number.

Acknowledgements

Research reported in this paper has been supported primarily by the Office of Naval Research under grant N00014-91-J1155. Partial support from grant N00014-91-J1614, also of the Office of Naval Research, is acknowledged. We are also grateful to Cray Research, Inc., for a computational grant funded through the University of California at Berkeley.

References

[1] Baba, E., "A new component of viscous resistance of ships," *Journal of the Society of Naval Architects of Japan*, Vol. 125, 1969, pp. 23–34.

[2] Suzuki, K., "On the drag of two-dimensional bodies semi-submerged in a surface flow," *Journal of the Society of Naval Architects of Japan*, Vol. 137, 1975, pp. 22–35.

[3] Honji, H., "Observation of a vortex in front of a half-submerged circular cylinder," *Journal of Physical Society, Japan*, Vol. 40, No. 5, 1976.

[4] Mori, K., "Necklace vortex and bow wave around blunt bodies," *Proc., Fifteenth Symposium on Naval Hydrodynamics*, Hamburg, Germany, 1984, pp. 303–317.

[5] Takekuma, K. and Eggers, K., "Effect of bow shape on free-surface shear flow," *Proc., Fifteenth Symposium on Naval Hydrodynamics*, Hamburg, Germany, 1984, 387–405.

[6] Osawa, Y., "Aufmessung des Geschwindigkeitsfeldes an und unter der freien Wasseroberfläche in der Bugumströmung eines stumpfen Körpers," *Bericht 476, Institut für Schiffbau*, Der Universität Hamburg, Germany, 1987. (In German).

[7] Miyata, H., Suzuki, A., and Kajitani, H., "Numerical explanation of nonlinear nondispersive waves around bow," *Proc., Third International Conference on Numerical Ship Hydrodynamics*, Paris, France, 1981, pp. 37–52.

[8] Grosenbaugh, M. A. and Yeung, R. W., "Flow structure near the bow of a two-dimensional body," *Journal of Ship Research*, Vol. 33, 1989, pp. 269–283.

[9] Cole, S. L. and Strayer, T. D., "Free-surface flow past a cylinder," *Mathematical approaches in hydrodynamics*, ed. T. Miloh, SIAM publication, Philadelphia, PA, 1991, pp. 335–348.

[10] Maruo, H. and Ikehata, M., "Some discussions on the free-surface flow around the bow," *Proc., Sixteenth Symposium on Naval Hydrodynamics*, Berkeley, CA, 1986, pp. 65–77.

[11] Dagan, G. and Tulin, M. P., "Two-dimensional free-surface gravity flow past blunt bodies," *Journal of Fluid Mechanics*, Vol. 51, 1972, pp. 529–543.

[12] Tuck, E. O. and Vanden-Broeck, J.-M., "Splashless bow flows in two dimensions?," *Proc., Fifteenth Symposium on Naval Hydrodynamics*, Hamburg, Germany, 1977, pp.293–301.

[13] Tuck, E. O. and Vanden-Broeck, J.-M., "Computation of near-bow and stern flows using series expansion in the Froude number," *Proc., Second International Conference on Numerical Ship Hydrodynamics*, Berkeley, CA, 1977, pp. 377–387.

[14] Madurasinghe. M. A. D., "Splashless ship bows with stagnant attachment," *Journal of Ship Research*, Vol. 32, 1988, pp. 194–202.

[15] Tuck, E. O., "Ship-hydrodynamic free-surface problems without waves," Thirteenth Georg Weinblum Memorial Lecture, *Journal of Ship Research*, v. 35, No. 4, 1991, pp. 277-287.

[16] Grosenbaugh, M. A. and Yeung, R. W., "Nonlinear free-surface flow at a two-dimensional bow," *Journal of Fluid Mechanics*, Vol. 209, 1989, pp. 57–75.

[17] Yeung, R. W., "Nonlinear bow and stern waves - inviscid and viscous solutions," *Mathematical approaches in hydrodynamics*, ed. T. Miloh, SIAM publication, Philadelphia, PA, 1991, pp. 349–369.

[18] Patel, V. C., Landweber,L., and C. J. Tang, C. J., "Free-Surface Boundary Layer and the Origin of Bow Vortices," *Report No. 284, Iowa Institute of Hydraulic Research*, The University of Iowa, Iowa, 1984.

[19] Lugt, H. J., "Local flow properties at a viscous free surface," *Physics of Fluids*, Vol. 30, 1987, pp. 3647–3652.

[20] Miyata, H., Baba, N., Kajitani, H., Sato, T., and Shirai, M., "Numerical and experimental analysis of nonlinear bow and stern waves of a two-dimensional body," Third report, *Journal of the Society of Naval Architects of Japan*, Vol. 156, 1984, pp. 1–12.

[21] Sarpkaya, T., "Trailing-vortex wakes on the free surface," *Proc., Sixteenth Symposium on Naval Hydrodynamics*, Berkeley, California, USA, 1986, pp. 38–49.

[22] Sarpkaya, T., Eltinsky, J., and Leeker, R. E., "Wake of a vortex pair on the free free surface," *Proc., Seventeenth Symposium on Naval Hydrodynamics*, The Hague, The Netherlands, 1988.

[23] Telste, J. G., "Potential flow about two counter-rotating vortices approaching a free surface," *Journal of Fluid Mechanics*, Vol. 201, 1989, pp.259–278.

[24] Yu, D. and Tryggvason, G., "The free surface signature of unsteady, two-dimensional vortex flows," *Journal of Fluid Mechanics*, Vol. 218, 1990, pp. 547–572.

[25] Marcus, D. L. and Berger, S. A., "The interaction between a pair of counter-rotating vortex pair in a vertical ascent and a free surface," *Physics of Fluids*, A 1, 1989, pp. 1988–2000.

[26] Ohring, S. and Lugt, H. J., "Interaction of a vortex pair with a free surface," *Journal of Fluid Mechanics*, Vol. 227, 1991, pp. 47–70.

[27] Bernal, L. P., Hirsa, A., Kwon, J. T., and Willmarth, W. W., "On the interaction of vortex rings and pairs with a free surface for varying amounts of surface active agent," *Physics of Fluids*, A 1(12), 1989, pp. 2001–2004.

[28] Wang, H. T. and Leighton, R. I., "Direct calculation of the interaction between subsurface vortices and surface contaminants," *Proc., Ninth Offshore Mechanics and Arctic Engineering Conference*, Houston, Texas, USA, vol. 1, Part A, 1990.

[29] Tryggvason, G., Abdollah-Alibeik, J., Willmarth, W. W., and Hirsa, A., "Collision of a vortex pair with a contaminated free surface," *Technical Report No. 90-1*, Program in Ship Hydrodynamics, College of Engineering, The University of Michigan, Ann Arbor, USA, 1990.

[30] Ananthakrishnan, P., "Surface waves generated by a translating two-dimensional body: effects of viscosity," *Ph.D. thesis*, Department of Naval Architecture and Offshore Engineering, University of California at Berkeley, USA, 1991.

[31] Wehausen, J. V. and Laitone, E. V., *Surface Waves*, Handbuch der Physik, ix, Springer-Verlag, 1960.

[32] Levich, V. G., *Physicochemical Hydrodynamics*, Prentice-Hall, Inc., EnglewoodCliffs, NJ, 1962.

[33] Batchelor, G. K., *An Introduction to Fluid Mechanics*, Cambridge University Press, 1970.

[34] Chorin, A. J., "Numerical solution of incompressible flow problems," *Studies in Numerical Analysis*, Vol. 2, 1968, pp. 64–71.

[35] Chorin, A. J., "Numerical solution of the Navier-Stokes equations," *Mathematics of Computations*, Vol. 22, 1968, pp. 745–762.

[36] Brackbill, J. U. and Saltzman, J. S., "Adaptive zoning for singular problems in two dimensions," *Journal of Computational Physics*, Vol. 46, 1982, pp. 342–368.

[37] Steinberg, S. and Roache, P. J., "Variational grid generation," *Numerical Methods in Partial Differential Equations*, Vol. 2, 1986, pp. 71–96.

[38] Yeung, R. W. and Ananthakrishnan, P., "Oscillation of a floating body is a viscous fluid," *Journal of Engineering Mathematics* Vol. 26, 1992, pp. 211–230.

[39] Yeung, R. W. and Vaidhyanathan, M., "Nonlinear interaction of water waves with submerged obstacles," *International Journal on Numerical Methods in Fluids*, Vol. 14, 1992, pp. 1111–1130.

[40] Ladyzhenskaya, O. A., *The Mathematical Theory of Viscous Incompressible Flow*, Gordon and Breach Science Publishers, New York, 1969.

[41] Temam, R., *Navier-Stokes Equations - Theory and Numerical Analysis*, North-Holland Publishing Company, 1979.

[42] Bell, J. B., Collela, P., and Glaz, H. M., "A second-order projection method for the incompressible Navier-Stokes equations," *Journal of Computational Physics*, Vol. 85, 1989, pp. 257–283.

[43] Beale, J. T., "The initial value problem for the Navier-Stokes equations with a free surface," *Communications in Pure and Applies Mathematics*, Vol. 34, 1981, pp. 359–392.

[44] Lamb, H., *Hydrodynamics*. Dover Publications, Inc., New York, 1932.

[45] Hirsch, C., *Numerical Computation of Internal and External Flows*, Vols. I & II, A Wiley-Interscience Publication, 1989.

DISCUSSION

K. Mori
Hiroshima University, Japan

It is very common to observe such a flow shown in Figure 10. It is a kind of turbulent flow which may require some different treatment from the method for the nonturbulent flow; an introduction of a model or an extremely fine grid. Otherwise the turbulent characteristics cannot be captured to lead a fake simulation. The production of turbulence may somehow absorb the accumulated energy on the crest which may change the phenomenon.

Could I have your comment on the dealing with such kind of turbulent vertical structured flow of the free surface?

AUTHORS' REPLY

We have stressed in our paper that the *initiation* of short bow waves is caused by inertial and gravitational effects, not viscosity. We believe that these short bow waves could become unstable and break at high Reynolds number. In such a scenario, the bow flow would be turbulent and contain much mixing. Proper turbulence modeling is necessary to analyze such breaking or post-breaking phenomena. We have yet to develop solution methods to tackle turbulent free-surface flows, but that is not quite the objective here.

DISCUSSION

M. Tulin
University of California at Santa Barbara, USA

In this remarkable and beautifully written paper, the authors have researched and developed computing algorithms, implemented them, and then made applications to treat 2-D free surface-body interactions for viscous flows including the effects of surface tension and contaminants on the free surface.

The special problem emphasized here is the deceptively simple one involving the flow immediately ahead of a blunt 2-D ship, which has attracted an increasing number of investigators since the first work by Dagan and Tulin. Their concern at that time was to understand the cause of the appearance of a strong spilling breaker in front of blunt ships at Froude numbers based on draft of $O(1)$. They suggested a local Taylor type instability. The work of Tuck and Vanden-Broeck, 1977, suggested the nonexistence of the inviscid flow, while other authors emphasized the role of viscous free-surface effects.

The present work would seem strongly to argue against viscous effects. This is an intuitively satisfying conclusion on the appearance in nature of violent spilling bow breakers at very large Reynolds numbers would suggest against the role of weak viscous effects initiating the breakers. It is, however, quite another story regarding the equilibrium of the spilling-breaking zone itself where it would seem quite clear that turbulent stresses acting beneath the breaker-eddy are required to maintain it in equilibrium. Two similar flows, which have already been well modeled, and for which the fundamentals are to a good extent understood, are the steady breaker in the flow above a hydrofoil, the separated flow behind bluff bodies (no free surface).

I would pose the treatment of this fully developed breaker flow before blunt bodies as a problem for the authors, even in the laminar case. In the case of the steady breaker above the hydrofoil, Tulin and Cointe (16th Symposium on Naval Hydrodynamics, Berkeley, 1986), have shown that beyond a certain critical condition (the incidence of a hydrofoil, for example) these flows may exist: (1) inviscid, (2) strong breaker, (3) weak breaker. Of these, the weak breaker is demonstrably unstable while experiments indicate that nature prefers the strong breakers over the inviscid flow.

Two questions for the authors: (1) Do they think they have done enough to answer the question as to the cause of the strong spilling breaker observed in nature? and (2) Can their numerical methods arrive at a bifurcated solution of the nature described by Tulin and Cointe? (A suggestion: treat numerically the active wave flow above a hydrofoil and see what happens.)

AUTHORS' REPLY

We want to thank Prof. Tulin for his generous and thoughtful comments. We would also like to thank Prof. Tulin for pointing out the relevance of his work (Tulin & Cointe, *16th Symposium on Naval*

Hydrodynamics, 1986) to the present study on the generation of bow waves. In the above paper, Tulin and Cointe had developed a model for *steady* spilling breakers, according to which the spiller was modeled as a stagnant eddy. Turbulent shear stress acting on the stream line, that divides the eddy and the uniform flow, was assumed to "support" this eddy. The shape of the spiller was determined based on the force balance between static pressure and the turbulent shear stress. The velocity was assumed to be discontinuous at the leading edge of the breaker and the dividing streamline to terminate at the crest which was taken to be the location of the stagnation point. The resistance associated with the breaking was also determined using linear potential-wave theory. The model was also validated by comparing its results with experimental results of Duncan (*Proc. R. Soc. Lond. A*, 1981). Many interesting results were obtained using this model, some of which that are relevant to our work has been outlined by Prof. Tulin in the above discussion.

As well pointed out in his discussion, the focus of our paper, at least in the case of surface-piercing body, is to demonstrate how effective, or more properly put, ineffective is the viscous effect in *initiating* the bow-wave breakers. Our low-Reynolds-number results indicate that even at low Froude number, bow waves are generated. Since such waves were observed in our earlier inviscid solutions also, we believe that generation of these bow waves is essentially because of inertial and gravitational effects. Although not reported in full here, such short upstream waves are not observed in the cases of a moving surface pressure or a translating submerged cylinder. The mechanism responsible for these short bow waves, we believe, is the interaction of a surface-piercing body with the stagnant fluid as it is in the case of bow flow. Although no high-Reynolds-number results are yet available at this time, we may still conjecture that these short waves would steepen further, with viscosity playing a weaker role, and could result in breaking as observed in Fig. 10. Much work remains to be done to understand how the occurrence of turbulence is related to the geometric steepness.

Despite its inability to describe post-breaking behavior, the present method has provided much insight to the pre-breaking process. However, we would like to point out here that only the incipience of breakers can be determined by the solution method (in the present form) but not the later stages of breaking. Perhaps a different solution method, especially from grid-generation point of view, is necessary to track the breakers. Thus, it appears that developing a solvable numerical model is crucial to obtain solutions corresponding to fully developed breakers. It is worthwhile to examine how physical models such as the one developed by Tulin and Cointe could be used to facilitate numerical studies. One also needs a proper turbulence model, not to mention proper constitutive relations or solution techniques to account for air-water mixing that occurs at the breakers. Considering all these complexities, we feel that our accomplishments are very modest, but we hope many more interesting findings will come forth in our future endeavors. We would like to thank Prof. Tulin for his suggestion of a few additional issues to examine, e.g., the bifurcated solutions of the type given in Tulin and Cointe. Once the numerical method is sufficiently extended, it is also worthwhile to consider flow over submerged hydrofoils, which is an ideal candidate problem for analyzing the physics of *steady* breakers.

Numerical Simulation of the Nonlinear Free-Surface Flow Around a Blunt Bow

M.-S. Shin. Y.-G. Lee, E.-C. Kim, S.-I. Yang
(Korea Research Institute of Ships and Ocean Engineering, Korea)

ABSTRACT

This paper presents simulated viscous flow fields with the free-surface around a two-dimensional body (semi-infinite body) and three-dimensional hull forms (Series 60 models and practical hull form). As the governing equation, Navier-Stokes equation and the continuity equation are adopted and solved by Marker And Cell (MAC) method. The flow around a semi-infinite body is simulated on the boundary- and body-fitted coordinate system while the others are on the variable spacing. The calculated results near the semi-infinite body show well the periodic oscillation of the free-surface and the interaction between the free-surface and induced viscous field. The simulated waves around hull forms show good agreement with the experimental results.

On the other hand, a critical condition for the appearance of sub-breaking waves is applied to the simulated bow waves, although the critical condition is derived from the inviscid instability analysis.

1. INTRODUCTION

It is important to verify the nonlinear characteristics around a blunt bow in the field of ship hydrodynamics. The clarification of this phenomena and the evaluation of its contribution to the resistance are important problems to ship hydrodynamics, especially in the wave resistance problem and the preliminary bow design stage.

Recently, many experimental and numerical results were presented as related to a bow wave in a uniform flow including breaking phenomenon. Under a certain Froude number, the oscillatory motion of the bow wave takes place and it becomes a wave-breaking in proportion to the increase of the uniform velocity.

The characteristics of nonlinear waves generated by an advancing two-dimensional rectangular cylinder was investigated by Miyata et al.[1,2]. From the experimental work, it was observed that the bow wave fluctuates periodically. As wave-breaking takes place on the forward face of the bow waves at a certain speed of advance, the wave fluctuates and moves periodically back and forth.

Grosenbaugh et al. [3,4] investigated the flow characteristics of bow waves of the piercing circular cylinder and the wing section. They reported that there was a critical flow velocity at which the appearance of the bow wave undergoes a transition from quiescent to turbulent condition. Above this critical velocity, the bow wave develops a periodic oscillation. This oscillation appears due to the balance between the rate at which fluid is being entrained into the separated region and the rate at which it is existing in quiescent condition.

Mori[5,6] suggested the sub-breaking waves as a free-surface turbulent flow which was transited from laminar to turbulent flow. Based on the direct observation of the free-surface and the analysis of measured data, it was clarified that the sub-breaking waves were neither overturning nor spilling.

Meanwhile, a number of methods has been developed to analysis the interaction problems between waves and bodies. Among them, the numerical methods by Finite Difference Method (FDM) is the most powerful tool for these nonlinear problems, because they can solve nonlinear differential equations with the nonlinear boundary condition under the least assumption.

Waves by a submerged hydrofoil was simulated by Mori et al. [7]. The boundary- and body-fitted coordinate system were adopted in the whole domain and the free-surface was expressed by means of the Lagrangian technique so that grid points move only up and down vertically.

The work was extended to the numerical simulation of the free-surface turbulent flow and the nonlinear free-surface waves by making use of the simplest turbulence model [8]. It was concluded that the simulated result by turbulence models with proper boundary condition at the free-surface is much similar to the experiment.

One of the numerical methods by FDM was developed for the simulation of ship waves. Nishimura et al.[9] calculated the flow around a practical hull

form of arbitrary waterline by TUMMAC(Tokyo University Modified Marker And Cell)-IV method. The particles on the free-surface are moved by Lagrangian technique. The computed waves are in good agreement with the measured results and the method is useful for the determination of better hull form with smaller wave resistance.

In the present paper, previous works are summarized concerning to the FDM applied for the explanation of the waves generated by blunt bows. Meanwhile, the instability analysis of free-surface flow is applied to the numerical results for the detection of the sub-breaking waves around a blunt bow in the critical flow velocity region. The qualitative accuracy of the calculated results is examined and the quantative availability of the instability analysis is discussed.

2. NUMERICAL ALGORITHM

2.1 Two-Dimensional Case

The main frame and the details are referred in the previous works [6,7,10]. The code to simulate the flow with a submerged hydrofoil is extended to a semi-infinite body with the free-surface.

The body- and boundary-fitted coordinate and H-shape and regular grid system are adopted rather than staggered while the free-surface is expressed by means of the Lagrangian techinique.

The Navier-Stokes equation and the continuity equation are directly solved by the MAC method and the equations with primitive variables are as follows.

$$\frac{\partial u}{\partial t}+u\frac{\partial u}{\partial x}+v\frac{\partial u}{\partial y}=-\frac{\partial P}{\partial x}+\frac{1}{Rn}\nabla^2 u \qquad (1)$$

$$\frac{\partial v}{\partial t}+u\frac{\partial v}{\partial x}+v\frac{\partial v}{\partial y}=-\frac{\partial P}{\partial y}-\frac{y}{Fn^2}+\frac{1}{Rn}\nabla^2 v \qquad (2)$$

$$\frac{\partial u}{\partial x}+\frac{\partial v}{\partial y}=0 \qquad (3)$$

All variables are on the Cartesian Coordinates system (x,y) where x and y are in the uniform flow direction and the vertical respectively ; u and v are the velocity components in the $x-$ and $y-$ directions respectively. P is the pressure. Rn and Fn are Reynolds and Froude numbers, and g, gravitational acceleration. All the variables are nondimensionalized by the draft of the body and the oncoming velocity U_0. The Laplacian operater is

$$\nabla^2=\frac{\partial^2}{\partial x^2}+\frac{\partial^2}{\partial y^2}. \qquad (4)$$

Differentiating equation (1) with respect to x and equation (2) to y, we have following equation with the forward time differencing :

$$\nabla^2\Phi=F_x+G_y-\frac{1}{\Delta t}(u_x^{n+1}+v_y^{n+1}) \qquad (5)$$

where

$$F=\frac{u^n}{\Delta t}+\frac{1}{Rn}\nabla^2 u-(u\frac{\partial u}{\partial x}+v\frac{\partial u}{\partial y}), \qquad (6)$$
$$G=\frac{v^n}{\Delta t}+\frac{1}{Rn}\nabla^2 v-(u\frac{\partial v}{\partial x}+v\frac{\partial v}{\partial y}),$$
$$\Phi=P+\frac{y}{Fn^2}$$

where the superscript denotes the time step and the last term in equation (5) is expected to be zero at every time step.

The Poisson equation for the pressure term is solved iteratively by relaxation method. The (n+1)th velocity components are obtained by solving equation (1) and equation (2) explicitly with the pressure given by equation (5). Then, the velocity components and moving marker particles are updated. As the initial condition, the still condition is used : the whole flow field is accelerated up to the given constant velocity.

The marker particles are moved by the Lagrangian technique as follows:

$$x^{n+1}=x^n+u^n\Delta t,\quad y^{n+1}=y^n+v^n\Delta t \qquad (7)$$

The wave elevations are obtained by interpolating between (n+1)th marker particles at the original coordinate, so that the grid points move only up and down vertically.

2.2 Three-Dimensional Case

The principal procedure of the TUMMAC-IV method are explained in references [1,2,9,15,16,17]. Therefore, very brief explanations are described here. The conservative formed Euler equation (8)~(10) and the continuity equation (11) for inviscid and incompressible fluid are represented in the finite-difference forms. These governing equations are solved as an initial-value and boundary-value problems including the free-surface condition using time-marching procedure and iteration methods.

$$\frac{\partial u}{\partial t}+\frac{\partial(u^2)}{\partial x}+\frac{\partial(uv)}{\partial y}+\frac{\partial(uw)}{\partial z}=-\frac{1}{\rho}\frac{\partial P}{\partial x} \qquad (8)$$

$$\frac{\partial v}{\partial t}+\frac{\partial(uv)}{\partial x}+\frac{\partial(v^2)}{\partial y}+\frac{\partial(vw)}{\partial z}=-\frac{1}{\rho}\frac{\partial P}{\partial y} \tag{9}$$

$$\frac{\partial w}{\partial t}+\frac{\partial(uw)}{\partial x}+\frac{\partial(vw)}{\partial y}+\frac{\partial(w^2)}{\partial z}=-\frac{1}{\rho}\frac{\partial P}{\partial z}+g \tag{10}$$

$$\frac{\partial u}{\partial x}+\frac{\partial v}{\partial y}+\frac{\partial w}{\partial z}=0 \tag{11}$$

In equations (8) $\sim$ (11), w is the velocity component in the z-direction and ρ is the density of water. The parameters are same as the two-dimensional case and used without nondimensionalization.

A Cartesian coordinate system is employed, in which the x-axis is the centerline on the design load waterplane of a ship. The ship advances in the negative x-direction. A grid system by staggered semi-variable rectangular meshes is used for the increase of computational accuracy and applicability. The Euler equation is represented by first-order forward differencing in time and second-order centered differencing in space except for the convection terms. The differencing of the convection terms are described by a hybrid scheme that is the combination of second-order centered differencing and donor-cell method. Also, the continuity equation is represented by second-order centered differencing in space.

The momentum equations and the continuity equation give the Poisson equation for the pressure distribution. The source term of the Poisson equation is determined from the velocity field at each time step. Therefore, the momentum equations and the Poisson equation are the principal equations to be solved in present computational procedure. The momentum equations are hyperbolic to be solved as an initial-value problem and the Poisson equation is elliptic to be solved as a boundary-value problem. That is, the former are solved by time-marching procedure and the latter is solved by iteration method at every time step.

The Poisson equation is iteratively solved by SOR (Succesive Over Relaxation) method with the following equation.

$$P^{m+1}_{i,j,k}=P^{m}_{i,j,k}+\omega(P^{m+1}_{i,j,k\ cal}-P^{m}_{i,j,k}) \tag{12}$$

where the superscripts m and $(m+1)$ denote iteration number and ω is a relaxation factor. $P^{m+1}_{i,j,k\ cal}$ is temporary pressure at each iteration step. The iteration is continued until the second term of equation (12) converges within an allowable error.

The term in the parenthesis in equation (12) is modified by eliminating P using the momentum equations. If the divergence $D^{m}_{i,j,k}$ is assumed in each staggered mesh, equation (12) is deformed as

$$P^{m+1}_{i,j,k}=P^{m}_{i,j,k}-\frac{\omega}{\Delta T\cdot A}\cdot D^{m}_{i,j,k} \tag{13}$$

where

$$A=2\{\frac{1}{(\Delta x)^2}+\frac{1}{(\Delta y)^2}+\frac{1}{(\Delta z)^2}\}. \tag{14}$$

In the above equation, Δx, Δy and Δz are the longitudinal length, transverse width and vertical height of a cell, respectively.

The method by equation (13) is called the simultaneous iterative method which is equivalent to the SOR method. In this method the velocity is successively updated through the iterated calculation of pressure field at a time step. This procedure is conveniently used to deal with the boundary condition for an arbitrary hull configuration.

Although this computational procedure is suitable to unsteady problems, it is applied to a steady problem of ship wave-making in this work by letting an unsteady solution approach to a steady state. The initial condition is a rested state, and the velocities in computational domain are gradually accelerated for a desired incident velocity at the inflow boundary. After the steps of acceleration the computation is continued for adequate time steps until a steady state is reached.

At the inflow boundary the velocity and pressure are given as a desired velocity and reference pressure, i.e., in case of a Dirichlet condition. The computational domain is bounded by a center plane of a ship, because the flow of a ship is symmetry. Namely, on the centerplane the condition of symmetry must be taken into account. The bottom boundary is usually located so deep that the fluid motion is very small. Therefore, the hydrostatic pressure and the velocity condition of zero gradient are given at the bottom boundary. At the sideward open boundary the velocities and pressures are set equal to the inner values so that their gradient in the direction normal to the boundary is set zero, i.e., in case of a Neumann condition. Also, at the downstream open boundary their gradient along the local flow direction is set zero.

The hull surface consists of waterlines and framelines. The former is approximated by a succession of straight segments, and the vertical variation within each cell is ignored for the latter. A free-slip body boundary condition is given in the body boundary cells (the cells include a body boundary segment). Namely, the velocity normal to the body surface is zero, and the tangential velocity does not have normal gradient, and finally the divergence of a body boundary cell is zero. Under these conditions, the pressure of a body boundary cell is computed by velocity-pressure simultaneous iterative method.

On the free-surface, the Lagrangian movement of marker particles is used for the fulfilment of the kinematic condition, and the irregular star technique of Chan and Street [10] is used for the dynamic condi-

tion. Some interpolation and extrapolation methods of velicities components at the position of a marker particle, i.e, four-point and nine-point interpolations and zero gradient extrapolations are used.

3. RESULTS AND DISCUSSIONS

3.1 Semi-infinite Body

Computations are carried out for a two-domensional semi-infinite piercing body. The coordinate system is shown in Fig.1 where the origin is set on the still water level and the bow while all of the parameters are non-dimensionalized by the draft and uniform velocity.

The grid system by boundary- and body-fitted coordinate is shown in Fig. 2 and the computational conditions are shown in Table 1. The computational domain is extended to eleminate the influence by the outflow boundary and the maximum grid spacing on the free-surface to x-direction is 0.1 to simulate the wave configuration precisely. The Reynolds Number is set to be 10^3 while the Froude number covers the range of 0.5 to 1.25.

Fig. 3 shows the time history of the drag coefficients, C_{DP}, during the calculation which are obtained by the intergration of the pressure at the fore face of a semi-infinite body. The steady state reaches after T=30 in case of Fn=0.5 and 0.75 while T=60 for Fn=1.0 and 1.25. The periodic oscillations are clearly observed at Fn=0.5, 0.75 and 1.0 as in the experiments by Grausenbaugh et al. [3,4]. In the experiment, sub-breaking is observed at $Fn \geq 1.0$ in front of the rectangular cylinder. It may be similar for the flow by the semi-infinite body too. However, the result at Fn=1.25 doesn't show the periodic oscillation. It should be pointed out that the numerical simulation including sub-breaking phenomena is important.

Fig. 4 shows the time evolution of the bow wave elevation at the bow of the body. The steady state reaches after T=30 at Fn=0.5 and 0.75, while T=60 at Fn=1.0 and 1.25.

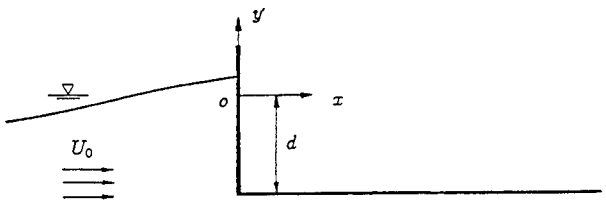

Fig. 1 Coordinate system

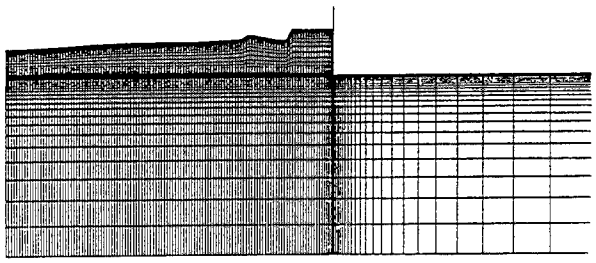

Fig. 2 Grid system for the semi-infinite body

Table 1 Computational condition

	Semi-infinite body
Domain of Computation	$-12 \leq x \leq 110$ $-9 \leq x \leq 0$
Reynolds number	10^3
Froude number	0.5 ~ 1.25
Maximum grid spacing to x-axis	0.1
Minimum grid spacing	0.02
Time increment	0.005
Aproximate Number of cell	7,500
Total time step	10,000 or 20,000
CPU time	1 or 2 hours

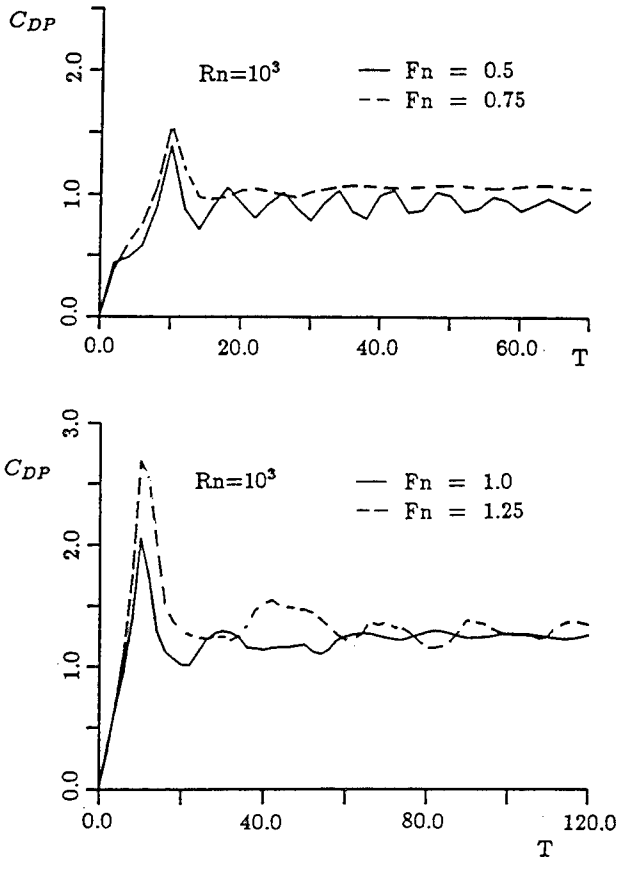

Fig. 3 Time history of the drag coefficients

Table 2 Comparison of periodic oscillation at the fore wall of body

Fn	Present calculation	Calculated result by Wehausen phenomenon [3]	Experimental result by by Miyata [1,2]	Experimental result by Grosenbaugh et al. [3]	
				Circular cylinder	Wing section
0.5	0.135	0.080			
0.75	0.082	0.053			
1.0	0.05	0.040	0.063		
1.1		0.036		0.06 ~ 0.07	0.09
1.25		0.032			

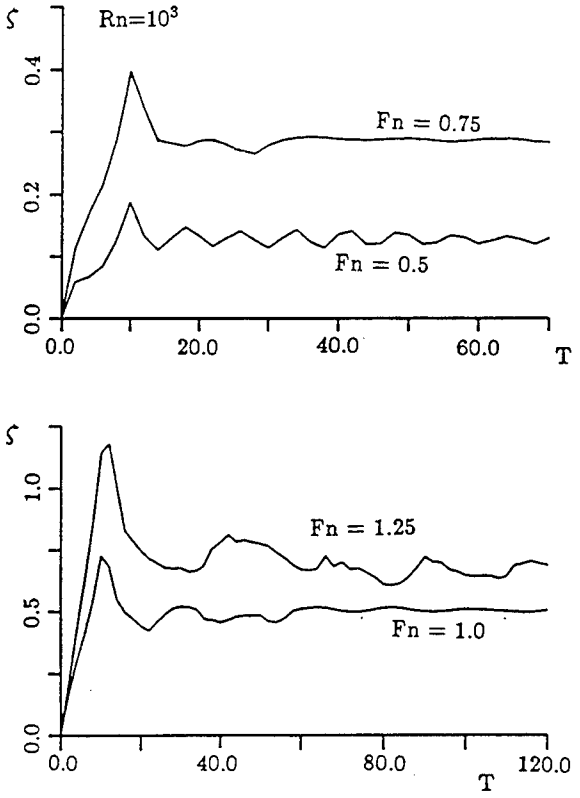

Fig. 4 Time evolution of the bow wave elevation at bow of the body (Rn=10^3)

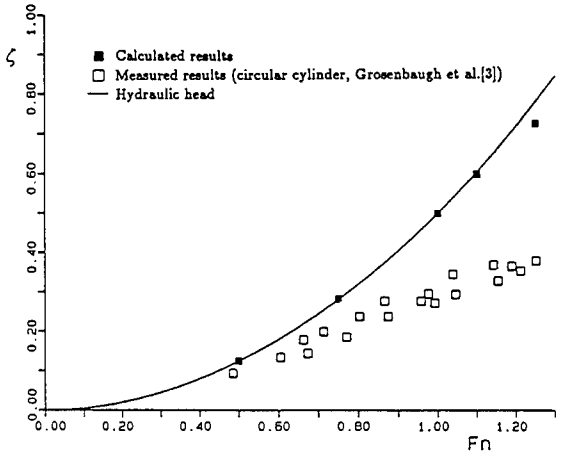

Fig. 5 Mean elevation of the bow wave

Table 2 shows the comparison of the oscillating periods at various Froude numbers. At Fn=1.0, the calculated periods are around 0.04~ 0.05 while the measured are 0.06~0.07.

The mean elevation of the bow wave is shown in Fig. 5 compared with the measured results by a circular cylinder [3]. The simulated results show fairly good agreement with the experiment at $Fn \leq 0.75$ in which the sub-breaking doesn't take place. Because the numerical scheme in this paper cannot contains the sub-breaking phenomena, reasonable agreement between hydraulic head and simulated results is observed only at $Fn \leq 1.0$.

Fig. 6 shows the wave profiles at various Froude numbers. The wave configurations is smooth at $Fn \leq 1.1$ but a steep slope is seen at $x \doteq -4.0$ in case of Fn=1.25 where the sub-breaking is experimentally observed in case of the rectangular cylinder [1].

The pressure contour maps of Fn=1.0 are shown in Fig. 7. The claculated period of bow wave was 20 (Table 2). The humps in the time history of wave elevation are at T=80 and 100 while the hollow was shown at T=90 (Fig. 4). Although the flow field under the body develops consequently at T=80 and 100, the wave elevation and the pressure contour in front of the body have almost same configuration. It is considered that the viscous flow under the body doesn't affect much to the flow in front of the body.

The calculated velocity vectors around the body are shown in Fig. 8. A counterclockwise vortex is observed under the body which differs noticeably at the two Froude numbers. Near the free-surface, an abrupt gradient of velocity is seen, which is similar to that in the boundary layer developed on a solid surface. This velocity distribution is also seen in the experimental result for a submerged hydrofoil [8].

The contour maps of the vorticity in front of the body are shown in Fig. 9. A horse shoe vortex is simulated and concentrated near the free-surface at Fn=1.25. Experimentally, the sub-breaking takes place at almost the same location ($x \doteq -4.0$) in case of the rectangular cylinder [2].

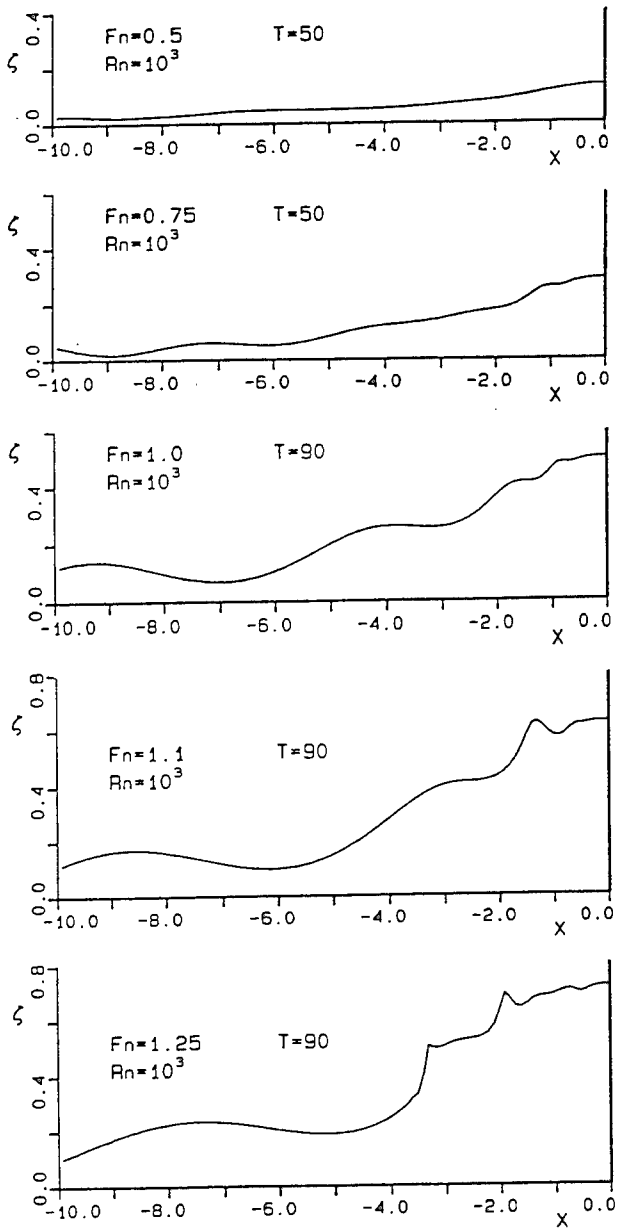

Fig. 6 Wave profiles at various Froude Numbers

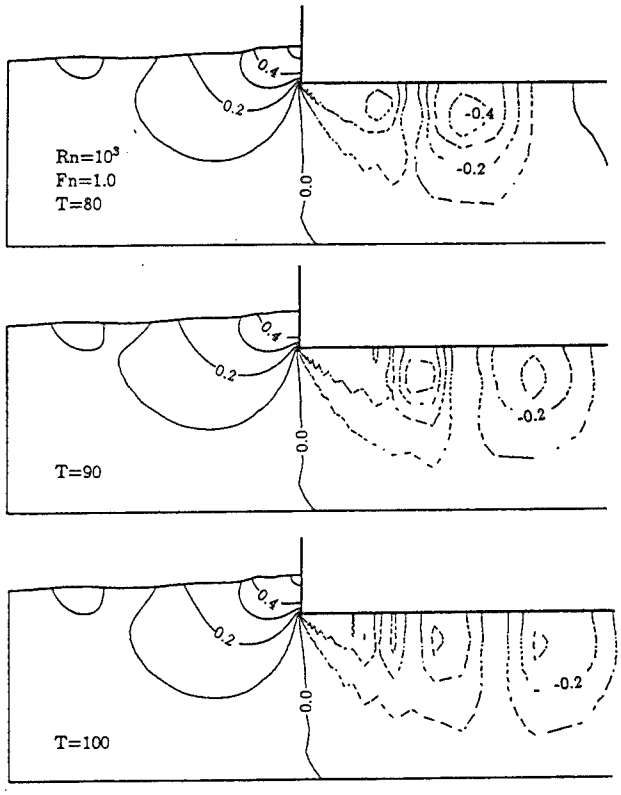

Fig. 7 Pressure contour maps (Fn=1.0)

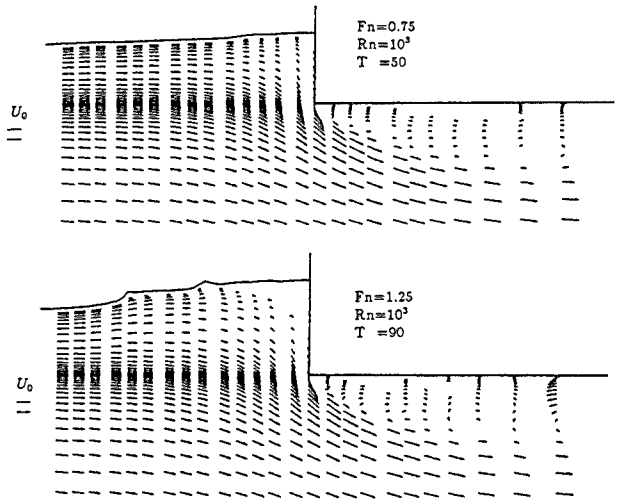

Fig. 8 Calculated velocity vectors around the body

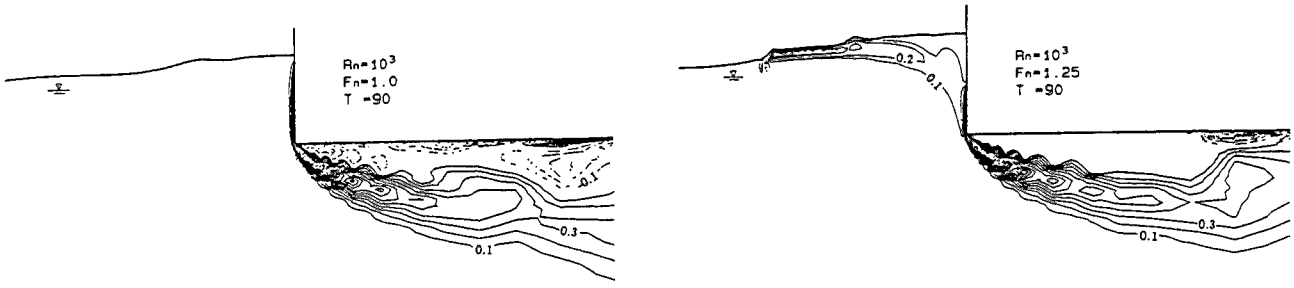

Fig. 9 Contour maps of the vorticity around the body

3.2 Ship Hulls

Three dimensional flows around Series 60 models and Afra-Max Class Tanker (designed by Daewoo Shipbuilding & Heavy Machinery Ltd.) as practical hull forms are simulated.

Fig. 10 show the lines of Series 60 hull whose block coefficients are 0.6 and 0.8. Fig. 11 shows the lines and principle dimensions of Tanker (Afra-Max Class) whose displacement, block and prismatic coefficients are 97,500 m^3, 0.8 and 0.81. The bulbous bow of this tanker is thin and large, while the center is higher than other conventional tanker. It will be an interesting subject to discuss the interaction between the bow and the free-surface.

Fig.12 shows the coordinate system and computational conditions are shown in Table 3 in detail. The number of grid points are 154,000 for Series 60 model of C_b=0.6, 60,000 for C_b=0.8 and 39,000 for tanker.

The comparison of the calculated and measured wave heights [18] along the hull surface for the Series 60 model of C_b=0.8 is shown in Fig. 13. The maximum wave heights [18] is about 2 cm at the same longitudinal position in both cases, but there is a little discrepancy near the shoulder. This may be due to the slip body boundary condition and no diffusion effect. On the whole length, the comparison shows qualitatively good agreement. Especially, better agreement is shown in the fore-body part.

Perspective views of computed waves which are magnified three times are shown in Fig.14. The difference of wave configuration affected by block coefficient is noticable.

Especially, near the soulder of the Series 60 model of C_b=0.8, a nonlinear wave formation is well simulated. The superior accuracy of the present method for the nonlinear wave problems had been shown in [15]. Fig.15 shows contour maps of computed waves for Series 60 models. Wave height around bow by Series 60 model of C_b=0.8 is higher than that of C_b=0.6. Also, the divergence angle of the bow wave by Series 60 model of C_b=0.8 is larger than that of C_b=0.6.

Fig.16 shows the perspective view of calculated

Table 3 Computational condition

	Series 60		Tanker
	$C_b = 0.6$	$C_b = 0.8$	Hull Form
Domain of Computation (m)			
Length	1.60	1.80	4.80
Breadth	0.385	0.60	1.58
Depth	0.42	0.43	0.86
Cell Size (m)			
DX	0.02	0.03	0.07
DY	0.007	0.015	0.04
DZ(Min.)	0.005	0.01	0.019
Number of Used Cell	154,000	60,000	39,000
Time Increment (sec)	0.0040	0.0027	0.0064 0.0057
Time Steps for Acceleration	300	400	300
Total Time Step	750	1000	500 500
Froude Number F_n	0.2	0.2	0.15 0.17
Length of Ship Model (m)	2.5	2.5	7.1341

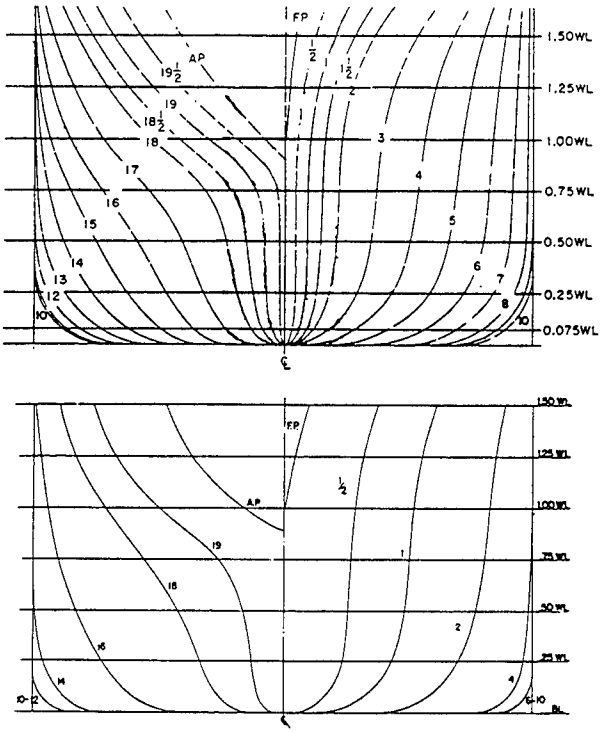

Fig. 10 Lines of Series 60 hull form (from above: C_b=0.6, 0.8)

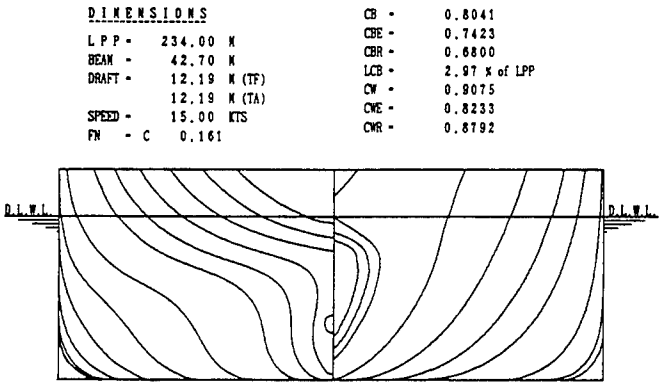

Fig. 11 Lines of Tanker (Afra Max Class)

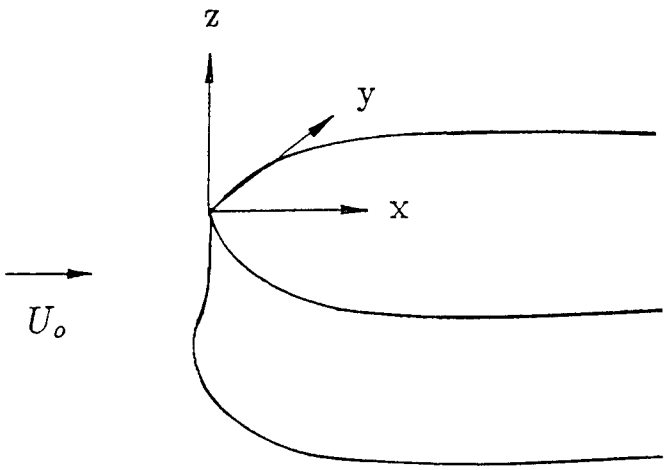

Fig. 12 Coordinate System

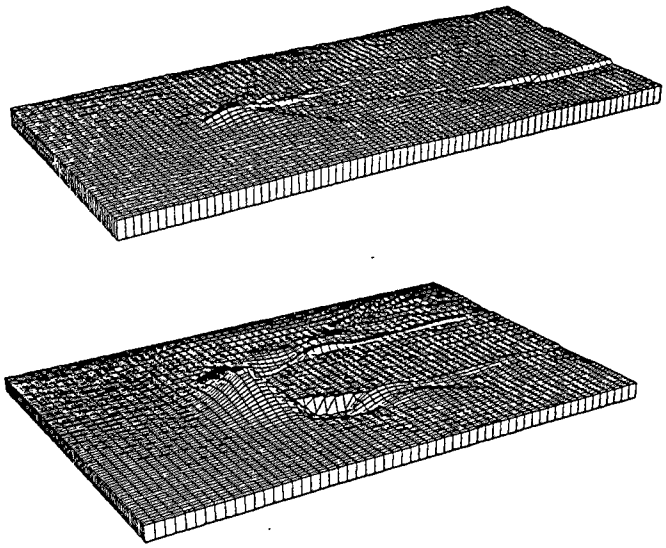

Fig. 14 Perspective views of computed waves (Series 60 models, Fn=0.2, from above: C_b=0.6, 0.8, wave height is three times magnified)

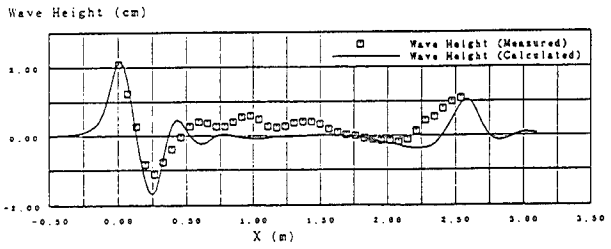

Fig. 13 Comparison of wave profiles along the hull (Series 60, C_b=0.8, Fn=0.167)

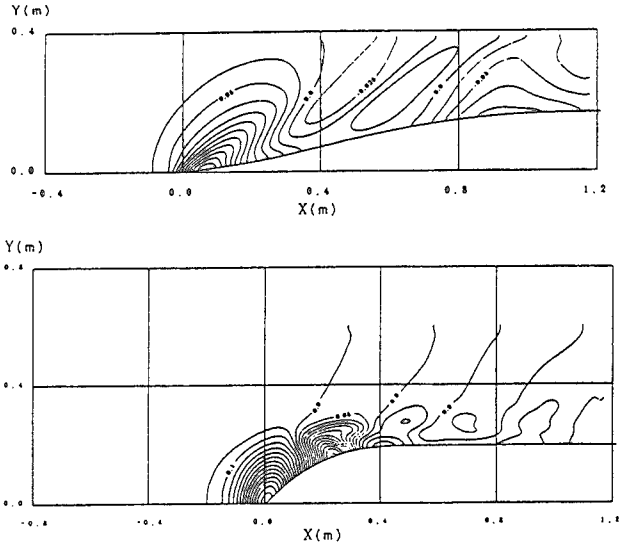

Fig. 15 Contour maps of computed waves (Series 60 models, Fn=0.2, from above: C_b=0.6, 0.8)

waves around a tanker at Fn=0.15 and 0.17 while Fig. 17 shows photographs of a running tanker model. The experiments for the tanker model have been conducted at the deep water towing tank of the KRISO. The tanker model which has the same dimensions as the condition of numerical simulation is towed by a eletric carriage. The tendency of wave configurations seems good in agreement. This is also noted in Fig. 18 for the wave contours, in which the wave formations do not show subtantial differnce between two Froude numbers. Sub-breaking waves are physically shown around a bow (Fig. 17) but calculated results (Fig. 16) don't show this phenomena. Although calculated result shows smooth free-surface (Fig.18) and the steady state is reached without any trouble, they are questionable. Therefore, it is necessary to adopt the numerical schemes for the sub-breaking waves or equivalent treatment.

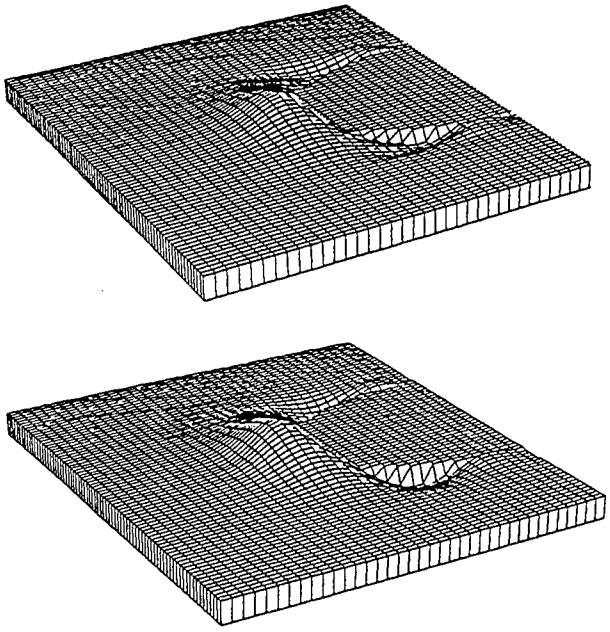

Fig. 16 Perspective views of computed waves (Tanker hull, from above: Fn=0.15, 0.17, wave height is three times magnified)

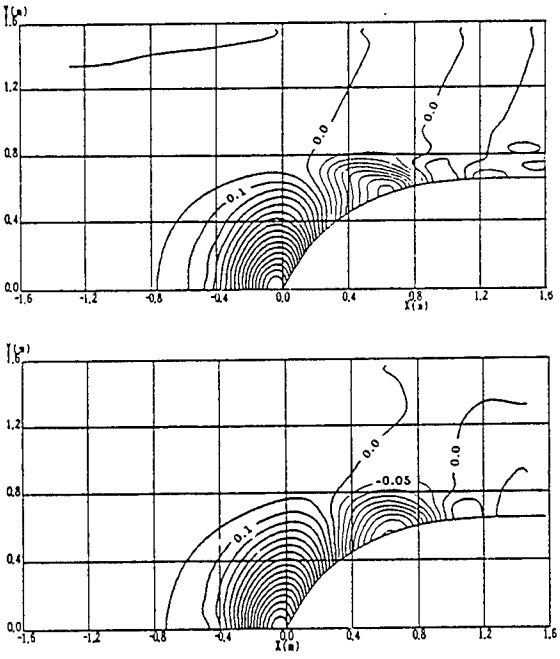

Fig. 18 Contour maps of computed waves (Tanker Hull, from above: Fn=0.15, 0.17)

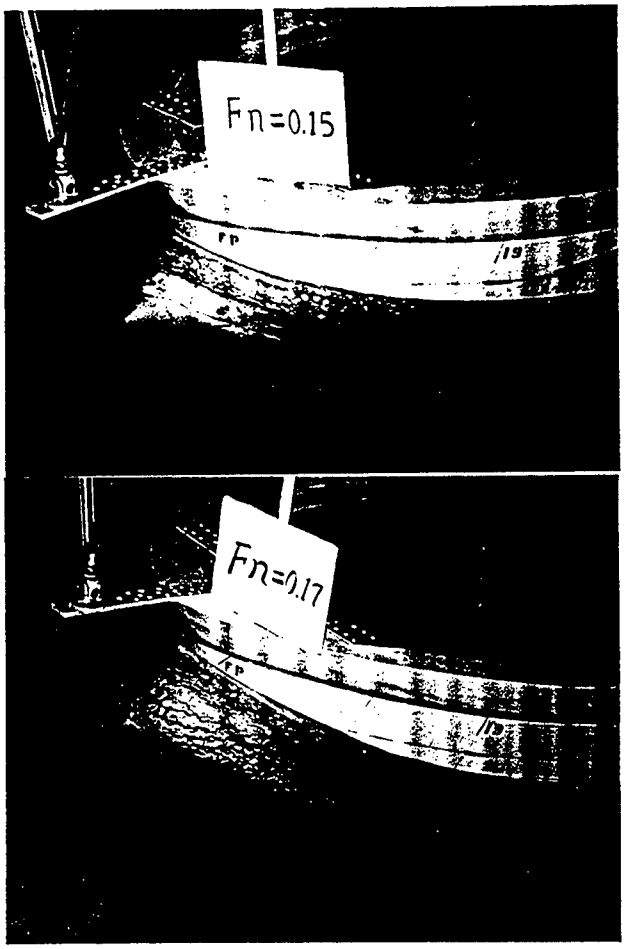

Fig. 17 Photographs of running ship model (Tanker Hull, from above: Fn=0.15, 0.17)

4. DETECTION OF SUB-BREAKING WAVES

The critical condition for the appearance of sub-breaking waves, proposed by Mori [5,6] is applied to the simulated results. The condition is given by

$$\frac{U}{M}\frac{\partial M}{h\partial S} - \frac{\partial U}{h\partial S} - \frac{1}{n_z}U\frac{\partial n_z}{h\partial S} > 0 \qquad (15)$$

where

$M = (\kappa U^2 - n_z g)n_z$,
U, W : Velocity components on stream line coordinate,
κ : Curvature of wave elevation,
h : Metric coefficients.

Near the wave crest, it is assumed $n_z \doteq 1$, $\frac{\partial}{h\partial S} \doteq \frac{\partial}{\partial x}$ and equation (15) can be approximately as follows :

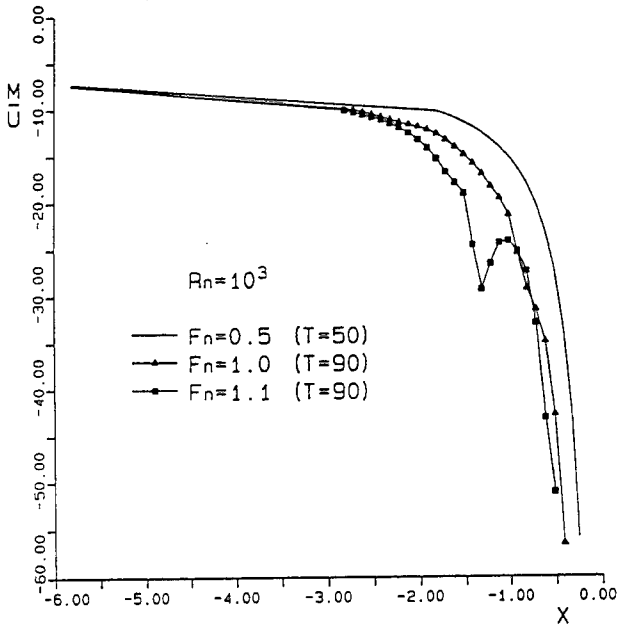

Fig. 19 M/U distributions at three different Froude numbers for the semi-infinite body.

$$\frac{U^2}{M}\frac{\partial}{\partial x}\left(\frac{M}{U}\right) > 0 \qquad (16)$$

where

$$M = \kappa U^2 - g$$

M is always negative in our problems. If the gradient of M/U with respect to the incidient flow direction shows negative gradient, the real flow field near the free-surface can be unstable.

In the experiment, sub-breaking with unsteadiness of the surface takes place at Fn=1.0. Fig. 19 shows the M/U distributions at three different Froude numbers for the semi-infinite body. For all cases, negative gradients are observed near the body which is due to the stagnant velocity component by the existence of the body which is not included in the present instability analysis. Comparing the M/U distributions at the three different Froude numbers, the M/U distributions of Fn=1.1 shows a sharp negative gradient around x=-1.5 compared with that of Fn=1.0, although the speed is slightly different. Thus it can be concluded that the sub-breaking takes place at Fn=1.1 and the scheme should have been switched into that capable for such turbulent flow. It should be also pointed out that the result at Fn=1.25 can be fake even if the computation has been carried out, the process of the sub-breaking phenomena is neglected.

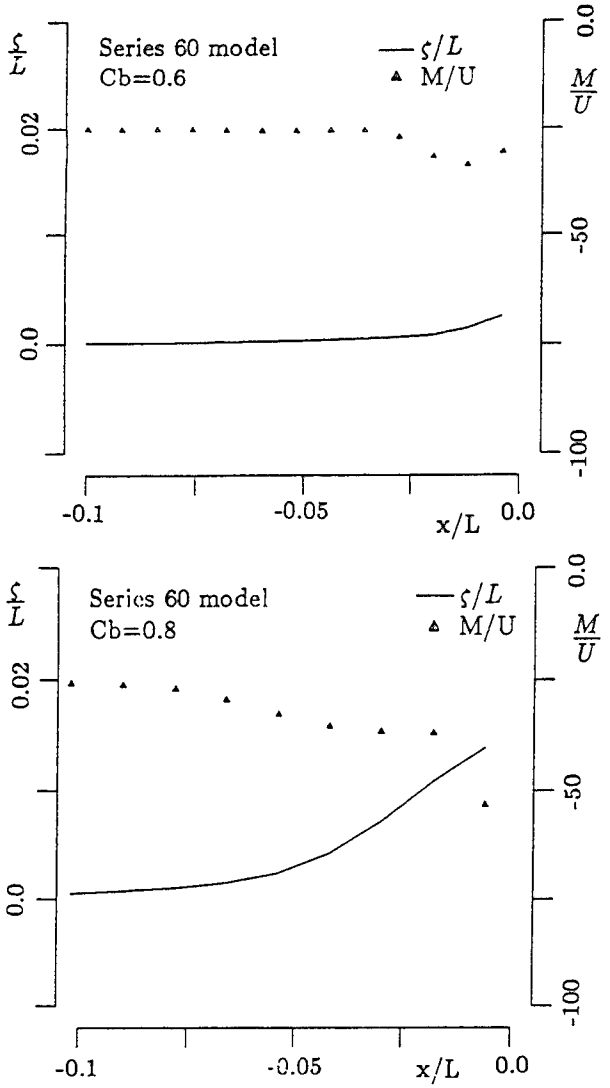

Fig. 20 Distributions of M/U along center line (Series 60 models,Fn=0.2, from above: C_b=0.6, 0.8)

The appearing condition of sub-breaking waves is applied to calculated results which is shown in Fig. 20. The gradient of plotted M/U along center line show almost flat at C_b=0.6, Fn=0.2. It means the sub-breaking looks like tanker (Fig. 17) doesn't appear at this Froude number.

Fig. 21 shows the M/U distributions applied to the calculated flow around a tanker hull. The abrupt negative gradient with respect to x is shown which means the sub-breaking waves can appear. But this negative gradient can be the consequence of the staganant velocity while the photographs at this Froude number show the sub-breaking.

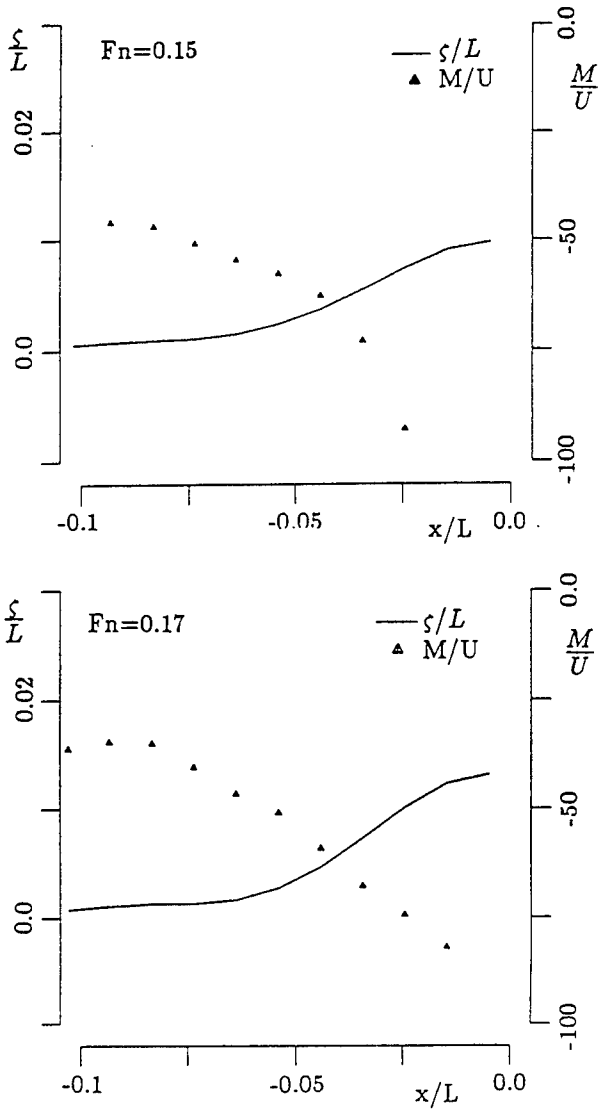

Fig. 21 Distributions of M/U along center line (Tanker hull, from above: Fn=0.15, 0.17)

5. CONCLUSIONS

The numerical simulations of the disturbed flow around a semi-infinite body and hull forms with free-surface are carried out and the detection of sub-breaking wave is applied to the simulated results. Through the present study, the findings are summarized as follows:

(1) The marker point moved by Lagrangian technique simulate well the free-surface formation around a blunt bow with the appropriate ship body boundary condition.

(2) An intensive interaction between the viscous flow with vortex motion and the free-surface is observed behind the semi-infinite body, but the bow waves are not so much affected by the viscous flow.

(3) The simulated bow wave elevation and its oscillation show generally good accordance with the experimental result.

(4) Detection of sub-breaking in front of the semi-infinite body is attempted by applying the criteria. It may have appeared at Fn=1.0.

The computations of semi-infinite body were executed by CRAY-2S at System Engineering Research Institute and the computations of hull forms were executed by IBM PC-386 with WEITEK coprocessor at KRISO

[ACKNOWLEDGEMENT]

This work was carried out under the sponsorship of the KRISO Elementary Research Program (Contract No. ED498).

Authors thank to Mr. Hochung Kim in Daewoo Shipbuilding & Heavy Machinery Ltd. who provided the drawings and informaton of Afra-Max Class Tanker.

[REFERENCES]

[1] Miyata, H., Kajitani, H., Matsukawa, C., Suzuki, N., Kanai, M. and Kuzumi, S., "Numerical and Experimental Analysis of Nonlinear Bow and Stern Waves of a Two-Dimensional Body (Second Report)," Journal of the Society of Naval Architects of Japan, Vol. 155, 1984, pp. 11-17.

[2] Miyata, H., Kajitani, H., Shirai, M., Sato, T., Kuzumi, S. and Kanai, M., "Numerical and Experimental Analysis of Nonlinear Bow and Stern Waves of a Two-Dimensional Body (Fourth Report)," Journal of the Society of Naval Architects of Japan, Vol. 157, 1985, pp. 15-33.

[3] Grosenbaugh, Mark A. and Yeung, Ronald W., "Flow Structure Near the Bow of a Two-Dimensional Body," Journal of Ship Research, Vol. 33, No. 4, Dec., 1989, pp. 269-283.

[4] Grosenbaugh, Mark A. and Yeung, Ronald W., "Nonlinear Bow Flows - An Experimental and Theoretical Investigation," Proceedings of 17th Symposium on Naval Hydrodynamics, Hague, Netherlands, 1988, pp. 195-214.

[5] Mori, K., "Critical Condition for Their Appearance of Steady Breakers on 2-Dimensional Wave Generaged by Submerged Foil," Nonlinear Water Waves, Springer-Verlag, 1987, pp. 145-150.

[6] Shin, M. and Mori, K., "Numerical Computation of 2-Dimensional Waves behind a Hydrofoil," Journal of the Society of Naval Architects of Japan, Vol. 163, 1988, pp. 19-24.

[7] Mori, K. and Shin, M., "Sub-Breaking Wave: Its Characteristics, Appearing Conditions and Numerical Simulation," Proceedings of 17th Symposium On Naval Hydrodynamics, Hague, Netherlands, 1988.

[8] Shin, M. and Mori, K., "On Turbulent Characteristics and Numerical Simulation of 2-Dimensional Sub-Breaking Waves," Journal of the Society of Naval Architects of Japan, Vol. 165, 1989, pp. 1-7.

[9] Nishimura, S., Miyata, H. and Kajitani, H., "Finite-Difference Simulation of Ship Waves by the TUMMAC-IV Method and Its Application of Hull-From Design," Journal of the Society of Naval Architects of Japan, Vol. 157, 1985, pp. 1-14.

[10] Chan, R. K. C. and Street, R. L., "A Computer Study of Finite-Amplitude Water Waves," Journal of Computational Physics, No. 6, June 1991, pp. 68-94.

[11] Mori, K., Kwak, S. -H., and Doi, Y., "Numerical Simulation of Ship Waves and Some Discussions on Bow Wave Breaking & Viscous Interactions of Stern Wave," Proceedings of 18th Symposium On Naval Hydrodynamics, Michigan, USA, 1988.

[12] Qi, Xu and Mori, K., "Numerical Simulation of 3-D Nonlinear Water Wave by Boundary Element Method," Journal of the Society of Naval Architects of Japan, Vol. 165, 1989, pp. 9-15.

[13] Shin, M., Lee, Y. -G. and Kang, K. -J., "Numerical Simulation of the Free-Surface Flow around a Floating Body," Proceedings of 6th International Workshop on Water Waves and Floating Bodies, Boston, USA, 1991.

[14] Baba, E., "A New Component of Viscous Resistance of Ships," Journal of the Society of Naval Architects of Japan, Vol. 125, 1988, pp. 23-34.

[15] Lee, Y. -G., Miyata, H. and Kajitani, H., "Some Applications of the TUMMAC Method to 3D Water-wave Problems," Journal of the Society of Naval Architects of Korea, Vol. 25, No. 4, 1988, pp. 13-27.

[16] Cho, K. J., Lee, K. -H. and Lee, Y. -G., "A Numerical Simulation of Ship Waves by using Finite Difference Method," Journal of the Society of Naval Architects of Korea, Vol. 28, No. 2, 1991, pp. 77-94 (in Korean).

[17] Miyate, H. and Nishimura, S. , "Finite-Difference Simulation of Nonlinear Ship Waves," Journal of Fluid Mechanics, Vol. 157, 1985, pp. 327-357.

[18] Kim, H. et al., "The Experimental Study on the Flow Characteristics around a Ship Hull", Seoul National University, SNUTT R9001, 1990 (in Korean).

DISCUSSION

K. Mori
Hiroshima University, Japan

The authors' approach to pay attention to the appearance of sub-breaking waves seems quite sound. This is because an experimental observation of the bow wave shows that the free surface becomes suddenly unsteady and ripple-like waves (which are called sub-breaking waves in the paper) appear beyond a certain advancing speed. In the numerical simulation, it should be considered that the energy may be absorbed for the turbulence production.

The authors applied Eq. (15) for the detection of the sub-breaking waves around the bow as a critical condition. The condition has been derived from the stability analysis and the steepness of the negative gradient gives the growth rate of the instability. Therefore, should we conclude from Figure 19 that all the flows at the three Froude numbers can be unstable in front of such a blunt bow although there are differences in its steepness?

How was the time evolution of the bow wave elevation for Fn=1.1? Were there any differences from that for Fn=1.0?

AUTHORS' REPLY

Thank you for your discussion and comment with kindness.

The balance between the increment of wave elevation by local wave length and the circumferential force by gravity composes the equation of the critical condition for the detection of sub-breaking waves. In case of the flow around a blunt bow, the velocity is reduced due to the stagnant flow and the local wave length becomes zero. As a result, the value of M/U near the body becomes minus infinity. This is due to the assumption that the basic wave in inviscid instability analysis is the sinuous wave. Although the negative gradient near the bow is shown, it cannot be said that all the flows are unstable. Because of the steep negative gradient and the discontinuous distribution of M/U of Fn=1.1, it can be said that the flow of Fn=1.1 is unstable.

The time evolution of the bow wave elevation of Fn=1.1 is additionally compared and the configuration of Fn=1.1 is similar to that of Fn=1.0 after T=90 as show in the figure below.

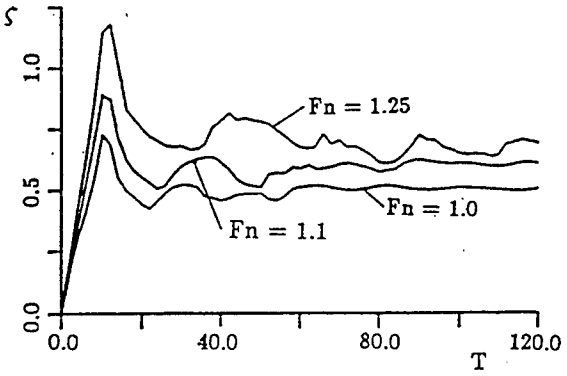

DISCUSSION

H. Miyata
University of Tokyo, Japan

Since water particles moving about a hull is under the influence of both free-surface waves and viscous motions, this kind of research is of increasing importance and may be developed into a useful tool for hull-form design.

The elucidation of the detailed phenomenon of nonlinear bow waves involving viscous motions is of another importance. However, the authors' discussions based on the simulation results seem to be insufficient, because the simulation is composed of numerous postulations and approximations. The viscous stresses on the free surface are ignored. The spacing is too coarse for these stresses. The grid system is incapable of representing the overturning motion. An appropriate turbulence model for the free-surface turbulence is not known. Further advanced research with smaller number of approximations and restrictions will provide us better understanding of the nonlinear mechanism of bow waves.

AUTHORS' REPLY

Thank you for your discussion.

The main aim of this paper is to predict the sub-breaking phenomena around a blunt bow. Our final goal is to simulate the wave breaking phenomena as a free-surface turbulent flow which can be used in the primary design stage of hull forms. In that sense, we thought that the viscous stresses can be ignored.

There are a lot of measured data in previous works around a piercing body. The measured data show the u velocity component in front of the body is always greater than zero and the distribution of the Reynolds stresses is similar to that in the boundary layer developed on the solid surface. Therefore, the wave-breaking phenomena should be represented as a turbulent flow, not as an overturning motion.

Author measured Reynolds stress near the free surface by a submerged hydrofoil and this work was extended to the numerical simulation by making use of the simplest turbulence model. It was concluded that the simulated result by turbulence models is much similar to the experiment and the proper boundary condition at the free surface is important. Much attention should be paid to get the proper free-surface boundary condition.

DISCUSSION

P. Ananthakrishnan
University of California at Berkeley, USA

I would like to commend the authors for their fine efforts on solution of this difficult. My comments/questions are as follows:

1. It has been pointed out by Grosenbaugh and Yeung (JSR, 1989) that the bow-wave oscillation observed in their experiments is not the same as the Wehausen phenomenon. The Wehausen phenomenon is used to refer to the starting transient generated by a body, as observed in the moving frame. These waves propagate upstream. On the other hand, the bow-wave oscillation phenomenon was observed to be a back and forth surging-type motion of the bow-wave front. This oscillation does not propagate upstream. As discussed in Grosenbaugh and Yeung, it may be irrelevant to compare these two different wave phenomena. The oscillation described in authors' results appear to be just the viscosity-modified Wehausen phenomenon.

2. Vorticity contours shown in Figure 9 indicate a pulsating type behavior. Could this be physical? Or is it due to an inappropriate difference scheme? Perhaps the authors can comment on this.

3. In your numerical method, grid points on the free surface are restricted to move only up or down. What is the consequence of such a restriction on the realism of the solution?

AUTHORS' REPLY

Thank you for your discussion and comment with kindness.

The periodic oscillation by present calculation should be compared to the experimental result. The periodic oscillation at $Fn=1.0$ is reasonable; present calculation is 0.05 while experimental results show around 0.06.

Vorticity contours are interpolated and drawn by a package subroutine. The discontinuous contours may be due to an interpolate procedure in this subroutine.

As I mentioned, the wavebreaking phenomena around a blunt bow should be treated as a free-surface turbulent flow. From the experimental result (19th ONR, Yeung and Ananthakrishnan), it is clearly shown. The wave face moves back and forth, but this behavior is not an overturning motion. the u-velocity on the free surface is always greater than zero so that the technique for an overturning motion isn't necessary.

Investigation on Scale Effect in Ship Viscous Flow by CFD

S. Abdallah (University of Cincinnati, USA), G. Caprino,
L. Sebastiani, A. Traverso (Italian Ship Research Center, Italy)

The present paper deals with viscous flow predictions around ship hull, with emphasis on the problem of scale effects on ship wake. A numerical methodology is described in which the solution for the three-dimensional turbulent flow is obtained the primitive-variable formulation. In this approach, the time averaged Navier-Stokes equations (RANSE) are solved for the velocity field using multi-step time dependent explicit schemes. The pressure field is calculated from a Poisson-type equation with Neumann boundary conditions, which is derived from the continuity equation. The Neumann pressure equation is guaranteed to converge, on non-staggered grids, by satisfying the compatibility condition using consistent finite-difference approximations for the pressure equation and the boundary conditions. The turbulent problem is closed by employing the Baldwin-Lomax turbolence model. Numerical results for the viscous wake at the propeller disk are obtained for a single-screw bulbous-bow gas carrier hull and compared with the model test results. In addition a computation at 1.0E+8 Reynolds number has been carried out, which is intermediate between model-scale and full-scale.

INTRODUCTION

Development in computational ship hydrodynamics is continuatively going on due to both the recent advance of high-speed computers and the refinement of numerical algorithms. From the ship designer point of view, the far most important application of such calculations is the evaluation of ship viscous wake at the propeller disk so to be able to predict the performances of the propeller in its operating conditions. Ship stern flow is currently calculated on the basis of viscous flow assumption, disregarding the presence of the propeller or considering eventually the hub influence on the flow. This way emphasis is given to the bare-hull wake, the so-called nominal wake, with respect to the wake actually present when the propeller is operating, the so-called effective wake. In the very last few years ever more ambitious attempts to a comprehensive treatment, which includes the effect of an operating propeller into viscous flow calculations with a free surface, are taking place within the CFD community but their final assessement is still far on the way. Even when propeller-hull and free-surface effects are not considered, that is the double-model nominal wake is addressed, the evaluation of the full-scale wake at the transverse section where the propeller is to be installed remains one of the major problem of ship hydrodynamics.

The common practice, and until the advent of numerical ship hydrodynamics the only feasible approach, to obtain information on the nominal wake at full scale is to measure nominal wake on models in towing-tanks and to extrapolate these model-scale results to the prototype. The Reynolds number scaling of ship stern viscous flow characteristics from model-scale to full-scale plays thererefore a central role in ship/propeller design. The difficulty of scaling from model-scale to full-scale Reynolds numbers is mainly due to the scarce availability of reliable and suitable full-scale data. Local observations of stern flow characteristics near the propller disk on full-scale ships are essentially obtained through Pitot probes or LDV measurements. Installation on board of the necessary equipment is not a routine task and requires a big preparation work besides mechanical interventions on the ship structure, so that few service ships are available for such a kind of measurements. Measurement techniques are in their turn very delicate and sensitive to external conditions.

Therefore full-scale data of wake distribution are a few and insofar the major empirical source on Reynolds-number wake scaling is represented by laboratory experiments on models. The situation is however not a satisfactory one at the moment, since these investigations are quite onerous both in terms of costs and time. More often than not available data are affected by measurement uncertainity or are not sufficiently detailed or testing conditions are not well documented. Besides the range of Reynolds numbers covered is not large enough to provide definitive information.

As a consequence of this general lack of empirical information, the reliability of CFD methodologies to predict scaling effects in ship wake is still not well assessed. It should be also noted that, due to the predominance of model-test data over full-scale data, up to now computational techniques have been tested and calibrated essentially in the model-scale Reynolds number range, up to 1.0E+6, while full-scale Reynolds numbers are of the order of 1.0E+9, among the largest values encountered in fluids engineering applications. Therefore the usual practice is to resort to using empirical or semi-empirical formulas for full-scale ship wake predictions.

There have been several formulas proposed for model-ship nominal wake correlation, as reported for istance in the 14th ITTC. Underlying theory is rather crude and it is essentially based on wake measurements on geosim models and simple boundary-layer considerations. The usual way of evaluating full-scale wake is to correct somewhat model data to compensate for the difference in Reynolds numbers. The advantage of such an approach is that an adequate scaling methodology can be in principle estabilished through extensive model tests. It should be however bearing in mind that this procedure is very expensive and its validity is limited to the class of ship forms for which the particular correlation formula has been estabilished.

As confirmed by the recent independent works of Tanaka [1] and Boccadamo [2], which gave a crictical examination of the various correlation techniques through wake measurements on geosims, the search for simple correction formulas for scale effects is still in progress. However it appears from the complexity of the flow phenomena taking place in the stern region of practical ship hulls, and revealed by the recent wake measurements carried out under the inititative of ITTC, that such attempts are doomed to fail due to the fact that conventional boundary-layer theory is not thoroughly valid in the thick wake stern region.

A more rational approach to the problem of Reynolds number scaling is therefore necessary and can be found by application of the recent CFD techniques. In principle there is no obstacle to the prediction of ship viscous flow at whatever Reynolds number provided that an efficient and reliable method is available to solve the governing equations, that is the the Navier-Stokes Equations (NSE) or more exactly the Reynolds Averaged Navier-Stokes Equations (RANSE). Actually, apart the previously mentioned scarcity of relevant experimental data necessary to calibrate/validate the code, this ambitious task cannot be completely fulfilled due to physical/ numerical reasons. These difficulties can be roughly summarised as uncertainties in the modelling of turbulence, approximations in the ruling equations and limitations of the numerical techniques in dealing with the sharp gradients in the near-wall region at high Reynolds numbers. Nevertheless the computational approach based on the numerical solution of RANSE equations seems the most promising one in the assessment of Reynolds numbers wake scaling, as it is confirmed by recent applications of CFD methods to Reynolds numers as high as five billion.

Our goal is to verify the reliability of CFD in the study of scale effects in ship wake. This goal requires the availability on one hand of a computer code with proven accuracy, validated against detailed experimental data, and on the other hand empirical wake data for at least two scales models of the same hull. In the study the first requirement is accomplished.

The present numerical methodology is based on the solution of the time-dependent 3D RANSE in primitive variables. Reynolds stresses are related to the means rate of strain on Boussinesq's hypothesis through the concept of the eddy-viscosity. Eddy viscosity is calculated by the algebraic model of Baldwin-Lomax [3], based on the distance normal to the hull. The governing equations are discretized on a non-staggered grid, and the incompressibility constraint is satisfied by employing the optimum pressure-Poisson approach developed by Sotiropoulos and Abdallah [4].

The computed results for a single-screw bulbous-bow gas carrier hull complete an extensive series of tests for verifying the present methodology. The importance of a high level of confidence in the computations must be stressed, as the study of scale effects will be based on the interpretation of the calculated results. In a forthcoming paper, the second requirement will be addressed.

To illustrate the actual possibilities of the methodology in the prediction of wake scaling, an additional calculation at a "full-scale" Reynolds number of 1.0E+8 has been however performed.

EXPERIMENTAL METHODOLOGY

Due to the major role of stern wake in ship hydrodynamics, measurements in ship boundary layers and wakes have been carried out over many years. Notwithstanding the huge amount of empirical information, in reality few of the available data are adequately detailed or well documented to provide a deep insight into the physics of stern wake and the mechanism of Reynolds numbers scaling. The main reason of this fact is that such measurements of local flow parameters are delicate, affected by several sources of uncertainity, expensive, time consuming and not included in the routine work of towing-tanks.

The basic experimental procedure to study wake scale effects still remains the use of geosim models. To this regard a series of toking-tank tests were carried out at the Naples University model-basin, DIN, on three ship models within a research program on geosim tests [5]. The choice of the model scales and of the test speeds has been done taking into account the blockage effect and the turbulence stimulation.

As regard the hull type a single-screw bulbous-bow tanker hull was selected. The main parameters of the prototype ship, designed and built by Fincantieri Merchantship Division, are the following:

Table 1. Main characteristics

parameter	load condition		
	full	trial	ballast
L/B	5.63	5.63	5.63
B/T	2.15	2.48	3.30
Cb	0.72	0.67	0.66
(δT/T)%	4.50	0.0	20.90

The corresponding model scale ratios are 28, 20, 15.7 and the modles were tested at Fn = 0.265. Wake at the propeller disk was measured by a rake of 6 Pitot tubes differentially spaced along the radius, which can rotate in order to cover the complete set of measurements over 360°. The differential value between the dynamic and static pressures of each tube wass measured by an HBM, type PD 1/0.1 differential pressure gauge, which signal was amplified by a 6-channel signal conditioning system. The measurement was simultaneously taken by the 6 tubes at each angular position.

System calibration was achieved through a series of carriage runs in open water, for a speed range from 0.2 up to 3.9 m/s with a 0.1 m/s increment. At each run the response in volts for the relative speed was recorded by the system and sent to the HBM signal conditioner. At the end of the series a regression was made on the recordered data to obtain the calibration curve of the Pitot tube.

The angular step of the rake, in the case of a single screw vessel, is kept at 5°, for a total of 37 positions to cover the entire propeller disc. At each angle the values at 6 different radial positions are recordered for a time of about 10 seconds. The acquisition system then provides the corresponding output in real time, converting the analogic signal into a physical quantity. The fluctuations of the measurements due to natural wake pulses at the propeller disc of a ship model makes data processing necessary in order to smooth out the results. This is done analytically by means of a mathematical spline adopted on the results along the radius at constant angle.

From the the measurements the following quantities were obtained for each of the three models tested in the towing-tank:

- the local nominal wake $1-w(x,\theta)$, relating to the different radius ratios $x=R/r$ and the various angles θ.

- the nominal wake curves for $1-w(x,\theta)$ for constant x radius ratio as a function of the angle θ.

- the circumferential mean wake for the various radius ratios and the total nominal volumetric wake.

- the iso-velocity curves on the propeller disc relating to 1-w ranging from 0.1 to 0.9 with step 0.1.

THEORETICAL METHODOLOGY

The progress of computational fluid dynamics (CFD) in the prediction of practical ship flows during the last decade is well illustrated by the results of the two comparative studies for numerical calculation of ship viscous flows, the 1980 SSPA-ITTC Workshop [6] and the 1990 SSPA-CTH-IIHR Workshop [7].

The workshops were addressed to give an assessment of the present state-of-the-art of ship viscous flow predictions by correlating computational results from different methodologies with detailed experimental flow data for selected test cases. The first Workshop showed a general breakdown in the capability of boundary-layer numerical methodologies to accurately predict ship stern flow, pointing out the need of further improvements in the modelling ship viscous flow. The results of the second Workshop clearly indicates what development direction has prevailed: in 1980 only one RANSE solver was presented, in 1990 only one boundary-layer method was presented.

A general conclusion which can be drawn from 1990 Workshop is that, nevertheless RANSE-based numerical methods are not still able to replace model tests in optimizing stern forms, they give already realiable qualitative information on the trend of stern flow characteristics according to changes in the stern geometry and could be a very precious tool in the evaluation of scale effects on ship wake.

In the following we will give an outline of the theoretical methodology used for the present investigation on ship wake scale effects.

General background

The main difficulties associated with the solution of the incompressible Navier-Stokes equations come from the continuity equation and the role played by the pressure. A better understanding of these difficulties can be achieved by looking at the basic governing equations for incompressible viscous flows.

Continuity Equation:

$$\text{div } \mathbf{V} = 0 \tag{1}$$

Momentum equation:

$$d\mathbf{V}/dt + (\mathbf{V} \text{ grad}) \mathbf{V} = - \text{grad } P + 1/Re \text{ grad}^2 \mathbf{V} \tag{2}$$

The structure of the above equations leads to the following remarks:

- continuity equation is not an evolution equation in time, which implies that the use of a time marching algorithm, such as for the compressible equation, is excluded;

- there is no physical boundary conditions for the pressure.

It can be concluded that continuity equation is essentially a constraint on the velocity field. Although it does not involve directly the pressure, which appears only in the momentum equation, the pressure is the only degree of freedom to impose the continuity equation. To approach this problem there are essentially two approaches, non-primitive variables ór primitive variables base equations. Within the first approach use of vorticity transport equation allows to eliminate the pressure from the governing equations. The present methology adopted the second approach, within which continuity equation is satisfied trhough a properly derived pressure equation.

Taking the time derivative of both hands of (1) and the divergence of both hands of (2), the following equation for the pressure is obtained:

$$\text{grad}^2 P = - \text{div} [(\mathbf{V} \text{ grad}) \mathbf{V} - 1/Re \text{ grad}^2 \mathbf{V}] \qquad (3)$$

This is a Poisson equation for the pressure which replaces the continuity equation (1) in the system of the governing equations. Equation (3) must be closed with a Neumann boundary condition which is derived by taking the normal component of the momentum equation (2) on the boundaries.

The Neumann boundary problem for the pressure is well-posed if a compatibility condition, derived by application of Green's theorem to the pressure equation, is satisfied. Whilst in continuum form this compatibility condition is identically satsfied, the same is not true when the discrete Neumann problem is considered depending on the discretization scheme adopted. If a staggered grid is adopted, the compatibility condition is automatically satisfied and thus a converged solution for the pressure exists. On a non-staggered grid the compatibility condition is not automatically satisfied and the pressure equation fails to converge. In the present approach, which adopts a non-staggered grid, the pressure equation is therefore uniformly modified to meet the compatibility condition by adding to its right hand side an artificial source term.

The corresponding time-averaged Navier-Stokes equations are derived modelling turbulent Reynolds stresses using the concept of algebraic eddy viscosity on Boussinesq hypothesis:

$$\langle V_i V_j \rangle = - 2/3 \, k \, d_{ij} + v_t \, (dV_i/dx_j + dV_j/dx_i) \qquad (4)$$

where the turbulent kinetic energy k is equal to the trace of Reynolds stress-tensor and the eddy viscosity vt is prescribed according to the turbulence model of Baldwin-Lomax as an empirical expression containing the distance normal to the hull.

The Baldwin-Lomax turbulence model has two advantages with respect to its popular competitor, the K-ϵ model: it does not require any additional differential equations and it can be prescribed up to the wall, so that the flow can be calculated by explicitly satisfying the no-slip condition.

Governing equations and numerical solution procedure

The 3D governing equations are written in cylindrical polar coordinates (x, r, θ) and then transformed to body-fitted, generalized, curvilinear coordinates (ξ , η , ζ) using the chain rule.

Continuity Equation:

$$J[\frac{\partial}{\partial \xi}(\frac{U}{J}) + \frac{\partial}{\partial \eta}(\frac{V}{J}) + \frac{\partial}{\partial \zeta}(\frac{W}{J})] = 0 \qquad (5)$$

Momentum Equation

$$\frac{1}{J}\frac{\partial Q}{\partial t} + A\frac{\partial Q}{\partial \xi} + B\frac{\partial Q}{\partial \eta} + C\frac{\partial Q}{\partial \zeta} = -H + \sigma + \frac{\partial E_1}{\partial \xi} + \frac{\partial E_2}{\partial \eta} + \frac{\partial E_3}{\partial \zeta} \qquad (6)$$

where:

$$Q = \begin{bmatrix} u \\ v \\ w \end{bmatrix} \qquad (A,B,C) = \frac{1}{J}\,\mathrm{diag}\,(U,V,W)$$

$$U = u\,\xi_r + \frac{v}{r}\,\xi_\theta + w\,\xi_x$$

$$V = u\,\eta_r + \frac{v}{r}\,\eta_\theta + w\,\eta_x \qquad (7)$$

$$W = u\,\zeta_r + \frac{v}{r}\,\zeta_\theta + w\,\zeta_x$$

The source terms H and σ are defined as follows:

$$H = \begin{bmatrix} \xi_r P_\xi + \eta_r P_\eta + \zeta_r P_\zeta - \dfrac{v^2}{r} \\ \dfrac{1}{r}(\xi_\theta P_\xi + \eta_\theta P_\eta + \zeta_\theta P_\zeta + uv) \\ \xi_x P_\xi + \eta_x P_\eta + \zeta_x P_\zeta \end{bmatrix} \qquad (8)$$

and:

$$\sigma = \frac{1}{J} \begin{bmatrix} -\frac{2\nu_t}{r}\left(R_{22} + \frac{u}{r}\right) \\ \frac{\nu_t}{r}\left(R_{12} + R_{21} - \frac{v}{r}\right) \\ 0 \end{bmatrix} \tag{9}$$

where:

$$R_{ij} = u^i_\xi \xi_{xj} + u^i_\eta \eta_{x_j} + u^i_\zeta \zeta_{x_j}$$

$$u^1 = u, \quad u^2 = v, \quad u^3 = w \tag{10}$$

$$x_1 = r, \quad x_2 = r\theta, \quad x_3 = x$$

$$i,j = 1, 2, 3$$

Finally the viscous flux vectors E_1, E_2 and E_3 are defined as:

$$E_j = \frac{\nu_t}{J} \begin{bmatrix} \alpha_{11} u_\xi + \alpha_{12} u_\eta + \alpha_{13} u_\zeta + S_{1j} \\ \alpha_{21} v_\xi + \alpha_{22} v_\eta + \alpha_{23} v_\zeta + S_{2j} \\ \alpha_{31} w_\xi + \alpha_{32} w_\eta + \alpha_{33} w_\zeta + S_{3j} \end{bmatrix} \tag{11}$$

where:

$$\begin{bmatrix} \alpha_{11} & \alpha_{12} & \alpha_{13} \\ \alpha_{21} & \alpha_{22} & \alpha_{23} \\ \alpha_{31} & \alpha_{32} & \alpha_{33} \end{bmatrix} = \begin{bmatrix} (\xi_r \epsilon^j_r + g^{1j})(\eta_r \epsilon^j_r + g^{2j})(\zeta_r \epsilon^j_r + g^{3j}) \\ (\frac{1}{r^2} \xi_\theta \epsilon^j_\theta + g^{1j})(\frac{1}{r^2} \eta_\theta \epsilon^j_\theta + g^2)(\frac{1}{r^2} \zeta_\theta \epsilon^j_\theta + g^{3j}) \\ (\xi_x \epsilon^j_x + g^{1j})(\frac{1}{r^2} \eta_x \epsilon^j_x + g^{2j})(\zeta_x \epsilon^j_x + g^{3j}) \end{bmatrix} \tag{12}$$

and:

$$\begin{Bmatrix} S_{1j} \\ S_{2j} \\ S_{3j} \end{Bmatrix} - \begin{Bmatrix} \epsilon_x^j R_{31} + \frac{1}{r} \epsilon_\theta^j (R_{23} - \frac{v}{r}) \\ \epsilon_x^j R_{32} + \epsilon_r^j R_{12} + \frac{1}{r} (\frac{2u}{r} \epsilon_\theta^j + v \epsilon_r^j) \\ \epsilon_r^j R_{13} + \frac{1}{r} \epsilon_\theta^j R_{23} \end{Bmatrix} \tag{13}$$

$$\epsilon^1 = \xi \ , \quad \epsilon^2 = \eta \ , \quad \epsilon^3 = \zeta$$

The metric coefficients g^{ij} and the Jacobian of transformation J are:

$$g^{ij} = \epsilon_r^i \epsilon_r^j + \frac{1}{r^2} \epsilon_\theta^i \epsilon_\theta^j + \epsilon_x^i \epsilon_x^j \tag{14}$$

and:

$$J = \frac{\partial(\xi,\eta,\zeta)}{\partial(r,r\theta,x)} \tag{15}$$

The pressure is calculated from the pressure Poisson equation (3), first obtained in cylindrical polar coordinates and then transformed to general curvilinear coordinates using the chain rule. The resulting equation is written as follows:

$$\begin{aligned} &\frac{\partial}{\partial\xi} [\frac{\Delta t}{J} (g^{11} \frac{\partial P}{\partial\xi} + g^{12} \frac{\partial P}{\partial\eta} + g^{13} \frac{\partial P}{\partial\zeta})] \\ &+ \frac{\partial}{\partial\eta} [\frac{\Delta t}{J} (g^{12} \frac{\partial P}{\partial\xi} + g^{22} \frac{\partial P}{\partial\eta} + g^{23} \frac{\partial P}{\partial\zeta})] \\ &+ \frac{\partial}{\partial\zeta} [\frac{\Delta t}{J} (g^{13} \frac{\partial P}{\partial\xi} + g^{23} \frac{\partial P}{\partial\eta} + g^{33} \frac{\partial P}{\partial\zeta})] = \nabla\cdot Q - G \end{aligned} \tag{16}$$

where:

$$\begin{aligned} G = &\frac{\partial}{\partial\xi} [\frac{\Delta t}{J} (\xi_r f^\xi + \eta_r f^\eta + \zeta_r f^\zeta)] \\ &+ \frac{\partial}{\partial\eta} [r \frac{\Delta t}{J} (\xi_\theta f^\xi + \eta_\theta f^\eta + \zeta_\theta f^\zeta)] \\ &+ \frac{\partial}{\partial\zeta} [\frac{\Delta t}{J} (\xi_x f^\xi + \eta_x f^\eta + \zeta_x f^\zeta)] \end{aligned} \tag{17}$$

and f^ξ, f^η and f^ζ are the convective and the diffusion terms in the momentum equations.

The governing equations are discretized on a non-staggered grid. We use 3-points central finite differencing for the continuity equation as well as for the pressure gradient and viscous terms while employ second order upwind differencing for the convective terms in the momentum equation. The upwind scheme eliminates the need for adding artifical dissipation terms, to the right hand side of the momentum equation.

The momentum equation (6) is solved by marching in time for the cylindrical polar velocity components Q. Time integration is performed by explicit four stage Runge-Kutta algorithm, enhanced with local time stepping and implicit residual smoothing. Pressure equation (16) is solved using the point successive relaxation method.

CALCULATION CONDITIONS

Grid definition

The numerical solution of RANSE equations requires in general an adequate discretization of the relevant fluid domain outside the hull through a grid of nodal points over which the ruling equations are actually solved. The algorithms based of finite difference or finite volume techniques want continuous and ordered grids whereon integrating the equation.

In particular a grid should be sufficiently regular to ensure an efficient numerical solution of the relevant equations, it should be orthogonal near hull surface to make easier the apllication of boundary conditions and it should be very fine in regions of sharp changes of geometry, in the thin boundary-layer at midship and generally in all the near-wall region. As a consequence of these strict requirements and of the geometry complexity for practical ship hulls and in consideration of its major role in the efficiency and accuracy of the numerical solution, numerical grid generation has developed to such a level of mathematical refinement that presently it does constitute a new sector of computational sciences.

The algorithm presently used to create the grids is based on the so-called body fitted coordinate system. That is a mesh which fits the shape of the computational domain where fluid flows. The basic idea underlying this methodology is to map the physical domain outside the ship hull into a fictious rectangular domain. It is immediate to generate an orthogonal grid on the trasformed domain, by simply drawing lines parallel to each coordinate axis. This grid of the physical domain is obtained by mapping backward the grid of the trasformed domain.

Numerically this is done by solving a set of three Poisson equations, where the dependent variables are the physical coordinates, the independent variables the transformed coordinates and the source terms are the grid control function that ensure the required grid distribution.

In order to solve the differential system one needs to apply a set of boundary conditions which are derived from the prescribed size of the physical domanin and the the number of points in the axial, radial and girthwise direction. The software used to perform these calculations is derived from the one originally developed at IIHR [8] and further improved [9].

The main goal of this technique is to achieve an orthogonal grid on every transversal section and it works very well if the number of point for each section is quiet small. As it increases the lines coming out of the hull, normal to the surface, move closer each other until they cross. In order to avoid this problem the first step of our calculation was to create a coarse orthogonal grid and then interpolate the mesh adding new points in radial and girthwise direction preserving cells orthogonality.

A better description of the boundary layer is obtained by thickening the grid points near the hull. Also the new radial distribution preserves orthogonality and the points are spaced according to a geometrical progression which ensures the desired number of grid point inside the boundary layer. Of course in the rear zone of the ship, where the cross section become more curved, preserving orthogonality is very hard if not impossible. In this case a good description of hull geometry is preferred, so the grid turns out to be more skewed. Continuity of grid cells, in the zone past ship sten, is obtained by introducing a false wake plane whose depth decrease smoothly in the sections near the hull and then remains constant.

For every case the ship length is the same as the distribution of section in the longitudinal direction. The influence of scale effects is taken into account thanks to the radial distribution of the radial points, which thicken as the Reynolds Number increase. The last radial section is placed at R/L=0.5 from the hull. The first grid section starts at X/L=0.51 the last is placed at X/L=1.7. Each grid has from 15 to 20 points inside the boundary layer, from 30 to 40 points in the girthwise direction.

Boundary conditions

Referring to the physical domain in Fig. 1, the relevant boundaries are the inlet plane (ABCD), the exit plane (EFGK), the water-plane (ABFEO') and keel-plane (DLKGC), wake centerplane (O'LKE), hull surface (ADLO') and outer boundary (BCGF).

The boundary conditions are applied as follows, in terms of the polar fluid velocity components u, v, w and the fluid pressure p:

ABCD)

u is specified from b'layer computations, while v and w are set to zero. The pressure is consequently computed from the normal momentum equation.

EFGK)

u = v = w = 0. The pressure is again computed from the normal momentum equation.

ABFEO'-DLKGC)

Simmetry is imposed by setting w and the normal derivatives of u,v and p to zero.

O'LKE)

SImmetry is imposed as above.

ADLO')

u = v = w = 0. The pressure is computed by setting its normal derivative to zero.

BCGF)

u = v = w = p = 0.

RESULTS AND CONCLUSIONS

For the correlation, the largest 15.7 model-scale was considered, corresponding to a model length of 5 meters and a Reynolds number of 9.0E+6. Ship dimensions are scaled by ship length and the velocity with respect to the maximum inlet velocity.

Numerical results are obtained using (75, 50, 32) grid points in the axial and tangential direction respectively. In Fig. 2 one half of the ship geometry is shown with 52 cross-sectional planesnoraml to the ship main axis. A typical finite-difference grid in the cross-sectional planes is shown in Fig. 3.

Fig. 4 shows the cross-velocity vectors at the propeller plane, x = 0.97. The computed results are in good agreement with the experimental data. Note that the computed and measured velocity vectors are not at the same space locations. It can be seen that the downward cross-flow near the vertical symmetry line is well predicted. In Fig. 5 the axial velocity contours are shown at the propeller plane. The axial velocity contours are well predicted for both the low and high velocity regions. In Figs. from 6 to 9 the non-dimensional velocity profiles at x = 0.5, 0.7, 0.9 and 1.0 are reported versus the angular position.

Besides the 9.0E+6 Reynolds number calculation, an additional calculation at a Reynolds number of 1.0E+8, which is intermediate between model-scale and full-scale, was carried out in order to investigate the applicability of the methodology to high Reynolds number in the scope of wake scaling effects analysis.

To this regards it should be noted that the central difficulty in applying RANSE to high Reynolds numbers is to mantain accuracy in the resolution of the increasing gradient of velocity and turbulence parameters within a layer of gradually diminishing thickness. On the other hand proper viscous and turbulent dynamics can be described with accuracy only if the vorticity generated within the wall layer is correctly predicted. As a matter of fact it results from the 1990 Workshop that only 3 methodologies over a total of 17 participated to the "full-scale" calculations on HSVA Tanker hull at Reynolds number of 2.0E+9.

It is however useful to recall the main conclusions which could be derived from the results of these calculations concerning Reynolds scaling. First at increasing Re the thinning of the boundary-layer was found not uniform in all regions, crossflows were found intensified and so longitudinal vorticity, measured by helicity density which is an index of the three-dimensionality of the flow. Besided it could be noted that at stern the transverse extent of vortical flow did not contract in the manner predicted by semi-empirical methods. In general correlation formulas resulted in overestimation of velocities in the wake centerplanes and ensured only a qualitative agreement for the velocity components at the propeller plane. This confirmed the limitation of scaling laws based on boundary-layer or simple wake concept in the ship stern region.

In Figs. 10 and 11 we report the trend of numerical error in the calculated pressure and axial velocity respectively versus iterations number to show the achievement of numerical convergence of the solution. In Figs. 12 and 13 we compare the isowake contours at the propeller disc at Re 9.0E+6 and 1.0E+8.

The computed results for Re = 9.0E+6 show that the present numerical apporach is adequate for predicting the complex turbulent flow around ship hulls. The method was already tested for several ship hulls and the present test case is a severe one due to the complex geometry involved. The achieved degree of accuracy ensures that the method is now ready to be applied for prediction of full scale ship hulls. This has been confirmed by the calculation presently carried out at an intermediate Reynolds number of 1.0E+8.

REFERENCES

[1] Tanaka, I., et al. - Investigations of scale effects on wake distributions using geosim models - KSNA - 1984.

[2] Lauro, G., Boccadamo, G., Cassella, P., "Scale effects on nominal wake at propeller disc", CETENA Technical Report N. 3504, 1989.

[3] Baldwin, B., Lomax, H., "Thin layer approximation and algebraic model for separated turbulent flows", 16th AIAA Meeting, 1978.

[4] Sotiropoulos, F., Abdallah, S., "Coupled fully implicit solution procedure for the steady incompressible Navier-Stokes equations", Journal of Computational Physics, 87, 1990.

[5] Boccadamo, G., Cassella, P., Lauro, G., "Geosim tests carried out at the department of Naval Engineering of Naples: research program and results", IMAEM '87, Varna, 1987.

[6] SSPA International Workshop on "Ship Boundary Layers", Gotheborg, Sweden, 1980.

[7] SSPA-CTH-IIHR INternational Workshop on "Ship Viscous Flows", Gotheborg, Sweden, 1990.

[8] Patel, V.C., Chen, H.C., Ju, S., "Ship stern and wake flows: solution of the fully elliptic RANSE and comparisons with experiments, IIHR Rep. 323, IOWA 1988.

[9] Caprino, G., Traverso, A., "Progress in multiblock technique for flow calculation around ship hull with PHOENICS",Italian PHOENICS User Conference, Genova, 1991.

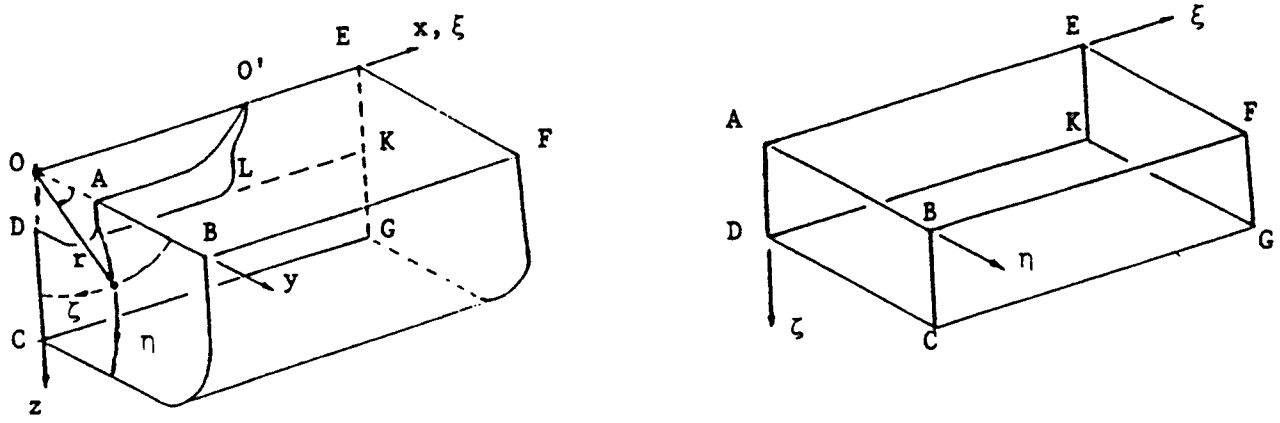

FIG. 1. PHYSICAL AND TRANSFORMED DOMAINS

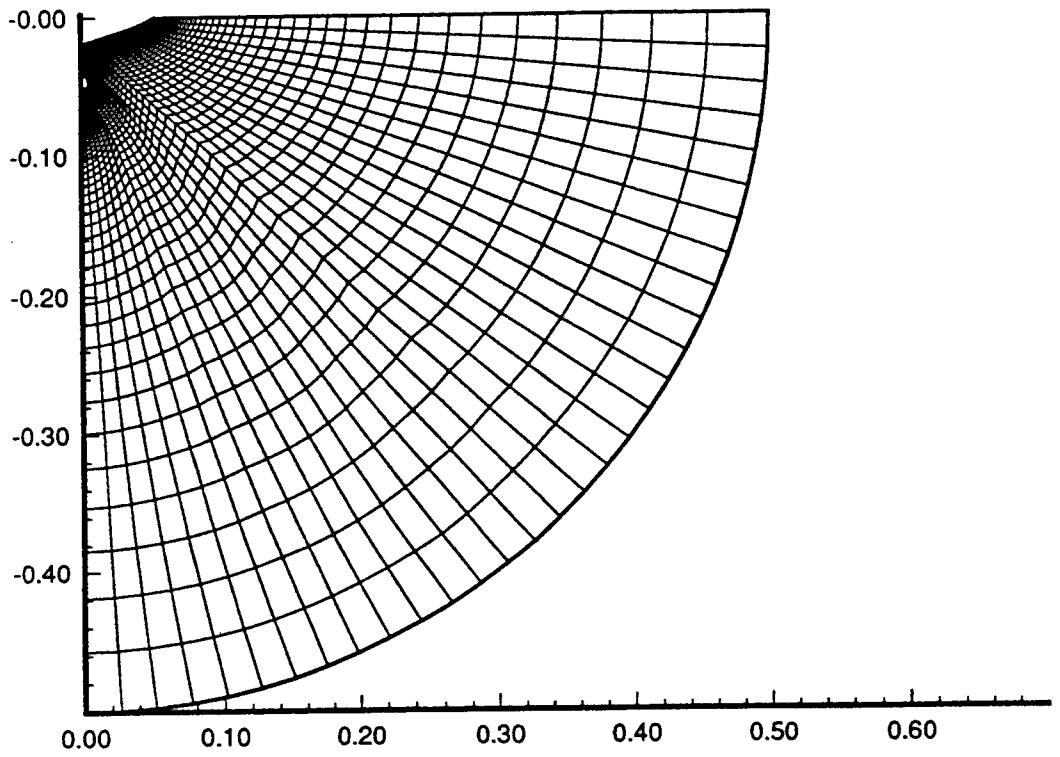

Fig. 2. Cross-sectional planes for one-half ship.

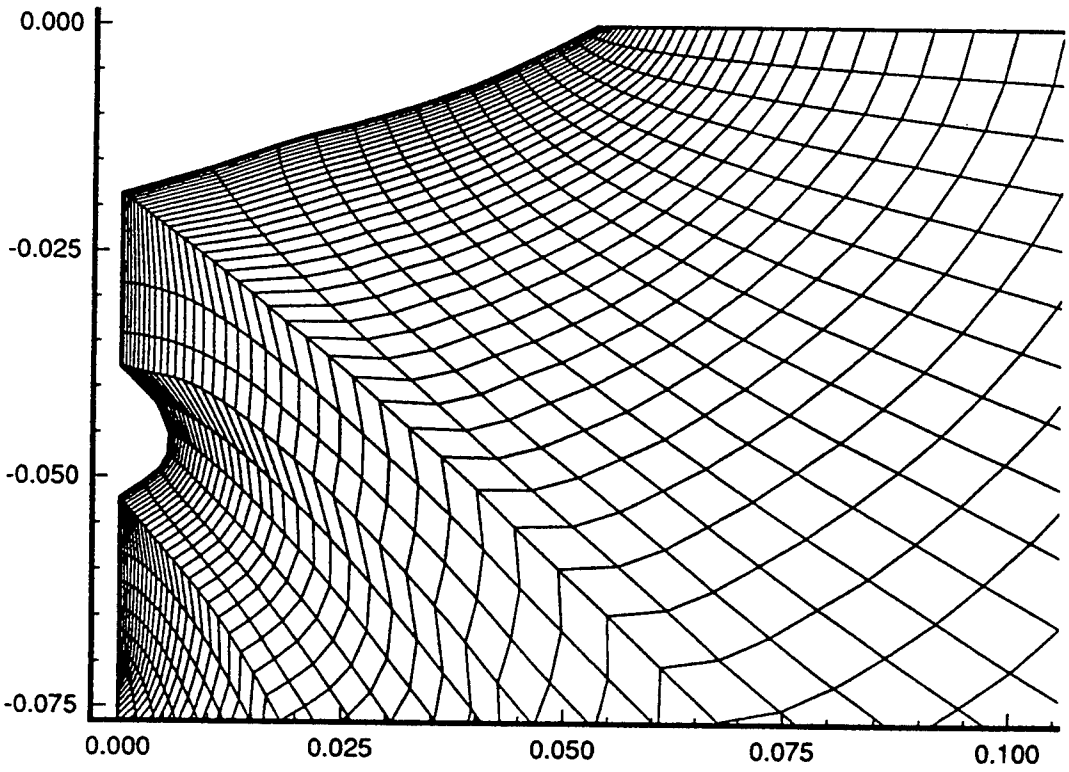

Fig. 3. Finite-difference grid on a cross-sectional plane.

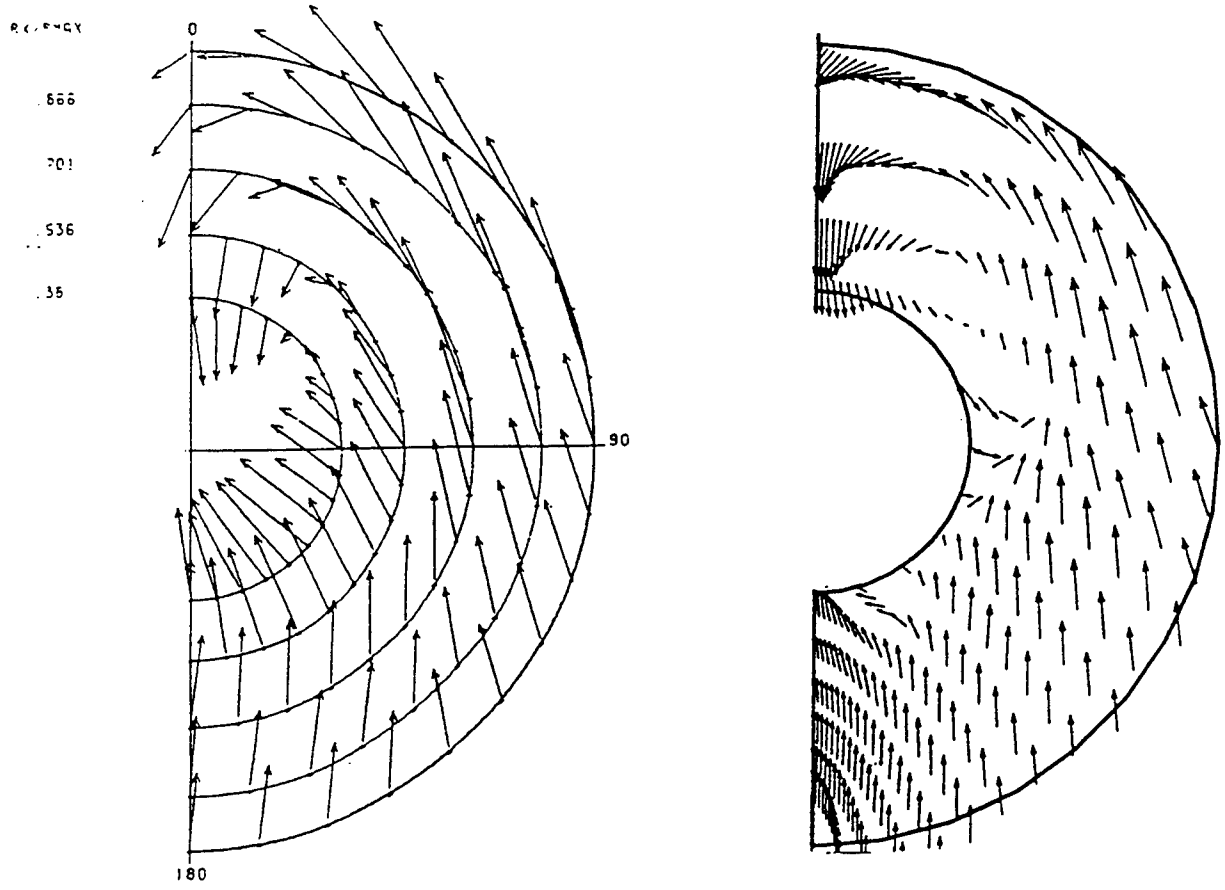

Fig. 4. Cross-velocity vectors at the propeller disc, x = 0.97.

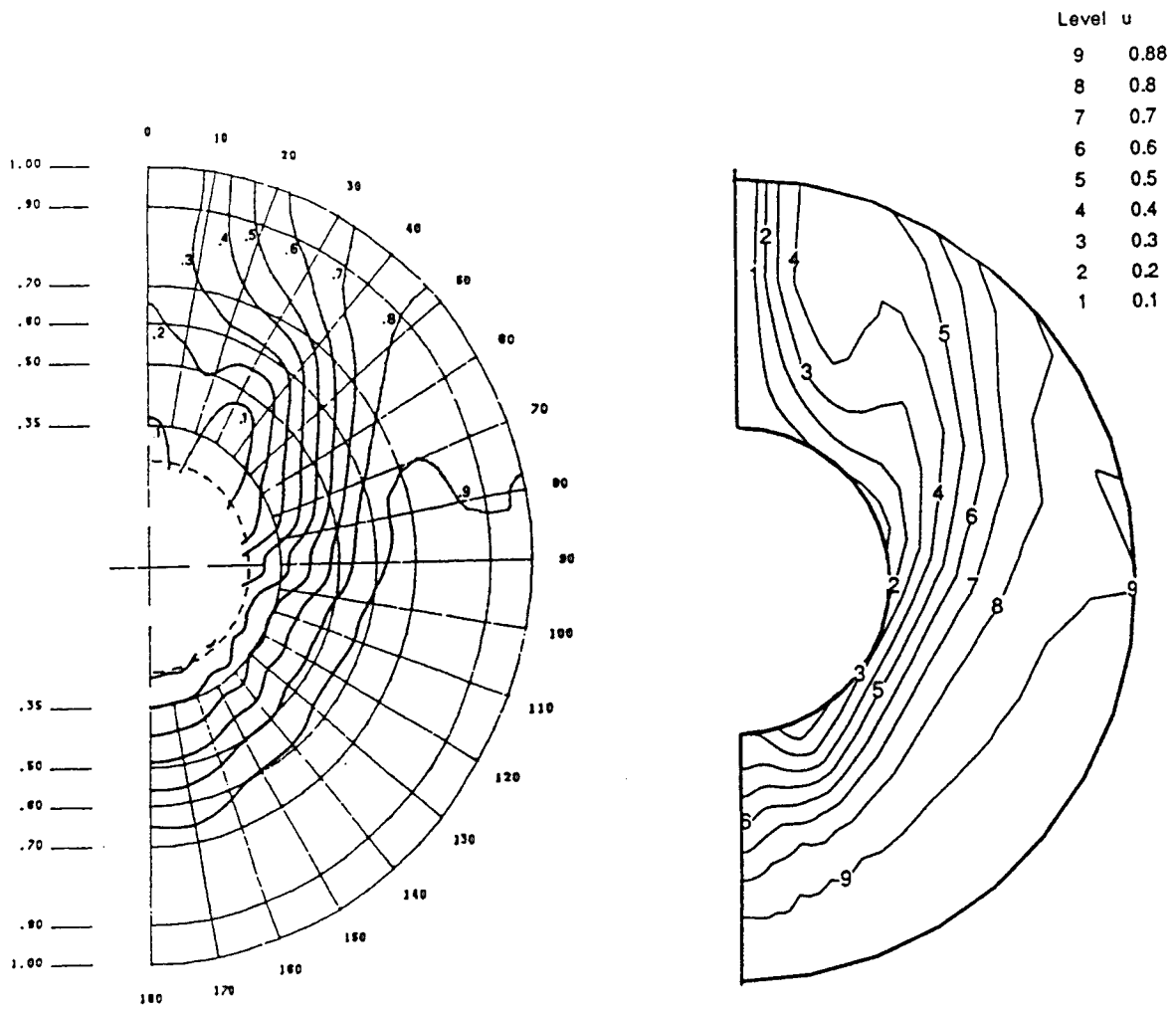

Fig. 5. Axial velocity contours at the propeller disc.

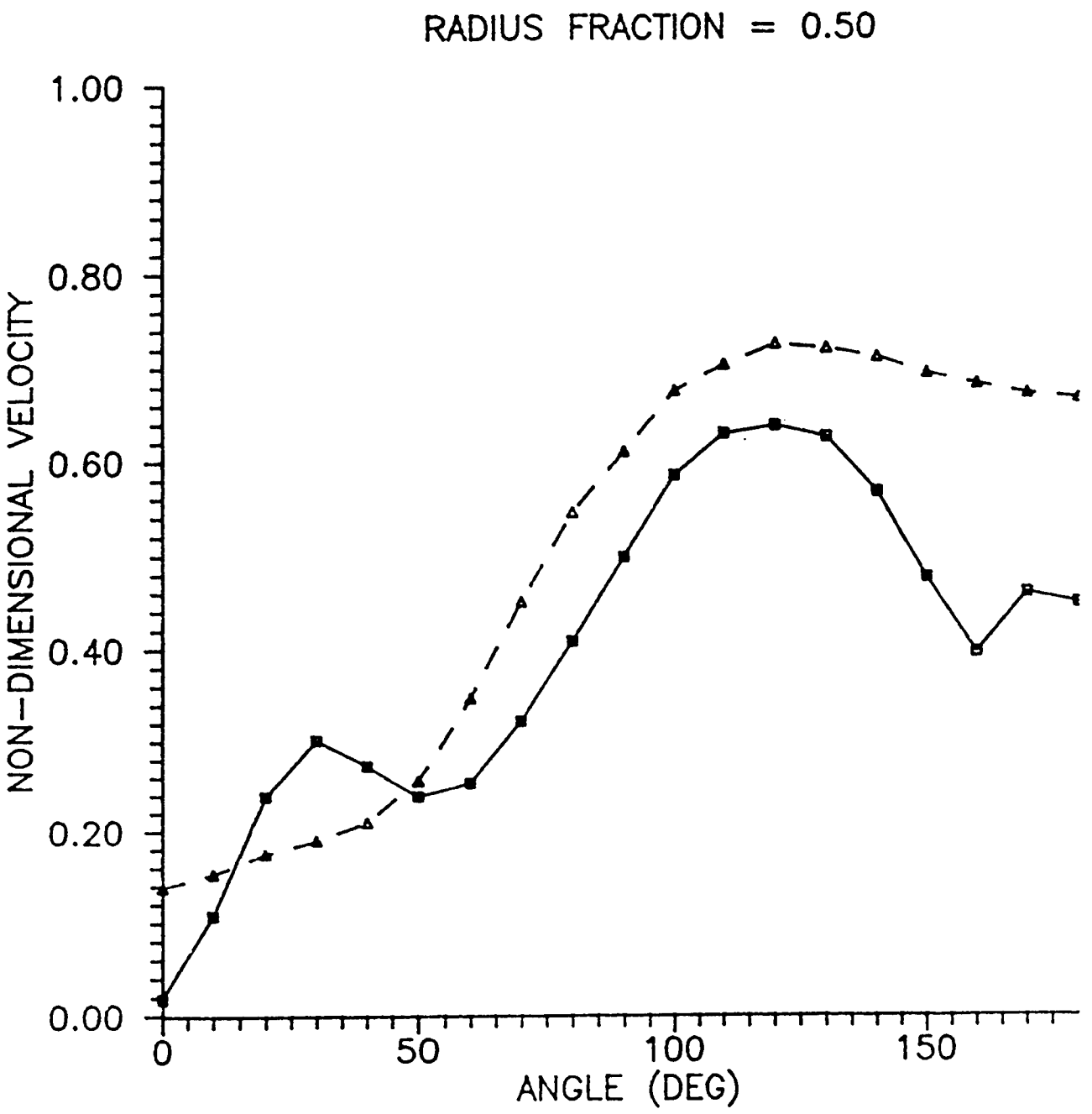

Fig. 6. Non-dimensional velocity profile at x = 0.5.

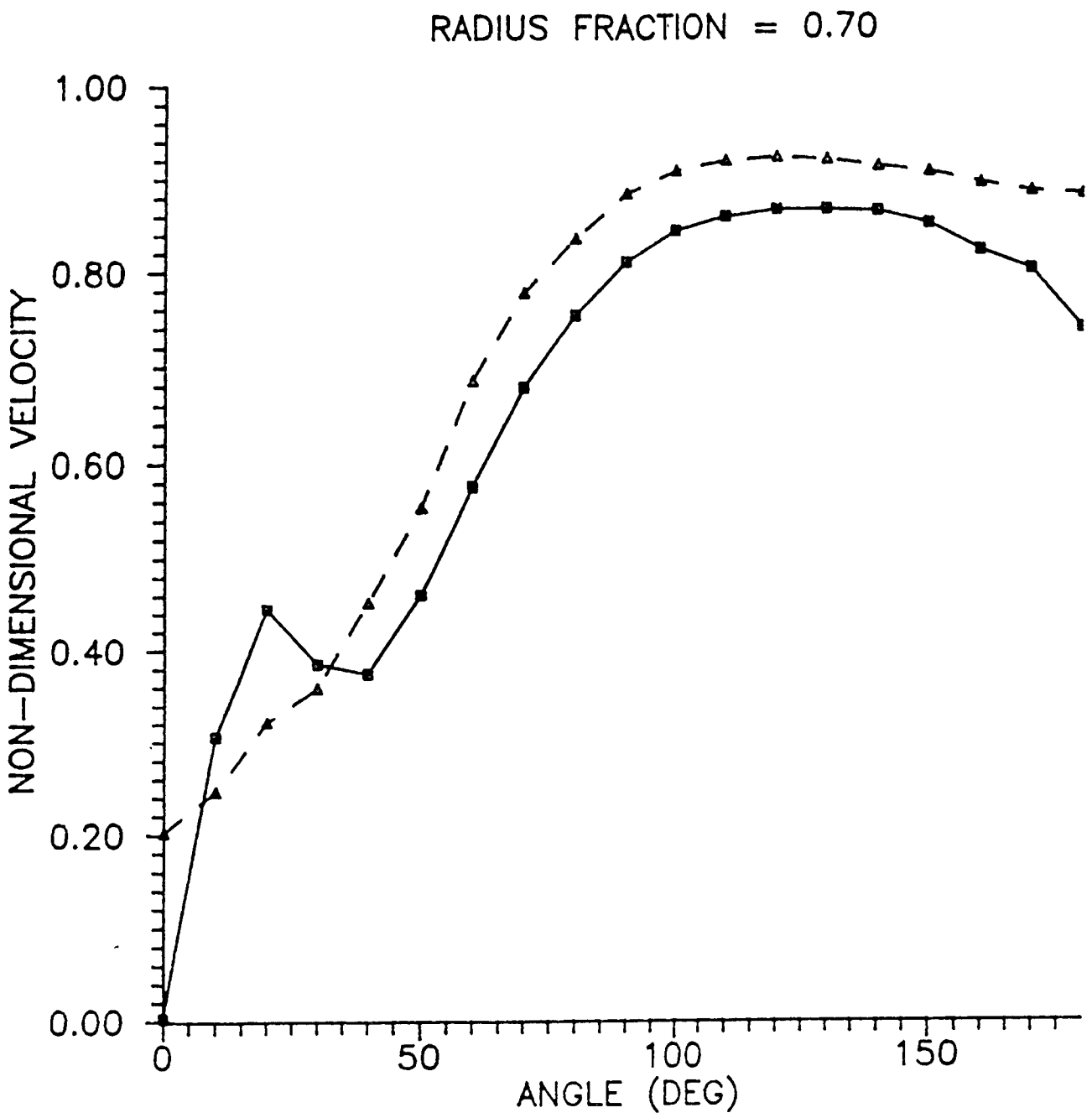

Fig. 7. Non-dimensional velocity profile at x = 0.7.

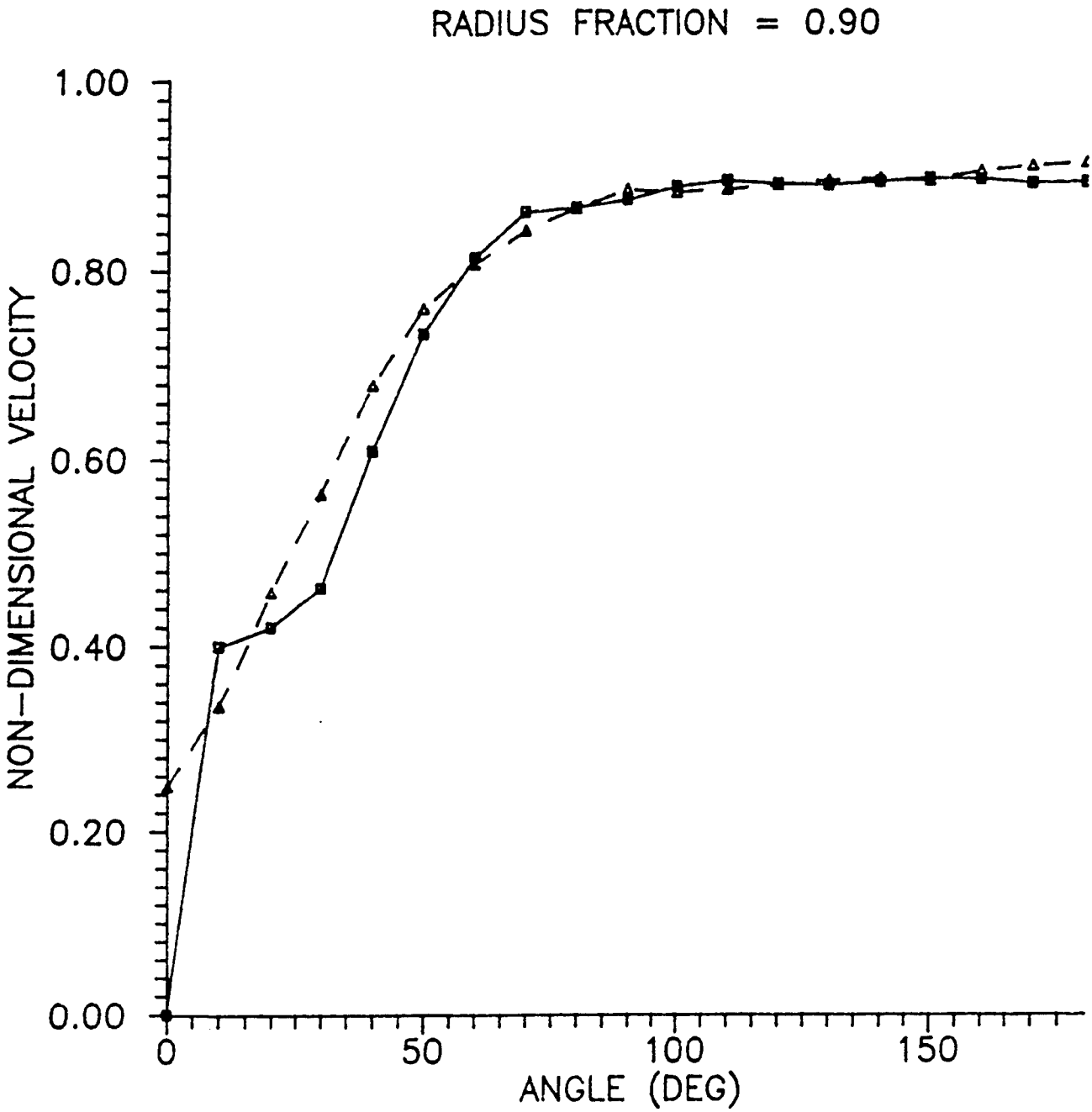

Fig. 8. Non-dimensional velocity profile at x = 0.9.

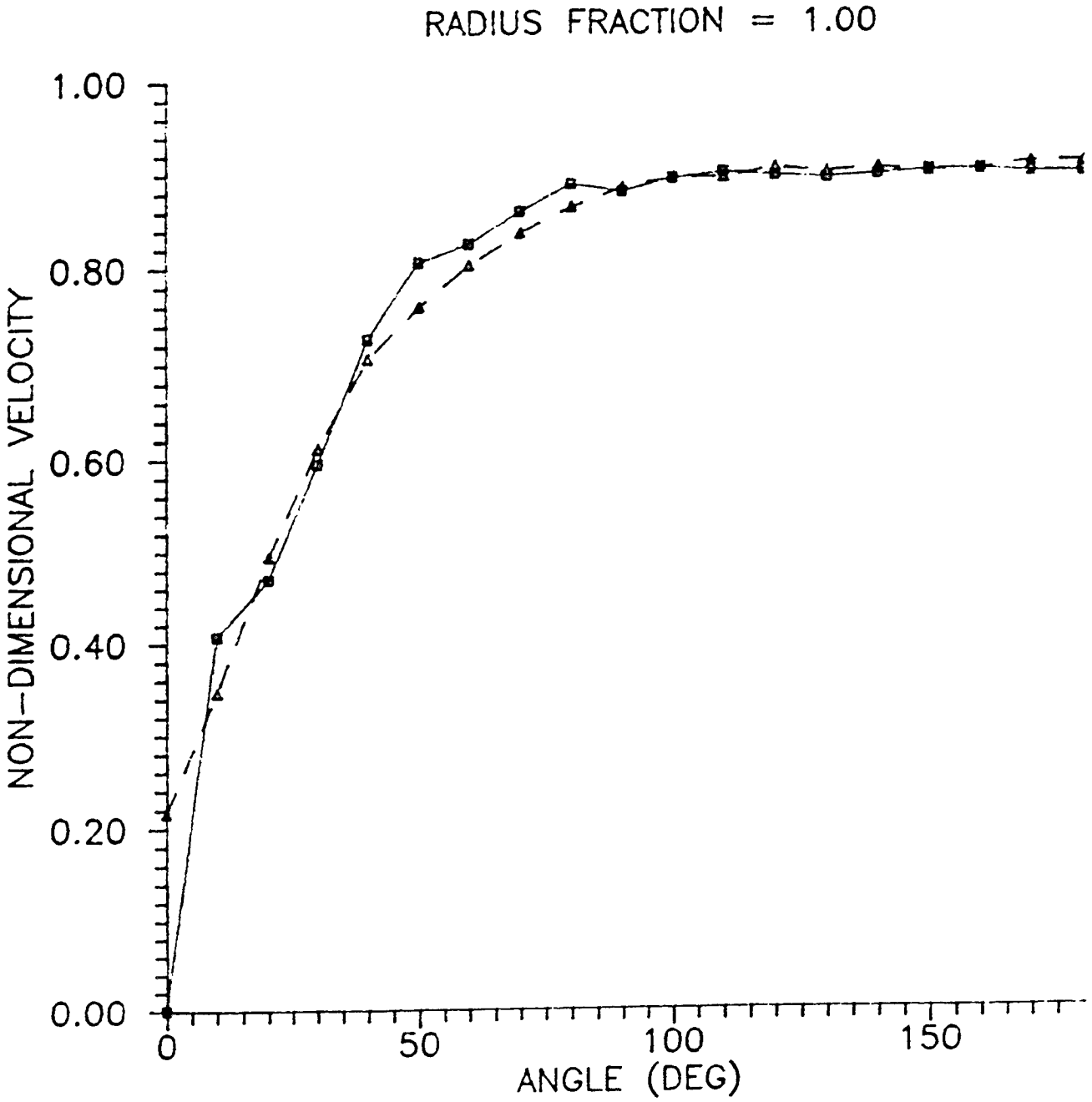

Fig. 9. Non-dimensional velocity profile at x = 1.0.

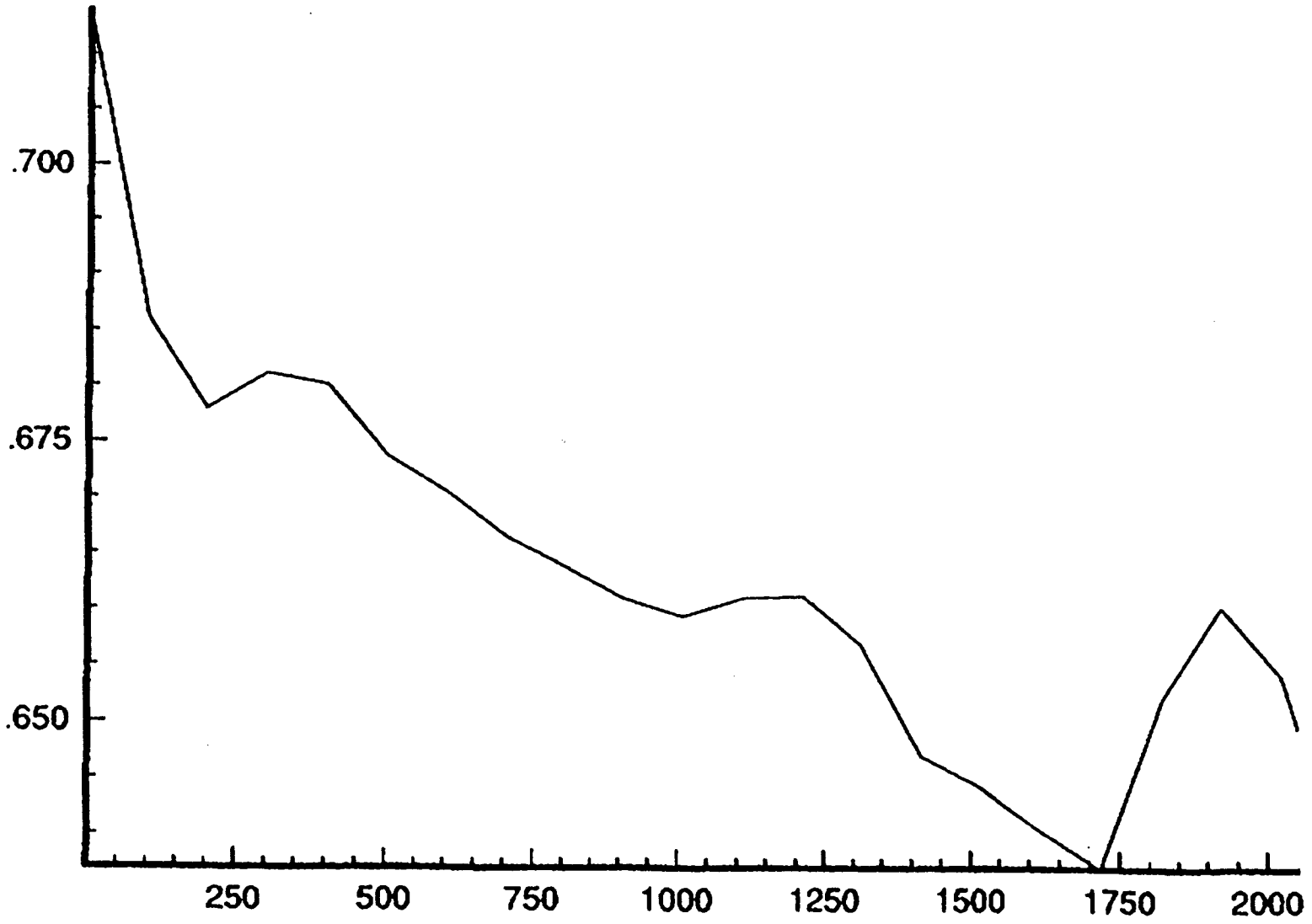

Fig. 11. Convergence of axial velocity calculation.

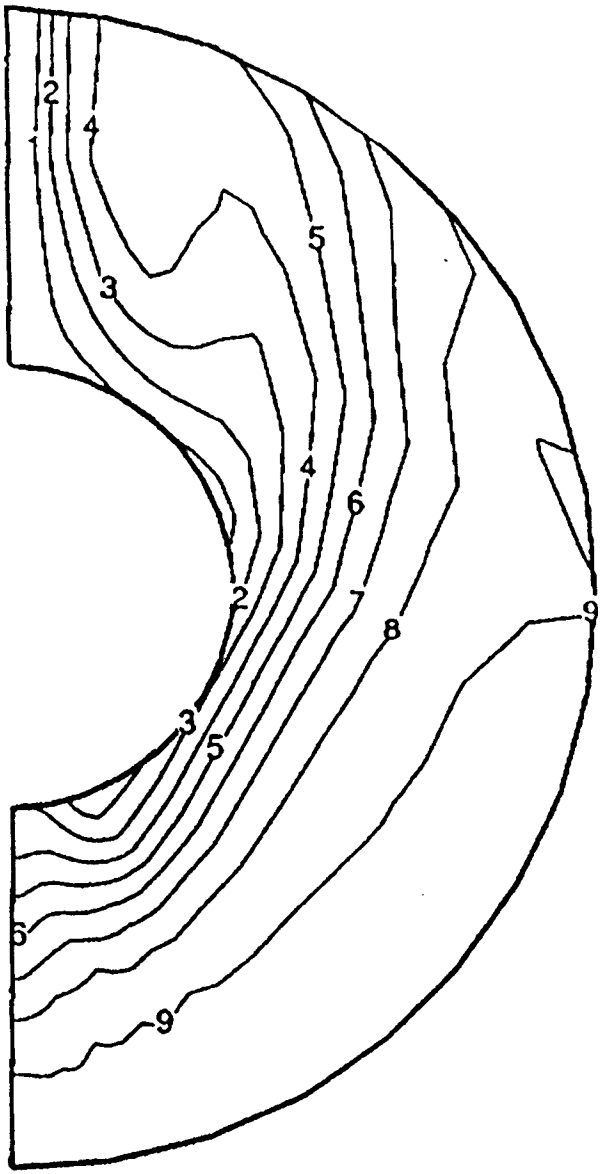

Level	u
9	0.88
8	0.8
7	0.7
6	0.6
5	0.5
4	0.4
3	0.3
2	0.2
1	0.1

Fig. 12. Axial velocity contours at the propeller disc, Re=9E+6.

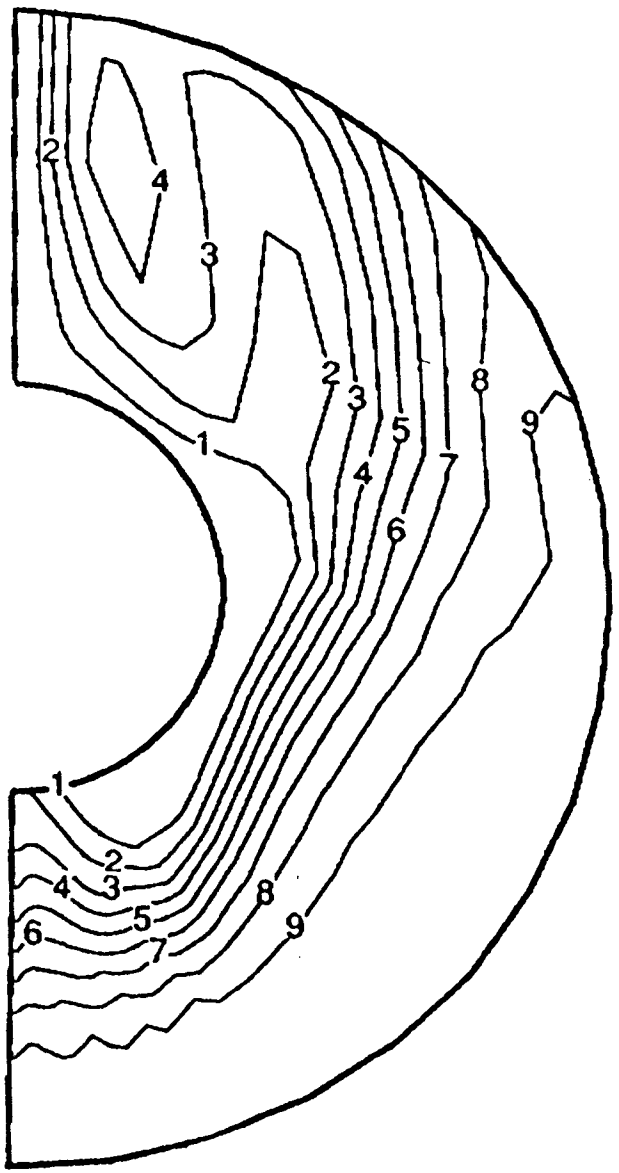

Fig. 13. Axial Velocity contours at the propeller disc, Re=1E+8.

DISCUSSION

V. Patel and S. Ju
University of Iowa, USA

In a recent paper (Ju and Patel, Journal of Ship Research, Vol 35, p. 101, 1991) a much more comprehensive study of high Re flow and scale effects was described. This paper carefully examined the application of a numerical method to high Re flow by comparisons with axisymmetric boundary-layer data of code R up to Re $\sim 10^5$, performed ship wake calculations for Re range $5x10^6$ to $5x10^9$, and used these results to assess the applicability of empirical scaling laws such as those of Tanaka and Himeno for Re scaling of ship wakes. This study led to conclusions similar to those of the present authors. What is surprising about the present paper, however, is that no reference is made to the previously published work and very similar conclusions are drawn from a much less detailed study in which the highest Re considered is only 10^8, an order of magnitude smaller than full scale! In particular, we do not see how the stated conclusions follow from the results (ex. scale effects) presented in Figures 12 and 13.

AUTHORS' REPLY

I fully appreciate the presentation of Prof. V.C. Patel and Dr. S. Ju and I wish to clarify that it was not our intention not to recognize the valuable work quoted in the Journal of Ship Research, 1991, which remains one of the most complete contributions to wake-scaling investigation to my knowledge. I, however, stated early in the paper, and I hope it appeared from my presentation as well, that our present work is still more dealing with validation rather than on high Re effects. Nevertheless, we performed a trial calculation at an intermediate Re (A.OE+8) between model (A.OE+6) and full-scale (A.OE+9) just to verify the present capability of our code to perform well at such Re. We need further work to really assess scale effects for practical hulls. About the conclusions you refer to, there is probably a misunderstanding. The consideration on Re scaling contained in the concluding chapter are not related to the present calculations. As a matter of fact, it is explicitly stated that they are state-of-the-art considerations drawn from the computation results of the 1990 Workshop on Ship Viscous Flow, to which you contributed also with a "full-scale" computation on HSVA tanker. I preferred to quote the workshop in place of your previously mentioned paper in order to give more generality to the considerations. I find it promising that two different methods seem to give good results at high Re for two different ships and I will be glad to see some further high Re calculations for other geometries.

DISCUSSION

H.-T. Kim
Chungnam National University, Korea

1. In the abstract, you stated that by using "consistent finite-difference approximation" for the pressure equation and the boundary conditions, the compatibility condition is satisfied and the pressure equation with Neumann B.C. is guaranteed to converge, but in the second paragraph below Eq. (3), it is stated that the pressure equation is uniformly modified to meet the compatibility condition by adding an artificial source term. Can you explain these seemingly inconsistent statements?

2. You used the Baldwin-Lomax zero Eq. model to close the RANS equation. But the Eq. (4) in the paper includes the turbulence kinetic energy and it confused me. Do you really include the turbulence kinetic energy term for the Reynolds stress? If so, how do you obtain them?

3. It is not clear to me how you obtain a discretized equation for pressure. Did you directly discretize the pressure Eq. (k)? Or, starting from the discrete form of the continuity Eq.?

AUTHORS' REPLY

1. Both the approaches, additional source introduction and finite difference consistent approximation, to get a consistent solution of the pressure Poisson-type equation have been analyzed in the development of the code and they are alternatives. At the end, the F.D. consistent scheme was selected to be implemented in the code.

2. I appreciate your question. In the general background description we refer to a 2 parameters turbulence model, but the formulation actually implemented uses Baldwin-Lomax turbulence model.

3. The pressure equation in curve linear coordinates (Eq. 16) is the one actually discretized in the code.

Session V

Viscous Ship Hydrodynamics

Longitudinal Vortices in a Turbulent Boundary Layer Along a Curved Wall

W. Kim, V. Patel (The University of Iowa, USA)

ABSTRACT

Laboratory and numerical experiments are performed to elucidate the influence of longitudinal surface curvature and pressure gradient on the growth and decay of longitudinal vortices immersed in a turbulent boundary layer. A pair of counter-rotating vortices, with their common induced flow towards the wall, is considered. Two cases are studied: vortices introduced in a flat-plate boundary layer, and vortices introduced in a boundary layer that is subsequently subjected to concave wall curvature and attendant pressure gradients in a rectangular duct with a 90° bend. In the former, computational results are compared with previous data. The same configuration of vortices is used in the latter study, in which both experiments and computations were carried out. The computational model solves the Reynolds-averaged Navier-Stokes equations in conjunction with a two-layer turbulence model. It is observed that there is a strong effect of curvature on the interaction between the vortices and the wall. The growth and decay of the vortices is affected. In particular, when vortices are introduced on the concave wall, secondary vortices of opposite sign arise outside the primary ones, forcing the primary vortices to stay close to each other. The vortex circulation decreases on the flat wall whereas it is increased on the concave wall.

NOMENCLATURE

A	area of half-delta wing (vortex generator)
C	chord length of half-delta wing
C_D, C_L	drag and lift coefficients
C_f	friction coefficient ($= \tau_w/\frac{1}{2}\rho U_o^2$)
C_p	pressure coefficient ($= \Delta\bar{p}/\frac{1}{2}\rho U_o^2$)
H	duct (curved-wall wind tunnel) width
k	turbulent kinetic energy, normalized by U_o^2
R_i, R_o	inner and outer radii of curved-wall tunnel
r	radial distance from center of vortex core
r_1	half-radius of the vortex wake
r_c	radius of the vortex core
S	half-span of vortex generator
U_o	reference velocity (= 16 m/sec)
U_τ	friction velocity, normalized by U_o
(U,V,W)	velocity components in (X,Y,Z) directions, normalized by U_o
$(\Delta U)_{max}$	maximum longitudinal velocity deficit, normalized by U_o
V_θ	circumferential velocity component
$(V_\theta)_c$	maximum circumferential velocity
$-\overline{uv}, -\overline{uw}, -\overline{vw}$	Reynolds shear stresses, normalized by U_o^2
X	streamwise distance from trailing edge of vortex generator
Y	normal distance from the wall
Z	spanwise distance from the symmetry plane
y^+	wall coordinate ($= U_\tau Y/\nu$)
y^*	distance of vortex center from the wall
z^*	distance of vortex center from symmetry plane
α	angle of attack of half-delta wing
β	apex angle of vortex generator
ε	rate of turbulent energy dissipation
Γ_c	circulation of vortex at trailing edge
Ω_x	peak longitudinal vorticity
$(\Omega_X, \Omega_Y, \Omega_Z)$	vorticity components in (X,Y,Z) directions
ν	kinematic viscosity
ν_t	eddy viscosity
τ_w	wall shear stress

INTRODUCTION

Longitudinal vortices, either arising naturally through separation or introduced artificially by vortex generators, imbedded in turbulent boundary layers, play an important role in a number of practical applications. Among naturally arising vortices in hydrodynamics are ship bilge vortices and the trailing legs of the horse-shoe vortex on a submarine appendage. Artificial vortex generators are often used to promote mixing and control separation, e.g., on the wings of the Boeing 737. The present paper is concerned with the development of artificially introduced vortices along a curved surface.

There have been several recent studies concerning vortices imbedded in turbulent boundary layers. In an effort to simulate ship stern vortices, Tanaka and Suzuki (1978) considered the interaction between a flat-plate turbulent boundary layer and the trailing vortex generated by the tip of a lifting wing. Although their measurements were somewhat limited, they showed, with the help of a parallel computational study, that the eddy viscosity for diffusion of the longitudinal vorticity was much smaller (by a factor of 6.33, supporting the earlier results of Batchelor (1964)) than the eddy viscosity in the parent boundary layer. Further experiments have been carried out at Imperial College, London, by Shabaka, Mehta, and Bradshaw (1985) with a single vortex in an otherwise two-dimensional turbulent boundary layer in zero pressure gradient. They also found, from measurements of mean velocities and Reynolds stresses, that empirical correlations used in traditional turbulence models were not likely to

accurately predict the development and decay of the vortex and its interaction with the boundary layer. Mehta and Bradshaw (1988) performed similar experiments with a vortex pair with common flow away from the wall, and found that large changes occur in the structural parameters of the turbulence. The same kind of experiments have since been carried out by Eibeck and Eaton (1985) and Pauley and Eaton (1988) at Stanford University. They showed that the rate of vorticity spreading in a vortex was greatly increased by proximity of other vortices, and vortices remaining close to the wall produced significant levels of spanwise skin friction and thus a greater rate of decay of circulation. In the above two sets of experiments, half-delta wings were used as vortex generators. The generators were put on the floor of the wind tunnel settling chamber in the experiments of Bradshaw et al., whereas Eaton et al. placed the generators near the start of the test section. Westphal, Eaton and Pauley (1985) have measured the development of a single vortex imbedded in a boundary layer subjected to an adverse pressure gradient and found that pressure gradients have a considerable effect on the structure of the vortex. In the area of computational modelling of the fate of artificial vortices, mention has been made already of the work of Tanaka and Suzuki (1978). Liandrat, Aupoix and Cousteix (1987) have calculated the development of longitudinal vortices in a flat-plate turbulent boundary layer using parabolized Reynolds-averaged Navier-Stokes equations, with mixing-length and Reynolds-stress models and compared with the measurements of Shabaka et al. (1985). They concluded that simple models of turbulence, based on eddy-viscosity concepts, provide satisfactory estimates of the main features of the flow in the case of a single vortex but are not satisfactory in describing the interaction among vortices. According to their study, Reynolds-stress models were somewhat better but they also underpredicted the stresses. The improvement they found by integration of the equations along streamlines with a simple diffusion model suggests that care must be exercised in numerical solution of flows with vortices. The authors are not aware of similar numerical studies elsewhere.

In spite of these previous studies, there remain several aspects of the physics of vortex development and decay that are not well understood. For example, the manner in which surface curvature affects the development and decay of longitudinal vortices imbedded in boundary layers is not known although curvature effects on turbulent boundary layers in the absence of secondary motion are well documented. Similarly, the influence of pressure gradients on streamwise vorticity in a turbulent boundary layer has not been explored. In the area of numerical modelling, there is no comprehensive attempt made to model either the flow induced by conventional vortex generators or its subsequent development. The present experimental and numerical study was designed to investigate these particular aspects of longitudinal vortices within turbulent boundary layers.

The previous experiments on vortices in flat-plate boundary layers are supplemented by similar experiments in vortices developing on a concave wall in the presence of pressure gradients. A simple semi-empirical model is proposed to describe the flow just downstream of a conventional half-delta-wing vortex generator, and this model is employed in a numerical method that solves the Reynolds-averaged Navier-Stokes equations, with a two-layer turbulence model, to predict the vortex evolution. Extensive comparisons between experiment and computations are made to elucidate the effects of streamwise wall curvature and pressure gradients on vortex growth and decay.

EXPERIMENTS

The experimental arrangement used by Pauley and Eaton (1988) is sketched in Figure 1. They made measurements behind a pair of half-delta-wing vortex generators placed on the wall of a straight rectangular duct. The boundary layer on this wall develops under nominally constant pressure, and has a momentum thickness Reynolds number, $R_\theta = 1700$ at the location of the vortex generators. Of the several different arrangements of vortex generators used in these experiments, the one chosen as the model for the present study is designated case 3 and 'common-down,' in which the generators are placed such that the common flow induced between them is towards the wall. The vortex generators are shown in Figure 2. Pauley and Eaton used a five-hole Pitot probe to measure mean-velocity components and hotwires to measure some of the Reynolds stresses. Their data are compared with the results of the corresponding numerical simulations in a later section.

The present experiments were conducted in the curved-wall wind tunnel shown in Figure 3. This open-circuit, suction-type wind tunnel has a 90° bend. The upstream straight section provides a developed turbulent boundary layer into which vortex generators are installed. The downstream straight section is provided to study recovery of the flow following the bend. The tunnel cross-section is rectangular with an aspect ratio of 6. Measurements and calculations of Kim (1991) revealed that, in the absence of vortex generators, the boundary layer on the middle two-third span of the outer (concave side) wall is essentially two-dimensional, i.e., free from secondary motion and corner effects. Two pairs of half-delta-wing vortex generators are installed symmetrically on this wall, 132 cm downstream of the boundary layers trip, which is a distance of 14C downstream of station U1, C (= 50 mm) being the generator chord. The location is shown in Figure 3. The generators are arranged so that the common flow between the vortices is towards the wall. Two pairs of generators placed symmetrically about the tunnel centerplane are chosen instead of a single pair at the tunnel center to minimize the length, and interference, of the probe traversing mechanism. The vortex generators have the same geometry as those of Pauley and Eaton (1988), shown in Figure 2, and therefore, generate comparable vortices. The experiment is performed with a free-stream velocity (U_o) at station U1 of 16 m/sec. The momentum thickness Reynolds number R_θ of the boundary layer at the location of the vortex generators is 3150.

In the presentation of experimental as well as computational results, unless otherwise indicated, all quantities are nodimensionalized with U_o, C, and fluid density ρ, as appropriate. Also, to facilitate comparisons among different experiments, the results are presented in coordinates which are referred to the location of the vortex generator, as shown in Figures 1 and 3. Thus, X is measured along the wall from the trailing edge of the vortex generator, Y is normal to the wall, and Z is spanwise, measured from the plane of symmetry between the two vortex generators. The mean-velocity components in the (X,Y,Z) directions are denoted by (U,V,W) and the corresponding fluctuating components by (u,v,w).

The pressure distribution along the inner (convex side) and outer (concave side) walls of the tunnel, measured with

wall pressure taps in the symmetry plane, without the vortex generators, is shown in Figure 4. It is clear that the vortices introduced on the outer wall just ahead of station U2 are subjected to an adverse pressure gradient at the start of the bend and a favorable pressure gradient at the exit from the bend. Within the bend, between stations 15 and 75, there is a fetch of nearly constant (slightly falling) pressure. In the upstream and downstream straight sections, there is a small favorable pressure gradient due to frictional losses.

A five-hole pressure probe, calibrated following the method of Treaster and Yocum (1979), is employed to measure the three mean-velocity components. The overall diameter of the probe is 0.13 inch (3.30 mm) and it has five 0.023 inch (0.584 mm) holes: one on the flat surface facing upstream and four equally-spaced on 45-degree facets.

The wall shear stress is determined by employing two different types of pressure probes at the same location. A total-head tube with inner and outer diameters of 0.047 and 0.065 inch (1.19 and 1.65 mm), respectively, is used in the manner of a Preston tube. However, the static pressure at the same point is obtained from a separate static-pressure probe. The difference between the readings of the two probes is used, along with the Preston tube calibration of Patel (1965), to obtain the wall friction coefficient.

A constant-temperature hotwire system is employed to measure the fluctuating velocity components. At the beginning of this study, it was thought that triple-sensor probes could be used to obtain all the necessary information in a single set of experiments. However, more detailed consideration of the flow to be measured in the present case soon led to the conclusion that commercially available triple-sensor probes are much too large to properly resolve the near-wall flow. Therefore, a miniature two-sensor (cross-wire) hotwire probe, whose overall size is less than 2 mm (DISA 55P61), is employed to improve resolution of the near-wall flow in the boundary layer. This probe is used in two orientations, namely, with the sensors in the UV or the UW planes, to obtain all except one ($-\overline{vw}$) component of the Reynolds stress tensor. King's law is employed to relate the output voltage to the effective cooling velocities along the wires. The cooling effect by the out-of-plane velocity component is ignored and the directional sensitivity coefficient is assumed to be a constant. Although the hotwire measurements also yield the mean-velocity components, the measurements with the pressure probe are generally more reliable. Therefore, only the pressure probe data are presented for the mean velocities. The pressure-probe and hotwire measurements are made in the upper half of the duct at five cross sections, namely, U2, 15, 45, 75, and D1, which are identified in Figure 3. The measured mean velocity and Reynolds stresses are compared with the computational results in a subsequent section.

NUMERICAL METHOD

The numerical method of Chen and Patel (1989) for the solution of the Reynolds-averaged Navier-Stokes equations is modified and used for the present work. This method uses a collocated grid with a PISO-like pressure-velocity coupling technique. However, in the original version, only the independent variables (i.e., the coordinates) are transformed into generalized curvilinear coordinates, leaving the vector components in Cartesian coordinates. For the present study involving a highly curved flow, it was felt desirable to consider the full-transformation approach, in which contravariant components of the velocity vector, following the direction of the numerically generated, nonorthogonal, curvilinear grid lines, are employed. The detailed tensor operations in transforming the Navier-Stokes equations can be found in Richmond, Chen and Patel (1986). Turbulence closure is effected by the two-layer turbulence model of Chen and Patel (1988) which combines a one-equation model near the wall with the standard k-ε model farther out. Details of the present version of the numerical method are given in Kim (1991).

The numerical method was employed to perform calculations for the flow within the entire duct, without any artificial disturbance, to study the development of the wall boundary layers and, in particular, the evolution of longitudinal vortices, naturally occurring on the convex wall induced by the pressure-driven secondary motion. The results are reported in Kim (1991). Although this portion of the overall study is not of concern here, it confirmed, as noted above, the experimentally observed two-dimensionality of the boundary layer over the mid-span of the outer wall. Comparisons between measurements and calculations also confirmed the ability of the numerical method to resolve the flow details, and limitations of the turbulence model in describing the effects of longitudinal curvature. These features will be commented upon in subsequent sections.

MODEL OF A HALF-DELTA-WING VORTEX GENERATOR

Although vortex generators are quite frequently used in practical applications, there is no model or method available for the prediction of the size, location and intensity of the vortex induced by a typical generator. If it is desired to study the fate of these vortices, and their interactions with the parent boundary layer, neighboring walls, and other vortices, it is clear that one must solve the full Reynolds-averaged Navier-Stokes equations for the flow downstream of the vortex generators. Solution of these equations to describe the flow around a vortex generator itself is a formidable task because it would require not only proper resolution of the boundary layer and the junction flow, but also the leading-edge vortex, its bursting, and transition to turbulence. To the authors' knowledge, such a solution has not been attempted and there are few, if any, successful solutions of the flow around even an isolated delta wing. An alternative to calculating the flow around the generator is to develop a model that relates certain overall characteristics of the vortex to the geometry of the generator. This alternative is followed here.

The flow behind a vortex generator is modeled by drawing upon the information that is available from studies on delta wings. In particular, a relation is sought between the geometrical and flow parameters of the generator and the parameters describing the resulting vortex, namely, the size, strength, and location of the vortex, as well as the distributions of velocity and turbulence parameters within the vortex. Such a model is then utilized to prescribe the initial conditions to calculate the downstream development of the flow.

To determine the position of the vortex center, it is assumed that it is the same as that observed on isolated slender delta wings, i.e., the effect of the wall is negligible. Lowson (1989) has carried out extensive visualization tests, compared his results with those of several previous experiments, and correlated the coordinates of the vortex

center with the ratio of the angle of attack (α) to the semi-apex angle (β) of the wing. Lowson's correlation is used here to determine the location of the vortex center at the trailing edge of the generator. For the present case, in which $\alpha/\beta = 0.825$, Lowson's correlation gives the following coordinates of the vortex center: $y^* = 0.6S$ and $z^* = 0.8S$, where S (= 0.4C) is the semi-span of the vortex generator (see Figure 2).

The velocity distribution within the vortex is determined by relating the drag and lift of the wing to parameters such as the maximum axial velocity deficit and the peak circumferential velocity, and assuming the shape of the velocity distributions. The profile used here is based on the experimental data of Leuchter and Solignac (1983), Phillips and Graham (1984), Mehta and Cantwell (1987), and Pauley and Eaton (1989), who measured detailed velocity profiles behind different types of vortex generators. According to Phillips and Graham, the axial velocity behind a vortex generator has a Gaussian distribution and the circumferential velocity can be represented by a Rankine vortex. This observation was supported by Pauley and Eaton. However, the presence of the solid wall near the vortex requires an image of the vortex in the wall. Another important observation made from the experimental data mentioned above is that the radius at which peak circumferential velocity occurs (i.e., radius of the vortex core, r_c) is about the same as the radius at which the axial velocity deficit is one-half of its maximum value (i.e., half-radius of the vortex wake, r_1). Thus, in the present study, it is assumed that the axial velocity profile is given by a Gaussian distribution and the circumferential velocity is represented by a Rankine vortex and its images. It is also assumed that the half-radius of the wake is the same as the radius of the vortex core. With these assumptions, the distribution of axial (longitudinal) velocity in the vortex behind a half-delta-wing generator is given by

$$U = 1 - (\Delta U)_{max} \exp\left\{- \ln 2 \left(\frac{r}{r_1}\right)^2\right\} \qquad (1)$$

Further, it is assumed that the center of the vortex core at the trailing edge of the vortex generator is a stagnation point (i.e., $(\Delta U)_{max} = 1.0$). The circumferential velocity with the Rankine-vortex model is given by

$$\begin{aligned} V_\theta &= (V_\theta)_c \frac{r}{r_c} \qquad \text{for } r < r_c \\ &= (V_\theta)_c \frac{r_c}{r} \qquad \text{for } r > r_c \end{aligned} \qquad (2)$$

with the circulation $\Gamma_c = 2\pi r_c (V_\theta)_c$ and $r_c = r_1$.

Once the shape of the axial velocity profile is assumed, conservation of mass and axial-momentum balance can be used to relate the drag of the vortex generator to the velocity distribution in the vortex. Any contribution from the pressure change induced by the vortex, and effects of the adjacent wall, are ignored in this model. This gives the drag coefficient

$$C_D = \frac{4\pi}{A} \int_0^\infty U\,(1 - U)\, r\, dr \qquad (3)$$

where A is the area of the vortex generator. Similarly, the lift of the generator is related to the circulation around the vortex, and the lift coefficient is given by

$$C_L = \frac{2\,\Gamma_c\, y^*}{U_o\, A} \qquad (4)$$

Polhamus (1971) gives the drag and lift coefficients of slender delta wings as functions of incidence, aspect ratio, and sweep angle. These relations are used here. For the present configuration of vortex generators shown in Figure 2, the resulting circulation Reynolds number (Γ_c/ν) is 18,700 and $r_1/C = r_c/C = 0.108$.

Vortices with the above velocity distribution are introduced inside the boundary layer, in which the streamwise velocity distribution (U component) is known. A simple superposition is adopted for this velocity component. However, introduction of the vortices leads to a transverse (spanwise) velocity component parallel to the wall which is not zero at the wall. This component is doubled due to the image vortex in the wall. To impose the no-slip condition for this spanwise velocity component at the solid wall, it is assumed that that component is related to the streamwise component by the inner leg of Johnston's triangular plot for crossflow in a three-dimensional turbulent boundary layer. Note that this inner leg, in which the velocity vector is assumed to be collateral, extends to U/U_τ of about 15, U_τ being the friction velocity.

For the turbulence model employed here it is also necessary to determine the distributions of k and ε within the vortex at the trailing edge of the vortex generator. Both the turbulent kinetic energy and the eddy viscosity are assumed to have Gaussian distributions, similar to the axial velocity. The peak values of k and ν_t (= $C_\mu k^2/\varepsilon$, C_μ being a model constant) are then related by assuring equilibrium between the production and dissipation of turbulent kinetic energy in the integral sense; i.e., the integrated production of turbulent kinetic energy is balanced by integrated dissipation rate at the plane in which the inlet velocity profiles are prescribed. Finally, the peak value of the eddy viscosity in the vortex is obtained from the formula of Owen (1970), which relates the eddy viscosity to the circulation Reynolds number Γ_c/ν.

The vortex model outlined above, along with the characteristics of the parent boundary layer (usually the thickness and friction coefficient), provide all of the initial conditions necessary to solve the Reynolds-averaged Navier-Stokes equations, starting from the trailing edge of the vortex generators. Thus, the model provides a means to introduce vortices of desired strength and configuration, at desired positions, in the Navier-Stokes solution method without having to resolve the flow around the generator itself. For vortex pairs, the model is used with appropriate overlaps and reflections in walls to obtain the combined velocity and turbulence profiles.

COMMON-FLOW DOWN VORTEX PAIR IN A FLAT-PLATE BOUNDARY LAYER

The numerical method and the vortex model outlined above are used first to simulate the experiments of Pauley and Eaton (1988). As shown in Figure 1, a pair of longitudinal vortices with their common flow toward the wall is introduced in a flat-plate turbulent boundary layer. The solution domain extends from the trailing edge of the vortex generator, X = 0, to X/C = 35 in the longitudinal direction, and is large enough in the normal ($0 \le Y/C \le 6$) and spanwise ($0 \le Z/C \le 10$) directions to exclude any effect of the tunnel walls. This domain is covered by a 42 x 65 x 57 nonuniformly distributed grid points. The vortex

model described in the previous section supplies the inlet conditions at X=0 and the downstream exit profiles are extrapolated. No-slip condition is imposed on the wall (Y=0), while symmetry conditions were imposed on Z=0 and the outer boundaries. The first grid point near the wall is located around y^+=1.0 and care is taken to ensure that the grid is dense in the region where the vortex core is located. It should be remarked that, in the presentation of results attention is confined to a small segment of the total solution domain, and also to a part of the wind tunnel cross-section, in which the vortices are not influenced by the side walls.

Two hundred iterations are required to obtain a converged solution. The CPU time required for calculations on the CRAY-YMP supercomputer was about 0.12 milliseconds per iteration per grid point, which translates into a total time of about one hour.

The calculated and measured contours of longitudinal velocity and vorticity are compared at four axial locations in Figure 5. The axial velocity contours clearly show strong distortion of the boundary layer by the vortices. The two vortices move apart as they grow in size and produce a region of a thin boundary layer between them. Convection of each vortex by the flow field of the other holds the vortices close to the wall, while the effect of the wall (the image vortices) is to force them apart. The boundary layer between the vortices is thinned by the strong downward flow and the lateral outflow of the boundary layer fluid. In the upwash region, the boundary layer is thickened because the vortex sweeps low momentum fluid away from the wall. The evolution of the vortices is best indicated by the longitudinal vorticity contours. These contours are flattened due to the impermeability of the wall even though their initial shape is circular. There is secondary vorticity with opposite sign to the primary one confined near the wall. The impermeability condition at the wall reverses the spanwise velocity component near the wall and is responsible for the production of vorticity of the opposite sign. The computations reproduce most of the features of the mean-velocity field except near the vortex center, where the calculations appear to diffuse the velocity deficit more rapidly than is observed in the experiment.

There is good agreement between the calculations and data with respect to the spanwise distributions of the (resultant) friction coefficient, shown in Figure 6. The downwash between the vortices thins the boundary layer and leads to higher friction there. The region of upwash, where low momentum fluid is lifted by the vortex, shows low friction coefficient, as expected from the axial velocity contours. It is also noticed that the troughs in the friction distribution indicate the lateral drift of the vortices. The agreement between the data and calculations at the first measurement station, namely, X/C = 1.7, is indicative of the success of the semi-empirical vortex model described in the previous section. The agreement further downstream, on the other hand, is a measure of the performance of the overall calculation method, including the numerical treatments and the turbulence model.

The circulation, and the magnitude and position of peak vorticity, are good characteristic parameters to describe the strength and the location of the vortices. For the experimental data, the circulation was obtained by integrating the longitudinal vorticity of primary sign over the domain of measurements, rather than performing a line integration of velocity around a contour. The circulation Γ and peak longitudinal vorticity Ω_x are plotted in Figure 7 as functions of the distance from the trailing edge of the generator. The position (y*,z*) of the center of the vortex core (i.e., the point of peak vorticity) is shown in Figure 8. It is clear that the calculations are in remarkable agreement with experiment with respect to the decay of circulation and drift in the vortex position. However, the peak vorticity is underpredicted by the computations. This, along with the difference in the axial velocity distributions noted above, suggests that the vortex diffuses more quickly in the numerical model than in the experiment, confirming the observation made by Tanaka and Suzuki (1978).

Figure 9 shows the comparison of three mean velocity components (U,V,W), the turbulent kinetic energy (k), and two Reynolds shear stresses ($-\overline{uv}$, $-\overline{uw}$), at the second measurement station which is 7.9C downstream from the trailing edge of the vortex generators. Four spanwise locations are chosen, representing the symmetry plane midway between the vortices, the center of the vortex core, a location in the upwash zone, and a location outside of vortex region, respectively. As was seen from the axial velocity and vorticity contours, the velocity deficit in the streamwise direction and the spanwise velocity component at the center of the vortex core is underpredicted in the computation. However, all velocity components at other locations are well predicted. The turbulent kinetic energy near the center of the vortex core is also underpredicted. Although the present turbulence model does not explicitly consider the individual Reynolds stresses, they are shown here to indicate the implications of using an eddy-viscosity model. It is interesting to note that, as expected, the primary shear stress $-\overline{uv}$ is predicted rather well except in the vortex core. The observed disagreements cannot be attributed entirely to the turbulence model or the vortex model used to set the initial conditions, however, because these are accompanied by disagreements in the mean-velocity gradients in the same locations. It is likely that the increased diffusion in the computations comes partly from the numerical method or insufficient grid points. This possibility is suggested because an arbitrary increase in the turbulent kinetic energy in the initial vortex failed to significantly improve the predictions. Finally, we note that the isotropic eddy-viscosity of the k-ε model does not predict the transverse Reynolds stress $-\overline{uw}$. Prediction of this detail would require an anisotropic model.

COMMON-FLOW DOWN VORTEX PAIR IN THE CONCAVE-WALL BOUNDARY LAYER

In this case, the numerical solution is obtained in a domain that starts at the trailing edge of the vortex generators (X = 0) and extends well downstream of station D1 (X = 150C) in the straight section of the wind tunnel (see Figure 3). In the spanwise direction, the solution domain extends from the symmetry plane between the vortices (Z = 0) to the side wall of the tunnel (Z = 6C). However, in these calculations, the side wall is also treated as a symmetry plane as there is negligible interaction between the vortices and the corner flow within the region of interest. This treatment enables more grid points to be placed near the vortices. In the normal direction, the solution domain extends from the concave side (Y = 0) to the convex side (Y = 4C) of the tunnel, and boundary layers on both walls are resolved using appropriate grid concentration. The grid spacing used in this curved-wall case is somewhat finer than that used in the previous case. In fact, a 57 x 76 x 75 grid is employed in the (X,Y,Z) directions, with the first grid point near the walls being at y^+ of the order of 1.0. Three hundred iterations are needed to obtain a converged solution.

Before presenting the results of the experiments and calculations, it is helpful to briefly review the transport equation for the longitudinal component of vorticity. In the coordinate system shown in Figure 3, this equation is

$$\frac{D\Omega_X}{Dt} = \left[\frac{R_o}{R_o - Y}\Omega_X \frac{\partial U}{\partial X} + \Omega_Y \frac{\partial U}{\partial Y} + \Omega_Z \frac{\partial U}{\partial Z} - \frac{V\,\Omega_X}{R_o - Y}\right]$$

R S1 S2 S3 S4

$$+ [\text{ Viscous terms} + \text{Turbulent terms }] \qquad (5)$$

Recall that X is along the outer, concave wall of the wind tunnel. The term on the left-hand side represents the total rate of change of longitudinal vorticity (Ω_X). The first term in the first bracket on the right-hand side represents the stretching of longitudinal vorticity in the X-direction, while the second and third terms represent the tilting of existing vorticity in the Y- and Z-directions into the X-direction by the gradients of the longitudinal velocity (U). The fourth term also comes from $(\Omega \bullet \nabla)V$, which represents the inviscid stretching or skewing of existing vorticity. This fourth term is absent in the flow over a flat surface considered in the previous section. Also, the sign of the velocity component normal to the wall (V) is important in determining the effects of the imposed curvature on the evolution of the longitudinal vorticity.

Figures 10(a) and (c) show the measured longitudinal velocity and vorticity contours. The first thing to notice from the vorticity contours is the strong secondary vorticity with opposite sign that is present outside of the primary vortices introduced by the vortex generators. When vortices were introduced in a flat-plate boundary layer, as discussed earlier, the secondary vorticity with opposite sign was found only near the wall. In the present case of the concave wall, however, the distribution of vorticity shows quite different features. From the contours of the longitudinal velocity, it is seen that the velocity defect in the vortex core decreases faster than in the flat-plate case. This acceleration is all the more surprising in view of the adverse pressure gradient that prevails at the beginning of curvature. It is likely that this is related to the fuller velocity profiles in the parent concave-wall boundary layer, as shown in Kim (1991) and will be discussed later. The symmetry of the experimental results shown in Figure 10 confirms that the vortex-pair development is not affected, at least up to station D1, by the asymmetry imposed by the side wall of the wind tunnel.

Figures 10(b) and (d) show the calculated longitudinal velocity and vorticity contours. It is immediately obvious from the velocity contours that the vortices no longer move apart from each other after station 75, as in the experiment. This phenomenon is attributed to the emergence of strong secondary vortices which surround the primary ones. The main difference in the vorticity contours from those in the flat plate is in the strength and size of these secondary vortices. The evolution of stronger secondary vortices is explained by the inviscid, curvature-related, vortex-stretching term (S4) in equation (5). Consider the downwash ($V < 0$) region between the two common-down vortices on the concave wall. The sign of S4 is the same as that of Ω_X, the implication of which is that vorticity is fortified between the two vortices. On the other hand, in the upwash zone ($V > 0$), the sign of S4 is different from that of Ω_X, so that primary vorticity decreases in this region. As the primary vorticity is weakened, secondary vorticity with opposite sign near the wall region is lifted by the upwash, intensifying the secondary vortices. It should be noted that even in the parent two-dimensional boundary layer in the curved duct, the normal velocity component (V) is directed from the outer to the inner wall between stations U2 and 15. The upwash flow is therefore strengthened further by this effect in the curved portion of the duct. Again, the lifted secondary vorticity is intensified due to the curvature-related term (S4), because the secondary vorticity and the upwash velocity have the same sign as that of the secondary vorticity. Thus, the induced velocity field increases near the primary vortex by intensification of the secondary flow during the curved portion. This increment of the induced velocity component plays a key role in fortifying the primary vortices. While this simple argument suffices to explain the overall trends, it does not of course take into account the complex interactions between curvature and turbulence that are contained in the remaining terms of equation (5).

Figure 11 compares the measured (longitudinal) friction coefficients with the calculated ones. It is found that the friction coefficients are somewhat underpredicted, particularly after station 15, where curvature effects set in. However, the shape and position of the peak values are in good agreement. The disagreement in the friction magnitude is similar to that observed by Richmond and Patel (1991), who employed the same turbulence model and a similar numerical method to study the effects of convex and concave curvatures on two-dimensional turbulent boundary layers. In particular, they found that the velocity profiles along concave surfaces were not predicted as full as those observed in experiments, and this correlated with the lower predicted friction coefficients. Thus, it appears that improved predictions would require a turbulence model that is more sensitive to surface curvature effects.

The circulation and peak vorticity of the primary and secondary vortices are shown in Figure 12. The circulation was obtained by integrating the vorticity of the appropriate sign rather than from contour integrals of velocity, and for direct and meaningful comparison of calculated and experimental values, the integration was carried out only over the measurement domain. It is seen that the computational results slightly overpredict the circulation of the primary and secondary vortices. However, the important observation to make here is that the circulation increases through the curved part both in the experiment and computation. Recall that, as shown in Figure 7, the circulation of the primary vortices on a flat plate decreased with downstream distance because of the losses due to spanwise friction. In the present case, a decrease of circulation is observed only before the curvature appears and after the curvature disappears. It should be noted that surface curvature begins at X/C = 3.6 and ends at X/C = 29.1. Concave curvature, therefore, acts to increase the circulation of the vortices. The peak vorticity of the primary vortex is also predicted well. Recall that the peak vorticity of the vortex introduced on a flat plate was underpredicted, as shown in Figure 7. The evolution of the secondary vortex is clearly seen from the corresponding plot of peak vorticity.

The positions of the centers of the primary and secondary vortex cores (i.e., the points of peak vorticity) are shown in Figure 13, even though the peak points are not as well defined as in the flat-plate case. The calculations are in fair agreement with the experimental data. It is again noticed that the lateral movement of the vortices

stops after station 75 (X/C = 24.9) according to the numerical solutions.

Figure 14 shows the profiles of the mean-velocity components (U,V,W), the turbulent kinetic energy (k), and two of the Reynolds shear stresses ($-\overline{uv}$, $-\overline{uw}$), at four spanwise positions, representing the symmetry plane, the center of the (measured) primary vortex core, the upwash zone, and outside of the vortex region, at station 15 (X/C = 7.8). The computational results show good agreement with experiment, and provide support for the vortex model used to construct the initial profiles just downstream of the vortex generator. The axial velocity defect near the center of the vortex core is much less than that in the flat-plate case. It is observed that the longitudinal velocity change due to the vortex is superimposed on the inviscid core of the basic curved-duct flow. The overall feature of the turbulence profiles is that the vortex is superimposed on the highly turbulent flow in the concave-wall boundary layer. It is well known that, in a two-dimensional boundary layer along a curved surface, convex curvature tends to reduce (stabilize) the turbulence, whereas concave curvature leads to an increase (destabilization). Obviously, this effect is not captured by the calculations. On the other hand, the shapes of the profiles of the turbulent kinetic energy and the primary shear stress $-\overline{uv}$ are predicted rather well throughout the flow domain.

SUMMARY AND CONCLUSIONS

The development of artificially-introduced vortex pairs in turbulent boundary layers was studied through physical and numerical experiments, particularly to elucide the influence of streamwise curvature and accompanying pressure gradients. Vortex pairs with the common flow between them down towards the wall were considered. Experiments were performed with such vortices in the boundary layer on the outer, concave wall of a curved-duct wind tunnel to complement similar ones conducted by Pauley and Eaton (1989) in a flat-plate boundary layer.

To conduct parallel numerical experiments, a semi-empirical model was developed to relate the size, strength, and location of vortices produced by conventional, half-delta-wing vortex generators, to the geometry of the vortex generators. The model also provides the velocity and turbulence distributions in the vortices just downstream of the generators, and these were used to determine the initial conditions for a subsequent solution of the Reynolds-averaged Navier-Stokes equations. Solutions were obtained for the geometries used in the two sets of experiments mentioned above using a modified version of the method of Chen and Patel (1989), described in Kim (1991).

The experimental and computational studies together lead to the following conclusions.

(1) The numerical solutions, with initial profiles obtained from the semi-empirical vortex model, provided good agreement with both sets of experimental data, particularly with regard to the size and location of the vortices.

(2) On a concave wall, strong secondary vortices form outside the primary ones introduced by the vortex generators. The secondary vortices originate from the underlying boundary-layer vorticity lifted by the upwash of the primary vortices. These secondary vortices also force the primary ones to stay close to the symmetry plane when compared with similar vortices on a flat plate.

(3) On a concave wall, the circulation of the common-flow-down vortices increases with downstream distance, whereas it decreases on a flat plate. This may be explained by the change of vorticity distribution due to the stretching applied by the wall curvature and the velocity field induced by the developing secondary vortex adjacent to the primary one.

(4) Measurements in the vortices on the concave wall indicate much higher levels of turbulent stresses compared to those measured in vortices on a flat plate. This indicates that concave curvature effects, which are known to be important in two-dimensional turbulent boundary layers, continue to play an important role in turbulent transport in more complex vortical flows. The numerical model could not capture the details of the flow in the eye of the vortex.

Before closing, it is important to note that the semi-empirical model of the vortex induced by a half-delta-wing vortex generator proposed here needs further verification and refinement. More detailed experiments, with larger and isolated vortex generators, are required to put the model on a firmer basis. However, it is also clear from the results presented here that the model can be used, in conjunction with advanced numerical methods, to study the fate of vortices introduced in complex turbulent shear flows. For example, the model may be used to investigate flow-control strategies on bodies at incidence where longitudinal vortices arise naturally from flow separation. Kim (1991) describes some additional numerical experiments in which other vortex pairs (with common flow away from the wall) were introduced in boundary layers on a flat plate as well as on convex and concave surface. Limitations of space, and lack of corresponding experimental data, preclude a discussion of these situations although the calculated results reveal quite interesting features. Finally, it is concluded that the numerical model employed here is successful in representing the overall features of the flows considered but further improvements are needed in the modelling of turbulence within the vortices. This is a subject of research in progress.

ACKNOWLEDGEMENTS

This research was sponsored by the Office of Naval Research under Grant N00014-89-J-1342 in support of the DARPA Subtech Program. The authors are grateful to Dr. E.P. Rood and Mr. J.A. Fein of ONR and Mr. G. Jones of DARPA for their support of this project. The calculations were performed on the supercomputers of the Numerical Aerodynamic Simulation facility located at NASA Ames Research Center.

REFERENCES

Batchelor G.K. (1964), "Axial flow in trailing line vortices," J. Fluid Mech., vol. 20, pp. 645-658.

Chen H.C. and Patel V.C. (1988), "Near-wall turbulence models for complex flow including separation," AIAA J., vol. 26, pp. 641-648.

Chen H.C. and Patel V.C. (1989), "The flow around wing-body junctions," Proc. 4th Symp. Numerical and Physical Aspects of Aerodynamic Flows, Long Beach, CA.

Eibeck P.A. and Eaton J.K. (1987), "Heat transfer effects of longitudinal vortex embedded in a turbulent boundary layer," J. Heat Transfer, vol. 109, pp. 16-24.

Kim W.J. (1991), "An experimental and computational study of longitudinal vortices in turbulent boundary lay-

ers," Ph.D. Thesis, Mechanical Engineering, Univ. Iowa, Iowa City, IA.

Leutcher O. and Solignac J. L. (1983), "Experimental investigation of the turbulence structure of vortex wakes," Proc. 4th Symp. Turbulent Shear Flows, Karlsruhe, Germany.

Liandrat J., Aupoix B., and Cousteix J. (1985), "Calculation of longitudinal vortices imbedded in a turbulent boundary layer," Proc. 5th Symp. Turbulent Shear Flows, Ithaca, N.Y.

Lowson M.V. (1989), "Visualization measurements of vortex flows," AIAA Paper 89-0191.

Mehta R.D. and Bradshaw P. (1988), "Longitudinal vortices imbedded in turbulent boundary layers. Part 2. Vortex pair with common flow upwards," J. Fluid Mech., vol. 188, pp. 529-546.

Mehta R.D. and Cantwell E.R. (1987), "Properties of a half-delta wing vortex," Proc. 6th Symp. Turbulent Shear Flows, Toulouse, France.

Mokhtari S. and Bradshaw P. (1983), "Longitudinal vortices in wind tunnel wall boundary layer," Aeronautical J., vol. 87, pp. 233-236.

Owen P.R. (1970), "The decay of a turbulent trailing vortex," Aeron. Quarterly, vol. 21, pp. 69-78.

Patel V.C. (1965), "Calibration of the Preston tube and limitations on its use in pressure gradient," J. Fluid Mech., vol. 23, pp. 185-208.

Pauley W.R. and Eaton J.K. (1988),"Experiments on the development of longitudinal vortex pairs embedded in a turbulent boundary layer," AIAA J., vol. 26, pp. 816-823.

Phillips W.R.C. and Graham J.A.H. (1984), "Reynolds stress measurements in a turbulent trailing vortex," J. Fluid Mech., vol.147, pp. 353-371.

Polhamus E.C. (1971), "Prediction of vortex-lift characteristics by leading edge suction analogy," J. Aircraft, vol. 8, pp. 193-199.

Richmond M.C., Chen H.C., and Patel V.C. (1986), "Equations of laminar and turbulent flows in general curvilinear coordinates," IIHR Rept. No.300, Univ. Iowa, Iowa City, IA.

Richmond M.C. and Patel V.C. (1991), "Convex and concave surface curvature effects in wall-bounded turbulent flows," AIAA J., vol. 29, pp. 895-902

Shabaka I.M.M.A., Mehta R.D., and Bradshaw P. (1985), "Longitudinal vortices imbedded in turbulent boundary layer. Part 1. Single vortex," J. Fluid Mech., vol. 155, pp. 37-57.

Tanaka I. and Suzuki T. (1978), "Interaction between the boundary layer and longitudinal vortices," Proc. Int. Symp. Ship Viscous Resistance, Gothenburg, Sweden.

Treaster A.L. and Yocum A.M. (1979), "The calibration and application of five-hole probes," ISA Trans., vol. 18, pp. 23-34.

Westphal R.V., Eaton J.K., and Pauley W.R. (1985), "Interaction between a vortex and a turbulent boundary layer in a streamwise pressure gradient," Proc. 5th Symp. Turbulent Shear Flows, Ithaca, N.Y.

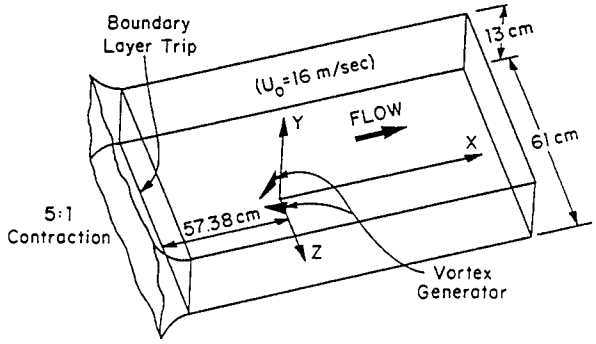

Figure 1 Wind tunnel of Pauley and Eaton(1989)

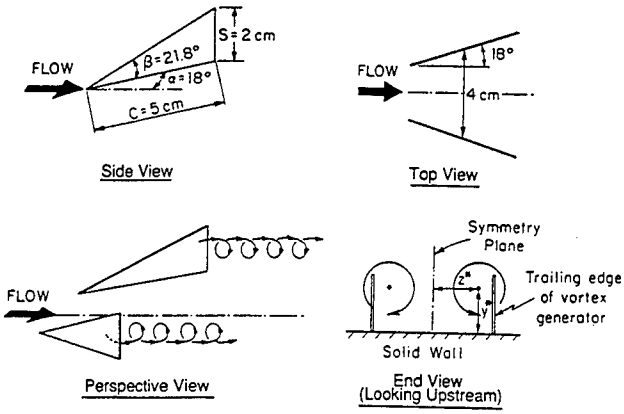

Figure 2 Half-delta-wing vortex generators

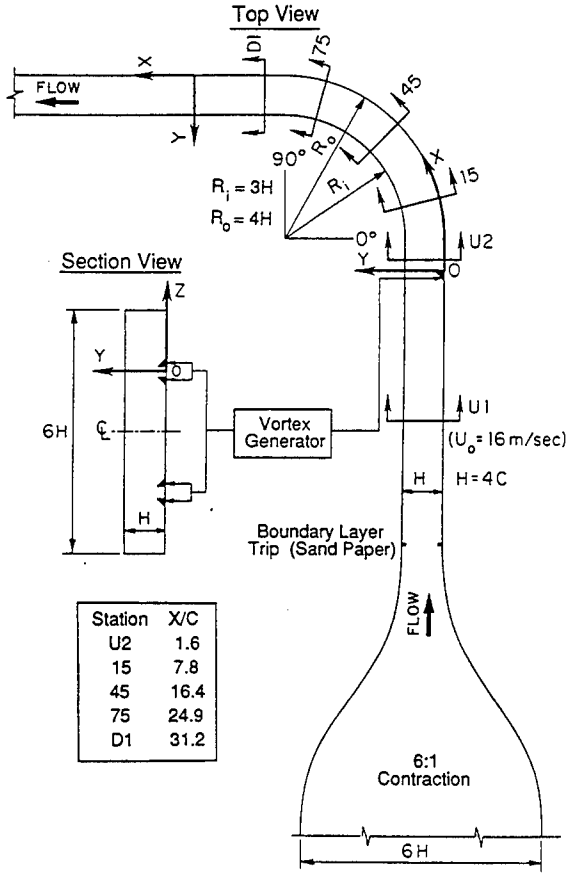

Station	X/C
U2	1.6
15	7.8
45	16.4
75	24.9
D1	31.2

Figure 3 Curved-wall wind tunnel; location of vortex generators and measurement stations

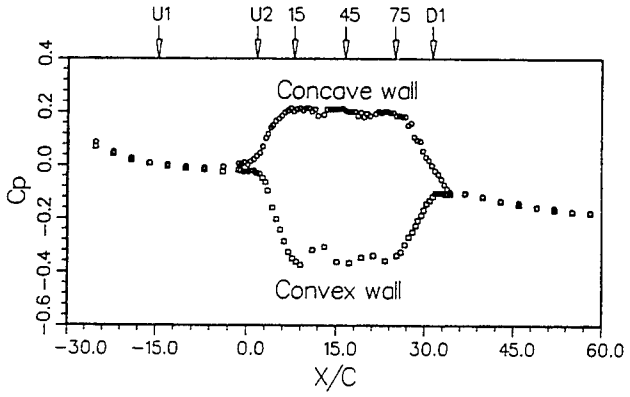

Figure 4 Pressure distribution along the curved-wall wind tunnel in the symmetry plane

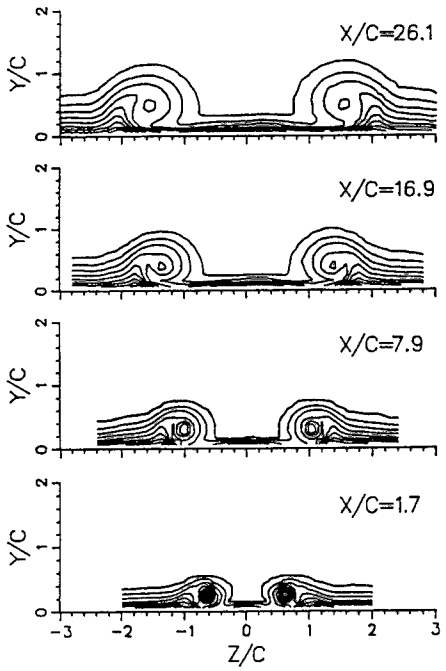

(a) Measured axial velocity (U)
(U= 0.99, 0.95, 0.9, 0.85, 0.8, 0.75, 0.7, 0.65, 0.6, 0.55)

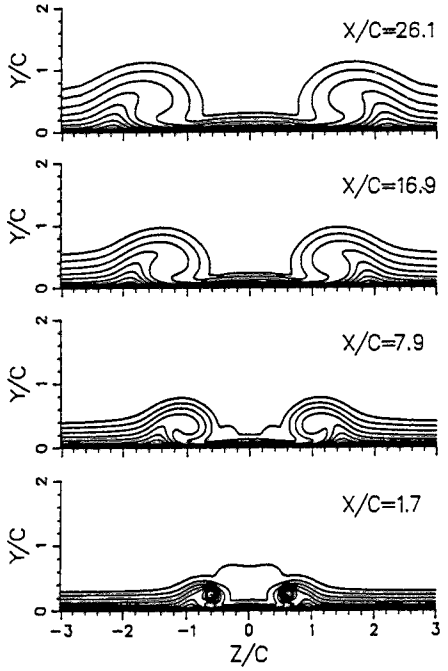

(b) Calculated axial velocity (U)
(U= 0.99, 0.95, 0.9, 0.85, 0.8, 0.75, 0.7, 0.65, 0.6, 0.55)

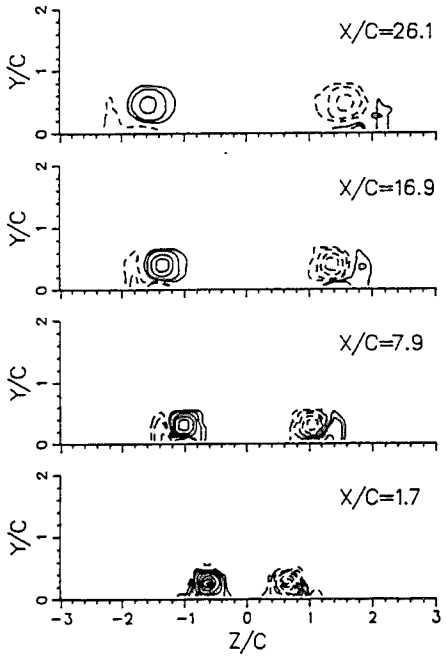

(c) Measured axial vorticity (Ω_X)
($\frac{\Omega_X C}{U_o}$= 0.1, 0.2, 0.5, 1.0, 2.0, 3.0, 4.0, 5.0, 6.0, 7.0, 8.0)

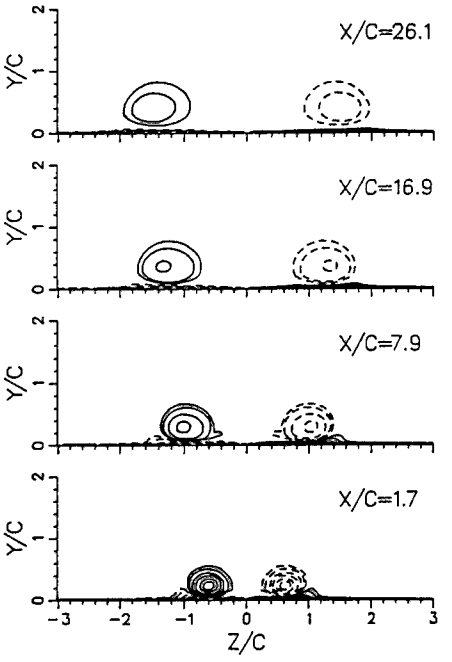

(d) Calculated axial vorticity (Ω_X)
($\frac{\Omega_X C}{U_o}$= 0.1, 0.2, 0.5, 1.0, 2.0, 3.0, 4.0, 5.0, 6.0, 7.0, 8.0)

Figure 5 Vortices in a flat-plate boundary layer

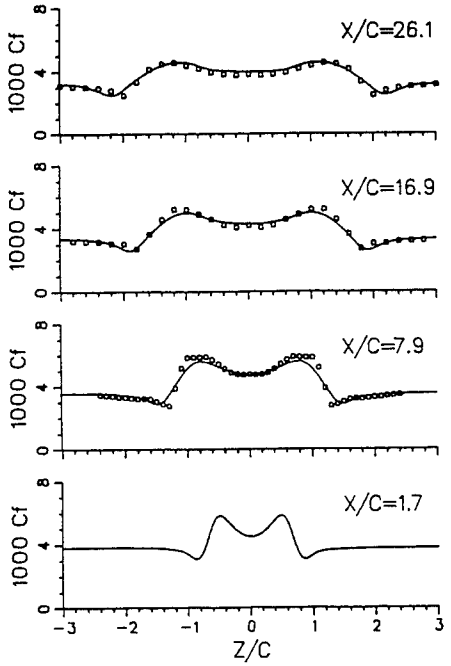

Figure 6 Friction coefficient with vortices in a flat-plate boundary layer

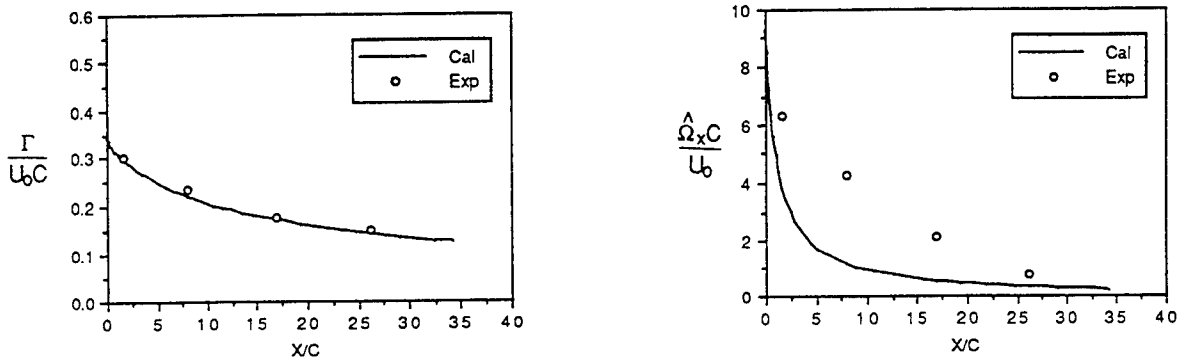

(a) Circulation

(b) Peak vorticity

Figure 7 Circulation and peak vorticity of vortices in a flat-plate boundary layer

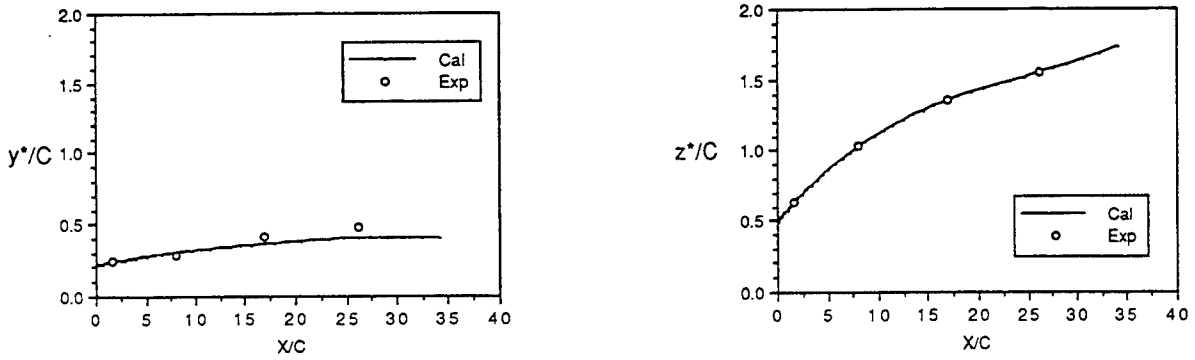

(a) Vertical location

(b) Spanwise location

Figure 8 Location of vortices in a flat-plate boundary layer

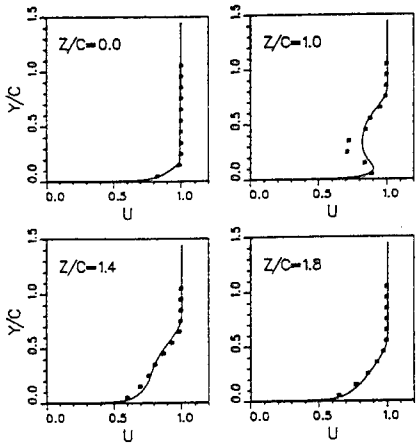

(a) Axial velocity (U)

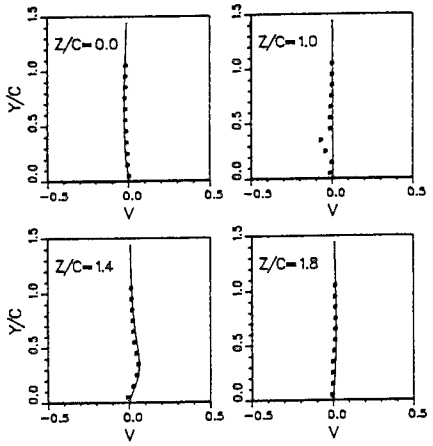

(b) Normal velocity (V)

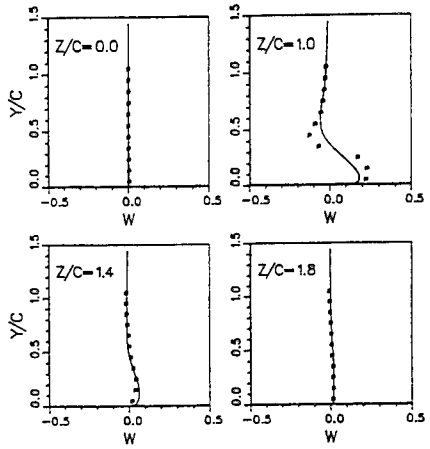

(c) Spanwise velocity (W)

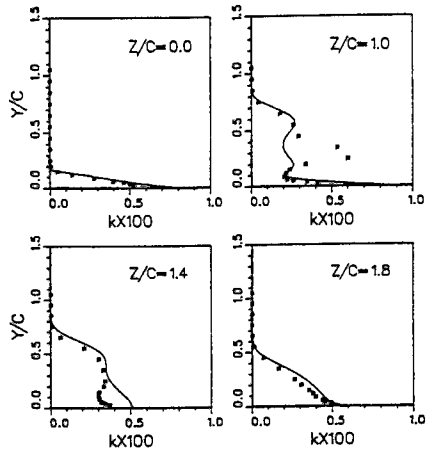

(d) Turbulent kinetic energy (k)

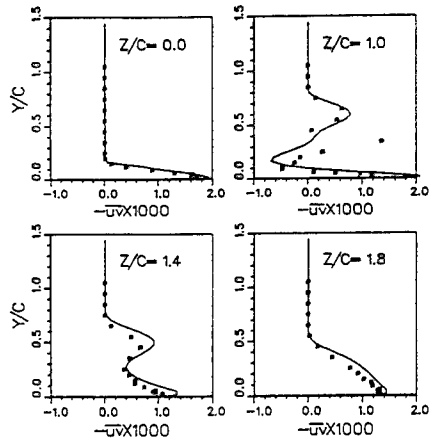

(e) Reynolds shear stress -$\overline{uv}$

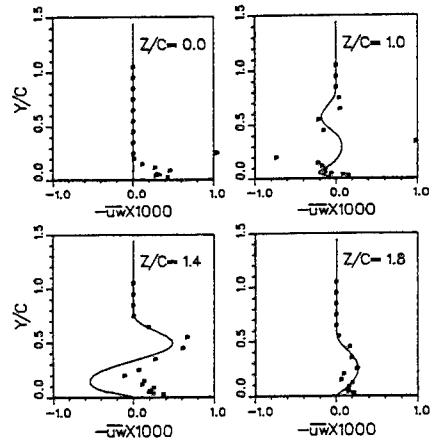

(f) Reynolds shear stress -$\overline{uw}$

Figure 9 Flow profiles in vortices on a flat-plate; X/C=7.9

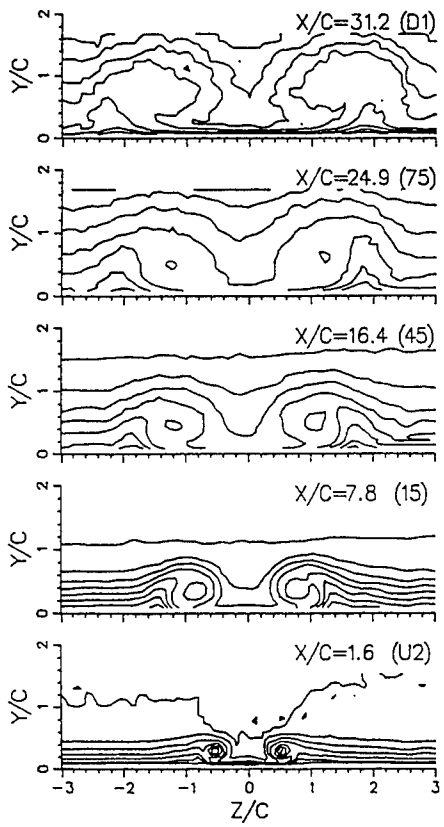

(a) Measured axial velocity (U)
(U= 1.01, 0.99, 0.95, 0.9, 0.85, 0.8, 0.75, 0.7, 0.65, 0.6)

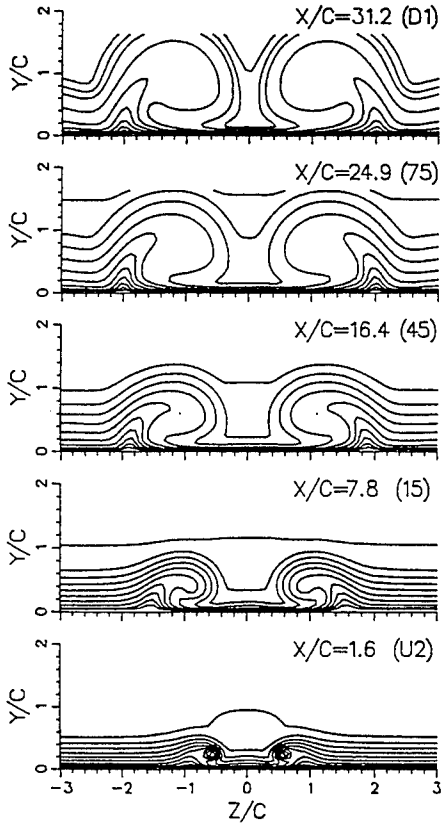

(b) Calculated axial velocity (U)
(U= 1.01, 0.99, 0.95, 0.9, 0.85, 0.8, 0.75, 0.7, 0.65, 0.6)

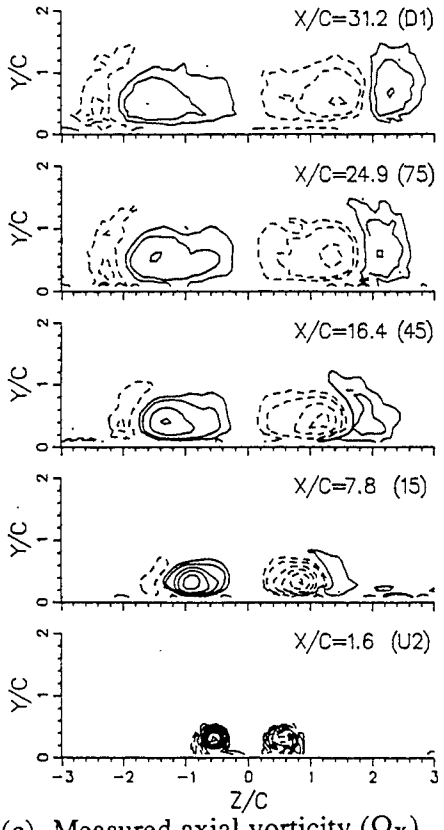

(c) Measured axial vorticity (Ω_X)
($\frac{\Omega_X C}{U_o}$= 0.1, 0.2, 0.5, 1.0, 2.0, 3.0, 4.0, 5.0, 6.0, 7.0, 8.0)

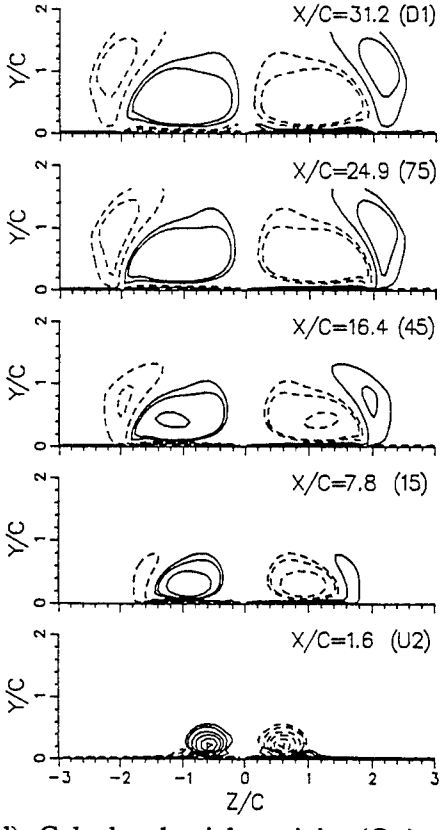

(d) Calculated axial vorticity (Ω_X)
($\frac{\Omega_X C}{U_o}$= 0.1, 0.2, 0.5, 1.0, 2.0, 3.0, 4.0, 5.0, 6.0, 7.0, 8.0)

Figure 10 Vortices in a concave-wall boundary layer

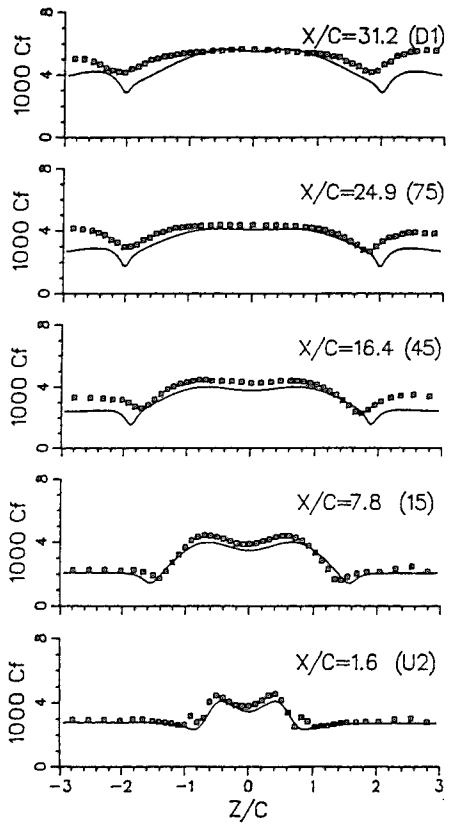

Figure 11 Friction coefficient of vortices in a concave-wall boundary layer

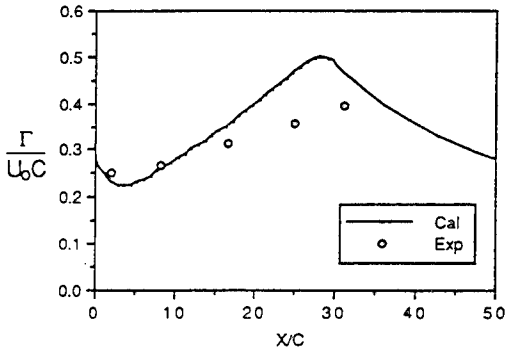

(a) Circulation of the primary vortex

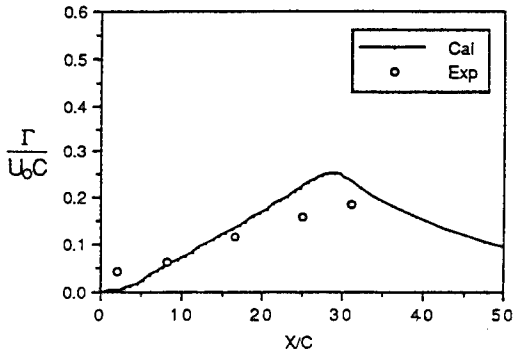

(b) Circulation of the secondary vortex

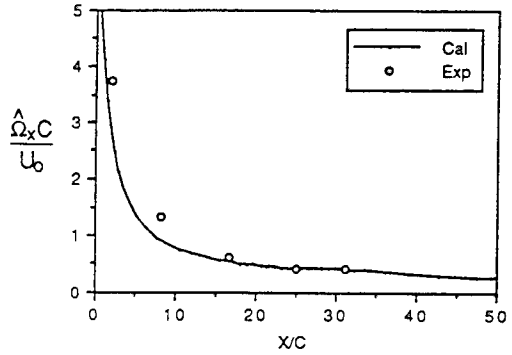

(c) Peak vorticity of the primary vortex

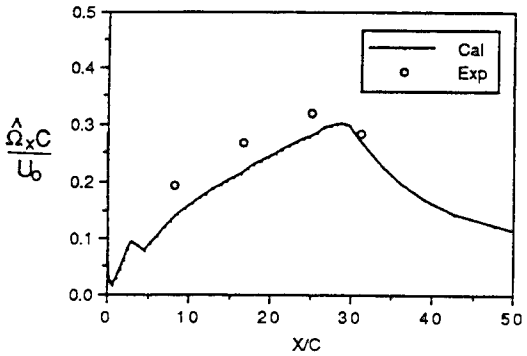

(d) Peak vorticity of the secondary vortex

Figure 12 Circulation and peak vorticity of vortices on a concave-wall boundary layer

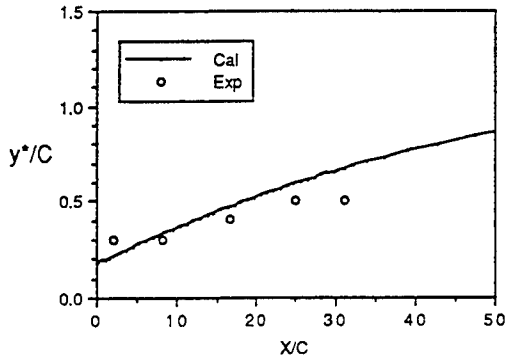

(a) Vertical location of the primary vortex

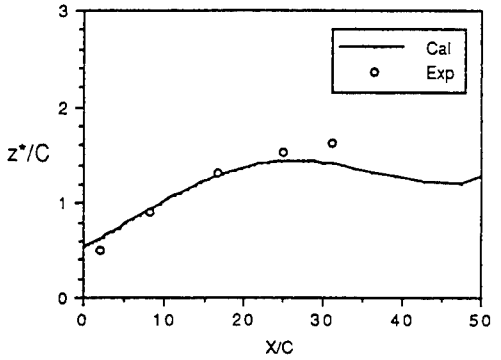

(b) Spanwise location of the primary vortex

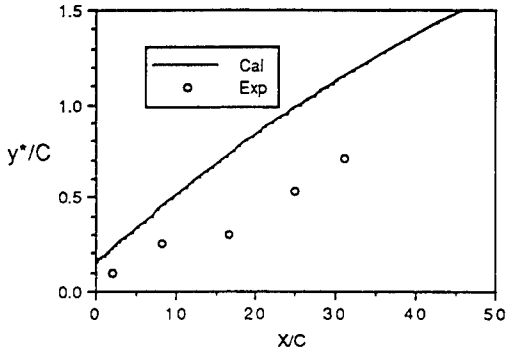

(c) Vertical location of the secondary vortex

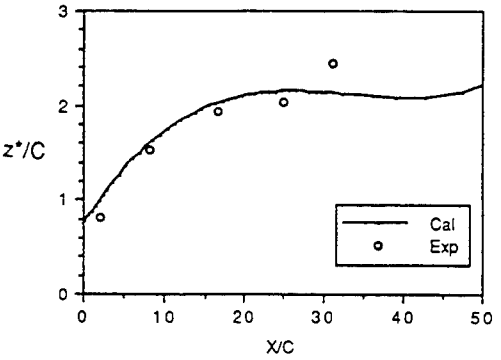

(d) Spanwise location of the secondary vortex

Figure 13 Location of the vortices on a concave wall

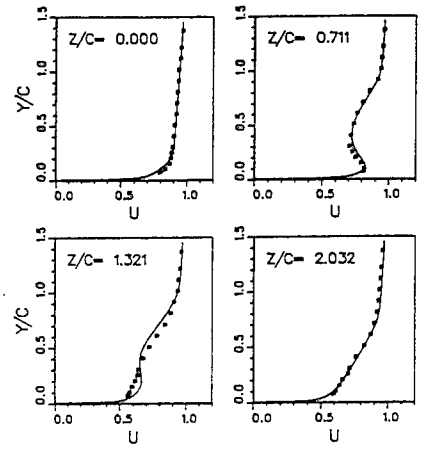

(a) Axial velocity (U)

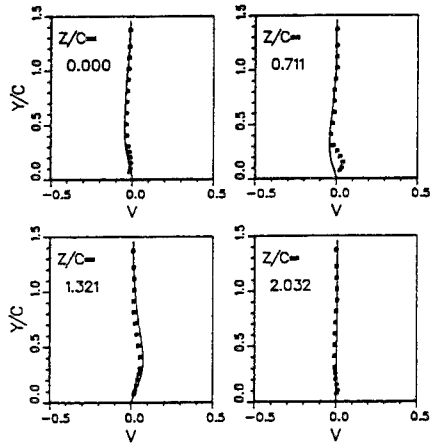

(b) Normal velocity (V)

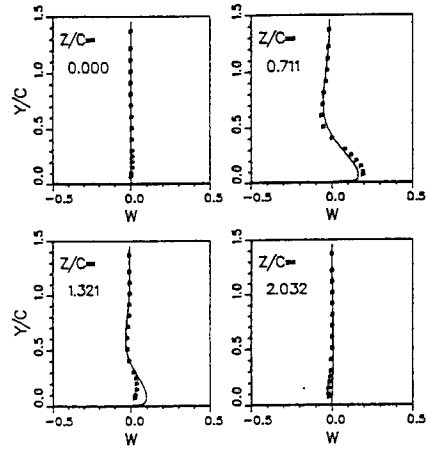

(c) Spanwise velocity (W)

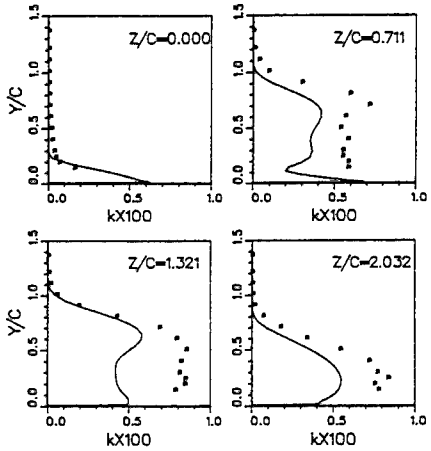

(d) Turbulent kinetic energy (k)

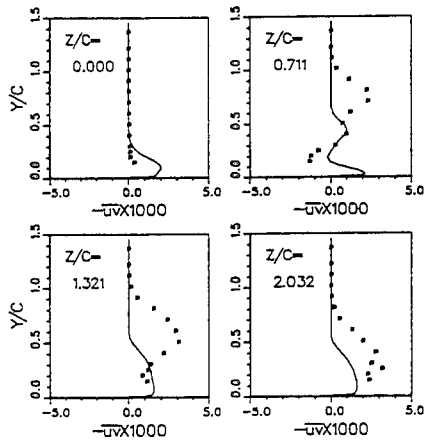

(e) Reynolds shear stress -$\overline{uv}$

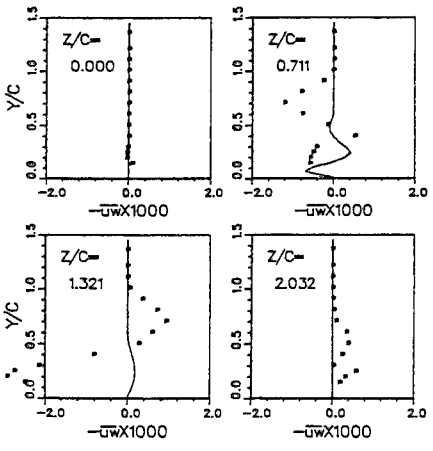

(f) Reynolds shear stress -$\overline{uw}$

Figure 14 Flow profiles in vortices on a concavewall; X/C=7.8

DISCUSSION

T. Huang
David Taylor Model Basin, USA

The agreement between the measured and predicted turbulent kinetic energy (k) and the Reynolds shear stresses ($-\overline{uv}$ and $-\overline{uw}$) shown in Figures 9 and 14 is not great. What is your measurement uncertainties of the measures quantities? Do you have enough grid resolution to capture the flow physics of viscous core? Can you assess the numerical dissipation of your computation? How to improve your computational technique to predict more accurately the flow field in the core regions of the vortices?

AUTHORS' REPLY

In the present study, two-sensor hot-wires (X-wire) were used without rotating the probe into the local mean-flow direction. The probe was aligned following the curvature of the wind tunnel. Measurement errors are expected due to the probe setting. About the grid resolution near the vortex core in the computational study, the location of vortex core is not known a priori, and therefore, it is not easy to ensure a fine grid near the vortex core. However, an attempt was made here to select a grid that would resolve the region of large velocity gradients. Probably an adaptive grid technique would help resolve the vortex core better.

DISCUSSION

Y. Himeno
University of Osaka Prefecture, Japan

Thank you for the very good experiment and computation. The measured peak vorticity value in Fig. 12(c), at x/c = 7.8, does not seem to coincide with the value in Fig. 10, x/c = 7.8. A similar inconsistency seems to appear in the peak vorticity values measured in Fig. 5 and Fig. 8(b). Would you explain the reason?

AUTHORS' REPLY

First of all, we apologize for an error since the contour level in figure 10(c) was misread. The corrected figure is shown below as figure A. The measured value of peak vorticity in figure 7(b) was given by Pauley and Eaton (1988). They calculated the vorticity using a cubic-spline interpolation, while the authors employed a quadratic interpolation. The recalculated value using quadratic interpolation is given in figure B. We thank Prof. Himeno for pointing out the error.

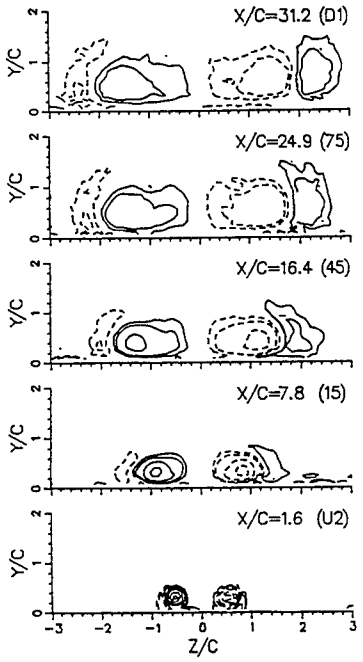

Fig A Measured axial vorticity (Ω_X) of vortices in a concave-wall boundary layer ($\frac{\Omega_X C}{U_o}$ = 0.1, 0.2, 0.5, 1.0, 2.0, 3.0, 4.0, 5.0, 6.0)

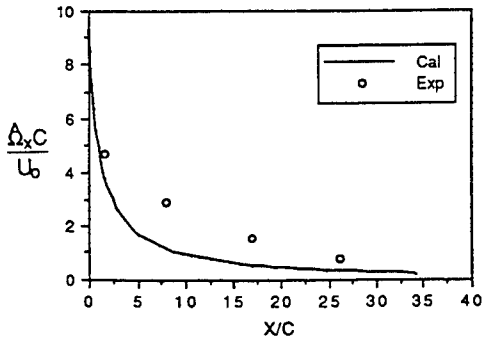

Figure B Peak vorticity of vortices in a flat-plate boundary layer

DISCUSSION

W. Devenport
Virginia Polytechnic Institute and State
University, USA

The authors have performed an impressive experimental and computational study of vortical boundary layer interaction. The results clearly show they have high quality measurements; the computational method uses a relatively robust turbulence model. In discussing their work, I would like to address some differences between computations and measurements in Figure 10 and 14, specifically, the fact that the measured contours of Figure 10 appear broader and flatter than those computed (especially at downstream locations) and turbulence levels near the vortex control in Figure 14 are significantly higher in the measurements than in the computations. Both these differences would be consistent with some side to side wandering of the experimental vortices. Could the authors comment on whether they observed any such motion?

AUTHORS' REPLY

Frankly speaking, we did not suspect any wandering of the vortices and therefore did not look for it during the measurements. However, meandering is much less likely when vortices are imbedded in a boundary layer, than when they exist in a freestream. The higher measured turbulence level in the vortex on the concave wall results not only from the vortex motion, but also from the mother boundary layer with which the vortices interact. It is well known that the k-ϵ model does not predict the increased production of turbulent kinetic energy in the boundary layer on a concave wall.

An Experimental Investigation of Interacting Wing-Tip Vortex Pairs

J. Zsoldos, W. Devenport
(Virginia Polytechnic Institute and State University, USA)

ABSTRACT

The interaction of turbulent trailing vortices shed from the tips of two rectangular wings have been studied through helium-bubble flow visualizations and extensive hot-wire velocity measurements made between 10 and 30 chordlengths downstream. The wings were placed tip to tip at equal and opposite angles of attack to generate pairs of co- and counter-rotating vortices. Meaningful hot-wire measurements could be made because the vortices were found to be insensitive to probe interference and subject only to very small wandering motions.

The co-rotating vortices were observed to roll around each other and merge. Upstream of the merger location the vortices have approximately elliptical cores. These are surrounded by the two wing wakes which join together at their ends. Flow in the vicinity of the cores appears fully developed. During the merging process the cores rotate rapidly about each other winding the wing wakes into a fine spiral structure. Merger roughly doubles the core size and appears to produced turbulence over a broad range of frequencies.

The counter-rotating vortices move sideways under their mutual induction and slightly apart, their flow structure changing little with streamwise distance. These cores remain fairly circular and do not become fully developed within the 30 chordlengths of the measurements.

INTRODUCTION

Interactions of vortices generated by lifting surfaces are commonly seen in the far wakes of marine vehicles. Understanding the turbulence structure of these flows is essential if they are to be successfully computed. Providing that understanding is the ultimate aim of the experiments described in this paper.

There have been few previous studies of the interaction of trailing vortices and none of these has addressed experimentally the turbulence structure. Donaldson and Bilanin (1975) examined various aspects of vortices produced by large scale aircraft including the roll up process and lift distributions, interaction of tip vortices with each other and with flap and tail vortices, various ways to increase vortex decay, and atmospheric effects. Most of their results presented were produced computationally with some velocity measurements from full scale aircraft. Crow (1970) developed an inviscid stability theory for counter-rotating vortices produced by large scale aircraft. He showed that for disturbances of certain wavelengths, the vortex pair would undergo a symmetric sinusoidal instability that caused the pair to join and form a train of vortex rings. Other work has concentrated on counter rotating vortices interacting with some type of wall or surface. Barker and Crow (1977) examined counter rotating vortices in a ground effect situation. Using two dimensional vortices, they compared the trajectories of the pairs against potential flow theory and to the results of full scale aircraft. Workers such as Sarpkaya et al. (1988) and Tryggvason et al. (1990) have studied qualitatively the interaction of vortex pairs and a free surface.

Because of the lack of previous work on vortex interaction we include here a brief review of relevant studies of isolated trailing vortices. Most previous workers have used one of two configurations to generate such vortices; the single wing and the split wing.

The mean velocity distributions of vortices shed from the tips of single wings have been measured by an number of workers over the last few decades (see for example Mason and Marchman (1972)). Instantaneous velocity distributions have also been examined by Corsiglia at al. (1973), using a flying hot wire, and by Green and Acosta (1991) using double-pulsed holography of small bubbles. Relatively few time averaged turbulence measurements are available, however. This is because trailing vortices generated in wind or water tunnels tend to meander (i.e. their core location is a function of time) and be sensitive to probe interference.

Meandering causes a fixed probe to greatly overestimate turbulence stresses in regions where there are significant mean velocity gradients across the vortex. In severe cases meandering also smooths mean velocity profiles significantly. Baker et al. (1974) conducted experiments on a trailing vortex generated by a rectangular wing in a water tunnel using laser Doppler velocimetry. They found that vortex meandering decreased the maximum tangential velocities by 30% and increased the measured core radius by a factor of 2.2. Baker attributed the meandering to freestream turbulence. Chigier and Corsiglia (1972) and Corsiglia et al. (1973) conducted triple hot-wire measurements on a trailing vortex in the NASA Ames 40x60 wind tunnel. They observed a spanwise meandering of about ± 2 chordlengths. As a result mean-velocity measurements made with a fixed hot-wire probe underestimated the peak tangential velocity by as much as 50%.

Probe interference problems in single-wing vortices have been reported by Orloff (1971), Gasparek (1960) and Mason and Marchman (1972). Orloff and Gasparek found that the trajectory of the vortex moved when a small diameter probe was inserted into the core. Mason and Marchman also

found that a probe changed the vortex trajectory but only if it was pitched or yawed relative to the free stream direction. Stifle and Panton (1991) examined the effects of passing a wire through the core of a single vortex produced by a delta wing. The found that disturbances introduced into the vortex core propagated both upstream and downstream with smaller disturbances produced by a slower moving wire.

Despite these problems there have been a few investigations of the turbulence structure of single-wing vortices. Singh and Uberoi (1976) measured the vortex generated by a laminar flow half wing with fixed hot-wire probes. They observed relatively high frequency unsteadiness in the core due to laminar flow instabilities but little or no low-frequency meandering. They inferred that the laminar flow instabilities had symmetric and helical modes with wavelengths of the same order as the core diameter. Helical, axisymmetric and other core instabilities in vortical flows have also observed been in flow visualizations by Sarpkaya (1992) and Maxworthy et al. (1985) and studied theoretically by a number of authors (see for example Kelvin (1880), Lundren and Ashurst (1989), Marshall (1991)). Devenport and Sharma (1991) and Devenport et al. (1992) studied the structure of a vortex generated by the roll up of a turbulent wing wake. Their vortex was shown, through visualizations, to be relatively stable (meandering less than ±0.05 chordlengths) and insensitive to probe interference. Detailed measurements, made with cross and triple hot-wire probes revealed in the mean velocity field and turbulence structure of the spiral wake surrounding the core over a range of conditions. Time average turbulence measurements made in the core were influenced by the small amount of meandering. However, spectral measurements here showed the core to be a region of very little turbulent activity at most conditions. Velocity fluctuations here appeared to be produced mostly by helical and axisymmetric waves traveling on the core.

In an attempt to generate stable single vortices, some workers have used a split wing configuration. Here the vortex is generated at the junction of two wings placed at equal and opposite angles of attack. A small nacelle is placed between the two wings and used to join the wing tips together. Although the split wing vortex is supposed to be more stable, its lacks the same initial turbulence or mean flow structure as that generated from a single wing. Hoffman and Joubert (1963) were among the first to use the split wing concept to generate a single vortex. They analyzed the circulation distribution of the vortex and found a region where the circulation is proportional to the logarithmic radius for various conditions. In addition they developed a circulation defect law in the inner region of the vortex analogous to a turbulent boundary layer. Leuchter and Solignac (1983) used a split wing to examine the effect of wind tunnel adverse pressure gradients on the decay of a vortex. Using laser doppler velocimeter, they obtained mean and turbulence quantities and found that with increased pressure gradients, vortex breakdown occurred much more rapidly. Bandyopadhyay et al.(1990) also made turbulence measurements using a split wing in various amounts of freestream turbulence. Using smoke flow visualizations and hot-wires, they observed that momentum transfer takes place between the core and outer region. They also discovered that turbulent fluid inside the core relaminarizes due to the rotational motion of the core. The most complete set of turbulence measurements for a split wing vortex to date is due to Phillips and Graham (1984). Using slant hot-wires they obtained mean velocities and Reynolds stresses for all three directions. Ways to increase the decay rate were also examined by introducing jets and wakes into the core.

In the present investigation two flows have been studied. The first involved the interaction of two trailing vortices of the same sign and strength (the co-rotating pair). The second also contained two vortices of the same strength but of opposite sign (the counter-rotating pair). Single rectangular wings were used to generate the vortices. The vortices were examined through helium bubble visualizations and detailed hot-wire measurements.

APPARATUS, INTRUMENTATION AND TECHNIQUES

Only brief descriptions are given here, for more details see Zsoldos (1992).

Wind Tunnel

Experiments were performed in the Virginia Tech Stability Wind Tunnel. It is a continuous, single return, closed-circuit subsonic wind tunnel with various interchangeable test sections. The test section used for the experiment (figure 1) is square with a cross section of 1.83m X 1.83m and a length of 7.33m. Flow in the empty test section is closely uniform with a turbulence intensity of less than .05% at 20m/s (see Choi and Simpson (1987)). One side of the test section is made of plexiglass and glass panels through which observations can be made.

Wings

Mason and Marchman's (1972) wing model was used along with an identical model produced on a numerical controlled milling machine. Each model has a rectangular planform, NACA 0012 airfoil section and a blunt wing tip. The chord and span are .203m and 1.22m respectively. Mason and Marchman's wing is made from solid brass while the other wing is made from solid aluminum. Surfaces of both wings are accurate to within ±.25mm. The wings were mounted vertically at the mid span of the test section from opposite walls perpendicular to the freestream (figure 1). The end of each wing ran through a turntable assembly mounted flush with each test section wall. The turntables allowed the wings to be rotated to any angle of attack about their quarter chord lines. The vertical location of each wing could be varied by sliding it through the turntable and clamping it to the turntable outside of the test section. The streamwise and lateral positions and the dihedral angle of the wings could also be adjusted, enabling their quarter chord lines to be made colinear.

The wings were initially placed at zero angle of attack, with an accuracy of ±0.2°, by using a removable wing tip holding 48 static pressure ports. Other angles of attack were measured relative to these locations.

To eliminate possible unsteadiness and non-uniformity that might result from natural transition, the boundary layer on the wings were tripped. Glass beads with a diameter of .5mm were glued to the wings in a random pattern in a strip extending between the 20% to 40% chord locations. Average density was 200 beads/cm^2.

Flow-visualization equipment

Flow visualizations were performed using a Sage Action Inc. Model 5 console helium bubble generator. The generator produces two separate streams of helium filled bubbles by supplying soap solution, helium and compressed air to two 'heads' (hypodermic tubes designed to form a continuous stream of bubbles). Bubbles were passed through two Sage Action vortex filters to centrifuge out heavier than air bubbles and were injected into the flow through two pieces of

4.8mm thick aluminum tubing of airfoil cross section located 1.0m upstream of the wing tips. At no time did the tubes or bubble streams appear to have any visible effects on the flow.

The bubbles were illuminated using a Varian arc lamp (Model p150S-7) supplied by Sage Action Inc. The arc lamp was mounted at the upstream end of the wind tunnel diffuser, well downstream of the test section. It was adjusted to produced a well defined narrow light beam aligned with the vortices. Photographs of the bubbles were taken using a Nikon N6006 camera with ASA 1600 color film using 2 and 8 second exposure times. Several hours of video film were also taken using a JVC camcorder.

Hot Wire Anemometry

Velocity measurements were made using single-sensor and four-sensor hot-wire probes. All sensors were operated using Dantec 56C01 and 56C17 bridge units interfaced through buck-and-gain amplifiers and an Analogic HSDAS-12 A/D converter to an IBM AT compatible computer. The HSDAS-12 can sample four hot-wire signals simultaneously at a maximum rate of 100kHz per channel. Two other channels of the A/D converter were used for digitizing the free-stream pitot static pressure and the flow temperature. Raw data was linearized and processed on line using an 18-8 Laboratories PL1250 array processor and also stored on optical disc cartridges.

A traversing gear mounted in the wind tunnel test section allowed the horizontal and vertical positions of probes to be controlled from the computer. The probe holder, a 23.6-mm diameter aluminum rod aligned with the free-stream, positioned the tip of the probe approximately 0.7m upstream of the traverse gear. Two 6.2-mm diameter rods were used to offset the axis of the probes from that of the holder by 114mm (see figure 2). Thus the probe holder did not have to be placed in or near the vortex core for the probes to be positioned there.

The single hot-wire probe (TSI type 1210T1.5) was used to measure profiles of mean velocity and turbulence intensity and spectra in the wing boundary layer as it left the trailing edge. A miniature quad hot-wire probe produced by Auspex Corporation (model AVOP-4-100) was used to measure mean velocities and Reynolds stresses at various planes downstream of the wings. A dummy probe, whose dimensions approximately matched those of the quad hot-wire probe was used to simulate the effects of a probe on the vortex during flow visualizations.

Three requirements led to the use of the quad-wire probe;

(i) The need to have simultaneous measurements of all three velocity components.

(ii) The need for a compact probe, to minimize probe interference and the size of the measurement volume.

(iii) The need to make measurements at large flow angles (such as at the edge of the core) without yawing or pitching the probe.

The probe (figure 2) consists of four wires arranged to form two orthogonal X-wire arrays, each sensor being inclined at a nominal angle of 45 degrees to the probe axis. Eight prongs position the wires some 70mm upstream of the main part of the probe within a measurement volume less than 1mm in diameter. Each wire is made of tungsten and is 0.8mm in length and 5μm in diameter.

The four simultaneous effective velocities output by the quad hot-wire probe were used to determine the 3 velocity components in a two stage process. First, initial estimates of the components were obtained using standard X-array hot-wire analysis, taking into account measured wire angles and pitch and yaw sensitivities. Second, corrections to these estimates, determined through direct calibration, were applied. This yielded instantaneous records of U, V, and W accurate to much larger values of instantaneous flow angles than the initial estimates.

The calibration involved pitching and yawing the quad wire probe through a total of 361 angle combinations in a uniform flow of 20m/s (the free stream velocity at which all measurements were made). Corrections were obtained by comparing the actual velocity components experienced by the probe, calculated from the flow velocity and pitch and yaw angles, with the initial estimates from the standard analysis. They were initially determined as functions of the actual components i.e.

$$\begin{aligned} \frac{V-V_e}{Q} &= f_1\left(\frac{V}{Q},\frac{W}{Q}\right) \\ \frac{W-W_e}{W} &= f_2\left(\frac{V}{Q},\frac{W}{Q}\right) \\ \frac{Q-Q_e}{Q} &= f_3\left(\frac{V}{Q},\frac{W}{Q}\right) \end{aligned} \qquad (1)$$

where $Q=\sqrt{U^2+V^2+W^2}$ and U, V and W refer to the velocity components, U being aligned with the probe axis. No subscript implies an actual value, subscript (e) identifies initial estimates obtained from the standard analysis. As an example, figure 3(a) shows contours of f_3. Note that even at moderate angles (e.g. 15°, W/Q = 0.27) the standard analysis requires significant if not substantial correction. To make use of these corrections it is necessary to express them as functions of the estimated rather than the actual components i.e.

$$\begin{aligned} \frac{V-V_e}{Q_e} &= g_1\left(\frac{V_e}{Q_e},\frac{W_e}{Q_e}\right) \\ \frac{W-W_e}{W_e} &= g_2\left(\frac{V_e}{Q_e},\frac{W_e}{Q_e}\right) \\ \frac{Q-Q_e}{Q_e} &= g_3\left(\frac{V_e}{Q_e},\frac{W_e}{Q_e}\right) \end{aligned} \qquad (2)$$

This was done by interpolating the corrections onto a square grid. Note that corrections for flow angles outside the acceptance cone of the quad wire were ignored in this interpolation. The acceptance cone and the function g_3 is illustrated in figure 3(b).

RESULTS AND DISCUSSION

The cartesian coordinate system (x,y,z) shown in figure 1 will be used in presenting results. The origin of this system is located midway between the wing tips on a line joining the wing leading edges at zero angle of attack. 'x' is measured in the downstream direction and 'y' and 'z' parallel and normal to the wing spans respectively. Most distances and velocities have been normalized on the wing chord 'c' of 0.203m and the free stream speed U_{ref} measured using a pitot-static probe located in the forward part of the test section.

Flow visualizations

The visualizations were performed to examine the interaction of the vortices, their wandering and sensitivity to probe interference over a broad range of conditions. The aim here was to select two cases, one with a co-rotating vortex pair and one with a counter-rotating vortex pair, for detailed velocity measurements. A full list of conditions is given in table 1 in

terms of the angles of attack of the wings α_1 and α_2 (measured according to the right-hand rule for the negative y axis, α_1 referring to the upper wing), wing-tip separation $\Delta y/c$ and chord Reynolds number $Re_c = U_{ref}c/\nu$. Counter- and co-rotating vortex pairs were generated by placing the wings at equal and opposite angles of attack respectively. Because of the volume of results only a representative sample will be presented here. For a full discussion see Zsoldos and Devenport (1991).

Figures 4(a) and (b) show visualizations of the co-and counter-rotating vortex pairs generated at $\Delta y/c$=0.25, Re_c = 130000 (U_{ref} = 10m/s) with the wings at 5° angle of attack. (Except for Reynolds number these were the cases selected for hot-wire measurements). These photo-mosaics were constructed from pictures taken over the course of several minutes, each component picture having an exposure time of 8 seconds. They are thus time averaged views of the vortex-core trajectories revealed by the lighter than air bubbles passing along them. Note that the flow is from right to left.

In the co-rotating case (figure 4(a)) the vortex cores, generated at the wing tips, rotate about each other as they move downstream. This is a consequence of the equal but opposite velocities they induce upon each other. Over their first few chord lengths the vortex cores move slightly apart, presumably as a result of the same conservation theorems (due to Betz (1933)) that cause an isolated wing tip vortex to initially move inboard. After reaching a maximum separation the cores begin moving towards each other, their rotation rate about each other increasing as they do. Ultimately, at about 20 chord lengths downstream of the wings, they merge and form a single vortex with a larger core. This merging process occurs over a distance of approximately 1.5 chord lengths and appeared to be associated with it a significant amount of high frequency, small scale turbulent motion. Merger occurs because the cores and wing wakes surrounding them are regions of distributed vorticity, not single point vortices. As a result the cores experience induced velocities that have a component that draws them together. Computational studies of inviscid vortices merging in this way have been performed by Rossow (1977) and Melander et al.(1988).

In the counter-rotating case (figure 4(b)) the interaction between the vortices is less dramatic. The vortex cores drift in the negative z direction (towards the camera) with distance downstream as a consequence of the equal velocities they induce upon each other in this direction. (Note that near x/c=20 the cores drift out of the illuminating light beam). The cores also move slowly apart as a consequence of Betz's (1933) conservation laws.

Figures 4(a) and (b) are qualitatively representative of the flow patterns seen at other conditions. Quantitatively, the interaction between the vortices, especially in the co-rotating case, decreased rapidly with increase in wing separation or decrease in angle of attack. We were surprised at just how close the wing tips had to be placed (<=0.375c at any angle of attack) for the co-rotating vortices to merge within the 30 chordlengths of the test section. This raises the question of whether some split-wing configurations with tip separations comparable to those of the present wings really produce a single vortex, as they are assumed to.

At none of the conditions was vortex wandering clearly visible by eye or in the photographs. Close examination of the video tapes, however, suggested that some small low frequency motions might be present. In the cases represented in figures 4(a) and (b) these motions were estimated to have an amplitudes of at most .05c and .09c respectively and typical frequencies of about fc/U_{ref}=0.004.

Probe interference was simulated at several sets of conditions by traversing the dummy probe through the vortex cores. Figures 5(a) and (b) are particularly clear visualizations performed with the dummy probe at $\alpha_1=\alpha_2=7.5°$ and Re_c=130000. In figure 5(a) the dummy probe is stationary at the center of the upper vortex core. Figure 5(b) is a long time exposure taken while the probe was traversed through this core (the location of the probe tip in this figure may be judged by comparison with figure 5(a)). In these pictures, and at all other conditions examined, the dummy probe had no visible effects on the vortex core at the measurement point. Effects were visible downstream of the measurement point but we saw no evidence of these disturbances propagating upstream.

Change in chord Reynolds number from 130000 to 400000 appeared to have no significant influence on the flow structure in any of the cases. One possible exception may be the amplitude of the vortex wandering which appeared even smaller at the higher Reynolds number.

Velocity measurements

The following flows were selected for detailed velocity measurements based on the flow visualization results.

Co-rotating vortices;

$\alpha_1 = -\alpha_2 = 5°$, Re_c = 260000

Counter-rotating vortices;

$\alpha_1 = \alpha_2 = 5°$, Re_c = 260000

Table 2 summarizes measurements made for these conditions at the wing trailing edges with the single hot-wire probe. Mean velocity and turbulence intensity profiles showed the boundary layers here to be fully turbulent. Spectra showed no peaks or other features that would suggest the presence of vortex-shedding or any other undesirable phenomena. In both cases the boundary layers on the two wings appeared similar with thicknesses between 0.038c and 0.063c.

Quad hot-wire measurements were made in four cross-sectional planes through the co-rotating vortex pair at x/c = 10, 15, 22 and 30 and in two planes through the counter-rotating pair at x/c = 10 and 30. (See figures 4(a) and (b) to visualize these positions). In each plane measurements were made at 600 to 900 points in nominally polar grids centered on the cores. At each point 614400 simultaneous samples of the three velocity components were taken at a rate of 30 kHz (sufficient to calculate a detailed low-uncertainty spectrum) over a total sampling time of about 2 minutes - about 33 gigabytes of raw data in total. Such a large quantity of data was needed to make possible the future removal of any small amplitude vortex wandering from the velocity measurements.

<u>The co-rotating vortex pair</u>

Figure 6 shows the overall mean flow and turbulence structure associated with the interaction and merger of the co-rotating vortex pair in terms of mean cross-flow velocity vectors and contours of turbulence kinetic energy k/U_{ref}^2. Figure 7 shows details of the flow in the core regions and includes, in addition, contours of mean streamwise vorticity $\omega_x c/U_{ref}$ and of the primary turbulent shear stress $\overline{v_r v_\theta}/U_{ref}^2$. V_r and V_θ are defined by the cylindrical coordinate system (r, θ, x) centered at the middle of the vortex cores and with the x direction aligned with the free stream.

By x/c=10 the co-rotating vortices have turned about their common center through an angle of about 135° (figures 6(a and b)). They

are separated by a distance almost equal to the wing-tip separation, 0.25c, having moved apart a short distance and then back towards each other by this stage (figure 4(a)). The mean velocity vectors of figure 6(a) show the strong rotational flows generated by the vortices and their mean interaction, which produces a crossflow stagnation point midway between the vortex centers. The contours of k/U_{ref}^2 (figure 6(b)) clearly show the wing wakes that surround the vortex cores. Even at this early stage the wakes have merged along a line midway between the cores. The wakes are rolled into brief spirals both by the rotational velocity fields of the individual vortices and by the turning of the vortices about one another. The resulting shear and distortion that the wakes experience is presumably responsible for the gradual reduction in peak turbulence levels along the wakes as the cores are approached.

Figures 7(a to d) show in detail the core region of one of the vortices, the flow being anti symmetric. (Note that the vectors of figure 7(a) do not appear on a perfectly polar grid due to corrections for absolute traverse-gear location applied after the experiments.) The core itself, marked by the solid line in figure 7(a) and defined as the locus of peak V_θ, is very slightly elliptical with its major axis aligned approximately normal to the line joining the two cores. The diameters are 0.080c and 0.075c measured along the major and minor axes respectively. Similarly distorted cores have been observed by Rossow (1977) in discrete vortex simulations of counter-rotating vortex pairs. The tangential velocities at the core edge vary substantially with circumferential location from 10.3% U_{ref} on the side closest to the plane of anti-symmetry to 20.4% U_{ref} on the opposite edge. This variation partly a consequence of the fact that the core axis lies at an angle to the freestream direction and thus the coordinate system in which these vectors have been resolved. (This is also why the point of zero cross flow velocity does not appear at the core center.) The contours of $\omega_x c/U_{ref}$ (figure 7(b)), being less affected by this skewing, are approximately elliptical in the core region and concentric with the core edge. They indicate a maximum normalized vorticity of 18.0 at the vortex center. These contours also show some positive vorticity in the wing wake curled around the core and a region of negative vorticity between the cores. Some details of the wake structure in the vicinity of the core are also visible in the turbulence kinetic energy and Reynolds shear stress contours (figures 7(c and d)). Within the core these contours show velocity fluctuations rising to a maximum. Those of t.k.e. are approximately concentric with the core and indicate a maximum of k/U_{ref}^2=0.0090. Those of shear stress are arranged in two lobes. The large fluctuation levels at the core center are mostly a consequence of the small amplitude wandering observed in the flow visualizations. If we assume that velocity fluctuations at the core center are entirely due to wandering we can estimate, using the measured mean velocity gradient, an upper bound for the amplitude of the core motions. This turns out to be 0.016c r.m.s. This length is marked on figure 7(a) to give a qualitative idea of the degree to which wandering may have smooothed the measured mean velocity field.

An alternative view of the turbulence structure in and around the core may be gained from velocity spectra. Figure 8(a) shows autospectra of V_r plotted as $G_{v_r v_r}/U_{ref}c$ *vs.* fc/U_{ref}, where f is frequency in Hertz, for various locations along the upper half of the radial profile labelled AA in figure 7(a). The spectrum at r/c = 0.52 shows velocity fluctuations (and some electrical noise) outside the turbulent region. Those at 0.24 and 0.16 show fluctuations in the region adjacent to the core occupied by the curled up wake of the lower wing. These, like others measured in the wake regions at x/c=10 show a peak in the vicinity of fc/U_{ref} = 4 and an inertial subrange at higher frequencies. The frequency fc/U_{ref}=4 implies a length scale (assuming Taylor's hypothesis) of 0.25 chordlengths - a probable size of large structures in a wake that, away from the vortex cores, is about 0.5 chordlengths in width (figure 6(b)). Devenport and Sharma (1992) have shown that in the wake region of an isolated vortex, autospectra of a given velocity component have identical shapes, regardless of where they are measured. The similarity in the shapes of the spectra at r/c=0.24 and 0.16 suggests that this may also be true in the present flow. Moving into the core the spectral peak at fc/U_{ref}=4 first becomes more pronounced (at r/c=0.09) and then disappears (r/c=0.04 and 0) as low-frequency energy levels rise. This rise is presumably a partial consequence of velocity fluctuations produced by vortex wandering. At higher frequencies (say fc/U_{ref}>20) spectral levels change little between r/c=0.09 and 0.04 and then fall slightly between r/c=0.04 and 0. This latter result, which implies that velocity fluctuations associated with small scale turbulence are only slightly weaker at the core center than elsewhere, is a surprising one bearing in mind the strong stabilizing effects of the core rotation. In isolated vortices it is an indication of a fully developed core region (Devenport and Sharma (1992)), i.e. one in which the flow is essentially independent of viscosity. This indication appears confirmed by the circulation profiles shown in figure 9. Circulation K was estimated from tangential velocities in those profiles measured normal to the line joining the two vortex cores. (At the time of going to press true integral calculations of circulation had not been performed.) The profiles are normalized on core circulation K_1 and radius r_1 and plotted in the manner of Hoffman and Joubert (1963). In this form the profiles clearly show Hoffman and Joubert's fully developed semi-logarithmic region.

That the flow in the co-rotating cores should be fully developed is surprising. Isolated split-wing vortices do not reach a fully developed state until the parameter $U_{ref}x/\Gamma_o$, where Γ_o is the total circulation, rises above a value of about 150 (Hoffman and Joubert). Isolated single-wing vortices must age by at least this amount (Devenport and Sharma (1992)). At x/c=10 $U_{ref}x/\Gamma_o$ is only 54 if Γ_o is taken as the root circulation about one of the wings. We are not sure at this stage why interaction between the co-rotating vortices should cause them to become fully developed so early.

By x/c=15 the co-rotating vortices have turned about their common center by a further 116° and moved significantly closer, being separated by only 0.17c here (figures 6(c and d)). The contours of turbulence kinetic energy in figure 6(d) show the distortion of the wing wakes brought on by the further turning of the vortices. Detailed views of one of the vortex cores (again that originating from the lower wing) show an even less axisymmetric flow than at x/c=10 (figures 7(e to h)). In both mean velocity vectors and vorticity contours the core appears more strongly elliptical. The diameters along its major and minor axes are 0.115c and 0.080c respectively, implying a core area about 50% greater than at x/c=10. Peak tangential velocities vary from 6.7%U_{ref} on the edge of the core facing the other vortex to 16.1%U_{ref} on the opposite side. The contours of vorticity, which

again are approximately concentric with the core indicate a maximum normalized vorticity of 15.7, 13% less than at x/c=10, and show a negative region between the cores. The turbulence kinetic energy contours and those of shear stress (figures 7(g and h)) show variations consistent with the convoluted wakes at this location, the small amplitude vortex wandering and the skewing of the vortex core with respect to the free stream direction. Velocity fluctuation levels at the core center (k/U_{ref}^2=0.0093) imply wandering motions with an r.m.s. amplitude less than 0.025c. This scale is shown alongside the mean velocity field in figure 7(e). Spectra measured in and around the cores at x/c=15 show a structure qualitatively identical to that at x/c=10 suggesting, as do the circulation profiles of figure 9, that the cores remain in a fully developed state. This is despite the fact that $U_{ref}x/\Gamma_o$ is only 81 here.

By x/c=22 the vortex cores appear to have merged, the mean-velocity vectors (figure 6(e)) showing the flow rotating about a single center. The core of this combined flow, illustrated in figure 7(i), is not circular but has an outline like that of two overlapping ellipses. It has diameters of 0.21c and 0.17c in the y and z directions respectively - about twice the linear dimensions of each of the unmerged cores. The tangential velocity at the core edge is also not axisymmetric, varying by about $\pm 1.3\%U_{ref}$ around the core edge around an average value of $12.6\%U_{ref}$. The contours of turbulence kinetic energy (figures 6(f) and 7(k)) show the wing wakes well wrapped up around the center of rotation forming a large turbulent region 1.25c in diameter at minimum. These contours do not do justice to the fine structure of this turbulent region which is more clearly seen in the profile of turbulence shear stress $-\overline{v_x v_r}/U_{ref}^2$ measured along the line BB and plotted in figure 10(a). The meaning of the complex variations in this profile become clear when one recognizes that a single passage through the wing wake produces an anti-symmetric $-\overline{v_x v_r}$ distribution consisting of one positive and one negative region. The profile therefore appears to pass at least 3 times through separate turns of the wing wake on both sides of the vortex center. This fine structure is probably a consequence of the rapid rotation of the vortex cores about each other as they merge. We would expect this rotation to wind up the wing wakes into a long double spiral which would then slowly merge into a single axisymmetric structure. Figure 10 suggests that this merger has barely begun at x/c=22.

The contours of mean vorticity and Reynolds shear stress (figures 7(j and l)) show some of the spiral structure extending well within the core edge. This non-axisymmetry implies that even in the core the merging process is not complete. Those of turbulence kinetic energy (figure 7(k)) show k/U_{ref}^2 reaching a maximum of .0019 at the core center. This is more than 4 times smaller than the peak values recorded in the unmerged cores and we are unconvinced that any of it is a consequence of lateral vortex wandering. If, however, it were it would imply motions with an r.m.s. amplitude of about 0.016c.

The spectral structure of the flow at this station is illustrated in figure 8(b) which shows V_r autospectra measured along the line CC through the center of the vortex. As in the unmerged cases the spectra measured in the wing wake outside the core (r/c=0.55 and 0.37) show broad peaks at frequencies likely to be associated with the passage of large wake structures. By x/c=22 this frequency has fallen to about fc/U_{ref} = 2. Moving into to the core, spectral levels at all frequencies rise. At lower frequencies, however, the rise is less dramatic than in the unmerged cores (figure 8(a)) and at higher frequencies it continues all the way to the vortex center. The implication of this is that the merging process generates turbulence in the core region over a broad range of scales. The circulation profile at x/c=22 (figure 9) has a surprisingly well developed form considering how incomplete the merging process appears and how small $U_{ref}x/\Gamma_o$ is. With the root circulations from the two wings now combined $U_{ref}x/\Gamma_o$ is only 59. Close examination of the circulation profile does show small variations from the semi-logarithmic region associated with the fine spiral structure of the wing wakes observed in the $-\overline{v_x v_r}$ profile.

At x/c=30, the most downstream station measured, the turbulence and mean flow measurements (figures 6(g and h)) show an overall structure much like that at x/c=22. Detailed views of the core region (figure 7(m to p)), however, show some relaxation and further development of the flow. The core here (figure 7m) is fairly circular with a diameter of 0.2c. The tangential velocities at its edge are fairly constant at $12.9\%U_{ref}$, varying by no more than ±0.38% - a range probably smaller than the uncertainty in this measurement. The large turbulent region surrounding the core (figure 6(h)) has grown and has a minimum diameter of about 1.5c. A profile of $-\overline{v_x v_r}$ through the vortex center (along line DD in figure 7(m)) still shows many of the positive and negative regions seen at x/c=22 but these are smaller in magnitude and less distinct (figure 10(b)). This merging of the wake spiral is also evident in the circulation profile at this station (figure 9) which, in addition to being fully developed, is much smoother than at x/c=22. The contours of mean vorticity are closely circular in the core region (figure 7(n)), the peak normalized vorticity at the vortex center being 5.6. Those of turbulence kinetic energy (figure 7(o)) are still slightly out of round and indicate a value of k/U_{ref}^2 of 0.0016 at the center. As at x/c=22 were are unconvinced that these fluctuations are even partly a consequence of meandering. The peak turbulence level in the core, if it were a consequence of meandering, would imply an r.m.s. amplitude of less than 0.017c. The spectral structure of the flow at x/c=30 is fairly similar to that at x/c=22 except that, as in the unmerged cores, high-frequency spectral levels at the core center are lower than in the immediately surrounding area. The implication here is that the rotation of the core ultimately stabilizes some of the turbulence generated in the merging process.

The counter-rotating vortex pair

Figures 11 through 13 show the flow structure produced by the counter-rotating vortex pair. In contrast to the co-rotating case this structure does not change dramatically with streamwise distance. The vectors shown in figures 11(a and c), like the visualization (figure 4(b)), show the cores moving slowly apart with distance downstream and across the test section in the negative z direction under their mutual induction. At x/c=10 the cores are separated by 0.45c (compared to a wing-tip separation of 0.25c) and are centered at z = -0.7c (the quarter chord location defining z/c=0). At x/c=30 these numbers are 0.52c and -1.7c respectively. This z-wise movement stretches the wing wakes (visible in the turbulence kinetic energy contours of figures 11(b) and (d)) which are forced into contact between the vortices. As in the co-rotating case this distortion produces a reduction in peak turbulence levels along the wing wakes as the

cores are approached.

The detailed views of the upper vortex core shown in figure 12, show it to be fairly circular with a diameter of about 0.088c at x/c=10 and 0.0108 at x/c=30. Peak tangential velocities at the core edge vary from 48%U_{ref} to 34%U_{ref} at x/c=10, the highest velocities being reached at closest to the plane of symmetry. These numbers are 36%U_{ref} and 25%U_{ref} at x/c=30. That these velocities are on the whole much larger than those produced by the unmerged co-rotating vortices is only partly a consequence of the difference in the velocity fields the vortices impose upon each other. It is also due to the fact that the root circulation associated with each of the counter rotating vortices is about 40% greater than that for the co-rotating vortices because of the mutual interference of the wings.

The vorticity contours (figures 12(b and f)) show the vortex cores to be embedded in an approximately oval region of vorticity that extends out towards the plane of symmetry. Within the core these contours are concentric and closely circular and indicate peak normalized vorticities of 35.1 and 33.1 at x/c=10 and 30 respectively, considerably higher than at any location in the co-rotating case. The contours of turbulence kinetic energy are also fairly circular in the core indicating large fluctuation levels at the core center, k/U_{ref}^2 = .0098 and .0285 at x/c=10 and 30. These are mostly due to vortex wandering, the implied r.m.s. amplitudes being .012c and .041c respectively. The relatively large amplitude at x/c=30 may have smoothed some parts of the measured mean velocity field here (figure 12(e)).

The spectral structure of the flow at these two locations is qualitatively identical. Figure 13 shows sample V_r autospectra measured along the profile EE indicated in figure 12(a). The biggest difference with similar spectra measured in the co-rotating case (figure 8(a)) is in the high frequency spectral levels at the core center (r/c=0.01). These are more than an order of magnitude smaller than spectral levels at the core edge (r/c=0.04) and in the surrounding region (r/c=0.09), suggesting very little small scale turbulent motion at the core center. In isolated trailing vortices this type of spectrum is associated with under-developed (i.e. viscosity-dependent) flow in the core region (see Devenport and Sharma (1992)). Circulation profiles for these vortex cores (figure 9) indeed show no fully-developed semi-logarithmic region outside the core. $U_{ref}x/\Gamma_o$ has values of 37.5 and 113 at x/c=10 and 30.

CONCLUSIONS, FUTURE WORK

The flow structure produced by pairs of co- and counter-rotating turbulent trailing vortices have been studied through helium-bubble visualizations and detailed three-component hot-wire velocity measurements. The vortices were generated by two rectangular wings placed tip to tip at equal or opposite angles of attack.

The flow visualizations were performed for a range of tip separations, angles of attack and Reynolds number. The helium bubbles clearly marked the cores of the interacting vortices. The co-rotating pair were seen to roll about each other and, if the wing separation was sufficiently small (<=0.375c) and the angle of attack sufficiently large, to merge within the 30 chordlengths of the wind tunnel test section. The counter-rotating pair moved slightly apart and across the test section under their mutual induction. These flows showed no significant effects of a 3:1 change in Reynolds number. At all conditions the vortices appeared completely insensitive to probe interference and subject only to very small amplitude wandering. Meaningful hot-wire velocity measurements could therefore be made.

The velocity measurements were made at a chord Reynolds number of 260000 with a wing tip separation of 0.25c. The wings were placed at equal angles of attack of 5°, producing a counter-rotating vortex pair, and at opposite angles of attack of 5°, producing a co-rotating pair. A 4-sensor miniature hot wire probe, calibrated directly for flow angle, was used to make detailed measurements at x/c = 10, 15, 22 and 30 in the co-rotating case and at x/c = 10 and 30 in the counter-rotating case.

Upstream of the merger location the co-rotating vortices have approximately elliptical cores. These cores are surrounded by the two wing wakes which join together at their ends and become wrapped up into spirals as the cores rotate about each other. The accompanying distortion appears to locally suppress turbulent motions in the wakes. The cores are, naturally, regions of high positive vorticity, but their interaction results in the formation of a region of negative vorticity between them. Autospectra of velocity fluctuations and circulation profiles suggest that flow in the vicinity of the cores is fully developed (i.e. viscosity independent). This is surprising since the vortex ages, measured as $U_{ref}x/\Gamma_o$, are only a third to a half of that required for fully developed flow in isolated vortices. During the merging process the vortex cores roll around one another rapidly winding up the wing wakes into a fine spiral structure that remains discernable for some distance downstream. Merger roughly doubles the core size and appears to produce turbulence over a broad range of frequencies. The merged core region recovers surprisingly rapidly to a fully developed state, especially considering its small age.

In contrast, the flow structure produced by the counter-rotating vortex pair does not change drastically with distance downstream. Their parallel movement across the test section stretches the wing wakes which are forced into contact between the cores. This distortion again appears to locally suppress turbulent motions in the wakes. Despite the strong velocity fields they impose upon each other the cores of these vortices remain closely circular and the vorticity and turbulence kinetic energy distributions within them are fairly axisymmetric. Autospectra and circulation profiles suggest that these vortices do not become fully developed within the 30 chordlengths of the measurements.

In this paper we have presented only a small sample of the measurements taken and the analyses that are possible on this large data set. For example, we are currently reprocessing the data to examine separately the turbulence structure in several different frequency ranges. One aim here is to remove as far as possible the effects of vortex wandering from those measurements made in the cores. Another aim is to reveal whether or not the cores are subject to the axisymmetric, helical and other instabilities seen in isolated vortices and, if they are, in what way those instabilities are affected by the presence of another vortex. These and other topics will be the subject of future papers.

ACKNOWLEDGEMENTS

The authors would like to thank Gautam Sharma, Mike Rife, Fabienne Glikson and Bill Hartwell for their assistance in taking many of the above measurements. The support of DARPA through ONR contracts N00014-90-J-1909 and N00014-91-J-1773 is also gratefully acknowledged.

REFERENCES

Baker G R, Barker S J, Bofah K K and Saffman P G, 1974, "Laser anemometer measurements of trailing vortices in water", Journal of Fluid Mechanics, vol 65, p 325-336.

Bandyopadhyay P, Stead D and Ash R, 1991, "Organized nature of a turbulent trailing vortex", AIAA Journal, vol. 29, no. 10, pp. 1627-1633.

Barker S J and Crow S C, 1977, "The motions of two-dimensional vortex pairs in a ground effect", Journal of Fluids Mechanics, vol 82, p659-671.

Betz D, 1933, "Behavior of vortex systems", NACA TM 713.

Chigier N A and Corsiglia V R, 1972, "Wind tunnel studies of wing wake turbulence", Journal of Aircraft, vol 9, p820-825.

Choi K and Simpson R L, 1987, "Some mean-velocity, turbulence, and unsteadiness characteristics of the VPI&SU Stability Wind Tunnel", Report VPI-AOE-161, VPI&SU, Blacksburg, VA.

Corsiglia V R, Schwind R G, and Chigier N A, 1973, "Rapid scanning, three-dimensional hot-wire anemometer surveys of wing-tip vortices", Journal of Aircraft, vol 10, p752.-757

Crow S C 1970, "Stability theory for a pair of trailing vortices", AIAA Journal, vol 8, p 2172-2179.

Devenport W J and Sharma G, 1991, "Far-field turbulence structure of the tip vortex shed by a single rectangular wing", Eighth Symposium on Turbulent Shear Flows.

Devenport W J, Glegg S A L and Sharma G, 1992, "Measurements in trailing vortices for BWI noise prediction. Part 1. Measurements", AOE Dept., VPI&SU, June 1991.

Donaldson C duP and Bilanin A J, 1975, "Vortex wakes of conventional aircraft", AGARD AG-204.

Gasparek E, 1960, "Viscous decay of a vortex", Masters thesis, Syracuse University, NY.

Green S I and Acosta A J, 1991, "Unsteady flow in trailing vortices", Journal of Fluid Mechanics, vol 227, pp 107-134.

Hoffman E R and Joubert P N, 1963, "Turbulent line vortices", Journal of Fluid Mechanics, vol 16, pp 395.

Lord Kelvin, 1880, "Vibrations of a columnar vortex", Mathematical and Physical Papers, vol. 4, Cambridge University Press.

Lamb H, 1932, "Hydrodynamics", 6th edition, Dover, p223.

Lundren T S and Ashurst W T, 1989, "Area-varying waves on curved vortex tubes with application to vortex breakdown", Journal of Fluid Mechanics, vol. 200, pp 283-307.

Leuchter O and Solignac J L, 1983, "Experimental investigation of the turbulence structure of vortex wakes", Proceedings of the 5th Symposium on Turbulent Shear Flows, Ithaca, NY, pp. 5.31-5.36.

Marshall J S, 1991, "A general theory of curved vortices with circular cross section and variable core area", Journal of Fluid Mechanics, vol. 229, pp 311.

Mason W H and Marchman J F, 1972, "Far-field structure of an aircraft trailing vortex, including effects of mass injection", NASA CR 62078.

Maxworthy T, Hopfinger E J and Redekopp L G, 1985, "Wave motions on vortex cores", Journal of Fluid Mechanics, vol. 151, pp 141-165.

Melander M V, Zabusky M J and McWilliams J C, 1988, "Symmetric vortex merger in two dimensions; causes and conditions", Journal of Fluid Mechanics, vol 195, p 303-340.

Orloff K L, 1971, "Experimental investigation of upstream influence in a rotating flowfield", PhD thesis, University of California, Santa Barbara.

Phillips W R C and Graham J A H, 1984, "Reynolds stress measurements in a turbulent trailing vortex", Journal of Fluid Mechanics, vol 147, pp 353-371.

Rossow V J, 1977, "Convective merging of vortex cores in lift generated wakes", Journal of Aircraft, vol 14, no 3, pp 283-290.

Sarpkaya T, Elnitsky J, and Leeker R E, 1988, "Wake of a vortex pair on the free surface", Proceedings of the 17th Symposium on Naval Hydrodynamics, National Academy Press, Washington D.C., pp. 47-54.

Sarpkaya T, 1992, "Three dimensional interactions of vortices with a free surface", AIAA 30th Aerospace Sciences Meeting, Jan 6-9, Reno, NV. Paper AIAA-92-0059.

Singh P I and Uberoi M S, 1976, "Experiments on vortex stability", Physics of Fluids, vol 19, p 1858-1863.

Stifle K E and Panton R L, "Experiments concerning the theories of vortex breakdown", AIAA 29th Aerospace Sciences Meeting, Reno, NV, Jan 6-9. Paper AIAA-91-0736.

Tryggvason G, Abdollahi-Alibeik J, Willmarth W and Hirsa A, 1990, "Collision of a vortex pair with a contaminated free surface", Report 90-1, University of Michigan.

Zsoldos J S, 1992, "The turbulence structure of trailing vortex pairs", MS thesis, VPI&SU.

Zsoldos J S and Devenport W J, 1991, "Flow visualization of interacting wing-tip vortex pairs", Report VPI-AOE-177, AOE Dept., VPI&SU, Blacksburg, VA.

Table 1. Flow conditions for visualizations.

Wing separation $\Delta y/c$	Angle of attack α_1, α_2	Reynolds number Re_c	Dummy probe
1.0	$\pm$2.5°	130,000	
1.0	$\pm$5.0°	130,000	
1.0	$\pm$7.5°	130,000	
1.0	$\pm$10.0°	130,000	
0.5	$\pm$2.5°	130,000	
0.5	$\pm$5.0°	130,000	
0.5	$\pm$7.5°	130,000	
0.5	$\pm$10.0°	130,000	
0.375	$\pm$2.5°	130,000	
0.375	$\pm$5.0°	130,000	yes
0.375	$\pm$7.5°	130,000	yes
0.375	$\pm$10.0°	130,000	yes
0.25	$\pm$2.5°	130,000	
0.25	$\pm$5.0°	130,000	yes
0.25	$\pm$7.5°	130,000	
0.25	$\pm$10.0°	130,000	
0.375	$\pm$5.0°	400,000	yes
0.375	$\pm$7.5°	400,000	yes
0.375	$\pm$10.0°	400,000	yes
0.25	$\pm$5.0°	400,000	yes

Table 2. Wing trailing edge characteristics.

	δ/c	δ^*/c	θ/c	Re_θ
Co-rotating y/c=1.2 pressure side	.04028	.00958	.00533	1289.1
Co-rotating y/c=1.2 suction side	.05631	.01344	.00742	1796.4
Co-rotating y/c=-1.2 pressure side	.04770	.01005	.00615	1486.9
Co-rotating y/c=-1.2 suction side	.06275	.01500	.00835	2018.5
Counter rotating y/c=1.2 pressure side	.03834	.00850	.00488	1180.1
Counter rotating y/c=1.2 suction side	.05949	.01535	.00822	1986.4
Counter rotating y/c=-1.2 pressure side	.04544	.00960	.00579	1400.2
Counter rotating y/c=-1.2 suction side	.06232	.01552	.00857	2072.4

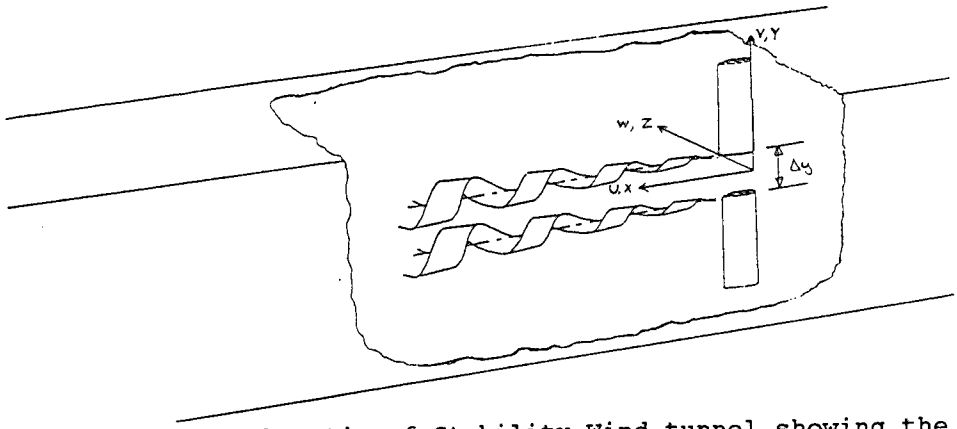

Figure 1. Schematic of Stability Wind tunnel showing the two wings and coordinate system.

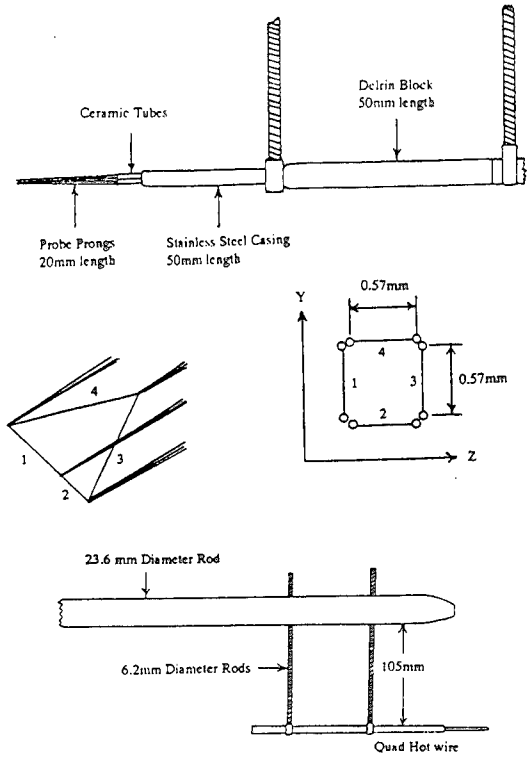

Figure 2. Quad hot wire probe showing wire arrangement and probe holder.

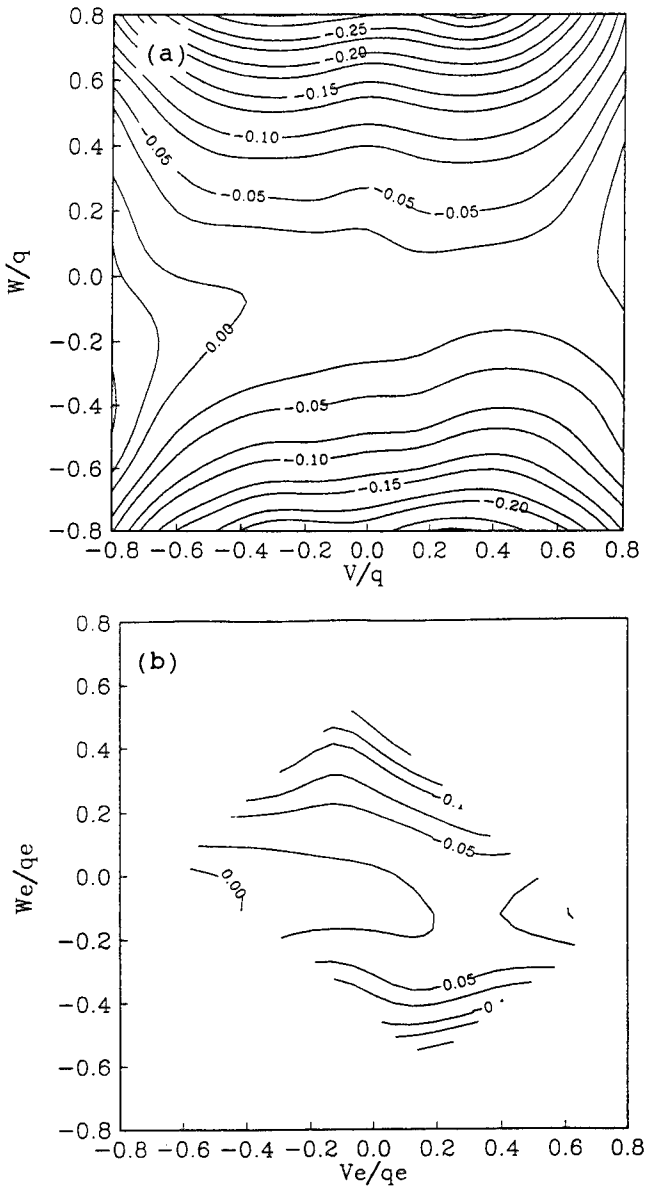

Figure 3. Contours of quad hot wire Q corrections (a) f_3 as a function of the actual velocities (b) g_3 as a function of the estimated velocities.

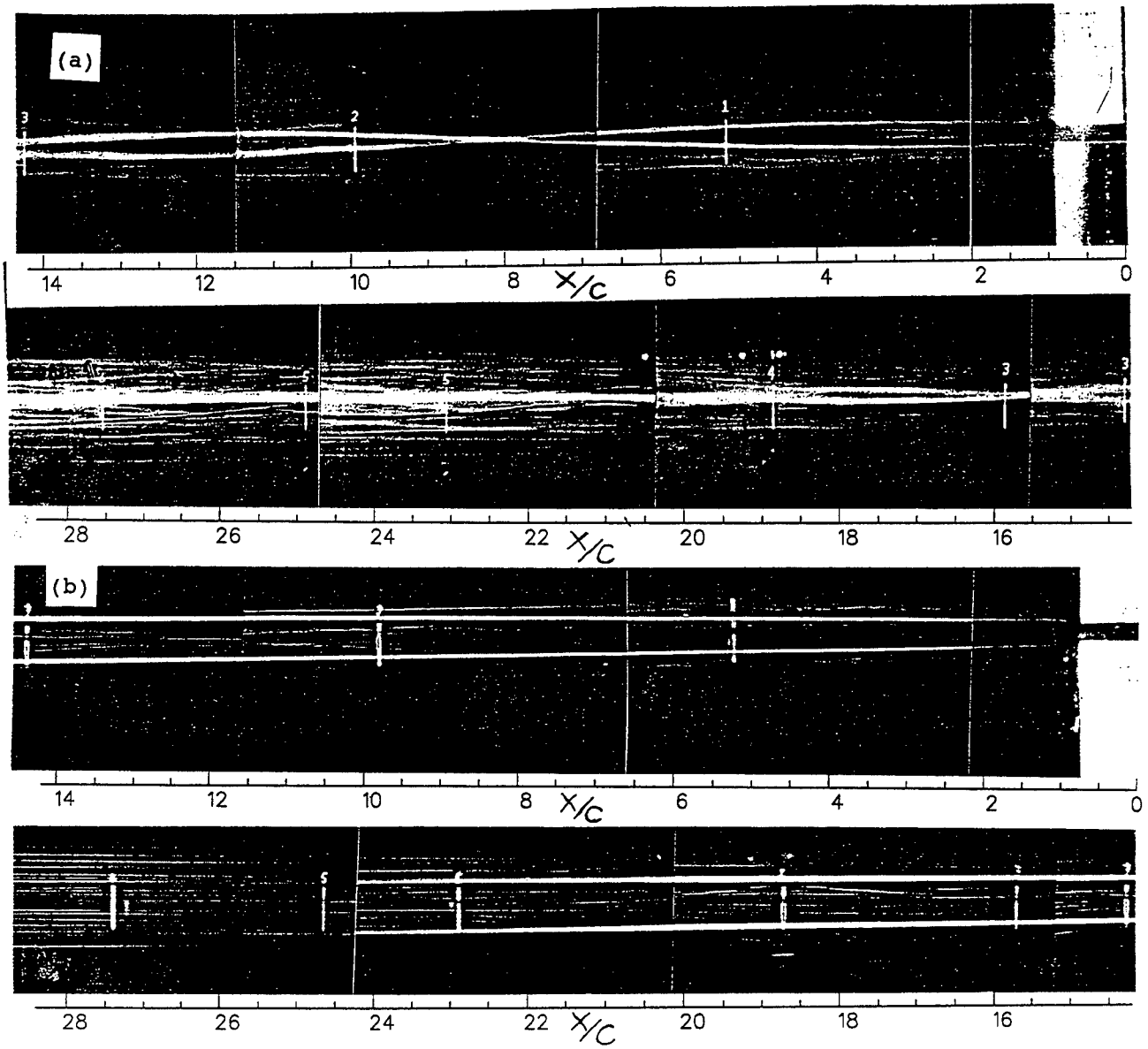

Figure 4. Photo mosaics of (a) co-rotating pairs and (b) counter rotating pairs (b) at 5° angle of attack, $\Delta y/c=.25$ $Re_c=130,000$. Flow is from right to left with the two wings on the far right of the photo.

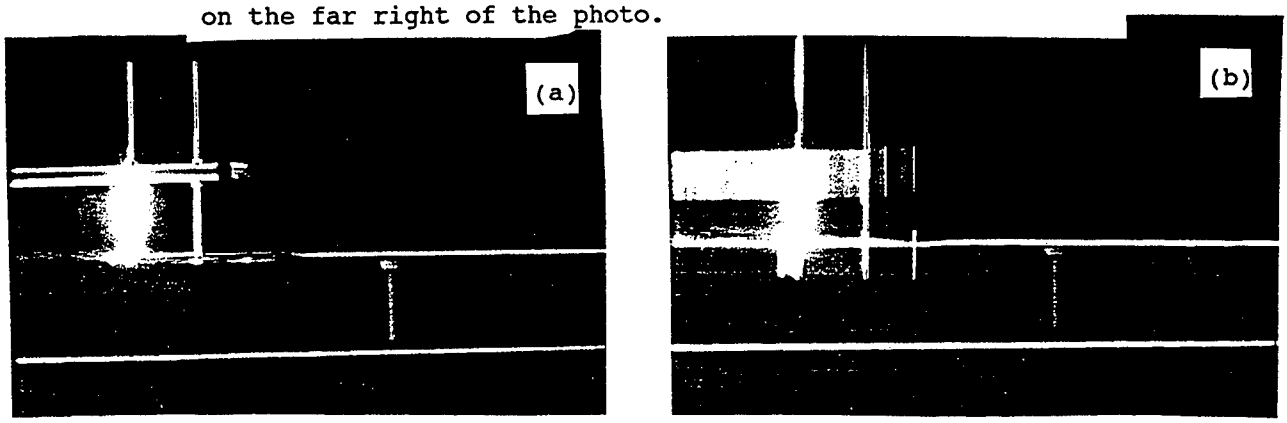

Figure 5. Probe interference effects in counter rotating pairs at 7.5° angle of attack, $Re_c=130,000$. (a) stationary probe (b) traversing probe. Note the lack of disturbances upstream of the probe tip.

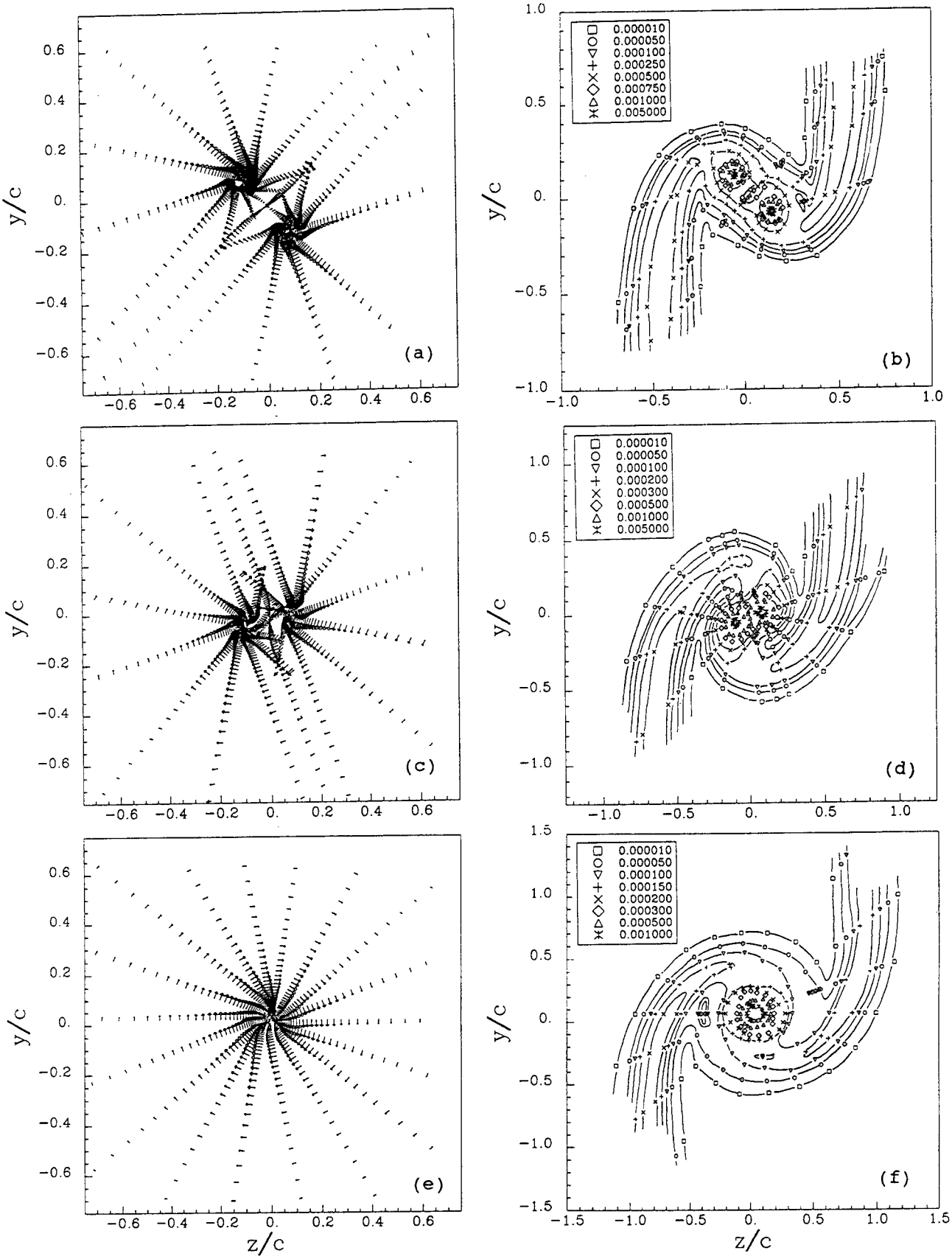

Figure 6. Co-rotating pairs angle of attack 5° Re_c=260,000 x/c=10 (a) secondary flow vectors (b) turbulent kinetic energy k/U^2_{ref}. x/c=15 (c) vectors (d) k/U^2_{ref}. x/c=22 (e) vectors (f) k/U^2_{ref}.

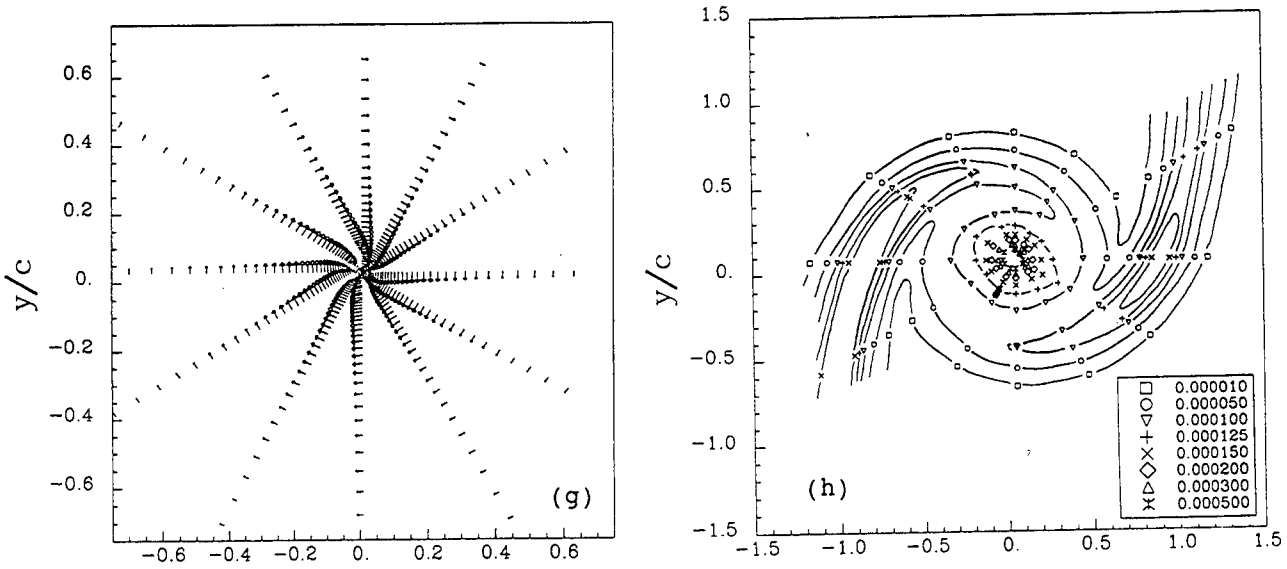

Figure 6. Co-rotating pairs angle of attack 5° Re_c=260,000 x/c=30 (g) vectors (h) k/U^2_{ref}.

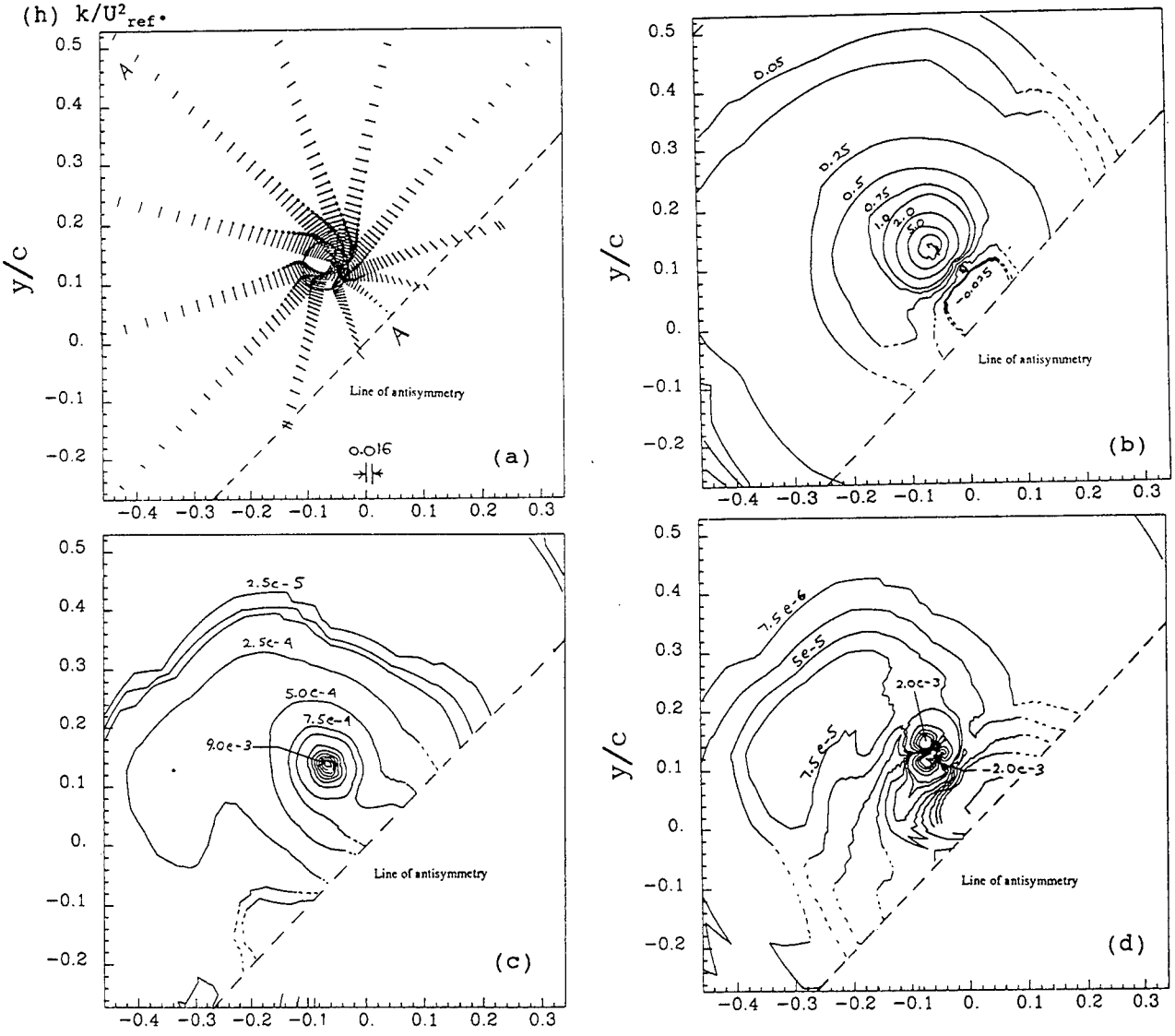

Figure 7. Co-rotating pairs x/c=10 core region (a) vectors (b) vorticity $\omega c/U_{ref}$ (c) k/U^2_{ref} (d) shear stress $\overline{v_\theta v_r}/U^2_{ref}$.

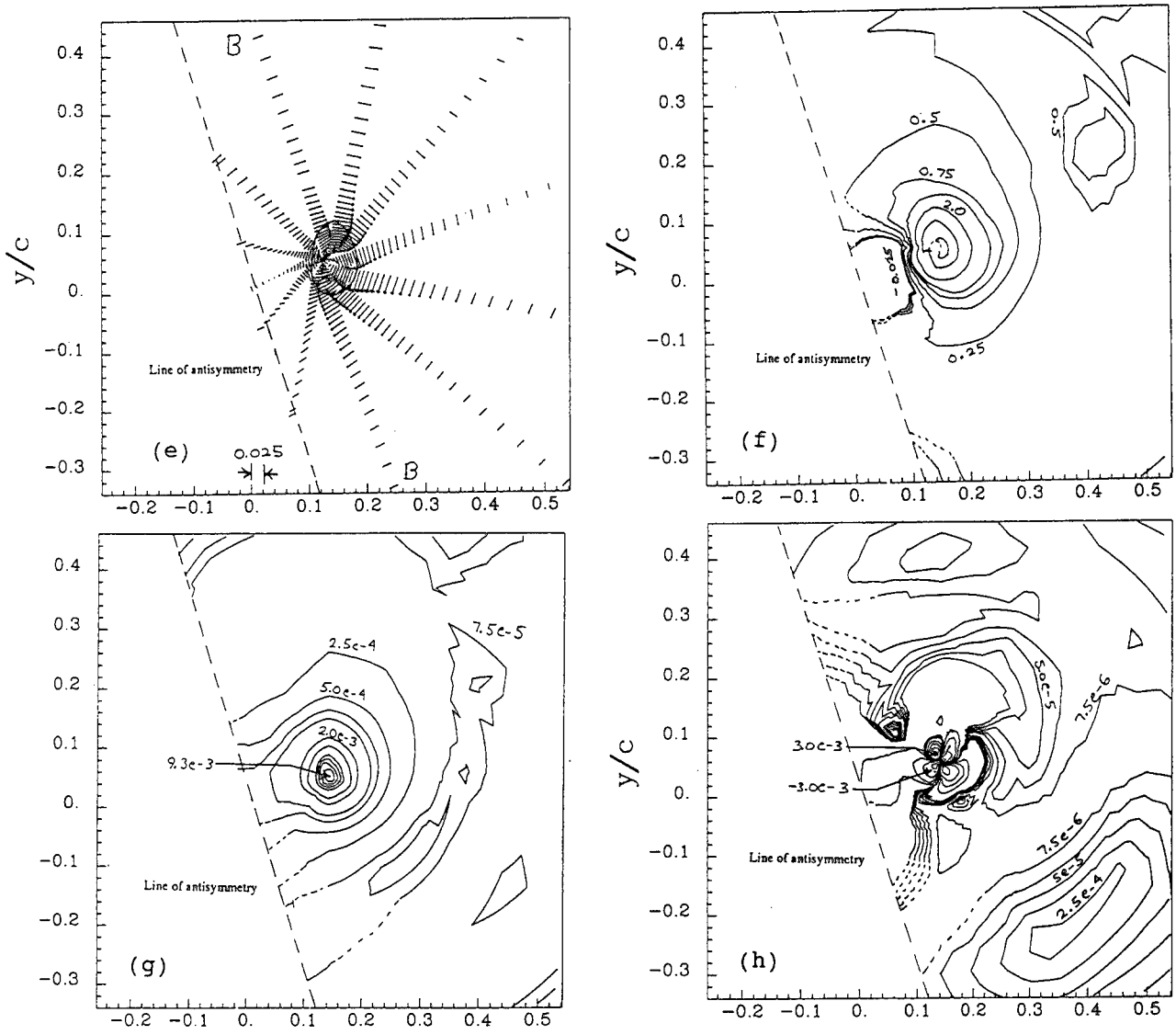

Figure 7. Co-rotating pairs x/c=15 core region (e) vectors (f) $\omega c/U_{ref}$ (g) k/U^2_{ref} (h) $\overline{v_\theta v_r}/U^2_{ref}$.

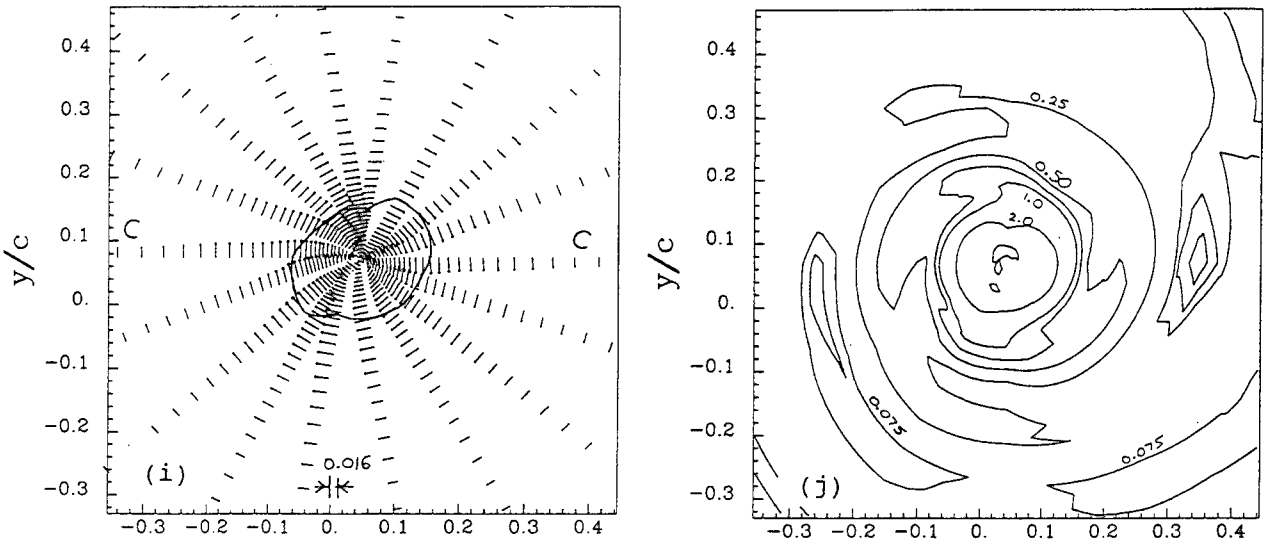

Figure 7. Co-rotating pairs x/c=22 core region (i) vectors (j) $\omega c/U_{ref}$.

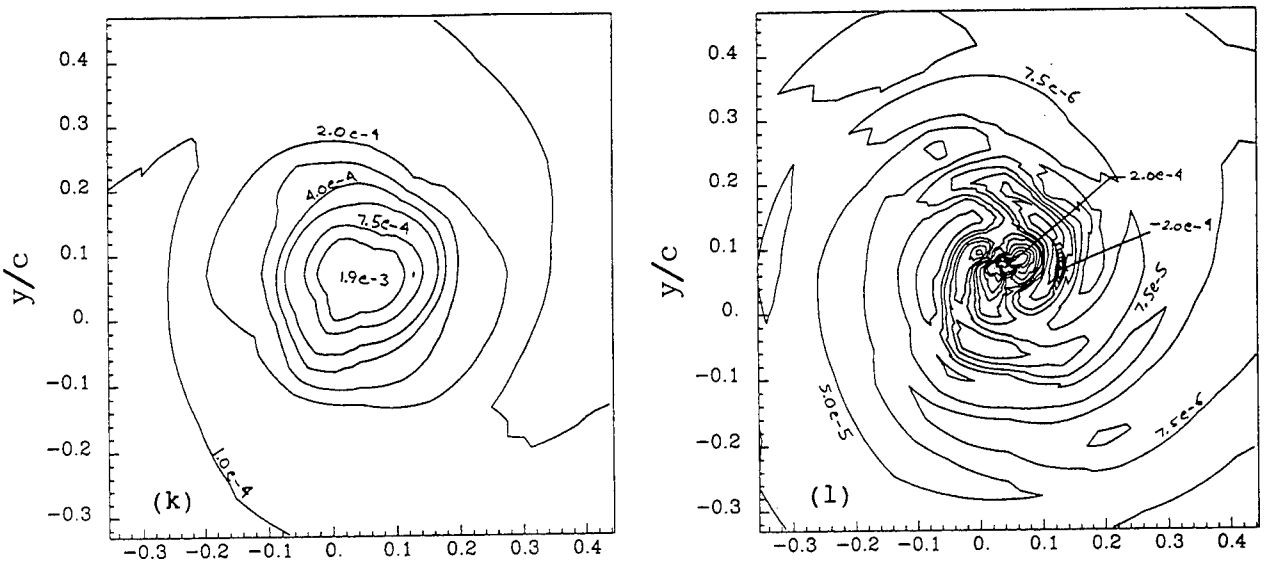

Figure 7. Co-rotating pairs x/c=22 core region (k) k/U^2_{ref} (l) $\overline{v_\theta v_r}/U^2_{ref}$.

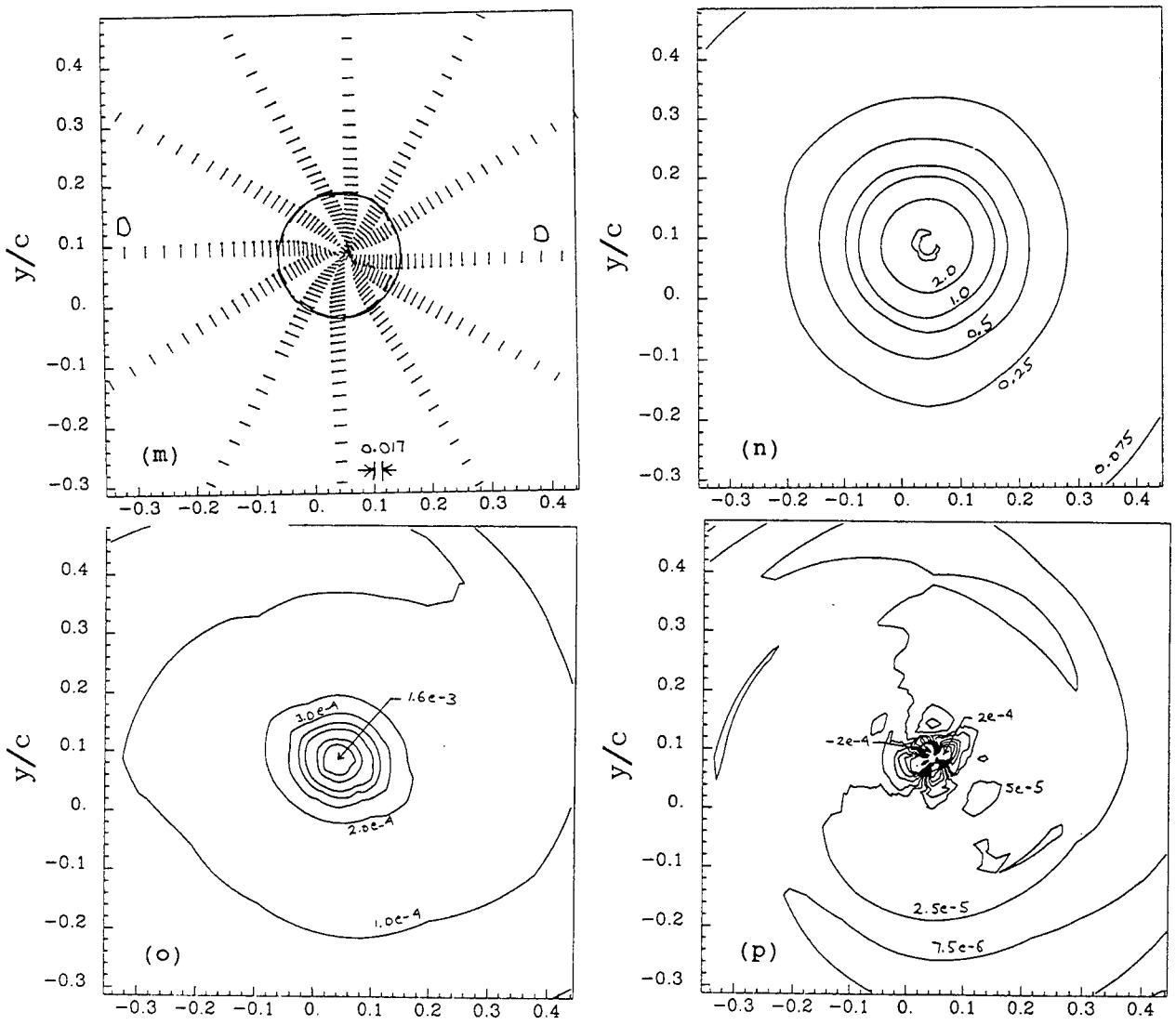

Figure 7. Co-rotating pairs x/c=30 core region (m) vectors (n) $\omega c/U_{ref}$ (o) k/U^2_{ref} (p) $\overline{v_\theta v_r}/U^2_{ref}$.

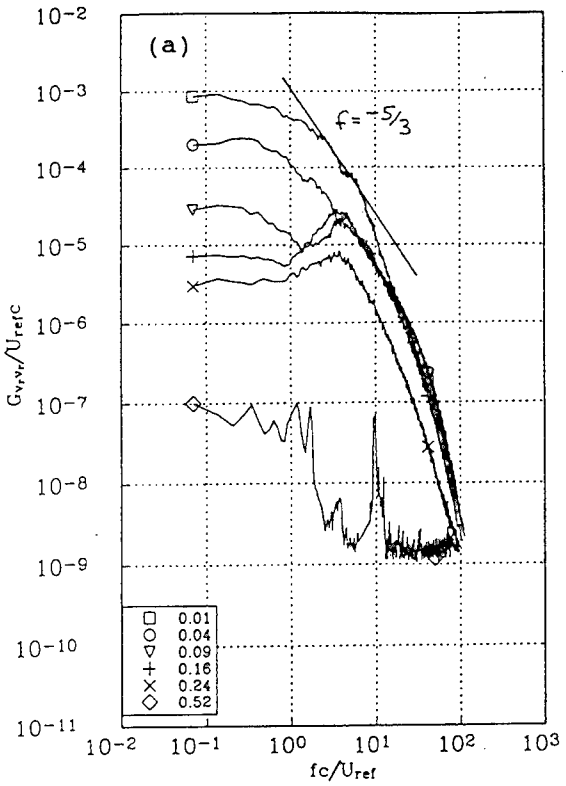

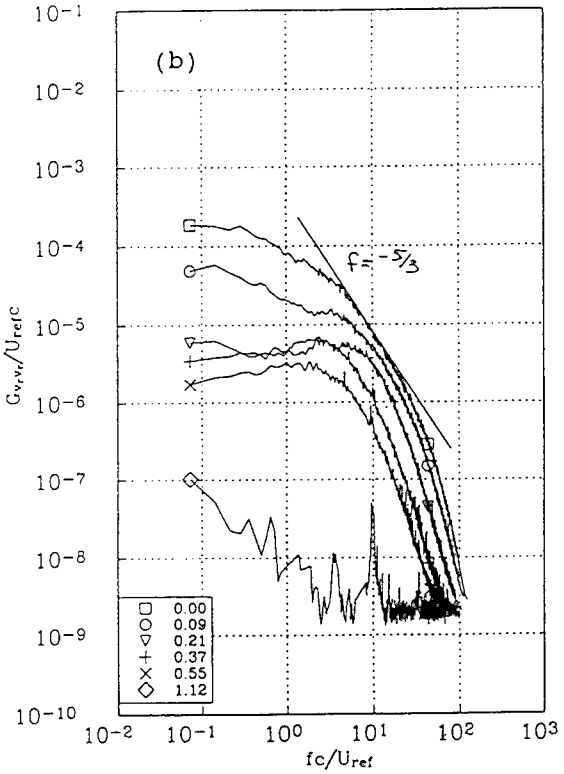

Figure 8. Autospectra G_{vrvr} at representative radial locations in the co-rotating pairs at (a) x/c=10 profile AA in figure 7a (b) x/c=22 profile CC in figure 7i.

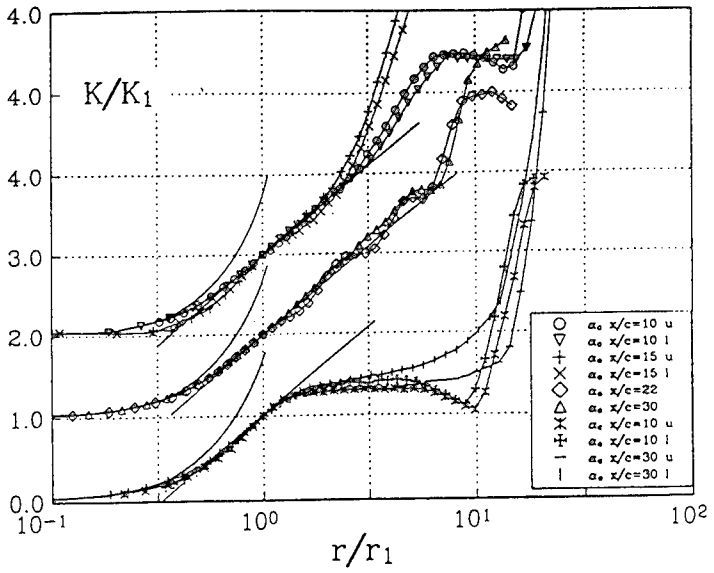

Figure 9. Circulation K of vortex pairs compared with Hoffmann and Joubert's circulation law (solid line). Subscript 1 is core location and u and l are upper and lower vortices in figure 6 and 12.

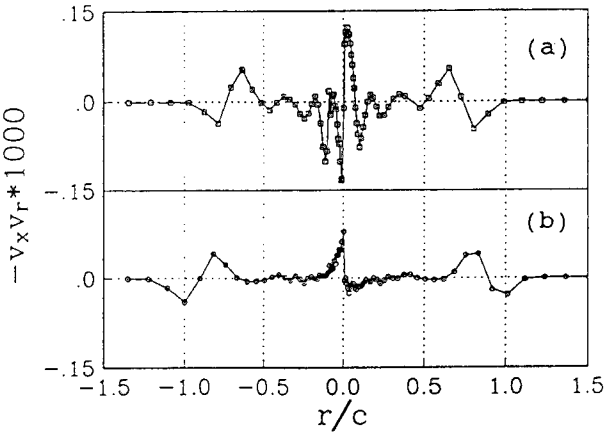

Figure 10. Profiles of $-\overline{v_x v_r}$ in the co-rotating pairs (a) x/c=22 profile CC in figure 7i (b) x/c=30 profile DD in figure 7m.

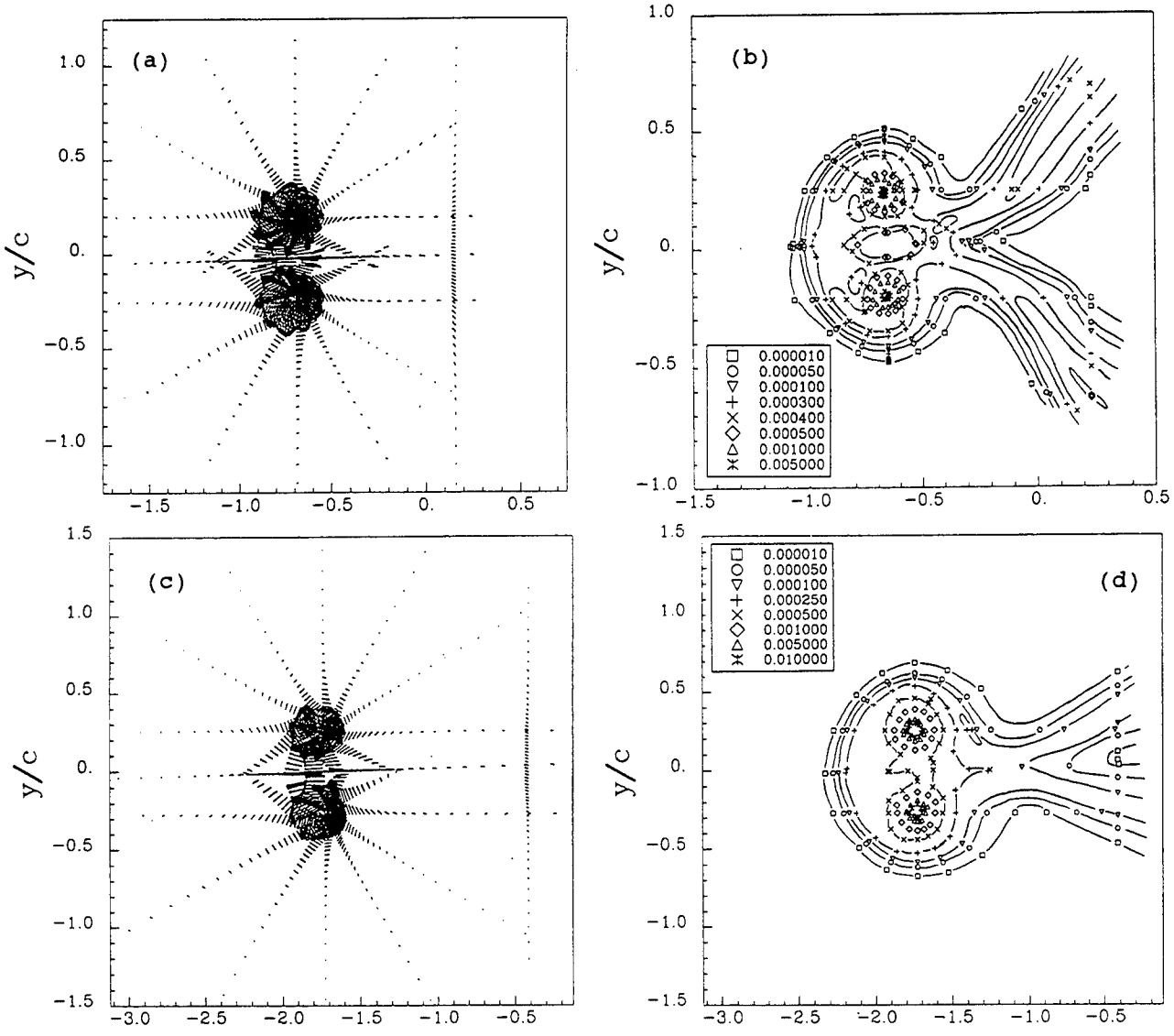

Figure 11. Counter rotating pairs angle of attack 5° Re_c=260,000 x/c=10 (a) secondary flow vectors (b) k/U^2_{ref}. x/c=30 (c) vectors (d) k/U^2_{ref}.

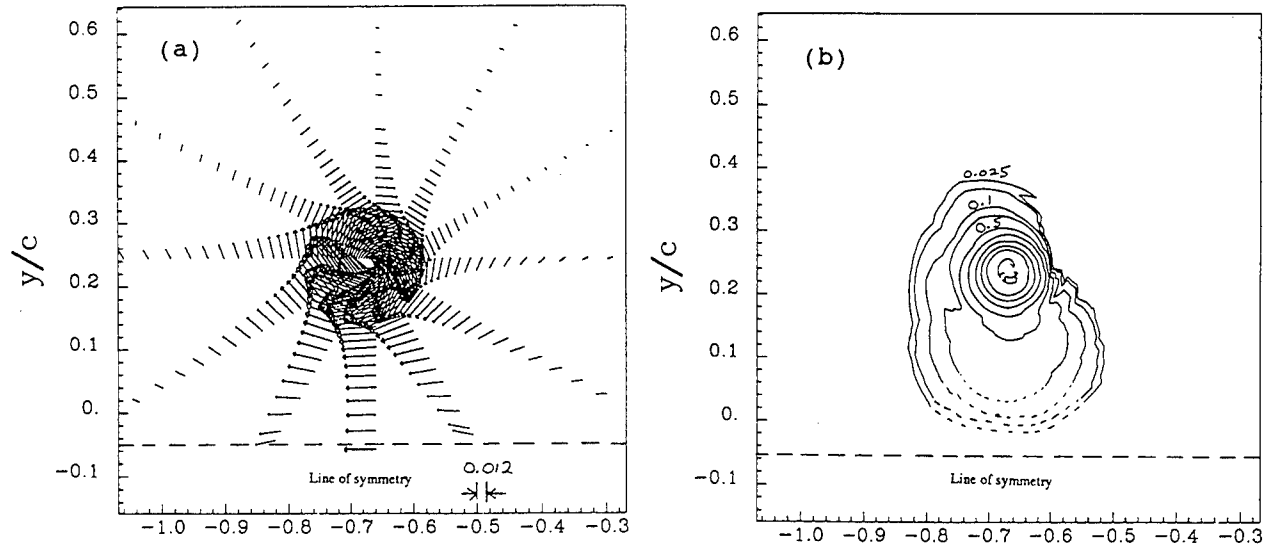

Figure 12. Counter rotating pairs core region x/c=10 (a) vectors (b) $\omega c/U_{ref}$

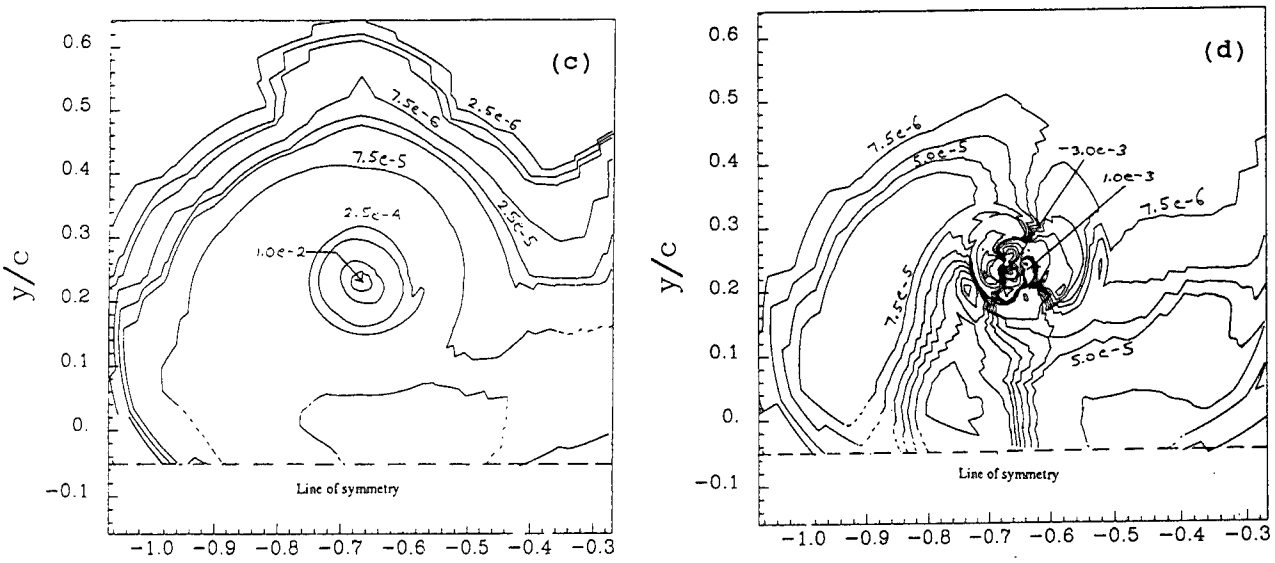

Figure 12. Counter rotating pairs core region x/c=10 (c)k/U^2_{ref} (d) $\overline{v_\theta v_r}$.

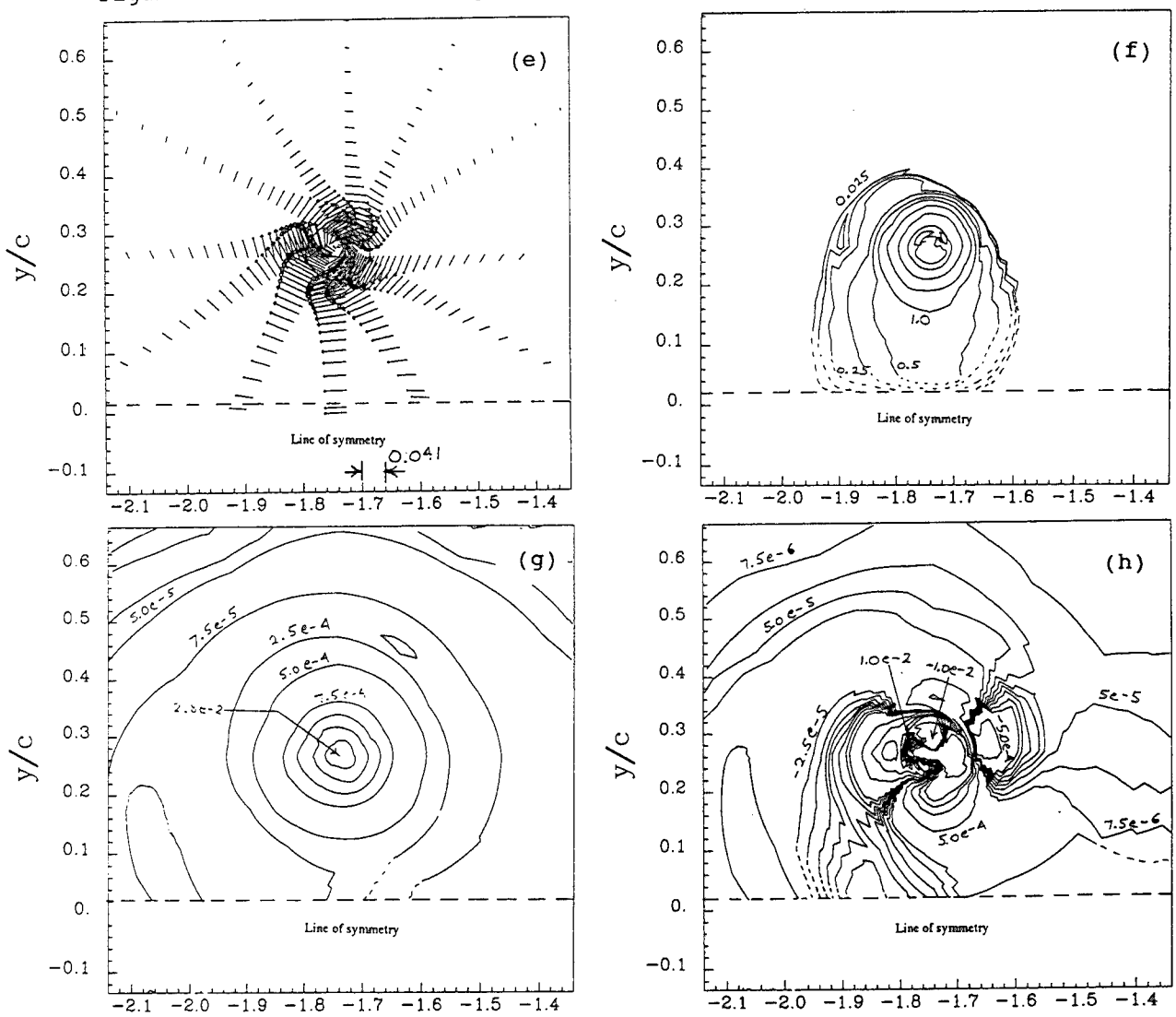

Figure 12. Counter rotating pairs core region x/c=30 (e) vectors (f) $\omega c/U_{ref}$ (g)k/U^2_{ref} (h) $\overline{v_\theta v_r}$.

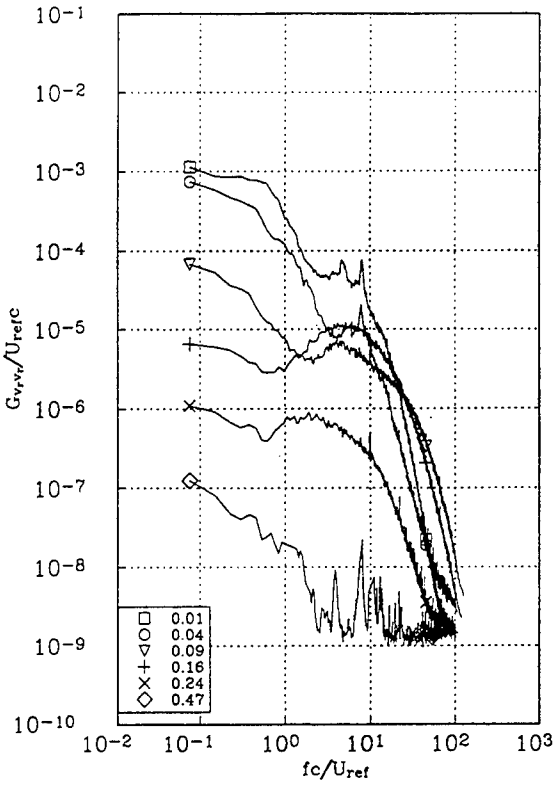

Figure 13. Autospectra G_{vrvr} at representative radial locations in the counter rotating pairs at x/c=10 profile EE in figure 12a.

DISCUSSION

T. Huang
David Taylor Model Basin, USA

It will be extremely valuable for the authors to include the turbulent shear stresses in the core regions of the vortices, excluding the effect of low-frequency vortex meandering.

AUTHORS' REPLY

We fully agree and expect to have these data in the near future.

Measurements of Flows Over an Axisymmetric Body With Various Appendages in a Wind Tunnel: the DARPA Suboff Experimental Program

T. Huang, H.-L. Liu, N. Groves, T. Forlini, J. Blanton, S. Gowing
(David Taylor Model Basin, USA)

ABSTRACT

Pressures, velocities, skin friction, and Reynolds stresses were measured in the stern boundary layer region of an axisymmetric body with and without appendages. These data are used to assess and further develop current computational fluid dynamics (CFD) capability for the prediction of flow fields around underwater bodies. The model configurations tested included an axisymmetric hull, a fairwater, one set of four identical stern appendages, and two axisymmetric ring wings. Analyses of measurement uncertainties of all the measured variables are presented. The data were corrected for tunnel effects. Comparison of the measured and computed mean axial velocity and turbulent shear stress profiles demonstrates the important influence of turbulence modeling in CFD predictions of the stern flows. The data illustrate the modifications by various appendages of the basic axisymmetric thick turbulent boundary layers over the stern.The spatial nonuniformity of mean axial velocities and redistribution of the normal and shear stresses are found to be caused by a pair of contrarotating longitudinal vortices generated by each appendage. These are imbedded in the inner stern boundary layer of the hull. The helical rotations of the vortices produce a transverse transport of axial momentum. The high momentum and low turbulence level fluid behind the appendage is pulled inward and the low momentum and high turbulence level fluid to each side of the appendage is pushed upward. The appendage-generated vortices redistribute axial-radial turbulent shear stresses but do not change their circumferential-average values. The imbedded vortices in the stern boundary layer show distinct characteristics of turbulent shear stresses with the mixing length scales governed by the core sizes of the vortices.

1. INTRODUCTION

The flow over an appended body during level flight is characterized by thick boundary layers, vortical flow structures generated by hull/appendage junctures, and appendage turbulent wakes. The spatial nonuniformity and temporal fluctuations of the flow into the propulsor significantly affect propulsor noise. Experimental data for CFD validation purposes have been obtained during the past 15 years but are limited. They are (1) thick stern boundary layer data for various axisymmetric configurations [1-6], (2) appendage/flat-plate juncture flow data [7,8], and (3) flow data for a curved body which simulates qualitatively the flow features of a turning body [9]. Experimental data for the flow field over an appended body are lacking and the validation of CFD numerical methods for submarine design applications cannot be adequately accomplished. A first goal of this project was to provide an experimental database for CFD code validation. Numerical predictions of the flow field over an axisymmetric hull model with and without various typical appendages could be compared with the experimental data. Comparisons were then made to assess the current CFD capability for design problems. The ultimate goal of this project is to acquire a fully-matured CFD capability that is user-friendly, cost effective and fully validated by comparison with detailed experimental data. This is called the DARPA SUBOFF Project.

As the flow approaches the stern of a typical underwater body, the boundary layer quickly thickens, viscous-inviscid flow interaction becomes pronounced, turbulence reacts to the change in mean flow, and conventional thin boundary-layer turbulence modeling is no longer applicable. Since the stern control surfaces are

generally immersed in this thick boundary layer, the numerical capability to predict the control effectiveness of the stern control surfaces and their adverse effect on the flow into the propulsor is limited. In addition, a large fairwater can generate a turbulent junction vortex from the fairwater/hull intersection and a pair of vortices which trail downstream into the propulsor. The flow unsteadiness around the fairwater and the vortex-induced spatial nonuniformity of the flow into the propulsor are of major concern. CFD capability to predict the flow nonuniformity at the propulsor location, caused by the fairwater and stern control surfaces, is lacking. The CFD capability to predict the propulsor noise arising from the spatial variations and temporal fluctuations of the propulsor inflow is also not well developed.

Part I of the first phase of the SUBOFF experiments was designed to accelerate the maturity of the current CFD capability for steady flow submarine applications. The experimental configurations covered eight simple but realistic representative configurations. They included steady flow field measurements in a large wind tunnel simulating straight and level flight, and straight flight at small angles of attack or drift conditions. The unique feature of the above experimental series is the quantification of the flow nonuniformities at the propeller location. The wake and vortical flow structures generated by various combinations of fairwater, stern control surfaces, and/or ring wings are the principal source of flow nonuniformity.

The massive amount of three-dimensional flow field data from the SUBOFF experiments has been organized, formatted and placed onto magnetic tapes. The data report and associated data files were prepared to provide CFD users with easy access to the measured data.

A simple and fully validated viscous-inviscid axisymmetric flow interaction procedure [17,18,19] was used to compute the flows of axisymmetric bodies without appendages in the free flight condition and inside the tunnel to assess tunnel wall effects during the design of the experiments.

The results computed by the viscous-inviscid procedure were also used to compare the experimental results and the results computed by more complete incompressible Reynolds-Averaged Navier-Stokes (RANS) solvers. The RANS results mentioned in this paper are limited to those available to the authors and are used to indicate the present status and potential of this approach. These limited comparisons of experimental data with the results computed by the RANS methods and the viscous-inviscid procedure are presented to promote further development of CFD methods to solve incompressible turbulent stern flows over axisymmetric bodies and three-dimensional ships with various appendages. Further validation of CFD computer codes using the present data base is expected to be continued.

The following sections present the SUBOFF models, experimental facilities and techniques used, wind tunnel blockage effects and corrections, measurement uncertainty analyses, typical results and discussion. Some of the details were reported in a series of DTRC reports [10-15]. A summary of the entire first phase of the SUBOFF experiments can be found in a DTMB report [16].

2. SUBOFF MODELS

The representative components of the DARPA SUBOFF body and their dimensions are shown in Fig. 1. A typical configuration is composed of an axisymmetric hull, a fairwater, one set of stern appendages, and two axisymmetric ring wings. Two SUBOFF models, DTRC Model Nos. 5470 and 5471, were used. The two models differ only in the location of the surface pressure taps. Model No. 5470 was designed for the towing tank and Model 5471 for the wind tunnel. The details of the model configurations have been described in Groves et al [10]. For completeness of this paper, the essential geometric features are repeated here. Each model component is described by equations giving either the axial and radial values for an axisymmetric component or the Cartesian coordinates (x, y, z) of nonaxisymmetric components. All equations and computer code listings give model scale coordinates in units of feet (1 ft.=0.3048 m). A grid representation of the axisymmetric hull, fairwater, and stern appendages is shown in Fig. 2.

2.1 Axisymmetric Hull

The axisymmetric hull has an overall length L of 14.292 ft (4.356 m) and a maximum diameter D of 1.667 ft (0.508 m). The hull is composed of a forebody of length 3.333 ft (1.016 m), a parallel middlebody section of length 7.313 ft (2.229 m), an afterbody of length 3.646 ft (1.111 m) and an afterbody cap of length 0.313 ft (0.095 m). Hull profiles are shown in Fig. 3.

2.2 Fairwater

The fairwater is located on the hull at top dead center with

its leading edge positioned at x=3.033 ft (0.924 m) and trailing edge at x=4.241 ft (1.293 m) for a total length of 1.208 ft(0.368 m). A cap attaches to the top of the fairwater at a height y=1.508 ft (0.460 m) and is a 2:1 elliptical cross-sectional shape. The fairwater cap, the fairwater is defined in terms of a forebody, a parallel middle body, and an afterbody region. Fig. 4 shows the fairwater section profile.

2.3 Stern Appendages

The stern appendages consist of four identical planes of NACA 0020 sections mounted on the model hull at angles of 0° (top dead center), 90°(port), 180°, and 270°(starboard). The circumferential angle,θ,in this report is defined positive counterclockwise viewed from the stern. The basic stern appendages, shown in Fig.5, can be attached to the hull at three different axial locations. The stern appendage location with the appendage trailing edge at x=13.146 ft (4.007 m) is designated the baseline stern appendage location. To provide clearance for stern appendage angular deflections, the appendages are slightly offset from the axisymmetric hull surface.

2.4 Ring Wings

Two ring wings, designated Ring Wing 1 and Ring Wing 2, have the same section shape of NACA 66 mod. with a 0.1 thickness-to-chord ratio and a=0.4 mean line, and differ only in their angle of attack. Figure 6 shows the placement of the wings relative to the axisymmetric hull.

2.5 Ring Wing Struts

Four separate, identical struts are mounted equally-spaced around the hull girth to support the ring wings. The struts were rotated 45° with respect to the stern appendages. The struts attach at the same axial position on the hull, x=13.589 ft (4.142 m). At the inner surface of each wing, the struts are contoured to match each wing.

2.6 Model Construction

The axisymmetric hull and fairwater were made of molded fiberglass. The hull was reinforced with a 10-in. (0.25 m) wide U-channel strongback. The stern appendages were made of Hysol, an epoxy and wood fiber-based compound that was both waterproof and easily machined. The ring wings, support struts, and stern hubs were machined from aluminum and anodized.

The various model components contain a large number of surface pressure taps. The taps were arranged to assist in wind tunnel alignment of the model with the flow and to provide a basic indication of surface flow variations as the model configuration, pitch, and drift were varied. Complete tap identification was provided in Groves et al. [10]. The finished model was checked for smoothness of the surface finishing. The model was measured for roughness at three positions on its circumference. The top centerline was at θ= 0°, the port seam was at 90° and starboard seam was at 270°. When the model was measured at five axial stations for the three angular positions, the port seam was the roughest and the top centerline the smoothest. The mean value for all 22 roughness readings was 0.00036 in. (0.0091 mm). These roughness measurements were made before the experiments.

The radii of the finished models were also measured. The radial measurements indicate a standard deviation in radius up to 0.07 in. (1.78 mm) in the bow region, less than 0.03 in. (0.762 mm) in the parallel middle body, and less than 0.05 in. (1.270 mm) in the stern region. The relatively large bow asymmetry occurs ahead of the trip wire and its impact is considered small. A complete analysis of the radial variations was given in Liu et al [13,16]. The overall uncertainty of the model radii was ± 0.03 in.(0.76 mm). The uncertainty of the total model length was 0.06 in.(1.59 mm). The overall model uncertainties (due to manufacturing errors) of ΔS/S and ΔV/V respectively were 0.3% and 0.6%, where S and V are the model surface area and volume.

3. EXPERIMENTAL FACILITIES AND MEASURING TECHNIQUES

The wind tunnel selected for the flow field measurements is the DTRC Anechoic Flow Facility (AFF). The measuring system employed in the AFF consists of four sub-systems: the probe traversing system, the computer, and the velocity and pressure measuring systems.

3.1 Wind Tunnel and Model Installation and Aligment

Eight DARPA SUBOFF model configurations were tested in the DTRC AFF with Model No. 5471. The wind tunnel has a closed-jet test section that is 8 ft. (2.4 m) square and 13.75 ft. (4.19 m) long. The corners have fillets which are carried through the contraction and allowance for boundary layer growth along the tunnel is made by tapering the corner fillets, starting from the test section entrance to the exit. The test section is followed by a large acoustically-tiled chamber 23.5 ft. (7. 16 m) square, normal to the flow, and 21 ft. (6.40 m) long. The forebody and most of the parallel

middle body were located in the closed-jet test section, and the afterbody protruded into the open-jet anechoic chamber as shown in Fig. 7.

Pretest analyses by Liu et al. [13] demonstrated that the effect of the open and closed jet model positioning had minimal effect on the flow parameters if the reference pressure and velocity were selected in the open-jet area, corresponding to x/L = 0.85. The model was supported by two thin NACA 0015 struts located at x/L = 0.24 and 0.63. The two supporting struts have a 6 in. (15 cm) chord. The strut bases were mounted below the tunnel floor for minimal flow disturbance. The model end of the strut was connected to a gimble secured to the model strongback to align the model for various angles of attack or drift. . For added stability, two 1/16-inch cables anchored the struts to the tunnel wall. Liu et al. [13] and the actual experimental results confirmed that the wake data at zero angles of attack and drift were essentially free from strut wake contamination except near $\pm 30^{o}$ of the strut. The analyses for the blockage of the model in the wind tunnel will be presented in the next section.

In order to align the model to the flow, the model center was first aligned to the tunnel centerline using a surveyor's transit located 32.8 ft. (10 m) downstream from the end of the model. After the model was physically aligned with the tunnel, pressures around the body circumference were measured at five axial locations for aerodynamic alignment. The pressure coefficients after the aerodynamic model alignment were within 0.003 of each other, which is about the accuracy of the pressure measurement system. An overall accuracy of model alignment with the flow is estimated to be better than 0.15 degree. The alignment procedure was detailed by Liu et al. [13].

3.2 Traversing System

A traversing system was built to move velocity or pressure probes radially in the stern region of the model. The probes angular position was automatically controlled in the radial direction and could be manually repositioned axially. The unit allowed a probe to be positioned anywhere within an annular volume 59 in.(1.5 m) in. length from 3 in (7.6 cm) to 28 in (71 cm) in radius. The traversing unit was mounted inside the anechoic chamber directly behind the model. This mounting location provided easy access to the model's stern region. Ward and Gowing [12] gave a complete description of the traversing system and its full capabilities.

3.3 Computer Data Acquisition System

A Unix-based Masscomp MC 5450-01 Scientific Laboratory System served as the data acquisition computer. In addition to collecting and analyzing the velocity and pressure data, the computer controlled the stepping motors of the traversing system and the rotary pressure scanners.

3.4 Velocity Measurement System

Velocity measurements utilized standard hot-film techniques and required the interaction of hot-film probes, a hot-film anemometer, the Masscomp computer, and the traversing system. The velocity magnitudes and directions obtained through the acquisition system were then used to calculate mean velocities, turbulence intensities, and Reynolds stresses in the wake of the model. A TSI Model IFA-100 (Intelligent Flow Analyzer) computer-controlled, hot-film anemometer and thin, cylindrical hot-film sensors were used to measure the flow in the AFF. Three types of probes were used to match the type of measurement required. A single sensor hot-film probe, TSI Model 1201-20, was selected to measure the time-varying response. A TSI 1249A-10 miniature "X" probe was used when the flow was two dimensional or in a boundary layer. The "X" probe measures two components of velocity, turbulence intensity and Reynolds stress. The "X" sensor was used for measurements close to the body surface and as a check for the three-sensor probe, A compact, three-sensor probe, TSI Model 1299-20-18 was used for most of the flow measurements since it yielded three velocity components with good spatial resolution. Velocity measurements were normalized using a reference velocity measured by pitot tubes in the free-stream at an axial location x/L = 0.85.

3.5 Wind Tunnel Wall Effects and Corrections

It is desirable to use the largest model possible to obtain the data at high Reynolds numbers. However, the wind tunnel blockage effect increases with model size. For a large model in a wind tunnel an area ratio of maximum model cross-section to tunnel cross-section of less than 5% is considered to be tolerable at low mach numbers (less than 0.2). Furthermore, if the blockage effect can be quantified and the wall effects can be removed from measured data by numerical computations, then the corrected data will simulate free flight conditions.

A potential-flow panel code computer program modified to include viscous effect in a simple viscous-inviscid interaction procedure [17, 18,19] was used to compute the flow field in the AFF. Only the bare axisymmetric body with the two supporting struts were

modeled. The effect of the open-jet was also estimated. Detailed determination of wind tunnel wall effects and corrections was given by Jiang et al.[20]. The computed pressure coefficient distribution C_p along the DARPA model represents the blockage effect in the AFF tunnel. An overall tunnel blockage was estimated as the average difference in the values of C_p over the body length. This difference in C_p is about 0.05 resulting in a velocity difference of about 0.025 of the freestream . To estimate the open-jet effect, a free surface boundary condition was assumed in the tunnel jet region to predict the pressure coefficient along the model. Velocity components in the flow direction on the panels of the open-jet region were iterated to achieve a constant value by allowing different normal velocities on the tunnel panels in the open-jet region [20]. The open-jet flow pressure distribution was found to locally follow the earlier open flow condition calculations. The velocities measured at the outer edges of the axial measuring locations with respect to the tunnel reference velocity were recorded and could be applied to correct small (1-3%) drifts of the hot-film anemometer.

The tunnel velocity and static pressure vary along the body length and across the tunnel section. Since viscous effects are important in the model stern region, the viscous-inviscid flow interaction computation procedure [17, 18,19] was used to compute these velocity and static pressure variations due to the axisymmetric body in the tunnel. The computed axial velocity and static pressure are uniform across the entire plane at x/L=0.85 with and without the presence of the tunnel walls. The presence of tunnel walls causes a 2.4% increase in axial velocity and a 4.8% increase in static pressure. The computed velocities and static pressures at the x/L=0.85 plane were equal to the free stream velocity and pressure for the open flow. Detailed velocity and static pressure measurements were made inside the tunnel in the presence of the axisymmetric body. It was found that, at the x/L=0.85 plane, the velocity variation was less than 0.5% and the static pressure coefficient variation was less than 1.0%. The velocity and static pressure at this plane were then used as the tunnel reference free stream velocity and static pressure. Two pitot probes, mounted at x/L=0.85 and r/Rmax = 3.6 were used to measure the tunnel reference velocity and static pressure for the entire experiment. The computed static pressure coefficients were obtained using the computed reference velocity and static pressure at x/L=0.85 for both with and without the tunnel walls. It was found that the tunnel blockage effect was nearly eliminated by using the reference velocity and static pressure at x/L=0.85. Therefore, all the measured velocities and static pressures were normalized by the reference velocity and static pressure measured at x/L=0.85 and r/Rmax=3.6.

3.6 Conditions of Inflow and Outflow Planes

The inflow plane selected was at x/L = -0.45, where there was no difference in the computed axial velocity with and without the model in the tunnel. The measured variation of the axial velocities across the inflow plane of the empty tunnel was found to be 0.5% U_{ref}. The outflow plane selected was at x/L = 1.2, where the difference in measured axial velocities with and without the model in the tunnel was about 0.5% U_{ref}. The measured variation of the axial velocities across the outflow plane of the empty tunnel was found to be 0.5% U_{ref}. Therefore, the inflow and outflow at x/L = -0.45 and 1.2, respectively, can be considered uniform outside of the wake region.

3.7 Longitudinal Flow Variation along the Tunnel

The variations of tunnel velocity and static pressure were measured along the ceiling at r/R_{max} = 3.6 with and without the model in the tunnel. A small favorable pressure gradient and a small velocity gradient along the tunnel was observed. When the small axial flow variation was removed from the measured data [16], the corrected data agreed better with the computed values where no flow variation was imposed in the computation. Thus, the flow over the model in the tunnel did simulate the free flight condition with minor effects of tunnel walls and axial pressure gradient. These effects were measured and presented [16]. However, no correction has been applied to the original measured pressure coefficients on the body. CFD users may apply the measured axial variations of velocities and pressure coefficients [16] to correct the raw data. The pressure coefficient corrections used to eliminate the effect of longitudinal flow variation along the tunnel and the corrected pressure coefficients on the body are given in Table 1.

4. MEASUREMENT UNCERTAINTY

Measurement error sources are usually identified either as bias (fixed) or precision (random) errors. The magnitude of bias and precision error sources were estimated individually and then combined to provide an estimate of the total measurement uncertainty [21, 22] . In this report, the 95%

confidence interval estimates [21,22] are used to present the bias and precision limits of the measurement errors. The final uncertainty analyses summarizing the uncertainties of the reported results measured by different systems were presented in detail [16] and are stated as follows.

4.1 Uncertainty of Hot-Film Velocity Measurements

Computer programs for calibration, data acquisition, probe traversing, data reduction, data archiving, and initial plotting of velocity were written by Blanton et al. [14] who estimated the uncertainties associated with using the hot-film measurement system. Bias uncertainties of velocity measurement, B_V, were found by perturbing the data reduction equation with estimates of individual uncertainty. The bias uncertainties considered by Blanton et al. [14] due to (1) temperature, (2) probe alignment, (3) analog to digital conversion, (4) speed calibration,and (5) angle calibration are summarized in Table 2, where S_V is the estimated sample standard deviation of the measured velocity. As shown in Table 2 the speed calibration and angle calibration are the major contributors of the bias uncertainty of the hot-film velocity measurements.The bias uncertainties due to hot-films for 10-20 points within the range of the measured velocity were found to be 1.5, 2.0, and 2.5% for a single, a two-component and a three-component hot-film probe, respectively. The variation of this uncertainty depends upon how carefully the values of n, A, and B were obtained [1 - 7, 9.].

Precision (random) uncertainty of the three-component hot-film measurements was determined from repeat measurements at one point in the free-stream and at another fixed point in a highly turbulent region (inside 10% of the boundary-layer thickness) of the model. The data acquisition system collected 1500 data points per transducer at 150 Hz. Therefore, a single measurement at each position required about 10-11 seconds to acquire data, analyze data, and move to the next position. At the two points thirty repeat measurements were taken consecutively. Another thirty repeat measurements were also taken over a typical time of 30 minutes (a representative time required for a typical constant radius velocity survey), the probe was moved to a different position and then returned to the same position (about 30% of the boundary layer thickness) inside the model boundary layer by the automatic traversing system. The $2S_V$, $2S_{V'}$ and $2S_{u'v'}$ precision uncertainties for the thirty repeat measurements for the three conditions are shown in Table 3, where S_V, $S_{V'}$ and $S_{u'v'}$ are sample standard deviations of the three mean and turbulent velocity components and the Reynolds stress, respectively. Table 3 indicates that the precision uncertainty of the present measuring system is much smaller than the bias uncertainty. The position uncertainty of the automatic probe traversing system therefore does not contribute significantly to the precision errors of the velocity measurements shown in Table 3. These thirty repeat measurements of mean velocity indicated that the precision uncertainty of the mean velocity was less than 0.3% of Uref. The total uncertainty of the measured mean velocity U_V with 95% confidence can be estimated from Tables 2 and 3 as $U_V = [B_V^2 + P_V^2]^{1/2}$. The total measurement uncertainty for each of the three mean velocity components with 95% confidence was 2.5% of U_{ref}. for the three-component hot-film probes. The total uncertainties for mean velocities were 1.5% and 2.0% of U_{ref} for a single and a two-component hot-film probe. The bias uncertainties of the measured turbulence Reynolds stresses are not significant because the use of differencing in the data reduction program removes most of the bias errors. The results of the thirty repeated measurements of three turbulence intensities and two Reynolds stresses shown in Table 3 indicated that the total measurement uncertainty for each of the three turbulence velocities with 95% confidence was less than 0.2% of U_{ref} ,and that for each of the two Reynolds stresses was less than $10^{-4} U_{ref}^2$ in the inner region of the turbulent boundary layer and wake and was less than $5x10^{-6}U_{ref}^2$ outside of the turbulent boundary layer and wake.

4.2 Uncertainty of Pressure and Shear Stress Measurements

The significant features of the pressure system were the ability for remote calibration at in situ temperatures, the measurement of tap and dynamic pressures with the same tranducer, and high scanning speeds to survey all pressures at constant tunnel conditions. Five rotary pressure scanners, Scanivalve Model 48J9GM were the heart of the pressure measuring system. Each scanner was connected to 48 pressure taps on one side and to a transducer on the other side. The calibration transducer was a Datametrics Type 570 Barocel sensor with a differential pressure range of 10 torr. Vishay Model 2310 signal conditioners were connected to the scanner transducers to provide excitation voltage, output signal amplification, and bridge balancing. This entire system was located inside the model. This arrangement reduced the length of the pressure lines from each of the surface pressure taps, decreased the response

time required for a measurement, and thus increased the allowable scanning rate. The analog output signal was conditioned, amplified, filtered, and finally connnected to the Masscomp MC5450 Scientific Laboratory System computer. The computer sampled the data from the five scanner transducers at 1 KHz for 100 ms for each tap.

Shear stress on a body in a flow can be measured with small obstacles that stagnate the velocity field near the surface to produce a pressure rise that is approximately proportional to shear stress [23] . This technique easily adapted to models that were already equipped with pressure taps for surveying pressure distributions. The pressure was measured at the tap with and without the obstacles. The measurement differences were used to compute the shear stress or friction coefficient at that location. Based on boundary-layer estimates, the blocks were less than 12% of the boundary layer thickness wherever they were used, and the top edge of the block is at a non-dimensional boundary layer height of $y^+ \cong 160$. Gowing [15] calibrated all the obstacle blocks with Preston tubes using the calibrations published by Patel as reported in Winter [24]. The blocks were calibrated on the wall of a wind tunnel and then calibrated on the SUBOFF model surface itself. In both cases, the blocks were placed midspan between two Preston tubes two inches apart and the average stress indicated by the tubes was the calibration value. This compensated for any spanwise variation in shear stress between the block and the tubes. The two calibrations (tunnel wall and model surface) on each block were compared and no significant differences in the values were found in the range of shear stress where the calibrations overlapped. Overall, the blocks produce a pressure rise that is about 75% of the pressure rise produced by a similar size Preston tube. If the obstacle block is not facing directly into the flow, the pressure rise will be different from that for an aligned block. This effect must be considered because some of the shear stress measurements are made near appendage and sail junctions where the surface flow is no longer parallel to the body. Instead of performing flow visualization, the blocks were aligned to the best estimate of the flow direction and this estimate is assumed to be within 15° of the true flow direction. The pressure rises on the blocks were measured by Gowing [15] during calibration at flow misalignment angles up to 35° in 5° increments. Up to a misalignment of 15°, the pressure rises, and hence the friction coefficient, will be within 5% of the value that would be measured with an aligned block. On the wall of the wind tunnel, the pressure rise on a block was measured with a second block placed 1.4, 2, 6 and 10 block widths away in the spanwise direction. No interference effects were observed with block separations of 3 block widths or greater. This minimum separation was used during the tests.

The major sources of error in the pressure and shear stress measurements were identified by Gowing [15]. The precision uncertainty of the repeated measurements was found to be smaller than the bias uncertainty. Misalignment of the reference pitot tubes and temperature drift in the electronics were the major sources of bias pressure measurement error. The pitot tube readings were compared during testing to check for misalignment and thermal drift in the electronics compensation by repeated calibrations at elevated tunnel temperatures. Over an estimated maximum tunnel temperature rise of $7^{\circ}C$, the true pressure coefficients were estimated to be within +0.01 and -0.0085 of the measured value. The greatest precision error source in the friction coefficient measurements was in measuring the small difference between two pressures with and without the block. The bias error sources were the accuracy limits of the published calibrations for Preston tubes and flow misalignment. Overall, Gowing [15] estimated the true friction coefficients with 95% confidence to be within ±0.0002 of their measured values. The total uncertainty of the measured pressure coefficients with 95% confidence was also estimated by Gowing [15] to be within ±0.015.

5. DATA PRESENTATION

A detailed summary of the test conditions for each individual test is presented in the appendix of Reference [16]. Flow field data were measured in the wind tunnel for the SUBOFF axisymmetric body with various appendages for nineteen model configurations identified in Table 4. Static pressure and skin friction (wall shear stress) measurements were made in the critical regions of the model surfaces. Velocity and off-body static pressure measurements were made in the stern boundary layers of the models. The stern flow parameters of importance are the boundary layer velocity profiles and Reynolds stresses at several axial locations for the CFD code validation, and mean spatial and time-dependent flow variations at the propeller plane for practical design consideration.

Model 5471 and its appendages contained 259 pressure taps for measuring the static pressures on the

surfaces.These surface pressure data were obtained to address the complex flow in the juncture region of the hull and appendages. Skin frictions were measured at selected pressure tap locations. Table 5 summarizes the measurement data for static surface pressure (denoted as P) and skin friction (denoted as S).

A summary of profile measurements in the stern region off the body, consisting of static pressure (denoted PP), stern boundary layer velocity (denoted VP) and mean spatial velocity variation (wake survey) in the propeller plane (denoted V), is presented in Table 6. Pressure and boundary layer velocity profiles were measured at various radial locations for a given axial and azimuthal position. In contrast, the mean wake data contained velocities at various circumferential angular positions for a given radial position at the propeller plane (X/L=0.978). The range of circumferential angles and radii is given in the appendix tables of Reference [16]. The massive raw data may be obtained from the DARPA Hydrodynamic/Hydroacoustic Technology Center located at the David Taylor Model Basin..

6. RESULTS AND DISCUSSION

Only typical results are presented to illustrate the general flow physics governing the modification of the basic turbulent stern flow field of a typical axisymmetric body by various appendages. The results computed by the viscous-inviscid flow interaction computation procedure [18,19] and by the incompressible RANS computer codes [25, 26, 27] are compared to some of the measured data.

6.1 Measured and Computed Static Pressure and Skin Friction Coefficients

The pressure coefficient is defined as $C_p=2(p-p_o)/\rho U_o^2$ for the unrestricted domain, where p is the local static pressure, p_o is the ambient pressure, U_o is the fream-stream velocity, and ρ is the mass density of the fluid.The corrected measured pressure coefficients shown in Fig. 8 agree well the values computed by a simple viscous-inviscid procedure [1,2,18,19] and a RANS calculation [27]. The measurement uncertainty of ± 0.015 for C_p is noted in the last line of Fig. 8 and for measured quantities in subsequent tables and figures as appropriate.

The measured pressure coefficients along the upper meridian line for various configurations are shown in Fig. 9. The effect of the appendages on the hull pressure is small except in the areas very close to the appendages. The measured static pressure coefficient distributions across the stern flow region of the axisymmetric bare hull are shown in Fig. 10. Good agreement between the measured and computed C_p values across the stern flow is also noted in Fig. 9. The measured pressure coefficients on the fairwater and on the stern appendages of various configurations are shown in Figs. 11 and 12. The computed C_p values based on the viscous-inviscid two-dimensional approximation of the section agree well with the measured values on the fairwater where the hull boundary layer is thin but overpredict the measured pressures on the stern appendages where the hull boundary layer is thicker. A general three-dimensional vicous-inviscid flow interaction computation procedure is expected to predict the pressures and the boundary layers over most of the fairwater. However, this simplification fails to predict two small tip vortices shed from the fairwater cap and the root vortices generated at the fairwater/hull juncture (see Section 6.3). Detailed comparison between the measured and computed C_p values on the fairwater and stern appendages remains to be made for the RANS codes in order to ascertain their capability to predict the entire flow field over and downstream of fairwater and stern appendages [16].

Comparison of the computed and measured skin friction coefficients along the upper meridian line is shown in Fig.13 for various configurations. Due to the increase of axial velocities behind the appendages the measured skin friction coefficients on the hull downstream of appendages are higher than those of the bare hull by 0.0004 (10-15%) for fairwater and by 0.001-0.0015 (about 3 times) for the stern appendages. The contribution of the higher skin friction to the total drag may not be significant since the hull area associated with the higher skin friction downstream of the stern appendages is small. As shown in Fig. 13 the agreement between the measured and computed values of C_τ is satisfactory for the bare hull.

6.2 Stern Boundary layer Velocity Profiles

The axisymmetric characteristics of the measured velocity profiles on the axisymmetric bare hull are shown in Fig. 14. The measured velocity profiles over various meridian lines of the bare hull at x/L=0.927 and 0.978 are used to illustrate that the stern flow over the bare hull in the wind tunnel is reasonably axisymmetric except in the wake region downstream of the supporting struts at $\theta=180^o$(Section 6.3).

Comparisons of the measured and computed velocity profiles at various axial locations of the axisymmetric bare hull are shown in Fig. 15; for bare hull

with two ring wings and bare hull and fairwater at 2° angle of attack or yaw are shown Fig.16; and, for axisymmetric bodies 1 and 2 [1,2] are shown in Fig. 17. Comparisons of the measured and computed Reynolds stresses - $-\overline{u_x'v_r'}/U_{ref}^2$ profiles are also shown in Figs. 15 and 17 . As shown in Figs. 15 and 17 both the viscous-inviscid flow interaction procedure and the RANS computer code [27] predict the measured axisymmetric stern boundary layer profiles rather well when the axisymmetric stern flow turbulence model [1, 2, 18,19] is incorporated in the computation. The importance of the turbulence model in the prediction of the turbulent stern flows is evident. Comparison of predicted and measured velocity and Reynolds stress profiles as illustrated in Figures 15 and 17 is essential and more revealing for the assessment of turbulence models used in CFD computations of stern flows.

6.3 Effect of Appendages on the Time-Averaged Stern Flows

Most appendages on an underwater body or a ship cause additional drag and turbulence, and usually generate longitudinal vortices, which are sources of spatial flow nonuniformity and temporal flow fluctuations at the propeller plane. Figs. 18 and 19 show the measured mean cross-flow velocity vectors and mean axial velocity contours at x/L=0.978 of the axisymmetric hull with three appendage configurations. As shown in Fig. 18 each appendage generates two contrarotating longitudinal vortices starting from the junctures of the hull and appendage. At x/L=0.978 the centers of the two vortices shed from the fairwater are estimated to be located at r/R_{max}=0.38 and $\theta = \pm 22^o$, where r is the radial distance from the body axis, R_{max} is the maximum radius of the hull, and θ is positive counterclockwise from the center plane of the fairwater. The centers of the eight vortices shed from the four stern appendages are estimated at r/R_{max}=0.22 and $\theta = \pm 17^o$ from the center plane of each appendage. The centers of vortices are also marked in Fig. 19. The adverse effects of the supporting struts on the measured mean velocities can be seen from Figs. 18 and 19 and are found to limit in the region of $150^o < \theta > 210^o$. The effects of fairwater and four stern appendages on the measured mean axial velocities at x/L=0.978 are shown in Fig. 20. As can be seen from Figs. 19 and 20 pairs of contrarotating longitudinal vortices generated by each appendage bring the high momentum fluid behind the appendage down to the hull. In the inner stern boundary layer the axial velocities behind the appendage are found to be higher than those to each side of the appendage. At outer radii slower axial velocities behind the appendage due to the appendage viscous wake are evident. It is important to note that the redistribution of the axial momentum by the appendage-generated vortices has only a small effect on the circumferential-average axial velocity profiles shown in Fig.16f.

6.4 Effects of Appendages on Turbulence Characteristics of Stern Flows

The turbulence characteristics of the stern flows can be represented by the distributions of Reynolds stresses, namely, $-\overline{u_x'v_r'}$, $-\overline{u_x'w_\theta'}$, $-\overline{v_r'w_\theta'}$, $\overline{u_x'^2}$, $\overline{v_r'^2}$, and $\overline{w_\theta'^2}$, where u_x', v_r', and w_θ' are the turbulence fluctuations in the axial, radial, and azimuthal directions, respectively. Fig. 21 shows the measured distibutions of one turbulent shear stress and three components of turbulence intensity at x/L=0.904, and 0.978 of the bare hull. As shown in Figure 21 the axial turbulence-velocity component has the highest intensity (2-5%) inside the stern boundary layer and the radial velocity component has the smallest intensity. The degree of anisotropy is not serious in the stern flows in general. The measured ratios of $[-\overline{u_x'v_r'}]/[\overline{u_x'^2}+\overline{v_r'^2}+\overline{w_\theta'^2}]$ are almost constant and are found to be about equal to the standard value of 0.15 [1,2,3,4,5,29].

Comparisons of circumferential variations of measured axial, radial and azimuthal turbulent normal stresses at x/L=0.978 of the axisymmetric hull with and without fairwater and four stern appendages are shown in Figures 22, 23, and 24, respectively. Recall that the trailing edge of the fairwater is at x/L=0.297, and that of the four appendages is at x/L=0.920. The influence of stern appendages on the measured turbulent normal stresses at x/L=0.978 is more pronounced than that of the fairwater. The helical rotation of the twin vortices pulls the low turbulence level fluid behind the appendages inward and pushes the high turbulence level fluid away from the appendages upward. The twin vortices generated by each appendage are responsible for the redistribution of turbulence normal stresses. The redistribution of turbulence normal stresses shown in Figs. 22, 23, and 24 correlate with the centers of the contrarotating vortices as inferred from Fig. 18 and the vortex induced pulling/pushing effect on the mean axial velocities shown in Fig. 20. The turbulence level inside the vortex core regions is higher than outside. The fairwater-generated vortices induce a 50%

circumferential variation in the three turbulence intensities. The vortices generated by stern appendages produce peak-to-valley circumferential variations of the three turbulence components by a factor of two at the inner radii. A small narrow viscous wake is detectable at the outer radii for each appendage.

Comparisons of the circumferential variations of two measured turbulent shear stresses are presented in Figs. 25 and 26 at x/L=0.978. The influence of the fairwater on the measured values of $-\overline{u_x'v_r'}$ (axial-radial) is small and on the $-\overline{u_x'w_\theta'}$ values is significant and can be traced to two contrarotating vortices imbedded in the inner stern boundary layer. The magnitude of the measured $-\overline{u_x'w_\theta'}$ attains equal peak value but the sign is opposite in the core regions of the two vortices as shown in Fig. 26. Distortions of the turbulent shear stresses by the eight vortices generated by the four appendages are more pronounced. The peak values of the measured turbulent shear stresses correlate with the centers of the vortices and the mixing length scales can be inferred from the core sizes. Redistributions of $-\overline{u_x'v_r'}$ are evident in Figs. 25 and 26, where lower turbulent shear stress in the inner stern boundary layer behind the appendage is induced by the pulling of high momentum and low turbulence level fluids inward. The reverse is true outboard of the two vortex centers. The fairwater does not affect at all the circumferential-average axial-radial shear stress at x/L=0.978. The effect of the stern appendages on the circumferential-average axial-radial shear stress is neglegible for $r/R_{max} \geq 0.5$ but is significant in the inner radii (about 30% higher). The imbedded longitudinal vortices in the inner stern boundary layer have their own distinct characteristics of turbulent shear stressess with the mixing length scales about equal to the core sizes of the vortices. These overall features of turbulent shear stresses can be incorporated into turbulence modeling for most CFD computer codes.

6.5 Spatial Wake Harmonics

The spatial variations of time-averaged velocities can be represented by a standard harmonic analysis. Figure 27 displays the results of the harmonic analysis of the mean axial velocities. High harmonic amplitudes at multiples of the number of the stern appendages are evident in Fig. 27. The fairwater causes increases in amplitude for a few low-order axial velocity harmonics. Measurement uncertainty of the harmonic amplitudes is estimated from the bare hull conditions and is found to be about $0.002U_{ref}$. Time-dependent flow interaction of appendage,hull, and propeller was investigated by Rood and Anthony [30].

7. CONCLUSION

We have described a recent extensive and comprehensive investigation of the three-dimensional flow field of an axisymmetric body with and without a fairwater, one set of four identical stern appendages, and two ring wings at small angles of attack and drift. These experiments were conducted in the DTMB Anechoic Flow Facility. The wall effects and corrections for the flow field measurement data with a large model in the wind tunnel were presented and measurement uncertainties were quantified. The massive data files of distributions of surface static pressure and skin friction and profiles of three velocity components, turbulence normal and shear stresses, and static pressure across the thick stern boundary layers have been placed onto magnetic tapes for easy access by the CFD users. Examples of a few experimental results were presented in this paper to illustrate the physical process governing the modification of thick axisymmetric stern boundary layers by various appendages. A few major conclusions can be drawn:

The turbulence modeling plays an important role in the prediction of the thick stern boundary layers for axisymmetric bodies [1,2,18,19]. Detailed comparison of the measured and computed velocity and turbulent shear stress profiles in the boundary layers is essential to assess the validity of the turbulence model used. Demonstration of CFD capability to predict time-averaged propulsor inflow distributions for a variety of body shapes is a prerequisite for using CFD as practical design tool.

The spatial nonuniformity of mean velocities and the redistribution of the turbulent normal and shear stresses are found to be caused by a pair of contrarotating vortices generated by each appendage that are imbedded in the inner boundary layer of the hull. The helical rotations of the vortices pull the high momentum and low turbulence fluid downstream and behind the appendage inward and push the low momentum and high turbulence level fluid away from the appendage upward. The appendage-generated vortices redistribute axial-radial turbulent shear stress but do not change their circumferential-average values . The imbedded vortices in the stern boundary layers show distinct characteristics of turbulent shear stresses with the mixing length scales governed by the core sizes of the vortices.

ACKNOWLEDGEMENT

This work was funded under DARPA's Task Area S1974-030, Program Element 63569N, The authors acknowledge with appreciation the continued support of DARPA area manager, Mr. Gary Jones. The authors thank Mr. Justin H. McCarthy for his critical review of the paper. The authors also thank their colleague, Dr. Ming- Shun Chang, Dr. David Fry, Dr. Chen-Wen Jiang, and Mr. William E. Smith, for their technical support. The NAS program at NASA-Ames Research Center provided their CRAY-2 and CRAY-YMP computers resources for this project.

REFERENCES

1. Huang, T.T.,Wang, H.T.,Santelli, N, and Groves, N. C.,"Propeller/Stern/Boundary-Layer Interactionon on Axisymmetric Bodies: Theory and Experiment," DTNSRDC Report 76-0113, December 1976.

2.. Huang, T.T.,Santelli, N. and Belt, G. S., "Stern Boundary-Layer Flow on Axisymmetric Bodies," Proceedings of the 12th Symposium on Naval Hydrodynamics,Wash. D. C., 1978, National Academy of Sciences, Washington, D.C., 1978, pp127-157.

3. Huang, T.T., Groves, N. C. and Belt, G.S., "Boundary Layer Flow on an Axisymmetric Body with an Inflected Stern," DTNSRDC Report 80/064, June 1980.

4. Groves, N.C.,Belt, G. S., and Huang, T. T., "Stern Boundary Layer Flow on a Three-Dimensional Body of 3:1 Elliptical Cross Section," DTNSRDC Report 82/022, April 1982.

5. Huang, T.T. and Groves, N. C., "Stern Boundary Layer Flow on a Three-Dimensional Body of 2:1 Elliptical Cross Section Section," DTNSRDC Report 84/022, October 1984.

6.Huang, T.T., and Groves, N. C., "Effective Wake:Theory and Experiment," Proceedings of the 13th Symposium on Naval Hydrodynamics, Tokyo, Japan, 1980, Shipbuilding Research Association of Japan, October 1980, pp. 651-673.

7. Dickinson, S.C., "An Experimental Investigation of Appendage-Flat Junction Flow, Vol.I: Description, and Vol.II: Elliptical Nose Appendage Data Base, DTNSRDC Report 86/051 and 86/052, December 1986.

8. Davenport, W.J. and Simpson, R.L., "The Turbulence Structure Near an Appendage-Body Junction," Proceedings of the 17th Symposium on Naval Hydrodynamics, The Hague, The Netherlands, 1988.,National Academy Press, Wash. D. C., 1989, pp 461-473.

9. Chang, M.S. and Purtell, L.P., "Three-Dimensional Flow Separation and the Effect of Appendages," proceedings of the 16th Symposium on Naval Hydrodynamics, Berkeley, California, 1986, National Academy Press, Wash. D. C.,1986, pp. 352-370.

10. Groves, N.C., Huang, T.T., and Chang, M.S., "Geometric Characteristics of DARPA SUBOFF Models," Report DTRC/SHD-1298-01, 1989.

11. Huang, T.T.,Liu, H.L., and Groves, N.C., "Experiments of DARPA SUBOFF Program," Report DTRC/SHD-1298-02, 1989.

12. Ward, K.C., and Gowing, S.,"Hardware and Instrumentation of the DARPA SUBOFF Experiments, " Report DTRC/SHD-1298-03,Feb. 1990.

13. Liu, H.L.,Jiang, C.W., Fry, D.J., and Chang, M.S., "Installation and Pretest Analysis of DAPRA SUBOFF Model in the DTRC Anechoic Wind Tunnel," Report DTRC/SHD-1298-04, Mar. 1990.

14.Blanton, J.N.,Forlini, T.J.and Purtell, L.P., "Hot-Film Velocity Measurement Uncertainty for DARPA SUBOFF Experiments" Report DTRC/SHC-1298-05, Mar. 1990.

15. Gowing, S., "Pressure and Shear Stress Measurement Uncertainty for DARPA SUBOFF Experiment," Report DTRC/SHD-1298-06, Jan. 1990.

16.Huang,T.T.,Liu,H.L.,Groves,N.C.,Forlini,T.J.,Blanton, J. N.,Gowing, S., and Smith,W. E.," Measurements of Flow Over an Axisymmetric Body with Various Appendages " DTMB Report, July, 1992.

17. Cebeci, T. and Smith, A.M.O., Analysis of Turbulent Boundary Layer, Academic Press, New York, 1974.

18.Wang,H.T.,and Huang,T.T.,"Calculation of Potential Flow/BoundaryLayerInteraction on Axisymmetric Bodies," ASME Symposium on Turbulent Boundary Layers, Niagara Falls, New York. pp. 47-57, 18-20 June 1979.

19. Huang, T. T., and Chang, M. S.," Computation of Velocity and Pressure Variation Across Axisymmetric Thick Turbulent Stern Flows," Chapter 18, Proceedings of a Symposium on Numerical and Physical Aspects of Aerodynamic Flows III, Edited by Tuncer Cebeci, Springger-Verlag, 1985, pp 341-359.

20. Jiang, C. W., Liu, H. L., and Huang, T. T., " Determination of Wind Tunnel Effects and Corrections," Paper presented at the 19th ITTC, Discussion of Cavitation Committee,s Report, Madrid, Spain, September 1990.

21. Moffat, R.J. "Contributions to the Theory of Single Sample Uncertainty Analysis," Trans. ASME J. Fluid Engineering, Vol. 104, pp. 250-260, 1982.

22. Measurement Uncertainty, ANSI/ASME PTC 19.1-1985, Part 1. 1986.

23. Elfstrom, G.M., "Indirect Measurement of Turbulent Skins Friction," reprinted from DME/NAE quarterly Bulletin No. 1979, Ottawa, Canada, April 1979

24. Winter, K.G., "An Outline of the Techniques Available for the Measurement of Skin Friction in Turbulent Boundary Layers," Progress Aerospace Science, Vol.18, pp. 1-57, 1977.

25. Gorski, J. J., Coleman,R. M., and Haussling,H. J.," Computation of Incompressible flow around the DARPA SUBOFF Bodies," Report DTRC-90/016, July, 1990.

26. Chen, H.-C., Korpus,R., Weems,K., and Fritts,M.," Calculation of Incompressible Viscous Flows about Submarine Configurations by a Multiblock RANS Method," Report SAIC-91/1239, October, 1991.

27. Tsai, J. F., Sung,C. H. , Huang,T. T. and Smith, W. E.," Effects of Turbulence Models on Axisymmetric Stern and Two-Dimensional Trailing Edge Flows Computed by an Incompressible Vicous Flow Solver," Report DTMB and/or paper in preparation, 1992.

28. Stern, F., Toda,Y., and Kim,H. T.," Computation of Viscous Flow around Propeller-Body Configurations: Iowa Axisymmetric Body," J. Ship Research, Vol. 35, No. 2, June, 1991, pp. 151-161.

29. Huang, T. T.," Measured similarity Properties of Eddy Viscosity and Mixing Length in Three-Dimensional Turbulent Stern Flows," paper presented at the 2nd International Symposium on Ship Viscous Resistance, SSPA, Goteborg, Sweden, 1985; also Report DTNSRDC-85/038, May, 1985.

30.Rood, E. P., and Anthony, D. G.,"An Experimental Investigation of Propeller/Hull/Appendage Hydrodynamic Interaction," Proceedings of the 17th Symposium on Naval Hydrodynamics, The Hague, The Netherlands, 1988, National Academy Press, Wash., D. C. 1989, pp 395-413.

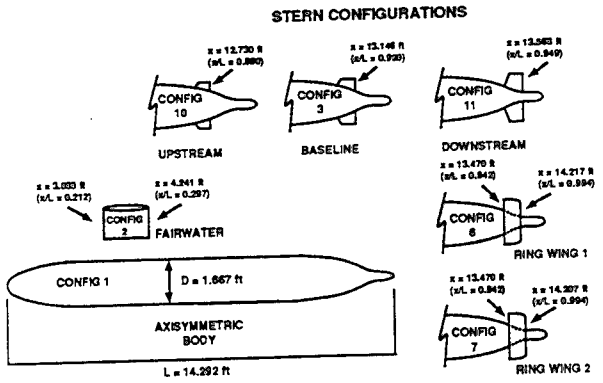

Fig. 1. Schematic of DARPA SUBOFF model components and stern configurations.

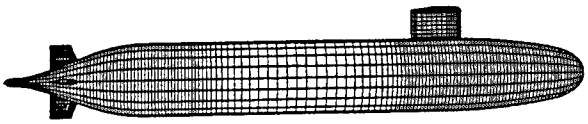

Fig. 2 Sample grid representation of Model Nos. 5470 and 5471

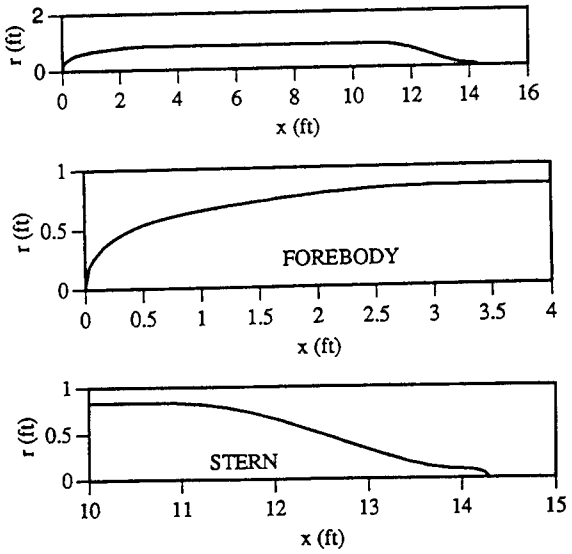

Fig. 3 Hull profile

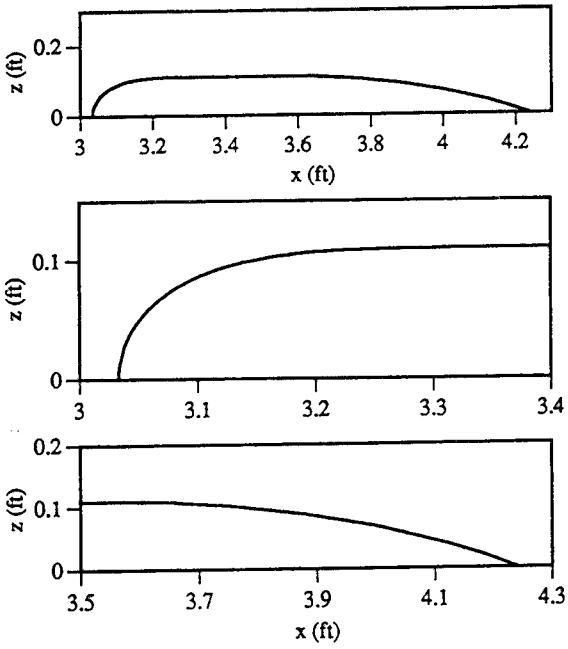

Fig. 4 Fairwater section profile

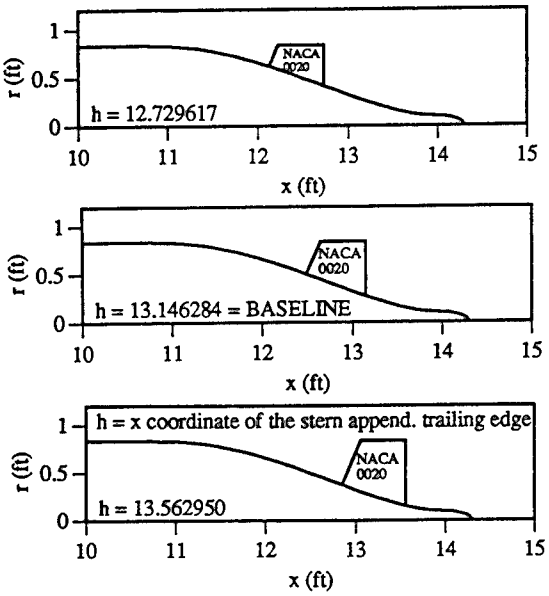

Fig. 5 Stern appendage locations

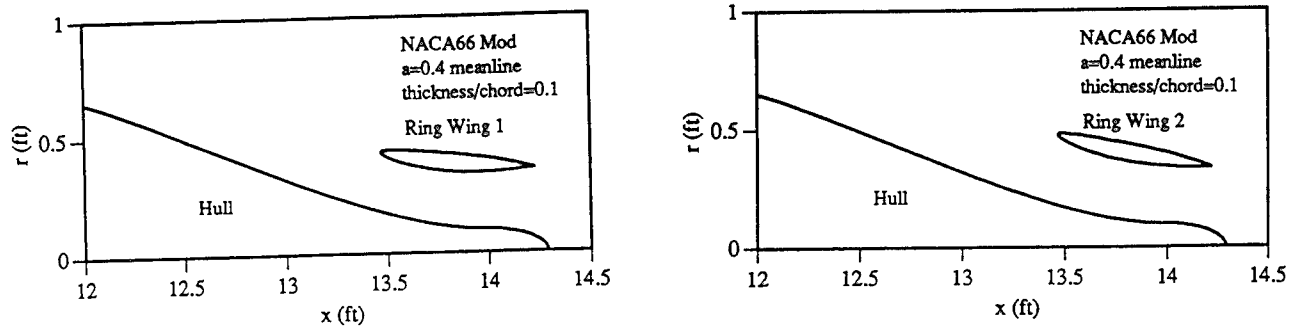

Fig. 6 Ring wing section profile and placement

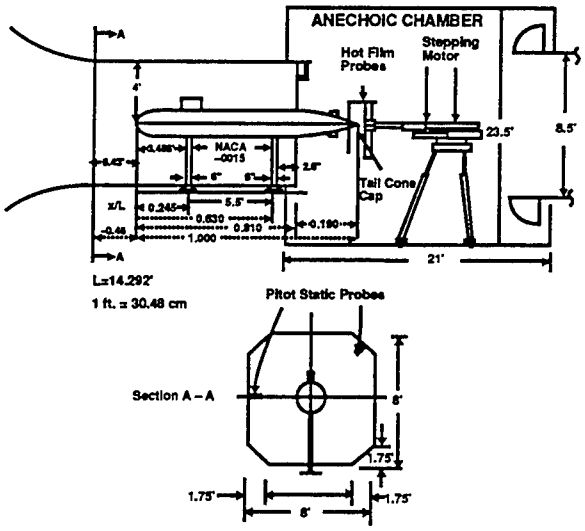

Fig. 7 Schematic view of Model in closed- and open-jet test section

Table 1 Example of Measured Surface Pressures Corrected by the Empty Tubnnel Axial Pressure Gradient

x/L	Δ C_p Empty Tunnel	Measured C_p On Body	Corrected C_p On Body
0.035	0.02776	-0.11398	-0.14174
0.070	0.02659	-0.07055	-0.09714
0.105	0.02578	-0.05479	-0.08057
0.181	0.02396	-0.09734	-0.12132
0.239	0.02367	-0.04317	-0.06684
0.402	0.02471	-0.01406	-0.03877
0.501	0.02144	-0.01303	-0.03447
0.601	0.01563	-0.02558	-0.04121
0.700	0.00937	-0.05175	-0.06112
0.741	0.00748	-0.11203	-0.11951
0.781	0.01043	-0.22959	-0.24002
0.805	0.01264	-0.20961	-0.22225
0.840	0.00852	-0.05445	-0.06297
0.857	0.00735	-0.006193	-0.01354
0.875	0.00656	0.08522	0.07866
0.904	0.00609	0.16067	0.15458
0.927	0.00646	0.18508	0.17862
0.956	0.00788	0.18326	0.17574
0.978	0.00963	0.14006	0.13043

$(C_p)_{corrected} = (C_p)_{measured} - \Delta C_p$

$C_p = (P - P_{ref}) / (1/2\ \rho\ U^2_{ref})$

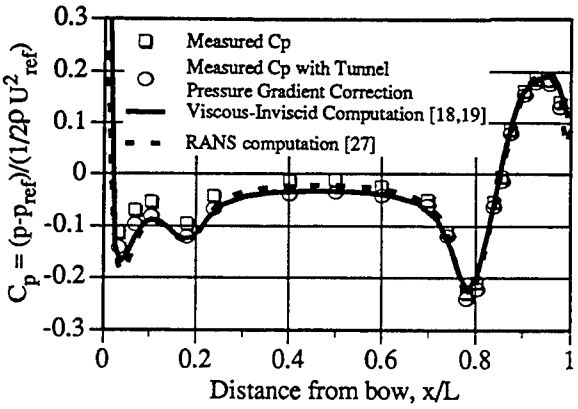

Fig. 8 Comparison of computed and measured static pressure coefficients on the axisymmetric hull
Measurement uncertainty of C_p: ±0.015

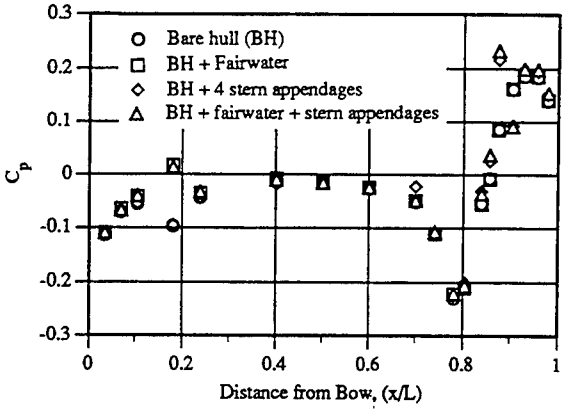

Fig. 9 Measured pressure coefficients along the upper meridian line for various configurations
Measurement uncertainty of C_p: ±0.015

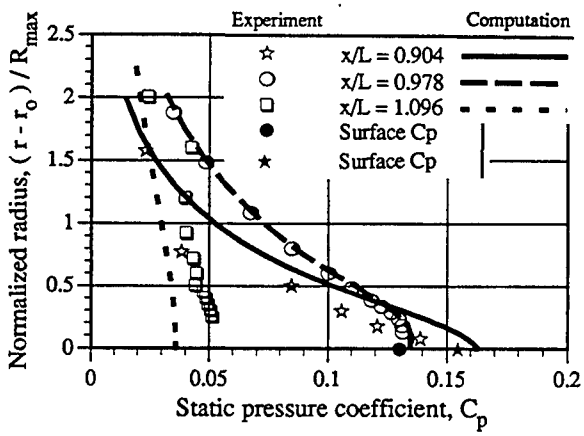

Fig. 10 Measured static pressure coefficient distributions across stern flow region of the axisymmetric hull
Measurement uncertainty of C_p: ±0.015

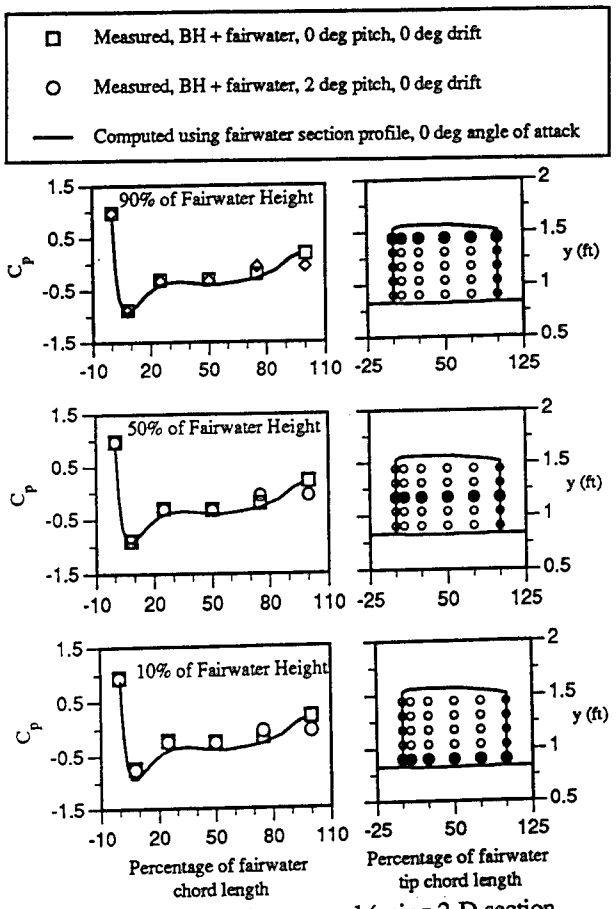

Fig. 11 Measured and computed (using 2-D section profile) pressure coefficient distribution of fairwater surface for various configurations
Measurement uncertainty of C_p: ±0.015

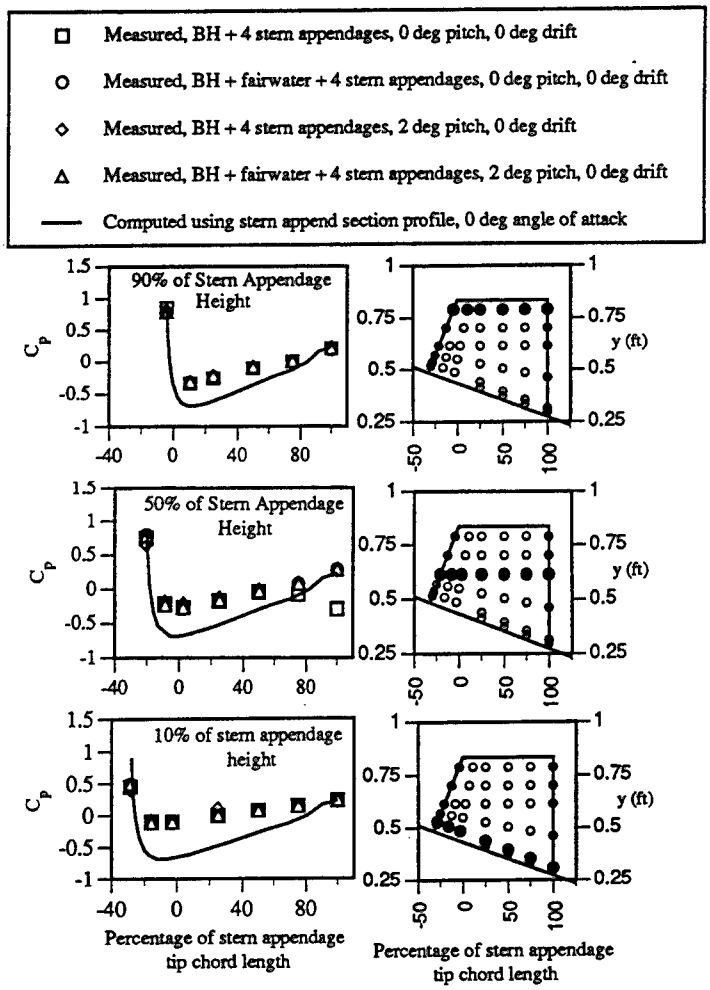

Fig. 12 Measured and computed (using 2-D section profile) pressure coefficient distribution on stern appendage surface (baseline position) for various configurations
Measurement uncertainty of C_p: ±0.015

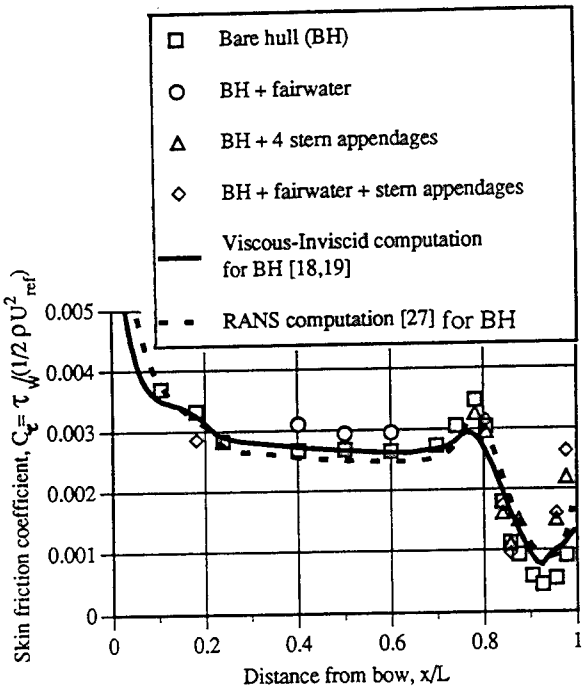

Fig. 13 Comparison of the computed and measured skin friction coefficients along the upper meridian line for various configurations
Measurement uncertainty of C_τ: ±0.0002

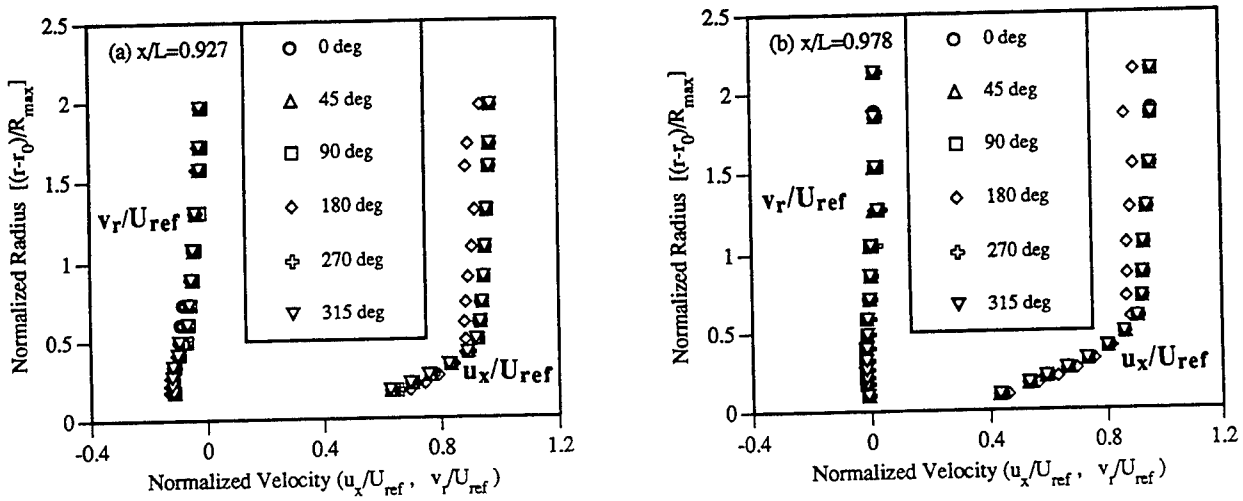

Fig. 14 Measured boundary layer velocity profiles over various meridian lines of the axisymmetric hull
Measurement uncertainties of u_x/U_{ref} and v_r/U_{ref}: ± 0.025

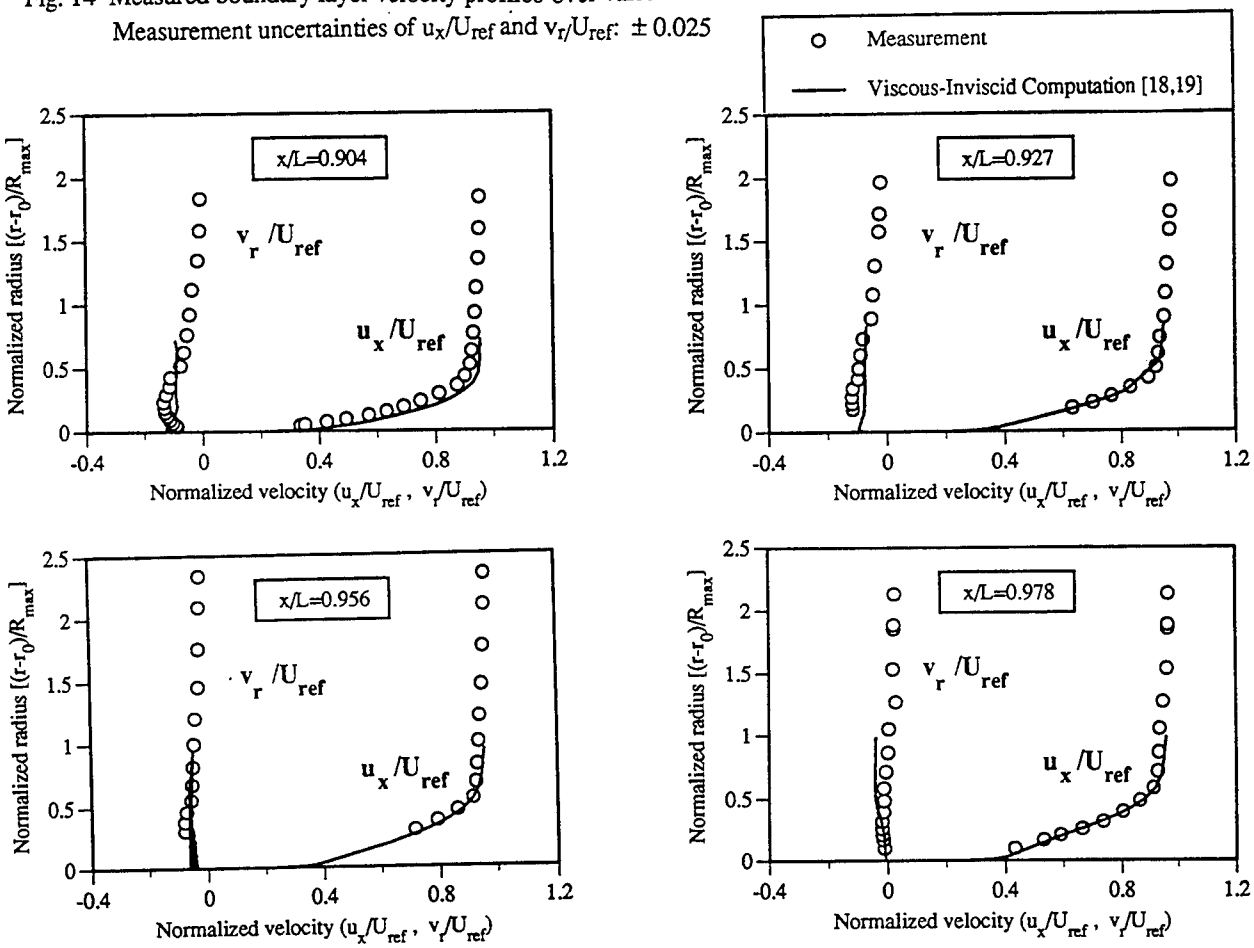

Fig. 15 a Comparison of measured and computed (viscous-inviscid) velocity profiles at various axial locations of the axisymmetric hull
Measurement uncertainties of u_x/U_{ref} and v_r/U_{ref}: ± 0.025

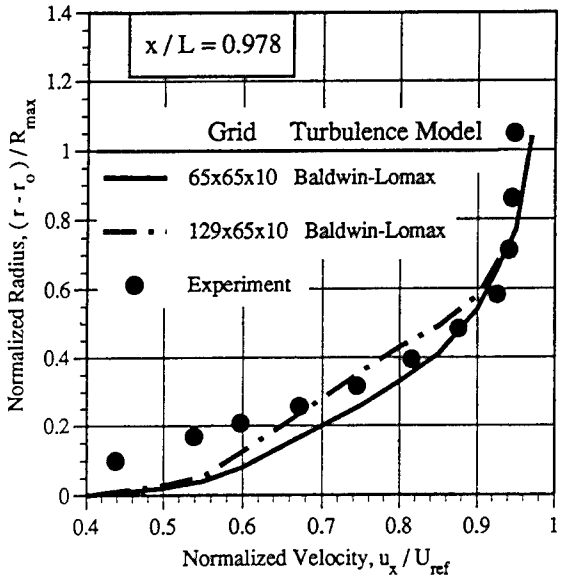

(a) RANS Computation [25]

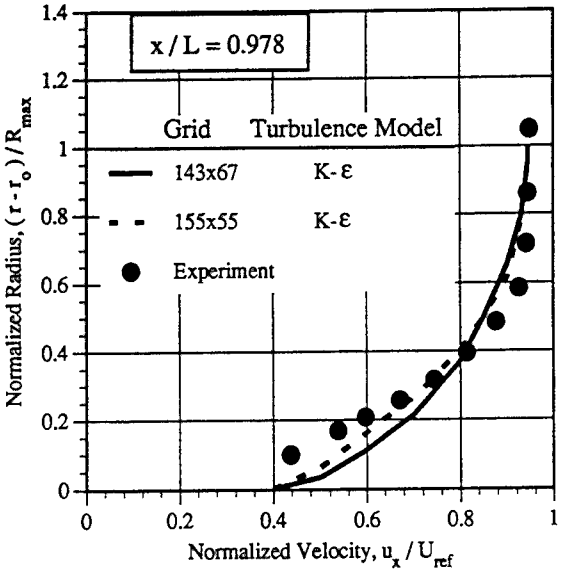

(b) RANS Computation [26]

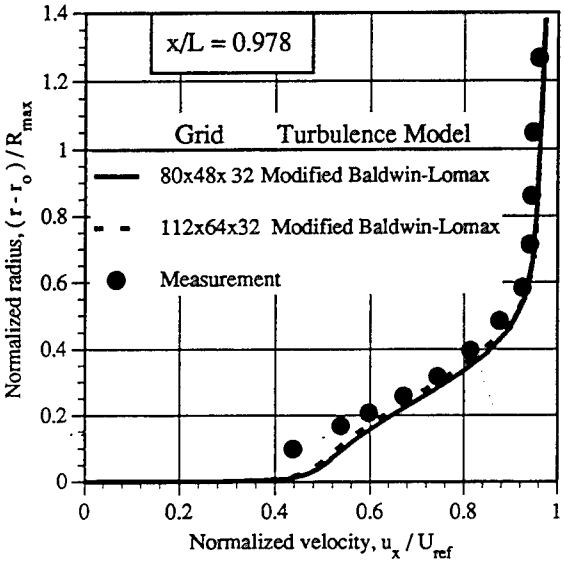

(d) RANS Computation [27]

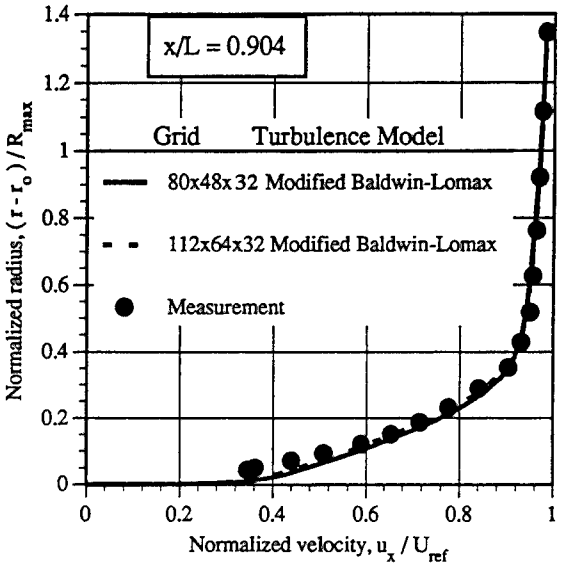

(c) RANS Computation [27]

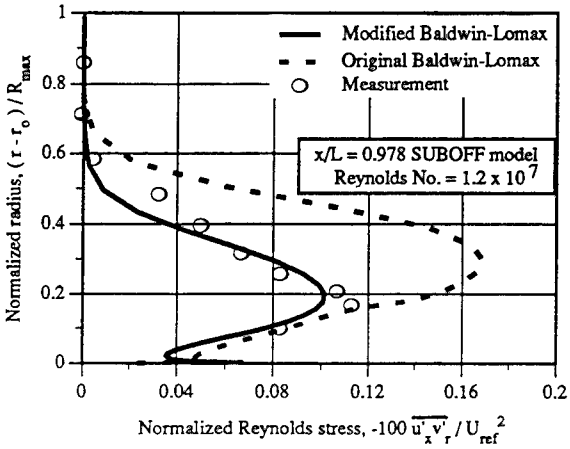

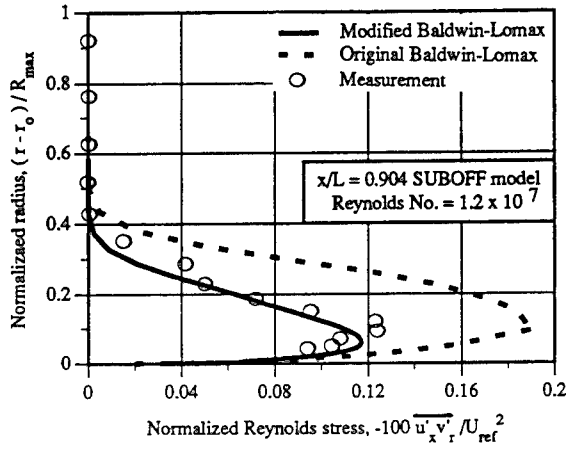

Fig. 15 b Comparison of measured and computed (RANS) velocity and Reynolds stress profiles at x/L=0.978 and 0.904 of the axisymmetric hull

Measurement uncertainties of u_x/U_{ref} : ± 0.025 and of $\overline{u_x'v_r'}/U_{ref}^2$: $\pm 10^{-4}$

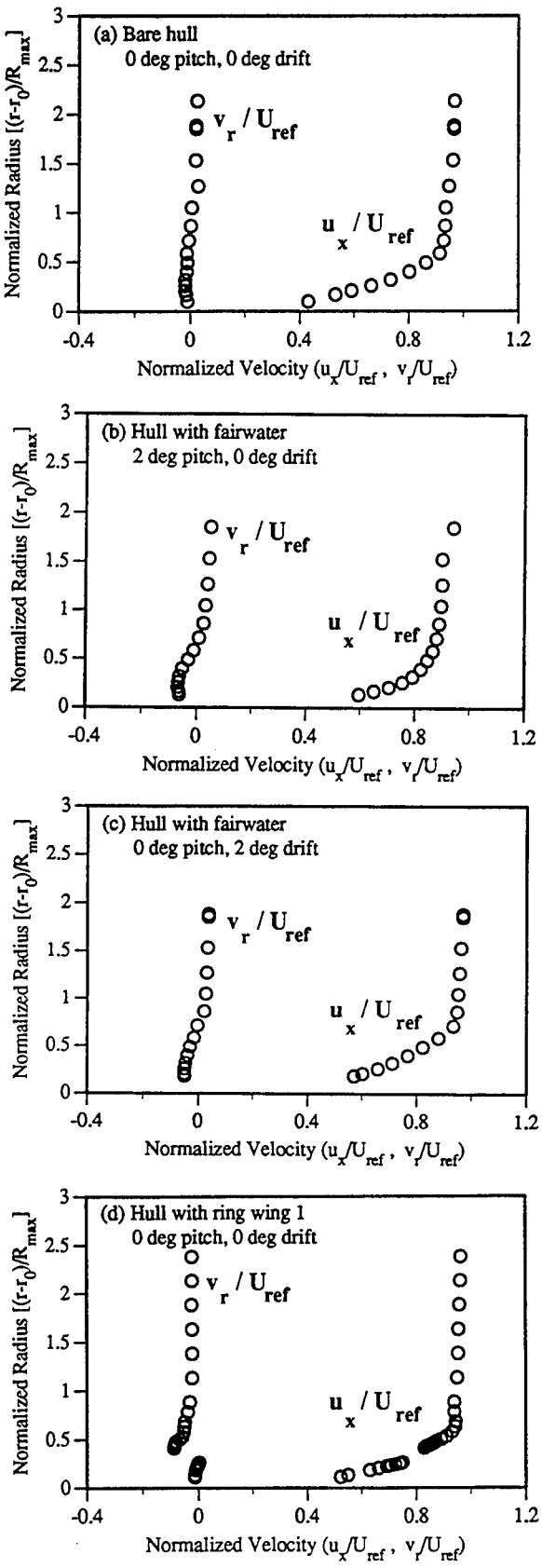

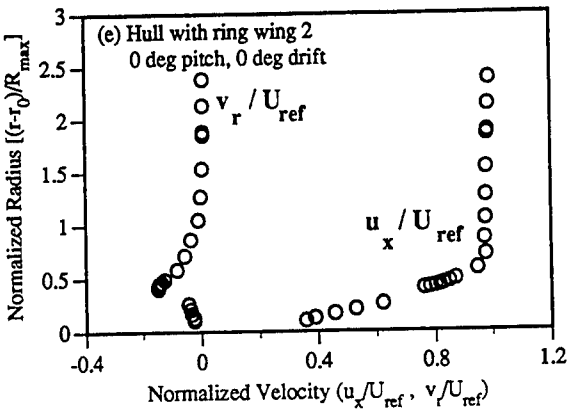

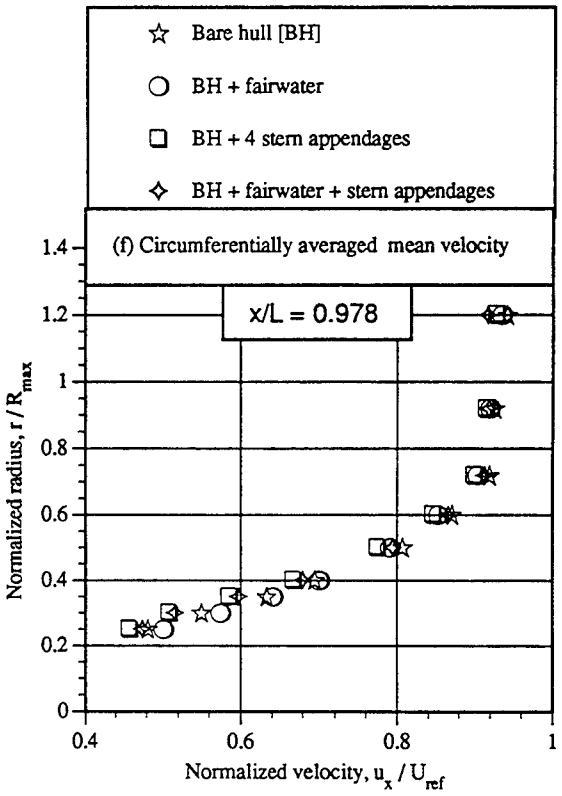

Fig. 16 Comparison of measured velocity profiles of various configurations at x/L=0.978 for θ=0° (a-e) or for circumferential-averaged (f)
Measurement uncertainties of u_x/U_{ref} and v_r/U_{ref}: ± 0.025

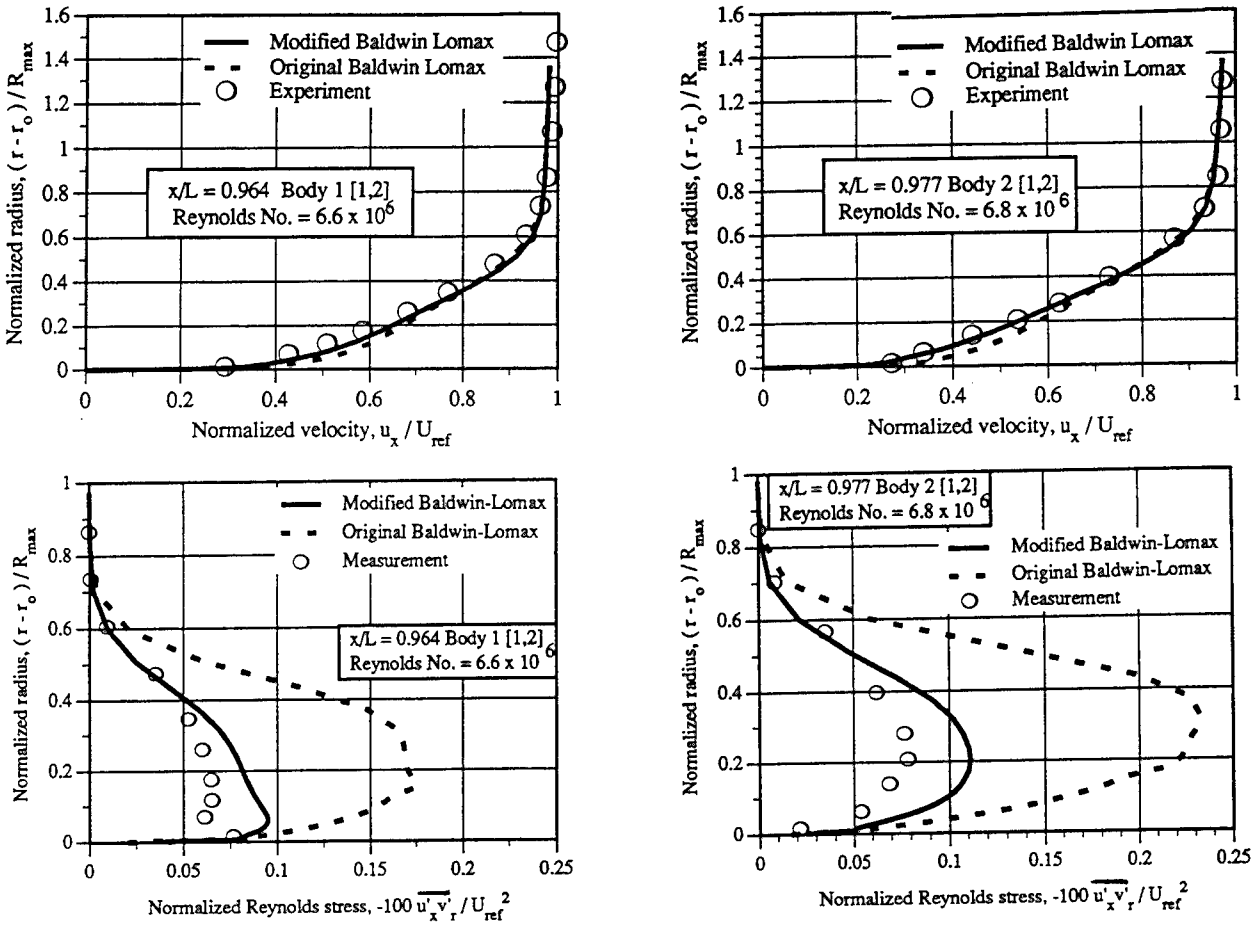

Fig. 17 Comparison of measured and computed (RANS) velocity and Reynolds stress profiles of axisymmetric bodies 1 and 2 [1,2]
Measurement uncertainties of u_x/U_{ref} : ± 0.020 and of $\overline{u_x'v_r'}/U_{ref}^2$: $\pm 10^{-4}$

Table 2. Bias Uncertainty of Three-Component Hot-Film Velocity Measurement (B_V = 2 Sv)

	u_x / U_{ref} %	v_r / U_{ref} %	w_θ / U_{ref} %
Temperature	0.32	0.32	0.32
Probe Alignment	-	0.50	0.50
Analog/Digital Conversion	0.07	0.13	0.12
Speed Calibration*	2.12	1.76	0.88
Angle Calibration	0.53	1.31	1.43
Total (Root Sum Square)	2.21	2.28	1.79

*10-points speed checks against the predetermined calibration curve

Table 3. Precision Uncertainty of Three-Component Hot-Film Velocity Measurement

	$P_V = 2S_V$			$P_{V'} = 2S_{V'}$			$P_{u'v'} = 2S_{u'v'}$	
	$\frac{u_x}{U_{ref}}$ %	$\frac{v_r}{U_{ref}}$ %	$\frac{w_\theta}{U_{ref}}$ %	$\frac{u'_x}{U_{ref}}$ %	$\frac{v_r'}{U_{ref}}$ %	$\frac{w_\theta'}{U_{ref}}$ %	$10^4 \frac{-u_x'v_r'}{U_{ref}^2}$	$10^4 \frac{-u_x'w_\theta'}{U_{ref}^2}$
Outside* BL Wake	0.04	0.04	0.06	0.02	0.04	0.02	0.01	0.01
Inside * turbulent wake	0.28	0.16	0.20	0.17	0.13	0.14	1.15	1.01
Outside* turbulent wake	0.16	0.06	0.04	0.09	0.05	0.06	0.05	0.05

* Fixed probe for repeated measurement
+ Probe moved and returned to the same point
Estimated from 30 repeated measurements using 1500 individual data at 150 Hz

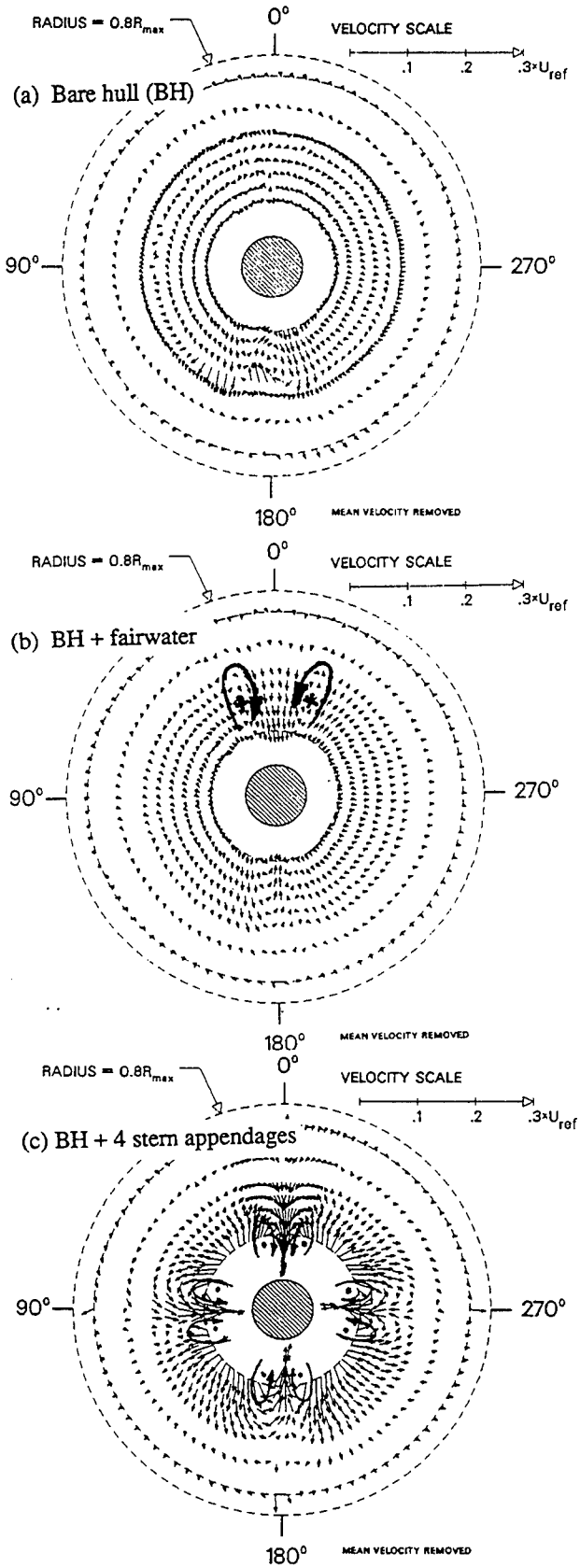

Fig. 18 Comparison of measured mean cross-flow velocity vectors at x/L=0.978 of the bare hull with various appendages
Measurement uncertainties of the cross-flow velocities: ±0.025 U_{ref}

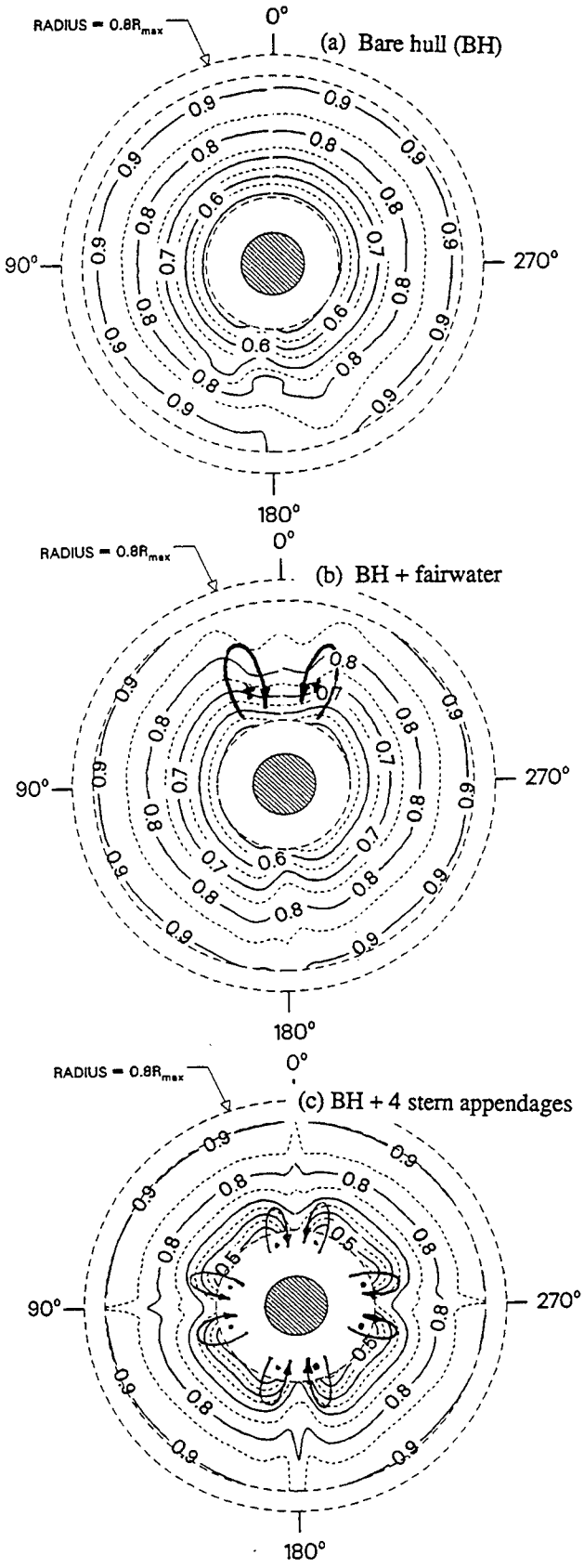

Fig. 19 Comparison of measured mean axial velocity contours at x/L=0.978 of the bare hull with various appendages
Measurement uncertainties of the mean axial velocities: ±0.025 U_{ref}

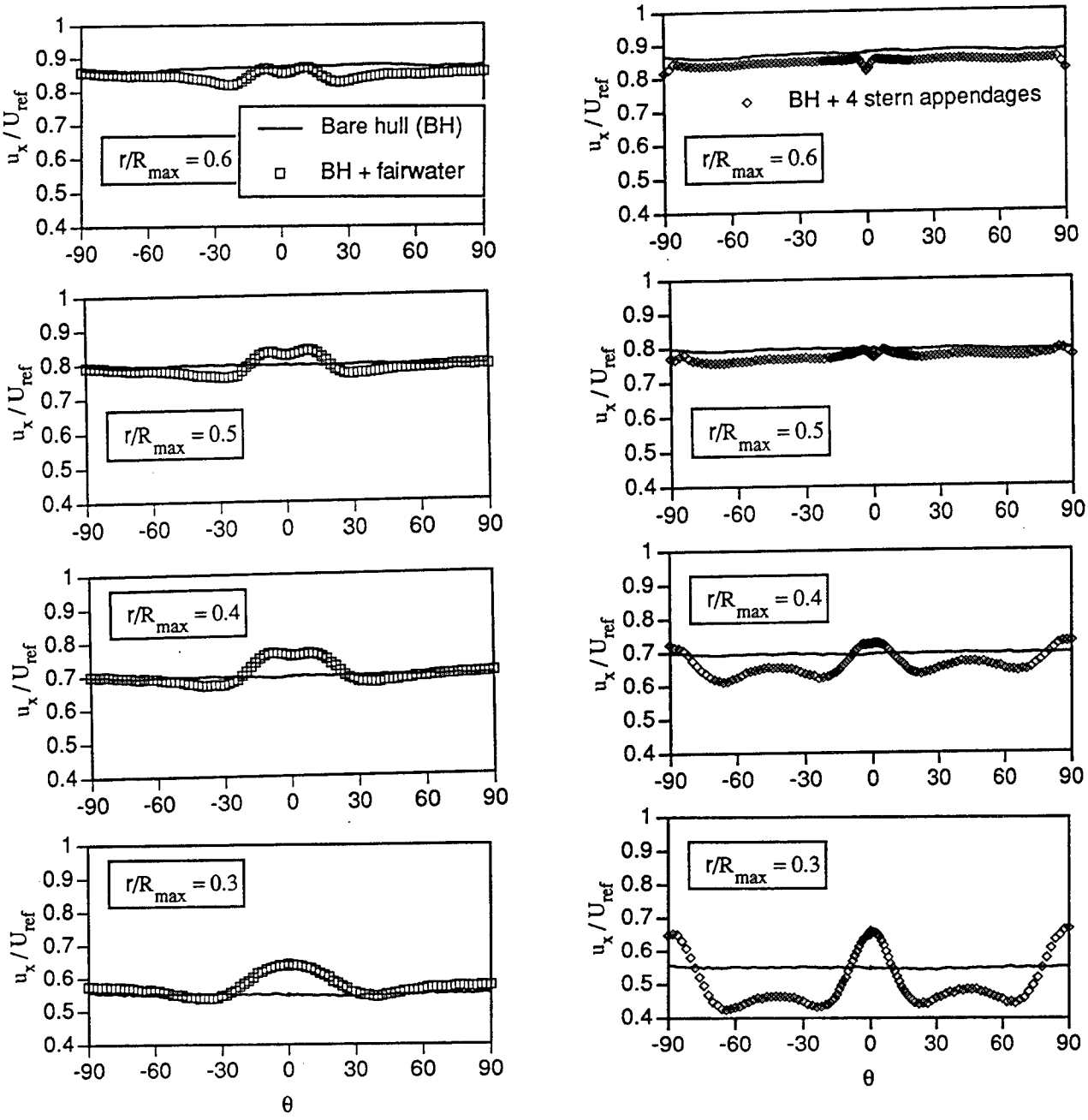

Fig. 20 Comparison of measured circumferential variation of mean axial velocities at x/L=0.978 for r/Rmax=0.3, 0.4, 0.5, and 0.6 of the bare hull with and without fairwater and four stern appendages
Measurement uncertainty of u_x/U_{ref}: ±0.025

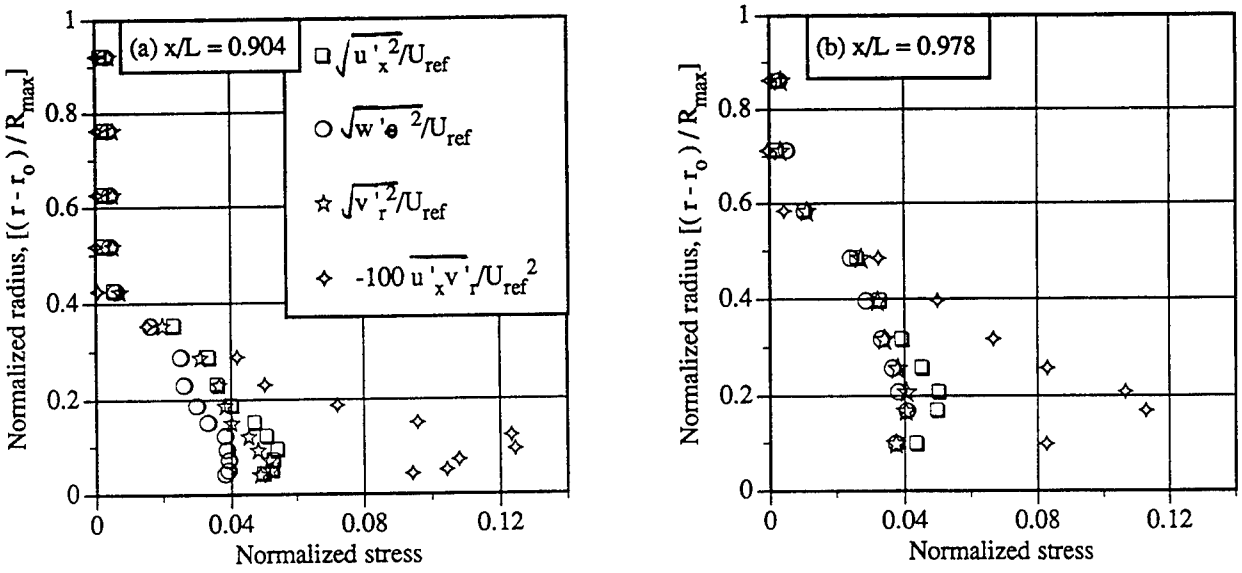

Fig. 21 Measurement distributions of Reynolds stresses on axisymmetric hull

Measurement uncertainty of turbulence level: ±0.002 and of $-\overline{u_x'v_r'}/U_{ref}^2$: 10^{-4}

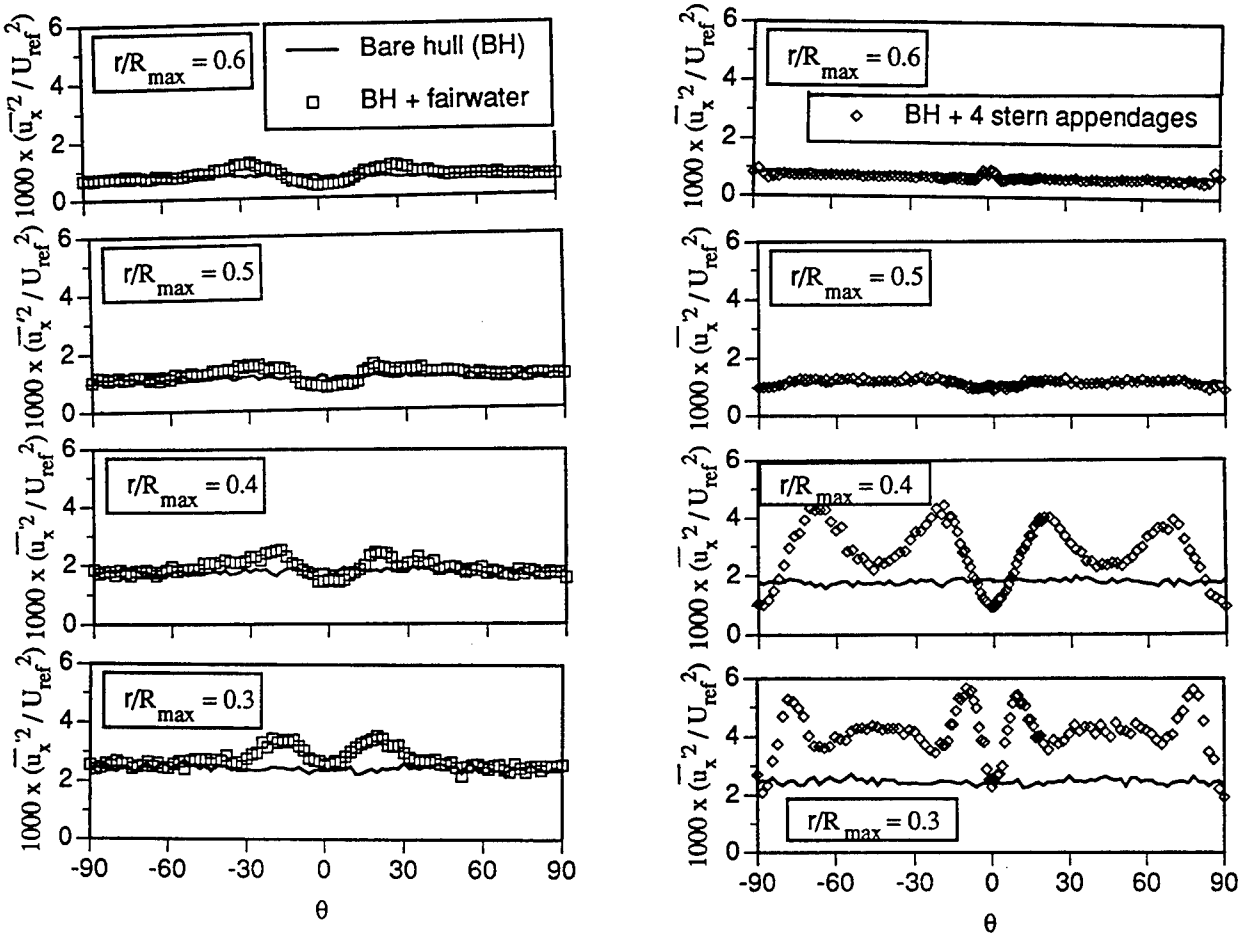

Fig. 22 Comparison of measured circumferential variation of axial normal stress at x/L=0.978 of the axisymmetric hull with and without fairwater or four stern appendages

Measurement uncertainty of $\sqrt{\overline{u_x'^2}}/U_{ref}$: 0.002

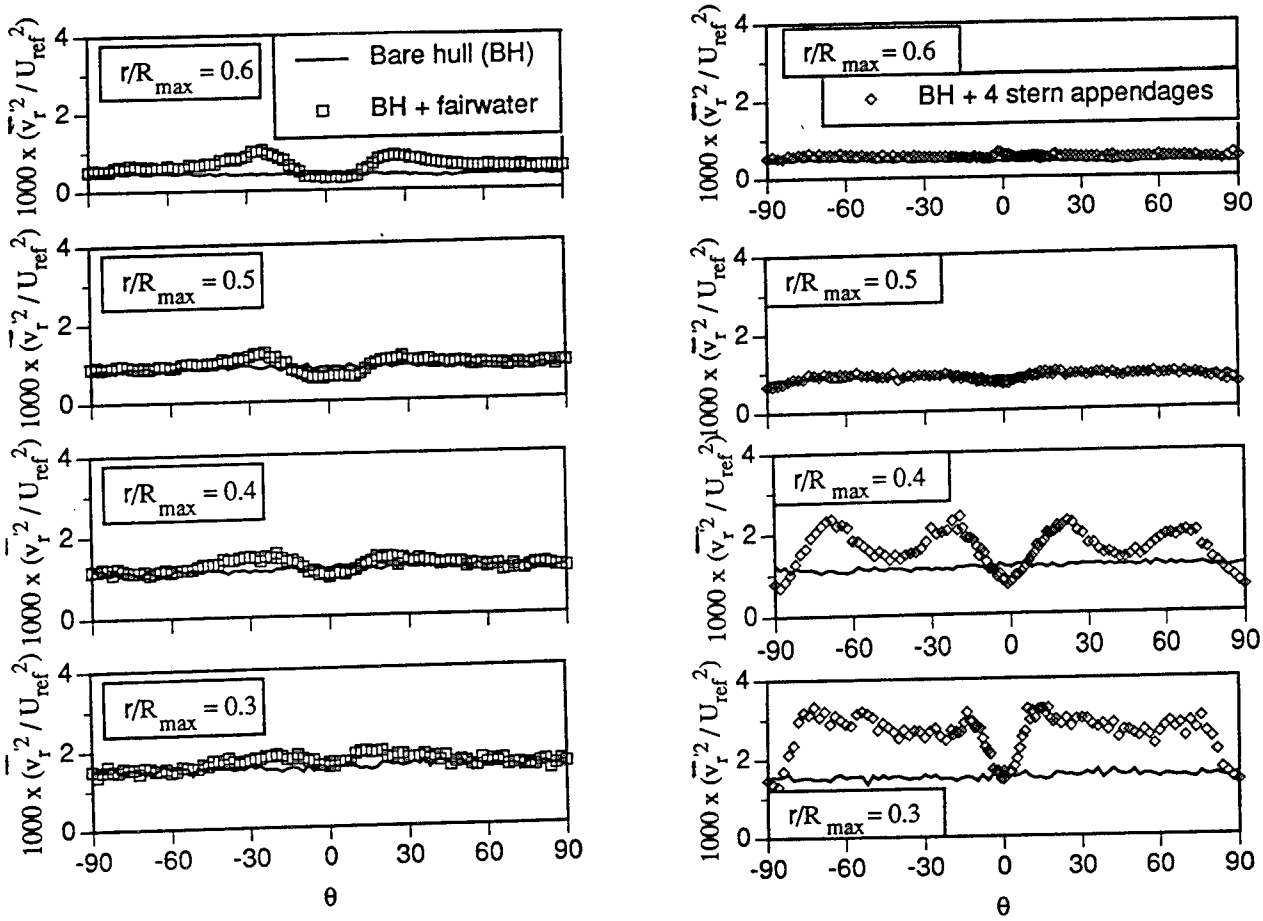

Fig. 23 Comparison of measured circumferential variation of radial normal stress at x/L=0.978 of the axisymmetrical hull with and without fairwater and four stern appendages

Measurement uncertainty of $\sqrt{\overline{v_r'^2}} / U_{ref}$: 0.002

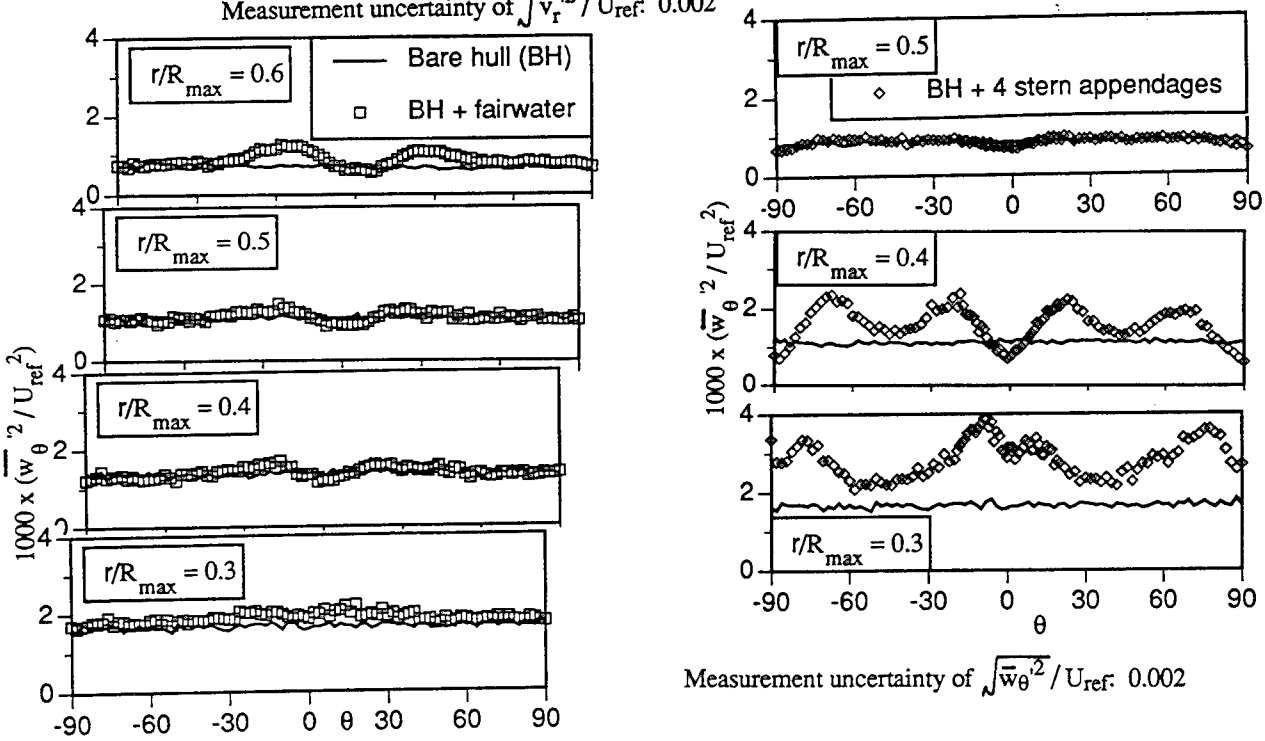

Measurement uncertainty of $\sqrt{\overline{w_\theta'^2}} / U_{ref}$: 0.002

Fig. 24 Comparison of measured circumferential variation of azimuthal normal stress at x/L=0.978 of the axisymmetrical hull with and without fairwater and four stern appendages

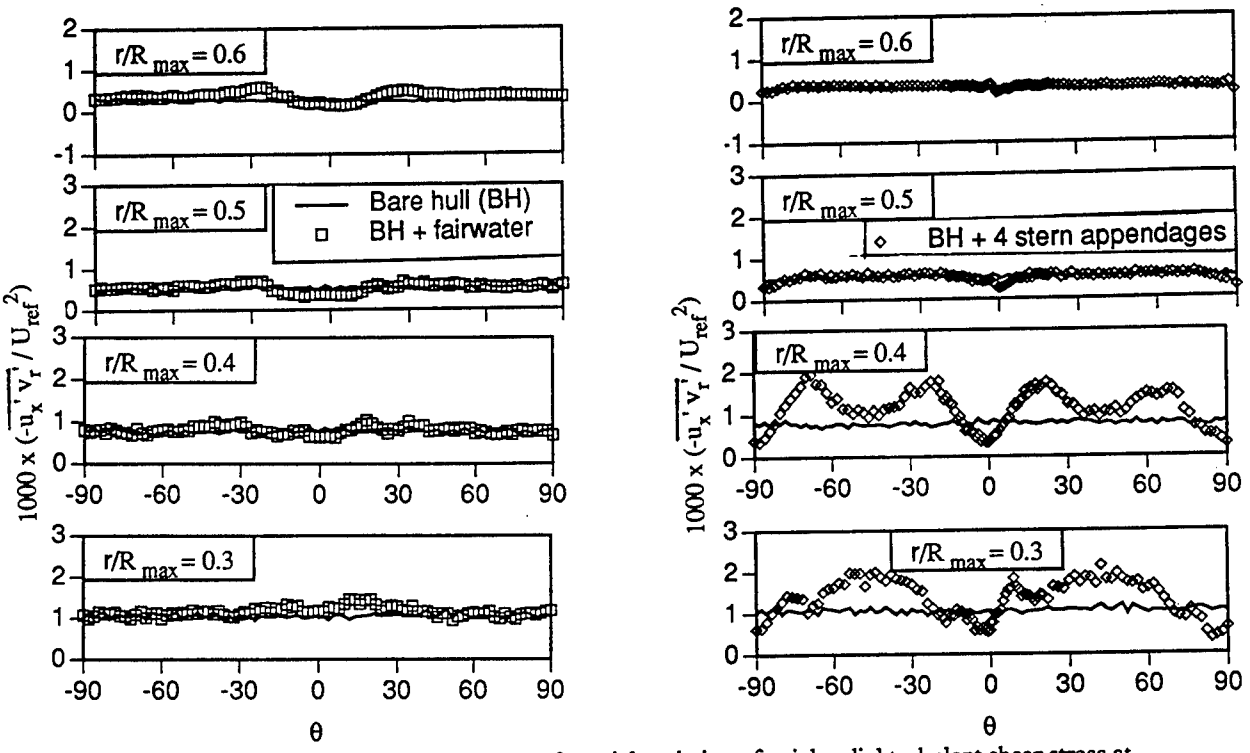

Fig. 25 Comparison of measured circumferential variation of axial-radial turbulent shear stress at x/L=0.978 of the axisymmetrical hull with and without fairwater and four stern appendages
Measurement uncertainty of $-\overline{u_x'v_r'}/U_{ref}^2$: $\pm 10^{-4}$

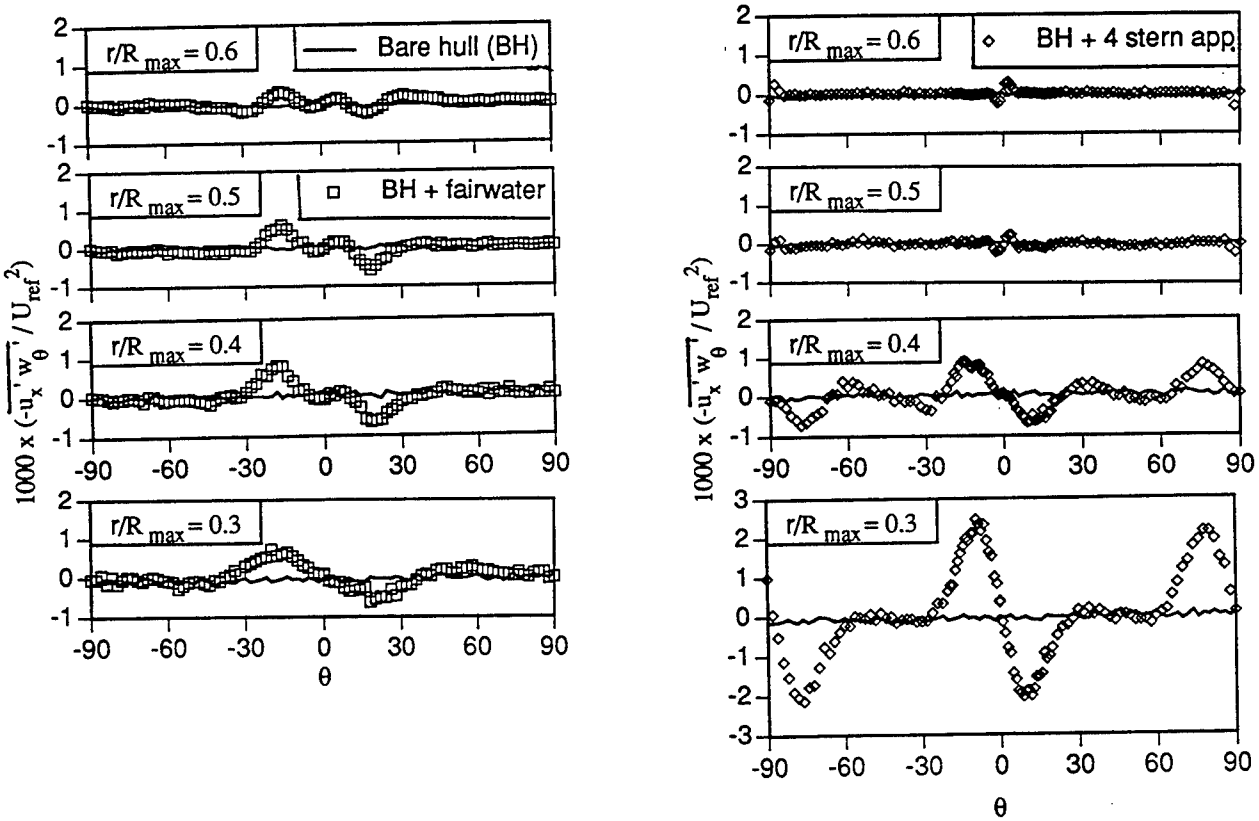

Fig. 26 Comparison of measured circumferential variation of axial-azimuthal turbulent shear stress at x/L=0.978 of the axisymmetrical hull with and without fairwater and four stern appendages
Measurement uncertainty of $-\overline{u_x'w_\theta'}/U_{ref}^2$: $\pm 10^{-4}$

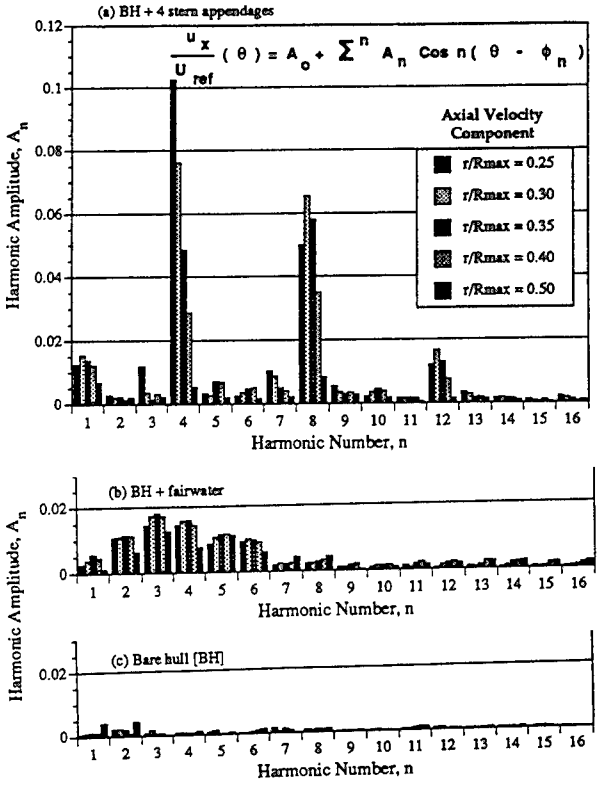

Fig. 27 Measured wake harmonics of the axisymmetric hull with and without fairwater or four stern appendages

Table 4. Summary of DTRC Model 5471 Configurations

Conf	BH	FW	SA			RW #1	RW #2	AOA		AOD	
			B	U	D			0°	2°	0°	2°
1	X							X		X	
2	X	X						X		X	
3	X		X					X		X	
4	X	X							X	X	
5	X	X						X			X
6	X					X		X		X	
7	X						X	X		X	
8	X	X	X					X		X	
9	X								X	X	
10	X			X				X		X	
11	X				X			X		X	
12	X	X				X		X		X	
13	X	X					X	X		X	
14	X		X						X	X	
15	X	X	X						X	X	
16	X					X			X	X	
17	X						X		X	X	
18	X	X				X			X	X	
19	X	X					X		X	X	

BH: Barehull; FW: Fairwater; SA: Stern appendages
B: Baseline; U: Upstream; D: Downstream
AOA : Angle of attack; AOD: Angle of drift

Table 5. Summary of Surface Flow Data Collected in AFF

Conf.	Surface Tap Designator											
	HU	HP	HS	HL	FH	FW	AH	SA	WU	WP	WS	WL
1	PS	PS	PS	P	PS		PS					
2	PS	P	P	P	PS	PS	P					
3	PS	P	P	P			PS	PS				
4	P	P	P	P	P	P	P					
5												
6	P								P	P	P	P
7	P								P	P	P	P
8	P	P	P	P	PS		PS	PS				
9	P	P	P	P	P		P					
10												
11												
12	P								P	P	P	P
13	P								P	P	P	P
14	P	P	P	P			P	P				
15							P	P				
16	P	P	P	P					P	P	P	P
17	P	P	P	P			P		P	P	P	P
18	P	P	P	P			P		P	P	P	P
19	P	P	P	P			P		P	P	P	P

P = Surface Pressure Measurements
S = Skin friction (Wall Shear Stress) Coefficients

Table 6. Summary of Profile Flow Data Collected in AFF

Conf	Profile Measurements at Each x/L								
	.875	.904	.927	.956	.978	.996	1.04	1.09	1.20
1	vp	vp v pp	vp	vp	vp v pp		v	v pp	v pp
2		v pp			v pp		v	v pp	v
3					v pp		vp	v pp	v
4		vp v			vp v			v	
5		vp v			vp v			v	
6					vp v	vp v	v	v	v
7					vp v	vp v	v	v	v
8					vp v		v vp	v vp	v
9					vp v				
10					v				
11					v				

VP = Boundary Layer Velocity Profile Data
V = Mean Velocity Wake Data
PP = Pressure Profile Data

DISCUSSION

E. Rood
Office of Naval Research, USA

I would like to thank the authors for presenting this paper. It is the product, I am sure, of a long and tedious measurement effort. Certainly this data base will serve as a valuable contribution for the validation of flow prediction methods. Nevertheless, the paper does not appear to present any new information. The description of the behavior of the flow instills confidence in the data although it does not explore new features of the flow. The authors hint that the data base will be used to develop CFD capability, but it is not clear how that will be done. Can the data base be used to separate errors due to numerical procedures from errors due to inadequate turbulence models? Do the authors have a preliminary assessment of the effects of, say, gridding versus turbulence model?

The action of the longitudinal vortices produced by the appendages is interesting. It has been known for a long time that the vortices tend to "invert" the boundary layer. However, the description of the motion in terms of vortices as it evolves downstream along the hull conjures an image that may not usefully serve in all cases. Would it also be appropriate to describe the effects of the appendages in terms of a jet? The inversion of the boundary layer places high momentum beneath low momentum in a region of small cross-section. This high-momentum fluid, then, is jetting through the otherwise slow moving boundary layer. I suggest that three-dimensional cross-section profiles of the axial velocity may conjure an image much different than a vortex. In this case, the emphasis is on the jet rather than the vortex, which merely serves as the transport mechanism.

AUTHORS' REPLY

We thank Dr. Rood for his interest in and comments on our paper. The paper represents a comprehensive database for the effects of typical appendages on the axisymmetric stern flows. The geometries of the hull and appendages are represented in simple mathematical forms so that computation grid resolution can be refined to any level without introducing discretization error on the body surface. The complete set of measurement data of mean flows and turbulence structures with clearly assessed measurement uncertainties is not available in any literature. It is true that some of the mean flow features have been known, but most available data are incomplete and are not suitable for CFD validation. The turbulence models for a thick stern boundary layer were investigated in this paper. However, the turbulence models for the appendages generated vortices have not been fully investigated.

Most CFD codes are not able to predict the stern flows of axisymmetric bodies with various appendages for design applications, because the grid resolutions are not fine enough in the juncture region and in the vortex cores, and most turbulence models that do not incorporate the special features of appendage induced vortices overpredict the decay rate of the vortices. In our experience, most grid generation schemes without local refinement may be used for qualitative prediction but are not adequate for quantitative prediction of vortical flows associated with hull/appendage junctures.

We have found that the first grid spacing normal to the body surface (y) must be set at a value of $u_\tau y/\nu$ slightly less than 10 in order to obtain a grid independent solution in our computation which uses a modified Baldwin-Lomax turbulence model, where u_τ is the frictional velocity and ν is the kinematic viscosity of the fluid. Inside the viscous cores of vortices at least 10 radial grid points are required. The standard Baldwin-Lomax turbulence model must be modified for a thick stern boundary layer and for the wake region of cross-flow separation associated with the body at a moderate angle of attack. Turbulence models for the appendage-generated vortices in the thick stern boundary layer have not been fully investigated. This paper is aimed at promoting research interest and activities in this special area.

It is well known that the pressure gradients in the hull/appendage juncture regions generate vortices. The vortex generation process and the three-dimensional interaction between the shed vortices and the thick stern boundary layer are expected to be described by solutions of the Reynolds-Averaged Navier-Stokes equations. Due to the limitations of the grid resolution and turbulence model used in most CFD codes, the numerical solutions are not fully satisfactory. The present measurement data are presented to assist the improvement of the current CFD capability.

To represent the effects of an appendage in terms

of a jet is not a sound approach. This analogy argument requires artificial input of a jet either on the boundary or in the flow field. Nevertheless, some aspect of the boundary layer inversion may qualitatively be simulated as a jet action in the boundary layer. A general quantitative solution for appendage flow is not likely to be obtained by a "jet" simulation.

DISCUSSION

V. Patel
University of Iowa, USA

1. You show well known axisymmetric (bare body) results along with calculations in Figures 1 and 15. The BL and the modified BL models give marginally different mean velocity profiles although the Reynolds stresses differ by a factor of two, or more. What does this mean? Do we conclude that the turbulence model is not very important (in the flow)?

2. We know that several groups have calculated the flow around the various DARPA configurations (fins, appendages, etc.). Can you tell us what has been concluded from these calculations?

AUTHORS' REPLY

We also thank Prof. V.C. Patel for his comments. It has been found [2, 19] that the standard Cebeci-Smith or Baldwin-Lomax turbulence model overpredicts eddy viscosity by as much as a factor of 4, mixing length by a factor of 2, and Reynolds stress by a factor of 2. These discrepancies will generally cause an overprediction of axial velocities in the propeller plane by 5 to 10 percent. The stringent requirements for the full-scale prediction of ship speed and propulsor rotation speed impose high standards of experimental and computational accuracy. Therefore, continued improvement of experimental and computational accuracy is essential to meet the design need. The turbulence model we propose and use in propulsor design to predict the propulsor inflows for the model- and full-scale ships is an interim rather than a final solution. It is essential to develop a more comprehensive and more rational turbulence model which can predict accurately the propulsor inflows. Critical examination of the measured and computed Reynolds stresses and velocity profiles, as illustrated in this paper, is extremely valuable to assess the validity of turbulence models. Without careful examination and thorough comparison, the utility of CFD can be seriously compromised.

The following are my personal assessments of the results of DARPA's CFD computations on the SUBOFF models. Except for the velocities in the region of the propeller plane, some CFD codes predicted reasonably well the entire flow fields of simple configurations (i.e., bare hull and bare hull with ring wings). However, only qualitative trends were predicted for more complex appended configurations. Some of the deficiencies of the present CFD capability are mentioned in the reply to Dr. Rood. The opportunity exists for substantial improvement of the current CFD capability to predict the entire flow field over a fully appended submarine. Grid resolution, computation/convergent efficiency, and turbulence modeling are a few areas that can be significantly improved.

Session VI

Hydrodynamics in Ship Design

A Practical Nonlinear Method for Calculating Ship Wavemaking and Wave Resistance

H. Raven (Maritime Research Institute Netherlands, The Netherlands)

Abstract

This paper presents a new method, developed at the Maritime Research Institute Netherlands, for predicting the wave pattern and wave resistance of a ship. A panel method is used to calculate the steady potential flow satisfying the fully nonlinear free surface boundary conditions. A particular feature is the use of source panels at a distance above the free surface. This has several practical advantages, but, as is shown analytically and numerically, also results in a quite accurate representation of surface waves. An iterative procedure is adopted to cope with the nonlinearity and free-surface character of the problem. The convergence problems typical of earlier methods seem not to occur with this method. Usually, 4 to 15 iterations are sufficient, making this approach most efficient. The computer program **RAPID** (**RA**ised **P**anel **I**terative **D**awson) is now being introduced in commercial ship design work.

The paper describes the basic decisions leading to the approach followed, outlines the method, and describes accuracy and sensitivity analyses. A few applications are shown, stressing the importance of nonlinear effects.

Nomenclature

Fn	Froude number
FSC	acronym for 'free surface condition'
$H(x,z)$	approximation of wave elevation
k	wave number
k_o	fundamental wave number, g/U_∞^2
$\hat{\mathcal{R}}_1$	Fourier transform of difference operator
t	time
u,v	velocity components on free surface
$\mathcal{W}_1$	boundary integral operator
x,y,z	Cartesian coordinates; x astern, y upward, z to port; origin on undisturbed waterplane at $\frac{1}{2}L_{pp}$
y_{f_s}	distance of panels above free surface
α	ratio of panel elevation to panel length,
ϵ_d	residual error in dynamic FSC
ϵ_k	residual error in kinematic FSC
$\Delta x, \Delta z$	free surface panel length and width
η	wave elevation (nondimensional)
η'	perturbation of wave elevation
σ	source strength
ϕ	total potential
Φ	base flow potential
φ'	perturbation of potential

1 Introduction

Computer calculations are playing a more and more important role in practical ship design. Hydrodynamics is one of the aspects for which the development of computer technology and Computational Fluid Dynamics have caused large changes and provided entirely new possibilities. It is mainly for potential flows, such as encountered in wave resistance, diffraction and propulsion problems, that reliable and practical computer codes are now available.

At the Maritime Research Institute Netherlands, the code DAWSON [1] in particular has taken a prominent place in the commercial ship design work. This method for computing the wave pattern and wave resistance of a ship is being used on a routine basis and applied to about 60 different hull forms per year in commercial projects. Much experience has been gained with its use during the last 5 years; experience that allows us to pre-optimize hull forms efficiently before model tests are conducted. Some examples of the application are given in [1] and [2].

However successful this program is, it does of course have its restrictions. Like almost all methods currently used for solving the wave resistance problem, it is based on a linearization of the free surface boundary conditions; specifically, it largely follows the formulation proposed by Dawson [3], which is a form of the slow-ship linearization. Such a simplification could not be avoided

until very recently, since the fully nonlinear problem was too difficult to be solved in general.

This linearization of the free surface conditions (FSC's) introduces errors, not only by the neglection of the nonlinear terms but also by the transfer of the boundary conditions from the actual towards the undisturbed water surface. In [4], the magnitude of these errors was estimated from the linear solution and found to be quite substantial in many cases. An example of this is shown in Fig. 1, which compares the error in the kinematic FSC (i.e. the residual normal velocity through the calculated free surface) with the vertical velocity on the free surface, for some different linearized formulations.

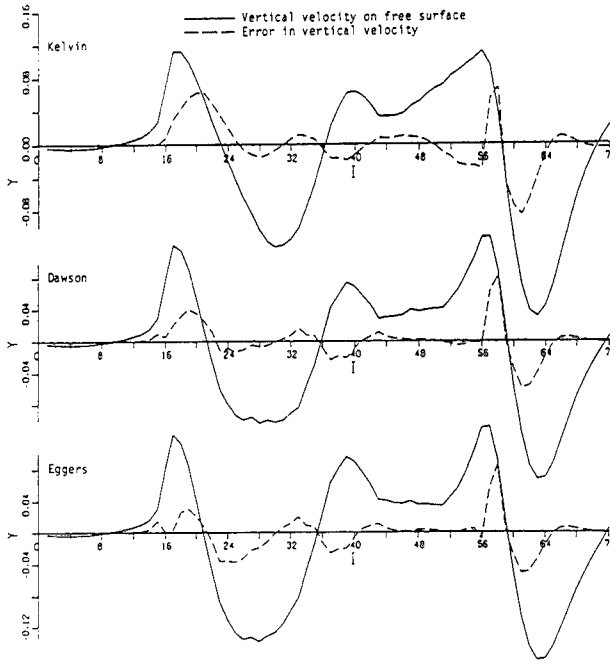

1. Error in kinematic free surface condition; Series 60 $C_b = 0.60$ model, $Fn = 0.35$.

An extreme case of the effect of these linearization errors was dealt with in [4]. It was shown that the neglected terms in the slow-ship linearization could in principle explain the paradoxical prediction of a *negative* wave resistance for slow, full-formed ships. The linearization allows an energy flux through the free surface, which would be prohibited by the exact free surface conditions. As a result of this supply of wave energy, the wave pattern predicted may be quite reasonable, but the predicted wave resistance is absolutely useless. A nonlinear method would eliminate this by imposing the exact FSC's, and thus hopefully lead to a positive and realistic wave resistance prediction.

Another shortcoming of linearized methods is the fact that they ignore certain effects that determine the flow field. The validity of the linearization is basically restricted to hull forms showing little section curvature and slope near the waterline. This in principle excludes a number of usual hull form features, such as strongly flared sections, flat sterns, transoms, and partly or slightly submerged bulbous bows. DAWSON-calculations for such hulls can still be performed but the realism of the predictions is impaired and a careful interpretation is necessary in such cases; optimization with respect to the features mentioned is not allowed.

A solution method for the fully nonlinear free surface problem is therefore desired, for its more complete and realistic flow field description and for the expected greater accuracy and reliability of the resistance prediction. With the advancing knowledge on numerical methods and the ever increasing computer power, such methods start being feasible now. The difficulty of this full, exact 'wave resistance problem' is caused not only by the nonlinearity of the free surface boundary conditions itself, but also by the fact that they must be applied at a surface that is initially unknown, and which shape and location depend nonlinearly on the solution in the field and reversely. Compared with the Dawson-like linearized methods, the extra requirements to be satisfied are:

- The free surface boundary conditions should include all nonlinear terms;
- They must be applied at the actual water surface;
- The hull boundary condition must be applied up to the actual waterline instead of the design waterline;
- The effect of the running trim and sinkage upon the wave resistance should be included.
- The correct conditions should be applied at the edge of a transom, if the water surface leaves the hull there.

Of these nonlinear effects, the second one is generally dominant [4] and will provide the largest difficulties in setting up a nonlinear method. The trim and sinkage effect is in most cases a rather modest change that can be accomodated in a linearized method as well (perhaps inconsistently). Transom conditions are in principle inconsistent with the assumptions underlying the FSC linearization. In the DAWSON-code, an option is available to impose such conditions in an ad-hoc fashion, but it has to be estimated beforehand whether the flow reaches the transom edge or detaches earlier. A nonlinear method ought to lead automatically to the right flow regime.

A new method for solving the fully nonlinear problem has now been developed at MARIN . All extensions

mentioned above are included, except the transom edge conditions which still have to be implemented. The method is based on a quite simple approach that is closely similar to Dawson's method, but relies on the use of source panels raised by a certain distance above the free surface. The program RAPID (RAised Panel Iterative Dawson) is currently being introduced in commercial ship design work. This paper presents the method and discusses the decisions taken in its development.

The number of available nonlinear methods is still quite limited, and little information was available on the best solutions for the many problems encountered. Therefore, prior to starting the development of a new method, we have seriously considered the various basic approaches to attack the nonlinear free surface potential flow problem. These considerations are briefly reported in Section 2, and lead to the choice of the class of methods that seems most efficient for the problem at hand. Section 2.3 summarizes the characteristics of earlier methods in this class. In Section 3, our decision to apply a panel method with the panels at a distance above the free surface is explained, and an analytical and numerical study of the accuracy of this approach is performed, leading to some surprising results. Section 4 then describes the basics of our new method. Results of a number of applications are discussed in Section 5, with an emphasis on the importance of nonlinear effects, and including some results of studies on the effect of the panel density. Conclusions are summarized in Section 6.

2 Basic decisions on the method

2.1 Laplace solver

The problem to be solved is that of a potential flow subject to boundary conditions on the hull and the free surface. The first decision to be taken is on the method to solve the Laplace equation for the velocity potential. Finite-Difference, Finite-Element or Finite-Volume methods could in principle be used (and are used in some methods, sometimes successfully). Still, the large number of variables to be handled in such field methods, and the necessity to generate a grid adapted to the free surface, suggest that these choices may not be optimal for potential flow problems, which can be entirely described in terms of boundary values. Therefore, not surprisingly, we have selected a Boundary Integral Method as the basic component of our method.

2.2 Steady iterative or time-dependent?

For the steady problem considered here, the free surface conditions require the pressure in the fluid at the free surface to be atmospheric, and the normal velocity through the free surface to vanish. The nonlinearity and free surface character of the problem preclude a direct solution procedure. There are two basic alternatives for solving this difficulty:

- to solve the equivalent time-dependent problem, starting from some initial state, and to continue the calculation until a steady state has been reached;
- to apply an iterative procedure to the steady problem, in which a sequence of linearized problems is solved until no further change occurs.

The time-dependent method might seem impractical, but still deserves due consideration. One advantage is that such a method can also be applied to many other problems that are actually time-dependent, such as ship motion and diffraction problems. Moreover, a quite straightforward and natural formulation is possible. The time-dependent terms occurring in the boundary conditions directly indicate a time-stepping process: in each time step the kinematic condition, which contains $\partial\eta/\partial t$, is advanced in time to obtain the free surface shape $\eta(x,z)$ for the next time-step, and the dynamic condition, containing $\partial\phi/\partial t$, is integrated in time to find the potential $\phi(x,z)$ at the free surface. This potential is subsequently imposed as a Dirichlet boundary condition. The Laplace equation is solved for the potential and velocities in the field at the new time level, and the whole cycle can be repeated for the next time step. This procedure has already often been applied successfully.

There are two principal drawbacks of the time-dependent approach. The first is the large number of time steps required before a steady solution is reached. Of course this depends on the initial conditions prescribed; probably the usual way of starting from rest and accelerating the model to its final speed is inefficient if only the steady solution is of interest. Anyway the calculation time needed is expected to remain a disadvantage of this approach.

The second difficulty is the necessity of specifying open-boundary conditions. In the unsteady problem, waves with all lengths and velocities can be generated, including those moving faster than the ship itself. Such waves should be allowed to leave the domain through the outer boundaries without too much reflection, since otherwise they will spoil the solution and delay the convergence to a steady result. But, particularly for 3D problems, no satisfactory non-reflective boundary conditions are known.

The steady iterative methods for solving the wave resistance problem are therefore expected to be in principle more efficient and perhaps less problematic. In the first place, the number of iterations does not depend on any physical evolution process, and may be much smaller than the number of time steps in a tran-

sient approach - provided that the iterative procedure is correctly formulated. But exactly this appears to be the principal difficulty, and all publications on existing methods in this class report cases of nonconvergence.

Compared with transient methods, the necessity of imposing non-reflective boundary conditions is less. In the steady approach all waves calculated satisfy the dispersion relation, and reflections only occur at the lateral and downstream boundaries of the calculation domain. By correctly dimensioning the latter, the reflections do not have any effect on the flow near the ship hull. But as opposed to time-dependent methods, a radiation condition must now be imposed, which prevents the occurrence of waves ahead of the ship. Experience is, however, available on ways to enforce this radiation condition in numerical methods, e.g. [1]

The convergence of the iterative process is, therefore, the central issue for steady iterative methods. Of course this convergence is strongly dependent on the precise formulation. Possible formulations can be divided in a few classes, to be briefly discussed below.

Two free surface conditions at $y = \eta$ are available:
- the kinematic condition, that the flow velocity at the free surface has no component normal to that surface:

$$\phi_x \eta_x + \phi_z \eta_z - \phi_y = 0 \qquad (1)$$

- the dynamic condition that the pressure, expressed in the velocities and wave elevation through Bernoulli's law, be constant (atmospheric) at the free surface:

$$\frac{1}{2} Fn^2 (1 - \phi_x^2 - \phi_y^2 - \phi_z^2) - \eta = 0. \qquad (2)$$

Here a coordinate system is supposed with the x-axis pointing astern, the y-axis vertically upward and z to port. All quantities have been nondimensionalized using a reference length (the ship length) and the ship speed.

Only one condition can be imposed upon the Laplace equation in each iteration; the other must be used to establish the relation between successive iterations, in such a way that it is satisfied upon convergence. Three options can then be distinguished.

The first option is, to impose the kinematic boundary condition in the solution of the Laplace equation under an approximate free surface. This gives rise to a Neumann condition for the potential that is easily implemented. The dynamic condition can then be used to deduce a new free surface elevation from the velocities calculated, and a new iteration can be started. Although this may seem a fairly obvious formulation of the iterative process, straightforward application will produce a solution without a trailing wave pattern. The only way to get the desired solution is to apply special, rather sophisticated prescriptions to deduce a new free surface from the calculated potential, e.g. [5]. For 3D cases, no examples of such a procedure are known to me.

The second possibility is just the other way round: impose the dynamic condition upon the solution of the Laplace equation in each iteration, and use the kinematic condition to update the free surface. This is possible in principle by integrating the dynamic condition, which contains ϕ_x, over x to find a new value of the potential at the free surface. This is subsequently imposed as a Dirichlet boundary condition for the Laplace equation; the resulting velocity field is substituted in the kinematic condition and integrated over x to find a new free surface shape. An example of a method attempting this approach is [6]. One may suppose this procedure to be susceptible to error accumulation due to the integrations.

In both approaches, the two free surface conditions, which *together* determine the wavelike behaviour, are uncoupled. The correct physical behaviour should thus be obtained by iteratively incorporating the interplay between them; a hard job for an iteration process. The third and final possibility eliminates this weak point by imposing a *combination* of both free surface conditions in the solution of the Laplace equation, and to use one of the conditions to update the free surface. Substituting the expression for the wave height (2) into the kinematic condition we obtain an expression in the potential only. This condition is basically Kelvin-like, and even more resembles the FSC according to Dawson. The success of the corresponding linearized formulation suggests that this single boundary condition includes already much of the physical behaviour. Therefore, the iterative procedure based on this combined condition is more "implicit" than the two previous possibilities, and may thus be expected to have better convergence properties. A possible drawback of this formulation is the structure of the resulting combined free surface condition, which precludes the application of iterative methods for solving the resulting set of equations.

Taking all this together, we think that a steady iterative method is preferable provided that the convergence problems can be overcome; and that in view of the latter, the formulation with the combined condition is most promising. These choices are directed by the wish to obtain an efficient and practical method, rather than a very general one. The resulting program will therefore be restricted to the steady forward-speed problem.

2.3 Previous experiences

A few methods already exist that are based on a Boundary Integral Method and apply a combined free surface

condition similar to that of Dawson. Ni [7] most closely followed the Dawson implementation. In his method, the free surface and hull are covered with source panels; in the collocation points in the free surface panel centres, the combined condition is imposed. After the solution of the Laplace equation, the free surface shape is updated using the dynamic condition. Thus the entire free surface panel distribution is displaced and deformed in every iteration. Ni found that a linear source distribution on quadratic panels was required to obtain an acceptable convergence. The method is rather complicated and, according to the first publications, sensitive to various numerical details. Still, possibly due to later improvements, the method performs well enough to be applied to some extent in practical problems [8].

Kim and Lucas [9] several years later came up with a very similar method. However, they state that explicit artificial damping is necessary to obtain a convergent procedure. Since the damping affects the final results as well, this approach is not acceptable in my opinion.

The other prominent method is that of Jensen et al. [10], [11], which contains several original ideas. In the first place, the singularity distribution is not located on the free surface itself, but in a horizontal plane at a fixed position, above the free surface. Point sources instead of source panels are used. The boundary condition includes the so-called transfer terms found from Taylor expansions, and is, therefore, fairly complicated. Good results have been obtained for a number of cases, but serious convergence problems are reported for several others. In particular, no convergence could be obtained for full hull forms such as tankers [10].

Another method perhaps to be mentioned is that of Musker [12]. In this method, source panels at a very small distance above the undisturbed free surface are used. The free surface condition is quadratic rather than fully nonlinear, and is tranferred to the undisturbed free surface using Taylor expansions. Thus it probably misses the dominant nonlinear effects. On the point of convergence of the iterative procedure this method cannot, therefore, be compared with fully nonlinear approaches.

This brief, and perhaps already incomplete, survey of existing methods again stresses that the convergence of the iterative process is the most critical point. It is noteworthy that this convergence is found to depend on small details of the numerical method and discretization, and on the precise formulation of the free surface condition.

In setting up our new method, the information on the importance of the distinct nonlinear terms gained from the studies reported in [4] appeared to be most helpful. In particular, the fact that the 'transfer terms', representing the difference between the flow quantities at the undisturbed free surface and those at the actual free surface, are generally the dominant nonlinear terms, requires them to be treated carefully and as implicitly as possible. At the same time they cannot be well represented by truncated Taylor expansions, since the convergence of these is poor in many cases; additionally, for usual singularity distributions large wiggles may occur in the Taylor terms. These studies have not only shown the desirability of a nonlinear method but have also partially directed its development.

3 The Raised-Panel Approach

3.1 Initial considerations

As has been mentioned in Section 2.1, a Boundary Integral or Panel method will be used. The usual procedure is, to cover the boundaries of the flow domain with a discretized singularity distribution; to choose a set of collocation points, as many as the number of degrees of freedom of the singularity distribution; to express the boundary conditions in these collocation points in the unknown singularity variables. Solving the resulting closed set of equations allows to determine the potential and velocity everywhere in the domain.

However, it is not necessary that the singularities are on the boundaries of the domain. It is allowed to position them *outside* the domain under certain conditions, provided that the collocation points remain on the boundary. For our particular application, we shall put the sources or source panels at some distance above the free surface. This has been applied originally by Jensen et al [10],[11] for the same free surface problem, and has several advantages for this application in particular:

- Since basically the distance from the panels to the free surface is arbitrary within certain limits, it is no longer necessary to adapt the source panels to the new free surface approximation in each iteration. This eliminates many geometric manipulations which may have a destabilizing effect on the convergence of the iterative process. With sources above the free surface we only have to move the free surface collocation points to the new approximation of the free surface, which is quite simple.
- Since the free surface panels do not move in each iteration, the influence coefficients (velocities induced by a unit source density) of free surface panels in hull collocation points do not change; this saves a considerable part of the calculation time.
- The fact that the potential field now extends above the free surface, uninterrupted by singularities on

the free surface, may somewhat facilitate the formulation of the iterative process.

- Due to the distance between the panels and the free surface, the velocity field induced in the fluid domain is much smoother than with a usual method.
- An additional benefit is the "desingularization", allowing the use of Gauss quadrature for integration over the panels instead of exact analytical expressions. This again saves computing time.

There is some general information from the literature on methods with such offset singularities. As just mentioned, the method by Jensen et al [10] uses point sources above the free surface, in a fixed horizontal plane at a distance of 1 to 3 source spacings above the undisturbed free surface. This distance is claimed to have only little influence on the results, but no theoretical study on the accuracy and order of this method seems to have been performed.

Other relevant papers concern simpler boundary conditions, of Dirichlet or Neumann type. In the method of Webster [13] for calculating the potential flow around closed bodies in an infinite fluid domain, triangular panels bearing a linear source distribution are located inside the hull, at a distance of less than half the panel edge length and half the local radius of curvature of the hull surface. The collocation points are chosen on the hull directly opposite to the panel cornerpoints. The method is successful, but has difficulty in representing the flow at corners such as a ship bow.

Schultz and Hong [14] proposed a formulation for 2D internal potential problems based on Cauchy's law. One of the alternatives studied was a method using sources outside the boundary. In general they found a decreasing discretization error for increasing distance to the boundary. For boundaries with sharp corners larger errors were found. Subsequently this method has been developed to solve 3D free surface problems by a transient approach [15]. Applications to moving submerged singularities have been shown. It is concluded that the distance of the panels to the free surface should be proportional to the square root of the panel dimension to obtain convergence for decreasing panel size; but this refers to the errors incurred by using Gauss quadrature instead of analytical integration over the panels.

It appears that for Dirichlet or Neumann conditions there is some information on the use of offset singularities, and fairly detailed studies of the accuracy have been performed. But for the particular application considered here, with a boundary condition of quite different form, little theoretical information is available. In particular, possible questions are:

- What is the accuracy for a free surface condition of the type considered?
- What is the effect of the distance of the singularities to the free surface upon the results?
- Is the poorer numerical conditioning of the equations acceptable?
- What are the limits on the distance? An analytical continuation of the potential field up to the level of the singularities must exist. Is an adequate representation of steep waves and of the flow field near the waterline possible?

Most of these questions will be answered in the following sections.

3.2 Accuracy Analysis

The accuracy aspect typical for our problem is the representation of surface waves. The main error sources involved are the discretization of the continuous free surface source distribution, and the difference scheme used for approximating the velocity derivatives occurring in the free surface condition. Besides, the truncation of the free surface distribution and the discretization of the hull source distribution introduce errors, but are less specific for our approach. In the effect of the former errors, a distinction can be made between numerical dispersion (a wavelength error) and numerical damping (an amplitude error). These errors have already carefully been considered for the standard approach, most systematically by Sclavounos and Nakos [16]. We shall now apply their methodology (and notation) to the solution of the linear wave resistance problem, with a Kelvin free surface condition, using singularities raised above the free surface. The analysis is restricted to 2D cases for simplicity.

For the sake of reference we first consider a *continuous* source distribution with infinite extension, at a distance y_{f_s} above the undisturbed free surface. The velocity components u, v on the undisturbed free surface $y = 0$ are expressed as integrals over the source plane, and substituted in the Kelvin condition $u_x + k_0 v = R.H.S.$. Here the right hand side incorporates the effect of other sources, e.g. those representing a body. The result is a boundary integral equation for σ, which can be represented by: $\mathcal{W}_1 \sigma = R.H.S.$.

The properties of the linear operator $\mathcal{W}_1$ are studied in Fourier space. The Fourier series representation

$$\sigma(x) = \frac{1}{2\pi} \int_{-\infty}^{+\infty} \tilde{\sigma}(k) e^{ikx} dk \qquad (3)$$

is substituted into the boundary integral equation. We then find

$$\tilde{\mathcal{W}}_1(k)\tilde{\sigma}(k) = R.\tilde{H}.S., \tag{4}$$

$$\tilde{\mathcal{W}}_1(k) = -\frac{1}{2}e^{-ky_{fs}}(1 - k/k_0). \tag{5}$$

The zero of the Fourier transform of the operator, $\tilde{\mathcal{W}}_1$, determines the wavelike behaviour of the solution in the far field; this has the wavenumber $k = k_0$ as expected.

We now consider the *discretized* problem with constant-strength source panels of uniform size. Infinite sums over the source panels now replace the integrations over the continuous source distribution, and discrete Fourier transforms of the source strength and operator are used. In analogy to Dawson's method the term u_x in the Kelvin condition is implemented by a difference scheme for the first derivative of the induced velocity. Therefore, also the discrete Fourier transform of the difference operator enters, which we shall denote by $ik\hat{\mathcal{R}}_1$. The resulting transform of the complete operator is:

$$\hat{\mathcal{W}}_1(k) = -\frac{1}{2\pi}[\Sigma_2(k\Delta x, \alpha) - \frac{k\hat{\mathcal{R}}_1(k)}{k_0}\Sigma_1(k\Delta x, \alpha)]. \tag{6}$$

Here, Δx is the panel length, and $\alpha = y_{fs}/\Delta x$. Σ_1 and Σ_2 represent the combined influence of the source panels. The root of the operator is:

$$k/k_0 = \frac{\Sigma_2}{\hat{\mathcal{R}}_1\Sigma_1}. \tag{7}$$

We shall now first leave out of account the errors introduced by the difference scheme by substituting $\hat{\mathcal{R}}_1 = 1$. Since both Σ_1 and Σ_2 are real, the discretization of the source distribution in constant-strength panels introduces an error in the wave length (numerical dispersion) but no numerical damping. To compute this error the infinite sums Σ_1 and Σ_2 must be evaluated numerically. The *order* of the dispersion error could not simply be deduced, but for a number of panel elevations and source panel sizes its value has been evaluated (Table 1). Keeping in mind that a usual panel length is $\Delta x = 0.1\pi/k_0$, we see that the raised-panel method is surprisingly accurate for panel elevations exceeding half the panel size, having a numerical dispersion of less than 0.6 %.

It is useful to compare this with the results of the same type of analysis for the standard method, with source panels *on* the undisturbed free surface, both with and without the dispersion correction described in [1]. This is a factor introduced into the free surface condition that exactly cancels the first terms of the expression for the numerical dispersion for the transverse wave component. As shown in Table 1, without dispersion correction considerable errors occur. The correction eliminates these, but only for the transverse wave components. E.g. for components at an angle of 60°, the wave number error is 29 % with dispersion correction, and 38 % without, for $\Delta x = 0.1\pi/k_0$. The raised-panel method, which does not have such a dependence on the wave direction, is found to be far superior.

It is interesting to carry out the same analysis for a raised point-source method. In a 2D case this then appears to reach the same level of accuracy as the raised-panel method, although for a somewhat larger elevation. However, this result is not necessarily representative of the performance of a 3D point-source method. The 2D point source method is analogous to a 3D method with transverse source *lines*; but in a 3D *point* source method these source lines are further discretized into an array of point sources (having equal strength in our 2D analysis). This introduces additional errors in the induced velocities, which do not occur in the raised-panel method.

The analysis has therefore been repeated by considering 2D point source arrays extending in $x-$ and $z-$direction. Evaluating the resulting double summations in the induced-velocity expressions we find that the 3D raised point-source method is substantially less accurate unless the aspect ratio of the 2D source array is kept close to unity. E.g. for $\Delta z/\Delta x = 2$, the wave length error is 2.5 % ; for $\Delta z/\Delta x = 3$, the error even amounts to 11.6 % (for $\Delta x = 0.1\pi/k_0$). Since keeping the aspect ratio close to unity generally requires a greater number of sources than usual and thus increases

Table 1: *Wavenumber ratio k/k_0 for raised-panel and standard method*

	$\alpha = 0.5$	$\alpha = 1.0$	$\alpha = 1.5$	$\alpha = 2.0$	Standard	Corrected
$k_0\Delta x = 0.1\pi$	0.9937	0.9997	1.0000	1.0000	1.0744	1.0003
$k_0\Delta x = 0.2\pi$	0.9819	0.9986	0.9999	1.0000	1.1608	1.0026
$k_0\Delta x = 0.3\pi$	0.9611	0.9957	0.9996	1.0000	1.2623	1.0090

the calculation time, this is a significant disadvantage of the point-source approach.

Up to this point we have left out of account the numerical errors introduced by the difference scheme. Since $\hat{\mathcal{R}}_1$ has real and imaginary parts, both dispersion and damping result. But the dispersion contribution is only of $\mathcal{O}(\Delta x^4)$ for the particular difference scheme used in our method; the leading-order dispersion thus results from the source discretization and not from the difference scheme. But the source discretization introduces *only* numerical dispersion and no damping. Therefore the errors due to the discretization and due to the differencing may be dealt with separately, as has been done in this study.

These conclusions, drawn from a 2D analysis, have all been confirmed by numerical experiments for 3D cases. In particular, as Fig.2 shows, with the raised source panel method the wave profile along the hull agrees fairly accurately with the result of the standard method with dispersion correction; but at a lateral distance from the path of the ship a significant phase difference is found, caused by the fact that the standard method contains a numerical dispersion error for diverging components.

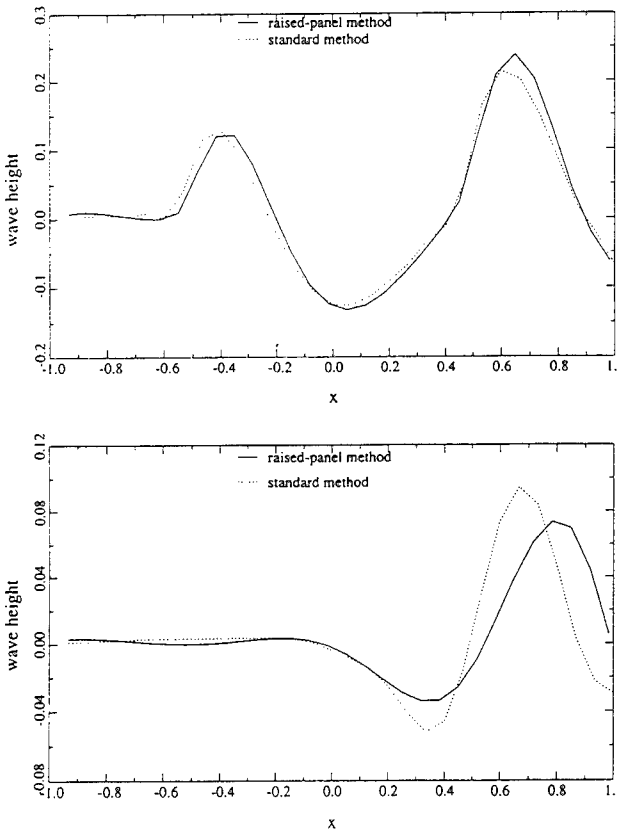

2. Wave profile along the hull (top) and at $z = 0.40L$, showing numerical dispersion of standard method. Kelvin FSC imposed. Wigley hull, $Fn = 0.40$.

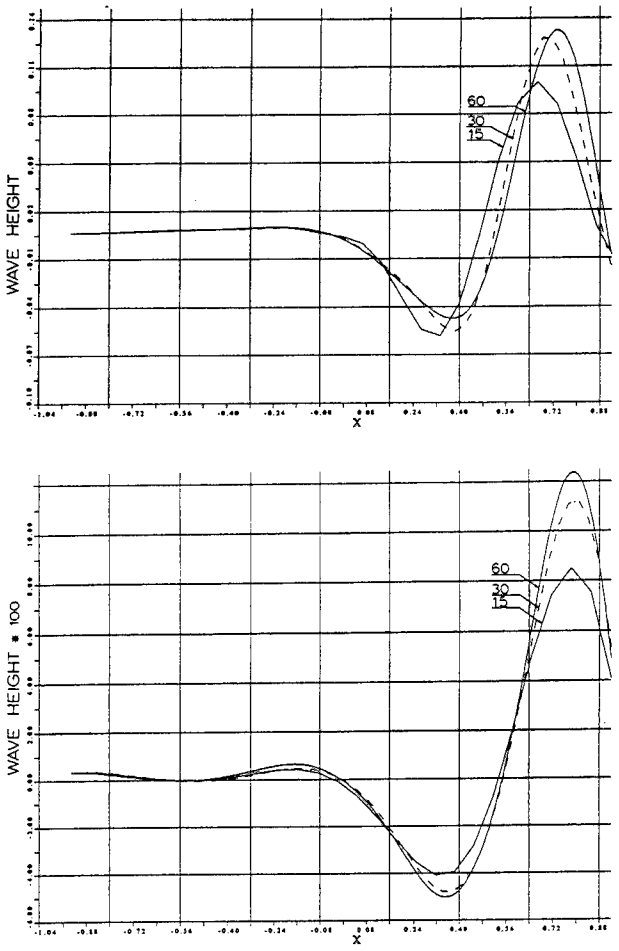

3. Wave cut at $z = 0.40L$, for 15, 30 and 60 panels per fundamental wave length. Standard method (top) and raised-panel method (bottom). Kelvin FSC imposed. Wigley hull, $Fn = 0.40$.

Fig.3 shows that for the raised-panel method the phase of the waves is absolutely insensitive to the panel length Δx, which indicates a negligible numerical dispersion. For the standard method (with dispersion correction) there is a forward shift that decreases upon longitudinal panel refinement. The effect of the aspect ratio of the source array or source panel distribution is shown in Fig. 4, where the longitudinal cuts at at distance from the hull are compared. The reduction of the aspect ratio from 2.6 to 1.0, here accomplished by increasing the number of free surface strips from 8 to 20, has no effect on the phase for the raised-panel method, but a substantial effect for the raised point-source method, exactly as theory predicts. (Apart from this, the increased resolution also appears to have a significant amplitude effect on both methods.)

Thus the raised-panel method appears to have the smallest dispersion error, much better than the method using panels on the undisturbed free surface (even with the explicit dispersion correction), while having the same

(small) numerical damping. The other issues mentioned in the previous section, concerning the conditioning of the equations and the effect of the panel elevation on the results, will be discussed in Section 4.3, in connection with the nonlinear solutions.

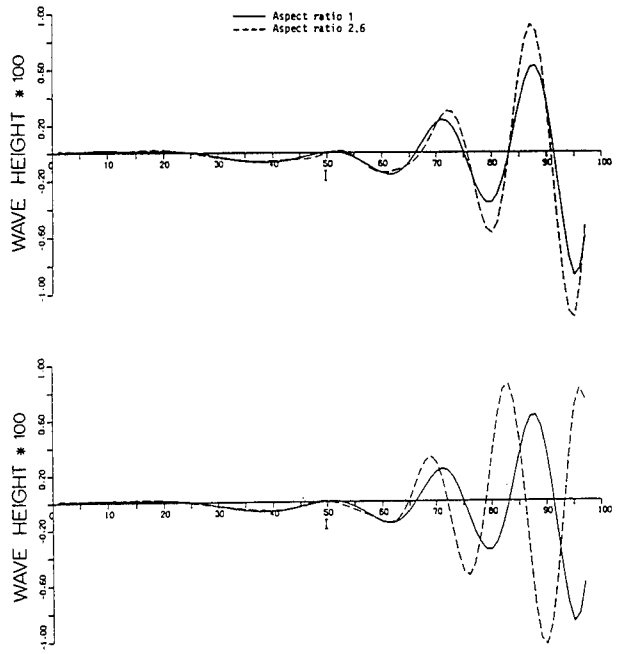

4. Effect of source distribution aspect ratio on numerical dispersion. Wave cut at $z = 0.46L$. Strut-like hull, $Fn = 0.25$. Raised source panels (top) and raised point sources (bottom).

4 R A P I D: RAised Panel Iterative Dawson

4.1 The Iteration Scheme

Based on the analytical and numerical study of the accuracy of various methods to solve the linear (Kelvin) problem, we can conclude that the raised-panel approach is the most promising candidate to go on with. The next step is to set up an iterative procedure in which a sequence of such linear problems is solved, until convergence to the solution of the complete, nonlinear problem is obtained. These linear problems are to be defined such that the free surface condition may be applied on a known, approximated surface instead of on the unknown free surface. On this surface a known 'base flow field' is assumed, just as is done in the derivation of the slow-ship FSC, but now to be updated in each iteration. The formulation of the updates of the surface and flow field largely determines the properties of the iterative process.

Regardless of the choice of the base flow and base surface, the iteration scheme will be as follows:

1. Define the panel distribution on the hull, and a free surface panel distribution well above the free surface.
2. Assume an initial approximation of the free surface, and an initial base flow on that surface.
3. Choose collocation points on the approximate free surface, e.g. right under the panel centres.
4. Impose the combined FSC, linearized with respect to this base flow and free surface, in the free surface collocation points. Impose the hull boundary condition in the hull collocation points.
5. Solve the linear problem in the usual way. Calculate the wave elevation from the dynamic condition.
6. Move the free surface collocation points to the new free surface.
7. Adapt the base flow to the new solution.
8. Calculate the residual normal velocity through the free surface and the residual pressure. If these exceed the specified tolerances, return to step 4. Usual tolerances are: 0.2 % of the ship speed, for the residual normal velocity, and 0.5 % of the stagnation pressure, for the residual pressure.

4.2 Formulation and implementation

The discretization of the source distributions is similar to that used in DAWSON. On the hull, flat quadrilateral panels with constant source density are used. The panel cornerpoints are defined directly on a digitizing table and stored on a hull geometry file. Similarly, the free surface singularities are flat quadrilateral panels with constant strength, usually positioned at about one panel length above the free surface. This free surface paneling is automatically generated based on the hull geometry.

The calculation is started with some initial flow-field and free surface shape. These have no influence on the final result, but may well influence the number of iterations needed. The simplest approach is to start from a flat free surface and a uniform flow. The first iteration then produces the Neumann-Kelvin approximation. Alternatively, one may start with a flat free surface with the double-body flow; the first iteration then leads to an incomplete slow-ship FSC. One step further is, to first run DAWSON, and then continue iterating with the free surface and flow field thus calculated. The number of iterations required to reach convergence with these alternatives generally decreases in this order. Still in all cases studied up to now, starting with a uniform flow was sufficient to get a converged result.

The linearized free surface condition to be imposed is derived as follows. For a known base flow field $\nabla\Phi$ and base surface $H(x,z)$, the velocity and free surface elevation to be calculated are decomposed as follows:

$$\nabla\phi = \nabla\Phi + \nabla\varphi', \tag{8}$$

$$\eta = H + \eta', \tag{9}$$

where $\nabla\varphi'$ and η' are (hopefully small) perturbations. The kinematic and dynamic boundary conditions, linearized in these perturbations, then read:

$$\Phi_x\eta_x + \Phi_z\eta_z + \varphi'_xH_x + \varphi'_zH_z - \Phi_y - \varphi'_y = 0 \tag{10}$$

$$\eta = \frac{1}{2}Fn^2(1 - \Phi_x^2 - \Phi_y^2 - \Phi_z^2 - 2\Phi_x\varphi'_x - 2\Phi_y\varphi'_y - 2\Phi_z\varphi'_z). \tag{11}$$

It is to be noted that these equations actually are to be satisfied on the new free surface $y = \eta$, but to allow a direct solution they must be transferred to the known surface $y = H$. Just as in slow-ship theory, consistency would require that a Taylor expansion in η' be used to incorporate this transfer [4]. But our insight in the nature of these terms indicates they are better discarded; we use the conditions in the form presented above. The ensuing inconsistency is, of course, meaningless for the converged result.

Next, the wave elevation η from the dynamic condition is substituted into the kinematic condition. The resulting combined condition then reads:

$$-\frac{1}{2}Fn^2(\Phi_x\frac{\partial}{\partial x} + \Phi_z\frac{\partial}{\partial z})(\Phi_x^2 + \Phi_y^2 + \Phi_z^2 + 2\Phi_x\varphi'_x + 2\Phi_y\varphi'_y + 2\Phi_z\varphi'_z) + \varphi'_xH_x + \varphi'_zH_z - \Phi_y - \varphi'_y = 0. \tag{12}$$

Another useful form may be

$$\varphi'_y - \varphi'_xH_x - \varphi'_zH_z + Fn^2(\Phi_x\frac{\partial}{\partial x} + \Phi_z\frac{\partial}{\partial z})(\Phi_x\varphi'_x + \Phi_y\varphi'_y + \Phi_z\varphi'_z) = -\epsilon_k + (\Phi_x\frac{\partial}{\partial x} + \Phi_z\frac{\partial}{\partial z})\epsilon_d, \tag{13}$$

where

$$\epsilon_k = \Phi_y - \Phi_xH_x - \Phi_zH_z, \tag{14}$$

$$\epsilon_d = \frac{1}{2}Fn^2(1 - \Phi_x^2 - \Phi_y^2 - \Phi_z^2) - H, \tag{15}$$

the residual errors in the kinematic and dynamic condition at the start of the iteration.

This quite straightforward derivation is valid irrespective of the definitions of the base flow and base surface; dependent on these, certain further reductions may be possible.

In the discretization of the FSC, again a close similarity to DAWSON exists, in that the derivatives of velocities and surface elevations are approximated by finite differences, directed upstream.

This simple basic method is sufficient for a class of cases, but some extensions are required for more difficult applications or, in particular, for finer free surface panel distributions. In the first place, applying the collocation point update as described in step 6 above may lead to a too drastic change and perhaps divergence. But the simplest form of underrelaxation has appeared to cure this: the collocation point is shifted to some weighted mean of the old and new positions. The relaxation factor generally is between 0.3 and 1.0, and may increase with the iteration number.

4.3 Free surface panel adaptation

A much more complicated modification is required when the opposing demands on the distance from the free surface panels to the surface cannot be met. As follows from the accuracy analysis in Section 3.2, the minimum distance amounts to about 0.5 panel length. The maximum distance is not dictated by these accuracy considerations, but by the conditioning of the resulting set of equations. If a collocation point, e.g. in a wave trough, is at a distance of several panel dimensions from the closest free surface panel, the matrix tends to become singular. That this can easily occur, can be deduced from the stagnation height expression

$$\eta_{max} = \frac{1}{2}Fn^2. \tag{16}$$

For the usual panel size of about 5 % of the fundamental wave length $\lambda_0 = 2\pi Fn^2$ (nondimensional), the stagnation height amounts to 1.6 panel length. Raising the panels by at least this amount in order to keep clear of the highest wave crests is likely to cause trouble near wave troughs.

The obvious solution is, to apply a form of adaptation of the free surface paneling to the wave surface. Although this might seem to destroy some of the principal advantages of the raised-panel methods, this is too pessimistic. Contrary to methods having the panels on the free surface itself, there is no need to apply the adaptation in every iteration; nor is it necessary to adapt the panels very carefully. The only requirement is to maintain a reasonable distance between the panels and the collocation points. Most of the advantages of the method are thus preserved; but not its amazing simplicity! If worked out, the panel adaptation turns out to require fairly tedious geometric manipulations, e.g. in the adaptation of the hull paneling to the modified intersection with the free surface panel distribution.

This panel adaptation in fact solves the conditioning problems. For a Series 60 Block 0.60 model, Fig. 5 compares the nonlinear wave profiles obtained with fixed and adapted free surface panels, respectively. The quite small difference is due to the better accuracy of the latter, and is found to increase with decreasing panel size for fixed y_{fs}, i.e. for a poorer conditioning of the version without panel adaptation.

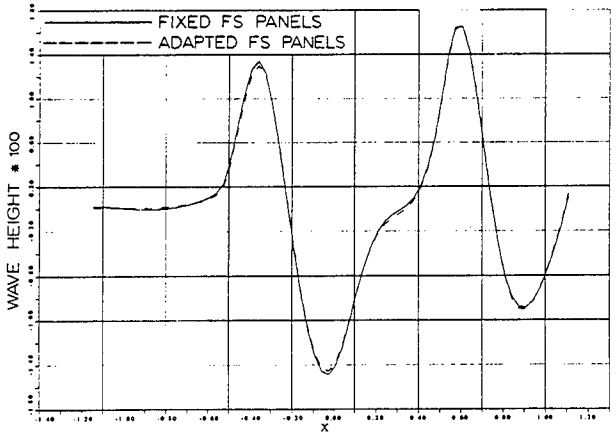

5. Wave profile along the hull, with and without free surface panel adaptation. Series 60 model, $Fn = 0.35$.

For the same case the effect of the distance of the panels above the free surface was tested, using the method with free surface panel adaptation. Fig. 6 shows the wave profile along the hull and at a transverse distance of about $0.41L$, for three different panel elevations. For the distances of $0.5\Delta x$ and $0.8\Delta x$ (which is about $0.9\Delta z$ and $1.4\Delta z$ along the hull), almost no difference is observed; the resistance difference amounts to 1 %. For the larger distance, $1.3\Delta x = 2.3\Delta z$, some deviations occur as a result of the poorer conditioning. The resistance difference now is 4 %. Similar experiences have been obtained for a number of cases. The general conclusion is that, with the free surface panel adaptation, reasonable limits for the elevation are 0.5 and 2 panel dimensions, respectively; and that within those limits the elevation has a quite small effect on the result. The condition number of the matrix equation is a reliable indication of the correctness of the elevation and the need to adapt the panels.

Although the adaptations of hull and free surface paneling are rather awkward, they do have the advantage of allowing an adaptation of the dynamic trim and sinkage of the hull without any additional cost or effort. The convergence of the trim and sinkage is exceptionally easy and produces no delay of the iterative process at all.

5 Results

During the last two years, a number of test cases has been run with the code RAPID that implements the method described before. Most of these tests served the purpose of validation or sensitivity studies. A number of applications in commercial projects has already been carried out. Below, a few of these calculations will be discussed.

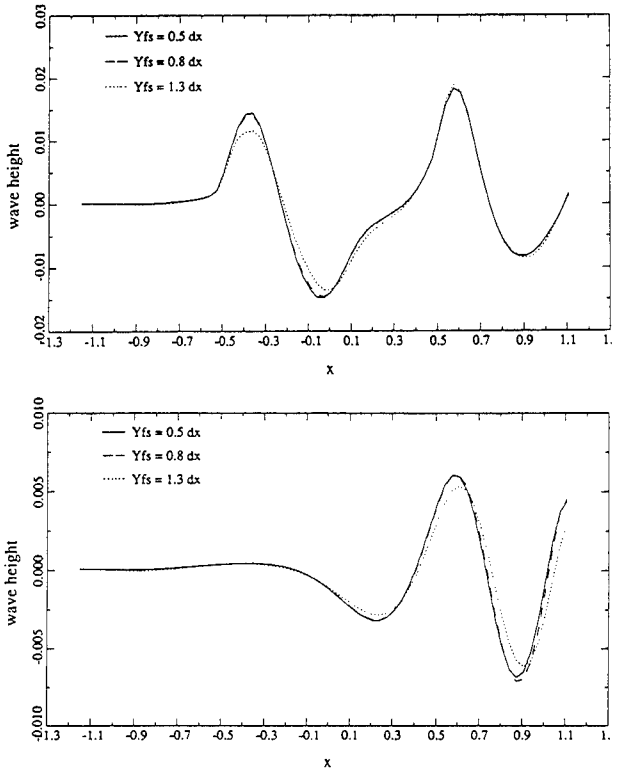

6. Effect of free surface panel elevation on wave profile along the hull (top) and at $z = 0.41L$ (bottom). Series 60 model, $Fn = 0.35$.

5.1 Wigley hull

For the Wigley parabolic hull at $Fn = 0.40$ fairly significant nonlinear effects are found, although the hull is quite slender. Fig. 7 shows the wave profile along the hull according to RAPID and the first iteration of RAPID, which is a Neumann-Kelvin approximation. The nonlinear result shows the expected higher and steeper bow wave, but otherwise agrees well with the Neumann-Kelvin result. The calculation required 4 iterations, and the CPU time amounted to 30 seconds on a CRAY-YMP4/464, for 140 hull panels and 304 FS panels.

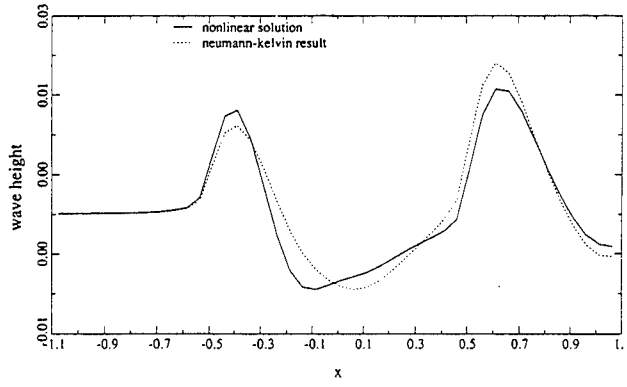

7. Effect of nonlinear terms on hull wave profile. Wigley hull, $Fn = 0.40$.

5.2 Series 60 model

For the Series 60 Block 0.60 hull at $Fn = 0.35$, some results will be shown of a study of the influence of the free surface panel density. The idea behind this study was that nonlinear effects will presumably be concentrated near the waterline, where perhaps even a weakly singular behaviour may occur. In that case, convergence of the iterative process, and convergence of the nonlinear solution for successive panel size reduction, would not be guaranteed.

First, the transverse panel distribution was successively refined, by twice decreasing by one half the distance between the waterline and the first row of collocation points adjacent to the hull. For the finest paneling, shown in Fig.8, this distance amounted to about 0.45 % of the ship length. Although for that grid both the underrelaxation and the free surface panel adaptation were necessary, no other problems occurred, and the tolerances were met after 9 iterations, taking some 350 CPU seconds (for 540 hull panels, 1104 FS panels). Fig.9 again compares the nonlinear and Neumann-Kelvin results; the nonlinear effects turn out to be more pronounced here.

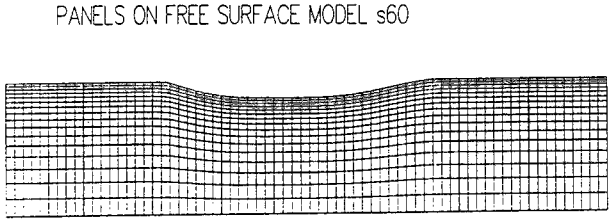

8. Free surface panel distribution for Series 60 model.

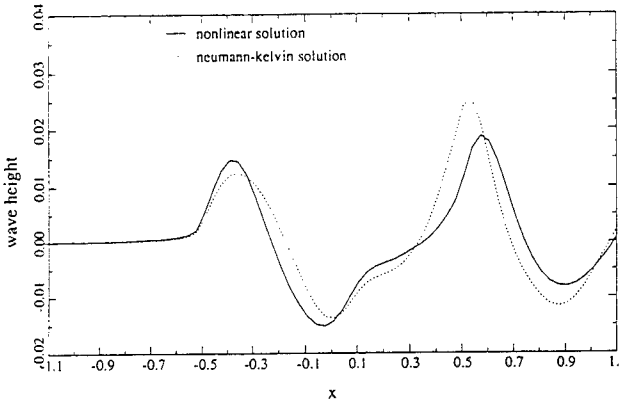

9. Effect of nonlinear terms on hull wave profile. Series 60 model, $Fn = 0.35$.

Fig. 10 compares the wave profiles along the hull, and the longitudinal cuts through the wave pattern at a transverse distance of 47 % of the ship length, obtained with the 3 different grids. In general an excellent convergence for decreasing free surface panel width is observed, in that the last refinement hardly has any effect at all. Only at the longitudinal position x = 0.20 something particular appears to happen in the hull wave profile; locally a grid-independent result has not yet been obtained. A closer inspection showed that the differences here are caused by the increasing resolution of a strongly diverging wave component, progressing in a direction making a large angle with the hull centreline and, therefore, having a very small wavelength. Such waves are only accurately resolved on the finest grids, but have no significant effect on the resistance and general flow pattern, and therefore are of little concern for applications in ship design. The differences in the predicted resistance with the three panelings considered amounted to 2.7 % for the nonlinear solution, against 6.2 % for the normal Neumann-Kelvin solution.

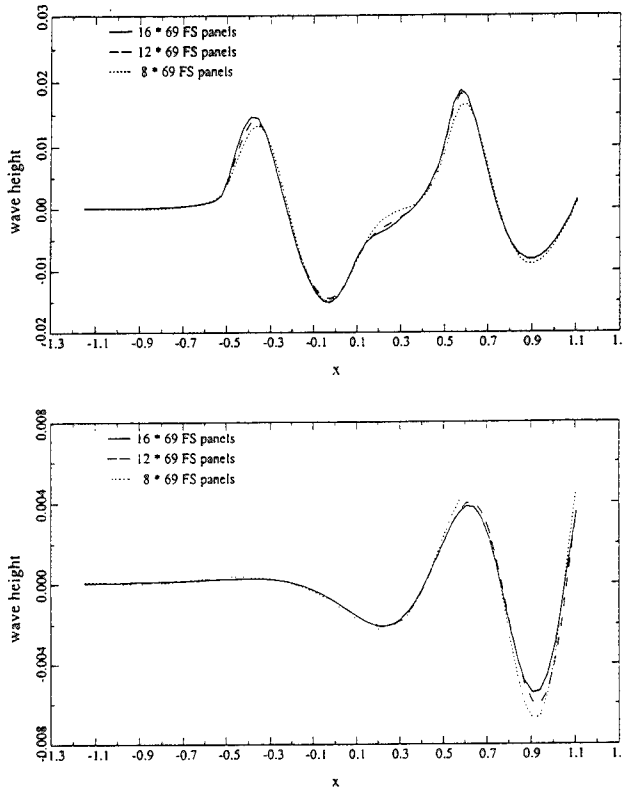

10. Effect of free surface panel width on wave profile along the hull (top) and at $z = 0.47L$ (bottom). Series 60 model, $Fn = 0.35$.

For the same model at $Fn = 0.35$, the free-surface paneling was also refined longitudinally. In the previous calculations there were 23 panels per fundamental wave length. Doubling this number produces only a small, but visible modification of the wave profile along the hull, and a somewhat larger difference at the transverse distance of 0.47L .

From these studies and a comparison with a parallel study for the linearized DAWSON-code, we conclude

that most of the discretization errors in RAPID are similar to, but perhaps somewhat smaller than, those in DAWSON. (As shown before however, the dispersion error is far smaller). In general a perfect grid-independence will be hard to reach in wave resistance problems, due to the existence of very short waves close to the path of the hull. Therefore a comparison between design variations should preferably be done with corresponding free surface panelings. In that case, the influence of the discretization errors as found here will be of no meaning from the practical point of view; particularly in comparison with the linearization errors which RAPID eliminates.

5.3 Tanker model

From publications on previous nonlinear methods it appears that generally the largest convergence problems occur for full hull forms at low speed, such as tankers. However, with RAPID no serious problems have been met in the calculations for several different tanker hulls. Figs 11 and 12 give a few results for the same tanker model as has been used in [4], at the same speed of $Fn = 0.177$. A large number of panels was used: 1258 per side on the hull and 2100 on the free surface. The converged result was obtained in 6 iterations, taking about 25 minutes of CPU time. (It is important to note here that the code used had not yet been optimized on the point of calculation time; significant improvements in efficiency will still be possible). Fig. 12 compares the wave profiles along the hull according to RAPID, DAWSON and the Neumann-Kelvin approximation. It appears that the slow-ship condition in DAWSON is a far better approximation of the exact result than the Kelvin condition. This is in agreement with the conclusions drawn from the error estimates in [4], and confirms that for this class of ships slow-ship theory is superior to the Neumann-Kelvin approach.

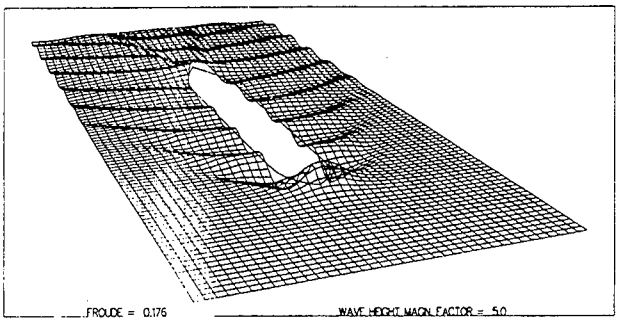

11. Wave pattern of tanker model at $Fn = 0.177$, calculated by RAPID.

For this tanker model the wave patterns predicted by DAWSON and by RAPID are qualitatively equal. However, a small longitudinal shift of the wave pattern can give rise to a large change of the resistance for full hull forms; therefore the small differences may still be quite significant. As is dealt with extensively in [4], DAWSON predicts a negative wave resistance for this tanker model (and for several others). This is at-

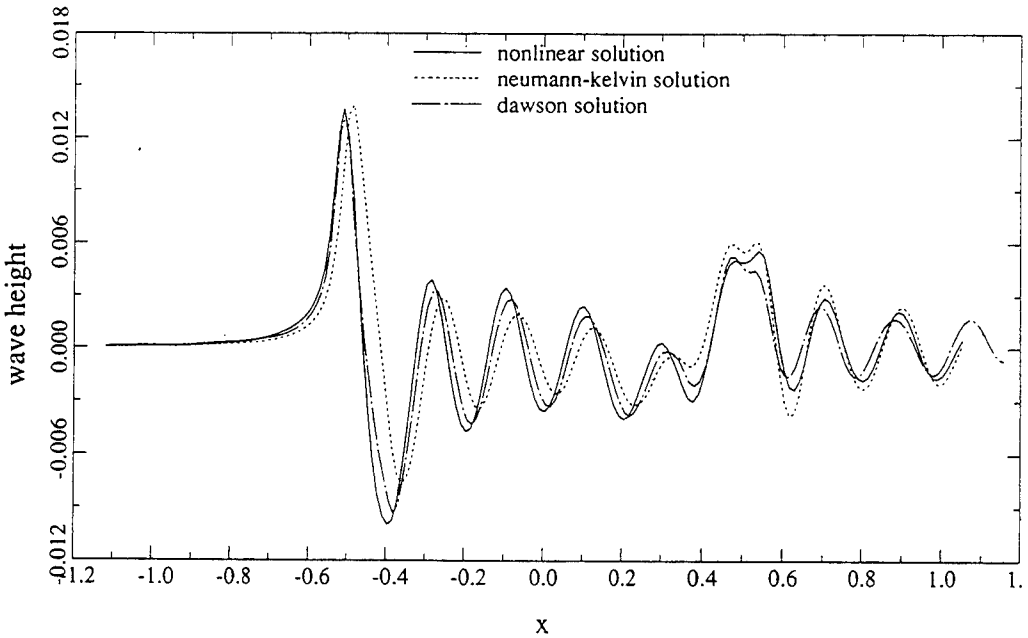

12. Hull wave profile predicted using Kelvin, Dawson and fully nonlinear free surface conditions. Tanker model, $Fn = 0.177$.

tributed to an energy supply through the free surface as a result of the linearization, a problem to be eliminated by RAPID. The resistance prediction deduced from the RAPID-result is therefore of particular interest.

As a matter of fact the large negative values did not occur, but the predicted wave resistance was close to zero. This may seem disappointing, since with a realistic wave pattern a zero resistance is just as paradoxical as a negative resistance. However, contrary to what is the case for the linearized calculations, I now have strong indications that the remaining error is attributable to an insufficient panel density on the hull; panel refinement (up to impractically large panel numbers) does result in a slow increase of the resistance to a positive value. Further publications on this issue will follow.

More RAPID-results for tanker models are discussed in [17].

5.4 Partly immersed bulbous bow

A very interesting application of RAPID is discussed next. In DAWSON, the free surface panels and collocation points are located on the undisturbed water surface. The hull form above that surface cannot have any effect. This is particularly disadvantageous in the case of a bulbous bow that pierces the undisturbed free surface. Experience shows that such bow forms can have very good properties. At a sufficiently high speed they become completely submerged by the bow wave, thus allowing a smooth flow over the top of the bulb and exerting a wave-height reducing effect. This phenomenon cannot well be incorporated in DAWSON since there the FSC is imposed at the undisturbed free surface. The procedure used until recently was, to increase the draft of the hull in the DAWSON calculations with an amount representing a reasonable estimate of the trim and sinkage.

In the present case however, this resulted in a submergence of the top of the bulb of only 0.01 m full scale. The hull panels and free surface panels then almost coincide; only due to the fact that the boundary conditions imposed on them are different a solution can be obtained. In principle, it is not justified to apply a linearized method to such a case; we should never completely trust such results. As a matter of fact substantial irregularities in the solution can be observed. The wave pattern calculated by DAWSON (Figs 13 and 14, top) would suggest a rather defective bulb action; although the flow near the bow is directed downward, it does not prevent the generation of a rather heavy bow wave around X = -0.4.

Repeating the calculations with RAPID however, substantially different results were obtained. RAPID does take into account the separation between the actual water surface and the bulbous bow, by imposing the FSC at the free surface itself. The iteration was started with a uniform base flow and flat free surface. The draft of the ship was increased first in order to guarantee a sufficient bow immersion. In the course of the iterative procedure, when the bow wave had assumed a sufficient height, the trim and draft were adapted step by step until the equilibrium of the vertical forces and trimming moments was reached.

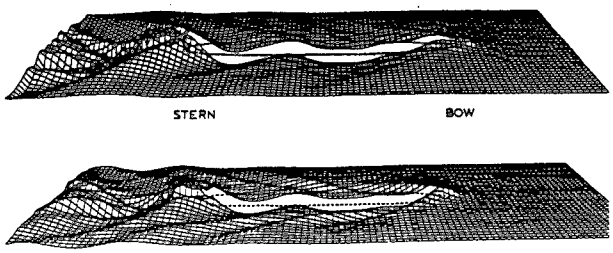

13. Wave patterns predicted by DAWSON (top) and RAPID (bottom). Hull with partially immersed bulbous bow. Wave heights 5 times magnified.

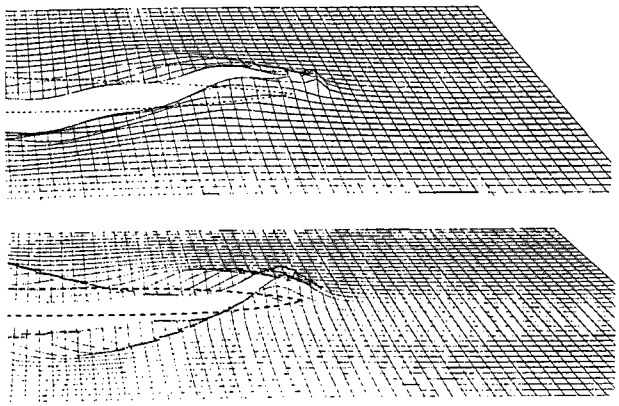

14. Close-ups of bow wave patterns predicted by DAWSON (top) and RAPID (bottom). Hull with partially immersed bulbous bow. Wave heights 5 times magnified.

The final result, obtained after 14 iterations, is shown in Figs 13 and 14 (bottom). (It is to be noted that near the stern, differences with DAWSON are largely caused by the absence of any transom stern modeling in RAPID). It is immediately clear that close to the bow a significantly different flow pattern is predicted, without the irregularities that are present in the DAWSON wave patterns (Fig. 15). The flow about the bulb is smooth and displays the correct flow pattern. The bow wave crest at X = -0.4 has disappeared; a crest now is positioned near the fore perpendicular. The better representation of the actual flow situation at the bow appears to influence a large part of the wave pattern, and results in substantially more pronounced diverging waves. Thus it affects the recommendations drawn

for improvement of the hull form. RAPID allows to optimize this class of bulbous bows, without the uncertainty on the limits of applicability that we always had to take into account in running DAWSON for such extreme cases.

It thus appears that even for slender hulls the nonlinear effects can be quite appreciable due to particular hull form features.

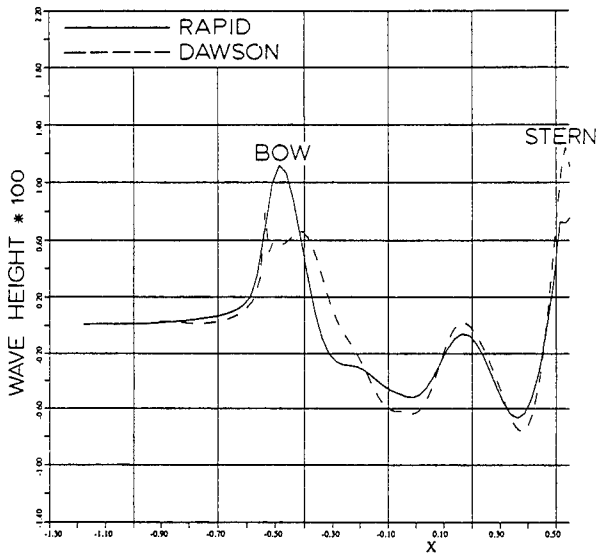

15. Hull wave profiles predicted by DAWSON and RAPID. Hull with partially immersed bulbous bow.

6 Conclusions

In this paper, a new and successful fully nonlinear procedure for solving the wave resistance problem has been presented. The RAPID-approach consists of the iterative application of a solution method for a steady linear problem. This solution method has several similiarities with Dawson's method, but a special feature is the use of source panels above instead of on the free surface. The main merits of the RAPID-approach are in my opinion:

- The convergence of the iterative procedure, which in most cases is automatic, even for notoriously difficult cases. Up to now, I have not yet met a realistic case for which no converged result could be obtained.
- The straightforward structure of the method, which is very similar to the Dawson approach; as a result of that, part of the extensive experience with that class of methods is still applicable.
- The absence of smoothing, artificial damping or tuning of any kind in the method. There are basically two free parameters for influencing the convergence properties: the relaxation factor, which is not critical at all and does not affect the final result; and the panel elevation, which within reasonable (and understandable!) bounds also has no effect on the final result.
- The quite small numerical dispersion of the raised-panel discretization for wave problems, as has been shown analytically and confirmed numerically.

The good convergence properties are probably due to the careful decisions on all aspects of the formulation of the method and its numerical implementation. In general, details of the numerics may have a dominant effect on the convergence behaviour of methods to solve the nonlinear free surface problem.

The RAPID code starts already being useful in the commercial ship design work at MARIN. In particular the example of the surface-piercing bulbous bow shows the value of the method to complement DAWSON. Even so, a number of improvements and extensions is still needed to make the code more generally applicable. In particular, a model and implementation of the flow off an immersed transom stern is to be added. Possibly, one day the step towards a higher-order panel distribution will be made to improve the numerical accuracy for a given panel number. Further study is needed to improve the accuracy of the prediction of the wave resistance itself; evaluating this by pressure integration is even much more difficult than in linearized methods.

It is useful to keep in mind that even with a solution of the full potential flow problem, several flow phenomena are not covered. In particular, wave breaking and its effect on the flow around the hull and wave pattern; and the effect of viscosity on the wave pattern around the stern. Still I believe that the possibility to solve the full, nonlinear potential flow problem means a significant step ahead in the consideration of wave resistance and wave pattern in ship design.

Acknowledgement

Part of the computing time involved in this development has been covered by a grant from the Dutch National Computing Facilities Foundation (NCF) under Project numbers SC-185 and SC-232.

References

[1] Raven,H.C.,"Variations on a Theme by Dawson", *Proc. 17th Symp. Naval Hydrod.*, The Hague, Netherlands, 1988, pp. 151-172

[2] Van den Berg,W., Raven,H.C. and Valkhof,H.H., "Free-surface Potential Flow Calculations for Merchant Vessels", *Proc. Int. Symp. on CFD and CAD in Ship Design*, Wageningen, Netherlands, 1990, pp. 165-181.

[3] Dawson,C.W., "A Practical Computer Method for Solving Ship-Wave Problems", *Proc. 2nd Int. Conf. Numerical Ship Hydrodynamics*, Berkeley, U.S.A., 1977

[4] Raven,H.C., "Adequacy of Free-Surface Conditions for the Wave-Resistance Problem", *Proc. 18th Symp. Naval Hydrod.*, Ann Arbor,Michigan, U.S.A.,1990.

[5] Salvesen,N. and Kerczek,C.H. Von, "Numerical Solution of Two-Dimensional Nonlinear Body-Wave Problems", *Proc. 1st Int. Conf. Numerical Ship Hydrodynamics*, Gaithersburg, U.S.A., 1975.

[6] Hess, J.L., "Progress in the Calculation of Nonlinear Free-Surface Problems by Surface-Singularity Techniques", *Proc. 2nd Int. Conf. Numerical Ship Hydrodynamics*, Berkeley, U.S.A., 1977, pp.278-284.

[7] Ni,S.-Y., "A Method for Calculating Non-linear Free Surface Potential Flows using Higher Order Panels", in: Ph.D. Thesis, Chalmers University, Gothenburg, Sweden,1987.

[8] Larsson,L., Broberg,L., Kim,K.-J., Zhang,D.-H., "New Viscous and Inviscid CFD Techniques for Ship Flows", *Proc. 5th Int. Conf. Numerical Ship Hydrodynamics*, Hiroshima, 1989.

[9] Kim,Y.-H. and Lucas,T., "Nonlinear Ship Waves", *Proc. 18th Symp. Naval Hydrodynamics*, Ann Arbor, Michigan, U.S.A., 1990.

[10] Jensen,G., "Berechnung der Stationären Potentialströmung um ein Schiff unter Berücksichtigung der nichtlinearen Randbedingung an der Wasseroberfläche", Thesis, IfS Bericht 484, 1988.

[11] Jensen,G., Bertram,V. and Söding,H., "Ship Wave-Resistance Computations", *Proc. 5th International Conf. Numerical Ship Hydrodynamics*, Hiroshima, Japan, 1989.

[12] Musker,A.J., "A Panel Method for Predicting Ship Wave Resistance", *Proc. 17th Symp. Naval Hydrod.*, The Hague, Netherlands,1988.

[13] Webster,W.C., "The Flow about Arbitrary Three-Dimensional Bodies", *Jnl. Ship Research*, Vol. 19-4, 1975.

[14] Schultz,W.W. and Hong,S.W., "Solution of Potential Problems using an Overdetermined Complex Boundary Integral Method", *Jnl. Comp. Phys.*, Vol. 84,1989.

[15] Schultz,W.W., Cao,Y. and Beck,R.F., "Three-Dimensional Nonlinear Wave Computation by Desingularized Boundary Integral Method", *Proc. 5th Workshop on Water Waves and Floating Bodies*, Manchester, U.K.,1990.

[16] Sclavounos,P.D. and Nakos,D.E., "Stability Analysis of Panel Methods for Free-Surface Flows with Forward Speed", *Proc. 17th Symp. Naval Hydrod.*, The Hague, Netherlands,1988, pp. 173-192.

[17] Ligtelijn,J.Th., Raven,H.C. and Valkhof,H.H., "Ship Design Today: Practical Applications of Computational Fluid Dynamics", *HADMAR'91 Symposium*, Varna, Bulgaria,1991.

DISCUSSION

S. Sharma
University of Duisburg, Germany

Michell's monumental theory of ship wave resistance has stubbornly resisted virtually all analytical attempts at improvement for nearly a hundred years. It seems that dedicated efforts of several researchers in various countries are now finally bearing fruit. We may soon have a reliable method of at least obtaining a numerical approximation to the exact nonlinear—but nonbreaking—ship waves in an ideal fluid. A significant part of the credit for this achievement goes to Dr. Raven for his series of contributions culminating in the present paper. I invite him to provide a few typical comparisons of his calculations with the best available model experiments. Only then will we be able to tell how much of the known gap between Michell's theory and real ship waves is closed by accounting for the nonlinear free surface condition and how much still remains due to neglect of viscosity (and possibly surface tension).

AUTHOR'S REPLY

Thank you for your kind remarks. As a matter of fact, the paper primarily discusses the convergence for increasing panel density, the dependence on numerical parameters, etc., rather than comparisons with experimental data. Now that I am confident that the results are fairly independent of the discretization, I have made a number of such comparisons. Because of the availability of extensive data, these mainly address standard test cases, the Wigley hull and the Series 60 parent form.

Fig. A shows the hull wave profiles for the Series 60 Cb=0.60 model at Fn=0.35. The data are those from the ITTC Cooperative Experimental Program. The full line represents the final nonlinear solution, while the markers indicate the result of the first iteration, which corresponds to a Neumann-Kelvin approximation (solved using Rankine panels of course). The Neumann-Kelvin solution significantly deviates from the data, by an underprediction of the bow wave, overprediction of the stern wave and a phase error. The slow-ship approach (DAWSON-code) (not shown) gives a wave profile which is somewhat closer to the experimental profile. But there is a definite improvement by taking into account the nonlinear effects: for the RAPID result, the agreement with the data is excellent.

For the Wigley hull at Fn=0.31 (Fig. B) and Fn=0.452 (Fig. C), again the RAPID-result is quite close to the experimental data, and the nonlinear effects account for most of the deficiencies of the linearized method. The only deviation visible in both cases (but not for the Series 60 hull) is an underprediction of the bow wave height by about 10 percent. This is a much better result than obtained with linearized methods, but raises the question of what else is causing this underprediction. It appears to me that it should be attributed to a jet-like flow in the immediate vicinity of the bow rather than to the neglect of viscosity or surface tension. This phenomenon cannot be covered by the present method and probably requires a separate treatment by a model still to be devised. Its effect on the wave profile and pattern is, however, quite small and localized.

Of course, further validations are desired and will be performed.

(See figures on the next page.)

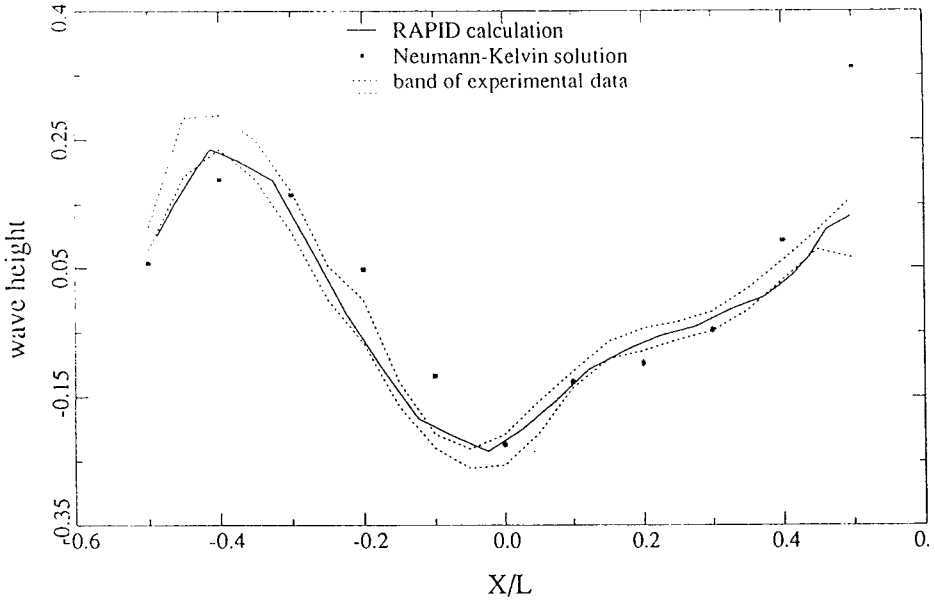

Fig. A. Wave profile for Series 60 C_B = 60 hull, Fn = 0.35, zero sinkage and trim.

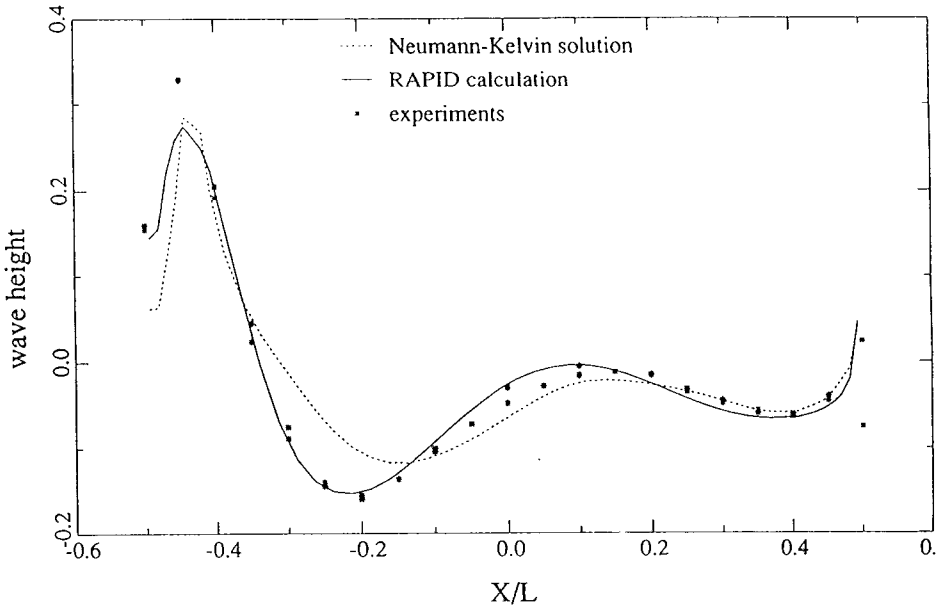

Fig. B. Wave profile for Wigley parabolic hull, Fn = 0.31, zero sinkage and trim.

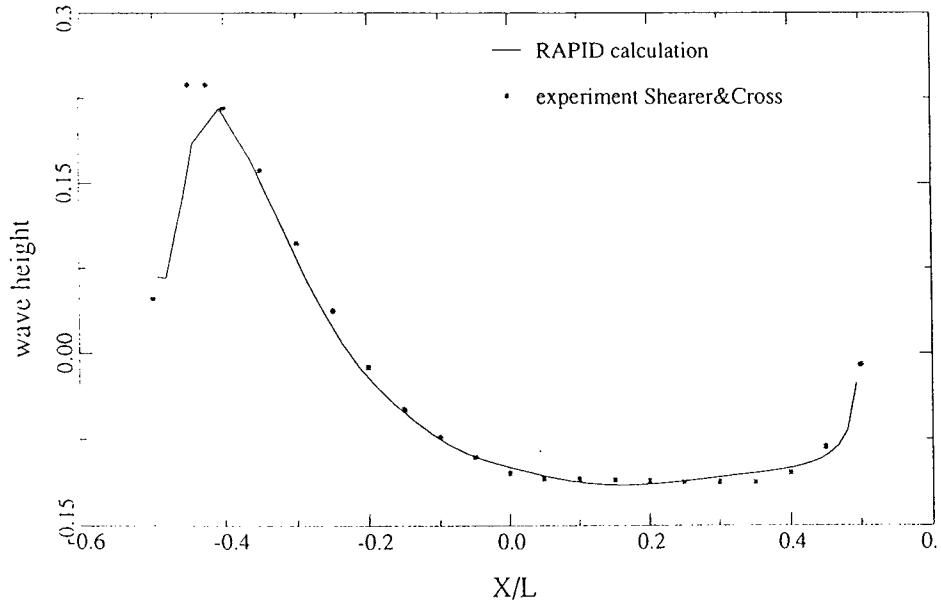

Fig. C. Wave profile for Wigley parabolic hull, Fn = 0.452, free sinkage and trim.

DISCUSSION

L. Larsson
FLOWTECH International, Sweden

The author is to be congratulated for his very interesting series of papers on Rankine source methods. The present idea to raise panels above the free surface was the first approach tested in the discussor's research group when we started the work on nonlinear methods in 1984. As appears from the enclosed figures from the thesis by Xia [A], a marked sensitivity was noted to the height of the (flat) source surface and the method was rejected. Xia's approach was a standard Dawson technique, but with a linearization about the previous solution. No transfer terms were included in the FSC, so the method should be very similar to the present one. One difference is that the source surface was never deformed, but is that really needed? Fig. 5 seems to indicate the opposite. Is there any other reason why the present method should be less sensitive to the source surface height than the standard Dawson technique as defined above?

[A] Xia, F., "Numerical Calculations of Ship Flows, with Special Emphasis on the Free Surface Potential Flow," PhD Thesis, Chalmers University of Technology, Gothenburg, Sweden, 1986.

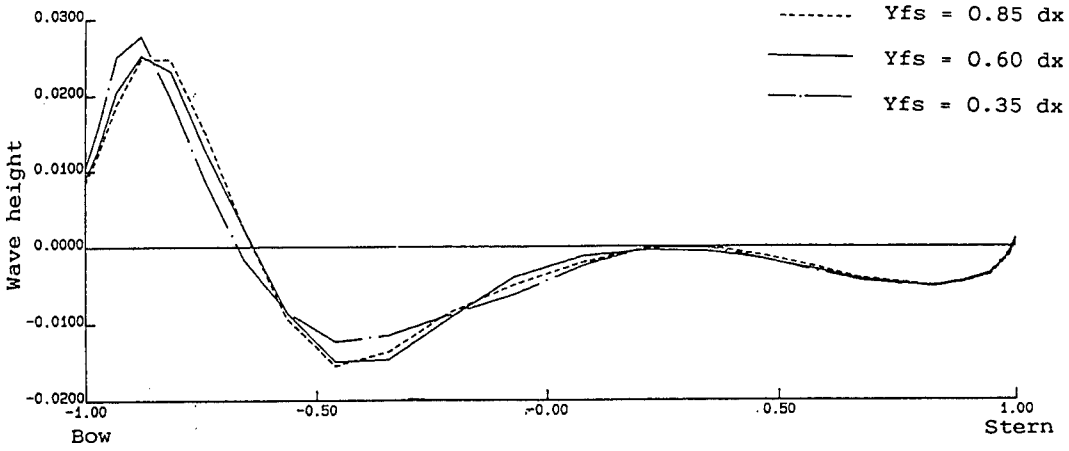

Figure A. Wave height for the Wigley hull at $F_n = 0.31$. Different locations of the source surface. From Xia [A].

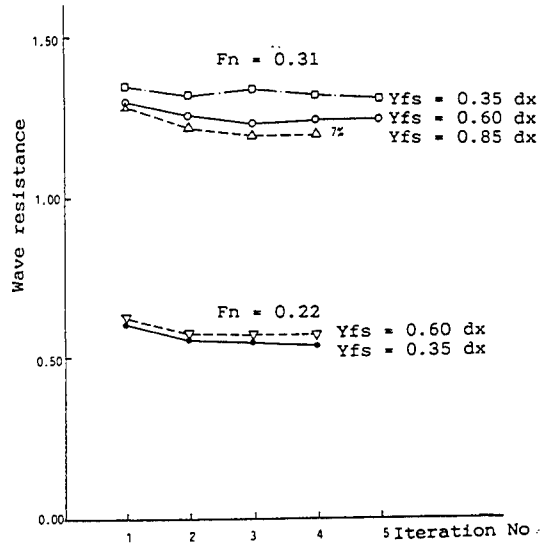

Figure B. Wave resistance for the Wigley hull at two Froude Numbers. Different locations of the source surface from Xia [A].

AUTHORS' REPLY

Thank you very much for your interesting remarks. Admittedly, I did not remember that Xia already had briefly studied a similar approach; I apologize for not referring to it. In my opinion, the results shown in your figures largely conform to mine. The smallest panel elevation (3 percent) amounts to 0.25 panel length; according to the analysis in Section 3.2, this introduces significant numerical dispersion, which may explain the deviations in the wave profile. The other two lines, for yfs=0.6Δx and 0.85Δx, are in much closer agreement. That the difference is somewhat larger than in my method may be due to the rather coarse discretization and the absence of free-surface panel adaptation (which ensures a high accuracy for a greater range of panel elevations). The differences in the resistance in Xia's calculations may have been magnified by inaccuracies in integrating up to the real waterline for the different hull panelings. Fig. 5 applies to a rather coarse paneling, with a fairly good conditioning even with fixed panels; it thus merely shows the insensitivity of the method for the panel shape and location. For finer free surface panelings, however, the same sort of figure shows larger differences due to inaccuracies in the fixed-panel method as a result of the increasing condition number.

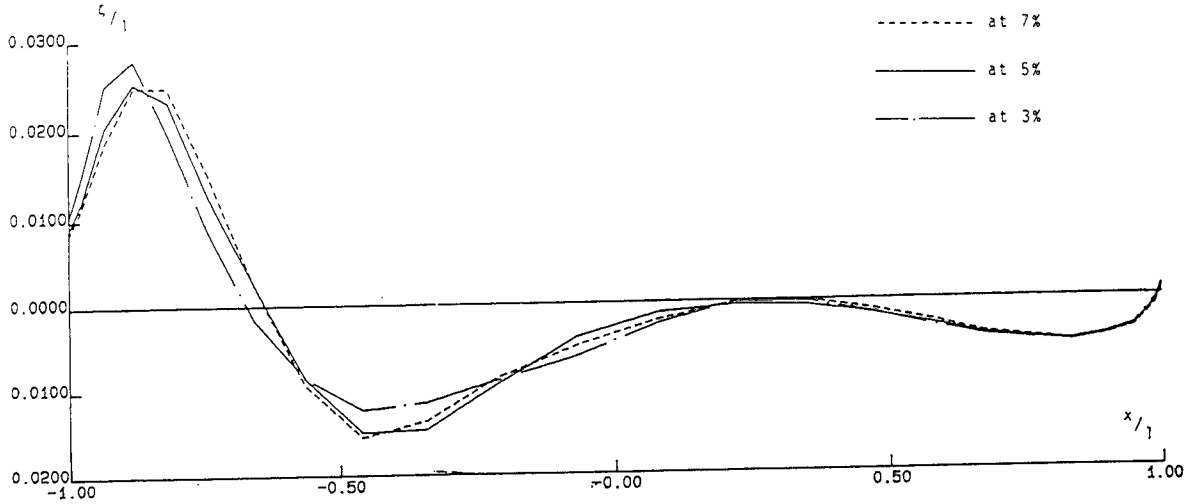

Figure 1. Comparison of the wave profiles, the Wigley hull, at $F_n = 0.3$.

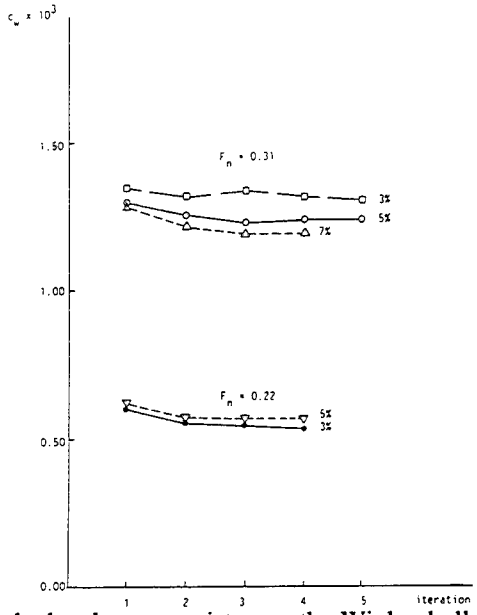

Figure 2. Convergence of the calculated wave resistance, the Wigley hull, at $F_n = 0.31$ and $F_n = 0.22$.

DISCUSSION

G. Jensen
The Hamburg Ship Model Basin HSVA, Germany

I want to congratulate the author for his valuable study. I also wish to ask a question and comment on a few things.

The author presents his method as a new one. It seems, however, that it is quite closely related to the method of Bertram, Jensen, and Sölding [10,11], the main difference being the neglect of some terms containing higher derivatives in the Taylor expansion of the free surface condition and the use of a Dawson type finite differencing scheme for second derivatives instead of analytical derivatives. Do you think this leads to a more general convergence?

I think general convergence cannot be expected by this class of methods which can only cover weak nonlinearities, due to the underlying assumption of a potential flow with a free surface described as a unique function. Thus, breaking waves and spray cannot be described. Although these phenomena occur on any practical ship hull, I agree that this method can be usefully applied as the critical region very close to the bow is not discretized. I claim, however, that for the limit of grid refinement, e.g., at the bow convergence, may not generally be reached.

In addition, there are a few other practical cases where larger areas of wave breaking occur, and where Jensen's method, as expected, does not converge and where x/ϕ, the method presented by the author, should not converge as well. These are as follows: Full block ships will generate a large breaking wave zone near the forward shoulder at high Froude numbers, especially on shallow water. Slightly submerged bodies often create breaking waves in the flow field. Catamarans often create breaking waves where the two wave systems interfere.

AUTHOR'S REPLY

Thank you for your useful comments. Different methods for solving this problem unavoidably seem to be closely related, as separate developments all tend to converge towards the same basic structure that is optimal for the problem. The actual similarities with your method are mostly mentioned in the paper; there are differences in the form of the FSC, the treatment of the radiation condition, the choice of the free-surface singularities, the free-surface panel adaptation, the hull discretization, and several other points. The transfer terms in the FSC are intentionally neglected in order to improve convergence. According to my experience, the convergence of RAPID is actually better than what has been published about your method, but perhaps later improvements in your code may have changed this. A direct comparison might be interesting. The designation "weak nonlinearities" seems not to do justice to their importance in practice. Anyway, this class of nonlinear effects appears to be well resolved, as Fig. 10 shows: the convergence for decreasing panel size is quite satisfactory. However, in an "inner region" in the immediate vicinity of the bow, the mathematical model may become singular, as an indication of the jet shooting up along the hull. The analogy with the 2D impulsively started wavemaker problem suggests that an insufficient resolution of this jet has only a very localized effect near the bow, while anything else is unaffected. If this is fact is the case, the method would be entirely satisfactory for the purpose it is intended for. Evidently, further study is needed to verify this hypothesis.

Undeniably, the method cannot cope with vertical wave faces or breaking. This does not seem to be a very important restriction since breaking cannot be incorporated in a potential flow model anyway. In cases in which extensive breaking occurs, I expect the method either not to converge, or to converge to a solution that is not physically realizable and unstable.

DISCUSSION

K. Nakatake
Kyushu University, Japan

I congratulate your completion of fully nonlinear method. According to our experience for the Rankine source method, it cannot be applicable to the very high speed range, say Fn=10.0. Did you apply your method to that case?

AUTHOR'S REPLY

In the first place, using Rankine sources is just one way of solving the uniquely posed potential problem, and is applicable regardless of the Froude

number. However, I presume you refer to your experience with applying Dawson's method to a submerged hydrofoil at high Fn. The possible shortcomings in that case may be either in the numerics or in the linearization. In the former case, they might be removed; in the latter case, they will be removed by the present method, provided that it converges. For the shallowest submergences, this might be problematic, but I have not tried it yet.

DISCUSSION

W. Schultz
University of Michigan, USA

Your statements about radiation conditions and open boundary conditions are confusing to me. Theoretically, radiation conditions are required for steady or periodic problems, not for initial value problems. Numerically, both methods may require open boundary conditions, but when material derivatives are used Cao, et al (1991)[Int J. Num. Meth. Fluid 12, 185] have shown no perceivable reflections without using any treatment at the open boundaries. While I agree that a time marching procedure is not usually efficient for steady flow, an adopted implicit procedure with large time steps is usually as efficient.

Your first conclusion that up to now you always get converged results for realistic cases—do those cases include flows with breaking waves? Also, it is my opinion that no procedure yet developed can adequately handle mesh refinement near the contact line.

AUTHOR'S REPLY

As a matter of fact, a radiation condition is only needed for steady problems, as stated in Section 2.3. Non-reflective ℓ.c.'s are in principle required for all free surface problems in truncated domains. But in steady problems the waves are confined to the Kelvin wedge; for a sufficient width of the free-surface domain, reflection only occurs at the downstream boundary, and the waves reflected there are unable to move back upstream into the domain. Such properties do not occur in general unsteady problems.

The reflection coefficient will be largely determined by the implied flow behavior outside the discretized free-surface domain; e.g., in Dawson's method, there is a sharp transition to a zero vertical velocity at the edge. With singularities above the free surface, however, this transition is much more gradual, and reflections could well be weaker. This may explain the good experiences with your raised point-source method.

For your remarks on wave breaking, I refer the reply to Jensen's comments; with the addition that problems seem to occur near the bow rather than at the entire contact line.

A Numerical Approach for Predicting the Total Resistance and Nominal Wakes of Full-Scale Tankers

S. Ju (Daewoo Shipbuilding & Heavy Machinery Ltd., Korea)
V. Patel (The University of Iowa, USA)

ABSTRACT

Recent advances in the power and speed of numerical methods for solution of the Reynolds-averaged Navier-Stokes equations to predict the flow around a ship hull have made it possible to consider their use in ship design. In this paper, one such method is applied to investigate its capabilities to predict the resistance components and the nominal wake at the propeller plane. A grid sensitivity study is first performed to determine the effect of grid numbers on the solution and the cost in terms of computer storage and time. The method is then applied to a tanker series with the same forebody and different afterbodies, at model- and full-scale, to show that such a method can be economically employed in the design environment to make a comparative assessment of different hull forms.

NOMENCLATURE

C_A	incremental resistance coefficient for model ship correlation
C_{AA}	air resistance coefficient
C_f	friction coefficient
C_p	local pressure coefficient
C_{fG}	integration of resistance due to C_f along the girth
C_{pG}	integration of resistance due to C_p along the girth
C_{F0}	frictional resistance coefficient of a plate
C_F	frictional resistance coefficient of the ship
C_{PP}	potential-flow pressure resistance
C_{PV}	viscous pressure resistance
C_R	residuary resistance
C_T	total resistance
C_V	total viscous resistance
C_W	wavemaking resistance
k	three dimensional form factor $\left(\frac{C_V - C_{F0}}{C_{F0}}\right)$

Subscripts

m	model
s	ship
a	afterbody (x > 0.35)
f	forebody (x < 0.35)

INTRODUCTION

In ship hydrodynamics, as distinct from aerodynamics, the major force component due to flow around the hull is resistance, rather than lift. It is one of the duties of a naval architect to design ships with hull forms having low resistance and, therefore, with minimum power requirements. The expected forces on a new ship and the ship response to these forces must be estimated as functions of the geometry and dimensions of the ship. These estimates are based on a combination of theoretical and empirical methods, and often require experimental confirmation. Design of a proper propulsion system for a given ship requires a knowledge of the flow field ahead of the propeller plane, in addition to the characteristics of the propeller, and involves a similar combination of theoretical and empirical techniques.

Current ship-resistance predictions are still based on the well-known suggestion of William Froude, who postulated that the full-scale ship resistance consists of two components, wavemaking resistance, which scales with the Froude number, and viscous resistance, which is Reynolds-number dependent. Model-scale Reynolds numbers are of the order of 10^6, while for full-scale ships they can be of the order of 10^9, which are among the largest values encountered in fluids-engineering applications. An outstanding practical problem in the prediction of the resistance of a full-scale ship is that of converting, or extrapolating, model results correctly to the full-scale ship.

Similarly, for determination of the flow into the propeller, current design practice relies heavily on model-scale experiments and prior experience based on experiments on similar hulls. Even in this case, there is considerable uncertainty in the prediction of the flow at full scale because the scaling methods used to extrapolate from model scale are based on notions of boundary-layer theory whereas, in reality, the wake flow is much more complex.

Although Computational Fluid Dynamics (CFD) is a long way from maturity for these and other applications in ship hydrodynamics, it is destined to play an increasing role in the ship design process. Over the past decade or so, much effort has been devoted at various organizations to the developmemt of CFD methods for prediction of the viscous flow over ship hulls. The Resistance and Flow Committee of the 19th ITTC (1990) concluded that some of the recent

computational methods for ship viscous flow using Reynolds-averaged Navier-Stokes (RANS) equations have succeeded in predicting the gross time-mean velocity field in the stern region with reasonable accuracy compared with model experiments. A similar observation was made following the 1990 SSPA-CTH-IIHR Workshop on Ship Viscous Flow (Larsson et al., 1991), where some 19 computational methods were compared with two sets of detailed model-scale data. One of the conclusions reached at the Workshop, however, was that none of the methods has become good enongh to be used by the designer to optimize the stern of full shaped ships, although many of them are promising and give qualitative information on how the flow around the stern is changed when the afterbody lines are modified. In addition, a very few methods succeeded in calculating the flow at full-scale Reynolds number, underscoring the additional difficulties that arise in using CFD methods at very high Reynolds numbers.

Although a great deal of effort has been devoted to development of CFD methods for ship hulls, relatively little attention has been paid to their use in the design environment. This paper is concerned with the practical applicability of the method of Patel, Chen and Ju (1988, 1990) to the prediction of resistance components and the nominal wake in the design context.

NUMERICAL METHOD AND ITS APPLICATIONS

The numerical method of Patel, Chen and Ju has been selected because it is one of the most widely tested methods. It has been compared with experiments on a variety of hull forms at model scale (Patel, Chen and Ju, 1990), and has been applied, in a preliminary way, to calculate the flow at full-scale Reynolds numbers (Ju and Patel, 1991) and the flow around a ship hull in yaw (Patel, Ju and Lew, 1990). In addition, this method has been combined with conventional propeller performance prediction methods based on inviscid fluid theories to study propeller-hull interaction (Stern et al., 1988), and a number of other extensions have been made to investigate different features of complex, three-dimensional shear flows. The method solves the RANS equations, along with the k-ε turbulence-model equations, in generalized, body-fitted coordinates which are also generated by numerical methods. The velocity components are retained in cylindrical-polar coordinates, and the wall boundary conditions are indirectly satisfied by using the wall-functions approach. Further details of the method are given in Patel, Chen and Ju (1988), Chen, Patel and Ju (1990) and Ju (1989).

A number of issues arise when such a method is used to assess its potential in the design environment. The first is to recognize its limitations. In this connection, we note that the method, in the form it is employed here, calculates the flow around a double body, assuming that the free surface is flat. Plane-of-symmetry conditions are imposed on that boundary. Thus, any Froude number effect is excluded. Secondly, the solutions are started at some location on the parallel middle body and, therefore, information on the forebody has to be obtained by other means, for example, by potential-flow or boundary-layer analyses. The second issue is that of the numerical performance of the method. In particular, it is important to establish the grid sensitivity of the method and the computer requirements to obtain grid-independent answers.

The next section is devoted to an evaluation of the grid sensitivity of the method, with particular reference to the prediction of the resistance components. In this case, extensive calculations were performed for the case of the HSVA tanker, which was one of the two test cases of the Ship Viscous Flow Workshop. The surface pressure and wall shear-stress data on this hull are used to assess the capability of the method to predict the viscous-pressure (C_{PV}) and frictional (C_F) resistance components, and the computer resources required to obtain grid-independent results.

Next, with the noted limitations of the numerical method in mind, calculations were performed for test hulls and conditions in which the double-body assumption is justified and the need for detailed calculations for the forebody flow is not critical. The test models selected are shown in Fig. 1. These series A tanker forms (A1,A2,A3) have the same forebody but different afterbodies, so that they are expected to have almost the same forebody viscous pressure (C_{PVf}) and frictional (C_{Ff}) resistance components. For these tankers, there exist data from towing-tank experiments at low Froude number for which the free-surface effects are small. Selected results for this tanker series are presented to demonstrate the general performance of the numerical method with respect to the predicition of resistance as well as the nominal wake at both model and full-scale Reynolds numbers.

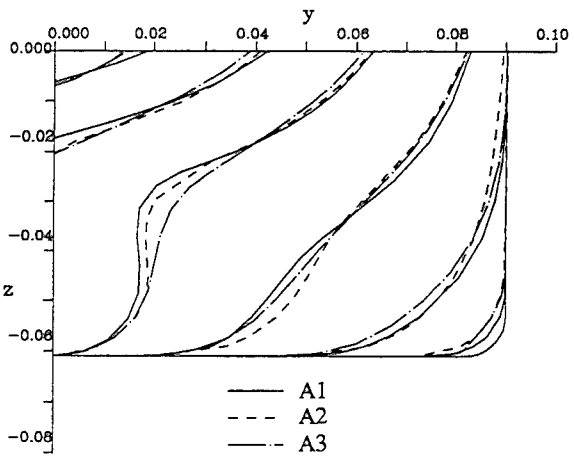

Fig. 1 Afterbody offset lines of Tanker series A

GRID DEPENDENCE AND COMPUTING RESOURCES

Even with the extensive comparisons that were made at the Ship Viscous Flow Workshop, it was not possible to isolate the effects of the many components of modern computational methods, such as grid number and topology, numerics, turbulence model, and boundary and initial conditions. For example, the number of grid points used for the calculations presented at the Workshop for the HSVA tanker at a Reynolds number of 5×10^6 ranged from a low of 8,000 to as high as 253,000. The grid topology also varied, particularly in the stern region. However, there was no clear cut correlation between the number of grid points and the quality of the results. The Workshop calculations made with the present method employed 23,000 grid points. Here, we make a more comprehensive assessment of the grid sensitivity of the method. Once again, the HSVA tanker is chosen as the test case.

In the calculations and results to be presented, all

coordinates and geometrical parameters are rendered dimensionless using the ship length L as the characteristic scale, and the coordinate x is measured from the bow. The velocity components (U,V,W) in (x,y,z) directions, respectively, and the friction velocity U_t are nondimensionalized by the ship speed U_0. The pressure is normalized by the ship speed and fluid density. The resistance coefficients are defined in the conventional manner (see Nomenclature). For ease of reference, and where appropriate, the results are plotted in the format used for the Ship Viscous Flow Workshop.

Table 1 summarizes the grid numbers for which calculations were performed, along with the number of iterations required to reach steady-state solutions, and computer storage and time. The number of grid points in the radial direction (JN), from the hull surface to the far field, was fixed at 30, while the number of points in the streamwise direction (IN) was varied from 54 to 151, and that around the girth was varied from 15 to 39. The total number of points used varied from 24,300 (54x30x15), comparable to that used for the Workshop calculations, to 176,670 (151x30x15). Fig. 2 shows some views of the coarsest and the finest grid. The increase in the required computer resources with increasing grid number is clear from Table 1.

The computed C_p and U_t, which are important for prediction of the resistance components, are compared with experiments in Figs. 3 and 4. The grid dependency in both directions is surprisingly small, and therefore the discrepancy between the calculations and experiments remains the same. It is noted that C_p along the waterline near x = 0.72 has a clearer wiggle as IN increases. This behavior is also observed in the potential-flow calculations shown in Fig. 5 when small enough panels are used near this location. This location is where the waterline starts to curve from the flat midbody. The comparisons of C_p obtained from the current viscous code and the potential code shows good agreement in the region of $0.6 < x < 0.8$ along both the keel and the waterline. The discrepancy around the midbody is associated with the initial conditions used at the inlet station at x = 0.3 in the viscous code. However, this discrepancy is not critical for the computation of the viscous pressure resistance, C_{PV}, since the component in the longitudinal direction of the pressure force is nearly zero due to the parallel mid body. The difference in C_p between the viscous and potential-flow calculations in the region of $x > 0.80$ is mainly responsible for the viscous pressure resistance.

Fig. 6 shows the convergence history of the resistance components calculated using four typical grids. In this figure, the resistance components are only those for $x > 0.35$, i.e., the forebody contributions are excluded. The surface area of the hull form is estimated using the numerical grid and includes about 1 % error compared to the real surface area. Usually, the surface area in the finer grid is larger than that in the coarser grid and this difference gives larger C_{Fa} for the finer grid. Two of the four calculations were started from the zero-pressure initial guesses, but the other two finer grid cases employed initial conditions based on the built-up pressure from the intermediate solutions of the coarser grids. The resistance coefficients were converged except in the finest grid case (151 x 30 x 39) which was stopped after 600 iterations due

Table 1. Summary of grid points and CPU memory and time

		KN = 15	KN = 21	KN = 27	KN = 39
IN= 54	total grid	24300	34020	43740	
	CPU memory (mb)	9.4	10.3	11.5	
	CPU sec. per iter.*	5.0	9.2	12.7	
	total no. of iter.**	100			
	total CPU hours*	0.2			
IN= 76	total grid	34200	47880	61560	88920
	CPU memory (mb)	10.6	15.1	18.0	25.6
	CPU sec. per iter.*	8.6	13.4	17.6	27.0
	total no. of iter.**		300		
	total CPU hours*		1.2		
IN= 107	total grid	48150		86670	
	CPU memory (mb)	13.4		25.5	
	CPU sec. per iter.*	11.8		24.6	
	total no. of iter.**			900	
	total CPU hours*			6.2	
IN= 151	total grid	67950			176670
	CPU memory (mb)	19.6			49.3
	CPU sec. per iter.*	15.9			48.0
	total no. of iter.**				2000***
	total CPU hours*				26.7***

note) * CPU time is based on CRAY2S. It takes approximately 22 times longer for DS5000 and 33 times for SPARC computer.
** convergence is based on the resistance components.
*** estimated after 600 iterations.

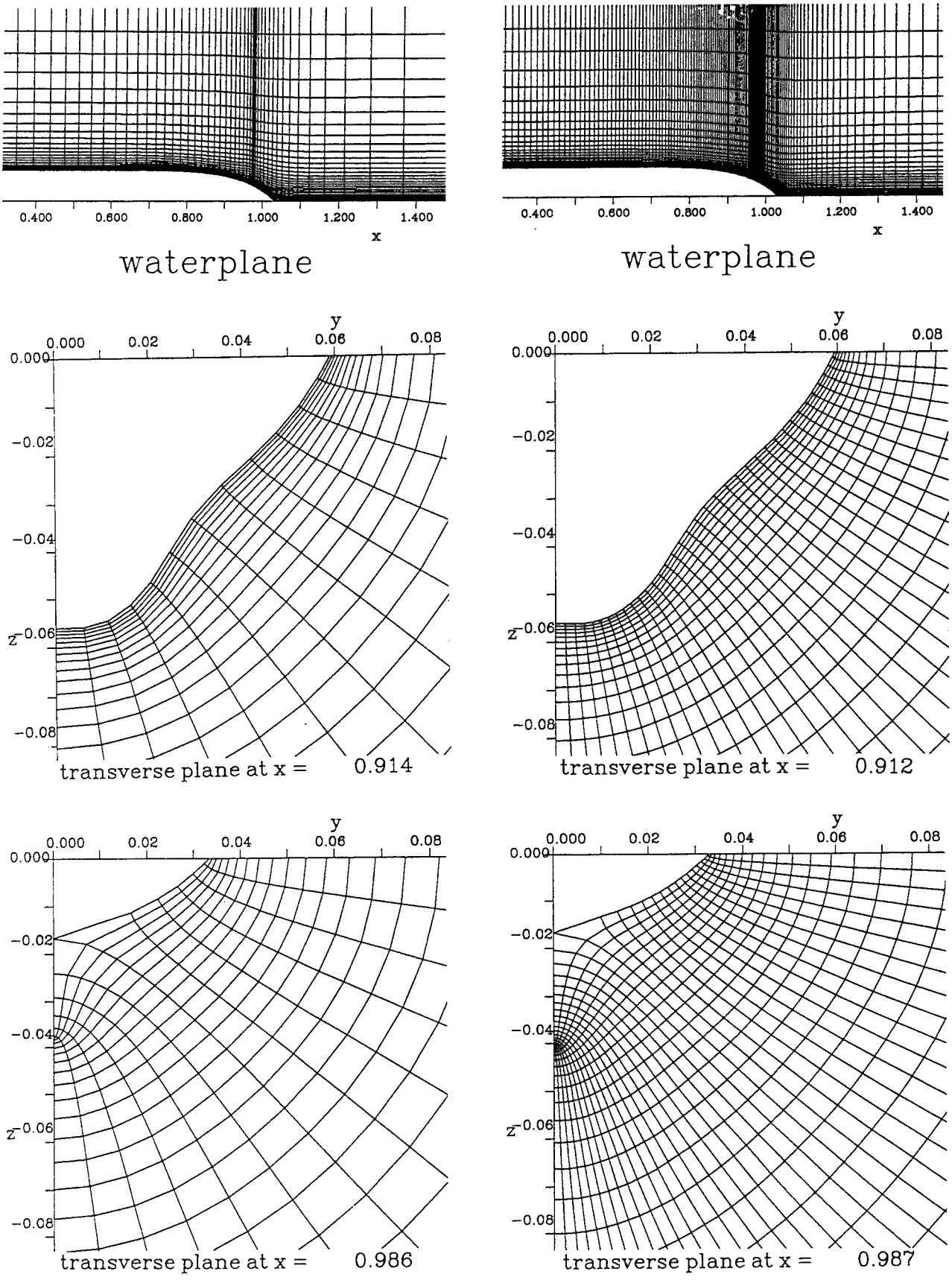

Fig. 2 Numerical grid (HSVA tanker)
Left : Coarse grid Right : Fine grid

to large computing time. The convergence of C_{Fa} is very fast, but the values of C_{PVa} converge very slowly, even when the residuals of the flow quantities (changes in velocity and pressure between successive iterations) are extremely small. For example, the value of C_{PVa} in the finest grid is 0.00079 after 600 iterations, but it is expected to decrease further by 0.00002, which is only about 1 % of C_T, after 2000 iterations.

Fig. 7 shows the influences of the grid number on the resistance components comparing the solutions obtained with four different grids. Both curves for C_{PVa} and C_{Fa} give convergent behavior as more grid points are used. The effect on C_{Fa} is not significant, say less than 0.00006, which is about 1.5 % of C_T. The coarse grid solution of C_{PVa} is 0.00040 (about 10 % of C_T) greater than that of the fine grid solution, which is assumed to be close to the final values. The higher values of C_{PVa} with the coarser grid are associated with not simulating the sharp pressure rise in the stern region. This behavior is also observed in the calculation of the potential-flow pressure resistance (C_{PPf}) for the forebody of the Tanker A, as shown in Fig. 8. Here, C_{PPf} is obtained by the Hess and Smith method (1962). Fig. 8 shows that more than 180 stations in the region $x < 0.5$ with more than 10 grid points in the girthwise direction are required to get a reasonable value of C_{PPf}. Even positive C_{PPf}'s are obtained with less than 70 stations. The grid dependency tests presented here clearly show the possibility to estimate the resistance components quantitatively by increasing the number of grid points.

The practical difficulty to use the viscous codes for predicting the resistance, however, is that the computing cost with the fine grids are still quite high, as shown in Table 1. Another approach to utilize the viscous codes considering the current level of the computing power and

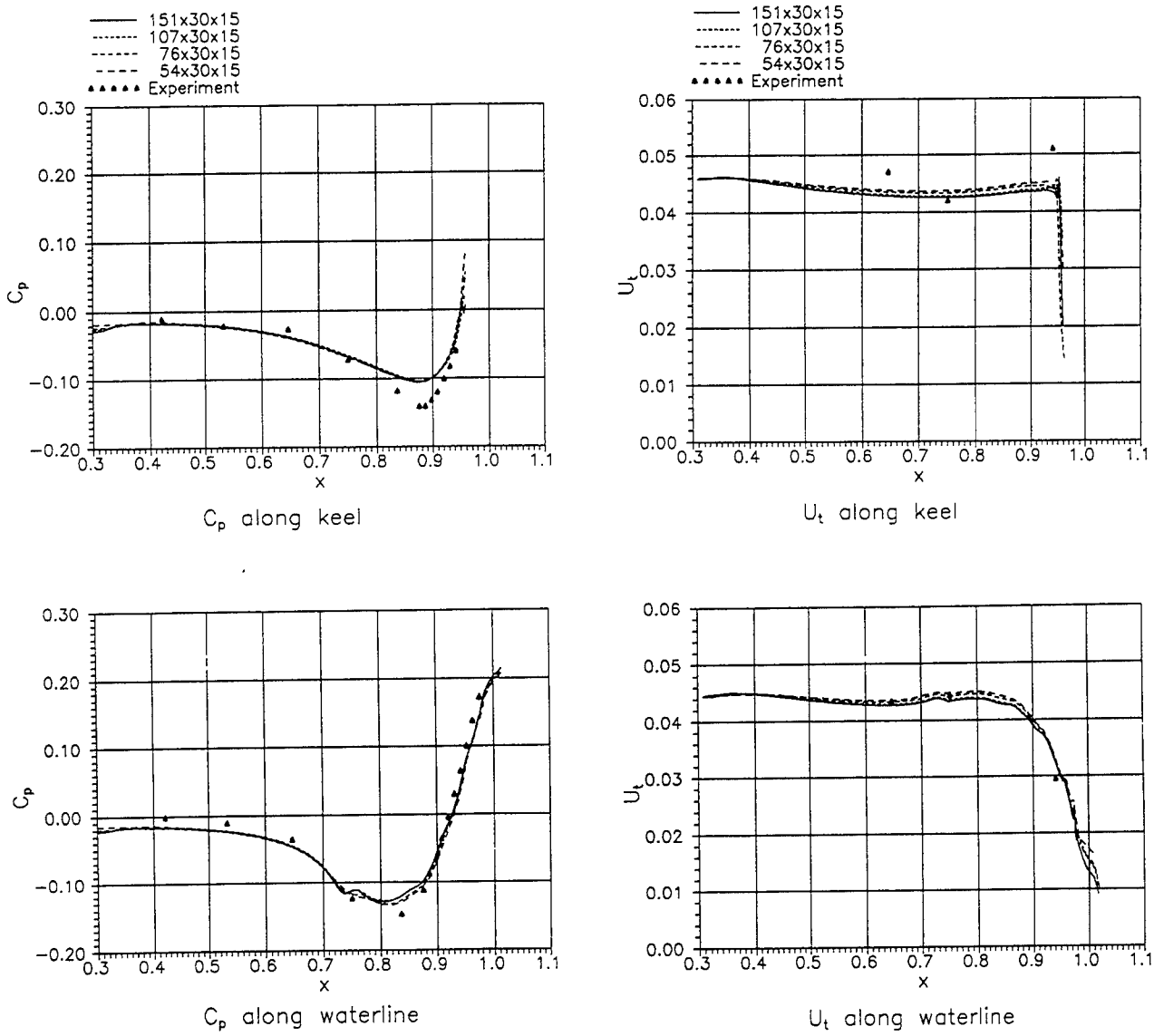

Fig. 3 Grid dependency test; grid refinement in the axial direction

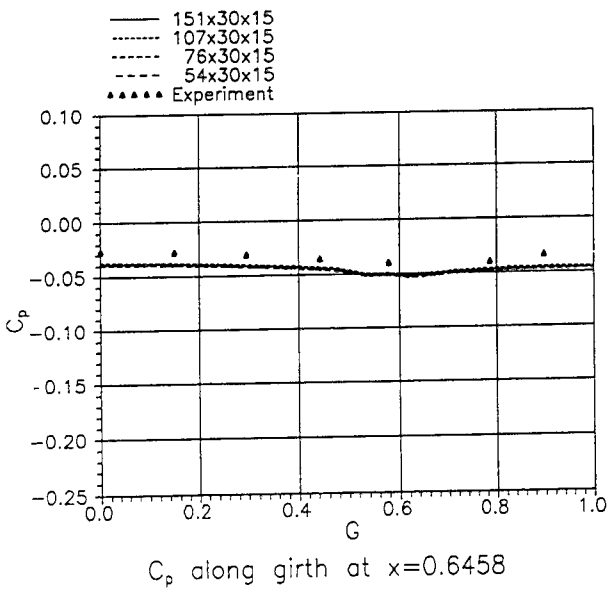

C_p along girth at x=0.6458

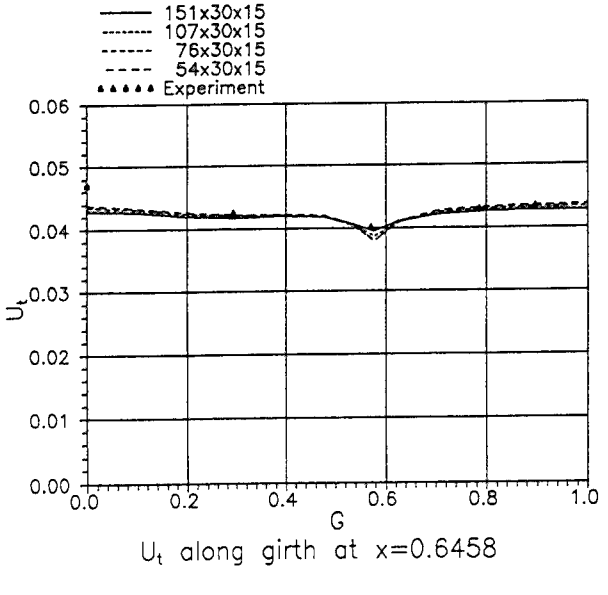

U_t along girth at x=0.6458

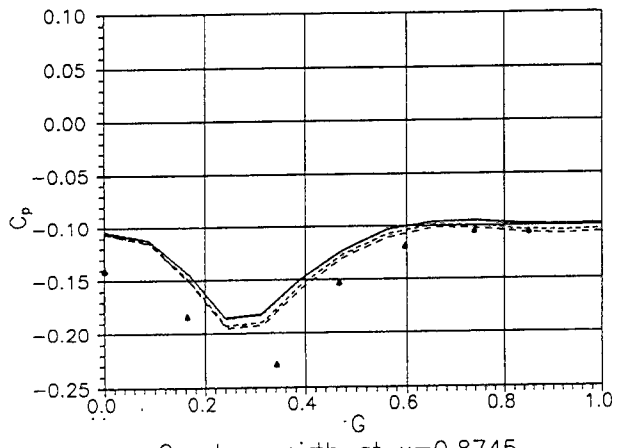

C_p along girth at x=0.8745

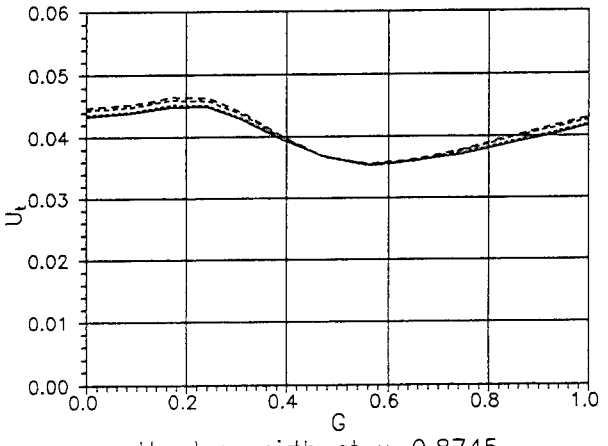

U_t along girth at x=0.8745

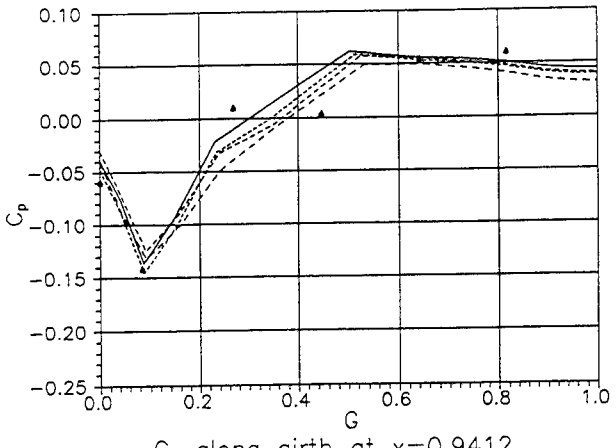

C_p along girth at x=0.9412

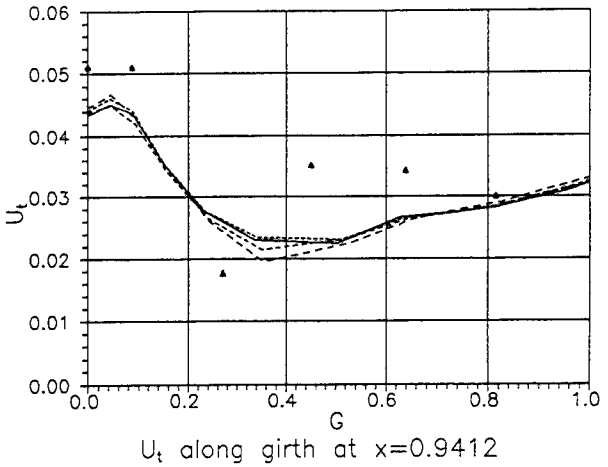

U_t along girth at x=0.9412

Fig. 3 (continued)

cost is to use them for comparative purposes only. This is explained and demonstrated with a commercial Tanker A in the next section.

MODEL-SHIP CORRELATION

For a comparative study of the Tanker series A (Fig. 1), a coarse and a fine grid, with (54x30x15) and (107x30x27) grid points, respectively, were employed. With three afterbody forms, and two Reynolds numbers, corresponding to model- and full-scale conditions, a total of 12 independent calculation were performed. For consistency of results, the same computing conditions during grid-generation and iteration procedures were used in all calculations.

Fig. 9 shows the finer grids for Tarker A3 at the model- and full-scale Reynolds numbers, which are 6.81 x 10^6 and 1.555 x 10^9, respectively. The considered Froude number for this tanker is 0.142. Table 2 provides a summary of the resistance calculations. Among the results shown, only the values of C_{PVa} and C_{Fa}, for the afterbody, $x > 0.35$, were obtained from the viscous-flow numerical method. All other quantities were deduced as explained in the table. In particular, the forebody pressure force C_{PPf} was obtained from potential-flow calculations, and the forebody frictional resistance C_{Ff} was obtained from the ITTC correlation line, and both were assumed to be the same for all three afterbody forms, The wave resistance C_W was also estimated with an inviscid free-surface method (Larsson et al., 1989).

With regard to the results of the viscous-flow method, it is observed that the afterbody frictional resistance (and therefore, the total frictional resistance) is insensitive to afterbody shape, but the effect of grid refinement is to

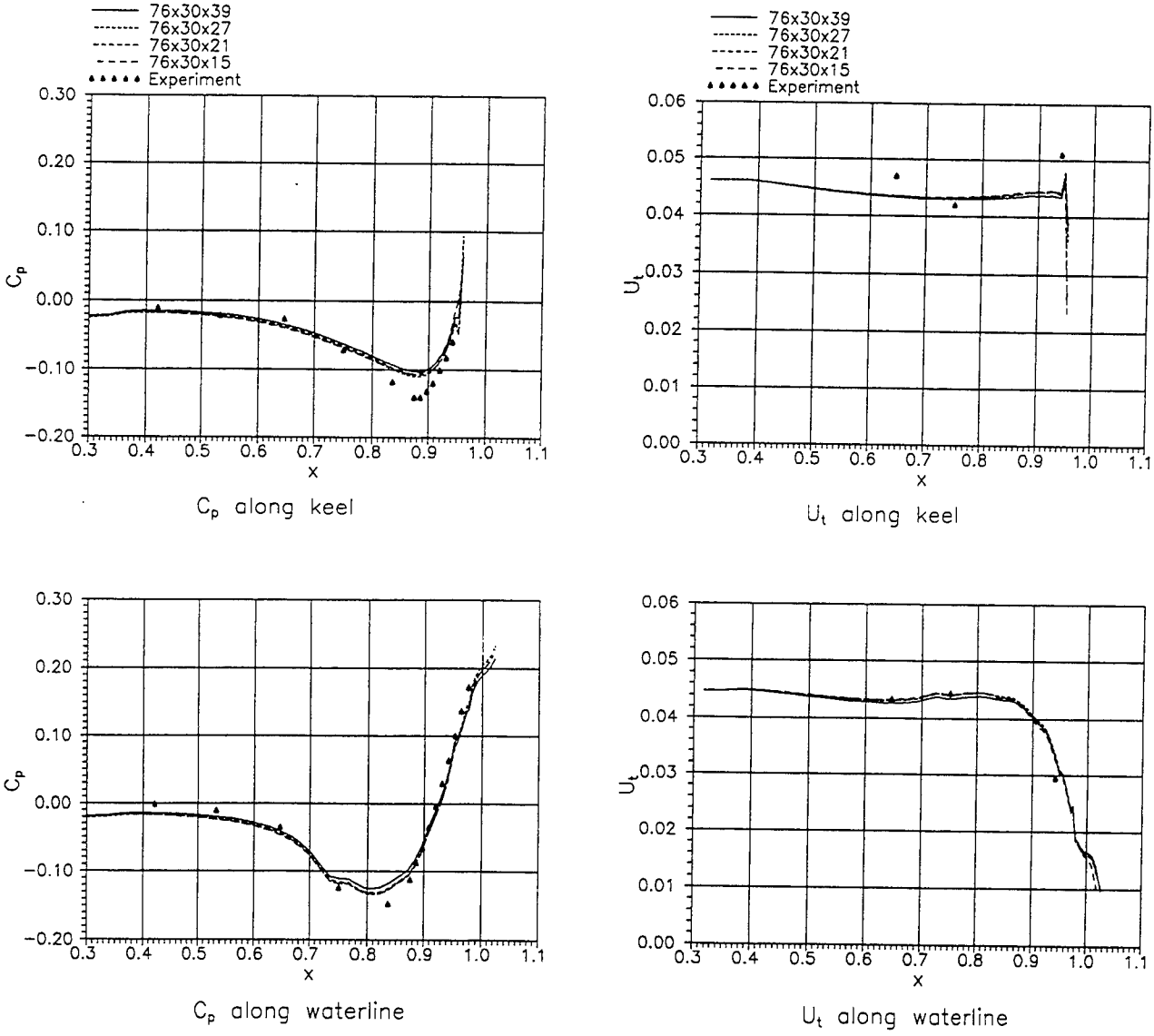

Fig. 4 Grid dependency test; grid refinement in the girthwise direction

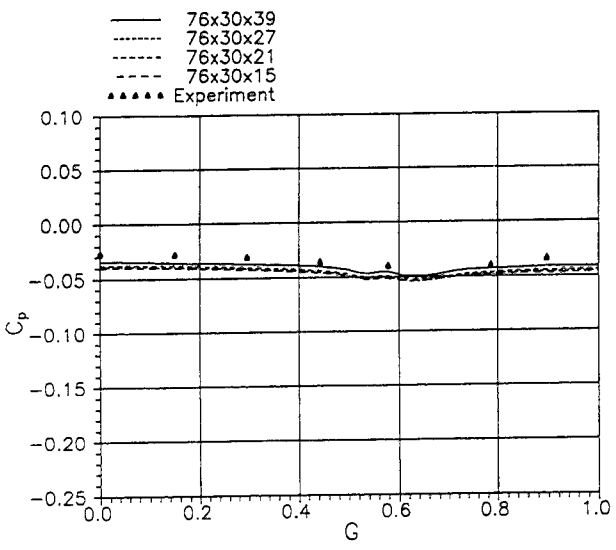

C_p along girth at x=0.6458

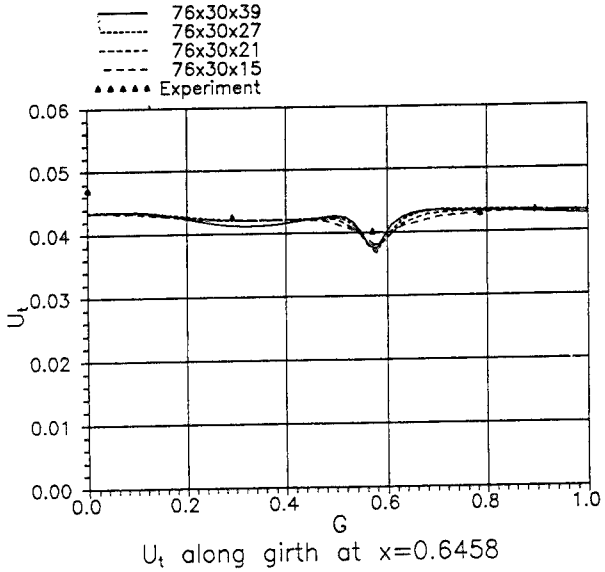

U_t along girth at x=0.6458

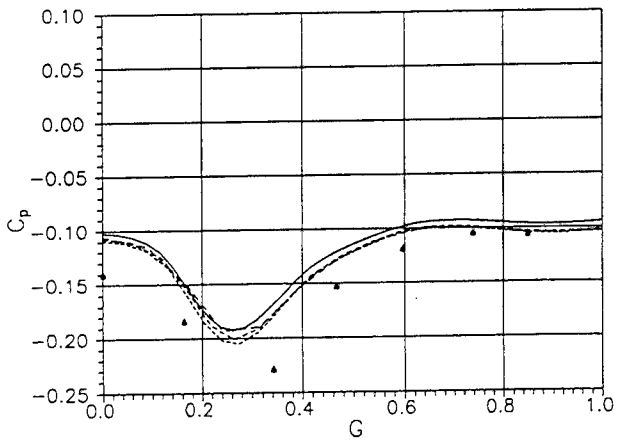

C_p along girth at x=0.8745

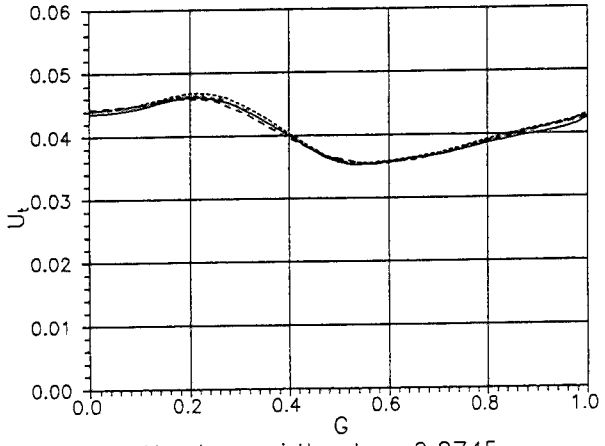

U_t along girth at x=0.8745

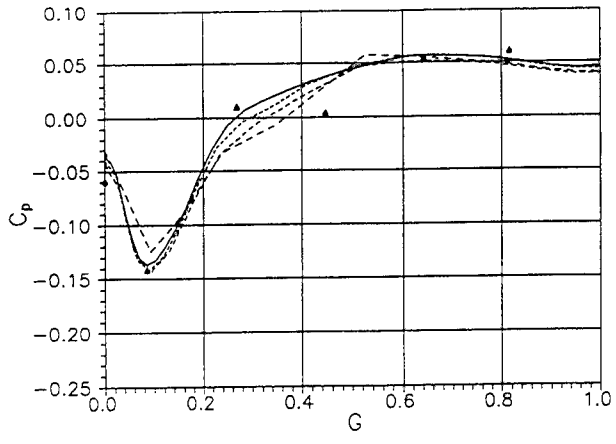

C_p along girth at x=0.9412

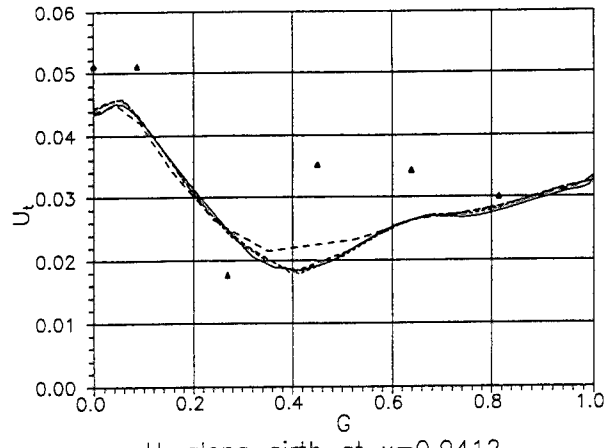

U_t along girth at x=0.9412

Fig. 4 (continued)

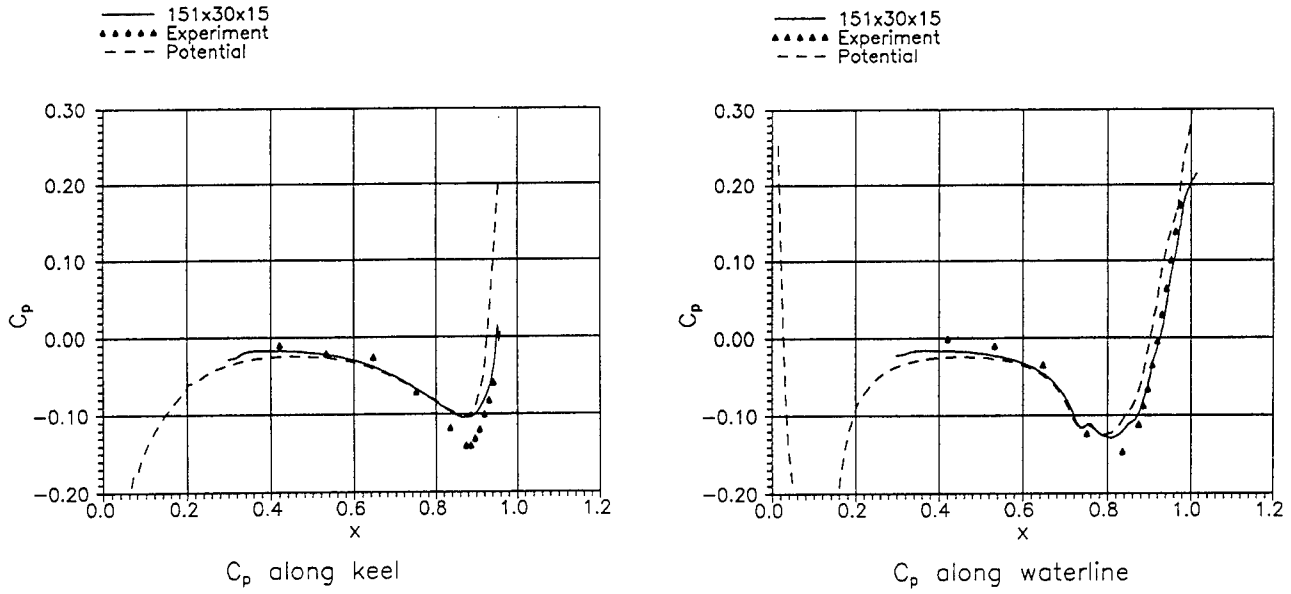

Fig. 5 Comparisons of Cp along lines of symmetry
(Viscous calculation, experiment and potential-flow calculation)

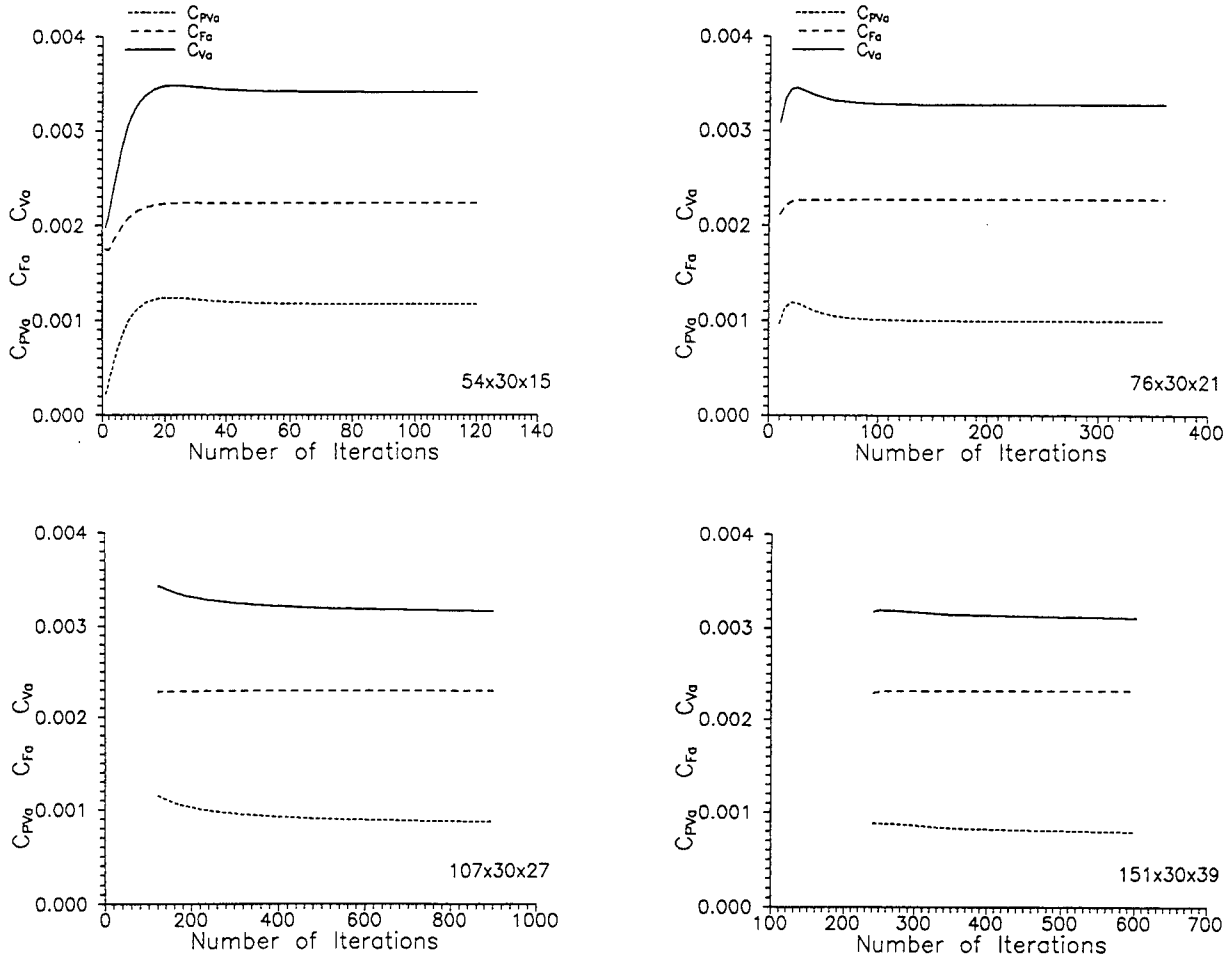

Fig. 6 Convergence history of the resistance components
with four different grids (C_{PVa}, C_{Fa} and C_{Va})

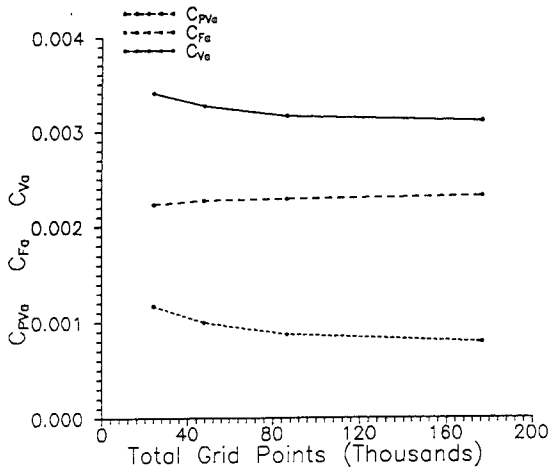

Fig. 7 Grid dependency test on the resistance components

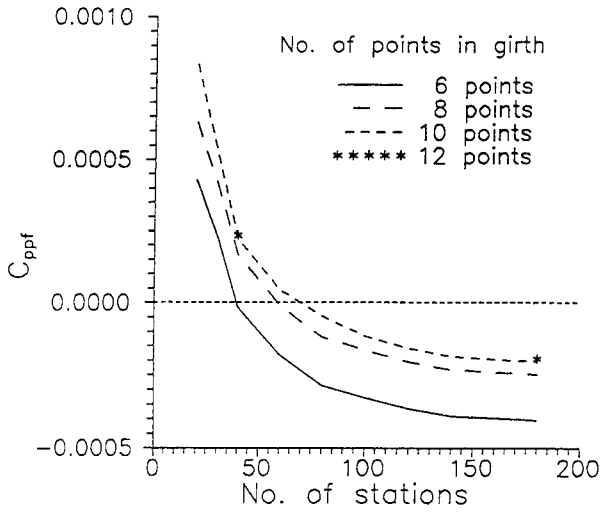

Fig. 8 Grid dependency test on C_{PPf} for the forebody

increase the estimated resistance by about 2% at model scale and about 7 to 8% at full scale. This suggests that more grid refinement is needed at full-scale Reynolds numbers. The effect of afterbody shape is clearly seen in the viscous pressure resistance, with Tanker A3 showing the smallest value and tanker A2 the largest. What is more significant, particularly for design calculations, is that, with the procedures employed, this ordering among the three hulls remains the same all the way to the estimate of the totoal resistance at model scale as well as full scale. The effect of grid refinement is to predict a smaller total resistance by about 5% at model scale and about 7 to 10% at full scale.

The results from towing tank resistance tests on models of this Tanker series are presented in Table 3. Here, only the total resistance at model scale was measured and the remaining quantities were estimated using standard practice based on 1978 ITTC performance prediction method for single screw ship. Here, $C_{Rm} = C_{Tm} - C_{FOm}$ and $C_{Ts} = C_{FOs} + C_{Rm} + C_A + C_{AA}$, where C_A is the incremental resistance coefficient for model-ship correlation and C_{AA} is the air resistance coefficient. Comparison of the measured total resistance in model tests with those calculated for model scale in Table 2 indicates that: (a) the measured values are about 5% lower than those predicted with the finer grid, indicating perhaps a need for further grid refinement; and (b) more importantly, the ordering of the three hulls with respect to their total resistance is the same in the measurements as that predicted, with A3 showing the smallest resistance and A2 the largest.

Comparison between the results obtained from the calculations (Table 2) and those deduced from towing-tank tests (Table 3) for the full scale ship requires further explanation. For this purpose, attention is drawn to the results for Tanker A1. Note that the total resistance predicted with the finer grid is $C_{Ts} = 0.00244$, whereas the measured value, accounting for the air resistance ($C_{AA} = 0.00005$) is only 0.00205, almost 20% lower. When the form-factor method is used for scaling from model to ship resistance, the form factor for Tanker A1 is estimated to be $k = 0.213$. With this value, $k\,C_{FOm} = 0.00068$ for the model and $k\,C_{FOs} = 0.00031$ for the ship. This indicates that the form factor must depend on the Reynolds number, a conclusion reached by many previous investigators using different arguments. This is further supported by a comparison of the calculated viscous-pressure resistance C_{PV} with $k\,C_{FO}$. At model scale, $C_{PVm} = 0.00078$, in substantial agreement with $k\,C_{FOm} = 0.00068$, but at full scale $C_{PVs} = 0.00072$ and does not decrease to the value (0.00031) predicted by the form-factor method.

Fig. 10 shows the longitudinal variations, for Tanker A3, of the contributions to the frictional (C_{FG}) and pressure (C_{PG}) resistance components at each section. These were determined by a girthwise integration, from the keel to the waterline, of the calculated friction and pressure distributions. In the case of the frictional resistance, no significant difference is observed between the result of the coarse and fine grids, at both the model and ship scales. The diminishing contribution of the stern to frictional resistance is also evident. In the case of C_{PG}, there are two regions, which give positive and negative contributions to the pressure resistance. The viscous pressure resistance is the difference between the areas under the curves in these two regions. This explains the difficulty of accurately predicting the viscous pressure resistance. The calculations indicate that the finer grid results in a higher predicted pressure recovery and decreasing viscous pressure resistance. Obviously, improvement in accuracy would require better resolution of the flow in the stern region.

Prediction of the stern flow is also of interest in matching the propeller to the hull and predicting propeller performance. Fig. 11 shows the axial-velocity contours and the transverse velocity vectors at the propeller plane of Tanker A3 calculated with the two grids at the two Reynolds numbers. The measurements at model scale are shown for comparison. In the calculations, the stern bulb shape was modelled, although not accurately enough to resolve the local flow details. However, the wake-rake support mounted into the propeller-shaft hole during the experiments was not considered. This, of course, has an effect on the flow in the center of the propeller disc. From the model-scale results it is clear that the calculations do not reproduce the details seen in the measurements, particularly with respect to the large velocity gradients below the propeller center. However, the finer-grid

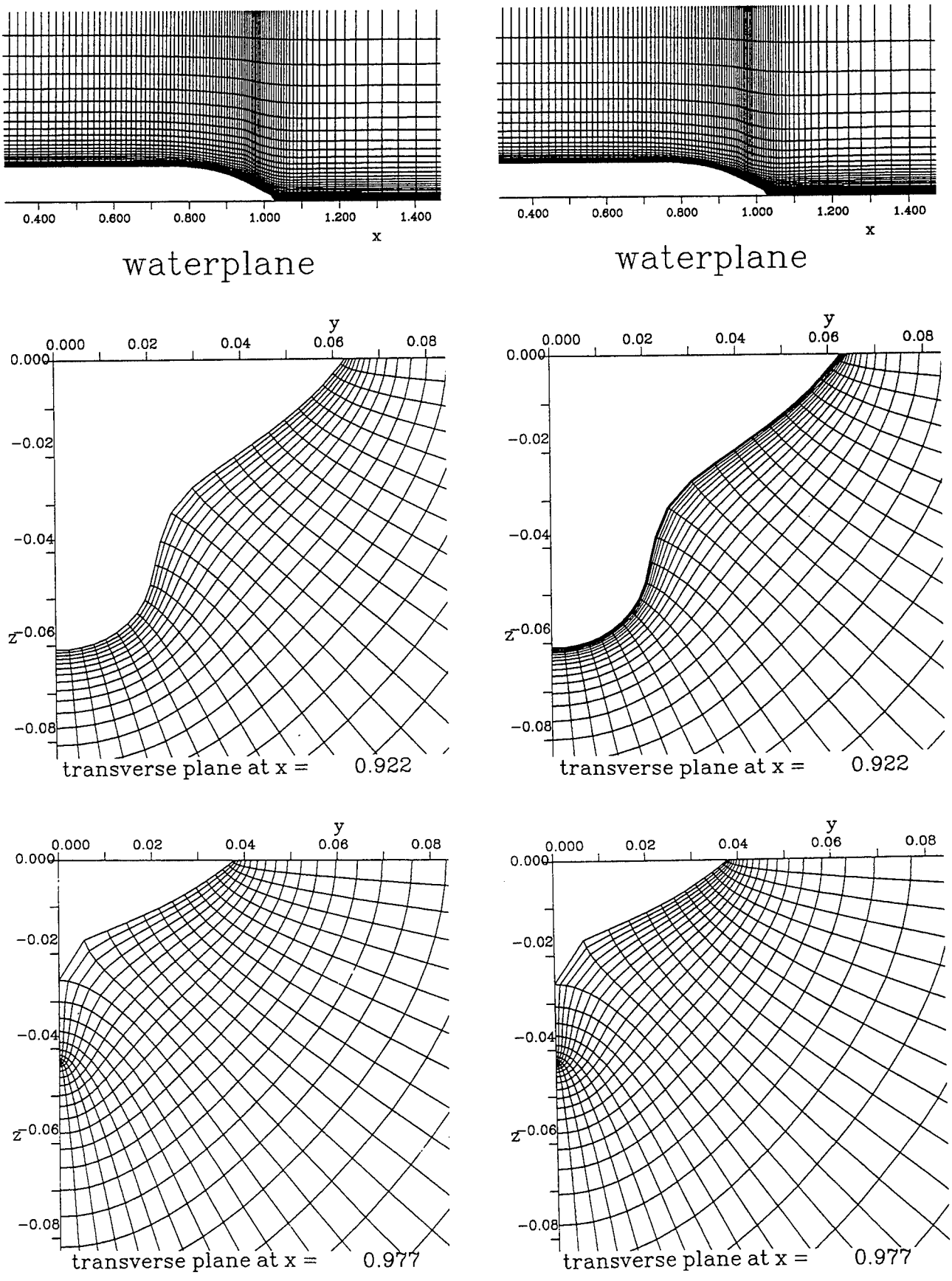

Fig. 9 Numerical grid (Tanker A3)
Left : Model-scale grid Right : Full-scale grid

Table 2. Calculated resistance components for Tanker series A

	(grid) INxJNxKN	model scale A1	model scale A2	model scale A3	full scale A1	full scale A2	full scale A3
$C_{PVa} \times 10^3$	54x30x15	1.33	1.37	1.25	1.28	1.38	1.19
x > 0.35	107x30x27	0.99	1.05	0.95	0.93	1.01	0.90
$C_{PPf} \times 10^3$ * x < 0.35		-0.21	-0.21	-0.21	-0.21	-0.21	-0.21
$C_{PV} \times 10^3$	54x30x15	1.12	1.16	1.04	1.07	1.13	0.98
($=C_{PVa}+C_{PPf}$)	107x30x27	0.78	0.84	0.74	0.72	0.80	0.69
$C_{Fa} \times 10^3$	54x30x15	1.98	1.98	1.98	0.86	0.86	0.86
x > 0.35	107x30x27	2.05	2.05	2.05	0.97	0.97	0.98
$C_{Ff} \times 10^3$ ** x < 0.35		1.24	1.24	1.24	0.56	0.56	0.56
$C_F \times 10^3$	54x30x15	3.22	3.22	3.22	1.42	1.42	1.42
($=C_{Fa}+C_{Ff}$)	107x30x27	3.29	3.29	3.29	1.53	1.53	1.54
$C_V \times 10^3$	54x30x15	4.34	4.38	4.26	2.49	2.55	2.40
($=C_{PV}+C_F$)	107x30x27	4.07	4.13	4.03	2.25	2.33	2.23
$C_W \times 10^3$ ***		0.19	0.19	0.19	0.19	0.19	0.19
$C_T \times 10^3$	54x30x15	4.53	4.57	4.45	2.68	2.74	2.59
($=C_V+C_W$)	107x30x27	4.26	4.32	4.22	2.44	2.52	2.42

note) * C_{PPf} was obtained by Hess and Smith method (1962).
** C_{Ff} was obtained from the 1957 ITTC model-ship correlation line considering the ratio of the surface area.
*** C_W was obtained by the X-PAN code of SHIPFLOW system (Larsson et al., 1989)

Table 3. Resistance results from towing tank tests (Van et al., 1991)

	model scale A1	model scale A2	model scale A3	full scale A1	full scale A2	full scale A3
$C_T \times 10^3$	4.07	4.12	3.99	2.10	2.15	2.02
$C_{F0} \times 10^3$ *	3.21	3.21	3.21	1.45	1.45	1.45
k	0.213			0.213		
k $C_{F0} \times 10^3$	0.68			0.31		
$C_R \times 10^3$	0.87	0.92	0.79	0.87	0.92	0.79
$C_A \times 10^3$	0.	0.	0.	-0.27	-0.27	-0.27
$C_{AA} \times 10^3$	0.	0.	0.	0.05	0.05	0.05
$(C_T-C_{AA}) \times 10^3$				2.05	2.10	1.97

note) * C_{F0} was obtained from the 1957 ITTC model-ship correlation line.

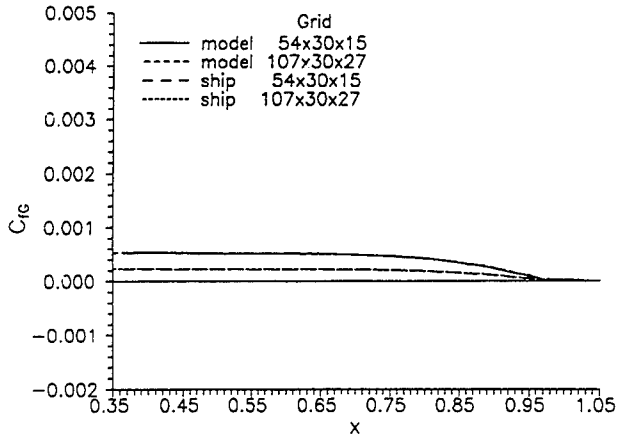

(a) C_{fG}

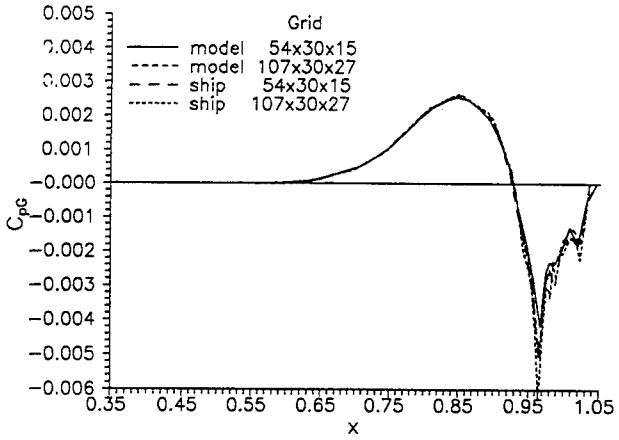

(b) C_{pG}

Fig. 10 Longitudinal distribution of C_{fG} and C_{pG} of Tanker A3

solution appears to indicate qualitative imporvements.

Comparison of the model and full-scale calculations indicate trends similar to those observed by Ju and Patel (1991) insofar as an increase in Reynolds number leads to a thinning of the viscous-flow region and intensified secondary flow. An analysis of these calculations along the lines suggested by Ju and Patel confirms their conclusion that these numerical calculations do not support the scaling laws based on classical boundary-layer and asymptotic-wake theories that are in current use.

CONCLUSIONS

This paper has been concerned with the use of a modern numerical method for calculation of the viscous flow around a ship hull, in conjunction with established procedures, for determining ship resistance and the flow at the propeller plane. An extensive numerical study was first conducted to establish the grid dependency of the solutions and computer requirements as both of these features determine the overall practicality of using CFD methods in the design environment. It is concluded that the method employed here would require further grid refinement and more grid points, with a concomitant increase in computer resources, to improve the quality of the predictions. Also, further development of this method along the lines suggested by the Ship Viscous Flow Workshop are necessary to enhance its numerical and physical performance.

The present calculations also indicate that, with moderate grid numbers and modest computer resourses, it is now possible to obtain useful predictions when changes in hull lines are evaluated at the preliminary design stage. The results for the Tanker series A presented here, and similar calculations performed for other series in the organization of the first author, suggest that this method can be usefully integrated into the design methodology to identify hull forms with improved resistance characteristics and tailored flow into the propeller. While the computer costs are still not low enough for routine and economical calculations, the numerical solutions have the advantage that many calculations can be performed in a short time and each solution provides details of the flow that are not readily obtained in standard towing tank tests.

ACKNOWLEDGEMENTS

The authors appreciate the assistance of Mr. S.E. Kim, Mr. J.K. Choi and Mr. Y.J. Park in the calculations and preparation of the figures. The computing time of CRAY2S was generously provided by SERI/KIST in Korea.

REFERENCES

Chen, H.C., Patel, V.C. and Ju, S. (1990), "Solutions of Reynolds-Averaged Navier-Stokes Equations for Three-Dimensional Incompressible Flows," J. Computational Physics, Vol. 88, No. 2, pp. 305-336.

Hess, J.L. and Smith, A.M.O. (1962), "Calculation of Non-Lifting Potential Flow about Arbitrary Three-Dimensional Bodies," Douglas Aircraft Company Report No. E S 40622, Long Beach.

ITTC (1990), "Report of the Resistance and Flow Committee," Proc. 19th ITTC (International Towing Tank Conference), Madrid, Spain, Vol. 1, pp. 55-107.

Ju, S. (1989), "Numerical Study of Ship Stern and Wake Flows at Model and Full-Scale Reynolds Numbers," Ph.D. Thesis, The University of Iowa, Iowa City, Iowa.

Ju, S. and Patel, V.C. (1991), "Stern Flows at Full-Scale Reynolds Numbers," J. Ship Research, Vol. 35, No. 2, pp. 101-113.

Larsson, L., Broberg, L., Kim, K.J. and Zhang, D.H. (1989), "SHIPFLOW - a CFD System for Ship Design," 4th International Symposium on Practical Design of Ships and Mobile Units, Varna, Bulgaria.

Larsson, 1., Patel, V.C. and Dyne, G. (editors) (1991), "Ship Viscous Flow - Proceedings of 1990 SSPA-CTH-IIHR Workshop," Flowtech International AB, Gothenburg, Sweden, Report No. 2.

Patel, V.C., Chen, H.C. and Ju, S. (1988), "Ship Stern and Wake Flows: Solutions of the Fully-Elliptic Reynolds-Averaged Navier-Stokes Equations and Comparisons with Experiments," Iowa Inst. Hydraulic Research, Uni. Iowa, IIHR Report No. 323.

Patel, V.C., Chen, H.C. and Ju, S. (1990), "Computations of Ship Stern and Wake Flow and Comparisons with

Experiment," J. Ship Research, Vol. 34, No. 3, pp. 179-193.

Patel, V.C., Ju, S. and Lew, J.M. (1990), "Viscous Flow Past a Ship in a Cross Current," Proc. 18th ONR Sym. Naval Hydrodyn., Ann Arbor, USA, August 20 - August 24, 1990.

Stern, F., Kim, H.T., Patel, V.C. and Chen, H.C. (1988), "A Viscous-Flow Approach to the Computation of Propeller-Hull Interaction," J. Ship Research, Vol. 32, No. 4, pp. 246-262.

Van, S.H., Yang, S.I., Kim, E.C., Kang, K.J., Shin, M.S. and Park, Y.J. (1991), "Hull Form Development for DW 150K Crude Oil Tanker," KRISO Model Test Report No. BSI839-1502E.D.

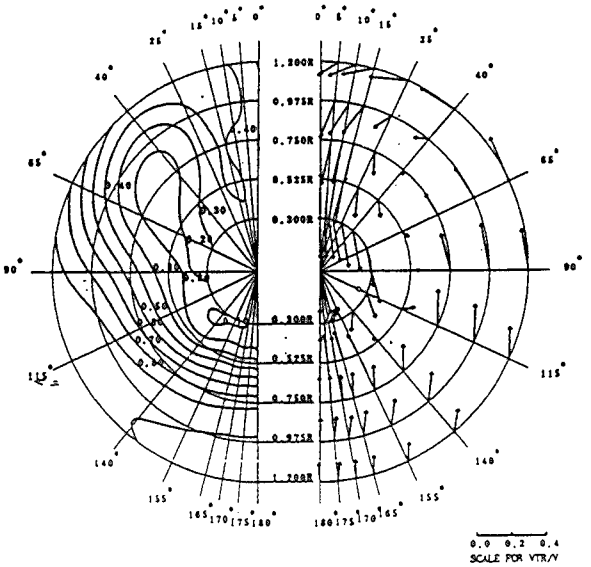

(c) model scale, experiment

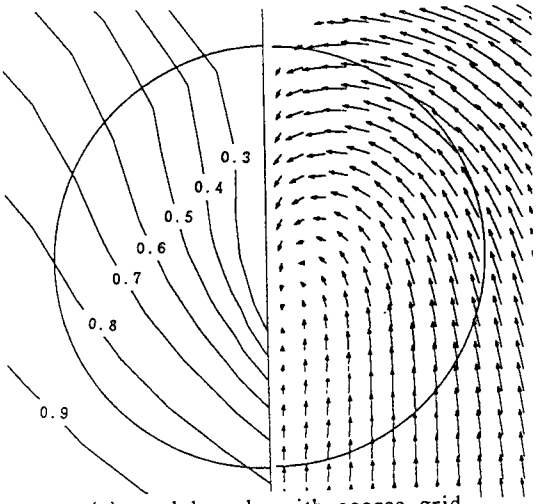

(a) model scale with coarse grid

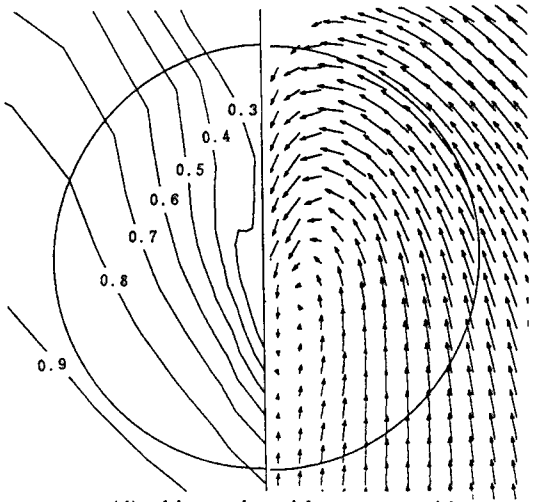

(d) ship scale with coarse grid

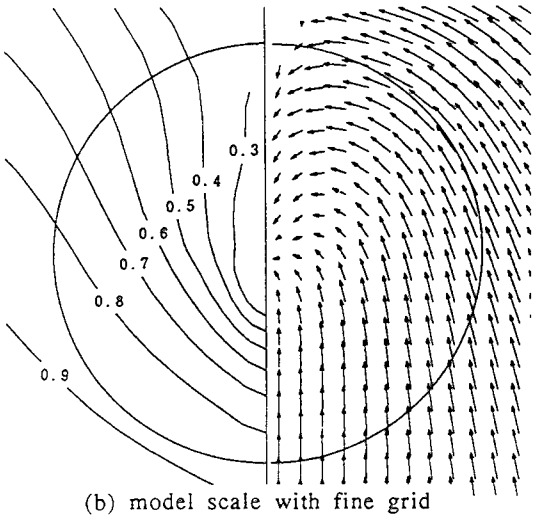

(b) model scale with fine grid

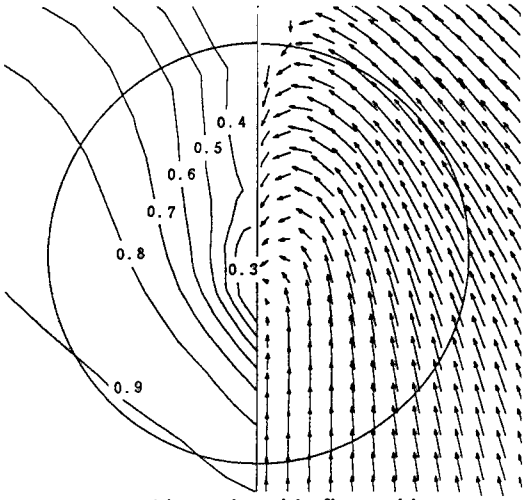

(e) ship scale with fine grid

Fig. 11 Axial velocity contours and transverse velocity vectors at propeller plane

DISCUSSION

L. Larsson
FLOWTECH International, Norway

This is an interesting study showing that the differences between fairly similar hulls can be predicted by CFD. Careful grid dependence studies have been made in the longitudinal and transverse directions, but why has no attention been paid to the normal direction? This is particularly important when scale effects are studied. At full scale a more stretched grid has been used, but is this adequate to cope with the reduction in viscous length scale of two orders of magnitude? There is no way the grid can be that much finer close to the hull. How does this worse resolution at full scale influence the conclusions drawn on the form factor?

A further general observation concerning full scale: It may well be that the difficulties in predicting the "hooked" wake contours of full ships is much alleviated at full scale, since the few measurements that exist indicate that the hooks are much less pronounced, or even non-existing, particularly with a working propeller.

DISCUSSION

H. Caprino
CETENA, Italy

The paper presented by Ju and Patel opens a new way to apply CFD to ship design. As it is the first attempt, as far as we know, to calculate the total resistance of a ship, some questions are obviously raised by this work.

1. Why did the authors not try to change the grid points in the radial direction where the strong velocity gradients in the near wall zone influence flow behavior?

2. To calculate the total resistance of a hull with CFD methods can give a good qualitative idea of ship behavior, above all during the preliminary phase of a project in order to compare different configurations, provided a considerable computational effort is made to achieve the integral quantities. Do the authors believe that a careful study of flow behavior, that means velocity and pressure values over and near the hull, can supply good qualitative information as well as with a lower computational effort?

3. We are pleased to observe that wake prediction at high Reynolds number does not support the scaling laws based on asymptotic-wake theories, as it turned out from the work on scaling effects that we present at this symposium.

DISCUSSION

L. Sebastiani
CETENA, Italy

In your grid sensitivity study, you vary grid points in the streamwise and girthwise direction, but you keep grid density fixed in the radial direction. Can you explain the reason for this choice? It seems to me that grid density in the radial direction should be investigated as it governs boundary-layer flow resolution.

Your attempt to derive global resistance characteristics from CFD calculations is very interesting. Still, the results are qualitative. In which way can they really help ship designers in selecting the best hull configuration? I wonder whether there is really a significant improvement with respect to simply looking at the local flow characteristics.

AUTHORS' REPLY

First of all, we would like to thank all discussors for their questions and comments. In reply to the questions on grid dependence in radial direction raised by all discussors, it is correct that the grid points in the radial direction influence the solution. Our previous study and experience show that the grid dependency on the resistance components in the radial direction is much less than the other two directions. Note that the current method employs the two-point wall-function approach, and the results are not so sensitive to the grid resolution near the wall because the solution is anchored at two near-wall mesh points on the law of the wall. Figure A.1 shows much less grid dependency on the C_p and U_t in the radial direction than those shown in Figs. 3 and 4. The number of grid points in the radial direction (JN) was varied from 30 to 60, while the number of points in the streamwise and girthwise directions (IN and KN) were fixed at 76 and 15. Also, the following table shows that the grid-dependency on the resistance components in the radial direction is negligible.

Grid	76x30x15	76x45x15	76x60x15
C_{PV_a}	.00101	.00102	.00102
C_{F_a}	.00227	.00227	.00227
C_{V_a}	.00328	.00329	.00329

The uncertainty of the wall-function approach pointed out by Prof. Larsson at high Reynolds numbers is that there are no firm guidelines that can be used to determine y+ values which should not be exceeded. The performance of the wall-function approach used in the present method at very high Reynolds numbers has been carefully examined with the aid of available experimental data on an axisymmetric body in Ju and Patel (1991), showing that the current boundary conditions could be applied at larger y+ values as the Reynolds number increases.

In reply to the questions regarding the applicability of CFD in ship design process, raised by Drs. Caprino, Traverso, and Sebastiani, the grid dependence on the friction velocity and pressure distributions on the hull is much less than that on the resistance components, particularly on the viscous pressure resistance. Also, we can get a general idea on the resistance without integrating the flow quantities, simply by comparing the deflections of the limiting streamlines in the stern region or the strengths of the vorticity in the wake of different hull forms. More deflected limiting streamlines and stronger vorticity generally indicate the increased resistance. We think that useful qualitative information with less computational effort can be obtained, demonstration of which was one of the purposes of this study.

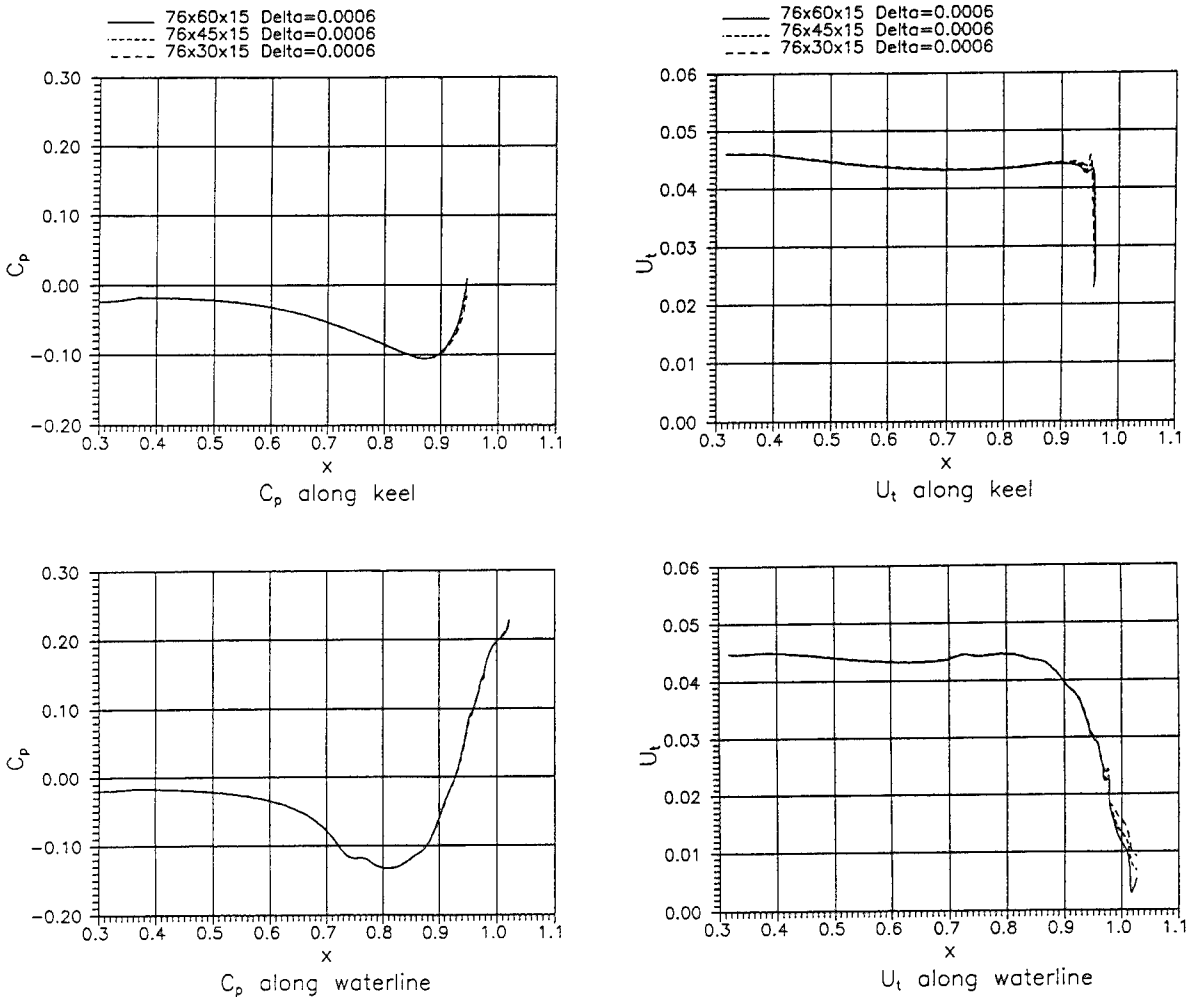

Figure A.1 Grid dependency test; grid refinement in the radial direction

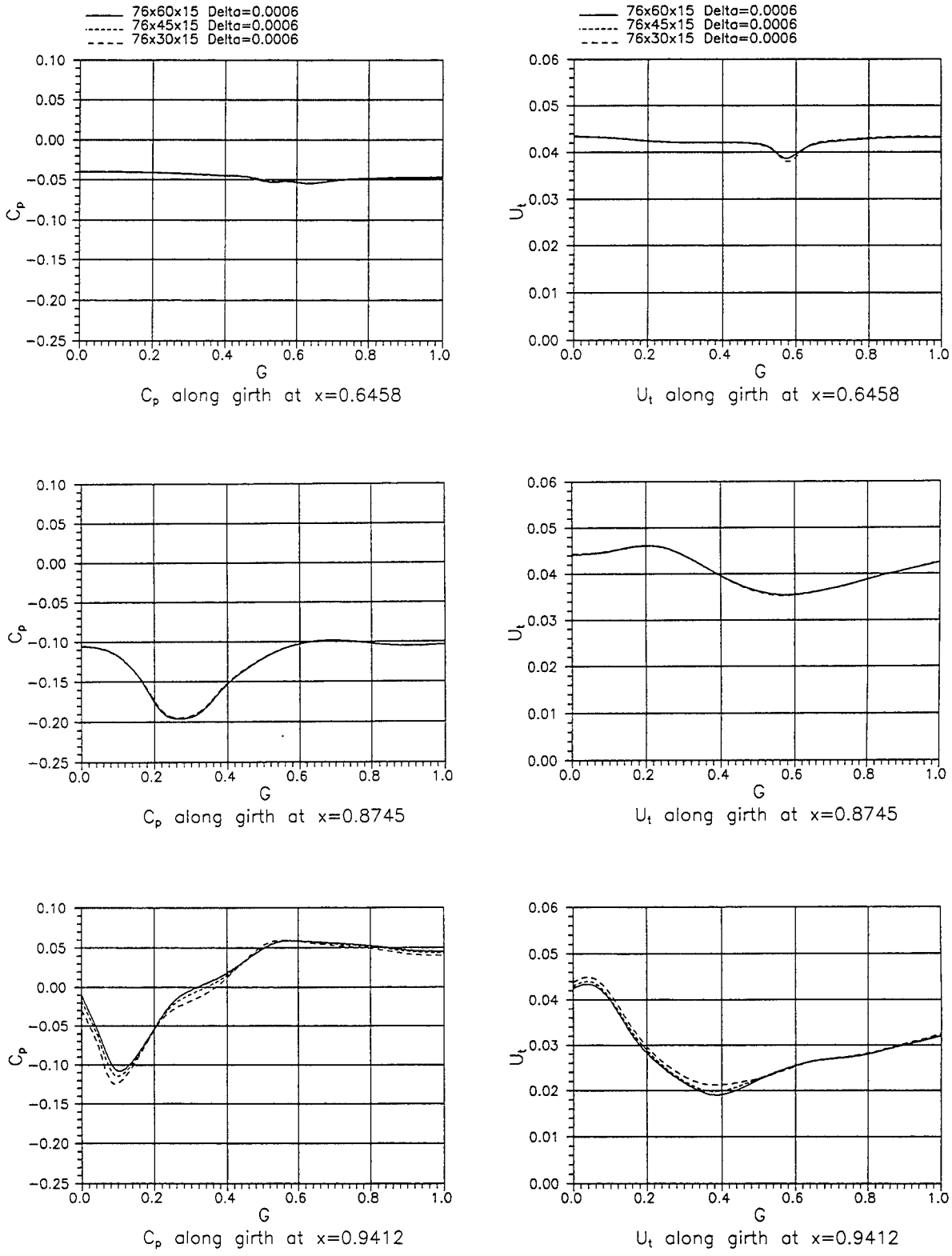

Figure A.1 (Continued)

Numerical Viscous Flow Computations for Complex Geometries

C.-W. Lin, S. Fisher, P. Impelluso (David Taylor Model Basin, USA)

ABSTRACT

An effective numerical technique for viscous flow computation has been developed, which allows the marine vehicle designer to model complex geometry, generate a detailed geometry database, create surface and three-dimensional volume grids, and model viscous flow phenomena. The whole process has been effectively integrated on a workstation network. The major goal of developing this numerical prediction capability is to obtain accurate computational results and reduce the turn-around time for real practical design applications. Several applications chosen for this paper illustrate the effectiveness and capability of this developed CFD technique. As rapid improvements occur in CFD technology and turbulence modelling, numerical prediction accuracy will be enhanced. In addition, advances in both computer CPU speed and memory size have enabled the use of more complex grid topologies which more accurately represent the real-life geometry. Future improvements in numerical methods and computer capabilities are anticipated to make time accurate flow solutions feasible. Improvements in visualization tools have also aided in the development of these complex grid structures, and the examination of the solution from a CFD analysis.

INTRODUCTION

The development of a practical ship design analysis system, by application of new technologies within the discipline of computational fluid dynamics (CFD), is a challenging task to CFD scientists. The capability of advanced CFD has been recognized as an effective tool to assist the design performance analysis of new and innovative designs [1]. Major challenges to CFD scientists include: how to model physically complex fluid flow such as the phenomenon of turbulence; how to deal with complicated real-life body geometry; and how to balance the requirements of accuracy, stability, and economy for numerical procedures. To achieve all of this capability for practical design applications, extensive research and development is still needed. This paper will focus on a description of the currently developed CFD numerical capability, especially concerning complex geometry applications. The modelling of complicated physical flow details such as turbulence is not the main subject in this paper; however, the importance of an accurate modelling of flow turbulence cannot be ignored. Only the steady state mean flow solution is concerned with here. The validation of computed results such as accuracy, numerical convergency and comparison with available experimental results will be briefly discussed.

In the past, simplification of modelled geometry or decomposition of complicated geometry into several simple components were the approaches to be adopted in hydrodynamic calculations. This was partly due to the limitation of numerical or analytic solution algorithms and partly due to the limitation of computer hardware capacity and speed. The disadvantage of this kind of approach occurs in either the loss of certain physical flow phenomena or ignoring the interference between simplified components. As numerical techniques of CFD have significantly improved along with the rapid development of powerful, high-speed computers, accurate viscous flow computations on quite complicated geometries have been achieved within a reasonable turn-around time. Hence, the CFD numerical capability is becoming an effective and feasible tool to support ship design analysis. This paper will discuss the current stage in CFD numerical capability, specifically on complex geometry applications. Several applications using this numerical prediction tool has been conducted and will be discussed in detail.

NUMERICAL FORMULATION

The numerical solution procedure is based on the conservation law form of the three-dimensional Reynolds-averaged Navier-Stokes equations. The pseudo-compressibility approach proposed by Chorin [2] is adopted in this work to formulate the incompressible steady-state viscous flow equations. The idea is to artificially change the propagating speed of pressure waves during the transient state. The time-accurate unsteady solution using this approach may not be physically valid, although some CFD investigators have tried to obtain time-accurate solutions using this approach. As for the work described in this paper, only the steady state solution is of interest.

This preconditioned incompressible Reynolds-averaged Navier-Stokes equations are thus,

$$Eq_t + F_x + G_y + H_z = 0, \qquad (1)$$

where the subscripts are partial derivatives with respect to the time t and the three Cartesian coordinates x, y, and z. The preconditioned matrix E and the column vectors of the variables q and of the three components of fluxes F, G, and H are defined as

$$E=\begin{bmatrix}\beta^{-2} & 0 & 0 & 0\\ (1+\alpha)\beta^{-2}u & 1 & 0 & 0\\ (1+\alpha)\beta^{-2}v & 0 & 1 & 0\\ (1+\alpha)\beta^{-2}w & 0 & 0 & 1\end{bmatrix},\quad q=\begin{bmatrix}p^{*}=p/\rho\\ u\\ v\\ w\end{bmatrix},\quad F=\begin{bmatrix}u\\ u^2+p^{*}-\tau_{xx}\\ uv-\tau_{xy}\\ uw-\tau_{xz}\end{bmatrix}$$

$$G=\begin{bmatrix}v\\ uv-\tau_{yx}\\ v^2+p^{*}-\tau_{yy}\\ vw-\tau_{yz}\end{bmatrix},\quad H=\begin{bmatrix}w\\ uw-\tau_{zx}\\ vw-\tau_{zy}\\ w^2+p^{*}-\tau_{zz}\end{bmatrix} \qquad (2)$$

where p is the pressure, ρ is the constant density, u, v, and w are the three Cartesian components of the velocity and the Reynolds stresses are defined as

$$\tau_{ij}=R_e^{-1}\nu\left(\frac{\partial u_i}{\partial x_j}+\frac{\partial u_j}{\partial x_i}\right),\qquad i,j\ =\ 1,2,3 \qquad (3)$$

where $(u_1, u_2, u_3) = (u, v, w)$, $(x_1, x_2, x_3) = (x, y, z)$, ν is the sum of the kinematic and the eddy viscosity and Re is the Reynolds number. The variables are nondimensionalized by the free stream condition at infinity in the following manner: u, v and w by u_∞, p and τ by $\rho_\infty u_\infty^2$, x, y and z by a characteristic length L and $Re = u_\infty L/\nu_\infty$. α and β^{-2} are the preconditioned parameters. The case $\alpha = -1$ reduces to the 3D version of Chorin's artificial compressibility model and β is analogous to the sound speed.

The idea is to choose a β for a given α such that the disparity in propagating speeds will be reduced during the transient state. The fact that the transient-state solution may not be physically valid is not relevant since only the steady-state solution is of interest. $\beta = 1$ has been chosen in this work which numerical experiments shows a good convergence rate.

The differential form of the Navier-Stokes equations (1) can then be integrated over a control volume and discretized by a finite-volume formulation. Therefore, the Eqs.(1) becomes

$$\frac{d}{dt}\begin{bmatrix}p^{*}\\ u\\ v\\ w\end{bmatrix}_{ijk}\Delta V_{ijk}=-\sum_{\ell=1}^{3}\left\{\begin{bmatrix}\beta^2\left(u\cdot\Delta s^{\ell}\right)\\ -\alpha u\left(u\cdot\Delta s^{\ell}\right)+p^{*}\Delta s_1^{\ell}-R_e^{-1}\nu\sum_{m=1}^{3}\left(\frac{\Delta s^m\cdot\Delta s^{\ell}}{\Delta V}\right)\frac{\partial u}{\partial\xi^m}\\ -\alpha v\left(u\cdot\Delta s^{\ell}\right)+p^{*}\Delta s_2^{\ell}-R_e^{-1}\nu\sum_{m=1}^{3}\left(\frac{\Delta s^m\cdot\Delta s^{\ell}}{\Delta V}\right)\frac{\partial v}{\partial\xi^m}\\ -\alpha v\left(u\cdot\Delta s^{\ell}\right)+p^{*}\Delta s_3^{\ell}-R_e^{-1}\nu\sum_{m=1}^{3}\left(\frac{\Delta s^m\cdot\Delta s^{\ell}}{\Delta V}\right)\frac{\partial w}{\partial\xi^m}\end{bmatrix}_{\ell(+)}\right.$$

$$\left.-\begin{bmatrix}\beta^2\left(u\cdot\Delta s^{\ell}\right)\\ -\alpha u\left(u\cdot\Delta s^{\ell}\right)+p^{*}\Delta s_1^{\ell}-R_e^{-1}\nu\sum_{m=1}^{3}\left(\frac{\Delta s^m\cdot\Delta s^{\ell}}{\Delta V}\right)\frac{\partial u}{\partial\xi^m}\\ -\alpha v\left(u\cdot\Delta s^{\ell}\right)+p^{*}\Delta s_2^{\ell}-R_e^{-1}\nu\sum_{m=1}^{3}\left(\frac{\Delta s^m\cdot\Delta s^{\ell}}{\Delta V}\right)\frac{\partial v}{\partial\xi^m}\\ -\alpha v\left(u\cdot\Delta s^{\ell}\right)+p^{*}\Delta s_3^{\ell}-R_e^{-1}\nu\sum_{m=1}^{3}\left(\frac{\Delta s^m\cdot\Delta s^{\ell}}{\Delta V}\right)\frac{\partial w}{\partial\xi^m}\end{bmatrix}_{\ell(-)}\right\} \qquad (4)$$

where ΔV is the volume of the cell ijk in the curvilinear coordinates $\xi^{\ell} = (\xi, \eta, \zeta)$, Δs^{ℓ} is the surface-area vector normal to the cell surface ξ^{ℓ} = constant and Δs_i^{ℓ} is its projection on the x_i coordinate. The notation $\ell(+)$ denotes that the terms inside the square bracket are evaluated at the midpoint of the right-hand-side cell surface $\xi^{\ell+1/2}$ = constant and $\ell(-)$ denotes that the same terms are evaluated at the midpoint of the left-hand-side cell surface $\xi^{\ell-1/2}$ = constant. For example, when $\ell = 1$, $\ell(+) = i+1/2, j, k$, and $\ell(-) = i-1/2, j, k$.

The computational domain is subdivided into a finite number of control volumes, and all the dependent variables defined at the geometrical center of the control volumes. The fluxes derived from the finite-volume formulation are evaluated at the midpoint of each cell surface using central difference. It is noted that a non-orthogonal curvilinear coordinate system is used with a non-staggered variable arrangement. It enables one to deal with quite arbitrary flow configurations with a better resolution in critical regions, which is especially valuable in three dimensional solutions where orthogonal grids are often difficult, and sometimes impossible to generate. The decomposition of the velocity vector is in the spatially fixed Cartesian directions, instead of in grid-oriented directions. It leads to the strong conservation form of the governing equations and totally eliminates the need to calculate the extremely grid-sensitive curvature terms.

The discretization procedure using finite volume formulation in Eq (4) leads to a set of coupled ordinary differential equations, which can have the form as

$$\frac{dq}{dt}\ =\ R(q) \qquad (5)$$

where R(q) is the vector of the residuals consisting of the flux balance from the convective and diffusive terms. The time integration is performed by using an explicit one-step multi-stage scheme derived from a generalization of the Runge-Kutta formulation. The multi-stage scheme of the Runge-Kutta method can be tailored to give the desired stability properties [3]. An implicit residual smoothing developed by Jameson [4] is implemented to relax the restriction on the time step imposed to explicit time-marching scheme applied to steady flow calculation. The CFL(Courant-Friedrichs-Lewy) number has been found to increase from 3.0 to 4.5 with the 4-stage Runge-Kutta scheme with 2 evaluations of implicit residual smoothing [5].

For steady flows, an acceleration technique known as local time stepping has also been used to enhance convergence to steady state solution. Local time stepping utilizes the maximum allowable time increment at each cell during the course of the solution. While this destroys the physical nature of the transient solution, the steady state solution is unaffected and can thus be obtained more efficiently.

MULTIBLOCK FLOW SOLUTION METHOD

The physical description of an actual marine vessel is typically a complex arrangement of several appendages with the vessel's hull. Structures such as skegs, struts, bilge keels, bulbous bows, control surfaces, etc. have a unique appearance when interacting with the

complex surface curvature of a hull. Due to this complex geometry arrangement, a single structured grid is not always feasible as a method of accommodating the entire flow field around an appended ship. Additional problems arise in the need for the grid not to be too skewed, and for good resolution of flow variables in regions of high gradients. The use of a single grid for a complicated flow domain also usually requires an inordinate amount of time to generate an acceptable representation. A multi-block approach, dividing the whole domain into simple subregions and solving for the flow concurrently in each of the different blocks, is an effective way to overcome these problems. In addition, different flow equations can be used in different blocks [6].

For a multi-block approach, additional boundaries between blocks are created inside the solution domain. The crucial element then becomes transferring appropriate information across these boundaries. Since the method in this multi-block procedure is designed specifically for the non-overlapping grid structure, the information at the interface boundary has to be computed and stored properly for the continuity of flow across the interface. All dependent variables at boundary points are computed using proper indices which define the interface locations between neighboring blocks. The first derivatives of velocity variables at boundary points are also calculated and stored, since they are needed for the computation of viscous diffusion terms in the equations. Due to fourth-difference artificial dissipation used in this work, extra first derivatives of velocity variables at the first grid cell surface of the connecting blocks are also computed and stored for the necessary fourth-difference calculation. Therefore, the grid cells close to the interface boundary will be integrated in a similar sense as those interior cells. A distortion-free flow movement can thus be achieved across the zonal interface. In fact, the scheme developed here is so flexible that a single block may connect to any number of blocks without increasing the tedious data bookkeeping process or reducing the effectiveness and accuracy at the interface boundary.

Boundary data at all surfaces of each block, in addition to the interface boundaries, are also computed and stored according to the boundary conditions provided. In comparison to the overlapping structured grid approach, the computer memory requirement of the multi-block method is not necessarily increased for storing this boundary data information. The overlapping structured grid approach also requires extra grids to store transferred information However, a scheme of non-overlapping grids provides a simpler way to book-keep all of the three-dimensional indices used in the computer code. Each block has a consistent index, the same as its grid points. Boundary data are responsible for the appropriate boundary conditions, as well as the information about neighboring blocks if it is an interface boundary. Since one block may interface with a number of blocks, the tracing of proper indices to connect blocks at proper locations is quite important. The book-keeping of the indices used in the current work has proven to be quite simple and the process of inputting to the computer quite easy. Only the starting index is necessary to identify the interface location between connecting blocks. To further simplify the effort of inputting those interface indices, the output of multi-block structured grid generator should provide this information. Although the current grid generators, GRIDGEN [7], used in this work has a similar capability, efforts are still needed in the future to effectively link the grid generator and the flow solver.

COMPUTATIONAL PROCEDURE

The procedure of numerical flow computation starts by modelling the proposed configuration in a CAD (computer aided design) environment specifically designed for ship geometries. Components of the whole configuration may be modelled separately with a consistent coordinate system, as is this case with a ship's appendages. However, overlapping sections are frequently a result and must be trimmed and aligned to the hull. Intersections of these appendages with the hull are successfully determined in the program REMESH developed in-house. The geometrical data base generated by REMESH becomes the main source to start generating a block structure. After the block topology is defined, surface grids on the six faces of each block are generated using either an algebraic or elliptical grid generator. As all the faces for every block has been generated, a three-dimensional volume grid is developed using a very efficient in-house algebraic interpolation program TRANS3D. Not only is the volume grid written out, but also a file containing values of the minimum, maximum, and negative grid volumes (if there are any), along with their locations within each block. Detailed procedures of grid generation are discussed in Lin, et al [8]. The three-dimensional grid around the proposed configuration is then used with the multi-block flow code for a steady-state solution of the incompressible Reynolds-Averaged Navier Stokes equations. The results of the computation are examined using visualization tools on the workstations. The whole process has been integrated and executed in a workstation/PC environment, while a supercomputer is available through the network.

Time marching procedure is used here which begins from some set of initial data. The initial data is usually specified as a uniform flow, or may be introduced from a previous solution. The time-marching procedure is applied iteratively to update the flow variables as the solution proceeds. Steady-state solutions are deemed converged as the root-mean-square (rms) of pressure residual has been reduced by a factor of 10^{-3}.

NUMERICAL APPLICATIONS

The application of advanced numerical technique into the practical design analysis for hydrodynamic performance prediction is feasible and may become a routine procedure in the near future. In this section, several different types of ship configurations are used to illustrate the capability of the numerical flow analysis tool for dealing with complex geometries. These configurations include; an oil tanker; an appended ship possessing a shaft and strut, a modified superstructure of a combatant for a study of air-wake, and an oceanographic testing device known as an Expendable Doppler Penetrometer.

The numerical accuracy is very important for the application of CFD techniques to design analysis support, although it is not the main subject for this paper. The prediction from the current numerical program has been compared with available experimental results for several different configurations [5,9]. Generally, the

prediction illustrates the main features of the flow quite well, compared with the measured results. Some details of flow quantities are still needed to be improved. It should be noted that numerical accuracy, as well as computational CPU speeds, is still being enhanced by implementing newly developed numerical algorithms or turbulence modelling for turbulent flow predictions.

A typical surface ship hull usually has complex curvature, and may be equipped with a number of appendages. Most commercial ships such as oil tankers or container ships, only have a few appendages, while combatants have a fair number of appendages. The capability to accurately model ship hull form is a necessary step to start a CFD flow computation. However, for practical design application, it requires effective and efficient representation of any arbitrary ship hull geometry in the computer environment. Even without any extruding appendages, it is sometimes not a trivial task to accurately model a real ship stern shape with a bulb bossing and a bulbous bow. As far as more complicated configurations such as ship hulls equipped with a number of appendages, the flow calculation around this appended ship becomes quite challenging to CFD scientists. In the following sections, four numerical applications on viscous flow calculations will be described. No free surface effect is concerned here. A symmetrical boundary condition is applied at the free surface, which is called a double-body solution.

BARE HULL

We chose an oil tanker with a bulbous bow and stern bulb bossing for this case. The ship is still in design stage. No substantial test data has been available, although more model tank experiments may be performed in the future. However, it is quite a good test case to illustrate how we model the complicated hull form and perform CFD flow calculations. Although a bulbous bow is designed for reducing wave-making resistance, the shape of bulbous bow for this non-free-surface viscous flow calculation is still carefully modelled. A typical C-type grid is used for better resolution of flow in ship bow area, see Fig. 1. Along the girth of tanker's cross section, i.e. from free surface to bottom keel line, it is divided into 2 grid blocks for better control of distribution of grid points on the hull. The grid points are thus able to be concentrated near the bilge and the bulbous bow. The resolution of viscous flow is therefore better at those areas of higher geometrical curvature. Although only half of the ships configuration is considered, the grid can be easily mirrored into the whole grid around the entire ship hull. A viscous flow with constant yaw angle with respect to the ship hull can be obtained in a straightforward extension of computation.

The tanker possesses a Gondola stern implying a bulbous bossing at the stern and a knuckle line along the hull at the after section of the ship. A careful modelling of this knuckle line is considered necessary. Surface grid distribution on the hull is carefully performed so as to preserve the accurate location of the knuckle line. Figure 2 shows the longitudinal velocity contours along the hull. The bilge vortex has been clearly shown its development along the hull. Figure 3 gives a cross-flow vector plot to see the bilge vortex at the end of middle parallel body.

FULLY APPENDED OPEN-STERN SHIP

The configuration is a typical open-stern ship equipped with a complete set of appendages, i.e. skeg, strut, shaft, propeller hub and bossing, is shown in Fig. 4. The complexity of geometry is obvious with a enlarged dome at the bow and pieces of appendages at the stern. The modelling of bow dome is similar to that of the bulbous bow mentioned in the previous section. A multi-block grid is needed for this complex appended stern configuration. Figure 5 gives an outline of block structure at this stern area. The hull and appendages are shown in Fig. 5 and are the geometrical data base generated by program REMESH. Figure 6 displays some surface grids on the hull and appendages.

Some preliminary flow results are presented here. Figure 7 shows flow particle tracing near the propeller fairwater along the shaft. A longitudinal velocity contour around propeller plane is given at Fig. 8. The color contour is defined as the sequence of blue, cyan, green, yellow, red and magenta with increasing velocity. Figure 9 shows the pressure contour on the surface of the appendages. At the present time, only qualitative results are presented. Quantitative comparisons with model-scaled experiment results will be made in the near future.

AIR WAKE

Due to the rapid development of CFD technology, interest has been raised in evaluating the air flow around the ship's superstructure. The wake due to the existence of this structure has been recognized as a primary factor in affecting the operation of a helicopter with the surface ship. Currently, the approach to identify this so called "operational envelope" for a helicopter/ship interface is to utilize full-scale trial results, which is expensive and time-consuming. A computational approach will save money and time. Although full-scale trials are definitely necessary, substantial efforts can thus be reduced with the assistance from computational predictions of air wake. Figure 10 shows a typical ship superstructure with some geometric simplifications. A complicated grid block topology is defined to cover the whole computational domain as shown in Fig. 11. A multi-block grid has been generated, which is given in Fig. 12. The is developed around the whole ship configuration, instead of a half ship body. Therefore, the same grid will be used to simulate the air flow around the superstructure at different angles of incoming wind. Although the flow computation is not available at the present time, the numerical capability to deal with such a complex superstructure is considered as feasible.

AFTER-BODY SHAPE DESIGN APPLICATION

An oceanographic device known as an Expendable Doppler Penetrometer (XDP) was designed to descend through the water and penetrate the sea bottom. As the probe penetrates the bottom of the sea, its velocity deceleration is measured as a change in acoustic signal frequency (Doppler shift). The frequency Doppler shift is analyzed to determine the bottom soil undrained shear strength. The terminal velocity of this device through the water is dependent on the hydrodynamic drag to its exterior shape. A design exercise was initiated to compare two configurations with a shape difference only at the tail section, Fig. 13. Since the configuration is symmetric, only a quarter of the body is modelled. Fig.

14 gives the block topology for the configuration. The pressure distribution contours and flow computations are shown in Fig. 15 for these two configurations. Both contour maps have the same levels with the sequence of blue, cyan, green, yellow, red, and magenta as increasing pressure. A substantially rapid change of pressure distribution was found with the short-tail configuration. It is believed that flow separation may occur there with that tail. A smooth distribution was found on the other long-tail configuration.

CONCLUSION

An effective numerical technique for viscous flow computation has been developed, which allows the marine vehicle designer to model complex geometry, generate a detailed geometry database, create surface and three-dimensional volume grids, and model viscous flow phenomena. The whole process has been effectively integrated on a workstation network. The major goal of developing this numerical prediction capability is to obtain accurate computational results and reduce the turn-around time for real practical design applications. Several applications chosen for this paper illustrate the effectiveness and capability of this developed CFD technique. As rapid improvements occur in CFD technology and turbulence modelling, numerical prediction accuracy will be enhanced. In addition, advances in both computer CPU speed and memory size have enabled the use of more complex grid topologies which more accurately represent the real-life geometry. Future improvements in numerical methods and computer capabilities are anticipated to make time accurate flow solutions feasible. Improvements in visualization tools have also aided in the development of these complex grid structures, and the examination of the solution from a CFD analysis.

REFERENCES

1. Verhoff, A., Melnik, R.E. and Carter, J.E., "Industry Warms to CFD," Aerospace America, AIAA, Feb. 1992.

2. Chorin, A.J., "A Numerical Method for Solving Incompressible Viscous Flow Problems," Journal of Computational Physics, Vol. 2, 1967.

3. Sung, C.H., Lin, C.W., and Hung, C.M., "An Explicit Runge-Kutta Method for 3D Turbulent Incompressible Flows," the 7th GAMM Conference on Numerical Methods in Fluid Mechanics, Louvain-la-Neuve, Sept. 1987.

4. Jameson, A., Schmidt, W., and Turkel, E., "Numerical Solutions of the Earlier Equations by Finite Volume Methods Using Runge-Kutta Time-Stepping Schemes," AZAA Paper No. 81-1529, 1981.

5. Lin, C.W., "Computation of Incompressible Stern Flow With Separation Using Explicit Runge-Kutta Finite-Volume Scheme," 6th International Conference on Numerical Methods in Lamina and Turbulent Flow, Swansea, U.K., July 1989.

6. Holst, T.L., Gandy, K.L., Flores, J., Chaderjian, N.M., Kaynak, U. and Thomas, S.D., "Numerical Solution of Transonic Wing Flows Using San Euler/Navier-Stokes Zonal Approach," AZAA Paper No. 85-1640, 1985.

7. Steinbrenner, J.P., Chawner, J.R., and Fouts, C.L., "The GRIDGEN 3D Multiple Block Grid Generation System, Volumes I and II," General Dynamics Corporation, Fort Worth, Texas, USA, 1990.

8. Lin, C.W., Smith, G.D., and Fisher, S.C., "Application of a Multiblock Grid Generation Approach to Ship Configuration," Proc. of Third International Conference on Numerical Grid Generation in CFD and Related Fields, Spain, Jun. 1991.

9. Lin, C.W., Smith, G.D., and Fisher, S.C., "Numerical Viscous Flow Simulation of Wind Tunnel Model-Scaled Experiments," The 2nd Osaka International Colloquium on Viscous Fluid Dynamics in Ship and Ocean Technology, Japan, Sept. 1991.

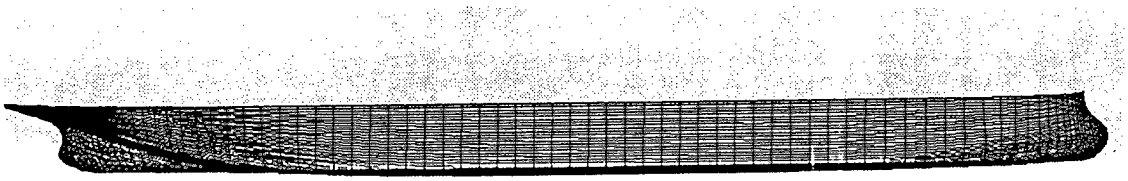

Fig. 1a Profile View of Oil Tanker

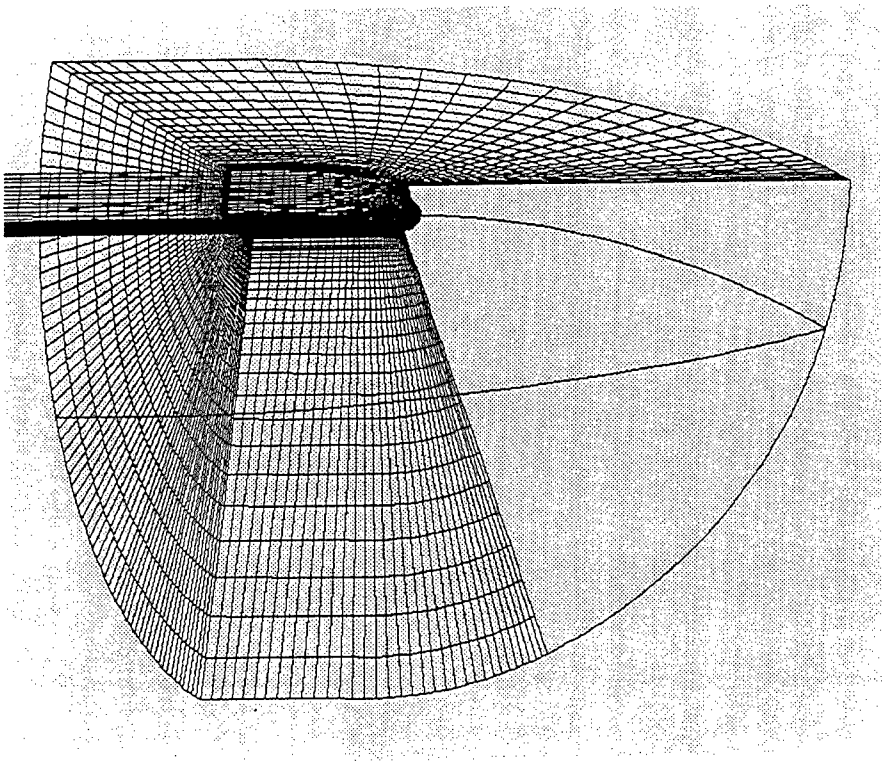

Fig. 1b Block Topology at the Bow

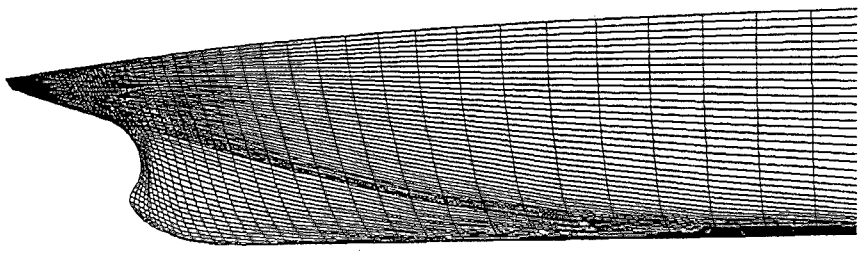

Fig. 1c Surface Grid at the Stern

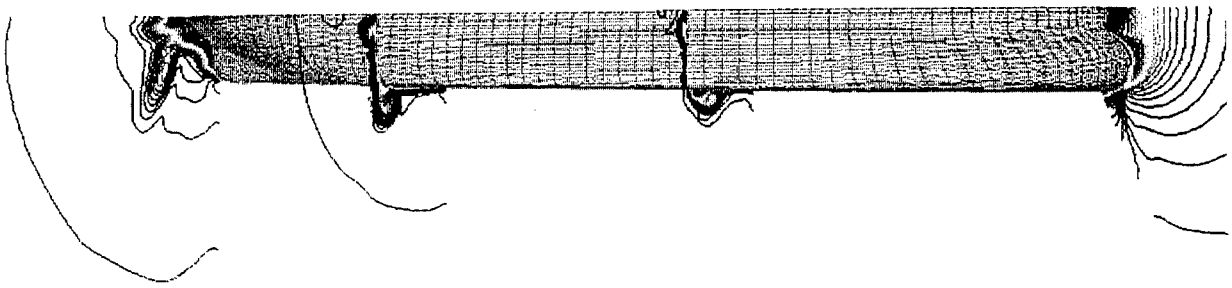

Fig. 2 Longitudinal Velocity Contours at Various Locations along the Hull

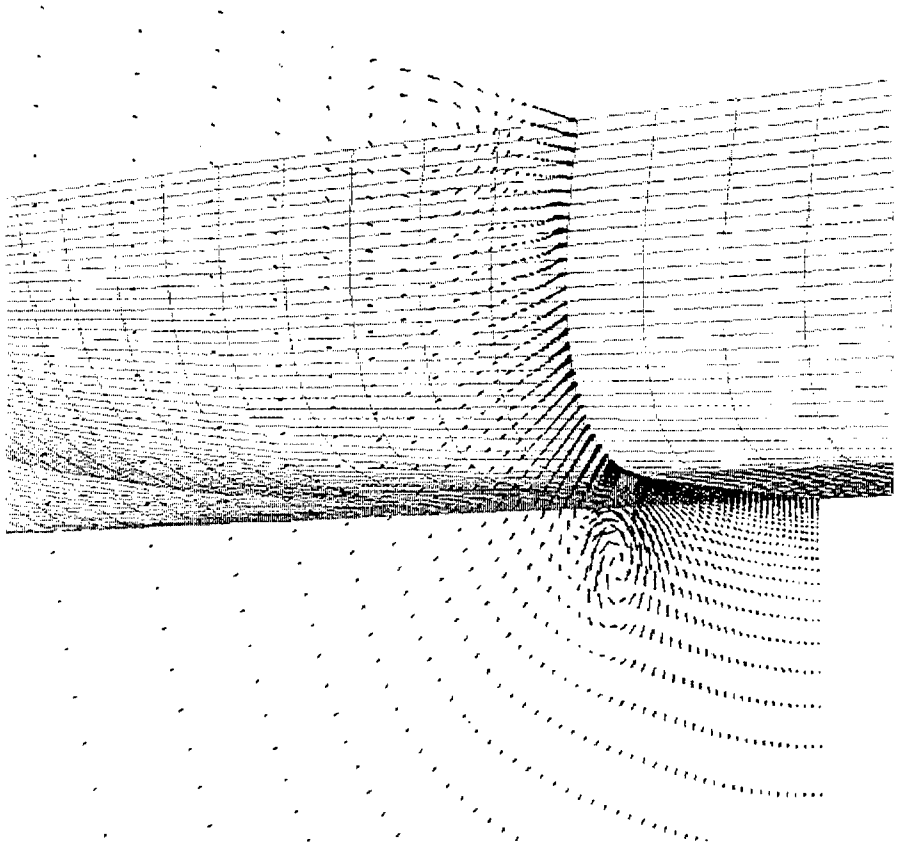

Fig. 3 Cross-Flow Vector at the End of Parallel Mid-Body

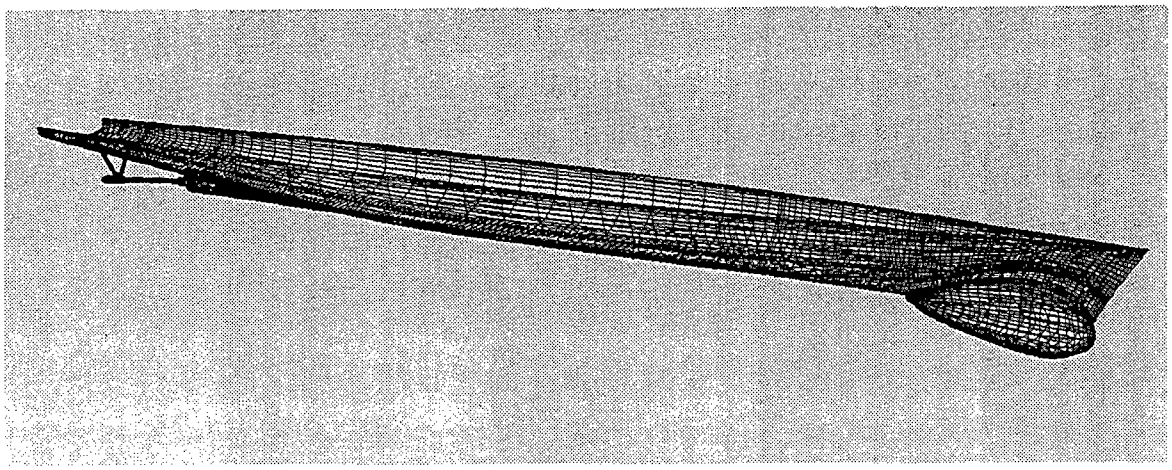

Fig. 4 Geometry for Fully Appended Open-Stern Ship Configuration

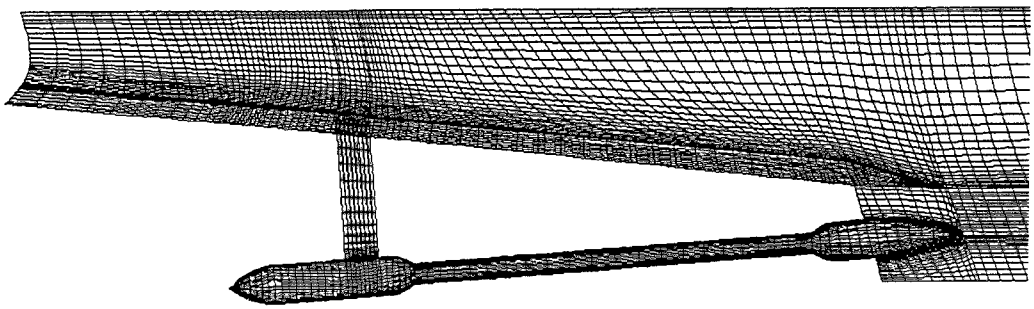

Fig. 5 Grid Block Topology for Appended Open-Stern Ship

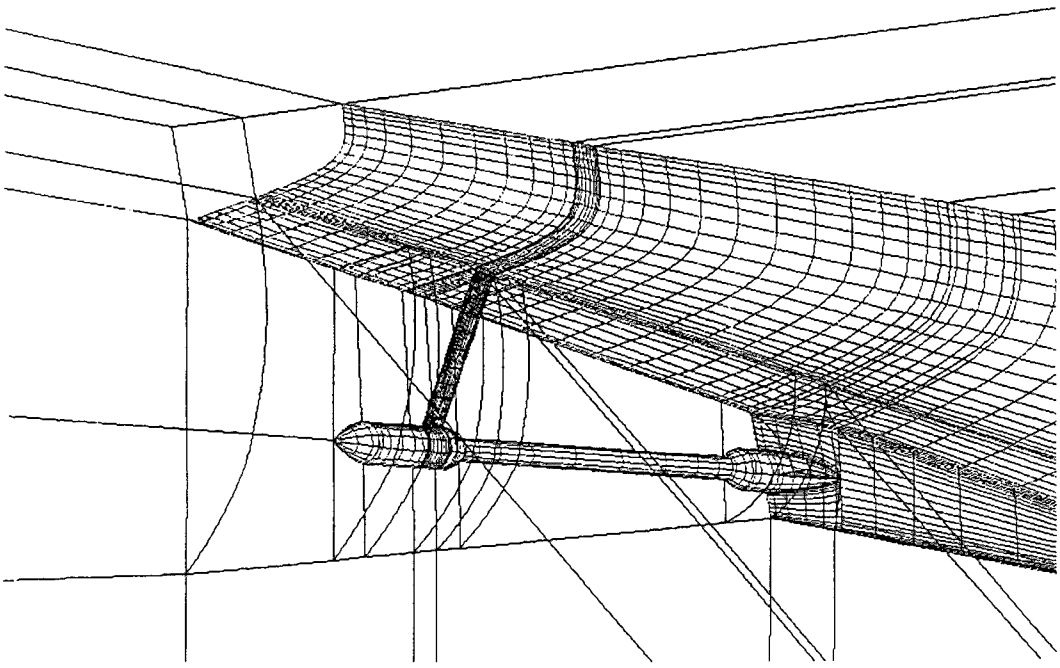

Fig. 6 Surface Grid on Appended Ship

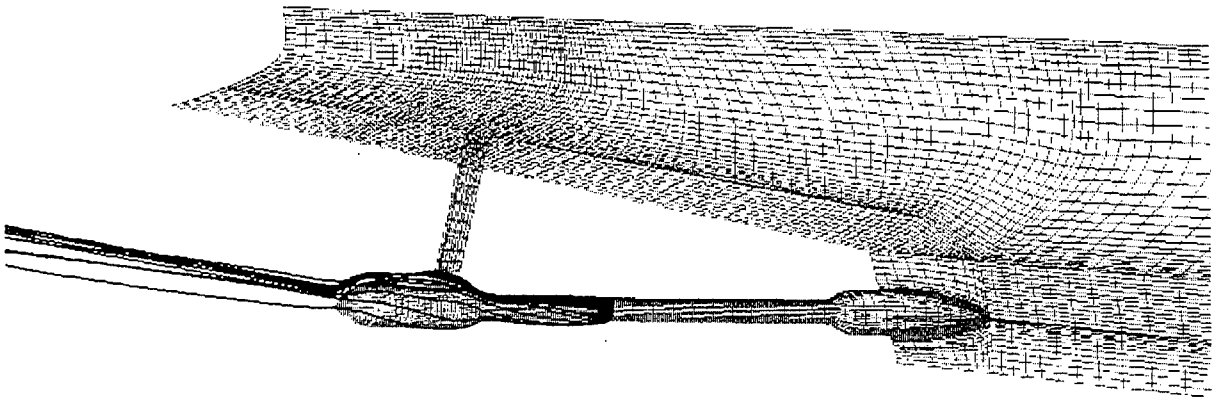

Fig. 7 Flow Partical Tracing along the Shaft

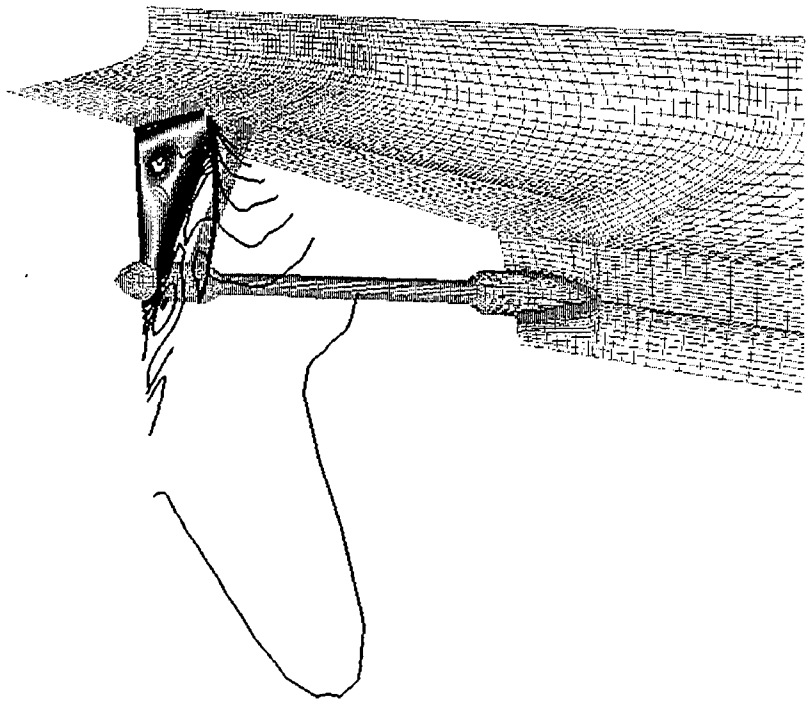

Fig. 8 Longitudinal Velocity Contour at Propeller Plane

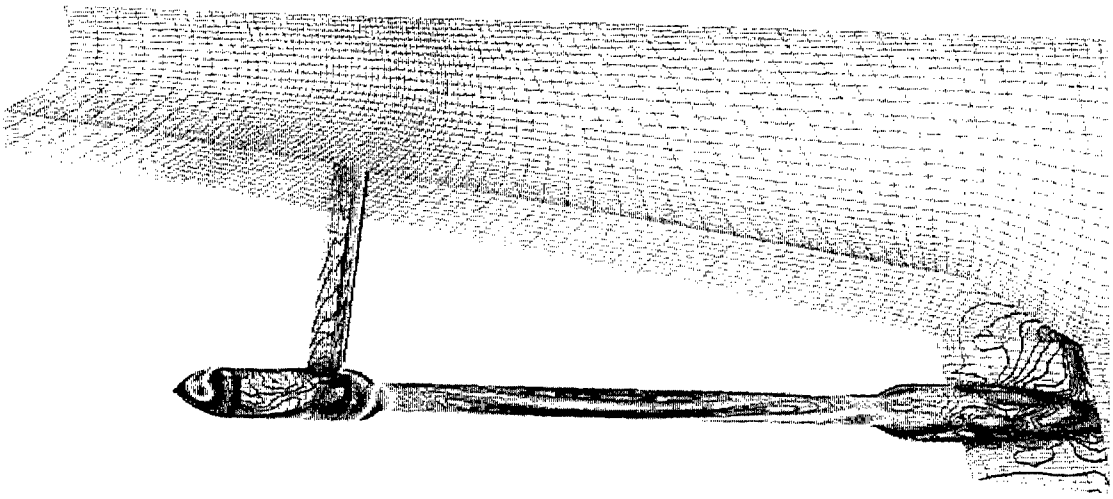

Fig. 9 Pressure Distribution on the Surface of Appendages

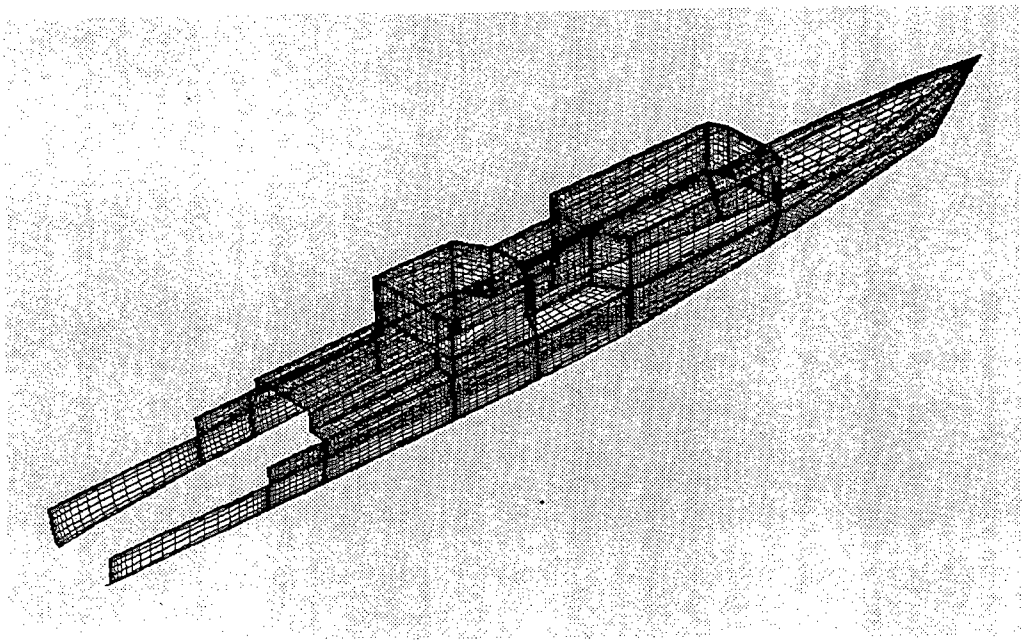

Fig.10 Geometry of Simplified Ship Superstructure

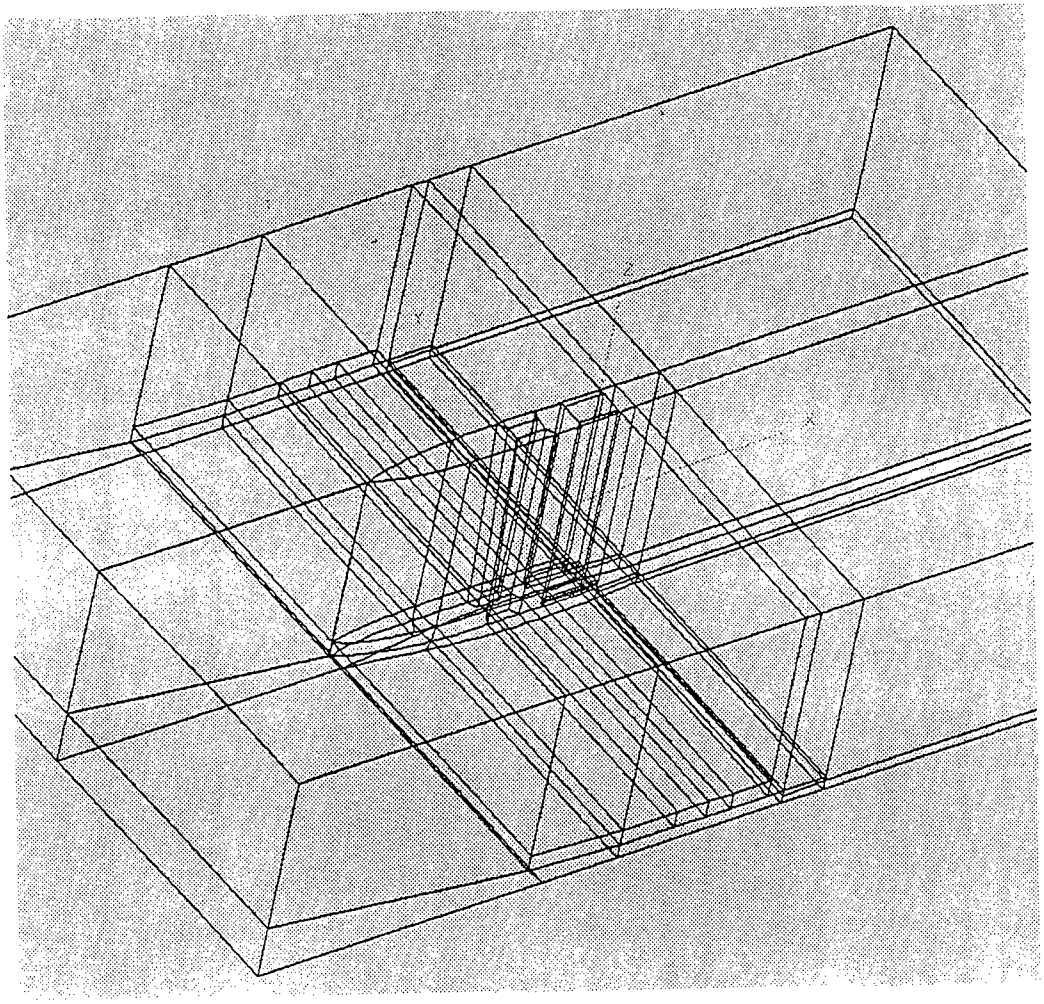

Fig.11 Grid Block Topology for Ship Superstructure

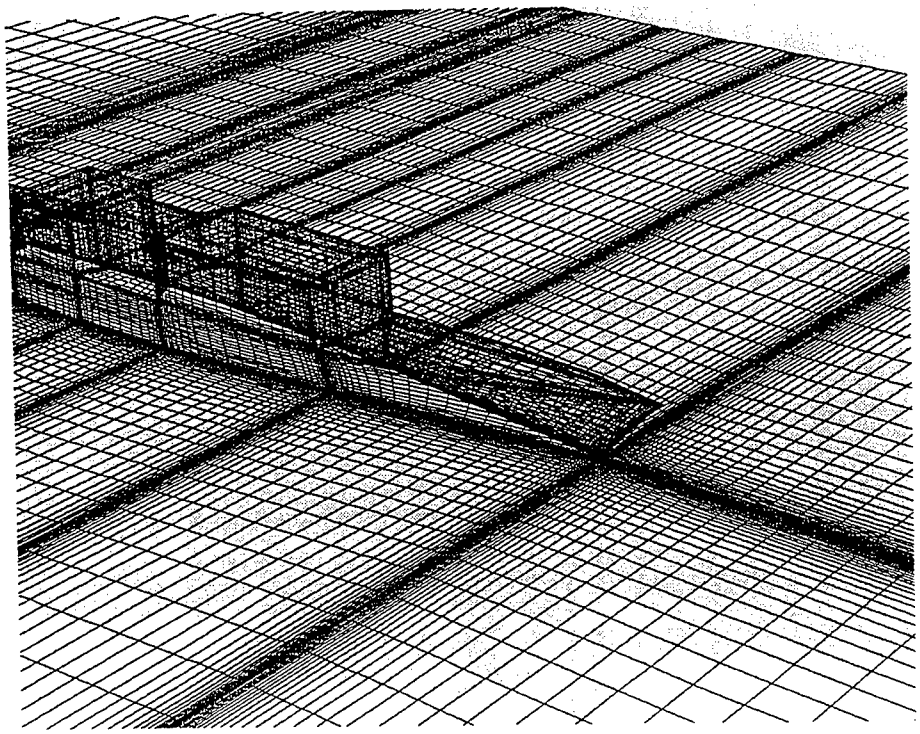

Fig.12 Multiblock Grid Distribution Around Ship Superstructure

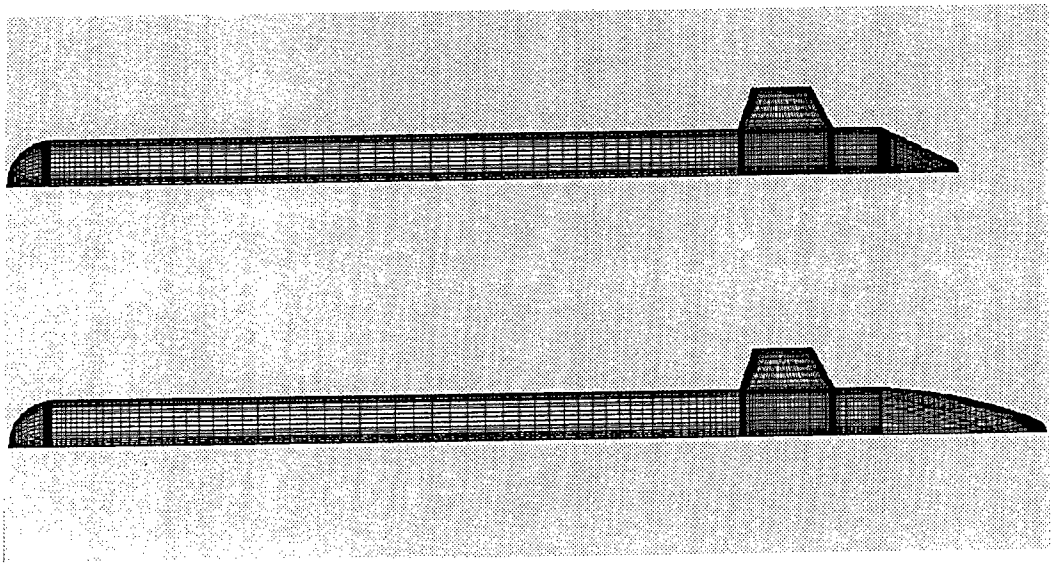

Fig.13 Geometrical Shapes for Two Different XDP Designs

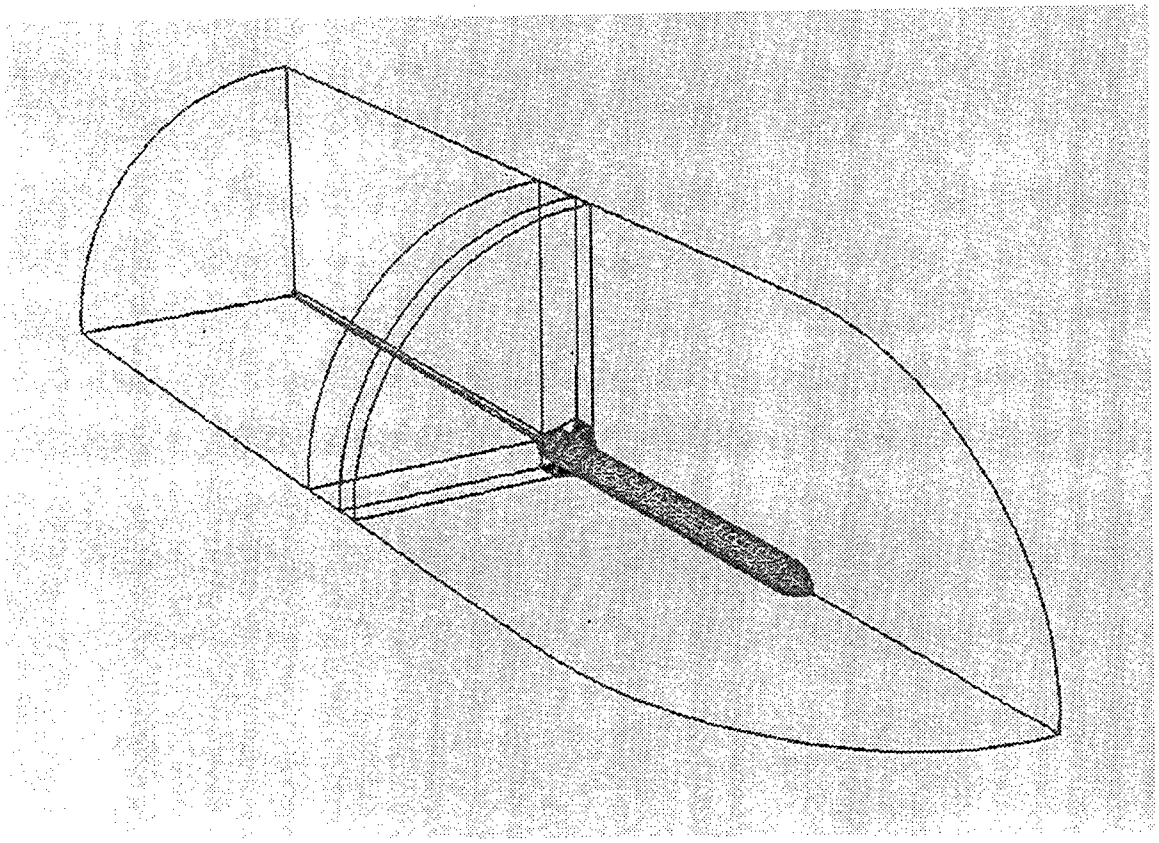

Fig.14 Grid Block Topology for XDP Body

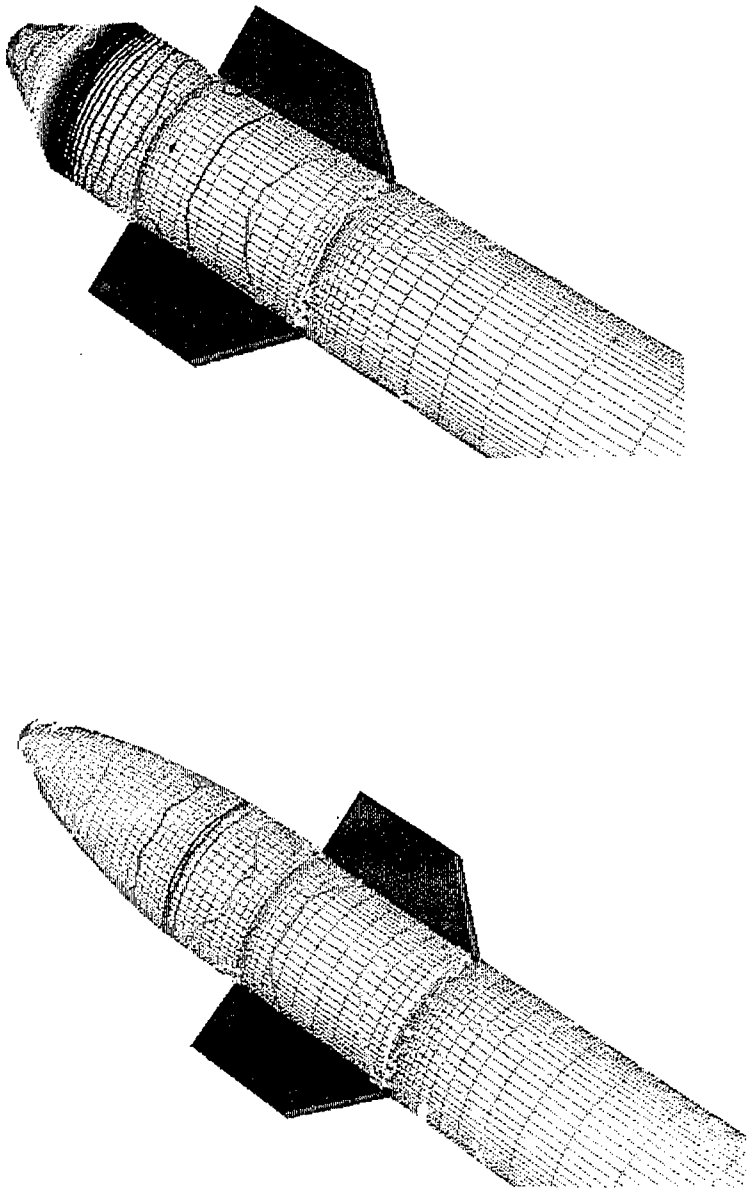

Fig.15 Pressure Contours on the Surfaces of Different XDP Designs

DISCUSSION

V. Patel
University of Iowa, USA

This paper appears to be quite similar to that presented last year at the Osaka Colloquium. Have you made comparisons with the data obtained at DTRC on the complex geometries of the DARPA SUBOFF experimental program? Also, I invite you to consider the ship hulls chosen for the SSPA-CTA-114R 1990 workshop to make comparisons between your calculations and experiment (as well as calculations with 19 other methods).

AUTHORS' REPLY

The main theme of this paper is to demonstrate how effectively we can deal with quite complicated geometry for CFD design applications. The comparison of predicated results with the DARPA SUBOFF experimental data has been clearly shown at the Osaka Colloquium. They were our first case of validation on the complex geometry. Since then, more validations have been conducted. However, they are not shown here since the validation is not the main subject for this paper. We clearly understand the importance of validation of CFD predicated results with experimental data, as I have mentioned in my oral presentation. Furthermore, the cases demonstrated in the paper are mostly surface ship type of CFD applications, instead of submarine-like body. It is our hope to encourage more CFD applications to a variety of complex configurations. The comparison of CFD predicated results for an appended ship with model experimental data is much more important to us, instead of just to a base HSVA tanker. However, we will perform HSVA tanker computations in the near future.

Session VII

Hydrodynamics in Ship Design

Investigation of Horizontal Motions of an SPM Tanker in Shallow Water Through Computation and Model Experiment

T. Jiang, S. Sharma (University of Duisburg, Germany)

ABSTRACT

In continuation of work reported at the 17th Symposium on Naval Hydrodynamics at The Hague in 1988, horizontal motions of a tanker single-point-moored in a steady current were further investigated. The present paper represents two major additional steps: (i) Model experiments in a towing tank for validating previous numerical investigations (nonlinear time-domain simulations and linearized stability analyses) based on a comprehensive mathematical model of the equations of motion in three degrees of freedom (surge, sway and yaw) and (ii) Transition from deep water to the practically more relevant case of shallow water. Various theoretically predicted phenomena (stable and unstable equilibria, self-sustained oscillations as limit cycles, and stabilizing effects of rudder deflection, reverse propeller rate and asymmetric mooring) were confirmed by experiment. Water depth was found to be a significant parameter, with a tendency toward stronger instability in shallow water.

NOMENCLATURE

A	Mooring line attachment point (fairlead)
C	Index for current
E	Index for equilibrium
F_A	Mooring line tension (horizontal component)
F_{AE}	Mooring line tension at equilibrium
G	Centre of gravity, also as index
h	Water depth
L_A	Instantaneous length of mooring line
L_{AU}	Unloaded length of mooring line
n	Propeller rate of turn
O	Midship point, also as index
$Oxyz$	Shipbound coordinate system
P	Effective mooring point (ship) Towing point (model)
$Px_oy_oz_o$	Earthbound coordinate system (ship) with x_o pointing against the current Carriagebound coordinate system (model) with x_o pointing in direction of tow
T	Draft of tanker
t	Time
u, v, r	Surge, sway, and yaw rate
V_C	Current speed (ship) Carriage speed (model)
X, Y, N	Net external horizontal force components along x,y axes and moment about z axis
x_Ay_A	Shipbound coordinates of A
x_G	Shipbound coordinate (LCB) of G
x_o, y_o	Coordinates of O (advance, transfer)
x_{oE}, y_{oE}	Coordinates of O at equilibrium
y_{oI}	Initial value of transfer
δ	Rudder angle
σ_c	Complex eigenvalue pair determining local stability of equilibrium
ψ	Heading angle
ψ_A	Direction of mooring line
ψ_E	Heading angle at equilibrium

INTRODUCTION

This paper deals with the horizontal motions of a large tanker single-point-moored (SPM) at an offshore terminal for loading or unloading, see Fig. 1. The obvious advantage of this nowadays popular configuration is that the ship hull is free to assume a favorable alignment to the prevailing current, wind or waves, thereby substantially reducing the mooring line tension compared to the values possible if its heading were constrained. The not so obvious disadvantage, however, is that under certain conditions the tanker may not attain a stable equilibrium even in a seemingly innocuous steady environment but indulge in large-amplitude low-frequency oscillations of periodic or aperiodic nature.

Needless to say that the problem is of great practical importance due to the formidable environmental implications of a tanker accident. The crucial aspect is not so much the space requirement for the large horizontal motions but rather the sometimes unpredictable peak tensions in the mooring line. At the same time, the

problem is also theoretically fascinating for it displays many exciting features of nonlinear dynamics: multiple equilibria, static and dynamic instability, limit cycles, self-sustained oscillations, multiple asymptotic response, deterministic chaos, strange attractors, basins of attraction with fractal boundaries, etc. Additional interest arises from the physical affinity of the problem to the case of a tanker under tow or after emergency anchoring in restricted waters.

Naturally, a considerable amount of research effort has been devoted to this problem during the last fifteen years or so. The earliest studies were apparently by Wichers (1976), Owen and Linfoot (1977), and Faltinsen (1979). Fairly complete bibliographies can be found in the doctoral dissertations of Papoulias (1987) and Wichers (1988). Among the more recent contributions worth mentioning are Obokata and Nakajima (1988), Aghamohammadi and Thompson (1990), and de Kat and Wichers (1991). But the number and range of parameters involved is so vast that we are still far from a satisfactory complete solution. To name only the most important factors, the dynamic response of the tanker would depend on design parameters (such as hull form and water depth), environmental parameters (such as current, wind and waves), operational parameters (such as loading condition and mooring configuration), and control parameters (such as rudder deflection and propeller rate of turn). The present paper focuses on the effect of water depth, a factor of obvious practical relevance, which to our knowledge has not been explicitly handled in published literature, except in the context of the related towing problem by Charters, Thomas and Latorre (1985), for instance.

CALCULATIONS FOR TANKER TOKYO MARU

In previous work we (1987, 1988a, 1988b, 1990 and 1991) consistently used supertanker TOKYO MARU as an exemplary ship for studying the dynamics of single-point mooring. Its principal particulars are reproduced in Table 1. The main reason for this choice was that the hydrodynamic control and response forces of this ship in deep water, including hull-propeller-rudder interactions and scale effects, had been very completely identified by extensive model tests at the Hamburg Ship Model Basin (HSVA) and documented by Oltmann and Sharma (1984). Our mathematical model for computing horizontal motions of an SPM ship in three degrees of freedom (surge, sway and yaw) - taking account of the effects of current, wind and waves - consists of an essentially nonlinear system of differential equations of order 18 (with memory effects) or order 6 (without memory). It was reported completely in (1988b) and will not be repeated here, except for the coordinate system (Fig. 2) for ready reference.

Numerical investigations conducted previously included determination of (i) multiple equilibria in state space, (ii) stability domains in parameter space, (iii) trajectories in state space, and (iv) practical measures for ensuring stability of asymptotic response. A selection of computer simulations for tanker TOKYO MARU is first reproduced here to illustrate certain characteristic phenomena (and for comparison with model experiments to follow). For each case the corresponding parameter values, equilibrium coordinates, equilibrium line tension, and the complex eigenvalue pair governing local stability of equilibrium (found by linear stability analysis) are compiled in Table 2.

All calculations are for the so-called autonomous case, i.e., for the tanker in a steady current, but without wind and waves, and ignoring memory effects as insignificant for the present purpose. Hydrodynamic force coefficients were input for the so-called model condition (i.e. without corrections for Reynolds number) to enable direct verification by comparison with model experiments, although all results are shown at actual ship scale (by simple Froude scaling) for easier practical assessment of the phenomena involved.

Each of the following Figs. 3 - 6 shows, starting from arbitrary initial conditions, two asymptotic responses (also called attractors), one converging on a stable static equilibrium and the other terminating in a self-sustained oscillation of large amplitude (about 40 m) and long period (about 20 min) accompanied by peaked fluctuation of line tension. The two members of each pair differ only in one parameter value, and simulated time histories and trajectories confirm the results of linearized stability analyses of equilibrium states which indicate a Hopf bifurcation as the corresponding parameter is varied, implying a transition from stable to unstable equilibrium.

Fig. 3 compares the reference case (rudder amidships, propeller freewheeling at zero torque, and fairlead at bow center: dotted line) with a modified case (rudder angle 35 deg to starboard: solid line). It illustrates the stabilizing effect of static rudder deflection as the simplest practical measure.

Fig. 4 compares the reference case (dotted line) with another modification (propeller operating at substantial reverse thrust: solid line) and illustrates basically the stabilizing effect of increased mean line tension.

Fig. 5 compares the reference case (dotted line) with yet another modification (fairlead moved off center to port: solid line) and is consistent with the general observation that asymmetric equilibria (from whatever cause) tend to be more stable than symmetric equilibria.

Fig. 6 compares two departures from the reference case: fairlead moved the same distance to port (solid line) or to starboard (dotted line). Each of these measures introduces an asymmetry into the system, in one case reinforcing and in the other case counteracting the inherent hydrodynamic asymmetry of the single-screw ship. The net effect is that the equilibrium is stable with fairlead to port but not to starboard.

MODEL EXPERIMENTS FOR TANKER ESSO OSAKA

Choice of Tank

Our previous experimental work, for instance, that leading to identification of a complete four-quadrant maneuvering mathematical model for tanker TOKYO MARU, was carried out in the large deep water tank (280 m × 18 m × 5.5 m) of the Hamburg Ship Model Basin (HSVA). By contrast, experiments reported here were performed in the main towing tank (200 m × 9.8 m × 1 m) of the shallow water research facility at Duisburg (VBD) for two reasons. First, since both of us have recently moved from Hamburg to Duisburg, the latter tank was more easily accessible to us. Second and more important, the Duisburg tank has two useful features typical of shallow water testing: water depth can be adjusted to any value from zero to one meter, and a true current can be generated by means of circulating water pumps installed at one end of the tank.

Choice of Tanker

The present work was conducted with a 1:65 scale model of tanker ESSO OSAKA, see Table 3 for its principal particulars. This departure from our previous exemplary tanker TOKYO MARU was motivated by three main reasons. First, thanks to a set of comprehensive full-scale trials sponsored by the United States Maritime Administration, the tanker ESSO OSAKA has meanwhile acquired the status of a standard ship for comparative maneuvering studies all over the world, see Crane (1979). Second, results of a comprehensive set of maneuvering tests with models at two scales (1:45 and 1:65), partly in four water depths (h/T = 16, 12, 1.5 and 1.2), carried out at Hamburg and Duisburg were accessible, see Oltmann, Wolff, Müller and Baumgarten (1986). Third, a suitable model, left over from a previous research project, was readily available for our study. Body plans and profiles of the two tankers, reproduced here in Figs. 7 and 8, respectively, display enough similarity of hull form to justify a tentative comparison of our calculations for TOKYO MARU with measurements for ESSO OSAKA.

Test Set-up

Purpose of model experiment was to dynamically simulate and record the asymptotic response of an SPM tanker in a steady current, as an autonomous system seeking its attractor after an arbitrary initial disturbance. Froude dynamic similarity was assumed, i.e., no attempt was made to compensate for the differences in Reynolds number between model and full-scale. Current was simulated by towing the model through still water; hence, initial conditions had to be carefully chosen to ensure a good approximation to the ultimate asymptotic response within the time limit imposed by the finite length of the tank. (It is intended to employ a true current generated by pumps in future experiments, thereby enabling arbitrarily long time records.) Specifically, following quantities were measured as functions of time: horizontal motion of the model in three degrees of freedom (surge, sway and yaw) and mooring line tension as well as elongation.

Fig. 9 shows a schematic of the test set-up. A camera mounted on top of the towing carriage took a sequence of bird's eye views of the model at programmable intervals (1,5 or 1 s) on a special film, yielding 300 to 500 frames per run of about 8 min duration (corresponding to about 1 hour at full scale). Each photograph identified two reference points on the carriage and two on the model. From each frame by photographic projection, semi-manual digitization and simple geometric transformation model heading angle and horizontal coordinates of midship point O were derived. In parallel, heading angle as indicated by a gyrocompass installed in the model was also recorded.

Fig. 10 shows a sample comparison of time history records of heading angle obtained by these two methods. That the discrepancy is generally much less than one degree gives us reasonable confidence in the accuracy of our simple improvised technique of trajectory measurement.

Mooring Line Model

A somewhat tricky part of the experiment was dynamically correct modeling of the highly nonlinear load-elongation characteristic of the full-scale mooring line (representing combined effects of elasticity of hawser and catenary action of anchored buoy or righting moment of articulated tower). This was finally achieved by employing, in series, a cascade of several (four for deep water, five for shallow water) linear springs of successively increasing stiffness and individually bounded extension, see Fig. 9. During the tests line elongation and tension were monitored by means of a potentiometer and force gauge, respectively. Such dynamic records (dots) from several runs are compared to static calibrations (circles) in Fig. 11 (top for deep water and bottom for shallow water). The two curves shown are fourth degree polynomials fitted to each data set and later used for corresponding computer simulations.

Results and Discussion

Results of nine selected test runs are presented in seven meaningful pairs in the following Figs. 12 - 18 (in essentially the same format as the previous computer simulations, cf. Figs. 3 -6). Corresponding values of relevant design, environmental and operational parameters are listed in Table 4. Three general comments are in order. First, all quantities are shown Froude scaled to ship size since model values would be arbitrary and fail to convey a feeling for the real magnitude of the practical problem. Second, a uniform current speed of 2 m/s was chosen as a realistic compromise between low speeds entailing

long eigenperiods and high speeds curtailing run duration, thus making optimum use of available tank length. Third, the two values of water depth equal to 3 and 1.5 times ship draft are to be understood as representing deep and shallow water, respectively.

Fig. 12 compares time histories and trajectories of the tanker in the reference condition (rudder amidships, propeller held fixed by friction, and fairlead at bow center) in deep water (solid line) and shallow water (dotted line). Both cases obviously reflect unstable equilibria. But motion amplitudes and line tension peaks are several times higher and the period substantially longer in shallow water than in deep water. This is in apparent contradiction to Charters, Thomas and Latorre (1985) whose calculations for the same tanker under tow indicate a stabilizing influence of shallow water over the speed range from 0.5 to 6 knots. Possible reasons for this discrepancy are differences in length and stiffness of mooring line versus tow line as well as deficiencies in mathematical modeling of hydrodynamic forces.

Fig. 13 demonstrates the stabilizing effect of rudder application by comparing the unstable reference case (rudder amidships: dotted line) with a modified case (rudder 35 deg to starboard: solid line). Similarly, Fig. 14 suggests a stabilizing effect of reverse propeller thrust by comparing the reference case (propeller held fixed by friction : dotted line) with a modified case (propeller operating at 20 rpm in reverse: solid line). Despite reservations owing to rather short time records in the tank and to some differences in hull form and size between the two ships, these experiments in deep water can be seen as essentially validating the calculations shown in Figs. 3 and 4.

Figs. 15, 16 and 17 demonstrate the effectiveness in shallow water as well of the theoretically predicted stabilizing measures rudder deflection, reverse propeller thrust and asymmetric fairlead, respectively, by comparing the unstable reference case (dotted line) with each of the corresponding modifications (solid line). Dramatic reductions of line tension peaks and ship motion amplitudes are achieved.

Fig. 18 is of special interest for it compares two records for the same unstable reference case but starting from different initial conditions. Normally, one would expect them to asymptotically converge on the same attractor (limit cycle). However, the recorded limited time history does not reflect this tendency, suggesting the possibility of competing attractors in state space with their associated separate basins of attraction.

CONCLUDING REMARKS

It is evident from the model experiment results shown that water depth has a significant influence on the horizontal motions of an SPM tanker in a steady current, with a tendency toward stronger instability in shallow water. Comparison of calculated trajectories for tanker TOKYO MARU in deep water with measured trajectories for tanker ESSO OSAKA in deep and shallow water generally confirms various theoretically predicted phenomena: stable and unstable equilibria, self-sustained oscillations, and stabilizing effects of rudder deflection, reverse propeller rate and asymmetric mooring.

For a more convincing validation of the theory it is necessary to do strictly comparable numerical simulations for ESSO OSAKA itself. We regret having been unable to finish these in time for the preprint but hope to present them in an addendum at the Symposium.

ACKNOWLEDGMENTS

The authors are grateful to Dipl.-Ing. A. Gronarz of Duisburg Ship Model Basin (VBD) for his invaluable assistance in conducting the model experiments reported here.

REFERENCES

Aghamohammadi, T. and Thompson, J.M.T. (1990): "An Experimental Study of the Large Amplitude Fishtailing Instabilities of a Tanker at a Single Point Mooring," Journal of Applied Ocean Research, Vol. 12, No. 1, pp. 25-33.

Charters, B., Thomas, G. and Latorre, R. (1985): "Analysis of Towed Vessel Course Stability in Shallow Water," Transactions of The Royal Institution of Naval Architects, Vol. 128, pp. 247-258.

Crane, C.L. (1979): "Maneuvering Trials of a 278000-DWT Tanker in Shallow and Deep Water," Transactions of The Society of Naval Architects and Marine Engineers, Vol. 87, pp. 251-283.

de Kat, J.O. and Wichers, J.E.W. (1991): "Behavior of a Moored Ship in Unsteady Current, Wind, and Waves," Marine Technology, Vol. 28, No. 5, pp. 251-264.

Faltinsen, O.M., Kjærland, O., Liapis, N., and Walderhaug, H. (1979): "Hydrodynamic Analysis of Tankers at Single-Point-Mooring Systems," Second International Conference on Behaviour of Off-shore Structures, London, Paper No. 59, pp. 177-206.

Jiang, T. (1991): "Investigation of Nonlinear Ship Dynamics Involving Instability and Chaos in Examples from Offshore Technology," PhD thesis, The University of Hamburg, IfS-Report No. 512 (in German).

Jiang, T., Schellin, T.E., and Sharma, S.D. (1987): "Maneuvering Simulation of a Tanker Moored in a Steady Current Including Hydrodynamic Memory Effects and Stability Analysis," Proceedings of the Int. Conf. on Ship Manoeuvrability, Royal Institution of Naval Architects, London, Vol. 1, Paper No. 25.

Jiang, T. and Schellin, T.E. (1988a): "Motion Prediction of a Single Point Moored Tanker Subjected to Current, Wind and Waves," Proceedings of the 7th Int. Symposium on Offshore Mechanics and Arctic Engineering,ASME, Houston, Vol. 2, pp. 317-326.

Obokata, J. and Nakajima, T. (1988): "On the Basic Design of Single Point System - Estimation of the Mooring Force," Journal of The Society of Naval Architects of Japan, Vol. 163, pp. 252-260.

Oltmann, P., Wolff, K., Müller, E., and Baumgarten, B. (1986): "On the Correlation Between Model and Full-Scale Ship for Maneouvring Tests in Deep and Shallow Water," Jahrbuch der Schiffbautechnischen Gesellschaft, Vol. 80, pp. 217-245 (in German).

Oltmann, P. and Sharma, S.D. (1984): "Simulation of Combined Engine and Rudder Maneuvers Using an Improved Model of Hull-Propeller-Rudder Interactions," Proceedings of the 15th Symposium on Naval Hydrodynamics, Hamburg, pp. 83-108.

Owen, D.G. and Linfoot, B.T. (1977): "Theoretical Analysis of Single Point Mooring Behavior," Trans. of The Society of Naval Architects and Marine Engineers, Vol. 85, pp. 315-324.

Papoulias, F.A. (1987): "Dynamic Analysis of Mooring Systems," PhD thesis, The University of Michigan, Ann Arbor, Michigan.

Schellin, T.E., Jiang, T., and Sharma, S.D. (1990): "Motion Simulation and Dynamic Stability of an Anchored Tanker Subject to Current, Wind and Waves," Journal of Ship Technology Research (Schiffstechnik), Vol. 37, No. 2, pp. 64-84.

Sharma, S.D., Jiang, T., and Schellin, T.E. (1988b): "Dynamic Instability and Chaotic Motions of a Single-Point-Moored Tanker," Proceedings of the 17th Symposium on Naval Hydrodynamics, The Hague, pp. 543-563.

Wichers, J.E.W. (1976): "On the Slow Motions of Tankers Moored to Single Point Mooring Systems," Proceedings of Offshore Technology Conference, Houston, Paper 2548.

Wichers, J.E.W. (1988): "A Simulation Model for a Single Point Moored Tanker," Maritime Research Institute Netherlands, Wageningen, Publication No. 797.

Table 1: Main dimensions of tanker TOKYO MARU[1]

Length between perpendiculars	290.0	m
Length of waterline	296.446	m
Beam	47.5	m
Draft forward	16.196	m
Draft aft	15.964	m
Block coefficient	0.805	
LCB fwd of midship section x_G	7.243	m
Radius of gyration (z-axis)	66.36	m
Number of propellers	1	
Diameter	7.91	m
Pitch ratio	0.745	
Expanded area ratio	0.6	
Number of blades	5	
Screw sense	righthanded	
Number of rudders	1	
Rudder area	73.5	m^2
Chord length	7.15	m
Aspect ratio	1.438	

[1]HSVA Model No. 2657, Scale 1:35

Table 2: System parameter values of computer simulations for TOKYO MARU shown in Figs. 3 - 6, including equilibrium states and complex eigenvalues from linear stability analysis (common parameters: $V_C = 2.0$ ms^{-1}, $L_{AU} = 75.0$ m)

Fig.	Case	x_A [m]	y_A [m]	δ [°]	n [rpm]	x_{oE} [m]	y_{oE} [m]	ψ_E [°]	F_{AE} [kN]	$\sigma_c \times 10^3$ [s^{-1}]
3	—	145	0	-35	1.4	-209	44.2	6.2	357	-0.40±i5.2
	···	145	0	0	1.4	-231	9.5	0.9	226	0.21±i5.7
4	—	145	0	0	-30.0	-216	31.4	8.2	510	-0.64±i6.4
	···	145	0	0	1.4	-231	9.5	0.9	226	0.21±i5.7
5	—	130	-13	0	1.4	-206	50.5	3.2	267	-0.16 ±i5.2
	···	145	0	0	1.4	-231	9.5	0.9	226	0.21±i5.7
6	—	130	-13	0	1.4	-206	50.5	3.2	267	-0.16±i5.2
	···	130	13	0	1.4	-212	-38.6	-1.8	240	0.06±i5.3

Table 4: System parameter values of model experiments for ESSO OSAKA shown in Figs. 12 - 18 (common parameter: $V_C = 2.0$ ms^{-1})

Fig.	Case	x_A [m]	y_A [m]	L_{AU} [m]	δ [°]	n [rpm]	h/T	y_{oI} [m]
12	—	162.5	0.0	78.0	0.0	0.0	3.0	32.5
	···	162.5	0.0	78.0	0.0	0.0	1.5	19.5
13	—	162.5	0.0	78.0	-35.0	0.0	3.0	32.5
	···	162.5	0.0	78.0	0.0	0.0	3.0	19.5
14	—	162.5	0.0	78.0	0.0	0.0	3.0	19.5
	···	162.5	0.0	78.0	0.0	-20.0	3.0	32.5
15	—	162.5	0.0	78.0	-35.0	0.0	1.5	32.5
	···	162.5	0.0	78.0	0.0	0.0	1.5	32.5
16	—	162.5	0.0	78.0	0.0	-30.0	1.5	32.5
	···	162.5	0.0	78.0	0.0	0.0	1.5	32.5
17	—	139.8	18.2	78.0	0.0	0.0	1.5	32.5
	···	162.5	0.0	78.0	0.0	0.0	1.5	32.5
18	—	162.5	0.0	78.0	0.0	0.0	1.5	19.5
	···	162.5	0.0	78.0	0.0	0.0	1.5	32.5

Table 3: Main dimensions of tanker ESSO OSAKA[1]

Length between perpendiculars	325.0	m
Length of waterline	335.0	m
Beam	53.0	m
Draft fwd	21.79	m
Draft aft	21.79	m
Block coefficient	0.829	
LCB fwd of midship section x_G	10.35	m
Radius of gyration (z-axis)	81.25	m
Number of propellers	1	
Diameter	9.10	m
Pitch ratio	0.715	
Expanded area ratio	0.682	
Number of blades	5	
Screw sense	righthanded	
Number of rudders	1	
Rudder area	124.65	m^2
Chord length	9.0	m
Aspect ratio	1.54	

[1]VBD Model No. 1238, Scale 1:65

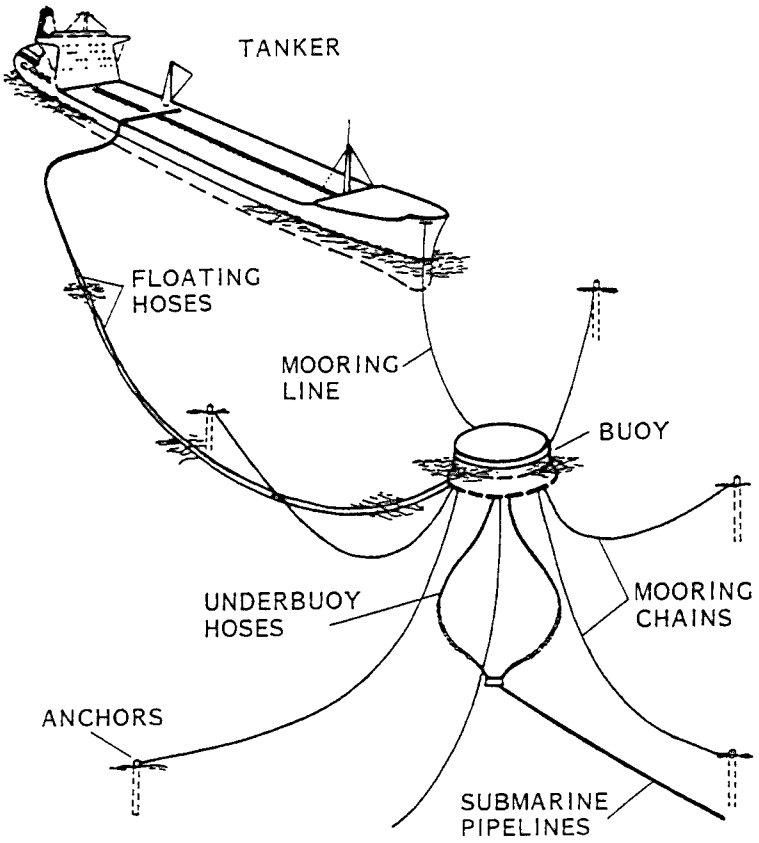

Fig. 1 Schematic of a single point mooring system

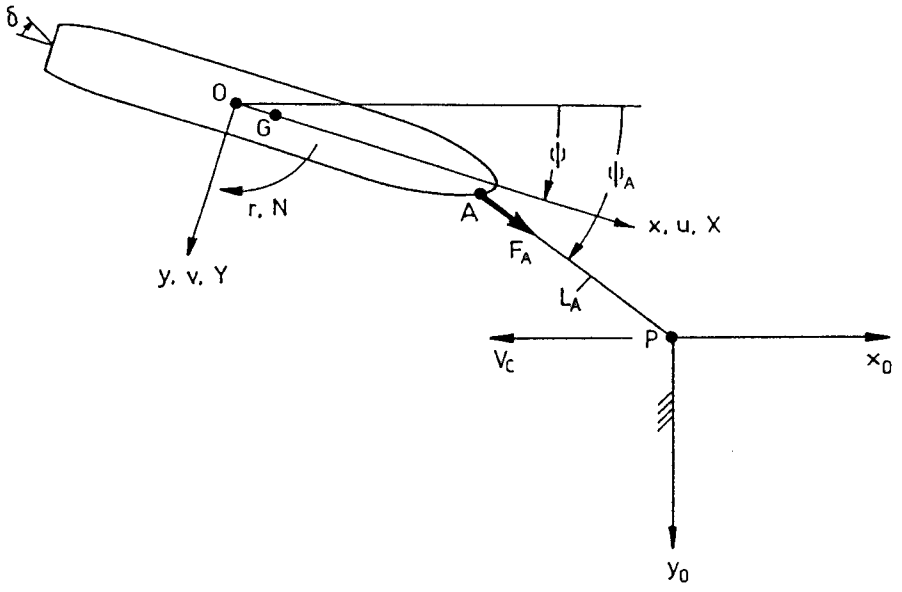

Fig. 2 Coordinate systems for SPM tanker

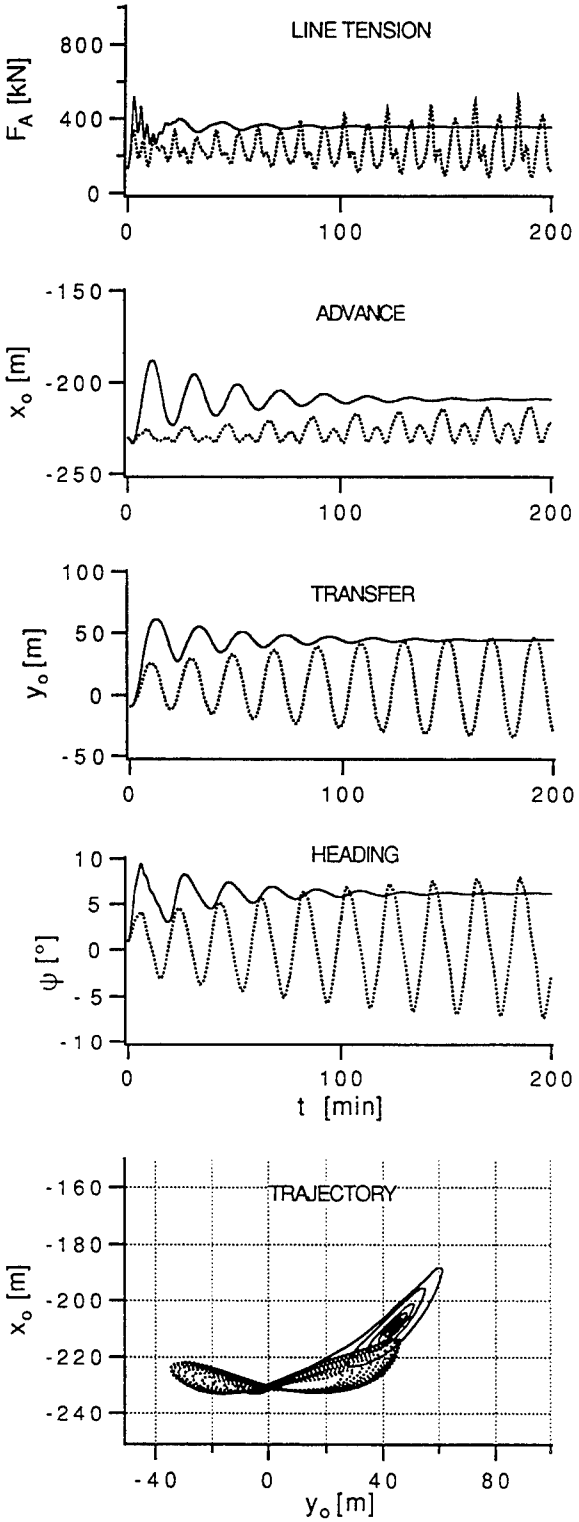

Fig. 3 Calculated time histories of SPM tanker in deep water with (—) and without (·····) rudder application

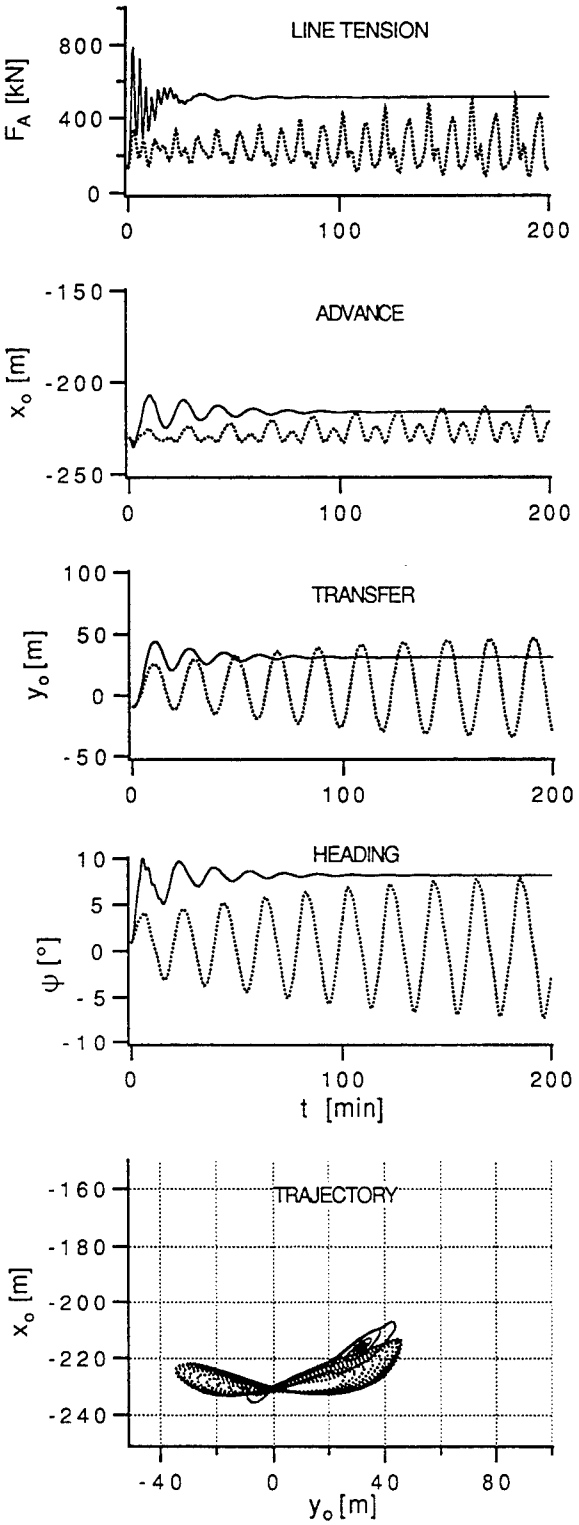

Fig. 4 Calculated time histories of SPM tanker in deep water with (—) and without (·····) reverse propeller torque

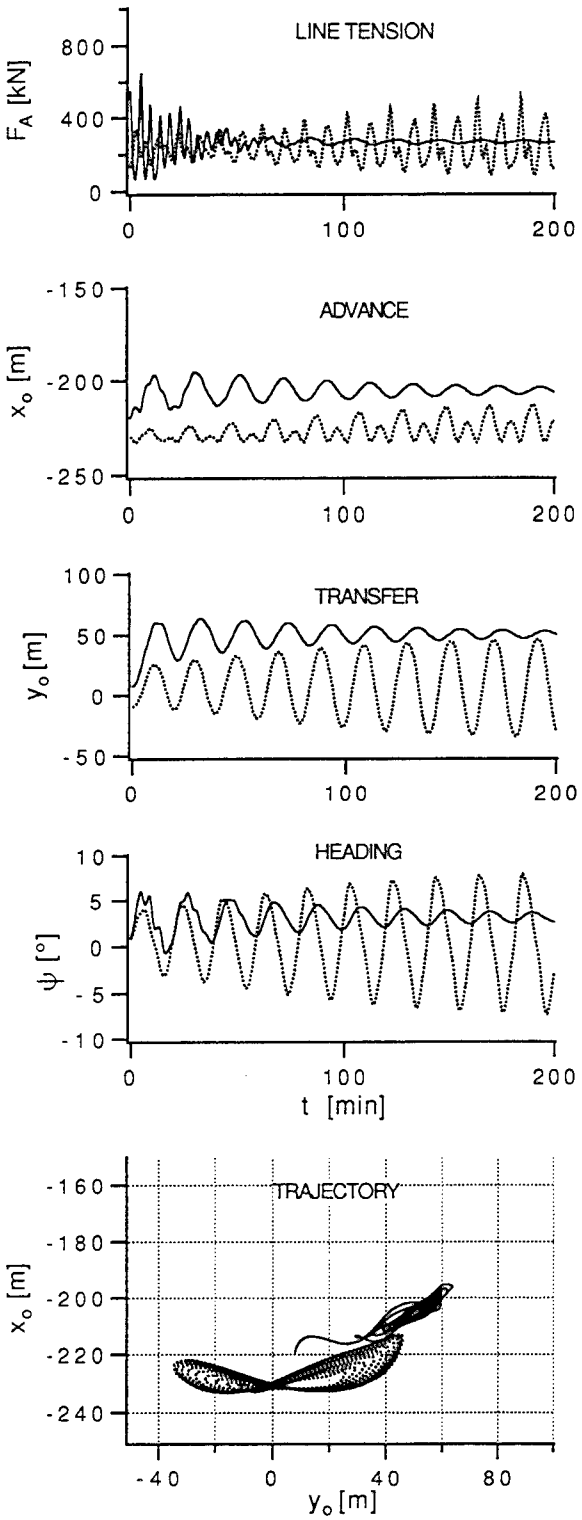

Fig. 5 Calculated time histories of SPM tanker in deep water with port (—) and symmetric (·····) fairlead

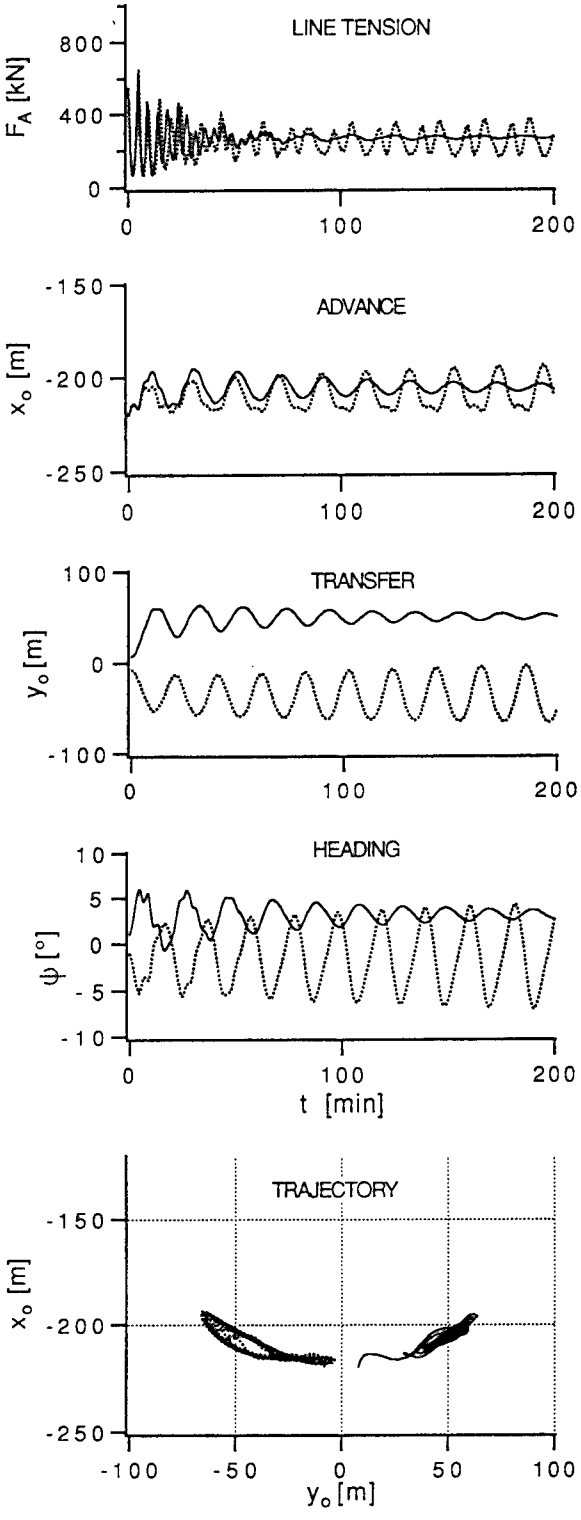

Fig. 6 Calculated time histories of SPM tanker in deep water with port (—) and starboard (·····) fairlead

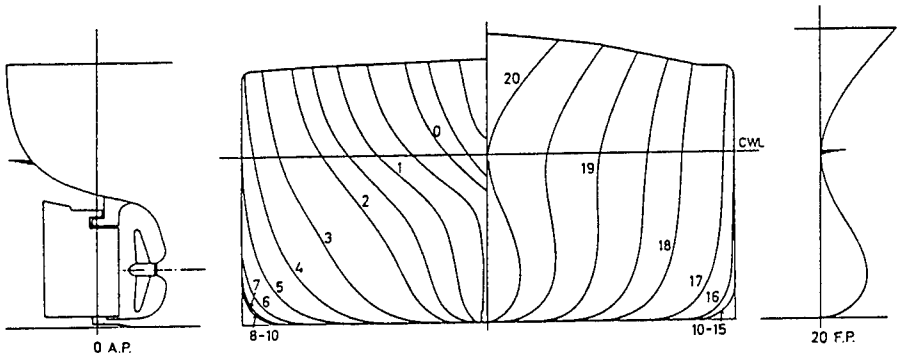

Fig. 7 Body plan and profile of tanker TOKYO MARU (HSVA Model No. 2507)

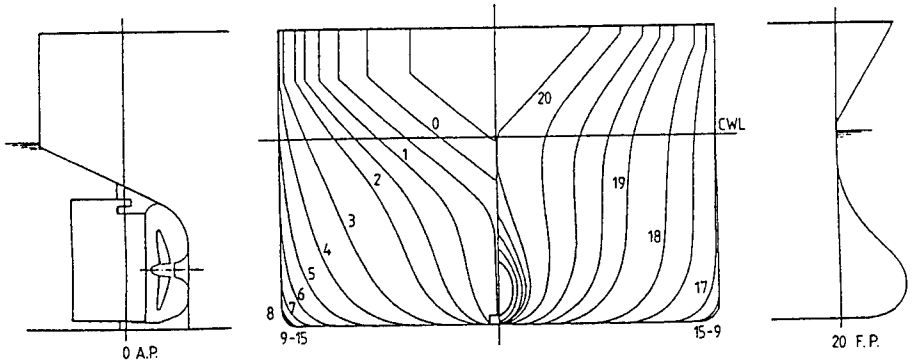

Fig. 8 Body plan and profile of tanker ESSO OSAKA (VBD Model No. 1238)

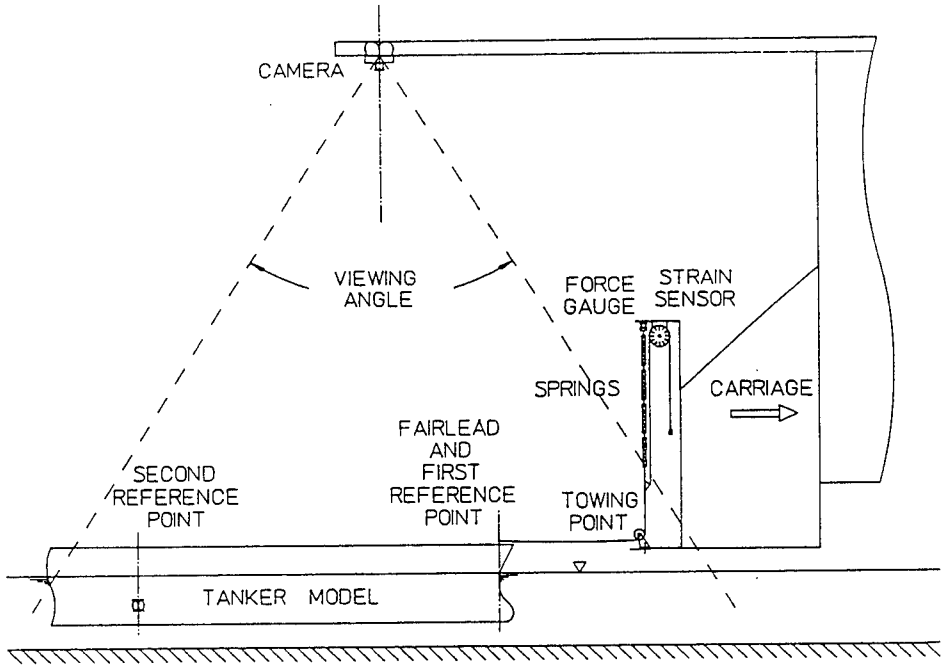

Fig. 9 Schematic of model test set-up in VBD

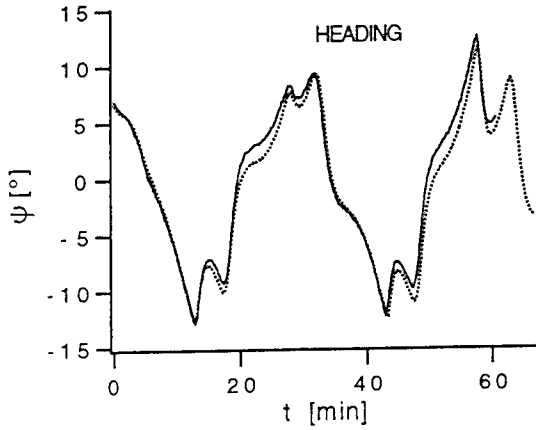

Fig. 10 Typical time history of heading angle as measured by photogrammetry (—) and by gyrocompass (·····)

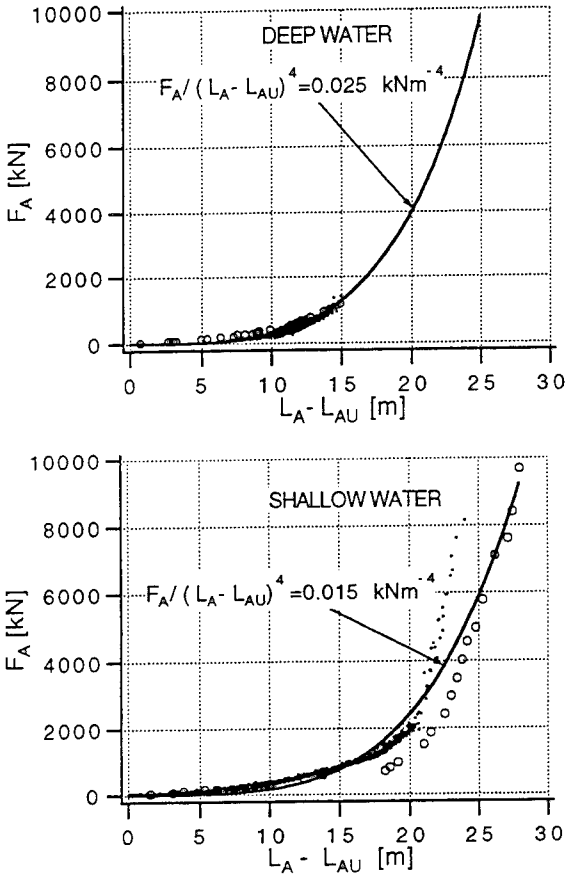

Fig. 11 Load-elongation characteristics of mooring line derived from dynamic records (·····) and static calibrations (ooo)

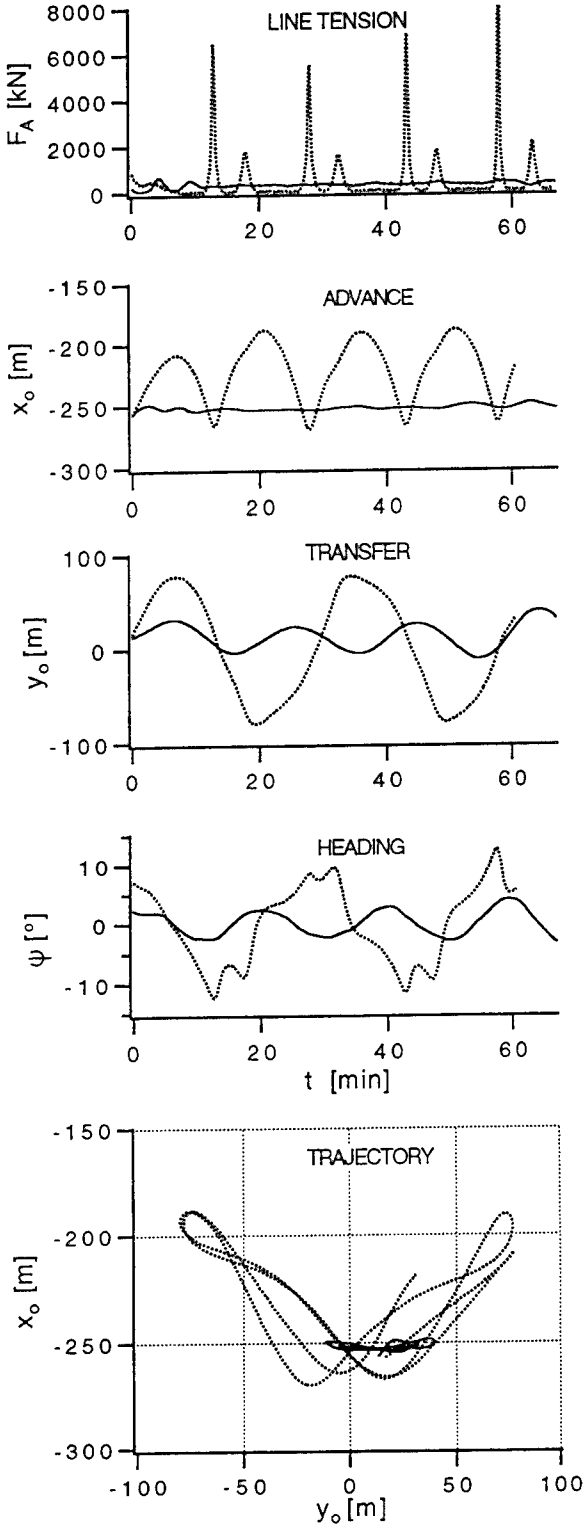

Fig. 12 Measured time histories of SPM tanker in deep (—) and shallow (·····) water

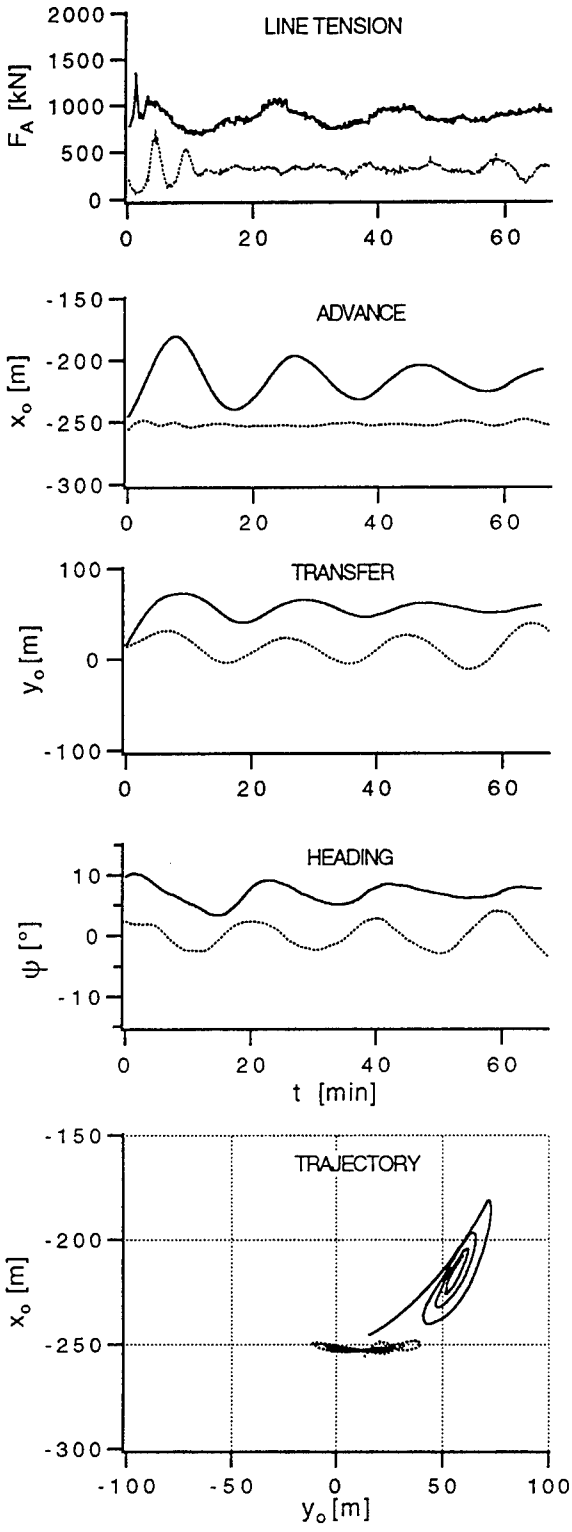

Fig. 13 Measured time histories of SPM tanker in deep water with (——) and without (·····) rudder application

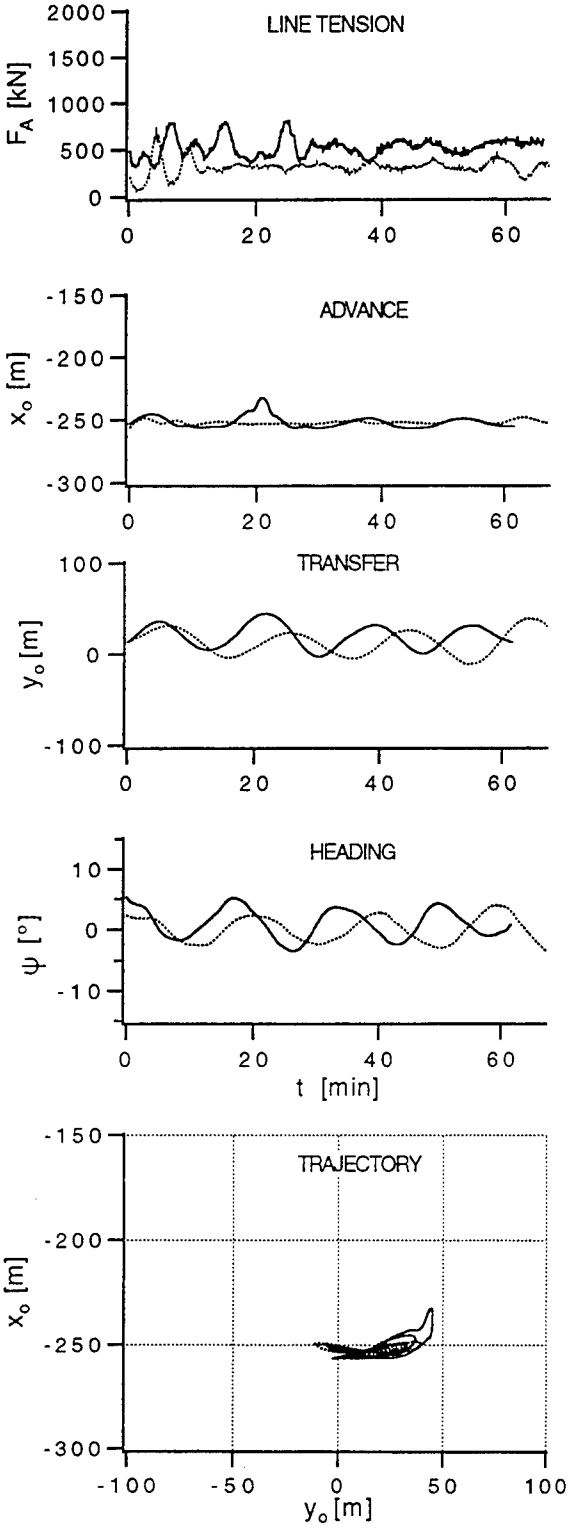

Fig. 14 Measured time histories of SPM tanker in deep water with (——) and without (·····) reverse propeller action

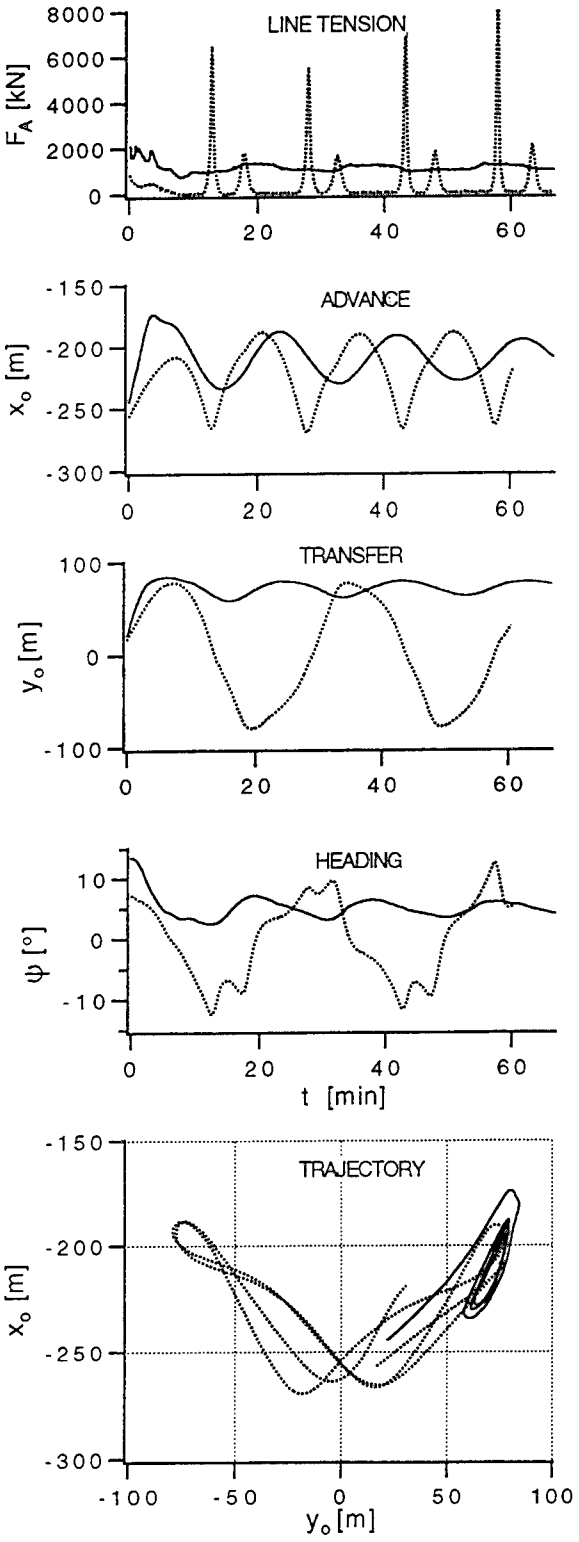

Fig. 15 Measured time histories of SPM tanker in shallow water with (——) and without (·····) rudder application

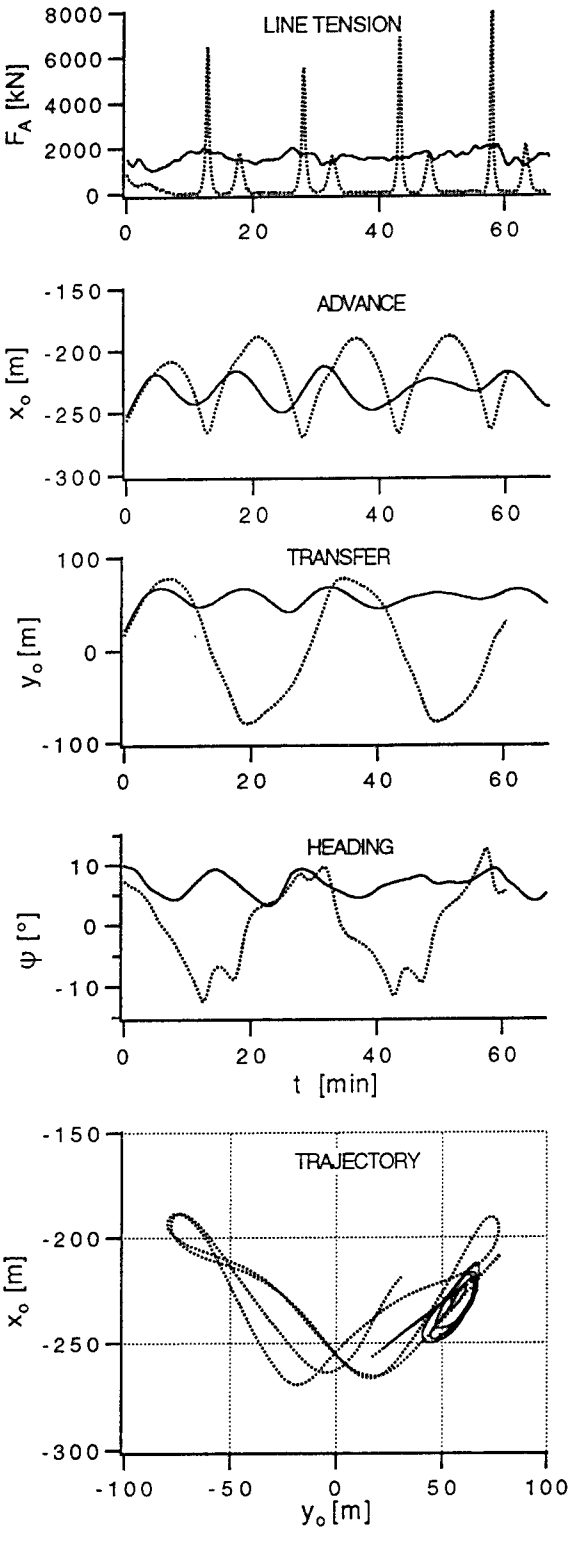

Fig. 16 Measured time histories of SPM tanker in shallow water with (——) and without (·····) reverse propeller action

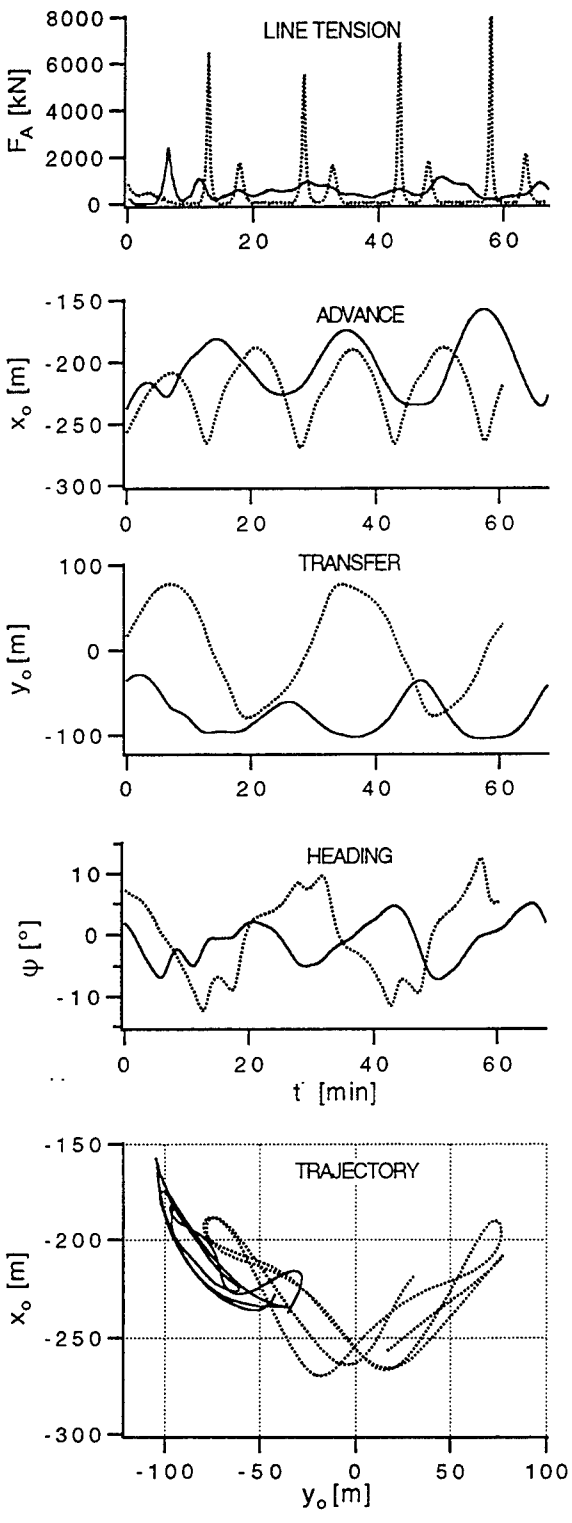

Fig. 17 Measured time histories of SPM tanker in shallow water with starboard (—) and symmetric (·····) fairlead

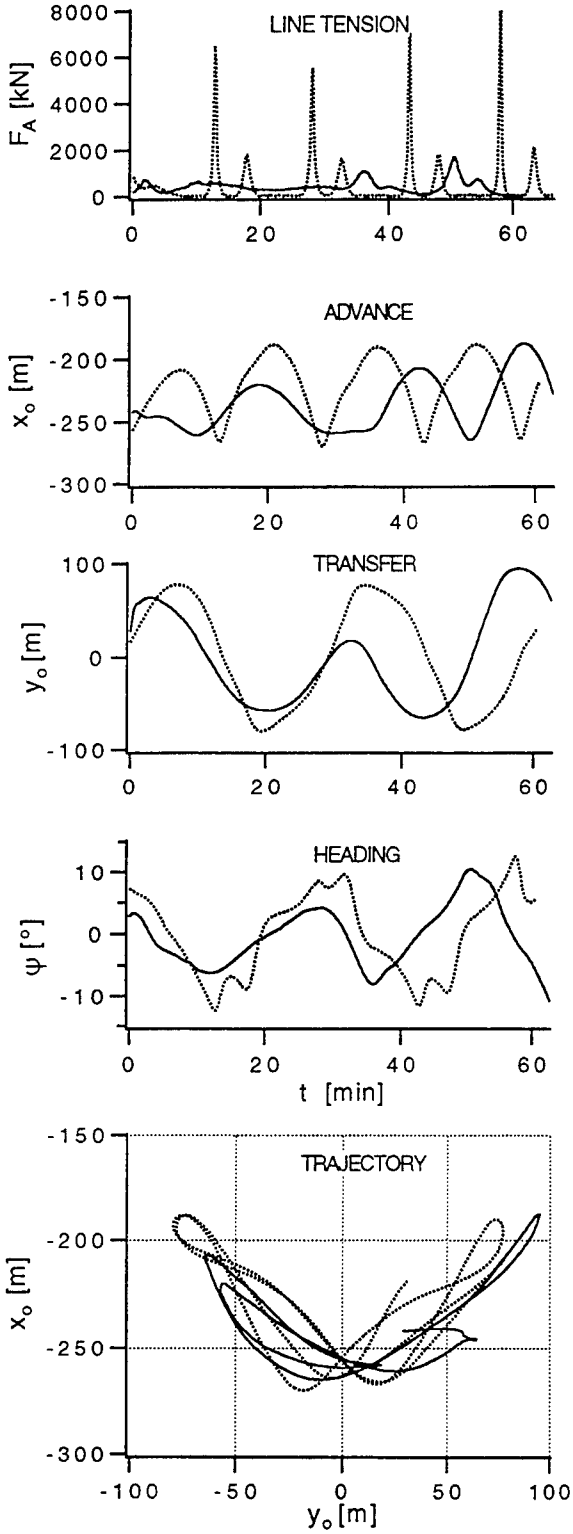

Fig. 18 Measured time histories of SPM tanker in shallow water, starting from two different initial conditions

ADDENDUM
CALCULATIONS FOR TANKER ESSO OSAKA

Parameter Identification

The basic input required for doing the necessary calculations for tanker ESSO OSAKA was a set of hydrodynamic coefficients constituting our so-called Four Quadrant Model of maneuvering. Fortunately, many of the coefficients were available from previous work at Hamburg (in deep water) and at Duisburg (in shallow water), see Oltmann et al.(1986). However, a closer scrutiny revealed that many of the coefficients, specially those for shallow water, needed verification or revision. Therefore, several additional PMM tests were conducted with a captive model of ESSO OSAKA (Scale 1:65) in the Duisburg tank. It turned out that a few of the more sensitive coefficients could not be definitively determined from force measurements alone and had to be adjusted by reference to trajectory measurements. Moreover, the experimentally determined hydrodynamic masses and damping coefficients were confirmed by comparison with theoretical calculations using the computer programm WAMIT acquired from Massachusetts Institute of Technology. The final values used for all calculations reported here are fully listed in Table 5.

Comparison with Measurements

All calculations were based on dynamic equations documented in our previous paper (1988b). Each calculation comprises: (i) Determination of equilibrium states, (ii) Local stability analysis, and (iii) Global time domain simulations. The parameter values of all cases studied here and associated equilibrium coordinates, line tension, and complex eigenvalue pairs governing local stability are compiled in Table 6.

Calculated time histories (dotted lines) are compared to corresponding measured time histories (solid lines) in Figs. 19 - 25. Initial values of coordinates were taken from model tests, with some adjustment of x_o-coordinate to ensure realistic line tension. Initial values of velocities were estimated by numerical differentiation of recorded coordinates.

Fig. 19 holds for deep water with no measures explicitly taken to stabilize the tanker. The instability identified by local stability analysis (see Table 6) is confirmed. Agreement between calculation and measurement is satisfactory, except that line tension is damped more strongly in experiment than in simulation. Fig. 20 holds for deep water with rudder applied. The intended stabilizing effect is confirmed both by experiment and by simulation. Fig. 21 also holds for deep water but now with reverse propeller action. Again the intended stabilizing effect is confirmed, although not as clearly in experiment as in simulation. A possible explanation may be that our mathematical model does not do full justice to the confused flow generated by the propeller

Table 5: System parameter values for four quadrant model of ESSO OSAKA in deep and shallow water (Symbols identical to those used by Oltmann and Sharma, 1984)

Parameters	$h/T = 3.0$	$h/T = 1.5$
Ideal Fluid Effects:		
$X''_{\dot{u}}$	-0.0693	-0.1400
X''_{vr}	0.5400	1.3000
X''_{rr}	0.0630	0.0630
X''_{vv}	0.0000	0.0000
$Y''_{\dot{v}}$	-1.0620	-2.0140
$Y''_{\dot{r}}$	-0.0240	-0.0480
$N''_{\dot{r}}$	-0.0570	-0.0790
$N''_{\dot{v}}$	-0.0240	-0.0480
Hull Lifting Effects:		
c	0.3860	0.8500
d	1.0000	1.0000
e	0.0895	0.0996
c'	0.5200	0.4000
d'	1.0000	1.0000
e'	0.1700	0.1500
k	0.4000	0.4000
Hull Cross-Flow Effects:		
a_0	0.9178	2.1410
a_7	1.3900	2.8000
a_8	1.8018	3.8410
a_9	-1.5000	-3.0000
Hull Resistance (Model Scale):		
R''_{Tu}	0.0018	0.0025
$R''_{\mathrm{Tu\|u\|}}$	0.0387	0.0240
R''_{Tuuu}	0.1173	0.3452
Interaction Factors:		
w (Model Scale)	0.6000	0.7000
t	0.1960	0.2430
$Y''_{\mathrm{PT}+}$	-0.0400	-0.0430
$N''_{\mathrm{PT}+}$	0.0294	0.0100
$Y''_{\mathrm{PT}-}$	0.1000	0.3300
$N''_{\mathrm{PT}-}$	-0.0500	-0.1000
k_{HR}	0.4000	0.3000
k_{PR}	0.8950	0.8950
Rudder Factors:		
k_{LR}	8.0000	12.5000
k_{DR}	3.7000	4.0000
k_{NR}	0.2000	0.2000
x''_{R}	-0.4700	-0.4700

Propeller Coefficients
$0 \le \epsilon \le 19.2°$
$C^*_{\mathrm{T}} = -0.630 + 0.815\cos\epsilon - 0.423\sin\epsilon$
$C^*_{\mathrm{Q}} = -0.101 + 0.122\cos\epsilon - 0.034\sin\epsilon$
$19.2° \le \epsilon \le 360°$
$C^*_{\mathrm{T}} = 0.126\cos\epsilon\|\cos\epsilon\| - 1.039\sin\epsilon\|\sin\epsilon\|$
$C^*_{\mathrm{Q}} = 0.018\cos\epsilon\|\cos\epsilon\| - 0.123\sin\epsilon\|\sin\epsilon\|$

Rudder Coefficients		
$\delta_{\mathrm{e}}[°]$	C°_{LR}	C°_{DR}
0	0.0000	0.0000
15	0.2083	0.0442
30	0.4034	0.1762
45	0.5547	0.2291
60	0.1952	0.2602
75	0.1146	0.2905
90	0.0340	0.3800

turning backward on a ship moving forward.

Fig. 22 holds for shallow water with no measures explicitly taken to stabilize the tanker. Again the instability identified by local stability analysis (see Table 6) is confirmed. Agreement between calculation and measurement is remarkable, including high peaks in line tension. Fig. 23 holds for shallow water with rudder applied. The intended stabilizing effect is confirmed both by experiment and by simulation. Fig. 24 also holds for shallow water but now with reverse propeller action. Once again the intended stabilizing effect is confirmed, although not as clearly in experiment as in simulation (see discussion of Fig. 21 above). Fig. 25 also holds for shallow water but now with fairlead offset to starboard. The intended stabilizing effect is weak but obviously present in both experiment and simulation.

Long-Term Behavior in Deep and Shallow Water

Fig. 26 compares calculated long-term time histories in deep and shallow water without use of explicit stabilizing measures, that is, extensions of previous Figs. 19 and 22 far beyond the range of experimental records, see also Fig. 12. The instabilities identified by local stability analyses are further confirmed. Note that motion amplitudes and line tensions are significantly higher in shallow water and that asymptotic behavior is qualitatively different: limit cycle in deep water versus strange attractor in shallow water.

Fig. 27 represents a further study of the strange attractor identified in Fig. 26. The two cases shown are for identical parameter values and initial conditions except for a difference of 0.0001° in the starting value of heading angle. Note that the time histories begin to diverge suddenly and unexpectedly after about 100 min, demonstrating long-term unpredictability characteristic of chaos.

Table 6: System parameter values of computer simulations for ESSO OSAKA shown in Figs. 19 - 26, including equilibrium states and complex eigenvalues from linear stability analysis (common parameters: $V_C = 2.0$ ms^{-1}, $L_{AU} = 78.0$ m)

Fig.	Case	x_A [m]	y_A [m]	δ [°]	n [rpm]	x_{oE} [m]	y_{oE} [m]	ψ_E [°]	F_{AE} [kN]	$\sigma_c \times 10^3$ [s^{-1}]
19	···	162.5	0	0	0	-251	5.1	0.3	377	0.19±i5.0
20	···	162.5	0	-35	0	-226	50.9	4.7	619	-0.36±i5.0
21	···	162.5	0	0	-20	-247	24.8	2.2	564	-0.21±i5.7
22	···	162.5	0	0	0	-252	14.0	0.4	425	1.04±i4.4
23	···	162.5	0	-35	0	-217	66.7	3.0	796	-0.25±i5.1
24	···	162.5	0	0	-30	-227	57.8	4.1	1159	-0.45±i6.3
25	···	139.8	18.2	0	0	-190	-90.1	-3.0	861	-0.22±i5.4
26	—	162.5	0	0	0	-251	5.1	0.3	377	0.19±i5.0
	···	162.5	0	0	0	-252	14.0	0.4	425	1.04±i4.4

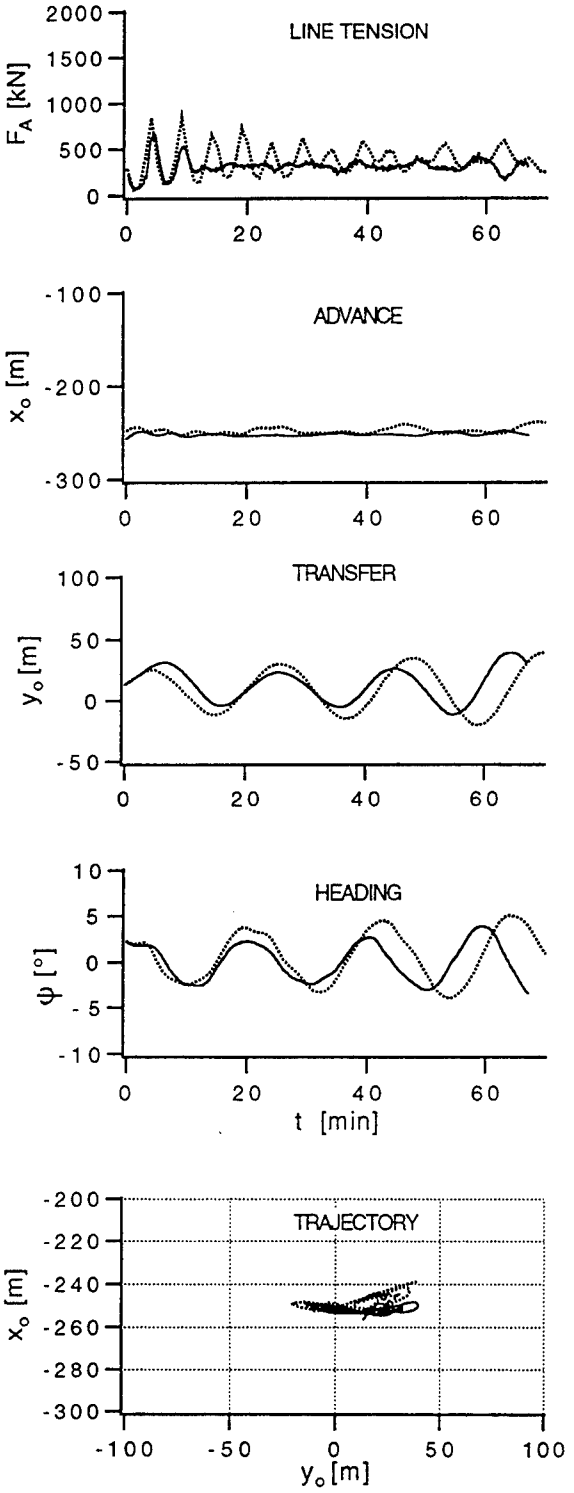

Fig. 19 Measured (—) and calculated (····) time histories of SPM tanker in deep water without explicit stabilizing measures

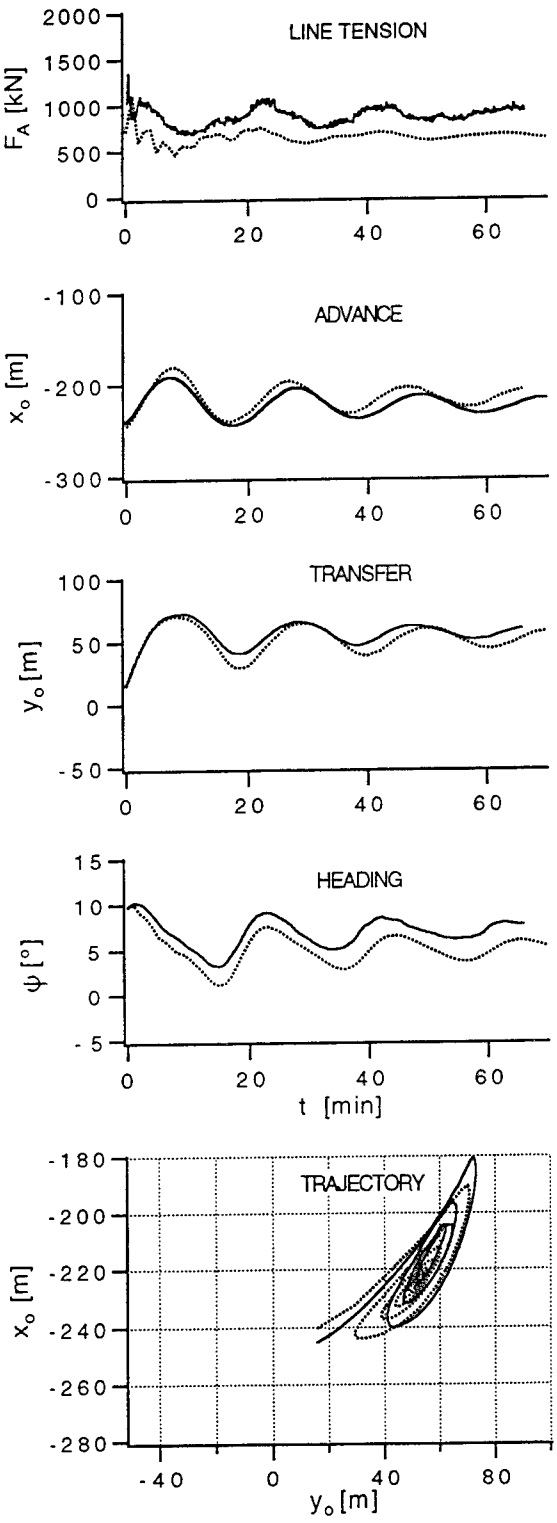

Fig. 20 Measured (——) and calculated (·····) time histories of SPM tanker in deep water with stabilization by rudder application

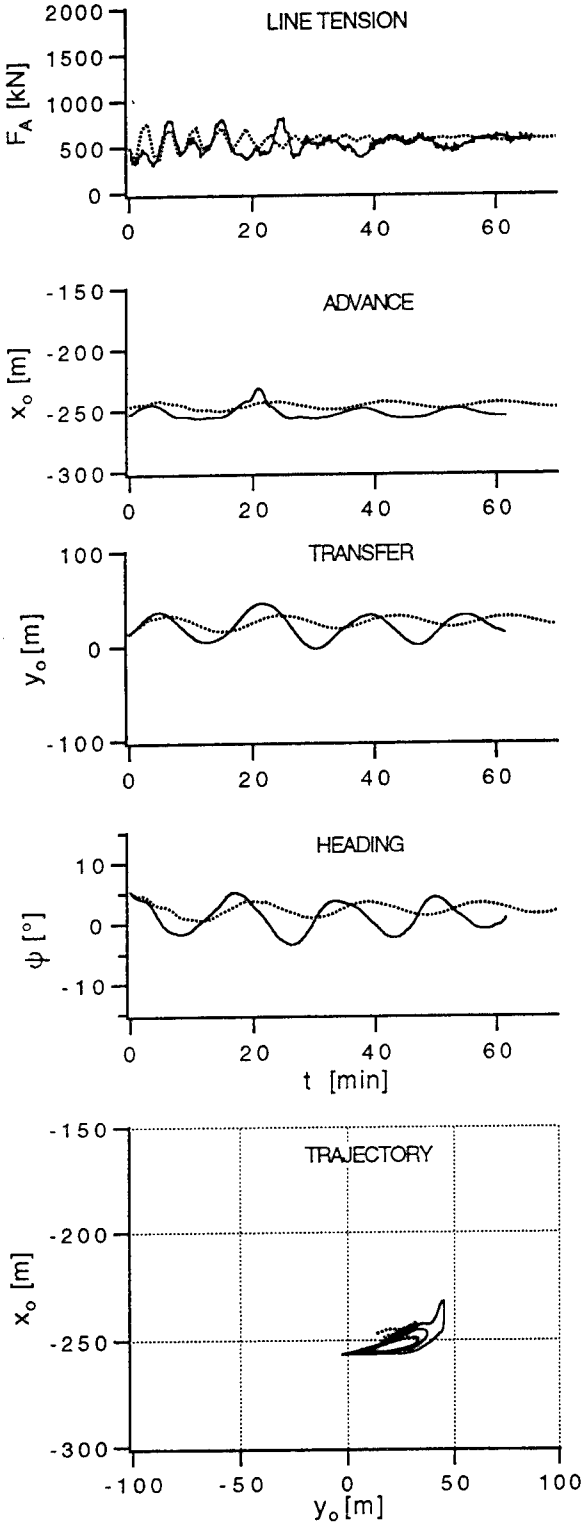

Fig. 21 Measured (—) and calculated (·····) time histories of SPM tanker in deep water with stabilization by reverse propeller action

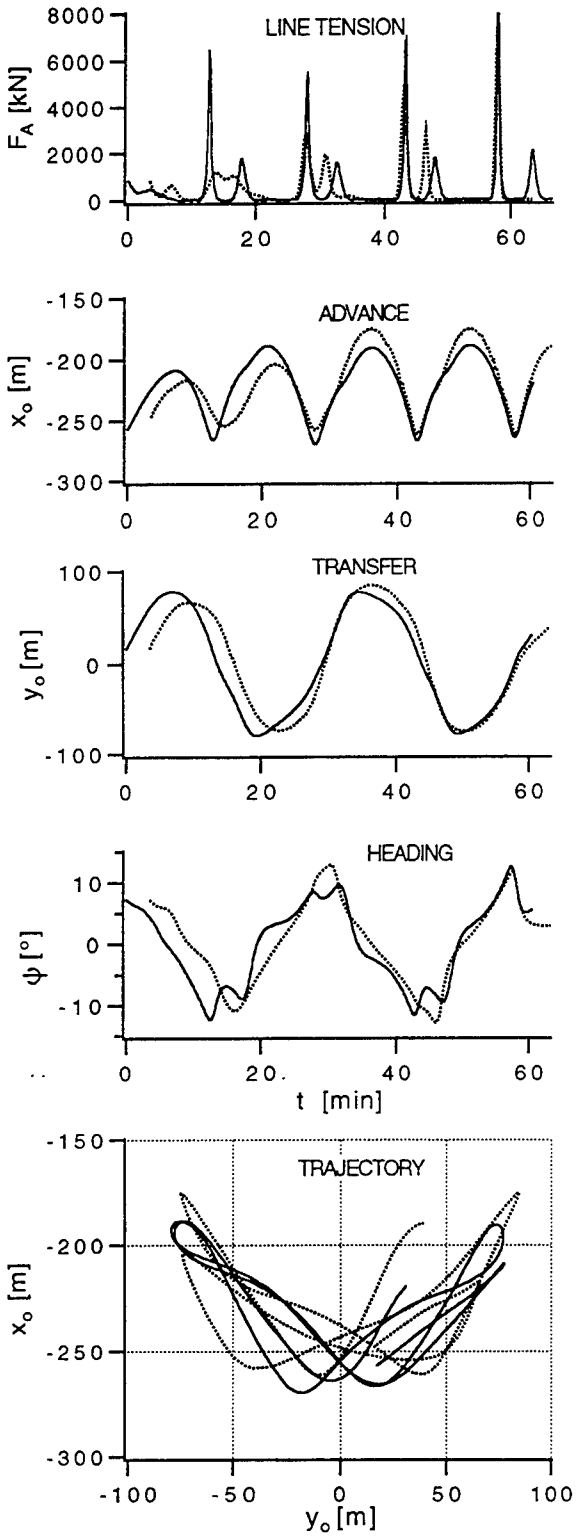

Fig. 22 Measured (—) and calculated (····) time histories of SPM tanker in shallow water without explicit stabilizing measures

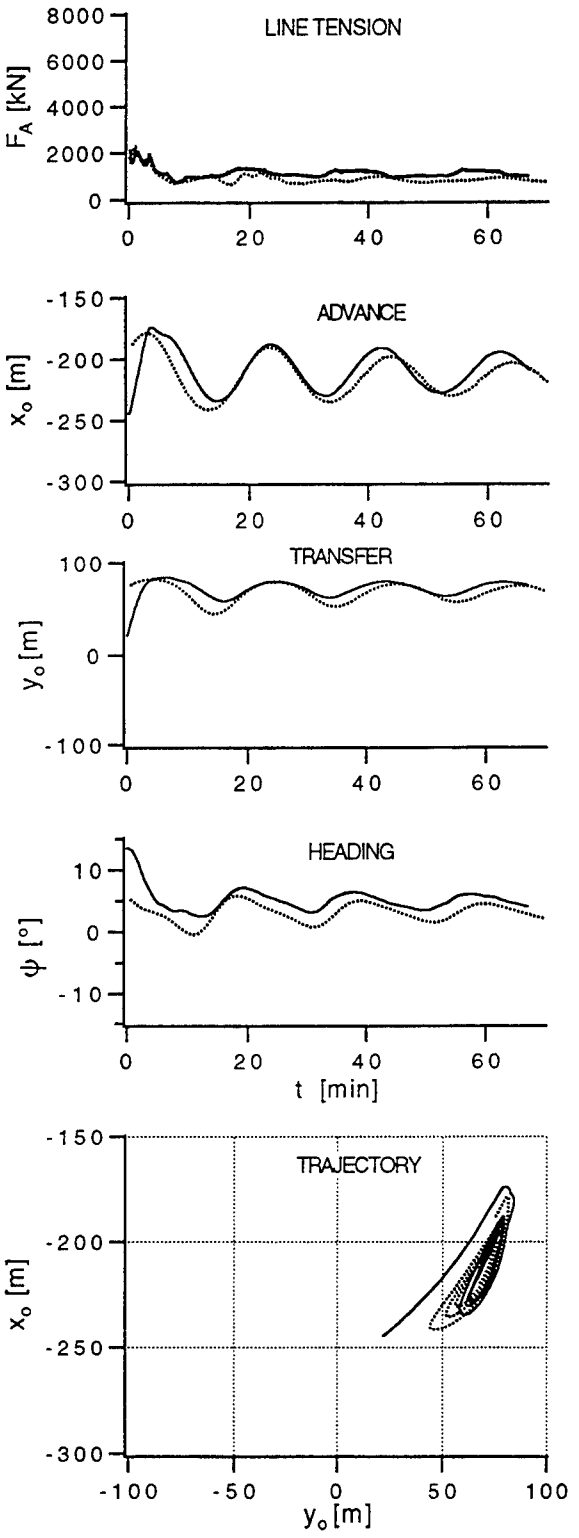

Fig. 23 Measured (—) and calculated (····) time histories of SPM tanker in shallow water with stabilization by rudder application

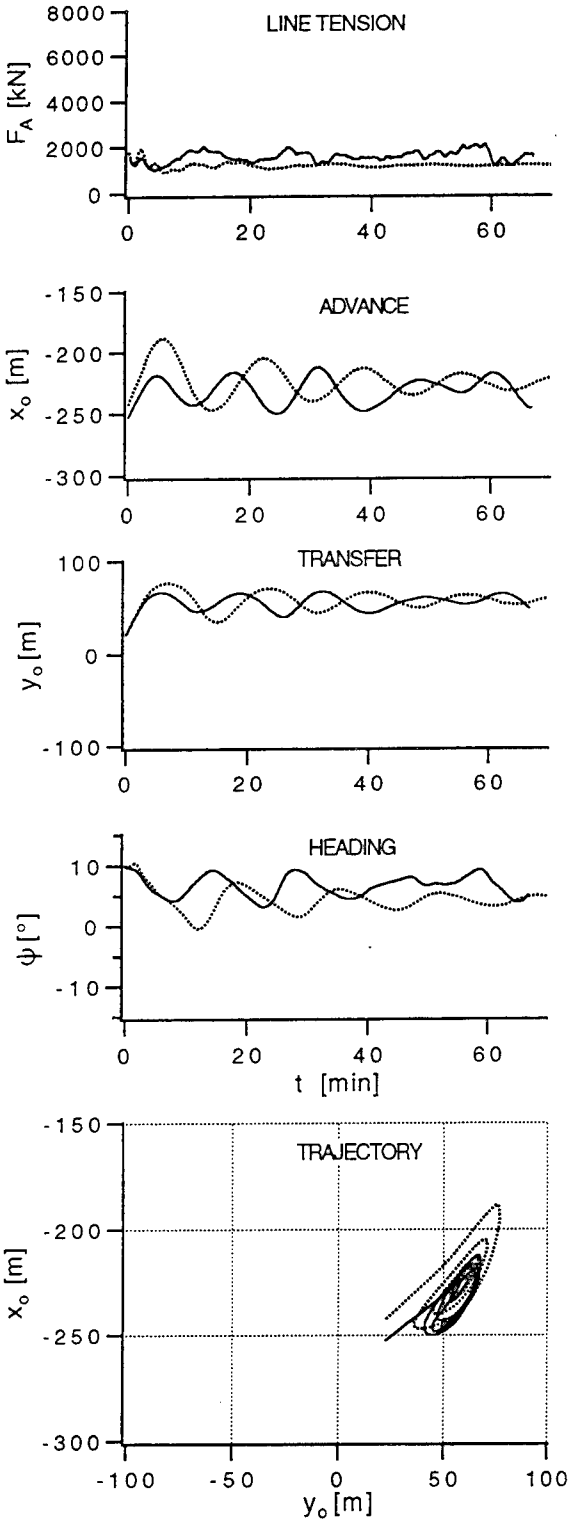

Fig. 24 Measured (—) and calculated (····) time histories of SPM tanker in shallow water with stabilization by reverse propeller action

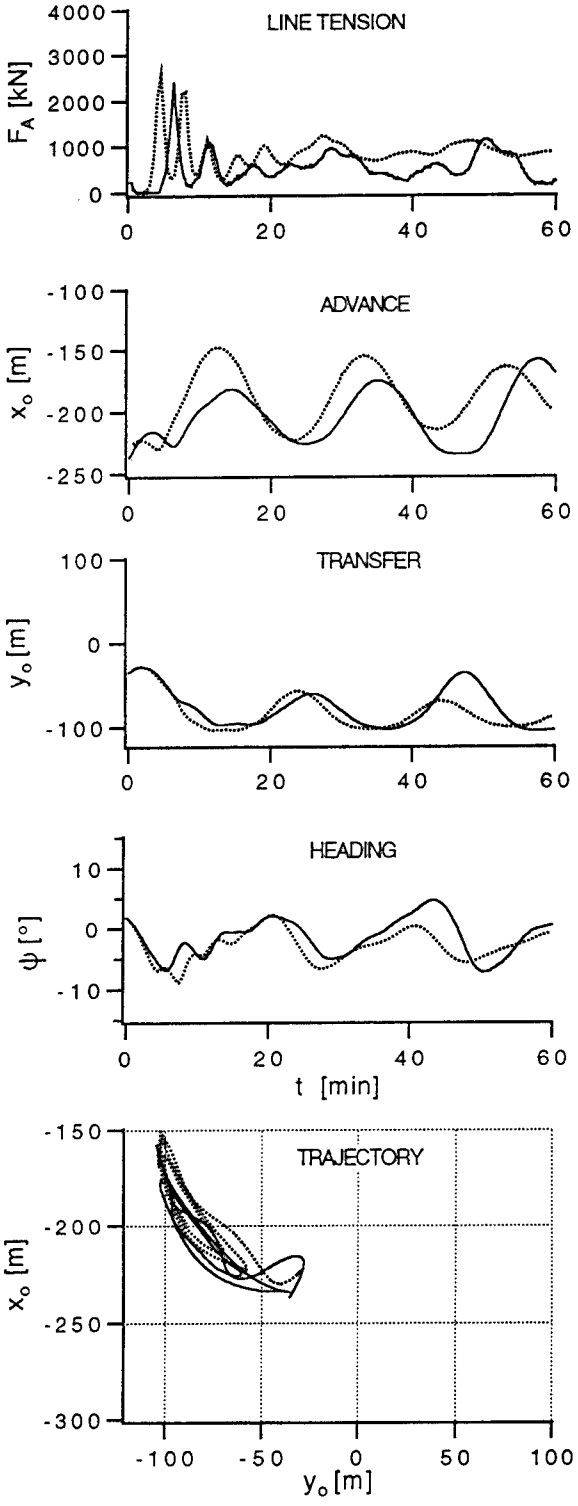

Fig. 25 Measured (—) and calculated (····) time histories of SPM tanker in shallow water with stabilization by fairlead offset to starboard

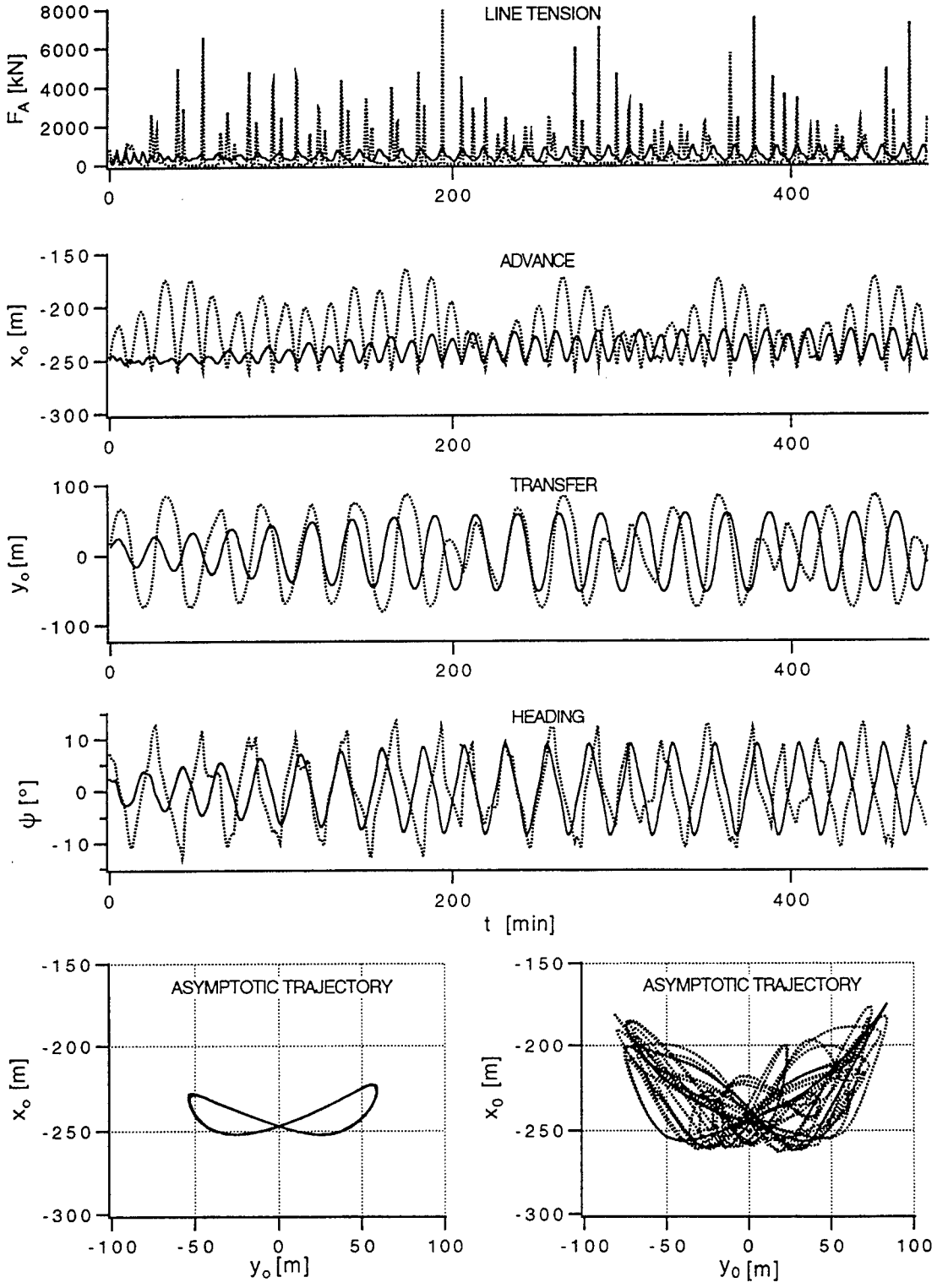

Fig. 26 Calculated long-term time histories of SPM tanker in deep (—) and shallow (·····) water without explicit stabilizing measures

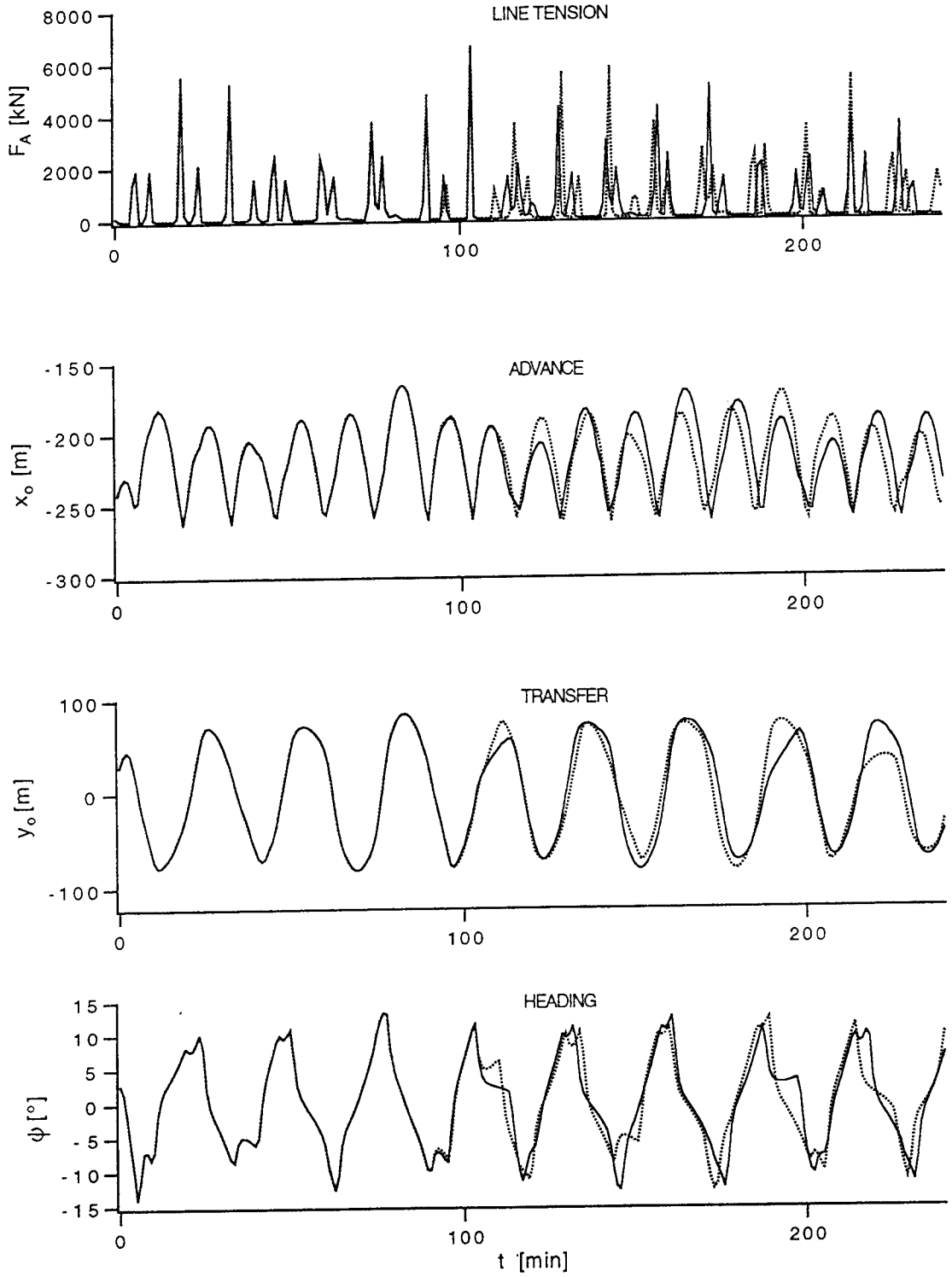

Fig. 27 Calculated time histories of SPM tanker in shallow water for the same parameter values as in Fig. 26, demonstrating extreme sensitivity of system response to initial conditions as evidence for chaos (the two cases shown differ only by 0.0001° in initial value of heading angle ψ)

DISCUSSION

T. Schellin
Germanischer Lloyd, Germany

The authors' previous work considered only theoretical prediction of horizontal motions of a single-point-moored tanker. Clearly, before theoretical results are used to derive practical recommendations for tanker operations, they should be validated by measurements. This has now been done, thereby generally confirming the various theoretically predicted phenomena, such as self-sustained oscillations, and associated stability states as well as the stabilizing effects of rudder deflection, asymmetric mooring, and reverse propeller rate. There is an additional parameter that concerns designers of turret mooring configurations, namely, the position of the mooring turret. Could the authors comment whether their results concerning asymmetric mooring are applicable to turret moored ships and, if so, what are the restrictions?

Although the presented experiments were performed with a model of a tanker different from that used for the theoretical investigations, its hull form was similar so that it seems fair to say that comparison of calculated trajectories for tanker TOKYO MARU were confirmed experimentally by model tests for tanker ESSO OSAKA. Naturally, for a convincing validation of the theory, strictly comparable numerical simulations for the tanker ESSO OSAKA are essential. Hopefully, the authors will be able to present results soon.

The paper represents a major step in that it deals with the practically relevant case of shallow water, especially since test results show that water depth had a significant influence on tanker motions with a tendency toward stronger instability in shallow water. This is of great interest as it relates to towing operations in estuary waters during a harbor approach and to emergency anchoring maneuvers of a tanker disabled in restricted waters. However, since it is known that there are scaling problems associated with the prediction of shallow water effects, it would be instructive if the authors could discuss the reliability of their predictions for full-scale operations in shallow water in more detail.

AUTHORS' REPLY

We thank Dr. Schellin, who is a renowned researcher in offshore mechanics, for his valuable comments and questions. Our response is as follows: (i) Having become sensitized to the phenomenon of small causes sometimes producing large effects in nonlinear systems, we hesitate to extrapolate from single-point mooring to turret mooring. Instead, we invite him to join us with his "knowhow" in a specific investigation of the dynamics of turret-moored ships. (ii) We concede that the Symposium deadline caught us in the midst of our transition from an older test tanker to a newer one. So, in the preprint we were forced to compare computer simulations for TOKYO MARU with tank experiments for ESSO OSAKA. But this inconsistency has now been corrected by our addendum. (iii) Our previous study for deep water had already indicated significant scale effects in the present problem. We agree that they may be even more important in shallow water, especially because, besides the usual Reynolds number discrepancy, the effect of a soft sea bottom in natural waters may also have to be considered. But in the present paper, all calculations and measurements are for model conditions only, including a hard tank bottom, although for ease of interpretation the results are presented for full-size ship by simple Froude scaling. We intend to pursue shallow water scale effects in subsequent work.

DISCUSSION

R. Latorre
University of New Orleans, USA

The unanticipated fishtailing of vessels moored to SPM installations in the 1970s resulted in attention given to the SPM analysis. With the use of available data, it is now possible to consider the behavior of the SPM in shallow water as the authors have done in their paper. I have a brief comment supporting the authors' experimental results.

Since the publication of the work of Charters et al (1985) cited by the authors, I have completed a number of studies on ship behavior in shallow water, Latorre (1992). I have performed a systematic study of the influence of shallow water on towed vessel trajectory in the towing tank. The results in Fig. A. indicate the towed vessel trajectory increases in both side excursion Y as well as towing length X transversed returning to centerline. Analysis has shown a rather consistent magnification of $1.5 < \gamma < 2.0$ where $\gamma = Y_{max}$ shallow water/Y_{max} deep water.

Looking at the authors' results for trajectory value Y_o of the ESSO OSAKA in Fig. 12. The magnification value of γ appears to be the same order. Our general conclusion is that it may be possible under some restrictions to be able to estimate the shallow water performance from deep water trajectory measurements.

Latorre, R., Developments at the University of New Orleans Towing Tank 1989-1992. Proceedings 23rd ATTC, New Orleans, June 11-12, 1992.

AUTHORS' REPLY

We are grateful for the corroborative evidence contributed by Prof. Latorre, a recognized authority on the related problem of towing stability including shallow water and canal effects. It is encouraging to observe that his experience with self-sustained oscillations of a towed ship agrees so well with ours. In shifting from water-depth to ship-draft ratio of 3.0 (which we call deep water) to 1.5 (which we call shallow water) the transverse excursions of the tanker in the unstable case are indeed magnified by about 50%. However, we would like to draw attention also to the qualitative difference in trajectory that might arise in shallow water as seen, for example, in our Fig. 26.

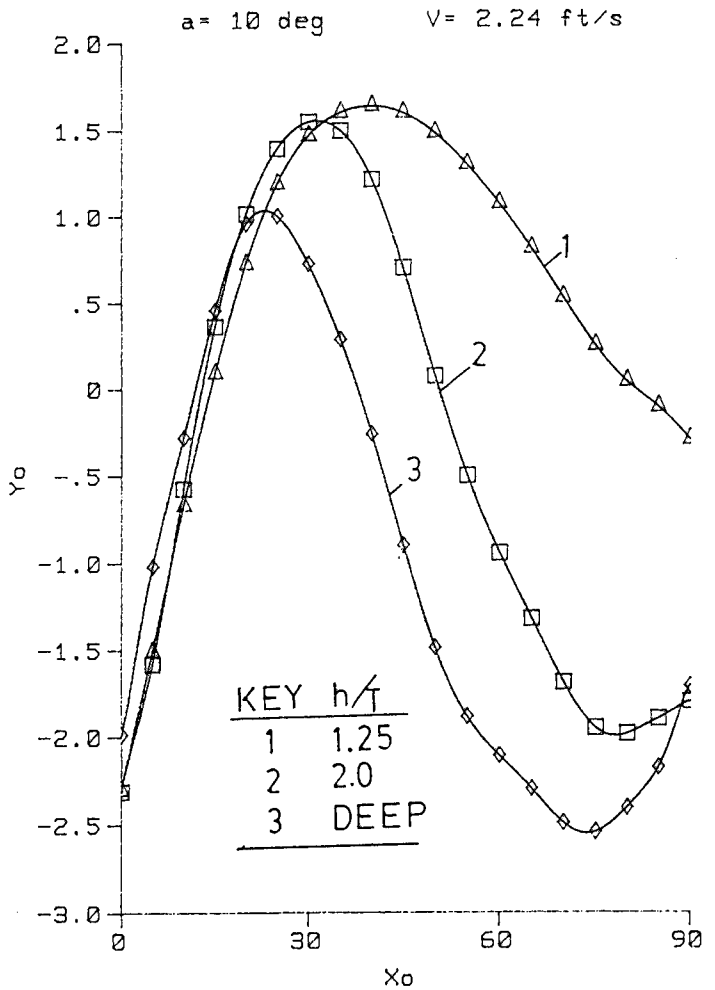

FIG. TOWED VESSEL TRAJECTORY

Design and Construction of the Long-Range High-Speed Foil-Catamaran Passenger Ship

K.-S. Min (Hyundai Heavy Industries Co., Ltd., Korea)

ABSTRACT

A study on the long-range high-speed foil-catamaran passenger ship design has been recently carried out for the open-sea service of 800 nautical miles round trip with top speed above 40 knots.

For the comfortability of passengers and crew, therefore, a great effort has been made to significantly improve the seakeeping quality in waves. The hydrofoil system, although adopted as an active motion control device, has been proved to be greatly beneficial to the improvement of resistance property too.

Extensive theoretical analyses and model tests were systematically carried out along the course of design for the system optimization and the verification. Extensive global and local structural analyses were also carried out simultaneously.

The ship is now under construction and it is expected to be completed by the end of August, 1992.

It is noted that this will be the first ship in the world for such a long-range open-sea service in this type and size of ships.

NOMENCLATURE

B	:	Mono Hull Beam
BR	:	Breadth of the Ship
C_B	:	Block Coefficient
C_F	:	Frictional Resistance Coefficient
C_M	:	Maximum Section Coefficient
C_P	:	Prismatic Coefficient
D	:	Depth of the Ship
d	:	Distance between Mono Hull Centerplanes
F_N	:	Froude Number
L	:	Ship Length in General or Total Lift from the Foil System
LCB	:	Longitudinal Center of Buoyancy
L_F	:	Lift by the Forward Foil
LOA	:	Length Over-All
LPP	:	Length between Perpendiculars
L_R	:	Lift by the Rear Foil
LWL	:	Length on Waterline
LWL/B	:	Length-Beam Ratio
LWL/T	:	Length-Draft Ratio
n_x	:	x-Component of the Unit Normal Vector on the Hull Surface
P	:	Pressure
R_F	:	Frictional Resistance
R_N	:	Reynolds Number
R_R	:	Residual Resistance
R_T	:	Total Resistance
R_W	:	Wave Resistance
S	:	Wetted Surface Area of the Mono Hull
T	:	Draft of the Ship
V	:	Ship Speed
∇	:	Underwater Volume of the Ship
$\triangle$	:	Total Displacement of the Ship
$\triangle_B$	:	Amount of Support by Buoyancy
λ, μ	:	Lagrangian Constant
ρ	:	Density of Sea Water
ϕ	:	Velocity Potential

1. INTRODUCTION

In response to the growing domestic request and the change of the overseas environment, our company has recently established a three-stage development plan for the high speed marine transportation system. The target of the first stage plan is the design and construction of the small high-speed passenger ship for the long-distance voyage with the capacity of more than 300 passengers.

In the beginning, some kinds of technical collaborations with experienced overseas organizations were seriously investigated. However, it has been realized that no suitable existing ships or designs were available for our purpose in the view points of endurance, seakeeping quality and structural reliability. As the result, the conclusion had been finally reached that it had to be developed by ourselves.

As the first step of the project, investigations were made for the selection of a proper ship type from the view points of seakeeping quality, resistance property and the possibility of increase in ship size. Along the

history, great efforts have been made by many naval architects to increase the ship speed. For the ships with conventional displacement type hull forms, however, it has been recognized that it is practically meaningless to try to increase the speed beyond a certain limit due to the rapid increase of wave resistance with the increase of ship speed.

In order to significantly increase the ship speed, therefore, it is necessary to prevent the rapid increase of wave resistance. This purpose could be achieved by at least two different ways. One way is to utilize the dynamic lift effect, and the other is to design the hull form of displacement type ships to be very fine. The hydrofoil boats and the surface effect ships together with the traditional planing hull ships are typical examples of the dynamic lift effect ships.

However, the dynamic lift effect ships have their own shortcomings. In general, they are less economical or poor in seakeeping quality. Furthermore, it is extremely difficult to increase the ship size beyond a certain limit, which may be regarded as the fatal disadvantage of this type of ships.

On the other hand, the hull form of catamaran ships could be made very fine so as to achieve the goal of high speed by preventing rapid increase of wave resistance. In fact, catamaran ships have attracted attention of naval architects due to many practical advantages such as large deck area, high stability, superior maneuverability, easy operation and maintenance, etc. However, the most noticable merit among many advantages is in the fact that ship size could be easily increased without any limitations and without sacrificing any other characteristics.

For this project ship, it is true that ship speed is one of the important design factors. However, the seakeeping quality is regarded as more important one for the comfortability of passengers and crew. Also, the possibility of the future increase of ship size should be seriously considered. From the overall view point, therefore, the conventional displacement type catamaran ship has been selected.

In this project, the design and the construction works are set to be progressed according to the following schedule :

- Conceptual Design and Initial Model Tests : From the middle of August to the end of December, 1990
- Model Tests for the Verification of the Performance Characteristic : From the beginning of January to the end of June, 1991
- Detail and Production Designs for the Actual Construction : From February, 1991
- Procurement of Hull Material : From June, 1991
- Commencement of Construction : From December, 1991
- Completion of Construction : End of August, 1992
- Sea Trial : From the end of August to the end of September, 1992

Due to the time limit, the author feels the lack of sufficient study or investigation. Considering such a short time and poor environment, however, the author is happy with the successful completion of the design work and the good progress in the construction.

In fact, the brief summary of the part of this work had been presented at the First International Conference on Fast Sea Transportation(FAST'91) held in Trondhein, Norway in June, 1991[1]*. However, the final configurations were not available at that time, since design work and test program had not been completed.

In this paper, the results of the theoretical and experimental studies, the final design configurations, and the status of the construction work shall be briefly summarized and discussed.

2. SELECTION OF THE MAIN DIMENSIONS

In the early stage of ship design, the most important and difficult task is the determination of main dimensions. To do this, the effect of variation in main dimensions on ship's overall performance characteristics should be systematically studied first. It should be pointed out that some characteristics may have more weight, of course. In any case, however, the basic requirements should always be satisfied. The basic requirements for this project are as follows :

- Number of passengers : not less than 300
- Endurance : not less than 800 nautical miles
- Service speed : not less than 35 knots

Due to the unusual requirement of such long voyage for this kind of ship, the seakeeping quality is considered to be more important than the speed quality.

The world-wide studies on the high speed displacement ship hull form have been actively carried out particularly from the middle of 1970's and valuable results have been obtained recently[2,3].

The results of recent studies could be briefly summarized as follows :

- The most important hull form design variable with respect to the seakeeping quality is the Length-Draft Ratio(LWL/T), and this ratio could be expressed as follows :

  $$LWL/T = (LWL/B) \cdot (B/T)$$

  Therefore, Beam-Draft Ratio(B/T) is also an important parameter for seakeeping. In general, the seakeeping quality is improved with the increase of this ratio.

- The most important hull form design variable with

* The numbers in brackets designate the numbers in references.

respect to the resistance property is the Length-Beam Ratio(LWL/B). In general, the resistance property is improved with the increase of this ratio.

- The block coefficient(C_B) does not have much effects either on the seakeeping quality or on the resistance property as long as it is within a certain range.

- There exist the ranges of the optimum prismatic coefficient(C_P), the maximum section coefficient(C_M) and the longitudinal center of buoyancy(LCB) for the given Froude Number(F_N).

Referring to the results of the world-wide studies, the initial selection on the main dimensions were made. However, they have been changed several times along the progress of the design work. Table 2.1 shows the changes of the main dimensions since the initial selection was made.

Table 2.1 Changes of Main Dimensions(in meters)

Items \ Version	I	IV	VII (Final)
LOA	35.0	45.0	45.5
LWL	32.5	42.0	42.0
Breadth	14.0	10.8	11.4
Mono Hull Beam	3.6	3.2	3.2
Distance between Mono Hull Centerlines	10.0	7.4	8.2
Draft	2.5	2.0	1.6
Depth	5.5	5.5	5.1

3. Hull Form Design

With the determination of the main dimensions, the hull form design work was started. Due to extremely tight time schedule, it was planned at first to immediately start the model tests after preparing 4 or 5 hull forms. However, it was decided to make use of this chance to perform the systematic theoretical and experimental studies on the hull form design of such high speed ships as much as possible even if a considerable amount of time and effort were spent.

In preparing basic hull forms, although not all of the cases, but generally the fore-body and the aft-body hull forms were designed separately and combined later to form a complete one. Particularly, the fore-body forms were prepared utilizing "the Wave Resistance Theory of Catamaran Ships" and "the Catamaran Hull Form Design by the Minimum Resistance Theory" developed by the author[4].

3.1 Fore-Body Hull Form

According to the traditional resistance theory, the total resistance of a ship could be expressed by the sum of frictional resistance and residual resistance as below:

$$R_T = R_F + R_R \qquad (1)$$

For such fine high-speed ships as considered in this project, however, residual resistance may be safely replaced by wave resistance, that is,

$$R_T \simeq R_F + R_W \qquad (2)$$

The basic concept and the design procedure could be summarized as follows :

- express each of resistance components in suitable form introducing proper assumptions.

- represent the hull form by the hull form equation with unknown coefficients.

- solve the unknown coefficients so that the total resistance, i.e., the sum of frictional resistance and wave resistance becomes minimum.

Particularly, the hull form with minimum wave resistance becomes to be longitudinally symmetric shape according to potential theory [5]. In practice, therefore, the fore-body hull form is obtained by first deriving longitudinally symmetric form with minimum total resistance whose length is two times of that of the entrance part, then by utilizing one-half of that form. In this project, however, the one-half of the derived form could be directly utilized as a complete form in many cases.

In order to present the ship body and the fluid motion around it, the general coordinate system has been introduced as shown in Figure 3.1.

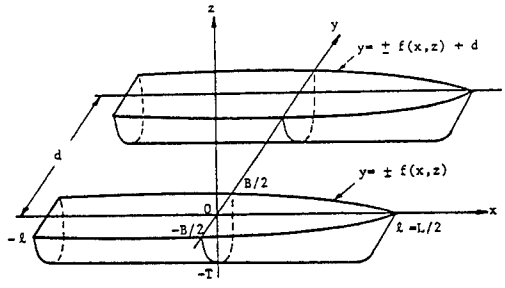

Fig. 3.1 General Coordinate System

3.1.1 Frictional Resistance

For frictional resistance, the traditional assumption has been introduced that the frictional resistance coefficient(C_F) is constant with the constant Reynolds Number(R_N). With this assumption, therefore, the least frictional resistance results from the least wetted surface area when ship length is fixed.

The frictional resistance(R_F) for catamaran ships is expressed as :

$$R_F = 2 \times \frac{1}{2} \rho S C_F V^2 \quad (3)$$

The exact expression for the mono hull wetted surface area is as follows :

$$S = 2 \int \int \sqrt{1 + f_x^2 + f_z^2} \, dx \, dz \quad (4)$$

Since the ship form is very fine, however, the following approximate expression of wetted surface area has been utilized in this study for the sake of convenience and consistancy with the expression of wave resistance :

$$S \simeq 2 \iint [1 + 1/2(f_X)^2 + 1/2(f_Z)^2] \, dx \, dz \quad (5)$$

The frictional resistance coefficent is determined from the 1957 ITTC correlation line as follows :

$$C_F = \frac{0.075}{(\text{Log } R_N - 2)^2} \quad (6)$$

3.1.2 Wave Resistance

It is well-known fact that present state-of-art on the wave-making resistance theory is such that theory itself is not sufficient and, hence, not generally used to obtain numerical predictions of wave resistance, although the result (obtained from the theory) is not grossly error. Nevertheless, it is still useful to qualitatively investigate the effect of hull form on wave resistance, and hence, could be well utilized in design problem instead of performance analysis problem. In this study, the wave resistance equation based on the linearized potential theory has been utilized.

Wave resistance is conceptually determined by integrating x-component of pressure over the entire underwater hull surface, i.e.,

$$R_W = \iint_S P \, n_x \, ds \quad (7)$$

From the linearized Bernoulli equation in this case,

$$P = - \rho \phi_t = - \rho V \phi_x \quad (8)$$

and equation (7) becomes,

$$R_W = - \rho V \iint_S \phi_x \, n_x \, ds \quad (9)$$

In order to derive the expression for wave resistance, therefore, the velocity potential of the steadily moving source under free surface should be obtained first by solving the Free Surface Boundary Value Problem. For this purpose, some basic assumptions concerning the fluid motion and the linearized wave should be introduced. Due to limited space, however, they will not be discussed here.

Seek the form of solution as :

$$2\pi \phi(\vec{x}) = \iint (G \frac{\partial \phi}{\partial n} - \phi \frac{\partial G}{\partial n}) \, ds \quad (10)$$

where $G(\vec{x};\vec{\xi})$ is the Green's Function, $\vec{x}=(x,y,z)$ and $\vec{\xi}=(\xi,\eta,\zeta)$ represent field and source points, respectively.

Green's Function should satisfy the following Boundary Value Problem :

- Governing Equation : $\nabla^2 G = 0$ for $Z < 0$
- Free-Surface Condition : $G_{xx} + kG_z = 0$ on $Z = 0$ $(k = g/v^2)$
- Radiation Condition : $\lim_{r \to \infty} [G_x^2 + G_y^2 + G_z^2] = 0$
- Bottom Condition : $\lim_{z \to -\infty} G_z = 0$, or $G_z(x,y,-h) = 0$

(11)

The Green's Function for infinite depth satisfying the above Boundary Value Problem can be expressed as [5,6] :

$$G(\vec{x};\vec{\xi}) = \frac{1}{r} + \frac{1}{r'} + \frac{4g}{v^2} \int_0^{\pi/2} d\theta \int_0^{\infty} dK \, e^{K(z+\zeta)} \times \times \frac{\cos[K(x-\xi)\cos\theta)] \cdot \cos[K(z-\zeta)\sin\theta]}{K\cos^2\theta - g/v^2} + \frac{4g}{v^2} \int_0^{\pi/2} d\theta \, \sec^2\theta \, e^{g/v^2(z+\zeta)\sec^2\theta} \times \times \sin[\frac{g}{v^2}(x-\xi)\sec\theta] \cdot \cos[\frac{g}{v^2}(z-\zeta)\sin\theta\sec^2\theta] \quad (12)$$

The first derivative of Green's Function for infinite depth satisfying the Boundary Value Problem can be expressed as follows after eliminating non-contributing terms [5,6] :

$$G_x(\vec{x};\vec{\xi}) = \frac{4g^2}{v^4} \int_0^{\pi/2} d\theta \, \sec^3\theta \, e^{g/v^2(z+\zeta)\sec^2\theta} \times \times \cos[\frac{g}{v^2}(x-\xi)\sec\theta] \cdot \cos[\frac{g}{v^2}(z-\zeta)\sin\theta\sec^2\theta] \quad (13)$$

In case of the catamaran ship composed of two identical hulls as shown in Figure 3.1, the centerplane of one hull coincides with x,z-plane with y=0 and that of another hull coincides with x,z-plane with y=d. In this case, the wave resistance on one hull will be generated by its own and the influence of the other one. Therefore, the velocity potential, and hence, the first derivative of Green's Function in x-direction should satisfy the boundary condition on the body surface, that is :

$$G_x = G_x\Big|_{\substack{y=0 \\ \eta=0}} + G_x\Big|_{\substack{y=d \\ \eta=0}} \quad (14)$$

Here, the first term of the right-hand side is related to the quantity generated by its own hull and the second term is related to that generated by the influence from the other one.

The precise expression is as follows :

$$G_x\Big|_{\substack{y=0\\ \eta=0}} = \frac{4g^2}{v^4}\int_o^{\pi/2} d\theta \sec^3\theta\ e^{g/v^2(z+\zeta)\sec^2\theta}\cos\left[\frac{g}{v^2}\right.$$
$$\left.(x-\xi)\sec\theta\right] \qquad (15)$$

$$G_x\Big|_{\substack{y=d\\ \eta=0}} = \frac{4g^2}{v^4}\int_o^{\pi/2} d\theta \sec^3\theta\ e^{g/v^2(z+\zeta)\sec^2\theta}\cos\left[\frac{g}{v^2}\right.$$
$$\left.(x-\xi)\sec\theta\right]\cos\left[\frac{g}{v^2}\, d\cdot\sin\theta\sec^2\theta\right] \qquad (16)$$

For the first approximation,

$$\phi = \frac{1}{2\pi}\iint_{S_o} G\,\frac{\partial\phi}{\partial n}\,ds \qquad (17)$$

$$\frac{\partial\phi}{\partial n} = \pm\frac{\partial\phi}{\partial y} = \pm V f_x \qquad (18)$$

$$n_x = f_x \qquad (19)$$

where, S_o represents centerplane.

Combining the above, the following results are obtained :

$$\phi_x = -\frac{V}{2\pi}\iint_{S_o} G_x(x,y,z;\xi,\eta,\zeta,)f_x(\xi,\zeta)d\xi d\zeta$$
$$= -\frac{V}{2\pi}\iint_{S_o}\frac{4g^2}{v^4}\int_o^{\pi/2} d\theta\sec^3\theta\ e^{g/v^2(z+\zeta)\sec^2\theta} \qquad (20)$$
$$\cos\left[\frac{g}{v^2}(x-\xi)\sec\theta\right]\left[1+\cos\left(\frac{g}{v^2}\, d\cdot\sin\theta\sec^2\theta\right)\right]$$

Finally, the wave resistance equation on one hull of the catamaran ship is obtained by substituting equation (20) into equation (9) :

$$\frac{1}{2}R_w = \frac{4\rho g^2}{\pi v^2}\iint_{S_o} dxdz\iint_{S_o} d\xi d\zeta f_x(x,z)f_x(\xi,\zeta)\times$$
$$\times\int_o^{\pi/2} d\theta\sec^3\theta\ e^{g/v^2(z+\zeta)\sec^2\theta}\cdot\cos\left[\frac{g}{v^2}\right. \qquad (21)$$
$$\left.(x-\xi)\sec\theta\right]\left[1+\cos\left(\frac{g}{v^2}d\cdot\sin\theta\sec^2\theta\right)\right]$$

If $\sec\theta$ is replaced by cosh u for the sake of convenience in integration and if overall catamaran ship is considered, then :

$$R_w = \frac{8\rho g^2}{\pi v^2}\int_o^{\infty} du\,\cosh^2 u\,[P^2(\cosh u) +$$
$$+ Q^2(\cosh u)]\,[1+\cos(\frac{g}{v^2}\, d\cdot\sinh u\cdot\cosh u)]$$
$$= R_s + R_I \qquad (22)$$

$$\left.\begin{matrix}P(\cosh u)\\ Q(\cosh u)\end{matrix}\right\} = \iint_{S_o} dxdz f_x(x,z)\cdot e^{g/v^2(\cosh^2 u)z}$$
$$\left\{\begin{matrix}\cos\\ \sin\end{matrix}\right\}\left(\frac{g}{v^2}\, x\,\cosh u\right) \qquad (23)$$

In equation(22), the first integral, Rs, represents the contribution from two independent single hulls and the second integral, R_I, represents the contribution from the interaction between two hulls. The following important facts could be deduced from equation(22) that :

- R_s depends on ship speed and ship form, while R_I depends on ship speed, ship form and separation ratio.
- R_s is always positive and can never be negative.
- R_I is either positive or negative. This implies the possibility to have favorable interactions depending on ship speed and separation.
- As ship speed increases, the interaction effect decreases, and finally there will be no interaction at very high speed.

The above important results from the theoretical study have been proved to be true by model experiments later.

3.1.3 Mathematical Expression of the Hull Form (Hull Form Equation)

As the next step to find out the ship form with minimum resistance, proper hull form equation(s) should be introduced to describe the hull shape mathematically. Such equation(s) should be not only able to describe the actual hull forms nicely, but also as simple as possible so that future mathematical treatment is possible. However, it is by no means easy to express the complicated hull forms nicely by a simple equation. For this purpose, therefore, the author has long adopted the separation of variable type equations. In other words, the hull forms are represented by a product of two functions as follows :

$$y = \pm f(x,z) = \pm X(x)\cdot Z(z) \qquad (24)$$

where X(x) and Z(z) represent waterline and body plans, respectively.

In order to derive the overall-optimized hull form, both waterline and body plans should be represented by proper equations containing unknown coefficients and the resistance equation should be solved for the unknown coefficients by the three-dimensional optimization technique.

However, it would take enormous effort and time, and almost impossible to carry out the necessary work within the limited time schedule for this project. Therefore, only one polynomial with unknown coefficients were adopted for the expression of waterline plan. The body plan was assumed to be one of four fixed shapes, and two-dimensional optimization technique was applied.

The hull form equations adopted in this study are as follows :

Waterline plan

$$X(x) = A_o + A_1|x| + A_2x^2 + A_3|x^3| + A_4x^4 \qquad (25)$$

Body plan

$$Z(z) = (1 + \bar{z})^2 \quad : \text{Concave type} \qquad (26\text{-a})$$
$$= 1 + \bar{z} \quad : \text{Straightline type} \qquad (26\text{-b})$$
$$= 1 - \bar{z}^2 \quad : \text{Parabolic type} \qquad (26\text{-c})$$
$$= \sqrt{1 - \bar{z}^2} \quad : \text{Elliptic type} \qquad (26\text{-d})$$

where $\bar{z} = z/T$.

Boundary conditions

$$X(\pm\ell) = 0$$
$$X(0) = B/2$$
$$X'(0) = 0$$
$$Z(0) = 1$$
$$Z(-T) = 0$$
$$2\int_{-\ell}^{\ell}\int_{-T}^{0} X(x)\cdot Z(z)dx\,dz = \nabla$$

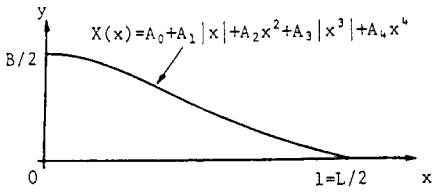

where A_i and ℓ denote the unknown hull form coefficients and one-half of ship length, respectively.

From the boundary conditions $X(0) = B/2$ and $X'(0) = 0$, the equation for the waterline plan is simplified as follows :

$$X(x) = \frac{B}{2}(1 + a_2 x^2 + a_3 |x^3| + a_4 x^4) \qquad (27)$$

where a_i's are the modified unknown coefficients.

3.1.4 Optimization Problem

In order to find the optimum set of coefficients in the hull form equation, Lagrangian Multiplier Method has been applied with proper constraints and constants as follows :

$$f_1 = R_T \quad : \text{Total resistance}$$
$$f_2 = f(a_i)=0 \text{ at } x=\ell \quad : \text{Boundary condition}$$
$$f_3 = 2\int_{-\ell}^{\ell}\int_{-T}^{0} X(x)\cdot Z(z)\,dx\,dz - \nabla = 0 \quad : \text{Fixed volume}$$
$$T(a_i, \lambda, \mu) = f_1 + \lambda f_2 + \mu f_3$$

where,

T = Lagrangian function (not ship draft)
a_i = unknown coefficients
λ, μ = Lagrangian constants

If partial differentiation of Lagrangian function is performed with respect to the unknown coefficients and the unknown constants, and the partial derivatives are set to be zero as shown below, then a system of linear equations for the unknown coefficients and the unknown constants is obtained :

$$\frac{\partial T}{\partial a_i} = 0$$
$$\frac{\partial T}{\partial \lambda} = 0$$
$$\frac{\partial T}{\partial \mu} = 0$$

The constants and the coefficients are obtained by solving the linear system.

3.2 Aft-body Hull form

Different from the fore-body area, much more space is needed at the aft-body area, and hence, the aft body hull form becomes much fuller than the fore-body hull form.

In this study, two different types of aft-body (non-reduced and reduced transom types) had been tried for each of three different section shapes, that is, straightline, parabolic and elliptic shapes. Figure 3.2 shows the section shapes and their combinations utilized for the systematic preparation of hull forms.

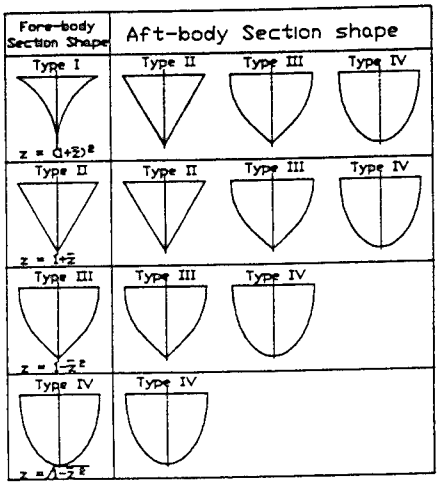

Fig. 3.2 The Section Shapes of the Fore-body and the Aft-body Hull Forms and their Combinations

3.3 Connection of the Fore-body and the Aft-body

In the case that the fore-body and the aft-body section shapes are identical, they are smoothly connected by nature. When they are different, however, the connection work has to be done.

The connection process has been arranged to be done using third order polynomial maintaining sufficient distance between two connection points not only so that both parts are connected very smoothly without any abrupt change in the section shape, but also so that the hydrostatic characteristics of the resulted hull form are not much different from those of initial target. Figure 3.3 shows this connection process schematically.

In practice, the relative difference between the block coefficients after connection and the target value

has been arranged to be greater than - 0.5% and less than 1.0%, that is,

$$0.995 < (C_B) \text{ actual } / (C_B) \text{ target } < 1.01$$

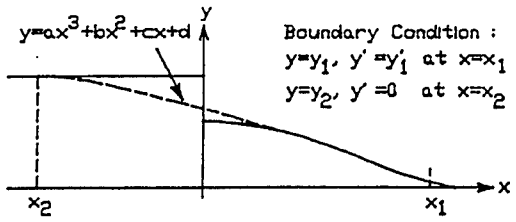

Fig. 3.3 Schematic Description of the Connection Process

3.4 Hull Forms

3.4.1 Initial Hull Forms

Before the actual design of hull forms, total 38 combinations of fore- and aft-parts were prepared and their practicability was investigated. Some of them were proved to be unpractical due to unsatisfaction of volume or LCB requirements.

Finally, 31 hull form combinations were chosen for the hull form design. These hull forms are called "the Initial Hull Forms". Figure 3.4 shows the 31 mono hull models of 31 initial hull forms.

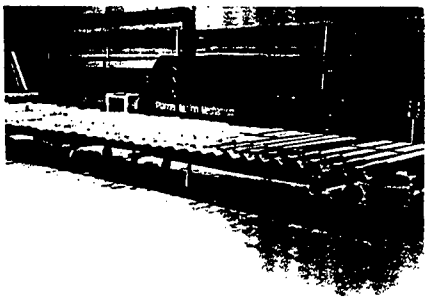

Fig. 3.4 Thirtyone(31) Initial Hull Form Models

3.4.2 The First Intermediate Hull Form

Originally, it was planned to choose about two(2) intermediate hull forms from 31 initial ones. Since more than half of the initial hull forms showed very similar resistance property, however, eight(8) intermediate hull forms were selected instead of two(2). The eight(8) selected hull forms are called "the First Intermediate Hull Forms", since one more intermediate hull form selection process was expected.

Also, there had been some changes in main characteristics such as lightship weight along the progress of design work. Therefore, these hull forms were prepared first by selecting superior hull forms from the test results and next by modifying them incorporating those changes. Figure 3.5 shows the mono hull models of the eight(8) selected hull forms.

Fig. 3.5 Eight(8) First Intermediate Mono Hull Models

3.4.3 The Second Intermediate Hull Form

The resistance and the trim control flap effectiveness tests were carried out for the eight(8) first intermediate hull form models, and two(2) second intermediate hull forms were selected based on the test results. Up to the first intermediate steps, only the mono hull forms were designed and tested. From the second intermediate steps, however, the complete catamaran hull forms were designed, models were constructed and tested as well as mono hull forms.

Figure 3.6 shows the catamaran models of these two(2) hull forms.

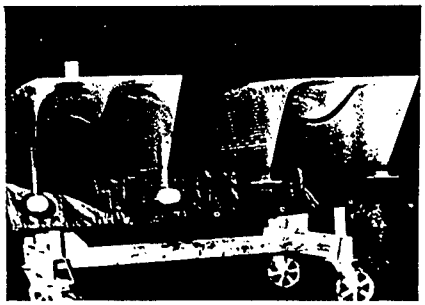

Fig 3.6 Catamaran Ship Models for the Second Intermediate Hull Forms

From the second intermediate hull forms, the model tests were carried out at both HMRI* and HSVA**, independently. Also, the tests were carried out not only for the resistance characteristics, but also for the seakeeping and the effect of motion control devices.

3.4.4 The Semi-Final Hull Form

After conducting the resistance, seakeeping and the effect of motion control device tests for two(2) second intermediate hull forms, one(1) hull form was selected based on the results of the overall evaluations.

* Hyundai Maritime Research Institute

** Hamburgische Schiffbau Versuchs Anstalt (Hamburg Ship Model Basin)

The selected hull form had the parabolic section shape both for the fore- and aft-bodies. Therefore, the bottom of the ship was a little bit sharp instead of flat or rounded. In fact, this hull form was going to be selected as the final hull form, and hence, the extensive theoretical analyses and model tests were carried out for this hull form.

However, the hull form had been finally revised due to the request from the Special Ship Department who was responsible for the actual construction. It was considered that the installation of the water inlet duct to the water-jet might be difficult for the section shape with sharp bottom.

The revised hull form had the elliptic section shape, and it was decided to call this hull form as "the Semi-Final Hull Form". Extensive theoretical analyses and model tests for the resistance and seakeeping characteristics were carried out again for this semi-final hull form.

3.4.5 The Final Hull Form

Basically, there are not much differences between the semi-final and the final hull forms. They have the same section shape. As the design work approached to the final stage, however, various initial estimations became to be clear, and hence, main characteristics also had to be modified. Incorporating all those up-to-dated information, the final hull form was re-designed.

The Figure 3.7 shows the catamaran ship model of the final hull form.

Fore - Body

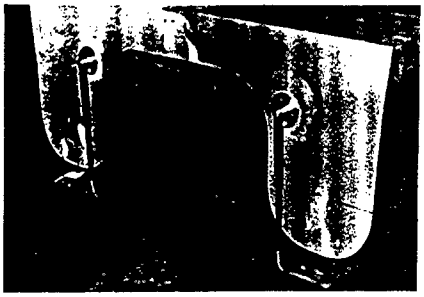

Aft - Body

Fig. 3.7 Catamaran Ship Model of the Final Hull Form with the Final (No.9) Foil System

4. MOTION CONTROL DEVICES

For the small-size high-speed catamaran ships, the motion in waves, particularly the vertical motion of bow is intrinsic and unavoidable unless ship size is much increased, and hence, there is an limitation in the improvement of motion characteristics purely by the proper selection of main dimensions and by the superior hull form design. In order to significantly improve the seakeeping quality, therefore, it is necessary to introduce some motion control devices.

Among control devices, an active control system would produce more significant effect. However, active systems also have disadvantages, that is, the system is more complicated, consumes more energy and requires higher costs for installation and maintenance. In this study, therefore, it had been tried to adopt the simplest-possible fixed control system as long as the final motion characteristics fell within the target range.

Following this design philosophy, three different motion control devices, that is, so-called motion control plate and motion control tank as the passive control device, and motion control hydrofoil as the active control device were decided to be tried individually and in combination. In fact, the passive control systems may be more accurately expressed by "Anti-Pitch Devices" rather than motion control ones. Therefore, the term of Anti-Pitch Plate and Anti-Pitch Tank may be used for the passive control devices.

4.1 Anti-Pitch Plate

This is nothing but the flat plate with simple shape as shown in Figure 4.1.

In this study, six(6) different plates in size and shape as shown in Table 4.1 were applied on each of mono hulls, and model tests were conducted for resistance and ship motion.

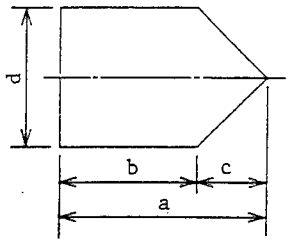

Fig. 4.1 Sketch of an Anti-Pitch Plate

Table 4.1 Six(6) Different Anti-Pitch Plates (All dimensions in meters)

No	a	b	c	d
1	3.0	2.0	1.0	1.6
2	4.5	3.0	1.5	2.4
3	6.0	4.0	2.0	3.0
4	3.0	2.0	1.0	2.0
5	4.5	3.0	1.5	3.0
6	6.0	4.0	2.0	4.0

The catamaran ship model with anti-pitch plates is shown in Figure 3.6.

4.2 Anti-Pitch Tank

This is the streamlined circular section tank as shown in Figure 4.2. This is also a multi-purpose tank not only as anti-pitch device but also as a fresh water or a fuel oil tank.

In this study, nine(9) different tanks in size and shape as shown in Table 4.2 were applied on each of the mono hulls, and model tests were also conducted for resistance and ship motion. In Table 4.2, $\triangle t$ represents the displacement of the tank.

Figure 4.3 shows the catamaran ship model with anti-pitch tanks.

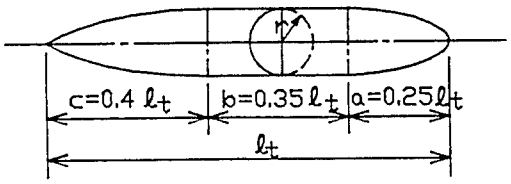

Fig. 4.2 Sketch of an Anti-Pitch Tank

Table 4.2 Nine(9) Different Anti-Pitch Tank

No.	ℓt (m)	r (m)	Vol. (m3)	△t/△ (%)
1	6.0	0.7	6.74	5.76
2		0.8	8.81	7.52
3		0.9	11.15	9.52
4	8.0	0.6	6.61	5.64
5		0.7	9.00	7.68
6		0.8	11.74	10.03
7	10.0	0.5	5.73	4.90
8		0.6	8.26	7.05
9		0.7	11.24	9.60

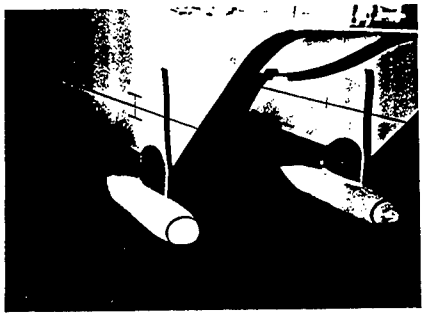

Fig. 4.3 Catamaran Ship Model with Anti-Pitch Tanks

4.3 Motion Control Hydrofoil

The hydrofoil system, that is, the forward and the rear foils with the struts connecting two mono hulls were introduced with the main purpose of motion control as an active control device.

At the same time, it was expected to be advantageous in resistance property also, since the ship hulls would be partially lifted up due to the dynamic lift generated by the foil system. This anticipation was proved to be achieved more than expected through the model tests later.

All together nine(9) different foil systems were designed. For four(4) foil systems among them, actual models were manufactured and model tests were conducted. The foil system has been adopted as the final motion control device and shall be discussed in more detail later.

4.4 Concluding Remark on the Motion Control Devices

There are two opposite aspects in the motion characteristics for the small high speed ships. While seakeeping quality should be improved as much as possible for the comfortability of passengers and crew, it is extremely difficult to improve the quality beyond centain level even if motion control devices of any kinds are introduced. In this project, therefore, the design target has been established so that most of passengers and crew may not feel great inconvenience with the extended sailing at Sea State 4. This target is such that the RMS value of the vertical acceleration at the bow at Sea State 4 is less than 1/10 of the gravitational acceleration(0.1g) for the frequency range of 3-10 Hz. This is rather an ambitious target.

Any device was going to be adopted if the results of model tests with the device satisfied this design target with the increase in resistance of about 10% range from the bare hull resistance. As shown in the results of model tests, it is true that the motion characteristics, particularly the vertical motion characteristics at the bow was significantly improved by the installation of the motion control devices. However, there were still considerable gaps between the test results with control devices and the design target. Here, it should be noted that the foil system would have the function of a passive control system like a large anti-pitch plate in model tests, since flap control is generally not possible during the model tests.

From the results of this study, the conclusion was reached that the design target could not be achieved without adopting the active control system. Therefore, the hydrofoil system with active flap control mechanism has been selected as the final motion control device.

5. HYDROFOIL SYSTEM

As mentioned previously, the hydrofoil system has been introduced as the device not only for the motion control, but also to achieve high speed. For this purpose, it has been decided for both forward and rear foils to have active flap control mechanism.

The present foil system has several important functions as follows :

- Motion control in heavy weather, that is, the reduction of heave, roll and pitch motion

- Prevention of the excessive heel during fast turning
- Reduction of resistance or increase of ship speed in favorable weather by producing the lift

It is well-known that the "Long-Range High-Speed Foil Catamaran Passenger Ship" developed in this study is the first catamaran in the world equiped with such multi-purpose and multi-function hydrofoil system. The basic concept, design philosoply and the actual design of the foil system shall be discussed.

5.1 Basic Design Concept

The difficulty in the early design stage of the foil system was to decide the ratio between the buoyancy and the basic lift* for the support of ship weight which led to the overall optimum compromization of resistance property and seakeeping quality. The answer to this question is by no means simple and could not be readily obtained even if model tests are carried out. There are many problems in model tests from the complicated physical phenomena to the test technique. The biggest problem among them is in the fact that the active control effect of the hydrofoil system could not be simulated in the model tests.

In the early design stage of this project, three(3) different foil systems with rectangular planform whose ratio between buoyancy and lift was 40:60, 30:70 and 20:80, respectively were designed. Both theoretical analyses and experimental investigations were carried out for these three foil systems. In theoretical analysis, however, the theory itself has not been satisfactorily established yet. In experimental investigation, the size of model was considered to be too small and tests were limited. Therefore, no definite conclusion or guideline could be derived. Nevertheless, this study, was not totally meaningless. Through this study, a rough qualitative indication was obtained as follows :

- In the first case (the case of 40:60 ratio), the seakeeping quality was the best, but resistance property was comparatively poor among three cases.

- In the third case(the case of 20:80 ratio), resistance property was quite good, but there was a high possibility that the forward foil might be emerged from the water during motion in heavy weather.

Reflecting the main purpose of the foil system as a motion control device and referring to the above indication, the ratio of 40:60 was selected initially as the tentative optimum compromization. However, this ratio has been changed to 30:70 later and maintained throughout the study.

The item to be decided next was how to assign this 70% basic lift to each of forward and rear foils, that is, how to determine so-called the "Share Ratio" of the basic lift between the forward and the rear foils. A design direction has been set up for this share ratio to be determined so that the ship would maintain the approximate even keel condition when sailing at the design cruising speed. This share ratio could be easily found from the locations of ship's center of gravity, longitudinal center of buoyancy(LCB) and from the position of the forward and the rear foils. The share ratio between the forward and the rear foils has been determined to be approximately 40:60.

The basic design concept discussed so far could be summrarized as follows :
At the design cruising speed, the total weight of the ship is to be supported in the following manner :

- 30% by the buoyancy
- 70% by the basic lift produced by the hydrofoil system with the flap positions in neutral
- the share ratio of the basic lift between the forward and the rear foils to be approximately 40:60 so that the ship would maintain the even keel condition approximately.

Figure 5.1 shows the summary of this basic design concept.

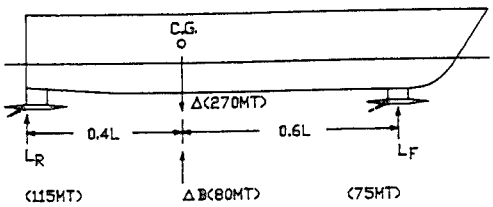

Fig. 5.1 The Basic Design Concept of the Hydrofoil System

5.2 Connection Method

In the early stage, the foil system was arranged to be rigidly connected to the two mono hulls by the two struts as shown in Figure 5.2 with the expectation that the installation of the foil system would help the overall structural system.

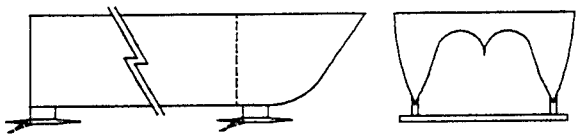

Fig. 5.2 The Initial Concept for the Installation of the Hydrofoil System

The structural analysis for this arrangement was performed so that the foil system might have enough strength against the design lift, dynamic load and deflection due to ship motion. The structural analysis itself shall be discussed later. According to the results of preliminary analysis, the thickness of the foils around the mid-span should be excessively large. Furthermore, some kinds of deflection or deformation at the fore-body of the ship were expected during fast maneuvering or motion in waves, since the fore-body of the ship is very thin. In this case, the fixed connection system may not

* Basic Lift means the lift produced by the foil system with the flaps in the neutral position.

be able to absorb the stress due to deformation. It was concluded, therefore, that this kind of the connection method had no advantages, but was harmful structurally.

In order to avoid the excessive thickness around the mid-span of the foils, it was decided to arrange one(1) strong strut at the mid-span of both forward and rear foils as shown in Figure 5.3. These struts shall be called the center struts. The hinge connection method was adopted for the side struts of the forward foil so that they may absorb certain amount of the transverse deflections. Two(2) watertight bulkheads were arranged in front of and behind the side struts at each of mono hulls for the extra safety when the foil system or struts were damaged. This arrangement has been adopted as the final system and is shown in Figure 5.3.

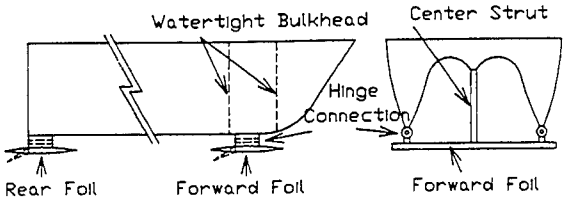

Fig. 5.3 The Final Concept for the Installation of the Foil System

The center struts have been arranged to be connected to the main hull by the flange connection method. Therefore, the entire foil system could be installed or removed easily*. Figure 5.4 shows the flange connection of the center strut and the hinge connection of the side struts.

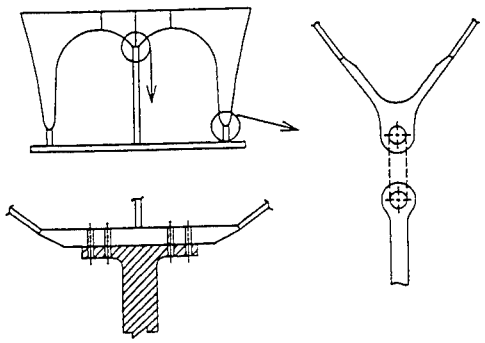

Fig. 5.4 The Final Connection Mechanism of the Forward Foil

5.3 Material of the Hydrofoil System

Some investigations were made on the possible foil materal, although the stainless steel was finally selected. First of all, the subject material should be non-corrosive.

Three different materials were selected for investigation in this study, that is, Ni-Al-Bronze alloy similar to the material used for the marine propeller, stainless steel and carbon fiber. Particularly, Ni-Al-Bronze alloy was selected for the economy study, and carbon fiber was selected for the study of the weight reduction and the possibility of the future application. The chemical composition and some important material properties for those three materials have been summarized in Table 5.1.

Table 5.1 Chemical Composition and Material Properties for the Three Different Materials

Item	Stainless Steel	Ni-Al Bronze Alloy	Carbon Fiber
Chemical Composition	16Cr 5Ni 1Mo	9Al 5Ni 4Fe	—
Tensile Strength (kgf/mm^2)	83 - 103	67 - 72	139
Yield Stress (kgf/mm^2)	62 - 67	25 - 32	54
Elongation(%)	> 15	20 - 30	15
Density(MT/m^3)	7.85	7.6	1.48
Elastic Modulus (kgf/mm^2)	1.8×10^4	$1.0\text{-}1.5\times10^4$	1.2×10^4
Fatigue Strength - Sea Water(kgf/mm^2)	25	21	—
Brinell Hardness (Bhn)	260 - 320	160 - 180	—

The results of this brief investigation are summarized as follows :

- When Ni-Al-Bronze alloy is utilized as the system material, the dimension, particularly the thickness of the foil system should be much increased to satisfy the required design strength. Therefore, the weight of the foil system and the resistance of the ship shall be increased.

- Carbon fiber has some superior properties to two other materials. However, general mechanical properties are not sufficiently determined yet. Further investigations on the material properties and the actual experiences would be necessary for the successful application.

Due to the limited time and for the sake of safety, therefore, the stainless steel has been selected as the foil material. It is the author's opinion, however, that carbon fiber could be successfully utitized as the foil material in the near future with the continuation of the necessary study.

5.4 Actual Design of the Hydrofoil System

Following the design concept and direction discussed so far, all together nine(9) systems were designed. In order to minimize the possibility of the cavitation inception and in order to minimize the induced drag, foil sections were designed to produce the lift by the optimum combination of camber and angle of attack. The camber and the angle of attack distributions were calculated by two different methods, that is, by lifting-line theory and by vortex lattice method, and compared each other.

* The required time for the installation or removal of the entire foil system is estimated to be less than three(3) hours.

The free-surface effect was not considered in any case. The results by two different methods were not much different each other. It has been found through the model tests that the final results obtained in this way sufficiently satisfy the design target in general.

For the design of foil section, "Foil Section Design Method by the Conformal Transformation Theory*" was going to be utilized. This method has many practical advantages and been being utilized for the propeller blade section design, but never been applied for the foil section design. In this study, therefore, NACA 66 thickness form and 0.8-a meanline have been used exclusively.

Figures 5.5, 5.6 and 5.7 show the planforms of No.1 to 3, No.5 and the final(No.9) foil systems.

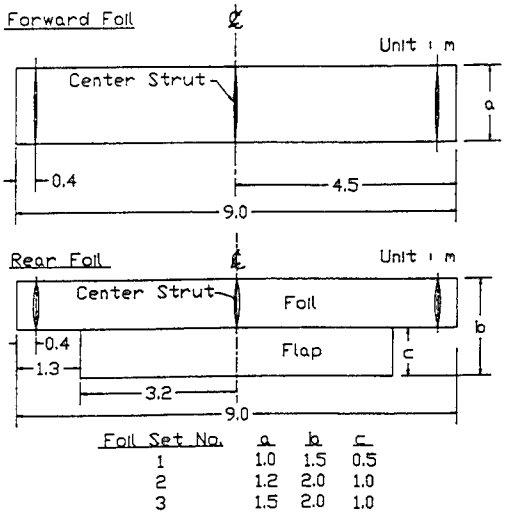

Foil Set No.	a	b	c
1	1.0	1.5	0.5
2	1.2	2.0	1.0
3	1.5	2.0	1.0

Fig. 5.5 Planforms of No.1, 2 and 3 Foil Systems

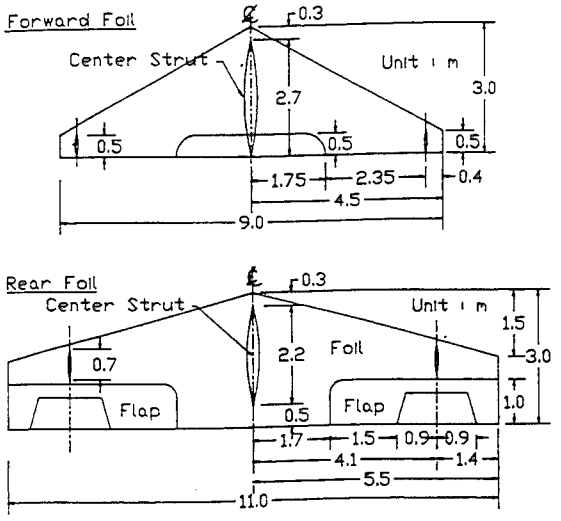

Fig. 5.6 Planforms of No.5 Foil System

* This method has been developed by the author for the first time in the world and proved to be superior through the various actual ship propeller design.

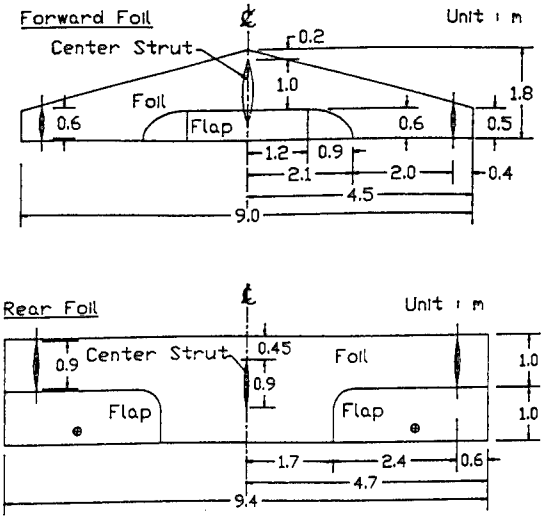

Fig. 5.7 Planforms of the Final(No.9) Foil System

6. MODEL TESTS

The importance of the model test cannot be overstressed for the successful completion of this project. The model tests for the initial and the first intermediate hull forms were carried out at HMRI only for the mono hull models. They may be regarded as the qualitative tests for the selection of superior hull forms. However, the tests for all other hull forms, that is, for the second intermediate, the semi-final and the final hull forms were conducted at both HMRI and HSVA.

Two different model ship sizes were used at HMRI, that is, 2.5 m and 2.8 m long models for the mono hulls and for the catamarans, respectively, while HSVA adopted only one model size. The model ship length at HSVA was 4.5 m.

Figure 6.1 shows the mono hull resistance test for one of the initial hull forms(Hull Form Ⅲ-3-S-R).

Figure 6.2 shows the catamaran bare hull resistance test for one of the second intermediate hull forms(Hull Form Ⅲ-3-N).

Figure 6.3 shows the seakeeping test for one of the second intermediate catamaran hull form(Hull Form Ⅲ-4-R) with No.1 foil system.

Figure 6.4 shows the resistance test for the final catamaran hull form with the final foil system. It is clearly shown in Figure 6.4 that about 70% of ship weight is lifted up above the water level.

Extensive model tests were carried out according to the carefully prepared model test program, and a vast amount of test data were obtained. Due to the limited space, however, only the limited test results shall be presented here.

Figures 6.5 and 6.6 comparatively show the typical resistance and seakeeping test results for the bare hull and for the ship with motion control devices,

respectively. the results shown in Figures 6.5 and 6.6 are for one of the second intermediate hull forms(Hull Form Ⅲ-4-R).

Table 6.1 shows the seakeeping test results for the bare hull and for the ship with motion control devices for the second intermediate hull form Ⅲ-4-R.

The seakeeping test results for the final catamaran bare hull and for the final ship with the final(No.9) hydrofoil system have been summarized in Table 6.2.

The resistance characteristics for the final hull form with and without the final(No.9) hydrofoil system are shown in Figure 6.7.

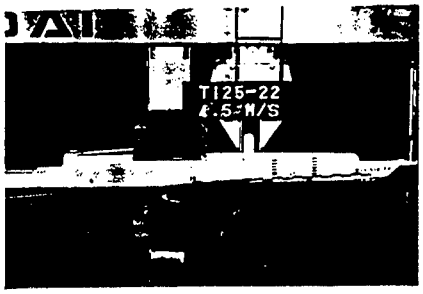

Fig. 6.1 Mono Hull Resistance Test for the Initial Hull Form Ⅲ-3-S-R

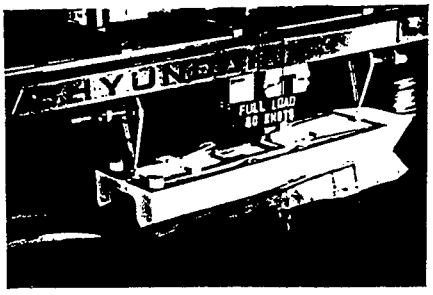

Fig. 6.2 Catamaran Bare Hull Resistance Test for the Second Intermediate Hull Form Ⅲ-3-N

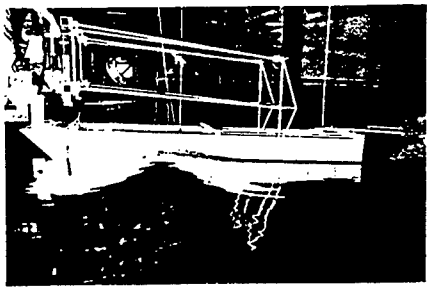

Fig. 6.3 Seakeeping Test for the Second Intermediate Catamaran Hull Form Ⅲ-4-R with the No.1 Foil System

As shown in the above tables and figures, it is true that the seakeeping quality is significantly improved with the motion control devices. However, it can also be concluded that the design target cannot be achieved without introducing the active control device.

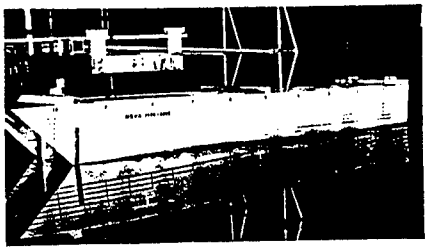

Fig. 6.4 Resistance Test for the Final Catamaran Hull Form with the Final Foil System

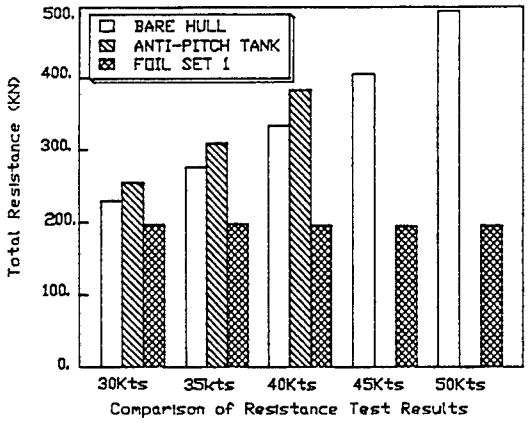

Fig. 6.5 Typical Resistance Test Results for the Bare Hull and for the Ship with Motion Control Devices for the Second Intermediate Hull Form Ⅲ-4-R

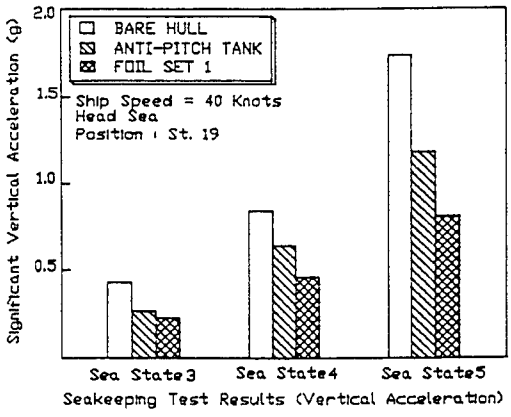

Fig. 6.6 Typical Seakeeping Test Results for the Bare Hull and for the Ship with Motion Control Devices for the Second Intermediate Hull Form Ⅲ-4-R

Table 6.1 Seakeeping Test Results for the Bare Hull and for the Ship with Motion Control Devices

The Second Intermediate Hull Form Ⅲ-4-R
Ship Speed = 40 knots
Free Trim Run
Head Sea

Approx. Sea State (Hs)	Motion Control Devices	Significant Heave Amplitude (m)	Significant Pitch Amplitude (deg)	Significant Vertical Acceleration at	
				St. 10 (in g)	St. 19 (in g)
3 (0.9 m)	Bare Hull	0.62	1.1	0.28	0.43
	Tank No. 5	0.43	0.7	0.19	0.27
	Foil Set 1	0.89	2.4	0.15	0.23
4 (1.9 m)	Bare Hull	1.22	2.1	0.50	0.84
	Tank No. 5	1.01	1.6	0.46	0.64
	Foil Set 1	1.17	2.9	0.34	0.46
5 (2.8 m)	Bare Hull	1.82	4.6	0.79	1.74
	Tank No. 5	1.67	3.1	0.67	1.18
	Foil Set 1	1.42	3.1	0.46	0.81

Table 6.2 Seakeeping Test Results for the Final Catamaran Bare Hull and for the Final Ship with the Final(No.9) Hydrofoil System

The Final Hull Form Ⅳ-4-F
Ship Speed = 40 knots
Even Keel Condition
Head Sea

Approx. Sea State (Hs)	Hull Condition	Significant Heave Amplitude (m)	Significant Pitch Amplitude (deg)	Significant Vertical Acceleration at	
				St. 10 (in g)	St. 19 (in g)
4 (1.9 m)	Bare Hull	1.26	2.56	0.43	0.74
	W/W the Final Foil Set	0.74	1.4	0.27	0.35
5 (2.8 m)	Bare Hull	2.21	4.7	0.65	1.08
	W/W the Final Foil Set	1.67	3.7	0.54	0.81

As shown in Figure 6.7, the resistance characteristics is remarkably improved by the hydrofoil system. Particularly, the resistance is continuously decreased with the increase of ship speed beyond a certain speed at the trim by stern conditions by about 2 degrees. It is also noted that the resistance could be further reduced if proper trim is maintained by adjusting the flap angles.

7. MOTION CONTROL SYSTEM

The next thing to do after the selection of motion control device was to decide the type of functions which the selected control device would have. In the beginning, most of effort was concentrated on the improvement of ship's vertical motion, particularly the vertical motion

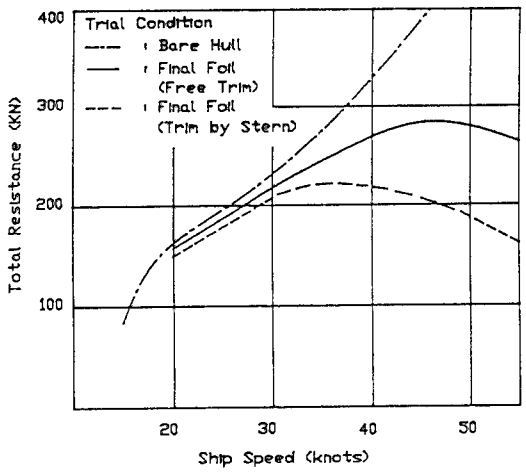

Fig. 6.7 The Resistance Characteristics for the Final Hull Form with and without the Final(No.9) Hydrofoil System

characteristics at the bow. Therefore, the forward and the rear foils were designed to have only one center flap, and a simple control system was going to be adopted which would have heave and pitch motion control functions utilizing the natural motion characteristics of the ship.

However, this idea was changed to the more active direction later. It was decided that the control system would have more functions as follows :

- Control of ship motions due to waves
  - Heave
  - Roll
  - Pitch
- Control of heel during maneuvering
- Control of flap deflection during astern operation

According to the above functions, the design of hydrofoil system had been revised. For the forward foil, one center flap was arranged so that the forward foil might have the major role of improving the vertical motion characteristics of the bow. For the rear foil, one each of port and starboard side flaps were arranged so that the rear foil might produce the transverse moment to control the roll and the heel as well as heave and pitch. The planform of the final(No.9) hydrofoil system is shown in Figure 5.7.

In the astern operation, there was a danger that the rear foil might be damaged by the impact of the strong water stream from the water-jet. The area exposed to such danger was once going to be cut out in advance as shown in Figure 5.6. However, the solution to this problem was improved by the following arrangement, since it was worried that the control system might not have sufficient control force or moment due to the reduction in the flap area :

- The rear foil system was moved 65 cm forward and 10 cm deeper from the initial position

- In astern operation, the tail flaps of the rear foil would be automatically deflected upward at their maximum position. In this case, the flaps are approximately in the parallel positions to the jet stream as shown in Figure 7.1.

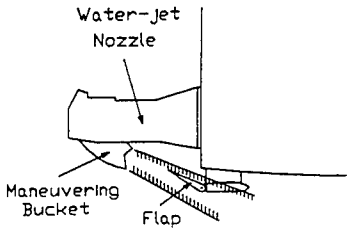

Fig. 7.1 Concept of Automatic Flap Control in Astern Operation

There is one thing to be mentioned here regarding the control system. The active motion control of the hydrofoil ship is achieved by the control of lift produced by the foil system, and the control of lift is made possible by the control of flaps. In this view point, the flap control mechanism is important for the effective control of motions. The conventional flap control mechanism is the complex system composed of several rotating shafts and gears similar to that of airplane wings. This is the proven system. However, there are several disadvantages as follows :

- System is complicated
- System is expensive(high cost)
- High power is required for the prompt operation (low effectiveness)

For the effective flap control, therefore, the author has developed the new control mechanism* for this project. In this system, the flaps are directly controlled by the motion of piston or bar connected to the hydraulic pump as shown in Figure 7.2.

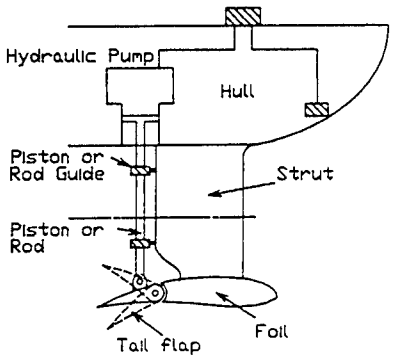

Fig. 7.2 Conceptual Description of the Flap Control System

Compared with the conventional mechanism, this system has several advantages as follows :

- System is very simple
- System is inexpensive(low-cost)
- Installation and maintenance of the system is easy
- Response(control speed) is extremely fast with low power(very high effectiveness)

In general, the piston or bar which controls the flap is long and made thin to reduce the extra resistance of water, and hence, it is apt to bend when pushing the flap. Therefore, one or two piston or bar guides are installed to prevent the bending of the piston or bar. The concept for this flap control system is described in Figure 7.2.

The overall outline of the motion control system is diagramatically described in Figure 7.3.

The overall concept for the motion control device and system has been developed by the author. The soft-ware for the control system shall be prepared by the Maritime Dynamics, Inc. in U.S.A. and the hard-ware such as foil and hydraulic systems shall be manufactured by Vosper Thornycroft in United Kingdom.

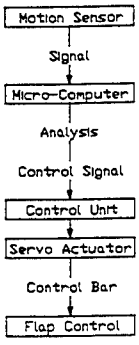

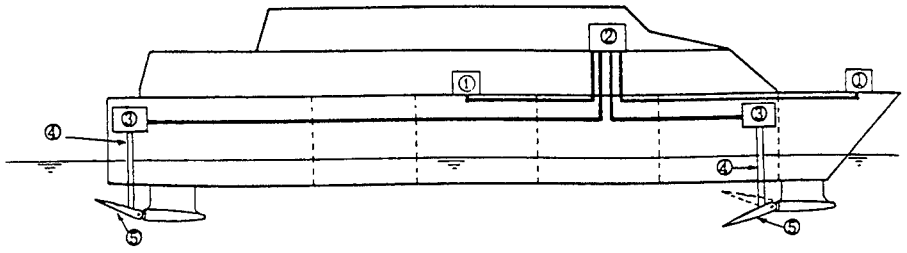

① Motion Sensor (Accelerometer or Gyro)
② Micro - Computer
③ Control Unit (Hydro Power Pack & Servo Actuator)
④ Control Bar
⑤ Flap

Fig. 7.3 Diagram of the Overall Motion Control System

* This new control system has been developed by the author and applied first time in the world in this project ship(Patent Pending).

8. PROPULSION SYSTEM

In order for a ship to sail, a sufficient thrust should be supplied by some kind of thrust-producing device to overcome the resisting forces from the water and air. For high speed ships, the selection of proper propulsion system is particularly important to achieve superior high speed performance characteristics.

At the initial stage of this project, the propulsion by screw propeller and that by water-jet were considered with equal weight. To reach the conclusion, therefore, a series of investigations were made as follows:

- Examination on the advantages and disadvantages of each system.
- Investigations regarding the propulsion system of recently constructed small high-speed crafts.
- Extensive discussions and investigations by visiting the major water-jet manufacturers in the world.
- Finally, on-board investigations by riding the actual ships propelled by the water-jet system.

From the result of the above investigations, the propulsion system was selected. It was the water-jet system.

In fact, this is the oldest type of mechanical propulsion for ships. As shown in Figure 8.1, the water-jet unit consists of an inlet channel(duct) leading the water to the impeller, a pump casing and an outlet part(nozzle), forming the jet.

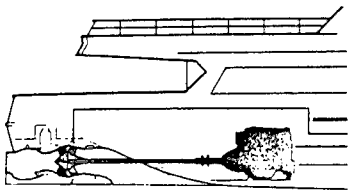

Fig. 8.1 General Arrangement of Water-Jet Propulsion System

There are many important advantages in water-jet propulsion system as follows :

1) Elimination of all external underwater appendages (reduced resistance)

2) Simple power transmission and compact installation
   - elimination of long and complex transmission lines
   - elimination of reverse gear
   - elimination of reduction gear in case of direct drive application
   - easier arrangements of multi-shaft configurations

3) High overall propulsive efficiency in a wide range of speed(negative thrust deduction fraction)

4) Outstanding navigability and maneuverability
   - very good acceleration and deceleration
   - excellent crash stop capability
   - lateral movement
   - rotation without forward motion

5) No risk of engine overload
   (cubic law power absorption, virtually independent of craft speed)

6) No problem in shallow draft design and shallow water operation

7) Protected propulsion system, particularly
   - in case of shallow water operation
   - even in case of grounding

8) Easy control of cavitation

9) Higher comfort for passengers and crew
   (low noise and vibration)

10) Low underwater noise
    (very important for Naval ships)

11) High reliability and easy maintenance
    (low maintenance cost)

Maneuvering is accomplished by a steering nozzle and astern thrust is achieved by a reversing bucket in the steering nozzle as shown in Figure 8.2.

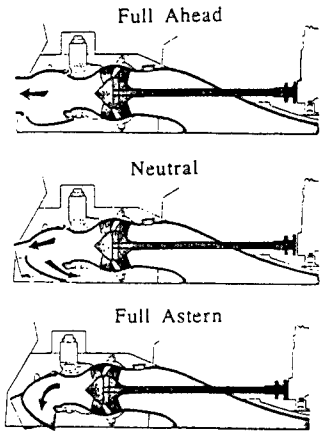

Fig. 8.2 Maneuvering with Water-Jet

In late 1960's to early 1970's when the water-jet became to be focused again as a marine propulsor for high speed vessels, the propulsive efficiency of the system was very poor that it was by no means comparable to that of the propeller propulsion system. Nowadays, however, the system has been so improved that for higher speed region, the efficiency of the water-jet propulsion system is even higher than that of propeller propulsion system as shown in Figure 8.3.

It is considered that Figure 8.3 shows the range of propulsive efficiency generally attainable with modern day's water-jet propulsion system.

The major disadvantages of water-jet propulsion are the loss of volume inside the ship due to ducting and impeller, or conversely the increase in size of the

ship to restore the displacement to its original value, and the relatively low propulsive efficiency at low speeds.

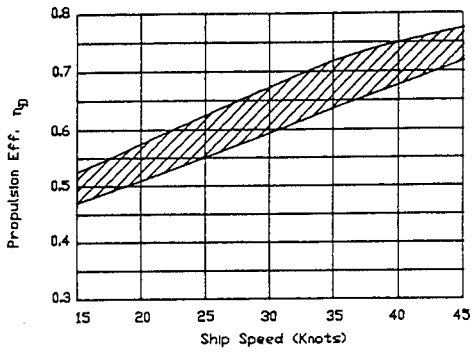

Fig. 8.3 Range of Propulsive Efficiency of Modern Water-Jet Propulsion System

9. STRUCTURAL DESIGN

9.1 Selection of the Material

9.1.1 Hull Material

The selection of the hull material for small high speed ships should be made based on the overall evaluation of various items such as performance, economy, weight and required strength.

In this project, preliminary midship sections were designed first for the three different cases of hull materials, that is, for the cases of general mild steel, higher tensile steel and aluminium. Various analyses were made with respect to hull weight, general strength, fatigue strength, cost of material and construction man-hour for each of cases and compared.

The material and processing costs per tonne of aluminium is much higher than those of the mild steel. It was estimated for this project ship that the total material cost and construction man-hour for the case of entire aluminium construction would be two and half(2.5) times and twice as high as those for the case of mild steel construction of the main hull. However, aluminium hull would definitely be more favorable in the weight. In fact, it was estimated that the hull weight of the aluminium construction would be about 30% less than that of mild steel construction, since the allowable stress-weight ratio of aluminium is 1.7 times higher than that of mild steel. In general, aluminium is inferior in fatigue strength to mild steel. When considering weight, however, aluminium is more advantageous, since the fatigue strength-weight ratio of aluminium is about 1.6 times higher than that of mild steel.

From the overall consideration, therefore, the aluminium was selected as the hull material. In order to improve the fatigue strength, much efforts were made in the structural design so that stress concentration at the high stress area could be avoided. At the same time, it was decided to conduct careful study on the fatigue strength through the prediction of fatigue life-span.

9.1.2 Material of the Hydrofoil System

The foil system is one of the important elements in weight control, since the weight of the foil system is about 10% of the total displacement of the ship. On the other hand, the structural safety of the foil system directly affects the safety of the ship. These two generally opposite aspects - weight and structural safety should be carefully considered in the material selection of the hydrofoil system.

As discussed in Chapter 5, the high strength stainless steel SS2387 was finally selected as the material for the foil system from the overall evaluations on the characteristics and properties such as yield stress, fatigue, absorbability of impact energy, corrosion, manufacturing and maintenance.

9.2 Midship Section Design

The design work on the midship section was started from almost the same stage as that of weight estimation. The difficulty in the early stage of the structural design was in the fact that no definite rule had been prepared from any classification society. The design guidelines from major classification societies were considered as suggestions, rather than rules. The initial midship section design was performed with such guidelines and various informations. In order to minimize the construction man-hour, to reduce the thermal deformation of aluminium material after welding and to avoid the occurance of cracks at the welding area, extruded profile was used as much as possible.

The longitudinal frame system was adopted with the frame spacing of 300 mm. The transverse frame spacing was arranged to be 1,000 mm. The upper deck as the main structural deck was arranged longitudinally throughout the ship length. Longitudinal girders are arranged against the slamming and transverse twisting moment. The bottom of deck connection under the potential slamming danger was designed to have arc shape to decrease the pressure due to slamming.

It was arranged that the ultimate longitudinal and transverse strengths of the ship were achieved by the main hull only without any contribution from the upper structure. In general, the structural design was carried out following the design guidelines from DnV and LR.

9.3 Structural Analysis

In order to confirm the local and global strength of the ship, the structural analyses were performed in accordance with the following steps :

(1) Load calculation according to the guidelines from the major classification societies
(2) Analysis of the transverse section at midship
(3) Overall three-dimensional hull structural analysis
(4) Detail analysis on the connecting parts of the hydrofoils to the hull
(5) Evaluation of safety according to the allowable stress

(6) Analysis and evaluation of fatigue strength

Three important steps among them shall be briefly discussed.

9.3.1 Overall Three-Dimensional Structural Analysis of the Hull

This project ship has rather complicated structural arrangement. First of all, two mono hulls are connected by the cross deck. Furthermore, one each of foils connecting two mono hulls are to be installed at the bow and the stern of the ship. For the twin-hull ships, the cross deck connection part is generally known to be relatively weak, and a large amount of concentrated loads are expected at both ends of the ship due to foil system. In order to investigate the structural response for this ship, therefore, it was decided to conduct the overall three-dimensional structural analysis of the hull by the finite element method.

About 5,840 grids and 10,430 elements were used for the modeling of the entire hull, and the analysis itself was done by MSC/NASTRAN program. Figure 9.1 shows the modeling for this analysis.

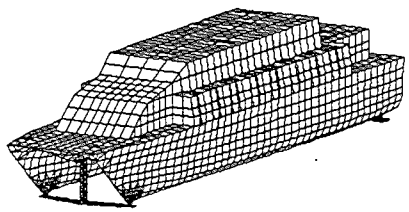

Fig. 9.1 Modeling for the Overall 3-Dimensional Structural Analysis

Four different load cases were selected as follows with the anticipation that they would be the most serious cases for the hull and foil structures :

- Load case 1 : Hull twisting moment
- Load case 2 : Crest landing bending moment
- Load case 3 : Design lift of the foils
- Load case 4 : Asymmetric lift of the foils

From the results of the analyses, it was concluded that the stresses generated at the hull for the given load cases are always less than the allowable values calculated by DnV guideline.

Figure 9.2 shows the stress distribution in the longitudinal direction under the load case 3, and Figure 9.3 shows the stress distribution in the forward foil under the load case 4.

9.3.2 Detail Analysis on the Connecting Parts of the Foils to the Hull

The connecting parts of the foils to the hull

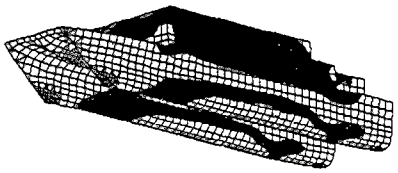

Fig. 9.2 Longitudinal Stress Distribution obtained by the Overall 3-Dimensional Structural Analysis under the Load Case 3

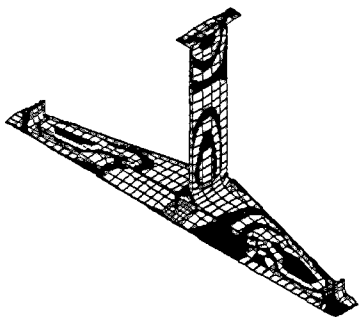

Fig. 9.3 Stress Distribution in the Forward Foil obtained by the Overall 3-Dimensional Structural Analysis under the Load Case 4

are considered to be the most sensitive area structurally in this project ship because of the large amount of the concentrated loads. Therefore, detail stress analysis was independently carried out in addition to the overall three-dimensional structural analysis. For this analysis, the hydrofoils were replaced by the solid elements, and the pin and flange joints of the connecting parts were modeled using rigid beam element.

In order to ensure that not complete damage, but only the partial damage might occur even in the extreme circumstances of unexpected collision with floating objects, the final strength analysis was separately performed. According to the result of the final strength analysis, the stress after damage at the remaining parts does not exceed yield stress except at the damaged part.

9.3.3 Analysis and Evaluation of the Fatigue Strength

The hydrofoils for this project are basically manufactured by the method of casting. However, both of forward and rear foils are too big to be casted as one piece. Therefore, it was decided to divide one foil into three sections - one center section and two side sections. Each of sections are to be manufactured by stainless steel casting and welded into one body.

It is considered that fatigue strength is most important for such welded areas. Therefore, it was decided to calculate and check the fatigue strength for those areas. Fatigue strength itself was calculated by two generally and widely used method, that is, stress-number of occurance(S-N) approach and fracture mechanics approach. The results of calculations are as follows :

- S-N approach : D = 0.046(10 year duration)

- Life-span of crack occurance : D = 0.019(10 year duration)

- Life-span of crack growth : 172 years(a_0=1mm, a_l=10mm)

Here, D represents the fatigue accumulation coefficient (damage ratio).

If D is equal to 1.0, it is generally considered that the fatigue failure is almost to occur. From the results of the above calculations, therefore, it is concluded that the hydrofoils in this project have more than enough fatigue strength with sufficient margin for the given load cases.

10. CONSTRUCTION

After completion of the conceptual design and obtaining the approval from the Classification Society for the major detail design drawings, procurement activity was immediately followed starting from the hull materials, and they arrived at our production shop in November, 1991. At last, the construction work was commenced on December 2, 1991 with aluminium plate cutting. The construction work has been and will be progressed according to the following general schedule:

- Work commencement : Dec. 2, 1991
- First sub-block assembly : Dec. 10, 1991
- Completion of the first main block : Jan. 20, 1992
- Turn over : Feb. 29, 1992
- Keel laying : Mar. 2, 1992
- Erection of the deck house block : May 30, 1992
- Completion of ship hull : June 20, 1992
- Launching : July 20, 1992
- Outfittings
  - · Main Engine : June 20, 1992
  - · Water-jet system : June 25, 1992
  - · Diesel generator : June 15, 1992
  - · Passenger cabin chairs : June 30, 1992
  - · Foil system : Sept. 15, 1992
- Dock trials : Aug. 14, 1992
- Sea trial(without Foil) : Aug. 25, 1992
- Overall evaluation of performance : Aug. 30, 1992 (without Foil) Sept. 30, 1992 (with foil)

For the efficient construction of the hull, it was decided to divide the complete hull into four(4) major blocks - three(3) main hull blocks, that is, forward-block, mid-block and aft-block, and one(1) deck bouse block.

Each of three main hull blocks except the deck house block were assembled in upside-down position first. After completion, they were turned over by 60 tonne capacity jib crane and erected. Finally, all the blocks are to be connected together by welding to form a complete hull. Semi-automatic MIG welding method has been applied for the aluminium welding. This hull construction concept is shown in Figure 10.1.

Figure 10.2 shows the construction of the forward-block of the main hull. Figure 10.3 shows the turning-over of the mid-block.

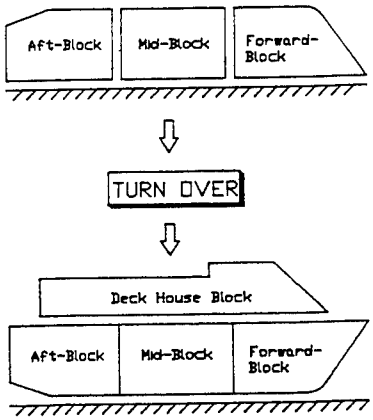

Fig. 10.1 Hull Construction Concept

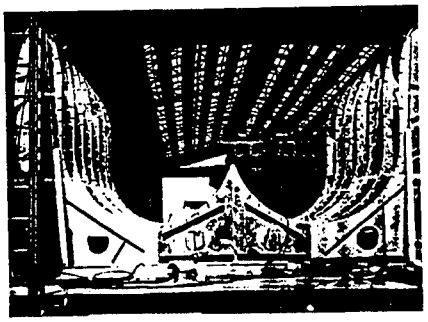

Fig. 10.2 Construction of the Forward-Block

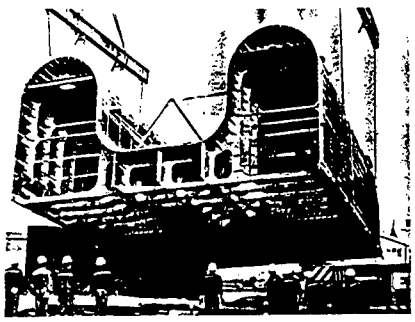

Fig. 10.3 Turn-Over of the Mid-Block

11. CONCLUSION

In this paper, discussions were made on the design and construction of "Long-Range High-Speed Foil-Catamaran Passerger Ship." A vast amount of theoretical and experimental studies have been systematically carried out for this purpose. Particularly, the conceptual design and the initial model test works had been completed within less than six(6) months since the start of design work in the middel of August, 1990.

This project ship is very difficult ship to design in several aspects compared with similar existing ships. Some of the difficult points are summarized in Table 11.1.

For small high speed ships, light weight is absolutely necessary. As shown in Table 11.1, however, this project ship is almost twice heavier than similar existing ships due to the owner's and operational requirements. Even if there is no definite requirement in seakeeping quality, furthermore, a great effort had to be made to significantly improve this characteristic due to the extended open-sea voyage.

In spite of such unfavorable conditions, it is considered that the design work has been completed quite successfully, and the construction work is under progress as scheduled. It has been predicted by the results of extensive model resistance tests that the ship could achieve the speed of more than 40 knots with almost the same propulsion power as that of other similar existing ships. Also, the design target in seakeeping quality seems to be most probably satisfied according to the results of computer simulation based on the seakeeping model test results. Furthermore, several new concepts have been developed and applied for this project ship first time in the world. This project ship is definitely the first ship in the world in this size and type of ships in the view points of the operational environment, design concept and some of ship systems. It could be concluded that the overall peformance of this project from the design to the construction is extremely efficient and successful.

However, it is a pity that the actual performance characteristics of the ship could not be presented here, since the construction work has not been completed at the time when this paper was being prepared. The sea trial is scheduled to be conducted from the end of August to the end of September, 1992 first without installing hydrofoil system and next with hydrofoil system installed. The author would like to have another opportunity in the near future to present the performance characteristics of this ship measured not only at the sea trial, but also through the actual operations.

Table 11.1 Some Typical Items to make Design Difficult(Compared with the similar existing ships of about 300 passenger capacity)

Item		This Project Ship	Similar Existing Ships
	Operational Area	Unrestricted Area	Coastal Area
Effects from the Operational Requirements	Endurance	Long Distance (800 N.M. Round Trip)	Short Distance (Less than 80 N.M.)
	Sailing Time	Long Time (about 10 hours)	Short Time (Less than 2 hours)
	Fuel Oil Capacity	About 30 MT	Less than 5 MT
	Main Dimensions (Considering the Seakeeping Quality)		
	LOA Breadth Depth	45.5 m 11.4 m 5.1 m	35 - 38 m 8 - 10 m 3.5 - 4.5 m
	Motion Control Device	Hydrofoil System with Automatic Flap Control	None
	Passenger Seat	Adjustable Back Type with Ample Space	Fixed Type
Design Cruising Speed at Design Draft		Over 40 knots	About 35 knots
Passenger with baggage (Based on 300 Passengers)		Total 39 MT (130 kg/ Person)	Total 22.5 MT (75 kg/ Person)
Main Engine (Based on about 4,000 HP)		PAXMAN VALENTA Diesel Engine About 11.0 MT x 2	Gas Turbine About 0.6 MT x 2
Total Displacement		About 270 MT	About 150 MT

REFERENCES

1. Min, K-S., "Long-Range High-Speed Catamaran Ship Design", Proceedings from the First International Conference on Fast Sea Transportation(FAST'91), Trondheim, Norway, June 1991, Vol. 1, pp. 591-606.

2. Bailey, D., "High Speed Displacement Ships ; Trends in Hull Form Design", Proceedings of the International Workshop on Developments in Hull Form Design, MARIN, Wageningen, the Netherlands, October 1985, Vol.1, pp.Ⅶ.1-10.

3. Oossanen, Peter van and Pieffers, Jan B. M., NSMB-Systematic Series of High-Speed Displacement Ship Hull Forms", Proceedings of the International Workshop on Developments in Hull Form Design, MARIN, Wageningen, the Netherlands, October 1985, Vol.1, pp.Ⅶ.1-16.

4. Min, K-S., "Catamaran Hull Form Design from the View Point of Wave Resistance", Proceedings of the 1st JSPC Symposium, Tokyo, Japan, July 1985., Proceedings of the International Workshop on Developments in Hull Form Design, MARIN, Wageningen, the Netherlands, October 1985, Vol.2, pp.258-273.

5. Wehausen, J. V., "Unpublished Lecture Note on Ship Hydrodynamics", University of California, Berkeley.

6. Havelock, T. H., "The Collected Papers on Ship Hydrodynamics", ONR/ACR-103.

A New Method of Calculating Unsteady Hydrodynamic Forces Acting Upon High-Speed Catamaran Ships

I. Watanabe (Ship Research Institute, Japan)

ABSTRACT

Modelling of the flow field around an oscillating catamaran in forward motion is discussed. Thin ship approximation is introduced to make the problem linear. It is shown that the flow field for each demihull can be treated separately as far as the vertical motion is concerned and the corresponding hydrodynamic forces are to be computed. The interaction effects between the hulls come first as generation of traction or repelling force between them. The antisymmetric forces arise on each demihulls due to interaction between the hulls even if the ship is making symmetric motion about the centerplane. The problem is solved by using unsteady lifting surface theory and an integral equation with repsect to pressure on the hull, taking into account of free surface wave effects, is solved numerically in order to determine its intensity of the interaction.

1 Introduction

The calcucation of hydrodynamic forces on a ship in waves is a still crucial problem in estimating ship safety margin in adverse seas in general. As for a catamaran ship, It is more so since the concept is rather new and conventional way of thinking for forces due to wave action is not appicable in most of the case. There are papers recently on hydrodynamic aspects of the multihull ships. Ohkusu has treated the problem by using slender body theory.[2] Kring et. al. has treated multihull ship problem by panel method.[1] This paper also concerns a catamaran ship, but with emphasis on linear hydrodynamic forces on it in oscillatory motion. It starts with discussion how to model unsteady flow field around a catamaran ship in symmetric motion in still water. Thin ship assumption is introduced to linearize the problem following Hanaoka's Theoretical approach.[3],[4] It will be shown next that the problem can be split into two problems, i.e. then symmetric problem and antisymmetric problem. The first problem is identical with the single hull problem and thus free from integral equation or cumbersome calculation to solve equations. Distortion of flow and radiating waves by one of demihulls induces on the other demihull antisymmetric flow about its centerplane. It may happen even if the ship is making symmetric motion orso called vertical motion. the antisymmetric flow problem is essentially unsteady lifting surface problem and an integral equation with repsect to pressure on the hull has to be solved in order to determine its intensity of the interaction. The paper discusses on how to determine hydrodynamic forces in vertical motion and then proceed to solve the integral equation and present with its numerical solution and hydrodynamic forces and moments acting on/between demihulls.

2 Basic Formulation

2.1 Statement of Problem

Consider a catamaran-type ship oscillating harmonically in a free stream of velovity U directed along the positive x-axis. Here x,y z are a left-handed set of Cartesian coordinates with the z axis upward, as illustratedin Fig. 1. The ship is comprised of two identical hulls of symmetric shape with respect to each centerplane. The Flow is assumed inviscid and irrotational.

The each hull may have any form under assumption that each hull is thin, namely the breadth and the draft are smaller in oder compared to the ship length. if we take ship length L, draft T and half breadth b and

$$\epsilon = \frac{b}{l}, \quad \lambda = \frac{T}{l}.$$

Then following order of smallness is assumed

$$\epsilon < \lambda < O(1).$$

Let the hull shape of a demihull be

$$y = \pm f(x, z). \tag{1}$$

Then entire full form is expressed by

$$y \pm f_0 = \pm f(x, z). \tag{2}$$

Here the distance between two hulls is denoted by $2f_0$.

Assume the ship is making only vertical motion of heaving and pitching. Take upward plus for heaving and bow up plus for pitching, then displacement of the hull becomes

$$z^* = h - x\theta. \tag{3}$$

The boundary condition on the hull surface becomes

$$\frac{\partial f}{\partial t} + (U + \frac{\partial \Phi}{\partial x})\frac{\partial f}{\partial x} + \frac{\partial \Phi}{\partial z}\frac{\partial f}{\partial z} - \frac{\partial \Phi}{\partial y} = 0 \tag{4}$$
$$\text{on } y \pm f_o = f(x, z - z^*).$$

If we expand the quantities included in the equation around the centerplane of the each demihull using the thin body assumption and take dominant linear terms, we get linear body boundary equation of the unsteady flow part as follows,

$$\frac{\partial \Phi}{\partial y} = -(\frac{\partial}{\partial t} + U\frac{\partial}{\partial x})(f_z z^*) \equiv Re\, w(x, z)e^{i\omega t}; \quad \text{at} \quad y = 0. \tag{5}$$

The equation tells us that the hull boundary condtion may be imposed not on the hull surface but on the centerplane of the each hull.

In addition, the ship may emit vortices of harmonically oscillating strength from each hulls because of the hull interaction. So we will impose Kutta condition at the trailing edge(at the AP) and null dynamic pressure condition across each trailing vortex sheets.

Further free surface condition will be linearised to get following well known formula

$$\left(\frac{\partial}{\partial t} + V\frac{\partial}{\partial x}\right)^2 \Phi + g\Phi_z = 0 \tag{6}$$

These three conditions plus the radiation condition and Laplace equation defines the problem to be solved here. Fig. 2 shows schematic view of the model to be treated in the paper.

2.2 Green's Theorem

Green's theorem may be utilized to get an expression of the velocity potential.We have seen that the body

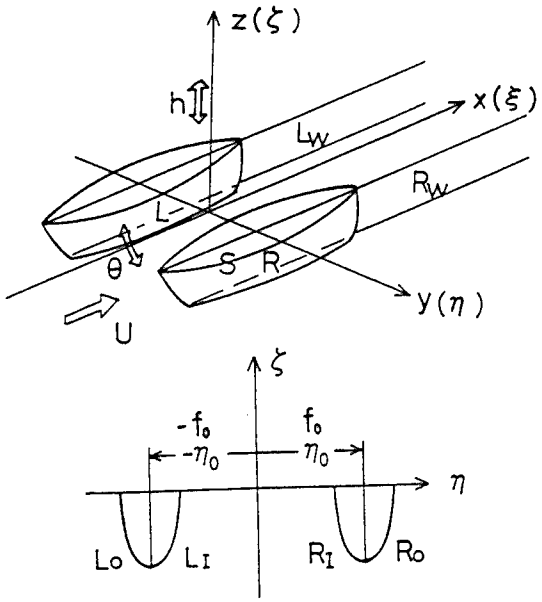

Fig. 1: Coordinate system

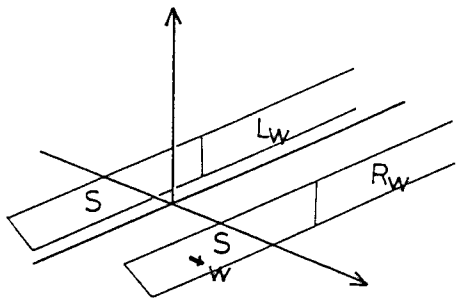

Fig. 2: Flow Model around the catamaran treated here

boundary condition and the wake condition is now to be imposed at $y = 0$ plane. Let us denote surfaces of the right side and left side demihull by $R_{i,o}$ and $L_{i,o}$ and subsequent vortex sheets of the both hulls by $R_{w\pm}$ and $L_{w\pm}$ respectively. The theorem reads

$$\begin{aligned} 4\pi\Phi &= \int\int_{R_{i,o}+R_{w\pm}} \left[\Phi' \frac{\partial G_0}{\partial n} - \frac{\partial \Phi'}{\partial n} G_0\right] ds \\ &+ \int\int_{L_{i,o}+L_{w\pm}} \left[\Phi' \frac{\partial G_0}{\partial n} - \frac{\partial \Phi'}{\partial n} G_0\right] ds \end{aligned} \tag{7}$$

Here subscripts i, o denote inner and outer hull surface of each demihull. The integration is made over the both sides of the centerplane($R_{i,o}$, $L_{i,o}$) and trailing vortex sheets of the two hulls extending to the infinity. ($R_{w\pm}$, $L_{w\pm}$) Integration over the other boundar vanishes because of the conditions there.

G_0 denotes velocity potential of unit strength source distribution and can be written in Michell's type of expression [3] as

$$\begin{aligned} G_0(x,y,x;x',y',z') &= \frac{2}{\pi}\int_{-\infty}^{\infty}\int_0^{\infty} \frac{e^{im(x-x')-|y-y'|\sqrt{m^2+n^2}}}{\sqrt{m^2+n^2}} \\ &\times \cos(nz+\varepsilon)\cos(nz'+\varepsilon) dn dm \\ &+2\{\int_{a_1'}^{a_2'} + \int_{a_3'}^{a_4'}\} \frac{D^2(m)}{K(m)} e^{im(x-x')+(z+z')D^2(m)-|y-y'|K(m)} dm \\ &-2i\{\int_{-\infty}^{a_1'} + \int_{a_2'}^{a_3'} + \int_{a_4'}^{\infty}\} \frac{\epsilon_p D^2(m)}{K(m)} \\ &\times e^{im(x-x')+(z+z')D^2(m)-i\epsilon_p|y-y'|K(m)} dm, \end{aligned} \tag{8}$$

where

$$\begin{aligned} &D^2(m) = (m+\nu/V)^2/\kappa', \\ &K(m) = \sqrt{|m^2 - D^4(m)|}, \\ &\varepsilon = \tan^{-1}\left(-D^2(m)/n\right), \\ &a'_{\{1\atop 2\}} = \kappa' \frac{-1-2\Omega \mp \sqrt{1+4\Omega}}{2}, \\ &a'_{\{3\atop 4\}} = \kappa' \frac{1-2\Omega \mp \sqrt{1-4\Omega}}{2}, \\ &\kappa' = \frac{g}{V^2}, \quad \Omega = \nu V/g, \\ &\epsilon_p = \begin{cases} 1, & \text{for } a_2' < m < \infty \\ -1, & \text{for } -\infty < m < a_1'. \end{cases} \end{aligned}$$

In order to limit the integration to finite region, the acceleration potential(ϕ) is introduced as

$$\Phi = \frac{1}{V}\int_{-\infty}^{x} e^{-i\frac{\nu}{V}(x-X)}\phi(X)dX. \tag{9}$$

Substitute this relation into (7) and make use of relation:

$$\begin{aligned} &\int_{-\infty}^{\infty} f(m)dm \int_{-\infty}^{\infty} dx' \int_{-\infty}^{x} e^{-i\frac{\nu}{V}(x-X)}\phi(X)dX e^{im(x-x')} \\ &= \pi f(-\frac{\nu}{V}) \int_{-\infty}^{\infty} e^{-i\frac{\nu}{V}(x-x')}\phi(x')dx' \\ &- i\oint_{-\infty}^{\infty} f(m)dm \int_{-\infty}^{\infty} \frac{e^{-im(x'-x)}}{m+\nu/V}\phi(x')dx' \end{aligned} \tag{10}$$

Since $phi(x)$ vanishes outside of the hull surface, we may restric integgration on the hull surfaces. Thus we have

$$\begin{aligned} 4\pi\Phi &= \int\int_{R_{i,o}} \left[\phi' \frac{\partial G_2}{\partial n} - \frac{\partial \Phi'}{\partial n} G_0\right] ds \\ &+ \int\int_{L_{i,o}} \left[\phi' \frac{\partial G_2}{\partial n} - \frac{\partial \Phi'}{\partial n} G_0\right] ds \end{aligned} \tag{11}$$

and

$$\begin{aligned} &G_2(x,y,x;x',y',z') = \\ &- \frac{2i}{V\pi}\oint_{-\infty}^{\infty}\int_0^{\infty} \frac{e^{im(x-x')-|y-y'|\sqrt{m^2+n^2}}}{\sqrt{m^2+n^2}(m+\nu/V)} \\ &\times \cos(nz+\varepsilon)\cos(nz'+\varepsilon) dn dm \\ &- \frac{2i}{V\sqrt{\kappa'}}\{\int_{a_1'}^{a_2'} + \int_{a_3'}^{a_4'}\} \frac{D(m)}{K(m)} \\ &\times e^{im(x-x')-|y-y'|K(m)+(z+z')D^2(m)} dm \\ &+ \frac{2i}{V\sqrt{\kappa'}}\{\int_{-\infty}^{a_1'} + \int_{a_2'}^{a_3'} + \int_{a_4'}^{\infty}\} \frac{\epsilon_p D(m)}{K(m)} \\ &\times e^{im(x-x')-i\epsilon_p|y-y'|K(m)+(z+z')D^2(m)} dm \\ &+ \frac{2}{V}\int_0^{\infty} \frac{e^{-|y-y'|\sqrt{(\frac{\nu}{V})^2+n^2}-\frac{i\nu}{V}(x-x')}}{(\nu/V)^2+n^2} \cos nz \cos nz' dn. \end{aligned} \tag{12}$$

By definition, the Φ_n' is symmetric to the $y = 0$ plane. However, the antisymmetric flow around the demi-hull exists even if the motion is symmtric because of the interaction of the hulls. Thus the pressure on the both sides on a demihull is not equal each other.

$$\phi'(f_o+) \neq \phi'(f_o-).$$

Since it is sufficient to concider one of the two demihulls due to symmetry. The right side demihull($y > 0$) is to be considered in the following.

In the outer side of the hull ,i.e. for $f_0 < y$

$$\begin{aligned} 4\pi\Phi &= \int\int_S (\phi_o' - \phi_i') \frac{\partial G_2}{\partial y'}(x,y,z:x',f_0,z')dx'dz' \\ &- 2\int\int_S \Phi_n' G_o(x,y,z:x',f_0,z')dx'dz' \\ &+ \int\int_S (\phi_i' - \phi_o') \frac{\partial G_2}{\partial y'}(x,y,z:x',-f_0,z')dx'dz' \\ &- 2\int\int_S \Phi_n' G_o(x,y,z:x',-f_0,z')dx'dz', \end{aligned} \tag{13}$$

where S denotes the projection of the centerplane to the demihull.

The y component of the perturbed velocity there is given by

$$
\begin{aligned}
&4\pi\frac{\partial\Phi}{\partial y}|_{y=f_0+} \\
&= \int\int_S(\phi_o'-\phi_i')\frac{\partial^2 G_2}{\partial y'\partial y}(x,f_0+,z:x',f_0,z)dx'dz' \\
&- 2\int\int_S w\frac{\partial G_o}{\partial y}(x,f_0+,z:x',f_0,z)dx'dz' \\
&+ \int\int_S(\phi_i'-\phi_o)\frac{\partial^2 G_2}{\partial y'\partial y}(x,f_0+,z:x',-f_0,z')dx'dz' \\
&- 2\int\int_S w\frac{\partial G_o}{\partial y}(x,f_0+,z:x',-f_0,z')dx'dz'.
\end{aligned}
\tag{14}
$$

Likeswise, on the inner side of the hull($0 < y < f_0$),

$$
\begin{aligned}
&4\pi\frac{\partial\Phi}{\partial y}|_{y=f_0-} \\
&= \int\int_S(\phi_o'-\phi_i')\frac{\partial^2 G_2}{\partial y\partial y'}(x,f_0-,z:x',f_0,z')dx'dz' \\
&- 2\int\int_S w\frac{\partial G_o}{\partial y}(x,f_0-,z:x',f_0,z')dx'dz' \\
&+ \int\int_S(\phi_i'-\phi_q)\frac{\partial^2 G_2}{\partial y\partial y'}(x,f_0-,z:x',-f_0,z')dx'dz' \\
&- 2\int\int_S w'\frac{\partial G_o}{\partial y}(x,f_0-,z:x',-f_0,z')dx'dz'.
\end{aligned}
\tag{15}
$$

It is to be noted that

$$
\begin{aligned}
\frac{\partial G_0}{\partial y}|_{y=f_0+} &= -\frac{\partial G_0}{\partial y}|_{y=f_0-} \\
\frac{\partial^2 G_2}{\partial y\partial y'}|_{y=f_0+} &= \frac{\partial^2 G_2}{\partial y\partial y'}|_{y=f_0-}
\end{aligned}
\tag{16}
$$

Thus, taking symmetric relation between the outer and inner side, there exists two distinct types of equations. One is equation for symmetric components. It is obtained by taking difference between (14) and (15) as,

$$
\frac{\partial\Phi}{\partial y} = -\frac{1}{2\pi}\int\int w\frac{\partial G_o}{\partial y}(x,f_0,z:x',f_0,z')dx'dz'. \tag{17}
$$

The equation shows the potential for symmetric component is determined solely by the body boundary value as is the case monohull problem. There is no need for solving integral equation. This is the main feature of the thin ship theory. It is easy to verfy that the solution of the above equation is

$$
\Phi = -\frac{1}{2\pi}\int\int wG_0(x,f_0,z:x',f_0,z')dx'dz'. \tag{18}
$$

No consideration is necessary to interaction effects as far as first order force in the vertical component is concerned. The interaction plays dominant role in the horizontal force calculation as the next formula shows.

If we add up (14)+(15), equation for antisymmetric component is derived as,

$$
\begin{aligned}
&\int\int(\phi_o-\phi_i)G_{2yy'}(x,f_0,z:x',f_0,z')dx'dz' \\
&+\int\int(\phi_i-\phi_o)G_{2yy'}(x,f_0,z:x',-f_0,z')dx'dz' \\
&= 2\int\int wG_{oy}(x,f_0,z:x',-f_0,z')dx'dz'.
\end{aligned}
\tag{19}
$$

This is an integral equation for the pressure distribution on the hull surface. The equation shows that the disturbance caused by one of hulls denoted by the righthand side term generates unsteady circulatory flow field around the other hull. This is one example of so called gust problem in the field of unsteady lifting surface problem, The kernel is much complicated since surface wave effect has to be taken into account though.

3 Symmetric Flow Problem

The velocity potential for the symmetric flow field can be written by Substituting (8) into G_0 of (18),

$$
\begin{aligned}
\Phi = Re\frac{e^{i\nu t}}{\pi}\iint w(x',z')\,[\,&-\frac{1}{X}\sum_{r=-\infty}^{\infty}\int_0^{\infty}\frac{1}{\sqrt{(\pi r/X)^2+\chi^2}} \\
&\times e^{-|y|\sqrt{(\pi r/X)^2+n^2}+i\frac{\pi r}{l}(x-x')}\cos(nz+\varepsilon)\cos(nz'+\varepsilon)dn \\
&-\{\int_{a_1'}^{a_2'}+\int_{a_3'}^{a_4'}\}\frac{D^2(m)}{K(m)}e^{(z+z')D^2(m)-|y|K(m)+im(x-x')}dm \\
&+i\{\int_{-\infty}^{a_1'}+\int_{a_2'}^{a_3'}+\int_{a_4'}^{\infty}\}\frac{\epsilon_p D^2(m)}{K(m)} \\
&\times e^{(z+z')D^2(m)-i\epsilon_p|y|K(m)+im(x-x')}dm\,]\,dx'dz'.
\end{aligned}
\tag{20}
$$

Here expression is changed in the form of double integral term of (20). Integration with repsect to m is replaced by summation. It is for ease of numerical evaluation. The change will be justified by the fact that, if we take the longitudinal domain length (X) lomg enough to cover all the appreciable fluid motion, finite Fourier series on that domain can approximate fouier tranform with good accuracy. This is closer to original Michell's approach since he devised the formula starting finite sum of the Fourier series.

3.1 Hydrodynamic Forces

It is easy to calculate hydrodymnamic Forces and moments of vertical motion if pressure distribution is known over the demihull. Within a framework of thin

ship theory, they are given by

$$F = -2 \iint p \frac{\partial f}{\partial z} \begin{Bmatrix} 1 \\ x \end{Bmatrix} dx dz. \tag{21}$$

p is pressure related to the velocity potential as

$$p = \left(\frac{\partial}{\partial t} + V \frac{\partial}{\partial x} \right) \Phi. \tag{22}$$

It is convenient to introduce dimensionless variables for further discussion as follows

$$\begin{aligned}
&\xi = x/l, \quad \eta = y/b, \quad \zeta = z/T, \\
&\mu = ml, \quad \chi = nl, \\
&\omega = \nu l/V, \quad \kappa = \kappa' l = gl/V^2, \\
&\Xi = X/\pi l, \quad \bar{D}^2(\mu) = (\mu + \omega)^2/\kappa \\
&\bar{K}(\mu) = \sqrt{|\bar{D}^4(\mu) - \mu^2|} \\
&\bar{\delta} = \delta/l, \\
&a_{1,2,3,4} = a'_{1,2,3,4} l.
\end{aligned}$$

If we integrate the potential (20) after substituting each corresponding values into $w(x', z')$, radiation forces(moments) for heaving and pitching ($F_{\theta\theta}$、$F_{\delta\delta}$、$F_{\theta\delta}$、$F_{\delta\theta}$) are obtained respectively.

Radiation Force for heaving, after some algebraic manipulation is given by

$$F_{\delta\delta} = \frac{2\rho g l^3 b^2 \bar{\delta}}{\pi T^2} \left[F_{\delta\delta S} \sin \nu t + F_{\delta\delta C} \cos \nu t \right], \tag{23}$$

where

$$\begin{aligned}
F_{\delta\delta S} = &\frac{\lambda}{\pi \Xi} \sum_{r=-\infty}^{\infty} \int_0^{\infty} \frac{H_{C\delta}^2 + H_{S\delta}^2}{\sqrt{(r/\Xi)^2 + \chi^2}} d\chi \\
&- \{ \int_{a_1}^{a_2} + \int_{a_3}^{a_4} \} \frac{C_\delta^2 + S_\delta^2}{\bar{K}(\mu)} d\mu,
\end{aligned} \tag{24}$$

and

$$F_{\delta\delta C} = \{ - \int_{-\infty}^{a_1} + \int_{a_2}^{a_3} + \int_{a_4}^{\infty} \} \frac{C_\delta^2 + S_\delta^2}{\bar{K}(\mu)} d\mu. \tag{25}$$

Likewise, radiation moment for pitching is written as

$$F_{\theta\theta} = \frac{2\rho g l^4 b^2 \bar{\theta}}{\pi T^2} \left[F_{\theta\theta S} \sin \nu t + F_{\theta\theta C} \cos \nu t \right], \tag{26}$$

where

$$\begin{aligned}
F_{\theta\theta S} = &\frac{\lambda}{\pi \Xi} \sum_{r=-\infty}^{\infty} \int_0^{\infty} \frac{H_{C\theta}^2 + H_{S\theta}^2}{\sqrt{(r/\Xi)^2 + \chi^2}} d\chi \\
&- \{ \int_{a_1}^{a_2} + \int_{a_3}^{a_4} \} \frac{C_\theta^2 + S_\theta^2}{\bar{K}(\mu)} d\mu,
\end{aligned} \tag{27}$$

and

$$F_{\theta\theta C} = \{ - \int_{-\infty}^{a_1} + \int_{a_2}^{a_3} + \int_{a_4}^{\infty} \} \frac{C_\theta^2 + S_\theta^2}{\bar{K}(\mu)} d\mu. \tag{28}$$

Coupling forces(moment) between heaving and pitching may be also derived by integration. For example, pitching moment due to heaving($F_{\theta\delta}$) can be calculated by

$$F_{\theta\delta} = \frac{2\rho g l^4 b^2 \bar{\delta}}{\pi T^2} \left[F_{\theta\delta S} \sin \nu t + F_{\theta\delta C} \cos \nu t \right], \tag{29}$$

where

$$\begin{aligned}
F_{\theta\delta S} = &-\frac{\lambda}{\pi \Xi} \sum_{r=-\infty}^{\infty} \int_0^{\infty} \frac{(H_{\theta C} H_{\delta C} + H_{\theta S} H_{\delta S})}{\sqrt{(r/\Xi)^2 + \chi^2}} d\chi \\
&- \left\{ \int_{a_1}^{a_2} + \int_{a_3}^{a_4} \right\} \frac{(C_\theta C_\delta + S_\theta S_\delta)}{\bar{K}(\mu)} d\mu \\
&- \left\{ - \int_{-\infty}^{a_1} + \int_{a_2}^{a_3} + \int_{a_4}^{\infty} \right\} \frac{(S_\theta C_\delta - C_\theta S_\delta)}{\bar{K}(\mu)} d\mu,
\end{aligned} \tag{30}$$

and

$$\begin{aligned}
F_{\theta\delta C} = &\frac{\lambda}{\pi \Xi} \sum_{r=-\infty}^{\infty} \int_0^{\infty} \frac{(H_{\theta S} H_{\delta C} - H_{\theta C} H_{\delta S})}{\sqrt{(r/\Xi)^2 + \chi^2}} d\chi \\
&+ \left\{ \int_{a_1}^{a_2} + \int_{a_3}^{a_4} \right\} \frac{(S_\theta C_\delta - C_\theta S_\delta)}{\bar{K}(\mu)} d\mu \\
&- \left\{ - \int_{-\infty}^{a_1} + \int_{a_2}^{a_3} + \int_{a_4}^{\infty} \right\} \frac{(C_\theta C_\delta + S_\theta S_\delta)}{\bar{K}(\mu)} d\mu.
\end{aligned} \tag{31}$$

Heaving force ($F_{\delta\theta}$) due to pitching can be obtained without calculation since it is related to $F_{\theta\delta}$ by following relation

$$\frac{F_{\delta\theta} l}{\theta} = \frac{F_{\theta\delta}}{\delta}. \tag{32}$$

These sets of formulas are all needed to calculate linear forces and moments in the vertical motion.

In the above formulas Hull form characteriastics function is used of which definition is as follows. Subscripts denote corresponding modes, e.g. δ for heaving and θ for pitching. H functions are used in double integral terms and C, S's are used in single integral terms. If we denote hull form by $\eta(\xi, \zeta)$ defined as

$$\eta(\xi, \zeta) = f(l\xi, T\zeta)/b,$$

then

$$H_{\delta C} + i H_{\delta S} = \bar{D}(\frac{r}{\Xi}) \int_{-1}^{1} \int_{-1}^{0} \frac{\partial \eta}{\partial \zeta} \cos(\chi\zeta + \varepsilon) e^{ir\xi/\Xi} d\xi d\zeta, \tag{33}$$

$$H_{\theta C} + iH_{\theta S} = \bar{\boldsymbol{D}}(\frac{r}{\Xi}) \int_{-1}^{1}\int_{-1}^{0} \frac{\partial \eta}{\partial \zeta} \xi \cos(\chi\zeta + \varepsilon) e^{i\tau\xi/\Xi} d\xi d\zeta, \tag{34}$$

$$C_\delta + iS_\delta = \bar{\boldsymbol{D}}^2(\mu) \int_{-1}^{1}\int_{-1}^{0} \frac{\partial \eta}{\partial \zeta}, e^{\bar{\boldsymbol{D}}^2(\mu)\zeta + i\mu\xi} d\xi d\zeta \tag{35}$$

$$C_\theta + iS_\theta = \bar{\boldsymbol{D}}^2(\mu) \int_{-1}^{1}\int_{-1}^{0} \frac{\partial \eta}{\partial \zeta} \xi e^{\bar{\boldsymbol{D}}^2(\mu)\zeta + i\mu\xi} d\xi d\zeta, \tag{36}$$

where

$$\chi = \lambda\chi, \quad \bar{\boldsymbol{D}}^2 = \lambda\bar{D}^2,$$
$$\tan\varepsilon = -\frac{(\frac{\tau}{\Xi} + \omega)^2}{\kappa\chi}.$$

3.2 Arbitray Hull Form

All the hydrodynamic forces can be determined if hull form functions are specified. It is covenient to introduce finite Fourier series as a mean to approximatearbitrary hull form. By doing so, analytical integration can be made if possible and forces can be expressed by combination of functions like Bessels Webers and so on, of which behavior is well known.

$$\eta = \frac{8}{(N+1)(K+1)} \sum_{j=1}^{N} \sum_{k=1}^{\frac{K+1}{2}} \sum_{n=1}^{N} \sum_{l=1}^{K} \epsilon_k \eta_{jk} \sin^2 \frac{l\pi}{2} \times \sin n\alpha_j \sin l\beta_k \sin n\alpha \sin l\beta, \tag{37}$$

where

$$\begin{aligned} \xi &= \cos\alpha, \quad \zeta = -\cos\beta \\ \alpha_j &= \frac{\pi j}{N+1}, \quad \beta_k = \frac{\pi k}{K+1} \\ \epsilon_k &= \begin{cases} 1, & \text{for } k \neq \frac{K+1}{2} \\ \frac{1}{2}, & \text{for } k = \frac{K+1}{2} \end{cases} \end{aligned}$$

It is known that η coicide given values η_{jk} at (α_j, β_k). When the above formula is substituted into $H_\theta, H_\delta, C_\theta, S_\theta$ and integration with respect to α, β is made, The hull form characteristic fuctions are expressed by combination of Bessel, Weber and Struve functions and so on, as shown,

$$H_{\delta C} + iH_{\delta S} = \bar{\boldsymbol{D}}(\frac{r}{\Xi}) \sum_{j=1}^{N} \sum_{k=1}^{\frac{K+1}{2}} \epsilon_k \eta_{jk} P_{\delta j}(\frac{r}{\Xi}) R_k(\chi) \tag{38}$$

$$H_{\theta C} + iH_{\theta S} = \bar{\boldsymbol{D}}(\frac{r}{\Xi}) \sum_{j=1}^{N} \sum_{k=1}^{\frac{K+1}{2}} \epsilon_k \eta_{jk} P_{\theta j}(\frac{r}{\Xi}) R_k(\chi) \tag{39}$$

$$C_\delta + iS_\delta = \bar{\boldsymbol{D}}^2(\mu) \sum_{j=1}^{N} \sum_{k=1}^{\frac{K+1}{2}} \epsilon_k \eta_{jk} P_{\delta j}(\mu) \bar{R}_k(\bar{\boldsymbol{D}}^2) \tag{40}$$

$$C_\theta + iS_\theta = \bar{\boldsymbol{D}}^2(\mu) \sum_{j=1}^{N} \sum_{k=1}^{\frac{K+1}{2}} \epsilon_k \eta_{jk} P_{\theta j}(\mu) \bar{R}_k(\bar{\boldsymbol{D}}^2) \tag{41}$$

where

$$P_{\delta j}(\frac{r}{\Xi}) = \frac{\pi}{N+1} \sum_{n=1}^{N} i^{n-1} \sin n\alpha_j \{J_{n-1}(\frac{r}{\Xi}) + J_{n+1}(\frac{r}{\Xi})\} \tag{42}$$

$$P_{\theta j}(\frac{r}{\Xi}) = -\frac{\pi}{2(N+1)} \sum_{n=1}^{N} i^{n} \sin n\alpha_j \{J_{n-2}(\frac{r}{\Xi}) - J_{n+2}(\frac{r}{\Xi})\} \tag{43}$$

$$R_k(\chi) = (\sin\varepsilon \bar{P}_k(\chi) - \cos\varepsilon \bar{Q}_k(\chi)) \tag{44}$$

$$\bar{P}_k(\chi) = -\frac{\pi}{K+1} \sum_{l=1}^{K} (-1)^{\frac{l-1}{2}} (2l) \sin^2 \frac{l\pi}{2} \sin l\beta_k J_l(\chi) \tag{45}$$

$$\bar{Q}_k(\chi) = -\frac{\pi}{K+1} \sum_{l=1}^{K} (-1)^{\frac{l+1}{2}} (2l) \sin^2 \frac{l\pi}{2} \sin l\beta_k \boldsymbol{E}_l(\chi) \tag{46}$$

$$\bar{R}_k(z) = \frac{2\pi}{K+1} \sum_{l=1}^{K} l \sin l\beta_k \sin^2 \frac{l\pi}{2} \sum_{r=0}^{\frac{l-1}{2}} \frac{(-1)^r A_r}{2^{2r} r!} \times \left[\left(\frac{2}{z}\right)^r \{I_{r+1}(z) - \boldsymbol{L}_{r+1}(z)\} - \frac{2^{r+1} r!}{\pi(2r+1)!} \right] \tag{47}$$

Here $J_l(z)$ is Bessel function, $\boldsymbol{E}_l(z)$ is Weber function, $I_r(z)$ is modified Bessel function and $\boldsymbol{L}_r(z)$ is modified Struve function and A_r is defined by

$$A_r = \prod_{k=1}^{r} [l^2 - (2k-1)^2], \qquad A_0 = 1 \tag{48}$$

Now it is clear that, once the hull form is specified by η_{jk}, $H_{C,S}$ and C, S are determined and then calculation of $F_{C,S}$'s is straight forward.

3.3 Numerical Example

Let us discuss some of the characteristics of the present formulation by taking numerical examples. Before doing so, it is worh while to note how to remove

singularity in the single integration terms of the force evaluation for accurate numerical integration. The integrands have square root singularity at the edges. This singular behavior can be removed easily by change ofintegration variables. The change of variable is made as follows. Take a case with sigular points at the edges

$$\int_a^b \frac{F(t)}{\sqrt{(t-a)(b-t)}}dt. \tag{49}$$

Then by changing μ to θ defined as follows

$$t = \frac{b-a}{2} + \frac{b+a}{2}\cos\theta. \tag{50}$$

The singular integral can be reduced to regular integral over $(-\pi/2, \pi/2)$.

Likewise, when integration of the next type is to be made over the semi-infinite region like

$$\int_a^\infty \frac{F(t)}{\sqrt{(t-a)(t-b)}}dt, \tag{51}$$

then, by changing variables from t to τ defined as follows

$$t = \frac{b-a}{2} + \frac{b+a}{2}\sqrt{\tau^2+1}, \tag{52}$$

The integration can be made regular defined over $(0, \infty)$.

Now characteristics of the present formula will be discused by taking numerical example. Let us take a catamaran ship. The hull shape is assumed to be that of conventional container ship (S-175). Parameters are as follows

$$F_n = 0.5, \quad \kappa = 2, \quad \omega = 1.75, \quad \Omega = 0.875.$$

Let us examine characteristics of integrands for vertical motion mode first. Integrand of the double integral is shown in Fig.3. The curve show integrands after ξ-integration. The line corresponds to heaving mode. It is seen that the integrand is limited in the very narrow range near the origin and thus is easy to evaluate numerically. Next integrands appearing in single integral terms are shown in Fig. 4 through 5. All the integrands are shown after change of variables mentioned above. Since $\Omega > 1/4$, a_3 and a_3 can not exists. only integations related a_1 and a_2 can exist. Fig. 4 shows that of finite integral between a_1 and a_2. The abscissa θ is related the original variable by abovementioned relation. It is seen that the change is smooth and easy to evaluate.

Fig. 5 shows integrands in semi-infinite integral terms, i.e.$(-\infty, a_1)$ and (a_2, ∞). By solid line, Both

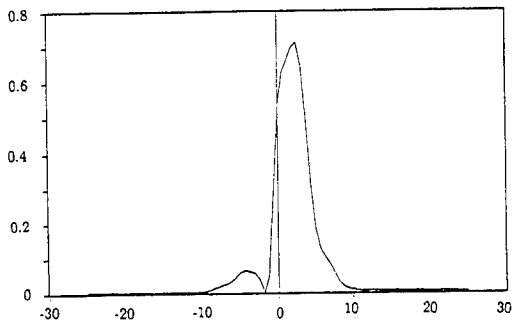

Fig. 3: Integrand of Double Integral vs. r, heaving mode, $Fn = 0.5$, $\omega = 1.75$, $\Omega = 0.875$

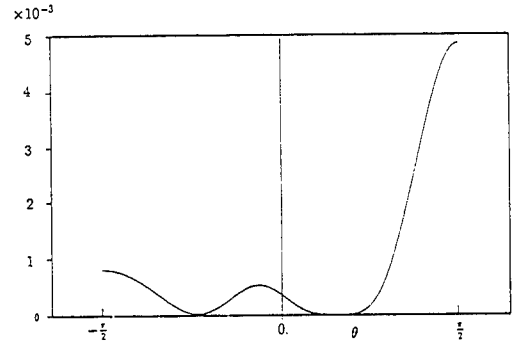

Fig. 4: Integrand of (a_1, a_2) Integral, $Fn = 0.5$, $\omega = 1.75$, $\Omega = 0.875$

ingegrands converges very rapidly enough easy numerical evaluation.

Hydrodynamic forces by present method is shown in Fig. 6 and 7. Radiation forces for heaving and pitching are shown in these figures together with strip method calculation. It is seen that present method give larger estimation than strip method does. Comparison with experimented results was not possible since those at high speed range were not at hand. It would be future task.

4 Antisymmetric Flow Problem

4.1 Integral Equation

The integral equation presented in the preceeding section is essentially unsteady lifting surface equation with surface wave effect as an extra term. Present equation is unique in the form that the kernel is expressed by Fourier integral.

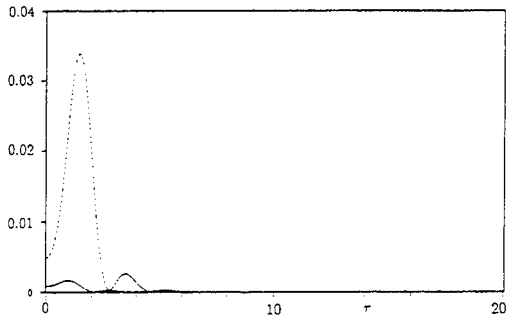

Fig. 5: Integrand of (a_2, ∞) by solid line, integrand of $(-\infty, a_1)$ integral dashed line. variable being changed from μ to τ, $Fn = 0.5$, $\omega = 1.75$, $\Omega = 0.875$

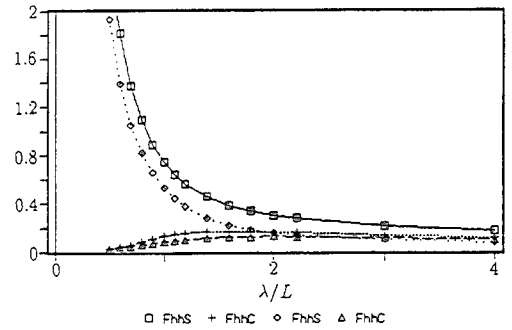

Fig. 6: Hydrodynamic Forces in Heaving, $\Diamond; F_{\delta\delta S}$, $\triangle; F_{\delta\delta C}$, $\square; F_{\delta\delta S}$(Strip Method), $+; F_{\delta\delta C}$(Strip Method) , $Fn = 0.5$, $\omega = 1.75$, $\Omega = 0.875$

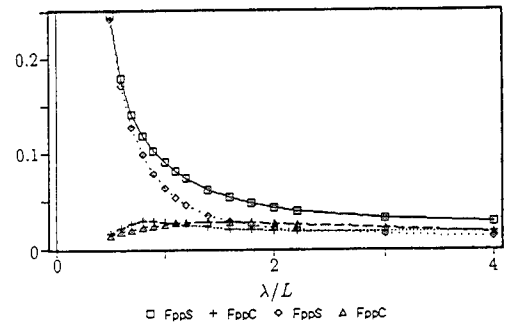

Fig. 7: Hydrodynamic Forces in Pitching, $\Diamond; F_{\delta\delta S}$, $\triangle; F_{\delta\delta C}$, $\square; F_{\delta\delta S}$(Strip Method), $+; F_{\delta\delta C}$(Strip Method) ,$Fn = 0.5$, $\omega = 1.74$, $\Omega = 0.87$

$$E(\xi,\zeta) = \int\int \Pi(\xi',\zeta') M(\xi,\zeta;\xi',\zeta') d\xi' d\zeta'. \qquad (53)$$

E shows disturbance to one demihull caused by the other demihull and vice versa.

$$\begin{aligned}
E(\xi,\zeta) &= \int_{-1}^{1}\int_{-1}^{0} \bar{w}\bar{G}_{0\eta}(\xi,\eta_o,\zeta;\xi',-\eta_o,\zeta')d\xi' d\zeta' \\
&= -\frac{2}{\pi}\int_{-\infty}^{\infty} d\mu \int_0^{\infty} e^{-2\eta_0\sqrt{\mu^2+\chi^2}}\cos(\chi\zeta+\epsilon)d\chi \\
&\times \int_{-1}^{1}\int_{-1}^{0} w(\xi',\zeta') e^{i\mu(\xi-\xi')}\cos(\chi\zeta'+\epsilon)d\xi' d\zeta' \\
&- 2\left\{\int_{a_1}^{a_2} + \int_{a_3}^{a_4}\right\} \bar{D}^2 e^{-2\eta_0\bar{K}(\mu)} d\mu \\
&\times \int_{-1}^{1}\int_{-1}^{0} w(\xi',\zeta') e^{i\mu(\xi-\xi')+\bar{D}^2(\zeta+\zeta')} d\xi' d\zeta' \\
&- 2\left\{\int_{-\infty}^{a_1} + \int_{a_2}^{a_3} + \int_{a_4}^{\infty}\right\} \bar{D}^2 e^{-2i\epsilon_p\eta_0\bar{K}(\mu)} d\mu \\
&\times \int_{-1}^{1}\int_{-1}^{0} w(\xi',\zeta') e^{i\mu(\xi-\xi')+\bar{D}^2(\zeta+\zeta')} d\xi' d\zeta' \qquad (54)
\end{aligned}$$

where

$$\eta_0 = f_0/l$$

The other symbols are defined as the last section.

The first and sedond terms represent local wave effects and the third term represents diverging wave component.

The kernel funtion(M) has a form

$$\begin{aligned}
M(\xi,\zeta;\xi',\zeta') &= \frac{2i}{\pi}\oint_{-\infty}^{\infty}\int_0^{\infty} \frac{\sqrt{\mu^2+\chi^2}}{\mu+\omega} Y(\sqrt{\mu^2+\chi^2}) \\
&\quad \times e^{i\frac{\nu}{\omega}(\xi-\xi')}\cos(\chi\zeta+\epsilon)\cos(\chi\zeta'+\epsilon)d\chi d\mu \\
&+ \frac{2i}{\sqrt{\kappa}}\left\{\int_{a_1}^{a_2} + \int_{a_3}^{a_4}\right\} \bar{D}\cdot\bar{K}\cdot Y(\bar{K}(\mu)) \\
&\quad \times e^{i\mu(\xi-\xi')+\bar{D}^2(\zeta+\zeta')} d\mu \\
&- \frac{2}{\sqrt{\kappa}}\left\{\int_{-\infty}^{a_1} + \int_{a_2}^{a_3} + \int_{a_4}^{\infty}\right\} \bar{D}\cdot\bar{K}\cdot \\
&\quad \times Y(i\epsilon_p\bar{K}(\mu)) e^{i\mu(\xi-\xi')+\bar{D}^2(\zeta+\zeta')} d\mu \\
&- 2\int_0^{\infty} \sqrt{\chi^2+\omega^2} Y(\sqrt{\chi^2+\omega^2}) \\
&\quad \times e^{-i\omega(\xi-\xi')}\cos\chi\zeta\cos\chi\zeta' d\chi
\end{aligned} \qquad (55)$$

where

$$Y(b) = 1 - e^{-2\eta_0 b}.$$

The first and forth terms represent main contribution as a lifting surface. The second and the third terms represent free surface wave effects.

4.2 Numerical Example

In order to solve the equation, the numerical scheme has to be be adopted. The equation is essentially

unsteady lifting surface equation for low aspect ratio wings. Thus experiences in the fields of the lifting surface equation problem may be made use of. Following the typical approach of the aerofoil theory, let the pressure distribution (Π) be given as a finite series of the trigonometric functions (Birnbaum series) like

$$\Pi(\alpha,\beta) = \tan\frac{\alpha}{2}\sum_{n=0}^{N}\sigma_n \cos n\alpha \sin\beta \qquad (56)$$

where α and β is defined as has been made in the former section as

$$\xi = \cos\alpha, \quad \zeta = -\cos\beta$$

This presentation denotes that the pressure has square root singularity at the leading edge(FP) and becomes null at the trailing edge to satisfy Kutta condition. Elliptic loading variation is assumed depthwise. The most variation in the vertical direction is taken based on the fact draft length ratio is very small for orgdinary hull configuration.

At the same time, approximation is introduced in the integration with respect to m of double integration terms. Same reasoning applies to this case as in the symmetric case except that the region length(Ξ) is taken longer taking into account of the flow property of the lifting problem.

Substitute (4.2) into (53) and integrate with respect to α' and β' , then we have as a coefficient for σ_n

$$\begin{aligned}
M_n(\xi,\zeta) = {} & \frac{2i}{\pi\Xi}\sum_{r=-\infty}^{\infty}\int_0^{\infty}\frac{\sqrt{(\frac{r}{\Xi})^2+\chi^2}}{\frac{r}{\Xi}+\omega}Y\left(\sqrt{(\frac{r}{\Xi})^2+\chi^2}\right)\\
\times\ & e^{i\frac{r}{\Xi}\xi}T_n(\frac{r}{\Xi})S_1(\chi)\cos(\chi\zeta+\epsilon)d\chi\\
+\ & \frac{2i}{\sqrt{\kappa}}\left\{\int_{a_1}^{a_2}+\int_{a_3}^{a_4}\right\}\bar{\boldsymbol{D}}\cdot\bar{K}\cdot Y(\bar{K})\\
\times\ & e^{i\mu\xi+\bar{\boldsymbol{D}}^2\zeta}T_n(\mu)S_2(\bar{\boldsymbol{D}}^2)d\mu\\
-\ & \frac{2}{\sqrt{\kappa}}\left\{\int_{\alpha}^{a_1}+\int_{a_2}^{a_3}+\int_{a_4}^{\alpha}\right\}\epsilon_p\bar{\boldsymbol{D}}\cdot\bar{K}\cdot Y(\bar{K})\\
\times\ & e^{i\mu\xi+\bar{\boldsymbol{D}}^2\zeta}T_n(\mu)S_2(\bar{\boldsymbol{D}}^2)d\mu\\
-\ & 2\int_0^{\infty}\sqrt{\chi^2+\omega^2}Y\left(\sqrt{\chi^2+\omega^2}\right)\\
\times\ & e^{-i\omega\xi}T_n(-\omega)S_1(\chi)|_{\epsilon=0}\cos\chi\zeta d\chi
\end{aligned} \qquad (57)$$

In the scheme of numerical evaluation , Simplification will be made to reduce ζ dependence by making average of the depthwise with elliptic loading as a weighting function. Thus only longitudinal variation remains to be determined by the equation. [6]

Let us multiply $\sin\beta$ to (54) and (55) and integration with respect to β is made. Then we have

$$\begin{aligned}
\bar{M}_n(\xi) = {} & \frac{2i}{\pi\Xi}\sum_{r=-\infty}^{\infty}\int_0^{\infty}\frac{\sqrt{(\frac{r}{\Xi})^2+\chi^2}}{\frac{r}{\Xi}+\omega}Y\left(\sqrt{(\frac{r}{\Xi})^2+\chi^2}\right)\\
\times\ & e^{i\frac{r}{\Xi}\xi}T_n(\frac{r}{\Xi})S_1^2(\chi)d\chi\\
+\ & \frac{2i}{\sqrt{\kappa}}\left\{\int_{a_1}^{a_2}+\int_{a_3}^{a_4}\right\}\bar{\boldsymbol{D}}\cdot\bar{K}\cdot Y(\bar{K})\\
\times\ & e^{i\mu\xi}T_n(\mu)S_2^2(\bar{\boldsymbol{D}}^2)d\mu\\
-\ & \frac{2}{\sqrt{\kappa}}\left\{\int_{\alpha}^{a_1}+\int_{a_2}^{a_3}+\int_{a_4}^{\alpha}\right\}\epsilon_p\bar{\boldsymbol{D}}\cdot\bar{K}\cdot Y(\bar{K})\\
\times\ & e^{i\mu\xi}T_n(\mu)S_2^2(\bar{\boldsymbol{D}}^2)d\mu\\
-\ & 2\int_0^{\infty}\sqrt{\chi^2+\omega^2}Y\left(\sqrt{\chi^2+\omega^2}\right)\\
\times\ & e^{-i\omega\xi}T_n(-\omega)S_1^2(\chi)|_{\epsilon=0}d\chi
\end{aligned} \qquad (58)$$

Same procedure will be applied to $E(\xi,\zeta)$ to give us with

$$\begin{aligned}
\bar{E}(\xi) = {} & -\frac{2}{\pi\Xi}\sum_{r=-\infty}^{\infty}\int_0^{\infty}e^{-\eta_0\sqrt{(\frac{r}{\Xi})^2+\chi^2}}\left(\frac{H_c-iH_s}{\bar{\boldsymbol{D}}}\right)\\
\times\ & e^{i\frac{r}{\Xi}\xi}S_1^2(\chi)d\chi\\
-\ & 2\left\{\int_{a_1}^{a_2}+\int_{a_3}^{a_4}\right\}e^{-2\eta_0\bar{K}(u)}(C-iS)\\
\times\ & e^{i\mu\xi}S_2^2(\bar{\boldsymbol{D}}^2)d\mu\\
-\ & 2\left\{\int_{-\infty}^{a_1}+\int_{a_2}^{a_3}+\int_{a_4}^{\infty}\right\}e^{-2i\epsilon_p\eta_0\bar{K}(\mu)}(C-iS)\\
\times\ & e^{i\mu\xi}S_2^2(\bar{\boldsymbol{D}}^2)d\mu
\end{aligned} \qquad (59)$$

Here S_1, S_2 and T_n are defined as follows

$$\begin{aligned}
S_1(\chi) = {} & \frac{\pi}{4}[\{J_0(\chi)+J_2(\chi)\}\cos\varepsilon\\
& \textit{nonumber}\\
& -\{E_0(\chi)+E_2(\chi)\}\sin\varepsilon]\\
S_2(\chi) = {} & \frac{\pi}{2x}\{I_1(x)-L_1(x)\}\\
T_n(\mu) = {} & \pi(-i)^n[J_n(\mu)+\frac{i}{2}\{J_{n+1}(\mu)-J_{n-1}(\mu)\}]
\end{aligned}$$

These formulas have been composed of functions whose behaviors are well known.

To determine σ_n numerically, a linear equation has to be set up. Easiest way is collocation method. A set of control point is selected like

$$\xi_j = \cos\frac{\pi j}{(N+1)}$$

Then N set of equations is set for determining N unknown σ_n at each points.

$$\sum_{n=1}^{N}\sigma_n\bar{M}_n(\xi_j) = \bar{E}(\xi_j) \quad (j=1,N) \qquad (60)$$

The components of the matrix may be evaluated numerically without much difficulty since the functions appearing there are expected to behave well.

4.3 Numerical Example

Let us discuss validity of the present method to estimate side force and yawing moment acting on demihulls by taking numerical example. The same model is taken as in the symmetric case. Parameters concerning motion is the same as the precedding section. Only heaving mode is treated. Side force and yawing moment(of a demihull) is integrating by integrating pressure distribution Π over the demihull surface. side force can be calculated as

$$\begin{aligned} F_y &= \rho \int_{-l}^{l} \int_{-T}^{0} (\phi_o - \phi_i) dx dz \\ &= \rho U^2 l T \int_{-1}^{1} \int_{-1}^{0} (\Pi d\xi d\zeta \\ &= \rho U^2 l T \frac{\pi^2}{4} (\sigma_0 - \frac{1}{2}\sigma_1). \end{aligned} \tag{61}$$

Yawing moment for each demihull is given as

$$\begin{aligned} M_z &= \rho \int_{-l}^{l} \int_{-T}^{0} (\phi_o - \phi_i) x dx dz \\ &= \rho U^2 l^2 T \int_{-1}^{1} \int_{-1}^{0} (\Pi d\xi d\zeta \\ &= -\rho U^2 l^2 T \frac{\pi^2}{8} (\sigma_0 - \sigma_1 + \frac{1}{2}\sigma_2). \end{aligned} \tag{62}$$

First behavior of integrands is shown by taking $G_2(\theta_1)$ of (59). Fig. 8 shows integrand of the double integration in there to $r/\Xi + \omega$. Solid line and dashoed line denote real and imaginary part respectively.

It is seen that the integrand is limited near $r/\Xi + \omega = 0$. Fig. 9, 10 and Fig. 11 show how the single integral term in the semi infinite region behave to τ of which definition is geven in the former section. The same variable conversion has been made prior to these calculation although the integration is relugar in this case.

In the integration of finite region, the integral varies smoothly.

But integrands of semi-infinite region make oscillatory motion as are shown in Fig. 10 and Fig. 11. Careful selection of increment of the numerical integration is necessary.

Fig. 12 shows magnitudes of σ_n's of the pressure distribution and how they behave as the number of terms included, N is increased. It is seen that higher order term diminished rapidly and they behave fairly well.

Fig. 13 shows how the side force and yawing moment converge with number of term, N. It is clear that the force and moment reach stable value when N excedds cetain limit, say $N = 9$.

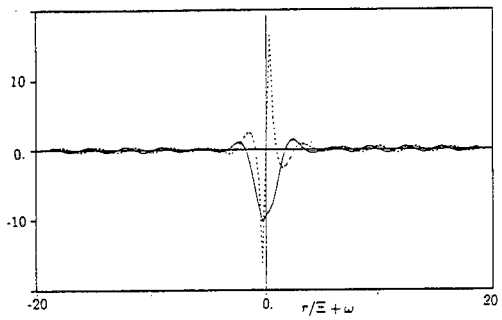

Fig. 8: Integrand Double Integral in $G_2(\xi_j)$ to $r/\Xi + \omega$, solid line for real part, dashed line for imaginary part of integrand, $Fn = 0.5$, $\omega = 1.75$, $\Omega = 0.875$

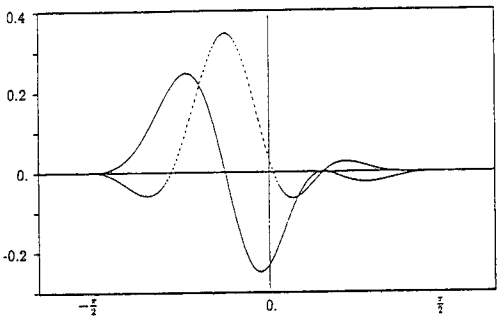

Fig. 9: Integrand of (a_1, a_2) Integral in $G_2(\xi_j)$, $Fn = 0.5$, $\omega = 1.75$, $\Omega = 0.875$

Fig. 14 shows how amplitude of the forces behaves to reduced frequency of motion, ω. It is seen that both the side force and moment diminish as the frequency ω increses.

Fig. 15 shows an example of presure distribution over the domihull. The higher pressure zone near the AP is due to square root singularity in the pressure distribution. It is seen that the pressure is high in the forepart and becomes low in the aftpart of the hull.

5 Conclusion

Discussion have been made on how to model unsteady flow field around a catamaran ship and to present a new calculation method of hydrodynamic forces on the ship in vertical motion in still water. Thin ship assumption was introduced to linearize the problem. It was shown then that the problem can be split into two problems, i.e. symmetric problem and antisymmetric problem for each demihull. It was shown that the symmetric

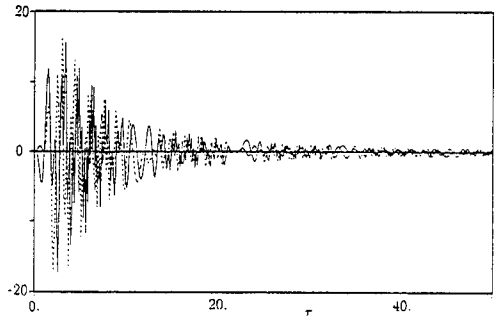

Fig. 10: Integrand of (a_2, ∞) in $G_2(\xi_j)$. Real part(solid line),Imaginary part(dashed line). Variable being changed to τ, $Fn = 0.5$, $\omega = 1.75$, $\Omega = 0.875$

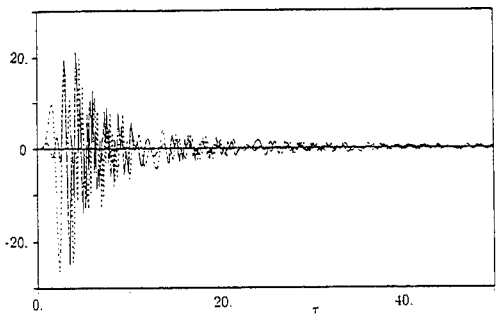

Fig. 11: Integrand of $(-\infty, a_1)$ $G_2(\xi_j)$. Real part(solid line),Imaginary part(dashed line). Variable being changed to τ, $Fn = 0.5$, $\omega = 1.75$, $\Omega = 0.875$

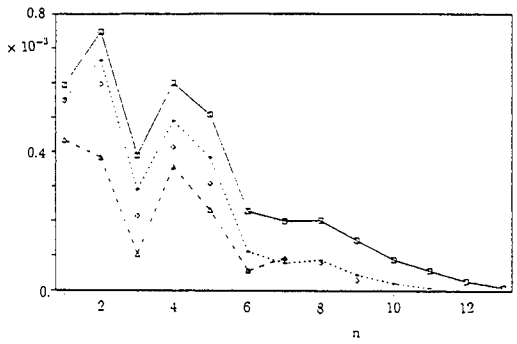

Fig. 12: Variation of Coefficients of Doulet Distribution to N,□;N=13,+;N=11 ◇;N=9,△;N=7. $Fn = 0.5$, $\omega = 1.75$, $\Omega = 0.875$

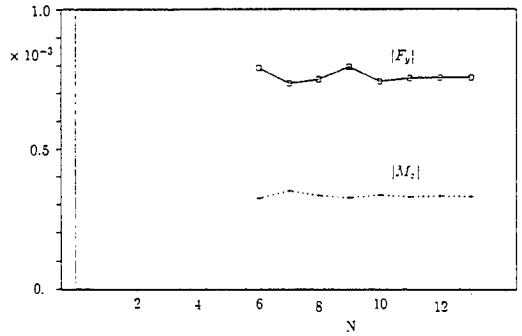

Fig. 13: Variation of Hydrodynamic Forces to N,□;Side Force +;Moment around the midship of the demihull, $Fn = 0.5$, $\omega = 1.75$, $\Omega = 0.875$

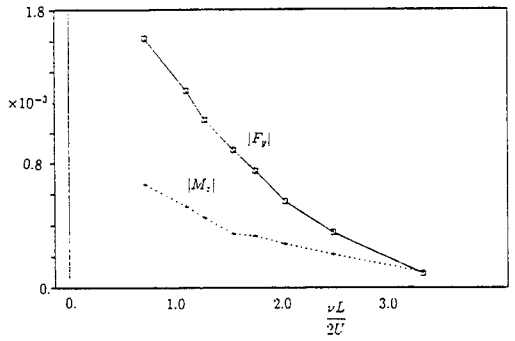

Fig. 14: Hydrodynamic Forces in Heaving vs. ω, □;Side Force +;Yawing Moment about the midship of the demihull, , $Fn = 0.5$, N=10

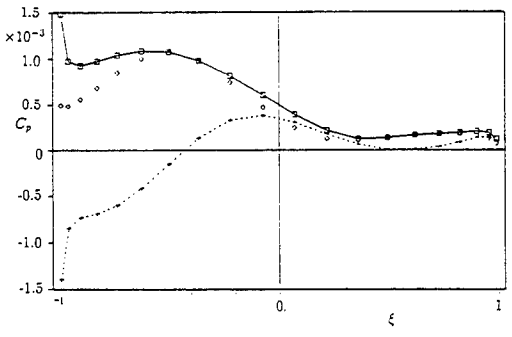

Fig. 15: Pressure Distribution in Heaving , □;Amplitude +;Real part, △;Imaginary part, , $Fn = 0.5$, $\omega = 1.75$, $\Omega = 0.875$, N=10

problem is identical with the single hull problem and thus the solution and forces and moments in vertical direction are written explicitly without difficulty. The antisymmetric flow arises due to interaction between demihulls even if the ship is making symmetric motion. The antisymmetric flow causes side force acting between demihulls. The integral equation of unsteady lifting surface to determine the flow was presented and solved numerically. The paper discussed the numerical characteristics of the method and solutions and comapred calculated horizontal forces and moments acting on the demihulls with other calculation.

Acknowledgement

The author wishes his sincere thanks to Dr.Tatsuro Hanaoka for his encouragements and suggestions during whole course of this research. It would have never been possible to reach its finish line without his presence. The author wishes to dedicate this paper to his late father who passed away in the middle of preparation of this paper.

References

[1] Kring, D., Sclavounos, P., "A New Method for Anlyzing the Seakeeping of Multi-Hill Ships", FAST'91 , 1991, pp429-444.

[2] Ohkusu,M., "Added Resistance of a Catamaran at High Froude Number", FAST'91 , 1991, pp679-691.

[3] Hanaoka,T. "On the Velocity Potential in Michell's System and the Configuration of the Wave-ridge due to a Moving Ship", Journal of Naval Architects of Japan, No.93, May, 1953, pp1-10.

[4] Hanaoka,T. "Theoretical Investigation Concerning Ship Motion in a Sea Waves", Proceedings of Symposium on the Behavior of Ships in a Seaway, Sept., 1957.

[5] Watanabe,I. "Calculation of Hydrodynamic Forces on a Ship in Waves Based upon Thin Ship Theory", Journal of Kansai Society of Naval Architects of Japan, No.217, March, 1922.

[6] Lawrence,H.R.,Gerber,E.H., "The Aerodynamic Forces on Low Aspect Ratio Wings Oscillating in an Incompressible Flow", Journal of Aeronautical Science, Vol.19, No.11, Nov., 1952, pp769-761.

[7] von Kármán, T. "Neue Darstellung der Tragflügeltheorie", ZAMM, Band 15, Heft 1, Feb., 1935, pp56-61.

DISCUSSION

R. Yeung
University of California at Berkeley, USA

I applaud the author's efforts of carrying through all analyses of this linearized problem and its successful implementation for design purposes. The decomposition to a thickness and a lifting problem used here requires a thin-body assumption. In traditional treatment of ship motion, this thin-body assumption is not needed and the body boundary condition is satisfied at the equilibrium hull surface rather than the "center-plane" of the hull(s). Such an additional "linearization" has been found to be inadequate for a single hull (Newman, 1959, J. Ship Res); hence, leading to the later development of ship theory. Inclusion of surface distribution on both sides of the demi-hull obviously complicates the analysis, but may well be needed if the author desires a realistic prediction of catamaran motion, even only for design evaluation purposes. Can the author comment on the adequacy of the thin-ship approximation used here?

AUTHOR'S REPLY

The author thanks Dr. Yeung's considerate comment. I would not argue that the thin-ship assumption adopted here can be applied on any kind of hull form or flow conditions since any kind of approximation has its field of validity. There are certain kinds of hull forms for high-speed vehicles which can be thought to have thin hull compared to conventional single-hull form. I expect the present method can give us good explanation of the flow field and forces on such kinds of flows, while keeping its merit of compact formulation of forces and clear insights on the flow.

DISCUSSION

T. Wu
California Institute of Technology, USA

In this paper, Dr. Watanabe makes a combined use of the velocity potential and acceleration potential in evaluating the hydrodynamic responses to high-speed catamaran ships undergoing steady motions which are symmetrical about the ship's centerplane. This appears to be a refreshingly innovative approach to achieving a resolution of the challenging problem since the terms of the surface integral equation over the trailing vortex sheets of the twin hulls are thus avoided. In this light, Dr. Watanabe deserves our strong recognition for this contribution of great significance.

For practical application, it is of interest to know if this method is so effective that the resulting savings of computational effort can be substantial. Further, would Dr. Watanabe comment if this method can be readily adapted to calculate solutions of hydrodynamic responses to unsteady motions of catamarans which may have small asymmetrical modes of motion such as yawing and rolling oscillations of small amplitudes.

AUTHOR'S REPLY

The author acknowledges Dr. Wu's long time contribution to our field and thanks for such an expert's comment to my paper. There are two points to which I should respond. The first point is about computation time. It only takes several minutes to calculate all the force components treated here with a modest size of work station and can be reduced further if integrations are optimized. Therefore, I think this CPU time is far shorter than any other method in this respect. As to the possibility to apply other modes of motion like rolling, sway, and yawing, we are working on those problems presently and would like to report it in the near future.

Model Testing of an Optimally Designed Propeller With Two-Sided Shifted End Plates on the Blades

K. de Jong[1,2], J. Sparenberg[2], J. Falcão de Campos[3,4], W. van Gent[4]
([1]Groningen Propeller Technology, The Netherlands; [2]University of Groningen, The Netherlands; [3]Maritime Research Institute Netherlands, The Netherlands; [4]Instituto Superior Técnico, Portugal)

SUMMARY

Model tests are carried out to investigate the hydrodynamic behaviour of an unconventional screw propeller with end plates. The end plate for each blade consists of two parts, one part attached to the pressure side of the bladetip, the other to the suction side. At the junction the end plate parts are positioned in a relatively shifted way with respect to each other. The propeller was optimized with respect to uniform inflow using variational calculus and was designed by lifting-surface theory. Open water experiments in a deep water towing tank are performed with the end plate propeller and with a state-of-the-art conventional propeller, used for reference. For the unconventional propeller also the case when the end plates were not yet fitted to the blades, is examined. Cavitation tests have been carried out in a cavitation tunnel for uniform inflow. The experimental results clearly reveal that the unconventional propeller with end plates meets some important design objectives, including the objective that a gain in propulsion efficiency can be achieved. Furthermore the propeller is free of cavitation within considerable margins around realistic levels of pressure and loading.

1. INTRODUCTION

The propeller investigated in this paper is a propeller with end plates. Its design is based upon an optimization method using variational calculus and upon a lifting-surface theory.

In the past a propeller with end plates according to such an optimization and design philosophy has already been manufactured and tested, see [1,2]. Extensions of the optimization theory were described in [3,4,5]. The implications of these extended optimization principles on the design method were reported in [6]. For a more detailed presentation of the theoretical considerations we refer to [7].

A concrete outcome of the theory of [7] is a propeller that is different from the one considered in [1,2]. A striking difference is that the new propeller has two-sided shifted end plates on the blades, whereas the propeller of [1,2] has two-sided symmetrically placed end plates. In the present paper we will discuss model testing of the propeller with the two-sided shifted end plates.

In Section 2 some particulars describing the geometry of the considered propellers used for testing are given. For the propeller with end plates we discuss shortly the geometry of the end plates and some of the underlying ideas.

In Section 3 propulsion characteristics in uniform onset flow, determined in open water model scale experiments, are presented. The propeller with end plates and an existing propeller model without end plates used for reference are considered. Both propellers have the same number of blades, equal diameter and should deliver equal thrust at a given advance speed. The propeller with end plates may operate at a lower rotation rate following from the optimization process. The reference propeller has been designed using state-of-the-art industrial practice. It has been built at full scale, and installed on a ship on which it operated satisfactory. The tests have been carried out in a towing tank.

For comparative purpose the end plate propeller was also tested when the end plates were not yet fitted to the blades. Evidently the so obtained propeller without end plates is not an optimum propeller according to the optimization and design theory. However, the extra test does give information about the influence of the end plates. A practical evaluation of the results is given. Also the propeller characteristics are compared with those of the Wageningen B-screw series. For the considered propellers without end plates a hydrodynamic analysis is carried out by means of the computer program ANPRO, based upon lifting-surface theory.

An additional verification of the hydrodynamic design principles is given in Section 4, where different kinds of cavitation are observed in a cavitation tunnel in uniform flow. It appears that in the conditions similar to full scale ship propulsion no cavitation is observed. Furthermore under operational conditions there have been shown to exist considerable

margins against cavitation for higher and lower loadings. For the purpose of flow vizualisation, the cavitational behaviour at considerable lower pressure has been observed. It turns out that some of the design objectives of the propeller with end plates are and others are not completely satisfied.

Finally in Section 5, on the basis of the experimental results, we state conclusions.

NOMENCLATURE:

A_e/A_0:	expanded blade area ratio
β:	reference pitch angle
C_D:	drag coefficient
C_T:	thrust coefficient $= (8T)/(\rho\pi D^2V^2)$
D:	propeller diameter
d:	hub diameter
η:	propeller efficiency $= (JK_T)/(2\pi K_Q)$
ϕ:	pitch angle
Γ_i:	circulation along blades and end plates, $(i=b,p,s)$
J:	advance coefficient $= V/(nD)$
K_T:	thrust coefficient $= T/(\rho n^2D^4)$
K_Q:	torque coefficient $= Q/(\rho n^2D^5)$
λ:	scale factor full scale versus model scale
$L.E.$:	leading edge
γ_i^j:	chordlines of end plate, $(i=p,s;\ j=1,\ldots,m)$
N_m:	rotation rate in open water experiments
n:	design rotation rate of propeller
p_a:	atmospheric pressure at water surface
p_w:	water column pressure
p_v:	vapour pressure
P_D:	delivered power
P/D:	pitch ratio of B-series propellers
Q:	torque
ρ:	fluid density
r:	radial position of a blade section
R:	maximum propeller radius
Rey:	Reynoldsnumber at 0.75 R
σ_n:	cavitation number
σ_p,σ_s:	spanwise length parameters of end plate
T:	thrust
$T.E.$:	trailing edge
Z:	number of propeller blades

2. PARTICULARS OF PROPELLERS

The tested propellers are designated as follows. The propeller with end plates is MARIN No. 6251. Since its design is a result of research carried out mainly in Groningen, The Netherlands, in this paper we sometimes speak of propeller No. 6251 as the Groningen Propeller. A photograph of this model propeller is shown in Figure 1. When referred to its status when the end plates are not yet fitted to the blades we write propeller No. 6251 (excl.epl.). The reference propeller model is MARIN No. 5869. The main data of these propellers are given in Table 1, while more details of the geometry can be seen in Figures 2 and 3. The intended full scale propeller has a diameter of 7.9 m, hence the length scale ratio of the propeller is 1 : 32.5.

Table 1. Some design data of the Groningen Propeller (MARIN No. 6251) and the reference propeller (MARIN No. 5869), both on model scale; scale factor $\lambda = 32.5$.

	No. 6251	No. 5869
n	4.85 Hz	7.60 Hz
A_e/A_0	0.483	0.517
J	0.624	0.399
K_T	0.425	0.173
D	243.08 mm	
d/D	0.178	
V	0.736 m/sec	
T	35.77 N	
Z	4	
ρ	1025 kg/m^3	

Because for the description of the geometry of the end plates there exists no commonly used notation, we now give a more precise impression of the shapes of the end plates of propeller No. 6251.

In Figure 4 for propeller No. 6251 the radially extrapolated tipprofile of the screwblade together with planforms of the end plate in the developed circular cylinder of diameter D are depicted. The end plate planform consists of two parts, one part in the foremost region of the screwblade, the anterior end plate part, the other part in the aftermost region, the posterior end plate part. As can be seen, in the case of Figure 4 the anterior end plate part is located at the suction side of the screwblade and the posterior end plate part at the pressure side. Along a number of chordlines denoted by γ_p^j and γ_s^j, where the subscripts p and s refer to pressure and suction side and with j=1,2,..., the profiles as depicted in Figure 5 are positioned. These profiles have to be interpreted as radial distances towards the smaller radii, measured from the chordlines γ_i^j, $(i=p,s)$, which are lying in the circular cylinder of diameter D.

We now shortly recapitulate from [7] some underlying principles that led to the nontrivial shapes of the two-sided shifted end plate. That the end plate planforms are taken as part of a circular cylinder through the bladetips, was motivated by the results

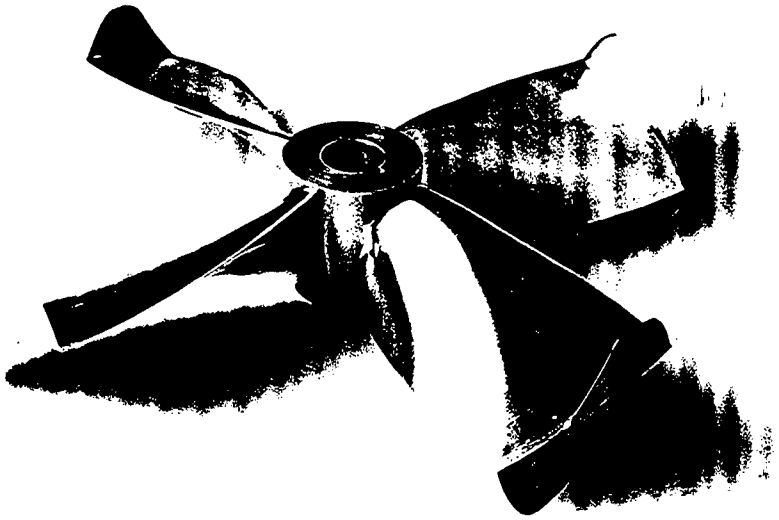

Figure 1. Groningen Propeller with two-sided shifted end plates, (MARIN No. 6251).

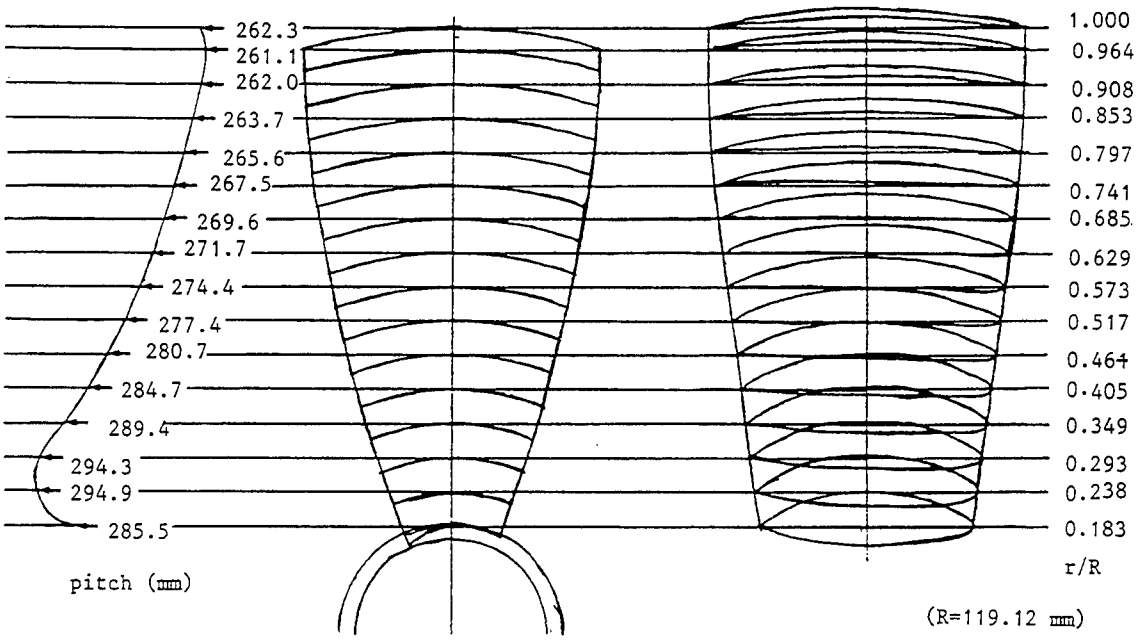

Figure 2. Blade geometry of propeller No. 6251.

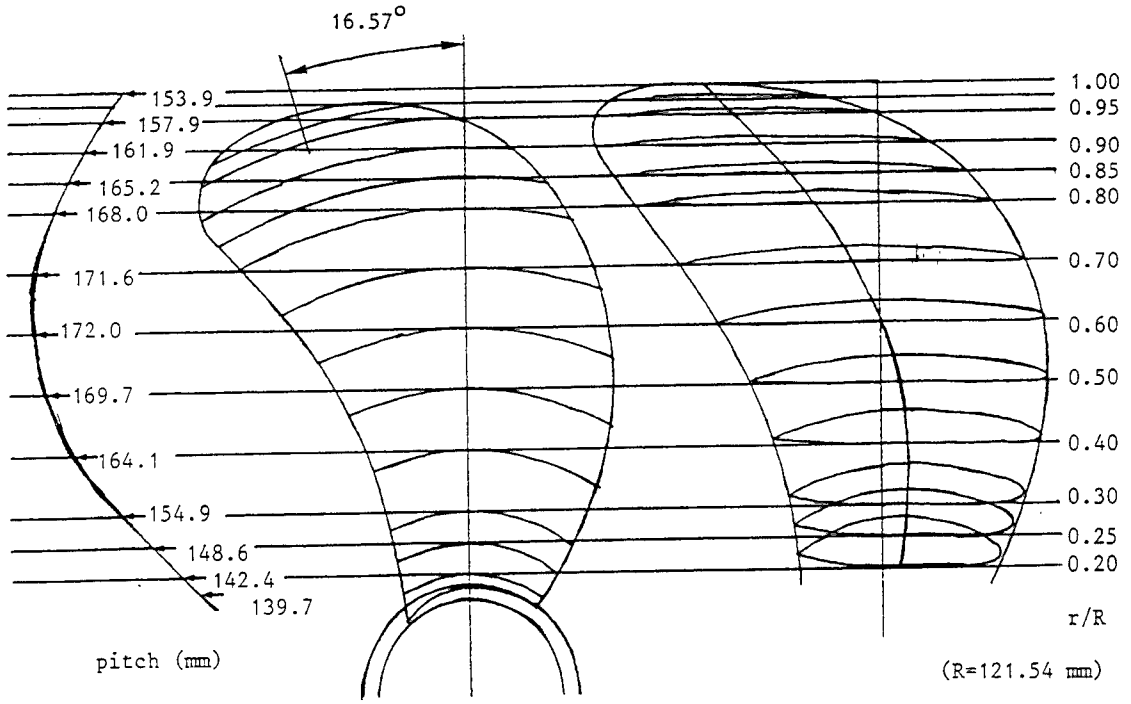

Figure 3. Blade geometry of reference propeller No. 5869.

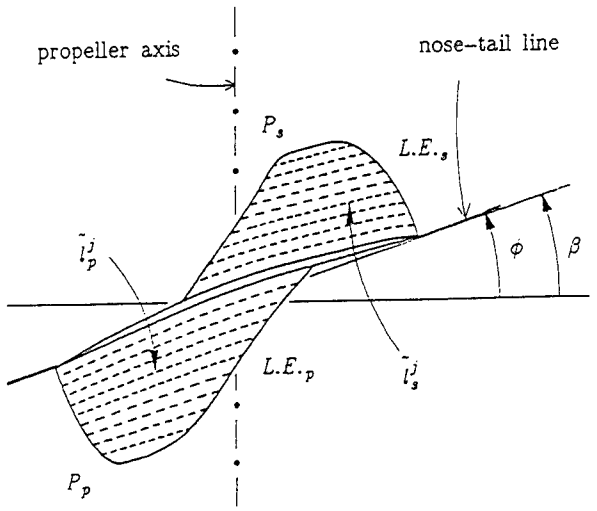

Figure 4. Propeller No. 6251; tipprofile of the blade, extrapolated to the cylinder with diameter D, and developed planforms P_p and P_s of the end plate parts; $\tilde{l}_i^j$ $(i=p,s;\ j=1,\ldots,m)$ are deformed chordlines along which the end plate profiles of Fig. 5 are positioned.

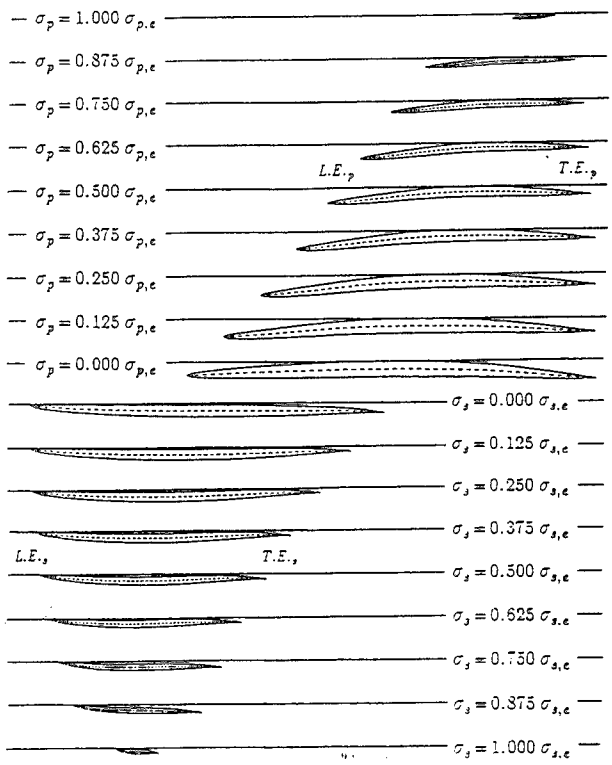

Figure 5. Propeller No. 6251; profiles at different spanwise stages of both end plate parts, to be located along the chords $\tilde{l}_i^j$ of Fig. 4;
horizontal lines ———— : at diameter D.
curved lines – – – – – : mean lines of profiles.

presented in [3]. Compared with the propeller of [1,2], the chordlengths of the end plate are reduced. The reduction of chord length is favourable because the end plates with their relatively high velocity with respect to the water, contribute substantially to the viscous energy loss of the propeller. However, the chordlengths can not be reduced too much, because in that case the danger of cavitation can become too large. Therefore a cavitation criterion was applied, that determines the chordlengths of the wingsections in connection with various section properties, such as lift and thickness influence.

The end plate parts with their roots have to cover completely the bladetip, in order to avoid in the vortex theory of the propeller the occurrence of a concentrated vortex segment at the bladetip. This is undesirable when lifting-surface design has to be carried out. Also an overlap between the roots of the end plate parts appeared necessary in order that on the one hand the vorticity can be conveyed smoothly from the blade to both end plate parts and that on the other hand favourable chordwise pressure jump distributions can be prescribed. Leading and trailing edge shapes of the end plate parts were chosen in such a way that at the thus obtained planforms the corresponding induced velocities do not exhibit unwanted singular behaviour.

That the anterior end plate part is at the suction side of the blade and the posterior part at the pressure side, has to do with the fact that for this situation the hydrodynamical lift forces cause in the blades and end plates lower internal stress levels than in the case when the anterior and posterior parts were positioned the other way round.

Observing the profiles it can be derived that the end plate part at the pressure side of the blade has the tendency to produce an "inwash", by which we mean that the water just downstream of the end plate part for the most part has a velocity component directed towards smaller radii. The end plate part at the suction side has the tendency to produce an "outwash", that is the water just downstream of its trailing edge has a velocity component directed mainly towards larger radii. The induced inwash and outwash, respectively, have a counteracting influence on the tendency of the fluid to flow around the tip from pressure to suction side (tipvortex), when no end plate would have been fitted to the bladetip. This simple and retrospective way of looking at the profiles agrees with the underlying optimization and design theory which aimed for an important part at spreading more evenly the trailing vorticity of a propeller by using extra wings in the form of the end plates, see [7].

That the end plates are two-sided and not one-sided is because the splitting of circulation at the bladetip into two parts to be conveyed from the blade to each end plate part in combination with the applied cavitation criterion, makes the surface area of the two-sided shifted end plate smaller than the surface area belonging to a comparable one-sided end plate. Of course this is important for keeping the viscous energy loss contribution of the end plates within bounds. The spans of the end plate were determined by an optimization method that minimized the sum of kinetic and viscous energy loss in order to find optimum circulation distributions. A number of design requirements of propeller No. 6251 were derived from a tuning process based upon the reference propeller No. 5869. The admitted underpressure at the suction sides of blades and end plates and the admitted maximum stresses in the material are examples of the design requirements.

The hub and blades of the Groningen Propeller have been manufactured at MARIN in a standard manner. The outer sections of the blades, about $2\,mm$ radial span, to which the end plates are attached, have been manufactured separately. The manufacture of the end plates required special attention. The shape of the end plates could not be described as a series of similar wing sections of which only the chord length, maximum thickness and camber varied in spanwise direction, as is mostly the case for the propeller blades. Instead, to allow fully for the merits of the theoretical design approach, the end plates are considered as hydrofoils of a general three-dimensional shape. A geometrical data file format suitable for Computer Aided Manufacturing has been used.

3. OPEN WATER TESTS

For the purpose of a reliable and accurate determination of the effect of end plates on the propeller performance, a clear specification of the test conditions is required. Moreover, tests with the different propellers should take place under identical circumstances. The open water tests have been carried out in the MARIN Deep Water Towing Tank.

For all final tests one and the same rotation rate has been used, that is $N_m = 800\,RPM$. This rotation rate has been chosen to be sufficiently high to avoid laminar flow effects on the propeller blades and to be sufficiently low to measure even the highest propeller loadings with one and the same calibrated measuring device. A check on the choice of the RPM-value has been made by repeating the tests on propeller No. 6251 (excl.epl.) at $N_m = 1000\,RPM$. The differences in the dimensionless thrust and torque coefficients were less than 1 percent except at the higher J-values. This is considered to be satisfactory.

Propeller No. 5869 has been used not only as a reference on which the design of the Groningen Propeller was tuned, see [6,7], but also as an experimental reference model during the tests. To check the repeatability of the test conditions propeller No. 5869 has been tested directly after propeller No. 6251 (excl.epl.), and again after propeller No. 6251 with end plates mounted. In between, some extra points have been measured for propeller No. 6251 (excl.epl.) to check the previous results. Again the repeatability is considered to be sufficient (ΔK_T and ΔK_Q less than 1 percent, except for some high J-values). The results of the open water tests are presented in numerical and graphical form. See Tables 2-4 and Figures 6 and 7. If we observe that the intended effect of the end plates is an increase of circulation around the propeller blades in the tipregions and that their unavoidable detrimental effect is extra viscous drag, the following comments can be given on the results.

First we compare propeller No. 6251 and propeller No. 6251 (excl.epl.), see Tables 2,3 and Figure 6. Over nearly the whole range of J-values K_T and K_Q are higher for the propeller No. 6251 with end plates. The maximum differences in comparison with propeller No. 6251 (excl.epl.) are about 0.047 and 0.0072, respectively, in the range between $J = 0.50$ and $J = 0.70$, which is about the design and operational condition.

For the high J-values the increase of K_T due to the effect of end plates becomes sligthly negative. The

Table 2. Open water model test results of propeller No. 6251 (excl.epl.); rotation rate 13.3 $Hz = 798$ *RPM*.

No. 6251 (excl.epl.)			
J	K_T	K_Q	η
.00	.5700	.08705	.000
.10	.5395	.08339	.103
.20	.5065	.08005	.201
.30	.4710	.07660	.294
.40	.4330	.07280	.379
.50	.3930	.06856	.456
.60	.3512	.06385	.525
.70	.3081	.05872	.585
.80	.2637	.05323	.631
.90	.2180	.04742	.659
1.00	.1705	.04128	.657
1.10	.1203	.03471	.607
1.20	.0658	.02745	.458
1.30	.0048	.01909	.052
1.307	.0000	.01841	.000

Table 3. Open water model test results of propeller No.6251 with end plates; rotation rate 13.3 $Hz = 798$ *RPM*.

No. 6251 with end plates			
J	K_T	K_Q	η
.00	.6038	.08566	.000
.10	.5733	.08342	.109
.20	.5441	.08171	.212
.30	.5132	.07991	.307
.40	.4788	.07760	.393
.50	.4402	.07456	.470
.60	.3975	.07067	.537
.70	.3508	.06593	.593
.80	.3009	.06039	.634
.90	.2481	.05410	.657
1.00	.1925	.04714	.650
1.10	.1334	.03948	.592
1.20	.0694	.03106	.427
1.297	.0000	.02192	.000

Table 4. Open water model test results of reference propeller No. 5869; rotation rate 13.3 $Hz = 798$ *RPM*.

No. 5869			
J	K_T	K_Q	η
.00	.3195	.03377	.000
.05	.3054	.03251	.075
.10	.2895	.03115	.148
.15	.2723	.02968	.219
.20	.2540	.02813	.287
.25	.2348	.02650	.353
.30	.2150	.02480	.414
.35	.1946	.02303	.471
.40	.1737	.02121	.521
.45	.1525	.01933	.565
.50	.1307	.01738	.599
.55	.1084	.01534	.619
.60	.0853	.01318	.618
.65	.0613	.01085	.584
.70	.0358	.00830	.480
.75	.0086	.00545	.187
.765	.0000	.00452	.000

effect on K_Q remains positive. These observations can be understood in view of the dominating viscous drag forces for ligthly loaded conditions, which situation is enhanced by the end plates.

For the low J-values it is remarkable that the increase in K_T due to the end plates remains, but the increase of K_Q disappears and becomes even negative at the highest loading condition. Similar tendencies of the curves of K_T and K_Q are also observed for the propeller with two-sided symmetrically end plates of [1], see [2]. Also these tendencies are known to occur for ringpropellers and propellers in ducts. A tentative explanation for this effect is that at the very high loading conditions the kinetic energy loss becomes far more important than the viscous energy loss. Then the presence of an additional winglike object in the tipregion of the blades can decrease, by spreading more evenly the trailing vorticity, the kinetic energy loss and hence the induced drag by a relatively large amount. This can be achieved at the cost of a relatively small increase of viscous drag.

The maximum increase of efficiency of propeller No. 6251 due to its end plates is 1.4 percent between $J = 0.4$ and 0.5. It has to be noted that an increase of efficiency in combination with increased K_T and K_Q is a tendency different from systematic series. In such series an increase of K_T and K_Q, obtained by a higher pitch to diameter ratio, is always connected with a reduction of efficiency.

As an example of comparison with series propellers we consider the B-series with the same number of blades $Z = 4$ and the same expanded blade area ratio $A_e/A_0 = 0.48$ as the Groningen Propeller. These B-series propellers are considered in the situation that they have the same power coefficient $(K_Q/J^3)^{\frac{1}{4}} = 0.732$ as propeller No. 6251 has in its design point $J = 0.624$. The data of the B-series propellers have been derived from the well-known polynomial expressions that are available for these propellers. Tabulated first in Table 5 is the B 4-48 propeller having at the same value $J = 0.624$ the same $K_Q = 0.0696$ as propeller No. 6251. It is the B-series propeller with pitch ratio $P/D = 1.33$. It is seen that the Groningen Propeller has a 5.4 percent higher efficiency and a 9.5 percent higher thrust coefficient C_T than this B-series propeller. To further illustrate the good efficiency of propeller No. 6251 we next select the B 4-48 propeller with the highest obtainable efficiency when, in satisfying the prescribed value $(K_Q/J^3)^{\frac{1}{4}} = 0.732$, the J-value is left

Table 5 Comparison between Groningen Propeller (MARIN No. 6251) with end plates and B-series propellers; all propellers have $Z = 4$, $A_e/A_0 = 0.48$, $(K_Q/J^3)^{\frac{1}{4}} = 0.732$.

	No. 6251	B-series ($Rey = 2.0*10^6$)	
		$P/D = 1.33$	$P/D = 0.815$
J	0.624	0.624	0.454
K_Q	0.0696	0.0696	0.0267
K_T	0.388	0.354	0.197
C_T	2.54	2.32	2.44
η	55.4 %	50.0 %	53.3 %

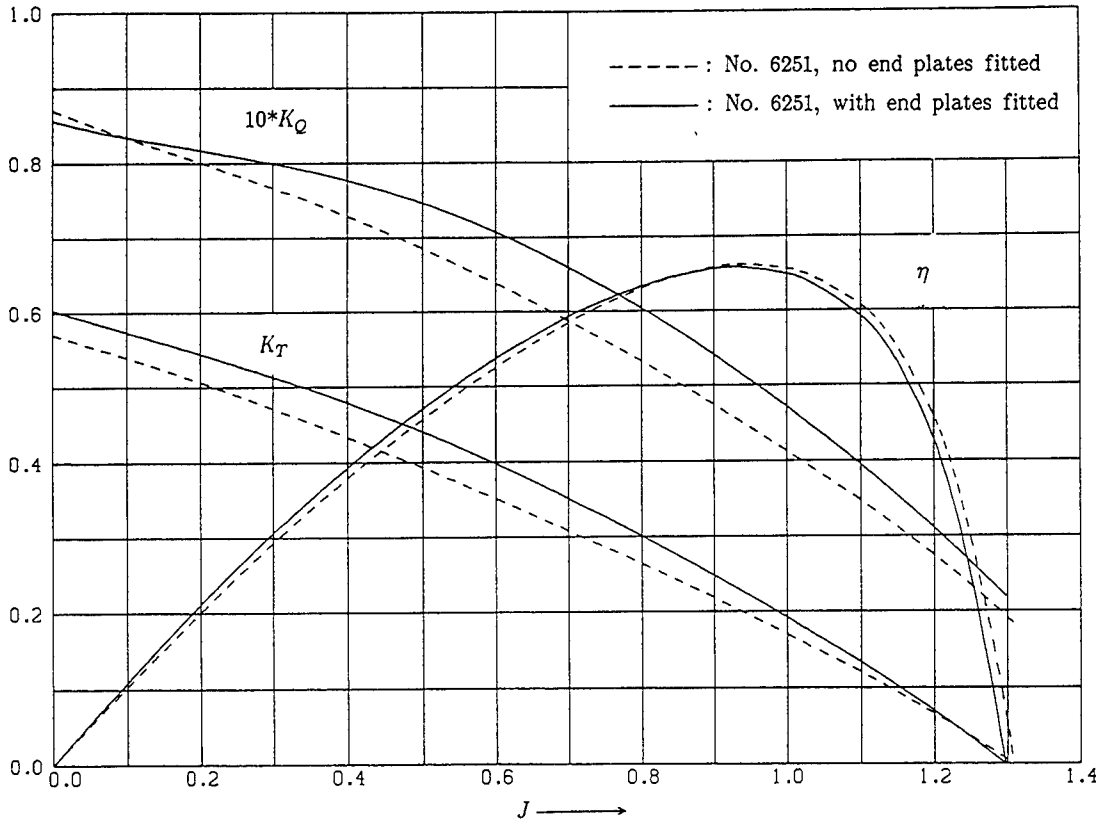

Figure 6. Open water characteristics of propeller No. 6251 (Groningen Propeller).

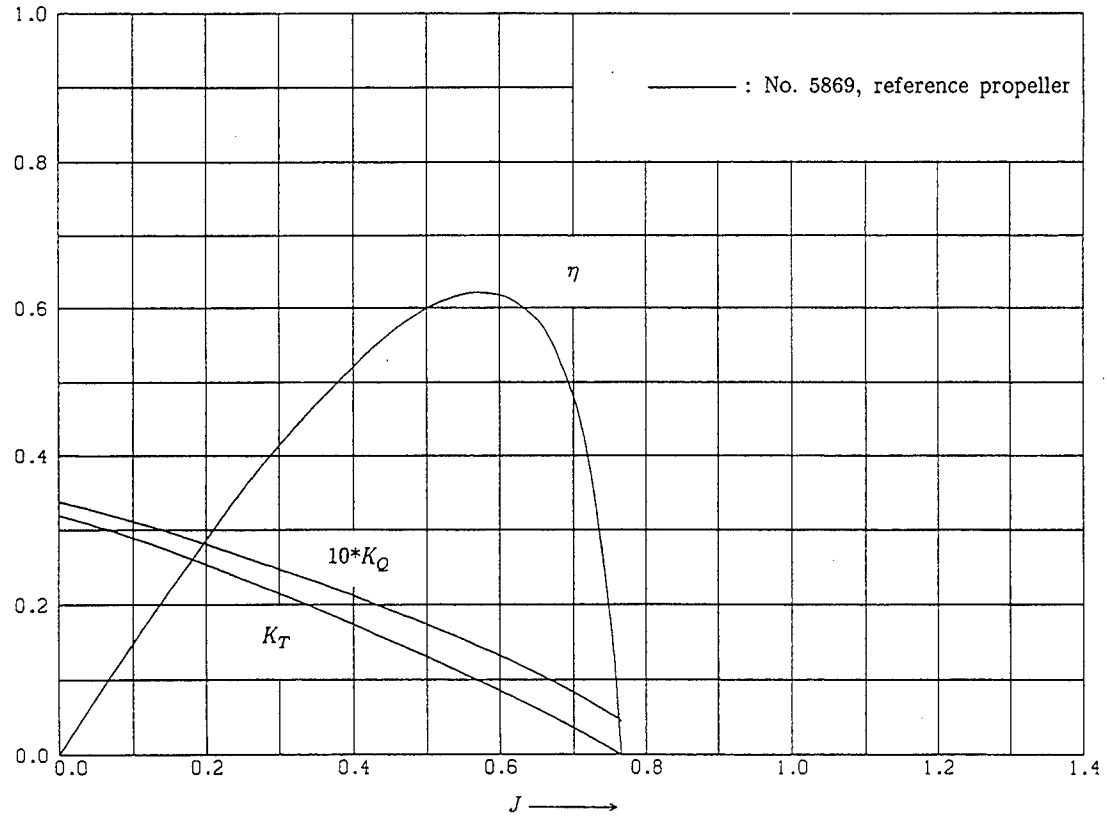

Figure 7. Open water characteristics of propeller No. 5869 (reference propeller).

free. We find that this is the B-series propeller with $P/D = 0.815$. The operational condition for this propeller is $J = 0.454$, see Table 5. Even with respect to this B-series propeller, propeller No. 6251 has a 2.1 percent higher efficiency and a 4.1 percent higher thrust coefficient C_T.

It has to be noted that for the Reynoldsnumber of the B-series propellers we have chosen $Rey = 2.0*10^6$. Actually this value is higher than for the propeller No. 6251 in its design point, for which holds $Rey = 0.15*10^6$. If we had chosen more suitable, lower Reynoldsnumbers for the B-series propellers, obviously the comparison would have been more in favour of the Groningen Propeller. However, since in this paper we did not actually check experimentally one B-series propeller under identical test conditions as for the other propellers, the comparison with the B-series propellers is only a qualitative one.

That a propeller with end plates can have a higher efficiency than any individual propeller of a complete class of propellers without end plates, as illustrated above with the B-series example, was already predicted in [7] from numerical calculations. The amounts of gain (5.4 and 2.1 percent, respectively) are in the same order of magnitude as the efficiency differences predicted in [7]. It is remarked that in [7] instead of the power coefficient the thrust coefficient C_T was prescribed.

The propeller with end plates does not meet its design conditions. At $J = 0.624$ a K_T of 0.425 was aimed at. The achieved value of K_T is 0.388. The thrust discrepancy must be attributed to shortcomings in the optimization and design theory. At the relatively heavy design loading condition of the Groningen Propeller the too simply modeled nonlinear effects become noticeable. Also the theoretical estimation of the viscous resistance of the propeller can play a role.

For an evaluation of the results of the tested propellers for practical application we consider two main possibilities, which only differ in one aspect. First, we compare for equal propeller power P_D, diameter D and ship speed V. Second, we compare for equal propeller thrust T, diameter D and ship speed V.

For equal power the non-dimensional base for comparison is

$$(K_Q/J^3)^{\frac{1}{4}} = \left(\frac{P_D}{2\pi\rho D^2 V^3}\right)^{\frac{1}{4}}$$

In Figure 8 the efficiencies of the propellers are plotted on this base. At the design point of the reference propeller the efficiency of the Groningen Propeller (MARIN No. 6251) is 53.58 percent and of the reference propeller 52.09 percent. The difference is 1.49 percent. The equal power condition corresponds to a value of $J = 0.60$ for propeller No. 6251, while its design value is $J = 0.624$. Hence to absorb the design power value the operational rotation rate of propeller No. 6251 has to be 4 percent higher than the design value.

For equal thrust the non-dimensional base for comparison is

$$C_T = \frac{8}{\pi}\frac{T}{\rho D^2 V^2} = \frac{8}{\pi}\frac{K_T}{J^2} \quad .$$

In Figure 9 the efficiencies of the three propellers are plotted on this base. At the design point of the reference propeller, where $C_T = 2.77$, the efficiency of propeller No. 6251 is 53.90 percent. The difference with the reference propeller is now 1.81 percent. The equal thrust condition corresponds to a value of $J = 0.603$ for propeller No. 6251 while the value at

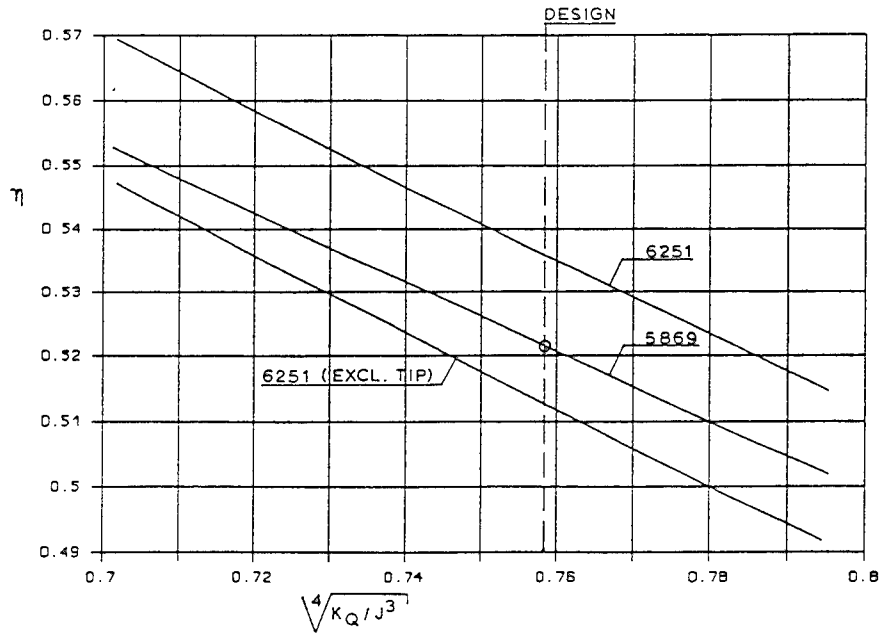

Figure 8. Comparison of propeller efficiencies on the basis of equal power.

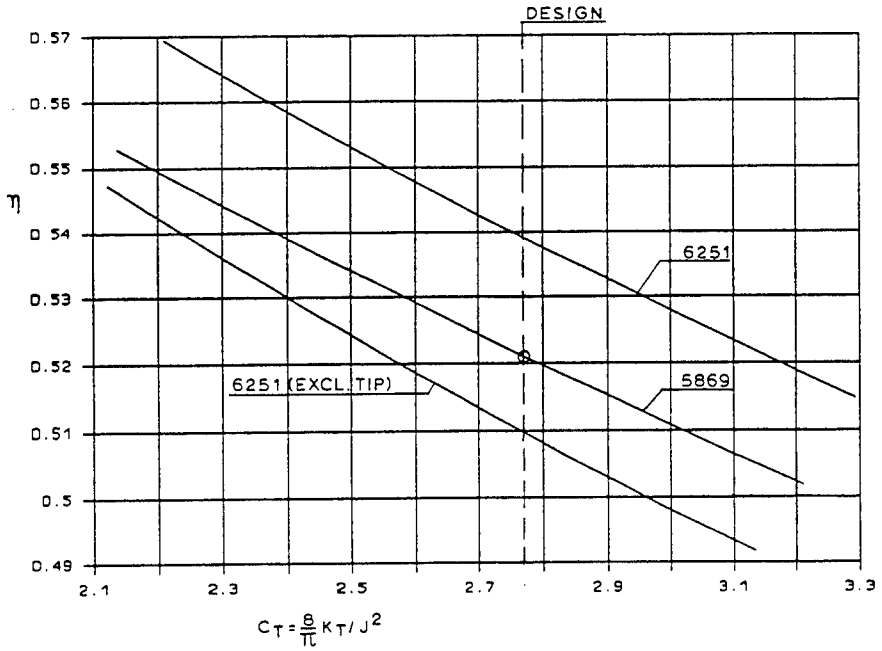

Figure 9. Comparison of propeller efficiencies on the basis of equal thrust.

design is $J = 0.624$. Hence to deliver the design thrust the operational rotation rate of propeller 6251 has to be 3.5 percent higher than the design value. From Figures 8 and 9 it can also be derived that the practical differences in efficiencies for propeller 6251 with end plates and without end plates, respectively, is between 2.3 and 3.0 percent.

For the reference propeller and for propeller No. 6251 (excl.epl.) a hydrodynamic analysis was carried out by means of the MARIN propeller analysis computer program ANPRO, based upon lifting-surface theory. The calculations were carried out for a Reynolds number corresponding to the model scale. For propeller No. 5869 the effective drag coefficient at a radial position $r/R = 0.7$ was taken equal to $C_D = 0.0113$.

If compared with the test results of Table 4 and Figure 7, it was noted that the agreement between theory and experiment was very good for the K_T-values. However, the theoretical values of K_Q were higher than the experimental ones. Some additional calculations were carried out to find the sensitivity of the calculations to the selected C_D-value. It appeared that a value of $C_D = 0.0070$ gave best agreement for the theoretical and experimental K_Q-values, while the agreement of K_T-values remained nearly unchanged.

Analogously for propeller No. 6251 (excl.epl.) the effective drag coefficient at a radial position $r/R = 0.7$ was taken equal to $C_D = 0.0133$. If compared with the test results of Table 2 and Figure 6, it was noted that the agreement between theory and experiment was very good for the K_T-values. The theoretical K_Q-values were lower than the experimental values, however. Some additional calculations were carried out to find the sensitivity of the calculations to the selected C_D-value. It appeared that a value of $C_D = 0.0180$ gave the best agreement.

It has to be noted that the discrepancies in K_Q-values between computational analysis and experimental results are different. Propeller No. 5869 seems to have a lower drag of the blades than expected theoretically and propeller No. 6251 (excl.epl.) seems to have a higher drag. The latter may have extra drag at the blade tip, due to its abrupt ending. This extra drag is not accounted for in the ANPRO computations. Another tentative explanation for the difference in K_Q between the analyzed propellers may be found in the differences in blade section profile shape. Then it could be concluded that the blade section profiles of propeller No. 6251 could possibly be improved.

4. CAVITATION OBSERVATIONS

Cavitation observations have been carried out in the MARIN Large Cavitation Tunnel. The cavitation number which has to be equal to real conditions is defined as follows

$$\sigma_n = \frac{p_a + p_w - p_v}{\frac{1}{2}\rho n^2 D^2} \quad .$$

The numerator contains pressures from ambient conditions, that is p_a is the atmospheric pressure at the water surface (about $1.0*10^5\ N/m^2$), p_w is the water column pressure at submergence depth and p_{v_2} is the vapour pressure in cavity (about $2.0*10^3\ N/m^2$). The denominator is a measure for the pressure created by the propeller action. For propeller No. 6251 we take the full scale values of rotational velocity n and propeller diameter D from Table 1 by dividing the small scale rotational velocity by $\lambda^{1/2}$ and by multiplying the small scale diameter by λ, respectively, where λ is the scale factor ($\lambda = 32.5$). Then, for a shaft submergence

depth of $8\,m$ the cavitation number becomes $\sigma_n = 7.69$. After correction for the required higher rotational velocity to absorb the design power, this number reduces to $\sigma_n = 7.15$.

When varying the tunnel water speed, a variation of propeller loading at constant cavitation number is obtained. By varying the pressure in the cavitation tunnel the cavitation number can be changed. In a diagram as given in Figure 10, different loading and cavitation conditions can be represented. On the vertical axis the value of σ_n is indicated and on the horizontal axis the value of K_T. The value of K_T at which propeller No. 6251 delivers the required thrust is $K_T = 0.40$ at $J = 0.60$. At this operational condition and the above value of $\sigma_n = 7.15$, no cavitation is observed, as indicated in Figure 10.

By means of variation of tunnel water speed and pressure (propeller rotation rate is kept constant at

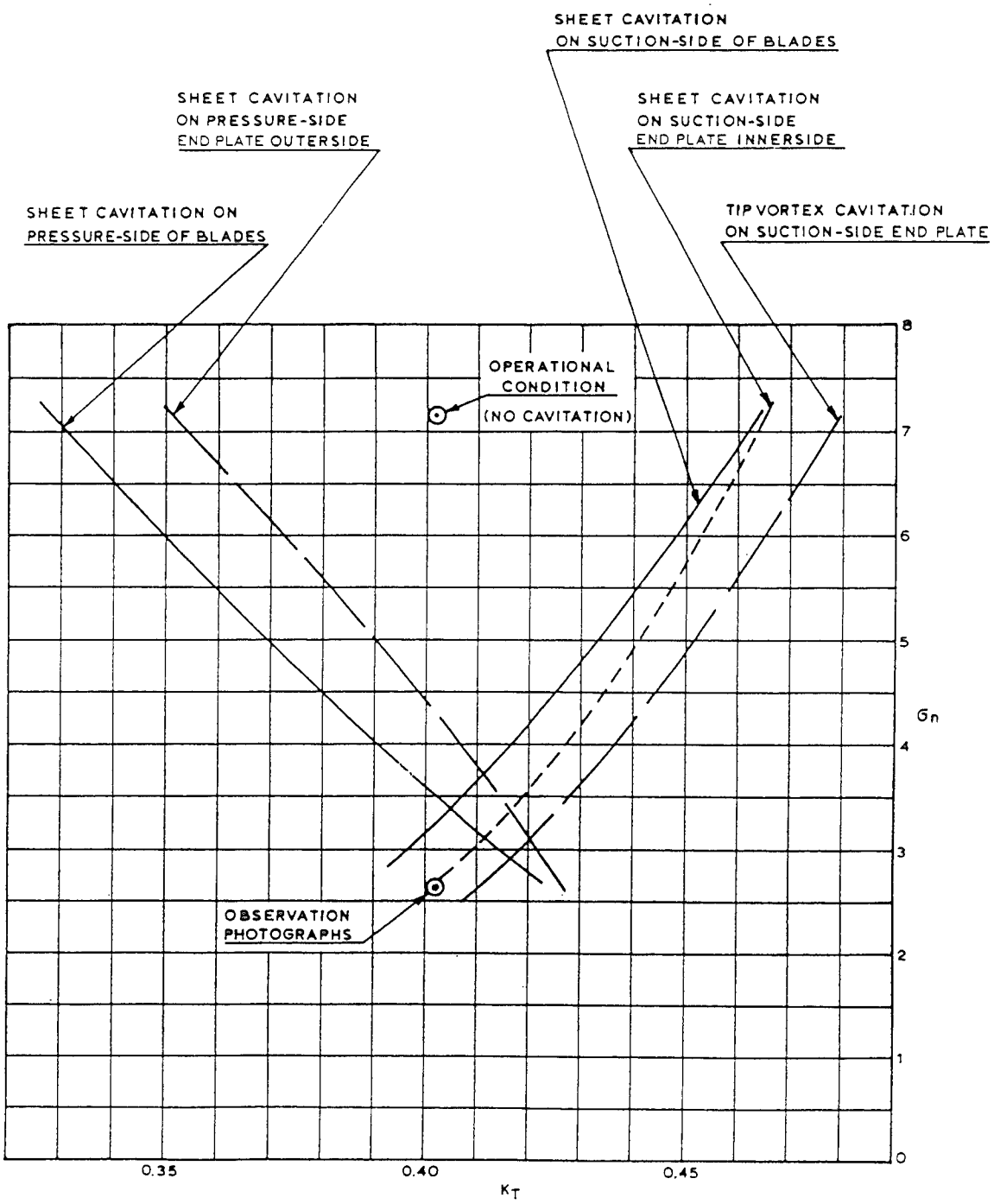

Figure 10. Cavitation inception diagram for propeller No. 6251 with end plates.

1500 *RPM*) the conditions have been observed and measured for which various types of cavitation start to occur. These conditions are also plotted in Figure 10 and data points for similar types are connected with lines. It can be concluded that the operational condition has considerable margins against cavitation for higher loadings (suction side cavitation) and for lower loadings (pressure side cavitation).

For one condition, $\sigma_n = 2.60$ and $K_T = 0.402$, photographs have been taken. Two photographs, one from the side and another from an oblique upstream position, have been taken for four blade positions, respectively blade 1, 2, 3 and 4 pointing to the side. See the photographs of Figure 11. The various types of cavitation can be seen; apparently small geometrical differences between the respective propeller blades lead to different sizes of the cavities. Also some differences between the upstream and side photographs occur; they are not taken simultaneously.

On the photograph with blade 1 pointing to the side it is seen that a vortex starts from the T-junction of the blades and the end plates. In the photograph from the side also a vortex from the tip of the suction side end plate can be seen.

On the photograph with blade 2 pointing to the side simultaneous occurrence (not on one and the same blade) of three vortices, from the blade junction and from the tips of the end plate parts can be seen.

On the photographs with blade 3 to the side it can be seen that the vortex from the pressure side plate tip has a lower pitch and a larger diameter than the vortex from the junction. The reverse situation has been observed for a high loading, $K_T = 0.60$, for about zero main flow velocity. In that case the vortex from the junction had the larger diameter and approximately zero pitch, while the vortex from the suction side end plate tip had a smaller diameter and a larger pitch. This mutation has not been photographed; the cavitation of the junction vortex appeared as very small bubbles.

The occurence of the weak vortices from the tips of the end plate parts at pressure and suction side, respectively, is in accordance with what was aimed at in the optimization and design method by which propeller No. 6251 was calculated. That is, theoretically, when the propeller has optimum circulation distributions, the trailing vorticity must have a square-root singularity at the tips of the end plate parts which has a small coefficient. The resulting vortices are the ones that are visible in the cavitation tunnel, but only for the low cavitation number.

That the vortices from the tips of the end plate parts at the pressure side are at larger radii than the vortices from the end plate part at the suction side is in agreement with the intended nature of the vortex wake of the end plates. In Figure 12 the planforms of one blade and end plate of propeller No. 6251 together with the corresponding vorticity and circulation distributions at the planforms and in the wake of the planforms are drawn. The calculated data belonging to these pictures followed from the optimization theory and from some design requirements. The data were used as input for the lifting-surface design method, see [6,7]. It is seen that in the wake of the end plate planforms the trailing vorticity of both end plate parts has the same sign in the helicoidal direction. Such a wake will have the tendency, by its own induced velocity, to show tipvortices, the one from the end plate part at the suction side of the blade rolling up towards smaller radii and the other rolling up towards larger radii, which is exactly what in the cavitation tunnel is observed.

An indication for this effect can already be seen from the shape of the calculated end plate tipprofiles, see Figure 5. It is seen from this figure that the direction of the mean line of the profile at the tail of the tip of the end plate part at the pressure side of the blade is towards larger radii and of the other end plate part towards smaller radii. Furthermore the tail of the tipprofile of the end plate part at the pressure side of the blade is at a larger radius than the tail of the tipprofile of the other end plate part.

The occurence of the vortex from the T-junction does not follow from the vorticity pattern of Figure 12. It must be realized that the vortex is not that strong as for conventional propellers without end plates, and that at the examined cavitation number $\sigma_n = 2.60$ which is considerably lower than the design cavitation number $\sigma_n = 7.15$, the cavitation that occurs in the tipregion of the screwblade at the suction side can easily feed the vortex with vapour.

Observing carefully the beginning of the vortex from the T-junction, it seems that it is shed from the root of the end plate part at the suction side of the blade. The shape of the end plate profiles at the suction side of the screwblade was given in Figure 5. It is observed that near the trailing edge the mean lines of the profiles have the tendency to be shaped in a more or less S-bend fashion. It appeared that this shape is due to a recently found error in the code of the lifting-surface design program that was used for the calculation of propeller No. 6251. After correcting the error in the code, the resulting calculated blades and end plates remained practically unchanged. The only noticeable deviation in geometry occurred for the end plate part at the suction side of the blade near the tail of the section profiles. It is found that the S-bend behaviour does not occur using the corrected code, as is shown in Figure 13, where the corrected end plate profiles are given. It is seen that the correction of the profiles is relatively larger near the root of that end plate part, hence nearer to the junction, than to its tip.

So a possible contribution to the occurence of the vortex from the T-junction might be the wrongly calculated end plate profiles near the junction, which might induce some unwanted extra circulation resulting in the shed vorticity from the root of the end plate part. If indeed the above explanation is true, not only the cavitational behaviour but also the efficiency of the propeller with end plates can possibly be improved somewhat. This is because the corrected end plate shapes are expected to yield then a slightly better spreading of the trailing vorticity in the sense of obtaining lower kinetic energy loss.

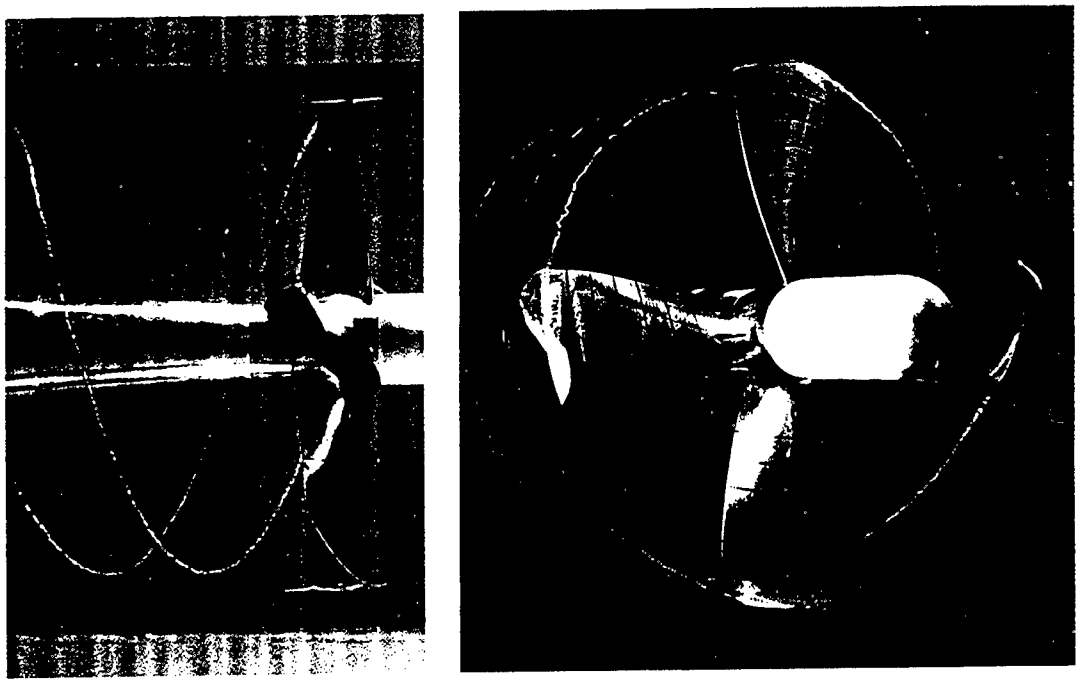

(a) blade 1 pointing to the side.

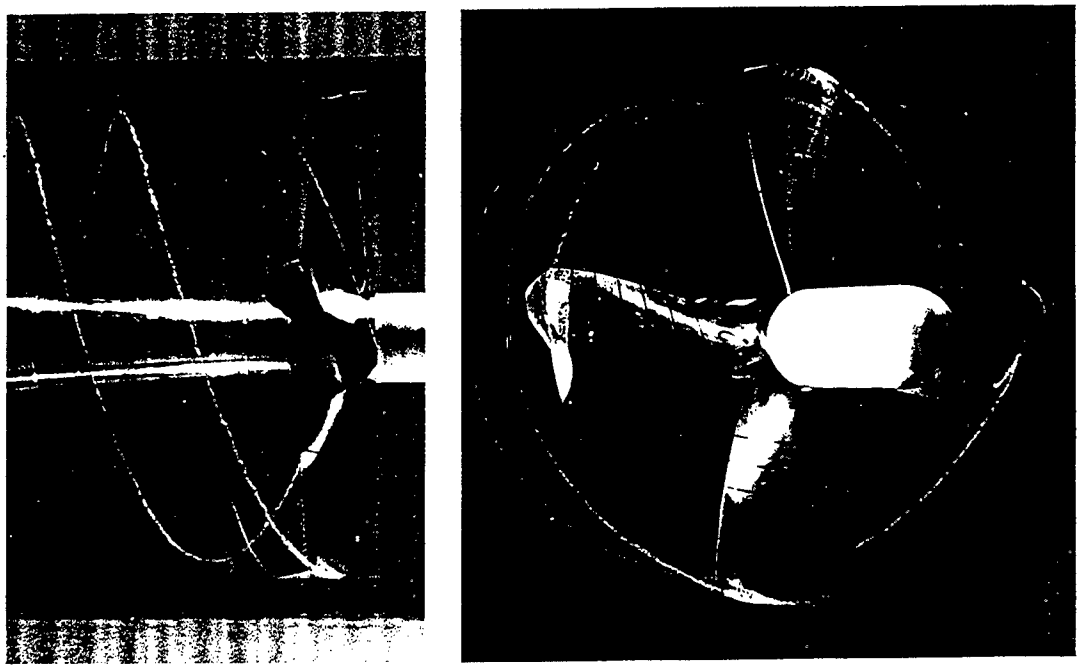

(b) blade 2 pointing to the side.

Figure 11. Observation of propeller No. 6251 for low cavitation number $\sigma_n = 2.60$ (design: $\sigma_n = 7.15$); $K_T = 0.402$
(see also next page)

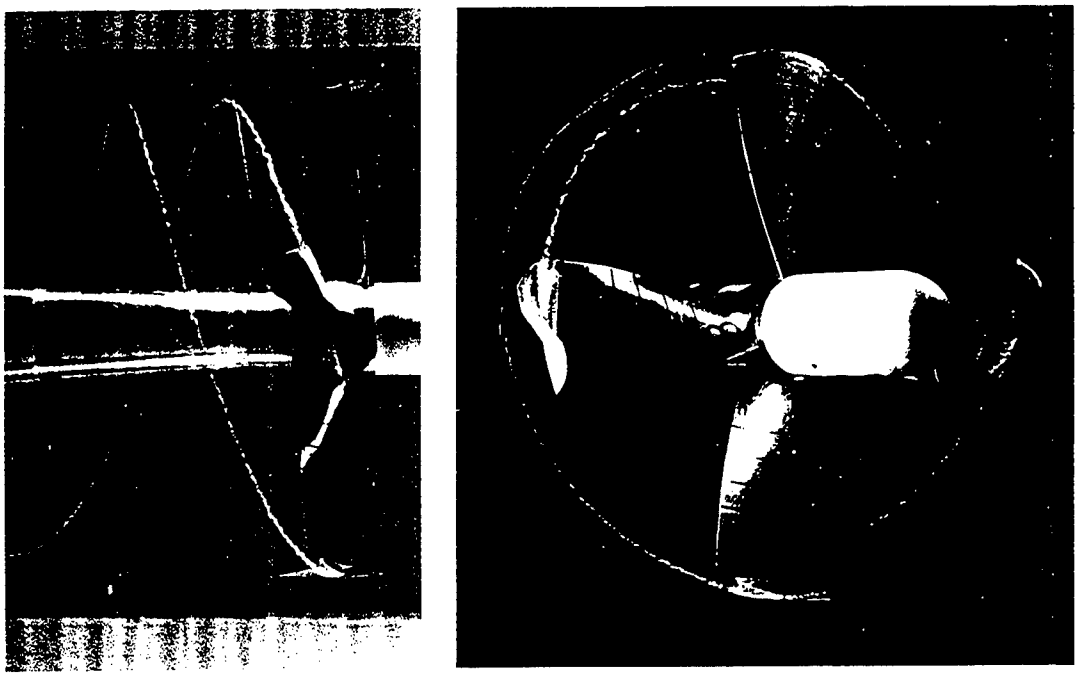

(c) blade 3 pointing to the side.

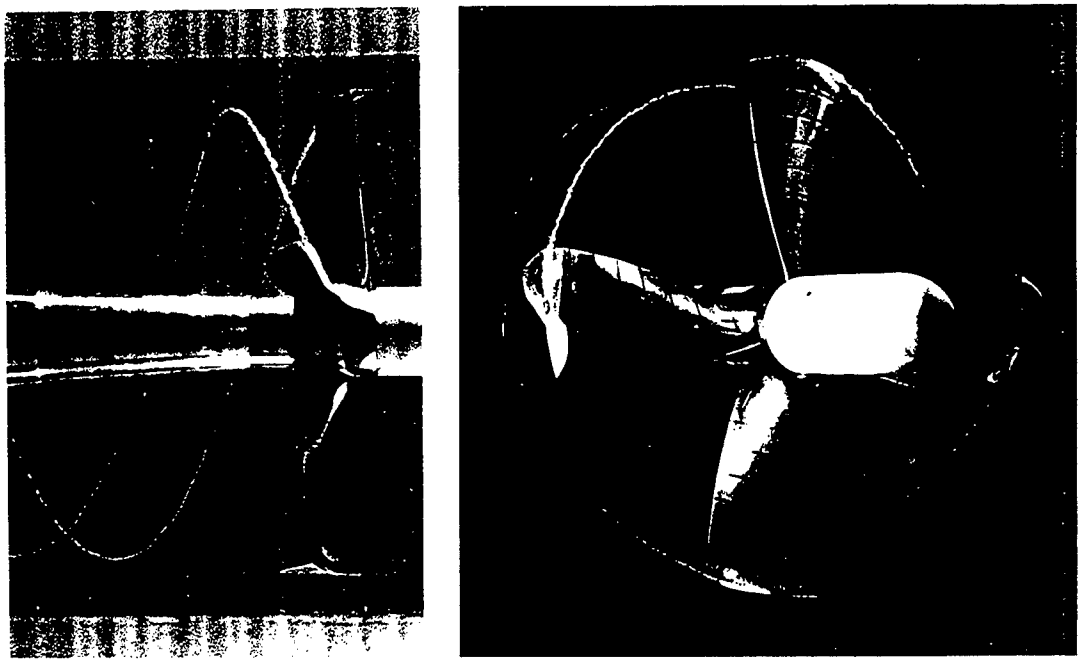

(d) blade 4 pointing to the side.

Figure 11. Observation of propeller No. 6251 for low cavitation number $\sigma_n = 2.60$ (design: $\sigma_n = 7.15$): $K_T = 0.402$
(see also previous page)

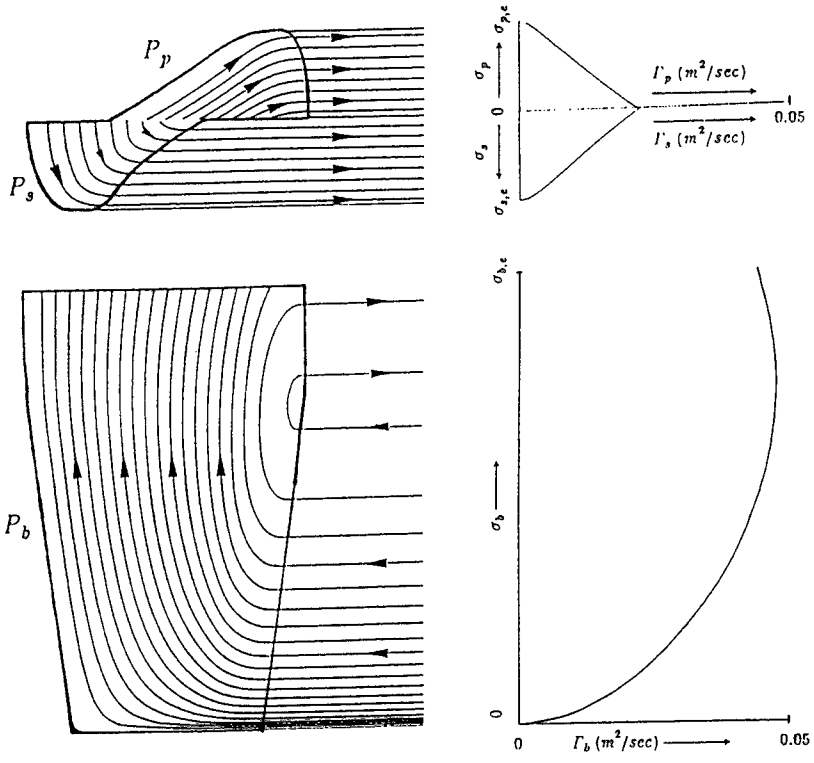

Figure 12. Propeller No. 6251; expanded planform P_b of blade and developed planforms P_p and P_s of end plate parts; distributions of vorticity and circulation distributions Γ_b, Γ_p and Γ_s along the spans.

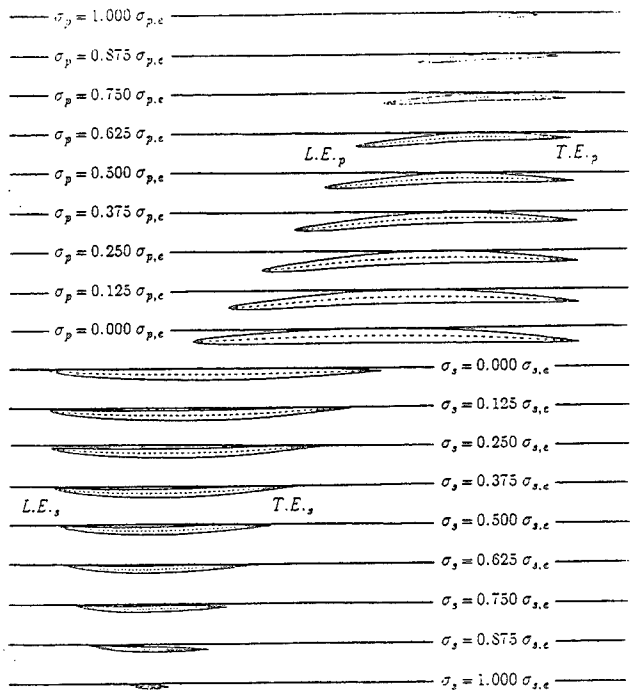

Figure 13. Propeller No. 6251; improved profiles of the end plate (original profiles were given in Fig. 5).

5. CONCLUSIONS

The reported test results of the Groningen Propeller with end plates confirm the design objective of conveying circulation from the screwblade in a continuous way to both end plate parts. The apparent effect on K_T and K_Q is measured over the complete range of propulsive J-values. In the range of J- and K_T-values for practical design there is an increase of efficiency. The related intended principle of spreading more evenly the trailing vorticity of the propeller is also confirmed by observations in the cavitation tunnel.

The design objective with respect to the value of K_T is not completely satisfied. The thrust discrepancy must be attributed to shortcomings in the optimization and design theory. To deliver the required thrust an increase of rotation rate by 4 % is necessary. If no increase of rotation rate is allowed, a practical adaptation of the pitch of the blades is necessary. A rule of thumb indicates 6 % increase of pitch. A better way to approximate the design thrust value better is to calculate the propeller again with the optimization theory, by demanding a somewhat larger thrust than the desired one.

In comparison with the reference propeller there is a clear increase in efficiency, for equal thrust condition, of about 1.8 %. It has to be noted that the propeller with end plates and the reference propeller have considerably different rotation rates. Therefore it is expected that gains in efficiency will be higher if propellers of both types are designed and compared for the same lower rotation rate. Furthermore it is expected that the gain in efficiency that is found by the discussed model scale experiments will be higher at full scale, due to the favourable influence on the viscous drag of the larger Reynoldsnumbers.

Because of the lower design rotation rate of the Groningen Propeller the rotational energy in the wake of the propeller will be larger than for a corresponding conventional propeller. The rotational energy can partly be transformed in thrust by a stator, such as a rudder. The lower rotation rate can possibly imply another advantage in view of reducing the extra cavitational danger caused by the inhomogeneous wake of a ship, in which the propeller with end plates rotates with a lower velocity.

Theoretical analysis of the propeller blades of the reference propeller and of the Groningen Propeller, when the end plates were not yet fitted to the blades, indicates differences between analysis and experiments. It has to be investigated whether the drag coefficients used in the analysis sufficiently represent the effect of the blade section profile shape. If this is true there might be room for improvement of the efficiency of the Groningen Propeller.

For realistic levels of pressure and loading no cavitation is observed in uniform flow. There are considerable margins for lower and higher loadings free of cavitation, but a test in a realistic wake field has to reveal whether these margins are sufficient. The type of cavitation which may appear on the suction side of the blades near the end plates indicates some risk of erosion of the blade material.

Because the end plate profiles can be slightly improved, the cavitational behaviour and the propeller performance can possibly be improved somewhat further.

ACKNOWLEDGEMENTS

This research was sponsored by the Technology Foundation, project number GWI59.0819.

REFERENCES

[1] Sparenberg, J.A., de Vries, J., "An Optimum Screw Propeller with End Plates", International Shipbuilding Progress, Vol. 34, July 1987, No. 395, pp. 124–133.

[2] van Gent, W., Falcão de Campos, J.A.C., de Jong, K., "Model Test Results of an Optimum Propeller with End Plates and Some Practical Aspects of Application", MARIN Jubilee Meeting, Wageningen, May 1992.

[3] de Jong, K., Sparenberg, J.A., "On the Influence of Choice of Generator Lines on the Optimum Efficiency of Screw Propellers", Journal of Ship Research, Vol. 34, No. 2, June 1990, pp. 79–91.

[4] de Jong, K., "On the Optimization, Including Viscosity Effects, of Ship Screw Propellers with Optional End Plates, Part I", International Shipbuilding Progress, Vol. 38, July 1991, No. 414, pp. 115–156.

[5] de Jong, K., "On the Optimization, Including Viscosity Effects, of Ship Screw Propellers with Optional End Plates, Part II", International Shipbuilding Progress, Vol. 38, September 1991, No. 415, pp. 211–252.

[6] de Jong, K., "On the Design of Optimum Ship Screw Propellers, Including Propellers with End Plates", International STG Symposium on Propulsors and Cavitation, Hamburg, June 1992.

[7] de Jong, K., "On the Optimization and the Design of Ship Screw Propellers with and without End Plates", Thesis, University of Groningen, Department of Mathematics, November 1991.

Session VIII

Wave and Wake Dynamics

Interaction of a Turbulent Vortex with a Free Surface

T. Sarpkaya (Naval Postgraduate School, USA)

ABSTRACT

The interaction of a single turbulent trailing vortex and its image with a deformable free surface has been undertaken for the purpose of exploring the origins of scars, striations, and three-dimensional instabilities. The experiments were conducted in a low turbulence water tunnel through the use of various vertically-mounted foils. The distance between the top of the test foil and the water surface was systematically varied. Velocity measurements with an LDV and photographic observations with LIF (laser induced fluorescence) of the vortices and free surface were made. Certain unusual characteristics of the remnants of the turbulent vortex tube – reconnection of normal vorticity with the free surface and the stretching out and quick dissipation of turbulent patches in the tangential direction – and their role in the creation of a quasi-two-dimensional whirl field have been explored. The numerical part of the investigation simulated the quasi-two-dimensional surface turbulence with vortex dynamics and explored the evolution of whirls, energy spectrum, and the fractal dimensions of the turbulence field.

INTRODUCTION

The wake/free-surface interaction and the mechanisms that affect the direct as well as remote observation of ship wakes have become major research topics in hydrodynamics.

Ship wakes produce a three-dimensional complex signature, comprised of a narrow dark band bordered by two bright lines in synthetic-aperture-radar (SAR) images. The dark band is the most prominent of all the signatures and is seen many kilometers downstream at all angles to the SAR azimuth direction even under severe weather conditions. It signifies the suppression of waves at the Bragg frequency as a consequence of various **short-wave-damping phenomena** such as turbulence, surface-active materials, and the redistribution of surface impurities to the surface by bubbles. The two bright lines, on the other hand, manifest themselves only in light winds and signify the occurrence of a range of waves which happen to be near the Bragg wavelength, possibly, as a consequence of the interaction between *quasi-two-dimensional and three-dimensional turbulent motions near the free surface and the restructuring and modulation of this interaction by wind,* unsteady Kelvin-wave-like disturbances, wave breaking, and momentum wake, just to name a few of the existing proposals. The central intent of this paper is neither a discussion of the remote sensing of surface-ship wakes nor the establishment of cause-and-effect relationships for the observed events noted above, but, rather, to describe a number of kernel experiments which could eventually serve to elucidate the basic fluid mechanics phenomena relevant to the understanding of near-surface turbulence structures.

BACKGROUND

Turbulent flow near surfaces is not uncommon and there has been intense interest in understanding the behavior of vortices near a wall and the physics of the mechanisms sustaining the turbulent behavior[-5]. Thus, it is not surprising that there should be turbulent flows at and near deformable surfaces or fluid interfaces, in addition to various types of waves, due to complex ship wakes. What is rather surprising is that the resulting turbulent wake (in part, due to vortical motions) should give rise to coherent structures capable of absorbing the incident electromagnetic waves (negative spectral perturbation) for unexpectedly long times even under real ocean ambient conditions. This leads to two generic questions regarding the behavior of turbulence at the free surface: (1) How are the coherent structures created at the interface and what dynamical processes are responsible for their life cycle? (2) What characteristics of these structures (e. g., scale, shape, motion, mutual interaction) are responsible for the absorption of the incident electromagnetic waves? This paper will be concerned only with the turbulent structures resulting from the interaction of a turbulent vortex with the free surface. Both the dynamical behavior,

through vortex dynamics, and the etiology of the coherent structures (what physical phenomenon causes them) are investigated in some detail.

Controlled laboratory experiments on free surface structures were first conducted by Sarpkaya in October 1983, as a continuation of his work on trailing vortices in homogeneous and density stratified media[6]. These observations and measurements were reported by Sarpkaya and Henderson[7-8] in 1984 and by Sarpkaya[9-10] in 1985. They have shown that a pair of ascending vortices shed by a lifting surface may interact with the free surface and give rise to scars and striations. The striations are essentially three-dimensional free-surface disturbances, normal to the direction of motion of the lifting surface. Sarpkaya and Suthon[11] have shown that the scars are small free-surface depressions, comprised of many randomly distributed whirls (normal vorticity connecting with the free surface), and come into existence towards the ends of the striations (see Figs. 1 and 2) and undergo mutual annihilation, dissipation, pairing, and merging. The striations come into existence as a subsurface instability, i.e., the free-surface proximity is not necessary but helps the striations to grow nonlinearly to larger amplitudes, depending on the prevailing free surface conditions (existing disturbances, contaminants, wind, current). In summary, an ascending laminar trailing vortex pair gives rise to two new components of vorticity: cross-axis vorticity in the striations and normal vorticity in the scars. The latter appears in part as distributed background vorticity and in (greater) part as randomly-distributed discrete structures (CW- and CCW-rotating whirls of various strengths), confined into a relatively narrow band.

When the vortices migrate large distances upward, they undergo various types of instabilities. Several theories have been proposed to explain the instabilities associated with the trailing vortices: Crow instability[12], Moore and Saffman instability[13], Batchelor's[14] swirling flow instability, Singh and Uberoi's[15] helical mode instability, and the free-stream turbulence proposals of Corsiglia et al.[16], and Baker et al.[17] Only the helical instabilities proposed by Singh and Uberoi[15] and observed by Sarpkaya[9] appear to provide a satisfactory explanation. In fact, as shown by Sarpkaya[18], tentacle-like sheets, resulting from the helical instabilities, are thrown away from the outer edges of the core of a turbulent vortex. In other words, **the vortex peels off randomly and sheds vorticity along its length.** These vortex sheets interact with the free surface and either connect normally with the free surface (resulting in whirls) or stretch out parallel to the free surface and dissipate quickly. These phenomena are further investigated in the present paper.

Numerical simulations of the domed region, formed by the rise of a Kelvin oval, attracted

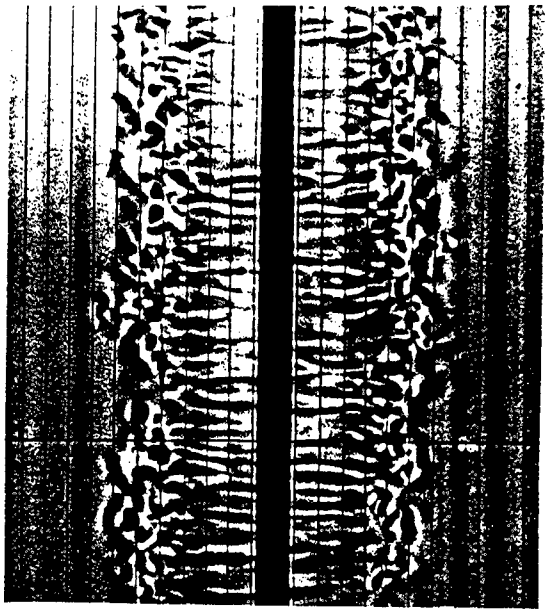

Fig. 1 Scars and striations above a trailing vortex pair.

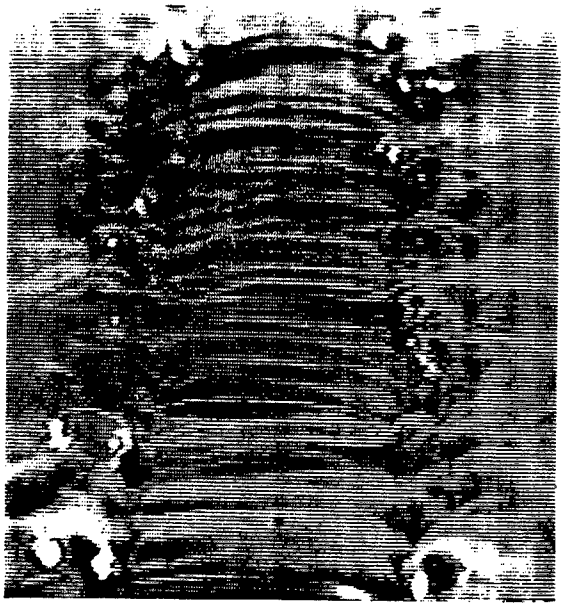

Fig. 2 Scars and striations due to a pair of vortices generated by a 2-D nozzle parallel to the free surface.

considerable attention. Sarpkaya et al.[19] modeled the vortex pair using two point vortices (with small cores) and line vortices to model the free surface without linearization. Subsequently, Marcus and Berger[20], Telste[21] and Ohring and Lugt[22] used different two-dimensional models to investigate the interaction between a couple of heterostophic line vortices and a free, initially planar, surface. In these calculations, the critical time at which the numerical instability manifests itself does not correspond to the instability of the free surface or to its maximum position. The calculations of Ohring and Lugt are

particularly noteworthy since they have presented results on the decay of the primary vortices and their paths, on the generation of surface vorticity and secondary vortices, on the development and final stages of the disturbed free surface, and on the influence of surface tension. They have also shown that, for an intermediate Froude number, the path of the primary vortex center portrays a complete loop (a special rebounding) due to the presence of secondary vortices .

Dommermuth and Yue[23] solved the linearized Navier-Stokes equations in three dimensions with a free surface to study the interaction of vortex tubes and vortex rings with slip- and no-slip rigid boundaries and a linearized free surface. Subsequently, Dommermuth[24] carried out numerical simulations of the interaction of laminar vortex tubes with no-slip walls to investigate the formation of U-shaped vortices without the complications of a free surface. They have concluded that two distinct types of vortices form: cam and snail vortices, as they preferred to call them. Cam vortices are formed as helical vorticity is stripped off of the primary vortex tubes. The helical vortex sheets are generated by the primary vortex tube due to the onset of a U-shaped instability previously identified by Sarpkaya[9] and by Sarpkaya and Suthon[11]. Dommermuth[25] extended his numerical analysis to the interaction of a pair of vortex tubes with a free surface and confirmed Sarpkaya and Suthon's[11] findings that the most interesting feature of the impingement of vortex tubes on a clean free surface is the reconnection of normal vorticity with the free surface, resulting in strong whirls. The simulation of more energetic transition[25] in vortices has tentatively shown that only the remnants of the primary vortex tube could be identified.

The interaction of jet flows with a free surface has attracted some attention[26-28] for the expressed purpose of determining the topology and dynamics of the resulting turbulent structures. Although instructive in understanding the conversion of the azimuthal vorticity (vortex rings) into streamwise vorticity, the jet flow is neither as complicated as the ship wake nor representative of the turbulent phenomena that occur in the ocean environment partly because there is **no normal vorticity generation** in the nominal plane of the free surface. Furthermore, the interaction of the jet flow with the free surface leads to the generation of **gravity-capillary waves** propagating in a direction almost perpendicular to the jet axis.

TURBULENT VORTEX AND FREE SURFACE

Even though there is still some work to be done on the three-dimensional nature of the laminar interaction, a number of kernel experiments, supported by analysis, is needed to elucidate the basic fluid mechanics of turbulent signatures, since turbulence is the current limit of resolution of our understanding of fluid motion. It is believed that one of the fundamental flows relevant to the dynamical processes in vorticity/free-surface interaction which can be carefully studied in isolation, without complications and competing influences that normally occur in a fully turbulent ship wake, is the interaction of a single turbulent vortex (and its image) with the free surface. This is expected to shed considerable light on the interaction between quasi-two-dimensional and three-dimensional turbulent motions. This is important not only near the free surface but also for the understanding of the processes of small-scale turbulence in the presence of highly stable stratification when three-dimensional turbulence shows a tendency to quasi-two-dimensional behavior due to the effect of buoyancy forces. Furthermore, the understanding of the properties of vortex-induced turbulence near the free surface will make it possible to explain the relationship between the spatial and temporal scales of turbulence, the evolution of surface inhomogeneities, and the characteristics of surface structures. It is this belief that led to a series of exploratory experiments and calculations reported by Sarpkaya[18] and to further studies reported herein.

Experiments were conducted in a low turbulence water tunnel with an open test section 45 cm wide, 60 cm deep (maximum), and 150 cm long. The turbulence management system was located upstream of the test section. It consisted of a honeycomb and fine-mesh screen. The turbulence intensity in the test section was less than 0.5% in the range of velocities used (from about 0.6 m/s to 2.5 m/s).

Several vertically mounted half Delta wings and rectangular foils (NACA 0012 and NACA 66-209 with no twist) were used to generate 'single' vortices shedding from the free end of the foil (see Fig. 3). The reason for the selection of the NACA 66-209 foil was that Green & Acosta[29] obtained extensive

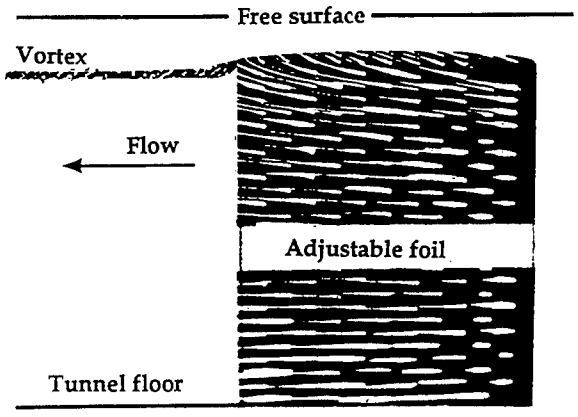

Fig. 3 NACA 66-209 foil section and the tip vortex.

velocity and some turbulence data for the **fully submerged vortex** through the use of a novel technique. Since some of their governing parameters are in the range of those encountered in the present investigation, their data for the fully-submerged vortex are used for comparison with those obtained in the present investigation.

The tip of each foil consisted of a smooth cap with an approximately semicircular cross-section. The interior of each model was hollowed and connected to a dye reservoir to seed the vortex cores with fluorescent dye[10] or fluorescent particles (about 10-20μm). The chord length of the model foils ranged from 5 cm to 10 cm. The distance from the test section floor (plane of reflection) to the top of the tip was either held constant at 38 cm, resulting in an effective aspect ratio of AR = 7.5, or varied, resulting in aspect ratios ranging from 7.5 to about 12. The leading edge of the foil was 4 chord lengths downstream of the test section entrance. The chord-based Reynolds number ranged from about 10^5 to 5.5×10^5.

In one series of experiments the foil was mounted in a rotatable cylindrical base, embedded into the bottom of the test-section floor. The bottom of the foil was flush with the tunnel floor. Then the water level was raised or lowered to adjust the position of the vortex relative to the free surface. This procedure was particularly helpful for LDV measurements, and, LIF and shadograph flow visualization experiments. In another series of experiments, the foil was made to protrude from the tunnel floor vertically upwards, to a desired height and angle of attack, while the water level was held constant. This was the reason for the change of the aspect ratio. However, the results have shown that, for models with large aspect ratios, the small change in AR, as the model tip approached the free surface, did not significantly change either the circulation of the vortex or the vortex/free-surface interaction. In this series of experiments the vertical positions of the LDV and shadograph screen were adjusted accordingly.

The angle of attack was varied from 5 to 10 degrees (well within the unseparated flow region). The total circulation of the **fully-submerged** trailing vortex was calculated from the tangential velocity distribution and from[29, 30]

$$\Gamma/Uc = [1.05\pi(\alpha - \alpha_0)]/(1 + 2/AR),$$

including a correction for the wall effect of the tunnel floor, as carefully noted by Green and Acosta[29]. The normalized vortex strengths Γ/Uc varied from about 0.30 to 0.65. The calculated values were within a few percent of those obtained from the tangential velocity distribution.

Green and Acosta[29] found that the normalized mean tangential velocity distribution is nearly independent of both the Reynolds number and downstream distance ($2\times10^5 < Re < 10^6$) and $2 < x/c < 10$. Of equal relevance to the present investigation is their conclusion that "the tangential velocity is θ-independent and the vortex is axisymmetric to within the experimental error. The unsteady component of the tangential velocity falls significantly with downstream distance." Two of their tangential velocity distributions at the same downstream distance and Reynolds number, but for different angles of attack, are shown in Figs. 4 and 5 together with those obtained in the present investigation. Clearly, the two sets of data are in fairly good agreement and the tangential velocity is significantly unsteady. The preliminary data[30] regarding the surface-proximity effects have shown that the unsteadiness in all velocity and turbulence

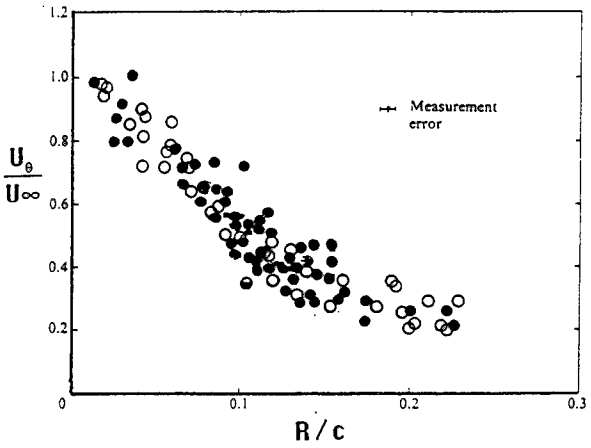

Fig. 4 Tangential velocity distribution: Green and Acosta[29]: ●, $x/c = 2$, $\alpha = 10^0$, $Re = 6.83\times10^5$; Present data: o, $x/c = 2$, $\alpha = 10^0$, $Re = 5\times10^5$

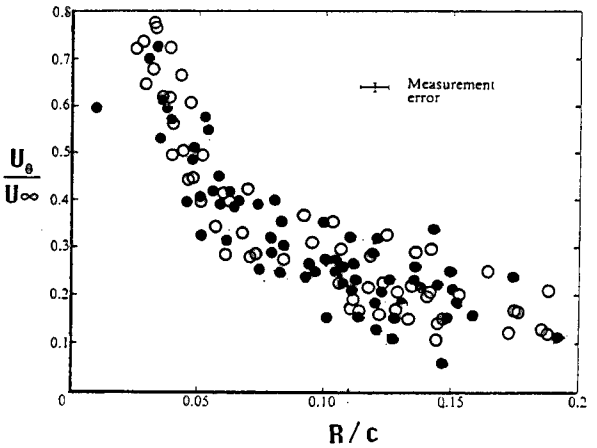

Fig. 5 Tangential velocity distribution: Green and Acosta[29]: ●, $x/c = 2$, $\alpha = 5^0$, $Re = 6.83\times10^5$; Present data: o, $x/c = 2$, $\alpha = 5^0$, $Re = 5\times10^5$

components increases dramatically and only the remnants of the primary vortex tube could be identified as the vortex approaches the free surface.

The structure of the vortex was video recorded through the use of LIF (Laser Induced Fluorescence, using fluorescent dyes or particles) at various speeds ranging from 60 frames/s to 10,000 fps at various downstream stations from the foil. Here only the sample results obtained at 500 frames/s at x/c = 7, for $Re = 4x10^5$ and $\Gamma/\nu = 1.8x10^5$ are shown.

Figures 6 and 7 show the vortex core and its surroundings in a 2 mm-thick laser light sheet in streamwise and transverse directions, respectively. The blur in the pictures is partly due to the vibration of the core, partly due to the photographing of the individual frames from a video monitor with a simple camera, partly due to the rapid motion of the secondary structures surrounding the core, and partly due to the reproduction of the paper. In any case, it is clear from these figures and from the viewing of hour-long video tapes that the vortex core and its immediate surroundings are not comprised of smooth axisymmetric surfaces. Vortex sheets peel off and some are thrown away from the core.

The core must be replenished with fresh fluid from the outer region, i.e., a turbulent exchange of momentum must take place between the outer region and the core. It is this **exchange of momentum that leads to the unsteadiness of the vortex core and the various velocity components.** As noted by Dommermuth and Yue[23], in their low-Reynolds number numerical simulations, "As a vortex tube interacts with itself and its neighbors, sheets of helical vorticity spiral off of the primary vortex tube. The origin of the sheets of helical vorticity appears to be the result of a helical instability that is initiated by large changes in curvature along the axes of the primary vortex tubes."

The evolution of the momentum exchange and the unsteadiness in various velocity components that result from it must certainly depend on the characteristics of the foil, transition in its boundary layers, Reynolds number, ambient turbulence, and the mutual interaction of the trailing vortices with each other or with their images across a deformable or rigid boundary. It is not the purpose of the present investigation to repeat some of the previous works which have dealt with the trailing vortices in an effectively infinite medium[6, 29], but rather, to present evidence that the turbulent vortex core is neither axisymmetric nor smooth and that the interaction of such a vortex with the free surface leads to quasi-two-dimensional turbulence dominated by whirls (reconnection of normal vorticity). The structures in the tangential direction dissipate quickly. .

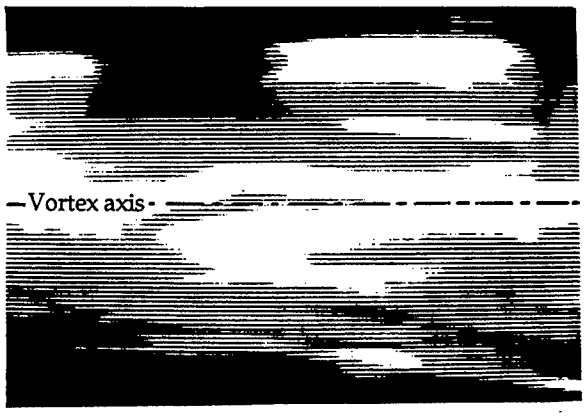

Fig. 6 A turbulent vortex in a streamwise light-sheet. The core is neither smooth nor axisymmetric. Shedding of turbulent patches is noted.

Fig. 7 The cross-section of a turbulent vortex as seen in 1/500 s, (deep submergence)

It is, therefore, instructive to look at the cross section of the vortex as the water level is brought closer to the tip of the hydrofoil. Aside from the primary characteristics of the fully submerged vortex, the said interaction is governed by the Froude number $F = V_0/\sqrt{2gh}$ where V_0 now represents the mutual induction velocity between the vortex and its idealized mirror image, across the fluid interface, ($V_0 = \Gamma/4\pi h$), and h is defined as the depth of submergence of the vortex axis (at the point of its generation) from the free surface . Thus, for a given Γ, the Froude number increases with decreasing h.

Figures 8 and 9 show two deeply-submerged ($F \approx 0.05$) vortex cores in a laser light sheet (**intersecting them at a 45-degree angle**, but photographed normal to the vortex axis). The vortex cores are surrounded by helical patches that could have only come from the vortex sheet (dye was introduced into the vortex

core, for details see Sarpkaya[6]). As the Froude number is increased, the vortex comes under the strong influence of the free surface. The events that follow will be described briefly through the use of representative figures, chosen randomly from among hundreds. It should be noted that the laser light sheet is intersecting the vortex axis at a 45-degree angle. The camera axis is normal to the vortex axis and looking slightly upwards from under the free surface so as to capture the reflection of the vortex and the reconnection of its tentacles.

Fig. 8 The cross section of a deeply-submerged vortex.

Fig. 9 The cross-section of the vortex shown in Fig. 8 after 0.01s. The shedding of turbulent patches is clearly evident in both pictures.

Figure 10 shows, for F = 0.32 and x/c = 2, the connection of a vortex patch with the free surface (and its image), (Re and Γ/ν have been held constant at the values cited previously). These connections are not always between the free surface and the vortex sheets still connected to the vortex core. In fact, many of the connections are between the free surface and the run-away patches of vorticity with no visible connection to the core (presumably, thrown away from the core). The earliest connections with the free surface are due to independently 'flying' patches (when the vortex core is not too close to the free surface).

Fig. 10 The connection of a vortex arm with the free surface (F = 0.32 and x/c = 2).

Figures 11a and 11b, separated by a time interval of about 0.02s, show at x/c = 7 (other parameters are held the same), the progression of the connection process and the evolution of whirls at the free surface. Clearly, the vortex core breaks up and spreads over a larger area as its proximity to the free surface increases. This is the mechanism whereby the three-dimensional turbulence below the free surface is transformed into a quasi-two-dimensional turbulence at the free surface.

Figures 12a and 12b show the multiple connections with the free surface at higher Froude numbers (F ≈ 1 and 2.8). The viewing of video tapes show that not all patches of vorticity are connected to the free surface. In fact some of these come close to the free surface rather quickly, stretch out in the horizontal plane (predominantly in the direction of largest strain), and then disappear just as fast. Another observation is that the larger the Froude number, the faster is the dissipation of the trailing vortex, as measured in terms of the extent of the whirls and scars at a given x/c. This would be

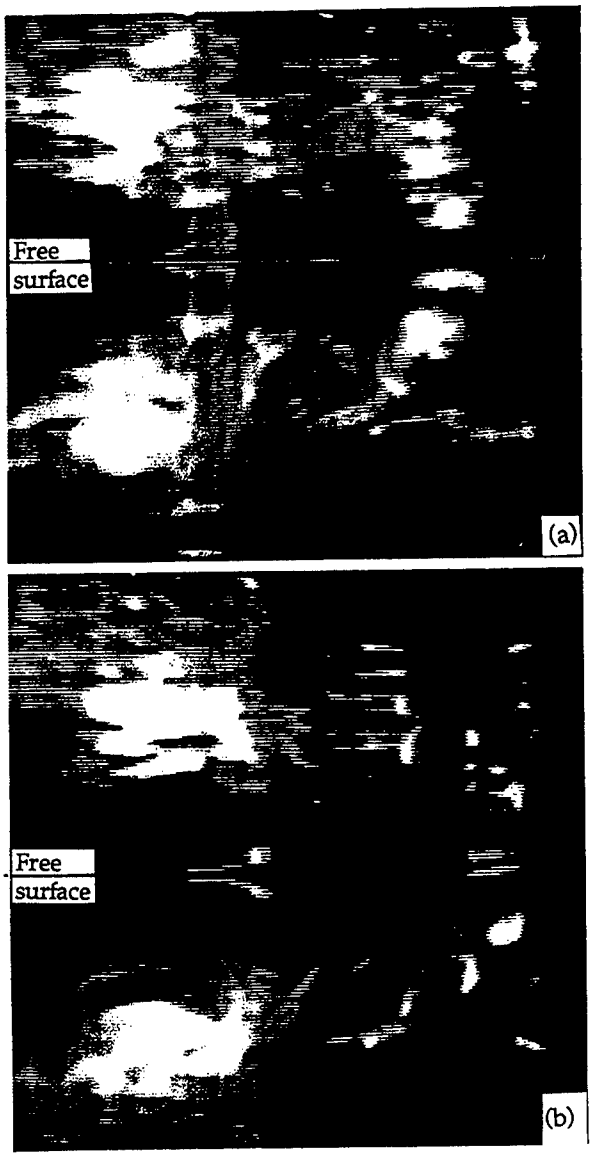

Figs. 11a and 11b The progression of the connection process and the evolution of whirls at the free surface (the two figures are 0.02 s apart).

somewhat expected since the tangential vorticity will be annihilated more in the overlapping regions of two closely situated counter-rotating turbulent vortices (real vortex and its 'mirror' image). In other words, the generation and dissipation of horizontal vorticity is enhanced at the expense of the normal vorticity. Figures 12a and 12b also show that the coherence of the vortex core is nearly lost and only the remnants of the original vortex may be seen. The numerical simulations of Dommermuth[25] of the more energetic transition in vortices near the free surface have also shown that only the remnants of the primary vortex tube could be identified (see Figs. 13a and 13b). Some resemblance may be noted between Figs. 12a-b and Figs. 13a-b. Clearly, the numerical model does not deal with finer structures of turbulence and with the whirls at the free surface.

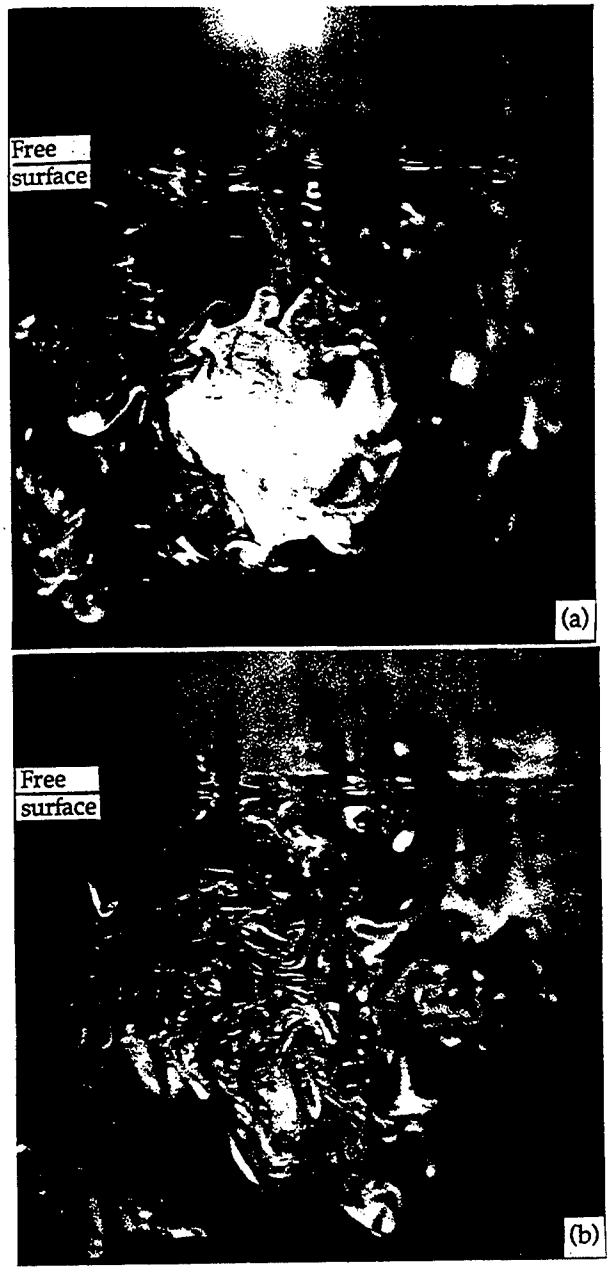

Figs. 12a and 12b The multiple normal connections with the free surface at higher Froude numbers.

Representative samples of the top view (taken with a laser light sheet, very near the free surface) of the surface structures are shown in Figs. 14a-c and 14d (the streaklines). The constellation of vortices seen in these figures emerged almost directly above, or slightly on the downwash side, of the trailing vortex. Two features of these whirls are particularly noteworthy. The first is the emergence of heterostophic vortices and the pairing of homostrophic vortices (these are best seen on the video films of our experiments). The second salient feature of the whirls is their persistence. It appeared as if the whirls became the 'black holes' of vorticity in a sea of otherwise featureless structures of vorticity. The structures that were not part of a whirl

dissipated quickly. It may thus be conjectured that the formation of whirls, as singularities of nearly concentrated vorticity, is a matter of survival of vorticity, either transported to the free surface or generated there. The tendency of the vortex couples of the same sign to transport energy from one area to another is severely limited partly by the swirling motion of the trailing vortex (directly below the scar), partly by the mutual interaction of the whirls, which keeps the scar intact, and partly by the uniform flow. Thus, the vortices created near the boundary of the scar cannot escape it but can unevenly modulate the edges of the scar.

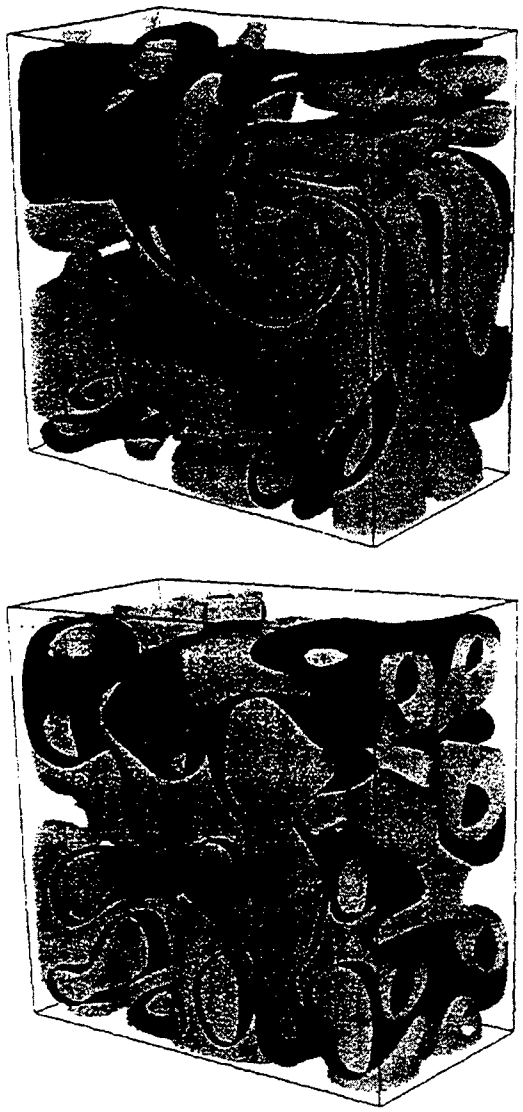

Figs. 13a and 13b The numerical simulations of the more energetic transition in vortices near the free surface (with permission of Dommermuth[25]).

Figs. 14a-d Evolution of a scar above a turbulent vortex (x/c = 7).

The foregoing points out the very important role played by the whirls and the danger of replacing the nonlinear–time–dependent free surface conditions with the more convenient assumption of "non-deforming surface" in numerical simulations of the interaction of vorticity with a free surface.

NUMERICAL SIMULATION OF SURFACE FLOW STRUCTURES VIA VORTEX DYNAMICS

The experiments have shown that the surface structures have the characteristic behavior of quasi-two-dimensional turbulence with energy cascading towards larger structures and stretched zones of weak vorticity dissipating slowly. The width of the wake above the trailing vortex increases slowly at the same rate at which the vortices grow in size through successive merging processes. Effective methods have been developed for structural and eddy center identification based on digital image analysis and

shadowgraph technique[11]. The size and angular velocities of the whirls were estimated from the video tapes in order to explore the statistics of the surface structures and to calculate the distribution of vorticity in the field of whirls. The instantaneous free-surface signatures are compared qualitatively with the predictions of a numerical model based on vortex dynamics[31].

The observations suggest that the two-dimensional numerical experiments can be started with 2n oppositely-signed vortices ($n \approx 1000$) each with a Gaussian distribution (initially placed in a scar band and then tracked in an unbounded domain). The total circulation is rendered zero in a suitable manner. Here, the uneven spacing and strength of the vortices correspond to the appearance of randomness with a large range of spatial and temporal frequencies.

One is particularly interested in the effects of the amalgamation of the vortices. In general, for a fairly wide parameter range, the vorticity field has a significant component made up of coherent vortices that are very long-lived compared with the typical flow timescales, such as a large scale advective time, or an eddy turnover time. The remainder of the field is a more characteristic turbulent background flow over which the coherent structures float. Typical flow diagnostics (fractal dimensions, energy spectra) are also calculated.

Figures 15-17 show at $V_0t/h = 1.6$ the streamlines, the energy spectrum, and the fractal structure of a representative scar. The energy spectral density for a system of N vortices (arbitrary signs and magnitudes) is given by Novikov[32], as

$$E_N = (4\pi k)^{-1}\left[\sum_{i}^{N}\Gamma_i^2 + 2\sum_{p<q}^{N}\Gamma_p\Gamma_q J_0(k\ell_{pq})\right]$$

in which k is the wave number, ℓ_{pq} is the absolute distance between any two vortices, and J_0 is a Bessel function. The first term corresponds to the vortex self energy and the second term to the energy of the interaction determined by the set of distances ℓ_{pq} between the vortices. The ratio of the second term to the first term is a measure of the scale of inhomogeneity of the turbulent flow field. The evolution of the energy spectral density was calculated from this equation.

The fractal dimension D is obtained by dividing the scar space into square meshes of size R and counting the number N of meshes containing at least one vortex. Then the fractal dimension is determined from $N \propto R^{-D}$.

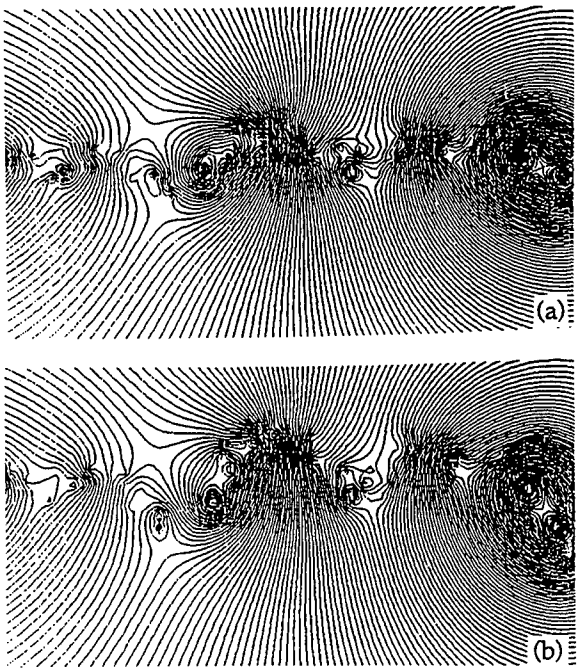

Figs. 15 The streamlines in a single evolving scar: (a) at $V_0t/h = 0.8$, and (b) at $V_0t/h = 1.6$.

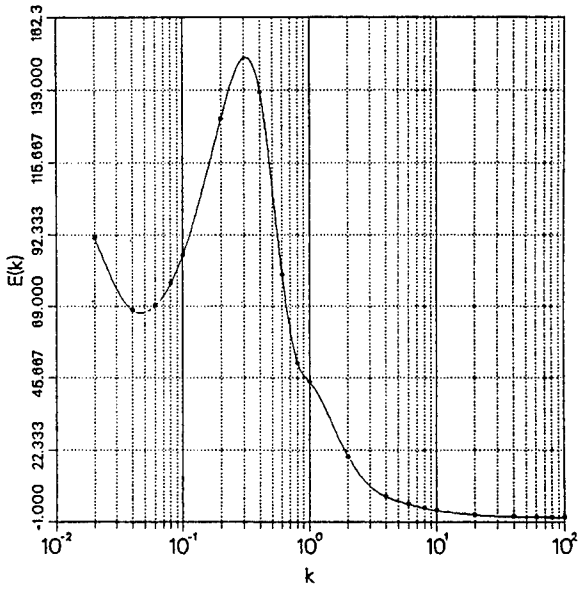

Figs. 16 Sample energy spectral density for a single scar at $V_0t/h = 1.6$.

The facts emerging from these figures are as follows: The whirls amalgamate up to a certain size as time increases (i.e., the amalgamation is self-limiting). It is remarkable that the band essentially retains its overall identity even though its width increases slightly due to the mutual interaction of the whirls. It is only rarely that one or two whirls leave the scar band due to mutual induction. The amalgamation process and, hence, the increase of the

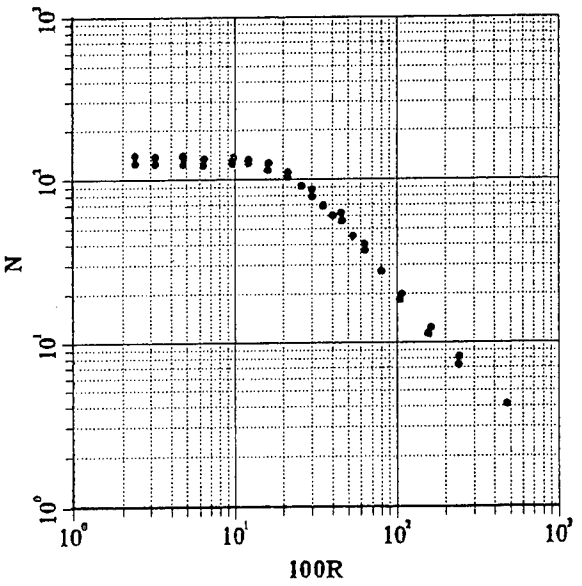

Fig. 17 Fractal structure of a single scar at V_0t/h =1.6.

number of large structures slow down or stop as time increases and the whirl system reaches an equilibrium without dissipation.

The whirl population has been doubled several times and the numerical experiments were carried out with different random-number seedings to ascertain that the results concerning the energy-density distribution and the cascading of the energy did not depend on either the number of the whirls or on their statistical distribution. It has been found that the population density and the number of random samplings are sufficiently large to arrive at statistically meaningful conclusions. The time variations of the distributions, therefore, allow one to estimate whether whirl-whirl interactions are important. The results presented above show that the shift in the size distribution toward larger structures and the concentration of energy in these structures are an important ingredient of the scar formation and life-span. The increase of the number of large structures slows down and nearly stops after a critical time, when the whirl concentration has fallen below a critical value, and the population of whirls becomes dominated by viscous decay process. Apparently, the two-dimensional topological features (whirls) of concentrated vorticity on the free surface are inherent products of the quasi-two-dimensionalization of the three-dimensional turbulence, prevailing just below the free surface. The results have also shown that the global maximum of the energy spectrum is shifted towards smaller wave numbers (larger wave lengths), as expected on the basis of amalgamations.

The fractal dimension D, as determined from figures such as Fig. 14 (experiments) have shown that the fractal dimension of the boundary of the LIF visulizations orthogonal to the vortex axis at various x/c and at various times at a given x/c is about 1.35 and the result is sensibly independent of the threshold. The fractal dimension D of the numerical simulations (e.g., Fig. 15) varied from about 1.29 to 1.36. The initial seeding of the vortices had very little or no influence on the simulated value of D. For a three-dimensional turbulence field, the accepted value of D is about 2.5. For a two-dimensional turbulence field, as in the present case, the value of D is almost halved. For example, the shape of the clouds yields a fractal dimension of about 1.35, the diffusion of a passive scalar quantity on the surface of turbulent water yields about D = 1.3, and the cross sectional pattern of the turbulent boundary layer is reported to give D = 1.37 (Takaki[33]). Evidently, the fractal dimension of the evolution of the whirls in a scar is in conformity with that of other nearly two-dimensional turbulent fields. Clearly, additional physical and numerical experiments are needed to delineate the characteristics of the turbulence field resulting from the interaction of a turbulent vortex with a free surface.

CONCLUSIONS

The interaction of a single turbulent trailing vortex and its image with a deformable free surface has been undertaken for the purpose of exploring the origins of scars, striations, and three-dimensional instabilities. The evidence presented herein shows that numerous tentacle-like vortex sheets of finite length, resulting from helical instabilities, stretch out or are thrown away from the outer edges of the vortex core. The vortex peels off randomly and sheds vorticity along its length. The core of a turbulent vortex is not a benign, smooth, axisymmetric, solid body of rotation. The exchange of momentum between the outer regions and the core leads to the oscillation of the vortex core and the various velocity components.

As the vortex sheets and turbulent patches (or finite regions of vorticity) interact with the free surface, they either give rise to whirls (reconnection of normal vorticity) or stretch out in the tangential direction and dissipate quickly. The closer the vortex to the free surface, the faster is its dissipation, as evidenced by the resulting scar at the free surface. This is expected on the grounds that the interaction of the vortex with its image across a shear-free boundary must result in the increased annihilation of vorticity.

The two fundamental modes of the vortex/free-surface interaction observed in the present investigation are suggestive of the 'spin' and 'splat' models of Bradshaw and Koh[34], Hunt[35], and Leighton et al.[36] Their spin model (vortical structures originating in the buffer layer and attaching to the free surface) and the splat model

(patches of vorticity or vortons impacting the free surface) in a turbulent open channel flow tend to support the observations made in the present investigation that the tentacles of vortex (helical sheets of vorticity) attach to the free surface and the patches of vorticity are thrown at the free surface. These similarities need to be explored further keeping in mind the fact that in the direct numerical simulations[36] the non-linear–time-dependent free surface conditions are linearized and the free surface is assumed to be non-deformable.

The numerical simulations of the scar band through the use of vortex dynamics have shown that the shift in the size distribution toward larger structures and the concentration of energy in these structures are an important ingredient of the scar formation and scar life-span.

The use of a turbulent vortex (and its image) near the free surface of an otherwise smooth uniform flow proved to be a 'kernel' experiment towards the elucidation of the dynamical processes in vorticity/free-surface interaction which can be studied in isolation, without complications and competing influences that normally occur in a fully turbulent ship wake. Clearly, detailed velocity and turbulence measurements and additional physical and numerical experiments are needed to delineate the characteristics of the scars and striations.

ACKNOWLEDGEMENTS

The author wishes to express his sincere appreciation to the Office of Naval Research and the Naval Postgraduate School for the support of the investigation. The project was monitored by Dr. Edwin P. Rood. The author also wishes to thank Mr. W. Lundblad and Mr. Jack McKay for their assistance with the experiments.

REFERENCES

1. Harvey, J. K. and Perry, F. J., "Flow Filed Produced by Trailing Vortices in the Vicinity of the Ground," *AIAA Journal*, Vol. 9, 1971, pp. 1659-1660.

2. Smith, C. R., Walker, J. D. A., Haidari, A. H., and Sobrun, U., "On the Dynamics of Near-Wall Turbulence," *Phil. Trans. Royal Soc. London* A, Vol. 336, 1991, pp. 131-175.

3. Peace, A. J. and Riley, N., "A Viscous Vortex Pair in Ground Effect," *J. Fluid Mechs.*, Vol. 129, 1983, pp. 409-426.

4. Doligalski, T. L. and Walker, J. D. A., "Boundary Layer Induced by a Convected Two-Dimensional Vortex," *J. Fluid Mechs.*, Vol. 139, 1984, pp. 1-28.

5. Robinson, S. K., "Coherent Motions in the Turbulent Boundary Layer," *Annual Review of Fluid Mechanics*, Vol. 23, 1991, pp. 601-639.

6. Sarpkaya, T., "Trailing Vortices in Homogeneous and Density Stratified Media," *J. Fluid Mechs.*, Vol. 136, 1983, pp. 85–109.

7. Sarpkaya, T., and Henderson, D. O., Jr., *Surface Disturbances Due to Trailing Vortices*, Technical Report No. NPS-69-84-004, 1984, Naval Postgraduate School, Monterey, California.

8. Sarpkaya, T., and Henderson, D. O., Jr., "Free Surface Scars and Striations Due to Trailing Vortices Generated by a Submerged Lifting Surface," AIAA 85-0445, presented at the 23rd Aerospace Sciences Meeting, Reno, Nevada, 14–17 January 1985.

9. Sarpkaya, T., "Surface Signatures of Trailing Vortices and Large Scale Instabilities," *Proceedings of the Colloquium on Vortex Breakdown*, (ed. R. W. Staufenbiel), pp. 145-187, Aachen, Germany, 11–12 February 1985.

10. Sarpkaya, T., "Trailing-Vortex Wakes on the Free Surface," *Proceedings of the 16th Symposium on Naval Hydrodynamics*, National Academy Press, Washington, D. C., 1986, pp. 38–50.

11. Sarpkaya, T., and Suthon, P. B. R., "Interaction of a vortex couple with a free surface," *Experiments in Fluids*, Vol. 11, 1991, pp. 205-217.

12. Crow, S. C., "Stability Theory for a Pair of Trailing Vortices," *AIAA Journal*, Vol. 8, No. 12, 1970, pp. 2172–2179.

13. Moore, D. W. and Saffman, P. G., "Axial Flow in Laminar Trailing Vortices," *Proc. Royal Soc. London*, Vol. A 333, 1973, pp. 491-508.

14. Batchelor, G. K., "Axial Flow in Trailing Line Vortices," *Jour,. Fluid Mechs.*, Vol. 20, 1964, pp. 645-658.

15. Singh, P. I. and Uberoi, M. S., "Experiments on Vortex Stability," *Physics of Fluids,*, Vol. 19, 1976, pp. 1181-1188.

16. Corsiglia, V. R., Schwind, R. G., and Chigier, N. A., "Rapid Scanning, Three-Dimensional Hot-Wire Anemometer Surveys of Wing-Tip Vortices," *J. Aircraft*, Vol. 10, 1973, pp. 752-757.

17. Baker, G. R., Barker, S. J., Bofah, K. K., and Saffman, P. G., "Laser Anemometer Measurements of Trailing Vortices," *Jour. Fluid Mechs.*, Vol. 65, 1974, pp. 325-336.

18. Sarpkaya, T., "Three-Dimensional Interactions of Vortices with a Free Surface," AIAA Paper No. 92-0059, January, 1992, (30th Aerospace Sciences Meeting of AIAA).

19. Sarpkaya, T., Elnitsky, J., Leeker, R. E., "Wake of a Vortex Pair on the Free Surface," Proc. 17th Symposium on Naval Hydrodynamics, Washington, D. C., pp. 53-60.

20. Marcus, D. L., and Berger, S. A., "The Interaction Between a Counter-Rotating Vortex Pair in Vertical Ascent and a Free Surface," *Physics of Fluids*, A-1, 1989, Vol. 12, pp. 1988–2000.

21. Telste, J. G. "Potential Flow about Two Counter-Rotating Vortices Approaching a Free Surface." *J. Fluid Mech.*, Vol. 201, 1989, pp. 259–278.

22 Ohring, S., and Lugt, H. J., "Interaction of a Viscous Vortex Pair with a Free Surface," *J. Fluid Mechs.*, Vol. 227, 1991, pp. 47-70.

23. Dommermuth, D. G. and Yue, D. K., "A Numerical Study of Three-Dimensional Viscous Interaction of Vortices with a Free Surface," *Proceedings of the 18th Symposium on Naval Hydrodynamics*, National Academy Press, Washington, D.C., 1991, pp. 727-788.

24. Dommermuth, D. G., "The Formation of U-Shaped Vortices on Vortex Tubes Impinging on a Wall with Applications to Free Surfaces," (to appear in *Physics of Fluids* A, 1992)

25. Dommermuth, D. G., "The Laminar Interactions of a Pair of Vortex Tubes with a Free Surface," (to appear in the *Journal of Fluid Mechanics*, 1992).

26. Ramberg, S. E., Swean, T. F., and Plesnia, M. W., "Turbulence Near a Free Surface in a Plane Jet," Naval Research Laboratory Memorandum Report 6367, 1989.

27. Madnia, K. and Bernal, L. P., "Interaction of a Turbulent Round Jet with the Free Surface," Technical Report No. 89-05, 1989, The University of Michigan.

28. Anthony, D. G., "The Influence of a Free Surface on the Development of Turbulence in a Submerged Jet," Technical Report No. 90-2, 1990, The University of Michigan.

29. Green, S. I. and Acosta, A. J., "Unsteady Flow in Trailing Vortices," *J. Fluid Mechs.*, Vol. 227, 1991, pp. 107-134.

30. Sarpkaya, T. and Neubert, D., "Velocity and Turbulence Measurements in a Turbulent Vortex in Free-surface Proximity," (to be presented at the 31st Aerospace Sciences Meeting, January 11-14, 1993).

31. Sarpkaya, T., "Computational Methods with Vortices—1988 Freeman Scholar Lecture," *Journal of Fluids Engineering, Transactions of ASME*, Vol. 111, No. 1, 1989, pp. 5–52.

32. Novikov, E. A., "Dynamics and Statistics of a System of Vortices," *Soviet Physics*, JETP, Vol. 41, 1974, pp. 937-943.

33. Takaki, R., "Statistical Treatment of Many Vortex Systems," *Advances in Turbulence* 2, Springer-Verlag, 1989, pp. 391-396.

34. Bradshaw, P. and Koh, Y. M., "A Note on Poisson's Equation for Pressure in a Turbulent Flow," *Physics of Fluids*, Vol. 24, 1981, pp. 777-779.

35. Hunt, J. C. R., "Turbulence Structure and Turbulent Diffusion Near Gas-Liquid Interfaces," in *Gas Transfer at Water Surfaces*, D. Reidel Pub. Co., 1984.

36. Leighton, R. I., Swean, T. F., Handler, R. A., and Swearingen, J. D., "Interaction of Vorticity with a Free Surface in Turbulent Open Channel Flow," AIAA Paper No. 91-0236, 1991, (23rd Aerospace Sciences Meeting of AIAA).

Numerical Investigation of an Oblique Collision of a Vortex Ring with a Clean Free Surface

M. Song (Hong Ik University, Korea),
G. Tryggvason (University of Michigan, USA)

Abstract

Experimental studies of the free surface signature of underwater vortical flows suggest that the reconnection or "opening-up" of vortex filaments at the surface is a major cause for generation of short wave on the free surface. To investigate this phenomena, numerical simulations of the collision of a vortex ring at an oblique angle of incident to the free surface have been performed. A nearly inviscid flow is assumed, and the vortex ring modeled by a collection of "vortons." This introduces a small amount of dissipation and allows the ring to reconnect with its image at the free surface. In most experimental studies the free surface deformation is very small, and here the free surface motion is assumed to be linear. The free surface deformation can then be solved separately after the evolution of the vortex ring has been computed. Following the first reconnection with the surface, the rings sometimes reconnect again, forming two half-rings that propagate parallel to the free surface. The computed free surface signature agree qualitatively with available experimental results. Based on the numerical investigation, we propose a simplified model which assumes that the major effect of the vortex reconnection to the free surface is a pressure impulse that generates short waves on the free surface.

Nomenclature

R	vortex ring radius
Γ	circulation of the ring
a	core radius
θ	incident angle
D	initial depth of the ring
ρ	fluid density
ν	fluid kinematic viscosity
g	acceleration of gravity
Re	Reynolds number (Γ/ν)
Fr	Froude number $(\Gamma/\sqrt{gR^3})$
S	surface tension
p	pressure
p^γ	surface pressure due to vortex motion
ω	vorticity vector
$\mathbf{u}$	local velocity vector
u, v, w	velocities in $x-$, $y-$ and $z-$directions
ω_j	unit vorticity vector of $j-th$ "vorton"
vol_j	volume of $j-th$ "vorton"
Ω	"vorton" vector
ε	"blob" size
σ	initial vorticity distribution parameter
Φ	wave potential
I	impulse
γ	total impulse
β	impulse shape parameter
h	surface elevation
r	radial distance
T'	dimensionless time

1 INTRODUCTION

The interaction of underwater vortical flows with a free surface has been an active area of research in recent years, motivated by a desire to understand the mechanisms responsible for the surface signature of ship wakes which are detected by remote sensing radars. Although the ship wake/free surface interaction is a very complicated phenomenon in which many competing processes modify each other, most of investigations have focused on simpler "canonical" problems such as underwater jets and vortex pairs, for example, with the anticipation that these studies will be helpful to understand the key aspect of the more complicated wake.

Bernal and Madnia [1] performed experimental studies of the interaction between a free surface and an underwater jet. They observed that the generation of short waves on the free surface appeared to be related to the apperence of surface dimples which signify vortex lines terminating at the free surface. To isolate this phenomenon and understand the details, Bernal and Kwon [2] and Kwon [3] looked at a single vortex ring colliding obliquely with the free surface. They found that the reconnection process of a vortex ring at the free surface is a direct cause for short wave generation

on the free surface. Song, Bernal and Tryggvason [4] discussed the surface signature associated with the evolution of a large vortex ring normal to the free surface. The experiments indicated that the later stage of the interaction was dominated by three-dimensional features associated with the development of a core instability and the eventual reconnection of the vortex core to the free surface. In their investigation, the vortex reconnection appeared to be a major mechanism for the generation of short waves on the free surface in agreement with Bernal and Kwon [2]. In this paper, we focus on the vortex ring/free surface interaction and address several issues by numerical simulations. We also propose a simplified model of this complicated phenomena, aiming at a fundamental understanding of the free surface behavior associated with the vortex ring evolution.

The reconnection of vortex filaments, by itself, is still not fully understood. Pumir and Kerr [5] simulated the interaction of vortex tubes of opposite signs by spectral methods. They considered a small periodic vortex segment and investigated the interaction of tubes. Their results showed complete reconnection at a low Reynolds number (1000) and the formation of vortex ribbons (flattened vortex cores) at a higher Reynolds number (4500). Ashurst and Meiron [6] solved the Navier-Stokes equation to simulate the reconnection process of two vortex rings with a Gaussian vorticity distribution over the core (core size was 0.1 of the ring radius) for Reynolds numbers less than 1000. They claimed that the reconnection took place on a convective time scale and conjectured that the initial conditions (the separation distance between the two rings and the incident angle) are important in determining the reconnection time. Kerr and Hussain [7] also performed similar calculations as Pumir and Kerr [5] and reviewed previous work. Saffman [8] briefly reviewed previous experimental and numerical investigations and suggested a simple model to explain the physics of the reconnection process.

A Lagrangian discretization of the vorticity equations is often used in numerical investigations of both two- and three-dimensional vortical flows. In two-dimensional cases, the discrete vortex elements are point vortices and in three-dimensional cases, they are usually called "vortons" (or vortex particles or vortex sticks). Despite some arguments regarding the consistency of the vorton modeling for vortical structures (Saffman and Meiron [9], Winckelmans and Leonard [10] and Greengard and Thomann [11]), the vortex particle modeling is attractive because when the vorticity is confined to a small region, only a small region needs to be considered numerically. The vorton modeling can also be easily incorporated into the free surface problem, and hence we use a vorton model to describe the vortex ring evolution in the present work. The method will be described briefly in section 2.1; for more details see Winckelmans [12].

Generally, free surface deformations due to underwater vortical flows are small for realistic Froude numbers. Therefore, the free surface waves are assumed to be linear here. By doing that, we can split the interaction problem into two separate parts: the vortex ring evolution with its image, and the free surface deformation which depends on the vortical structure calculated without any effect from the surface deformation. As a result, the problem becomes much simpler and requires considerably less computing time than if we attempted the fully nonlinear problem.

In the following section we describe the mathematical formulation of the problem and its numerical implementations. Section 3 is devoted to the presentation and discussion of results including a simplified model of the interaction. At the end we summarize the work presented in this paper. Preliminary results of this study were briefly discussed at APS meetings (Song, Tryggvason and Bernal [13], Song and Tryggvason [14]).

2 FORMULATION OF THE PROBLEM

2.1 Vortex Ring Modeling

In order to simulate the vortex reconnection where a vortex ring "opens up" at the free surface and forms an U-vortex, we use a vorton method which is basically an inviscid model. Even though the reconnection process of the vortex core is not fully understood, viscosity is believed to play a key role in the process (Kerr and Hussain [7]). The role of viscosity is not to modify the large scale behavior of the flow but to initiate a local cancellation of vorticity of opposite signs. This local behavior produces a pressure imbalance along the axis of the vortex core near the reconnection region, and this pressure imbalace causes the vorticity to be swept outward (Saffman [8]). The experimental studies of Kwon [3] showed that the reconnection time is not sensitive to the Reynolds number variation as long as Re is roughly larger than 2000, and hence we may speculate that while vorticity diffusion is important, the absolute magnitude of the viscosity has small effects.

Knowing this, we expect that an essentially inviscid simulation with a small diffusive mechanism can successfully accomplish the reconnection which, in reality, is a phenomenon where viscosity plays an important role. Indeed, inviscid numerical simulations using vorton model with a careful treatment of the problem caused by the discretization of the vorticity (Winklemans and Leonard [15] and Winklemans [12]) have successfully simulated the reconnection of vortex filaments. This is because the finite blob used for the vortex particles exhibits a somewhat dissipative role when the particles are very close to each other.

Guided by the weak dependency of the reconnection process on the Reynolds number, as long as it is reasonably large, we introduce viscosity in the vorticity evolution following Winklemans and Leonard [15]. Their treatment of the viscous term in the vorticity equation was based on Degond and Mas-Gallic [16]

where the ∇^2 operator is approximated by local averaging of the vorticity. This additional viscosity makes the vortical structure evolve smoother without changing the global evolution and also makes simulation with the free surface possible for a significant period of time after the reconnection.

Following Winckelmans and Leonard [15] and Winckelmans [12], a brief description of the problem follows: The dimensionless governing equation is the Navier Stokes equation in vorticity form,

$$\frac{\partial \omega}{\partial t} + (\mathrm{u} \cdot \nabla)\omega = (\omega \cdot \nabla)\mathrm{u} + \frac{1}{Re}\nabla^2 \omega. \qquad (1)$$

Here u is the velocity vector, $\omega = \nabla \times \mathrm{u}$ is the vorticity, and Re is the Reynolds number defined by Γ/ν. As shown by Winckelmans and Leonard [15], an alternative form of Eq. (1) is

$$\frac{\partial \omega}{\partial t} + (\mathrm{u} \cdot \nabla)\omega = (\omega \cdot \nabla^T)\mathrm{u} + \frac{1}{Re}\nabla^2 \omega, \qquad (2)$$

and is known to provide better flow behavior when a discretized vortex model is applied. If the vorticity field is written as a summation of vortex particles of finite number, N, we have

$$\begin{aligned} \omega(\mathrm{x}) &= \sum_{j=1}^{N} (\omega_j vol_j)\delta(\mathrm{x} - \mathrm{x}_j) \\ &\equiv \sum_{j=1}^{N} \Omega(\mathrm{x}_j)\delta(\mathrm{x} - \mathrm{x}_j). \end{aligned} \qquad (3)$$

Here ω_j and vol_j are the unit vorticity vector and the volume of the j-th vorton respectively, and $\Omega(\mathrm{x}_j) \equiv \omega_j vol_j$. The velocity field induced by the above discretized vorticity is

$$\cdots \mathrm{u}(\mathrm{x}) = \sum_{j=1}^{N} \nabla\Big(\frac{1}{|\mathrm{x} - \mathrm{x}_j|}\Big) \times \Omega(\mathrm{x}_j)\delta(\mathrm{x} - \mathrm{x}_j), \qquad (4)$$

Here x is the Lagrangian field point which moves according to the kinematic relation

$$\frac{d\mathrm{x}}{dt} = \mathrm{u}(\mathrm{x}). \qquad (5)$$

Since the above formulation is too singular to implement numerically, a regularized formulation where the δ function is replaced by a properly smoothed function ζ_ϵ satisfying certain conditions (Greengard [17], Winckelmans and Leonard [15]) is used. The vorticity, Eq. (3), is modified by a "blob" of size ϵ, so that

$$\omega(\mathrm{x}) \approx \omega_\epsilon(\mathrm{x}) = \sum_{j=1}^{N} \Omega(\mathrm{x}_j)\zeta_\epsilon(\mathrm{x} - \mathrm{x}_j) \qquad (6)$$

$$\text{where } \zeta_\epsilon(\mathrm{x} - \mathrm{x}_j) = \frac{15\epsilon^4}{8\pi(|\mathrm{x} - \mathrm{x}_j|^2 + \epsilon^2)^{7/2}}, \qquad (7)$$

and the velocity field induced by this regularized vorticity is

$$\mathrm{u}(\mathrm{x}) = -\sum_{j=1}^{N} \frac{\chi_\epsilon(\mathrm{x} - \mathrm{x}_j)}{|\mathrm{x} - \mathrm{x}_j|^3}(\mathrm{x} - \mathrm{x}_j) \times \Omega(\mathrm{x}_j), \qquad (8)$$

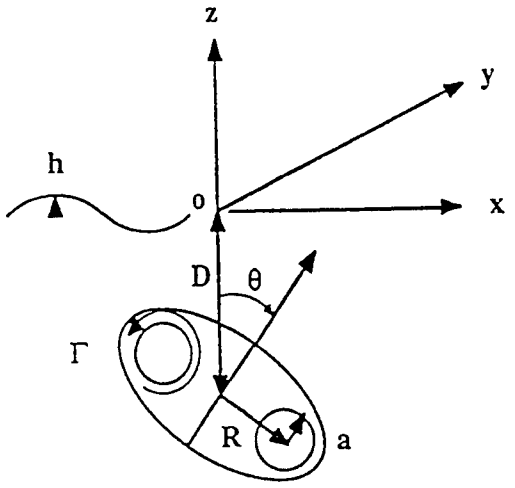

Fig. 1 Schematic diagram of the flow and the coordinate system.

$$\text{where } \chi_\epsilon(\mathrm{x} - \mathrm{x}_j) = \frac{|\mathrm{x} - \mathrm{x}_j|^3(|\mathrm{x} - \mathrm{x}_j|^2 + 5\epsilon^2/2)}{4\pi(|\mathrm{x} - \mathrm{x}_j|^2 + \epsilon^2)^{5/2}}. \qquad (9)$$

The evolution equation for the strength of each vorton, including the viscous diffusion, is

$$\begin{aligned} \frac{d\Omega}{dt} &= \frac{1}{4\pi}\sum_{j=1}^{N} \frac{(|\mathrm{x} - \mathrm{x}_j|^2 + \frac{5}{2}\epsilon^2)}{(|\mathrm{x} - \mathrm{x}_j|^2 + \epsilon^2)^{\frac{5}{2}}}(\Omega(\mathrm{x}) \times \Omega(\mathrm{x}_j)) + \\ &(\mathrm{x} - \mathrm{x}_j)\frac{3(|\mathrm{x} - \mathrm{x}_j|^2 + \frac{7}{2}\epsilon^2)}{(|\mathrm{x} - \mathrm{x}_j|^2 + \epsilon^2)^{\frac{7}{2}}}(\Omega(\mathrm{x}) \cdot ((\mathrm{x} - \mathrm{x}_j) \times \Omega(\mathrm{x}_j))) \\ &+ \frac{105\epsilon^4}{Re(|\mathrm{x} - \mathrm{x}_j|^2 + \epsilon^2)^{\frac{9}{2}}}(vol(\mathrm{x})\Omega(\mathrm{x}_j) - vol(\mathrm{x}_j)\Omega(\mathrm{x})). \end{aligned} \qquad (10)$$

In order to conserve the volume of the vortons, we keep $(\varepsilon(\mathrm{x})^2|\Omega(\mathrm{x})|)$ constant in time.

The coordinate system used is shown in Fig. 1 with the flow geometry. To save computing time the vortex ring is initiated close to the free surface and symmetry about $y = 0$ axis is used. The initial vorticity distribution is Gaussian, defined by

$$|\omega(r)| = \frac{1}{2\pi\sigma^2}\exp\{-\frac{r^2}{2\sigma^2}\}, \qquad (11)$$

where r is the perpendicular distance to the core of the ring.

2.2 Free Surface Calculation

Assuming that the flow outside of the vortex ring is inviscid, incompressible and irrotational, a velocity potential for wave motion can be introduced. This velocity potential, $\Phi(x, y, z, t)$, satisfies the Laplace equation in the fluid domain. From the Bernoulli equation the pressure field can be expressed as

$$p = -\rho\{\frac{\partial \Phi}{\partial t} + \frac{1}{2}(\nabla\Phi)^2 + gz\} \qquad (12)$$

where ρ is the density, g is the acceleration of gravity. This pressure also satisfies the following relation at the free surface

$$p = P - S(\frac{1}{R_1} + \frac{1}{R_2}). \quad (13)$$

Here S is the surface tension, R_1 and R_2 are the two principal radii at the free surface, positive when the center of curvature is above the free surface, and $P = p^\gamma + p_a$, where p_a is the atmospheric pressure and p^γ is the pressure which is obtained from the vortex ring motion. Recalling that experimental results showed generation of very small waves at low Froude number vortex ring/free surface collisions (Song et.al. [4], for example), the above dynamic free surface boundary condition can be linearized with the assumption of zero atmospheric pressure (Yih [18]). We therefore have the following partial differential equation for Φ at the free surface.

$$\frac{\partial \Phi}{\partial t} = -\frac{p^\gamma}{\rho} - gz + \frac{S}{\rho}(\frac{\partial^2 h}{\partial x^2} + \frac{\partial^2 h}{\partial y^2}) \quad \text{at } z = 0\,. \quad (14)$$

The kinematic free surface condition is

$$\frac{\partial h}{\partial t} = \frac{\partial \Phi}{\partial z} - (\frac{\partial \Phi}{\partial x}\frac{\partial h}{\partial x} + \frac{\partial \Phi}{\partial y}\frac{\partial h}{\partial y}) \quad \text{at } z = h\,, \quad (15)$$

and is also linearized:

$$\frac{\partial h}{\partial t} = \frac{\partial \Phi}{\partial z} \quad \text{at } z = 0\,. \quad (16)$$

To complete the boundary conditions $\Phi = \nabla\Phi = 0$ is imposed far away from the interaction region.

To nondimmensionalize these equations we scale time by R^2/Γ, length by R, velocity potential by Γ, velocity by Γ/R and the pressure by $\rho\Gamma^2/R^2$, giving the following dimensionless partial differential equations for the update of the wave potential and the free surface elevation

$$\frac{\partial \Phi}{\partial t} = -p^\gamma - \frac{h}{Fr^2} + \frac{1}{We}(\frac{\partial^2 h}{\partial x^2} + \frac{\partial^2 h}{\partial y^2}) \quad (17)$$

$$\text{and} \quad \frac{\partial h}{\partial t} = \frac{\partial \Phi}{\partial z}. \quad (18)$$

Here, $Fr = \Gamma/\sqrt{gR^3}$ and $We = \rho\Gamma^2/(RS)$.

As mentioned before the pressure p^γ at the free surface in the dynamic free surface boundary condition is obtained from the vortex ring calculation, where the free surface is taken as flat. Once the vortex filaments connect to the free surface, it is no longer possible to take the flow at the free surface as irrotational, hence we estimate the pressure due to the vortex motion directly from the Navier-Stokes equations. Dimensionless Navier-Stokes equations in the velocity form are

$$\begin{aligned}
\frac{\partial u}{\partial t} + u\frac{\partial u}{\partial x} + v\frac{\partial u}{\partial y} + w\frac{\partial u}{\partial z} &= -\frac{\partial p^\gamma}{\partial x} + \frac{\nabla^2 u}{Re} \\
\frac{\partial v}{\partial t} + u\frac{\partial v}{\partial x} + v\frac{\partial v}{\partial y} + w\frac{\partial v}{\partial z} &= -\frac{\partial p^\gamma}{\partial y} + \frac{\nabla^2 v}{Re} \quad (19) \\
\frac{\partial w}{\partial t} + u\frac{\partial w}{\partial x} + v\frac{\partial w}{\partial y} + w\frac{\partial w}{\partial z} &= -\frac{\partial p^\gamma}{\partial z} + \frac{\nabla^2 w}{Re} - \frac{1}{Fr^2}.
\end{aligned}$$

Taking partial derivatives of the first and second equations in Eq.(19) with respect to x and y respectively and adding we have a two-dimensional Poisson equation for the surface pressure due to vortex motion,

$$\nabla^2_{2d} p^\gamma = \frac{\partial^2 p^\gamma}{\partial x^2} + \frac{\partial^2 p^\gamma}{\partial y^2} \quad (20)$$

$$= \frac{\partial}{\partial t}\frac{\partial w}{\partial z} - \frac{\partial}{\partial x}(u\frac{\partial u}{\partial x} + v\frac{\partial u}{\partial y}) - \frac{\partial}{\partial y}(u\frac{\partial v}{\partial x} + v\frac{\partial v}{\partial y}) - \frac{1}{Re}\nabla^2\frac{\partial w}{\partial z}$$

where we have used continuity and the fact that the free surface is flat as far as the vortex motion is concerned. All the terms on the right hand side of Eq.(20) can be determined from the vortex calculation and then the Poisson equation is solved by a fast solver.

To determine the $\partial\Phi/\partial z$ term in Eq.(18), Φ is expressed by a truncated Fourier series. The physical domain of the problem which is infinite is truncated at a finite distance from the collision point and a damping layer used to dissipate the outward propagating waves. Outside of this layer the wave potential and the surface elevation are set to zero. Time integration is done by a high order predictor-corrector scheme with variable step size.

3 RESULTS AND DISCUSSIONS

3.1 Characteristic of Numerical Vortex Rings

The characteristics of the vortex rings used in our numerical experiments were investigated in several preliminary tests with different initial parameters. Physical parameters that characterize the rings are the dimensionless radius of the vortex core (a) and the distribution of vorticity (σ) in the core. Numerical parameters are the number of vortex particles and the size of the blob used. The influence of these numerical parameters on the convergence of the solution has also been investigated by Greengard [17], Winckelmans and Leonard [15] and others.

To characterize the rings, we first investigated the speed of the ring and several invariants of the ring motion without viscosity. We used 231 and 1045 vortex particles for two different cases. The vortex ring is divided into 33 (55 for the 1045 particle case) segments in the azimuthal direction and each segment consists of 2 layers (3 layers when 1045 particles were used). At the cross section of the ring, one vortex particle is located at the center of the core, and the second and third layers are composed of 6 and 12 particles respectively. Since there is little information from experiments about the detailed structure of the vortex core we use equation (11) with $a = 0.25$ and $\sigma = 0.1$ for for most of our calculation. This leads to a dimensionless propagation speed that approximately matches the one in the experiments of Kwon [3].

The computed mean velocities of the vorticity centroid were steady but slight oscillations in the axial speeds were observed due to the discretization and also partially due to the initial vorticity distribution.

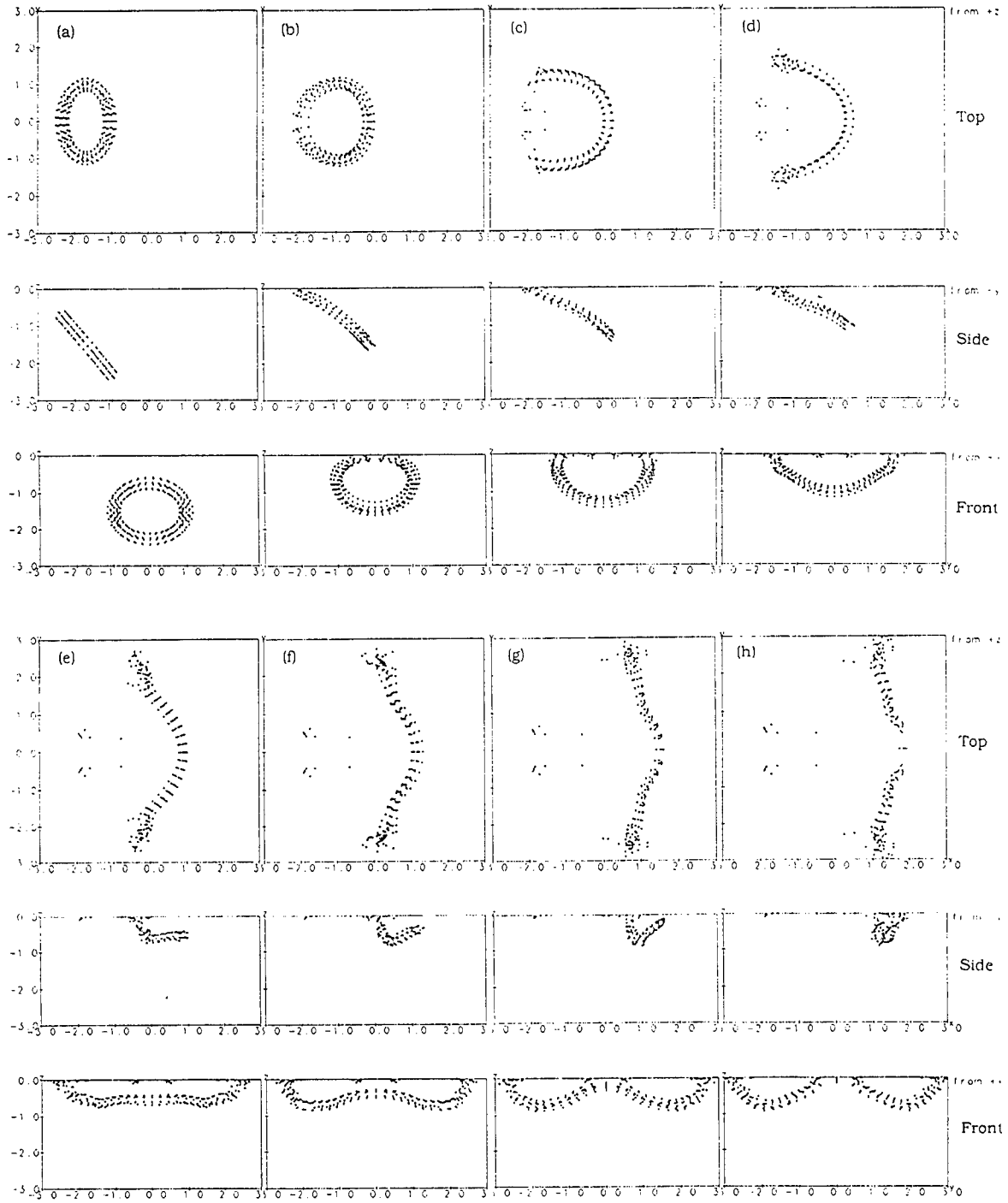

Fig. 2 Typical vortex ring evolution. $Re = 1000$. $\theta = 50°$. $\sigma = 0.1$ and $a = 0.25$. 231 vortex particles. Top row: Top view, Second row: Side view and Third row: Front view. From (a), $T' = 0.0$, 6.0, 8.0, 10.0, 14.0, 16.0, 18.0 and 20.0.

As the number of particles is increased, the axial speed converges to a value which is close to the estimate of Saffman [19] and the oscillations are also reduced.

If we include viscous effect and set $Re = 5000$, the propagation speed decreased slightly with increasing time due to vorticity diffusion. The rate of decrease of propagation speed are comparable to Saffman's [19] result. These numerical experiments showed that the modeling of the vortex ring is well under control and addition of viscosity does not affect the global behavior of the ring.

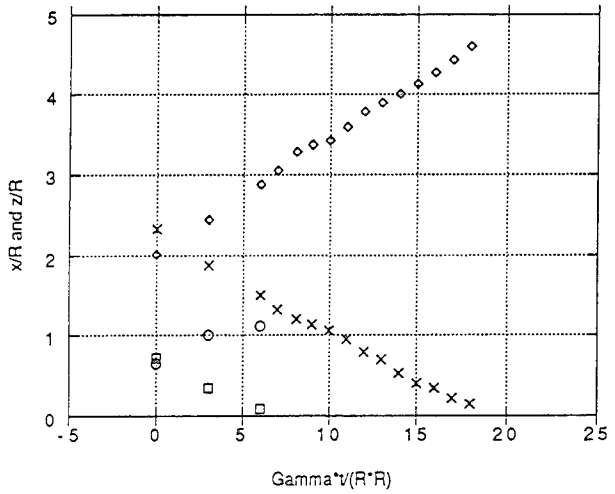

Fig. 3 Position of vortex cores at the center plane ($y = 0$) as a function of dimensionless time. ○: X_u/R, ◇: X_l/R, □: Z_u/R and ×: Z_l/R. $Re = 1000$. $\theta = 50°$. $\sigma = 0.1$ and $a = 0.25$. 231 vortex particles.

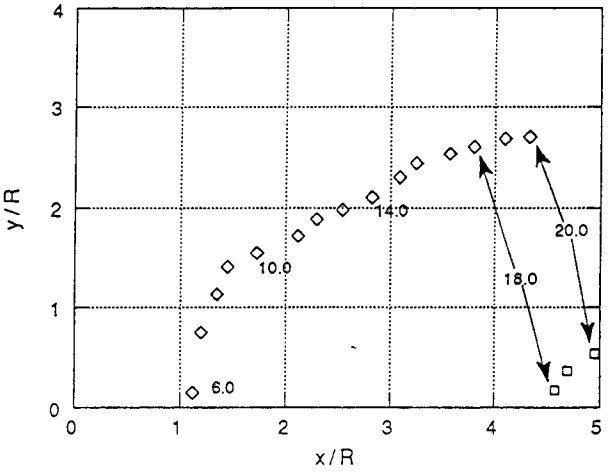

Fig. 4 Trajectory of vortex reconnection point on the free surface. ◇: Upper vortex core and □: Lower vortex core. $T' =$ from 6.0 to 20.0 by 1.0. $Re = 1000$. $\theta = 50°$. $\sigma = 0.1$ and $a = 0.25$. 231 vortex particles.

3.2 Reconnection of two vortex rings

In contrast to the single ring propagation, the reconnection process can not be realized successfully relying only on the diffusive mechanism naturally included in the inviscid vortex particle modeling when a somewhat modest number of vortons is used. When two vortex filaments interact with each other a dramatic stretching of vorticity occurs near the reconnection region and this, generally, prevents the calculation from being continued further. This is a significant problem if we want to see the second reconnection and the pressure field between the two rings, which will be used for the wave motion in our case, also becomes unrealistically large. Hence, we need a small amount of real viscosity to investigate the vortex reconnection with the present method, and the inclusion of a small amount of viscosity is believed to cause little change in the global picture of the ring evolution.

Typical evolution of two vortex rings colliding obliquely with each other is shown in Fig. 2 The first, second and third rows are a top view, side view and the front view of the ring below the image plane, $z = 0$, respectively. The initial incident angle (θ) is 50° and the Reynolds number is 1000.

As the upper part of the ring approaches the top surface, it starts to move toward the negative x-direction due to its image (frame (b)). The upper part of the ring opens up between frames (b) and (c), and reconnects with its image ring. After the first reconnection, the U-shape vortex ring propagates along the positive x-axis with its legs separating ((c) and (d)). As time increases, the lower part of the ring approaches the surface again ((e) and (f)) and eventually reconnects with its image at the surface. In frame (h) two separate half rings have formed and are propagating outward, leaving a few particles behind.

In Fig. 3 the evolution of the vortex core in the double reconnection process is shown by plotting the dimensionless downstream location of the core and the distance of the core to the image plane as a function of dimensionless time. The symbols ○ and □ represent the downstream location and depth of the upper core, respectively, and ◇ and × are for the lower core. The speed of propagation of both the upper and lower cores is essentially constant (0.21) until they disappear from the center plane ($y = 0$). The trajectories of the vortex cores on the $z = 0$ plane in normalized coordinates are plotted in Fig. 4. The diamonds are for the reconnected upper core and the squares are for the lower core. Right after the first reconnection the two cores move away from the $y = 0$ plane very rapidly (from $T' = 6.0$ to 9.0), and then they move steadily downstream and away from the center plane until the second reconnection occurs. At $T' = 18.0$ the lower core reconnects at the $z = 0$ plane and the two cores form half rings that move obliquely away from the center plane.

Our numerical experiments show that the secondary reconnection of the lower core is very sensitive to the initial conditions (such as the incident angle, core size and viscosity). This sensitivity was also found in the experimental studies of Kwon [3] and the numerical studies of Ashurst and Meiron [6]. More detailed simulations of reconnection of two vortex rings by vorton methods can be found in the works of Winckelmans and Leonard [15] and Winckelmans [12].

One of the important parameters that characterizes the reconnection process is the time scale of the reconnection. To define the reconnection time, we evaluate the circulation of the upper core of the ring at the center plane ($y = 0$) and estimate the difference be-

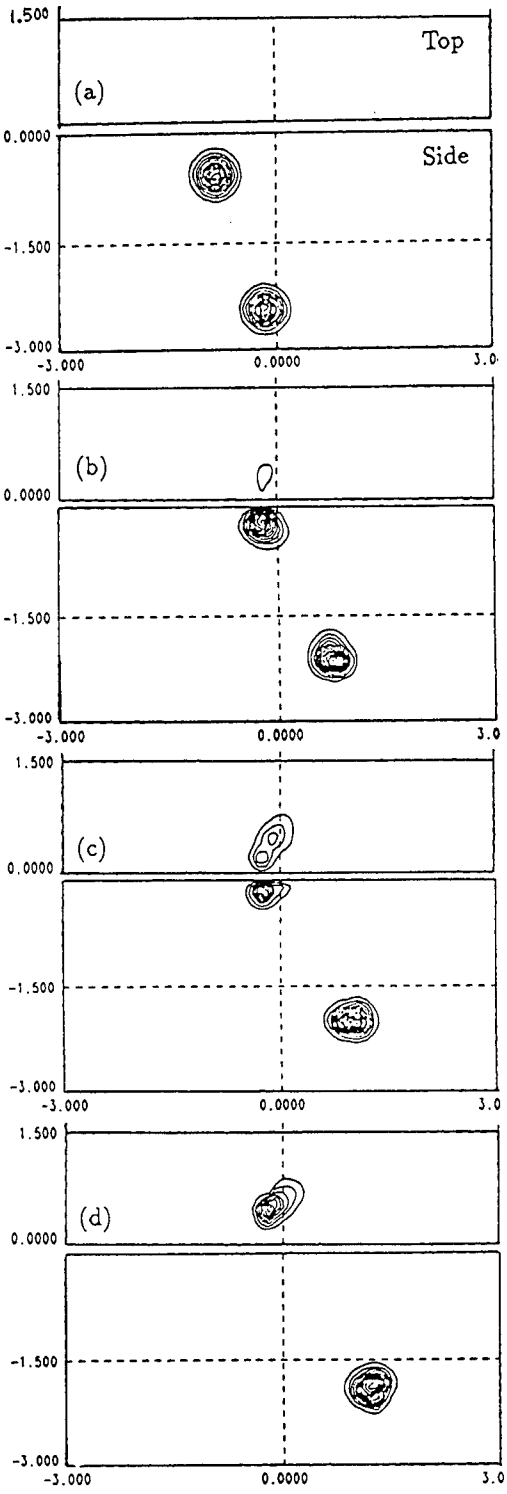

Fig. 5 Vorticity contours at the center plane ($y = 0$) and the free surface. $Re = 5000$. $\theta = 70°$. $\sigma = 0.1$ and $a = 0.25$. $T' = 0.0$, 4.139, 5.290 and 6.328.

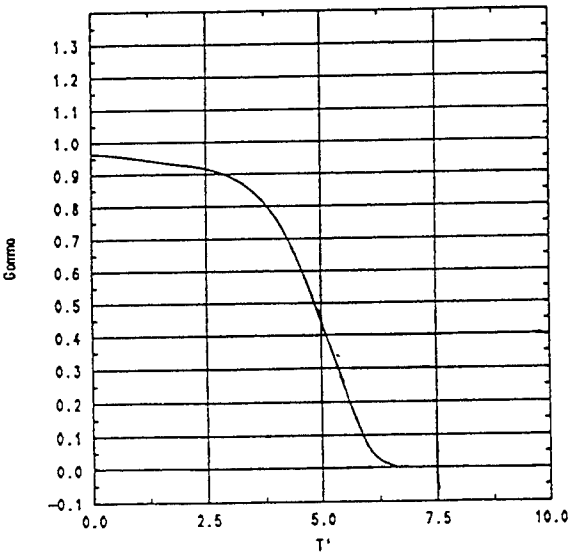

Fig. 6 Circulation of the upper part of the ring as a function of dimensionless time. $Re = 5000$. $\theta = 70°$. $\sigma = 0.1$ and $a = 0.25$.

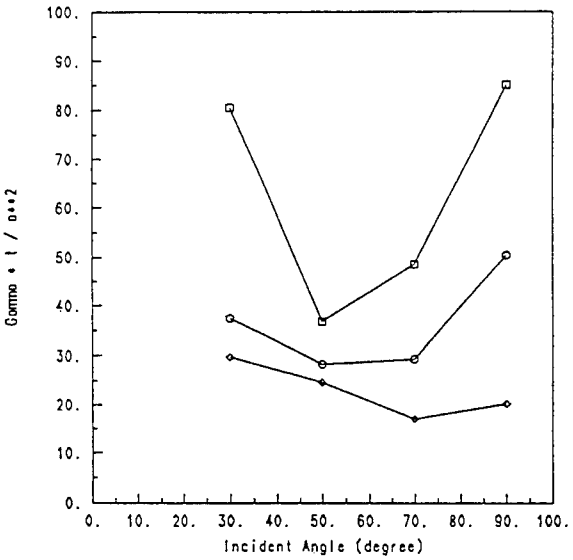

Fig. 7 Nondimensional reconnection times as a function of incident angle. ○: inviscid, $\sigma = 0.1$. ◇: inviscid, $\sigma = 0.05$. □: $Re = 5000$, $\sigma = 0.1$.

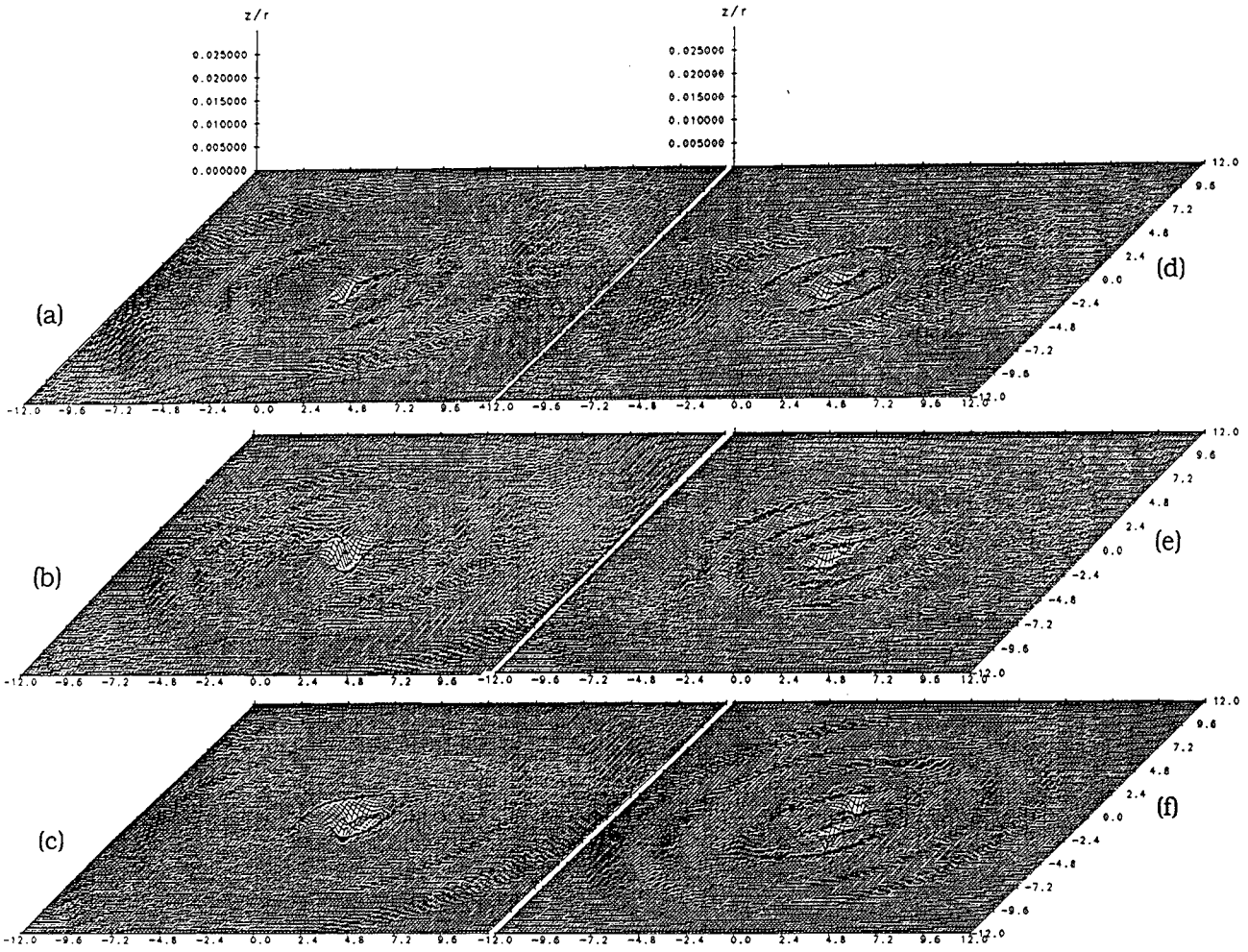

Fig. 8 Perspective views of free surface deformation. $Fr = 0.2$. $Re = 5000$. $\theta = 70.0°$. $T' = 5.0, 6.0, 7.0, 8.0, 9.0$ and 11.0.

tween the times of 90% and 10% circulations. Fig. 5 shows the vorticity contours at the center plane ($y = 0$) and at the top surface ($z = 0$ and $y > 0$), that will be used for the free surface calculation ($\theta = 70°, a = 0.25, D = 1.5$, $\sigma = 0.1$ and $Re = 5000$). Once the upper part of the core attaches to the free surface, vertical vorticity appears on the free surface and eventually no noticeable y-component of the vorticity in the upper part of the core is detected at the center plane. Fig. 6 shows the change of the circulation of the upper part of the ring at the center plane.

To summarize our numerical results for the time scale of the first reconnection, we plot the dimensionless reconnection time ($\Gamma t/a^2$) as a function of the incident angle (θ) in Fig.7 for three different cases: two inviscid calculations with different vorticity distributions ($\sigma = 0.05$ and 0.1) and one viscous calculation for $\sigma = 0.1$ and $Re = 5000$. Even though we do not have many data points and the definition of the reconnection time is somewhat arbitrary, three things are noticeable. First, there is an incident angle at which reconnection takes place in a shortest time. This angle depends on the initial vortex structure, and in our experiments is between 50° and 70°, bigger for a more concentrated vortex ring ($\sigma = 0.05$). Secondly, it takes a longer time for a ring of rather uniform vorticity ($\sigma = 0.1$) to accomplish the reconnection than the concentrated ring. Thirdly, there is an angle (about 50°) at which the reconnection time is not significantly affected by the initial condition (viscosity and vorticity distribution).

3.3 Free Surface Waves

Based on results from the preliminary calculations, the initial condition for the ring and the computational parameters for the free surface were selected for one well resolved calculation. A vortex ring (a = 0.25, $\sigma = 0.1$ and $Re = 5000$), which is the same an in Fig.5, is now located at 1.5 dimensionless distances below the free surface with 70° incident angle. The Froude number is 0.2 and the Weber number is 100. The computational domain on the free surface is truncated to a square plane whose side is $48 \times R$ with a 256×256 grid on it. The calculation is stopped when the first reconnection

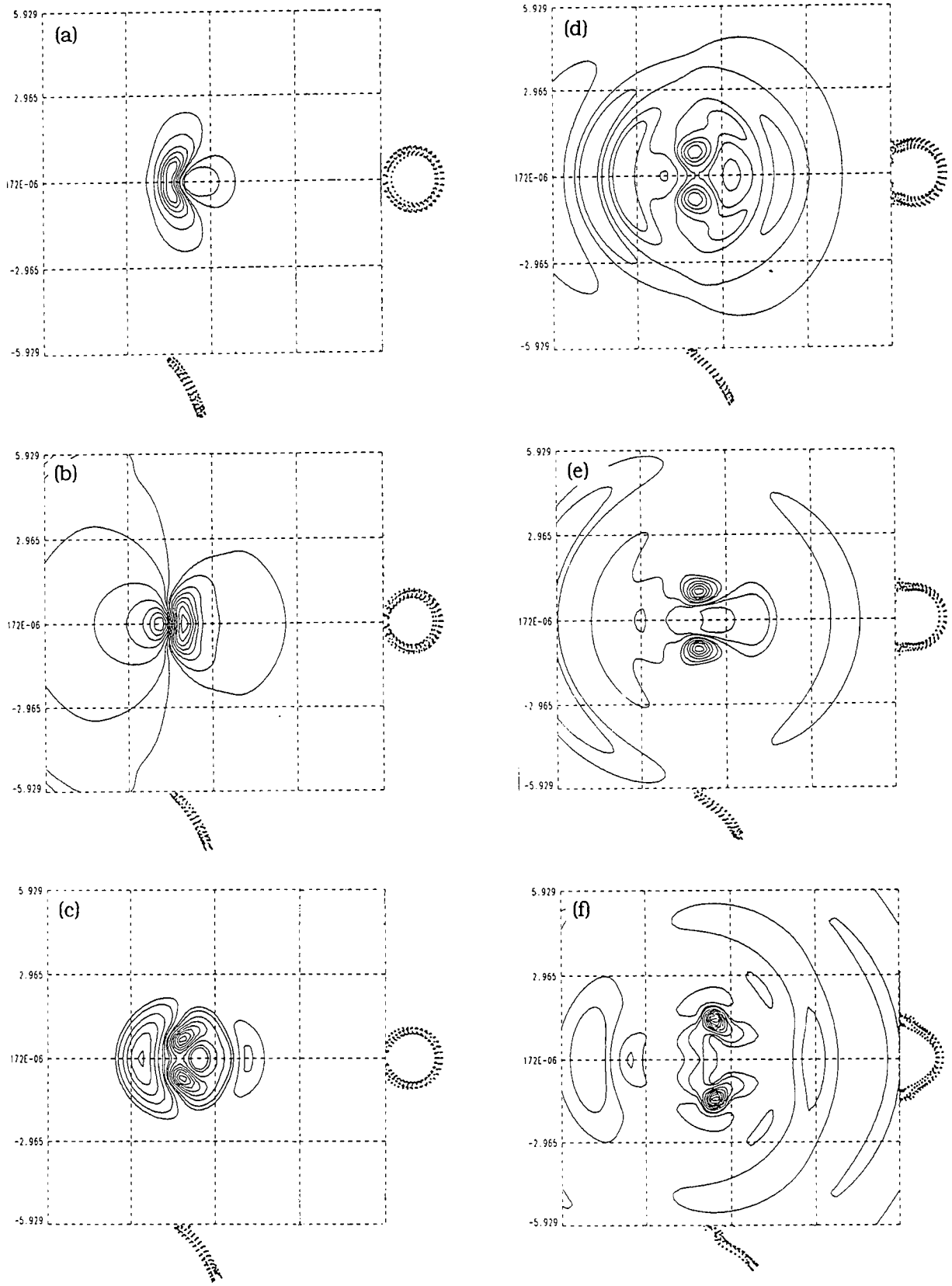

Fig. 9 Free surface contours and front/side views of ring. $Fr = 0.2$. $Re = 5000$. $\theta = 70.0°$. $T' = 5.0$, 6.0, 7.0, 8.0, 9.0 and 11.0.

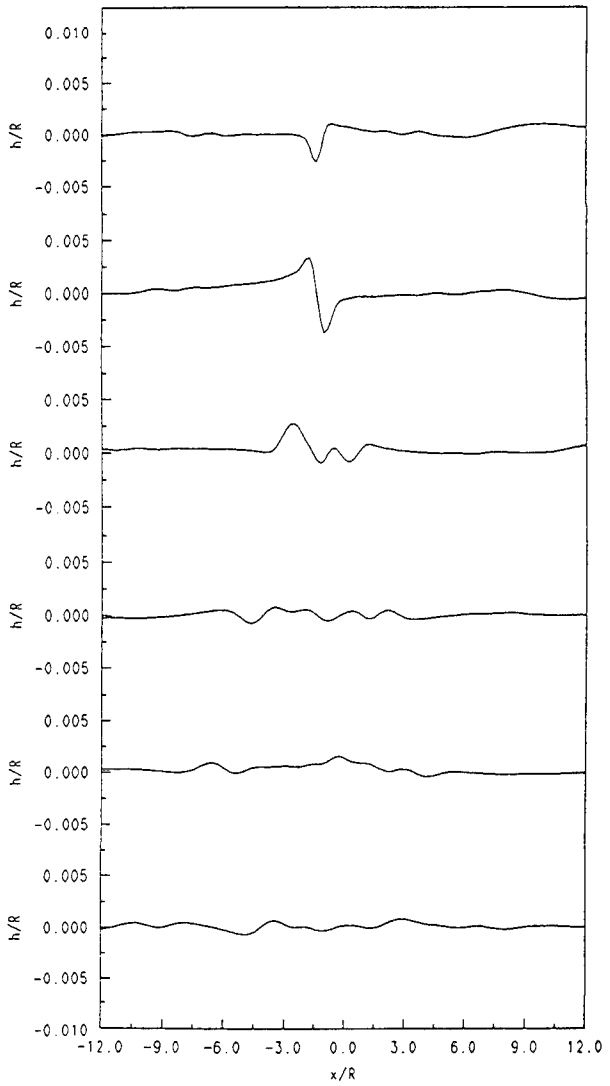

Fig. 10 Surface elevations at $y = 0$. $Fr = 0.2$. $Re = 5000$. $\theta = 70.0°$. From the top, $T' = 5.0$, 6.0, 7.0, 8.0, 9.0 and 11.0.

is completed.

Fig. 8 shows perspective pictures of the free surface at several times. The z-axis is stretched 240 times compared to the x- and y-axis. The first two frames show the free surface deformations that are mostly due to the upper part of the ring. This signature becomes more clear as time increases. In the next three frames, two dimples due to the reconnected vortex cores at the free surface appear. Notice the waves generated during this reconnection process. Once two distinguished dimples (sixth frame) are established, there is no more surface wave generation but the generated waves propagate outward from the reconnection region. In addition to the waves generated due to the reconnection process, there are slowly varying surface deformation near the two distinct dimples, which seem to be related to the flow induced by the lower part of the reconnected ring.

In order to obtain more detailed information about the correlation between the free surface signature and the vortex ring evolution, contour plots of the surface elevation and side/front views of the ring are shown together in Fig. 9. As the vortex ring approaches the free surface, the upper part of the core starts to move locally in the negative x-direction due to its image. The dominant surface deformation at this stage is the depressed free surface near and parallel to the axis of the upper part of the core and the slight elevation near the center of the ring. This surface pattern grows as time increases, even when the dimples appear. Indeed, the dimples are related to the low pressure regions on the free surface and the pressure imbalance along the vortex core accelerate the reconnection process. However, since there is still considerable y-component vorticity in the center plane, the depression of the free surface due to the upper part of the core remains. The most dramatic topological change in the vortical structure occurs between the third and fourth frames in Fig. 9. In the fourth frame, no vortex particles belonging to the upper part of the core are observed at the center plane. Moreover, the vortex lines at the free surface are almost perpendicular to the surface, indicating a full reconnection of the vortex core. Once there is no noticeable y-component vorticity in the upper part of the core at the center plane, the depressed free surface is released and moves upward. This is clearly captured in the contour plot in the fourth frame. The following free surface motion is similar to the Cauchy-Poisson's wave problem with a single negative surface depression as an initial condition. The next few frames of contour plots show wave propagations in the positive and negative x-directions. The last frame shows two distinct dimples and a slight modification of the surface profile near the reconnection region.

Another description of the evolution of the free surface can be seen in Fig. 10 where the surface profile at the center plane at times corresponding to Fig. 9 is shown. The development of the depression associated with the upper part of the vortex core continues up to the second frame ($T' = 6.0$), when the depression is suddenly released and waves that propagate in the positive/negative x-direction appear.

3.4 Pressure impulse modeling

3.4.1 Mathematical Formulation

In the previous sections we have noticed that most of the short waves on the free surface are generated by the reconnection process during which a significant pressure impulse acts on the free surface. This observation suggests that it may be possible to model the effect of the vortical motion simply by a pressure pulse (or pulses) acting on the surface at the reconnection point. If such a model produces the right wave patterns, considerable simplifications result and, in particular, the wave pattern due to many reconnections could be computed rel-

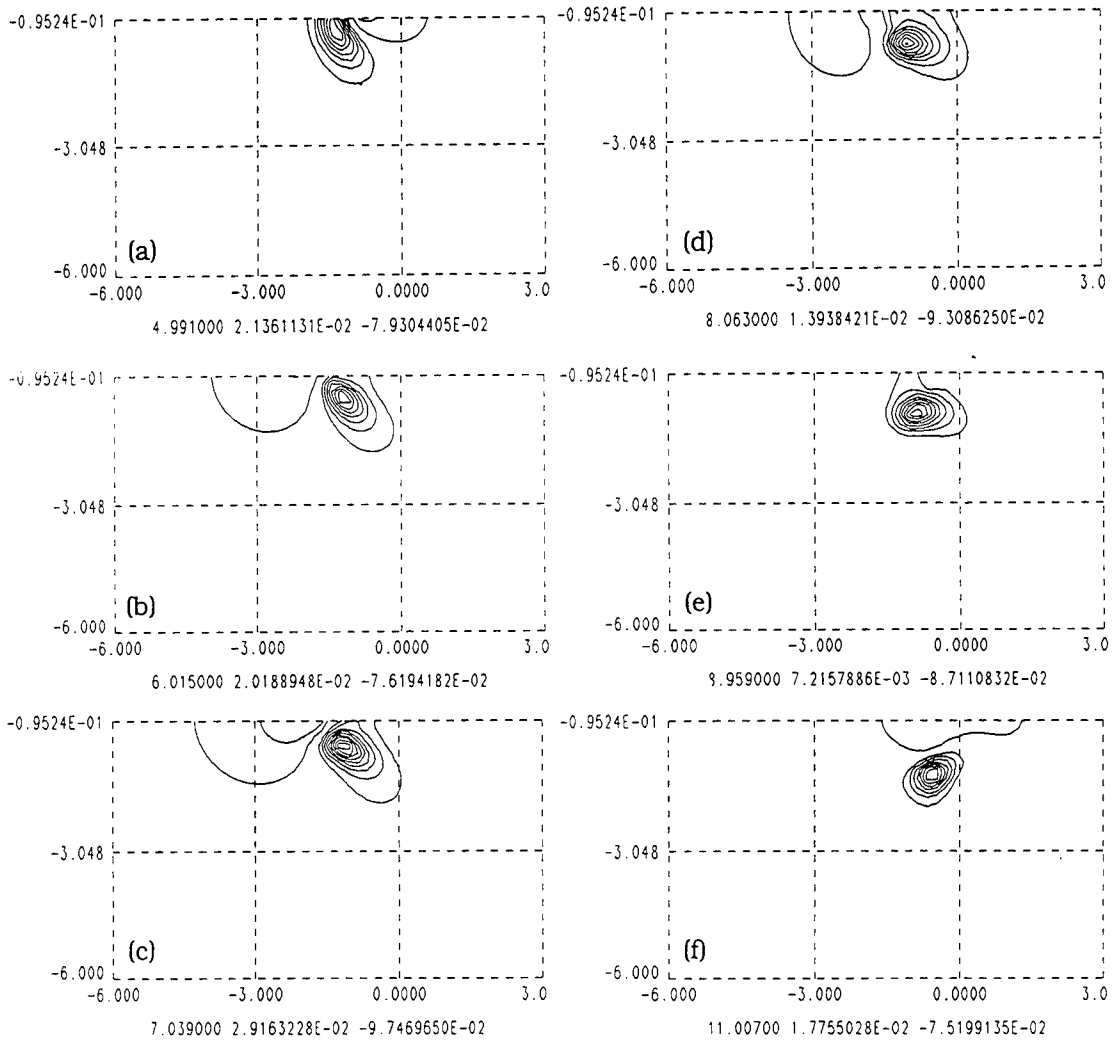

Fig. 11 Distribution of surface pressure due to vortex evolution. Only $y < 0$ side is shown. $Fr = 0.2$. $Re = 5000$. $\theta = 70.0°$. From (a), $T' = 5.0$, 6.0, 7.0, 8.0, 9.0 and 11.0.

atively cheaply. Based on this ideas we introduce below an analytical model that is basically a Cauchy-Poisson wave problem with a known pressure impulses.

The governing equation for the wave-velocity potential is

$$\frac{\partial^2\Phi}{\partial r^2} + \frac{1}{r}\frac{\partial\Phi}{\partial r} + \frac{\partial^2\Phi}{\partial z^2} = 0 \tag{21}$$

in cylindrical coordinates. Following Sneddon's [20] notation, zeroth order Hankel transformation is given as

$$\tilde{\Phi}(\xi, z, t) = \int_0^\infty r\ \Phi(r, z, t) J_0(\xi r)\ dr. \tag{22}$$

Taking the Hankel transform of Eq.(21) gives

$$\frac{\partial^2\tilde{\Phi}}{\partial z^2} - \xi^2\tilde{\Phi} = 0. \tag{23}$$

Corresponding Hankel transformed linearized free surface boundary condition is

$$\frac{\partial^2\tilde{\Phi}}{\partial t^2} + g\frac{\partial\tilde{\Phi}}{\partial z} = 0 \tag{24}$$

at $z = 0$, and its dimensionless form, using the same variables which were used to nondimensionalize the equations in previous sections, is

$$\frac{\partial^2\tilde{\Phi}}{\partial t^2} + \frac{1}{Fr^2}\frac{\partial\tilde{\Phi}}{\partial z} = 0. \tag{25}$$

From now on, all equations are in dimensionless forms. If we let

$$\tilde{\Phi} = A(\xi, t)\exp(\xi z), \tag{26}$$

Eq. (23) is satisfied and, substituting Eq. (26) into Eq. (25), we have

$$\frac{\partial^2 A}{\partial t^2} + \frac{\xi}{Fr^2}A = 0. \tag{27}$$

Once we obtain $A(\xi, t)$ which satisfies Eq. (27) and the proper initial conditions, we perform an inverse Hankel transform to get a wave potential that can be used to obtain surface elevations with the linearized kinematic free surface boundary condition.

Now, if an impulse at the free surface is given at $t = 0$, we can write $I(r) = \Phi(r, 0, 0)$, and from Eq. (26)

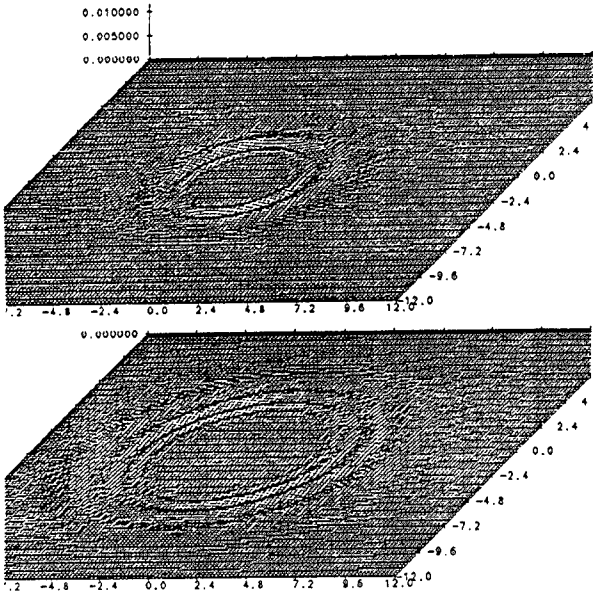

Fig. 12 Perspective views of surface wave propagation due to a pressure impulse at (-1.5, 0.0). $\gamma = 0.006$. $\beta = 0.3$. $T' = 3.0$ and 5.0.

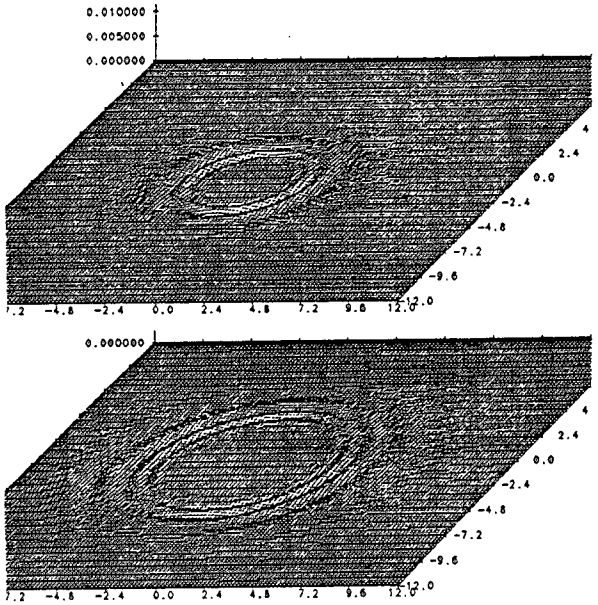

Fig. 13 Perspective views of surface wave propagation due to three pressure impulses. At (-1.5, 0.0): $\gamma = 0.006$, $\beta = 0.3$. At (-1.2, 0.3): γ = -0.003, $\beta = 0.3$. At (-1.2, -0.3): γ = -0.003, $\beta = 0.3$. $T' = 3.0$ and 5.0.

we have the initial conditions for $A(\xi, t)$,

$$A(\xi, 0) = \tilde{\Phi}(\xi) = \int_0^\infty I(r) r J_0(\xi r) dr \qquad (28)$$

$$\text{and} \quad \frac{\partial A(\xi, 0)}{\partial t} = 0 \qquad (29)$$

Solving Eq. (27) with the above initial conditions,

$$A(\xi, t) = \tilde{I}(\xi) \cos\left(\sqrt{\frac{\xi}{Fr^2}} t\right) \qquad (30)$$

$$\text{and } \tilde{\Phi}(\xi, z, t) = \tilde{I}(\xi) \cos\left(\sqrt{\frac{\xi}{Fr^2}} t\right) \exp(\xi z). \qquad (31)$$

An inverse Hankel transform finally gives

$$\Phi(r, z, t) = \int_0^\infty \xi \tilde{I}(\xi) \cos\left(\sqrt{\frac{\xi}{Fr^2}} t\right) J_0(\xi r) \exp(\xi z) d\xi \qquad (32)$$

$$\text{and } h(r, t) = Fr \int_0^\infty \xi^{\frac{3}{2}} \tilde{I}(\xi) \sin\left(\sqrt{\frac{\xi}{Fr^2}} t\right) J_0(\xi r) d\xi. \qquad (33)$$

If the impulse given on the free surface can be approximated as

$$I(r) = \frac{\gamma}{2\pi\beta^2} \exp\left(-\frac{r^2}{2\beta^2}\right), \qquad (34)$$

where $\gamma = \int_0^\infty I(r) 2\pi r dr$, from Gradshteyn and Ryzhik [21],

$$\begin{aligned} \tilde{I}(\xi) &= \int_0^\infty r I(r) J_0(\xi r) dr \\ &= \frac{\gamma}{2\pi} \exp\left(-\frac{\xi^2 \beta^2}{2}\right) \end{aligned} \qquad (35)$$

Substitution of Eq. (35) into expression (33) gives

$$\begin{aligned} h(r, t) &= -\frac{\gamma Fr}{2\pi} \int_0^\infty \xi^{\frac{3}{2}} J_0(\xi r) \exp\left(-\frac{\beta^2 \xi^2}{2}\right) \\ &\quad \sin\left(\sqrt{\frac{\xi}{Fr^2}} t\right) d\xi \\ &= -\frac{\gamma Fr}{\pi^2} \int_0^\infty \int_0^{\frac{\pi}{2}} \xi^{\frac{3}{2}} \exp\left(-\frac{\beta^2 \xi^2}{2}\right) \\ &\quad \sin\left(\sqrt{\frac{\xi}{Fr^2}} t\right) \cos(\xi r \cos\alpha) d\xi d\alpha. \end{aligned} \qquad (36)$$

To evaluate the above integral we use the method of stationary phase (Stoker [22]) and obtain the final form of the free surface deformation due to the initial impulse given by Eq. (34) as

$$h(r, t) = -\frac{\gamma t^3}{2^{\frac{7}{2}} \pi r^4 Fr^2} \exp\left(-\frac{\beta^2 t^4}{32 r^4 Fr^4}\right) \sin\left(\frac{t^2}{4 r Fr^2}\right) \qquad (37)$$

provided $t^2/(4rFr^2)$ is large. Eq. (37) states that at fixed t and r wave height is proportional to γ/Fr^2 and the wave frequency decreases as Fr increases.

3.4.2 Wave Propagations

Fig. 11 shows the distribution of surface pressure associated with the evolution of the ring in Figs. 8-10 (only $y < 0$ side is shown). Frame (a) shows that the minimum pressure above the upper part of the ring. After the sudden topological change of the ring configuration during the reconnection, the local minimum

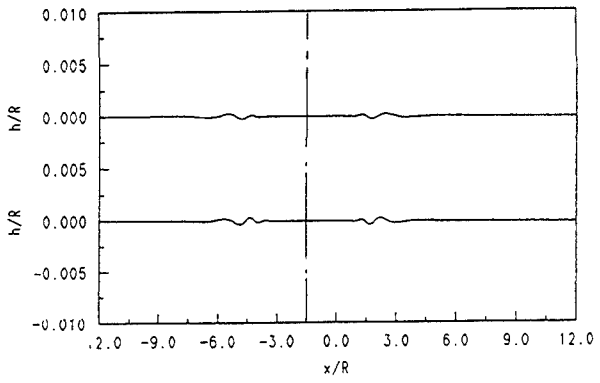

Fig. 14 Surface deformations at the center plane (y = 0). T' = 3.0. Top: Single impulse. Bottom: 3 impulses.

pressure region moves outward from the center line following the motion of the reconnected vortex core (frame (b)). Once the first reconnection is fully accomplished the local pressure minimum is clearly depicted far away from the center line (y = 0). Note that there is no wave-like variation of the pressure over the surface but only changes in shape and location of its maximum and minimum.

From Fig. 11 we determine the magnitude and shape of the impulse to be given on the free surface. First we give one impulse at the center of the reconnection region (-1.5, 0.0) with γ = 0.006 and β = 0.3. In Fig. 12 we show perspective views of the wave profile at two different dimensionless times. The top picture is at T' = 3.0 and shows two distinct wave crests traveling radially outward. Comparing this wave profile to frame (e) in Fig. 8, the modeled wave looks little shorter than in the full simulation and the traveled distance is also shorter in the modeled case. Except for the modification of the surface near the reconnection region due to the two dimples associated with the reconnected cores, both pictures show qualitatively similar shape with the afore-mentioned slight differences. The bottom picture at T' = 5.0 shows, basically, propagation of the wave shown in the top with a slight modification around the inner and outer boundaries of the wave packet. This wave is also a little bit shorter and slower compared to the wave in frame (f) of Fig. 8.

If we look closely at the variation of the surface pressure during the reconnection process the real pressure impulse seems more like three impulses than single impulse at the center. At the instance when the upper part of the ring is ready to open up, the pressure at the center reaches its minimum and the shape of low pressure region is elongated and curved toward downstream. Right after the reconnection, the local minimum pressure region becomes a local maximum, and the minimum pressure region splits into two, on either side of the center and a little downstream.

In order to model this procss more realistically we use three impulses near the reconnection region as initial conditions. One impulse at the center, (-1.5, 0.0), with γ = 0.006 and β = 0.3, and two impulses just outside of the center and little downstream, (-1.2, 0.3) and (-1.2, -0.3), with γ = -0.003 and β = 0.3. Fig. 13 shows the wave profiles at T' = 3.0 and 5.0. Wave patterns similar to Fig. 12 are seen in these calculation. In order to make more detailed comparison between the wave patterns of Fig. 12 and Fig. 13, we show wave profiles at the center plane in Fig. 14. The top is for the single impulse case and the bottom is for three impulse case at T' = 3.0. A broken line at x/R = -1.5 indicates the location where the initial impulses are given. First thing we notice is that the waves at the bottom are slightly larger and shorter. Contrary to the symmetry about the broken line for the single impulse case the bottom shows flatter downstream waves travelling a little faster than the upstream ones. Since our full interaction simulation (Fig. 10) includes a considerable effect from the base flow induced by the lower part of the ring it is difficult to see this detailed differences in Fig. 14. However the shadowgraph images obtained by Kwon [3] show these longer downstream and shorter upsream waves.

4 CONCLUSION

The generation of surface waves due to the reconnection of a vortex ring with a free surface is investigated with a vortex particle model for the ring and linearized free surface conditions. The first reconnection of the vortex ring can be successfully computed with a modest number of viscous vortex particles and the reconnection time scale for the first reconnection is comparable to the experimental results of Kwon [3]. A reconnection occurs faster when the incident angle is between 50° and 70° than when the ring is more normal or more parallel to the free surface. While the first reconnection occurs as long as the ring is initially not nearly parallel to the free surface, the secondary reconnection is more sensitive to the initial conditions (the incident angle, the distribution of vorticity, and the Reynolds number).

From the experimental studies of Bernal and Madnia [1] and Kwon [3], it is known that short wave generation is associated with a rapid change of pressure near the vortex reconnection region. A linearization of the free surface conditions, based on a small Froude number assumption, retains the pressure effects due to the vortex motion as the most dominant term. Consequently, the free surface deformations can be obtained without solving the full boundary value problem, which is very expensive. The present numerical study shows that surface waves are generated when a vortex core opens up at the free surface and the depressed surface region is released. As long as the Weber number is chosen realistically (in our case, larger than 50), surface tension effects on the free surface deformation appear to be negligible.

Based on the numerical results we propose a simplified model of the wave generation due to the vor-

tex reconnection. Preliminary results suggest that the waves generated are similar to those produced by the full problem. However, before the model can be applied by any confidence to a more complicated problem, such as multiple reconnection, more work is required to connect the model parameters to the influence of the ring.

Acknowledgements

This work was supported under the Program in Ship Hydrodynamics (PSH) at the University of Michigan, funded by the University Research Initiative of the Office of Naval Research, Contract number N000184-86-K-0684. The numerical simulations were performed on the computers at the San Diego Supercomputing Center, which is supported by the NSF. We would like to thank the members of the PSH for constructive discussions. We also express special thanks to Prof. Bernal for his valuable discussions and suggestions. MS has been supported partially by the Korea Science Foundation.

References

[1] Bernal, L. P. and Madnia, K., "Interaction of a turbulent round jet with the free surface," Proc. 17th Symposium on Naval Hydrodynamics, The Hague, The Netherlands, 1989.

[2] Bernal, L. P. and Kwon, J. T., "Vortex ring dynamics at a free surface," Phys. Fluids A, Vol. 1, 1989, pp. 449-451.

[3] Kwon, J. T., "Experimental study of vortex ring interaction with a free surface," Ph.D. Thesis, University of Michigan, 1989.

[4] Song, M., Bernal, L.P. and Tryggvason, G., "Head on collision of a large vortex ring with a free surface," Phys. Fluids A, To appear.

[5] Pumir, A. and Kerr, R. M., "Numerical simulation of interacting vortex tubes," Phys. Rev. Let., Vol. 58, 1987, pp. 1636-1639.

[6] Ashurst, Wm. T. and Meiron, D. I., "Numerical study of vortex reconnection," Phys. Rev. Let., Vol. 58, 1987, pp. 1632-1635.

[7] Kerr, R. M. and Hussain, F., "Simulation of vortex reconnection," Physica D, 1988.

[8] Saffman, P. G., "A model of vortex reconnection," J. Fluid Mech., Vol. 212, 1990, pp. 395-402.

[9] Saffman, P. G. and Meiron, D. I., "Difficulties with three-dimensional weak solutions for inviscid incompressible flow," Phys. of Fluids, Vol. 29, 1986.

[10] Winckelmans, G. and Leonard, A., "Weak solutions of the three-dimensional vorticity equation with vortex singularities," Phys. Fluids, Vol. 31, 1988.

[11] Greengard, C. and Thomann, E., "Singular vortex systems and weak solutions of the Euler equations," Phys. of Fluids, Vol. 5, 1988, pp. 1156-1162.

[12] Winckelmans, G., "Topics in vortex methods for the computation of three- and two-dimensional incompressible unsteady flows," Ph.D. Thesis, California Institute of Technology, 1989.

[13] Song, M., Tryggvason, G. and Bernal, L., "Interaction of vortex rings with a free surface," Bull. Am. Phys. Soc., Vol. 34, 1989, pp. 2295. (abstract only)

[14] Song, M. and Tryggvason, G., "Free Surface Waves due to the "Opening-Up" of a Vortex Ring," Bull. Am. Phys. Soc., Vol. 35, 1990. (abstract only)

[15] Winckelmans, G. and Leonard, A., "Improved vortex methods for three-dimensional flows," Proc. SIAM Workshop on Vortex Dynamics, Leesburg, Virginia, 1988.

[16] Degond, P. and Mas-Gallic, S., "The weighted particle method for convection-diffusion equations - Part I," Submitted to Math. Comput., 1988.

[17] Greengard, C. A., "Three-dimensional vortex method,". Ph.D. Thesis, University of California Berkeley, 1984.

[18] Yih, C.-S., Fluid Mechanics, McGraw-Hill, Inc., 1969.

[19] Saffman, P. G., "The velocity of viscous vortex rings," Stud. Appl. Math., Vol. XLIX, No. 4, 1970, pp. 371-380.

[20] Sneddon, I.N., Fourier Transforms, McGraw-Hill, New York, 1951.

[21] Gradshteyn, I.S. and Ryzhik, I.M., Table of Integrals, Series, and Products, Academic Press, 1980.

[22] Stoker, J.J., Water Waves, Interscience Publishers, Inc., NY, 1957.

DISCUSSION

K. Mori
Hiroshima University, Japan

What boundary conditions are used on the free surface in your computation of the vorticity equation? On the free surface, from the tangential condition, we have, for example, in linearized form,

$$\frac{\partial w}{\partial x}+\frac{\partial u}{\partial z}=0$$

which may lead

$$Wy = 0.$$

This means that a boundary layer-like layer for vorticity may develop on the free surface which may change the development of vorticity.

AUTHOR'S REPLY

Wave calculation is based on velocity potential as stated in the paper and linearized free-surface conditions are used. In linearized formulations, the effect of the surface deformation on the motion of the ring is neglected.

DISCUSSION

A. Weigand
University of California at San Diego, USA

In Fig. 5c (top view of vorticity, reconnected to the free surface), two separate vorticity peaks are visible? What causes these two peaks? Are they related and due to the numerical procedure, or do you think that they exist in reality and, therefore, are physically relevant?

AUTHOR'S REPLY

While sufficiently large number of vortices is capable of predicting the core deformation accurately, we have used a relatively small number in the computations presented here. Therefore, although the large-scale motion is fully conveyed, we caution the reader not to attach major significance to small-scale phenomena in these results such as the transient appearance of two peaks in the surface vorticity in Fig. 5c.

DISCUSSION

D. Dommermuth
Science Applications International Corporation, USA

At low Froude numbers, when the time scale of the vortical motions is longer than the time scale of the wavy motions, the free-surface elevation is hydrostatically balanced with the vortical pressure. The dispersive waves that you observe in your numerical simulations may be due to an imbalance in your initial conditions. Suppose you have a vortex ring that is initially very deep (say, more than 100 diameters). As this vortex ring nears the free surface, would you expect the same dispersive waves to be generated as your shallowly-submerged vortex ring? (Here, the deep initial depth is only meant to give the free surface sufficient time to adjust to the presence of the vortex ring.)

AUTHOR'S REPLY

The waves are not due to an impulsive introduction of the ring close to the free surface. In order to avoid problems caused by the introduction of the ring, the effective circulation of the ring was increased gradually from zero to its full strength during short start-up period. We examined several initial depths and weighting functions and concluded that the treatment we used was adequate for our purpose.

Experimental Studies of Vortex Reconnection to a Free Surface: A Physical Flow Model

M. Gharib, A. Weigand, C. Willert, D. Liepmann
(University of California at San Diego, USA)

ABSTRACT

An experimental investigation of the reconnection process of a vortex ring obliquely approaching a free surface is presented. This investigation focused on the early stages of the interaction process. Using Digital Particle Image Velocimetry (DPIV), the vorticity field was mapped. The results depict the formation of a secondary vortex that plays an important role in the reconnection process. A physical model was developed to describe the reconnection process based on the temporal and spatial measurements of the velocity and vorticity fields.

NOMENCLATURE

D	Core-to-core diameter of vortex ring
D_0	Nozzle diameter
Fr	Froude Number ($\Gamma/\sqrt{gD^3}$)
g	Gravitational acceleration
h	Depth of the nozzle centerline
P	Pressure at free surface
R	Radius of curvature
Re	Reynolds Number (Γ/ν)
s,r,z	Curvilinear coordinate system
u	Velocity vector
u,v,w	Cartesian velocity components
u_s,u_r,w	Curvilinear velocity components
We	Weber Number ($\rho\Gamma^2/\sigma D$)
x,y,z	Cartesian coordinate system
α	Angle of vortex generator with surface
Γ	Circulation
μ	Dynamic viscosity
ν	Kinematic viscosity
ω	Vorticity vector
$\omega_x,\omega_y,\omega_z$	Cartesian vorticity components
ρ	Density
σ	Surface Tension
τ	Shear stress

1. INTRODUCTION

Recent satellite images of the ocean surface by synthetic aperture radar have revealed interesting, but puzzling features of complex shear flows interacting with the ocean surface. Persistence of some of the observed features are specially intriguing, since they do not obey any known decay laws for fully submerged shear flows. The flow field of a ship wake is quite complex and its full simulation in the laboratory is difficult, if not impossible, to perform. Therefore, experimental and computational approaches that focus on elementary shear flows provide better understanding of the nature of this complex flow.

In this regard, vortex rings and vortex couples have received much attention as generic elementary shear flows. The problem of a vortex ring or a vortex couple approaching a boundary with or without no-slip condition whether it is solid or deformable is challenging since it involves three-dimensional vortex reconnection. The first important steps toward understanding the process of vortex/free-surface interaction were undertaken by Sarpkaya (1), Ohring and Lugt (2), and Dommermuth (3) on the vortex couple problem and by Bernal and Kwon (4), Bernal *et al.* (5) and Leighton and Swean (6) on the vortex ring problem.

Bernal and Kwon showed that as a vortex ring approaches the free surface at an oblique angle, the upper part of the vortex ring deforms and opens its ends to reconnect to the surface. Their intriguing observations raised many important fundamental questions regarding vortex-ring interaction with a free surface which is drastically different from the case of a vortex ring interacting obliquely with a solid wall (7).

In this paper, we focus on the processes that lead to the reconnection process of a laminar vortex ring approaching at an angle to the free surface. In our investigations, we employed Digital Particle Image Velocimetry (DPIV) (8) to map the velocity and vorticity fields of the approaching vortex. The mapping process was carried out on the free surface and at various two-dimensional cross-sections in the flow. DPIV measurements allowed us to investigate the spatial and temporal evolution of the vortex ring and its interaction with the free surface.

2. EXPERIMENTAL SETUP AND PROCEDURES

Figure 1 shows the experimental setup. The vortex-ring generator is placed in a water tank of 81x38x81cm. For the purpose of dye flow-visualization, shadowgraphs, and DPIV, the tank has optical windows on five sides.

The nozzle of the vortex-ring generator has a diameter (D_0) of 30 mm and incorporates a piston to drive the flow. The piston is driven by an air-pressurized water reservoir and activated by a solenoid valve. The apparatus can generate vortex rings with diameters from 30 to 43 mm within a Reynolds number range of 600 to 1800. The experiment is computer controlled (IBM-PC AT) which allows precise timing and synchronization (time resolution better than 1 millisecond) of the vortex-ring generator, dye injector and DPIV camera.

For the purpose of repeatability, the tank was filled with deionized water which has a relatively constant surface tension compared to tap water. To make sure that the water surface is as clean as possible within the laboratory environment, we used two wipers to remove the aged water surface before each measurement. Additionally, before and after each experimental run the surface tension was measured with a Fisher Surface Tensiomat (Ring Tensiometer).

For the experiments reported in this paper, the centerline of the vortex-ring generator was one nozzle-diameter ($h = 30$ mm) below the surface and inclined at an angle (α) of 7°. The generated vortex ring had a core-to-core diameter (D) of 37 mm. The Reynolds number ($Re = \Gamma/\nu$) for all of our experiments was 1150 with the circulation (Γ) of 11.5 cm^2/seconds. Also, the Froude number ($Fr = \Gamma/\sqrt{gD^3}$) and Weber number ($We = \rho\Gamma^2/\sigma D$) had values of 0.051 and 0.53, respectively.

3. RESULTS

3.1 Flow Visualization

The shadowgraph visualization showed a small depression of the free surface followed by the appearance of two round surface depressions that enlarge with time (Fig. 2). These observations which are similar to those of Bernal and Kwon (4), give the impression that the appearance of two symmetrical surface depressions are associated with the reconnection of the primary vortex; in this case, the opening of the upper portion of the main vortex ring to the free surface. In order to connect these observations to the crucial stages of the reconnection process we decided to map the temporal and global behavior of the velocity and vorticity fields on the surface and in planes normal to it.

3.2 Free-Surface Velocity Mapping

Using DPIV we were able to obtain the velocity field on the free surface. The vortex ring parameters (Froude and Reynolds numbers) were chosen so that any surface deformations would be of the order of the laser sheet thickness. This allowed us to position the laser sheet very close to the surface. After reviewing several hundred velocity fields in conjunction with their associated vorticity and strain fields, it was decided to present only the frames that are crucial in identifying the important milestones of the reconnection process. In our presentation of the results, we refer to these milestones as stages.

Figure 3a shows the initial motion at the surface due to the induced inviscid velocity field of the approaching vortex (Stage 1). In this early stage, a stagnation point (marked as S_1) appears at $x \approx 41$ mm and $y \approx 0$ mm. From this point flow accelerates spatially backward in the negative x-direction and then through a spatial deceleration converges towards a second stagnation point (marked as S_2) at $x \approx 1.4$ mm and $y \approx 0$ mm. For a normal angle ($\alpha = 90°$) approach of the vortex ring to a free surface, one would expect a symmetric outward spatial acceleration with a circular stagnation region surrounding S_1. But for an oblique approach, only a small arc portion of the primary vortex interacts with the free surface, thus the observed pattern is a manifestation of the induced velocity of this portion of the vortex ring on the free surface. With time, the size of the stagnation area (S_1) increases and becomes more well-defined. However its location remains unchanged as the second stagnation point moves forward in the positive x-direction. Therefore, the flow turns at sharper angles which result in a sink-source (dipole) pattern for the velocity vector field (Fig. 3b). Between Stages 2 and 3 a qualitative change occurs in the flow behavior. At Stage 3 (Fig. 3c), S_2 moves forward even closer to S_1 and changes the dipole into a vortex-pair pattern on the surface by reversing the direction of the flow between S_1 and S_2 (Stage 4, Fig. 3d). Note that the magnitude of the velocity vectors along the center line (connecting S_1 and S_2) decreases between Stages 2 and 3.

With time the vortex-pair pattern is enhanced by a strong forward current at the center which clearly separates the two counter rotating elongated regions (Fig. 3e). At Stage 5, these elongated regions go through a procession which reshapes them back to circular form. Stage 6 (Fig. 3f) shows completion of the reconnection process and formation of two distinct circular vortices at the surface. This stage corresponds to the shadowgraph image in Figure 2.

So far, the described series of surface velocity patterns shows the early stages of the vortex interaction with the free surface. The later stages involve the fold-up and splitting of the lower portion of the vortex ring which result in the formation of two half-vortex rings as was reported by Bernal and Kwon (4). We observed a similar behavior for the later stages of the flow evolution. However, in this paper we focus on the early, but crucial stages of the vortex interaction with the free surface.

It has been generally assumed that the reconnection of the main vortex to the surface is directly associated with the appearance of the two identifiable surface depressions in the shadowgraph picture. The interesting behavior of the stagnation points on the free surface raised the suspicion that some other important events might occur before the main vortex reconnects to the free surface. Therefore, we decided to extract the vorticity field from the velocity field measurements.

3.3 Vorticity Field

Figure 4 shows the temporal and spatial evolution of the vorticity field on the free surface. Figure 4a shows the appearance of a symmetric vorticity field. With time, the vortex pair grows until a tail pattern appears behind each vortex (Stage 3). These tails grow into a new vortex pair whose strength exceeds that of the initial pair (Stages 4 and 5). During Stages 3-5, the initial pair interacts with the new pair until they merge and create a new and larger vortex pair in Stage 6.

These observations reveal the dynamic nature of the surface flow that was not obvious in the velocity and shadowgraph pictures and raise the question of whether the initial vortex pair belongs to the main vortex ring. To answer this question, we tagged the core of the vortex ring with fluorescent dye at two positions close to the point where it would contact the free surface. This experiment showed that the first vortex pair appeared at the free surface before the marked core of the vortex ring could contact the water surface. These observations indicated that a secondary vortex must have been formed near the surface prior to the arrival of the primary vortex, and the appearance of the first vortex pair on the surface might have been related to the early reconnection of the secondary vortex to the free surface. To confirm the existence of this secondary vortex, we conducted DPIV measurements of the velocity field in the symmetry plane ($z = 0$) of the approaching primary vortex.

Figure 5 depicts the evolution of the vorticity field in the symmetry plane ($z = 0$). As is evident in these figures, a secondary vortex with its axis parallel to the free surface exists very near the surface. Initially (Stage 1), this vortex with clockwise (negative) vorticity is fairly weak and is located behind and above the upper core of the main vortex. At Stage 2 the vorticity field shows a large vorticity gradient near the free surface by the compression of the constant vorticity contours. At Stage 3, the large vorticity gradient against the free surface disappears, but a new region of strong vorticity gradient appears where the two counter rotating vortices join. In Stage 4 the secondary vortex disappears. The corresponding surface vorticity at this stage (Fig. 4d) shows how the previously mentioned tail pattern evolves into a complete vortex pair.

3.4 Peak Vorticity Behavior of the Primary and Secondary Vortices

In order to correlate the sequence of events on the free surface to the events in the symmetry plane we present Figures 6a and 6b that show the variations of the peak vorticity with time in the symmetry plane (ω_z) and on the surface (ω_y). In the following discussion we regard the magnitude of the peak vorticity as a general representation of the vorticity associated with each vortex.

For the secondary vortex, the vorticity parallel to the surface, $|\omega_z|$, (Fig. 6a) and normal to the surface, $|\omega_y|$, (Fig. 6b) increase between Stages 1 and 2. During this time, $|\omega_y|$ for the primary vortex on the surface stays negligible while $|\omega_z|$ decreases slightly. Note that between Stages 2 and 3 we observe a weak appearance of the primary vortex on the surface (the tail pattern in Figure 4c). This first appearance of the primary vortex on the surface coincides with the qualitative changes of the velocity vector patterns from a dipole to a vortex-pair, i.e., completion of the flow deceleration and reversal of the flow direction along the centerline. Also, during this period both primary and secondary vortices show increases in their peak vorticity values in the symmetry plane, $z = 0$. Between Stages 3 and 4 a drastic decrease occurs in the peak value of $|\omega_z|$ for both the primary and secondary vortices in the symmetry plane to the degree that the secondary vortex disappears from the symmetry plane after Stage 5 in Figure 6a. However, in Figure 6b $|\omega_y|$ for the primary vortex continues to increase. The secondary vortex pair on the free surface maintains its vorticity value in this period. For the primary vortex, coincidence of an increase in $|\omega_y|$ on the surface with a reduction of $|\omega_z|$ clearly indicates a direct connection between the reconnection process and these components of vorticity.

Between Stages 5 and 6, $|\omega_y|$ of the primary vortex reaches its maximum value marking completion of the reconnection process. This completion is more evident in the $|\omega_z|$ component of vorticity where its value reduces to zero after a preceding mild increase. It is interesting to note that this mild increase in $|\omega_z|$ for the primary vortex coincides with the disappearance of the secondary vortex from the symmetry plane.

Figure 7a shows the temporal and spatial evolution of the ω_z-component of the vorticity field in the symmetry plane for Stages 3 through 5. This figure shows that between Stages 4 and 5, the secondary vortex disappears ($t = 5.4$ s) while the primary vortex retains some of its peak value which corresponds to the generation of a tertiary vortex. It seems that this tertiary vortex is not strong enough to play a role in the further development of the primary vortex.

3.5 Normal-Strain Field in the X-Y Symmetry Plane

Figure 7b shows the temporal and spatial evolution of the normal strain rate field ($\partial w/\partial z$) in the symmetry plane ($z = 0$) for the corresponding time steps of Figure 7a. The normal strain rate is a measure of the out-of-plane stretching of the vorticity vector. In Figure 7b a strong and concentrated positive strain rate field is present near the free surface in a region above and between the cores of the primary and secondary vortices. The concentrated strain field moves into the region between the two vortices while its strength reduces and its area increases. This behavior covers Stages 3 and 4 where the peak vorticity values of the primary and secondary vortices rapidly decreases.

4 A FLOW MODEL FOR THE RECONNECTION PROCESS

In order to illustrate the dynamics of the vortex ring interaction with the free surface, we developed a descriptive flow model that provides the kinematic and dynamic conditions necessary to generate the observed velocity and vorticity fields during the reconnection process.

4.1 Generation and Reconnection of the Secondary Vortex

In the previous section we presented experimental evidence that should prove the existence of a secondary vortex and its reconnection to the free surface prior to the reconnection of the primary vortex to the free surface. The role of this secondary vortex in the reconnection process will be discussed in this section. In this respect, we need to discuss the mechanisms that might be responsible for the generation of the secondary vortex.

The conventional approaches to the issue of vorticity generation and vorticity flux at solid boundaries usually deal with situations where the no-slip condition is involved. The issue of vorticity generation and flux at a free surface has only recently received recognition through the works of Lugt (9,10), Lundgren (11), Saffman (12) and Rood (13) . In this regard, a brief review of vorticity generation mechanisms at the free surface will be discussed.

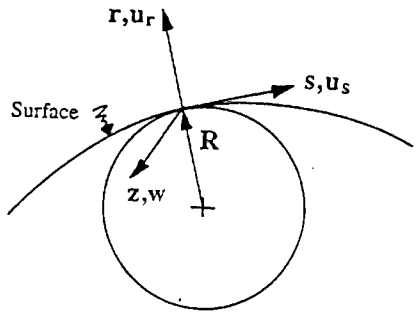

Schematic 1 Curvilinear coordinate system at the free surface.

The parallel component of the vorticity (ω_z) at the free surface can be obtained in a curvilinear coordinate system (see Schematic 1) as:

$$\omega_z = -\frac{\tau_{rs}}{\mu} - \frac{1}{\mu}\frac{\partial \sigma}{\partial s} - 2\frac{u_s}{R} + 2\frac{\partial u_r}{\partial s}, \qquad (1)$$

where τ_{rs} is the surface shear stress in the s -direction , R is the local radius of curvature of the surface, and σ is the surface tension.

For the air-water interface, the shear imposed by air on water can be neglected (i.e. $\tau_{rs} \approx 0$, see Lugt (9,10)). Now, consider the primary vortex ring as it approaches the free surface before Stage 1 (Schematic 2).

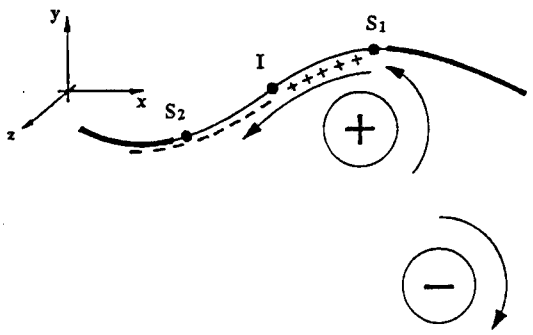

Schematic 2 Approach of the primary vortex ring and generation of vorticity at the free surface.

The velocity field induced by the primary vortex can cause a local and unsteady change in the surface slope. It can also redistribute the contaminants on the surface which will result in the generation of surface tension gradients at the free surface. The schematic shows the local surface slope change and regions of expected high concentration of contaminants (thick line). By inspecting the schematics in conjunction with Eqn. 1, one can identify regions that can possess positive or negative vorticity near the free surface. For the region between point S_1 and I where S_1 is assumed to be locally close to the maximum height of the free surface and point I is the approximate location of the inflection point, the radius of curvature (R) is positive and the surface velocity (u_s) is negative. Therefore, ($-u_s/R$) will be positive and results in the generation of positive vorticity between S_1 and I. In this region $\partial\sigma/\partial s$ is negative, and, therefore $-1/\mu(\partial\sigma/\partial s)$ is positive which also contributes to the positive vorticity generation. To the left of I, R is negative and both $-u_s/R$ and $-\partial\sigma/\partial s$ are negative and would generate negative vorticity near the free surface.

The role of $\partial u_r/\partial s$ can be clarified by inspecting the normal velocity component at the free surface. Figure 8 shows the surface normal strain rate field ($\partial v/\partial y$) obtained from the surface velocity field. For an initially still surface ($v = 0$), Figure 8 indicates that an upward motion region is trailed by a region of downward motion. Since the surface slopes in our experiments were small, it is a good approximation to accept the iso-velocity contours as representative of the magnitude the normal velocity component (v). Therefore, by inspecting the iso-velocity contours in Figure 8, one can conclude that $\partial u_r/\partial s$ is positive between S_1 and S_2 and is negative in the region to the left of the S_2. The contribution of this term also supports positive vorticity generation between S_1 and I; counteracts contributions of the other two terms in the region between I and S_2; and finally supports generation of negative vorticity beyond point S_2.

It follows from our previous discussion that once vorticity is generated at the free surface by the aforementioned mechanisms, the positive vorticity region will mix with its immediate positive sign primary vortex. Similarly, the negative vorticity region should spiral into a vortex by self-induction in a region below S_2 (see Schematic 3).

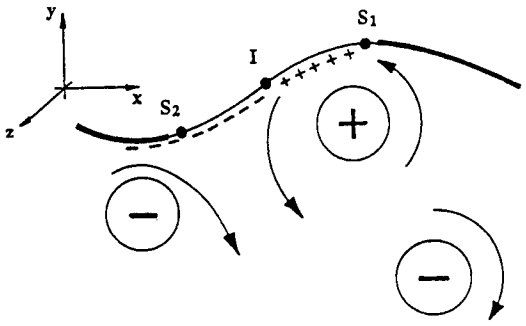

Schematic 3 Approach of the primary vortex ring and formation of the secondary vortex.

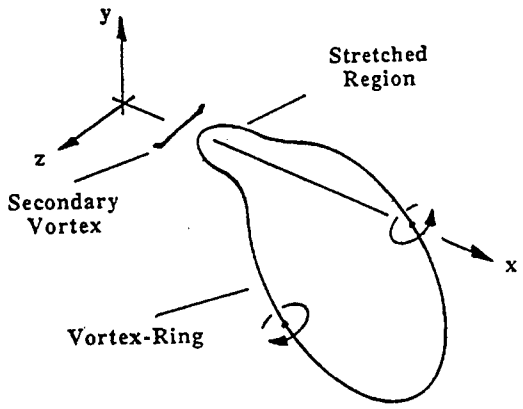

Schematic 4 Deformation of the primary vortex ring as it approaches the free surface.

In this respect, Figures 5a and 5b show a high concentration of positive vorticity on the top portion of the primary vortex and the presence of a negative vorticity region approximately to the left of the point I. These observations qualitatively support our conjectures regarding generation mechanisms and probable location of the secondary vortex near the free surface.

The induced velocity field of the approaching primary vortex has finite span on the free surface (see Fig. 3a). Therefore the secondary vortex is generated over a finite length. The kinematic condition for the free surface prompts reconnection of the two ends of the secondary vortex to the free surface with a normal incident angle. This reconnection event manifests itself as the initial vortex pair on the free surface (Fig. 4a).

The secondary vortex reconnects to the surface like a half ring. Our velocity measurements below the surface (y = -4 mm) confirm that the vertical component of the vorticity exists with smaller peak values compared to its value at the free surface, which indicates a gradual bending of the secondary vortex toward the surface. Therefore, the secondary vortex moves forward in the positive x-direction under its self-induced velocity, which is responsible for the second stagnation point, S_2, to move toward the first stagnation point, S_1. This behavior can be easily recognized in Figures 5a and 5b where the region between the two vortices narrows and its top region (i.e. S_2) moves forward.

4.2 Dynamics of the Approaching Primary Vortex Ring

Let us consider the primary vortex as it approaches the free surface but is not yet close enough to be influenced by the presence of the secondary vortex or deformation of the free surface. The flow visualization studies of the primary vortex during these early stages (Stages 1 and 2) show that the top portion of this vortex staggers backward (in the negative x -direction) and forms a narrow stretch towards the secondary vortex (see Schematic 4).

As has been shown by Ashurst and Meiron (14), this stretching action is due to the interaction of the primary vortex with its image vortex ring above the symmetry plane (see Figure 1 of the Ashurst & Meiron). A similar behavior is expected for the cases where two vortex rings approach each other in an oblique angle (15). In our case the undeformed free surface acts as a shear free symmetry plane.

As it was discussed in Section 3.2, the surface velocity field has a distinct sink-source pattern which illustrates the initial interaction of the tip of the primary vortex with the secondary vortex and enlargement of S_1 region due to the further rearward motion of the tip region. At these stages the secondary vortex has already reconnected to the free surface.

Figures 6b and 3a indicate that reconnection of the primary vortex starts at Stage 3. This is the stage that the first normal component of vorticity due to the primary vortex appears on the surface and the parallel component of the primary vortex in the symmetry plane starts to decrease dramatically. Figure 6a shows that the reduction of $|\omega_z|$ for the primary vortex in the symmetry plane occurs in two distinct steps. The first step starts with Stage 3 and the second with Stage 5. The latter has a shallower slope than the former. Similarly, the increase in the peak vorticity value of the primary vortex on the surface occurs at two steps with the steeper slope starting at Stage 3 followed by the shallower slope starting at Stage 5.

The scenario that we seek to construct should be able to explain processes that result in the production of the normal component of the vorticity at the free surface and degeneration of the parallel component of the primary vortex in the symmetry plane. Recently, Ashurst *et al.* (16) have shown that the shearing strain-rates induced on the stretched section of the primary vortex by the undeformed portion of the ring can rotate the vorticity components. It is important to note that in our flow situation the secondary vortex is in close proximity to the stretched section of the primary vortex and its induced shear strain-rate field would have an additional effect. Because after Stage 4 the secondary vortex disappears from the symmetry plane at $z = 0$ and its strength on the free surface starts to decrease, this additional effect is expected to lose its importance to the reconnection process in the later stages

(from Stages 4 to 6). The reaction of the stretched portion of the primary vortex to the combined influence of the secondary vortex and the undeformed volume of the primary vortex will depend on whether their actions enhance or cancel each other.

As was described in the previous section, after the initial reconnection of the secondary vortex to the free surface, its normally reconnected portion at the free surface moves in the positive x-direction. However, its parallel segment is held back by the rearward motion of the stretched portion of the primary vortex. This action causes a situation where the top portion of the primary vortex is under direct influence of the secondary vortex (see Schematic 5).

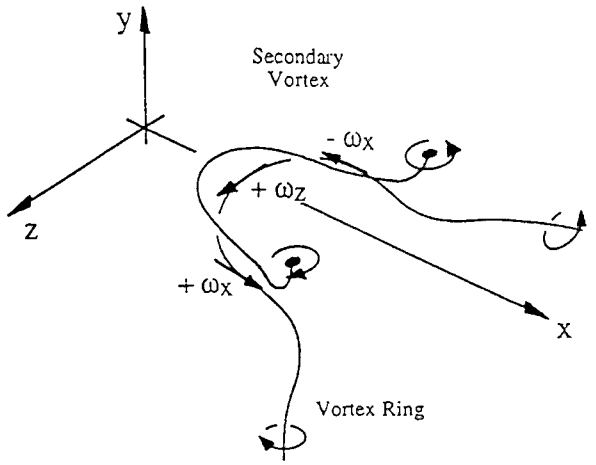

Schematic 5 Interaction of the primary and secondary vortices during the reconnection process.

Let us try to visualize the shear strain-rate field of the secondary vortex as the primary vortex approaches it. First, consider the material changes in the various components of the vorticity. If we ignore viscous effects in the early stages, the vorticity equation becomes:

$$\frac{D\underline{\omega}}{Dt} = (\underline{\omega} \cdot \nabla)\underline{u}. \tag{2}$$

Let us start with the rate of change for the y-component of the vorticity:

$$\frac{D\omega_y}{Dt} = \omega_x \frac{\partial v}{\partial x} + \omega_y \frac{\partial v}{\partial y} + \omega_z \frac{\partial v}{\partial z}. \tag{3}$$

According to the schematics, near the tip of the stretched part of the primary vortex, the z-component of the vorticity (ω_z) is dominant, i.e., $|\omega_z| >> |\omega_x|$ and $|\omega_y|$. Therefore, we only consider the z-component of vorticity near the tip region of the primary vortex. According to the schematic, the y-component of the induced velocity by the secondary vortex should have a symmetric distribution near the symmetry plane ($z = 0$) which requires $\partial v/\partial z = 0$ close to the $z = 0$ region. Therefore, near the tip regions we expect:

$$\frac{D\omega_y}{Dt} \approx 0. \tag{4}$$

This means that the reconnection of the vortex to the free surface should not be expected in this region. Farther away from the tip region, the two legs of the stretched section of the vortex ring are mainly composed of x-component of the vorticity (ω_x). Therefore, we can write:

$$\frac{D\omega_y}{Dt} \approx \omega_x \frac{\partial v}{\partial x}. \tag{5}$$

This region is mainly under the influence of the curved-up section of the secondary vortex. Schematic 5 shows that in the x-z plane for the side where $z < 0$:

$$\omega_x < 0 \text{ and } \frac{\partial v}{\partial x} < 0, \tag{6}$$

therefore,

$$\frac{D\omega_y}{Dt} > 0. \tag{7}$$

Due to the upward inclination of the stretched-back section of the primary vortex, ω_y in the $z < 0$ region is positive and we should expect production of positive ω_y. For $z > 0$ we find $\partial v/\partial x < 0$ and $\omega_x > 0$ which results in $D\omega_y/Dt < 0$ and production of negative ω_y. This means that we should expect the reconnection process to occur on both sides of the symmetry plane. This behavior can be easily seen in Figures 4c and 4d where the surface vorticity shows the appearance of the tail patterns symmetrically off the x- axis. The sense of rotation of these reconnected vortices is negative for $z > 0$ and positive for $z < 0$ as was predicted by the equations. It is interesting to check whether this action is consistent with the action of the undeformed portion of the vortex ring on the stretched part. Ashurst *et al.* (16) find that $D\omega_y/Dt$ is positive for $z < 0$ and negative for $z > 0$ regions in the x-z plane. It is now clear that due to the consistency of the action of the secondary vortex and undeformed part of the primary vortex ring, we observe a steep slope for the growth of $|\omega_y|$ of the primary vortex in the early stages of the reconnection (Stages 3-5 in Fig. 6b). This growth becomes milder in the later stages where only the action of the undeformed part of the primary vortex supports the reconnection process.

Now we need to understand the evolution of the tip portion of the primary vortex where ω_z is dominant and, then, connect it to the flux of vorticity at the free surface. In Figure 6a we can identify a two-step reduction in the peak vorticity value of the ω_z component.

We start with the vorticity transport equation in the z-direction:

$$\frac{D\omega_z}{Dt} = \omega_x \frac{\partial w}{\partial x} + \omega_y \frac{\partial w}{\partial y} + \omega_z \frac{\partial w}{\partial z} + \nu\left(\frac{\partial^2 \omega_z}{\partial x^2} + \frac{\partial^2 \omega_z}{\partial y^2}\right). \quad (8)$$

In the symmetry plane, only ω_Z is present, therefore, we can safely write:

$$\frac{D\omega_z}{Dt} \approx \frac{\partial w}{\partial z}\omega_z + \nu\left(\frac{\partial^2 \omega_z}{\partial x^2} + \frac{\partial^2 \omega_z}{\partial y^2}\right). \quad (9)$$

In the initial Stages 1 and 2 the viscous terms can be expected to play a minor role in the absence of large vorticity gradients. According to the results in Section 3.5, the normal strain rate $\partial w/\partial z$ in the symmetry plane is positive. Also for the primary vortex, $\omega_Z > 0$ in the symmetry plane. Therefore:

$$\frac{D\omega_z}{Dt} \approx \omega_z \frac{\partial w}{\partial z} > 0. \quad (10)$$

This means that the primary vortex should initially experience stretching or extensional strain which should result in an increase in its peak vorticity value. Figure 6a shows an initial increase in the peak vorticity value between Stages 2 and 3. The secondary vortex will experience a similar extension and its peak value will increase correspondingly. The generation of the normal strain rate $\partial w/\partial z$ can be attributed to two independent processes. The first process, suggested by Ashurst (16), is due to the mutual action of the top region of the primary vortex with its image which is similar to the action of a vortex ring that approaches its image at a normal angle. The second process which is suggested by Saffman (17) relies on the cancellation of vorticity by the fusion between the tip region of the primary vortex and the parallel section of the secondary vortex. The vorticity cancellation decreases the rotation inside the core, leading to an increase in pressure relative to the pressure at large distances from the region which in fact leads to a positive strain normal to the symmetry plane. The Ashurst model explains the existence of the normal strain outside the core, while Saffman's is more suitable for the action in the core region.

We still need to explain the large reduction of ω_Z between Stages 3 and 4 and the relatively mild reduction between Stages 5 and 6. Either vorticity is lost to the field at the free surface, diffused and canceled by the secondary vortex or convected out of the symmetry plane. In order to understand this process, we need to examine the vorticity flux equation. Following Lugt (9) and Rood (13), the vorticity flux equation at the free surface in a curvilinear coordinate system can be obtained as:

$$\nu\left(\frac{\partial \omega_z}{\partial r}\right) = -\frac{\partial u_s}{\partial t} - \frac{1}{2}\frac{\partial u_s^2}{\partial s} - \frac{1}{\rho}\frac{\partial P}{\partial s} - g\cos\theta. \quad (11)$$

Near the tip of the primary vortex, the velocity measurements show that the spatial surface-velocity changes are small, i.e., the contribution of the second term on the right-hand side of Eq. 11 is small. Since the surface-tension distribution between points S_1 and S_2 can be considered to be uniform, the normal pressure distribution will be uniform and thus the contribution of the third term will also be small. In our experiments the surface slopes are mild (i.e. $\theta \approx 90°$). Therefore, it can be assumed that $g \cos \theta$ is small. These assumptions leave the surface acceleration term, $\partial u_S/\partial t$, as the main player in removing or adding vorticity to the flow field through the free surface. The surface velocity along the line that connects S_1 and S_2 decreases with time to a finite negative value from its initial rest state (i.e. $\partial u_S/\partial t < 0$). This can be seen in Figure 3a. Therefore, the negative acceleration which results in a positive value for the term $-\partial u_S/\partial t$, should initially cause a positive vorticity flux to the region between S_1 and S_2. Evidence of the initial positive vorticity concentration can be seen in Figures 5a and 5b. However, Figure 3b shows a reduction in the overall magnitude of the velocity vector with time. This means that $\partial u_S/\partial t$ is positive beyond Stage 1 and thus a negative flux of vorticity to the field through the free surface should occur.

The action on the surface is due to the kinematics of the flow and the consequent flux of vorticity is due to viscous diffusion. Therefore, the vorticity field reacts to the kinematics with some time lag. For this reason, the vorticity field (ω_Z) of the tip region of the primary vortex (see Fig. 6a) starts to decrease in Stage 3 in response to the deceleration of the surface velocity field in Stage 2 (see Fig. 3b). Now, Figures 5b and 5c indicate that high vorticity regions of the primary vortex have counter sign vorticity of the secondary vortex in their neighborhood. Therefore, one expects additional loss of vorticity due to the diffusion within the neighboring regions. In the later stages (as is evident in Figure 5c) only this interdiffusion of the counter sign vorticity regions is important and not the loss of vorticity to the free surface. This can explain why at the later stages the tip of the primary vortex loses its vorticity (ω_Z) at a lower rate than in the earlier stages.

5. CONCLUSION

The described physical model suggests that the reconnection of the primary vortex occurs in two steps. First, the combined action of shear strain rate of the secondary and the undeformed portion of the primary vortex reconnect the stretched portion of the primary vortex to the free surface. The completion of the reconnection occurs at a slower rate through the sole action of the undeformed part of the vortex ring as suggested by Ashurst.

Our physical model suggests that the disconnection of the tip of the stretched back portion of the primary vortex, also occurs in two steps. In the first step, the loss of vorticity to the free surface (as suggested by Rood) and diffusive flux of vorticity to the secondary vortex (as suggested by Saffman) cause a large reduction of the vorticity. In the later stages it is the latter mechanism which is responsible for the milder rate of the vorticity reduction in the symmetry plane.

ACKNOWLEDGMENTS

The authors gratefully acknowledge valuable discussions with W. Ashurst, L. Bernal, and E. Rood. This work has been sponsored by ONR (contract number N00014-89-1529).

REFERENCES

1. Sarpkaya, T., "Trailing-Vortex Wakes on the Free Surface," Sixteenth Symposium on Naval Hydrodynamics, University of California, Berkeley, 1986.

2. Ohring, S. and Lugt, H.J., "Interaction of a Viscous Vortex Pair with a Free Surface," Journal of Fluid Mechanics, Vol. 127, 1991, pp.

3. Dommermuth, D.G., "The Formation of U-Shaped Vorticies on Vortex Tubes Impinging on a Wall with Applications to Free Surfaces," Physics of Fluids A, Vol. 4, No. 4, April, 1992, pp.757-769.

4. Bernal, L.P. and Kwon, J.T., "Vortex Ring Dynamics at a Free Surface," Physics of Fluids A, Vol. 1, No. 3, March 1989, pp.449

5. Bernal, L.P., Hirsa, A., Kwon, J.T. and Willmarth, W.W., "On the Interaction of Vortex Rings and Pairs with a Free Surface for Varying Amounts of Surface Active Agents," Physics of Fluids A, Vol. 1, 1989, pp. 2001-

6. Leighton, R.I. and Swean, T.F.Jr., "The Enstrophy Balance During the Interaction of a Vortex Ring with a Shear-Free Boundary," Dynamics of Bubbles and Vorticies Near a Free Surface, AMD-Vol. 119, ASME, 1991, pp.

7. Lim, T.T., "An Experimental Study of a Vortex Ring Interacting with an Inclined Wall," Experiments in Fluids, Vol. 7, 1989, pp.453-468.

8. Willert, C.E. and Gharib, M., "Digital particle image velocimetry," Experiments in Fluids, Vol. 10, pp.181-193.

9. Lugt, H.J., "Local flow properties at a viscous free surface," Physics of Fluids, Vol. 30, 1987, pp. 3647-3652.

10. Lugt, H.J., "Fundamental viscous flow properties at a free surface," Fluid Dynamics Transactions, Vol. 14, 1988, pp. 1-20.

11. Lundgren, T.S., "A Free Surface Vortex Method with Weak Viscous Effects," Mathematical Aspects of Vortex Dynamics, Proceedings of the Workshop on Mathematical Aspects of Vortex Dynamics, Leesburg, Virginia, April 25-27, 1988, pp. 68-79.

12. Saffman, P.G., "Approach of a Vortex Pair to a Rigid Free Surface in Viscous Fluid," Physics of Fluids A, Vol. 3, 1991, pp. 984-985.

13. Rood, E.P., "Vortex Interactions with a Free Surface," International Wake Vortex Symposium, FAA, Washington DC, Oct 29-31, 1991.

14. Ashurst, W.T. and Meiron, D.I., "Numerical Study of Vortex Reconnection," Physical Review Letters, Vol. 58, No. 16, April, 1987, pp. 1632-1635..

15. Schatzle, P.R., "An Experimental Study of Fusion of Vortex Rings," PhD Thesis, California Institute of Technology, Pasadena, 1987.

16. Ashurst, W.T., Gharib, M., and Liepmann, D. "Surface Vortex Reconnection." Bulletin of the American Physical Society, Vol. 36, No. 10, Nov. 1991, pp. 2717.

17. Saffman, P.G., "A Model for Vortex Reconnection," Journal of Fluid Mechanics, Vol. 212, 1989, pp. 395-402.

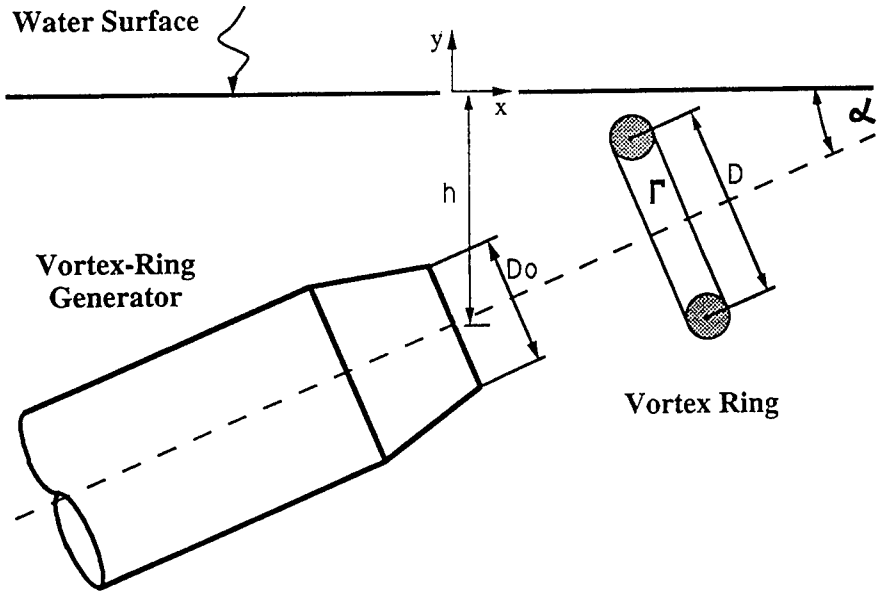

Figure 1 Experimental Setup.

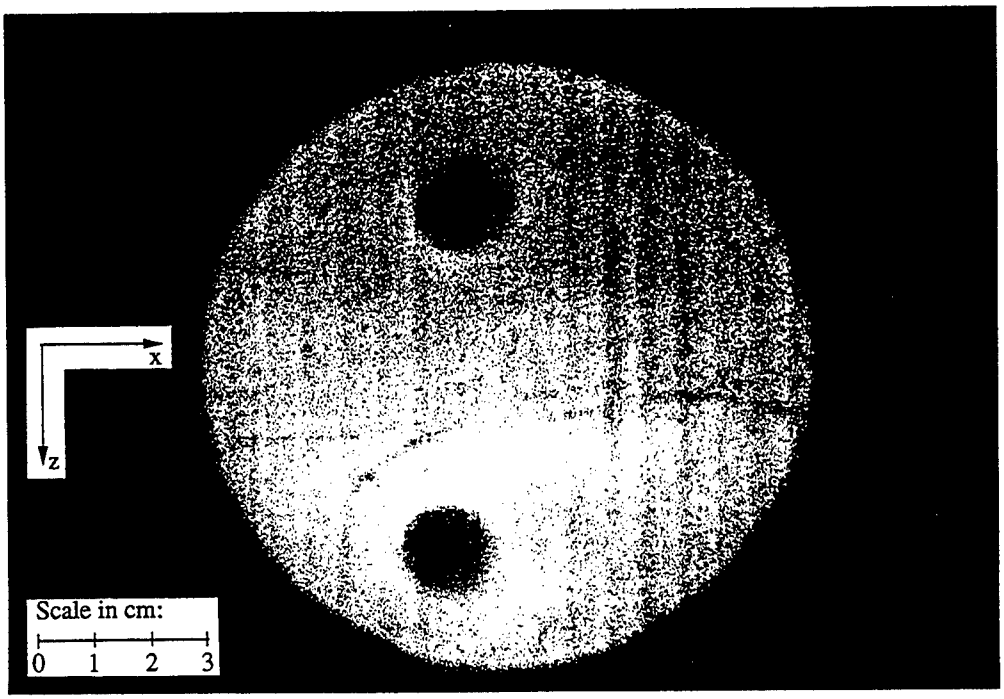

Figure 2 Typical shadowgraph picture of a vortex ring reconnected to a free surface.

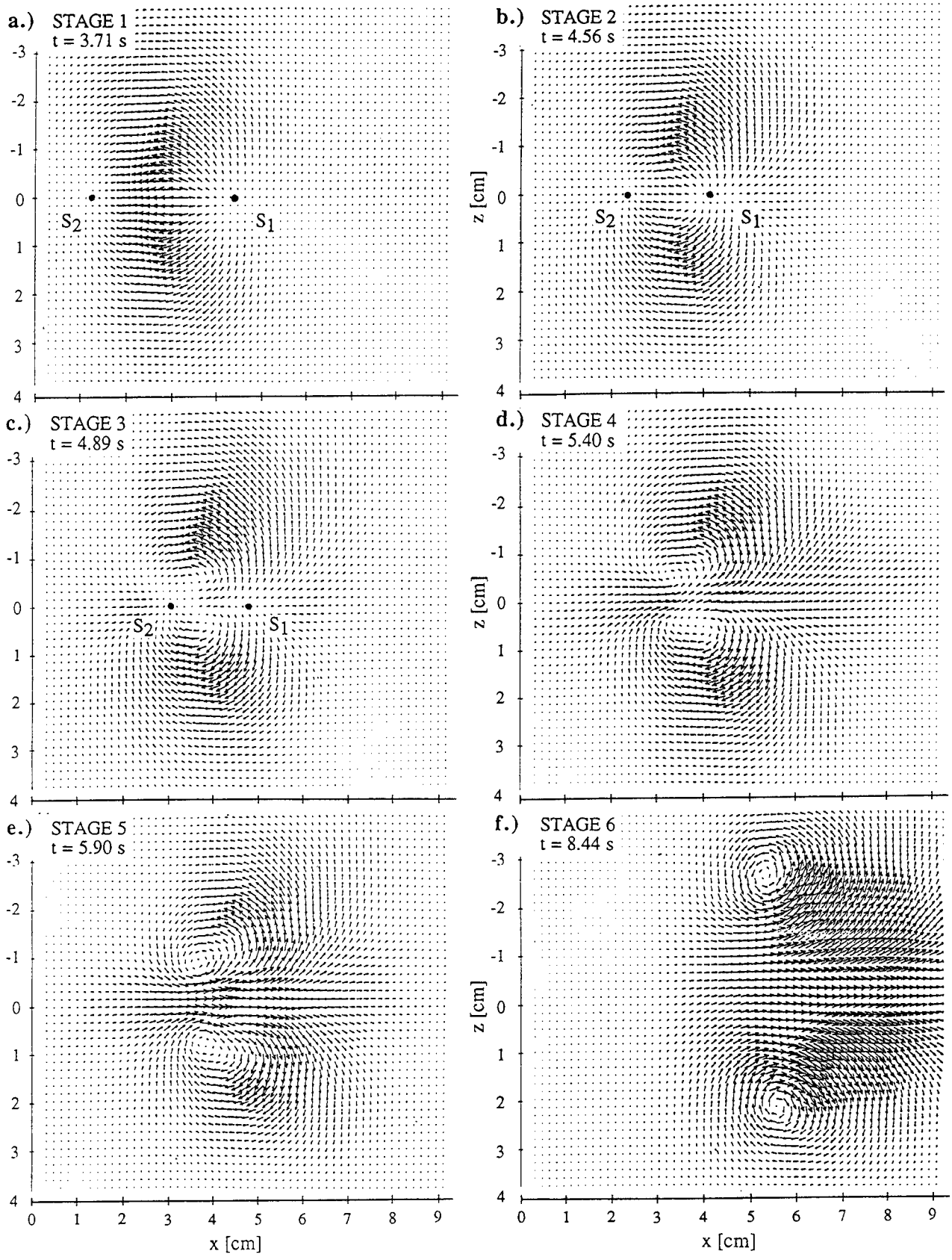

Figure 3a - 3f Velocity field at the free surface during the reconnection process (stages 1 to 6).

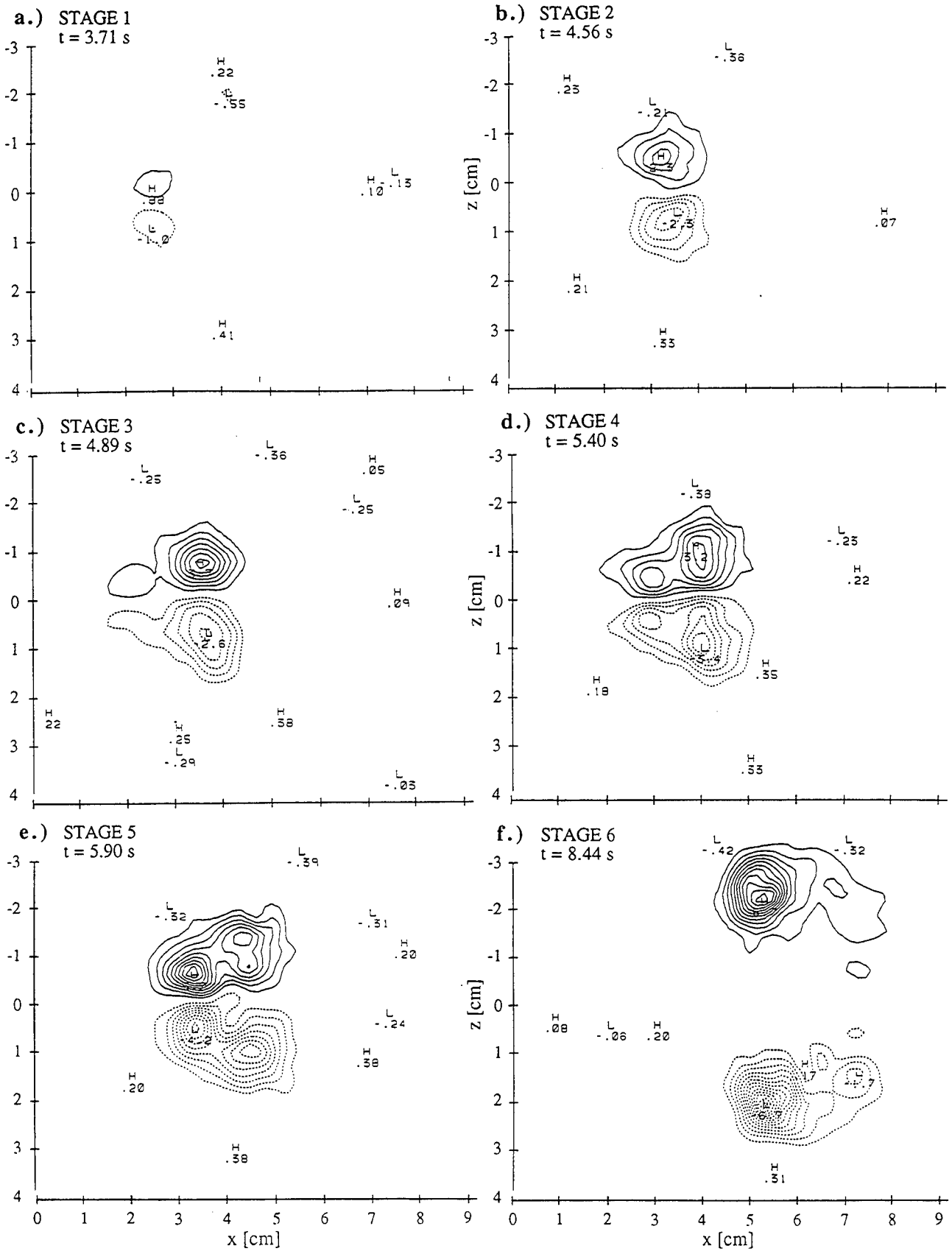

Figure 4a - 4f Vorticity field (ω_y -component) at the free surface during the reconnection process (stages 1 to 6).

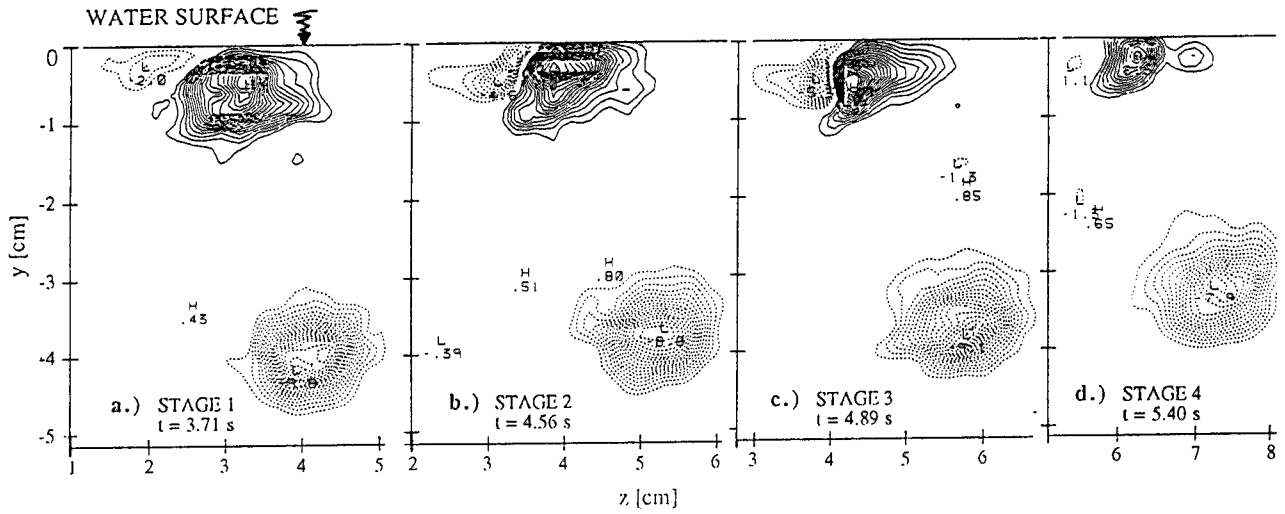

Figure 5a - 5d Vorticity field (ω_z -component) in the symmetry plane ($z = 0$) during the reconnection process (stages 1 to 4).

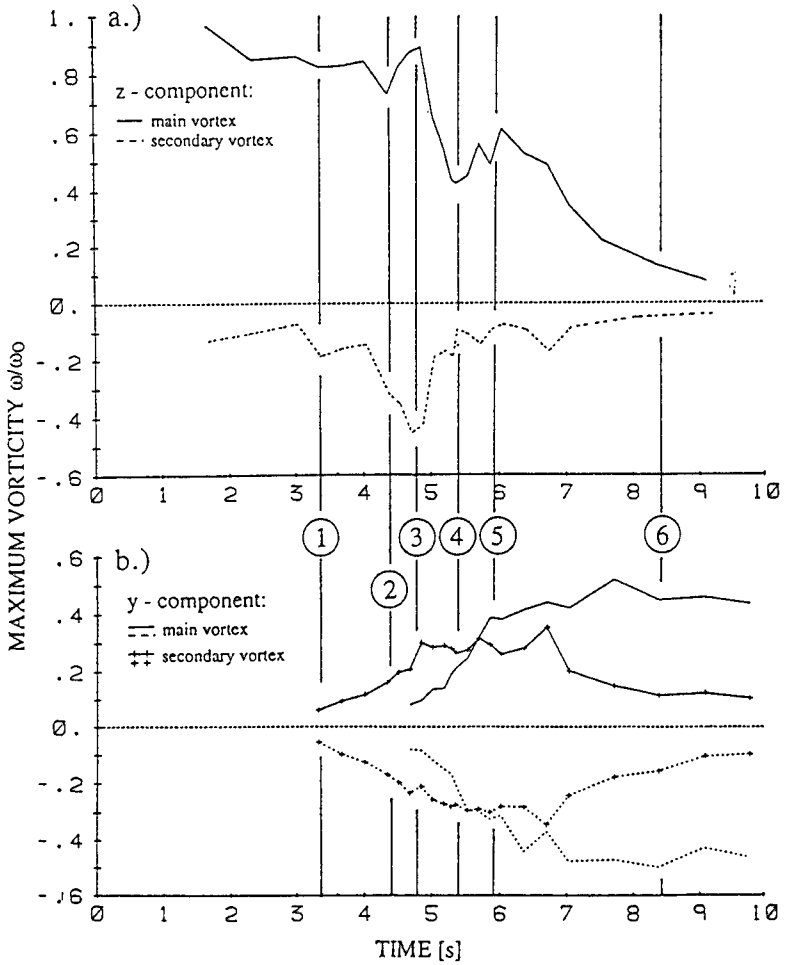

Figure 6 Temporal development of the peak vorticity normalized with the initial peak vorticity of the vortex ring ($\omega_0 = 11.0\ s^{-1}$).
a.) ω_z - component in the symmetry plane ($z = 0$).
b.) ω_y - component at the free surface.

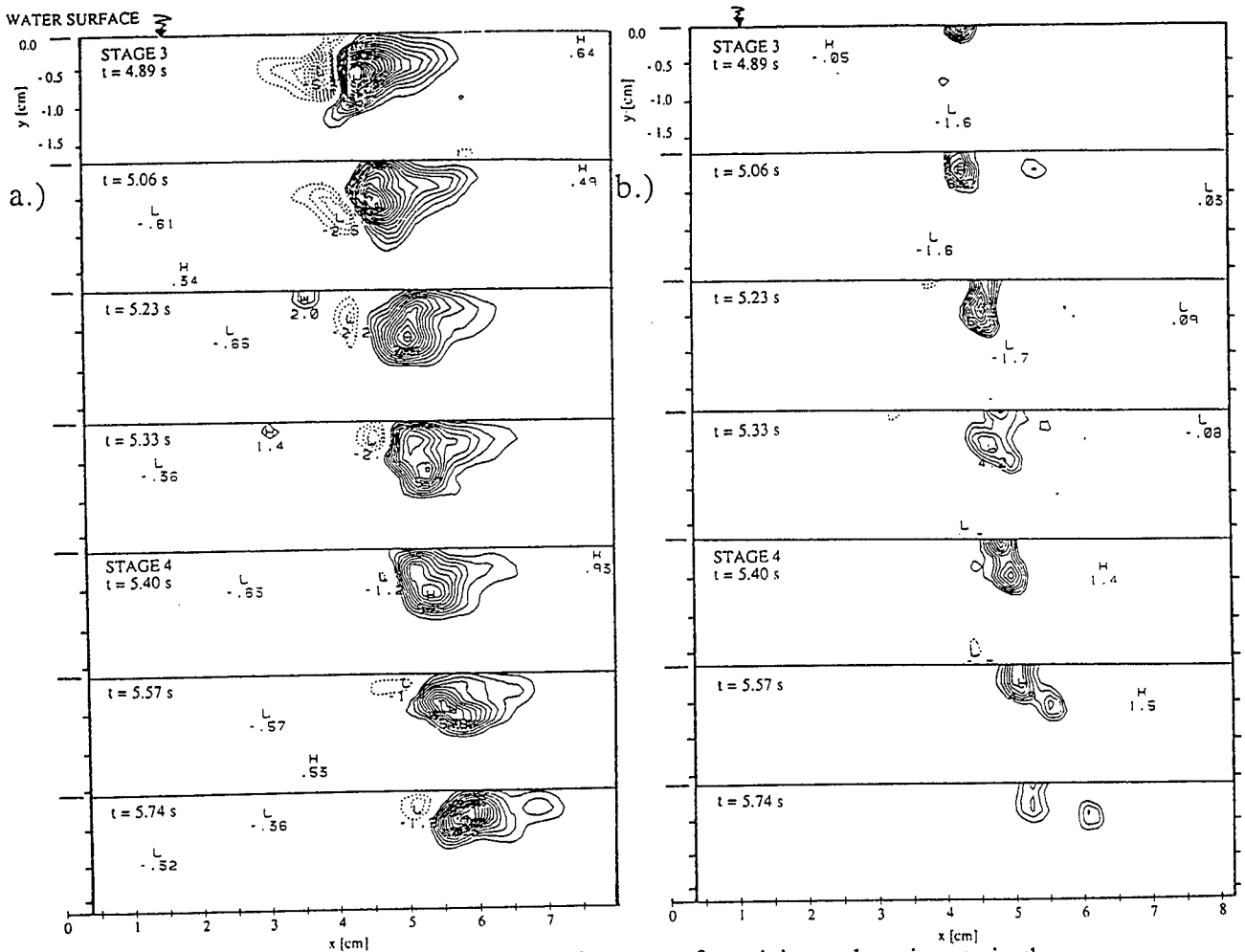

Figure 7 Spatial and temporal development of vorticity and strain rate in the symmetry plane ($z = 0$) during stage 3 - 5.
a.) ω_z - component.
b.) $\partial w/\partial z$ - component.

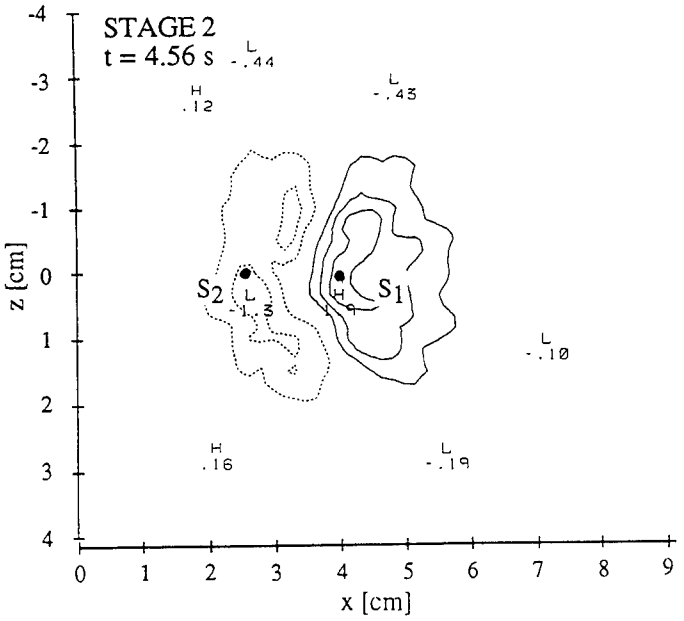

Figure 8 Strain rate $\partial v/\partial y$ at the free surface during stage 2.

DISCUSSION

K. Mori
Hiroshima University, Japan

Thank you for your interesting paper.

Did you use the tangential stress condition on the free surface in your analysis? If it is considered, the tangential components of vorticity may be zero and a boundary layer-like flow region may develop (see the text book by Batchelor). Did you observe any phenomena to support this in your measurement?

AUTHORS' REPLY

As it was stated in the paper (eqn. 1), the condition of shear stress $\Gamma = \sigma$ does not necessarily imply that the tangential component of vorticity is equal to σ ($\omega_z = \sigma$) at the surface. This is because surface parallel vorticity can exist due to surface tension gradients or other terms in eqn. 1. Our data was obtained in a real experiment and does not include any specific assumptions. A boundary layer-like flow is plausible for non-zero shear stress conclusions. However, we did not observe that in our experiments.

Session IX

Wave and Wake Dynamics

Turbulent Structure in Free-Surface Jet Flows

D. Walker, C.-Y. Chen, W. Willmarth
(The University of Michigan, USA),
D. Anthony (David Taylor Model Basin, USA)

ABSTRACT

This paper examines the evolution of a turbulent jet beneath a free surface using a three-component laser velocimeter. Reynolds- and Froude-number effects in the interaction of the jet with the free surface are identified. At low Froude number, the anisotropy of the turbulence near the free surface is increased. The outward velocity near the surface, which gives rise to a surface-current layer, is larger at low Froude number. An increase in Reynolds number further increases the magnitude of this outward velocity. At low Froude number, the mean velocity profiles exhibit spatial variations which may be due to coherent vorticity attached to the free surface. These variations are absent at high Froude number, probably due to changes in vorticity/free-surface interaction, caused by the larger surface deflections. These changes in vorticity/free-surface interaction may also result in the smaller outward velocity observed at high Froude number. Near the free surface, the high-mean-shear regions of the flow exhibit locally elevated Reynolds shear stress which contributes to surface current.

INTRODUCTION

The interaction of turbulent flow with a free surface has received increasing attention in recent years. A significant portion of this interest has come as a result of recent advances in remote sensing which are expected to allow world-wide monitoring of maritime traffic in the foreseeable future. Techniques such as synthetic-aperture radar (s.a.r.) are capable of detecting the free-surface disturbances created by a surface ship many kilometers behind a vessel, and sometimes many hours after the ship has passed (see e.g. Munk, *et al.*, 1987). Presently there is a significant lack of understanding of the ways in which a turbulent flow creates free-surface disturbances, and how the structure of the underlying turbulence is modified by the presence of the free surface. The purpose of this work is to develop some understanding of the nature of the interaction of an axisymmetric turbulent jet with a free surface.

Extensive turbulence measurements in axisymmetric jets have been reported by Wygnanski & Fiedler (1969) and others. The study of turbulent jet flow near a free surface, however, has been relatively limited. Swean, *et al.* (1989) made turbulence measurements in a developing planar surface-jet and noted a decrease in vertical velocity fluctuations near the free surface. The interaction of a round turbulent jet issuing parallel to a free surface was examined by Bernal & Madnia (1988). In the region where the jet first interacts with the free surface, the jet scaling depends on the depth below the free surface. Significant surface disturbances occurred in the interaction region, where the large scale structure of the jet first interacts with the free surface. These disturbances form approximately plane waves which propagate away from the jet axis. The angle at which the waves propagate varied with jet exit velocity and jet depth—the angle increasing with increasing velocity or decreasing depth. They also noted the appearance of small circular dimples on the free surface using shadowgraph visualization. These dimples are typical of the signature of a vortex with its axis normal to the free surface (see Sterling *et al.*, 1987) and indicate that vortex reconnection (where a vortex breaks and "reconnects" with its image vortex above the free surface) has occurred.

The study of Anthony & Willmarth (1992) examined a circular jet issuing two jet-diameters below, and parallel to, a free surface using a three-component laser velocimeter. They also noted that the vertical velocity fluctuations were damped near the free surface and identified several other interesting effects. Most notable was the existence of a thin surface-current layer, identified in near-surface velocity measurements, which propagated away from the jet centerline. It was concluded on the basis of flow visualization that the surface current was comprised mainly of vortical structures ejected from the main jet.

A similar surface-current layer was observed by Walker & Johnston (1991) in moderate- to high-Reynolds-number model-ship wakes. This suggests that the mechanisms of generation of this surface current layer are basic fluid dynamic phenomena associated with the interaction of turbulent vorticity with the free surface.

Vortex reconnection has also been observed in model-ship wakes by Walker & Johnston. In these flows, it appears that the reconnection process occurs primarily at the smaller turbulent scales.

The purpose of this study is to gain an understanding of the effects of variation in the two primary parameters which govern the behavior of turbulent free-surface flows, the Reynolds number and the Froude number. The ultimate goal is to use this understanding facilitate prediction of the free-surface features of a ship wake. It is therefore important to understand what range of these parameters is relevant in turbulent ship wakes. If it is assumed that the turbulent wake of a surface ship is made up primarily of the boundary layer from the ship, then twice the boundary-layer thickness at the stern is a reasonable approximate length scale for the wake. Assuming that the ship is a flat plate 140 m in length moving at 30 knots (both length and velocity typical of a modern destroyer), the boundary layer thickness at the trailing edge is about 1 m. The resulting Reynolds number for the wake is about $3(10^7)$ and the Froude number is about $3(10^0)$.

The above values of Froude and Reynolds number hold at the origin of the wake. Further aft of the ship, the length scale for the wake increases and the velocity scale decreases. This results in a decrease in the local Froude number. Classical scaling for an axisymmetric wake (or a co-flowing jet) suggests that the Reynolds number will decrease also, but only slowly (see e.g. Hinze, 1978). Hence, to understand the evolution of a turbulent ship wake, one must understand the interaction with the free surface of a turbulent shear flow at a Reynolds number on the order of 10^8 and Froude numbers of order 10^1. For the far wake, important in remote sensing of ship wakes, the Froude number can become very small, while the Reynolds number changes only slightly.

Laboratory experiments (Anthony & Willmarth, 1992, Bernal & Madnia, 1988) are typically limited to Reynolds numbers of order 10^4. At these low Reynolds numbers, the primary limitation is that the smaller scales are absent so that the range of length scales present in the turbulence is typically small. This obscures possible differences in free-surface interaction between the largest and smallest scales of turbulence.

In what follows, data is presented on the structure of turbulence in jets issuing parallel to a free surface. A high-Reynolds-number (10^5) jet is examined. (Flow-visualization results presented by Walker, *et al.*, 1991 show that there is a marked increase in the small-scale turbulence present in this high-Reynolds-number jet relative to that seen at Reynolds numbers of about 10^4.) The Froude number of this jet is of order 10^0. These results will be compared to those of Anthony & Willmarth (1992) for Reynolds number of order 10^4 and Froude number of order 10^1. Since both the Reynolds and Froude numbers vary between these two cases, the effect of these parameters is identified by reference to a third case which matches the Reynolds number of Anthony & Willmarth and the Froude number of the present high-Reynolds-number jet. In this way, the range of Froude numbers present in a ship wake are covered and a Reynolds number which is sufficient to introduce a broad range of length scales is attained. The study

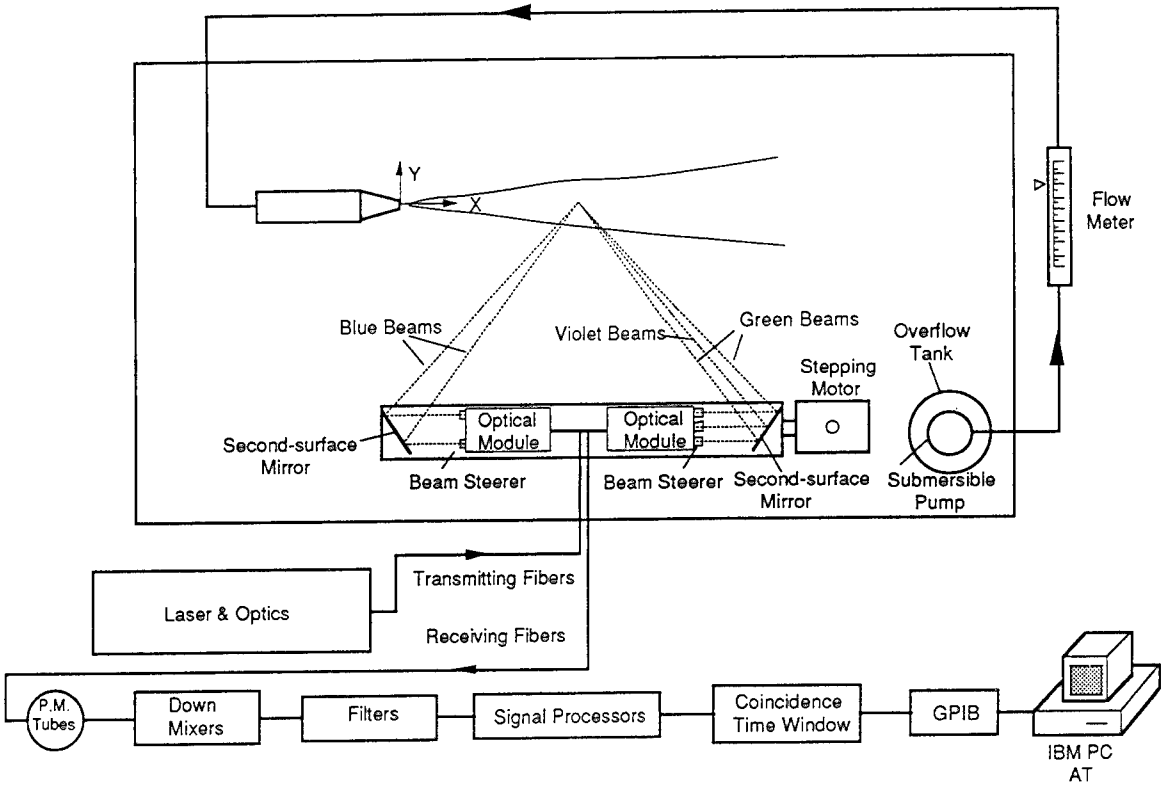

Figure 1 Schematic of experimental apparatus showing arrangement of 0.0254 m jet and laser velocimeter.

concentrates on quantifying the near-surface turbulent structure using laser velocimeter measurements and identification of the effects of Froude and Reynolds number on the nature of, and evolution of, the flow.

EXPERIMENTAL APPARATUS AND PROCEDURES

For part of this study, the jet apparatus used by Anthony & Willmarth (1992) was reused, but the experiments were conducted in a different tank with a larger nozzle. A set of results at high Reynolds number was obtained using a large-scale jet operating in the University of Michigan towing tank. The three-component laser velocimeter was the one used by Anthony & Willmarth. In what follows, the jets are described briefly, followed by a description of the different tanks in which they were operated. The laser velocimeter is then described followed by a discussion of the methods used for calculation of the statistics, ensemble sizes and averaging times.

Jet Apparatus

Different combinations of Reynolds number and Froude number were obtained by using three different combinations of jet nozzle diameter and exit velocity. The nozzle diameters used were 0.102 m, 0.0254 m and 0.00635 m. (The 0.00635 m nozzle was used only in the study of Anthony & Willmarth.) All of the jet nozzles were similar; the nozzle profile was a fifth-degree polynomial having specified diameter at inlet and exit and both zero slope and curvature at inlet and exit. The 0.0254 m and 0.00635 m jet nozzles were described in detail by Anthony (1990). For the present study, the 0.0254 m jet was supplied by a submersible pump and the flowrate was continuously monitored via a calibrated rotameter. This system is shown schematically in Figure 1.

The 0.102 m jet (designed and built by W.W.W.) was driven by a four-bladed propeller located on the axis of the jet. Downstream of the propeller was an expansion, followed by a honeycomb flow straightener and several screens. The nozzle was constructed of fiberglass and has a contraction ration of 9:1. This jet has a maximum exit velocity of 3 m/s and is capable of attaining Reynolds numbers in excess of 300 000. Initial measurements showed a turbulence intensity of about 0.5 percent at the jet exit plane and no measurable swirl in the jet.

The design of all the jets was such that they were free to entrain fluid from all directions, in contrast to those emanating from solid walls, e.g. the jet of Bernal & Madnia (1988).

Tank Facilities

The three jets were operated in three different tanks. The study of Anthony & Willmarth (1992), which used the 0.00635 m jet, was done in a long towing tank with a 0.610 m x 0.610 m cross-section and the details can be found in Anthony (1990).

Because of physical size of the 0.102 m jet, the measurement were made in the towing tank in the Ship Hydrodynamics Laboratory of University of Michigan. The tank is 6.7 m wide, 3.1 m deep and 110 m long. To reduce seeding requirements, plastic curtains were located 48 jet diameters upstream and 128 diameters downstream of the jet exit plane. A swimming-pool-type skimmer, connected to the tank filter system, was operated continuously at the downstream end of this region to clean the free surface.

For the 0.0254 m jet, a smaller tank (3.7 m x 2.4 m x 0.61 m deep) was used. The pump for the jet was located in a smaller "overflow" tank placed in the main tank (see Figure 1). This overflow tank served to maintain a constant free-surface level during the experiments and also to continuously, mechanically clean the free surface during the course of the experiment.

A comparison between the three different tanks is shown in Figure 2. All tanks are shown in dimensions of jet diameters, based on the exit diameter of the jet operated in that particular tank.

Laser Velocimeter

The velocity field of the jet was examined using a three-component laser velocimeter designed for use in a towing tank (Willmarth, 1987). The system uses three

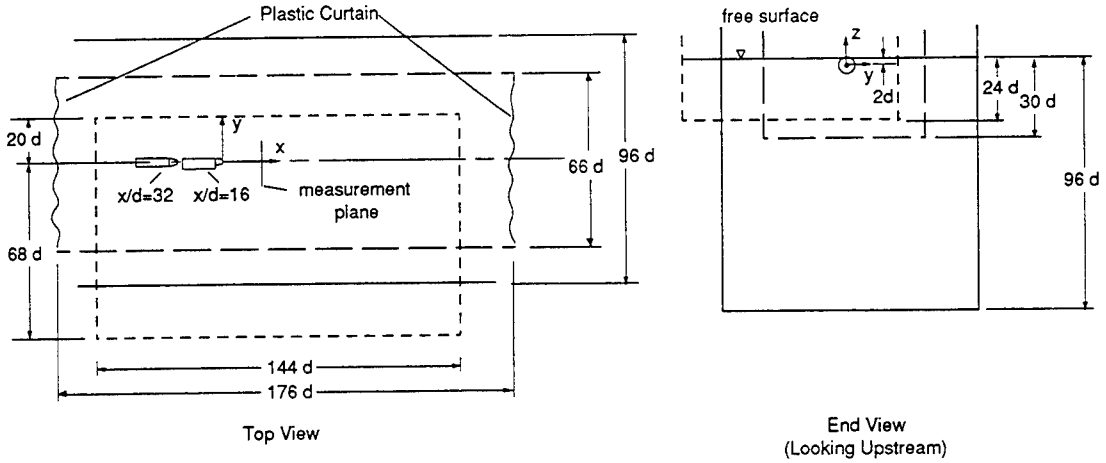

Figure 2 Schematic showing arrangement of jet apparatus in various tanks: — — , 0.102 m jet; - - - - , 0.0254 m jet; ——— , 0.00635 m jet (Anthony & Willmarth, 1992).

different lines of an Argon ion laser to obtain measurements of three independent components of velocity. The three colors used are green (514.5 nm), blue (488.5 nm), and violet (476.5 nm); the green and blue beam pairs determined two velocity components in a plane, and the violet beam pair determined the third component which is perpendicular to this plane. Bragg cells were used to shift the frequency of one beam of each pair by 40 MHz in order to distinguish negative velocities on all components.

In this design, the transmitting and receiving optics were contained in two water-tight modules mounted inside a submerged cylindrical housing (see Figure 1). Optical fibers were used to transmit light between the above-water and underwater optics. Beam steerers and second-surface mirrors were mounted just after these two modules to allow crossing of the six beams. Each beam pair formed an effective measuring volume approximately 200 μm in diameter. The scattering particles used were titanium dioxide of rutile crystalline form and were approximately 3 μm in size. The light scattered from the measuring volume was collected off-axis, each module receiving scattered light from transmitted beams of the other module. This arrangement was chosen for improved spatial resolution and results in measurement volumes with lengths of approximately 500 μm.

The signals from the photomultipliers were down-mixed to yield effective shift frequencies of 200 kHz on green and blue and 500 kHz on violet for the 0.102 m diameter jet. The 0.0254 m diameter jet experiments used effective shift frequencies of 50 kHz on green and blue, and 100 kHz on violet in order to maintain the resolution of the velocity measurements for the lower velocities encountered in this case. The resulting signals were filtered using Krohn-Hite band-pass filters, and were sent to counter-type signal processors (TSI 1980B). The outputs from the three counters were then checked for temporal coincidence. The coincidence check functioned as follows: A data set was valid only if all three processors had reported valid measurements during a specific time window. The length of this window was set equal to the average transit time of a particle passing through the measuring volume. The data were transferred to a Lecroy MM8206A CAMAC digital memory and were then transferred over an IEEE-488(GPIB) interface to an IBM PC-AT computer.

Data Analysis

The data reported below are based on ensembles of individual realizations of the instantaneous three-component velocity vector. Initially, the mean and standard deviation for each measured velocity component were calculated. Realizations that were more than three standard deviations removed from the mean on any component were eliminated. The velocities were then resolved into the appropriate coordinate system and final statistics were calculated. The required coordinate transformations are detailed in the thesis by Anthony (1990). All final statistics were corrected for velocity bias by weighting each velocity measurement with the reciprocal of the magnitude of the instantaneous velocity vector as proposed by McLaughlin & Tiederman (1973).

The results of Anthony & Willmarth (1992), included below for comparison purposes, were calculated using ensembles of 1000 elements. For this study, both jets examined had velocities which were lower than that of Anthony & Willmarth. Since the seed material was the same and the seed densities were comparable or lower, and the same laser velocimeter was used, this reduction in velocity resulted in a significantly lower data rate, and hence a longer time to acquire a similar ensemble size.

For the 0.0254 m jet, the velocity was reduced by a factor of four compared to the results of Anthony & Willmarth (0.50 m/s vs. 2.0 m/s). This resulted in a four-fold decrease in data rate. Initially measurements were done for this case using 500 point ensembles. This yielded acceptable results at the first measurement station, located 16 diameters downstream of the jet exit. Measurements further downstream exhibited significant scatter. Ensemble sizes were then increased to 1000 and better results were achieved.

The requirement of a larger ensemble size appears to actually be a requirement that the averaging time be sufficiently long. Comparison of the characteristic time scale for this jet and that of Anthony & Willmarth shows that the time scale has increased by a factor of sixteen. Since the data rate has only decreased by a factor of four, the averaging time for a comparable size ensemble has only increased by a factor of four. The net result is a four-fold decrease in the averaging time for a comparable size ensemble when measured in jet characteristic time scales. In the results presented below for this flow, vertical profiles were calculated based on 500 point ensembles, and the horizontal profiles used 1000 point ensembles. Based on the characteristic time scale of the jet, a further increase in averaging time (ensemble size) would be desirable.

For the 0.102 m jet, the ensemble size used for the calculation of statistics was reduced to 500. The large volume of water seeded for this experiment resulted in lower seed densities and, hence, larger averaging times. For this case, the smaller ensembles appear to have had only minimal effect on the quality of the data.

RESULTS

Profiles of turbulence quantities were obtained from three-component velocity measurements. In the results presented below, instantaneous velocities are designated using upper-case letters (U,V), fluctuations about the mean use lower-case letters (u,v), time-average quantities are indicated by an overbar ($\overline{U}$,$\overline{V}$,$\overline{uv}$), and r.m.s. velocities are designated using a prime (u',v'). In these results, x is distance measured along the jet axis with $x = 0$ at the jet exit plane; the positive x-direction will be referred to as the streamwise direction and the corresponding velocity component U is the streamwise velocity. The surface-normal direction is defined as the z-direction, positive upward, with the origin on the jet axis. This will be referred to as the vertical direction with velocity component W. The transverse, or horizontal, coordinate is y. The origin is again at the jet axis and the positive direction is defined so as to result in a right-handed coordinate system. The transverse velocity is given the symbol V.

For this study, water was the working fluid and the air-water interface will be referred to as the free surface. The Froude number (Fr) was 1.0 based on jet-exit velocity U_o and jet exit-nozzle diameter d. The Reynolds numbers (Re) were 102 000 and 12 700, again based on U_o and d. These Reynolds numbers resulted from an exit

distance $h = 2d$ below the free surface. This places the free surface at $z = 2d$.

Table 1 Experimental conditions.

Exit Diameter d	Exit Velocity U_o	$Re = \frac{U_o d}{\nu}$	$Fr = \frac{U_o}{\sqrt{gd}}$
0.102 m	1.00 m/s	102 000	1.0
0.0254 m	0.50 m/s	12 700	1.0
0.00635 m	2.00 m/s	12 700	8.0

The above conditions were chosen to complement the results of Anthony & Willmarth (1992). They examined a jet located $2d$ below the free surface with Re = 12 700 and Fr = 8.0 (U_o = 2.0 m/s and d = 0.00635 m). The combined set of data, therefore has a *high-Reynolds-number* case (Re = 102 000, Fr = 1.0), *high-Froude-number* case (Re = 12 700, Fr = 8.0), and an *intermediate* case (Re = 12 700, Fr = 1.0). In the interest of brevity, these names will be used hereafter to refer to the different conditions.

Classical scaling arguments for a round turbulent jet in an infinite medium say that the maximum velocity in a turbulent jet is proportional to x^{-1} while the characteristic length (usually the full width at half the maximum velocity) is proportional to x (see e.g. Hinze, 1978). For the self-preserving region of a turbulent jet, therefore, universal behavior will be found in the profiles of turbulence quantities if vertical and lateral distances (z and y) are normalized by x, and all velocities are normalized by $U_o d/x$. Presentation of the data in this manner will allow ready comparison of the evolution of the near-surface jet to the self-preserving behavior of a deep jet. It is also a consistent normalization for comparing the different cases to be examined in this study as well as examining the streamwise evolution of the jet for a given set of conditions.

Profiles of turbulence quantities were obtained at two downstream locations, x/d = 16 and 32. The closer location, x/d = 16, is just downstream of where the jet first begins to interact with the free surface; x/d = 32 is far enough downstream that the surface current identified by Anthony & Willmarth (1992) is well established. Vertical profiles were obtained in the symmetry plane of the jet (y = 0) and horizontal profiles were obtained along a line just below the free surface, nominally at z/d = 2. In what follows, the results for x/d = 16 are presented first, then those for x/d = 32.

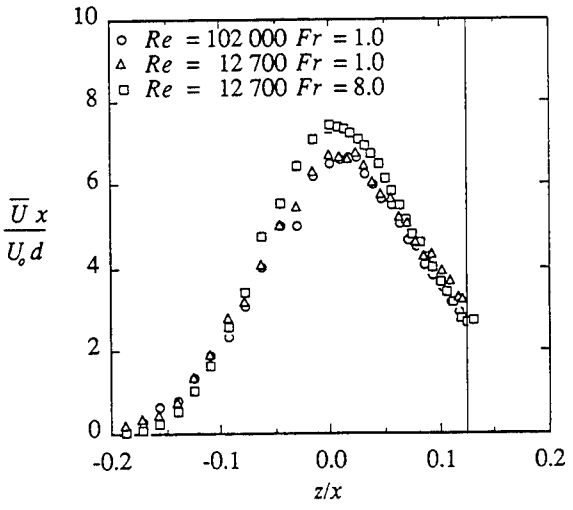

Figure 3 Vertical profiles of mean streamwise velocity $\overline{U}$ at x/d = 16, y/d = 0.

Results for x/d = 16

Figure 3 shows vertical profiles of the streamwise velocity at x/d = 16 on the jet symmetry plane. Far below the surface the velocity profiles are in good agreement, as one would expect since this region is least affected by the presence of the free surface. The maximum velocity of the high-Froude-number jet is about ten percent higher than that of the other two cases and occurs at about z/x = 0, the jet centerline. For the other two cases, both

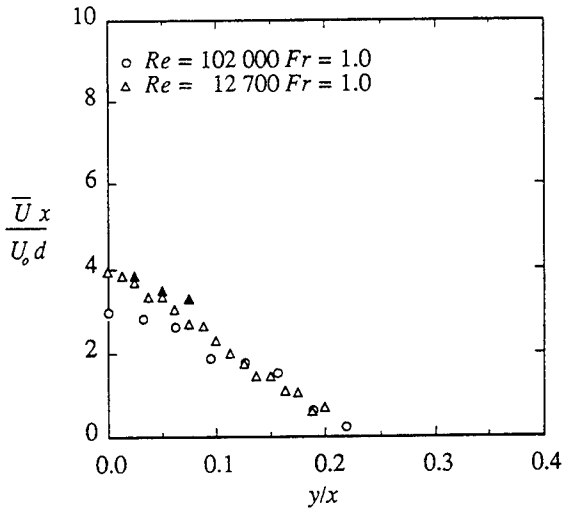

Figure 4 Horizontal profiles of mean streamwise velocity $\overline{U}$ at x/d = 16, z/d = 2. Solid symbols are for $-y/x$.

with lower Froude number, the maximum velocity occurs slightly nearer the surface. At the surface, the intermediate case exhibits a slightly higher velocity than that of the other two. This is confirmed in Figure 4 where horizontal profiles at the surface are shown. (The result of Anthony & Willmarth do not include horizontal profiles at x/d = 16 and z/d = 2.) Further from the jet axis, the mean velocities approach similar values.

Figures 5 and 6 show vertical and horizontal profiles of the mean transverse velocity, respectively. For all cases, the vertical profile shows a near-zero velocity, as would be expected on the symmetry plane of the jet. The horizontal profiles (again excluding the high-Froude-number results) show that there is a significant transverse velocity, its positive magnitude indicating that the flow is outward, away from the jet axis. Far from the centerline, the intermediate case exhibits a larger outward velocity than the high-Reynolds-number case.

Profiles of the vertical velocity are shown in Figures 7 and 8. The mean velocities for the high-Froude number

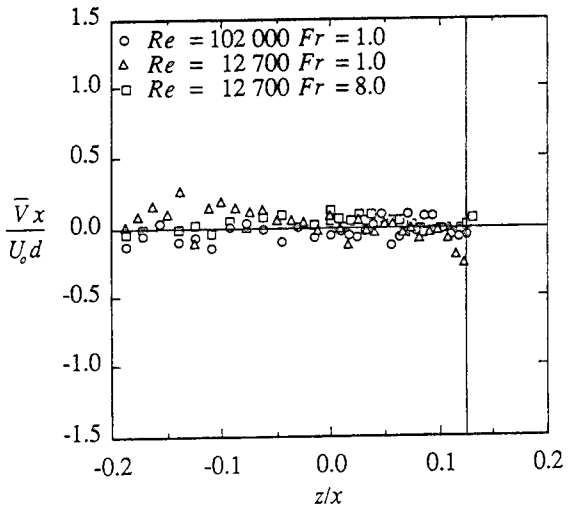

Figure 5 Vertical profiles of mean transverse velocity $\overline{V}$ at $x/d = 16, y/d = 0$.

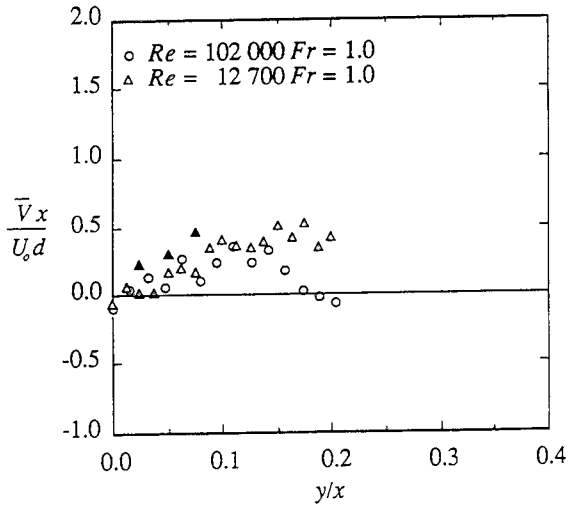

Figure 6 Horizontal profiles of mean transverse velocity $\overline{V}$ at $x/d = 16$, $z/d = 2$. Solid symbols -$\overline{V}$ are for -y/x.

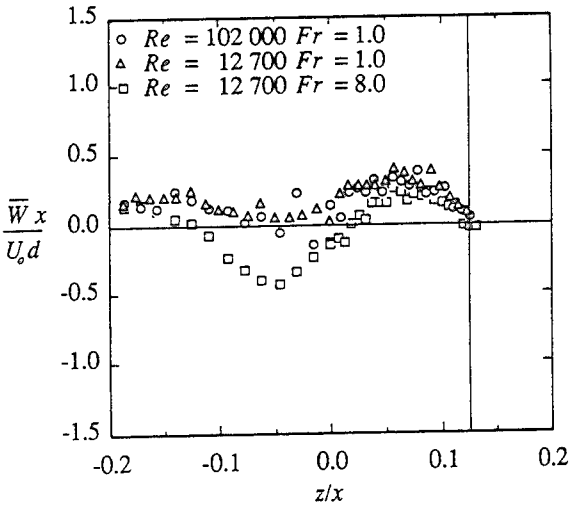

Figure 7 Vertical profiles of mean vertical velocity $\overline{W}$ at $x/d = 16, y/d = 0$.

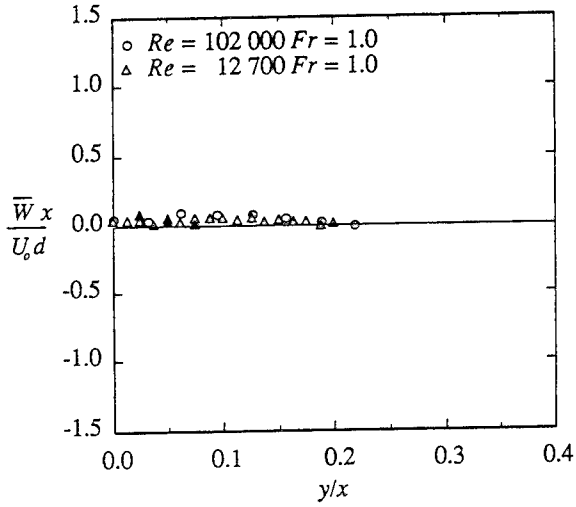

Figure 8 Horizontal profiles of mean vertical velocity $\overline{W}$ at $x/d = 16, z/d = 2$. Solid symbols are for -y/x.

outward, away from the jet axis. Far from the centerline, the intermediate case exhibits a larger outward velocity than the high-Reynolds-number case.

Profiles of the vertical velocity are shown in Figures 7 and 8. The mean velocities for the high-Froude number results are negative immediately below the jet axis. This is typical of a jet in an infinite medium (see, e.g. Wygnanski & Fiedler, 1969). Near the jet axis, the flow is outward because the centerline velocity is decreasing, while in the outer part of the jet the flow is inward due to entrainment. For the two low-Froude-number cases, the mean vertical velocity is consistently positive, except in a small region just below the jet axis for the high-Reynolds-number case. (This small difference in $\overline{W}$ for the two low-Froude-number cases may explain the differences in $\overline{V}$ seen in Figure 6.) This indicates that the effects of the free surface, in particular the formation of the surface current with its strong outward velocity may be more pronounced at low Froude number. The strong outward flow at the surface, evident in Figure 6, is sufficient to reverse the natural flow downward away from the jet axis for negative z values. This indicates that at low Froude number, the jet interacts more strongly with the free surface at $x/d = 16$ than at high Froude number. Figure 8 shows that the mean vertical velocity is essentially zero at the free surface, as would be expected.

The r.m.s. velocity profiles for $x/d = 16$ are shown in Figures 9 through 14. Figures 9 and 10 show the r.m.s. streamwise velocity. The results are generally similar for all three cases, however, there is a slight elevation of the

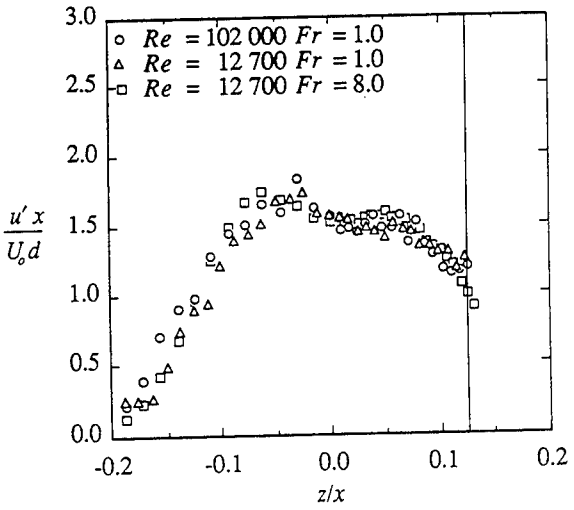

Figure 9 Vertical profiles of r.m.s. streamwise velocity u' at $x/d = 16, y/d = 0$.

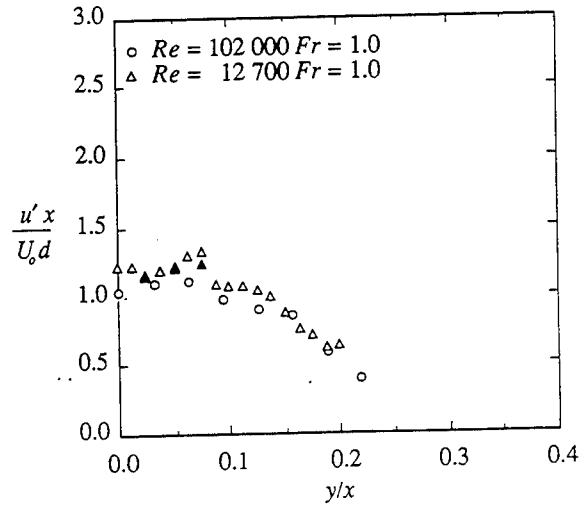

Figure 10 Horizontal profiles of r.m.s. streamwise velocity u' at $x/d = 16$, $z/d = 2$. Solid symbols are for $-y/x$.

r.m.s. velocity below the jet axis ($-0.15 < z/x < -0.07$) in the high-Froude-number case which is probably related to the negative $\overline{W}$ velocity below the jet axis. The high-Reynolds-number jet also exhibits a higher r.m.s. velocity at large depths ($z/x < -0.1$) which may be a Reynolds-number effect. There is also about a twenty percent elevation of the r.m.s. u and v velocities at the free surface for the low-Froude-number cases. Figure 10 shows that there is substantial agreement between the two low-Froude-number cases at the free surface.

Vertical profiles of the r.m.s. transverse velocities are shown in Figure 11. In general, the levels of v' are about ten to twenty percent lower than u'. However the r.m.s. velocity at the free surface for the low-Froude-number cases is still larger than that for the high-Froude-number case by about twenty percent. The high Reynolds number jet exhibits slightly elevated v' levels at all locations relative to the other two cases. Horizontal profiles (Figure 12) show that, again, there is reasonable agreement between the two low-Froude-number cases at the free surface.

Figures 13 and 14 show vertical and horizontal profiles of the r.m.s. vertical velocity, respectively, at $x/d = 16$. The behavior of w' is similar to the other r.m.s. velocities for $z/x < 0$ in the two low-Reynolds-number cases; i.e. there is a slight elevation of w' for $-0.15 < z/x < -0.07$ for the high-Froude-number case. For $z/x > 0$, the intermediate case exhibits slightly lower values of w' than the high-Froude-number case. Again the high-Reynolds-number jet exhibits an elevated r.m.s.

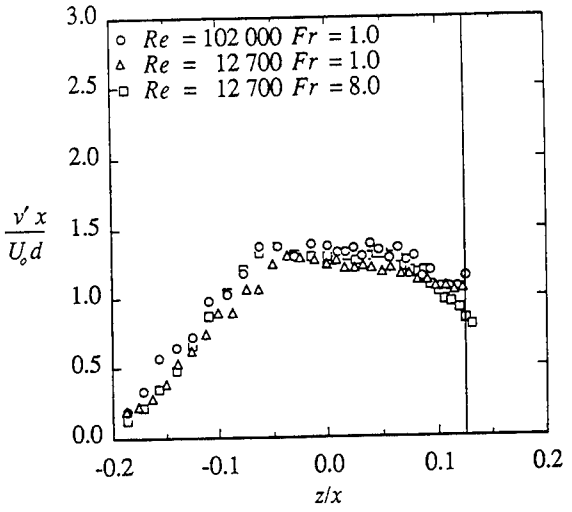

Figure 11 Vertical profiles of r.m.s. transverse velocity v' at $x/d = 16, y/d = 0$.

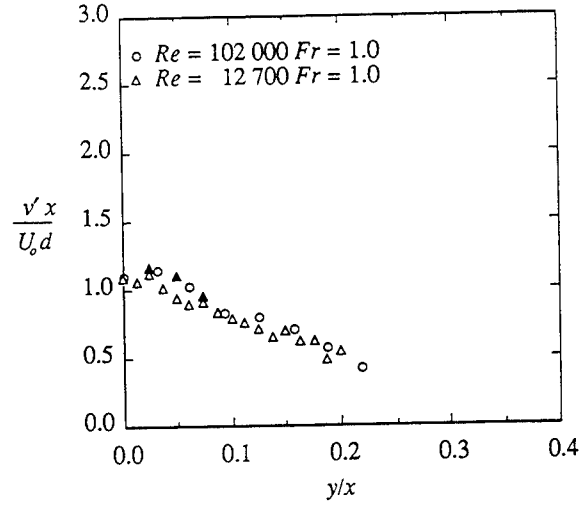

Figure 12 Horizontal profiles of r.m.s. transverse velocity v' at $x/d = 16$, $z/d = 2$. Solid symbols are for $-y/x$.

level, but it is more pronounced than for the other velocity components. Since the r.m.s. levels tend to increase slightly with increasing x/d, this may indicate that the high-Reynolds-number jet develops more quickly than the others. For $z/x > 0$, the trend is distinctly different; w' is reduced by as much as thirty percent in the low-Froude-number cases. The horizontal profiles in Figure 14 show that the two low-Froude-number cases exhibit similar behavior at the free surface for $x/d = 16$.

One striking feature of Figures 9, 11 and 13 is the disparity in r.m.s. levels at the free surface for the high- versus low-Froude-number cases. For the low-Froude-number cases, the tangential velocity fluctuations are increased by 30 to 40 percent over the high-Froude-number case, and the vertical fluctuations are reduced by a similar amount. As a result, the turbulence in the low-

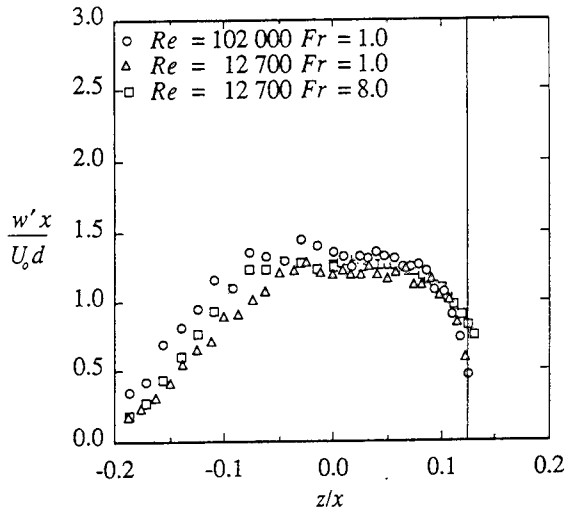

Figure 13 Vertical profiles of r.m.s. vertical velocity w' at $x/d = 16, y/d = 0$.

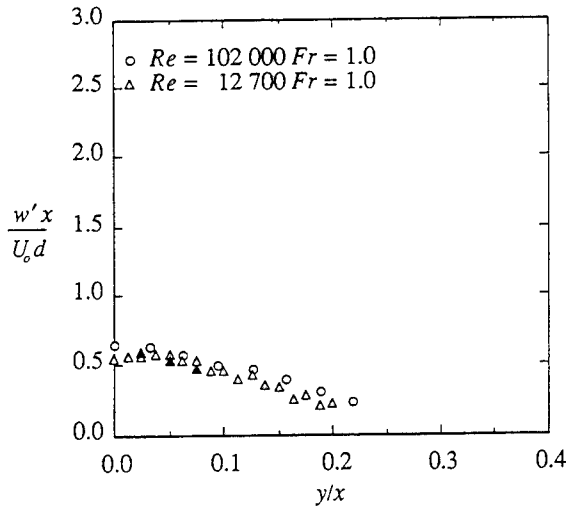

Figure 14 Horizontal profiles of r.m.s. vertical velocity w' at $x/d = 16, z/d = 2$. Solid symbols are for $-y/x$.

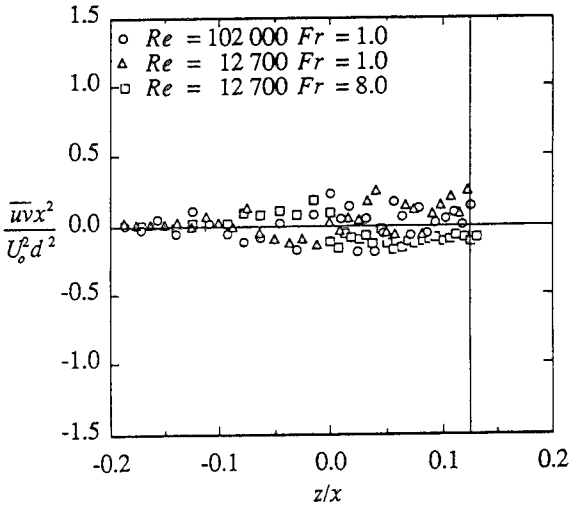

Figure 15 Vertical profiles of $\overline{uv}$ Reynolds stress at $x/d = 16, y/d = 0$.

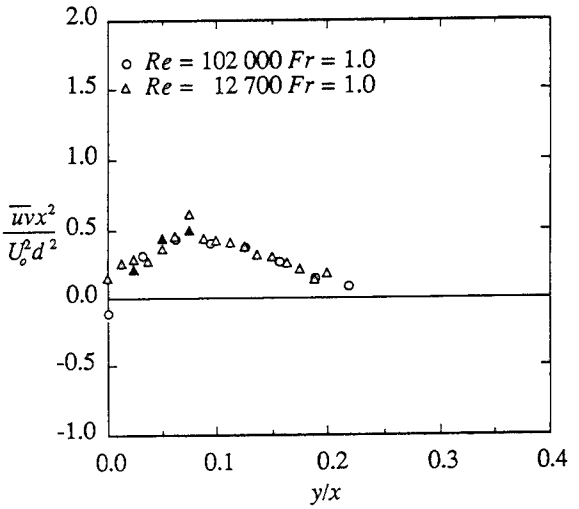

Figure 16 Horizontal profiles of $\overline{uv}$ Reynolds stress at $x/d = 16, z/d = 2$. Solid symbols are $-\overline{uv}$ for $-y/x$.

Froude-number jets is much more anisotropic at the free surface. For these cases the free-surface behaves much more like a rigid, shear-free boundary and, hence, vertical momentum is deflected in the horizontal direction by the free surface. This results in a reduction in w' and an increase in u' and v'.

Figure 15 shows vertical profiles of the $\overline{uv}$ Reynolds stress at $x/d = 16$. Since these measurements are located in the vertical symmetry plane of the jet, any cross-stream transport of momentum ($\overline{uv}$) should be zero. Near the surface, there is some systematic deviation from zero in the results. The high-Froude-number results are consistently negative and the other two cases are positive. This is probably due to slight misalignment of the jet

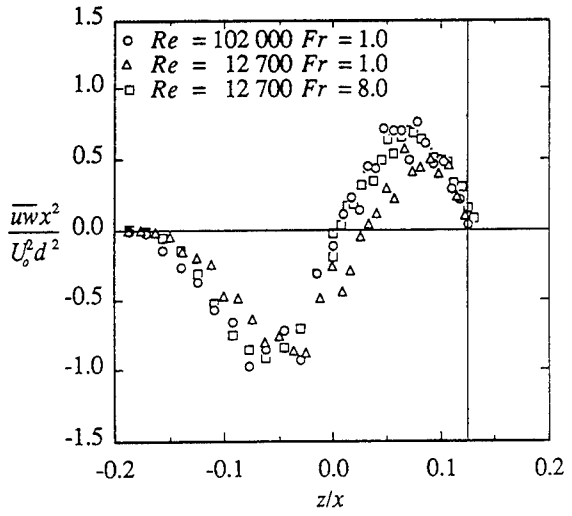

Figure 17 Vertical profiles of $\overline{uw}$ Reynolds stress at $x/d = 16$, $y/d = 0$.

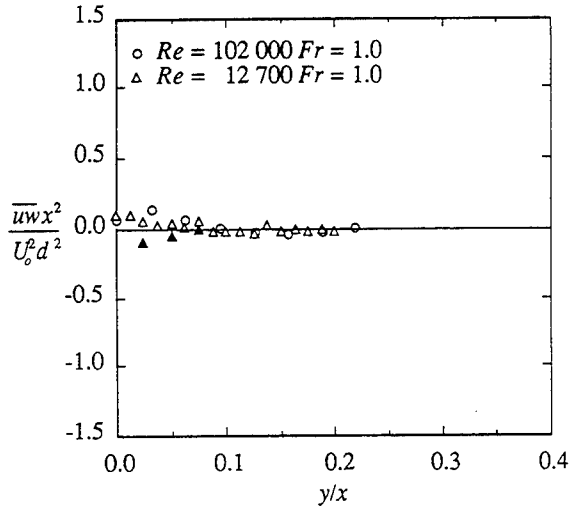

Figure 18 Horizontal profiles of $\overline{uw}$ Reynolds stress at $x/d = 16$, $z/d = 2$. Solid symbols are for $-y/x$.

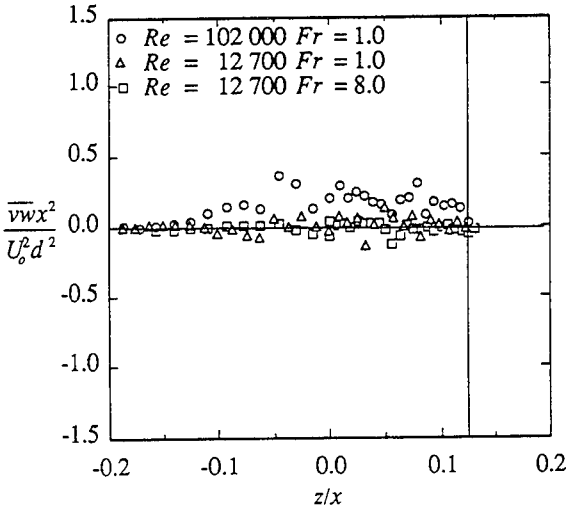

Figure 19 Vertical profiles of $\overline{vw}$ Reynolds stress at $x/d = 16$, $y/d = 0$.

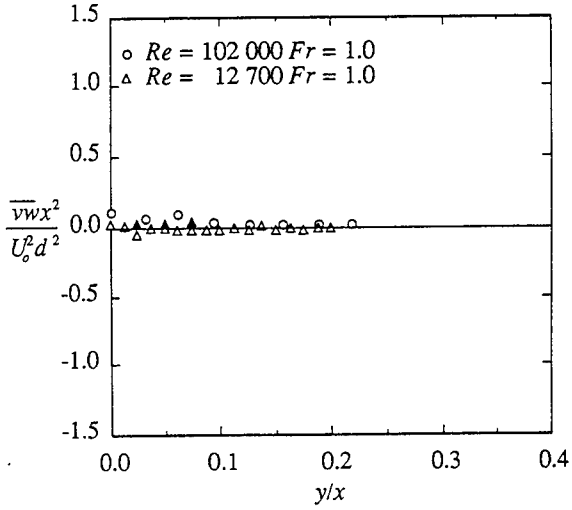

Figure 20 Horizontal profiles of $\overline{vw}$ Reynolds stress at $x/d = 16$, $z/d = 2$. Solid symbols are $-\overline{vw}$ for $-y/x$.

resulting in measurements slightly off the jet centerline. There is also some scatter in the results. Figure 16 shows the horizontal $\overline{uv}$ profiles at the free surface for the two low-Froude-number cases. Again, there is substantial agreement.

The $\overline{uw}$ Reynolds stress is shown in Figure 17. The intermediate case differs considerably from the other two cases which are in substantial agreement. This reduction is probably due to the smaller mean velocity gradients in the $\overline{U}$ profile for this case and the reduced level of the vertical velocity fluctuation w'. The product of these two quantities is the dominant production term for the $\overline{uw}$ Reynolds stress (see Bradshaw, 1978). At the free surface, one would expect this Reynolds stress to be zero and this is shown to be so in Figure 17, and further confirmed by the horizontal profiles at the free surface shown in Figure 18.

Figures 19 and 20 show vertical and horizontal profiles of the $\overline{vw}$ Reynolds stress. One would expect that this Reynolds stress would be zero for both profiles. This is true in the horizontal profile shown in Figure 20, but again the vertical profile shows a consistent deviation near the surface (particularly in the high-Reynolds-number case) which is, again, probably due to a slight misalignment of the jet.

Results for $x/d = 32$

Similar horizontal and vertical profiles of turbulence quantities were obtained at $x/d = 32$. Profiles of the mean streamwise velocity are shown in Figures 21 and 22.

In analyzing the results from the horizontal profiles for the intermediate case, it became apparent that the symmetry plane of the jet was located at about $y/x = 0.015$. This would correspond to an angular misalignment of less than one degree. What is not clear is whether this is due to a "physical" misalignment of the jet apparatus, or is due to the effect of the wall located at $y/x = 0.625$, which corresponds to $y/d = 20$ (see Figure 2). The presence of the wall could cause the maximum in the the velocity profile to move toward the wall (to positive z/x) due to the Coanda effect. For ease in interpretation, the data for the horizontal profiles has been plotted with y/x measured relative to the observed symmetry plane of the jet. Vertical profiles for this case were obtained slightly off the symmetry plane. This is no major problem for most statistics since the jet exhibits a broad maximum near the centerline. However, for quantities which change sign at the jet centerline (i.e., $\overline{V}$, $\overline{vw}$, $\overline{uv}$), sharp transverse gradients are present and a slight deviation from the symmetry plane can result in major changes in the measured turbulence quantities. The implications of these effects will be discussed, as necessary, below.

The vertical profile of $\overline{U}$ shown in Figure 21 shows good agreement between the results of the two low Froude number cases, even though the Reynolds numbers are very different. The velocity is relatively uniform between the jet axis $z/x = 0$ and the free surface for these two cases. For the high-Froude-number case, the maximum velocity is at $z/x = 0$ and there is a velocity gradient below the free surface. The maximum velocity for the high-Froude number jet is about ten to fifteen percent higher than the other two cases, similar to the results at $x/d = 16$. The scatter evident in the intermediate case results is most likely due to insufficient averaging time. (The r.m.s. velocity results, to be presented below,

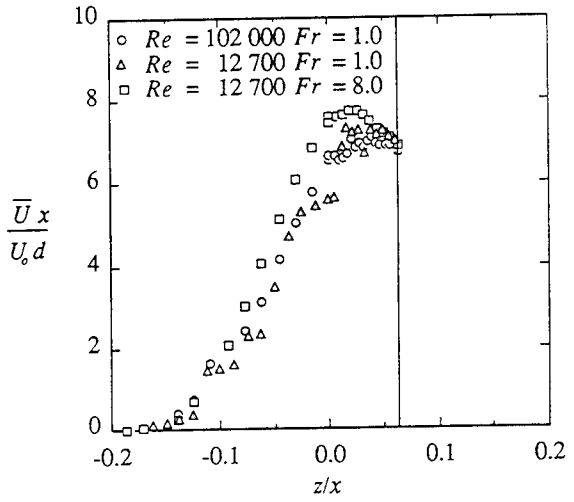

Figure 21 Vertical profiles of mean streamwise velocity $\overline{U}$ at $x/d = 32$, $y/d = 0$.

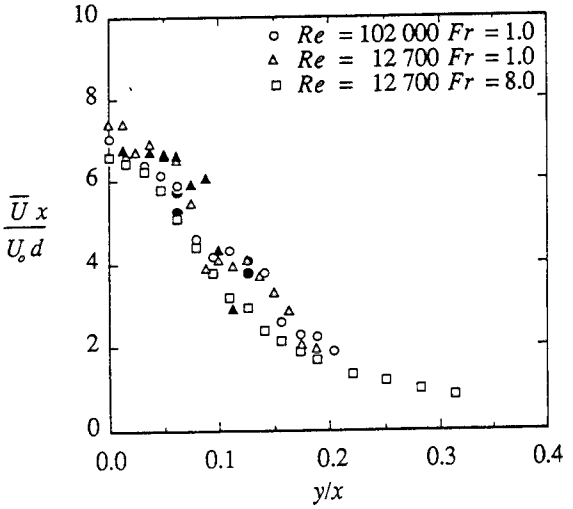

Figure 22 Horizontal profiles of mean streamwise velocity $\overline{U}$ at $x/d = 32$, $z/d = 2$. Solid symbols are for $-y/x$.

are comparable to those of Anthony & Willmarth, 1992; this indicates that the accuracy of the individual velocity measurements is acceptable. However, the time scales in this jet are a factor of 16 longer than those of Anthony & Willmarth while, for the vertical profile, the sampling time was only a factor four longer. Hence, the scatter in the data can be attributed to the length of the sampling time, as discussed earlier.)

Horizontal profiles of $\overline{U}$ are shown in Figure 22. The results from the intermediate case, which include several points for $y/x < 0$ (indicated by the solid symbols), show that the flow is essentially symmetric. For the two low-Froude-number cases shown in Figure 22, the velocities agree for $y/x > 0.1$ but the intermediate case exhibits noticeably higher velocity for $y/x < 0.1$ than

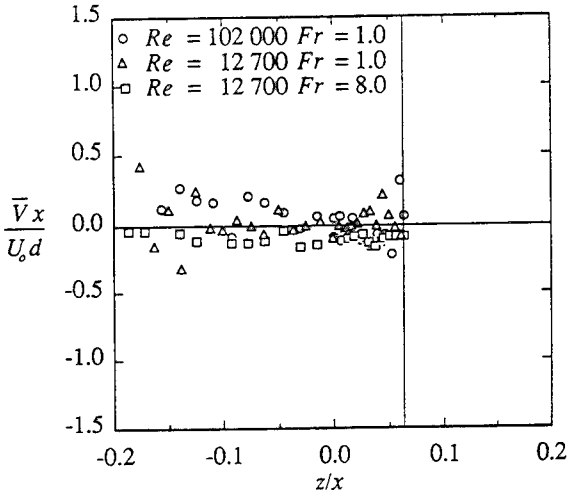

Figure 23 Vertical profiles of mean transverse velocity $\overline{V}$ at $x/d = 32$, $y/d = 0$.

either the high-Reynolds-number or the high-Froude-number case.

Vertical profiles of the mean transverse velocity are shown in Figure 23. The results scatter about zero, the expected value for $\overline{V}$ on the symmetry plane. The scatter is, again, attributable to inadequate averaging time; this is particularly evident at large negative z/x locations where the flow is very intermittent. Horizontal profiles of $\overline{V}$ are shown in Figure 24. For $y/x < 0.1$, the behavior of the two low-Froude-number jets is similar at $x/d = 32$. The intermediate case has a smaller transverse velocity than the high-Reynolds-number case at $x/d = 32$ for $y/x > 0.1$, but it is slightly larger than than $\overline{V}$ for the high-Froude-number case. Comparison of these results to those at $x/d = 16$ indicates that the intermediate case initially (at $x/d = 16$) spreads faster than the high-Reynolds-number case but by $x/d = 32$ this situation is reversed.

Profiles of the mean vertical velocity are shown in Figures 25 and 26. The vertical profiles exhibit no

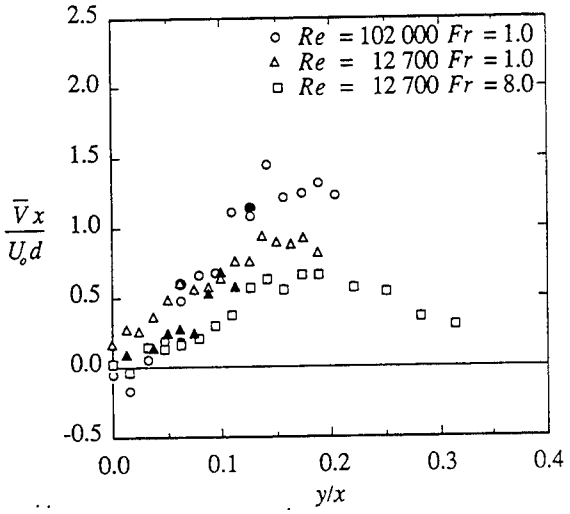

Figure 24 Horizontal profiles of mean transverse velocity $\overline{V}$ at $x/d = 32$, $z/d = 2$. Solid symbols are $-\overline{V}$ for $-y/x$.

significant difference for the three cases. The similarity in the $\overline{W}$ profiles indicates that the differences in the mean horizontal and vertical $\overline{U}$ profiles can be almost completely attributed to to the differences in $\overline{V}$ at the surface. The low-Froude-number jets spread more rapidly (larger $\overline{V}$) and this causes a smaller streamwise velocity below the surface. At the surface, the increased $\overline{U}$ for the low-Froude-number cases may be due to the same mechanism which causes increased $\overline{V}$. The horizontal profiles show that the vertical velocity is essentially zero at the free surface, as would be expected.

Horizontal and vertical profiles of r.m.s. streamwise velocities, shown in Figures 27 and 28, clearly show that for $y/x > 0.1$, the two low-Froude-number cases exhibit an increased level of u'. For $y/x < 0.1$, there is some scatter and slight inconsistencies between the vertical and horizontal profiles; however, the vertical profiles indicate

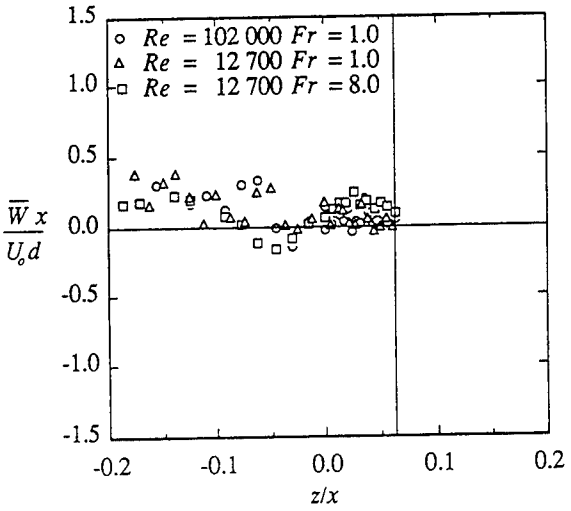

Figure 25 Vertical profiles of mean vertical velocity $\overline{W}$ at $x/d = 32$, $y/d = 0$.

that the two low-Froude-number cases exhibit larger r.m.s. streamwise velocity fluctuations near the free surface. Comparison to $x/d = 16$ shows that the r.m.s. level has increased for all cases by 30 to 40 percent, and that the difference near the free surface between the high- and low-Froude-number cases is similar, but more pronounced at $x/d = 32$.

The r.m.s. transverse velocities v' are presented in Figures 29 and 30. The horizontal profile, shown in Figure 30, shows that near the surface, the high-Reynolds-number flow exhibits the largest transverse velocity fluctuations, with the two low-Reynolds-number cases having the smallest. Compared to $x/d = 16$, all three cases have exhibited an increase in v', but the increases are largest for the high-Reynolds-number case.

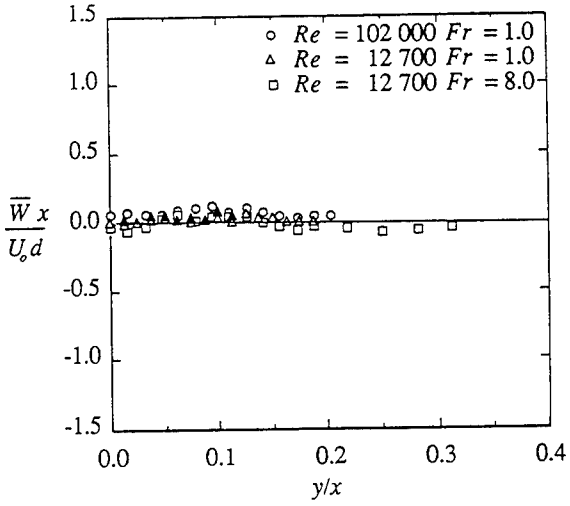

Figure 26 Horizontal profiles of mean vertical velocity $\overline{W}$ at $x/d = 32$, $z/d = 2$. Solid symbols are for $-y/x$.

This has resulted in significant difference in v' between the two low-Froude-number cases—a major change between $x/d = 16$ and $x/d = 32$.

Figure 31 shows vertical profiles of the r.m.s. vertical velocity. The two low-Froude-number cases appear to exhibit vertical velocity fluctuations which are about twenty percent higher than the high-Froude-number case near the jet centerline; however, this behavior is reversed at the free surface. The horizontal profiles (Figure 32) show that at low Froude number, there is an approximate fifty percent reduction in w' when compared to the high-Froude-number case at $x/d = 32$. This is somewhat more than what was seen at $x/d = 16$, but the difference is primarily due to an increase in w' for the high-Froude-number case; the other results are virtually unchanged

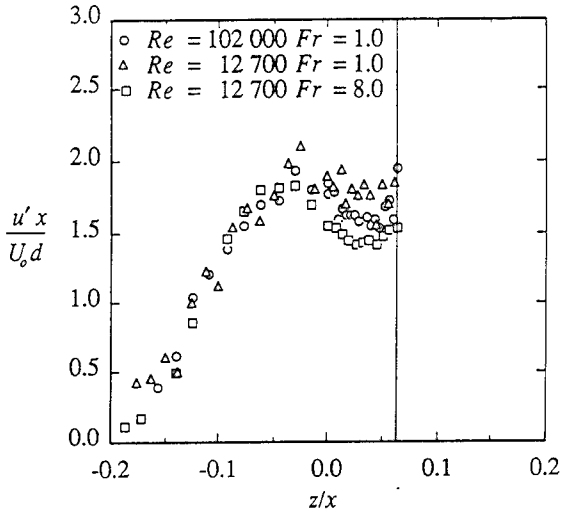

Figure 27 Vertical profiles of r.m.s. streamwise velocity u' at $x/d = 32$, $y/d = 0$.

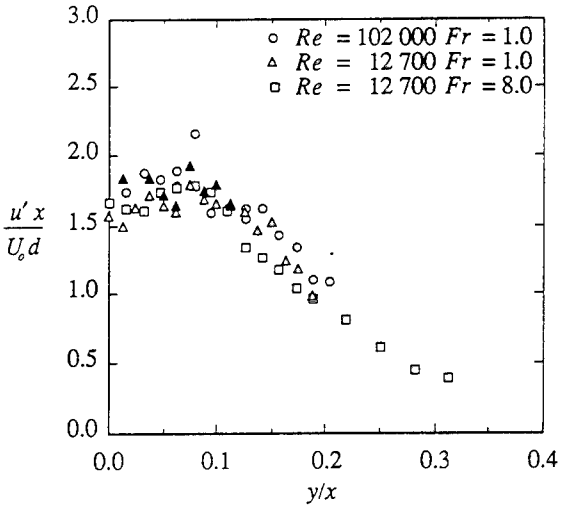

Figure 28 Horizontal profiles of r.m.s. streamwise velocity u' at $x/d = 32$, $z/d = 2$. Solid symbols are for $-y/x$.

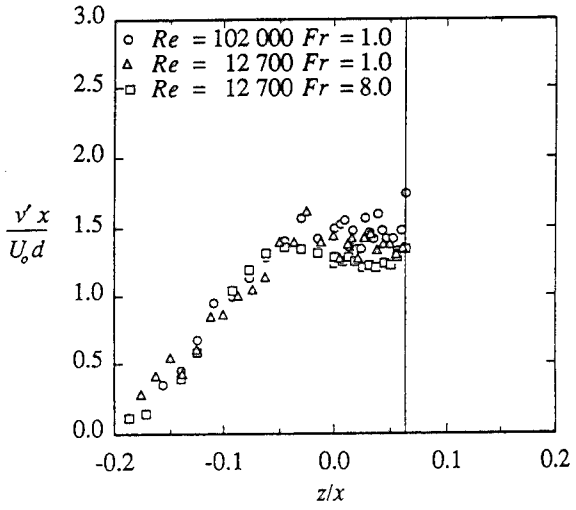

Figure 29 Vertical profiles of r.m.s. transverse velocity v' at $x/d = 32$, $y/d = 0$.

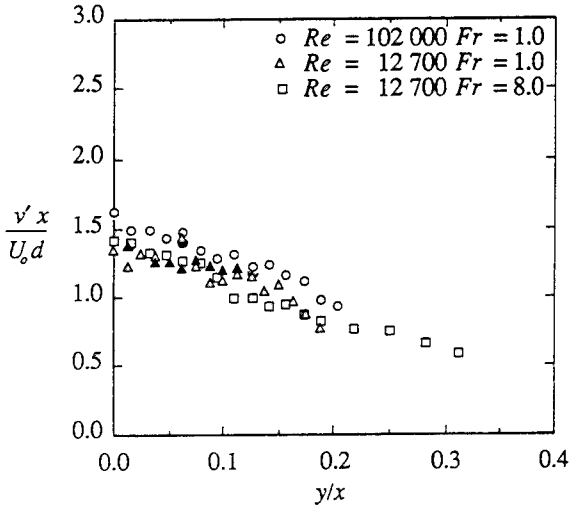

Figure 30 Horizontal profiles of r.m.s. transverse velocity v' at $x/d = 32$, $z/d = 2$. Solid symbols are for $-y/x$.

from $x/d = 16$. At $x/d = 32$ the anisotropy of the turbulence has remained unchanged for the high-Froude-number case relative to $x/d = 16$. This is due to the uniform rise in all r.m.s. velocity fluctuations, For both the low-Froude-number cases, the transverse and streamwise velocity fluctuations have increased a similar amount, but the vertical r.m.s. velocity has remained the same.This results in the increased anisotropy for these cases at $x/d = 32$ relative to $x/d = 16$.

Horizontal and vertical Reynolds shear stress profiles are shown in Figures 33 through 38 for $x/d = 32$. Figure 33 shows the vertical profile of the $\overline{uv}$ Reynolds stress. The results for the high-Reynolds-number case and the high-Froude-number case are near zero; however the results for the intermediate case are consistently negative. This is due to the slight misalignment of the jet

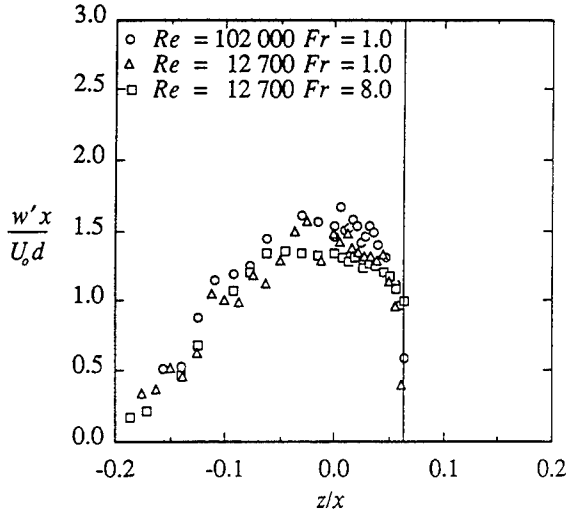

Figure 31 Vertical profiles of r.m.s. vertical velocity w' at $x/d = 32, y/d = 0$.

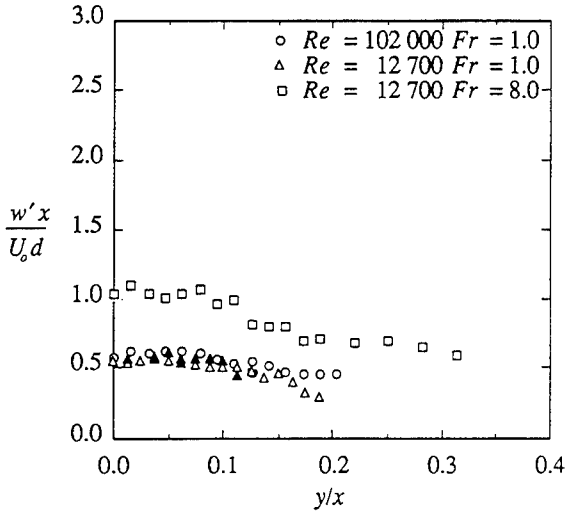

Figure 32 Horizontal profiles of r.m.s. vertical velocity w' at $x/d = 32, z/d = 2$. Solid symbols are for $-y/x$.

symmetry plane noted earlier. In the horizontal profiles of $\overline{uv}$, shown in Figure 34, it appears that the high-Reynolds-number results are consistently higher than the high-Froude-number case. There is considerable variation in the results from the intermediate case but they appear to be in agreement with the high-Froude-number results for $y/x < 0.1$ and approach the high-Reynolds-number results for $y/x > 0.1$. The peak level of $\overline{uv}$ in the horizontal profiles for the two low-Reynolds-number cases is comparable to the results for $x/d = 16$. This indicates that there has been a relative increase in $\overline{uv}$ for the high-Reynolds-number case. This would be expected due to the slightly higher level of v' for this case.

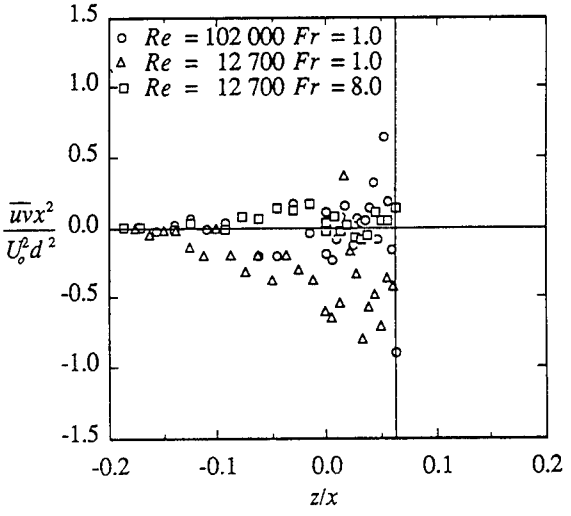

Figure 33 Vertical profiles of $\overline{uv}$ Reynolds stress at $x/d = 32, y/d = 0$.

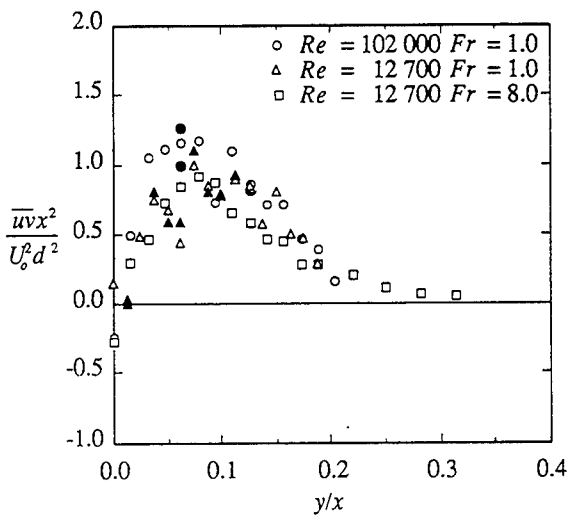

Figure 34 Horizontal profiles of $\overline{uv}$ Reynolds stress at $x/d = 32, z/d = 2$. Solid symbols are $-\overline{uv}$ for $-y/x$.

The "scatter" in the $\overline{uv}$ profile for the intermediate case shown in Figure 34 is probably not "bad data" or "random noise". If one examines the $\overline{U}$ velocity profile for this flow shown in Figure 22, it is clear that the profile exhibits several local maxima. The locations of these maxima correlate roughly with the locations of local minima in the $\overline{uv}$ profile. Further, the location of the high-mean-shear regions in Figure 22 correlate roughly with the local peaks in $\overline{uv}$. It is clear that the profiles are not dense enough to resolve the details of this phenomenon, but the results appear to be internally consistent. Similar variations in the $\overline{U}$ and $\overline{uv}$ profiles also occur in the other low-Froude-number case;

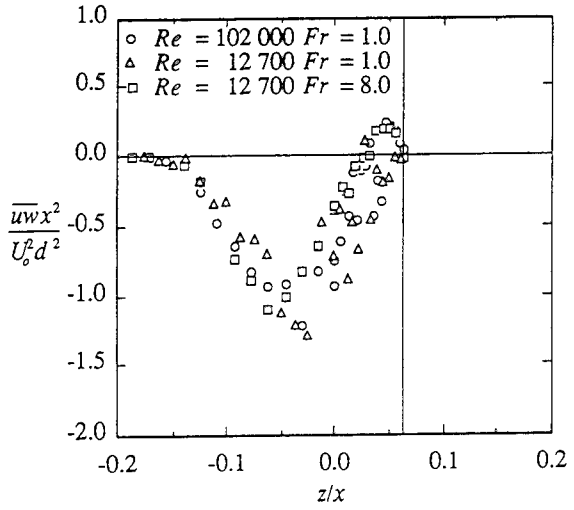

Figure 35 Vertical profiles of $\overline{uw}$ Reynolds stress at $x/d = 32$, $y/d = 0$.

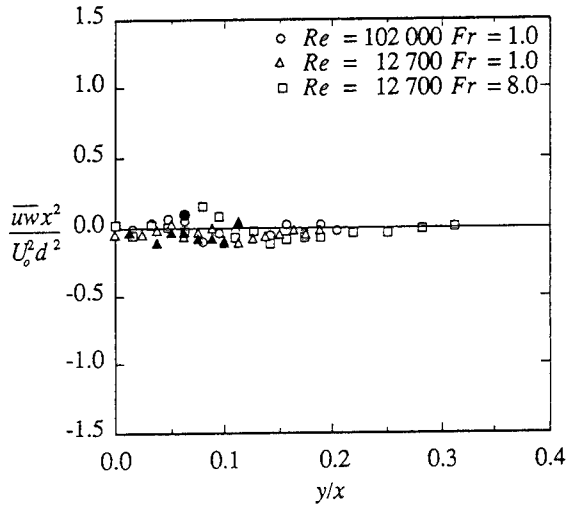

Figure 36 Horizontal profiles of $\overline{uw}$ Reynolds stress at $x/d = 32$, $z/d = 2$. Solid symbols are for $-y/x$.

however, they are less pronounced. In contrast, the results for the high-Froude-number case are smooth and monotonic. The variations seen in the low-Froude-number cases may result from reconnection to the free surface of the vorticity associated with the large-scale structures in the jet as visualized by Walker, *et al.* (1991). The differences between the high- and low-Froude-number cases may result from the pronounced wave making seen in the high-Froude-number case by Walker, *et al.*. and Anthony & Willmarth (1992).

Vertical profiles of $\overline{uw}$, shown in Figure 35 exhibit the same similarities between the two low-Froude-number cases which were evident in the profiles at $x/d = 16$. Similar differences between the low- and high-Froude number cases are also present. These differences reflect generally the differences in the mean velocity profiles

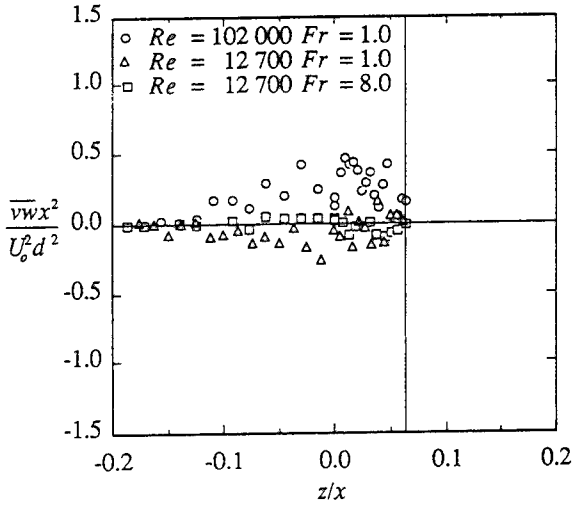

Figure 37 Vertical profiles of $\overline{vw}$ Reynolds stress at $x/d = 32$, $y/d = 0$.

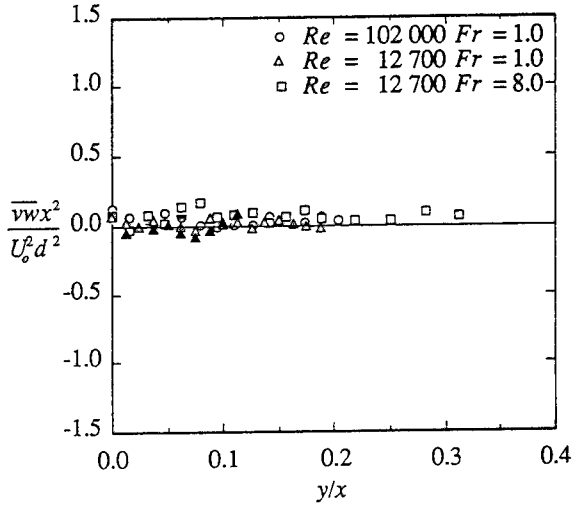

Figure 38 Horizontal profiles of $\overline{vw}$ Reynolds stress at $x/d = 32$, $z/d = 2$. Solid symbols are $-\overline{vw}$ for $-y/x$.

where for the two low-Froude-number cases the maximum velocity has shifted nearer the surface. Horizontal profiles of $\overline{uw}$ are essentially zero, as would be expected, and profiles of $\overline{vw}$ shown in Figures 37 and 38 are, as expected, also near zero.

SUMMARY AND CONCLUSIONS

This study examined the effects of the main parameters, Froude number and Reynolds number on the structure of turbulence in near-surface turbulent jets. Measurements of all six Reynolds stresses as well as the three mean velocity components were obtained using a three-component laser velocimeter. The study examined

two jet flows: $Re = 12\,700$ with $Fr = 1.0$ and $Re = 102\,000$ with $Fr = 1.0$. These results are combined with those of Anthony & Willmarth (1992) for $Re = 12\,700$ and $Fr = 8.0$. This combined set of results allows a comprehensive evaluation of the effects of these parameters over a meaningful range. The measurements were confined to vertical profiles on the jet axis and horizontal profiles at the free surface for two streamwise locations $x/d = 16$ and 32.

Examination of the mean velocity profiles shows that the two low-Froude-number jets appear to evolve more quickly than the other case. As a result the maximum $\overline{U}$ velocity decreases more quickly, and the location of this maximum moves toward the surface more quickly. Horizontal profiles of $\overline{U}$ at $x/d = 32$ are smooth for the high-Froude-number case, but exhibit spatial variations for the low-Froude-number cases. The variations are most pronounced in the intermediate case, and probably result from the large-scale vortical structure of the jet attaching to the free surface. This would result in significant coherent vorticity oriented normal to the free surface. The fact that the spatial fluctuations are less pronounced in the high-Reynolds-number case may be due to the increased amount of small-scale vorticity present in this flow acting to smooth out the velocity variations. In the high-Froude-number case, the large free-surface deformations may change the way in which the large-scale structure interacts with the free surface, or at least "randomize" the location of the interactions in such a way at to yield a smooth velocity profile.

At $x/d = 32$, the intermediate case exhibits the highest $\overline{U}$ velocity, overall. It is followed by the high-Reynolds-number case, while the high-Froude-number case has the lowest velocity. At $x/d = 16$ the transverse velocity $\overline{V}$ is the same for the two low-Froude-number cases. Of the two low-Froude-number results, the high-Reynolds-number case exhibits the largest $\overline{V}$ at $x/d = 32$. At this location the high-Froude-number case has the lowest $\overline{V}$. Hence, for the two low-Froude-number cases, the vertical $\overline{U}$ and $\overline{W}$ velocity profiles are similar for $x/d = 32$, and the differences in the horizontal $\overline{U}$ profiles are accounted for by the differences in the $\overline{V}$ profiles. It is not clear at this time why this difference exists but it is most likely a Reynolds-number effect.

In all the results, the turbulence became more anisotropic at the free surface; the horizontal and streamwise velocity fluctuations were increased and the vertical velocity fluctuation levels were decreased due to the presence of the free surface. Initially, the two low-Froude-number cases exhibited a greater degree of anisotropy, due to higher u' and v' levels, and lower w', than the high-Froude-number case. For all the cases, u' and v', as normalized here, increased with streamwise distance. For the high-Froude-number case w' increased a similar amount and so, the anisotropy for that case was similar at both streamwise locations. For the low Froude number cases, w' was roughly the same at both locations. Hence due to the increase in u' and v', the degree of anisotropy near the free surface increased significantly for the low-Froude-number cases at the downstream location. This behavior indicates that the effects of the free-surface on the turbulent velocity fluctuations is much stronger at low Froude number, causing more energy to be transferred from the vertical velocity fluctuations to those tangent to the surface.

At both streamwise locations, the vertical profiles of the $\overline{uw}$ Reynolds stress reflect the differences in the mean velocity profiles for the different values of Froude number. Horizontal profiles of the $\overline{uv}$ Reynolds stress show that the maximum values of this stress are obtained for the high-Reynolds-number flow, while the lowest are for the high-Froude-number case. This is reflective of the relative values of $\overline{V}$ at the surface (i.e., the spreading rate) for the different flows. For the intermediate case, local maxima in the Reynolds stress profile appear to correlate with the high-mean-shear regions in the mean velocity profile—further evidence that the fluctuations in the mean velocity profiles are due to coherent vortices connected to the free surface. The larger $\overline{uv}$ values for the two low-Froude-number flows is probably related to the vorticity connected to the free-surface. The observation of the highest levels of $\overline{uv}$ in the high-Reynolds-number case is, most likely, due to the increased amount of small-scale vorticity connected to the free-surface (seen in the visualizations of Walker, *et al.* (1991). The low levels of $\overline{uv}$ in the high-Froude-number case may be due to the large free-surface deformations inhibiting vortex reconnection to some degree, or some other form of wave-vorticity interaction.

ACKNOWLEDGEMENT

This work was supported by the University Research Initiative/Program in Ship Hydrodynamics sponsored by the Office of Naval Research under contract number N00014-86-K-0684.

REFERENCES

Anthony, D.G. & Willmarth, W.W. 1992 Turbulence measurements in a round jet near a free surface. *J. Fluid Mech.* (in press).

Anthony, D.G. 1990 *The influence of a free surface on the development of turbulence in a submerged jet.* PhD Thesis, University of Michigan.

Bernal, L.P. & Madnia, K. 1988 Interaction of a turbulent round jet with the free surface. *Proc. 17th Symposium on Naval Hydrodynamics.* National Research Council, Washington, D.C.

Bradshaw, P. 1978 *Topics in Applied Physics Vol. 12—Turbulence, 2nd Edition.* Springer-Verlag, Berlin.

Hinze, J.O. 1978 *Turbulence, 2nd Edition.* Mcgraw-Hill, New York.

McLaughlin, D.K. & Tiederman, W.G. 1973 Biasing correction for individual realization laser anemometer measurements in turbulent flow. *Phys. Fluids* **16**, 2082-2088.

Munk, W.H., Scully-Power, P., & Zachariasen, F. 1987 Ship wakes from space: The Bakerian Lecture, 1986. *Proc. Royal Soc. London A* **412**, 231-254.

Swean, T.F., Ramberg, S.E., Plesnia, M.W. & Stewart, M.B. 1989 Turbulent surface jet in a channel of limited depth. *J. Hydraulic Eng.* **115**, 1587-1606.

Sterling, M.H., Gorman, M., Widmann, P.J., Coffman, S.C., Strozier,J. & Kiehn, R.M. 1987..Why are these disks dark? The optics of Rankine vortices. *Phys. Fluids*, **30**, 3624-3626.

Walker, D.T. & V.G. Johnston 1991 Observations of turbulence near the free surface in the wake of a model ship. In: *Dynamics of Bubbles and Vortices Near a Free Surface AMD -119*. I. Sahin & G. Tryggvason, eds., ASME, New York.

Walker, D.T., Willmarth, W.W. & Anthony, D.G. 1991 Observations of the interaction of turbulent jets with a free surface. *Bull. Amer. Phys. Soc.* **36**, 2680.

Willmarth, W.W. 1987 Design of a three component fiber optic laser Doppler anemometer for wake measurements in a towing tank. *Proc. Int'l Towing Tank Conf.*, ITTC, Tokyo.

Wygnanski, I. & Fiedler, H. 1969 Some measurements in the self-preserving jet. *J. Fluid Mech.* **38**, 577-612.

Wave-Wake Interactions About a Body of Revolution Advancing Beneath the Free Surface

J.-C. Park, H. Miyata, Y. Tsuchiya, M. Kanai
(University of Tokyo, Japan)

ABSTRACT

Forces and flow phenomena about a body of revolution are studied both experimentally and numerically. The revolutional body is towed at Fn=0.11 to 0.44 with different depth of submergence. It is shown that the lift force varies with the Froude number in close connection with the variation of the drag force, which is attributable to the variation of the pressure distribution on the upper surface of the body. The interaction of the viscous flow with the wave motion is simulated by a finite-difference method in the framework of an inflexible rectangular coordinate system. Some interesting features of the vortices about the revolutional body are revealed in both cases of straight and oblique flows.

1. INTRODUCTION

A cylindrical body is often used as an important component of offshore structures and ships. Significant number of the oil-drilling platforms are supported by a pair of lower hulls, SWATH ships are supported by a pair of submerged bodies of revolution and the submarines have the most typical configuration of revolution.

In order to design the optimal configuration of the cylindrical body the hydrodynamical forces should be satisfactorily clarified. Not only the drag force but also other forces and moments are important for the dynamic properties of the system. When it is operated in the vicinity of the free-surface the forces and moments show some nonlinear behaviors.

Physical experiments of measuring the forces at an experimental tank is very useful to grasp the hydrodynamical properties of the system. However, the understanding of the physical phenomena, that is, fluid-motions which cause the forces and moments, is more important, since it gives more substantial informations. The sound understanding of the physical phenomena that connect body configuration with the forces and moments seems to be most important for the designers of hydrodynamical systems. The most significant physical phenomena are free-surface waves and viscous flows about a body of revolution moving beneath the free-surface. In case the body does not pierce the free-surface the wave motion may be of the linear system, but in case it interacts with the viscous flow or in case it makes steep slopes nonlinear features become important. The viscous flow which dominates the flow about the aftpart of the body is intrinsically nonlinear.

For the elucidation of the nonlinear fluid motions both experimental and numerical investigations are effective and analytical ones may be of limited usefulness. Proper use of these investigations seems to provide satisfactory knowledge necessary for the understanding of the nonlinear mechanism of fluid motions. The numerical and physical experiments are very advantageous for the qualitative understanding of the structure of vortices. By the recent advances of the technology of computational fluid dynamics the nonlinear features of viscous flow are going to be clarified in details.

Two kinds of CFD techniques have been developed at the authors' laboratory in the past 10 years. One is the TUMMAC method that employs the inflexible rectangular coordinate

system and the other is the WISDAM method that employs the boundary-fitted, curvilinear coordinate system. Both methods solve the Navier-Stokes equation by the time-marching procedure with finite-difference and finite-volume discretization, respectively. The WISDAM method is suitable for the simulation of the complicated viscous flow in the boundary layer and in the separated flow about a smooth body surface [1]~[3] and the TUMMAC method is suitable for a body of extreme complexity and for a free-surface motion with extreme nonlineality [4]~[8].

In this paper the waves and viscous flow about a body of revolution are studied. The complicated vortex shedding mechanism is explained with the simulation results by the WISDAM-V method in Section 2. The experimental study of forces is described in Section 3 for the body set in the vicinity of the free-surface. The new CFD technique based on the TUMMAC-VII code is described in Section 4 for the present condition of a body of revolution moving beneath the free-surface. The numerical simulations are presented in Sections 5 and 6 for two cases of the body in steady straight course and steady oblique course. Brief concluding remarks are mentioned in Section 7.

2. 3D STRUCTURE OF SEPARATED FLOW IN AN INFINITE FLUID REGION

Experimental and computational studies are performed for the elucidation of the 3D structure of the separated flow past a body of revolution in an infinite fluid region. A body of simple configuration as shown in Fig.1 is chosen so that the results can be extended to various engineering problems concerning 3D separated flows. The forebody has a smooth parabolic profile, so that no separation would take place at this part of the body. Its length is 283 mm and the cylindrical middle section is an acrylic tube of 540 mm in length and 160 mm in diameter. Drag measurements were conducted with this model having various afterbodies of straight conical profile of different semi-apex angles.

The measured drag coefficients are shown in Fig.2. It suddenly increases when the semi-apex angle (β) of the conical afterbody increases from 20° to 24° and then the doubly increased coefficient is kept at the constant value when the semi-apex angle increases up to 60° . The critical geometry of a revolutional body with a conical afterbody advancing parallel to its axis is present when β is in between 20° and 24° . This does not seem to be dependent on the Reynolds number.

For the case of 30° semi-apex angle a numerical simulation was performed by the WISDAM-V method in a curvilinear coordinate system shown in Fig.3. The so-called O-type grids are used for the transverse sections of the computational domain and the so-called H-type grids for the horizontal planes. The first grid point is located so close to the body surface that the spacing in the lateral direction is about 5×10^{-5} ,while length is made dimensionless with respect to the length of the main part of the body which is 832 mm. Since the simulation is performed at the Reynolds number 1×10^6 , this distance corresponds to 2 to 3 viscous units, which implies that the first grid points are located inside the viscous sublayer. This is important for the present method without using the wall-function in the boundary layer.

Equi-pressure surfaces in the vicinity of the afterbody are shown in Fig.4 at various time levels. Since the iso-surfaces of the negative pressure on the afterbody are intimately related with those of vorticity, the variation of the iso-pressure surface is supposed to be caused mostly by vortex shedding. The prominent structure of the vortices is made of ring-shaped vortices followed by longitudinal ones which are horseshoe-shaped or spindle-shaped. A longitudinal vortex tube usually makes a pair with another one of opposite sense of rotation. It is noted that the longitudinal vortices are generated inside of the ring vortices in the vicinity of the body surface. It is supposed that the ring vortices made of the spanwise components of vorticity is deformed or splitted on the way to dissipation. Such mechanism of vortex shedding seems to have some common features with the cases of bodies with similar configuration.

3. FORCES AND PRESSURE DISTRIBUTION

The experimental set-up for the measurement of drag and lift is shown in Fig. 5. The diameter of the tested body is denoted D and the clearance between the top surface of the body and the free-surface is h. Since the tested body is supported by a sword, the forces exerted on it are extracted in the measurement.

The cylindrical body with the afterbody of 20° semi-apex angle is chosen for the study of

the wave-wake interaction problem. The Froude number based on the length of the body is varied from 0.11 to 0.44. Due to the restriction of the experimental set-up the parameter of submergence (h/D) is varied from 0.25 to 1.00. Therefore the free-surface effect is still present on the condition of the deepest submergence.

The variation of lift coefficient is summarized in Fig.6, in which the lift coefficient is made dimensionless with respect to the horizontal projected area. The overall tendency of lift coefficient is to increase abruptly with the decrease of submergence and to increase with the increase of Froude number. However, the latter increase is not monotonous and the smallest value is recorded at the highest Froude number. The variation of drag and lift coefficients versus Froude number is shown in Fig.7, in which the coefficients are made dimensionless with respect to the surface area of the body.

The variation is very wavy due to the wave resistance especially when the body is shallowly submerged. It is noted that the phase of lift variation is quite contrary to that of drag for almost all cases. It is presumably due to the fact that the high wave drag is caused by the small wave elevation on the afterbody, which causes relatively smaller angle of upward flow resulting in the small lift force.

Pressure distribution is measured at Fn = 0.44 on three longitudinal lines, that is, two on the vertical plane that includes the axis of the body (one $\theta = 0°$ on the top surface, the other $\theta = 180°$ on the bottom surface) and one on the horizontal surface that includes the axis of the body ($\theta = 90°$ on the side surface). The results are compared in Fig.8. As is naturally anticipated the variation of the pressure due to the difference of the depth of submergence is most noticeable on the upper surface of the body. The quite particular distribution on the upper surface at h/D=0.25 is attributable to the breaking phenomenon of the waves above the afterbody.

The measured wave contours are shown in Fig.9 for three degrees of submergence. The wave height is made dimensionless with respect to the water head of the uniform stream at the advance speed. While the Froude number based on the length of the body is set at 0.44, the wave formation varies with the depth of submergence. In the shallowest case the waves on the afterbody are broken and the wave formation shows more complicated features involving unsteady variation.

4. COMPUTATIONAL METHOD TUMMAC-VII

4.1 Grid System

A rectangular staggered mesh system is employed, as shown in Fig.10. Since the degree of accuracy is less higher than the curvilinear, boundary-fitted coordinate system for the implementation of the body boundary conditions, resolution of the physical phenomena in the vicinity of the body surface is not very satisfactory. However, this system has the advantage of high adaptability and robustness. Furthermore, the elaborate efforts of grid generation are almost entirely eliminated, which is most important for engineering applications. The equally-spaced grid system gives better resolution in the far-field than the boundary-fitted coordinate system, which provides coarser grid spacing there for the resolution of separated flow far behind a body. As described in the subsequent sections, most of the efforts are focused on the treatment in the body boundary cells.

4.2 Computational Procedure

The governing equations are the continuity equation and the Navier-Stokes equation, as follows.

$$\partial_i u^i = 0, \tag{1}$$

$$\partial_t u^i = -\partial_j P + a^i . \tag{2}$$

Here, ∂_i denotes space-differencing in the x_i direction, ∂_t time-differencing, P the pressure divided by the density of water, and the last term a^i is written as

$$a^i = - u^j \partial_j u^i + (Re^{-1} + \nu_s)\, \partial_j \partial_j u^i + M^i + \partial_j \nu_s (\partial_j u^i + \partial_i u^j) + f^i$$

where, ν_s is the eddy viscosity of the subgrid-scale (SGS) turbulence model, M^i is the controllable numerical dissipation introduced to stabilize the solution [9], and f^i is the external force including the gravity force.

The algorithm of the computation is same with the previous TUMMAC method [4, 5, 6, 8]. Updating of the velocity field is made after

updating the pressure field by solving the Poisson equation, and this cycle is repeated in a time-marching procedure. However, in the region composed of B-cells the following simultaneous iterative method is used, because it is very suitable for the implementation of the zero-divergence condition in the body boundary-cells.

$$P^{m+1} = P^m + \frac{\omega}{A} D \quad , \tag{3}$$

$$A = \Delta t + \left[\frac{\gamma_{i+1} + \gamma_{i-1}}{(\Delta x_1)^2} + \frac{\gamma_{j+1} + \gamma_{j-1}}{(\Delta y)^2} + \frac{\gamma_{k+1} + \gamma_{k-1}}{(\Delta z)^2} \right], \tag{4}$$

where, ω is the relaxation factor, D is the divergence of a cell and γ is the volume porosity defined in the subsequent section. The velocity field is updated by the following equation

$$u^{i\,(n+1)} = u^{i\,(n)} + \Delta t \left(- \partial_j P + a^i \right). \tag{5}$$

4.3 Body-Boundary Conditions

In order to represent the complicated configuration of a 3D body two kinds of porosity are introduced, i.e., volume-porosity (γ) and surface-porosity (β) [8], the ratio of the fluid portion of each boundary cell to the total volume and that of surface area, respectively. Since the location of the body-boundary is approximately represented by these scalar values, they are used not only for the flagging of cells and for the drawing of the body configuration but also for the flux and divergence calculations as well as the choice of differencing scheme.

The boundary-cell (B-cell) is defined as a cell in which volume-porosity is greater than 0.5 but less than 1.0. A cell of which volume-porosity is less than 0.5 is defined as an empty cell (E-cell), where the pressure is not computed. A full-of-fluid cell (F-cell) facing an E-cell is defined as a special B-cell (B*-cell) with the porosity of 1.0. The choice of computational method for the pressure from Eq. (5) or (6) is determined by this flagging.

The velocity point located at the center of each surface of a cell is assumed to be present if the surface-porosity is greater than 0.5. The choice of the differencing scheme is also dependent on the surface-porosity. The velocity on a cell surface for which surface-porosity is unity is normally calculated by the momentum equation (5), while that on a cell surface for which surface is greater than 0.5 but less than 1.0 is extrapolated from the neighboring velocities u^{i*} in Eq. (6) (see Fig.11).

$$u^{i*} = \frac{\sum \beta^k u^k}{\sum \beta^k} \quad , \tag{6}$$

where, the velocities u^k are not themselves extrapolated and the surface-porosity β^k of the cell where neighboring velocities are suitable is used as a weighting function. The extrapolated velocity $u^{i\#}$ is calculated by a quadratic equation (7),

$$u^{i\#} = u^{i*} \sqrt{\frac{(\beta^i - 0.5)}{(\beta^i + 0.5)}} \quad . \tag{7}$$

Therefore, the extrapolation is made approximately in the direction normal to the body.

4.4 Free-Surface Condition

This condition is the same with that of the previous TUMMAC-IV method [4] [5]. For the fulfillment of the free-surface condition, the dynamic and kinematic conditions are given as

$$P = P_0 = 0 \qquad \text{on } z = h, \tag{8}$$

$$\partial_t F + u^j \partial_j F = 0 \qquad \text{on } z = h, \tag{9}$$

where $F(x^i,t)$ is the equation of free-surface and P_0 is the atmospheric pressure divided by the density of water.

The dynamic condition expressed by Eq. (8) is implemented by the irregular-stars technique by Chan & Street [10] in the procedure of pressure computation and the kinetic condition expressed by Eq. (9) is fulfilled by the Lagrangian movement of marker particles on the free-surface.

5. NUMERICAL SIMULATION(I)
- STRAIGHT COURSE AT Fn = 0.44 -

The condition of computation is listed in Table 1. The computational domain is 1.80 m × 0.48 m × 0.59 m, the degree of submergence h/D is 0.5 and the Froude number based on the body length is 0.44.

The simulated results of overall flow-field are shown in Fig.12 and the details are presented in Fig.14 on the cross-sectional planes at the longitudinal location shown in Fig.13. In all figures it is clearly observed that the flow due to the waves on the free-surface is closely related with the viscous flow about the body. Fig.12 indicates that the wake on the afterbody is attracted upward and that the pressure field is very complicated in the region between body and free-surface. The wake contours are not of the form of circle but it is deformed and the contours of vorticity about the axis of the longitudinal coordinate show complicated features of vortex shedding. Some pairs of longitudinal vortices with counterrotating components are formed behind the revolutional body. However, due to the inadequate degree of accuracy and due to the predominant pressure field by the waves the separated vortices give only very gentle influences on the pressure field.

6. NUMERICAL SIMULATION (II)
- OBLIQUE COURSE AT Fn = 0.11 -

By giving horizontal velocity component at the inflow boundary the oblique flow is generated. The flow field is simulated when the oblique flow angle β is 10° at Fn=0.11 and the results are shown in Figs.15 to 17. The depth of submergence is same with the previous case.

The pressure field is seriously influenced by the presence of the free-surface even at this low Froude number as shown in Fig.16. The structure of the longitudinal vortex component seems to be extremely complicated as observed in Fig.17. A pair of longitudinal vortex tubes which is predominant on the face surface of the forepart of the body is abruptly decomposed and partly connected with another pair of longitudinal vortices on the back surface of the aftpart of the body. The latter pair of vortices are shed far downstream.

The structure of longitudinal vortices is compared between the cases of straight and oblique flows with equi-vorticity surface drawings. One of the typical features of the complicated flow phenomenon is visualized by the numerical simulation. The sound understanding of the complicated structure and mechanism of the flow in addition to the estimation of forces and moments will be of significant importance for the design of a body moving beneath the free-surface.

7. CONCLUSIONS

One of the most complicated fluid phenomenon of wave-wake interaction is studied for the case of a body of revolution advancing beneath the free-surface. It is demonstrated that the nonlinear forces are caused by the variation of pressure distribution mostly on the upper surface of the aft-part of the body and that this is partly due to the deformation of the wake by the presence of the free-surface. Although the degree of accuracy of the present CFD technique is not satisfactory, the large-scale vortical motions under the influences of the free-surface or of the oblique flow are qualitatively well simulated. The numerical simulations seem to be very useful for the understanding of the fluid mechanics which cause nonlinear forces on a moving body.

REFERENCES

1. H. Miyata, T. Sato and N. Baba, "Difference Solution of a Viscous Flow with Free-Surface Wave about an Advancing Ship", J. Comput. Phys, vol. 72, no. 2, 1987.

2. H. Miyata, M. Zhu and O. Watanabe, "Numerical Study on a Viscous Flow with Free-Surface Waves about a Ship in Steady Straight Course by a Finite-Volume Method", J. Ship Research, to appear.

3. H. Miyata and N. Ogawa, "3D Vortical Flow Past Bodies of Revolution with Conical After bodies", J. Numerical Methods in Fluids (submitted), 1991.

4. H. Miyata and S. Nishimura, "Finite Difference Simulation of Nonlinear Ship Waves", J. Fluid Mech., vol. 157, 1985.

5. H. Miyata, S. Nishimura and A. Masuko,"Finite Difference Simulation of Nonlinear Waves Generated by Ships of Arbitrary Threemsional Configuration", J. Comput Phys, vol. 60, No. 3, 1985.

6. H. Miyata, "Finite-Difference Simulation of Breaking Waves", J. Comput. Phys. , vol. 65, No.1, 1986.

7. H. Miyata, M. Katsumata, Y. G. Lee and H. Kajitani, "A Finite-Difference Simulation Method for Strongly Interacting Two-Layer

Flow", J. Soc. Naval Archit. , Japan, vol. 163, June 1988.

8 H. Miyata and Y. Yamada, "A Finite-Difference Method for 3D Flows About Bodies of Complex Geometry in Rectangular Coordinate Systems", J. Numerical Methods in Fluids, (to appear in 1992).

9. N. Baba and H. Miyata, "Effect of the Form of Navier-Stokes Equation on Large-scale Vortex Dynamics", Proc. 1st Symposium on Numerical Fluid Dynamics, Chuo-University, Tokyo, 1987.

10. R. K. -C. Chan and R. L. Street, "A Computer Study of Finite-Amplitude Water Waves", J. Comput. Phys. vol. 6, 1970.

Table1 Condition of computation for the case of straight course.

Number of used cell	101 × 49 × 59 = 291,991
Cell size	$\Delta x = 0.018\ m$, $\Delta y = 0.01\ m$ $\Delta z = 0.01 \sim 0.030\ m$
Reynolds number (*L-base*)	1.26×10^6
Froude number (*L-base*)	0.44 ($u = 1.4\ m/s$)
Time increment T^*	2.8×10^{-4}
Time for Acceleration	1.0 (2600 *step*)
Total Time	2.0 (5200 *step*)
CPU Time (TITAN - III)	*about 160 hours*

Table2 Condition of computation for the case of oblique course.

Number of used cell	91 × 46 × 34 = 142,324
Cell size	$\Delta x = 0.026\ m$, $\Delta y = 0.016\ m$ $\Delta z = 0.016 \sim 0.048\ m$
Reynolds number (*L-base*)	3.67×10^5
Froude number (*L-base*)	0.11 ($u = 0.35\ m/s$)
Time increment T^*	1.73×10^{-3}
Time for Acceleration	0.5 (870 *step*)
Total Time	2.5 (4350 *step*)
CPU Time (RS - 3330)	*about 62 hours*

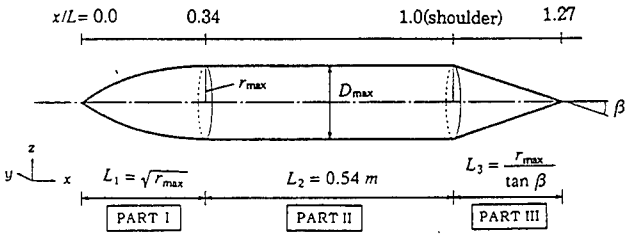

Fig. 1 Configuration of the tested body of revolution advancing to the left.

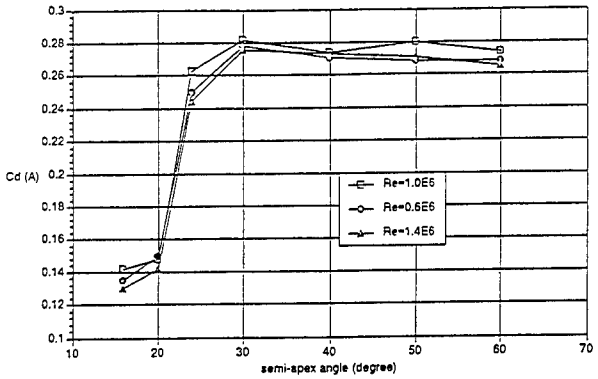

Fig. 2 Variation of drag coefficient at various semi-apex angles, Cd is made dimensionless with respect to the forward projected area.

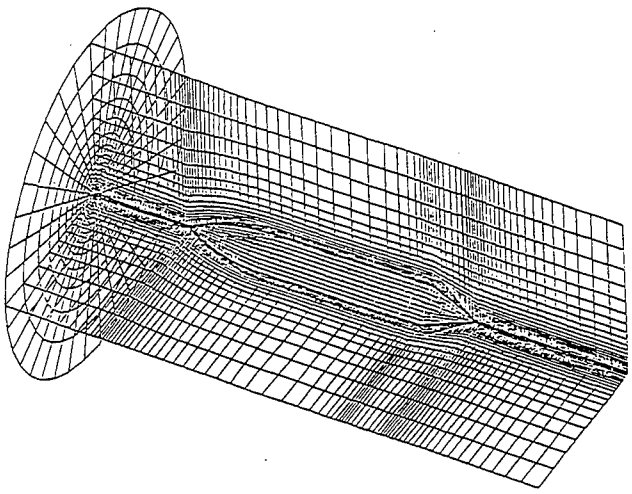

Fig. 3 Boundary-fitted grid system for the case of a flow in an infinite fluid domain.

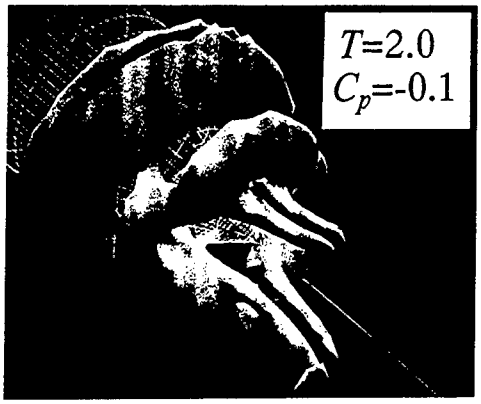

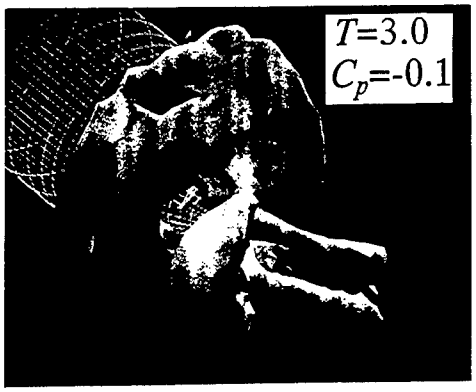

Fig. 4 Computer-graphics drawing of equi-pressure (Cp at - 0.10) surface at T = 1.7, 2.0 and 3.0 from above.

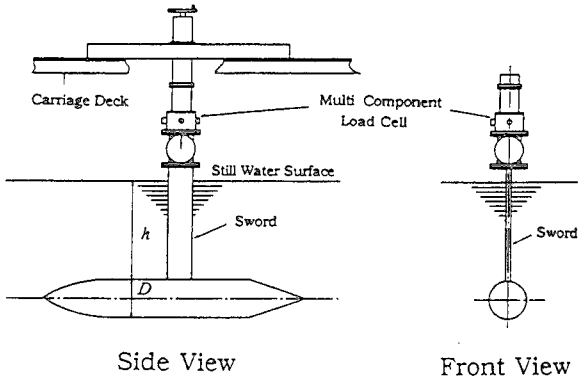

Fig. 5 Experimental set-up.

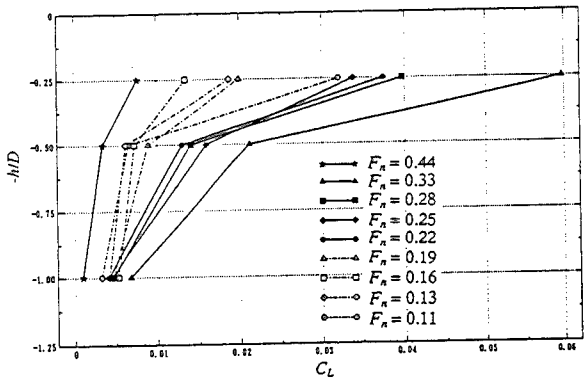

Fig. 6 Variation of lift coefficient at various depth of submergence and Froude numbers.

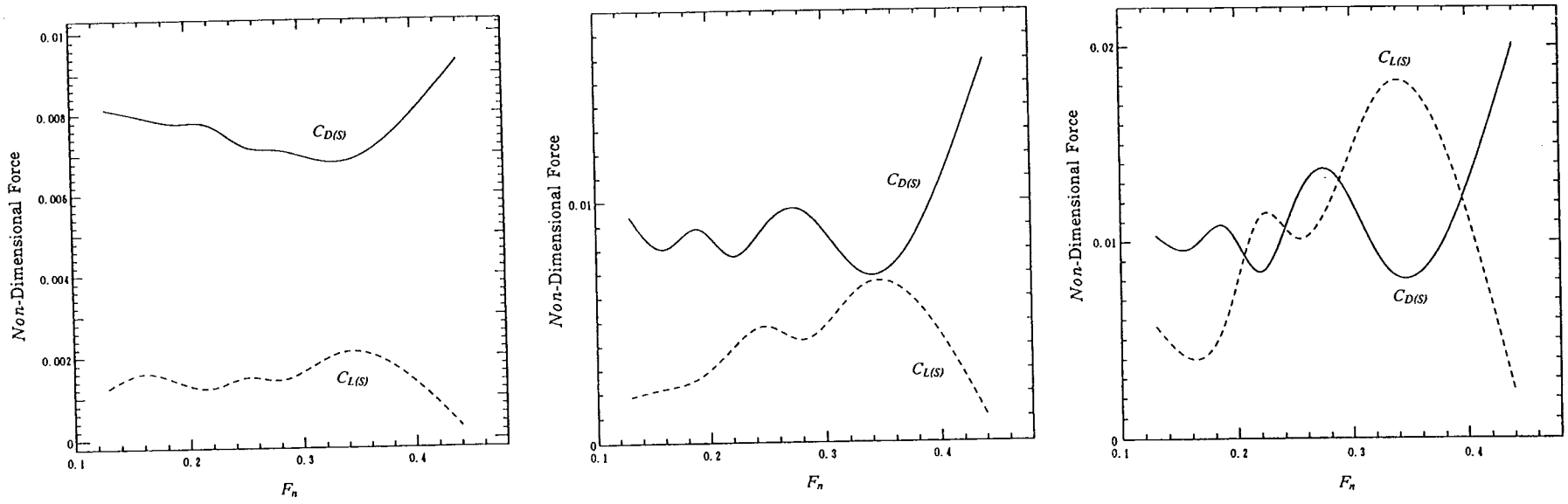

(a) $h/D = 1.0$ (b) $h/D = 0.5$ (c) $h/D = 0.25$

Fig. 7 Drag and lift variation at three shallowly-submerged conditions, the values are made dimensionless with respect to the surface area.

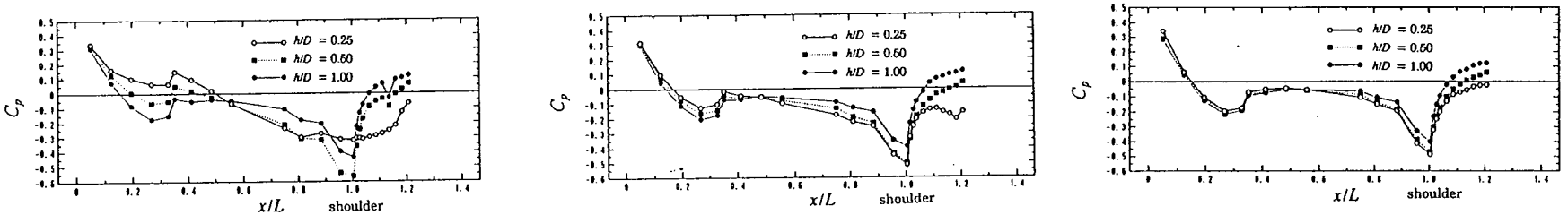

(a) upper (b) side (c) bottom

Fig. 8 Longitudinal distribution of pressure coefficient on the lines at $\theta = 0°$ (upper), 90° (side) and 180° (bottom), Fn = 0.44.

(a) $h/D = 1.0$

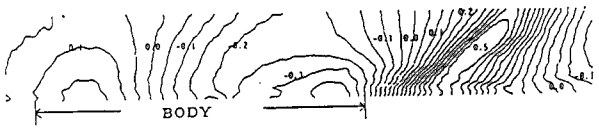

(b) $h/D = 0.5$

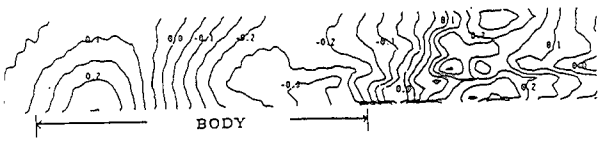

(c) $h/D = 0.25$

Fig. 9 Contours of waves generated by the body advancing at Fn = 0.44 at three degrees of submergence.

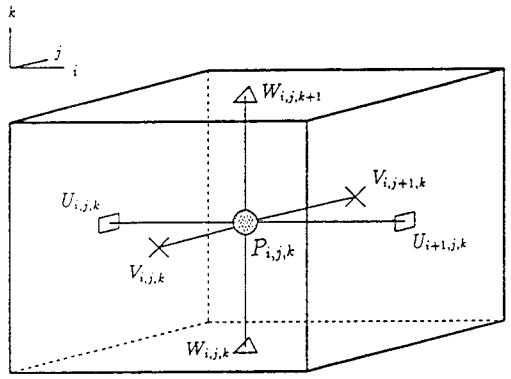

Fig. 10 The staggered grid system.

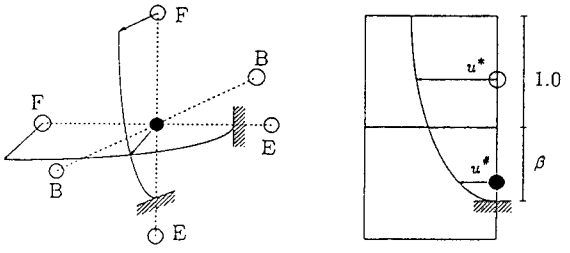

Fig. 11 Schematic sketch of velocity extrapolation on the body surface by use of the porosity technique.

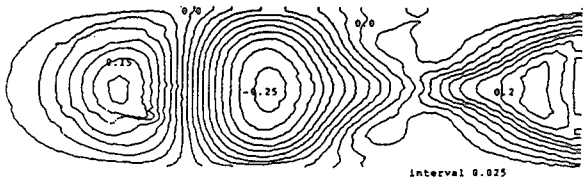

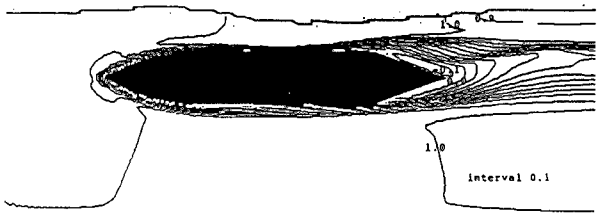

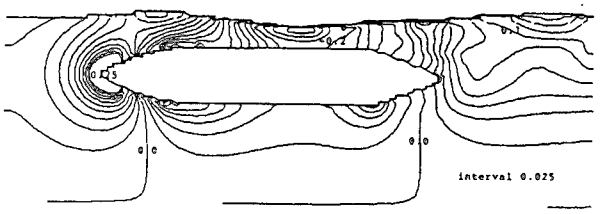

Fig. 12 Computed contours of wave, longitudinal velocity component and pressure coefficient, the latter two are or the centerplane, Fn = 0.44.

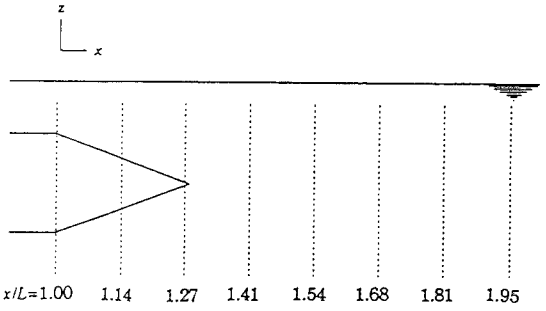

Fig. 13 Schematic sketch for the longitudinal location of cross-sectional planes.

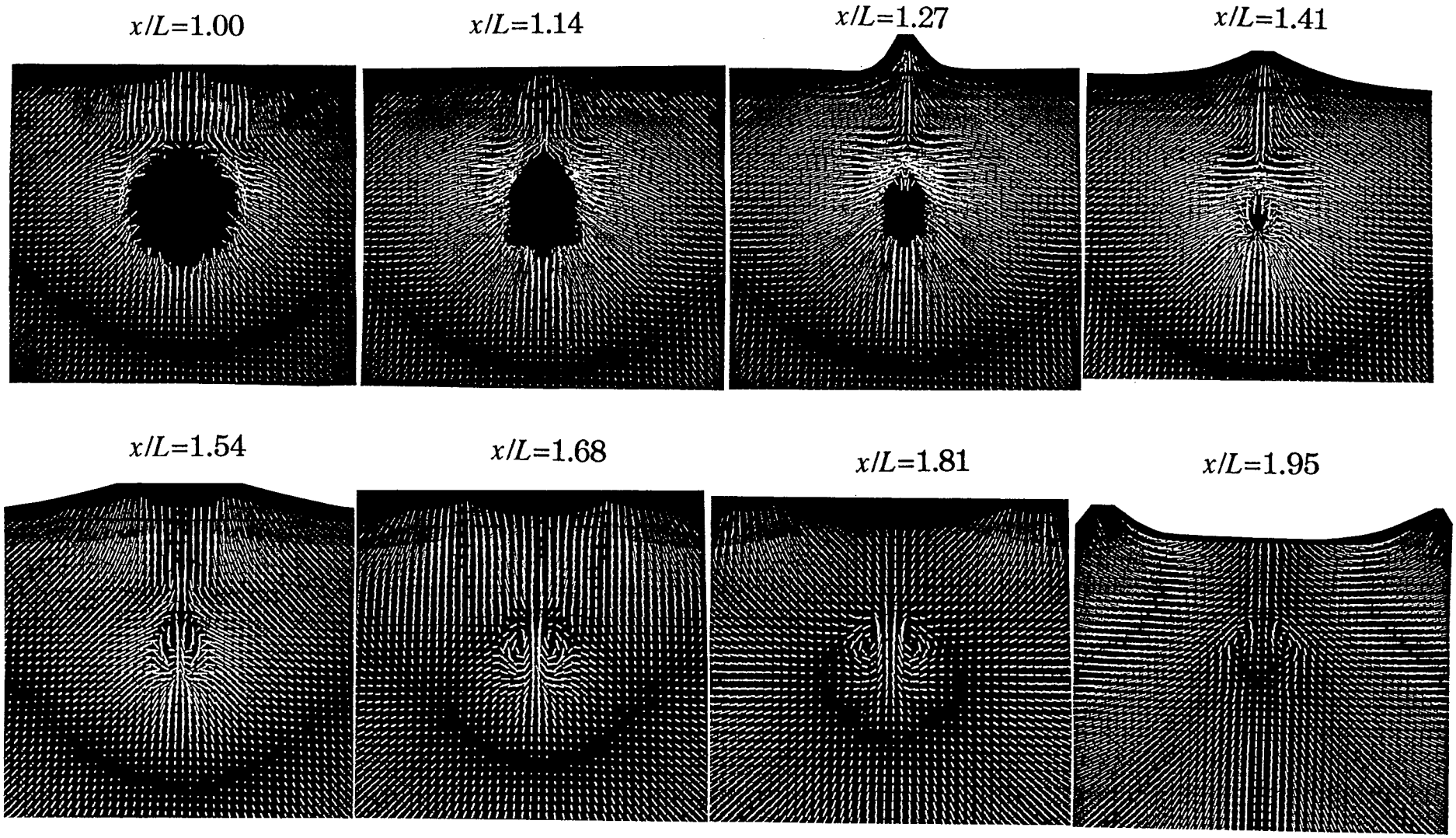

Fig. 14(a) Simulated velocity vector fields on the cross-sectional planes at Fn = 0.44.

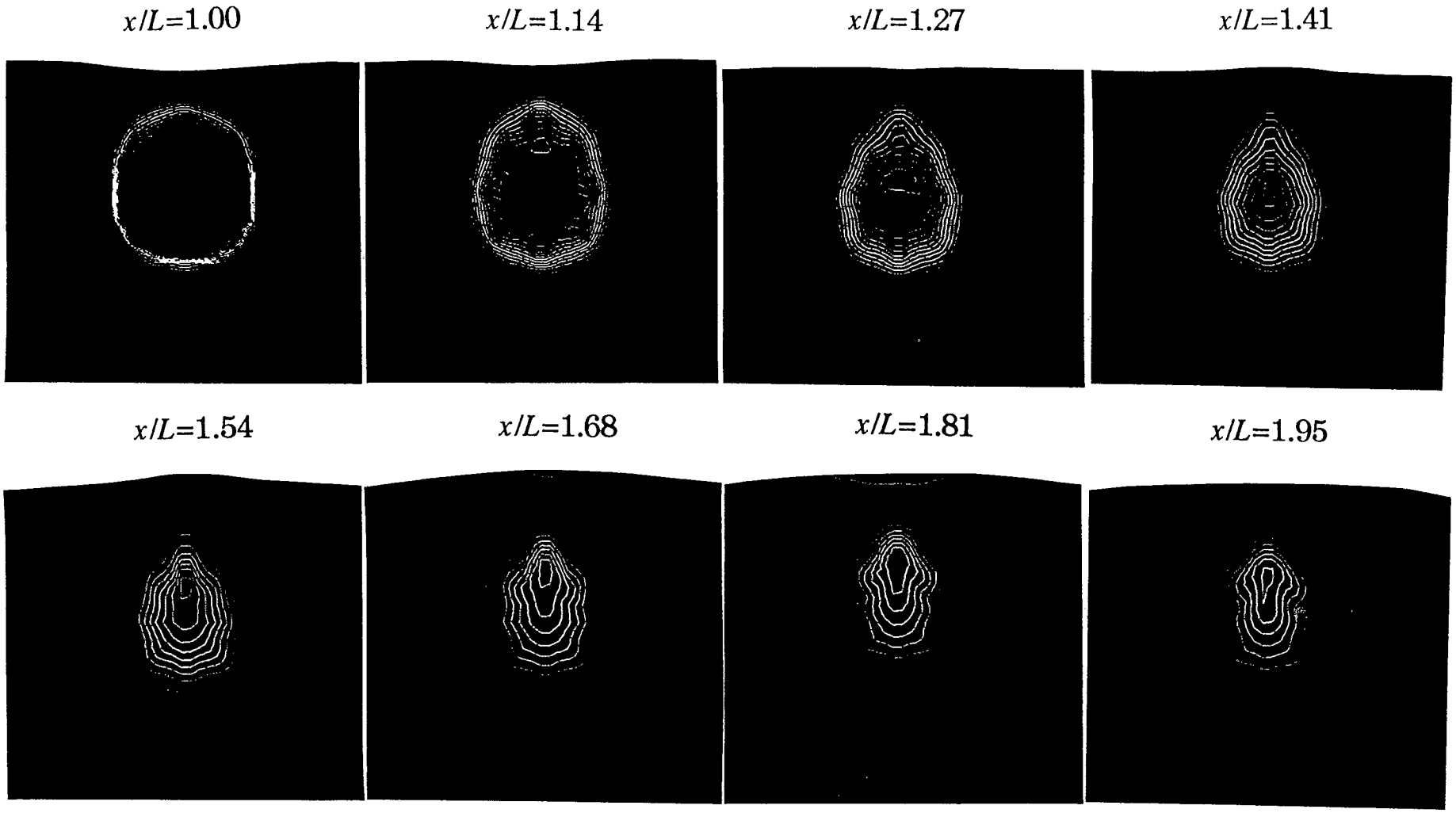

Fig. 14(b) Contours of u^1 on the cross-sectional planes, contour values are from - 0.2 to 1.0 with the interval 0.1.

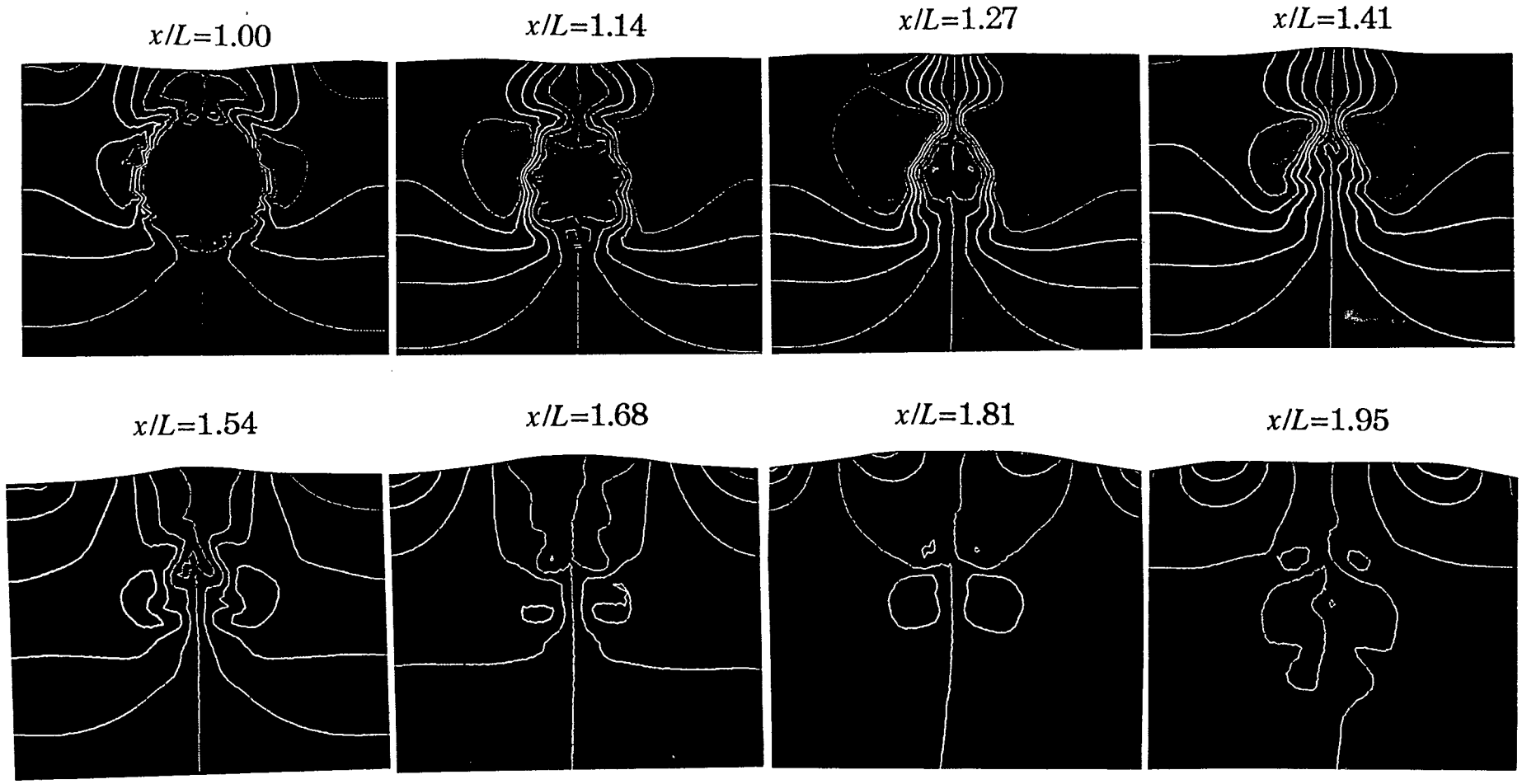

Fig. 14(c) Contours of u^2 on the cross-sectional planes, contour value are from - 0.12 to 0.12 with the interval 0.02.

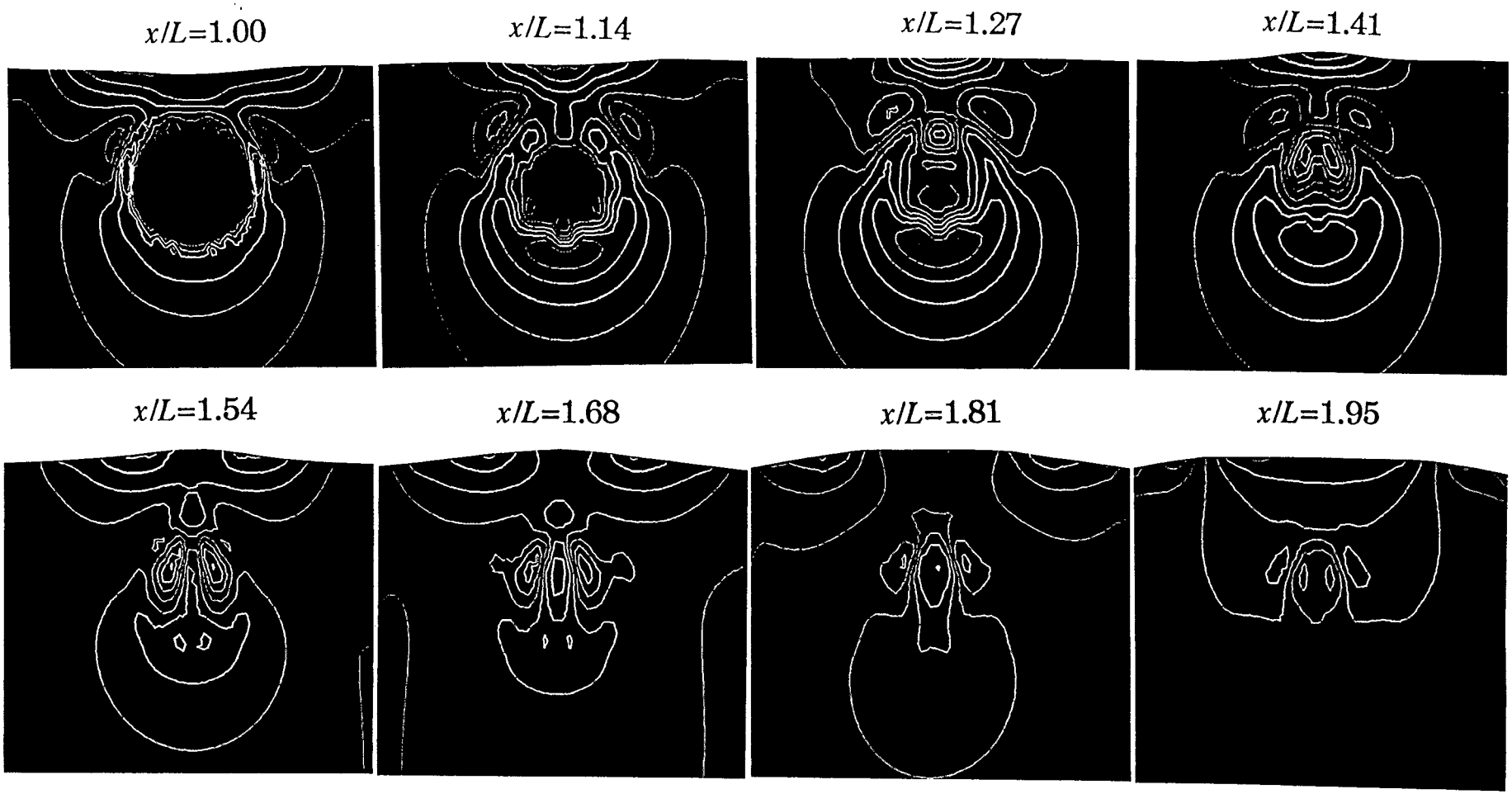

Fig. 14(d) Contours of u^3 on the cross-sectional planes, contour values are from - 0.12 to 0.12 with the interval 0.02.

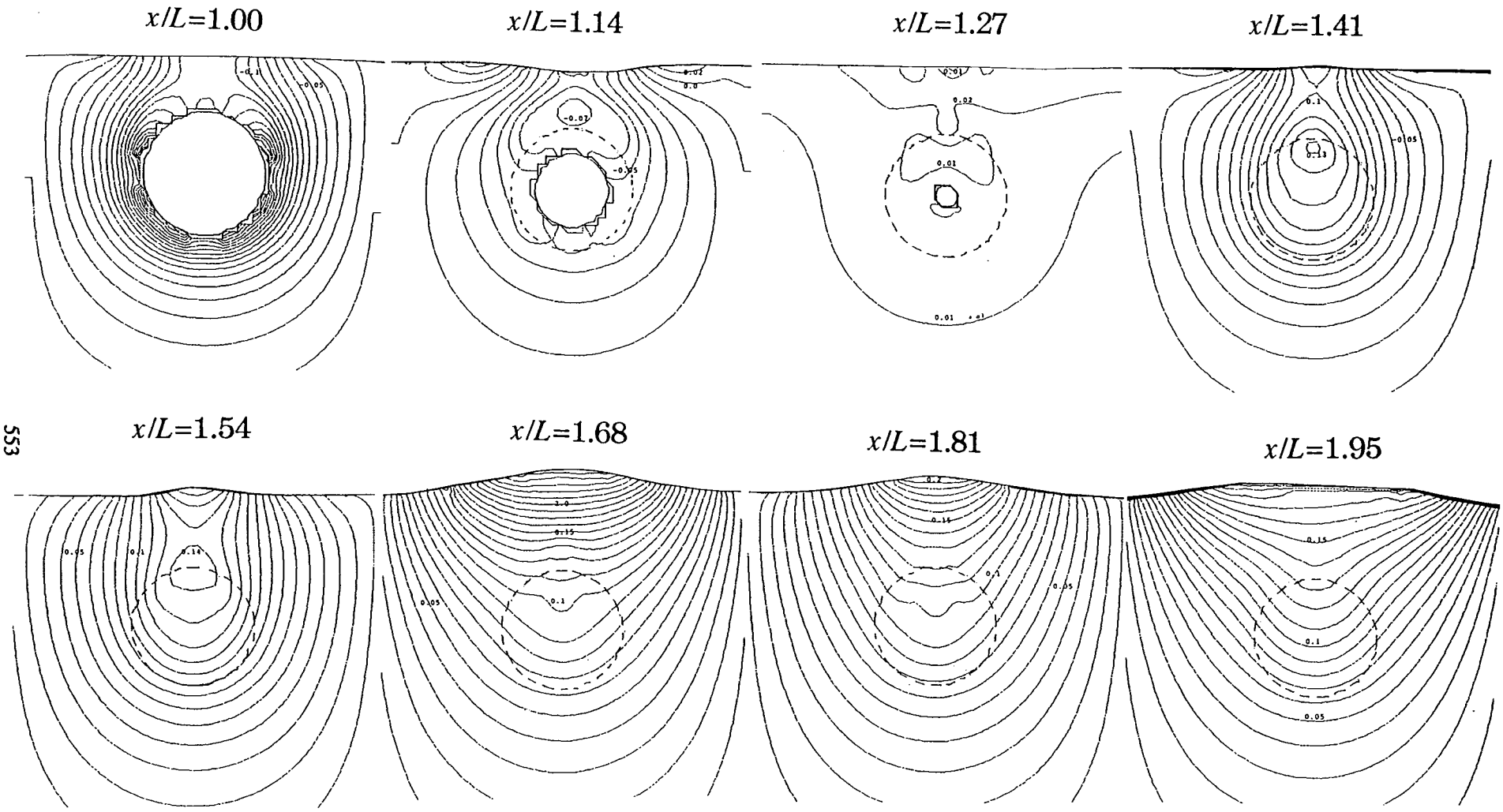

Fig. 14(e) Contours of pressure coefficients on the cross-sectional planes, the contour interval 0.01.

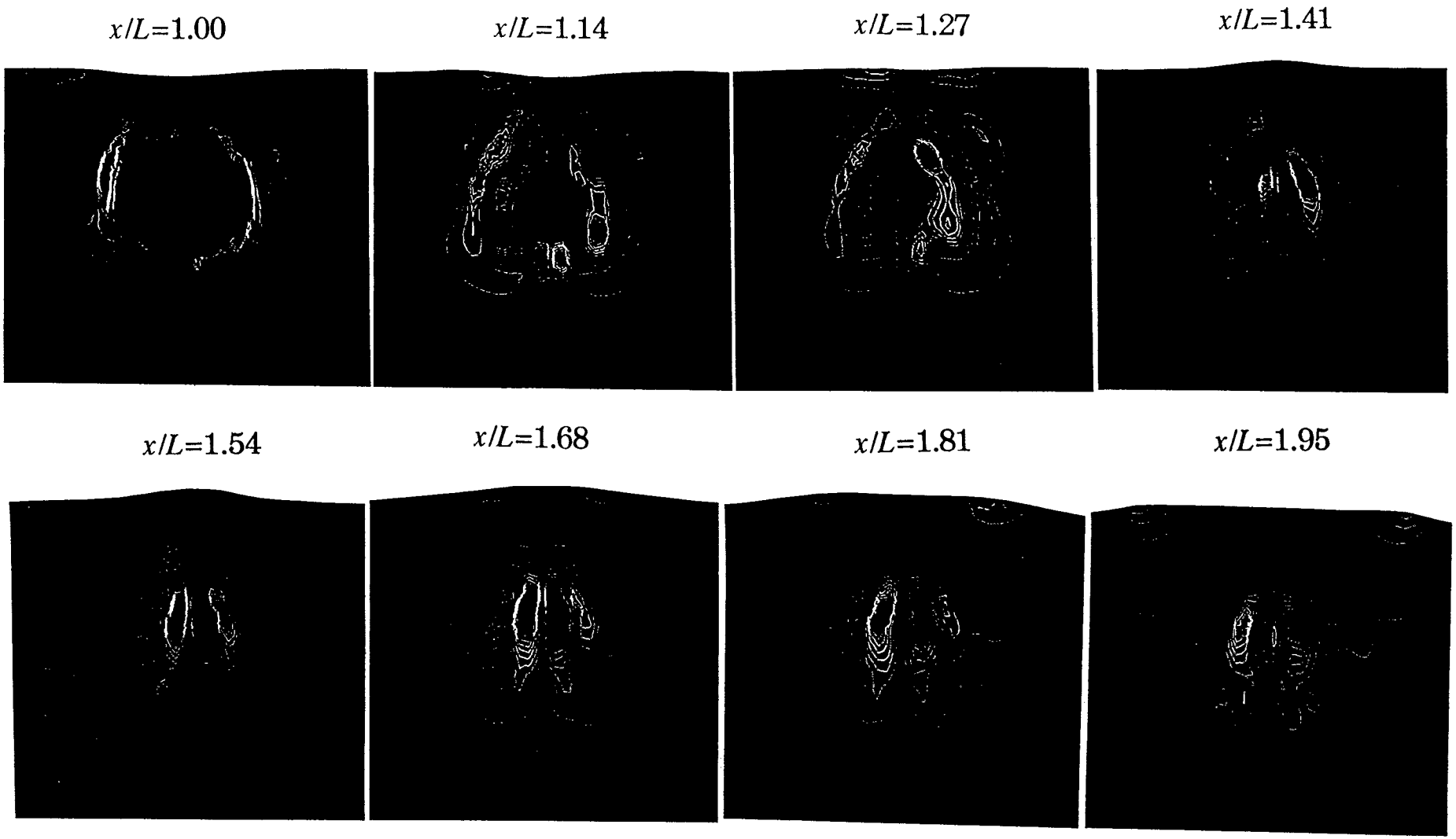

Fig. 14(f) Contours of ω' on the cross-sectional planes, the contour values are from - 4.0 to 4.0 with the interval 0.5.

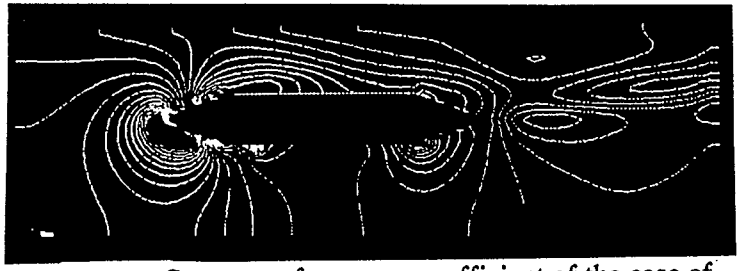

Fig. 15 Contours of pressure coefficient of the case of oblique flow at Fn = 0.11 on a horizontal plane that includes the axis of the body, contour values are from - 0.3 to 0.3 with the interval 0.02, the oblique flow is in the upward direction.

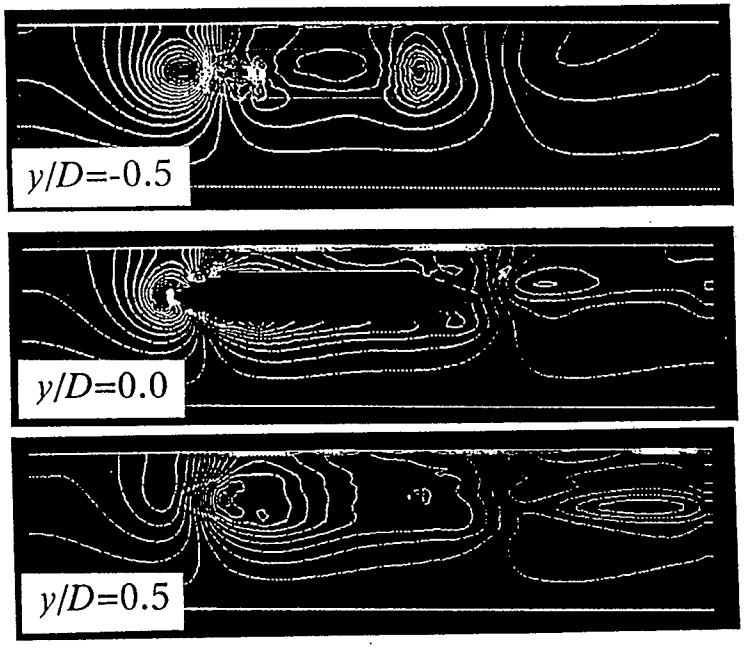

Fig. 16 Contours of pressure coefficient of the case of oblique flow at Fn = 0.11 on three vertical planes, contour values are from - 0.3 to 0.3 with the interval of 0.02, the oblique flow is in the positive y-direction.

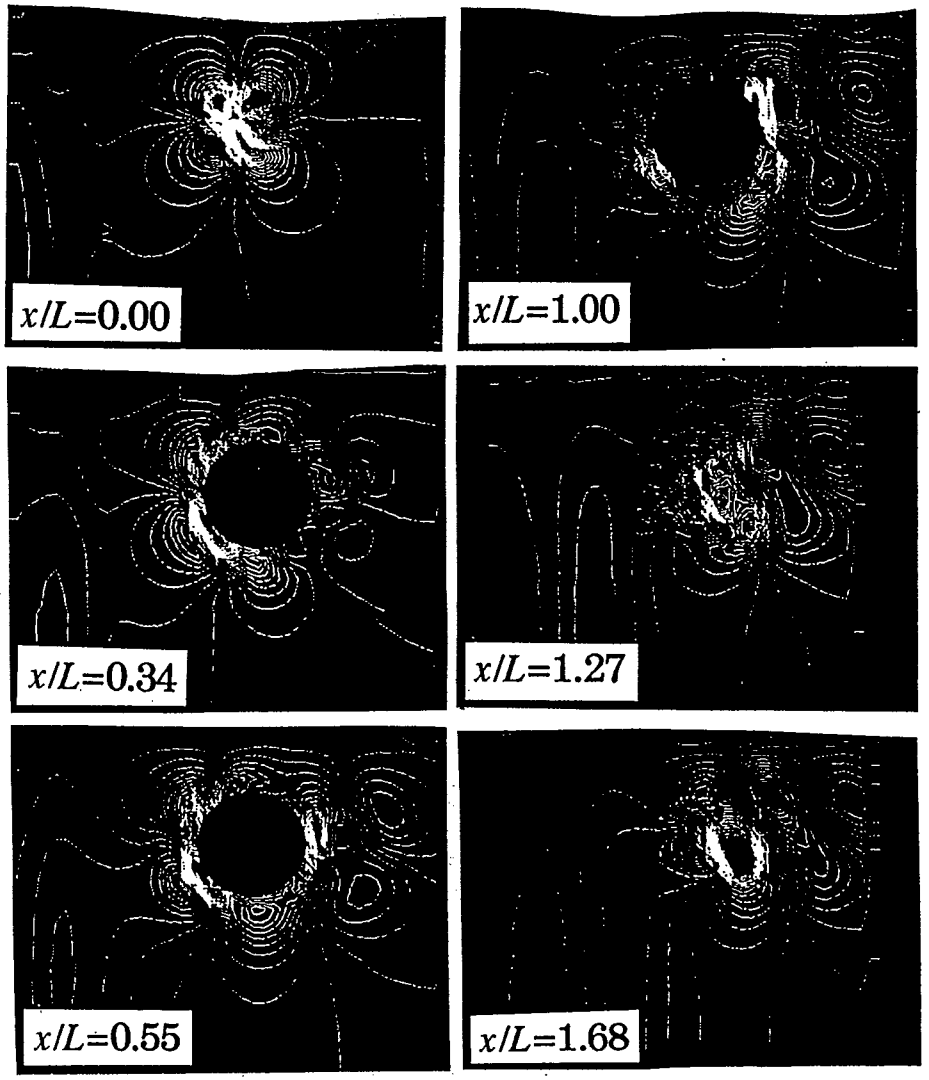

Fig. 17 Contours of pressure coefficient of the case of oblique flow at Fn = 0.11 on cross-sectional planes, the contour values are from - 4.0 to 4.0 with the interval 0.2, the oblique flow is from left to right.

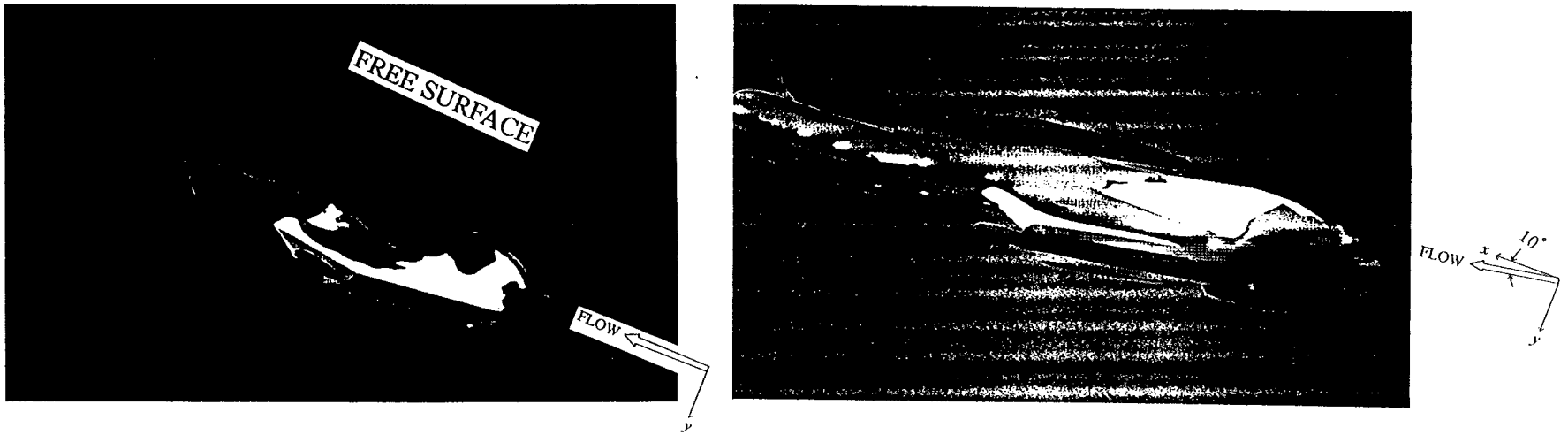

Fig. 18 Computer-graphics drawing of equi-vorticity surfaces at 3.0 (red) and - 3.0 (blue).

DISCUSSION

H. Raven
MARIN, The Netherlands

You performed 2 sets of calculations with different Navier-Stokes solvers. Without free surface, the WISDAM method leads to an inherently unsteady result containing large-scale periodic vortex shedding. With free surface, the TOMMAC method converges to a steady result. I do not suppose this is entirely a genuine effect of the free surface. Do you have an explanation for this startling difference between the behavior of the methods? Do you have any comparisons of the results of both methods under identical conditions?

AUTHORS' REPLY

Thank you for your discussion. Both of the numerical methods employ time-accurate solution algorithm. The N.S. equation is explicitly discretized, and the time-increment is 10^{-3} to 10^{-4} of the nondimensional time. With the increase of the number of grid points, we can have more interesting features of unsteady vortex shedding. One example is shown in Ref [8] for the case of vortex shedding from a sphere.

Session X

Wave and Wake Dynamics

Numerical Evaluation of Fins Acting Near the Free Surface

S. Fontaine, S. Huberson, J. Montagne
(Bassin d'Essais des Carènes, France)

ABSTRACT

A lifting surface method associated with vortex particles modeling the vortical wake is presented to calculate the unsteady flow around stabilization fins. Typically, fins are used on submarines and the assumption is made that the waves affect the fins but that the free surface is not influenced by them. The effectiveness of the fins at low speed is studied, so that the orbital motion of the flow and the nonlinear interaction with the vortical wake are addressed. In the last part, an approach for dealing with fin/wave interactions when the diving plane happens to get too close to the free surface is discussed.

I. Introduction

We want to compute the hydrodynamic characteristics of a diving plane of a submarine in water waves. In particular, we are interested in the unsteady global forces which take an important place in the manœuvrability. A second interest is to determinate the wake generated by a diving plane and its interaction with other appendices.

The optimization of fins working near the free surface becomes a difficult problem at lower speed.

- The first property of the flow to be considered in that work is that it is an unsteady flow. The local conditions in which the fins have to operate are governed by the waves and the vortical wake are far from equilibrium at each time in the wave cycle. Praticularly, when the instantaneous incidence is not small, let us say larger than 5 degrees, the vortices wich develop at the tips of the fins can not be neglected. Moreover, they are responsible for non linear effects wich have to be correctly modelled.
- Due to the relative magnitude of the wave induced velocity and of the velocity of the fin itself, the latter can experience very high angle of attack during a part of the wave cycle. As a result, the boundary layer of the fin can separate far upstream of the trailing edge, sometimes at the leading edge. The numerical approximation of such flow require an accurate account for viscous effects and the numerical solving of Navier Stokes equations seems to be unavoidable.
- As it has been previously mentioned, we are interested in cases where the submarine is close to the free surface. It is obvious that the surface can be affected by this proximity and the hydrodynamics characteristics of fin are strongly altered. A full description of this phenomenon would require a combined model for the flow induced by the fin and for the description of the unsteady free surface.
- The last point is that if one wants to study the interaction effects between all the foils of a complete submarine, the full development of the vortical wake of each fin as to be computed on very long time, specially for those which are located upstream. During their development, these vortical wakes are submitted to two different effects, both due to the presence of the submarine hull. First, their trajectory will be affected by the deviation of the streamlines due to the presence of the hull. The second point is that this vortical wake is partially embeded within the ship boundary layer and can be analysed as a concentrated vortex interacting with a shear flow.

It is not the aim of the present paper to address all the above described problems. Our attention will be focussed on those wich can be relevant of an inviscid analysis of the vorticity dynamic. This restriction is mainly imposed by the limitation of the numerical method which has been chosen. Because of the necessity to establish as

clearly as possible the level of confidence one can have in the numerical results, comparison with experimental data have been made to complete the description of the flow. These experiments are used in two different ways. First we check the validity of our model by a direct comparison between experimental and numerical results. Second, we use the discrepancy of these two different appproach to draw the outline of the domain in which the different parameters value do not allow to expect good results from the numerical model. This last remark only concerns the present method and does not indicate that no method can work for those cases.

In section two of the paper, the numerical method is described. Because it has already been used in other studies (ref [4],[7]), the particles method presentation will be very short. Larger emphasis will be devoted to the description of the method used to compute the flow around the submarine hull which is rather new. The numerical study is presented in section three. It consist of three different subsection. The description of the flow around an isolated fin in waves is split in two parts: the effect of the orbital velocity field due to the waves, and the effect of the free surface. A third subsection will be devoted to the study of the influence of the submarine hull on long time development of the diving planes vortical wakes. Only the inviscid flow approximation will be considered in all cases.

II. The numerical methods.

The outlines of the method result from the above mentioned assumptions that the velocity field can be expressed in the frame moving with the submarine as the sum of several terms:

$$\underline{U}_T = \underline{U}_\infty + \underline{U}_w + \underline{U}_G + \underline{U}_{l_s} + \underline{U}_\omega \qquad (1)$$

The velocity of the submarine $\underline{U}_\infty$ and the velocity field of the waves $\underline{U}_w$ are given. The perturbation due to the submarine and its diving planes is split into three terms: $\underline{U}_G$ the contribution of the hull, $\underline{U}_{l_s}$ the contribution of the diving planes and $\underline{U}_\omega$ the contribution of the vortical wake. These flow fields derive from potentials ϕ_G, ϕ_{l_s} and ϕ_ω. We use three different methods for describing these potentials, a lifting surface method for the fins, a particle method to describe the wake, and a discontinuous Galerkin method for the hull. This yield three coupled methods that we describe hereafter, before giving the global resolution algorithm.

2.1 Description of the fins by the lifting surfaces.

The fins are taken into account by using an integral description through a distribution of doublet on their skeleton. Typically, we use a mesh as given in figure 3. This is a well known vortex lattice method in which we can use equivalence between a surface distribution of doublets and a linear distribution of vorticity on the edges of the cells. In order to take into account the influence of the other part of the body the potential ϕ_{l_s} has to match the boundary condition on the fin:

$$\frac{\partial \phi_{l_s}}{\partial n} = -(\underline{U}_\infty + \underline{U}_w + \underline{U}_G + \underline{U}_\omega) \cdot \underline{n} \qquad (2)$$

2.2 The particle method.

The vortex particles concept has already been used to compute three dimensional unsteady flows around wings and helicopter rotors [1]. Particle methods have been introduced as early as 1931 [2] in order to compute two dimensional flows of incompressible inviscid fluids involving a singular vorticity distribution. Chorin [3] proposed an extension of the method to account for viscous effect both within the flow field and along the boundaries. Rehbach [4] extended the method to three dimensionnal flows.

The method consists in discretizing the vorticity support with a set of particles and to compute their motion. This is achieved by using a lagrangian coordinate system to express the Euler equations.

$$\begin{aligned} \frac{d\underline{X}}{dt} &= \underline{U}_T(\underline{X}, t) \\ \frac{d\underline{\omega}}{dt} &= (\underline{\omega} \cdot \underline{\nabla})\underline{U}_T \end{aligned} \qquad (3)$$

The vorticity distribution is discretized in particles. The particles are defined by two quantities: their circulation $\underline{\Omega}_i$ which is the amount of vorticity initially contained in the particle and a point $\underline{X}_i$ which can be the geometrical center of the particle or any other point representative of the particle location. For instance, they represent the following averages:

$$\begin{aligned} \underline{\Omega}_i &= \int\int\int_{P_i} \underline{\omega} d\sigma \\ \underline{\Omega}_i \wedge \underline{X}_i &= \int\int\int_{P_i} \underline{\omega} \wedge \underline{x} d\sigma \end{aligned} \qquad (4)$$

The velocity field is obtained from the vorticity distribution by using the Biot-Savart integral law:

$$\underline{U}_\omega(\underline{x}) = \frac{1.}{4\Pi} \int\int\int_{R^3} \frac{\underline{\omega}(\underline{y}) \wedge (\underline{x} - \underline{y})}{|\underline{x} - \underline{y}|^3} d\sigma \qquad (5)$$

The vorticity creation

The vorticity creation model establishes the link between the solid walls discretization and the particle wake. Particles are created along given lines in order to satisfy a condition formaly derived from the Joukovski condition. First, we use the Hess relation between the doublet distribution and vorticity to obtain a linear distribution of vorticity on the lattice of the surface $\underline{\omega}_{s_w}$. Then, this vorticity is assumed to be emitted within the fluid at a mean velocity computed along the separation lines.

Here, the separation line is the trailing edge of the fin which is discretized in small segments σ_e which are represented by their mid point $\underline{X}_e$. At each point $\underline{X}_e$ and at each time step Δt, a particle is created according to the following relations:

$$\begin{aligned} \underline{X}_i &= \underline{X}_e + \Delta t/2 \underline{U}_T(\underline{X}_e) \\ \underline{\Omega}_i &= \int_{\sigma_e} \omega_{e\omega} dx \Delta t \mid \underline{U}_T(\underline{X}_e) \mid \end{aligned} \tag{6}$$

Coupling the particle method to the general procedure

Here, the velocity to be used U_T is the sum of all contribution defined in (1). Then, the discrete equations to be solved are:

$$\begin{aligned} \frac{d\underline{X}_i}{dt} &= \underline{U}_T(\underline{X}_i) \\ \frac{d\underline{\Omega}_i}{dt} &= (\underline{\Omega}_i \cdot \underline{\nabla})\underline{U}_T(\underline{X}_i) \\ \underline{U}_\omega(\underline{X}_i) &= \frac{1.}{4\Pi} \sum_{j \neq i} \frac{\underline{\Omega}_j \wedge (\underline{X}_i - \underline{X}_j)}{\mid \underline{X}_i - \underline{X}_j \mid^3} \\ (\underline{\Omega}_i \cdot \underline{\nabla})\underline{U}_\omega(\underline{X}_i) &= \frac{3}{8\Pi} \sum_{j \neq i} \frac{1}{\mid \underline{X}_i - \underline{X}_j \mid^5} \\ & [((\underline{X}_i - \underline{X}_j) \cdot \underline{\Omega}_i)((\underline{X}_i - \underline{X}_j) \wedge \underline{\Omega}_j) + \\ & (((\underline{X}_i - \underline{X}_j) \wedge \underline{\Omega}_j) \cdot \underline{\Omega}_i)(\underline{X}_i - \underline{X}_j)] \end{aligned} \tag{7}$$

In three dimensional case, the vorticity transport equation has a non-zero right hand side which is called the deformation term. This term can be obtained through an integral relation by derivating the Biot-Savart law.

2.3 The use of the discontinuous Galerkin method for the hull.

The contribution to the potential flow of the body of the submarine and of the sail is calculated through a discontinuous Galerkin method on boundary elements. The use of this method is motivated by the fact that the body surface in generally produced by a CAD system. The discontinuous Galerkin method allows to take advantage of the high degree of approximation used in CAD, and can use directly the unstructured approximation surface panel definition obtained with standard CAD designs.

We give hereafter a short description of the method as it has been implemented for our application. We want to solve the problem:

$$\begin{aligned} \Delta \Phi_G &= 0 \\ \frac{\partial \Phi_G(P)}{\partial n_P} &= -(\underline{U}_\infty + \underline{U}_\omega + \underline{U}_\omega + \underline{\nabla}\phi_{t_e}) \cdot \underline{n}_P \\ &= -\underline{U}_{ext} \cdot \underline{n}_P \end{aligned} \tag{8}$$

The point P belongs to S_*, the surface of the submarine, n_p is the exterior normal to S_*, and $\underline{U}_{ext}$ is a given velocity field. For instance $\underline{U}_{ext}$ can be the sum of the velocities given by the lifting surface, the vorticity particles and the global advance $\underline{U}_\infty$. This problem is solved through a boundary element method, by looking for the potential distribution on S_* satistafying the equation:

$$\begin{aligned} \phi(M) - \frac{1}{2\pi} \int_{S_*} \phi(P) \frac{\partial}{\partial n_P} \left(\frac{1}{|M-P|}\right) d\sigma_P = \\ -\frac{1}{2\pi} \int_{S_*} (\underline{U}_{ext}, \underline{n}_P) \frac{1}{|M-P|} d\sigma_P \end{aligned} \tag{9}$$

This equation can be reformulated in a concise form:

$$(I - K)\phi = f \tag{10}$$

where I is indentity, K and f are the integral operators.

At first, we define the approximation of the surface of the body as a set of curved panels Γ_i covering the surface. Each panel can be obtained by a polynomial transformation of the unit simplex. Each point P of the panel is obtained from a point $\hat{P}$ by $P = \Psi_i(\hat{P})$, Ψ_i is a polynomial in $(\hat{x}, \hat{y})$ of degree r. The main requirement of this representation of the surface is that there is no hole. The panels resulting from a CAD design may not necessary connect at their vertices, as we can see on the mesh used for our example (figure 1). Then, the potential approximation Φ_h on the boundary elements is search as an element of the space V_h of functions u_h, defined as:

$$V_h = (u_h , \forall i \in I_* , u_{h_{\Gamma_i}} = \hat{P}_i \circ \Psi_i^{-1} , \hat{P}_i \in P_p)$$

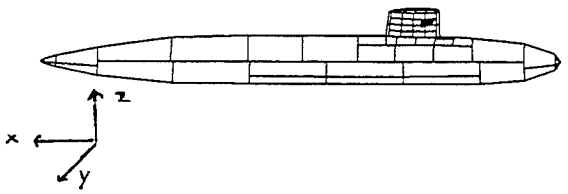

Figure 1: Discretization of a submarine hull.

P_p is the space of polynomials of degree inferior or equal to p with respect to the variables $\hat{x}$,$\hat{y}$ on the unit simplex, I_* is the index space of all panels. In this method, p is restricted by p< r, in order to be consistent with the discretisation of S_*. We can note that this definition of V_h does not impose any continuity on u_h at the interface of the panels. The approximate solution Φ_h is obtained by projection of the equation (11):

$$\begin{cases} \forall v_h \in V_h \\ \int_{S_*} (I - K_h)\phi_h . v_h d\sigma = \int_{S_*} f d\sigma \end{cases} \tag{11}$$

K_h is the integral operator applied to the fonction Φ_i on the panel distribution. This equation leads to a linear system which can be solved with standard matrix inversion methods.

One is refered to [5] for a complete discussion of the application of the method. For practical purpose, the main issue, appart from the mesh generation, is to set up quadrature formulae which are consistent with the degree of approximation and which are not too much

time consuming. This is the main discussion of the report [6]. An other issue is the choice of the degree of approximation p. Our experience is that the value p=2 is an optimum with respect to efficiency and accuracy. Moreover it allows to derive directly the pressure and the velocities on the body. However, p=1 is often usefull because the CAD system can give too many panels to be handled with the p=2 approximation.

Coupling the Galerkin approximation to the general procedure.

The Galerkin approximation is introduced in the flow of the general procedure as a standard boundary element method. The flow field given by $\underline{U}_\infty$, the lifting surfaces and the particles at the previous time step introduces a right hand side term in the equation treated explicitly. Then, the flow field induced by the body must be taken into account to implement the particles and the lifting surface. The computation of velocities at points outside of the surface S_* is obtained by quadrature formulae which use far field approximation or interpolation between the value on the body and the far field approximation.

2.4 The global time stepping algorithm.

We use a time marching approach, either for steady or unsteady problems. Then, we use a fractional time step algorithm in order to decouple the problems. Knowing the values of ${\phi_G}^{n+2/3}$, ${\phi_l}_*^n$ and ${\phi_\omega}^{n+1/3}$ at time step, the values at time step n+1 are obtained following the loop:

- Compute ${\phi_l}_*^{n+1}$ with conditions imposed by ${\phi_\omega}^{n+1/3}$, ${\phi_G}^{n+2/3}$
- Compute ${\phi_\omega}^{n+4/3}$ with conditions imposed by ${\phi_l}_*^{n+1}$, ${\phi_G}^{n+2/3}$
- Compute ${\phi_G}^{n+5/3}$ with conditions imposed by ${\phi_l}_*^{n+1}$, ${\phi_\omega}^{n+4/3}$

For unsteady problems, this algorithm is consistent and is accurate enough for small time steps. Owing to the hyperbolic nature of the flow this algorithm happens to converge to a steady solution when it exists.

2.5 The wave model.

As it has been mentioned in the introduction, we assume that the free surface is not disturbed by the submarine and the depth is infinite so the wave model is a simple two dimensional Stokes model. We just recall hereafter the explicit formula which are used to express the velocity potential. The free surface is assumed to be sinusoidal, according to the following equation:

$$y = a\sin(mx - nt) \qquad (12)$$

It is a progressive wave with a wavelength $\lambda = 2.\pi/m$ and a period $\tau = 2.\pi/n$. The expression of the velocity potential is

$$\phi = \frac{acm}{\mathrm{sh}(mh)}\mathrm{sh}(my)\sin(mx - nt)$$

III. Validation tests.

3.1 Problem description .

The results coming from a test campaign on the efficiency of the diving planes of a submarine near the free surface gave us a lot of information in order to assess the method. During the tests, a model of a submarine with the fins mounted on the sail has been towed near the free surface (figure 2). The efforts on the fins and the hull were measured during the tests. Several experimental conditions were used by varying the towing speed, the depth, the wave parameters and the period of oscillation of the fins. At the stage of development of the numerical method, it is not feasable to run all the test cases with the complete geometry. On the other hand, since the tests were not made in order to validate a numerical method, they don't cover systematically the range of variation of the different parameters.

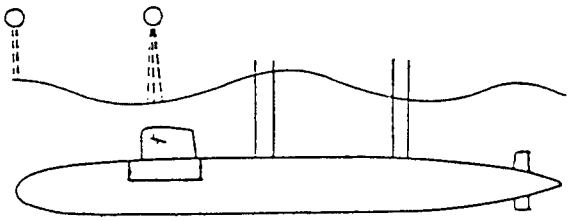

Figure 2: Experimental conditions

For these reasons, the numerical results are splitted into three parts. First, we compare the lift measured in the experiment and the lift calculated on isolated diving planes with the same geometry and the same flow parameters, for particular conditions. These comparisons indicate large unsteady effects when the variation of incidence is due to oscillations of the diving planes. Since, the comparisons show some discrepency between experimental and numerical results, two other kinds of tests have been performed in order to assess the effect of the hull and of the free surface.

The free surface interaction with the fin is addressed an experiment on a flat plate at a steady incidence performed in the tunnel of the Laboratory of Fluid Mechanics of Le Havre University. The results compared with different numerical approximations show that the effect of the free surface is negligible for the application considered.

One case has been run with the hull and the fins for a fixed angle of incidence. It has been run sufficiently in order to see the effect of the hull on te roll up of the vor-

tex. For the lift, with no waves, the effect is negligible. These three tests are discussed hereafter.

3.2 An isolated diving plane.

The numerical conditions are specially designed to be representative of the conditions experienced by a submarine. To reduce computing time, we only considered the diving plane in the calculations and the effect of the submarine is neglected. The results are the global forces on the foil. Experimental results used in the validation are obtained in the towing tank of Paris for different wave conditions. The diving plane has been discretized in a 12×5 mesh. This mesh is illustrated on figure 3. The dashed part has been added in order to simulate the submarine hull.

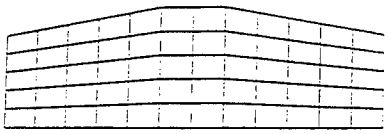

Figure 3: Diving plane discretization

An oscillating diving plane.

We consider that the incoming flow is uniform and that the diving plane is oscillating. The characteristics are given in (13); β is the angle of incidence of the diving plane with the flow, ω the pulsation, c the chord of the fin.

$$\begin{cases} \beta = 9.9^0 cos(\omega t + 12^0) \\ \omega = 0.668 \quad rad/s \\ depth \quad of \quad fin = \frac{5}{3}c \quad m \end{cases} \tag{13}$$

The results obtained with these conditions are presented in Table 1. They are given in terms of the Cz amplitude and of the phase difference with the oscillation. The quasi-unsteady results correspond to an approximation considering that the unsteady lift is simply the steady lift (figure 4) at the angle of incidence β and the velocity at time t. We can observe that the amplitude is in concordance with experimental data. The unsteady effect have an influence in term of difference of phase.

Table 1:

	Experiment	quasi-unsteady	unsteady
amplitude (Cz)	0.6	0.54	0.62
difference of phase	$+13^0$		-22^0

Diving plane in water waves.

An unsteady flow results from the composition of the wave induced velocity field and the submarine velocity. The time evolution of the angle of incidence of the diving

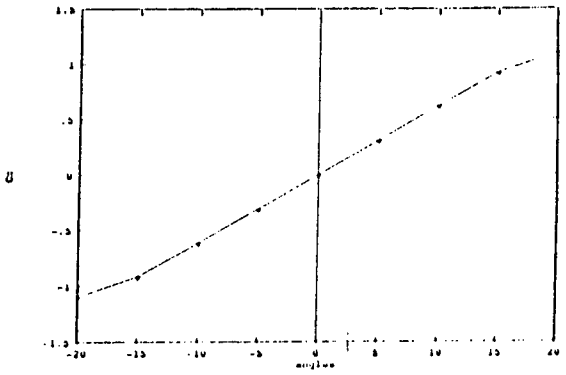

Figure 4: Lift of the diving plane with respect to the angle of incidence

plane of the submarine with this flow is:

$$\theta = \tan^{-1}((\mid \underline{U}_\infty \mid + u_w)/v_w)$$

The speed of the submarine is constant and the wave characteristics are given in (14),(15); h_{cc} is the total height between crest and though, λ the wave length. T the period, Tc the characteristic period which correspond to c/V the time for a particle to cross the diving plane. The wave lengths are large compared to the size of fin.

The maximum angle of incidence of the fin θ is about 10^0 for the first case and about 20^0 for the second.

$$case \quad 1 \begin{cases} h_{cc} = 4.3 \quad m \\ \lambda = 138 \quad m \\ T = 9.4 \quad s \\ Tc = 0.58 \quad s \\ depth \quad of \quad fin = \frac{5}{3}c \quad m \end{cases} \tag{14}$$

$$case \quad 2 \begin{cases} h_{cc} = 3.3 \quad m \\ \lambda = 200 \quad m \\ T = 11.3 \quad s \\ Tc = 2.3 \quad s \\ depth \quad of \quad fin = \frac{23}{3}c \quad m \end{cases} \tag{15}$$

These two cases differ principally by the depth of the fin and by the speed of the submarine. The results are given in Table 2. We can observe that the unsteady effects are negligible in the first case, and are important for the second. In the latter, the vorticity emitted along the edges of the plane at time t_0 is convected downstream and will remain above the wing for a time ranging from 0 for the trailing edge to Tc for the region close to the leading edge. This effect is a memory effect due to the presence of the vortex core above the plane. Moreover the large maximun angle of incidence in the second case induced a loss of lift which is not taken into account in the present method.

An oscillating diving plane in water waves.

We have made a test which consider the two effects: oscillations and water waves. The conditions are the following:

Table 2:

case 1

	Experiment	quasi-unsteady	unsteady
amplitude (Cz)	0.55	0.6	0.63
difference of phase	$+9^0$		-5^0

case 2

	Experiment	quasi-unsteady	unsteady
amplitude (Cz)	1.05	1.18	1.35
difference of phase	-20		-20

$$\begin{cases} h_{cc} = 4.3 \quad m \\ T = 9.4 \quad s \\ \lambda = 138 \quad m \\ \beta = 2.2^0 + 10.6^0 cos(\omega t - 10^0) \\ \omega = 0.668 \quad rad/s \\ depth \quad of \quad fin = \frac{6}{3} c \quad m \end{cases} \tag{16}$$

and the results are given in figure 5. The maximum angle of incidence between the diving plane and the flow is about 20^0. It seems that when the effects are coupled, there is less unsteady phenomena.

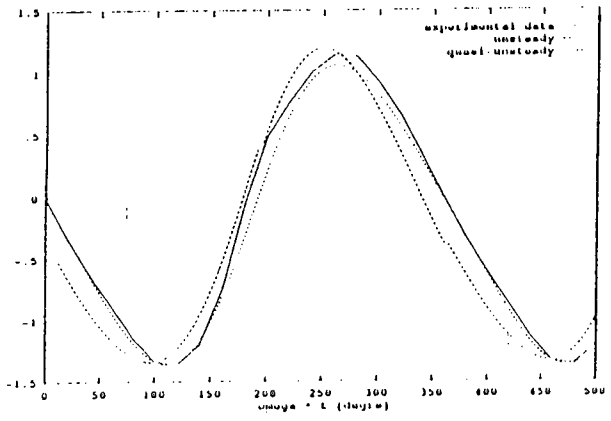

Figure 5: Time evolution of the lift during one period.

3.3 Influence of the free surface.

In this part, the wave velocity is not accounted for. This is not required by the numerical method: the stokes wave model which is used in section 3.1 is linear so that the free surface is a plane. As a result it is compatible with the double model approximation which is used to model pressure effect in the present section. However, as it has been claim in the introduction, our goal was to combine experimental and numerical approach in order to give a description of the flow as realistic as possible. In that connection, we have retain flow conditions which are compatible with both numerical computation and measurements. Presently, the experimental study only concerns fins in a uniform stream. This limitation has been chosed in order to simplify the flow because we plan to combine velocity field measurements and free surface determination. The results to be described hereafter have to be considered as the first step of this particular study.

The computer code is the code which as been used for section 3.1. The external flow is assumed to be uniform and the free surface effect is correctly approximated by the double model assumption: a symetrical condition is imposed on the free surface; this condition is satisfied by using a second fin as described on figure 6.

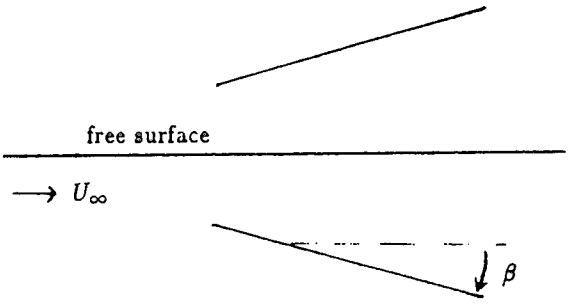

Figure 6: Double model assumption

For the experimental work, we have used a water tunel with a free surface. The fin has been placed on the side wall of the tunel and is equipped with a two components balance. Experiments have been performed for Reynold numbers ranging from 2.2 10^4 to 3.5 10^4. The fin has been placed at three different height under the free surface: 0.45 c, 0.72 c and 1.32 c where c is the chordlentgh of the fin. On figure 7 we compare the numerical results to the measured value of the lift coefficient:

$$C_z = \int_{fin} p\vec{n} \cdot \vec{e_z}$$

where $\vec{e_z}$ is a vertical unit vector, $\vec{n}$ is the unit normal to the fin. No viscous correction has been applied. It can be observed that a good agreement is obtained even if the fin is rather close to the surface. Nevertheless, a slight divergence of the two curves for the lower value of the immersion parameter indicate that we are close to the limit of validity of the method.

3.4 Influence of the submarine hull.

We have also tried to estimate the influence of the submarine hull. This was achieved by assuming that the perturbation caused by the presence of the hull could be modelled by the potential formulation. The hull of the submarine is discretized into a set of 150 curved panels

(figure 1).
The panels are described with a CAD system by a polynomial chart which the degree r is included between 5 and 12. Those high degrees are due to the definition of the tips of the submarine. The middle part of the hull is described with small degree panels.

The degree of approximation of the potential is equal to 1 s not to consume too much time. The computing time for calculating the integrals defined in (13) is about a half hour on a computer Alliant FX80.
The submarine has a constant velocity and is set in infinite depth. The angle of incidence of the diving plane with the incoming undisturbed flow is 10 degres. The vortex particles are emitted along trailing edge and tips in order to well represent the wake.

At first, we study the wake position without the submarine hull. We compute this case during 30 chord length, this represents about 200 time steps. The vortical wake is represented on figure 8a in the plane (x,y) and on figure 8b in the plane (x,z). The rolled up wake can be observed.
We consider the similar computation with the submarine hull. The results are presented on figures 8c and 8d, where the hull is plotted. It can be observed that the presence of the submarine disturbes the wake. The particles are moving around the sail and are convected with the velocity due to the hull.

The interest of this result is to show that interaction between the appendices can occur. Then, it becomes necessary to know locally the flow. We present on figure 9, 10 the velocities distribution and the vorticity in a plane (y,z) in the rear of the submarine. Those informations are adequately in order to evaluate the interaction between the appendices.

IV. Conclusion.

A first step of our programme has been accomplished, since we wanted to show the feasability of a method coupling boundary elements and the vortex particles concept to compute efforts for maneuvrability purpose. This method can be helpful to simulate non linear interactions, specially memory effects. In order to assess in a better way the interaction with the free surface we intend to pursue the systematic comparison briefly presented in section 3.3.
Now we have a complete procedure to describe the submarine within the perfect fluid assumption, and we are looking for optimizing its time efficiency in order to improve its capabilities.

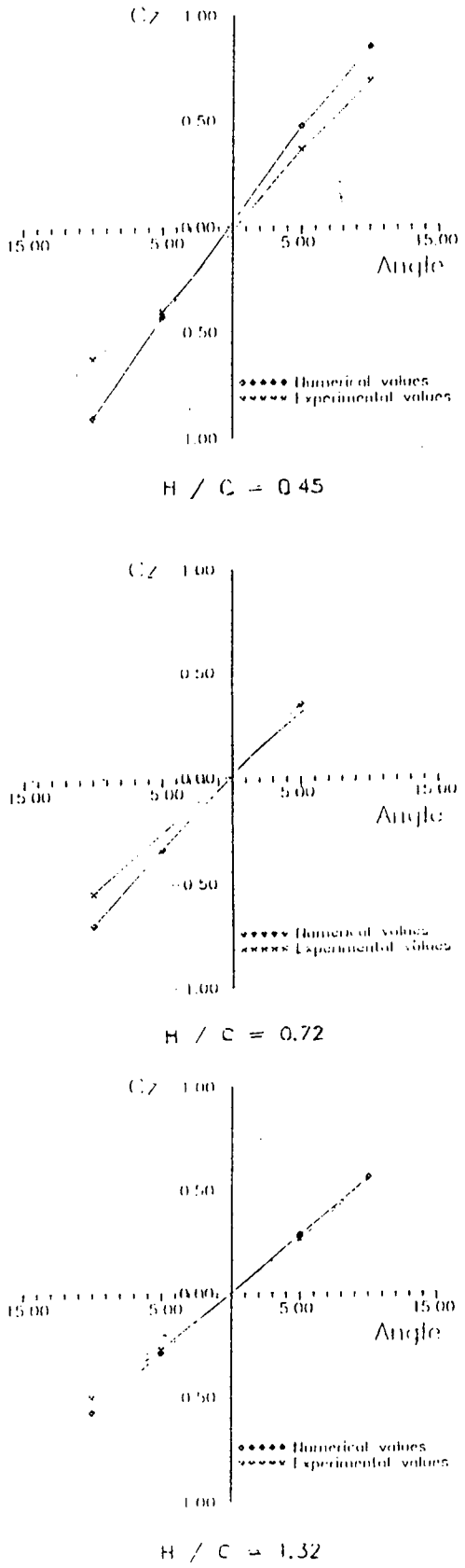

Figure 7: Lift coefficient of a fin near the free surface for different immersion

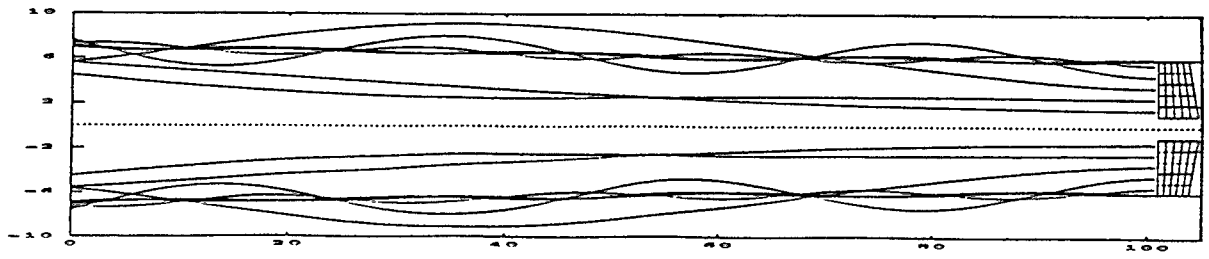

a)

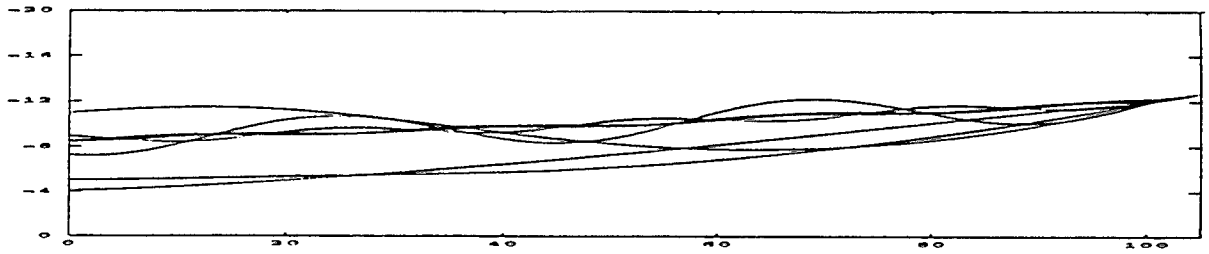

b)

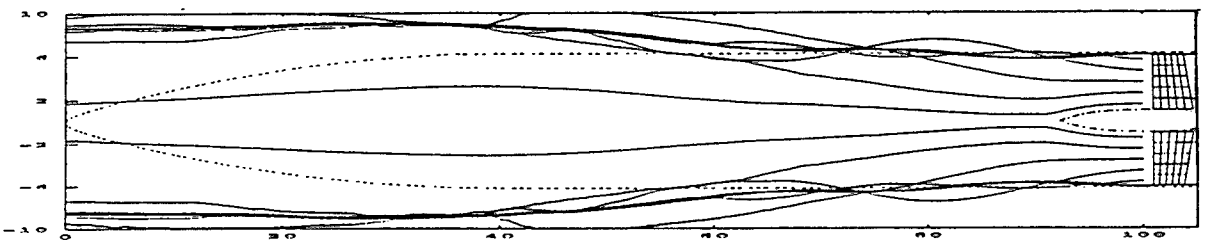

c)

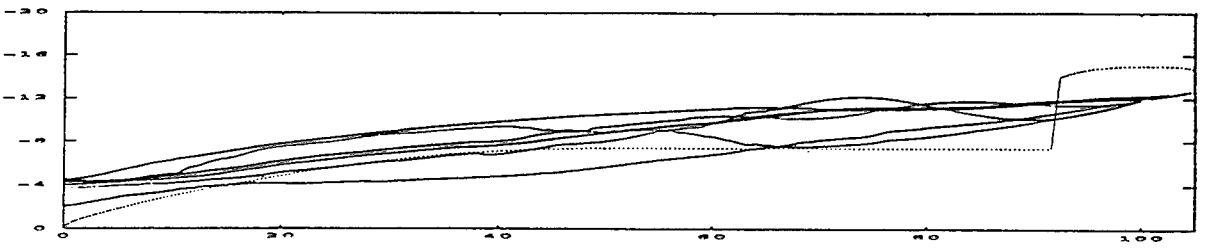

d)

Figure 8: Evolution of the wake position.

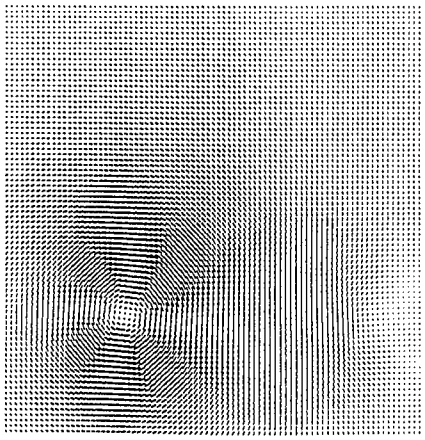

Figure 9: Velocities distribution

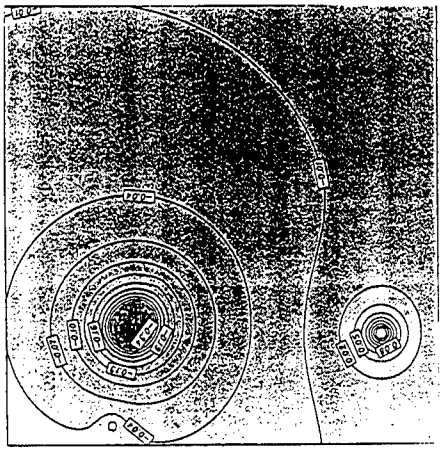

Figure 10: Vorticity distribution

References

[1] Cantaloube B. and Huberson S. A new approach to compute the flow around helicopter rotors, 9^th European Helicopter Forum, Stresa, 1983.

[2] Rosenhead. The formation of vortices from a surface discontinuities, Proc. of the Roy. Soc, Vol A 134, pp 170,192, 1931.

[3] Chorin A.J. Numerical study of slightly viscous flow, J. Fluid Mech., Vol57, 1973, pp 785-796

[4] Rehbach C. A numerical calculation of three dimensionnal unsteady flows with vortex sheets, AIAA 16th aerospace Sciences Meeting, Huntsville, 1978.

[5] Fontaine S. ,Guermond J.L. Une approximation de Galerkin discontinue de type h-p des écoulements potentiels ,La Recherche Aerospatiale, 1991, N^0 4, pp37,49.

[6] Fontaine S. Report DRET, 91/1033J.

[7] Fontaine S. ,Huberson S.,Montagné J.L. Numerical Computation of the Flow Around a Diving Plane in Water Waves.CADMO 1991.

Inner-angle Wavepackets in an Unsteady Wake

Y.-S. Cao, W. Schulz, R. Beck (University of Michigan, USA)

Abstract

The phenomenon of the inner-angle wavepackets in the wake of a ship is investigated. The three most probable causes of the wavepackets are: interference of the wave systems by the bow and stern; free-surface nonlinear effects; and wake unsteadiness due to translation and oscillation of the disturbance. The phenomenon is studied with nonlinear calculations using a desingularized boundary integral method, linear calculations using a time-domain Green function, and the method of stationary phase. It is shown that nonlinear effects are not essential to the generation and persistence of inner-angle wavepackets; the unsteadiness of the wake can cause the inner-angle wavepackets. The unsteadiness is one possible explanation for the phenomenon.

Introduction

In addition to the normal Kelvin wave pattern, a relatively isolated wavepacket is sometimes observed in the wake of a ship. The wavepacket, referred to as the inner-angle wavepacket or inner-angle soliton, appears at an angle less than 19.5°, the angle of the normal Kelvin cusp line from the course of the ship. The wavepacket can persist for several kilometers behind the ship. A typical example is the experimental observation and measurement in the wake of the U.S. Coast Guard cutter Point Brower (Brown *et al.* 1989). In the experiment, the inner-angle wavepacket was observed at an angle of approximately 11°. Although the generation mechanism responsible for this wave feature is not entirely clear, the most probable hypotheses for the causes for the inner-angle waves are: 1) a linear interference pattern due to the wave fields generated by the bow and the stern; 2) nonlinear free surface effects; and 3) unsteadiness of the wake as referenced to the coordinate system attached to ship.

The linear interference has been studied by Hall & Buchsbaum (1990) using a submerged source-sink pair as well as a line source distribution to model the ship. The linear free surface boundary condition was used. They were able to generate an inner-angle wavepacket using this model. However, the wavepacket amplitude decayed faster than the observed data. Brown *et al.* (1989) also found that the decay rate of the amplitude of the interference pattern predicted by linear steady Kelvin wake theory was higher than the observed decay rate.

Nonlinear effects have been claimed to play an important role in the generation of the inner-angle waves (Hall & Buchsbaum 1990, Brown *et al.* 1989, and Akylas *et al.* 1989). No comprehensive nonlinear models have been developed to calculate the entire wave field of a ship, although considerable research has been conducted on certain aspects. Most nonlinear studies use a perturbation method to account for nonlinear effects (Akylas *et al.* 1988, Brown *et al.* 1989, and Hall & Buchsbaum 1990). A two-dimensional nonlinear Schrödinger equation for the wave envelope is derived assuming a narrow band of frequencies for the carrier waves along the ray of the inner-angle wavepacket. The wave envelope from the nonlinear Schrödinger equation can support solitary wave solutions (hence the terminology inner-angle soliton). However, the use of the envelope equation implies that the wavelengths of the carrier waves are much smaller than the envelope width, which seems not to be supported by visual observations. Moreover, as pointed out by Wu (in a discussion of Akylas *et al.* 1988), the carrier waves are not perpendicular to the envelope track and hence it is an open question whether the asymptotic radiation of the envelope wave packets can be satisfactorily explained by local group velocity considerations. An overview of the research into the inner-angle wavepacket is given by Hall (1991).

The studies mentioned assume a steady wake in the coordinate attached to the ship. However, the observed wake of the Coast Guard cutter was distorted by ambient waves, limiting the comparison to averaged properties (Brown *et al.* 1989). There was still variability in the reduced data even when the components due to the ambient waves were filtered. This could be due to, in addition to the ambient waves, 1) variation in ship speed or heading; 2) time-dependent ship motions; 3) interaction with the transverse Kelvin wave and the time-dependency or instability of the "solitary" wave envelope. Other sources of unsteadiness could be the propeller induced flow field, vortex shedding (von Kármen vortex street type) and the turbulent flow in the near field. Unsteady features of

the wake may play a very important role in this phenomenon and may be an alternative explanation for the phenomenon. It is therefore desirable to investigate the unsteady features of the wake.

Time-harmonic unsteady waves have long been studied in seakeeping problems. However, the main objective there is to determine the hydrodynamic forces acting on the ship and the resulting ship motions, while little attention is given to the far-field wave patterns. Eggers (1957) studied the wave pattern due to a translating pulsating source and described several systems of constant phase curves. Recent work by Noblesse & Hendrix (1990) showed similar results. These studies show that the wave pattern geometry and its polar angular boundary for the far field waves essentially depends on the nondimensional Brard parameter $\tau = V\omega/g$, where V is the translating speed of the disturbance, ω is the pulsating frequency of the disturbance as observed from the coordinate system attached to the disturbance, and g is the acceleration of gravity. These studies used the method of stationary phase. Recently, Nakos and Sclavounos (1990) calculated the time-harmonic wave patterns due to a modified Wigley hull model translating and oscillating in heave using a Rankine source panel method. However, none of the described work on unsteady wave patterns specifically tried to explain the inner-angle wavepacket phenomenon. Only recently, Mei (1991a,b) used a unsteady, nonlinear Schrödinger equation to study the phenomenon.

In our study, the following three methods are used to examine causes for the inner-angle wavepacket with the emphasis given to the unsteadiness of the wake:
1) Linear wave calculations: The time-domain Green function satisfying the linear free surface conditions and radiation conditions (Liapis & Beck 1986, King 1987, Beck & Magee 1990) is used to calculate the wave elevation.
2) Method of stationary phase: Although it is not easy to evaluate wave elevation by the method of stationary phase, the wave field boundaries and the rate of decay can be obtained without a great deal of computational effort. These lines are obtained in a similar manner as Eggers (1957).
3) Nonlinear wave calculations: The time-stepping procedure following material particles (Longuet-Higgins & Cokelet 1976), combined with a desingularized boundary integral method (Cao 1991 and Cao *et al.* 1991), is used to calculate the waves with fully nonlinear free surface boundary conditions. It has been shown that the method is fast, accurate and numerically stable.

Since in this study we are primarily interested in far-field waves, we simply model a ship either by a source-sink pair moving below the free surface or a moving pressure distribution on the free surface.

Initial-Boundary Value Problem

In the following, all quantities are made dimensionless by the fluid density ρ, the gravitational acceleration g, and a proper length scale L. Therefore, the speed V is replaced by Froude number $F_\tau = V/\sqrt{gL}$.

We assume that the fluid is incompressible and inviscid and the flow is irrotational. This implies the existence of a velocity potential $\phi(\bar{\mathbf{x}}, t)$ with the fluid velocity $\mathbf{u}$ given by $\mathbf{u}(\bar{\mathbf{x}}, t) = \nabla\phi$, where $\bar{\mathbf{x}} = (\bar{x}, \bar{y}, \bar{z})$ is a field point and t is time. The surface tension is neglected.

Two coordinate systems are used (Fig. 1). $O\bar{x}\bar{y}\bar{z}$ is the earth fixed coordinate system and $Oxyz$ is the moving coordinate system attached to the disturbance which advances with speed V the -$\bar{x}$ direction. Therefore, $\bar{x} = x - F_\tau t, \bar{y} = y, \bar{z} = z$. The plane $O\bar{x}\bar{y}$ and Oxy coincide with the mean position of the free surface and the $\bar{z}-$axis and $z-$axis point upwards. A system of polar coordinates R, β will be introduced in the Oxy plane as an alternative. The problem under consideration is the flow generated by a disturbance starting from rest. The disturbance can be the motion of a singularity below the free surface (representing a submerged solid body), or a free surface pressure distribution. The fluid domain D is bounded from above by the free surface S_f and a contour S_∞ sufficiently far from the disturbance.

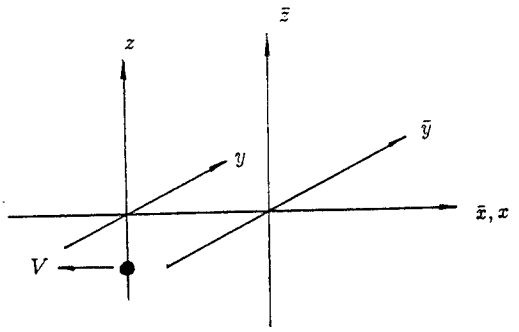

Fig. 1. The coordinate systems.

The continuity equation requires that the potential ϕ satisfy the Laplace equation,

$$\Delta\phi = 0 \qquad (\text{in } D). \tag{1}$$

The free surface boundary is not known *a priori*, it is determined through two boundary conditions. The kinematic condition ensures that a fluid particle on the free surface remains on it,

$$\frac{D\vec{X}_f}{Dt} = \nabla\phi \qquad (\text{on } S_f) \tag{2}$$

where

$$\frac{D}{Dt} = \frac{\partial}{\partial t} + \nabla\phi \cdot \nabla$$

is the substantial derivative following a fluid particle, $\vec{X}_f = (\bar{x}_f, \bar{y}_f, \bar{z}_f)$ is the position vector of a free surface particle and $\bar{z}_f = \eta(\bar{x}, \bar{y}, t)$ is the free surface elevation. The dynamic condition requires that the pressure on the free surface is zero (without loss of generality), unless the disturbance is represented by an ambient pressure p_a over some finite part of S_f. Bernouli's equation can be transformed to

$$\frac{D\phi}{Dt} = -p_a - \eta + \frac{1}{2}|\nabla\phi|^2 \qquad (\text{on } S_f) \qquad (3)$$

At infinity, a proper far-field condition is required. For a three-dimensional initial-boundary value problem, $\phi \to 0$ implies that the flow due to a disturbance vanishes at infinity.

In our time-dependent problems, we study the flow generated by disturbances starting from rest. For initial conditions, we pose

$$\phi = 0 \qquad (\text{in } D \text{ for } t \le 0)$$

and

$$\eta = 0 \qquad (\text{on } S_f \text{ for } t \le 0). \qquad (4)$$

Linear Calculations

Our above problem can be linearized by conventional perturbation methods, with ϕ and η being considered as small quantities. Then ϕ has to satisfy the linearized free surface condition

$$\frac{\partial^2\phi}{\partial t^2} + \frac{\partial\phi}{\partial\bar{z}} = 0 \qquad (\text{on } \bar{z} = 0), \qquad (5)$$

in our dimensionless notation and η can be found from

$$\eta = -\frac{\partial\phi}{\partial t} \qquad (\text{on}\bar{z} = 0). \qquad (6)$$

Considering the simplified case of a flow generated from singularities of given strength rather than by a ship, we need only the potential due to a source-type singularity. General problems can always be represented through linear superposition of the fundamental solution. The time-domain Green function due to an impulsive source $G(P, P', t, t')$ at time t' and location P' is given by

$$G(P, P', t, t') =$$

$$\left(\frac{1}{r} - \frac{1}{\hat{r}}\right)\delta(t - t') + \tilde{G}(P, P', t, t')\, H(t - t'). \qquad (7)$$

where

$$\tilde{G}(P, P', t, t') =$$

$$\int_0^\infty dk\sqrt{k}\sin\left(\sqrt{k}(t - t')\right)e^{k(\bar{z}+\bar{z}')}J_0(k\bar{R}) \qquad (8)$$

is the wavy part, $P = (\bar{x}(t), \bar{y}(t), \bar{z}(t))$ is the field point, and $P' = (\bar{x}'(t'), \bar{y}'(t'), \bar{z}'(t'))$ is the source point. $r = [(\bar{x}-\bar{x}')^2+(\bar{y}-\bar{y}')^2+(\bar{z}-\bar{z}')^2]^{\frac{1}{2}}$ is the distance between the field and source points, $\hat{r} = [(\bar{x}-\bar{x}')^2+(\bar{y}-\bar{y}')^2+(\bar{z}+\bar{z}')^2]^{\frac{1}{2}}$ is the distance between the field point and the image of the source point, and $\bar{R} = [(\bar{x} - \bar{x}')^2 + (\bar{y} - \bar{y}')^2]^{\frac{1}{2}}$. Here, J_o is the zero-order Bessel function, $\delta(t)$ is the delta function, and $H(t)$ is the unit step function.

The Green function $G(P, P', t, t')$ satisfies the following governing equation,

$$\nabla^2 G = -4\pi\delta(P - P')\,\delta(t - t'),$$

with the linear free surface condition on $z = 0$,

$$\frac{\partial^2 G}{\partial^2 t} + \frac{\partial G}{\partial z} = 0 \qquad (\text{on } z = 0),$$

and the initial and far-field conditions,

$$G,\ \frac{\partial G}{\partial t} = 0 \qquad t - t' < 0$$
$$\nabla G \to 0 \qquad \text{as } r \to \infty$$

The potential due to a point source of strength $\sigma(t)$ moving in the path $(\bar{x}' = \bar{x}'(t'), \bar{y}' = \bar{y}'(t'), \bar{z}' = \bar{z}'(t'))$ with zero intensity for $t < 0$ is then

$$\phi(P, t) = \int_0^t \sigma(t')G(P, P', t, t')dt'. \qquad (9)$$

The free surface elevation in the fixed coordinate system is,

$$\eta(\bar{x}, \bar{y}, t) = -\frac{\partial\phi}{\partial t} \qquad (\text{on } z = 0). \qquad (10)$$

For flow in the coordinate system attached to the disturbance, it is adequate to replace $\bar{x}$ by $x - F_\tau t$ and $\frac{\partial}{\partial t}$ by $\frac{\partial}{\partial t} - F_\tau\frac{\partial}{\partial x}$. Then one obtains the wave elevation in the coordinate system moving with velocity F_τ in the $-x$ direction as

$$\eta(x, y, t) = -(\frac{\partial\phi}{\partial t} - F_\tau\frac{\partial\phi}{\partial x}) \qquad (\text{on } z = 0). \qquad (11)$$

We use the subroutine initially developed by Liapis and Beck (1986) and later improved by King (1987) and Magee (1990) to calculate $G(P, P', t, t')$. The time convolution integral in (9) is performed using a simple trapezoidal rule.

Since discretization of the free surface is not necessary in the linear calculations, we are able to consider a large free surface area with a fine grid. The disturbance used is a translating and pulsating source-sink pair. The submergence depth is chosen to be unity as is the separation of the source and sink. Figures 2 to 6 show the wave patterns by the source-sink pair with zero-mean strength for the Froude number based on separation distance $F_\tau = 1.0$ and different values of τ. For $\tau = 0$ (and $F_\tau \neq 0$), we recover the classical Kelvin wave system within the wave cusp angle $\beta_k = \tan^{-1}\frac{1}{\sqrt{8}}$ (Fig. 31). For increasing τ, the system splits up into *two*, bounded by cusp angles β_1 and β_2, with β_1 of the inner system slightly decreasing. The boundary angle β_2 of the outer system approaches a max-

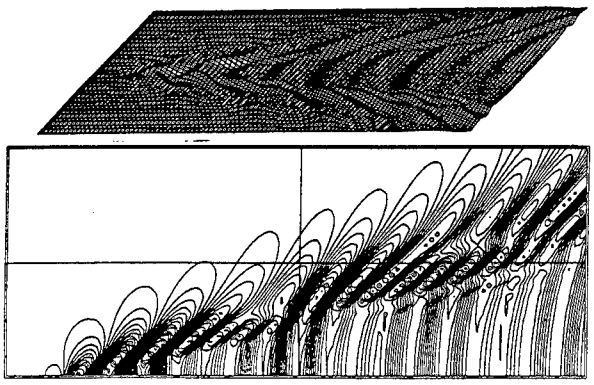

Fig. 2. Waves due to a translating and pulsating source-sink pair with zero-mean strength and τ = 0.125; linear calculation.

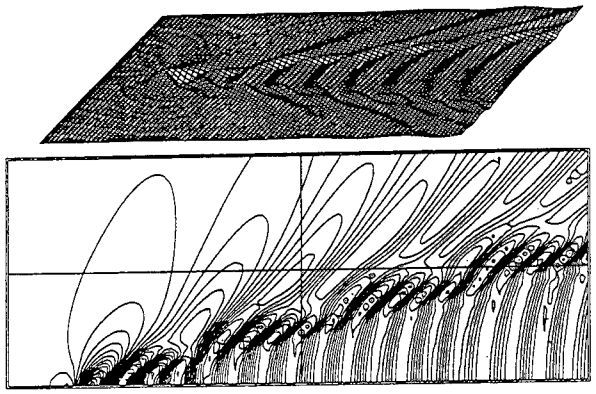

Fig. 3. Waves due to a translating and pulsating source-sink pair with zero-mean strength and τ = 0.25; linear calculation.

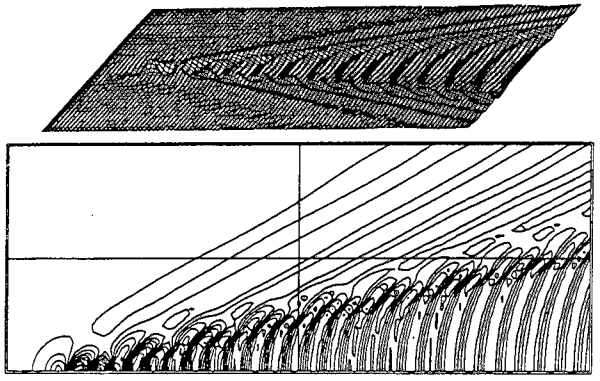

Fig. 4. Waves due to a translating and pulsating source-sink pair with zero-mean strength and $\tau = 0.5$; linear calculation.

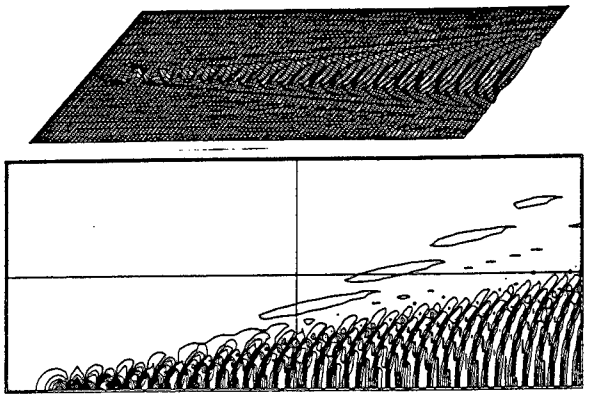

Fig. 5. Waves due to a translating and pulsating source-sink pair with zero-mean strength and $\tau = 1.0$; linear calculation.

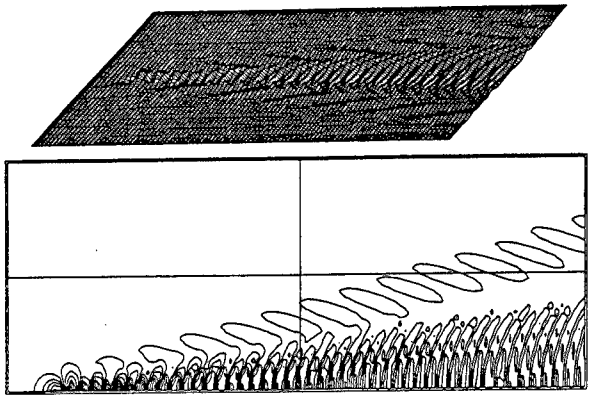

Fig. 6. Waves due to a translating and pulsating source-sink pair with zero-mean strength and $\tau = 2.0$; linear calculation.

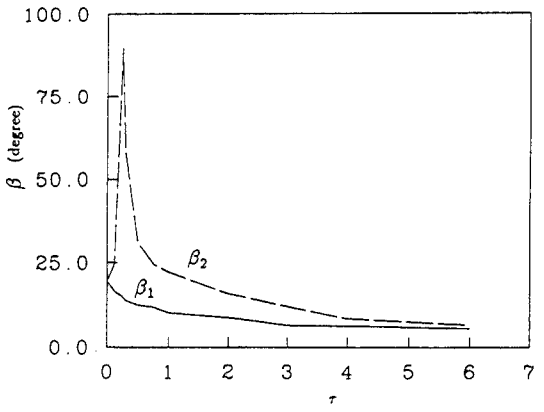

Fig. 7. Bounding line angles *vs.* τ (measured from figures 2 to 6).

imum of order $\pi/2$ for $\tau \approx 1/4$ and then falls off towards β_1 with τ increasing. Fig. 7 shows the angles β_1 and β_2, measured from figures 2 to 6, as functions of τ. From Fig. 7, we may guess that the inner-angle of the Point Brower observations corresponds to β_1 for $1.0 < \tau < 1.5$.

Fig. 8 shows isometric and contour plots of the far-field waves generated by a translating and pulsating source-sink pair with nonzero mean strength and τ=1 which may correspond to the surge motion of a ship. The pulsation amplitude is the same as the mean value. As can be seen, an inner-angle wavepacket is well separated from the Kelvin diverging waves at about 14°.

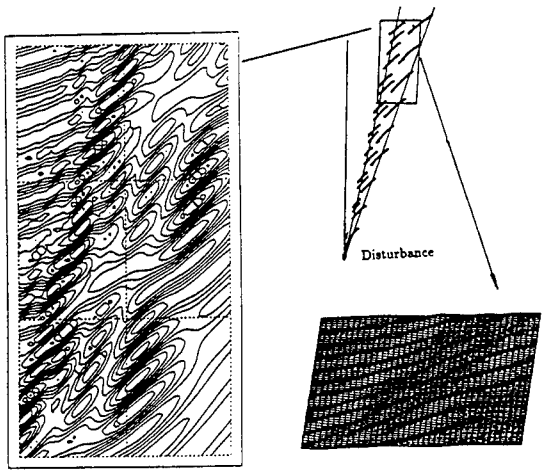

Fig. 8. Far-field waves due to a translating and pulsating source-sink pair with non-zero-mean strength and $\tau = 1.0$; linear calculation.

Far-field Wave Pattern by Method of Stationary Phase

The method of stationary phase provides an easy way to determine far-field wave patterns in terms of curves of constant phase. In this analysis, the particularity of the disturbance does not affect the establishment of the formulas for determining the phase lines as will be shown in the following. Therefore, if the region under consideration is sufficiently far from the disturbance, the far-field wave pattern obtained is independent of the local disturbance details.

Assuming the wake is linear and has reached a time-harmonic state, we can express the velocity potential $\phi(\vec{x},t)$ as

$$\phi(\vec{x},t) = Re\{\varphi(\vec{x})e^{i\omega t}\}, \tag{12}$$

Clearly, the spatial function φ also satisfies Laplace equation. The linearized free surface boundary condition for ϕ in the coordinate system moving with the disturbance in the $-\bar{x}$ direction is

$$\frac{\partial\phi}{\partial z} + \left(\frac{\partial}{\partial t} - F_\tau\frac{\partial}{\partial x}\right)^2\phi = 0 \qquad (\text{on } z = 0). \tag{13}$$

Substituting (12) into (13) gives the free surface condition for φ,

$$\frac{\partial\varphi}{\partial z} + F_\tau{}^2\frac{\partial^2\varphi}{\partial x^2} - 2iF_\tau\omega\frac{\partial\varphi}{\partial x} - \omega^2\varphi = 0 \qquad (\text{on } z = 0). \tag{14}$$

Separation of variables gives

$$\varphi \propto e^{kz}exp\left[i\left(k_x x + k_y y\right)\right] \tag{15}$$

where the wavenumber vector is given by

$$(k_x, k_y) = k(\cos\theta, \sin\theta). \tag{16}$$

Substituting (16) and (15) into (14) gives the relation between k and θ,

$$k = (kF_\tau\cos\theta - \omega)^2. \tag{17}$$

Solving (17) for k gives

$$k_j = \frac{1 + 2\tau\cos\theta + \delta_j\sqrt{1 + 4\tau\cos\theta}}{2F_\tau{}^2\cos^2\theta} \tag{18}$$

with its first derivative

$$\frac{dk_j}{d\theta} = k_j\tan\theta\frac{(\sqrt{1 + 4\tau\cos\theta} + \delta_j)}{\sqrt{1 + 4\tau\cos\theta}} \tag{19}$$

where $\tau = F_\tau\omega$ again is the Brard number and $\delta_j = (-1)^{j+1}, (j = 1, 2)$. Since k is real, we have $(1+4\tau\cos\theta) \geq 0$. So, the region for θ must be restricted to $-\theta_o \leq \theta \leq \theta_o$, where

$$\theta_o = \begin{cases} \pi & \text{if } \tau \leq 0.25 \\ \pi - \cos^{-1}\left(\frac{1}{4\tau}\right) & \text{if } \tau > 0.25 \end{cases}$$

The spatial potential φ can then be expressed as

$$\varphi(\vec{x}) = \sum_{j=1}^{2}\int_{-\theta_o}^{\theta_o} d\theta A_j(\theta)e^{k_j z}e^{i\left(k_{xj}x + k_{yj}y\right)}, \tag{20}$$

where $A_j(\theta)$ is a function depending on the particular disturbance. The wave elevation $\bar{\eta}(\vec{x},t)$ has a form similar to ϕ,

$$\bar{\eta}(\vec{x},t) = Re\{\eta(\vec{x})e^{i\omega t}\} \tag{21}$$

and

$$\eta(\vec{x}) = \sum_{j=1}^{2}\int_{-\theta_o}^{\theta_o} d\theta B_j(\theta)e^{i\left(xk_{xj} + yk_{yj}\right)}$$

$$= \int_{-\theta_o}^{\theta_o} d\theta B_j(\theta)e^{i\,R\psi_j(\beta,\theta)} \tag{22}$$

where $B_j(\theta)$ is a function depending on the the particular disturbance, R and β are the polar coordinates of the field point,

$$(x, y) = R(\cos\beta, \sin\beta)$$

and

$$\psi_j = k_j(\cos\beta\cos\theta + \sin\beta\sin\theta).$$

Evaluation of (22) by the method of stationary phase (Copson 1965) gives

$$\eta(R,\beta) \approx$$

$$\sum_{j=1}^{2}\sum_{m}^{M} B_j(\bar{\theta}_m)\left[\frac{2\pi}{R|\psi_j''(\beta,\bar{\theta}_m)|}\right]^{\frac{1}{2}} e^{iR\psi_j(\beta,\bar{\theta}_m)\pm\frac{1}{4}\pi i} + O(\frac{1}{R}) \tag{23}$$

where $\bar{\theta}_m$ are the stationary points given by

$$\frac{d}{d\theta}\left(\psi_j(\beta,\theta)\right) = 0$$

or

$$x\, dk_{xj} + y\, dk_{yj} = 0. \tag{24}$$

The choice of the "$\pm$" sign in (23) is the same as the sign of the second derivative $\psi''(\beta,\bar{\theta}_m)$. For simplicity, the subscripts m and j and the bar over θ are omitted hereafter.

The curve of constant phase can be obtained without knowing $A(\theta)$ and $B(\theta)$. The curve of constant phase C is given by

$$R\psi(\beta,\theta) \pm \frac{\pi}{4} = C$$

or

$$k_x x + k_y y = c \tag{25}$$

where $c = C \mp \frac{\pi}{4}$. Solving (24) and (25) simultaneously for x and y gives

$$(x, y) = \frac{c\,(dk_y, -dk_x)}{k_x\, dk_y - k_y\, dk_x}\ . \tag{26}$$

With the use of (16), (26) becomes

$$(x, y) = \frac{c}{k^2}\left(k\cos\theta + \frac{dk}{d\theta}\sin\theta\ , k\sin\theta - \frac{dk}{d\theta}\cos\theta\right). \tag{27}$$

Substituting (18) and (19) into (27) gives the parametric equations for the curves of constant phase c,

$$\frac{(x, y)}{{F_\tau}^2} =$$

$$\frac{2c\left[(\delta_j\sin^2\theta + \sqrt{1+4\tau\cos\theta})\cos\theta,\ -\delta_j\sin\theta\cos^2\theta\right]}{(1+2\tau\cos\theta+\delta_j\sqrt{1+4\tau\cos\theta})\sqrt{1+4\tau\cos\theta}} \tag{28}$$

with θ being the parametric variable. Choosing values of C separated by 2π gives a set of phase lines separated by one wavelength. Equation (28) shows that the constant phase lines, further scaled by ${F_\tau}^2$, only depend on τ.

The lines of constant phase developed in (28) do not yet satisfy the radiation condition that all waves must have a group velocity that moves away from the disturbance when referenced to the moving coordinate system. Because of symmetry about y, we will only consider the case of $y > 0$ (thus $\theta > 0$). At first glance, there seems to be two sets of constant phase lines since $j = 1, 2$. By carefully examining (28), we find that for $j = 1$ in (28) positive c satisfies the radiation condition for $0° \le \theta \le 90°$ but not for $90° < \theta < \theta_o$. The constant c must be negative for $90° < \theta \le \theta_o$ to satisfy the radiation condition. So (28) with $j = 1$ gives two systems of constant phase lines which we refer to as the first and second wave systems hereafter. For $j = 2$ in (28), positive c satisfies the radiation condition for $0° \le \theta \le \theta_o$, giving only one system of constant phase lines (the third wave system). Hence, there are three different wave systems in the wake.

Figures 9 to 16 show lines of constant phase C for several values of τ with $F_\tau \neq 0$. For a given value of τ, each figure contains three distinct systems of waves similar to those in Noblesse & Hendrix (1990) using a different approach. For $\tau = 0$ (steady waves), the third system disappears (the wavelength becomes infinitely large), while the first and second systems of the phase lines are identical and the same as the normal Kelvin wave pattern. For $\tau > 0$, the first system is very similar to the Kelvin wave pattern consisting of transverse waves and diverging waves and has a cusp line whose angle is less than the Kelvin angle $\beta_k = 19.5°$. The second system also consists of transverse waves and diverging waves. For $\tau < 0.25$, the cusp line is at an angle larger than 19.5°; for $\tau > 0.25$, the transverse waves in the second system disappear. The third system has ring-type waves for $0 < \tau < 0.25$ and for $\tau > 0.25$, part of the ring-type waves transform into diverging waves.

A line of constant phase C is disconnected at the cusp line of a wave system since the constant c has a jump of $\pi/2$ across the cusp. This is because the second derivative of ψ, ψ'', changes sign across the cusp. Because of this jump, the crests (or troughs) of the transverse waves and the crests (or troughs) of the diverging waves do not meet on the cusp line. The phase lines shown in Noblesse & Hendrix (1990) correspond to the lines of constant c and are continuous at the cusp.

From (28), we have

$$\frac{|y|}{x} = f\frac{\sin\theta|\cos\theta|}{\sin^2\theta + \delta_j\sqrt{1+4\tau\cos\theta}}\ , \tag{29}$$

where

$$f = syn\{c\ \frac{1+2\tau\cos\theta+\delta_j\sqrt{1+4\tau\cos\theta}}{cos\theta}\} \tag{30}$$

Equation (29) for $j = 1$ is plotted in Fig. 17 for various values of τ. The curves for $0° < \theta \le 90°$ correspond to the first system of phase lines and those for $90° < \theta \le \theta_o$ correspond to the second system of phase lines as explained above. Eq.(29) for $j = 2$ is plotted in Fig. 18 for various values of τ.

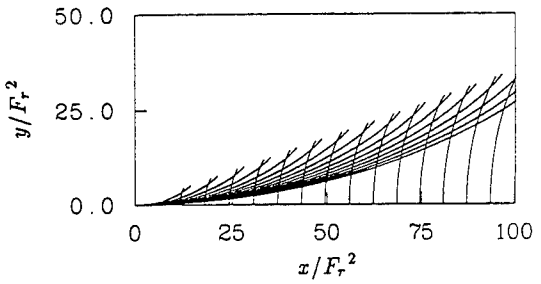

Fig. 9. Constant phase lines of Kelvin wake, $\tau = 0$.

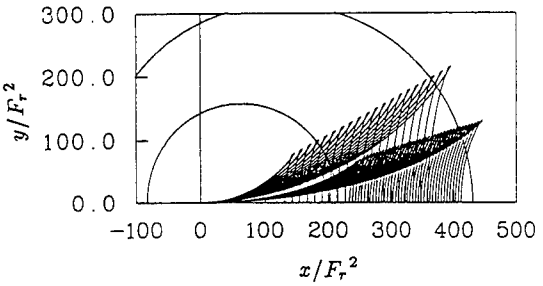

Fig. 10. Constant phase lines, $\tau = 0.2$.

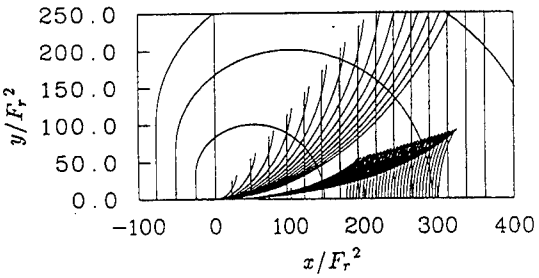

Fig. 11. Constant phase lines, $\tau = 0.25^-$.

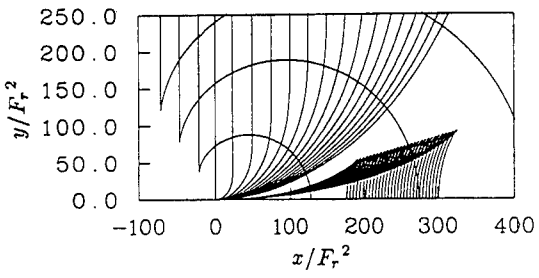

Fig. 12. Constant phase lines, $\tau = 0.25^+$.

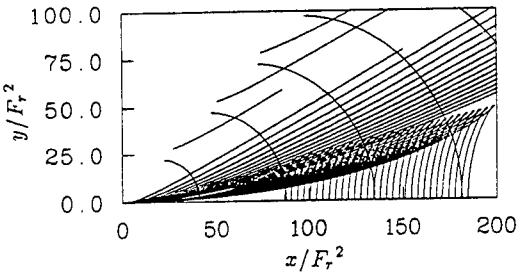

Fig. 13. Constant phase lines, $\tau = 0.5$.

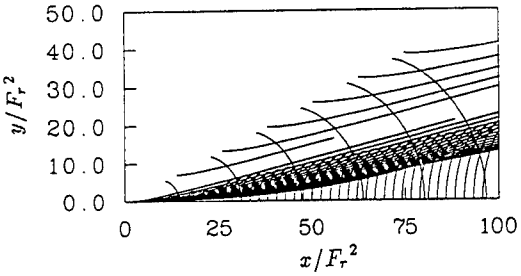

Fig. 14. Constant phase lines, $\tau = 1.0$.

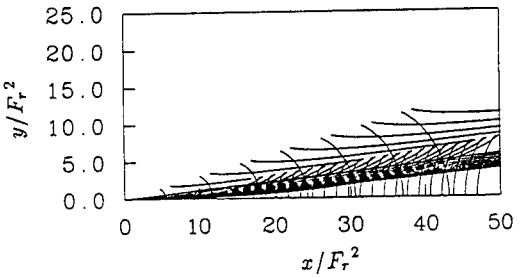

Fig. 15. Constant phase lines, $\tau = 2.0$.

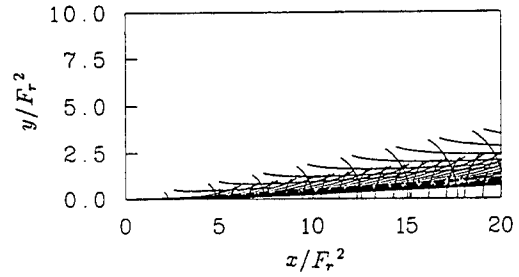

Fig. 16. Constant phase lines, $\tau = 4.0$.

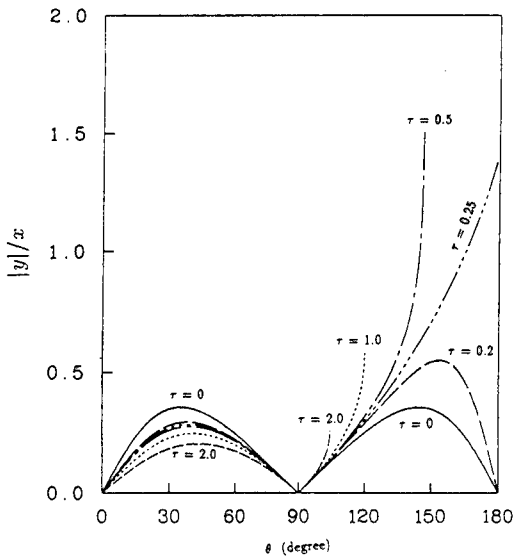

Fig. 17. $|y|/x$ *vs.* θ for the first and second systems.

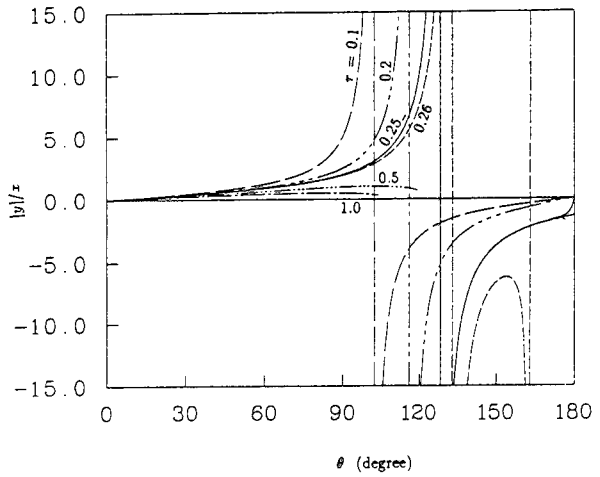

Fig. 18. $\tan^{-1}(|y|/x)$ *vs.* θ for the third system.

The bounding angle for each system can be determined from Fig. 17 and Fig. 18, or from (28) directly. The maximum $|y|/x$ of each system gives the bounding angle $\bar{\beta} = \tan^{-1}(|y|/x)$. For the first system, $0° < \theta < 90°$ in Fig. 17, $|y|/x$ has one maximum which is also a local maximum (*i.e.* the derivative of $|y|/x$ is zero). For the second system, $90° < \theta < \theta_o$ in Fig. 17, $|y|/x$ also has one maximum which, however, is not a local maximum when $\tau > 1/4$. For the third system, Fig. 18, $|y|/x$ can have a maximum of $\pm\infty$ for τ less than a certain value. $|y|/x$ has a jump from ∞ to $-\infty$ (or $-\infty$ to ∞) across an angle θ_c which is the root of $\sin^2\theta_c - \sqrt{1+4\tau\cos\theta_c} = 0$. The infinity of $|y|/x$ does not correspond to the angle of the bounding line. The angle of the bounding line in this system only comes from the local maximum of $|y|/x$ where the derivative of $|y|/x$ is zero. Fig. 19 shows $\tan^{-1}(|y|/x)$ as a function of θ for the third system. From Fig. 19, it is easier to determine the angle of the bounding line by finding the global maximum of $\tan^{-1}(|y|/x)$.

Fig. 20 shows the bounding angles for the three systems (denoted by $\bar{\beta}_1$, $\bar{\beta}_2$ and $\bar{\beta}_3$ respectively) as functions of τ. $\bar{\beta}_1$ is a continuous function of τ. $\bar{\beta}_2$ has a jump from 54.74° to 90° and $\bar{\beta}_3$ has a jump from 180° to 126.26° when τ changes from 0.25− to 0.25+. Fig. 20 can be used conveniently to determine the angles of the inner-angle wavepackets.

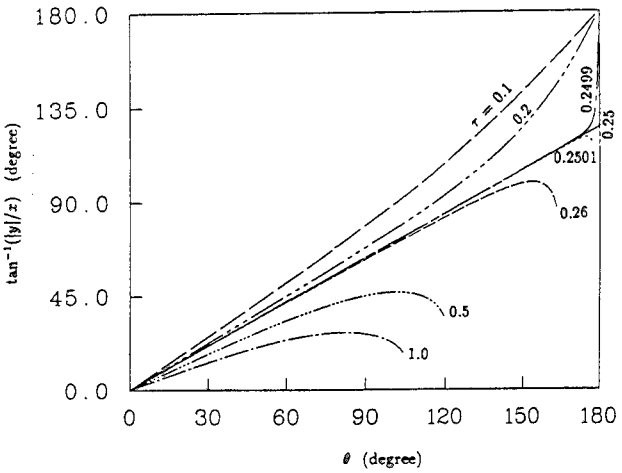

Fig. 19. $\tan^{-1}(|y|/x)$ *vs.* θ for the third system.

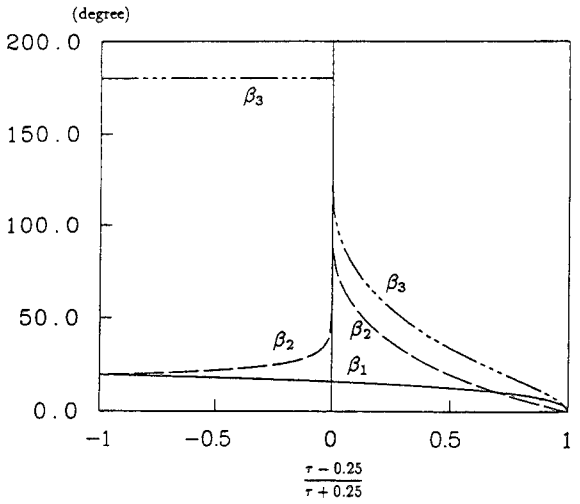

Fig. 20. Bounding line angles β_1, β_2 and β_3 as functions of τ .

The wave decay rate for large R can be estimated by applying the method of stationary phase to (22) without knowing $B(\theta)$ (Copson 1965). The decay rate is closely related to the second derivative of ψ (corresponding to the first derivative of $|y|/x$, Newman 1977). Fig. 17 and Fig. 18 are helpful since they allow one to visualize the first derivatives of $|y|/x$. At a cusp line ($\beta = \bar{\beta}_i$, i=1,2,3), if $\psi_j'' = 0$ but $\psi_j''' \neq 0$, then (23) should be replaced by, (see Copson, 1965),

$$\eta(R,\bar{\beta}_i) \approx \sum_{j=1}^{2}\sum_{m}^{M} 2B_j(\bar{\theta}_m)\Gamma(\frac{4}{3})\{\frac{6}{R|\psi_j'''(\bar{\beta}_i,\theta_m)|}\}^{\frac{1}{3}} e^{iR\psi_j(\beta_i,\theta_m)\pm\frac{\pi}{6}i} + O(\frac{1}{R^{2/3}}) \quad (31)$$

The decay rate along different β can be determined by (23) and (31) with the information on ψ_j'' provided by figures 17 and 18.

- Along β, in which $\beta \neq \bar{\beta}_i$ and $\beta < max(\bar{\beta}_i)$, $i = 1,2,3$, the wave elevation is given by (23) since the second derivative of ψ, ψ'', does not vanish at the stationary points. The waves decay at a rate of $R^{-1/2}$. For simplicity, we express this decay as

$$\eta(R,\beta) \propto \frac{1}{R^{1/2}} + O(\frac{1}{R}). \quad (32)$$

- If β is greater than $\max(\beta_i)$, there are no stationary points and the waves decay faster,

$$\eta(R,\beta) \propto \frac{1}{R} + O(\frac{1}{R^2}). \quad (33)$$

- The decay rates along the bounding angles of the wave systems are as follows:
  - Along $\beta = \bar{\beta}_1$, for all τ, ψ'' is zero for the first wave system at the stationary point while ψ'' is not zero for the other two wave systems. The contribution from the first system dominates and decays as $R^{-1/3}$, while the contributions from the other two systems decay as $R^{-1/2}$. Therefore, the decay rate along $\beta = \bar{\beta}_1$ is

$$\eta(R,\beta) \propto \frac{1}{R^{1/3}} + O(\frac{1}{R^{1/2}}). \quad (34)$$

  - Along $\beta = \bar{\beta}_2$, ψ'' is zero for the second system at the stationary point only when $\tau < 0.25$. When $\tau \geq 0.25$, ψ'' is not zero. Also, ψ'' is also not zero for the other two systems for all τ. Therefore, the decay rate along $\bar{\beta}_2$ is

$$\eta(R,\beta) \propto \begin{cases} \frac{1}{R^{1/3}} + O(\frac{1}{R^{1/2}}) & \text{if } \tau < 0.25 \\ \frac{1}{R^{1/2}} + O(\frac{1}{R}) & \text{if } \tau \geq 0.25. \end{cases}$$

  - Along $\beta = \bar{\beta}_3$, ψ'' is zero for the third system for $\tau > 0.25$. ψ'' is not zero for the other two wave systems for all τ. Therefore, the waves decay as

$$\eta(R,\beta) \propto \begin{cases} \frac{1}{R^{1/3}} + O(\frac{1}{R^{1/2}}) & \text{if } \tau > 0.25 \\ \frac{1}{R^{1/2}} + O(\frac{1}{R}) & \text{if } \tau \leq 0.25. \end{cases}$$

Nonlinear Calculations

In the nonlinear calculations, a time-stepping procedure is employed to solve the initial-boundary value problem. In this procedure, a boundary value problem with the free surface position and the potential known at a given instant of time is solved by the desingularized method to find the velocity on the free surface. Then the position of the free surface and the potential are updated by integrating the nonlinear free surface boundary conditions (2) and (3) with respect to time in a Lagrangian fashion. Computations are conducted in the fixed coordinate system with the use of a moving computational window (Cao 1991).

The indirect version of the desingularized method is used (Cao 1991 and Cao *et al.* 1991). For the waves due to a source-sink pair, the potential ϕ is constructed by the disturbance singularity (a source-sink pair) and a simple Rankine source distribution over an auxiliary surface S_f' of finite extent above the free surface,

$$\phi(\vec{X}) = \frac{-\sigma_o}{4\pi|\vec{X}-\vec{X}_{o1}|} + \frac{\sigma_o}{4\pi|\vec{X}-\vec{X}_{o2}|} + \int\int_{S_f'} \sigma(\vec{X}_s)\frac{1}{|\vec{X}-\vec{X}_s|}ds \quad (35)$$

where $\vec{X}_{o1}$ and $\vec{X}_{o2}$ are the locations of the source and sink respectively. The strength of the pair, σ_o, is given. The strength of the the Rankine source distribution $\sigma(\vec{X}_s)$ on S_f' is determined by satisfying the Dirichlet condition for ϕ on the free surface. To ensure the convergence of the numerical solution, when the integral equation (35) is discretized, the local desingularization distance L_d (distance between the corresponding nodal points on S_f and S_f') is chosen to be related to the local mesh size such that

$$L_d = l_d(D_m)^\nu \quad (36)$$

where D_m is the local mesh size (usually the square root of the local mesh area in a three-dimensional problem). The parameter l_d is independent of the discretization and reflects how far the integral equation is desigularized. The parameter ν affects the accuracy of the numerical integration. A proper choice of l_d and ν is: $1.0 < l_d < 2.0$ and $\nu = 0.5$ (Cao 1991 and Cao *et al.* 1991).

Because of the desingularization, the Rankine source distribution can be replaced by concentrated Rankine sources at the nodal points on S_f', thus reducing the CPU time for the calculation of the influence matrix. A fast iterative solver, GMRES, is used to solve the matrix equation. Since we are interested in the far-field waves, a large computational domain is required resulting in a large matrix equation (number of unknowns $N > 3000$). To accelerate the convergence, a simple and effective preconditioning technique is adapted. We use the influence

matrix at the first time step as the preconditioner (Cao 1991). The preconditioning can make solving the matrix equation 10 times faster. The time integration of the free surface boundary conditions is performed using a fourth-order Runge-Kutta-Fellhberg method.

We first calculate the waves generated by a submerged source-sink pair. The separation, the depth of the submergence, and the strength of the source and the sink are chosen to approximately model the Coast Guard cutter. The cutter has a 25.3m waterline length, $5.2m$ beam, $1.8m$ draught, and the ship speed V was $7.7m/s$ (Brown *et al.* 1989). The source-sink pair starts to move horizontally in the $-\bar{x}$ direction from rest. We use the same separation (87.7% of the waterline length), submerged depth (50% of the draught) and strength (VA_w, where $A_w = 3.3m^2$ is the submerged cross-sectional area near midship) of the source-sink pair as used by Hall & Buchsbaum (1990). The problem is made dimensionless based on the ship's waterline length. The strength of the pair is multiplied by $(1 - e^{-\mu t})$ where μ=2.0. The time simulation is sufficiently long so that the waves behind the pair achieve a steady state. Fig. 21 shows the isometric and contour plots of the waves when the pair has traveled about 16 ship lengths. The wake has essentially become a Kelvin wake although there is an interference between the wave systems by the source and the sink. This interference is not at an angle significantly less than the Kelvin angle in contrast to the observed inner angle of 11° for the Point Brower experiment. In addition, as discussed in a later section, the interference pattern decays at a faster rate than observed.

Steady waves due to two moving free surface pressure patches are shown in figures 22 and 23. Each patch has a length 1 and beam 0.2. The pressure distribution for each patch is

$$p_a(\hat{x},\hat{y},t) = p_o P^x(\hat{x}) P^y(\hat{y}) \tag{37}$$

where

$$P^x(\hat{x}) = \begin{cases} 1 & |\hat{x}| \le 0.8 \\ \frac{1}{2}\{\cos[5\pi(\hat{x} \mp 0.8)] + 1\} & 0.8 < |\hat{x}| \le 1 \\ 0 & |\hat{x}| > 1.0 \end{cases} \tag{38}$$

$$P^y(\hat{y}) = \begin{cases} 1 & |\hat{y}| \le 0.1 \\ \frac{1}{2}\{\cos[10\pi(\hat{y} \mp 0.1)] + 1\} & 0.1 < |\hat{y}| \le 0.2 \\ 0 & |\hat{y}| > 0.2 \end{cases}$$

and $(\hat{x},\hat{y})$ are the local coordinates attached to the centroid of a patch. The centroids of the two pressure patches are separated by 1.8. Froude number based on the patch length is 0.4. In Fig. 22, the pressure is small ($p_o = 0.001$) so the waves are essentially linear. In Fig. 23, the pressure is 20 times larger so the waves are nonlinear (the maximum wave slope is about 0.30). Fig. 24 compares the longitudinal wave cuts of the linear and nonlinear steady waves at different y when the linear waves of Fig. 22 are multiplied by 20. It is surprising in Fig. 24 that the linear and nonlinear waves are so close. A much larger pressure disturbance leads to wave breaking causing the nonlinear calculation to stop. If the nonlinear calculation could have been performed allowing local wave breaking near the disturbance, we would expect to see much larger differences between the linear and nonlinear far-field waves.

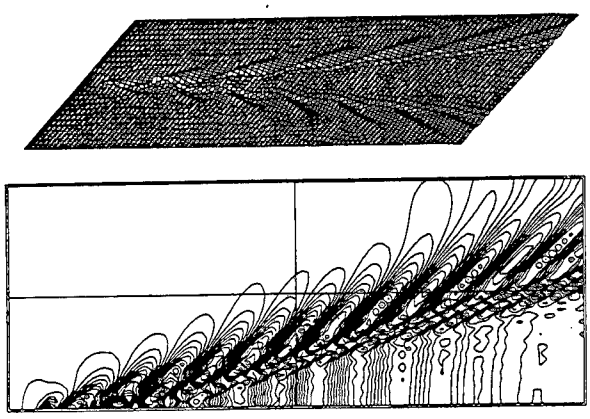

Fig. 21. Waves due to Point Brower (modeled by a translating, non-pulsating source-sink pair); F_r=0.49; nonlinear calculation; free surface domain: ($0 \le x \le 11$ $0 \le y \le 4.5$); Contour lines are apart by 0.005.

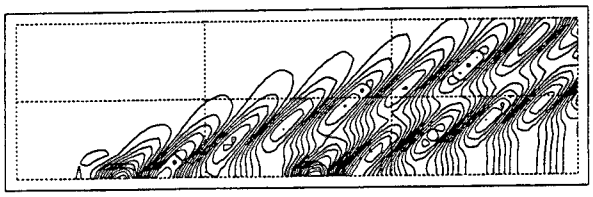

Fig. 22. Waves due to two translating, non-pulsating surface pressure patches (weak disturbance); nonlinear calculation; free surface domain: ($0 \le x \le 5.2$, $0 \le y \le 1.6$); Contour lines are apart by 0.0002.

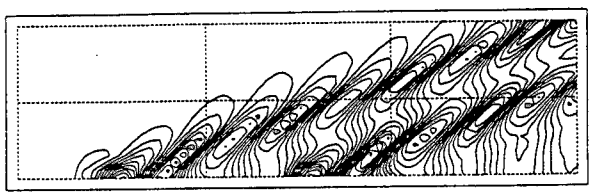

Fig. 23. Waves due to two translating, non-pulsating surface pressure patches (strong disturbance); nonlinear calculation; free surface domain: ($0 \le x \le 5.2$, $0 \le y \le 1.6$); Contour lines are apart by 0.004.

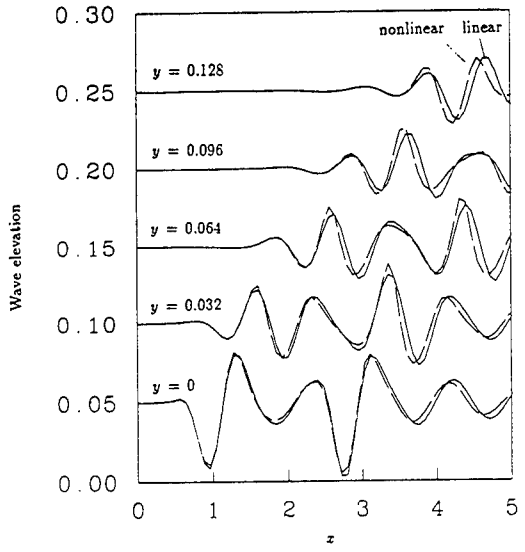

Fig. 24. Comparison of nonlinear waves to "linear" waves due to two translating, non-pulsating surface pressure patches (strong disturbance).

The nonlinear calculation shown in Fig. 23 does not reveal any inner-angle wavepacket at an angle significantly less than the Kelvin angle. Instead, the two wave systems formed by the forward and aft disturbances seem parallel to each other. The computations (not shown here) using other values of the separation distance of the two patches, aiming at the effects of interference of the bow and stern waves, reveal the same feature except when the separation distance is so small that the two wave systems merge into one Kelvin-type wave system.

We then calculate the unsteady wake generated by one pressure patch of form (38) translating at the same speed as that in Fig. 23 in the $-\bar{x}$ axis and pulsating with a frequency ω such that $p_o = p_o \sin \omega t$. Figures 25 to 30 show the waves for different values of τ. For small τ, two wave systems can be seen, one with a bounding angle larger than the Kelvin angle $\beta_k = 19.5°$ and the other smaller than β_k. As τ increases, only one wave system with the smaller bounding angle is visible. Although it is not easy to measure bounding angles precisely from these contour plots, it is clear that both angles decrease with increasing disturbance frequency.

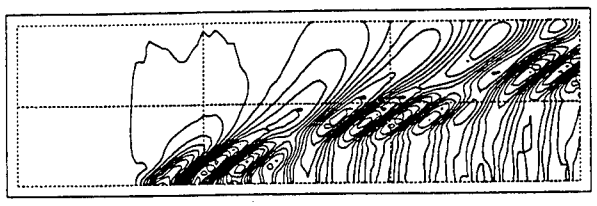

Fig. 25. Waves due to a translating and pulsating surface pressure patch with zero mean,$\tau = 0.25$, $F_n = 0.4$; free surface domain: $(0 \leq x \leq 5.2,\ 0 \leq y \leq 1.6)$; Contour lines are apart by 0.0001.

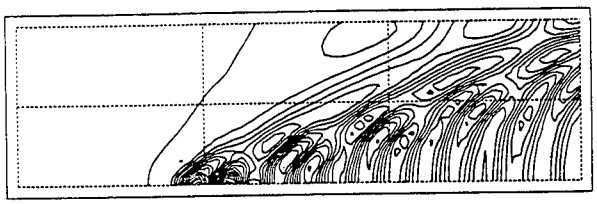

Fig. 26. Waves due to a translating and pulsating surface pressure patch with zero mean,$\tau = 0.5$, $F_n = 0.4$; free surface domain: $(0 \leq x \leq 5.2,\ 0 \leq y \leq 1.6)$; Contour lines are apart by 0.0001.

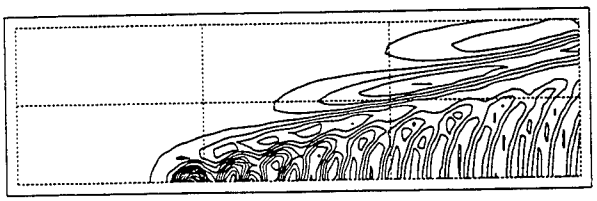

Fig. 27. Waves due to a translating and pulsating surface pressure patch with zero mean,$\tau = 1.0$, $F_n = 0.4$; free surface domain: $(0 \leq x \leq 5.2,\ 0 \leq y \leq 1.6)$; Contour lines are apart by 0.0001.

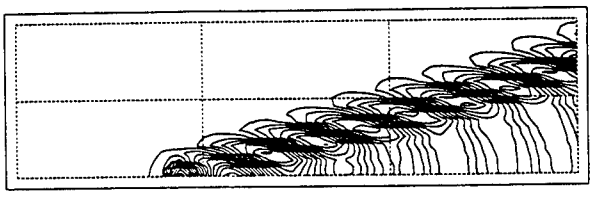

Fig. 28. Waves due to a translating and pulsating surface pressure patch with zero mean,$\tau = 2.0$, $F_n = 0.4$; free surface domain: $(0 \leq x \leq 5.2,\ 0 \leq y \leq 1.6)$; Contour lines are apart by 0.00005.

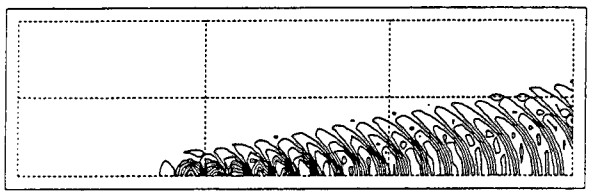

Fig. 29. Waves due to a translating and pulsating surface pressure patch with zero mean,$\tau = 4.0$, $F_n = 0.4$; free surface domain: $(0 \leq x \leq 5.2,\ 0 \leq y \leq 1.6)$; Contour lines are apart by 0.00005.

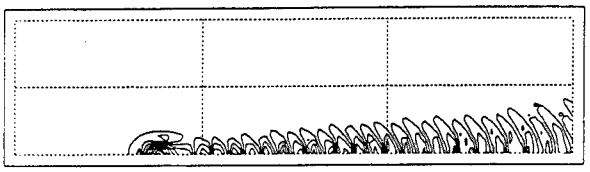

Fig. 30. Waves due to a translating and pulsating surface pressure patch with zero mean,$\tau = 6.0$, $F_n = 0.4$; free surface domain: $(0 \leq x \leq 5.2,\ 0 \leq y \leq 1.6)$; Contour lines are apart by 0.000001.

Comparisons and Discussions

We now can compare the results of the nonlinear calculations, the linear calculations and the stationary phase analysis; and compare the steady and unsteady waves.

Fig. 31 shows the contour plot of the waves generated by the same source-sink pair used in Fig. 21 to simulate the cutter Point Brower using the linear calculation. Both the nonlinear (Fig. 21) and linear (Fig. 31) calculations show similar interference of the wave system caused by the source and the sink. The interference is not clearly separated from the Kelvin diverging waves. Fig. 32 and Fig. 33 show results of the linear and nonlinear wave calculations for the same source-sink pair used in Fig. 21 and Fig. 31 but for unsteady flow. As an example, the unsteadiness is introduced by allowing the source-sink pair to heave with an amplitude of 25% of the mean depth of submergence and τ=0.5. An inner-angle wavepacket is seen separated from the Kelvin diverging waves at an angle between 13.5° and 14.5° in both linear and nonlinear calculations. The wavepacket by the nonlinear calculation seems more isolated. Besides

The unsteadiness could also come from the large eddy separation in the turbulent wake. Rough calculation using the frequency of the vortex shedding from a cylinder at high Reynolds number ($Re = \frac{\rho V d}{\mu}$=$10^4$ to 10^7) (White, 1979) indicates the corresponding τ's in the range of 1.0 to 2.0 are possible. There are obviously many sources of unsteadiness that are in the proper range to give an inner-angle wavepacket between 10° to 15°. The heave example shown in Fig. 32 and Fig. 33 is just one.

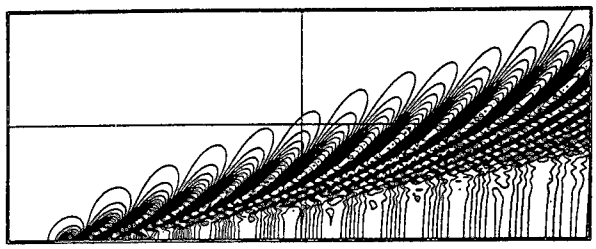

Fig. 31. Steady Waves due to Point Brower (modeled by a translating, non-pulsating source-sink pair); F_τ=0.49; linear calculation; free surface domain: $(0 \leq x \leq 11\ \ 0 \leq y \leq 4.5)$; Contour lines are apart by 0.005.

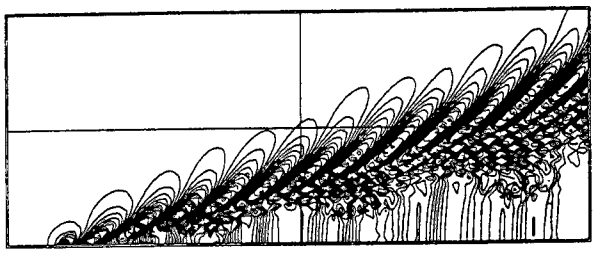

Fig. 32. Unsteady Waves due to Point Brower (modeled by a translating, pulsating source-sink pair); F_τ=0.49; $\tau = 0.5$; linear calculation; free surface domain: $(0 \leq x \leq 11\ \ 0 \leq y \leq 4.5)$; Contour lines are apart by 0.005.

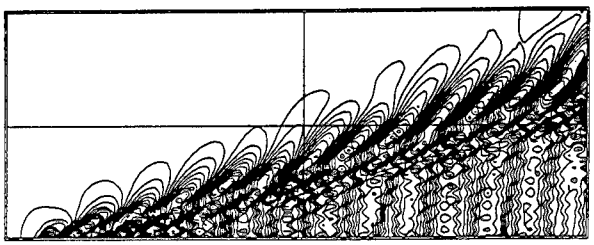

Fig. 33. Unsteady Waves due to Point Brower (modeled by a translating, pulsating source-sink pair); F_τ=0.49; $\tau = 0.5$; nonlinear calculation; free surface domain: $(0 \leq x \leq 11\ \ 0 \leq y \leq 4.5)$; Contour lines are apart by 0.005.

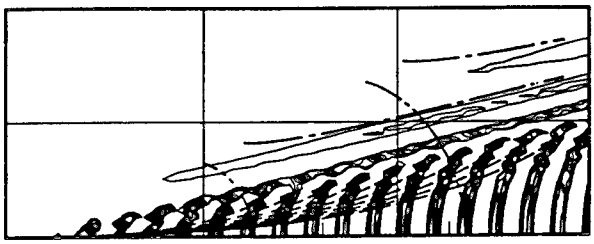

Fig. 34. Comparison of wave contour lines and constant phase lines for linear waves due to a translating and pulsating source-sink pair with zero-mean; $\tau = 1.0$.

Three wave systems are identified in the stationary phase analysis. However, the phase lines do not give the quantitative information about the wave elevation. To calculate the wave elevation, it is necessary to know $A(\theta)$, or $B(\theta)$, which depends on the particular disturbance. It is possible that one may not be able to identify all the three wave systems in the isometric and contour plots of the wave elevation. At low frequency, we see the first and second systems in the plots of the linear and nonlinear waves. The third system is not seen most likely because it has a large wavelength, a small amplitude, or is outside the computational window. At an intermediate frequency, the third system can be identified while it is difficult to distinguish the second system from the first system because the bounding lines of the two systems are close and the waves interact. At high frequency, the second system has a very short wavelength, shorter than our computational grid can resolve. We can see the third system or the combination of the first and third systems but it is difficult to distinguish them from the plots of wave elevation. Fig. 34 shows a contour plot of wave elevation due to a translating, pulsating source-sink pair with a zero-mean strength and $\tau = 1.0$ using the linear calculation. The corresponding constant phase lines are overlayed on the contour lines (note: only positive values of the wave elevation are plotted for a better comparison). The agreement in the wavelength, wave orientations, and the phase in the inner region and outer region is fairly good.

Figures 35 to 39 show the waves due to the same source-sink pair used in Fig. 34 but with $\tau = 0.5$ at five different times within one period of the oscillation, beginning at time $t = 12.0$ when the pair has traveled 18 ship lengths. The period is $100\Delta t$ where $\Delta t = 0.02$ is the time step used in the calculation. As can be seen, the initial transient effects have died out and the waves have almost achieved the time-harmonic state since Fig. 35 and Fig. 39 are nearly identical. To examine how these unsteady waves move, the wave elevation along the symmetry plane and the ray of the inner-angle wavepacket of 14 degrees within one period is shown in Fig. 40 and Fig. 41 respectively. In Fig. 40 and Fig. 41, R is the distance from the center of the source-sink pair. As expected, the transverse waves (Fig. 40) radiate from the disturbance. The waves along the 14° line (Fig. 41) also radiate from the disturbance but with a lower frequency fluctuation. From Fig. 40 and Fig. 41, it can be seen that the wave amplitude along the wavepacket is larger and decays at a slower rate than that along the symmetry plane.

The wave motions can be seen more clearly from the animation of the waves (shown by a video tape). The animation clearly shows that the inner-angle wavepacket originates from the disturbance and moves away from it. The wavepacket fluctuates about the 14° line, which agrees with the observed sinuous fluctuation along the "solitary" feature in the wake of the cutter Point Brower (Brown *et al.* 1989). The animation also shows that there are long-crest waves moving away from the wavepacket periodically, corresponding to the diverging waves of the third wave system in the constant phase analysis. As a wave (*e.g.*, a wave crest) in the wavepacket moves along the 14° line, half of it merges into one of the long-crested waves and the other half keeps moving along the wavepacket.

Fig. 42 shows the peak wave amplitude within the diverging wave system of the steady wake in Fig. 21 by nonlinear calculation. The peak wave amplitude at a distance x is obtained by searching for the maximum wave amplitude in the y direction within the diverging-wave region ($15° < \beta < 19.5°$). Fig. 43 shows the peak wave amplitude within the region ($10° < \beta < 15°$) of the interference between the bow and stern wave systems in Fig. 21. Fig. 44 and Fig. 45 show the peak wave amplitudes within the diverging wave and interference regions for the steady wake in Fig. 31 by linear calculation. Both linear and nonlinear results show that the waves within the interference region decay at $O(R^{-1/2})$, faster than the waves within the diverging-wave region ($O(R^{-1/3})$). This is consistent with the results of the linear steady Kelvin wake theory (Ursell 1960).

For an unsteady wake, Fig. 46 shows the peak amplitudes within the inner-angle wavepacket of the waves in Fig. 33 by nonlinear calculations. The results for three different times are shown by three different symbols. Fig. 47 shows the the peak amplitudes within the the inner-angle wavepacket of the linear wake (at five different times, figures 35 to 39). The upper envelope of the amplitude in each figure gives the decay rate of the wavepacket amplitude. A straight line showing the algebraic decay rate by the stationary phase analysis is drawn at the upper bound of the peak amplitude in each of the figures. As can be seen, the waves by both nonlinear and linear calculations decay at a rate close to $O(R^{-1/3})$ within the inner-angle wavepacket. This is consistent with the result of the stationary phase analysis for the unsteady wake.

The experimental data of Brown *et al.* (1989) are also redrawn in Fig. 48 to show the algebraic decay of the peak amplitude. The observed decay rate is closer to the $O(R^{-1/3})$ decay rate given by the unsteady theories for the unsteady inner-angle wavepacket.

Conclusions

The nonlinear and linear computations, as well as the stationary phase analysis for the waves due to the source-sink pair or surface pressure patch, have shown that the nonlinear effects are not essential to the generation and persistence of inner-angle wavepackets. The unsteadiness of the wake due to the translation and pulsation of a disturbance can cause the inner-angle waves. The angle of the the inner-angle wavepacket decreases with the reduced frequency. The inner-angle wavepacket decays at the same rate as the Kelvin diverging cusp line. The

generation and persistence of the inner-angle wavepacket can be explained by linear unsteady wave theory. The observed inner angle of 11 degrees in the full scale measurement on the Coast Guard cutter Point Brower corresponds to $1.0 < \tau < 1.5$.

Acknowledgment

This work was supported under the Program in Ship Hydrodynamics at The University of Michigan, funded by The University Research Initiative of the Office of Naval Research, Contract Number N000184-86-K-0684. Computations were made in part using a Cray Grant, University Research and Development Program at the San Diego Supercomputer Center.

References

Akylas, T.R., Kung, T.J. & Hall, R.E. 1988 Nonlinear groups in ship wakes. *proc. 17th Symp. on Naval Hydrodynamics*, The Hague, pp. 422-489.

Beck, R.F. and Magee, A.R. 1990 Time-domain analysis for predicting ship motions. *Proc. of the IUTAM symp. on Dynamics of Marine Vehicles and Structures in Waves*, Uxbridge, U.K.: Brunel University, pp. 49-64.

Brown, E.D., Buchsbaum, S.B., Hall, R.E., Penhune, J.P., Schmitt, K.F., Watson, K.M. and Wyatt, D.C. 1989 Observations of a nonlinear solitary wave packet in the Kelvin wake of a ship. *J. Fluid Mech.* **204**, pp.263-293.

Cao, Y. 1991 Computations of nonlinear gravity waves by a desingularized boundary integral method. Ph.D. Diss., Dept. of Naval Architecture and Marine Engineering, The University of Michigan, USA.

Cao, Y., Schultz, W.W., and Beck, R. F. 1991 Three-dimensional desingularized boundary integral methods for potential problems. *Int. J. Num. Meth. Fluids* **12**, pp. 785-803.

Copson, E.T. 1965 *Asymptotic Expansions.* Cambridge University Press.

Eggers, K. 1957 Uber das wellenbild einer pulsierenden strorung in translation. *Schiff and Hafen* **11**, Hamburg.

Hall, R. 1991 Solitons in ship wakes. in *Of Fluid Mechanics and Related Matters*, (edited by Salmon, R. and Betts, D.), Scripps Institution of Oceanography, Reference series 91-24, pp. 237-248.

Hall, R. and Buchsbaum, S. 1990 A model for the generation and evolution of an inner-angle soliton in a Kelvin wake. *Proc. 18th Symp. on Naval Hydrodynamics*, Ann Arbor, Michigan, USA, pp. 453-464.

King, B.K. 1987 Time-domain analysis of wave exciting forces on ships and bodies. Ph.D. Diss., Dept. of Naval Architecture and Marine Engineering, The University of Michigan, USA.

Liapis, S.J. and Beck, R.F. 1985 Seakeeping computations using time domain analysis. *Proc. of 4th International Conference on Numerical Hydrodynamics*, Washington, D.C.,: National Academy of Sciences, pp.34-55.

Longuet-Higgins M.S., and Cokelet,C.D. 1976 The deformation of steep surface waves on water: I. A numerical method of computation. *Proc. R. Soc. London* **A350**, pp. 1-26.

Magee, A. 1991 Large-amplitude ship motions in the time domain. PhD Diss., Dept. Naval Architecture and Marine Engineering, The University of Michigan, USA.

Mei, C.C. 1991a Ship oscillations and wake solitons. *6th International Workshop on Water Waves and Floating Bodies*, Woods hole, Massachusetts, USA, pp. 179-182.

Mei, C.C. & Naciri M. 1991b Note on ship oscillations and wake solitons. *Proc. R. Soc. London* **A 432**, pp.535-546.

Nakos, D.E. and Sclavounos, P.D. 1990 Ship motions by a three-dimensional Rankine panel method. *Proc. 18th symp. on Naval Hydrodynamics*, Ann Arbor, Michigan, USA, pp. 21-40.

Newman, J.N. 1977 *Marine Hydrodynamics.* The MIT Press.

Noblesse, F. and Hendrix, D. 1990 Fourier-Kochin representation of the flow due to a ship advancing in regular waves. *Proc. of the IUTAM symp. on Dynamics of Marine Vehicles and Structures in Waves*, Uxbridge, U.K., Brunel University, pp. 181-196.

Ursell, F. 1960 On Kelvin's ship wave pattern. *J Fluid Mech.* 8, pp. 418-431.

White, F.M. 1979 Fluid Mechanics. McGraw-Hill, New York.

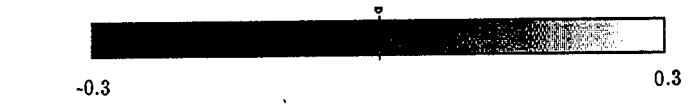

Fig. 35. Unsteady wake due to a translating and pulsating source-sink pair with zero-mean; τ = 0.5; t = 12.0.

Fig. 36. Unsteady wake due to a translating and pulsating source-sink pair with zero-mean; τ = 0.5; t = 12.5.

Fig. 37. Unsteady wake due to a translating and pulsating source-sink pair with zero-mean; τ = 0.5; t = 13.0.

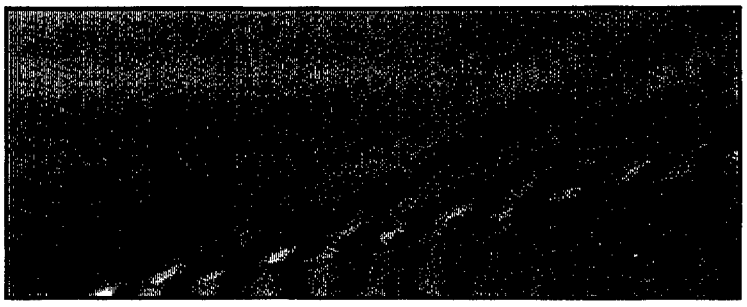

Fig. 38. Unsteady wake due to a translating and pulsating source-sink pair with zero-mean; τ = 0.5; t = 13.5.

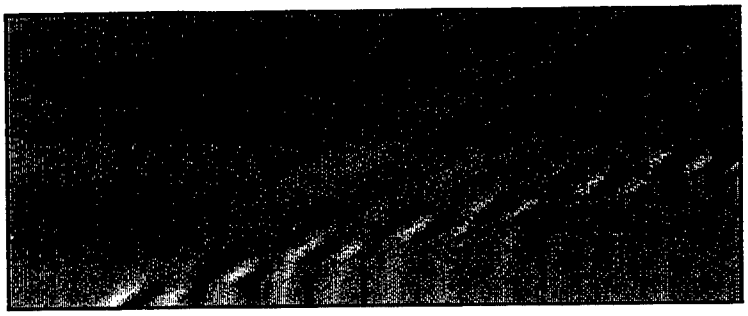

Fig. 39. Unsteady wake due to a translating and pulsating source-sink pair with zero-mean; τ = 0.5; t = 14.0.

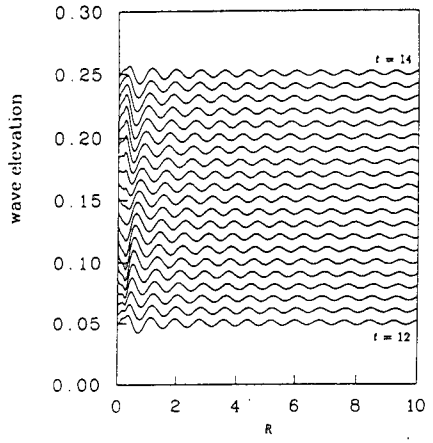

Fig. 40. Wave elevation of figures 35 to 39 along the symmetry plane.

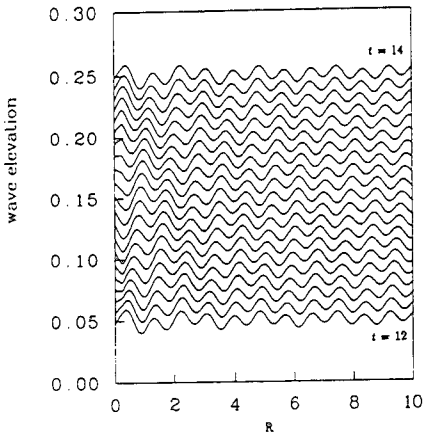

Fig. 41. Wave elevation of figures 35 to 39 along the inner-angle wavepacket.

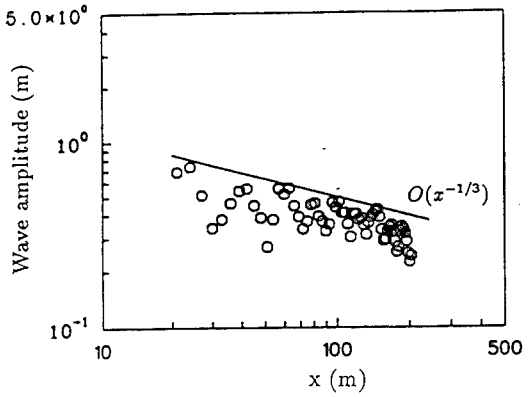

Fig. 42. Peak wave amplitude within the diverging wave region of nonlinear steady wake of Fig. 21.

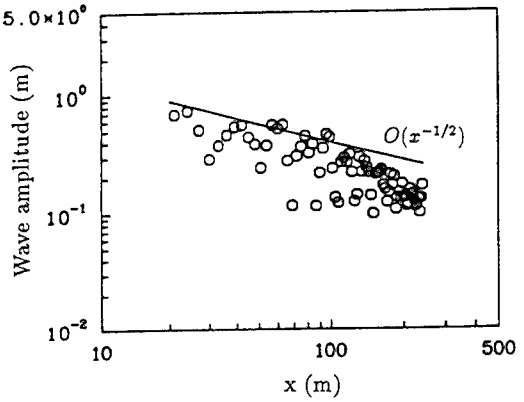

Fig. 43. Peak wave amplitude within the interference region of nonlinear steady wake of Fig. 21.

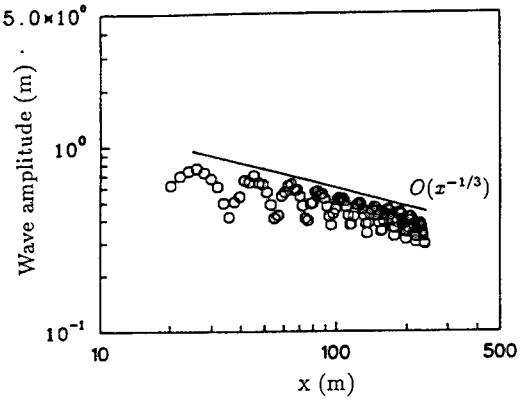

Fig. 44. Peak wave amplitude within the diverging wave region of linear steady wake of Fig. 31.

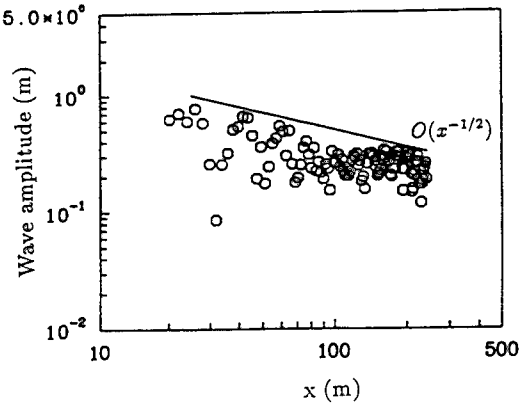

Fig. 45. Peak wave amplitude within the interference region of linear steady wake of Fig. 31.

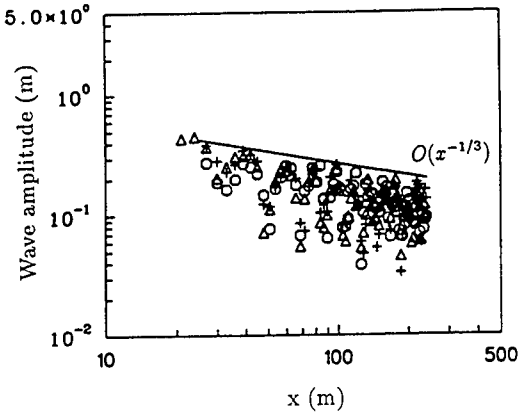

Fig. 46. Peak wave amplitude within the inner-angle interference region of nonlinear unsteady wake of Fig. 21.

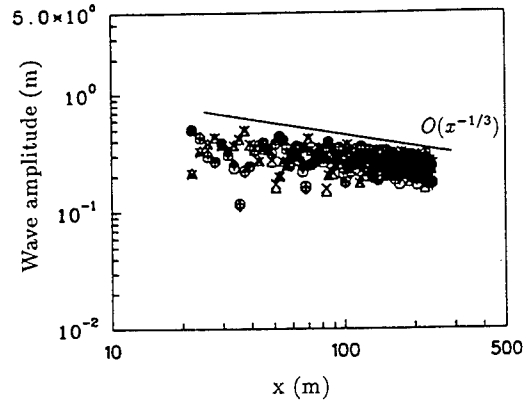

Fig. 47. Peak wave amplitude within the inner-angle interference region of linear unsteady wake of Fig. 31.

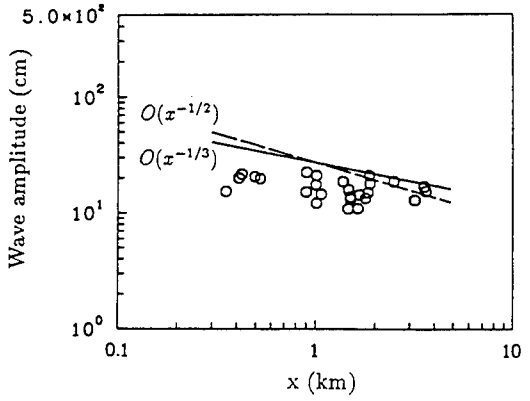

Fig. 48. Peak wave amplitude within the inner-angle wavepacket in the wake of the cutter Point Brower (experimental data of Brown *et al.* redrawn to show the algebraic decay rate).

DISCUSSION

J.-W. Kim
Seoul National University, Korea

Congratulations on your successful explanation for the inner-angle wave packets observed in the Point Brower experiment. I would like to give you two questions. I think the comparison of dispersion parameters, such as wavelengths and frequencies, are important to decide whether this phenomenon is unsteady or not. Have you tried this? My second question is why the inner-angle wave packets cannot be seen in general observations if they can be predicted by linear theories?

AUTHORS' REPLY

A careful to your first question cannot be given because the experiments reported in Brown et al (1989) did not directly measure the wave packet angle but inferred that angle based on steady Kelvin theory. Hence, it is difficult to directly ascertain the importance of the unsteady effects.

We do not mean to claim that these inner-angle wave packets are generally seen. They appear in a minority of all wakes, but seem to be found only on certain ships in moderate seas.

DISCUSSION

M. Tulin
University of California at Santa Barbara, USA

The Point Brower observations have offered a scientific mystery with some practical consequences. I have myself felt uneasy with previous non-linear wave explanations; they seemed strained. The authors are to be congratulated on explaining the inner wave front to unsteady wave generation. The correlation between the observed modulations in the wave front (sinuosity) with the theoretical predictions, for the given angle of the front (11°), is convincing. It remains to offer some explanation of the origin of the unsteady waves. A suggestion: compare the detailed wave structure observed behind the Point Brower with the unsteady wave theory; this is not done in the paper.

The authors do not mention that the inner wave front is a caustic (therefore the $x^{-1/6}$ decay). This is important to realize, since the angle of a caustic front can usually be calculated rather easily from a knowledge of the dispersion relation. The calculation of the entire wave pattern is much more complicated. A historical note: the wave patterns behind a pulsating disturbance for a wide range of τ have been given in the 1950s and 1960s by Hanaoka (as I remember) in a volume published by the Soc. of Naval Architects of Japan (in English).

AUTHORS' REPLY

We would like to thank Prof. Tulin for his kind comments and valuable suggestions.

Sufficient Point Brower experimental data is not available to conduct a detailed wave structure comparison. We would like to do so when the data is available. The cusp (or caustic) angle can be found in the extrema of Eq. 29, but not in a closed form as for steady waves.

We are working on a revision and extension of this work with Prof. Eggers. He has made us aware of the many fine early works by the Japanese in this area.

Wavemaking by Heaving Bodies in Long Tanks, Including Nonlinear Group Formation Near Resonance

M. Tulin, Y. Yao (University of California at Santa Barbara, USA)

ABSTRACT

In view of several practical ramifications of this problem, computational-analytical techniques for calculating waves induced by heaving arbitrary bodies in narrow tanks have been developed. These feature computational nearfield solutions matched with appropriate far field solutions. In the linear case, the far field is provided by linear mode superposition. In the non-linear case, the far field is described by a suitable non-linear evolution equation of the cubic Shrödinger type. Matching techniques were developed. Calculations were successfully carried out on an IBM 2000. The results confirm the important effect of tank walls on added mass and damping.

Results of computations have been compared with some data obtained with a conical wavemaker in a narrow tank. Pronounced wave groups were obtained near resonance, and these are very well reproduced in considerable detail by the non-linear theory and computations, without considering any effects of dissipation.

INTRODUCTION

We have carried out, some years ago, our first experimental studies of shaped wavemakers, Kolaini (1989), and Tulin & Kolaini (1988); the majority of our observations were for a cone which heaved on the tank centerline. The observed wave patterns change dramatically in the vicinity of the frequency corresponding to the first (symmetrical) natural transverse mode (first cut-off frequency), & we observed striking effects there, including the suppression of the planar mode and the generation of nonlinear groups of sloshing (transverse) waves. Subsequently we have carried out analyses & numerical computations to explain these observations quantitatively.

This study is closely related to two areas of related work in the literature. The first area concerns analytical studies of wave effects due to oscillations of a truncated cylinder in a tank, utilizing the linear free surface approximation, see Yeung and Sphaier (1989a; 1989b). The second area concerns theoretical and experimental studies of non-linear wave group formation by a symmetrical wavemaker operating near the first cut-off: Kit, Shemer & Miloh (1987). The first set of authors focussed on the prediction of added mass & damping for heave as well as surge, pitch & sway, over a wide range of frequencies, utilizing linear analytical solutions in series form. In their impressive work, they found sharp but finite peaks and sometimes discontinuities in the computed values of their dimensionless coefficients at the successive cut-off frequencies. The second set of authors concentrated on the measurement & prediction of the non-linear modulated sloshing wave patterns in the tank near the first cut-off frequency; these were produced by a segmented symmetric paddle wavemaker which was operated so as always to produce zero mean paddle displacement & thus avoid the production of planar waves.

The force on oscillating bodies are the integration of pressures resulting from the near field motions, while the wave patterns in the body of the tank themselves define the far field motions. Yeung & Sphaier have avoided the problem of connecting the near & far fields by choosing a body, the truncated cylinder, for which they are able, rather marvelously, to obtain analytical solutions, including both propagating & evanescent modes,

satisfying the linear boundary conditions on both the wavemaker, the free surface & the tank walls. Kit, *et al*, are largely concerned with the wave groups in the far field, which they model with an appropriate non-linear evolution equation. They have attempted connection between this far field model and the wavemaker itself by linearizing the wavemaker boundary conditions and applying them on the back wall of the tank. The resulting theory was able to produce intermittent wave group behavior only after the introduction of large damping, empirically determined.

In our own work we have dealt with both the linear regime (L) of Yeung & Sphaier and the non-linear regime (NL) of Kit, *et al*. For both regimes we distinguish between the near & far fields. In the near field we employ a boundary element plus multiple image computational method; for (L), linearized BC's were satisfied on the undisturbed body & free surface; in (NL) the exact BC's were satisfied on the real boundaries. In the far field we employ different representations in the two cases. In (L) we utilize a series in terms of normal (free wave) modes, omitting only evanescent modes with rapid decay near the wavemaker. In (NL), which applies near a cut-off frequency, we utilize the free propagating wave mode plus a non-linear evolution equation which describes the behavior of the resonant sloshing mode. This equation is determined using a multiple scale analysis following the technique used by Jones (1984) to treat cross waves; the original derivation of the non-linear cubic Schrödinger equation for wave problems in ducts goes back to Aranha, Yue & Mei (1982).

In both (L) & (NL) the near and far field solutions are required to match on a suitable downtank plane across the tank & the solutions are found simultaneously. The method has the advantage that it may be applied to arbitrary bodies.

In (L) we have made computations for a series of bodies of conical shape with elliptic cross section; these were for a range of shapes and relative axis: downtank/crosstank $\gtrless 1$, The cone represents the present body and was studied most extensively, as it was the subject of earlier experiments. These calculations were originally suggested to explain the observed disappearance of the planar mode during oscillation of the cone at the first cut-off, & they did succeed in confirming this observation. As we shall see, however, this striking phenomena is not at all general, depending for a given tank on both the cross section area & shape of the heaving body. For the cone, we have made calculations of added mass & damping up to & near the first cut-off, & found behavior very similar to that found by Yeung & Sphaier for the truncated cylinder. In particular, we have found that the sharp peaks in added mass and damping near the first cut-off have a finite value, which we believe to be actual & not a result of numerical difficulties near the resonant singularity.

In (NL) we have made computations for the heaving cone tested by Kolaini (1989). These calculations reproduced the observed phenomena very well, including : wave group size, shape, spacing & propagation speed, & including the observed amplitude cut-off effect. No dissipation or other empirical adjustments to the theory were required.

In this paper we describe the theoretical & numerical methods and the major results briefly.

BASIC EQUATIONS

Consider a heaving wavemaker with characteristic length scale D, operating at one end of a uniform horizontal channel of breadth b in which the undisturbed depth of liquid is d, the angular frequency of the periodic motion of the wavemaker is ω, a is the stroke of the wavemaker and g is the acceleration due to gravity. The flow is assumed to be incompressible, inviscid and irrotational. Dimensionless variables are defined using a as an amplitude scale, $k=g/\omega^2$ as a lengthscale and ω^{-1} as a timescale. Then the exact equations to be satisfied are

$$\nabla^2\Phi = 0 \tag{2.1a}$$

$$\frac{\partial\Phi}{\partial z} - \frac{\partial\eta}{\partial t} = \varepsilon \frac{\partial\Phi}{\partial x_i}\frac{\partial\eta}{\partial x_i} \qquad \text{at } z = \varepsilon\eta \tag{2.1b}$$

$$\frac{\partial\Phi}{\partial t} + \eta = -\frac{1}{2}\varepsilon \frac{\partial\Phi}{\partial x_i}\frac{\partial\Phi}{\partial x_i} \qquad \text{at } z = \varepsilon\eta$$

where $\varepsilon = ka$

$$\frac{\partial\Phi}{\partial y} = 0 \qquad \text{at } y = \pm\frac{bk}{2} \text{ (side walls)} \tag{2.1c}$$

$$\frac{\partial\Phi}{\partial z} = 0 \qquad \text{at } z = -dk \text{ (bottom)} \tag{2.1d}$$

$$\frac{\partial\Phi}{\partial n} = n_z(x,y,z)\sin(t) \tag{2.1e}$$

$$\text{at } x = f(y, z, \varepsilon \sin t) \text{ (wavemaker surface)}$$

$$\frac{\partial\Phi}{\partial n} = 0 \qquad \text{at } x = 0 \text{ (backwall)} \tag{2.1f}$$

We shall consider separately here two problems:

NL, Nonlinear: ε, δ (= a/D) not small.
Initial boundary value problem;
oscillations started from rest:

$$\Phi(x,y,z;\,0) = 0 \qquad (2.1g)$$

L, Linear: ε, δ small.
Frequency Domain.

In the case of problem NL, the radiation condition is applied downtank:

$$\Phi(x,y,z,t) \rightarrow 0 \quad \text{as } x \rightarrow \infty \qquad (2.1h)$$

In the case of the frequency domain calculation (L), it is assumed that the wave energy is flowing down-tank only (no reflections considered).

Problem NL is especially appropriate in the vicinity of resonant frequencies where the solutions of problem L become unbounded.

The approach used for both problems is to divide the flow field into a near-field (near the wavemaker) and a far-field (down-tank) where the two separate solutions are matched at an appropriate cross section ($x = x_0$) (See Fig 1), which is chosen to be far enough from the wavemaker that the decaying wave modes generated there may be neglected. The near-field is to be determined by the boundary element method, while the far-field is to be described in an analytic manner.

Assuming a flow symmetric about the channel centerplane, the field to be computed may be taken as bounded by the centerplane, wavemaker surface, matching plane and the side, bottom, & back walls. The effects of the centerplane, bottom and back wall may be taken into account by use of suitable image systems. There are seven images of the near-field boundary elements, see Fig 1.

We note that in the general case of a non-symmetric wavemaker shape, one can use three images of the near-field boundary elements to remove the bottom and back walls.

NEAR FIELD

Problem NL :

The near-field $\Phi(s_o)$ and the velocity normal to s_o, $\Phi_n(s_o)$, are related through Green's Third Formula :

$$2\pi\Phi(p)+\int_{s_o}\int [\Phi(q)\frac{\partial G(p,q)}{\partial n} - G(p,q)\frac{\partial \Phi(q)}{\partial n}]ds = 0$$

$$p,q \in s_o \qquad (3.1)$$

where $s_o = s_w + s_f + s_{sw} + s_m$; $\vec{n}$ is the normal to the boundary in the outward direction from the fluid domain; $p = \vec{x}_p$ and $q = \vec{x}_q$; the Green's function G(p,q) is a simple source ($\frac{1}{|p-q|}$) plus its seven similar source images.

In (3.1), $\Phi_n(s_{sw})$ and $\Phi_n(s_w)$ are known (2.1c,e). The exact free surface shape η, and $\Phi(s_f)$ may be determined at each time step through integration of the following relations which apply exactly on s_f:

$$\frac{D\eta}{Dt} = \frac{\partial \Phi}{\partial z} \qquad (3.2a)$$

$$\frac{Dx}{Dt} = \varepsilon\frac{\partial \Phi}{\partial x} \quad \text{and} \quad \frac{Dy}{Dt} = \varepsilon\frac{\partial \Phi}{\partial y} \qquad (3.2b)$$

$$\frac{D\Phi}{Dt} = -\eta + \frac{1}{2}\varepsilon\left[\left(\frac{\partial \Phi}{\partial x}\right)^2 + \left(\frac{\partial \Phi}{\partial y}\right)^2 + \left(\frac{\partial \Phi}{\partial z}\right)^2\right] \qquad (3.2c)$$

where $\nabla\Phi(s_f)$ is known at the previous time step; therefore $\Phi(s_f)$ can be taken as known.

However, both $\Phi(s_m)$ & $\Phi_n(s_m)$ are unknown. They must, however, match their corresponding far-field values on s_m & are therefore related through far-field relationships. These relationships will be discussed subsequently.

Problem L :

In this case, ε is taken as zero in (2.1); $\Phi = \phi\, e^{-it}$, where ϕ is complex; and the equivalence of (3.1) is:

$$2\pi\phi(p)+\int_{s_o}\int [\phi(q)\frac{\partial G(p,q)}{\partial n} - G(p,q)\frac{\partial \phi(q)}{\partial n}]ds = 0$$

$$p,q \in s_o \qquad (3.3)$$

where G(p,q) is the same as above.

In the linear case, $\phi(s_f) = \phi_n(s_f)$, where s_f is the undisturbed free surface. As in (NL), $\phi(s_m)$ and $\phi_n(s_m)$ are known. On s_m, we will require matching of the near and far field, see Matching & Numerical Details.

FAR FIELD

Problem L :

The linear far field free wave modes in the tank are well known, and are represented by three series (in dimensional form):

$$\Phi = \Phi_I + \Phi_{II} + \Phi_{III} \qquad (4.1)$$

where

$$\Phi_I = \sum_{n=0}^{n^*} A_n e^{i(k_{xn} x - \omega t)} \cos (k_{yn} y) \cosh k_z (z + d)$$

$$\Phi_{II} = \sum_{n=n^*+1}^{\infty} B_n e^{-k_{xn} x - i\omega t} \cos (k_{yn} y) \cosh k_z (z + d)$$

$$\Phi_{III} = \sum_{m=1}^{\infty} \sum_{n=0}^{\infty} C_{mn} e^{-k_{xmn} x - i\omega t} \cos (k_{yn} y) \cos k_{zm} (z + d)$$

where,

$$k_{yn} = \frac{n\pi}{b}$$

$$\text{I:} \quad k_{xn}^2 = k_z^2 - k_{yn}^2 \geq 0 \qquad (n \leq n^*) \qquad (4.2)$$

$$\text{II:} \quad k_{xn}^2 = k_{yn}^2 - k_z^2 \geq 0 \qquad (n > n^*)$$

$$\text{III:} \quad k_{xmn}^2 = k_{zm}^2 + k_{yn}^2$$

The wavenumber, k_z, and k_{zm} in (4.2) are given by the set of dispersion relations:

$$\omega^2 = g k_z \tanh (k_z d) ; \quad \omega^2 = - g k_{zm} \tan (k_{zm} d) \qquad (4.3)$$

The first compatibility equation (4.2I) reveals that a sequence of propagating wave solutions exists. Each successive solution begins at a cut-off frequency, $\Omega_{n/2}$, for which k_z (given by 4.3) is equal to transverse wavenumbers, k_{yn}, which are multiples of the half tank wavenumber, $n\pi/b$, see Figure 2.

In the solution, (4.1), the first term comprises a finite series of propagating modes for transverse wavenumbers up to and including the preceding cut-off wavenumber, the second comprises an infinite series of evanescent modes for transverse wavenumbers larger than the preceding cut-off wavenumber, the third comprises a double infinite series of evanescent modes for all combinations of transverse & vertical wavenumbers. An asterisk in (4.1) denotes the cut-off condition.

In the case where the wavemaker operates just below (subcritical) or above (supercritical) the first (symmetrical) cut-off frequency, $\Omega_1 = (2\pi g/b)^{1/2}$, only two of the wave solutions given by (4.1) are important in the far-field, where most of the evanescent waves have died.

$\omega < \Omega_1$:

$$\phi = A e^{ix} \cosh (z+kd) + B e^{-\sqrt{\lambda'} x} \cos (\frac{2\pi}{kb} y) \cosh (z+kd) \qquad (4.4a)$$

$\Omega_1 < \omega < \Omega_2$:

$$\phi = A e^{ix} \cosh (z+kd) + B e^{i\sqrt{-\lambda'} x} \cos (\frac{2\pi}{kb} y) \cosh (z+kd) \qquad (4.4b)$$

where $$\lambda' = \frac{\Omega_1^4 - \omega^4}{\omega^4} = \left(\frac{2\pi}{bk} \right)^2 - 1 \qquad (4.5)$$

is a small parameter of the problem, and the complex numbers A & B are to be determined by solving the entire problem coupling the near and far field.

It is seen that the B component in (1.1) changes across the cut-off frequency, Ω_1, from a decaying mode (subcritical) to a propagating mode (supercritical). Since only propagating modes are associated with damping, this has the consequence that B contributes to the damping only for supercritical conditions; resulting in a discontinuity in damping across Ω_1. The added mass is associated with modes of Φ out of phase with the stroke, both propagating and decaying.

It is fundamental that energy supplied to a given mode (the damping) will propagate downtank at the group velocity c_g of that mode. As a result, for a given quantity of modal damping, the modal energy density within the far field will vary as $(c_g b)^{-1}$.

It is easily shown that within the framework of linear theory, c_g varies as $(-\lambda')^{1/2}$, and thus disappears at Ω_1. As a result, unbounded energy density normally appears at the cut-off frequency & destroys the validity of the linearized theory. It is interesting to realize that this occurs even in the case of finite damping.

Problem NL :

Here we consider only tanks sufficiently deep ($d>b/2$) so that the deep water approximation suffices near the first cut-off. As discussed in the Introduction, an evolution equation for the intermittent wave groups may be determined by a multiple scale analysis. Following Jones (1989), the slow variables which correctly scale the wave group phenomena are:

$$X = \varepsilon x \qquad \tau = \varepsilon^2 t \qquad (4.6)$$

The potential and wave elevation are expanded in ε:

$$\Phi = \Phi_1 + \varepsilon \Phi_2 + \varepsilon^2 \Phi_3 + O (\varepsilon^3) \qquad (4.7a)$$

$$\eta = \eta_1 + \varepsilon \eta_2 + \varepsilon^2 \eta_3 + O (\varepsilon^3) \qquad (4.7b)$$

Multiple scale analysis produces first and second order solutions. The latter are very lengthy in the case where a planar wave coexists near Ω_1 ($A \neq 0$). For the sake of brevity we give here only the case $A=0$ for Φ_2 and η_2:

$$\Phi_1 = A\, e^z\, e^{i(x-t)} + \cos(y)\, e^z[C(X,\tau)\cos(t) + D(X,\tau)\sin(t)] \quad (4.8)$$

$$\eta_1 = iA\, e^z\, e^{i(x-t)} + \cos(y)\, e^z[C(X,\tau)\sin(t) - D(X,\tau)\cos(t)] \quad (4.8b)$$

$$\Phi_2 = [\, 2CD\cos(2t) + (D^2 - C^2)\sin(2t)\,] / 4 \quad (4.9a)$$

$$\eta_2 = \cos(2y)[(D^2 - C^2)\sin(2t) - 2CD\sin(2t) + (D^2+C^2)] / 4 \quad (4.9b)$$

where C, D are defined in terms of a complex evolution function: $F(X,\tau;\lambda) = C + iD$. The detuning parameter λ arises naturally, and defines the closeness to the resonant frequency. It is:

$$\lambda = \frac{\Omega_1^2 - \omega^2}{\varepsilon^2\omega^2} = \frac{\frac{2\pi}{bk} - 1}{\varepsilon^2} \quad (4.10)$$

where we note $\lambda = \lambda'/2\varepsilon^2$.

A third order solvability equation is found in the form of a non-linear partial differential evolution equation for $F(X,\tau;\lambda)$. We have found:

$$i\frac{\partial F}{\partial \tau} + \frac{1}{4}\frac{\partial^2 F}{\partial X^2} - \frac{1}{2}JF + \frac{1}{8}\,|F^2|\,F = 0 \quad (4.11)$$

where

$$J = \lambda + \frac{4\sqrt{2}-5}{14}|A^2|$$

so that in the presence of planar waves J replaces λ as the detuning parameter ; it expresses the influence of already existing planar waves of amplitude A upon the generation & propagation of the sloshing wave groups.

MATCHING & NUMERICAL DETAILS

Problem L :

Boundary conditions on s_o are given except on s_m, where the near & far field are required to match. For $\omega<\Omega_2$, the far field is represented by only two modes, A & B, see (4.4). The matching is accomplished by requiring $\phi_n(\text{near}) = \phi_n(\text{far})$ at each grid point on s_m and requiring two integrals of ϕ over s_m to match in the near and far fields. These integrals are:

$$\int_0^{\frac{bk}{2}}\int_{-dk}^{0} \phi(\text{near})\cosh(z+kd)\,dzdy$$

$$= \int_0^{\frac{bk}{2}}\int_{-dk}^{0} \phi(\text{far})\cosh(z+kd)\,dzdy$$

$$= A\, e^{ix_o}\frac{bk}{2}\left(\frac{\sinh(2dk) + 2dk}{4}\right) \quad (5.1a)$$

$$\int_0^{\frac{bk}{2}}\int_{-dk}^{0} \phi(\text{near})\cos(\frac{2\pi}{bk})\cosh(z+kd)\,dzdy$$

$$= \int_0^{\frac{bk}{2}}\int_{-dk}^{0} \phi(\text{far})\cos(\frac{2\pi}{bk})\cosh(z+kd)\,dzdy$$

$$= B\, e^{i\sqrt{-\lambda'}\,x_o}\frac{bk}{4}\left(\frac{\sinh(2dk) + 2dk}{4}\right) \quad (5.1b)$$

As a consequence, $\phi_n(\text{near}) = \phi_n(\text{far})$ on s_m,

All of the variables in (3.3) & (4.4) are complex, so separation into real and imaginary parts doubles the number of equations. The resulting matrix needs only to be solved separately for each frequency, & was solved by the generalized minimal residual method; approximately 60 seconds CPU time per frequency were required on the IBM 2000. Constant boundary elements were utilized & the control points were taken at the panel center. Convergence tests were carried out. Approximately 700 panels were utilized on s_o and convergence within 5% is estimated.

Problem NL :

The non-linear evolution equation is discretized by a semi-implicit finite-difference scheme of the Crank-Nicolson type. The nonlinear term is quasi-linearized by the explicit estimation as Aranha *et al.* did (1982). The space step for the far-field was chosen as $\Delta X = 0.2$, and the time-step (Δt) was chosen as one twentieth of the wavemaker period. In order to eliminate the influence of the far end of the tank, the domain of calculation was two to three times as long as actual. The solution, F, was taken as zero at the end of the tank. The motion started from rest and F was determined simultaneously with the solution of the near field problem.

Matching was accomplished by requiring $\Phi_n(\text{near}) = \Phi_{1n}(\text{far})$ on s_m and that two integrals of the fields match at s_m, One of these is an integral of Φ over s_m, as in (L), and the other an integral of η over the tank width at x_o:

$$\int_0^{\frac{bk}{2}}\int_{-dk}^{0} \Phi(\text{near})\cos(y)\, e^z\,dzdy$$

$$= \int_0^{\frac{bk}{2}}\int_{-dk}^{0} \Phi_1(\text{far})\cos(y)\, e^z\,dzdy$$

$$= [\, C(x_o,\tau)\cos(t) + D(x_o,\tau)\sin(t)]\,\frac{bk}{8} \quad (5.2a)$$

$$\int_0^{\frac{bk}{2}} \eta(\text{near}) \cos(y)\, dy$$

$$= \int_0^{\frac{bk}{2}} \eta_1(\text{far}) \cos(y)\, dy$$

$$= [\, C(x_o,\tau) \sin(t) - D(x_o,\tau) \cos(t)] \frac{bk}{4} \qquad (5.2b)$$

These integrals allow the determination of $C(x_o,t)$ and $D(x_o,t)$ through the matrix solution at each time step.

The number of panels in the near field was approximately two third of that in (L), and the number of equations one third.

Each complete case shown in Figure 7 (about 7000 time steps) involved 10 hrs CPU time on the IBM 2000; or about 7 seconds per time step.

NUMERICAL RESULTS & COMPARISONS

The experiments of Kolaini (1989) were carried out in a wave tank of cross-section *3 ft* square and length *75 ft* with a conical wavemaker of 76 degrees total angle; the average water depth was *60 cm*, the average draft of the wavemaker was *23 cm* and the diameter was 33.3 *cm*.

Problem L :

The amplitude of the propagating planar wave was observed to disappear at Ω_1 during tests. In Figure 3, the results of linear calculations confirm a very small value of the wave amplitude there (about .5% of the stroke). However, in the case of the widest tank calculated (b/D=6.0), the wave amplitude at Ω_1 is only slightly smaller than its maximum value.

The behavior of the planar wave amplitude approaching Ω_1 was found to depend upon the body shape. The results of calculations for conical bodies of constant total volume but of various elliptical cross sections are shown as Figure 4; we note that the depth in this case was increased over Figure 3, in order to accentuate the effects. These reveal that elongation of the body along the wavemaker alleviates the tendency for the wave to disappear, whereas its elongation downtank accelerates its disappearance. These results show, too, that the observation of disappearance at the cut-off frequency for the cone wavemaker was fortuitous.

If the force on the oscillating body is: $F=F_I \sin\omega t + F_R \cos\omega t$, than the added mass coefficient, $\mu_{33}=F_R/\rho V a\omega^2$, where V is the body volume. The force was calculated by appropriate integration of the body pressures, $\rho\Phi_t$. The results are shown as Figure 5. All of the wave modes, both propagating & evanescent contribute to the added mass, but the rapid rise to a peak at Ω_1 is due to the contribution of the B mode which also peaks there; we estimate that about 60-70% of μ_{33} at Ω_1 is due to the B mode, decaying rapidly on either side of Ω_1. It is interesting that the tank width has a very profound influence on the added mass, everything else constant. This was already computed & noted by Yeung & Sphaier. They have also shown as we show in Figure 5 that narrowing the tank decreases the sharpness of the B peak, and for very narrow tanks causes the peak entirely to disappear.

The damping factor, $\lambda_{33} = F_I/a\omega$, is shown in Figure 6 for the cone. The damping decay approaching Ω_1 is due to the suppression of the planar wave, previously noted. The discontinuity across Ω_1 is due to the propagation of the B wave beyond Ω_1 and not below it. Again, the effect on damping near Ω_1 is exaggerated in the case of wider tanks.

Problem NL :

Kolaini (1989) showed that the heaving motion of the conical wavemaker (b/D=2.7; d/b=.23) near Ω_1 generally resulted in the continuous intermittent propagation of sloshing wave groups downtank, see Figure 7(top). Our major result here is to show that these experimental results are closely reproduced by the present theory, which contains no disposable parameters.

An interesting phenomenon first noted by Kolaini is the suppression of the wave group propagation for strokes below a certain value & the linear increase of wave group speed with stroke above this value, see Figure 7(a). The present theory reproduces the experimental results remarkable well. The same is true of the amplitude, spacing, & shape of the groups, see Figure 8(b).

With increasing stroke, Kolaini found that some of the wavegroups become increasingly deformed in shape with the increasing distance downtank. Utilizing the present non-linear theory we have tested the hypothesis that these deformations might be the result of small variations in tank effective width. The results of a simulation of the effect of width variations of .5% with a period of 4.4 tank widths is shown in Figure 9 (c). The resulting wavegroup shape deformations are suggestive of

those actually measured, see Fig 9(a), and are certainly highly noticeable when compared to the case of uniform width, see Fig 9(b). These results suggest the importance of tank precision in such experiments.

The calculated results for large strokes, Figure 9(b), also reproduce the vertical asymmetry of the measured wave group; this is a consequence of including the second order solution.

DISCUSSION & SUMMARY

The success of the computations presented here demonstrates the utility of near-far field matching to deal with problems of wave generation in tanks by large & rather arbitrarily shaped bodies. The present paper shows, furthermore, how to carry out the matching.

The results obtained in the linear case confirm many of the findings of Yeung & Sphaier (1989) concerning the strong effect of tank walls on the added mass and damping of oscillating bodies. Our own interest in the linear calculation of the planar propagating wave was motivated by the experimental finding of Kolaini (1989) that this wave disappeared at the first symmetric cut-off frequency in the case of a cone of 76° total angle with a diameter/tankwidth about .36. This striking observation was confirmed by the linear computations. But they also revealed that disappearance could occur at sub-critical frequencies for bodies elongated in the downtank direction. There is clearly more to learn about these phenomena in tanks, and it would seem important to do so for the proper interpretation of wave induced forces on bodies in tanks.

When oscillating a body near the first symmetric resonance, large sloshing waves can be generated near the body, which intermittently leave the body to propagate down tank as a wave group. These had previously been observed & studied by Kit, *et al* (1987). Kolaini (1989) has measured these wave groups & found that they were generated only for sufficiently large heaving strokes, & that they propagated with speeds increasing linearly with further increase in stroke. The theoretical prediction of these properties has not been possible based on previously existing theory. It was for this reason that we instituted the near-far field approach, involving a boundary element computation in the near field based on non-linear boundary conditions on the body and the free surface. This approach seems to have succeeded, as not only do the calculations result in propagating wave groups without the introduction of viscous dissipation, but the qualitative behavior of these groups is reproduced surprising well. This sets the stage for the computational studies of such wave groups. It needs to be commented, however, that since the computation for a complete run (7000 time steps) requires 10 hrs CPU time on an IBM 2000, so that the wave tank seems an equally efficient research tool.

In the course of the non-linear research, we have obtained the far field evolution equation for sloshing waves in the presence of propagating planar waves. The result shows that the detuning parameter is increased by addition of planar waves. This is likely to reduce the strength or even eliminate the resonance. This may explain why we have not seen evident wave groups when operating at the second or higher cut-off frequencies.

Finally we should note that the propagating of directional modes by heaving shaped bodies between tank walls can be used for the generation of directional seas in narrow wave tanks for testing purposes, as suggested originally by Tulin & Kolaini (1988). We have been experimenting with specially shaped wavemakers, driven stochastically, for several years now.

ACKNOWLEDGEMENTS

We wish gratefully to acknowledge that the research reported here was carried out under a research grant with the Ocean Technology Division of the Office of Naval Research, Dr Steve Ramberg, Director. We also thank the Computer Center at UCLA for free computation time. And finally, the authors acknowledge useful and important discussions of these problems with both Professor Touvia Miloh of Tel Aviv University and Professor Ronald Yeung of the University of California at Berkeley.

REFERENCES

Aranha, J.A., Yue, D.K.P. and Mei, C.C., 1982, "Nonlinear waves near a cut-off frequency in an acoustic duct - a numerical study", *J. Fluid Mech.*, *121*, pp 456-485.

Jones, A.F., 1984, "The generation of cross-waves in a long deep channel by parametric resonance", *J. Fluid Mech.*, *138*, pp 53-74.

Kit, E., Shemer, L. and Miloh, T.,1987,"Experimental and theoretical investigation of nonlinear sloshing waves in a rectangular channel", *J. Fluid Mech., 181*, pp 265-291

Kolaini, A.R., 1989, "Nonlinear waves near the cut-off frequency", *Ph.D Dissertation, Chapter 5, UCSB.*

Tulin, M.P. & Kolaini, A., 1988, "Steep short-crested waves produced by a simple three dimensional wavemaker", *Proceedings of the 22nd American Towing Tank Conference*, National Academy Press, pp 203-207.

Yeung, R. W. & Sphaier S. H., 1989, "Wave-interference effects on a truncated cylinder in a channel", *J. Eng. Mathematics*, 23, pp 95-117.

Yeung, R. W. & Sphaier S. H., 1989, "Wave-interference effects on a floating body in a towing tank", *PRADs '89*, Varna, Bulgaria, Oct. 23-28, 1989.

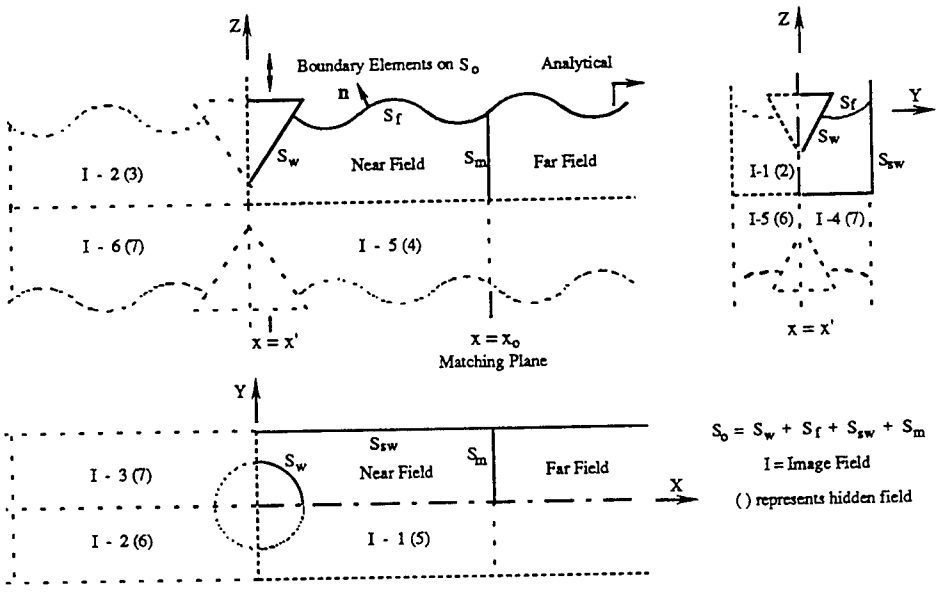

Figure 1. Side, Front, & Top Views of a Large Body in a Tank Showing the Division of the Fields into Near, Far, and Image

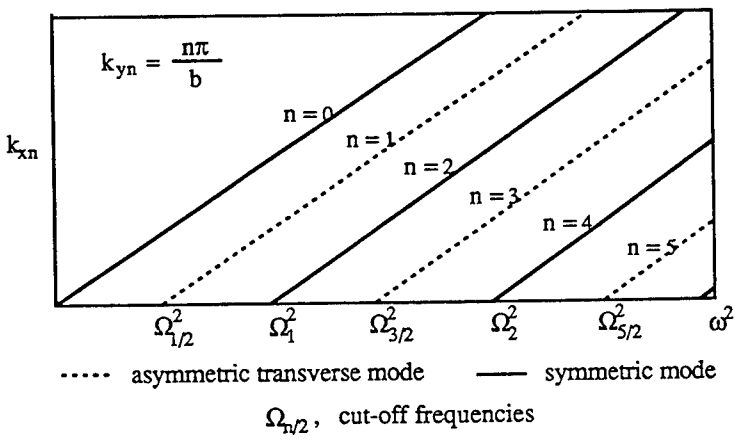

Figure 2. Dispersion Relation for Surface Gravity Waves in a Tank (Schematic)

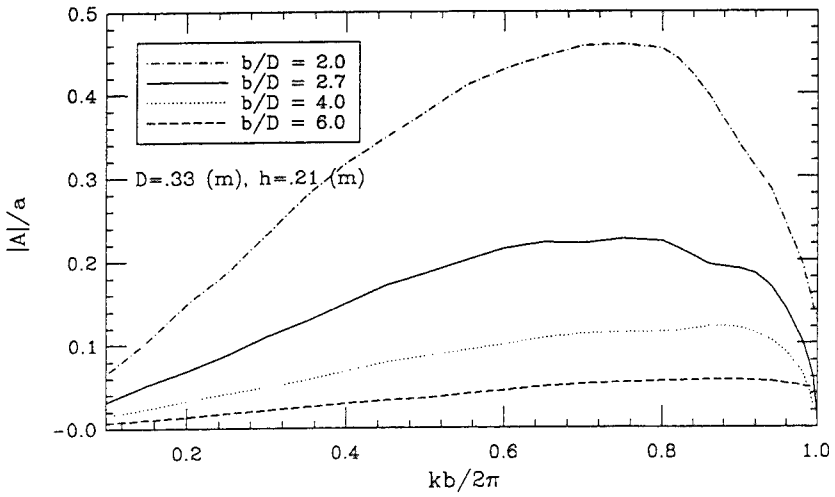

Figure 3. Nondimensional amplitude of the planar wave versus frequency for a half cone wavemaker with various tank widths.

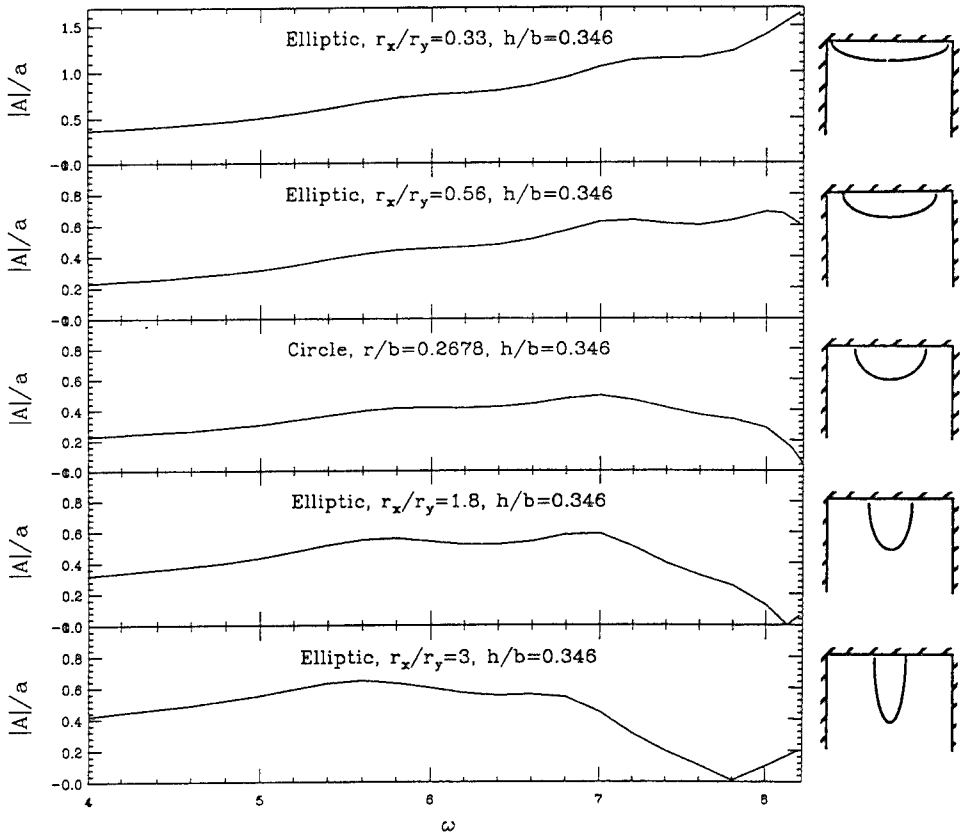

Figure 4. Nondimensional amplitude of the planar wave versus frequency for various wavemakers with constant total volume. (cut-off frequency $\Omega_1 = 8.223$; tank width b = .91 *m*).

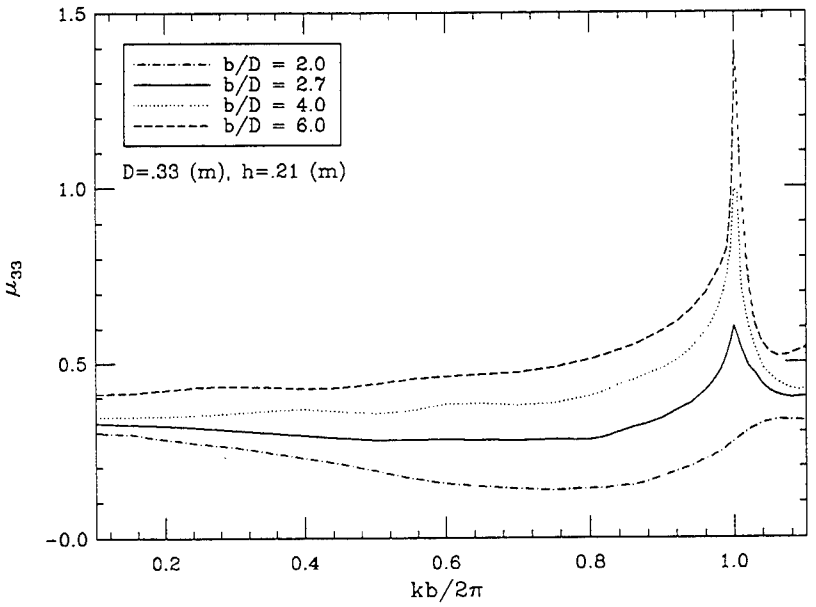

Figure 5. Nondimensional added mass coefficient as a function of kb/2π for a half cone wavemaker with various tank widths.

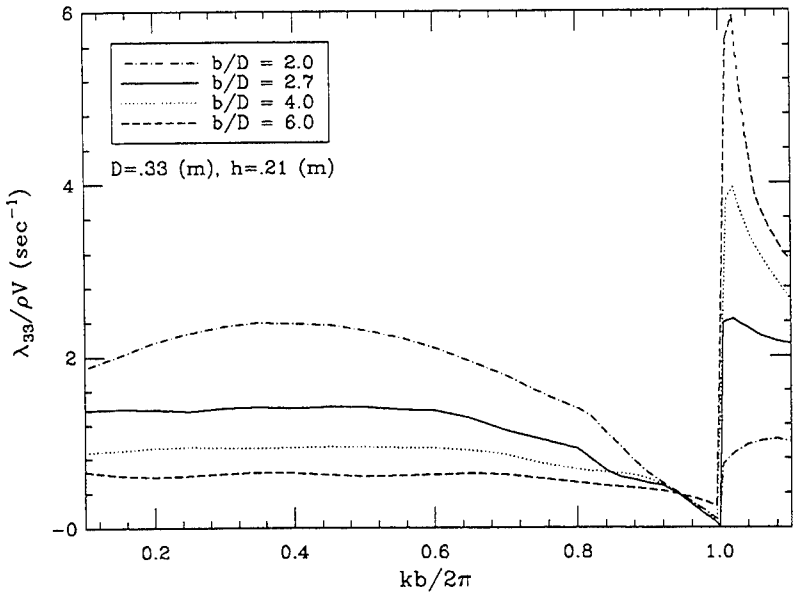

Figure 6. Damping factor as a function of kb/2π for a half cone wavemaker with various tank widths.

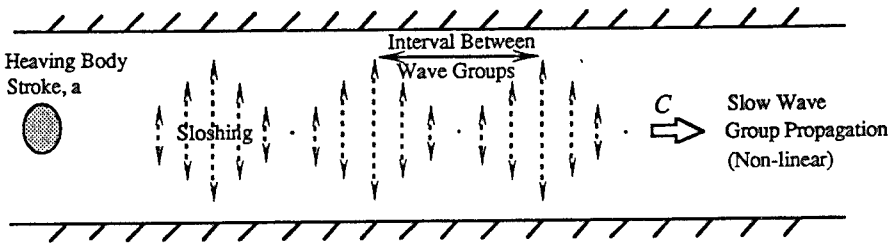

The Situation Near Tank Resonance

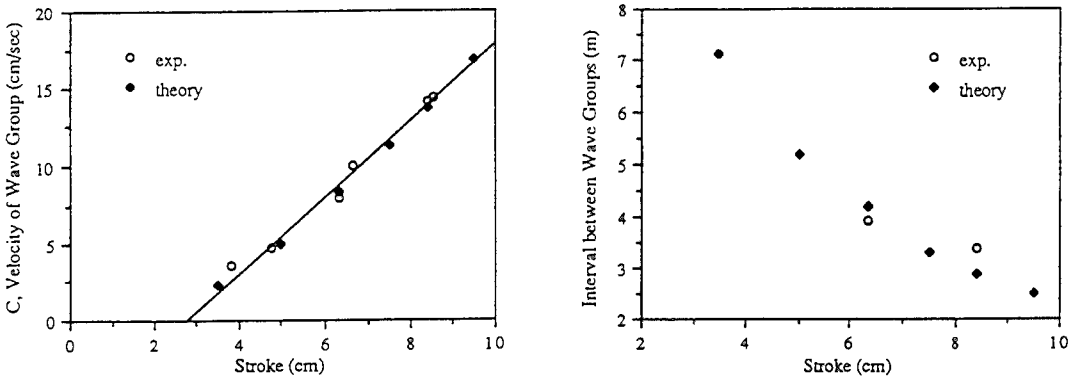

(a) (b)

Figure 7. Non-linear sloshing wave group propagation in the channel with various wavemaker strokes at frequency *1.299 Hz* (cut-off frequency $f_1 = 1.308\ Hz$). (a) - group speed ; (b) - group interval.

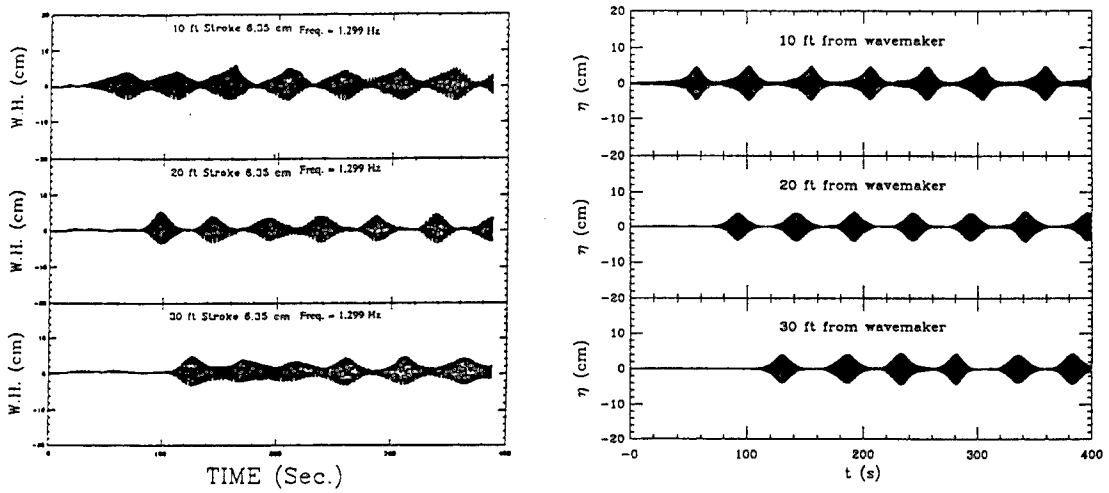

(a) (b)

Figure 8. Sloshing wave heights as a function of time at various locations along the channel with a wavemaker stroke of *6.35 cm* at frequency *1.299 Hz* (cut-off frequency $f_1 = 1.308\ Hz$). (a) - experiment ; (b) - theory.

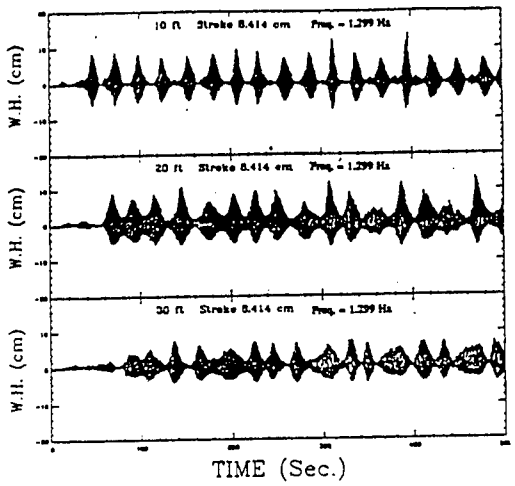

(a)

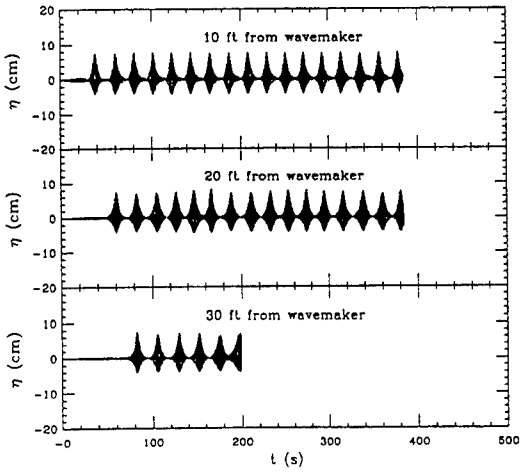

(b)

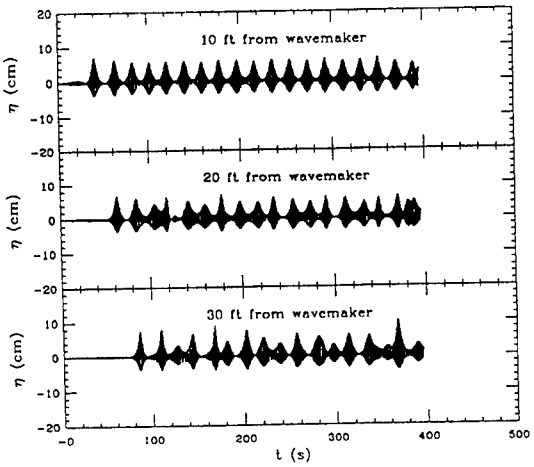

(c)

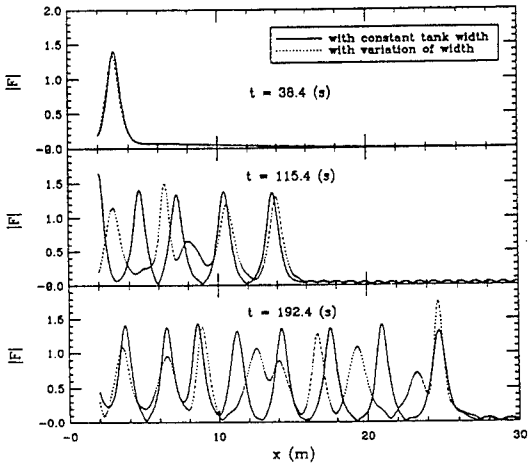

(d)

Figure 9. Sloshing wave heights as a function of time at various locations along the channel with a wavemaker stroke of *8.41 cm* at frequency *1.299 Hz* (cut-off frequency f_1 = *1.308 Hz*). (a) - experiment ; (b) - theory (constant width) ; (c) - theory (wavy width). Numerical solution for sapce-time evolution of | F | (d).

DISCUSSION

R. Yeung
University of California, USA

I want to congratulate the authors for a very fine paper covering both linear and nonlinear behavior of waves near the cross-mode resonance. In the case of linear results, we are most gratified to see that one interesting aspect of our earlier works (Yeung & Sphaier, 1989) is confirmed in the present work, namely, when the body size approaches $\sim 50\%$ of the tank width, it inhibits the occurrence of the first "spike" of the added mass curve. We were fascinated but concerned with the results at the time.

Because of the occurrence of the spikes and "discontinuities" we have also been puzzled by how the actual wave fields will evolve as one crosses the first cut-off. The authors have provided an elegant nonlinear (evolution) model to explain the experimental observations. Can the authors comment on whether or not such a model would also be applicable at the higher cut-off frequencies?

AUTHORS' REPLY

We thank Prof. Yeung for his kind discussion. As he has observed, the results of our calculations of wall effects (Problem L) are quite consistent with his own and have very interesting and even surprising features. More work is desirable, including experimental validation.

It is possible, in principle, to study higher resonances. Of course, the derivation of the evolution equation becomes increasingly more tiresome. It may be of interest that we have not observed any striking resonance effects while operating at the second cut-off and higher, although we did not attempt precise measurements; of course, at these higher resonances, the lower nodes are in general present and can mask subtle higher mode effects.

Session XI

Cavitation and Bubbly Flows

Analysis of a Two-Dimensional Partially- or Supercavitating Hydrofoil Advancing Under a Free Surface With a Finite Froude Number

C.-S. Lee, J.-M. Lew, Y.-G. Kim
(Chungnam National University, Korea)

ABSTRACT

A potential-based boundary element method is presented for the analysis of a super- or partially-cavitating two-dimensional hydrofoil at a finite submergence beneath a free surface, treating without approximation the effects of the finite Froude number and the hydrostatic pressure.

Free surface sources and normal dipoles are distributed on the foil and cavity surfaces, their strength being determined by satisfying the kinematic and dynamic boundary conditions on the foil-cavity boundary. The cavity surface is determined iteratively as a part of the solution.

Numerical results show that the wave profile is altered significantly due to the presence of the cavity. The buoyancy effect due to the hydrostatic pressure, which has usually been neglected in most of the cavitating flow analysis, is found playing an important role, especially for the supercavitating hydrofoil; the gravity field increases the cavity size in shallow submergence, but decreases when deeply submerged, while the lift is reduced at all depth.

INTRODUCTION

Recently the need for a fast ship is increasing not only for the military purpose but also for the transportation of passengers and of modern commercial products[1]. Hull forms of new concept are now under investigations, the hydrofoil being considered a useful means of producing lift in many cases. At a high speed it is impossible to avoid the cavitation on and around the hydrofoil, and hence we should be able to predict with a sufficient accuracy such behavior of cavity as the inception, the extent and the shape, for the proper design of the hydrofoils. Furthermore the hydrofoil-generated wave profile, altered by the presence of the cavity, has to be correctly predicted for the propulsor and/or tandem hydrofoil design.

Researches on the cavity around the body were initiated by Helmholtz in 1868 and Kirchoff in 1869 by the hodograph method. Then in 1907 Levi-Civita extended the method for the flow around the curved obstacle. The first engineering application of these works was made possible half a century later by Tulin[2] for the analysis of the supercavitating flow, and followed by numerous investigations (see, for example, Tulin[2] for the review of general papers related to the cavity flow).

Analysis on the cavitation in practice is carried out under various assumptions. The fluid is assumed incompressible, inviscid and irrotational. The angle of attack, the cavity thickness and the wave amplitude are assumed small to enable the linearization. The cavity termination condition has to be suitably specified. The influence of the hydrostatic pressure term in the cavitating free surface wave analysis has usually been neglected. Our aim is to analyze the cavity flow past a hydrofoil, advancing with a finite Froude number, and at the same time to show the importance of the buoyancy effect, that is, the gravity effect on the submerged foil-cavity system, in the cavity analysis. We therefore review the existing papers in three categories as follows:

- Literature where the buoyancy effect in unbounded fluid is neglected.
- Literature where the buoyancy effect in unbounded fluid is considered.
- Literature where the buoyancy effect in a free surface flow is neglected.

Linear theory for the first category was typically developed by Geurst[3] and Tulin[2] under the assumption that the thickness of the body and the cavity is small compared to the dimension of the body in the main stream direction. Nonlinear analysis was carried out analytically by Wu[4] for the supercavitating flow of infinite cavity length. Numerical analysis to solve the integral equation, formulated based on Green's identity, was first performed by Golden[5], using the discrete vortex/source distribution method for the two-dimensional hydrofoil. This was extended to the supercavitating hydrofoil of the finite span by Jiang[6] and further to the unsteady cavitating pro-

peller by Lee[7], enabling the prediction of cavity extent and volume variation. Analysis up to this point was based on the linear theory. Nonlinear analysis considering the exact cavity and hydrofoil thickness was done by Uhlman[8][9] for the two-dimensional hydrofoil in partially- and supercavitating conditions by the method of vorticity distribution. A new nonlinear boundary element method based on the potential formulation is recently reported by Lee[10], Kim et al[11] and Lee et al[12] for the analysis of the partially- and supercavitating flow around the hydrofoil by using the normal dipole and source distribution on the cavity and foil surfaces. Similar works are also done simultaneously by Kinnas and Fine[13].

The effect of the transverse gravity field, that is, the buoyancy effect, upon the cavity flow in unbounded fluid was first considered by Street[14][15]. He solved the linearized supercavitating flow around a symmetric wedge section, including the hydrostatic pressure, and found that the gravity effect produces the negative lift in the supercavitating flow. Kiceniuk and Acosta[16] then verified the results experimentally. By applying the conformal mapping technique, Larock and Street[17] developed a nonlinear theory and solved a mixed-boundary-value-problem to find that the gravity effect reduces the lift and cavity size. In their analysis they adopted the single spiral model, which permits the sudden velocity jump at the cavity termination point (see Tulin[2] for description of the termination modelings).

The cavity flow beneath a free surface has been dealt with many authors. In early sixties, linear theories were developed treating single flat-plate hydrofoil with a finite cavity near the free surface (see, for example, Yim[18]), and Green and Street[19] subsequently treated by the linear theory two supercavitating hydrofoils of finite cavity length at infinite Froude number. Larock and Street[20] also analyzed the supercavitating flow past a two-dimensional flat plate by using Riemann-Hilbert mapping technique. They treated the finite cavity length problem and adopted the double-spiral cavity termination model. For the hydrofoil of arbitrary section, Furuya[21] applied the nonlinear theory and solved the problem in an iterative manner. It should be noted that the works up to this point are all carried out for the infinite Froude number flow, neglecting the buoyancy effect. Applying Green's theorem, Doctors[22] recently introduced the method of the free surface source distribution on the body and cavity surfaces for the hydrofoil advancing at a finite Froude number. Although he could satisfy the linearized free surface condition, the radiation condition and the infinite depth bottom boundary condition by using the free surface sources, he suffered from a numerical difficulties in his velocity-based formulation, and had to resort to the least square fitting method to remove the highly oscillating behavior of the source strength along the cavity surface. He also neglected the buoyancy effect, while dealing with the finite Froude number problem.

In the present study, we treat the partially- or supercavitating flow past a two-dimensional hydrofoil advancing under a free surface with a finite Froude number. We applied Green's identity to derive the integral equation for the unknown velocity potential on the foil and cavity surfaces. By introducing the free surface dipoles and sources, we satisfy the linearized free surface condition and the radiation condition at the outset. We include the hydrostatic pressure term in evaluating the dynamic condition on the cavity surface and show the significance of this buoyancy effect. The present paper may be regarded as an outgrowth of the authors' series of works [10] [11] [12], where additional details, especially on numerical procedures, may therefore be found.

STATEMENT OF THE BOUNDARY VALUE PROBLEM

Let's consider a two-dimensional cavitating hydrofoil be placed in an inviscid, incompressible and irrotational fluid. A Cartesian coordinate system is chosen as shown in Fig. 1, with the x-axis placed on the undisturbed free surface, S_F, and with the positive y-axis pointing the opposite of the gravitational acceleration. The hydrofoil of the chordlength c is inclined by an angle of attack α relative to the uniform oncoming free stream in the positive x-direction. The leading edge of the foil is located at $x = 0$ and below the undisturbed free surface at $y = -d$, d being the submergence.

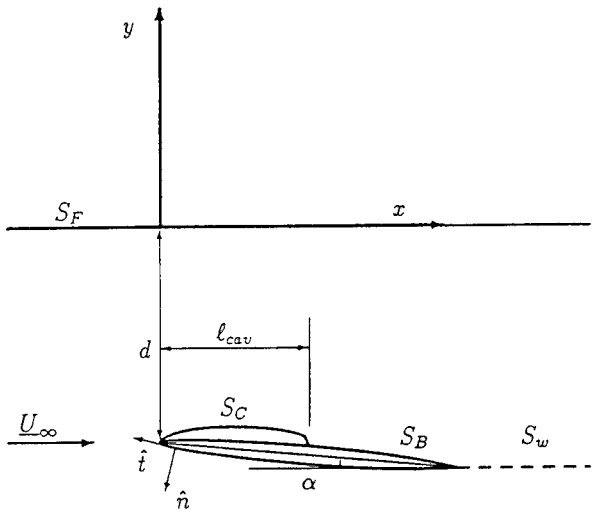

Figure 1: Coordinate system and definition sketch of a cavitating hydrofoil.

The total velocity, $\underline{V}$, may be expressed in terms of the total velocity potential, Φ, which is defined using the oncoming velocity, $\underline{U}_\infty$, the position vector, $\underline{x}$, and the perturbation potential, ϕ, as follows:

$$\underline{V} = \nabla\Phi \tag{1}$$

where

$$\Phi = \underline{U}_\infty \cdot \underline{x} + \phi \tag{2}$$

Conservation of the mass applied to the potential flow gives the Laplace equation as a governing equation, that is,

$$\nabla^2 \Phi = 0 \ , \quad \text{throughout the fluid} \tag{3}$$

We assume that the amplitude of the free surface, ζ_w, or the disturbance is small so that the boundary condition on the free surface may be linearized. Motion of the fluid can be uniquely defined by imposing the boundary conditions on the boundary surfaces as follows:

1. Linearized free surface condition on the free surface:

$$\Phi_{xx} + \nu \Phi_y = 0 \ , \quad \text{on the free surface} \quad S_F \tag{4}$$

where, with $U_\infty = |\underline{U}_\infty|$,

$$\nu = \frac{g}{U_\infty^2} \tag{5}$$

The free surface elevation may be expressed as

$$\zeta_w = -\frac{U_\infty}{g} \phi_x \ , \quad \text{on the free surface} \quad S_F \tag{6}$$

2. Radiation condition at infinity:

$$\lim_{x \to -\infty} |\nabla \Phi| = |\underline{U}_\infty|$$
$$\lim_{x \to +\infty} |\nabla \Phi| < \infty \tag{7}$$

3. Flow tangency condition on the body surface:

$$\hat{n} \cdot \underline{V} = \frac{\partial \Phi}{\partial n} = 0 \ , \quad \text{on the body surface} \quad S_B \tag{8}$$

where $\hat{n}$ is the unit vector normal to the boundary, defined positive when pointing into the fluid region.

4. Quiescence condition at infinite depth:

$$\lim_{y \to -\infty} \nabla \Phi \to \underline{U}_\infty \tag{9}$$

5. Kutta condition:

$$|\underline{V}_{T.E.}| < \infty \ , \quad \text{at the trailing edge} \tag{10}$$

where $T.E.$ stands for the trailing edge.

For the partially cavitating flow, the Kutta condition requires that the magnitude of the velocity be finite at the trailing edge as in the subcavitating flow. The same condition may, however, be implemented in a different way for the supercavitating case, since the trailing edge is the junction point of the two distinct flow regions. The Kutta condition may be restated that the flow across the trailing edge be smooth and continuous. See Lee et al[12] and Wu[4][23] for additional description of the requirement at the junction point, that is, the detachment condition at either the leading or the trailing edges.

With the presence of cavity around the hydrofoil, we have to apply the kinematic and dynamic boundary conditions on the cavity surface, the cavity closure condition at the cavity trailing end and the cavity detachment condition.

6. Kinematic condition on the cavity surface:

$$\frac{DF}{Dt} = 0 \ , \quad \text{on the cavity surface} \quad S_C \tag{11}$$

where $F(x, y)$ is a function expressing the cavity surface.

7. Dynamic condition on the cavity surface:

$$p = p_v \ , \quad \text{on the cavity surface} \quad S_C \tag{12}$$

where p_v is the vapor pressure inside the cavity.

8. Cavity closure condition:

$$T^c(x_{cte}) = 0 \ , \quad \text{at the cavity trailing end} \tag{13}$$

where $T^c(x)$ denotes the cavity thickness function and x_{cte} denotes the x-coordinate of the cavity trailing end.

9. Detachment condition at the trailing edge of the foil in supercavitating flow is the continuity of the velocity vectors at the trailing edge:

$$\lim_{A \to T.E.} \underline{V}_A = \lim_{B \to T.E.} \underline{V}_B \tag{14}$$

where A and B are points positioned on the lower part of the hydrofoil and cavity surfaces connected at the trailing edge, respectively.

Using the Bernoulli equation, we get relations between the surface pressure, p, the tangential speed on the foil-cavity surface, $|\underline{V}_t|$, the cavitation number, σ, and the pressure coefficient, C_p, as follows:

1. Case when the buoyancy effect is not included:

$$C_p \equiv \frac{p - p_\infty}{\frac{1}{2}\rho U_\infty^2} = 1 - \left(\frac{|\underline{V}_t|}{U_\infty}\right)^2 \quad \text{on foil/cavity surface} \tag{15}$$

$$\sigma \equiv \frac{p_\infty - p_v}{\frac{1}{2}\rho U_\infty^2} = -C_{p_v} = \left(\frac{|\underline{V}_c|}{U_\infty}\right)^2 - 1 \quad \text{on the cavity surface} \tag{16}$$

where ρ is the density of water, p_∞ is the ambient pressure at the depth of the leading edge upstream infinity, that is, $p_\infty = p_{atm} + \rho g d$, p_{atm}

being the atmospheric pressure, and $|\underline{V}_c|$ is the tangential speed on the cavity surface.

2. Case when the buoyancy effect is included:

$$C_p \equiv \frac{p-p_\infty}{\frac{1}{2}\rho U_\infty^2} = 1-(\frac{|\underline{V}_t|}{U_\infty})^2 - \frac{2(y-y_{ref})/c}{F_c^2} \quad (17)$$

$$\begin{aligned}\sigma &\equiv \frac{p_\infty - p_v}{\frac{1}{2}\rho U_\infty^2} \\ &= -C_{p_v} = (\frac{|\underline{V}_c|}{U_\infty})^2 - 1 + \frac{2(y_c-y_{ref})/c}{F_c^2} \\ &\qquad \text{on the cavity surface}\end{aligned} \quad (18)$$

where c the chordlength, y_c and y_{ref} the y-coordinates of the cavity surface and the leading edge, respectively, and $F_c = U_\infty/\sqrt{gc}$ the Froude number of the oncoming flow.

In this paper, we are interested in the lift, L, the drag, D, and the moment, M, acting on the hydrofoil in cavitating condition and also the cavity volume, Vol (or, the cavity section area in the present two-dimensional problem).

The nondimensional coefficients of these quantities are defined following the expression of Uhlman[8].

The lift coefficient, C_L, is given as

$$C_L \equiv \frac{L}{\frac{1}{2}\rho U_\infty^2 c} = -\oint_{S_B} C_p \hat{t}\cdot\frac{U_\infty}{U_\infty}\,ds \quad (19)$$

the drag coefficient, C_D, is

$$C_D \equiv \frac{D}{\frac{1}{2}\rho U_\infty^2 c} = -\oint_{S_B} C_p \hat{n}\cdot\frac{U_\infty}{U_\infty}\,ds \quad (20)$$

and the moment coefficient, C_M, about the leading edge of the hydrofoil is

$$C_M \equiv \frac{M}{\frac{1}{2}\rho U_\infty^2 c^2} = -\oint_{S_B} C_p \underline{r}\times\hat{n}\,ds \quad (21)$$

where c denotes the chordlength and $\underline{r}$ denotes a vector from the leading edge to a point on the foil surface; $\hat{t}$ is the unit tangential vector defined in the clockwise direction along the foil surface as shown in Fig. 1.

The cavity volume, Vol, is calculated from the cavity thickness function, $T^c(x)$, as

$$Vol = \int_0^{\ell_{cav}} T^c(x)\,dx \quad (22)$$

where ℓ_{cav} is the cavity length defined along the x-axis as shown in Fig. 1. For supercavitating flow, $T^c(x)$ becomes the vertical extent of the upper and lower cavity surfaces.

SINGULARITY DISTRIBUTION METHOD

From the Green's theorem, we may derive an expression for the potential in the flow field by distributing the normal dipoles and sources on the body surface, or alternatively by distributing only either the normal dipoles or sources as shown by Lamb[24]. From various literatures (see, for example, Moran[25]), we know the lifting airfoil problem can be treated successfully by adopting only the normal dipoles on the foil surface and on the wake sheet. To deal with the cavity flow problem in the present method, in addition to the normal dipoles, we introduce the sources to represent the presence of the cavity on the cavitating portion of the foil. We expect that the sources will serve as a normal flux generator, which may be integrated in the streamwise direction to form the cavity shape, in a similar manner as in the thickness problem of the thin wing theory.

The total potential in the fluid region may now be expressed as follows:

$$\begin{aligned}\Phi(\underline{x}) = U_\infty x &+ \int_{S_B\cup S_C}\frac{\mu(\underline{\xi})}{2\pi}\frac{\partial}{\partial n_\xi}G(\underline{x};\underline{\xi})\,dS \\ &+ \int_{S_C}\frac{q(\underline{\xi})}{2\pi}G(\underline{x};\underline{\xi})\,dS \\ &+ \int_{S_w}\frac{\mu_w}{2\pi}\frac{\partial}{\partial n_\xi}G(\underline{x};\underline{\xi})\,dS\end{aligned} \quad (23)$$

where

$$\begin{aligned}q(\underline{\xi}) &= \text{free-surface source strength}\\ \mu(\underline{\xi}) &= \text{free-surface normal dipole strength}\\ \underline{x}(x,y) &= \text{field point where the induced potentials are calculated, } (x+iy)\\ G(\underline{x};\underline{\xi}) &= \ln(\underline{x}-\underline{\xi}) + \ln(\underline{x}-\underline{\xi}')\\ &\quad + 2\int\frac{e^{-ik(\underline{x}-\underline{\xi}')}}{k-\nu}\,dk - 2\pi i e^{-i\nu(\underline{x}-\underline{\xi}')}\\ \frac{\partial}{\partial n_\xi} &= \text{normal derivative with respect to the point } \underline{\xi}\\ \underline{\xi}(\xi,\eta) &= \text{point where the singularity is located, } (\xi+i\eta)\\ \underline{\xi}'(\xi,\eta) &= \text{complex conjugate of } \underline{\xi}, (\xi-i\eta)\end{aligned}$$

and also S_B, S_C and S_w denote the body surface, the cavity surface and the wake sheet surface, respectively, and μ_w denotes the dipole strength on the wake sheet surface, S_w, which is negative of the jump of potentials across the wake sheet surface. The direction of the dipole in the wake sheet surface, S_w, is defined positive when pointing upward.

For dipole only distribution, we may convert the flow tangency condition (8), $\partial\Phi/\partial n = 0$, in the fluid side of the boundary into the zero total potential condition, for the fictitious internal flow,

$$\Phi^-(\underline{x}) = 0 \quad (24)$$

where the superscript denotes that the velocity potential is to be calculated on the interior to the foil surface (see, for example, Breslin et al[26]). If we apply this

conversion across the dipole and source sheet, we will inevitably introduce errors in the flow tangency boundary condition or nonzero normal flux due to the influence of the sources. Indeed, this normal flux on the current dipole and source sheet is in essence the thickness correction function necessary in searching the cavity shape. If this error term vanishes through iterations, due to the vanishing source strengths, the kinematic condition on the cavity surface will then be satisfied by the alternative form of the kinematic boundary condition for the internal flow (24).

Equation (23) may now be reformed and applied to a point on and inside the foil-cavity surface to meet the alternative form of the kinematic boundary condition (24) as

$$\begin{aligned}\Phi^-(\underline{x}) = 0 = U_\infty x &+ \frac{\mu(\underline{x})}{2} \\ &+ \oint_{S_B \cup S_C} \frac{\mu(\underline{\xi})}{2\pi} \frac{\partial}{\partial n_\xi} G(\underline{x};\underline{\xi})\, \mathrm{d}S \\ &+ \int_{S_C} \frac{q(\underline{\xi})}{2\pi} G(\underline{x};\underline{\xi})\, \mathrm{d}S \\ &+ \int_{S_w} \frac{\mu_w}{2\pi} \frac{\partial}{\partial n_\xi} G(\underline{x};\underline{\xi})\, \mathrm{d}S \end{aligned} \quad (25)$$

In case of partially cavitating flow, μ_w is the negative of the potential jump at the trailing edge, whereas, in fully cavitating flow, μ_w is that at the cavity trailing end. For a steady lifting flow, the negative of μ_w is equivalent to the circulation around the hydrofoil and constant along the wake surface, S_w.

The Kutta condition (10) is replaced by Morino's condition [27] for the present potential based method as

$$\mu_w = -(\Delta\Phi)_w \quad (26)$$

where $(\Delta\Phi)_w$ is the potential jump across the wake sheet surface, S_w, which extends to downstream infinity either from the trailing edge in the partially-cavitating flow or from the cavity trailing end in the supercavitating flow.

Due to the characteristics of singularities, the governing equation (3), the free surface boundary condition (4), and the quiescence condition (9), will automatically be satisfied.

Since $U_\infty x$ in (25) is known, the equation (25) becomes an integral equation for the unknown strengths of source and normal dipole distributions.

By the definition of the velocity potential, we may express the potential on the cavity surface as follows:

$$\Phi^{u,l} = \Phi^{u,l}_{cdp} + \int_0^{l_g} |\underline{V}_c|\, \mathrm{d}s \quad (27)$$

where the superscripts, u and l, represent the upper and lower surfaces of the cavity, respectively, and the subscript *cdp* denotes the cavity detachment point and l_g denotes the girth length along the cavity surface from the cavity detachment point to the point where the potential is calculated.

Thus, Φ^u and Φ^l denote the velocity potentials on the upper and lower surfaces of the cavity in case of the fully cavitating flow, respectively. Φ^u_{cdp} and Φ^l_{cdp} become the velocity potentials at upper and lower cavity detachment point, respectively. For the partially cavitating flow with positive angle of attack, only the velocity potentials on the upper surface of the cavity, Φ^u and Φ^u_{cdp}, are considered.

Equation (27) relates the tangential speed on the cavity surface to the velocity potential, which is really a useful form, since the speed on the cavity surface, $|\underline{V}_c|$, is related to the unknown variables Φ or μ.

The source strength representing the thickness of the cavity or, more correctly, the function to relocate the current cavity surface position in an iterative process may be related, in a linearized sense, to the product of the oncoming velocity and the first derivative of cavity thickness correction function, t^c, as in the case of thin wing theory,

$$q = V_n = U_\infty \frac{dt^c}{dx} \quad (28)$$

$$t^c = T^c_{(i)} - T^c_{(i-1)} \quad (29)$$

where V_n is the normal component of the total velocity on the cavity surface, which is expected to be nonzero when the tangency boundary condition (8) is replaced by the zero total potential condition (24), and the subscript (i) denotes the iteration index. Equation (29) shows that t^c is the difference of the cavity surfaces between two successive iterations. Note that the source strength, $q(\underline{\xi})$, vanishes upon convergence.

Since the cavity thickness, T^c, is to satisfy the closure condition (13), the thickness correction function, t^c, should also satisfy the same condition. Integrating (28), we get expressions for the cavity thickness correction and an alternative form of the cavity closure condition as follows:

$$t^c(l) = \int_0^l \frac{q}{U_\infty}\, dx \quad (30)$$

$$t^c(\ell_{cav}) = \int_0^{\ell_{cav}} \frac{q}{U_\infty}\, dx = 0 \quad (31)$$

Once the equation (25) is solved, the cavity source strengths, $q(\underline{\xi})$, are known, and hence the new cavity shape may be obtained by correcting the ordinate of the cavity surface at the current iteration, as schematically shown in Fig. 2.

NUMERICAL IMPLEMENTATION OF THE PROBLEM

Discrete representation of the hydrofoil and cavity surfaces

For numerical computation, the foil and cavity surfaces are replaced by a set of straight line segments of finite length as shown in Figs. 3 and 4 for partially- and supercavitating flows, respectively.

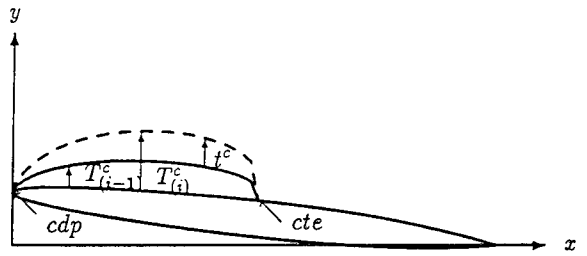

Figure 2: Definition sketch of the cavity surface position at each iteration.

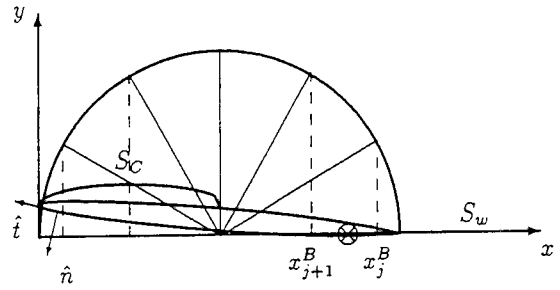

Figure 3: Discretization of the foil and cavity surfaces for partially-cavitating flow.

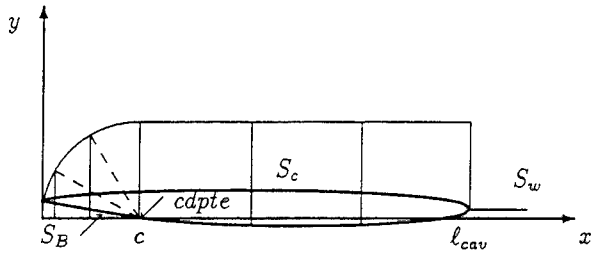

Figure 4: Discretization of the foil and cavity surfaces for supercavitating flow.

The flow near the leading edge varies more rapidly than any other region around the foil, and hence the surface panel size should be smaller in this region. We adopted, to represent the x-coordinate of the panel boundary, x^B, two different discretization functions for the partially- and supercavitating flows as follows:

1. For the partially-cavitating flow,

$$x^B = \frac{c}{2}(1 - \cos\theta) \ , \quad 0 \le \theta \le \pi \qquad (32)$$

2. For the supercavitating flow,

$$x^B = c(1 - \cos\theta) \ , \quad 0 \le \theta \le \tfrac{\pi}{2} \qquad (33)$$

In the above equations, the lower and upper limits of θ corresponds to the leading edge and trailing edge, respectively.

The x-coordinate of the cavity, x^C, is the same as the coordinate of the panel boundary above the upper surface of the foil, that is, $x^C = x^B$, whereas each surface panel on the supercavitating portion has the same horizontal extent as the panel on the foil next to the trailing edge. The vertical coordinate of the hydrofoil, y^B, is computed by using the offset of the hydrofoil section, and that of the cavity, y^C, is obtained as a part of the solution. Figures 3 and 4 show the typical discretized foil and cavity surfaces for the partially- and supercavitating cases, respectively.

Approximation of the integral equation

Assume that the strengths of sources and normal dipoles are constant on each panel, that is,

$$\mu(\underline{\xi}) = \mu_j \ , \quad \text{on panel } j, \ j = 1, \ldots, N^D + 1 \qquad (34)$$

$$q(\underline{\xi}) = q_k \ , \quad \text{on panel } k, \ k = 1, \ldots, N^S \qquad (35)$$

where $N^D + 1$ and N^S denote the number of panels on which normal dipoles and sources are distributed, respectively. Since the source panels always coincide with the dipole panels, the total number of panels to represent the foil-cavity system will be N^D. We will not count the dipole for the wake sheet surface just for convenience, since it is always represented as a function of the other dipole strengths.

The control point on the foil-cavity surface, $\underline{x}^P$, where the boundary conditions are to be satisfied, is positioned at the center of each element, such that

$$\underline{x}^P_i = \frac{1}{2}(\underline{x}_i + \underline{x}_{i+1}) \ , \quad i = 1, \ldots, N^D \qquad (36)$$

where $\underline{x}_i$ may either be the panel boundary coordinate of the hydrofoil, $\underline{x}^B = (x^B, y^B)$, or that of the cavity, $\underline{x}^C = (x^C, y^C)$.

Distributing the normal dipoles on the surfaces of both hydrofoil and cavity and the sources on the cavity surface, we can express for the partially-cavitating foil the total velocity potential at the i-th control point as follows:

$$\begin{aligned} \Phi^-_i = 0 = U_\infty x^P_i \ &+ \sum_{j=1}^{N^D} \frac{\mu_j}{2\pi}\beta_{ij} \\ &+ \sum_{k=1}^{N^S} \frac{q_k}{2\pi}\alpha_{ik} \\ &+ \frac{\mu_w}{2\pi}\beta_{iw} \end{aligned} \qquad (37)$$

where

$$\beta_{ij} = \begin{cases} \pi & , \ \text{if } i = j \\ \int_{C_j} \frac{\partial}{\partial n_j} G(\underline{x}_i; \underline{\xi}_j) \, \mathrm{d}S & , \ \text{if } i \ne j \end{cases}$$

$$\alpha_{ik} = \int_{C_k} G(\underline{x}_i; \underline{\xi}_k) \, \mathrm{d}S$$

$$\beta_{iw} = \int_{S_w} \frac{\partial}{\partial n_w} G(\underline{x}_i; \underline{\xi}_w) \, \mathrm{d}S$$

where the subscripts i and j denote the i-th control point and the j-th singularity point, respectively, and

the subscript w represents the wake surface.

For the supercavitating flow, in accordance with the smooth flow detachment condition of Kutta type as described earlier, the slope of the lower surface of the cavity at the detachment point must be equal to that on the lower surface of the hydrofoil at the trailing edge, and hence we have

$$q_{cdpte} = |\underline{U}_\infty|\{\frac{d}{dx}h^l(x)\}_{T.E.} \tag{38}$$

where q_{cdpte} is the source strength at the cavity detachment point near the trailing edge and $h^l(x)$ denotes the function expressing the lower surface of the foil.

Thus, in case of supercavitating flow, the equation (37) may be rewritten as

$$\begin{aligned}\Phi_i^- = 0 = U_\infty x_i^P + \frac{q_{cdpte}}{2\pi}\alpha_{i\ (cdpte)} &+ \sum_{j=1}^{N^D}\frac{\mu_j}{2\pi}\beta_{ij} \\ &+ \sum_{k=1}^{N^S-1}\frac{q_k}{2\pi}\alpha_{ik} \\ &+ \frac{\mu_w}{2\pi}\beta_{iw}\end{aligned} \tag{39}$$

where the subscript *cdpte* denote the panel index immediately downstream from the trailing edge of the hydrofoil.

An approximate expression for the Kutta condition (10) is obtained, following the Morino's condition (26), as

$$\mu_w = -(\Delta\Phi)_w = \Phi_1 - \Phi_{N^D} = -(\mu_1 - \mu_{N^D}) \tag{40}$$

where the subscripts 1 and N^D link the values to the lower and upper surface panels, respectively, adjacent to either the trailing edge for the partially cavitating flow or the cavity trailing end for the supercavitating flow.

Before converting (27) into a discrete form, it is necessary to review the relation of the tangential speed on the cavity, $|\underline{V}_c|$, with the constant pressure dynamic boundary condition for the cases with or without including the gravity effect in the pressure equation. When neglecting the buoyancy effect, according to (15) and (16), the dynamic condition on the cavity surface (12) can be replaced by the kinematic condition that the tangential speed on the cavity surface, $|\underline{V}_c|$, is constant. With the effect included as in (17) and (18), however, the dynamic boundary condition can no longer be simply replaced by a single tangential speed value due to the difference in the hydrostatic pressure on the cavity surface. Expecting an iterative procedure to determine the cavity surface, we may assume the speed on the cavity be represented by a reference speed at the leading edge, $|\underline{V}_{ref}|$, multiplied by a correction factor as a function of girthwise position, $a(s)$. The tangential speed on the cavity surface may therefore be expressed as:

$$|\underline{V}_c| = \begin{cases} \text{const.} & \text{without buoyancy effect} \\ a(s)\,|\underline{V}_{ref}| & \text{with buoyancy effect} \end{cases} \tag{41}$$

By equating the pressures on the cavity surface and the reference point, equation (18) relates the speed, $|\underline{V}_c|$, on the cavity surface, y_c, with the reference speed $|\underline{V}_{ref}|$ at y_{ref} as

$$(\frac{|\underline{V}_c|}{U_\infty})^2 + \frac{2(y_c - y_{ref})/c}{F_c^2} = (\frac{|\underline{V}_{ref}|}{U_\infty})^2 \tag{42}$$

By substituting $|\underline{V}_c| = a(s)|\underline{V}_{ref}|$ into (42), we may derive an expression for the correction factor, $a(s)$, as follows:

$$a = \sqrt{1 - \frac{2g(y_c - y_{ref})}{|\underline{V}_{ref}|^2}} \tag{43}$$

From (27) and (41), the total velocity potential at the control point of the *j-th* source panel along the cavity surface in the streamwise direction can be expressed as follows:

$$\Phi_j^{u,l} = \begin{cases} \Phi_{cdp}^{u,l} + |\underline{V}_c|\sum_{k=1}^{j}\Delta s_k^{u,l} \\ \quad \text{without buoyancy effect} \\ \Phi_{cdp}^{u,l} + |\underline{V}_{ref}|\sum_{k=1}^{j}a(s_k)\,\Delta s_k^{u,l} \\ \quad \text{with buoyancy effect} \end{cases} \tag{44}$$

where $\Phi_{cdp}^{u,l}$ denotes the total velocity potential on the cavity detachment points at the leading edge and the trailing edge of the hydrofoil, and $\Delta s_k^{u,l}$ denotes the length of the *k-th* source panel along the upper and lower cavity surfaces, respectively.

Since $\Phi_j = \Phi_j^- - \mu_j = -\mu_j$, the above relation becomes

$$\mu_j^{u,l} = \begin{cases} \mu_{cdp}^{u,l} - |\underline{V}_c| l_g & \text{without buoyancy effect} \\ \mu_{cdp}^{u,l} - |\underline{V}_{ref}| l_g^* & \text{with buoyancy effect} \end{cases} \tag{45}$$

where

$$l_g = \sum_{k=1}^{j}\Delta s_k, \quad l_g^* = \sum_{k=1}^{j}a(s_k)\,\Delta s_k \tag{46}$$

Equation (45) shows that strengths of normal dipoles on the cavity surface can be expressed as a function of the dipole strengths at the cavity detachment point and the representative tangential speed on the cavity surface, $|\underline{V}_c|$ or $|\underline{V}_{ref}|$; that is, there is no unknown dipole strength on the cavity surface. It should however be noted that the correction factor, $a(s)$, can be approximated by using $|\underline{V}_{ref}|_{(i-1)}$ of the previous *(i-1)-st* iteration.

Upon discretization, the cavity closure condition (31) for the partially-cavitating flow will be recast as

$$\sum_{k=1}^{N^S} q_k \Delta s_k = 0 \tag{47}$$

In case of supercavitating flow, applying (38), the above relation can be rewritten as

$$\sum_{k=1}^{N^S-1} q_k \Delta s_k = -q_{cdpte}\Delta s_{cdpte} \tag{48}$$

where Δ_{cdpte} denotes the length of the cavity panel con-

nected to the trailing edge.

The total number of unknowns for the partially cavitating flow is N^D+1, which consists of (N^D-N^S) unknown dipoles, (N^S) sources and $|\underline{V}_c|$ or $|\underline{V}_{ref}|$. To determine the unknowns we need the same number of equations, which may be formed by applying (37) to N^D control points defined in (36) and by applying the closure condition (47). For the super-cavity, the number of unknowns is reduced to N^D, since one of the source strength q_{cdpte} is known from (38). The equations may similarly be formed by using (39) to the control points except the one immediately downstream from the trailing edge and by using the closure condition (48).

Discussion on the solution procedure

Upon formation of the linear system of algebraic equations, we may solve the simultaneous equations with the aid of high speed computer, determining the strengths of sources and normal dipoles. The cavity thickness may be computed by integrating the source strengths in accordance with (30) and by using (29). In this paper, only the vertical coordinate of the cavity surface is evaluated. Once the cavity surface is found for the present step, the sources and normal dipoles are to be relocated on the newly obtained cavity surface, and then the whole process is repeated until a sufficient convergence is achieved. Upon convergence, the strength of the sources vanishes and the converged cavity shape is obtained.

For the first iteration, it is necessary to assume the initial cavity geometry. A simple quadratic cavity shape with maximum thickness to be equal to the foil thickness was assumed for the partial cavity case. To satisfy the cavity detachment condition (14), for the supercavitating flow, the slope of the cavity is matched with that of the lower surface of the trailing edge and again the lower surface was initialized with a quadratic function, whereas the upper surface of the cavity was assumed as a straight line with a slope of $\frac{1}{2}\alpha$. The vertical coordinate of the cavity trailing end is initially located above the x-axis by $\ell_{cav}\times\frac{1}{2}\alpha$, but this point is free to move up and down depending on the integrated cavity shape. The initial approximation of the cavity geometry is found irrelevant to the final solution, as long as the shape is represented by a smooth simple curve. Based on this numerical experimentation, we conclude that the solution is convergent to a common solution regardless of the initial guess of the cavity shape. For most of the engineering calculations, the first few iterations are found sufficient, but for most of sample calculations, the number of iterations, N^{iter}, is set to 10. Typical numbers of panels used are $N^D\approx 200$ or 100 for the supercavitating or partially cavitating flows, respectively.

Once we get the dipole distribution, then we can compute the tangential speed $|\underline{V}_t|$ by differentiating the total potential values (which is negative of the dipole strength) along the foil-cavity surface. We use a simple quadratic differentiation formula to take derivatives. Equation (15) is then used to compute the pressure coefficient, from which the lift, drag and moment coefficients are obtained by evaluating (19) through (21), and the cavity volume is obtained by (22). The cavitation number, σ or σ_{comp}, is computed by substituting into (16) or (18) the tangential speed on the cavity surface, $|\underline{V}_c|$, which is obtained directly by solving the simultaneous equation.

NUMERICAL CALCULATIONS AND DISCUSSIONS

Non-cavitating free surface flow

The present paper is the outgrowth of Lee et al[12], who applied the present method to the cavitating flow past a hydrofoil advancing in an unbounded fluid. The numerical procedure are described in detail and evaluated in Lee et al[12] for the case of the unbounded fluid. The difference of the present application occurs only with the presence of the additional free boundary, that is, the free surface in contact with the atmosphere.

The first step in validating the present numerical procedure is, therefore, to analyze the flow past a hydrofoil advancing beneath a free surface in non-cavitating condition. We selected a 12% thick Joukowski section, for which a numerical result by Bai[28] and experimental data are available. Figure 5 shows the pressure distribution around this Joukowski hydrofoil

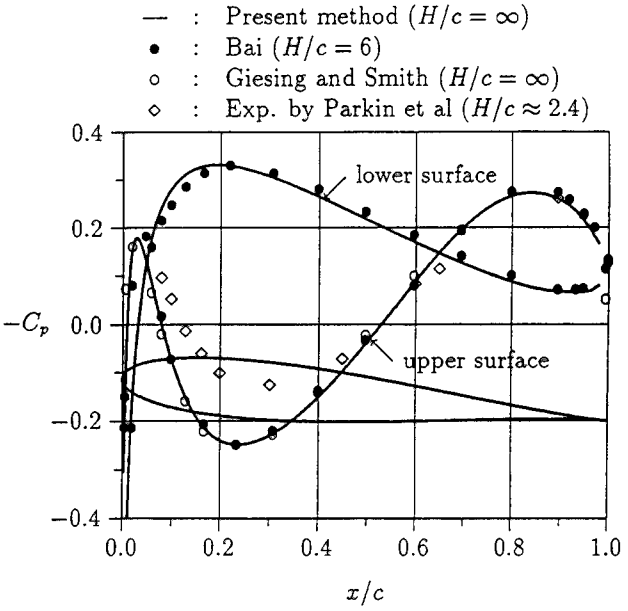

Figure 5: Pressure distribution on a 12% thick Joukowski hydrofoil at $\alpha=5$ deg, $F_c=0.617$, and the leading edge submergence $d/c=0.113$. Fluid depth, H, is infinite. Data taken from Bai[28].

under the condition of $\alpha = 5$ deg, $F_c = 0.617$, and the leading edge submergence $d/c = 0.113$, together with the comparison with existing data. It is shown that the result correlates well at least with existing numerical methods for the fluid of infinite depth.

Supercavitating flow

A symmetric wedge in transverse gravity field in unbounded fluid

To show the effect of the transverse gravity field upon the cavitating flow, we selected a symmetric wedge placed horizontally in uniform flow. Figure 6 shows the computed (negative) lift, L, non-dimensionalized with the displaced weight of the wedge, B, versus the cavity length relations for the wedge with apex angles, $\beta = 1$ deg and $\beta = 7.5$ deg, together with the linear theoretical result of Street[14] and experiments of Kiceniuk and Acosta[16]. It is first of all observed that the magnitude of the negative lift, that is, the loss of the lift, increases with the increase of the cavity length. It is shown that, for the small apex angle, $\beta = 1$ deg, the computed result $(- \cdot -)$ falls on the theoretical line of Street (——) up to the cavity length, $\ell_{cav}/c = 2.0$. The two results deviate from each other, from $\ell_{cav}/c = 2.0$ and above, showing the evidence of the blockage effect upon the lift force of the long buoyant cavity.

Kiceniuk and Acosta[16] carried out experiments with a symmetric $\beta = 7.5$ deg wedge for three Froude numbers, $F_c = 5.0, 6.2$ and 7.5, and their results are reproduced in Fig. 6. Our computational results for the same condition are also added in Fig. 6, showing little dependency upon Froude number variation. It is noted that the experimental results scatter considerably, which indicates the unsteadiness of the high speed flow condition, while showing the similar trend as the present computation. Figure 7 shows the results for the apex angle, $\beta = 15$ deg, for the same Froude numbers. Deviation between the experiments and the numerical computation increases, which indicates that the wall blockage effect appears more significant with the increase of the apex angle and the transverse thickness of the cavity.

A deeply submerged flat plate

Another computation is made for the flow past a flat plate deeply submerged beneath a free surface, but unlike the existing results such as Lee et al[12], including in the present study the hydrostatic pressure variation due to the gravity in the vertical direction. Figure 8 show the cavity shapes, predicted by considering or without considering the buoyancy effect, for the assumed cavity length, $\ell_{cav}/c = 4.4$. For the same cases with pre-assigned cavity length, the computed lift, drag coefficients and the computed cavitation number, σ, and the cavity volume are compared in Table 1. It may be noted that, for this deeply submerged case, the lift and the cavity size are reduced slightly, although not significant, due to the transverse gravity field variation around the foil and cavity boundary as predicted by Larock and Street[17].

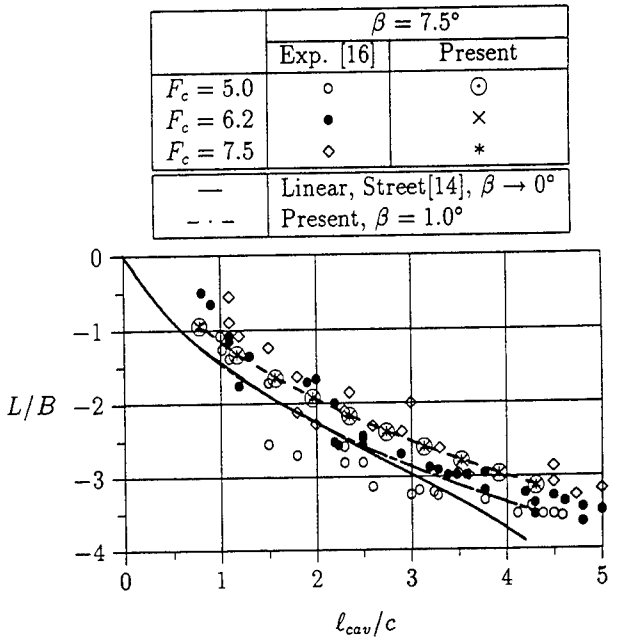

Figure 6: Ratio of the buoyancy induced lift to the displaced weight of the wedge versus the cavity length for $\beta = 7.5$ deg. Comparison with the linear theory of Street[14] and experiments of Kiceniuk and Acosta[16].

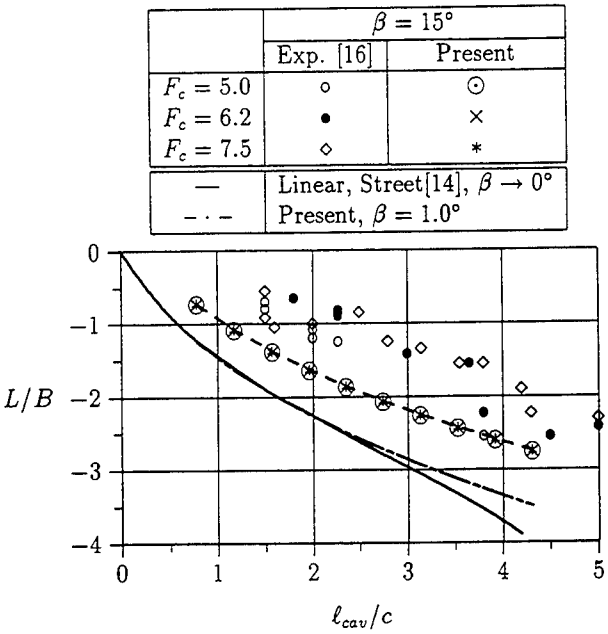

Figure 7: Ratio of the buoyancy induced lift to the displaced weight of the wedge versus the cavity length for $\beta = 15$ deg.

Table 1: Comparison of the lift, drag coefficients, the cavitation number and cavity volume coefficients, predicted with and without considering the buoyancy effect, for a prescribed cavity length, $\ell_{cav}/c = 4.4$. $N^D = 190$.

	Without buoyancy effect	With buoyancy effect
C_L	0.324	0.307
C_D	0.057	0.054
σ	0.190	0.174
Vol	1.240	1.203

A hydrofoil beneath a free surface

Up to now, the influence of the free surface boundary in contact with the atmosphere is not considered, that is, the effect of the free wave upon the flow around the hydrofoil has been neglected. To the authors' knowledge, there is no published evidence dealing with the transverse gravity effect upon the cavity flow past a hydrofoil advancing at a finite Froude number near a free surface, and hence only the results of the present method will be presented. Figure 9 shows that, for the similar condition as Fig. 8 except the finite submergence depth, $d/c = 0.53$, the cavity shape and wave profile are altered significantly. When the hydrostatic pressure term is considered into computation, the position of the cavity upper surface near the leading edge is lowered compared to the surface obtained without considering the gravity effect, but the cavity turns slightly upwards downstream due to the buoyancy effect. Remember that the pressure constant dynamic boundary condition on the cavity surface is equivalent to requiring the velocity being constant when neglecting the buoyancy effect, but on the contrary with the buoyancy effect, the tangential speed on the cavity surface is no longer constant. The tangential speed on the upper surface is less than the speed on the lower surface due to the difference in the hydrostatic pressure. Moreover, the effect is more significant on the upper cavity surface than on the lower surface. It is expected, therefore, that the wave pattern will be influenced to the same degree and should be analyzed with the buoyancy effect into consideration.

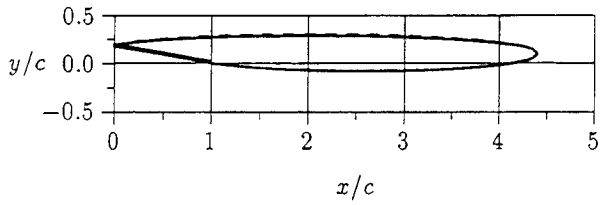

Figure 8: Effect of the transverse gravity field upon the cavity shape on a supercavitating flat-plate hydrofoil at $\alpha = 10$ deg, $F_c = 4.0$ and $d/c = \infty$; Predicted with(——) and without(− − −) the hydrostatic pressure.

We, then, carried out a parametric study to see the influence of the submergence depth and Froude number. Figure 10 shows the cavity volume, the cavity length, and the lift and drag coefficients variations as a function of the cavitation number for three depth conditions, that is, $d/c = 0.5, 1.0$ and 2.0, for a flat-plate hydrofoil at $\alpha = 10$ deg and $F_c = 3.0$. Figure 11 also shows the similar quantities for the same hydrofoil at $\alpha = 10$ deg and the submergence depth, $d/c = 1.0$, for three Froude numbers, that is, $F_c = 3.0, 4.0$ and 5.0. In both figures, the results obtained with or without considering the hydrostatic pressure term in computations are compared. It is noted that the buoyancy effect, due to the depth difference between the upper and lower cavity surfaces, appears most significantly in the cavity volume and the cavity length. At the same cavitation number, by including the buoyancy effect, the cavity volume and the cavity length are reduced when the submerged depth is large, roughly when $d/c > 1.0$, in a similar manner as we observed for the deeply submerged hydrofoil, whereas the trend is reversed for the case of shallow submergence. The lift and drag coefficients decrease at most of the submerged depths when the buoyancy effect is considered.

From Fig. 11, we may observe that the buoyancy effect decreases with increase of Froude number, as expected from (17) and (18). The buoyancy effect appears are most pronounced at lower Froude numbers when the hydrofoil advances at shallow draft, when $d/c = 1.0$, contrary to the negligible influence for the cavity flow in deeply submerged condition.

The most noticeable consequence of including the hydrostatic pressure in the computation may be evidenced from Fig. 12, which shows the change of the wave elevation for different cavitating conditions. A

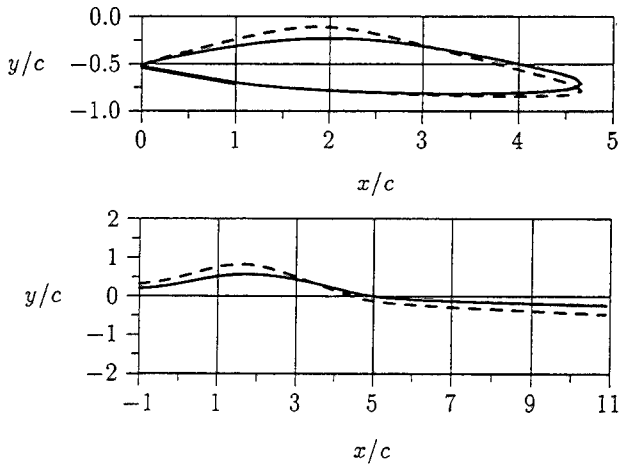

Figure 9: Effect of the transverse gravity field upon the cavity shape(above) and wave profile(below) past a supercavitating flat-plate hydrofoil at $\alpha = 10$ deg, $F_c = 4.0$ and $d/c = 0.53$; Predicted with(——) and without(− − −) the hydrostatic pressure term.

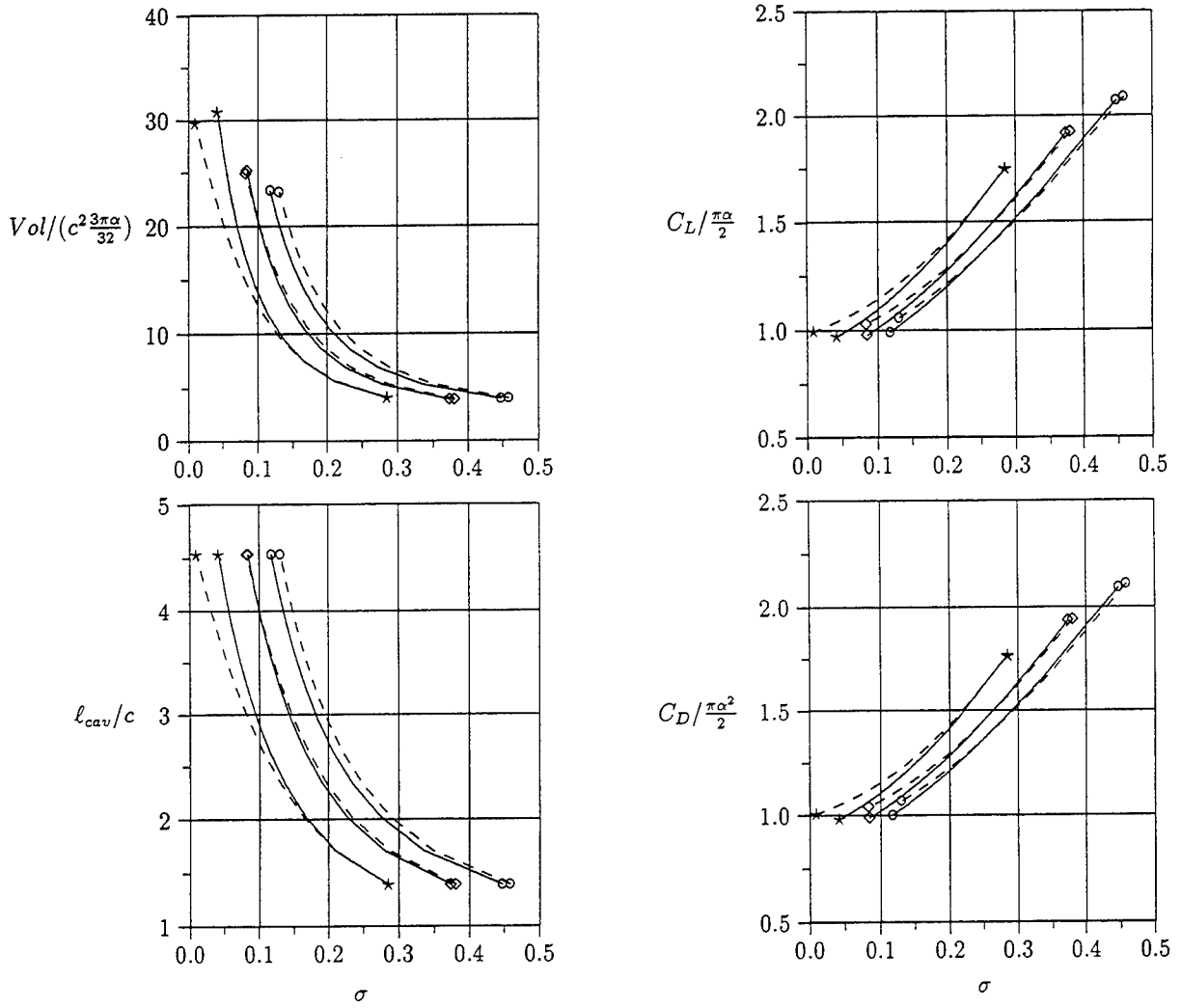

Figure 10: Effect of the transverse gravity field upon the cavity volume, the cavity length, the lift coefficient and the drag coefficient for a supercavitating hydrofoil at $\alpha = 10$ deg, $F_c = 3.0$, for three submergence depths, $d/c = 0.5(\star), 1.0(\diamond)$ and $2.0(\circ)$; Predicted with(——) and without(– – –) the buoyancy effect.

flat-plate hydrofoil is operating at $\alpha = 10$ deg and $d/c = 1.0$ for two Froude numbers, $F_c = 2.0$ and 3.0. Added together in the figure is the wave elevation generated by a symmetric hydrofoil with 1 % thick biconvex foil section. It may be seen that the wave elevation decreases in general with inclusion of the buoyancy effect, presumably due to the cushioning effect of the constant pressure cavity.

The lift and drag coefficients and the cavity length and volume coefficients obtained for the corresponding cases to Fig. 12 are summarized in Table 2. We observe that the buoyancy effect is the same as we have seen in the parametric study. Table 2 also shows that due to the buoyancy effect the lift and the cavity volume reduced by $1.4 \sim 3\%$ and about 20%, respectively, for both Froude number cases.

Partially-cavitating flow

A computation is made for a partially-cavitating hydrofoil with an NACA 16-006 section advancing at Froude number, $F_c = 0.5$, with $\alpha = 5.0$ deg beneath a free surface at $d/c = 0.6$. Figure 13 shows the cavity shape and the wave profile for the assumed cavity extent of $\ell_{cav}/c = 0.5$, together with the wave pattern generated when the cavity is absent. It is observed that the wave amplitude increases considerably compared to the non-cavitating case, due to the additional thickness effect of the cavity. It is also seen that the cavity and wave profiles, with and without considering the buoyancy effect, are indistinguishable in the partially cavitating case. This is due to the small cavity size and also due to the relatively large Froude number

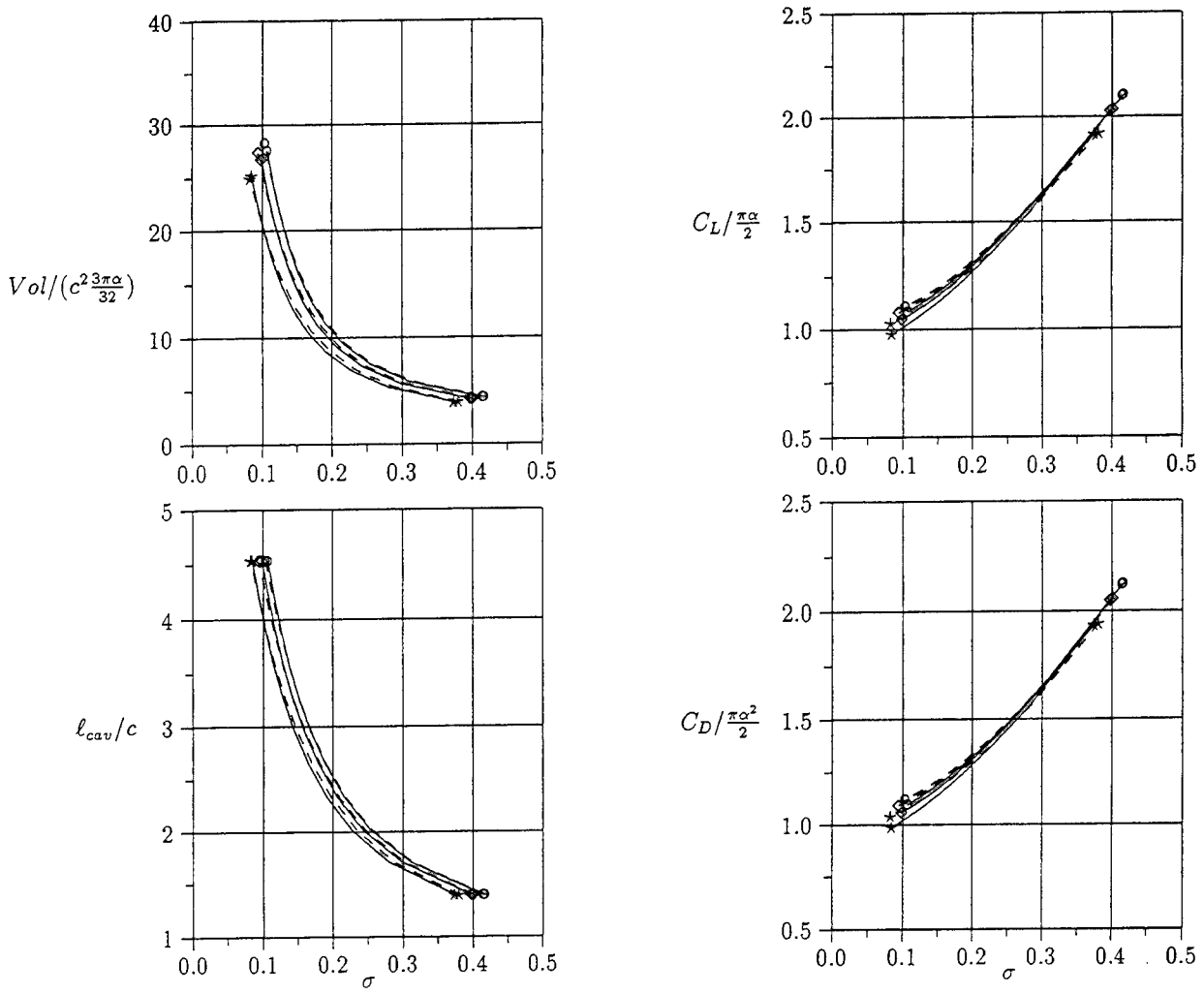

Figure 11: Effect of the transverse gravity field upon the cavity volume, the cavity length, the lift coefficient and the drag coefficient for a supercavitating hydrofoil at $\alpha = 10$ deg, $d/c = 1.0$, for three Froude numbers, $F_c = 3.0(\star), 4.0(\diamond)$ and $5.0(\circ)$; Predicted with(——) and without(– – –) the buoyancy effect.

Table 2: Buoyancy effect upon the lift and drag coefficients and the cavity length and volume coefficients for a supercavitating hydrofoil at $\alpha = 10$ deg and $d/c = 1.0$ for two Froude numbers, $F_c = 2.0$ and 3.0. Comparison with the non-cavitating case is given.

		Without buoyancy effect	With buoyancy effect	Non-cavitating condition
$F_c = 2.0$ $\sigma = 0.148$	C_L	0.296	0.292	0.665
	C_D	0.052	0.051	0.107
	ℓ_{cav}/c	3.042	2.570	N/A
	Vol	0.563	0.467	N/A
$F_c = 3.0$ $\sigma = 0.142$	C_L	0.313	0.303	0.725
	C_D	0.055	0.053	0.115
	ℓ_{cav}/c	3.081	3.042	N/A
	Vol	0.694	0.677	N/A

compared to the supercavitating case.

CONCLUSIONS

A potential-based boundary element method is presented for the analysis of a super- or partially-cavitating two-dimensional hydrofoil advancing at a finite submergence beneath a free surface, treating without approximation the effects of the finite Froude number and the hydrostatic pressure.

The present paper employs the free surface source and normal dipole distribution method for the solution of the mixed-boundary-value problem. The strength of singularities is determined by satisfying the boundary conditions on the body and cavity surfaces; the cavity geometry is determined through an iterative process.

Numerical results show that the wave profile is al-

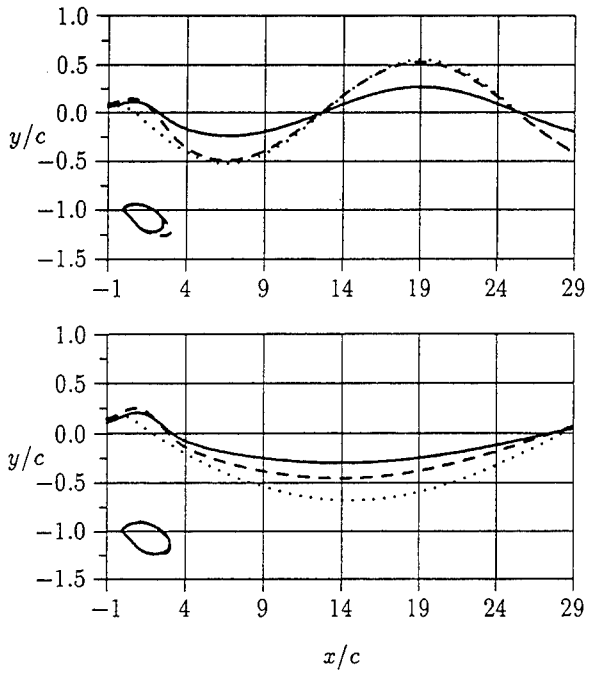

Figure 12: Buoyancy effect upon the cavity and wave profiles past a supercavitating flat-plate hydrofoil at $\alpha = 10$ deg, $d/c = 1.0$ for two Froude numbers, $F_c = 2.0$(upper) and 3.0(lower); Predicted with(——) and without(− − −) the buoyancy effect. Non-cavitating case(· · · · ·) is added for comparison.

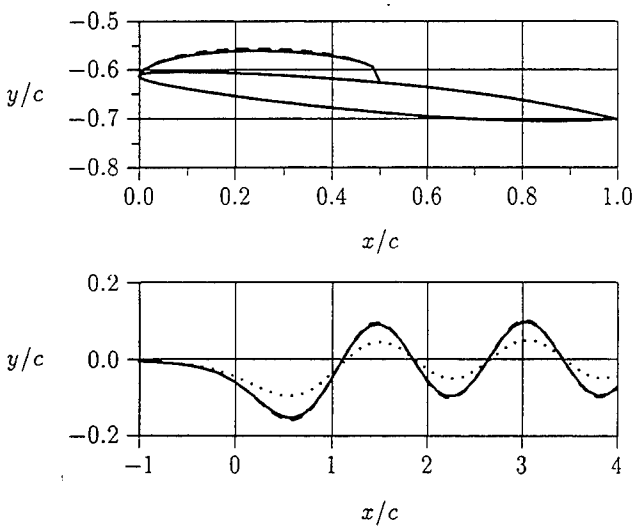

Figure 13: Effect of the transverse gravity field upon the cavity shape and the wave profile past a partially cavitating hydrofoil with NACA 16-006 section at $d/c = 0.6$, $\alpha = 5$ deg and $F_c = 0.5$, for a cavity length, $\ell_{cav}/c = 0.5$. The cavity and wave profiles predicted with(——) and without(− − −) the hydrostatic pressure term are not distinguishable. Non-cavitating case (· · · · ·) is added for comparison. $N^D = 200$.

tered significantly due to the presence of the cavity. The buoyancy effect due to the hydrostatic pressure, which has usually been neglected in most of the cavitating flow analysis, is found playing an important role, especially for the supercavitating hydrofoil, showing the dependency of the cavity shape upon the submergence depth, while leading to the reduction of the lift and drag for all submerged depth. The cavity length and the cavity volume decrease when the buoyancy effect is considered for the case of deep submergence, whereas those quantities increase for the case of shallow submergence.

The present potential-based boundary element method, developed for the two-dimensional case, may be extended for the analysis of the three-dimensional lifting hydrofoil by replacing the free surface Green function without any difficulty.

ACKNOWLEDGEMENTS

Financial support from Korea Science and Engineering Foundation and Hyundai Maritime Research Institute is greatly acknowledged.

REFERENCES

[1] "First International Conference on Fast Sea Transportation," Norwegian Inst. of Tech., Trondheim, Norway, 1991.

[2] Tulin, M.P., "Supercavitating Flows - Small Perturbation Theory," J. of Ship Research, Vol. 7, No. 3, Jan., 1964, pp.16-37.

[3] Geurst, J.A., "Linearized Theory of Two Dimensional Cavitating Lifting Flow," Ph.D. Thesis, Delft Technical Institute, The Netherlands, 1961.

[4] Wu, T. Y., "Inviscid Cavity and Wake Flows," Basic Developments in Fluid Dynamics, Vol. 2, Academic Press Inc., New York, 1968.

[5] Golden, D.W., "A Numerical Method for Two Dimensional, Cavitating, Lifting Bodies," S.M. Thesis, Department of Ocean Engineering, M.I.T., 1975.

[6] Jiang, C.W., "Experimental and Theoretical Investigation of Unsteady Supercavitating Hydrofoils of Finite Span," Ph.D Thesis, Department of Ocean Engineering, M.I.T., Cambridge, Mass., 1977.

[7] Lee, C.-S., "Prediction of Steady and Unsteady Performance of Marine Propellers with or without Cavitation by Numerical Lifting Surface Theory," Ph.D. Thesis, Department of Ocean Engineering, M.I.T., Cambridge, Mass., 1979.

[8] Uhlman, J.S., The Surface Singularity Method Applied to Partially Cavitating Hydrofoils," J. of Ship Research, Vol. 31, No. 2, June, 1987, pp. 107-124.

[9] Uhlman, J.S., The Surface Singularity or Boundary Integral Method Applied to Supercavitating Hydrofoils," J. of Ship Research, Vol. 33, No. 1, March 1989, pp. 16-20

[10] Lee, C.-S., "A Potential-Based Panel Method for the Analysis of a 2-Dimensional Partially Cavitating Hydrofoil," J. of SNAK, Vol. 26, No. 4, Dec., 1989, (in Korean), pp. 27-34.

[11] Kim, Y.-G., Lee, C.-S., Lee, J.-T., "A Potential-Based Panel Method for the Analysis of a Two Dimensional Super-Cavitating Hydrofoil," SNAK Autumn meeting, 1990; also available in J. of SNAK, Vol. 28, No. 2, Oct. 1991, pp. 159-173 (in Korean).

[12] Lee, C.-S., Kim, Y.-G., Lee, J.-T., "A Potential-Based Panel Method for the Analysis of a Two Dimensional Super- or Partially Cavitating Hydrofoil," J. of Ship Research, Vol. 36, No. 2, June 1991.

[13] Kinnas, S.A., Fine, N.E., "Nonlinear Analysis of the Flow Around Partially or Super-Cavitating Hydrofoils by a Potential Based Panel Method," IABEM-90 of the International Association for Boundary Element Method, 1990.

[14] Street, R.L., "Supercavitating Flow About a Slender Wedge in a Transverse Gravity Field," J. of Ship Research, Vol. 7, No. 1, June, 1963, pp. 14-24.

[15] Street, R.L., "A note on Gravity Effects in Supercavitating Flow," J. of Ship Research, Vol. 8, No. 4, March, 1965, pp. 39-46.

[16] Kiceniuk, T., Acosta, A.J., "Experiments on Gravity Effects in Supercavitating Flow," J. of Ship Research, Vol. 10, June, 1966, pp. 119-121.

[17] Larock, B.E., Street, R.L., "A nonlinear theory for a fully cavitating hydrofoil in a transverse gravity field," J. of Fluid Mechanics, Vol. 29, 1967, pp. 317-336.

[18] Yim, B., "On a fully cavitating two-dimensional flat plate hydrofoil with nonzero cavitation number near a free surface," *Hydronautics, Tech. Rep.* no. 463-4, Laurel, Md, 1964.

[19] Green, T. III, Street, R.L., "Two Supercavitating Hydrofoils Near a Free Surface," J. of Fluid Mechanics, Vol. 27, 1967, pp. 1-28.

[20] Larock, B.E., Street, R.L., "A Nonlinear Solution for a Fully Cavitating Hydrofoil Beneath a Free Surface," J. of Ship Research, Vol. 11, No. 2, June, 1967, pp. 131-139.

[21] Furuya, O., "Nonlinear calculation of arbitrarily shaped supercavitating hydrofoils near a free surface," J. of Fluid Mechanics, Vol. 68, 1975, pp.21-40.

[22] Doctors, L.J., "Effects of a Finite Froude Number on a Supercavitating Hydrofoil," J. of Ship Research, Vol. 30, No. 1, March, 1986, pp. 1-11.

[23] Wu, T. Y., "Cavity and Wake Flows," Annual Review of Fluid Mechanics, Vol. 4, 1972, pp. 243-284.

[24] Lamb, H., "*Hydrodynamics*," Dover Publications, N.Y., 1945, pp. 59-60.

[25] Moran, J., " An Introduction to the Theoretical and Computational Aerodynamics," John Willey & Sons, 1984, pp. 118-123.

[26] Breslin, J.P., Van Houten, R.J., Kerwin, J.E. & Johnsson, C.A., "Theoretical and Experimental Propeller-Induced Hull Pressures Arising from Intermittent Blade Cavitation, Loading, and Thickness," SNAME Trans. Vol. 90, 1982, pp. 111-151.

[27] Morino, L. and Kuo, C.-C., " Subsonic Potential Aerodynamic for Complex Configurations: a General Theory," AIAA J., Vol. 12, No. 2, 1974, pp. 191-197.

[28] Bai, K.J., " A Localized Finite-Element Method for Two-Dimensional Steady Potential Flows with a Free Surface," J. of Ship Research, Vol. 22, No. 4, Dec. 1978, pp. 216-230.

Cavitation Scaling Experiments With Headforms: Bubble Acoustics

Y. Chizelle[1], S. Ceccio[2], C. Brennan[1], Y. Shen[3]
([1]California Institute of Technology, USA; [2]University of Michigan, USA;
[3]David Taylor Model Basin, USA)

ABSTRACT

Recently Ceccio and Brennen [1][2][3] have examined the interaction between individual traveling cavitation bubbles and the structure of the boundary layer and flow field in which the bubble is growing and collapsing. They were able to show that individual bubbles are often fissioned by the fluid shear and that this process can significantly effect the acoustic signal produced by the collapse. Furthermore they were able to demonstrate a relationship between the number of cavitation events and the nuclei number distribution measured by holographic methods in the upstream flow. Kumar and Brennen [4][5] have further examined the statistical properties of the acoustical signals from individual cavitation bubbles on two different headforms in order to learn more about the bubble/flow interactions. All of these experiments were, however, conducted in the same facility with the same size of headform (5.08cm in diameter) and over a fairly narrow range of flow velocities (around 9m/s). Clearly this raises the issue of how the phenomena identified change with speed, scale and facility. The present paper will describe further results from experiments conducted in order to try to answer some of these important questions regarding the scaling of the cavitation phenomena. These experiments (see also Kuhn de Chizelle *et al.* [6][7]) were conducted in the Large Cavitation Channel of the David Taylor Research Center in Memphis Tennessee, on similar Schiebe headforms which are 5.08, 25.4 and 50.8cm in diameter for speeds ranging up to 15m/s and for a range of cavitation numbers.

NOMENCLATURE

C_p	pressure coefficient, $(P-P_o)/0.5\rho U_o^2$
D	headform diameter
I*	dimensionless acoustic impulse
P	static local pressure
P_o	static free-stream pressure
P_v	water vapor pressure
R	Radius of the base of the hemispherical cap of the bubble
Re	Reynolds number, U_oD/ν
t	time
Δt^*	dimensionless bubble travel time between electrodes 1 and 2
U_o	free-stream velocity
X_c	collapse coordinate along the axis of revolution
δ	bubble thickness in the direction normal to the headform surface
γ_i	dimensionless electrode duration parameter for electrode i
γ	global coverage parameter
ν	kinematic viscosity
ρ	density
σ	cavitation number, $(P_o-P_v)/0.5\rho U_o^2$
σ_i	inception cavitation number
τ_w	acoustic impulse duration

1. INTRODUCTION

The purpose of the experiments described herein is to investigate the effects of scale in the cavitation occurring on a simple axisymmetric headform. The focus is on traveling bubble cavitation, and the interaction between the flow and the dynamics and acoustics of individual bubbles. Experiments by Ceccio and Brennen [2][3] on 5.08cm diameter axisymmetric headforms had revealed a surprising complexity in the flow around single cavitation bubbles. Among the phenomena observed during those previous experiments were the fact that the bubbles have an approximately hemispherical shape and are separated from the solid surface by a thin film of liquid. This general conformation persists during the growth phase though, especially with the larger bubbles, the thin film appears to become unstable and may begin to shear off the underside of the bubble leaving a cloud of smaller bubbles behind. On the other hand, the collapse phase is quite complex and consists of at least three processes occurring simultaneously, namely collapse, shearing due to the velocity gradient near the

surface and the rolling up of the bubbles into vortices as a natural consequence of the first two processes. These processes tend to produce small transverse vortices with vapor/gas filled cores. It was noted that the collapse phase was dependent on the shape of the headform and the details differed between the ITTC headform (Lindgren and Johnson, [8]) which possesses a laminar separation and the Schiebe body (Schiebe, [9]; Meyer, Billet and Holl, [10]) which does not. The current investigation employed Schiebe headforms with a minimum pressure coefficient on the surface of Cp_{min}= -0.78.

Several other features of the flow around individual cavitation bubbles were noted in those earlier experiments and need to be mentioned here. On the ITTC headform, when some of the larger bubbles passed the point of laminar separation they would induce an attached "streak" of cavitation at both the lateral extremes of the bubble as indicated in Figure 1. These streaks would stretch out as the bubble proceeded downstream, being anchored at one end to a point on the body surface along the laminar separation line and at the other end to the "wing-tips" of the bubble. The main bubble would collapse, leaving the two streaks it induced to persist longer.

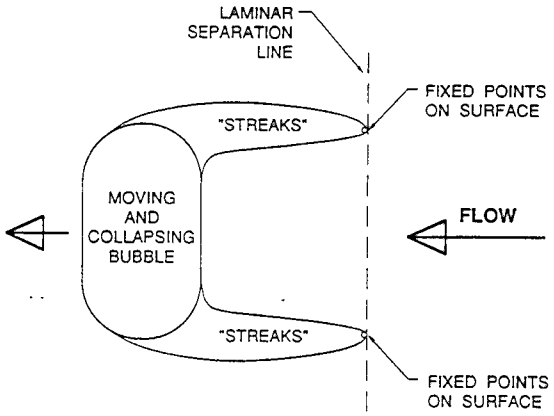

Fig. 1 Schematic diagram indicating the conformation of a cavitating bubble induced separation streaks.

One of the important consequences of these variations in the details of the collapse processes is the effect on the noise produced by a single cavitation event (Ceccio and Brennen, [2][3]; Kumar and Brennen, [4][5]). Bubble fission can produce several bubble collapses and therefore several acoustic pulses. Presumably this would also effect the cavitation damage potential of the flow. However it is important to reiterate that these earlier experiments were all conducted with 5.08cm diameter headforms and utilized only a very narrow range of tunnel velocities of 8-9m/s. Consequently there are very real questions as to how the observed phenomena might scale with both headform size and with tunnel velocity. The experiments described here represent one effort to answer some of these questions.

We digress briefly to note that questions on the scaling of cavitation have been asked for many years but particularly in the aftermath of the ITTC comparative tests conducted by Lindgren and Johnsson [8] who showed how disparate the appearance of cavitation was at different speeds, in different facilities and at different water "qualities". The latter characterization refers to the number of cavitation nuclei present in the water where most of these nuclei usually consist of very small air bubbles in the range of 5 to 300μm. As O'Hern *et al.* [11][12] have shown, the nuclei are similar in size distribution in most deaerated water tunnels and in the ocean. This causes one set of scaling questions since the ratio of body size to the nuclei size will change with the body size. The other set of scaling issues derives from the complex interactions between the bubbles and the flow close to the headform. Since the flow is Reynolds number dependent, scaling effects will also be caused by the changes in both body size and tunnel velocity. As a guide to interpretation of the results of the experiments a panel method was developed to solve the axisymmetric potential flow around the Schiebe headform in the absence of cavitation. Some results from these calculations are presented in Figure 2, which shows the isobars in the low pressure region on the surface of the headform.

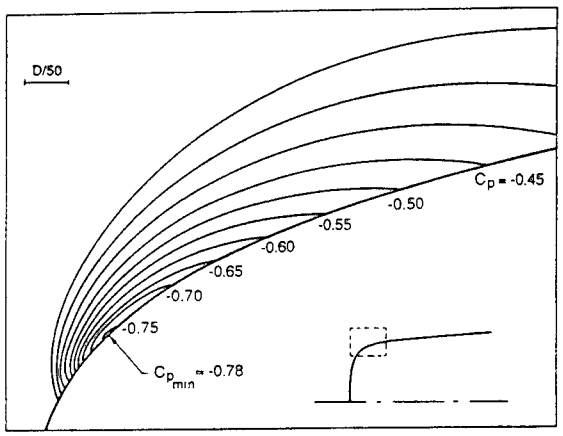

Fig. 2 Pressure distribution near the minimum pressure point in the potential flow around the Schiebe headform.

2. EXPERIMENTS

The data presented in this paper was taken during tests conducted in the Large Cavitation Channel of the David Taylor Research Center in Memphis, Tennessee (Morgan, [13]). Three geometrically similar axisymmetric Schiebe headform (Schiebe, [9]) measuring 5.08cm, 25.4cm and 50.8cm in diameter were installed on the centerline of the tunnel and cavitation tests were conducted over a range of tunnel speeds from 9m/s to 15m/s and dissolved oxygen contents (30 to 80% saturation at atmospheric pressure). The experimental

arrangements are described by Kuhn de Chizelle *et al.* in greater detail in other papers [6][7] and will not be repeated here. It is sufficient to indicate (i) that a larger number of still photographs and a substantial quantity of video was taken for each operating condition (the video was synched to a strobe light to improve time resolution), (ii) that surface electrodes were used to detect the presence of a bubble immediately over that electrode, (iii) that a hydrophone placed inside the headform recorded the cavitation noise (the headform was made of lucite and filled with water in order to provide a short and relatively reverberation free path for the noise between the cavitation and the hydrophone).

Figure 3 presents the observed cavitation inception numbers, σ_i, as a function of the headform diameter, D, tunnel velocity, U_o, and air content relative to saturation at atmospheric pressure. Inception was based on an arbitrarily chosen event rate of about 50 cavitation events per second. The events were detected by means of flush mounted electrodes, the current from which was moderated by the presence of a bubble [1][3].

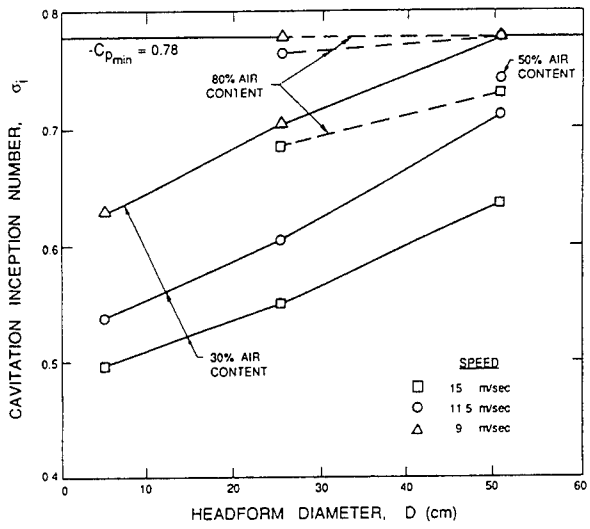

Fig. 3 Cavitation inception numbers σ_i, for the various headform sizes, velocities and air contents.

The trends in Figure 3 are fairly clear. The inception number increases with increasing headform size and the curves may well asymptote a value equal to the magnitude of the minimum pressure coefficient on the surface of the headform (Cp_{min}= -0.78). This headform size effect is simply a consequence of the fact that the larger the headform, the more nuclei are available for cavitation and, therefore, for a specific event rate the value of σ_i will be larger. The values of σ_i also increase with an increase in air content for a similar reason, namely more nuclei at the larger air contents. Figure 3 also demonstrates that the cavitation inception number increases with decreasing tunnel velocity. This effect is not so readily explained. However it is clear that to achieve the same cavitation number at a lower velocity one requires a lower tunnel pressure and it may be that the nuclei concentration in the tunnel increases considerably with decreasing operating pressure. We shall discuss this and other effects later in the paper.

3. EVENT RATE OBSERVATIONS

Both the photographs and the video tapes were analyzed in order to explore the variations in the cavitation event rates with headform size and tunnel velocity. The event rates were evaluated by counting the number of individual bubbles (or events) observable in a single frame and averaging this number over many frames. This allowed construction of Figure 4 in which the average number of observable events is plotted against the cavitation number, σ, for each of three velocities (9, 11.5 and 15m/s) for the three headforms (this data is for 30% dissolved oxygen content and we shall focus attention on these conditions). Not surprisingly the number of events increases with decreasing cavitation number and with increasing headform size. Not so predictable is the tendency for the number of events to decrease with increasing speed.

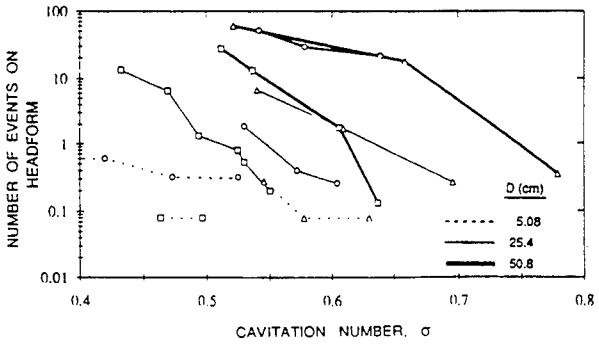

Fig. 4 Average number of observable events on the headform as a function of the cavitation number for all headform sizes and tunnel velocities.
□ U_o=15m/s; ○ U_o=11.5m/s; △ U_o=9m/s

The data on the number of events may be converted to cavitation event rates using bubble lifetimes obtained from knowledge of the velocity (from potential flow calculations using the panel method) and the measured locations of bubble appearance and collapse as a function of σ (see Kuhn de Chizelle *et al.*, [6]). The resulting event rate data for 30% dissolved oxygen content is presented in Figure 5 and it is clear that this is consistent with the cavitation inception data of Figure 3 given the selected criterion of 50 events/sec.

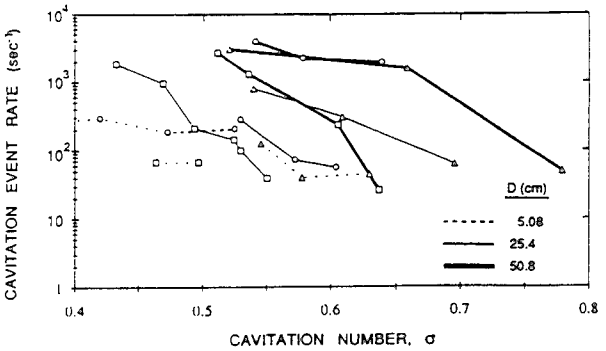

Fig. 5 Cavitation event rate as a function of the cavitation number for all headform sizes and tunnel velocities.

□ U_o=15m/s; ○ U_o=11.5m/s; △ U_o=9m/s

As previously stated, one of the purposes of the present investigations was to demonstrate the connection between the event rate (and by implication the inception number) and the nuclei number distribution. While the details of this analysis will be left until a later paper, it is instructive to present the event rate data of Figure 5 in the following modified form. Let us estimate that all the nuclei which pass through an annular stream-tube bounded on the inside by the headform and on the outside by the stream-surface which just touches the C_p=-σ isobar (see Figure 2) cavitate and therefore form observable bubbles. Then, using the potential flow velocity in this stream-tube (therefore neglecting boundary layer effects) and using the data of Figure 2 to estimate the thickness of the stream-tube at each cavitation number, we can calculate the volume flow rate of liquid in the stream-tube for each operating condition. Dividing the data of Figure 5 by these values we obtain an estimate of the number of cavitation nuclei per unit liquid volume; this data is presented in Figure 6.

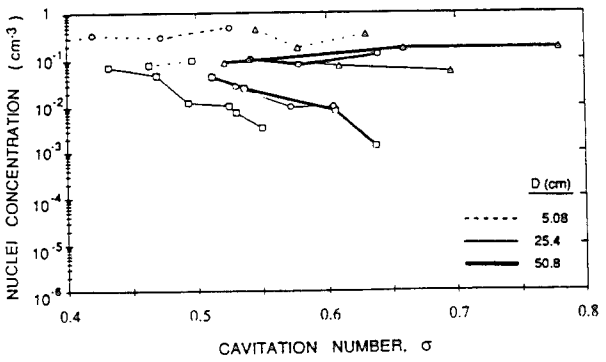

Fig. 6 Number of exited nuclei per unit liquid volume as a function of the cavitation number for all headform sizes and tunnel velocities.

□ U_o=15m/s; ○ U_o=11.5m/s; △ U_o=9m/s

It is significant that some of the variation with cavitation number, headform size and tunnel velocity which was present in Figures 4 and 5 has now been substantially removed. Indeed, with several exceptions, a fair fraction of the data of Figures 4 and 5 would now appear to correspond to a nuclei concentration of 0.1 nuclei/cm^3. The most noticeable deviation from this uniform value occurs at the highest speed (15m/s) with the two larger headforms.

The fact that most of the data appears to correspond to the same nuclei concentration is simultaneously encouraging and puzzling. It is encouraging because it suggests that a more careful analysis which begins with the same nuclei number distribution and follows each nucleus along its streamline may allow synthesis of the event rates and the inception numbers. But it is also puzzling because the concentration of 0.1 nuclei/cm^3 is at least an order of magnitude smaller than most of the measurements of cavitation nuclei would suggest.

Referring to Billet's [14] useful review of the subject of nuclei concentrations and distributions we note that the most reliable observations of nuclei (micro-bubbles and particles) have been obtained by systematically surveying the reconstructed holograms of volumes of tunnel water taken while the tunnel is in operation (for example Gates *et al.*, [15]). For de-aerated tunnel water, such inspections typically reveal concentrations of the order of 20 nuclei/cm^3 with sizes ranging from about 5μm to about 200μm. However the next question to ask is what fraction of these potential nuclei do, in fact, cavitate when subjected to sub-critical pressures. Here the answer is quite unclear. The other principal method for counting nuclei is the cavitation susceptibility meter in which the liquid is drawn through an orifice (or other device) in which the water is subjected to low pressures. The device is of sufficiently small size so that cavitation events occur individually. Then the concentration of actual cavitation nuclei (as opposed to potential nuclei) is obtained from the measured event rate and the known volume flow rate. Billet's review indicates that the typical concentrations measured by susceptibility meters is usually of the order of 2 nuclei/cm^3, significantly smaller than the concentrations obtained by holographic methods. While this may suggest that only a fraction of the potential nuclei actually cavitate, the data is, as yet, inadequate to support any firm conclusion.

In a later paper we shall present a model for the cavitation event rate which is based on a known nuclei number distribution function and follows all the possible sizes of nuclei along the streamlines on which cavitation might occur. This model is similar to that described by Ceccio [1] but corrects some errors in that previous analysis and includes other effects which may be important such as the effect of the boundary layer and the screening effect which occurs in the stagnation point flow and was first described by Johnson and Hsieh [16]. A brief preview of these results is given here. If one assumes a typical nuclei number distribution function, N(R) in m^{-4} of the form $N(R) = 10^{-5} / R^{3.5}$ for

$R < 2x10^{-4}$ m, then typical event rates for the Schiebe headform are shown in Figure 7. This data does not include the screening effect which reduces the event rate by about a factor 2 to 5. Nor does it include boundary layer effects which are small.

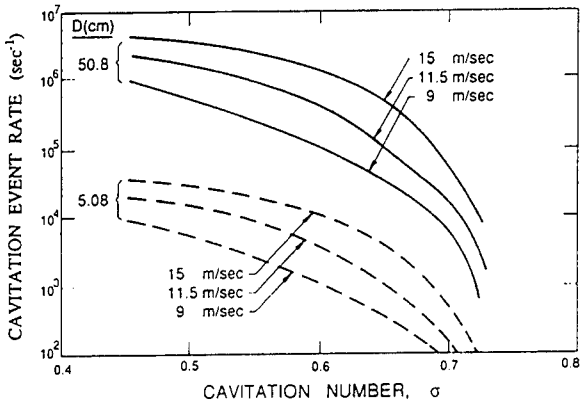

Fig. 7 Calculated event rates for the Schiebe headform for various headform sizes and tunnel velocities. Bubble screening effect not included.

Qualitative comparison of Figure 7 with Figure 5 reveals significant areas of both agreement and disagreement. Note first that the trend in event rate with headform size and with cavitation number are quite similar. However the trend with tunnel velocity produced by the model is contrary to the trend in most of the experiments. Perhaps this discrepancy is caused by assuming a common nuclei distribution for all operating conditions when, in fact, the nuclei population may be much higher at the low tunnel velocities than at the high since, to reach the same cavitation numbers, one must operate the tunnel at much lower pressures at the low velocities. The other area of disagreement to which reference was made earlier is that the event rates in the model are much higher than in the experiments.

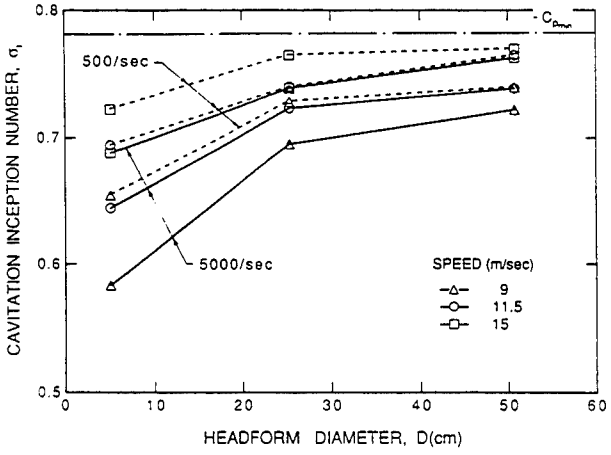

Fig. 8 Calculated cavitation inception numbers for various headform sizes and tunnel velocities and based on two different critical event rates of 5000/sec and 500/sec.

Given a model for the event rate one may the obtain cavitation inception numbers simply by establishing some critical event rate criterion. Figure 8 presents some typical cavitation inception numbers calculated in the way for criteria of 5000 events per second and 500 events per second. Comparing this with Figure 3 we note the same areas of disagreement that were manifest in the comparisons of event rates.

4. CAVITATION APPEARANCE

A typical bubble cavitation event consists of the growth and collapse of a bubble as it travels through the low pressure region close to the headform surface. The shape and size the bubble will assume are dependent on the cavitation number and the pressure coefficient history it experiences along its trajectory. In this section we shall describe in more detail the observations made during a study of the photographs and video recordings. The following observations were made at a dissolved oxygen content of 30%.

Bubble shape

For cavitation numbers close to the minimum pressure coefficient σ=0.78, the bubble life-time is very short. In Figure 3 we noted that the highest inception cavitation numbers occur for the largest bodies at the lowest velocities. Figure 9a shows a cavitation bubble for such conditions (σ_i=0.77; D=50.8cm; 9m/s; 30% dissolved oxygen content). All the bubbles assume a very thin disk-like geometry. For such cavitation numbers there is little or no growth normal to the headform surface. The bubbles grow almost entirely in the plane parallel to the headform. In its final phase the center of the bubble does not collapse first. Instead we observe the evanescence of the bubble's leading edge. There seems to be a location on the headform at which the cavity collapses, creating a fairly straight leading edge on the bubble. At these cavitation numbers we can see from Figure 2, that the critical isobar Cp=-σ is very elongated and close to the body surface. The region below vapor pressure is quite similar to the shape the bubbles assume. It appears that the bubbles are prevented from growing in the direction perpendicular to the body surface by the high normal pressure gradients normal to the surface. On the other hand, since the smallest headform has much smaller cavitation inception numbers (significantly less than 0.78), the bubbles observed on this headform do not assume such a flattened shape, even under inception conditions.

As the cavitation number is decreased below σ_i, the bubbles grow in volume (in diameter and in height) and assume the roughly hemispherical shape typified by Figure 9b. The maximum volume is mostly cavitation number dependent. As the bubbles approach their collapse phase their thickness, δ, normal to the headform surface decreases faster than their base radius, R, and the leading edge collapses most rapidly along a fairly straight

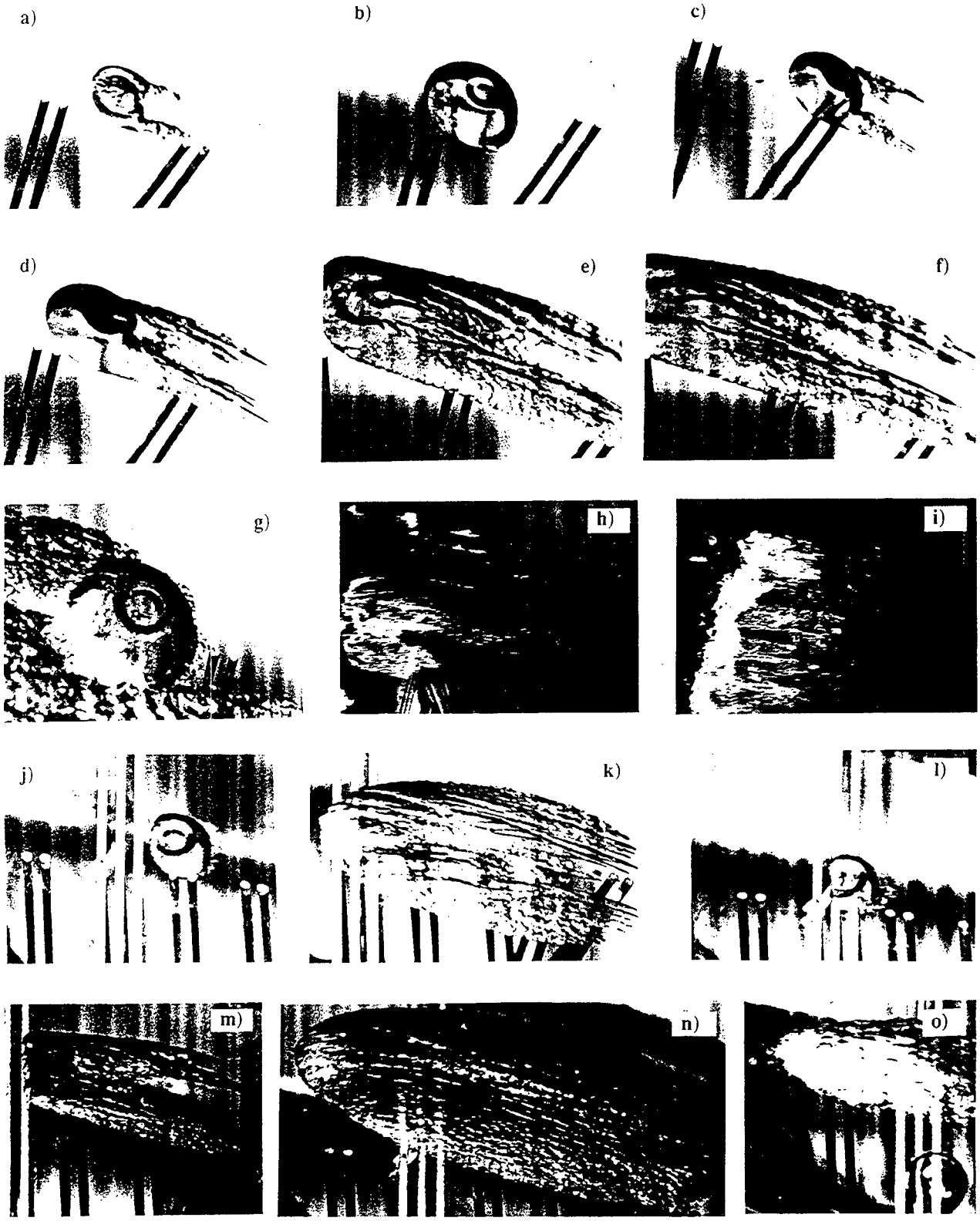

Fig. 9 High speed photography of cavitation events taken at a 30% saturation dissolved air content:
50.8cm diameter headform (distance between the two pairs of patch electrodes: 2.54cm) :
Figure **a**: U_O=9m/s, σ=0.77; Figures **b-c-d-e-f**: U_O=15m/s, σ=0.60; Figures **g-h**: U_O=15m/s, σ=0.54; Figure **i**: U_O=15m/s, σ=0.51
25.4cm diameter headform (distance between the two pairs of patch electrodes: 1.27cm) :
Figures **j-k**: U_O=15m/s, σ=0.55; Figures **l-m-n**: U_O=15m/s, σ=0.53; Figure **o**: U_O=15m/s, σ=0.49

front (Figures 9j, 9l). At this stage they appear thin and close to the headform surface (see also Ceccio, [1]) and look similar to the bubbles observed under inception conditions.

One unique feature of the present observations was the appearance of wave-like circular dimples on the top of the hemispherical cap (Figures 9b, 9e, 9f, 9g, 9j, 9l, 9m). The dimples seem to become more pronounced as the volume of the bubble increases. They are absent during the growth phase as seen in Figure 9c, and appear early in the collapse phase. Their ring shape could be interpreted as a precursor of a collapsing reentrant jet, but we note that the center of the dimple retains a concave curvature at all times. The dimple seems quite stable, and remains on the bubble until the very last stage of collapse. On the 50.8cm headform the dimples sometimes appear in pairs on the largest bubbles. On the smallest headform they do not form as distinctly, but occasionally a single rough depression in the center of the bubble may be observed.

Measurements of the bubbles on all three headforms show that the radius at the base of the hemispherical cap, R, scales linearly with the headform diameter, D (Kuhn de Chizelle *et al.*, [6]). At the same cavitation number, the ratio R/D, appears to be the same for all three headforms. We do not observe any variation of R/D with the velocity U_o. Furthermore the dimensionless collapse location X_c/D is approximately the same for all headforms. This appears to be true as long as the interactions between bubbles, or between bubbles and patch cavities remains limited. Therefore simple size scaling of the base diameter of the bubble cap with the headform size seems to be possible. This simple scaling applies only to the bubble's base radius though, since the shape of the bubble, its thickness δ, the amount of shear on its base and the cavitation event rate vary greatly from one headform to the other.

Bubble tail and patches

Figure 9a shows the presence of streaks of vapor or "tails" extending behind both sides of the bubble. It appears as though the bubble is sheared in the region extremely close to the headform surface leaving the tails behind in its wake. The undersides of some bubbles appear roughened towards the trailing and leading edges. The structure of the tails is always extremely wavy, turbulent and they seem to be attached to the headform surface (Fig. 9c). They appear early in the growth phase of the bubble. As the bubble is convected downstream it continues to "feed vapor" into the tails, allowing them to extend in length and height (Figures 9c, 9d, 9e, 9f). Ultimately the larger bubbles will collapse leaving behind patch-like cavities. It seems clear that whether a bubble will be sheared or not is determined early in the growth phase. If a bubble does not exhibit the trailing edge streaks early in its passage as seen in Figure 9c, it will grow and collapse with a smooth cap shape (Fig 9b, 9j, 9l). For this reason, for fixed cavitation conditions, the streaks always occur around the same position on the headform (Fig. 9c, 9d, 9e, 9f) and so will the leading edge of the patches. If the thickness of those streaks is small, the dynamic of the final collapse of the bubble appears unaffected by them and appears similar to the process described in the previous paragraph and seen in Figure 9m. However, for small enough cavitation numbers the patch can out-grow the bubble and swallow it leaving behind a patch-like cavity (Fig. 9k, 9n). At this point it is not clear if all the patch cavitation structures are generated by traveling bubbles. Some of them evidently are, and can be recognized by a planform shape, similar to a "V" with its vertex pointing downstream. The final length and thickness of the patch cavity are dependent on the bubble that generated it, and therefore vary with the headform diameter and cavitation number. For cavitation numbers close to the minimum pressure coefficient $-Cp_{min}=0.78$, no patches and very few bubble tails are observed as in Figure 9a. For these conditions the tails seem unable to grow sufficiently to form a patch-like cavity. Figures 9k, 9n show two typical patches at lower cavitation numbers. We notice that the patch on Figure 9k is thinner and ends sooner for higher cavitation numbers. The collapse mechanism of the patch itself is quite unclear. In the video recordings they vanish entirely between two frames (1/30 seconds). Is the entire patch swept downstream once the bubble head has vanished, or does it entirely collapse on the headform? The current investigation has not, as of yet, been able to answer these questions.

The number of sheared bubbles seems to increase with the cavitation number, headform diameter and flow velocity. Since the ratio of the laminar boundary layer thickness to headform size will scale with $Re^{-1/2}$, we would expect that the shearing of the cavitation bubbles would increase as the relative boundary layer thickness decreases. However, at the highest Reynolds number of 10^7, we note that the theoretical laminar to turbulent transition comes close to the low pressure region and might cause further disruptive effects.

Bubble-patch interactions

When the cavitation number is sufficiently reduced, the transient patches become fairly stable and remain on the headform, thus creating attached cavities for periods of up to a few seconds. As their number increases the patches will merge to create larger attached structures. Favre and Avellan [17] have shown that those attached cavities disturb the initial pressure distribution in such a way that they actually extend downstream beyond the original $Cp=-\sigma_i$ isobar. The cavitation number at which this phenomenon happens varies considerably from one headform to the other. It can be seen in Figure 9i at a cavitation number of about 0.5 for the 50.8cm headform. By contrast, at the same cavitation number, the 25.4cm headform produces just a few bubbles and patches (Figure 9o) and the 5.08cm headform shows no cavitation. At this point we note that the transient cavitation patch phenomenon was never observed on the smallest headform. That headform seems to exhibit an abrupt switch from traveling bubble cavitation (some of which have long trailing tails) to persistent attached

cavities. The attachment location of these cavities on that headform is fixed, and usually corresponds to a roughness element. This has not been observed on the larger headforms, even though the polished finish was identical to that of the 5.08cm body. Roughness appears to be a very critical parameter for the attached cavitation scaling of these bodies.

For all test conditions at cavitation number below 0.7 we noticed the coexistence of the two different kinds of cavitation patterns: traveling bubbles and transient patches. Quite remarkably, even for the conditions at which we observe many patch-type cavities, some very smooth hemispherical traveling bubbles are still present (Figure 9b, 9h). We can see in Figures 9g, 9h, 9i bubble type cavitation riding above attached cavities.

Comparing the shape of the bubbles encountering patch cavities with those which do not, it is clear that the shapes differ because the former are not subjected to the boundary layer shear which the latter experience. Bubbles which do encounter patches or attached cavities will eventually collapse and merge completely with the larger structure upstream of its closure region. By doing so they appear to perturb the attached cavity shape, as has been observed by Briancon-Marjollet *et al.* [18].

5. CAVITATION NOISE

For a range of cavitation numbers between inception and a value at which the cavitation patches persisted, it was possible to identify in the hydrophone output the signal produced by each individual bubble collapse. It was found necessary to digitally high pass filter the signals using a cut-off frequency of 5kHz in order to reduce the effect of vibration and noise caused by cavitation at the top of the supporting strut. This filtering did not, however, substantially effect the results. The processing amplifier gain response was calibrated and applied to the results. The noise from the cavitation was analyzed in several ways. We present first a spectral analysis which is the traditional approach normally taken toward cavitation noise. However more fundamental information can be gained from an analysis of the pressure pulses produced by individual cavitation events as will be described later.

Spectral analysis

FFT analyses of the signals from individual events were performed for different cavitation conditions for Nyquist frequencies up to 500kHz. In order to compare the shape of the power spectral density for different cavitating conditions the values have been non-dimensionalized by the number of sampled points, N, multiplied by the mean squared power amplitude, $\overline{PSD}$, where

$$\overline{PSD} = \frac{1}{N^2}\left[C^2(f_0) + C^2(f_{N/2}) + 2\sum_{i=1}^{i=N/2-1} C^2(f_i)\right].$$

The dimensionless PSD curves are presented in Figure 10 and consist of data averaged over several cavitation events.

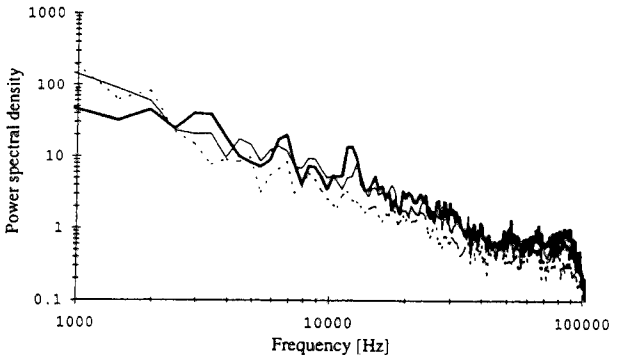

Fig. 10 Averaged dimensionless power spectral density signals for the 50.8cm headform:

——— U_o=9m/s, σ=0.66; ——— U_o=11.5m/s, σ=0.64; -------- U_o=15m/s, σ=0.61.

First we notice that for all headforms and tests conditions the measured spectral shape varies little with the operating condition and cavitation number as was reported by Arakeri and Shanmuganathan [19]. Most of the data represented here was taken close to inception. The influence of the hydrophone cutoff frequency above 80kHz can be observed in all signals. The measured decay between 1kHz and 80kHz in the present data appears roughly constant, with a value of about -22dB/dec. for all conditions. This value is similar to the value of -24dB/dec. (or $f^{-6/5}$) obtained earlier by Kumar and Brennen [5] and by Ceccio and Brennen [2][3] in the Caltech Low Turbulence Water Tunnel. By way of comparison we note that the spectra obtained by Blake *et al.* [20] for cavitation on a hydrofoil show a comparable frequency dependence of -20dB/dec. (or f^{-1}) though there is also a consistent dip in their spectra at 10kHz. Arakeri and Shanmuganathan [19] have presented data with a similar frequency dependence though the slope also increases from about -12dB/dec. (or $f^{-3/5}$) to -30dB/dec. (or $f^{-3/2}$) as the bubble interactions increase. None of this data is very close to the value of -8dB/dec. which Fitzpatrick and Strasberg [21] predicted for the range 10 to 100kHz based on a Rayleigh-Plesset analysis. Taking fluid compressibility into account yields decays as low as -40dB/dec. (f^{-2}) for the very high frequencies (around 100kHz and up), but these frequencies are beyond the capability of the hydrophone used in the present experiments.

Measurement of the frequency decay as a function of the cavitation number for different cavitating conditions is shown in Figure 11. We observe that this slope seems to decrease as the cavitation number value is reduced below 0.6. For some cavitation conditions the slope can be as low as -35dB/dec. This change is consistent with the effects of bubble interactions observed by Arakeri and Shanmuganathan [19].

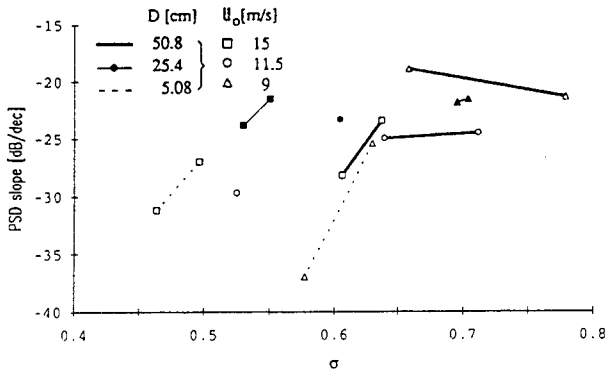

Fig 11. Average power spectral density slope decay between 1kHz and 80kHz [dB/dec.]. Measurements for different headform diameters and velocities as a function of the cavitation number.

Acoustic pressure pulses

The amplitudes of the acoustic pressure pulses were measured by defining the impulse, I, as the integral under that instantaneous pressure time history from the beginning of the collapse pulse to the moment when the pressure returns to its mean value. Since the impulse will vary inversely with the distance of the hydrophone from the noise source, we multiply I by the appropriate headform radius D/2 and form a dimensionless impulse, I*, by dividing by the headform radius, free stream velocity and the fluid density as indicated by the Rayleigh-Plesset analysis, so that the dimensionless impulse, $I^* = 4\pi I/\rho U_o$. The hydrophone output for each of the experimental conditions was examined in order to identify at least 40 of the larger pulses associated with a bubble collapse. The average values of the non-dimensional impulses obtained in this way are plotted against cavitation number in Figure 12.

The non-dimensional impulse is of the same order of magnitude for all three headforms. It initially increases as the cavitation number is decreased below inception. However most of the data also indicates that the average impulse ceases to increase and, in fact, decreases when σ is decreased below a certain value (about 0.43, 0.50 and 0.62 for the 5.08cm 25.4cm and 50.8cm diameter headform). The decrease at low cavitation numbers might be caused by the increasing presence of attached cavitation patches, damping the bubble collapse mechanism. The location of the peaks appears to be somewhat influenced by the velocity: they are shifted towards higher cavitation numbers for lower velocities. This trend is consistent with previous observations (Kuhn de Chizelle *et al.*, [6]) of the average void fraction over the headform at constant cavitation numbers, which exhibited an increase with a decrease in velocity. The conditions at which the impulses, I*, are maximum seem to correspond to circumstances in which the cavities cover about 20% of the surface area of the headform in the neighborhood of the minimum pressure point. Higher void fractions increase the interactions between the bubbles and the patches and considerably reduce the acoustic impulse. Such an effect was previously reported by Arakeri and Shanmuganathan [19] who noticed strong interaction effects for void fraction values larger than 25%.

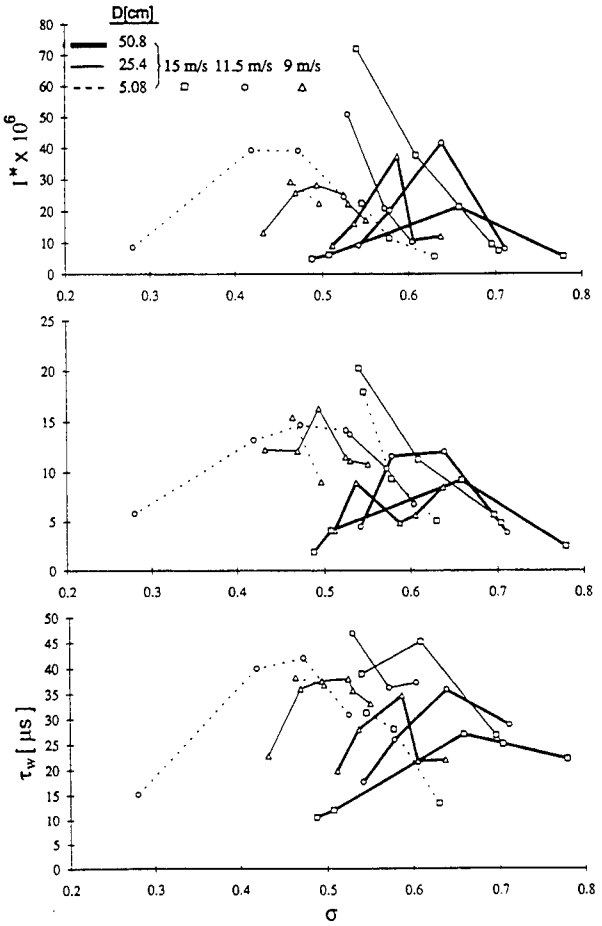

Fig. 12 Average dimensionless maximum acoustic impulse I*, standard deviation and impulse duration τ_w [μs] for all three headforms as a function of the cavitation number.

The standard deviation for the impulse is substantial, around 40% of the average value. Therefore for identical cavitation conditions the cavitation noise may vary considerably from one event to another. The duration of the impulse, τ_w, is also presented in Figure 12 and reveals a cavitation number dependence similar to that observed for the impulse. It appears to be of the same order of magnitude for all velocities and diameters. Examining this data it should be recalled that the typical response time of the hydrophone is about 3μs and is not negligible compared with the measured duration.

In summary, we find that the acoustic impulse produced by a single bubble collapse, while exhibiting considerable variability, nevertheless scales with headform size and tunnel velocity in the way which is expected on the basis of the Rayleigh-Plesset analysis.

Moreover, when the bubble concentration exceeds a certain value the noise from individual events becomes attenuated.

Electrode signal analyses

When a bubble is located over a particular electrode denoted by the index "i", it produces a perturbation in the voltage signal, $v_i(t)$, from that electrode. Figure 13 presents an example of the signals from the first and second patch electrodes (located at axial distances of 5.08 and 7.62cm from the headform stagnation point). The corresponding noise signal is plotted on the same Figure, time shifted by 170μs which corresponds to the time necessary for the acoustic noise to travel from the headform surface to the hydrophone. The signals from an unsheared bubble (seen in photograph 9b) and from a sheared bubble developing attached streaks (seen in photograph 9d) are contrasted in this Figure.

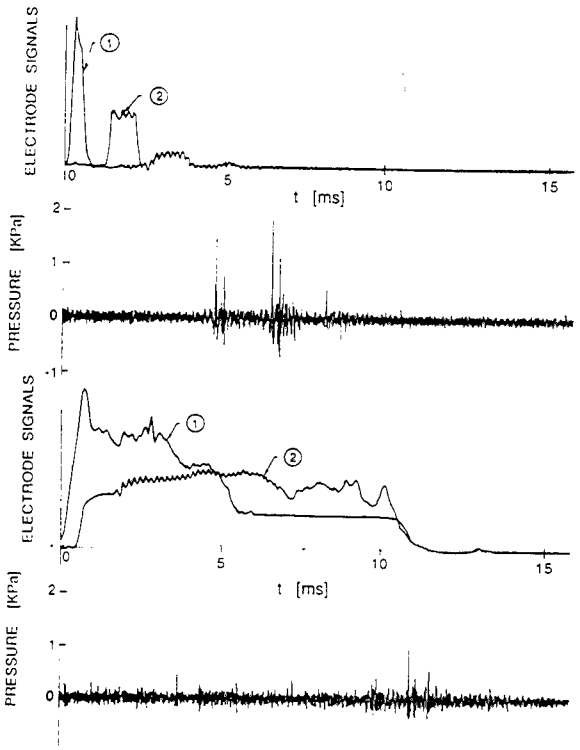

Fig. 13 Electrode signals from upstream patch electrodes 1 and 2 and the corresponding acoustic noise signals. The signals plotted correspond to the bubbles presented in photographs 9b and 9d.

Analyses of these electrode signals shed additional light on the mechanism of the bubble collapse. Sheared bubbles produce much longer electrode signals. Moreover, the trace from the first electrode will vanish before that from the second electrode, indicating that the collapse mechanism always proceeds in a downstream direction. Whether the cavity disappears by collapsing on the headform itself or detaches and is convected away by the flow is unclear. The time interval between the ends of the two electrode signals is often comparable to that measured for the case of unsheared traveling bubbles. This suggests that the leading edge of the patch detaches first and cavity is convected away by the flow.

The typical time for which a bubble covers an electrode is given by

$$\tau_i = \int_{t=0}^{t=\text{end of electrode signal}} v_i(t)dt \Big/ v_{i_{max}}$$

and can be written in dimensionless form by defining an electrode signal duration parameter $\gamma_i=\tau_i U_0/D$. Clearly a bubble with attached streaks or patches will yield substantially larger γ_i values than single unattached bubbles. Therefore γ_i provides a valuable indicator of the type of event which has occurred. The global coverage parameter γ defined as $\gamma=\sqrt{\gamma_1\gamma_2}$ groups both electrode duration parameters. Non-sheared bubbles typically have coverage parameters less than 0.01.

For single traveling bubbles, the duration parameters over the first and the second upstream patch electrode are strongly correlated. Figure 14 represents a plot of γ versus the dimensionless electrode duration for the first electrode, γ_1 ,for a wide range of cavitation numbers and velocities. Clearly there exists a strong correlation between both electrodes durations γ_1 and γ_2. It follows that a long (or short) duration at the first electrode leads to a long (or short) duration at the second electrode. Therefore we may conclude from Figure 14 that trailing streaks or tails (which cause larger durations) only appear early in the bubble evolution and that, if they do not appear, the bubble will continue without tail for the rest of its lifetime. This was also the conclusion reached from studies of photographs and video observations (Kuhn de Chizelle *et al.*, [6][7]). Note that the above implies that the leading edges of the attached patches are always upstream of the first electrode.

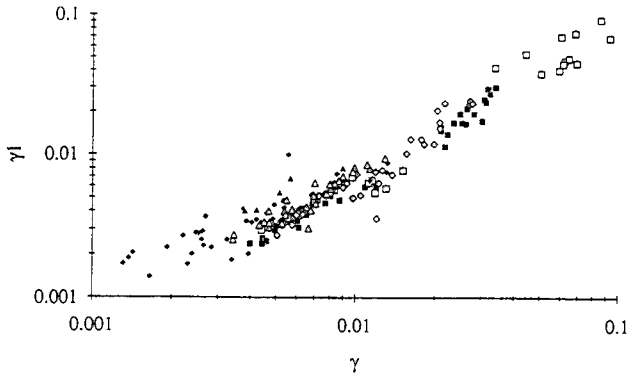

Fig. 14 Non-dimensional electrode signal duration time on the first and second patch electrodes for all flow velocities and cavitation numbers

The time of passage over the electrode "i" is denoted by t_i and may be defined by the quantity

$$t_i = \int_{t=0}^{t=\text{end of signal}} v_i(t)t\,dt \Big/ \int_{t=0}^{t=\text{end of signal}} v_i(t)\,dt.$$

Then the non-dimensional interval (or bubble travel time) between the signals from electrodes 1 and 2 can be defined as $\Delta t^*=(t_2-t_1)U_o/D$ and data on this quantity is presented in Figure 15.

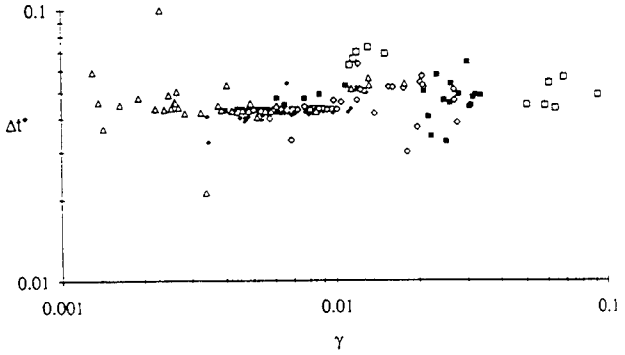

Fig. 15 Non-dimensional electrode peak interval, Δt^*, for all flow velocities and cavitation numbers.

For all conditions the non-dimensional interval is concentrated around a value of $\Delta t^*=0.043$. Panel method calculations of the non-dimensional travel time along a streamline between electrode 1 and electrode 2 yield an identical value of $\Delta t^*=0.043$ for the streamline closest to the headform. Also the travel time increases slightly as the streamline is located further from the headform. From the photographs Kuhn de Chizelle *et al.* [6] estimated that a typical non-dimensional bubble thickness for cavitation numbers around 0.65 is about $\delta\approx 0.01$ and the potential flow travel time for streamlines located at that distance above the headform surface is $\Delta t^*=0.044$. The agreement between the measured travel time for non-sheared bubbles (represented by γ values less than 0.01) and the potential flow calculation indicates that there is no slip between the bubble and the inviscid flow outside the boundary layer. The bubbles appear to ride over the boundary layer and travel at the same velocity as the outer flow.

For shear factors less than 0.005 which correspond to the highest cavitation numbers ($\sigma \geq 0.70$) some scatter can be observed. For those conditions photographs indicate that many bubbles collapse before they reach the second electrode. The signals measured on the second electrode may therefore be generated by rebounded bubbles. At the other extreme the large values of γ (>0.01) correspond to long sheared bubbles with tails. Note from Figure 15 that the scatter in Δt^* increases significantly with γ and that there is a trend toward greater travel times indicating that the bubble velocity is slower than that of the flow outside the boundary layer. This is consistent with part of the bubble being within the boundary layer.

Since the electrodes and the hydrophone signals were recorded simultaneously, it is possible to correlate the acoustic output of each event with the γ value for that event in order to explore the effect of bubble attachment on the noise. Figure 16 presents γ as a function of the non-dimensional acoustic impulse, I*, for the 50.8cm headform at 30% dissolved oxygen content. Most of the data is confined to cavitation numbers close to inception (low event rates) in order to ensure no overlap between events.

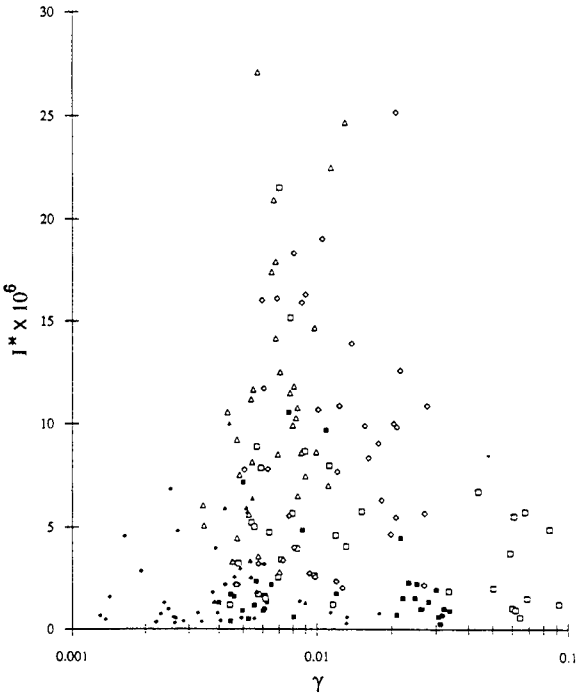

Fig. 16 Dimensionless acoustic impulse, I*, for the 50.8cm headform as a function of the electrode signal coverage parameter γ.

■ σ=0.64, U_o=15m/s; □ σ=0.60, U_o=15m/s;
◆ σ=0.71, U_o=11.5m/s ◇ σ=0.64, U_o=11.5m/s;
▲ σ=0.78, U_o=9m/s; △ σ=0.66, U_o=9m/s

Figure 16 leads to several conclusions. First we focus on the data on the left hand side for values of γ less than 0.01. These correspond to unattached bubbles with the smallest bubbles having the smallest values of γ. In this regime the impulse increases with increasing γ (i.e. decreasing cavitation numbers and increasing bubble size) as previously suggested by many authors, for example Fitzpatrick and Strasberg [21] and Hamilton *et al.* [22]. Ceccio and Brennen [2][3] also demonstrated that the impulse may be much smaller than this maximum. The data here clearly exhibit an upper bound

or envelope on the impulse. Vogel *et al.* [23] have also reported that the cavitation noise increases for the case of unsheared bubbles as the ratio of the distance to the headform and the maximum bubble radius decreases.

The present data adds to these earlier studies in that it shows a clear decline in the impulse when the value of γ exceeds about 0.02. These γ values correspond to bubbles which have attached streaks and patches and it is apparent that this results in a decrease in the impulse associated with the collapse of these events. The largest coverage parameters, γ, correspond to the lowest cavitation numbers and thus to the largest patch cavities. The reduction in cavitation noise for these types of events can probably be attributed to the fact that the collapse is much less coherent, producing high pressure nodes which are much smaller in magnitude.

6. CONCLUSIONS

In this paper we have presented some of the results from a series of experiments carried out in the Large Cavitation Channel (LCC) to investigate the scaling of the dynamics and acoustics of individual cavitation bubbles in flows around headforms. Many of the phenomena observed by Ceccio and Brennen [2][3] in experiments on 5.08cm headforms were seen again in the present experiments. Such micro-fluid mechanical phenomena included the hemispherical shape of individual cavitation bubbles, the thin film separating them from the surface, the destabilization of that film, the occasional production of attached streaks in the wake of the bubbles and the complex processes during the bubble collapse including bubble fission and roll-up into vortices.

The present experiments yielded substantially lower cavitation inception numbers for the larger headforms. One result of this was that for the same air content, velocity and cavitation number, we observed bubble inception on the smallest headform and fully developed attached cavitation on the largest. Some of the differences in the appearance of individual bubbles on the three headforms could be attributed to this large difference in inception numbers since it implied quite different locations for the critical C_p=-σ isobars. The most noticeable effect of scale on the appearance of cavitation was the increase in bubble-generated attached streaks and patches for the larger headforms. On the 5.08cm headform a traveling bubble would occasionally generate two attached streaks or tails at the lateral extremes of the bubble. These would disappear almost immediately after the bubble collapsed. On the larger headforms at higher speeds (larger Reynolds numbers) and low cavitation numbers the streaks began to occur more frequently and extend behind the entire width of the bubble. The streaks would tend to produce a transient patch of attached cavitation which would disappear shortly after the bubble collapsed. For low enough cavitation numbers , however, the patches would persist almost indefinitely and create larger attached cavitation structures. It is possible that this is the mechanism of formation for most patch cavitation.

Another new observation during the present experiments was the appearance of a remarkably repeatable "dimple" on the exterior surface of the traveling bubbles on the two larger headforms. These seem to appear when the bubble (or headform) is sufficiently large which suggests that the dimples are influenced by surface tension effects.

Cavitation event rates were also evaluated from the photographs and videotapes and this data clearly complements the observations of cavitation inception since inception was based on a chosen event rate. The event rates increase with increasing headform size and with decreasing cavitation number in the expected fashion if one assumes a fixed nuclei concentration. However the observed increase in the event rates with decrease in tunnel velocity are contrary to that which one would expect from the lower nuclei flux at lower speeds. It suggests that the nuclei population is substantially larger when the facility is operated at the lower pressures needed to achieve the same cavitation numbers at a lower velocity. It is also demonstrated that the event rates appear to correspond to a nuclei population of the order of 0.1 nuclei/cm^3 which is at least an order of magnitude lower than the expected nuclei population. We are continuing to investigate possible explanations for this discrepancy including the bubble screening effect first suggested by Johnson and Hsieh [16].

The noise generated by individual events and the variations in the noise with the type of event were also investigated. We first demonstrate that the acoustic impulse generated by individual traveling bubbles scales quite well with headform size and tunnel velocity and that this scaling is in accord with that expected from the Rayleigh-Plesset or Fitzpatrick-Strasberg analysis. As expected lower cavitation numbers lead to larger bubbles and larger impulses as long as the bubbles do not interfere with one another or with larger patch cavities.

As in the previous study by Ceccio and Brennen [2][3] the impulses generated are less than about a third of the magnitude predicted by the Rayleigh-Plesset analysis. It seems likely that the shearing and fission the bubble experiences prior to collapse leads to a less highly focused and less "efficient" noise-producing event. The present study has added to this information. We have shown that the events which generate attached "streaks" or "tails" and which represent a greater fraction of the events at higher Reynolds numbers also produce significantly smaller acoustic impulses. This correlation was observed by special cross-correlation of the surface electrode signals and the hydrophone output. The above observation has clear implications for the scaling of cavitation noise.

Some additional observations were made for those conditions at which the cavitation number was small enough for persistent attached patches to form and at which the void fraction of bubbles in the cavitation region became significant. First it was clear that when a traveling bubble encountered (or rode over) a patch its dynamics were altered and its acoustic output

substantially diminished. Secondly like Arakeri and Shanmuganathan [19] we also observed a significant decrease in the noise when the void fraction was sufficiently large so that the bubbles covered about 20% of the area in the cavitation region.

ACKNOWLEDGMENTS

Large scale experiments like these require help of many people and the authors are very grateful to all of those who helped in this enterprise. We are very grateful to the ONR for their support under contracts N00014-91-J-1426 (SLC) and N00014-91-J-1295 (CEB, YKdC). We are also extremely grateful to the David Taylor Research Center (DTRC) and to their staff including W.B. Morgan for making the use of the LCC possible for us and to both Scott Gowing and James Blanton of DTRC for extensive help with the experiments. Po-Wen Yu from the U. of Michigan also provided important help with the photography.

REFERENCES

1. Ceccio, S.L. 1989. "Observations of the dynamics and acoustics of traveling bubble cavitation." Ph.D. Thesis, California Institute of Technology.
2. Brennen, C.E. and Ceccio, S.L. 1989. "Recent Observations on cavitation and cavitation noise." Proc. ASME Third Int. Symp. on Cavitation Noise and Erosion in Fluid Systems, San Francisco, FED-Vol. 88, pp. 67-78.
3. Ceccio, S.L. and Brennen, C.E. 1991. "The dynamics and acoustics of traveling bubble cavitation." J. Fluid Mech., Vol. 233, pp. 633-660.
4. Kumar, S. and Brennen, C.E. 1991. "Statistics of noise generated by traveling bubble cavitation." ASME Cavitation and Multiphase Flow Forum, Portland OR, June 1991, FED Vol. 109, pp. 55-62.
5. Kumar, S. and Brennen, C.E. 1992. "An acoustical study of traveling bubble cavitation." Submitted to J. of Fluid Mech.
6. Kuhn de Chizelle, Y., Ceccio, S.L., Brennen, C.E. and Shen, Y. 1992. "Cavitation scaling experiments with headforms: Bubble dynamics." Proc. Second International Symposium on Propeller and Cavitation, Hangzhou, China.
7. Kuhn de Chizelle, Y., Ceccio, S.L., Brennen, C.E. and Shen, Y. 1992. "Scaling experiments on the dynamics and acoustics of traveling bubble cavitation." Proc. Institution of Mechanical Engineers, Cambridge, UK.
8. Lindgren, H. and Johnsson, C.A. 1966. "Cavitation inception on headforms. ITTC comparative experiments." Proc. 11th Int. Towing Tank Conf., pp. 219-232.
9. Schiebe, F.R. 1972. "Measurements of the cavitation susceptibility of water using standard bodies." St. Anthony Falls Hydraulic Lab., Univ. of Minnesota, Rep. No. 118.
10. Meyer, R.S., Billet, M.L. and Holl, J.W. 1989. "Free-stream nuclei and cavitation." Proc. ASME Third Int. Symp. on Cavitation Noise and Erosion in Fluid Systems, San Francisco, FED-Vol. 88, pp. 52-62.
11. O'Hern, T., D'Agostino, L. and Acosta, A.J. 1988. "Comparison of holographic and counter measurements of cavitation nuclei in the ocean." ASME J. Fluids Eng., Vol, 110, pp. 200-207.
12. O'Hern, T., Katz, J. and Acosta, A.J. 1985. "Holographic measurements of cavitation nuclei in the sea." ASME Cavitation and Multiphase Flow Forum Booklet, FED Vol. 23, pp 39-42.
13. Morgan, W.B. 1990. "David Taylor Research Center's Large Cavitation Channel." Proc. Int. Towing Tank Conference, Madrid, Spain, pp. 1-9.
14. Billet, M.L. 1985. "Cavitation nuclei measurement - A review." ASME Cavitation and Multiphase flow Forum, Booklet, pp. 31-38.
15. Gates, E.M., Billet, M.L., Katz, J., Ooi, K.K., Holl, W. and Acosta A.J. 1979. "Cavitation inception and nuclei distribution. Joint ARL-CIT experiments." Rep. E244-1, Calif. Inst. of Tech., Div. of Eng. and Appl. Sciences, Pasadena, CA 91125.
16. Johnson, V.E. and Hsieh, T. 1966. "The influence of gas nuclei on cavitation inception." Proc. Sixth Symposium on Naval Hydrodynamics, Washington D. C.
17. Favre, J.N., Avellan, F., Ryhming, I.L. 1987. "Cavitation performance improvement using a 2-D inverse method of hydraulic runner design." Proc. Int. Conf. on Inverse Design Concepts and Optimization in Engineering Science-II., Penn. State Univ.
18. Briancon-Marjollet, L. and Franc, J.M. 1990. "Transient bubbles interacting with an attached cavity and the boundary layer." J. Fluid Mech., Vol. 218, pp. 355-376.
19. Arakeri, V.H. and Shanmuganathan, V. 1985. "On the evidence for the effect of bubble interference on cavitation noise." J. Fluid Mech., Vol. 159, pp. 131-150.
20. Blake, W.K., Wolpert, M.J. and Geib, F.E. 1977. "Cavitation noise and inception as influenced by boundary layer development on a hydrofoil." J. Fluid Mech., Vol. 80, pp. 617-640.
21. Fitzpatrick, H.M. and Strasberg, M. 1956. "Hydrodynamic sources of sound." First Symp. on Naval Hydrodynamics, Washington D.C., pp. 241-280.
22. Hamilton, M.F., Thompson, D.E. and Billet, M.L. 1982. "An experimental study of traveling bubble cavitation and noise." ASME Int. Symp. on Cavitation Noise, pp. 25-33.
23. Vogel, A., Lauterborn, W. and Timm, R. 1989. "Optical and acoustic investigations of dynamics of the Laser-produced cavitation bubbles near a solid boundary layer." J. Fluid Mech., Vol. 206, pp. 299-338.

Tip Vortex Roll-Up and Cavitation

D. Fruman[1], C. Dugué[1*], A. Pauchet[2], P. Cerruti[3], L. Briançon-Marjolet[2]
([1]Ecole Nationale Supérieure de Techniques Advancées, France;
[1*]University of Minnesota [on leave from Ecole Nationale Supérieure];
[2]Bassin d'Essais des Carènes, France;
[3]Laboratoire d'Hydrodynamique, France)

ABSTRACT

Experiments conducted in three cavitation tunnels with elliptical planform hydrofoils, of area ratio 3.8 and mid-span chord ranging from 40 to 475 mm, allowed to investigate the effects of Reynolds numbers, comprised between $4x10^5$ to $6.8x10^6$, on tip vortex cavitation. The hydrodynamic forces of the hydrofoil were measured for Reynolds numbers ranging from $2.5x10^5$ to $2.4x10^6$. The tangential velocity profiles were measured in each one of the cavitation tunnels for numerous stations situated between the tip of the foil and the trailing edge at mid-span and some other stations beyond the trailing edge. Axial velocities and turbulence levels were also measured. The critical cavitation numbers were determined in the two largest cavitation tunnels. From the values of the tangential component of the velocity, the local intensity of the vortex and the radius of the inner, solid body rotation, region are determined. Using their values at the position corresponding to the minimum pressure along the vortex path, the minimum pressure coefficient is computed and its absolute value compared to the desinence cavitation number for several flow situations. This comparison is very satisfactory and sheds new light on tip vortex cavitation interpretation.

NOMENCLATURE

a	distance to the vortex axis for maximum tangential velocity
b	half span
c_{max}	maximum chord
C_l	lift coefficient
C_p	pressure coefficient at the vortex axis
C_{pmin}	mimum pressure coefficient at the vortex axis
i	incidence angle
p_∞	pressure of the unperturbed flow
p_0	pressure at the vortex axis
r, y	distance to vortex axis
V_∞	free stream velocity
V_t	tangential velocity
V_a	axial velocity
δ	boundary layer thickness
Γ	tip vortex intensity
ν	liquid kinematic viscosity
ρ	liquid density
σ_i	incipient cavitation number
σ_d	desinent cavitation number

1. INTRODUCTION

Onset of cavitation occurs on the axis of a tip vortex when the pressure there reaches a value equal or below that of the vapor pressure of the flowing liquid. The pressure on the vortex axis depends on the process leading to the roll-up of the vortex sheets and, in particular, on how the vortex intensity and the vortex core develops along the vortex path. A considerable amount of work has been devoted to these matters but, in spite of much effort, a conclusive approach allowing to interprete test results on cavitation inception and desinence and to extrapolate them to Reynolds numbers such as those encountered in propeller application has not yet been offered.

The major ingredients of the alchemy of the phenomenology of tip vortex cavitation is in the seminal paper by McCormick (1962) published exactly thirty years ago. In it, McCormick rules out the possibility of estimating the critical cavitation conditions from either a completely rolled-up vortex sheet model (far downstream) or of a nondistorded vortex sheet model (very near the wing). He thus proposes a semiempirical approach in which he considers, for the first time, that the boundary layer developed over the lower surface of the foil near the tip determines the extent of the vortex core. He then postulates a power law relation, $\delta \approx Re^{-r}$, between the boundary layer thickness, δ, and the local Reynolds number, Re. However, since no detailed velocity measurements in the region very near the tip were available at that time, in McCormick's original work (McCormick (1954)) the flow at the tip of the foil is analyzed as being the result of the velocity field induced

by the distribution of circulation along the wing span. The flow is then very much similar to the one around the edge of a flat plate so that the maximum "tangential" velocity at a distance from the tip a, supposed to be the core radius and small as compared to the half span, is proportional to $a^{-0.5}$. It should be pointed out that this computation assumes, wrongly (see Van Dyke (1964)), that the lifting line theory is valid up to the tip of the foil. Since the minimum pressure coefficient will scale with the square of the maximum velocity, the critical cavitation number will be roughly inversely proportional to the core radius This leads McCormick to establish, based on his experiemental data for Reynolds numbers, computed with the free stream velocity and the chord, ranging from $2x10^5$ to $3x10^6$, that the power index r is 0.35, different from the values of 0.5 and 0.2 for respectively laminar and turbulent boundary layer over a flat plate. This situation is resolved by McCormick (1962) by saying that the value obtained is reasonable because comprised between the two referred extreme values. The fact that McCormick's data extend from the laminar to the turbulent regime does not justifies that the power index should be comprised between these values. Indeed, Billet and Holl (1979) have already pointed out that the critical cavitation number should scale as the inverse of the square of the vortex core radius if a potential vortex behaviour is postulated. In that case the critical cavitation number should scale as Reynolds to the power 0.4 if a turbulent boundary layer behaviour is assumed. This is what the direct plotting of McCormick (1962) results show for rectangualr foils at 4 and 8° incidence. Moreover, in a recent investigation, Fruman *et al.* (1991) have related the core radius to the desinent cavitation numbers, σ_d, of elliptical planform wings having identical cross sections and operating at the same incidence angle by the same relationship, $a \approx \sigma_d^{-1/2}$. They showed that a behave very much as the thickness of a flat plate boundary layer in the transitional regime (Schlichting (1979)) for Reynolds numbers comprised between 0.6 and $6x10^5$ and can not, thus, be fitted by a power law. Moreover, beyond the transitional regime, the evolution of the vortex core radius is analogous to that of a turbulent boundary layer ($a \approx Re^{-0.2}$). These results were further substantiated by detailed laser velocimetry measurements of the tangential velocity profiles along a vortex path from the tip of an elliptical wing to a distance downstream where roll-up has been completed. These measurements allowed to determine the evolution of the local core radius with distance and to compare it with the mid-span boundary layer thickness (assumed to be equal to that of a flat plate of equal length). The order of magnitude of the core radius is indeed comparable to the boundary layer thickness. McCormick's introduction of the boundary layer thickness concept is thus highly justified despite the fact that there is a disagreement concerning its variation with Reynolds numbers.

The minimum pressure coefficient on the axis of the vortex will be also directly related to the local vortex circulation at the point of minimum pressure. This leads to two different problems. First, the vortex intensity to be taken into account is proportional to the mid-span bound circulation of the foil. Therefore, a good knoweledge of the actual lift coefficient is necessary to fully interpret results which otherwise display quite unexpected behaviours. This question has been recognized by Platzer and Souders (1979), but effects of Reynolds number and free stream turbulence seem to have been underestimated in many cases. As an exemple, Arndt *et al.* (1991) found, based on a theoretical value of the lift coefficient, only a fraction of the bound circulation in the vortex while more recent experimental results by Arndt and Dugué (1992) show that actual lift of the foil is only 75% of the theoretical one. Second, there is a controversy about where the minimum pressure occurs along the vortex and how far downstream of the tip one has to perform tangential velocity measurements in order to determine its location.

Several contributions to the computation of the minimum pressure on the vortex have been recently published. In all cases, the way authors operated was to measure, either by Laser Doppler Velocimetry (LDV) (Stinebring *et al.* (1991), Arndt *et al.* (1991), Fruman *et al.* (1991)) or double pulse holography (Green (1988, 1991)), the "tangential" velocity profiles of the vortex at varied distances from the tip of the hydrofoils and to integrate the radial momentum as if the vortex was axisymmetrical. This procedure can certainly be criticized because the velocity profiles are not, at the selected stations, those of an axisymmetrical vortex and, therefore, account of the whole velocity field has to be taken. However, and in spite of this limitation, the results obtained are very interesting and a review of these recent contributions will be highly valuable.

Arndt *et al.* (1991) used an elliptical planform hydrofoil with area ratio of 3, Reynolds numbers, based on the free stream velocity and the base chord length, comprised between $3x10^5$ and $11.5x10^5$, and LDV systems for measuring the axial and "tangential" velocities. It should be pointed out that the velocities were measured on a direction normal to both the free-stream direction and the axis of the hydrofoil at distances from the tip comprised from 0.47 to 3.77 maximum chord and a Reynolds number of $5.6x10^5$. Notice that 0.47 maximum chord from the tip correspond to the foil trailing edge at mid-span, thus, far from the tip. Cp_{min} was computed by numerically integrating the radial equilibrium equation for the velocity distribution on each side of the vortex axis. The results show that the minimum pressure coefficient for the suction side of the velocity profile are generally smaller than those for the pressure side and that on both sides they vary with downstream location. Moreover, even if the value of the inception cavitation number is bracketed by the estimates of $-Cp_{min}$ the authors claim that other effects should be considered. They argue that although the incipient cavitation number will tend to diminish if the operating pressure of the cavitation tunnel is larger prior to the tests, this tension effect will be cancelled by the contribution of the fluctuating component of the pressure field. However, a more recent result by Arndt and Dugué (1992) show a good agreement with the incipient cavitation number, "raising a question concerning Arndt and Keller's (1992) conclusion that the measured differences between $-Cp_{min}$ and σ_i can be accounted for by flow unsteadiness in the vortex". Moreover, and as it was signaled above, Arndt *et al.* (1991) questioned the validity of estimating $-Cp_{min}$ by the techniques used in the presence of a strong asymmetrical velocity profile and possibly large axial flow

velocities in the vortex core (not shown in the referred paper but in Arndt and Keller (1991)).

Green's (1991) work differs from the above because he employed the double pulsed holography technique to determine the axial and tangential velocity profiles and the single pulse holography to obtain the pressure on the vortex axis at distances from the tip larger than one chord. Tests were performed with a rectangular planform hydrofoil with aspect ratio of 2.3 in a cavitation tunnel characterized by a very low free stream turbulence level. Velocity measurements were reported for a Reynolds number of 6.83×10^5 and cavitation inception data for a Reynolds number of about 10^6. By partly using the tangential velocity data for a 10° incidence angle, the author makes an estimation of $-Cp_{min}$ leading to a value of 4.38±0.4. From single pulse holography of bubbles he determines a value of 3.3±0.5, which he claims to be independent of distance, much lower than the one estimated from the velocity profiles. After some discussion his best estimate of $-Cp_{min}$ is set equal to 3.8±0.6; "inferring the mean core pressure from measurements of tangential velocity seems to be viable". The values of the incipient cavitation number, for the same incidence angle, are comprised between 4.2 and 2.6 depending on the air content of the recirculating water. Either surface tension effects or pressure unsteadiness are considered by Green to explain the disagreement between the cavitation data and the minimum pressure coefficient (3.8±0.6). In Green (1988) it is signaled that the trailing vortices meander laterally by 0.01 or 0.02 m (up to 14 % of the chord length) at about a mean location for a distance larger than three chords.This is a situation which seems unique to these experiments. In Arndt *et al.* (1991) and Green (1991), the pressure coefficients on the vortex axis were computed from velocity profiles determined far from the tip and their values are not in agreement with the critical cavitation numbers.

Stinebring *et al.* (1991) conducted tests with a trapezoidal planform hydrofoil with an aspect ratio of 1.28 for Reynolds numbers close to 5×10^6 (well in the turbulent regime) and measurements of the three components of the velocity (axial, parallel to the foil span (radial) and normal to both (tangential)) were made by means of a three components LDV system at 0.073 and 0.667 tip chord downstream the tip. They mapped the velocity field on a plane normal to the axial flow at 0.067 tip chord (where cavitation onset occurs) and showed that the flow outboard of the hydrofoil follows nearly a circumferential path about the vortex center while, inboard, there is a strong radial flow away from the vortex center. This means that, outside the hydrofoil wake, the radial component is negligible small on a straight line drawn horizontally (the foil is also horizontal) through the vortex center. An estimate of the minimum pressure coefficient, Cp_{min}, in the vortex center (-0.82) was obtained by numerically integrating the radial equilibrium equation for the tangential velocity profile obtained nearest the tip. Its absolute value compares favorably to those of the incipient (0.6) and desinent (0.8) cavitation numbers. It should be noted that, since the absolute value of the pressure coefficient is in both cases larger than the critical cavitation number, the difference can be accounted for by surface tension effects on the nuclei. No explicit mention of vortex wandering was made by the authors.

In their approach of the problem Fruman *et al.* (1992) determined the critical cavitation conditions of an elliptical planform hydrofoil of area ratio 3.8 and symmetric NACA 16020 cross section. They also measured the "tangential" velocity distribution, over axes parallel to the foil span, for 5 and 10° incidence angles and, respectively, 15 and 13 m/s, corresponding to Reynolds numbers of 1.2 and 1.0×10^6, for stations comprised between the tip of the wing and four maximum chord downstream (four stations were comprised between the tip and the mid-span trailing edge). Instead of conducting a numerical integration of the radial equilibrium equation using the velocity data, as for Stinebring *et al.* (1991), Arndt *et al.* (1991) and Green (1991) the authors proceeded in the following way : first, the profile outside the wake is fitted with a Lamb (1945) model and simultaneously corrected for image effects due to the lateral tunnel walls; second, the local vortex circulation is made non dimensional with the mid-span bound circulation (computed from actual lift measurements); third, the vortex core is made non dimensional with the mid-span boundary layer thickness (assumed to be equal to that of a flat plate of equal length); fourth, from the local vortex intensity and the vortex core radius the local minimum pressure is computed by replacing their values in the integration of the radial equilibrium equation for a Lamb velocity profile. The following conclusions were drawn from the results of the above procedure : i) vortex roll-up leads to a local circulation of about 25% of the mid-span bound circulation at the tip of the wing; ii) the vortex core radius is very close to the mid-span boundary layer thickness (computed as for a flat plate) at one half of the maximum chord from the foil tip; iii) a minimum of Cp_{min} occurs at a distance of about one eight of a chord downstream of the tip and iv) $-Cp_{min}$ is in agreement with the desinent cavitation number of the foil for the same incidence angles and test velocities. The good agreement between the cavitation results and the ones issued from the "tangential" velocity profiles led to a detailed analysis of data obtained during these tests and previous ones for much smaller Reynolds numbers with a geometrically similar foil. The main conclusions of this analysis have already been detailed in the beginning of this introduction. Finally, in Stinebring *et al.* (1991) and Fruman *et al.* (1991) there is good agreement between the minimum pressure coefficient computed at the position where cavitation occur along the vortex path; that is to say in the region very near the tip of the wing.

It can thus be said that there are still major unresolved questions concerning tip vortex cavitation and that there is ample room for other contributions. The objective of the present one is to make use of the rationale developed by Fruman *et al.* (1992) to conduct tests in three different cavitation tunnels on geometrically similar hydrofoils, of elliptical planform and cross section NACA 16020, for flow conditions allowing a large range of Reynolds numbers to be investigated. The program encompasses several tasks which are summarized below :

a) Measurement of the hydrodynamic forces of two of the foils in order to fully characterize the Reynolds number effects on, in particular, the lift coefficient. In this investigation, Reynolds numbers have been increased up to the situation where a near plateau was obtained for the lift coefficients. The details of the lift coefficient versus Reynolds number and incidence angles evolution are essential for interpreting and discussing the critical cavitation number data on one hand and the Cp_{min} values on the other.

b) Measurement of the "tangential" velocity profiles in each one of the cavitation tunnels for a given incidence angle ($\approx 10°$) of the foils. They were performed for numerous stations comprised between the tip and the trailing edge at the mid-span, allowing a very detailed description of the roll-up process in the very near region, and for stations sufficiently far downstream to obtain information on the completion of the vortex roll-up. Axial velocity and turbulence data were also obtained in two of the cavitation tunnels. These detailed measurements complete and extend those presented by Fruman *et al.* (1991).

c) Measurements of both the incipient and desinence cavitation numbers in the three cavitation tunnels as a function of incidence angle and Reynolds numbers. As in McCormick's work (1962) the analysis of cavitation data was limited to desinent conditions.

The analysis of the data is conducted in the following way:

1) From the lift coefficients it is easy to obtain the mid-span bound circulation value for all flow conditions investigated.

2) From the "tangential" velocity profiles the local vortex intensity can be obtained and related to the mid-span bound circulation. Also, either by considering the distance to the axis where the maximum of the velocities occur or by fitting a Lamb profile through the whole velocity profile, the radius of the local core can also be reached. The core radius is then related to the thickness of the boundary layer, assumed to be that of an equal length flat plate.

3) With the results from 2), the minima of the pressure coefficient at the vortex axis, Cp_{min}, along the vortex path is obtained and compared to the desinent cavitation number.

2. EXPERIMENTAL FACILITIES AND PROCEDURES

Experiments were conducted in three cavitation tunnels, whose geometry and operating conditions are given later, using elliptical planform hydrofoils of area ratio 3.8 and identical NACA 16020 cross sections. The foils are scaled according with the test section dimensions of the tunnels. Table 1 summarizes the foils dimensions and the free stream velocity range.

A limited number of tests were also conducted at the Bassin des Carènes with a hydrofoil of identical planform but cross section NACA 0020.

Table 1 : Foils dimensions and free stream velocity range.

FACILITY	Chord, mm	Half-span, mm	Min. veloc, m/s	Max. veloc, m/s
ENSTA	40	60	3	10
Ecole Navale	80	120	3	15
Bassin des Carènes	475	712.5	2	20

2.1. Tests in the ENSTA cavitation tunnel (ECT)

The hydrofoil was mounted horizontally on one of the vertical walls of the 150 mm height and 80 mm width test section of the ENSTA cavitation tunnel. The tangential components of the velocities of the vortex issued from the tip of the foil were measured for 10.6° incidence angle and a free stream velocity of 9 m/s (Reynolds number of about 3.6×10^5) at fourteen stations situated at a distance, measured from the leading edge at the mid-span, of 0.5, 0.525, 0.55, 0575, 0.625, 0.675, 0.75, 0.875, 1, 1,5, 3, 5.5, 8 and 10.5 maximum chord.

The LDV system operated in the backscatter mode using a 150 mW nominal laser, a TSI fiber optics and a Intelligent Flow Analyser IFA 550 from TSI. For the optical arrangement chosen, the measuring volume is about 200 μm long. The displacement of the optics is controlled automatically by means of a Macintosh II with step widths as small as 20 μm. The data rate, was increased by seeding the circulating water with Iriodine. The axial turbulence level in the test section, measured in the absence of the hydrofoil, was less than 2%. Lift and drag measurements were performed using a two components strain gage balance.

2.2. Tests in the Ecole Navale cavitation tunnel (ENCT)

The hydrofoil was mounted horizontally on one of the vertical walls of the 192 mm side and 1 m long square test section of the Ecole Navale cavitation tunnel at 300 mm from the entrance. Air content was keep in the 2 to 3 ppm range. The free stream turbulence was 1.5%. All instantaneous values of the operating parameters were recorded in order to compute the actual Reynolds and cavitation numbers.

Lift and drag forces were measured using a two-component strain gauge balance whose calibration, prior to the tests, showed a linear response in the range of forces expected, up to 170 daN for lift and up to 18 daN for drag. In order to extend the range of Reynolds numbers for which force coefficients were known, measurements were conducted with a homothetic hydrofoil of 80 mm half span and 60 mm chord for free stream velocities comprised between 15 and 40 m/s at the Institut de Machines Hydrauliques et de Mécanique des Fluides (IMHEF) of Lausanne (Switzerland).

The axial and "tangential" components of the velocity of the tip vortex were measured at stations situated at 0.5, 0.525, 0.55, 0.575, 0.625, 0.675, 0.75, 0.875, 1.0, 1.25, 1.5, 2, 2.5 and 4 maximum chord

downstream the leading edge at mid-span using a Dantec two components (three beams) LDV operating in the backscatter mode with a 5 W Argon ion laser source. For the optical configuration selected, the measuring volume is 0.5 mm long and 0.04 mm wide. The backscattered signal, acquired by two photomultipliers and treated by two Dantec enhanced Burst Spectrum Analyzers (BSA) 57N20 and 57N35, is processed by an IBM PS/2 microcomputer using the Dantec Burstware software. The liquid was seeded with Iriodine in order to increase the data rate. Velocities were measured on four hundred positions separated by a minimum step width of 30 μm for a 10° incidence angle and a free stream velocity of 13.5 m/s.

2.3. Tests in the Bassin des Carènes Cavitation Tunnel (GTH)

The hydrofoil hangs vertically from the top horizontal wall of the 1.14 m side square test section of the GTH (Grand Tunnel Hydrodynamique) (see Lecoffre *et al.* (1987) and Briançon and Frechou (1992)). The tip of the foil was situated at 1.26 m from the entrance and the tip vortex cavitation could be then visualized over the remaining 4.74 m of the test section length. The foil incidence was modified manually through a mechanical system installed on the test section cover. Since no force balance was available for these tests, the zero incidence angle was set by geometrically checking, prior to installing the cover, its position with respect to the cover lateral sides. Once in the test section, the zero incidence angle was verified by performing tip vortex desinence experiment at negative and positive angles of attack and determining the position insuring the symmetry of the results. The zero position is known with a precision of ±0.5°. Incidence angles were varied between 0 and 13.5°. Data reported here were obtained without nuclei injection at oxygen contents of about 3.2 ppm. The axial free stream turbulence level was between 0.3 and 0.5 %. Operating conditions were continuously monitored and recorded on the video images used to determine "off-line" the critical cavitation conditions.

Axial and "tangential" velocities were measured with a two components (three beams) forward scattering LDV system using a 15 Watt Argon source at stations situated at 0.58, 0.6, 0.7, 0.8, 1, 1.7, 2.6, 3.5 and 4 maximum chord downstream the mid-span leading edge. Because of the extremely large distance between the emission and reception optics, their position was simultaneously monitored by two three-axis independent computer-controlled (Dantec) traversing mechanism systems. The measuring volume, of 4.7 mm long and 0.18 mm wide, was positioned with a precision of ±50 μm and the steps size (0.25 to 5mm) were adapted to the local tangential velocity gradients. LDV data were analyzed using two Dantec BSA and stored on a PC computer for further treatment.

2.4. Critical cavitation number measurements procedure

Tip vortex cavitation inception and desinence were obtained from direct visual observation of the test section or by delayed inspection of video recordings of the region close to the tip of the wing (for the GTH tests). In all cavitation tunnels, visualization was improved using stroboscopic light sources. Except when otherwise specified, test were conducted at constant cavitation number (constant free stream velocity and test section pressure) by slowly varying the incidence angle of the foil until cavitation onset occurred. The incidence was then increased slightly to obtain a well developed tip vortex cavitation and desinence conditions were obtained by reducing the incidence angle. Cavitation inception is critically dependent, Arndt *et al.* (1991), upon the water quality characterized, essentially, by the nuclei and gaz content. Thus, in the present work desinent cavitation numbers have been used throughout since, as already mentioned by McCormick (1962), they are much less sensible to changes in water quality.

2.5. Velocity measurements procedure

Figure 1 shows the coordinate axis and the way the velocity profiles were determined in the three cavitation tunnel.

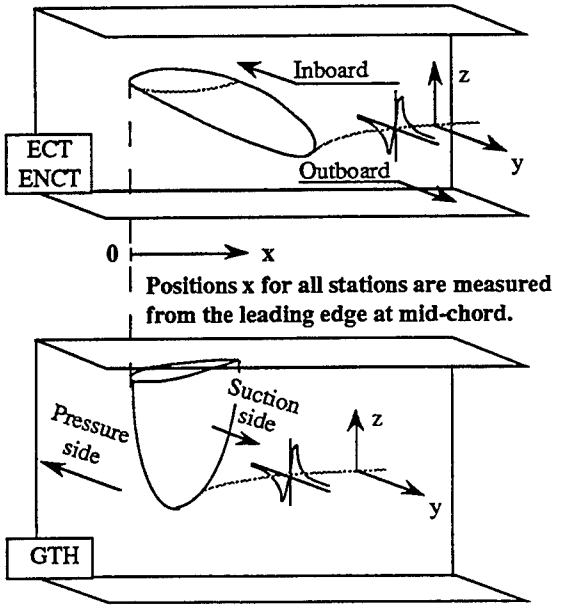

Fig. 1 : Foil arrangement, coordinate system and velocity components measured in the three cavitation tunnels.

One of the major problems associated with the LDV measurements is to be sure that the measuring volume coincides with the center of the vortex. This was done by first making the point of crossing of the laser beams to coincide with the cavities convected in the vortex path for a cavitation number slightly below critical. Second, the vertical velocity component on a vertical axis was determined for a short distance on both sides of this position. The extremum of the velocity corresponds to the effective location of the vortex axis.

It should be mentioned that vortex wandering was very limited in all the tests reported here. For example, a comparison of photographs of a cavitating tip vortex taken

in the ENCT at low (10^{-5} s) and high (0.5 s) exposure times for the same flow conditions indicates that the amplitude of the vortex meandering can be estimated in the near region (about one chord from the tip) to be less than 100 μm. In the GTH, at about the same position, the amplitude is about 1 mm, roughly scaling with the foil size. For the farthest velocity profile obtained, the maximum wandering amplitude was about 5 mm. This is only one percent of the foil chord, well below the vortex meandering (14 % of the chord length) reported by Green (1988) for tests performed with a rectangular foil at Reynolds numbers probably within the transitional regime.

3. RESULTS

3.1. Force measurements

Figure 2 shows the lift and drag coefficients as a function of the incidence angles determined from measurements conducted at the ENCT. Reynolds number effects are particularly dramatic on the lift coefficient since, at 10° incidence angle for example, it falls from 0.75 at $Re=2.5x10^5$ to 0.3 for $Re=1.2x10^6$. Tests conducted at the Institut de Machines Hydrauliques et de Mécanique des Fluides (IMHEF) of Lausanne have fully confirmed the data obtained at the ENCT on one side and have allowed to obtain data for Reynolds numbers of up to $2.4x10^6$. Figure 3 shows for several incidence angles the lift coefficients as a function of Reynolds numbers. For Reynolds numbers lower than those for which laminar to turbulent transition is expected to occur ($\approx 4x10^5$) the lift increases very rapidly, besides for the very small angles, while it remais nearly constant for Reynolds numbers exceeding 10^6. The results obtained in the ECT in the range of $Re<4x10^5$ are in general agreement, although a little bit smaller, with those measured at the lowest range of Reynolds in the ENCT. The difference in the lift coefficient values can be due essentially to the difference in the wing confinement in the two test sections. When analyzing the results, the mid-span bound circulation will be computed from the lift coefficients by,

$$\Gamma_0 = \frac{C_l(i,Re)\, V_\infty\, c_{max}}{2}$$

3.2. Velocity Measurements

3.2.1. Tangential velocities

Figure 4 shows results obtained in the ECT at an incidence angle of 10.6 and a free stream velocity of 9 m/s. The vertical (≈ tangential) component of the velocity, V_t, normalized with the free stream velocity V_∞, is plotted for stations comprised between the tip of the wing and the trailing edge at mid-span. It should be pointed out that even if as much as 320 measurements have been made over spanwise positions comprised between $y/c_{max}=\pm 0.4$ with a minimum radial step of 40 μm, only a reduced number of data points have been reported in order to make the figure easily readable. Even though, there is a remarkable good definition of the velocity profiles, in particular in the core region. It has also to be signaled that, because the short distance between the tip and the lateral wall of the test section (only 20 mm) the raw results have been corrected to account for image effects.

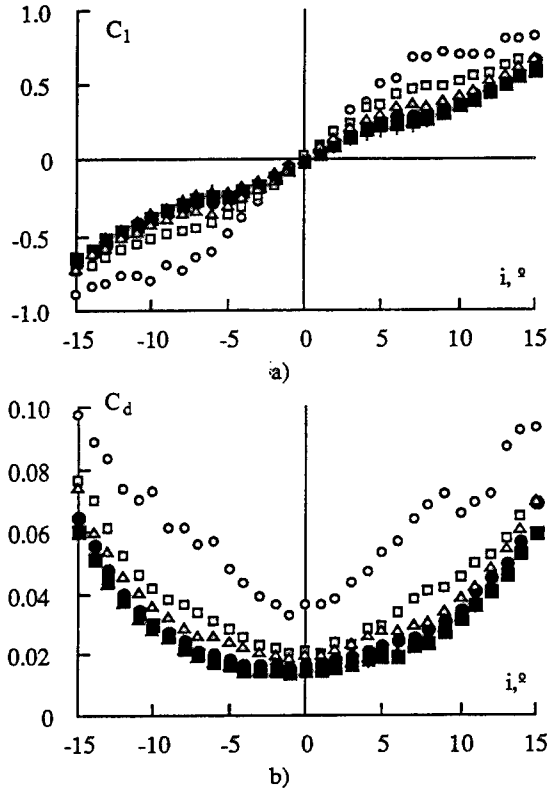

	○	□	△	●	■	▲	+
10^{-5} Re	2.5	4.1	5.5	7.1	8.9	10.4	12.0

Fig. 2 : Hydrodynamic coefficients versus incidence angle for the elliptical foil NACA 16020 cross section and different Reynolds numbers. a) lift coefficients, b) drag coefficients. Data obtained in the ENCT.

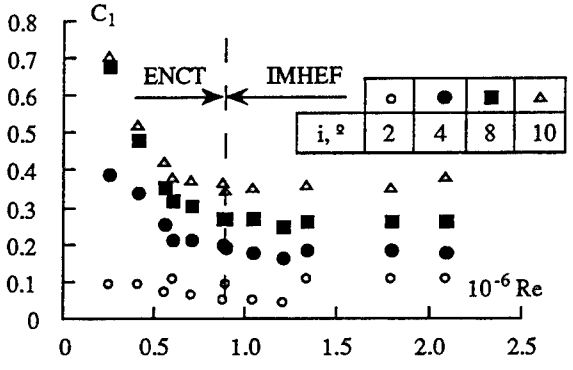

Fig. 3 : Lift coefficients as a function of the Reynolds number for different incidence angles. Data obtained in the ENCT and the IMHEF cavitation tunnel.

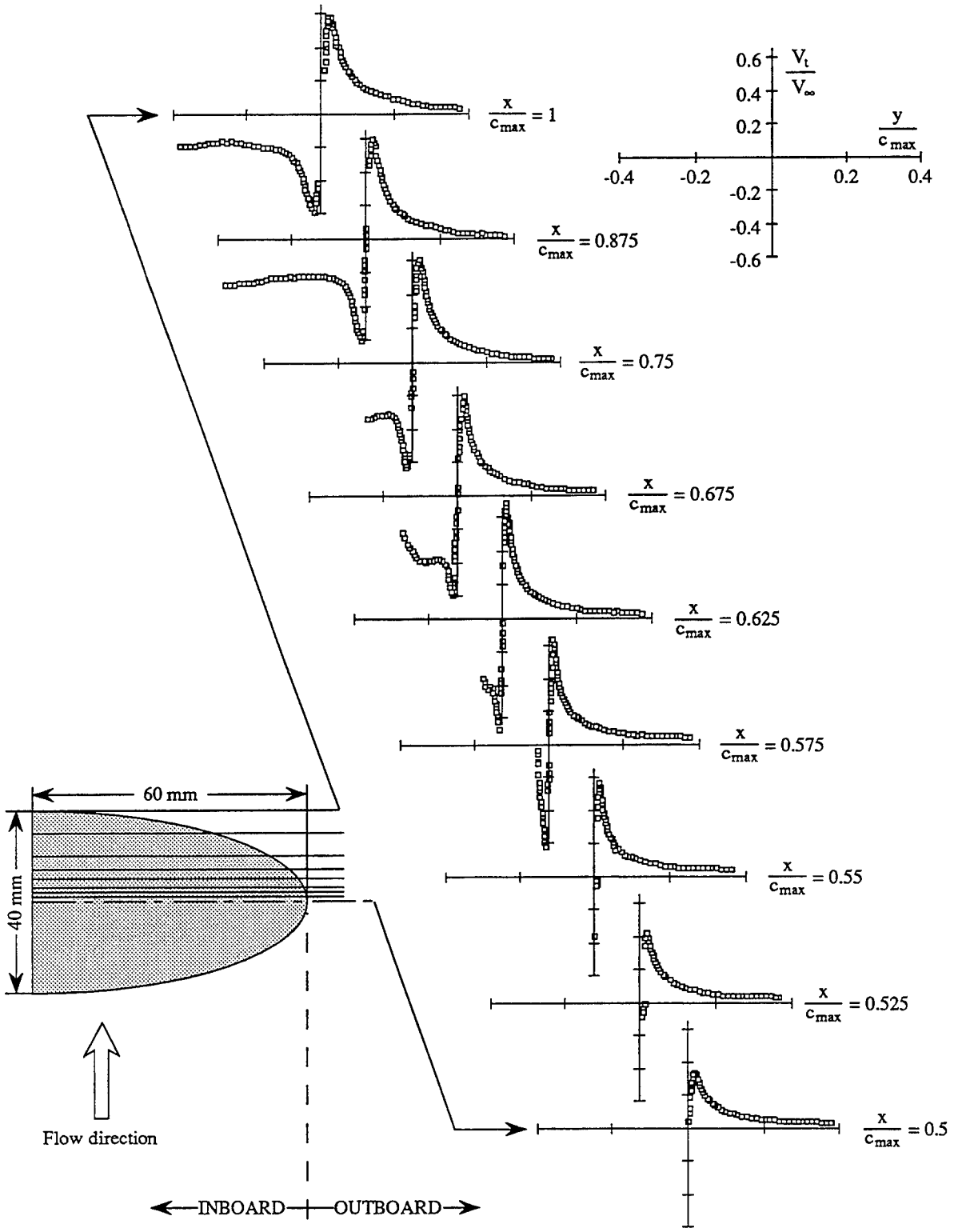

Figure 4 : Tangential velocities as a function of distance to the vortex axis for different axial stations. ECT data for i=10.6° and V_∞= 9 m/s.

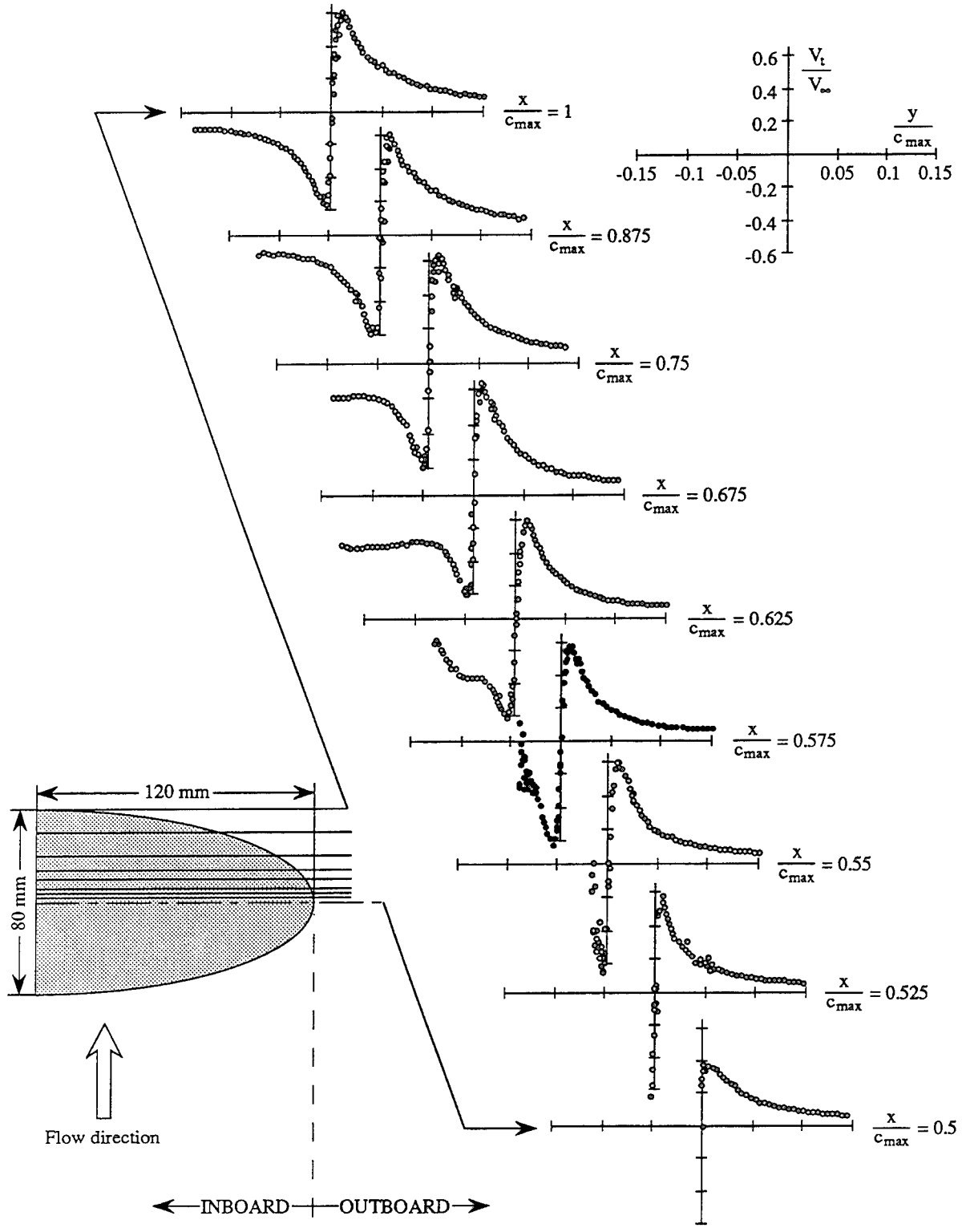

Figure 5 : Tangential velocities as a function of distance to the vortex axis for different axial stations. ENCT data for i=10° and V_∞=13.5 m/s.

These results improve considerably those presented by Fruman *et al.* (1991) and show some very interesting features of the flow in the very near region of roll-up. At the wing tip, there is already a clear indication of the initiation of a vortical structure, comprising a rotational zone where the velocities are proportional to the radial distance, and, as it will be shown later, a potential region outside. The maximum velocity, very precisely measured, increases when moving downstream and, simultaneously, the rotational zone develops for negative values of the spanwise distance (inboard). For x/c_{max}=0.575, only 3 mm downstream the tip, the rotational zone is well developed and the beginning of the symmetrical potential region occurs. From there on the maximum and the minimum of the velocities are nearly equal (to within 0.3%), showing thus that the square of the ratio between the two extremum can not be used in here as a parameter pertaining to vortex roll-up completion, as suggested by Stinebring *et al.* (1991). At x/c_{max}=0.625, the maximum velocity is the largest and the influence of the wing wake inboard becomes evident as shown by the downwash velocities already present. The wake effect develops downstream while the maximum velocity reaches a near plateau whose value is slightly larger than 0.6 V_∞. Since the pressure on the vortex axis will be closely related to the square of the maximum tangential velocity, whatever the velocity distribution is and even if the flow is not axisymmetrical, it is clear that measurements not conducted in the very near field, less than a chord from the point of initiation of the vortex roll-up, will be meaningless from the point of view of its cavitation implications. These results show also the need to conduct measurements with an extremely good spatial definition in order not to miss the pecularities of the velocity profiles in the core region, where good quality data are necessary to obtain reasonable estimates of the vortex core size, and to achieve a good description of the whole transitional and potential region.

In Figure 5 the results obtained in the ENCT for an incidence angle of 10° and a free stream velocity of 13.5 m/s are shown. The distance investigated on both sides of the vortex axis has been reduced to ±0.15 c_{max}. Comparison with the velocity profiles of Figure 4 shows that the vortex roll-up is also already initiated at the wing tip. Moving downstream clearly demonstrate that the velocities behave nearly in the same way in both cavitation tunnels in spite of the fact that the Reynolds number has been increased by a factor of three ($3.6x10^5$ in the ECT and $10.8x10^5$ in the ENCT). The absolute values of the maximum and minimum velocity are nearly equal from the station x/c_{max}=0.525 on and are very close to 0.6 V_∞. The solid body rotation region extends inboard from this same station. Figure 6 shows that for the velocity profile obtained at x/c_{max}=2.5, symmetry has been achieved on both sides of the tip vortex axis.

The improvement in the spatial definition of the tangential velocity profiles in the ECT and the ENCT, as compared with earlier results by Fruman *et al.* (1991), is remarkable and offers new insights on the way roll-up develops in the very near region. In perticular, the present results clearly demonstrate that symmetry is achieved very rapidly downstream of the tip.

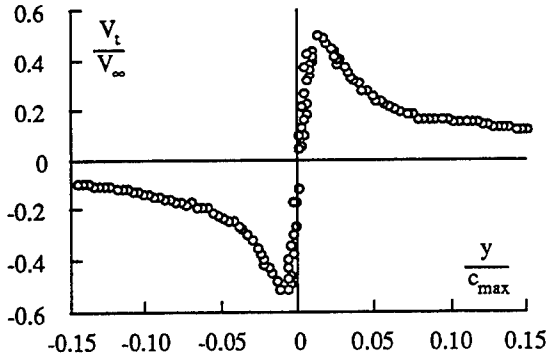

Fig. 6 : Tangential velocities as a function of distance to the vortex axis for x/c_{max} = 2.5. ENCT data for i =10° and V_∞ =13.5 m/s.

Since the velocity profiles obtained at the GTH were measured along axes at 90° from those used in the ECT and the ENCT, there are marked differences as can be seen in Figure 7 for a 10° incidence angle and 10 m/s free stream velocity. The most significant is the strong disymmetry between the measurements conducted on the suction and on the pressure side. On the suction side the maximum velocity increases considerably over a very short distance, from x/c_{max}=0.58 to 0.60, and decreases steadily from there on. On the pressure side, the maximum of the absolute value of the velocity is very small for the first velocity profile (x/c_{max}=0.58) and increases steadily up to a distance x/c_{max}=1.7. It is very interesting to note that for the station situated at x/c_{max}=0.6, a small "accident" occurs on the pressure side very near the axis. This accident moves outside, as can be seen by considering the velocity profiles in Figure 7, and fades away for a distance of about two chords downstream. Figure 8 shows that this "accident" persist in the velocity profiles obtained at x/c_{max}=0.8 for three flow conditions. This "accident " is very much analogous to the one signaled by Arndt and Keller (1991), who performed their measurements in the same way that at the GTH and attributed it to a secondary vortex. However, we recall that no such "accident" has been noticed in the results obtained at the ECT and the ENCT.

3.2.2. Axial velocities

The measurements conducted in the ENCT have demonstrated that the axial velocity profiles remain nearly equal to the free stream velocity everywhere but in a region very close to the vortex axis, Figure 9. An excess velocity of about 30% exists on the axis of the vortex at the wing tip and is conserved two millimeters downstream. However, it rapidly fades away to finally show, at a distance of two chords downstream, a weak velocity defect. In the GTH the behavior is much more complex. Indeed, in the region very near the tip, Figure 10 shows that the velocities increase by about 10% for distances comprised between y/c_{max}=±0.1 and that, around the axis, strong defect and excess velocities, the former of about 0.85 V_∞ and the later of up to 1.63 V_∞, are superimposed.

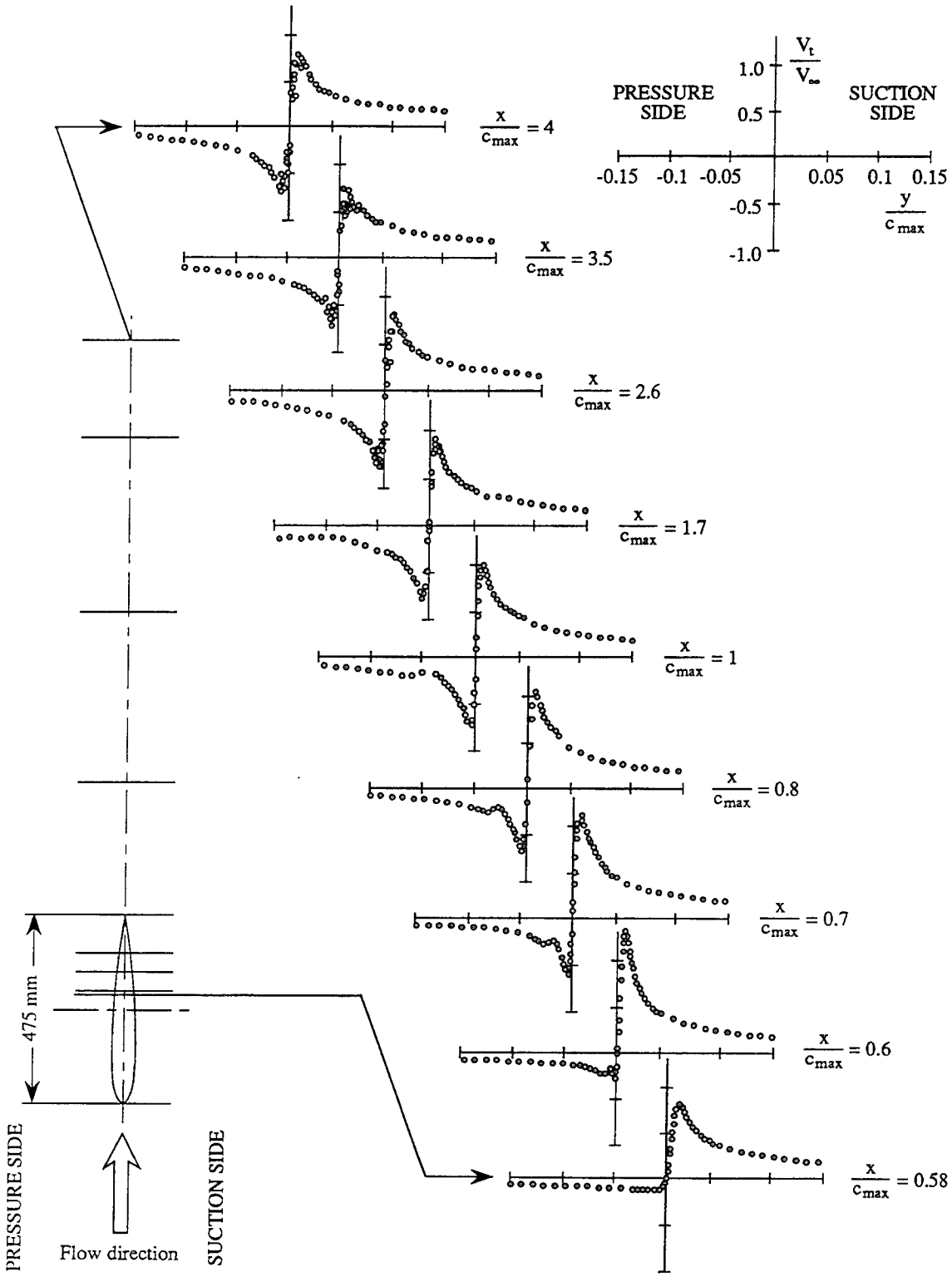

Figure 7 : Tangential velocities as a function of distance to the vortex axis for different axial stations. GTH data for i=10° and V_∞=10 m/s.

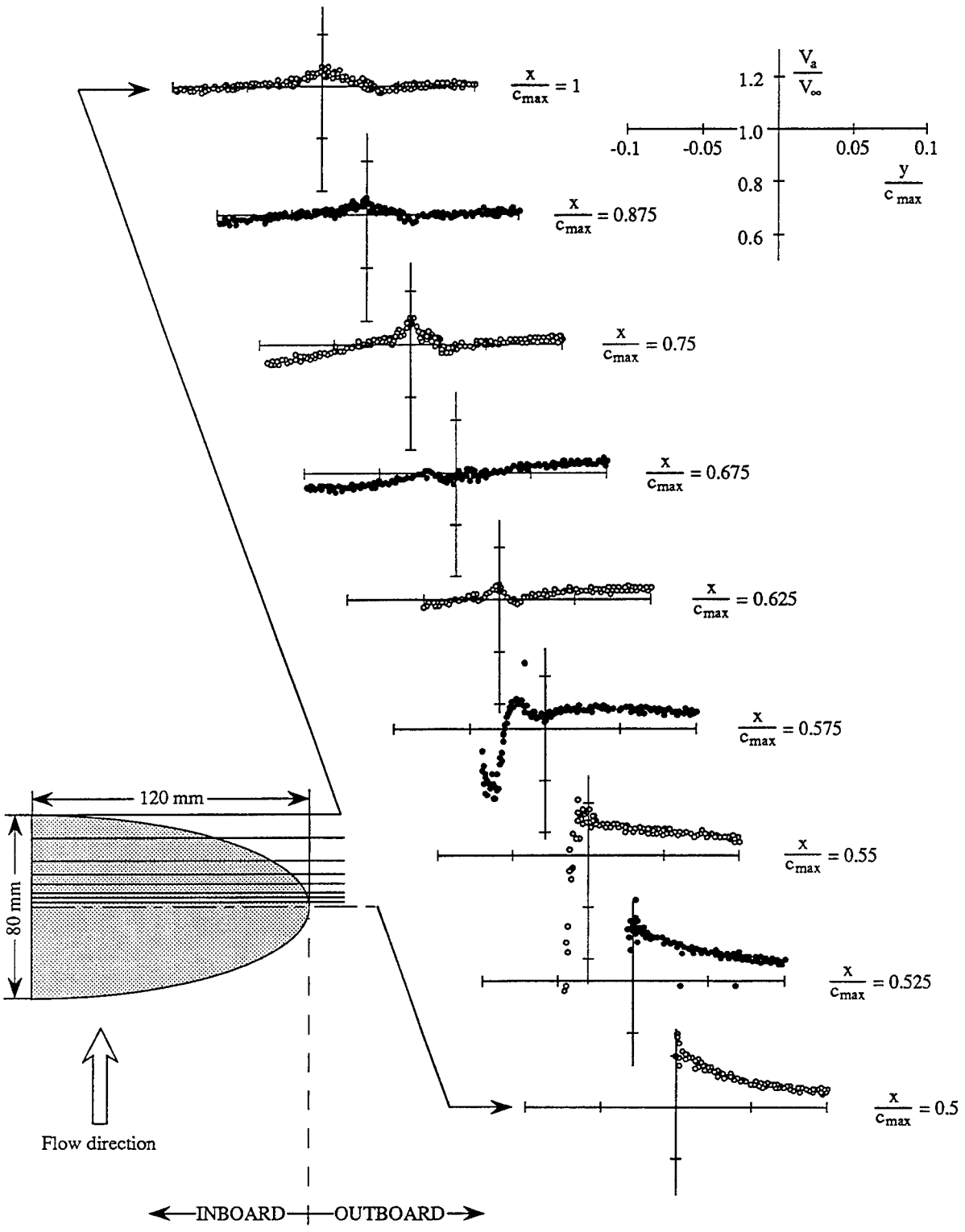

Figure 9 : Axial velocities as a function of distance to the vortex axis for different axial stations. ENCT data for i=10° and V_∞=13.5 m/s.

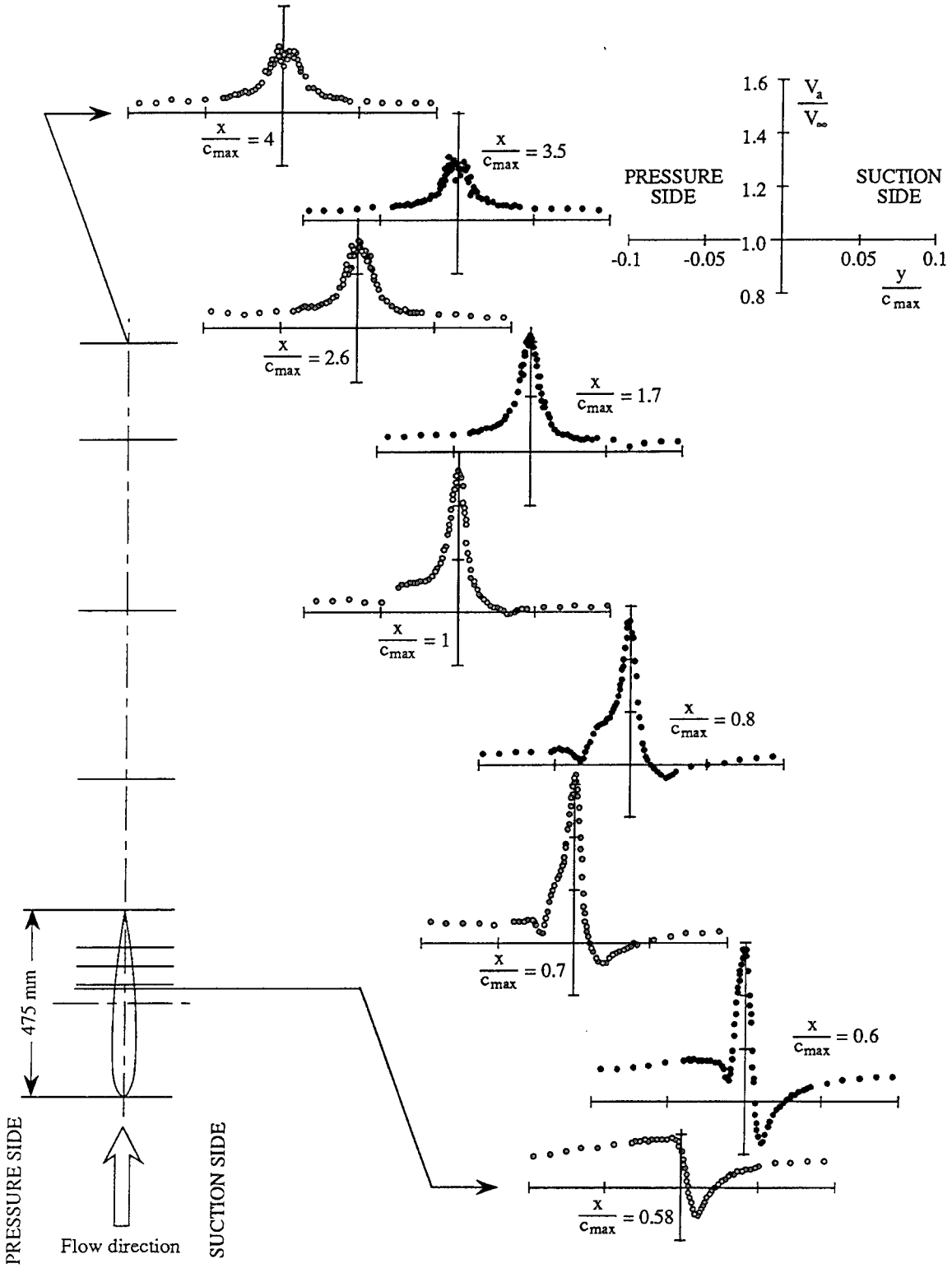

Figure 10 : Axial velocities as a function of distance to the vortex axis for different axial stations. GTH data for i=10° and V_∞=10 m/s.

The profiles relax downstream but, even at a distance of four cords, a jet behavior with an excess velocity of 1.25 V_∞ persists. The signature of the secondary vortex of Arndt and Keller (1991) is seen on the pressure side for a distance of about half chord downstream the tip.

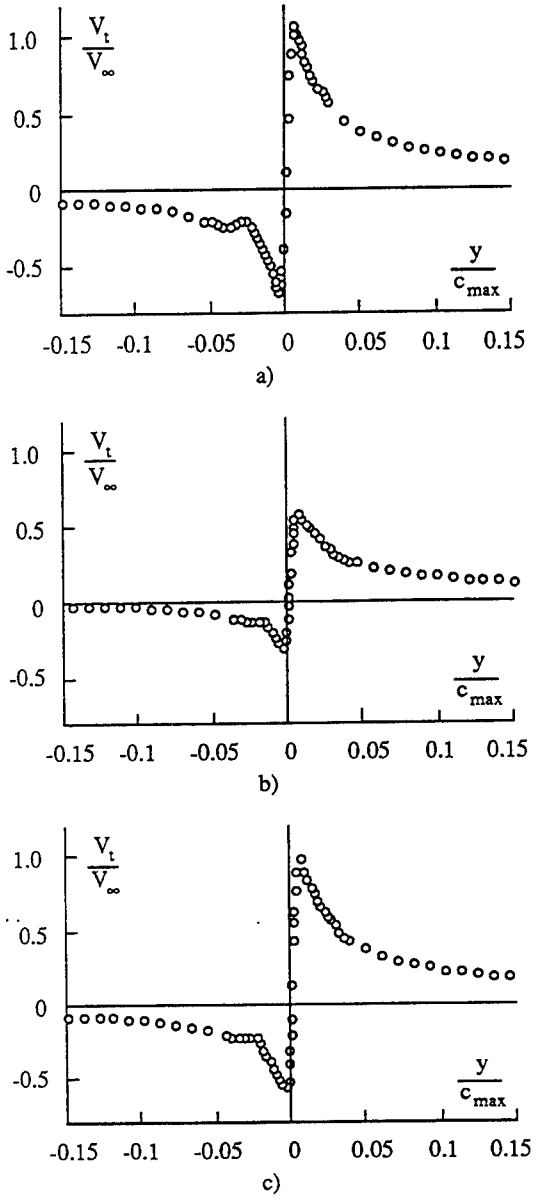

Fig. 8 : Tangential velocities as a function of distance to the vortex axis for x/c_{max} = 0.8. GTH data for a) i=10° , V_∞ =10 m/s, b) i=6° , V_∞ =10 m/s and c) i=10° , V_∞ =6 m/s.

3.2.3. Tangential and axial turbulence

Figure 11 gives the RMS value of the tangential component divided by V_∞ at x/c_{max}=1.0 in the three cavitation tunnels. As shown, the background level is comparable, of the order of 1 to 1.5%, outside a radius of about 0.05 maximum chord. Within this region the turbulence level increases up to slightly more than 20% in the ECT, to slightly more than 55% in the ENCT and up to 62% in he GTH. It is interesting to note that being on the wake side (as in the ECT and ENCT) does not introduce any significant change of the background turbulence in spite of the fact that, as shown above, the induced velocities are quite important. It should also be mentioned that a maximum relative fluctuation of 78% was measured in the GTH for the station situated at x/c_{max}=0.6.

The behavior of the RMS of the axial component in the GTH is analogous to those of the tangential component. This is shown in Figure 12 were it can be seen that the background turbulence is about the same for both components, that the maximum of the relative RMS of the axial component is close to 55% and is situated on the axis (as for the tangential component) and that the lateral extension of the region where the increase occurs is the same for both components. A small but noticeable "accident" can be seen on the pressure side in the immediate vicinity of the axis. This accident is the turbulence counterpart of the one signaled already in §§ 3.2.1 and 3.2.2..

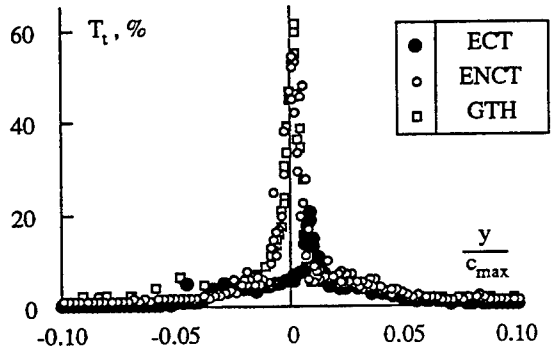

Fig. 11 : RMS value of the tangential component divided by V_∞ as a function of distance to the vortex axis for x/c_{max} = 1 in the three cavitation tunnels.

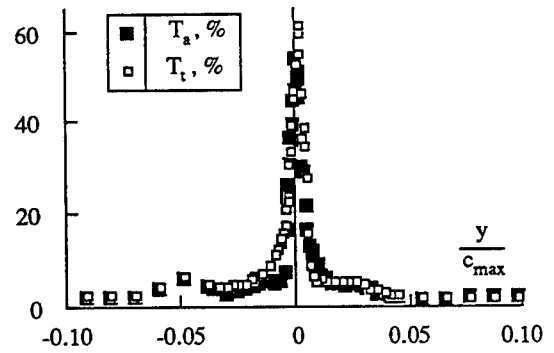

Fig. 12 : RMS value of the axial component compared to the RMS of the tangential component (both divided by V_∞) as a function of distance to the vortex axis for x/c_{max} = 1 at GTH.

3.3. Critical cavitation numbers

The cavitation number is defined as usual by,

$$\sigma = 2\frac{p_\infty - p_v}{\rho V_\infty^2} \qquad (1)$$

where p_v is the vapor pressure at the temperature of the flowing water. Indices i and d are used for inception and desinence conditions respectively.

As an example, Figure 13 presents the inception and desinence cavitation numbers obtained for free stream velocities of 10 m/s in the GTH and the ENCT with the NACA 16020 cross section wings. The scatter of the results in the ENCT gives a good idea of the error associated with the visual detection of the cavitation onset and desinence. It should be pointed out that tests performed by different manipulators have shown a remarkable good repeatability of the results. This is shown in Figure 14 where data presented by Fruman *et al.* (1991) for desinence condition are compared to those of the present tests.

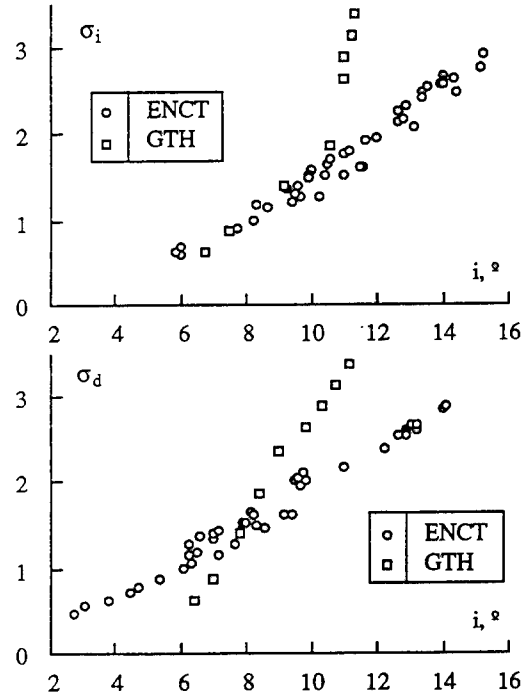

Fig. 13 : Incipient and desinence cavitation numbers as a function of incidence angle. ENCT and GTH data. V_∞=10 m/s.

By interpolating through the data points, it is possible to establish the curves giving the critical desinence number for constant incidence angle as a function of Reynolds numbers. For 8, 10 and 12°, Figure 15 shows the results obtained in the ENCT and the GTH.

In order to demonstrate the very strong influence of the wing cross section on the desinence conditions, Figure 16 reports the results obtained with the two elliptical foils with cross section NACA 16020 and 0020 at a Reynolds number of 5.2 10^6 in the GTH. The differences are as dramatic as those shown by Arndt and Dugué (1992) for another elliptical foil of area ratio 3 and cross section NACA 66_2-415, a=0.8, compared to one of our NACA 16020 foil results.

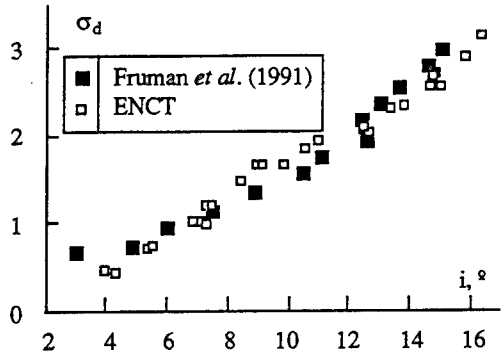

Fig. 14: Desinence cavitation numbers as a function of incidence angle for tests performed at ENCT. Comparison of Fruman *et al.* (1991) and present results.

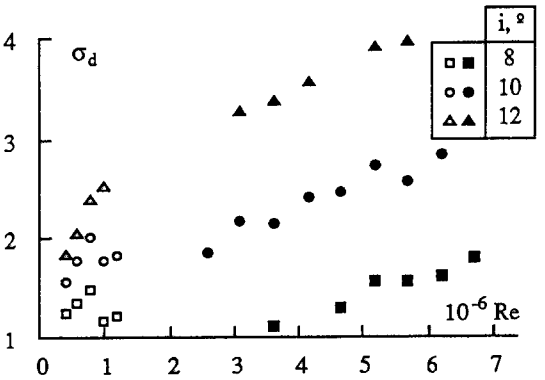

Fig. 15 : Desinence cavitation numbers as a function of Reynolds numbers at constant incidence angle for tests performed at ENCT (open symbols) and GTH (black symbols).

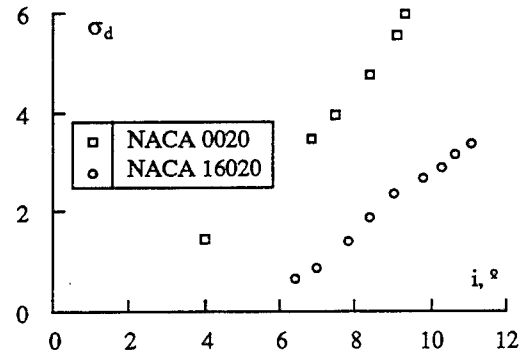

Fig. 16 : Desinence cavitation numbers as a function of incidence angle for a Reynolds number 5.2x10^6. NACA 16020 and NACA 0020 cross section wings. GTH data.

4. ANALYSIS AND DISCUSSION

4.1. Tangential velocities

From a close inspection of the tangential velocity results it is clear that the flow is very much three-dimensional in the region extending from the tip to the trailing edge at mid-span. From this position on the hypothesis of axisymmetry can be considered as a good approximation although it is only after about two chords that it is fully valid. Whatever the precise shape of the velocity profile is, the pressure on the vortex axis will always be proportional to the square of the ratio between the maximum of the tangential velocity and the free stream velocity,

$$C_p(x) = -2\int_0^{\infty} \frac{V_t(x)^2}{V_\infty^2}\frac{dr}{r} \approx -k\left[\frac{V_{tmax}(x)}{V_\infty}\right]^2 \qquad (2)$$

where k depends on the shape of the velocity profile. Figure 17 is a plot of the square of $V_{tmean}=0.5\ (V_{tmax}-V_{tmin})$ for all of the profiles shown in figures 4, 5 and 7 (provided V_{tmin} is actually measured) and of the maximum non dimensional tangential velocity for the data presented in figures 4 and 5. It clearly shows that, in spite of the very significant differences of Reynolds numbers, covering more than two decades, of lift coefficients and of experimental configurations, there is a clear analogy between all these results. The smallest value of $Cp_{min}(x)$ should occur at the station where the maximum tangential velocity is the largest; thus, for short distances downstream the tip.

Because the maximum velocity data shows a relatively good qualitative agreement, it seems natural to pursue further our analysis of the data.

Let us assume that, in spite of the 3-D character of the velocity field in the near region, a good approximation of the local vortex intensity, $\Gamma(x)$, and of the local viscous core radius, $a(x)$, can be inferred from the information contained in the "tangential" velocity profiles. To do this, we proceed as follows :

i) for the velocity profiles obtained in the ECT and the ENCT the angular momentum, product of the tangential velocity and the distance to the vortex axis, is plotted as a function of the distance to the vortex axis. Figure 18 shows the data of figures 4 and 5 for $x/c_{max}=0.75$ and demonstrate that a nearly constant value is achieved outside the solid body and transition region for the outboard data. For the velocity profile obtained in the GTH this procedure is meaningless because of the strong disymmetry between the pressure and suction sides (see Arndt *et al.* (1991)). Instead, and without an *a priori* justification, we select, as the local vortex intensity, the mean of the extrapolated angular momentums on the pressure and suction sides, as indicated in Figure 19.
ii) from the position of the maximum of the tangential velocity, an estimate of the vortex core radius is readily available.
iii) using the values of $\Gamma(x)$, $a(x)$ and $V_{tmax}(x)$ it is easy to verify if the experimental velocity profile can be approached by a Lamb type by verifying that,

$$\frac{0.714\ \Gamma(x)}{2\pi\ a\ (x)\ V_{tmax}(x)} \approx 1$$

If this condition is well satisfied, the experimental data for the ECT and the ENCT can be fitted using a Lamb (1945) velocity profile given by,

$$V_t(x, y) = \frac{\Gamma(x)}{2\pi y}\left[1 - \exp\left(-1.255\ \left(y/a\right)^2\right)\right] \qquad (3)$$

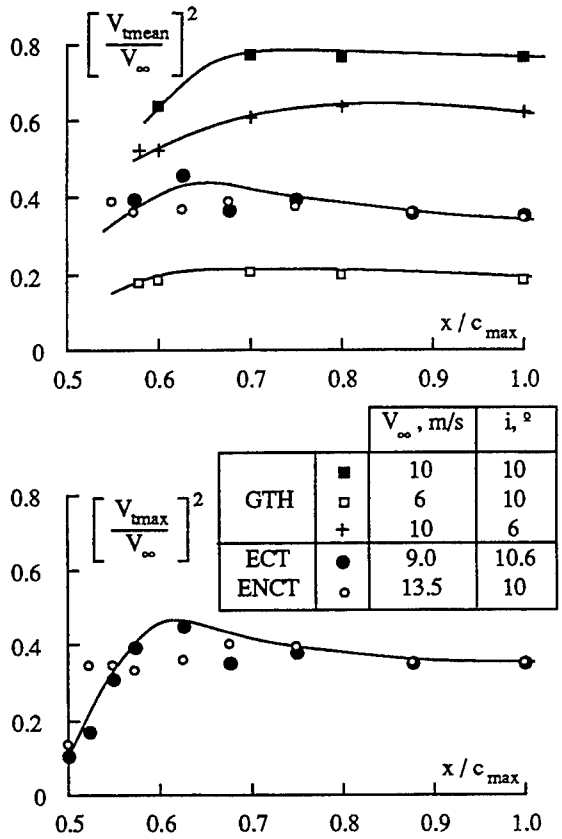

Fig. 17 : Non dimensional mean ($0.5\ (V_{tmax}-V_{tmin})$) and maximum (V_{tmax}) tangential velocity squared as a function of distance downstream.

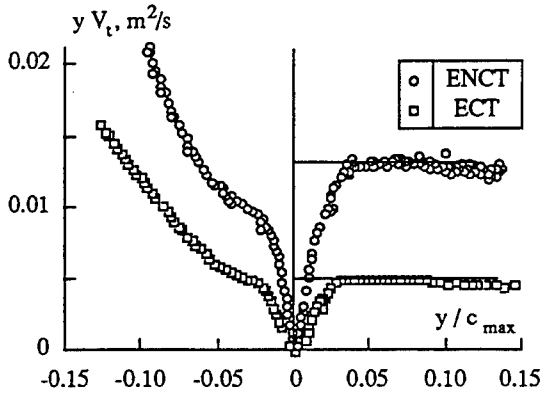

Fig. 18 : Angular momentum of velocities obtained at ECT and ENCT as a function of distance to the vortex axis for $x/c_{max} = 0.75$.

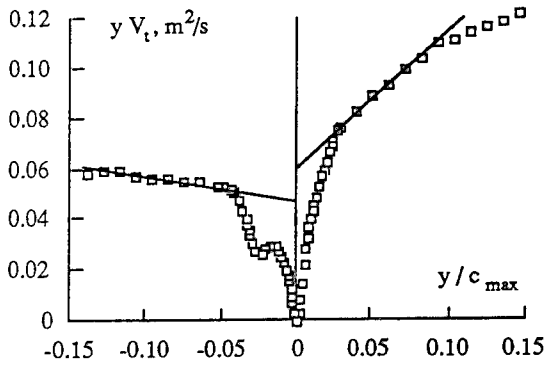

Fig. 19 : Angular momentum of velocities obtained at GTH as a function of distance to the vortex axis for $x/c_{max} = 0.8$.

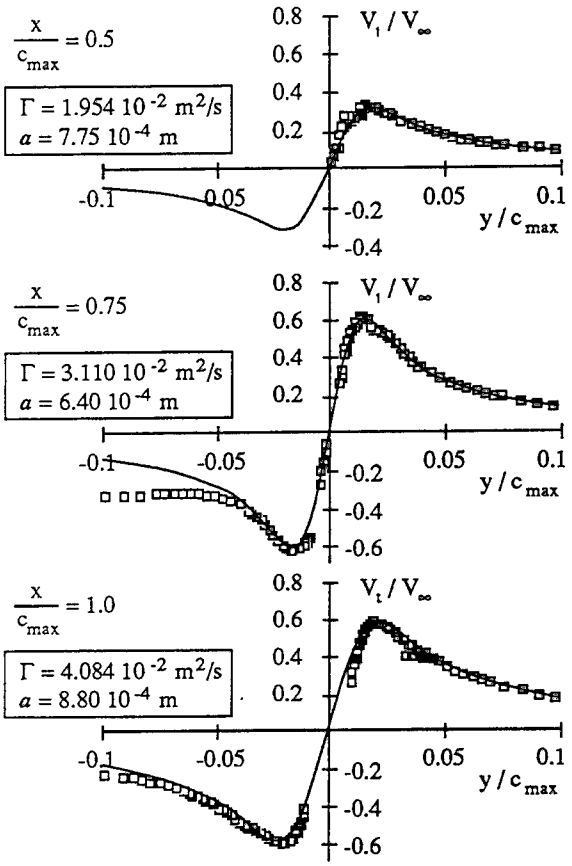

Fig. 20 : Exemple of fitting of the experimental data with a Lamb (1945) velocity profile. ECT data.

The fitting is improved by manually modifying the value of $\Gamma(x)$ and $a(x)$. As an example, Figure 20 shows for some of the velocity profiles the experimental data and the fitted curve. The adjustment is remarkable good on the outboard side and approaches very nicely the inboard side at a distance of half a chord from the tip. For the GTH data the mean of the pressure and suction side local velocites are fitted in order to obtain a better estimate of the vortex core radius. This procedure can not be justified *a priori*.

The values of $\Gamma(x)$ are made non dimensional with the mid-span bound circulation computed from the lift coefficient and those of $a(x)$ are made non dimensional with the boundary layer thickness at mid-span, δ, computed as for a fully turbulent boundary layer over a flat plate (Schlichting (1979)) by,

$$\delta = 0.37\ c_{max}\left[\frac{V_\infty c_{max}}{\nu}\right]^{-0.2} \qquad (4)$$

The values obtained from the present tests are plotted in Figure 21(a). Again, in spite of the variety of the flow conditions tested, these results are in quantitative agreement and provide interesting informations concerning the roll-up process in the near region. Indeed, Figure 21(a) clearly demonstrate that the roll-up is well initiated at the tip of the wing where the local vortex intensity reaches $0.25\ \Gamma_0$. At the wing trailing edge, half a chord downstream the tip, the local vortex intensity has increased by a factor of two and is still half way from the conditions of roll-up completion. These results are in fully agreement with those presented by Fruman *et al.* (1991). Concerning the radius of the core region, Figure 21(b), it is worth noting that a minimum of about $0.5\ \delta$ appears in the vicinity of the tip and that at the wing trailing edge it reaches roughly 70% of the boundary layer thickness. This value is smaller that the one inferred from previous results (Fruman *et al.* (1991)).

On the basis of these and previous results, it appears that the local vortex intensity and core radius are respectively a fraction of the mid-span bound circulation and boundary layer thickness. The pressure coefficient can thus be expressed as,

$$C_p(x) \approx -k\left[\frac{V_{tmax}(x)}{V_\infty}\right]^2 \approx -K(x)\,C_l^2\left[\frac{V_\infty c_{max}}{\nu}\right]^{0.4} = -K(x)\,C_l^2\,Re^{0.4} \qquad (5)$$

where the constant K accounts, in particular, for the achieved fraction of the roll-up.

4.2. Critical cavitation numbers

Figure 22 shows the desinence cavitation number divided by the Reynolds number to the power 0.4 as a function of the incidence angle for the NACA 0020 foil tested in the GTH ($Re=5.2x10^6$). In the same figure, data from McCormick (1962) ($Re\approx 7x10^5$) and Falcao dos Santos *et al.* (1989) ($Re=2.2x10^6$) for a NACA 0015 elliptical foil with area ratio of 4 have been also plotted. The agreement is remarkable taking into account the two order of magnitude range of Reynolds numbers ($7x10^5<Re<5.5x10^6$) covered by the data, the difference in relative foil thickness and the fact that tests were conducetd in three different facilities by independant investigators. Additional data sustaining this correlation with Reynolds number to the power 0.4, or close, is provided by Billet and Holl (1979) who present data for a rectangular and a quasi elliptical foil with area ratio equal to 4 and NACA 0015 and 0010 (cambered) cross section respectively. It should also be mentionned that McCormick (1962) data for rectangular foils at 4 and 8° incidence display also an analogous behaviour as a function of Reynolds number; the power computed from his data is

very close to 0.41. Therefore, it seems clear that a correlation based on a simple relation between the core size and the turbulent boundary layer is satisfactory.

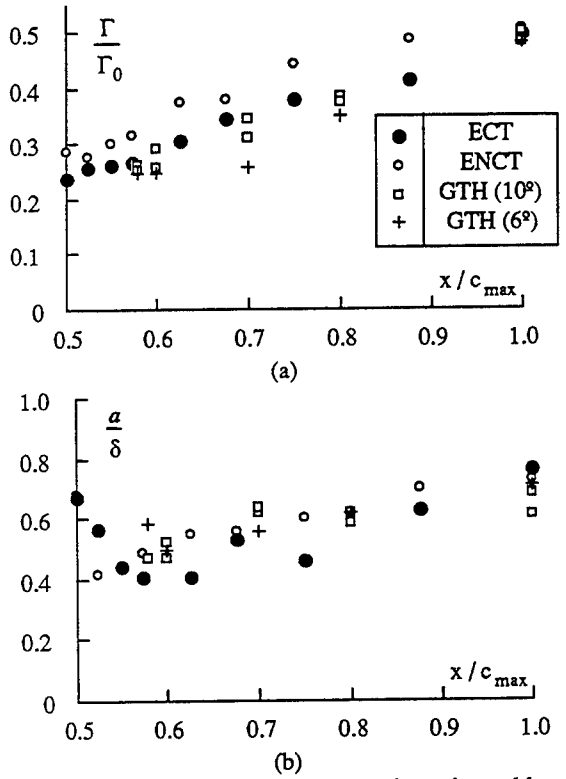

Fig. 21 : Non dimensional local vortex intensity and local vortex core radius as a function of downstream distance for data obtained at ECT, ENCT and GTH.

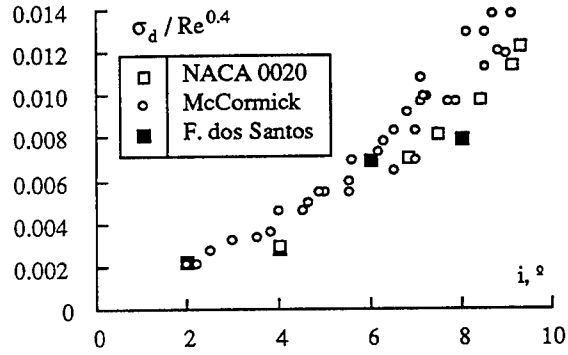

Fig. 22 : Desinence cavitation number divided by Reynolds number to the power 0.4 as a function of incidence angle for the NACA 0020 elliptical foil. Comparison of present data and previous data by McCormick (1962) and Falcao dos Santos *et al.* (1989) for a NACA 0015 elliptical foil.

For the elliptical NACA 16020 foil, the desinence cavitation number divided by the Reynolds number to the power 0.4 for the ENCT tests conducted in the range of $5.6x10^5<Re<1.2x10^6$ are plotted in Figure 23(a) as a function of the lift coefficient. The data correlates rather well in spite of the existence of some scattered points for the lowest velocity on this graph, 7 m/s. It is suspected that this situation arises from the quite substantial modification of the boundary layer for Reynolds numbers below about $6x10^5$ as indicated by the alteration of both the lift and the drag coefficient. A correlation as a function of C_l^2, as suggested by expression (5), did not provide for a more satisfactory presentation. The results for the tests conducted in the GTH ($2.6x10^6<Re<6.8x10^6$) are plotted in the same way in Figure 23(b). It should be recalled that the lift coefficients are the asymptotic values for large Reynolds numbers in Figure 3. Again, there is a remarquable good alignement of the data points when the lifft coefficient is used as the abscissa and the slope is very close to that of the ENCT data.

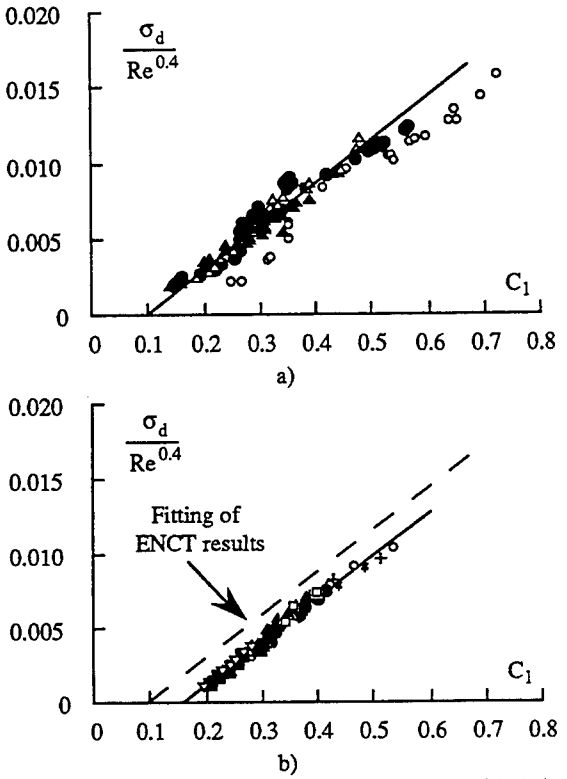

Fig. 23 : Desinence cavitation number divided by Reynolds number to the power 0.4 as a function of lift coefficient for NACA 16020 elliptical foil. a) ENCT data; b) GTH data.

Although the ENCT and the GTH data plotted independently are satisfactory, they do not strictly coincide as shown in Figure 23b. The reason for this discrepancy can be traced down to different problems. It may be possible that the extrapolated values of lift coefficients, over more than a decade of Reynolds numbers, are slightly overestimated; it may also be possible that some, as yet unknown, effects at very large Reynolds numbers tend to reduce the desinence cavitation number relative to those at smaller Reynolds numbers. This is very much evident in Figure 13b where, for incidence angles of less than 8°, the GTH desinence cavitation numbers fall below those at the

ENCT. In any event, there is thus a clear indication that cavitation numbers obtained by extrapolating test results performed at low, but still high enough if compared to the transition values, Reynolds numbers will be overestimated.

The final question to be addressed concerns the computation of the minimum pressure from the velocity measurements. If a Lamb velocity profile is assumed, the pressure coefficients is simply given by,

$$C_p = -\frac{1.255}{2\pi^2 a^2}\left[\frac{\Gamma}{V_\infty}\right]^2 \ln 2 = -0.0441\left[\frac{\Gamma}{V_\infty a}\right]^2 \qquad (6)$$

From Figure 21 we have for the conditions of minimum pressure along the vortex path,

$\Gamma = \alpha\,\Gamma_0 = 0.5\,\alpha\,V_\infty\,C_l\,c_{max}$ with $\alpha = 0.35$

and

$a = \beta\,\delta(c_{max})$ with $\beta = 0.48$

By introducing the turbulent boundary layer thickness given by expression (4) , we have finally,

$$C_{pmin} = -0.043\ C_l^2\ Re^{0.4}$$

For 10° incidence and 13.5 m/s the desinence cavitation number obtained at ENCT is 1.5 and the computed value of C_{pmin} with C_l=0.35 is -1.36. For the GTH results at 10° incidence and 10m/s we have σ_d=2.5 and, with C_l=0.34, C_{pmin}=-2.4. For 10° and 6m/s σ_d=2.2 and, with C_l=0.34, C_{pmin}=-2.0. No comparison has been attempted with the results issued from ECT tests since, as already signaled in Fruman *et al.* (1991), they are mostly situated in the transition region and, thus, the Reynolds dependency is not as for fully turbulent results. Moreover, for small incidence angles, 6° for exemple, the computed value of $-C_{pmin}$ overestimates the desinence cavitation number obtained at the GTH. Even though, considering the variety of experimental facilities, the numerous operating personnel involved in performing the experiments and the amount of data that needed to be processed in order to obtain these results the agreement between the desinence cavitation number and the absolute value of the minimum pressure coefficient is extremely reasonable for incidence angles corresponding to moderately loaded lifting surfaces.

This agreement brings a strong support to the earlier conclusion of Fruman *et al.* (1991) that pressure fluctuations do not contribute significantly to tip vortex cavitation occurrence. In this respect, it is gratifying to see that we have been rejoined by others on this specific matter. Moreover, it does not seem that the jet behaviour in the vortex core, which has been observed in the GTH tests, is responsable of a significant modification of the cavitation occurrence. By the same token, using the actual lift measurements in the discussion and interpretation of tip vortex cavitation results, as it has been done in the revised version of Fruman *et al.* (1991) and here, has shown to be very important and has also been recognized as such by other authors

V. CONCLUSIONS

A considerable amount of data concerning i) the force coefficients of the elliptical hydrofoils used in the experiments, ii) the velocities induced by the roll-up of the tip vortex in the very near region (within half a chord downstream the tip) and iii) the tip vortex cavitation inception and desinence have been obtained in several cavitation tunnels. The tangential velocity profiles have allowed to establish, by fitting the data to a Lamb velocity profile, the evolution of the local vortex intensity and core radius along the vortex path. The minimum of the pressure on the vortex axis occurs in the vicinity of the tip, at a distance of about 1/8th of the maximum chord. At this position, the local vortex intensity is about 35% of the mid-span bound circulation and the vortex core radius is about 45% of the thickness of the turbulent boundary layer computed as for a flat plate of length equal to the maximum chord. For a Lamb velocity profile, the pressure coefficient on the vortex axis is computed - using the values of the local vortex intensity , the local vortex radius and the boundary layer thickness - as a function of the square of the lift coefficient and the power 0.4 of the Reynolds number. For large enough incidence angles (10°) the agreement between the minimum pressure coefficient on the vortex axis and the desinence cavitation numbers is remarkable good. This agreement makes unnecessary to account for pressure fluctuation effects to advance cavitation occurrence ($\sigma_d > |C_{pmin}|$) or for interfacial tension effects to account for cavitation occurrence delay ($\sigma_d < |C_{pmin}|$). Moreover, data obtained al low (but larger than those corresponding to the laminar to turbulent transition) values of the Reynolds numbers seems to give slightly overestimated values when extrapolated to a tenfold larger Reynolds number.

ACKNOWLEDGEMENTS

This work was conducted with the financial support of the Direction de Recherches, Etudes et Techniques (DRET) of the Ministery of Defense, France, and is part of the "Action Concertée Cavitation" program headed by DRET. The authors wish to express their gratitude to Mr. G. Fernandez and Mrs. Bourgeois-Gaffié of DRET for their continuous support. The contribution of Mr. T. Pichon, who conducted the experiments at the ENCT, has been essential for the program. Dr. F.Avellan and P. Dupont, from the IMHEF, Lausanne, have contributed with the force data at high Reynolds numbers. Finally, Mrs. Janine Indeau has been in charge of the word processing, data plotting, graphics and final printing. Without her contribution this work would have never being completed in time.

REFERENCES

Arndt, R.E.A. and Keller, A.P., (1991). Water quality effects on cavitation inception in a trailing vortex. Cavitation '91, ASME FED 116, pp 1-8 .

Arndt, R.E.A. and Keller, A.P., (1992). Water quality effects on cavitation inception in a trailing vortex. Journal of Fluids Engineering, June.

Arndt, R.E.A.and Dugué, C., (1992). Recent advances in tip vortex cavitation research. International Symposium on propulsors and cavitation. June 22-25, Hambourg.

Arndt, R.E.A., Arakeri, V.H. and Higuchi, H., (1991). Some observation of tip-vortex cavitation. Journal of Fluid Mech., 229, pp 269-289.

Billet, M.L. and William Holl, J., (1979). Scale effects on various types of limited cavitation. International Symposium on Cavitation Inception, ASME Winter Annual Meeting, New York, Dec 2-7.

Briançon, L. and Frechou, D., (1992). Cavitation in 'Le Grand Tunnel Hydrodynamique'. ISPC, China, Sept.

Falcao de Campos, J.A.C., George, M.F. and Mackay, M., (1989). Experimental investigation of tip vortex cavitation for elliptical and rectangular wings. Cavitation and multiphase flow forum. ASME FED 79, pp. 25-30.

Fruman, D.H., Dugué, C. and Cerrutti, P., (1991,). Tip vortex roll-up and cavitation. Cavtation and multiphase flow forum, ASME FED 109, pp 43-48. Revied version submitted for publication to the Journal of Fluids Engineering.

Green S.I., (1988). Tip vortices-single phase and caviting flow phenomena. PhD Thesis, California Institute of Technology.

Green S.I., (1991). Correlating single phase flow measurements with observations of trailing vortex cavitation. Journal of Fluids Engineering, March, 113, pp 125-129.

Lamb, H., (1945). **Hydrodynamics**, Cambridge University Press. London and New York .

Lecoffre,Y., Chantrel, P. and Teiller, J., (1987). Le Grand Tunnel Hydrodynamique. ASME winter annual meeting, Boston.

McCormick, B.W., (1954). A study of the minimum pressure in a trailling vortex system. PhD Thesis, The Pennsylvania State University, June.

McCormick, B.W., (1962). On vortex produced by a vortex trailing from a lifting surface. Journal of Basic Engineering, Sept , pp. 369-379.

Platzer, G.P.and Souders, W.G., (1979). Tip vortex cavitation delay to marine lifting surfaces - a literature survey. D.W.T. Naval Ship R&D Center Report 79/051, August.

Schlichting, H., (1979) **Boundary Layer Theory**, McGraw-Hill Co.

Stinebring, D.R., Farrell, K.J. and Billet, M.L., (1991). The structure of a three-dimensional tip vortex at high Reynolds numbers. Journal of Fluids Engineering, September, 113, pp 496-503.

Van Dyke, M., (1964). **Perturbation methods in Fluid Mechanics**, Academic Press, New York.

DISCUSSION

C. Hsu, David Taylor Model Basin, USA

I have read the paper with great interest. Thick NACA sections used in the model test are known to be susceptible to flow separation. The flow characteristics of such sections depend very much on flow conditions (laminar, transitional, or turbulent), ambient turbulence intensity, surface roughness, etc. The scattering of the lift data of the small ECT and ENCT models can therefore be attributed to the effects of transitional flow instabilities and flow separation. Such model data may not be at all useful for full-scale predictions, since only thin foil sections are of practical interest and full-scale Reynolds numbers are also generally two or three orders of magnitude larger the model Reynolds numbers.

Some of the experimental data are, however, of fundamental interest. The peak tangential velocity is seen in Fig., 4, 5, and 7 to attain maximum values very near the wing tip and to decay farther downstream. The existence of inner vortex core can also be inferred from the tangential velocity measurements. According to Hsu, the tangential velocity near the wing tip (thus by ignoring the axial gradient effects) in the inner viscous region for elliptical wings can be approximated as

$$V_t = \frac{\bar{\Gamma}}{2\pi} K^{1-n}(\nu t)^{-n/2} V_\eta = \frac{\bar{\Gamma}}{2\pi} K^{1-n}(-4\eta)^{n/2} V_\eta r^{-n}$$

with

$$\bar{\Gamma} = \Gamma_0 (2/b)^{1-n}$$
$$\Gamma_0 = 0.5 V_\infty c_{max} C_L$$
$K = 2-n$
b = *semi-span*
c_{max} = *the maximum chord length*
n = 0.5 *for elliptical wings*
$$V_\eta = 2^{-n}\Upsilon(3/2-n/2)\, M(1/2+n/2.\ 2.\ \eta)\, (-\eta)^{1/2}$$
M = *hypergeometric function of the first kind*
Υ = γ *function*
$$\eta = \frac{r^2}{4\nu t} = \textit{similarity variable}$$

For a first approximation $t = x/V_\infty$ (i.e. the tip vortex is assumed to be convected downstream with free stream speed). r can then be expressed by

$$\begin{aligned} r &= (-4\eta)^{1/2}(\nu x/V_\infty)^{1/2} \\ &= (-4\eta^{1/2}(x/c_{max})^{1/2}(\nu/V_\infty c_{max})^{1/2} c_{max} \\ &= (-4\eta)^{1/2}(x/c_{max})^{1/2} Re^{-1/2} c_{max} \end{aligned}$$

Calculated tangential velocity profiles for ENCT and GTH models are given in Figures 1 and 2. Calculations are based

$c_{max} = 80.0mm$ $b = 120.0mm$ $\alpha = 10.0^0$
$V_\infty = 13.5m/sec$ $Re = 1.08 \times 10^6$
$C_L = 0.335$ (*measured data*)
$x/c_{max} = 0.675$ *and* 1.000

for ENCT model, and

$c_{max} = 475.0mm$ $b = 712.5mm$ $\alpha = 10.0^0$
$V_\infty = 10.0m/sec$ $Re = 4.75 \times 10^6$
$C_L = 0.463$ (*postulated*)
$x/c_{max} = 0.600,\ 1.000$ *and* 1.700

for GTH model. Calculated peak tangential velocities are seen to be in good agreement with measurements.

The cavitation inception measurements performed at GTH are also of great interest. The data, as reproduced in Fig. 3 can be fitted with curves given by

$$\sigma = \begin{cases} 0.00062 \times Re^{0.5} & 8.0^0 \\ 0.00114 \times Re^{0.5} & \textit{for } \alpha = 10.0^0 \\ 0.00173 \times Re^{0.5} & 12.0^0 \end{cases}$$

Such Reynolds dependence conforms with Hsu's scaling law for the tip vortex cavitation inception of elliptical wing.

It is to be noted that, in Hsu's approach, the cavitation inception of tip vortex is assumed to occur very near wing tip and to be characterized by the maximum tangential velocity. Such assumptions, in view of authors' measurements, seem to be justified. These assumptions may, however, not be viable for wings of complicated planforms or with tip flow control devices: further studies on tip vortex problems seem warranted.

Ref. Hsu, C.C., (1991). Studies of scaling of tip vortex cavitation inception on marine lifting surface. Journal of Fluid Engineering, Vol. 113, Sept, pp. 504-508.

AUTHORS' REPLY

I would very much like to thank Dr. C.C. Hsu for taking the time to read our paper and preparing detailed comments. Since he is not asking any specific questions, I do not have any answer to give. However, I would like to take this opportunity to make some comments. Indeed, we agree with the discussor that the foil we have used is prone to all the problems he mentioned; this is not a reason for not trying to accurately predict tip vortex cavitation occurrence. However, the data on lift and drag given in Fig. 2 of our paper is not "scattered"; it does reflect the physics very accurately and, in particular, the strong effect of Reynolds number. Fig. 3 shows that for large enough Reynolds numbers, there is a near plateau that can be extended with a good degree of confidence to the tests performed in the GTH.

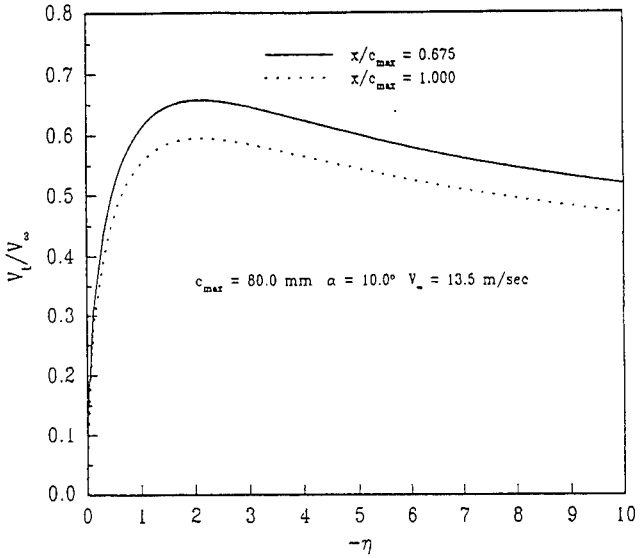

Figure 1 - Tangential Velocity Profile in the Viscous Inner Region of the Tip Vortex for a Elliptical Wing with Span-Maximum Chord Length Ratio = 3.0

The form 6 velocity profile we have used is as good as any. It allows a good fitting of the velocity data and gives access to the local vortex intensity and the local core radius; two quantities whose physical significance is evident. The use of a more complicated velocity model did not seem necessary at the present stage of our analysis. We would like to point out that the velocity data plotted in Fig. 7 of our paper shows in the very near region downstream the tip a very marked dissymmetry of the velocity profiles. We think that it is not appropriate to use, as the discussor does, the data for the section side only (and thus ignoring what happens on the pressure side) to justify the results obtained by means of this suggested velocity distribution approximation. Experimental results have to be used very carefully in order to avoid jumping to biased conclusions.

Finally, the conditions of data presented in Fig. 22 and 23 of our paper seem to demonstrate that the desinent cavitation numbers do follow a 0.4 power dependence on the Reynolds number.

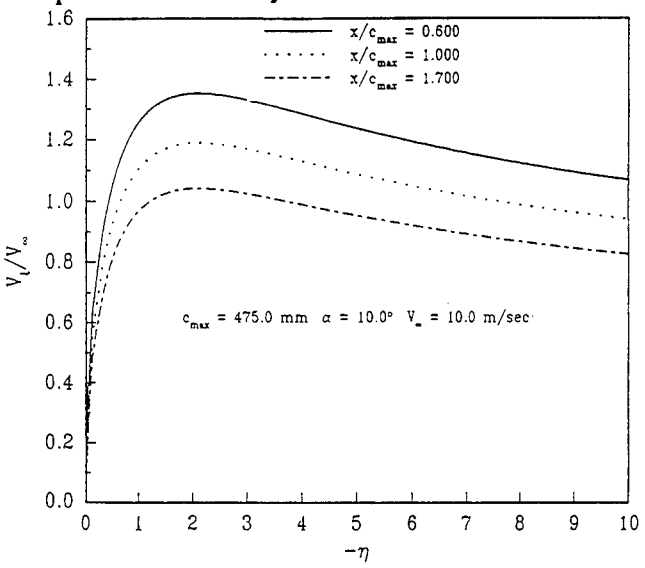

Figure 2 - Tangential Velocity Profile in the Viscous Inner Region of the Tip Vortex for a Elliptical Wing with Span-Maximum Chord Length Ratio = 3.0

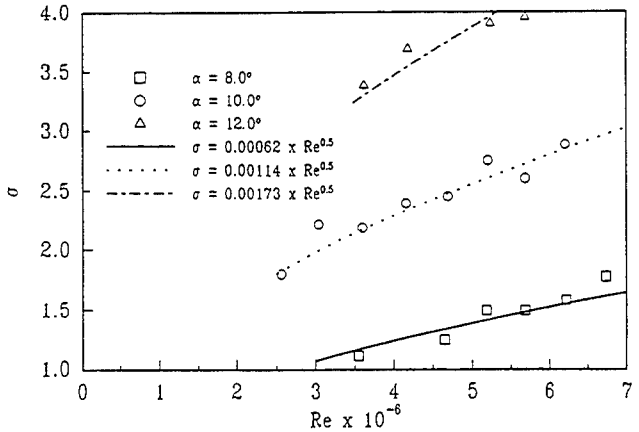

Figure 3 - Cavitation Number as a Function of Reynolds Numbers for Test Performed at GTH

DISCUSSION

C. Brennan
California Institute of Technology, USA

I would like to congratulate the authors of this paper for their excellent research on scaling effects on tip vortices and tip vortex cavitation. In many ways, this complements our paper on the scaling effects in travelling bubble cavitation.

In their paper, the authors chose to focus on desinent cavitation numbers because of the greater repeatability of this data. But I would be most interested if the authors would comment on the inception number data that was obtained and its dependence not only on Reynolds number but also on other factors such as nuclei size, nuclei population, and air content. Will this be part of a later presentation?

rationale for investigating scale effects on travelling bubble cavitation (Prof. Brennen's paper) and tip vortex cavitation is similar.

The effect of a large nuclei seeding on tip vortex desinence has been shown in the video. The critical cavitation number increases considerable, and, under such circumstances, it is hard to distinguish between "gaseous" or "vaporous" cavitation. Some data for cavitation inception are given in Fig. 13 of our paper, and it can be seen that there are differences between inception and desinent conditions. We have accumulated a very large data base on critical cavitation conditions, and this will be the subject of a subsequent paper.

Let me use this opportunity to give some detail on the scientific program we are conducting on tip vortex cavitation (Figure). As you can see, most of the factors that may affect tip vortex cavitation will be investigated during a four year research effort.

AUTHORS' REPLY

We very much appreciate the compliments of Prof. Brennen concerning our work. Indeed, the

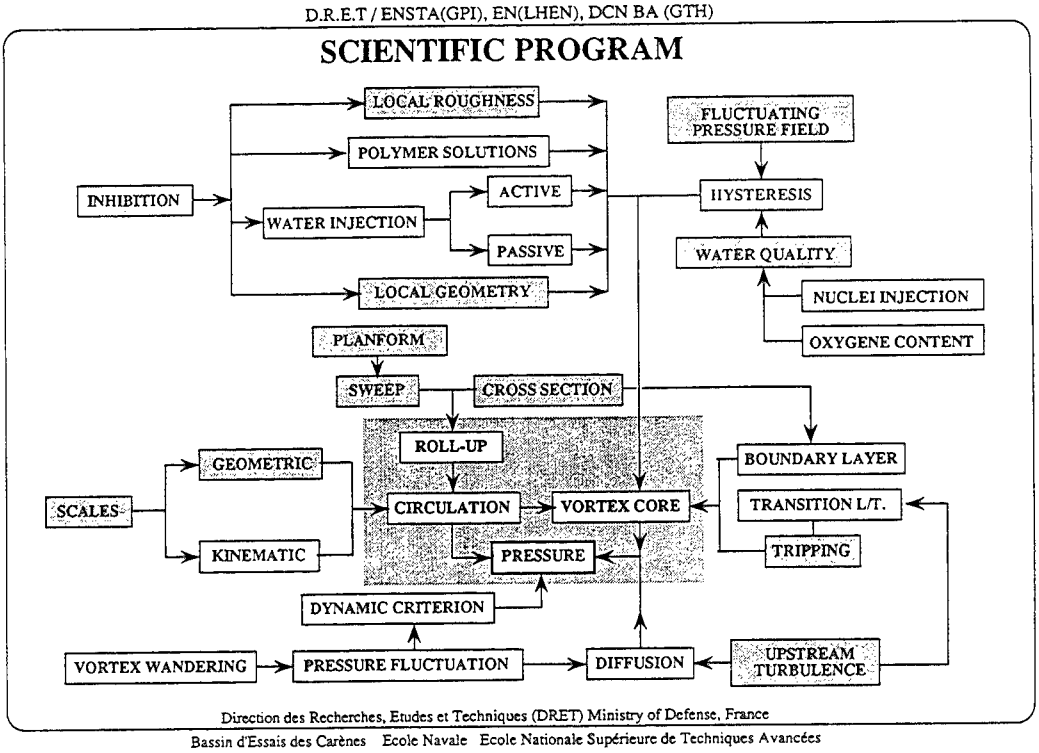

Session XII

Cavitation and Bubbly Flows

A Systematic Investigation of Viscous Scale Effects on Cavitation Inception

Y. Ye, D.-Z. Wang, F. Lu, S. Huang
(China Ship Scientific Research Center, China)

ABSTRACT

Viscous scale effects on cavitation inception were systemetically investigated by using several series of axisymmetric bodies, two dimensional foil sections and propellers. Tests included LDV flow measurement, oil film flow visualization, surface mean and fluctuating pressure measurement, thrust, torque and noise measurement and cavitation observation. Theoretical computation was also performed. LDV flow measurement was successfully used to determine the thin boundary-layer transition as a supplementary flow visualization measure, by which a regular size effect on boundary-layer transition on the Schiebe bodies was revealed. The similar size effect on transition on propeller models was also found by the oil film method. A quasi-critical Reynolds number was defined to analyze this size effect on transition. A much thicker separated bubble was measured on the hemispherical model for a Reynolds number of $R_{eD} = 1.68 \times 10^6$. Typical scaling trends for travelling bubble cavitation and attached small bubble-band cavitation on hydrofoils were observed. The preliminary result of the blackboard paint used as a tripping device is encouraging. From the very limited propeller cavitation data, the Reynolds number exponent n of propeller tip vortex cavitation scaling rules was found to be dependent upon the blade surface condition, the stage of development of TVC and the thrust loading of propeller models.

NOMENCLATURE

α_c	radius of the cavitating core
A_E / A_o	propeller disc area ratio
$C_{0.7}$	chord length of a propeller section at 0.7 radius
$C_p = \frac{P - P_o}{\frac{1}{2}\rho V_p^2}$	pressure coefficient
D	propeller diameter
h	radial distance from body surface
H	shape factor of boundary-layer velocity profile
$J = \frac{V}{nD}$	advance ratio
K	roughness height
$K_T = \frac{T}{\rho n^2 D^4}$	propeller thrust coefficient
L	reattachment length
m	exponent
n	exponent number of revolutions per second
P	pressure, pitch
P_v	vapor pressure
P_o	pressure at infinity
r	local radius on a propeller
R	radius of propeller
$R_{eD} = \frac{VD}{\nu}$	Reynolds number
$R_{eK} = \frac{u_K \cdot K}{\nu}$	roughness Reynolds number
$R_{en} = \frac{nD^2}{\nu}$	propeller Reynolds number
$R_{e_{0.7}} = C_{0.7}\frac{\sqrt{V^2 + (0.7\pi nD)^2}}{\nu}$	section Reynolds number at 0.7 radius
T	propeller thrust
u	axial fluctuating velocity
u_K	smooth laminar boundary-layer velocity at the top of roughness height
v	radial fluctuating velocity
V	free stream velocity
V_p	section inflow velocity
x	axial distance, non-dimensional radius
y, Δy	vertical or radial distance from body surface
α	angle of attack, air content
α/α_s	air content ratio
δ	boundary-layer thickness
$\sigma = \frac{P_o - P_v}{\frac{1}{2}\rho V^2}$	cavitation number
$\sigma_n = \frac{P_o - P_v}{\rho n^2 D^2}$	propeller cavitation number

ABBREVIATION AND SUBSCIPT:

carb	carborundum
crit	critical
d	desinent
i	incipient
LDV	Laser Doppler Velocimeter
L.E.	leading edge
min	minimum
q.crit	quasi critical
r	reattachment
RPM	revolutions per minute
s, sep	separation
T.E.	trailing edge
TVC	tip vortex cavitation
2D	two dimensional
3D	three dimensional
0	desinent TVC
1	unattached TVC, diplacement
2	attached TVC, momentum
3	developed TVC, energy
4	fully-developed TVC

INTRODUCTION

Cavitation inception prediction is of vital importance in the research and design of modern high speed naval ships and underwater weapons. In order to correctly predict the full scale cavitation performance, not only the precise and reliable model cavitation test data must be obtained, but also the corresponding scaling rules should be established from the gradually accumulated correlation information between model test and prototype trial. For this purpose some basic concepts of the cavitation scale effects must be well understood. Departures from the classic rule $\sigma_i = -C_{P\min}$ for the cavitation number at inception are called "scale effects", which can be chiefly divided into the viscous and nuclei effects. The present work at CSSRC only concerns with the viscous scale effects on cavitation. Based on the significant progress achieved in the past, especially during the recent 20 years (see, for example [1-3]), we have confined ourselves to few topics of the subject such as the transition detection, size effect (unit Reynolds number effect) and scaling rules. This extensive systematic experimental investigation has been conducted since 1984. It mainly consisted of the following three parts:

1. Study of axisymmetrical bodies --
Theoretical computation using two different appoaches was performed for the flow field around the hemispherical headforms considering the blockage effect of the water tunnel and the viscosity. Three series of Schiebe bodies, hemispherical headforms and blunt circular cylinders of diameters of D=50, 100, 150 and 200 mm were tested at the Large Cavitation Tunnel of CSSRC. Flow measurements were made using a two-channel three-beam LDV operated in forward-scatter mode. In addition to the cavitation obersvation with and without turbulence stimulators, surface mean and fluctuating pressure were also measured.

2. Study of two-dimensional foil sections
LDV measurement and cavitation observation were conducted at the cavitation tunnel of Shanghai Ship and Shipping Research Institute for a series of NACA 16-012 foil section models with chord lengths of C=100, 200, 300 and 400 mm respectively.

3. Study of propellers --
Viscous scale effects on propeller tip vortex cavitation were investigated by testing a series of three geosim propeller models of diameters of D=200, 280 and 350 mm in the Large Cavitation Tunnel of CSSRC without and with two diferent turbulence stimulators. Tests included flow visualization by oil film method, repeated measurement of thrust and torque, noise measurement and cavitation observation for five different conditions of propeller tip vortex cavitation: desinent, unattached, attached, developed and fully developed TVC. The present paper is a final report to summarize the main results of this systematic investigation of viscous scale effects.

II. STUDY OF AXISYMMETRIC BODIES

Since early fifties of the present century cavitation scale effects studies caused by the model scale, free stream velocity and fluid properties have developed step by step [1-3]. In the recent twenty years some important viscous effects on cavitation inception were successfully revealed by utilization of different suitable flow visualization techniques. Of particalar importance here is the pioneer work done at CIT by Arakeri and Acosta [4]. They developed the schlieren technique of flow visualization of the thermal boundary layer for water tunnel use, by which they clearly showed the existence of previously unreported laminar separation bubble on two headforms up to very high laboratory Reynolds numbers. Van der Meulen impressively introduced a three-dimensional imaging technique of in-line holography to visualize boundary-layers both on axisymmetric headforms and two-dimensional hydrofoils [5, 6]. It consisted of making holograms when injecting small amounts of a sodium chloride solution into the flow at the position of or close to the stagnation point on the model. The laminar separation points on axisymmetric bodies on

two-dimemsional hydrofoils can be quite clearly demonstrated by either of the schlieren or holographic methods. However, there exist some difficulties in detection of both the transition of thin boundary-layer on streamlined bodies and reattachment in the large separated regions by these two methods. As a starting-point of the present study we tried to use LDV to determine the separation, reattachment and especially transition points on axisymmetric headforms in cavitation tunnels.

Experimental Arrangement and Models

Although in 1975 Acosta and Parkin [7] already indicated that it appeared feasible to use LDV for determination of the gross characteristics of the surface boundary layer, especially for transition detection. However, before we started our flow measurement, we hardly could find any reference pursued along this thought. At the first stage of our study we had to check this feasibility. The following four axisymmetric headforms of diameter of 64 mm were tested: a 1.5 cal. ogive, a Schiebe body of $C_{Pmin} = -0.75$, a longitudinal blunt circular cylinder and a hemispherical headform body with a downstream facing step at the tangency point, Fig.1. The initial tests were performed in a cavitation tunnel with a test section of $600 \times 600\,mm^2$. Test Reynolds number ranged from 0.75×10^5 to 6×10^5. Flow measurements were made using a two-channel three-beam LDV operated in forward-scatter mode. It consisted of a Spectra-Physics 15 mW He-Ne Laser and TSI optics. The feasibility test turned out to be successful [8]. At the second stage of the present study three series of headforms were tested with a test section of diameter of $\phi 800\,mm$. Test Reynolds number ranged from 0.6×10^5 to 1.68×10^6. The main difference of the test set up used were as follows:

a) a lens of 500 mm focal length was used, the measurement volume was 0.162 mm wide,

b) mean and fluctucting pressure on the body surface were measured. The transducers used were TEAC PGM-2KC, the diameter of diaphragm was about $\phi 5.5\,mm$.

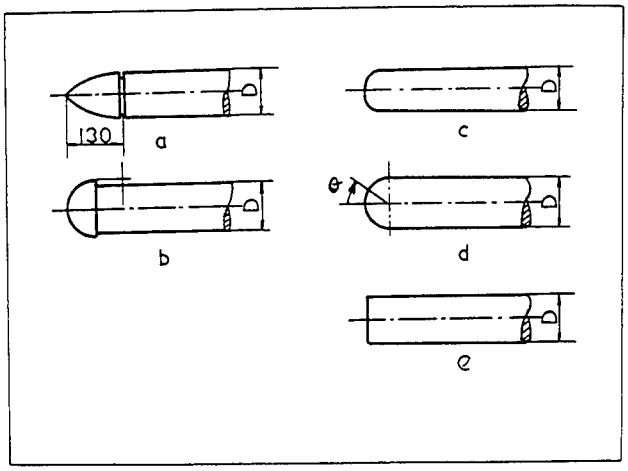

Fig.1. Configuration of test models
a: 1.5 cal ogive
b: hemispherical headform with step
c: Schiebe body ($C_{P_{min}} = -0.75$
d: hemispherical body
e: blunt body

Theoretical Computation

At first, the laminar separation point of an hemispherical headform in an infinite flow field was calculated, the predicted separation angle was $\theta_{sep} = 84^0 04'$, θ see Fig.1. The maximum diameter used in the series tests was $\phi 200\,mm$, therefore the blockage effect was too big to be neglected. Then flow field around the axisymmetric headforms considering the blockage effect of the water tunnel was calculated. Two approaches were performed. The first approach consisted of irrotational flow and laminar boundary layer calculation successively. The second aproach consisted of direct numerical solution for viscous flow around an axisymmetric nose in water tunnel.

1). The first Approach

For H200, the predicted separation point by the first approach is $\theta_{sep} = 87.5^0$. Flow measurement by LDV indicated that at $V = 2.5 m/s$, non-dimensional velocity distribution, separation angle and boundary layer thickness were all nearly in agreement with the prediction, Fig.2. However, at $V = 10.5 m/s$, although the measured separation angle $\theta = 87^0$ was in agreement with the prediction, but there exsisted big difference both in the non-dimensional velocity distribution and boundary layer thickness, Fig.3,4.

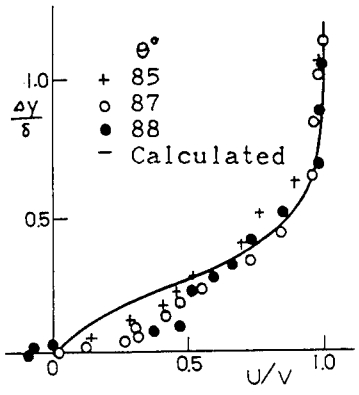

Fig.2. Comparison of laminar boundary-layer calculation and LDV mesurement results, H200, V 2.5m/s

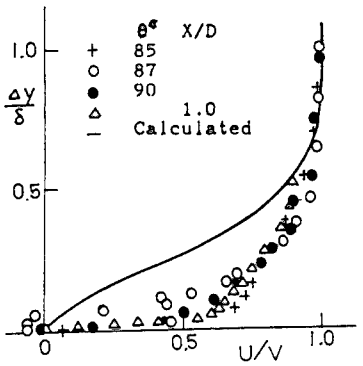

Fig.3. Comparison of laminar boundary-layer calculation and LDV measurement results, H200, V 10.5m/s

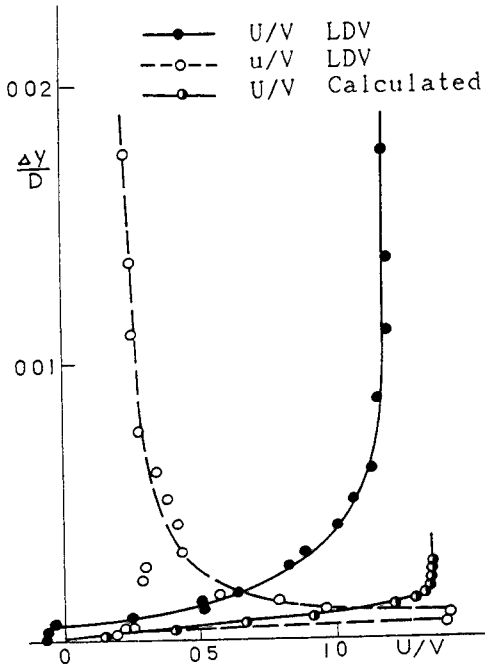

Fig.4. Comparison of laminar boundary-layer calculation and LDV measurement results, H200, V 10.5m/s θ87°

2). The Second Approach

Viscous flows around the three hemispherical noses were calculated. The diameter ratios were 1/3, 1/4 and 1/8 respectively. Reynolds numbers of the flow based on the diameters of noses were 2×10^3. Primary results show that due to the blockage effect the computed surface pressure distributions are changed in the same way as the measured ones and the velocity distributions measured by the LDV method. For the real flow of high Reynolds number, criterion of transition and turbulence model must be invoked.

LDV Measurement and Signal Analysis

We were not interested in the survey of the whole flow field around the test models, so we confined ourselves to measure the flow at few selected positions in order to find some characteristic points such as points of boundary layer separation, reattachment and transition. By using the present LDV set up with frequency shift the reverse flow could well be measured. Therefore during our initial tests the separation and reattachment points of separated region both of the blunt circular sylinder and the step body were easily founded. Our effort was mainly concentrated on how to use LDV to determine the transition from laminar to turbulence. We analyzed the LDV signals at positions close to the maximum intensity point inside the near wall region of the boundary layer. Signal analysis consisted of spectrum analysis and comparison of the ratio of low pass filtered RMS value to higher pass filtered one of the velocity fluctuation.

Although both the axial and radial components of the velocity fluctuations were measured. Some main tendencies could be found from the signal analysis of the axial component alone. By careful comparison of many power spectra and ratios the correlation between these spectra and ratios with velocity distributions of different flow regime gradually became clear. When transition occurred, in addition to the well-known large RMS value associated with transition, spectrum analysis of the LDV signals of fluctuating velocity indicated that the velocity level was increasing almost linearly with decrease of the frequency in a log-log plot of the power spectrum. On the other hand, the ratios of low pass filtered RMS value of the LDV signals to high pass filtered one often reached a maximum. Transition detection on the 1.5 cal. ogive and the Schiebe body shows

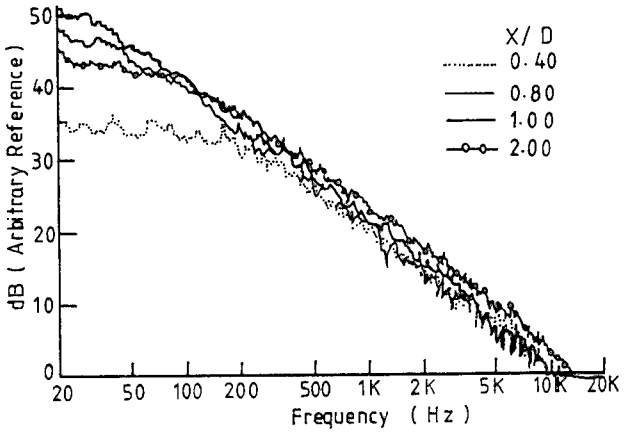

Fig.5. Power spectra of axial fluctuating velocity for V=1.5m/s, Schiebe body

good agreement with results of schlieren and in-line holography methods [8].

Some results of the present LDV measurement related to transition detection on the Schiele body will be presented here. The Schiebe body used in the present study has a minimum pressure coefficient of -0.75. Figs. 5,6 are the power spectra of axial fluctuating velocity at different locations for V=1.5 and 7.0 m/s. The ratios of RMS values obtained with different band pass filters of 2-200 Hz, 2Hz-1 KHz, 200 Hz - 20 KHz and 1 KHz - 20 KHz are given in Table 1.

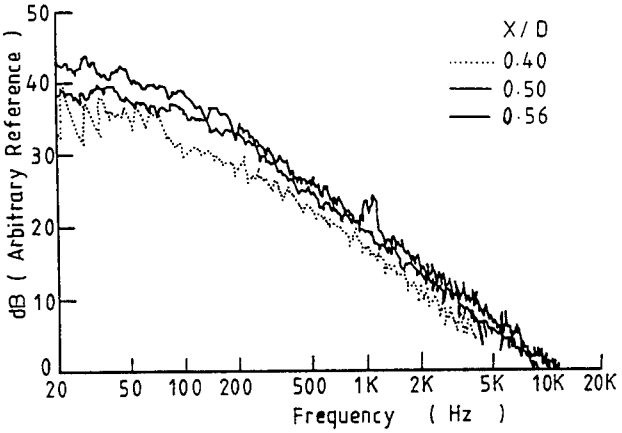

Fig.6. Power spectra of axial fluctuating velocity for V=7.0m/s, Schiebe body

The power spectra presented here seem similar to the spectra of axial velocity fluctuation downstream of a roughness rod from a classical study on transition by Klebanoff and Tidstrom [9]. From Fig.5 at the lowest Reynolds number, close to the nose of Schiebe body, we can see that the fluctuation is composed of relatively high frequencies and in a downstrem direction there appears a gradual change to lower and lower frequencies until transition occurs. Fig.7 is a comparison of transition measurement results by different methods of Schiebe bodies. In

Table 1. Comparison of Ratios of RMS Values of Axial Fluctuating Velocity Using Different Band Pass Filters, Schiebe Body ($C_{p_{min}} = -0.75$), D=64mm

X/D	u m/s	$\sqrt{\overline{u_2}}$ m/s	$\sqrt{\overline{u_2}}/U_0$	$\frac{2Hz-1KHz}{1K-20KHz}$	$\frac{2-200Hz}{200-20KHz}$	$\frac{2-200Hz}{1K-20KHz}$
U_0 = 1.5 m/s, R_{e_D} = 1.10×10^5						
0.4	0.961	0.269	0.179	1.97		
0.8	0.920	0.468	0.312	2.93	1.75	2.80
0.9	1.239	0.481	0.320	2.76	1.79	2.66
1.0	1.165	0.708	0.472	4.08		
1.1	0.775	0.623	0.415	4.25	2.00	4.15
1.2	1.252	0.578	0.385	4.46	2.10	4.05
2.0	0.782	0.587	0.391	3.00	1.33	2.81
U_0 = m/s, R_{e_D} = 2.20×10^5						
0.70	2.883	0.320	0.107	3.12	1.43	2.73
0.75	2.598	0.363	0.120	3.12	1.60	2.84
0.80	2.722	0.327	0.109	2.60	1.30	2.44
1.00	2.728	0.237	0.079	2.12	1.28	2.06
U_0 = 5 m/s, R_{e_D} = 3.66×10^5						
0.60	4.924	0.439	0.088	3.21	1.36	2.91
0.65	4.677	0.426	0.085	3.40	1.56	3.11
U_0 = 7 m/s, R_{e_D} = 5.13×10^5						
0.40	7.625	0.228	0.033	1.64	1.02	2.15
0.50	7.242	0.482	0.069	3.18	1.36	2.88
0.56	7.278	0.365	0.052	2.48	1.19	2.31

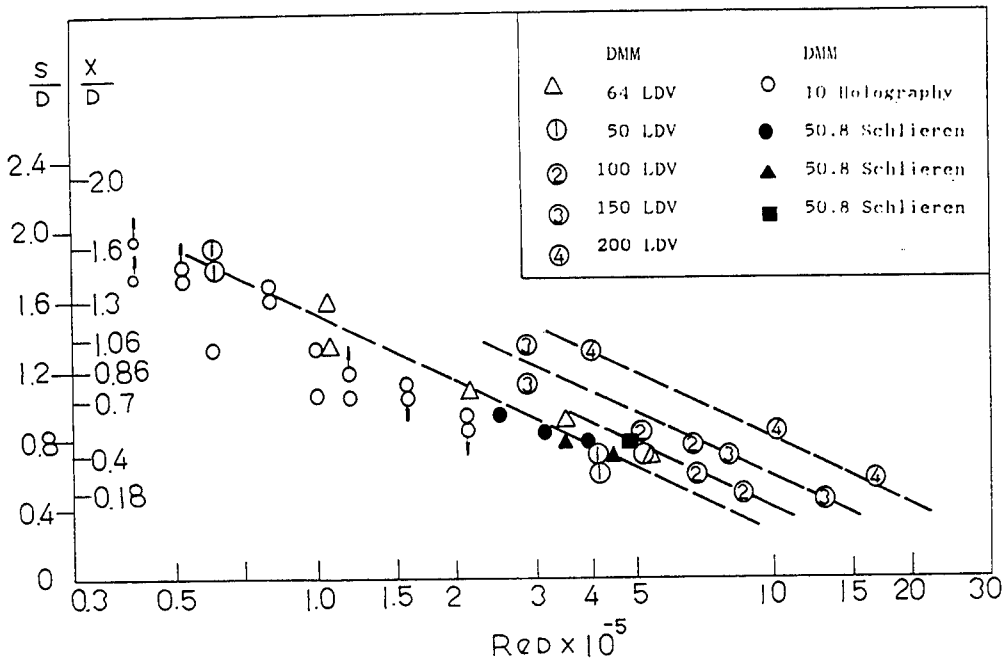

Fig.7. Comparison of transition measurement results by diferent methods of Schiebe headforms and its size effect

the same figure transition positions by LDV method of a series of four different sized Schiebe bodies with $C_{P\min} = -0.75$ were also given (D = 50, 100, 150 and 200 mm) [10]. From this figure it can be seen that, generally speaking, transition location detected by LDV is a little bit downstream than detected by in-line holography. If holography gives the position where transition from laminar to turbulence just starts, then LDV measurement gives the position where turbulence has already further developed.

The present series flow measurements by LDV clearly revealed a regular size effect or unit Reynolds number effect on boundary-layer transition on the Schiebe headforms, namely at the same Reynolds number, the smaller the diameter of the model, the shorter the distance of the transition point downstream from the minimum pressure point. This is thought to be caused by the bigger relative surface roughness on the smaller models. If model surface was hydrodynamically smooth, then the bigger the model size, the nearer should be the transition from the $C_{P\min}$ point.

In addition to this Schiebe headform series with transition, the other two headform series used in this study also represent different typical flow fields with separation of thin boundary layer or large separated region respectively. For all four models of the hemispherical headform series a negative axial velocity was measured near the wall in a range from $\theta = 79^\circ$ to $\theta = 90^\circ$. For H200, the measured separation point was $\theta = 87^\circ$. The LDV flow measurement result was comparable to the laminar boundary layer calculation result in the low speed range. But for V = 6.5 and 10.5 m/s, the measured boundary layer thickness was equivalent to 5-6 times the theoretically predicted laminar boundary layer thickness, and the velocity distribution was much fuller than the laminar distribution, see Fig.2-4. Fig.8 is a comparison of the calculated and measured boundary layer momentum thickness δ_2, the difference between these values is quite evident. Obviously, separation did exist in this case, but the velocity profile can not be regarded as a laminar profile. Besides, the relationship between the ratio of displacement thickness to momentum thickness H_{12} and the ratio of energy thickness to momentum thickness H_{32} was not in agreement with a relation deduced from experimental results by Rotta [11], so this velocity profile did not belong to a one-parameter turbulent family, whereas most of the velocity profile of the Schiebe headforms measured followed this relationship. Therefore, strictly speaking, this kind of separation on the hemispherical headforms can only be considered in very general terms as a transitional or viscous separation. On the other hand, we compared the power spectra of LDV signal at V=10.5 m/s for $\theta = 85^\circ, 87^\circ, 90^\circ$ (upstream from the separation point, separation point, downstream from the separation point and near the reattachment zone). We also compared the ratios of the RMS values from two different pass filters, see Table 2. By comparison, it was found that when boundary layer separation occurred, the characteristics of the power spectrum are very much like those of the power spectrum when boundary layer transition occurred. In both cases they only appeared in a very thin layer close to the body surface. However, these characteristics manifested themselves most strongly in the large separated region and near the reattachment point on the longitudinal blunt circular cylinder not only for the axial fluctuating velocity component but also for the radial one. Table 3 gives the ratio

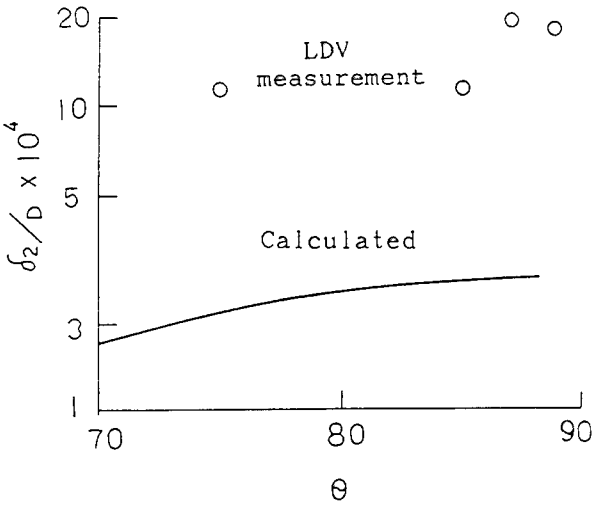

Fig.8. Comparison of boundary-layer momentum thickness

Table 2. Comparison of Ratios of RMS Values of Axial Fluctuating Velocity Using Different Band Pass Filters, (2Hz-1KHz)/(1K-20KHz).

Model	$l_{m/s}$	θ°	Axial Distance X/D	Radial Distance h_{mm}	Low Pass Filtered	High Pass Filtered	Ratio
H200	10.5	85		0.20	0.092	0.032	2.00
H200	10.5	87		0.23	0.237	0.052	4.55
H200	10.5	90	0.5	0.08	0.257	0.094	2.73
S150	10.5		0.4	0.10	0.235	0.042	5.60

Table 3. Comparison of Ratios of RMS Values of Axial and Radial Fluctuating Velocity Using Different Band Pass Filters, (2Hz-1KHz)/(1K-20KHz), Blunt Cylinder, D=64mm

Axial Distance X/D	Radial Distance h mm	$R_{rD} \times 10^{-5}$ 1.23 u	1.23 v	2.46 u	2.46 v	3.84 u	3.84 v	6.07 u	6.07 v
0	0	2.69	2.27			3.60	6.09	2.49	2.52
0.917	0.04			8.18	4.63	6.08	4.04	6.78	3.15
	12.00			5.09	7.38				
Xr/D	0.04			7.88	4.91	7.13	5.14	6.49	5.22

of RMS values by different band pass filters of 2Hz-1KHz and 1KHz-20KHz of a blunt model of diameter of 64 mm. These values are apparently bigger than the corresponding values related to the thin boundary layer transition or separation. The measuring point at X/D=0.917 and h=12mm was close to the maximum shear layer of the fluctuating velocity. The reattachment length L on this blunt cylinder was decreasing with the increase of the free stream velocity. The values of X_r/D were 1.584, 1.540, 1.505 and 1.472 for $R_{eD} \times 10^{-5}$ of 1.23, 2.46, 3.84 and 6.07 respectively.

Due to the high air content ratio $\alpha/\alpha_s \cong 1$ with the flow measurement around the blunt cylinder series, the free stream was basically saturated in the large cavitation tunnel. The measured reattachment length beame about 2/3 of the measured value at the small cavitation tunnel ($600 \times 600\, mm^2$) with low air content ratio, L/D decreased from 1.6 to 1. This fact was very much similar to the test results of a hemispherical headform with a backward facing step tested at two different air content ratios in the small tunnel. From the series flow measurement around the blunt cylinders it was found that the reattachment length L/D was increased with the increase of model size, it varied from L/D=0.86 for model B50 to L/D=1.05 for model B150 and L/D basically did not change with free stream speed for the same sized model. These differences between L/D measured at different conditions of air content ratio in fact revealed an impressive bubble/flow structure interaction of real fluid effects on the non-cavitating flow inside the large separated region.

Spectrum Analysis of Pressure Signal

Figs.9 and 10 are the spectra of pressure signal from surface transducers on the hemispherical nose H200. Transducers were located at four positions respectively: A) X/D=0.55, B) X/D=0.50, $\theta = 90°$, C) $\theta = 78.5°$, D) $\theta = 75°$. Power density in the lower frequency band differed most significantly at X/D=0.50, $\theta = 90°$ for V=2.5 m/s and 10.5 m/s. Measurement indicated that the increase of power density in the lower frequency band for V=10.5 m/s appeared just downstream from the separation point $\theta = 87°$ and near the reattachment zone. Evidently, there exist points of similarity between the power spectra of pressure and velocity signal. The higher power density in the lower frquency band appeared to be a common feature in cavitation prone areas such as in transition, separation and reattachment zones.

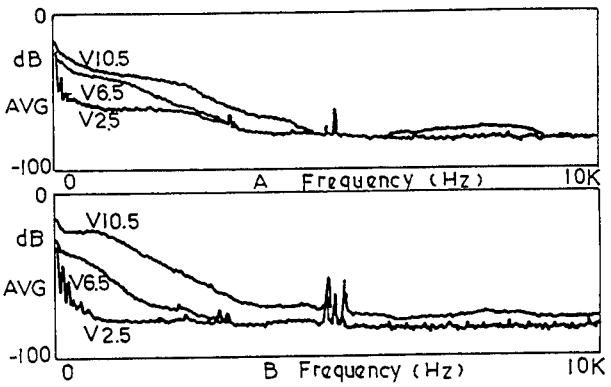

Fig.9. Power spectra of surface pressure fluctuation of hemispherical headforms H200, Trans. A(X/D, 0.55), B(X/D, 0.50)

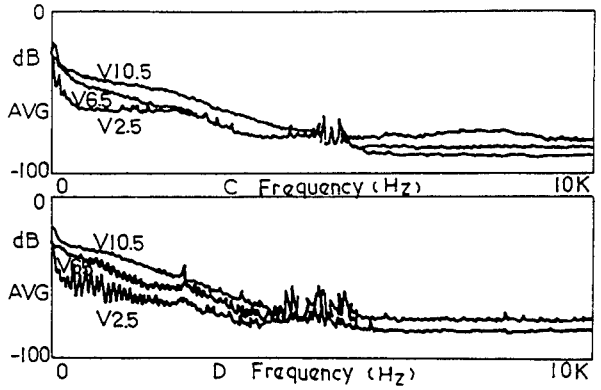

Fig.10. Power spectra of surface pressure fluctuation of hemispherical headforms H200, Trans. C(θ78.5°), D(θ75°)

Cavitation Tests

Figs. 11 and 12 are limited cavitation curves of Schiebe and hemispherical headforms respectively. These two curves remind the common characteristics of several sets of existing data for limited surface cavitation on hydrofoils and headforms.

In our tests travelling bubble cavitation appeared at lower velocity for Schiebe models. But when velocity or model diameter increased a little bit, fixed patch cavitation appeared. Especially for large sized models the number of fixed patches with a triangular leading edge increased with the velocity. It clearly revealed the roughness effects. For models S200 and S50, 60 μm distributed carborundum was used as turbulence stimulator near the stagnation point within a range of 0.7 D. Observation indicated that the number of fixed patches usually increased in the downstream region from distributed carborundum in comparison with the non-stimulated model. Cavitation index

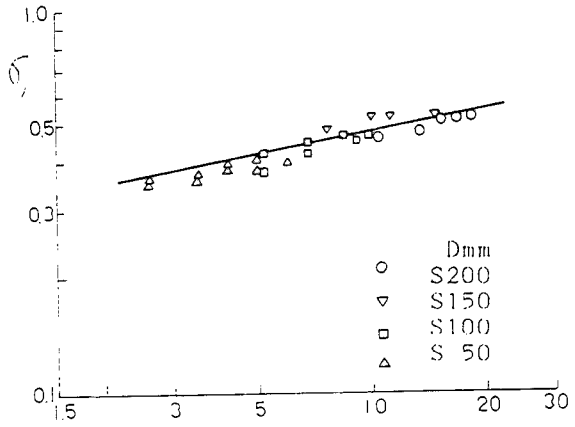

Fig.11. Limited cavitation curves of Schiebe headforms

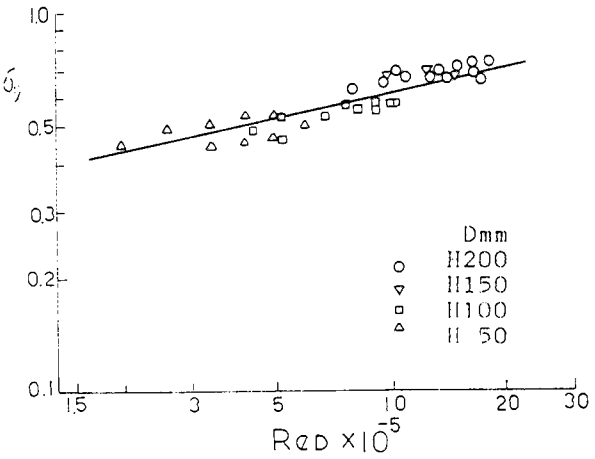

Fig.12. Limited cavitation curves of hemispherical headforms

and location did not change significantly. Cavitation inception occurred in the transition region of the Schiebe models and cavitation index could be approximately correlated with the nagative value of the pressure coefficient there.

For the hemispherical models, band or bubble-ring cavitation have never been observed in this tunnel. At lower test speed, treavelling bubble cavitation appeared, at high test speed, fixed patch cavitation appeared. The number of the fixed patches became more and bubble cavitation disappeared with the further increase of speed. For models H200 and H50, 60 μm distributed carborundum was used as turbulence stimulator from the stagnation point up to $\theta = 80°$. For model H100 a wax ring of 0.3 mm in height and 4 mm in width was used as a turbulence stimulator. For model H200, travelling bubble or fixed patch cavitation occurred at $\theta = 86° - 88°$ without stimulator, but a thin piece of densely distributed cavitation on roughness appeared at $\theta = 81° - 84°$ with stimulator used, in the later case cavitation quite often started from the trailing edge of the distributed carborundum. The limited cavitation index without stimulator could be correlated with the nagative value of the pressure coefficient at $\theta = 87°$. For model H100, cavitation observation was made with the upper half model having a wax half ring and lower half model having 60 μm carborundum distributed from the stagnation point down to X/D=0.55. At the middle speed range the travelling bubble and fixed patch cavitation existed simultaneously on the upper half model, but cavitation attached to the roughness appeared on the lower half model, Fig.13. In this case the limited cavitation index could be correlated with the measured value of the minimum pressure coefficient. For the blunt circular cylinder, the cavitation type belonged to vortex cavitation. Fig.14 is the cavitation

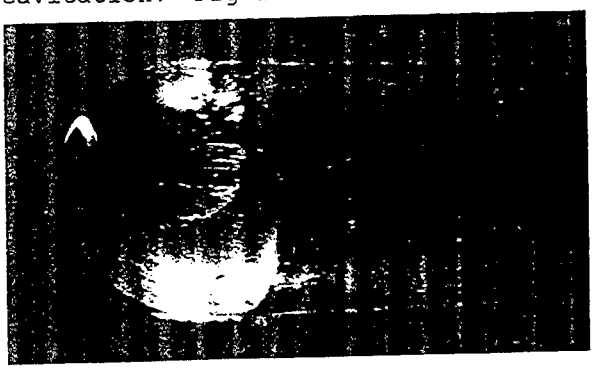

Fig.13. Limited cavitation with different turbulence stimulators on hemispherical headform H100, V 6.5m/s σ 0.54

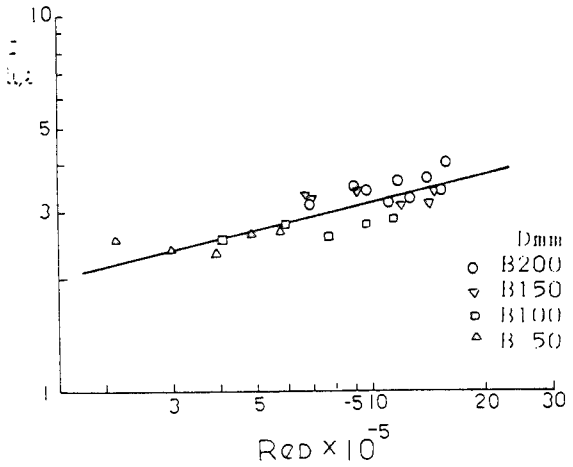

Fig.14. Cavitation curve of blunt cylinders

curve of blunt circular cylinders. $\bar{\sigma}$ is the average value of desinent and inception cavitation indices. It is interesting to notice that the cavitation curves for hemispherical and Schiebe headforms and blunt circular cylinders have almost the same slope from the present measurements in a log-log plot of σ versus R_{e_D}.

As already mentioned, power spectra of the LDV signals in cavitation prone regions had a common feature which strongly suggested that there might exist large-scale coherent structure of turbulence. High-speed cavitation photos under stroboscopic light indeed made these line vortices of turbulence visible. Figs. 15 and 16 recorded the typical cavitation pattern downstream from the fully developed attached cavity end both of Schiebe and hemispherical bodies. This pattern looked like consisted of many large horseshoe or hairpin vorticies, especially a number of U shaped and Ω shaped vortex cavitation could be observed which inclined at almost 45° with respect to the boundary. They clearly revealed the coherent structure of turbulent boundary layer. Fig.17 gives a rare case of a very large Ω shaped vortex cavity inside the large separated region of blunt circular cylinder.

Fig.15. Horseshoe vortex cavities downstream from the end of developed cavity of Schiebe headform, S 100, V 9.5 m/s, σ 0.29

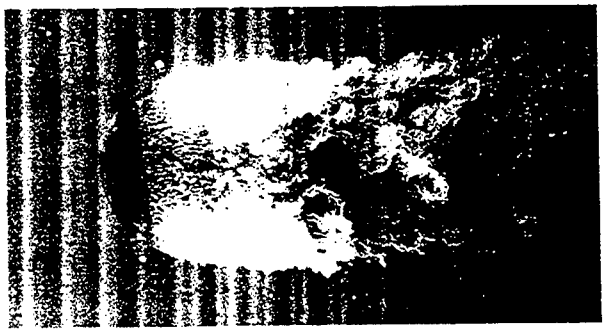

Fig.16. Horseshoe vortex cavities downstream from the end of developed cavity of hemispherical headforms, H100, V 12.5m/s, σ 0.35

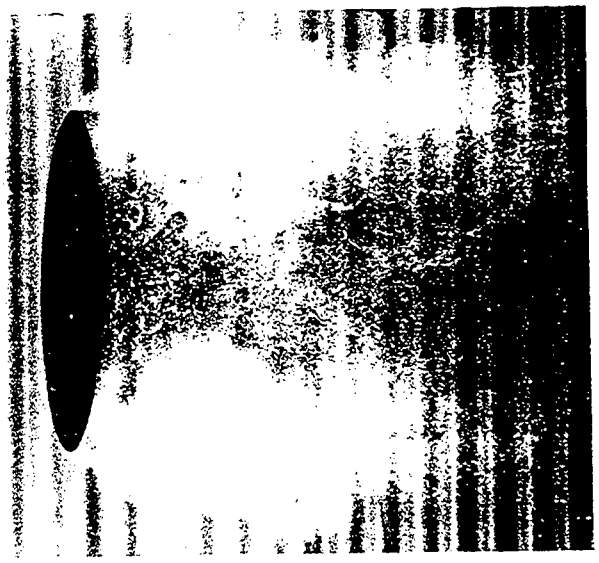

Fig.17. Horseshoe vortex cavities in the cavitation region on blunt circular cylinder B200, V 5.0m/s, σ 1.44

III. STUDY OF TWO DIMENSIONAL FOIL SECTIONS

In the early fifties the scale effects study on cavitation on hydrofoils was initiated both at the CIT and PSU. In the late eighties some more hydrofoil cavitation data were published by the PSU and MARIN. These data showed the different scale effects on the different types of cavitation. Billet and Holl observed clear trends for attached cavitation from several series tests of hydrofoils. However, for travelling-bubble cavitation on hydrofoils, the velocity scale effect was observed where as the size scale effect was not observed [12]. Van der Meulen studied the boundary layer and cavitation phenomena on two hydrofoils NACA 16-012 and NACA 4412 by using an in-line holographic technique. He found that there existed a certain correlation between the cavitation appearance and the viscous flow behaviour [6]. Van der Meulen and Ye conducted an experimental investigation of artificial means to eliminate both viscous and nuclei effects on bubble cavitation on a NACA 4412 hydrofoil [13]. In the late nineties both experimental and numerical studies on hysrofoil cavitation were performed at the DTRC and elsewhere. Shen and Dimotakis investigated the viscous and nuclei effects on hydrodynamic loadings and cavitation of a NACA 66 (MOD) foil section. Their study concerned two different types of pressure loadings representing a propeller blade section operating at design and off-design conditions. They used a viscous/inviscid interation code developed by Cebeci et al. to compute the viscous flow field on

the foil section [14]. Latorre and Baubeau carried out a numerical study of wall influence on boundary-layer transition for two-dimensional NACA 16-012 and 4412 hydrofoil sections [15]. The main objective of the present experimental hydrofoil cavitation study is trying to further understand the different scaling trends for attached leading edge cavities and bubble cavitation and their correlation with the viscous flow behavious. A series of four two-dimensional NACA 16-012 hydrofoil section models having chord length of C=100, 200, 300 and 400 mm were tested at two angles of attack $\alpha = 2°$ and $7°$. Tests comprised LDV measurement and cavitation observation. Test section of the cavitation tunnel of SSSRI is $600 \times 600\, mm^2$. Foil models were made of bronze.

LDV Measurement

LDV measurement was made at two free stream speeds V=1 m/s and 5 m/s. Figs.18,19 are the measured pressure distribution on the biggest foil model at two values of angle of attack $\alpha = 2°$ and $7°$ respectively. Because it was impossible to measure the boundary-layer near the leading edge of the smallest model the angle of attack has to be increased to $\alpha = 3.2°$, Fig.20 is the measured result. Comparison of the pressure distribution was made with the computed results of Latorre and Baubeau. The boundary-layer measurements indicated that all the velocity profiles could be attributed to turbulent profiles except for very few profiles of two small foil models measured at $\alpha = 2°$ and V=1m/s near the leading edge of the foils. By comparison with the experimental results of Van der Meulen [6] and computed results of Latorre and Baubeau [15] transition from laminar to turbulence occurred earlier in the present test.

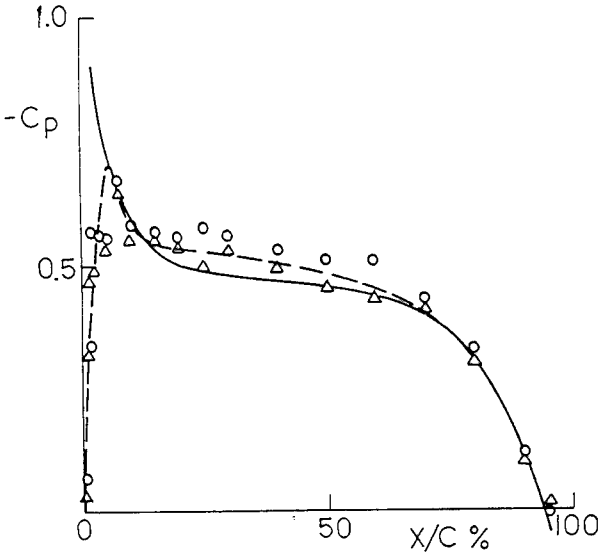

Fig.18. Pressure distribution, NACA 16-012 at $\alpha = 2°$, C=400mm
—△— V=1m/s, LDV measurement
--o-- V=5m/s, LDV measurement
—— Calculated (Latorre and Baubeau $\alpha = 2°$)

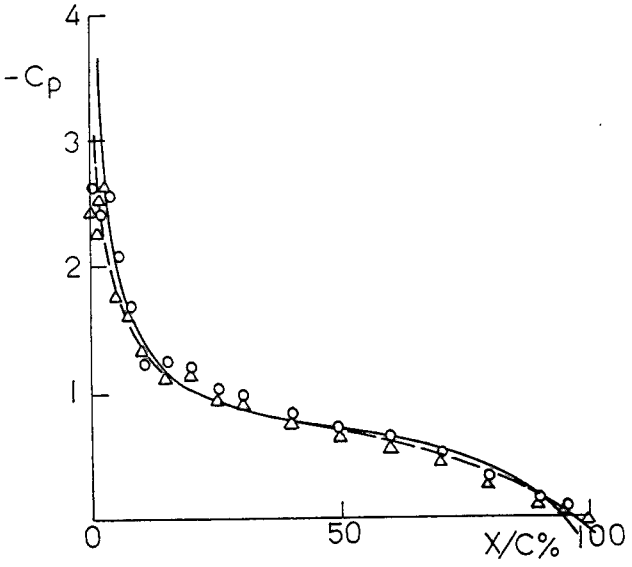

Fig.19. Pressure distribution, NACA 16-012 at $\alpha = 7°$, C=400mm
—△— V=1m/s, LDV measurement
—o— V=5m/s, LDV measurement
—— Calculated (Latorre and Baubeau $\alpha = 6°$)

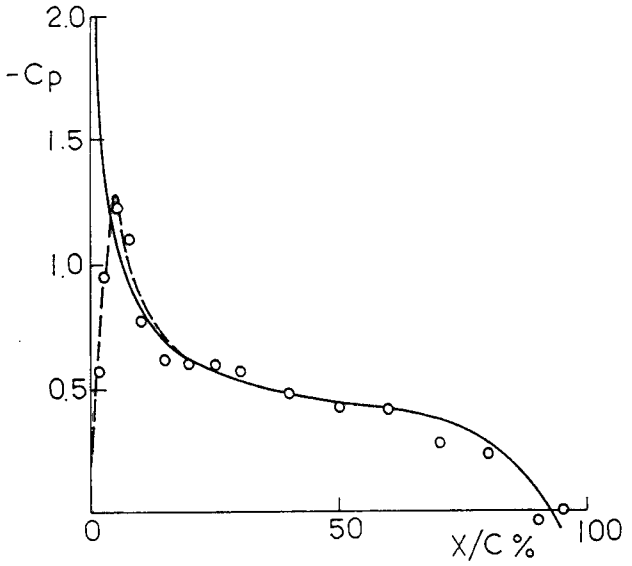

Fig.20. Presure distribution, NACA 16-012 at $\alpha = 3.2°$, V=1m/s, C=100mm
--o-- LDV measurement
—— Calculated (Latorre and Baubeau, $\alpha = 4°$)

Cavitation Observation

Cavitation experiments were conducted in routine procedure to determine the type of cavitation, the desinent cavitation number σ_d and the incipient cavitation number σ_i. Besides, for the sheet cavitation appeared in the case of $\alpha = 7°$, another two cavitation numbers were recorded, σ_1 was the cavitation number corresponding to a developed sheet cavity having a length of about 1/8 of the chord length and σ_2 was the cavitation number corresponding to a more developed sheet cavity having a length of about 1/4 of the chord length. When sheet cavity appeared, all the measurements were performed not only for smooth foil surface but also for painted foil surface.

The type of cavitation occurring at $\alpha = 2°$ was typical travelling bubble cavitation, Fig.21. The bubble cavitation started to appear usually at a position of about x/c=20% from the leading edge. The largest bubbles could reach the trailing edge. Fig.22 gives the desinent and incipient bubble cavitation data which clearly demonstrate both velocity and size effect. Cavitation index decreased with increasing Reynolds number for a given foil model and increased with increasing chord length for a fixed Reynolds number. Furthermore, the smaller the chord length, the bigger the slope of variation of cavitation index versus Reynolds number and the bigger the difference in cavitation indices of different sized models at a given Reynolds number.

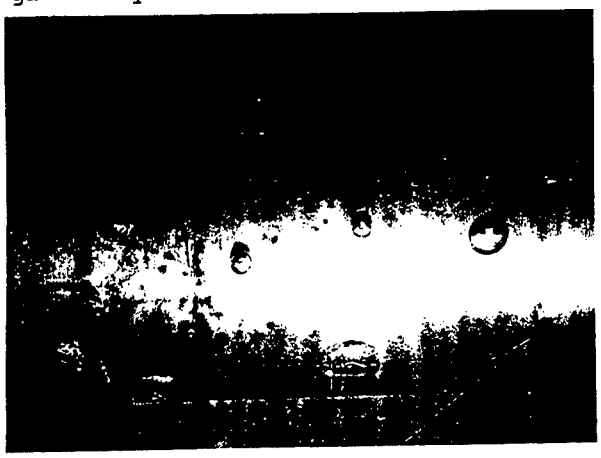

Fig.21. Travelling bubble cavitation, NACA 16-012, C=200mm, $\alpha = 2°$, V=5.5m/s, $\sigma = 0.430$

The cavitation appearance for $\alpha = 7°$ was attached bubble-band cavitation started from the leading edge, Fig.23. This type of cavitation looked like a transition case from sheet cavitation to cloud

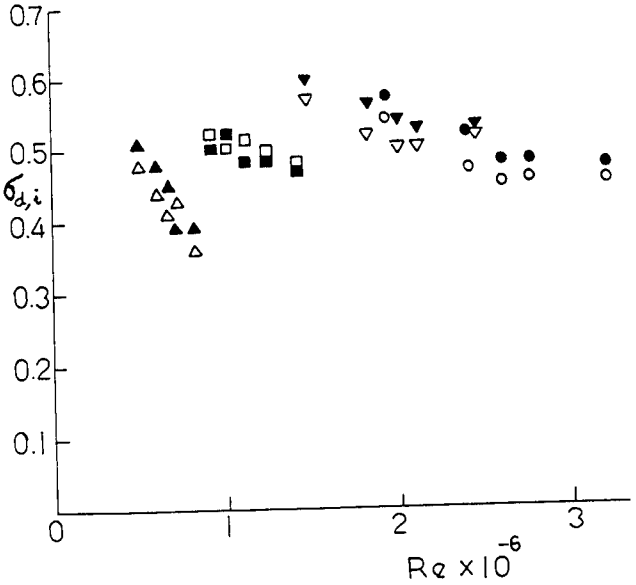

Fig.22. Desinent and incipient cavitation data for NACA 16-012, $\alpha = 2°$

Cmm	100	200	300	400
desinent	▲	■	▼	●
incipient	△	□	▽	○

Fig.23. Attached small bubble-band cavitation, NACA 16-012, C=200mm, $\alpha = 7°$, V=7m/s, $\sigma = 1.48$

cavitation. Figs.24 and 25 show desinent and incipient cavitation data on smooth and painted surfaces respectively. Cavitation index increases with increasing Reynolds number for a given foil model. Due to the scatter of the data no definite size effect was observed. A more clear Reynolds number effect appeared in the case of painted surface. The viscous scale effects on developed cavitation was smaller than those on desinent, incipient cavitation, Fig.26. The size effect on the developed (σ_1) and more developed attached bubble-band cavitation (σ_2) is similar to the size effect on travelling bubble

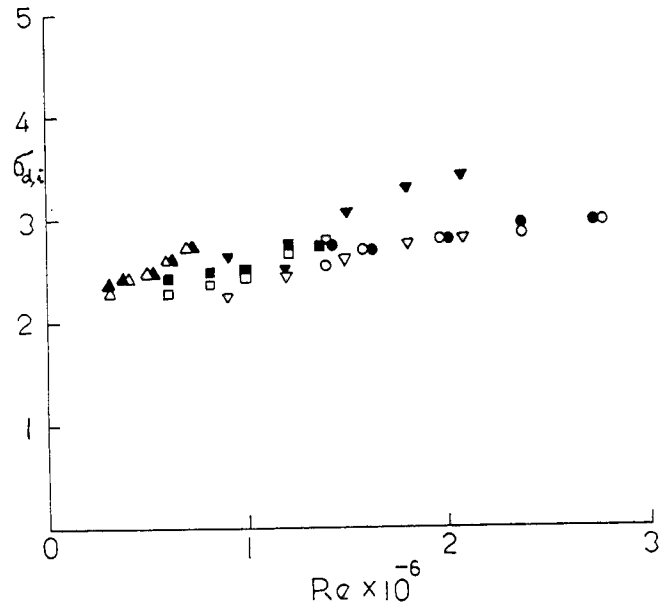

Fig.24. Desinent and incipient cavitation data for NACA 16-012, $\alpha = 7°$, smooth

Cmm	100	200	300	400
desinent	▲	■	▼	●
incipient	△	□	▽	○

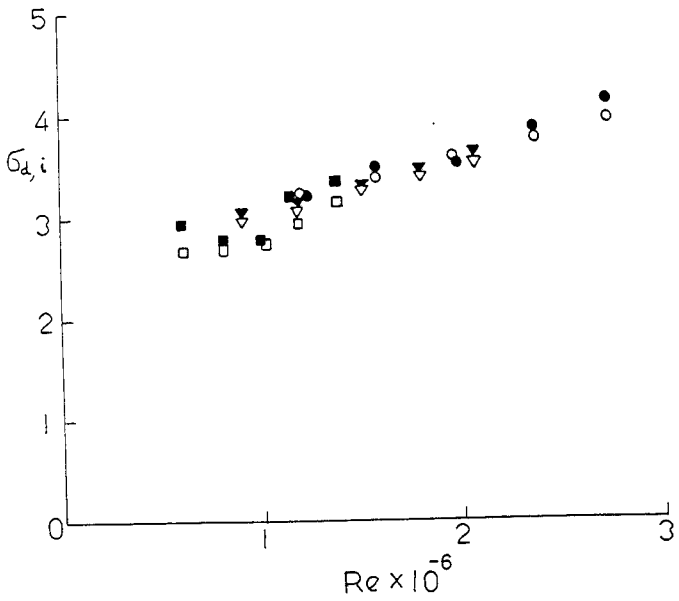

Fig.25. Desinent and incipient cavitation data for NACA 16-012, $\alpha = 7°$, painted

Cmm	200	300	400
desinent	■	▼	●
incipient	□	▽	○

cavitation, namely cavitation number for fixed cavity length increases with increasing chord length of the model except for the largest foil. This kind of size effect is thought to be caused by the time effects, at a fixed Reynolds

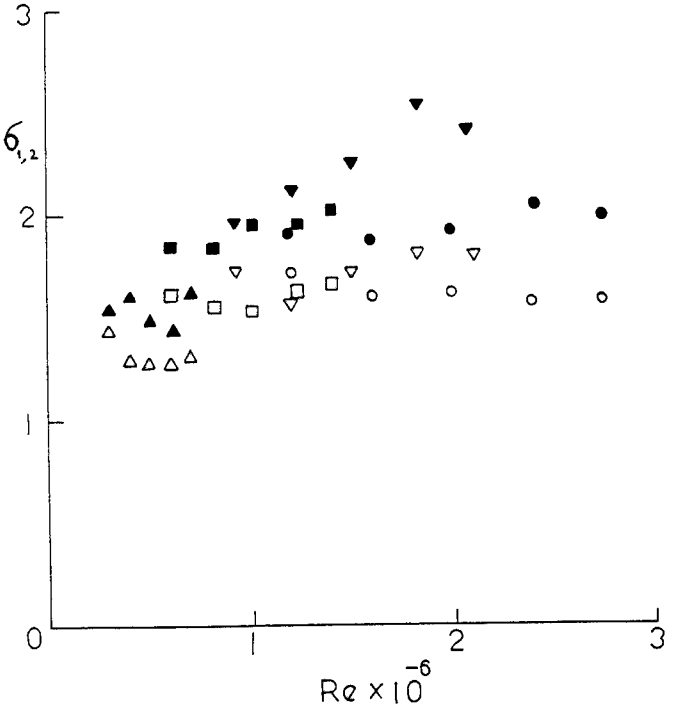

Fig.26. Developed and more-developed cavitation data for NACA 16-012, $\alpha = 7°$

Cmm	100	200	300	400	
developed σ_1	▲	■	▼	●	$(\frac{1}{4}c)$
more-developed σ_2	△	□	▽	○	$(\frac{1}{8}c)$

number the residence time of bubbles in the low pressure region is shorter for a smaller foil with higher free stream speed.

An interesting process was observed during the cavitation test for the smallest model at angles of attack betwen $\alpha = 2°$ to 3.2°. Tests started from a low speed of V=5m/s with a large number of developed bubble cavitation near the foil surface. When the pressure was increased the bubble cavitation disappeared first, then attached transient sheet cavitation came into sight on the smooth foil surface from the leading edge and so did the streak cavitation on the painted surface a little while later. Next the pressure was further increased till all these cavitation diappeared. After the desinent cavitation was measured the pressure was decreased to measure the incipient cavitation. First the same process appeared as just mentioned about the sheet cavitation on smooth and painted surfaces. As the pressure was further lowered, all of a sudden these cavitation grew very rapidly downstream. As soon as the cavity length became close to 2/3 of the chord length, a strong vibration of the sheet cavity end began to appear and at the same time the bubble cavitation came into view. When the pressure was further lowered causing the

bubble cavitation to develope, the sheet cavitation disappeared gradually. At last the foil surface was full of bubble cavitation. Afterwards tests were conducted with increasing speed up to V=8m/s. The cavitation process was basically the same as with V=5m/s, but more streak cavitation occurred on the painted surface and it became more difficult for transient sheet cavitation to disappear on the smooth surface, consequently both bubble and sheet cavitation appeared simulataneously. Figs.27-29 are some of the photos taken during this interesting process at an angle of attack $\alpha = 3.2°$.

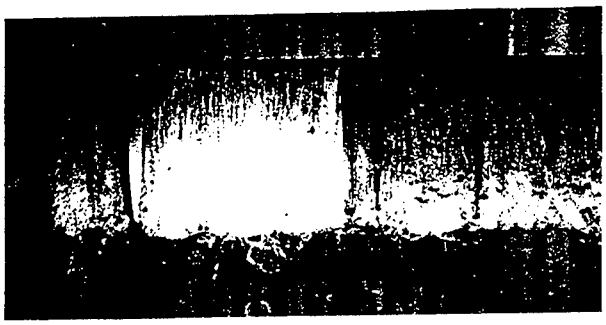

Fig.27. Cavitation appearance, NACA 16-012, C-100mm, $\alpha = 3.2°$, V=6m/s, $\sigma = 0.53$

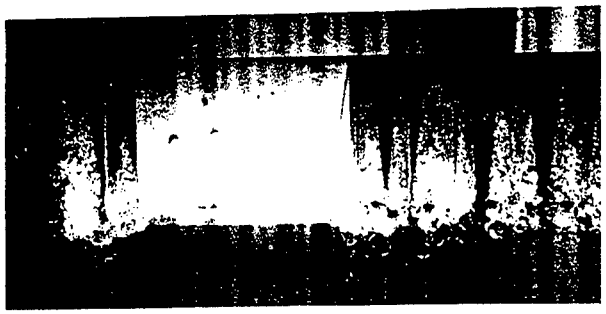

Fig.28. Cavitation appearance, NACA 16-012, C=100mm, $\alpha = 3.2°$, V=6m/s, $\sigma = 0.47$

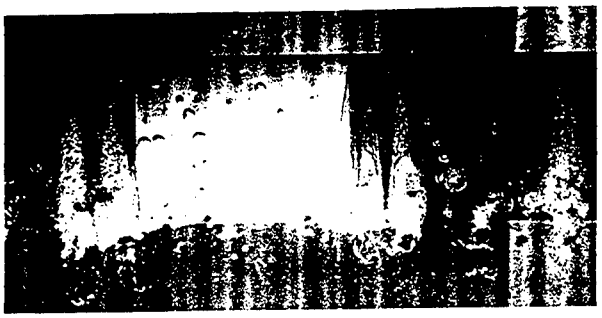

Fig.29. Cavitation appearance, NACA 16-012, c=100MM, $\alpha = 3.2°$, V=6m/s, $\sigma = 0.36$

Few similar findings were reported before. Arakeri and Acosta found disappearance of cavitation on a tripped 2-inch hemispherical headform with increase of speed and decrease of pressure [16]. Van der Meulen demonstrated change of cavitation type from bubble to sheet cavitation by a slight increase of angle of attack around $\alpha = 3°$ on a NACA 16-012 hydrofoil [6]. Shen and Dimotakis showed the strong influence of speed on cavitation appearance on a NACA 66 (MOD) foil section at $\alpha = 3°$, leading edge attached cavities appeared at high speed but midchord bubble cavitation occurred at low speed [14].

This kind of unusual cavitation process has forced scientists to further study not only viscous and nuclei effects but also their interaction. In the present test, at $\alpha = 2°$ there existed a weak peak in the pressure distribution which did not cause laminar separation, however this peak became strong enough to induce separation when roughness spot or dirty particle attached to the leading edge or when angle of attack was slightly increased. Then streak cavitation or transient spot or patch cavitation emerged. When the pressure was lowered abundunt nuclei inside the free stream possibly would bring about the disappearance of laminar separation and consequently the leading edge cavities would vanish.

IV. STUDY OF PROPELLERS

Recently there clearly appears a new surge of interest in the vortex structure and vortex cavitation of marine lifting surface and propeller. Interesting reports on the subject have been issued one after another (see for example the Proceedings of the 21st and 22nd American Towing Tank Conference). In order to further study the cavitation scale effects and to give a correct prediction of cavitation performance on prototype it is necessary for each facility to develope its own database and to accumulate its own experience. This part of our systematic investigation is dealing with the viscous scale effects on propeller tip vortex cavitation.

In the present paper only few interesting findings from the boundary-layer visualization and cavitation observation will be reported.

Boundary-Layer Visualization

As far as the flow visualization of the boundary-layer on rotating propeller blades is concerned, even though a three-dimensional LDV can be used to measure the boundary-layer, it is quite a time-consuming work to do. Instead, a much more time-saving method - the oil film method is used[24].

In the present investigation we have used a series of three different sized propeller models. This propeller was selected from a cavitating propeller series which was designed for high speed vessels [17]. The blade outline can be seen on Fig.30, which was taken just before the oil film test. The first blade of the propeller was smooth. The second one was roughened at the leading edge with 60 microns carborundum over about 3% of the chord on the suction side. The whole third blade surface was painted with a kind of blackboard paint. The oil paint used for flow visualization was a kind of castor oil mixed with red lead oxide. The paint should be mixed about in the proportion of one part of caster oil to five parts of red lead oxide. Paint tests were made at J=0.996, 0.86 (effective slip ratio 0.3, 0.4) of several speeds, namely, V=3.5, 5.0, 6.4 and 8.0 m/s for D=220 mm and V=3.5, 4.0, 5.0 and 6.25 for D=280 mm and D=350 mm. Theoretical calculation was performed for these two advance ratios. Figs.31,32 are the calculated pressure distribution results. For both values of J at r/R=0.7 the pressure distribution on the suction side is near shock-free entrance condition, but a peaked condition appears on the pressure side. Figs.33-36 are the photos and sketches of the paint tests. The shade line area indicates laminar boundary-layer, the remains represent either turbulent boundary-layer or boundary-layer separation.

The oil film flow visualization of the geosiom propeller models revealed that a laminar boundary-layer region always appeared near the leading edge of blade root on smooth blades of all the propeller models in the whole tested range with a maximum Reynolds number of $R_{e0.7R} = 3 \times 10^6$.

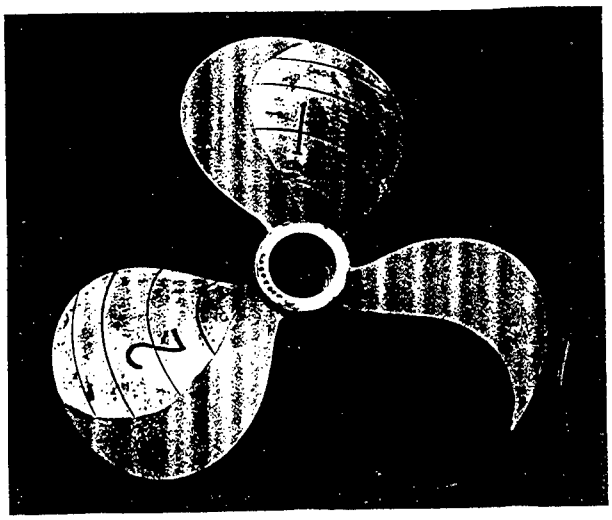

Fig.30. The propeller model before oil film test

This laminar region diminished very slowly with the increase in free stream speed. If no suitable boundary-layer stimulator was used it would be quite difficult to remove this laminar region away by the increase of speed only. The effect of carborundum at the leading edge was so significant that almost in all conditions tested the laminar region disappeared. According to Huang et al, incipient cavitation numbers on the axisymmetric headforms with isolated roughness bands were found to approximate the computed values of $-C_{P\min}$ when the roughness numbers R_{eK} were equal to or greater than 600 [18]. Huang and Shen

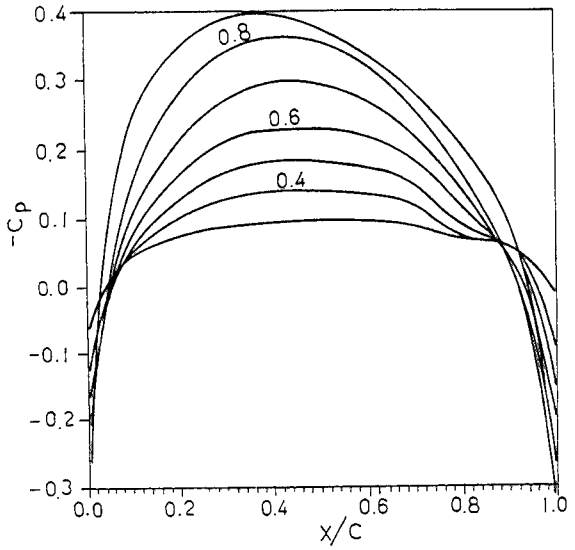

Fig.31. Calculated pressure distribution on propeller at J=0.996 (suction side)

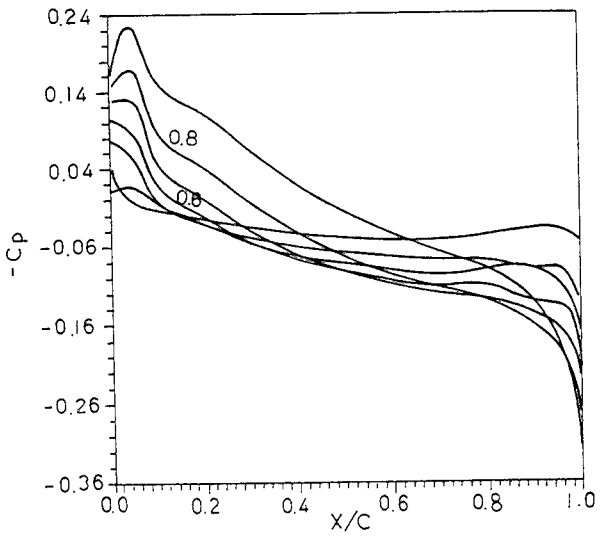

Fig.32. Calculated pressure distribution on propeller at J=0.996 (pressure side)

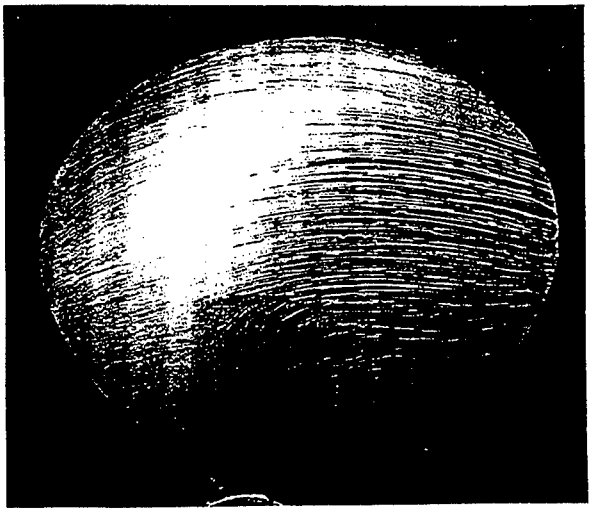

Fig.33. The paint pattern on propeller D=280mm at V=5m/s, J=0.996 (suction side)

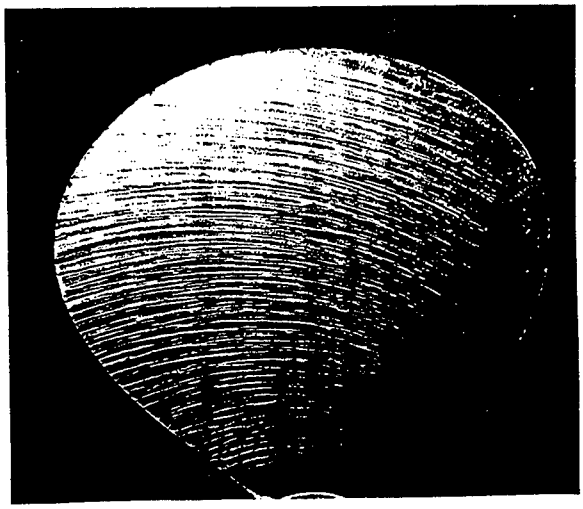

Fig.34. The paint pattern on propeller D=280mm at V=5m/s, J=0.996 (pressure side)

reported that leading-edge roughness with roughness Reynolds numbers $R_{eK}=\frac{u_K \cdot K}{\nu}$ about equal to 600 was found to reduce the difference between the measured incipient sheet cavitation numbers and the computed values of $-C_{Pmin}$ on three hydrofoils, one propeller at two values of J in steady flow, and a hydrofoil under pitching oscillation [19]. A minimum roughness Reynolds number of 300 to stimulate boundary-layer transition on model propellers was recommended by the 18 the ITTC [20]. In fact, direct systematic measured transition data of boundary-layer on propeller models is rather rare to be found in the literature in comparison with the ones on flat plate, axisymmetric bodies and foil sections.

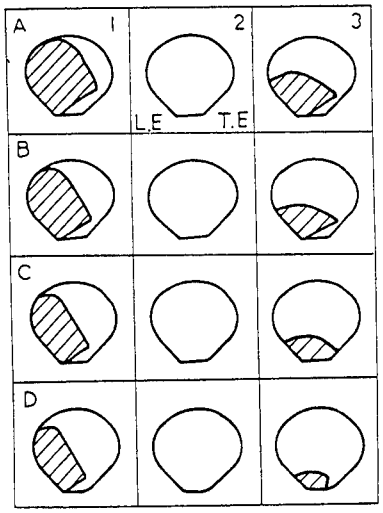

Fig.35. The paint test sketch on propeller of D=220mm at various speeds
Column: 1-smooth, 2-with carborundum, 3-painted
Row: A-V=3.5m/s B-V=5.0m/s
C-V=6.4m/s D-V=8.0m/s

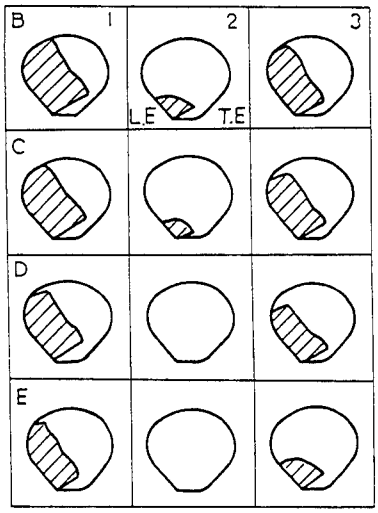

Fig.36. The paint test sketch on propeller of D=350mm at various speeds
Column: 1-smooth, 2-with carborundum, 3-painted
Row: B-V=3.5m/s C-V=4.0m/s
D-V=5.0m/s E-V=6.25m/s

In the present study approximate values of the critical roughness Reynolds numbers may be estimated. According to the calculated pressure distribution, for the leading edge roughness at r/R=0.7, the smooth laminar boundary-layer volocity u_K at the top of the roughness of height K equals about 1.05

V ($C_p = -0.1$). Table 4 gives the measured and estimated results of the critical Reynolds numbers both at 0.7 radius and for the leading edge roughness used (60 μm carborundum).

Table 4. The Measured and Estimated Critical Reynolds Number at 0.7 Radius for Roughened Models with Carborundm

J	0.996			0.86		
Dmm	220	280	350	220	280	350
$R_{e0.7} \times 10^{-6}$	0.92	1.68	2.62	1.04	1.89	2.36
R_{eK}	476	681	850	538	766	765
R_{eK} / D	2.16	2.43	2.43	2.45	2.74	2.19

The oil film results disclosed that the critical roughness Reynolds number R_{eKcrit} is approximately proportional to the propeller diameter D. On average a rough estimation of R_{eKcrit} / D can be given as $R_{eKcrit} / D = Const = 2.4 \frac{1}{mm}$. Thus, for a propeller of D=250mm, R_{eKcrit} will be equal to about 600. Coincidently, this value is double the minimum roughness Reynolds number of 300 to stimulate boundary-layer transition recommended by the 18th ITTC. The difference in this value may be caused by the different pressure distribution. The ratio of R_{eKcrit} can be used to give a rough estimation of the critical roughness Reynolds number for different sized propeller models to stimulate the whole suction side boundary-layer into turbulent for a near shock-free entrance pressure distribution at 0.7 radius. Usually a roughness height of K=60 μm or 30 μm has been found suitable, in this case K=Const we have R_{eK}/D=Const, $R_{e0.7} / D^2$=Const, namely the critical Reynolds number at 0.7 radius is roughly proportional to the square of the diameter. This size effect is larger than in the case of $R_{eK} = \frac{u_K \cdot K}{\nu}$=Const, $R_{e0.7} / D$=const which is implied in the constancy of the critical Reynolds number $R_{eK} = \frac{u_K \cdot K}{\nu}$=Const for different sized models as appeared in a relation recommended by the 18th ITTC for the peaked pressure distribution $R_{e0.7}$/C=K/450 [20]. In addition to the application of 60 μm carborundum at the leading edge of the propeller models, a kind of blackboard paint was used to paint the whole blade as an alternative to induce transition of the boundary-layer. The preliminary result of the blackboard paint used as a tripping device was encouraging.

The laminar region was always diminished considerably in all conditions tested. This stimultor became more effective at higher speeds on the smaller propeller, in this case either the laminar region was totally removed or only a very small laminar region existed near the leading edge of the blade root.

The oil film flow visualization of the geosim propeller models strongly suggested that there existed a similar size effect on boundary-layer transition as in the case of the Schiebe bodies, namely, for a given Reynolds number, the smaller the propeller diameter, the smaller the laminar boundary-layer region on the propeller blades. This size effect is thought to be caused by the difference in relative roughness height of the blade surface. This effect is most evident in the case of painted blades. Here a quasi-critical Reynolds number R_{eqcrit} is defined in a practical manner as the Reynolds number at which boundary-layer transition occurs close to the leading edge at all outer ratii of r/R>0.4 (R being the radius of the propeller model). According to this definition table 5 gives some paint test results of the present study.

Table 5. The Measured and Estimated Quasi-critical Reynolds Number at 0.7 Radius for Different Blade Surface Conditions

Blade surface condition	Dmm	220	280	350
	J	$R_{eqcrit} \times 10^{-6}$		
roughened with carborudum	0.996 0.86	0.92 0.90	1.18 1.14	2.19 1.66
painted	0.996 0.86	1.65 1.04	2.35 1.89	2.86 2.36
smooth	0.996 0.86		~2.7	~4.3

From this table it is clear enough to show that for a given smaller laminar region on the propeller blade at inner radii r/R<0.4, the quasi-critical Reynolds number is increasing with the propeller diameter in the tested range. Roughly speaking, for the two types of roughened blades this size effect can be expresssed as $R_{e0.7} / D^{1.5}$=const. This constant is dependent on both the blade surface condition and the thrust loading of the propeller models. Fig.37 is the variation of the separation radius with Reynolds number. Here for the near shock-free condition the separation radius may still be defined as in the peaked condition, even there was neither the separation bubble near the leading edge nor distinct "cut off" of the paint streaks of the laminar flow region. However transition occured more gradually than on a propeller blade with a peaked pressure distribution. An increase in the Reynolds number shifted

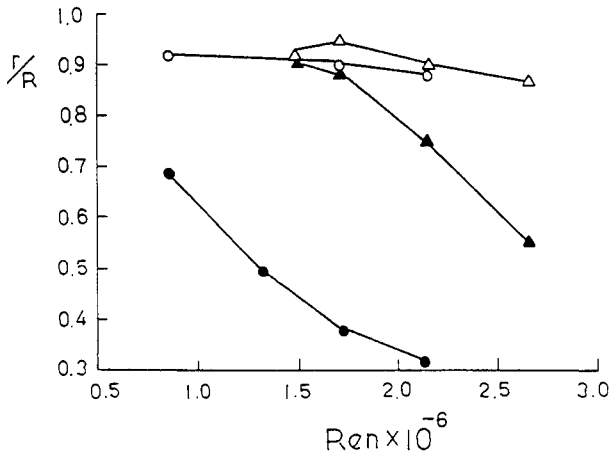

Fig.37. Variation of separation radius with Reynolds number and surface condition (J=0.996)

Dmm	Smooth	painted
220	o	●
350	△	▲

the transition region towards the leading edge, the chordwise movement of the transition edge was more evident than the radial one. The separation radius was not constant, it only varied slightly on the smooth blades but significantly on the painted blades. The laminar region on the painted blades was smaller than on the smooth blades, especially when the Reynolds number was increasing this boundary-layer stimulator became more effective. It is interesting to mention that in our tests the boundary-layer on the whole pressure side was turbulent. This agreed with the calculated peaked pressure distribution with a very strong adverse pressure gradient at the leading edge. As far as the cavitation tunnel test is concerned, it is not generally true to say that the bigger the propeller model, the smaller the scale effects. In order to reduce the scale effects caused by viscosity and blockage, it is preferably to choose a testing scheme using a comparatively smaller model with a higher RPM of the propeller. In this case the test Reynolds number either may become closer to the critical Reynolds number with smooth blades or may easily reach on exceed a much lower critical one with roughened blades.

Scale Effects on Propeller TVC

McCormick's semi-expirical scaling relationship for tip vortex cavitation inception on hydrofoils in the form of $\sigma_i = R_e^n \cdot \alpha^m$ has been widely used to predict full scale propeller TVC inception based on model tests [21]. Here α is the angle of attack of the hydrofoil. The determination of the Reynolds number exponent n is important for the TVC scaling. The lack of necessary propeller model series test data has forced us to tentatively utilize the existed hydrofoil data, though there exists apparent distinction between the TVC on hydrofoils and propellers. It would be much better to accumulate sufficient propeller data to develope a proper scaling relationship for propeller TVC inception. Our effort is just the first step to develope our own database to determine such a scaling law.

It has been found from many investigations that the inception of TVC depends strongly on both the tip boundary-layer and the dissolved air content of the water. The present study deals with the viscous scale effects on propeller TVC only. In order to reduce the possible nuclei scale effects all the cavitation tests were performed at an almost constant value of α/α_s ($0.85 \lesssim \alpha/\alpha_s \lesssim 0.90$). Cavitation tests were conducted at three speeds V=3.5, 5.0 and 6.5 m/sec for two values of J=0.996 and 0.86. Five different stages of development of TVC were measured with naked eyes under stroboscopic light at fixed values of V and J. The conditions measured were 1). desinent TVC, σ_0, 2). unattached TVC, σ_1, 3). attached TVC, σ_2, 4). developed TVC, σ_3 (the first stage of developed TVC), 5). fully developed TVC with mid chord small bubble band cavitation from r/R=0.4 up to the propeller tip, σ_4 (the second stage of developed TVC, this stage will be simply designated as fully developed TVC in this paper). Due to the design limitation of the tunnel sometimes it was impossible to arrive at the above mentioned conditions. Figs.38 is a tpical photo of the fully developed TVC. The cavitation appearance on painted blades under the fully developed TVC condition

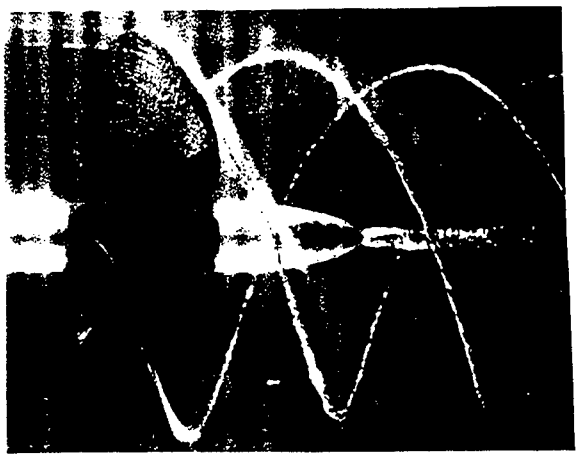

Fig.38. The fully developed TVC on painted propeller D=350mm at V=6.5m/s and J=0.996

is worth mentioning. The mid-chord cavitation bubble appeared to be a fine bubble band which looks like closer to what expected to be the full scale pattern.

The performance tests of these propeller models indicated that the tunnel blockage effects were not negligible due to the limited size of the tunnel. The tunnel blockage of the three configurations tested were 5.3, 8.6 and 13.4% respectively (the area ratio of the propeller disc area to the tunnel cross area). In order to compare the test TVC results under the same thrust loading, a simple K_T indentity method was used to correct the measured cavitation data. Figs.39-42 are some of the corrected TVC data. Table 6 gives the exponents n of the results of linear regression analysis of these data.

Table 6. The Reynolds Number Exponents n for TVC Scaling Rules for Different Blade Surface Conditions and Stages of Development of TVC.

J=0.996	smooth	with carb.	painted
attached	0.20	0.08	-0.07
unattached	0.15	-0.05	0.06
desinent	0.08	0.02	0.24
J=0.86	smooth	with carb.	painted
attached	0.43	0.10	-0.03
unattached	0.22	0.02	0.13
desinent	0.17	0.14	0.20

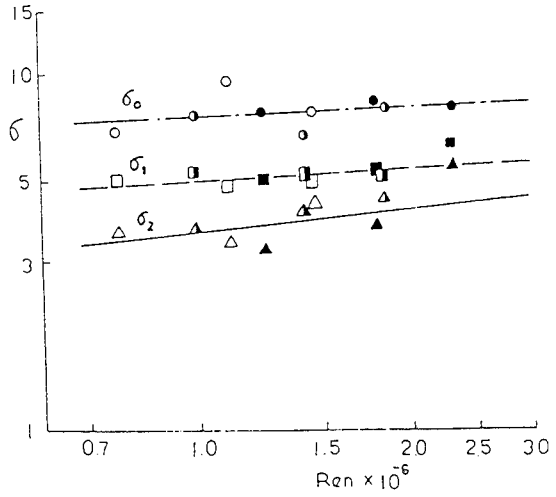

Fig.39. Cavitation numbers versus Reynolds number for a series of propeller models at different stages of development of TVC (smooth blades, J=0.996)

Dmm desinent unattached attached

220 ○ □ △

280 ◑ ◨ ◭

350 ● ■ ▲

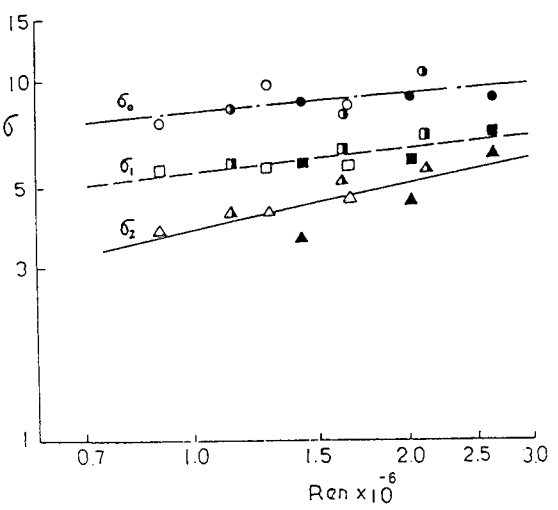

Fig.40. Cavitation numbers versus Reynolds number for a series of propeller models at different stages of development of TVC (smooth blades, J=0.86)

Dmm desinent unattached attached

220 ○ □ △

280 ◑ ◨ ◭

350 ● ■ ▲

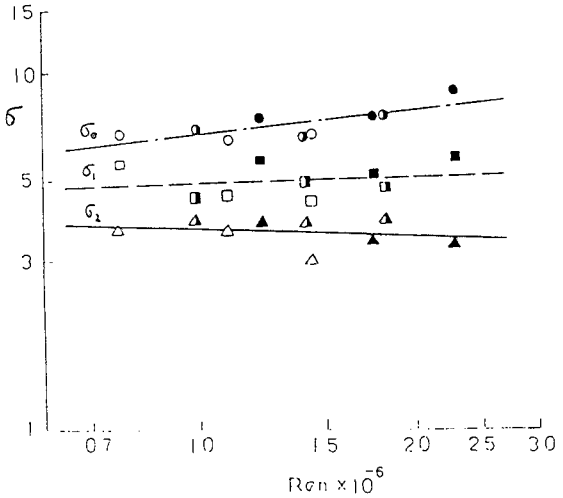

Fig.41. Cavitation numbers versus Reynolds number for a series of propeller models at different stages of development of TVC (roughened with leading edge carborundum, J=0.86)

Dmm desinent unattached attached

220 ○ □ △

280 ◑ ◨ ◭

350 ● ■ ▲

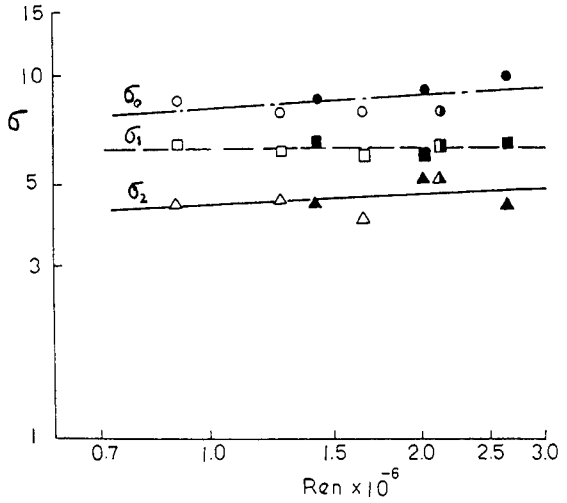

Fig.42. Cavitation numbers versus Reynolds number for a series of propeller models at different stages of development of TVC (painted baldes, J=0.996)

Dmm	desinent	unattached	attached
220	○	□	△
280	◐	◨	▲
350	●	■	▲

Based on the above mentioned experimental results some of the main viscous scale effects on TVC may be discussed as follows:

1. The Effect of the Reynolds Number

After the tunnel blockage correction was made, a clear Reynolds number effect on the cavitation data appeared. No clear size effect was observed. This was possibly caused by the fact that during the cavitation tests the boundary-layer on both the suction and pressure sides was turbulent near the propeller tip, and the inception of TVC was mainly effected by the boundary-layer development near the tip. Thus the size effect of boundary-layer transition turned out to be a secondary effect on the inception of TVC, here the dominant effect was the Reynolds number effect.

2. The Effects of Blade Surface Condition and Cavitation Development

If we use the exponential scaling law as $\sigma_i \propto R_e^n$, here the Reynolds number Re is based on the blade chord length and the resultant blade inflow velocity at 0.7 radius, then the exponents n for different test conditions can be determined from the very limited data available. Even though the values of n should not be regarded as very accurate quantities, they will still be useful for us to understand some basical aspects of TVC scaling rules, at least, qualitatively. From table 6, it is evident that for all three blade surface conditions and three types of TVC the exponents n differ from each other. The values of n are strongly dependent on both the types of TVC measured and the blade surface conditions of the propeller models. Generally speaking, the real values of n found at this tunnel were smaller than the usual range of n=0.36-0.60 reported in the literature. The effects of blade surface condition on TVC manifested itself first in the cavitation inception numbers. In comparison with the smooth blades TVC was delayed on the painted blades in general. For the roughened blades with carborundum the desinent TVC was often delayed but the attached TVC was often hastened. Secondly, the blade surface condition also had an effect on the exponent n. The values of n for the desinent, unattached and attached TVC on the smooth blades were the highest among three different blade surfaces with few exceptions. The effect of cavitation development was quite regular for the smooth blades: the exponent n was the highest for the attached TVC and n was the lowest for the desinent TVC. On the other hand, the exponent n was increasing with the thrust loading of the propeller for the smooth blades. The cavitation development still exerted an certain regular effect on the exponent n for the painted blades, however it was just the opposite to the effect on smooth baldes: the exponent n was the lowest for the attached TVC and n was the highest for the desinent TVC. This effect became irregular for the roughened blades with leading edge carborundum. During the cavitation tests the boundary-layer condition on the suction side of the smooth blades was far from quasi-critical: the laminar region was either close to the blade tip (J=0.996) or near r/R=0.6-0.7 (J=0.86). However, the boundary-layer condition on the suction side of the roughened blades was either near critical (with carburundum) or near quasi-critical (painted), the laminar region was completely disappeared with carborundum or only a small laminar region existed close to the painted blade root. For the same cavitation development the highest exponent n of the smooth blades may be related to the biggest laminar boundary-layer region on the suction side of propeller baldes [22].

In order to further improve the accuracy of the TVC inception measurement and to establish a more solid scaling relationship, there appears an apparent need to use some more objective method

of defining TVC inception like Kuiper's method [23] of determination of the TVC inception from the radius of the cavitating core (α_c=0.25 mm) or Ye's improved method [24] based on Kuiper's method ($\alpha_c = 0$).

V. CONCLUSION

The main conclusions are as follows:

1. LDV flow measurement was successfully used to determine the thin boundary-layer transition as a supplementary but quantitative flow visualization measure. When transition occurred, in addition to the well-known large RMS value associated with transition, spectrum analysis of the LDV signals of fluctuating velocity indicated that the velocity level was increasing almost linearly with decrease of the frequency in a log-log plot of the power spectrum. On the other hand, the ratio of low pass filtered RMS value of the LDV signals to high pass filtered one often reached a maximum. These features of the LDV sinals also appeared in some extent in the measurements at other cavitation prone regions such as reattachment points of separated boundary-layer or region. Transition detection by the present LDV method showed good agreement with the results of schlieren and in-line holography methods.

2. The present series flow measurements by LDV clearly revealed a regular size effect or unit Reynolds number effect on boundary-layer transition on the Schiebe headforms, namely at the same Reynolds number, the smaller the diameter of the model, the shorter the distance of the transition point downstream from the minimum pressure point. This is thought to be caused by the bigger relative surface roughness height on the smaller models.

3. Spectrum analysis of the LDV signals in cavitation prone regions implied that there might exist large-scale coherent structure of turbulence. Downstream from the fully developed attached cavity end both of Schiebe and hemispherical bodies cavitation pattern looked like consisted of many large horseshoe or heirpin vortices (Ω-shape, U-shape). Most of these large scale structure of vortex cavities inclined at almost 45° with respect to the flow boundary. They clearly revealed the coherent structure of turbulence.

4. Boundary-layer separation was found at $\theta = 87°$ of the hemispherical model H200 for a Reynolds number of $R_{eD} = 1.68 \times 10^6$. But the measured boundary layer thickness was equivalent to 5-6 times the predicted one, and velocity profile was much fuller than the laminar one. Preliminary analysis indicated that this separation was neither laminar nor turbulent, it can be considered in very general terms as transitional or viscous separation. It seems that in comparison with the laminar separated bubble this much thicker viscous separated bubble will offer much more time for gaseous micro-bubble growth to occur. As far as the mechanism of cavitation inception inside the separated zone is concerned, it seems not general to consider the pressure fluctuation near reattachment point as the only possible reason.

5. Typical scaling trends for travelling bubble cavitation and attached small bubble-band cavitation on hydrofoils were observed. The size effect on developed attached bubble-band cavitation was similar to the size effect on desinent and incipient travelling bubble cavitation except for the largest foil.

6. The preliminary result of the blackboard paint used as a tripping device is encouraging. The laminar region was always diminished considerably in all conditions tested. This stimulator became more effective at higher speed on the smaller propeller, in this case either the laminar region was totally removed or only a very small laminar region existed near the leading edge of the blade root.

7. The oil film flow visualization of the propeller models strongly suggested that there existed a similar size effect boundary-layer transition as in the case of Schiebe bodies. A quasi-critical Reynolds number Reqcrit was defined to analyze this size effect. For a near shock-free condition, roughly speaking Req.crit was found to be proportional to $D^{1.5}$ for propeller models either painted or roughened with leading edge carborundum.

8. From the very limited data of the present study, the Reynolds number exponent n of propeller TVC scaling rules was found to be dependent upon the blade surface condition, the stage of development of TVC and the thrust loading of propeller models. Much remains to be done before some more solid propeller TVC scaling rules may be established.

ACKNOWLEDGMENTS

This investigation was sponsored by the National Natural Science Foundation of China and the China State Shipbuilding Corporation. The authors would like to thank Messrs. X.X. Shan and W.G. Gao of Shanghai Jiao Tong University for their technical assistance with the LDV measurement. Special thank goes to Mr. J.D. Chen of CSSRC for his calculation of the propeller performance. The first author would like to express his sincere

appreciation and to pay great respect to Prof. W.J. Fang for his continuous attention, support and encouragement during the years-long course of this cavitation research at CSSRC.

REFERENCES

1. Acosta, A.J., "Cavitation Inception and Internal flow with Cavitation". The Fourth DAVID TAYOR LECTURE, DTNSRDC 79/011, Oct.1979.

2. Arndt, R.E.A., "Recent Advances in Cavitation Research". Advances in Hydroscience, Vol.12, Academic Press, 1981.

3. Rood, E.P., "Review-Mechanisms of Cavitation Inception". Journal of Fluids Engineering, Vol.113, June 1991, pp.163-175.

4. Arakeri, V.H. and Acosta, A.J., "Viscous Effects in the Inception of Cavitation on Axisymmetric Bodies". Journal of Fluids Engineering, Transactions ASME, Vol.95, Dec.1973, pp.519-527.

5. Van der Meulen, J.H.J., "A holographic Study of Cavitation on Axisymmetric Bodies and the Influence of Polymer Additives", Ph.D. Thesis, Enschede, 1976.

6. Van der Meulen, J.H.J., "Boundary Layer and Cavitation Studies of NACA 16-012 and NACA 4412 Hydrofoils", 13th Symp. on Naval Hydrodynamics, 1980.

7. Acosta, A.J. and Parkin, B.R., "Cavitation Inception-A Selective Review", J. of Ship Research, Vol.19, 1975, pp.193-205.

8. Ye, Y.P. and Wang, D.Z., "Laser Velocimeter Measurements and Cavitation Observation on Two Axisymmetric Bodies", Int. Symp. on Cavitation, Sendai, 1986, pp.139-143.

9. Klebanoff, P.S. and Tidstrom, K.D., "Mechanism by which a Two-Dimensional Roughness Element Induces Boundary-Layer Transition", The Phisics of Fluids, Vol.15, 1972, No.7, pp.1173-1188.

10. Ye, Y.P., Wang, D.Z., and Huang, S., "Visous Effects Study by LDV of Cavitation on Sixteen Axisymmetric Bodies", 17th Int. Congress on Theoretical and Applied Mechanics, Grenoble, 1988, and J. of Hydrodyanmics, Beijing, Ser. B, 4(1990), pp.1-13.

11. Rotta, J. "Schubspannung Verteilung und Energiedissipationbei turbulenten Grenzschichten", Ing. Arch, 20, pp.195-207.

12. Billet, M.L. and Holl, J.W., "Scale Effects on Various Types of Limited Cavitation", International Symposium on Cavitation Inception, ASME, New York, December 1979, pp.11-24.

13. Van der Meulen, J.H.J. and Ye, Y.P., "Cavitation Inception Scaling by Roughness and Nuclai Generation", 14th Symposium on Naval Hydrodynamics, Ann Arbor, Michigan, 1982.

14. Shen, Y.T. and Dimotakis, P.E., "Viscous and Nuclei Effects on Hydrodynamics Loadings and Cavitation of a NACA 66 (MOD) Foil Section", Journal of Fluisds Engineering, ASME. Vol.111, pp.306-316.

15. Latorre, R., Baubeau, R., "Numerical Study of Wall Influence on Boundary-layer Transition for Two-Dimensional NACA 16-012 and 4412 Hydrofoil Dections", Journal of Ship Research, Vol.34, No.1, March 1990, pp.38-47.

16. Arakeri, V.H. and Acosta, A.J., "Cavitation Inception Observations on Axisymmetric Bodies at Supercritical Reynolds Numbers", Journal of Ship Research, Vol.20, No.1, March 1976, pp.40-50.

17. Zhu, H.S., "A Cavitating Propeller Series", Shipbuilding of China, CSNAME, Shanghai, No.4, 1981.

18. Huang, T.T., Belt, G.S. and Groves, N.C., "Cavitation Inception Observations on Axisymmetric Headforms with Turbulence Stimulators", DTNSRDC-83/071, Bethesda, 1983.

19. Huang, T.T. and Shen, Y.T., "Application of Turbulence Stimulator to Reduce Scale Effect on Cavitation Inception", Int. Symp. on Propellers and Cavitation, Wuxi, 1986.

20. ITTC "Report of Cavitation Committee", Proc. 18th ITTC, Kobe, 1987.

21. McCormick, B.W. Jr., "On Cavitation Produced by a Vortex Trailing from a Lifting Surface", J. Basic Engineering, ASME, Sept. 1962, pp.369-379.

22. Ye, Y.P., Lu, F., Shi, M.G. and Qiang, D.X., "Viscous Scale Effects on Tip Vortex Cavitation of Propellers", to be presented at the 2nd Int. Symp. on Propeller and Cavitation, Hangzhou, Sept. 1992.

23. Kuiper, G., "Cavitation Inception on Ship Propeller Models", Ph.D. Thesis, Delft University, 1981.

24. Ye, Y.P., "Some Aspects of Hub Vortex Cavitation", ASME, Int. Symp. on Cavitation, FED Vol.16, 1984, pp.177-189.

Analytical and Numerical Study of Large Bubble/Bubble and Bubble/Flow Interactions

G. Chahine, R. Duraiswami, M. Rebut (DYNAFLOW, Inc., USA)

Abstract

The presence of cavities in a liquid can have significant effects on its behavior and its flow characteristics. In practical flow situations, these effects cannot be fully understood or predicted without addressing complicated, but nonetheless fundamental phenomena associated with the dynamics, interactions, and deformation of bubbles. The importance of these phenomena has long been recognized, but has largely been neglected due to the difficulty of the associated mathematical problems. In this contribution, bubble shape oscillations in response to nonuniform flow fields and/or due to their interaction with other bubbles are considered using both a matched asymptotic expansions technique and a fully three-dimensional boundary integral method.

Results from both approaches in a few particular cases are compared, and the limits of application of these methods for these cases is assessed.

Nomenclature

r_{b0},	characteristic bubble size,
τ_{b0},	characteristic bubble time scale
L_0,	*outermost* characteristic flow length scale
τ_0,	characteristic flow time scale
l_0,	bubble/boundary distance scale
T_0,	interaction time scale,
ϵ,	ratio between r_{b0} and l_0
t,	time
ϕ,	bubble velocity potential in moving frame
ϕ_b,	bubble velocity potential $= \phi' - \phi_0$
ϕ',	total velocity potential
ϕ_0,	basic velocity potential
$\mathcal{G}$,	velocity gradient scale
$\mathcal{H}$,	velocity bigradient scale
R_i,	ith component of the bubble radius

Introduction

The presence and dynamics of bubbles and cavities in a flow field can have significant effects of relevance to engineering applications. These effects include erosion, noise generation, damping of acoustic signals, degradation of performance...etc [1, 2, 3, 4]. This has instigated a great interest in the study of the problem, and thousands of publications have been devoted to the study of cavity flows since the early work of Rayleigh [5] and Besant [6]. Due to the complexity of the general mathematical and physical problem, most approaches have, however, been limited to the study of spherical, isolated bubbles, or to elongated linearized two-dimensional cavities. More recently, with the advent of new mathematical and computational tools, increasing attention has been given to the study of more practical cavity configurations: namely nonspherical bubbles and bubble clouds. Nonspherical axisymmetric bubble dynamics, such as in the vicinity of a solid wall or a free surface were most particularly studied [7, 8, 9, 4]. All these studies were restricted to the simplified case where the bubble is in a quiescent fluid and where external forces, if any are potential, and act in a direction perpendicular to any nearby rigid or free boundary. Advantage was taken of the axisymmetry of the resulting problem. Deviations from these simplifying assumptions could significantly influence the results. In fact, in most practical cases bubbles are neither isolated, nor in a uniform flow or in a quiescent fluid. Common examples include cavitation bubbles near propeller blades, large cavity dynamics near complex geometries in a gravity field, dynamics of bubble clouds, and bubble dynamics in a shear or boundary layers.

The dynamics of bubble clouds have also recently received a lot of attention [10, 11, 12, 13], especially since they have been observed to produce dramatic deleterious effects, which cannot be explained with approaches based on single bubble dynamics.

All these studies but [9, 11], have considered only the contribution of the bubble volume change on the cloud dynamics, and have either neglected bubble fluid relative motion and bubble deformation, or restricted their approach to acoustic perturbations.

In a first approach, based on the method of matched asymptotic expansions, we consider these effects in the limiting configuration where the bubble size is small compared to inter-bubble distance (small void fraction), or where the bubble size is much smaller than some characteristic length scale of the surrounding flow.

These include problems of bubble dynamics in nonuniform flow fields (bubble dynamics in the flow field of a vortex or near a headform) and the inclusion of compressibility. In these cases, the small perturbation is chosen to express small but not negligible interactions.

This limitation is removed in a second parallel approach where a fully three dimensional numerical method is developed. This method has been tested for bubble dynamics in a quiescent fluid [14, 15], and has been recently used for the investigation of bubble dynamics in complex flow fields such as vortical, boundary and shear flows [16, 17].

In this contribution we will present first the model used for the bubble dynamics (Section 1). We will highlight effects taken into account and attempt to describe the limits of validity of the model. We will then describe in general terms the asymptotic approach used (Section 2). In Sections 3 to 5 bubble behavior in nonuniform flow fields, particularly the flow about a headform and in a vortex flow are described. In Section 6 the same method is used to describe the particular configurations of multibubble clouds with a particular note on the extension of the method to the case where the bubbly medium is slightly compressible. In the following sections the studies described above will be extended to very large deformations and interactions. The numerical method used will be described in Section 7 while Sections 8 will consider the particular cases of bubble behavior in a sheared flow field near a solid wall, in a vortex flow, and for a multibubble configuration. Finally some conclusions are drawn from the results.

1 Bubble Dynamics Model

We will consider mostly cavitation bubbles where relatively large bubble wall velocities are involved and where, as a result, viscosity has no appreciable effect on the growth and collapse of the bubbles. The study will also be restricted to the case where the flow velocities remain small compared to the speed of sound in water, and as a result, we can neglect or approximately account for compressibility effects. This is usually valid until the latest collapse phase. The above two assumptions, classical in cavitation bubble dynamics studies, result in a flow *due to bubble dynamics* that is potential (velocity potential, $\phi_b(\mathbf{x},t)$) so that $\mathbf{u}_b = \nabla\phi_b$, and which satisfies the Laplace equation,

$$\nabla^2\phi_b = 0. \tag{1}$$

In our numerical work this assumption is not imposed on the "basic flow," i.e. to the underlying flow existing in absence of the bubble, . In addition, compressibility of the liquid, or of the bubbly medium in the case of a bubble cloud, can be considered in an "ad-hoc" fashion through a delay time for the propagation of information between the source and a field point, as well as through a compressible model for the *spherical component* of the bubble oscillations. The solution must in addition satisfy boundary conditions at infinity, at the bubble walls and at the boundaries of any nearby bodies. At all moving or fixed surfaces (such as a bubble surface or a nearby boundary) an identity between fluid velocities normal to the boundary and the normal velocity of the boundary itself is to be satisfied. For instance, at the bubble-liquid interface, the normal velocity of the moving bubble wall must equal the normal velocity of the fluid, or,

$$\nabla\phi_\mathbf{b}\cdot\mathbf{n} = \mathbf{V_s}\cdot\mathbf{n}, \tag{2}$$

where $\mathbf{n}$ is the local unit vector normal to the bubble surface and $\mathbf{V_s}$ is the local velocity vector of the moving surface. This equation expresses the fact that the bubble surface, $\mathcal{B}(r,\theta,\phi,t)$, is a material surface of the liquid

$$\frac{D\mathcal{B}}{Dt} = 0. \tag{3}$$

The bubble is assumed to contain noncondensible gas as well as vapor of the surrounding liquid. The pressure within the bubble at any given time is considered to be the sum of the partial pressures of the noncondensible gases, P_g, and that of the vapor, P_v. Vaporization of the liquid is assumed to occur at a fast enough rate so that the vapor pressure remains constant throughout the simulation and equal to the equilibrium vapor pressure at the liquid ambient temperature. In contrast, since time scales associated with gas diffusion are much larger, the amount of noncondensible gas inside the bubbles is assumed to remain constant and the gas is assumed to satisfy the polytropic relation, $P_g\mathcal{V}^k = constant$, where $\mathcal{V}$ is the bubble volume and k the polytropic constant, with $k = 1$ for isothermal behavior and $k = c_p/c_v$ for adiabatic conditions. In previous studies the influence of heat transfer [18], and gas diffusion [19] on the dynamics of a bubble cloud was considered. We will neglect these effects in this presentation.

The pressure in the liquid at the bubble surface, P_L, is obtained at any time from the following pressure balance equation:

$$P_L = P_v + P_{g_0}\left(\frac{\mathcal{V}_0}{\mathcal{V}}\right)^k - \mathcal{C}\sigma, \tag{4}$$

where P_{g_0} and $\mathcal{V}_0$ are the initial gas pressure and volume respectively, σ is the surface tension, $\mathcal{C}$ the local curvature of the bubble, and $\mathcal{V}$ the instantaneous value

of the bubble volume. Here P_{g_0} and $\mathcal{V}_0$ are known quantities at $t = 0$. The curvature and the normal, n, to the surface $\mathcal{B}$ are given by:

$$\mathcal{C} = \nabla \cdot \mathbf{n} \qquad \mathbf{n} = \frac{\nabla \mathcal{B}}{|\nabla \mathcal{B}|}. \tag{5}$$

2 Asymptotic Theory for Bubble Flow Interactions

The asymptotic method that we have developed is centered on the following approach. Whether the problem considered is that of bubble interactions in a cloud or that of the interaction between bubbles and a nonuniform complex flow, the problem is addressed by a decomposition of both time and space domains into multiple scales. For instance, the dynamics of any bubble is obtained by considering an *inner* problem of scales r_{b0}, a characteristic bubble size, and τ_{b0}, a characteristic bubble time scale. The overall flow field, on the other hand is addressed by considering an *outermost* problem with scales L_0, a characteristic flow length scale, and T_0, a characteristic flow time scale. Using the same procedure, an intermediate *outer* problem is introduced with *outer* scales such as a characteristic length scale of interbubble distances or bubble/boundary distances, l_0, and an interaction time scale, τ_0. Finally, a *far-field* acoustic field scale can be introduced based on the length, $c\tau_{b_0}$, where c is the sound speed in the liquid.

An asymptotic analysis of the problem can be developed when these various scales are of different orders of magnitude. For instance, for bubble/bubble interactions in a cloud or for bubble/flow interactions near a boundary an asymptotic approach can be introduced when r_{b0} is much smaller than l_0, in which case one could use the ratio between r_{b0} and l_0 as the small perturbation parameter, ϵ.

$$\epsilon = \frac{r_{b0}}{l_0} \tag{6}$$

The *outer problem* is associated with the macroscopic behavior of the bubbles in a bubble cloud or in a complex flow geometry. A bubble then appears as a superposition of singularities of various orders. If more then one bubble is involved, the summation is to be carried out over all the bubbles. The *inner problem* obtained when the lengths are normalized by r_{b0}, provides the microscopic details of the behavior of the flow in the vicinity of an individual bubble center (B_i). The presence of the other bubbles or boundaries, all considered to be at infinity in the *inner problem*, is sensed only by means of the matching condition with the *outer problem*. The boundary conditions at infinity for the *inner problem* are therefore obtained at each order of approximation by the asymptotic behavior of the outer solution in the vicinity of B_i. Thus, if one knows the behavior of all bubbles except B_i, the motion, deformation and pressure field due to this cavity can be determined by solving linearized forms of the equations presented in the previous section. At the lowest order, $\epsilon = 0$, each bubble (of index i) behaves spherically as if in an infinite medium and the time dependence of its radius, $a_0^i(t)$, is given by the Rayleigh-Plesset equation if the medium compressibility is neglected, [20], or by the Keller-Herring equation [21, 24] for example if a slight compressibility of the medium is taken into account (see section 6).

The combination of all these first approximations of each *inner* problem provides a description of the whole first order flow field (i.e. a distribution of sources or sinks representing all bubble oscillations). The behavior of this *outer* flow field in the vicinity of each bubble sets the boundary conditions at infinity at the following order of approximation, ϵ, for the corresponding *inner* problem. The same process is then repeated for the successive orders.

At all orders solutions of the Laplace equation are expanded in general form as spherical harmonics and the bubble radius equation is expanded in surface harmonics:

$$\phi(r,\theta,\varphi,t) = \sum_{j=0}^{\infty} \sum_{m=-j}^{j} (A_{Ijm} r^j + \frac{B_{Ijm}}{r^{j+1}}) Y_{jm}(\theta,\varphi), \tag{7}$$

$$r = \mathcal{R}(\theta,\varphi,t) = \sum_{j=0}^{\infty} \sum_{m=-j}^{j} R_{Ijm}(t) Y_{jm}(\theta,\varphi), \tag{8}$$

In what follows, quantities indicated with a superscript $\tilde{}$ are inner variables, while those with a superscript $\bar{}$ refer to outer variables. The Y_{jm} are given by:

$$Y_{jm} = \begin{cases} P_j^m(\cos\theta)\ \cos m\varphi; & \text{for } m \geq 0 \\ P_j^{|m|}(\cos\theta)\ \sin |m|\varphi; & \text{for } m < 0 \end{cases} \tag{9}$$

Then all quantities, χ, particularly $\tilde{\phi}, \bar{\phi}, and \tilde{R}$, are expanded in powers of ε as follows:

$$\chi = \chi_0 + \varepsilon\chi_1(r,\theta,\varphi,t) + \varepsilon^2\chi_2(r,\theta,\varphi,t) + O(\varepsilon^3). \tag{10}$$

3 Bubble Behavior in a Nonuniform Flow Field

Let us consider a *basic* flow field (flow in absence of the bubble) that is potential and steady, with a velocity vector $\mathbf{V_0}$ deriving from the potential ϕ_0. Let the pressure be p_0 and the liquid density ρ. The velocity potential satisfies the Laplace equation and the Bernoulli equation:

$$\nabla^2\phi_0 = 0, \qquad \frac{1}{2}(\nabla\phi_0)^2 + \frac{p_0}{\rho} = \text{constant}. \tag{11}$$

Let ϕ' and p' be the potential, the speed and pressure in presence of the bubble. We now have similar equations as (11-12) with these complete flow variables. In addition, far away from the bubble, we have

$$\phi' = \phi_0,$$

and the continuity of the normal velocities at the bubble wall can be written:

$$\{\nabla\phi' \cdot \mathrm{n}\}_{r=\mathcal{R}} = \left\{\frac{\partial \mathcal{R}}{\partial t}\mathrm{e}'_r \cdot \mathrm{n}\right\}_{r=\mathcal{R}}, \tag{12}$$

We will consider now the *bubble potential*, ϕ_b, difference of the potentials ϕ' and ϕ_0.

$$\phi_b = \phi' - \phi_0. \tag{13}$$

Since at infinity V_b and ϕ_b decay to zero, and the pressure is p_0, the Bernoulli equation becomes:

$$\{\frac{\partial \phi_b}{\partial t} + \frac{1}{2}(\nabla\phi_b)^2 + \frac{1}{2}V_0^2 \;+\; \nabla\phi_b \cdot V_0 + \frac{p'}{\rho}\}_{r=\mathcal{R}} = \\ = \left\{\frac{1}{2}V_0^2 + \frac{p_0}{\rho}\right\}_{M=\infty}, \tag{14}$$

where we have limited ourselves to the case where the *basic* flow is steady. The right hand side of the equation is a constant of the *basic* flow field.

At this time we can transform the above equations to those in a coordinate system with origin o moving with a velocity *prescribed* $\mathbf{V}_M$, and decompose this velocity as

$$\mathbf{V}_M = \mathbf{V}_e x + \vec{\omega} \times \mathrm{oM}, \tag{15}$$

where $\mathbf{V}_e$ is the translation velocity of o, and $\vec{\omega}$ is the rotation velocity with respect to the fixed frame.

Making the transformation, the system of equations of the problem becomes, ϕ being the velocity potential of the *bubble flow* in the moving frame:

$$\Delta\phi = 0; \quad \lim_{\infty}\phi = 0; \quad \{\nabla\phi \cdot \mathrm{n}\}_{wall} = 0,$$

$$\left\{\nabla\phi \cdot \mathrm{n} = \frac{\partial R}{\partial t} + (\mathbf{V_e} - \mathbf{V_0}) + \vec{\omega} \times \mathrm{oM} \cdot \mathrm{n}\right\}_{r=\mathcal{R}},$$

$$\left\{\frac{\partial \phi}{\partial t} + \frac{1}{2}(\nabla\phi)^2 + (\mathbf{V}_0 - \mathbf{V}_e - \vec{\omega} \times \mathrm{oM}) \cdot \nabla\phi + \right.$$

$$\left. + \frac{1}{2}(V_0^2 - V_e^2) + \frac{p}{\rho}\right\}_{r=R} = \frac{p_0(\mathrm{o})}{\rho}. \tag{16}$$

The pressure at the bubble wall and the pressure inside the bubble are related through Equation (4).

Nondimensionalizations

All equations can be normalized using the following scales. In the *outer* problem:

r	$= l_0\,\bar{r}$	l_0 : the initial bubble wall distance
ϕ	$= \phi_{ext}\,\bar{\phi}$	ϕ_{ext} : outer velocity potential scale

In the *inner* problem:

R	$= r_0\,\tilde{R}$	r_0 : the initial bubble radius
p	$= \Delta p\,\tilde{p}$	Δp : pressure change scale
t	$= T_0\,\tilde{t}$	T_0 : characteristic collapse time
ϕ	$= r_0^2\tilde{\phi}/T_0$	r_0^2/T_0 : inner velocity potential scale
V_0	$= v_0\tilde{V}_0$	v_0 : basic flow velocity scale
∇V_0	$= \mathcal{G}\,\tilde{\nabla}V_0$	$\mathcal{G}$: basic velocity gradient scale

The matching conditions between the *inner* and the *outer* solutions is obtained by formally writing that there exists an intermediate region characterized by r^*, $r_0 \ll r^* \ll l_0$ where both solutions are valid. This leads to:

$$\frac{r_0^2}{T_0}\,\tilde{\phi}(\frac{r}{r_0}) = \phi_{ext}\,\bar{\phi}(\frac{r}{l_0}). \tag{17}$$

Taylor series expansions of the basic velocity

Since we are considering the case where the size of the *inner* region is small compared to the characteristic length of the *basic* flow, we can express the velocity field in the *inner* region as a Taylor series expansion about the moving origin o.

$$\mathbf{V}_0(\tilde{\mathrm{r}}) = \mathbf{V}_0|_{\mathrm{o}} + \tilde{\mathrm{r}} \cdot \tilde{\nabla}\mathbf{V}_0\Big|_{\mathrm{o}} + \frac{1}{2}\tilde{\mathrm{r}} \cdot \tilde{\nabla}\tilde{\nabla}\mathbf{V}_0\Big|_{\mathrm{o}} \cdot \tilde{\mathrm{r}} + O(\epsilon^3)$$

In order to compute the various terms in Equation (16) we need the following quantities:

$$\mathbf{V}_0(\mathrm{r}) - \mathbf{V}_e \;=\; \mathcal{G}\,r_0\,\tilde{\mathrm{r}} \cdot \tilde{\nabla}\mathbf{V}_0(\mathrm{o}) + \\ \frac{1}{2}r_0^2\,\mathcal{H}\,\tilde{\mathrm{r}} \cdot \tilde{\nabla}\tilde{\nabla}\mathbf{V}_0(\mathrm{o}) \cdot \tilde{\mathrm{r}} + \cdots \tag{18}$$

$$(\mathbf{V}_0(\mathrm{r}) - \mathbf{V}_e) \cdot \tilde{\nabla}\phi \;=\; \frac{r_0^2}{T_0^2}\,\tilde{\nabla}\tilde{\phi} \cdot (\mathcal{G}T_0\tilde{\mathrm{r}} \cdot \tilde{\nabla}\mathbf{V}_0(\mathrm{o}) + \\ \frac{1}{2}\,\mathcal{H}T_0^2 r_0\,\tilde{\mathrm{r}} \cdot \tilde{\nabla}\tilde{\nabla}\mathbf{V}_0(\mathrm{o}) \cdot \tilde{\mathrm{r}} + \cdots$$

$$\frac{1}{2}(\mathbf{V}_0^2(\mathrm{r}) - \mathbf{V}_e^2) \;=\; \frac{r_0^2}{T_0^2}(\mathcal{G}\,T_0^2\frac{v_0}{r_0}\,\tilde{\mathrm{r}} \cdot \tilde{\nabla}V_0(\mathrm{o}) \cdot \mathbf{V_0}(\mathrm{o}) + \\ \tfrac{1}{2}\;\; T_0^2 v_0\,\mathcal{H}\,\tilde{\mathrm{r}} \cdot \tilde{\nabla}\tilde{\nabla}\mathbf{V}_0(\mathrm{o}) \cdot \tilde{\mathrm{r}} \cdot \mathbf{V_0}(\mathrm{o}) + \\ \tfrac{1}{2}\;\; \left(\mathcal{G}\,T_0\,\tilde{\mathrm{r}} \cdot \tilde{\nabla}\mathbf{V}_0(\mathrm{o})\right)^2 + \cdots \tag{19}$$

where v_0 is the characteristic velocity of the flow field, $\mathcal{G}$ the characteristic dimension of the velocity gradient and $\mathcal{H}$ the characteristic dimension of the velocity bigradient.

4 Problems with a Plane of Symmetry

We now consider the problem of a bubble in a flow in the case where there is a plane of symmetry. This assumption is not fundamental and has been made to simplify the analysis. The general theory is first developed, and is then applied to the problem of a bubble collapsing near a semi-infinite bluff axisymmetric body in a uniform flow field.

Problem formulation

We will choose a coordinate system $Oxyz$ fixed to a streamline, $\mathbf{V_e} = \mathbf{V_0}(\mathrm{o}(t))$, so that the x-axis is parallel to $V_0(\mathrm{o})$; $\tilde{\mathbf{V}}_0 = v_x(t)\mathrm{e}_x$. If we consider the case where

the problem is symmetrical about the (Oxz) plane then

$$\tilde{\nabla}\mathbf{V}_0(\mathbf{o}) = \begin{bmatrix} \alpha_1 & 0 & \alpha_2 \\ 0 & 0 & 0 \\ \alpha_2 & 0 & -\alpha_1 \end{bmatrix}_{\mathbf{e_x},\mathbf{e_y},\mathbf{e_z}} \tag{20}$$

As a result $\tilde{\mathbf{r}}\cdot\nabla\mathbf{V}_0(\mathbf{o})$ and $\tilde{\mathbf{r}}\cdot\nabla\nabla\mathbf{V}_0(\mathbf{o})\cdot\tilde{\mathbf{r}}$ can be written:

$$\tilde{\nabla}\mathbf{V}_0(\mathbf{o})\cdot\begin{bmatrix} x \\ y \\ z \end{bmatrix}_{\mathbf{e_x},\mathbf{e_y},\mathbf{e_z}} = \begin{bmatrix} \alpha_1 x + \alpha_2 z \\ 0 \\ -\alpha_1 z + \alpha_2 x \end{bmatrix}_{e_x,e_y,e_z} = r\begin{bmatrix} G_r(\theta,\psi) \\ G_\theta(\theta,\psi) \\ G_\psi(\theta,\psi) \end{bmatrix}_{e_r,e_\theta,e_\psi}$$

$$\begin{bmatrix} x \\ y \\ z \end{bmatrix}_{e_x,e_y,e_z} \cdot\nabla\nabla\vec{V}_0(O)\begin{bmatrix} x \\ y \\ z \end{bmatrix}_{e_x,e_y,e_z} = \begin{bmatrix} \gamma_1 z^2 + 2\gamma_3 xz \\ 0 \\ \gamma_4 x^2 + 2\gamma_3 xz \end{bmatrix}_{e_x,e_y,e_z} = r^2\begin{bmatrix} H_r \\ H_\theta \\ H_\psi \end{bmatrix}_{e_r,e_\theta,e_\psi}$$

where we have transformed the quantities from cartesian coordinates (x,y,z) to spherical coordinates (r,θ,ψ) with the polar axis along the z axis. In the above equations:

$$\gamma_1 = \frac{\partial\alpha_2}{\partial z}, \quad \gamma_2 = \frac{\partial\alpha_2}{\partial x}, \quad \gamma_3 = \frac{\partial\alpha_1}{\partial z}, \quad \gamma_4 = \frac{\partial\alpha_1}{\partial x}. \tag{21}$$

Since the problem has a plane of symmetry, we shall take $\vec{\omega} = \omega(t)\mathbf{e}_Y$,

$$\vec{\omega}\times\mathbf{oM} = \omega\, r\,(\mathbf{e}_Y\times\mathbf{e}_r). \tag{22}$$

We nondimensionalize ω as $\omega = \Omega\tilde{\omega}$, where Ω is the characteristic rotation speed of the frame.

Domain of validity of the asymptotic solution

The choice of the relative sizes of the six nondimensional parameters of the problem to consider was determined first by application of the least degeneracy principle. This was then relaxed in order to obtain solutions in some practical physical configurations. The analytical and numerical solutions presented below are based on the following sizes of these parameters relative to ε.

1. The characteristic length of the *inner* problem is smaller than that of the *outer* problem, $r_0/l_0 << 1$.

2. The characteristic velocity of the initial flow, v_0, is of same order as the characteristic collapse velocity, $v_0 = O(r_0/T_0)$.

3. The characteristic basic velocity gradient is of the order of ε in the *inner* problem: $\mathcal{G}T_0 = O(\varepsilon)$.

4. The characteristic velocity bigradient at the scale of the *inner* problem is far smaller than that of the *inner* problem: $\mathcal{H}T_0 r_0 = O(\varepsilon^2)$.

5. The characteristic rotation speed at the scale of the *inner* problem is smaller than the collapse velocity: $\Omega T_0 = O(\varepsilon)$.

6. The collapse velocity is directly related to the local pressure by $\rho v_{collapse}^2/\Delta p = O(1)$.

The bubble is considered to be close enough to the submerged body so that at leading order, ε^0, in the *outer* problem, the body appears as an infinite flat wall. At subsequent orders, the curvature is taken into account. This means that the ratio of the bubble standoff distance to the local radius of curvature of the body is of order ε. In the *inner* problem, the effect of the wall is seen first at order ε for the potential and at order ε^2 for the bubble radius. The effect of the curvature only intervenes at order ε^2 on the potential and only adds a constant to the equations.

Order ϵ^0

The system of equations described above reduces at order ϵ^0 in the *inner problem* to that of an oscillating spherical bubble:

$$\tilde{\phi}_0 = q/\tilde{r} \quad \text{with} \quad q = -\tilde{R}_0{}^2\dot{\tilde{R}}_0, \tag{23}$$

where $\tilde{R}_0$ is determined by the Rayleigh-Plesset equation

$$\tilde{R}_0\ddot{\tilde{R}}_0 + \frac{3}{2}\dot{\tilde{R}}_0^2 = \mathcal{P}\left(\tilde{R}_0{}^{-3K} - 1\right) - 2\mathcal{W}^{-1}\left(\frac{1}{\tilde{R}_0} - \tilde{R}_0{}^{-3K}\right) - \Delta\tilde{p}, \tag{24}$$

where $\mathcal{W} = \Delta P R_0/\sigma$ and $\mathcal{P} = (p_\infty - p_v)/\Delta P$, with the initial conditions: $\tilde{R}_0 = 1$ and $\dot{\tilde{R}}_0 = 0$. In the *outer problem* the general solution (7) reduces to

$$\tilde{\phi}_0 = B_0(\tilde{t})\,P_0(\cos\theta)\,(\frac{1}{\tilde{r}^{n+1}} + \frac{1}{\tilde{r}'^{n+1}}) \tag{25}$$

The matching condition between the two problems can be written

$$\frac{r_0^2}{T_0}\left[\tilde{\phi}_0(\tilde{r}) + \varepsilon\tilde{\phi}_I(\tilde{r}) + \varepsilon^2\tilde{\phi}_{II}(\tilde{r}) + O(\varepsilon^3)\right] = \phi_{ext}\left[\bar{\phi}_0(\bar{r}) + \varepsilon\bar{\phi}_I(\bar{r}) + \varepsilon^2\bar{\phi}_{II}(\bar{r}) + O(\varepsilon^3)\right] \tag{26}$$

which leads to:

$$\phi_{ext} = \varepsilon\frac{r_0^2}{T_0}; \quad B_0(\tilde{t}) = q(\tilde{t}); \quad \lim_{\tilde{r}\to\infty}\tilde{\phi}_I = \frac{q}{2} \tag{27}$$

Order ε

After accounting for the solution at $O(\varepsilon^0)$ the equations of the problem at $O(\varepsilon)$ become:

$$\Delta\tilde{\phi}_1 = 0; \qquad \lim_{\tilde{r}\to\infty}\tilde{\phi}_1 = \frac{q}{2}$$

$$\left\{\frac{\partial\tilde{\phi}_1}{\partial\tilde{r}} + \tilde{\phi}_1\frac{\partial^2\tilde{\phi}_0}{\partial\tilde{r}^2}\right\}_{\tilde{r}=\tilde{R}_O} = \frac{\partial\tilde{\phi}_1}{\partial\tilde{r}} - G_r\tilde{R}_O$$

$$\left\{ \frac{\partial \phi_1}{\partial \tilde{t}} + \phi_1 \frac{\partial^2 \tilde{\phi}_0}{\partial \tilde{t} \partial \tilde{r}} + \frac{\partial \phi_1}{\partial \tilde{r}} \frac{\partial \tilde{\phi}_0}{\partial \tilde{r}} + \phi_1 \frac{\partial \tilde{\phi}_0}{\partial \tilde{r}} \frac{\partial^2 \tilde{\phi}_0}{\partial \tilde{r}^2} + \right. \quad (28)$$

$$\left. \tilde{R}_O G_r \frac{\partial \tilde{\phi}_0}{\partial \tilde{r}} + \mu v_x(t) \tilde{R}_0 F(\theta, \psi) \right\}_{\tilde{r}=\tilde{R}_O} = 3K\mathcal{P}\phi_1 \tilde{R}_O^{-3K-1}$$

where

$$\begin{aligned} G_r &= 2\alpha_2 \cos\theta \sin\theta \cos\psi + \alpha_1(\sin^2\theta \cos^2\psi - \cos^2\theta) \\ F &= \alpha_1 \sin\theta \cos\psi + \alpha_2 \cos\theta \end{aligned} \quad (29)$$

Resolution of the order ε

Using the general solution of the Laplace equation, the limit condition at infinity on ϕ_1 leads us to take:

$$A_{1jm} = \delta_{j,0}\, q/2, \quad (30)$$

Since the problem is symmetrical about the (Oxz) plane, there are no terms in $\sin\psi$,and we do not have to consider $m < 0$. Equation (16) becomes:

$$\begin{aligned} -\frac{j+1}{\tilde{R}_O^{j+2}} B_{1jm} Y_{jm} &+ \frac{2q}{\tilde{R}_O^3} R_{1jm} Y_{jm} = \dot{R}_{1jm} Y_{jm} + \\ &- \frac{2}{3}\tilde{R}_O \alpha_2 Y_{21} + \alpha_1 \tilde{R}_O (Y_{20} - \frac{Y_{22}}{6}), \\ \frac{\dot{q}}{2} + \frac{\dot{B}_{1jm}}{\tilde{R}_O^{j+1}} Y_{jm} &- \frac{\dot{q}}{\tilde{R}_O^2} R_{1jm} Y_{jm} + q \frac{j+1}{\tilde{R}_O^{j+4}} B_{1jm} Y_{jm} + \\ &- 2\frac{q^2}{\tilde{R}_O^5} R_{1jm} Y_{jm} - \frac{2}{3\tilde{R}_O} q \alpha_2 Y_{21} + \\ -\frac{q}{\tilde{R}_O}\alpha_1(\frac{Y_{22}}{6} - Y_{20}) &+ \mu \tilde{R}_0 v_x(\alpha_1 Y_{11} + \alpha_2 Y_{10}) \\ &= \dot{R}_{100} Y_{00} 3K\mathcal{P}\tilde{R}_0^{-3K-1} \end{aligned} \quad (31)$$

For $j > 2$ we have a homogeneous linear differential system where the initial conditions are zero. The solution is therefore $R_{1jm} = B_{1jm} = 0;\ \forall j > 2$.

The equations for the non-zero terms at order ϵ as well as all equations obtained at order ϵ^2 can be found in Reference [22]. At order ϵ the bubble behavior is modified by both the presence of the wall, which at this order only appears as a flat plate, and the presence of a pressure gradient. At the following order ϵ^2 the curvature of the wall comes into play as well as the velocity bigradient.

Application to Bubble Dynamics near a Headform

We consider now the dynamics of a bubble near a semi-infinite bluff body. The velocity potential considered is that due to a superposition of a uniform flow and a source of intensity Q located at the origin:

$$\phi_0 = V_\infty x + \frac{Q}{r} \quad (32)$$

This simulates the flow field about a Rankine body of radius, $R = \sqrt{\frac{Q}{\pi V_\infty}}$ and stagnation point at $X = -R/2$.

At order ε^0, the outside pressure $\Delta p(t)$ is taken to be the pressure in the fluid in absence of the bubble along the trajectory of a fluid particle. At higher orders of ε, the gradient and bigradient are also taken into account while following a fluid particle.

A fourth order Runge-Kutta procedure is used to solve the ordinary differential equations presented earlier. To illustrate the method, a Rankine body with a radius of 10 centimeters with flow at infinity advancing at a velocity of 1.15 m/s was selected. Figures 1 through 4 show some results obtained on bubble behavior near the Rankine body. Figures 1a through 1c show a case where the interaction between the bubble and the flow field is significant. The initial bubble radius is $r_0 = 1$ cm. and its distance, l_0, from the wall is such that $\varepsilon = r_0/l_0$ is equal to 0.3.

Figure 1b shows the trajectory of the bubble center along the body, and Figure 1c shows the pressure and velocity variations with time. In the initial phase $t < 2.0$ the bubble sees a pressure drop. Later, the pressure rises back towards the ambient pressure. This velocity is also that chosen for translating the origin of coordinates in which the bubble shape is prescribed. Figure 1a shows, overlaid on each other, the bubble contours at different times (from $t = 0.1T_0$ to $2T_0$ during the bubble growth and collapse. The orientation of the bubble relative to the body is the same as illustrated in Figure 1b which shows bubble positions versus time. It is apparent from the contour plots that the bubble moves toward the body wall during its collapse. Due to the velocity and pressure gradient around the body the bubble elongates and in fact rotates around its center of mass. Initially, the side of the bubble surface facing an intermediary direction between the downstream direction and the wall direction flattens out. A reentrant jet is then produced perpendicular to that face. The direction of the jet appears to change with time in a fashion indicating increased influence of the presence of the wall. The computations shown in the figure stopped when the bubble wall touched the origin of coordinates. This moment will be delayed in future computations by selecting an adequate translation of the origin of coordinates that is perpendicular to the wall.

Figure 2 shows the influence of the distance of the bubble to the wall, or ε, on its shape history. Bubble collapse contours are shown for $\varepsilon = 0.15, 0.3$ and 0.6. As expected, deviation from sphericity increases with the proximity to the wall. Due to stronger shearing action closer to the body approaching the wall has the effect of increasing bubble stretching and elongation during its growth, then reinforcing the reentrant jet formation during the collapse. For $\varepsilon = 0.3$ and $\varepsilon = 0.6$ the computation stopped when the bubble surface touched the origin of coordinates. However, due to the weak nature of the interaction for $\varepsilon = 0.15$ the collapse is completed with no reentrant jet and is followed by a bubble re-

bound or second growth that is not shown on the figure.

Also, as expected, a similar effect as in figure 2 is obtained if the distance to the body is maintained constant while the bubble size is changed. Figure 3 shows such a case, where the distance between the bubble center and the wall is maintained at 3.333 cm, while the bubble size is varied from 0.5 cm ($\varepsilon = 0.15$), to 1 cm ($\varepsilon = 0.3$), to 2 cm ($\varepsilon = 0.6$). Here too the jet is seen to rotate to become closer and closer to perpendicular to the wall.

5 Bubble/Vortex Interaction

One of the most fundamental phenomena observed in flow cavitation is the capture of bubbles/nuclei by vortices. The problem of the interaction of a single gas bubble and a Rankine line vortex is amenable to treatment via analytical techniques. Here we also apply to this problem the method of matched asymptotic expansions described above. To do so we assume that the length scale characteristic of the bubble, r_{bo} is small compared to the initial distance from the bubble to the vortex, d.

The analytical results have been tested for a plausible set of parameters, and yield physically reasonable solutions. The solution shows that the bubbles are attracted towards the vortex center, and that a jet appears on the side of the bubble opposite to the flow direction. Further investigation of the parameter space and computation of higher order corrections are currently underway.

Problem formulation

Consider a spherical bubble initially at rest in an incompressible, inviscid liquid at a distance d from a line vortex of strength Γ. The pressure at infinity is p_∞ and the velocity due to the vortex alone (i.e. excluding any bubble effects) is$\mathbf{V_0}$. To perform the calculations we consider, as in the previous section, two coordinate frames. The first is a *fixed frame* which is convenient for describing the overall flow, one axis of which coincides with the vortex axis. The second is a *moving frame* which has its origin initially at the center of the bubble and moves at the liquid velocity in the absence of the bubble. We denote the location of the moving origin by o.

With the same assumptions as in the previous section the equations of the problem, both for the flow and the boundary conditions on the bubble are the ones presented in Section 1. Since we are interested in the modification in the flow caused by the presence of the bubble, it is convenient to introduce as in Section 3 the *reduced* or *bubble potential* ϕ_b, defined by

$$\phi_b = \phi' - \frac{\Gamma}{2\pi}\beta = \phi' - \phi_v, \tag{33}$$

where ϕ_v is the velocity potential due to the isolated vortex and β is the angular cylindrical coordinate in the fixed frame. The quantity ϕ_b represents the change to the potential of the flow because of the presence of the bubble. Because of linearity, the function ϕ_b also satisfies Laplace's equation and conditions described in Section 3.

We now consider the moving system of coordinates. The coordinates are initially coincident with the bubble center, and move with the flow at that location in the absence of the bubble while the Cartesian axes remain parallel to those in the fixed frame. Let ϕ denote the *bubble velocity potential* in the moving frame.

$$\phi_b(\mathbf{x}, t) = \phi_b(\mathbf{x}' + \mathbf{o}, t) = \phi(\mathbf{x}', t) \tag{34}$$

where $\mathbf{x}'$ is $\mathbf{x}$ referred to the moving frame. The velocity $\mathbf{V}$ is expressed in the moving frame as

$$\mathbf{V} = \frac{\Gamma}{2\pi l}\mathbf{e}_{z'} \times \mathbf{e}_l, \tag{35}$$

where $\mathbf{e}_l$ is a unit vector along the shortest line joining the point at which the velocity is to be measured and the z axis of the fixed system, and l the length of this line. The velocity of the moving coordinate system is then:

$$\mathbf{V}_O = \frac{\Gamma}{2\pi d}\left[-\sin\omega t\ \mathbf{e}_{1'} + \cos\omega t\ \mathbf{e}_{2'}\right], \tag{36}$$

By maintaining the moving cartesian axis parallel to the fixed frame axis we obtain the same equations for ϕ as in Section 3, with $\omega \equiv 0$.

Dimensional Analysis

As in the previous section the flow is assumed to be divided into two regions, an external region where the effects of the vortex dominate, while the region close to the bubble is dominated by its dynamics. The length scale characteristic of the bubble region is r_{bo}, the initial bubble radius, while the *outer problem* has as scale d. We will consider the case where $\epsilon = r_{bo}/d$ is small. The physical quantities entering the problem are p_{g0} and r_{bo} (from the bubble), and p_∞, Γ, and ρ_l from the liquid.

The matching between the *inner* and *outer* problem and the application of the principle of least degeneracy leads to the condition that the scaling for the velocity $\mathbf{V}$ be such that it is of the same order as the bubble deformation velocity

$$|\mathbf{V}| \sim \frac{\Gamma}{2\pi d} \sim \frac{r_{bo}}{T_0}. \tag{37}$$

The nondimensional velocity is then defined by

$$\mathbf{V} = \Omega\tilde{\mathbf{V}}\frac{r_{bo}}{T_0} \text{ with } \Omega = \frac{\Gamma/2\pi d}{\sqrt{p_\infty/\rho}}. \tag{38}$$

This imposes the following restriction on the gradient of the vortex velocity field

$$(\mathbf{V}|_{\mathcal{R}} - \mathbf{V}_O) \sim r_{bo}|\nabla\mathbf{V}| \sim \varepsilon\frac{r_{bo}}{T_0}. \tag{39}$$

We will denote

$$\mathbf{V} - \mathbf{V}_O = \varepsilon\frac{r_{bo}}{T_0}\Omega\tilde{\mathbf{V}}_d, \tag{40}$$

An important quantity is the rotation frequency of a particle around the vortex line. This is given by

$$\omega = \frac{\Gamma}{2\pi d^2}. \tag{41}$$

The ratio of this frequency and the Rayleigh frequency is seen to be

$$\omega T_0 = \frac{r_{bo}}{d}\frac{\Gamma/2\pi d}{\sqrt{p_\infty/\rho_l}} \sim O(\varepsilon). \tag{42}$$

Asymptotic expansions

After expanding the equations of the problem described earlier as indicated in Section 2 these are solved up to and including terms of $O(\varepsilon)$. As in the previous section problem upon introducing the expansions, the leading order problem ϵ^0 reduces to the spherical oscillating bubble problem. This problem has solution

$$\phi_0 = q_0/r = -R_0^2\dot{R}_0/r, \tag{43}$$

which yields the following Rayleigh-Plesset equation for R_0

$$R_0\ddot{R}_0 + \frac{3}{2}\dot{R}_0{}^2 = \mathcal{P}_g R_0^{-3k} - \frac{2\mathcal{W}^{-1}}{R_0} + \left(\mathcal{P}_v + \Omega^2 - 1\right), \tag{44}$$

where

$$\mathcal{P}_g = \frac{p_{g0}}{p_\infty}; \qquad \mathcal{P}_v = \frac{p_v}{p_\infty}, \tag{45}$$

Order ε^1

The equations at $O(\varepsilon)$ are

$$\nabla^2\phi_1 = 0 \tag{46}$$

subject to

$$\frac{\partial\phi_1}{\partial r} - 2\frac{\dot{R}_0}{R_0}R_1\Big|_{r=R_0} = \frac{\partial R_1}{\partial t} + \Omega\mathbf{V}_d\cdot\mathbf{e}_r, \tag{47}$$

and

$$\frac{\partial\phi_1}{\partial t} + \dot{R}_0\frac{\partial\phi_1}{\partial r} + R_1\left(2\frac{\dot{R}_0{}^2}{R_0} + \ddot{R}_0\right) + +51$$
$$+\dot{R}_0\Omega\mathbf{V}_d\cdot\mathbf{e}_r + \mathbf{V}_0\cdot\mathbf{V}_1\Big|_{r=R_0} = 3k\mathcal{P}_g\frac{r_{100}}{R_0^{3k+1}} +$$
$$-\frac{2\mathcal{W}}{R_0}\sum_{l=1}^{\infty}\sum_{m=-l}^{l}\frac{r_{1lm}}{R_0}\left(1 - \frac{(l-1)(l+2)}{2}\right) \tag{48}$$

Introducing the expansion for the function R_1 and ϕ_1 similar to that in Section 2, with the difference that the $Y_{lm}(\theta,\varphi)$ are defined here as

$$Y_l^m(\theta,\varphi) = \sqrt{\frac{(n-|m|)!}{(n+|m|)!}}P_n^{|m|}(\cos\theta)\exp(im\varphi).$$

the dynamic boundary condition becomes:

$$\frac{R_0}{l+1}\left\{\ddot{r}_{1lm} + 2\left(\frac{\dot{R}_0}{R_0}\dot{r}_{1lm} - \left(\frac{\dot{R}_0}{R_0}\right)^2 r_{1lm} + \frac{\ddot{R}_0}{R_0}r_{1lm}\right) +\right.$$
$$\left.+\Omega(\dot{A}\delta_{l2}^{m2} + \dot{A}^*\delta_{l2}^{m,-2})\right\} + \frac{\dot{R}_0}{l+1}\left(\dot{r}_{1lm} + 2\frac{\dot{R}_0}{R_0}r_{1lm} +\right.$$
$$\left.+\Omega(A\delta_{l2}^{m2} + A^*\delta_{l2}^{m,-2})\right) - \left(2\frac{\dot{R}_0^2}{R_0} + \ddot{R}_0\right)r_{1lm} =$$
$$-3k\mathcal{P}_g\frac{r_{100}\delta_{l0}^{m0}}{R_0^{3k+1}} + \frac{2\mathcal{W}}{R_0}\frac{r_{1lm}}{R_0}\left(1 - \frac{(l-1)(l+1)}{2}\right) +$$
$$+\Omega(A\delta_{l2}^{m2} + A^*\delta_{l2}^{m,-2}) + \Omega^2(R_{0l}\delta_{l1}^{m1} + R_{0l}^*\delta_{l1}^{m,-1}),$$

where

$$\alpha = \frac{-R_0}{\sqrt{2}}(\cos\omega t - i\sin\omega t). \tag{49}$$

Examination of the above equation reveals that, except for $(l,m) = (2,2)$, $(2,-2)$, $(1,1)$, and $(1,-1)$ the equations are homogeneous second order linear differential equations (initial value problems). Since we have assumed the bubble starts from a spherical shape, and is initially at rest, the solutions to these equations will vanish identically. For the four non-trivial cases, the differential equation satisfied by the particular radial component may be written as follows:

$$R_0\ddot{R}_{111} + 3\dot{R}_0\dot{R}_{111} - 4\frac{\dot{R}_0^2}{R_0}R_{111} =$$
$$4\frac{\mathcal{W}R_{111}}{R_0^2} - 2\sqrt{2}\Omega^2 R_0\cos\omega t; \tag{50}$$

$$R_0\ddot{R}_{11,-1} + 3\dot{R}_0\dot{R}_{11,-1} - 4\frac{\dot{R}_0^2}{R_0}R_{11,-1} =$$
$$4\frac{\mathcal{W}R_{11,-1}}{R_0^2} + 2\sqrt{2}\Omega^2 R_0\sin\omega t; \tag{51}$$

$$\frac{R_0}{3}\ddot{R}_{122} + \dot{R}_0\dot{R}_{122} - \left(2\frac{\dot{R}_0^2}{R_0} + \frac{1}{3}\ddot{R}_0\right)R_{122} =$$
$$-\frac{\mathcal{W}R_{122}}{R_0^2} + 2\sqrt{\frac{2}{3}}\Omega\left(\frac{R_0\dot{R}_0}{3}\sin 2\omega t - \frac{2\omega R_0^2}{3}\cos 2\omega t\right); \tag{52}$$

$$\frac{R_0}{3}\ddot{R}_{12,-2} + \dot{R}_0\dot{R}_{12,-2} - \left(2\frac{\dot{R}_0^2}{R_0} + \frac{1}{3}\ddot{R}_0\right)R_{12,-2} =$$
$$-\frac{\mathcal{W}R_{12,-2}}{R_0^2} + 2\sqrt{\frac{2}{3}}\Omega\left(\frac{R_0\dot{R}_0}{3}\cos 2\omega t + \frac{2\omega R_0^2}{3}\sin 2\omega t\right), \tag{53}$$

where

$$R_{111} = r_{111} + r_{11,-1} \qquad R_{11,-1} = \frac{r_{111} - r_{11,-1}}{i},$$
$$R_{122} = r_{122} + r_{12,-2} \qquad R_{12,-2} = \frac{r_{122} - r_{12,-2}}{i}, \tag{54}$$

In terms of these new coefficients the surface of the bubble (in the moving coordinate system) is given by

$$r = R_0 + \varepsilon\left[(R_{111}\cos\varphi - R_{11,-1}\sin\varphi)\sin\theta +\right.$$
$$\left.(R_{122}\cos 2\varphi - R_{12,-2}\sin 2\varphi)\sin^2\theta\right] + O(\varepsilon^2). \tag{55}$$

Results and Conclusions

We present here some results from a numerical study using the above equations. The equations involve 4 parameters – $\mathcal{P}_g, \mathcal{P}_v, \Omega, \mathcal{W}$ and the perturbation parameter ε. In the following we have not attempted to map the parameter space of the above equations, but rather demonstrate the characteristics of their solutions for a particular choice of the parameters and show that they make physical sense. We choose the following for the physical parameters: $P_\infty = 1.03 \times 10^5 Pa$, $R_0 = 10^{-3} m$, $d = 5 \times 10^{-2} m$, $\Gamma = 1.2 m^2/s$, $P_v = 2 \times 10^3 Pa$, $\sigma = 7 \times 10^{-2} N/m$, $P_{g0} = 3 \times 10^4 Pa$, $\rho = 10^3 kg/m^3$, $k = 1.4$.

This yields the following for the non-dimensional parameters: $\mathcal{P}_g = 2.9126 \times 10^{-1}$, $\mathcal{P}_v = 1.94174 \times 10^{-2}$, $\mathcal{W}^{-1} = 6.7961158 \times 10^{-4}$, $\Omega = 3.764 \times 10^{-1}$, $T_0 = 9.85 \times 10^{-5}$, $\varepsilon = 0.05\omega = 7.53 \times 10^{-3}$.

The equation systems at $O(1)$ and $O(\varepsilon)$ are integrated using a simple fourth-order accurate Runge-Kutta scheme. The results from this trial run are shown in Figures 4-6. The results indicate that the expression for the bubble becomes multivalued for times after $4.6T_0$, i.e. the origin of the local coordinates lies outside the bubble after this time. Thus results of the integration up to this time are shown. Figure 4 shows a cross-sectional view of the bubble in the x, y plane at various times. The bubble motion and deformation, and the formation of the jet are clearly seen. The bubble initially collapses almost spherically (while moving with the vortex flow), and reaches a minimum at approximately $1.55T_0$, and grows till it reaches a maximum size at $2.9T_0$. It subsequently collapses and shows the formation of a jet on the side opposite to its direction of motion, and directed towards the vortex axis. The computations are stopped at $4.6T_0$ when the bubble no longer contains the origin of coordinates. Figure 5 shows the trajectory of the $\varphi = 0$ and $\varphi = \pi$ points in this cross-section. Finally Figure 6 shows cross-sectional views of the bubble at the same times, but in a normal plane. This plane contains the z axis and the line connecting the moving coordinate origin and the vortex. The fact that the jet is directed towards the vortex axis becomes apparent in this view.

Quite obviously a more systematic study of the parameter space is required. Also, as in Reference [28] the results of the asymptotic analysis and of the 3D boundary element program **3DynaFS** must be compared. Qualitatively the same types of results are observed. The expression used for the motion of the moving coordinate system must be refined to prevent bubble function becoming multi-valued so early in the collapse. These and related aspects are items of current research.

6 Bubble Cloud Study

Consider a cloud of N bubbles of radius r_b^i, $i = 1, \cdots, N$ immersed in a liquid. The bubbles are initially assumed to be at rest and at equilibrium with the surrounding fluid. The characteristic radius of the bubbles is r_{b0}. We denote the distance between bubbles i and j as l_{ij}, which we take to be of the order of the characteristic distance l_0. We define as before ϵ as r_{b0}/l_0.

The matched asymptotic expansions method described in the previous sections was implemented earlier in [11, 25] to study the behavior of such a bubble cloud. Here we will only sketch an outline of the model. We assume that the characteristic geometric scale of the cloud (l_0), is small compared to the outside driving pressure field scale (L_0), but is much larger than the typical bubble radius r_{b0}. Therefore, to first approximation, the same driving pressure is assumed to be felt at the same time by all bubbles in the cloud. Variations of this pressure due to the position of each bubble are only seen at the higher orders. In a more general case, the pressure felt by each bubble is dependent on the bubble location and on the modification of the outside flow field by the presence of the bubble cloud. We are presently implementing such an approach which accounts for the compressibility of the two-phase bubbly medium.

Since ϵ is the ratio r_{b0}/l_0, it is directly related to the void fraction here assumed to be low. At the lowest order, $\epsilon = 0$, each bubble (of index i) behaves spherically as if in an infinite medium and the time dependence of its radius, $a_0^i(t)$, is given by the Rayleigh Plesset equation, [20]. If the compressibility of the medium is to be included, then an equivalent equation such as in [24] can be used. This first approximation of the whole flow field (a distribution of sources or sinks representing all bubble oscillations) sets the boundary conditions at infinity at the following order of approximation. The same process is then repeated for the successive orders. *Up to the order* $O(\epsilon^3)$, one can show, [11, 25], that the influence of the remaining bubbles on each bubble B_i, can be schematically replaced by the influence of a single equivalent bubble centered at G_i. The growth rate and position of this equivalent bubble are determined by the distribution and the growth rate of the other cavities. In general, this fictitious bubble equivalent to the "rest-of-the-cloud" and the corresponding "cloud center" and "equivalent bubble intensity" are different for each bubble. If θ_{ig} is the angle between the centers' direction $\mathbf{B_iG_i}$ and the direction of a field point $\mathbf{B_iM}$, the equation of the surface of the axisymmetric bubble B_i can be written in the form:

$$R(\theta_{ig}, \varphi, t) = a_0^i(t) + \epsilon a_1^i(t) + \epsilon^2[a_2^i(t) + f_2^i(t).\cos\theta_{ig}] + \epsilon^3[a_3^i(t) + f_3^i(t).\cos\theta_{ig} + g_3^i(t)\mathcal{P}_2(\cos\theta_{ig})] + o(\epsilon^3),$$

where $\mathcal{P}_2$ is the Legendre polynomial of order 2, and argument $\cos\theta_{ij}$. The components, a_n^i, f_n^i and g_n^i, satisfy

linear second order differential equations which can be written in symbolic form as follows:

$$\mathcal{D}_2(y_n^i) = \sum_j^{'} \left(\frac{l_0}{l_0^{ij}}\right)^m \mathcal{F}_j^i(y_0^i, ..., y_{n-1}^i)\mathcal{P}_m(\cos\theta_{ig}). \quad (56)$$

Here $\mathcal{D}_2(y_n^i)$ represents a differential operator of the second order in time acting on the radius component y_n^i (one of a_n^i, f_n^i, g_n^i) of the bubble i ; l_0^{ij} is the initial distance between the bubbles B_i and B_j; $\mathcal{F}_j^i(y_0^i, ..., y_{n-1}^i)$ is a known function of the terms (y_k^i), determined at the preceding orders; m is an integer indicating the order of the spherical harmonic; θ_{ig} is the polar angle measured wth respect to the line connecting the center of the bubble i and the center of the equivalent bubble B_g; and n is an integer indicating the order of the approximation.

The detailed expressions can be found in Reference [11]. The behavior of B_i can then be computed by integration of the obtained system of differential equations using a multi-Runge-Kutta procedure. The behavior of the whole cloud is thus obtained. Earlier studies [11, 25, 18] have shown that collective bubble behavior can have a dramatic effect on both bubble growth and implosion. Specifically, bubble growth is inhibited by bubble interactions, while bubble collapse is enhanced. This cumulative effect comes from the fact that the interaction reduces any driving pressure drop as a result of the other bubble growth, while it increases the collapse driving pressure as a result of the other bubble collapse. Due to the cumulative effects of the collapse of all the bubbles in the cloud, each bubble ends its collapse under the influence of a pressure which is orders of magnitude higher than that for an isolated bubble (see Figure 9 described below and corresponding discussion)

Extension to a slightly compressible liquid

The incompressibility approximation assumed above can be relaxed. In this section we extend our asymptotic treatment of a bubble cloud to the case of a slightly compressible liquid. Briefly the method followed is that of expansion in two parameters - the Mach number $\mathcal{M}$, and the parameter ϵ introduced earlier. We derive $O(\mathcal{M})$ corrections to the incompressible equations (valid till $O(\epsilon^3)$ discussed above.

To consider the effect of compressibility we consider the following equations of motion:

$$\frac{1}{\rho}\left(\frac{\partial\rho}{\partial t} + (\mathbf{u}\cdot\nabla)\rho\right) + \nabla\cdot\mathbf{u} = 0 \quad (57)$$

$$\left(\frac{\partial\mathbf{u}}{\partial t} + (\mathbf{u}\cdot\nabla)\mathbf{u}\right) + \frac{1}{\rho}\nabla p = 0 \quad (58)$$

$$\frac{dp}{d\rho} = c_\infty^2 \qquad h = \int_{p_\infty}^{p}\frac{dp}{\rho} \quad (59)$$

The flow is assumed irrotational, so that we can define a velocity potential

$$\mathbf{u} = \nabla\phi. \quad (60)$$

Substituting from (59) for the velocity in the equations of motion we obtain

$$\nabla^2\phi + \frac{1}{\rho c_\infty^2}\left[\frac{\partial h}{\partial t} + (\nabla\phi\cdot\nabla)\,h\right] = 0, \quad (61)$$

and

$$\frac{\partial\phi}{\partial t} + \frac{1}{2}|\nabla\phi|^2 + h = 0 \quad (62)$$

We now consider the cases where the length scale $L_0 = c_\infty\tau_{b0}$ is much larger than the length scales l_0 and r_{b0}, so that

$$r_{b0} \ll l_0 \ll L, \quad (63)$$

and define a new parameter $\mathcal{M}$ such that

$$\mathcal{M} = \frac{r_{b0}}{L} = \frac{r_{b0}/\tau_0}{c_\infty}. \quad (64)$$

We can identify $\mathcal{M}$ with the Mach number, and use it as a perturbation parameter. The details of this calculation will be demonstrated in a later paper [29], and we only outline the approach here, and present some preliminary results.

The problem can be decomposed into an acoustic part and a hydrodynamic part. The acoustic part consists of the "far" field corresponding to the pure liquid far away from the cloud region, while the "near" field is that in the neighbourhood of the bubbles, and corresponds to the hydrodynamic part of the problem. The near field can be decomposed, as before, into an "inner" (corresponding to the neighborhood of a bubble) and "outer" field (corresponding to the rest of the cloud).

It turns out that if we take $\mathcal{M} \sim \epsilon^3$ the inner equations are almost identical to the incompressible ones until $O(\mathcal{M})$, except that they account for the time retardation due to the compressibility of the medium.

Performing the analysis with this assumption yields that the preceding equations hold, with the equation of the bubble radius at $O(\epsilon^0)$ modified from a Rayleigh-Plesset form to a Keller-Herring form [21]

This equation can be written as

$$\rho\left[(1-\frac{\dot a}{c})a\ddot a + \frac{3}{2}\left(1-\frac{\dot a}{3c}\right)\dot a^2\right] = \frac{1}{\rho}\left(1+\frac{\dot a}{c}+\frac{a}{c}\frac{d}{dt}\right)[p_B - p_\infty], \quad (65)$$

where

$$p_B = p_{g0}\left(\frac{V_0}{V}\right)^k + p_v - \frac{2\sigma}{a}, \quad (66)$$

and c is the sound speed.

This model is being used in in combination with the bubble interaction model to extend the study to the case where a slight compressibility of the liquid is taken into account. Figure 7, for instance shows the influence of a finite sound speed on the behavior of a bubble in a 6-bubble configuration.

7 Boundary Element Method for Three-Dimensional Bubble Dynamics

In order to enable the simulation of bubble behavior in complex geometry and flow configurations including the full non-linear boundary conditions, a three-dimensional Boundary Element Method was developed. This method uses Green's identity to solve Laplace's equation. If the velocity potential, ϕ, or its normal derivative is known on the fluid boundaries (points M), and ϕ satisfies the Laplace equation, then ϕ can be determined anywhere in the domain of the fluid (field points P) using the identity:

$$\int\int_s \left[-\frac{\partial \phi}{\partial n} \frac{1}{|\,\mathrm{MP}\,|} + \phi \frac{\partial}{\partial n} \left(\frac{1}{|\,\mathrm{MP}\,|} \right) \right] ds = a\pi\phi(P), \quad (67)$$

where $a\pi = \Omega$ is the solid angle under which P sees the fluid.

$a = 4$, if P is a point in the fluid

$a = 2$, if P is a point on a smooth surface

$a < 4$, if P is at a corner of the discretized surface.

The advantage of this integral representation is that it effectively reduces the dimension of the problem by one. If the field point P is selected to be on the boundary of the fluid domain (a bubble surface or on any other boundary), then a closed system of equations can be obtained and used at each time step to solve for values of $\partial\phi/\partial n$ (or ϕ) assuming that all values of ϕ (or $\partial\phi/\partial n$) are known at the preceding step.

To solve Equation (66) numerically, it is necessary to discretize the bubble into panels, perform the integration over each panel, and then sum up the contributions to complete the integration over the entire bubble surface. To do this, the initially spherical bubble is discretized into a geodesic shape using flat, triangular panels. After discretizing the surface, Equation (66) becomes a set of N equations (N is the number of discretization nodes) of index i of the type:

$$\sum_{j=1}^{N} \left(A_{ij} \cdot \frac{\partial \phi_j}{\partial n} \right) = \sum_j (B_{ij} \cdot \phi_j) - a\pi\phi_i, \quad (68)$$

where A_{ij} and B_{ij} are elements of matrices which are the discrete equivalent of the integrals given in Equation (66). To evaluate the integrals in (66) over any particular panel, a linear variation of the potential and its normal derivative over the panel is assumed. In this manner, both ϕ and $\partial\phi/\partial n$ are continuous over the bubble surface, and are expressed as a function of the values at the three nodes which delimit a particular panel. Obviously higher order expansions are conceivable, and would probably improve accuracy at the expense of additional analytical effort and numerical computation time. The two integrals in (66) are then evaluated analytically. The resulting expressions, too long to present here, can be found in [27]. In order to proceed with the computation of the bubble dynamics several quantities appearing in the above boundary conditions need to be evaluated at each time step. The bubble volume presents no particular difficulty, while the unit normal vector, the local surface curvature, and the local tangential velocity at the bubble interface need further development. In order to compute the curvature of the bubble surface a local bubble surface three-dimensional fit, $f(x,y,z) = 0$, is first computed. The unit normal at a node and the local curvature can then be expressed using Equations (5).

To obtain the total fluid velocity at any point on the surface of the bubble, the tangential velocity, $\mathbf{V_t}$, must be computed at each node in addition to the normal velocity, $\mathbf{V_n} = \partial\phi/\partial n\ \mathbf{n}$. This is also done using a local surface fit to the velocity potential, $\phi_l = h(x,y,z)$. Taking the gradient of this function at the considered node, and eliminating any normal component of velocity appearing in this gradient gives a good approximation for the tangential velocity

$$\mathbf{V_t} = \mathbf{n} \times (\nabla\phi_l \times \mathbf{n}). \quad (69)$$

With the problem initialized and the velocity potential known over the surface of the bubble, an updated value of $\partial\phi/\partial n$ can be obtained by performing the integrations outlined above, and solving the corresponding matrix equation. The unsteady Bernoulli equation can then be used to solve for $D\phi/Dt$, the total material derivative of ϕ,

$$\frac{D\phi}{Dt} = \frac{\partial\phi}{\partial t} + |\,\nabla\phi\,|^2 = \frac{P_a - P_L}{\rho} - gz + \frac{1}{2}\,|\,\nabla\phi\,|^2 . \quad (70)$$

$D\phi/Dt$ provides the total time variations of ϕ at any node during its motion with the fluid. The second term on the right hand side is the hydrostatic pressure and is introduced to account for cases where the influence of the gravitational acceleration is not negligible. Using an appropriate time step, all values of ϕ on the bubble surface can be updated using ϕ at the preceding time step and $D\phi/Dt$. In the results presented below the time step was based on the ratio between the length of the smaller panel side, l_{min} and the highest node velocity, V_{max}. This choice limits the motion of any node to a fraction of the smallest panel side. It has the great advantage of constantly adapting the time step, by refining it at the end of the collapse – where l_{min} becomes very small and V_{max} very large – and by increasing it during the slow bubble size variation period. New coordinate positions of the nodes are then obtained using the position at the previous time step and the displacement,

$$d\mathrm{M} = \left(\frac{\partial\phi}{\partial n}\mathbf{n} + \mathbf{V_t} \right) dt. \quad (71)$$

This time stepping procedure is repeated throughout the bubble oscillation period, resulting in a shape history of the bubbles.

8 Presence of a Viscous Basic Flow

Cavitation bubbles seldom grow and collapse in a quiescent fluid or in a uniform flow field. To the contrary, cavities are most commonly observed in shear layers, boundary layers and vortical structures. To study bubble dynamics in a nonuniform flow field, let us consider the case where the "basic flow" of velocity $\mathbf{V_0}$ is known and satisfies the Navier Stokes equations:

$$\frac{\partial \mathbf{V_0}}{\partial t} + \mathbf{V_0} \cdot \nabla \mathbf{V_0} = -\frac{1}{\rho}\nabla P_0 + \nu \nabla^2 \mathbf{V_0} \ . \tag{72}$$

If the basic flow is potential the application of the Boundary Element Method is straightforward and there is no need for any additional assumptions.

In the presence of the oscillating bubbles, the velocity field is given by $\mathbf{V}$ which also satisfies the Navier Stokes equation:

$$\frac{\partial \mathbf{V}}{\partial t} + \mathbf{V} \cdot \nabla \mathbf{V} = -\frac{1}{\rho}\nabla P + \nu \nabla^2 \mathbf{V} \ . \tag{73}$$

Both $\mathbf{V}$ and $\mathbf{V_0}$ also satisfy the continuity equation. We can now define bubble flow velocity and pressure variables, $\mathbf{V_b}$ and P_b, as follows:

$$\mathbf{V_b} = \mathbf{V} - \mathbf{V_0}, \qquad P_b = P - P_0. \tag{74}$$

If we assume that this bubble flow field ($\mathbf{V_b}$ and P_b) is potential, we can use a method similar to the one described in the previous section to study the dynamics. This assumption implies that, even though the basic flow is allowed to interact with the bubble dynamics and be modified by it, no new vorticity is allowed to be generated by the bubble behavior. Within this restriction, we have

$$\mathbf{V_b} = \nabla \phi_b, \qquad \nabla^2 \phi_b = 0. \tag{75}$$

By subtracting (72) from (71), and accounting for (74) we obtain

$$\nabla \left[\frac{\partial \phi_b}{\partial t} + \frac{1}{2}\mathbf{V_b}^2 + \mathbf{V_0} \cdot \mathbf{V_b} + \frac{P_b}{\rho} \right] = \mathbf{V_b} \times (\nabla \times \mathbf{V_0}). \tag{76}$$

This equation, once integrated, may be considered the equivalent of the classical unsteady Bernoulli equation in potential flow. As an illustration consider the case where the basic flow field is that of a two-dimensional Rankine vortex, $\mathbf{V_0} = V_\theta \mathbf{e}_\theta$, with

$$V_\theta = \frac{\Gamma}{2\pi r}; \qquad r \geq a_c;$$

$$V_\theta = \omega r = \frac{\Gamma r}{2\pi a_c^2}; \qquad r \leq a_c, \tag{77}$$

where a_c is the radius of the viscous core, Γ the vortex circulation and V_θ the tangential velocity. In that case the Bernoulli equation can be replaced by:

$$\frac{\partial \phi_b}{\partial t} + \frac{1}{2}|\mathbf{V_b}|^2 + \frac{P_b}{\rho} = \text{constant along radial direction}. \tag{78}$$

Accounting for at-infinity conditions, the pressure at the bubble wall, P_L, is related to the pressure field in the Rankine vortex, P_0, by:

$$\left[\frac{P_L}{\rho} = \frac{P_O}{\rho} - \frac{\partial \phi_b}{\partial t} - \frac{1}{2}|\mathbf{V_b}|^2 \right]_{at\ bubble\ wall} \tag{79}$$

The nondimensional basic flow pressure, $\overline{P}_0$, normalized with the ambient pressure, P_∞, is known and is given by:

$$\overline{P}_O(\overline{r}) = 1 - \Omega \left[1 - \frac{1}{2}\left(\frac{\overline{r}}{\overline{a}_c}\right)^2 \right]; \qquad \overline{r} \leq \overline{a}_c$$

$$\overline{P}_O(\overline{r}) = 1 - \frac{\Omega}{2}\left(\frac{\overline{a}_c}{\overline{r}}\right)^2; \qquad \overline{r} \geq \overline{a}_c,$$

where lengths are normalized by R_{max}, the maximum radius the bubble would achieve in an infinite medium if the pressure drops to the value on the vortex axis. The swirl parameter Ω, defined as,

$$\Omega = \frac{\rho}{P_\infty}\left(\frac{\Gamma}{2\pi a_c}\right)^2, \tag{80}$$

characterizes the intensity of the rotation-generated pressure drop relative to the ambient pressure. The pressure on the vortex axis is $(1 - \Omega)$ and goes to zero if $\Omega = 1$.

9 Computational Results and Discussion

We present in this section some results obtained with the Boundary Element Method code (**3DynaFS**), and compare them with results from the asymptotic expansion method. The accuracy of the numerical code was evaluated by using simple test cases known in the literature such as the collapse of spherical and axisymmetric bubbles. For spherical bubbles, comparison with the Rayleigh-Plesset "exact" solution revealed that numerical errors were less than 0.14 percent for a discretized bubble of 162 nodes. The error dropped to 0.05 percent for 252 nodes. The two discretizations – 162 nodes (320 triangular panels) or 252 nodes (500 panels) – are usually selected for most of our nonspherical bubble dynamics runs. However, for the purpose of studying multibubble interactions we were limited to 102 node bubbles (200 panels) due to the limitations of our 32 MBytes MIPS RC3240 computer. For an 8-bubble configuration the code uses about 30 MBytes for 102-node bubbles. With this "coarse" discretization the error is about 2 percent on the achieved maximum radius, but is very small, 0.03 percent, on the bubble period. (This can be seen in figure 9). Comparisons were also made with studies of axisymmetric bubble collapse available in the literature [8, 4], and have shown, for the coarse discretization, differences with these stud-

ies on the bubble period of the order of 1 percent. Finally, comparison with actual test results of the complex three-dimensional behavior of a large bubble collapse in a gravity field near a cylinder shows very satisfactory results, [15] (see Figure 8). The observed difference in the period was shown to be related to the confinement of the experimental bubble in a cylindrical container [27].

Figure 9 compares the results obtained with the 3D code with those given by the asymptotic approach. The bubble cloud is subjected to a sudden pressure drop, and for ease of interpretation, only symmetric cloud configurations are considered. Results for one, two, four and eight-bubble symmetric configurations are shown. For the two-bubble case the bubble centers are separated by a distance l_0, and the initial gas pressure in each bubble is such that the bubble would achieve a maximum radius $R_{max} = R_{b0} = 0.07 l_0$ if isolated. The four-bubble configuration considers similar bubbles centered on the corners of a square with sides of dimension l_0. Finally, the eight bubbles are located on the corners of a cube of side l_0. The figure presents the variations with time of the distance between an initial bubble center and both the point closest to (< 0), and the point farthest (> 0) from the "cloud center". These points are selected because they lie along the direction of development of the reentrant jet the farthest point becoming the tip of the jet which penetrates the bubble during the collapse. As we can see from the figure, the BEM method clearly shows that for bubbles *oscillating in phase* the period of oscillation increases with the number of interacting bubbles. The maximum bubble size along the jet axis is however not significantly modified. The jet advancement towards the "cloud center" increases with the number of bubbles. This is seen by the crossing of the $r = 0$ line by the upper curves on the graph which becomes more and more pronounced with an increase in the number of bubbles. This effect is more pronounced for larger values of ϵ (see Figure 10).

Figure 9 also compares the results of the BEM code with the asymptotic approach. It illustrates the limitations of the incompressible asymptotic approach as it stands now. When the number of bubbles increases the method diverges towards the end of the collapse and predicts either a much faster collapse than obtained with the more accurate BEM method (N=2 and 4), or an unexplained early bubble rebound ($N = 8$). This behavior occurs earlier when either the number of bubbles or the value of ϵ increases.

Figure 10 shows the influence of ϵ on the bubble dynamics for a 4-bubble configuration. Using the BEM 3D results enables one to study the influence of reducing bubble inter-distance on the dynamics of each bubble. Increasing the proximity between the bubbles, or increasing the number of bubbles is seen to increase the lengthening effect on the bubble period, while enhancing the reentrant jet formation, as in the more classical case of bubble collapse near a solid wall. In all cases, the reentrant jet formed is directed towards the center of the bubble cloud, or here, the center of the square. As expected, the asymptotic approach gives a very good approximation at low values of ϵ, but fairs poorly for high values of ϵ (note that for $\epsilon = 0.5$ the bubbles touch at their maximum size). The above conclusions on the asymptotic approach have to be tempered by the fact that all cases presented addressed relatively intense bubble collapse (with a strong reentrant jet formation). The relevant nondimensional parameter to characterize the collapse intensity is the ratio, $\mathcal{P}_{gm}$, of the gas pressure to the outside pressure at maximum bubble size. This ratio is about 0.06 for the cases shown above. For higher values of $\mathcal{P}_{gm}$ a smoother collapse followed by a rebound occurs, and the asymptotic approach fairs much better [28]. Figures 11 and 12 illustrate further the three-dimensional behavior of the bubble, using 198-node bubbles. Figure 11 shows two cross-sectional views of the bubble shapes at various times during the collapse for a strong interaction case ($\epsilon = 0.498$), for a 4-bubble configuration. The first view shows bubble contours in the $Z = 0$ plane, plane of the four bubble centers. In this plane all four bubbles can be seen, and the reentrant jet appears very wide giving the bubble at the end of the collapse the appearance of a "deflated balloon". The second view is a diagonal cut though the centers of two of the bubbles. In this view, the reentrant jet appears much more pronounced. The combination of the two views illustrates very clearly the reentrant jet formation, its direction towards the center of the square, and gives a qualitative idea about the intensity of the collapse. In this case, due the geometry of the configuration, the jet has a two-dimensional flat shape, rather than a conical axisymmetric shape. This clearly provides one reason for the failure of the asymptotic approach for this case, since the expansions in that approach were stopped to an order (ϵ^3) which does not allow the description of any azimuthal bubble shape variations. Figure 12 presents a 3D view of the bubbles towards the end of a relatively weak collapse of a 4-bubble configuration ($\epsilon = 0.185$). Since the case shown is symmetrical and all bubbles have the same shape, this diagonal view can be interpreted as showing the shape of the same bubble from different view angles. The reentrant jet is here again seen to be wide, pointed, and well advanced towards the other side of the bubble. A complete history of the advancement of the jet in the bubble can be deduced from figure 10. Figures 13 through 17 illustrate various important effects due to either asymmetries in the bubble configuration, or due to the presence of an underlying nonuniform flow. Figure 13 shows the case of an asymmetric five bubble configuration. All bubbles have the same initial radius and internal pressure, and are initially spherical and located in the same plane. The most visible effect observed is that on the center bubble. Its growth is initially similar to that of the other bubbles, but it ends up being

the least deformed. Later on, as the collapse phase advances with the development of a reentrant jet directed towards the central bubble, this bubble appears to be shielded by the rest of the cloud. Its period appears to be at least double that of the other bubbles. Unfortunately, the code cannot presently follow the dynamics beyond this point since it fails following the touchdown of the first reentrant jet on the other bubble side. Here, this occurs before any significant progress of the collapse of the central bubble is observed. The issue of continuing the computations beyond this point is clearly important and is presently the subject of an ongoing research at DYNAFLOW. Reference [30] gives results of our first attempt towards solving this problem. Figure 14 shows a 4-bubble configuration where the bubbles are centered on the corners of a square. All bubbles were chosen so that they would behave identically if in an infinite medium. However, a time delay between the bubble oscillations was imposed. As a result, at $t = 0$ the bubbles had relative initial sizes in the ratios $2, 1, 3, 1$ counter-clockwise starting from the bubble centered at the origin. This results in a very asymmetric behavior of the cloud configuration. The bubble periods appear to be lengthened the most for the larger bubbles at $t = 0$. The "delayed" bubbles (the smaller at $t = 0$) are prevented by the other bubbles from growing significantly, and end up collapsing very early in their history. These bubbles on the other hand significantly influence the "earlier" ones by increasing at some point the pressure drop these bubbles sense and then by preventing them later on from collapsing. Since the code presently breaks down before a significant collapse, we can only speculate that a very strong collapse of the larger bubbles would ensue, because of the large pressure produced by the collapse of the smaller bubbles. This can be illustrated by observing the modification of the imposed pressure drop by the behavior of an individual bubble. As shown in figure 15, the bubble growth initially reduces the effective pressure drop that would be felt by a second bubble at the distance l_0, this trend is later reversed, and is followed by a significant pressure rise during the bubble collapse.

Figure 16 shows the three-dimensional behavior of a bubble in a line vortex. The bubble is initially positioned at a distance of $2R_{max}$ from the vortex axis located at $\overline{X} = 2$. The normalized core size is 4 in this case. Figure 16*a* gives a view in the XOY plan of the bubble at different instants. The bubble is seen spiraling around the vortex axis (perpendicular to the figure) while approaching it. At the same time, due to the presence of the pressure gradient, the bubble strongly deforms and a reentrant jet is formed directed towards the axis of the vortex. Figure 16*b* shows the same bubble seen from the OX axis. Here some elongation is observed along the axis of the vortex as well as a very distinct side view of the re-entrant jet. This result is totally contrary to the usually held belief that bubbles constantly grow during their capture until they reach the axis and elongate along it. Finally, Figure 17 shows in the XOY plane perpendicular to the vortex axis the motion of two particular points on the bubble, A and B, initially along OY. Also shown is the motion of the mid point, C. While C seems to follows a path similar to the classical logarithmic spiral, A and B follow more complicated paths, even moving away from the vortex axis at some point in time.

Figures 18 and 19 , address the behavior of a bubble near a solid wall in the presence of a nonuniform flow field and as a result of a relative velocity between the bubble and the flow. In the example shown a simple linear velocity profile is used to simulate the the boundary layer flow near the wall in which the bubble dynamics is considered. The *basic* flow velocity varies from a value, V_{shear} at a distance r_{b0} from the wall to zero at the wall. The *basic* pressure is assumed constant across the shear layer and is an input of the problem, P_{amb}, as is the initial gas pressure inside the bubble, P_{g0}. The bubble center is located at a distance l_0 from the wall, the ratio r_{b0}/l_0 being a key parameter characterizing the bubble / wall interaction. Here, another important parameter is the ratio between the characteristic *shear velocity* and a characteristic bubble dynamics velocity [16], for instance $\chi = V_{shear}/\sqrt{\Delta P/\rho}$. Figure 18 shows an example of bubble growth and collapse shape contours obtained with **3DynaFS** near a solid wall in the absence of shear. Figure 19 shows for the same conditions the bubble collpase in the presence of the nonuniform flow. A very significant effect of the wall flow is seen on the development of the reentrant jet. The jet is seen to be much weakened and delayed. Since we have made these *numerical* observations in 1990 in [16], tests conducted by other researchers in the Large Cavitation Channel appears to confirm experimentally at least some aspects of these observations.

Figure 20 shows the strong interaction between a growing and collapsing bubble and a vortex ring. Figure 20a shows a high speed movie sequence where the vortex ring, the axis of which is on the left edge of the successive pictures, was generated using the impulsive motion of a piston in a tank where a reduced ambient pressure was imposed [45]. The bubble was spark-generated using submerged electrodes positionned where the initial bubble center is sought. The figure shows that the bubble grows initially almost spherically, then the shear flow due to the vortex ring becomes very important leading to a stretching and elongation of the bubble along a stream line of the vortex flow. The bubble then collapses in a very unusual manner producing a constriction along the vortex flow line, then decomposing into two bubble clouds. A set of various bubble / vortex interaction intensities is presented in [45]. Figure 20b is a direct numerical simulation of the experimental case shown in figure 20a. The vortex ring flow was simulated assuming a Rankine model and a viscous core size as observed from other tests where microbubble motion inthe vortex flow were visualized. Given such a crude

model of the vortex ring and given that the modification of the vortex flow by the bubble dynamics neglected, the similitude between the numerical simulation and the experimental result is quite satisfactory and is able to capture most of the feature of the bubble behavior. An improved viscous model and the inclusion of the *basic* flow modification will enable an even better correspondence. The study of such an interaction is essential to the understanding of the the interaction between microbubble and large organized viscous structures which occur in boundary layers. These interactions are expected to be much more significant at full scale than in the laboratory, particularily due to a significant increase of the ratio between hydrodynamics scales and bubble scales.

10 Conclusions

In this contribution the dynamics of the interaction between bubbles and nearby boundaries (other bubbles or complex geometries) or nonuniform flows was considered using an asymptotic method and a three-dimensional Boundary Element model. Both approaches enabled us to address aspects of the bubble dynamics that have been ignored to date due to their mathematical difficulty. The asymptotic approach, valid for the case of *weak* interactions, enables a better understanding of the general trends without recourse to an extensive analysis of test cases, since it provides analytical expressions from parts of the solutions. On the other hand direct 3D simulation have the advantage of enabling the study of *strong* interactions where the asymptotic expansion metod fails. Comparison of the two methods provides a means of mutual validation of the methods.

From the application of both methods the following conclusions can be drawn from the study:

1. When compared to the dynamics of a single bubble, significant modification of the bubble dynamics and shape is observed for multibubble interaction. For identical bubbles acting in concert, an increase in the bubble period is observed without significant modification of the bubble maximum size when the number of bubbles increase or when their separation distance decreases.

2. A shielding effect of the bubbles was observed leading to an increased period and maximum size of the bubbles in the center of the cloud.

3. While very large pressures are computed using the asymptotic method with bubble clouds composed of the same size bubbles, more moderate pressures are obtained when the bubbles are not exactly in phase and when large deformations are taken into account.

4. Bubble collapse near a solid wall and in the presence of a nonuniform flow field is seen to be significantly modified by the presence of this flow field. Reentrant jet formation is seen to be delayed and weakened when not eliminated.

5. Bubble capture, growth and collapse in a line vortex flow field is seen to involve significantly non spherical effects which have been systematically neglected by previous studies. For instance, noise generation at the inception of tip vortex cavitation can probably be explained by the deformation, collapse and splitting of the bubble while being captured.

6. The study of the interaction between bubbles and large organized structures provides some hints about the complexity of bubble dyanmics in real full scale flow fields.

On-going areas of improvement of this study include extension of the asymptotic approach to the case of a compressible fluid and coupling of the multibubble approach to a two-phase medium model. The Boundary Element Method approach is being improved to include the full description of the reentrant jet piercing of the bubble and its subsequent advancement in the fluid. The 3D code **3DynaFS** is also being exercised on a Cray Y-MP and implemented on a parallel Connection Machine in order to significantly improve computation time, and to allow practical consideration of a much larger number of elements than at present.

Acknowledgments

We would like to acknowledge the support of the Office of Naval Research, Contract N00014-89-C-0025, and the interest and technical discussions with Dr. Edwin Rood. The authors would like to acknowledge the many contributions and significant discussions of several colleagues at DYNAFLOW, INC.

References

[1] YOUNG, F.R., "Cavitation," *McGraw-Hill, London.* 1989.

[2] ROOD, E.P., "Review - Mechanics of cavitation inception," *ASME Journal of Fluids Engineering,* Vol. **113**, 163-175, 1991.

[3] HAMMITT, F.G., *Cavitation and Multiphase Flow Phenomena,* McGraw-Hill, New York, 1980.

[4] BLAKE, J. R, AND GIBSON, D. C., "Cavitation Bubbles Near Boundaries," *Annual Review of Fluid Mechanics*, Vol. **19**, pp. 99-123, 1987.

[5] RAYLEIGH LORD,"On the Pressure Developed in a Liquid During Collapse of a Spherical Cavity," *Phil. Mag.*, pp. 34, 94-98, 1917

[6] BESANT, W., "A Treatise on Hydrodynamics", *Cambridge University Press*, pp. 198, 1859.

[7] SHIMA, A. AND NAKAJIMA, K., "The Collapse of a Non-Hemispherical Bubble Attached to Solid Wall," *Journal of Fluid Mechanics*, Vol. **80**, pp. 369-391, 1977.

[8] GUERRI, L., LUCCA, G., AND PROSPERETTI, A., "A Numerical Method for the Dynamics of Non-Spherical Cavitation Bubbles," *Proceedings 2nd International Colloquium on Drops and Bubbles, JPL Publication 82-7, Monterey CA*, Nov 1981.

[9] CHAHINE, G. L., "Experimental and Asymptotic Study of Nonspherical Bubble Collapse," *Applied Scientific Research*,38, pp. 187-197, 1982.

[10] VAN WIJNGAARDEN, L. , "On the Collective Collapse of a Large Number of Gas Bubbles in Water," *Proceedings of the 11th International Congress of Applied Mechanics, Springer, Berlin*, pp. 854-865, 1964.

[11] CHAHINE, G.L., "Cloud Cavitation: Theory," *14th Symposium on Naval Hydrodynamics, Ann Arbor, Michigan, National Academy Press, Washington, D.C.*, pp. 165-195. 1983.

[12] D'AGOSTINO, L. AND BRENNEN, C.E.,"On the Acoustical Dynamics of Bubble Clouds," *ASME Cavitation and Polyphase Flow Forum, Houston, Texas*, pp. 72-76. 1983.

[13] KUMAR, S. AND BRENNEN, C.E., "Some nonlinear interactive effects in bubbly cavitation clouds," submitted to *Journal of Fluid Mechanics.*

[14] CHAHINE, G.L. AND PERDUE, T.O., "Simulation of the Three-Dimensional Behavior of an Unsteady Large Bubble Near a Structure," *Proc. 3rd Int. Coll. on Drops and Bubbles, Monterey CA, Sept. 1988.*

[15] CHAHINE, G.L., "A Numerical Model for Three-Dimensional Bubble Dynamics in Complex Geometries," *22nd American Towing Tank Conference, St. Johns, Newfoundland, Canada, August 1989.*

[16] CHAHINE, G.L., "Numerical Modelling of the Dynamic Behavior of Bubbles in Nonuniform Flow Fields," *ASME 1990 Cavitation and Multiphase Flow Forum, Toronto, Canada*, 1990.

[17] CHAHINE, G.L., "Nonspherical bubble dynamics in a line vortex," Proceedings of ASME Cavitation and Multiphase Flow Forum, Toronto 1990,(ed. O. FURUYA) *ASME*, pp. 121-126, 1990.

[18] CHAHINE, G. L. AND LIU, H. L.,"A Singular Perturbation Theory of the Growth of a Bubble Cluster in a Super-heated Liquid," *Journal of Fluid Mechanics*, Vol. **156**, pp. 257-274, 1985.

[19] KALUMUCK, K.M. AND CHAHINE, G.L, "The Influence of Gas Diffusion on the Growth of a Bubble Cloud,"*ASME Cavitation and Multiphase Flow Forum, Cincinnati, Ohio*, pp. 17-21, June 1987.

[20] PLESSET, M.S. AND PROSPERETTI, A., "Bubble Dynamics and Cavitation," *Annual Review of Fluid Mechanics*, Vol. **9**, pp. 145-185, 1977.

[21] PROSPERETTI, A. AND LEZZI, A.M., "Bubble Dynamics in a Compressible Liquid. Part 1. First Order Theory." *Journal of Fluid Mechanics* **168**, pp. 457-478, 1986.

[22] REBUT, M. AND CHAHINE, G.L., "Asymptotic Study of Bubble Dynamics in a Nonuniform Potential Flow", ASME Cavitation and Multiphase Flow Forum, Los Angeles 1992.

[23] DURAISWAMI, R. AND CHAHINE G.L., "Analytical study of a gas bubble in the flow field of a line vortex," *ASME Cavitation and Multiphase Flow Forum, Los Angeles 1992.*

[24] HERRING, C., "Theory of the Pulsations of the Gas Bubble Produced by an Underwater Explosion" *Columbia University NDRC Reo. C-4 SR 20-010*, 1941.

[25] CHAHINE, G. L., "Pressure Field Generated by the Collective Collapse of Cavitation Bubbles," *Proceedings, IAHR Symposium on Operating Problems of Pump Stations and Power Plants, Amsterdam, Holland*, **2-1**, pp. 1-12., 1982.

[26] G.L. CHAHINE, K.M. KALUMUCK, AND T.O. PERDUE, "Cloud Cavitation and Collective Bubble Dynamics," *Tracor Hydronautics, Technical Report 83017-1*, 1986.

[27] CHAHINE, G. L., PERDUE, T. O. AND TUCKER, C.B., "Interaction Between an Underwater Explosion Bubble and a Solid Submerged Body," *DYNAFLOW, Inc. Technical Report 89006-1*, 1989.

[28] CHAHINE, G.L. AND DURAISWAMI, R. "Dynamical Interactions in a multi-bubble cloud." in "Proceedings of the ASME Cavitation and Multiphase Flow Forum, Portland 1991" (ed. O. FURUYA) *ASME*, 49-54, (also *To appear in the Journal of Fluids Engineering*), 1991.

[29] DURAISWAMI, R. AND CHAHINE, G.L., "Multiple bubble dynamics in a slightly compressible liquid," *in preparation.*

[30] ZHANG, S., DUNCAN, J., AND CHAHINE, G.L., "Dynamics of a bubble past the point of collapse," *Asme Cavitation and Multiphase Flow Forum, Los Angeles, 1992.*

[31] SNAY, H.G., GOERTNER J.F., AND PRICE, R.S.,, "Small Scale Experiments to Determine Migration of Explosion Bubbles Towards Submarines," *Navord Rep. 2280*, 1952.

[32] CHAHINE, G.L,"Dynamics of the interaction of nonspherical cavities," in "Mathematical approaches in hydrodynamics," ed. T. MILOH, *SIAM, Philadelphia*, 1991.

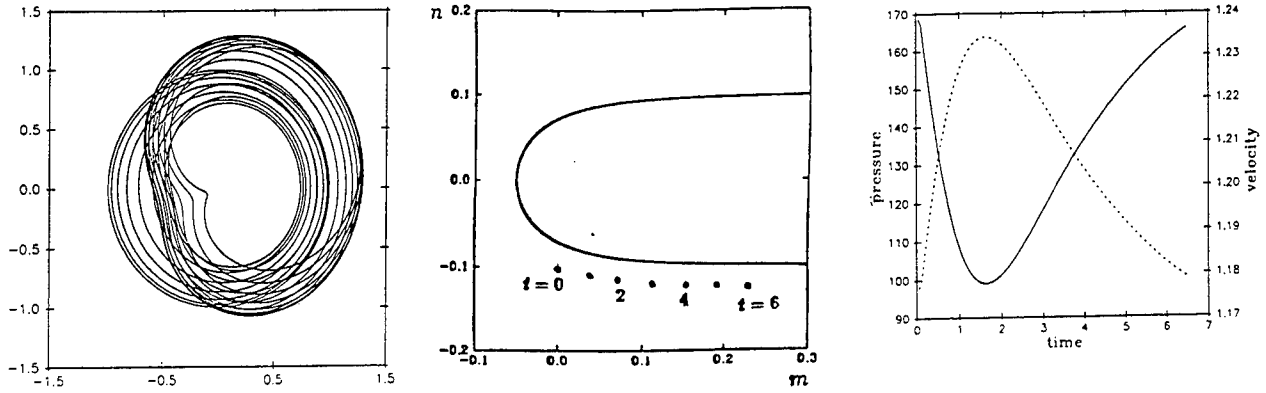

a b c

Figure 1a-c: Fig. 1b and Fig. 1c show the geometry and flow field of the problem considered. The trajectory of the bubble center along the headform (of radius 10 cm) is indicated in Fig. 1b. The pressure (in $Pa - y$ axis) and the velocity (in ms^{-1} – right y axis) of the basic flow along this streamline, are plotted against the non-dimensional time. The free stream velocity is 1.15 ms^{-1}. Fig. 1a shows the computed bubble contours for $\epsilon = 0.3$, and time between $0.1T_0$ to $2T_0$. Bubble translation, rotation and re-entrant jet formation are clearly seen.

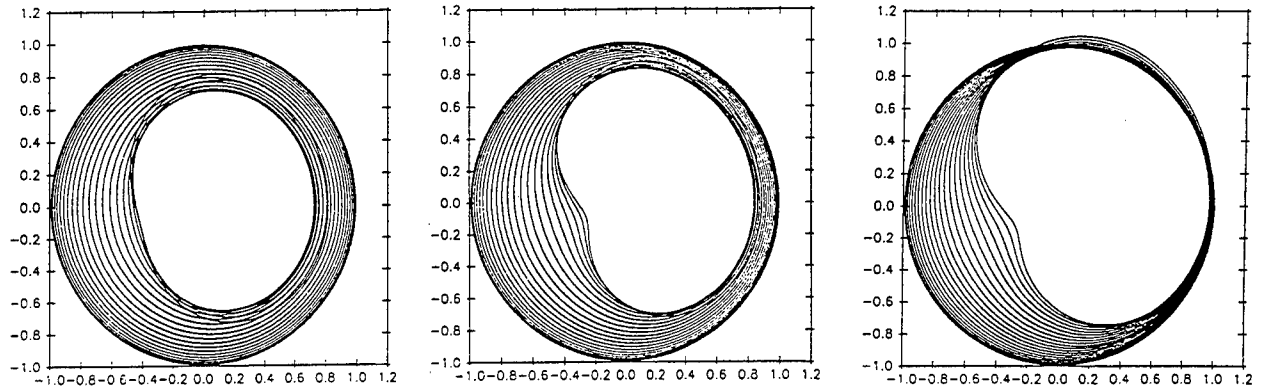

a b c

Figure 2a-c: Bubble contours at various times for $\epsilon = 0.15, 0.3$ and 0.6. Here the initial bubble radius was kept constant at 1 cm, while the initial standoff from the head form was varied to change ϵ. Increasing interaction is seen with decreasing standoff.

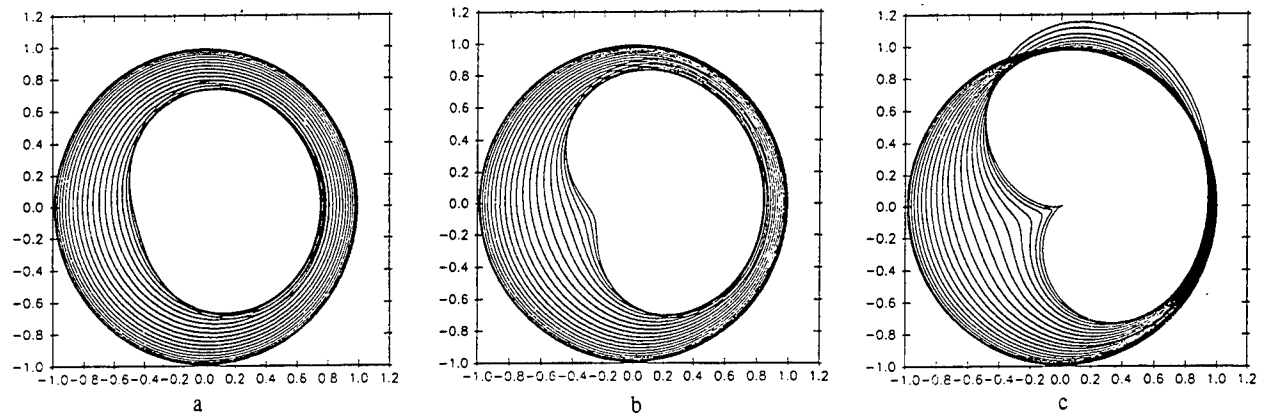

a b c

Figure 3a-c: Bubble contours at various times for $\epsilon = 0.15, 0.3$ and 0.6. Here the initial standoff distance l_0 was kept constant at 3.333 cm, while the initial radius was varied to change ϵ. Increasing interaction is seen with increasing initial bubble size.

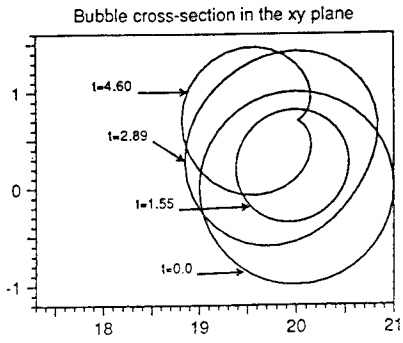

Figure 4:

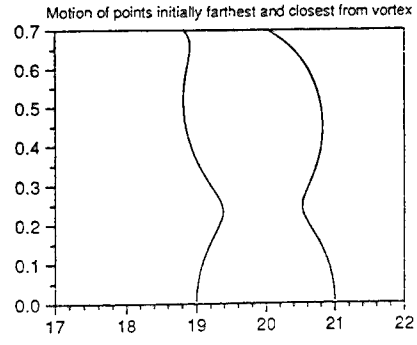

Figure 5:

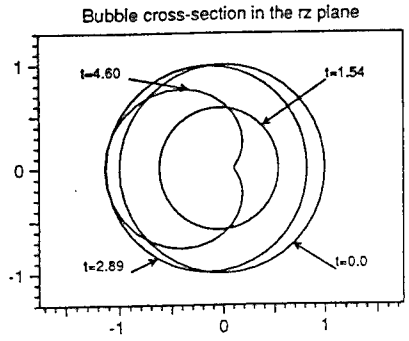

Figure 6:

Figures 4-6: The interaction of the bubble with a line vortex is shown in these figures (see Section 5). Fig. 4 shows the cross-section of the predicted bubble shape in the $x-y$ plane (normal to the vortex axis). The vortex passes through $(x,y)=(0,0)$ along the z axis (normal to the plane of the paper). Fig. 5 indicates the motion of the points initially farthest from and closest to the vortex axis in Fig. 4. Fig. 6 shows the cross-section of the predicted bubble shape in a plane containing the vortex line and the center of the moving coordinate system. The vortex axis is at -20, on the abscissa.

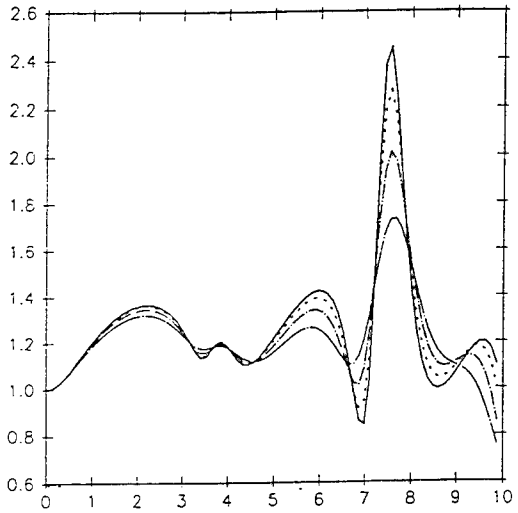

Figure 7: Influence of compressibility on the dynamics of a 6-bubble cloud. The figure shows $R(\theta_{ig}=0,t)$ vs. time for one bubble. The bubbles have an initial radius of 0.01 cm and are arranged at equal distances from the origin along the coordinate axes, so that $\varepsilon=0.07$. The bubbles are at equilibrium at $t=0$ when they are subjected to a sudden pressure drop. Here $\mathcal{P}=2.0$, and $\mathcal{W}=679$. The solid line indicates the incompressible solution. Also plotted is the corresponding curve for $\mathcal{M}$ =0.01 (small dashes), $\mathcal{M}$ =0.03 (small dash-dot), and $\mathcal{M}$ =0.07 (dash-dot). The strong effect of increasing compressibility can be seen.

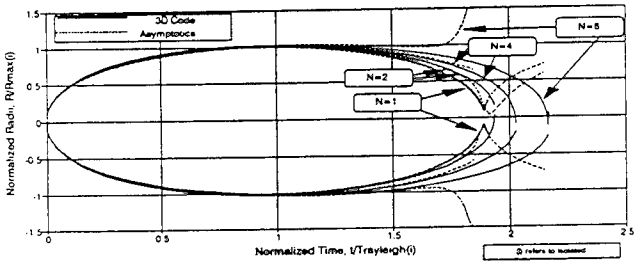

Figure 9: Motion of the bubble points farthest and closest to the cloud center versus time for 1,2,4 and 8-bubble symmetric configurations. Comparison between 3D code results and the asymptotic analysis. $\varepsilon=0.07$, $P_{g0}/P_{amb}=283$.

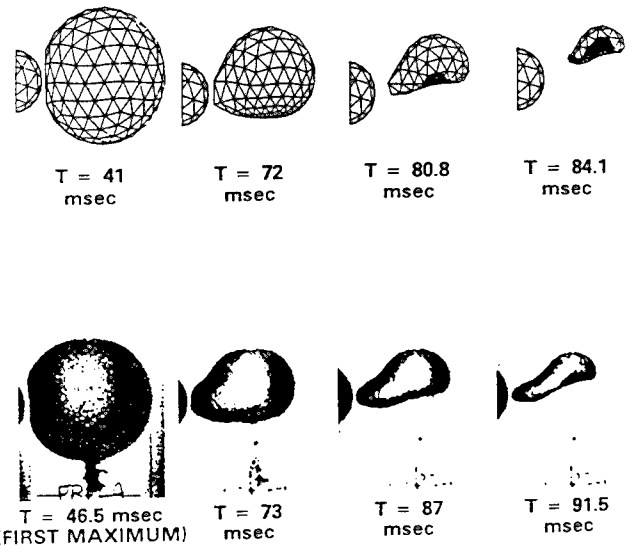

Figure 8: Large bubble collapse near a cylinder. Comparison between our three-dimensional BEM code and the experimental results of Goertner *et al.*

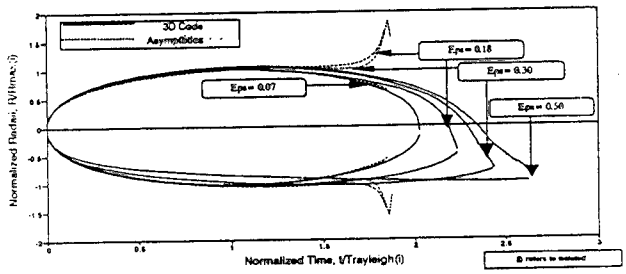

Figure 10: Motion of the bubble points farthest and closest to the cloud center versus time for a 4-bubble symmetric configuration. Comparison between 3D code results and the asymptotic analysis. Influence of bubble proximity or ε. $P_{g0}/P_{amb}=283$.

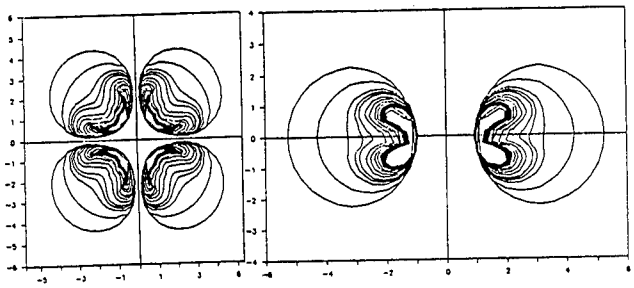

Figure 11: Bubble contours during collapse of a 4-bubble configuration. a) Cross sectional view in the plane $Z = 0$. b) Cross sectional view in the plane $Y = X$. $\epsilon = 0.498$ based on the maximum radius. Note the non-axisymmetric shape of the jet during collapse.

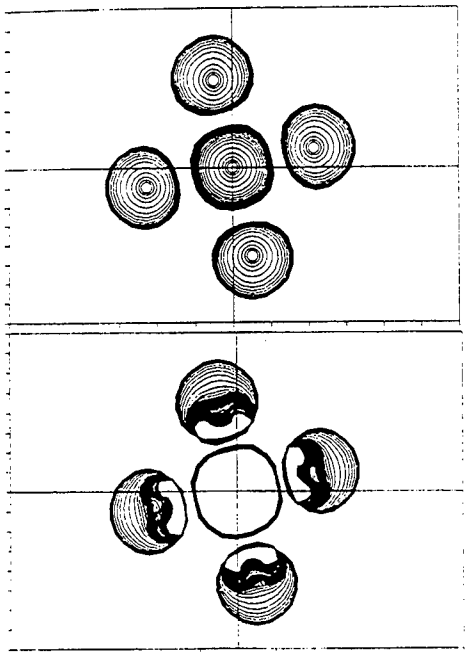

Figure 13: Growth and collapse of 5 bubbles having the same initial size and internal pressure. Influence of the initial bubble geometry on dynamics. $\epsilon = 0.474$ based on the maximum radius. The center bubble is seen to have a remarkably different behavior.

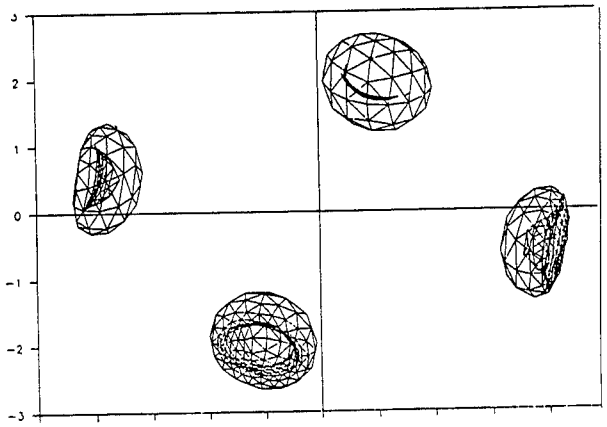

Figure 12: Bubble Contours for the collapse of a 4-bubble cloud for $\epsilon = 0.185$. Since the case shown is symmetrical and all bubbles have the same shape, this diagonal view can be interpreted as showing the shape of the same bubble from different view angles.

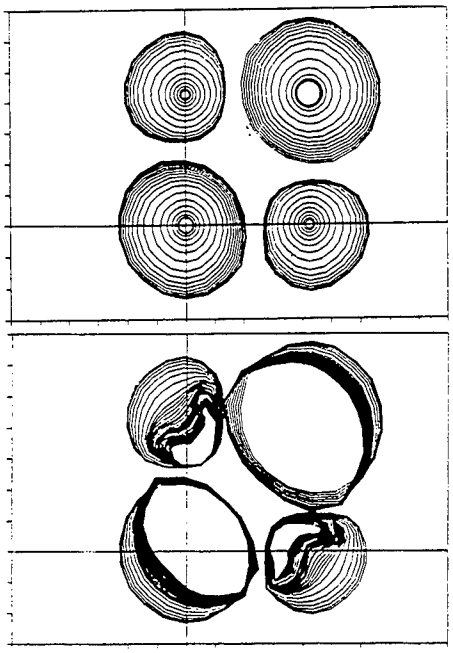

Figure 14: Growth and collapse of 4 identical bubbles initially symmetrically distributed but with different initial radii (2,1,3,1 clockwise starting from origin). The figure shows the influence of 'phasing' on the dynamics.

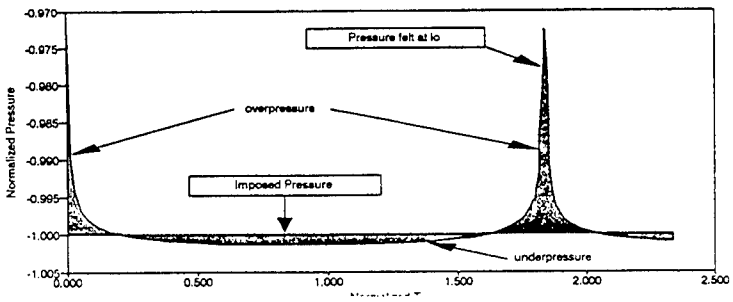

Figure 15: Pressure at distance l_0 from a bubble following a sudden pressure drop. $\epsilon = 0.3$, $P_{g0}/P_{amb} = 283$.

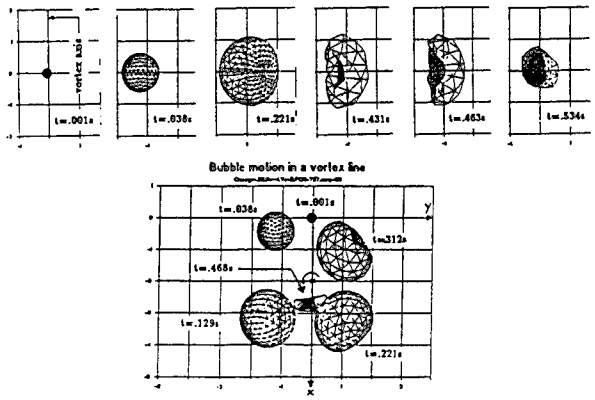

Figure 16:

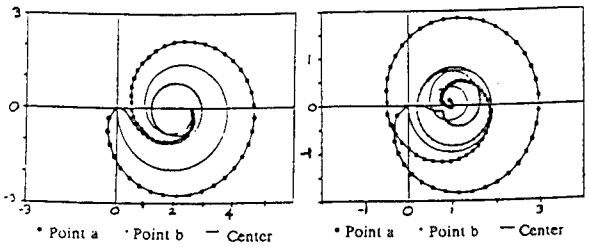

Figure 17:

Figure 16-17: These figures show bubble vortex interaction for $\Omega = 0.948$, $a_c = 4R_{max}$, and $P_{g0}/P_{amb} = 584$. Figure 16 shows three dimensional bubble shapes at various times during bubble capture in a vortex line. a) View in the XOY plane. b) View in the XOZ plane. Figure 17 shows the motion of the two bubble points initially on axis OY and their mid-point vs. time. a) Vortex at $X = 2$. b) Vortex at $X = 1$.

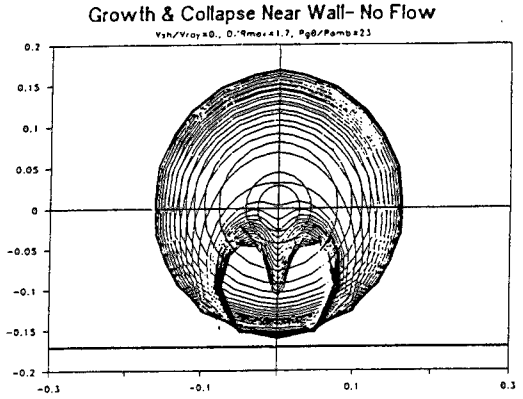

Figure 18:

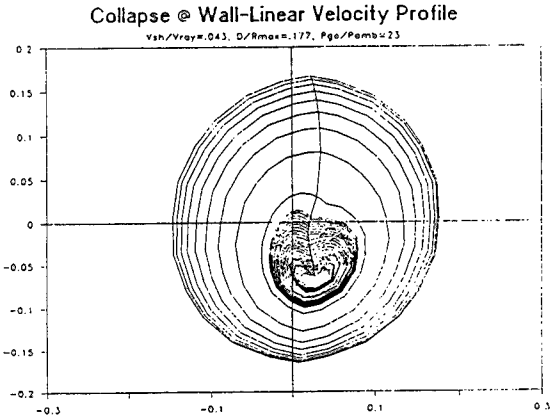

Figure 19:

Figure 18-19: These figures show the influence of a shear flow in the growth and collapse of a bubble in the vicinity of a wall. $P_{g0}/P_{amb} = 23$. $L/R_{max} = 1.77$ Fig. 18 shows a case where and there is no shear flow. Fig. 19 shows the same case for $V_{shear}/V_{Rayleigh}$=0.042.

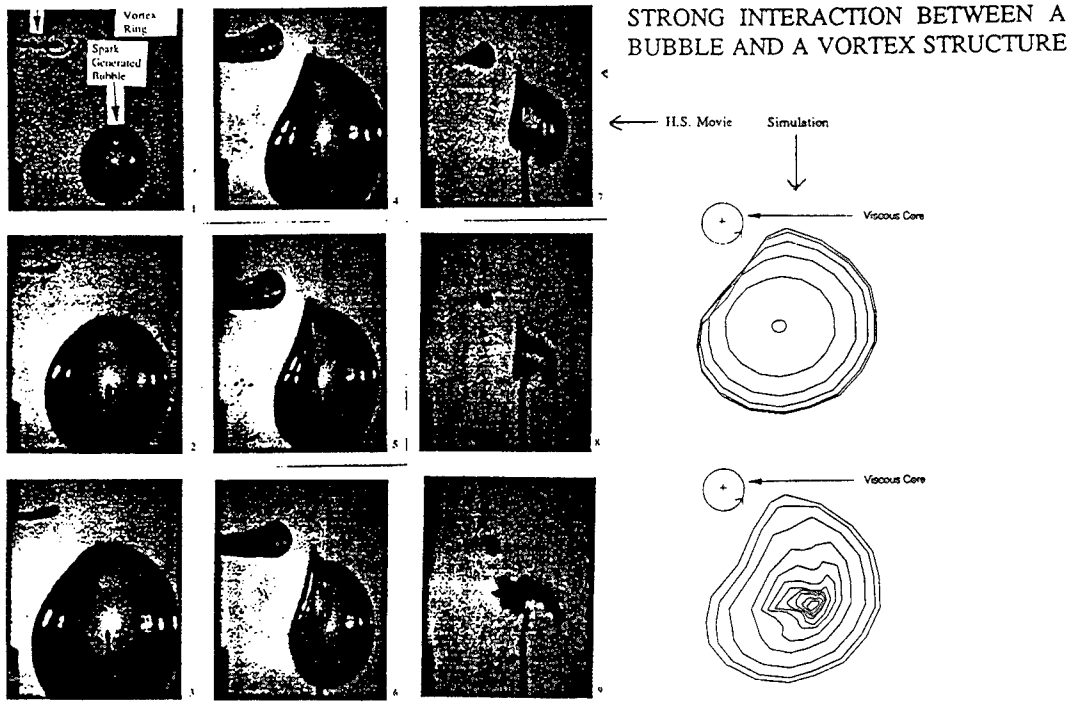

Figure 20: Comparison of 3D BEM simulation and high speed movie sequence for the interaction between a bubble and a vortex ring. The bubble is spark generated and the vortex ring piston generated.

DISCUSSION

R. Yeung
University of California at Berkeley, USA

I would like to congratulate the authors for a fine contribution. In your numerical procedure for treating the interaction of multiple bubbles, I anticipate a singular force, potential value, and possibly even more singular velocities would occur when the cavities make the initial contact as a point. Can you explain in some detail how you handle the treatment of this singular behavior, or its avoidance?

AUTHORS' REPLY

Thank you, Prof. Yeung, for your comments. If a contact point occurs as you describe, singular behavior leading to termination of the computations occur. In fact, in all computations presented in the paper, this did not occur and it appears that a fluid layer remains between the bubbles. Singular behavior is seen only if the time step is coarse. The adaptive time stepping in our code based on the minimum distance between any two points in the computational domain enables avoidance of the problem. However, we encounter this difficulty when a reentering jet is formed, crosses the bubble, and touches the other side of the bubble. Presently, the computation stops at this point for the 3 DynaFS. For the axisymmetric code, we have made progress in solving the problem beyond that point by modeling the bonded surfaces as a surface of shear discontinuity that is followed from that point on using a hypersingular formulation of the boundary integral method [1,2]

[1] Zang, Duncan, and Chachine, 1992 a.
[2] Zang, Duncan, and Chachine, 1992 b.

DISCUSSION

C. Brennan
California Institute of Technology

I would like to congratulate the authors on a very interesting paper. The efforts to understand the way in which cavitation bubbles are deformed by the large shear rates and pressure gradients near the surface of a body have clearly been heightened by the experimental observations of Ceccio and myself (JFM, 1991). I would like, if I may, to show a view-graph of some calculations that a student of mine, Yan Kuhn de Chizelle, has recently produced, which shows results somewhat similar to those of the authors. A boundary integral method was used to solve the unsteady axisymmetric flow of a toroidal source/sink being corrected along a streamline very close to the body surface. The "bubble" clearly shows the shape similar to those of the experiments of Ceccio and Brennen with a thin film separating it from the surface and a characteristic wedge shape at the front. As in the authors' calculations, the collapse causes a jet to develop on the anterior surface of the wedge.

AUTHORS' REPLY

I would like to thank Prof. Brennen for his comments and confirming independently our findings. Since submission of our paper, we have conducted some 3-D computations on bubble behavior near a blunt body, which tends to confirm further these findings. A Rankine body was used for the computations. The flow was given by combining a uniform flow with a source and sink flow. The resulting body was discretized and bubbles were followed in their motion around the body. Fig. 1 shows the flow field used. The velocity near the body was assumed to decay from the inviscid solution to zero at the body wall in a simulated boundary layer. Fig. 2 shows the results obtained, which are able to reproduce several of the features of the paper of the discussor in these proceedings. These are generation of a dimple on the bubble during its growth, which rotates to become almost perpendicular to the body at buSK maximum. Also, the downstream bottom of the bubble is seen lifting from the surface, while the upstream friction is seen to present a characteristic trailing portion of the bubble that tends to stick to the wall. These could be due to the numerics but also reproduce previously observed configuration. See Fig. 3 showing a buSK near a foil with its image in its foil.

Broadband Noise of the Cavitating Marine Propellers: Generation and Collapse of the Free Bubbles Downstream of the Fixed Cavitation

J. Matusiak (Technical Research Centre of Finland, Finland)

ABSTRACT

A method of evaluating generation and collapse of free cavitation bubbles in the propeller flows is presented. The number and size of free, spherical cavitation bubbles are related to the variation of propeller-blade-attached cavitation. The beta type probability density distribution of the initial bubble size is proposed. This distribution is normalized with respect to the sheet cavitation thickness. The method of calculating the low-frequency pressures induced by fixed blade cavitation and high-frequency broadband noise caused by the collapse of free bubbles in propeller flows is presented. The method yields noise spectra in the frequency range from the blade-passing frequency to tens of kilohertz. Computed pressure and noise induced by the cavitating propellers are compared to the values measured in model- and full-scale experiments. The fractal structure of the bubble cloud and the proposed method of evaluating the collapse of the bubble cloud downstream of the fixed cavities yield noise spectra which correlate well with the experimental results of full- and model-scale measurements.

NOMENCLATURE

a	velocity of sound
A_c	cavity area
B	constant of the barotropic equation
C	constant
D	pressure gradient
f	density function, frequency
h_0	depth of propeller shaft
H	pressure function at the bubble wall
l	relative length of sheet cavitation
l_c	chordwise length of sheet cavitation
L_p	noise level
n	number of bubbles, exponent of the barotropic equation
m	parameter of the beta distribution
p	pressure
p_0	ambient pressure
P	pressure at the bubble wall
$P(f)$	discrete Fourier transform of pressure
r	radial ordinate of field point
R	bubble radius, distance from the control point on the blade to the field point
R_0	propeller radius
s	non-dimensional chordwise distance
S	surface tension, power spectral density
T_b	blade-passing period
t	time
t_c	time to the first rebound
t_t	time of travel of a flow particle from the cavity sheet to the blade trailing edge
U	velocity of the propeller blade section
V	cavity volume
v	non-dimensional volume
Z	number of propeller blades
x	dimensionless ordinate of the beta distribution
β	ratio of volumetric gas concentration
γ	exponent of the isentropic process
η	thickness of sheet cavitation
ρ	spanwise distance, density
σ	cavitation number
τ	collapse time
θ	angular position
Ω	angular velocity of propeller

Subscripts

c	cavitation
f	fluid
g	gas
l	blade loading
m	model
s	ship
t	blade thickness
v	vapour, volume
x	dimensionless bubble radius
0	initial
∞	at infinity, external

Superscript

*	complex conjugate

Operators

$\dot{A}$	time derivative of A
ΔA	finite difference of A
d(A)	in the figures, first time derivative of A
dd(A)	in the figures, second time derivative of A

INTRODUCTION

Marine screw propeller located at the stern of a ship operates in a flow affected by the hull. The ship wake, which is a decelerated, non-uniform inflow into the propeller disc, has certain negative effects on its operation. Apart from the desired steady thrust component developed by the propeller, an unwanted unsteady loading is experienced by propeller and ship. These periodic loads, called "bearing forces", are transferred through the shaft and the bearings to the ship structure. The magnitude of these unsteady loads depends mainly on the non-uniformity of the wake and usually does not exceed 5% of the steady components, i.e. thrust and torque. A rotating propeller induces an unsteady pressure field which affects the submerged part of the hull as "surface pressures and forces".

In general, propellers of surface vessels are designed to carry the loading at which cavitation is unavoidable. The occurrence and extent of this cavitation depends on the angular position of the blades. The main reasons for cavitation unsteadiness are a non-homogeneous inflow into the propeller disc (ship wake), resulting in unsteadiness of blade loading, and hydrostatic pressure variation experienced by the rotating blades. Fluctuating cavitation is responsible for the fact that the vertical surface force considerably exceeds the vertical bearing force. Thus unsteady cavitation is usually the main cause of ship vibration problems. The pressure induced by unsteady cavitation decreases much slower with distance than the contributions of the non-cavitating propeller. Moreover, this pressure also comprises high-frequency components and thus it is the main source of the underwater noise generated by vessels. The primary source of high-frequency noise is the collapse of free cavitation bubbles. This noise contributes to crew discomfort, may interfere with the sonar systems of a research vessel and may promote the detection of a naval vessel by enemy sensors [1].

Fig. 1 is the illustration of the above described effects on the propeller-induced pressure. Description of the evaluation of pressure induced by the non-cavitating propeller and the method of calculating the cavitation fixed with the blades can be found in the literature [2 - 11]. The details of the approach adopted in the following are given in reference [12].

Scope of the work

The problem of theoretically evaluating the broadband pressure induced by the cavitating marine screw propeller is considered in the following. The method of evaluating the number and mean size of free cavitation bubbles generated by a break-off of the unsteady sheet cavitation of a screw propeller is presented. The size distribution of bubbles thus generated is proposed. The collapse of free bubbles downstream of the blade-fixed cavities is discussed and the formulae for numerical evaluation are given. In particular, the formula for the collapse time of a bubble subjected to the linearly increasing pressure is derived. The computer implementation of the presented method is outlined. The computed results in the form of noise level spectra are presented and compared to the experimental data.

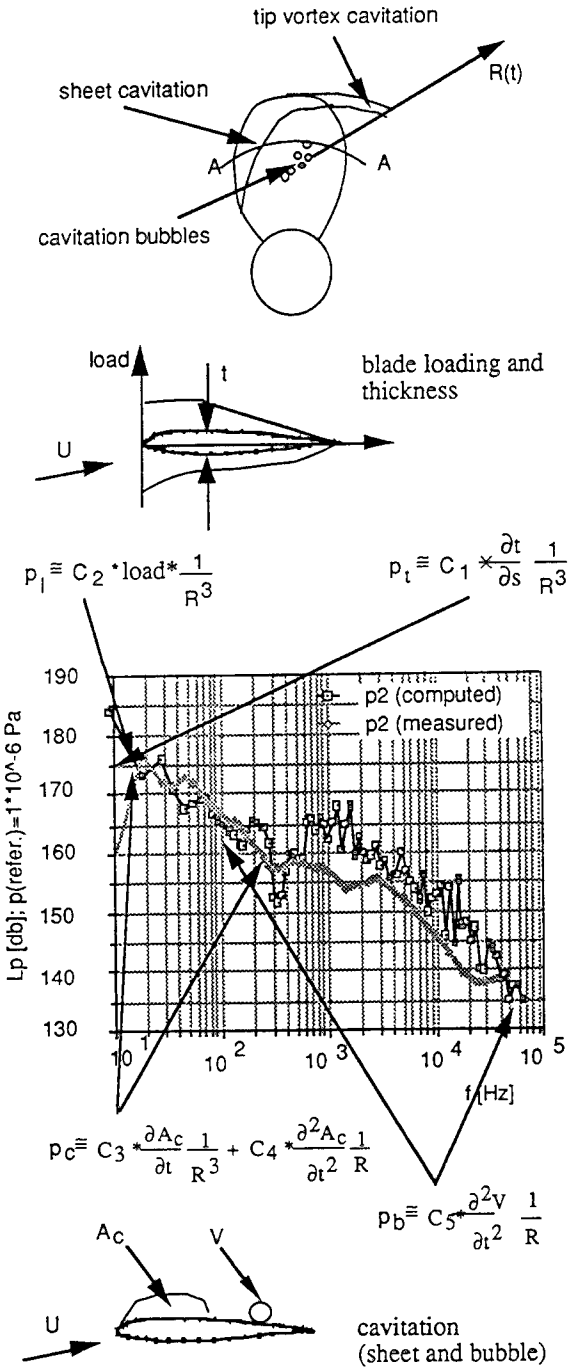

Fig. 1 Components of the propeller-induced unsteady pressure- schematic summary.

CAVITATION-INDUCED HIGH FREQUENCY NOISE

General

The literature survey of the methods of evaluating the propeller cavitation noise conducted by Pylkkänen [13] summarizes the published approaches. Most of them rely on model-scale cavitation tests. Thus there is a relatively large number of publications dealing with the scaling of propeller noise. A theoretical approach to the problem presented by Gravastrand [14] considers cavitation bubble growth and collapse in a partially constant pressure field. Okamura & Asano [15] use a semi-empirical approach. This allows an estimation of the high-frequency noise from the main particulars of the propeller and from the global sheet cavitation information. Weitendorf [16] and Isay [17] suggest the use of the so-called bubble tracing method. In this method the growth and collapse of the bubbles, when passing the low pressure region of the propeller blade suction side, is evaluated.

Ross [18] presented an analytical method of evaluating the pressure induced by a collapsing cavitation bubble at the instant of the rebound. Morozov [19] pointed out that the broadband character of the noise spectrum is the result of a large number of bubbles collapsing nearly simultaneously. Assuming random time intervals between the pressure peaks of assumed analytical form, Morozov derived the formulae for the power spectral density of the entire process of bubble cloud collapse.

Bark [20] conducted cavitation observations and pressure measurements for the harmonically pitching hydrofoil and model propellers operating in a ship model wake. His observations relate the collapse of the disintegrated fixed cavities to the induced pressures.

Fixed cavitation break-off

Experimental results indicate that bubble cavitation and in particular bubble collapse are responsible for high-frequency noise induced by screw propellers [21]. The volume variation of attached sheet cavitation is far too slow to induce high-frequency noise. Free bubble generation is associated with the break-off of fixed cavitation at the downstream end. The phenomenon is discussed by Knapp et al in reference [21] for cavitating axially symmetric bodies. Even for stationary flow conditions, an unsteadiness of fixed cavitation is observed. This is attributed to the re-entrant flow at the downstream end of the cavity. When reaching the upstream end of the cavity, this re-entrant jet may in an extreme case suppress the cavitation. Less violent contacts of the re-entrant jet with the inner surface of the cavity cause periodic break-offs of the latter. This break-off mechanism as well as diffusion of the air nuclei from the liquid flowing into the cavity [22] generate free cavitation bubbles. These bubbles are convected by the flow into the higher pressure region and collapse, inducing noise. An experimentally obtained distribution of damaging cavitation blows in relation to the attached sheet cavity, presented in reference [21], supports this hypothesis. The cycling of cavitation of the lifting surfaces (struts, hydrofoils and propeller blades), in steady flow conditions, is far more limited. The re-entrant jet thickness in relation to the cavity length is smaller, which might be the reason for stability of the partial cavitation of the hydrofoils for cavity relative lengths $\ell < 0.75$. The instability region $0.75 < \ell < 1.15$ can be understood as cavitation cycling. However, this uncertainty region is limited to a restricted range of flow parameters which are irrelevant for a well-designed propeller. For these reasons this phenomenon will not be discussed further, although it might be the main source of noise induced by a poorly designed screw propeller operating in a strongly non-homogeneous wake field.

Generation of free bubbles in unsteady flow conditions

Bark [20] observed in model scale the disintegration of cavities and their collapse in unsteady flow conditions. The break-off of the fixed cavitation, filmed during the tests, was complex and often took place in stages. Although the collapse of the attached and disintegrated patches of sheet cavitation were noted, spherical, small-diameter bubbles were also observed. The collapse of these spherical bubbles was associated with violent pressure peaks. The rebound of collapsing cavities was observed and a generation of sharp pressure peaks associated with it was noted.

The following model of free cavitation bubble generation is proposed. The attached cavity grows in the low ambient pressure region through the expansion of air nuclei convected to it by surface diffusion and the re-entrant jet, and by the liquid vaporization. At this phase there is no net generation of free cavitation bubbles. Propeller cavitation observations reported in references [23, 24, 25, 5] can be considered to support this model.

The decrease in the sheet cavitation volume is associated with cavity break-off. At this stage the re-entrant flow is insignificant. The downstream end of the cavity tears itself off into free bubbles. This is illustrated in Fig. 2.

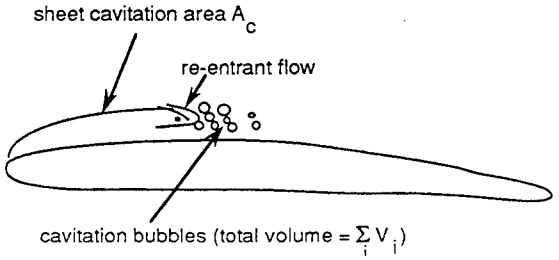

Fig. 2. Generation process of free cavitation bubbles.

The volume rate of bubbles generated in the process equals the rate at which the sheet cavity volume decreases times the relative gas & vapour volume β in the sheet, and it can be expressed as follows

$$\frac{d}{dt}\left(\sum_{i=1}^{n} V_i\right) = -\beta \frac{d}{dt}(A_c)\, d\rho \quad \text{for } \frac{dA_c}{dt} < 0$$
$$\frac{d}{dt}\left(\sum_{i=1}^{n} V_i\right) = 0 \quad \text{for } \frac{dA_c}{dt} > 0 \qquad (1)$$

where V_i is the volume of ith bubble, $d\rho$ is the blade span differential and and n is the total number of bubbles.

Size distribution of the cavitation bubbles shed from the fixed cavity

The initial size of the bubbles generated as an effect of the fixed cavity tearing-off is proposed to be represented by the beta distribution [26]. Its density probability function is of the form

$$f_x(x) = m\,(1 - x)^{m-1} \qquad (2)$$

where

$$x = R/(0.5\,\eta_c) \tag{3}$$

is the dimensionless bubble radius and η_c is the fixed cavitation thickness at the point of the break-off. m is a constant.

The proposed density function (2) is presented in Fig. 3 for the value of constant m = 9.

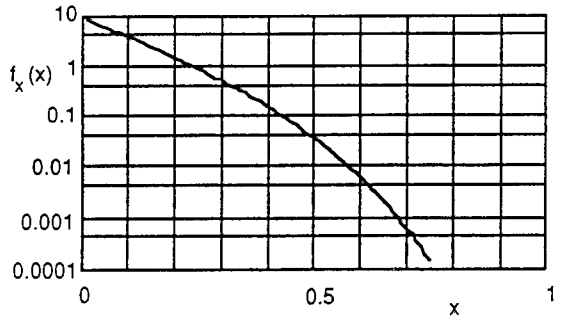

Fig. 3. The proposed probability density function of the cavitation bubbles radius generated as the result of the tearing-off of the fixed cavity.

Thus it is assumed that the diameter of the bubbles leaving the trailing edge of the sheet cavitation does not exceed the maximum thickness of the fixed cavity. This assumption and the feature of the maximum size limit of the applied density function (2) is in agreement with the proposed model of the free bubble generation. Moreover, this function has the following attractive features. It describes a fractal form with a dimension m - 1. Hence the number of bubbles increases rapidly with the decreasing radius. Although there is no quantitative experimental evidence available on the matter, photographs presented in reference [27] support qualitatively this type of a bubble cloud distribution. In reference [28] the structure of a bubble cloud is described which can be regarded as fractal. There is no reference made to the type of process which generated the cloud. Using the means of the parametric study, the constant m in formula (2) was chosen to be m = 9. This study involved the computation of noise for three marine screw propellers for which the experimental data was available [29, 25, 30].

Stereophotogrammetry of the sheet cavitation at the break-off [31] indicates that its chordwise thickness distribution $\eta(s)$ can be approximated by the shape function of the turbulent boundary layer on a flat plate, i.e. $\eta(s) = \text{constant}*s^{4/5}$. Thus the maximum thickness of the fixed cavity at the point of the break-off is obtained from the length and area of the sheet cavitation

$$\eta_c = 1.8\,(A_c/l_c). \tag{4}$$

Four other initial bubble size distributions were also tried. They are presented in reference [12]. The beta distribution with m = 9 gave the best numerical agreement with the experimental values. The final results of these computations are presented in the next section. The high fractal dimension of this distribution (m - 1 = 8) indicates that the formation of the bubble cloud is a very complex dynamic process. However, the detailed mathematical modelling of this process is beyond the scope of this paper and will not be discussed here. Instead the globally better understood vapour-gas-mixture continuity relation and the deduced bubble size distribution is used. Qualitatively the cavitation break-off process and the complexity of it are described by Bark [20]. Different modes and stages of the attached cavitation disintegration and the fact that the thickness of the bubble cloud exceeds the thickness of the sheet cavitation [20] indicate that break-off is indeed the result of a complex process. The proposed model can be considered to represent the final stage of sheet cavitation disintegration.

For the beta type of bubble size distribution given by formula (2), the mean value of the bubble dimensionless radius is

$$\bar{x} = 9\int_0^1 x\,(1-x)^8\,dx = 0.1\ . \tag{5}$$

The spherical bubble non-dimensional volume equals $v(x) = 4/3\,\pi x^3$ and thus the derived volume density function in terms of the radius is

$$f_v(x) = f_x(x)\,\frac{dx}{dv} = \frac{m}{4\pi}\,\frac{(1-x)^{(m-1)}}{x^2}. \tag{6}$$

For m = 9 the mean value of the bubble volume is

$$\bar{v} = \int_0^{v(x=1)} v\,f_v(v)\,dv$$
$$= 12\pi\int_0^1 x^3(1-x)^8\,dx = v(x = 1.6565\,\bar{x})\ . \tag{7}$$

The integrand of (7) is plotted in Fig. 4 showing that the main part of the free cavitation volume is shed downstream of the fixed cavity in the form of bubbles of the diameter close to 10% of the sheet cavitation thickness at the point of the break-off.

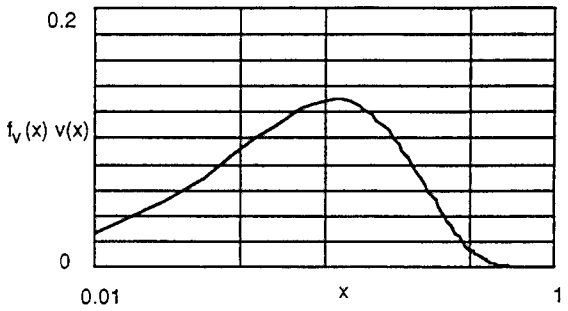

Fig. 4. Volume distribution of the free bubbles generated as the result of the sheet cavity break-off.

The condition (1) of the vapour & gas mixture continuity yields

$$\frac{d}{dt}(n\,\bar{V}) = -\beta\,\frac{d}{dt}(A_c)\,d\rho \tag{8}$$

where

$$\overline{V} = (\eta_c/2)^3 \overline{v} . \qquad (9)$$

Assuming that the mean value of the bubble volume is constant within the finite time increment Δt, equation (8) yields the total number Δn of the generated bubbles for the blade length $d\rho$ and within time step Δt

$$\Delta n = \frac{-\beta}{\overline{V}} \left[A_c(t + \Delta t) - A_c(t) \right] d\rho . \qquad (10)$$

This model of free bubble generation excludes the vapour liquidisation. Moreover, spanwise flow of the vapour and gas mixture contained by the cavitation sheet towards the blade tip is disregarded. The latter is expected to be of importance in the case of highly skewed propellers. This three-dimensional effect, which stabilizes fixed cavitation, might be the reason for the reduced pressures and noise of propellers with skewed blades.

Collapse of free bubbles

The bubbles generated as a result of the fixed cavitation break-off are rapidly accelerated by the water flow downstream of the fixed cavity. The bubbles are assumed to be spherical in shape. Their radii are small compared with their relative distances, and their velocity is assumed to be equal to the local flow velocity. These assumptions allow us to disregard their interaction and coalescence in particular. Rapid films of reference [27] support the assumption of zero slip velocity. Thus collapse of the bubble cloud can be treated as collapse of the individual bubbles. Moreover, the effect of the solid boundary, which is the blade surface, on the dynamics of the bubbles is disregarded, too.

Partial cavitation cuts off the sharp pressure peak at the leading edge of the blade. The pressure at the non-cavitating portion of the hydrofoil increases monotonically from the vapour value p_V to the static pressure value p_0 at the trailing edge. For the sake of simplicity, this pressure growth is assumed to be linear, that is of the form

$$p_\infty(t) = p_V + \frac{t}{t_t} (p_0 - p_V) \qquad (11)$$

where $t_t = (c - l_c)/U$ is the time of travel of a flow particle from the downstream end of the sheet cavity to the trailing edge of the hydrofoil, c is chord od the hydrofoil, l_c is the chordwise length of the sheet cavitation and U is velocity of the blade section. The above assumption means that the perturbed flow velocity is neglected when evaluating the chordwise position of a bubble. Moreover, the effect of the boundary layer downstream of the fixed cavity on the bubble translational motion is disregarded, too. p_∞ will be called the external pressure in the following. The ∞ index means that this bubble-collapse-driving pressure extends in space as constant over the radial distance $r >> R$.

Relation (11) can also be written as

$$p_\infty(t) = p_V + \frac{t}{c - l_c} \frac{1}{2} \rho_f U^3 \sigma(\rho,\theta) \qquad (12)$$

where $\sigma(\rho,\theta)$ is the cavitation number at the blade section located at the radius ρ and angular position θ, ρ_f is water density.

Collapse time of vapour bubble

In references [21, 32], the time of collapse of a bubble subjected instantaneously to a pressure jump is shown to be

$$\tau = 0.91468 \, R_0 \sqrt{\rho_f / p_\infty} . \qquad (13)$$

This formula was derived by Rayleigh. Viscosity, liquid compressibility and bubble surface tension were disregarded. Assuming that pressure variation given by formula (12) is slow when compared with the bubble collapse time, disregarding surface tension, compressibility and viscosity effect the following generalization of the Rayleigh equation

$$\frac{dR}{dt} = \sqrt{\frac{2 (p_V - p_\infty)}{3\rho_f} \left[1 - \frac{R_0^3}{R^3} \right]} \qquad (14)$$

for the bubble wall velocity is proposed

$$\frac{dR}{dt} = \sqrt{\frac{2 (p_0 - p_V) \, t \, (R_0^3 - R^3)}{3\rho_f \, t_t \, R^3}} . \qquad (15)$$

Formula (15) yields after integration an estimate of the time of bubble collapse due to linearly increasing external pressure

$$t_c = (3\tau/2)^{2/3} (t_t)^{1/3} \text{ for } t_t > t_c . \qquad (16)$$

For the fully cavitating foil sections, $t_c = \tau$ is taken.

Vapour bubble collapse in a linearly increasing pressure field

The equation for bubble collapse, including the effect of liquid compressibility,

$$\begin{aligned} &R \ddot{R} \left(1 - \frac{\dot{R}}{a}\right) + \frac{3}{2} \dot{R}^2 \left(1 - \frac{\dot{R}}{3a}\right) \\ &= H \left(1 + \frac{\dot{R}}{a}\right) + R \frac{\dot{H}}{a} \left(1 - \frac{\dot{R}}{a}\right) \end{aligned} \qquad (17)$$

was derived by Gilmore and quoted here after reference [21]. In this equation

$$a = a_0 \left[\frac{P + B}{p_\infty(t) + B} \right]^{\frac{n-1}{2n}} \qquad (18)$$

is the local velocity of sound in the liquid and

$$H = \frac{n (p_\infty + B)}{(n-1)\rho_f} \left[\left(\frac{P + B}{p_\infty + B} \right)^{(n-1)/n} - 1 \right] \qquad (19)$$

is the pressure function at the bubble wall with the assumption of isentropic compression. For water, constants

$B = 3*10^8$ Pa, n = 7 and a_0 = 1450 m/s are taken.

For the special case of linearly increasing external pressure, which is given by formula (11), disregarding viscosity, gas compression within the bubble and wall surface tension, it can be shown that the time derivative of the pressure function is given by

$$\dot{H} = \frac{D}{p_v + Dt + B} H - \frac{D}{\rho_f}\left[\frac{P+B}{p_v + Dt + B}\right]^{\frac{n-1}{n}} \qquad (20)$$

where $D = (p_0 - p_v)/t_t$ is the slope of the external pressure increase. Moreover, the pressure at the bubble wall was taken to be constant and equal to the vapour value, that is $P = p_v$.

Inclusion of the surface tension and isentropic compression of the gas contained by the bubble leads to a pressure at the bubble wall in the form of

$$P(R) = p_{g0}\left[\frac{R_0}{R}\right]^{3\gamma} - \frac{2S}{R}. \qquad (21)$$

In formula (21) p_{g0} is the initial pressure within the bubble and S is surface tension.

The time derivative of the pressure function in the case of linearly varying external pressure equals

$$\dot{H} = \frac{D}{p_v + Dt + B} H - \frac{D}{\rho_f}\left[\frac{P+B}{p_v + Dt + B}\right]^{\frac{n-1}{n}} + \frac{R}{\rho_f R}\left[\frac{p_v + Dt + B}{P+B}\right]^{\frac{1}{n}}\left[\frac{2S}{R} - 3\gamma p_{g0}\left(\frac{R_0}{R}\right)^{3\gamma}\right] \qquad (22)$$

where $p_{g0} = p_v$ for the compressible, non-condensable vapour is taken.

In the case of supercavitation, the bubble is subjected to an instant increase in pressure up to the value p_0 at the trailing edge. In this case the above formulae can be used by substituting in (22) vapour pressure p_v by the pressure at the trailing edge p_0 and setting D = 0. Although the static pressure at the trailing edge is time dependent, this dependence is much weaker than the pressure variation acting on a bubble due to a chordwise travel, i.e. $dp_0/dt << D$. Thus it is justifiable to neglect the former dependence when time derivatives explicitly present in bubble dynamics equations are evaluated.

The case of a partially cavitating foil is simulated using the bubble collapse model presented above. The conditions are realistic for a full-scale propeller. The distance from the point of break-off to the trailing edge is 1 m and the propeller diameter is 5 m. The rate of propeller revolution is 118 rpm, the radial hydrofoil location is at $\rho = 2$ m and the considered blade is at the uppermost position. The propeller submergence is h_0 = 3.5 m. The fourth-order Runge-Kutta method was used in solving the Gilmore equation for bubble collapse. The surface tension and compression of the vapour were taken into account. The initial radial velocity of the bubble was taken to be zero, that is $dR_0/dt = 0$ and the initial bubble radius was taken to be $R_0 = 1$ mm. The results of the computations are presented in Figs. 5 to 8. In the following figures, d(R) and dd(R) denote the first and second time derivatives of the bubble wall radius, that is bubble wall velocity and acceleration. Volumetric acceleration is denoted by dd(V).

The collapse time of the bubble yielded by formula (16) is $t_c = 0.877$ ms for the case presented above. Thus compressibility of the liquid and vapour slightly increases the collapse time.

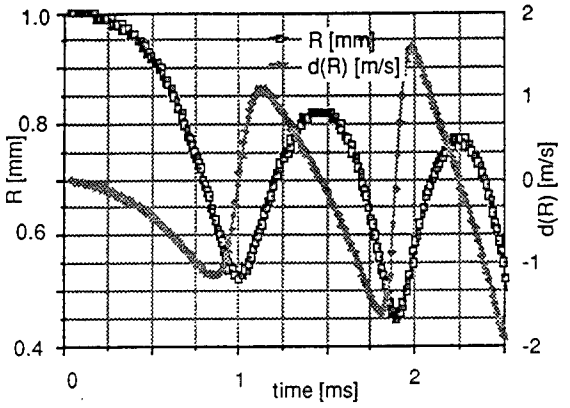

Fig. 5. Spherical bubble collapse and rebounds in linearly increasing pressure field downstream of the partial cavity (bubble radius and wall velocity).

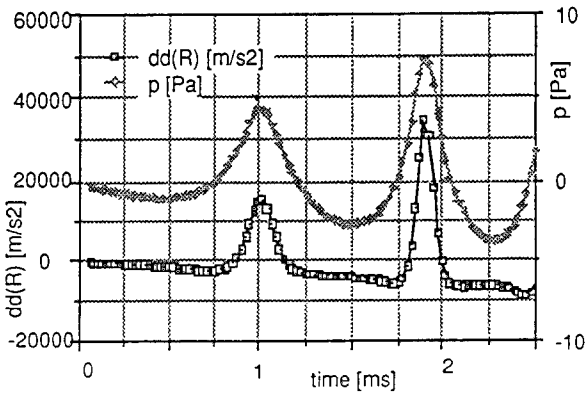

Fig. 6. Spherical bubble collapse and rebounds in linearly increasing pressure field downstream of the partial cavity (bubble radial accelerations and field pressure at 1 m distance).

The consecutive rebounds require shorter times. The volumetric acceleration associated with them gets narrower and the maximum bubble radius decreases. Thus each consecutive rebound induces higher frequency noise of decreasing power. This is seen in Fig. 7 as the peaks of the noise spectrum at the frequencies exceeding 1.2 kHz. At the instant of rebound the radial velocity of the bubble equals zero and thus volumetric acceleration and noise are directly related to the radial acceleration. The peak value of the latter is governed by the gas compression within the bubble. In Fig. 7 the power spectral density of the pressure induced by the collapsing bubble of Figs. 5 and 6 are presented. A single bubble of 1 mm radius and a cloud of one hundred bubbles of the same initial size, leaving the fixed cavity at random instants within 24 degrees of propeller rotation, in the external pressure field increasing linearly from the vapour value with the rate of 2.8 MPa/s, are considered. The spectra do not differ by the constant factor only. Their shapes are different, too. In the high-frequency range ($f > 1/t_c$) this difference is related directly to the bubble number ($10 \log 100 = 20$). At the frequencies $f < 1/t_c$ the difference in the height of the spectra is larger and it grows inversely with the frequency. This is because the bubbles do not leave the fixed cavity at the same time. Each of them is at a different phase

of collapse. As a result an irregular time-history of the induced pressure forms. A sample of this pressure signal is shown in Fig. 8.

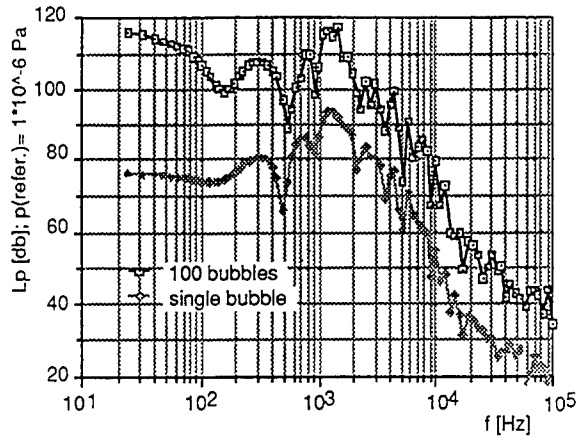

Fig. 7. Power spectral density of the pressure at 1 m distance from a collapsing single bubble and from a cloud of one hundred bubbles of 1 mm radius in the linearly increasing external pressure (partially cavitating blade section).

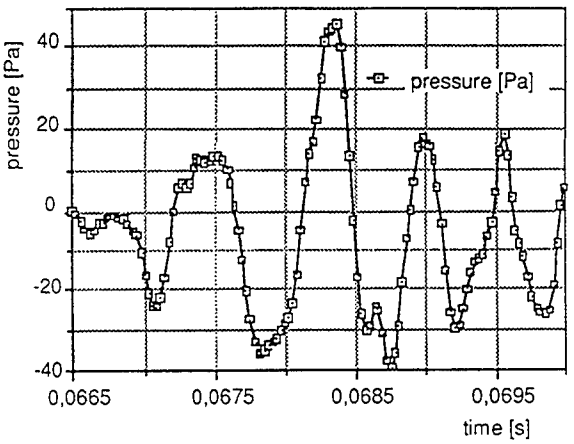

Fig. 8. A sample of the pressure time-history induced by a collapsing cloud of one hundred cavitation bubbles of 1 mm radius (partially cavitating blade section).

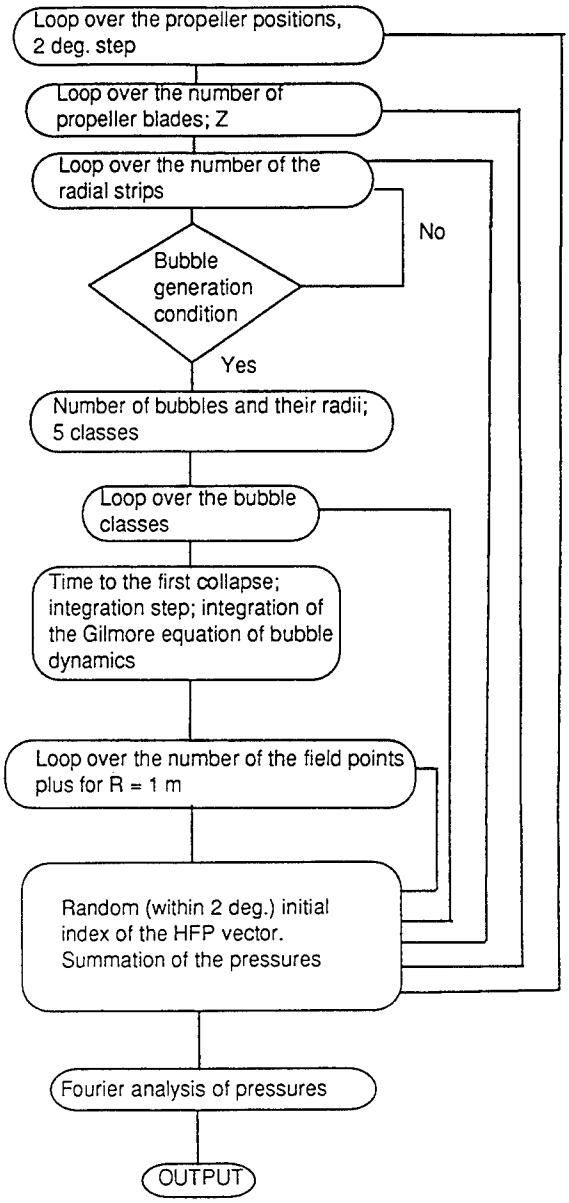

Fig. 9 Block diagram of the numerical scheme for the evaluation of the high-frequency noise induced by a cavitationg propeller.

Computer implementation of the numerical simulation of the propeller-induced noise

The method was computer coded using the FORTRAN 77 programming language. The code is vectorized in order to minimize the execution time on the CRAY X-MP EA/432 supercomputer. The total length of the computer program is 5309 lines. Thus it is not feasible to present a detailed description of the code here. Only the main features of it and the crucial details concerning the numerical implementation and the form of results presentation are given in the following. The procedure is illustrated in Fig. 9.

Having the results of the unsteady lifting surface computation [33], in the form of the unsteady load at the eight equally spaced strips the blade is divided into, fixed cavitation is evaluated with the spacing of the blade angular position of two degrees, that is $\Delta\theta = 2$ deg. The quasi-steady, two-dimensional and linear approach of Geurst [3] is used when evaluating sheet cavitation. Differentiation of the fixed cavitation volume is conducted using the three point symmetric finite difference scheme. Low-frequency pressures induced by the blade thickness and loading, and by the

fixed cavitation, are calculated for each of the 180 blade positions, that is for the 180/Z angular positions of propeller. Thus the time history of the propeller-induced pressure is computed for the blade-passing period $T_b = 2\pi/(\Omega Z)$ and for the points for which coordinates are given as the input data. An additional, fictious field point located at 1 m distance from the propeller disc is considered, too. For this point the far field solution is applied, in which only the effect of cavitation is considered. Thus the distance R from the control point on the blade to this fictious point is taken to be constant and equal to 1 m. In the results presented in the next section this point is depicted on the figures by "p at 1 m". These values can be extrapolated to higher distances with an assumption of the linear acoustics and the undisturbed pressure propagation in an unbounded, homogeneous medium

$$p(r,t) = \frac{\rho_{f0}}{4\pi r} \ddot{V}(t - r/a_0) \tag{23}$$

where

$$\ddot{V} = 4\pi (R^2\ddot{R} + 2R\dot{R}^2) \tag{24}$$

is volumetric acceleration of bubble.

For each blade position and for each blade section condition (1) is checked. The total number of cavitation bubbles (10) and their mean volume (9) are evaluated for the cases of sheet cavitation shrinking. The ratio of gas & vapour volume to the total volume of the sheet is assumed to be β = 0.8. The probability density function (2) is discretized by the five bubble dimensionless radii. For each bubble class determined by the radius R and time t_t the time to the first rebound t_c is evaluated using the formula (16). Integration of the Gilmore equation (17) is conducted for each bubble class using the fourth-order Runge-Kutta method. The simulation period is set to 3.5 t_c. The time step Δt of this integration is selected as follows. The blade-passing period is divided into the 131072 instants. Thus the sampling period of the computed noise is $\Delta t_n = T_b$ /131072. The integration step is selected to be the smaller of the two values: Δt_n and 3.5 t_c/4000. The computed time history of the induced high-frequency pressure caused by a single bubble class is added as many times as there are bubbles in the class into the total pressure vector HFP which covers the entire blade-passing period. The first element of the HFP vector, during this copying scheme, is governed by the angular position of the propeller and by a random integer value. This insures a random instant of bubble generation within a 2 deg. interval of blade angular position. This summation is repeated for all bubble clouds and bubble classes resulting in the time-history of a broadband pressure.

The results of computations are presented in the raw form without any attempt to scale them. In order to cover a sufficiently broad bandwidth and to reveal all relevant features of data the frequency axis is given in a logarithmic scale. The ordinate is given in a logarithmic scale as well, with the following definition of noise level [34, 18]

$$L_p(f)\ [db] = 20 \log[P(f)/p_{refer.}] \tag{25}$$

where the reference pressure is taken to be $p_{refer.}$ = 1 μPa and P(f) is understood as the root-mean-value (rms).

Computation of (25) is conducted using the standard procedures of signal processing [35]. The Fourier transform of the broadband pressure is evaluated using the Fast Fourier Transform method yielding the complex pressure spectrum P(f) discretized with the frequency resolution $\Delta f = 1/T_b$. The one-sided power spectral density of the pressure is obtained from the following

$$S_p(f) = 2\ T_b\ P(f)\ P^*(f) \tag{26}$$

where $P^*(f)$ is the complex conjugate of the P(f).

The noise level is thus finally obtained from the following expression

$$L_p(f) = 10 \log[S_p(f)\ \Delta f/p^2_{refer}] \tag{27}$$

The resolution Δf, which equals the blade-passing frequency, does not allow the presentation of the low-frequency part of the noise spectrum as distinct peaks. Instead a broken line connecting the peak values is plotted in the results presented in the next section. The high frequency portion of the spectra is smoothed by calculating the mean of eleven adjacent values for each spectral line.

Results of the numerical simulation of the propeller-induced noise measurements

The method described above was verified by conducting the computations of noise for a number of marine propellers for which the experimental results are available in the open literature and for a coastal service boat. This simulation included both the full- and model-scale measurements. In these experiments low frequency pressure and noise were measured by the transducers and hydrophones mounted at the ship and model sterns close to the propeller. For this reason computations were conducted taking into account the effects of blade thickness and loading on the induced pressures. In the case of the coastal service boat the measurements were conducted with stationary hydrophones.

In Figs. 10 and 11 the results of computations are compared to the measured values in terms of the noise level for the product tanker M/T Pasadena. She was the subject of the Nordic co-operative project dealing with structure-borne sound in ships from propellers and diesel engines [30]. Noise measurements in the full-scale and tests in the cavitation tunnels were conducted. The results of the measurements are plotted as the interpolated values read from the figures and tables of references [36] and [30]. The model-scale experimental values are the "mean levels" of reference [36]. The advance ratio J in the following figures is based on the mean value of the axial velocity in the propeller plane.

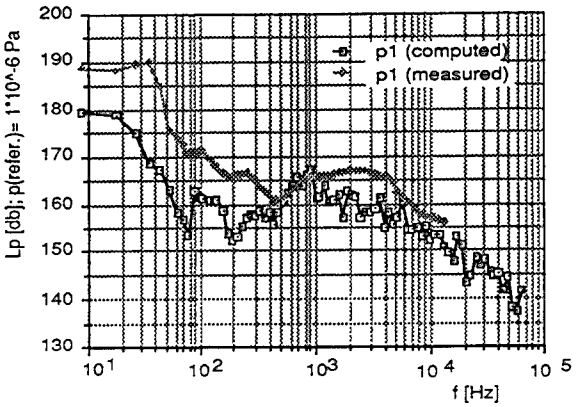

Fig. 10. Noise spectrum of the M/T Pasadena (full-scale). Measuring point 1 at the condition B of the reference [36] (V_S = 16,3 kn, Ω = 132 rpm).

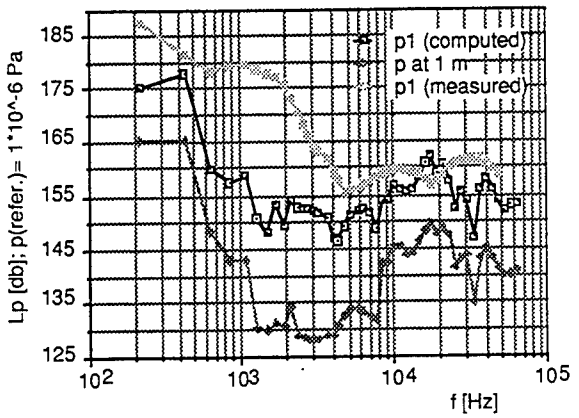

Fig. 11. Noise spectrum of the M/T Pasadena (model test in scale λ = 23,7 in the cavitation tunnel). Measuring point 1 at the condition B of reference [36] (Ω_m = 3227 rpm and J = 0,385 corresponding to the full-scale values V_s =16,3 kn and Ω_s = 132 rpm).

The main features of the measured noise spectra are well reproduced. That is, the maxima and minima are of nearly the same value and they are located at the same frequencies. Also the slopes of the spectra are of similar values. The biggest discrepancy is in the frequency bandwidth starting approximately at twice the blade-passing frequency and extending to the local minimum of the spectra (300 Hz in the full-scale). In the model test the effect of noise reflection from the tunnel walls may be affecting the measured values [37]. Another explanation for these differences is the inaccuracies in the evaluation and numerical differentiation of the fixed cavitation volume. In this intermediate frequency region the form of the noise spectrum is primarily governed by the higher harmonics of the pressure induced by the fixed cavitation (Fig. 1) and secondarily by the number of free bubbles. The pressure induced by the fixed cavitation is related to the second time derivative of the volume, while the number of free bubbles is related to the finite difference of the volume (formula (10)). Moreover, as there is good agreement of the noise in the high frequency region, it can be concluded that the main reason for the discrepancies, apart the spurious noise of the measurements, is the inaccuracies in the evaluation of fixed cavitation. The assumption of the sheet cavitation's quasi-steady character, which results in a distortion of the details of cavitation volume time history, can be blamed for the differences in the intermediate frequency range.

The results of the computed noise for the containership Sydney Express and her models are presented in Figs. 12 to 14. The measured values are read from the figures of the references [29] and [25]. The detailed propeller and other relevant data were also taken from these references. Model experiments of Sydney Express were conducted following the cavitation and Froude similarity test conditions [25, 29]. The noise level up to the frequency 10 kHz is rather well reproduced by computations in the bigger model propeller case. For the smaller model propeller the bandwidth of good agreement is significantly smaller.

The results of the noise induced by the single screw coastal service boat are presented in Figs. 15 and 16. Measurements were conducted in shallow water (approximate depth of 25 m).

The clear effect of the reflections from the water surface and sea bottom is a deformation of the noise spectra at the low frequency range (up to 1 kHz). The high-frequency noise propagates without significant distortion. Propagation of the higher frequencies can not be regarded as being either a pure plane or purely spherical acoustic waves. This transmission loss effect in shallow water is discussed by Urick [38]. In reference [38] at short distances spherical spreading is applied. For higher ranges the sound pressure attenuation is lower and is given by the formula $p^2(r) = p_0^2 r^{-3/2}$. For still higher distances the cylindrical spreading of noise is assumed leading to the pressure attenuation of the form $p^2(r) = p_0^2 r^{-1}$. The computed results were obtained with the assumption of ideal spherical spreading. Judging from the measured noise level difference at these two field locations the cylindrical spreading is more suitable in this shallow water case and the considered range.

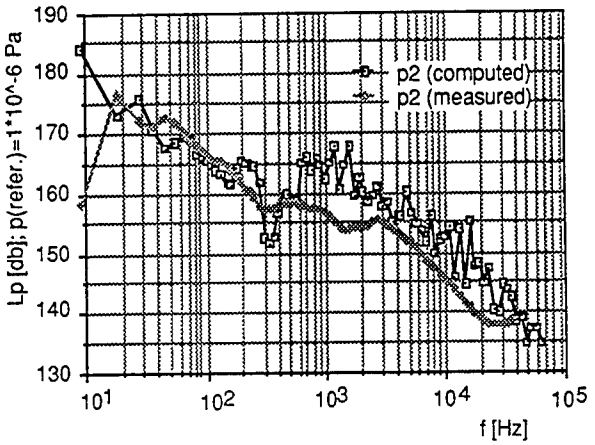

Fig. 12. Noise spectrum of the Sydney Express (full-scale). Measuring point 2 at a speed of 22 knots and propeller-shaft speed of 110 rpm.

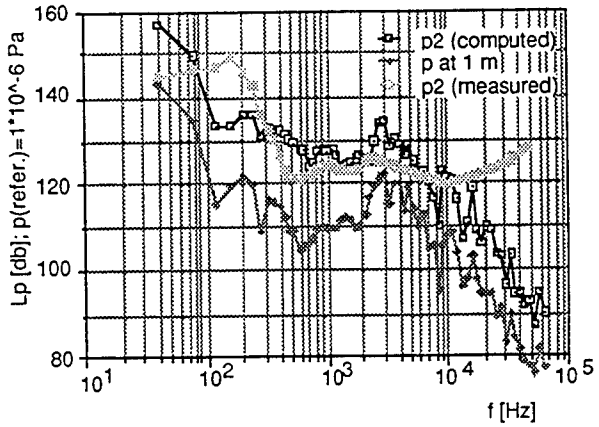

Fig. 13. Noise spectrum of the Sydney Express (model test in scale λ = 18,7 in the cavitation tunnel). Measuring point 2 at a speed of 22 knots and propeller-shaft speed of 110 rpm, corresponding to the model condition of Ω_m = 474 rpm, J = 0,654.

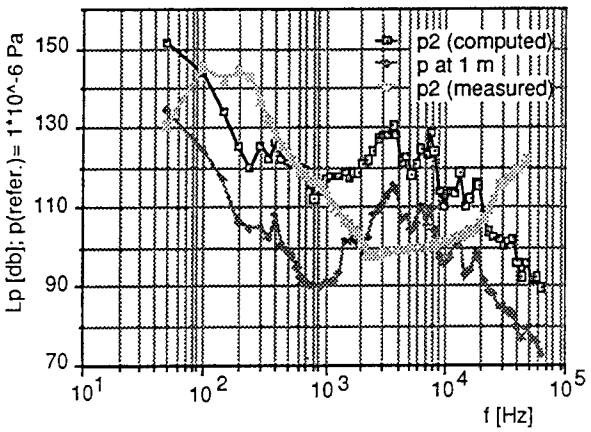

Fig. 14. Noise spectrum of the Sydney Express (model test in scale $\lambda = 28$ in the cavitation tunnel). Measuring point 2 at a speed of 22,4 knots and propeller-shaft speed of 109,5 rpm, corresponding to the model condition of $\Omega_m = 580$ rpm, $J = 0{,}677$.

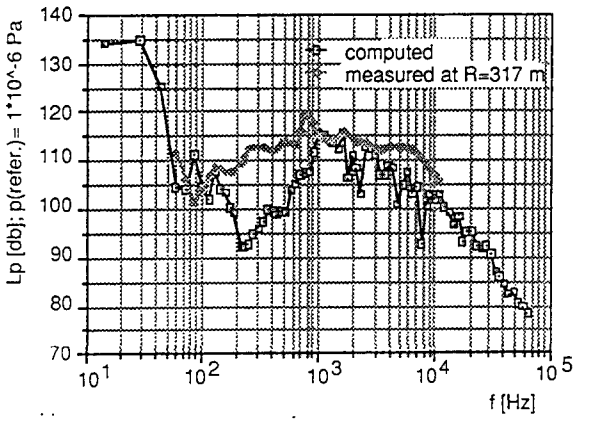

Fig. 15. Noise level of the coastal service boat. Measurement conducted 317 m port of the ship.

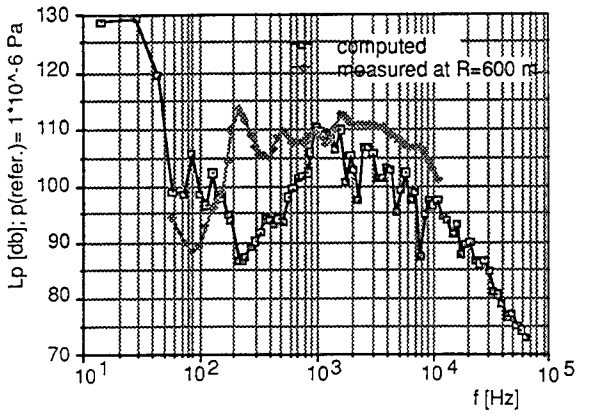

Fig. 16. Noise level of the coastal service boat. Measurement conducted 600 m port of the ship.

CONCLUSIONS

The approach presented results in broadband propeller-induced pressures which agree well with the available measured results. The method is applicable for cavitating marine screw propellers of normal type. High-frequency noise due to a non-cavitating propeller is not dealt with. The reason for this is its minor importance in the case of normally operating surface vessel. Although the method is theoretical, it requires certain experimentally obtainable data. This is the nominal model wake of the vessel and the results of the model self-propulsion test. That is, the same data are needed as are used in preparing the cavitation model test. Although the method requires much computer effort (approximately 12 min CPU time of the CRAY X-MP EA/432 supercomputer) it is cheaper than the cavitation tests. Calculations directly yield the prediction of the full-scale values and they are not affected by other deficiencies of experimental methods, such as spurious noise, reflections and other experimental errors.

There are, however, several open questions left. The tested cases were normal marine propellers of surface vessels which exhibited a moderate amount of the sheet type cavitation. It can be questioned whether this method can be used for the modern highly-skewed propellers. For these propellers the relation between the fixed cavitation volume variation and the volume of the generated free bubbles is probably affected by the three-dimensional effect of the spanwise flow. Moreover, as the method is based on potential flow approximation, it does not take into account viscous effects. As a result it fails to predict the noise measured at low Reynolds numbers. The lack of viscous effects may further contribute to the problems with dealing with the leading edge cavitation of highly-skewed propellers. For propellers exhibiting very short leading edge cavitation the linear approach which disregards blade thickness will result in too pessimistic prediction. Effects such as propeller-hull-vortex (PHV) and tip-vortex cavitation induced noise are disregarded. It remains uncertain whether the rather poor agreement in the intermittent frequency range is caused by the above-mentioned deficiencies of the measurements, or whether it is a problem of the fixed cavitation evaluation. The simplified model of the break-off, neglecting the collapse of non-spherical patches of sheet cavitation detached from the main cavity [20], may also be responsible for the poor agreement of the noise spectra in the intermediate frequency range. Some of these questions can be verified when the appropriate measured data are available.

The noise propagation model adopted in this method is that of the linear acoustic approximation yielding spherical spreading, for the unbounded, homogeneous medium. The vicinity of water and hull surfaces, sea bottom or water tunnel walls reflecting sound results in directional sensitivity, transmission anomalies and loss. These effects have a great influence, especially on the long pressure waves and noise at large distances. In this respect predicting the high-frequency noise generated by the cavitating propeller of a vessel in restricted waters is of importance also for hydroacoustic investigations.

ACKNOWLEDGEMENT

The generous assistance of the Finnish Navy in making it possible to verify the theory with measurements is very much appreciated.

REFERENCES

1. Keane, R. G. Jr. & Sandberg, W.C., "Naval architecture for combatants". Naval Engineers Journal, September 1984, pp. 47 - 64.

2. Gent, W. van & Oossanen, P. van, "Influence of wake on propeller loading and cavitation." International Shipbuilding Progress. 20(1973)228.

3. Geurst, I. A., "Linearized theory of two-dimensional cavity flows". Doctoral thesis, Delft University. 1961 Rijswijk Z-H. 209 p.

4. Hsu, C. C. & Shen, Y. T., "Unsteady partial cavity flows on foils." Proceedings of the Seventeenth Symposium on Naval Hydrodynamics. The Hague, Netherlands, Aug 1988. Vol 2. Pp. 31 - 46.

5. Johnsson, C.-A. & Søntvedt, T., "Propeller excitation and response of 230 000 twd tankers." Det Norske Veritas, publication No. 79. Nov 1972. 47 p.

6. Kaplan, P. et al, "Theoretical analysis of propeller radiated pressure and blade forces due to cavitation." Symposium on Propeller Induced Ship Vibration. London, 10 - 13 Dec., 1979. RINA. Pp. 133 - 146.

7. Lee, C.-S., "Prediction of the transient cavitation on marine propellers by numerical lifting-surface theory." Proceedings of the Thirteenth Symposium on Naval Hydrodynamics. Tokyo, Japan. Oct 1980. Published by The Shipbuilding Research Association of Japan. Pp. 41 - 64.

8. Matusiak, J., "Pressure fluctuations induced by a cavitating propeller." Seminar on Ship Vibration. Espoo 1982, VTT Symposium 24. Pp. 7 - 28.

9. Noordzij, L., "Considerations on the hull excitation force induced by a cavitating propeller." International Shipbuilding Progress 25(1978)288. Pp. 199 - 211.

10. Tamborski, L., "A study of the fluctuating hull surface forces induced by a cavitating propeller." Proceedings of the 4th Lips Propeller Symposium. Drunen, The Netherlands, October 1979. Pp. 21 - 51.

11. Tulin, M., P. & Hsu, C. C., "New application of cavity flow theory." Proceedings of the Thirteenth Symposium on Naval Hydrodynamics. Tokyo, Japan. Oct 1980. Published by The Shipbuilding Research Association of Japan. Pp. 107 - 130.

12. Matusiak, J., Pressure and noise induced by a cavitating marine screw propeller. Espoo 1992. VTT Publications. 80 p. + app. 22 p.

13. Pylkkänen, J., "Calculation of high frequency cavitation noise of marine screw propellers." Espoo 1991, Technical Research Centre of Finland, Ship Laboratory, Technical report LAI90102TR-1/2. 18 p.

14. Gravastrand, P.-T., "Sound pressure levels from cavitating propellers." 1981, Det Norske Veritas, Technical report 81-1070. 19 p.

15. Okamura, N. & Asano, T., "Prediction of propeller cavitation noise and its comparison with full-scale measurements." Naval Architecture and Ocean Engineering, 27(1989). Pp. 19 - 33.

16. Weitendorf, E.-A., "Cavitation phenomena, propeller excited hull pressure amplitudes and cavitation scale effect." Ocean Engineering 8(1981)5, pp. 517 - 539.

17. Isay, W. H., Kavitation. Hamburg, 1981, Schiffahrts-Verlag "Hansa" C. Schroedter & Co. 441 p.

18. Ross, D., Mechanics of underwater noise. 1976, Pergamon Press Inc. 375 p.

19. Morozov, V. P., "Cavitation noise as a train of sound pulses generated at random times." Soviet Physics, Acoustics. 14(1968). Pp. 361 - 365.

20. Bark, G., On the mechanisms of propeller cavitation noise. Doctoral thesis. Göteborg 1988, Chalmers University of Technology, Division of Mechanics. 267 p.

21. Knapp, R. T. et al., Cavitation. New York 1970, McGraw-Hill Book Company. 578 p.

22. Rozdzestwienskij, V.V., Cavitation. Leningrad 1977. Published by Sudostrojenie. 246 p., (in Russian)

23. "Cavitation photography and propeller-induced pressure measurements of the MS Arcturus." Espoo 1982, Technical Research Centre of Finland, Ship Laboratory, Research report LAI-286/82.

24. Chao, K.-Y., "Development of a practical computer program for the prediction of pressure fluctuations on the shell plating induced by a cavitating propeller in a wake field." Hamburg 1982, Forschungszentrum des Deutschen Schiffbaus, Report No. 137. 35 p. (in German).

25. Goetz, V. von, "Scaling effects on propeller cavitation." Hamburg 1986. Forschungszentrum des Deutschen Shiffbaus, report 175. 7 p. (in German).

26. Ang, A. H-S & Tang, W. H., Probability concepts in engineering planning and design. Volume 1. Basic principles. USA, 1975. 409 p.

27. Briancon, L. et al, "Transient bubbles interacting with an attached cavity and boundary layer." Journal of Fluid Mechanics 20(1990). Pp. 355 - 376.

28. Agrest, E. M. & Kuznetsov, G. N., "Dynamics of the bubble-size distribution in sound fields." Soviet Physics, Acoustics, 20(1974)3, pp. 213 - 216.

29. Goetz, V. von, "Investigations on acoustic observations of propeller cavitation." Hamburg, 1986. Forschungszentrum des Deutschen Shiffbaus, report 174. 12 p. (in German).

30. Nilsson, A. C. & Tyvand, N. P., ed. Noise sources in ships. Part 1 Propellers. Final report from a Nordic cooperative project: Structure borne sound in ships from propellers and diesel engines. Nordforsk, miljövårdsserien 1981:2.

31. Søntvedt, T. & Frivold, H., "Low frequency variation of the surface shape of tip region cavitation on marine propeller blades and corresponding disturbances on nearby solid boundaries." 1976. Det Norske Veritas, publication No. 95. 12 p.

32. Lamb, H., Hydrodynamics. Cambridge University Press, Sixth edition. London, 1975. 738 p.

33. Tsakonas, S. et al, "Propeller blade pressure distribution due to loading and thickness effect." Hoboken N.J., 1976, Stevens Institute of Technology, Report DL-1869, vol. 1. 61 p.

34. ISO 1683. Acoustics- preferred reference quantities for acoustic levels. International Standard Organization, 1983. 2 p.

35. Newland, D. E., An introduction to random vibrations and spectral analysis. London 1975, Longman. 285 p.

36 Fuldskalamålinger af kavitatiosstøj på M/T "PATAGONIA" og M/T "PASADENA". 1980, Skibsteknisk Laboratorium, Danish Maritime Institute, Udført for: NORDFORSK og Teknologirådet, report No SL 78912.30/3.

37. Sammenlignin mellem fuldskala- og modelskalamåinger af kavitatiosstøj på M/T "PATAGONIA" og M/T "PASADENA". Lyngby 1980. Skibsteknisk Laboratorium, Danish Maritime Institute. Udført for: NORDFORSK og Teknologirådet, report No SL 78912.30/4.

38. Urick, J. R., Principles of underwater sound. 3rd edition. 1983, McGraw-Hill Book Company. 423 p.

DISCUSSION

C. Brennan
California Institute of Technology, USA

The author presents an interesting attempt to synthesize the noise from sheet cavitation. The basic approach seems quite appropriate and represents an extension of the procedure first put forward by Fitzpatrick and Strasberg at the very first Naval Hydrodynamics Symposium in Washington, D.C., in 1956. (I am a little surprised at the lack of reference to this paper or the extensive work of Blake as described in his recent book on the subject.) While I would not differ with the basic philosophical approach presented by the author, there are some places where I would question the details: (a) The empirical formula used to determine the size of the bubbles is crucial in determining the noise spectra. The author correlates this size with the thickness of the sheet cavity. Would it not be more appropriate to scale it with some turbulent eddy size as strongly suggested by the recent studies of entrainment by Prosperetti, Duncan, Chachine, and others? (b) The bubble cloud shed by a sheet cavity usually has a high enough void fraction for cloud effects to be important. The author seems to dismiss these effects rather too quickly. (c) I am concerned when I examine the typical bubble history shown in Fig. 5. This shows typical ratios of minimum to maximum bubble size of the order of 0.5. Such ratios are typical of gas bubbles but not of cavitation bubbles in which the ratios are typically 10^{-5} or smaller. It is this range of ratios that is necessary to produce significant cavitation noise.

AUTHOR'S REPLY

Thank you Prof. Brennen for your comments and questions. I am sorry I did not refer explicitly to the single bubble dynamics and its effect on the noise spectrum presented by Fitzpatrick and Strasberg. The book of Blake, which is referred by me, covers this subject and other matters that are relevant to my paper. This book includes also further references and the one referred by you. There is a large number of papers on the single bubble dynamics published. The pioneering work in this field was done by Lord Rayleigh in the last century.

(a) I do not know the publication referred to by you. There is unfortunately very little experimental evidence of the bubble size distribution in the cloud. Reference [28] of my paper and the recent measurements conducted at the University of Tokyo by Prof. Kato and one of his students indicate that a fractal form suggested by me seems to be an appropriate choice. The assumption that the maximum diameter of a bubble shed from the fixed cavity does not exceed the sheet thickness seems reasonable to me. If you have any evidence to the contrary, I would be very glad to see it. (b) My assumption that the bubbles do not interact is not quite suitable for large bubbles. This may be the reason for poor correlation of the computations with the experimental data in the intermediate frequency range (from 300 Hz to 1 kHz). However, the bulk of the created bubbles is of a very small size. Each of them is of a different radius and each of them is created, shed downstream, and collapses at a different instant. Thus, their significant interaction is very unlikely. Assumption of the spherical form of the bubbles is good also for small size bubbles as the significance of the surface tension grows rapidly with the curvature. (c) My assumption was that during a very rapid collapse, the vapor behaves as a compressible gas, that is, it does not condense. The inclusion in the numerical model of the effects of vapor condensation and of the partial gas pressure in the bubble is possible if the appropriate experimental data are available. I am afraid that such data are different for each cavitation test facility. The ratio of minimum to maximum bubble size quoted by you (10^{-5}) seems to me too low. A bubble of the initial diameter of 1 m compressing to 10 μm is difficult to accept. The photographs of the collapsing bubbles shown us by Dr. Chahine and those that can be found in the literature (Ref 121 of my paper) indicate that this ratio is much closer to the one presented by me.

I attempted to develop a method that leads to a practical result, which is a noise spectrum generated by a cavitating propeller. If I included the effects of factors that are unknown or different for each test facility, I would not be able to reach my goal.

DISCUSSION

Spyros Kinnas
Massachusetts Institute of Technology, USA

The author is making use of a quasi-steady two-dimensional cavity theory in order to determine the sheet cavity on the blade. I am wondering how good this approximation may be, especially at the tip region (even for conventional propellers).

AUTHOR'S REPLY

Quasi-steady two-dimensional cavity theory produces surprisingly good results, especially in terms of sheet cavitation extent. It underpredicts cavitation thickness at the blade tip region. In order to take into account the three-dimensional nature of the flow at the tip, the following is done. The intermittent tip vortex cavitation radius is evaluated in a quasi-steady manner using the method of Betz. Cavitation at the blade tip is related to the tip vortex cavitation using the circulation conservation principle and simple geometrical considerations. The approach is described in detail in reference [12] of my paper.

DISCUSSION

R. Latorre
University of New Orleans, USA

The author has presented a very interesting result of his study on cavitation noise from marine propellers. I have a comment and a question.

In the work of Osborne, Latorre (1992), we considered the development of a numerical model of single bubble growth and collapse along with the digital processing of the noise signal into a power spectra similar to the one shown by the author in Fig. 7. One main conclusion is that Equation (13) is in good agreement with our numerical results.

I would like to ask the author to describe the signal processing he used. In our development, we utilized a digital filter based on the Hanning window to obtain the 1/3 octave band pass frequency. Our intent was to replicate the instrumentation used in experimental measurements.

Osborne, G., Latorre, R., "Development of Numerical Modeling of Cavitation Bubble Behavior and Noise," Naval Engineers Journal, Vol. 104, No. 1, pp. 36-45, January 1992.

AUTHOR'S REPLY

Thank you Prof. Latorre for your comments and your question concerning processing the numerically simulated pressure signal. Because of the complex nature of this signal, which comprises both the slowly varying in time, deterministic part, and a large number of random peaks, I decided to use Fast Fourier Transform (FFT) technique, which resulted, in my case, in 65536 spectral lines. Another reason for this choice was the fact that low frequencies of the measured propeller-induced pressure are usually analyzed by the spectral analyzers that utilize the FFT algorithm. This enabled me to present the pressure level at the low frequency range (from the blade passing frequency to 15 times the blade frequency) with the resolution equal to the blade frequency value. Thus, a comparison of the measurements and computation was made possible. For higher frequencies, a special processing of the raw discrete Fourier transform data was conducted, which enables a comparison of the results with the measured noise level data and which also reveals the main features of the simulated noise. The procedure is as follows:

- Noise level is evaluated (formula [27]) for each spectral line.
- Spectrum is smoothed by calculating the mean of eleven adjacent values for each spectral line.
- For each frequency decade, 25 equally spaced frequencies are selected and for each of them the mean noise level is evaluated.

This procedure leads to 1/7 octave analysis of the signal.

Session XIII

Propulsor Hydrodynamics and Hydroacoustics

A Nonlinear Boundary Element Method for the Analysis of Unsteady Propeller Sheet Cavitation

S. Kinnas, N. Fine (Massachusetts Institute of Technology, USA)

ABSTRACT

The unsteady flow around a cavitating marine propeller is treated in nonlinear theory by employing a low-order potential-based boundary element method and a time-marching scheme. The kinematic and dynamic boundary conditions, which are fully three-dimensional and time-dependent, are satisfied on the propeller surface beneath the cavity and on the portion of the blade wake surface which is overlapped by the cavity. The formulation and algorithm are developed to treat arbitrary cavity planforms in an efficient and robust manner. The results from the numerical method are shown to converge quickly with number of panels and with number of time steps per propeller revolution. The produced cavity shapes are validated and shown to satisfy the imposed dynamic boundary condition within acceptable accuracy. Computed cavity planforms are compared to those from linear theory and linear theory with leading edge corrections.

1 INTRODUCTION

Unsteady propeller cavitation has always been a major concern in marine propeller design. In recent years, when quite often the presence of cavitation is inevitable, the use of an analytical tool to identify the cavitation characteristics of a particular propeller geometry has become an essential part of the design process. With the evolution of faster computers and more accurate methods of analysis, the improvement of the prediction of unsteady propeller *sheet* cavitation was natural. In the present work, a nonlinear boundary element method for the analysis of the unsteady flow around cavitating propellers will be presented.

Cavitating or free-streamline flows were first addressed in nonlinear theory via the hodograph technique as introduced by Helmholtz, Kirchoff and Levi-Civita [1]. Due to the difficulty of this technique to treat general shape three dimensional geometries, the linearized cavity theory, introduced by Tulin [25] became quickly very popular, and this is proven from the vast amount of publications[3] on applications of linearized cavity theory. In particular, the three-dimensional flow effects around cavitating finite span hydrofoils have been treated in linear theory, either via a strip-theory/ lifting-line approach [22,20,27,30], or via the numerical lifting surface approach [24,9].

The first effort to analyze the complete three dimensional unsteady flow around a cavitating propeller subject to a spatially non-uniform inflow was carried out by C-S. Lee [18]. He employed a source and vortex lattice lifting surface scheme and he applied the unsteady three dimensional *linearized* boundary conditions on the cavity. The cavity planform was determined at each blade strip and each time step (i.e., blade angle) by searching for the cavity length which would produce the desired vapor pressure inside the cavity. The effect of the other strips was accounted for in an iterative sense by "sweeping" along the spanwise direction of the blade back and forth until the cavity shape converged. Unfortunately, this method was hampered by the inherent inability of linear cavity theory to predict the correct effect of blade thickness on cavity shape [26,28]. This deficiency was recently corrected in two dimensions by Kinnas [12,11], who introduced the *leading edge correction* in the linearized dynamic boundary condition on the cavity. The leading edge correction was subsequently applied to the three dimensional propeller solution [10]. The numerical scheme was also improved by employing a more robust arrangement of the vortex and source lattice and their required control points. The method (which is incorporated in the code PUF-3A) has been found to predict the gross unsteady cavity characteristics on propellers within reasonable qualitative agreement with experimental or full-scale observations [2]. However, details of the cavity flow at the blade leading edge and tip cannot be computed reliably, especially in the case of highly skewed propellers, due to the breakdown of either the linear cavity theory or the employed leading edge corrections. The accurate prediction of the cavity flow at the tip is important since this is where much of the action occurs, especially in the onset of tip vortex cavitation.

[1]Principal Research Engineer & Lecturer.

[2]Doctoral Graduate Student.

[3]A complete list of which may be found in [26].

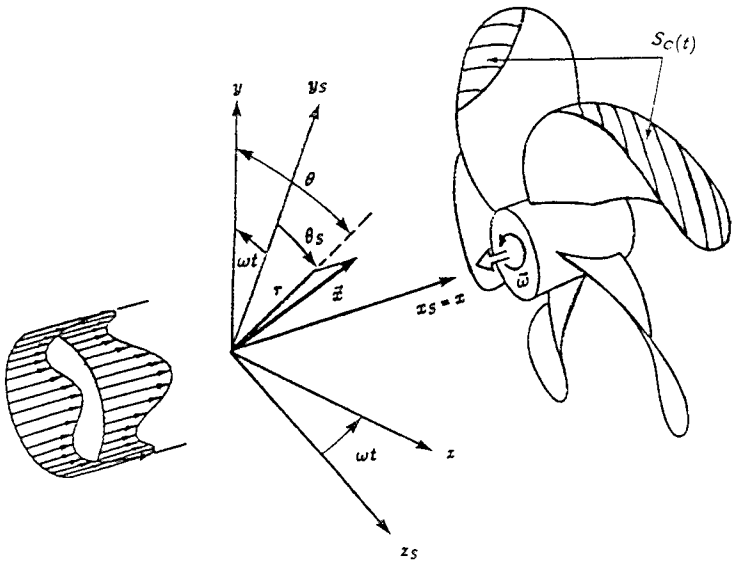

Figure 1: The cavitating propeller in a circumferentially nonuniform wake inflow.

Very recently we have completed a (potential based) Boundary Element Method (BEM) for the prediction of the unsteady (fully wetted) flow around either open or ducted propellers [16,8]. The method has proven to be very robust and able to compute unsteady pressure distributions at the propeller leading edge and tip at a broad range of reduced frequencies, even in the case of extreme propeller geometries [15]. The present paper deals with the extension of the BEM to analyze, in nonlinear theory, unsteady propeller sheet cavitation.

Various velocity-based BEM's have been applied for the nonlinear analysis of the flow around 2-D and 3-D partially and supercavitating hydrofoils. These include methods by Pellone and Rowe [23], for supercavitating 3-D hydrofoils, by Uhlman [28,29], for partially and supercavitating 2-D hydrofoils, and by Lemonnier and Rowe [7], for partially cavitating 2-D hydrofoils. In each of these BEM's, the panels are placed on the cavity boundary whose shape is determined by an iterative process which terminates when both the kinematic and the dynamic boundary conditions are satisfied.

Recently, a potential-based boundary element method (*i.e.*, one based on Green's third identity for the perturbation potential) was developed by Kinnas and Fine [14] for the nonlinear analysis of the flow around partially and supercavitating 2-D hydrofoils. This method, when applied to partially cavitating hydrofoils (with the cavity length known and the cavitation number unknown) has been found to converge to the final cavity shape with fewer iterations than velocity-based BEM's. In particular, it has been found that the first step in the iterative method, in which the dynamic boundary condition is satisfied on the hydrofoil surface beneath the cavity, predicts a cavity shape which is remarkably close to the "exact" nonlinear shape. More recently this method was extended for the analysis of the flow around 3-D cavitating hydrofoils [13,5]. In the present work, this method is further extended for the analysis of unsteady propeller sheet cavitation.

2 FORMULATION

Consider a propeller subject to a circumferentially nonuniform inflow $\mathbf{U}_W(x_S, r_S, \theta_S)$, as shown in Figure 1. The wake inflow is expressed in terms of the absolute (ship fixed) system of cylindrical coordinates x_S, r_S, θ_S. In analyzing the flow around the propeller we use the propeller fixed system (x, y, z), also shown in Figure 1. We assume that the propeller is right-handed and that it rotates with angular velocity ω. The inflow relative to the propeller, $\mathbf{U}_{in}$, will be time dependent and given as

$$\mathbf{U}_{in}(x, y, z, t) = \mathbf{U}_W(x, r, \theta - \omega t) + \omega \times \boldsymbol{x}, \quad (1)$$

where $r = \sqrt{y^2 + z^2}$, $\theta = \arctan(z/y)$ and $\boldsymbol{x} = (x, y, z)$.

We assume that the propeller cavitates, and the time dependent cavity sheet surface is denoted by $S_C(t)$. We also assume at this point, that the resulting flow is incompressible and inviscid, and that the inflow $\mathbf{U}_W$ is the effective wake, *i.e.* it includes the interactions between the vorticity of the inflow in the absence of the propeller (nominal wake) and the vorticity due to the propeller. Then, the time dependent total flow velocity relative to the propeller fixed system, $\mathbf{q}(x, y, z, t)$, can be written in terms of the perturbation potential, $\phi(x, y, z, t)$, as follows:

$$\mathbf{q}(x,y,z,t) = \mathbf{U}_{in}(x,y,z,t) + \nabla\phi(x,y,z,t). \quad (2)$$

In the next four sections, we outline the necessary equations and conditions for determining $\phi(x,y,z,t)$ as well as the cavity planform and shape.

2.1 The Green's Formula

By applying Green's third identity for $\phi(x,y,z,t)$ at any time t, we get the following integral equation for the perturbation potential $\phi_p(t)$ at any point p on the *wetted* part[4] of the propeller blade (or hub) surface, $S_{WS}(t)$, or on the cavity surface, $S_C(t)$, both shown in Figure 2:

$$\begin{aligned} & 2\pi\phi_p(t) = \\ = & \int_{S_{WS}(t)\cup S_C(t)} \left[\phi_q(t)\frac{\partial G(p;q)}{\partial n_q(t)} - G(p;q)\frac{\partial \phi_q(t)}{\partial n_q(t)}\right] dS \\ + & \int_{S_W(t)} \Delta\phi(r_q,\theta_q,t)\frac{\partial G(p;q)}{\partial n_q(t)} dS; \quad p \in (S_{WS}\cup S_C) \end{aligned} \quad (3)$$

with the subscript q corresponding to the variable point in the integrations; $\mathbf{n}_q(t)$ is the unit vector normal to the propeller wetted surface, the cavity surface or the wake surface; $\Delta\phi$ is the potential jump across the wake sheet, $S_W(t)$, and $G(p;q)$ is the Green's function. In the case of unbounded three dimensional fluid domain $G(p;q) = 1/R(p;q)$, with $R(p;q)$ being the distance between points p and q.

Equation (3) expresses the potential on the combined wetted propeller and cavity surface, $S_{WS}(t) \cup S_C(t)$, as the superposition of the potentials induced by a continuous source distribution, G, and a continuous dipole distribution, $\frac{\partial G}{\partial n}$, on $S_{WS}\cup S_C$, and a continuous dipole distribution on the trailing wake surface $S_W(t)$, also shown in Figure 2. Note that all the involved surfaces in equation (3) are time dependent, either because their shapes and/or because their line boundaries are functions of time. On the combined wetted blade and cavity surface, $S_{WS}(t)\cup S_C(t)$, as will be described in the next sections, either the source distribution is known (a *Neumann* condition) or the dipole distribution is known (a *Dirichlet* condition). The remainder of the unknown dipole or source distribution is determined from the application of equation (3).

At first, the strength of the source distribution on the wetted propeller surface may be expressed, via the kinematic boundary condition, as[5]

$$\frac{\partial\phi_q}{\partial n_q} = -\mathbf{U}_{in}(x_q,y_q,z_q,t)\cdot\mathbf{n}_q; \quad q \in S_{WS}(t) \quad (4)$$

where x_q, y_q, z_q are the coordinates of point q with respect to the propeller fixed system.

[4]Another name for the *non-cavitating* part.

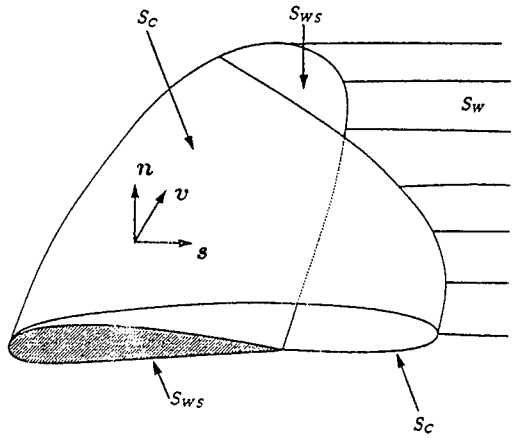

Figure 2: Definition of the wetted blade, the cavity and the trailing wake surfaces.

In the case of partial cavitation (when the cavities do not extend behind the blade trailing edge[6]) the trailing wake, S_W, is treated the same way as in the case of fully wetted unsteady flows [15]. In more detail, the geometry of the wake is assumed to be invariant with time and taken to be the same as the steady-flow relaxed wake corresponding to the circumferentially averaged inflow [6]. The dipole strength $\Delta\phi(r,\theta,t)$ in the wake, is convected along the assumed wake model with angular speed ω, in order to ensure that the pressure jump in the wake is equal to zero, i.e.,

$$\begin{aligned} \Delta\phi(r,\theta,t) &= \Delta\phi_T\left(r, t - \frac{\theta-\theta_T(r)}{\omega}\right); \\ & \qquad t \geq \frac{\theta-\theta_T(r)}{\omega} \\ \Delta\phi(r,\theta,t) &= \Delta\phi^S(r); \; t < \frac{\theta-\theta_T(r)}{\omega} \end{aligned} \quad (5)$$

where r,θ are the cylindrical coordinates of the wake surface, S_W, and $\theta_T(r)$ is the θ coordinate of the propeller blade trailing edge at radius r. $\Delta\phi^S(r)$ is the steady flow potential jump in the wake when the propeller is subject to the circumferentially averaged inflow. For $t < 0$ we assume that the propeller is subject to the circumferentially averaged inflow. The unsteady inflow is "turned on" at $t = 0$.

[5]A special numerical treatment is required to determine the source strength at the wetted part of the blade in the vicinity of the moving cavity trailing edge, as will be discussed in Section 3.2

[6]The geometry of the trailing wake in the case of supercavitation will be discussed in Section 2.2.

The value of the dipole strength, $\Delta\phi_T(r,t)$, at the trailing edge of the blade at time t, will be given by

$$\Delta\phi_T(r,t) = \phi_T^+(r,t) - \phi_T^-(r,t) = \Gamma(r,t) \qquad (6)$$

where $\phi_T^+(r,t)$ and $\phi_T^-(r,t)$ are the values of the potential at the upper (suction side) and lower (pressure side) blade trailing edge, respectively, at time t. The difference in those potentials is also equal to the circulation Γ at time t around the blade section at radius r. The condition (6) is equivalent to requiring the shed vorticity from the blade trailing edge to be proportional to the time rate of change of the circulation around the blade.

2.2 The Dynamic Boundary Condition

The dynamic boundary condition (DBC) requires that the pressure everywhere inside and on the cavity be constant and equal to the known cavity pressure, p_c. Bernoulli's equation with respect to the propeller fixed system becomes:

$$\frac{p_o}{\rho} + \frac{1}{2}|\boldsymbol{U}_w|^2 = \frac{\partial\phi}{\partial t} + \frac{p_c}{\rho} + \frac{1}{2}|\boldsymbol{q}_t|^2 - \frac{1}{2}\omega^2 r^2 + g y_S. \quad (7)$$

where ρ is the density of the fluid and r is the distance from the axis of rotation. Here $\boldsymbol{U}_w$ is the total "effective" wake velocity and $\boldsymbol{q}_t$ is the total cavity velocity. p_o is the pressure far upstream on the shaft axis; g is the acceleration of gravity and y_S is the ship fixed coordinate, shown in Figure 1, defined as negative in the direction of gravity. After some manipulation, and using the definition of the cavitation number:

$$\sigma_n \equiv \frac{p_o - p_c}{(\rho/2)n^2D^2}, \qquad (8)$$

where $n = \omega/2\pi$ and D are the propeller revolutions and diameter, respectively, the cavity velocity may be written

$$\begin{aligned} |\boldsymbol{q}_t|^2 &= n^2D^2\left[(1+\sigma_n)[1-f(s)]^2 - 1\right] \\ &+ |\boldsymbol{U}_W|^2 + \omega^2 r^2 - 2gy_S - 2\frac{\partial\phi}{\partial t} \end{aligned} \qquad (9)$$

The function f corresponds to a pressure recovery law in front of the trailing edge of the cavity along the arc s on the surface of each spanwise blade section. This pressure law is intended to simulate the real fluid effects at the end of the cavity. It is given from

$$f(s) = \begin{cases} 0 & s < s_T \\ A\left[\frac{s-s_T}{s_L-s_T}\right]^\nu & s_T \le s \le s_L \end{cases} \qquad (10)$$

Here, s is the arclength of the blade section beneath the cavity measured from the cavity leading edge, s_L is the arclength at the end of the cavity, and s_T is the arclength at the beginning of the transition zone where the pressure recovery law is applied. The extent of the transition zone is given in terms of the parameter $\lambda = (s_L - s_T)/s_L$. The parameters A ($0 < A < 1$) and ν ($\nu > 0$) are arbitrary constants. The effect of these parameters on the cavity shape has been shown for hydrofoils in [14], and in the case of propellers in [4].

Due to the particulars of our algorithm, the cavity boundary is most naturally considered in two parts: the first being the portion which overlaps the propeller blade, and the second —which occurs in the case of supercavitation — the portion which overlaps the blade wake surface. The application of the dynamic boundary condition on each of these parts will be considered separately.

DBC on the Cavitating Part of the Blade

In addition to the expression (9), the velocity $\boldsymbol{q}_t$ may also be expressed in terms of the directional derivatives of the perturbation potential and the components of the inflow along the same curvilinear coordinates. The coordinate system[7] on the cavity surface consists of s (chordwise) and v (spanwise), as shown in Figure 2:

$$\begin{aligned} \boldsymbol{q}_t &= \\ &= \frac{\left(\frac{\partial\phi}{\partial s} + U_s\right)[\boldsymbol{s} - (\boldsymbol{s}\cdot\boldsymbol{v})\boldsymbol{v}] + \left(\frac{\partial\phi}{\partial v} + U_v\right)[\boldsymbol{v} - (\boldsymbol{s}\cdot\boldsymbol{v})\boldsymbol{s}]}{\|\boldsymbol{s}\times\boldsymbol{v}\|^2} \\ &+ \left(\frac{\partial\phi}{\partial n} + U_n\right)\boldsymbol{n} \end{aligned} \qquad (11)$$

with $\boldsymbol{s}$ and $\boldsymbol{v}$ being the unit vectors corresponding to the coordinates s and v, respectively, and with $\boldsymbol{n}$ being the unit normal vector to the assumed cavity. U_s, U_v, and U_n are the s, v and n components of the relative inflow, $\boldsymbol{U}_{in}$.

If s, v and n were located on the correct cavity surface, and if the flow was steady, then the normal velocity, $\frac{\partial\phi}{\partial n} + U_n$, would vanish. However, this is not the case since the cavity surface is not known *a priori* and its location is approximated, as will be described in the next section. Nevertheless, in applying the dynamic boundary condition, the normal velocity is assumed to be vanishingly small[8]. Equations (9) and (11) may then be combined to form an equation which is quadratic in the unknown chordwise perturbation velocity, $\frac{\partial\phi}{\partial s}$. Solving this quadratic[9], we can express $\frac{\partial\phi}{\partial s}$ in terms of the cavitation number, the inflow velocity, and the *unknown* crossflow $\frac{\partial\phi}{\partial v}$ and time derivative $\frac{\partial\phi}{\partial t}$:

[7] In general non-orthogonal.

[8] This term could very easily be included in a iterative numerical scheme for determining the cavity shape. Its effect on the solution is expected to be insignificant though.

[9] The root which corresponds to cavity velocity vectors pointing downstream is selected.

$$\frac{\partial \phi}{\partial s} = -U_s + \left(\frac{\partial \phi}{\partial v} + U_v\right)\cos\theta + \sin\theta\sqrt{|\boldsymbol{q}_t|^2 - \left(\frac{\partial \phi}{\partial v} + U_v\right)^2} \qquad (12)$$

with θ being the angle between s and v, as shown in Figure 2, and where $|\boldsymbol{q}_t|$ is given by equation (9). Equation (12) is integrated once to form a Dirichlet boundary condition on ϕ:

$$\phi(s) = \phi(0) + \int_0^s [\text{right-hand-side of (12)}]ds \qquad (13)$$

The integral on the right-hand-side of equation (13) is determined by trapezoidal quadrature. The lower limit of the integral corresponds to the cavity detachment point at each blade section, whose location is considered to be an independent parameter in the present work. A discussion on the location of the detachment point is offered in Section 6. The value of $\phi(0)$ in equation (13) is unknown and is expressed via a cubic extrapolation in terms of the unknown potentials on the wetted panels on the same strip in front of the cavity.

The dynamic boundary condition (13) is transcendental since ϕ depends on both its spanwise and time derivatives. These terms are treated as knowns and are updated in an iterative time-stepping scheme which will be discussed later. The convergence of the crossflow term $\frac{\partial \phi}{\partial v}$ has been studied for the case of steady cavitating three dimensional hydrofoils and reported in [13]. To summarize the result, it was found that the global dependence of the solution on the crossflow term was small and only a single additional iteration was required for convergence. The convergence of the time-derivative, as well as its effect on the solution, will be discussed in Section 3.2.

DBC in the Supercavitating Wake

Equation (13) also applies on the upper or lower part of the supercavity. As already mentioned, though, the cavity surface is not known and has to be determined as part of the solution. In this work, however, we will apply our dynamic and kinematic boundary conditions on an approximate cavity surface, as shown in Figure 3. This surface is defined as follows:

- It coincides with the blade surface under the cavity in the cavitating part of the blade in front of the trailing edge. We denote this surface with $S_{CB}(t)$
- In the case of supercavitating flow, the two sides of the supercavity behind the trailing edge coincide with the two sides of the zero thickness trailing wake sheet. We denote this surface with $S_{CW}(t)$.

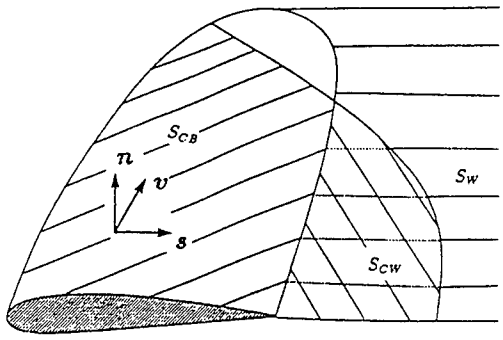

Figure 3: The approximate cavity surface on which the boundary conditions are applied.

A justification for making this approximation as well as a measure of its effect on the cavity solution will be given in Appendix A and in Section 4. In this case, requiring the pressures on the upper and lower parts of the supercavity to be the same (since both have to be equal to the cavity pressure p_c), is equivalent to the force-free wake condition, which has been enforced by satisfying the vorticity convection equation (5). In other words, the supercavitating part of the wake, $S_{CW}(t)$, and the rest of the wake behind the cavity, $S_W(t)$, can both be treated as *one*. As in the case of the fully wetted unsteady (or partially cavitating) flow, the potential jump at the trailing edge is determined by equation (6) and is convected downstream according to equation (5).

Having treated the wake as mentioned, we need to satisfy a dynamic boundary condition only on one of two sides of the supercavity. In this case we choose the "upper" (suction) side of S_{CW}. The dynamic boundary condition on the cavitating portion of the wake, S_{CW}, may also be written as a Dirichlet condition on φ. However, in this case we will assume that the coordinate s follows the streamlines and that the total cross flow velocity normal to s and in the plane of the wake is small compared to the mean velocity of the wake sheet at the same point. This assumption is justified from our experience with the cross flow in the case of partially cavitating flows, mentioned earlier. The dynamic boundary condition on S_{CW} may thus be written

$$\boldsymbol{V} \cdot \boldsymbol{s} = \frac{\partial \phi^+}{\partial s} + U_s = |\boldsymbol{q}_t|. \qquad (14)$$

Equation (14) may be integrated once to form a Dirichlet boundary condition on ϕ^+, similar to (13). The value of $|\boldsymbol{q}_t|$ is given, as in the case of the cavitating part of the blade, by equation (9).

On the other hand, equation (3) needs special treatment when $p \in S_{CW}$. This will render the following expression for ϕ_p^+, the perturbation potential on the "upper" side of the wake surface, as proven in [5]:

$$
\begin{aligned}
4\pi\phi_p^+(t) &= 2\pi\Delta\phi_p(t) \\
&+ \int_{S_B}\left[\phi_q(t)\frac{\partial G(p;q)}{\partial n_q} - G(p;q)\frac{\partial\phi_q(t)}{\partial n_q}\right]dS \\
&- \int_{S_{CW}(t)} q_w(t)G(p;q)dS \\
&+ \int_{S_{TW}} \Delta\phi(r_q,\theta_q,t)\frac{\partial G(p;q)}{\partial n_q}dS; \quad p \in S_{CW}(t) \qquad (15)
\end{aligned}
$$

where $S_B \equiv S_{WS}(t) \cup S_{CB}(t)$ is the surface of the blade, and $S_{TW} \equiv S_W(t) + S_{CW}(t)$ is the total surface of the trailing wake, with the normal vector n_q defined as positive when pointing to the suction side. Note that S_B and S_{TW} do not depend on time. In addition, we have introduced the cavity source in the wake, q_w, defined as:

$$
q_w(t) = \frac{\partial\phi^+(t)}{\partial n} - \frac{\partial\phi^-(t)}{\partial n} \qquad (16)
$$

The original Green's formula (3) for $p \in S_B$ will also be modified to:

$$
\begin{aligned}
2\pi\phi_p(t) &= \\
&= \int_{S_B}\left[\phi_q(t)\frac{\partial G(p;q)}{\partial n_q} - G(p;q)\frac{\partial\phi_q(t)}{\partial n_q}\right]dS \\
&- \int_{S_{CW}(t)} q_w(t)G(p;q)dS \\
&+ \int_{S_{TW}} \Delta\phi(r_q,\theta_q,t)\frac{\partial G(p;q)}{\partial n_q(t)}dS; \quad p \in S_B \qquad (17)
\end{aligned}
$$

Note that in both equations (15) and (17) the Green's functions G and $\frac{\partial G}{\partial n_q}$ do not depend on time, since they are located on the approximate cavity surface, which is assumed to be fixed in time. The consequences of this will be better understood in Section 3.

2.3 The Shape of the Cavity

Since the dynamic boundary condition is applied on the portion of the flow boundary which is encompassed by the cavity, the other boundary condition (namely the kinematic condition) may be used to determine the position of the actual cavity surface once the singularity strengths are known. In this section, the most useful form of the kinematic boundary condition (KBC) will be derived. As in the previous section, the cavity boundary will be divided into two zones which will be considered separately.

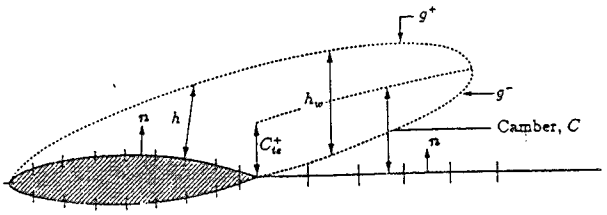

Figure 4: Definition of the cavity camber and height for a supercavitating section of the propeller blade.

KBC on the Cavitating Part of the Blade

The kinematic boundary condition on the cavity is the requirement that the velocity normal to the cavity is zero (in the case of steady flows) , or, more generally (also valid in the case of unsteady flows), the statement that the substantial derivative of the cavity surface is zero. Using the latter statement of the condition as a starting point, the kinematic boundary condition may be written

$$
\begin{aligned}
&\frac{D}{Dt}(n - h(s,v,t)) = \\
&= (\frac{\partial}{\partial t} + \boldsymbol{q}_t \cdot \nabla)(n - h(s,v,t)) = 0 \qquad (18)
\end{aligned}
$$

where n is the coordinate normal to the blade surface (with unit vector $\boldsymbol{n}$) and $h(s,v,t)$ is the thickness of the cavity normal to the blade at the point (s,v) at time t. Expressing the gradient in terms of the local directional derivatives

$$
\nabla = \frac{[\boldsymbol{s} - (\boldsymbol{s}\cdot\boldsymbol{v})\boldsymbol{v}]\frac{\partial}{\partial s} + [\boldsymbol{v} - (\boldsymbol{s}\cdot\boldsymbol{v})\boldsymbol{s}]\frac{\partial}{\partial v}}{\|\boldsymbol{s}\times\boldsymbol{v}\|^2} + \boldsymbol{n}\frac{\partial}{\partial n}, \qquad (19)
$$

and performing the dot product with $\boldsymbol{q}_t$ (as defined in (11)) and finally substituting the result in (18) yields the following partial differential equation for the cavity thickness:

$$
\begin{aligned}
\frac{\partial h}{\partial s}[V_s - \cos\theta V_v] + \frac{\partial h}{\partial v}[V_v - \cos\theta V_s] &= \\
= \sin^2\theta(V_n - \frac{\partial h}{\partial t}) \qquad (20)
\end{aligned}
$$

where

$$
\begin{aligned}
V_s &\equiv \frac{\partial\phi}{\partial s} + U_s \\
V_v &\equiv \frac{\partial\phi}{\partial v} + U_v \\
V_n &\equiv \frac{\partial\phi}{\partial n} + U_n.
\end{aligned}
$$

KBC in the Supercavitating Wake

The kinematic boundary condition on the cavity surface in the wake may be derived in a similar fashion:

$$\frac{D}{Dt}\left(n - g(s,v,t)\right) = 0 \qquad (21)$$

where $g(s,v,t)$ defines the cavity surface. The upper and lower cavity surfaces, $g(s,v,t)^{\pm}$, may be written

$$g(s,v,t)^{\pm} = C(s,v,t) \pm \frac{1}{2}h_w(s,v,t),$$

where C is the cavity camber in the wake and h_w is the cavity thickness. The quantities g, C and h_w are all taken along the normal to the trailing wake surface, as shown in Figure 4.

Assuming again that the spanwise crossflow velocity is small, the kinematic boundary condition (21) can be shown to reduce to

$$q_w(t) - \frac{\partial h_w}{\partial t} = |\boldsymbol{q}_t|\frac{\partial h_w}{\partial s}. \qquad (22)$$

where q_w is the cavity source distribution, defined by equation (16). Note that the cavity height on the blade and in the wake, both shown in Figure 4, are defined differently and so they are given separate symbols.

Once all of the singularities on the blade and in the wake have been determined, the cavity thickness is found by solving the PDE (20) and the ODE (22). This is done by replacing the partial derivatives of h and h_w with two-point backwards difference formulae and solving for h and h_w recursively [13,5]. The treatment of the time derivatives will be described in Section 3.2.

2.4 The Cavity Planform

The extent (planform) of the unsteady cavity is not known and has to be determined as a part of the solution. The cavity length at each radius r (defined as the arclength of the intersection of the cavity with a cylinder of radius r whose axis is the axis of rotation) is given by the function $l(r,t)$. For given cavitation number σ_n, this function must be determined from the requirement:

$$\begin{aligned} &\delta(l(r,t), r; \sigma_n) \equiv \\ \equiv\ &h(l(r,t), r, t) \ [\text{or } h_w(l(r,t), r, t)] = 0 \end{aligned} \qquad (23)$$

Equation (23) requires the unsteady cavity shape to close at its trailing edge. A discussion on this requirement will be given in Section 6. As will be described in the next section the cavity and wetted blade are discretized into M spanwise strips. In that case, equation (23) becomes:

$$\delta_m(l_1(t), l_2(t), ..., l_M(t); \sigma_n) = 0; \quad m = 1, ..., M \qquad (24)$$

where δ_m is the openness of the cavity trailing edge at the m^{th} strip and l_m is the value of $l(r,t)$ at midspan of the same strip. At each time t the vector $\boldsymbol{L} = [l_1, l_2, ..., l_M]^T$ must be determined from satisfying the M nonlinear equations (24). The algorithm to do that is described in detail in [13]. We summarize it in the following steps:

Step 1: Make a guess for the shape of the cavity trailing edge, $\boldsymbol{L}$, (a very good guess is the cavity planform from the previous time step).

Step 2: Invert equations (17) and (15) subject to the conditions (4), (13), (14) and (6).

Step 3: Integrate equations (20) and (22) to determine the cavity openness, δ_m, for all m at the assumed cavity trailing edge.

Step 4: If $\delta_m \neq 0$ then update the cavity planform $\boldsymbol{L}$ by applying a Newton-Raphson (secant method) scheme on equations (24) and repeat Steps 1 to 4, until the openness of the cavity $\delta_m = 0$ for *all* m, within a prescribed tolerance δ_{TOL}.

The algorithm is also depicted in Figure 5 in the case of a two-dimensional and a rectangular hydrofoil, where the corresponding cavity openness is shown for several planform guesses, including the "correct" planform. The effect of the magnitude of δ_{TOL} on the cavity planform is investigated in Appendix B. A discussion on the multiplicity of solutions for the cavity planform is offered in Appendix C.

3 NUMERICAL IMPLEMENTATION

The objective of the numerical analysis is to invert equations (17) and (15) subject to the conditions (4), (13), (14) and (6). The numerical implementation is very similar to that for the cavitating flow around two and three dimensional hydrofoils [14,13,5] and will be described in detail in [4]. A summary of the numerical implementation is given next.

The combined wetted blade and cavity surface is discretized into N panels in the chordwise and M panels in the spanwise direction, as shown in Figure 6. The trailing wake (and supercavity) is discretized into panels at constant angular intervals $\Delta\theta_W = \omega\Delta t$ with Δt being the time step. The trailing wake panels are also shown in Figure 6. The blade and trailing wake discretization is *identical* to that in the case of fully wetted unsteady flows [16,8,15]. Therefore, the involved influence coefficients are time independent and thus need only to be computed once. This is a consequence of the approximation of the cavity surface, already mentioned in

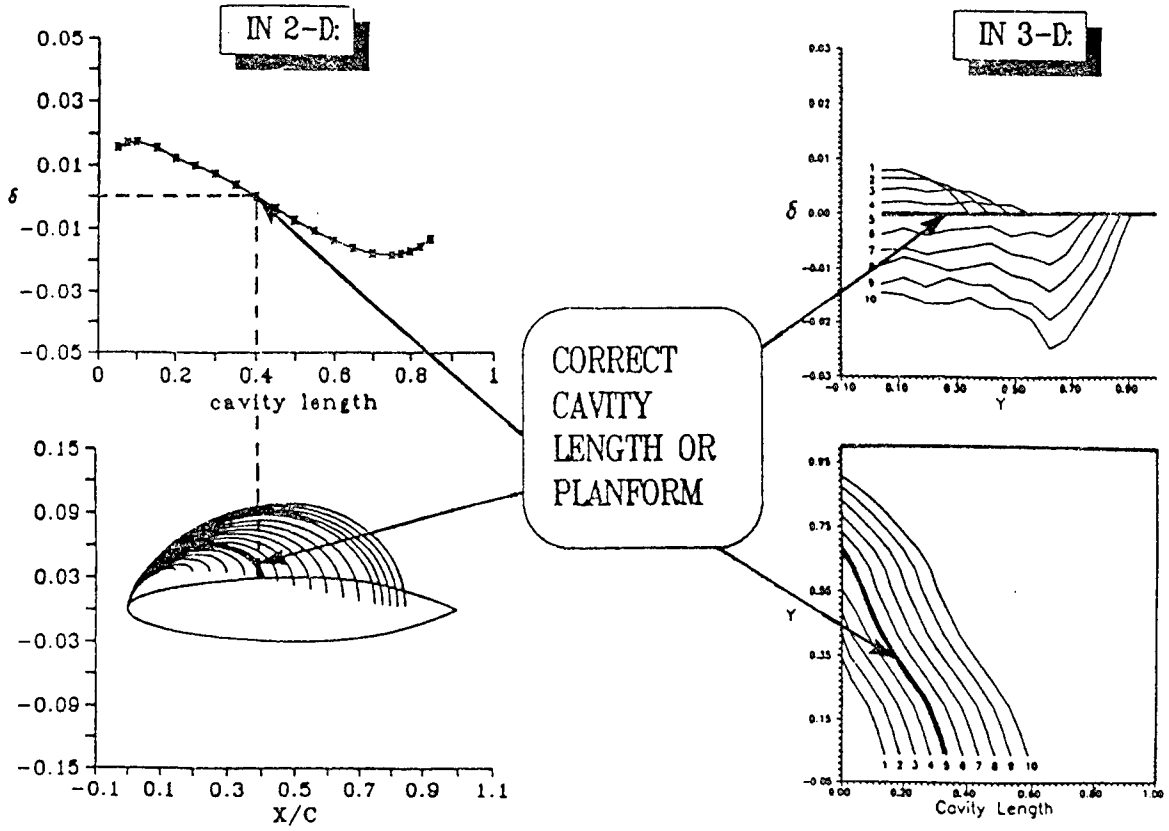

Figure 5: The algorithm for determining the cavity planform for fixed cavitation number.

Section 2.2. The source or dipole distributions on each of these panels is approximated with constant strength distributions. The involved influence coefficients for the unit strength dipoles and sources are computed by utilizing the formulas in [21] and [8]. If we call:

N_{WS} = No. of wetted panels
N_{CB} = No. of cavitating panels on the blade
N_{CW} = No. of cavitating panels in the wake

then among the discrete sources and dipoles we have

- N_{WS} known source strengths, via equation (4),
- N_{CB} known dipole strengths, via equation (13), and
- N_{CW} known dipole strengths, by integrating equation (14).

The *unknown* strengths of the

- N_{WS} dipoles on the wetted blade,
- N_{CB} sources on the cavitating blade, and
- N_{CW} cavity sources in the wake

are determined by inverting the discretized form of equations (17) and (15). The treatment of the unsteady potential jumps in the trailing wake is identical to that for fully wetted unsteady flows [8,15] and will also be described in detail in [4]. In summary, the potential jump in the wake is either known from previous time steps or from applying equation (6) or an unsteady pressure Kutta condition at the trailing edge of the blade.

3.1 The Split Panel Technique

As mentioned already the discretization for the unsteady cavitating propeller flow is identical to that for the unsteady fully wetted flow, *i.e.* fixed in time. To keep it this way, however, we would have to force the unsteady cavity to end at panel boundaries. Unfortunately, we found that approximating the cavity trailing edge with the closest panel boundaries in the chordwise direction, either produced uneven cavities in the spanwise direction or more often was causing the process of determining the cavity planform to diverge. To circumvent

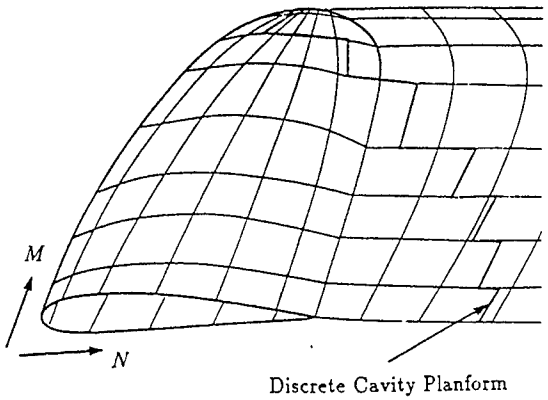

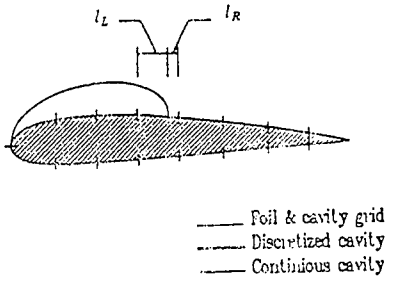

Figure 6: Discretization of the propeller blade, the cavity and their trailing wakes; $N = 12$, $M = 8$, $\Delta\theta_W = 6^o$.

this problem we utilize the split panel technique, which was introduced in [13]. This technique is depicted in Figure 7. The panels whose midspan segment (defined as the segment connecting the midpoints of the spanwise panel sides) is intersected by the continuous cavity trailing edge line, are *split* into a "left" cavitating and "right" wetted panel, as shown in Figure 7. Ideally, we could treat these panels as two separate panels. This, however, would introduce an additional number of influence coefficients, which would have to be computed at every iteration of determining the cavity planform and every time step. To avoid this, we treat the split panel as *one*. The values for the dipole and source strength on the split panel are taken as the weighted averages of the strengths of its "left" and its "right" part. For example the cavity source is defined as:

$$\left[\frac{\partial\phi}{\partial n}\right]_{SPLIT} = \frac{\frac{\partial\phi}{\partial n_L} l_L + \frac{\partial\phi}{\partial n_R} l_R}{l_L + l_R} \qquad (25)$$

where l_L and l_R are the lengths of the "left" and "right" parts of the split panel at midspan of each strip, as shown in Figure 7. The value of $\frac{\partial\phi}{\partial n_R}$ is known, via equation (4), and the value for $\frac{\partial\phi}{\partial n_L}$ is expressed, via extrapolation[10], in terms of the unknown source strengths in front of the split panel. This is also depicted in Figure 7. A similar technique is applied to determine the dipole strength of the split panel. In addition, since the dipole and source strengths on the split panels have been expressed in terms of unknowns at neighboring panels, we do *not* apply equation (17) or (15) at any of these panels. The split panel technique is described in more detail in [13] and will be described as applied to propellers in [4].

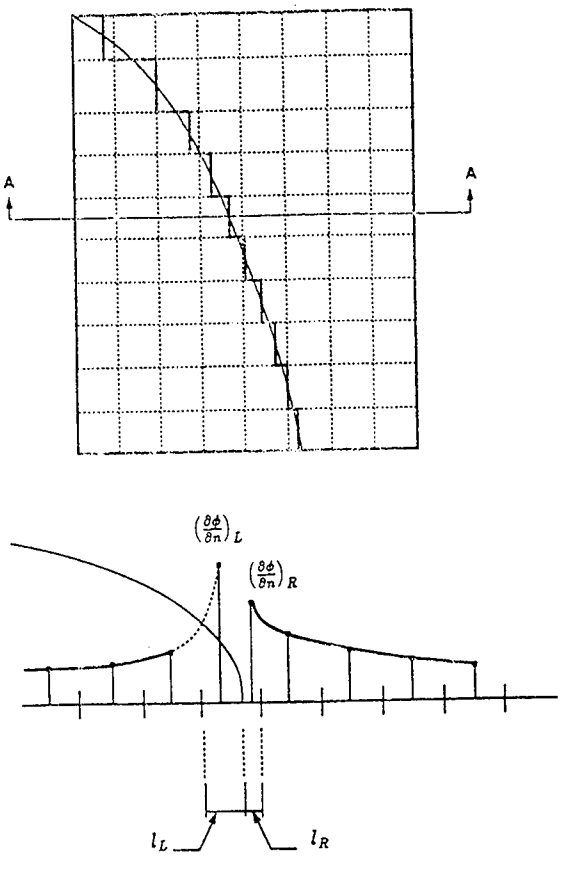

Figure 7: The split panel technique.

3.2 Treatment of the Unsteady Terms

The dynamic and kinematic boundary conditions, (13), (14), (20) and (22), include time derivatives of the potential and the cavity thickness. The numerical treat-

[10]The cavity source is assumed to behave like $1/\sqrt{x}$ with x being the distance from the cavity trailing edge.

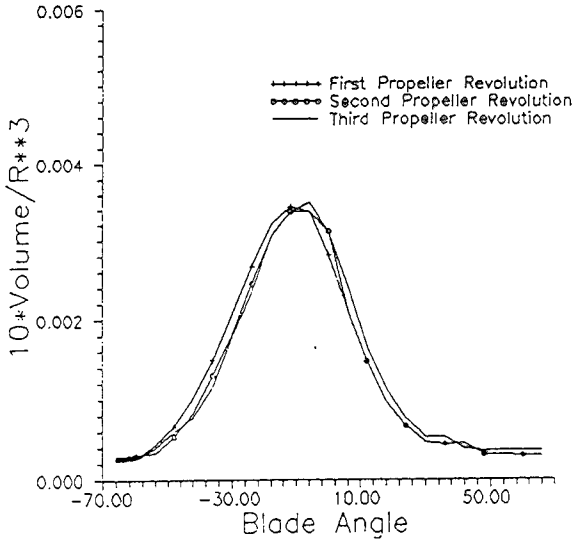

Figure 8: Cavity volume vs blade angle θ for the trial one-bladed propeller at $\sigma_n = 3.5$. Shown are the solutions from the first three revolutions, with the differences due mostly to convergence of $\frac{\partial \phi}{\partial t}$.

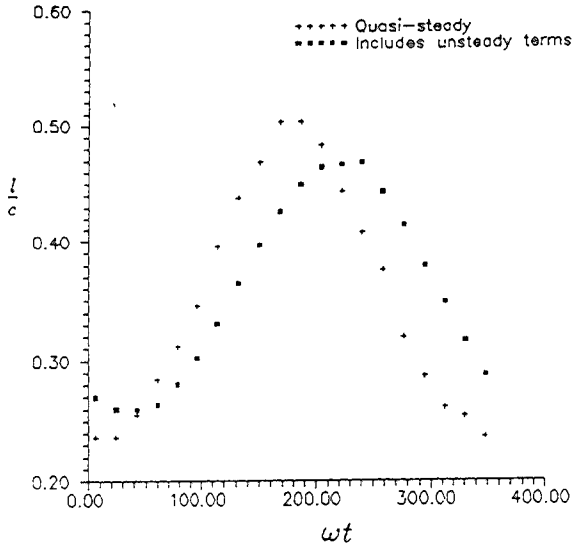

Figure 9: Cavity length vs ωt for a NACA16006 2-D section at $\alpha = 4°$ and $\sigma(t) = 1.2 + 0.2\cos\omega t$. Shown are the quasi-steady and the fully unsteady cavity solution.

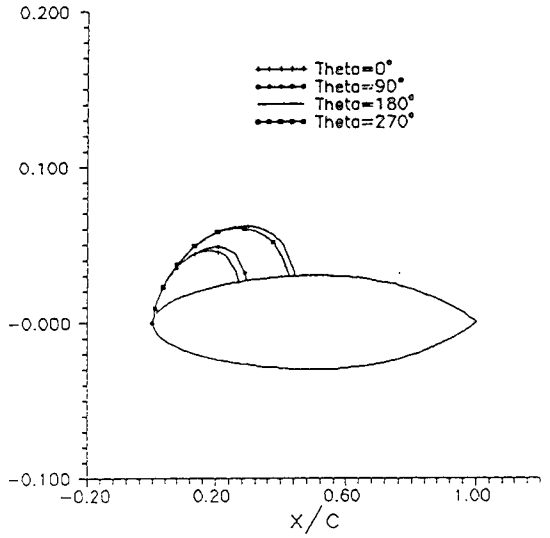

Figure 10: Cavity shapes from several time steps of the fully unsteady solution shown in the previous figure.

ment of these terms and their effect on the solution will be described in this section.

As we mentioned in Section 2.2, the dynamic boundary condition (13) expresses ϕ as a function of, among other parameters, the time derivative $\frac{\partial \phi}{\partial t}$. At a given time step, $\frac{\partial \phi}{\partial t}$ is assumed to be known and equal to its value computed after the solution was obtained when the propeller was at the same angular position during the previous rotation. The derivative is computed numerically by implementing a fourth-order-accurate backward finite difference scheme[11]. During the first propeller revolution, $\frac{\partial \phi}{\partial t}$ is assumed to be zero. A better approximation for $\frac{\partial \phi}{dt}$, though, would be its value from the fully wetted flow and this will be implemented in the future. Therefore, the solution will take several revolutions to converge to the steady-state oscillatory solution. However, several revolutions are already necessary for the solution to converge, since, according to the time-marching algorithm, it takes one full revolution for all of the blades to "see" the unsteady inflow and thus several revolutions for the solution to converge. The fact that the value of $\frac{\partial \phi}{\partial t}$ lags by one revolution is not expected to slow the convergence of the overall solution. As an example, Figure 8 shows the time-history of the cavity volume for a one-bladed propeller operating in a non-uniform inflow wake, both described in Section 4, for the first three revolutions.

The implementation of the time derivatives of the cavity thickness $\frac{\partial h}{\partial t}$ and $\frac{\partial h_w}{\partial t}$ in the kinematic boundary conditions (20) and (22) are numerically straightforward and will not be discussed in further detail here. These boundary conditions are used in the computation of the cavity thickness, which occurs after the solution at the current time step when the source strengths are known. In addition, these terms must also be included in determining the strength of a source panel which is wetted at the current time step, but which was cavitating during the previous time step. In other words, a

[11] Various finite difference schemes have been investigated for the computation of the fully wetted unsteady pressure distribution and the fourth-order scheme was chosen for reasons of robustness [15].

collapsing cavity has an *additional* source strength on the panels which lie between the trailing edge of the cavity from consecutive time steps. The magnitude of the total source will be given as

$$\frac{\partial \phi}{\partial n} = -U_n + \frac{\partial h}{\partial t}. \qquad (26)$$

In order to understand the importance of the unsteady terms of the boundary conditions, an unsteady two-dimensional model of a partially cavitating hydrofoil is investigated, wherein the cavitation number is allowed to vary harmonically ($\sigma(t) = \sigma_0 + \sigma_g \cos\omega t$) while the inflow is steady and uniform and the wake is quasi-steady (no shed vorticity, but the wake dipole strength changes each time step). Although this model is not an accurate representation of the physical flow, it allows us to see the relative effects of the various unsteady terms on the global 2-D solution. To this end, we have computed the time history of the cavity length on a NACA16006 hydrofoil operating at an angle of attack of 4° and with a time-dependent cavitation number equal to $\sigma(t) = 1.2 + 0.2\cos\omega t$ at a reduced frequency of $k = \frac{\omega c}{2U} = 1.0$. Figure 9 shows the cavity length as a function of ωt for one cycle for two different solutions. The first solution contains no history at all; the time derivatives of both the potential and the cavity thickness are zero. The second solution includes all the unsteady terms as well as the additional source terms during the collapse stage. Note that the curve from the fully unsteady solution is shifted to the right, *i.e.* the growth stage lasts longer than the collapse stage, a well known characteristic of unsteady cavitation.

Figure 10 shows cavity shapes from several time steps during the second cycle of the fully unsteady solution discussed above. Of particular interest is the difference between the cavity shapes at $\omega t = 90°$ and 270° for which *the cavitation numbers are identical.* The difference between the shapes is due entirely to the unsteady terms.

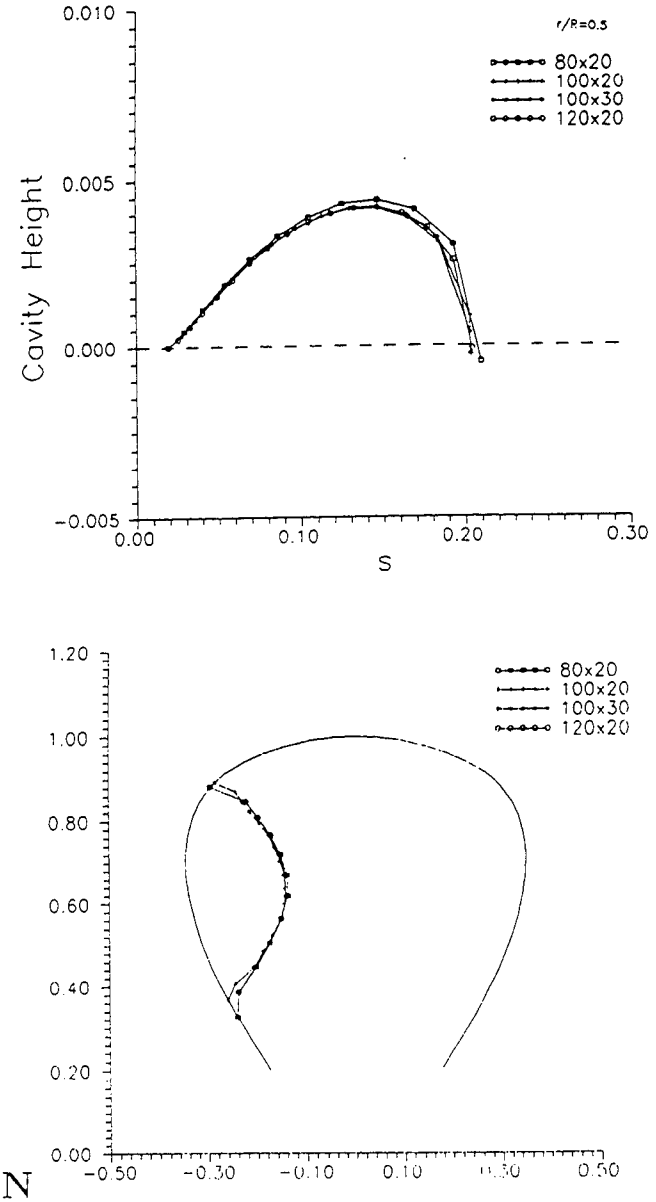

Figure 11: Convergence of the blade cavity planform with number of panels; predicted from the present method. The corresponding cavity shapes at $r/R = 0.5$ are also shown. Uniform flow with $J_S = 0.8$; $\sigma_n = 2.7$. Cavity detachment is set at 2.45% of the local chord at all spanwise locations.

4 RESULTS AND VALIDATION

The numerics of the present method have been extensively validated when applied to two or three dimensional hydrofoils, and the results are reported in [14, 13,5]. We next test the numerics of our method when applied to propellers. We apply the method on a one-bladed propeller, whose the geometry characteristics are given in Appendix D. The propeller is operating at an advance ratio $J_S = V_S/(nD) = 0.8$, with V_S being the ship speed, and a cavitation number $\sigma_n = 2.7$. We first run the propeller in uniform inflow and ignore the hydrostatic terms ($g = 0$). In this case, the cavity shape is steady in time. The resulting cavity planforms and the cavity heights at one blade section are shown in Figure 11 for different number of chordwise and spanwise panels.

To validate the solution, we analyze the blade with the computed cavity added to its suction side, as one modified blade in fully wetted flow. In doing so we apply a fully wetted boundary element method [19] by utilizing a panel arrangement which is adapted to the cavity trailing edge, which is known at this stage. The pressure distribution at $r/R = 0.75$ is shown in Figure 12 together with the pressure distribution from the present method. Note that the pressure distribution from the present method is constant over the cavity, as it should be, since the same formulation is utilized in computing the pressure as in the dynamic boundary condition. Most remarkable, though, is the agreement of that pressure to the one from the validation test. This good agreement indicates that the predicted cavity shape is a very good approximation to the cavity shape that would result from a completely non-linear theory, in which the "exact" cavity shape is determined in an iterative sense by repanelling the updated shapes, until convergence. This result supports the assumption we made in Section 2.2, where we applied the boundary conditions on the approximate cavity surface. Finally, the cavity planform from applying the present (PROPCAV) and other methods (PUF-3A), which have been mentioned in the introduction [18,10], are shown in Figure 13. Note that the original PUF-3A (linear) overpredicts the cavity extent in both the spanwise and chordwise directions, especially at the inner propeller radii. On the other hand, the modified PUF-3A (with the leading edge corrections) seems to underpredict the cavity planform, even though it produces more "accurate" cavity shapes than the original.

We then apply our method for the same propeller in a non-uniform axial wake inflow, U_{W_x}, of which the circumferential variation is given in Figure 14. In this case the hydrostatic terms are turned on ($Fr = n^2D/g = 10.45$). The advance coefficient and the cavitation number are kept the same as in the uniform inflow case. The computing time on a DEC9000 computer for $N = 80$, $M = 20$ and $\Delta\theta_W = 6°$, was approximately three hours per revolution. The convergence of the cavity volume with the size of the time step is shown in Figure 15.

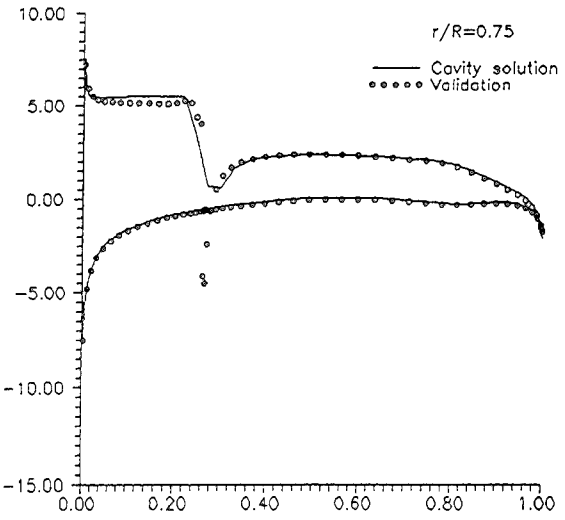

Figure 12: Chordwise pressure distributions on the cavitating blade at $r/R = 0.75$. Uniform flow with $J_S = 0.8$; $\sigma_n = 3.5$. The pressure coefficient is defined as $C_P = (p - p_o)/(\rho/2)/V_S^2$, with V_S being the ship speed.

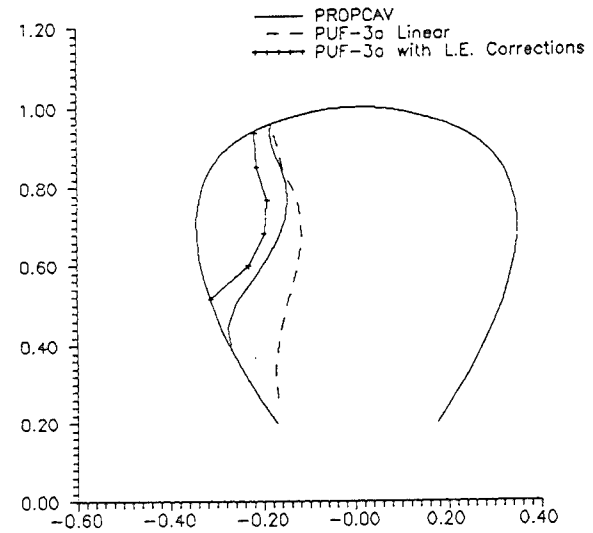

Figure 13: Cavity planforms predicted from PUF-3A (with and without the leading edge correction) and the present method (PROPCAV). Uniform inflow with $J_S = 0.8$; $\sigma_n = 3.5$.

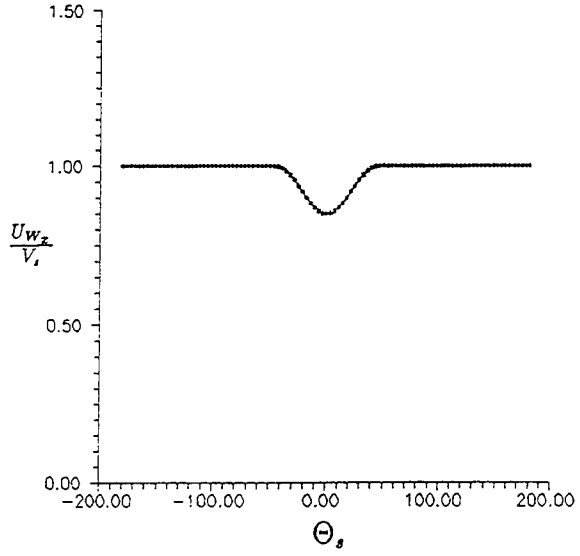

Figure 14: The wake inflow as a function of θ_S; $\theta_S = 0$ corresponds to the "12 o'clock" position. The same at all propeller radii.

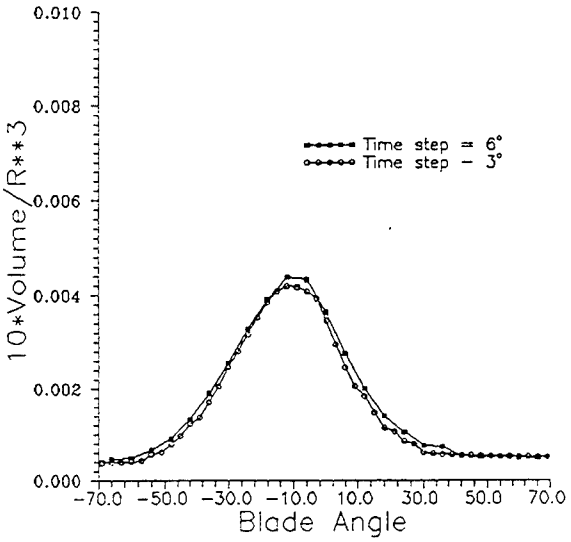

Figure 15: Cavity volume as function of blade angle: predicted from present method (PROPCAV). Non-uniform flow with $J_S = 0.8$; $\sigma_n = 3.5$. Convergence with time step $\Delta\theta_W = \omega\Delta t$.

5 CONCLUSIONS

A potential-based boundary element method has been developed for the analysis of unsteady propeller sheet cavitation. The method is able to treat, in a computationally efficient and robust way, arbitrary unsteady cavity shapes on a blade discretization which is fixed in time. Applying the cavity boundary conditions on the blade surface under the cavity rather than on the "exact" cavity surface, is shown (here and in the cited references) to have little effect on the predicted cavity extent and volume. The non-linear character of the solution is thus preserved, while substantial savings in the computing time are accomplished. The method, implemented in the computer code PROPCAV, provides the user with more accurate blade cavity shapes than a previous method (PUF-3A) which was based on a linearized lifting surface formulation.

6 FUTURE WORK

As mentioned in Section 2.2, the location of the detachment point at each blade section is an arbitrary parameter. These points could be determined from further knowledge of the viscous flow in front of the cavity. In addition, we have made the assumption that the unsteady cavity closes at its trailing edge. In reality, though, there is a trailing wake behind the cavity of some finite thickness. The detachment point as well as the open wake behind the cavity could be determined from coupling the method described in the present paper with a boundary layer solver. Systematic boundary layer LDV measurements in front and behind unsteady cavities in two and three dimensions would be enlightening in learning more about the physics of the flow. Viscous flow numerical simulations of cavity flows in two-dimensions would also be useful at this stage [17]. In addition to the boundary layer coupling, there is also a need for the numerical treatment of the tip vortex cavitation, especially at off-design conditions. We have already faced this problem when applying our method to some propeller geometries, in which the predicted cavity shapes and planforms do not close and seem to need to be matched by a local tip vortex solution. In addition, the present method could readily be extended to treat the effects of a hub and/or a duct as well as the effects of another component.

7 ACKNOWLEDGEMENTS

Support of this research has been provided by the Applied Hydromechanics Research Program administered by the Office of the Naval Research (Contract: N00014-90-J-1086). The authors would like to thank Randall A. Villeneuve, a graduate student in the Department of Ocean Engineering at MIT, for his help in producing the cavitating rectangular hydrofoil results.

References

[1] G. Birkhoff and E.H. Zarantonello. *Jets, Wakes and Cavities.* Academic Press Inc., New York, 1957.

[2] W.M. Blake, K. Meyne, J.E. Kerwin, E. Weitendorf, and J. Friesch. Design of APL C-10 propeller with full-scale measurements and observations under service conditions. *Trans. SNAME*, 98:pp. 77–111, 1990.

[3] T. Brockett. *Minimum Pressure Envelopes for Modified NACA-66 Sections with NACA a=0.8 Camber and Buships Type I and Type II Sections.* Report 1780, DTNSRDC, Teddington, England, Feb 1966.

[4] N. E. Fine. *Nonlinear Analysis of Cavitating Propellers in Nonuniform Flow.* PhD thesis, Department of Ocean Engineering, MIT, October, 1992.

[5] N.E. Fine and S.A. Kinnas. A boundary element method for the analysis of the flow around 3-d cavitating hydrofoils. *Journal of Ship Research*, 1992 (year of acceptance). to appear.

[6] D.S. Greeley and J.E. Kerwin. Numerical methods for propeller design and analysis in steady flow. *Trans. SNAME*, vol 90, 1982.

[7] Lemonnier H. and Rowe A. Another approach in modelling cavitating flows. *Journal of Fluid Mechanics*, vol 195, 1988.

[8] Ching-Yeh Hsin. *Development and Analysis of Panel Method for Propellers in Unsteady Flow.* PhD thesis, Department of Ocean Engineering, MIT, September 1990.

[9] C.W. Jiang. *Experimental and Theoretical Investigation of Unsteady Supercavitating Hydrofoils of Finite Span.* PhD thesis, M.I.T., Department of Ocean Engineering, May 1977.

[10] J.E. Kerwin, S.A. Kinnas, M.B. Wilson, and McHugh J. Experimental and analytical techniques for the study of unsteady propeller sheet cavitation. In *Proceedings of the Sixteenth Symposium on Naval Hydrodynamics*, Berkeley, California, July 1986.

[11] S.A. Kinnas. Leading-edge corrections to the linear theory of partially cavitating hydrofoils. *Journal of Ship Research*, 35(1):pp. 15–27, March 1991.

[12] S.A. Kinnas. *Non-linear Corrections to the Linear Theory for the Prediction of the Cavitating Flow Around Hydrofoils.* PhD thesis, Department of Ocean Engineering, MIT, May 1985.

[13] S.A. Kinnas and N.E. Fine. A numerical nonlinear analysis of the flow around 2-D and 3-D partially cavitating hydrofoils. *Journal of Fluid Mechanics*, 1993 (year of acceptance). to appear.

[14] S.A. Kinnas and N.E. Fine. Non-Linear Analysis of the Flow Around Partially or Super-Cavitating Hydrofoils by a Potential Based Panel Method. In *Boundary Integral Methods-Theory and Applications, Proceedings of the IABEM-90 Symposium, Rome, Italy, October 15-19, 1990*, pages 289–300, Springer-Verlag, Heidelberg, 1991.

[15] S.A. Kinnas and C-Y. Hsin. A boundary element method for the analysis of the unsteady flow around extreme propeller geometries. *AIAA Journal*, 30(3):688–696, March 1992.

[16] S.A. Kinnas, C-Y. Hsin, and D.P. Keenan. A potential based panel method for the unsteady flow around open and ducted propellers. In *Proceedings of the Eighteenth Symposium on Naval Hydrodynamics*, pages 667–685, Ann Arbor, Michigan, August 1990.

[17] A. Kubota, H. Kato, and H. Yamaguchi. Finite difference analysis of unsteady cavitation on a two-dimensional hydrofoil. In *Proceedings of the Fifth International Conference on Numerical Ship Hydrodynamics*, pages 667–683, Hiroshima, Japan, September 1989.

[18] Chung-Sup Lee. *Prediction of Steady and Unsteady Performance of Marine Propellers with or without Cavitation by Numerical Lifting Surface Theory.* PhD thesis, M.I.T., Department of Ocean Engineering, May 1979.

[19] Jin-Tae Lee. *A Potential Based Panel Method for The Analysis of Marine Propellers in Steady Flow.* PhD thesis, M.I.T., Department of Ocean Engineering, August 1987.

[20] P. Leehey. Supercavitating hydrofoil of finite span. In *IUTAM Symposium on Non-Steady Flow of Water at High Speeds*, pages 277–298, Leningrad, June 1971.

[21] J.N. Newman. Distributions of sources and normal dipoles over a quadrilateral panel. *Journal of Engineering Mathematics*, vol 20:pp 113–126, 1986.

[22] T. Nishiyama. Lifting line theory of supercavitating hydrofoil of finite span. *ZAMM*, 50:645–653, 1970.

[23] C. Pellone and A. Rowe. Supercavitating hydrofoils in non-linear theory. In *Third International Conference on Numerical Ship Hydrodynamics*, Basin d'essais des Carènes, Paris, France, June 1981.

[24] Widnall S.E. Unsteady loads on super-cavitating hydrofoils. *Journal of Ship Research*, 9:pp. 107–118, 1966.

[25] M.P. Tulin. *Steady Two-Dimensional Cavity Flows About Slender Bodies.* Technical Report 834, DTMB, May 1953.

[26] M.P. Tulin and C.C. Hsu. New applications of cavity flow theory. In *13th Symposium on Naval Hydrodynamics*, Tokyo, Japan, 1980.

[27] J.S. Uhlman. A partially cavitated hydrofoil of finite span. *Journal of Fluids Engineering*, 100(3):pp. 353–354, September 1978.

[28] J.S. Uhlman. The surface singularity method applied to partially cavitating hydrofoils. *Journal of Ship Research*, vol 31(No. 2):pp. 107–124, June 1987.

[29] J.S. Uhlman. The surface singularity or boundary integral method applied to supercavitating hydrofoils. *Journal of Ship Research*, vol 33(No. 1):pp. 16–20, March 1989.

[30] R.J. Van Houten. The numerical prediction of unsteady sheet cavitation on high aspect ratio hydrofoils. In *14th Symposium on Naval Hydrodynamics*, 1982.

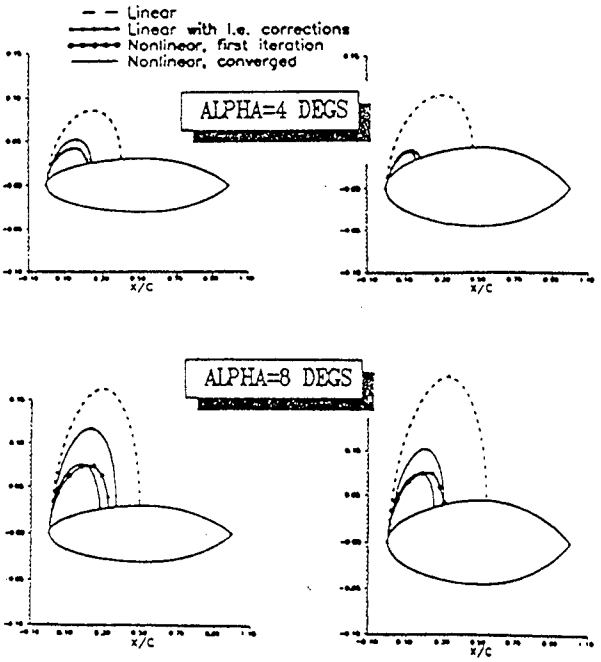

Figure 16: Cavity shapes, predicted from linear (with and without the leading edge correction) and from the present non-linear method (with and without cavity re-panelling). NACA-16 hydrofoil at $\alpha = 4°$ (top), $\alpha = 8°$ (bottom), with thickness to chord ratio 6% (left) and 9% (right). The ratio α/σ is kept constant and equal to 0.055.

A Non-linear Character of Solution

Effect of Re-panelling on Solution

As mentioned several times in the main body of this paper, the dynamic and kinematic boundary conditions on the cavity are applied on an approximate surface. We have investigated the effect of this approximation on the solution in two dimensions, for partially and supercavitating flows, where we iterated to determine the "exact" cavity surface on which both conditions are met [14,13,5]. In conclusion we found that:

- For fixed cavity length, the cavitation number and cavity shape converge quickly (often in two iterations) to the "exact" nonlinear result. This is much faster than a previously developed surface vorticity-based boundary element method [28]. Even the first iteration is very close to the exact result [14].
- For fixed cavitation number, the first iteration (panels on the hydrofoil) cavity is also close to the "exact", as reported in [13]. This may also be seen in Figure 16, in which the cavity shapes are

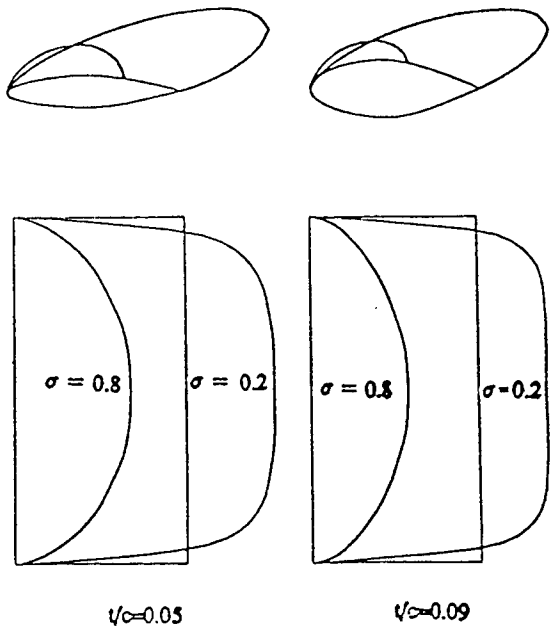

Figure 17: Non-linear effect of blade thickness on cavity solution. Cavity planforms and shapes at midchord, predicted by the present method, are shown. Rectangular hydrofoils, $\alpha = 5°$, $A = 5$, $t/c = 0.05, 0.09$ (span and chord are not in scale).

shown for two hydrofoil sections at two angles of attack, as predicted from linear theory, with and without the leading edge correction, and from the present method without (first iteration) and with (converged solution) re-panelling. In the same figure, also note the substantial improvement on the

linear theory, when the leading edge corrections are included.

In addition, we have validated the cavity solution resulting from the present method when applied to two and three dimensional hydrofoils. To accomplish that, we add the computed cavity heights normal to the hydrofoil suction side to produce a new hydrofoil, which we then analyze in fully wetted flow. In this case we locate the panels on the computed cavity surface. The resulting pressure distribution on the new foil has been found to be nearly constant, equal to the desired cavitation number, within acceptable accuracy. This is a strong indication that the "tested" cavity shape provides a very good approximation of the "exact" cavity surface. This validation test has also been applied in the case of the propeller, as described in Section 4.

Non-linear Dependence of Solution on Blade Thickness

The present method has also been found to manifest the correct non-linear effect of blade thickness on the shape of the cavity. This is shown in Figure 17 where the cavity planforms and shapes at midspan are shown for two rectangular hydrofoils at two cavitation numbers. Both hydrofoils have an aspect ratio $A = 5$, zero camber and a NACA65a thickness section of which the maximum thickness is varying elliptically to zero in the spanwise direction. They are both at an angle of attack $\alpha = 5°$. The first has a thickness to chord ratio at midspan $t/c = 5\%$, and the second with $t/c = 9\%$. Note that the present method predicts a smaller cavity (in extent and volume) for the thicker foil at the same cavitation number. The predicted effect of foil thickness on the cavity size appears to be less pronounced in the case of supercavities.

B Effect of δ_{TOL} on Solution

As mentioned in Section 2.4 the "correct" cavity planform for a given cavitation number is determined via an iterative process until the thickness at the trailing edge of the cavity vanishes at all spanwise locations within some prescribed tolerance δ_{TOL}. The effect of that tolerance (made non-dimensional on the chord) on the predicted cavity planform is shown in Figure 18 for a rectangular hydrofoil of $t/c = 0.05$. The planform No. 1 (which also happens to be the converged planform for $\delta_{TOL} = 0.1$) has been used as the initial guess for all

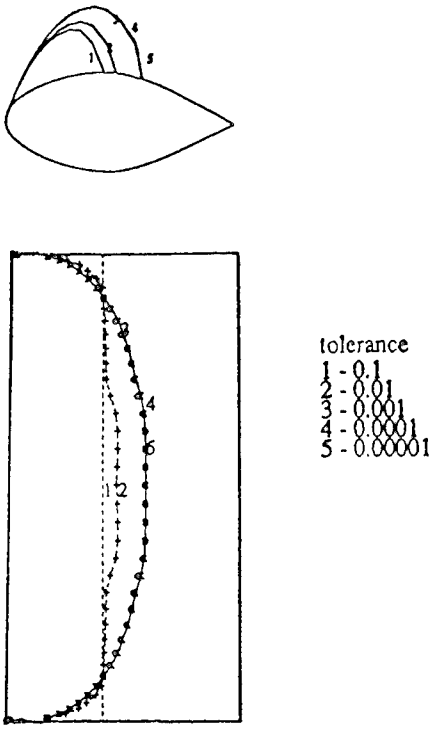

Figure 18: Cavity planforms, predicted from the present method, for several values of δ_{TOL}. The corresponding cavity and foil sections at midspan are shown at the top. Same hydrofoil as in Figure 17, $\alpha = 5°$, $t/c = 0.05$, $\sigma = 0.8$ (span and chord are not in scale)

these cases. The results shown in Figure 18 suggest that at least a tolerance $\delta_{TOL} = 0.001$ must be utilized.

C Multiplicity of Solutions for Hydrofoils

Equations (24) may accept more than one solution, *i.e* cavity planform, for some values of cavitation number. For example, this is a very well known fact in two dimensions, where for some cavitation numbers there are three solutions (two partial cavities and one supercavity). Our method has also been found to predict multiple solutions in three dimensions [5], as can be seen in Figure 19. Note that for $\sigma = .74, .76, .78$ we predict two cavity planforms, one partial cavity and one mixed cavity (supercavity at midspan). The partial cavities were produced when the initial guess was a partial cavity and the supercavities when the initial guess was a supercavity. The cavity length at midchord vs α/σ is also shown in Figure 20, together with the corresponding curves for two other rectangular hydrofoils with aspect

ratios $A = 2$ and $A = 10$. Notice the striking similarity of these curves to the well known characteristic curve for a two dimensional cavitating flat plate (not shown in the Figure), especially for the larger aspect ratio hydrofoils. Further research and/or experiments are required in determining the stability and physical existence of the multiple solutions. The reader is also referred to [13] and [5] for more discussion on this issue. The multiplicity of solutions for propeller blades will be addressed in the future [4].

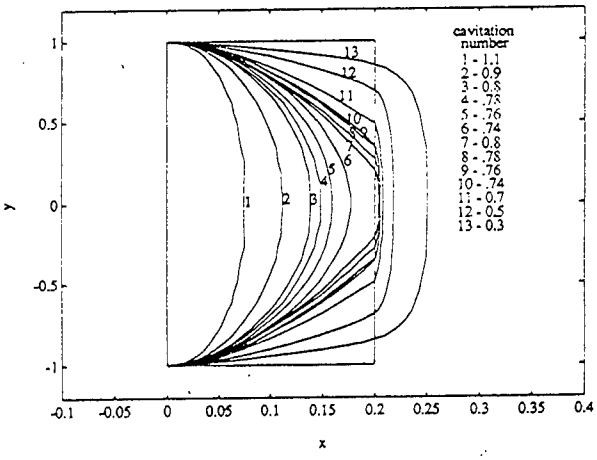

Figure 19: Cavity planforms, predicted from the present method, for several cavitation numbers. Rectangular hydrofoil, $t/c = 0.05$, $\alpha = 5°$, aspect ratio $A = 5$.

r/R	P/D	$rake/D$	$skew(deg.)$	l_c/D	f_{max}/l_c	τ_{max}/D
0.2	1.332	0.	0.	0.174	0.0351	0.0651
0.25	1.338	0.	0.	0.202	0.0369	0.0594
0.3	1.345	0.	0.	0.229	0.0368	0.0537
0.4	1.358	0.	0.	0.275	0.0348	0.0441
0.5	1.350	0.	0.	0.312	0.0307	0.0360
0.6	1.310	0.	0.	0.337	0.0245	0.0286
0.7	1.250	0.	0.	0.347	0.0191	0.0219
0.8	1.150	0.	0.	0.334	0.0148	0.0157
0.9	0.950	0.	0.	0.280	0.0123	0.0101
0.95	0.750	0.	0.	0.210	0.0128	0.0072
1.0	0.500	0.	0.	0.	0.0120	0.0044

Table 1: The trial propeller geometry.

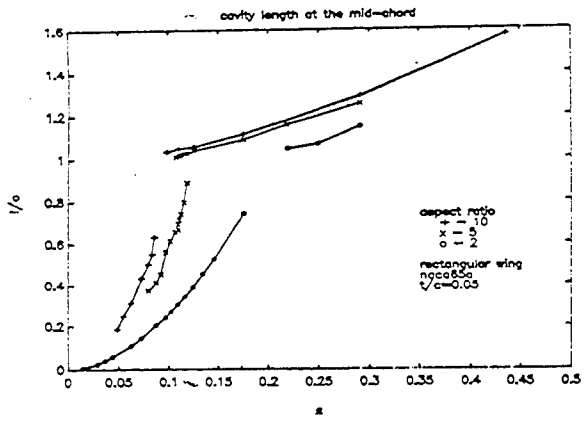

Figure 20: Effect of aspect ratio on multiplicity of solutions for rectangular hydrofoils ($t/c = 0.05$, $\alpha = 5°$). The cavity length at midspan is shown vs α/σ for three aspect ratios $A = 2, 5, 10$.

D Geometry of the Propeller

The propeller geometry is given on Table 1. R is the radius and D the diameter of the propeller. P is the pitch of the propeller helix, l_c is the blade chord at r, f_{max} is the maximum camber and, τ_{max} the maximum thickness. The camber distribution is a $NACA\ a = 0.8$ meanline and the thickness distribution a modified $NACA$ 66 form [3].

DISCUSSION

Chang-Sup Lee
Chungnam National University, Korea

The authors should be praised for their fine piece of work. I feel they are keeping a good pace to lead researchers in propeller hydrodynamics. I would like to ask a question in connection with the cavity planform shown in Fig. 17. We observe that the cavity length at the tip is zero; or in other words the tip region is not cavitating contrary to a usual observation in cavitation tunnel experiments. We, at Chungnam National University, are working on the same problem, using almost same procedure as described in the present paper. Our results always showed a tendency to supercavitate at the tip. We feel that the behavior may be associated strongly with the crossflow component, or the spanwise velocity component. We wish to hear how the authors treated the flow in the tip region. Did you make any approximation to compute velocity in the tip region? And also we would like to hear whether there is any effort to resolve the tip flow or tip vortex cavitation. Again we congratulate the authors for their excellent achievement.

AUTHORS' REPLY

We would like to thank Dr. Lee for his kind comments and for his interest in the presented work. He asks about the cavity planform shown in Figure 17. For the (rectangular planform) foil and conditions shown in Figure 17, the method predicted a cavity shape whose length reduced to zero near the tip. We have done extensive validation of similar results, including "pressure validation", mentioned in section 4. In addition, we have also made some water tunnel observations of a similar wing — one which is shaped like the keel of a sailboat —and found that the sheet cavity did taper to zero near the tip. A cavitating tip vortex, separate from the sheet cavity, was also observed. We can imagine that the tip vortex and sheet cavity may in other conditions be connected, which may explain the observations which Dr. Lee refers to.

For elliptic planform foils (or any foil whose chord length tapers to zero at the tip) the predicted planforms *do* tend to supercavitate at the tip. An example of this is shown in Figure 21 (taken from [5]) where the planform is predicted to increase near the tip. Perhaps it is this type of supercavitation to which Dr. Lee refers. In addition, for rectangular foils at higher angles of attack or lower cavitation numbers, we also predict supercavitation throughout the span, but without the increase in cavity length near the tip seen in Figure 21. Regarding the crossflow term in the dynamic boundary condition, no approximation has been made; the crossflow has been included in an iterative sense. In any case, as shown in [4], the crossflow terms have little effect on the predicted cavity shapes.

Dr. Lee also asks about our plans for incorporating a model for tip vortex cavitation. We have made preliminary plans to couple the current solution with an inner tip vortex solution in the vicinity of the blade tip. However, details of this method have yet to be developed.

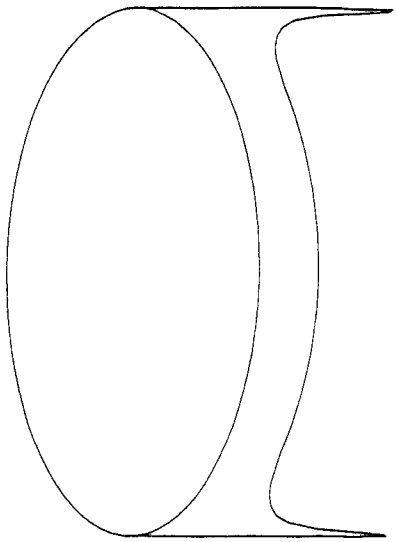

Figure 21: Predicted cavity planform for an elliptic hydrofoil, showing large cavity lengths near the tip.$t/c = 0,04$, $\alpha/\sigma = 0.327$, $\alpha = 3°$. The span to maximum chord ratio is 5.9. (Taken from [5])

DISCUSSION

C. Brennen
California Institute of Technology, USA

I applaud the authors' effort to construct analytical methods to analyze sheet cavitation on a propeller. I am however concerned that their methods are not capable of tackling the most dramatic phenomenon associated with unsteady sheet cavitation, namely the detachment of the sheet and the production of a cavitation cloud whose subsequent collapse is a very violent phenomenon. While I recognize that the authors do not claim to address this phenomenon, nevertheless it raises the question of the conditions governing free streamline separation at the leading edge (see Furuya, JFM, 1975), a critical issue which, in steady flows, determines whether or not a sheet cavity will form. I am curious to know whether the authors are considering this important issue of cavity separation at the leading edge in order to broaden the applicability of their methodology.

AUTHORS' REPLY

We would like to thank Dr. Brennen for his constructive comments. He first comments on the inability of our method to treat the important phenomenon of cloud cavitation and the apparent neglect of the importance of the cavity detachment point. As he recognizes, in the present work our objective was to develop a robust and efficient method for the prediction of sheet cavitation on propellers which operate in a nonuniform ship wake. This type of cavitation is commonly observed in the case of propellers operating close to design conditions. The kind of "violent" cavitation he refers to tends to be more common in situations where the geometry (foil) is pitching and the flow is stationary as opposed to our applications where the flow is

non-stationary and the geometry (propeller) is stationary. In several propeller applications (especially at design conditions) a time dependent sheet cavity appears to occur throughout the full propeller revolution. By using the panel method and by applying the three dimensional nonlinear boundary conditions, we are confident that we can obtain the correct inviscid solution even for extreme propeller geometries. However, we acknowledge that the location of the cavity detachment plays a very important role in determining the global flow, including the shape of the sheet cavity. As we mentioned in section 6, we plan to employ an interactive boundary layer analysis in front of and behind the cavity. Using a detachment criterion similar the one suggested by Franc and Michel (JFM, 1985), the dependence of the detachment point on viscosity will be captured. Work on implementing this for two dimensional flows has already begun.

For propellers operating at off-design conditions, cloud cavitation is known to have a large effect on the induced vibrations, radiated noise, and surface erosion. A further coupling of the present method with a bubble or cloud cavity model deserves consideration, especially as hardware and software advances yield faster run times and permit the use of more complex codes. However, the phenomenon is very complex and adequate modeling of the physics may be outside the scope of potential flow theory, even when the viscous boundary layer is accounted for.

DISCUSSION

Tetsuji Hoshino
Mitsubishi Heavy Industries, Japan

I would like to congratulate the authors on developing the very sophisticated theory of unsteady propeller cavitation. I would like to ask one question. The calculations shown here look like that the cavity always appears from the leading edge of the blade. The pressure at the leading edge would be always lower than the vapour pressure in the lifting surface theory but not always lower in the panel method. Therefore, you should determine the starting point of the cavity by the pressure condition that the pressure on the blade becomes lower than the vapor of the water.

AUTHORS' REPLY

We want to thank Dr. Hoshino for his comments. He addresses the issue of cavity detachment, noting that our detachment points should coincide with the minimum pressure points from the fully wetted flow. It is true that the minimum pressure point is always at the leading edge in linearized hydrofoil theory. However, when the leading edge corrections are included [11], the minimum pressure point is not at the leading edge any longer. As mentioned in the previous discussion, we recognize the importance of the detachment point. It has been shown that the actual detachment point depends strongly on the nature of the boundary layer near the blade leading edge. Our ultimate goal is to develop the detachment criterion mentioned above, thereby incorporating the effect of viscosity. Our present goal, however, was to numerically validate the *inviscid* result for given locations of detachment points.

DISCUSSION

William B. Morgan
David Taylor Model Basin, USA

It seems that one of the principal problems with this theory is determining the cavity detachment point. Can the authors give any insight to how to estimate this detachment point for an arbitrary shape? I am interested in some of the new sections being developed for propellers. Another question concerns cavities of 0.7 to 1.0 chord length. Does your theory show an instability in this area as observed in experiments?

AUTHORS' REPLY

We thank Dr. Morgan for his comments. He first asks about the cavity detachment. We hope that we have answered his question in the previous discussions. He also asks whether the so-called "three-quarter chord instability", which has been observed in experiments, has been predicted by our theory. In two dimensional flows, there is an observed instability of cavities which have length greater than roughly three quarters of the chord. In analysis, this instability is manifested by the occurrence of multiple solutions. In other words, for a given cavitation number there correspond more than one cavity length. Our theory also predicts multiple solutions for two dimensional foils and for high aspect ratio three dimensional foils (see Appendix C of the paper). However, our method has not predicted multiple solutions for propellers. This is in agreement with the fact that no corresponding instability has been observed for propeller flows.

DISCUSSION

K. Nakatake
Kyushu University, Japan

I congratulate your completion of the method for this difficult problem.

1. Is U_W equal to U_w ?
2. You wrote U_W (effective wake) includes the interaction between the vorticity of the inflow and the vorticity due to the propeller. Do you mean that the propeller creates vorticity flow in front of the propeller? How could you obtain?

AUTHORS' REPLY

We thank Dr. Nakatake for his comments. He asks if U_W is the same as U_w. In fact, the use of U_w in equation (7) is incorrect; it should say U_W. He also seeks a clarification of our definition of the effective wake, which the symbol U_W represents. We say that the effective wake includes the interaction between the vorticity in the inflow in the absence of the propeller (the nominal wake) and the vorticity due to the propeller (distributed on the propeller blades and their wakes). This interaction does not create vorticity in front of the propeller. It redistributes it though and as a result changes the flow field seen by the propeller.

DISCUSSION

Chen-Wen Jiang
David Taylor Model Basin, USA

It will be valuable to see the improvement of current approach compared with your lifting surface theory. The propeller used in Ref. [10] could be used for this purpose. There are two questions regarding this paper:

1. How do you treat the boundary condition at the cavity/propeller surface junction area?
2. Our experience indicates that the wake alignment is important to the unsteady pressure condition. I expect it is critical in the unsteady pressure calculation. Probably the influence of wake alignment is more important than the items mentioned in "future work" section. What is your opinion on this?

AUTHORS' REPLY

We thank Dr. Jiang for his comments. One comparison of the present method to the lifting surface method is given for a no-skew propeller in Figure 13. Another comparison may be seen in Figure 22. In these comparisons it can be seen that the lifting surface method (PUF-3A) predicts cavities which are within reasonable bounds to those predicted by the present panel method (PROPCAV) only when the leading edge corrections are included. We have also carried a comparison for the high-skew AO-177 propeller used in Ref. [10]. In that case we have found that the cavity planforms compare well to those from lifting surface theory (with leading egde corrections) at inner radii but that the panel method predicts shorter supercavities than the lifting surface method at the outer radii. We suspect that in this case the results from the lifting surface method need more panels in the spanwise direction. We plan to make a more thorough comparison between the two methods in the future.

Dr. Jiang's question on the treatment of the cavity/propeller junction is addressed in Section 3.1 and in more detail in the cited references in the same section. Finally, his question on wake alignment. Wake alignment would affect the cavity solution in a similar way wake alignment affects the loading on the blade in fully wetted flow. This effect, however, has been found to be minimal at design conditions.

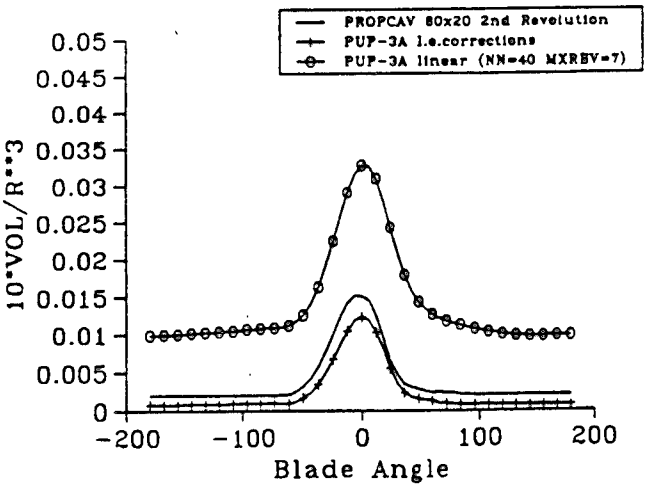

Figure 22: Cavity volume histories predicted by PUF-3A (with and without the leading edge correction) and the present method (PROPCAV) on the test propeller at $J_S = 0.8$ and $\sigma = 2.7$ in nonuniform flow.

DISCUSSION

H. C. Raven
MARIN, The Netherlands

I first want to congratulate the authors with completing this 3-D unsteady panel method for propeller cavitation. There may be discussion, though, on its being nonlinear. Because only the first iteration is carried out, the cavity conditions are applied on the foil surface instead of on the cavity. As a result, terms of first order in the cavity thickness are missing in both the kinematic and the dynamic boundary conditions. Incorporating these "transfer terms" leads to a linearized consistent formulation recently proposed by Buist and Raven [Ref]. In that paper it was shown that the linearized method gives results quite close to that of nonlinear method. The additional transfer terms improve the agreement. Your results do show that incorporating the fully wetted flow without approximation already yields a satisfactory method, but one should be aware of its leading order inconsistency. Can you comment on this?

[Ref] J. Buist, H.C. Raven "A consistently linearized approach for the calculation of partial sheet cavitation", ASME cavitation Forum, 1991.

AUTHORS' REPLY

We thank Dr. Raven for his comments. The presented method has been formulated as an iterative method (this is more clear in [14] and [13]) in which the cavity shape is updated by an additional cavity height which is taken normal to the cavity surface from the previous iteration. The first iteration cavity is taken to coincide with the foil surface underneath it. It has been found (see [14]) that the cavity shape from the first iteration is very

close to the final. So it has been decided to stop the iterative process after the first iteration, especially when we applied the method to the unsteady cavitating flow around propellers. Dr. Raven's formulation (in his Ref. with Buist) treats the cavity solution as a linear perturbation to the fully wetted flow. We do not do that. Our problem is formulated as a perturbation to the inflow instead. In our formulation there is *no assumption* about the magnitude of the perturbation potential ϕ. In the next lines a proof is given that our first iteration cavity solution is indeed a *consistently* linearized formulation with respect to the cavity thickness h. We will limit ourselves in two dimensions:

Consider a 2-D hydrofoil with s being its arclength, measured from the leading edge, with $\boldsymbol{n}$ and $\boldsymbol{s}$ being the normal and tangent to the foil unit vectors, respectively. Call q_n and q_s the components of the total velocity vector, $\boldsymbol{q}$, normal and tangent to the foil, respectively, resulting from the first iteration cavity solution. These velocities are thus evaluated on the foil surface. The velocity vector, $\boldsymbol{q}^h$, on the cavity surface (of height $h(s)$) may be found from the following expansion:

$$\boldsymbol{q}^h = \boldsymbol{q} + \frac{\partial \boldsymbol{q}}{\partial n} h + O(h^2) \tag{1}$$

The normal vector, $\boldsymbol{n}^h$, on the cavity surface is given [14]:

$$\boldsymbol{n}^h = \boldsymbol{n} - \frac{dh}{ds}\boldsymbol{s} + O(h^2) \tag{2}$$

Making use of the equations:

$$\frac{\partial q_n}{\partial n} = -\frac{q_n}{R} - \frac{\partial q_s}{\partial s} \tag{3}$$

$$\frac{\partial q_s}{\partial n} = -\frac{q_s}{R} + \frac{\partial q_n}{\partial s}, \tag{4}$$

with R being the radius of curvature of the hydrofoil, it can proven that:

$$\boldsymbol{q}^h \cdot \boldsymbol{n}^h = q_n - q_s \frac{dh}{ds} + O(h^2), \tag{5}$$

Omitting second order terms in equation (5) renders our kinematic boundary condition which requires:

$$q_n - q_s \frac{dh}{ds} = 0 \tag{6}$$

Note from equation (6) that $q_n = O(h)$. This has been used in deriving equation (5).

Similarly it can proven for the dynamic boundary condition, that:

$$q_s^h = q_s(1 - h/R) + O(h^2) \tag{7}$$

Including the curvature term $(-h/R)$ has a very small effect on the solution, because the curvature of hydrofoils is relatively small, except at the leading edge where, however, the height is small.

Numerical Simulation and Experimental Study of the Hydrodynamic Characteristics of a Hydrofoil-Strut-Pod Configuration with Inlets (I)

L. Baiqi, Z. Dexiang, Y. Xiaozhong, H. Shan, C. Zhongyao
(China Ship Scientific Research Center, China)

ABSTRACT

Under the linearized water surface condition, a numerical method based on the doublet distribution for predicting hydrodynamic characteristics of a foil-strut-pod configuration is presented in this paper. The theoretical formula derived by the authors previously for the calculation of induced velocity caused by a horseshoe vortex with arbitrary orientation beneath the water surface is applied. The computer executive time for calculating the complex exponential integral is obviously reduced by using a new method proposed. It is found that good agreement between calculated and experimental results can be achieved.

In addition to the numerical approach, a new test set-up for experimentally studying the integrated hydrofoil waterjet propulsion system has been developed. The lift and drag of foil-strut-pod configuration with inlet flow and the net propulsive force produced by integrated hydrofoil waterjet propulsion system were obtained from the experiments. It has been shown that the performance of the test set-up is satisfactory, the effects of inlet velocity on lift and drag can not be neglected, and the net propulsive force is useful for predicting the speed of prototype craft.

NOMENCLATURE

A_i	cross-sectional area of inlet
c	chord length of foil section
C_P	pressure coefficient
C_L	lift coefficient
C_D	drag coefficient
D	drag
$E_1(z)$	complex exponential integral
F_{rc}	Froude number based on chord c $(U/\sqrt{gc})$
g	acceleration of gravity
$G(p,q)$	velocity potential of the Havelock-Kelvin source
h	submergence depth of leading edge of foil
$\bar{h}$	relative depth of submergence (h/c)
k	wave number (g/U^2)
L	lift
L_P	length of pod in axial direction
L_S	chord length of strut
M	number of horseshoe vortexes
N	number of elements on body surface
$\vec{n}$	unit vector normal to body surface, pointing outward
$\vec{n}_i$	unit vector normal to ith element, pointing outward
$\vec{n}_w$	unit vector normal to wake surface, pointing to negative direction of y axis for vertical plane or negative direction of z axis for other plane
P	pressure acting on body surface
P_∞	static pressure in undisturbed coming flow
p	point in fluid domain
q	point on body surface
Q	flowrate
S_b	body surface
S_{bj}	jth element on body surface
S_w	wake surface
$S_{w\ell}$	ℓth horseshoe vortex strip
S	representive area
T	thrust produced by waterjet propulsion system
T_n	net propulsive force of integrated hydrofoil waterjet pro-

	pulsion system
U	velocity of free stream
V_i	mean velocity at inlet
V_j	mean velocity at nozzle exit
$\overline{V}_i^j$	inlet velocity ratio (V_i/U)
$\overline{V}_j^i$	exit velocity ratio (V_j/U)
X_f	longitudinal force measured by fore dynamometer
X_a	longitudinal force measured by aft dynamometer
Z_f	vertical force measured by fore dynamometer
Z_a	vertical force measured by aft dynamometer
AR	aspect ratio of foil
α	angle of attack of foil
$\gamma(q)$	distribution of doublet strength on S_b
$\gamma_w(q)$	distribution of doublet strength on S_w
$\gamma(q_j)$	strength of the jth vortex lattice on S_b
$\gamma_w(q_\ell)$	strength of the ℓth horseshoe vortex on S_w
Ω	fluid domain
$\phi(x,y,z)$	induced velocity potential
ρ	water density
∇_{S_b}	gradiant operator defined on S_b

PART 1 NUMERICAL SIMULATION OF THE HYDRODYNAMIC CHARACTERISTICS OF A HYDROFOIL-STRUT-POD CONFIGURATION

INTRODUCTION

There are many published papers dealing with numerical simulation of flow past a body in unbounded flow field, but few works have been focused on the flow problem of a 3-D lifting configuration beneath the water surface. When the lifting configuration, such as foil-strut-pod configuration of a hydrofoil craft, operate close to the water surface, the surface effects cannot be ignored. So it is desirable to develop a numerical method for predicting the hydrodynamic characteristics of a 3-D lifting configuration moving beneath the water surface.

The numerical method based on doublet distribution presented in present paper was developed from the method in reference [1] and can be used to predict the pressure distribution and other hydrodynamic characteristics of a general 3-D lifting configuration under the linearized free surface condition.

Because the doublet distribution with constant density is equivalent to the vortex lattice, so one of the key points of the problem is to derive the theoretical formula of induced velocity caused by a horseshoe vortex with arbitrary orientation beneath the water surface in uniform flow. The formula has been derived previously from the Havelock-Kelvin source by the authors [2] and provides a theoretical basis of numerical simulation.

Another key point is how to reduce the computer executive time with satisfactory accuracy. For this effort a new method to calculate the complex exponential integral $E_1(z)$ was presented in the study. It has been found that the computational time was obviously reduced, while good accuracy was achieved by using this new method.

As a numerical example, the hydrodynamic characteristics of the aft foil-strut-pod configuration of hydrofoil craft PS30 were calculated, and the results showed good agreement with the experiment data.

BASIC EQUATIONS

We consider a lifting body in an inviscid, imcompressible, irrotational flow with a uniform velocity U far upstream. A Cartesian rectangular coordinate system O-xyz is adopted, where x is parallel to the free stream direction, z-axis points upward, and the y-axis complies with right handed coordinate system, as shown in Fig.1. The induced velocity potential caused by the body satisfies the following equations and conditions:

$$\nabla^2\phi(x,y,z)=0, \quad (x,y,z)\in\Omega \tag{1}$$

$$\frac{\partial^2\phi}{\partial x^2}+k\frac{\partial\phi}{\partial z}=0, \quad z=0 \tag{2}$$

$$\left.\frac{\partial\phi}{\partial n}\right|_{S_b}=-\vec{U}\cdot\vec{n} \tag{3}$$

$$\lim_{z\to-\infty}\phi,\nabla\phi=0 \tag{4}$$

radiation condition and Kutta condition (5)

There is trailing vortex sheet S_w extending from the trailing edge of body to infinity downstream. Across the sheet, the induced velocity potential ϕ is discontinuous, but its normal derivative is continuous.

According to the Green theorem, the solution satisfying (1), (2), (4) and the radiation condition can be expressed as

$$\phi(p)=\iint_{S_b}\gamma(q)\frac{\partial G(p,q)}{\partial n}dS(q)$$

$$+\iint_{S_w}\gamma_w(q)\frac{\partial G(p,q)}{\partial n_w}dS(q) \quad (6)$$

Substituting (6) to (3), we obtain

$$\vec{n}\cdot\nabla\left[\iint_{S_b}\gamma(q)\frac{\partial G(p,q)}{\partial n}dS(q)\right.$$

$$\left.+\iint_{S_w}\gamma_w(q)\frac{\partial G(p,q)}{\partial n_w}dS(q)\right]=-\vec{U}\cdot\vec{n} \quad (7)$$

The formula (7) is an essential control equation for solving the problem of uniform flow past the body by using the doublet distribution method. The doublet distribution can be derived from equation (7) and Kutta condition.

Once the distribution of $\gamma(q)$ and $\gamma_w(q)$ are obtained, the distribution of the induced velocity on the S_b, the pressure distribution and the lift coefficient can be calculated by the following formulas:

induced velocity on the body surface

$$\nabla\phi(p)=-\frac{1}{2}\nabla_{S_b}\gamma(p)+\iint_{S_b}\gamma(q)\nabla\frac{\partial G}{\partial n}dS$$

$$+\iint_{S_w}\gamma_w(q)\nabla\frac{\partial G}{\partial n_w}dS \quad (8)$$

pressure distribution on the body surface

$$C_P=\frac{P-P_\infty}{\frac{1}{2}\rho U^2}=1-\frac{(\vec{U}+\nabla\phi)\cdot(\vec{U}+\nabla\phi)}{U^2} \quad (9)$$

hydrodynamic lift coefficient

$$C_L=\frac{L}{\frac{1}{2}\rho U^2 S}=-\iint_{S_b}(P\vec{n}\cdot\vec{k})dS/\frac{1}{2}\rho U^2 S \quad (10)$$

C_L can also be calculated by the vortex distribution on S_b according to the Kutta-Joukowski theorem.

NUMERICAL METHOD

In order to obtain an approximate solution for equation (7), the body surface S_b is approximated by a number of small quadrilateral elements, and the wake surface S_w is divided into a series of semi-infinite strips correspondingly. The quadrilateral elements and strips are replaced by the doublet distribution. The centroid of each element is taken as the control point satisfying boundary condition. Accordingly, the boundary integral equation (7) is transformed into a set of linear equations

$$\vec{n}_i\cdot\left[\sum_{j=1}^{N}\gamma(q_j)\nabla\iint_{S_{bj}}\frac{\partial G(p_i,q)}{\partial n}dS(q)\right.$$

$$\left.+\sum_{\ell=1}^{M}\gamma_w(q_\ell)\nabla\iint_{S_{w\ell}}\frac{\partial G(p_i,q)}{\partial n_w}dS(q)\right]=-\vec{U}\cdot\vec{n}_i$$

$$i=1,2,\ldots,N \quad (11)$$

In order to solve the set of equations (11), the Kutta condition must be added which requires no concentrated vortex at trailing edge, i.e.

$$\gamma_{w\ell}=\gamma_{\ell k}-\gamma_{\ell 1}, \quad \ell=1,2,\ldots,M \quad (12)$$

where the $\gamma_{\ell 1}$ and $\gamma_{\ell k}$ denote the vortex strength of two sides at trailing edge of the body respectively, $\gamma_{w\ell}$ denotes the strength of ℓth horseshoe vortex.

The key point to solve the set of equations (11) is the calculation of influence coefficients

$$\nabla\iint_{S_{bj}}\frac{\partial G(p_i,q)}{\partial n}dS(q) \text{ and}$$

$$\nabla\iint_{S_{w\ell}}\frac{\partial G(p_i,q)}{\partial n}dS(q).$$

So it is needed to derive the theoretical formulas of induced velocity potential caused by vortex lattice and horseshoe vortex with arbitrary orientation beneath the water surface in uniform flow. As fundamental solutions, they are useful for solving the wave-making problem caused by a lifting configuration. The formulas have been derived by the authors previously under the linearized free surface condition. Details about these formulas can be found in reference [2].

Because the calculation of the complex exponential integral $E_1(z)=\int_z^\infty[e^{-t}/t]dt$, ($|\arg z|<\pi$) is rather time-consuming and very frequent in solving wave-making problem, a numerical method has been employed to calculate the $E_1(z)$ for improving computational efficiency. In this method the $E_1(z)$ was calculated directly from its asymptotical expansion for $|z|>20$, for $|z|\leq 20$, the value of the $E_1(z)$ was calculated by interpolation from relevant discrete points at which the values of

$E_1(z)$ were computed previously. The numerical examples presented in this paper show that the numerical method is efficient and accurate.

NUMERICAL EXAMPLES

Unbounded Flow past a Sphere

Fig.2 shows the numerical results and analytical solution of the pressure distribution on the surface of a sphere in the unbounded uniform flow. It can be found that the numerical results coincide well with the analytical solution.

Unbounded Flow past a Foil of Finite Span

The flow past the foil with section NACA0012 and AR=10 was simulated. The calculated pressure distribution on the foil surface at $\alpha=6.75°$ is shown in Fig.3 and Fig.4. The surface of the foil is divided into 320 quadrilateral elements with 10 segments spanwise and 32 segments along the contour of foil section. The computed results are compared with the measured ones, and good agreement has been achieved.

Flow past a Hydrofoil of Finite Span beneath the Water Surface

The pressure distribution on the hydrofoil with section NACA16 series in uniform flow beneath the water surface was calculated. The aspect ratio AR and Froude number F_{rc} are 4.08 and 8.23 respectively. In computation, the surface of the hydrofoil is divided into 340 quadrilateral elements with 10 segments spanwise and 34 segments along the contour of foil section. The computed results of pressure distributions on the hydrofoil surface for various relative submergence depth $\bar{h}$ are shown in Fig.5. It has been found that the water surface has much more effects on the upper side of the hydrofoil than on the lower side, it is in accord with the experience. The lift coefficients were also calculated and compared with experimental ones, as shown in Fig.6. The lift coefficients calculated by present method are in good agreement with the experimental data.

Flow past a Hydrofoil-Strut-Pod Configuration

As a main numerical example, the hydrodynamic characteristics of the aft hydrofoil-strut-pod configuration of hydrofoil craft PS30 were calculated. The contour and paneling of the configuration are illustrated in Fig. 7, where the yaw angle is assumed to be zero.

The configuration consists of a hydrofoil, two struts, two pods and two end-plats. Paneling of the configuration surface is performed in such a way that firstly, the configuration surface is divided into 14 regions in our case, secondly, each region is divided into a number of quadrilateral elements. The total number of elements on the configuration surface is 648.

According to the symmetry and the Kutta condition (12), the set of equations (11) can be transformed into the following form including the Kutta condition (12):

$$\begin{bmatrix} B_{11} & B_{12} & \cdots & B_{17} \\ B_{21} & B_{22} & \cdots & B_{27} \\ \vdots & & & \\ B_{71} & B_{72} & & B_{77} \end{bmatrix} \cdot \begin{bmatrix} \vec{\Gamma}_1 \\ \vec{\Gamma}_2 \\ \vdots \\ \vec{\Gamma}_7 \end{bmatrix} = -\vec{U} \cdot \begin{bmatrix} \vec{N}_1 \\ \vec{N}_2 \\ \vdots \\ \vec{N}_7 \end{bmatrix} \tag{13}$$

$$B_{ij} = \begin{bmatrix} b_{11} & b_{12} & \cdots & b_{1m_j} \\ b_{21} & b_{22} & \cdots & b_{2m_j} \\ \vdots & & & \\ b_{m_i1} & b_{m_i2} & \cdots & b_{m_im_j} \end{bmatrix} \tag{14}$$

$$\vec{\Gamma}_i = [\gamma_{i1} \ \gamma_{i2} \ \cdots \ \gamma_{im_i}]^T \tag{15}$$

$$\vec{N}_i = [\vec{n}_{i1} \ \vec{n}_{i2} \ \cdots \ \vec{n}_{im_i}]^T \tag{16}$$

where $[B_{ij}]$ is the influence coefficient matrix;

$b_{\ell k}$ is the induced normal velocity at ℓth control point in the ith region caused by the kth vortex lattice with unit strength in the jth region;

γ_{ij} denotes the strength of the jth vortex lattice in the ith region;

$\vec{\Gamma}_i$ is the column vector composed of γ_{ij} $(j=1,2,\ldots,m_i)$;

$\vec{n}_{ij}$ denotes the unit normal vector of the jth element in ith region pointing outward;

$\vec{N}_i$ is the general column vector composed of $\vec{n}_{ij}$ $(j=1,2,\ldots,m_i)$.

Because the order of the matrix $[B_{ij}]$ is relatively large, it is time-consuming to solve the set of equations (13) directly. In order to save the computation time, we calculate,

instead, the inverse matrix B_{ii} on the main diagonal directly, and solve the set of equations (13) interatively. The numerical procedure is as follows:

$$\vec{\Gamma}_i^{(1)}=B_{ii}^{-1}[-\vec{U}\cdot\vec{N}_i-\sum_{j=1}^{i-1}B_{ij}\vec{\Gamma}_j^{(1)}-\sum_{j=i+1}^{7}B_{ij}\vec{\Gamma}_j^{(0)}] \quad (17)$$

$$\vec{\Gamma}_i^{(p)}=A_i^{(p)}\tilde{\vec{\Gamma}}_i^{(p)}+(E-A_i^{(p)})\vec{\Gamma}_i^{(p-1)} \quad p\geq 2,\ i=1,2,\ldots,7 \quad (18)$$

where superscript p is the number of iteration;

E is the unit matrix;

$\vec{\Gamma}_j^{(0)}$ $(j=1,2,\ldots,7)$ is the initial values of $\vec{\Gamma}_j$;

$$\tilde{\vec{\Gamma}}_i^{(p)}=B_{ii}^{-1}[-\vec{U}\cdot\vec{N}_i-\sum_{j=1}^{i-1}B_{ij}\vec{\Gamma}_j^{(p)}-\sum_{j=i+1}^{7}B_{ij}\vec{\Gamma}_j^{(p-1)}];$$

$$A_i^{(p)}=\begin{bmatrix}\alpha_{i1}^{(p)} & 0 & \cdots & 0\\ 0 & \alpha_{i2}^{(p)} & \cdots & 0\\ \vdots & & & \\ 0 & 0 & \cdots & \alpha_{im_i}^{(p)}\end{bmatrix};$$

$\alpha_{ij}^{(p)}$ is a relaxational factor.

The iteration method mentioned above is so called controlled successive over relaxation method (CSOR), it is much better than the other known iterative methods.

The numerical results are shown in Fig.8 to Fig.13. Fig.8 and Fig.9 show the lift coefficient depending on the relative submergence depth and angle of attack. The numerical and experimental data of lift coefficient at $\bar{h}=1.59$ are shown in Table 1. The pressure distribution on some sections of the configuration are shown in Fig.10 to Fig.13. It can be found that these numerical results are reasonable, although there are not experimental data to check the numurical results of pressure distribution.

Table 1 Comparison of numerical results with experimental data for lift coefficient

α	2°	3°	4°
C_{Lc} (calculation)	0.345	0.435	0.519
C_{Le} (experiment)	0.347	0.422	0.500
C_{Lc}/C_{Le}	0.994	1.03	1.038

PART 2 EXPERIMENTAL STUDY OF INTEGRATED HYDROFOIL WATERJET PROPULSION SYSTEM

INTRODUCTION

The fore and aft hydrofoils of a waterjet propelled hydrofoil craft are usually arranged in canard type, in which over 65% of the craft weight is borne by the aft foil. The aft hydrofoil-strut-pod configuration should provide not only a lift enough to support most of craft weight but also one or two inlets for the waterjet propulsion system. The water inlet is generally imbeded in the pod and may be regarded as a part of the foil-strut-pod configuration. In operation, the water enters through the inlet and duct system, then energy is added to flow by the pump, finally the water exhausts at the nozzle exit with a high velocity and a thrust propelling the craft forward is produced. It can be seen that the mutual hydrodynamic interference between the aft hydrofoil -strut-pod configuration and the waterjet propulsion system can not be neglected. However, there is not much published information on the mutual interference at present. This is due to the fact that most of the model tests for hydrofoil and waterjet were conducted separately.

In order to investigate experimentally the effects of inlet flow on hydrodynamic characteristics of the hydrofoil-strut-pod configuration and to obtain the net propulsive force of waterjet propulsion system with the hydrofoil-strut-pod configuration, a new test set-up has been developed for the towing tank at CSSRC. It has been found from the experiments that the performance of the test set-up is quite satisfactory. Test results also demonstrate that the effects of inlet velocity must be taken into account in design of the hydrofoil-strut-pod configuration, and the measured net propulsive force of the integrated hydrofoil waterjet propulsion system can be used to predict the craft speed. Compared with the similar test facility described in reference [3], the present test set-up seems to be more reasonable, and a new dimension is added to the experimental technique in dealing with hydrodynamic problem of hydrofoil craft. The test set-up can be used to directly measure net propulsive force and lift of the hydrofoil configuration within an extensive flowrate range.

DESCRIPTION OF THE TEST SET-UP

The experiments were conducted at the towing tank of CSSRC. The towing tank is 474m long, 7m deep, 14m wide. The carriage can be operate at speed up to 20m/s.

The test set-up fixed to the carriage is composed of a foil-strut-pod configuration model, a waterjet propulsion system, adjustment units and measuring instruments, as shown in Fig.14.

A 1/12 linear scale model of a full scale foil-strut-pod configuration with one foil, two struts and two pods was adopted in tests. The scaled model was kept geometrically similar to full scale prototype in all respects except internal duct imbeded in the struts.

The waterjet propulsion system of the test set-up consists of centrifugal pump, flexible joint, piping, valve, flowmeter, nozzle, inlet and internal duct. The pump driven by a 4kW motor provides flowrate of 8×10^{-3} m^3/s and lift of 24m under nominal condition. The valve and flowmeter are respectively used to regulate and measure flowrate. A flexible rubber corrugated pipe is used as a joint between the model and pump which not only allows a flow path and easy connection but also isolates transmission of the force normal to its axis (e.g. foil lift). Exit of the nozzle is of round shape. Internal cross-sectional area of the exit equals its full scale value times the square of scale ratio 1/12 in order to simulate the thrust performance of waterjet propulsion system.

Two altitude adjustment units and one angle adjustment unit were used to adjust submergence depth of the model, altitude of the waterjet propulsion system and angle of attack of the model. The model and waterjet propulsion system were fixed to the carriage by means of the adjustment units.

The measuring instruments include fore dynamometer, aft dynamometer, flowmeter and associated pen recorders. In the tests, they can be employed to measure fore vertical force Z_f, fore longitudinal force X_f, aft vertical force Z_a, aft longitudinal force X_a and flowrate Q.

METHOD AND RESULTS OF EXPERIMENT

The main purposes of conducting model tests on the integrated hydrofoil waterjet propulsion system are:

1. To predict the hydrodynamic characteristics of the foil-strut-pod configuration with inlet flow and to study the mutual hydrodynamic interference between the hydrofoil configuration and waterjet propulsion system, particularly the effects of inlet velocity (or flowrate) on hydrodynamic characteristics of the configuration.
2. To investigate the thrust performance of the integrated hydrofoil waterjet propulsion system. The net propulsive force produced by the integrated system, which equals thrust produced by the waterjet propulsion system minus external drag exerted on the configuration, is very useful for the interpretation of test result and predicting the speed of craft.

To fulfill the above purposes, the geometrical similarity between the model and the full scale prototype regarding the external form of inlet lip, nozzle exit and foil-strut-pod configuration must be maintained, except those internal components such as pump and duct etc. The deletion of the requirement for the pump and duct is due to the fact that in our case problems related to the duct loss from inlet to nozzle exit and the propulsion efficiency are beyond our study. In case only the hydrodynamic characteristics of the foil-strut-pod configuration is studied, even the similarity for nozzle exit is not necessary. In addition to the geometrical similarity, it is also necessary in conducting model tests to comply as nearly as possible with the laws of dynamic similarity. The dynamic similarity in terms of Froude number was maintained in tests, while Reynolds scaling law was given up as usual because it is impossible to meet both requirements simultaneously. However, the size of model should be as large as possible so as to attain a sufficient Reynolds number within the interested test speed range.

Prior to conducting the test program in the towing tank, all the instruments including one flowmeter and two dynamometers were carefully calibrated. All calibrated curves were linear within the test range.

The model tests in towing tank for a given set of submergence depth and angle of attack were carried on in such a way that the flowrate was changed one by one from the maximum to zero by regulating the valve for a given carriage speed. The forces Z_f, X_f, Z_a, X_a and the flowrate Q were measured for each run.

The lift L of the foil-strut-pod configuration with inlet flow and the net propulsive force T_n of the inte-

grated hydrofoil waterjet propulsion system can be directly derived from measured values,

$$L = Z_f + Z_a = Z_f \quad (19)$$

$$T_n = -(X_f + X_a) \quad (20)$$

However, the drag D of the configuration with inlet flow can not be directly measured because D is included in T_n in such a way that it is difficult to be separated. It is well known that T_n plus D is equal to the thrust T produced by waterjet propulsion system. Assuming that T can be calculated in terms of the formula given in [4]

$$T=\rho Q(V_j-U)-\tfrac{1}{2}\rho A_i(V_i-U)^2 \quad (21)$$

then $$D = T-T_n = T+X_f+X_a \quad (22)$$

Owing to the fact that it is difficult to calculate T exactly, so the accuracy of D is somewhat lower than that of L and T_n.

It must be stressed that D is defined as the resultant of all the external wetted surface forces acting on the foil-strut-pod configuration in the free steam direction, and T is the resultant of all the internal wetted surface forces exerted on the waterjet propulsion system in the advancing direction of the carriage, while the stream surface generated from the stagnation points on inlet lip separates the internal flow ingested by the inlet from the external flow [5].

The test program covered the variation of the following parameters: (1) carriage speed from 0 to 6.7m/s; (2) flowrate from 0 to about 6.5×10^{-3} m^3/s, which respectively correspond to the closed and totally opened condition of the valve; (3) angle of attack equal to 0.45° and 1.65°; (4) submergence depth of foil equal to 0.152 m.

Some experimental results on the lift and drag of the configuration with two inlets operating are given in Fig.15 and Fig.16. It may be noted that the effects of inlet velocity ratio on the lift and drag can not be neglected. The lift coefficient C_L decreases slowly with increase of inlet velocity ratio. When $F_{rc}=6.94$, C_L at $\overline{V}_i=0.7$ is lower than C_L at $\overline{V}_i=0$ by about 9.5% for $\alpha=0.45°$ and by about 6% for $\alpha=1.65°$. When $F_{rc}=5.18$, C_L at $\overline{V}_i=0.7$ is lower than C_L at $\overline{V}_i=0$ by about 7% for $\alpha=0.45°$ and by about 3% for $\alpha=1.65°$. It may well be that the reducing of water flow past foil due to the presence of inlets leads to the loss of foil lift. The drag coefficient C_D varies with inlet velocity ratio more obviously, which is probably related to the suction force pointing forward produced on inlet lip surface.

The tests of the configuration with streamlined caps at the fore end of pod for blocking inlet flow were conducted in the same way as the conventional hydrofoil test. The measured lift and drag forces are also given in Fig.15 and Fig.16 for comparison. The lift coefficients in this case are all a little lower than the corresponding ones of the configuration without caps. On the opposite, the drag coefficients in this case are all higher, it can be attributed to absence of the suction force on inlet lip surface when mounting streamlined caps to inlets.

The net propulsive force T_n of integrated hydrofoil waterjet propulsion system measured at various speed and flowrate is shown in Fig.17 and Fig.18. It is clear that for a given speed, if the net propulsive force is just equal to the sum R of the drag of fore foil unit, the additional drag due to the interference of fore foil unit on aft foil unit and the air drag of hull, then the hydrofoil craft will navigate under foilborne condition with constant speed. So the curves of T_n versus U and Q can be used to evaluate speed of a waterjet propelled hydrofoil craft. As long as T_n and R are plotted against the speed under certain design operation conditions including flowrate, angle of attack and depth of submergence, then the speed value corresponding to intersection of both curves is just the speed which can be attained by the craft.

CONCLUSIONS

The numerical method presented in this paper can be used to predict the hydrodynamic characteristics (including pressure distribution) of foil-strut-pod configuration under the linearized water surface condition. Comparison of calculations with experiments shows that good agreement between them can be achieved.

The theoretical formula of induced velocity caused by a horseshoe vortex with arbitrary orientation deduced from Havelock-Kelvin source provides a important basis for numerical simulation of present problem.

The proposed new method calculating $E_1(z)$ reduces obviously the

computer executive time and can be used in solving wave-making problem.

The integrated hydrofoil waterjet propulsion system test set-up developed at CSSRC has been shown to be satisfactory. The test set-up can be used to investigate the effects of inlet flow on hydrodynamic characteristics of the foil-strut-pod configuration and to obtain the net propulsive force of the integrated hydrofoil waterjet propulsion system.

The effects of inlet velocity ratio on the lift and drag must be taken into consideration in design of foil-strut-pod configuration. The measured net propulsive force is very useful for predicting the speed of craft.

REFERENCES

[1] Huang Shan, Li Baiqi, "A doublet distribution method for predicting the hydrodynamic characteristics of a hydrofoil of finite span", Proceedings of International Symposium on Ship Resistance and Powering Performance, Shanghai, China, April 11-14, 1989.

[2] Zhu Dexiang, Li Baiqi, "Induced velocity potential of an arbitrary horseshoe vortex in the uniform flow field with free surface", Journal of Hydrodynamics, Ser.A, Vol.6, No.1, 1991 (in Chinese).

[3] Thoms T. Huang, et al., "Development of a hydrofoil waterjet propulsion system test facility", AD 707075, May, 1970.

[4] Li Baiqi, "Thrust, moment and propulsive efficiency of waterjet propulsion system for hydrofoil craft", CSSRC Technical Report No. 85087, 1984 (in Chinese).

[5] R.J.Etter, V.Krishnamoorthy and J.O.Scherer, "Model testing of waterjet propelled craft", Proceedings of the 19th Meeting of ATTC, 1980.

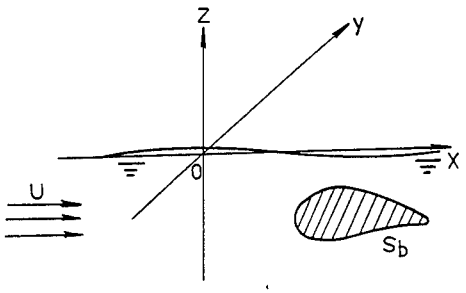

Fig.1 Body and coordinate system

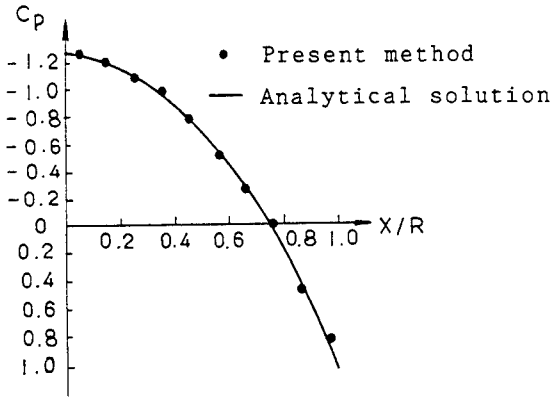

Fig.2 Pressure distribution on the sphere surface

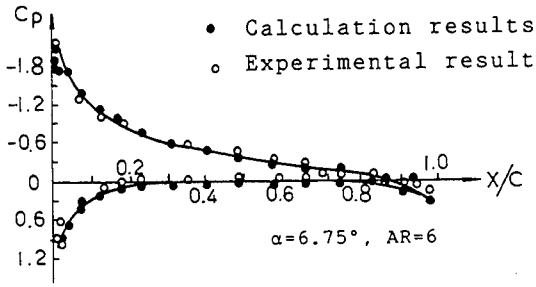

Fig.3 Pressure distribution on mid-section of the foil

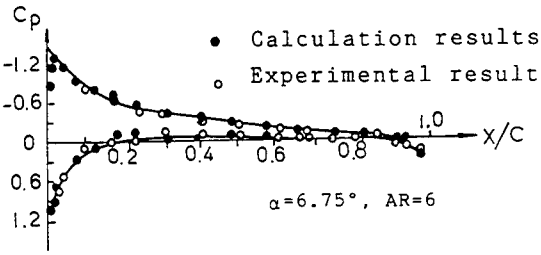

Fig.4 Pressure distribution on tip-section of the foil

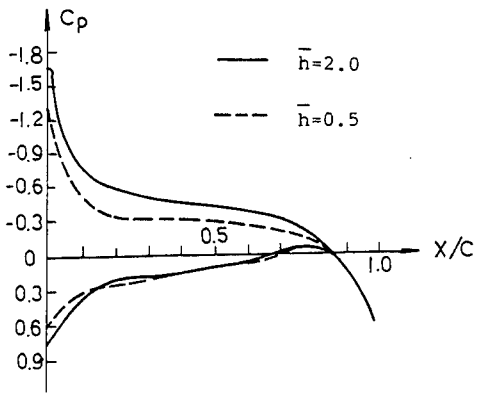

Fig.5 Pressure distribution on mid-section of the hydrofoil

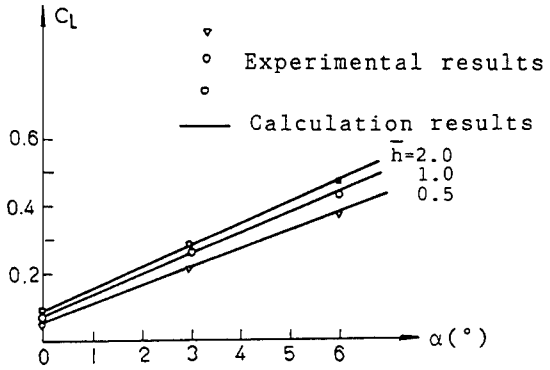

Fig.6 Lift coefficient of the hydrofoil

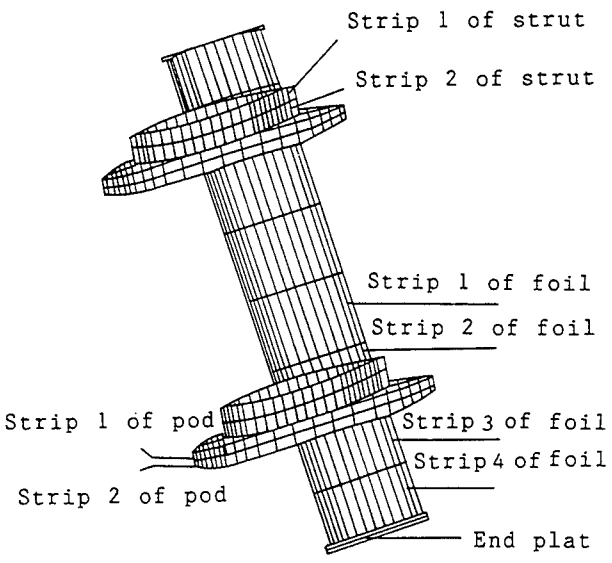

Fig.7 Contour and paneling of the foil-strut-pod configuration

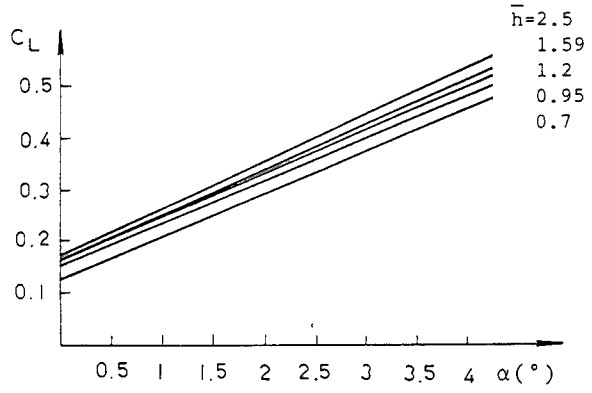

Fig.8 Lift coefficient of the foil-strut-pod configuration

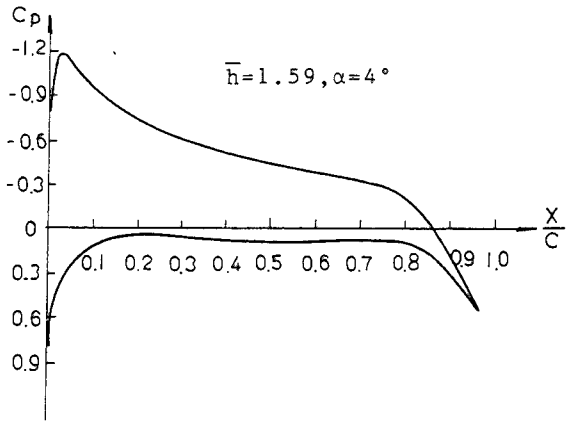

Fig.10 Pressure distribution on strip 2 of foil of the configuration

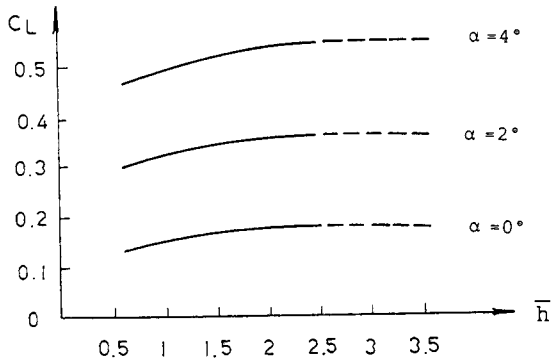

Fig.9 Lift coefficient of the foil-strut-pod configuration

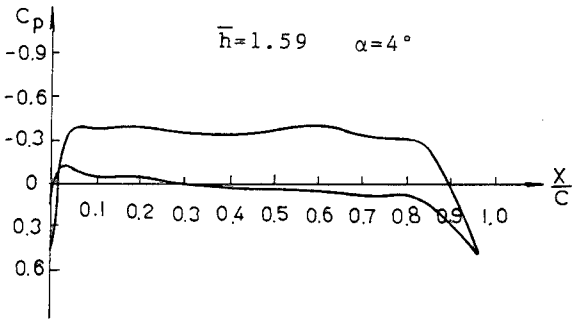

Fig.11 Pressure distribution on strip 3 of foil of the configuration

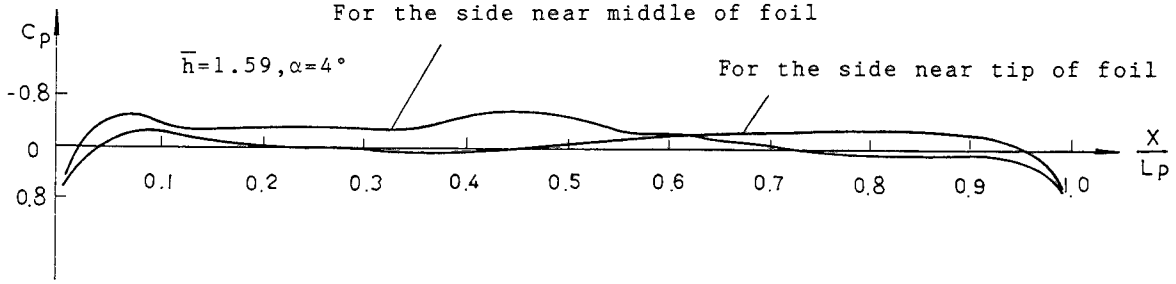

Fig.12 Pressure distribution on strip 1 of pod of the configuration

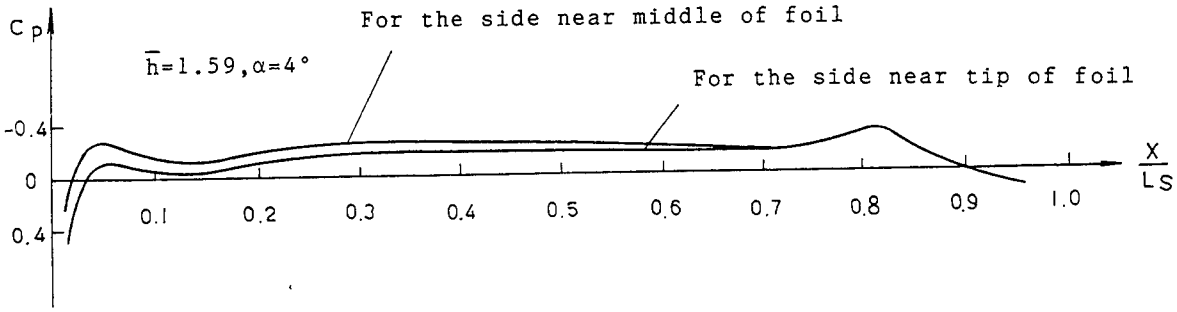

Fig.13 Pressure distribution on strip 2 of strut of the configuration

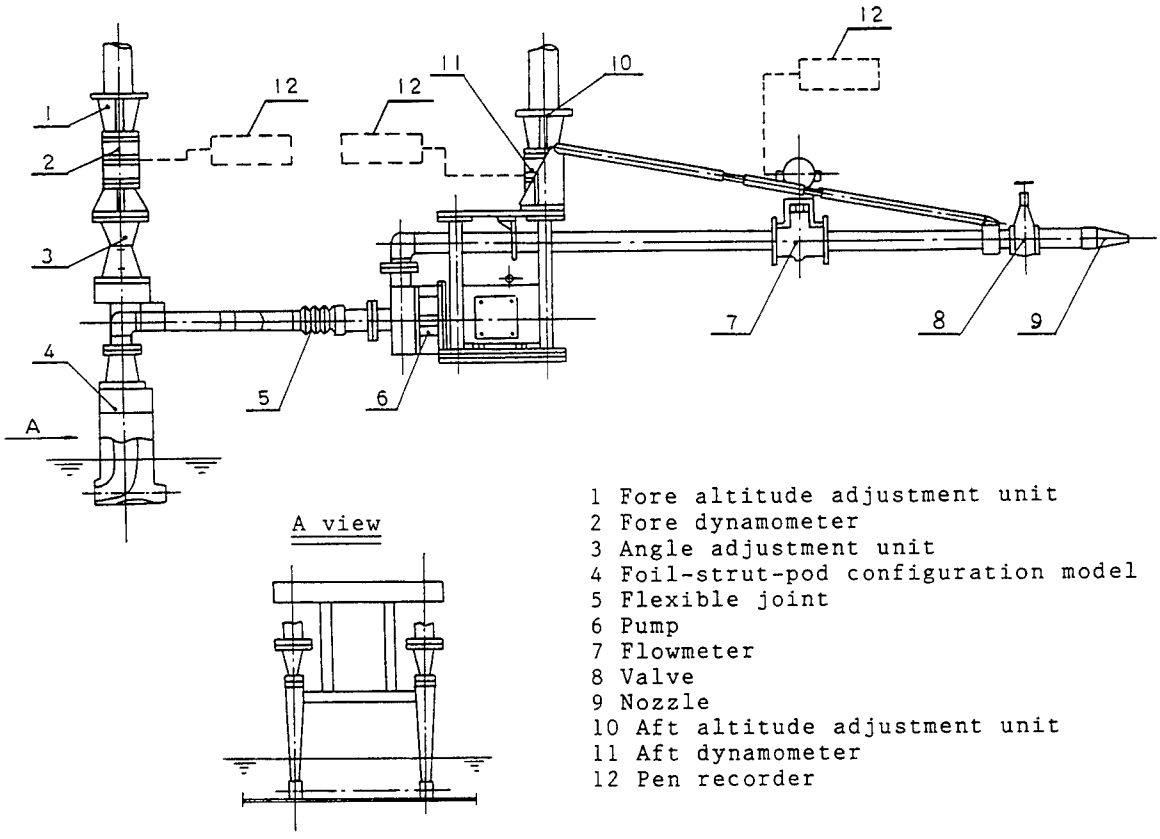

1 Fore altitude adjustment unit
2 Fore dynamometer
3 Angle adjustment unit
4 Foil-strut-pod configuration model
5 Flexible joint
6 Pump
7 Flowmeter
8 Valve
9 Nozzle
10 Aft altitude adjustment unit
11 Aft dynamometer
12 Pen recorder

Fig.14 Test set-up

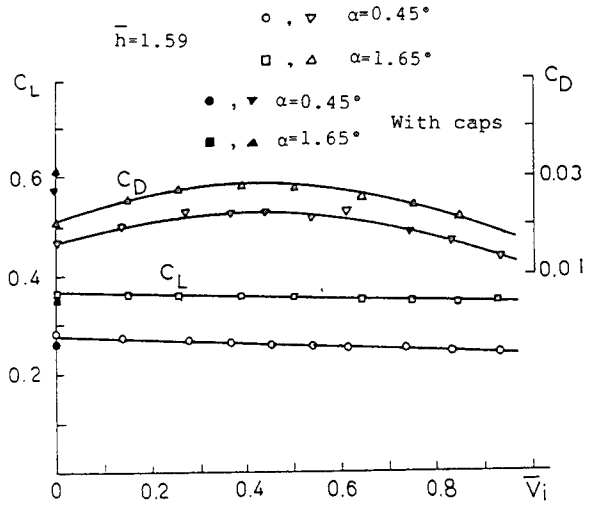

Fig.15 Experimental results of lift and drag (F_{rc}=5.18)

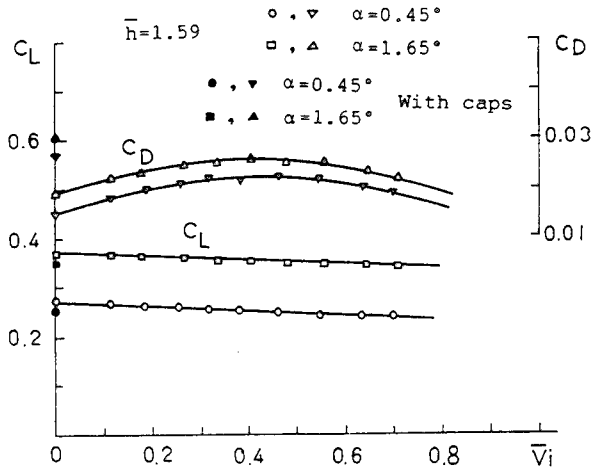

Fig.16 Experimental results of lift and drag (F_{rc}=6.94)

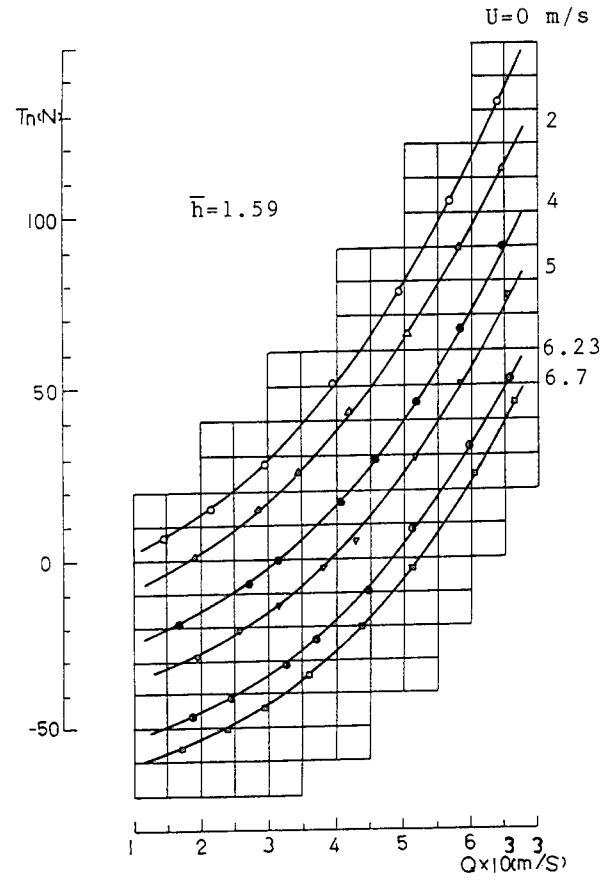

Fig.17 Experimental results of net propulsive thrust (α=0.45°)

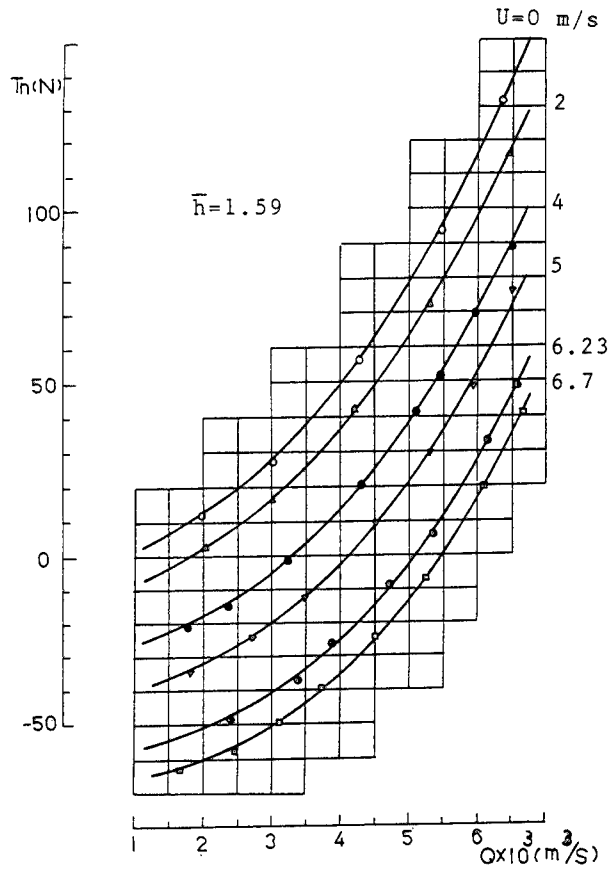

Fig.18 Experimental results of net propulsive thrust (α=1.65°)

The Effect of Turbulence Ingestion on Propeller Broadband Forces

C.-W. Jiang, M. Chang, Y. Liu (David Taylor Model Basin, USA)

ABSTRACT

This paper presents the theoretical prediction of the low frequency unsteady broadband forces for propellers in a turbulent flow, such as those on any surface ship. Broadband forces are predicted by the use of a new correlation method and are compared with existing theoretical models based on both correlation and spectrum approaches. In contrast to the available theories, the new theory predicts low blade rate humps and broadband forces simultaneously. For a homogeneous and isotropic turbulent inflow and for a given advance coefficient, turbulence length scale and turbulence level, the present theory produces an unsteady broadband thrust level which is proportional in the high frequency region to the third power of ship speed. At low frequencies, predictions of propeller unsteady thrust spectra show peaks near the first and second blade rate frequencies and those peaks skew to the higher frequency side of the blade rate frequencies. Side forces demonstrate the same phenomena but at a lower level. The physics of the phenomena are discussed and numerical results are compared with limited experimental data.

NOMENCLATURE

A_s	Filter function
b	Blade spacing
C	Blade section chord length
D	Propeller diameter
f(r)	Longitudinal velocity correlation function
f_M	Meanline shape function
F_i	Propeller force at i direction
g(r)	Transverse velocity correlation function
$G_{ij}(\omega)$	Velocity correlation in frequency domain
$H(\omega)$	Aerodynamic response function
i_T	Total rake
$J = V_s/nD$	Advance coefficient
$K(\omega)$	Sears function
k	Wave number
L	Blade lift force
$\ell(t)$	Hydrodynamic force
n	Propeller rotational speed, rps
P	Pitch of blade section
r	Radial coord. or dist. between two points
R	Propeller radius
$R_{ij}(\tau)$	Velocity correlation in time domain
u	Root mean square of turbulence
u_i	Turbulent velocity in i-th direction
U(r)	Resultant velocity at propeller radius r
V_a	Axial vel. at prop. plane for a given radial loc.
V_s	Ship speed
#	Lbs
ω	Frequency
Ω	Shaft rate frequency
Ω'	Blade rate frequency
Λ	Turbulence integral length scale
ρ	Fluid density
ϕ	Propeller blade pitch angle
ϕ_i	One dimensional turbulence spectrum
Φ	Wave number spectrum of turbulence
Ψ	Broadband unsteady thrust spectrum
Ψ^*	Broadband unsteady thrust/ω^3

INTRODUCTION

The unsteady forces generated by a propeller consist of periodic force components and a broadband force component. The narrowband periodic force components occur at multiples of the blade passage frequency and are considered to result from the unsteady pressure distribution on the propeller blades. These unsteady pressures are caused by the non-uniform inflow or by cavitation, such as for the propellers on surface ships. Force spectra from this non-uniform inflow are narrowband at the blade rates. The high frequency broadband noise is due to vortex shedding

by the propeller blades. Although designers are careful to reduce these unsteady force sources, laboratory experiments indicate that an unexpected broadband force occurs at first and second blade rate frequencies. This low frequency broadband force is due to the interaction of the inflow turbulence with the propeller blades. The inflow turbulence ingested on the propeller blades is generated in the hull boundary layer and in the boundary layers on all the appendages upstream of the propeller, superposed on the ambient free-stream turbulence. Therefore, the inflow turbulence may contain a broad range of length scales. This paper addresses the effects of turbulence on broadband forces generated by propeller blades regardless of the source of the turbulence.

The unsteady force caused by turbulence ingestion has been studied by several investigators in the past. Most previous studies are based upon special assumptions and, thus, lack generality. Sevik [1] considered the forward speed to be much greater than the propeller rotational speed and, therefore, regarded the blades as rotationally stationary with respect to the turbulence. This assumption implied that the blades are rotationally uncorrelated. He measured the unsteady thrust on a ten-bladed rotor operating in a water tunnel downstream of screen-generated turbulence. The experimental measurements show humps near blade rate frequencies and its multiples which were not predicted from Sevik's theory. Thompson [2] extended this theory and performed additional experiments for rotors with different numbers of blades. The experimental results show that the magnitude of the broadband humps increases when the blade-to-blade spacing decreases. He included in his analysis the blade to blade circumferential correlations in a zero forward speed sense. In comparison to the experiments, his theoretical results produced consistently higher humps. Chandrashekhara [3] examined only the cases for which the circumferential correlation length was larger than a blade spacing. Mani [4], Homicz and George [5], Amiet [6], and Blake [7] considered the rotor forces and noises radiated by turbulence with a given wave spectrum. Mani [4] showed that the radiated sound spectrum from a rotor operating in a turbulent inflow has humps centered at the blade rate frequencies and its multiples. The width of those humps was found in his experiments to be related to the ratio of the turbulence length scale to the blade spacing. Blake [7] considered the case of a rotor with a small advance coefficient and a turbulence length scale considerably smaller than the length of the blade span. Simple results are obtained from asymptotic expansion of small and large correlation lengths. The small correlation result approaches the result of Sevik's analysis, and the large correlation theory predicts the narrow bandwidth humps at blade rate frequencies. Although Blake's model predicts the humps at the blade rate frequency, the hump amplitudes above the smooth broadband force spectrum curve do not exhibit the decay phenomena observed in experiments.

In the present paper, the correlation analysis follows Sevik's approach [1], but removes the simplification of the velocity correlation tensor used in [1]. The blade rotational effect is correctly preserved in the analysis and the results resemble the experimental observation. Numerically, for a given turbulence correlation function, the statistical properties of the unsteady angle of attack encountered by the moving blade are evaluated at each time step. Then the force spectrum is obtained from a Fourier transformation of the computed time history of those unsteady angles of attack. The next two sections outline the fundamental approaches and the corresponding computational procedures. Numerical examples are included for the thrust, side force and torque spectra of a rotor in an isotropic turbulence flow. These results are compared with existing experiments. A flow chart of the present numerical turbulence ingestion model is given in Figure 1; the blade surface is divided into chordwise strips along the span. Each strip is considered as a two-dimensional (2-D) section with unsteady lift concentrated at the quarter-chord of that section. As is indicated in Figure 1, the two critical components of the model are the inflow turbulence characteristics and the transfer function between the turbulence intensity spectrum and the unsteady forces. In the given examples, the Sears function is used as the fluid dynamic transfer function.

THEORETICAL APPROACH

The analysis of turbulence-generated propeller broadband force can be approached with two different techniques. One is the spectrum approach and the other is the correlation approach. These two approaches should lead to the same results if the specified spectrum form and correlation function describe the same turbulence characteristics. The authors prefer the correlation method because it is the more direct approach and is easier to apply numerically. However, for completeness of the study, the spectrum approach is included in this paper. Results from both approaches will be compared in the discussions.

Spectrum Approach

This section follows the procedure described in Blake [7], which assumes that the turbulence is convected frozen (Taylor's hypothesis) and the turbulent characteristics are represented as a product of functions

in each direction (separation of variables). With the turbulent inflow component normal to the blade, u_2 in Figure 2, expressed in terms of its Fourier transform:

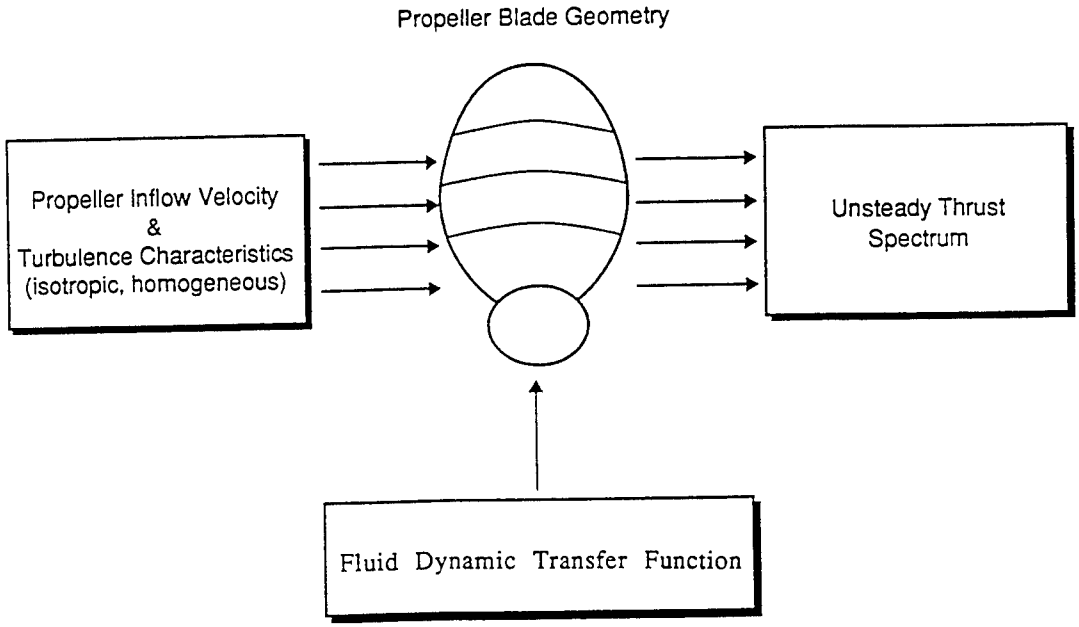

Fig. 1. Flow chart of excitation force model.

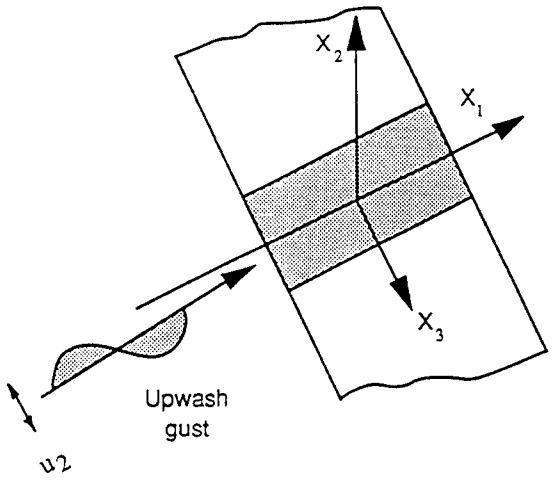

Fig. 2. Definition of local coordinate system.

$$u_2(\vec{k},\omega) = \frac{1}{(2\pi)^3}\int\int\int\int u_2(\vec{x},t)e^{-i(\vec{k}\cdot\vec{x}-\omega t)}d\vec{x}dt \quad (1)$$

where $\vec{}$ denotes the vector in terms of the coordinates in the propeller plane (x_1, x_3) and its normal (x_2), the lift per unit radius on the s-th blade written in terms of the Fourier components of the incident upwash, $u_2(\vec{k},\omega)$, is

$$dL_s(\omega)/dr = \rho\pi C u_2(\vec{k},\omega)U(r)L_{2D}(k_1C/2) \; e^{i(k_3 r + k_{12} sb - \omega t)} \quad (2)$$

where L_{2D} is the two-dimensional lift due to a unit disturbance, C is the blade chord length, b is the blade spacing at the radius r, k_{12} equals $k_1\cos\phi + k_2\sin\phi$, ϕ is the blade pitch angle, and U(r) is the resultant velocity into the blade at radius r. The net force on an N-bladed propeller in the i-th direction due to the $(\vec{k},\omega)$ turbulence contribution is found by summing over all the blades and integrating over the radius from the propeller hub (R_H) to tip (R_T)

$$F_i(\vec{k},\omega) = \int_{R_H}^{R_T} \rho\pi C u_2(\vec{k},\omega)U(r)n_i(\phi)L_{2D}(k_1C/2) \sum_{s=0}^{N-1} e^{i(k_3 r + k_{12} sb - \omega t)}dr \quad (3)$$

where $n_i(\phi)$ is the direction cosine in the i-th direction of the blade. The summation over the N blades in equation (3) is called a filtering function, denoted A_s, and is

$$A_s(k_{12}b) \equiv \sum_{s=0}^{N-1} e^{ik_{12}sb} = \frac{\sin(Nk_{12}b/2)e^{[i(N-1)k_{12}b/2]}}{\sin(k_{12}b/2)} \quad (4)$$

Substituting this expression back into equation (3), the net force becomes

$$F_i(\vec{k},\omega) = \int_{R_H}^{R} \rho\pi C u_2(\vec{k},\omega)U(r)n_i(\phi)L_{2D}(k_1C/2) A_s(k_{12}b)e^{-i(k_3 r - \omega t)}dr \quad (5)$$

and the frequency spectrum of the fluctuating force, $\Psi_{ii}(\omega)$, becomes

$$\Psi_{ii}(\omega) = \int_{k_1}\int_{k_2}\int_{k_3}\int_{R_H}^{R}\int_{R_H}^{R} \rho^2\pi^2C^2 \mid L_{2D}(k_1C/2) \mid^2 \mid A_s(k_{12}b) \mid^2 U(r_1)U(r_2)\Phi_{22}(\vec{k},\omega) n_i(\gamma_1)n_i(\gamma_2)e^{ik_3(r_2-r_1)}dr_2dr_1d\vec{k} \quad (6)$$

where $\Phi_{22}(\vec{k},\omega)$ is the wave number spectrum of the turbulent field. Equation (6) is the fundamental form of the spectrum approach. It is clearly seen that the major task of the analysis is in the specification of the wave number spectrum of the turbulent field $\Phi_{22}(\vec{k},\omega)$ and the evaluation of the multiple integrals. In general, the spectrum form $\Phi_{22}(\vec{k},\omega)$ associated with a moving body is not known, and the prediction of $\Psi_{ii}(\omega)$ with triple integration over $\vec{k}$ is impractiable. Nevertheless, the analytical results associated with some simple forms of $\Phi_{22}(\vec{k},\omega)$ could provide a good approximation to reality and lead to a better understanding of the overall features of $\Psi_{ii}(\omega)$.

By applying Taylor's hypothesis that the turbulence convects over the blade with the resultant velocity and without decay, and by assuming that the wave number spectrum can be separated into directions along the resultant velocity (k_1), the radial direction (k_3), and the normal direction (k_2), the turbulence spectrum becomes

$$\Phi_{22}(\vec{k},\omega) = \bar{u_2^2}\phi_1(k_1)\phi_2(k_2)\phi_3(k_3)\delta[\omega - U(r)k_1] \quad (7)$$

Furthermore, we assume that $\phi_i(k_i)$ takes a form of

$$\phi_i(k_i) = \frac{1}{\pi}\frac{\Lambda_i}{1+(\Lambda_i k_i)^2} \quad (8)$$

where $2\Lambda_i$ represents the integral length scale of u_2 in the i-th wave vector direction. When the radial integral length scale is small with respect to the blade span, i.e.,$\phi_3(k_3) \simeq \Lambda_3/\pi$ and the radial direction wave number is small, i.e., $k_3R \ll 1$, the force spectrum , equation (6) becomes

$$\Psi_{ii}(\omega) = \int_{k_1}\int_{k_2}\int_{R_H}^{R_T} \rho^2\pi C^2\Lambda_3 \mid L_{2D}(k_1C/2) \mid^2 \mid A_s(k_{12}b) \mid^2 U^2(r)\bar{u_2^2}\phi_1(k_1)\phi_2(k_2)n_i^2(\phi) \delta[\omega - U(r)k_1]drdk_1dk_2$$

$$= \int_{k2}\int_{R_H}^{R_T} \rho^2\pi C^2\Lambda_3 \mid L_{2D}(\frac{\omega C}{2U}) \mid^2$$
$$\mid A_s[(k_2\sin\phi + \frac{\omega}{U}\cos\phi)b] \mid^2$$
$$U^2(r)\bar{u_2^2}\phi_1(\omega/U)\phi_2(k_2)n_i^2(\phi)drdk_2 \quad (9)$$

For simplification, the average spanwise lift amplitude as a function of wave number has been used in the last formulation. Then the turbulence spectrum can be moved outside of the radial integral. The discrete, numerical expression of equation (9) becomes

$$\Psi_{ii}(\omega) = \sum_{\delta k_2}\phi_2(k_2)\sum_{\delta R}\rho^2\pi C^2\Lambda_3 \mid L_{2D}(\frac{\omega C}{2U}) \mid^2$$
$$\mid A_s[(k_2\sin\phi + \frac{\omega}{U}\cos\phi)b] \mid^2$$
$$U^2\bar{u_2^2}\phi_1(\omega/U)n_i^2(\phi) \quad (10)$$

Equation (10) entails summation over the blade elements and the wave number and it is numerically more managable than equation (6). The application of this model will be presented in a later section and the results will be discussed. For the case of small advanced coefficient and small hub, $R_T \gg R_H$, equation (9) can be further reduced to

$$\Phi_{ii}(\omega) = \frac{\pi^2}{3}[\rho(\Omega R_T)^2]^2(CR_T)^2\bar{u_2^2}/(\Omega R_T)^2 \mid L_{2D}(\frac{\omega C}{U_T})$$
$$\mid^2 (2\Lambda_3/R_T)n_i^2(\gamma)\frac{1}{U_T}\phi_1(\frac{\omega}{U_T})$$
$$\int_{-\infty}^{\infty} \mid A_s[(k_2\sin\gamma + \frac{\omega}{U_T}\cos\gamma)b] \mid^2$$
$$\phi_2(k_2)dk_2 \quad (11)$$

where U_T is the resultant tip speed $\sqrt{V^2+(R_T\Omega)^2}$ (V is axial inflow velocity). Blake[7] obtained the asymptotic solutions of the above equation. Evaluation of the integral is determined by the relative width of the turbulence spectrum, $\phi_2(k_2)$, and the filter function, $\mid A_s[(k_2\sin\gamma + \frac{\omega}{U_T}\cos\gamma)b] \mid^2$. When the band of $\phi_2(k_2)$ is greater than the range of the filter function, i.e., the axial integral length parameter, $2\Lambda_2$, is smaller than the blade spacing projected in the axial direction (small correlation length), the last equation can be simplified to

$$\Phi_{ii}(\omega) = \frac{8\pi^2}{3n_s}(\frac{1}{2}\rho V^2)^2 R_T{}^4(\frac{C}{R_T})^2(\frac{\pi}{J})^2\frac{\bar{u_2^2}}{V^2}\frac{2\Lambda_3}{R_T}$$
$$\frac{\Lambda_1/\pi R_T}{1+(\Lambda_1\omega/\Omega_s R_T)^2}\frac{1}{1+\pi\omega C/\Omega_s R_T} \quad (12)$$

On the other hand, when the axial integral length parameter, $2\Lambda_2$, is greater than the blade spacing projected in the axial direction (large correlation length), equation (11) becomes

$$\Phi_{ii}(\omega) = \frac{8N\pi^2}{3n_s}(\frac{1}{2}\rho V^2)^2 R_T{}^4(\frac{C}{R_T})^2(\frac{\pi}{J})^2\frac{\bar{u_2^2}}{V^2}\frac{2\Lambda_3}{R_T}$$
$$\frac{\Lambda_1/\pi R_T}{1+(\Lambda_1 mN/R_T)^2}\frac{\mid A_s[(k_2\sin\gamma + \frac{\omega}{U_T}\cos\gamma)b] \mid^2}{1+\pi mNC/R_T} \quad (13)$$

where m is the number of the blade rate frequency; otherwise, $\Phi_{ii}(\omega)$ equals zero.

In examining equations (12) and (13), it is seen that equation (12) is a monotonically decreasing function of ω and it resembles the rotational uncorrelated results of Sevik [1]. Equation (13) contains only the blade rate humps with non-decayed amplitude above the rotational uncorrelated results. Neither of these approximations can be applied to predict the complete measured phenomena. In order to obtain a meaningful prediction, one has to go back to at least equation (11). Numerical results show that even (11) does not give satisfying predictions; only the results of equation (10) are in reasonable agreement with the measurements. Further discuissions of the spectrum approach will be given in the results section.

Correlation Approach

The derivations of the frequency spectrum of propeller thrust using the correlation approach are briefly discussed here. These derivations follow the theory of Sevik [1] except that the velocity correlation has been modified to incorporate propeller rotational effects. In order to calculate the characteristics of the fluctuating force over the blade surfaces, the blade is divided into a number of surface elements. The time-dependent forces acting on the various surface elements are related by virtue of spatial and temporal correlation of the velocity fluctuations in the approach stream as well as by virtue of the induced effects that take place between adjacent elements. In the following tensor equations, subscripts are used to denote the direction along the coordinate axes, while superscripts are used to denote the blade element involved. For example, $F_{ij}^{\alpha\beta}(t,\tau)$ denotes the hydrodynamic force acting on the α-th element in the direction i at the instant of time t caused by a velocity fluctuation of unit magnitude in the direction j on the β-th element at the instant τ. With this convention, the hydrodynamic

force acting on the α-th element at time t in the direction i, $\ell_i^\alpha(t)$, due to the influence of velocity fluctuation at all elements, β, and in all the directions, j, over all the time, τ, is expressed as

$$\ell_i^\alpha(t) = \int_{-\infty}^{t} F_{ij}^{\alpha\beta}(t-\tau) u_j^\beta(\tau) d\tau \qquad (14)$$

where

$$\begin{aligned} i,j &= 1,2,3 \\ \alpha,\beta &= 1,2,...n \end{aligned}$$

Since $\ell_i^\alpha(t)$ is a random function of time in a turbulent flow, a statistical approach must be employed. If the inflow turbulence is time-invariant, the correlation function of unsteady forces, $\Phi_{ij}^{\alpha\beta}$, becomes

$$\begin{aligned} \Phi_{ij}^{\alpha\beta}(\tau) &\equiv E[\ell_i^\alpha(t)\ell_j^\beta(t+\tau)] \\ &= \lim_{T\to\infty}\frac{1}{T}\int_0^T\int_0^\infty\int_0^\infty F_{ik}^{\alpha\gamma}(\tau_1)F_{jm}^{\beta\delta}(\tau_2) \\ &\quad u_k^\gamma(t-\tau_1)u_m^\delta(t+\tau-\tau_2)d\tau_1 d\tau_2 dt \\ &= \int_0^\infty\int_0^\infty F_{ik}^{\alpha\gamma}(\tau_1)F_{jm}^{\beta\delta}(\tau_2)R_{km}^{\gamma\delta}(\tau+\tau_1-\tau_2) \\ &\quad d\tau_1 d\tau_2 \qquad (15) \end{aligned}$$

where

$$\begin{aligned} R_{km}^{\gamma\delta}(\tau+\tau_1-\tau_2) &\equiv \lim_{T\to\infty}\frac{1}{T}\int_0^\infty u_k^\gamma(t-\tau_1) \\ &\quad u_m^\delta(t+\tau-\tau_2)dt \end{aligned}$$

The corresponding frequency spectrum of the correlated force fluctuations on the α-th element in the direction i due to the β-th element in the direction j can be found by taking the Fourier transform of the above correlation tensor:

$$\begin{aligned} \Psi_{\ell_i\ell_j}^{\alpha\beta}(\omega) &= \frac{1}{2\pi}\int_{-\infty}^{\infty}\Phi_{ij}^{\alpha\beta}(\tau)e^{-i\omega\tau}d\tau \\ &= \frac{1}{2\pi}\int_{-\infty}^{\infty}\int_0^\infty\int_0^\infty F_{ik}^{\alpha\gamma}(\tau_1)d\tau_1 F_{jm}^{\beta\delta}(\tau_2)d\tau_2 \\ &\quad R_{km}^{\gamma\delta}(\tau+\tau_1-\tau_2)d\tau \\ &= [H_{ik}^{\alpha\gamma}(\omega)]^*[H_{jm}^{\beta\delta}(\omega)]G_{km}^{\gamma\delta}(\omega) \qquad (16) \end{aligned}$$

where

$$H_{ik}^{\alpha\gamma}(\omega) \equiv \int_0^\infty F_{ik}^{\alpha\gamma}(\tau)e^{-i\omega\tau}d\tau$$

and

$$G_{km}^{\gamma\delta}(\omega) \equiv \frac{1}{2\pi}\int_{-\infty}^{\infty} R_{km}^{\gamma\delta}(\tau)e^{-i\omega\tau}d\tau$$

$H_{ik}^{\alpha\beta}(\omega)$ is the hydrodynamic frequency response function and $G_{km}^{\gamma\delta}(\omega)$ is the Fourier transform of the velocity correlation function. Equation (16) is the formula for predictions of unsteady forces due to inflow turbulence. When we apply this equation to the propellers, we have to specify $H_{ik}^{\alpha\beta}(\omega)$ and $G_{km}^{\gamma\delta}(\omega)$ according to the enviroments in which the rotors are operating. A computer code has been written to compute the $G(\omega)$ and $\Psi(\omega)$ for specified turbulence characteristics. To demonstrate the computation procedure, the analysis of an isotropic turbulence is given below for general discussion.

ISOTROPIC TURBULENCE

In the present method, we shall first derive the velocity correlation function between points α and β. A detailed derivation for isotropic turbulence is given by Hinze [9] and is briefly described below. Longitudinal correlation refers to the coordinate system in Figure 3. The origin of the coordinate system is at α and r is the distance between points α and β with components ξ_i along the axis x_i. In the plane of the $\alpha\beta$-line and the x_1-axis, the velocities at α and β can be resolved into the components u_{1*}, directed between these two points, and the components u_{2*}, which are perpendicular to the line-$\alpha\beta$. The velocity components along the x_1-axis at these two points are:

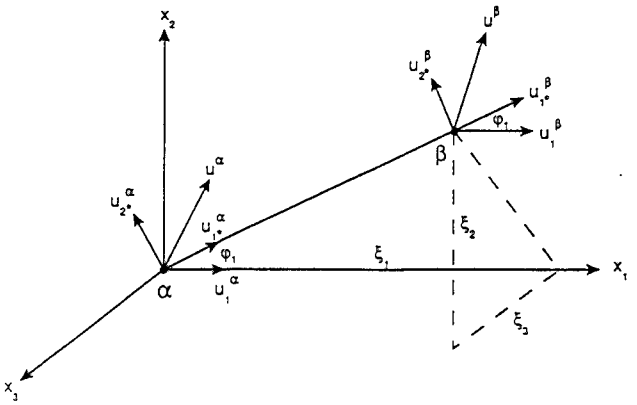

Fig. 3. Geometrical definition of $\overline{u_1^\alpha u_1^\beta}$

$$u_1^\alpha = u_{1*}^\alpha \cos\varphi_1 - u_{2*}^\alpha \sin\varphi_1$$

$$= u_{1*}^\alpha \frac{\xi_1}{r} - u_{2*}^\alpha \sqrt{1 - \frac{\xi_1^2}{r^2}}$$

$$u_1^\beta = u_{1*}^\beta \frac{\xi_1}{r} - u_{2*}^\beta \sqrt{1 - \frac{\xi_1^2}{r^2}} \qquad (17)$$

Let us define

$$\overline{u_{1*}^\alpha u_{1*}^\beta} \equiv u^2 f(r)$$

$$\overline{u_{2*}^\alpha u_{2*}^\beta} \equiv u^2 g(r)$$

where u is the root-mean-square of turbulence and r is the distance along these two points. Because of invariance conditions, we have

$$\overline{u_{1*}^\alpha u_{2*}^\beta} = \overline{u_{2*}^\alpha u_{1*}^\beta} = 0$$

When we multiply u_1^α by u_1^β and take the mean value of the product, we get

$$R_{11} \equiv \overline{u_1^\alpha u_1^\beta}$$

$$= u^2 [\frac{f(r) - g(r)}{r^2} \xi_1 \xi_1 + g(r)] \qquad (18)$$

Next, let us consider $\overline{u_1^\alpha u_2^\beta}$. From Figure 4, we have

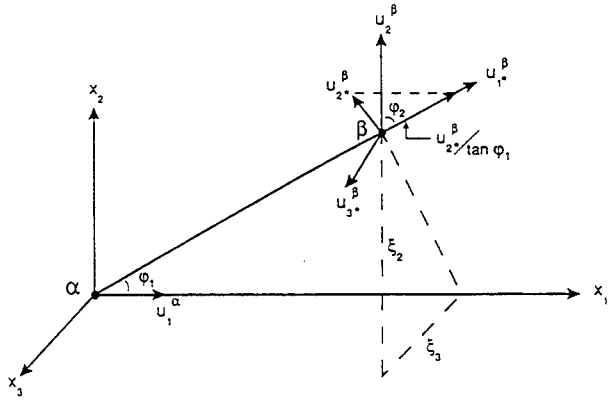

Fig. 4. Geometrical definition of $\overline{u_1^\alpha u_2^\beta}$

$$u_1^\alpha = u_{1*}^\alpha \frac{\xi_1}{r} - u_{2*}^\alpha \sqrt{1 - \frac{\xi_1^2}{r^2}}$$

$$u_2^\beta = u_{1*}^\beta \cos\varphi_2 + u_{2*}^\beta \frac{\cos\varphi_2}{\tan\varphi_1} + F(u_{3*}^\beta)$$

$$= u_{1*}^\beta \frac{\xi_2}{r} + u_{2*}^\beta \frac{\xi_1 \xi_2}{r^2 \sqrt{1 - \frac{\xi_1^2}{r^2}}} + F(u_{3*}^\beta) \qquad (19)$$

where $F(u_{3*}^\beta)$ is the term associated with the velocity component u_{3*}^β. This term is not given in detail because the invariance and isotropy conditions provide the zero mean for all terms containing the u_{3*}^β component. The invariance and isotropy conditions yield

$$\overline{u_{1*}^\alpha u_{2*}^\beta} = \overline{u_{1*}^\alpha u_{3*}^\beta}$$
$$= \overline{u_{2*}^\alpha u_{1*}^\beta}$$
$$= \overline{u_{2*}^\alpha u_{3*}^\beta}$$
$$= 0$$

The correlation of u_1^α and u_2^β is determined as

$$R_{12} = \overline{u_1^\alpha u_2^\beta}$$

$$= u^2 \frac{f(r) - g(r)}{r^2} \xi_1 \xi_2 \qquad (20)$$

In general, combining equations (18) and (20), we can write the velocity correlation as

$$R_{ij} = u^2 [\frac{f(r) - g(r)}{r^2} \xi_i \xi_j + g(r) \delta_{ij}] \qquad (21)$$

where δ_{ij} is the Kronecker delta. The relationship between $f(r)$ and $g(r)$ can be derived from the continuity condition of fluid incompressibility,

$$\frac{\partial R_{ij}}{\partial \xi_j} = 0 \qquad (22)$$

Substituting R_{ij} of equation (21) into equation (22) yields

$$f(r) + \frac{r}{2} \frac{\partial f(r)}{\partial r} = g(r) \qquad (23)$$

From this relation between $f(r)$ and $g(r)$, the velocity correlation function can be expressed in terms of one scalar function, either f(r) or g(r), which gives

$$R_{ij} = u^2 [-\frac{1}{2r} \frac{\partial f(r)}{\partial r} \xi_i \xi_j + (f(r) + \frac{r}{2} \frac{\partial f(r)}{\partial r}) \delta_{ij}] \qquad (24)$$

The longitudinal correlation function, $f(r)$, can be approximated by an exponential function

$$f(r) = e^{-r/\Lambda} \tag{25}$$

where Λ is the integral scale of the turbulence. This is equivalent to assuming that the turbulence spectrum is in the form as it is used in the spectrum approach. As has been verified by screen-generated turbulence, this is a good approximation for homogeneous and isotropic flow field.

For blades rotating in a turbulent field with rotational speed Ω, $r(\tau)$ is

$$r(\tau) \equiv \sqrt{(V\tau)^2 + r_\alpha^2 + r_\beta^2 - 2r_\alpha r_\beta \cos(\theta_\alpha - \theta_\beta + \Omega\tau)} \tag{26}$$

Equation (24) can be rewritten as:

$$R_{ij} = u^2[\frac{1}{2r\Lambda} r_i r_j + (1 - \frac{r}{2\Lambda})\delta ij]e^{-\frac{r(\tau)}{\Lambda}} \tag{27}$$

or in the algebraic form

$$\begin{aligned} R_{11} &= u^2[\frac{1}{2r\Lambda}\xi^2 + (1 - \frac{r}{2\Lambda})]e^{-\frac{r(\tau)}{\Lambda}} \\ R_{22} &= u^2[\frac{1}{2r\Lambda}\eta^2 + (1 - \frac{r}{2\Lambda})]e^{-\frac{r(\tau)}{\Lambda}} \\ R_{12} &= u^2[\frac{1}{2r\Lambda}\xi\eta]e^{-\frac{r(\tau)}{\Lambda}} \end{aligned} \tag{28}$$

By taking numerical Fourier transformations of the time domain correlation function (equation (27)), one obtains the frequency spectrum of the velocity correlation function, $G_{ij}(\omega)$, as

$$G_{ij}(\omega) = \frac{1}{2\pi}\int_{-\infty}^{\infty} R_{ij}(\tau)e^{-i\omega\tau}d\tau \tag{29}$$

where the omitted superscripts are the indices of two points for convenience.

In examining equation (27), it is clear that R_{ij} is periodic with respect to blade rotation due to the presence of the cosine term in the correlation function. This periodic term is most dominant when V/Ω is small. As τ or V increases, the importance of the cosine term decreases and R_{ij} becomes a monotonically decreasing function of τ. The spectrum represented by equation (29) should thus contain both a broadband and a blade rate hump spectrum in general. It resembles the experimental measurements and will be discussed in detail in the results section.

Sevik [1] studied special cases of the above equation when ΩR is much smaller than V, and he approximated equation (27) by

$$r(\tau = 0) \equiv \sqrt{r_\alpha^2 + r_\beta^2 - 2r_\alpha r_\beta \cos(\theta_\alpha - \theta_\beta)} \tag{30}$$

The corresponding velocity correlation then becomes

$$R_{ij} \simeq e^{-\frac{r(\tau=0)}{\Lambda}} R_{ii}(V\tau) \tag{31}$$

The components of the velocity correlation tensor are

$$R_{11} = u^2 e^{-(\frac{V\tau}{\Lambda} + \frac{r(\tau=0)}{\Lambda})} \tag{32}$$

and

$$R_{22} = u^2(1 - \frac{V\tau}{2\Lambda})e^{-(\frac{V\tau}{\Lambda} + \frac{r(\tau=0)}{\Lambda})} \tag{33}$$

The effect of the angular location of the blade, $\Omega\tau$, is totally absent in Sevik's correlation model; $e^{-r(\tau=0)/\Lambda}$ is a time independent term. The solution for G_{ij} contains no blade humps and may be expressed analytically; that is,

$$\begin{aligned} G_{11} &= \frac{2}{\pi}u^2\frac{\frac{V}{\Lambda}}{(\frac{V}{\Lambda})^2 + \omega^2}e^{-r/\Lambda} \\ G_{22} &= \frac{2}{\pi}u^2\frac{\frac{V}{\Lambda}}{(\frac{V}{\Lambda})^2 + \omega^2}(1 - \frac{1}{2}\frac{(\frac{V}{\Lambda})^2 - \omega^2}{(\frac{V}{\Lambda})^2 + \omega^2})e^{-r/\Lambda} \end{aligned} \tag{34}$$

Hoping to recover the blade rate humps without losing the simplicity of the analysis, Martinez [8, Appendix A] modified Sevik's analysis by including the propeller rotational speed through the approximation

$$r(\tau) \cong \sqrt{r_\alpha^2 + r_\beta^2 - 2r_\alpha r_\beta \cos(\theta_\alpha - \theta_\beta + \Omega\tau)} \tag{35}$$

Then the velocity correlation function becomes

$$R_{11} = u^2 e^{-(\frac{V\tau}{\Lambda} + \frac{r(\tau)}{\Lambda})} \tag{36}$$

and

$$R_{22} = u^2(1-\frac{V\tau}{2\Lambda})e^{-(\frac{V\tau}{\Lambda}+\frac{r(\tau)}{\Lambda})} \quad (37)$$

which still preserves the exponential form of the correlation function used by Sevik [1]. As is true for the spectrum approach, simplification of the correlation function implies a filtering process in the physics. For practical applications, the search for an analytical solution could have prevented the advancement of unsteady force prediction methods in the past. Later, Martinez and Weissman [8, Appendix B] followed the recommendation of the authors of the present paper and used the same correlation function (equation (27)) to perform analytical study. They were able to form a closed form solution and the solution contains Bessel functions. Their numerical results obtained from computing the various order of Bessel functions compared well with the present computational results. The present analysis adapts both theoretical and numerical techniques. For individual cases, the theoretical analysis will be carried to its full extent, in this case to equation (29), and then numerical analysis will follow.

FLUID DYNAMIC RESPONSE FUNCTION - $H(\omega)$

The next step of the computation is the establishment of a transfer function, $H(\omega)$, defined in equation (16). The simplest computation is based on two-dimensional, incompressible and inviscid aerodynamics theory. Sears [10] derived the response function for a zero skew, discrete sinusoidal gust convected in the plane of a foil at zero angle of attack. The resulting aerodynamic unsteady force is represented as

$$H(\omega) = 2\pi\rho U\frac{C}{2}K(\omega) \quad (38)$$

where $K(\omega)$ is the Sears' function and is in terms of cylindrical functions $H_0^{(2)}(k)$ and $H_1^{(2)}(k)$;

$$K(\omega) = \frac{H_1^{(2)}(k)}{H_1^{(2)}(k)+iH_0^{(2)}(k)} \quad (39)$$

where k is the normalized reduced frequency $(\omega C/2U)$.

Equation (38) was derived for an isolated foil operating with sinusoidal velocity disturbances normal to the foil surface. When applying the equations to propellers or small aspect ratio foils, the results of using a two-dimensional approximation may not valid. However, the two-dimensional theory will give satisfactory predictions providing the value of the local lift slope is appropriately corrected. This means that the coefficient 2π of equation (38) be replaced by the steady state local lift slope as described by Sevik [1].

Applying the above Sears' function to a 2-D blade, the angle between the inflow and the direction of advance also has to be considered. This gives

$$H_p(\omega) = H(\omega)\cos\phi \quad (40)$$

where H_p denotes the two-dimensional response function for a propeller in its direction of advance and ϕ is the inflow angle with respect to that direction. When operating near design conditions, ϕ may be approximated by the pitch angles of blade sections for most marine propellers.

NUMERICAL PROCEDURES

With a specified correlation function, equation (28), and a chosen transfer function, equation (40), we may proceed to perform the numerical unsteady force computations as given in equation (16). Since propeller unsteady forces are generated from the unsteady velocity relative to the blades, the velocity spectrum components $G(\omega)$ in equation (16) should be expressed in a rotational cylindrical coordinate system which is fixed on the blade. Let the mean inflow to the propeller be denoted by $\overline{u^\alpha}$. Then the unsteady angle of attack becomes

$$\begin{aligned}\alpha(\tau) &\simeq \tan^{-1}\frac{u_N^\alpha}{\overline{u^\alpha}} \\ &\simeq \frac{u_N^\alpha}{\overline{u^\alpha}}\end{aligned} \quad (41)$$

with

$$u_N^\alpha = u_x^\alpha\cos\phi_\alpha + u_\theta^\alpha\sin\phi_\alpha \quad (42)$$

and

$$\begin{aligned}u_N^\alpha u_N^\beta &= (u_x^\alpha\cos\phi_\alpha + u_\theta^\alpha\sin\phi_\alpha)(u_x^\beta\cos\phi_\beta + u_\theta^\beta\sin\phi_\beta) \\ &= u_x^\alpha u_x^\beta\cos\phi_\alpha\cos\phi_\beta + u_x^\alpha u_\theta^\beta\cos\phi_\alpha\sin\phi_\beta + \\ &\quad u_\theta^\alpha u_x^\beta\sin\phi_\alpha\cos\phi_\beta + u_\theta^\alpha u_\theta^\beta\sin\phi_\alpha\sin\phi_\beta\end{aligned} \quad (43)$$

where ϕ_α is the propeller inflow angle at point α.

The velocity correlation of equation (16), thus, becomes

$$R^{\alpha\beta}_{NN} = R^{\alpha\beta}_{xx}\cos\phi_\alpha\cos\phi_\beta + R^{\alpha\beta}_{x\theta}\cos\phi_\alpha\sin\phi_\beta + R^{\alpha\beta}_{\theta x}\sin\phi_\alpha\cos\phi_\beta + R^{\alpha\beta}_{\theta\theta}\sin\phi_\alpha\sin\phi_\beta \quad (44)$$

The calculation of $R^{\alpha\beta}_{xx}$ is straight forward as

$$R^{\alpha\beta}_{xx} = u^2[\frac{1}{2r\Lambda}dx^2 + (1-\frac{r}{2\Lambda})]e^{-\frac{r(\tau)}{\Lambda}} \quad (45)$$

where $dx = V\tau$ and

$$r(\tau) \equiv \sqrt{(dx)^2 + r_\alpha^2 + r_\beta^2 - 2r_\alpha r_\beta\cos(\theta_\alpha(0) - \theta_\beta(0) + \Omega\tau)}$$

The calculations of $R^{\alpha\beta}_{x\theta}$ and $R^{\alpha\beta}_{\theta\theta}$ in terms of τ has to be further expressed through the instantaneous angular locations of the blade elements. For the coordinate system shown in Figure 5, the tangential velocity component is

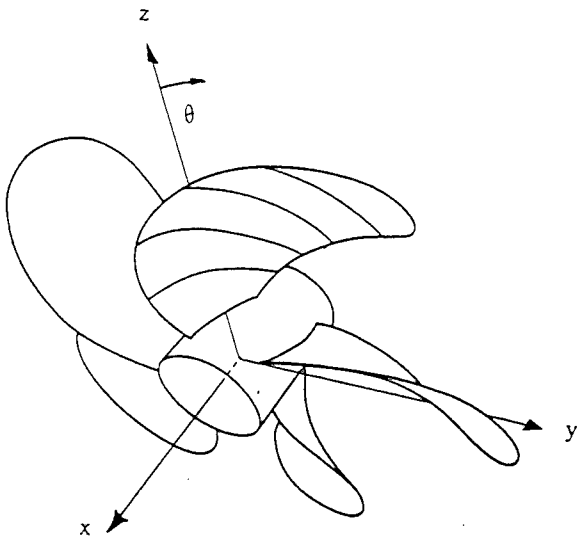

Fig. 5. Chordwise strips on propeller blade

$$u^\beta_\theta = u^\beta_y\cos\theta_\beta(\tau) - u^\alpha_z\sin\theta_\beta(\tau) \quad (46)$$

and the velocity correlations $R^{\alpha\beta}_{x\theta}$ and $R^{\alpha\beta}_{\theta\theta}$ are

$$R^{\alpha\beta}_{x\theta} = R^{\alpha\beta}_{xy}\cos\theta_\beta(\tau) - R^{\alpha\beta}_{xy}\sin\theta_\beta(\tau) \quad (47)$$

and

$$R^{\alpha\beta}_{\theta\theta}(\tau) = R^{\alpha\beta}_{yy}\cos\theta_\alpha(0)\cos\theta_\beta(\tau) + R^{\alpha\beta}_{xz}\sin\theta_\alpha(0)\sin\theta_\beta(\tau) - R^{\alpha\beta}_{yz}\cos\theta_\alpha(0)\sin\theta_\beta(\tau) - R^{\beta\alpha}_{yz}\sin\theta_\alpha(0)\cos\theta_\beta(\tau) \quad (48)$$

where

$$\begin{aligned} R^{\alpha\beta}_{yy} &= u^2[\frac{1}{2r\Lambda}dy^2 + (1-\frac{r}{2\Lambda})]e^{-\frac{r(\tau)}{\Lambda}}, \\ R^{\alpha\beta}_{xy} &= u^2(1-\frac{r}{2\Lambda}dxdy)e^{-\frac{r(\tau)}{\Lambda}}, \\ R^{\alpha\beta}_{xz} &= u^2(1-\frac{r}{2\Lambda}dxdz)e^{-\frac{r(\tau)}{\Lambda}}, \\ R^{\alpha\beta}_{zz} &= u^2[\frac{1}{2r\Lambda}dz^2 + (1-\frac{r}{2\Lambda})]e^{-\frac{r(\tau)}{\Lambda}}, \\ dy &= r_\alpha\cos\theta_\alpha(0) - r_\beta\cos\theta_\beta(\tau), \end{aligned}$$

and

$$dz = r_\alpha\sin\theta_\alpha(0) - r_\beta\sin\theta_\beta(\tau).$$

Since turbulence has been assumed to be homogeneous, $R^{\alpha\beta}_{\theta\theta}(\tau)$ is only a function of τ, and can be evaluated at $\theta_\alpha(0)$ and $\theta_\beta(\tau)$.

Based on the above definition of R_{NN}, correlation functions are numerically evaluated at given ω values as

$$G^{\gamma\delta}_{NN}(\omega) \equiv \frac{1}{2\pi}\int_{-\infty}^{\infty} R^{\gamma\delta}_{NN}(\tau)e^{-i\omega\tau}d\tau$$

The thrust spectrum tensor, equation (16), between blade elements α and β is then calculated as:

$$\Psi^{\alpha\beta}_{\ell_x\ell_x}(\omega) = [H^{\alpha\gamma}_{xx}(\omega)]^*[H^{\beta\delta}_{xx}(\omega)][G^{\gamma\delta}_{NN}(\omega)] \quad (49)$$

Assuming the unsteady force generated at each individual strip is two dimensional, the last equation becomes

$$\Psi^{\alpha\beta}_{\ell_x\ell_x}(\omega) = [H^{\alpha\alpha}_{p}(\omega)]^*[H^{\beta\beta}_{p}(\omega)][G^{\alpha\beta}_{NN}(\omega)]$$

with H_p given by equation (39). The total unsteady force spectrum is obtained from summing $\Psi^{\alpha\beta}_{\ell_1\ell_1}(\omega)$ over all elements of α and β. In this computation, the mean flow angle ϕ has to be estimated before the unsteady thrust can be determined. This angle can be obtained from propeller computer codes. For near-design operating conditions, the pitch of the blade may be used for ϕ for most marine propellers, as mentioned earlier.

Similarly, the side force spectrum can be numerically calculated by using equation (16), it becomes

$$\Psi^{\alpha\beta}_{\ell_y\ell_y}(\omega) = \frac{1}{2\pi}\int_{-\infty}^{\infty}\int_0^{\infty}\int_0^{\infty} F^{\alpha\gamma}_{yN}(\tau_1)d\tau_1 F^{\beta\delta}_{yN}(\tau_2)d\tau_2$$

$$R^{\gamma\delta}_{NN}(\tau+\tau_1-\tau_2)e^{-i\omega\tau}d\tau$$

$$= \frac{1}{2\pi}\int_{-\infty}^{\infty}\int_0^{\infty}\int_0^{\infty} F^{\alpha\gamma}_{NN}(\tau_1)sin\phi_\alpha$$

$$sin(\theta_\gamma(0)+\theta_0)d\tau_1 F^{\beta\delta}_{NN}(\tau_2)$$

$$sin\phi_\beta sin(\theta_\delta(0)+\theta_0+\Omega\tau)d\tau_2$$

$$R^{\gamma\delta}_{NN}(\tau+\tau_1-\tau_2)e^{-i\omega\tau}d\tau$$

$$= [H^{\alpha\gamma}_{NN}(\omega)sin\phi_\alpha]^*[H^{\beta\delta}_{NN}(\omega)sin\phi_\beta]$$

$$[\overline{G}^{\gamma\delta}_{NN}(\omega)] \qquad (50)$$

where θ_0 is the blade reference angular location, and

$$\overline{G}^{\gamma\delta}_{NN}(\omega) \equiv \frac{1}{2\pi}\int_{-\infty}^{\infty} R^{\gamma\delta}_{NN}(\tau)sin(\theta_\gamma(0)+\theta_0)$$

$$sin(\theta_\delta(0)+\theta_0+\Omega\tau)e^{-i\omega\tau}d\tau$$

Since

$$\frac{1}{2\pi}\int_0^{2\pi} sin(\theta_\gamma(0)+\theta_0)sin(\theta_\delta(0)+\theta_0+\Omega\tau)d\theta_0 =$$

$$\frac{1}{2}cos(\theta_\delta(0)-\theta_\gamma(0)+\Omega\tau)$$

Then

$$\overline{G}^{\gamma\delta}_{NN}(\omega) = \frac{1}{4\pi}\int_{-\infty}^{\infty} R^{\gamma\delta}_{NN}(\tau)cos(\theta_\delta(0)-\theta_\gamma(0)+\Omega\tau)$$

$$e^{-i\omega\tau}d\tau$$

Again, assuming the unsteady force generated at each individual strip is two-dimensional, then the side force spectrum becomes

$$\Psi^{\alpha\beta}_{\ell_y\ell_y}(\omega) = [H^{\alpha\alpha}_{NN}(\omega)sin\phi_\alpha]^*[H^{\beta\beta}_{NN}(\omega)sin\phi_\beta]$$

$$[\overline{G}^{\alpha\beta}_{NN}(\omega)] \qquad (51)$$

Followed the same procedures, the total torque due to the ingested turbulence can be derived in final form as

$$\Psi^{\alpha\beta}_{qq}(\omega) = [H^{\alpha\alpha}_{NN}(\omega)cos\phi_\alpha]^*[H^{\beta\beta}_{NN}(\omega)cos\phi_\beta][G^{\alpha\beta}_{qq}(\omega)]$$

where

$$G^{\gamma\delta}_{qq}(\omega) \equiv \frac{1}{2\pi}\int_{-\infty}^{\infty} R^{\gamma\delta}_{NN}(\tau)r_\gamma r_\delta e^{-i\omega\tau}d\tau$$

where r_γ is radial distance of element γ. Numerical calculations of thrust, side force and torque spectra are performed and presented in the following section.

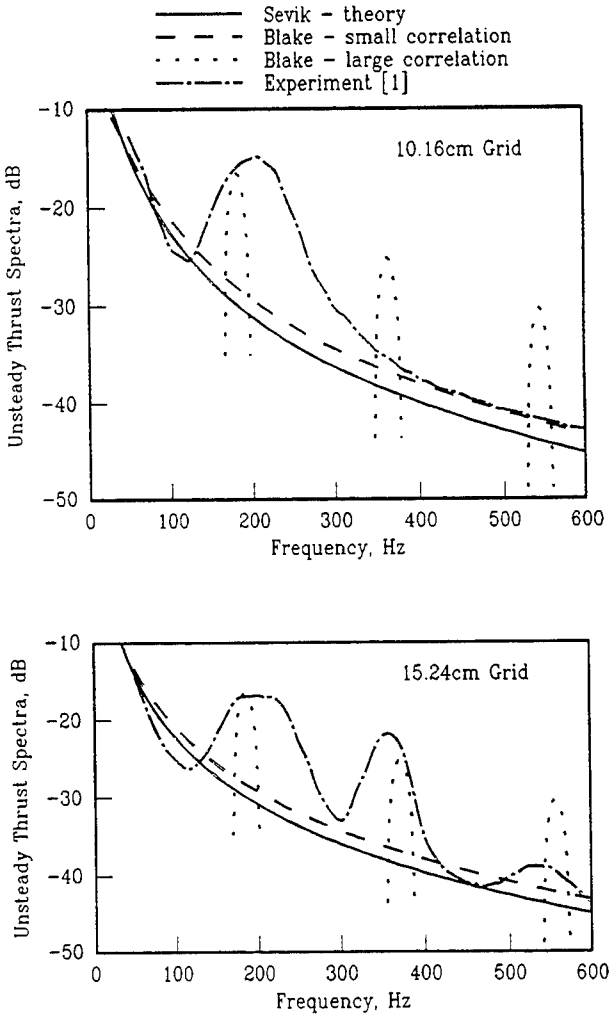

Fig.6 Comparison of Existing Methods

RESULTS AND DISCUSSIONS

Sevik's experiment [1] is used to study the present approach and to demonstrate the differences between the present computation and previous results. The experiment was conducted in the 1.22m (48") diameter water tunnel at Pennsylvania State University. The propeller used for this investigation has ten blades with a constant chord length of 2.54cm (1") and a radius of 10.16cm (4"). The turbulence level in the test section without the grid was about 0.1%. Two grids were used with mesh sizes of 10.16cm (4") and 15.24cm (6"), respectively, to generate the turbulence level of about 3% with two different integral length scales at the propeller plane. The distance between the grid and the propeller plane was twenty times the grid sizes. Data were taken at a tunnel speed equal to 4.57m/sec (15ft/sec) and the advance ratio was 1.22. Power spectral density of the propeller thrust due to turbulence was measured and compared with theoretial results of Sevik [1], Figure 6. The measured spectra show significant humps at the first blade rate frequency while the humps at the higher blade rates were observable only for the 15.24cm grid case. The theoretical results of Sevik compared well with the measurements with respect to the broadband part of the spectrum while the humps were missing. Later, Blake [7] compared those data with his asymptotic solutions of equation (12) and equation (13), derived to improve the prediction on blade rate humps. His results are also given in Figure 6. The smooth broken line in Figure 6 shows the asymptotic results of small correlation (equation (12)) and the dotted line provides the large correlation results (equation (13)). It is seen that the small correlation results approach Sevik's theory as expected since they are equivalent to omitting the rotational correlation from the analysis. The large correlation asymptotic results give humps centered at multiples of the blade rate frequency without the broadband part of the spectrum. The comparison of the asymptotic solutions and measurement indicate that the basic approach is correct and that numerical simplification should be avoided.

Computations based on equation (10) and equation (11) were performed numerically for the two grid sizes, and the results are given in Figures 7 and 8. The results of equation (11), Figure 7, show that the center frequencies of the humps shift and skew to higher frequencies when compared with Blake's calculations. The amplitudes of the humps do not decay at higher blade rates for either grid size. Also, the results using equation (11) show ditches between the humps quite below the measured results. Since equation (11) did not have the radial dependence of the filtering function (A_s), Sears' function and Taylor's hypothesis, it over emphasizes the blade rotational effect. By removing the small advance coefficient assumption, including the radial dependence on filtering and Sears' functions, and numerically integrating equation (10), the hump amplitude and ditch depth are reduced and the hump bandwidth is increased as shown in Figure 8. It is thus demonstrated, in a practical application, that the radial dependence should be included in the analysis. Neverthless, including this effect in the wave number integration complicates the computation and the spectrum approach is not recommended at present.

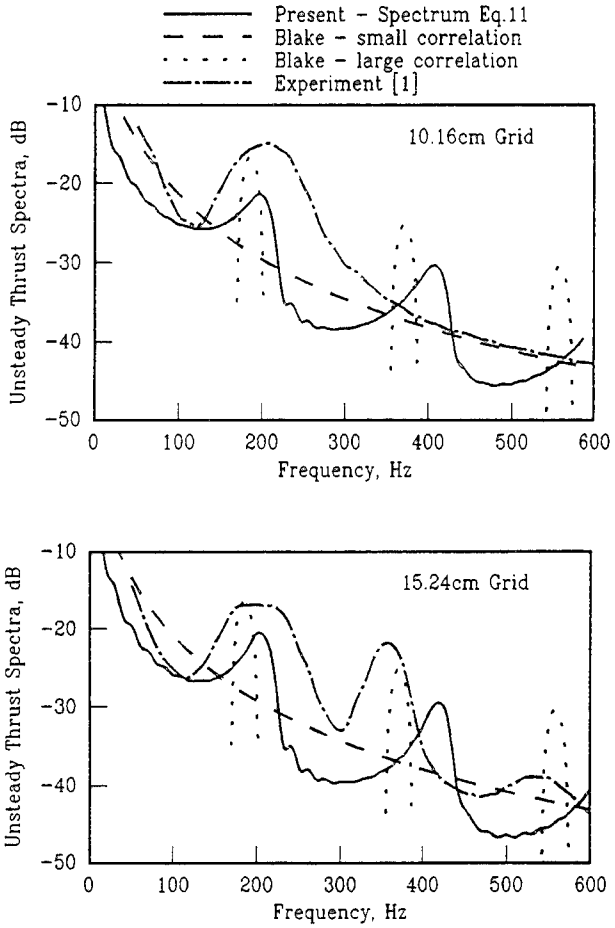

Fig.7 Comparison of Simplified Spectrum Approaches

Figures 9a and 9b present the comparisons between the results of the present correlation theory and the experiment. The current correlation theory predicts both the humps which were demonstrated in the experiment and the broadband part of the spectrum. The broadband part of the spectrum compares well while the hump amplitudes and center frequencies of higher harmonics do not agree. The cause of the

hump discrepancy could be in the uncertainty of the inflow turbulence. The experiments show the inconsistency in the results between 10.16cm (4") and 15.24cm (6") grids. The 15.24cm (6") grid results have humps at both first and second blade rate frquencies while 10.16cm (4") grid results show only one hump near the first blade rate. These differences could reflect deviations from the design homogeneous and isotropic grid turbulent inflow. Since the characteristics of the inflow were not measured, no further comparisons are possible. However, from the general features of the comparsion and the other computations which are not included, the authors are certain that the present model should predict the spectrum reasonably well if the inflow turbulence is given.

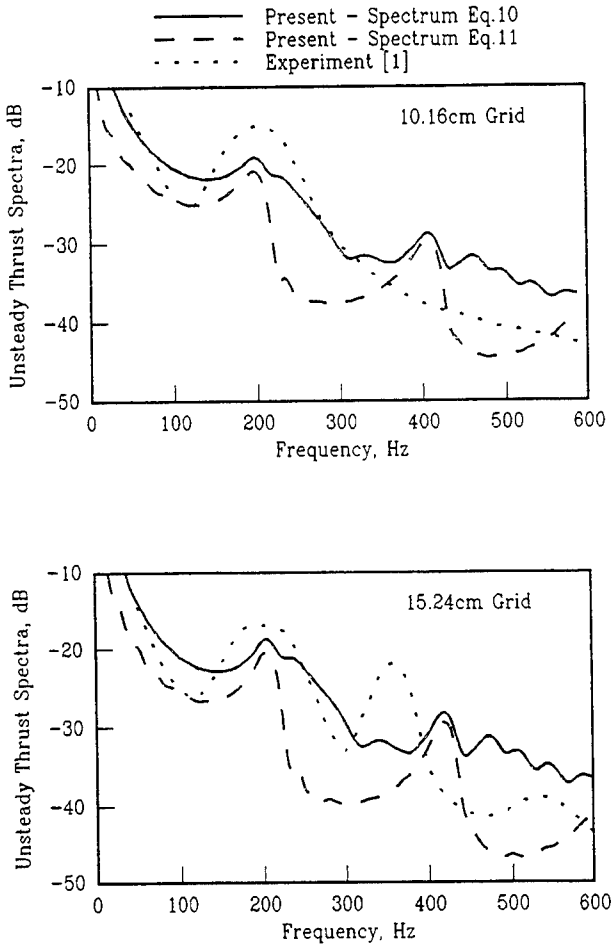

Fig.8 Comparison of Unified Spectrum Methods With Experiment

Martinez's [8] analytical model decomposed the axial and propeller-plane velocity correlations to investigate the contribution of each component. The same investigation can be performed numerically. Figure 10 gives the spectra combination of $x-x$ with $x-\theta$ and $x-x$ with $\theta-\theta$ forces. It demonstrates that the $x-x$ component provides the basic shape and level of the thrust spectrum. The frequency shift is due to the

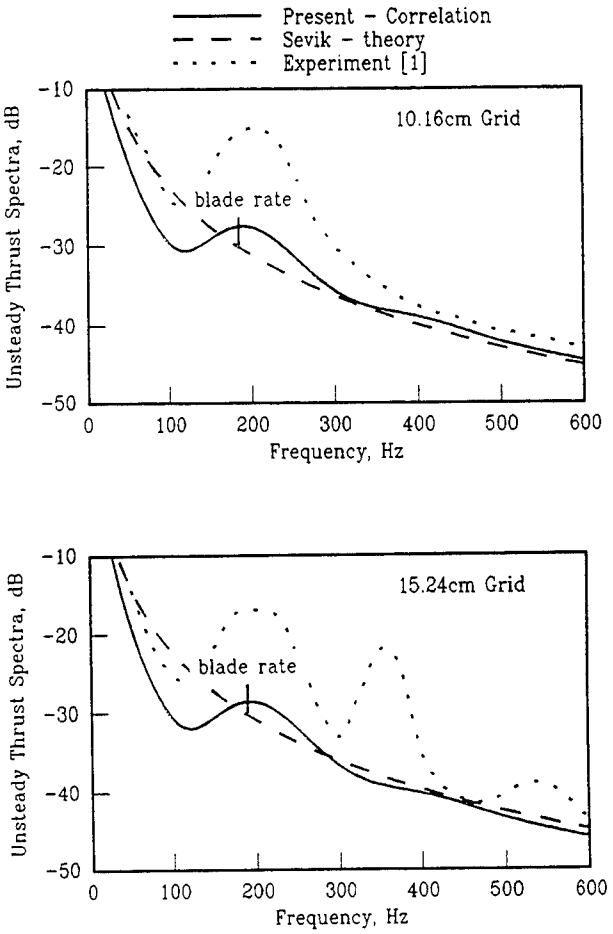

Fig.9 Comparison of Correlation Methods With Experiment

$x-\theta$ effect and the level increase at lower frequency is due to the $\theta-\theta$ effect. Due to the phase shift of the $x-\theta$ component velocity correlation, the $x-\theta$ term subtracts from the $x-x$ term at the left of blade rate frequency, while to the right it adds to the $x-x$ term.

Side force and torque spectra, Figure11, have shapes similar to the thrust spectrum. The differences in spectrum levels are due to the velocity correlation functions, $G(\omega)$, and components of fluid transfer function. The level of side force spectrum is about 10dB below the thrust spectrum.

The characteristics of the unsteady force spectrum may be generalized from the study of isotropic turbulence. The present isotropic results show that the spectrum can be normalized in terms of the param-

eters $V/\Lambda\Omega, \Lambda/R$ and ω/Ω. Their influence on the resulting unsteady force is demonstrated in Figures12 and 13, and is summarized as follows:

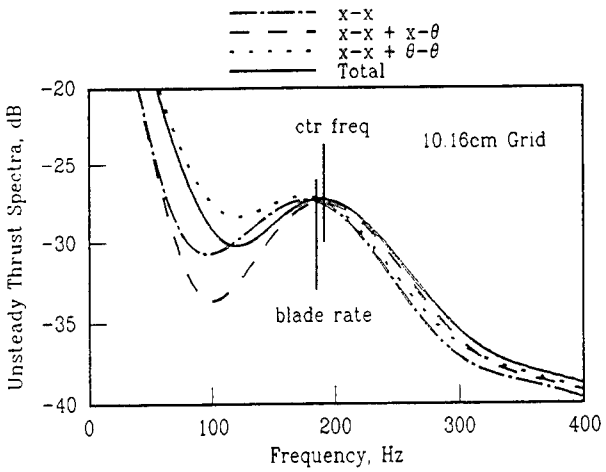

Fig.10 Thrust Spectrum Components

1) The effect of the inflow turbulence scale, Λ/R: In general, the smaller the turbulence length scale, the higher the broadband unsteady spectrum. However, both amplitudes and bandwidths of the blade rate humps decrease with decreasing turbulence scale as the result of faster decay of the rotational correlations, while the variation of the turbulence length scale has only a minimal effect on the hump center frequencies, Figure12.

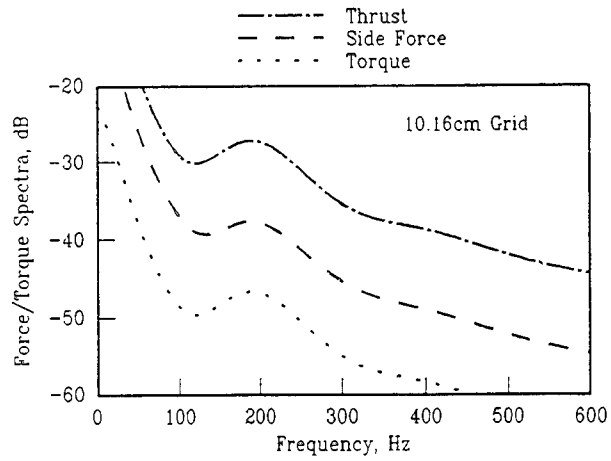

Fig.11 Forces and Torque Spectra

2) The effect of advance coefficient, $V/\Lambda\Omega$: With other nondimensional parameters held constant, Figure 13 shows that as the advance coefficient decreases, the blade rate humps become more pronounced. The

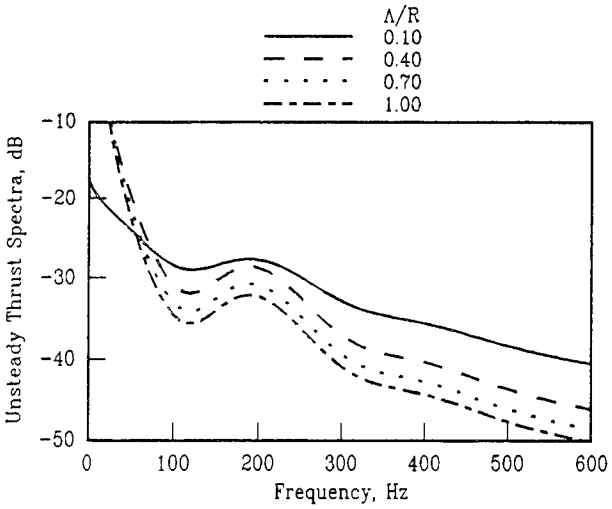

Fig.12 Effect of Turbulence Length Scale (Λ/R) on Unsteady Thrust
(Turbulence Level = 0.03; V/RΩ=0.39)

higher blade rate humps become significant at low advance coefficients as shown by Blake[7] and discussed previously. In the normal operating condition ($V/\Lambda\Omega$ greater than 0.5), only the first blade rate hump is expected.

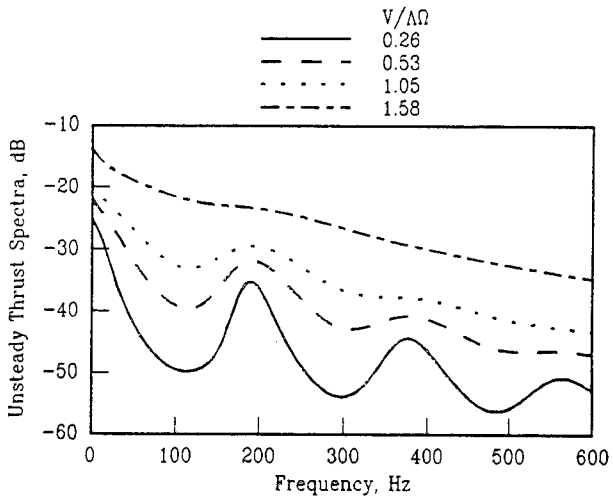

Fig.13 Effect of Advance Coefficient (V/ΛΩ) on Unsteady Thrust
(Turbulence Level = 0.03; Λ/R=0.28)

3) Skew of the hump center frequencies: The center frequencies of the humps shown in Figure 14 are not at blade rate frequencies and are skewed to the right.

The skew is caused by the geometrical pitch of the blade combined with $x-\theta$ correlation. The larger the pitch, the greater the skew will be. The first order estimate of this skewness may be approximated from the second and third terms of equation (47) and given in Figure 10.

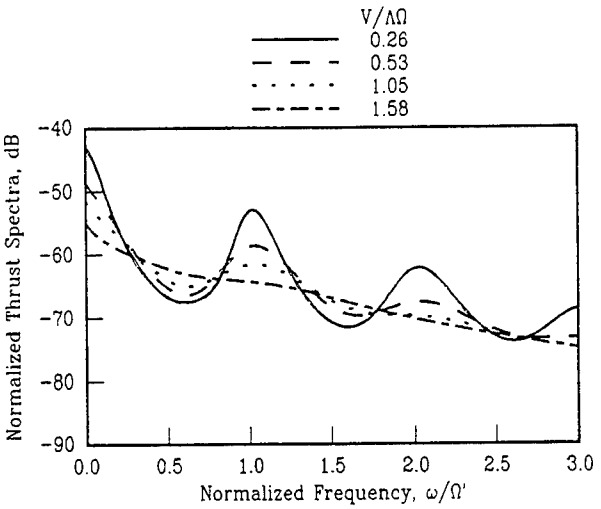

Fig.14 Normalized Effect of Advance Coefficient (V/ΛΩ) on Unsteady Thrust (Turbulence Level = 0.03; Λ/R=0.28)

4) Inverse cubic dependency on the high frequencies: To demostrate the spectrum behavior at high frequencies, the theoretical results of the grid turbulence for 10.16 cm and 15.24 cm screens are re-plotted in normalized form in Figure 15. The frequency is normalized by the blade rate frequency and the thrust

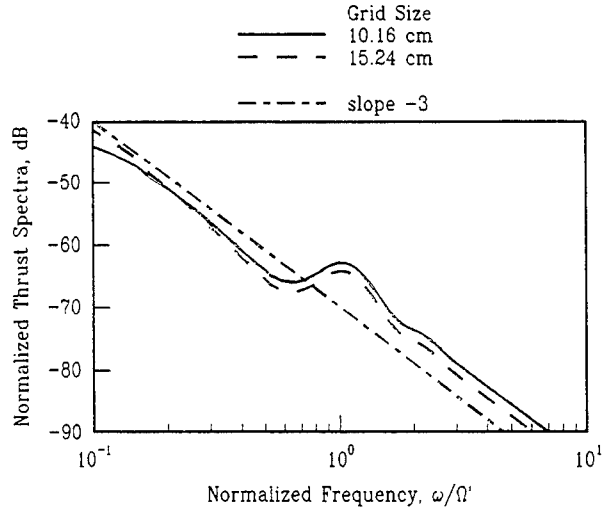

Fig.15 Normalized Unsteady Thrust (Turbulence Level = 0.03; V/nD=1.22)

spectrum is normalized by the third power of the velocity. At high frequencies, past the second hump, the slope of these normalized curves approaches minus three as expected from equation (12) or equations (34) and (38) for a given advance coefficient and turbulence level. The two grids used in the experiment did not cover enough of a range in turbulence lengths to make as substantial alterations near the hump as the theoretical calculation provided in Figure12.

Because ships normally operate at a nearly constant advance coefficient, it is of interest to present the thrust spectrum in dimensional form as a function of ship speed or propeller rpm with a given advance coefficient. The behavior of the thrust spectra at different speeds for the 10.16 cm grid turbulence is shown in Figure 16. It is seen that the hump bandwidth at

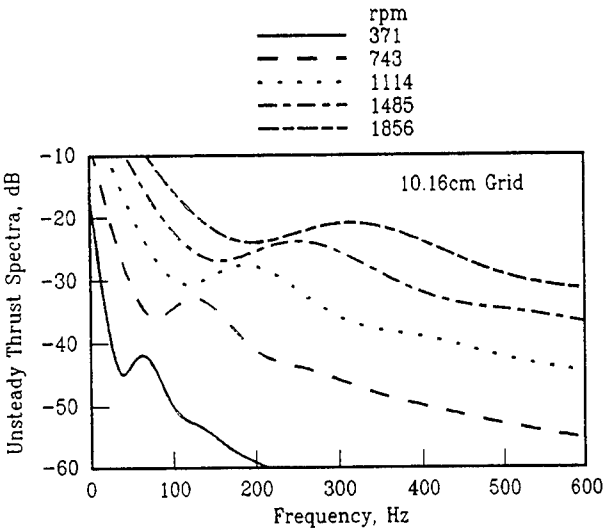

Fig.16 Unsteady Thrust at Constant Advance Ratio (Turbulence Level = 0.03; V/nD=1.22)

the first blade rate frequency increases as ship speed increases. In practice, one should anticipate a sharp hump during lower speed operation.

CONCLUSIONS

Theoretical predictions of broadband thrust forces in a turbulent flow are presented. The calculations are carried out using a correlation method and a spectrum method. The results of the correlation theory provide a better correlation with experiment than the spectrum theory, computed from an assumption of homogeneous and isotropic turbulence. Turbulence velocity correlation can be considered as the combination of transverse and rotational correlation. The effect of transverse correlation produces an unsteady thrust proportional to the third power of ship speed. The rotational correlation is inversely proportional to a ro-

tational parameter given by $V/\Lambda\Omega'$. The rotational correlation distorts the V^3 power relation and causes the unsteady thrust spectra to show humps near the first and second blade rate frequencies; these humps skew to the higher frequency side of the blade rate frequencies. Since the hump phenomena were not explained previously, only limited, inconclusive experiments are available to verify the theory. Future experiments should include simultaneous measurement of unsteady force and turbulence in order to validate the theory.

The spectrum method is not as easy to apply as the correlation method because it involves higher order integration. When the integration order was reduced through simplification, the results were also degraded as shown in Figures 6 through 8. The correlation method gives good results, Figure 9, and can be adapted to more complex cases with little numerical difficulty.

In addition to improving the inflow turbulence assumptions, the analytical methods can be further improved by including the effect of finite span, camber and angle of attack. A parametric investigation of the turbulence inflow and propeller unsteady response should be done under laboratory conditions before the theory is applied to a complex propeller/rotor geometry.

REFERENCES

1. Sevik, M., "Sound Radiation From a Subsonic Rotor Subjected to Turbulence," Int. Symp. Fluid Mech. Des. Turbomach., NASA SP-304, Part II 1974, Pennsylvania State University, University Park, PA.

2. Thompson, D. E., "Propeller Time-Dependent Forces Due to Nonuniform Flow," PhD Thesis, May 1976, The Pennsylvania State University.

3. Chandrashekhara, N., "Tone Radiation From Axial Flow Fans Running in Turbulent Flow," J. Sound Vib., 18, 1971, pp.533-543.

4. Mani, R., "Noise Due to Interaction of Inlet Turbulence With Isolated Stators and Rotors," J. Sound Vib., 17, 1971, pp.251-260 .

5. Homicz, G. F., and George, A. R., "Broadband and Discrete Frequency Radiation From Subsonic Rotors," J. Sound Vib., 36, 1974, pp.151-177.

6. Amiet, R., "Noise Produced by Turbulent Flow into a Propeller or Helicoper Rotor," AIAA J., 15, 1977, pp.307-308.

7. Blake, W. B., Mechanics of Flow-Induced Sound and Vibration, Vol. II Complex Flow-Structure Interactions, Academic Press, Inc. 1986.

8. Martinez, R., "Analysis of the Right Shift of the Blade-Rate Hump in Broadband Spectra of Propeller Thrust," U-1993-381.9, 1991, Cambridge Acoustical Associates.

9. Hinze, J. O., Turbulence, an Introduction to Its Mechanics and Theory, McGraw-Hill, New York, 1959.

10. Sears, W. R., "Some Aspects of Non-Stationary Air Foil Theory and Its Practical Application," J. Aeron. Sci., Vol. 8, 1941.

DISCUSSION

J.-C. Suh
Korea Research Institute of Ships and Ocean Engineering, Korea

I would like to express a great congratulation to the authors for their excellent paper. I have two questions about obtaining a transfer function of the propeller unsteady forces. It seems that the authors have used the linearized analytic solution only for a vertical gust of onset flow (Sear's function). However, there are two components of onset flow to a blade section in concern, say vertical and horizontal gust. I think that both components should be included to make a sort of consistent calculation. Is there any reason for excluding the horizontal component?

At off design conditions, incidence angles to a blade section would be large. The linearized analytic solution that the authors have chosen might be inappropriate for obtaining the global propeller forces in the cases of off design conditions. How did the authors include this nonlinear effect on the calculations?

AUTHORS' REPLY

The unsteady lift is due to the unsteady angle of attack, which is the angle between the direction of relative velocity and the blade section. Equation (42) is the unsteady blade normal velocity due to both the axial and the tangential components. The unsteady force due to the perturbation velocity along the blade section is a higher order; that is,

$$\frac{V+v'}{U+u'}=\frac{V+v'}{U}[1-(u'/U)+\cdots]\approx\frac{V}{U}+\frac{v'}{U}-\{\frac{V}{U}\frac{u'}{U}\}\approx\frac{V}{U}+\frac{v'}{U}$$

where V/U is the mean angle of attack and v'/U is the unsteady angle of attack. This approach should be a good approximation as long as the variation of angle of attack is inside the linear region. The linearized theory breaks down, and a higher-order approach has to be developed when the operation mean angles of attack are outside the limits of the linear region. The term within the bracket, {}, becomes important when V/U is large. However, in that case we will expect the separation phenomenon to dominate the physics of thrust, and a totally different transfer function will have to be applied.

DISCUSSION

E. Rood
Office of Naval Research, USA

The authors have presented a very interesting paper formally accounting for rotational correlation. It is clear that this development will produce blade rate humps. However, I wonder about the quantitative comparison with the experimental data.

How were the correlations obtained in the referenced experiment? What is the variation in the integral length scale with position in the propeller plane? Were two-point correlations obtained?

Has the experiment been repeated? Should it be? What does the prediction tell us to guide another experiment?

AUTHORS' REPLY

Dr. Rood's questions were our questions. The experimental results used in this paper were performed more than twenty years ago, and the turbulence characteristics were not measured at that time. In order to verify this theory, an experiment is being conducted at the Applied Research Laboratory, Penn State University. Both inflow turbulence and unsteady thrust are measured in this experiment. The experiments have been repeated for grid generated turbulence and presented at this symposium. Those results will be published in the near future. The problem with Dr. Sevik's experiments could be the instrumentation and/or blade resonance frequency. Indeed, the dynamometer has been redesigned for ARL/PSU's test.

DISCUSSION

R. Martinez
Durham, New Hampshire, USA

This paper represents an important contribution to our current understanding of how a rotor filters out a broadband force from the turbulence that it chops. The authors consider two approaches to this random-gust/blade interaction problem: (1) a wavenumber-

spectral one, which is then applied to cases of anisotropic flows characterized by three independent integral scales, i.e., one for each spatial direction; and (2) a spatial-domain solution, applied to frozen isotropic turbulence. The predicted peak levels display a slight shift to the right of the blade-rate frequency and its overtones, due to the cross-correlation of flows normal and tangential to the rotor plane. Everything is well explained. There are only two minor comments:

(1) Have the authors had a chance to apply the wavenumber approach to isotropic turbulence so as to provide an apples-to-apples check for that method against the spatial correlation solution?

(2) The author of Ref. 8 has recently derived an asymptotic expression for the maximum, or latent, shift of the cross-correlation component. This is (where B is the number of blades)

$$shift = \frac{1}{\sqrt{5}}\frac{J}{\pi}\sqrt{\nu^2+\left(\frac{R_t/\Lambda}{B}\right)^2}$$

where v = 1 and 2 for the blade-rate frequency and its first harmonic, respectively. J is the advance ratio. R_t is the rotor tip radius. The question is, did the calculations of the cross-correlation component by itself follow the above equation, as has been the case for the predictions in Ref. 8?

AUTHORS' REPLY

(1) The correlation approach is easy to understand and follow. Comparisons of the spectrum and correlation approaches are not valid because of the simplification used after Equation (6) for the spectrum method. As mentioned in the paper, the triple integrals of wave number in the spectrum method is impractical to solve and is not performed. This integration would be necessary to compare with correlation method results.

(2) Dr. Martinez recently derived an analytical asymptotic expression for hump ship to higher than the blade rate. We have checked our x-θ numerical correlation results, which indicate the peak shift on this component follows your formula.

DISCUSSION

D. Thompson
Pennsylvania State University, USA

This paper presents an important improvement to the theory of propeller unsteady response to a turbulent inflow. The investigation is thorough, and the paper is well organized and written with the exception of some minor grammatical and typographical errors.

It would have been interesting to see the results of the study of the unsteady thrust sensitivity to advance ratio change, Figure 13, plotted in terms of nondimensional values. For instance, in Figure 13 the variations in advanced ratio were obtained for constant shaft RPM; otherwise, the center of the spectral humps would move with frequency. A good nondimensional frequency would perhaps be frequency divided by blade rate frequency. Operating at off-design advance ratio changes the steady thrust. A good nondimensional unsteady thrust would perhaps be through division by the steady thrust at each advance ratio considered. A presentation of the results in this fashion would add to the interpretation.

AUTHORS' REPLY

We appreciate Dr. Thompson's comment. Fig. 14 is a nondimensional plot of Fig. 13, where the frequency is nondimensionalized by the blade rate frequency as suggested by Dr. Thompson, and the force is normalized by the velocity's third power. The unsteady thrust is not rendered by the steady thrust because the unsteady loading is not proportional to the steady force mathematically. For practical purposes, we could have also plotted the unsteady thrust in terms of percentage of the steady thrust. Thank you for your suggestion.

DISCUSSION

M. Sevik
David Taylor Model Basin, USA

It is with pleasure that I comment on an excellent paper that deals in a comprehensive manner with the unsteady forces generated by a turbulent flow on a rotating propeller. This subject, which was also of interest to me, resulted in a paper that first appeared

in the Proceedings of the Seventh Symposium on Naval Hydrodynamics, held in Rome, Italy, in 1968. The humps in my experimental data were not explained by my theory. They are explained in the present paper, however, by the time-dependent terms in equation (26) which were omitted in my original equation (30). In addition, the authors also predict time-dependent side forces, while my paper only dealt with the fluctuating thrust. I agree with the authors that future experiments should include simultaneous measurements of unsteady force and turbulence. The characteristics of the turbulent flow were not measured in my experiments on the assumption that a distance of 20 mesh sizes between the propeller and the grids would ensure reasonable isotropy of the turbulence.

The practical application of the theory in the wake of a ship will require knowledge of the governing flow parameters, which are difficult to measure or predict. The theory will also require changes in order to deal with flows that are much more complex than heretofore considered. The authors' task is, therefore, only partly finished.

AUTHORS' REPLY

We thank Dr. Sevik, who is a pioneer in this subject, especially noted for his contribution to the correlation approach we adopted here, for his discussion. We agree with Dr. Sevik's comments that the application of this theory to the wake of a ship is more complex than we considered here. A study of the importance of turbulence characteristics for this kind of flow field is being conducted at ARL/PSU. Preliminary data indicate that the effect of appendages on thrust spectrum is very small.

Session XIV

Propulsor Hydrodynamics and Hydroacoustics

Numerical Calculation of the Viscous Flow Around a Rotating Marine Propeller

K.-J. Oh (Kyungnam University, Korea),
S.-H. Kang (Seoul National University, Korea)

ABSTRACT

Reliable and accurate prediction of viscous flow around a marine propeller operating at the stern is of pratical importance for design and performance prediction of propellers. A computer code was developed in the present study for the full viscous flow simulation around the marine propeller at the stern and it's performance was investigated using the available data. The continuity and Navier-Stokes equations with a standard k-ε model in the rotating coordinate fixed on the propeller are numerically solved using FVM.The predicted profiles of circumferentially averaged velocity and turbulent kinetic energy show a good agreement with the measured ones at the downstream of the propeller, while there are significant discrepancies in the near wake. A vortex-like core with low velocity inside associated with the formation of the tip vortex and the location of maximum axial velocity on the suction side of the blade were observed in the simulation. Flow structure observed in the experiment were confirmed in the simulation, however not quantitatively. The blade wake was diffused too much in comparison with the measured one.

NOMENCLATURE

a_i	coefficients in the descretized eq.
b_j^i	transformation matrix
C_μ, C_D, C_1, C_2	turbulence model constants
D_p	diameter of the propeller
E	constant
J	advance ratio or Jacobian
k	turbulent kinetic energy
L	body length
m	mass flow rate
N	rotational speed of the propeller
n	normal distance from the surface
M_{xx}	axial momentum deficit parameter
$M_{\theta x}$	tangential momentum parameter
P	pressure
R_e	radius of the external boundary
R_h	radius of the hub
R_p	radius of the propeller
S_ϕ	source term for each variables
U,V,W	velocity component in x,r,θ dir.
x,r,θ	cylindrical coordinate
ε	dissipation rate of kinetic energy
ϕ	specific variable
Γ_ϕ	diffusion coefficient of ϕ
κ	von Karman constant
ρ	density
σ_k, σ_e	turbulence model constants
τ_w	wall shear stress
ω	rotational speed of the propeller
ξ, η, ς	boundary fitted coordinate

INTRODUCTION

Modern propeller design methods are mainly based on the inviscid flow theory, with various viscous effects taken into account only through empirical information concerning balde drag and wake. The hull and propeller interaction, which is also one of the most important phenomena to understant the ship propulsion efficiency, is strongly influenced by viscous effects. Reliable and accurate prediction of viscous flow around a marine propeller operating at the stern is of pratical importance for design and performance prediction of propellers. The function and geometry of a propeller are similar to those of general turbomachines, but the flow features become more complicated due to unsteadiness, three-dimensionality, and high level of turbulence. It is also still difficult job to reasonably simulate the vortex type of flow near the tip and hub.

Various numerical methods have been developed in the past for the two or three dimensional flows, compressible or incompressible flows, inviscid or viscous flows, and steady or unsteady flows. Techniques for turbomachinery flow computations have reached a high level of maturity. However, there is still a need of calibration of the computation even for the two-dimensional cascade flow[1]. Only a few cases of viscous flow simulation of marine propeller have been reported in the past. Recently, Stern and Kim[2] presented the

calculation results of the flow through a propeller with rectangular blades using Navier-Stokes analysis.

On the other hand, very little information is available on the details of the unsteady, turbulent flow behind a body-propeller combination, not only for the physical understanding of the flow structure but also for the assesment of numerical methods. The detailed measurement around the propeller is very difficult to carry out in the rotating blades as well as in the wake. Recently, Hyun[3], Hyun and Patel[4, 5] experimentally investigated flows behind a propeller operating on the axisymmetric body in the wind tunnel. They reported interesting features of the propeller wake and provided extensive data, i.e. circumferentially averaged and 3-dimensional phase averaged values of mean velocity components and Reynolds stresses. Any numerical investigations for the above measurements are not reported yet.

The objectives of the present study is to develope a computer code for the three-dimensional viscous flow simulation around the marine propeller at the stern and investigate the performance using the available data [4,5]. The continuity and Navier-Stokes equations with a standard k-ε model were solved using Finite Volume Method. The simulated results are to be discussed below.

GOVERNING EQUATION

Configuration of the propeller mounted on the axisymmetric stern is shown in Fig. 1. Goveming equations for the incompressible, steady, and turbulent flow are given by the continuity and the Reynolds averaged Navier-Stokes equations. They are written in the rotating cylindrical coordinate system (x, r, θ) fixed on the propeller blade of constane angular velocity ω. Reynolds stresses are modelled using a standard k - ε model. The values of k and ε are obtained from their transport equations. Modified version of k - ε model for low- intensity turbulence, anisotropic turbulence, rotating effects on turbulence, etc. have been investigaed. Since they are not well developed yet for the general purposes, a simple one is used in this study. The general form of the governing equations can be written as follow.

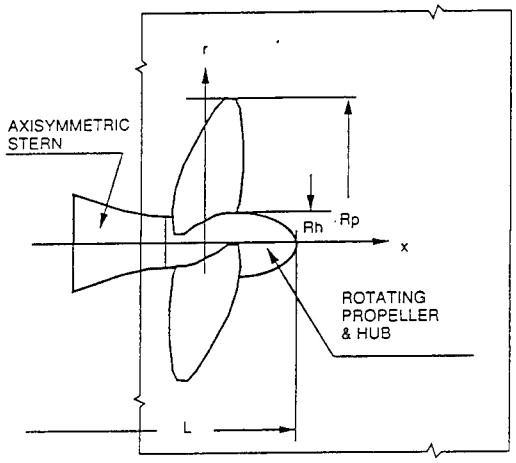

Fig.1 Configuration of a body-propeller, flow domain for simulation and cylindrical coordinate.

$$\frac{\partial}{\partial x}(U\phi)+\frac{1}{r}\frac{\partial}{\partial r}(rV\phi)+\frac{1}{r}\frac{\partial}{\partial \theta}(W\phi)=\frac{\partial}{\partial x}\left(\Gamma_\phi\frac{\partial \phi}{\partial x}\right)+\frac{1}{r}\frac{\partial}{\partial r}\left(r\Gamma_\phi\frac{\partial \phi}{\partial r}\right)+\frac{1}{r^2}\frac{\partial}{\partial \theta}\left(\Gamma_\phi\frac{\partial \phi}{\partial \theta}\right)+S_\phi \quad (1)$$

where ϕ, Γ_ϕ, and S_ϕ denote the flow variables, diffusion coefficients and source terms respectively (cf. Table 1).

TRANSFORMATION OF GOVERNING EQUATIONS

The flow domain is schematically shown in Fig. 1, which is bounded by the propeller blade passage, the propeller hub and body surface, the axis of wake, upstream and downstream sections, and the outer boundary. A non-orthogonal boundary fitted coordinate system (ξ, η, ζ) is used to transform the phycal domain to a rectangular computational domain. The transformation of the independent variables (x, r, θ) in the governing equations, leaving the flow variables ϕ in the original cylindrical coordinate, can be expressed as follow [6,7].

$$\frac{\partial}{\partial \xi}\left(b_1^1U\phi+b_2^1V\phi+b_3^1W\phi\right)+\frac{\partial}{\partial \eta}\left(b_1^2U\phi+b_2^2V\phi+b_3^2W\phi\right)+\frac{\partial}{\partial \zeta}\left(b_1^3U\phi+b_2^3V\phi+b_3^3W\phi\right)=\frac{\partial}{\partial \xi}\left(\Gamma_\phi Jg^{11}\frac{\partial \phi}{\partial \xi}\right)+\frac{\partial}{\partial \eta}\left(\Gamma_\phi Jg^{22}\frac{\partial \phi}{\partial \eta}\right)+\frac{\partial}{\partial \zeta}\left(\Gamma_\phi Jg^{33}\frac{\partial \phi}{\partial \zeta}\right)+S_\phi \quad (2)$$

where b_j^i is the transformation matrix which is represented by the partial derivatives of (x, r, θ) with respect to (ξ, η, ζ). J is Jacobian, g^{ij} is metric tensor, and S_ϕ is the source term in the transport equation for each variables.

BOUNDARY CONDITION

Bonudary conditions imposed on each boundaries are as follow;

(1) Upstream section; The values of the 3 components of velocity and the turbulent kinetic energy and its dissipation rate are prescribed. The pressure is not required, since the staggered grid system is chosen in the present calculation. Determination of the upstream condition is dependent of the interaction between the hull and the propeller. A simple viscous flow calculation is carried out for the extended region around the axisymmetric body with the propeller modelled by the

uniform distribution of momentum source corresponding to the propeller thrust.

(2) Downstream section; The downstream section is located far from the body and the propeller, and zero gradient condition is assumed for all variables.

(3) Blade and hub surface; To avoid the difficulty in resolving the near wall turbulent flow, the wall function is used at the surface. The grid points next to the wall are located in the fully turbulent layer where the logarithmic law is satisfied and the velocity vectors are assumed to be collateral. Then the wall shear stress τ_w and the turbulence quntities at the wall are estimated as follows.

$$\frac{\tau_w}{\rho} = \kappa V_t C_\mu^{1/4} \frac{\sqrt{k}}{\ln(E \cdot n^+)}, k = \frac{\tau_w}{\rho\sqrt{C_\mu}}, \varepsilon = \frac{C_\mu^{3/4} k^{3/2}}{\kappa \cdot n} \tag{3}$$

where V_t is the magnitude of the velocity at the first grid point from the wall, n is normal distance from the wall, and k and E are 0.42 and 9.793 respectively.

(4) External boundary; It is placed sufficiently far from the propeller. Uniform free stream without turbulence is assumed there.

$$U = U_0, W = -\omega R_e, k = \varepsilon = 0, P = P_0 \tag{4}$$

The value of radial velocity at the external boundary is determined from the continuity equation.

(5) Periodic surfaces; Periodic boundary conitions are enforced on the periodic surfaces.

Table 1. ϕ, Γ_ϕ, and S_ϕ in the governing equations.

ϕ	Γ_ϕ	S_ϕ
1	0	0
U	ν_e	$-\frac{1}{\rho}\frac{\partial P}{\partial x}+\frac{\partial}{\partial x}\left(\nu_t\frac{\partial U}{\partial x}\right)+\frac{1}{r}\frac{\partial}{\partial r}\left(r\nu_t\frac{\partial V}{\partial x}\right)+\frac{1}{r}\frac{\partial}{\partial \theta}\left(\nu_t\frac{\partial W}{\partial x}\right)$
V	ν_e	$-\frac{1}{r}\frac{\partial P}{\partial r}+\frac{\partial}{\partial x}\left(\nu_t\frac{\partial U}{\partial r}\right)+\frac{1}{r}\frac{\partial}{\partial r}\left(r\nu_t\frac{\partial V}{\partial r}\right)+\frac{1}{r}\frac{\partial}{\partial \theta}\left(\nu_t\frac{\partial W}{\partial r}\right)-\frac{1}{r^2}\frac{\partial}{\partial \theta}(\nu_t W)-\frac{2\nu_e}{r^2}\frac{\partial W}{\partial \theta}-\nu_e\frac{V}{r^2}-\nu_t\frac{V}{r^2}+\frac{W^2}{r}+r\omega^2+2\omega W$
W	ν_e	$-\frac{1}{\rho r}\frac{\partial P}{\partial \theta}+\frac{\partial}{\partial x}\left(\frac{\nu_t}{r}\frac{\partial U}{\partial \theta}\right)+\frac{1}{r}\frac{\partial}{\partial r}\left(\nu_t\frac{\partial V}{\partial \theta}\right)+\frac{1}{r}\frac{\partial}{\partial \theta}\left(\frac{\nu_t}{r}\frac{\partial W}{\partial \theta}\right)-\frac{1}{r}\frac{\partial}{\partial r}(\nu_t W)+\frac{2}{r}\frac{\partial}{\partial \theta}\left(\frac{\nu_t}{r}V\right)-\nu_e\frac{W}{r^2}-\frac{VW}{r}+\frac{\nu_t}{r}\frac{\partial W}{\partial r}+\frac{\nu_t}{r^2}\frac{\partial V}{\partial \theta}-2\omega V$
k	$\frac{\nu_e}{\sigma_k}$	$G-C_D\varepsilon$
ε	$\frac{\nu_e}{\sigma_\varepsilon}$	$\frac{\varepsilon}{k}(C_1 G-C_2\varepsilon)$

note: $G=\nu_t\left[2\left\{\left(\frac{\partial U}{\partial x}\right)^2+\left(\frac{\partial V}{\partial r}\right)^2+\left(\frac{1}{r}\frac{\partial W}{\partial \theta}+\frac{V}{r}\right)^2\right\}+\left(\frac{\partial U}{\partial r}+\frac{\partial V}{\partial x}\right)^2+\left(\frac{1}{r}\frac{\partial U}{\partial \theta}+\frac{\partial W}{\partial x}\right)^2+\left(\frac{1}{r}\frac{\partial V}{\partial \theta}+\frac{\partial W}{\partial r}-\frac{W}{r}\right)^2\right]$

$$\nu_e = \nu + \nu_t, \nu_t = C_\mu\frac{k^2}{\varepsilon}$$

$$C_\mu = 0.09; C_D = 1.0; C_1 = 1.44; C_2 = 1.92; \sigma_k = 1.0; \sigma_\varepsilon = 1.3$$

NUMERICAL SCHEME

The governing equations are discretized using the Finite Volume Method and the hybrid scheme for the convective terms in the staggered grid system [8]. The scalar variables P, k, ε are located at grid node, while velocity components are placed between scalar nodes. Such a grid system has a benefit of having the velocity at the boundaries of the scalar cells where they are needed in integrating the convection term. Furthermore, the pressure nodes are located on either side of the velocity node and it is easy to calculate the pressure gradient term in the momentum equations. The final form of the discretized equations can be expressed as below [6,7,8].

$$a_p\phi_p = a_N\phi_N + a_S\phi_S + a_E\phi_E + a_W\phi_W + a_D\phi_D + a_U\phi_U + \overline{S}_\phi \tag{5}$$

The subscript P refers to a grid node to be considered and the subscript U, D correspond to the upstream and downstream grid points respectively. The neighbouring grid point in the section are denoted by N, S, E, W, and a_N, a_S, a_E, a_W etc. represent the diffusion and convection coefficients at each corresponding surface of the control volume.

Since the velocity field obtained using the previous values of pressure at each iteration does not satisfy the continuity equation, they are corrected using the corrected values of pressure, which are obtained using the continuity equation, i.e. the SIMPLE algorithm [8]. The discretized form of pressure correction equation is obtained in the form of eq. (5).

CALCULATIONS

Model Propeller

The developed numerical method is applied to the propeller investigated by Hyun [2] and Hyun and Patel

[3, 4] in the wind-tunnel. The propeller was mounted at the stern of an axisymmetric body, which was designed modifying the Afterbody 5 of Huang *et al.* [9]. The total length is L=151.61 cm. The diameter of the propeller $D_p=2R_p$=10.16 cm, and the hub-tip ratio of the propeller is R_H/R_p=0.2187. The propeller has three blades, the sections of which have NACA-66 thickness distributions. It was mounted at x/L=0.9755. The value of the freestream velocity and the number of rotations were U_o=16.5 m/s , N=200 rps respectively. The advance ratio of the the propeller J (= ND_p/U_o) was 0.812. The Reynolds numbers based on the based on the body length and the cord length at r/R_p of the propeller blade were 1.55×10^6 and 1.44×10^5.

Extensive measurements were carried out at the down stream of the propeller using a five hole pitot tube and a hot-wire anemometer. Measured data, i.e. mean velocity, static pressure, the turbulent kinetic energy, and Reynolds stresses, are available for the assesment of the present numerical method.

Grid Generation and Estimation of Inlet Conditions

Since the propeller operates at the stem, the calculation domain should cover the whole field of the flow including the body as well as the propeller. However, the number of grid point is still limited by the computer capacity and the main interest of the present study is to simulate the flow near the propeller. The computational grid was algebraically generated in the limited domain, which is bounded by two neighbouring blades, the sections of x/D_p = - 0.15 at the upstream and of x/D_p = 6.0 at the downstream locations. The external boundary is located at r/D_p= 5.5 , which is far enough from the propeller. The numbers of grid point were 132, 40, and 20 in the streamwise, radial, and circumferential (blade-to-blade) directions respectively. The finer meshes are allocated near the leading and trailing edges, propeller tip, and the blade and body surfaces considering rapid changes in the velocity fields. The generated meshes at the ξ =1, η =2, and ζ =1 surfaces are shown in Fig2.

Since the inlet section of x/D_p=-0.15 locates near the propeller, the flow is strongly distorted due to the body and propeller interaction. The boundary conditions, i.e. the values of each velocity components and the turbulent kinetic energy and it's dissipation rate should be properly estimated there. The boundary conditions were estimated by axisymmetric viscous flow calculation in the whole domain including the body and the propeller. The interaction of the body and the propeller was taken into account in the calculation, assumming the acting propeller to be the uniform distribution of momentum source corresponding to the propeller thrust. The calculated streamwise and radial components of velocity at the inlet position with and without the propeller are compared with measured values in Figs. 3 and 4. The flow near the body is axially accelerated and radially inward motion is induced due to the propeller suction

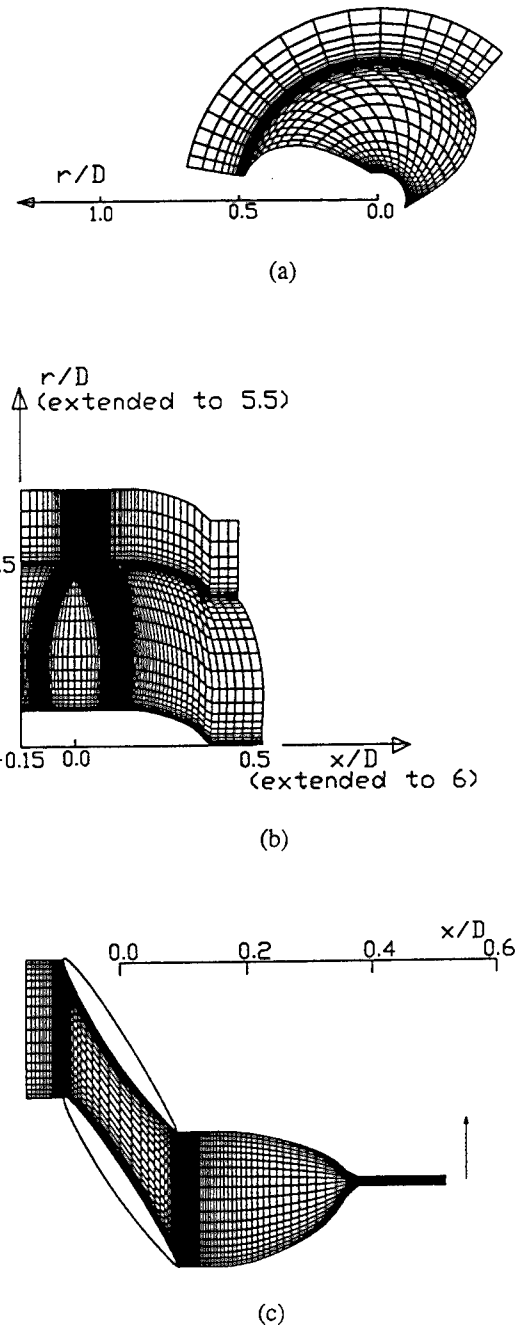

Fig.2 Parts of the generated mesh on (a) ξ =1.0, (b) η =2.0, (c) ζ =1.0 planes.

effect. The streamwise component of velocity are reasonably predicted in comparison with measured values, except near the tip of the propeller.

Solutions are assumed to be converged when the residual sources of each variables reduce to 1% of the reference values, and the converged solution is obtained after about 1000 iterations and CPU time of 5.5 hours on CRAY-2S supercomputer.

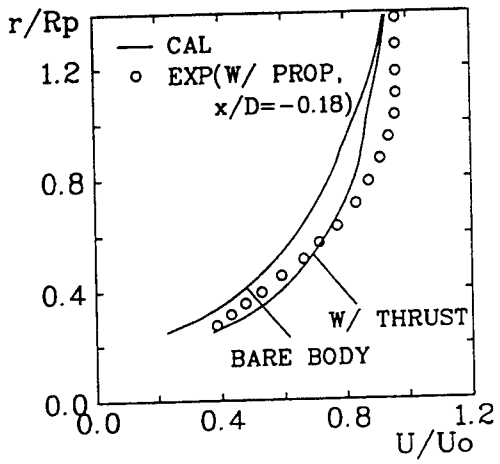

Fig.3 Streamwise velocity components at the inlet with and without the propeller.

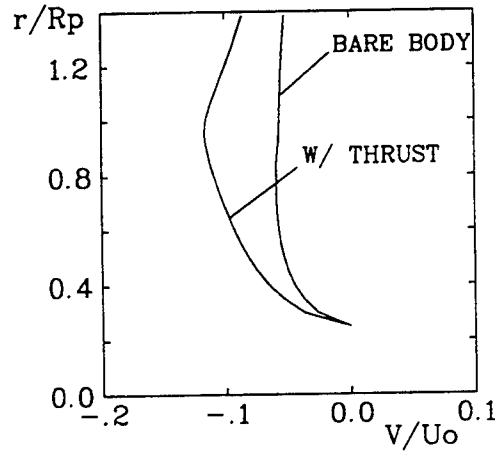

Fig.4 Radial components of velocity at the inlet with and without the propeller.

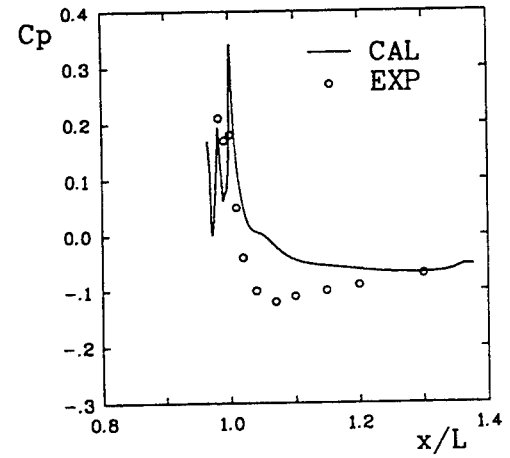

Fig.5 Calculated and measured[2] circumferentially averaged values of pressure coefficient along the hub and wake center line.

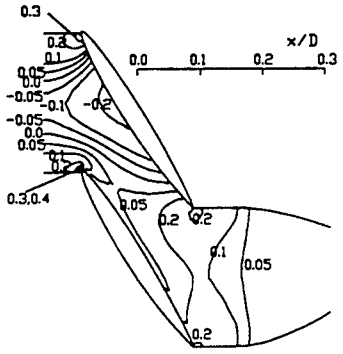

Fig.6 Contours of equi-pressure coefficient on the blade to blade surface of the hub.

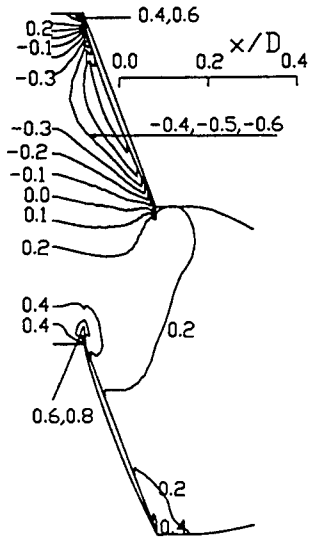

Fig.7 Contours of equi-pressure coefficient on the blade to blade surface of r/R_p=0.7.

RESULTS AND DISCUSSION

The circumferentially averaged values of the pressure coefficient along the hub and the wake center line are presented and compared with measured values in Fig.5. The pressure at the upstream of the propeller is higher than the ambient pressure due to the deceleration over the stern and rapidly increses through the propeller. The pressure significantly changes over the tail and in the the wake. After rapid decrease in pressure due to the propeller, the pressure increases again up to the stagnation point at the tail. It monotonically recovers to

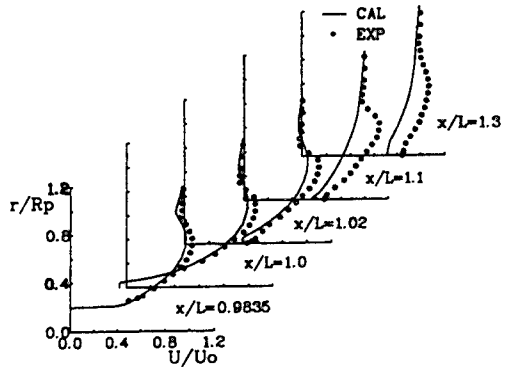

Fig.8 Calculated and measured[2] circumferentially averaged profiles of axial velocity compenent.

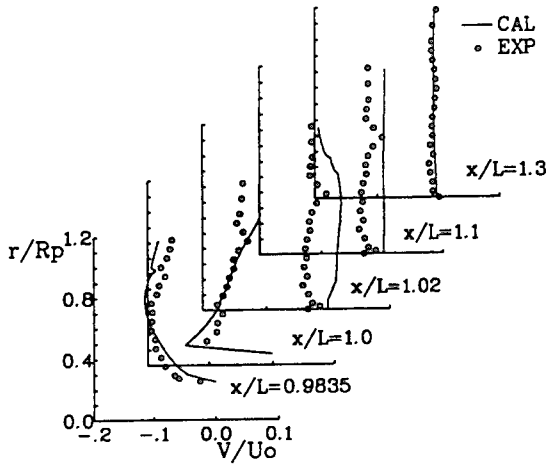

Fig.9 Calculated and measured[2] circumferentially averaged profiles of radial velocity compenent.

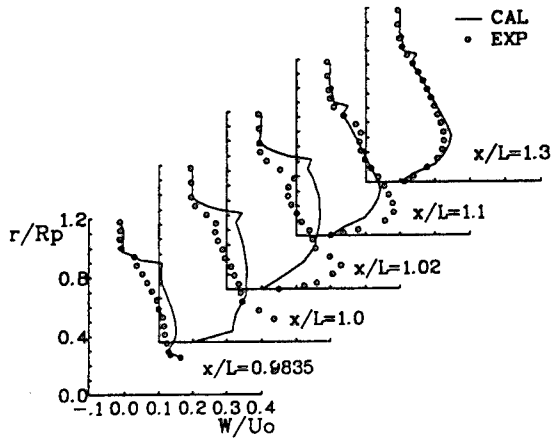

Fig.10 Calculated and measured[2] profiles of tangential velocity compenent.

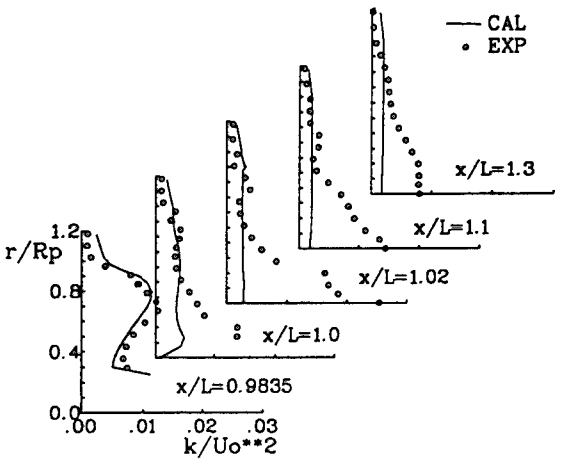

Fig.11 Calculated and measured[2] circumferentially averaged profiles of turbulent kinetic energy.

the value of the ambient pressure in the wake, however the measured values recovers after showing the minimum value (Fig.5). The reason of the discrepancy is not clear, and the flow acceleration and rotational effect of the propeller and hub may be not fully taken into accout in the simulation. Figs. 6 and 7 show the pressure coefficient distributions in the blade to blade surfaces of the hub and r/R_p=0.7 respectively. The staganation point appears near the leading edge of the pressure side. The pressure variations over the pressure side are not large along the blade. However, there appears strong adverse pressure gradient over the suction side. The location of the minimum pressure on the suction side moves to the trailing edge as the radial distance increases.

Circumferentially averaged values of mean velocities at the downstream of the propeller are compared with measured values in Figs. 8, 9 and 10. The axial acceleration of the flow due to the propeller is observed in the axial velocity profiles at x/L = 0.9835, 1.0, 1.02 in Fig.8. The axial velocities have their maximum values at r/R_p=0.7, and approaches to the free stream velocity. At the tail of body, x/L=1.0, a small separation region is observed in the prediction. Comparison of the predicted with the measured velocity profiles shows a reasonable coincidence up to the one diameter downstream of the propeller, while there are significant discrepancies in the wake. At x/L=1.1 and 1.3, the flow maintains the acceleration effect of the propeller and have a peak value in the axial velocity, however the prediction does not show this feature at near wake. As mentioned befor, it is because the flow acceleration and rotational effect of the propeller and hub may be not fully taken into accout in the simulation. Radial velocitie profile at x/L=0.983 shown in Fig.9 has it's maximum values at r/R_p=0.75. At x/L=0.983 and 1.0, the predicted values show good agreement with the measured profiles and rapid changes in the radial velocity was simulated near the hub. At x/L=1.02 and

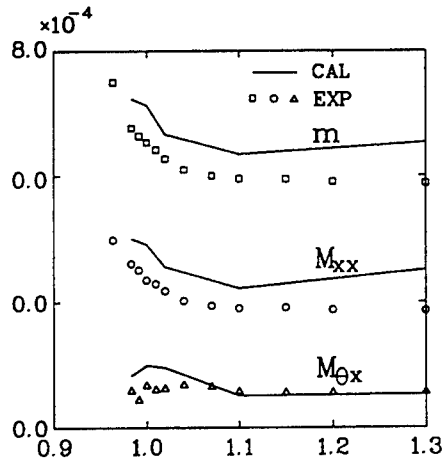

Fig.12 Variations of mass and momentum deficit parameters.

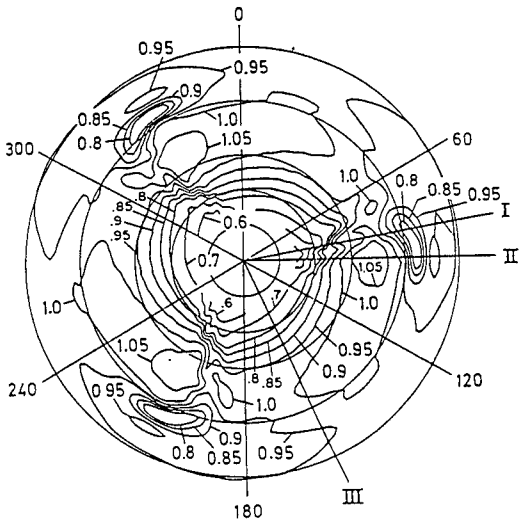

(a)

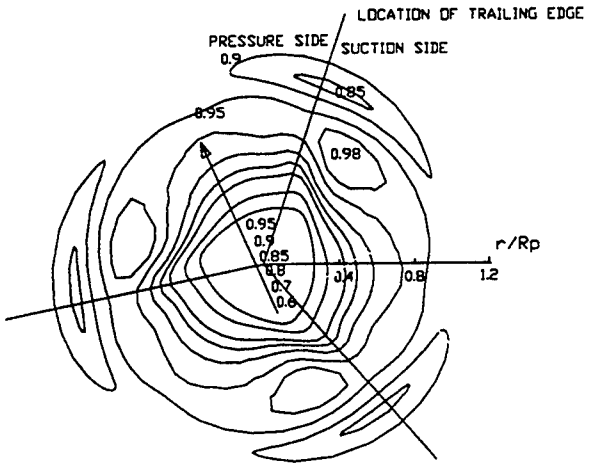

(b)

Fig.13 Axial velocity distributions at $x/L = 0.9835$; (a) measured [2], (b) calulated values.

1.1, the flows are almost parallel to the axis in the calculation, and these are the consistant with the under-estimation of the axial velocity profiles. Averaged values of swirl velocities are reasonably predicted in the comparison with the measured profiles in Fig.10. The prediction of rapid variations of swirl velocity near the tip confirms the measurements. The magnitudes of circumferential velocity increase from the outside to the hub like a free vortex type of flow, however they reduce to zero on body surface and the centerline of the wake.

Averaged turbulence kinetic energy distributions are compared with measured profiles in Fig.11. At the just downstream of the propeller, the turbulence kinetic energy distribution was nicely calculated and showed it's maximum value at the location of the maximum axial velocity. This is due to the large value of generation rate of the turbulence kinetic energy over this region. However, in the downstream of the wake, predicted values of the turbulence kinetic energy is considerably smaller than those of the measured ones.

Momentum deficit parameters in the wake are important to estimate the propeller thrust and torque. Integral parameters for the mass and the momentum deficts are defined as follows.

$$m = \frac{2\pi\rho}{U_o L^2}\int_0^{\delta}(U_o - U)rdr \tag{6}$$

$$M_{xx} = \frac{2\pi\rho}{U_o^2 L^2}\int_0^{\delta} U(U_o - U)rdr \tag{7}$$

$$M_{\theta x} = \frac{2\pi\rho}{U_o^2 L^2}\int_0^{\delta} UWrdr \tag{8}$$

The estimated values of these parameters and measureed ones are shown in Fig.12. The mass and axial momentum deficts rapidly decrease in the near wake and are gradually decrease to have asymtotic values in the far wake. On the other hand, the circumferential momentum generated by the swirlling flow remains constant in the wake. The values of the mass and axial momentum deficts from the prediction are somewhat higher than those of the measurements. This discrepancy is partiallay due to the difference between the estimated and measured values of the inlet boundary conditions. Over-all simulation errors are accumulated in these integral parameters. Considering the error in the parameters at the inlet location, the prediction error is not so significant.

Measurements of three-dimensional phase-averaged mean velocity field and Reynolds stresses were made with a triple sensor hot wire [3,4,5]. They provide the true information of complexity of the flow and

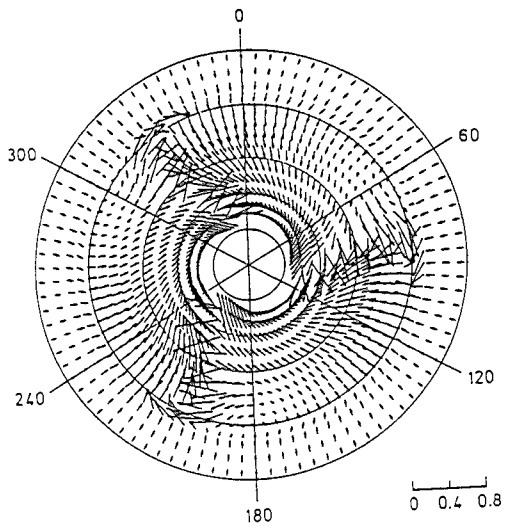

(a)

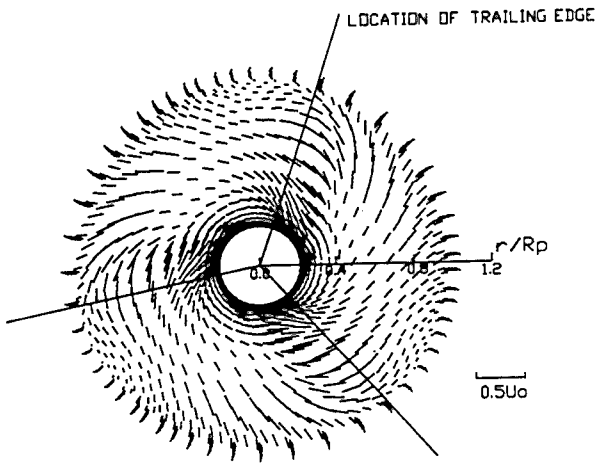

(b)

Fig.14 Vetor plots of cross flow at $x/L = 0.9835$;
(a) measured [2], (b) calulated values.

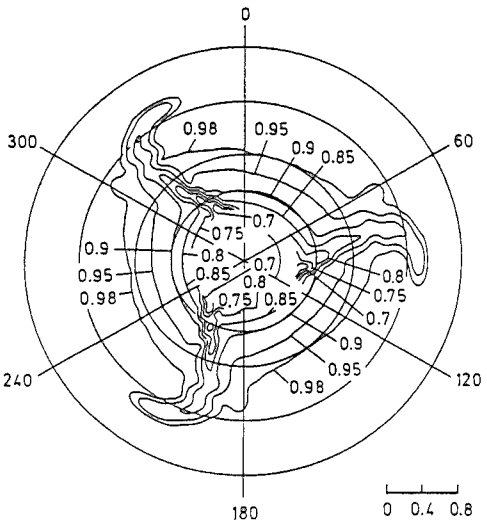

(a)

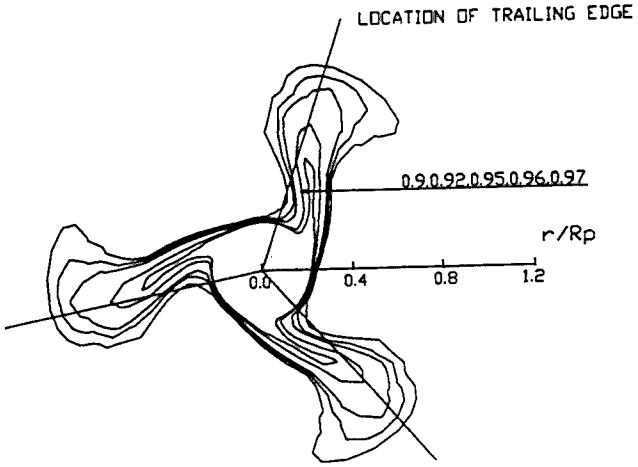

(b)

Fig.15 Streamwise velocity contours at $x/L = 0.9835$ in moving pitchline coordinate;
(a) measured [2], (b) calulated values.

contribution of local aspects of the flow in the blade wake, at the intersection of the hub and the blade, and near the tip. The calculated and measured axial velocity contours at x/L=0.983 are shown in Fig.13. Measurement shows a vortex-like core with low velocity inside near r/R_p=0.96, which is associated with the formation of the tip vortex. The wake of the main span of the propeller appears in the region between 75 to 90 degrees in the phase plane. The location of maximum axial velocity was observed on the suction side and was indicated by a core of high velocity around 95 degree and r/R_p=0.96, where the propeller was disigned to produce maximum circulation. All the aspects of the flow are confirmed in the simulation. However, the minimum value of the velocity in the tip vortex is 0.85 (the measured value was 0.80) and the maximum value of the velocity in the main core is 0.98 (the measured value was 1.05). The changes in axial velocity across the blade wake observed in the experiment do not appear in the calculation. The projection of the velocity vectors are presented in Fig.14. Out side the blade wakes, the radial velocity is generally negative. Within the blade wakes, the flow direction radially inward on the suction side and outward on the pressure side. The simulated trend of radial velocity variation is coinside with the measurement, however no outward motion on the pressure side. The rapid change in circumferential velocity across the wake is also confirmed. The swirling velocity rapidly reduces near the tip, however the formation of the hub and tip vortex do not observed in the

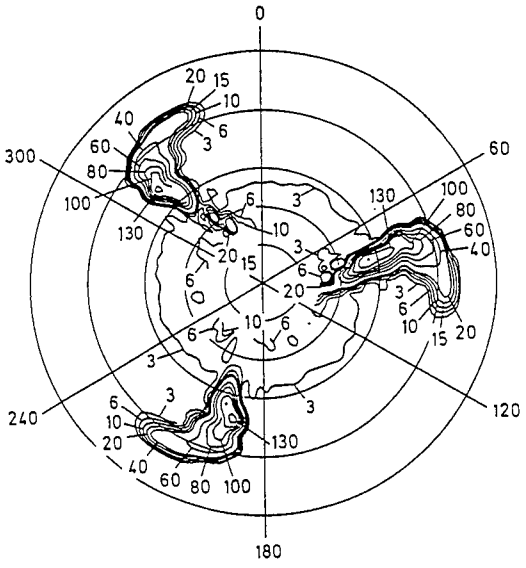

(a)

(b)

Fig.16 Turbulent kinetic energy distributions at $x/L = 0.9835$; (a) measured [2], (b) calulated values.

simulation. Meshes in the study seems not enough to have fine resolution.

Hyun and Patel plotted velocity component in the planes perpendicular to the constant pitch surface of the propeller, which is to capture the flow structure more accurately. Measured and calculated streamline components of velocity are shown in Fig.15. The general view of velocity contour shows the shape and the thickness of the wake center plane and tip vortex formation. Finally turbulent kinetic energy distributions are shown in Fig.16. The figure shows that high turbulence levels are confined within the blade wake. There is large discrepancy between the calcualted and measured contours. The maximun value of kinetic energy was as high as 0.130 at the maximum load radius of the suction surface, where the radial and circumferential gradients of mean velocity are large. Simulated maximum values is 0.030 at the same location. If we remember that the circumferentially averaged distribution of kinetic energy was in good agreement with measured one in Fig.11, the total kinetic energies coinside each other. The layer of turbulent kinetic energy was diffused too much across the blade wake in comparison with the measured one.

CONCLUSION

Three dimensional viscous flow simulation around the marine propeller was carried out and compared with the available data. The important results and conclusion are summarized below.

1. Comparison between the predicted and the measured velocity profiles shows a reasonable agreement in the downstream of the propeller, while there are significant discrepancies in the near wake. At the just downstream of the propeller, the turbulence kinetic energy distribution was nicely calculated and showed it's maximum value at the location of the maximum axial velocity. However, in the downstream of the wake, predicted values of the turbulence kinetic energy is considerably smaller than those of the measured ones.

2. A vortex-like core with low velocity inside associated with the formation of tip vortex and the location of maximum axial velocity on the suction side were observed in the simulation. All the aspects of the flow were confirmed in the simulation, however not quantitatively.

3. The maximun value of kinetic energy (0.130 in measurement) was underpredicted as low as 0.030 at the same location. The layer of turbulent kinetic energy was diffused too much across the blade wake in comparison with the measured one.

ACKNOWLEDGEMENT

The present work was partially supported from the Turbo and Power Machinery Research Center founded by the Korea Science and Engineering Foundation. Dr. B.S. Hyun provided the measured data file.

REFERENCE

1. Kang, S.H., Lee, J.S., Kim , Y.H., and Kim, K.Y., "Numerical Calculations of the Turbulent Flow through a Controlled Diffusion Compressor Blade in Cascade", Proceeding of ISROMAC-4, 1992.

2.Stern, F. and Kim, H.T., "Computation of Viscous Flow Around a Propeller-Shaft Configuration with Infinite-Pitch Rectangular Blades," Proc. 5th Int. Conf. Numerical Ship Hydrodynamics, Hiroshima, Japan. 1990.

3. Hyun, B.S., "Measurements in the Flow Around a Marine Propeller at the Stern of an Axisymmetric Body," Ph. D. Thesis, The University of Iowa, 1990.

4. Hyun, B.S. and Patel, V.C., "Measurements in the flow around a marine propeller at the stern of an axisymmetric body, Part 1: Circumferentially-averaged flow", Experiments in Fluids, 11, 1991, pp.33-44.

5. Hyun, B.S. and Patel, V.C., "Measurements in the flow around a marine propeller at the stern of an axisymmetric body, Part 2: Phase-averaged flow", Experiments in Fluids, 11, 1991, pp.105-117.

6. Kang, S.H., Oh, K.J. and Kobayashi,T., " A Viscous Flow Calculation of the Stern Flow", KSME Journal, 5(1), 1991, pp.36-44.

7. Oh, K.J. and Kang,S.H., "Full scale Reynolds number effects for the viscous flow around the ship stern", Computational Mechanics, 9(2), 1992.

8. Patankar, S.V., Numerical Heat Transfer and Fluid Flow, Mcgraw-Hill Book Company,1980.

9. Huang, T.T., Groves, N.C., and Belt, G.S., "Boundary Layer Flow on an Axisymmetric Body with an Inflected Stern," DTNSRDC Report 801064, David Taylor Research Center, MA. ,1980.

Unsteady Nonlinear Vortex Lattice Method for Prediction of Propeller Performances

G.-Q. Wang[1], L.-X. Xu[2], C.-J. Yang[1], M. Tamashima[3], M. Ogura[3]
([1]Shanghai Jiao Tong University, China; [2]Shanghai Merchant Ship Design and Research Institute, China; [3]West Japan Fluid Engineering Laboratory Co., Ltd., Japan)

ABSTRACT

The paper presents an unsteady nonlinear vortex lattice method (UNVLM) for calculations of propeller hydrodynamic performances, in which the shape and rollup of the wake vortex sheet are not known as a priori, but determined as part of solution by the time-dependent vortex shedding procedure. Calculations for the performances of a conventional propeller DTNSRDC-4118 and a highly skewed propeller DTNSRDC-4383 are performed by this method. The influence of the blade tip vortex separation upon the performances of propeller is investigated. Comparison of these predictions with experimental data indicates that the agreement is satisfactory. In addition, the time-dependent deformation of shed vortex sheet and its final stable geometric shape are also shown clearly. Such information may be of practical value in studying the geometric shape of free vortex wake and establishing a reasonable free vortex wake model.

NOMENCLATURE

a_{ij}^k — Normal component of velocity at the ith control point, induced by the bound vortex ring with unit strength circulation around the jth element on the kth blade, also called influence coefficient;
b_{ij}^k — Influence coefficient of the trailing vortex ring Γ_{wj} on the kth blade;
c — Subscript denoting blade camber surfaces;
$C_{0.75R}$ — Chord length at $0.75R$;
c_{ij}^k — Influence coefficient of the tip or leading edge separated vortex ring Γ_{sj} on the kth blade;
C_f — Friction drag coefficient;
C_p — Pressure coefficient;
C_s — Leading edge suction coefficient;
D — Propeller diameter;
d_{ij}^k — Influence coefficient of the jth line source element Q_j on the kth blade;
$f(s)$ — Camber distribution, see Fig.1;
K — Number of propeller blades;
K_T, K_Q — Thrust and torque coefficients;
L — Number of separated vortex rings shed from tip and leading edges, or the number of tip separated vortex rings without leading edge separation;
M — Number of trailing vortex rings shed from the trailing edge;
M_B — Number of spanwise intervals;
$\mathbf{n}$ — Normal vector on camber surface;
$\mathbf{n}_i$ — Unit normal vector at the ith control point;
$\mathbf{n}_{nm}$ — Unit normal vector of the nmth vortex element;
n — Rate of revolution (rps);
N — Number of bound vortex rings, $N = M_B \times N_B$;
N_B — Number of chordwise intervals;
Q_j — Strength of jth concentrated line source representing blade thickness;
Q_{nm} — Strength of line source element;
R — Blade tip radius ($= D/2$);
r_H — Hub radius;
s — Nondimensional chordwise coordinate, $s = 0$ at the leading edge, $s = 1$ at the trailing edge;
$\mathbf{s}_0$ — Direction of the chordwise elements closest to the leading edge, positive towards the leading edge;
t — Time variable;
T, Q — Thrust and torque;
u, l — Subscripts denoting upper and lower sides of blade camber surfaces;
$\mathbf{U}$ — Local inflow velocity vector under

open water condition;

$\mathbf{U}_i$ — Inflow velocity at the ith control point;

$\mathbf{V}$ — Total velocity vector;

$\mathbf{V}_A$ — Advance velocity;

$(\mathbf{V}_m)_i$ — Mean value of resultant velocity on both sides of the camber surface at the ith control point;

$\mathbf{V}_{nm}$ — Total velocity at the nmth bound vortex element;

$x_m(r)$ — Blade rake, i.e. x-coordinate of midchord line;

x, y, z — Cartesian coordinates fixed on the propeller;

x, r, θ — Cylindrical coordinates fixed on the propeller;

Γ_{fj} — Strength of the jth bound vortex ring;

Γ^s_{lm} — Strength of the lmth spanwise vortex element;

Γ_{nm} — Strength of the nmth bound vortex element;

Γ_{sj} — Strength of the jth tip or leading edge separated vortex ring;

Γ_{wj} — Strength of jth trailing vortex ring;

ΔA_{nm} — Area of the nmth bound vortex ring;

δ_k — Blade index, $\delta_k = 2\pi(k-1)/K$, $k = 1, 2, ..., K$;

Δl_{nm} — Length of the nmth bound vortex or source element;

Δt — Time increment;

$\Delta \mathbf{V}_i$ — Tangential velocity jump across the camber surface;

$\theta_m(r)$ — Skew angle, i.e. angular coordinate of midchord line as measured from y-axis;

ρ — Density of fluid;

Φ — Velocity potential;

Ω — Angular speed of propeller, $\Omega = 2\pi n$;

1. INTRODUCTION

The effect of highly skewed propellers on reducing vibration forces and noise has been recognized and accepted by people gradually since 1960's. Investigations on the hydrodynamic performances of highly skewed propeller and its application to large or high speed ships have attracted growing attention of researchers in the world with the rapid increase in ship size and engine power and the development of computer techniques. However, the problems related to the hydrodynamic performances and strength analysis of highly skewed propeller are more complicated than conventional one due to its particular geometrical contour, so the further improvement on propeller theory is required, which promotes the development of propeller theory to a certain extent.

Two numerical lifting surface approaches have been developed and widely used in the predictions of hydrodynamic performances of the propeller, i.e. the mode function method and the discrete vortex lattice method. Recently much attention has been paid to the panel method to improve the accuracy of calculating pressure distributions on the propeller blades. The common shortcoming of those approaches is that the nonlinear effects of the wake shape are ignored and the geometric shape of free vortex wake, namely wake model has to be presumed. Obviously, it is unreasonable to apply the same presumed wake model to different propeller types and loads.

A new numerical lifting surface method, termed as an unsteady nonlinear vortex lattice method (UNVLM), has been developed for calculating the steady and unsteady flow about a three-dimensional thin wing with or without leading edge separation in the field of aerodynamics[1,2]. This method has also been applied successfully to the hydrodynamic performance prediction of the ship rudder and theoretical design of additional thrusting fins[3,4]. The present paper describes how the UNVLM has been extended to the calculation of hydrodynamic characteristics of propeller, in which the shape and rollup of the wake vortex sheets are not known as a priori, but are determined as part of solution by the time-dependent vortex shedding procedure. It is possible by using this method that the time-dependent deformation of shed vortex sheet and its final stable geometric shape are illustrated clearly, and the unsteady performances of propeller can be directly calculated. This method may also be used to investigate the dynamic characteristics of propellers at short start and stop conditions, and to consider problems of the tip and leading edge or only tip edge vortex separations on the propeller blades, provided that the location of the separating line and the vortex strength of the separation are specified in advance.

In present study, calculations for hydrodynamic performances of a conventional propeller DTNSRDC-4118 and a highly skewed propeller DTNSRDC-4383 with 72-degree skew angle are performed by UNVLM, in which two cases are investigated: one is under the condition of the attached flow, the other is the steady flow with tip separation on the propeller blades. The influence of tip separation on propeller performances is shown. Comparison of calculated

results with experimental data indicates that the agreement is satisfactory.

2. BLADE GEOMETRY AND SINGULARITY ARRANGEMENTS[5]

2.1 Blade Geometry

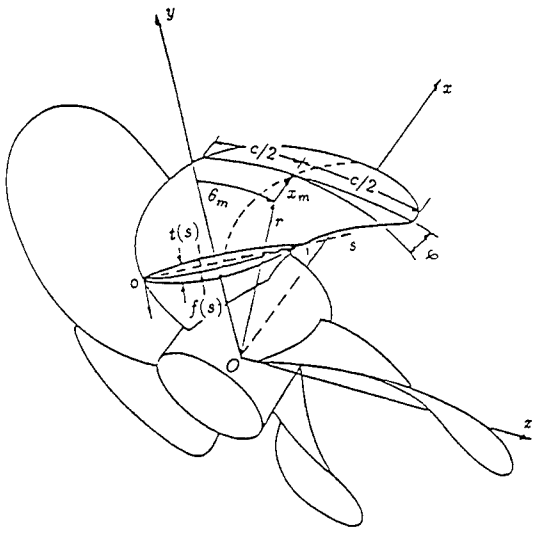

Fig.1 Coordinate system and blade geometry notation

As shown in Fig.1 the Cartesian coordinate system $O-xyz$ for the expression of blade geometry is fixed on the propeller, with x- axis defined as positive downstream, y-axis located on the reference line of a specified blade, and z-axis directed by right hand rule. To facilitate computation, a cylindrical coordinate system $O-xr\theta$ is defined in the usual way, with the angle θ measured clockwise from y-axis when viewed in the positive direction of x-axis, and the radial coordinate r given by $r=\sqrt{y^2+z^2}$. The correlation between the two coordinate systems is as follows:

$$\begin{cases} x = x \\ y = r\cos\theta \\ z = r\sin\theta \\ \theta = \tan^{-1}(z/y) \end{cases} \tag{1}$$

The expressions of blade camber surface are derived as:

$$\begin{cases} x_c(r) = x_m(r) + C(r)(s-\frac{1}{2})\sin\varphi(r) \\ \qquad -f(s)\cos\varphi(r) \\ \theta_c(r) = \theta_m(r) + C(r)(s-\frac{1}{2})\cos\varphi(r)/r \\ \qquad +f(s)\sin\varphi(r)/r + \delta_k \\ y_c(r) = r\cos\theta_c(r) \\ z_c(r) = r\sin\theta_c(r) \end{cases} \tag{2}$$

2.2 Blade Singularity Arrangement

A continuous distribution of sources and vortices representing blade thickness and loading is replaced by a set of discrete line source and vortex ring elements of constant strength with endpoints of each element located on the camber surface. The radial interval from the hub, r_H, to the tip, R, is divided into M_B equal intervals, with the chordwise vortex elements forming vortex rings located at radii:

$$\rho_m = r_H + (R-r_H)\frac{4m-3}{4M_B+2} \qquad m=1,2,...,M_B+1 \tag{3}$$

The intersections of the spanwise vortex elements forming vortex rings or the discrete spanwise line source elements and chordwise vortex elements can be written as:

$$s_n = \frac{n-\frac{3}{4}}{N_B} \qquad n=1,2,...,N_B \tag{4}$$

The control point is chosen at the center of vortex ring, i.e. the mid-point of the line joining $(s_{n+\frac{1}{2}},\rho_m)$ and $(s_{n+\frac{1}{2}},\rho_{m+1})$, where the boundary condition, i.e. the total normal velocity of the flow should be zero on the camber surface, is satisfied.

3. MATHEMATICAL DESCRIPTION OF THE METHOD AND CALCULATIONAL PROCEDURE

The UNVLM applied in the present paper is based on the potential flow theory. Bound vortex rings are placed on the lifting surface, and the free vortices are time-dependently shed from the edges of lifting surface (the trailing edge, tip or leading edge of the propeller blades). The geometric shapes of free vortex wake are unknown as a priori, but determined as part of solution. The fluid viscous effect is represented by tip or leading edge vortex separations.

Assume that the flow is incompressible, irrotational, and homogeneous in the fluid domain excluding the propeller blades and their wakes. A velocity potential exists and satisfies the continuity equation

$$\Delta\Phi = 0 \tag{5}$$

and is subjected to the following boundary conditions:

1). The radiant condition.

The induced velocity of the propellers decays far from the blade, everywhere except near the wakes, that is

$$\text{when } |r| \to \infty, \qquad \nabla\Phi = 0 \tag{6}$$

2). Tangency condition on the camber surface.

The total normal velocity of flow should be equal to zero on the camber surface, i.e.

$$\mathbf{V} \cdot \mathbf{n} = 0, \quad \text{or} \quad \mathbf{n} \cdot (\nabla\Phi + \mathbf{U}) = 0 \tag{7}$$

The local inflow velocity vector under the open water condition, $\mathbf{U}$, is written as

$$\mathbf{U} = \mathbf{V}_A + \mathbf{\Omega} \times \mathbf{r} \tag{8}$$

3). The Kutta Condition.

At the trailing edges and at tip and leading edges where free vortex separations exist, the Kutta condition should be satisfied.

$$\nabla\Phi < \infty \tag{9}$$

4). Kelvin's theorem of circulation conversion.

$$\text{At any time step ,} \qquad \frac{D\Gamma}{Dt} = 0 \tag{10}$$

5). The pressure difference between upper and lower surfaces of free vortex wake sheets is equal to zero, that is

$$\Delta C_p|_w = 0 \tag{11}$$

To model the viscous effects of separated flow properly, both the location of the separating line and the vortex strength of the tip and leading edge separation have to be provided in advance. Usually this is done by experiments, flow visualization technique or the theoretical calculation of the viscous flow.

Two cases are investigated in this paper. One is that free vortex sheets are shed only from the trailing edges of blades, which are composed of trailing vortex rings, the other is that bound vortex sheets are separated at the tip edges and convected down in the trailing wake, forming into a set of tip edge separated vortex rings in addition to trailing vortex rings. Both of them are referred to free vortex rings, the strengths of which are determined by those of the adjacent bound vortex rings at previous time step.

As the above-mentioned numerical model of combined vortex rings and source lines has been established, the equation (5) and its boundary conditions, except (7), are satisfied automatically. According to (7) a set of linear algebraic equations is obtained to determine the strength of bound circulation:

$$[A_{ij}]\begin{bmatrix}\Gamma_{f1}\\ \cdot\\ \cdot\\ \cdot\\ \Gamma_{fj}\\ \cdot\\ \cdot\\ \cdot\\ \Gamma_{fN}\end{bmatrix} + [B_{ij}]\begin{bmatrix}\Gamma_{w1}\\ \cdot\\ \cdot\\ \cdot\\ \Gamma_{wj}\\ \cdot\\ \cdot\\ \cdot\\ \Gamma_{wM}\end{bmatrix} + [C_{ij}]\begin{bmatrix}\Gamma_{s1}\\ \cdot\\ \cdot\\ \cdot\\ \Gamma_{sj}\\ \cdot\\ \cdot\\ \cdot\\ \Gamma_{sL}\end{bmatrix}$$

$$+ [D_{ij}]\begin{bmatrix}Q_1\\ \cdot\\ \cdot\\ \cdot\\ Q_j\\ \cdot\\ \cdot\\ \cdot\\ Q_N\end{bmatrix} = -\mathbf{U}_i \cdot \mathbf{n}_i \tag{12}$$

where the values of Γ_{wj} and Γ_{sj} are known from those of adjacent bound vortex rings at previous time step, and

$$A_{ij} = \sum_{k=1}^{K} a_{ij}^k ,$$

$$B_{ij} = \sum_{k=1}^{K} b_{ij}^k ,$$

$$C_{ij} = \sum_{k=1}^{K} c_{ij}^k ,$$

$$D_{ij} = \sum_{k=1}^{K} d_{ij}^k .$$

Because the blade shape is not varying during whole computation procedure, the coefficients A_{ij} and D_{ij} are both constant and their calculations are performed only once. The calculational effort of B_{ij} and C_{ij} increases with time as the number of free vortex elements grows. This must be performed at each time step since wake rollup changes the geometry involved in its induced velocity calculations.

Move all known terms of equation (12) to the right side of equation, the linear equations used to determine bound circulations are derived as

$$\sum_{j=1}^{N} A_{ij}\Gamma_{fj} = -\mathbf{U}_i \cdot \mathbf{n}_i - \sum_{j=1}^{M} B_{ij}\Gamma_{wj} - \sum_{j=1}^{L} C_{ij}\Gamma_{sj} - \sum_{j=1}^{N} D_{ij}Q_j \qquad i = 1, 2, ..., N \tag{13}$$

As soon as the unknown strengths of vortex rings Γ_{fj} are obtained at each time step, the downwash at each vortex edge location $(u,v,w)_i$ (i.e. the nodal points of all the free vortex rings) is calculated by the following equation:

$$(u,v,w)_i = [\mathbf{A}_{wij}] \begin{bmatrix} \Gamma_{f1} \\ \cdot \\ \cdot \\ \cdot \\ \Gamma_{fj} \\ \cdot \\ \cdot \\ \cdot \\ \Gamma_{fN} \end{bmatrix} + [\mathbf{B}_{wij}] \begin{bmatrix} \Gamma_{w1} \\ \cdot \\ \cdot \\ \cdot \\ \Gamma_{wj} \\ \cdot \\ \cdot \\ \cdot \\ \Gamma_{wM} \end{bmatrix}$$

$$+[\mathbf{C}_{wij}] \begin{bmatrix} \Gamma_{s1} \\ \cdot \\ \cdot \\ \cdot \\ \Gamma_{sj} \\ \cdot \\ \cdot \\ \cdot \\ \Gamma_{sL} \end{bmatrix} + [\mathbf{D}_{wij}] \begin{bmatrix} Q_1 \\ \cdot \\ \cdot \\ \cdot \\ Q_j \\ \cdot \\ \cdot \\ \cdot \\ Q_N \end{bmatrix} + \mathbf{U}_i \qquad (14)$$

The new location of the free vortex nodes for the next time step $\mathbf{r}_i = (x,y,z)_i$ is then determined by

$$\mathbf{r}_i(x,y,z,t+\Delta t) = (u,v,w)_i \cdot \Delta t + \mathbf{r}_i(x,y,z,t) \qquad (15)$$

where $\mathbf{A}_{wij}$, $\mathbf{B}_{wij}$, $\mathbf{C}_{wij}$ and $\mathbf{D}_{wij}$ are the influence coefficients of the bound vortex ring, trailing vortex ring, tip or leading-edge separated vortex ring and line source element on each free vortex node respectively.

To demonstrate the calculational procedure of propeller open water characteristics, it is assumed that at $t = t_0$ the propeller starts impulsively from rest to steady advance velocity $\mathbf{V}_A$ and rate of revolution n, and no free vortex rings exist at the moment. Once the bound vortex strengths are solved, a time increment Δt is added and a new raw of free vortex rings are shed. The shedding procedure was illustrated in detail in reference (3).

The time increment Δt is prescribed as:

$$\Delta t = \frac{C_{0.75R}}{0.75\pi N_B n D} \qquad (16)$$

where $C_{0.75R}/N_B$ is the chordwise length of an element at $0.75R$.

4. CALCULATIONS OF HYDRODYNAMIC FORCES

Once the strengths of bound vortex rings are obtained, the forces acting on the propeller blades can be calculated, which consist of the potential forces and viscous forces.

4.1 Potential Forces

The potential forces acting on the propeller blades are composed of following three parts:
1). Kutta-Joukowsky force acting on the spanwise and chordwise vortex elements.

$$\delta\mathbf{F}^K_{nm} = \rho\Delta l_{nm}\mathbf{V}_{nm} \times \mathbf{\Gamma}_{nm} \qquad (17)$$

It should be noted that $\mathbf{\Gamma}_{nm}$ denotes the array of discrete chordwise and spanwise vortex elements[5] which are different from the value of bound vortex rings $\mathbf{\Gamma}_{fj}$, but can be obtained from the latter easily.
2). The Lagally force acting on the line source elements.

$$\delta\mathbf{F}^L_{nm} = -\rho\Delta l_{nm} Q_{nm}\mathbf{V}_{nm} \qquad (18)$$

3). The force proportional to the time rate of the change of the velocity potential, which may be evaluated in the following way:

$$\delta\mathbf{F}^t_{nm} = \rho\mathbf{n}_{nm}\frac{\partial}{\partial t}\Big(\sum_{l=1}^{n}\Gamma^s_{lm}\Big)\Delta A_{nm} = \rho\mathbf{n}_{nm}\frac{\partial}{\partial t}\big(\Gamma_{f[(m-1)N_B+n]}\big)\Delta A_{nm} \qquad (19)$$

4.2 Viscous Force

$$\delta\mathbf{F}^F_{nm} = \frac{1}{2}\rho C_f \Delta A_{nm}|\mathbf{V}_{nm}|\mathbf{V}_{nm} \qquad (20)$$

The increase in viscous resistance under off-design conditions is properly balanced by deducting 1/3 of leading-edge suction force from total force. The leading-edge suction force can be calculated as follows:

$$\delta\mathbf{F}^s_{1m} = \frac{1}{4}\pi\rho C_s^2 \Delta r_{1m}\cdot\mathbf{s}_0 \qquad (21)$$

where C_s is defined as

$$C_s = \frac{1}{2}\Gamma^s_{1m}(\sqrt{s_{1m}} - \sqrt{s_{0m}}) \qquad (22)$$

with s_{1m} and s_{0m} representing the coordinates of the ends of the first chordwise interval on the leading edge, and Γ^s_{1m} is the strength of the first discrete spanwise vortex element[5].

To sum up, the x, θ, and r components of the hydrodynamic forces acting on the propeller can be expressed as follows:

$$F_{x,\theta,r} = \sum_{k=1}^{K}\sum_{m=1}^{M_B}\Big[\sum_{n=1}^{N_B}(\delta\mathbf{F}^K_{nm} + \delta\mathbf{F}^L_{nm} + \delta\mathbf{F}^t_{nm} + \delta\mathbf{F}^F_{nm}) - \frac{1}{3}\delta\mathbf{F}^s_{1m}\Big]_{x,\theta,r} \quad (23)$$

The propeller thrust and torque can be written respectively as

$$T = -\sum_{k=1}^{K}\sum_{m=1}^{M_B}\Big[\sum_{n=1}^{N_B}(\delta\mathbf{F}^K_{nm} + \delta\mathbf{F}^L_{nm} + \delta\mathbf{F}^t_{nm} + \delta\mathbf{F}^F_{nm}) - \frac{1}{3}\delta\mathbf{F}^s_{1m}\Big]_x \quad (24)$$

$$Q = \sum_{k=1}^{K}\sum_{m=1}^{M_B}\Big[\sum_{n=1}^{N_B}(\delta\mathbf{F}^K_{nm} + \delta\mathbf{F}^L_{nm} + \delta\mathbf{F}^t_{nm} + \delta\mathbf{F}^F_{nm})_\theta \cdot \mathbf{r}^c_{nm} - \frac{1}{3}(\delta\mathbf{F}^s_{1m})_\theta \cdot \mathbf{r}^c_{1m}\Big] \quad (25)$$

The coefficients of propeller thrust and torque are then respectively:

$$K_T = \frac{T}{\rho n^2 D^4} \quad , \quad K_Q = \frac{Q}{\rho n^2 D^5}$$

To understand the difference caused by various numerical approaches, calculations of above mentioned potential forces also are performed by integrating pressure distribution. The computational points of the pressure are defined at the control points on the propeller camber surface. The pressure jump across the surface of blade may be obtained from the unsteady Bernoulli's equation as following:

$$\begin{aligned}\Delta P_i &= (P_u)_i - (P_l)_i \\ &= -\rho\frac{\partial}{\partial t}(\Phi_u - \Phi_l)_i \\ &\quad - \frac{1}{2}\rho(\mathbf{V}_u \cdot \mathbf{V}_u - \mathbf{V}_l \cdot \mathbf{V}_l)_i \end{aligned} \quad (26)$$

Noting that

$$(\Phi_u - \Phi_l)_i = \Gamma_{fi} \ ,$$
$$\mathbf{V}_u = \mathbf{V}_m + \frac{1}{2}\Delta\mathbf{V} \ ,$$
$$\mathbf{V}_l = \mathbf{V}_m - \frac{1}{2}\Delta\mathbf{V} \ ,$$

the pressure jump can be rewritten as:

$$\Delta P_i = -\rho\frac{\partial}{\partial t}\Gamma_{fi} - \rho(\mathbf{V}_m \cdot \Delta\mathbf{V})_i \quad (27)$$

where $(\mathbf{V}_m)_i$ is the vector sum of the inflow velocity and the velocities induced by vortex rings and line source elements.

Then the potential force will be

$$\delta\mathbf{F}^P_i = -\Delta P_i \Delta A_i \cdot \mathbf{n}_i \quad (28)$$

Similarly the expressions of thrust and torque of the propeller can be derived as follows:

$$T = -\sum_{k=1}^{K}\Big[\sum_{i=1}^{M_B\times N_B}\delta\mathbf{F}^P_i + \sum_{m=1}^{M_B}(\sum_{n=1}^{N_B}\delta\mathbf{F}^F_{nm} + \frac{2}{3}\delta\mathbf{F}^s_{1m})\Big]_x \quad (29)$$

$$Q = \sum_{k=1}^{K}\Big\{\sum_{i=1}^{M_B\times N_B}(\delta\mathbf{F}^P_i)_\theta \cdot \mathbf{r}^c_i + \sum_{m=1}^{M_B}\Big[\sum_{n=1}^{N_B}(\delta\mathbf{F}^F_{nm})_\theta \cdot \mathbf{r}^c_{nm} + \frac{2}{3}(\delta\mathbf{F}^s_{1m})_\theta \cdot \mathbf{r}^c_{1m}\Big]\Big\} \quad (30)$$

5. EXAMPLES AND RESULTS

Calculations are performed by UNVLM without and with tip vortex separations for a conventional propeller DTNSRDC-4118 and a highly skewed propeller DTNSRDC-4383 with 72° skew angle to verify the present method. The corresponding calculated results are shown in Tab.1 and Tab.2.

Table 1 Results for DTNSRDC-4118

J		0.833		0.500	
Formulas		(24),(25)	(29),(30)	(24),(25)	(29),(30)
Case 1	K_T	0.149	0.145	0.260	0.244
	K_Q	0.0272	0.0272	0.0396	0.0400
Case 2	K_T	0.153	0.140	0.283	0.265
	K_Q	0.0279	0.0278	0.0438	0.0440

Table 2 Results for DTNSRDC-4383

J		0.889		0.600		0.470	
Formulas		(24),(25)	(29),(30)	(24),(25)	(29),(30)	(24),(25)	(29),(30)
Case 1	K_T	0.239	0.227	0.360	0.321	0.412	0.357
	K_Q	0.0474	0.0474	0.0614	0.0610	0.0663	0.0655
Case 2	K_T			0.362	0.321	0.422	0.363
	K_Q			0.0620	0.0610	0.0687	0.0678

Notes: Case 1 — Without tip separation
Case 2 — With tip separation

The comparisons between calculated results for the open water characteristics under the condition of tip separation and the existing experimental data are shown in Fig.2 and Fig.3 for propellers DTNSRDC 4118 and 4383 respectively.

Fig.4 indicates the transient K_T and K_Q for the propeller DTNSRDC-4118 at J=0.833 under the conditions without and with tip separations.

Fig.5 shows comparisons of the results by two ways of calculating forces mentioned above for the DTNSRDC-4383 at $J = 0.6$.

The variations of the geometric shape of the free vortex sheets at time step $t = t_0 + 10\Delta t$, $t_0 + 30\Delta t$, and $t_0 + 60\Delta t$ for DTNSRDC-4118 at $J = 0.833$ under condition without tip separation are shown in Figs. 6, 7, and 8.

Fig.9 shows the shape and rollup of the wake vortex sheet at time step $t = t_0 + 40\Delta t$ for the DTNSRDC-4118 propeller at $J = 0.833$ under condition with tip separation.

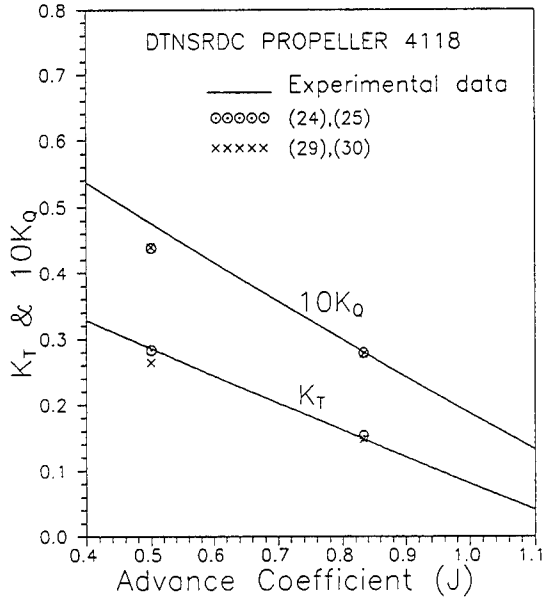

Fig.2 Comparison of open-water characteristics for propeller DTNSRDC-4118

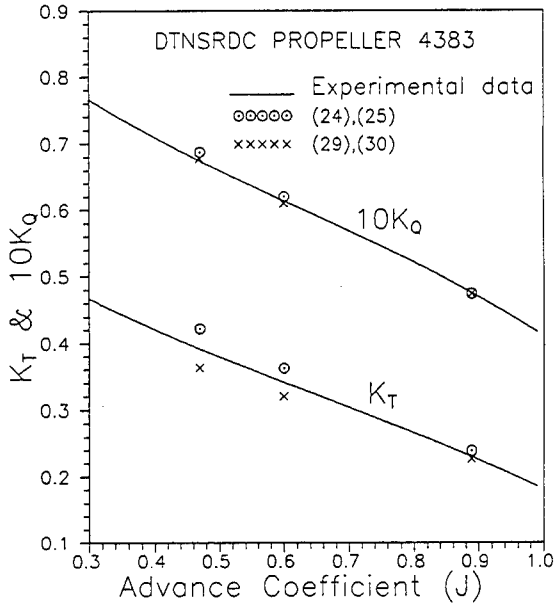

Fig.3 Comparison of open-water characteristics for propeller DTNSRDC-4383 (72° skew)

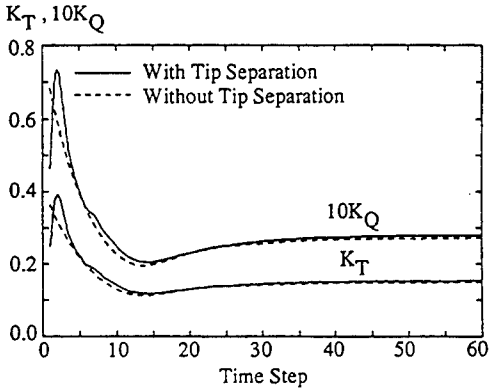

Fig.4 Variation of K_T and K_Q with time when impulsively started (DTNSRDC-4118, $J = 0.833$)

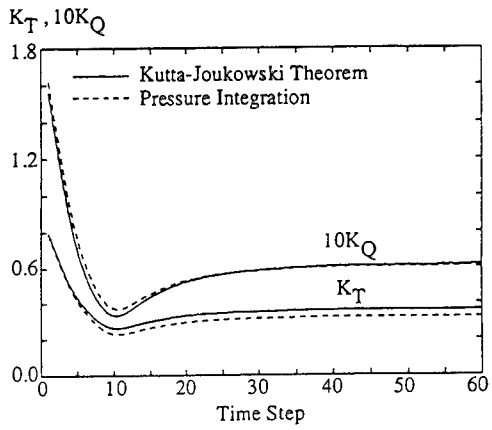

Fig.5 Variation of K_T and K_Q with time when impulsively started (DTNSRDC-4383, $J = 0.6$)

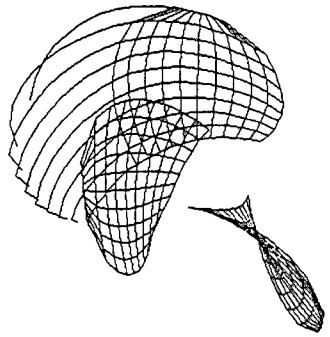

Fig.6 Geometric shape of free vortex wake (DTNSRDC-4118, $J = 0.833$, $t = t_0 + 10\Delta t$)

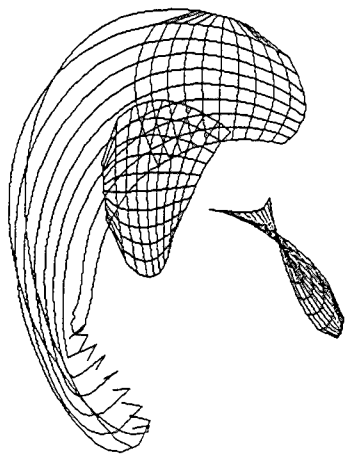

Fig.7 Geometric shape of free vortex wake (DTNSRDC-4118, $J = 0.833$, $t = t_0 + 30\Delta t$)

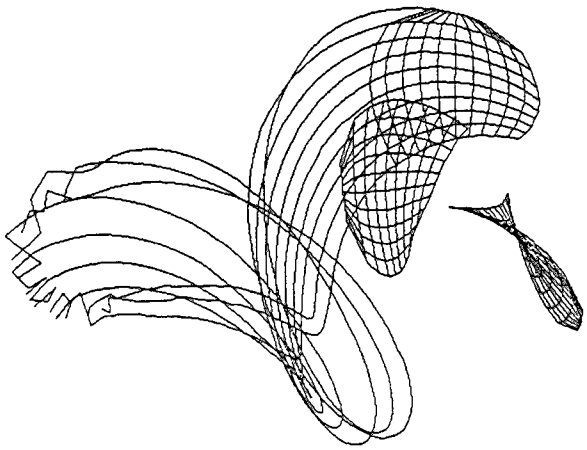

Fig.8 Geometric shape of free vortex wake (DTNSRDC-4118, $J = 0.833$, $t = t_0 + 60\Delta t$)

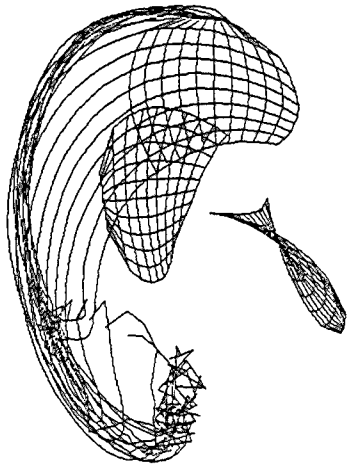

Fig.9 Geometric shape of free vortex wake (DTNSRDC-4118, $J = 0.833$, $t = t_0 + 40\Delta t$)

6. CONCLUSIONS

1. UNVLM is a valuable tool for predictions of propeller hydrodynamic performances. It may be applied not only to predictions of both steady and unsteady performances, but also to investigations on the dynamic variation performances of the propeller at short start and stop conditions.
2. This numerical method provides a good way to analyse the influence of the tip and leading edge separations. The present results show that values of K_T and K_Q increase slightly, when tip vortex separation is taken into consideration.

However, the influence on the skewed propeller DTNSRDC-4383 is smaller than on the conventional propeller DTNSRDC-4118, especially at low advance coefficient J. Further research is needed for the explanation of this phenomenon.

The calculated results indicate that the influence of tip separation on values of K_T and K_Q of DTNSRDC-4118 propeller is significant at $J = 0.5$. The K_T and K_Q are still a little lower than experimental data, even though the tip vortex separation is taken into account. That means it may be necessary to consider the leading edge separation for this case. Anyhow, the computational program provided in the present paper can be used to study the leading-edge separation problem, which will be conducted later on.

3. The present results show that the prediction accuracy of open water characteristics for highly skewed propellers is improved considerably by using UNVLM.
4. The geometric shape of free vortex sheets and their variation in the shedding process are illustrated in the present paper. Such information may be of practice value in measuring and analyzing the structure and geometric shape of the free vortex wake, and then in establishing a rational wake model.
5. As a time-dependent wake shedding and rollup numerical procedure is applied, it can be imagined that the UNVLM needs more computer time than the traditional lifting-surface methods. That means, frankly speaking, it can not be considered very worthwhile applying the method only to the prediction of open water characteristics of propellers. However, as mentioned above, this numerical method provides a possibility to investigate some problems related to propellers, such as tip and leading edge separations, unsteady performances of propeller at start and stop conditions etc., for which other methods could do nothing. Thus, it is expected that the UNVLM will be an important part in the development of propeller theories.

REFERENCES

1. Kandil, O. A., Mook, D. T., and Nayfey, A. H., "Nonlinear Prediction of the Aerodynamic Loads on Lifting Surfaces", Journal of Aircraft, Vol.13, Jan. 1976, pp.22–28.
2. Katz, J., "Lateral Aerodynamics of Delta Wings with Leading Edge Separation", AIAA Journal, Vol.22, No.3, 1984, pp.323–328.
3. Wang Guoqiang and Zhang Tianfeng, "A Nonlinear Vortex Lattice Method for Calculating Hydrodynamic Forces of Rudder with Tip Edge Separation", The IMAEM'87, IV Congress, Varna, Bulgaria, 1987, pp.23-1–23-7; also Journal of Shipbuilding of China, No.97, 1987, pp.14–21.
4. Wang Guoqiang and Zhang Tianfeng, "Design of Additional Thrusting Fin with Nonlinear Vortex Lattice Method", The PRADS'87, Trondheim, Norway, 1987, pp.202–210.
5. Wang Guoqiang and Hu Shougen, "Improvement of Prediction Method for Propeller Characteristics and Blade Pressure Distribution", Selected Paper of CSNAME, Vol.3, 1988, pp. 135–151; also Journal of Shipbuilding of China, No.100, 1988, pp.22–35.

Pressure Distribution and Blade Stress on a Highly Skewed Propeller

Y. Ukon (Ship Research Institute, Japan),
H. Yuasa (Mitsubishi Engineering and Ship Building Co., Ltd., Japan)

ABSTRACT

This paper describes the extensive investigations on pressure and stress on the blade of a highly skewed propeller of the "Seiun-Maru". The measurement of pressure distribution on the blades of propeller models working in uniform flow and non-uniform flow behind wire mesh screen and the measurement of pressure distribution and stress on the propeller blades of the highly skewed propeller in full scale were performed. These were carried out on a conventional propeller as well, of which various full scale measurements have been conducted. On the highly skewed propeller, complicated and peculiar phenomena in the pressure measurements were found, which could not be predicted by the existing theory. Furthermore, the measurement of blade stress was performed on the highly skewed propeller working behind the complete ship model with flow liners in the cavitation tunnel. The measurements on the model corresponded well with those on the full scale.

The present measurements indicated that there still remain some problems to be improved on propeller theories particularly for a highly skewed propeller.

NOMENCLATURE

C_p	;	Pressure coefficient = $(P_i-P_\infty)/\frac{1}{2}\rho n^2D^2$
D	;	Propeller diameter
E	;	Young's modulus, Modulus of elasticity
J	;	Advance ratio = V/nD
K_Q	;	Torque coefficient = $Q/\rho n^2D^5$
K_T	;	Thrust coefficient = $T/\rho n^2D^4$
n	;	Revolution rate of propeller
P_c	;	Pressure at center of propeller shaft
P_i	;	Local pressure on propeller blade
P_v	;	Vapor pressure
P_∞	;	Reference pressure at infinity
Q	;	Torque
T	;	Thrust
V	;	Advance velocity
w	;	Wake fraction
ϵ	;	Strain
Θ	;	Angular position of propeller blade (Zero deg = 12 o'clock, positive to clockwise, looking forward)
σ^*	;	Non-dimensionalized Stress = $\epsilon E/\rho n^2D^2K_T$
σ_n	;	Cavitation number = $(P_\infty-P_v)/\frac{1}{2}\rho n^2D^2$
ρ	;	Density of water

1. INTRODUCTION

Recently highly skewed propellers, HSP in short, are often utilized for various kinds of ships. It is well known that this type of propeller reduces not only ship hull vibration and noise remarkably but also fuel consumption in some cases. The hydrodynamic characteristics of HSP, however, have not been fully understood yet, unlike those of a conventional propeller, CP in short. To highlight the difference of hydrodynamic aspects between them clearly, a comparison of the pressure distribution on the blades of two kinds of propeller models was made in detail, because cavitation occurrence depends on the pressure distribution and FEM (Finite Element Method) analysis for propeller strength employs it as input data. For this purpose, a sophisticated technique to measure the pressure distribution on the blades of a propeller model was newly developed. The pressure measurement was performed on two kinds of propeller models working in uniform flow and non-uniform flow generated by wire mesh screen at the SRI (Ship Research Institute) large cavitation tunnel. In this paper, the pressure distribution especially on HSP is discussed comparing the measurements with the calculation by an existing propeller theory.

The progress of numerical techniques such as propeller lifting surface theory [1,2,3], lifting body theory [4,5] and CFD [6] to calculate propeller performance is so remarkable that some of them are applied to the design of marine propellers effectively. In order to evaluate newly developed numerical techniques, experimental data at high Reynolds number play an important role. It has been indirectly confirmed only by measuring ship speed, power, thrust, torque and others at sea trials or full scale measurement whether propeller theories can predict the pressure distribution or cavitation extent with sufficient accuracy. Comparing with thrust and torque, pressure distribution is of more microscopic quantity and most suitable for the evaluation of theory in detail. According to the recent development of measuring instruments, more precise pressure measurement has been carried out on the blade of propeller models working in non-uniform flow. The measured data on the pressure distribution of a full scale propeller for a merchant ship have not been published at all. An exceptional example was presented by Allison [7]. He carried out the measurement of both pressure and blade stress on the surface propellers of the SES-100B at speeds up to 85 kts.

Lately, it is reported that 6 % of installed HSP have been broken or bent in the vicinity of the tip.

According to the report, the break-off of the propeller tip was caused by rapid fatigue crack growth even in ahead conditions. Then, a research program was proposed to measure the pressure distribution and the blade stress near the propeller tip on the blades of CP and HSP. The research project SR206 included the measurement of three-dimensional wake distribution by Tracer/Multi-TV-Camera method [8] as a two-years program from 1989 to 1990. Simultaneously the wake measurement by LDV was performed in 1989 [9]. In these measurements, a training ship "Seiun-Maru" was employed, which is operated by the Institute for Sea Training, Ministry of Transport. On this ship, the measurements of hull surface pressure and cavity thickness on both propellers, and blade stress at the root of HSP were conducted in 1982 [10]. The measurement of pressure distribution and blade stress on the blades of two full scale propellers was charged by three organazations. The Ship Research Institute has already measured the pressure distribution on propeller models in a cavitation tunnel [11,4]. ALM (Akishima Laboratory, Mitsui Eng. & Ship Building Co. Ltd.) has experienced to measure the blade stress of a CPP at full scale [12] and Nakashima Propeller Co. Ltd. has advanced techniques and experts to manufacture propellers.

In the present research project, the blade stress measurement on the HSP model was also performed using a complete ship model of the Seiun-Maru in the SRI cavitation tunnel. In this measurement, not only the estimated wake distribution by the flow liners [13] but also cavitation pattern were simulated. The blade stress and cavitation pattern on the model were compared with the full scale measurements.

2. MEASUREMENT OF PRESSURE ON PROPELLER MODEL

2.1. Recent Progress of Pressure Measurement

Pressure on a propeller blade is one of the most important parameters not only to characterize the performance of a propeller but also to evaluate propeller theory. Several researchers have proposed the measurement techniques of blade pressure on propeller models together with the development of miniature pressure transducers.

One of them was to fit pressure gauges flush-mounted to the blade surface directly. Takei [11] measured the pressure distribution on a model propeller working not only in uniform flow but non-uniform flow. Takahashi [14] and Vermissen [15] also carried out the measurement of pressure distribution by this type of method.

Recently Jessup [16] and Ling [17] have developed a new technique to measure at numerous pressure taps on the blade surface through connecting channels to the pressure gauge with sequential plugging and unplugging of holes. This technique can not be applied to the measurement in non-uniform flow.

Koyama [4] measured the pressure distribution on a propeller model with rather thick blades by using the pressure pick-ups with Helmholtz cavity chamber. The pressure transducers were embedded on the surface opposite to the surface where the pressure distribution is to be measured. These transducers were fitted to the propeller blades, to make Helmholtz cavity chambers. The major advantages of this type of pressure pick-ups are the ability to measure unsteady pressure with high accuracy, without disruption to the measuring blade surface and even under cavitating conditions.

2.2. Measurement Technique

Tested Propellers

In this paper, three propeller models were used. The principal particulars of the model propellers are given in Table 1. The pressure distribution measurement was carried out using 400 mm diameter propellers, MP No. 251 and 252, not only in uniform flow but in non-uniform flow generated by wire mesh screen, while the blade stress was measured using about 221 mm diameter propeller, MP No. 323, in non-uniform flow behind a complete ship model of the Seiun-Maru written in the following section. The principal particulars of the ship model are given in Table 2. Both measurements were conducted in the SRI large cavitation tunnel.

Pressure Pick-up

In the present measurement, pressure transducers (Sankei Eng. P303-1S) were used, whose specifications

Table 1 Principal Particulars of Model Propellers

Type	CP	HSP	
Model Propeller No.	251	323	252
Diameter [m]	0.400	0.22095	0.400
Pitch Ratio at 0.R	0.950	0.944	
Expanded Area Ratio	0.650	0.700	
Boss Ratio	0.1972		
Number of Blades	5		
Blade Thickness Ratio	0.0442	0.0496	
Mean Blade Width Ratio	0.2465	0.2739	
Skew Angle [deg]	10.5	45	
Rake Angle [deg]	6.0	-3.03	
Blade Section	MAU	Modified SRI-B	
Material	Anodized Aluminum		
Direction of Rotation	Right		

Table 2 Principal Particulars of Model Ship

M. S. No.	500
Length bet. P.P. [m]	6.444
Breadth [m]	0.984
Depth [m]	0.491
Draft [m]	0.356
C_B [-]	0.577
Material	Wood

Table 3 Specification of Pressure Gauge for Model Propeller

Type	P303-1S
Capacity	$\pm$1kg/cm^2
Resp. Freq.	7kHz
Output Voltage	50mV/6VFS
Non-Linearity	0.5% FS
Repeatability	0.2% FS
Bridge Voltage	6VDC(8VDCmax)

are shown in Table 3 and the same installations of the pressure transducers were adopted in earlier measurement [4]. The measured pressure values in some places, however, were unfavorably affected by the stress due to the deformation of propeller blades. In order to remove such a detrimental effect, a special care was taken on the attachment of pressure transducers to the blade. These were supported by soft adhesive filler to isolate the pressure gauges from blade stress. Fig. 1 shows the improved attachment to measure the pressure on a propeller blade without any effects from blade stress and deformation. The Helmholtz cavity chamber was filled with silicone sealant whose viscosity was 10 cs.

In order to check this newly developed attachment, the following test was performed. The pressure taps were covered with a rigid metallic tap and tiny amount of air was supplied into the cavity chamber. By sealing off the pressure pick-ups from the surrounding pressure, the output of pressure transducers was checked. If a pressure pick-up was affected by blade stress, the output of the pressure transducer should change during the revolution of propeller model. Little influence was found for most of pressure pick-ups under the respective experimental conditions. A few of them were slightly affected by the propeller loading. Corrections to the measured pressure coefficients for them were made by subtracting those due to loading which were obtained by this procedure. This correction, however, amounted so small that this was less than the corresponding errors of the measurements.

For both propellers, the pressure pick-ups were arranged mainly along 0.7 R (radius) as well as 40 %C (chord length) from the leading-edge. The arrangement of the pick-ups for each propeller is shown in Table 4. Eighteen and Seventeen pressure pick-ups were installed for CP and HSP, respectively. A few of them were provided at geometrically similar positions to evaluate the reliability of measurement. In order to examine whether the present pressure pick-up can measure unsteady pressure significantly, the response of the pressure pick-ups was examined using an underwater speaker which emits sinusoidal pressure at the frequencies from 100 Hz to 1 kHz. In the frequency range from 100 Hz to 700 Hz, the decay of the transferred pressure amplitude was within 3 dB and no shift of the phase was observed. From the measurement in uniform flow, the response of the pressure pick-ups can be also estimated from the static pressure variation during rotation.

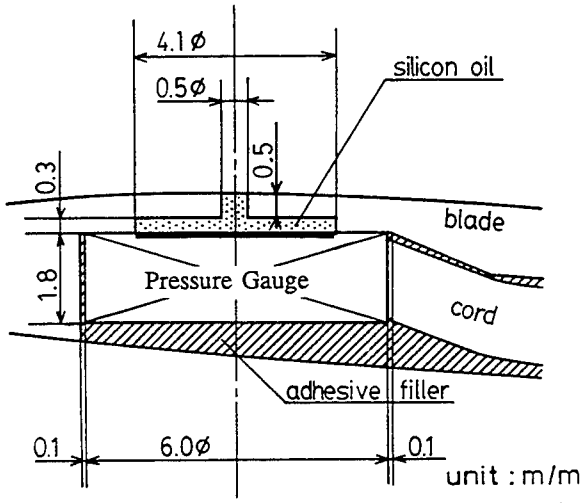

Fig. 1 Newly Developed Helmholtz Cavity Chamber and Pressure Gauge

Measurement Procedure

The measurements were performed in the No. 1 working section of the SRI large cavitation tunnel. The capacity of a dynamometer for thrust and torque was 200 kg and 10 kg-m, respectively. Pressure signals from the gauges were transmitted through 6 ch. wired FM telemeter. Calibrations were conducted in the cavitation tunnel not only by varying the static pressure in the range of 80 mmHg with keeping the tunnel water velocity and the propeller shaft speed at zero but also by turning the propeller very slowly, i.e., 0.1 rps. These calibrations were done before and after each set of runs at given six pressure pick-up locations. The accuracy of the present calibration was expected within ± 0.2 mmHg and the accuracy of measurement was enhanced by such frequent calibrations. The calibration factor varied little throughout the experiments.

The present measurements were made at three revolution rates of propeller, those were, 3.63, 6.63 and 8.00 rps. To determine the measurement condition, the respective propeller characteristics were measured in the cavitation tunnel and the correction of wall effect was made [18]. The corrected curves of propeller characteristics on thrust and torque agree well with the results of propeller open water test in a towing tank as shown in Fig. 2. For the measurement in uniform flow, the tested advance coefficients were 0.50, 0.60, 0.70 and 0.90, based on the thrust identity method.

The measurement conditions in non-uniform flow for CP and HSP were K_T=0.207 and 0.201, respectively. These conditions were determined by the reading of thrust meter equipped to the Seiun-Maru in the full scale

Table 4 Arrangement of Pressure Gauge on Model Propeller

(a) CP

chord-wise position	side of blade	radial position		
		0.5R	0.7R	0.9R
10%	back face		* *	
25%	back face		*	
40%	back face	* *	* *	* *
60%	back face		*	
80%	back face		* *	

(b) HSP

chord-wise position	side of blade	radial position		
		0.5R	0.7R	0.9R
10%	back face		* *	
17.5%	back face		*	
25%	back face		*	
40%	back face	* *	* *	* *
60%	back face		*	
70%	back face		*	
80%	back face		* *	

measurement in 1982 and corresponded to 163 rpm of the engine. The simulated wake from the estimated one of the Seiun-Maru by wire mesh screen is shown in Fig. 3.

2.3. Measurements in Uniform Flow

The measured pressure in the chordwise and radial directions in uniform flow for CP at advance ratio J=0.5 and 0.7 are shown in Figs. 4 and 5, respectively. The present measurements were carried out at three different revolution rates of propellers to investigate the Reynolds effects except J=0.5. In each figure, the pressure distributions computed by an existing lifting surface theory, "kernel function expansion method" [1] with the "equivalent two-dimensional profile method" [19] are demonstrated. The present calculation method of blade surface pressure is a kind of "strip theory". The hydrodynamically equivalent camber-line at given radial positions is computed from three-dimensional upwash given by the lifting surface theory. The equivalent thickness is given by two-dimensional geometrical offsets. Then, the pressure distribution of the equivalent two-dimensional wing section can be calculated by Moriya's non-linear wing theory [20].

Except 3.63 rps, two measurements at higher rate of propeller revolution, that is, 6.63 rps and 8.0 rps agreed well with each other within the measurement error. Good agreements between theory and measurement were observed at the suction side, while the computed values were considerably lower than the experiments at the pressure side except near the leading edge.

The measured results in the chordwise and radial directions for HSP are shown in Figs. 6 and 7. Roughly speaking, the tendency between theory and experiment on the chordwise pressure distributions of HSP was similar to

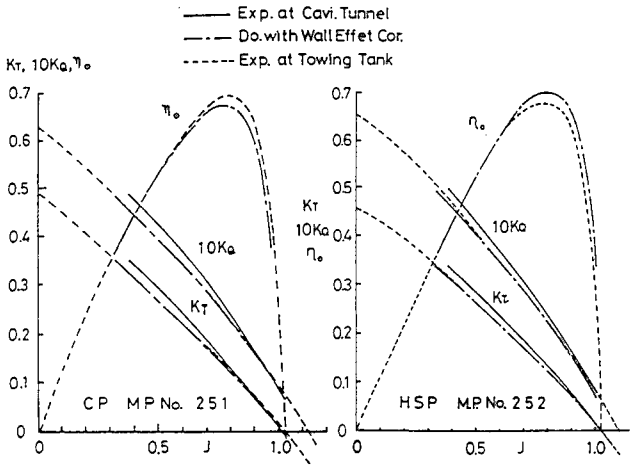

Fig. 2 Propeller Open Water Characteristics

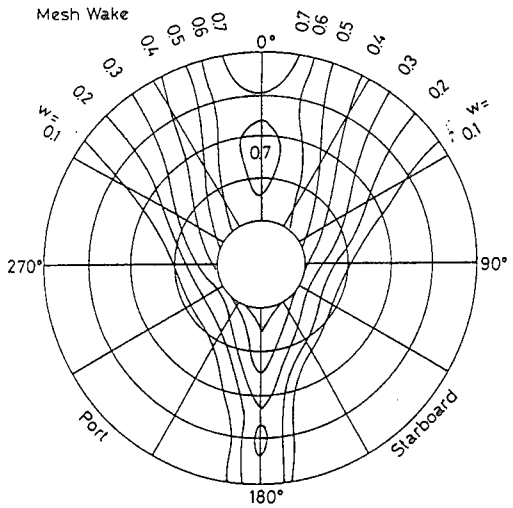

Fig. 3 Seiun-Maru Full Scale Wake Distribution Simulated by Wire Mesh Method

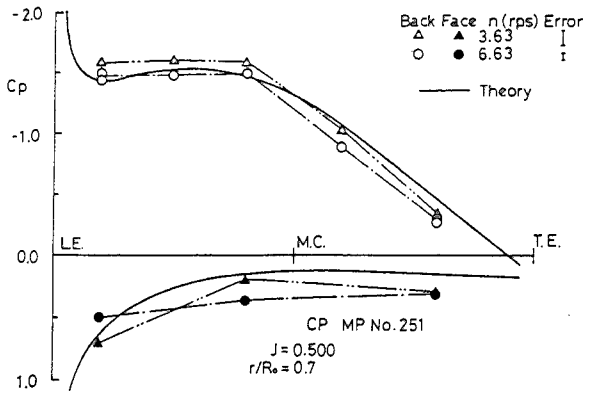

Fig. 4 (a) Chordwise Pressure Distribution on CP in Uniform Flow: J=0.5, r/R_0=0.7

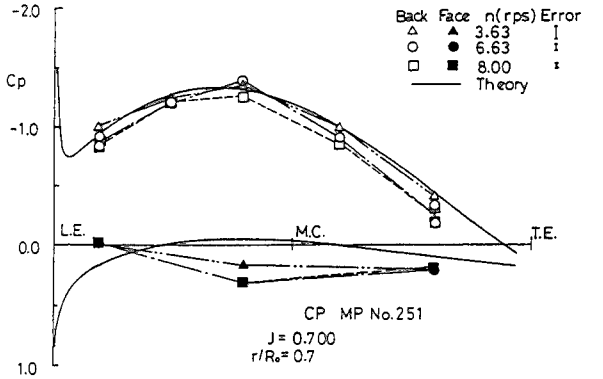

Fig. 4 (b) Chordwise Pressure Distribution on CP in Uniform Flow: J=0.7, r/R_0=0.7

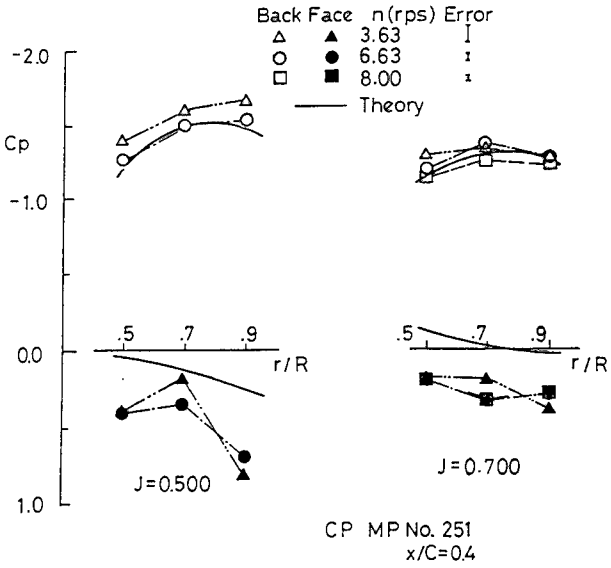

Fig. 5 Radial Pressure Distribution on CP in Uniform Flow: J=0.5 & 0.7, x/C=0.4

those of CP for both suction and pressure sides except the propeller tip. From the present measurements, the following two interesting findings were obtained. Wavy pressure distributions at the suction side for HSP were found at each advance ratio. Such distributions were not observed in the measurement on CP. With respect to the radial pressure distribution at 40 %C position, a good correlation between theory and measurement was found both on HSP and CP, except near the tip. At the advance coefficient 0.5 and o.6, the pressure on the back side at 0.9 R was extremely less than the theoretical value, while the pressure on the face side at 0.9 R for J=0.9 became extremely higher than that given by the theory.

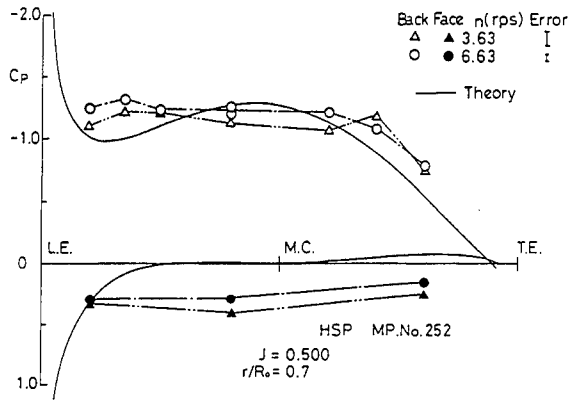

Fig. 6 (a) Chordwise Pressure Distribution on HSP in Uniform Flow: J=0.5, r/R_0=0.7

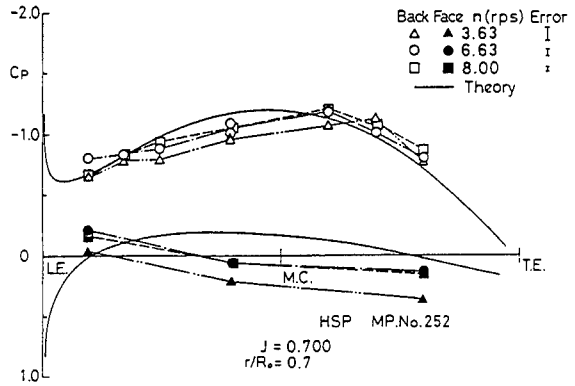

Fig. 6 (b) Chordwise Pressure Distribution on HSP in Uniform Flow: J=0.7, r/R_0=0.7

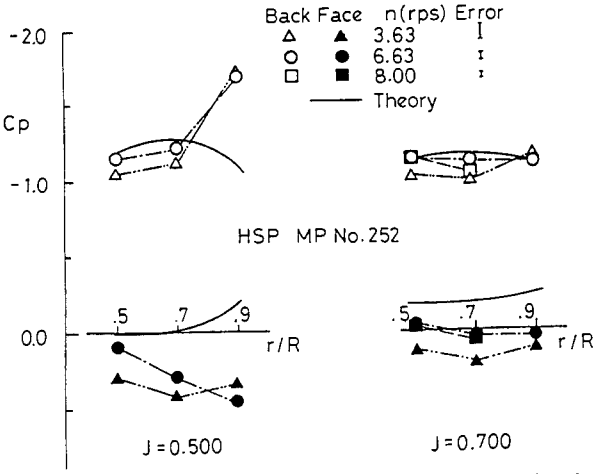

Fig. 7 Radial Pressure Distribution on HSP in Uniform Flow: J=0.5 & 0.7, x/C=0.4

2.4. Measurements in Non-uniform Flow

From the evaluation of effects on the pressure pick-up due to blade stress by the above-mentioned procedure and natural frequency of the pressure pick-up, it is expected that the present measurement technique has reasonable accuracy for unsteady measurements.

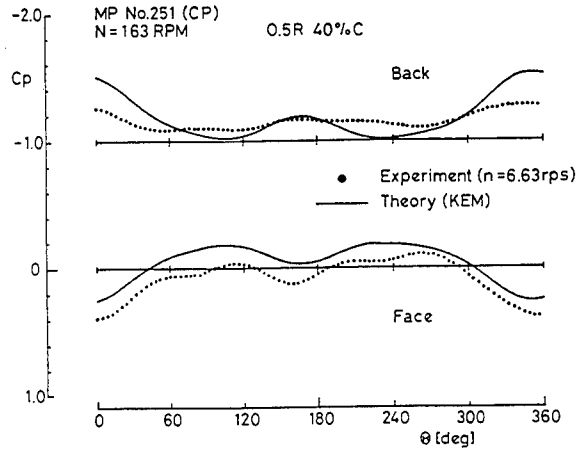

(a) r/R_0=0.5, x/C=0.4

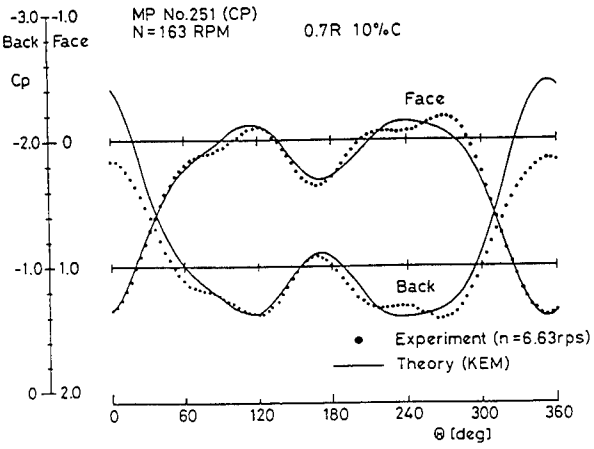

(b) r/R_0=0.7, x/C=0.1

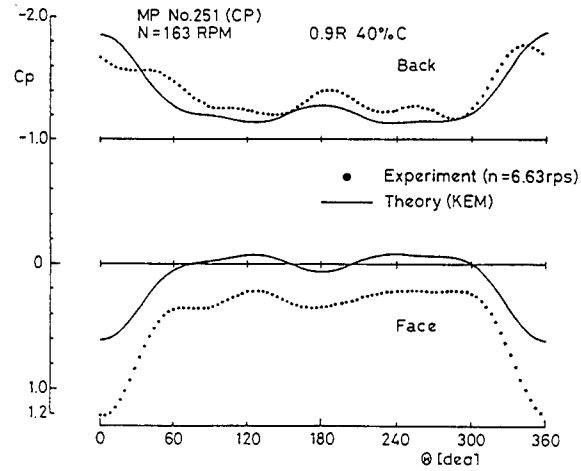

(c) r/R_0=0.9, x/C=0.4

Fig. 8 Blade Pressure Variation during One Rotation of CP in Non-Uniform Flow

In Fig. 8, several measurements of pressure variation on the blade of CP are shown during one rotation of the propeller in non-uniform flow. At 40 %C of 0.5 R, the mean value of pressure coefficient on the suction side showed close agreement between measurement and theory. Smaller amplitude of the measured pressure variation may be caused by laminar viscous effect. On the pressure side, good qualitative agreements were observed between measurement and theory. The present theory overpredicted the pressure coefficient as seen in the measurements in uniform flow. At 10 %C of 0.7 R, excellent agreements between the measured and the computed values were obtained at both sides. At 40 %C of 0.7 R and 0.9 R, a similar tendency was observed on the correlation between measurement and computation to that at 40 %C of 0.5 R. As a common tendency in the measurements, negative peak near the angular position of zero degrees was smaller than that of the theory. With respects to the chordwise pressure distributions, the same tendency in the relation between experiment and theory was found.

The measured pressure variation of HSP is compared with the computed values in Fig. 9. The correlation between theory and experiment were similar among 40 %C of 0.5 R and 0.7 R and 10 %C of 0.7 R. At 40 %C of 0.9 R, however, extraordinary discrepancy between theory and measurement was obtained. The theory entirely underpredicted the amplitude of the pressure coefficients not only at suction side but also at pressure side.

2.5. Discussions

Reynolds Effects

In the present investigation, the measurements in uniform flow were performed at three different shaft speeds except at lower advance ratio for the highest revolution rate of n=8.0 rps because of the capacity on the measurement apparatus. For CP, marked differences on the pressure distribution were found at the lowest speed from those at other higher speeds. Those were greater than the estimated error band. Roughly speaking, at the higher velocity, the measured pressure became higher. The similar tendency was observed in the measurements by Jessup [16]. It might be said that this tendency was due to Reynolds effects. For both propellers, little influence of propeller revolution rate on the pressure distribution could be observed at higher speeds.

Skew Effects

Comparing the chordwise pressure distribution between CP and HSP, the latter distribution became wavy. From flow visualization by oil film method, however, no significant difference was observed in the pattern between CP and HSP.

On the radial pressure distribution, the measured pressure near the tip of HSP rapidly changed and differed from the predicted one except for the case of J=0.7, where the propeller operated at the shock free condition.

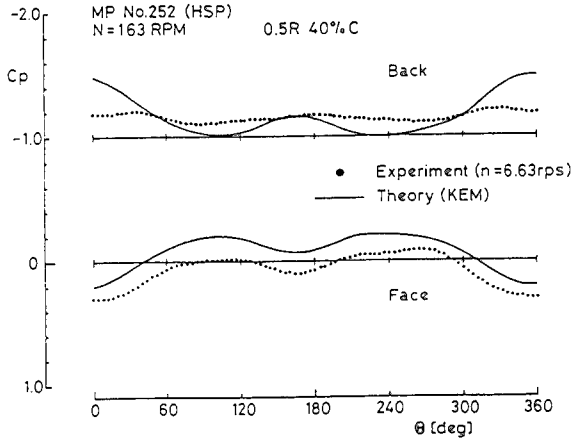

(a) $r/R_0=0.5$, $x/C=0.4$

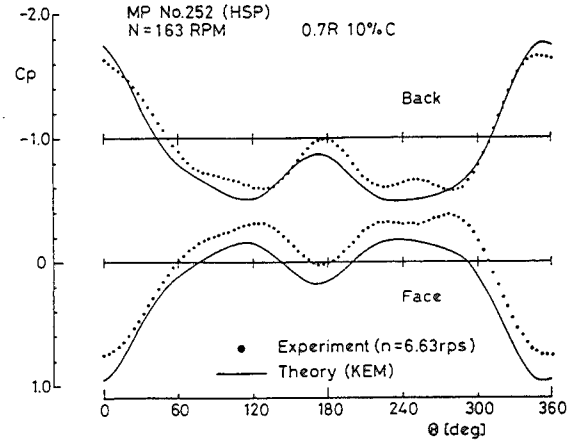

(b) $r/R_0=0.7$, $x/C=0.1$

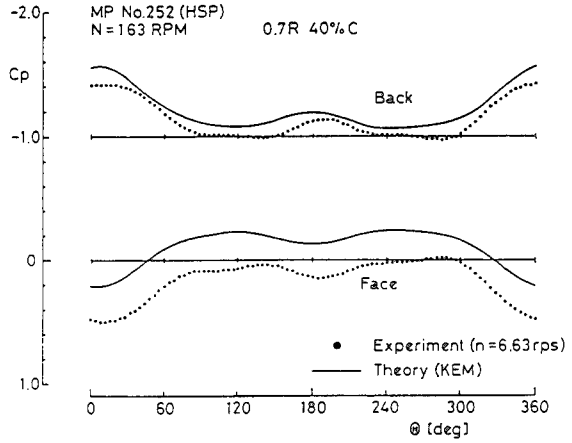

(c) $r/R_0=0.7$, $x/C=0.4$

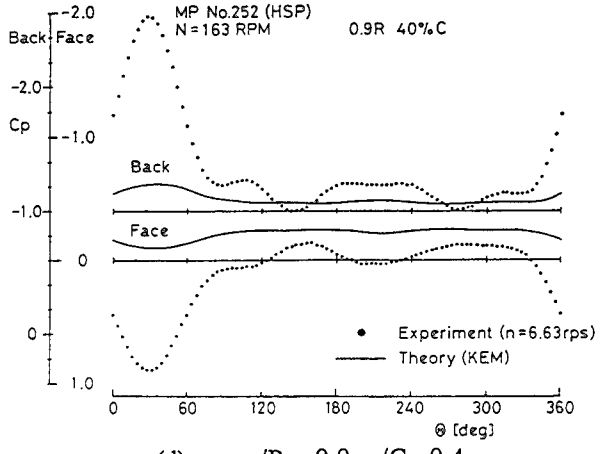

(d) $r/R_0=0.9$, $x/C=0.4$

Fig. 9 Blade Pressure Variation during One Rotation of HSP in Non-Uniform Flow

One of the reasons is thought that the pressure tap at 40 %C of 0.9 R was covered with the vortex generated by leading edge separation.

With respect to the pressure distribution in non-uniform flow, both distributions of two propellers showed similar behavior, except near the tip. In the vicinity of the tip, the negative pressure peak was moderate for CP, while that for HSP was extremely sharp. This tendency might be also explained by the above-mentioned reason.

Comparison with Computation

In the present paper, the pressure distribution was computed by using a current lifting surface theory. In this computation, viscous correction was made using a simple method by multiplying an empirical constant with drag coefficients for given thickness. A detailed comparison between the computation and the measurements on the suction side showed the discrepancies that for lower J than 0.7 the theory predicted lower values in the aft part of the chord, while for higher J it did lower values in the fore part of the chord. This might be caused by neglecting the displacement effect due to boundary layer thickness around the blade in the calculation.

The present theory overpredicted the pressure distribution on the face side in most cases. Since the other theories [4,5,17] based on a surface pannel method presented higher pressure coefficients than the present theory did, it is expected that a better agreement could be obtained by employing the above-mentioned improved theories. For HSP, an existing theory could not reasonably predict the pressure distribution not only near the tip but also at the angular position around zero degrees. The theory which takes account of leading edge vortex separation or tip vortex [21] could give us breakthrough to predict to flow field around the blades of HSP.

3. MEASUREMENT OF PRESSURE ON FULL SCALE PROPELLER

3.1. Measurement System and Procedure

Sensor for Full Scale Measurement

From the view points of full scale measurement, the Helmholtz chamber method as utilized in the model measurement, was also adopted to the present pressure measurement. Since less drift of standard pressure and robustness against rough treatment were inevitable to a pressure transducer for full scale measurement, two kinds of strain gauge-type pressure transducers (Kyowa PS-5KB and 2KB for CP, and PS-5KB-M306 for HSP) [22] were employed for this measurement.

On the contrary, this pressure gauge has a shortcoming that the output voltage is relatively not so high. It was, however, judged that the measurement with sufficient accuracy would be possible owing to the recent rapid progress of a strain amplifier. From the experience of the above-mentioned model experiments, it is inevitable to remove the influence of blade deformation into the output of a pressure gauge and to protect the gauge with specially designed adapter [22]. The adapters were made of stainless steel for the prevention of corrosion due to sea water. In order to confirm the effectiveness of this adapter, preliminary tests [22] were performed, in which full scale conditions were simulated to some extent.

Arrangement of Pressure Pick-ups

Twenty-four pressure pick-ups were equipped for each propeller from the limitation of number of channels of the present telemeter. The arrangement of pressure pick-ups on the blades of full scale propellers of the Seiun-Maru is shown in Table 5. From No. 2 to No. 5 blade, six pressure pick-ups were equipped on each blade. On No. 1 blade, three double-axis strain gauges were fitted. Among twenty-four pressure gauges, four pairs of gauges were fitted to the similar locations of other blades to evaluate the measurement accuracy and to examine the influence of capacity of the pressure gauge. It was not possible to arrange the pressure pick-ups at nearer positions to the leading edge than those in Table 5, because of the adapter size and the evaluation of measurement accuracy. The Helmholtz cavity chamber was filled with silicone sealant with the viscosity of 25 cs.

The cords of pressure pick-ups and strain gauges were installed into copper tubes to protect them from the periodical deformation of a propeller blade operating in non-uniform flow. The copper tubes were embedded in recesses with adhesive and filler, and faring was made along the blade surface to keep the original blade shape of the propellers.

Measuring System

The wired FM telemeter method [12] was adopted to transmit pressure and strain signals and the number of channels of the telemeter limited to thirty. Twenty-four channels among them were employed to measure the pressure on the propeller blades. Pressure signals were transmitted from the pressure pick-ups through waterproof connectors, pre-amplifiers, distributors, the telemeter for transmission, slip rings to the telemeter for receiver as shown in Fig. 10. The receiver had five switches corresponding to each blade so that the measurement at six channels can be performed simultaneously. The measured data were stored by an analogue data recorder. After A-D conversion, the measured pressure and strain signals were analyzed by a micro computer.

3.2. Tested Ship and Experimental Conditions

As a tested ship, the Seiun-Maru [22] was selected and employed for the present measurements by courtesy of the Institute for Sea Training. The propeller with three strain gauges and twenty-four pressure pick-ups was equipped to the ship in the dock as shown in Fig. 11. The transmitter of FM telemeter and the slip ring were attached to the propeller shaft as shown in Fig. 12 and the

Table 5 Arrangement of Pressure Pick-up on Full Scale Propeller

* Number Indicates Blade Number of Propeller

chordwise position	side of blade	radial position			
		0.5R	0.7R	0.9R	0.95R
10%	back		2 & 4		
	face		3		
15%	back			2	
	face			3	
25%	back		5	5	
	face				
40%	back	4	2 & 4	2	4
	face	5	3 & 5	3	5
60%	back		4	5	
	face				
80%	back		2 & 4	2	
	face		3	3	

receiver was placed in the exercise room on the upper deck. CP in 1989 and HSP in 1990 were tested. The pressure pick-ups and strain gauges were fitted to both propellers in Nakashima Propeller Co. Ltd. by engineers of three organizations (SRI, ALM and Nakashima).

In the 1989 measurement, the ship was operated with searching calm sea area. The change of draft during the measurement would be a few centimeters, estimating from fuel consumption. The thrust and torque coefficients for CP were analyzed to be 0.210 and 0.0339, respectively [22]. The advance ratio J was estimated as 0.62 from the data of a propeller open water test. The ship conditions of mean draft, trim and displacement for CP were 5.42 m, 0.08 B/S and 5,260 ton, respectively.

In the 1990 measurement, the Seiun-Maru with HSP was operated similarly to that with CP. Experimental conditions of ship speed, thrust and power versus the rate of propeller revolutions are plotted in Fig. 13. The relation between revolution rate and ship speed was almost linear. The measured thrust and power were roughly proportional to square and cubic of revolution rate, respectively. Roughly speaking, HSP was operated at almost constant advance ratio as CP. The advance ratio J for HSP was estimated as 0.66 under the conditions of 110 and 149 rpm. The thrust and torque coefficients under these conditions for HSP corresponded to 0.190 and 0.0303, respectively. The ship conditions of mean draft, trim and displacement for HSP were 5.17 m, 0.90 B/S and 4,942 ton, respectively.

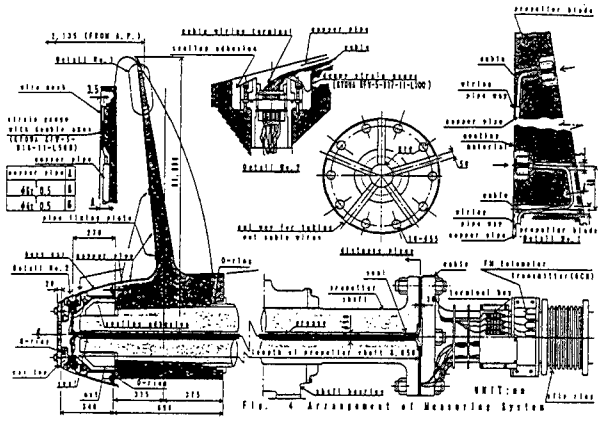

Fig. 10 Measuring System for Pressure and Stress in Full Scale

Fig. 11 Highly Skewed Propeller Equipped with Pressure Pick-ups and Strain Gauges

3.3. Measurement Procedure and Analysis Method

Before the measurement of pressure distribution at sea, the calibration of pressure pick-ups was performed in the dock. After filling sea water into the dock, floating the ship and settling the current down for one hour, the

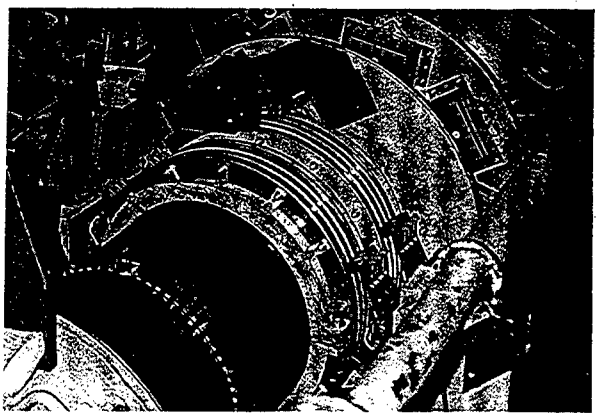

Fig. 12 Transmitter and Slip Ring

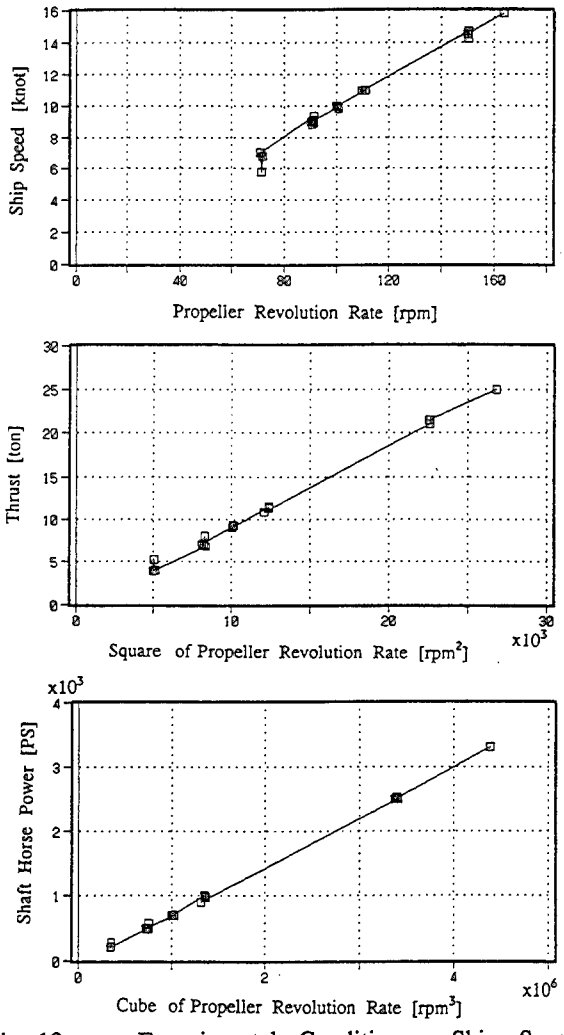

Fig. 13 Experimental Condition - Ship Speed, Thrust and Power versus Propeller Revolution Rate -

calibration was made. Regression analysis with the head calculated from the geometrical position of the pressure pick-ups was applied to get the calibration constants for each pressure gauge.

At the calibration of CP, some pressure pick-ups had been already out of order. On other pressure pick-ups of CP, the linearity between the head and the output of pressure pick-up was quite good. At the calibration of pick-ups for HSP, the coefficients of correlation were relatively worse than those of CP [22]. Only one pick-up was out of order for HSP.

Just before and after every pressure measurement, the standard pressure was measured without turning the propeller blade and with the ship speed less than 0.2 knots. Analogue pressure and strain signals and the position pulses of the blade were recorded by a data recorder. Some of the data were analyzed on board. The measurement was initiated when the revolution rate of a propeller and the ship speed became almost steady. Since the measurement was accomplished by sequentially changing the blade to be measured from No. 1 to No. 5 blade, simultaneous measurement could be conducted for the blade of interest. The measurement, however, was not performed simultaneously for other blades. Based on the position pulses of the propeller, the pressure signals were averaged, assuming that they were harmonic.

3.4. Measurements

Data Quality Evaluation

From the examination of the standard pressure measured immediately before and after the pressure measurement, little drift was observed for the present measurements, except two pick-ups (0.95 R, 40 %C, face and 0.9 R, 40 %C, face) of CP. The error of the averaged pressure measurements was estimated ± 0.01 kg/cm^2 except those at the top position of the propeller and under cavitating condition. Since the data analysis on the extremely low pressure equal to vapor pressure was carried out by the extrapolation using the calibration constants at dock and the measurement of the standard pressure, the error of the present measurements should be estimated to be ± 0.03 kg/cm^2 finally. Representing it by the pressure coefficient, it amounts to ± 0.12 for 110 rpm and ± 0.07 for 149 rpm, respectively. The error due to the trim of the ship during the full scale measurement was supposed negligible, because of little change of the draft at the stern.

The drift of standard pressure for HSP was relatively larger than that for CP throughout the entire full scale measurement of HSP. The influence of the drift on the pressure measurement, however, was negligible even for HSP owing to the measurement of the standard pressure at every runs. The error of the pressure measurements for HSP was also estimated to be the same as CP. Among the data in which the drift of standard pressure was negligible, the analyzed data were determined by taking account of sea state, steering angle and the stability of propeller revolution rate.

Variation of Blade Pressure during One Revolution

The variations of the measured pressure on HSP during one revolution at 110 and 149 rpm are shown in Figs. 14 (a) and (b), together with the computed values by one of Koyama's lifting surface theories [1]. Figs. 15 (a) and (b) show the pressure variation on CP at the same revolution rate of the propeller. The solid lines and broken lines show the measured and the computed results, respectively. The abscissa and the ordinate show angular position of the blade and the pressure coefficient, respectively. Zero degrees of the propeller angular position is defined as the generator line of the blade locates 12 o'clock. In these figures, the data for the pressure gauges which became out of order are excluded. The difference of measured pressure between two pairs at 40 %C of 0.7 R was very small, while that at 80 %C of 0.7 R was more remarkable.

In Figs. 14 and 15, the pressure at the back side of 0.7 R increases with the increase of angular position, while the pressure at the face side of 0.7 R decreases. This tendency is given by the tangential component of the wake and agrees with not only experimental results of pressure on the blade of propeller models in a towing tank [14] but also theoretical calculation. This explains one of the reasons why wider extent of cavitation on propeller blades working behind a ship appears mainly at starboard side.

In both figures, the plateau of the pressure variation at 15 %C from the leading edge on the back side at 0.9 R can be found. These pressure pick-ups were expected to be covered with unsteady sheet cavity. The slight virtual decrease of this pressure with the turning of the propeller blade was given by the correction of static pressure due to head variation. Under the condition higher than 90 rpm, sheet cavitation occurred near the tip. The measured pressure in the cavity on HSP was relatively higher than vapor pressure. This might be raised by more intermittent occurrence of cavitation or difference of cavity structure. On the other hand, the measured pressure in the cavity on CP was nearly equal to vapor pressure.

In the present measurement, little influence of difference of propeller revolution rate into the pressure coefficients was observed and a similarity law was established except the region of cavitation. From the view point of the measurement of absolute pressure, it is expected that these measurements are surely reliable.

In the pressure variation on the face side during one revolution at 80 %C of 0.9 R under 149 rpm as shown in Figs. 14 (b) and 15 (b), an interesting phenomenon was observed. At the angular position between 30 and 40 deg for CP and 60 and 80 deg for HSP, fluctuating pressure was detected by a pressure pick-up on the face side where cavitation did not exist. This pressure might be brought about by unsteady cavitation on other blades in the propeller slip stream such as the break-down of tip vortex cavitation.

Among these pressure variations, the pressure curve in the back side at 80 %C of 0.9 R on HSP was very peculiar, since it moved once to the positive direction and then stepwise shifted toward the negative direction at the angular position of about 50 degrees. Similar but less remarkable behavior could be found in the pressure variation not only at 60C % of 0.9 R of HSP but also at 60 %C and 80 %C of 0.9 R of CP. In the measurement of HSP, three pairs of pressure pick-ups were alive.

Chordwise and Radial Pressure Distribution

The chordwise pressure distributions at 0.7 R and 0.9 R, and radial ones at 40 %C for each 90 degrees of angular position under the condition of 110 rpm for CP and HSP are shown in Figs. 16 and 17, respectively. In these figures, theoretical values given by the lifting surface theory are included. Discussion on the correlation between the experiment and the theory will be presented later.

The chordwise pressure distributions at 0.7 R and

0.9 R, and radial ones at 40 %C for 110 rpm are shown in Figs. 16 (a) and (b), respectively. As an interesting characteristic of the chordwise pressure distribution, it can be cited that the pressure distribution at 0.7 R of HSP is similar to that of CP, while the pressure on the back side at 0.9 R becomes lower towards the trailing edge. Even turning normally, the loading at the trailing edge of HSP is extremely higher than expected as if the propeller would operate under the astern condition. On the other hand, the loading at the tip of HSP locally becomes higher than that of the inner position not like CP.

In Fig. 17 (a), the chordwise pressure distribution of 0.9 R at 90 and 180 degrees of angular position looks like the letter "M". Similar pressure distributions were observed in the pressure measurements on HSP model of the Seiun-Maru as shown in Fig. 6 (a). It seems that

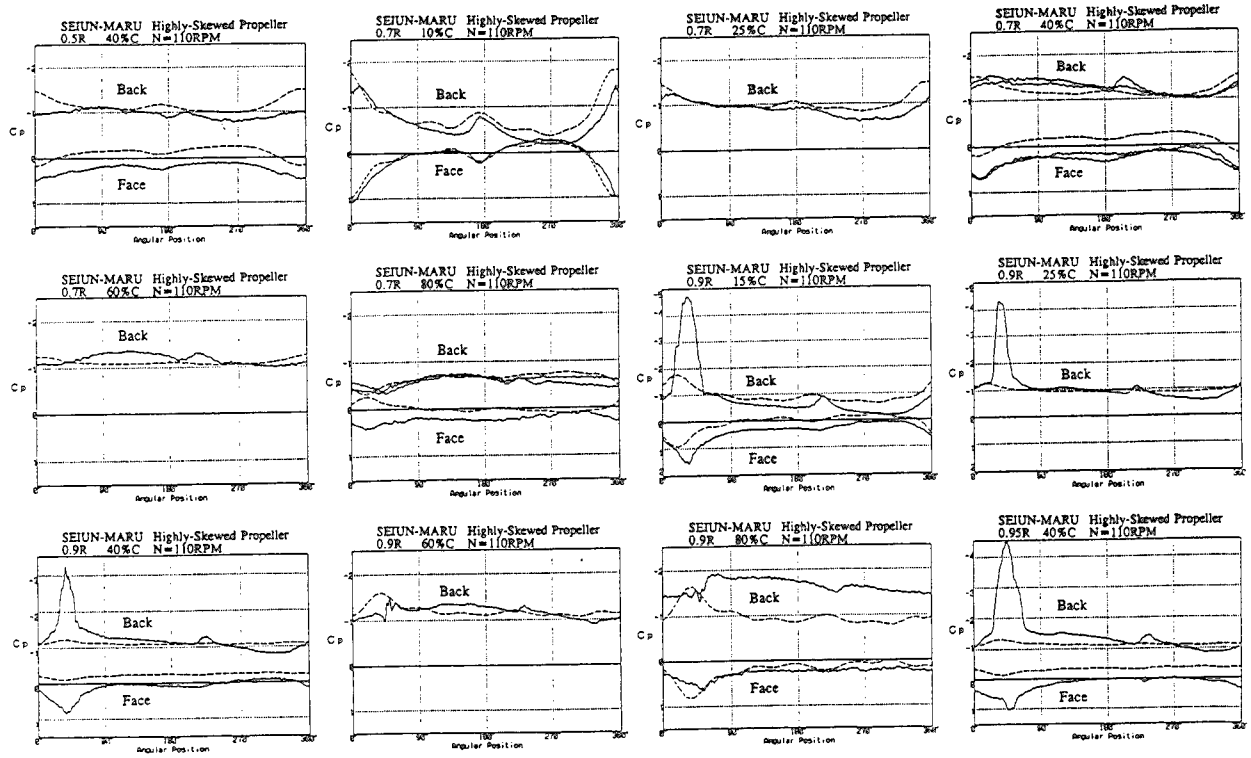

Fig. 14 (a) Variation of Averaged Pressure during One Revolution - HSP, 110 rpm

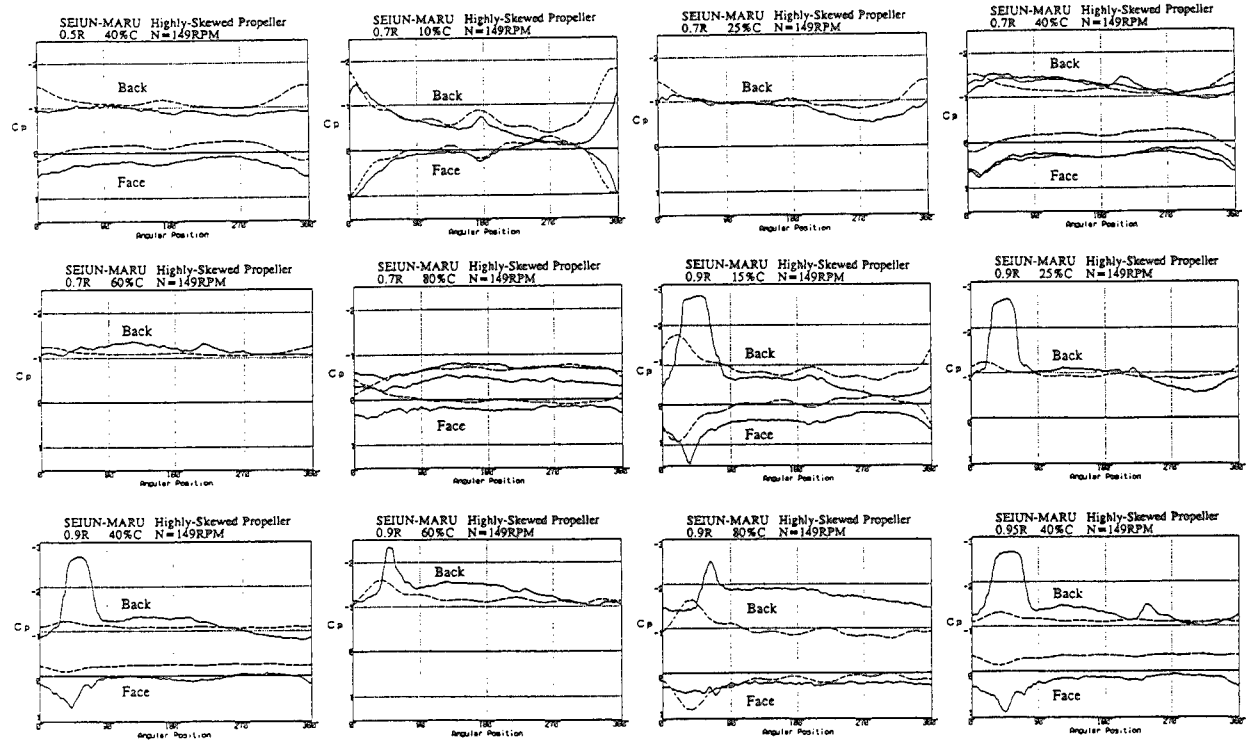

Fig. 14 (b) Variation of Averaged Pressure during One Revolution - HSP, 149 rpm

these interesting phenomena might be caused by transient behavior of laminar separation bubble or radial vortex formed by leading edge separation.

Concerning radial pressure distribution in Fig. 16 (b), peculiar characteristics that the pressure at 0.95 R on the face side of HSP rapidly jumped to negative pressure were found independently of angular position. Although the loading at the tip on CP would be very light, it could not be concluded definitely because some pressure pick-ups in the vicinity of tip were broken out.

3.5. Discussions

Theoretical Calculation and Estimated Wake Distribution

The comparison of measured pressure distribution with the theory is very important to evaluate the reliability

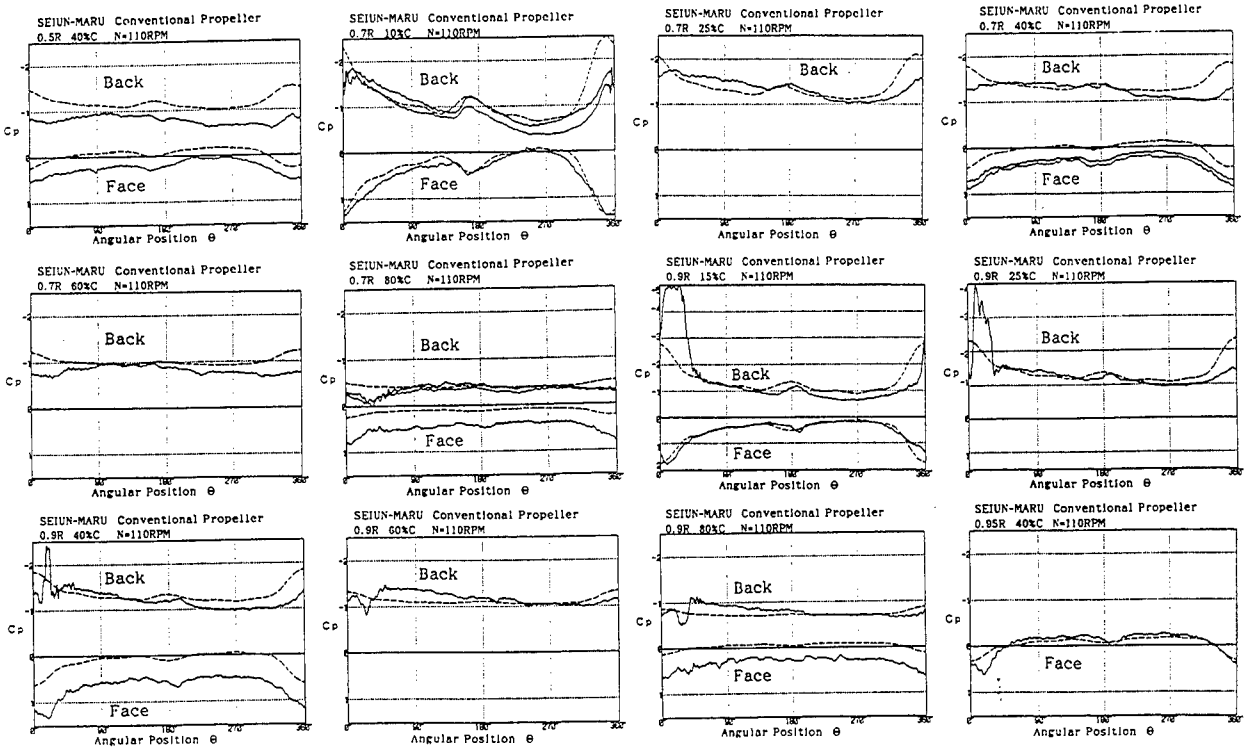

Fig. 15 (a) Variation of Averaged Pressure during One Revolution - CP, 110 rpm

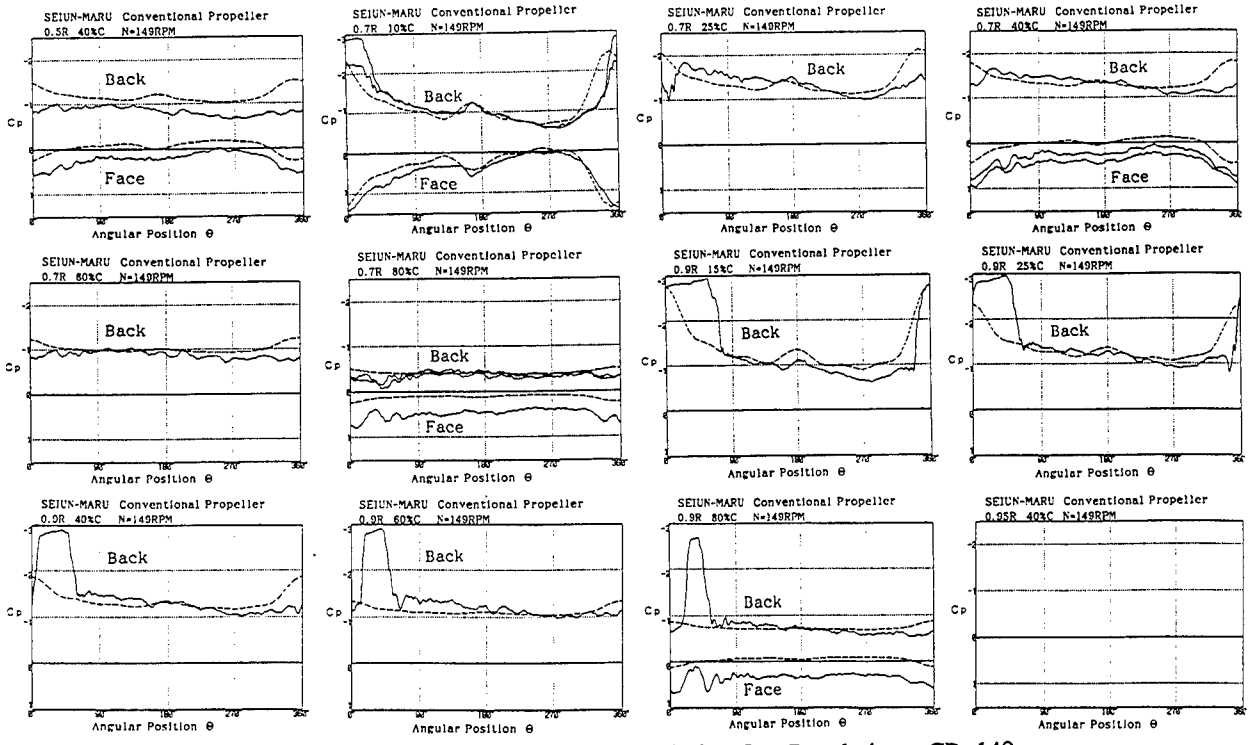

Fig. 15 (b) Variation of Averaged Pressure during One Revolution - CP, 149 rpm

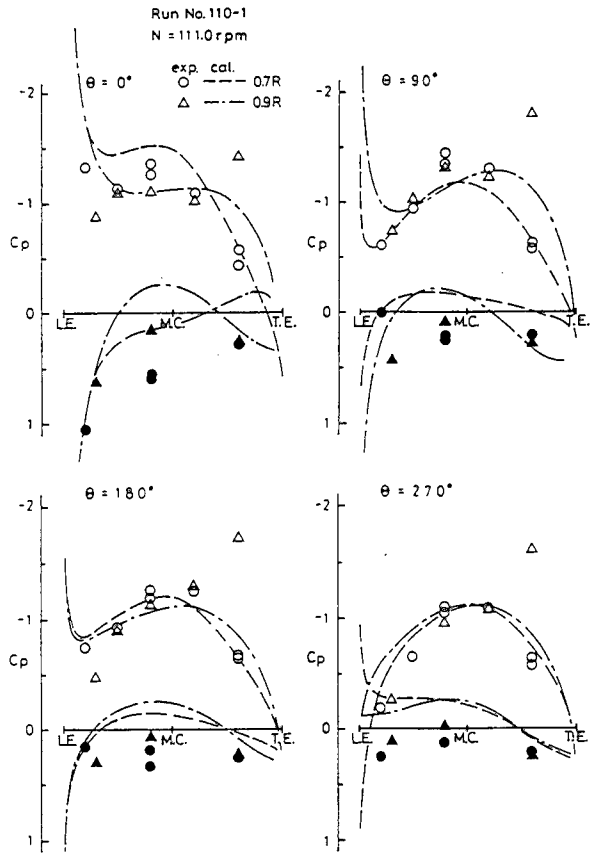

Fig. 16 (a) Chordwise Pressure Distribution at 0.7 R and 0.9 R on HSP

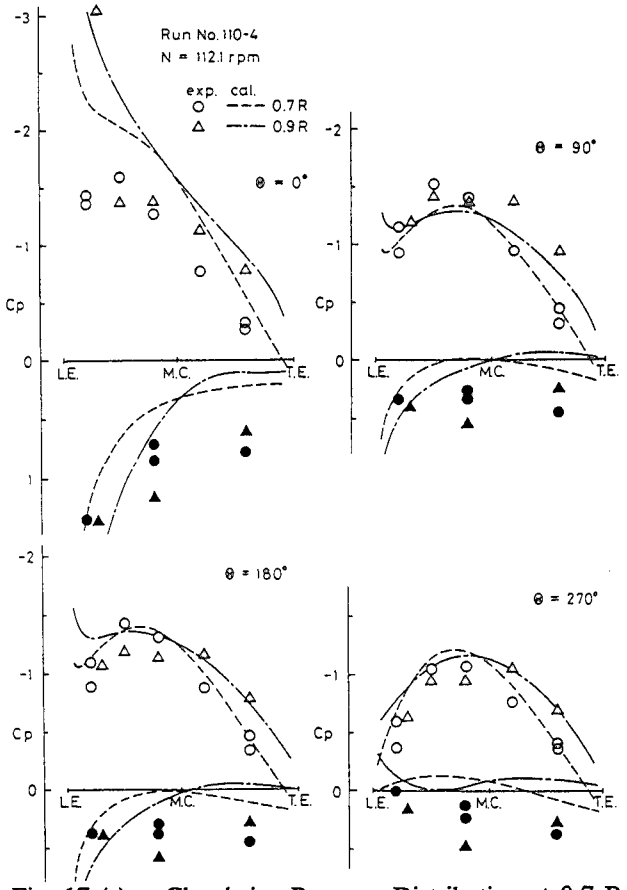

Fig. 17 (a) Chordwise Pressure Distribution at 0.7 R and 0.9 R on CP

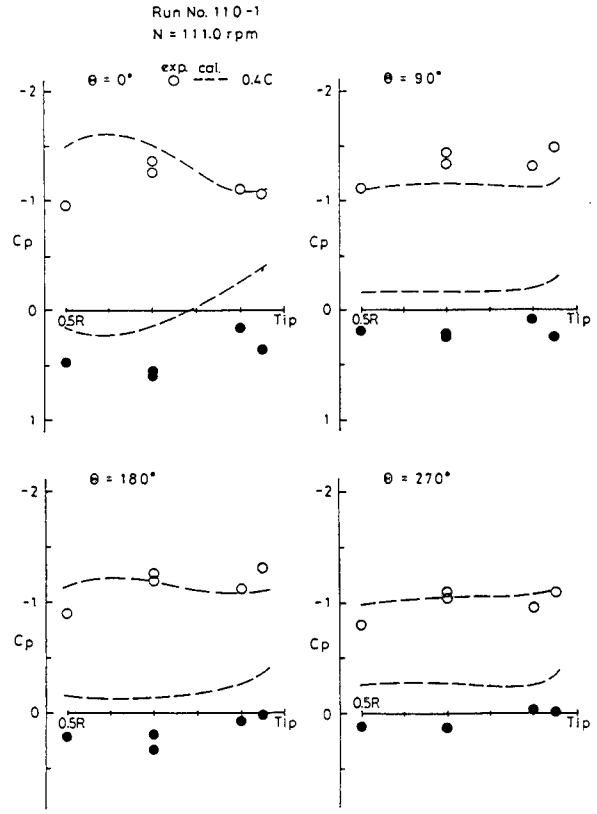

Fig. 16 (b) Radial Pressure Distribution at 40 % Chord on HSP

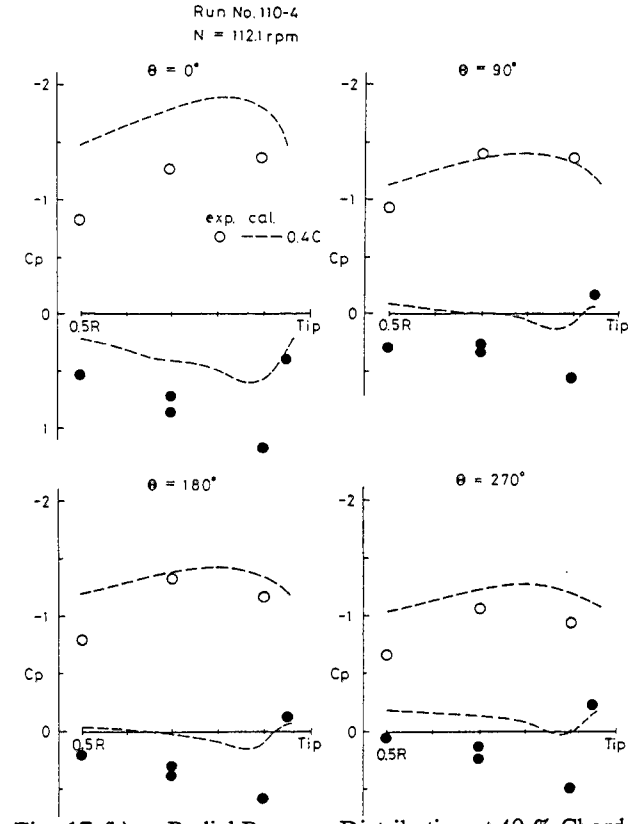

Fig. 17 (b) Radial Pressure Distribution at 40 % Chord on CP

of the present measurement and an existing propeller lifting surface theory [1]. As input data of the wake distribution, the estimated one [23] by Sasajima's method was derived from the measured wake distribution in a towing tank. This wake is shown in Fig. 18. The tangential component of wake distribution measured in a towing tank was applied to this estimation without modification.

Operating conditions of each propeller were determined to be K_T = 0.210 for CP and 0.190 for HSP, respectively. These conditions correspond to the condition of 110 rpm and 149 rpm for both propellers. Under these conditions, cavitation extent was not so large for 110 rpm and the revolution rate of the propeller was stable, and then the output of pressure pick-ups was sufficiently large. The thrust at each operating condition was obtained by reading the thrust meter equipped to the Seiun-Maru.

In the present calculation, symmetric estimated wake distribution as shown in Fig. 18 was used as input data. In the full scale measurements, however, some instruments for the wake measurements [8,9] were installed on the hull surface at the starboard side as shown in Fig. 19. The wake measurement was performed using the complete ship model and simulating the miniature models of the instruments for full scale wake measurements for HSP in the cavitation tunnel. The measured nominal wake distributions at the propeller disk without and with instruments are shown in Figs. 20 (a) and (b), respectively. The latter wake was asymmetric and the wake peak revealed at the starboard side. Using this wake, the pressure distribution on the HSP was recalculated and the calculated pressure variation during one revolution at two locations (10 %C, 0.7 R and 15 %C, 0.9 R) is shown in Fig. 21 with the measurements. The calculation was conducted by the thrust identity method. Slight improvement on the correlation between the measurements and theory was found. The difference considerably decreased in the phase delay of the negative pressure peak between the measurements and the calculations. At other locations, negligible change in the calculated values was observed due to the difference of the input wake, comparing with the data in Fig. 14 (a).

Variation of Blade Pressure during One Revolution

Comparison of the pressure between measurement

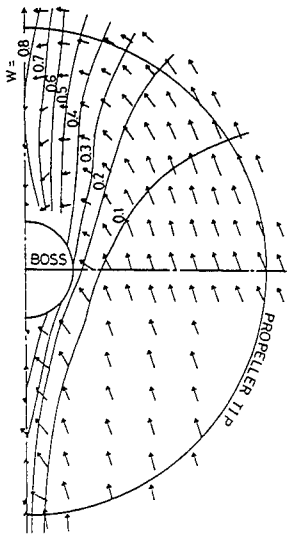

Fig. 18
Axial and Tangential Wake Distribution Estimated by Sasajima and Tanaka's Method (1-w = 0.816)

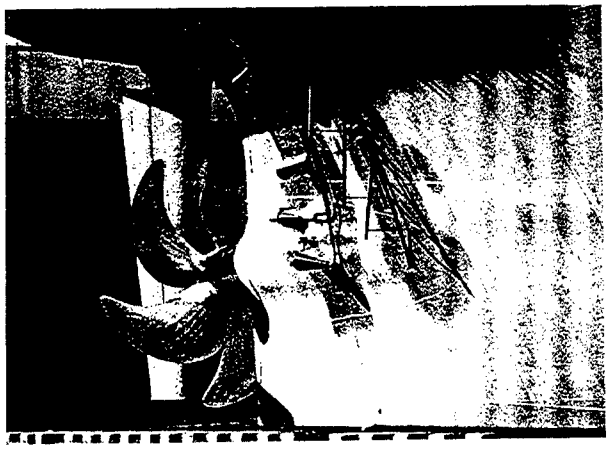

Fig. 19 Arrangement of Measurement Instrument around Ship Stern with HSP

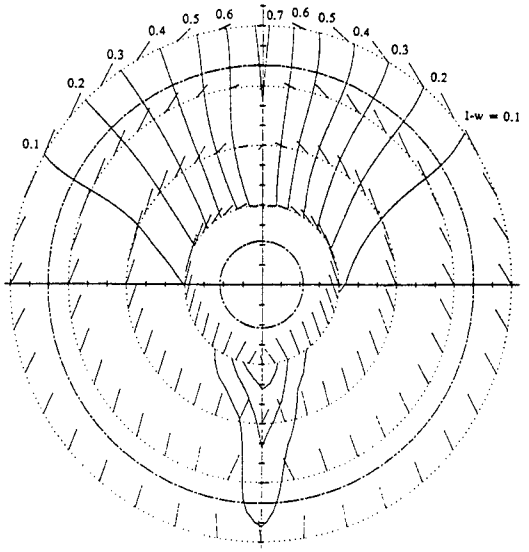

(a) behind Ship Model without Measurement Instrument (1-w = 0.822)

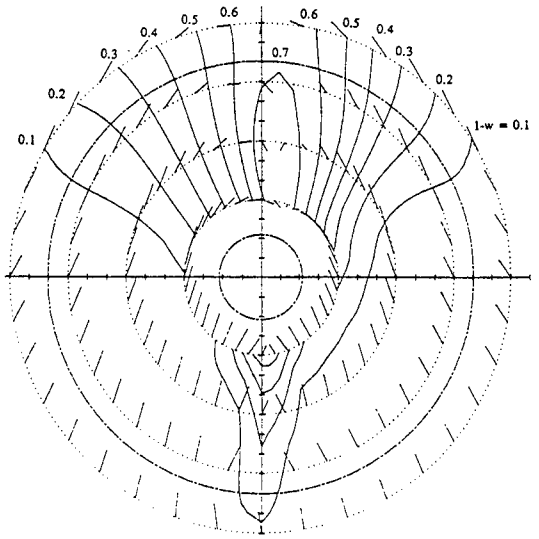

(b) behind Ship Model with Measurement Instrument (1-w = 0.790)

Fig. 20 Simulated Wake Distribution in Cavitation Tunnel

and theory for both propellers is shown in Figs. 14 and 15. Theoretical pressure variation at 40 %C of 0.5 R is lower than the experimental one on both back and face sides. Since both agreed with each other qualitatively, the difference between them was brought about by excess computation of induced velocity due to displacement effects which was calculated by the "equivalent two-dimensional profile" method similar to the "strip theory". The same discrepancy was observed in the comparison between the theory and the model measurement on the Seiun-Maru propellers. Therefore, it can be concluded that the present pressure calculation method has room to be improved.

At 10 %C of 0.7 R, excellent agreement between theory and measurement was obtained not only on the back side but also on the face side for both propellers except cavitation region. In the vicinity of the top position of a propeller blade, however, the pressure peak given by the theory was lower than then measured one of 110 rpm. This discrepancy was expected to be caused by the decrease of wake peak due to the propeller suction. At other positions on the back side of 0.7 R, close agreement was obtained except near the top position of the propeller. On the other hand, the same tendency as that of 0.5 R was found on the face side at 40 %C and 80 %C of 0.7 R.

At each location 0.9 R on the back side for CP, the present theory also corresponded well to the measured pressure except the region where sheet cavity might cover the pressure pick-up. At 15% C of 0.9 R on the face side of CP, excellent agreement was observed.

Sharp peaks were found in the pressure variation in the fore part of the blade on the back side at 0.9 R of HSP for 110 rpm and might be given by intermittent cavitation or low pressure of the vortex core. At other positions on the back-side of 0.9 R for HSP, the theory predicted the measured pressure very well. Under these conditions, three-dimensional effects due to cavity on pressure distribution were considered to be small from the present measurements. On the face side of each propeller, the same discrepancy at 0.9 R was presented as found at 0.5 R and 0.7 R.

There existed remarkable difference of the pressure variation between CP and HSP at 80 %C of 0.9 R for both propeller revolution rates. At about fifty degrees of angular position of the propeller blade, the pressure once shifted positively and then jumped stepwise and negatively. This measured pressure variation can not be predicted by the theory. This pressure jump was not found in the measurement of CP even in full scale clearly. Examining the pressure variation on other pick-ups of not only CP but also HSP carefully, similar but very tiny jump can be found at 60 %C of 0.9 R for both propellers and at 80 %C of 0.9 R for CP. This might be caused by the crossing of the tip vortex or the "part-span vortex" stemmed from leading edge separation above the pressure pick-ups as shown in Fig. 22. This type of vortex was expected to be similar one to that observed in the face cavitation.

The pressure variation at 0.95 R on the back side was affected by sheet cavitation. In the non-cavitation region, the discrepancy between the theory and the measurement was found as observed in the measurement of HSP model in Fig. 9 (d), and it is supposed that the present theory can not predict the pressure near the tip significantly.

Chordwise and Radial Pressure Distribution

As shown in Figs. 16 and 17, excellent agreement between the theory and the full scale measurements of the pressure on the back side of 0.7 R and 0.9 R for CP were obtained except at the angular position of zero deg, while the theory predicted fairly lower pressure distribution on the face side than that of the measurements. Since the same trend was observed on the propeller model, the theory should be to blame for the discrepancy.

The theory agreed well with the measurements of chordwise pressure distribution at 0.7 R of HSP as shown in Fig. 16 (a). On the contrary, the measured pressure in the aft part of 0.9 R became extremely lower with approaching to the trailing edge and deviated completely from the computed one. This indicates that the load around the trailing edge near the tip of HSP was surprisingly higher than that expected by the theory. This pressure drop in the vicinity of the trailing edge at 0.9 R is supposed to be affected by the existence of vortex stemmed from leading edge separation. To simulate such flows around the propeller blades, the development of a new propeller theory including the modelling of leading

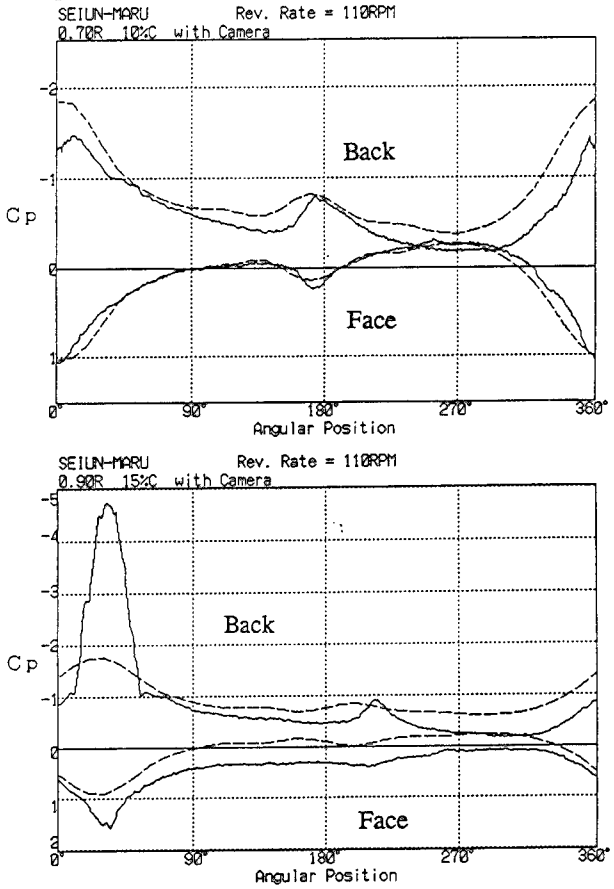

Fig. 21 Comparison of Pressure Variation during One Revolution between Measurement and Calculation with Corrected Wake

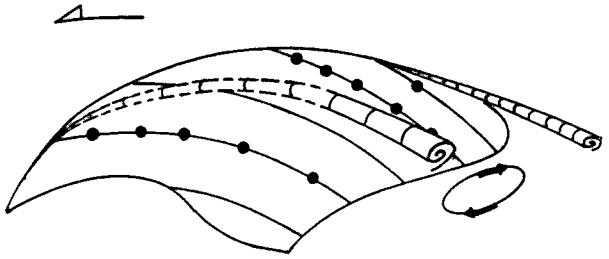

Fig. 22 A Model of Leading Edge Separation Vortex

edge separation as shown in Fig.22 is necessary (for example, [21]). The present measurements suggeste that even if a propeller rotates normally, the tip of HSP is heavily loaded stepwise and twisted to the inverse direction against the expectation. Therefore, if a crack happens to occur at the trailing edge of the blade near the tip, the crack on HSP would grow much more rapidly than CP due to such repeated high loadings near the tip.

As shown in Fig. 16 (b) of the radial pressure distribution at 40 %C of HSP, the present measurements also suggested that the measured propeller load at the tip was higher than the computed one by the lifting surface theory. This HSP was specially designed to make much thicker than the NK rule and to decrease the geometrical pitch at the tip, though.

The comparison between the theory and the measurement clearly indicates that there still remain some problems to be improved for the existing propeller lifting surface theory and the design of HSP from the view point of propeller strength.

4. MEASUREMENT OF BLADE STRESS ON FULL SCALE PROPELLER

4.1. Measurement Procedure

In the measurement of blade stress on the full scale propellers, two kinds of strain gauges were employed. One of them was waterproof double-axis strain gauge (Kyowa KFW-5-D16-11-L500) as an active gauge for the measurement and embedded on the blade. The other was triple-axis strain gauge (Kyowa KFW-5-D17-11-L100) as a dummy gauge for temperature compensation and installed into the boss cap. In order to prevent the strain gauges from the separation due to the flow above the blade surface, the active strain gauges were embedded to the hollow blade surface dug with 3.5 mm deep with adhesive, and covered with wire mesh screen and soldered as shown in Fig. 23. The diameter of the follow surface was determined 50 mm to depress the influence on the measurement due the change of blade section within 10 % error. The cords were surrounded with copper tubes and tubes was attached to the blade with pipe fixing plate and adhesive. The recesses were coated with adhesive and filler, and finally the coated portion was finished to present a smooth flush surface by a grinder after hardening of the coating.material. Three strain gauges for the measurement were stuck on 70 % chordwise position at 70, 80 and 90 % radial positions of the No. 1 blade on the face side for each propeller as shown in Fig. 24.

To coincide one of the strain gauge axes with the direction of principal stress, each of them was arranged parallel to the tangents of 70 %C line, while another of the strain gauge axes were put to the normal to the chord line. In this paper, the respective directions are denoted as R and T. Two triple-axis strain gauges were stuck on the hollow place of the boss cap where the measurements were not to be influenced due to deformation of a propeller. At each stage of the preparation work, the line resistance and the earth resistance were measured by a digital voltmeter and checked. Finally the load test to the propeller blade was performed by using an oil pressure jack and the response of each gauge was examined.

The measurement system of blade stress was the same as that of pressure in full scale. The signals of strain gauges on the blade were transmitted to the receiver of the wired FM telemeter through the waterproof connection, the cords in the hollow propeller shaft and the slip ring attached to the propeller shaft and analyzed by a micro computer.

4.2. Measurements

Calibration and Measuring Procedure

Calibration of the strain gauges was carried out by impressing the voltage equivalent to 500 μ strain at the terminal of the telemeter in the dock. Even under the static condition when the blades are not operating, it is expected that the measured strain are affected by the strain due to the weight of the blade itself. Little difference, however, in the measured strain was found between the angular position at 0 deg (top) and 180 deg (bottom) within the accuracy of measurement. In the same manner as the pressure measurement, the acquired data during 8.2 sec were averaged and the variation of blade strain during one revolution was obtained. Just before and after the measurements, zero strain was measured under the condition that the propeller stopped and the ship speed was less than 0.2 knots.

Measured Results

CP. The measurements of blade stress on CP were performed for various propeller revolution rates of 70, 90, 110, 149 and 163 rpm as in the measurements of pressure distribution. Fig. 25 shows typical measured strain values at 0.7, 0.8 and 0.9 R during one revolution at 112.4 rpm. Positive and negative values are tension and compression, respectively.

Since the measured strain decreased with approaching to the propeller tip, this tendency agreed with the existing measurements. For the measurement on the radial direction, only tension stress acted to the blade during one revolution at each radial position, while for

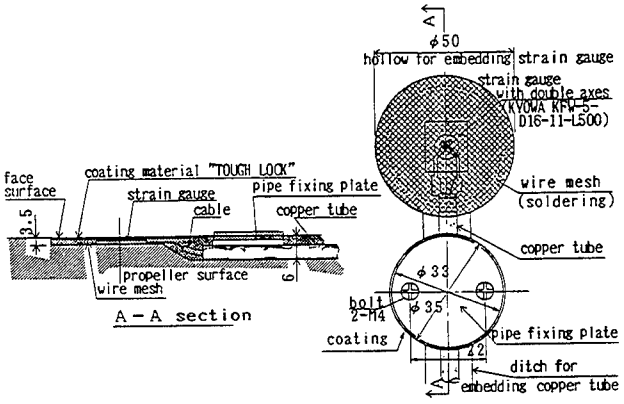

Fig. 23 Fitting of Strain Gauge on Blade Surface

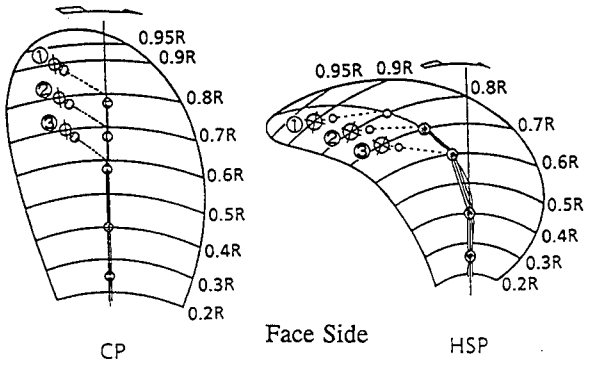

Fig. 24 Location of Active Strain Gauge

tangential direction, the strain at each radial position was very low. It proved that each strain gauge was stuck on so that one of the axes coincided with the direction of principal stress. Comparing the maximum principal stress at 70 %C at each radial position with the calculated values by FEM at the design of the propeller [23], the former was higher than the latter by about 7 ~ 20 % as shown in Table 6.

HSP. The measurements were conducted at the propeller revolution rates of 70, 90, 110 and 149 rpm. Fig. 26 shows the variation of measured strain during one revolution at 0.7 R for 110 rpm. Tension stress was found in the radial direction R and in the tangential one T as well. One of the reasons may be due to disagreement of the direction between the principal stress and the axis of strain gauge. This might be caused by that the lifting surface calculation could not predict the pressure distribution in the vicinity of the propeller tip accurately.

At the angular position of 45 deg, sharp peak of the radial strain was found. Near the bottom, the strain values in both direction were constant. At the port side, the strain values become minimum. Radial strain values at three radial positions varied with corresponding to the pressure variation at 40 % of 0.95 R as shown in Fig. 14 (a). A strong correlation of the measurements was found between the strain and the pressure variation during one revolution. A comparison of mean principal stress at 70%C between the measurement and FEM analysis at the design of HSP was shown in Table 6. Except 0.9 R, the measured values were less than the predicted ones by the FEM. The pressure distribution as the input data for the FEM calculation was calculated by Yamasaki's lifting surface theory [24] using the estimate wake without the tangential wake as shown in Fig. 18.

4.3. Discussions

Comparison of Measurements between CP and HSP

From the comparison of two measurements on CP and HSP, it was observed that the radial strain at 0.7 ~ 0.9 R of CP was more predominant than tangential one. The radial strain of HSP was also more predominant than the tangential one, while the tangential one was negligible. Although one of the axes of the strain gauges on HSP did not coincide with that of the principal stress and the blade thickness was different between them, qualitative comparison might be possible. Introducing non-dimensionalized stress and comparing two measurements, the mean stress on CP was larger than that of HSP, while each amplitude was comparable as shown in Fig. 27. Roughly speaking, the measured stress on HSP was constant independent of the propeller revolution rate, while that of CP tended to slightly decrease with the increase of the revolution rate.

Comparison between Measurements and FEM Computation

To discuss how accurately the FEM can predict the blade stress distribution on full scale propellers, FEM computation on the HSP was performed by using the MSC/NASTRAN [25]. The propeller blades were modelled by 528 quadrilateral elements and divided by twenty-four in the radial direction and twenty-two in the chordwise direction. The number of connection point was 575. The boundary condition at 0.2 R was given as fixed support. Since the accuracy of FEM computation became worse due to the rapid decrease of the blade thickness and the use of constant thickness element in the vicinity of the

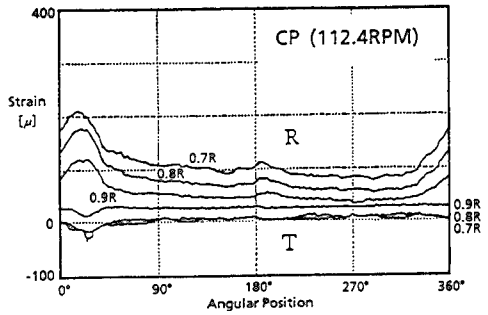

Fig. 25 Variation of Blade Strain during One Revolution on Full Scale CP

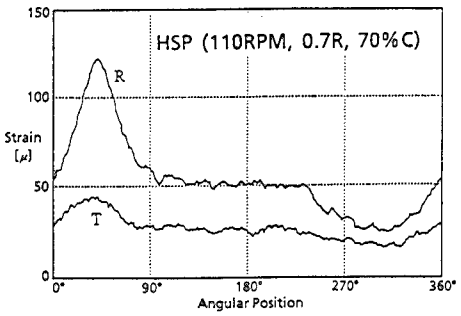

Fig. 26 Variation of Blade Strain during One Revolution on Full Scale HSP

Table 6 Comparison of Blade Stress along 70% C between Measurement and calculation by FEM

Radial Position	Measured Value [kg/mm²]	Predicted Value [kg/mm²]
CP (Max. Stress, 163rpm)		
0.7R	4.8	4.5
0.8R	3.6	3.1
0.9R	1.8	1.5
HSP (Mean Stress, 149rpm)		
0.7R	1.2	1.5
0.8R	0.9	1.2
0.9R	0.6	0.6

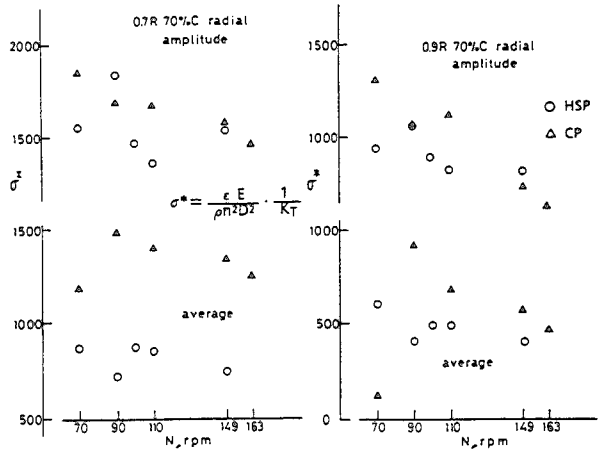

Fig. 27 Comparison of Non-Dimensionalized Blade Stress between Full Scale CP and HSP versus Propeller Revolution Rate

tip, the blade shape of the leading edge near the tip was slightly modified.

The loadings to the blade are considered to be composed of hydrodynamic force and centrifugal one. Two kinds of hydrodynamic loadings were employed as input data. One of them was the calculated results of pressure distribution by Koyama's unsteady propeller lifting surface theory [1]. These results were employed in the comparison of pressure between the measurement and the theory described in the previous chapter. Another loading was the pressure distribution modified by the measured pressure in the vicinity of the propeller tip.

A comparison of the radial and tangential strain variation at three radial positions between the measurements and FEM calculation is shown in Fig. 28 under the condition of 110 rpm. In this figure, the computed strain was transformed to the respective axial components of the used strain gauges. The FEM computations agreed well with the measurements qualitatively and they were predicted smaller than those of the measurement. Fig. 29 demonstrates the variation of the maximum stress during one revolution. The region of relatively large stress extended to the trailing edge of the propeller blades. It is an inherent phenomenon to HSP [26]. At the angular position of 20 degrees, large peak of the stress revealed.

In Fig. 30, the blade stress distribution calculated by FEM with the modified pressure distribution at the angular position of 40 degrees is compared with the calculated distribution by the lifting surface theory. The calculations with the correction using the measured values indicated the higher stress area at the trailing edge of 0.7 R than those without the correction. From the present calculation, it was recognized the tendency that the corrected pressure distribution predicted more accurate blade stress distribution than that without the correction quantitatively. To improve the prediction of the blade stress, more precise and advanced program code of lifting surface theories are needed. Therefore, the introduction of leading edge separation vortex and tip vortex to a lifting surface theory is inevitable and the vortex lattice method is more suitable because the modelling of separation vortex is easier than the mode function method.

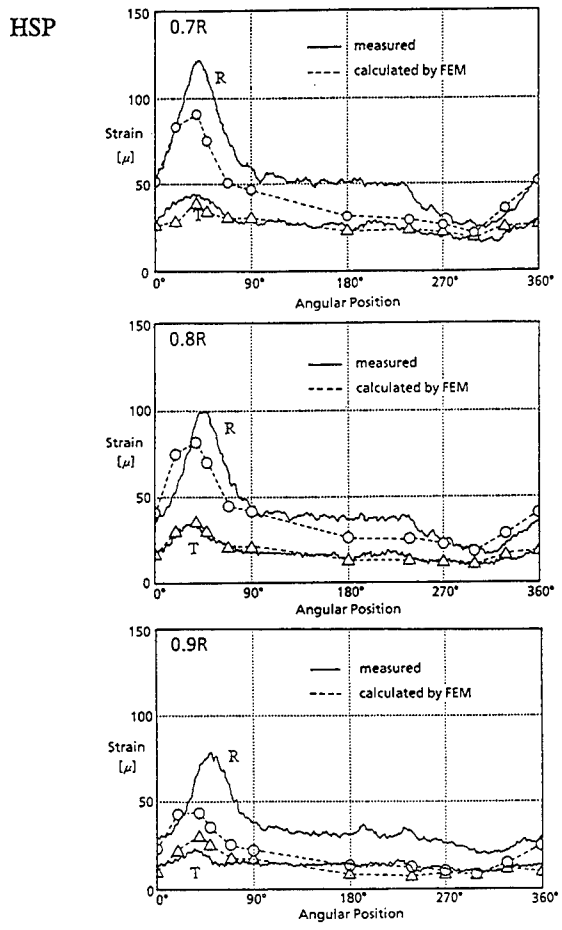

Fig. 28 Comparison of Blade Strain Variation during One Revolution between Measured and Calculated Values by FEM (110 rpm)

5. Blade Stress Measurement on the Propeller Model

5.1. Tested Model

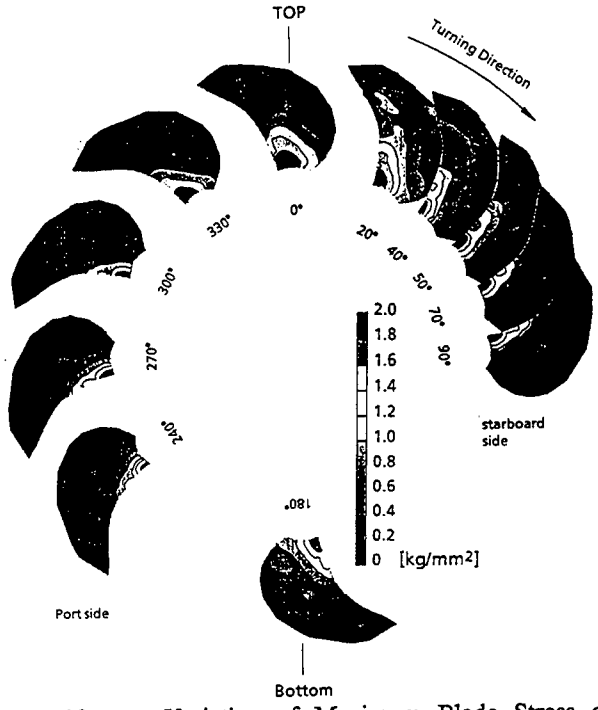

Fig. 29 Variation of Maximum Blade Stress on HSP during One Revolution Calculated by FEM (110 rpm)

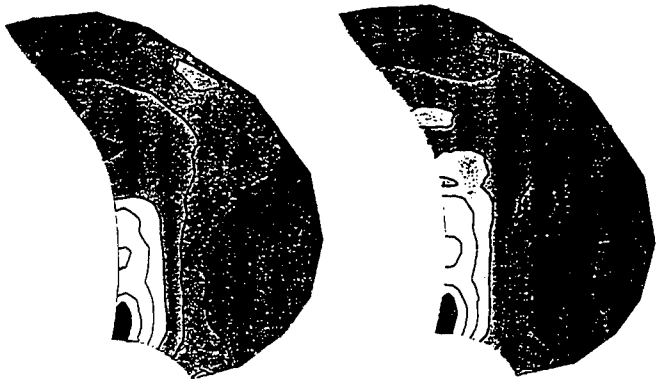

Fig. 30 Comparison of Stress Distribution between FEM Calculation Results by Two Kinds of Pressure Distribution (110 rpm, 40 deg)

The measurements of blade stress on the propeller model have been performed by a number of researchers. Since most of the measurements were made in a towing tank, the wake distribution was model one, Reynolds number at the measurement was considerably low and neglected the influence of cavitation, e.g. [26]. The present measurements was conducted in the No. 2 working section of SRI large cavitation tunnel using a complete ship model. To simulate the estimated wake for the full scale in the cavitation tunnel, a pair of the flow liners was employed [13] as shown in Fig. 31. The simulated wake is shown in Fig. 20 (a). The principal dimensions of ship and propeller model are shown in Tables 1 and 2.

Five waterproof double-axis strain gauges (Kyowa, KFG-1-120-D16-23 N30C2) were stuck on the blades by two kinds of methods. Two of the gauges were stuck on the blade surface directly and covered with the coating for waterproofing the gauges and smoothing the surface profile. Three of them were embedded on the hollow blade surface whose diameter and depth were 7 mm and 0.5 mm like the full scale measurement, respectively. The gauges were covered with a synthetic compound and finished to get a smooth flush surface. The former is called "On-blade method", while the latter is called "In-blade method" in this paper. The direction of the gauge axes was set in the same manner as the full scale. The arrangement of five gauges is shown in Fig. 32. Dummy gauge for the temperature compensation was installed into the propeller boss cap.

5.2. The Measurement Apparatus

For the present measurement, a transmitter and a receiver for the wired FM telemeter system with five channels were provided. The transmitter in a waterproof airtight case was installed into the ship model and connected to the propeller driving system (Kempf and Remmers) as shown in Fig. 33. The inside of the model was filled with water and the pressure was reduced to the given low pressure. Five strain signals were acquired simultaneously with the position pulses of the propellers and recorded by an analogue data recorder. Then, the whole measurements on five double-axis strain gauges could be accomplished by twice measurements.

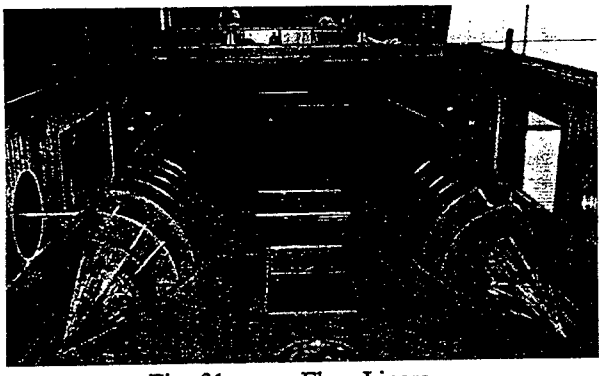

Fig. 31 Flow Liners

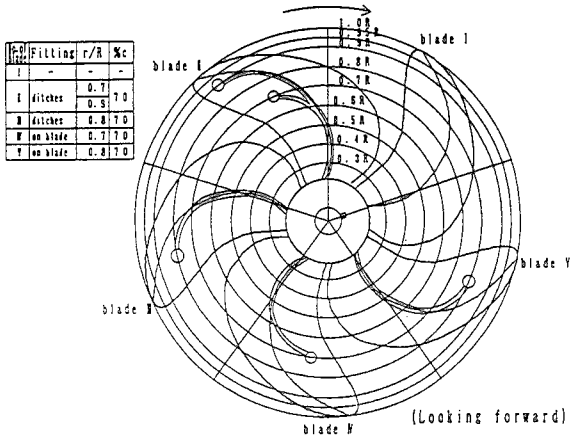

Fig. 32 Arrangement of Strain Gauges on HSP Model

5.3. Experimental Condition and Procedure

The experimental conditions of the model measurement were determined according to those of the full scale measurement. The revolution rate of the propeller model at the measurement was determined so that the relation between the hydrodynamic load to the blade and the strain for the model was kept to be similar to that for the full scale. The ratio $\rho n^2 D^2/E$ of the model was determined to be equivalent to that of the full scale under the conditions of 70, 90,110 rpm. For 149 rpm, it was impossible to conduct the measurement at the propeller revolution rate given by the present similarity law because of the strength of the models and the telemeter. Young's modulus for the model and the propeller were 12,000 and 7,000 kg/mm^2, respectively. The pressure was determined as the cavitation number at the shaft center was equal for both cases. Cavitation patterns on the model were similar to those on the full scale in the angular positions when the observation was possible in the full scale. The inflow velocity was determined by K_T identity method. K_T values were given by the full scale measurement. These experimental conditions were determined by using another propeller model without strain gauges.

5.4. Measurements

Just before and after the measurement, the drift of zero strain at each gauge was measured. Throughout the measurement, it was very small and the maximum value was 3 μ strain. The data analysis was for about 2000 data per one channel was made by the same procedure as in the full scale measurement. The scatter of the measurements were extremely smaller than those of the full scale and 5 μ strain in standard deviation. As a representative example, the variation of the measured strain is presented during one revolution at the propeller revolution rate of 110 rpm as shown in Fig. 34. For other conditions, similar distribution were obtained except that sharp peak of the strain became flat due to cavitation. Comparing these data with those in full scale, excellent agreements were found.

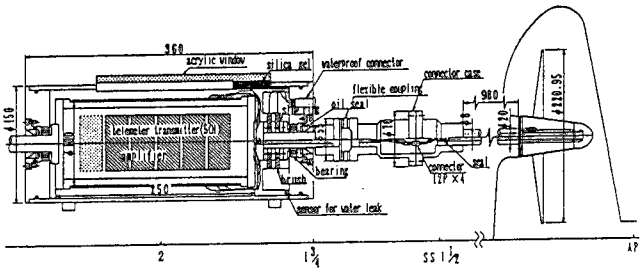

Fig. 33 Measuring System of Blade Stress on Model Propeller

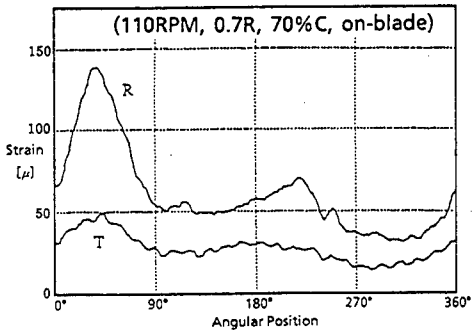

Fig. 34 Variation of Measured Blade Strain during One Revolution on HSP Model

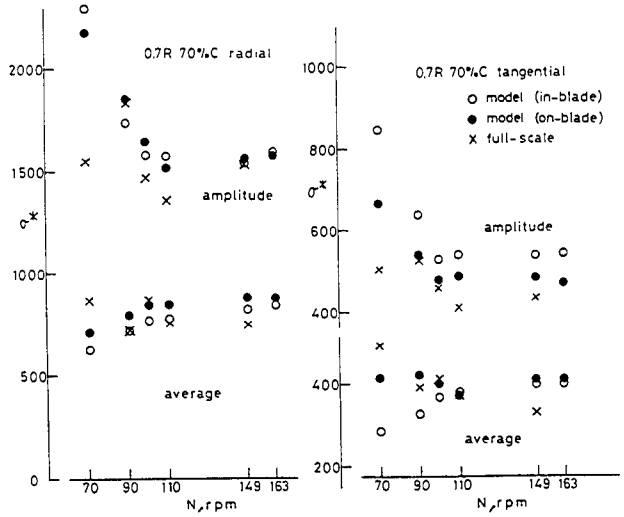

Fig. 35 Comparison of Non-Dimensionalized Blade Stress of HSP between Model and Full Scale

Non-dimensionalized blade stress measurements at 0.7 R on HSP model are demonstrated in Fig. 35, with the full scale measurements as a function of the propeller revolution rate in full scale. The amplitude of blade stress except 0.9 R agreed well between the model and the full scale, while close agreements were found on the mean values at 0.7 R. The measurements in full scale and those on model by two kinds of methods agreed well each other, except on the mean value at 0.8 R. On-blade method, if anything, presented closer correlations than In-blade method. The present model test including the simulation of cavitation can predict the full scale phenomena very well not only qualitatively but also quantitatively.

CONCLUSIONS

First of all, in this paper, sophisticated measurement techniques have been developed to measure the pressure distribution on the propeller model. The pressure distributions were measured on CP and HSP working not only in uniform flow but also non-uniform flow. From the measurement and the comparison with a lifting surface theory, the following conclusions can be drawn.

1. The present measurement technique using Helmholtz cavity chamber typed pressure transducers can measure pressure on propeller models without the effects of blade deformation.
2. The measured pressure distribution on the blades of a propeller model agrees well with the theory not only in uniform flow but also in non-uniform flow except near the tip. On the pressure side, however, the theory underpredict the pressure regardless of advance ratio, skew and flow.
3. The measured pressure distribution of HSP seems to be affected by the complicated flow field around the blades. It is recognized that the existing propeller theory can not compute the pressure at the tip with sufficient accuracy for HSP.

Secondly, from the present full scale measurement and the comparison with an existing propeller lifting surface theory on the pressure distribution of the full scale propeller, the following conclusion can be drawn.

4. The theory with use of estimated full scale wake distribution predicts well the pressure on the back side for HSP except 80 %C of 0.9 R but lower pressure on the face side except the cavitation region. At 80 %C of 0.9 R, the pressure on HSP tendes to drastically lower than that given by the theory. This pressure drop is expected to be caused by the vortex stemmed from leading edge separation. It is clearly demonstrated that there still remaine some problems to be improved for the existing propeller theory essentially. Taking account of the wake induced by the wake measurement instrument improves the correlation of the phase of pressure variation between the theory and the measurements.
5. The measured pressure in the cavity on the blade of CP in full scale is almost vapor pressure, while that of HSP is rather higher than the vapor pressure.

Finally, from the measurement of blade stress on the full scale propellers and the HSP model, the following conclusion can be obtained.

6. Strong correlations are observed between the variation of the pressure and the blade stress during one revolution for CP and HSP. FEM analysis on HSP using the corrected pressure from the pressure measurement as input data improves the correlation with the measurements and predicts higher blade stress in the wider area than that using only the computed pressure does.
7. The stress measurements on the propeller model behind a complete ship model with flow liners in the cavitation tunnel showed good agreements with the full scale measurement. This method is useful for the prediction of blade stress.

The present study provides a number of invaluable standard data to validate the computational techniques on marine propellers and important suggestion on the damage mechanism of HSP.

ACKNOWLEDGMENTS

The present research was performed as a part of the cooperative researches between the Ship Research Institute and the Japan Shipbuilding Research Association of Japan. The authors express their deep acknowledgements to the Japan Shipbuilding Research Association of Japan, the Japan Shipbuilding Industry Foundation and the Ship Promotion Foundation for their financial support.

The authors wish to express their gratitude to Prof.

H. Kato, University of Tokyo, who was the chairman of the research panels and Dr. Y. Sasaki, Nippon Kaiji Kyokai, for their suggestion and encouragement and to Mr. Y. Kurobe, T. Kudo, the Ship Research Institute, H. Kamiirisa, Akishima Laboratory, Mitsui Engineering & Shipbuilding Co. Ltd., H. Kubo and Y. Itadani, Nakashima Propeller Co. Ltd. for their cooperation on the measurements.

Finally thanks are also due to those members of the staff at the SRI and ALM.

REFERENCE

1. Koyama, K.,"A Numerical Method for Propeller Lifting Surface in Non-Uniform Flow and Its Application", J. of the Soc. Nav. Arch. Japan, Vol. 137, June 1975, pp.78-87
2. Yuasa, H., Ishii, N., Persson, B., Frydenlund, O., and Holden, K.,"Practical Applications of the Discrete Vortex Element Method for Calculation of Propeller Induced Excitation Forces", Proc. of 13th Symp. on Naval Hydrodynamics, Tokyo, Oct. 1980, pp.65-88
3. Hoshino, T.,"Application of Quasi-Continuous Method to Unsteady Propeller Lifting Surface Problems", J. of the Soc. Nav. Arch. Japan, Vol. 158, Dec. 1985, pp.48-68
4. Koyama, K., et al.,"Experimental Investigation of Flow around a Marine Propeller and Application of Panel Method to the Propeller Theory", Proc. of the Symp.on Naval Hydrodynamics, Berkeley, 1986
5. Hoshino, T.,"Hydrodynamic analysis of Propellers in Steady Flow Using a Surface Panel Method", J. of the Soc. Nav. Arch. Japan, Vol. 165, May 1989, pp.55-70
6. Uto, S., Kodama, Y.,"Application of CFD to the Flow Conputation around a Marine Propeller - Grid Generation and Invisicid Flow Computation Using Euler-Equation", J. Kansai Soc. N. A., Japan, No.230, 1992
7. Allison, J. L.,"Propellers for High-Performance Craft", Marine Technology, Volume 15, Number 4, October 1978, pp.335-380
8. Komura, T., Kato, H. and Yamaguchi, H.,"A New Velocity Measurement Method for Field Use by Tracer / Multi TV Camera System", Proc. of Fluid Measurement and Instrumentation Forum - 1991-, Vol. 108, ASME, Portland, June. 1991, pp.105-110
9. Tanibayashi,H. et al.,"Development of Means for Radical Improvement of Predicting Propeller Excited Vibratory Forces", Proc. of 4th International Marine System Design Conference, Kobe, May 1991
10. Takahashi, H.,"Full-Scale Measurements on Training Ship 'Seiun-Maru'", Proc. of 17th ITTC, Vol. 2, Group Discussion, Göteborg, 1984, pp323-334
11. Takei, Y. et al.,"Measurement of Pressure on a Blade of a Propeller Model", Papers of Ship Research Institute, No. 55, 1979
12. Uchida, M., Nishikawa, E., Nakai, N., Kamiyama, H. and Kamiirisa, H.,"An Attempt on Measure the Blade Stress of Controllable Pitch Propeller of an Actual Ship", J. Kansai Soc. N. A., Japan, No. 211, Mar. 1989, 69-76
13. Ukon, Y. et al.,"Comparative Model Measurements on Pressure Fluctuations Induced by Propeller Cavitation", Proc. of International Symposium on Cavitation Noise and Erosion in Fluid Systems-1989, FED-Vol. 88, ASME, San Francisco, Dec. 1989, pp.11-17
14. Takahashi, M. and Oku, R.,"The Cavitation Characteristics of MAU Type Propeller (The 1st and 2nd Report)", J. of the Soc. of Nav. Arch. Japan, Vol. 141, 1977, pp.17-27 and 143, 1978, pp.61-68
15. Vermissen, G.G.P. and van Gent, W., "Hydrodynamic Pressure Measurements on a Ship Model Propeller", Proc. of 14th Symp. on Naval Hydrodynamics, Washington, 1982
16. Jessup, S.D.,"Further Measurements of Model Propeller Pressure Distributions Using a Novel Technique", DTNSRDC-86/011, 1986
17. Ling, Z. et al.,"Analysis of Three-Dimensional Flow around Marine Propeller by Direct Formulation of Boundary Element Method (3rd Report)", J. of the Soc. Nav. Arch. Japan, Vol. 160, Dec. 1986, pp.40-53
18. Lindgren, H.,"Propeller Cavitation Experiments in Uniform Flow, A Note on Test Procedure, Corrections and Presentation", Proc. of 10th ITTC, Teddington, Cavitation Committee Report, Appendix 1, Vol. 1, Sep. 1963, pp.114-126
19. Sugai, N.,"A Method for Calculating the Hydrodynamic Characteristics of Marine Propellers", J. of the Soc. Nav. Arch. Japan, Vol. 128, Dec. 1970, pp.61-83
20. Moriya,T.,"A Method of Calculating Aerodynamic Characteristics of an Arbitrary Wing Section", J. of the Japan Society for Aeronautical Science, Vol.5, No.33, Jan. 1938, pp.7-17
21. Ishii, N.,"The Influence of Tip Vortex on Propeller Performance", J. of the Soc. Nav. Arch. Japan, Vol. 168, Dec. 1990, pp.77-88
22. Ukon, Y. et al.,"Measurement of Pressure Distribution on Full Scale Propellers", Proc. of Propellers/Shafting '91 Symp., SNAME, Virginia Beach, Sep. 1991, pp.13 (1-15)
23. SR183 Panel,"Study on Propellers and Stern Hull Forms Aiming at Reducing the Stern Vibration and Noise", Report of the Ship Building Association, No. 358, 1983
24. Yamasaki, S.,"Research on Highly Skewed Propeller", Doctor Thesis, Hiroshima University, July 1983
25. Ship & Ocean Project Division,"Stress Analysis of Highly Skewed Propeller Blades", Mitsui Zosen Technical Review, No. 138, Oct. 1989, pp.27-32
26. Yamasaki, S. et al.,"Research on Highly Skewed Propeller (3rd Report Model Tests on Static and Dynamic Propeller Blade Stress", J. of the Soc. Nav. Arch. Japan, Vol. 150, Dec. 1981, pp.110-120

DISCUSSION

W. Morgan
David Taylor Model Basin, USA

This is a very interesting paper and a valuable addition to the literature. When we developed the "modern" highly skewed propeller in the 1960s, one concern we had was the strength in backing due to static divergent. At that time we did a lot of work including extensive model tests and came to the conclusion that "most" highly skewed propellers should be thickened near the blade tip (0.8K to 1.0R) to have adequate strength in backing. This was discussed in a SNAME paper on "Highly Skewed Propellers" by Cumming, Boswell, and myself in 1972. Could the authors comment on our earlier observations relative to their present work?

AUTHORS' REPLY

Thank you very much for Dr. Morgan's comments. Considering the strength in backing, most highly skewed propellers seem to be thickened near the blade tip. Discussor's earlier works are invaluable to design highly skewed propellers and the basis for the design. Our conclusion is that, if one would like to design the blade thinner near the tip to improve the propeller efficiency, he should take into account the strength not only in the backing but also in ahead condition. Concerning the latter strength, it is not appropriate to analyze the propeller blade strength based on any existing propeller theories without considering such an impulsive periodic loading in ahead condition given in this paper, because the propellers are entirely employed in ahead condition. Since our present measurements were not performed at the fully loaded condition, more serious phenomena might occur on the blade under this condition.

DISCUSSION

T. Hoshino
Mitsubishi Heavy Industries, Ltd., Japan

First of all, I would like to congratulate the authors on successfully conducting the very difficult measurements of pressure distributions on propeller blades and blade stress on both model and full scales. Measurements of pressure distribution are very important to confirm and/or improve the existing propeller theory.

1. Fig. 7 and 9 show that the theory underestimated the pressure on the face side, but overestimated on the back side at $\gamma/R_u = 0.9$. This means that the thrust calculated by the theory was lower than the experiment. Did you compare the thrust of HSP between the calculation and the experiment?

2. In full scale measurement of pressure distribution, the correction of static pressure increase due to wave elevation would be important. How did you correct the effect of wave deviation at each speed?

AUTHORS' REPLY

Thank you for Dr. Hoshino's questions.

For the first question, we calculated the thrust by the theory and compared with the measurements. For the design condition of $J=0.6$ in uniform flow, the theory agrees with the measurements, and we calculated the pressure distribution by adjusting the thrust by K_T identity method. Locally, at some measuring points the theory overpredicted, and at other points the theory underpredicted. The authors expect that the thrust given by the theory corresponded to the measurements totally.

As the authors have mentioned in this paper, usually the present theory predicted lower pressure than the theory on the face side. The reason should be attributed to the use of "equivalent two-dimensional hydrofoil theory." Therefore, you feel the theoretical one was lower than the experiment. We did not calculate the thrust from the pressure difference between the face and the back side.

Second question: For the present measurements, we did not correct the effect of wave elevation at each speed. After the full scale measurement, we have performed the self-propulsion test with adjusting the draft and measured the change of ship condition. The variation of sinkage of the ship at aft peak was small, and the wave elevation was not so remarkable for this ship under the condition that the author presented the data in this paper. From the full scale measurement, we can estimate that the effect of the ship condition was so small because of the similarity law on the pressure coefficients established at each propeller revolution rate except at the non-cavitating region. The correction method of wave elevation was not so simple and easy.

DISCUSSION

W. Morgan
David Taylor Model Basin, USA

This is a very interesting paper and a valuable addition to the literature. When we developed the "modern" highly skewed propeller in the 1960s, one concern we had was the strength in backing due to static divergent. At that time we did a lot of work including extensive model tests and came to the conclusion that "most" highly skewed propellers should be thickened near the blade tip (0.8K to 1.0R) to have adequate strength in backing. This was discussed in a SNAME paper on "Highly Skewed Propellers" by Cumming, Boswell, and myself in 1972. Could the authors comment on our earlier observations relative to their present work?

AUTHORS' REPLY

Thank you very much for Dr. Morgan's comments. Considering the strength in backing, most highly skewed propellers seem to be thickened near the blade tip. Discussor's earlier works are invaluable to design highly skewed propellers and the basis for the design. Our conclusion is that, if one would like to design the blade thinner near the tip to improve the propeller efficiency, he should take into account the strength not only in the backing but also in ahead condition. Concerning the latter strength, it is not appropriate to analyze the propeller blade strength based on any existing propeller theories without considering such an impulsive periodic loading in ahead condition given in this paper, because the propellers are entirely employed in ahead condition. Since our present measurements were not performed at the fully loaded condition, more serious phenomena might occur on the blade under this condition.

DISCUSSION

T. Hoshino
Mitsubishi Heavy Industries, Ltd., Japan

First of all, I would like to congratulate the authors on successfully conducting the very difficult measurements of pressure distributions on propeller blades and blade stress on both model and full scales. Measurements of pressure distribution are very important to confirm and/or improve the existing propeller theory.

1. Fig. 7 and 9 show that the theory underestimated the pressure on the face side, but overestimated on the back side at $\gamma/R_u = 0.9$. This means that the thrust calculated by the theory was lower than the experiment. Did you compare the thrust of HSP between the calculation and the experiment?

2. In full scale measurement of pressure distribution, the correction of static pressure increase due to wave elevation would be important. How did you correct the effect of wave deviation at each speed?

AUTHORS' REPLY

Thank you for Dr. Hoshino's questions.

For the first question, we calculated the thrust by the theory and compared with the measurements. For the design condition of $J=0.6$ in uniform flow, the theory agrees with the measurements, and we calculated the pressure distribution by adjusting the thrust by K_T identity method. Locally, at some measuring points the theory overpredicted, and at other points the theory underpredicted. The authors expect that the thrust given by the theory corresponded to the measurements totally.

As the authors have mentioned in this paper, usually the present theory predicted lower pressure than the theory on the face side. The reason should be attributed to the use of "equivalent two-dimensional hydrofoil theory." Therefore, you feel the theoretical one was lower than the experiment. We did not calculate the thrust from the pressure difference between the face and the back side.

Second question: For the present measurements, we did not correct the effect of wave elevation at each speed. After the full scale measurement, we have performed the self-propulsion test with adjusting the draft and measured the change of ship condition. The variation of sinkage of the ship at aft peak was small, and the wave elevation was not so remarkable for this ship under the condition that the author presented the data in this paper. From the full scale measurement, we can estimate that the effect of the ship condition was so small because of the similarity law on the pressure coefficients established at each propeller revolution rate except at the non-cavitating region. The correction method of wave elevation was not so simple and easy.

Session XV

Propulsor Hydrodynamics and Hydroacoustics

Application of a Panel Method to the Unsteady Hydrodynamic Analysis of Marine Propellers

K. Koyama (Ship Research Institute, Japan)

ABSTRACT

A panel method for analysis of unsteady flow around a propeller is presented. The purpose of the study is to simulate the potential flow around a propeller operating in arbitrary motion. The numerical calculation is carried out for the unsteady flow by time marching with the development of the vortex wake.

Kutta condition at trailing edge of the blade is discussed and an explanation is made on the doublet matching numerical Kutta condition of the potential based surface panel method. This is proved by simple numerical calculation for two dimensional steady flow. The numerical condition is applied to the calculation for propellers.

Numerical validation of the method is performed by the calculation for three propellers. Numerical accuracy of paneling and time marching is investigated.

Some flow characteristics such as the effect of neighbour blades and the effect of existance of hub are discussed.

A propeller operating in the non-uniform flow is investigated. Calculations are carried out for sinusoidal inflow. The result is compared with unsteady method based on frequency domain analysis.

1. INTRODUCTION

The purpose of this study is to develop the simulator for hydrodynamics of marine propellers. Study on CFD is very active now under favorable conditions of high speed computers. This situation of computer utility stimulates us to develop the application of potential theory to further wide field. In order to accomplish the simulator for hydrodynamics of marine propellers, we are developing the calculation program for the unsteady hydrodynamic analysis of marine propellers using a panel method.

In the field of hydrodynamic analysis of marine propellers the lifting surface theory has been developed and applied successfully. In the early stage of the study the mode function method was used but recently almost all numerical methods employ the vortex/doublet lattice method. This change is owing to the development of high speed computers and to the demand for analysis of complicated shape of blades. Recently the application of the panel method to the hydrodynamic analysis of marine propellers becomes active. Useful information on the flow and pressure on the propeller blade can be obtained by the method. The lifting surface theory treats the thin wing, whereas the panel method treats the thick wing. So unknowns for panel method are 2 times more than unknowns for lifting surface theory. Considering that some calculations are necessary to be added for including thickness effect in case of the lifting surface theory and that the panel method treats exactly thick wings, 2 times more unknowns for panel method is considered to be preferable.

Application of the panel method to the hydrodynamic analysis of marine propellers becomes active gradually(1)-(11). The method treats numerically the potential flow around the lifting body as exactly as possible. The viscous effect of the flow is concentrated in the infinitesimal thin vortex wake behind the blade. The geometry of the lifting body can be treated as accurately as wanted by the numerical calculation of the panel method. There are some directions to be developed in the field of this method. One direction is to develop new methods such as velocity based panel method. Other direction is to improve the numerical methods such as higher order panel method. The direction of this paper is different from these. A simple method, potential based low order panel method is used. Our direction is to expand the application of the panel method to the unsteady hydrodynamic analysis of marine propellers. Recently the

study in the same direction was presented(11).

Kutta condition at trailing edge of blades is very important in case of numerical calculation of panel method. Because the condition is very severe in case of panel method, although the treatment of the condition was easy in case of the mode function method of the lifting surface theory.

In this paper a panel method for unsteady flow around propeller blades is presented. Kutta condition at the trailing edge of the blade is discussed. The calculation is carried out by time marching with the development of the vortex wake. Numerical validation of the method and the comparison of the results with the experiment are shown. Effect of neighbour blades and effect of hub are discussed. Propeller operating in sinusoidal inflow is calculated and discussed.

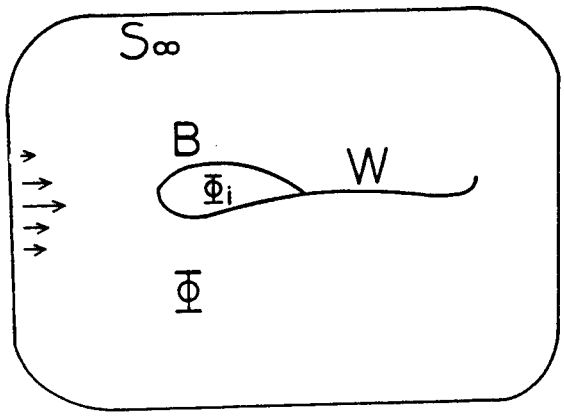

Fig.1 Flow Domain and Boundary

2. FORMULATION FOR THE UNSTEADY POTENTIAL FLOW AROUND A PROPELLER

2.1. Boundary Integral Equation

We consider a propeller operating in unbounded flow field (Fig.1). It is assumed that the vortex wake emanating from the trailing edge of the blades is infinitesimally thin and that the flow field except vortex wake is incommpressible, inviscid and irrotational. Then there exists the velocity potential Φ and the velocity vector $\mathbf{v}$ is expressed as

$$\mathbf{v} = \nabla \Phi \tag{1}$$

According to the condition of continuity of the flow Laplace equation is obtained for the potential

$$\nabla^2 \Phi = 0 \tag{2}$$

According to Green's identity formula, the velocity potential in the flow field is expressed as

$$\Phi = -\frac{1}{4\pi} \int\int \frac{\partial \Phi}{\partial n'} \frac{1}{r} dS + \frac{1}{4\pi} \int\int \Phi \frac{\partial}{\partial n'} \left(\frac{1}{r}\right) dS \tag{3}$$

where the integral domain includes all boundary surface which bounds the flow field and r is defined to be the length of the vector $\mathbf{r}$ from integral point to observer point. Symbol $\partial / \partial n'$ is the normal derivertive to the integral surface directed into the flow field.

If we set fictitious velocity potential Φ_i inside the blade,

$$0 = -\frac{1}{4\pi} \int\int_B \frac{\partial \Phi_i}{\partial n_i} \frac{1}{r} dS + \frac{1}{4\pi} \int\int_B \Phi_i \frac{\partial}{\partial n_i} \left(\frac{1}{r}\right) dS \tag{4}$$

Then the velocity potential can be written as

$$\begin{aligned} \Phi = & -\frac{1}{4\pi} \int\int_B \sigma \frac{1}{r} dS + \frac{1}{4\pi} \int\int_B \mu \frac{\partial}{\partial n'} \left(\frac{1}{r}\right) dS \\ & - \frac{1}{4\pi} \int\int_W \frac{\partial \Phi}{\partial n'} \frac{1}{r} dS + \frac{1}{4\pi} \int\int_W \Phi \frac{\partial}{\partial n'} \left(\frac{1}{r}\right) dS \\ & - \frac{1}{4\pi} \int\int_{S\infty} \frac{\partial \Phi}{\partial n'} \frac{1}{r} dS + \frac{1}{4\pi} \int\int_{S\infty} \Phi \frac{\partial}{\partial n'} \left(\frac{1}{r}\right) dS \end{aligned} \tag{5}$$

where

$$\mu = \Phi - \Phi_i \tag{6}$$

$$\sigma = \frac{\partial \Phi}{\partial n'} + \frac{\partial \Phi_i}{\partial n_i} = \frac{\partial}{\partial n'} (\Phi - \Phi_i) \tag{7}$$

Then finally we obtain the expression

$$\Phi = \Phi_D + \Phi_S + \Phi_W + \Phi_\infty \tag{8}$$

$$\Phi_D = \frac{1}{4\pi} \int\int_B \mu \frac{\partial}{\partial n'} \left(\frac{1}{r}\right) dS \tag{9}$$

$$\Phi_S = -\frac{1}{4\pi} \int\int_B \sigma \frac{1}{r} dS \tag{10}$$

$$\Phi_W = \frac{1}{4\pi} \int\int_W \Delta\Phi_W \frac{\partial}{\partial n'} \left(\frac{1}{r}\right) dS \tag{11}$$

$$\Phi_\infty = -\frac{1}{4\pi} \int\int_{S\infty} \frac{\partial \Phi}{\partial n'} \frac{1}{r} dS + \frac{1}{4\pi} \int\int_{S\infty} \Phi \frac{\partial}{\partial n'} \left(\frac{1}{r}\right) dS \tag{12}$$

where

Φ_D is velocity potential induced by doublet distribution on body surface.
Φ_S is velocity potential induced by source distribution on body surface.
Φ_W is velocity potential induced by vortex wake
Φ_∞ is velocity potential in case of unperturbed field without a propeller
Φ_i is fictitious velocity potential inside the propeller
$_B$ is the surface of a propeller such as blades or hub.
$_W$ is one side of the surface of vortex wake
$_{S\infty}$ is the boundary surface far from the propeller.
$\Delta\Phi_W$ is the potential jump on the vortex wake

In the case where the observer point is on the blade surface, the integral for Φ_D becomes singular. The potential on the blade surface inside the flow field induced by doublet distribution Φ_{D+} and the fictitious potential on the blade surface inside the blade induced by doublet distribution Φ_{D-} are expressed as

$$\Phi_{D\pm} = \pm \frac{1}{2}\mu + \frac{1}{4\pi} \text{=}\!\!\int\!\!\int_B \mu \frac{\partial}{\partial n'}\left(\frac{1}{r}\right) dS \qquad (13)$$

where the symbol $\text{=}\!\!\int\!\!\int$ indicates that the integration excludes the singular point at which the observer point coincides with the integral point.

From these equations we can get the boundary integral equation

$$-\frac{1}{2}(\Phi - \Phi_i) + \frac{1}{4\pi} \text{=}\!\!\int\!\!\int_B (\Phi - \Phi_i) \frac{\partial}{\partial n'}\left(\frac{1}{r}\right) dS = \Phi_i - \Phi_S - \Phi_W - \Phi_\infty \qquad (14)$$

The fictitious potential inside the blade Φ_i is assumed suitably and Φ_S, Φ_∞ are determined by the boundary condition. Then the equation (14) becomes a Fredholm integral equation of the second kind with the unknown $\Phi - \Phi_i$.

In the present method the fictitious potential Φ_i is assumed to be equal to Φ_∞

$$\Phi_i = \Phi_\infty \qquad (15)$$

Then the integral equation becomes

$$-\frac{1}{2}(\Phi - \Phi_\infty) + \frac{1}{4\pi} \text{=}\!\!\int\!\!\int_B (\Phi - \Phi_\infty) \frac{\partial}{\partial n'}\left(\frac{1}{r}\right) dS = -\Phi_S - \Phi_W \qquad (16)$$

$$\Phi_S = -\frac{1}{4\pi}\int\int_B \frac{\partial}{\partial n'}(\Phi - \Phi_\infty)\frac{1}{r} dS \qquad (17)$$

$$\Phi_W = \frac{1}{4\pi}\int\int_W \Delta\Phi_W \frac{\partial}{\partial n'}\left(\frac{1}{r}\right) dS \qquad (18)$$

$\partial\Phi/\partial n'$ is given by the boundary condition on the blade surface B according to the movement of the blade.

$$\partial\Phi/\partial n' = \mathbf{V}\cdot\mathbf{n} \qquad (19)$$

where $\mathbf{V}$ is the vector of the velocity of the moving blade and $\mathbf{n}$ is the unit vector normal to the blade surface.

$\partial\Phi_\infty/\partial n'$ is given by the inflow velocity

$$\partial\Phi_\infty/\partial n' = \mathbf{W}\cdot\mathbf{n} \qquad (20)$$

where $\mathbf{W}$ is the vector of the velocity of the non-uniform inflow. Detail of these expressions are shown in Ref.(12). These give the value Φ_S.

Present analysis is for unsteady flow. Above equation shows the instance of the flow phenomena. Vortex wake is developed with time step. $\Delta\Phi_W$ is given by the value at previous time step in general, because the vortex wake is flowed by the induced velocity and the value $\Delta\Phi_W$ on the vortex wake is kept in its value. However the value $\Delta\Phi_W$ on the panel nearest to the trailing edge of the blade is decided by the Kutta condition. This is discussed in Section 3.

2.2. Low Order Panel Method

In the panel method the integral surface S, W is devided into many small panels. Integation is performed for each panel. There are low order panel method and higher order panel method according to the order of approximation of integral over the panel (6). In this paper we use simple low order panel method, in which we assume that the panel is a plane and that the singularity such as doublet and source is constant in its value on the panel. In this case integral over a panel becomes (12)

$$\Phi_{Di} = \frac{1}{4\pi} \text{=}\!\!\int\!\!\int_{Bi} \mu \frac{\partial}{\partial n'}\left(\frac{1}{r}\right) dS = -m_{00}\, Z\, H_{0.0.-3} = -m_{00}\frac{-1}{4\pi} Z\, H(0,0,3) \qquad (21)$$

$$\Phi_{Si} = -\frac{1}{4\pi}\int\int_{Bi} \sigma \frac{1}{r} dS = s_{00}\, H_{0.0.-1}$$

$$= \quad s_{00} \frac{-1}{4\pi} \quad H\ (0,0,1) \qquad (22)$$

$$H_{mnk} = \frac{-1}{4\pi} \iint_{B1} X'^{m}\, Y'^{n} \rho^{k}\, dX'dY' \qquad (23)$$

$$H\ (M,N,K) = \iint_{B1} \frac{(X-X')^{M}(Y-Y')^{N}}{\rho^{K}}\, dX'dY' \qquad (24)$$

$$H_{0.0.k} = \frac{-1}{4\pi} H\ (0,0,-k) \qquad (25)$$

$$H\ (0,0,1) = \Sigma\ (R_{12}\, Q_{12} + |Z|\, J_{12}) - |Z|\, \Delta\theta \qquad (26)$$

$$H\ (0,0,3) = \frac{sgn(Z)}{Z}\ (-\Sigma\ J_{12} + \Delta\theta) \qquad (27)$$

$$\left.\begin{aligned} Q_{12} &= \log \left| (\rho_2 + s_2) / (\rho_1 + s_1) \right| \\ J_{12} &= \arctan\ (|Z|\, s_2 / R_{12}\rho_2) \\ &\quad - \arctan\ (|Z|\, s_1 / R_{12}\rho_1) \\ R_{12} &= S_{12}\ (X'-X) + C_{12}\ (Y'-Y) \\ s &= C_{12}\ (X'-X) + S_{12}\ (Y'-Y) \\ C_{12} &= (X_2-X_1)/d_{12},\quad S_{12} = (Y_2-Y_1)/d_{12} \\ d_{12} &= ((X_2-X_1)^2 + (Y_2-Y_1)^2)^{1/2} \\ \rho_1 &= ((X-X_1)^2 + (Y-Y_1)^2 + Z^2)^{1/2} \\ \rho_2 &= ((X-X_2)^2 + (Y-Y_2)^2 + Z^2)^{1/2} \\ \Delta\theta &= \begin{cases} 2\pi & \text{point}(X,Y,0) \text{ is inside the panel} \\ 0 & \text{point}(X,Y,0) \text{ is outside the panel} \end{cases} \end{aligned}\right\} \qquad (28)$$

where suffix $_1$ of $_{D1}$, $_{S1}$ indicates a plane panel expressing a part of integral surface. X,Y,Z are the coordinates on the plane panel.

2.3. Pressure and Forces

Pressure on the blade is expressed as

$$\frac{p}{\rho} + \frac{1}{2} q_r^2 + gy + \frac{\partial \Phi}{\partial t} - \frac{1}{2} V^2 = C(t) \qquad (29)$$

where y is upward vertical coordinates, ρ is density of water, g is gravity acceleration and

$$q_r = |\mathbf{v} - \mathbf{V}|, \quad V = |\mathbf{V}| \qquad (30)$$

As the value in far front of a propeller is the same as the value at the propeller position without the propeller, using suffix ∞ for the value, pressure coefficient is expressed as

$$C_p = \frac{p-p_\infty}{(1/2)\rho V_\infty^2}$$

$$= q_{r\infty}^2 / V_\infty^2 - q_r^2 / V_\infty^2 - (2g / V_\infty^2) \cdot (y - y_\infty) - (2 / V_\infty^2) \cdot \frac{\partial (\Phi - \Phi_\infty)}{\partial t} \qquad (31)$$

where

$$q_{r\infty} = |\nabla\Phi_\infty - \mathbf{V}| \qquad (32)$$

$$V_\infty = |\nabla\Phi_{\infty M} - \mathbf{V}| \qquad (33)$$

$$\nabla\Phi_{\infty M} = \text{mean}\ (\nabla\Phi_\infty) \qquad (34)$$

In the numerical calculation we separate the effect of gravity and approximate $q_{r\infty}$ equal V_∞, resulting

$$C_p = 1 - q_r^2 / V_\infty^2 - (2 / V_\infty^2) \cdot \frac{\partial (\Phi - \Phi_\infty)}{\partial t} \qquad (35)$$

By integrating the pressure over the blade surface, we can get the value of forces and moments such as thrust, torque, scaft forces and moments. Details are shown in Ref.(12)

3. KUTTA CONDITION

Kutta condition which makes the separation point coincide with the trailing edge, is very important because it controls the whole flow around the blade. In the present method this condition is set by equating both pressure of upper and lower surface of blade at the trailing edge.

$$p_u = p_l \quad \text{at trailing edge of blade} \qquad (36)$$

$$\frac{p_u - p_l}{\rho} = -\frac{\partial}{\partial t}\ (\Phi_u - \Phi_l) - \frac{1}{2}\ (q_{ru}^2 - q_{rl}^2) = 0 \qquad (37)$$

$$q_r = |\mathbf{v} - \mathbf{V}| \qquad (38)$$

where suffix $_{u,l}$ means upper and lower surface of a blade. If we write

$$V^* = (q_{ru} + q_{rl}) / 2 \qquad (39)$$

equation (37) becomes

$$\partial / \partial t\ (\Phi_u - \Phi_l) + V^*\ (q_{ru} - q_{rl}) = 0 \qquad (40)$$

Theoretical analysis for the Kutta condition at the trailing edge of a casped wing shows the delicate flow around the trailing edge. Almost in all cases for three dimensional wing(13) or for unsteady flow(14), flow leaves trailing edge to the direction tangential to either upper or lower surface of wing. But in many cases the angle of trailing edge is small and it is difficult for numerical method to treat the delicate flow exactly. So it is assumed in the present numerical method as in other numerical methods that the flow leaves the trailing edge to the direction tangential to the bisector of trailing edge.

In our numerical method it is assumed that the flow near the trailing edge is two dimensional and following notations are used (Fig.2)

$$\frac{\partial}{\partial t}\ (\Phi_u - \Phi_l) = \frac{(\Phi_{0u} - \Phi_{0l}) - (\Phi_{wu} - \Phi_{wl})}{\Delta s_w / V^*_w} \qquad (41)$$

$$q_{ru} - q_{rl} = \left(\frac{(\Phi_{0u} - \Phi_{Tu})}{\Delta s_u} - \mathbf{V} \cdot \mathbf{e}_u\right) - \left(\frac{(\Phi_{0l} - \Phi_{Tl})}{\Delta s_l} - \mathbf{V} \cdot \mathbf{e}_l\right)$$

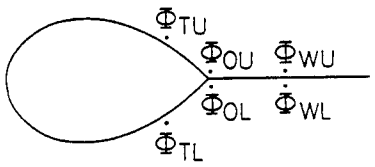

Fig.2 Potential at Trailing Edge

$$= \frac{(\Phi_{Ou}-\Phi_{Ol})-(\Phi_{Tu}-\Phi_{Tl})}{\Delta s} - \mathbf{V}\cdot(\mathbf{e}_U-\mathbf{e}_L) \qquad (42)$$

where
$\Delta s_W, \Delta s_U, \Delta s_L$ are the length $_{Ou\to Wu}$, $_{Tu\to Ou}$, $_{Tl\to Ol}$,
$\mathbf{e}_U, \mathbf{e}_L$ are the unit vector along $_{Tu\to Ou}$, $_{Tl\to Ol}$
V^*_W is the mean velocity between $_{Ou\to Wu}$
and further

$$\Delta s_U = \Delta s_L = \Delta s$$

is assumed. Then Kutta condition becomes

$$\frac{(\Phi_{Ou}-\Phi_{Ol})-(\Phi_{Wu}-\Phi_{Wl})}{\Delta s_W / V^*_W} + V^*\left(\frac{(\Phi_{Ou}-\Phi_{Ol})-(\Phi_{Tu}-\Phi_{Tl})}{\Delta s} - \mathbf{V}\cdot(\mathbf{e}_U-\mathbf{e}_L)\right) = 0 \qquad (43)$$

then

$$\Phi_{Ou}-\Phi_{Ol} = \frac{\Delta s_W/V^*_W}{\Delta s/V^* + \Delta s_W/V^*_W}(\Phi_{Tu}-\Phi_{Tl}) + \frac{\Delta s/V^*}{\Delta s/V^* + \Delta s_W/V^*_W}(\Phi_{Wu}-\Phi_{Wl}) + \frac{\Delta s_W/V^*_W}{\Delta s/V^* + \Delta s_W/V^*_W}\mathbf{V}\cdot(\mathbf{e}_U-\mathbf{e}_L)\Delta s$$
$$= (1-k)(\Phi_{Tu}-\Phi_{Tl}) + k(\Phi_{Wu}-\Phi_{Wl}) + (1-k)\mathbf{V}\cdot(\mathbf{e}_U-\mathbf{e}_L)\Delta s \qquad (44)$$

$$k = \frac{\Delta s/V^*}{\Delta s/V^* + \Delta s_W/V^*_W} \qquad (45)$$

$\Phi_{Ou}-\Phi_{Ol}$ is used for the potential jump on the vortex wake adjacent to the trailing edge in the integral equation. The first term of expression (44) is main term. $(\Phi_{Tu}-\Phi_{Tl})$ is unknown in the integral equation. The second term is the unsteady term. $(\Phi_{Wu}-\Phi_{Wl})$ is known in the previous time step. The third term is the term corresponding to the effect of blade thickness. The third term becomes zero when wing thickness is zero or when the inflow velocity vector coincides with the mean camber line at the trailing edge. In case of steady flow the value k in condition (44) should be set zero.

If we neglect the third term and set k=0 then

$$\Phi_{Ou}-\Phi_{Ol} = \Phi_{Tu}-\Phi_{Tl} \qquad (46)$$

This is the same as the potential continuous Kutta condition which is used in Morino's method(15).

In order to make clear this theory for Kutta condition, calculations for two dimensional steady flow were carried out. In this case the boundary integral equation corresponding to equation(16) becomes

$$\frac{1}{2}\Phi = \frac{-1}{2\pi}\oint_B \Phi\frac{\partial}{\partial n'}\log r\,ds + \frac{1}{2\pi}\int_B \frac{\partial\Phi}{\partial n'}\log r\,ds + \frac{-1}{2\pi}\int_{WU}\Delta\Phi_w\frac{\partial}{\partial n'}\log r\,ds \qquad (47)$$

where $\Phi_\infty = 0$ was assumed.

In order to make clear the meaning of the third term of expression (44), the calculation of the circular cylinder with circulation was performed. The angle between the direction of motion and the direction of potential cut line is 135° (Fig.3).

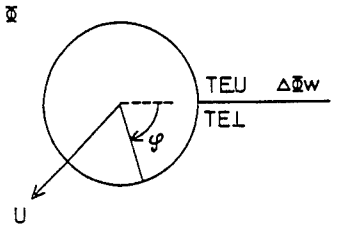

Fig.3 Motion of Circular Cylinder

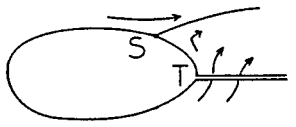

Fig.4 Potential Cut Point T and Separation Point S

The results of the calculation based on the condition (46) are shown in Fig.5(a),(b),(c). In the figure the velocity potential Φ, velocities V, V_I, V_T, and pressure coefficient C_p are shown. Following notations are used for the velocities in the figure.

$$V = \mathbf{t}\cdot\mathbf{v}, \quad \mathbf{v} = \nabla\Phi$$
$$V_I = \mathbf{t}\cdot(-\mathbf{V})$$
$$V_T = V + V_I$$

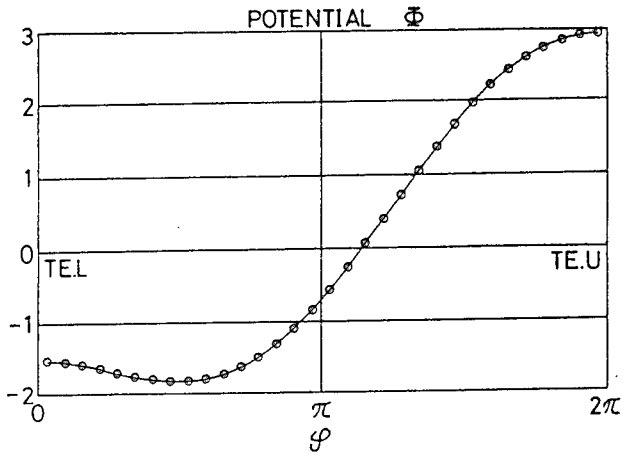

Fig. 5(a) Potential on Cylinder(Eq. 46)

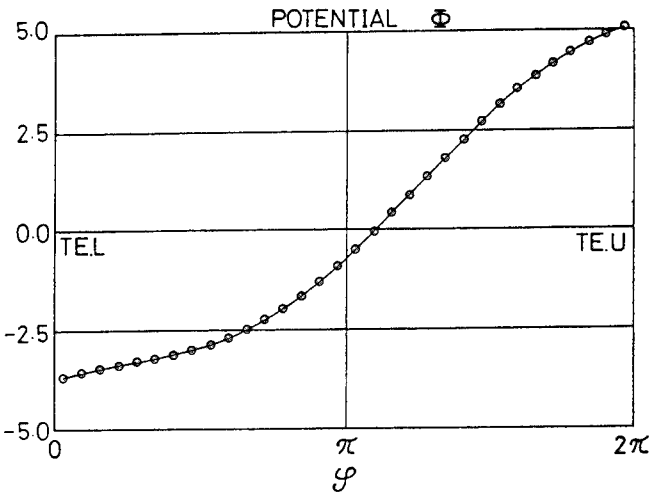

Fig. 6(a) Potential on Cylinder(Eq. 44)

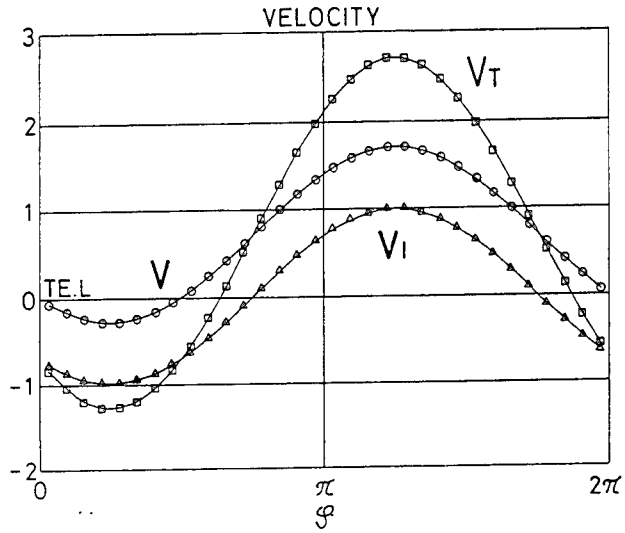

Fig. 5(b) Velocity on Cylinder(Eq. 46)

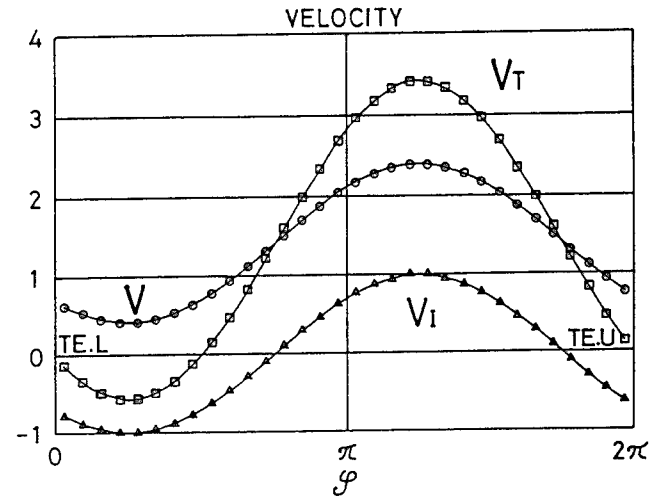

Fig. 6(b) Velocity on Cylinder(Eq. 44)

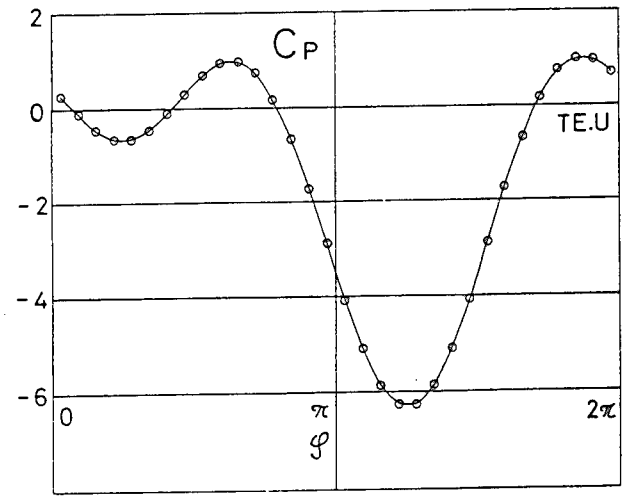

Fig. 5(c) Pressure on Cylinder(Eq. 46)

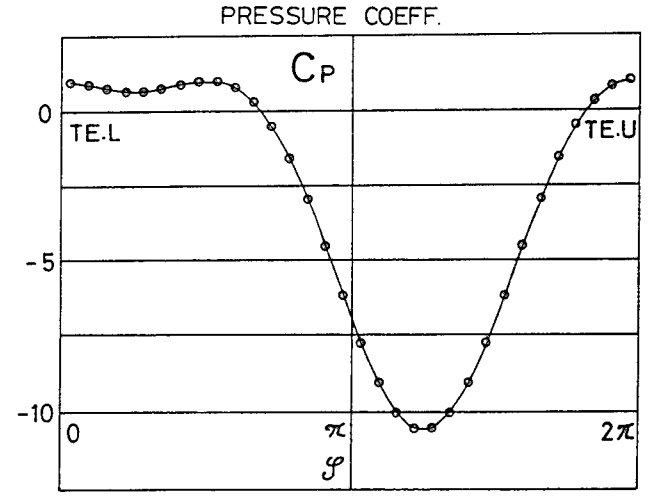

Fig. 6(c) Pressure on Cylinder(Eq. 44)

Where **t** is tangential unit vector to the surface. The abscissa is the angle φ corresponding to the position on the cylinder surface. The definition of the direction of the velocity is the same as that of the angle. Around the trailing edge T that is both tips of the abscissa, the value Φ is constant and disturbance velocity V is nearly zero. The results are considered to be the appearance of the effect of the condition (46). But the separation point S which is the position $V_T=0$, aparts from the point T which is the intersecting point of the cylinder surface and potential cut line (Fig.4), because the flow velocity observed on the cylinder V_T is the summation of the disturbance velocity V and relative velocity V_I. So it comes to the conclusion that in case of circular cylinder, the condition (46) or the condition (44) without the third term cannot control the condition that the separation point S coincides with the point T although the solution is decided uniquely.

Next the results of the calculation by the condition (44) with k=0 is shown in Fig.6(a), (b), (c). As expected by the theory both velocities V_T on the upper and on the lower surface around the point T are nearly equal in the absolute value, very small in the absolute value and opposite in the sign. Then this method can control the condition that the separation point S coincides with the point T. This means that the method based on the condition (44) can treat correctly the Kutta condition at the trailing edge of the airfoil.

Next the calculation for the airfoil was performed using condition (46). The profile of the airfoil is expressed by

$$Y = a + \Sigma a_n \cos(n\theta) + \Sigma b_n \sin(n\theta)$$
$$X = \cos(\theta)$$

a_1 =	0.001135	b_1 =	0.069427
a_2 =	-0.018741	b_2 =	-0.010211
a_3 =	-0.001486	b_3 =	-0.007872
a_4 =	0.000036	b_4 =	0.000029
a_5 =	-0.000017	b_5 =	-0.001110

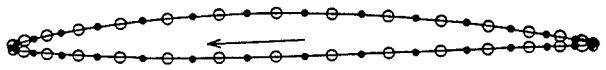

Fig.7 Panel of Airfoil

The panel arrangement is shown in Fig.7. The number of the panels is 32. The calculated results for potential, velocity, and pressure in case of the angle of attack $\alpha=2°$ are shown in Fig.8(a), (b), (c). Similarly to the case of

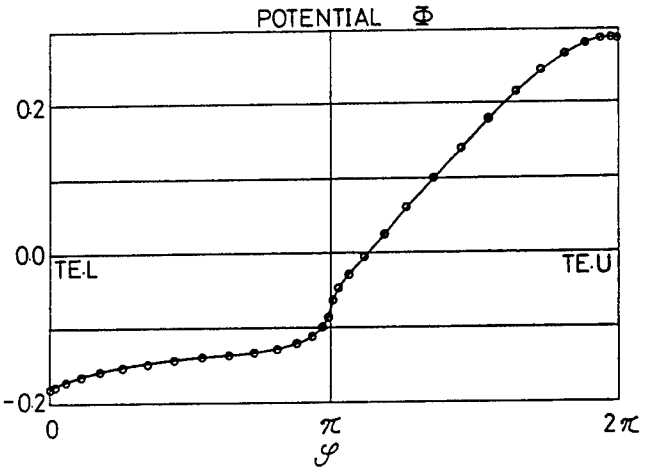

Fig.8(a) Potential on Airfoil (Eq.46)

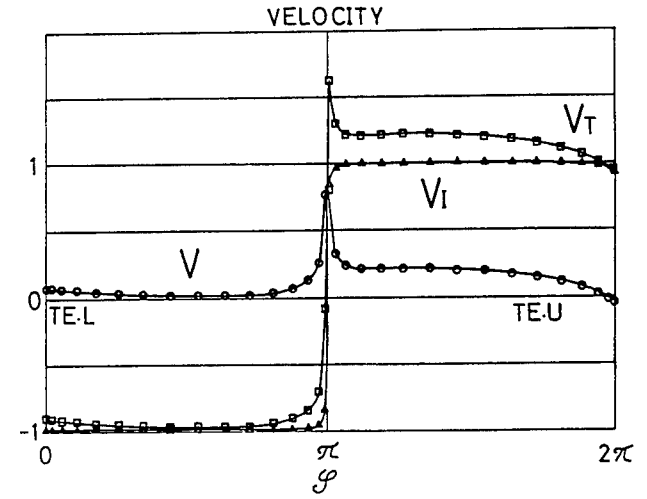

Fig.8(b) Velocity on Airfoil (Eq.46)

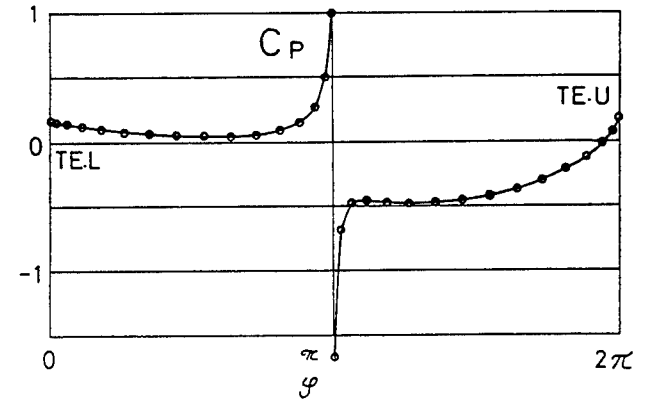

Fig.8(c) Pressure on Airfoil (Eq.46)

the circular cylinder, the disturbance velocity potential is constant and the disturbance velocity is nearly zero near the trailing edge T which is the cross point of airfoil line and potential cut line. The effect of relative velocity corresponding to the motion of the airfoil is quite different from the case of the circular cylinder. Because the trailing edge angle θ_T is very small in case of airfoil in contrast to the circular cylinder in which the angle is large $\theta_T=\pi$. As shown in the figure the relative velocities on the upper and lower surface are nearly equal in the absolute value and opposite in the direction, which is exactly realized in case $\theta_T=0$. As a result the Kutta condition at the trailing edge T is almost satisfied. Except the case of very large θ_T , the separation point S is located between the trailing edge T and the control point of the panel tangent to the trailing edge . This shows that the condition (46) works well for the calculation of the thin wing.

The calculation for the same airfoil by the method based on the condition (44) was performed and the results was similar to the results by condition (46) and the discrepancy was less than 1% in the value of the lift coefficient.

The pressure distribution for the angle of attack α = -4° ,0° 2° ,4° ,6° based on the condition (46) are shown in Fig.9 with the comparison with the calculation by Imai's conformal mapping method (16). The agreement is satisfactory.

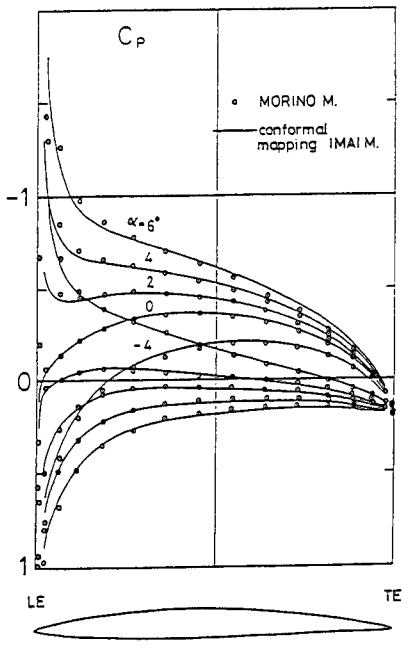

Fig.9 Comparison with Conformal Mapping Method

4. NUMERICAL CALCULATION

4.1 Propellers and Paneling

Numerical calculation was performed for three propellers MP221, DTRC4119, MP218. Their principal particulars and operation conditions are shown in Table 1. Figures of paneling for the propellers are shown in Figs.10, 11, 12.

Propeller MP221 is a simple model propeller which has three blades of low aspect ratio. The blade has no camber and the form of blade section is NACA 4 digit type. Measurement of pressure near tip on the blade was presented(6). For the propeller the comparison of the calculation by the present panel method with the lifting surface theory and with the measurement is shown in the following sections.

Propeller DTRC4119 is also three bladed propeller of simple geometry but with camber. Section meanline is NACA a=0.8 and section thickness form is NACA66 (DTRC Modified). Measurement of pressure on the blade had been performed using LDV flow velocity data near the blade surface(17). For the propeller the comparison of the present calculation with the measurements and with other panel method(VSAERO) is shown. For the propeller the effect of the hub is also discussed.

Propeller MP218 is conventional 5 bladed propeller. Blade section is MAU. The propeller was designed for a training ship " Seiun-maru " Many studies had been performed for the propeller in Japan. The calculation for the propeller operating in non-uniform flow is performed and comparison is made with other unsteady panel method (BEM) and with unsteady lifting surface theory. Both unsteady analysis are based on frquency domain analysis, whereas the present method is based on time domain analysis.

Table 1 Particulars of Model Propellers

Propeller No.	MP221	DTRC4119	MP218
Diameter (m)	0.3	0.305	0.221
Hub Ratio	0.313	0.2	0.197
Pitch Ratio	0.85	1.084(.7R)	0.95(.7R)
No. Blade	3	3	5
Blade Section	NACA4digit	NACA66a=.8	MAU
Advance C. J=	0.6	0.833	0.658
KT Measured	0.082	0.146	0.195

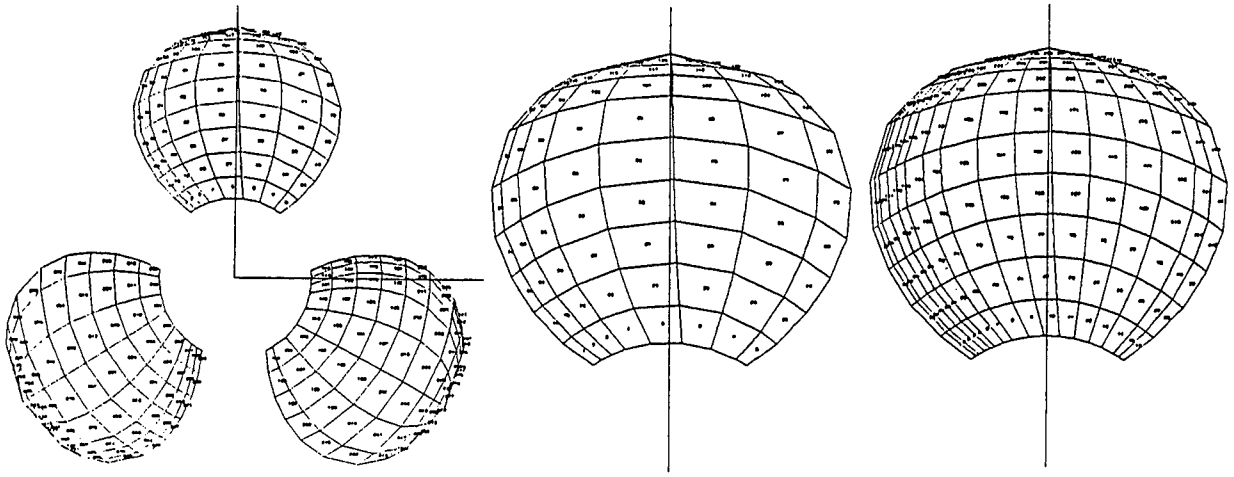

Fig. 10 Paneling of blade surface for MP221 NR × NC = 9×8 , 9×16

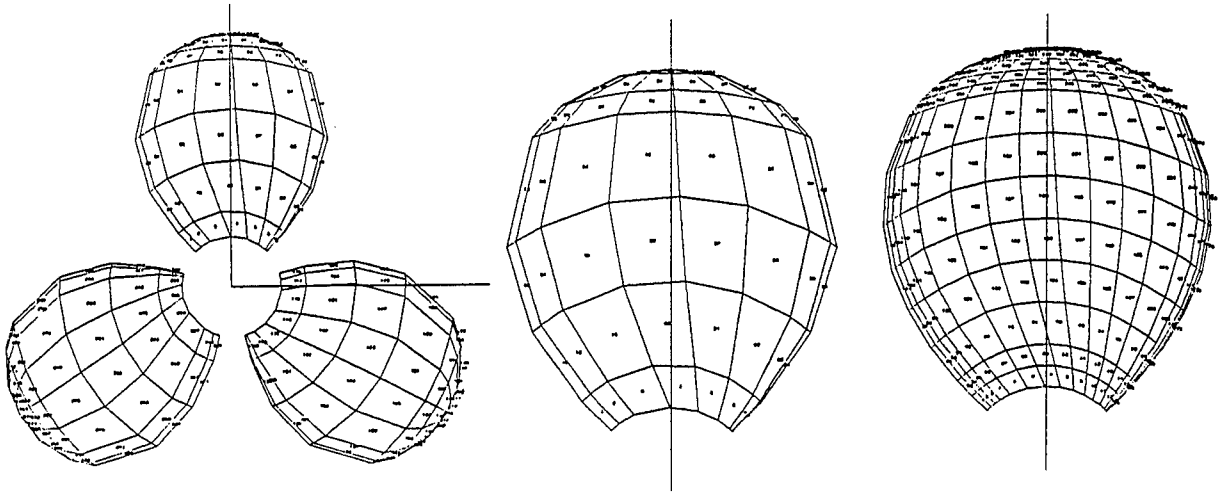

Fig. 11 Paneling of blade surface for DTRC4119 NR × NC = 7×8 , 14×16

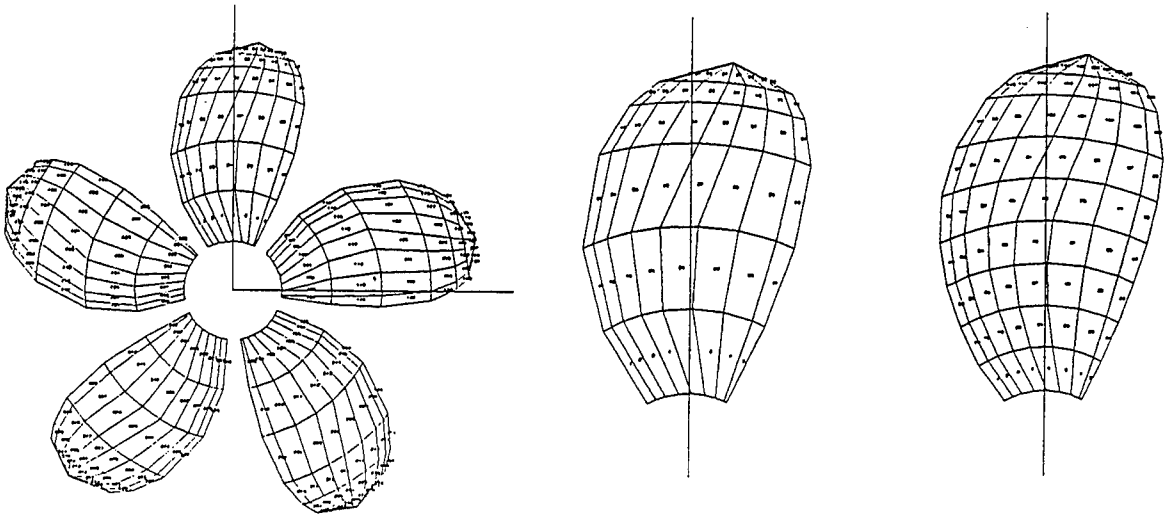

Fig. 12 Paneling of blade surface for MP218 NR × NC = 6×8 , 9×8

4.2 Time Step Calculation

Present calculation is carried out by time marching. Watching the calculation results on each time step reveals the phenomena and is useful for us to check the numerical results. Here we will see the calculation results on time step for propeller MP221.

At the begining of time marching there is no vortex wake behind blades. The potential and the pressure on blade are shown in Fig.13. There is no potential jump at trailing edge of blade and no force from the flow.

Next step the vortex wake is emanated from the trailing edge (Fig.14). Kutta condition presented in section 3 is used at the trailing edge. The results are shown in Fig.15. Potential jump at the trailing edge is appeared and the pressure jump at the trailing edge becomes very small and the lift is generated on the blade.

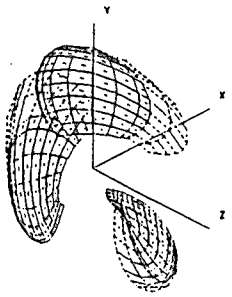

Fig.14. Propeller with Wake (MP221)

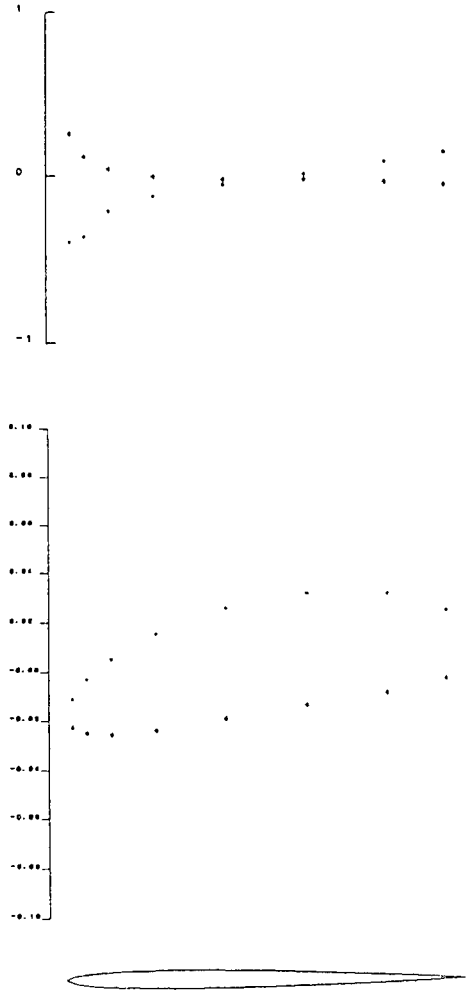

Fig.13 Potential and Pressure without Wake
(MP221 , r/R = 0.85)

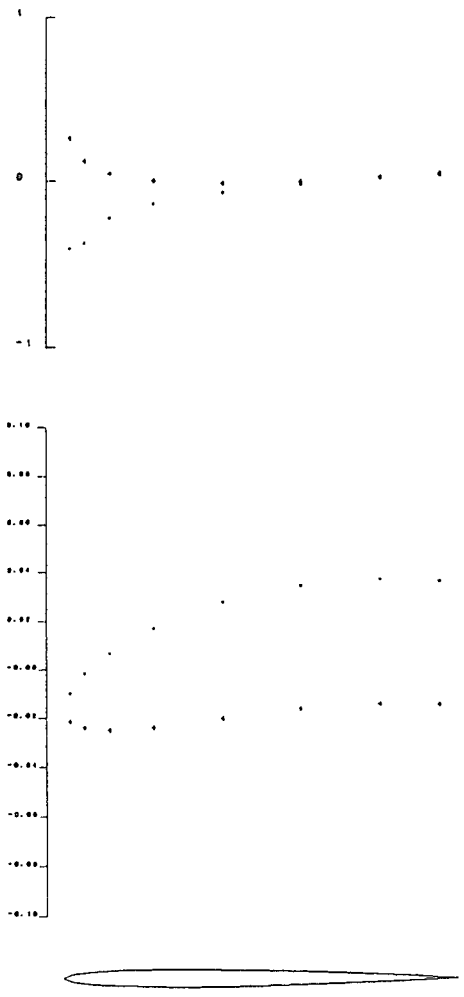

Fig.15 Potential and Pressure with Wake
(MP221 , r/R = 0.85)

4.3 Effect of Number of Panels

In order to evaluate the present scheme, we have to know the effect of number of panels and length of the vortex wake on the accuracy of the calculation.

The offset presenting the geometry of the blade is constructed from the manufacturing point of view. Offset points are distributed more to the region with high curvature. In case of numerical calculation there is the optimum distribution of location presenting the geometry of blades. In general the location of optimum points is different from the offset points. As errors may occur in interpolating the geometry for the numerical points from the offset points, we don't interpolate the geometry but select the most effective points from the offset.

Calculations for 3 paneling cases of MP221 presented in Fig.10 are shown in Fig.16. One case is for the propeller with whole blades, whereas other cases are for the propeller with only one blade for convenience. In the figure thrust coefficient KT for one blade is plotted for time steps. Development of vortex wake is shown in Fig.17.

Calculations for 3 paneling cases of DTRC4119 presented in Fig.11 are shown in Figs. 18, 19. Similar calculations for MP218 are shown in Figs.20, 21.

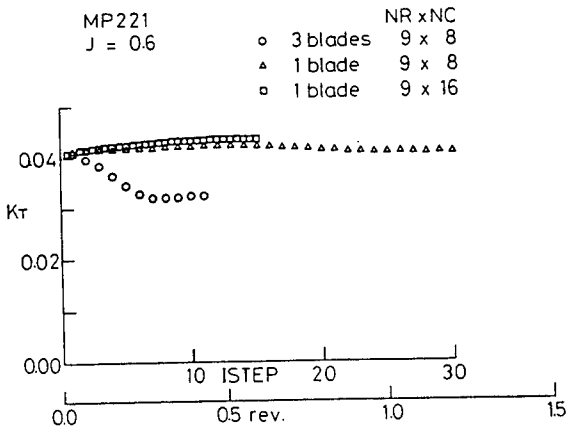

Fig.16 Thrust Coefficient for one blade (MP221)

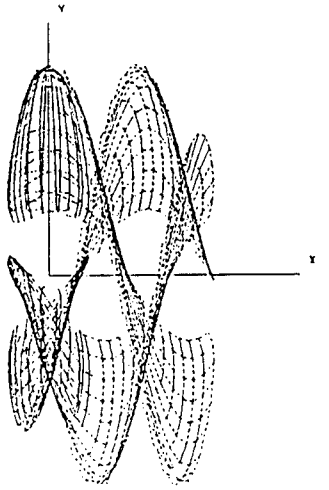

Fig.17(a) Propeller with Vortex Wake
(MP221 , ISTEP=11)

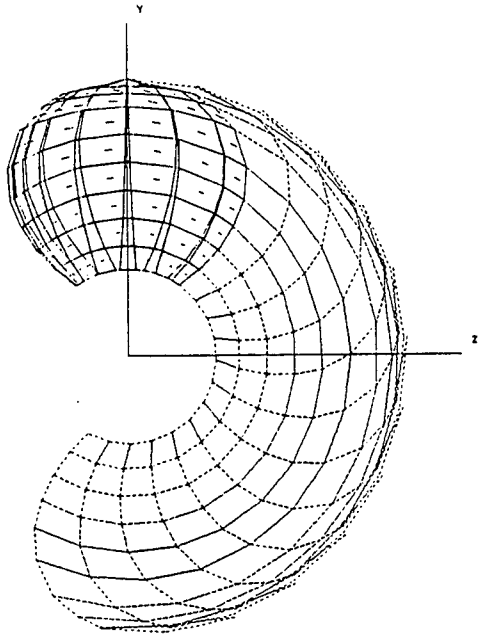

Fig.17(b) Propeller with Vortex Wake
(MP221 , ISTEP=11)

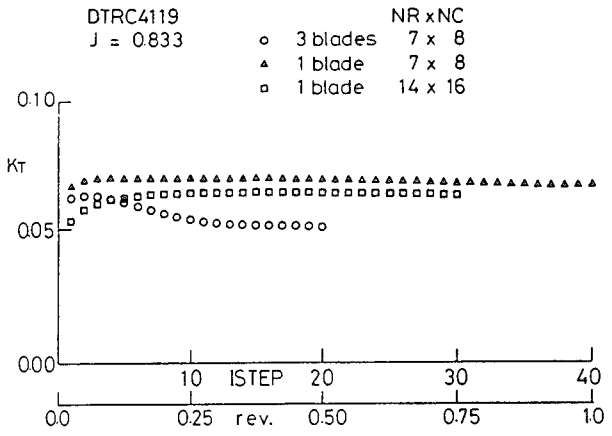

Fig. 18 Thrust Coeff. for one blade (DTRC4119)

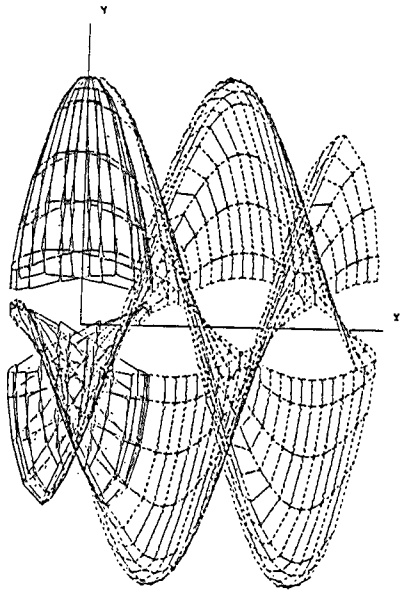

Fig. 19(a) Propeller with Vortex Wake
(DTRC4119 , ISTEP=20)

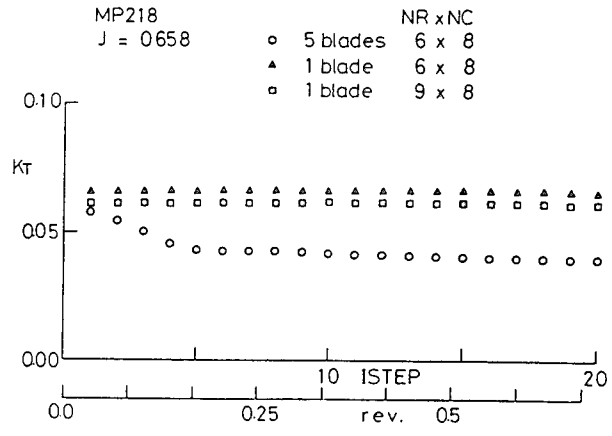

Fig. 20 Thrust Coeff. for one blade (MP218)

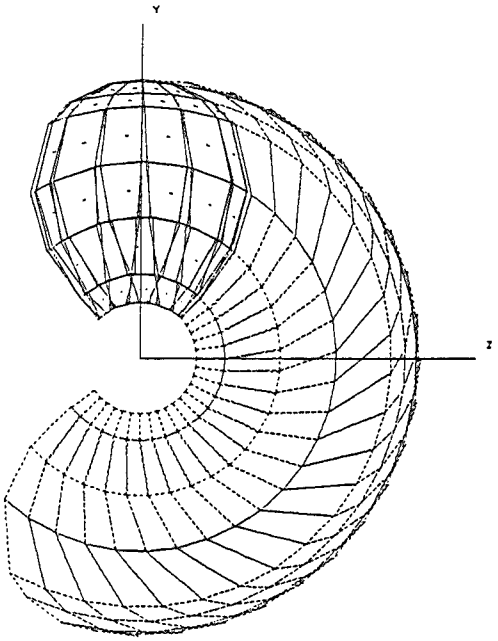

Fig. 19(b) Propeller with Vortex Wake
(DTRC4119 , ISTEP=20)

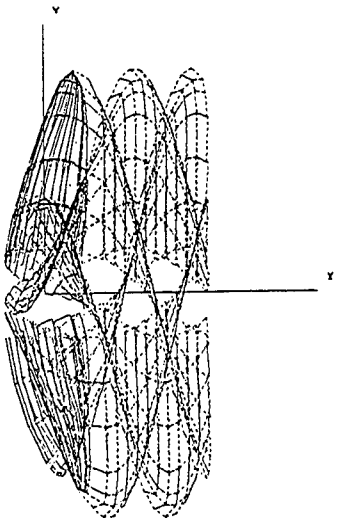

Fig. 21(a) Propeller with Vortex Wake
(MP218 , ISTEP=10)

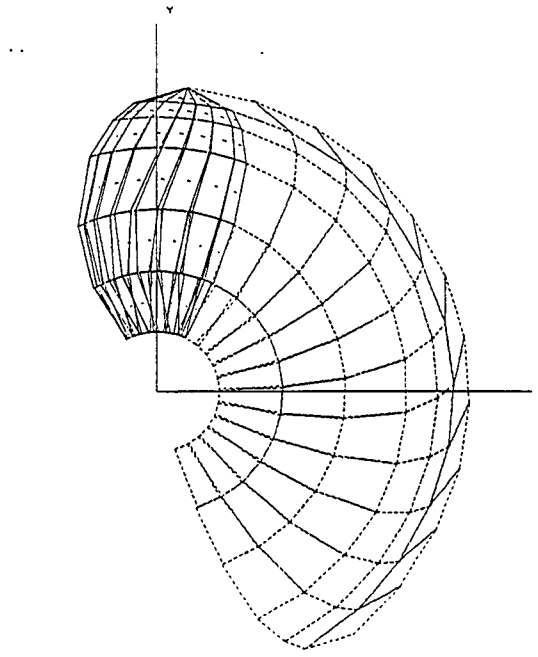

Fig. 21(b) Propeller with Vortex Wake
(MP218 , ISTEP=10)

KT value increases gradually in fore half revolution and decreases in aft half revolution . The variation is very small and the effect of length of vortex wake is not so strong but the total decrease in revolutions should be noticed. Discrepancy of KT value for different paneling can be seen in these figures . The value of the discrepancy should be noticed when the calculation results are used.

Comparison between the propeller with all blades and the propeller with one blade shows the effect of other blades. As shown in the figures the effect of the other blades grows in the first few time steps. This is explained by the reach of the vortex wake from the neighbour blade.

4.4. Comparison with Lifting Surface Theory

In this section calculation results for pressure distribution of MP221 are shown (Fig. 22) and comparison with the ordinary method based on lifting surface theory is discussed.

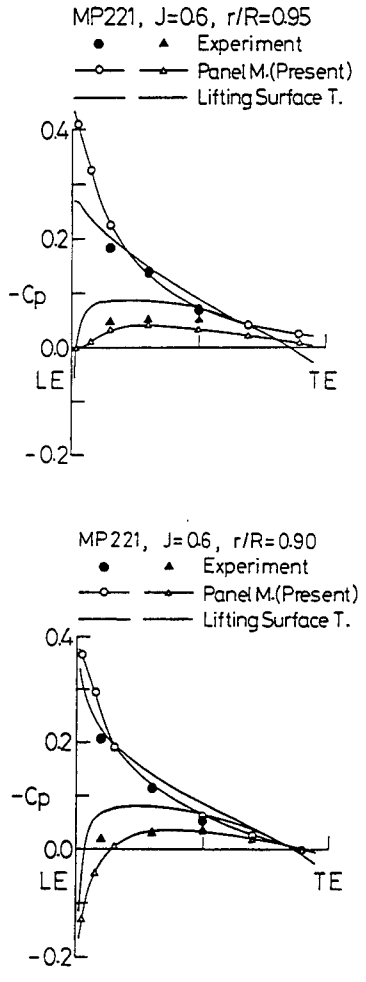

Fig. 22 Pressure Distribution (MP221)

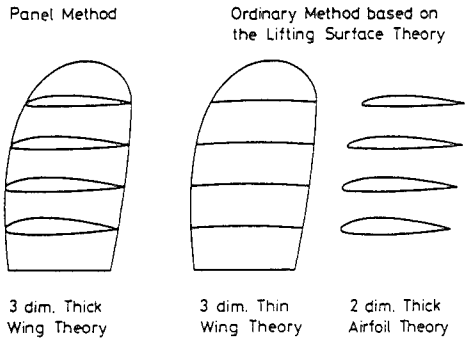

Fig. 23 Ordinary Method Based on Lifting Surface Theory

As shown in Fig. 22 the result by the present panel method is close to the experiment, whereas $-C_p$ value by the ordinary method based on lifting surface theory is higher than the experiment. These results prove very well a shortcoming of the ordinary method based on lifting surface theory and the improvement by panel method.

In the ordinary method based on lifting surface theory, the camber effect and the thickness effect are treated separately (Fig. 23) and lifting surface theory and thick airfoil theory are used. The camber effect is calculated by lifting surface theory which is available for three dimensional thin wings. The calculation supplies hydrodinamic camber line which is different from the geometrical camber line. The hydrodinamic camber line and the thickness distribution compose the two dimensional thick airfoil. The pressure on the two dimensional thick airfoil can be calculated by nonlinear thick airfoil theory, in which the pressure distribution has no singularity at leading edge. It is noteworthy that the three dimensional effect of thickness is not taken into consideration in the ordinary method based on lifting surface theory. This had already been pointed out(18). This is proved very well in Fig. 22.

4.5. Effect of Hub

Calculation results for pressure distribution of DTRC4119 at 20 time step are shown in Fig. 24. Comparisons with experiment (17) and with other panel method(VSAERO) show generally satisfactory agreement. In detail the present panel method gives higher value for $-C_p$ near the leading edge on the back side. The present panel method gives higher value for $-C_p$ also on the face side at r/R=0.3. The reason for the discrepancy is not clear.

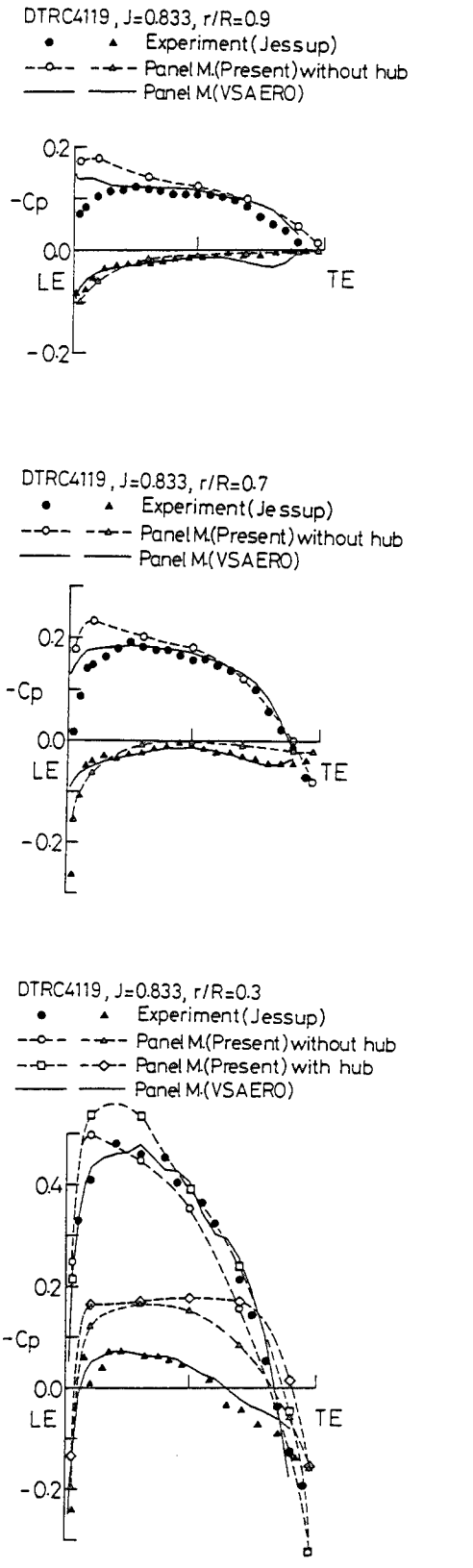

Fig. 24 Pressure Distribution (DTRC4119)

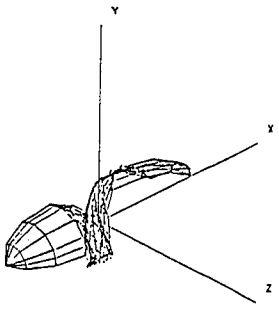

Fig. 25 Paneling of Hub

For propeller DTRC4119 calculations were performed for both cases without hub and with hub. Comparison of both calculations shows the effect of hub. Paneling for the hub is shown in Fig. 25. As shown in Fig. 24 for r/R= 0.3, flow velocity in case of with hub is faster and the pressure is lower according to the effect of hub. Comparison of circulation distribution between with/without hub is shown in Fig. 26. According to the effect of hub, the circulation around blade section near hub is higher than that for the calculation without hub. This is considered to be the results of mirror effect by the hub. On the other hand circulation on the other part in case of with hub is lower than that for the blade in case of without hub. KT value for the propellers with and without hub is 0.149 and 0.152 respectively

This is considered to be the results of higher inflow velocity from the effect of existence of hub. This explanation has already presented by some papers(19), (20). Actual flow around blade root and hub may be complicated. Vortex wake from blade root may be developed along hub surface and connected to hub vortex. So further improvement of vortex wake model is necessary for the analysis of a propeller with hub.

4.6 Propeller Operating in the Non-Uniform Flow

As marine propellers operate behind ship hull, the inflow to the propeller is not uniform. So it is important to know the characteristics of propellers operating in non-uniform flow.

Calculation of propeller MP218 operating in non-uniform flow was carried out. Simple sinusoidal axial wake was chosen for the non-uniform flow

$$V_S(1-W_x)=V_S(1-(0.3+0.3\cos 4\theta))$$

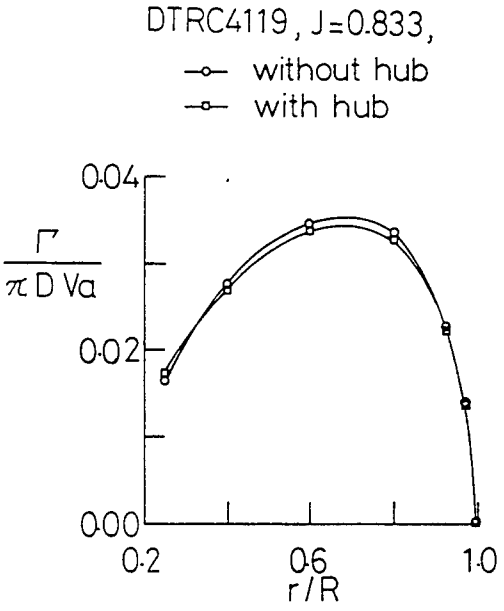

Fig. 26 Circulation Distribution

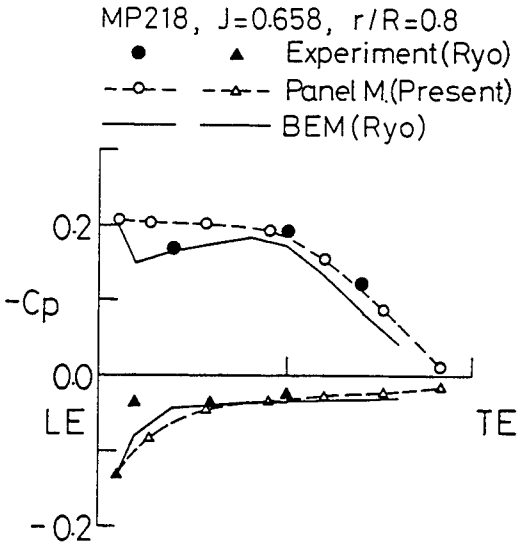

Fig. 27 Pressure Distribution (MP218)

Sinusoidal axial wake is useful for the study of unsteady characteristics of a propeller.

The results are compared with the calculation by frequency domain BEM by Ryo(2), which is a kind of panel method, and comparison is also made with the calculation by the lifting surface theory.

Before discussing non-uniform flow, calculation result for MP218 in uniform flow is shown in Fig. 27 and compared with other panel method and experiment(3). Comparisons show satisfactory agreement in general and in detail the present panel method gives higher value for $-C_p$ around 20% chord on the back side.

Result of the calculation for propeller MP218 operating in sinusoidal axial inflow is shown in Fig. 28. KT value for each blade and KT value for all blades are plotted for time step. KT value for one blade oscillates corresponding to sinusoudal inflow. KT value for all blades doesn't oscillate because the sinusoidal inflow is proportional to $\cos 4\theta$ and MP218 is 5 bladed propeller. The value for early time step corresponds to quasisteady calculation, whereas the value for latter time step approaches the unsteady calculation. The decrease of KT value for all blades with time step is not small in contrast to the case of uniform flow (Fig. 20). Comparison with unsteady analysis by BEM and lifting surface theory is shown in Fig. 29. The two methods employ frequency domain analysis, whereas the present method use time domain analysis. The comparison shows satisfactory agreement in general but in detail in latter time step, where the comparison should be made, the lower value of the oscillation by the present method is too low compared with other two methods.

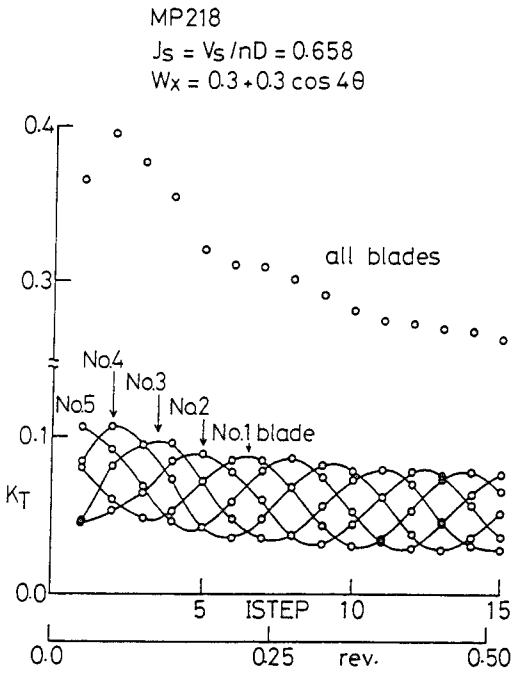

Fig. 28 Variation of Thrust Coeff.
MP218 Operating in Sinusoidal Inflow

5. CONCLUDING REMARKS

A panel method for analysis of unsteady flow around a propeller was presented. Calculation was carried out at each time step with the development of vortex wake. The method was discussed with numerical validation and with the comparison with other method and experiment for three propellers. Some flow characteristics such as the effect of neighbour blades and the effect of existance of hub were discussed. The verification was accomplished in the uniform inflow cases. The method was applied to a propeller operating in sinusoidal axial non-uniform inflow field. The result was compared with unsteady method based on frequency domain analysis. The method can treat the analysis of a propeller operating in arbitrary motion in non-uniform inflow. The treatment of the deformation of vortex wake according to induced velocity was left to be studied later.

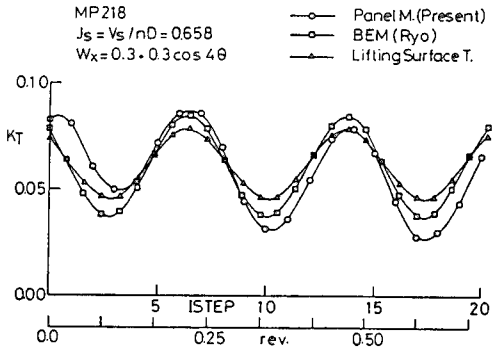

Fig. 29 Comparison with Other Methods
MP218 Operating in Sinusoidal Inflow

The development of computer program used in the present paper was performed as a cooperative research project "No Vibration High Quality Ship". The project was supported by the technology development fund of Ship & Ocean Foundation. The author would like to express sincere gratitude to Prof. H. Tanibayashi, who was the chief of author's group in the project.

REFERENCES

1. Ling, Z., Sasaki, Y., and Takahashi, M., "Analysis of Three-Dimensional Flow around Marine Propeller by Direct Formulation of Boundary Element Method (1st Report : in Uniform Flow)," J. of the Society of Naval Architects of Japan, Vol. 157, June 1985

2. Ling, Z., Sasaki, Y., and Takahashi, M., "Analysis of Three-Dimensional Flow around Marine Propeller by Direct Formulation of Boundary Element Method (2nd Report : in Steady Ship's Wake)," J. of the Society of Naval Architects of Japan, Vol. 159, June 1986

3. Ling, Z., Sasaki, Y., and Takahashi, M., "Analysis of Three-Dimensional Flow around Marine Propeller by Direct Formulation of Boundary Element Method (3rd Report : Comparison of Pressure Distributions on Propeller Blade between Caiculation and Model Test)," J. of the Society of Naval Architects of Japan, Vol. 160, Dec. 1986

4. Hoshino, T., "Hydrodynamic Analysis of Propellers in Steady Flow Using a Surface Panel Method", J. of the Society of Naval Architects of Japan, Vol. 165, June 1989

5. Hoshino, T., "Numerical and Experimental Analysis of Propeller Wake by Using a Surface Panel Method and a 3-Component LDV", 18th Symposium on Naval Hydrodynamics, AnnArbor 1990

6. Koyama, K., Kakugawa, A., and Okamoto, M., "Experimental Investigation of Flow around a Marine Propeller and Application of Panel Method to the Propeller Theory", 16th Symposium on Naval Hydrodynamics, Berkeley 1986

7. Hess, J. L., and Valarezo, W. O., "Calculation of Steady Flow About Propellers Using a Surface Panel Method," J. Propulsion and Power, Vol. 1, No. 6, Nov.-Dec. 1985

8. Yang, C. I. and Jessup, S. D., "Benchmark Analysis of a Series of Propellers with a Panel Method," Propellers'88, SNAME, Sept. 1988

9. Kerwin, J. E., Kinnas, S. A., Lee, J. T., and Shih, W. Z., "A Surface Panel Method for the Hydrodynamic Analysis of Ducted Propellers," SNAME Trans., Vol. 95, 1987

10. Hsin, C. Y., Kerwin, J. E., and Kinnas, S. A., "A Panel Method for the Analysis of the Flow Around Highly Skewed Propellers," Propellers/Shafting'91, SNAME, Sept. 1991

11. Kinnas, S., Hsin, C.-Y., and Keenan, D., "A Potential Based Panel Method for the Unsteady Flow Around Open and Ducted Propellers," 18th Symposium on Naval Hydrodynamics, AnnArbor 1990

12. Koyama, K., "A Numerical Method for Analyzing Potential Flow Around a Screw Propeller Based on the Lifting Body Theory (first report)," Papers of Ship Research Institute, Vol. 25, No. 5, Sept. 1988

13. Mangler, K. W. and Smith, J. H. B., "Behaviour of the Vortex Sheet at the Trailing Edge of a Lifting Wing," The Aeronautical J. of the Royal Aeronautical Society, Vol. 74, Nov. 1970

14. Giesing, J. P., "Vorticity and Kutta Condition for Unsteady Multi-energy Flows," J. Applied Mech., Sept. 1969

15. Morino, L. and Kuo, C. C., "Subsonic Potential Aerodynamics for Complex Configurations : A General Theory," AIAA J., Vol. 12, No. 2, Feb. 1974

16. Imai, I., "A Theory of General Aerofoil," J. Society of Aeronautical Science of Nippon, Vol. 9, No. 88, 1942

17. Jessup, S. D., "An Experimental Investigation of Viscous Aspects of Propeller Blade Flow," The Catholic University of America, Dissertation for PHD, 1989

18. Koyama, K., Takei, Y., Kurobe, Y., and Kakugawa, A., "A Method for Treating the Singularity at the Blade Tip of Marine Propellers (Third Report)," J. of the Society of Naval Architects of Japan, Vol. 153, June 1983

19. Chattopadhyay, S., Kato, H., and Yamaguchi, H., "A Study on Performance and Cavitation of Propellers for High Speed Crafts Including Effect of Boss (1st Report : Analysis in Uniform Flow)," J. of the Society ofNaval Architects of Japan, Vol. 158, Dec. 1985

20. Yang, C.-J. and Tamashima, M., " A Simplified Method to Predict Marine Propeller Performance Including the Effect of Boss ", Trans. the West-Japan Society of Naval Architects, No. 80, 1990

DISCUSSION

S. Kinnas
Massachusetts Institute of Technology, USA

First, I would like to congratulate the author for his continuing efforts in developing panel methods for propellers. I would like to raise the following questions/comments though:

The author discretizes the trailing wake with piecewise constant strength dipoles. We have found (by applying a similar method Ref. [11]) that it was necessary to keep the strength of at least the first panel in the wake linear in order for the results to be insensitive to the size of the wake panel (i.e., time step). For example, the author may look in Fig. 6 and 7 of [21] where it is shown that the results are strongly dependent on the time step size, unless a linear panel in the wake is employed. How does the predicted unsteady circulation distribution around a 2-D foil subject to a transverse gust behave with the ratio of the length of the first panel in the wake to that of the last panel on the hydrofoil, for the same (or similar) conditions to those shown in Fig. 6 of [21]?

Concerning his Kutta condition: We have also found that the correction to Morino's condition (third term in equation 44) is necessary (also sufficient) in 2-D in order to render zero pressure jump at the trailing edge, especially for thick sections at high angles of attack [22]. However, we have found that this condition is not always sufficient in 3-D for guaranteeing that the pressure jump at the trailing edge is equal to zero at all spanwise locations (especially in the presence of strong spanwise flow). Namely, in 3-D we had to apply an iterative pressure Kutta condition [21] in order to explicitly require that the pressure jump be equal to zero at all spanwise locations. Has the author checked the pressure jump at the trailing edge at all spanwise locations for his propeller runs? For example, the pressure distributions shown in Fig. 24 for r/R=0.7 do not seem to match at the trailing edge.

Concerning the comparison of the lifting surface (LSM) and the panel method (PM) against experiments given in section 4.4, it is beyond dispute that the PM will capture the potential flow effects more accurately than the LSM. Before comparing with experimental results though, the effects of viscosity should be included (for example via a boundary layer connection). In most cases, the PM will predict a higher circulation than LSM. On the other hand, the boundary layer effects will reduce the inviscid flow circulation (because, in most occasions, the thickness of the boundary layer on the pressure side is smaller than that on the suction side). Thus, in some instances those two effects will cancel, and the LSM will produce a circulation that is closer to experiment than that from the PM. This is the reason why the lifting surface method has been so successful in designing conventional (no skew or rake) propellers. The discussor does not imply that comparisons with experiments should not be done; he only wants to stress out that we should be careful in drawing conclusions about the two methods (PM or LSM) before the viscous flow effects are included. To put it in different words, we should not always expect the PM results to be close to experiments. The discussor would like to listen to the authors' comments on this issue.

[21] Kinnas, S.A. and Hsin, C.-Y. "Boundary Element Method for the Analysis of the Unsteady Flow Around Extreme Propeller Geometries," AIAA Journal, Vol. 30, No. 3, March 1992, pp 688-696.

[22] Lee, J.-T. "A Potential Based Panel Method for the Analysis of Marine Propellers in Steady Flow," PhD Thesis, MIT, Dept. of Ocean Engineering, August 1987.

AUTHOR'S REPLY

Thank you, Dr. Kinnas, for your important discussion. I would like to reply to each item.

Fig. 21(b) of the main body shows the vortex wake paneling for the propeller in uniform flow. Paneling for the propeller in sinusoidal non-uniform flow $Wx = 0.3 + 0.3 \cos 4\theta$ is shown in Fig. B. Although strength of dipole is constant in the wake panel, the size of the first panel in the wake is small compared with other panels in the wake. The size is almost the same as the last panel on the blade as shown in Fig. B. The strength of dipole is set as expression (44) of the main body. The length of the other wake panel is $\Delta t \bullet n = 0.0343$ ($n = 17.15$ rps), so there are about 7 panels in the 0.25 rotation (this corresponds to one period of $\cos 4\theta$). This balance is considered to be reasonable for the calculation, although the numerical check might be necessary as the discussor pointed out.

As the discussor pointed out for the pressure

distribution near the trailing edge in Fig. 24, the pressure Kutta condition might not be complete, although the pressure jump near the trailing edge is very small. Considering that the condition (44) is valid for 2D case as shown in numerical calculation in Section 3, it is reasonable to interpret that the reason for the incompleteness may be 3D effect. But the numerical results cannot explain this. For example, the pressure condition near the trailing edge for r/R = 0.7 is worse than that for r/R = 0.9, although 3D effect is considered to be stronger for 4/R = 0.9. So the author thinks it should be studied further to make clear the incompleteness.

It goes without saying that a new method should be compared with ordinary methods and shown with its advantage when it is proposed. Why is it necessary to use a panel method? The author intended to show an example of the advantage of the panel method in Section 4.4. The author thinks Fig. 22 shows the advantage of the panel method very well. Mechanism of difference between the two methods was explained by the 3D effect from thickness for lifting surface theory, which was discussed in Ref. (6). The conclusion shown in Fig. 22 will not alter even if the viscous effect is taken into consideration, because both calculations for -Cp will go up if the boundary layer thickness is taken into account.

Thank you.

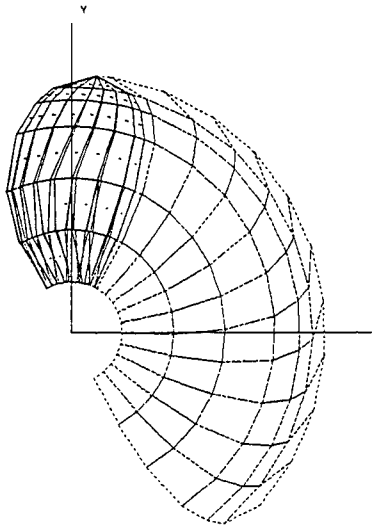

Fig. B Paneling for the propeller in non-uniform flow

DISCUSSION

B. Maskew
Analytical Methods, Inc., USA

The panel method described in the paper applied the well established Dirichlet condition, which sets a fictitious internal potential equal to that of the onset flow. With this approach, the doublet and source distributions provide the *perturbation* potential of the flow. I have two comments on the paper: the first concerns the ensuing discussion on the Kutta condition, where it was noted that, if the third term in Eq. 44 is omitted, then the Kutta condition is not satisfied for thick trailing edges. If, in fact, the *total* potential, i.e., $\rho+\rho\infty$, is used in each of the quantities in Eq. 46 rather than the *perturbation* potential, then the *steady* Kutta condition on the thick sections can be satisfied (this essentially restores the third term in Eq. 44 in a simple manner).

My second comment concerns the very low panel densities used on the blades. In general, it is found that at least 20 (and preferably 30 or more) panels are needed across the blade chord on the upper and lower surfaces to adequately capture the pressure distribution. This is particularly important if the blade section includes an "aft loaded" camber line or if the blade is operating in a highly curved flow field. In these situations, even a sophisticated explicit Kutta condition that equalizes the upper and lower trailing edge pressures will not give the correct pressure distribution on a low order method unless the surface geometry is well represented. If boundary layer effects are to be included, then at least 30 chordwise panels on the upper and lower surfaces are needed.

AUTHOR'S REPLY

Thank you, Dr. Maskew, for your important discussion. If the total potential is used in Eq. (46), the steady Kutta condition on the thick airfoil can be satisfied, as you said in your first comment. If velocity vector V in Eq. (19) is set zero and inflow velocity W in Eq. (20) is set some finite constant value in my formulation, the potential Φ gives the total potential. And the third term of Eq. (44) vanishes because of V=0. This is useful for the case of a wing that doesn't rotate. So this idea cannot be applied to a propeller blade.

As for your second comment, I should investigate

the effect of number of panels with finer paneling as you said. But it was happy for me to have the chance to compare the calculations with fine paneling by some other researchers. The workshop on surface panel method for marine propellers organized by the 20th ITTC Propulsor Committee was held in this hotel last Sunday. Some researchers including the discussor use very fine paneling. Fig. A is the example of the comparison of our calculation with other calculations. This discrepancy shows the degree of error or degree of accuracy for our calculation. This should be noticed when our calculation results are used.

Thank you.

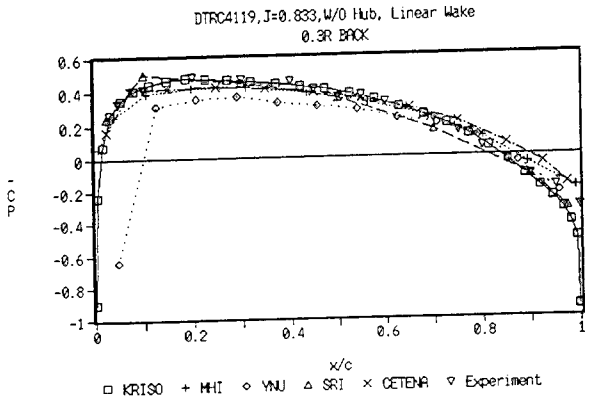

Fig. A Comparison with Other Calculations Pressure Distribution

DISCUSSION

T. Hoshino
Mitsubishi Heavy Industries, Ltd., Japan

I would like to congratulate the author for the excellent paper presenting the method to analyze the unsteady characteristics of propeller by surface panel method. I would like to ask one question. Calculation of several rotations of propeller is necessary to get the converged solution in time domain analysis. How many rotations did you calculate to obtain the final solution?

AUTHOR'S REPLY

Thank you, Dr. Hoshino, for your important discussion. I calculated about 0.5 rotation of time steps to obtain the KT, KQ, CP value presented in this paper. As you can see in Figs. 16, 18, 20, the effect of the vortex wake emanating from the neighbor blade is very significant. That is about early 0.25 rotation in these calculation cases. Calculation was performed about 1.0 rotation for one blade, and the result showed very small variation of KT value. But I think it should be confirmed by the calculation with more long vortex wake. Thank you.

A Bilinear Source and Doublet Distribution Over a Planar Panel and Its Applications to Surface Panel Methods

J.-C. Suh, J.-T. Lee, S.-B. Suh
(Korea Research Institute of Ships and Ocean Engineering, Korea)

Abstract

This paper presents closed-forms for computing the induced potentials and velocities due to a bilinear density distribution of source and/or doublet singularities over a planar panel. The surface integrals associated with Green's scalar identity can be transformed into contour integrals using Stokes' formulas. The present analysis includes, of course, the cases of constant or linear distributions. The closed-forms are more computer-oriented and explicit than those derived previously so that we can obtain, with much easier implementation, the matrix elements of the linear system of algebraic equations in application of surface panel methods.

NOMENCLATURE

A	constant in equation for the vorticity component of a Hill's spherical vortex flow, $\omega = Ar\sin\theta$
$\underline{A}$	vector, Eq. (11)
a	constant defined by $\underline{e}\cdot\underline{r}$
a_0, a_1, a_2, a_3	coefficients for specification of bilinear source distributions
a, b, c	lengths of the semi-axes of an ellipsoid
$\underline{B}$	vector, Eq. (7)
b_0, b_1, b_2, b_3	coefficients for specification of bilinear doublet distributions
C_i	perimeter of a planar panel with the index i denoting the side in concern
$\underline{e}$	unit vector independent of a source-point, especially taken as $\pm\underline{n}$, Eqs. (7) and (11)
$\underline{e}_{\ell i}$	unit direction vector along sides of a panel
$\underline{e}_\xi, \underline{e}_\eta$	unit vectors in ξ- and η-direction in the local coordinate system (ξ,η,ς)
$\underline{e}_\phi$	unit vector in ϕ-direction in a spherical polar coordinate system (ρ,θ,ϕ)
ℓ	arclength along each side of a planar panel
N_S	number of sides of a polygon panel
$\underline{n}$	unit normal vector to a planar panel
Q_i	corner points (vertices) of a panel
$\underline{q}$	velocity
q_s	surface speed
q_o	undisturbed speed of onset flow
q_x, q_y	x-and y-component of velocity in the symmetric plane of a Hill's vortex flow
q_θ	speed at the interior surface of a sphere for a Hill's vortex flow
R	radius of a sphere for a Hill's spherical vortex flow
R_i	distance between a vertex of a panel and a field point
$\underline{r}$	distance vector between a source-point and a field-point, $\underline{x}_\xi - \underline{x}_p$; as a scalar, distance between the two points
s_i	length of each side of a panel, Fig. 1
t	maximum thickness of a circular wing
x, y, z	Cartesian coordinates of a field point measured from the origin of (ξ,η,ς)-coordinate system
(x', z')	local plane coordinate system, Fig. 2
$\underline{x}_p$	position vector of a point where potential and velocity are evaluated, i.e. of a field-point
$\underline{x}_\xi$	position vector of a point where a singularity is located, i.e. of a source-point
(U,V,W)	onset flow velocity
α	angle of attack
μ	surface doublet density, equivalently defined by $\mu = -\phi$

(ρ, θ, ϕ)	spherical polar coordinate system used for representation of a Hill's spherical vortex flow
σ	surface source density
ϕ	velocity potential
$\triangle\phi$	jump of velocity potential at trailing edge
(ξ, η, ς)	local Cartesian coordinate system where a singularity is located at the plane of $\varsigma = 0$
$\underline{\omega}$	vorticity; as a scalar, vorticity component of a Hill's spherical vortex flow

1. INTRODUCTION

The main task for computing the potential flow about arbitrary bodies is to determine velocity potential ϕ in a fluid domain. Using Green's scalar identity, the velocity potential can be represented from distributions of sources and doublets on the boundary surfaces. Applying the normal boundary condition at the collocation points results in a linear system of algebraic equations to be solved for unknown doublet strengths on each panel with known source strengths. The associated surface integrals should be evaluated at the collocation points to obtain the matrix elements of the linear system. A fast and accurate computation of these elements is, therefore, very important in the numerical solution.

The potential ϕ within the fluid domain can be expressed approximately as a sum of each contribution in terms of the surface value of the potential ϕ and its normal derivative $\underline{n} \cdot \nabla\phi$ on each panel of the discretized boundary surfaces S_i;

$$\phi(\underline{x}_p) = -\frac{1}{4\pi} \sum_i \iint_{S_i} \left\{ \frac{1}{r} \underline{n} \cdot \nabla\phi - \phi \, \underline{n} \cdot \nabla\left(\frac{1}{r}\right) \right\} dS \quad (1)$$

The velocity can be derived by differentiating Eq. (1) with respect to the coordinates of the field point. Here r is distance between the integration point $\underline{x}_\xi$ on S_i and the field point $\underline{x}_p$ located in the fluid domain. The first and the second term represent the potential due to a surface distribution, respectively, of source-type singularity with a density $\sigma \equiv \underline{n} \cdot \nabla\phi$ and of doublet-type singularity with a density $\mu \equiv -\phi$. We may take without loss of generality one planar panel as the integration region in concern herein, which can be regarded as a part of the discretized boundary surface.

The closed-form expressions of the surface integrals for constant source distributions over flat quadrilateral panels have been introduced by Hess & Smith (1). They expressed the surface integrals as a superposition of line integrals for each side of the panels, with independent treatment of the contribution from the side. Webster (2) has extended the Hess and Smith analysis to a triangular panel in order to eliminate the discontinuity problem for a flat quadrilateral source panel by allowing a linear variation of the source strength across the triangular panel. These two approaches are concerned with only the source distributions and the resultant expressions are considerably complicated to employ a computer code. A simpler and more unified derivation has been provided by Newman (3) for computing the potential due to a constant doublet or source distribution. His analyses are based on the elementary plane geometry related to the solid angle of a panel. He defined four infinite sectors (for a quadrilateral panel), bounded by semi-infinite extensions of the two adjacent sides of the panel with respect to the corresponding vertices, such that the difference between the domains of the four sectors is the domain of the panel. Then the surface integral over each infinite sector is evaluated in terms of the included angle of the corresponding vertex projected onto the unit sphere with center at the field point. He has also described the more general recursive scheme for computing the potential due to a source or doublet distribution of linear, bilinear or higher order form, using the basic results for the case of the constant distribution. However the computer-oriented results for the induced velocities due to the higher-order distributions do not appear explicitly to be appreciated.

Another elegant approach based on mathematical formulations has been presented by Cantaloube & Rehbach (4). They introduced more explicit expressions of the surface integrals for the source or doublet distribution. With vector operations of the integrands for using Stokes' formulas, they show that the surface integrals for the constant or linear distributions of sources and doublets over a planar facet can be transformed into line integrals along the contour of the panel. The major advantages of their study are that the formulations are valid for a planar curve-sided panel and that the resultant equations are expressed in a global coordinate system while the aforementioned analyses require the transformation of the local coordinate system. Thus the expressions derived by Cantaloube & Rehbach may be regarded as a more computer-oriented form. They have proposed the direct numerical integrations of the line integrals by an integration quadrature (e.g. Simpson rule or Gaussian quadrature). However when a field point is very close to the sides or vertices of a panel, a large number of the quadrature base points and considerable effort to choose these points suitably would be needed in order to achieve good accuracy. Such numerical implementation in a computer code may lead to a large amount of extra-computer time. Any attempt for finding closed form expressions of the line integrals even for a polygon panel does not appear in their study. Suh (5) obtained, as an extension of Cantaloube & Rehbach's work, the closed-forms for computing the induced potentials and velocities due to constant and/or linear distributions of the singularities. He expressed them as a sum of contribution from each side of the panel, in terms of appropriate basic integrals.

As an another extension (but of the different approach) the present paper deals with a *bilinear* singularity distribution over *a planar polygon panel.* In numerical implementation of the potential-based panel method for solving the potential flow around a lifting body, the trailing wake sheet is represented approximately as the doublet distribution of potential jump. One possible way to include the effect of the local variation of these doublet strengths is with the use of a bilinear distribution over each wake panel (which is uniquely determined from imposed potential jump values at its four vertices). The use

of the bilinear distribution over quadrilateral panels (or the linear distribution over triangular panels) eliminates the discontinuity problem of singularity for the piecewise constant distribution. Then the singularity strength will be chosen to vary bilinearly (or linearly) across the panel. The main scope of the present work is therefore to derive explicit and elegant closed-forms of the induced potential and velocity due to a bilinear distribution. The bilinear distribution case includes, of course, both the constant and the linear distribution cases.

Alternative forms of the associated integrands for the bilinear distribution of sources and doublets over a planar panel are presented in Section 2, from which we can transform the associated surface integrals into line integrals along contour of the panel by using Stokes' formulas. For a planar polygon panel, the derived line integrals can be reduced to closed-form expressions which are presented in Section 3. They are expressed compactly as a sum of contribution from each side of the panel, in terms of appropriate basic integrals. It will be shown that each contribution depends on the relative position of a field point from the side. Section 4 is devoted to analytical evaluations of the basic integrals. In section 5, for the purpose of checking the convenience and accuracy of the present approach, we apply the derived expressions to some flow problems, as listed below, related to surface panel methods: (i) an axisymmetric rotational flow inside a sphere (a Hill's spherical vortex flow) (ii) a non-lifting flow around an ellipsoid and (iii) a lifting flow around an elliptic wing.

2. ALTERNATIVE FORMS OF INTEGRANDS FOR STOKES' FORMULAS

Without loss of generality we will consider the domain of one planar panel for the integration region as a part of the discretized boundary surface in Eq. (1). We take an orthogonal coordinate system (ξ, η, ς) to specify a bilinear form, such that the panel is in the plane $\varsigma = 0$ and the direction of ς-axis is the same as that of the unit normal vector, $\underline{n}$, of the panel, as shown in Fig. 1. The unit vectors in the direction of ξ-axis and η-axis are denoted by $\underline{e}_\xi$ and $\underline{e}_\eta$, respectively. These two axes may be chosen arbitrarily in the directions but lying on the panel surface. The coordinates (x, y, z) of the field point $\underline{x}_p$ are measured relatively from the origin of the coordinate system.

The potentials and the velocities at a field point $\underline{x}_p$ induced by a bilinear source distribution $\sigma = a_0 + a_1\xi + a_2\eta + a_3\xi\eta$ and by a doublet distribution $\mu = b_0 + b_1\xi + b_2\eta + b_3\xi\eta$, respectively, can be written as,

$$\phi^{(\sigma)} = -\frac{1}{4\pi}\iint_S \Big[c_0\frac{1}{r} + c_1\frac{\xi - x}{r} + c_2\frac{\eta - y}{r} + c_3\frac{(\xi - x)(\eta - y)}{r}\Big]\, dS \tag{2}$$

$$\underline{q}^{(\sigma)} = \frac{1}{4\pi}\iint_S \Big[c_0\nabla(\frac{1}{r}) + c_1(\xi - x)\nabla(\frac{1}{r}) \tag{3}$$

$$+c_2(\eta - y)\nabla(\frac{1}{r}) + c_3(\xi - x)(\eta - y)\nabla(\frac{1}{r})\Big]\, dS \tag{4}$$

$$\phi^{(\mu)} = -\frac{1}{4\pi}\underline{n}\cdot\iint_S \Big[d_0\nabla(\frac{1}{r}) + d_1(\xi - x)\nabla(\frac{1}{r}) + d_2(\eta - y)\nabla(\frac{1}{r}) + d_3(\xi - x)(\eta - y)\nabla(\frac{1}{r})\Big]\, dS \tag{5}$$

$$\begin{aligned}\underline{q}^{(\mu)} &= -\frac{1}{4\pi}\{\oint_C \mu\nabla(\frac{1}{r})\times d\underline{\ell} + \iint_S (\underline{n}\times\nabla\mu)\times\nabla(\frac{1}{r})dS\} \\ &= -\frac{1}{4\pi}\Big[\oint_C (b_0 + b_1\xi + b_2\eta + b_3\xi\eta)\nabla(\frac{1}{r})\times d\underline{\ell} \\ &\quad + \iint_S \{(b_1 + b_3\eta)\underline{e}_\eta \supset q(b_2 + b_3\xi)\underline{e}_\xi\}\times\nabla(\frac{1}{r})dS\Big]\end{aligned} \tag{6}$$

where for shortness of expressions we have defined the constants $c_0 = a_0 + a_1x + a_2y + a_3xy, c_1 = a_1 + a_3y, c_2 = a_2 + a_3x, c_3 = a_3$ and $d_0 = b_0 + b_1x + b_2y + b_3xy, d_1 = b_1 + b_3y, d_2 = b_2 + b_3x, d_3 = b_3$. Equation (6) has been changed into the form of the vortex distribution equivalent to the doublet distribution (6, 7).

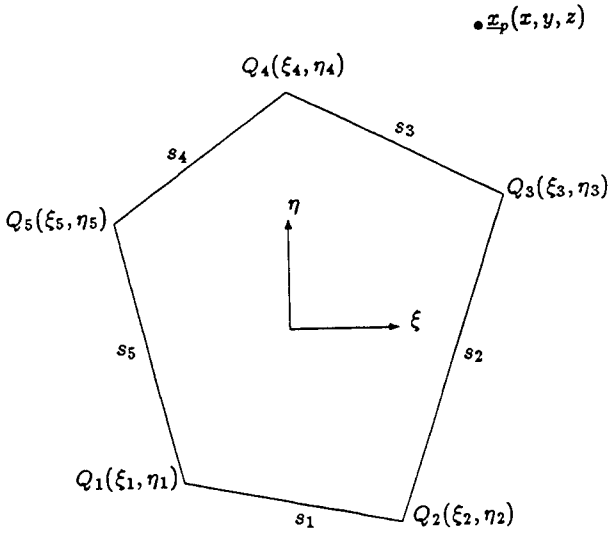

Fig. 1 A planar panel defined in a local coordinate system

In the case of a bilinear singularity distribution, eight different integrands are involved in the surface integrals in Eq. (1). For use of Stokes' formulas, all integrands can be transformed into equivalent ones either in curl-form of a vector or in cross product-form of a vector with the normal $\underline{n}$ as follows:

$$\frac{1}{r} = \underline{e}\cdot(\nabla\times\underline{B}) \tag{7}$$

$$\frac{\xi - x}{r} = \underline{e}_\eta\cdot(\underline{n}\times\nabla r) \tag{8}$$

$$\frac{\eta - y}{r} = -\underline{e}_\xi\cdot(\underline{n}\times\nabla r) \tag{9}$$

$$\frac{(\xi - x)(\eta - y)}{r} = \underline{e}_\eta\cdot\Big[\underline{n}\times\nabla\{(\eta - y)r\}\Big] \tag{10}$$

$$\nabla(\frac{1}{r}) = -\nabla\times\underline{A} \tag{11}$$

$$\begin{aligned}(\xi - x)\nabla(\frac{1}{r}) &= \Big[\underline{e}_\eta\cdot\{\underline{n}\times\nabla(\frac{\xi - x}{r})\} - \frac{1}{r}\Big]\underline{e}_\xi \\ &\quad - \Big[\underline{e}_\xi\cdot\{\underline{n}\times\nabla(\frac{\xi - x}{r})\}\Big]\underline{e}_\eta \\ &\quad - z\Big[\underline{e}_\eta\cdot\{\underline{n}\times\nabla(\frac{1}{r})\}\Big]\underline{n}\end{aligned} \tag{12}$$

$$(\eta-y)\nabla(\frac{1}{r}) = \Big[\underline{e}_\eta\cdot\{\underline{n}\times\nabla(\frac{\eta-y}{r})\}\Big]\underline{e}_\xi - \Big[\underline{e}_\xi\cdot\{\underline{n}\times\nabla(\frac{\eta-y}{r})\}+\frac{1}{r}\Big]\underline{e}_\eta + z\Big[\underline{e}_\xi\cdot\{\underline{n}\times\nabla(\frac{1}{r})\}\Big]\underline{n} \quad (13)$$

$$(\xi-x)(\eta-y)\nabla(\frac{1}{r}) = -\underline{e}_\xi\cdot\Big[\underline{n}\times\nabla\{\frac{(\xi-x)^2}{r}\}\Big]\underline{e}_\xi + \underline{e}_\eta\cdot\Big[\underline{n}\times\nabla\{\frac{(\eta-y)^2}{r}\}\Big]\underline{e}_\eta + z\,\underline{e}_\xi\cdot\Big[\underline{n}\times\nabla(\frac{\xi-x}{r})\Big]\underline{n} \quad (14)$$

where

$$\underline{A}=\frac{\underline{e}\times\underline{r}}{r(r+\underline{e}\cdot\underline{r})}\,,\quad \underline{B}=\frac{\underline{e}\times\underline{r}}{r+\underline{e}\cdot\underline{r}}$$

The distance vector $\underline{r}$ is defined as $\underline{x}_\xi-\underline{x}_p$ where the subscripts ξ and p refer to the source point and the field point, respectively. Equations (7) and (11) have been introduced by Suh (5) and Guiraud (8) respectively, which can be also derived by direct manipulation with starting from the right sides. The remaining equations have been derived by a similar deduction, under hypothesis of planarity of the panel. While Eqs. (7) and (11) hold for any $\underline{e}$ independent of the integration point $\underline{x}_\xi$ more generally, the unit vector $\underline{e}$ is taken as $\pm\underline{n}$ for application of Stokes' transformation where the sign is chosen such that $\underline{e}\cdot\underline{r}$ is not negative. Of course, these two relations can be simply used if one wants to compute the induced potentials and velocities due to the constant source and doublet distributions. In this case, the present approach using these key relations will be shown to consider consistently simpler than those presented in (1, 2, 3, 4).

Using Stokes' formulas of the surface integrals with the alternative forms for a polygon panel, we can express the surface integrals as a sum of the associated line integrals for each side of the panel with independent treatment of the contribution from the side. Each contribution can be written as closed-forms in term of only the geometrical parameters of the side as will be described in the following sections.

3. INDUCED POTENTIALS AND VELOCITIES

By using Eqs. (7) through (10) for the corresponding integrands and then by performing Stokes' transformations, Eq. (2) can be written as, in terms of line integrals,

$$\phi^{(\sigma)} = -\frac{1}{4\pi}\Big[c_0\oint_C\frac{\underline{r}\cdot(d\underline{\ell}\times\underline{n})}{r+\underline{e}\cdot\underline{r}}+c_1\underline{e}_\eta\cdot\oint_C r\,d\underline{\ell} - c_2\underline{e}_\xi\cdot\oint_C r\,d\underline{\ell}+c_3\underline{e}_\eta\cdot\oint_C(\eta-y)r\,d\underline{\ell}\Big] \quad (15)$$

The term $\underline{r}\cdot(d\underline{\ell}\times\underline{n})/d\ell$ represents the projection of the distance vector $\underline{r}$ onto the vector perpendicular to both $d\underline{\ell}$ and $\underline{n}$. Because it is constant for each side of a straight line and $\underline{e}\cdot\underline{r}$ is a non-negative constant ($\equiv a$) for all sides of the planar panel (that represents the normal distance of the field point from the panel), Eq. (15) can be written

$$\phi^{(\sigma)} = -\frac{1}{4\pi}\sum_{i=1}^{N_S}\Big[c_0t_i\int_{C_i}\frac{1}{r+a}d\ell+c_1v_i\int_{C_i}r\,d\ell - c_2u_i\int_{C_i}r\,d\ell+c_3v_i\int_{C_i}(\eta-y)r\,d\ell\Big] \quad (16)$$

The index i denotes the integer for identification of the side in concern, N_S is the number of sides of the polygon panel (e.g., $N_S=3$ for triangular panels), $t_i=\underline{r}\cdot(\underline{e}_{\ell_i}\times\underline{n})$, $u_i=\underline{e}_\xi\cdot\underline{e}_{\ell_i}$ and $v_i=\underline{e}_\eta\cdot\underline{e}_{\ell_i}$. The directional vector $\underline{e}_{\ell_i}=d\underline{\ell}/d\ell$ is chosen in a counterclockwise direction as the convention of the contour integral. Rewriting the last integral in Eq. (16) in terms of the local coordinates of the nodes, we finally obtain the expression for the source-induced potential:

$$\phi^{(\sigma)} = -\frac{1}{4\pi}\sum_{i=1}^{N_S}\Big[c_0t_i\int_{C_i}\frac{1}{r+a}d\ell+\{c_1v_i-c_2u_i+c_3v_i(\eta_i-y)\}\int_{C_i}r\,d\ell+c_3v_i^2\int_{C_i}\ell r\,d\ell\Big] \quad (17)$$

Here ℓ is the integral variable representing the arclength along each integration path C_i. The vertices composed of the panel (ξ_i,η_i) and the sides are also defined in a counterclockwise order as illustrated in Fig. 1. It is seen that the integral term for each side is related to the relative position of the field point from the side. Each integral, as will be shown, depends only on the coordinates of the two end points of the corresponding side. Equation (17) can be directly used even in the cases of that the field points are just at the panel surface (i.e., in the self-induction cases), by setting $a=0$ in Eq. (17) since $\underline{n}\cdot\underline{r}=0$. Furthermore, when the field point is just at the side of the panel, the first term vanishes because t_i decays faster than the integral with r approaches zero, while the other terms have finite values.

For the source-induced velocity, we first re-arrange the first integrand in Eq. (3) for use of Stokes' transformations:

$$\nabla(\frac{1}{r})=\underline{n}\,\{\underline{n}\cdot\nabla(\frac{1}{r})\}-\underline{n}\times\{\underline{n}\times\nabla(\frac{1}{r})\}$$

Using Eqs. (11) through (14) and rearranging the resulting expressions give us the corresponding expression for the source-induced velocity:

$$\begin{aligned}\underline{q}^{(\sigma)} = \frac{1}{4\pi}\sum_{i=1}^{N_S}\Big[&-c_0\Big\{\underline{n}(\underline{n}\cdot\underline{e})t_i\int_{C_i}\frac{1}{r(r+a)}d\ell\\ &+(\underline{n}\times\underline{e}_{\ell_i})\int_{C_i}\frac{1}{r}d\ell\Big\}+(v_i\underline{e}_\xi-u_i\underline{e}_\eta)\Big\{\{c_1(\xi_i-x)\\ &+c_2(\eta_i-y)\}\int_{C_i}\frac{1}{r}d\ell+\{c_1u_i+c_2v_i\}\int_{C_i}\frac{\ell}{r}d\ell\Big\}\\ &-t_i(c_1\underline{e}_\xi+c_2\underline{e}_\eta)\int_{C_i}\frac{1}{r+a}d\ell\\ &+z\underline{n}(c_2u_i-c_1v_i)\int_{C_i}\frac{1}{r}d\ell+c_3\Big\{-\underline{e}_\xi u_i(\xi_i-x)^2\\ &+\underline{e}_\eta v_i(\eta_i-y)^2+\underline{n}u_iz(\xi_i-x)\Big\}\int_{C_i}\frac{1}{r}d\ell\\ &+c_3\Big\{-2\underline{e}_\xi(\xi_i-x)u_i^2+2\underline{e}_\eta(\eta_i-y)v_i^2\underline{n}zu_i^2\Big\}\int_{C_i}\frac{\ell}{r}d\ell\Big\}\\ &+c_3\Big\{\underline{e}_\eta v_i^3-\underline{e}_\xi u_i^3\Big\}\int_{C_i}\frac{\ell^2}{r}d\ell\Big]\end{aligned} \quad (18)$$

For a bilinear doublet distribution $\mu = b_0 + b_1\xi + b_2\eta + b_3\xi\eta$, the induced potentials and velocities can be obtained in a straightforward manner as in the cases of the source distribution. The final results can be written, for the induced potentials,

$$\begin{aligned}\phi^{(\mu)} &= -\frac{1}{4\pi}\sum_{i=1}^{N_s}\Big[-d_0(\underline{n}\cdot\underline{e})t_i\int_{C_i}\frac{1}{r(r+a)}d\ell \\ &\quad +\{d_2u_i - d_1v_i + d_3u_i(\xi_i - x)\}\int_{C_i}\frac{1}{r}d\ell \\ &\quad +d_3u_i^2 z\int_{C_i}\frac{\ell}{r}d\ell\Big] \qquad (19)\end{aligned}$$

and, for the induced velocities,

$$\begin{aligned}\underline{q}^{(\mu)} &= \frac{1}{4\pi}\sum_{i=1}^{N_s}\Big[(\underline{r}\times\underline{e}_{\ell_i})\Big\{(b_0 + b_1\xi_i + b_2\eta_i + b_3\xi_i\eta_i) \\ &\quad \int_{C_i}\frac{1}{r^3}d\ell + \{b_1u_i + b_2v_i + b_3(\xi_iv_i + \eta_iu_i)\} \\ &\quad \int_{C_i}\frac{\ell}{r^3}d\ell + b_3u_iv_i\int_{C_i}\frac{\ell^2}{r^3}d\ell\Big\} \\ &\quad +(\underline{n}\cdot\underline{e})t_i(d_1\underline{e}_\xi + d_2\underline{e}_\eta)\int_{C_i}\frac{1}{r(r+a)}d\ell \\ &\quad +\underline{n}(d_1v_i - d_2u_i)\int_{C_i}\frac{1}{r}d\ell + d_3\Big[\underline{n}\{v_i(\eta_i - y) \\ &\quad -u_i(\xi_i - x)\} + z(\underline{e}_\eta v_i - \underline{e}_\xi u_i)\Big\}\int_{C_i}\frac{1}{r}d\ell \\ &\quad +d_3\underline{n}(v_i^2 - u_i^2)\int_{C_i}\frac{\ell}{r}d\ell\Big] \qquad (20)\end{aligned}$$

It is easily found that the expression for the induced potential $\phi^{(\mu)}$ has the same form as the normal component of $\underline{q}^{(\sigma)}$ except notation of the singularity distribution.

4. CLOSED-FORMS OF THE BASIC INTEGRALS

In the preceding sections, we have expressed the induced potentials and velocities in forms of a sum of the more simplified line integrals given in Eqs. (17), (18), (19) and (20). We will derive here closed-forms of the following line integrals involved in those expressions:

$$\begin{aligned}&\mathrm{I1}_i = \int_{C_i}\frac{1}{r}d\ell,\quad \mathrm{I2}_i = \int_{C_i}\frac{1}{r+a}d\ell,\quad \mathrm{I3}_i = \int_{C_i}\frac{1}{r(r+a)}d\ell, \\ &\mathrm{I4}_i = \int_{C_i}\frac{1}{r^3}d\ell,\quad \mathrm{J1}_i = \int_{C_i}\frac{\ell}{r}d\ell,\quad \mathrm{J2}_i = \int_{C_i}\frac{\ell}{r^3}d\ell, \\ &\mathrm{J3}_i = \int_{C_i} r\,d\ell,\quad \mathrm{K1}_i = \int_{C_i}\frac{\ell^2}{r}d\ell,\quad \mathrm{K2}_i = \int_{C_i}\frac{\ell^2}{r^3}d\ell, \\ &\mathrm{K3}_i = \int_{C_i}\ell r\,d\ell\end{aligned}$$

The line integrals for each side of the polygon can be treated independently by the geometric parameters of that side. It is sufficient, therefore, to consider only one side of the panel, say $i = 1$, for the purpose of these evaluations. For simplicity of the presentation, we drop the subscript i used for identifying the side. We take, without loss of generality, a local plane coordinate system (x', z') in the plane through the field point $\underline{x}_p$ and the side in concern, such that the side lies on the x'-axis, one end point of the side is at the origin and the integration path is performed along the positive x'-axis, as shown in Fig. 2. Then the local coordinates (x', z') can be expressed, in terms of the global coordinates, as $|z'| = |\underline{e}_\ell \times \underline{Q_1x_p}|$ and $x' = \underline{e}_\ell\cdot\underline{Q_1x_p}$. In the following development, we define the distances between the end points and the field point by $R_1 \equiv |\underline{Q_1x_p}| = \sqrt{x'^2 + z'^2}$ and $R_2 \equiv |\underline{Q_2x_p}| = \sqrt{(s-x')^2 + z'^2}$. Expressing the integrals in terms of the local coordinates x' and z' and performing the integration (9), we get the following results for the integrals.

$$\begin{aligned}&\mathrm{I1} = \ln\frac{R_2 + s - x'}{R_1 - x'},\quad \mathrm{I2} = \mathrm{I1} - \frac{a}{\sqrt{z'^2 - a^2}}\sin^{-1}H, \\ &\mathrm{I3} = \frac{1}{a}(\mathrm{I1} - \mathrm{I2}),\quad \mathrm{I4} = \frac{1}{z'^2}\Big\{\frac{s-x'}{R_2} + \frac{x'}{R_1}\Big\}, \\ &\mathrm{J1} = R_2 - R_1 + x'\mathrm{I1},\quad \mathrm{J2} = \frac{1}{R_1} - \frac{1}{R_2} + x'\mathrm{I4}, \\ &\mathrm{J3} = \frac{1}{2}\{(s-x')R_2 + x'R_1 + z'^2\mathrm{I1}\}, \\ &\mathrm{K1} = \frac{1}{2}\{(s-x')R_2 + x'R_1 - z'^2\mathrm{I1}\} + 2x'\mathrm{J1} - x'^2\mathrm{I1}, \\ &\mathrm{K2} = -\Big(\frac{s-x'}{R_2} + \frac{x'}{R_1}\Big) + \mathrm{I1} + 2x'\mathrm{J2} - x'^2\mathrm{I4}, \\ &\mathrm{K3} = \frac{1}{3}(R_2^3 - R_1^3) + x'\mathrm{J3},\end{aligned}$$

where $H = \dfrac{\sqrt{z'^2 - a^2}\{z'^2 s + a(s-x')R_1 + ax'R_2\}}{z'^2(R_1 + a)(R_2 + a)}$ and I2 is replaced by $\mathrm{I1} - \dfrac{a}{\sqrt{z'^2 - a^2}}(\pi - \sin^{-1}H)$ if $\Big(\dfrac{z'^2 + aR_2}{R_2 + a}\Big)^2 + \Big(\dfrac{z'^2 + aR_1}{R_1 + a}\Big)^2 \le z'^2$ holds. In the cases of $a = 0$ and/or $z = 0$, we can take the limit forms of the expressions. The expressions involve only three transcendental functions for each side (or vertex) to evaluate, including the square-root function for the distance R_i, the logarithmic function and the arc sine function.

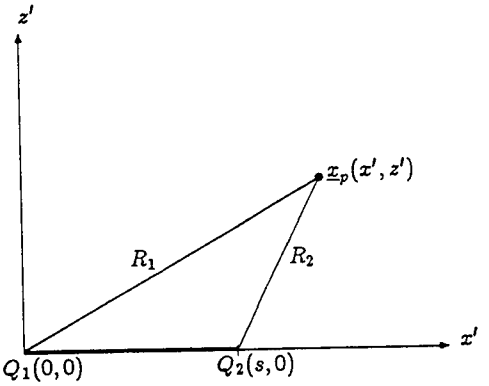

Fig. 2 A local plane coordinate for each side of a panel

Finally the closed-forms of Eqs. (17) through (20) can be written as, in terms of the basic integrals retaining the index i for identification of the side and vertex:

$$\phi^{(\sigma)} = -\frac{1}{4\pi}\sum_{i=1}^{N_S}\Big[c_0 t_i \mathrm{I2}_i + \{c_1 v_i - c_2 u_i + c_3 v_i(\eta_i - y)\}\mathrm{J3}_i + c_3 v_i^2 \mathrm{K3}_i\Big] \quad (21)$$

$$\begin{aligned}\underline{q}^{(\sigma)} = \frac{1}{4\pi}\sum_{i=1}^{N_S}\Big[&-c_0\Big\{\underline{n}(\underline{n}\cdot\underline{e})t_i\mathrm{I3}_i + (\underline{e}_\eta u_i - \underline{e}_\xi v_i)\mathrm{I1}_i\Big\} \\ &+(\underline{e}_\xi v_i - \underline{e}_\eta u_i)\Big\{\{c_1(\xi_i - x) + c_2(\eta_i - y)\}\mathrm{I1}_i \\ &+(c_1 u_i + c_2 v_i)\mathrm{J1}_i\Big\} - (c_1\underline{e}_\xi + c_2\underline{e}_\eta)t_i\mathrm{I2}_i \\ &+(c_2 u_i - c_1 v_i)\underline{n}z\mathrm{I1}_i + c_3\Big\{\{-\underline{e}_\xi u_i(\xi_i - x)^2 \\ &+\underline{e}_\eta v_i(\eta_i - y)^2 + \underline{n}u_i z(\xi_i - x)\}\mathrm{I1}_i \\ &+\{-2\underline{e}_\xi(\xi_i - x)u_i^2 + 2\underline{e}_\eta(\eta_i - y)v_i^2 + \underline{n}z u_i^2\}\mathrm{J1}_i \\ &+\{-\underline{e}_\xi u_i^3 + \underline{e}_\eta v_i^3\}\mathrm{K1}_i\Big\}\Big]\end{aligned} \quad (22)$$

$$\phi^{(\mu)} = \frac{1}{4\pi}\sum_{i=1}^{N_S}\Big[d_0(\underline{n}\cdot\underline{e})t_i\mathrm{I3}_i + \{d_1 v_i - d_2 u_i - d_3 u_i(\xi_i - x)\}\mathrm{I1}_i - d_3 z u_i^2 \mathrm{J1}_i\Big] \quad (23)$$

$$\begin{aligned}\underline{q}^{(\mu)} = \frac{1}{4\pi}\sum_{i=1}^{N_S}\Big[&\Big\{\{(\xi_i - x)v_i - (\eta_i - y)u_i\}\underline{n} \\ &+z(v_i\underline{e}_\xi - u_i\underline{e}_\eta)\Big\}\Big\{(b_0 + b_1\xi_i + b_2\eta_i + b_3\xi_i\eta_i)\mathrm{I4}_i \\ &+\{b_1 u_i + b_2 v_i + b_3(\xi_i v_i + \eta_i u_i)\}\mathrm{J2}_i + b_3 u_i v_i \mathrm{K2}_i\Big\} \\ &+(d_1\underline{e}_\xi + d_2\underline{e}_\eta)(\underline{n}\cdot\underline{e})t_i\mathrm{I3}_i + (d_1 v_i - d_2 u_i)\underline{n}\mathrm{I1}_i \\ &+d_3\underline{n}\Big\{\{v_i(\eta_i - y) - u_i(\xi_i - x)\}\mathrm{I1}_i \\ &+(v_i^2 - u_i^2)\mathrm{J1}_i\Big\} + d_3(\underline{e}_\eta v_i - \underline{e}_\xi u_i)z\mathrm{I1}_i\Big]\end{aligned} \quad (24)$$

These expressions cover, of course, the results for the case of constant/linear singularity distributions. Equations (21) through (24), are relatively much simpler and more explicit than those given in (1), (2), (3) and (4), although are not shown precisely the identities (because of the different manipulation) which exist among their expressions and the present ones. These explicit simple expressions (even for the linear distributions) may reduce computing time significantly for formation of a set of simultaneous linear equations in application of singularity methods. In the potential-based panel methods, for example, the calculated potentials form the fundamental matrix elements of the linear system to be solved and thus such a formation is the primary factor of the computing time. Also the present expressions may be used to find potential and velocity in order to include mutual interaction in complex-flow problems for compound propulsors. In some problems we should often put a careful effort for field points located inevitably in the extreme vicinity of the panel edges.

5. APPLICATIONS TO SURFACE PANEL METHODS

To validate the formulation described in the preceding sections, for the following three potential flow problems we compared the numerical results obtained using surface panel methods with the analytic solutions: (i) simulation of a Hill's spherical vortex flow, (ii) non-lifting flow about an ellipsoid, and (iii) lifting flow about a circular wing.

5.1 Simulation of a Hill's Spherical Vortex Flow

The newly useful relation Eq. (7) can be applied directly to evaluate the volumetric integral of vorticity distributions, namely, the Biot-Savart integral. Sample calculation is applied to a Hill's spherical vortex flow as demonstrated below. For axi-symmetric flow without swirl motion inside a sphere, the vorticity has only a component in the ϕ direction in spherical polar coordinates (ρ, θ, ϕ). As a simple solution to the governing equation for the scalar vorticity component, we may set $\omega = A\rho\sin\theta$. Then the constant vortex-lines are circles of radius $\rho\sin\theta$ with center along the x-axis ($x = \rho\cos\theta$). This flow is called *a Hill's spherical vortex flow* (10). Typical streamline patterns are shown in Fig. 3. From the relation between the stream function and the scalar vorticity component, we can find the velocity components in the symmetric xy-plane of $\phi = 0$ (7):

$$\begin{aligned} q_x &= \frac{A}{5}(R^2 - \rho^2)\cos^2\theta + \frac{A}{5}(R^2 - 2\rho^2)\sin^2\theta \\ q_y &= \frac{A}{10}(R^2 - \rho^2)\sin 2\theta - \frac{A}{10}(R^2 - 2\rho^2)\sin 2\theta \end{aligned}$$

where R is radius of a sphere.

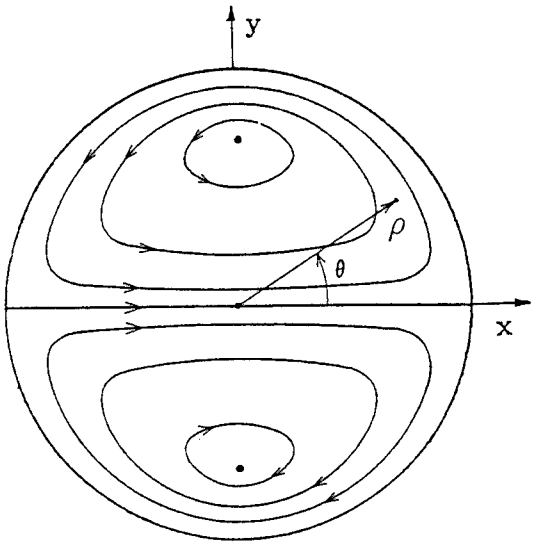

Fig. 3 Streamline pattern of a Hill's spherical vortex flow

With the given velocity field, we will now recover this vortex flow by the integral representation in the form of the vector identity for velocity. A velocity field $\underline{q}$ can be written as,

$$\begin{aligned}\underline{q} = \frac{1}{4\pi}\Big[&-\iint(\underline{n}\cdot\underline{q})\nabla(\frac{1}{r})dS - \iint(\underline{n}\times\underline{q})\times\nabla(\frac{1}{r})dS \\ &+\iiint(\nabla\cdot\underline{q})\nabla(\frac{1}{r})dV + \iiint(\nabla\times\underline{q})\times\nabla(\frac{1}{r})dV\Big]\end{aligned}$$

Knowing that the normal component $(\underline{n}\cdot\underline{q})$ is assumed to be zero at the boundary surface and the fluid is incompressible (i.e., $\nabla\cdot\underline{q}=0$), we simplify the above equation as

$$\underline{q}=\frac{1}{4\pi}\Big[-\iint(\underline{n}\times\underline{q})\times\nabla(\frac{1}{r})dS+\iiint\underline{\omega}\times\nabla(\frac{1}{r})dV\Big]$$

As an approximation, we may assume $(\underline{n}\times\underline{q})$ and $\underline{\omega}$ are piecewise constant over the subdivided elements. We can then transform the volume integral over each cell into surface integrals over its enclosed faces (i.e. six planar faces) by Gauss theorem. The integrand of the transformed surface integrals becomes $1/r$. Equation (7) (with $\underline{e}=\pm\underline{n}$) can be used to transform each surface integral into line integrals expressed in a form analogous to the first integral term in Eq. (17). The final form becomes

$$\begin{aligned}\underline{q} &= -\frac{1}{4\pi}\Big[\sum_n(q_\theta\underline{e}_\phi)_n\times\iint\nabla(\frac{1}{r})dS_n\\ &\quad-\sum_i(\omega\underline{e}_\phi)_i\times\{\sum_{k=1}^{6}\underline{n}_k\iint\frac{1}{r}dS_k\}_i\Big]\end{aligned}\qquad(25)$$

Here q_θ is the speed at the interior surface of the sphere and $\underline{e}_\phi$ is unit vector in ϕ-direction. The first summation is performed for the panels on the interior surface of the sphere and the second for all divided cells. The surface integrals represent, respectively, the velocity and the potential induced by the constant source distribution over the corresponding planar panels with unit density, as described in the preceding sections.

In order to show that such representation of the velocity in terms of the surface integrals and the volume integrals can recover the given velocity distribution, the comparisons of the simulated velocity with the given velocity are made along two rays of constant polar angles $\theta_c=28^\circ$ and $\theta_c=88^\circ$ as shown in Table, where the velocity direction is defined by $\tan^{-1}(q_y/q_x)$ in the symmetric xy-plane of $\phi=0$. Here we take $R=1$, $A=1$ and $N_\rho\times N_\theta\times N_\phi$=20 × 36 × 36 as number of the subdivided elements. The good agreements between the given and the simulated velocity components are observed. These agreements mean that the present expressions for the constant singularity distributions are valid. When we calculate the shear-flow interaction terms in rotational flow problems about a three-dimensional body by using the vorticity-velocity formulation (11), such a Biot-Savart integration would be necessary to find the velocity field for a (given) vorticity field.

Table: Simulation of a Hill's spherical vortex flow

(a) $\theta_c=28^\circ$

ρ	Speed q_s =		Direction (deg.)	
	simulated	given	simulated	given
0.010	0.199	0.200	0.007	0.002
0.050	0.198	0.199	0.038	0.060
0.100	0.196	0.198	0.218	0.240
0.150	0.193	0.195	0.527	0.549
0.200	0.189	0.190	0.978	0.999
0.250	0.183	0.185	1.588	1.607
0.300	0.177	0.178	2.386	2.400
0.350	0.169	0.170	3.410	3.417
0.400	0.160	0.161	4.712	4.711
0.450	0.150	0.152	6.375	6.362
0.500	0.139	0.141	8.516	8.482
0.550	0.127	0.129	11.31	11.24
0.600	0.114	0.116	15.02	14.91
0.650	0.101	0.103	20.08	19.88
0.700	0.089	0.090	27.17	26.81
0.750	0.077	0.078	37.25	36.64
0.800	0.068	0.069	51.46	50.47
0.850	0.064	0.064	69.84	68.45
0.900	0.067	0.067	89.57	88.04
0.950	0.078	0.078	106.43	105.17
0.975	0.086	0.085	112.78	112.12

(b) $\theta_c=88^\circ$

ρ	Speed q_s =		Direction (deg.)	
	simulated	given	simulated	given
0.010	0.198	0.200	0.001	0.000
0.050	0.198	0.199	0.003	0.005
0.100	0.195	0.196	0.018	0.020
0.150	0.190	0.191	0.045	0.047
0.200	0.183	0.184	0.085	0.087
0.250	0.174	0.175	0.141	0.143
0.300	0.163	0.164	0.218	0.219
0.350	0.149	0.151	0.323	0.324
0.400	0.134	0.136	0.471	0.470
0.450	0.117	0.119	0.684	0.680
0.500	0.098	0.100	1.010	0.998
0.550	0.077	0.079	1.558	1.529
0.600	0.054	0.056	2.649	2.564
0.650	0.029	0.031	5.807	5.413
0.700	0.004	0.005	64.28*	39.68*
0.750	0.028	0.025	171.93	171.03
0.800	0.059	0.056	175.67	175.43
0.850	0.092	0.089	176.88	176.75
0.900	0.127	0.124	177.46	177.39
0.950	0.164	0.161	177.78	177.76
0.975	0.184	0.180	177.80	177.89

* The relatively poor agreement occurs near the stagnation point where the very small difference in magnitude of the velocity produces the large difference in its direction.

5.2 Non-Lifting Flow about an Ellipsoid

The analytic solutions of the perturbation potentials of an ellipsoid at zero angle of attack are given in reference (10). By superposing the analytic solutions at zero angle of attack relative to the different axes, we obtain the analytic solutions for an arbitrary oblique onset flow $\underline{q}_o=(U,V,W)$. Then the surface speeds are found by differentiating the potential along the surface. The final result is given herein for comparisons of the numerical solutions.

For an ellipsoid whose geometry is specified as $(x/a)^2 + (y/b)^2 + (z/c)^2 = 1$ where a, b, c are the lengths of the semi-axes of the ellipsoid, the total velocity $\underline{q}_s$ on the surface becomes

$$\underline{q}_s(x,y,z) = \left(\frac{x^2}{a^4} + \frac{y^2}{b^4} + \frac{z^2}{c^4}\right)^{-1} \cdot$$
$$\cdot\Big[U(1+\frac{\alpha_0}{2-\alpha_0})\Big\{(\frac{y^2}{b^4}+\frac{z^2}{c^4})\underline{i} - \frac{xy}{a^2b^2}\underline{j} - \frac{zx}{c^2a^2}\underline{k}\Big\}$$
$$+V(1+\frac{\beta_0}{2-\beta_0})\Big\{(\frac{z^2}{c^4}+\frac{x^2}{a^4})\underline{j} - \frac{yz}{b^2c^2}\underline{k} - \frac{xy}{a^2b^2}\underline{i}\Big\}$$
$$+W(1+\frac{\gamma_0}{2-\gamma_0})\Big\{(\frac{x^2}{a^4}+\frac{y^2}{b^4})\underline{k} - \frac{zx}{c^2a^2}\underline{i} - \frac{yz}{b^2c^2}\underline{j}\Big\}\Big]$$

where

$$\alpha_0 = abc\int_0^\infty (a^2+\lambda)^{-3/2}(b^2+\lambda)^{-1/2}(c^2+\lambda)^{-1/2}d\lambda$$
$$\beta_0 = abc\int_0^\infty (a^2+\lambda)^{-1/2}(b^2+\lambda)^{-3/2}(c^2+\lambda)^{-1/2}d\lambda$$
$$\gamma_0 = abc\int_0^\infty (a^2+\lambda)^{-1/2}(b^2+\lambda)^{-1/2}(c^2+\lambda)^{-3/2}d\lambda$$

The linear and the bilinear singularity distributions over the triangular panels and the quadrilateral panels respectively, were applied to obtain the surface speed on a sphere. No-penetration condition is applied at the nodes of the panels (as collocation points) in the potential based panel method. The resulting linear system of equations form for the unknown nodal values of the perturbation potential. In Fig. 4, the surface speeds calculated numerically using a second order fitting of the potential are compared with the analytic solutions. Both cases of the triangular panels and the quadrilateral panels give the accurate solutions. These comparisons imply that the calculations for the induced potentials due to the linear and the bilinear distributions are valid.

Similarly we applied the bilinear distribution to calculate the surface speed of an ellipsoid in an oblique onset flow. Figure 5 shows the chordwise distribution of the surface speed at the three different spanwise positions. In Fig. 5, the numerical results have good agreement with the analytic solutions. Some discrepancy is observed near the leading edge and the trailing edge where the numerical resolution does not follow the rapid change in the potential.

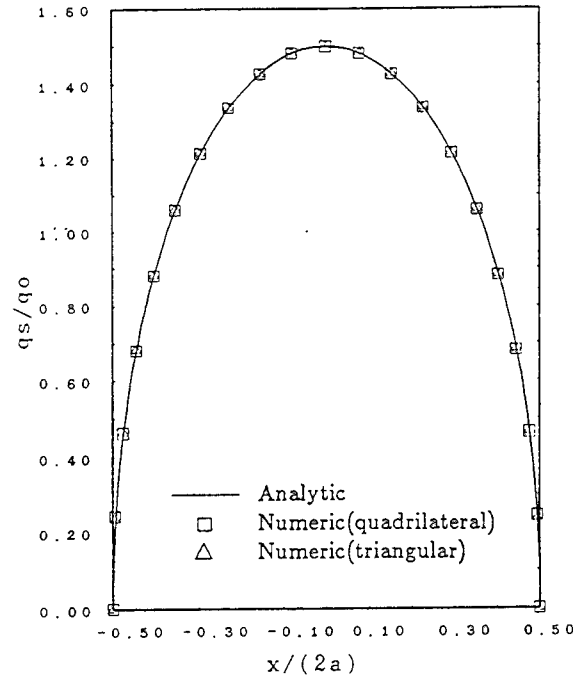

Fig. 4 The surface speed of a sphere calculated by using the triangular panels and the quadrilateral panels with the linear and the bilinear singularity distribution respectively. The number of chordwise and spanwise panels: $N \times M = 40 \times 40$.

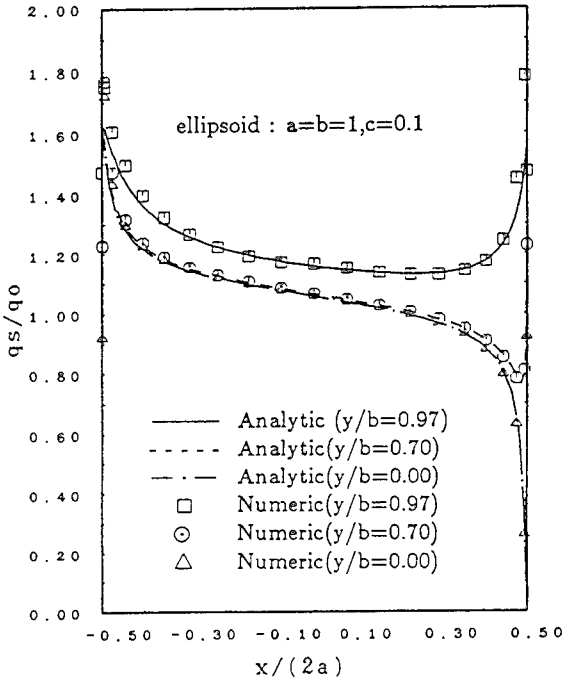

Fig. 5 The surface speed of an ellipsoid in an oblique onset flow by using the quadrilateral panels with the bilinear singularity distribution. The onset flow velocity: $\underline{q}_o = (1, 0, 0.1736)$; The number of chordwise and spanwise panels: $N \times M = 40 \times 40$.

5.3 Lifting Flow about a Circular Wing

We calculated the circulation distribution for a circular wing, for which the linearized analytic solutions are given in reference (12). Numerical and analytical circulation distributions for circular wings with NACA 4-digits section at 5° angle of attack are compared in Fig. 6. For

easy implementation of the Kutta condition described in Appendix, the constant singularity density was used for wing panels and the bilinear distribution for wake sheet elements extending on the xy-plane. It is seen that the numerical method gives fair values compared to the linearized analytic solution using the moderate number of panels. Particularly the numerical results are in good agreements with the analytic ones near the tip where the circulation changes rapidly. The bilinear representation of the wake sheet singularity in the numerical method would be appropriate to include this local variation. Fig. 6 shows that the circulation decreases as the thickness-chord ratio increases. This feature is also found in the results provided by Lee (6).

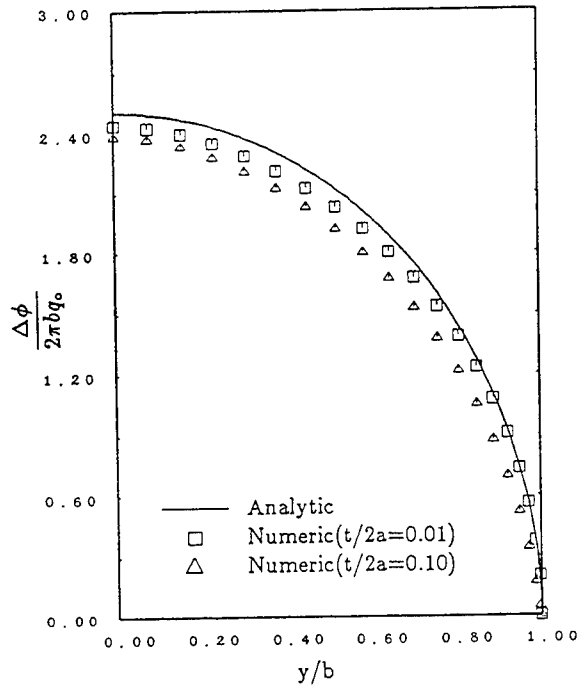

Fig. 6 Circulation distribution of a circular wing at $\alpha = 5^o$ angle of attack. The number of chordwise and spanwise panels: $N \times M = 40 \times 40$.

6. CONCLUDING REMARKS

The major purpose of this paper is to derive the closed-forms for computing explicitly the induced potential and velocity due to singularity distributions. Especially for constant distributions, the resultant expressions from Eqs. (17) through (20) do not have any local coordinate terms so that we may use directly a global coordinate system. This aspect is a great advantage of the present study over those presented previously. The elegant closed-forms for evaluating the Biot-Savart integral are additionally presented. Through the several applications of the present analysis to surface panel methods, we have shown the formulation to be valid. The Kutta condition (described in Appendix) based on the local behavior of the trailing edge flow gives reasonable numerical solution under the stated assumptions, by including the spanwise variation of the potential jump along the trailing edge.

Although the present work has mainly concerned with a flat panel, the doublet potential for constant distribution is valid for hyperboloidal panels bounded by straight edges. In this case the vector $\underline{e}$ in Eq. (11) may be taken as other unit vector independent of the singularity position and we must ensure the correct jump of the potential when the field point crosses the panel surface. Eventually, future work should address the treatment of such a higher-order representation of geometry.

ACKNOWLEDGEMENTS

This work was carried out under the sponsorship of the Korea Research Institute of Ships and Ocean Engineering Elementary Research Program (Contract No. ED499).

REFERENCES

1. Hess, J. L. and Smith A. M. O., "Calculation of Potential Flow about Arbitrary Bodies," Progress in Aeronautical Science Series, Vol. 8, Pergamon Press, 1966, pp. 1-137.
2. Webster, W. C., "The Flow About Arbitrary, Three-Dimensional Smooth Bodies," Journal of Ship Research, Vol. 19, No. 4, 1975, pp. 206-218.
3. Newman, J. N., "Distributions of Sources and Normal Dipoles over a Quadrilateral Panel," Journal of Engineering Mathematics, Vol. 20, 1986, pp. 113-126.
4. Cantaloube, B. and Rehbach, C., "Calcul des Integrales de la Methode des Singularites," Recherche Aerospatiale, No. 1, 1986, pp. 15-22.
5. Suh, J. C., "Analytical Evaluation of the Surface Integral in the Singularity Methods," Transactions of the Society of Naval Architects of Korea, Vol. 29, No. 1, 1992, pp. 14-28.
6. Lee, J. T., "A Potential Based Panel Method for the Analysis of Marine Propellers in Steady Flow," Ph. D. dissertation, Department of Ocean Engineering Report No. 87-13, M. I. T., 1987, pp. 144-147.
7. Brockett, T. E., "NA 520 Lecture Notes," (unpublished) Department of Naval Architecture and Marine Engineering, The University of Michigan, 1986
8. Guiraud, J. P., "Potential of Velocities Generated by a Localized Vortex Distribution," Aerospace Research, English Translation-ESA-TT-560, 1988, pp. 105-107
9. Gradshteyn, I. S. and Ryzhik, I. M., Table of Integrals, Series and Products, Academic Press, Inc., New York and London, 1965, pp. 81-84.

10. Milne-Thomson, L. M., Theoretical Hydrodynamics, 5th edition, Macmillan, London, 1968, pp. 534-536, 578-579.

11. Brockett, T. E., "Propeller Interaction with Axisymmetric Sheared Onset Flow," Proceedings of the 16th Symposium on Naval Hydrodynamics, Office of Naval Research, 1986.

12. Jordan, P. F., "Exact Solutions for Lifting Surfaces," AFOSR Scientific Report, AFOSR-TR-72-1737, 1972.

13. Mangler, K. W. and Smith, J. H. B., "Behaviour of the Vortex Sheet at the Trailing Edge of a Lifting Wing," Aeronautical Journal of the Royal Aeronautical Society, Vol. 74, 1970, pp. 906-908

14. Morino, L., Kaprielian, Z. and Sipcic, S. R., "Free Wake Analysis of Helicopter Rotors," Vertica, Vol. 9, No. 2, 1985, pp. 127-140

15. Ingham, D. B., Heggs, P. J. and Manzoor, M., "The Numerical Solution of Plane Potential Problems by Improved Boundary Integral Equation Methods," Journal of Computational Physics, Vol. 42, 1981, pp. 77-98.

16. Batchelor, G. K., An Introduction to Fluid Dynamics, Cambridge University Press, Cambridge, 1967, p.105.

APPENDIX: Implementation of the Kutta Condition

The Kutta condition has been applied originally in the steady two-dimensional flow case for uniqueness of solution mathematically and for regular flow in the vicinity of the trailing edge (T. E.) physically. It eventually implies that the rear stagnation point is at the T. E. for a non-cusped sharp-edged foil in order to satisfy both the pressure-equality condition and the condition of finite velocity at the T. E.. But if we applied this interpretation in steady three-dimensional flow, the two conditions of pressure equality and finite velocity can not be satisfied exactly at the T. E., since there is inherently a velocity difference across the sharp T. E..

There is no rigorous numerical model of the Kutta condition for general three-dimensional potential flow unless the viscous effect is fully investigated, in the viewpoint of that the physical features behind the Kutta condition are complex. However it is considered acceptable to employ a numerical scheme by which a resulting solution should satisfy nearly the condition of finite velocities and the condition of zero loading in the neighborhood of the T. E. or at the T. E.. Following the concepts based on the pressure-equality condition and the finiteness of velocity, Mangler & Smith (13) have investigated the trailing-edge flow (the so-called 'Maskell' trailing-edge flow), for steady three-dimensional lifting problems. As an extension of Mangler and Smith's approach to the unsteady three-dimensional flow case, the trailing-edge flow is discussed by Morino et al. (14). The essential result is that the flow leaves the T. E. parallel to either the upper or lower surface depending on the sign of the vorticity in the sheet as it leaves the T. E.. The possible orientation of the sheet is limited to be between the tangents of the surface at the T. E., otherwise an infinite velocity will occur.

The Kutta condition suggested in the present numerical method is (i) to introduce the wake sheet as a 'barrier' for the existence of a physical discontinuity in the fluid region about a lifting body, (ii) to assume a fitting form for potential values (ϕ) along the upper and lower surfaces so that the potential can be extrapolated to the T. E. as points on the surface approach the T. E. and the stagnation point can be located at either the upper or the lower trailing edge, and (iii) to satisfy the pressure equality condition at the T. E..

Let us approximate the disturbance potential distributions (ϕ) on the upper and the lower surfaces near the T. E. as a linear form of the local coordinates (geometrical parameters) ξ and η:[1]

$$\phi_u(\xi_u, \eta) = a_u\, \xi_u + b_u\, \eta + c_u\,, \tag{26}$$

$$\phi_\ell(\xi_\ell, \eta) = a_\ell\, \xi_\ell + b_\ell\, \eta + c_\ell\,, \tag{27}$$

where the parameter η is arclength along the T. E. positive taken as spanwise direction (see Fig. 2 in reference (13)) and the parameters ξ_u and ξ_ℓ are arclength along the upper surface and the lower surface, respectively, measured from the T. E. and normal to the T. E.. Here the subscripts u and ℓ refer to the upper and the lower surface, respectively. Then the potential jump at the T. E. from (26) and (27) can be written, including its spanwise variation term,

$$\triangle\phi = \phi_u\,(0,\eta) - \phi_\ell\,(0,\eta) = c_u - c_\ell + (b_u - b_\ell)\eta$$

This potential jump is expressed in terms of unknown quantities in the panel-method approximation as:

$$\triangle\phi = (\phi_1 - \phi_N) - (a_u\xi_{u1} - a_\ell\xi_{\ell N}) - (b_u\eta_1 - b_\ell\eta_N) + (b_u - b_\ell)\eta \tag{28}$$

where ϕ_1 and ϕ_N are the (unknown) disturbance potential, respectively, at the control points of the two adjacent panels to the T. E. (i.e., the 1st panel from the T. E. on the upper surface and the N-th panel on the lower surface). $\xi_{u1}, \xi_{\ell N}, \eta_1, \eta_N$ are the local coordinates of the control points. Then taking the gradient of (26) and (27) and then including the undisturbed velocity $\underline{q}_o$ give the total tangential speeds on the upper and the lower surface near the T. E.:

$$q_u^2 = (\underline{q}_o \cdot \underline{e}_{\xi u} + a_u)^2 + (\underline{q}_o \cdot \underline{e}_\eta + b_u)^2 \tag{29}$$

$$q_\ell^2 = (\underline{q}_o \cdot \underline{e}_{\xi\ell} + a_\ell)^2 + (\underline{q}_o \cdot \underline{e}_\eta + b_\ell)^2 \tag{30}$$

where $\underline{e}_{\xi u}$, $\underline{e}_{\xi\ell}$ and $\underline{e}_\eta$ are the unit vectors of the local coordinate system at the trailing edge point.

According to the Mangler and Smith's analysis, vanishing the tangential speed at the T. E. either on the upper or the lower surface allows us to determine the unknown coefficients a_u and a_ℓ in (28):

[1] Similar procedure has been presented by Ingham et al. (15) for the problems with two regions of different physical features, in which the two analytical solution forms of the Laplace equation for the two regions in the neighborhood of the discontinuity are introduced and then the appropriate physical matching conditions at the common interface are enforced to determine the coefficients associated with those forms. Also this procedure has been applied to irrotational solenoidal flow near a stagnation point (16).

$$\begin{cases} a_u = -\underline{q}_o \cdot \underline{e}_{\xi u} + \sqrt{-D}\,, \; a_\ell = -\underline{q}_o \cdot \underline{e}_{\xi \ell}, & \text{if } D < 0 \\ a_u = -\underline{q}_o \cdot \underline{e}_{\xi u}\,, \; a_\ell = -\underline{q}_o \cdot \underline{e}_{\xi \ell} + \sqrt{D}, & \text{if } D > 0 \\ a_u = -\underline{q}_o \cdot \underline{e}_{\xi u}\,, \; a_\ell = -\underline{q}_o \cdot \underline{e}_{\xi \ell}, & \text{if } D = 0 \end{cases}$$

where $D = 2(\underline{q}_o \cdot \underline{e}_\eta)(b_u - b_\ell) + (b_u^2 - b_\ell^2)$. Here b_u and b_ℓ are still unknown representing variation of the perturbation potential in η-direction on the upper surface and the lower surface at the T. E. panels. Consequently this model requires an iteration procedure to determine these coefficients by fitting the potential values at the T. E. panels in that direction.

As a special case of two-dimensional steady flow, (for which a stagnation point should be located at the T. E.) it holds $q_u = 0$ and $q_\ell = 0$. Applying these constraints to (29) and (30) gives

$$a_u = -\underline{q}_o \cdot \underline{e}_{\xi u} \;\text{ and }\; a_\ell = -\underline{q}_o \cdot \underline{e}_{\xi \ell}$$

With these coefficients, (28) reduces to

$$\Delta\phi = \phi_1 - \phi_N + \underline{q}_o \cdot \Delta\underline{r}$$

where $\Delta\underline{r}(= \underline{r}_1 - \underline{r}_N)$ denotes difference of position vectors of the control points of the two adjacent panels. Lee (6) suggested this equation as the Kutta condition for steady two-dimensional lifting flow, by which he has shown significant improvement on accuracy of numerical solutions compared to those obtained by the so-called Morino's Kutta condition. Accordingly Eq (28) contains the Kutta condition for the two-dimensional flow.

Session XVI

Frontier Experimental Techniques

The Flow Structure in the Lee Side of an Inclined Prolate Spheroid

T. Fu, R. Shekarriz, J. Katz (The Johns Hopkins University, USA)
T. Huang (David Taylor Model Basin, USA)

Abstract

Particle Displacement Velocimetry is used for measuring the velocity and vorticity distributions around an inclined prolate spheroid. The objective is to determine the effects of boundary layer tripping, incidence angle and Reynolds number on the flow structure. It is shown that when the flow is not tripped, separation causes formation of a pair of vortex sheets. The sizes of these sheets increase with increasing incidence angle and axial location. Rollup of a primary vortex occurs in some cases. The rest of the lee side remains almost vorticity free proving that the flow can be characterized as open separation. Tripping causes earlier separation, brings the primary vortex closer to the body, and spreads the vorticity over a larger region.

Introduction

The structure of three dimensional separated flows has baffled researchers for quite some time and is still not clearly understood. Extended efforts by Wang (1972, 1983) and by Peake and Tobak (1982) led to the understanding that two distinct types of flow separation can exist behind inclined bodies of revolution. The first type, typically defined as "closed separation", involves an *enclosed* region bounded by a stream surface that intersects with the body at the separation and reattachment lines. The second type, "open separation", involves detachment of stream surfaces from a body at the separation line, but without reattachment of the same surface further downstream. Consequently, the flow field does not necessarily contain an enclosed separated region (bubble), and except for the detaching stream surface, the flow can remain attached to the body. According to some references (Costis et al., 1989; and Wang et al. ,1992, for example) both forms of separation can occur on the same body, depending on the incidence angle.

One type of model, inclined prolate spheroids, has received considerable attention, but unfortunately the length to diameter ratios have varied. Unlike the computed results that provide detailed distribution of the velocity and vorticity (Kim and Patel, 1991a and b; as well as Gee et al., 1992; are a few examples), most of the experimental studies are limited to measurements of surface shear stresses (Meier and Kreplin, 1980) and surface flow visualization (Han and Patel, 1979; Costis et al., 1989, Wang et al., 1990). Velocity measurements away from the body, such as the data provided by Meier et al. (1983) as well as by Barber and Simpson (1990) are scarce. Both studies were performed with point measurement techniques, the former with a multi-port pitot tube, and the latter with combined hot wires and a pitot tube for turbulence and mean velocity measurements. Some flow visualization experiments with laser sheet and dye (Meier et al., 1983; Costis et al., 1989; Han and Patel, 1979) were also performed. Consequently, the currently available experimental data are insufficient for comparison with the computed results.

Almost all of the available sources claim that changes in the Reynolds number cause considerable changes in the

location of separation, a trend mostly attributed to boundary layer transition (Han and Patel, 1979, for example). Secondary vortex structures that can be easily identified at low Reynolds numbers are hard to detect when the flow becomes unsteady, particularly when point measurement techniques are utilized. As a result, Meier et al. (1983) had no difficulties in plotting the cross flow topology at low velocities, but could not decide whether the vortex pair located near the surface disappeared, or the flow became unsteady to the level that they could not identify them. This particular problem can only be solved by mapping the instantaneous velocity distribution, an option made possible by implementing the Particle Displacement Velocimetry (PDV) method. This approach can overcome smearing of data caused, for example, by meandering of structures.

Detailed mapping of the flow structure in the lee side of an inclined prolate spheroid is the primary focus of this paper. As the results show, the instantaneous velocity and vorticity distributions enable identification of primary and secondary vortex structures even when the flow is unsteady and turbulent. The effect of several parameters, such as the incidence angle, Reynolds number and boundary layer tripping are investigated.

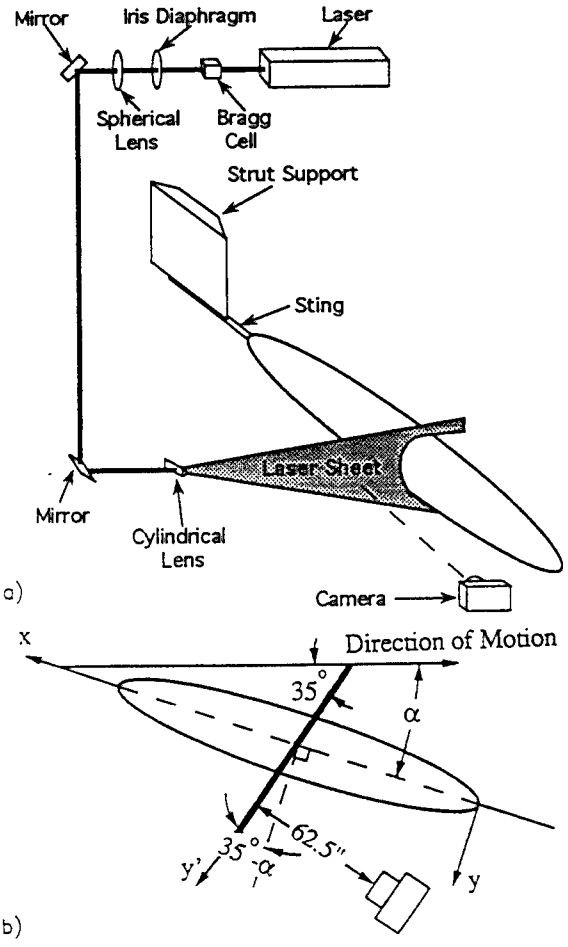

Figure 1: A sketch of: a) the experimental setup in the towing tank; b) orientation of the laser sheet and coordinate system.

Experimental Setup

The experiments were performed in a 140 ft long and 10x5 ft cross section towing tank located at the David Taylor Model Basin. The test model was a sting mounted, 9 inch diameter (D_{max}), 6:1 prolate spheroid. Most of the measurements were performed at 10^0 and 20^0 incidence, and at carriage velocities (U) ranging between 1 to 5 ft/sec (corresponding to Reynolds numbers, based on the model length, ranging between 0.42×10^6 to 2.1×10^6). A 2 mm diameter wire, cemented to the surface at x/L=0.2 (x is the axial distance from the nose, and L is the length of the model), was used for tripping the boundary layer during some of the experiments.

As noted before, the velocity distribution was measured by using PDV. Detailed descriptions of the experimental setup and analysis procedures are provided by Shekarriz et al. (1992a and b), and Dong et al. (1992a and b). Briefly (see sketches in Figure 1), PDV consists of illuminating desired sections of the flow field with a laser sheet, while seeding the water with microscopic (~25 microns in diameter), neutrally buoyant (specific gravity varying between 0.95 and 1.05) particles containing imbedded fluorescent dye. These particles are practically invisible in most of the flow field, but they respond with intense fluorescence while being illuminated by a green laser (Argon ion in the present study). By pulsing the laser more than once while recording a single image each particle leaves multiple traces on the same film. Most images are recorded by a submerged 35 mm camera, primarily since the film meets the required resolution (3500x2500 pixels per negative). Video images are recorded for qualitative observations, and for determining the location of the separation point.

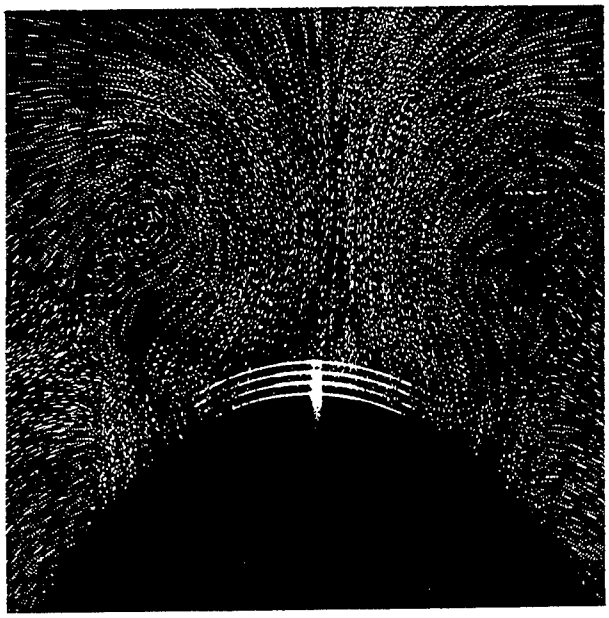

After being developed the negatives are digitized by a diode array scanner. Two types of analysis procedures have been developed. The first consists of matching traces of the same particle and measuring the distance between them ("Particle Tracking"). The second procedure consists of dividing the image into a large number of small sections, and determining the average displacement of all particles within each section by computing the auto-correlation function of the intensity distribution ("Auto-Correlation" method). All the present data has been analyzed by using this procedure. Calibration experiments (Dong et al., 1992a) have shown

Figure 2: a) An image of the flow on the lee side of a inclined prolate spheroid at $Re_L=2.1x10^6$, $\alpha=20^o$ and x/L=0.90; b) The velocity distribution computed from the image in part a.

a)

b)

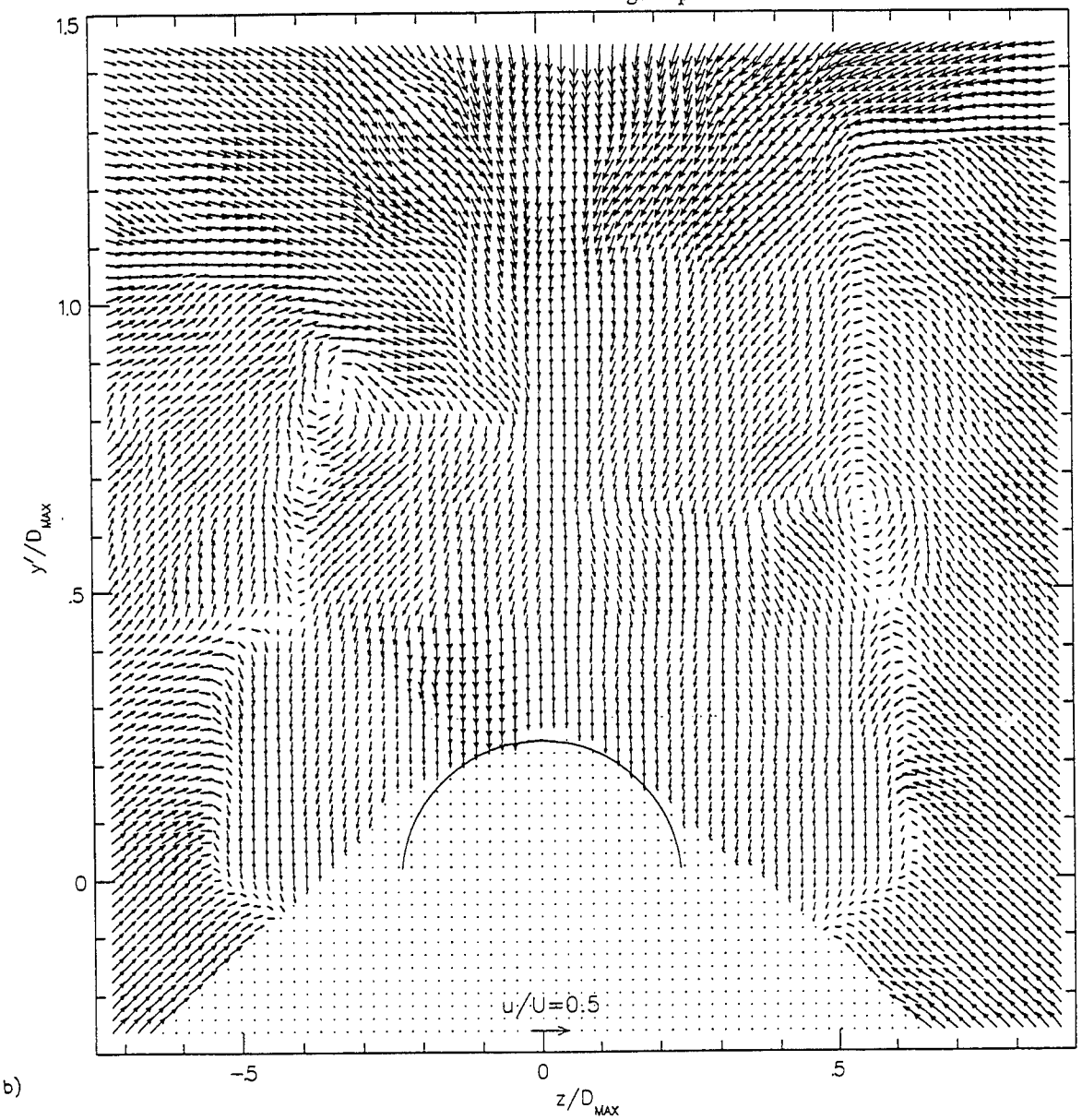

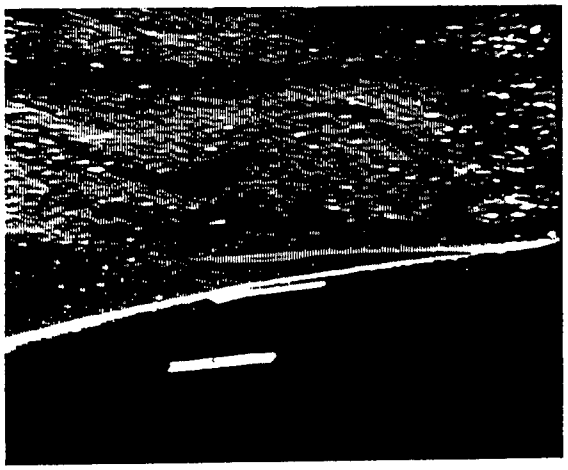

Figure 3: An image of an axial sheet containing dye traces used to determine the location of separation.

that the error level can be kept at about 1%, provided several conditions, such as particle density and magnification, are satisfied.

In the present study the laser sheet and the recording equipment were kept at a fixed position. Due to the geometry of the body, and our desire to measure the velocity up to x/L=1.0, it was necessary to position the camera ahead of the model, and incline the laser sheet at an angle of 35^0 to the axis of the tank. Consequently, when the model was at 20^0 incidence, there was a 15^0 angle between the illuminated plane and the normal to the axis of the model. This arrangement also increased the residence time of each particle within the light sheet. It simplified the recording procedures by enabling us to increase the delay between exposures, which for most of the data presented here, was 1 msec. No attempt was made in this paper to interpolate or add data to regions with insufficient particle seeding, or when the body blocked part of the image.

A sample photograph recorded by exposing the film four times, and the corresponding velocity vector map are presented in Figure 2a and b, respectively. The presence of two "major" vortex structures (foci) and the saddle points below them are clearly evident. Note that the locations of these singular points depend on the orientation of the laser sheet. In this particular case (20^0 incidence) there is only a 15^0 angle between the light sheet and the cross planes (see Figure 1b). Thus, there is only about 3.4% difference (1-cos15^0) in the velocities, and the flow structures should be quite similar. Several co-rotating secondary vortices can be identified below the primary structure on the left side of the model. A similar phenomenon has been identified by Ward and Katz (1989 a and b) during qualitative visualization experiments in the lee side of a nose cone with a sharp tip.

The instantaneous velocity distribution in Figure 2b appears to be asymmetric. Examination of numerous images, some of which will be presented later, leads to the conclusion that the asymmetry is a result of vortex meandering. In other images the primary structure on the right side is higher, and in some they are symmetric. When averaged, the flow structure in the lee side of the model appears to be symmetric. Note also that due to narrowing of the body, the velocity is not zero even outside of the region affected by flow separation.

The location of separation on the body was determined by recording video images of light sheets oriented parallel to the direction of motion, and by distributing fluorescent dye in the water. This choice was a result of several attempts to determine the angle at which the location of separation was most clearly evident. A sample image of dye traces focusing on the area near the separation point is presented in Figure 3.

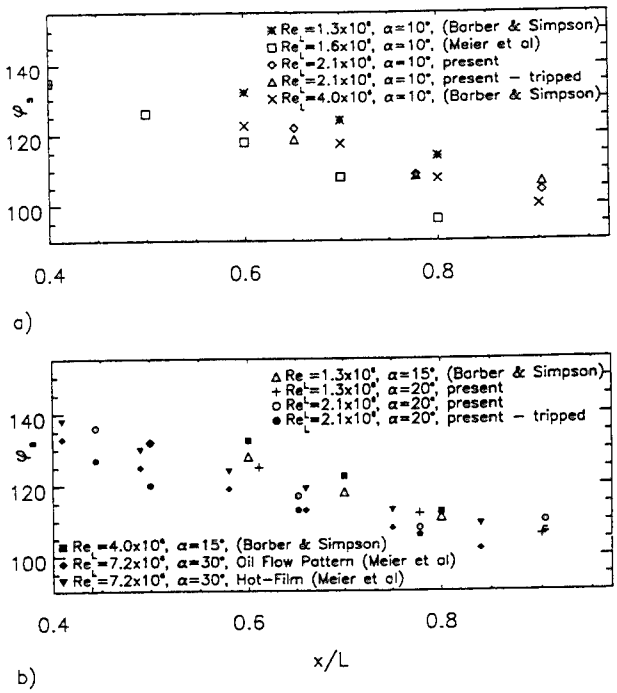

Figure 4: The location of boundary layer separation.

Results

Location of Separation

The location of boundary layer separation is presented and compared to other measurements in Figures 4a and b (ϕ is the azimuthal angle, 0^0 being the windward meridian). At 10^0 incidence, the present separation line at $Re_L=2.1x10^6$ agrees with the results of Barber and Simpson (1990) at $Re_L=4.0x10^6$, but is considerably below (smaller ϕ) their data at $Re_L=1.3x10^6$. Tripping seems to have very little effect at such a low incidence. At 20^0 (Figure 4b), tripping causes separation at a lower azimuthal angle up to x/L=0.7, and has much less effect on the location of separation beyond this point. Since there is no other source of information at this angle, the results are compared to other measurements at 15^0 and 30^0. On a smooth body the separation point moves slightly towards the windward meridian as the Reynolds number is increased from $1.3x10^6$ to $2.1x10^6$. At $Re_L=1.3x10^6$ the results fall slightly below the 15^0 data of Barber and Simpson (1990). Meier et al. (1983) provide two data sets at 30^0 incidence. The first set is measured with flush mounted hot wires, and the second, with substantially earlier separation, is determined by surface oil visualization. They do not explain this discrepancy. The present results at 20^0 incidence are close to their hot film data (at 30^0) and above their surface oil results. Since the present locations of separation fall between available data at 15^0 and 30^0, one can at least conclude that the results are consistent.

Qualitative Observations

Selected images aimed at demonstrating the characteristic flow structure in the lee side of the model are presented in Figure 5-9. The first (Fig. 5a) is a low velocity ($Re_L=4.2x10^5$) image containing multiple secondary vortices. As the Reynolds number is increased, the presence of these secondary vortices becomes less evident, as shown in Figure 5b (see also Figure 2). These structures do not disappear, as the vorticity distributions show (Figure 11 for example), but their scale and form are such that it is hard to identify them from qualitative observations. Axial variations in the size and location of flow structures are presented in Figure 6, while incidence angle effects can be observed by comparing Figures 7a and b. As expected, the

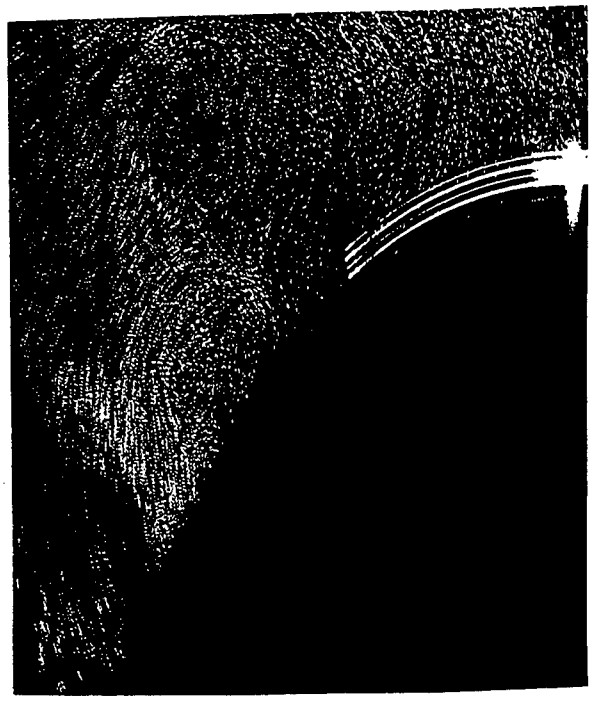

a)

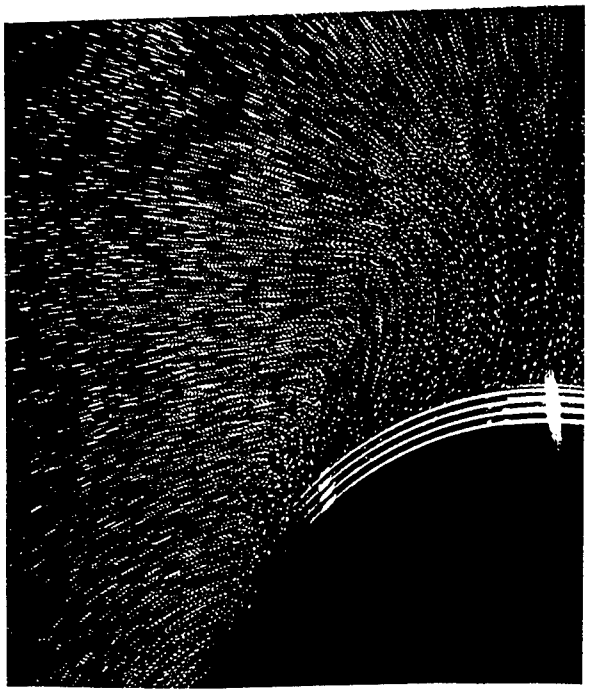

b)

Figure 5: Images demonstrating the Reynolds number effect at x/L=0.78 and $\alpha=20^o$; a) $Re_L=4.2x10^5$ and b) $Re_L=2.1x10^6$.

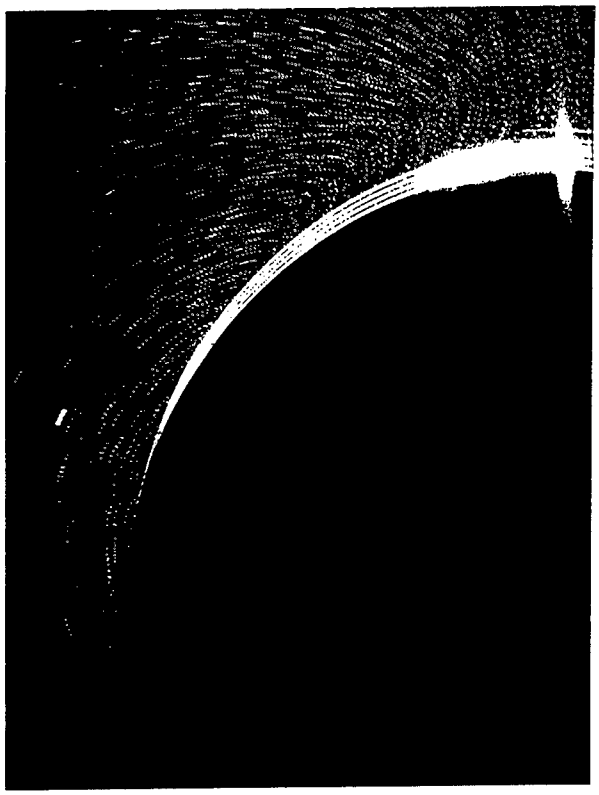

a)

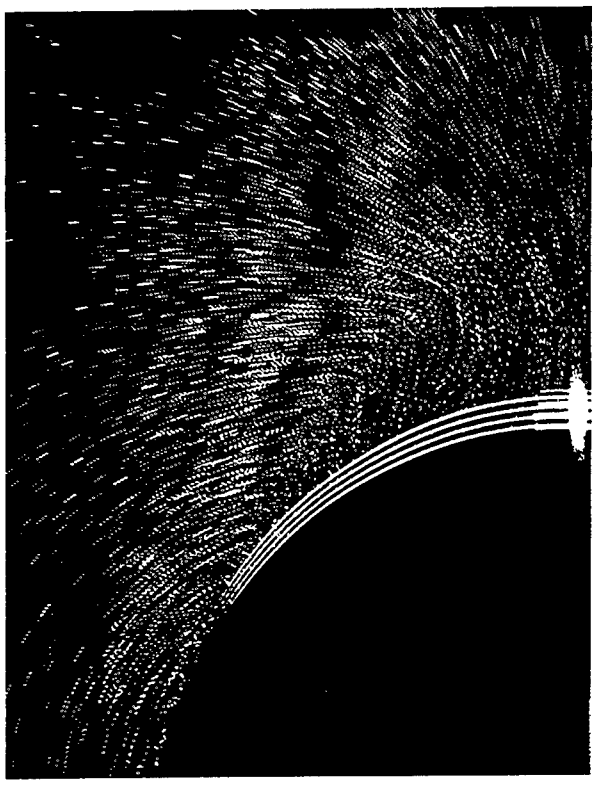

b)

Figure 6: Images demonstrating axial variations in the flow structure at $\alpha=20^o$ and $Re_L=2.1x10^6$; a) x/L=0.5 and b) x/L=0.65.

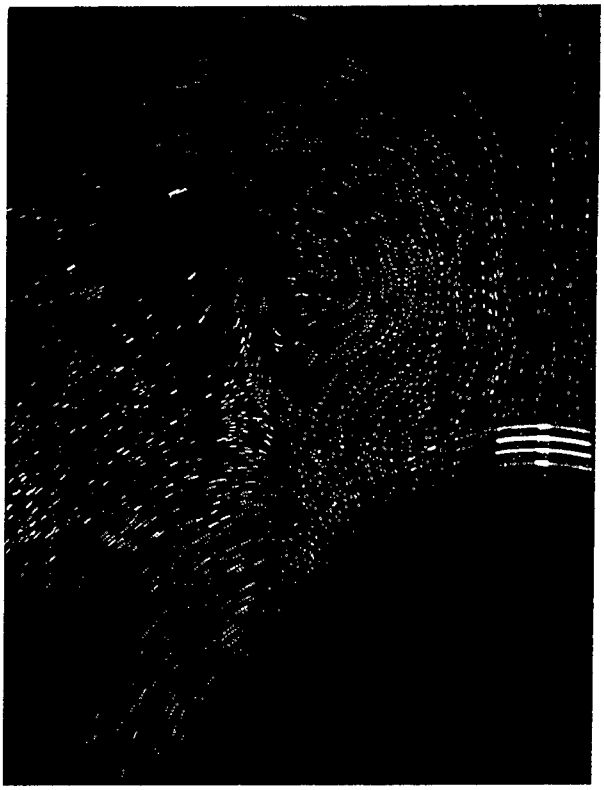

a)

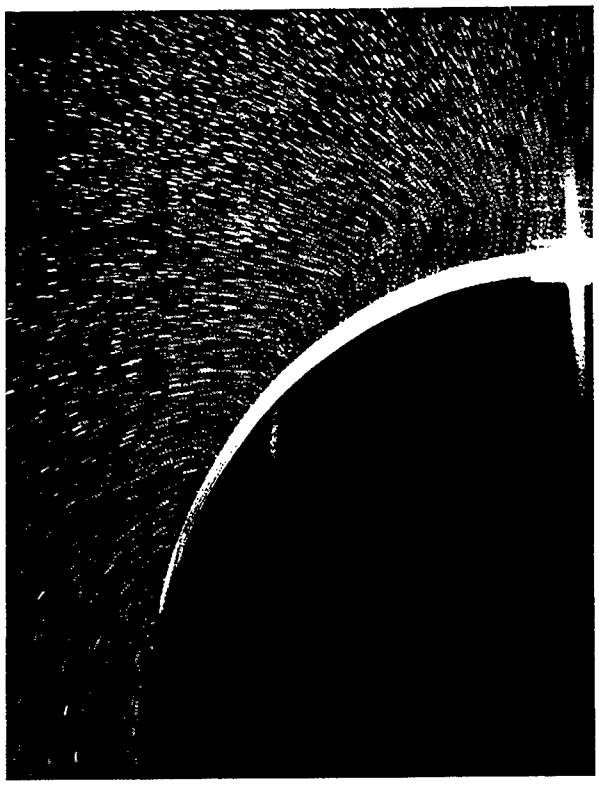

b)

Figure 7: Incidence angle effects on the flow structure at x/L=0.90 and $Re_L=2.1x10^6$; a) $\alpha=20^o$ and b) $\alpha=10^o$.

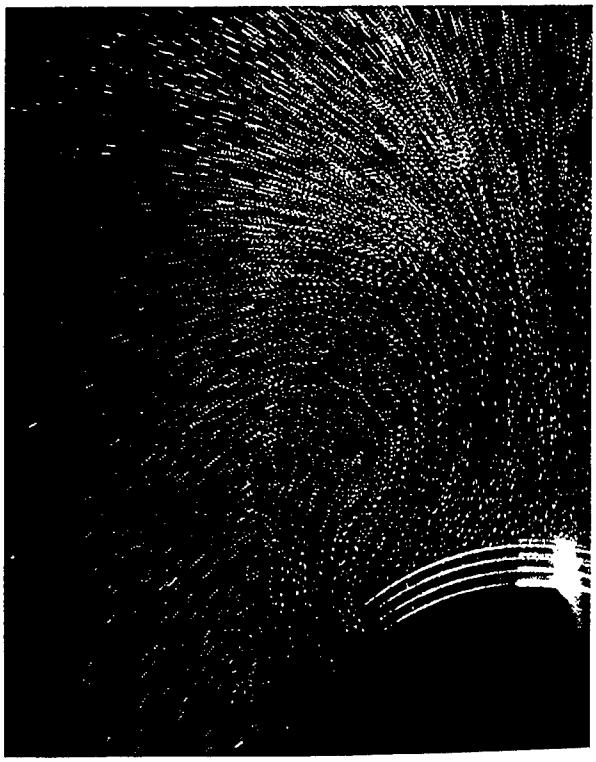

Figure 8: The flow structure when the boundary layer is tripped at x/L=0.90, Re_L=2.1x10^6, and α=20°.

dimensions of the region affected by boundary layer separation increase with increasing x/L and increasing incidence angle. Finally, the effect of boundary layer tripping is demonstrated by comparing Figure 7b to Figure 8. With tripping the secondary structures seem to disappear and the primary vortices are located much closer to the surface. This qualitative assessment is only a clue to major changes in the velocity and vorticity distributions.

Figure 9 contains several close-up views of specific sections in order provide clearer details of the flow structure. The first image shows the flow in the vicinity of a saddle point, and the second provides clear evidence for the existence of secondary vortices below the primary

a)

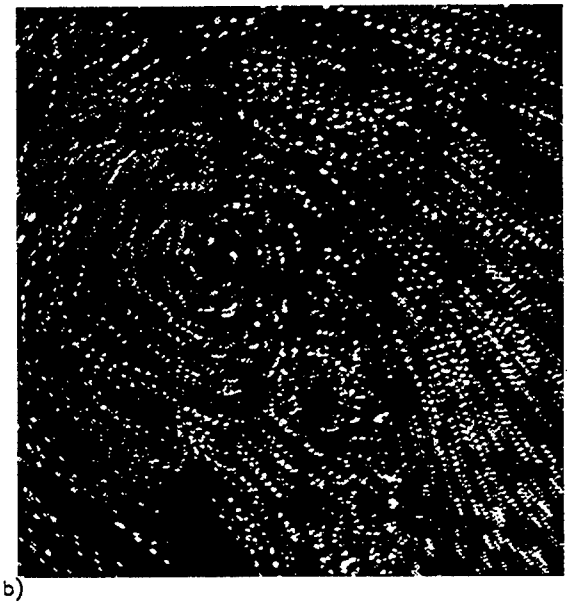

b)

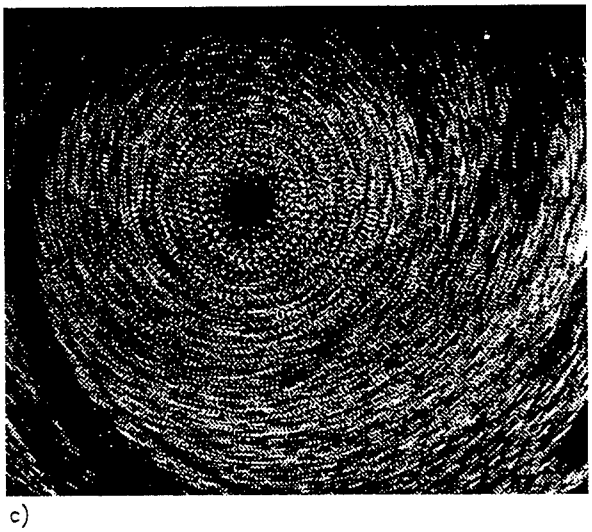

c)

Figure 9: Magnified sections focusing on: a) a saddle point; b) primary and secondary structures. Both are at x/L=0.90, Re_L=2.1x10^6 and α=20°; c) Tip vortex behind an elliptical wing at Re_c=5x10^5, α=5° and x/c=1.5.

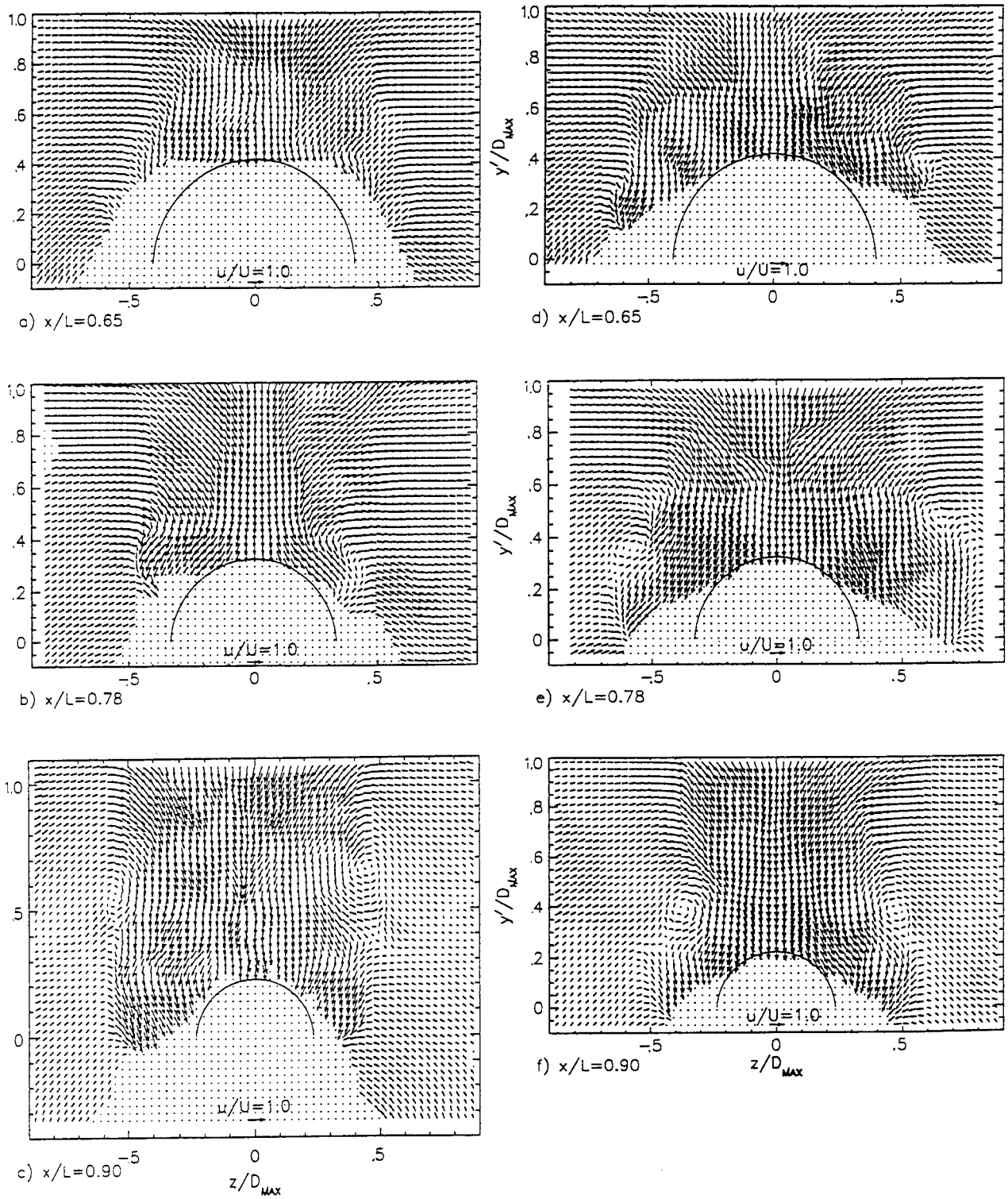

Figure 10: Instantaneous velocity distributions at $Re_L=2.1x10^6$ and $\alpha=20^o$. a, b and c are smooth body distributions; d, e and f are tripped boundary layer results.

structure (distinction between primary and secondary vortices is made based on their size and repeatability). Note that none of the vortices shown here has the structure that one would expect to see in a typical vortex with a clearly defined core. In order to emphasize this point, a typical image of a tip vortex is also provided in Figure 9c. This issue will be discussed later while presenting the quantitative results.

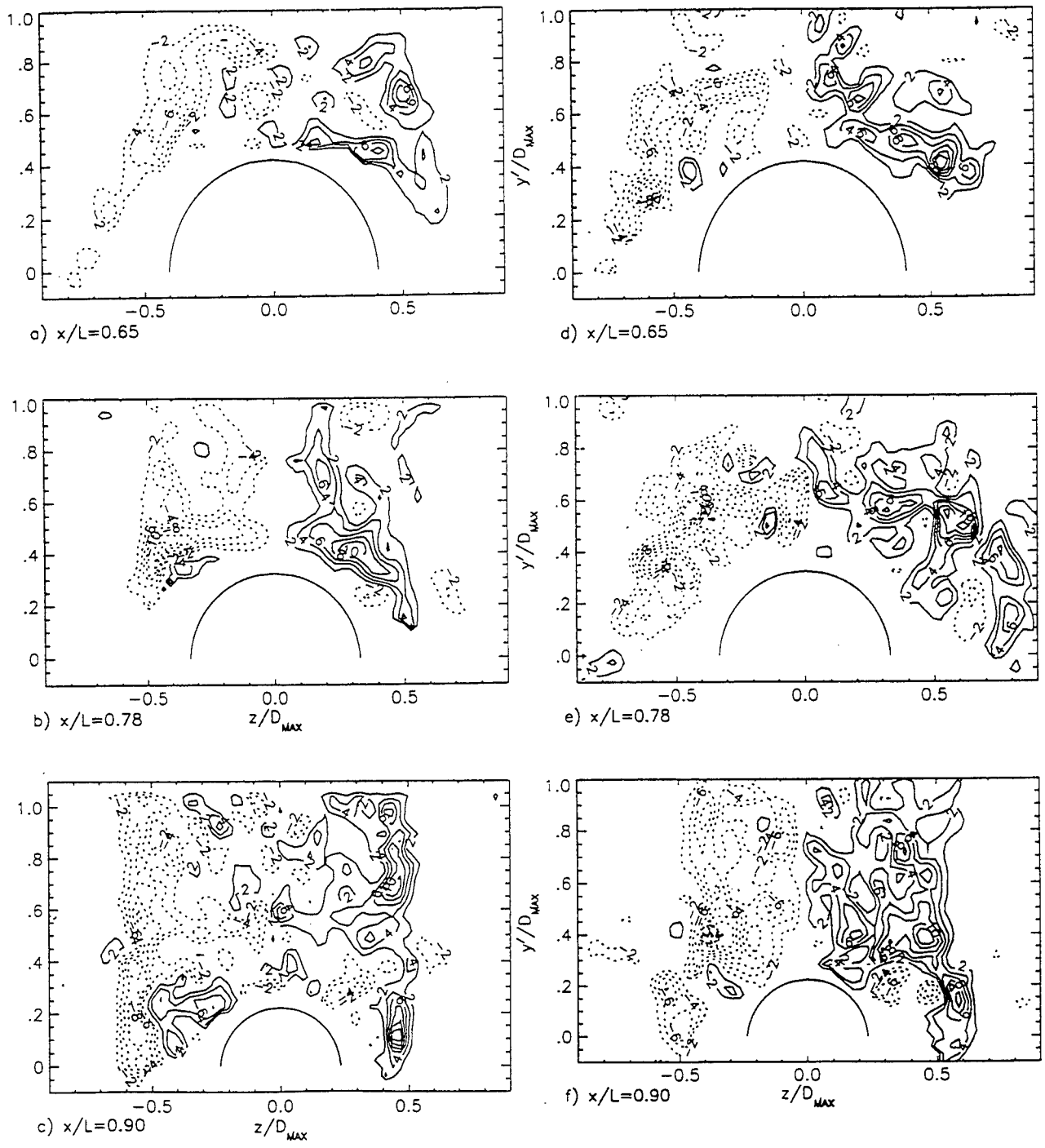

Figure 11: Vorticity distribution computed from the data presented in Figure 10.

Velocity and Vorticity Distributions

Selected computed instantaneous vector maps, illustrating axial variations in the flow structure, with and without boundary layer tripping, are presented in figure 10. The corresponding vorticity contour plots, determined by computing $\omega=\Delta v/\Delta z-\Delta w/\Delta y'$, where v and w are the velocity components in the y' and z directions, respectively, are presented in Figure 11. The accuracy of the vorticity is only about 10%, since its computation involves a comparison between fairly close numbers. Several trends become clearly evident from the results. First, in agreement with the previous qualitative observations, the region affected by flow separation (identified by the presence of rotational flow) increases with x/L only in the y' direction, whereas the change in

the z direction is minimal. Second, boundary layer tripping not only changes the location of the primary vortices, but it also alters the entire vorticity distribution . On the smooth body the vorticity seems to be concentrated within clearly defined regions, that at x/L=0.9 resemble two symmetric vertical vortex sheets with several discrete peaks. The highest peak, which is consistent with the location of the primary structure, has a dimensionless vorticity ($\omega D_{max}/U$) of about 6 at x/L=0.65, and at least 10 at x/L=0.78 and 0.9. The space between the "vortex sheets" contains much less vorticity, and in some cases (not shown here), it contains predominantly irrotational flow. These results indicate that the fluid located between the "vortex sheets" does not pass near the surface of the body and as a result remains vorticity free. This phenomenon can only happen if the region contains "freshly" entrained external fluid, namely this zone cannot be a part of an enclosed separated bubble. Thus, the flow in the lee side of the model under these conditions can be characterized as open separation.

On the tripped body the vorticity is distributed more uniformly over the entire lee side of the model. This trend should be expected since boundary layer tripping causes a considerably higher level of turbulent diffusion (mixing), and as a result more uniformly distributed vorticity. At x/L=0.65 there are still sites with irrotational flow, whereas further downstream, at x/L=0.78 and 0.9, the vorticity is non zero almost everywhere, and the contour plots contain several peaks with values ranging from 6 to 8. The highest peaks (at x/L=0.78 and 0.9), whose locations are consistent with the sites of the primary vortices (see the velocity distributions), are located much closer to the surface, but their magnitudes remain at the same levels as the smooth body results. Due to the reduced distance from the surface, one would expect also a considerable change in the forces acting on the body. These forces will be calculated following completion of data analysis. This dramatic change in flow structure has been consistently evident in all the data analyzed during the present study. To the best of our knowledge, such a phenomenon has not been reported anywhere in the literature. However, as noted before, practically any experimental study performed with inclined bodies of revolution (Meier et al., 1983 and Han and Patel, 1979; for example), shows sensitivity to the Reynolds number, presumably due to the characteristics of the boundary layer on the surface of the model.

Although not always obvious from the velocity maps, the presence of counter-rotating secondary vortex pairs near the surface is clearly evident from the vorticity distribution. These structures exist even when the boundary layer is tripped, as shown for example in Figure 11f. As noted before, Meier et al. (1983) could identify these vortices only at very low Reynolds numbers, but the present PDV results show that these structures exist even when the boundary layer is turbulent. Identification of these vortices with point measurement techniques is difficult because of meandering, the extent of which is discussed later. Note that these so called "secondary structures" are not always

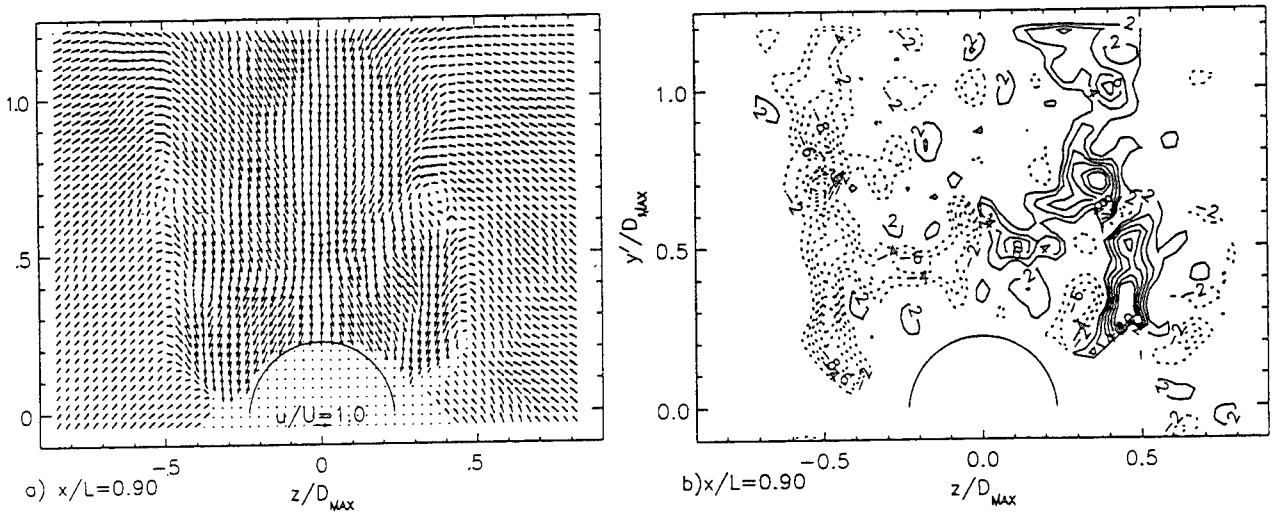

Figure 12: a) Velocity and b) vorticity distributions on a smooth body at x/L=0.90, Re_L=2.1x10^6, and α=20°.

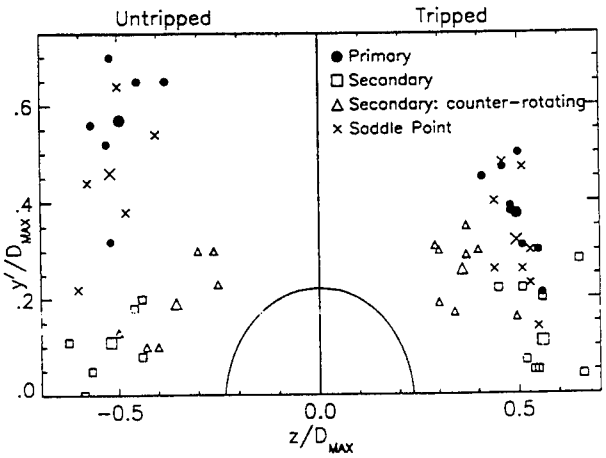

Figure 13: The location of foci and saddle points determined from several images at x/L=0.90, Re_L=2.1x10^6, α=20°, with (right side) and without tripping (left side). Larger symbols indicate mean values.

small, and the magnitudes of the vorticity peaks within them are comparable to those of the primary vortices. Since they are located closer to the surface, they may have a greater impact on the forces acting on the body.

Vector and vorticity plots at the same conditions as the data in Figures 2b and 10c, are presented in Figures 12a and b to demonstrate variations between runs. Compared to Figure 10c the vorticity in Figure 12 is even more concentrated within the two "vortex sheets" and a considerable portion of the flow in the middle is irrotational. The "secondary" structures are located further away from the surface, and are similar in size and magnitude to the "primary" vortices. Note that an additional weaker vortex pair exists also at y'/D_{max}=0.5 and z/D_{max}=±0.1. Traces of a similar pair are evident also in Figure 10c, but have not been observed in other

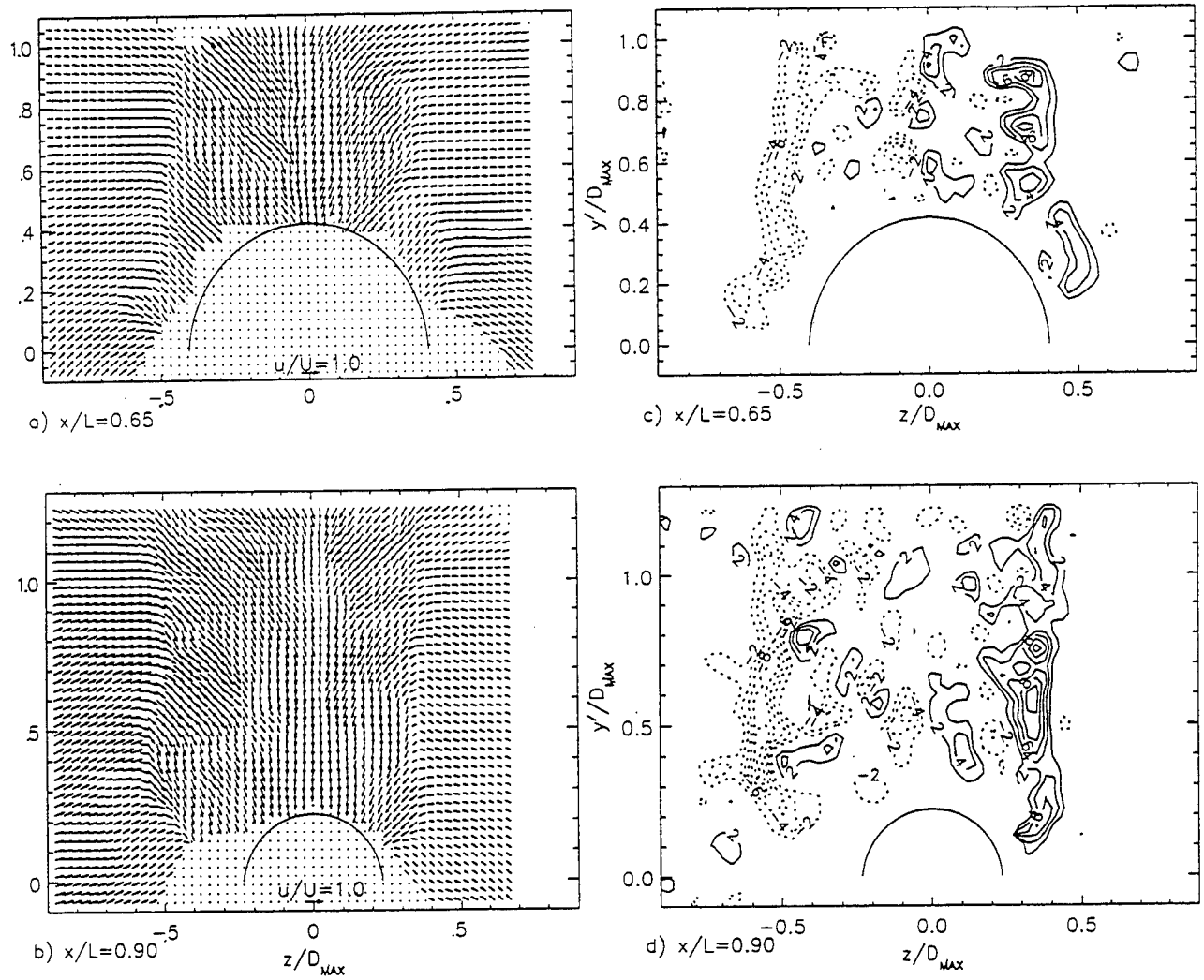

Figure 14: a-b) Velocity and c-d) vorticity distributions at Re_L=1.3x10^6 and α=20°.

distributions (data not shown). Meandering of structures occurs both behind the smooth body and to a lesser extent, also when the boundary layer is tripped. This trend is illustrated in Figure 13, that compares the locations of singular points (foci and saddle points) in several vector maps. As noted before, the unsteady nature of this flow is the main reason for the difficulties in resolving the size and strength of secondary vortices from time averaged point measurements. In spite of these variations, Figure 13 confirms that boundary layer tripping consistently shifts the location of the primary vortex and the saddle point below it closer to the surface.

When the Reynolds number is reduced to $1.3x10^6$, as shown in Figure 14, the smooth body results are not substantially different. The pairs of "vortex sheets" still exist, but it is difficult to identify the primary structure since the vorticity distributions contain several peaks with similar size and strength. This phenomenon exists in both examples, but is more pronounced at x/L=0.65. The dimensionless vorticity peaks are also lower by about 20%. This trend is expected, since the vorticity produced in a laminar boundary layer is proportional to $U^{3/2}$, or $\omega/U \propto U^{1/2}$.

Two sample velocity and vorticity distributions at 10^0 incidence are presented in Figure 15 to demonstrate differences from the data at 20^0. Here the size of the region with rotational flow is considerably smaller, with peak values of less than half of those at 20^0. The peak magnitudes are consistent with Barber and Simpson's (1990) hot wire measurements. At x/L=0.78 the vortex sheet appears to be wrapped around the body, and each side contains at least three centers, the largest of which is only slightly more powerful than the other two. At x/L=0.9 the vortex sheet detaches from the surface and major vorticity peaks appear on each side of the body.

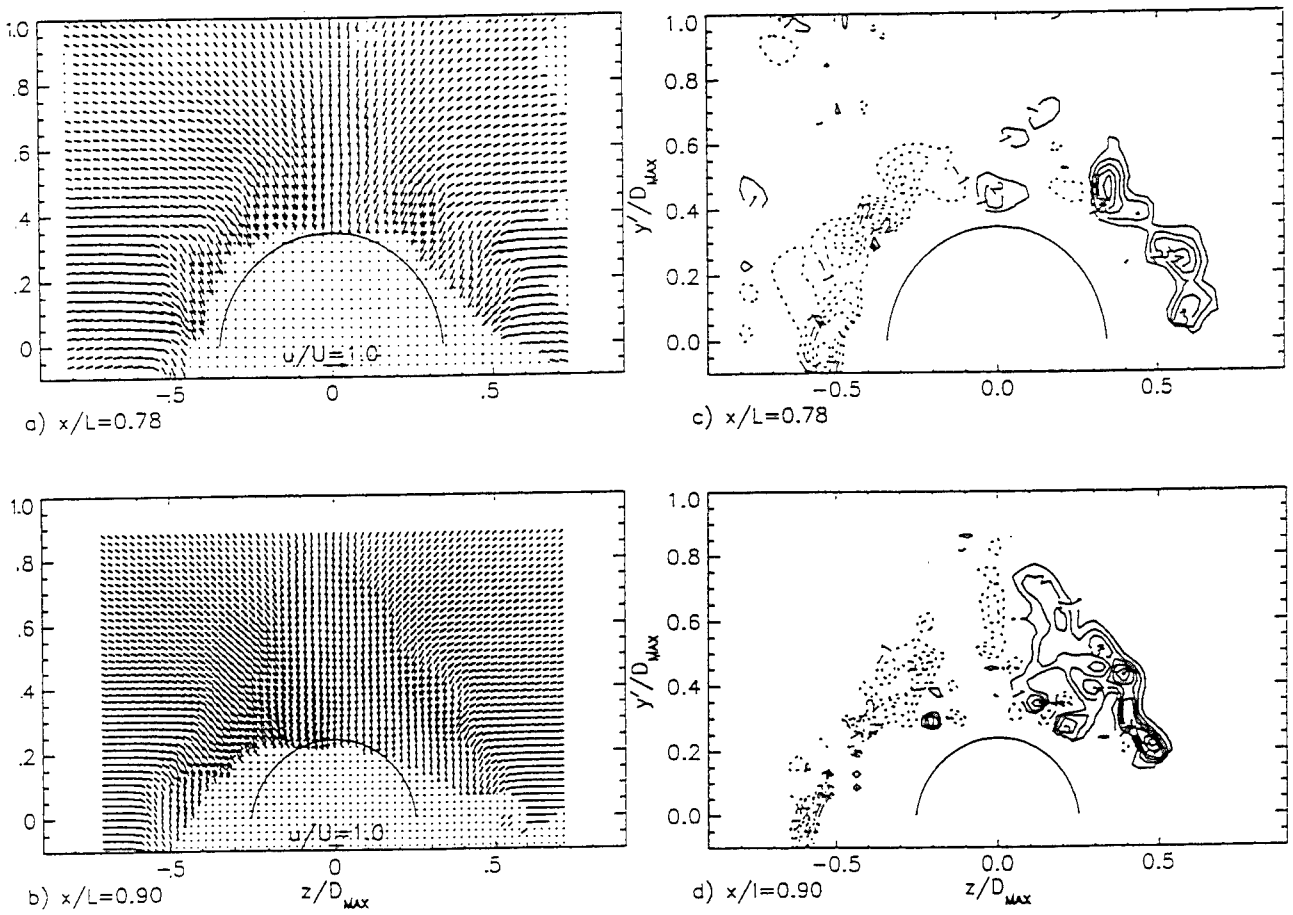

Figure 15: a - b) Velocity and c-d) vorticity distributions at $\alpha=10^o$ and $Re_L=1.3x10^6$.

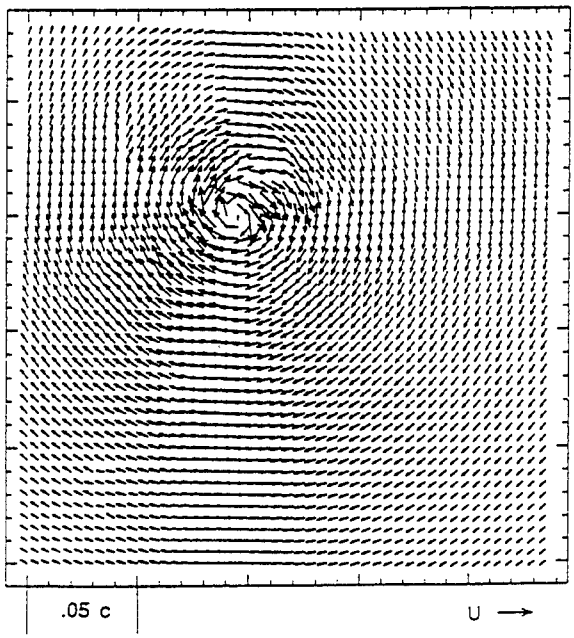

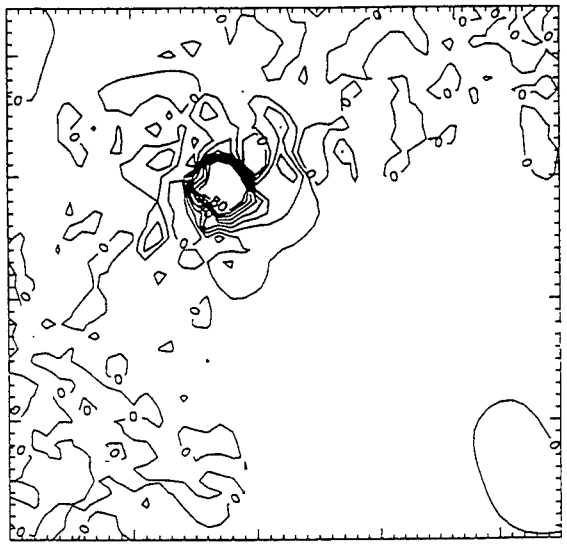

Figure 16: Velocity and vorticity distributions of the tip vortex shown in Figure 9c.

Discussion

Throughout the entire paper the terms "primary and secondary vortices" have been used to describe either peaks in the vorticity distributions, or centers of regions with a predominantly circular motion. Yet, in many cases the primary peaks are only slightly larger than the secondary ones, and both have comparable magnitudes to other peaks within the vortex sheets. This phenomenon is more pronounced when the boundary layer is tripped (Figures 10d, e and f). Thus, the location and strength of the primary vortex provide us with insufficient information on the flow structure, and its effect on the forces acting on the body.

The lee flow structure is fundamentally different from other vortex-dominated flows, such as a tip vortex, for which most of the vorticity is concentrated within a clearly defined core. This difference can be clearly observed by comparing the present results to a sample velocity and vorticity distribution of a tip vortex shown in Figures 16a and b. The vorticity within the tip vortex core is higher by almost two orders of magnitude than the surrounding fluid. In the lee side of an inclined body additional vorticity is constantly added into the flow as the boundary layer fluid detaches from the surface. The resulting vortex sheet is unstable and breaks into several distinct vortices, which often do not form a clearly dominating structure. Each time a local rollup occurs, a saddle point appears below it. Unlike the tip vortex, this flow structure is "fragile" and sensitive to small changes, such as turbulence, surface tripping and injection, as well as minute geometric changes in the case of sharp nose cones. When the body is very long, such as in some of the classical nose cone measurements (see Allen and Perkins, 1951 and a review by Peake and Tobak, 1982), the lee side contains a large number of trailing vortices.

Conclusions

It is demonstrated in this paper that by using PDV one can map the lee side velocity and vorticity distributions even when the flow is unsteady. Measurements performed with and without boundary layer tripping, at Reynolds numbers between 0.42×10^6 to 2.1×10^6 and incidence angles of 10^0 and 20^0 lead to the following conclusions:

1. When the boundary layer is untripped, the flow structure contains a pair of "vortex sheets" located on each side of the model. Each sheet contains several vorticity peaks. Typically the largest one is defined as the primary vortex, but in some cases there are several vorticity peaks with comparable sizes and magnitudes and no peak is dominating. As part of the vortex sheet rolls up into a distinct vortex, a saddle point appears below it in the velocity field. The space between the sheets contains primarily irrotational flow. Hence the lee side flow can be characterized as open separation. The entire

flow structure is unsteady. Vortex meandering causes the instantaneous distributions to appear asymmetric, but when averaged over time the flow is symmetric.

2. Boundary layer tripping changes the overall flow structure greatly. Primary vortices move closer to the surface, without significantly changing their size or magnitude. The vorticity distribution becomes more uniform, and additional vorticity peaks appear randomly over the entire lee side. At 20^0 incidence tripping also causes the boundary layer to separate earlier.

3. Pairs of counter rotating "secondary vortices" appear near the surface on both sides of the model. They have been seen before (refs. 10 and 18), but only at very low Reynolds numbers because they meander. Their sizes and magnitudes also vary substantially, and in some cases are comparable to the "primary vortices".

4. The dimensions of the vortex sheet and the magnitude of the vorticity peaks within it increase with x/L. A small change in the velocity (between 3 to 5 ft/sec) causes an expected reduction in the magnitude of the peaks, but does not change the overall flow structure. Qualitative observations at lower velocities show that the vortex sheet breaks into a series of co-rotating vortices.

5. The structures in the lee side do not have clearly defined cores containing most of the vorticity, as typically occurs in tip vortices. Instead, the vorticity is distributed more uniformly, and in some cases it is difficult to identify the presence of major peaks.

Acknowledgment

This work was supported by DARPA, Submarine Technology Program. The authors would to thank Mr. G. Jones, the area manager for his continued support. Thanks are also due to Ed Pogozelski for his assistance.

References

1. Allen, H.J., Perkins, E.W., "Characteristics of Flow Over Inclined Bodies of Revolution", NACA RM A50L07.

2. Barber, K.M., Simpson, R.L., (1990), "Mean Velocity and Turbulence Measurements of Flow Around a 6:1 Prolate Spheroid", VPI report No. VPI-AOE-174.

3. Costis, C.E., Hoang, N.T., Telionis, (1989), "Laminar Separating Flow Over a Prolate Spheroid", J. Aircraft, Vol. 86, No. 9, pp. 810-816.

4. Dong, R., Chu, S., Katz, J., (1992), "Quantitative Visualization of The Flow Structure Within The Volute of a Centrifugal Pump, Part A: Technique", Accepted For Publication in The Journal of Fluids Engineering.

5. Dong, R., Chu, S., Katz, J., (1992), "Quantitative Visualization of The Flow Structure Within The Volute of a Centrifugal Pump, Part B: Results", Accepted For Publication in The Journal of Fluids Engineering.

6. Gee, K., Cummings, R.M., Schiff, L.B., "Turbulence Model Effects on Separated Flow About a Prolate Spheroid", AIAA J., Vol. 30, No. 3, March, pp. 655-664.

7. Han, T., Patel, V.C., (1979), "Flow Separation on a Spheroid at Incidence, J. Fluid Mechanics, Vol. 92, Part 4, pp. 643-657.

8. Kim, S.E., Patel, V.C., (1991), "Laminar Flow Separation on a Spheroid at Incidence", AIAA paper No. 91-1803.

9. Kim, S.E., Patel, V.C., (1991), "Separation on a Spheroid at Incidence: Turbulent Flow", Second Osaka International Colloquium on Viscous Fluid Dynamics in Ship and Ocean Technology, Osaka, Japan, Sept. 27-30.

10. Meier, H.U., Kreplin, H.P., (1980) "Experimental Investigation of The Boundary Layer Transition and Separation on a Body of Revolution", Z. Flugwiss. Weltraumforschung, Vol. 4 No. 2, pp. 65-71.

11. Meier, H.U., Kreplin, H.P., Vollmers, H., (1983), "Development of Boundary Layers and Separation Pattern on a Body of Revolution at incidence", 2nd Symposium on Numerical and Physical Aspects of Aerodynamic Flows, State University, Long Beach CA, January.

12. Peake, M., Tobak, D.J., (1982), "Topology of Three dimensional Separated Flow", Annual Review of Fluid Mechanics, Vol. 14, PP. 61-85.

13. Shekarriz, A., Fu, T.C., Katz, J., Liu, H.L., Huang, T.T., (1992), "Quantitative Visualization of Junction Vortices Using Particle Displacement Velocimetry", AIAA J., Vol. 30, No. 1, pp. 145-152.

14. Shekarriz A., Fu, T.C., Katz, J., Huang, T.T., (1992), "Near Field Behavior of a Tip Vortex", accepted for publication at the AIAA Journal.

15. Wang , K.C., (1972), " Separation Patterns of Boundary Layer Over an Inclined Body of Revolution", AIAA J., Vol. 10, No. 8, pp. 1044-1050.

16. Wang , K.C., (1983), "On the Dispute About Open Separation", AIAA paper No. 83-0296.

17. Wang , K.C., Zhou, H.C., Hu, C.H., Harrington, S., (1990), "Three-Dimensional Separated Flow Structure Over Prolate Spheroids", Proc. R. Soc. London, A 421, pp. 73-90.

18. Ward, K.C., Katz, J., (1989), ``Topology of the Flow Structures Behind an Inclined Projectile: Part A", *The Journal of Aircraft*, Vol. 26, No. 11, pp. 1016-1022.

19. Ward, K.C., Katz, J., (1989), ``Topology of the Flow Structures Behind An Inclined Projectile: Part B", *The Journal of Aircraft*, Vol. 26, No. 11, pp. 1023-1031.

New Experimental Techniques on Ship Motions in Directional Spectrum Waves

S. Takezawa, T. Hirayama (Yokohama National University, Japan)

ABSTRACT

Real sea surface is expressed by short crested irregular waves with continuous directional spectrum. These waves will be called as directional spectrum waves.

For conducting running ship experiment in short crested irregular waves, we developed new type of directional spectrum wave generator for a towing tank.

Furthermore, other than wave probe array, we developed non touch type new wave surface probe for obtaining the encounter directional wave spectrum especially for high speed running condition.

Finally, we developed a new estimation method of directional transfer function of ships or floating bodies from experiments in directional spectrum waves.

This paper reports above three new experimental techniques.

NOMENCLATURE

S:power spectrum
D:directional distribution function
H:frequency response function
B:breadth of segmented wave generator
ω:wave frequency. suffix o means absolute and suffix e means encounter
k:wave number
θ:wave direction of propagation
χ:encounter wave angle
ε, ψ:random phase angle
():column vector
[]:matrix

INTRODUCTION

About seakeeping research,the one of main objects is to become able to estimate ship behavior in actual ocean wave condition. Real sea is mainly composed of two wave systems namely wind waves and swell. Here,the swell is very similar to long crested waves, on the other hand, wind waves are short crested waves and can be expressed by continuous directional spectra concerning to wave direction of propagation. We call such waves as directional spectrum waves.

Of course the characteristics of directional spectrum of actual ocean waves are not clear yet, but theoretical calculations can be conducted for regular waves with arbitrary encounter direction (oblique waves) and this means that theoretical calculation is also available in directional spectrum waves with arbitrary shape. This results are not examined enough by experiments ,so experiments in directional spectrum waves are needed.

Long crested oblique waves are relatively easy to generate in a square basin by so called snake type wave maker and also easy to analyze. For example see reference(1). About the generation of short crested directional spectrum waves ,there was a trial(2) that such waves were generated in a long tank by changing rotation speed of each electric motor for segmented flap type wave generator mounted on one side of longitudinal tank wall and running ship tests were conducted. However directional spectrum waves were not so easy to be generated, because each segment of snake type wave generator must be driven independently and arbitrarily. Furthermore large number of reliable segmented wave generator were needed for this case.

Some square basins that can generate directional spectrum waves can be seen today (for example 1,3), but running ship test is difficult to conduct because they don't have enough area (3) for running. So, the generation of arbitrary directional spectrum waves in narrow long tank is desired for conducting running ship test.

On the other hand, in our conventional towing tank of Yokohama National University (YNU), recently we succeeded to generate the directional spectrum waves with arbitrary symmetrical directional distribution following to a new concept(4,5). And this was confirmed by new measuring and analyzing techniques for directional spectrum waves developed by ourselves. About directional wave measurement,we developed laser beam type wave surface probe(LAWSURP). This is so called non-touch

type and suitable for encounter wave measurement in high speed running condition.

Our new wave generating technique utilize the reflection of tank side walls positively, and from this reason, there is a restriction that directional distribution become symmetrical and main direction of encounter directional spectrum waves must be head or following sea.

Of course, we conducted experiments of running ship models and models of floating offshore structures in such directional spectrum waves and compared measured motion spectra with theoretical ones and we also developed a new technique to estimate directional frequency transfer functions directly from measured data of motions of ship or offshore structures in such waves.

This latter technique is applicable to estimate directional transfer functions of actual ships or floating offshore structures if measurement of directional spectra of incoming ocean waves can be conducted.

Of course realization of generation of directional spectrum waves in narrow long tank is useful not only in checking results from linear theory but also investigating nonlinear phenomena that can not be treated by linear theory.

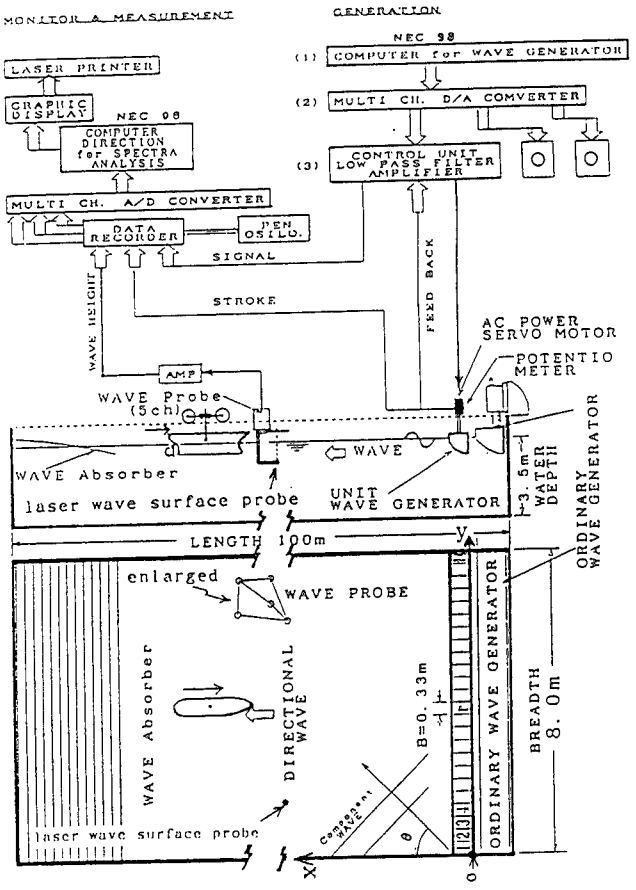

Fig.1 Generating system for directional spectrum waves in the towing tank of Yokohama National University(YNU).

So ,our report on new experimental techniques namely (1): directional spectrum wave generation, (2): laser type wave surface probe for directional spectrum wave analysis and (3) direct estimation method of directional frequency transfer functions of motions of a running ship from experiments, will be very useful for studying seakeeping problem.

GENERATION OF DIRECTIONAL SPECTRUM WAVES IN A TOWING TANK

Wave Generator

Up to this time, it had been considered that generation of directional spectrum waves with arbitrary directional function will be very difficult in a towing or narrow long tank, because of wave reflection at the tank side walls. On the other hand snake type wave maker installed in a square basin or rectangular tank can realize only a limited small area of uniform directional spectrum wave.

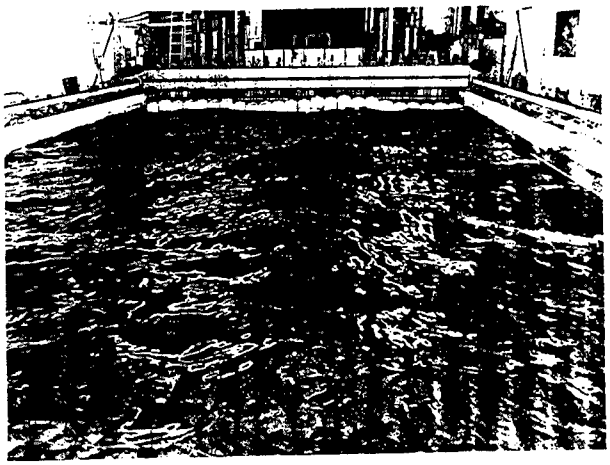

Photo 1. Directional spectrum wave generator installed at the end of the towing tank (L=100m,B=8m,d=3.5m) of Yokohama National University (YNU) . Snake motion of 24 segmented plunger type wave generator can be seen.

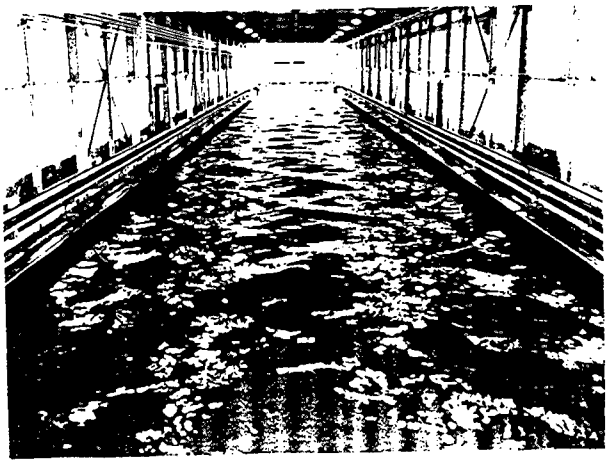

Photo 2. Generated directional spectrum wave. Looking toward the end beach. Side beaches, now lifted condition, are seen.

For generating uniform directional spectrum waves along a long towing tank ,from the view point of new concept ,a new wave maker which consist of 24 segmented independently driven plunger type wave maker was installed at the end of the towing tank of YNU(4). See the fig.1 and photo.1. The type of this wave maker is so called snake type and each segmented wave maker is plunger type . Furthermore the most important point is that this wave maker utilize the tank side walls reflection positively as mirror image generator.

Namely, fluid disturbances are limited within the both side walls of the towing tank but those walls are considered to have mirror effect if the reflection occurs at that walls. So we can understand that the measured wave elevation in a towing tank can be expressed as the sum of the results of the infinite series of directional plane wave generator with finite span(this case 8m) or in other words as the results of linear array of oblique plane wave generator. So, relatively homogeneous directional wave fields are realized along the towing tank .

From this results, we can recognize that by the YNU type wave generator, we can conduct running ship test in directional spectrum waves by relatively small number of segmented wave generator using conventional towing tank.

The wave directional characteristics and uniformity of this tank are already confirmed (5).This can be seen in fig.2. Left hand side figure correspond to the position of 15 m from wave generator and right hand side figure to 60 m . Between these two figures we can see no significant difference from the view point of practicality.

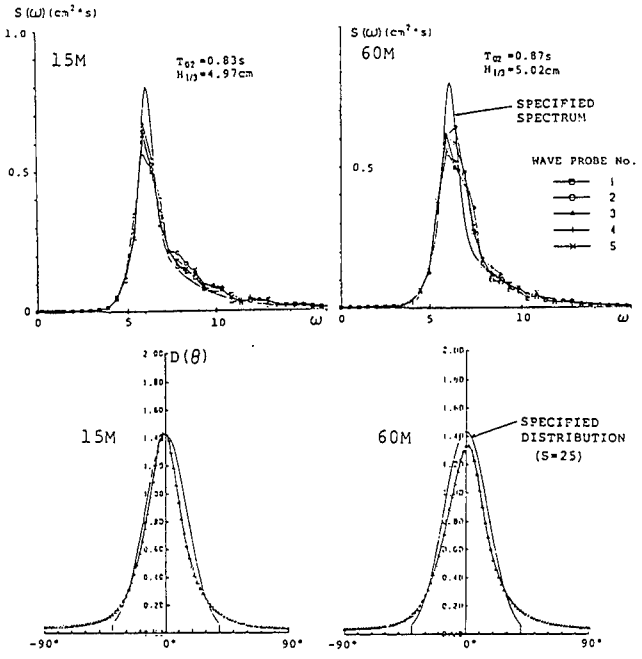

Fig.2 Directional wave spectra measured at different point(15m & 60m from wave generator) in the towing tank of YNU.

Each unit driven by electric servo motor can be controlled independently according to digital signals through D/A converter. Digital wave signal is pre-calculated as described in the next section and stored in the floppy disk of a personal computer.

Signal for segmented wave generator

Expression of directional wave spectrum

Usually ,directional spectrum of sea waves are expressed by the following formula.

$$S(\omega,\theta)=D(\omega,\theta)\cdot S(\omega) \qquad (1)$$

In general , the directional distribution function D is the function of both direction and frequency, but here it is assumed that this is only the function of direction following to the ITTC's and ISSC's directional spectrum standard.

As directional distribution function D ,next two expressions are familiar and here we adopted those expressions.

$$\text{Type(i)} \quad D(\omega,\theta)=D(\theta) \qquad (2)$$
$$=D_0\cos^{2n}\theta \quad :|\theta|\leq\frac{\pi}{2}$$

$$\text{Type(ii)} \quad D(\omega,\theta)=D(\theta) \qquad (3)$$
$$=D'_0\cos^{2s}\left(\frac{\theta}{2}\right) \quad :|\theta|\leq\pi$$

Parameters n and s are both concentration or peakedness parameter and inverse of those parameters will be called as directional or angular spreading factor. Between those two parameters there is an approximated relation as s=4.3n (19). Do are coefficient for normalization. This can be seen in fig.3. Usually n=1, namely cos-square distribution, is adopted for the field of seakeeping problem. As one dimensional wave spectrum we adopted so called P-M type wave spectrum.

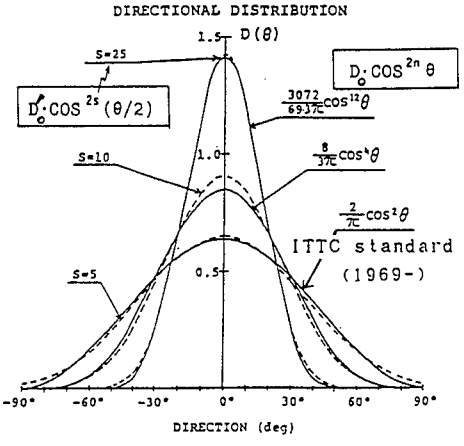

Fig.3 Comparison of two kinds of directional distribution function.

Calculation of signal

The directional spectrum waves can be considered as the superposition of long crested plane waves with various kind of frequencies and directions of propagation, so the elevations of such waves at arbitrary position (x,y) is expressed from the same consideration.
The motion of snake type wave generator is decided by considering wave elevation at the position of wave generator (x=0, about coordinate system see fig.1), in double summation expression.

$$\eta(0,rB,t)=\sum_{i=1}^{I}\sum_{j=1}^{J} a_{ij}\cos(\omega_i t - k_i rB\sin\theta_j+\varphi_{ij}) \quad (4)$$

where $a_{ij}=\sqrt{2S(\omega_i,\theta_j)\Delta\omega\Delta\theta}$

and furthermore taking into account of the directional transfer function of directional plain wave generator with finite span. Finally the voltage timehistory for the r-th segmented wave generator becomes

$$V(r,t)=\sum_{i=1}^{I}\sum_{j=1}^{J}\frac{a_{ij}}{|G(\omega_i,\theta_j)|}\times\cos(\omega_i t-k_i rB\sin\theta_j+\varepsilon_{ij}) \quad (5)$$

where G is transfer function between driving signal and generated regular wave. Generally speaking ,G is the function of both frequency and wave direction.
Of course YNU type wave generator have limitation that we can not generate directional waves which has unsymmetrical directional distribution, because of mirror effect and range of wave direction is limited as +90 to -90 deg. The number I of frequency of component wave was selected as 150 to 200. Directional interval is made 2 degrees and time interval of digital signal is made as 0.935 sec (0.1 sec for the model of 2/175 scale).

MEASUREMENT OF DIRECTIONAL SPECTRUM WAVES

Laser Wave Surface Probe (LAWSURP)

Directional spectra are estimated from measured wave timehistory by applying so called MLM (Maximum Likelihood Method) (6,7),because it is said that directional resolution is relatively high .

If we want to adopt this method for encounter waves of running ship , we must know the wave number or wave length from measured encounter frequency for calculation. But in following sea condition one to one correspondence is broken between encounter wave frequency and wave length, so conventional MLM can not be applied directly as described later(8,9,10,11).

For the wave measurement, we used array of capacitance type five wave probes at the first time (8.9) and this can be seen in the fig.1, but such probes like water surface piercing type are not suitable for high speed running case. Furthermore, basically, there is no need to measure only wave height for obtaining directional spectrum, and we also desired to measure wave slope more precisely ,so the wave probe for measuring wave height and wave slope by using laser light was developed by our group(12). We call this as laser wave surface probe (LAWSURP).

Schematic description of laser surface probe is illustrated in fig.4. Basically, this is non touch type wave probe. Wave height is measured from the scanning lines of the TV image showing the air-water boundary by laser beam shot from the under water point. Resolution of wave height is about 1 mm. And wave slope component (longitudinal and transverse direction) is obtained from using the relation of wave slope (s) and horizontal movement (R) of the laser spot on the horizontal projection board about 0.5m over the water level. R is measured using TV camersa.

The relation between s and R is expressed as follows

$$\sin^{-1}(n\sin s)-s=\tan^{-1}\left(\frac{R}{h}\right) \quad (6)$$

where n is refractive index. About the water n is 1.33. Furthermore h is obtained from wave height, so we can obtain wave slope s.
This probe system is mounted on a carriage and can measure encounter waves moving in high speed, because laser beam does not disturb the water surface.

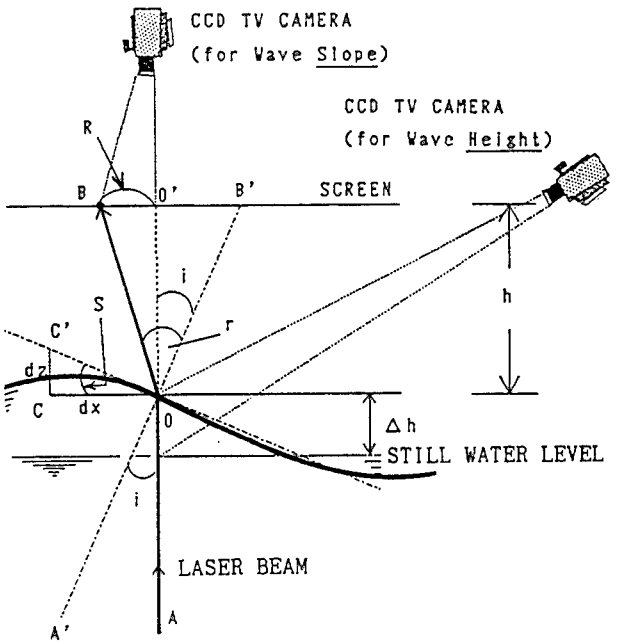

Fig.4 Measuring principle of wave elevation and wave slopes by the laser wave surface probe (LAWSURP).

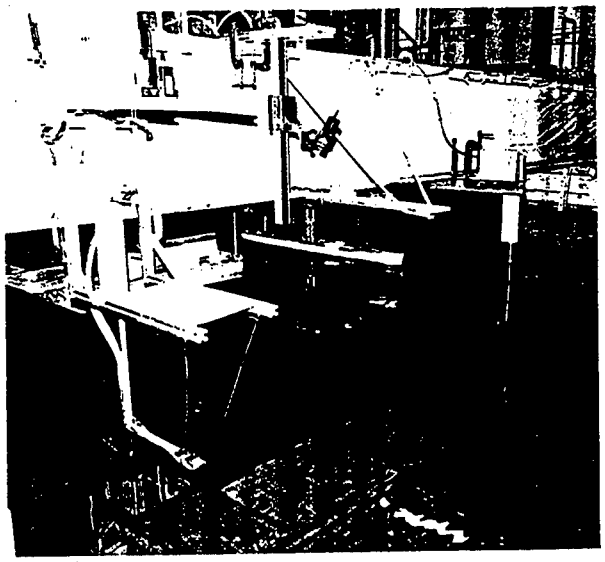

Photo 3. System of Laser Wave Surface Probe (LAWSURP). Laser beam is introduced to the under water point through optical fiber.

This probe gives three kinds of informations on surface elavation namely wave height and two components of wave slope, and we applied those data to MLM.

Example of generated directional spectra.

Example of directional spectrum wave at rested condition can be seen in fig.5 . (a) is wave height and (b),(c) correspond to wave slope in transverse plain and longitudinal plain. Fig.6 is estimated directional wave spectrum. This is the case close to the cos-square distribution(dotted line). (b) is directional distribution at several frequencies, and (c) is mean distribution function ,namely the integrated result along the frequency.

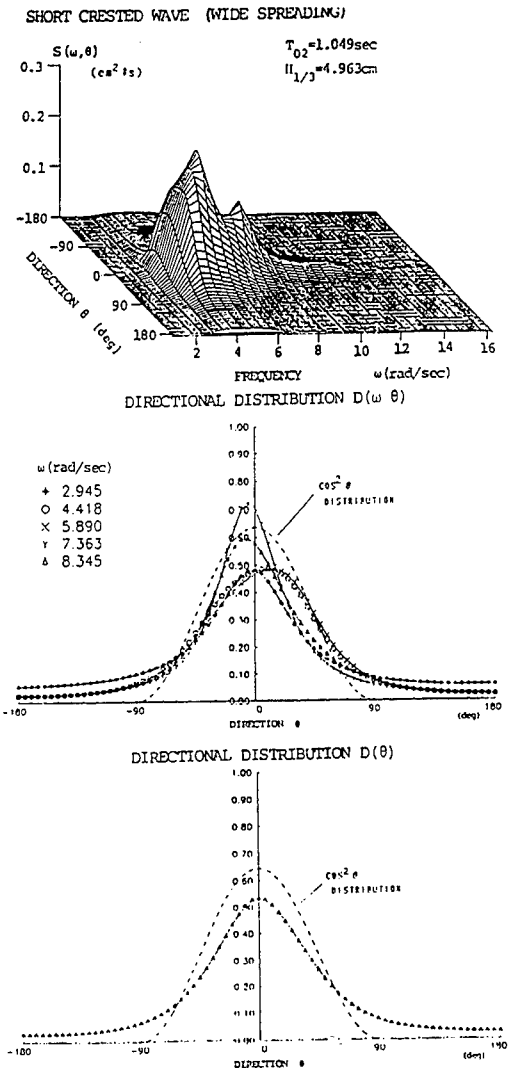

Fig.6 Directional distribution of a wide spreading directional wave spectrum obtained by a laser wave surface probe (LAWSURP).

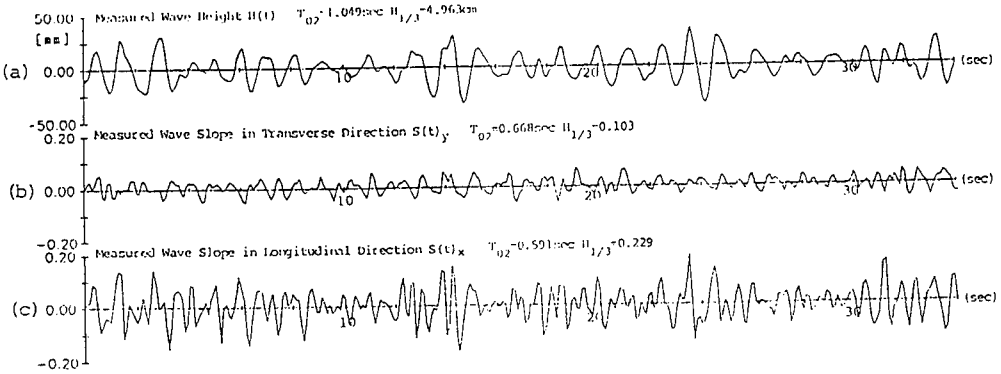

Fig.5 An example of measured timehistory of directional spectrum wave with wide spreading directional distribution function using a laser wave surface probe (LAWSURP). (a)is wave elevation (mm),(b)is wave slope (rad)in transverse direction and (c) is wave slope in longitudinal direction.

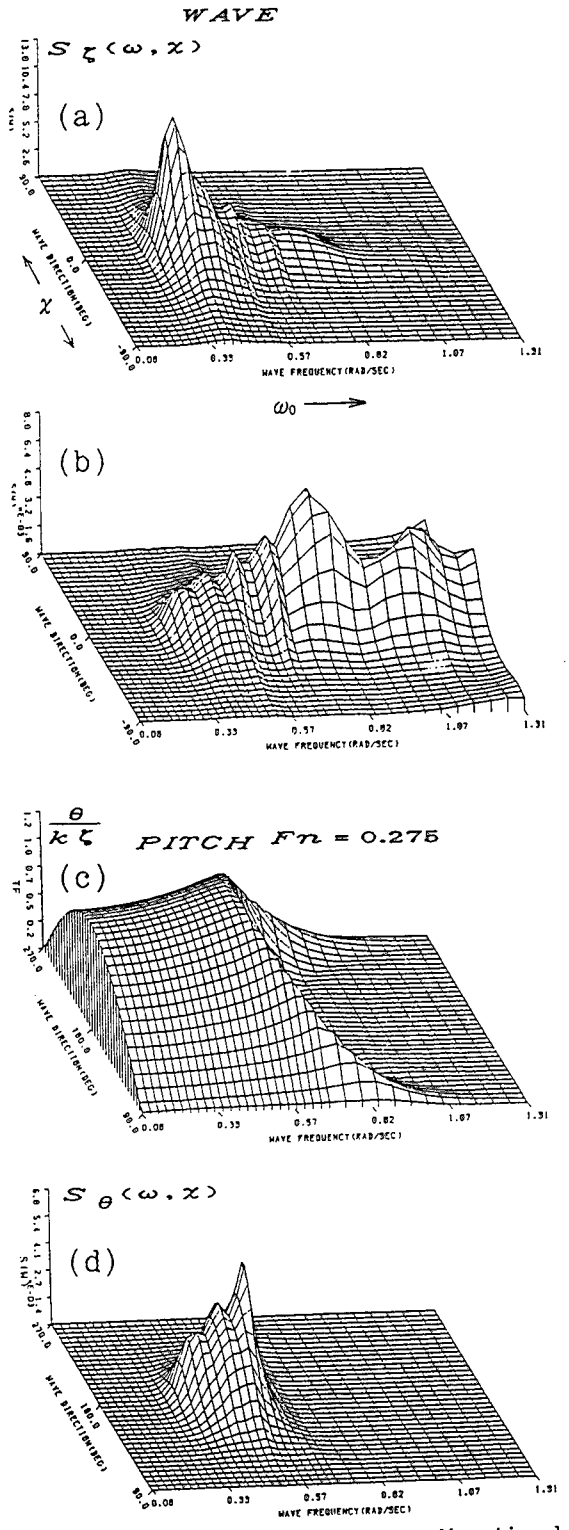

Fig.7 Theoretically estimated directional spectrum of pitch of a container ship. (a)is analyzed directional wave spectrum from experiment at zero forward speed and (b) is corresponding directional wave slope spectrum. (c) is theoretical directional transfer function of pitch by a strip method(NSM) and (d)is calculated response spectrum of pitch using wave slope spectrum (b) and response function(c). Frequency is in ship scale.

EXAMPLES OF MODEL SHIP TESTS IN DIRECTIONAL SPECTRUM WAVES AND COMPARISON WITH THEORY.

Some problems in theoretical estimation

For head sea case

In fig.7, we show two dimensional spectra and two dimensional frequency response functions . Abscissa shows absolute (not encounter) wave frequency and ordinate shows component wave direction. Principal(or main) wave direction corresponds to zero degree.

(b) is "wave slope" spectrum transformed from wave elevation spectrum of Fig.7(a) at zero forward speed condition. This expression is consistent to the transfer function nondimensionalized by wave slope like pitch or roll. (c) is theoretical transfer functions of pitch at Froude number of 0.275. Theoretical calculations by a strip method (NSM) is done on the base of absolute wave frequency namely on wave length. Considering experimental condition of this time, sway and yaw are fixed.

From wave slope spectrum multiplied by square of transfer functions ,we can obtain theoretically estimated response directional spectrum as Fig.7(d). In the general form, this process is expressed as follows.

$$S_z(\omega_0, \chi, V)=|H_z(\omega_0, \chi, V)|^2 S_\zeta(\omega_0, \chi) \qquad (7)$$

where $S_\zeta(\omega_e, \chi)$= wave spectrum at $V=0$

For following sea case

In following seas we can not apply MLM because of one to one correspondence in frequency domain can not be realized (18).

This situation is described in fig.8.

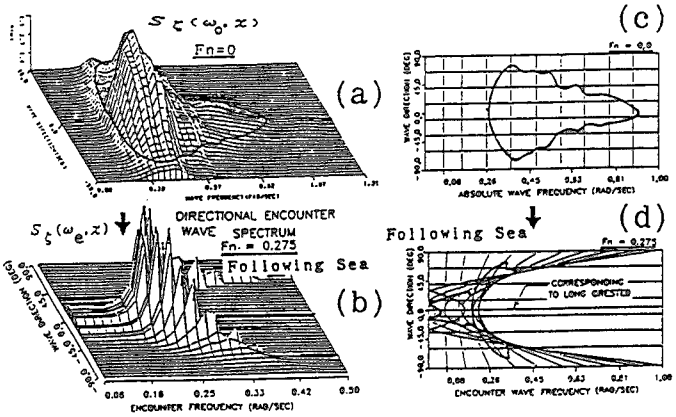

Fig.8 Example of transformation of directional wave spectrum in following sea condition. (a) is obtained spectrum at rested condition and (b) is transformed results from (a) under the following sea condition (Fn=0.275). (c) show the mesh and a contour curve in (a) and (d) shows the transformed results of that mesh and the contour curve.

Fig.8(a) is an example of estimated directional spectrum from wave records at standing condition. Abscissa is circular frequency and ordinate is wave direction. On the other hand (b) is directional encounter wave spectrum in following sea condition transformed from (a). This transformation is made by the following formula

$$S_z(\omega_e, \chi)=\frac{S_z(\omega_0, \chi, V)}{1-\frac{2\omega_0}{g}V\cos\chi} \qquad (8)$$

The suffix 0 means absolute and e means encounter. Spectrum in the right hand side does not include V for the wave case.(Expression (8) including V is used for motion spectrum estimated by the transfer function expressed in absolute wave frequency.)
The relation between absolute wave frequency and encounter wave frequency is given by

$$\omega_e=\omega_0-\frac{\omega_0^2}{g}V\cos\chi \qquad (9)$$

Fig.8(c) shows one of contour curves of spectrum (a),and this curve is transformed into a thick solid curve in Fig.8(d). Others are transformed results of the lattice in (c). As can be seen in this figure, corresponding frequency area is modified and folded, so one to one correspondence can not be realized in such a following sea case. So, MLM can not be applied for these following sea case.

From this reason, in following sea case, we adopted directional wave spectrum estimated at standing condition as input wave spectrum for obtaining response spectrum as shown equation (7)

After this ,the obtained spectrum is transformed into encounter frequency expression by expression (8).

Model and experimental condition

Model ship and experimental setup

As an example, we used a container ship model of 2.0m length. Scale ratio is 2/175. This ship type was adopted in the ITTC's comparative study on ship motion. Froude number of this ship speed is 0.275(22.1 knots) .

The model ship is towed through heaving guide rod with gymbal mounted at the center of gravity of the model, and the heave ,pitch and roll motions are measured. This case surge ,yaw and sway motions are fixed and theoretical calculations are also conducted following to this condition.

Generally speaking , for obtaining stable statistical values ,about 200 encounter wave peaks are requested in irregular waves, so 8 to 14 times runs were executed for following sea experiment.

Typical Examples

Head Sea Condition

For the running condition ,in case of head seas ,we can estimate encounter directional wave spectrum by introducing small correction into MLM for standing condition

Theoretically estimated two dimensional spectrum ,as shown in Fig.7(d) , can not be compared directly with experiment, because measured motion timehistory results in one dimensional spectrum. In other words this is the integrated results of two dimensional spectrum as following equation.

$$S_z(\omega_e)=\int_{-\pi}^{\pi}S_\zeta(\omega_e, \chi)|H_z(\omega_e, \chi)|^2 d\chi \qquad (10)$$

So ,here, comparisons between one dimensional spectra is made. Fig.9 is drawn in the actual ship scale. Fn=0.275. Cal means estimation by NSM, using measured wave spectra as input wave data.

About heave motion in the directional spectrum waves in which principal wave direction is head sea, the effects of directional spreading of waves are not so large considering from both experimental results and theoretical calculations , but rolling motions appear even if the main direction of directional spectrum waves is head sea as shown in fig.9(d) and this is the most characteristic feature.

Following sea condition

Similar to fig.9, fig.10 correspond to following sea case of Fn=0.275. Directional function is s=10 type. Cal means calculated results ,as already described, using theoretical directional transfer function and directional spectrum of waves estimated from the measured waves at standing condition.

FFT means that the one dimensional spectrum is obtained by Fast Fourier Transformation method and MEM means by Maximum Entropy Method. Results in fig.10 are averaged results according to run number. Both methods show about the same results but relatively sharp peaks are obtained by MEM than by FFT.

Cal is smaller than experiments for rolling, and there seems two peaks ,one correspond to peak of wave spectrum and the other to roll natural frequency noted by an arrow.

Similar to the results in head sea, in following directional spectrum waves there also appear rolling motion which can hardly seen in long crested following (encounter angle=0 degree) irregular waves except nonlinear phenomena. The encounter mean wave period (23 sec) of this case is close to natural period of rolling so about 40 degrees maximum double amplitude was seen from time history. On the other hand pitch is reduced by 8%.

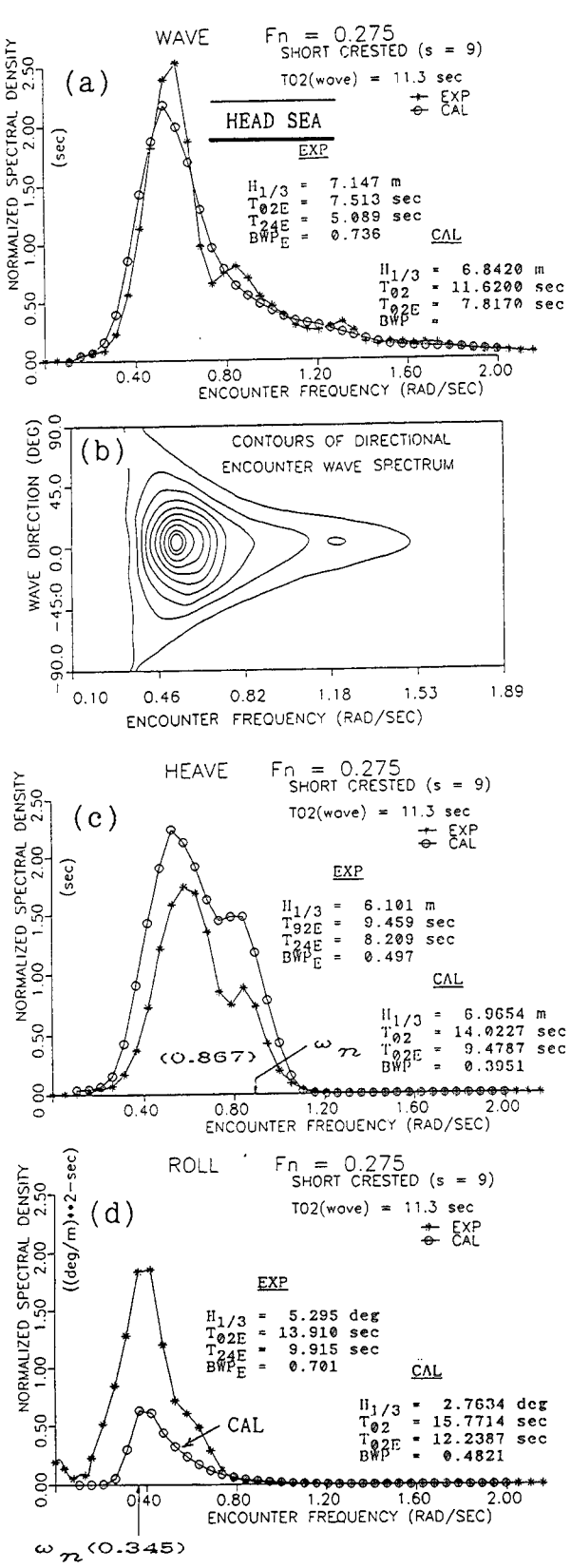

Fig.9 Comparison of one dimensional motion (heave & roll) spectra in directional spectrum wave (s=9) with that from theoretical estimation noted by cal. Head sea condition and Fn=0.275. All in ship scale.

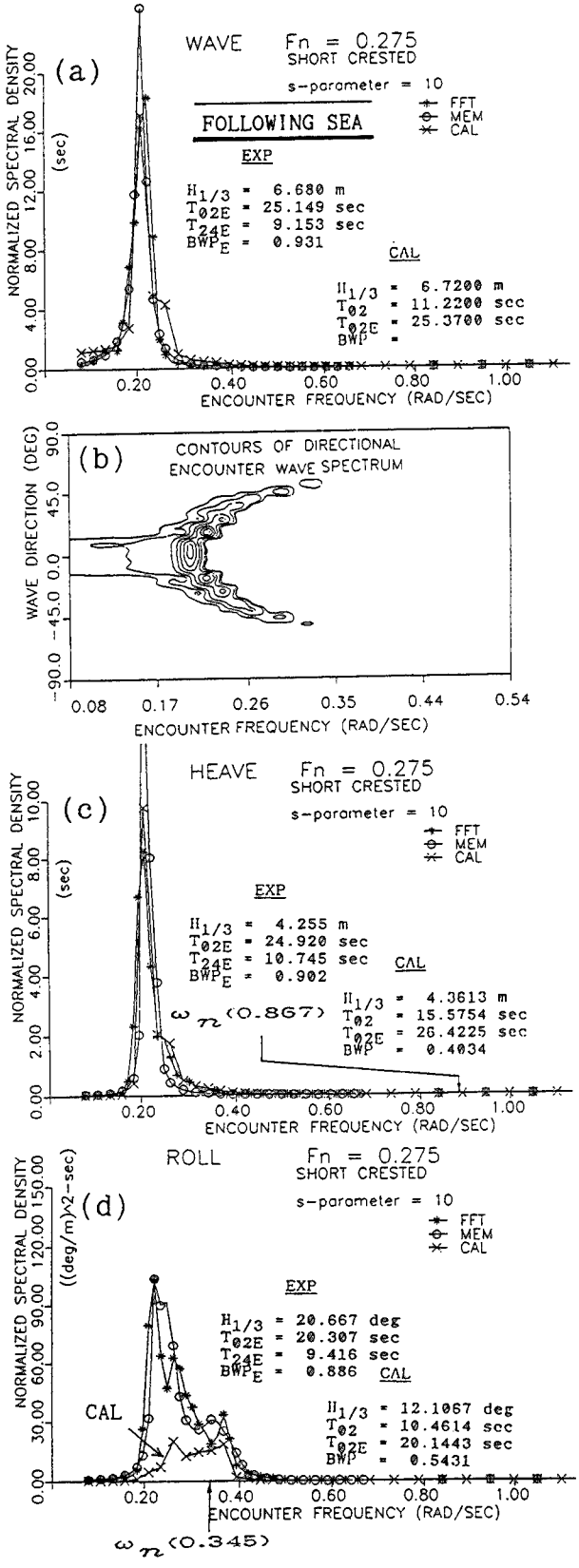

Fig.10 Comparison of one dimensional motion (heave & roll) spectra in directional spectrum wave (s=10) with that from theoretical estimation. Following sea condition and Fn=0.275. All in ship scale.

In following sea case,heave natural frequency is far out of wave frequency as shown by downward arrow.

Encounter mean wave period is changed from that absolute value and become longer in following sea condition. Furthermore, from analysis ,encounter mean period of directional spectrum waves becomes shorter than that of long crested irregular waves in following sea condition by about 10% for this case, and this tendency is reasonable.

Effect of angular spreading parameter

To see the effect of wave directional spreading on motions ,we show fig.11. The abscissa is angular spreading factor defined by 1/s, and s is parameter used in equation (3). Four kind of s is considered including long crested waves. Cos-square directional function correspond to 1/s=0.2 approximately.

Ordinate is defined by square root of Mo(motion)/Mo(wave). Here Mo means area of spectrum, so if this value equal 4.0 then by a wave with significant height of 1.0 meter, 4.0 degrees significant roll angles are excited.

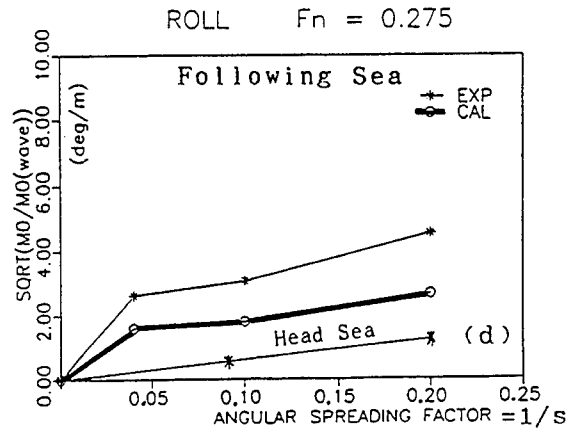

Fig.11 Effect of angular spreading factor(1/s) on roll response in following directional spectrum waves.

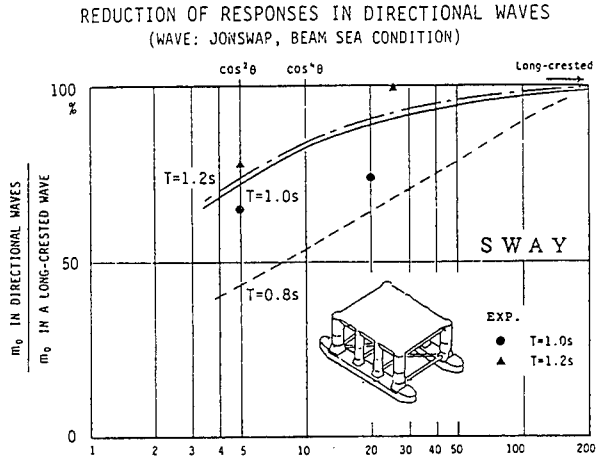

Fig.12 Reduction of response in directional spectrum waves of a moored semisubmersible platform model. Abscissa is peakedness parameter s in log scale.

For roll the effect of angular spreading factor is very large in experiment and so very important factor, and the experimental results show larger change than calculated results.

The motions of a moored semi-submersible platform (8 columns and 2 lower hulls type) are also affected by the directional spreading characteristics of directional spectrum waves and some examples are shown in fig.12 (13,14,15). This case, abscissa is s in log-scale. About 30% reduction of sway motion can be seen for cos-square distribution case.

ESTIMATION OF DIRECTIONAL FREQUENCY TRANSFER FUNCTION OF MOTIONS FROM MEASURED RESPONSES IN DIRECTIONAL SPECTRUM WAVES

As often tried in long crested regular ,irregular or transient water waves (TWW)(21) , it is important to estimate directional response transfer functions of models by using a measured wave and responses. However, for the case of directional spectrum wave, it is not so easy to conduct such inverse estimations ,because obtained response spectrum is the results of integration in each wave direction like equation (10).

About this estimation problem we proposed new practical methods(10,11,16,20).

Response spectra is expressed by equation (10). This case we want estimate H from integrated value S. For this we discretize equation (10) as follows.

$$s=(w_n)^T(|h_n|^2)\delta x \qquad (11)$$

where w_n is wave spectrum and h_n is the directional response function at ω, and here $\delta\chi$ is the width of encounter wave angle. Suffix n is the number of wave direction. Superscript T means transposition of matrix.

Next, we expand H by Fourier series as

$$|H(\omega_e, \chi)|^2 \approx \sum_{k=0}^{N} a_k(\omega_e)\cos k\chi \qquad (12)$$

and discrete expressions becomes as

$$(|h_n|^2) \equiv \begin{bmatrix} 1 & \cos\chi_1 \cdots \cos N\chi_1 \\ 1 & \cos\chi_2 \cdots \cos N\chi_2 \\ \vdots & \vdots \quad \ddots \quad \vdots \\ 1 & \cos\chi_n \cdots \cos N\chi_n \end{bmatrix} \begin{pmatrix} a_0 \\ a_1 \\ \vdots \\ a_N \end{pmatrix} \equiv [C](a) \qquad (13)$$

From this the condition for making minimizing the square of estimation error of response one dimensional spectrum become as follows.

$$\begin{bmatrix} ([W][C])^T([W][C])(\delta x)^2 & c_l^T \\ c_l & 0 \end{bmatrix} \begin{pmatrix} (a_N) \\ \lambda \end{pmatrix} = \begin{pmatrix} ([W][C])^T(s)\delta x \\ (|h_n|^2)_l \end{pmatrix} \qquad (14)$$

c_l is the l-th row vector of matrix C

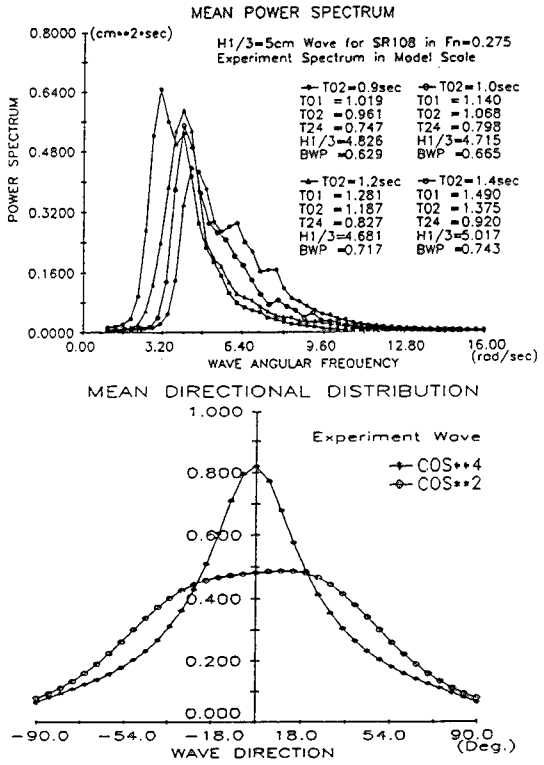

Fig.13 Variety of measured directional wave spectra (one dimensional and directional distribution function) used for directional transfer function estimation.

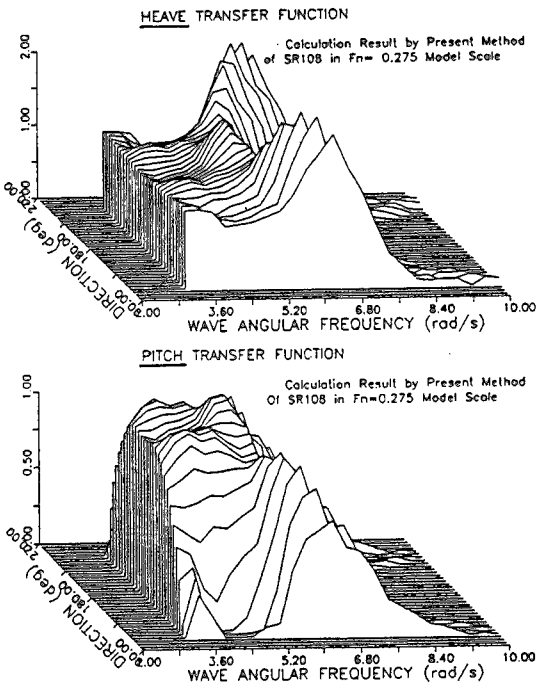

Fig.14 Estimated directional transfer function of heave and pitch.

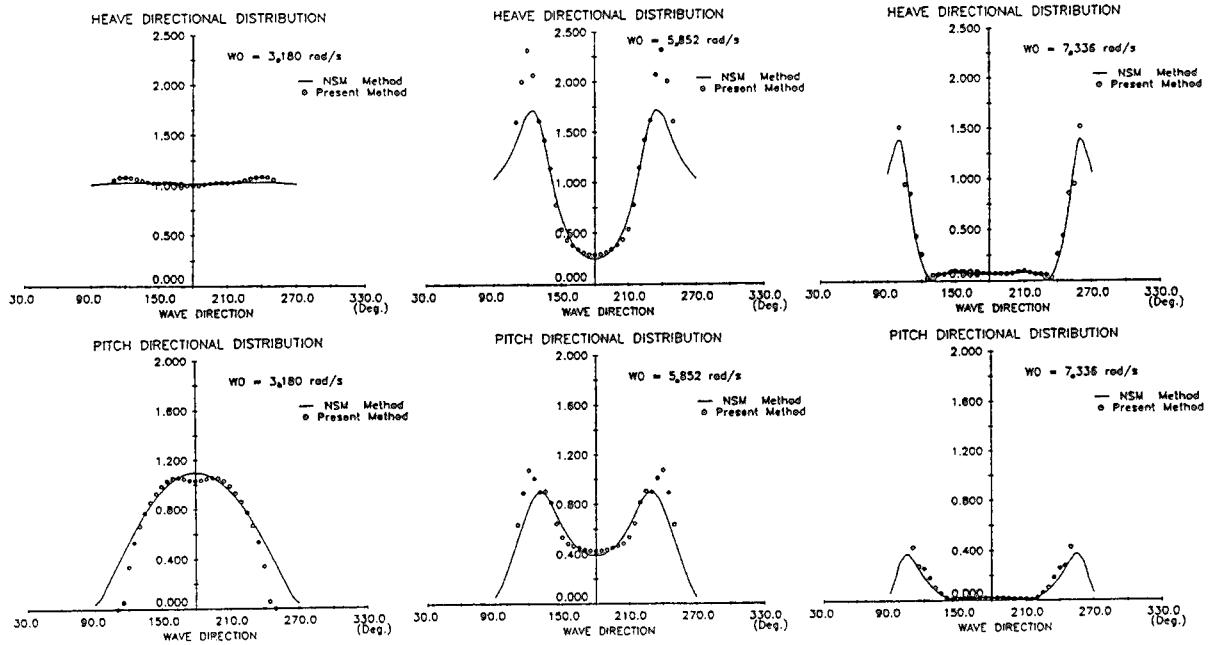

Fig.15 Comparison of estimated directional transfer function and calculation shown by the sectional shape at the point of three frequencies.

where.

$$[W]=\begin{bmatrix}(w)_1^T\\(w)_2^T\\\vdots\\(w)_m^T\end{bmatrix} \qquad (15)$$

Here, m means the number of wave kind. λ is the Lagrangian multiplier for introducing restraint condition when we know the response function at direction χ_1 .

Example of estimated directional transfer functions

Fig13 shows directional wave spectra used for estimation . We used four cases of one dimensional frequency spectra , and two cases of directional distribution function , so the total 8 cases of wave spectra are used.

Fig.14 is estimated heave and pitch directional transfer functions expressed in three dimensional figure at the heading sea condition of Fn=0.275. Fig.15 is sectional shape of directional transfer functions at three frequencies. Constraint is introduced at 180 deg.(head sea) by the results obtained from experiments in Transient water waves (21). Solid curves are theoretical ones by NSM and they show relatively good coincidence with each other. So this method can be applied for the ship or floating offshore structures in real sea if the incident directional wave spectra can be measured.

CONCLUSION

About the recently developed new experimental techniques on ship motions in directional spectrum waves, following conclusions are obtained.

1) We could realized practically homogeneous directional spectrum wave fields in a conventional long towing tank by the small number of segmented wave generator mounted at the end of the tank, from taking into consideration of the reflection of side walls.

Although such wave generating system is restricted to such waves that the principal direction of directional spectrum wave is parallel to the tank side wall, various applications will be possible, and new results will be expected especially about non linear phenomena in the field of ship hydrodynamics.

2) Generated directional spectrum waves were confirmed by the newly developed Laser Wave Surface Probe(LAWSURP) and by so called MLM analysis method. LAWSURP is suitable for high speed running condition and measurement of wave local slope.

3) We also developed a new estimation method of directional transfer functions from measured motion responses and directional wave spectra.

4) Experiments in directional spectrum waves showed the effect of angular spreading factor on response, especially on the motion of semi submersible platform and on ship roll motions in following sea condition.

ACKNOWLEDGMENT

The authors would like to acknowledge to Mr.K.Miyakawa and Mr.T.Takayama in developing new wave maker and new wave probe (LAWSURP) and execution of experiment.The authors also acknowledge the contribution from Dr.K.Kobayashi who developed computer program of NSM and prepare digital signals of wave maker and furthermore the contributions from Associate Prof.S.Ueno, and post graduate course student A.Kasahara, S.Acharrya, M.Itabashi, H.Inagaki, G.Chen, X.Wang, S.Kim, S.A.Tuzcuoglu, T.Suganuma, H.Kajiwara, A.Suzano.

REFERENCES

(1)Ishida,S.and Watanabe,I., "Properties of Oblique Waves Generated by Snake Motion of Segmented Wavemaker," Transactions of The West-Japan Society of Naval Architects, No.69, March, 1985

(2)van Lammeren,W.P.A and Vossors,G.,"The Seakeeping Laboratory of the Netherlands Ship Model Basin ,"Int. Shipbuilding Progress, vol.4, No29, 1957

(3)Mynett,A.E., Bosma,J., Keuning,J.A. and Gerritsma,J., "Laboratory Simulation of Ship Motions in Directional Seas,"BOSS'88,1988

(4)Takezawa,S., Hirayama,T., Miyakawa,K. and Takayama,T., "The Directional Spectrum Water Wave Generator for Towing Tanks ,"Journal of Kansai Society of Naval Architects, Japan. No.211, 1988

(5)Takezawa,S., Kobayashi,K. and Kasahara,A. , "Directional Irregular Waves Generated in a Long Tank, " Journal of Society of Naval Architects, Japan, Vol.163, 1988

(6)Capon,J., "High Resolution Frequency Wavenumber Spectrum Analysis," Proc.IEEE. vol.57, No.8, August,1969

(7)Jefferys,E.R. et al., "Measuring Directional Spectra With the MLM, "Conference on Directional Spectra Applications,1981

(8)Takezawa,S., Hirayama,T.:"Towed Ship Motion Test in Directional Spectrum Waves in a Long Tank",Journal of Society of Naval Architects, Japan, Vol.165, 1989

(9)Takezawa,S., Hirayama,T. and Acharrya,S. "Towed Ship Motion Test in Directional Spectrum Waves in a Long Tank (part 2)," Journal of Society of Naval Architects, Japan, Vol.166, 1989

(10)Takezawa,S., Hirayama,T. and Acharyya,S., "Towed Ship Motion Test in Directional Spectrum Waves in a Long Tank(part 3)," Journal of Society of Naval Architects, Japan, Vol.167, 1990

(11)Takezawa,S.,Hirayama,T. and Acharyya,S., "On Large Rolling in Following Directional Spectrum Waves," STAB'90, 1990

(12)Takezawa,S., Miyakawa,K., Takayama,T. and Itabashi,M., "On the Measurement of Directional Wave Spectra by the New Wave Measuring System using Laser Beams," Journal of Society of Naval Architects, Japan, Vol.166, 1989

(13)Takezawa,S. and Kobayashi,K., "On the Motion Characteristics of Semi-Submersibles

in Short-Crested Irregular Waves," BOSS'88, 1988
(14)Takezawa,S. and Kobayashi,K., "On the Motion Response of Offshore Floating Structures in Directional Spectra Waves-The 1st-order responses-", Journal of Naval Architects,Japan, Vol.165, 1989
(15)Takezawa,S. and Kobayashi,K., "On the Motion Responses of Offshore Floating Structures in Directional Spectra Waves-The 2nd-order responses-", Journal of Naval Architects, Japan, Vol166, 1989
(16)Takezawa,S., Hirayama,T., Ueno,S. and Chen,G., "Estimation of Directional Frequency Response Functions of a Floating Offshore Structure Based on Experiments in Directional Spectrum Waves,"
(17)Maeda,H. & Kasahara,A., "Generation and analysis of 2-dimensional irregular water waves.JKSNA Japan," No.202, 1986,pp.13-21
(18)Takaishi,Y.,Yoshino,T.,Takagi,M. Saitou,K. ,"On the motions of a high speed container ship with a single screw in oblique waves.JSNA JAPAN, No.129,1971,pp 76-81
19)Mituyasu et al,On directional spectra of ocean waves, 21th Coastal Engineering Symposium,(Japan),1974
20)Takezawa,S.,Hirayama,T.,Ueno,S.,& Wang,X., "Estimation of Directional Frequency Response Functions of a Running Ship Based on Experiments in Directional Spectrum Waves," Journal of Society of Naval Architects, Japan,Vol.170,1991
21)Takezawa,S., Takekawa,M. & Hirayama,T., "Advanced Experimental Techniques for Testing Ship Models in Transient Water Waves (Part1 & 2)," Eleventh Symposium on Naval Hydrodynamic, London ,1976

Research on Unsteady Wave Field Generated by Ships With Advance Velocity by Transverse Cut Method

S. Naito[1], N. Yamama[2], T. Seto[1]
([1]Osaka University, Japan; [2]Mitsubishi Heavy Industries, Ltd., Japan)

ABSTRACT

The mutual relation exists between unsteady wave field and forces - that is wave exciting forces, added resistance and wave damping force - . As well known, Kochin function shows the characteristics of unsteady wave field and when we want to obtain the forces it is also needed. Hence, the experimental techniques to get the function must be developed. Two method could be thought, one is the longitudinal cut method which means that the unsteady wave field is cut on the parallel line to ship course, the other is the transverse cut method. The former has already established by Ohkusu, the later is presented by the authors with experiment results obtained with the new equipments, and we show the asymptotic behaviors of unsteady waves at far field and give a consistent explanation of the mutual relation among them.

NOMENCLATURE

$H_j(\theta)$	:	Kochin function
D_w	:	space of wave probes
V_{wp}	:	speed of wave probe
L	:	ship length
K	:	wave number $= \omega^2/g$
K_0	:	wave number $= g/V^2$
g	:	gravitational acceleration
V	:	model ship speed
α_0	:	critical angle $= \cos^{-1}(\frac{1}{4\Omega})$
Ω	:	$= \omega \cdot V/g$
ω	:	wave frequency
$\sigma(x)$	:	singularity distribution
ζ	:	wave elevation
θ	:	propagating direction of elementary waves
R	:	horizontal distance between (0,0) and (x,y)

1 INTRODUCTION

It is important to know the characteristics of unsteady wave field generated by oscillating ships for the detailed investigation on seakeeping in waves, because the relation between the wave forces acting on ships and/or floating bodies and generated waves by them is close. In the research field on steady wave making resistance, the wave pattern analysis has been successful. Also in the research field on unsteady wave making resistance, the wave pattern analysis must be considered. Ohkusu has already presented the method of the unsteady wave field analysis by the parallel cut with the ship's course[7]. We say it longitudinal cut method.

In this paper, we present the wave pattern analysis method with the transverse cut of the wave field, namely transverse cut method. Even if either method is used, some wave probes are necessary. In case of the former method, the wave probes can be set up at the fixed point in space, and the truncated correction, that is a restricted water tank correction, is necessary, because waves propagated behind the ship exist at far field[20]. In case of the later method, the wave probes must be set up at the moving coordinate with ships, and the method does not need the correction, because the wave amplitude gets almost to 0 very rapidly near the edge of unsteady wave field.

We carried out the experiments of wave pattern analysis by the transverse cut method with the new facility which is on the moving coordinate with ships and has a small carriage with five wave probes moving perpendicular to ship's course. As the results the amplitude functions, namely Kochin function, of fine ships like container and full ships like tanker can be obtained experimentally. For the unsteady wave pattern analysis, it is suitable to investigate the asymptotic behavior of the unsteady wave field by using the stationary phase method which is one of the approximated integration method. With this method, the decaying order of wave amplitude at the edge of unsteady wave field is obtained analytically, and we have confirmed that the approximated results are available. The calculated results are useful to understand what is the dominant characteristics of the wave field and to know how to make the wave pattern analysis.

The experimental results of Kochin function of the ship with blunt bow do not coincide with the calculated results based on the slender-body assumption. Especially under the diffraction condition, the difference is large. As the one method to solve the problem, we distribute the isolated sin-

gularity at fore point of ships, which presents the bluntness of ships, and compare the experiment results with calculated one of Kochin function. Good agreement is obtained.

We also carried out the wake measurement of the blunt ship and took picture of wave breaking behaviors in front of it. The mutual relation among the blunt bow, the wake and the wave breaking is discussed. The authors will also show the overview on the research of the unsteady wave field.

2 WAVE GENERATED BY PERIODICAL SINGULARITY WITH CONSTANT ADVANCE VELOCITY

2.1 Co-ordinate system and two kinds of waves [13,14,15,18]

The wave number of waves generated by periodical singularity with advance velocity of V can be obtained in the co-ordinate system in fig.1. In the view of the space co-ordinate system $(O_s - X_sY_s)$ and the moving co-ordinate system$(o - xy)$ with the singularity, the relation between them is as follows.

$$X_s = x + Vt \quad : \quad Y_s = y \tag{1}$$

The waves that have amplitude unit and satisfy the free surface condition and also propagate in the direction of θ in $o - xy$ system can be shown as follows.

$$\zeta(\theta) = e^{i\{\omega t - k(x\cos\theta + y\sin\theta)\}} \tag{2}$$

Transforming the equation to $O_s - X_sY_s$ system gives

$$\begin{aligned} \tilde{\zeta}(\theta) &= e^{i(\omega t - k\cdot X_s\cdot\cos\theta + k\cdot Vt\cdot\cos\theta - k\cdot Y_s\sin\theta)} \\ &= e^{i(\omega + k\cdot V\cdot\cos\theta)t} e^{-ik(X_s\cdot\cos\theta + Y_s\sin\theta)} \end{aligned} \tag{3}$$

The waves propagate in the direction of θ in $o - xy$ system also propagate in the direction of θ in $O_s - X_sY_s$ system. Considering the time term, the wave phase velocity C in $O_s - X_sY_s$ system is

$$C = \frac{\omega + k\cdot V\cdot\cos\theta}{k} = \frac{\omega}{k} + V\cdot\cos\theta$$

And the wave dispersion relation is given as follows.

$$C^2 = \frac{g}{k} \tag{4}$$

Solving these two equations, the wave number k can be obtained

$$k_j(\theta) = \frac{K_0\{1 - 2\Omega\cos\theta \pm \sqrt{1 - 4\Omega\cos\theta}\}}{2\cos^2\theta} \tag{5}$$

Positive is when j=1, negative is when j=2 : where $\Omega = \omega V/g$, $K = \omega^2/g$, $K_0 = g/V^2$. The waves generated by periodical singularity with constant velocity are composed of these two waves having wave number $k_j(\theta)$ j=1,2 mentioned above and can be explained as follows.

1. The one wave is the deformed Kelvin wave generated when a singularity advances with a constant velocity.
2. The other wave is a deformed ring wave generated when a singularity oscillates without velocity.

Although the wave mentioned in (1) above is called k_1 wave and (2) is k_2 wave usually, they have various names and are not specified.

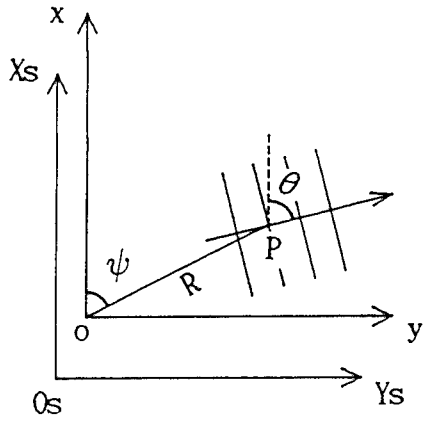

Fig.1 Co-ordinate system

Since the term within the root shown in eq.(5) must be positive, the following condition should be satisfied.

$$1 - 4\Omega\cos\theta \geq 0 \tag{6}$$

In case of $\Omega \geq 0.25$, namely $\cos\theta \leq 0.25 \leq \Omega$, then θ should exist within $\cos^{-1}(0.25/\Omega) \leq |\theta| \leq \pi$.
Since θ means wave propagating direction, the waves do not propagate in the direction of outside of this range. Write α_0 for $\cos^{-1}(0.25/\Omega)$, and name it the critical angle. In case of $\Omega \leq 0.25$, the value within the root is always positive, therefore waves propagate to every direction.

These wave numbers, k_1, k_2, correspond to each wave number of Kelvin wave and ring wave, that is, when a singularity does not oscillate k_2 wave disappears and k_1 wave number coincides with Kelvin wave number. On the other hand when a singularity does not have advance velocity, k_1 wave disappears and k_2 wave number coincides with ring wave number. To make it easy to understand, rewrite the wave number shown in eq.(5) as follows.

$$\begin{aligned} k_1 &= K_0\cdot\sec^2\theta\left(\frac{1 + \sqrt{1 - 4\Omega\cos\theta}}{2}\right)^2 \\ k_2 &= K\cdot\left(\frac{2}{1 + \sqrt{1 - 4\Omega\cos\theta}}\right)^2 \end{aligned} \tag{7}$$

Therefore it is clear as

1. When $\omega = 0$, the singularity does not oscillate but translates in a constant advanced velocity, hence $K = 0$ and $k_2 = 0$, $\Omega = 0$ so that $k_1 = K_0\cdot\sec^2\theta$. This is the wave number of Kelvin wave.
2. When $V = 0$, the singularity does not translate but oscillates, hence $K_0 = \infty$ and $k_1 = \infty$, $\Omega = 0$ so that $k_2 = K$. This is the wave number of ring wave.

When $V = 1.0(m/s)$, $\omega = 6.0(1/s)$, $\Omega = 0.61$, $K_0 = 9.8(1/s)$, $\alpha_0 = 66°$, as the typical condition in this calculation, the results of k_1 and k_2 are shown in fig.2.

When $\theta = 90°$, the wave number of k_1 wave is infinity, namely wave length is infinitesimal. When waves propagating in direction of θ are getting to α_0, the wave length of k_2 wave is getting shorter. The k_1 wave number coincides with the k_2 wave number at $\theta = \alpha_0$.

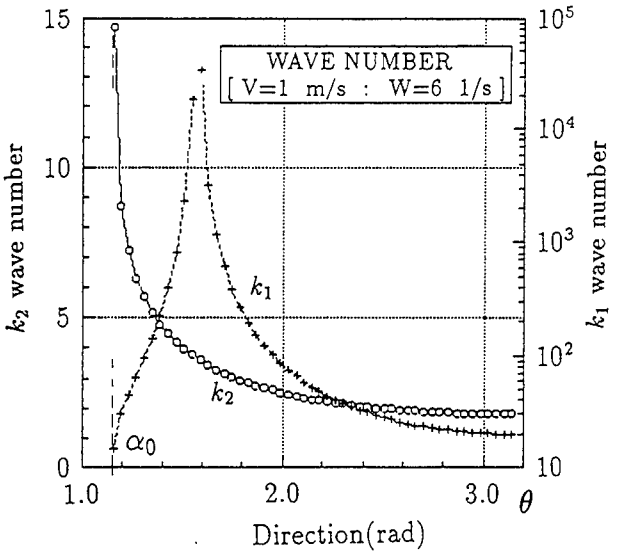

Fig.2 Wave number of k_1 and k_2 waves

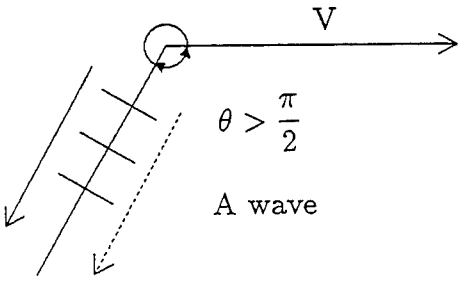

Fig.3

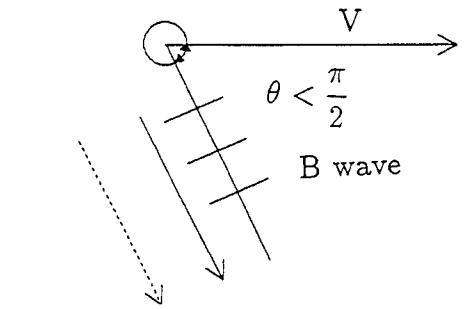

Fig.4

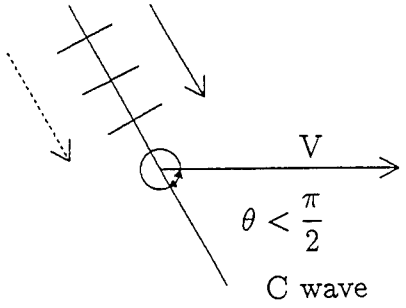

Fig.5

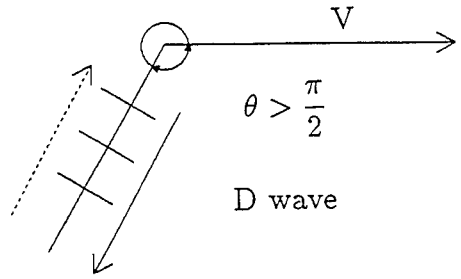

Fig.6

(Propagating direction of $A, B, C,$ and D waves represented in $o - xy$ system and $O_S - X_S Y_S$ system)

2.2 Parameter Ω

According to these formulas we can find that parameter Ω plays an important role. As it is indicated $\Omega = \sqrt{K/K_0}$, K shows the wave number generated by oscillation and K_0 shows the wave number generated by a constant velocity, thus Ω indicates the ratio of wave number of unsteady wave to steady wave. Namely the parameter Ω shows the degree of unsteadiness of wave field, and various phenomena of unsteady wave field can be settled by Ω. When the value of Ω becomes beyond the certain value, that is Ω =0.25, the critical angle α_0 emerges. Any elementary waves do not propagate in the direction of $\theta \leq \alpha_0$. This phenomenon is named as Doppler effect of water wave which effect is usually used in the acoustic research field. It means the effect of velocity on wave number.

2.3 Fundamental property of k_1 and k_2 waves

When we divide unsteady waves into two wave systems and divide each system into two kinds of waves, we can well understand the property of waves generated by the periodical singularity, that means ships, with constant velocity.

Although we call each wave as A, B, C, D wave for convenience, they do not have particular names. A, B, C and D waves can be described as follows.

[1] A wave (k_2 wave system) : Fig.3
It propagates behind the singularity in both $o - xy$ and $O_s - X_s Y_s$ systems. The mark $\longleftarrow$ shows the direction of propagation in $o - xy$ system and the mark $\leftarrow\cdots$ shows the direction of propagation in $O_s - X_s Y_s$ system.

[2] B wave (k_2 wave system) : Fig.4
It propagates toward the front in both $o - xy$ and $O_s - X_s Y_s$ systems. It exists in front of the singularity because both phase and group velocities are faster than the one of singularity.

[3] C wave (k_1 wave system) : Fig.5
It propagates toward the front of the singularity in both $o-xy$ and $O_s-X_sY_s$ systems. Although group velocity is slower than the velocity of singularity, it exists behind of the singularity.

[4] D wave (k_1 wave system) : Fig.6
It propagates behind of the singularity in $o-xy$ system, on the other hand in $O_s-X_sY_s$ system it propagates toward the front. Both phase and group velocities are slower than the velocity of singularity.

The magnitude of wave length is $A > B > C > D$.
Here we can find an interesting point as follows.
Since A wave propagates behind in $O_s-X_sY_s$ system, a singularity is expected to get thrust as the reaction of sending out that wave. T his thrust is called wave propulsion generally.

2.4 Concept of elementary waves

The structure of wave system generated when ship navigates in still water is explained by the conception of elementary waves originated from the idea of Kelvin. This is very effective idea to understand the complicated wave field generated by ships, and also very successful idea. His idea shows wave field which looks very complicated can be presented by means of summing up two dimensional waves which propagate in various directions. We call the two dimensional wave an elementary wave, which constructs the wave field.

The parameter characterizing an elementary wave is simple, it is an amplitude (ζ), period (T) and propagating direction (θ). The wave field generated by the advancing and oscillating ships in waves is explained by the mathematical procedure like superposition of elementary waves like A,B,C, and D waves as mentioned at section (1.3), and this method is established to explain an unsteady wave field.

2.5 Wave pattern

When we see the waves generated by ships, they are not elementary waves but their superposed wave field. The wave field we see at this moment is the crest and trough lines where phase of elementary waves matches , hence they are called equi-phase lines or wave pattern. The wave pattern generated by ships with constant velocity without oscillation is well known as Kelvin wave pattern. Then let's obtain what kind of wave pattern is generated by ships with constant velocity with oscillation.

The elevation of water surface ζ_p at an arbitrary point P, the direction ψ and distance R from origin, occurred by elementary waves can be explained as follows. (refer to fig.1 expressing co-ordinate system)

$$\zeta_p(R,\psi) = A(\theta)e^{i\{\omega t - k_j(\theta)R\cos(\theta-\psi)\}} \tag{8}$$

If $R = 0$ is substituted into the eq.(8) (where a singularity or a ship exists),

$$\zeta_p = A(\theta)e^{i\omega t} \tag{9}$$

In order to equalize the phase of wave at the point P with the one at the origin, phase part $k_j(\theta)R\cos(\theta-\psi)$ should be satisfied the relation as follows.

$$k_j(\theta)R\cos(\theta-\psi) = 2n\pi \ : \ n = 0, \pm1, \pm2, \cdots \tag{10}$$

By differentiating eq.(10) with respect to θ, one equation is obtained. The envelop line of equi-phase line group satisfies it and eq.(10) simultaneously. Wave pattern can be drawn by indicating the point P presenting the unknown co-ordinates (x,y), that is ψ and R, respect of given θ. Finally wave pattern can be drawn as using the next relations,

$$\begin{aligned} x &= \frac{2n\pi q_j(\theta)}{k_j(\theta)[\cos\theta \cdot q_j(\theta) + \sin\theta]} \\ y &= \frac{2n\pi}{k_j(\theta)[\cos\theta \cdot q_j(\theta) + \sin\theta]} \end{aligned} \tag{11}$$

where

$$q_j(\theta) = -\tan\theta \pm \sqrt{1 - 4\Omega\cos\theta}(\cot\theta + \tan\theta) \tag{12}$$

Fig.7 shows the wave patterns under the condition $\Omega = 0$, that is $V = 0$ or $\omega = 0$. These wave patterns are named as when $\omega = 0$, the Kelvin wave pattern[17] and when $V = 0$, ring wave pattern respectively.

In the case that the singularity pulsates($\omega \neq 0$) or advances ($V \neq 0$), that is $\Omega \neq 0$, the wave pattern changes gradually as following figures.

The wave pattern drawn in the dotted lines and real lines in fig.8 are constructed by elementary A wave [in the range $\pi \geq \theta \geq \pi/2$] and B wave [in the range $\pi/2 \geq \theta \geq \alpha_0$] respectively belonging to k_2 wave system.

In fig.9, the wave pattern drawn in real lines and dotted lines are constructed by elementary C waves [in the range $\pi/2 \geq \theta \geq \alpha_0$] and D wave [in the range $\pi \geq \theta \geq \pi/2$] respectively belonging to k_1 wave system.

Fig.10 shows the relation between the velocity of singularity and k_2 wave pattern. From the viewpoint of wave pattern, the increase of velocity is equivalent to the increase of ω. The increase of V or ω, that is $\Omega = \omega V/g$ has large value, makes the forms of equi-phase lines more parallel to the longitudinal direction, that means more parallel to the ship. Thus the phenomena in unsteady wave field should be discussed from not ω or V but the parameter Ω.

3 CONSTRUCTION OF UNSTEADY WAVE FIELD

3.1 Theoretical equation of unsteady waves

The theoretical equation of unsteady waves is given as follows.

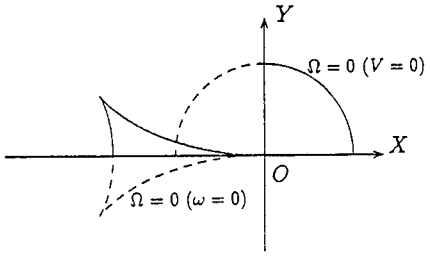

Fig.7 Ring wave pattern [$V = 0$] and Kelvin wave pattern [$\omega = 0$]

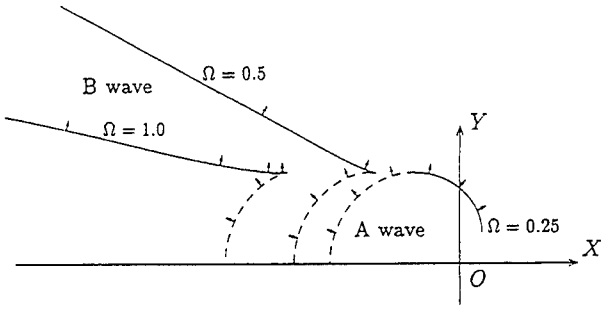

Fig.8 k_2 wave patterns generated by periodical singularity

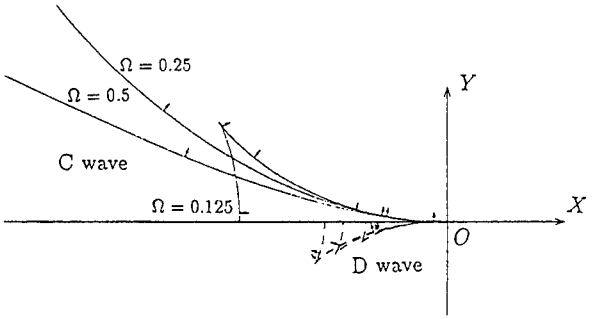

Fig.9 k_1 wave patterns generated by periodical singularity

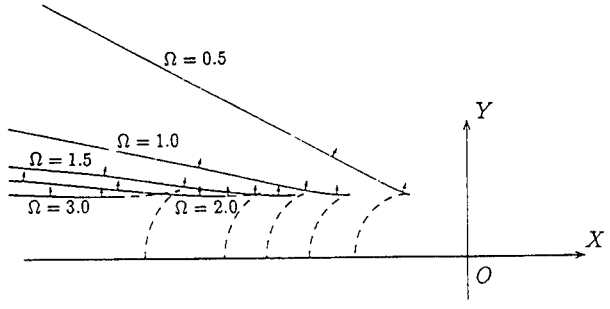

Fig.10 Variation of k_2 wave patterns according to Ω value

$$\zeta = \frac{2\omega}{g}\left[\int_{-\pi/2}^{a} - \int_{\pi/2}^{b}\right] W_1(\theta)H_1(\theta)\exp\{-iRg_1(\theta)\}d\theta + \frac{2\omega}{g}\left[\int_{a}^{b}\right] W_2(\theta)H_2(\theta)\exp\{-iRg_2(\theta)\}d\theta \quad (13)$$

$$W_j(\theta) = \left(1 + \frac{k_j(\theta)\cos\theta}{K_0\Omega}\right)\frac{k_j(\theta)}{\sqrt{1 - 4\Omega\cos\theta}} \; : \; j = 1,2$$

Where $a = \psi - \pi/2$, $b = \psi + \pi/2$, $\Omega = \omega V/g$, $K = \omega^2/g, K_0 = g/V^2$, and $k_j(\theta)$ is shown in eq.(5). Here $g_j(\theta)$ is an important function to know the unsteady wave behavior at far field and to obtain the approximated value of eq.(13) and given as follows.

$$g_j(\theta) = k_j(\theta)\cdot\cos(\theta - \psi) \quad (14)$$

The first term in eq.(13) means the surface elevation caused by k_1 wave and the second term means k_2 wave. $H_j(\theta)$ is the Kochin function showing the property of the periodical singularity, that is ships, as follows under the slender body assumption.

$$H_j(\theta) = \int_{-L/2}^{L/2} \sigma(x)\cdot e^{i\cdot k_j(\theta)\cdot\cos\theta\cdot x}dx \; : \; j = 1,2 \quad (15)$$

$\sigma(x)$ is singularity distribution along the center line of a ship which is determined by solving the two dimensional problem of each section of the ship, namely Ursell-Tasai method. This equation is Fourier transform of $\sigma(x)$.

Near the θ=α_0, the $W_j(\theta)$ value becomes large by the order $1/\sqrt{\theta}$. By the well known variable transformation, that singularity can be removed[25].

3.2 Approximated formula on unsteady waves

Eq.(13) is generally expressed as following form.

$$I = \int_{\alpha}^{\beta} f(\theta)\exp\{-iRg(\theta)\}d\theta \quad (16)$$

Where

$$f(\theta) = H_j(\theta)\cdot W_j(\theta) \quad ; \quad j = 1,2$$
$$= H_j(\theta)\cdot\left(1 + \frac{k_j(\theta)\cos\theta}{K_0\Omega}\right)\frac{k_j(\theta)}{\sqrt{1 - 4\Omega\cos\theta}} \quad (17)$$

This integral form is well known, and when the value of R is large, the approximated method to obtain the integral result is recommended. Although the calculation of unsteady wave field is not so difficult by using computer recently, for understanding the structure of unsteady wave it is necessary to extract some dominant components from eq.(13).

Since the value of $\exp\{-iRg(\theta)\}$ fluctuates very rapidly when R becomes large, the integrated value is nearly 0. Only in the neighborhood of special point θ where $g'(\theta) = 0$ is satisfied, the integrated value would be exist. That point is called as stationary phase point.

Differentiating eq.(14) respect to θ and make it 0, the following relation is obtained, which gives stationary phase points.

$$\cot\psi = -\tan\theta \pm \frac{\sqrt{1-4\Omega\cos\theta}}{\cos\theta\cdot\sin\theta} \tag{18}$$

The minus sign and the plus sign mean k_1 wave, k_2 wave respectively. This relation is same as eq.(12) which is needed to obtain the wave pattern. The equation has the validity when R becomes large, namely the approximated wave presents the behavior of unsteady waves at the far

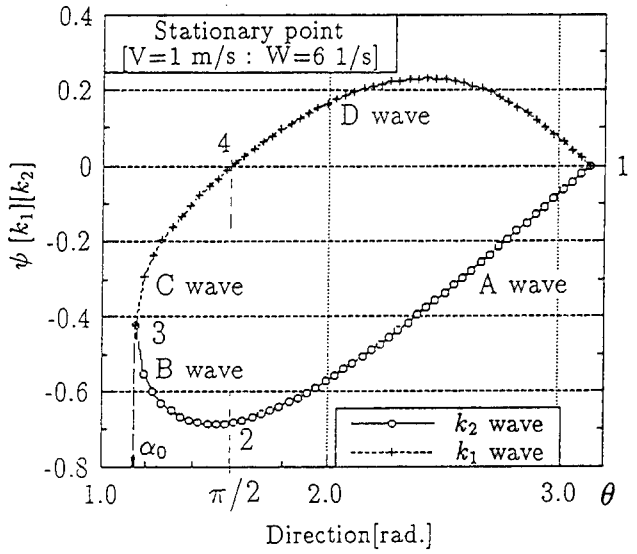

Fig.11 Stationary phase point of k_1 and k_2 waves

field. The calculated results of the stationary phase point are shown in fig.11.

The taylor expansion of $g(\theta)$ around the stationary phase point θ_0 is

$$g(\theta) = g(\theta_0) + g'(\theta_0)\cdot(\theta-\theta_0) + \frac{g''(\theta_0)\cdot(\theta-\theta_0)^2}{2} + \frac{g'''(\theta_0)\cdot(\theta-\theta_0)^3}{6} + \cdots \tag{19}$$

There are several ways to approximate $g(\theta)$ around $\theta=\theta_0$ as follows[26].

(1) $g'(\theta_0)=0$ and we consider the 1st and 3rd terms.
(2) $g'(\theta_0)=g''(\theta_0)=0$ and we consider the 1st and 4th terms.
(3) $g'(\theta_0)=0$ and we consider the 1st, 3rd and 4th terms.
(4) $g''(\theta_0)=0$ and we consider the 1st, 2nd and 4th terms.
[In this case, there is no solution of $g'(\theta)=0$]

Therefore $f(\theta)$ around θ_0 is slowly varying function, let's be $f(\theta)\simeq f(\theta_0)$.

The case (1) is the most popular case. Eq.(16) is approximated by substituting the first and third terms of right hand side in eq.(19) to eq.(16) as follows.

$$I \simeq f(\theta_0)\exp\{-iRg(\theta_0)\} \times \int_\alpha^\beta \exp\{\frac{-iRg''(\theta_0)\cdot(\theta-\theta_0)^2}{2}\}d\theta \tag{20}$$

The well known integrated result is given as

$$I \simeq f(\theta_0)\exp\{-iRg(\theta_0)\}\sqrt{\frac{2\pi}{R|g''(\theta_0)|}}\cdot\exp\left(\pm\frac{\pi}{4}\right) \tag{21}$$

The $\pm$ sign in front of $\pi/4$ corresponds to the plus and minus of $g''(\theta_0)$.

Therefore integrated result can be determined easily by obtaining the stationary phase point. Even though the integrated result gives a good approximated value when R is very large, it is important to investigate the conditions when you need to get more accurate value. In the case that some stationary points exist, each integrated value should be added.

When $g''(\theta_0)=0$, it is impossible to use the approximated formula shown in eq.(21), because the denominator is 0. In this case next equation is valid.

$$I \simeq f(\theta_0)\exp\{-iRg(\theta_0)\} \times \int \exp\{\frac{-iRg'''(\theta_0)\cdot(\theta-\theta_0)^3}{6}\}d\theta \tag{22}$$

When variable transformation is performed as eq.(23), this integrated result is shown by Gamma function.

$$\frac{g'''(\theta_0)\cdot(\theta-\theta_0)^3}{6} = \xi^3 \tag{23}$$

This result is only valid at $g'(\theta_0)=g''(\theta_0)=0$ corresponding to the case (2).
When $g''(\theta_0)\simeq 0$, two stationary phase points are close, therefore the another method must be used[27]. This method corresponds to the case (3) in which both $g''(\theta)$ and $g'''(\theta)$ can not be neglected. Although this integral calculation is complicated, it can be shown with Airy function by using Chester-Friedman- Ursell method[16].

$$\alpha = g''(\theta_0)/2, \quad \beta = g'''(\theta_0)/6$$

$$g(\theta) \simeq g(\theta_0) + \alpha\cdot(\theta-\theta_0)^2 + \beta\cdot(\theta-\theta_0)^3 \tag{24}$$

Around the double stationary point, there are two roots of $g'(\theta)=0$ and one point approaches the other point. The function $g'(\theta)$ and $g(\theta)$ could be approximated as a

quadratic and cubic expression respectively.
Performing the co-ordinate transformation as follows

$$\theta - \theta_0 = a_1 \cdot \bar{\theta} + a_2 \tag{25}$$

Substituting eq.(25) to eq.(24)

$$\begin{aligned} g(\theta) - g(\theta_0) &= \beta a_1^3 \cdot \bar{\theta}^3 + (\alpha a_1^2 + 3\beta a_1^2 a_2) \cdot \bar{\theta}^2 \\ &+ (2a_1 a_2 \alpha + 3a_1 a_2^2 \beta) \cdot \bar{\theta} \\ &+ a_2^2(\alpha + \beta a_2) \end{aligned} \tag{26}$$

Near the θ_0, this equation can be approximated as a cubic expression

$$g(\theta) - g(\theta_0) = \frac{1}{3} \cdot \bar{\theta}^3 - \xi \cdot \bar{\theta} + \gamma \tag{27}$$

Comparing each power,a_1,a_2,ξ and ζ are determined as follows.

$$a_1 = \sqrt[3]{\frac{2}{g'''(\theta_0)}}\ ,\ \xi = \frac{g''(\theta_0)^2}{2g'''(\theta_0)}\sqrt[3]{\frac{2}{g'''(\theta_0)}} \tag{28}$$

$$a_2 = -\frac{g''(\theta_0)}{g'''(\theta_0)}\ ,\ \gamma = g(\theta_0) + \frac{g''(\theta_0)^3}{3g'''(\theta_0)^2} \tag{29}$$

Wave elevation is shown by using Airy function and the relation $d\theta/d\bar{\theta} = a_1$.

$$Airy\quad function\ :\ Ai(\pm x) = \frac{1}{\pi}\int_0^\infty \cos(\frac{t^3}{3} \pm xt)dt$$

$$\begin{aligned} \zeta &\simeq \frac{2\omega}{g} f(\theta_0) e^{iRg(\theta_0)} \cdot 2\pi \sqrt[3]{\frac{2}{Rg'''(\theta_0)}} \cdot e^{i\frac{Rg''(\theta_0)^3}{3g'''(\theta_0)^2}} \\ &\times\ Ai\left(-\sqrt[3]{\frac{R^2}{4}} \cdot \frac{g''(\theta_0)^2}{g'''(\theta_0)^{4/3}}\right) \end{aligned} \tag{30}$$

Wave motion shown by this equation indicates the characteristics of wave behaviors around the edge of unsteady wave field.

Also the case (4) in which $g''(\theta_0) = 0$, namely a stationary phase point does not exist. We consider up to $g'(\theta)$ and $g'''(\theta)$, the result also can be obtained with Airy function. This function is important to calculate behavior at the front of water waves. In this case the detail calculated method will be described at section 2.3.2. Case (3) and (4) are important for the investigation of asymptotic behaviors of unsteady wave field.

The dominant component of unsteady waves is evaluated with the methods mentioned above. We need to estimate the range of the validity of these results. Since $\lceil g''(\theta_0) \simeq 0 \rfloor$ and/or $\lceil g''(\theta)$ and $g'''(\theta)$ can not be neglected $\rfloor$ are uncertain, it is not so easy to estimate the validation range. Therefor there are some opinions computing the exact formula (13) directly is more accurate than the approximated method. The approximated calculation gives us the important and dominant informations of the unsteady wave field, though.

When $\theta \simeq \alpha_0$ (α_0 is the critical angle), the amplitude part of the integrand becomes large very rapidly. In this region the approximated relation $f(\theta) \simeq f(\theta_0)$ breaks.

3.3 Asymptotic behavior of unsteady waves

We can understand more deeply the seakeeping theory by knowing the asymptotic behavior of unsteady waves.

3.3.1 Asymptotic behavior of unsteady waves at x→ −∞

When x→ -∞, where is far behind away from ships, the dominant elementary wave is the propagating wave to direction π, namely the function $g(\theta_0)$ tends to $-k_2(\pi)$. As the result wave elevation is

$$\begin{aligned} \zeta &\simeq f(\theta_0)\exp\{-iRk_2(\pi)\}\sqrt{\frac{2\pi}{R|g''(\pi)|}}\exp(\pm\pi/4) \\ &\sim O\left(\frac{1}{\sqrt{R}}\right) \end{aligned} \tag{31}$$

This result tells us that the amplitude of the propagating wave to direction π decays with order $O(1/\sqrt{R})$. This is the basic background of the truncated modification for the longitudinal cut method.

3.3.2 Asymptotic behavior of unsteady waves at $y \to +\infty$ and $x \to +\infty$

When $y \to +\infty$ under x = - const., the value $\cot(\psi) = \cot(x/y)$ tends to 0_- (Minus of 0_- means that the value tends to 0 from negative value.), and also when $x \to 0_-$ under y=+const., the value $\cot(\psi)$ tends to 0_- and when $x \to +\infty$, the value $\cot(\psi)$ tends to $+\infty$. So the behavior of unsteady waves at far field can be considered on referring to the value of $\cot(\psi)$.

Under the both conditions, $x \to 0_- \to +\infty$ (where is in the forward direction from a singularity) and $y \to +\infty$ (where is in the transverse direction from a singularity), a stationary phase point does not exist.

So, the behavior of wave motion around the edge of unsteady wave field ($x \to +\infty$, y =const. and $y \to +\infty$, x =const.) can be investigated simultaneously.
At these region, the solution $g'(\theta) = 0$ does not exist. So the θ_s satisfied $g''(\theta_s) = 0$ is used, that is $g'(\theta_s)$ and $g'''(\theta_s)$ terms are considered to evaluate eq.(13) as follows.

$$\begin{aligned} \zeta &\simeq \frac{2\omega}{g} f(\theta_s) e^{iRg(\theta_s)} \\ &\times \int_{-\infty}^{\infty} e^{iR\left(g'(\theta_s)(\theta-\theta_s)+g'''(\theta_s)\frac{(\theta-\theta_s)^3}{6}\right)} d\theta \end{aligned} \tag{32}$$

This equation can be calculated with Airy function because it is consisted 1st and 3rd order terms. The result is

$$\zeta \simeq \frac{2\omega}{g} f(\theta_s) e^{iRg(\theta_s)} \sqrt[3]{\frac{2}{Rg'''(\theta_s)}} \times Ai\left(Rg'(\theta_s)\sqrt[3]{\frac{2}{Rg'''(\theta_s)}}\right) \quad (33)$$

When y in eq.(32) becomes large, that is R becomes large, the wave motion is investigated by knowing the asymptotic behavior of Airy function. Asymptotic behavior of Airy function when $\xi \to \infty$ is shown.

$$Ai(\xi) \sim \frac{1}{2\sqrt{\pi}} \frac{1}{\sqrt[4]{\xi}} \exp(-\frac{2}{3} \cdot \xi \cdot \sqrt{\xi}) \quad (34)$$

An independent variable ξ is shown

$$\xi = Rg'(\theta_s)\sqrt[3]{\frac{2}{Rg'''(\theta_s)}} \simeq C_0 R^{2/3} \sim O(R^{2/3}) \quad (35)$$

Substitute ξ into the eq.(33)

$$Ai(x) \simeq \frac{1}{2\sqrt{\pi}} \cdot (C_0 R^{2/3})^{-1/4} \cdot \exp\left(-\frac{2}{3}(C_0 R^{2/3})\right)^{3/2}$$
$$\simeq \frac{1}{2\sqrt{\pi}} \cdot (C_0)^{-1/4} \cdot (R)^{-1/6} \cdot \exp(-\beta R)$$
$$\therefore \quad \beta = \frac{2}{3} \cdot (C_0)^{3/2}$$

Substituting this into eq.(33), the asymptotic value of the wave amplitude near the edge of unsteady wave field is shown as follows

$$\zeta \sim O(\frac{e^{-\beta R}}{\sqrt{R}}) \quad (36)$$

where $R = \sqrt{x^2 + y^2}$.

This decay order is very high. When x or $y \to +\infty$, wave amplitude damps rapidly. This remarkable decay order indicates that a truncated correction of wave data is not necessary when the unsteady wave pattern analysis is carried out with the transverse cut method, which is one of the merits of this method. The investigation of this section shows the asymptotic behaviors of unsteady wave at the edge of unsteady wave field.

Fig.12 shows these general states of decaying order at the edge of unsteady wave field.

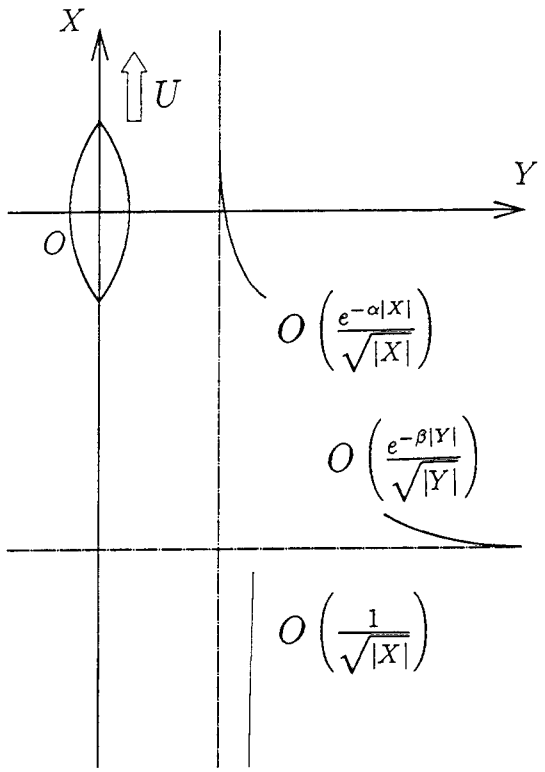

Fig.12 General states of decaying order of asymptotic waves at the edge of unsteady wave field

4 UNSTEADY WAVE PATTERN ANALYSIS –TRANSVERSE CUT METHOD–

For obtaining the wave elevation $\zeta(x_0, y)$ which does not depend on time, needed some experimental equipments and analytical theory are needed. In this experiment we use the small carriage with five wave probes which is on moving co-ordinate system, namely on the ship fixed co-ordinate system, and it moves in transverse direction. As the result we can get five wave data. With these data, $\zeta(x_0, y)$ can be obtained by the analysis theory mentioned below and is substituted to eq.(37) or (38). Finally $H(\theta)$ can be determined.

In this analysis, the steady wave elevation ζ_0 is also obtained. Detail investigations on the mutual interaction between unsteady and steady waves will be possible.

4.1 Analysis formula of transverse cut method

Unsteady wave pattern analysis has presented firstly by Ohkusu. His method is the parallel cut method with the ship course shown BB' line in fig.13. Naito and Zhang[12] have shown the transverse cut method of the wave field shown AA' line in fig.13. Each method has merits and demerits respectively.

The longitudinal cut method does not measure an elementary wave propagating to $\pi/2$ because the setting line of wave probes is parallel to $\pi/2$. On the contrary, the transverse cut method does not measure an elementary wave propagating to π because the setting line of wave probes is parallel to π.

In the research field on steady wave making resistance, the wave pattern analysis is successful. By the unsteady wave pattern analysis, we can obtained the Kochin function experimentally. As the result, the discussion on ⌈ Which theory is the most suitable ? ⌋ and ⌈ How to correct the theory ? ⌋ turns to be real.

The wave pattern analysis formula is obtained by the Fourier transformation of the unsteady wave formula shown

by eq.(13). After rather complicated calculus, the wave pattern analysis formula by the transverse cut method can be obtained as follows.
[1] Analysis formula of symmetrical unsteady wave field generated by symmetrical ship motions (heave, pitch, surge) is as follows.

$$H_i(\theta) = \frac{g}{2\omega}\int_0^\infty \zeta(x_0,y)\cdot\cos(k_i(\theta)y\sin\theta)dy$$
$$\times\underline{\frac{\sin^2\theta \pm \sqrt{1-4\Omega\cos\theta}}{\cos\theta(1+k_i(\theta)\Omega\cos\theta/K)}}\cdot e^{ik_i(\theta)x_0\cos\theta} \qquad (37)$$

[2] Analysis formula of unsymmetrical unsteady wave field generated by unsymmetrical ship motions (roll, yaw, sway) is as follows.

$$H_i(\theta) = \frac{g}{2\omega}\int_0^\infty \zeta(x_0,y)\cdot\sin(k_i(\theta)y\sin\theta)dy$$
$$\times\underline{\frac{\sin^2\theta \pm \sqrt{1-4\Omega\cos\theta}}{\cos\theta(1+k_i(\theta)\Omega\cos\theta/K)}}\cdot e^{ik_i(\theta)x_0\cos\theta+\pi/2} \qquad (38)$$

$i = 1,2$ means k_1, k_2 wave system respectively. x_0 is the position of transverse cut plane.
When $\theta \to \pi/2$, the limited value of under line part exists as $2K$ when $i = 1$, and 2Ω when $i = 2$ respectively.
If we could determine $\zeta(x_0,y)$ by experiment, Kochin function $H_j(\theta)$ can be obtained with eq.(37) or eq.(38). The method to get $\zeta(x_0,y)$ is shown at section 3.3.

4.2 New system of the experiment

We built up the new experimental system shown in fig.14 and fig.15. It has the small carriage moving the transverse direction beneath the main towing carriage. This small carriage is driven by DC motor and has five super-sonic-type wave probes. They are setted with an equal space [Dw]. The space Dw among probes and the moving speed [Vwp] of them can be changed arbitrary with the control unit. When the first probe passes the longitudinal center line of the model the starting signal is generated which is the reference input time.

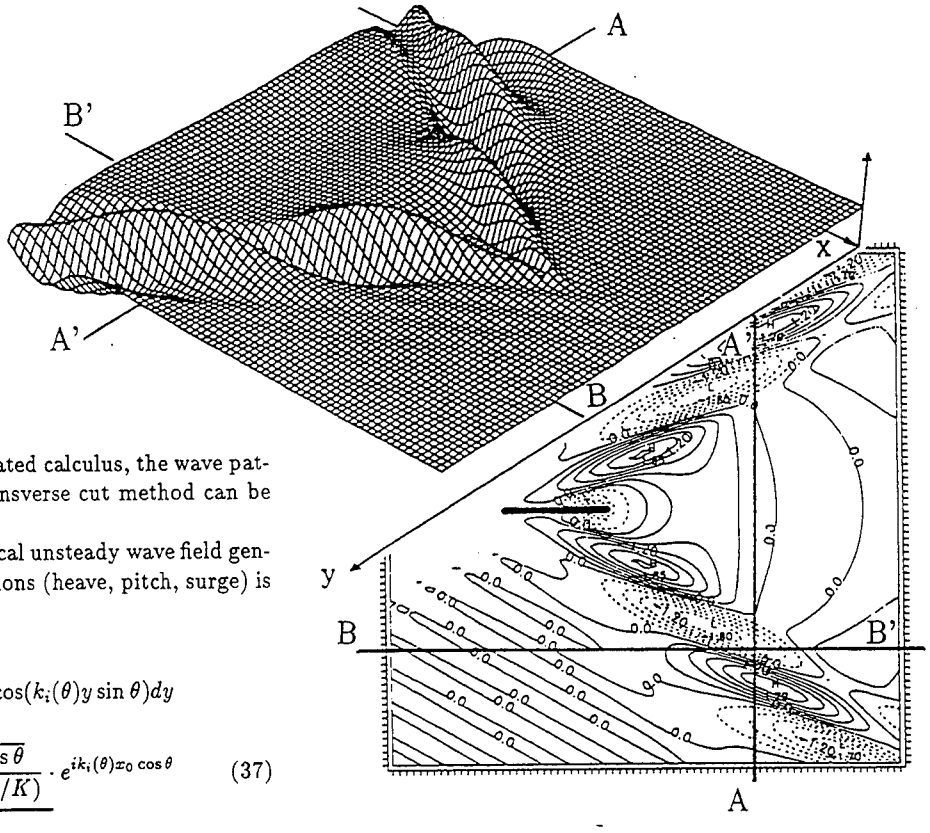

Fig.13 Perspective view of unsteady wave field generated by ships [cos component]

4.3 Technique to obtain wave amplitude $\zeta(x_0,y)$

The water surface at an arbitrary point in unsteady wave field oscillates with the encounter period Te in case of diffraction condition, in case of radiation condition oscillates with the period T. Since the carriage speed must be determined as that every

T_e/[number of wave probes N : in our case 5] (second),

each probe must cross the point(x,y). As the result, five data of surface elevation every one period is obtained. The speed of wave probe V_{wp} is decided as follows.

$$V_{wp} = \frac{N\cdot D_w}{T_e}$$

N=5 is used in our experiments. If this speed is high for the system, V_{wp} divided by (N-1),(N-2),...,{ N-(N-2)} can be used.

[a] Radiation experiment
Getting the value of $\zeta(x_0,y)$ on the line $x=x_0$ is easy by the least square method because the water surface fluctuation is regular and we take wave data five times during one period.